

Mahmood Aliofkhazraei
Abdel Salam Hamdy Makhlouf
Editors

Handbook of Nanoelectrochemistry

Electrochemical Synthesis
Methods, Properties and
Characterization Techniques



SpringerReference

Handbook of Nanoelectrochemistry

Mahmood Aliofkhazraei
Abdel Salam Hamdy Makhlouf
Editors

Handbook of Nanoelectrochemistry

Electrochemical Synthesis Methods,
Properties, and Characterization
Techniques

With 753 Figures and 131 Tables

 Springer Reference

Editors

Mahmood Aliofkhazraei
Department of Materials Engineering
Tarbiat Modares University
Tehran, Iran

Abdel Salam Hamdy Makhlouf
Manufacturing Engineering Department
College of Engineering and Computer
Science
University of Texas Pan-American
Edinburg, TX, USA

ISBN 978-3-319-15265-3 ISBN 978-3-319-15266-0 (eBook)
ISBN 978-3-319-15267-7 (print and electronic bundle)
DOI 10.1007/978-3-319-15266-0

Library of Congress Control Number: 2015949631

Springer Cham Heidelberg New York Dordrecht London
© Springer International Publishing Switzerland 2016

This work is subject to copyright. All rights are reserved by the Publisher, whether the whole or part of the material is concerned, specifically the rights of translation, reprinting, reuse of illustrations, recitation, broadcasting, reproduction on microfilms or in any other physical way, and transmission or information storage and retrieval, electronic adaptation, computer software, or by similar or dissimilar methodology now known or hereafter developed.

The use of general descriptive names, registered names, trademarks, service marks, etc. in this publication does not imply, even in the absence of a specific statement, that such names are exempt from the relevant protective laws and regulations and therefore free for general use.

The publisher, the authors and the editors are safe to assume that the advice and information in this book are believed to be true and accurate at the date of publication. Neither the publisher nor the authors or the editors give a warranty, express or implied, with respect to the material contained herein or for any errors or omissions that may have been made.

Printed on acid-free paper

Springer International Publishing AG Switzerland is part of Springer Science+Business Media
(www.springer.com)

Preface

Nowadays, human cannot still expand the frontiers of knowledge by having an unchanged usual view to the natural, chemical and biological processes. In order to develop and grow the human knowledge, it is necessary to see from different views and in various aspects. Looking from the large and broad scales such as the mapping of cities and countries with satellite, etc., give us the information which are unachievable by the normal vision. However, looking to the nature, from the perspective of micron and nanometer (at atomic scales) provides the information which can more easily discover the mystery of that phenomenon. What is now known as nanotechnology is becoming familiar and controlling many phenomena at the atomic and angstrom dimensions which is a difficult way with promising future and very amazing results. For instance, the recent progress in fabrication of carbon nanotubes, microelectronic chips, bimolecular engines, and nanomachines, nanosensors, microfilters and other cases have resulted in changes and developments in computers, electronics, aerospace, biochemistry, ecology, chemistry and other sciences. Electrochemistry beside the presence of powerful microscopic methods and electrodes with nanometer dimensions helped us for microstructural investigation and identification of nanostructured surfaces.

Nanotechnology has also contributed in developing and progressing of analytical electrochemistry which is very widespread scientific field. Any non-uniformity in the surfaces causes to the lack of repeatability in the obtaining of expected results. For example, information surrounding the surfaces, interfaces, corrosion, failure or abrasion of the surfaces, non-uniformity of the surfaces, recognition of the existed components in the surfaces and the degree of their oxidation are much more necessitated to study the processes. This vital information can be obtained by nanotechnology, and different microscopic techniques have been improved and developed in order to analyze the surfaces at atomic scales.

Electrochemical deposition of the metals is an ancient art which is one of the primary processes in the protection using nanosized materials. Electrochemical deposition, electroless deposition and substitution reaction which are used for the deposition of metallic alloys and metallic composite materials, taking advantage of the electrochemical reactions. Multilayered thin film, nanowires, nanowires with

nanometer layers, nanotubes, nanoparticles located in the metallic matrix and nanoparticles containing membranes can be fabricated by nanoelectrochemistry. The topics covered in this field of science are very broad. The progress in nanoelectrochemistry increased sharply during the recent years. As a result, this handbook aims to gather different aspects of nanoelectrochemistry beside its advances.

The editors of this handbook would like to appreciate all of contributors to this handbook and thank them for their hard work, patience during preparation of this handbook and also their high quality chapters. We wish publishing of this handbook will help all researchers to benefit from this collection and further progress of nanoelectrochemistry.

Summer 2015

Mahmood Aliofkhazraei
Abdel Salam Hamdy Makhoulouf

Contents

Volume 1

Part I Synthesis and Fabrication of Nanostructured Materials.....	1
1 Electrochemical Fabrication of Graphene-Based Nanomaterials	3
Alina Pruna, Daniele Pullini, and David Mataix Busquets	
2 Electrochemical Fabrication of Nanostructures	23
R. Abdel-Karim	
3 Electrochemical Preparation of Nanoresonators	47
Andrzej Kudelski	
4 Electrochemically Fabricated Nanostructures in Energy Storage and Conversion Applications	71
Kafil M. Razeeb, Maksudul Hasan, Mamun Jamal, and Alan Mathewson	
5 Electrochemical Synthesis of Metal Chalcogenide Nanorods, Nanotubes, Segmented Nanorods, and Coaxial Nanorods	101
Néstor L. Chévere-Trinidad, Serkan Gurbuz, Jessica Kramer, and Dhandapani Venkataraman	
6 Nanomaterials Produced by Electrocrystallization Method	135
Maria Trzaska and Zdzislaw Trzaska	
7 Formation and Characterization of Bimetallic Nanoparticles in Electrochemistry	169
Chun-Jern Pan, Loka Subramanyam Sarma, and Bing-Joe Hwang	

8	Synthesis, Modification, and Characterization of Nanocarbon Electrodes for Determination of Nucleic Acids.....	241
	David Hynek, Katerina Tmejova, Jiri Kudr, Ondrej Zitka, Lukas Nejd, Pavel Kopel, Branislav Ruttkay-Nedecky, Jindrich Kynicky, Jaromir Hubalek, Rene Kizek, and Vojtech Adam	
9	Porous Indium Phosphide: Preparation and Properties	283
	Suchikova Yana	
Part II Synthesis and Fabrication of Nanostructured Coatings and Thin Films		
		307
10	Recent Approaches for Designing Nanomaterials-Based Coatings for Corrosion Protection	309
	Nedal Abu-Thabit and Abdel Salam Hamdy Makhlouf	
11	Electrodeposited Zn-Nanoparticles Composite Coatings for Corrosion Protection of Steel	333
	Liana Maria Muresan	
12	Electrochemical Fabrication of Multi-Nanolayers.....	355
	Paul McCloskey, Terence O'Donnell, Brice Jamieson, Donald Gardner, Michael A. Morris, and Saibal Roy	
13	Electroless Nanocomposite Coatings: Synthesis, Characteristics, and Applications.....	389
	Sankara Narayanan T.S.N., Seshadri S.K., Il Song Park, and Min Ho Lee	
14	Self-Assembled Monolayers on Nanostructured Composites for Electrochemical Sensing Applications.....	417
	Nada F. Atta, Ekram H. El-Ads, and Ahmed Galal	
15	Nanostructured Hybrid Graphene-Conducting Polymers for Electrochemical Supercapacitor Electrodes	479
	Punya A. Basnayaka, Manoj K. Ram, Elias K. Stefanakos, and Ashok Kumar	
16	The Electrochemistry of Peptide Self-Assembled Monolayers	503
	Emanuela Gatto, M. Caruso, and M. Venanzi	
17	Electrophoretic Deposition (EPD): Fundamentals and Applications from Nano- to Microscale Structures	561
	Pouya Amrollahi, Jerzy S. Krasinski, Ranji Vaidyanathan, Lobat Tayebi, and Daryoosh Vashaee	

18 Nanoporous Anodic Aluminum Oxide: Fabrication, Characterization, and Applications.....	593
Wojciech J. Stepniowski and Zbigniew Bojar	
19 Electrodeposition of ZnO Nanostructures: Growth, Doping, and Physical Properties	647
M. Allan Thomas and Jingbiao Cui	
20 Nanostructured Transition Metal Oxides Produced by Electrodeposition for Application as Redox Electrodes for Supercapacitors.....	681
M. Fátima Montemor, S. Eugénio, N. Tuyen, R.P. Silva, T.M. Silva, and M.J. Carmezim	
21 Nanoscale Electrodeposition of Metals and Semiconductors from Ionic Liquids Probed by Scanning Tunneling Microscopy	715
Hong-Dan Peng, Yu Zhao, and Ge-Bo Pan	
Volume 2	
Part III Electrochemical Properties and Characterization of Nanostructured Materials.....	739
22 Characterization of Nanomaterials in Electrochemistry	741
Giorgia Greco	
23 Electrochemical Control of the Core-Shell Cobalt-Platinum Nanoparticles.....	769
S. Grau, E. Gómez, J.M. Feliu, and E. Vallés	
24 Metal Oxide Nanoparticle Engineering for Printed Electrochemical Applications.....	783
Pawel Jerzy Wojcik, Luis Pereira, Rodrigo Martins, and Elvira Fortunato	
25 Microstructural Aspects of Ionic Conductivity in Nanocrystalline Zirconia.....	819
Mirosław M. Bućko	
26 Wet Chemical Approaches for Chemical Functionalization of Silicon and Titanium Nanomaterials	849
Kerrilee A. Stewart and Harinder Pal Singh Missan	

Part IV Electrochemical Properties and Characterization of Nanostructured Coatings and Thin Films	867
27 Electron Transfer and Charge Storage in Thin Films of Nanoparticles	869
Krzysztof Winkler and Emilia Grądzka	
28 Electroforming and Electrodeposition on Complex 3D Geometries: Special Requirements and New Methods	941
Anne Jung, Martin Weinmann, and Harald Natter	
29 Modeling of Metal Electrodeposition at the Nanoscale	971
O.A. Oviedo and E.P.M. Leiva	
Part V New Properties	1011
30 Plasmonic Nanostructured Supports for Spectro-Electrochemistry of Enzymes on Electrodes	1013
Inez M. Weidinger	
31 Self-Organized Nano- and Microstructure of Electrochemical Materials by Design of Fabrication Approaches	1033
Zhenyu Chu, Lei Shi, and Wanqin Jin	
32 Application of Two-Dimensional Heisenberg Model to Electrochemical Nucleation Theory	1057
Serghei A. Baranov	
Part VI Applications	1071
33 Scanning Electrochemical Microscopy: A Multiplexing Tool for Electrochemical DNA Biosensing	1073
Mohtashim Hassan Shamsi and Heinz-Bernhard Kraatz	
34 Implementation of Nanostructured Catalysts in the Electrochemical Promotion of Catalysis	1095
Holly A.E. Dole and Elena A. Baranova	
35 Self-Assembled Peptide Nanostructures for the Development of Electrochemical Biosensors	1125
Jaime Castillo-León, Kinga Zór, and Winnie E. Svendsen	
36 Electrochemical Sensors Based on Nanostructured Materials	1143
Iuliana Moldoveanu, Raluca-Ioana Stefan-van Staden, and Jacobus Frederick van Staden	

37	Biocomposite Nanomaterials for Electrochemical Biosensors	1161
	Stelian Lupu, Paul Cătălin Balaure, Cecilia Lete, and Constantin Mihailciuc	
38	Development of Nanostructures by Electrochemical Method for Chemical Sensors	1195
	Surajit Kumar Hazra and Sukumar Basu	
39	Nanomaterials in Solar Cells	1251
	Razika Tala-Ighil	
40	Characterization of Metallic Micro(Nano)cluster-Based Contacts for High-Effective Photovoltaic Devices	1271
	Viktor Laptev and Halyna Khlyap	
41	Anodically Grown TiO₂ Nanotube Membranes: Synthesis, Characterization, and Application in Dye-Sensitized Solar Cells	1299
	Adriano Sacco, Andrea Lamberti, Stefano Bianco, and Elena Tresso	
Part VII	Future Prospects of Nanostructured Materials and Coatings	1327
42	Frontiers of Nanoelectrochemistry and Application of Nanotechnology: A Vision for the Future	1329
	Sukanchan Palit	
43	New Insights in Nanoelectrodeposition: An Electrochemical Aggregative Growth Mechanism	1349
	Jon Ustarroz, Annick Hubin, and Herman Terryn	
44	Recent Advances in Synthesis, Modification, and Applications of TiO₂ Nanotube Arrays by Electrochemical Anodization	1379
	Jianying Huang, Keqin Zhang, and Yuekun Lai	
45	New Approaches to the Study of Spinel Ferrite Nanoparticles for Biomedical Applications	1417
	Noppakun Sanpo, Christopher C. Berndt, Cuie Wen, and James Wang	
Index		1443

About the Editors



Mahmood Aliofkhazraei Department of Materials Engineering, Tarbiat Modares University, Tehran, Iran

Dr. Mahmood Aliofkhazraei is assistant professor in materials engineering department at Tarbiat Modares University. Dr. Aliofkhazraei's research interests include nanotechnology and its use in surface and corrosion science. One of his main interests is plasma electrolysis, an area in which he published more than 40 papers and a book. In total, he has published more than 12 books and 90 journal papers. He has given

invited talks including several keynotes in several countries. Dr. Aliofkhazraei has received several awards including the Khwarizmi award, IMES medal, INIC award, best thesis award (multiple times), best book award (multiple times), and the best young nanotechnologist award of Iran (twice). He is on the advisory editorial board of several materials science and nanotechnology journals. He is a member of the national association of surface sciences, Iranian corrosion association, and national elite foundation of Iran.



Abdel Salam Hamdy Makhoulf Manufacturing Engineering Department, College of Engineering and Computer Science, University of Texas Pan-American, Edinburg, TX, USA

Prof. Dr. Abdel Salam Hamdy Makhoulf, Ph.D., P.ENG., is RGV STAR Professor in the Department of Manufacturing Engineering, University of Texas-Pan American, in Edinburg, Texas, USA. He is the founder

of Surface Engineering Laboratory and a leading faculty of the Rapid Response Manufacturing Center. His research interests include preparation and characterization of advanced coatings, corrosion, nano/biomaterials, renewable energy, and advanced materials and polymers. Prof. Makhoulf was able to make breakthroughs in several highly important areas of materials science and corrosion engineering.

Prof. Makhlof is a multiple-award winner for his academic excellence: He received several prestigious awards in **Germany** (Humboldt Research Award for Experienced Scientists at Max Planck Institute); **USA** (Fulbright Visiting Scholar, NSF Fellow, and Department of Energy Fellow); **Belgium** (Belgian Federal Science Research Fellowship); **Arab League** (Arab Youth Excellence Award in Innovation 2013); **Jordan** (Abdul Hameed Shoman Award in Engineering Science 2012); **Egypt** (National Prize of Egypt in Advanced Science and Technology 2006; Egyptian Prize of Excellence in Surface Technology and Corrosion 2006; and Egyptian Prize of Excellence and Innovation in Materials Science and their Applications 2009); and **Palestine** (An-Najah Prize for Research 2014). Prof. Makhlof's biography was selected to be included in *Who's Who in the World*® 2015, 2007, and 2006.

Prof. Makhlof is a persistent journal reviewer, advisor, and judge of the work of his peers. He is a referee for over 30 international journals of a high caliber, and a continued board member of over 20 journals. He is also an experienced editor with board titles at journals published by Springer and Elsevier, an expert evaluator for the EU's FP7, with an estimated budget of over €50.521 billion, DAAD and German Aerospace Center, the US Fulbright Commission, the Qatar National Research Fund, the Kuwait Foundation for the Advancement of Sciences, and a consultant at Innosquared GmbH, Germany. He is a reviewer/panelist for the NSF programs: Manufacturing Machines and Equipment, Materials Engineering and Processing, and CREST; with an estimated budget of over \$7.6 billion. He is a member of the advisory committee of Australia – EU initiative “Corrosion Matters” through the EU program H2020.

Prof. Makhlof has organized and served as a head speaker at highly prestigious international symposiums and conferences over 30 times. His publication list (+170) includes studies and review papers authored in journals from top publishers. He is the editor of 12 books, 17 book chapters, and has 2 US patents. He supervised 11 Ph.D. and master's students, and 5 postdoctoral fellows.

Contributors

R. Abdel-Karim Department of Metallurgy, Faculty of Engineering-Cairo University, Giza, Egypt

Nedal Abu-Thabit Department of Chemical and Process Engineering Technology, Jubail Industrial College, Jubail, Saudi Arabia

Vojtech Adam Department of Chemistry and Biochemistry, Faculty of Agronomy, Mendel University in Brno, Brno, Czech Republic, European Union

Central European Institute of Technology, Brno University of Technology, Brno, Czech Republic, European Union

Pouya Amrollahi Helmerich Advanced Technology Research Center, School of Material Science and Engineering, Oklahoma State University, Tulsa, OK, USA

Nada F. Atta Chemistry Department, Faculty of Science, Cairo University, Giza, Egypt

Paul Cătălin Balaure Department of Organic Chemistry, Faculty of Applied Chemistry and Materials Science, University Politehnica of Bucharest, Bucharest, Romania

Elena A. Baranova Department of Chemical and Biological Engineering, and Centre for Catalysis Research and Innovation, University of Ottawa, Ottawa, ON, Canada

Serghei A. Baranov Institute of Applied Physics AS RM, Chisinau, Moldova
Dnester University, Tiraspol, Moldova

Punya A. Basnayaka Department of Mechanical Engineering and Clean Energy Research Center, University of South Florida, Tampa, FL, USA

Department of Engineering and Engineering Technology, Cuyahoga Community College, Cleveland, OH, USA

Sukumar Basu IC Design and Fabrication Centre, Department of Electronics and Telecommunication Engineering, Jadavpur University, Kolkata, WB, India

Christopher C. Berndt Faculty of Engineering and Industrial Sciences, Swinburne University of Technology, Hawthorn, VIC, Australia

Stefano Bianco Center for Space Human Robotics@PoliTO, Istituto Italiano di Tecnologia, Torino, Italy

Applied Science and Technology Department, Politecnico di Torino, Torino, Italy

Zbigniew Bojar Department of Advanced Materials and Technologies, Faculty of Advanced Technologies and Chemistry, Military University of Technology, Warszawa, Poland

Mirosław M. Bućko Faculty of Materials Science and Ceramics, University of Science and Technology, Krakow, Poland

David Mataix Busquets Universidad Politécnica de Valencia, Valencia, Spain

M.J. Carmezim Centro de Química Estrutural, Instituto Superior Técnico, Universidade de Lisboa, Avenida Rovisco Pais, Lisbon, Portugal

ESTSetúbal, Instituto Politécnico de Setúbal, Setúbal, Portugal

M. Caruso Department of Chemical Sciences and Technologies, University of Rome “Tor Vergata”, Rome, Italy

Jaime Castillo-León Sol Voltaics AB, Lund, Sweden

Néstor L. Chévere-Trinidad Department of Chemistry, University of Massachusetts Amherst, Amherst, MA, USA

Zhenyu Chu State Key Laboratory of Materials-Oriented Chemical Engineering, Nanjing Tech University, Nanjing, People’s Republic of China

Jingbiao Cui Department of Physics, University of Memphis, Memphis, TN, USA

Holly A.E. Dole Department of Chemical and Biological Engineering, and Centre for Catalysis Research and Innovation, University of Ottawa, Ottawa, ON, Canada

Ekram H. El-Ads Chemistry Department, Faculty of Science, Cairo University, Giza, Egypt

S. Eugénio Centro de Química Estrutural, Instituto Superior Técnico, Universidade de Lisboa, Avenida Rovisco Pais, Lisbon, Portugal

J.M. Feliu Departamento de Química Física, Instituto de Electroquímica, Universidad de Alicante, Alicante, Spain

Elvira Fortunato CENIMAT/I3N, Departamento de Ciência dos Materiais, Faculdade de Ciências e Tecnologia, FCT, Universidade Nova de Lisboa (UNL), Caparica, Portugal

Ahmed Galal Chemistry Department, Faculty of Science, Cairo University, Giza, Egypt

Donald Gardner Intel Corporation, Santa Clara, USA

Emanuela Gatto Department of Chemical Sciences and Technologies, University of Rome “Tor Vergata”, Rome, Italy

E. Gómez Ge-CPN, Departament de Química Física, Institut de Nanociència i Nanotecnologia (IN2UB), Universitat de Barcelona, Barcelona, Spain

Emilia Grażdzka Institute of Chemistry, University of Białystok, Białystok, Poland

S. Grau Ge-CPN, Departament de Química Física, Institut de Nanociència i Nanotecnologia (IN2UB), Universitat de Barcelona, Barcelona, Spain

Giorgia Greco Department of Science, University of Roma Tre, Rome, Italy

Serkan Gurbuz Department of Chemistry, University of Massachusetts Amherst, Amherst, MA, USA

Maksudul Hasan Tyndall National Institute, University College Cork, Cork, Ireland

Surajit Kumar Hazra Department of Physics and Materials Science, Jaypee University of Information Technology, Wagnaghat, Solan, HP, India

Jianying Huang National Engineering Laboratory for Modern Silk, College of Textile and Clothing Engineering, Soochow University, Suzhou, People’s Republic of China

Jaromir Hubalek Department of Chemistry and Biochemistry, Faculty of Agronomy, Mendel University in Brno, Brno, Czech Republic, European Union
Central European Institute of Technology, Brno University of Technology, Brno, Czech Republic, European Union

Annick Hubin Department Materials and Chemistry, Research Group Electrochemical and Surface Engineering (SURF), Vrije Universiteit Brussel (VUB), Brussels, Belgium

Bing-Joe Hwang Nanoelectrochemistry Laboratory, Department of Chemical Engineering, National Taiwan University of Science and Technology, Taipei, Taiwan

National Synchrotron Radiation Research Center, Hsinchu, Taiwan

David Hynek Department of Chemistry and Biochemistry, Faculty of Agronomy, Mendel University in Brno, Brno, Czech Republic, European Union
Central European Institute of Technology, Brno University of Technology, Brno, Czech Republic, European Union

Mamun Jamal Tyndall National Institute, University College Cork, Cork, Ireland

Brice Jamieson ELIX Wireless Charging Systems, Vancouver, Canada

Wanqin Jin State Key Laboratory of Materials-Oriented Chemical Engineering, Nanjing Tech University, Nanjing, People's Republic of China

Anne Jung Applied Mechanics, Saarland University, Saarbruecken, Germany

Halyna Khlyap University of Stuttgart, Kaiserslautern, Germany

Rene Kizek Department of Chemistry and Biochemistry, Faculty of Agronomy, Mendel University in Brno, Brno, Czech Republic, European Union

Central European Institute of Technology, Brno University of Technology, Brno, Czech Republic, European Union

Pavel Kopel Department of Chemistry and Biochemistry, Faculty of Agronomy, Mendel University in Brno, Brno, Czech Republic, European Union

Central European Institute of Technology, Brno University of Technology, Brno, Czech Republic, European Union

Heinz-Bernhard Kraatz Department of Physical and Environmental Sciences, University of Toronto Scarborough, Toronto, ON, Canada

Department of Chemistry, University of Toronto, Toronto, ON, Canada

Jessica Kramer Department of Chemistry, University of Massachusetts Amherst, Amherst, MA, USA

Jerzy S. Krasinski Helmerich Advanced Technology Research Center, School of Electrical and Computer Engineering, Oklahoma State University, Tulsa, OK, USA

Andrzej Kudelski Faculty of Chemistry, University of Warsaw, Warsaw, Poland

Jiri Kudr Department of Chemistry and Biochemistry, Faculty of Agronomy, Mendel University in Brno, Brno, Czech Republic, European Union

Central European Institute of Technology, Brno University of Technology, Brno, Czech Republic, European Union

Ashok Kumar Department of Mechanical Engineering, University of South Florida, Tampa, FL, USA

Clean Energy Research Center, University of South Florida, Tampa, FL, USA

Jindrich Kynicky Central European Institute of Technology, Brno University of Technology, Brno, Czech Republic, European Union

Yuekun Lai National Engineering Laboratory for Modern Silk, College of Textile and Clothing Engineering, Soochow University, Suzhou, People's Republic of China
Physikalisches Institute and Center for Nanotechnology (CeNTech), Westfälische Wilhelms-Universität Münster, Münster, Germany

Andrea Lamberti Applied Science and Technology Department, Politecnico di Torino, Torino, Italy

Viktor Laptev New Russian University, Moscow, Russia

Min Ho Lee Department of Dental Biomaterials and Institute of Biodegradable Materials, Institute of Oral Bioscience and BK21 Plus Program, School of Dentistry, Chonbuk National University, Jeonju, Republic of Korea

E.P.M. Leiva Instituto de Investigaciones en Físico-Química de Córdoba (INFIQC-CONICET), Departamento de Matemática y Física, Facultad de Ciencias Químicas, Universidad Nacional de Córdoba, Córdoba, Argentina

Cecilia Lete Laboratory of Electrochemistry, Institute of Physical Chemistry “Ilie Murgulescu” of the Romanian Academy, Bucharest, Romania

Stelian Lupu Department of Analytical Chemistry and Environmental Engineering, Faculty of Applied Chemistry and Materials Science, University Politehnica of Bucharest, Bucharest, Romania

Abdel Salam Hamdy Makhlof Manufacturing Engineering Department, College of Engineering and Computer Science, University of Texas Pan-America, Edinburg, TX, USA

Rodrigo Martins CENIMAT/I3N, Departamento de Ciência dos Materiais, Faculdade de Ciências e Tecnologia, FCT, Universidade Nova de Lisboa (UNL), Caparica, Portugal

Alan Mathewson Tyndall National Institute, University College Cork, Cork, Ireland

Paul McCloskey Tyndall National Institute, University College Cork, Cork, Ireland

Constantin Mihailciuc Department of Physical Chemistry, Faculty of Chemistry, University of Bucharest, Bucharest, Romania

Harinder Pal Singh Missan Fuel Cell Materials Research Lab, Department of Physics, University of the West Indies, Trinidad and Tobago, West Indies

Iuliana Moldoveanu Laboratory of Electrochemistry and PATLAB Bucharest, National Institute of Research for Electrochemistry and Condensed Matter, Bucharest, Romania

Faculty of Applied Chemistry and Materials Science, Politehnica University of Bucharest, Bucharest, Romania

M. Fátima Montemor Centro de Química Estrutural, Instituto Superior Técnico, Universidade de Lisboa, Avenida Rovisco Pais, Lisbon, Portugal

Michael A. Morris University College, Cork, Ireland

Liana Maria Muresan Department of Chemical Engineering, Babes–Bolyai University, Cluj–Napoca, Romania

Sankara Narayanan T.S.N. Department of Dental Biomaterials and Institute of Biodegradable Materials, Institute of Oral Bioscience and BK21 Plus Program, School of Dentistry, Chonbuk National University, Jeonju, Republic of Korea

Harald Natter Physical Chemistry, Saarland University, Saarbruecken, Germany

Lukas Nejd Department of Chemistry and Biochemistry, Faculty of Agronomy, Mendel University in Brno, Brno, Czech Republic, European Union

Terence O'Donnell University College Dublin, Dublin, Ireland

O.A. Oviedo Instituto de Investigaciones en Físico-Química de Córdoba (INFIQC-CONICET), Departamento de Matemática y Física, Facultad de Ciencias Químicas, Universidad Nacional de Córdoba, Córdoba, Argentina

Sukanchan Palit Department of Chemical Engineering, University of Petroleum and Energy Studies, Dehradun, India

Haridevpur, Kolkata, India

Chun-Jern Pan Nanoelectrochemistry Laboratory, Department of Chemical Engineering, National Taiwan University of Science and Technology, Taipei, Taiwan

Ge-Bo Pan Division of Interdisciplinary Research, Suzhou Institute of Nano-tech and Nano-bionics (sinano), Chinese Academy of Sciences, Suzhou, China

Il Song Park Division of Advanced Materials Engineering and Institute of Biodegradable Materials, Chonbuk National University, Jeonju, Republic of Korea

Hong-Dan Peng Division of Interdisciplinary Research, Suzhou Institute of Nano-tech and Nano-bionics (sinano), Chinese Academy of Sciences, Suzhou, China

Luis Pereira CENIMAT/I3N, Departamento de Ciência dos Materiais, Faculdade de Ciências e Tecnologia, FCT, Universidade Nova de Lisboa (UNL), Caparica, Portugal

Alina Pruna University of Bucharest, Magurele, Bucharest, Romania

Universidad Politécnica de Valencia, Valencia, Spain

Daniele Pullini Centro Ricerche Fiat, Torino, Orbassano, Italy

Manoj K. Ram Clean Energy Research Center, University of South Florida, Tampa, FL, USA

Nanotechnology Research and Education Center, University of South Florida, Tampa, FL, USA

Kafil M. Razeeb Tyndall National Institute, University College Cork, Cork, Ireland

Saibal Roy Tyndall National Institute, Cork, Ireland

Branislav Ruttkay-Nedecky Department of Chemistry and Biochemistry, Faculty of Agronomy, Mendel University in Brno, Brno, Czech Republic, European Union
Central European Institute of Technology, Brno University of Technology, Brno, Czech Republic, European Union

Seshadri S.K. Department of Metallurgical and Materials Engineering, Indian Institute of Technology Madras, Chennai, India

Adriano Sacco Center for Space Human Robotics@PoliTO, Istituto Italiano di Tecnologia, Torino, Italy

Noppakun Sanpo Faculty of Engineering and Industrial Sciences, Swinburne University of Technology, Hawthorn, VIC, Australia

Loka Subramanyam Sarma Department of Chemistry, Yogi Vemana University, Kadapa, Andhra Pradesh, India

Mohtashim Hassan Shamsi Department of Physical and Environmental Sciences, University of Toronto Scarborough, Toronto, ON, Canada

Department of Chemistry, University of Toronto, Toronto, ON, Canada

Lei Shi State Key Laboratory of Materials-Oriented Chemical Engineering, Nanjing Tech University, Nanjing, People's Republic of China

R.P. Silva Centro de Química Estrutural, Instituto Superior Técnico, Universidade de Lisboa, Avenida Rovisco Pais, Lisbon, Portugal

T.M. Silva Centro de Química Estrutural, Instituto Superior Técnico, Universidade de Lisboa, Avenida Rovisco Pais, Lisbon, Portugal

Department of Mechanical Engineering, GI-MOSM, Instituto Superior de Engenharia de Lisboa (ISEL), Lisbon, Portugal

Elias K. Stefanakos Clean Energy Research Center, University of South Florida, Tampa, FL, USA

Wojciech J. Stepniowski Department of Advanced Materials and Technologies, Faculty of Advanced Technologies and Chemistry, Military University of Technology, Warszawa, Poland

Raluca-Ioana Stefan-van Staden Laboratory of Electrochemistry and PATLAB Bucharest, National Institute of Research for Electrochemistry and Condensed Matter, Bucharest, Romania

Faculty of Applied Chemistry and Materials Science, Politehnica University of Bucharest, Bucharest, Romania

Kerrilee A. Stewart Fuel Cell Materials Research Lab, Department of Physics, University of the West Indies, Trinidad and Tobago, West Indies

Winnie E. Svendsen DTU Nanotech, Technical University of Denmark, Kgs. Lyngby, Denmark

Razika Tala-Ighil Unité de recherche matériaux, procédés pour l'environnement, URMPE Institute of Electrical and Electronic Engineering, University M'Hamed Bougara, Umbb, Boumerdes, Algeria

Lobat Tayebi Helmerich Advanced Technology Research Center, School of Material Science and Engineering, Oklahoma State University, Tulsa, OK, USA

Department of Developmental Sciences, Marquette University School of Dentistry, Milwaukee, WI, USA

Herman Terryn Department Materials and Chemistry, Research Group Electrochemical and Surface Engineering (SURF), Vrije Universiteit Brussel (VUB), Brussels, Belgium

M. Allan Thomas Department of Physics and Astronomy, University of Arkansas at Little Rock, Little Rock, AR, USA

Katerina Tmejova Department of Chemistry and Biochemistry, Faculty of Agronomy, Mendel University in Brno, Brno, Czech Republic, European Union
Central European Institute of Technology, Brno University of Technology, Brno, Czech Republic, European Union

Elena Tresso Center for Space Human Robotics@PoliTO, Istituto Italiano di Tecnologia, Torino, Italy

Applied Science and Technology Department, Politecnico di Torino, Torino, Italy

Maria Trzaska Institute of Precision Mechanics, Warsaw, Poland

Zdzislaw Trzaska University of Ecology and Management, Warsaw, Poland

N. Tuyen Centro de Química Estrutural, Instituto Superior Técnico, Universidade de Lisboa, Avenida Rovisco Pais, Lisbon, Portugal

Jon Ustarroz Department Materials and Chemistry, Research Group Electrochemical and Surface Engineering (SURF), Vrije Universiteit Brussel (VUB), Brussels, Belgium

Ranji Vaidyanathan Helmerich Advanced Technology Research Center, School of Material Science and Engineering, Oklahoma State University, Tulsa, OK, USA

E. Vallés Ge-CPN, Departament de Química Física, Institut de Nanociència i Nanotecnologia (IN2UB), Universitat de Barcelona, Barcelona, Spain

Jacobus Frederick van Staden Laboratory of Electrochemistry and PATLAB Bucharest, National Institute of Research for Electrochemistry and Condensed Matter, Bucharest, Romania

Daryoosh Vashaee Helmerich Advanced Technology Research Center, School of Electrical and Computer Engineering, Oklahoma State University, Tulsa, OK, USA
Electrical and Computer Engineering Department, North Carolina State University, Raleigh, NC, USA

M. Venanzi Department of Chemical Sciences and Technologies, University of Rome “Tor Vergata”, Rome, Italy

Dhandapani Venkataraman Department of Chemistry, University of Massachusetts Amherst, Amherst, MA, USA

James Wang Faculty of Engineering and Industrial Sciences, Swinburne University of Technology, Hawthorn, VIC, Australia

Inez M. Weidinger Institut für Chemie, PC 14, Technische Universität Berlin, Berlin, Germany

Martin Weinmann Physical Chemistry, Saarland University, Saarbruecken, Germany

Cuie Wen Faculty of Engineering and Industrial Sciences, Swinburne University of Technology, Hawthorn, VIC, Australia

Krzysztof Winkler Institute of Chemistry, University of Bialystok, Bialystok, Poland

Pawel Jerzy Wojcik CENIMAT/I3N, Departamento de Ciência dos Materiais, Faculdade de Ciências e Tecnologia, FCT, Universidade Nova de Lisboa (UNL), Caparica, Portugal

Suchikova Yana Berdyansk State Pedagogical University, Berdyansk, Zaporizhia Oblast, Ukraine

Keqin Zhang National Engineering Laboratory for Modern Silk, College of Textile and Clothing Engineering, Soochow University, Suzhou, People’s Republic of China

Yu Zhao Division of Interdisciplinary Research, Suzhou Institute of Nano-tech and Nano-bionics (sinano), Chinese Academy of Sciences, Suzhou, China

Ondrej Zitka Department of Chemistry and Biochemistry, Faculty of Agronomy, Mendel University in Brno, Brno, Czech Republic, European Union

Central European Institute of Technology, Brno University of Technology, Brno, Czech Republic, European Union

Kinga Zór DTU Nanotech, Technical University of Denmark, Kgs. Lyngby, Denmark

Part I

**Synthesis and Fabrication
of Nanostructured Materials**

Electrochemical Fabrication of Graphene-Based Nanomaterials

1

Alina Pruna, Daniele Pullini, and David Mataix Busquets

Contents

Introduction.....	4
Electrochemical Synthesis of Graphene Nanomaterials from Aqueous Solution.....	5
Surface-Mediated Electrodeposition of Graphene Nanomaterials	7
Liquid-Phase Electrosynthesis of Graphene Nanomaterials.....	10
Synthesis of Graphene Nanomaterials by Electrodeposition from Nonaqueous Solution	11
Electrochemical Unzipping of Carbon Nanotubes	14
Synthesis of Graphene Nanomaterials by Electrophoretic Deposition.....	16
Composite Nanomaterials Obtained by Electrodeposition of Graphene	18
Conclusions.....	18
References.....	19

Abstract

Its unique nanostructure and extraordinary thermal, mechanical, and electrical properties such as good biocompatibility, high-surface area, excellent electrical conductivity, electron mobility at room temperature, and flexibility have made graphene a popular research subject in the recent past in many fields such as batteries, supercapacitors, fuel cells, and sensors, to name only a few.

A. Pruna (✉)
University of Bucharest, Magurele, Bucharest, Romania

Universidad Politécnica de Valencia, Valencia, Spain
e-mail: ai.pruna@gmail.com

D. Pullini
Centro Ricerche Fiat, Torino, Orbassano, Italy
e-mail: daniele.pullini@crf.it

D.M. Busquets
Universidad Politécnica de Valencia, Valencia, Spain
e-mail: dbusquets@mcm.upv.es

Since the micromechanical cleavage of graphite, various deposition approaches were followed for the development of graphene-based devices. Nevertheless, all of these approaches have their own advantages and disadvantages. Among the deposition methods, electrochemical approach is potentially the simplest and least expensive method; it is a fast and green approach, suitable for mass production and for large-area applications.

This chapter proposes to review on the electrochemical synthesis of graphene as an alternative to a more convenient, efficient, and greener route to fabricate graphene-based nanomaterials with lower oxygen content.

Keywords

Graphene oxide • Reduction • Electrodeposition • Electrophoresis • Composites

Introduction

Graphene sheets, an intriguing novel two-dimensional carbon material, have attracted more and more attention because of its unique properties such as high-surface area, excellent mechanical stiffness and flexibility, exceptional electrical properties, and electrochemical sensing presenting considerable potential for applications in fields such as biosensors, catalysis, electrochemical energy storage, and electronics [1].

Graphene-based nanomaterials exhibit many exciting properties which could be useful for fabrication of many novel devices. However, in order to fully realize these properties and applications, consistent, reliable, and inexpensive methods for growing high-quality graphene layers in excellent yields are crucial, as the existence of residual defects will heavily impact their electronic properties, despite their expected insensitivity to impurity scattering.

Various technologies were reported for the fabrication of graphene materials since the elegant “scotch tape” method, but many concerns were raised along. For example, the large-scale fabrication of graphene by chemical vapor deposition and subsequent transfer protocols make it a limiting alternative due to the special equipment and conditions used. Chemical reduction of exfoliated graphene oxide (GO) may offer the advantages of being cheap and upscalable as reported by deoxygenation of GO with various agents such as hydroquinone [2], NaBH_4 [3], hydrazine hydrate [4], hydrazine vapor [5], or hydrazine with NH_3 [6]. Since these reducing agents, and in particular the hydrazine, are toxic and should be used with extreme care, green reducing agents got highly desired [7]. On the other hand, the method of drop casting solution deposition of graphene films on a conductive substrate [8] presents difficulties, as well, due to bad dispersion of graphene, poor adhesion to substrate, and low reproducibility. Anyhow, it is rather difficult to derive relatively pure graphene from chemical reduction.

Therefore, developing a convenient and efficient route to produce graphene film on the conductive substrate is still a challenge. Moreover, the deposition techniques

should be fully compatible with plastic substrates, low-temperature processes, and solution-processable materials, suitable for flexible substrates for large-area manufacturing technologies.

Electrochemical methods are known as an effective tool to modify electronic states by adjusting the external power source to change the Fermi energy level of the surfaces of electrode materials [9]. In recent years, the electrochemical synthesis of graphene materials has drawn considerable attention, in spite of the necessity of a conducting substrate and limitations due to the scale of preparation thanks to obvious advantages in comparison with the methods listed previously. First, this method offers the advantages of simplicity, time efficiency, and environmental friendliness [10–12]; thus, it will not result in contamination of the reduced material. More importantly, the highly negative potentials used in the electrochemical method, which can be easily controlled via changing the electrochemical parameters, can overcome the energy barriers to efficiently reduce the oxygen-containing functional groups in GO [10], more than it is possible via chemical methods. In addition, the reaction conditions are generally mild and the direct immobilization of the as-prepared nanomaterials on the conducting substrate easily facilitates further applications.

This chapter explores the electrochemical synthesis approaches to produce graphene nanomaterials and their properties for various applications. Some of the previous works on the electrochemical synthesis of graphene nanomaterials are summarized in Table 1 in regard to the main conditions of the synthesis and the applications of the obtained materials.

More details on each specific approach for the synthesis of graphene nanomaterials based on electrochemical methods are given in the following subsections. Nevertheless, this work is not intended as an extensive review of research performed up to date but rather as an insight into the synthesis approaches followed on the topic.

Electrochemical Synthesis of Graphene Nanomaterials from Aqueous Solution

The decorative oxygen functional groups of GO such as hydroxyl, carboxyl, or epoxides make it hydrophilic and easily dispersible in water [7]. Therefore, many aqueous electrolytes including NaCl [25], Na₃PO₄ [12], Na₂SO₄ [26], NaNO₃ [16], PBS [10], KNO₃ [27], and KCl [28] aqueous solutions have been investigated as mediums for electrochemical reduction of GO. The removal of these functional groups by electrochemical reduction was generally reported as partial and the recovery of sp² structure by healing of the sp³ defects in GO is still a challenge [10] requiring thus further treatments of the electroreduced GO materials.

Although the mechanism of electrochemical reduction is not fully understood and it requires further study, it was found that the electrochemical reduction process is pH dependent. This suggests the following mechanism of reduction [12, 29]:

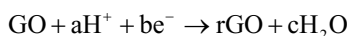


Table 1 Overview of graphene nanomaterials obtained by electrochemical methods

Material	Fabrication type	Electrolyte	Electrochemical method	Application	References
Sodium dodecyl sulfate-intercalated rGO	Substrate mediated	Aqueous	Constant potential	–	Alanyaloğlu et al. [13]
rGO	Substrate mediated	Aqueous	Cyclic voltammetry	Electrocatalysis	Kakaei [14]
rGO	Substrate mediated	Aqueous	Cyclic voltammetry	Catalase sensor	Ting et al. [15]
rGO	Substrate mediated	Aqueous	Constant potential	Supercapacitor	Peng et al. [16]
rGO/polyaniline composite	Substrate mediated	Aqueous	Cyclic voltammetry	–	Tang et al. [17]
RGO/Ni(OH) ₂ composite	Substrate mediated	Aqueous	Electrophoretic deposition	Supercapacitor	Zhang et al. [18]
Graphene/MnO ₂ nanowall hybrid	Substrate mediated	Aqueous	Cyclic voltammetry	Supercapacitor	Zhu et al. [9]
rGO/SWCNT composite	Substrate mediated	Aqueous	Electrophoretic deposition	–	Bittolo Bon et al. [19]
rGO	Solution exfoliation	Aqueous	Constant potential	Field-effect transistor	Su et al. [20]
rGO	Solution exfoliation	Ionic liquid	Constant potential	–	Liu et al. [21]
rGO/Au composite	Substrate mediated	Ionic liquid	Constant potential	–	Fu et al. [22]
Unzipped MWCNT	Substrate mediated	Aqueous	Constant potential	–	Shinde et al. [23]
Unzipped SWCNT	Substrate mediated	Aqueous	Cyclic voltammetry	–	John et al. [24]

The strategies to fabricate graphene nanomaterials by electrochemical method followed different routes as depending on the necessity of a substrate or the steps involved.

Surface-Mediated Electrodeposition of Graphene Nanomaterials

Graphene sheets have the ability to strongly adhere to various substrates due to their high van der Waals attraction, large surface area, and flatness [27]. As dictated by the application envisioned for such materials, the electrodeposition of graphene on various substrates was performed by either direct mode or by two-step electrosynthesis.

Direct Electrodeposition

Hilder et al. [30] studied the effect of conductivity of deposition medium direct electrochemical reduction of GO from aqueous suspension by applying reduction voltages exceeding -1.0 to -1.2 V. According to the tests carried out, he observed that the optimum conductivity values for the deposition to produce ranged 4 – 25 mS cm^{-1} irrespective of system parameters such as concentration and history of the GO sample or electrolyte.

On the basis of pulse voltammetry and cyclic voltammetry measurements, Guo et al. [10] described how hydroxyl and epoxide groups on GO sheets can be reduced more quickly at an applied potential of -1.5 to 0 V compared with -1.3 to 0 V. Similarly, a constant potential reduction at -1.2 V was carried out by Peng et al. [16] to reduce GO film and fabricate a capacitor with the electrochemically rGO which achieved a specific capacitance of 128 F g^{-1} .

Strongly alkaline solutions were reported as effective for the deoxygenation of GO [29]. The electrodeposition of rGO from GO suspension by cyclic voltammetry technique in 6 mol L^{-1} KOH aqueous solution in the range of 0.9 – 0 V (vs. Hg/HgO) showed an O/C ratio as low as 1.29 %. This material showed good electrochemical performance upon cycling. After $3,000$ cycles, the electrode preserved 99 % of its initial capacitance of 152 F g^{-1} at a current density of 5 A g^{-1} .

Chen et al. [31] directly deposited graphene nanosheets onto a glassy carbon electrode (GCE) through cyclic voltammetric (CV) reduction of a GO colloidal solution. Prior to CV deposition, the GO material was exfoliated in a phosphate buffer solution by ultrasonication and further subjected to N_2 bubbling. The irreversible electrochemical reduction of GO was identified by the presence of a cathodic peak at -1 V in the CV curves (Fig. 1), while the other cathodic and anodic peaks were attributed to active oxygen-containing groups on graphene planes that were too stable to be reduced by the CV method. The charge-transfer property of the rGO electrode evaluated with the help of carbon-material surface chemistry-sensitive redox probe $\text{Fe}(\text{CN})_6^{3-/4-}$ showed increased electrochemical active sites after deposition of rGO on GCE. The rGO-modified GCE showed high-resolution capacity to hydroquinone and catechol, therefore indicating graphene as a promising sensing platform for isomer determination.

Fig. 1 CVs depicting electrochemical reduction of 1.0 mg mL⁻¹ GO in PBS (0.067 M, pH 9.18) on a GCE at 10 mV s⁻¹ (Reprinted with permission from Chen et al. [31]. Copyright (2011) Elsevier)

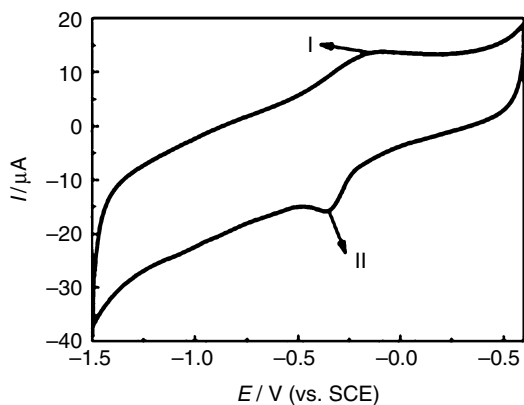
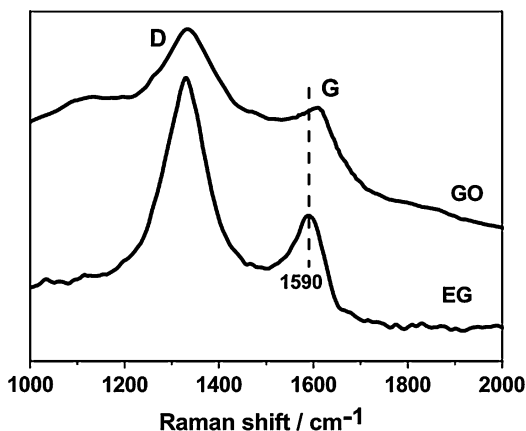


Fig. 2 Raman spectra of GO and electroreduced GO (Reprinted with permission from Liu et al. [32]. Copyright (2011) WILEY-VCH)



Liu et al. [32] reported the direct deposition of rGO onto GCE by electrolysis of GO suspensions as a function of pH. According to their results, the electrodeposition could occur in over the pH range 2.0–10, while at higher pH values such as pH 11.0 and 13.0, no deposition was observed on the surface of the electrode. The Raman spectra of the electroreduced GO show that the G band associated with graphite lattice is red shifted in comparison with GO as the reduction to graphene leads to an increased in-plane crystalline order of sp² carbon atoms and thus increased π -electron conjugation within the sp² carbon network (see Fig. 2).

On the other hand, Ye et al. [33] applied constant potential mode and pulsed electrodeposition to directly obtain rGO film on GCE from a phosphate buffer solution (PBS) containing 0.1 mg mL⁻¹ GO. Two pulses were used as shown in the Fig. 3: a constant potential of 0.6 V to deposit GO sheets on GCE and -1.2 V to electrochemically reduce the as-deposited GO sheets to rGO sheets. His study showed that electrodeposited rGO film could be used as an effective support for the electrodeposition of Pt microspherical particles resulting in a modified electrode (Pt/rGO/GCE)

with superior electrocatalytic activity and improved stability for methanol oxidation than the Pt/GCE electrode.

Two-Step Electrodeposition

Two-step electrochemical depositions typically involved the preparation of a modified electrode followed by electrodeposition. One popular way of fabricating modified electrode is by spin coating, drop casting, or dipping the electrode in the GO solution.

By applying this technique, Yu et al. [34] studied the electrodeposition of rGO using GO-drop-casted GCE electrodes and applied potential windows of -1.0 to 1.6 V, -1.5 to 0 V, and -1.0 to 1.0 V. According to their results, the distribution of the residual functional groups in the electrodeposited rGO obtained under different potentials had a marked effect on the specific capacitance of the electrode. That is, applying the window -1.5 to 0 V greatly decreased the number of epoxy groups

Fig. 3 (a) Pulsed electrodeposition mode for the deposition of rGO on GCE. (b) Constant potential mode for the deposition of GO on GCE [33]

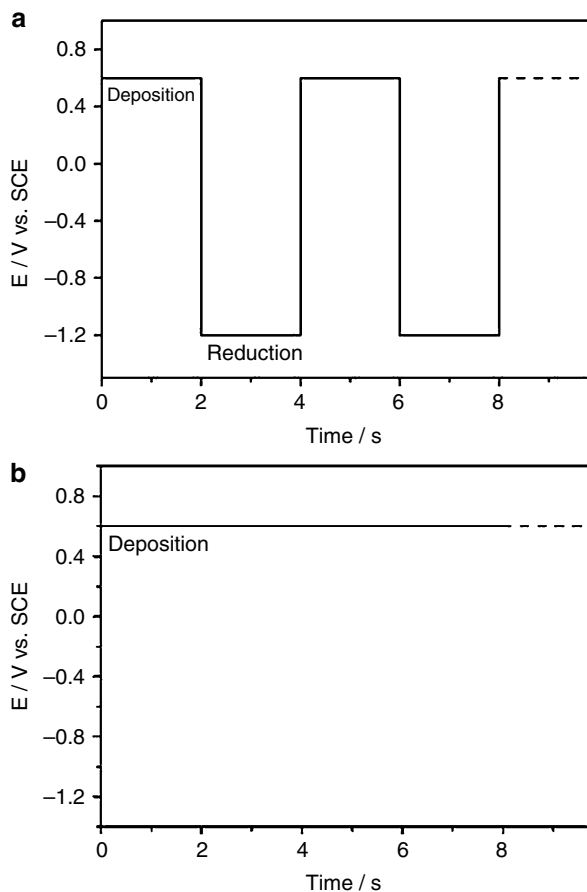


Table 2 Fitting results (%) of the C1s XPS spectra before and after electrochemical prereduction of GO (Reprinted with permission from Yu et al. [34]. Copyright (2013) Elsevier)

Treatment	COOR 289 eV	C–O 286.6 eV	C–OH 285.7 eV	C–C (sp ²) 284.5 eV
Before	40.6	40.1	7	12.3
–1.0 to 1.6 V		37.6	19.2	43.2
–1.0 to 1.0 V		19.2	19.7	61.1
–1.5 to 0 V		15.4	35.9	48.7

and resulted in small new sp² domains, while sp² carbon groups increased. On the other hand, the reduction at –1.0 to 1.0 V for 4,000 s enhanced sp² carbon to 61.1 %, and large sp² domains were formed. Consequently, the specific capacitances were 246 and 164 F/g, in agreement with Raman and X-ray photoelectron spectroscopy (XPS) results – see Table 2.

Another modified electrodes reported for the electrodeposition of graphene-based nanomaterials are, for instance, modified gold electrodes with GO by using self-assembled monolayers of cystamine and further electrochemically reduced it to obtain reduced GO layers [27]. Wang et al. [25] reported a study on electrochemical reduction of GO monolayers on 3-aminopropyltriethoxysilane (APTES)-modified electrodes.

As compared to hydrazine-reduced rGO, Wang et al. claimed that the morphology of single-layer electrodeposited rGO was similar for the films adsorbed on 3-aminopropyltriethoxysilane (APTES)-modified solid substrates such as GCE or ITO [35]. Raman spectra showed that the G band for fresh electrochemical rGO shifted from 1,600 to 1,587 cm⁻¹ compared with GO and together with results from the negative charge testing with [Fe(CN)₆]^{3-/4-} proved that the electrochemical method is more effective than the hydrazine vapor reduction method to reduce the GO films.

Filik et al. [36] reported the fabrication of an electrochemical sensor based on graphene–Nafion composite for detection of acetaminophen. He coated a GCE with GO suspension mixed with Nafion–isopropyl alcohol which was further immersed in 0.02 M KH₂PO₄ solution and subjected to a cathodic potential of –0.7 V for 10 min. Cyclic voltammetry was used to investigate the electrochemical behavior of acetaminophen on the bare GCE and the modified GCE in 0.1 M ammonia buffer solution at a scan rate of 50 mVs⁻¹, respectively. The graphene–Nafion-modified electrode exhibited excellent electrochemical activity on the oxidation of acetaminophen having a detection limit of 0.025 μM.

Liquid-Phase Electrosynthesis of Graphene Nanomaterials

Suspensions of graphene-based materials are typically obtained electrochemically by oxidation of graphite in various electrolytes. For example, Wang et al. [37] and Lee et al. [38] prepared graphene sheets on the graphite surface by electrolysis in

poly(sodium-4-styrene-sulfonate) (PSS) solution with the formation of stable graphene/polymer suspensions, while Dilimon and Sampath [39] exfoliated graphite in acetamide–urea–ammonium nitrate melt.

Su et al. [20] investigated the exfoliation of graphite by applying varying biases such as constant switching in the range -25 to 25 V in different electrolytes. They observed that only the electrolytes containing H_2SO_4 exhibit ideal exfoliation efficiency. However, as the exfoliation using only H_2SO_4 induces large amounts of defects in the graphene sheets, KOH was added to lower the exfoliation rate. Regarding the bias, low and inefficient exfoliation was produced by applying bias up to 10 V, while fast rate was observed upon increasing the bias larger than 10 V. The obtained graphene sheets were reported to be bilayered with A–B stacking exhibiting a lateral size of $30\ \mu\text{m}$. Transparent films obtained with the self-assembled graphene sheets showed good potential for flexible electronics, as per the sheet resistance of $\sim 210\ \Omega/\text{sq}$ at 96% transparency.

Further, Zhang et al. [40] reported the synthesis of single-layer or bilayer electrochemically functional graphene nanocomposites with good electrocatalytic activity toward hydrogen peroxide (H_2O_2) and β -nicotinamide adenine dinucleotide (NADH), in sheet or ribbon shapes, by one-step liquid-phase exfoliation of natural flake graphite with methylene blue and applied ultrasonic treatment.

A stable colloidal graphene/sodium dodecyl sulfate (SDS) suspension was reported by Alanyalıoğlu et al. [13] by a two-step route (see Fig. 4): first, an electrochemical intercalation of SDS into graphite and further, the electrochemical exfoliation of an SDS-intercalated graphite electrode. They observed that the electrochemical intercalation process in 0.01 M SDS solution occurred with simultaneous water electrolysis even at low intercalation potential values, while no water electrolysis was produced at a large anodic potential range in 0.1 M SDS solution. The current fluctuations in the current–time transient obtained during the potentiostatic intercalation at 1.6 V versus Pt were attributed to repeated exfoliation of graphene sheets from the graphite surface and formation of fresh surface to the electrolyte during SDS intercalation into graphite electrode [41]. Based on their results, the graphene sheets with high structural order and low number of layers can be obtained by using relatively high intercalation potentials.

Synthesis of Graphene Nanomaterials by Electrodeposition from Nonaqueous Solution

Since the electroreduction of GO from aqueous suspensions requires the use of a fixing agent onto electrode that presents difficulties to be removed [27, 42], some organic solvents replacing water were examined as a medium for electrochemical reduction of GO [43].

According to the study performed by Harima et al. [43], their sweep-voltammogram I–V results (see Fig. 5) show that GO can be successfully electroreduced onto fluorine-doped–tin-oxide (FTO) substrate in acetonitrile, dimethylformamide, dimethylsulfoxide, and propylene carbonate from which the

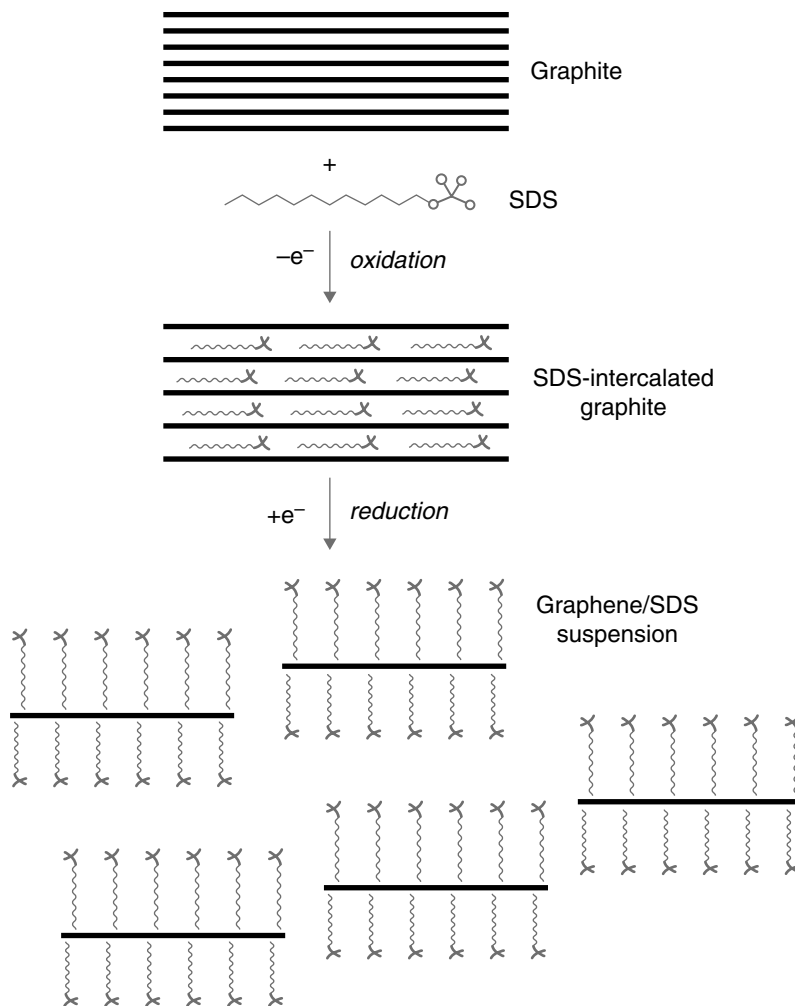


Fig. 4 Representative view of electrochemical route to produce graphene/SDS suspension (Reprinted with permission from Alanyalioğlu et al. [13]. Copyright (2012) Elsevier)

amount of electricity necessary to reduce almost complete 1 mg GO was determined as 2.0 C. The film obtained in polycarbonate showed a specific capacitance of 146 F g^{-1} .

Ping et al. [44] reported the electroreduction of GO onto ionic-liquid n-octylpyridinium hexafluorophosphate-doped screen-printed electrode (IL-SPE) from nitrogen-purged solution under magnetic stirring at -0.8 V (vs. Ag/AgCl) for 600 s. The fabricated glucose biosensor based on the modified rGO/IL-SPE electrode showed good analytical performance with a linear detection range from $5 \text{ }\mu\text{M}$ to 12 mM , with a detection limit of $1 \text{ }\mu\text{M}$.

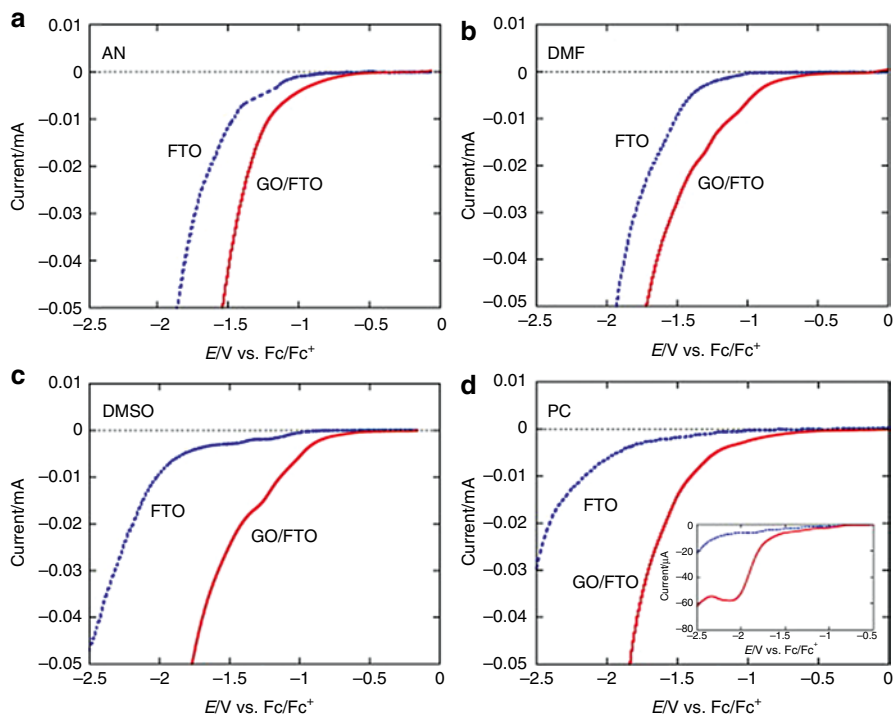


Fig. 5 Linear-sweep voltammograms of FTO and GO (0.1 mg)/FTO electrodes in organic solvents containing 0.5 M Et_4NBF_4 at 10 mV s^{-1} : (a) acetonitrile (AN), (b) dimethylformamide (DMF), (c) dimethylsulfoxide (DMSO), and (d) propylene carbonate (PC). The inset of (d) denotes current–voltage curves in the same conditions as in (d), but with a thinner GO layer on FTO (Reprinted with permission from Harima et al. [43]. Copyright (2011) Elsevier)

A one-step electrochemical approach was performed by Liu et al. [21] for the preparation of ionic-liquid-functionalized graphene sheets with the assistance of an ionic liquid and water. The properties of graphene sheets obtained by applying constant potentials of 10–20 V to two high-purity graphite electrodes were analyzed as a function of ionic liquid and ratios of ionic liquid/water employed. According to their results, the ionic-liquid-treated graphite sheets could be exfoliated into functionalized graphene nanosheets allowing individualization and homogeneous distribution into polar aprotic solvents, without further reduction.

Kauppila et al. [45] studied the electroreduction of GO spin-coated onto SnO_2 substrates by using cyclic voltammetry between 0 and -0.8 V at pH 2 and from 0 to -1.3 V at pH 12. The type of deposition solution that was aqueous solutions or organic ones – propylene carbonate and acetonitrile – and varying pH values proved to have a marked influence: given the broader potential window for organic solvents, the reduction process started at more negative potentials in organic solutions with respect to aqueous ones.

Electrochemical Unzipping of Carbon Nanotubes

Shinde et al. [23] reported another electrochemical approach to transform multi-walled carbon nanotubes (MWCNTs) to graphene nanoribbons (see scheme in Fig. 6) by first oxidizing the MWCNT and further reducing them (see Fig. 7).

The electrochemical unzipping of CNTs has the advantages of eliminating the limitations of over-oxidation and edge defects in chemical unzipping by careful control of the electric field. After spreading a suspension of CNT onto GCE electrodes, the modified electrodes were oxidized at constant potential for 2–12 h in 0.5 M H_2SO_4 solution. Further, the oxidized-CNT/GCE electrode was subjected to -0.75 V for 2–12 h. Their results underlined the unique advantage of the unzipping treatment of CNTs in the presence of an interfacial electric field with respect to the orientation of CNTs, by the fabrication of graphene sheets with controlled widths and fewer defects.

John and colleagues [24] reported an in situ Raman spectroscopic and microscopic investigation of the electrochemical unzipping of single-walled carbon nanotubes. According to their Raman spectral mapping results, metallic SWCNTs are opened up rapidly followed by gradual electrochemical unzipping of semiconducting SWCNTs. Considering the resonant Raman scattering theory, it was found that two metallic SWCNTs with chiralities (10, 4) and (12, 0) get unzipped first at a lower electrode potential (-0.36 V) followed by the gradual unzipping of another

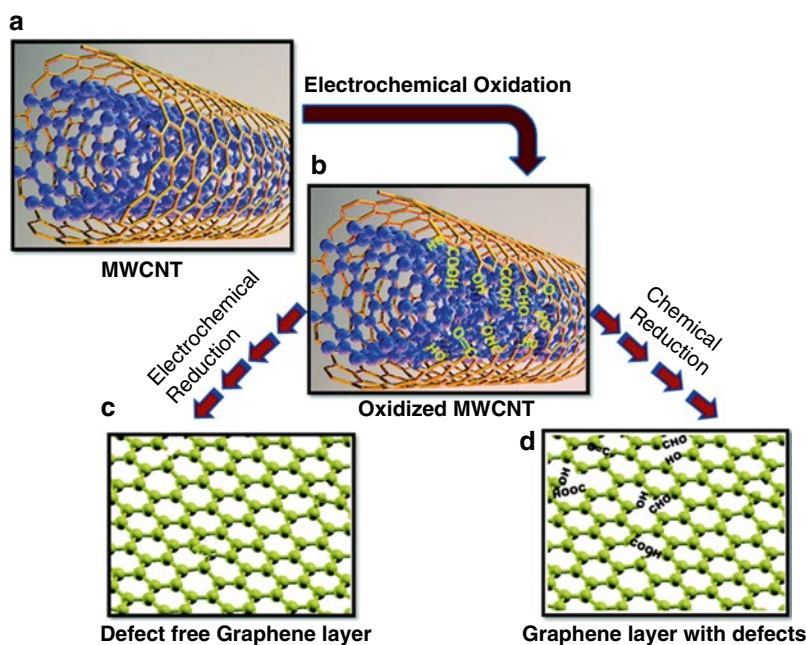


Fig. 6 Diagram of the electrochemical approach for unzipping the CNTs to graphene sheets (Reprinted with permission from Shinde et al. [23]. Copyright (2011) American Chemical Society)

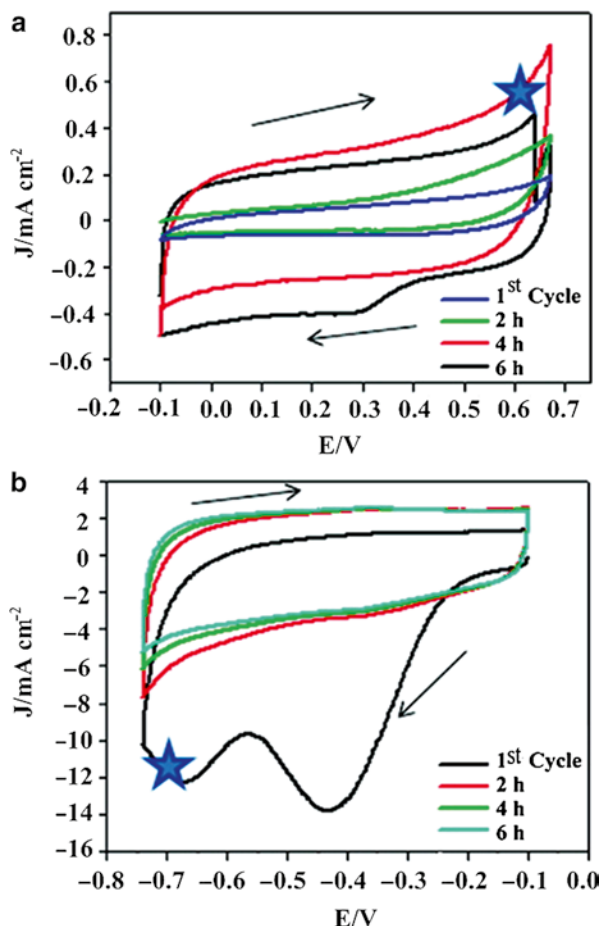


Fig. 7 (a) Cyclic voltammograms (oxidation) of MWCNTs in the potential window from 0.1 to 0.7 V in 0.5 M H_2SO_4 using glassy carbon electrode at 100 mV/s scan rate. (b) Cyclic voltammograms (reduction) of MWCNTs in the potential window from -0.1 to -0.75 V in 0.5 M H_2SO_4 at 100 mV/s scan rate. Regions marked with a *star* indicate the potentials at which the CNTs have been selectively oxidized or reduced (Reprinted with permission from Shinde et al. [23]. Copyright (2011) American Chemical Society)

two metallic tubes, (9, 3) and (10, 1), at a relatively higher potential (-1.16 V). The semiconducting SWCNTs with chiralities (11, 7) and (12, 5), however, got open up gradually at (-1.66 V).

Recently, Huang et al. [46] reported on the capacitance properties of layer-by-layer spray-deposited SWCNTs and observed that vacuum and H_2 heat treatment resulted in a hybrid microstructure of SWCNTs and multilayer graphene sheets from unzipped SWCNTs with increased capacitance of 151 F g^{-1} at 2 mV s^{-1} .

Synthesis of Graphene Nanomaterials by Electrophoretic Deposition

Electrophoretic deposition (EPD) gained much interest in deposition of graphene-based materials, being employed as a pretreatment and followed by electroreduction. Thus, rGO films on an indium tin-oxide (ITO) sheet electrode has been realized via EPD technique followed by subsequent in situ electrochemical reduction by constant potential method [47, 48].

Wu et al. [48] deposited graphene sheets by the electrophoretic method using a bias voltage of 100–160 V after the previous addition of a charger to render the sheets positively charged, while Chen et al. [49] reported the electrophoretic deposition of graphene starting from an ethanol colloidal suspension and applied bias of 50 V.

The electrophoretic method was also applied to combine the graphene and carbon nanotubes in a flexible, transparent, and conductive novel hybrid material [19] starting from a 1-ethyl-2-pyrrolidinone stable suspension by applying lower biases and deposition time with respect to the data existing in the literature [50] and resulted in the appearance of a thin paperlike structure with good transparency.

Liu et al. [28] showed that rGO films obtained this way (denoted with GS; see Fig. 8) resembled GO in terms of morphology, but most of the oxygen-containing functional groups were removed according to their XPS results for non-oxygenated groups C=C/C–C that increased from 49.1 in GO to 74.2 % in rGO. Moreover, the rGO obtained by Liu and his colleagues showed also a π - π^* shakedown feature at 290.6 eV, confirming the existence of conjugated carbons. The specific capacitance still remained at high level of 93 F g⁻¹ after 400 times of cycling, demonstrating that the prepared film electrode possessed the excellent stability and lifetime as supercapacitor material (Fig. 9).

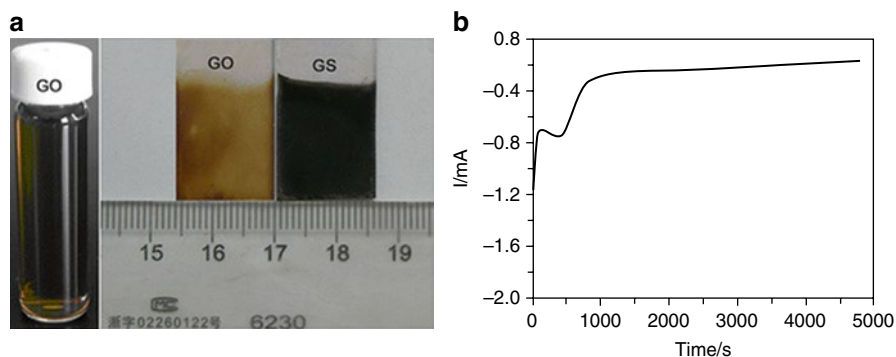


Fig. 8 (a) Optical images of the GO aqueous suspension (0.6 mg mL⁻¹) and the as-deposited GO film and GS film on ITO sheet, respectively; (b) Typical i - t curve for electroreduction of GO film on the ITO electrode in the 0.1 M KCl aqueous solution at -0.9 V (Reprinted with permission from Liu et al. [28]. Copyright (2011) Springer)

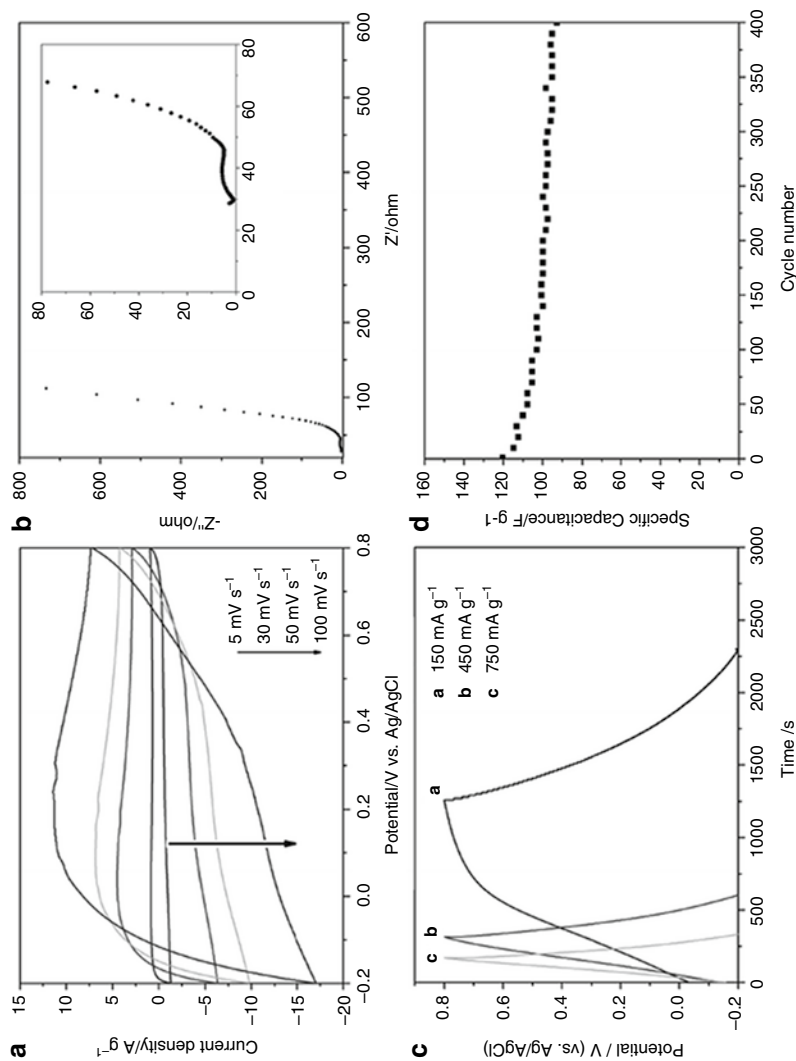


Fig. 9 (a) Cyclic voltammogram and (b) Nyquist plots of GS films in $0.1 \text{ M Na}_2\text{SO}_4$ electrolyte; (c) galvanostatic charge/discharge curves of GS films at different current densities; (d) the specific capacitance change at a constant current density of 750 mA g^{-1} as a function of cycle number (Reprinted with permission from Liu et al. [28]. Copyright (2011) Springer)

Composite Nanomaterials Obtained by Electrodeposition of Graphene

Graphene-based nanocomposites have attracted great attention due to the synergistic contribution of two or more functional components. Considering an appropriate design, nanocomposites can exhibit the beneficial properties of each parent component, resulting in a material with improved performance.

Up to now, many studies were devoted to the incorporation of graphene into composite materials and exploration of their applications in various fields, including quantum dots [25], metal nanoparticles [51], metal oxides [52], carbon nanotubes [53], and conducting polymers [54] or biopolymers such as polysaccharides [55] peptides [56], proteins [57], and nucleic acids [58].

Zhu et al. [9] reported one-step electrochemical reduction for the synthesis of graphene/MnO₂ nanowall hybrids by subjecting a GO-drop-casted GCE electrode immersed in 0.1 mol/L Na₂SO₄ containing 0.05 mol/L Mn(OAc)₂ to potential cycling in the range 0 to -1.5 V (vs. Ag/AgCl) at a scan rate of 50 mV/s for ten cycles. Their composite resulted in an amorphous conductive network with potential in electrochemical supercapacitor and biosensor applications.

Tang and colleagues [17] reported on the electrochemical reduction of GO simultaneously with aniline electropolymerization for the fabrication of graphene-polyaniline hybrid film by cyclic voltammetry. The superior electrical conductivity and electroactivity in acidic and even in neutral and alkaline media of their alternate-layered graphene-polyaniline films make them promising for applications in sensors, catalysis, and energy conversion devices.

Fu et al. [22] obtained graphene/Au composite by electrochemical co-reduction of GO and chloroauric acid in ionic liquid and claimed it exhibited enhanced electrochemical activity and stability toward the redox of Fe³⁺/Fe²⁺, while the composite of reduced GO with CNTs obtained by Lu et al. [59] by electrophoretic deposition at constant DC voltage of 30 V was reported to achieve the highest capacitance for a 40 % CNT content.

Nevertheless, the development of facile and effective approaches still remains a great challenge as both the introduction of insulating GO and the lengthy experimental procedure will definitely limit the practical applications of graphene-based composite.

Conclusions

Graphene-based nanomaterials exhibit many exciting properties which could be useful for fabrication of many innovative devices. However, in order to fully realize these properties and applications, consistent, reliable, and inexpensive methods for growing high-quality graphene layers in excellent yields are crucial, as the existence of residual defects will heavily impact their electronic properties, despite their expected insensitivity to impurity scattering. Electrochemical approach proved a

high potential under this aspect. Nevertheless, it should be noted that the uncontrollable problems of random size and shape (sheets vs. ribbons) in liquid-phase exfoliation may be a limit for specific applications of graphene. Although the electrochemical unzipping of CNTs to fabricate graphene sheets has size limitations due to the CNTs' diameter and the electronic characteristics might be affected by the adsorption of cations, anions, and solvent molecules at defect site, this approach opens new pathways for the preparation of high-quality graphene in good yield.

The encouraging results of the current electrochemical synthesis of graphene nanomaterials have already determined the direction of future research efforts. Anyhow, reliable electrochemical synthesis approaches to yield defect-free graphene structures with tailored properties have not been fully referred to and need further grope for. The role of oxygen functional groups of GO on its electrochemistry and the mechanism of the electrochemical reduction [60] still need to be understood thus requiring further detailed research investigation.

Acknowledgments Financial support is gratefully acknowledged from the Romanian Ministry of Education, CNCS-UEFISCDI, through the project number PN-II-RU-PD-2012-3-0124.

References

1. Carrera-Cerritos R, Baglio V, Aricò AS, Ledesma-García J, Sgroi MF, Pullini D, Pruna AJ, Mataix DB, Fuentes-Ramirez R, Arriaga LG (2014) Improved Pd electro-catalysis for oxygen reduction reaction in direct methanol fuel cell by reduced graphene oxide. *Appl Catal B Environ* 144:554–560
2. Wang G, Yang J, Park J, Gou XL, Wang B, Liu H, Yao J (2008) Facile synthesis and characterization of graphene nanosheets. *J Phys Chem C* 112:8192
3. Lomeda JR, Doyle CD, Kosynkin DV, Hwang WF, Tour JM (2008) Diazonium functionalization of surfactant-wrapped chemically converted graphene sheets. *J Am Chem Soc* 130:16201
4. Stankovich S, Dikin DA, Piner RD, Kohlhaas KA, Kleinhammes A, Jia Y, Wu Y, Ruoff RS, Nguyen ST (2007) Synthesis of graphene-based nanosheets via chemical reduction of exfoliated graphite oxide. *Carbon* 45:1558
5. Wu SX, Yin ZY, He QY, Huang X, Zhou XZ, Zhang H (2010) Electrochemical deposition of semiconductor oxides on reduced graphene oxide-based flexible, transparent and conductive electrodes. *J Phys Chem C* 114:1816
6. Li D, Muller MB, Gilje S, Kaner RB, Wallace GG (2008) Processable aqueous dispersions of graphene nanosheets. *Nat Nanotechnol* 3:101
7. Pruna A, Pullini D, Busquets D (2013) Influence of synthesis conditions on properties of green-reduced graphene oxide. *J Nanopart Res* 15:1605
8. Pumera M, Ambrosi A, Chng ELK, Poh HL (2010) Graphene for electrochemical sensing and biosensing. *Trends Anal Chem* 29:954–965
9. Zhu C, Guo S, Fang Y, Han L, Wang E, Dong S (2011) One-step electrochemical approach to the synthesis of graphene/MnO₂ nanowall hybrids. *Nano Res* 4:648–657
10. Guo HL, Wang XF, Qian QY, Wang FB, Xia XH (2009) A green approach to the synthesis of graphene nanosheets. *ACS Nano* 3:2653
11. Wang Z, Zhang J, Chen P, Zhou X, Yang Y, Wu S, Niu L, Han Y, Wang L, Chen P, Boey F, Zhang Q, Liedberg B, Zhang H (2011) Label-free, electrochemical detection of methicillin-resistant staphylococcus aureus DNA with reduced graphene oxide-modified electrodes. *Biosens Bioelectron* 26:3881

12. Zhou M, Wang Y, Zhai YM, Zhai JF, Ren W, Wang FA, Dong SJ (2009) Controlled synthesis of large-area and patterned electrochemically reduced graphene oxide films. *Chem Eur J* 15:6116
13. Alanyaloğlu M, Segura JJ, Oró-Solè JO, Casan-Pastor N (2012) The synthesis of graphene sheets with controlled thickness and order using surfactant-assisted electrochemical processes. *Carbon* 50:142–152
14. Kakaei K (2013) One-pot electrochemical synthesis of graphene by the exfoliation of graphite powder in sodium dodecyl sulfate and its decoration with platinum nanoparticles for methanol oxidation. *Carbon* 51:195–201
15. Ting SW, Periasamy AP, Chen SM, Saraswathi R (2011) Direct electrochemistry of catalase immobilized at electrochemically reduced graphene oxide modified electrode for amperometric H₂O₂ biosensor. *Int J Electrochem Sci* 6:4438–4453
16. Peng XY, Liu XX, Diamond D, Lau KT (2011) Synthesis of electrochemically-reduced graphene oxide film with controllable size and thickness and its use in supercapacitor. *Carbon* 49:3488–3496
17. Tang Y, Wu N, Luo S, Liu C, Wang K, Chen L (2012) One-step electrodeposition to layer-by-layer graphene–conducting-polymer hybrid films. *Macromol Rapid Commun* 33:1780–1786
18. Zhang H, Zhang X, Zhang D, Sun X, Lin H, Wang C, Ma Y (2013) One-step electrophoretic deposition of reduced graphene oxide and Ni(OH)₂ composite films for controlled syntheses supercapacitor electrodes. *J Phys Chem B* 117:1616–1627
19. Bittolo Bon S, Valentini L, Kenny JM, Peponi L, Verdejo R, Lopez-Manchado MA (2010) Electrodeposition of transparent and conducting graphene/carbon nanotube thin films. *Phys Status Solidi A* 207:2461–2466
20. Su CY, Lu AY, Xu Y, Chen FR, Khlobystov AN, Li LJ (2011) High-quality thin graphene films from fast electrochemical exfoliation. *ACS Nano* 5:2332–2339
21. Liu N, Luo F, Wu H, Liu Y, Zhang C, Chen J (2008) One-step ionic-liquid-assisted electrochemical synthesis of ionic-liquid-functionalized graphene sheets directly from graphite. *Adv Funct Mater* 18:1518–1525
22. Fu C, Kuang Y, Huang Z, Wang X, Du N, Chen J, Zhou H (2010) Electrochemical co-reduction synthesis of graphene/Au nanocomposites in ionic liquid and their electrochemical activity. *Chem Phys Lett* 499:250–253
23. Shinde DB, Debgupta J, Kushwaha A, Aslam M, Pillai VK (2011) Electrochemical unzipping of multi-walled carbon nanotubes for facile synthesis of high-quality graphene nanoribbons. *J Am Chem Soc* 133:4168–4171
24. John R, Shinde DB, Liu L, Ding F, Xu Z, Vijayan C, Pillai VK, Pradeep T (2014) Sequential electrochemical unzipping of single-walled carbon nanotubes to graphene ribbons revealed by in situ Raman spectroscopy and imaging. *ACS Nano* 8:234–242
25. Wang ZJ, Zhou XZ, Zhang J, Boey F, Zhang H (2009) Direct electrochemical reduction of single-layer graphene oxide and subsequent functionalization with glucose oxidase. *J Phys Chem C* 113:14071
26. Shao YY, Wang J, Wu H, Liu J, Aksay IA, Lin YH (2010) Graphene based electrochemical sensors and biosensors: a review. *Electroanalysis* 22:1027–1036
27. Ramesha GK, Sampath S (2009) Electrochemical reduction of oriented graphene oxide films: an in situ Raman spectroelectrochemical study. *J Phys Chem C* 113:7985
28. Liu S, Ou J, Wang J, Liu X, Yang S (2011) A simple two-step electrochemical synthesis of graphene sheets film on the ITO electrode as supercapacitors. *J Appl Electrochem* 41:881–884
29. Zhang X, Zhang D, Chen Y, Sun X, Ma Y (2012) Electrochemical reduction of graphene oxide films: preparation, characterization and their electrochemical properties. *Chin Sci Bull* 57:3045–3050
30. Hilder M, Winther-Jensen B, Li D, Forsyth M, MacFarlane DR (2011) Direct electrodeposition of graphene from aqueous suspensions. *Phys Chem Chem Phys* 13:9187–9193
31. Chen L, Tang Y, Wang K, Liu C, Luo S (2011) Direct electrodeposition of reduced graphene oxide on glassy carbon electrode and its electrochemical application. *Electrochem Commun* 13:133–137

32. Liu C, Wang K, Luo S, Tang Y, Chen L (2011) Direct electrodeposition of graphene enabling the one-step synthesis of graphene–metal nanocomposite films. *Small* 7:1203–1206
33. Ye W, Zhang X, Chen Y, Du Y, Zhou F, Wang C (2013) Pulsed electrodeposition of reduced graphene oxide on glass carbon electrode as an effective support of electrodeposited Pt microspherical particles: nucleation studies and the application for methanol electro-oxidation. *Int J Electrochem Sci* 8:2122–2139
34. Yu H, He J, Sun L, Tanaka S, Fugetsu B (2013) Influence of the electrochemical reduction process on the performance of graphene-based capacitors. *Carbon* 51:94–101
35. Wang Z, Wu S, Zhang J, Chen P, Yang G, Zhou X, Zhang Q, Yan Q, Zhang H (2012) Comparative studies on single-layer reduced graphene oxide films obtained by electrochemical reduction and hydrazine vapor reduction. *Nanoscale Res Lett* 7:161
36. Filik H, Çetintaş G, Avan AA, Koç SN, Boz İ (2013) Electrochemical sensing of acetaminophen on electrochemically reduced graphene oxide-Nafion composite film modified electrode. *Int J Electrochem Sci* 8:5724–5737
37. Wang G, Wang B, Park J, Wang Y, Sun B, Yao J (2009) Highly efficient and large-scale synthesis of graphene by electrolytic exfoliation. *Carbon* 47:3242–3246
38. Lee SH, Seo SD, Jin YH, Shim HW, Kim DW (2010) A graphite foil electrode covered with electrochemically exfoliated graphene nanosheets. *Electrochem Commun* 12:1419–1422
39. Dilimon VS, Sampath S (2011) Electrochemical preparation of few layer-graphene nanosheets via reduction of oriented exfoliated graphene oxide thin films in acetamide–urea–ammonium nitrate melt under ambient conditions. *Thin Solid Films* 519:2323–2327
40. Zhang D, Fu L, Liao L, Liu N, Dai B, Zhang C (2012) Preparation, characterization, and application of electrochemically functional graphene nanocomposites by one-step liquid-phase exfoliation of natural flake graphite with methylene blue. *Nano Res* 5:875–887
41. Xu Q, Schwandt C, Chen GZ, Fray DJ (2002) Electrochemical investigation of lithium intercalation into graphite from molten lithium chloride. *J Electroanal Chem* 530:16–22
42. Shao YY, Wang J, Engelhard M et al (2010) Facile and controllable electrochemical reduction of graphene oxide and its applications. *J Mater Chem* 20:743–748
43. Harima Y, Setodoi S, Imae I, Komaguchi K, Ooyama Y, Ohshita J, Mizota H, Yano J (2011) Electrochemical reduction of graphene oxide in organic solvents. *Electrochim Acta* 56:5363–5368
44. Ping J, Wang Y, Fan K, Wu J, Ying Y (2011) Direct electrochemical reduction of graphene oxide on ionic liquid doped screen-printed electrode and its electrochemical biosensing application. *Biosens Bioelectron* 28:204–209
45. Kauppila J, Kunnas P, Damlin P, Viinakanoja A, Kvarnström C (2013) Electrochemical reduction of graphene oxide films in aqueous and organic solutions. *Electrochim Acta* 89:84–89
46. Huang C, Grobert N, Watt AAR, Johnston C, Crossley A, Young NP, Grant PS (2013) Layer-by-layer spray deposition and unzipping of single-wall carbon nanotube-based thin film electrodes for electrochemical capacitors. *Carbon* 61:525–536
47. Hasan SA, Rigueur JL, Harl RR, Krejci AJ, Gonzalo-Juan I, Rogers BR, Dickerson JH (2010) Transferable graphene oxide films with tunable microstructures. *ACS Nano* 4:7367–7372
48. Wu ZS, Pei S, Ren W, Tang D, Gao L, Liu B, Li F, Liu C, Cheng HM (2009) Field emission of single-layer graphene films prepared by electrophoretic deposition. *Adv Mater* 21:1756
49. Chen Y, Zhang X, Yu P, Ma YW (2009) Stable dispersions of graphene and highly conducting graphene films: a new approach to creating colloids of graphene monolayers. *Chem Commun* 30:4527
50. Lee V, Whittaker L, Jaye C, Baroudi KM, Fischer DA, Banerjee S (2009) Large-area chemically modified graphene films: electrophoretic deposition and characterization by soft x-ray absorption spectroscopy. *Chem Mater* 21:3905–3916
51. Pasricha R, Gupta S, Srivastava AK (2009) A facile and novel synthesis of Ag–graphene-based nanocomposites. *Small* 5:2253–2259
52. Yin Z, Wu S, Zhou X, Huang X, Zhang Q, Boey F, Zhang H (2010) Electrochemical deposition of ZnO nanorods on transparent reduced graphene oxide electrodes for hybrid solar cells. *Small* 6:307–312

53. Qiu L, Yang X, Gou X, Yang W, Ma ZF, Wallace GG, Li D (2010) Dispersing carbon nanotubes with graphene oxide in water and synergistic effects between graphene derivatives. *Chem Eur J* 16:10653–10658
54. Xu J, Wang K, Zu SZ, Han BH, Wei Z (2010) Hierarchical nanocomposites of polyaniline nanowire arrays on graphene oxide sheets with synergistic effect for energy storage. *ACS Nano* 4:5019–5026
55. Guo Y, Guo S, Ren J, Zhai Y, Dong S, Wang E (2010) Cyclodextrin functionalized graphene nanosheets with high supramolecular recognition capability: synthesis and host-guest inclusion for enhanced electrochemical performance. *ACS Nano* 4:4001–4010
56. Han TH, Lee WJ, Lee DH, Kim JE, Choi EY, Kim SO (2010) Peptide/graphene hybrid assembly into core/shell nanowires. *Adv Mater* 22:2060–2064
57. Liu J, Fu S, Yuan B, Li Y, Deng Z (2010) Toward a universal “adhesive nanosheet” for the assembly of multiple nano-particles based on a protein-induced reduction/decoration of graphene oxide. *J Am Chem Soc* 132:7279–7281
58. Lv W, Guo M, Liang MH, Jin FM, Cui L, Zhi L, Yang QH (2010) Graphene-DNA hybrids: self-assembly and electrochemical detection performance. *J Mater Chem* 20:6668–6673
59. Lu T, Pan L, Li H, Nie C, Zhu M, Sun Z (2011) Reduced graphene oxide–carbon nanotubes composite films by electrophoretic deposition method for supercapacitors. *J Electroanal Chem* 661:270–273
60. Kashimura S, Ishifune M (2004) Reduction of Oxygen containing compounds. In: *Encyclopedia of Electrochemistry* (A. J. Bard, M. Stratmann Eds.). Wiley-VCH, Weinheim, Germany, p 199

R. Abdel-Karim

Contents

Introduction.....	24
Theory of Electrodeposition	25
Nucleation.....	26
Growth of Nuclei	28
Modes of Thin-Film Growth.....	29
Microstructures of Electrodeposits	31
Nanoelectrodeposited Metals and Alloys and Their Properties	33
Gold-Based Deposits	33
Co-Based Alloys	34
Copper-Based Deposits.....	37
Nickel-Based Deposits.....	38
Template-Assisted Electrodeposition	41
Conclusions.....	42
References.....	43

Abstract

Electrodeposition is a unique technique in which a variety of materials can be produced including metals, ceramics, and polymers. In the current chapter, the advantages of electrochemical deposition techniques in fabricating various nano-materials with superior properties compared with conventional materials will be highlighted. The properties of various nanostructured coatings produced by electrodeposition are discussed. Some models describing nucleation and growth mechanism are presented. Finally, the importance of some nanocrystalline electrodeposits in many industrial applications as well as their potential role in the

R. Abdel-Karim (✉)

Department of Metallurgy, Faculty of Engineering-Cairo University, Giza, Egypt

e-mail: randaabdelkarim@gmail.com

planned future technologies is emphasized. The potential of highly ordered nanomaterials for future technological applications includes the field of various nanophotonic, catalytic, microfluidic, and sensing devices, as well as functional electrodes and magnetic recording media. Another application is template-assisted electrodeposition employing a variety of nanoporous membranes and films such as nanoporous alumina membranes used for the synthesis of high-density, ordered arrays of nanodots, nanotubes, and nanowires.

Keywords

Electrocrystallization • Nucleation and growth • Metals • Alloys • Nanocomposites • Nanorods • Nanowires • Nanoporous membranes

Introduction

Nanocrystalline materials with grain size of less than 100 nm are a new and novel class of advanced materials, which are intensively applied in the scientific and business communities. Since their introduction in the early 1980s [1], intensive scientific activity in the areas of production, microstructural characterization, and property determination of these materials has resulted in the development of a number of manufacturing techniques capable of producing various materials with superior properties over conventional materials [2]. Consequently, several industrial applications and hence new market opportunities have emerged from this field and are continuing to increase in numbers. Most current efforts on large-scale production of nanostructured materials are concerned with consolidating nanocrystalline precursor powders produced by techniques such as gas condensation, ball milling, or spray conversion. Film deposition techniques such as physical and chemical vapor deposition, sol-gel techniques, etc. are also under intensive research activities.

A thin coating (thickness up to $\sim 100 \mu\text{m}$) electroplated onto on a substrate to modify specific surface properties is probably the most widely known application of electrodeposition technologies. However, it should be noted that there are several other processes (e.g., brush plating, electrowinning, and electroforming) which can be used to produce nanocrystalline materials as thick coatings (several mm or cm thick) or in freestanding forms such as sheet, foil, tubes, wire, mesh, plate, and foam [3]. Table 1 summarizes the nano products obtained from each process.

The production of nanomaterials requires a deposition process on the atomic level and extreme control over the deposition. The obvious advantages of this century-old process of electrodeposition are as follows:

- (a) High production rate and low cost
- (b) Free from porosity and high purity
- (c) Industrial applicability

Table 1 Different techniques for production of nanomaterials

Nanoproduct	Production techniques
Powders	Gas condensation, ball milling, or spray conversion
Thin coatings	Physical and chemical vapor deposition, sol-gel techniques, electrodeposition
Thick coatings Freestanding forms such as sheet, foil, tubes, wire, mesh, plate and foam	Brush plating, electrowinning and electroforming

- (d) Ability to overcome shape limitations or allow the production of freestanding parts with complex shapes
- (e) Coating on widely differing substrates
- (f) Ability to control structural features with sizes ranging from nm to μm
- (g) Control of the alloy composition and the ability to produce alloys with composition unattainable by other methods
- (h) The possibility of forming of simple low-cost multilayers in many different systems
- (i) No requirements of postdeposition treatment [3]

Electroplating is a technologically feasible and economically superior technology for the production of nanostructured pure metals and alloys as well as nanocomposites [2]. Electrochemical deposition of polycrystalline metals and alloys exhibits several types of growth forms such as layers, blocks, ridges, pyramids, spiral growth, dendrites, powders, and whiskers [4]. Mohanty [5] has demonstrated the electrodeposition of various nanostructure materials, such as nanoparticles, nanowires of Au, Pt, Ni Co, Fe, Ag, etc., for example, the synthesis of nanocrystalline pure metals e.g., Ni [6], Co, and Cu [7], binary alloys e.g., Ni-P [8], Ni-Fe [9], Zn-Ni [10], and Co-W [11], and ternary alloys e.g., Ni-Fe-Cr [12] and Ni-Mo-Fe [13]. Even multilayered structures or compositionally modulated alloys (e.g., Cu-Pb and Ni-P, metal matrix composites e.g., Ni-Si C, and ceramics e.g., ZrO_2 have been successfully produced by electrodeposition techniques [14].

Theory of Electrodeposition

The mechanism of electrodeposition is similar to the crystal growth of conventional metals and is developed in two steps:

- (i) Formation of nuclei covering electrode with few atomic layers of metal
- (ii) Growth of deposits

Formation of nuclei requires high voltage although once formed, nuclei will grow fast at low voltage. The atoms (adatoms), which are formed during the

electroplating on the crystal plane quickly, occupy suitable sites, such as kink sites where atoms interact with three neighbors or edge sites (two neighbors) and sometimes occupy terrace sites (one neighbor).

The growth takes place through the following steps:

- (a) Mass transport in solution by diffusion of ions to the surface of cathode
- (b) Electron transfer to form an adatom (a mobile or absorbed atom)
- (c) Diffusion of adsorbed atoms across the surface to kink sites [15]

Nucleation

The nucleation and growth processes taking place during electrodeposition of metal coatings are similar to that occurring during any conventional crystallization process. They differ in that, in the case of electrocrystallization, the metal atoms required for nucleation must first be present. The hydrated metal ions transfer across the metal-solution interface and then neutralize at the cathode surface, forming the local crystal nuclei. On the other hand, in the case of crystallization from molten metal, the uncharged metal atoms collect to form crystal nuclei, which then grow spontaneously, as soon as a critical size is reached [16].

Homogeneous Nucleation

When the temperature falls below the melting point, the molten metal is cooled, and the first crystal nuclei are formed. The process results in thermal energy change, as the state changes from liquid to solid. The so-called Gibbs free energy (G) of all elements is then equal to zero. However, this is true only for each element in a defined state (liquid, solid, gaseous) and at a given temperature. As metal atoms solidify, the kinetic energy, ΔG_v , is designated with a minus sign due to contraction in volume.

On the other hand, as a solid nucleus is formed, an interface must be formed between this nucleus and the surrounding melt. For this, some surface work (ΔG°) is required, which therefore is positive. The surface energy γ between the crystal surface and the deposited layer depends on the type of metal as well as the surface area of the nucleus. The total change in Gibbs free energy, ΔG , for the formation of a spherical nucleus of radius r , volume $V_K = (4/3) \pi r^3$, and surface area $= 4 \pi r^2$ is the sum of volume energy and surface energy, ΔG_v and ΔG°

$$\Delta G = \Delta G_v + \Delta G^\circ = -\left(4/3\right)\pi r^3 \cdot \Delta G_v + 4\pi r^2 \gamma \quad (1)$$

The crystal nuclei with $r > r^*$ are thermodynamically stable and will probably continue growing. On the other hand, if $r < r^*$, the nucleus is not thermodynamically stable and is likely to contract in size, and it dissolves. Further growth of such small nuclei is accompanied by an increase in Gibbs free energy [16].

Heterogeneous Nucleation

In this case, nucleation and growth initiates at the mold wall or perhaps around solid impurities in the melt. These are known as initiation sites and act as active centers, reducing activation energy need for formation of nuclei of greater than the critical size. The change in free energy ΔG^{**} is not only a function of the radius of the nucleus but also of the wetting angle θ .

If $\theta=0$, a complete wetting of the wall surface by the nascent crystal nucleus occurs and $\Delta G^{**}=0$, which corresponds to spontaneous crystallization from the melt, without any activation energy barrier.

If $\theta=180$, there is no wetting of the container wall by the growing nuclei, and the relationship $\Delta G^{**}=\Delta G^*$ is obtained. This condition represents a homogeneous nucleation and requires the highest energy of formation of a nucleus. The formation of nuclei of at least the critical size can result when the metal ions pass directly to the cathode surface at nucleation sites, where this is energetically favored. Another option is that they pass through sites which are energetically less favorable. In the latter case, lateral movement of adsorbed atoms across the surface is necessary to form nuclei of the critical size [15].

As adatoms reach the cathode, the hydrated metal ions lose a part of their hydration sheath and thus retain a partial charge. In this especially low-energy state, they diffuse across the cathode surface to the nearest growth site. Depending on the location and state of the resulting crystal nucleus, four different types of site are recognized. These are zero-dimensional sites and one-, two-, and three-dimensional sites (edge, plane, or corner sites, respectively).

1. Zero-dimensional nuclei:

This represents the deposition of individual adatoms onto an active site at the cathode surface. Formation of such nuclei requires the smallest of all energies of nucleation.

2. One-dimensional nuclei:

When a series of adatoms accumulate along the edge of a monoatomic step at the cathode surface, the nucleation energy required for this is somewhat higher than in case 1.

3. Two-dimensional nuclei:

This situation illustrates a planar agglomeration of adatoms, the orientation of which will often depend on that of the underlying substrate. This effect is known as "epitaxy," where the lattice structure of the deposit is either identical to that of the cathode or very similar.

4. Three-dimensional nuclei:

The lattice structure of the deposit differs from that of the cathode. In practice, the conditions for forming such nuclei are extremely complex. The interaction between a crystal nucleus and the substrate depends on their lattice structures. This is in the case of a totally smooth and featureless substrate.

The nucleation may exhibit epitaxial behavior if the lattice structures of substrate and deposited metal are identical or similar. In case of three-dimensional

nucleation, lattice defects such as edges, corners, and steps are presented at the cathode surface. The nucleation energy for three-dimensional nuclei is always larger than that for two-, one-, or zero-dimensional types [15].

The rate of nucleation dN_k/dt is presented as follows:

$$\frac{dN_k}{dt} = a_k \cdot \exp\left(-\frac{\Delta G^*}{RT}\right) \quad (2)$$

where a_k is a constant of the system.

According to the following equation, the critical nucleus size decreases as the crystallization overvoltage η_k , increases:

$$\eta_k = \frac{2\gamma V}{zF \bar{r}^*} = \frac{RT}{zF} \ln \frac{c_{ad}}{c_{ad}^o} \quad (3)$$

where

V is the molar volume of a crystal nucleus of critical size.

z is the number of electrons transferred.

c_{ad} is the concentration of adatoms at a growth site.

c_{ad}^o is the concentration of adatoms in the equilibrium state.

Increasing the concentration of adatoms will lead to increase in both the crystallization overvoltage and the rate of nucleation [17, 18].

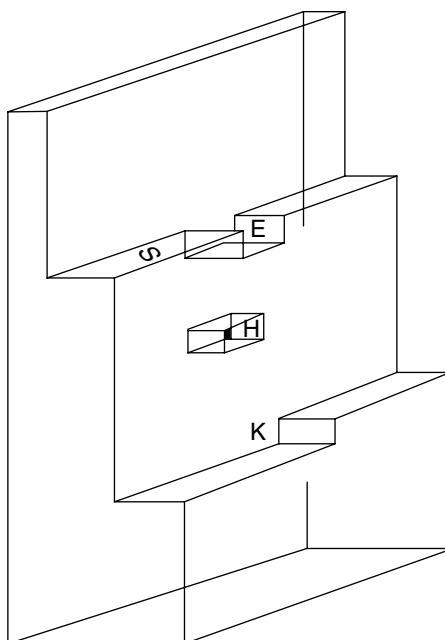
Growth of Nuclei

The electrodeposit formation takes place by the following steps:

- Ions of the solvent move through the cathode by diffusion, migration, and convection.
- There is an electron transfer between the cathode and the ions.
- There is partial or total loss of the solvation spheres and adatom formation.
- The adatoms are absorbed by the surface and spread till they find suitable sites.
- There is cluster formation.
- There is crystallographic development of the crystal grain [15].

According to the model of Kossel and Stansky, the crystal growth occurs through competition between vertical growth, depending on two-dimensional nucleation rate, and horizontal growth, depending on the rate of the repeatable step [19]. The Kossel-Stansky model assumed that the strength of binding of an atom to the surface depends on its number of nearest neighbors. They applied this to a simple cubic crystal, which is also known as a Kossel crystal. According to this theory, metal atoms are preferentially deposited at sites on the cathode surface where their incorporation in the lattice releases the most energy. On this basis, preferential growth of

Fig. 1 Different growth sites at a substrate.
E=corner; H=recess;
K=edge; S=step [17]



nuclei is expected at the locations such as edges, corners, steps, and kinks. Metal atoms at the surface of the lattice have unbound valence bonds that exert an effect on their immediate environment which is most pronounced at the topographic features listed above, where it is said that individual atoms are more exposed. That's why preferential metal deposition occurs at these locations, where the free energy required is at a minimum. These locations are also known as semicrystalline. At these topographic features, the highest current density is observed, which motivates the crystal growth rate [16]. According to the Terrace-Ledge-Kink (TLK) model, metal atoms are preferentially deposited at edges, corners, steps, and kinks (Fig. 1) where overall the free energy needed is minimum [17].

Incoming adatoms build up, either directly or after lateral diffusion, at the defect sites presented on the cathode surface. The stability of growing nuclei formed at these locations is determined by the local lattice energy required to incorporate more atoms into the metal matrix at the cathode. Later on, it was realized that crystal growth can occur by means of the rotational movement of a growing spiral at a screw dislocation [15].

Modes of Thin-Film Growth

These are monolayer overgrowth, nuclear growth, and the growth mode that has both features of the former two. The monolayer overgrowth mode is described in Fig. 2b and is also called Frank-van der Merwe mode (FvdM mode).

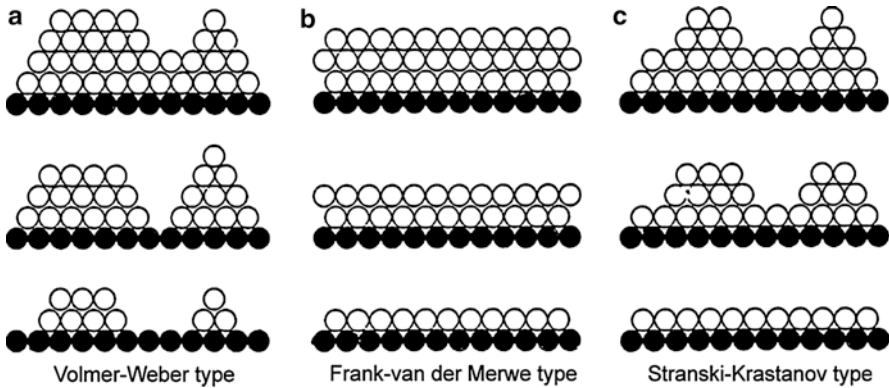


Fig. 2 Different modes of thin-film growth; (a) Volmer-Weber (V-W) type, (b) Frank-van der Merwe (F-M) type, and (c) Stranski-Krastanov (S-K) type [19]

The deposited atoms (or molecules) cover the substrate uniformly by one atom thickness, and the deposit grows layer by layer. This growth mode occurs when the substrate material and the growth material have good amicability and low surface tension [19].

Another mode is called island growth or Volmer-Weber mode (VM mode). When the desorption process is not strong, the atoms, which reach the substrate, form two-dimensional gases on it, and they condense forming a nucleus with high density. High density of nucleus leads to touch and combine each other, and they grow to an island. When it further grows, it becomes a channel state, a whole state, and finally makes a uniform thin layer as shown in Fig. 2a. The VM mode differs from FvdM mode in that VM mode does not grow layer by layer. This mode is chosen in case of high surface tension of the growth material and low amicability between the substrate materials and the growth deposit.

Stranski-Krastanov growth mode is an intermediate process consisting of both 2D layer and 3D island growth. Transition from the layer-by-layer to island-based growth occurs at a definite critical coating thickness which depends mainly on the chemical and physical properties, such as surface energies and lattice parameters, of the substrate and the coating layer [20–22].

The growth of epitaxial (homogenous or heterogeneous) layers on a single crystal surface depends critically on the interaction strength between adatoms and the substrate. In Volmer-Weber (VW) growth mode, adatom-adatom interactions are stronger than those of the adatom with the substrate material, resulting in the formation of three-dimensional adatom clusters or islands [21]. Growth of these clusters, accompanied with coarsening, will lead to rough multilayer film formation on the substrate. On the other hand, during Frank-van der Merwe (FM) growth mode, adatoms are attached preferentially to surface sites resulting in the formation of atomically fully smooth layers. This layer-by-layer growth is two dimensional leading to complete film formation before the growth of subsequent layers [22].

Markov [23] proposed an equation for the layer chemical potential per atom as

$$\mu(n) = \mu_{\infty} + [\varphi_a - \varphi'_a(n) + \varepsilon_d(n) + \varepsilon_e(n)] \quad (4)$$

where μ_{∞} is the bulk chemical potential of the adsorbate material, φ_a the desorption energy of an adsorbate atom from a wetting layer of a material similar to the substrate material, $\varphi'_a(n)$ the desorption energy of an adsorbate atom from the substrate, $\varepsilon_d(n)$ the misfit dislocation energy per atom, and $\varepsilon_e(n)$ the homogeneous strain energy per atom. In general, the value of φ_a , $\varphi'_a(n)$, $\varepsilon_d(n)$, and $\varepsilon_e(n)$ is dependent in a complex way on the thickness of the growing layers and lattice misfit between the substrate and adsorbate layer.

In case of small strains, $\varepsilon_{d,e}(n) \ll \mu_{\infty}$, the criterion that determines the film growth mode depends on the chemical potential change per unit atom $\frac{d\mu}{dn}$.

- For VW growth mode, $\frac{d\mu}{dn} < 0$ (adatom cohesive force is higher than surface adhesive force)
- For FM growth mode, $\frac{d\mu}{dn} > 0$ (surface adhesive force is higher than adatom cohesive force)

SK growth can be characterized by both of these inequalities. While initial deposit growth follows a FM mechanism, i.e., positive differential μ , nontrivial amounts of strain energy accumulate in the deposited layers. At a critical thickness, this strain induces a sign reversal in the chemical potential, i.e., negative differential μ , leading to a change in the growth mode. At this point, it is energetically preferred to nucleate islands, and additional growth is favored by a VW mode [23].

Attachment of the thinner deposit to the thicker substrate causes a misfit strain “ ϵ ” at the interface given by

$$\epsilon = (a_f - a_s)/a_s \quad (5)$$

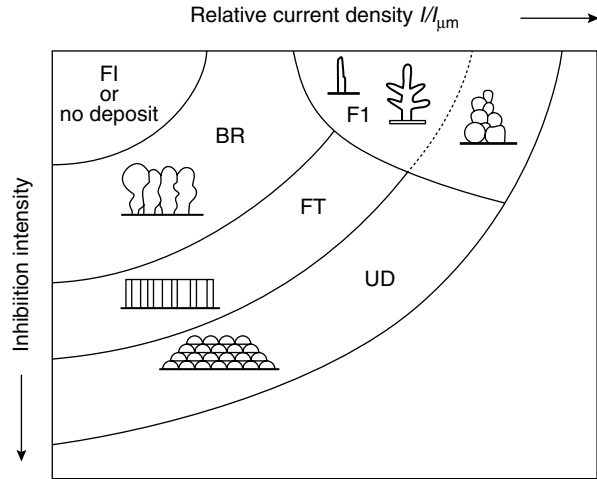
where a_f and a_s are the deposit and substrate lattice constants, respectively.

As the wetting layer thickness is higher, the resulting strain energy increases rapidly. In order to lower the strain, island formation can take place in either a dislocated or coherent mode. In dislocated islands, strain relief results from interfacial misfit dislocations. The reduction in strain energy accommodated by forming a dislocation is generally greater than the effect of increasing surface energy associated with creation of the new clusters. The thickness of the wetting layer at which island nucleation is formed, called the critical thickness h_c , is strongly dependent on the lattice mismatch between the layer and substrate. Higher mismatch leads to smaller critical thicknesses for deposit formation [24].

Microstructures of Electrodeposits

Fischer [25] recognized five main growth morphology types for polycrystalline electrodeposits: field-oriented isolation, basis-oriented reproduction, twinning intermediate, field-oriented texture, unoriented dispersion type. This model was based on previous work of Winand [18], which is summarized in Fig. 3.

Fig. 3 Winand diagram of surface morphology depending on current density and inhibition activity [18]



- (i) **Field-oriented isolated crystal type (FI)**
At low overvoltage (0–10 mV), a one-dimensional nucleation is observed. The nuclei grow to form individual crystallites, usually oriented in the axis of the current field. Growth occurs slowly at the side faces of these crystallites, and dendritic layers are deposited. These deposits have no useful technical properties.
- (ii) **Base-oriented reproduction type (BR)**
At higher overvoltage of 10–100 mV, a two-dimensional nucleation occurs, and flat-faced crystallites grow. The technical properties of these deposits are interesting because they are similar to those of the underlying substrate.
- (iii) **Field-oriented texture type (FT)**
In the range of 100–150 mV of overvoltage, single crystallites initially form. If the overvoltage increases, the crystallites become three-dimensional, which grow parallel to the electric field lines and whose bounds are crystallites.
- (iv) **Unoriented dispersion type (UD)**
At overvoltage higher than 200 mV, small crystals are formed as a result of high rates of electrocrystallization. The result is a microstructure of very fine randomly oriented crystallites with two visible grain structures. Deposits of this type are ideal for technical applications, due to their excellent properties.
- (v) **Twinning transition type (Z)**
This type of growth represents the transition between FT and BR type. This structure is formed when the crystallization overvoltage is large enough to allow formation of two-dimensional nuclei. Twinning may cause a reduction of the ductility of the deposited metal.

Nanoelectrodeposited Metals and Alloys and Their Properties

As indicated in Table 2, the electrodeposition technology has been used to produce a wide range of nanostructured materials, e.g., metal nanoparticles, nanowires, nanofilms, bulk NC metals, laminated composites, multilayered coatings, and nanoparticle-reinforced composite coatings. The electrodeposited nanostructured layers could be pure metals, alloys, composites, or sandwich layers.

Gold-Based Deposits

Au

A lot of intensive research was directed toward gold nanostructures, which is applied for many applications as substrates for surface-enhanced Raman scattering (SERS), super-hydrophobicity catalysis or sensors, selective solar absorbers, antireflection coatings, or diffraction gratings. The surface morphology of gold, especially the roughness, influences their functional properties. The catalytic activity of metal nanostructures is dependent on surface morphology [26].

Bossini et al. [29] studied the galvanostatic electrodeposition of nanogold using cyanocomplex Au(I) baths with citrate additives. The structural effects of organic

Table 2 Different electrodeposited nanomaterials, properties and applications [3, 26–28]

Materials	Properties and applications
Au based alloys	
Au, Au–Cu	Substrates for surface-enhanced Raman scattering (SERS) technique, super-hydrophobicity catalysis or sensors, selective solar absorbers, antireflection coatings or diffraction gratings
Pd-based alloys	
Pd, Ni–Pd	Hydrogen storage and purification, electrodes for hydrogen evolution and fuel cells
Co-based alloys	
Co, Co–W, Co–P	Good candidates for the replacement of the highly toxic hexavalent chromium in plating baths, due to their excellent mechanical and wear resistant properties. These materials have high saturation magnetization, good thermal stability and extraordinary hardness
Co–Ni–Cu	Good catalyst for hydrogen evolution
Ni-based alloys	
Ni, Ni–W, Ni–P, Ni–Mo, Ni–Co, Ni–Cu, Ni–Zn, Ni–Mg, and Ni–B	Good magnetic properties, corrosion protection, stress corrosion and Electrocatalytic activity for hydrogen evolution
Ni–Al ₂ O ₃ , Ni–SiC	Corrosion protection, wear resistance
Ni–Fe–Cr	Cracking resistance, soft magnets, catalysts

additives have been explained on the basis of competitive adsorption and cathodic reaction of the organics. In situ SERS measurements have explained the molecular aspects of grain growth inhibition and related stabilization of adatom clusters and nanocrystalline structures. The adsorption behavior of cyanide during the electrodeposition of gold has been investigated by in situ Raman spectroscopy.

The codeposition of nanocrystalline Au/B₄C composites has been investigated by Bicelli [30]. Considerable stabilization of nanosize under prolonged heat treatment can be obtained by dispersion of ceramic particles within the nanocrystalline matrix. Hardness values typical of nanometric systems can be preserved even after prolonged heat treatment in composite systems. Instrumented indentation measurements have been used for evaluation of hardness, Young's modulus, and plasticity of freestanding nanocrystalline metal and composite foils. The wear behavior of nanodeposited Au and composites has been evaluated by the pin-on-disk technique.

Au-Cu

Bossini et al. [31] developed baths based on Au(CN)₂⁻, Cu(I)-CN⁻, Cu(II)-EDTA, and Cu(II) for the electrodeposition of equiatomic alloys. The effects of the dispersion of ceramic particles on structure evolution kinetics have been investigated. In another work, Bossini et al. [32] investigated the hydrogen-related nanometric voids and their annealing behavior using thermal desorption spectroscopy and SAXS. The effects of the nature of chelating agents on geminate density were studied by XRD peak analysis. Tensile test results showed the mechanical effects connected to the use of different Cu(II) chelating agents, which can be explained with different densities of hydrogen-related nanovoids present in the electroformed alloys.

Co-Based Alloys

According to Bartlett et al. [27] and Herrasti et al. [28], nanocrystalline cobalt and cobalt-based are good candidates for the replacement of the highly toxic hexavalent chromium in electroplating baths, due to their excellent mechanical and wear-resistant properties. These materials have high saturation magnetization and good thermal stability. Improving hardness levels for nanocrystalline cobalt and its alloys over the polycrystalline counterparts has been reported. Electrochemically prepared Co nanodeposits have three to five times higher coercivity (H_c) than conventional polycrystalline Co.

Co-Fe

Koay et al. [33] have studied the magnetic properties, such as M_s and H_c , of Co-Fe alloys based on their different alloy compositions in electrolytes. It was found that the values of M_s and H_c increased linearly with additional contents of Fe. The increase in the M_s value was correlated to the crystal structure or phases of the films. The coexistence of both Co-Fe face-centered cubic (FCC) was confirmed.

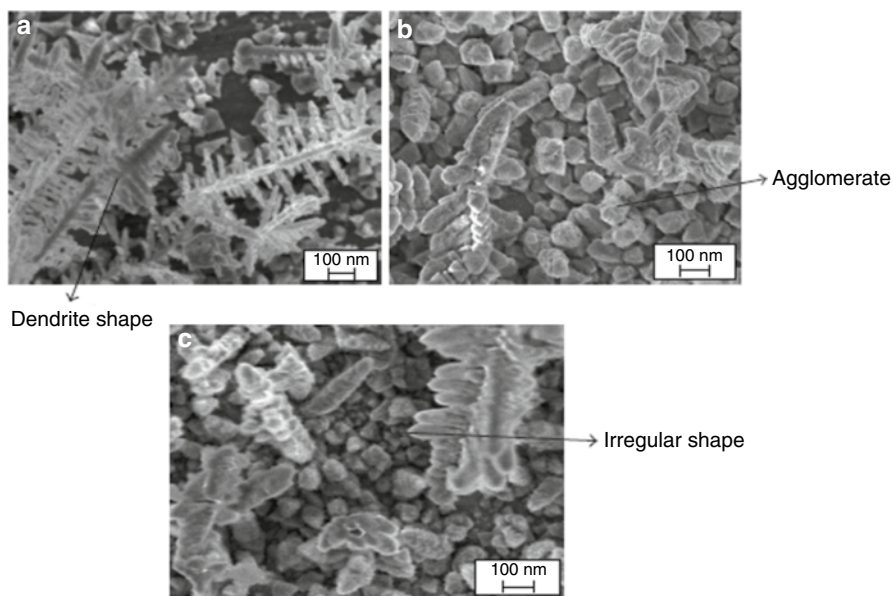


Fig. 4 FESEM micrographs of Co-Fe nanocoatings as a function of deposition time: (a) 30, (b) 60, and (c) 90 min [33]

Additionally, initial research works reported that, for nanocrystalline materials, there was a large reduction in M_s with finer grain size formation. It was stated that 40 % decrease in M_s for nanocrystalline Fe compared to its bulk polycrystalline was confirmed. Figure 4 illustrates the dendritic microstructure of Fe-Co nanodeposits, as a function of deposition time [33].

Co-Ni-Cu

Wang et al. [34] studied the electrodeposition of Co-Ni-Cu ternary nanodeposit using a mixture of CoCl_2 , NiCl_2 , and CuCl_2 . Three-dimensional CoNiCu nanonetwork structure exhibited good performance as a catalyst for hydrogen evolution reaction (HER). Figure 5 shows the dendritic microstructure of such deposits.

Co-Ni-P

Ternary Co-Ni-P nanodeposits were successfully prepared by electrodeposition using a chloride bath containing boric acid and NaH_2PO_2 . The morphology of the obtained layer was dependent on the concentration of Hypophosphite. As the concentration of Hypophosphite was increased, smooth deposits successively changed to dendritic, nodular, and again smooth. The crystalline structure can be either fcc or hcp, according to the dominating Fe-group metal content. The preferred orientation varies in a complex way with the bath and alloy composition. The deposition conditions have limited effects on the grain size of the alloys (ca. 50 nm). The magnetic properties are mainly dependent on the amount of codeposited P [35].

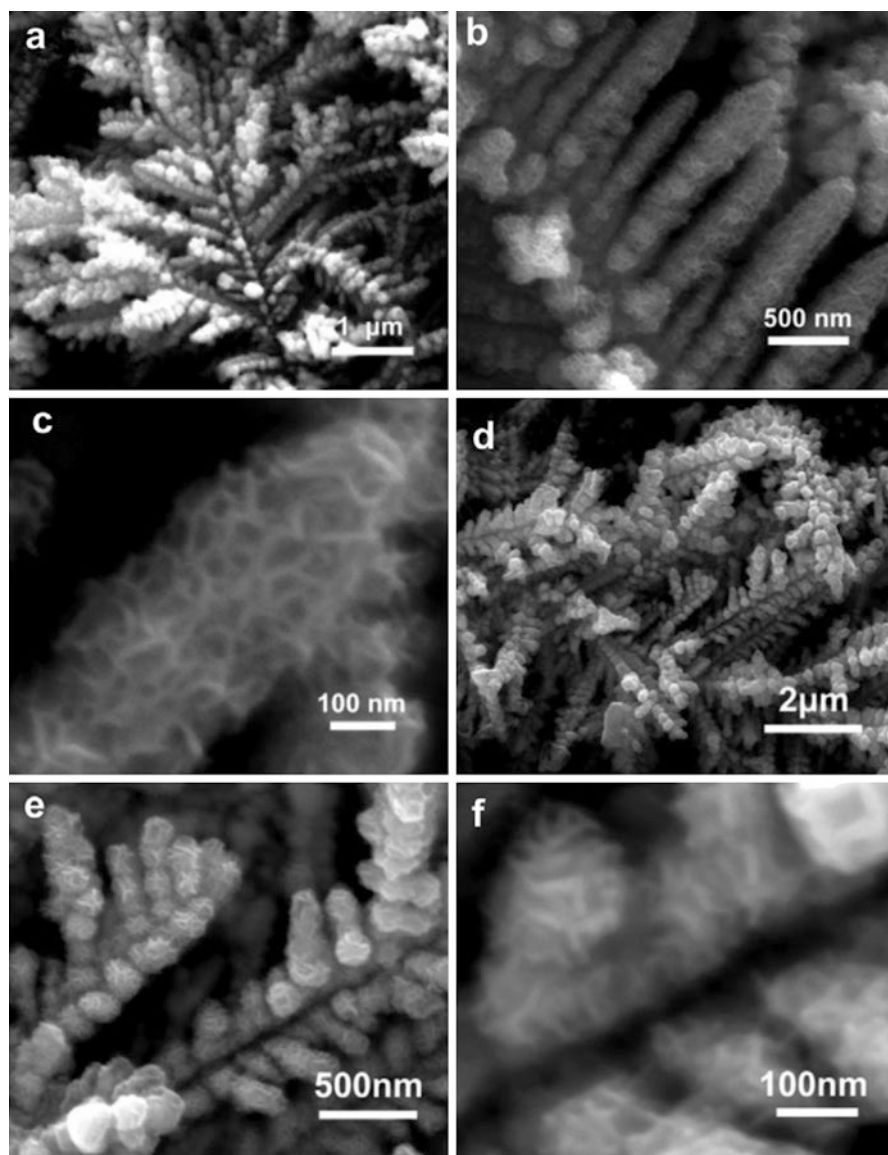


Fig. 5 SEM of the as-deposited dendritic-like morphology of CoNiCu alloy deposited in a mixed solution with $0.02\ \text{mol/L}\ \text{CoCl}_2$, $0.02\ \text{mol/L}\ \text{NiCl}_2$ and $0.01\ \text{mol/L}\ \text{CuCl}_2$ for 15 min [34]

Copper-Based Deposits

Coarse-grain copper is widely used in electrical and electronic devices despite the fact that it readily corrodes in a variety of environments [28]. Delplancke et al. [36] studied the electrodeposition of bimodal nanograin structures, with simultaneous presence of coarse (500 nm) and n-metric (100 nm) copper grains [36]. Natter et al. [37] reported significant tensile strength of copper nanodeposits due to small grain size and high defect density. The nature and concentration of organics added to the electrodeposition bath affecting the nanograin dimensions. Bicelli et al. [30] stated that room-temperature recrystallization behavior has a significant bearing on the stability of the electrical quantities of electronic devices implementing electrodeposited Cu, which tends to exhibit time-dependent properties. Annealing at moderate temperature is therefore common practice to avoid uncontrolled aging of these materials. The development of a $\langle 100 \rangle$ texture under low-temperature annealing has been reported. Ebrahimi et al. [38] stated that the annealing of 100 nm grain copper deposits up to 423 K displayed a limited (ca. 20 %) grain growth and no measurable variation of yield strength; concomitantly, a notable improvement of ductility and ultimate tensile strength was observed. Hall–Petch behavior of hardness was reported.

Cu-Fe

“Nanocrystalline two-phase” Cu-Fe alloys (0–60 w% Cu) consisting of a mixture of fcc Cu {111} preferred orientation and bcc Fe {211} preferred orientation have been electrodeposited using sulfate-citrate bath. For the lowest content of Fe, the details of the evolution of the magnetic moment of the alloys were obtained by SQUID magnetometry. Increase of CuSO_4 concentration led to grain refinement [39].

Cu-Ni

Cu-Ni nanodeposits were obtained by pulse plating, and single-phase fcc alloys (26–36 w% Cu) with grain size in the range 2.5–28.5 nm and $\langle 111 \rangle$ texture have been obtained. Adjusting the pulse plating parameters can lead to formation of smooth, bright, and nodular surface morphology. Tensile stress layers galvanostatically deposited are higher in comparison with pulse-plated ones. The residual tensile macrostress of a range of Ni-Cu alloys was studied by spiral contractometry and the microstresses measured by the peak-broadening of XRD peaks [30]. Wolf et al. [40] stated that hyperfine interactions were detected due to a disordered grain boundary structure. The presence of Ni precipitates below the detectability limit of XRD was inferred from PAC measurements. Low current densities, higher temperatures, and addition of saccharin can improve the homogeneity of the NiCu alloy.

Nickel-Based Deposits

The electrochemical behavior of nickel and its oxides is important for applications such as rechargeable batteries, fuel cells, catalysis, and decorative coatings. Among various electrodeposited nanocrystalline metals, Ni-based alloys have been extensively researched due to their distinct properties such as being five times harder, reduction in coefficient of friction by 50 %, improved corrosion resistance, increased wear resistance by a factor of 170, improved electrocatalytic activities for hydrogen evolution and hydrogen oxidation reactions, and higher hydrogen diffusion [2]. Pure Ni film and eight Ni-based alloy films (Ni-W, Ni-P, Ni-Mo, Ni-Co, Ni-Cu, Ni-Zn, Ni-Mg, and Ni-B) were deposited and characterized. More systematic studies were conducted for Ni-W and Ni-P films, along with pure Ni film as a baseline [6].

NC nickel of about 17 nm size produced by ED significantly enhances the electrocatalytic activity for hydrogen evolution due to the increased density of active surface sites [41].

According to Rashidi et al. [6], at the current densities higher than 75 mA/cm², in the absence of saccharin the nickel layer exhibits a pyramidal-like morphology (Fig. 6a) while it changes to a colony-like morphology in presence of saccharin. An increase in current density results in larger colonies and brighter appearance (Fig. 6b, c).

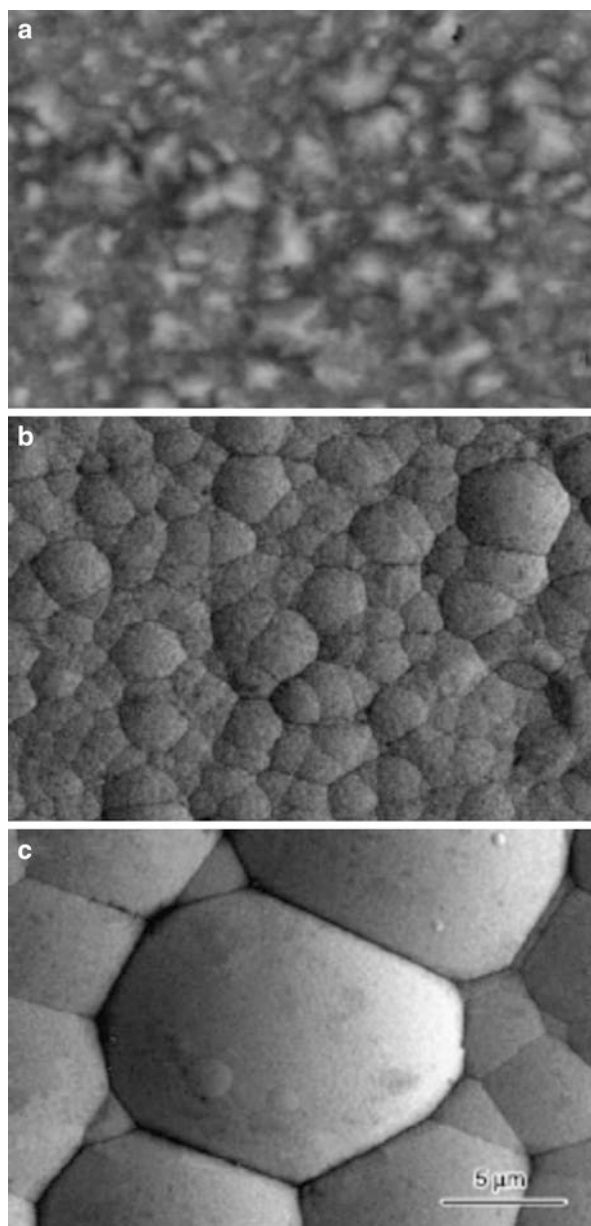
Ni-W Alloys

Weston et al. [42] studied the properties of Ni-W nanodeposits. Ni-W alloy was introduced to replace chromium coatings because they are environmentally friendly. Ni-W alloys have various industrial applications because of their excellent material and physical properties. First, the deposited Ni films exhibit hardness of a range from 2 to 7 GPa, depending on the actual grain size. Second, these nanocrystalline Ni-W films exhibit excellent corrosion rates as low as ~2.5 % of that of a typical conventional stainless steel. Third, these Ni-W alloys would be used as diffusion barriers between copper and silicon in ultralarge-scale integration (ULSI) circuits and microelectromechanical systems (MEMS). Nickel–tungsten alloys with grain size of around 20 nm lead to low friction and wear, and the hardness of nickel–tungsten electrodeposits increases significantly as the crystallite size is reduced from around 50 to 10 nm.

The W dopants were introduced by adding a tungsten salt into nickel sulfate (NiSO₄) to form Ni-W alloys; interestingly, it is rather difficult to deposit pure W films without depositing Ni simultaneously. Usually, ammonium chloride (NH₄Cl) and/or citric acid (Cit) are also added into the deposition bath to improve Faradaic efficiency (FE), to control the pH value, and to increase solubility of metal ions.

A characteristic relationship between composition and grain size has been illustrated, which is explained from the W segregation that reduces the grain boundary energy as the driving force for grain growth. Some studies stated that when tungsten atomic percentage is increased from 2.5 % to 23 %, the corresponding grain size is

Fig. 6 SEM micrographs of nickel coatings deposited as a function of working parameters: (a) saccharin-free bath at $i = 100 \text{ mA/cm}^2$, (Pyramidal-like) (b) bath containing 5 g/L saccharin at $i = 100 \text{ mA/cm}^2$, (colony-like) (c) bath containing 5 g/L saccharin at $i = 300 \text{ mA/cm}^2$ (large colony-like) [6]



decreased from >100 to <10 nm. In addition to XRD peak broadening that is associated with reducing grain size, shifts in XRD peak position were also observed. This is because the solution of larger tungsten atoms increases the lattice parameter of the FCC alloys [43].

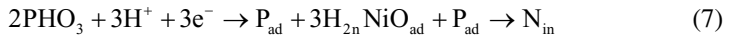
Ni-Co Alloys

Alloys of iron group metals, Fe, Co, and Ni, have been considered as very good magnetic materials. These alloys are known to possess much better permanent magnetic properties than pure metals. Ni-Co alloys have been investigated as important engineering materials for several decades because of their unique properties, such as high strength, good wear resistance, heat conductivity, and electrocatalytic activity. Electrodeposited Ni-Co thin films have been intensively studied due to their application in MEMS. Thin and thick Ni-Co films form important parts of magnetic-MEMS devices including sensors, microactuators, or micromotors because of their excellent physical properties. Fine Ni, Co, and Ni-Co alloy powders are required for developing magnetoresistive sensors in thick-film form [44].

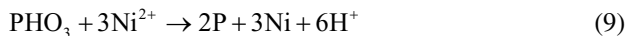
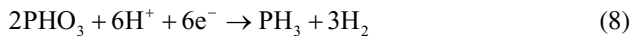
Liping et al. [45] showed that Co content affects the morphology and grain size of alloys. The phase structure of Ni-Co alloys gradually changed from fcc to hcp structure with the increase of Co content. The hardness of Ni-Co alloys with a maximum around 49 wt% Co followed the Hall-Petch effect. It was found that the improvement of wear resistance of Ni-rich alloys with hardness increase followed Archard's law. In addition, the Co-rich alloys exhibited much lower friction coefficient and higher wear resistance than Ni-rich alloys. It has been concluded that hcp crystal structure in Co-rich alloys contributed to the remarkable friction-reduction effect and better antiwear performance under the dry sliding wear conditions. According to Rafailovic [46], the structure morphology was converted from platelet to cauliflower structure by increasing Ni²⁺/Co²⁺ ratio.

Ni-P Alloys

Ni-P deposits obtained from electrodeposition are good catalysts for hydrogen evolution, special paramagnetic properties, excellent microhardness, and corrosion resistance [47]. Ni-P alloys have been studied to a less extent than Ni-W alloys. Nevertheless, a similar relationship between the P content and resultant grain size has been reported. Like W, although it is feasible to add P dopants into the iron-group metals during electrodeposition, deposition of P alone is difficult [48]. Two possible deposition mechanisms were suggested for electrodeposition by Erb et al. [49]. The "direct" deposition mechanism assumes that the phosphorus element forms from the reduction of phosphorus oxyacid in the aqueous solutions;



However, this mechanism is not convincing, because direct deposition of pure elemental phosphorus is not possible. Alternatively, the "indirect" deposition mechanism assumes that the reduced phosphine from phosphorus oxyacid reacts with Ni²⁺H in the bath and produces Ni-P alloys, i.e.,



Nanocrystalline Ni-P alloys and coatings have excellent corrosion resistance, electrochemical catalytic properties [50], and nonmagnetic character [51]. Amorphous Ni-P coatings that contain more than 10 at.% P were found to be highly effective for corrosion resistance [52]. In addition, Ni-P alloys are used in MEMS devices and electronics.

Ni-Mo Alloys

According to Schulz et al. [53], the enhanced HER kinetics of Ni-nanodeposits are due to the high area fraction of grain boundaries (and to some extent, triple junctions) intersecting the free surface of the electrode. The HER kinetics can be further enhanced by alloying nanocrystalline Ni with molybdenum. Ni-Mo deposits are good catalysts for hydrogen production from water by electrolysis as well as by steam reforming of hydrocarbons. Halim et al. [54] prepared nodular Ni-Mo nanocrystalline deposits (Fig. 7) by galvanostatic electrodeposition from citrate-ammonia solutions. According to XRD analysis, a single Ni-Mo solid solution phase was detected. The size of the nodules increased as electroplating current density increased. From EDX analysis, as the current density increased from 5 to 80 mA·cm⁻², the molybdenum content in the deposits decreased from ~31 to 11 wt%. Nanolayers with 23 % Mo exhibited the highest microhardness value (285 Hv). Mo content values between 11 % and 15 % are recommended for obtaining high corrosion resistance and better electrocatalytic activity for HER.

Nickel-based composite coatings are characterized by their high catalytic activity for hydrogen evolution (HER) and electrocatalytic oxygen evolution (OER) as well as good corrosion resistance in aggressive environments. Ni-Mo nanocomposite layers (18–32 nm) were prepared by galvanostatic electrodeposition from a nickel salt bath containing suspended Mo nanoparticles. According to XRD analysis, the nanodeposits consisted of crystalline Mo incorporated into Ni matrix. The molybdenum content decreased by increasing the deposition current density and ranged between ~6 % and ~17 % Mo. The crystallite size and the surface roughness increased by increasing the current density (Fig. 8). The corrosion rate of Ni-Mo composites increased with increasing Mo content due to crystallite size-refining and surface roughness effect. Electrocatalytic effect for hydrogen production was improved mainly due to higher surface roughness and thus providing more accessible surface area [55].

Template-Assisted Electrodeposition

Nanowires and nanorods of defined dimension were successfully prepared using templated synthesis. Several techniques of forming nanomaterials using templates have been developed such as chemical vapor deposition (CVD), sol-gel deposition, polymerization, and electrochemical deposition. The template-assisted electrodeposition has been successfully used to prepare 1D nanostructures of various metals, semiconductors, and conductive polymers. Template synthesis in nanoporous membranes have been carried out in anodic aluminum oxide, polycarbonate, and diblock copolymer membranes [56, 57].

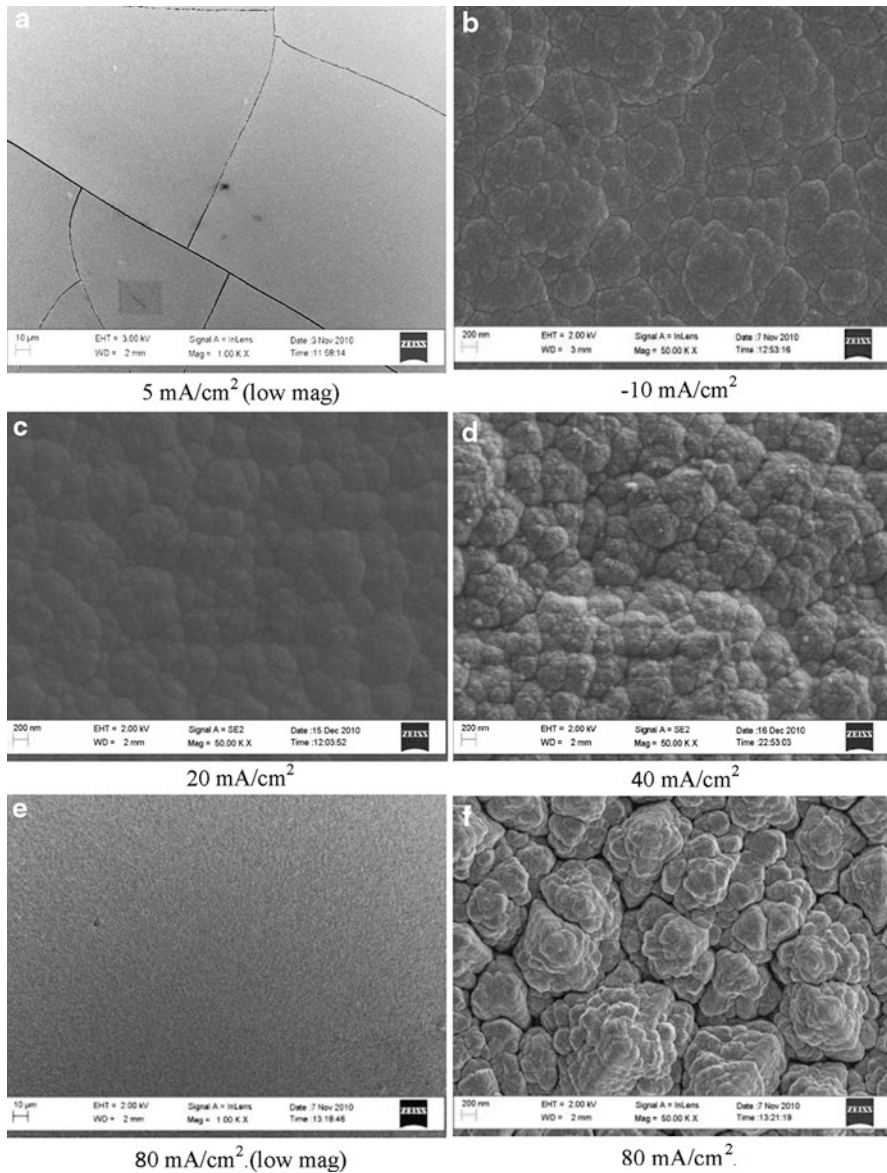


Fig. 7 SEM micrographs of Ni-Mo nanodeposits showing nodular shaped microstructure [54]

Conclusions

Electrodeposition has been identified to be a technologically feasible and economically superior technique for the production of nanocrystalline pure metals and alloys as well as nanocomposites. Electrodeposition of polycrystalline metals and alloys exhibits several types of growth forms including layers, blocks, ridges, dendrites,

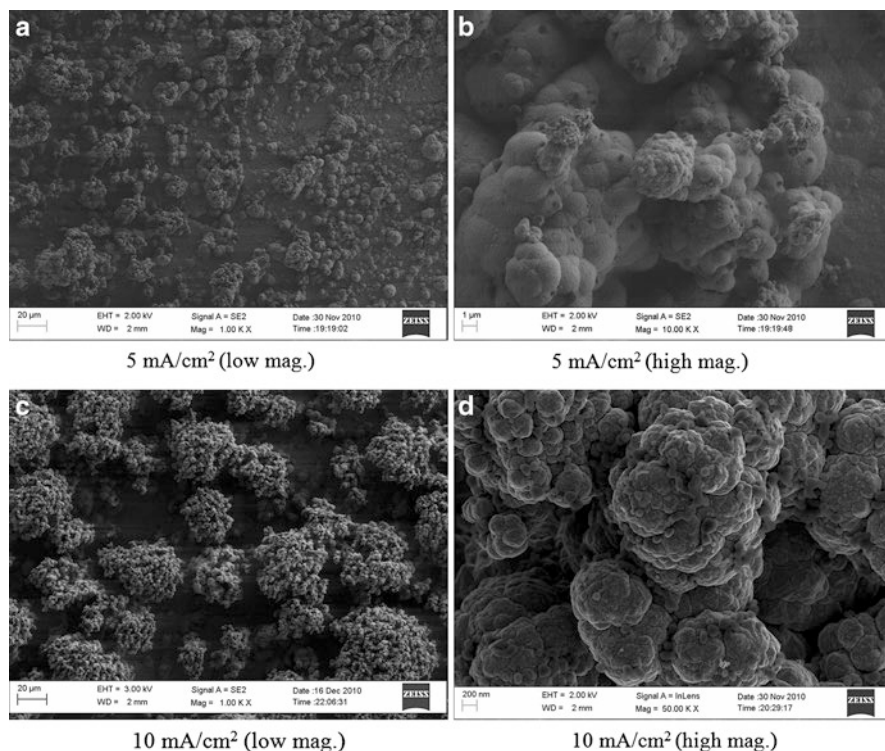


Fig. 8 SEM micrographs for electrodeposited Ni-Mo Nanocomposites showing clusters formation [55]

pyramids, spiral growth forms, powders, and whiskers. Research on the structure–property–performance relationships of these materials has indicated many promising properties which can be exploited for commercial purposes. Of all the nanoprocessing techniques, electrodeposition appears to be a promising technique due to its relatively low cost, ability to produce compositions unattainable by other techniques, and the possibility of forming of simple low-cost multilayers in many different systems. Consequently, new markets and business opportunities are expected to emerge for the electroplating industry.

References

1. Gleiter H (1981) Deformation of polycrystals: mechanisms and microstructures. In: Hansen N, Horsewell A, Liholt H (eds) Proceedings of the 2nd Riso international symposium on metallurgy and materials science. Riso National Laboratory, Roskilde, p 15
2. Rofagha R, Wood D, Erb U (1993) Industrial applications of nanocrystalline electrodeposits. In: Yacamán MJ, Tsakalakos T, Kear BH (eds) Proceedings of the first international conference on nanostructured materials, Cancun. Nanostructured materials, vol 3. pp 1–6
3. Gurrappa I, Binder L (2008) Electrodeposition of nanostructured coatings and their characterization – a review. *Sci Technol Adv Mater* 9:043001 (11 pp)

4. Bockris JOM (1964) Modern aspects of electrochemistry, vol 3. Butterworths, London, p 224
5. Mohanty US (2011) Electrodeposition: a versatile and inexpensive tool for the synthesis of nanoparticles, nanorods, nanowires, and nanoclusters of metals. *J Appl Electrochem* 41:257–270
6. Rashidi AM, Amadeh A (2010) Effect of electroplating parameters on microstructure of nanocrystalline nickel coatings. *J Mater Sci Technol* 26(1):82–86
7. Bakonyi I, Toth-Kadar E, Toth J, Tarnoczi T, Cziraki A (1996) In: Suryanarayana C (ed) Processing and properties of nanocrystalline materials. TMS, Warrendale, PA, pp 465–471
8. McMahon G, Erb U (1989) Structural transitions in electroplated Ni-P alloys. *Microstruct Sci* 17:447–455
9. Abdel-Karim R, Reda Y, Muhammed M, El-Raghy S, Shoeib M, Ahmed H (2011) Electrodeposition and characterization of nanocrystalline Ni-Fe alloys. *J Nanomater* 2011:519274
10. Alfantazi AM, El-Sherik AM, Erb U (1994) The role of nickel in the morphology evolution of pulse plated Zn-Ni alloy coatings. *Scr Metall Mater* 30(10):1245–1250
11. Osmola D, Renaud E, Erb U, Wong L, Palumbo G, Aust KT (1993) Synthesis of nanocrystalline Co-W alloys. *Mater Res Soc Symp Proc* 286:191–196
12. Cheung C, Erb U, Palumbo G (1994) Application of grain boundary engineering concepts to alleviate stress corrosion cracking in alloys 600 and 690. *Mater Sci Eng* 185A:39–43
13. El-Raghy SM, Abdel-Karim R, Khalaf A, Ayman K, Aziz L (2012) Surface characterization and corrosion properties of nanocrystalline Ni-based coatings. In: International conference on corrosion mitigation and surface protection technologies, Hurghada, 10–13 Dec
14. Boukherroub R, Szunerits S (2009) Wet chemical approaches for chemical functionalization of semiconductor nanostructures. In Schmuki P, Virtanen S (eds) *Electrochemistry at the nanoscale*. New York: Springer, chapter 5
15. Albert Calbetó S (2011) Nickel matrix micro/nano SiC composite electrodeposition. Escola Tècnica Superior d'Enginyeria Industrial de Barcelona, Master thesis, Spain
16. Khalaf A, Ayman K, Aziz L (2012) Electrodeposition and characterization of nanocrystalline Ni-based deposits. BSc Graduation Project, Department of Metallurgy, Cairo University
17. Kanani N (2004) *Electroplating – basic principles, processes and practice*. Elsevier, Amsterdam
18. Winand R (1994) Electrodeposition of metals and alloys-new results and perspectives. *Electrochem Acta* 39(8/9):1091–1105
19. Watanabe T (2004) Nano-plating- microstructure control, theory of plated film and data base of plated film microstructure. Elsevier, Amsterdam, chapter 2
20. Venables J (2000) *Introduction to surface and thin film processes*. Cambridge University Press, Cambridge
21. Oura K, Lifshits VG, Saranin AA, Zotov AV, Katayama M (2003) *Surface science: an introduction*. Springer, Berlin
22. Pimpinelli AO, Villain J (1998) *Physics of crystal growth*. Cambridge University Press, Cambridge
23. Markov IV (1995) *Crystal growth for beginners: fundamentals of nucleation, crystal growth, and epitaxy*. World Scientific, Singapore
24. Matthews JW (1975) *Epitaxial growth*. Academic, New York
25. Fischer H (1954) *Elektrolytische Abscheidung und Elektrokrystalabsatz von Metallen* Berhn. Springer, Berlin, p 729
26. Elias J, Gizowska M, Brodard P, Widmer R, deHazan Y, Graule T, Michler J, Philippe L (2012) Electrodeposition of gold thin films with controlled morphologies and their applications in electrocatalysis and SERS. *Nanotechnology* 23:255705 (7 pp)
27. Bartlett PN, Birkin PN, Ghanem MA, Groot P, Sawicki M (2001) The electrochemical deposition of nanostructured cobalt films from lyotropic liquid crystalline media. *J Electrochem Soc* 148:C119–C123
28. Herrasti P, Ponce de León C, Walsh FC (2012) The corrosion behavior of nanograined metals and alloys. *Rev Metal* 48(5):377–394
29. Bozzini B, Fanigliulo A, Serra M (2001) Electrodeposition of star-shaped gold crystallites. *J Cryst Growth* 231:589–598

30. Bicelli LP, Bozzini B, Mele C, D'Urzo L (2008) A review of nanostructural aspects of metal electrodeposition. *Int J Electrochem Sci* 3:356–408
31. Bozzini B, Giovannelli G, Cavallotti PL (2000) Part II – baths not containing free cyanide. *J Appl Electrochem* 30:591–594
32. Bozzini B, Giovannelli G, Natali S (2000) Metastable structures in electrodeposited AuCu. *Scr Mater* 43:877–880
33. Koay MH, Wan Normimi RA, Azrina Resali N, Chong WT, Salleh Z, Ghani MA (2013) The physical and magnetic properties of electrodeposited Co-Fe nanocoating with different deposition times. *J Nanomater* 2013, Article ID 680491, (6 pp)
34. Wang C, Li W, Lu X, Xie S, Xiao F, Liu P, Tong Y (2012) Facile synthesis of porous 3D CoNiCu nano-network structure and their activity towards hydrogen evolution reaction. *Int J Hydrog Energy* 37:18688–18693
35. Park D-Y, Myung NV, Schwartz M, Nobe K (2002) Electrodeposited CoNiP films. *Electrochim Acta* 47:2893–2900
36. Delplancke JL, Sun M, O'Keefe TJ, Winand R (1989) Nucleation of electrodeposited copper on anodized titanium. *Hydrometallurgy* 23:47–66
37. Natter H, Hempelmann R (1996) Nanocrystalline copper by pulsed electrodeposition. *J Phys Chem* 100:19525–19532
38. Ebrahimi F, Zhai Q, Kong D (1998) Mechanical properties of Cu/Ag multilayered composition. *Mater Sci Eng A* 255:20–32
39. Williams JM, Blythe HJ, Fedosyuk VM (1996) An investigation of electrodeposited granular Cu Fe alloyed films. *J Magn Magn Mater* 155:355–357
40. Wolf H, Guan Z, Li X, Wichert TH (2001) Magnetic properties of grain boundaries of nanocrystalline Ni and of Ni precipitates in nanocrystalline NiCu alloys. *Hyperfine Interact* 136/137:281–287
41. Haseeb A, Blanpain B, Wouters G, Celis JP, Roos JR (1993) Electrochemical deposition: a method for the production of artificially structured materials. *Mater Sci Eng A* 168:137–140
42. Weston DP, Shipway PH, Harris SJ, Cheng MK (2009) Friction and sliding wear behavior of electrodeposited cobalt and cobalt–tungsten alloy coatings for replacement of electrodeposited chromium. *Wear* 267:934–943
43. Park H (2008) Electrodeposition of nanocrystalline Ni-based alloys. Master thesis, Clemson University
44. Lidija D, Dragica R, Mnicic M (2009) Deposition and characterization of nanostructured nickel-cobalt alloys. *Hem Ind* 63(5a):557–569
45. Liping W, Yan G, Qunji X, Huiwen L, Tao X (2005) Microstructure and tribological properties of electrodeposited Ni–Co alloy deposits. *Appl Surf Sci* 242:326–332
46. Rafailovic LD, Maricic AM, Artner W, Nauer GE, Minic DM (2009) Morphology and microstructure of annealed Ni-Co alloy powders electrodeposited on copper substrates. *Sci Sinter* 41:135–142
47. Daly BP, Barry F (2003) Electrochemical nickel-phosphorous alloy formation. *J Int Mater Rev* 48:326–338
48. Doyle DM, Palumbo G, El-Sherik AM, Erb U, Aust KT (1992) Proceedings of the nanophases nanocrystalline structure, California, Mar 1992, p 51
49. Erb U, Aust KT, Palumbo G (2002) Nanostructured materials processing, properties and technologies. William Andrew Publishing, Norwich, p 179
50. Siegel RW, Thomas GJ (1992) Grain boundaries in nanophase materials. *Ultramicroscopy* 40:376–384
51. Ciubotariu AC, Benea L, Varsanyi ML, Dragan V (2008) Electrochemical impedance spectroscopy and corrosion behavior of Al₂O₃-Ni nano composite coatings. *Electrochim Acta* 53:4557–4563
52. Brooks I, Erb U (2001) Hardness of electrodeposited microcrystalline and nanocrystalline gamma-phase Zn-Ni alloys. *Scr Mater* 44:853–858
53. Schulz R, Huot J, Trudeau M (1994) Nanocrystalline Ni-Mo alloys and their application in electro catalysis. *J Mater Sci* 9:2998–3008

54. Halim J, Abdel-Karim R, El-Raghy S, Nabil M, Waheed A (2012) Electrodeposition and characterization of nanocrystalline Ni-Mo. *J Nanomater* 2012:845673, 10 pp
55. Abdel-Karim R, Halim J, El-Raghy S, Nabil M, Waheed A (2012) Surface morphology and electrochemical characterization of electrodeposited Ni-Mo nanocomposites as cathodes for hydrogen evolution. *J Alloys Compd* 530:85–90
56. Guangwei S, Lixuan M, Wensheng S (2009) Electrodeposition of one-dimensional nanostructures. *Recent Pat Nanotechnol* 3:182–191
57. Liu GQ, Zhao XS (2004) Nanoporous materials – science and engineering, vol 4, Series on chemical engineering. Imperial College Press, London, chapter 1

Andrzej Kudelski

Contents

Introduction.....	48
Surfaces Containing a Large Number of Electromagnetic Nanoresonators.....	50
Electrochemically Roughed Metal Electrodes.....	50
Electroplated Flat Surfaces.....	55
Metal Nanostructures Synthesized Using Templates.....	57
Electromagnetic Nanoresonators Covered by a Thin Layer of Other Metals.....	60
Single Active-Site Nanoresonators.....	61
Conclusions.....	63
References.....	64

Abstract

In 1970s it was observed that the efficiency of Raman scattering for molecules placed in the optical nanoresonators may increase even more than seven orders of magnitude. Later, large increase of the efficiency of other optical processes (e.g., infrared absorption, fluorescence, or second harmonic generation) has been also reported for molecules placed in nanoresonators. Therefore, fabrication of electromagnetic nanoresonators and their applications for the construction of various analytical sensors are studied in many laboratories in the world. The first practically used electromagnetic nanoresonators have been formed electrochemically, and, although other methods have been developed since then, various types of such nanostructures are still being formed using different electrochemical methods.

In this review different approaches used for the electrochemical formation of electromagnetic nanoresonators are discussed. Methods of the formation of single

A. Kudelski (✉)

Faculty of Chemistry, University of Warsaw, Warsaw, Poland

e-mail: akudel@chem.uw.edu.pl

active-site nanoresonators, and of nanostructured surfaces containing a large number of places where the optical energy is concentrated, are presented. Fabrication of composite nanoresonators composed of at least two different materials is also briefly described.

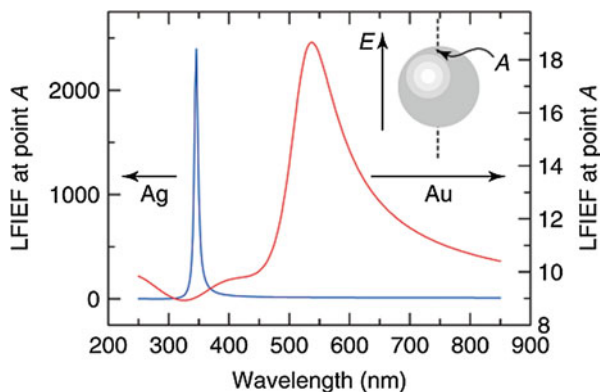
Keywords

Electrochemistry • Electromagnetic Nanoresonators • Gold • SERS • Silver • SPR • Surface Plasmon Resonance • Surface-Enhanced Raman Scattering • TERS • Tip-Enhanced Raman Spectroscopy

Introduction

When electromagnetic radiation interacts with a nanostructured surface of metal with a negative real and small positive imaginary dielectric constant (e.g., silver and gold), they induce a collective oscillation of surface conduction electrons called surface plasmons [1–4]. Plasmons lead to enhanced electromagnetic fields at some places of the illuminated surface [1–4]. This field enhancement is highly localized at the nanoparticle and decays rapidly away from the nanoparticle/dielectric interface into the dielectric background [1–4]. In order to calculate local electromagnetic field enhancement in the proximity of a metallic nanoparticle irradiated with light, one has to solve either Maxwell's or Helmholtz's equation [3]. This can be, in general, a rather difficult undertaking. Full analytical solutions of Maxwell's equations exist for simple geometries, and they are useful for understanding basic concepts and ideas. For example, the plot of the local field intensity enhancement factor (LFIEF) for spheres of either Au or Ag at the point immediately above the surface of the sphere and for different wavelengths is shown in Fig. 1. The points of the largest LFIEFs on the surface of the sphere are along the main symmetry axis in the direction defined

Fig. 1 Local field intensity enhancement factor (LFIEF) at point A (*inset*) on a sphere of either Au or Ag in the electrostatic approximation (Reprinted from [2] with permission from Wiley-VCH)



by the polarization of the electric field E . LFIEF reaches maximum when $\text{Re}[\varepsilon_{\text{met}}(\lambda) + 2\varepsilon_{\text{en}}(\lambda)] = 0$ (where $\varepsilon_{\text{met}}(\lambda)$ and $\varepsilon_{\text{en}}(\lambda)$ are the wavelength-dependent (complex) dielectric constants of the metal and the environment around, respectively) and is limited only by how small $\text{Im}[\varepsilon_{\text{met}}(\lambda)]$ is at that particular λ [1, 2]. Calculations of LFIEF have been carried out for many various systems [1–5]. These simulations have shown that LFIEF is significantly different at various positions of the particle and strongly varies with respect to many parameters, such as the electric properties of the material, the actual shape and size of the particle, and the illumination geometry [3, 4]. It is worth to note that very large values of LFIEF can be achieved in narrow gaps between metal nanoparticles [5].

Local enhancement of the intensity of the electromagnetic field may cause in some cases significant enhancement of the surface effectiveness of several optical phenomena including fluorescence, infrared absorption, Raman scattering, Raman optical activity, hyper-Raman scattering, coherent anti-Stokes Raman scattering, and second harmonic generation (see Table 1) [1, 6–28]. From the practical point of view the most important is the application of nanoresonators in increasing the sensitivity of Raman spectroscopy. For many decades Raman spectroscopy has not been considered a useful analytical tool because of the very low efficiency of the “normal” Raman scattering. A typical total Raman scattering cross section is ca. 10^{-29} cm² per molecule, whereas typical cross sections for absorption in ultraviolet and infrared are ca. 10^{-18} and 10^{-21} cm² per molecule, respectively [1]. Therefore, to

Table 1 Optical spectroscopic techniques for which the measured signal may be significantly enhanced by the metallic nanoresonators

Spectroscopic technique	Spectroscopic technique utilizing nanoresonators	Abbreviation	References
Fluorescence	Surface-enhanced fluorescence, surface plasmon-enhanced fluorescence, metal-enhanced fluorescence, surface plasmon field-enhanced fluorescence ^a	SPFS, MEF ^b	[6–12]
Infrared absorption	Surface-enhanced infrared absorption	SEIRA	[1, 13]
Second harmonic generation	Surface-enhanced second harmonic generation	SESHG	[14–16]
Raman scattering	Surface-enhanced Raman scattering	SERS	[1, 14, 17]
Resonance Raman scattering	Surface-enhanced resonance Raman scattering	SERRS	[18, 19]
Hyper-Raman scattering	Surface-enhanced hyper-Raman scattering	SEHRS	[20–23]
Raman optical activity	Surface-enhanced Raman optical activity	SEROA	[24, 25]
Coherent anti-Stokes Raman scattering	Surface-enhanced coherent anti-Stokes Raman scattering	SE-CARS	[15, 26–28]

^aVarious names are used in the literature

^bVarious abbreviations are used in the literature

record conventional Raman spectra, analytical concentrations greater than 0.01 M are usually required. However, by utilizing special electromagnetic nanoresonators constructed from metal nanoclusters, the Raman scattering cross sections can be significantly increased (for Raman bands with a small Raman shift, this increase is roughly proportional to the fourth power of the field enhancement [1, 19]) making possible the observation of Raman spectra even of a single molecule [29–31]. Because of the extremely low detection limit of resonator-enhanced Raman scattering (for the historical reasons called surface-enhanced Raman scattering – SERS) and the fingerprint-like character of recorded spectra, SERS has become one of the most widely used analytical and/or surface tools. This is reflected in the number of scientific publications on the subject. In the database “Web of Knowledge,” in the 10-year period of 2004–2013, the keyword “SERS” produces more than 10^4 hits.

The first practically used electromagnetic nanoresonators have been formed electrochemically [17, 32, 33], and various types of such nanostructures are still being formed using different electrochemical methods. In this chapter different approaches used for the electrochemical formation of electromagnetic nanoresonators are discussed. Both the formations of the single active-site nanoresonators and nanostructured surfaces containing a large number of active places are presented. Because the majority of practical applications of electromagnetic nanoresonators are connected with the enhancement of the efficiency of Raman process, the properties of nanostructures presented in this chapter are usually optimized to maximize surface enhancement of Raman scattering.

This chapter is organized as follows:

1. In section “[Surfaces Containing a Large Number of Electromagnetic Nanoresonators](#),” technologies of electrochemical formation of surfaces containing a large number of places where the optical energy is concentrated are described.
2. In section “[Single Active-Site Nanoresonators](#)” the electrochemical methods of the formation of nanoresonators with only single active-site are presented. Such nanoresonators are used when an optical spectroscopic technique (usually Raman) is coupled with scanning probe microscopy (*scanning tunneling microscope*, STM, or *atomic force microscope*, AFM), forming spectroscopic–microscopic tool allowing to overcome the Abbe’s diffraction limit of the optical measurements [34, 35].
3. Finally, section “[Conclusions](#)” presents some conclusions and summarizes this chapter.

Surfaces Containing a Large Number of Electromagnetic Nanoresonators

Electrochemically Roughed Metal Electrodes

The first practical application of electromagnetic nanoresonators in the spectroscopic measurements was realized in 1974 by Fleischmann et al., who reported observation of strong Raman signal for pyridine adsorbed on the surface of a silver

electrode electrochemically roughened in a KCl solution [17]. As mentioned in the previous section, this report by Fleischmann et al. launched broad using of nanoresonators to increase efficiency of many optical processes. Since silver is the best material to construct nanoresonators for visible radiation (the imaginary part of the dielectric constant of silver is small in the practically whole visible range of the electromagnetic radiation and silver is relatively inert chemically), nanostructured silver surfaces are used in many laboratories in the world. Nanostructuring of silver surfaces is usually carried out electrochemically by the oxidation–reduction (OR) cycling, and the applied potential is changed linearly from the most negative value toward the most positive one and again to the most negative value. During the oxidation part of the cycle, silver at the surface is oxidized (usually roughening is carried out in chlorides, so produced Ag^+ ions are deposited on the electrode surface as AgCl), whereas during the reduction part of the cycle, silver cations are reduced and deposited on the surface of the electrode, producing a highly developed structure.

The morphology of roughened silver surface, and hence the average field enhancement factor, depends on many parameters of the roughening procedure (e.g., potential range in which the roughening is carried out, sweep rate, and number of potential cycles – for details see Kruszewski S, Skonieczny [36] and Kruszewski [37]). Since variation of the roughening parameters often causes relatively small changes of the efficiency of the formed nanoresonators, one may find in the literature many slightly different procedures of the electrochemical nanostructuring of silver electrodes. According to our experience, very efficient silver nanoresonators may be obtained by three successive OR cycles in a 0.1 M KCl aqueous solution from -0.3 to $+0.3$ to -0.3 V (versus a 0.1 M KCl AgCl/Ag electrode) at a sweep rate of 5 mV s^{-1} . As mentioned above, different groups nanostructure silver electrodes using procedures which may differ in practically all experimental parameters: concentration of KCl, the extreme positive and negative potentials, the sweep rate, and the number of cycles. For example, silver electrodes may be effectively nanostructured by 3 OR cycles in a 0.2 M KCl solution from -0.7 to $+0.25$ at a sweep rate of 5 mV s^{-1} [38], ca. 450 OR cycles in a 0.1 M KCl solution from -0.3 to $+0.2$ at a sweep rate of 0.5 V s^{-1} [17], or a single OR cycle in a 0.1 M KCl solution from -0.2 to $+0.2$ at a sweep rate of 10 mV s^{-1} [39].

The scanning electron microscopic (SEM) image of the silver electrode nanostructured by a typically used procedure of 3 OR cycles from -0.3 to $+0.3$ at a sweep rate of 5 mV s^{-1} carried out in a 0.1 M KCl solution is shown in Fig. 2. As can be seen in Fig. 2, the outermost layer of the roughened silver electrode looks like a sponge formed from silver nanoclusters with a dimension typically in the range of 50–300 nm.

Chlorides are adsorbed very strongly on silver surfaces; therefore, in the case of silver electrodes nanostructured in KCl solution, some chlorides are present on their surface in spite of very careful rinsing of electrodes with water after the electrochemical nanostructuring. Therefore, when the surface of formed Ag nanoresonators should be chloride-free, the nanostructuring is carried out in other electrolytes. For example, nanostructured silver surface may be prepared by six successive positive–negative cycles in 0.1 M Na_2SO_4 solution from -0.5 to $+0.5$ to -0.5 V (versus a 0.1 M KCl AgCl/Ag electrode) at a sweep rate of 50 mV s^{-1} [40].

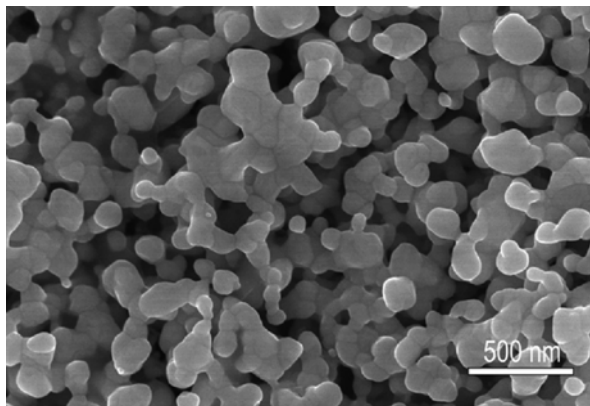


Fig. 2 Scanning electron microscopic (SEM) image of a silver electrode roughened by three successive oxidation–reduction cycles in a 0.1 M KCl aqueous solution from -0.3 to $+0.3$ to -0.3 V (versus a 0.1 M KCl AgCl/Ag electrode) at a sweep rate of 5 mV s^{-1} (Reprinted from [24] with permission from Elsevier)

The other metal often used for the formation of nanoresonators is gold. Gold electrodes are usually nanostructured using relatively similar methods as for roughening of silver electrodes: carrying out some number of OR cycles in KCl aqueous solution. However, contrary to the described above nanostructuring of Ag, electrochemical oxidation of Au in KCl solution leads to creation of soluble gold complexes (e.g., AuCl_4^-). Therefore, after the roughening procedure, the electrolyte and the counter electrode may be significantly contaminated with gold. According to our experience, very efficient gold nanoresonators may be obtained by 20 successive OR cycles in a 0.1 M KCl aqueous solution between -0.6 and $+1.25$ V (versus a saturated calomel electrode) at a sweep rate of 0.2 V s^{-1} [41]. A scanning electron microscopic image of a gold electrode roughened by oxidation–reduction cycling in 0.1 M KCl solution is shown in Fig. 3c. As in the case of silver, some groups use slightly different procedures for roughening of gold electrodes which also give efficient system of nanoresonators. For example, Russell et al. nanostructured Au electrode by 25 OR cycles from -0.3 to $+1.2$ V at a sweep rate of 1 V s^{-1} , holding the potential at 1.2 V for 30 s, sweeping back to -0.3 V at a sweep rate of 0.5 V s^{-1} , and then holding the potential at -0.3 V for 1.2 s [43].

Efficient nanoresonators, although unfortunately chemically significantly less stable than those from gold and silver, may be formed from copper. Contrary to silver and gold, there is no one prevalent method for the nanostructuring of copper electrodes. In general, four kinds of significantly different procedures are used:

- (a) Potential cycling of a copper electrode in a solution containing a copper salt (e.g., solution of CuCl_2 or $\text{CuCl}_2 + \text{LiCl}$) [44, 45]. In this case, the potential range is chosen in such a way that more metallic copper is deposited during the reduction part of the cycle than it is later dissolved during the oxidation part. A typical example of such roughening procedure is roughening of the Cu electrode in 0.2 M LiCl and 0.01 M CuCl_2 solution by 50 successive positive–negative scans between -0.55 and $+0.05$ V versus saturated calomel electrode at a sweep rate of 20 mV s^{-1} [45].

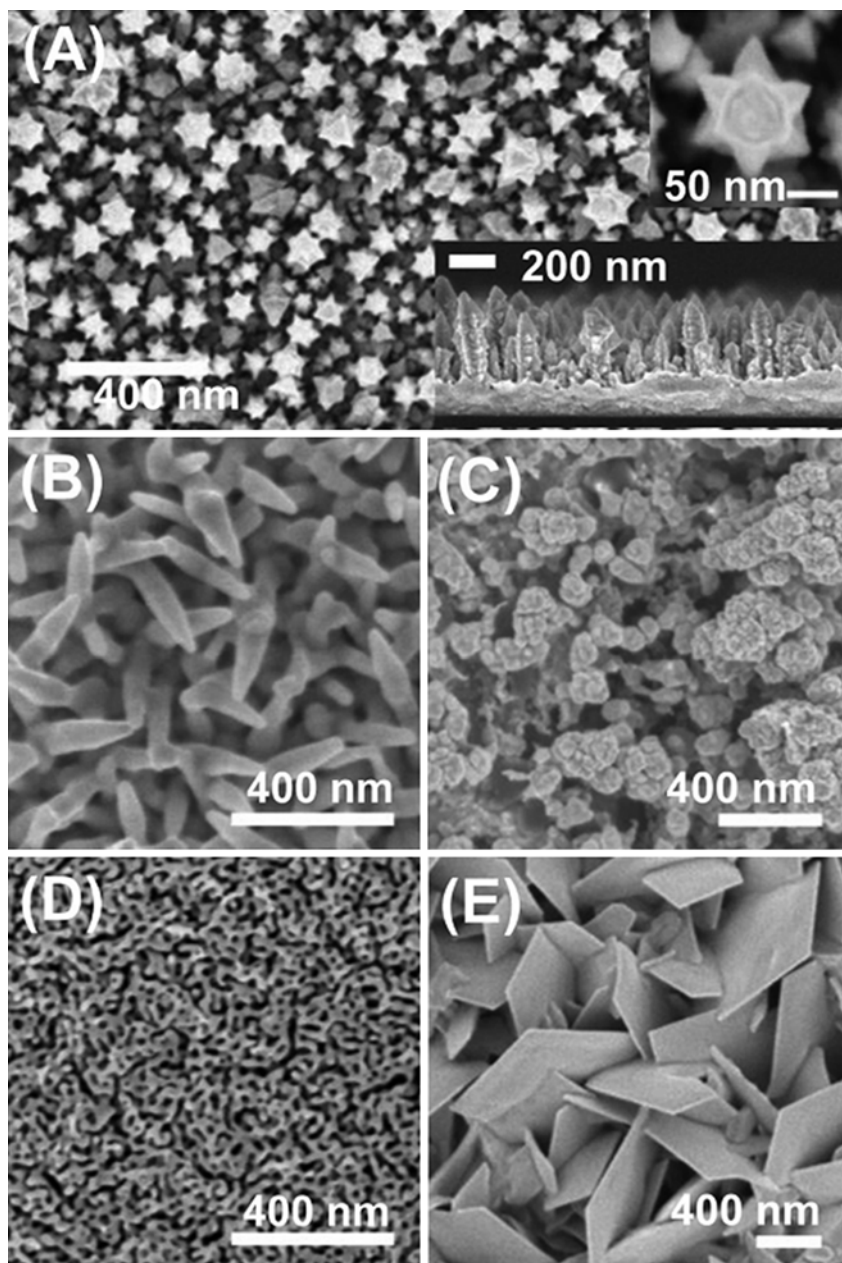


Fig. 3 Scanning electron microscopic (SEM) images of differently nanostructured gold surfaces: (a) dendritic rod gold nanostructures formed by one-step gold electrodeposition from a solution containing Au(I) ions complexed with sulfite anions, (b) nanospike gold clusters deposited from a solution containing HAuCl_4 and $\text{Pb}(\text{CH}_3\text{COO})_2$, (c) gold electrode prepared by a standard electrochemical oxidation–reduction cycling in a 0.1 M KCl solution, (d) surface obtained the dealloying of Ag from Ag/Au alloy, and (e) nanoplate Au surface prepared by an electrodeposition from a solution containing $\text{KAu}(\text{CN})_2$ and Na_2CO_3 (Reprinted from [42] with permission from Elsevier)

- (b) Cycling of copper electrodes in electrolytes containing ions that form complexes with copper cations of very low solubility (e.g., KI) [46–48]. This method of roughening of copper is similar to the standard roughening of silver by the oxidation–reduction cycling in chlorides during which nearly insoluble AgCl is formed.
- (c) OR cycling in electrolytes that do not form complexes or low-solubility salts with Cu^{2+} cations (e.g., KCl, LiCl, Na_2SO_4) [45]. An example of such nanostructuring is roughening by 50 successive positive–negative scans at 20 mV s^{-1} from -0.50 to $+0.13 \text{ V}$ in a 0.1 M KCl solution. This method of roughening of copper is similar to the standard roughening of gold during which soluble (AuCl_4^-) complexes are formed.
- (d) Rapid anodic dissolution of copper in an acidic electrolyte accompanied by a disproportionation of the dissolving Cu^+ , thus produced at the electrode, to Cu^{2+} and Cu^0 . Such copper roughening may be carried out in $0.2 \text{ M CuSO}_4 + 0.4 \text{ M H}_2\text{SO}_4$ solution at the current density of ca. 1 A cm^{-2} [45]. Copper surfaces nanostructured in this way contained significantly less oxygen than surfaces produced by standard oxidation–reduction cycling [45].

Highly efficient nanoresonators for the visible radiation are formed practically only from IB metals (Ag, Au, and Cu). Therefore, when one does not study adsorbate–adsorbent interactions (as in analytical applications), practically always nanoresonators from IB metals are used. However, in some cases, the problem to be solved is to identify species adsorbed on the surfaces of a specific metal (especially on surfaces of very important in catalysis VIII B metals), to determine their orientation with respect to the particular surface, and to observe how the strength of various chemical bonds changes upon this adsorption. In such cases nanoresonators formed from other metals (e.g., VIII B group) may be very useful, and hence, production of such nanoresonators is also of practical significance.

Various methods leading to the formation of nanoresonators from many VIII B group metals (Pt, Ru, Rh, Pd, Fe, Co, Ni) important in catalysis and their alloys have been developed by Tian et al. [49]. The produced nanoresonators are relatively efficient, for example, the surface enhancement factor for the Raman scattering can achieve even two to four orders of magnitude [49] (for comparison, the respective surface enhancement factor for the Raman scattering on the nanostructured silver is in the range from six to seven orders of magnitude [50]). In the majority of cases the roughening procedure is carried out electrochemically and consists of a number of rectangular oxidation–reduction cycles carried out in a $0.5 \text{ M H}_2\text{SO}_4$ aqueous solution. For example, to produce nanoresonators on the platinum surface, the Pt electrode has been cycled with the frequency of 1.5 kHz with upper and lower switching potentials of 2.4 V and -0.2 V for a period ranging from 5 s to 10 min [51]. The rhodium surface can be effectively roughened by applying a square-wave current of 1.6 A cm^{-2} and -0.95 A cm^{-2} at a frequency between 200 and 800 Hz for about 2 min [52]. Thereafter, the rhodium electrode should be held at 0.2 V until the completion of the surface electroreduction [52].

Electroplated Flat Surfaces

Nanoresonators from various metals can be also formed by the electrodeposition of metal films on flat surfaces. Contrary to the electrodeposition procedures typically used in the commercial electroplating, in which one is trying to obtain a coherent and smooth metal coating, formation of metal island films or dendrite-like structures is preferred during the production of nanoresonators. Synthesis of nanoresonators using electroplating has been carried out for various metals using many different procedures. Below some examples of procedures applied for the most widely used metals are presented.

Oriňáková et al. studied morphological and electromagnetic properties of silver films deposited on the stainless steel from an electrolyte containing 0.01 M AgNO₃, 0.1 M KNO₃, and 0.1 M KCN (pH = 10.25) by the electrochemical cycling between -700 and -1550 mV (versus Ag/AgCl/ 3 M KCl) [53]. They found that the morphology and the electromagnetic properties of the formed silver nanostructures significantly depend on the number of deposition cycles and the potential scan rate [53]. An increase in both size and density of the Ag nanoparticles with increasing number of deposition cycles was observed. A decrease in size and aggregation ability of Ag nanoparticles and clusters, resulting in lower coverage of the working electrode, was registered with an increase in potential scan rate. The optimal “electromagnetic” properties of Ag films deposited at the experimental conditions used were obtained for 30 scans at the scan rate of 100 mV s⁻¹ [53].

An interesting approach for the electrochemical formation of silver nanoresonators was developed by Liu et al. [54]. In the first stage of the synthesis, Liu et al. deposited silver clusters on the surface of the electrode by immersing of the electrode in the aqueous colloidal suspension of silver nanoparticles [54]. Then the electrochemical deposition of silver was carried out at room temperature under current density of 5 μA cm⁻² from the solution containing AgNO₃ and polyvinylpyrrolidone [54]. Just formed silver film is composed of relatively large nanoplates (several tens to several hundred of nanometers in dimension) [54]. The density of nanoplates covering on the substrate can be controlled by adjusting the amounts of seed. All the nanoplates are distributed on the substrate uniformly even at very high density. Such Ag nanostructured surfaces show high SERS activity and hence are suitable materials for the microdetection devices based on the SERS effect.

Formation of copper nanostructured films by the electrodeposition of copper on the platinum electrodes from acidic and ammonia bath was recently investigated by Cejkova et al. [55]. These investigations show that even small modification of the deposition procedure (such as the bath compositions, applied current densities, and the duration of individual steps) may cause large differences in the morphology of the formed nanoparticles and in the efficiency of obtained structures to locally concentrate the energy of the incident electromagnetic wave – this property was tested by the measurement of the surface enhancement of the Raman signal [55]. Cejkova et al. found that good surface enhancement of the efficiency of Raman scattering

can be achieved on the copper substrates prepared by the electrochemical deposition from ammonia baths. Copper nanoresonators fabricated from acidic baths are significantly less efficient. The results of microscopic measurements demonstrated that the average surface roughness does not play a substantial role, whereas the shape of the surface nanostructures is a key parameter [55].

Gold nanostructured surfaces are also important from the practical point of view. Comparison of many different methods of the formation of such nanostructures has been recently carried out by Kim et al. [42]. This group compared gold surfaces prepared by five different procedures: (i) a standard electrochemical oxidation–reduction cycling in a 0.1 M KCl aqueous solution, (ii) dealloying of Ag from Ag/Au alloy, (iii) electrochemical deposition of nanopikes, (iv) electrochemical deposition of nanoplates, and (v) electrochemical formation of dendritic rod surfaces [42]. Morphologies of compared gold nanostructures are shown on Fig. 3. Dendritic rod surfaces were produced by a simple one-step electrodeposition at -0.85 V from a solution containing 36 mM Au(I) ions complexed with sulfite anions; the total deposition charge density was 0.45 C cm $^{-2}$ [42, 56, 57]. Nanospike Au surfaces were electrodeposited at 0.05 V with a deposition charge density of 0.31 C cm $^{-2}$ from a solution containing 7 mM HAuCl $_4$ and 0.5 mM Pb(CH $_3$ COO) $_2$ [42, 58]. Nanoplate Au surfaces were electrodeposited at -1.1 V from a solution containing 15 mM KAu(CN) $_2$ and 0.25 M Na $_2$ CO $_3$, with a deposition charge density of 0.61 C cm $^{-2}$ [42, 59]. All mentioned above potential values are given versus Ag/AgCl/ 3 M KCl reference electrode. Comparison of SERS activities between all described above nanostructured Au surfaces revealed that the highest electromagnetic enhancement factors are achieved using gold dendritic rod surfaces and that the highly faceted sharp edge sites play a critical role in inducing high SERS activity of Au surfaces [42]. Some other types of Au nanostructures are also used practically. For example, Duan et al. reported that very promising electromagnetic properties revealed flowerlike gold nanoarchitectures [60] formed by the gold electrochemical deposition. Deposition of flowerlike gold nanostructures may be carried out at the cathodic current density of 0.25 mA cm $^{-2}$ from solution containing 25 mM HAuCl $_4$ and 20 g dm $^{-3}$ polyvinylpyrrolidone [60].

In some cases nanoresonators are also fabricated by the electrodeposition of the platinum group metals. For example, Pt nanoresonators may be obtained by the electrodeposition of platinum carried out from 0.06 M H $_2$ PtCl $_6$ aqueous solution using current density of ca. 5 mA cm $^{-2}$ for a period of 20 s to 2 min [51]. Relatively similar methods may be used to form nanoresonators from ruthenium, rhodium, and palladium. Nanostructured films from these metals have been formed by the electrochemical potentiostatic deposition from solutions containing 0.01 M RuCl $_3$, RhCl $_3$, and PdCl $_2$, respectively, in which 0.1 M KCl has been added as the supporting electrolyte [61]. For the electrodeposition of nanostructured metal films, the electrode has been held at -0.8 V for 10 min for Ru, at -0.4 V for 5 min for Rh, and at -0.2 V for 5 min for Pd, respectively (all potentials are quoted versus saturated calomel electrode) [61].

Metal Nanostructures Synthesized Using Templates

For some (mainly analytical) applications, very high reproducibility of nanostructured surfaces is required. Therefore, the auxiliary templates from other materials are sometimes used to improve reproducibility of the obtained metal nanoresonators. Generally, in the first step of the template-assisted synthesis of nanoresonators, the substrate, on which metal clusters will be deposited, is regularly nanostructured. Such nanostructuring may be obtained by the regular covering (shielding) of some parts of the substrate (e.g., by the monolayer of nanospheres or by a thin film with regularly distributed hollows), or the material of the substrate is itself chemically nanostructured. In the next step, the metal that supports surface plasmon resonance is deposited on such nanostructured substrate. The synthesis of nanoresonators may be finished at this stage (in such a case the auxiliary nanostructured features are remaining in the obtained composite material). However, the auxiliary nanostructures may also be removed after deposition of the metal supporting surface plasmon resonance.

The simplest method of the template-assisted formation of electromagnetic nanoresonators is deposition of metal that supports surface plasmon resonance on the regularly nanostructured substrate. Many groups use as reproducibly nanostructured substrates Ti or Al electrodes on which tubular arrays of oxides nanotubes are formed [62–68]. For example, Janik-Czachor et al. produced tubular arrays of TiO_2 or Al_2O_3 nanotubes with different diameters and deposited Ag, Au, or Cu clusters on them (see Fig. 4) [62–65]. The nanotubes were fabricated by the electrochemical anodization (oxidation) of Ti or Al electrodes. In the case of Ti, the anodization was performed in the mixture of aqueous solution of NH_4F and glycerol with applied voltage in the range 10–25 V [62–65]. The aluminum oxide nanotubes were fabricated by the electrochemical oxidation of Al samples at a constant voltage of 15 V in a mixture of aqueous solutions of $(\text{NH}_4)_2\text{SO}_4$ and NH_4F [65]. Janik-Czachor et al. found that when metal clusters were deposited on the nanotubes with very low diameter (below 50 nm), the just formed nanoresonators are significantly more reproducible and active than nanoresonators formed by the standard method of the electrochemical roughening of metal electrodes [65]. Moreover, deposition of metal clusters on different substrates may induce changes in their electronic structure, which influence many important properties of metal nanoparticles [64].

The most typical example of the electrochemical synthesis of metal nanostructures using an auxiliary template, which is removed after deposition of the metal layer, is fabrication of regularly arranged metal nanoparticles by the so-called template-defined electrochemical deposition [43, 69]. In this case, the close-packed monolayer of monodispersed spheres is used as a template [43, 69]. Figure 5b–d shows nanostructured surfaces prepared by the gold electrodeposition through such close-packed monolayer of polystyrene spheres with the diameters of 600 nm assembled onto evaporated gold electrodes [43]. The thickness of the electrodeposited film was controlled by varying the charge passed and was in the range of 150–460 nm. After gold electrodeposition the polystyrene was removed to leave the thin structured gold films containing a regular hexagonal array of uniform segment

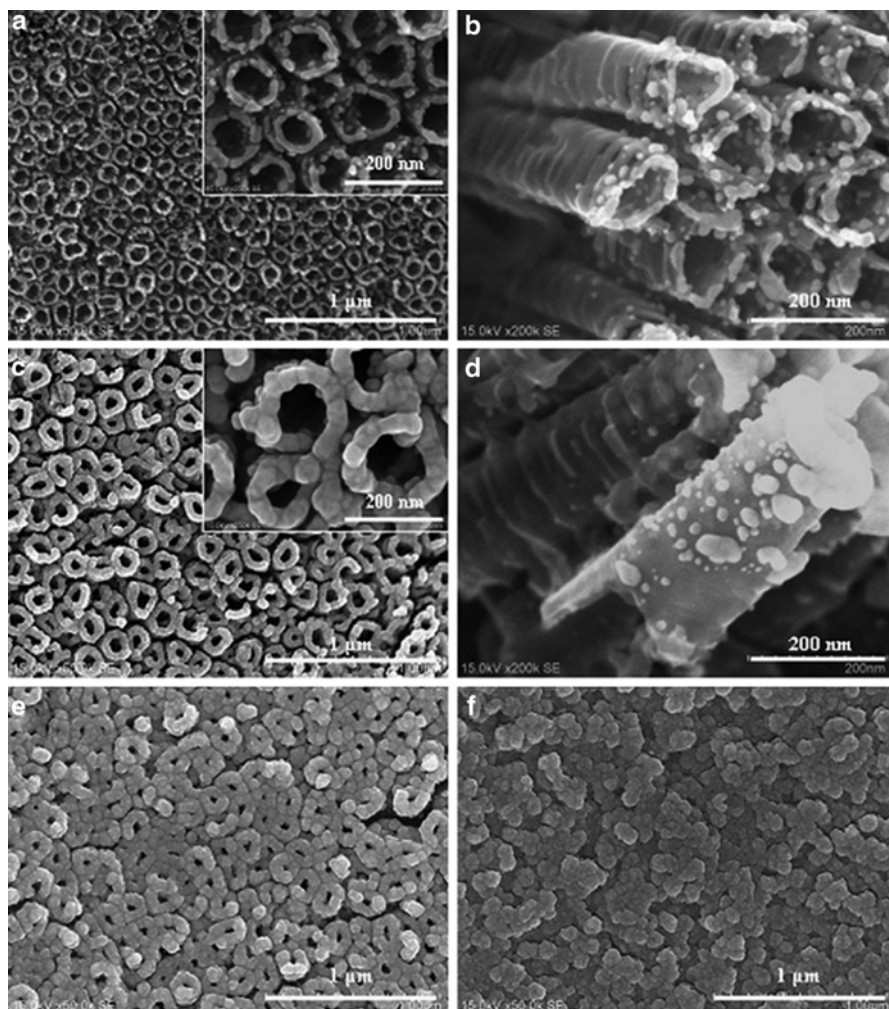


Fig. 4 Scanning electron microscopic (SEM) images of a TiO_2 nanotube layer covered with different amounts of silver. (**a, b**) 0.01 mg cm^{-2} of Ag, (**c, d**) 0.06 mg cm^{-2} of Ag, (**e**) 0.09 mg cm^{-2} of Ag, and (**f**) 0.2 mg cm^{-2} of Ag (Reprinted from [65] with permission from Elsevier)

sphere voids [43]. The procedures of the electrochemical deposition of other metals (silver, copper, and platinum) on the surface of the electrode covered by the monolayer of nanospheres may be found, for example, in Yang et al. [69]. Nanostructured substrates obtained by the template-defined electrochemical deposition are stable, reusable, and very reproducible [43].

Interesting modification of the described-above nanoshell-controlled deposition of regular metal nanostructures is using a template which itself is obtained electrochemically [70]. For example, Kondo et al. prepared ordered gold

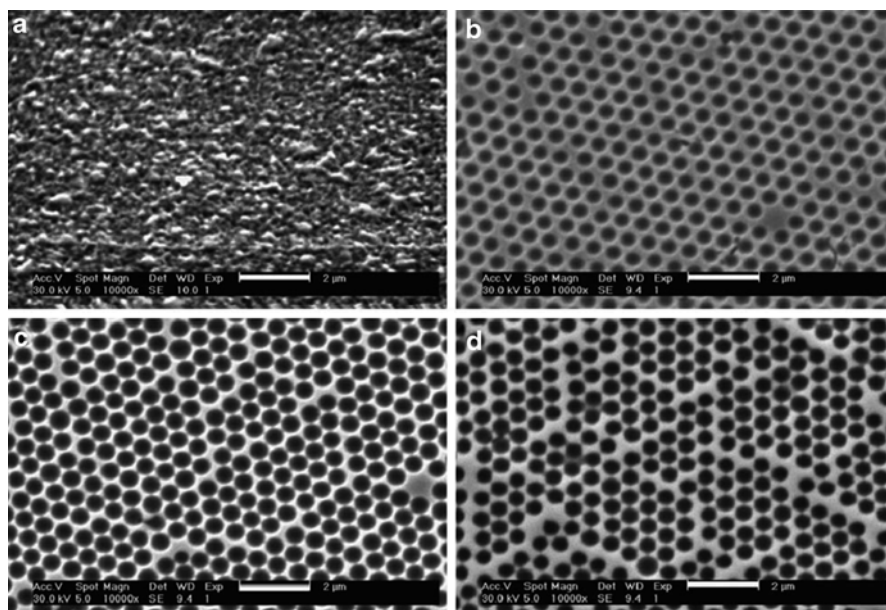


Fig. 5 Scanning electron microscopic (SEM) images of (a) gold electrode prepared by a standard electrochemical oxidation–reduction cycling in a 0.1 M KCl solution and (b–d) gold surfaces nanostructured by the so-called template-defined electrochemical deposition. The structured gold surfaces were produced using 600 nm diameter template spheres and have thicknesses of (b) 150 nm, (c) 260 nm, and (d) 460 nm, respectively. The scale bar is 2 μm in each case (Reprinted from [43] with permission from Elsevier)





nanodot arrays by the gold deposition through the alumina mask with regularly arranged through holes. The alumina mask has been prepared by the anodization of Al in acidic solution (as mentioned above, the array of Al_2O_3 nanotubes is formed in this condition). Then, Al substrate, on which Al_2O_3 nanotubes have been formed, is selectively dissolved in saturated I_2 methanol solution followed by the dissolution of the bottom part of the porous alumina films in phosphoric acid solution [70].

Electrochemically formed thick nanotube Al_2O_3 or TiO_2 layers may be also used as templates to form some metals into electromagnetic nanoresonators in the form of nanowires. For example, Joo and Suh reported formation of Ag nanoresonators by the electrochemical deposition of silver from solution containing silver nitrate and boric acid in the aluminum oxide nanotemplates and then by the subsequent removal of the auxiliary oxide layer [71]. Joo and Suh showed that using nanotemplates results in very good control over the size and dispersion of formed Ag nanoparticles [71]. Further investigations show that such a procedure of the formation of electromagnetic nanoresonators is very effective for the transition metals [49].

Electromagnetic Nanoresonators Covered by a Thin Layer of Other Metals

Important limitation in a wider application of optical nanoresonators for surface investigations is the restriction of the materials from which very efficient nanoresonators may be formed to the IB metals (Ag, Au, and Cu) [1, 50]. As already mentioned, the construction of nanoresonators from other metals (including commercially very important platinum group metals) is also possible, but the achieved enhancement factors of the electromagnetic field are significantly smaller [49, 72, 73]. Interesting strategy to overcome this problem was proposed by Fleischmann et al. who coated nanostructured Ag and Au surfaces with thin films of other metals [74, 75]. Using such substrates Fleischmann et al. recorded SERS spectra characteristic for adsorbates interacting with a thin layer of electrochemically deposited metal [74, 75]. This approach was further improved for the Pt group metals by Weaver et al., who proposed using ultrathin (2–5 monolayer) pinhole-free electrodeposits of such metals on mildly nanostructured gold surfaces [76, 77]. The initially developed method of the preparation of transition-metal overlayers on nanostructured gold involved constant-potential cathodic electrodeposition from dilute (ca. 0.1–0.5 mM) metal salt solution in aqueous HClO_4 [76, 77]. For example, 2-monolayer Pd film may be formed on the gold surface by Pd cathodic deposition from 5 mM PdCl_2 in 0.1 M HClO_4 solution (current density was 0.08 mA cm^{-2} for 12 s) [78]. Similar procedure (using 5 mM RhCl_3 instead of PdCl_2) was applied with comparable success to prepare rhodium films [78]. Further investigations showed that more uniform layers from platinum group metals (Pt, Pd, Rh, and Ir) may be

Table 2 A schematic illustration of electrochemically nanostructured metal surfaces typically used for plasmonic applications

Electrochemically roughened electrodes	
Electroplated flat surfaces	
Nanostructures synthesized using templates	
Electromagnetic nanoresonators covered by a thin layer of other metals	

formed using spontaneous redox replacement of an underpotential-deposited (upd) auxiliary copper or lead monolayer with a Pt group metal cations [79]. To prepare upd copper monolayer the nanostructured gold electrode was immersed in 1 mM $\text{CuSO}_4 + 0.1 \text{ M H}_2\text{SO}_4$ solution. Then the electrode was immersed in this solution at a potential just above $\sim 0.01 \text{ V}$ where bulk Cu deposition commences, to ensure full monolayer coverage, and was then transferred to a deaerated solution containing the transition-metal cation of interest (typically 5 mM Pt or Pd salt in 0.1 M HClO_4). Just formed (< 2 monolayers) Pt or Pd films displayed pinhole-free characteristics [67]. In the case of rhodium and iridium films, significant improvement of their properties was observed when an auxiliary upd Pb monolayer was used instead of a upd Cu monolayer [79].

A schematic comparison of all nanostructured metal surfaces described in section “[Surfaces Containing a Large Number of Electromagnetic Nanoresonators](#)” is shown in Table 2.

Single Active-Site Nanoresonators

The previous section “[Surfaces Containing a Large Number of Electromagnetic Nanoresonators](#)” presents electrochemical formation of nanostructures containing many places in which energy of the incident electromagnetic radiation is concentrated. However, for some purposes nanoresonators containing only one active area (as sharp metallic tips) are required. The first practical application of the one “hot spot” nanoresonator was independently demonstrated by Zenobi et al. [34] and Anderson [35]. They showed that when a fine tip made of a metal that supports surface plasmon resonances is brought within a nanometer range to a sample, a strong enhancement of Raman signal from molecules being in the close proximity to the tip is observed. This spectroscopic–microscopic tool, the so-called tip-enhanced Raman spectroscopy (TERS), can be used for molecular analysis with excellent spatial resolution, only limited by the tip apex size and shape. Further investigations showed that tips made of metals that support surface plasmon resonance may be also used to enhance locally other optical processes, such as second harmonic generation [80, 81], coherent anti-Stokes Raman scattering [82, 83], fluorescence [84], or infrared adsorption [85]. Production of suitable tips (nanoresonators) is a key issue in these spectroscopic–microscopic measurements.

Usually “single hot spot” nanoresonators used for the local concentration of the electromagnetic radiation are made of gold. Sharp gold tips have many important applications; therefore, even before they have been applied for the “tip-enhanced” spectroscopic–microscopic measurements, various groups have developed different methods of their preparation. For example, gold tips have been fabricated by etching the gold wire in a CaCl_2 solution of 10–50 % saturation at the etching voltage of 30 V [86], etching the gold wire in a 3 M NaCl and KCl solution at 10 V [87], or etching the gold wire in a 0.8 M KCN solution at the etching voltage of 12 V [88]. Abbou et al. developed a simple method to produce gold tips to be used as

an ultramicroelectrode [89]. They etched a gold wire for about 2 min at 7 V in a mixture of saturated CaCl_2 , water, and ethanol in a proportion of 2:8:1 [89].

The first work aimed on the preparation of gold tips optimized for the plasmonic applications was published by Ren et al. in 2004 [90]. In this contribution Ren et al. proposed a method for the production of gold tips with the tip apex radius lower than 30 nm by the direct current electrochemical etching of the gold wire in the mixture of concentrated HCl and ethanol. The influence of the solution composition and the etching voltage on the surface structure and sharpness has been investigated [90]. Ren et al. found that a tip with a smooth surface can be obtained in a solution of equal content of hydrochloric acid and ethanol, while the tips obtained from solutions with significantly different contents of both compounds show grainy structures [90]. In the next contribution Ren et al. proposed improved procedure of the preparation of gold tips by using the etching current as ending point control [91]. This resulted in a significant increase of the success rate of the preparation of highly active nanoresonators to 90 % [91]. Many groups tested other electrolytes. For example, Gingery and Buhlmann reported producing of 15 nm gold tips using NaCl in a 1 % perchloric acid [92]. Williams and Roy etched gold wire in a 37 % fuming HCl acid using square pulses at 3 kHz (30 μs on and 300 μs off) with starting amplitude of 8 V and a dc offset of 500 mV [93]. Richards et al. proposed a method of fabricating smooth gold tips with a radius of curvature of ca. 40 nm and with an aspect ratio suitable for shear force measurement (see Fig. 6) by a single-step direct current electrochemical etch (at 2.4 V dc) in 1:1 mixture of 37 % fuming HCl acid and high-purity water [94]. Richards et al. found that replacement of the ethanol (previously used for preparation of Au tips for TERS experiments) with high-purity water yields tips with a smoother surface. Hommelhoff et al. prepared sharp gold tips with high surface quality by the electrochemical etching in 90 % saturated aqueous solution of KCl [95]. Radii of curvature of the formed tip lie in the range of 20–40 nm, and the surface roughness was measured to be less than 0.8 nm [95]. High-quality gold tips with smooth surface and a radius curvature of about 20 nm have been also formed by Xu et al. by a single-step constant current electrochemical etch in 1:1 mixture of 37 % concentrated HCl and ethanol [96].

Tips for AFM/STM microscopic–optical spectroscopic measurements have been also formed from other metals supporting surface plasmon resonance, especially from silver. For example, silver tips for local Raman measurements may be formed by etching of a silver wire in a mixture (from 1:1 to 1:4) of concentrated HClO_4 and methanol at an anodic voltage between 1.6 and 8 V [97–100]. Local enhancement of the electromagnetic field caused by the Ag tip is usually stronger than that caused by the Au tip; however, due to the oxidation when exposed to air, Ag tips often lose enhancement effects after 2 or 3 days [101]. Moreover, when illuminated with the intensive laser radiation, the shape of the Ag tips changes due to the significant temperature increase, which causes that some Ag tips lost their strong “plasmonic activity” within just a few minutes [102]. Therefore, the majority of the optical spectroscopic–STM microscopic measurements are still carried out with gold tips.

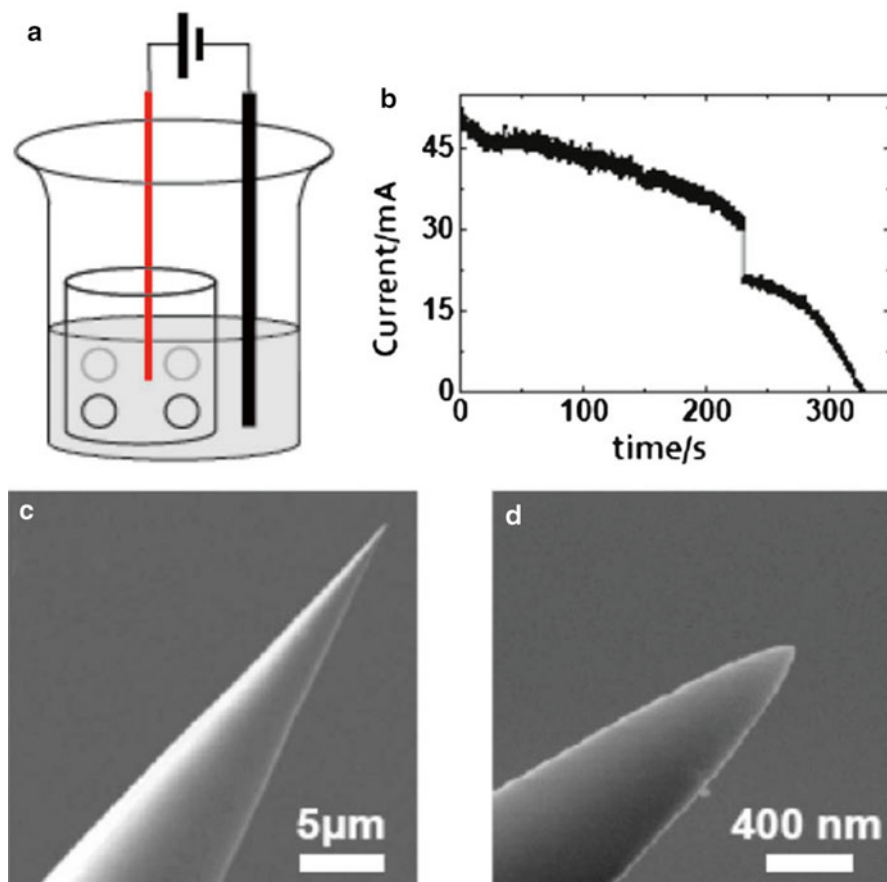


Fig. 6 (a) Schematic diagram of the experimental setup used for the fabrication of smooth gold tips. (b) Typical current–time etch curve obtained in a 1:1 mixture of 37 % fuming HCl acid and water at the etching voltage of 2.4 V dc. (c, d) Scanning electron microscopic (SEM) images of an etched Au tip, indicating an apex of ca. 50 nm (Reprinted with permission from [94]. Copyright 2009 American Institute of Physics)

Conclusions

Discovering in 1970s that the efficiency of Raman scattering for molecules placed in the optical energy concentrators (nanoresonators) may be increased by six to seven orders of magnitude launched intensive research aimed at the production of efficient electromagnetic nanoresonators. Further investigations showed that the electromagnetic nanoresonators may also be used to enhance significantly the surface sensitivity of several other spectroscopic measurements (especially infrared absorption), which initialized development of the electromagnetic nanoresonators

optimized for other regions of the electromagnetic radiation. The spectroscopic technique which gains the most due to the application of metal electromagnetic nanoresonators is still, however, Raman spectroscopy, from which the great success of nanoresonator-enhanced surface measurements started. As mentioned in the “Introduction,” the efficiency of generation of Raman signal for molecules placed in the electromagnetic nanoresonators is in some cases so high that it is possible to observe Raman spectrum even of a single molecule [29–31]. For a large system, a single analyte molecule would seldom be adsorbed at the highly active part of the resonator; therefore “simple” single-molecule Raman spectroscopy cannot be treated as a reliable analytical technique (Raman signal from a single molecule reveals strong temporal fluctuations and is not reproducible). However, for some analytes, even when only about 50–100 analyte molecules are contained in the sample, reproducible nanoresonator-enhanced Raman signal can be measured. Therefore, SERS is one of the most sensitive analytical tools with the limit of detection for some analytes of the order of 10^{-18} mol dm⁻³ [50]. Due to large practical significance of nanoresonators, chemically stable gold surfaces nanostructured specifically to form efficient electromagnetic nanoresonators are already available commercially [103].

As mentioned in the section “Surfaces Containing a Large Number of Electromagnetic Nanoresonators,” the first practical application of electromagnetic nanoresonators has been realized for nanoresonators formed electrochemically [17]. Although also other methods of the production of electromagnetic nanoresonators have been developed, electrochemical nanostructuring of metal surfaces is still very often used to prepare electromagnetic nanoresonators. The aim of this chapter was to present an overview of various methods typically used for the formation of both the single active-site nanoresonators and nanostructured surfaces containing a large number of places where the optical energy is concentrated. We hope that this short review should help researchers, who are interested in carrying out nanoresonators-enhanced surface spectroscopic measurements, to find a method of the formation of nanoresonators which will be the most suitable for their system.

References

1. Aroca R (2006) Surface-enhanced vibrational spectroscopy. Wiley, Chichester
2. Etchegoin PG, Le Ru EC (2011) Basic electromagnetic theory of SERS. In: Schlücker S (ed) Surface enhanced Raman spectroscopy: analytical, biophysical and life science applications. Wiley-VCH, New York, pp 1–37
3. Bailo E, Deckert V (2008) Tip-enhanced Raman scattering. *Chem Soc Rev* 37:921–930
4. Kottmann JP, Martin OJF, Smith DR, Schultz S (2001) Dramatic localized electromagnetic enhancement in plasmon resonant nanowires. *Chem Phys Lett* 341:1–6
5. Xu H, Bjerneld EJ, Käll M, Börjesson L (1999) Spectroscopy of single hemoglobin molecules by surface enhanced Raman scattering. *Phys Rev Lett* 83:4357–4360
6. Pompa PP, Martiradonna L, Della Torre A, Della-Sala F, Manna L, De Vittorio M, Calabi F, Cingolani R, Rinaldi R (2006) Metal-enhanced fluorescence of colloidal nanocrystals with nanoscale control. *Nat Nanotechnol* 1:126–130

7. Song JH, Atay T, Shi S, Urabe H, Nurmikko AV (2005) Large enhancement of fluorescence efficiency from CdSe/ZnS quantum dots induced by resonant coupling to spatially controlled surface plasmons. *Nano Lett* 5:1557–1561
8. Stranik O, McEvoy HM, McDonagh C, MacCraith BD (2005) Plasmonic enhancement of fluorescence for sensor applications. *Sens Actuators B* 107:148–153
9. Yu F, Yao D, Knoll W (2003) Surface plasmon field-enhanced fluorescence spectroscopy studies of the interaction between an antibody and its surface-coupled antigen. *Anal Chem* 75:2610–2617
10. Neumann T, Johansson ML, Kambhampati D, Knoll W (2002) Surface-plasmon fluorescence spectroscopy. *Adv Funct Mater* 12:575–586
11. Aslan K, Gryczynski I, Malicka J, Matveeva E, Lakowicz JR, Geddes CD (2005) Metal-enhanced fluorescence: an emerging tool in biotechnology. *Curr Opin Biotechnol* 16:55–62
12. Touahir L, Jenkins ATA, Boukherroub R, Gouget-Laemmel AC, Chazalviel JN, Peretti J, Ozanam F, Szunerits S (2010) Surface plasmon-enhanced fluorescence spectroscopy on silver based SPR substrates. *J Phys Chem C* 114:22582–22589
13. Imae T, Torii H (2000) In situ investigation of molecular adsorption on Au surface by surface-enhanced infrared absorption spectroscopy. *J Phys Chem B* 104:9218–9224
14. Brolo AG, Germain P, Hager G (2002) Investigation of the adsorption of L-cysteine on a polycrystalline silver electrode by surface-enhanced Raman scattering (SERS) and surface-enhanced second harmonic generation (SESHG). *J Phys Chem B* 106:5982–5987
15. Addison CJ, Konorov SO, Brolo AG, Blades MW, Turner RFB (2009) Tuning gold nanoparticle self-assembly for optimum coherent anti-Stokes Raman scattering and second harmonic generation response. *J Phys Chem C* 113:3586–3592
16. Park B, Kim MS, Kim YD, Jung EC, Jung CS (1993) Charge-transfer effect on surface-enhanced second-harmonic generation. *J Phys Chem* 97:5080–5084
17. Fleischmann M, Hendra PJ, McQuillam AJ (1974) Raman spectra of pyridine adsorbed at a silver electrode. *Chem Phys Lett* 26:163–166
18. Faulds K, Barbagallo RP, Keer JT, Smith WE, Graham D (2004) SERRS as a more sensitive technique for the detection of labelled oligonucleotides compared to fluorescence. *Analyst* 129:567–568
19. Maher RC, Cohen LF, Etchegoin P (2002) Single molecule photo-bleaching observed by surface enhanced resonant Raman scattering (SERRS). *Chem Phys Lett* 352:378–384
20. Li WH, Li XY, Yu NT (1999) Surface-enhanced hyper-Raman spectroscopy (SEHRS) and surface-enhanced Raman spectroscopy (SERS) studies of pyrazine and pyridine adsorbed on silver electrodes. *Chem Phys Lett* 305:303–310
21. Hulteen JC, Young MA, Van Duyne RP (2006) Surface-enhanced hyper-Raman scattering (SEHRS) on Ag film over nanosphere (FON) electrodes: surface symmetry of centrosymmetric adsorbates. *Langmuir* 22:10354–10364
22. Leng W, Kelley AM (2006) Surface-enhanced hyper-Raman spectra and enhancement factors for three SERS chromophores. SEHRS spectra on Ag films at pulse energies below 2 pJ. *J Am Chem Soc* 128:3492–3493
23. Milojevich CB, Silverstein DW, Jensen L, Camden JP (2013) Surface-enhanced hyper-Raman scattering elucidates the two-photon absorption spectrum of rhodamine 6G. *J Phys Chem C* 117:3046–3054
24. Osińska K, Pecul M, Kudelski A (2010) Circularly polarized component in surface-enhanced Raman spectra. *Chem Phys Lett* 496:86–90
25. Kneipp H, Kneipp J, Kneipp K (2006) Surface-enhanced Raman optical activity on adenine in silver colloidal solution. *Anal Chem* 78:1363–1366
26. Steuwe C, Kaminski CF, Baumberg JJ, Mahajan S (2011) Surface enhanced coherent anti-Stokes Raman scattering on nanostructured gold surfaces. *Nano Lett* 11:5339–5343
27. Kim H, Taggart DK, Xiang C, Penner RM, Potma EO (2008) Spatial control of coherent anti-Stokes emission with height-modulated gold zig-zag nanowires. *Nano Lett* 8:2373–2377
28. Nambodiri V, Nambodiri M, Cava Diaz GI, Oppermann M, Flachenecker G (2011) Surface-enhanced femtosecond CARS spectroscopy (SE-CARS) on pyridine. *Vib Spectrosc* 56:9–12

29. Kneipp K, Wang Y, Kneipp H, Perelman LT, Itzkan I, Dasari RR, Feld MS (1997) Single molecule detection using surface-enhanced Raman scattering (SERS). *Phys Rev Lett* 78:1667–1670
30. Nie S, Emory SR (1997) Probing single molecules and single nanoparticles by surface-enhanced Raman scattering. *Science* 275:1102–1106
31. Michaels AM, Nirmal M, Brus LE (1999) Surface enhanced Raman spectroscopy of individual rhodamine 6G molecules on large Ag nanocrystals. *J Am Chem Soc* 121:9932–9939
32. Jeanmaire DL, Van Duyne RP (1977) Surface Raman spectroelectrochemistry: part I. Heterocyclic, aromatic, and aliphatic amines adsorbed on the anodized silver electrode. *J Electroanal Chem* 84:1–20
33. Albrecht MG, Creighton JA (1977) Anomalously intense Raman spectra of pyridine at a silver electrode. *J Am Chem Soc* 99:5215–5217
34. Stockle RM, Suh YD, Deckert V, Zenobi R (2000) Nanoscale chemical analysis by tip-enhanced Raman spectroscopy. *Chem Phys Lett* 318:131–136
35. Anderson MS (2000) Locally enhanced Raman spectroscopy with an atomic force microscope. *Appl Phys Lett* 76:3130–3132
36. Kruszewski S, Skonieczny J (1993) Influence of atomic- and micro-roughness variations on the surface enhanced Raman scattering signal. *Opt Appl* 23:51–60
37. Kruszewski S (1994) Dependence of SERS signal on surface roughness. *Surf Interface Anal* 21:830–838
38. Brolo AG, Sanderson AC (2004) Surface-enhanced Raman scattering (SERS) from a silver electrode modified with oxazine 720. *Can J Chem* 82:1474–1480
39. Bryant MA, Pemberton JE (1991) Surface Raman scattering of self-assembled monolayers formed from 1-alkanethiols at Ag. *J Am Chem Soc* 113:3629–3637
40. Michota A, Kudelski A, Bukowska J (2000) Chemisorption of cysteamine on silver studied by surface-enhanced Raman scattering. *Langmuir* 16:10236–10242
41. Kudelski A (2003) Structures of monolayers formed from different HS-(CH₂)₂-X thiols on gold, silver and copper: comparative studies by surface-enhanced Raman scattering. *J Raman Spectrosc* 34:853–862
42. Choi S, Ahn M, Kim J (2013) Highly reproducible surface-enhanced Raman scattering-active Au nanostructures prepared by simple electrodeposition: origin of surface-enhanced Raman scattering activity and applications as electrochemical substrates. *Anal Chim Acta* 779:1–7
43. Abdelsalam ME, Bartlett PN, Baumberg JJ, Cintra S, Kelf TA, Russell AE (2005) Electrochemical SERS at a structured gold surface. *Electrochem Commun* 7:740–744
44. Chase B, Parkinson B (1991) A study of the wavelength and potential dependence of surface enhanced Raman scattering on Cu, Ag, and Au electrodes. *J Phys Chem* 95:7810–7813
45. Kudelski A, Bukowska J, Janik-Czachor M, Grochala W, Szummer A, Dolata A (1998) Characterization of the copper surface optimized for use as a substrate for surface-enhanced Raman scattering. *Vib Spectrosc* 16:21–29
46. Kudelski A, Bukowska J (1996) Temporal evolution of Raman intensities on surface-enhanced Raman scattering active copper and gold electrodes at negative potentials. *Vib Spectrosc* 10:335–339
47. Irish DE, Stolberg L, Shoesmith DW (1985) Surface enhanced Raman spectroscopy and electrochemistry at the copper/iodide, water interface. *Surf Sci* 158:238–253
48. Rubim JC, Gutz IGR, Sala O (1984) Surface-enhanced Raman scattering (SERS) and fluorescence spectra from mixed copper(I)/pyridine/iodide complexes on a copper electrode. *Chem Phys Lett* 111:117–122
49. Tian ZQ, Ren B, Wu DY (2002) Surface-enhanced Raman scattering: from noble to transition metals and from rough surfaces to ordered nanostructures. *J Phys Chem B* 106:9463–9483
50. Kudelski A (2008) Analytical applications of Raman spectroscopy. *Talanta* 76:1–8
51. Cai WB, Ren B, Li XQ, She CX, Liu FM, Cai XW, Tian ZQ (1998) Investigation of surface-enhanced Raman scattering from platinum electrodes using a confocal Raman microscope: dependence of surface roughening pretreatment. *Surf Sci* 406:9–22

52. Tian ZQ, Yang ZL, Ren B, Li JF, Zhang Y, Lin XF, Hu JW, Wu DY (2006) Surface-enhanced Raman scattering from transition metals with special surface morphology and nanoparticle shape. *Faraday Discuss* 132:159–170
53. Oriňáková R, Škantárová L, Oriňák A, Demko J, Kupková M, Andersson JT (2013) Electrochemical deposition of SERS active nanostructured silver films. *Int J Electrochem Sci* 8:80–99
54. Liu G, Duan G, Jia L, Wang J, Wang H, Cai W, Li Y (2013) Fabrication of self-standing silver nanoplate arrays by seed-decorated electrochemical route and their structure-induced properties. *J Nanomater* 2013:365947
55. Cejkova J, Prokopec V, Brazdova S, Kokaislova A, Matejka P, Stepanek F (2009) Characterization of copper SERS-active substrates prepared by electrochemical deposition. *Appl Surf Sci* 255:7864–7870
56. Hyun M, Choi S, Lee YW, Kwon SH, Han SW, Kim J (2011) Simple electrodeposition of dendritic Au rods from sulfite-based Au(I) electrolytes with high electrocatalytic and SERS Activities. *Electroanalysis* 23:2030–2035
57. Ahn M, Kim J (2012) Electrochemical behavior of dopamine and ascorbic acid at dendritic Au rod surfaces: selective detection of dopamine in the presence of high concentration of ascorbic acid. *J Electroanal Chem* 683:75–79
58. Plowman B, Ippolito SJ, Bansal V, Sabri YM, O'Mullane AP, Bhargava SK (2009) Gold nanospikes formed through a simple electrochemical route with high electrocatalytic and surface enhanced Raman scattering activity. *Chem Commun* 2009:5039–5041
59. Seo B, Choi S, Kim J (2011) Simple electrochemical deposition of Au nanoplates from Au(I) cyanide complexes and their electrocatalytic activities. *ACS Appl Mater Interfaces* 3:441–446
60. Duan G, Cai W, Luo Y, Li Z, Li Y (2006) Electrochemically induced flowerlike gold nanoarchitectures and their strong surface-enhanced Raman scattering effect. *Appl Phys Lett* 89:211905
61. Gao JS, Tian ZQ (1997) Surface Raman spectroscopic studies of ruthenium, rhodium and palladium electrodes deposited on glassy carbon substrates. *Spectrochim Acta A* 53:1595–1600
62. Roguska A, Kudelski A, Pisarek M, Opara M, Janik-Czachor M (2011) Surface-enhanced Raman scattering (SERS) activity of Ag, Au and Cu nanoclusters on TiO₂-nanotubes/Ti substrate. *Appl Surf Sci* 257:8182–8189
63. Roguska A, Pisarek M, Kudelski A, Lewandowska M, Kurzydłowski KJ, Janik-Czachor M (2009) In situ spectroelectrochemical surface-enhanced Raman scattering (SERS) investigations on composite Ag/TiO₂-nanotubes/Ti substrates. *Surf Sci* 603:2820–2824
64. Pisarek M, Roguska A, Kudelski A, Andrzejczuk M, Janik-Czachor M, Kurzydłowski KJ (2013) The role of Ag particles deposited on TiO₂ or Al₂O₃ self-organized nanoporous layers in their behavior as SERS-active and biomedical substrates. *Mater Chem Phys* 139:55–65
65. Roguska A, Kudelski A, Pisarek M, Opara M, Janik-Czachor M (2011) Raman investigations of SERS activity of Ag nanoclusters on a TiO₂-nanotubes/Ti substrate. *Vib Spectrosc* 55:38–43
66. Li X, Chen G, Yang L, Jin Z, Liu J (2010) Multifunctional Au-coated TiO₂ nanotube arrays as recyclable SERS substrates for multifold organic pollutants detection. *Adv Funct Mater* 20:2815–2824
67. Huang Y, Sun L, Xie K, Lai Y, Liu B, Ren B, Lin C (2011) SERS study of Ag nanoparticles electrodeposited on patterned TiO₂ nanotube films. *J Raman Spectrosc* 42:986–991
68. Chen Y, Tian G, Pan K, Tian C, Zhou J, Zhou W, Ren Z, Fu H (2012) In situ controlled growth of well-dispersed gold nanoparticles in TiO₂ nanotube arrays as recyclable substrates for surface-enhanced Raman scattering. *Dalton Trans* 41:1020–1026
69. Yang S, Lapsley MI, Cao B, Zhao C, Zhao Y, Hao Q, Kiraly B, Scott J, Li W, Wang L, Lei Y, Huang TJ (2013) Large-scale fabrication of three-dimensional surface patterns using template-defined electrochemical deposition. *Adv Funct Mater* 23:720–730

70. Kondo T, Matsumoto F, Nishio K, Masuda H (2008) Surface-enhanced Raman scattering on ordered gold nanodot arrays prepared from anodic porous alumina mask. *Chem Lett* 37:466–467
71. Joo Y, Suh JS (1995) SERS on silver formed in anodic aluminum oxide nanotemplates. *Bull Korean Chem Soc* 16:808–810
72. Tian N, Zhou ZY, Sun SG, Cui L, Ren B, Tian ZQ (2006) Electrochemical preparation of platinum nanothorn assemblies with high surface enhanced Raman scattering activity. *Chem Commun* 2006:4090–4092
73. Abdelsalam ME, Mahajan S, Bartlett PN, Baumberg JJ, Russell AE (2007) SERS at structured palladium and platinum surfaces. *J Am Chem Soc* 129:7399–7406
74. Fleischmann M, Tian ZQ, Li LJ (1987) Raman spectroscopy of adsorbates on thin film electrodes deposited on silver substrates. *J Electroanal Chem* 217:397–410
75. Mengoli G, Musiani MM, Fleischmann M, Mao BW, Tian ZQ (1987) Enhanced Raman scattering from iron electrodes. *Electrochim Acta* 32:1239–1245
76. Leung LWH, Weaver MJ (1987) Extending surface-enhanced Raman spectroscopy to transition-metal surfaces: carbon monoxide adsorption and electrooxidation on platinum- and palladium-coated gold electrodes. *J Am Chem Soc* 109:5113–5119
77. Leung LWH, Weaver MJ (1988) Adsorption and electrooxidation of carbon monoxide on rhodium- and ruthenium-coated gold electrodes as probed by surface-enhanced Raman spectroscopy. *Langmuir* 4:1076–1083
78. Zou S, Weaver MJ (1998) Surface-enhanced Raman scattering on uniform transition-metal films: toward a versatile adsorbate vibrational strategy for solid-nonvacuum interfaces? *Anal Chem* 70:2387–2395
79. Mrozek MF, Xie Y, Weaver MJ (2001) Surface-enhanced Raman scattering on uniform platinum-group overlayers: preparation by redox replacement of underpotential-deposited metals on gold. *Anal Chem* 73:5953–5960
80. Zayats AV, Sandoghdar V (2000) Apertureless scanning near-field second-harmonic microscopy. *Opt Commun* 178:245–249
81. Neacsu CC, van Aken BB, Fiebig M, Raschke MB (2009) Second-harmonic near-field imaging of ferroelectric domain structure of YMnO_3 . *Phys Rev B* 79:100107
82. Ichimura T, Hayazawa N, Hashimoto M, Inouye Y, Kawata S (2004) Tip-enhanced coherent anti-Stokes Raman scattering for vibrational nanoimaging. *Phys Rev Lett* 92:220801
83. Furusawa K, Hayazawa N, Catalan FC, Okamoto T, Kawata S (2012) Tip-enhanced broadband CARS spectroscopy and imaging using a photonic crystal fiber based broadband light source. *J Raman Spectrosc* 43:656–661
84. Hui YY, Lu YC, Su LJ, Fang CY, Hsu JH, Chang HC (2013) Tip-enhanced sub-diffraction fluorescence imaging of nitrogen-vacancy centers in nanodiamonds. *Appl Phys Lett* 102:013102
85. Huth F, Chuvilin A, Schnell M, Amenabar I, Krutokhvostov R, Lopatin S, Hillenbrand R (2013) Resonant antenna probes for tip-enhanced infrared near-field microscopy. *Nano Lett* 13:1065–1072
86. Melmed AJ (1991) The art and science and other aspects of making sharp tips. *J Vac Sci Technol B* 9:601–608
87. Ito T, Buehlmann P, Umezawa Y (1998) Scanning tunneling microscopy using chemically modified tips. *Anal Chem* 70:255–259
88. Baykul MC (2000) Preparation of sharp gold tips for STM by using electrochemical etching method. *Mater Sci Eng B* 74:229–233
89. Abbou J, Demaille C, Druet M, Moiroux J (2002) Fabrication of submicrometer-sized gold electrodes of controlled geometry for scanning electrochemical-atomic force microscopy. *Anal Chem* 74:6355–6363
90. Ren B, Picardi G, Pettinger B (2004) Preparation of gold tips suitable for tip-enhanced Raman spectroscopy and light emission by electrochemical etching. *Rev Sci Instrum* 75:837–841

91. Wang X, Liu Z, Zhuang MD, Zhang HM, Wang X, Xie ZX, Wu DY, Ren B, Tian ZQ (2007) Tip-enhanced Raman spectroscopy for investigating adsorbed species on a single-crystal surface using electrochemically prepared Au tips. *Appl Phys Lett* 91:101105
92. Gingery D, Buhlmann P (2007) Single-step electrochemical method for producing very sharp Au scanning tunneling microscopy tips. *Rev Sci Instrum* 78:113703
93. Williams C, Roy D (2008) Fabrication of gold tips suitable for tip-enhanced Raman spectroscopy. *J Vac Sci Technol B* 26:1761–1764
94. Eligal L, Culfaz F, McCaughan V, Cade NI, Richards D (2009) Etching gold tips suitable for tip-enhanced near-field optical microscopy. *Rev Sci Instrum* 80:033701
95. Eisele M, Krüger M, Schenk M, Ziegler A, Hommelhoff P (2011) Production of sharp gold tips with high surface quality. *Rev Sci Instrum* 82:026101
96. Xu G, Liu Z, Xu K, Zhang Y, Zhong H, Fan Y, Huang Z (2012) Constant current etching of gold tips suitable for tip-enhanced Raman spectroscopy. *Rev Sci Instrum* 83:103708
97. Zhang W, Yeo BS, Schmid T, Zenobi RJ (2007) Single molecule tip-enhanced Raman spectroscopy with silver tips. *J Phys Chem C* 111:1733–1738
98. Sonntag MD, Klingsporn JM, Garibay LK, Roberts JM, Dieringer JA, Seideman T, Scheidt KA, Jensen L, Schatz GC, Van Duyne RP (2012) Single-molecule tip-enhanced Raman spectroscopy. *J Phys Chem C* 116:478–483
99. Paulite M, Blum C, Schmid T, Opilik L, Eyer K, Walker GC, Zenobi R (2013) Full spectroscopic tip-enhanced Raman imaging of single nanotapes formed from β -amyloid(1–40) peptide fragments. *ACS Nano* 7:911–920
100. Stadler J, Schmid T, Zenobi R (2011) Nanoscale chemical imaging of single-layer graphene. *ACS Nano* 5:8442–8448
101. Yi KJ, He XN, Zhou YS, Xiong W, Lu YF (2008) Tip-enhanced near-field Raman spectroscopy with a scanning tunneling microscope and side-illumination optics. *Rev Sci Instrum* 79:073706
102. Zhang W, Schmid T, Yeo BS, Zenobi R (2008) Near-field heating, annealing, and signal loss in tip-enhanced Raman spectroscopy. *J Phys Chem C* 112:2104–2108
103. Vernon KC, Davis TJ, Scholes FH, Gómez DE, Lau D (2010) Physical mechanisms behind the SERS enhancement of pyramidal pit substrates. *J Raman Spectrosc* 41:1106–1111

Electrochemically Fabricated Nanostructures in Energy Storage and Conversion Applications

4

Kafil M. Razeeb, Maksudul Hasan, Mamun Jamal,
and Alan Mathewson

Contents

Introduction.....	72
Nanostructured Electrode Materials for Pseudocapacitor and Fuel Cell.....	73
Pseudocapacitor.....	73
Fuel Cells.....	74
Fabrication of the Electrode Materials.....	76
Synthesis of Coaxial Ni/NiO Nanowires for Pseudocapacitor.....	76
Synthesis of Core/Shell Ni/NiO/Pt NWA for Fuel Cell.....	76
Material Characterization.....	77
Electrochemical Characterization of Ni/NiO NWA for Supercapacitors.....	77
Electrochemical Characterization of Ni/NiO NWA/Pt for Fuel Cells.....	78
Results and Discussions.....	78
Elemental Characterization of the Electrodes.....	78
Electrochemical Characterization of the Electrodes.....	84
Conclusions.....	96
References.....	97

Abstract

In order to move away from the carbon-based energy technologies, electrochemical energy production and storage is under serious consideration as an alternative energy/power source. The future success of this global effort is under review, and researchers are looking forward to designing more sustainable

K.M. Razeeb (✉) • M. Hasan • M. Jamal • A. Mathewson
Tyndall National Institute, University College Cork, Cork, Ireland
e-mail: kafil.mahmood@tyndall.ie; maksudul.hasan@tyndall.ie; mamun.jamal@tyndall.ie;
alan.mathewson@tyndall.ie

and environmentally friendly electrochemical energy storage and conversion (EESC) systems. Electrochemical energy storage and conversion systems in the broadest sense have three variants: batteries, fuel cells, and electrochemical capacitors, also known as supercapacitors. The energy storage and conversion mechanisms in these three systems are different, but the energy – providing processes in these systems – all follow solid state and surface interface chemistry, taking place in active electrode materials and at the phase boundary of the electrode/electrolyte interface. Also, all three systems consist of two electrodes which are in contact with the electrolyte but separated by a membrane. Conventional materials used in these systems cannot meet the ever-increasing demand for energy. Thereby, designing efficient and miniaturized EESC devices that achieve high energy storage or delivery at high charge and discharge rates and with lifetimes capable of matching the specific requirements of applications is one of the major challenges facing today's research community.

Thereby, this chapter will review some of the recent developments (2010–2012) in the fabrication of nanostructured electrode materials by electrochemical methods and their application in the fuel cells and supercapacitors. Furthermore, novel nanowire-/nanoparticle-based electrodeposited nano-heterostructures (Armand M, Tarascon JM, *Nature* 451:652, 2008; Chmiola J, Largeot C, Taberna PL, Simon P, Gogotsi Y, *Science* 328:480, 2010; Tarascon JM, Armand M, *Nature* 414:359, 2001) and their advantages over conventional electrode materials will be discussed.

Keywords

Energy storage • Energy conversion • Nanowire • Supercapacitor • Fuel Cell

Introduction

1D nanowires represent an attractive architecture for electrochemical power applications owing to their novel anisotropic morphologies and self-supporting arrays grown directly on a current collector. Active materials structuring into 1D nanostructures offers short diffusion paths and large electrolyte contact area for ionic transport and electronic conduction which results in reduced internal resistance as well as longer durability and stability. Template-mediated fabrication is one attractive method for highly ordered array fabrication of nanowires on metallic current collector substrates. Furthermore, template-based electrodeposition is an easy and efficient technique for fabricating freestanding nanowires on any substrate that requires large surface area for electrochemical reactions. So, most of the discussion of this chapter is related to the usability of these freestanding nanowire arrays as electrode materials in supercapacitor (pseudocapacitor) and fuel cell applications.

Nanostructured Electrode Materials for Pseudocapacitor and Fuel Cell

Pseudocapacitor

Recently, electrochemical capacitors (ECs), also known as supercapacitors, have attracted considerable attention owing to their much higher power delivery or uptake ($>10 \text{ kW kg}^{-1}$) capability when compared to batteries ($<1 \text{ kW kg}^{-1}$ for Li-ion). The major challenges in designing an efficient and miniaturized electrochemical energy storage device are to achieve high energy storage and delivery at high charge/discharge rates, with lifetimes matching the specific requirements of applications [1–3]. The development of these high-performance supercapacitor devices is crucial for the powering of contemporary and future electronic systems. The application areas for these supercapacitors include multifunctional portable equipment, wireless sensor modules deployed in smart environments, hybrid electric vehicles (HEVs), and large industrial equipment. There are different types of electrochemical energy storage devices. Among them, pseudocapacitor is a particular type of supercapacitor where the charge is stored using Faradaic process through electron charge transfer between electrode and electrolyte. These supercapacitors are usually fabricated using nanostructured electrode materials, because the nanostructured pseudocapacitor electrodes are beneficial in asymmetric and/or hybrid configurations due to their high specific capacitance (F g^{-1}) and high volumetric capacitance (F cm^{-3}) that result from their high packing density and large active surface areas, respectively [4, 5]. Specifically, one-dimensional (1D) nanostructured materials, e.g., nanotubes (NTs) or nanowires (NWs), fabricated directly on to a substrate may eliminate the use of ancillary materials and increase the active surface area as well as the energy capacity of the electrodes. In recent years, there has been extensive research in developing alternative pseudocapacitor electrode materials, such as cobalt oxide [6], manganese oxide [7, 8], nickel hydroxide [9] and nickel oxide [10–13], either as porous and/or one-dimensional (1D) nanostructures. Due to its low cost, high specific capacitance, and good capacity retention, NiO is one of the most promising materials [4]. It is also environmentally friendly. Unfortunately, nickel oxide is an electrically poor conductive material (p-type semiconductor), and therefore, in order to improve the maximum utilization of NiO, the introduction of a conductive metal as a coaxial supporting structure is essential [14].

In recent work, NiO–TiO₂ nanotube (NT) arrays were created by electrochemical anodization of Ni–Ti alloy foils followed by thermal annealing (at 600 °C) where the Ti component in the foil was used as the core supporting structure [11]. However, achieving a high aspect ratio and porous nanostructures through the anodization of Ni–Ti foil is quite difficult, and the reported NT film thickness was only 200 nm to 500 nm (maximum aspect ratio is 13:1 with pore diameter of 38 nm) resulting in a film porosity of 49 %, where the capacitance was 4 mF cm^{-2} [11, 15]. Additionally, this alloy foil is quite expensive and requires long processing time and complicated processing steps to fabricate the final electrodes. In another approach, NiO nanorod

arrays were fabricated by thermal hydrolysis of a mixture of urea and nickel salts on a Ni foam substrate at 100 °C for 12 h followed by annealing at 250–400 °C for 3 h to facilitate NiO crystallization to be able to show pseudocapacitance [16]. Since simple and low-cost fabrication methods are always desired, hence, we have adopted a convenient method for the fabrication of the electrode by a simple electrodeposition of Ni NWs using template and controlled conversion of the deposited Ni NWs into Ni/NiO core/shell structure by low-power oxygen plasma annealing within a few minutes. The coaxial Ni/NiO NW arrays demonstrated an excellent capacity retention as well as high capacitance, both are important properties for supercapacitor applications [14].

Fuel Cells

In recent years, alkaline direct ethanol fuel cells (ADEFEC) have attracted increasing interest as an ideal power source [17–21] due to the relatively high energy densities that can be achieved (8.1 kW/kg vs. 6.1 kW/kg for methanol). Furthermore, the kinetics of ethanol oxidation [22] and oxygen reduction [23, 24] reactions are faster in alkaline than in acid media. Pt is considered to be the best electrocatalyst for low-temperature fuel cells [25], and consequently, Pt and Pt-based nanoelectrocatalysts have been extensively studied for the anodic electrooxidation of ethanol [20, 21, 26–29] and the cathodic reduction of oxygen [23, 24, 30–33] in fuel cell applications. However, the conclusion was that Pt-based electrocatalysts are still far beyond being ideal because of a number of fundamental reasons such as low electron transfer kinetics for cathodic oxygen reduction reactions, inefficient electrooxidation of ethanol to CO₂, catalytic poisoning, and also high cost and limited availability of Pt materials [29, 32, 34–36]. In practice, there appears to be few or even no alternative electrocatalysts that can break the C–C bond completely to the end products of CO₂. The recent research trends have been focused on tackling the poisoning issue (by the adsorption of CO-like species) by the modification of Pt noble metal with foreign metals such as Ru, Ni, Co, Mo, and Sn [35–37]. In concomitant research, Pt-decorated Ru bimetallic nanostructures are reported to be the most active anode materials for the electrooxidation of alcohols [38], and these have also been shown to improve the CO tolerance of the electrocatalyst [39, 40]. Since, a high loading of the precious metals is generally required to achieve reasonable fuel cell performance, whereas factors such as commercialization and maximizing the activity of the electrocatalyst necessitate a reduction of this loading into the electrode. Therefore, a catalytic system with high surface area and cheap supporting structure should potentially be able to optimize the efficiency of these electrocatalysts without sacrificing their performance. The core/shell nanostructures forming layers of Pt onto cheap materials have emerged as an effective way of increasing electrocatalytic activity [17, 26, 41–44]. One-dimensional (1D) nanostructures, particularly carbon nanotubes (CNT), have been widely used as a supporting material for Pt nanoparticles (NPs) due to their high electrochemical surface area (ECSA) and unique physical

properties [45, 46]. However, the inherent agglomeration nature of CNT significantly reduces the surface area of the electrocatalytic support and increases contact resistance which results into low performance [47]. Additionally, there are a number of challenges associated with the synthesis of these systems that need to be overcome if Pt NPs are to be reliably deposited onto the walls of such support structures. On the other hand, using 1D metal nanowire arrays as a supporting structure is potentially more attractive for fuel cell applications, since noble metals can be coated or deposited on the nanowire surface of cheap materials [48–50].

Oxide-supported Pt electrocatalysts are shown to be efficient for direct ethanol electrooxidation both in acid and alkaline media. Metal oxide-supported Pt electrocatalysts such as Pt/SnO_x [51], Pt–MgO/C [52], Pt–CeO₂/C [53, 54], Pt–ZrO₂/C [55], CNT/SnO₂/Pt thin films [56], Pt–Mo/CNT@TiO₂ [57], and Pt–ATO (platinum–antimony tin oxide)/MWCNT [58] have been shown to improve electrocatalytic activity and stability for ethanol electrooxidation compared to pure Pt or Pt/C electrocatalysts. NiO is a very attractive material for various applications such as Li-ion battery anode [59], supercapacitors [14, 60], and fuel cell electrodes [61, 62]. In this chapter, we demonstrate a novel hybrid electrocatalyst synthesized using highly ordered conductive metal/metal oxide (Ni/NiO) nanowire arrays (NWA) as a support for porous Pt NP. A simple method is reported here using the combination of electrodeposition of Ni nanowires inside a porous template and oxygen plasma annealing to convert into a core/shell Ni/NiO nanowires. The Pt NPs are reduced onto the Ni/NiO NWA surface by chemical reduction using a borohydride technique, thereby forming a 1D Ni/NiO NWA/Pt electrocatalyst. The synthesized material has been evaluated and the results suggest that Ni/NiO NWA/Pt could be used as an efficient nanoelectrocatalyst for ethanol electrooxidation in ADEFC [63]. Table 1 summarizes some of the recent publications on nanowire-based anode electrocatalysts for fuel cell applications and compared the materials in terms of their specific activity and Co tolerance.

Table 1 Comparison of typical Pt-based anode electrocatalysts for fuel cell applications

Catalyst/electrode	Specific activity (mAcm ⁻²)	CO tolerance I _f /I _b	References
Ni@NiO/porous Pt hybrid nanowires	126	1.2	[63]
Pt–Co alloy nanowires	5.57	0.88	[49]
Te/Pt hybrid nanowires	1	1.2	[48]
Pt–Co alloy NPs	1.7	–	[35]
C/Pt NP commercial	1.26	0.76	[35]
Ni–Cu alloy nanowires	10.30	–	[64]
AuPdPt alloy nanowires	107	1.5	[65]
PdNi alloy NPs/C	4.35	0.83	[66]
Ni@Pt nanotubes	82.6	1	[67]

Fabrication of the Electrode Materials

Synthesis of Coaxial Ni/NiO Nanowires for Pseudocapacitor

Alumina templates (Anodisc 47, Whatman, nanopore diameter of $\sim 250\text{--}300$ nm, length ~ 60 μm , and density of $\sim 1 \times 10^9$ cm^{-2}) were obtained from GE Healthcare UK Ltd. A 400 nm layer of Ni film was evaporated (Temescal FC-2000) onto one side of the template, which served as the working electrode. A copper wire was connected to the Ni backside of the template using silver paste from Radionics Ltd. Ireland and left overnight to dry before use. A low-stress nickel sulfamate bath was prepared using nickel sulfamate (0.37 mol dm^{-3}), boric acid (0.64 mol dm^{-3}), nickel bromide (0.18 mol dm^{-3}), and wetting agent ANKOR (R) F (10 ml l^{-1}). The pH of the solution was adjusted to 3.8 by adding 1 mol dm^{-3} sulfonic acid at room temperature. The deposition was conducted at a constant temperature of 50 $^{\circ}\text{C}$, while the solution was stirred at 100 rpm. A two-electrode cell was used with Ni/porous alumina template as a working electrode (cathode) and Ni pellets in a Ti basket as an anode. A 50 mA cm^{-2} (the ratio of the total template area) constant current was applied to the working electrode. The deposition rate was found to be 0.6 μm per minute. After deposition, the template was dissolved in 1 mol dm^{-3} KOH solution for 1 h, to release the vertically aligned Ni nanowire array film. The array was then washed with copious amount of deionized water and dried in air. A thin film of Ni ($3\text{--}4$ μm) had also been deposited onto the back side of the seed layer while Ni nanowires grew inside the pores. This film eventually prevented the NWs from collapsing after removal of the template. The film of Ni NW arrays was attached onto a silicon substrate by adhesive tape (Kapton tapes, DuPontTM, USA) at the edge, so that the back side was not exposed to the plasma during annealing and thereby only the surface of Ni NWs should convert to oxides. The fabricated Ni NW arrays were annealed in plasma (March Plasmod GCM 200) at power input ranging from 25 to 50 W at a constant oxygen flow (30 cc min^{-1}) by varying the annealing time. At the front side of the seed layer (the NWs' side), only a small fraction of the seed could be exposed to the plasma owing to very high density of NWs ($\sim 1 \times 10^9$ cm^{-2} with wire diameter of $250\text{--}300$ nm). Afterward, the plasma-treated samples were detached from the Si substrate and cut into pieces and preserved for characterization [14].

Synthesis of Core/Shell Ni/NiO/Pt NWA for Fuel Cell

The porous Pt NPs were deposited onto core/shell Ni/NiO nanowires by a hydrothermal reduction method from a solution containing a metal precursor salt (5 mM $\text{Na}_2\text{PtCl}_6 \times 6\text{H}_2\text{O}$) and a reducing agent (30 mM NaBH_4). Ni/NiO NWA sample was immersed in a 5 mL glass tube containing 500 μL aliquots of the Pt metal precursor salt at 80 $^{\circ}\text{C}$ and stirred for 20 min. The resulting hybrid electrocatalyst was removed from the mixture and washed with deionized water for the complete removal of residual Cl^- ions (the filtrate water was tested by 1 M silver nitrate solution and no

white colored precipitate (AgCl) was observed). To compare the electrocatalytic activities, Pt NPs were also deposited onto the metallic Ni NWA, using the NaBH_4 -reduction method described above. The samples were dried in an oven at 100 °C for 1.5 h before starting to measure the electrocatalytic performances. The amount of Pt reduced was measured using a high precision microbalance (Mettler Toledo, XS 105 Dual Range, repeatability (SD), $d=0.01$ mg) from the weight difference before and after the reduction of Pt [63].

Material Characterization

The crystal structures of the nanowires were characterized by X-ray diffraction (XRD, Philips PW3710-MPD diffractometer with Cu-K α radiation, $\lambda=1.54$ Å). The nanostructures and morphology were examined by scanning electron microscopy (SEM, FEI Nova 630 Nano-SEM or QUANTA FEG 650) and high-resolution transmission electron microscopy (HR-TEM, JEOL 2100 HR-TEM instrument operating at an acceleration voltage of 200 kV) coupled with energy dispersive X-ray spectroscopy (EDS Oxford Instruments INCA energy system). Cross section samples were prepared using focused ion beam (FIB, FEI DualBeam FIB Helios Nanolab 600i) for TEM characterization. Protective layers of carbon and platinum were deposited onto a lamella by electron beam-induced deposition (EBID). After deposition the lamella was cut and attached to a TEM grid. FIB at 30 kV was used to thin down the lamella to approximately 100–150 nm. In order to minimize the FIB induced damage, the final polishing was performed at 2 kV for 2 nm per side. The targeted final thickness was in the range of 30–60 nm. The cross sections were analyzed by HR-TEM at 200 kV. The bright-field (BF) images were taken with a medium-sized objective aperture to increase the contrast. EDS line scans were taken in scanning TEM (STEM) mode with medium spot size (40–60 nm sphere diameter of analyzed volume). STEM analysis was performed at 30 kV and dark-field images were taken in high-angle annular dark-field (HAADF) mode. In all cases, the elemental analysis was performed using the INCA software [14].

Electrochemical Characterization of Ni/NiO NWA for Supercapacitors

The electrochemical measurements of Ni/NiO nanowire arrays were performed using a CH Instruments 660C potentiostat. Electrodes comprised of 20 μm long Ni/NiO NWs, arrayed in 1×1 cm² surface areas. The electrochemical results are expressed in terms of the geometrical surface area. Chronopotentiometry (CP) and potentiostatic cyclic voltammetry (CV) were performed with a three-electrode glass cell setup filled with 1 mol dm⁻³ KOH as an electrolyte. The active material (Ni/NiO NW arrays) served as the working electrode, platinized titanium mesh as the counter, and Ag/AgCl/3 mol dm⁻³ KCl as the reference electrode. Cyclic voltammetry measurements were carried out in the potential range of 0.0–0.52 V (vs. Ag/AgCl)

at different scan rates of 5–50 mV s⁻¹ and conditioned at the initial potential for 20 s. CP charge–discharge measurements were carried out at a fixed current density of 5 mA cm⁻² [14].

Electrochemical Characterization of Ni/NiO NWA/Pt for Fuel Cells

A test cell was constructed with 1 M ethanol (EtOH) and 0.5 M KOH electrolyte at a temperature of 21 ± 1 °C using a platinized titanium mesh and a Hg/HgO (1 M KOH solution) as the counter and reference electrodes, respectively. Cyclic voltammetry (CV) and chronoamperometry (CA) were performed as main tools for the electrochemical characterization. Each electrode (0.5 × 0.5 cm²) comprised of 13 μm long 1D Ni/Pt NWA and Ni/NiO/Pt NWA was attached onto the Ni-coated polymer substrate by conductive glue (silver paste, Radionics Ltd. Ireland) and covered by nail varnish at the edge to avoid electrolyte leakage to the back side. CV measurements were carried out within the potential range of 0.4 to -1.0 V at different scan rates of 2–100 mV/s and conditioned at the open circuit potential (-0.65 V, OCP) for 20 s. CA measurements were carried out at a fixed potential of -0.2 V [63].

Results and Discussions

Elemental Characterization of the Electrodes

The fabrication of Ni/NiO NW arrays was done by direct electrochemical deposition of Ni inside nanoporous Al₂O₃ template and the subsequent conversion of outer shell into oxide by oxygen plasma annealing [14]. Figure 1a shows the SEM images of as-deposited Ni NWs, and plasma-annealed Ni NWs at 50 watt (W) for 60 s is shown in Fig. 1b after removal from the template and dispersion onto Au/Si substrate. The surface morphologies of the as-deposited and plasma-annealed NWs are different. The surface roughness of the annealed samples is increased due to oxide formation. A thin oxide layer is formed around the circumference of Ni nanowires, and hence, oxygen plasma annealing is found to be efficient in the conversion of the deposited metallic Ni into NiO. Figure 2 shows the effect of annealing time on the as-deposited vertically aligned Ni NWs. Figure 2a–c shows the SEM images taken at a 45° perspective view for different annealing times of 120, 300 and 600 s, respectively. In the short-time annealed Ni NWs, the oxide layer thickness cannot be distinguished easily. However, a high-magnification HR-TEM bright-field (BF) image (inserted into Fig. 2d) clearly shows the presence of a thin oxide layer at the outer surface of Ni. With the increased annealing time of Ni NWs and by keeping the input power constant at 50 W, the resulting oxide layer thickness around the metallic Ni circumference increased gradually (see Fig. 2d–f) [14].

Subsequently, the annealing time (at a fixed input power of 50 W) was varied to achieve an optimized thickness of the outer shell oxide layer, so that it can

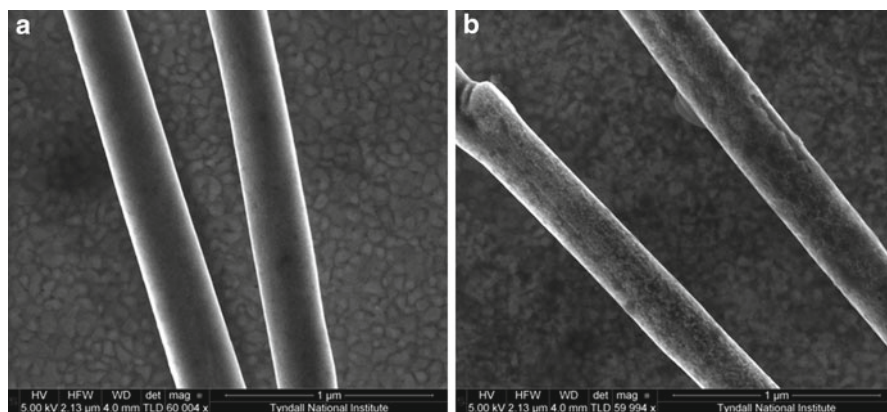


Fig. 1 SEM images after removal from the template and dispersion onto Au/Si substrate of (a) as-deposited Ni NWs and (b) Ni/NiO NWs that were prepared by oxygen plasma annealing at 50 W for 60 s. SEM images clearly show the formation of oxide layer around the circumference of the Ni NWs (Reproduced with permission from Ref. [14])

maintain a good electrical connection with the inner core of the metallic Ni. However, when the annealing time was increased to 300 and 600 s as shown in Fig. 2b, c, the surface morphology of the resulting oxide layers becomes inhomogeneous compared to those annealed for shorter time (i.e., 120 s; see Fig. 2a). In addition, Ni NWs annealed for 300 s or higher were found to be agglomerated as bundles of fused wires that consume the interspaces between wires. These eventually reduce the total electroactive surface area available for electrochemical reactions [14].

Elemental mapping by scanning transmission electron microscopy–energy dispersive X-ray spectroscopy (STEM–EDS) reveals the presence of both Ni and O in the annealed Ni nanowires as can be seen in Fig. 3. Nanowire arrays obtained at 50 W for 120 s annealing showed homogeneous surface morphology and the one-dimensional vertical nanostructures being well preserved (see Fig. 2a) and therefore used for the subsequent studies [14]. The HR-TEM image in Fig. 4a reveals domains of different crystallites or grains of shell. Figure 4b is the high-magnification image showing NiO crystallites in the shell. Figure 4c reveals another area where the interface between the Ni (core) and NiO (shell) is clearly visible with lattice fringes in the shell. Figure 4d, e shows the EDS spectra of Ni core (D1) and NiO shell (D2), respectively. The EDS data revealed the composition of these regions, where Ni and O ratios are 6.5:3.5 (D2) and 19:1 (D1), i.e., showing the presence of small quantity of O in the core of the annealed Ni nanowires but a large quantity of O in the shell [14].

A simple hydrothermal NaBH_4 -reduction method was applied to the 1D Ni/NiO nickel nanowire array (NWA) to coat Pt NP and form a novel Ni/NiO NWA/Pt hybrid nanoelectrocatalyst. Figure 5a, b shows the SEM images of the Ni/NiO NWA after reaction with the metal precursor salt solution. These clearly reveal that Pt NPs

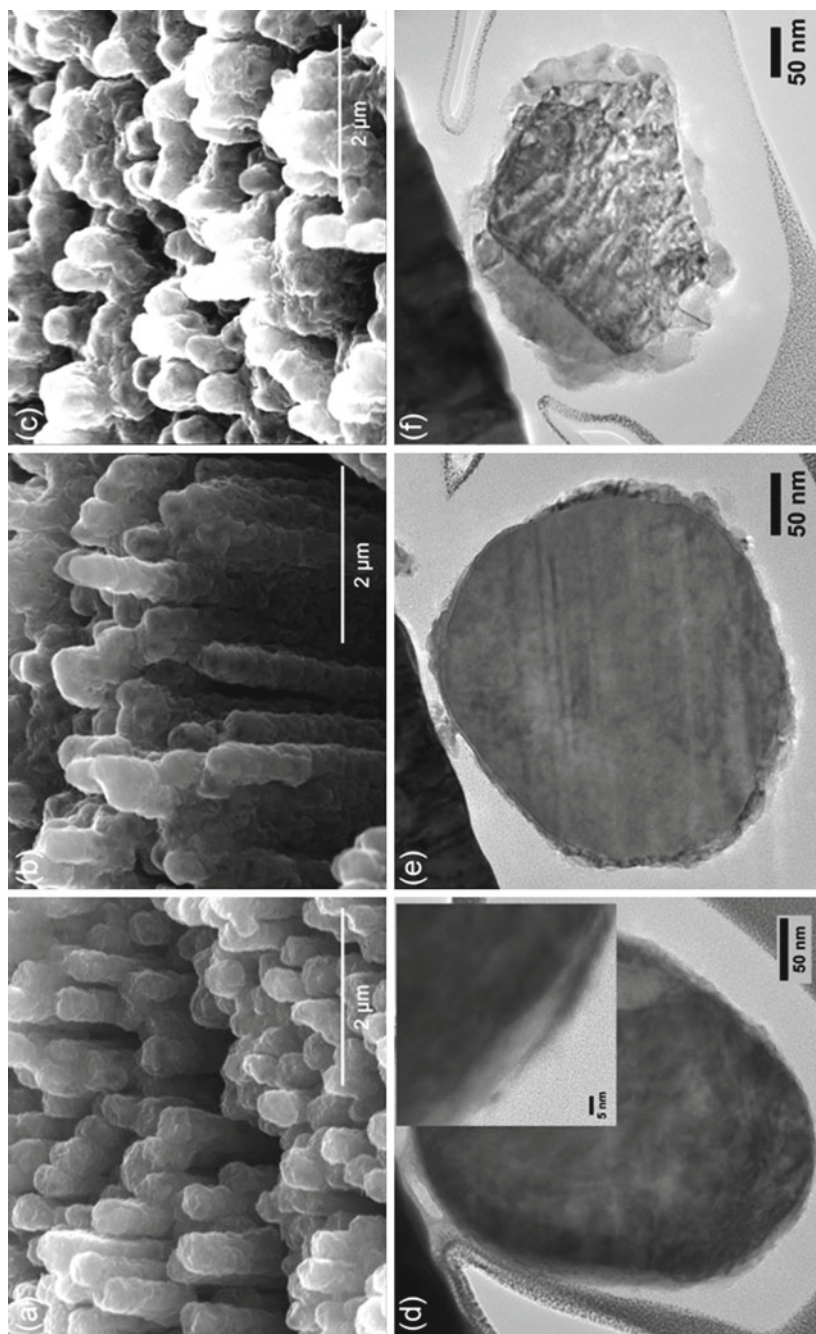


Fig. 2 SEM images at 45° perspective view of the Ni/NiO NW arrays obtained from metallic Ni NWs after oxygen plasma annealing at 50 W for 120 s (a), 300 s (b), and 600 s (c). TEM bright-field (TEM-BF) images of the corresponding coaxial Ni/NiO NWs annealed for 120 s (d), 300 s (e), and 600 s (f) show the gradual increase in thickness of the outer shell oxide layers and thinning of the metallic Ni (Reproduced with permission from Ref. [14])

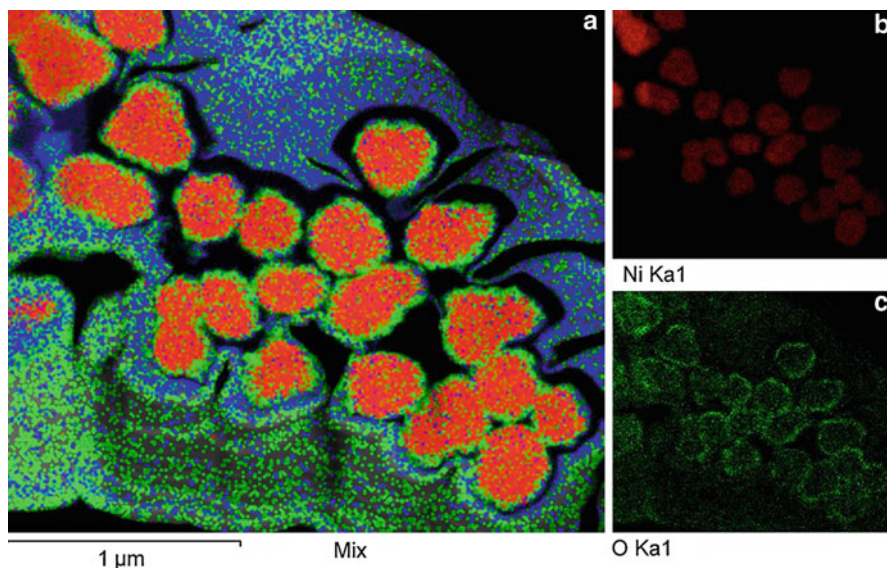


Fig. 3 STEM-EDS elemental mapping shows the presence of a thin oxide layer around the Ni circumference annealed at 50 W for 600 s: dark-field (DF) images of (a) coaxial Ni/NiO NWs, (b) nickel at the inner core, and (c) oxygen at the outer shell (Reproduced with permission from Ref. [14])

are adsorbed on the surface of the NiO. Further insight into the microstructure of the NiO and Pt NP formed at the surface of the Ni/NiO nanowires was obtained by TEM.

Figure 6a–c as the bright-field (BF) TEM images shows different regions of the Pt NP-supported Ni/NiO nanowires at increasing magnification. It can be seen that Pt NP attached at the surface of the core/shell Ni/NiO nanowires. The grain size of the Pt NP varies from ~3 to 15 nm although some NPs (often at the core of the 75 nm agglomerates) are somewhat larger at ~30 nm. The diffraction pattern shown in Fig. 6d was acquired from a common region of the Pt NP attached onto nanowires and exhibits the presence of face-centered cubic (fcc) Pt for which the measured (111), (200), (220), and (311) spacings are 0.2256, 0.1957, 0.1385, and 0.1208 nm, respectively.

The Pt NP also contains a reasonably homogeneous distribution of fine pores. A higher magnification through focal series of BF images shown in Fig. 7 presents the reverse Fresnel effects as a function of the defocus conditions, which are consistent with a distribution of fine pores. The diameter of these pores found in the region is 2–3 nm. The NiO shell has a characteristically “ribbon-like” morphology with a typical thickness of ~15 nm and consists of irregular grains that vary in diameter from ~3 to 15 nm. The d-spacing for the (111), (200), (220), and (311) fcc oxides is measured to be 0.2399, 0.2077, 0.1468, and 0.1253 nm, respectively.

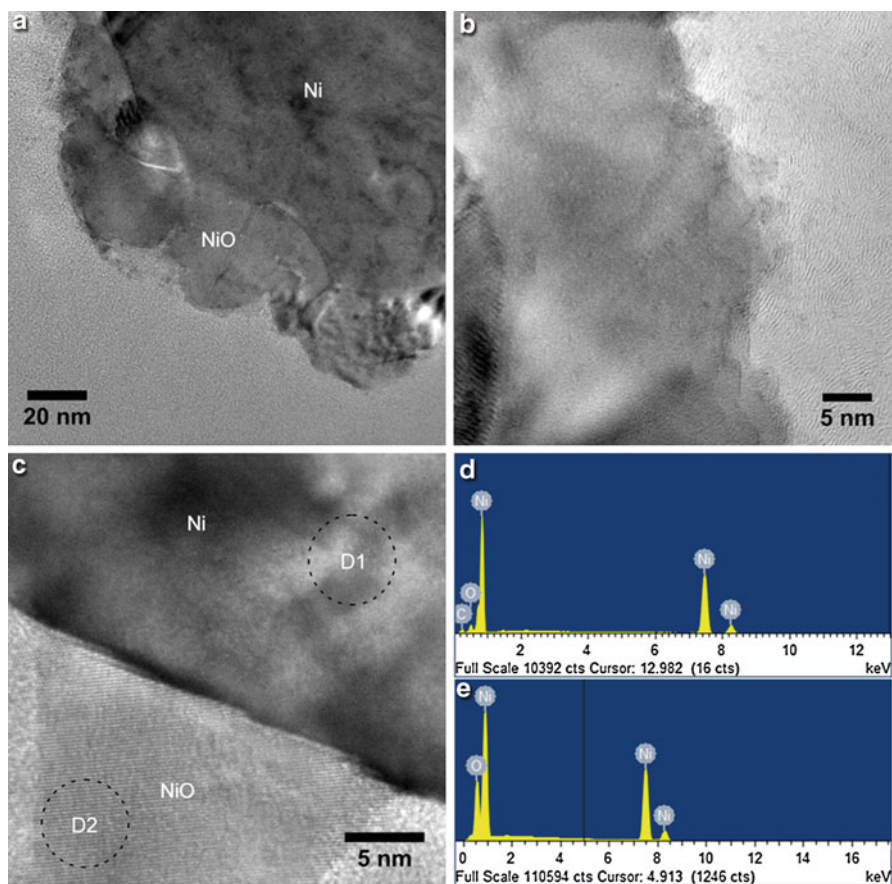


Fig. 4 HR-TEM images of the coaxial Ni/NiO NW (annealed for 600 s at 50 W) show (a) NiO crystallites or grains in the shell, (b) magnified view of NiO crystallites, and (c) magnified view of the interface of Ni and NiO showing the lattice fringes in the shell. EDS spectra of D1 (d) and D2 (e) correspond to domains of Ni (core) and NiO (shell) (Reproduced with permission from Ref. [14])

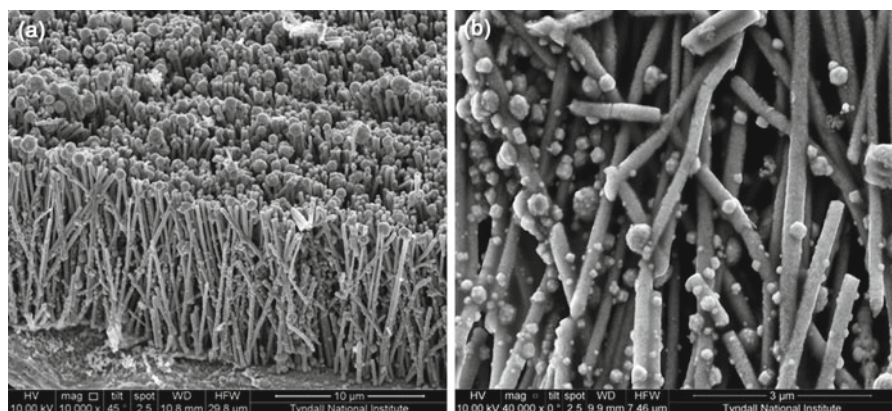


Fig. 5 SEM images of 1D Ni/NiO NWA-supported Pt NP cross-sectional (a) low and (b) higher magnified view (Reproduced with permission from Ref. [63])

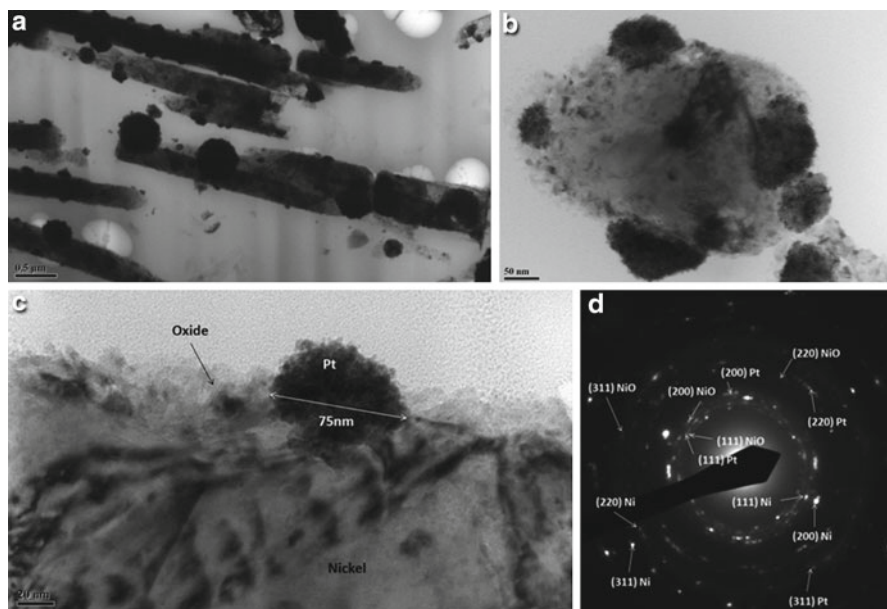


Fig. 6 BF TEM images of (a, b) Pt-supported Ni/NiO NWA where Pt NP can be seen at both the sidewalls and tip of the elongated core/shell Ni/NiO nanowires. (c) A higher-magnification BF image of a sidewall Pt NP at a Ni/NiO nanowire surface where the irregular NiO layer formed at the surface of the Ni can be distinguished. (d) A diffraction pattern confirming the presence of Ni, NiO, and Pt for which the lattice parameters of the NiO and Pt are found to be 0.4120 and 0.3936 nm, respectively (Reproduced with permission from Ref. [63])

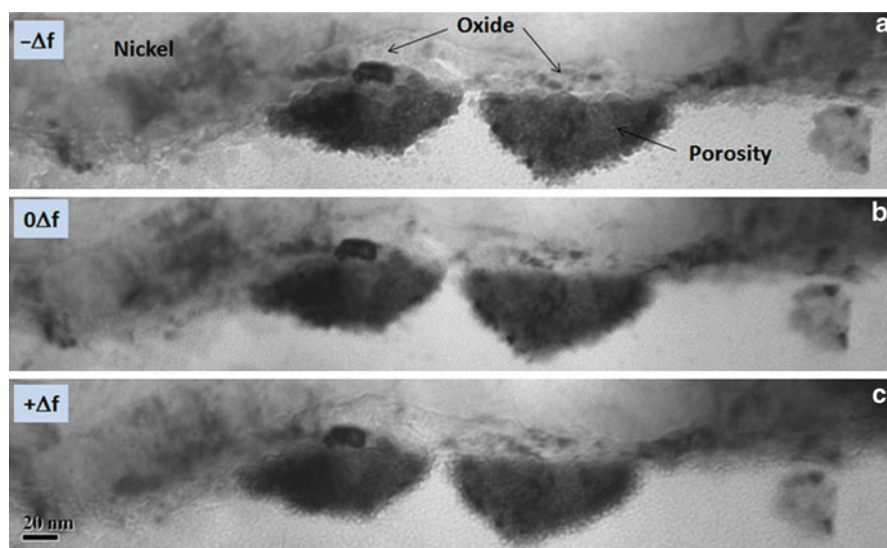
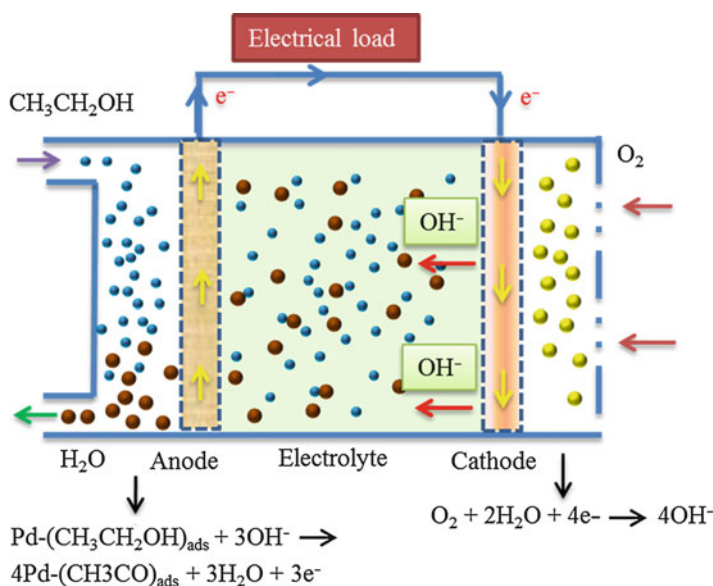


Fig. 7 Higher-magnification BF images of a sidewall Pt NP agglomerate taken in an (a) under-focus, (b) in-focus, and (c) over-focus condition showing a distribution of 2–3 nm pores. Note the reverse Fresnel effects as a function of the defocus conditions (Reproduced with permission from Ref. [63])

Electrochemical Characterization of the Electrodes

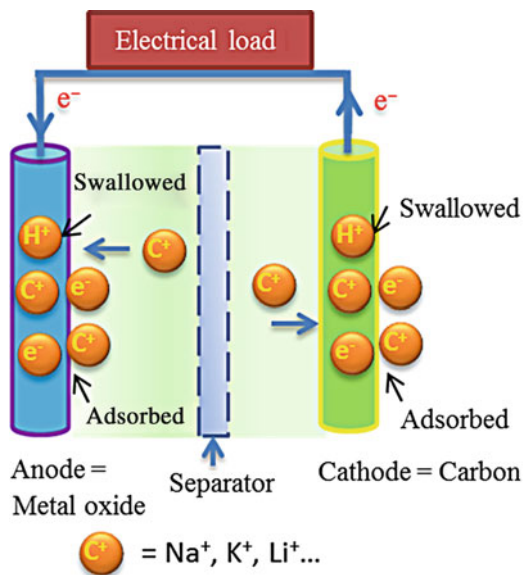
In order to understand the electrochemical characterization of the electrode materials, it is imperative that we understand the working principle of the electrodes in an alkaline fuel cell as well as in a pseudocapacitor. Schematic 1 shows the diagram of the working principle of the alkaline ethanol fuel cell. Here, ethanol is being used as a fuel that produces electrical energy due to electrochemical oxidation at the anode materials. The electrical energy generated in the form of electrical current in this way is used for the application load and in turn reaches at the cathode to complete the electrochemical cycle.

Schematic 2 shows the diagram of the working principle of pseudocapacitor that stores and releases electrical energy in the chemical forms through the redox reaction on the surface or near the surface of active (electrode) materials, in a similar fashion to other electrochemical energy storage device such as batteries. On discharge, the device releases its stored electrical energy that passes through the external load and used by the application, and ions pass through the separator toward the anode, where they either adsorbed or swallowed depending on the materials and electrolyte system applied. On charging, ions are released from the anode, move toward cathode, and are stored in a similar fashion.



Schematic 1 Working principle of alkaline fuel cell technology – electron ions generated in anode passed through the external load to the cathode where O_2 is reduced to OH^- ions

Schematic 2 Working principle of pseudocapacitor. On discharging, electrons passed through external load and ions through separator toward anode, where they adsorbed. On charging, ions move toward cathode and are stored in a similar fashion

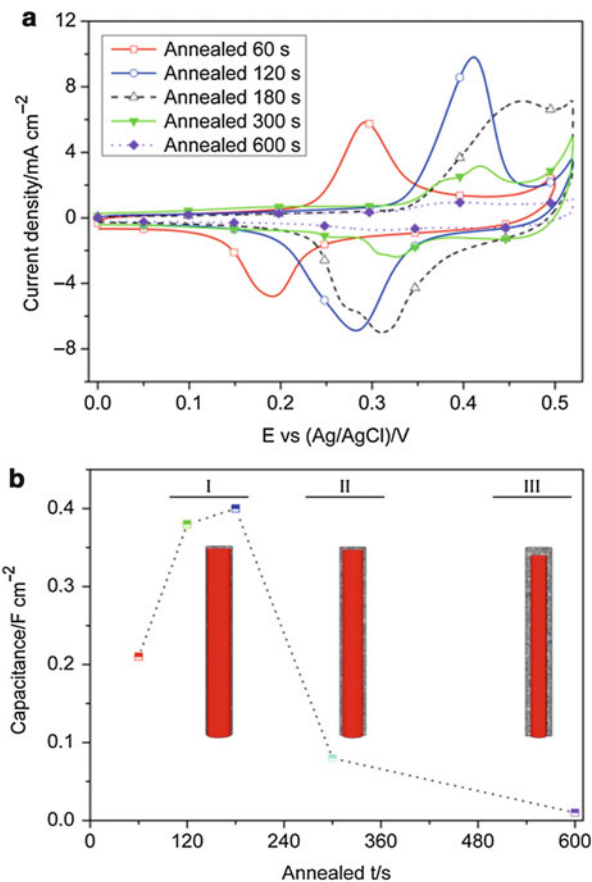


In the next few sections, Ni/NiO and Ni/NiO NWA/Pt array as electrode materials for supercapacitors and fuel cells will be discussed in some details.

Ni/NiO Nanowire Array as Electrode for Pseudocapacitor

Figure 8a shows the effect of annealing time (at a constant input power of 50 W) on the CVs (at a scan rate of 10 mV s⁻¹). A change in the electrochemical behavior has been observed with increasing the annealing time. The CV of the coaxial Ni/NiO NW arrays (annealed for 60 s) shows an anodic peak at 0.294 V and a cathodic peak at 0.193 V (vs. Ag/AgCl). This redox couple is associated with the pseudocapacitive behavior of the NiO component in Ni/NiO NW arrays. It originates from the surface Faradaic oxidation and reduction reactions ($\text{NiO} + \text{OH}^- \leftrightarrow \text{NiOOH} + \text{e}^-$), where the anodic peak is due to the oxidation of NiO to NiOOH and the cathodic peak is for the reverse process [10–12]. After increasing the annealing time to 120 s, the peak current intensities of the corresponding redox reactions are increased and the peak potentials shift to higher values at 0.41 and 0.28 V, respectively, as can be seen in Fig. 8a. The increase in the charge–discharge current intensity is due to the formation of a thicker oxide (i.e., larger amount) around the circumference of the Ni nanowires. There is a sharp increase in the anodic and cathodic peak currents, indicating that the outer shell of NiO film has higher electrochemical activity, which maintains a good electrical contact with the inner metallic Ni core. For the 180 s annealed sample, the redox potentials shift further to the higher potentials (oxidation peak at 0.465 V and reduction peak at 0.31 V). However, the peaks become

Fig. 8 (a) Cyclic voltammograms of the annealed Ni NW arrays measured at the potential scan rate of 10 mVs^{-1} in 1 mol dm^{-3} KOH. The annealing time ranges from 60 to 600 s at a constant input power of 50 W and oxygen flow of 30 cc min^{-1} in the plasma chamber. (b) Capacitance of the coaxial Ni/NiO NW arrays plotted as a function of the annealed time (Reproduced with permission from Ref. [14])



wider, indicating the low electrochemical activity of the redox-active material. The maximum peak potential separation (ΔE_p) increases with increasing the annealing time (0.1 V for 60 s annealing to 0.13 and 0.16 V for 120 and 180 s annealing, respectively), while the redox peaks shift to the right side of the scale. This observation infers that the redox reaction at or near the surface of Ni/NiO is quasi-reversible for the samples annealed for a longer time; this may be further attributed to the solution–electrode and/or core–shell interface resistance [68, 69]. The capacitance is increased to 0.4 F cm^{-2} of the sample annealed for 180 s compared to 0.38 F cm^{-2} and 0.21 F cm^{-2} of the samples annealed for 120 and 60 s, respectively, as can be seen in Fig. 8b. As more metallic Ni is converted to NiO, the capacitance initially increases, which is indicative of pseudocapacitive behavior of the redox-active NiO component in the electrodes [68]. However, as the amount of NiO content increases further (beyond 180 s annealing time), the capacitance decreases (Fig. 8b). This is

due to the decrease in electrical conductivity with the inner core (Ni), which reduces the rate of charge transport as the thickness of NiO (shell) increases [68].

The electrodes annealed for longer time exhibit low electrochemical activity, which can be fairly attributed to the consumption of the interspaces between wires by the oxide, which increasingly reduces the total electroactive surface area for charge storage and redox reactions as discussed earlier with reference to Fig. 2. Therefore, these results can be summarized as follows: (1) With increasing annealing time, more Ni is turned into NiO and this thins the inner conductive core of Ni. Thereby the electrical resistance of the individual NW is increased as is evident from shifting of the redox peaks. (2) The electrical conductivity between outer shell NiO and inner core Ni metallic support might reduce considerably. Therefore, thick and poorly conductive NiO in the outer shell becomes practically in electrical isolation from the conductive inner core Ni, which results in a decrease in capacitance to 0.08 and 0.01 F cm⁻² for samples annealed for 300 and 600 s [14].

The CVs of 120 s annealed Ni/NiO NW arrays at scan rates between 5 and 50 mV s⁻¹ are shown in Fig. 9a. It can be observed that the pair of anodic and cathodic peak curves is symmetric over the entire range of scan rates, indicating reversibility of the redox reactions at or near the coaxial Ni/NiO NW surfaces. Here, the peak current intensity increases linearly with the scan rate [14], indicating that the redox process associated with NiO active component in the Ni/NiO NW system is diffusion controlled. This linear response of the peak current intensity is also an indication of the fast electronic and ionic transport rates. However, the maximum peak potential difference (ΔE_p) between anodic and cathodic peak increases (0.10 V for 5 mV s⁻¹ to 0.22 V for 50 mV s⁻¹) with scan rate, which implies that the redox reactions are quasi-reversible. Figure 9b shows the rate capability performance (in terms of capacitance) of the electrode used in Fig. 9a, where the electrodes show good rate capability over the entire range of scan rates. As an example, at the scan rate of 50 mV s⁻¹, the capacitance (0.36 F cm⁻²) of the Ni/NiO NW arrays retained up to 94 % of that measured at a lower scan rate of 5 mV s⁻¹ (0.38 F cm⁻²). Ni/NiO NW arrays annealed for very short time of 60 s and thereby consisting of thinner oxide shell can be cycled even at a higher scan rate of 100 mV s⁻¹ without any decrease in capacitance [14].

However, it was observed that the 60 s annealed sample showed almost 50 % lower capacitance compared to 120 s samples as can be seen in Fig. 8b. At the higher scan rate, high capacitance retention indicates the rapid ionic and electronic transport rates of the Faradaic redox reactions and the faster charge–discharge kinetics is attributed to the unique core/shell nanoarchitecture with a large electroactive surface area, which offers a highly conductive and robust core for reliable connection to the NiO shell. This high aspect ratio structure also ensures easy electrolyte access to a large volume of redox-active materials [11, 68].

A set of charge–discharge experiments were carried out using chronopotentiometry in order to investigate the reaction kinetics and to measure the capacitance. 120 s annealed Ni/NiO NW arrays were used as the electrode, and the measurements were performed at a constant current density of 5 mA cm⁻². The first few cycles of the representative charge–discharge potential profiles are shown in

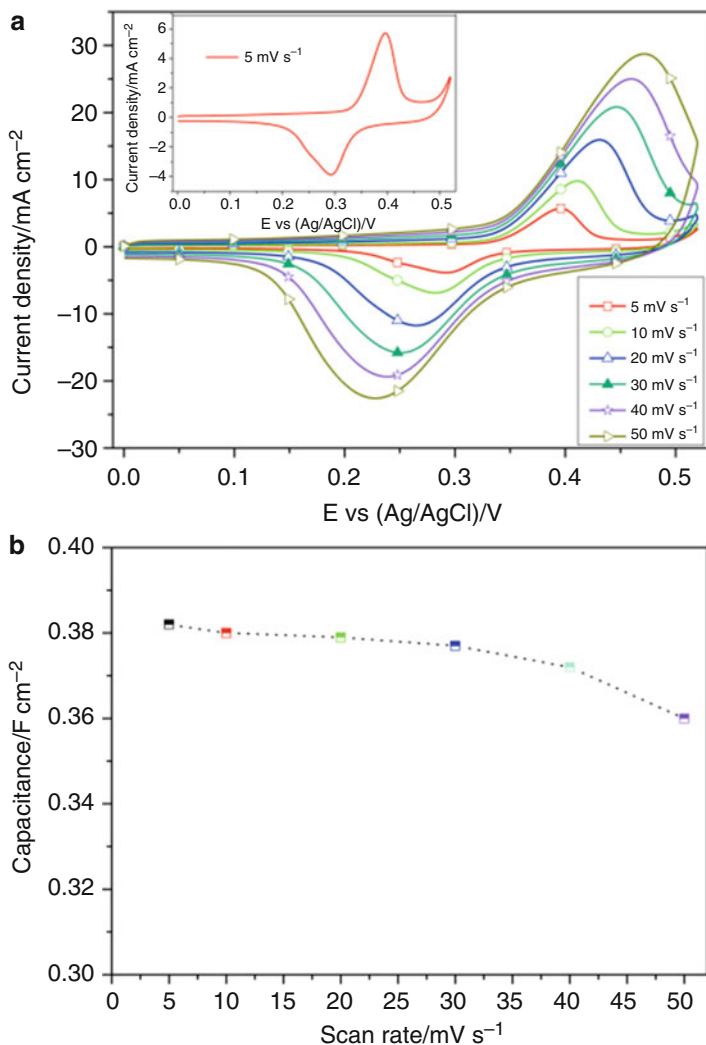
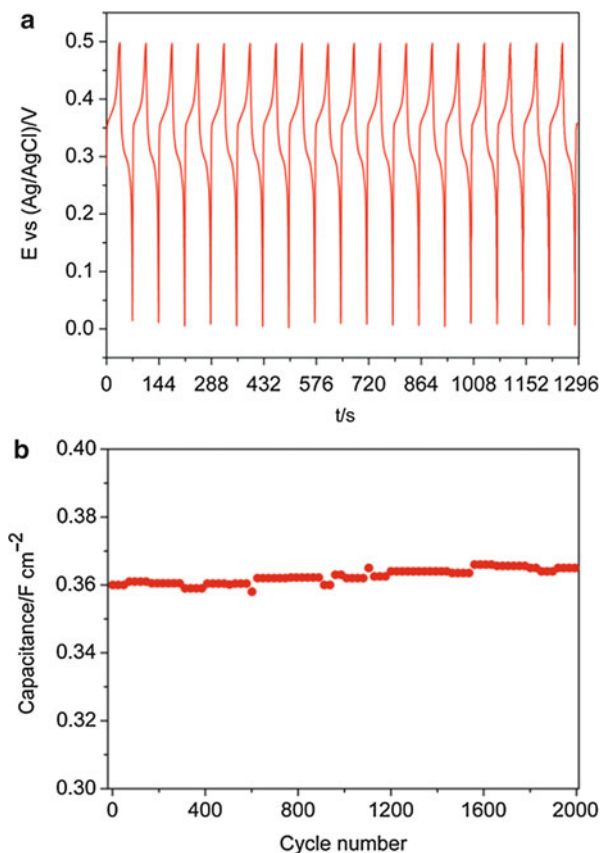


Fig. 9 (a) Cyclic voltammograms of 120 s oxygen plasma annealed Ni/NiO NW arrays measured at scan rates from 5 to 50 mV s^{-1} . Inset shows CV taken at a low scan rate of 5 mV s^{-1} . (b) Capacitance as a function of the scan rate (Reproduced with permission from Ref. [14])

Fig. 10a. Even at a high charging–discharging current, the curves are symmetric enough, implying that the electrode has fast charge–discharge properties with an excellent electrochemical reversibility. The charging and discharging for similar time duration confirm that the reversible Faradaic redox reactions occurred at or near the electroactive surfaces. The measured capacitance is 0.36 F cm^{-2} , which conforms to the value calculated from CV measurements at a high scan rate of

Fig. 10 (a) First few cycles of the typical charge–discharge potential profiles of 120 s oxygen plasma annealed Ni/NiO NW arrays measured with chronopotentiometry at a charging–discharging current of 5 mA cm^{-2} . (b) Capacitance as a function of the cycle number (Reproduced with permission from Ref. [14])



50 mV s^{-1} as can be seen in Fig. 9b. Figure 10b depicts the cycling performance for the first 2,000 cycles of the coaxial Ni/NiO NW arrays shown in Fig. 10a. As an electrode material, the Ni/NiO NW arrays exhibited long-term cycling performance, and no deterioration in capacitance was observed over the entire cycling period. The small variation in capacitance may be attributed to the heating effect, generated in the long range cycles or other physical factors rather than chemical or structural changes associated with the electrode materials. This was further confirmed by observing the samples under SEM before and after exposure to the cycling [14].

The core/shell Ni/NiO NW-based nanoarchitecture provides a unique combination of entirely exposed, high aspect ratio, one-dimensional vertical structures with a highly conductive metal in the core. This leads to homogeneous electrolyte accessibility even to remote sites and resulted in a large electroactive surface area for charge storage and redox reactions and high rates of electronic and ionic conductivity. We believe by optimizing the fabrication parameters that the capacitive performance of the coaxial Ni/NiO NW can be enhanced further. Furthermore, these core/shell nanostructures can be directly grown on thin conductive as well as on flexible substrates,

which enable in realization of an efficient and cost-effective one-step approach for binder-free fabrication of supercapacitor electrodes [14].

Ni/NiO NWA/Pt as Electrode in Fuel Cell

Figure 11 shows cyclic voltammograms taken after 20 scans. The typical features of hydrogen adsorption/desorption and oxide formation/reduction are seen for both the 1D Ni NWA and the Ni/NiO NWA-supported porous Pt NP electrocatalysts. Nevertheless, electrocatalytic activities for the bare Ni NWA and Ni/NiO NWA support structures are not being observed in the same electrochemical window. The electrochemical surface area (ECSA) has been calculated from the following expression, $ECSA = (Q_H/Q_M W_{Pt})$ [70], where Q_M is the charge due to the monolayer adsorption of hydrogen (0.21 mCcm^{-2} for Pt), Q_H is the charge (mCcm^{-2}) due to hydrogen absorption onto the electrode, and W_{Pt} is the Pt loading in the electrocatalyst. The hydrogen desorption peak is being used to calculate ECSA within the potential region of -0.9 to -0.4 V in the anodic direction (see Fig. 11) and is summarized in Table 2.

The ECSA of Pt-supported Ni/NiO NWA ($120 \text{ m}^2/\text{g}_{Pt}$) is 1.3 times higher than that of the Ni NWA ($92 \text{ m}^2/\text{g}_{Pt}$) structure. It should also be noted that the ECSA for the Ni/NiO NWA/Pt electrocatalyst is considerably higher than the reported values for Pt nanorods ($30 \text{ m}^2/\text{g}_{Pt}$) synthesized by galvanic displacement reaction [50] as well as a commercially available carbon-supported Pt NP electrocatalyst ($\sim 53 \text{ m}^2/\text{g}_{Pt}$) [35], which obviously suggest higher utilization efficiency of the Pt NP on core/shell metal/metal oxide NWA. The increase in the ECSA value is

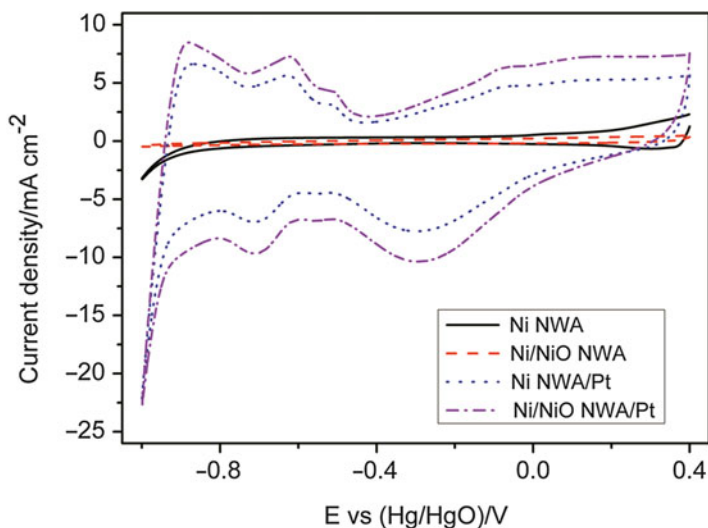


Fig. 11 Comparison of cyclic voltammograms of 1D Ni NWA, Ni/NiO NWA, Ni NWA/Pt, and Ni/NiO NWA/Pt in 0.5 M KOH solution at 21 °C, scan rate 50 mVs^{-1} (Reproduced with permission from Ref. [63])

Table 2 Cyclic voltammetry analysis of the Ni/NiO NWA-supported Pt electrocatalysts. The specific and mass activities are measured at the respective peak potential (E_p) (Reproduced with permission from Ref. [63])

Electrocatalyst	ECSA ($\text{m}^2/\text{g}_{\text{Pt}}$)	Specific activity (mAcm^{-2})		Mass activity ($\text{mA}/\text{mg}_{\text{Pt}}$)	
		Fw. scan, E_p/V	Rev. scan, E_p/V	Fw. scan	Rev. scan
Ni NWA/Pt*	92	84, 0.068	75, -0.14	350	312
Ni/NiO NWA/Pt*	120	126, 0.062	103, -0.16	525	429

*Pt loading in both electrodes is $0.24 \text{ mg}/\text{cm}^2$

due to the 1D nanostructure which is free from any surfactants/ancillaries and is enhanced by the homogenous fine porous microstructure of the Pt NP at the surface of the conductive robust core. The favorable properties are likely to be further enhanced by the obtainable interspacing of the nanowires for the fast ion adsorption/desorption.

Cyclic voltammetry and chronoamperometry were used to investigate the electrocatalytic activity for ethanol electrooxidation on porous Pt NP-supported Ni/NiO NWA. The typical activities for ethanol electrooxidation on Pt-based electrocatalysts are observed in Fig. 12a with the forward oxidation peak (i.e., under anodic condition) and the backward oxidation peak (i.e., under cathodic condition). The oxidation current peak in the forward scan is denoted as the electrooxidation of the freshly chemisorbed ethanol species onto the Pt surface, while the peak in the backward scan is attributed to the reduction of the oxidized Pt oxide and the removal of the incompletely oxidized CO-like carbonaceous species formed in the forward scan [34].

The electrooxidation of ethanol on the Ni/NiO NWA/Pt electrocatalyst surface starts at a more negative potential than that of Ni NWA/Pt, as shown in Fig. 12b, c signifying that the NiO nanoshell around the metallic Ni NWA influences the faster electrode kinetics. The current of Ni/NiO NWA/Pt for both in forward and backward peaks increases considerably (see Fig. 12a) and is almost 1.5 times higher than that of Ni NWA/Pt (see Table 1). The promotional effect due to oxide inclusion for the electrooxidation of ethanol is also realized in the thin-film electrode version of Ni/NiO/Pt, as shown in Fig. 12d. The specific peak current density of the Ni/NiO/Pt electrocatalyst is 5 mAcm^{-2} based on the forward anodic peak, which is ~ 1.5 times higher than that of the Ni/Pt (3 mAcm^{-2}) electrode. Hence, the electrooxidation of ethanol suggests that the inclusion of oxide to the Ni/Pt system significantly promotes the electrocatalytic activity for the electrooxidation of ethanol with the same amount of Pt loading. The specific peak current densities (based on the forward anodic peak, I_f) of 1D Ni NWA/Pt and Ni/NiO NWA/Pt electrocatalysts are 84 and 126 mAcm^{-2} , and their mass peak current densities are 350 and $525 \text{ mA}/\text{mg}_{\text{Pt}}$, respectively. The higher specific and mass activity of Ni/NiO NWA/Pt electrocatalyst could potentially be understood in terms of the active role played by the NiO nanoshell around the conductive Ni core. It is worth noting that the specific activity of the 1D Ni/NiO NWA/Pt electrocatalyst is much higher than the corresponding

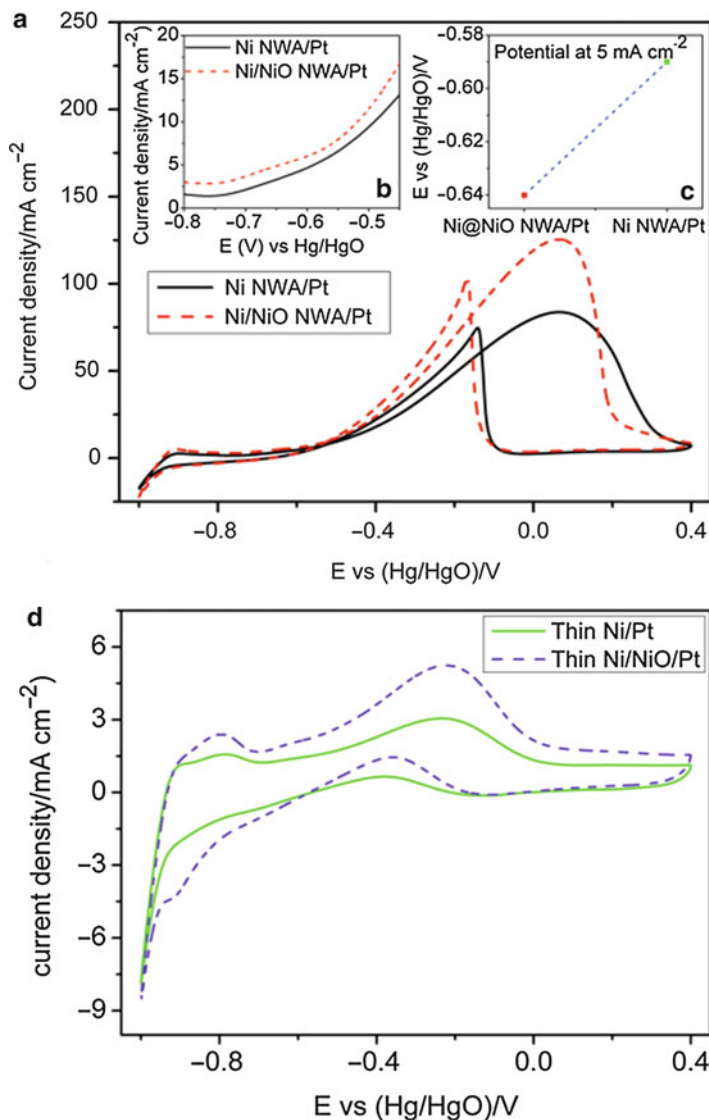


Fig. 12 (a) Cyclic voltammograms of 1D Ni NWA/Pt and Ni@NiO NWA/Pt electrocatalysts in 0.5 M KOH/1 M ethanol solution at 21 °C, scan rate 20 mVs⁻¹ (Pt loading, 0.24 mgcm⁻²). (b) Magnified view of onset potential region of cyclic voltammograms. (c) Electrooxidation potential of the respective electrocatalyst at 5 mAcm⁻². (d) Cyclic voltammograms of thin Ni/Pt and NiO/Pt electrocatalysts in 0.5 M KOH/1 M ethanol solution at 21 °C, scan rate 20 mVs⁻¹ (Pt loading, 0.1 mgcm⁻²) (Reproduced with permission from Ref. [63])

activities reported for Te/Pt hybrid nanowires (~1 mA cm⁻²) [48], commercial Pt/C NP (~1 mA cm⁻²), and Pt–Co alloy NP (~2 mA cm⁻²) [35]. The specific activity of the oxide-promoted 1D core/shell Ni/NiO NWA/Pt electrocatalyst is approximately

100 times higher than those reported for the commercial Pt/C NP electrocatalysts. The results obtained in this study suggest that even with a reduced Pt loading within the Ni/NiO NWA/Pt electrode system, it could be possible to replace the commercial Pt/C NP anode electrocatalysts currently used in ADEFC.

The enhanced electrocatalytic activity due to the oxide support is due to the synergistic interaction between the finely porous Pt NP and the NiO nanoshell formed at the outer surface of the conductive 1D metallic Ni core [58, 62]. The ratio of the forward anodic peak current density (I_f) to the backward anodic peak current density (I_b) is usually considered as the provision of a measurement of the poisoning tolerance to CO-like carbonaceous oxidative intermediates formed during the electrooxidation of alcohols (in the forward scan). The I_f/I_b value of the Ni/NiO NWA/Pt electrocatalyst was found to be 1.2, and this value is higher than those reported for 1D Pt/Co nanowires (0.88) and commercial Pt/C NP (0.76) electrocatalysts [35, 49]. The higher I_f/I_b value indicates a greater poisoning tolerance, and this potentially credited to the dual effects of the NiO nanoshell and the nanoporous Pt NP at the surface of the core/shell 1D nanostructure.

The mass transport behavior of the Ni/NiO NWA/Pt electrocatalyst has also been investigated as shown using a series of cyclic voltammograms at different scan rates in Fig. 13a. The peak current density (in the forward scan) and the square root of the scan rates of the Ni/NiO NWA/Pt electrode are shown in Fig. 13b in which a linear relationship can be seen at the start of the 20 mVs⁻¹ scan. The linear observation implies that the electrocatalytic process for the electrooxidation of ethanol on the Ni/NiO NWA/Pt structure is not controlled by mass transport or by the concentration polarization until the scan rate is higher than 20 mVs⁻¹. However, at lower scan rates, the electrooxidation of ethanol is dominated generally by the activation polarization of the electrode materials.

The electrode kinetic parameters for ethanol electrooxidation are determined from the Tafel plots, as shown in Fig. 14. A linear region of the Tafel plots is observed on both Ni NWA/Pt and Ni/NiO NWA/Pt electrocatalysts, and Tafel slopes are measured to be 199 mV/dec and 155 mV/dec, respectively. This similar behavior in the Tafel slopes indicates that reaction mechanism occurs on both electrocatalysts alike. It is supposed that a higher charge transfer rate occurred on Ni/NiO NWA/Pt structure during the electrooxidation of ethanol compared to Ni NWA/Pt electrocatalyst.

The stability of the electrocatalysts has been investigated by chronoamperometry experiments at different temperatures as shown in Fig. 15. The working electrode was held at -0.2 V (vs. Hg/HgO), and the changes in ethanol electrooxidation current with time were measured. The initial current densities are high for both electrocatalysts which is due to double layer charging. The current due to ethanol electrooxidation was found to decay continuously for both electrocatalysts, most likely due to electrode poisoning by chemisorbed CO-like carbonaceous oxidative intermediates. Generally, chemisorbed CO starts to accumulate on the electrocatalyst surface if the kinetics of its removal becomes significantly slower than that of the electrooxidation of ethanol. Thus, a more steady decay rate of the electrooxidation current with time implies a higher stability of the electrocatalyst and a

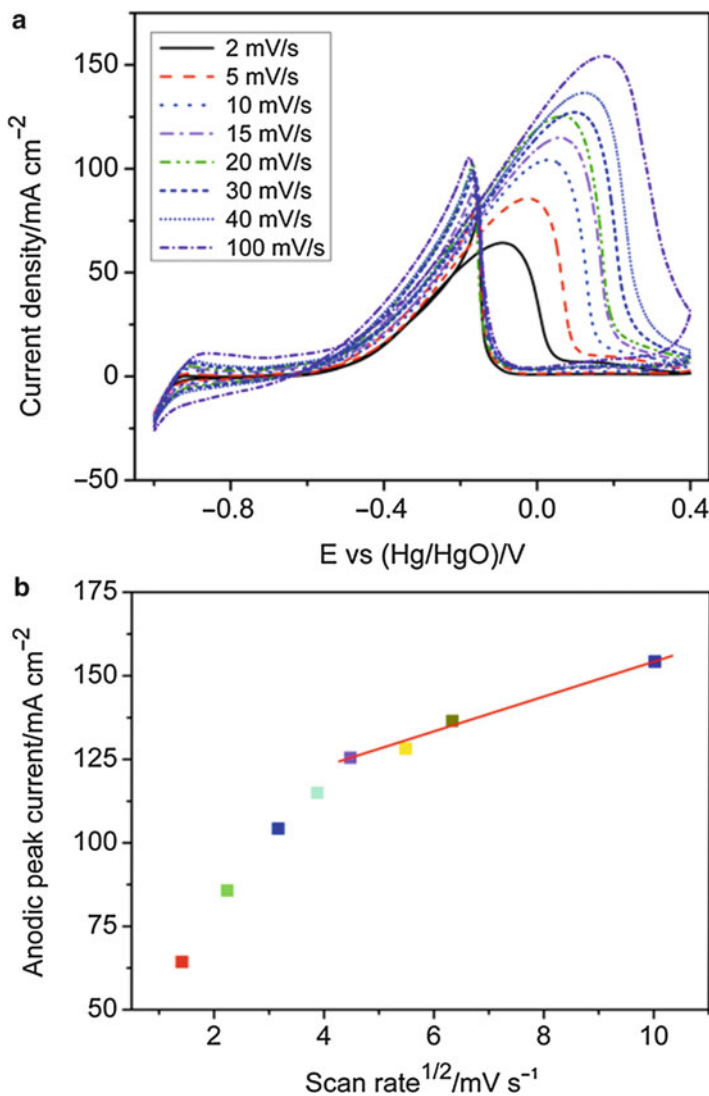


Fig. 13 (a) Cyclic voltammograms of 1D Ni/NiO NWA/Pt electrocatalysts at different scan rates in 0.5 M KOH/1 M ethanol solution at 21 °C. (b) Plot of forward anodic peak current density and the square root of the scan rate (Reproduced with permission from Ref. [63])

greater tolerance to poisoning. However, a rapid current decay is observed on Ni NWA/Pt electrocatalyst at low temperature (21 °C) by comparison at higher temperature of 50 °C. The rate of electrooxidation current decay for the Ni/NiO NWA/Pt system was found to be much lower and consistent at both low and higher

Fig. 14 Tafel plots for ethanol electrooxidation of 1D Ni NWA/Pt and Ni/NiO NWA/Pt electrocatalysts measured in 0.5 M KOH/1 M ethanol solution at 21 °C, scan rate 2 mV/s (Reproduced with permission from Ref. [63])

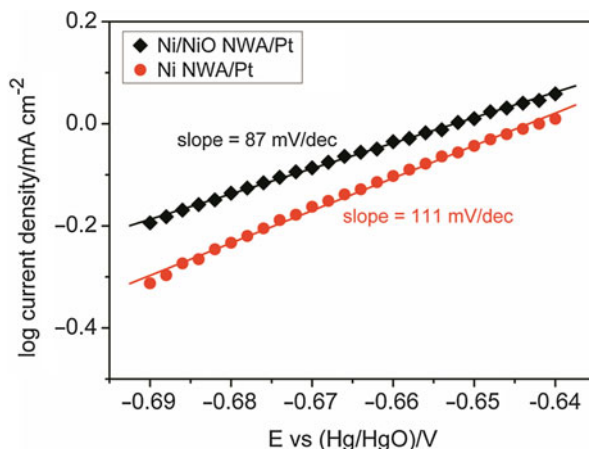
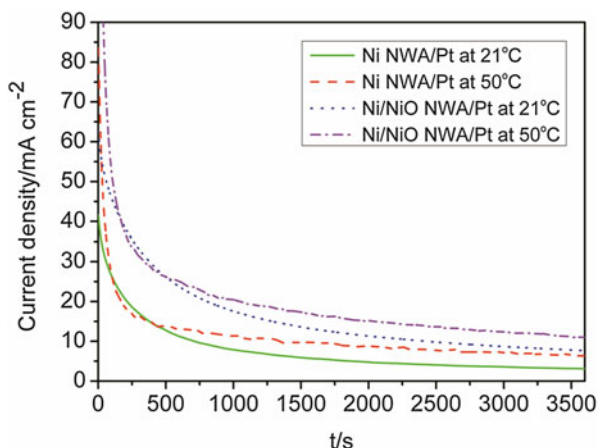


Fig. 15 Chronoamperograms for the electrooxidation of ethanol on 1D Ni NWA/Pt and Ni/NiO NWA/Pt at -0.2 V (vs. Hg/HgO) in 0.5 M KOH/1 M ethanol solution at 21 °C and 50 °C (Reproduced with permission from Ref. [63])



temperatures. The electrooxidation current densities at the end of 3,600 s test at 21 °C are 3 and 8 mAcm⁻² for the Ni NWA/Pt and Ni/NiO NWA/Pt electrocatalysts, respectively, whereas at 50 °C, these current densities rise to 6 and 11 mA cm⁻², respectively. The core/shell metal/oxide NWA as the support exhibits the higher electrocatalytic stability toward ethanol electrooxidation at both operating temperatures investigated.

Conclusions

A simple, low-cost, and effective fabrication process has been demonstrated for the construction of one-dimensional, vertical, and core/shell Ni/NiO nanostructures for pseudocapacitor electrodes. The fabrication of the electrode is based on direct electrochemical deposition of Ni inside a nanoporous alumina template and the subsequent conversion of the outer shell into oxide by oxygen plasma annealing after template removal. The crystal structure, morphology, and shell thickness were found to be dependent on the annealing conditions (input power and annealing time). The electrode annealed at 50 W for 120 s demonstrated high capacitance (0.36 F cm^{-2}) with high charge–discharge kinetics. For the same electrode, a high degree of stability was attained for long-term cycling (over 2,000 cycles). The high charge–discharge kinetics and high capacitance resulted from the unique core/shell Ni/NiO nanoarchitecture, which offers a highly conductive and robust core for enhanced electronic transports to the NiO shell and a large electroactive surface area for charge storage and redox reactions. The fabrication method of the core/shell nanowire array electrodes is both simple and effective, and thereby it can potentially be applied for volume production of integrated electrochemical capacitors [14].

Modified Ni/NiO NW arrays with porous Pt nanoparticles have been used as anode material in a fuel cell. The hybrid nanoelectrocatalyst has been reported to exhibit excellent electrocatalytic activity and stability for the electrooxidation of ethanol in alkaline media. The enhancement in electrocatalytic performance compared to the commercial Pt/C NP anode electrocatalysts as reported in literature can be attributed to few facts such as (i) uniform free-standing nanowires which are free from any surfactants/ancillaries, (ii) porous Pt NP at the NiO surface which is supported by a conducting robust core of metallic Ni nanowire, and (iii) interspacing of the nanowires ensuring the access of alcohol for fast ion adsorption/desorption. The specific and mass activity for the electrooxidation of ethanol on the Ni/NiO NWA/Pt structure is approximately 1.5 times higher than that on Ni NWA/Pt at the same Pt loading. The higher stability and tolerance to CO-like poisoning of Ni/NiO NWA/Pt electrocatalyst has been observed both at low and higher temperatures. The oxide promotion effect in electrocatalytic activity can be attributed to the synergistic interaction between the Pt NP and the NiO nano-shell formed at the outer surface of conductive 1D metallic Ni core. The work described in this chapter is new in terms of the fabrication of a highly active and stable 1D Ni/NiO NWA/Pt electrocatalyst, which can lead as alternative electrocatalyst system to commercial Pt/C NPs currently used in ADEFC. The developed porous 1D Ni/NiO NWA/Pt nanostructure similarly has the potential applications in chemical sensors for the detection of gaseous or aqueous species such as NO_2 , CO , CO_2 , or $\text{C}_2\text{H}_5\text{OH}$.

Acknowledgments This work is financially supported by Enterprise Ireland (EI) under the commercialization fund CFTD/2008/322.

References

1. Armand M, Tarascon JM (2008) Building better batteries. *Nature* 451(7179):652–657. doi:10.1038/451652a
2. Chmiola J, Largeot C, Taberna PL, Simon P, Gogotsi Y (2010) Monolithic carbide-derived carbon films for micro-supercapacitors. *Science* 328(5977):480–483. doi:10.1126/science.1184126
3. Tarascon JM, Armand M (2001) Issues and challenges facing rechargeable lithium batteries. *Nature* 414(6861):359–367
4. Zhang Y, Feng H, Wu XB, Wang LZ, Zhang AQ, Xia TC, Dong HC, Li XF, Zhang LS (2009) Progress of electrochemical capacitor electrode materials: a review. *Int J Hydrog Energy* 34(11):4889–4899. doi:10.1016/j.ijhydene.2009.04.005
5. Zhang CX, Hu J, Cong J, Zhao YP, Shen W, Toyoda H, Nagatsu M, Meng YD (2011) Pulsed plasma-polymerized alkaline anion-exchange membranes for potential application in direct alcohol fuel cells. *J Power Sources* 196(13):5386–5393. doi:10.1016/j.jpowsour.2011.02.073
6. Wei TY, Chen CH, Chang KH, Lu SY, Hu CC (2009) Cobalt oxide aerogels of ideal supercapacitive properties prepared with an epoxide synthetic route. *Chem Mater* 21(14):3228–3233. doi:10.1021/cm9007365
7. Brousse T, Toupin M, Dugas R, Athouel L, Crosnier O, Belanger D (2006) Crystalline MnO₂ as possible alternatives to amorphous compounds in electrochemical supercapacitors. *J Electrochem Soc* 153(12):A2171–A2180. doi:10.1149/1.2352197
8. Lei Y, Daffos B, Taberna PL, Simon P, Favier F (2010) MnO₂-coated Ni nanorods: enhanced high rate behavior in pseudo-capacitive supercapacitor. *Electrochim Acta* 55(25):7454–7459. doi:10.1016/j.electacta.2010.03.012
9. Zhao DD, Bao SJ, Zhou WH, Li HL (2007) Preparation of hexagonal nanoporous nickel hydroxide film and its application for electrochemical capacitor. *Electrochem Commun* 9(5):869–874. doi:10.1016/j.elecom.2006.11.030
10. Tao BR, Zhang JA, Miao FJ, Hui SC, Wan LJ (2010) Preparation and electrochemistry of NiO/SiNW nanocomposite electrodes for electrochemical capacitors. *Electrochim Acta* 55(18):5258–5262. doi:10.1016/j.electacta.2010.04.057
11. Kim JH, Zhu K, Yan YF, Perkins CL, Frank AJ (2010) Microstructure and pseudocapacitive properties of electrodes constructed of oriented NiO-TiO₂ nanotube arrays. *Nano Lett* 10(10):4099–4104. doi:10.1021/nl102203s
12. Wang DC, Ni WB, Pang H, Lu QY, Huang ZJ, Zhao JW (2010) Preparation of mesoporous NiO with a bimodal pore size distribution and application in electrochemical capacitors. *Electrochim Acta* 55(22):6830–6835. doi:10.1016/j.electacta.2010.05.084
13. Wu MS, Huang YA, Yang CH, Jow HH (2007) Electrodeposition of nanoporous nickel oxide film for electrochemical capacitors. *Int J Hydrog Energy* 32(17):4153–4159. doi:10.1016/j.ijhydene.2007.06.001
14. Hasan M, Jamal M, Razeem KM (2012) Coaxial NiO/Ni nanowire arrays for high performance pseudocapacitor applications. *Electrochim Acta* 60:193–200. doi:10.1016/j.electacta.2011.11.039
15. Liu H, Ye J, Xu C, Jiang SP, Tong Y (2007) Kinetics of ethanol electrooxidation at Pd electrodeposited on Ti. *Electrochem Commun* 9(9):2334–2339. doi:10.1016/j.elecom.2007.06.036
16. Lu Z, Chang Z, Liu J, Sun X (2011) Stable ultrahigh specific capacitance of NiO nanorod arrays. *Nano Research* 4(7):658–665. doi:10.1007/s12274-011-0121-1
17. Gao HL, Liao SJ, Liang ZX, Liang HG, Luo F (2011) Anodic oxidation of ethanol on core-shell structured Ru@PtPd/C catalyst in alkaline media. *J Power Sources* 196(15):6138–6143. doi:10.1016/j.jpowsour.2011.03.031
18. Antolini E (2007) Catalysts for direct ethanol fuel cells. *J Power Sources* 170(1):1–12. doi:10.1016/j.jpowsour.2007.04.009
19. Zhou WJ, Song SQ, Li WZ, Zhou ZH, Sun GQ, Xin Q, Douvartzides S, Tsiakaras P (2005) Direct ethanol fuel cells based on PtSn anodes: the effect of Sn content on the fuel cell performance. *J Power Sources* 140(1):50–58. doi:10.1016/j.jpowsour.2004.08.003

20. Lai SCS, Koper MTM (2009) Ethanol electro-oxidation on platinum in alkaline media. *Phys Chem Chem Phys* 11(44):10446–10456. doi:10.1039/b913170a
21. Vigier F, Coutanceau C, Perrard A, Belgsir EM, Lamy C (2004) Development of anode catalysts for a direct ethanol fuel cell. *J Appl Electrochem* 34(4):439–446. doi:10.1023/B:JACH.0000016629.98535.ad
22. Xu CW, Cheng LQ, Shen PK, Liu YL (2007) Methanol and ethanol electrooxidation on Pt and Pd supported on carbon microspheres in alkaline media. *Electrochem Commun* 9(5):997–1001. doi:10.1016/j.elecom.2006.12.003
23. Spendelov JS, Wieckowski A (2007) Electrocatalysis of oxygen reduction and small alcohol oxidation in alkaline media. *Phys Chem Chem Phys* 9(21):2654–2675. doi:10.1039/b703315j
24. Elezovic NR, Babic BM, Radmilovic VR, Vracar LM, Krstajic NV (2011) Nb-TiO(2) supported platinum nanocatalyst for oxygen reduction reaction in alkaline solutions. *Electrochim Acta* 56(25):9020–9026. doi:10.1016/j.electacta.2011.04.075
25. Steele BCH, Heinzel A (2001) Materials for fuel-cell technologies. *Nature* 414(6861):345–352. doi:10.1038/35104620
26. Huang M, Dong G, Wang N, Xu J, Guan L (2011) Highly dispersive Pt atoms on the surface of RuNi nanoparticles with remarkably enhanced catalytic performance for ethanol oxidation. *Energy Environ Sci* 4(11):4513–4516. doi:10.1039/c1ee02044g
27. Yano J, Takatsuka Y, Harima Y, Kitani A (2011) Pt and Sn-dispersed polyaniline electrodes for the anodes of the direct ethanol fuel cell. *Electrochemistry* 79(5):424–427
28. Leger JM, Rousseau S, Coutanceau C, Hahn F, Lamy C (2005) How bimetallic electrocatalysts does work for reactions involved in fuel cells? Example of ethanol oxidation and comparison to methanol. *Electrochim Acta* 50(25–26):5118–5125. doi:10.1016/j.electacta.2005.01.051
29. Rousseau S, Coutanceau C, Lamy C, Leger JM (2006) Direct ethanol fuel cell (DEFC): electrical performances and reaction products distribution under operating conditions with different platinum-based anodes. *J Power Sources* 158(1):18–24. doi:10.1016/j.jpowsour.2005.08.027
30. Ghosh S, Raj CR (2010) Facile in situ synthesis of multiwall carbon nanotube supported flowerlike Pt nanostructures: an efficient electrocatalyst for fuel cell application. *J Phys Chem C* 114(24):10843–10849. doi:10.1021/jp100551e
31. Cheng N, Li H, Li G, Lv H, Mu S, Sun X, Pan M (2011) Highly active Pt@Au nanoparticles encapsulated in perfluorosulfonic acid for the reduction of oxygen. *Chem Commun* 47(48):12792–12794. doi:10.1039/c1cc15203c
32. Morozan A, Jusselme B, Palacin S (2011) Low-platinum and platinum-free catalysts for the oxygen reduction reaction at fuel cell cathodes. *Energy Environ Sci* 4(4):1238–1254. doi:10.1039/c0ee00601g
33. Wang D, Xin HL, Yu Y, Wang H, Rus E, Muller DA, Abruna HD (2010) Pt-decorated PdCo@Pd/C core-shell nanoparticles with enhanced stability and electrocatalytic activity for the oxygen reduction reaction. *J Am Chem Soc* 132(50):17664–17666. doi:10.1021/ja107874u
34. Manoharan R, Goodenough JB (1992) Methanol oxidation in acid on ordered NiTi. *J Mater Chem* 2(8):875–887
35. Koenigsmann C, Wong SS (2011) One-dimensional noble metal electrocatalysts: a promising structural paradigm for direct methanol fuel cells. *Energy Environ Sci* 4(4):1161–1176. doi:10.1039/c0ee00197j
36. Zhao X, Yin M, Ma L, Liang L, Liu C, Liao J, Lu T, Xing W (2011) Recent advances in catalysts for direct methanol fuel cells. *Energy Environ Sci* 4(8):2736–2753. doi:10.1039/c1ee01307f
37. Watanabe M, Motoo S (1975) Electrocatalysis by ad-atoms: part II. Enhancement of the oxidation of methanol on platinum by ruthenium ad-atoms. *J Electroanal Chem* 60(3):267–273. doi:10.1016/s0022-0728(75)80261-0
38. Chen C-H, Sarma LS, Wang D-Y, Lai F-J, Al Andra C-C, Chang S-H, Liu D-G, Chen C-C, Lee J-F, Hwang B-J (2010) Platinum-decorated ruthenium nanoparticles for enhanced methanol electrooxidation. *ChemCatChem* 2(2):159–166. doi:10.1002/cctc.200900051
39. Sasaki K, Wang JX, Balasubramanian M, McBreen J, Uribe F, Adzic RR (2004) Ultra-low platinum content fuel cell anode electrocatalyst with a long-term performance stability. *Electrochim Acta* 49(22–23):3873–3877. doi:10.1016/j.electacta.2004.01.086

40. Ianniello R, Schmidt VM, Stimming U, Stumper J, Wallau A (1994) CO adsorption and oxidation on Pt and PtRu alloys: dependence on substrate composition. *Electrochim Acta* 39(11–12):1863–1869. doi:10.1016/0013-4686(94)85176-x
41. Mahendiran C, Maiyalagan T, Scott K, Gedanken A (2011) Synthesis of a carbon-coated NiO/MgO core/shell nanocomposite as a Pd electro-catalyst support for ethanol oxidation. *Mater Chem Phys* 128(3):341–347. doi:10.1016/j.matchemphys.2011.02.067
42. Kristian N, Yu Y, Lee J-M, Liu X, Wang X (2010) Synthesis and characterization of Co(core)-Pt(shell) electrocatalyst prepared by spontaneous replacement reaction for oxygen reduction reaction. *Electrochim Acta* 56(2):1000–1007. doi:10.1016/j.electacta.2010.09.073
43. Strasser P (2009) Dealloyed core-shell fuel cell electrocatalysts. *Rev Chem Eng* 25(4):255–295. doi:10.1515/revce.2009.25.4.255
44. Strasser P (2008) Fuel cell catalyst particles have platinum-rich shell, copper core. *Adv Mater Process* 166(1):13–13
45. Li Y, Hu FP, Wang X, Shen PK (2008) Anchoring metal nanoparticles on hydrofluoric acid treated multiwalled carbon nanotubes as stable electrocatalysts. *Electrochem Commun* 10(7):1101–1104. doi:10.1016/j.elecom.2008.05.025
46. Zhao Y, Fan L, Zhong H, Li Y, Yang S (2007) Platinum nanoparticle clusters immobilized on multiwalled carbon nanotubes: electrodeposition and enhanced electrocatalytic activity for methanol oxidation. *Adv Funct Mater* 17(9):1537–1541. doi:10.1002/adfm.200600416
47. Rauhe BR, McLarnon FR, Cairns EJ (1995) Direct anodic-oxidation of methanol on supported platinum ruthenium catalyst in aqueous cesium carbonate. *J Electrochem Soc* 142(4):1073–1084. doi:10.1149/1.2044547
48. Guo S, Dong S, Wang E (2010) Novel Te/Pt hybrid nanowire with nanoporous surface: a catalytically active nanoelectrocatalyst. *J Phys Chem C* 114(11):4797–4802. doi:10.1021/jp909623x
49. Liu L, Pippel E, Scholz R, Goesele U (2009) Nanoporous Pt-Co alloy nanowires: fabrication, characterization, and electrocatalytic properties. *Nano Lett* 9(12):4352–4358. doi:10.1021/nl902619q
50. Mohl M, Kumar A, Reddy ALM, Kukovec A, Konya Z, Kiricsi I, Vajtai R, Ajayan PM (2010) Synthesis of catalytic porous metallic nanorods by galvanic exchange reaction. *J Phys Chem C* 114(1):389–393. doi:10.1021/jp9083508
51. Zhou W-P, Axnanda S, White MG, Adzic RR, Hrbek J (2011) Enhancement in ethanol electro-oxidation by SnO(x) nanoislands grown on Pt(111): effect of metal oxide-metal interface sites. *J Phys Chem C* 115(33):16467–16473. doi:10.1021/jp203770x
52. Xu CW, Shen PK, Ji XH, Zeng R, Liu YL (2005) Enhanced activity for ethanol electro oxidation on Pt-MgO/C catalysts. *Electrochem Commun* 7(12):1305–1308. doi:10.1016/j.elecom.2005.09.015
53. Bai Y, Wu J, Qiu X, Xi J, Wang J, Li J, Zhu W, Chen L (2007) Electrochemical characterization of Pt-CeO₂/C and Pt-CexZr1-xO₂/C catalysts for ethanol electro-oxidation. *Appl Catal B Environ* 73(1–2):144–149. doi:10.1016/j.apcatb.2006.06.026
54. Xu CW, Shen PK (2005) Electrochemical oxidation of ethanol on Pt-CeO₂/C catalysts. *J Power Sources* 142(1–2):27–29. doi:10.1016/j.jpowsour.2004.10.017
55. Bai YX, Wu JJ, Xi JY, Wang JS, Zhu WT, Chen LQ, Qiu XP (2005) Electrochemical oxidation of ethanol on Pt-ZrO₂/C catalyst. *Electrochem Commun* 7(11):1087–1090. doi:10.1016/j.elecom.2005.08.002
56. Tabet-Aoul A, Saidani F, Rochefort D, Mohamedi M (2011) Pulsed laser synthesis of SnO(2)-Pt nano-thin films onto carbon nanotubes and their electrocatalytic activity towards ethanol oxidation. *Int J Electrochem Sci* 6(12):6385–6397
57. Wang X-y, Zhang J-c, Cao X-d, Jiang Y-s, Zhu H (2011) Synthesis and characterization of Pt-MoO(x)-TiO(2) electrodes for direct ethanol fuel cells. *Int J Miner Metall Mater* 18(5):594–599. doi:10.1007/s12613-011-0483-0
58. Guo D-J (2011) Electrooxidation of ethanol on novel multi-walled carbon nanotube supported platinum-antimony tin oxide nanoparticle catalysts. *J Power Sources* 196(2):679–682. doi:10.1016/j.jpowsour.2010.07.075

59. Wang XH, Li XW, Sun XL, Li F, Liu QM, Wang Q, He DY (2011) Nanostructured NiO electrode for high rate Li-ion batteries. *J Mater Chem* 21(11):3571–3573. doi:10.1039/c0jm04356g
60. Lu Q, Lattanzi MW, Chen YP, Kou XM, Li WF, Fan X, Unruh KM, Chen JGG, Xiao JQ (2011) Supercapacitor electrodes with high-energy and power densities prepared from monolithic NiO/Ni nanocomposites. *Angew Chem Int Edit* 50(30):6847–6850. doi:10.1002/anie.201101083
61. Xu CW, Shen PK, Liu YL (2007) Ethanol electrooxidation on Pt/C and Pd/C catalysts promoted with oxide. *J Power Sources* 164(2):527–531. doi:10.1016/j.jpowsour.2006.10.071
62. Xu C, Tian Z, Shen P, Jiang SP (2008) Oxide (CeO₂, NiO, Co₃O₄ and Mn₃O₄)-promoted Pd/C electrocatalysts for alcohol electrooxidation in alkaline media. *Electrochim Acta* 53(5):2610–2618. doi:10.1016/j.electacta.2007.10.036
63. Hasan M, Newcomb SB, Razeeb KM (2012) Porous core/shell Ni@NiO/Pt hybrid nanowire arrays as a high efficient electrocatalyst for alkaline direct ethanol fuel cells. *J Electrochem Soc* 159(7):F203–F209. doi:10.1149/2.015207jes
64. Xi-ke T, Xiao-yu Z, Li-de Z, Chao Y, Zhen-bang P, Su-xin Z (2008) Performance of ethanol electro-oxidation on Ni–Cu alloy nanowires through composition modulation. *Nanotechnology* 19(21):215711
65. Zhu C, Guo S, Dong S (2012) Facile synthesis of trimetallic AuPtPd alloy nanowires and their catalysis for ethanol electrooxidation. *J Mater Chem* 22(30):14851–14855. doi:10.1039/C2JM32663A
66. Zhang Z, Xin L, Sun K, Li W (2011) Pd–Ni electrocatalysts for efficient ethanol oxidation reaction in alkaline electrolyte. *Int J Hydrog Energy* 36(20):12686–12697. doi:http://dx.doi.org/10.1016/j.ijhydene.2011.06.141
67. Ding L-X, Li G-R, Wang Z-L, Liu Z-Q, Liu H, Tong Y-X (2012) Porous Ni@Pt core-shell nanotube array electrocatalyst with high activity and stability for methanol oxidation. *Chem A Eur J* 18(27):8386–8391. doi:10.1002/chem.201200009
68. Liu JW, Essner J, Li J (2010) Hybrid supercapacitor based on coaxially coated manganese oxide on vertically aligned carbon nanofiber arrays. *Chem Mater* 22(17):5022–5030. doi:10.1021/cm101591p
69. Jiang J, Kucernak A (2002) Electrochemical supercapacitor material based on manganese oxide: preparation and characterization. *Electrochim Acta* 47(15):2381–2386. doi:10.1016/S0013-4686(02)00031-2
70. Singh RN, Singh A, Anindita (2009) Electrocatalytic activity of binary and ternary composite films of Pd, MWCNT and Ni, part II: methanol electrooxidation in 1 M KOH. *Int J Hydrog Energy* 34(4):2052–2057. doi:10.1016/j.ijhydene.2008.12.047

Electrochemical Synthesis of Metal Chalcogenide Nanorods, Nanotubes, Segmented Nanorods, and Coaxial Nanorods

Néstor L. Chévere-Trinidad, Serkan Gurbuz,
Jessica Kramer, and Dhandapani Venkataraman

Contents

Introduction.....	102
Background.....	104
Synthetic Methods.....	104
Optimization of the Electrochemical Synthesis of Cadmium Selenide.....	105
Electrodeposition on Metallic Surfaces and Other Materials.....	108
Role of the Templates.....	111
Role of the pH.....	122
Segmented Nanorods.....	124
Coaxial Nanorods.....	126
Conclusions.....	131
References.....	132

Abstract

Electrodeposition is a key technique to create nanostructures of metals and inorganic semiconductors. Unlike the electrodeposition of metals, the fabrication of nanostructures of binary semiconductors with desired crystallinity and stoichiometry is not straightforward. Herein, we describe the optimization of conditions for the electrodeposition of stoichiometry and crystalline cadmium selenide (CdSe), cadmium telluride (CdTe), and CdSe/CdTe nanostructures. We first identified the optimal conditions for the electrodeposition of CdSe and CdTe with 1:1 stoichiometry by varying the concentrations of Cd²⁺ and SeO₂ (or TeO₂) and optimizing the electrodeposition potential. We then optimized the pH of the

N.L. Chévere-Trinidad • S. Gurbuz • J. Kramer • D. Venkataraman (✉)
Department of Chemistry, University of Massachusetts Amherst, Amherst, MA, USA
e-mail: nestor.chevere@aic.edu; serkangurbuz232@gmail.com; jkramer@sandiego.edu;
dv@chem.umass.edu

electrolysis solution for increasing the crystallinity of the deposited structures. We then tested the efficacy of our electrodeposition conditions on substrates such as gold, nickel, and indium tin oxide. We used the optimized conditions to electrodeposit semiconductors within anodic aluminum oxide (AAO) membranes to create oriented CdSe and CdTe nanorods, CdSe/CdTe segmented nanorods, and CdSe/CdTe coaxial nanorods. These optimized electrodeposition conditions add a valuable tool in the synthetic toolbox for the synthesis of crystalline semiconductor nanostructures for solar cell applications.

Keywords

Cadmium selenide • Coaxial nanorods • Nanorods • Porous templates

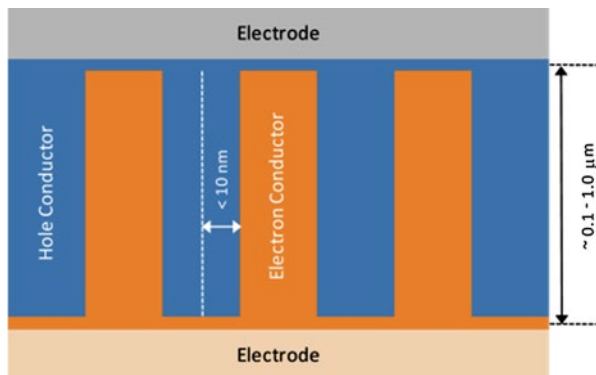
Introduction

In recent years, metal chalcogenides have attracted much attention due to their unique physical properties as a semiconducting material with promising applications to electronic devices [1–3]. These materials have been widely used as biological fluorescence labels [4–6] and as active layers in light-emitting diodes [7, 8] and lasers [9]. For the past decade, metal chalcogenides (especially cadmium selenide and cadmium telluride) have been extensively studied for high-efficiency and low-cost hybrid solar cells [10–12]. (Table 1 shows a summary application and the materials used.) Typically, nanoparticles are chemically synthesized and dispersions of nanoparticles in organic solvents are used to formulate the active layer in hybrid cells. However, it has been difficult to consistently obtain the required nanoscale morphologies using this approach. In this regard, we believe that electrochemical synthesis of chalcogenide semiconductors can provide a viable

Table 1 Representative examples of applications of inorganic semiconductor nanostructures

Applications	Materials	References
Electronic devices	Semiconductor clusters, nanocrystals, and quantum dots	Alivisatos [1]
	Quantum dots	Bawendi [2]
	Metal dichalcogenide nanosheets	Chhowalla [3]
Biological fluorescence labels	Semiconductor nanocrystals	Bruchez [4]
	Quantum dot bioconjugates	Chan [5]
	CdSe-ZnS quantum dot bioconjugates	Mattoussi [6]
Light-emitting diodes	Single monolayers of nanocrystals	Coe [7]
	Nanocrystal quantum dots	Klimov [8]
Lasers	Polymer/quantum dot nanocomposites	Park [9]
Hybrid solar cells	Nanocrystals	Gur [10]
	Nanocrystal-polymer composites	Liu [11]
	CdSe nanocrystals	Han [12]

Fig. 1 Schematic representation of the ideal architectures for a photovoltaic device



pathway to create nanoscale morphologies for solar cell applications. In this chapter, we provide protocols for the electrochemical synthesis of chalcogenide semiconductors.

In a hybrid device, inorganic nanoscale semiconductors and organic conjugated polymers are blended and cast as thin film. Figure 1 shows a representation of a cross section of commonly targeted architecture for a hybrid device. This architecture, termed as ordered heterojunction, provides an interface within the exciton diffusion distance (typically < 10 nm) and consists of parallel and regular cylinders or sheets of semiconductors.

In hybrid solar cells, nonorganic semiconductors can be used as the electron donor material or the electron acceptor depending on the location of the valence and conduction bands relative to the conjugated polymer. Typically the organic conjugated polymer acts as the hole conductor and the inorganic semiconductor acts as electron conductor. Inorganic electron conductors have certain advantages over organic electron conductors (such as C_{60} -based molecules) due to their high charge-carrier mobility and stability [13]. One of the most important requirements that inorganic semiconductors must meet is the inherent crystallinity of the semiconductor. High crystallinity is directly related to high charge-carrier mobility, which mean charges (electron and holes) are quickly transported to the electrode with the reduction of current lost via exciton recombination [14].

Several methods have been developed to fabricate oriented, highly crystalline semiconductor nanostructures. Examples of these methods are vapor-liquid-solid (VLS) [15], solution-liquid-solid (SLS) [15, 16], and thermal reduction process [17, 18]. In these methods, precursors of the semiconductor, or the semiconducting material itself, are converted into a vapor (VLS) or are taken from a solution (SLS) and solidified into a single crystal material. In order to convert the materials to the vapor phase, high-temperature and/or high-vacuum systems are needed. Due to the slow crystallization process, these methods offer an alternative to obtain highly crystalline materials. However, it has been difficult to fabricate such systems over large areas.

Another promising method to fabricate these materials is electrochemical deposition [19–24]. This technique involves an electrochemical reaction of the precursors in solution which are deposited as the final material on an electrode surface. One of the most important advantages of this technique is that it does not require high vacuum and can be performed at room temperature. However, poor crystallinity of the final materials, control of the phase, and stoichiometric problems are found using electrochemical synthesis. Herein, we report the protocols for the electrochemical synthesis of highly crystalline-oriented cadmium selenide and cadmium telluride.

Background

Synthetic Methods

There are several methods reported for the synthesis of cadmium selenide (CdSe) and cadmium telluride (CdTe) including molecular beam epitaxy (MBE) [25], metal-organic vapor chemical deposition (MOCVD) [26], organometallic vapor phase epitaxy (OMVPE) [27], solvothermal methods [28, 29], and hydrothermal methods [30–32]. Vapor-liquid-solid (VLS) process is also a widely used method for the synthesis of non-binary semiconductors such as silicon or germanium [33]. Although highly crystalline materials are obtained with these methods, they require high temperature and high vacuum making them not suitable for a facile synthesis of CdSe or CdTe nanostructures.

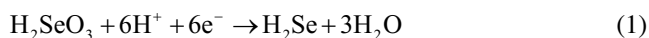
Electrodeposition has been studied as an alternative because it offers a convenient and an inexpensive synthetic way for the preparation of cadmium chalcogenides from aqueous or nonaqueous solutions of the appropriate precursors [34, 35]. Electrodeposition has the advantage of being a low-temperature method so it can be used in systems containing thermal unstable materials. Another major advantage of using room temperature is that the electrodes and the semiconductors may have different thermal expansion coefficients. Refer to Table 2.

Table 2 Synthetic methods for metal chalcogenide semiconductors

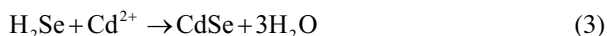
Method	Binary semiconductor	References
Molecular beam epitaxy (MBE)	ZnCdSe quantum dots	Zhang [25]
Metal-organic vapor chemical deposition (MOCVD)	ZnSe quantum dots	Liao [26]
Organometallic vapor phase epitaxy (OMVPE)	ZnSe epitaxial layers	Bourret-Courchesne [27]
Solvothermal	ZnS and ZnSe nanocrystallites	Deng [28]
	CdS nanorods	Li [29]
Hydrothermal	ZnSe and CdSe nanocrystals	Wang [30]
		Peng [31]
	Amorphous cluster and nanocrystalline CdSe	Ge [32]
Electrodeposition	Thin film semiconductors	Lokhande [35]

Optimization of the Electrochemical Synthesis of Cadmium Selenide

In order to synthesize CdSe, the method reported by Kressin and Sailor [21] was used. In this protocol, CdSe was electrochemically synthesized from an aqueous solution of cadmium chloride (CdCl_2) and selenium dioxide (SeO_2). Hydrochloric acid (HCl) was used as the supporting electrolyte for the electrodeposition. Reactions 1 and 2 show the electrochemical reaction of SeO_2 in acidic conditions. Hydrogen selenide (H_2Se) is formed after a potential is applied to the solution (Reaction 1). Reaction 2 shows the reaction of H_2Se with H_2SeO_3 to form elemental selenium (Se).



The net reaction for the electrodeposition of CdSe is stated to occur via the reaction of H_2Se and Cd^{2+} (Reaction 3). Figure 2a shows formation of CdSe at atomic levels.



In order to avoid the formation elemental Se, a large stoichiometric excess of Cd^{2+} was used. This creates a competition reaction between reactions 1 and 2 and the Cd^{2+} in the solution. Mishra and Rajeshwar [36] have postulated a direct

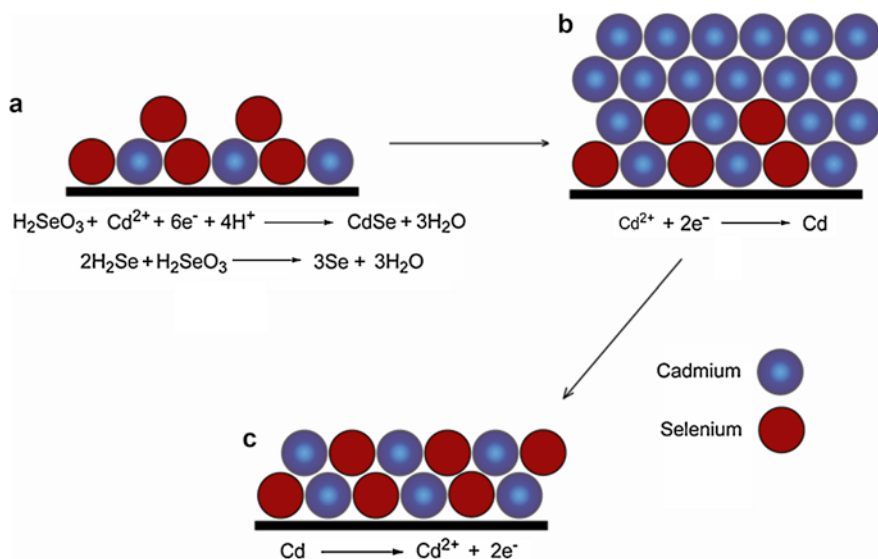
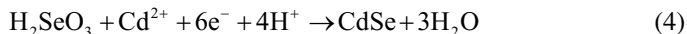


Fig. 2 Schematic representation of the CdSe electrodeposition by cyclic voltammetry (Figure redrawn from Kressin et al. [21])

$6e^-$ deposition process as a mechanism for the CdSe electrochemical synthesis. This process is represented on the reaction 4.



This procedure deposits a submonolayer of CdSe and a large layer of metallic Cd (Fig. 2b). Then the electrode is swept to a positive potential in order to strip the excess of elemental Cd (Fig. 2c).

Figure 3 shows the cyclic voltammogram for the electrodeposition of CdSe over nickel as a working electrode. The region A corresponds to the electrodeposition of CdSe. Region B is the potential range where the cathodic electrodeposition of elemental Cd occurs. Region C is the region where the excess of Cd is stripped off by sweeping the electrode to a positive potential.

CdSe was deposited at room temperature with a three-electrode setup, using silver/silver chloride reference electrode (Ag/AgCl) and a Pt wire as the counter or auxiliary electrode. Titanium and nickel were used as working electrode. The electrodeposition solution contained 0.1 M of CdCl₂, 0.2 M HCl, and 0.1 mM SeO₂. The concentration of Cd²⁺ is 100 times larger than the concentration of SeO₂. As explained above, the excess of cadmium ions is needed to avoid the formation of elemental Se. Cyclic voltammetry technique was used in the early experiments. The potential range typically used was between -0.355 and -0.755 V versus Ag/AgCl at a scan rate of 100 mV/s.

The work by Sailor et al. [21] was done using a rotating disk electrode (RDE). In their work they deposited a film of CdSe over nickel. They calculated that in the reduction process, which corresponds to region B on Fig. 3, the excess of Cd is about

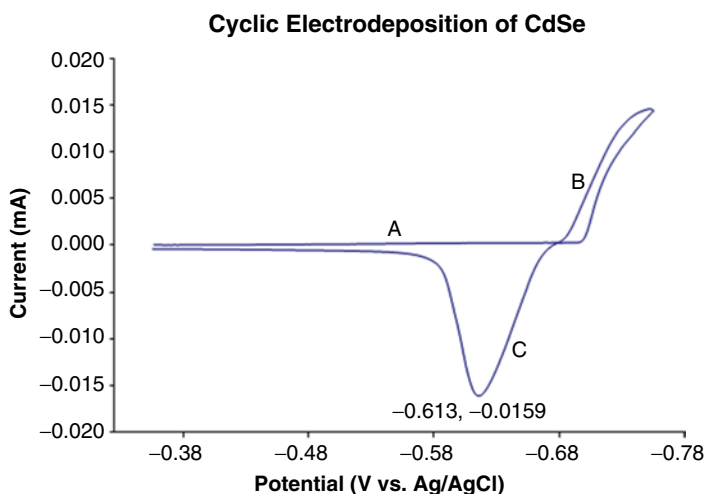


Fig. 3 Cyclic voltammogram of the electrochemical deposition of CdSe. Three-electrode setup cell: Pt wire as the auxiliary electrode, Ni plate as the working electrode, and Ag/AgCl as the reference electrode. Potential range -0.355 to -0.755 V, scan rate=100 mV/s, and Bioanalytical Systems C50W potentiostat

five atoms of Cd per atom of Se. This value was obtained under their conditions. During the stripping process, where the excess of Cd is oxidized to Cd^{2+} , the formed CdSe is thermodynamically and kinetically stable that it cannot be stripped in the process. They assumed that CdSe deposition was limited by diffusion of the Se-containing species to the electrode. With this assumption and using the Levich equation (Eq. 1), they calculated the amount of CdSe that can be deposited per cycle.

$$I_{\text{lim}} = 0.62 n F A D^{2/3} \nu^{-1/6} C * \omega^{1/2} \quad (5)$$

In Eq. 1, I is the Levich current, n is the number of electrons transferred in the half reaction, F is the Faraday constant ($96485.3415 \text{ s A/mol}$), A is the area of the electrode, D is the diffusion coefficient, ν is the scan rate, ω is the spin rate of the electrode, and C is the concentration. For a solution of $0.4 \text{ mM H}_2\text{SeO}_3$, with diffusion coefficient of $7.0 \times 10^{-6} \text{ cm}^2 \text{ s}^{-1}$, spin rate of 1000 rpm for the RDE, and a scan rate of 10 V/s with a potential range from -0.4 to -0.8 V versus SCE, they obtained a maximum of $1.6 \times 10^{-10} \text{ mol/cm}$ or 1.7 monolayers of CdSe per cycle.

In our work the number of monolayer deposited per cycle could not be calculated because we were using a fix electrode and porous membranes. Samples were analyzed with the use of energy dispersive X-ray spectroscopy (EDS) to calculate the composition of Cd and Se. The resulting values were compared with Sailor's work. We obtained a Se:Cd ratio = 1.09 in most of the cases and they obtained a Se:Cd ratio = 1.03 .

Direct current (DC) potentiostatic electrodeposition was also investigated. In order to select the optimal working potential, several potentials were tested (from -0.520 to -0.640 V). An example of the DC voltammogram for the deposition of CdSe at -0.590 V is showed on Fig. 4. Figure 5 shows the X-ray powder diffraction (XRD) pattern of the final material (CdSe) deposited at various potentials.

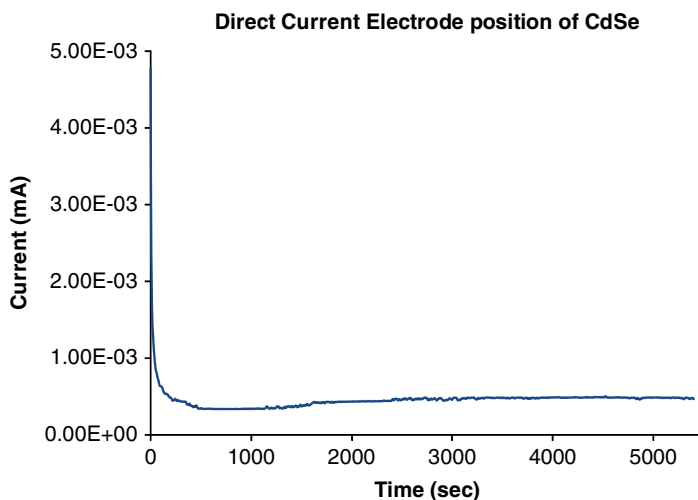


Fig. 4 Direct current voltammogram of the electrochemical deposition of CdSe. Three-electrode setup cell: Pt wire as the auxiliary electrode, Ni plate as the working electrode, and Ag/AgCl as the reference electrode. Potential -0.590 V and a Bioanalytical Systems C50W potentiostat

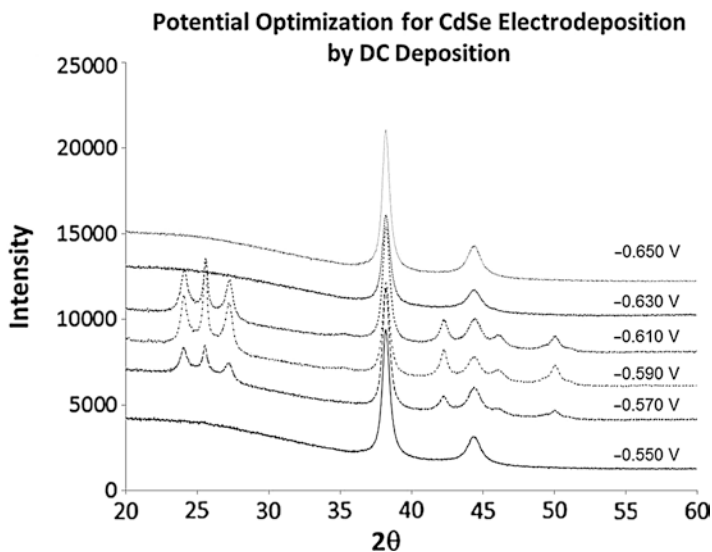


Fig. 5 X-ray powder diffraction pattern of hexagonal CdSe electrodeposited at different potentials. Sample annealed @ 450 °C for 8 h

From the analysis of the XRD pattern for CdSe electrodeposition at various potentials, it can be concluded that the optimal working potential is -0.590 V. The same experimentation was performed for CdTe resulting -0.570 V the optimal working potential for its electrodeposition. DC electrodeposition was chosen to be used as the default deposition technique due to its simplicity.

Electrodeposition on Metallic Surfaces and Other Materials

CdSe and CdTe were deposited over metal surfaces such as Ni, Ti, or Au or over materials such as indium tin oxide (ITO) using cyclic voltammetry or direct current electrodeposition. A scanning electron microscopy (SEM) image of the CdSe deposited over Ni by CV voltammetry is shown in Fig. 6. In this image it can be clearly seen the CdSe nodules formed on the surface of the metal.

The crystallinity of the obtained product was ascertained by X-ray powder diffraction (XRD). Figure 7 shows the XRD pattern for the cubic phase of CdSe. According to Debye-Scherrer formula, full width at half maximum (FWHM) is indirectly proportional to crystallite size. An extremely broad peak is often defined as polycrystalline with most crystallites at few nanometer scales. Sharp peaks are labels for large crystallites in the deposit. From figure below, electrodeposit obtained with CV over nickel is polycrystalline with few nanometer crystallites.

In order to improve the crystallinity of the CdSe, the sample was annealed at 450 °C for 8 h. Additionally, the phase of the material changed from cubic to hexagonal which is the most stable thermodynamic phase of the CdSe. Figure 8 shows

Fig. 6 Scanning electron microscope (SEM) image of CdSe over nickel. Deposition done by cyclic voltammetry

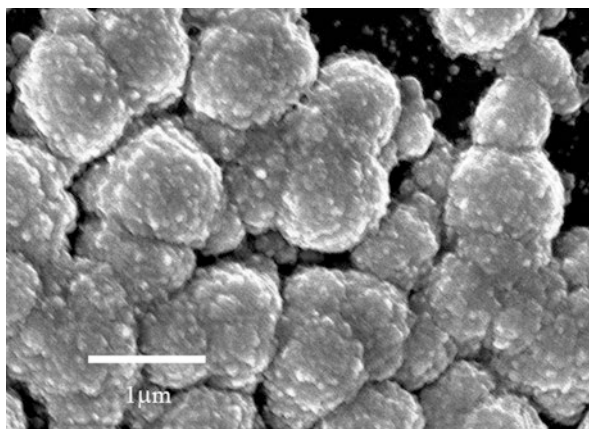
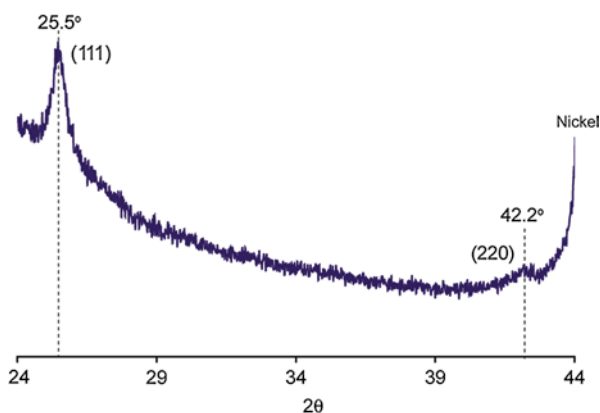


Fig. 7 X-ray powder diffraction for cubic CdSe deposited over nickel



the X-ray powder diffraction pattern of a more crystalline CdSe with lower FWHM values.

The electrodeposition of CdSe was also tested inorganic substrates such as ITO. The deposition was done using an ITO-coated glass as the working electrode by direct current technique at -0.590 V for 45 min (Fig. 9).

The deposition of cadmium telluride was also investigated. Its deposition was done using Au-coated glass as a working electrode by DC technique at a constant potential of -0.570 V for 1 h. CdTe films were characterized by X-ray powder diffraction. Figure 10 shows the XRD pattern for CdTe. Peaks at 38.4° and 44.5° correspond to gold and the three other peaks correspond to the cubic phase of CdTe. These experiments were used to set the optimal parameters to follow for the next experiments done.

In separate experiments, synthesis of semiconductors such as ZnTe, ZnSe, and CdS was done. Zinc chalcogenides were synthesized using the CdSe synthesis but

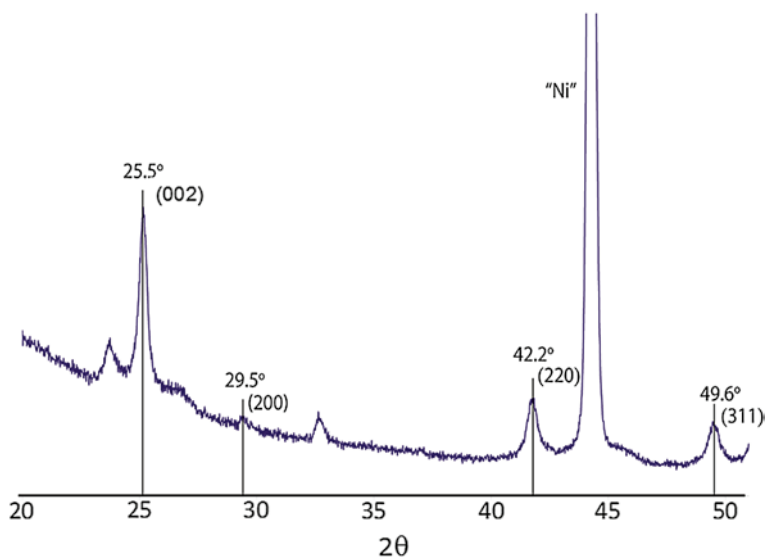


Fig. 8 X-ray powder diffraction for hexagonal CdSe over nickel after annealing at 450 °C for 8 h

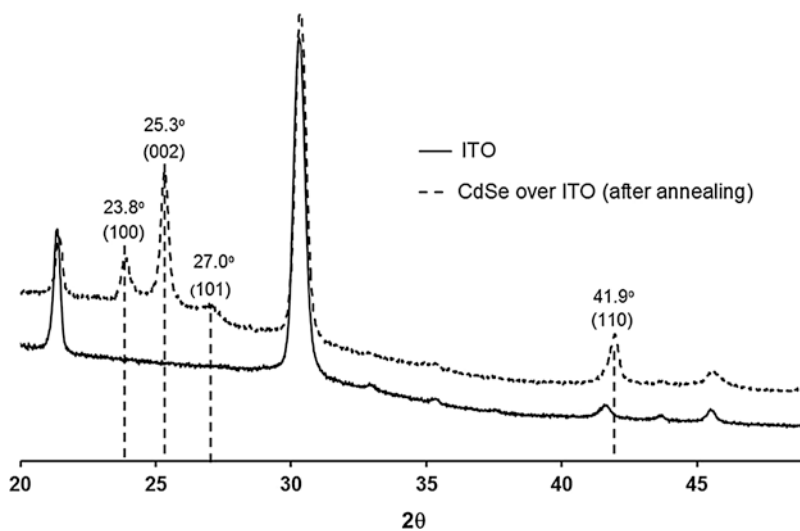


Fig. 9 X-ray powder diffraction for hexagonal CdSe over ITO after annealing at 450 °C for 8 h

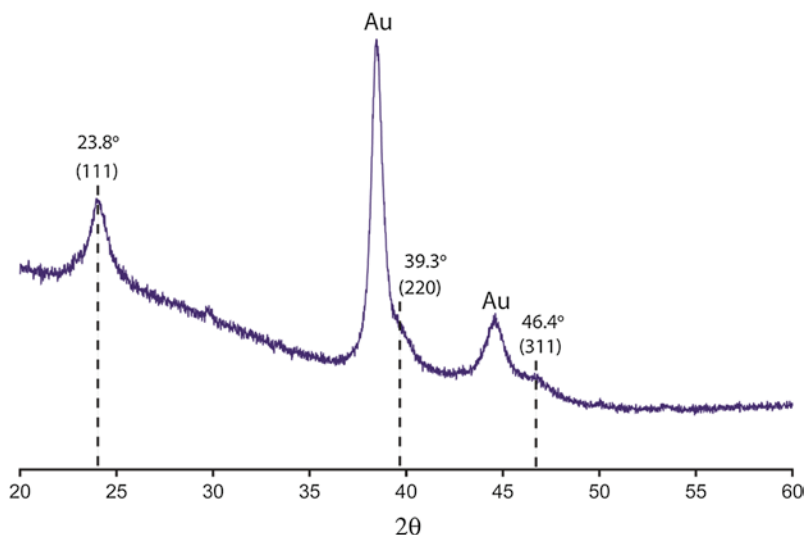


Fig. 10 X-ray powder diffraction for cubic CdTe deposited over gold-coated glass

replacing CdCl_2 for ZnCl_2 . The corresponding ZnTe or ZnSe were not obtained as expected. On the other hand, we tried the electrodeposition of CdS from a solution of CdCl_2 and elemental sulfur in dimethylsulfoxide. In contrast to the electrodeposition of CdSe, CdS was deposited using a high voltage system with a potential of 50 V ac applied between the nickel working electrode and a graphite counter electrodes at 75 °C for 60 min [37]. The product obtained was a fine yellow powder. This product was characterized by X-ray powder diffraction (Fig. 11). No further synthesis of CdS was done.

Role of the Templates

Electrodeposition of CdSe was performed on gold-coated porous membranes such as polycarbonate (PC) and anodic aluminum oxide (AAO). These membranes were used as the working electrode and were prepared by sputtering gold over the membrane surface for 1, 5, 10, or 20 min.

Polycarbonate membranes of 100 or 400 nm pores and approximate 7 μm thicknesses from Millipore and anodic aluminum oxide with 200 or 35 nm pores and 70 μm thicknesses were used as templates. SEM images of the 100 and 400 nm pore polycarbonate membranes are shown in Figs. 12 and 13, respectively. A drawback of the polycarbonate membranes is that there is a distribution of the pore size and the pores are not oriented perpendicular to the surface of the membranes. However,

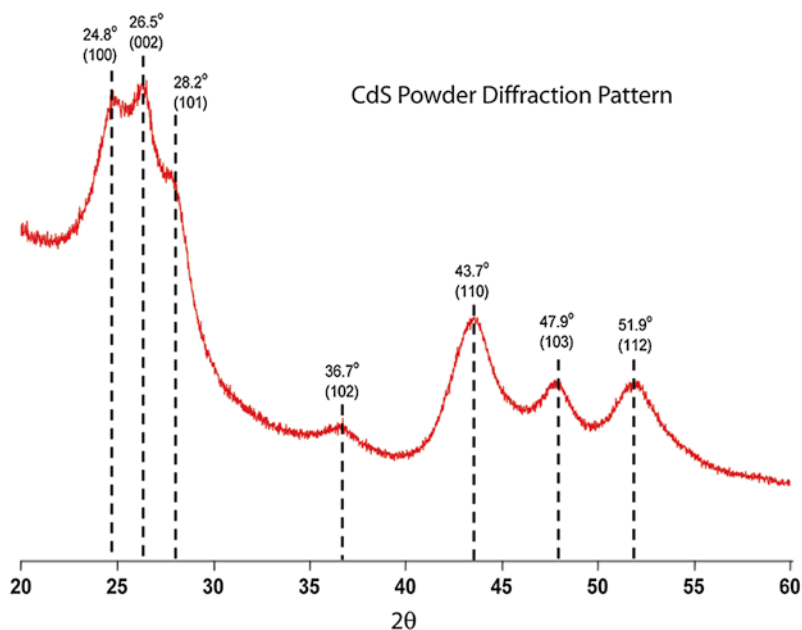
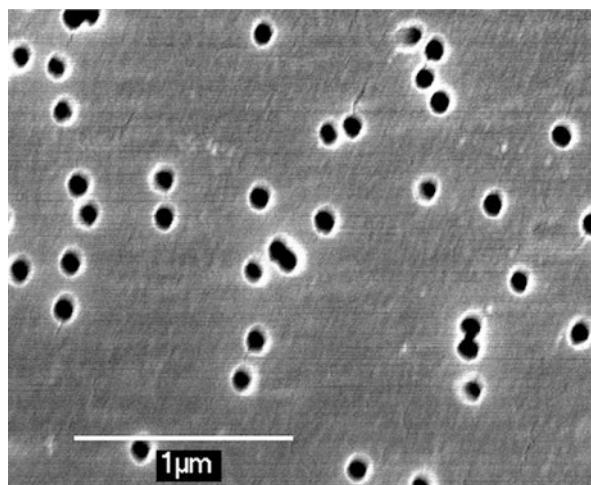


Fig. 11 X-ray diffraction pattern for CdS

Fig. 12 Scanning electron microscopy image of the 100 nm pore-size PC membrane



the easy removal of the template after the electrodeposition made them useful for our research purpose.

In order to achieve more oriented nanostructures, in-house fabricated AAO membranes with 35 nm were used as they oriented pores (Fig. 14). Commercial AAO membrane does not have an even hexagonal array but was used to optimize nanostructure synthesis (Fig. 15).

Fig. 13 Scanning electron microscopy image of the 400 nm pore-size PC membrane

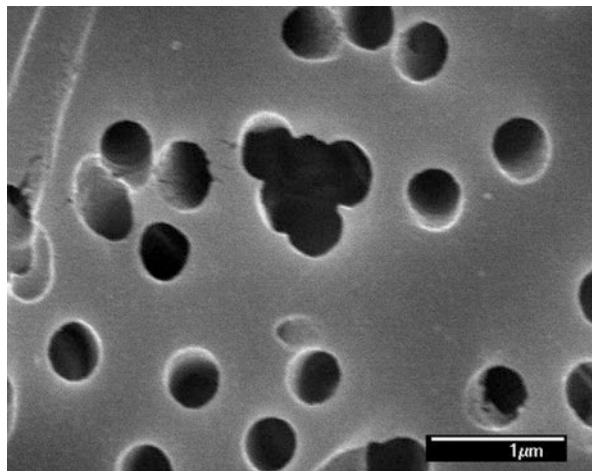


Fig. 14 Scanning Electron Microscopy image of the ~35 nm pore-size AAO membrane (Prepared at Russell's Lab, PSE Department at UMass Amherst)

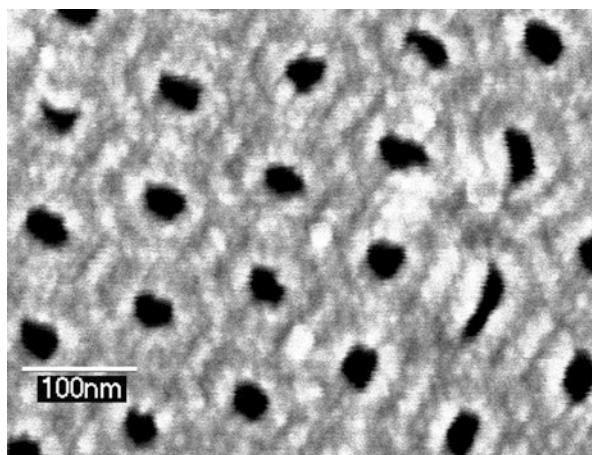
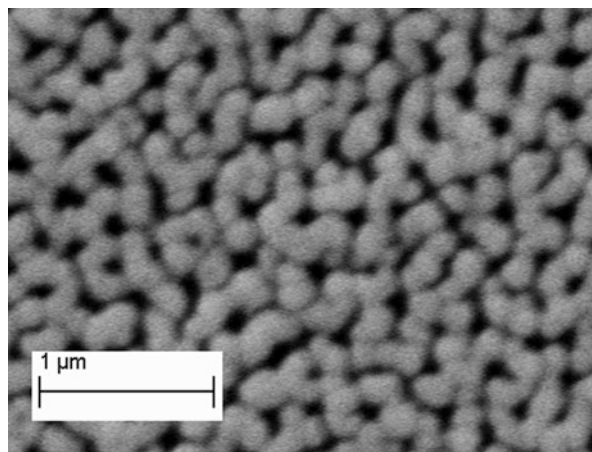


Fig. 15 Scanning electron microscopy image of the 200 nm pore-size AAO membrane (Whatman, Inc.)



Cadmium selenide was deposited by direct current electrodeposition at -0.590 V using the above-described membranes as the working electrode. The established potential was held for 1 h. Then, the polycarbonate membrane was washed out with dichloromethane. In the case of anodic aluminum oxide, the membrane was removed by washing with 3 M NaOH for 30 min. Samples were characterized by SEM. Figure 16 shows the process for the template fabrication of the nanorods.

CdSe nanorods were obtained from the 100 nm pore polycarbonate membranes. On the other hand, CdSe nanotubes were achieved with the 400 nm pore polycarbonate membranes. CdSe nanorods and nanotubes are shown in Figs. 17 and 18, respectively.

Figure 19 shows the formation of CdTe nanorods deposited by DC techniques at -0.570 V on the 100 nm pore-size polycarbonate membrane.

When the AAO membranes are used, instead of PC membranes, nanostructures with a higher degree of organization are obtained. Figures 20 and 21 show the CdSe nanorods formed when the 200 nm pore anodic aluminum oxides were used.

Why is there a difference of the achieved nanostructures when a different polycarbonate membrane is used? After several trials, nanotubes were obtained from the 400 nm pore-size PC membrane and nanorods were obtained from the 100 nm pore PC membranes. We hypothesized that this observation can be rationalized by the deposition of gold during the sputtering process. If gold were to infiltrate the pores during the sputtering process, it can create a tubular-gold initiator. Figure 22 shows a scheme of the infiltration phenomenon.

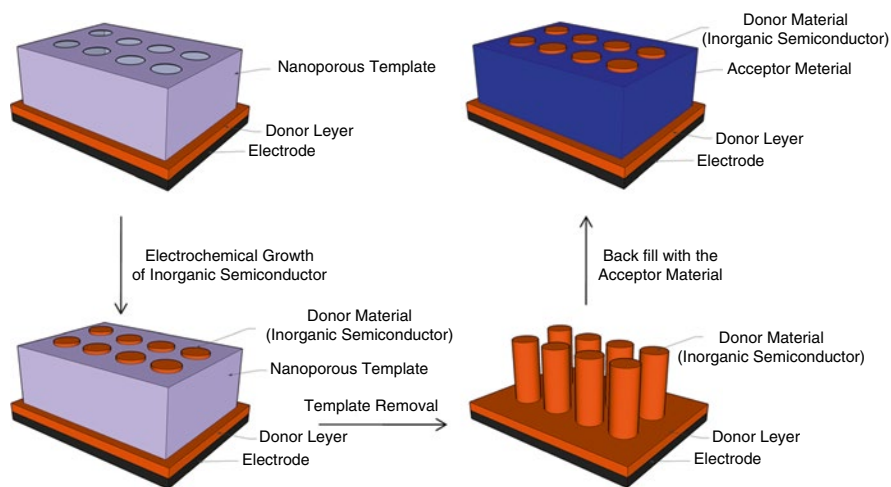


Fig. 16 Schematic procedure for the fabrication of oriented nanorods

Fig. 17 Scanning electron microscopy image of CdSe nanorods deposited on the 100 nm pore-size PC membrane

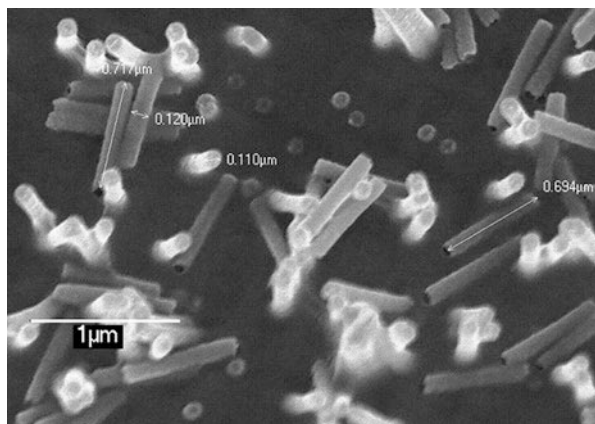


Fig. 18 Scanning electron microscopy image of CdSe nanotubes deposited on the 400 nm pore-size PC membrane

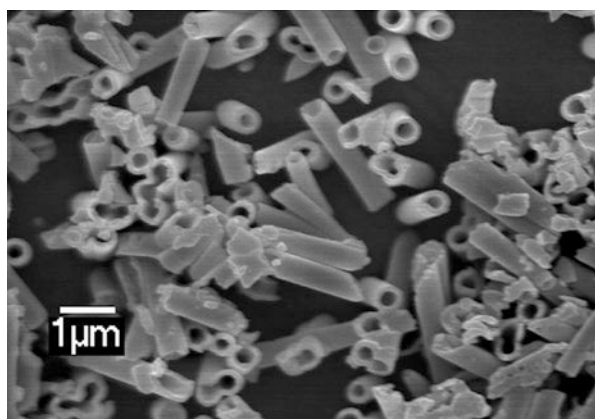


Fig. 19 Scanning electron microscopy image of CdTe nanorods deposited on the 100 nm pore-size PC membrane

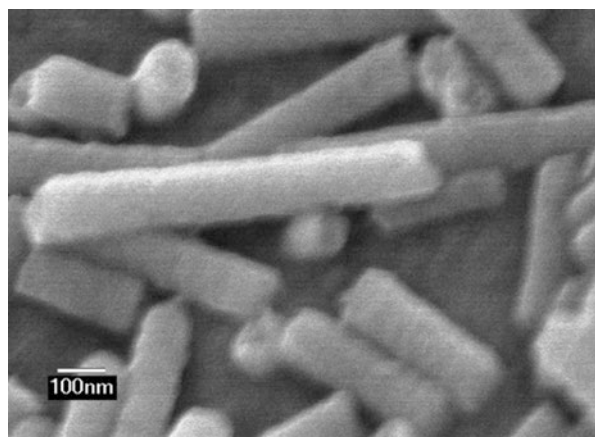


Fig. 20 Scanning electron microscopy image of the CdSe nanorods deposited on 200 nm pore-size anodic aluminum oxide membrane (Whatman, Inc.) (*top view*)

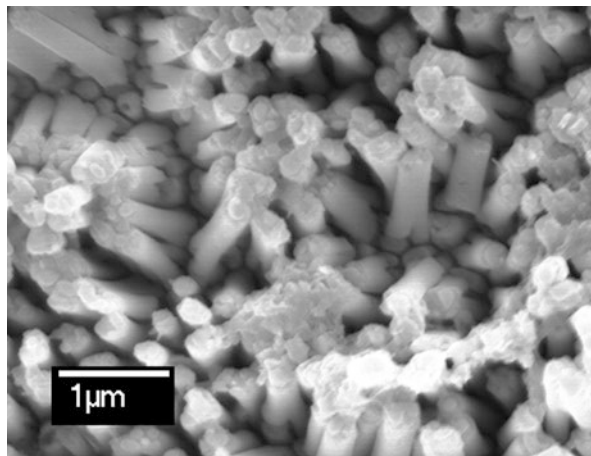
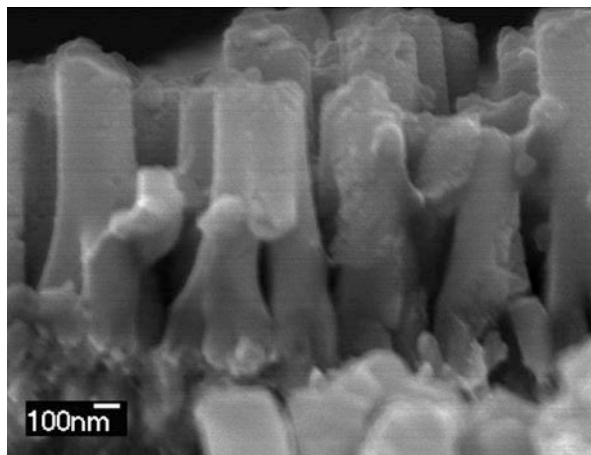


Fig. 21 Scanning electron microscopy image of the CdSe nanorods deposited on 200 nm pore-size AAO membrane (Whatman, Inc.) (*side view*)



The most critical observation was that only the 400 nm pore PC membranes produce nanotubes. Both the 100 nm pore PC membranes and the 200 nm pore AAO membranes form nanorods. To prove our hypothesis, 100 nm pore PC membranes were gold coated at different times. Since the pore size is small compared to 400 nm pores, it was expected pores be completely covered during gold sputtering process. Figure 23 shows the scanning electron microscopy images of the 100 nm pore PC membranes coated with gold at 1, 2, 5, and 20 min. Notice that between 1 and 5 min, there are pores that are not completely filled. However, nanorods were obtained from each of the templates.

In the case of the 200 nm pore AAO membrane, the scenario was different; bigger pore size always achieved nanorods. It is relevant to note the work done by Whitesides and coworkers [38] where they fabricated metal nanotubes by sputtering

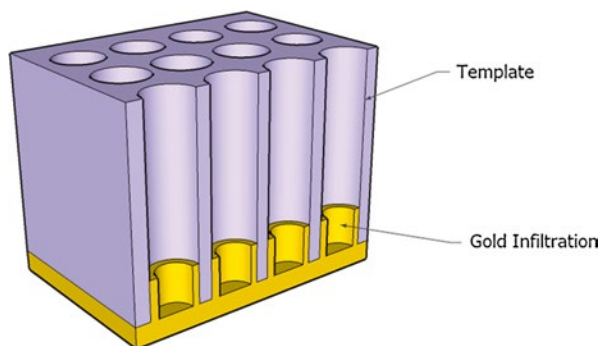


Fig. 22 Representation of the gold infiltration on the pores of a membrane

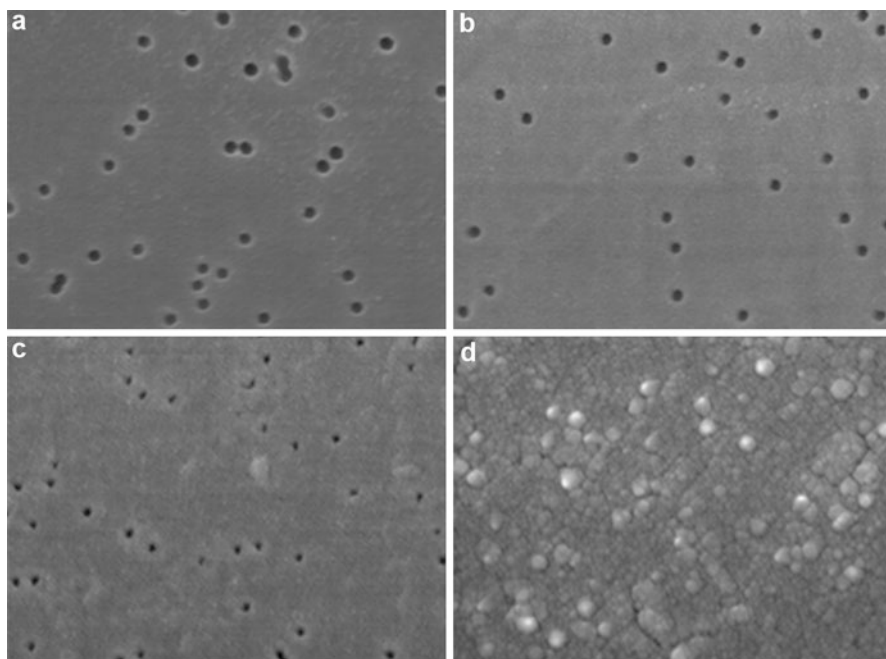


Fig. 23 Scanning electron microscopy image of the gold-coated side of the 100 nm pore polycarbonate membrane. A=1 min, B=2 min, C=5 min, and D=20 min

gold, platinum, or ITO over AAO membrane. In our case, the 200 nm pore AAO membranes were sputtered with gold. This experiment was performed in order to understand the gold infiltration effect. The template was washed out with 3 M NaOH solution for 45 min. The sample was analyzed by scanning electron microscopy. Figure 24 shows the resulting nanostructures produced by exposing the AAO membranes for 10 min of gold deposition. These structures have an appearance of small tubes.

Fig. 24 Scanning electron microscopy image of the nanostructures of the Au sputtering over 200 nm pore-size anodic aluminum oxide membrane obtained after membrane removal (Whatman, Inc.)

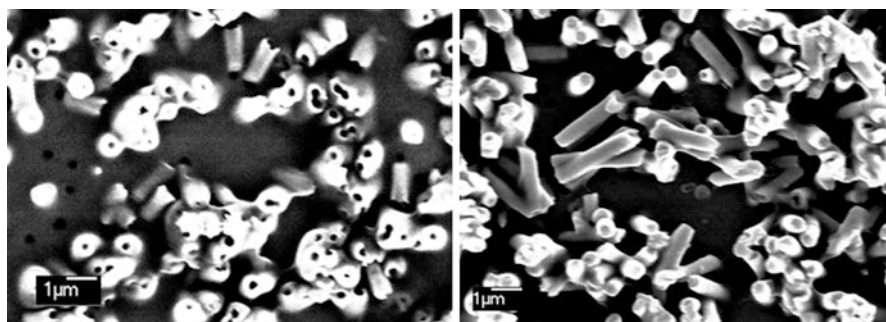
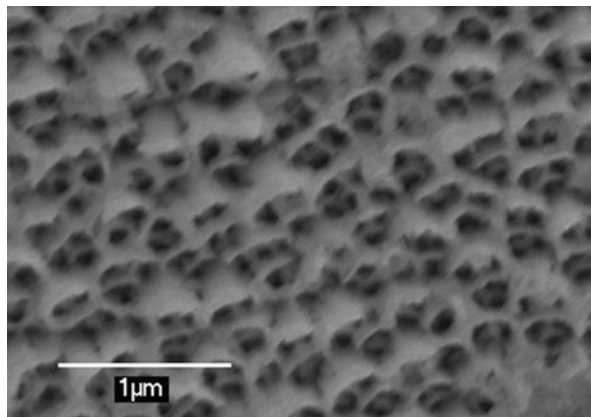


Fig. 25 Scanning electron microscope images of electrodeposited CdSe on a 400 nm PC membrane. Nanotubes (*left*) obtained by no stirring; nanorods (*right*) obtained by stirring

On one of the first electrodeposition experiments done in the PC membrane, we found that if the solution is stirred during electrodeposition, nanorods were obtained. On the other hand, when no stirring was used, nanotubes were achieved (Fig. 25).

One of the questions that came out of these experiments was: “What parameters can we control to obtain either nanorods or nanotubes?” Some of the parameters that were taken in consideration for evaluation were: stirring rate, polarity of the solvent, concentration of CdCl_2 and concentration of SeO_2 .

In the first parameter, stirring, CdSe precursor’s solution was stirred at 0, 200, 400, 600, and 800 rpm while the potential was applied. CdSe was deposited by CV method at -0.355 to -0.755 V for 200 cycles (~ 26 min). Samples were analyzed by SEM. To calculate the nanorods/nanotubes ratio, the inner diameter was divided by the outer diameter. The raw data was obtained by measuring the inner and the outer diameter of an average of 20 nanostructures on the SEM images obtained from the different

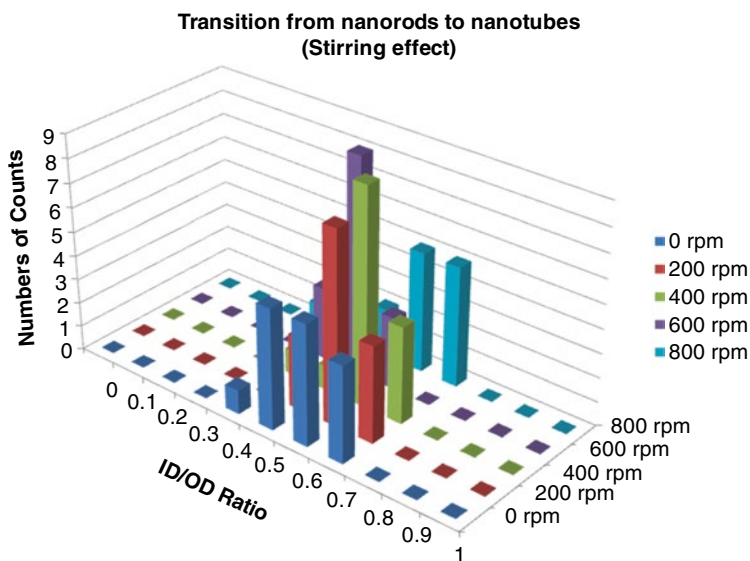


Fig. 26 Stirring effect on the transition from nanorods to nanotubes. Stirring rates: 0, 200, 400, 600, and 800 rpm

experiments at different stirring revolutions. Figure 26 shows a correlation between nanorods and nanotubes formed on each experiment. From the graph, if values are close to zero, it means that the structure has more nanorod character. On the other hand, if values are close to one, it means that the inner diameter is almost equal to the outer diameter and the nanostructure is a nanotube. On these experiments, we were expected to obtain more nanorods at high rpm and more nanotubes at low rpm.

In the data shown on the graph above, there is no an expected trend. Most of the nanostructures formed at different stirring revolution have almost the same dimensions, nanotubes with thick wall.

Figure 27 represents the ideal expected trend for the transition from nanotubes to nanorods. In this graph the first parameter refers, for example, to 0 rpm; the second parameter represents 200 rpm and so on, up to the fifth parameter that represents 800 rpm. This graph would be also true for the expected results obtained from experiments changing the other parameters explained before. From this graph, in the first parameter there is a high amount of nanorod character nanostructures. Moving through the graph, a transition from nanorods to nanotubes can be seen. At the last parameter the amount of nanotubes is high.

Thinking about the possibility that the diffusion of the species into the pore was limited by the hydrophobicity of the PC membrane, experiments changing the polarity of the solvent were done. The use of an organic solvent such as ethanol would help the CdSe precursors to be delivered into the pores easily. Solvent ratios used for these experiments were: 0 % water/100 % ethanol, 25 % water/75 % ethanol, 50 % water/50 % ethanol, 75 % water/25 % ethanol, and 100 % water/0 % ethanol.

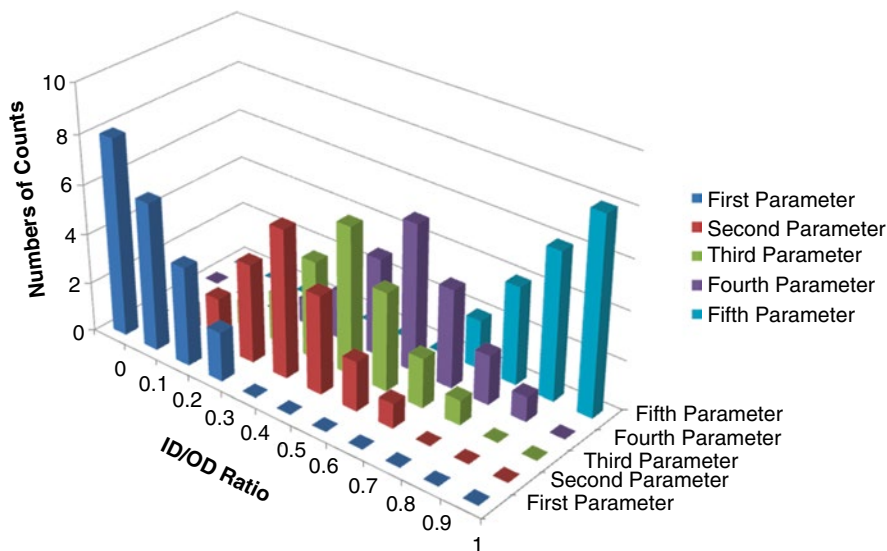


Fig. 27 Ideal behavior for the transition from nanorods to nanotubes

Figure 28 shows the solvent effect in the transition from nanorods to nanotubes of the nanostructures obtained in the 400 nm pore PC membrane. Data was obtained the same way as previous comparison experiments (see Appendix for raw data). Basically, the amount and the wall thickness of nanotubes obtained from all the five solution were comparable with the stirring effect experiments.

Taking in consideration that the steps for the electrodeposition process using CV deposition are (a) formation of CdSe, (b) reduction of Cd^{+2} (to ensure the formation of CdSe), and (c) stripping the excess of metallic Cd back to the solution by oxidation (Fig. 1), we decided to change the concentration of CdCl_2 in the solution. We expected to have more metallic Cd to oxidize with an increase in the concentration of the cadmium ions in the electrodeposition solution. Consequently, we expected that the stripping process should produce more nanotubes than nanorods. Solutions containing concentrations of 0.01, 0.05, 0.1, and 0.3 M were prepared for the electrodeposition. Figure 29 shows the results obtained when the concentration of Cd^{+2} was changed in electrodeposition solution. Similarly to the previous experiments there is not a significant trend that explains why we obtain either nanorods or nanotubes.

Similarly, experiments containing SeO_2 solutions with concentrations of 0.01, 0.05, 0.1 and 0.3 M were done. In this case, SeO_2 in the normal solution was 100 times less than the concentration of CdCl_2 . One of the possible explanations why nanotubes were obtained in the large-pore-size PC membranes was that the solution ran out of SeO_2 and the formation of CdSe ceased. An increase in the SeO_2 concentrations may provide more reactant to be used to produce more CdSe and fill up more nanotubes. Figure 30 shows the unexpected results obtained from solutions of

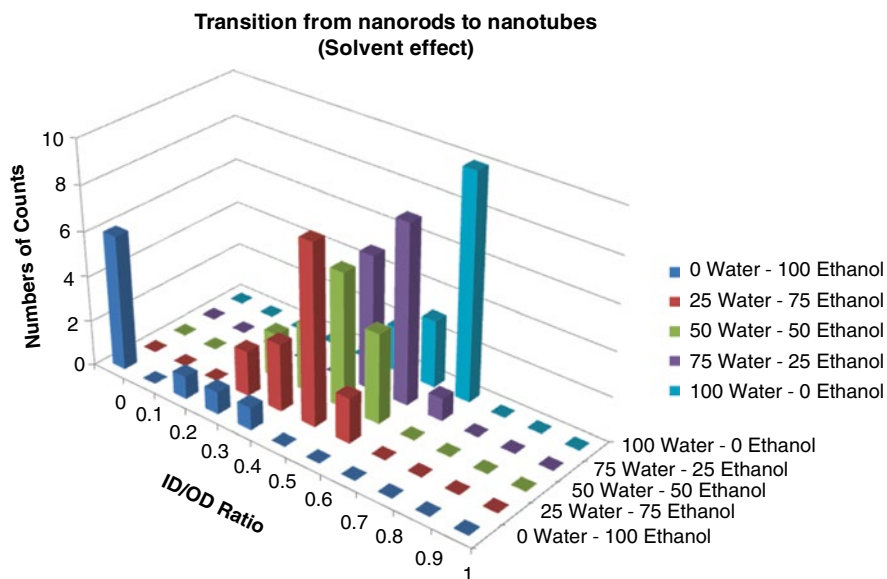


Fig. 28 Solvent effects on the transition from nanorods to nanotubes. Solvent ratios: 0 %/100 %, 25 %/75 %, 50 %/50 %, 75 %/25 %, and 100 %/0 % water/ethanol

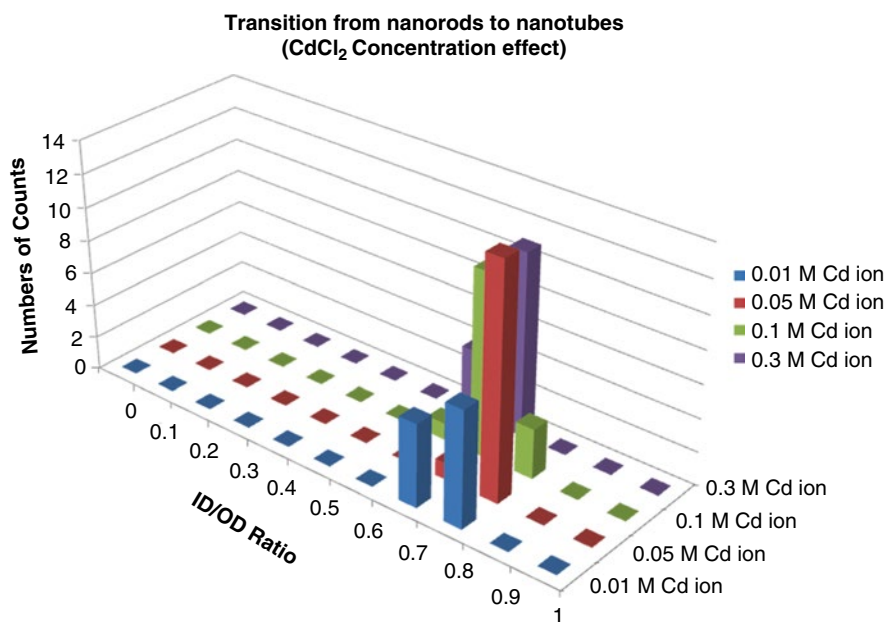


Fig. 29 Cd²⁺ ion effect on the transition from nanorods to nanotubes CdCl₂ concentrations: 0.01, 0.05, 0.1, and 0.3 M

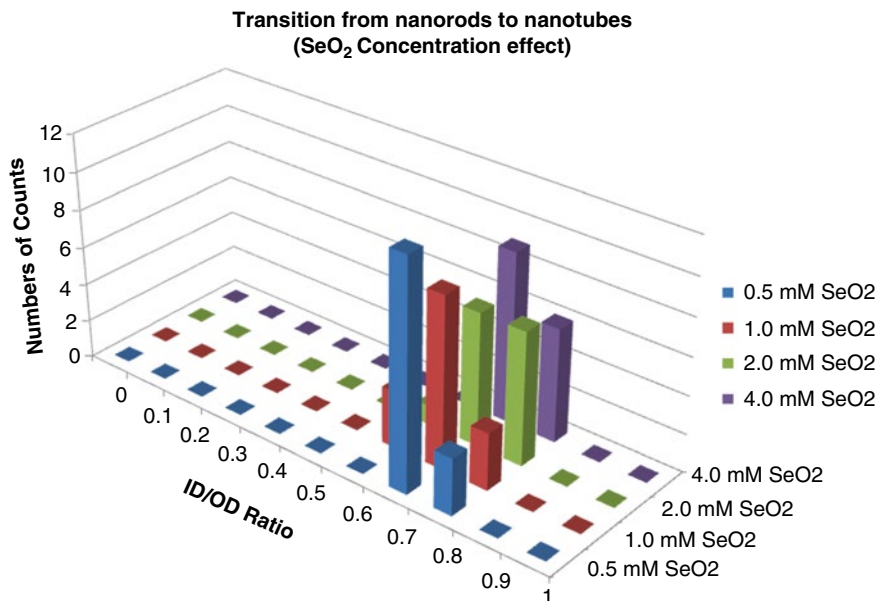


Fig. 30 Concentration effect of SeO₂ on the transition from nanorods to nanotubes SeO₂ concentrations: 0.5, 1.0, 2.0, and 4.0 mM

concentrations of 0.5, 1.0, 2.0, and 4.0 mM of SeO₂. The amount of nanotubes obtained from all solutions was almost the same in all the cases. No trend was found to explain why nanotubes were achieved on the 400 nm pore PC membranes and nanorods on the 100 nm pore PC membranes.

Summarizing this section, no clear explanation about which parameters are needed to achieve either nanotubes or nanorods was found. The only consistent finding was that nanorods can be obtained on the small-pore-size PC membrane and nanotubes can be obtained on the large-pore-size PC membrane.

Role of the pH

The crystallinity of the semiconductor is an important characteristic because it is related with the charge mobility of a material. In order to have high crystalline material, high-temperature and high-vacuum techniques such as VLS or CVD have to be used. With electrochemistry, the obtained material exhibits poor crystallinity. The most common way to improve its crystallinity is by annealing the samples at high temperatures. This process faces problems with temperature-sensitive materials.

One methodology tested to improve the crystallinity of a material was a change on the pH of the precursor's solution. It was believed that with an increment in the acidity of the solution, the obtained product is redissolved in the solution and then recrystallized slowly achieving a better crystalline material.

CdSe precursor's solution was prepared with different concentrations of HCl varying from 0.01 to 1.0 M. The deposition was done by DC electrodeposition using surfaces such as Ni, Au-coated AAO, and PC membranes and Au-coated glass as working electrodes. The characterization was performed by X-ray powder diffraction (XRD). AAO and PC membranes were analyzed on the Au-coated side. Figures 31, 32, 33, and 34 show the obtained results.

From the analysis of these results, it can be concluded that there is a change in the phase of the CdSe. At low concentration of HCl, the cubic phase is more predominant; a change in the phase can be observed when the HCl concentration is increased. In the range from 0.01 to 0.2 M, there is a transition from cubic to hexagonal phase. Surprisingly, when the HCl concentration is further increased, the hexagonal phase is reverted to the cubic phase with sharper peaks referring larger crystallite sizes. This phenomenon was not clearly understood but these

Fig. 31 X-ray powder diffraction of the electrodeposition of CdSe over Ni at different pH

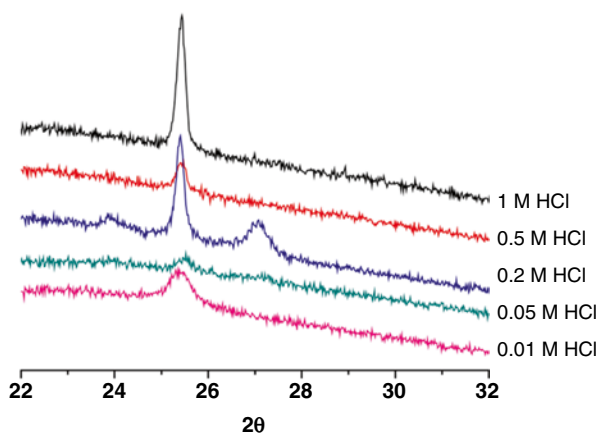


Fig. 32 X-ray powder diffraction of the electrodeposition of CdSe over the Au side of the AAO membrane at different pH

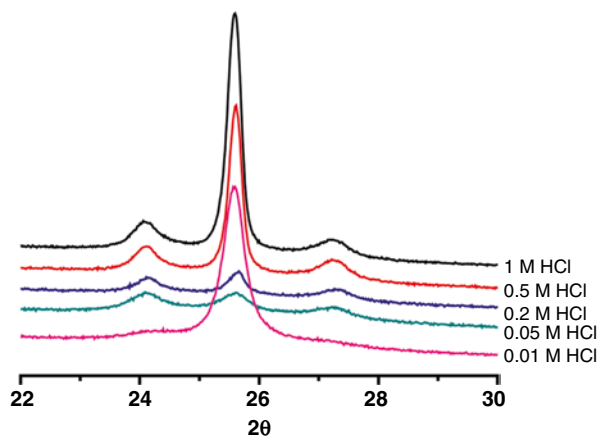


Fig. 33 X-ray powder diffraction of the electrodeposition of CdSe over the Au side of the PC membrane at different pH

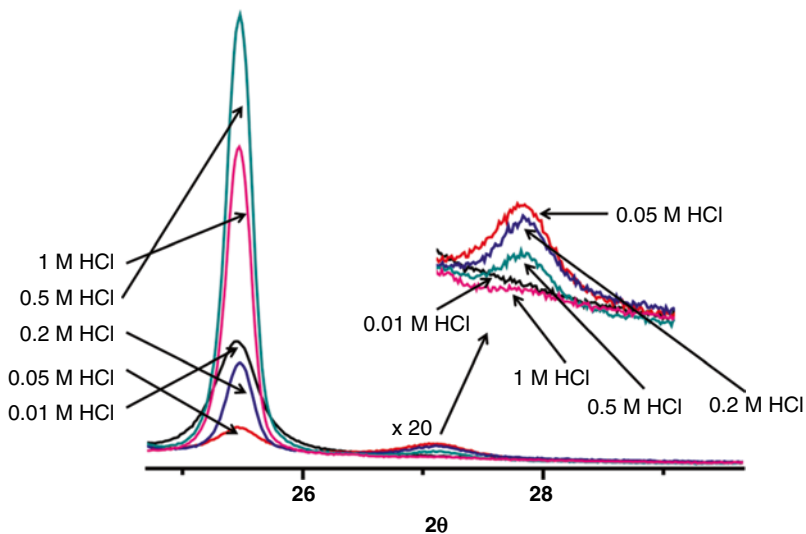
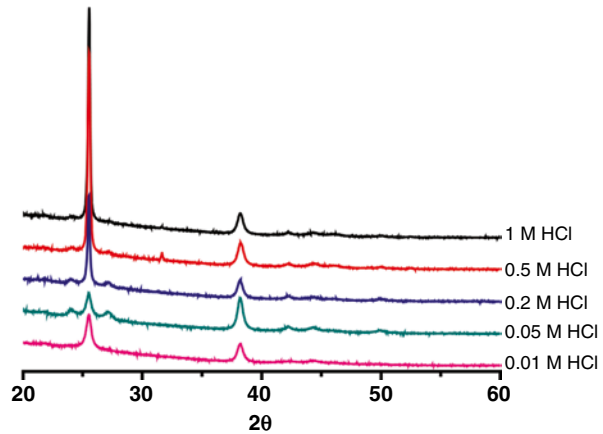


Fig. 34 X-ray powder diffraction of the electrodeposition of CdSe over the Au on glass at different pH

experiments were useful to select the best HCl concentration needed to obtain the most appropriate phase, in this case hexagonal.

Segmented Nanorods

Inorganic semiconductor nanorods can be modified by the addition of a different material such as a metal [39] or another inorganic semiconductor [20] to create segmented nanostructures. In the case of CdSe, addition of a metal has been shown

to increase the electronic conductivity of the semiconductor by a factor of 15 when they are illuminated by visible light [39]. The use of different inorganic semiconductors such as CdSe and CdTe will provide to a device a way to absorb in more than one region of the solar spectrum.

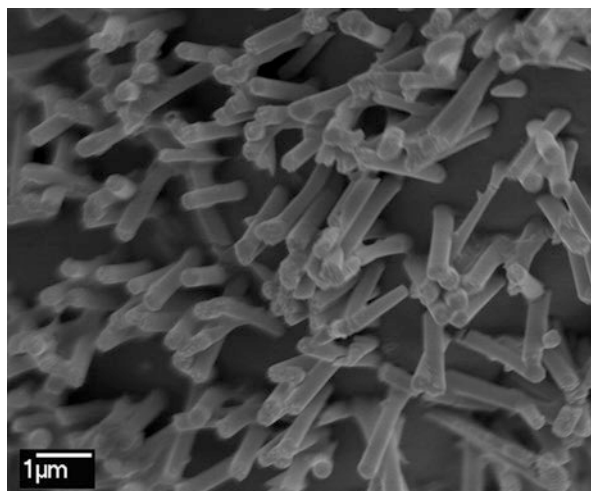
CdSe nanorods were synthesized using the modification described by Kressin and Sailor [21]. The semiconducting material was electrodeposited on a template, in our case a gold-coated PC membrane. Then, the template was washed with dichloromethane. Figure 16 shows a schematic sequence of the fabrication of an inorganic semiconductor (donor material) such as CdSe.

After the template removal, the sample was characterized by scanning electron microscopy (SEM). In Fig. 35 the CdSe nanorods obtained from the electrodeposition on a 100 nm pore PC membrane can be seen. In this case, the electrode (gold-coated template) was kept under a potential of -0.590 V for 1 h. Figure 36 shows a schematic sequence of the fabrication of a segmented inorganic semiconductor (donor material) such as CdSe/CdSe [20] or CdTe/CdSe.

In order to fabricate segmented nanorods, CdSe was deposited on a 100 nm pore gold-coated polycarbonate membrane. The electrodeposition was performed at -0.590 V for 45 min. Then, the same electrode was submerged in a CdTe precursor's solution and a potential of -0.570 V was applied for 45 min. The template was washed out with dichloromethane and the sample characterized by scanning electron microscopy (SEM). Figure 37 shows a SEM image of an isolated segmented nanorod. Electron diffraction analysis by X-ray (EDAX) shows a different composition on each end of the nanorod (Figs. 38 and 39).

To summarize this section, segmented nanorods consisting of CdSe and CdTe were obtained from the 100 nm PC template. The EDAX characterization confirms the identity of each extreme of the nanostructure showing CdSe in one extreme and CdTe in the other extreme.

Fig. 35 Scanning electron microscopy image of CdSe nanorods deposited on the 100 nm pore-size polycarbonate membrane at -0.590 V for 1 h



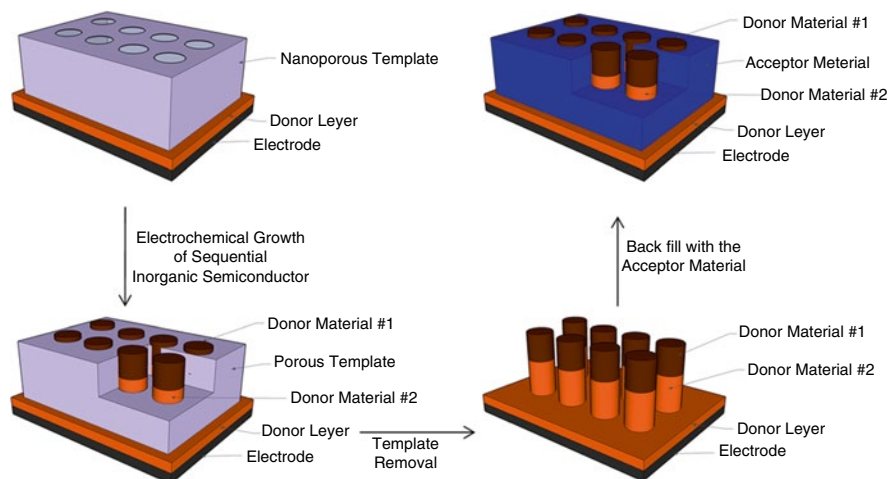
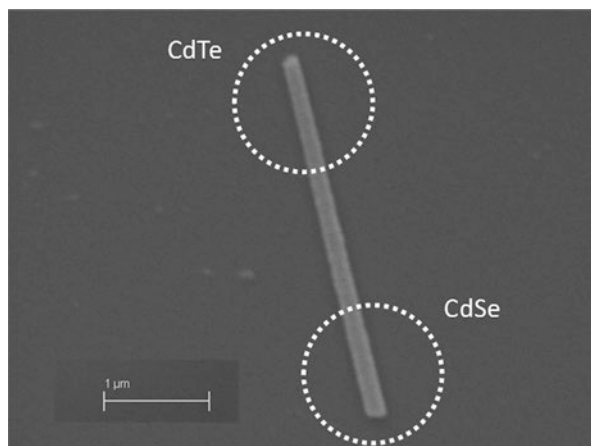


Fig. 36 Sequence for the fabrication of segmented nanorods

Fig. 37 Scanning electron microscopy image of CdSe/CdTe segmented nanorods deposited on a 100 nm pore-size polycarbonate membrane by sequential electrodeposition at -0.590 V for 45 min and -0.570 V for 45 min, respectively



Coaxial Nanorods

Axial heterojunctions have been shown to be important building blocks in nano-electronics and photonics [40]. One-dimensional nanowires with controlled radial compositions [41, 42] or controlled axial composition [40, 43–46] have been synthesized mostly by chemical vapor deposition or vapor-liquid-solid techniques. Some examples are SiC nanowires on Cu nanotubes [47], ZnO-Ge axial nanorods [48], Au(Si)-filled Ga_2O_3 nanotubes [49], In_2O_3 nanowire covered with SnO_2 [50], and ZnSe-ZnTe [51].

Fig. 38 Electron diffraction analysis by X-ray pattern of CdTe over gold-coated glass as the substrate after template removal (*top* part of the nanorod on Fig. 35)

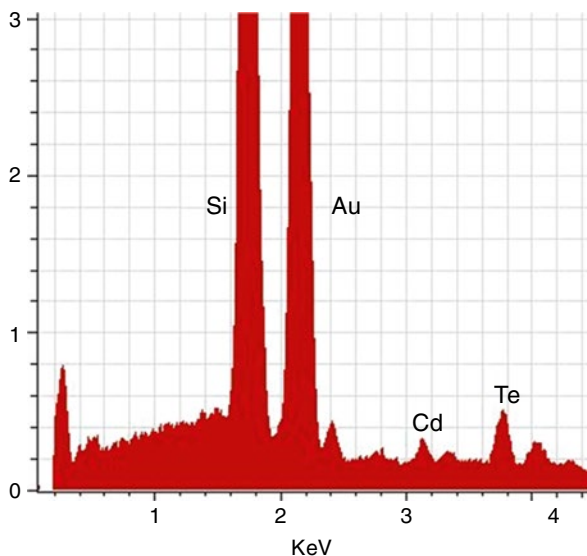
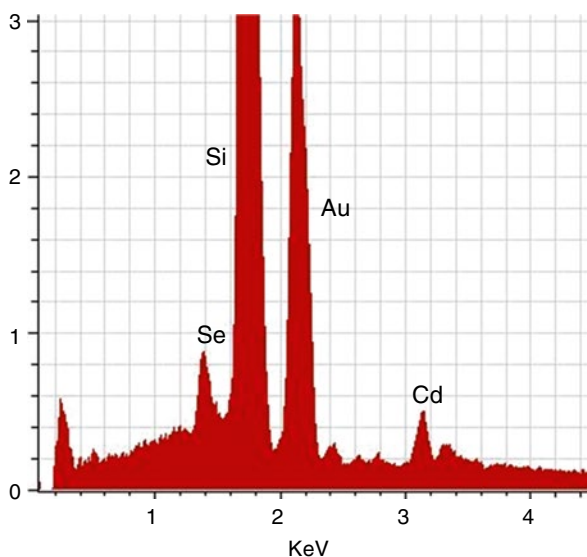


Fig. 39 Electron diffraction analysis by X-ray pattern of CdSe over gold-coated glass as the substrate after template removal (*bottom* part of the nanorod on Fig. 35)



In this section we present the fabrication of radial heterojunctions by electrochemistry as the principal deposition technique. Figure 40 shows a generic view of the process for the fabrication of the coaxial nanorods.

CdSe was deposited on a 400 nm pore gold-coated polycarbonate membrane. The electrodeposition was performed at -0.590 V for 1 h. Then, the template was washed with dichloromethane. With the use of the 400 nm PC template, we achieved the formation of CdSe nanotubes (Fig. 41).

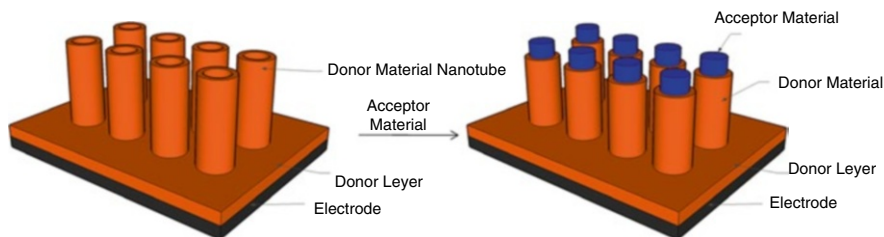
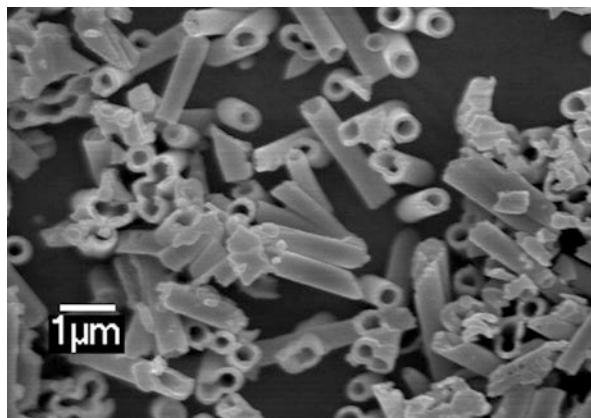


Fig. 40 Fabrication of the radial heterojunction nanorods

Fig. 41 Scanning electron microscopy image of CdSe nanotubes deposited on the 400 nm pore-size polycarbonate membrane at -0.590 V for 1 h



CdSe was deposited on a 400 nm pore gold-coated polycarbonate membrane. The electrodeposition was performed at -0.590 V for 45 min. Then, the same electrode was submerged in a CdTe precursor's solution and a potential of -0.570 V applied for 45 min. The template was washed with dichloromethane and the sample characterized by scanning electron microscopy (SEM). Figure 42 shows an image of the coaxial nanorods. Electron diffraction analysis by X-ray (EDAX) shows a different composition of each semiconductor on the outside (Fig. 43) part of a nanorod and the inside (Fig. 44) part of a nanorod.

In addition, CdSe nanotubes were filled with small organic molecules. The idea was to fabricate a coaxial nanorod with an organic material in the center. We decided to start with a small conductive molecule such as triphenylamine and tri-4-tolylamine. The first step was the electrodeposition of CdSe nanotubes in the 200 nm anodic aluminum oxide (AAO) membrane. Then the sample (working electrode) was rinsed with water and ethanol to help it to dry fast. The membrane was cut into two pieces, one for the SEM characterization and the other piece to be exposed to the small organic materials. Figure 45 shows the nanotubes formed in the 200 nm

Fig. 42 Scanning electron microscopy image of CdSe/CdTe coaxial nanorods deposited on a 400 nm pore-size polycarbonate membrane by sequential electrodeposition at -0.590 V for 45 min and -0.570 V for 45 min, respectively

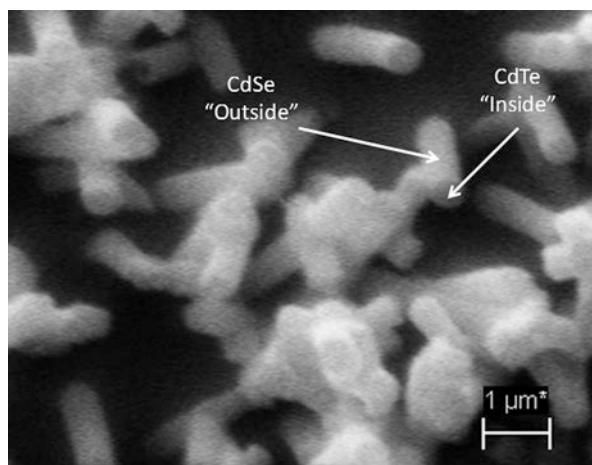
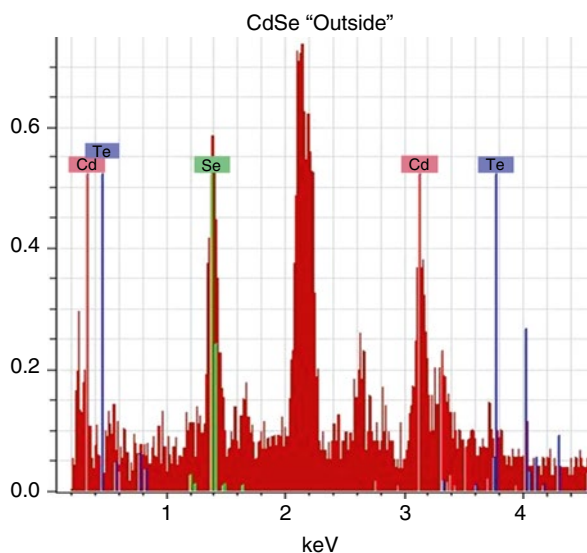


Fig. 43 Electron diffraction analysis by X-ray pattern of CdSe/CdTe coaxial nanorod over gold as the substrate after template removal (outside point on the CdSe/CdTe coaxial nanorod)



AAO template. The organic compounds were placed over the piece of template and molten on an oven at 200 °C for 8 h. The slow process was thought to deliver the material into the pores efficiently.

The excess of organic material was removed from the template surface with dichloromethane. AAO template was washed out with 3.0 M NaOH solution for 1 h. Samples were characterized by SEM. Figures 46 and 47 show the scanning electron microgram of CdSe nanotubes filled with triphenylamine (TPA) and

Fig. 44 Electron diffraction analysis by X-ray pattern of CdSe/CdTe coaxial nanorods over gold as the substrate after template removal (inside point on the CdSe/CdTe coaxial nanorod)

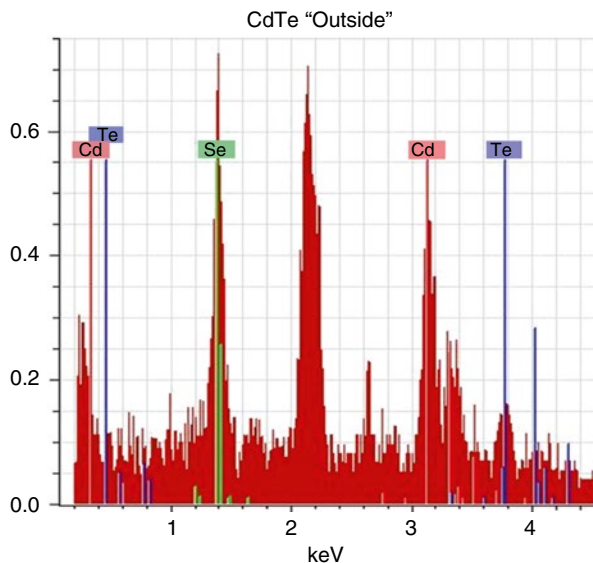
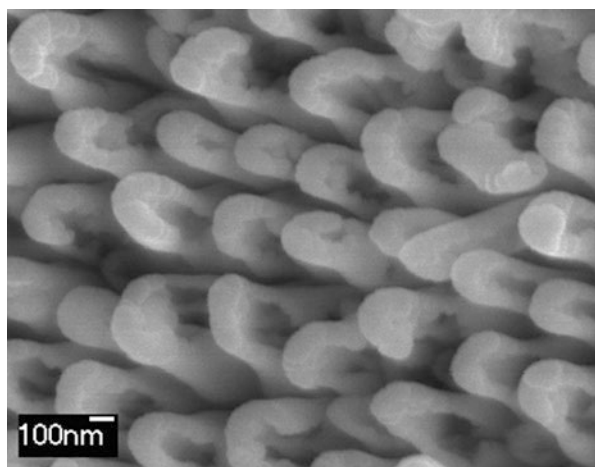


Fig. 45 Scanning electron microscopy image of CdSe nanotubes deposited on a 200 nm pore-size anodic aluminum oxide membrane deposited for 45 min



tri-4-tolylamine, respectively. The long structures that can be appreciated on Fig. 17 are crystals formed during the crystallization of TPA.

To summarize, the identity of the external region and the internal region of the coaxial nanorods was confirmed by EDAX. It shows higher concentration of CdTe in the inside of the rods which confirms that possibly the CdSe nanotubes have been filled with CdTe. On the other hand, the trial to fill the CdSe nanotubes with either metals or organic semiconductors was not what we were expecting. For some reason the characterization of the obtained structures did not prove that the CdSe nanotubes were filled.

Fig. 46 Scanning electron microscopy image of CdSe nanotubes deposited on a 200 nm pore-size anodic aluminum oxide membrane deposited for 45 min. Triphenylamine molten over the electrode

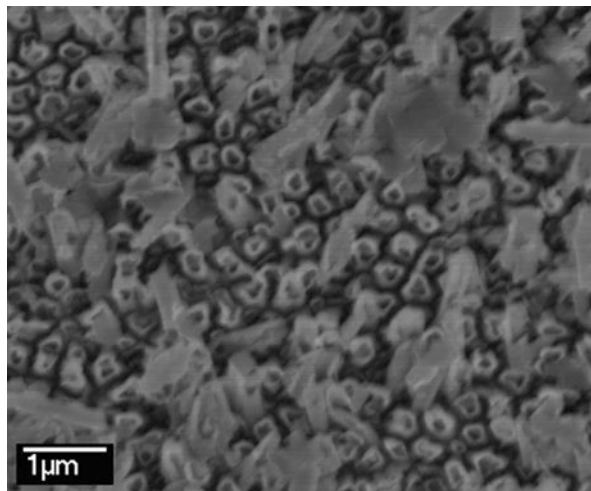
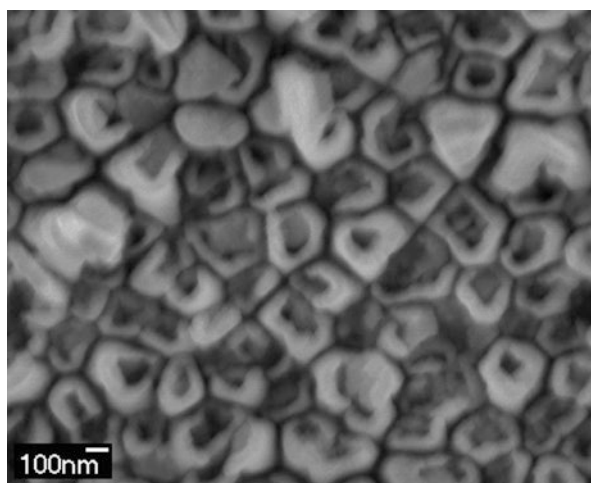


Fig. 47 Scanning electron microscopy image of CdSe nanotubes deposited on a 200 nm pore-size anodic aluminum oxide membrane deposited for 45 min. Tri-4-tolylamine molten over the electrode



Conclusions

In summary, we optimized parameters for the electrodeposition of cadmium chalcogenides using an aqueous solution of CdCl_2 and SeO_2 or TeO_2 with 0.2 M HCl. The optimal working potential found for the deposition of CdSe and CdTe by DC electrodeposition was -0.590 V and -0.570 V, respectively. It was found that nanorods can be obtained on the small-pore-size PC membrane (100 nm) and nanotubes can be obtained on the large-pore-size PC membrane (400 nm).

In conclusion, we have optimized the electrodeposition process to tune the crystallinity of the chalcogenide semiconductor. Additionally, we have shown that the electrodeposition process can be used to obtain nanotubes, nanorods, segmented nanorods, and coaxial nanorods using electrochemical deposition.

References

1. Alivisatos AP (1996) Semiconductor clusters, nanocrystals, and quantum dots. *Science* 271(5251):933–937
2. Bawendi MG, Steigerwald ML, Brus LE (1990) The quantum mechanics of larger semiconductor clusters (“quantum dots”). *Annu Rev Phys Chem* 41(1):477–496
3. Chhowalla MSS, Hyeon SS, Eda G, Li L-J, Loh KP, Zhang H (2013) The chemistry of two-dimensional layered transition metal dichalcogenide nanosheets. *Nat Chem* 5:263–275
4. Bruchez M Jr et al (1998) Semiconductor nanocrystals as fluorescent biological labels. *Science* 281(5385):2013–2016
5. Chan WC et al (1998) Quantum dot bioconjugates for ultrasensitive nonisotopic detection. *Science* 281(5385):2016–2018
6. Mattoussi H et al (2000) Self-assembly of CdSe-ZnS quantum dot bioconjugates using an engineered recombinant protein. *J Am Chem Soc* 122(49):12142–12150
7. Coe S et al (2002) Electroluminescence from single monolayers of nanocrystals in molecular organic devices. *Nature* 420(6917):800
8. Klimov VI et al (2000) Optical gain and stimulated emission in nanocrystal quantum dots. *Science* 290(5490):314–317
9. Park JH et al (2004) White emission from polymer/quantum dot ternary nanocomposites by incomplete energy transfer. *Nanotechnology* 15(9):1217–1220
10. Gur I et al (2005) Air-stable all-inorganic nanocrystal solar cells processed from solution. *Science* 310(5747):462–465
11. Liu J et al (2004) Employing end-functional polythiophene to control the morphology of nanocrystal-polymer composites in hybrid solar cells. *J Am Chem Soc* 126(21):6550–6551
12. Han L et al (2006) Synthesis of high quality zinc-blende CdSe nanocrystals and their applications in hybrid solar cells. *Nanotechnology* 17:4736–4742
13. Huynh WU et al (2003) Controlling the morphology of nanocrystal-polymer composites for solar cells. *Adv Funct Mater* 13(1):73–79
14. Huynh WU, Dittmer JJ, Alivisatos AP (2002) Hybrid nanorod-polymer solar cells. *Science* 295:2425–2427
15. Meieszawaska AJ et al (2007) The synthesis and fabrication of one-dimensional nanoscale heterojunctions. *Small* 3(5):722–756
16. Ouyang L et al (2007) Catalyst-assisted solution-liquid-solid synthesis of CdS/CdSe nanorod heterostructures. *J Am Chem Soc* 129(1):133–138
17. Goldberger J et al (2005) ZnO nanowire transistors. *J Phys Chem B Lett* 109:9–14
18. Hu JQ et al (2003) Thermal reduction route to the fabrication of coaxial Zn/ZnO nanocables and ZnO nanotubes. *Chem Mater* 15:305–308
19. Choi S-J et al (2001) Electrochemical preparation of cadmium selenide nanoparticles by the use of molecular templates. *J Electrochem Soc* 148(9):C569–C573
20. Klein JD et al (1993) Electrochemical fabrication of cadmium chalcogenide microdiode arrays. *Chem Mater* 5(7):902–904
21. Kressin AM et al (1991) Synthesis of stoichiometric cadmium selenide films via sequential monolayer electrodeposition. *Chem Mater* 3:1015–1020
22. Li Q et al (2006) Luminescent polycrystalline cadmium selenide nanowires synthesized by cyclic electrodeposition/stripping coupled with step edge decoration. *Chem Mater* 18:3432–3441
23. Ma C et al (2004) Single-crystal CdSe nanosaws. *J Am Chem Soc* 126:708–709
24. Shen CM, Zhang XG, Hi L (2001) DC electrochemical deposition of CdSe nanorods array using porous anodic aluminum oxide template. *Mater Sci Eng A* 303:19–23
25. Zhang BP, Yasuda T (1997) Naturally formed ZnCdSe quantum dots on ZnSe (110) surfaces. *Appl Phys Lett* 70(18):2413
26. Liao MCH, Chang YH (1997) Fabrication of ZnSe quantum dots under Volmer-Weber mode by metalorganic chemical vapor deposition. *Appl Phys Lett* 70(17):2256

27. Bourret-Courchesne ED (1996) Incorporation of hydrogen in nitrogen and arsenic doped ZnSe epitaxial layers grown by. *Appl Phys Lett* 68(17):2418
28. Deng ZX et al (2002) Structure-directing coordination template effect of ethylenediamine in formations of ZnS and ZnSe nanocrystallites via solvothermal route. *Inorg Chem* 41(4):869–873
29. Li YD et al (1998) Nonaqueous synthesis of CdS nanorod semiconductor. *Chem Mater* 10(9):2301–2303
30. Wang C et al (1999) An aqueous approach to ZnSe and CdSe semiconductor nanocrystals. *Mater Chem Phys* 60(1):99–102
31. Peng Q et al (2001) Low-Temperature Elemental-Direct-Reaction Route to II-VI Semiconductor Nanocrystalline ZnSe and CdSe. *Inorg Chem* 40(16):3840–3841
32. Ge J-P, Li Y-D, Yang G-Q (2002) Mechanism of aqueous ultrasonic reaction: controlled synthesis, luminescence properties of amorphous cluster and nanocrystalline CdSe. *Chem Commun* 17:1826–1827
33. Duan X, Lieber CM (2000) General synthesis of compound semiconductor nanowires. *Adv Mater* 12(4):298–302
34. Licht S (1987) A description of energy conversion in photoelectrochemical solar cells. *Nature* 330:148–151
35. Lokhande CD, Pawar SH (1989) Electrodeposition of thin film semiconductors. *Phys Status Solidi (a)* 111(1):17–40
36. Mishra KK, Rajeshwar K (1989) A re-examination of the mechanisms of electrodeposition of CdX and ZnX (X=Se, Te) semiconductors by the cyclic photovoltammetric technique. *J Electroanal Chem* 273(1–2):169–182
37. Routkevitch D et al (1996) Electrochemical fabrication of CdS nanowire arrays in porous anodic aluminum oxide templates. *J Phys Chem* 100:14037–14047
38. Dickey MD et al (2008) Fabrication of arrays of metal and metal oxide nanotubes by shadow evaporation. *ACS Nano* 2:800–808
39. Peña DJ et al (2002) Template growth of photoconductive metal-CdSe-metal nanowires. *J Phys Chem* 106:7458–7462
40. Gudiksen MS et al (2002) Growth of nanowire superlattice structures for nanoscale photonics and electronics. *Nature* 415(6872):617–620
41. Lauhon LJ et al (2002) Epitaxial core-shell and core-multishell nanowire heterostructures. *Nature* 420(6911):57–61
42. Li Y et al (2006) Dopant-free GaN/AlN/AlGaIn radial nanowire heterostructures as high electron mobility transistors. *Nano Lett* 6(7):1468–1473
43. Bjork MT et al (2002) One-dimensional steeplechase for electrons realized. *Nano Lett* 2(2):87–89
44. Verheijen MA et al (2006) Growth kinetics of heterostructured GaP-GaAs nanowires. *J Am Chem Soc* 128(4):1353–1359
45. Wu Y et al (2004) Single-crystal metallic nanowires and metal/semiconductor nanowire heterostructures. *Nature* 430(6995):61–65
46. Yang C, Zhong Z, Lieber CM (2005) Encoding electronic properties by synthesis of axial modulation-doped silicon nanowires. *Science* 310(5752):1304–1307
47. Ho GW et al (2004) Self-assembled growth of coaxial crystalline nanowires. *Nano Lett* 4(10):2023–2026
48. Yin L-W et al (2007) Tailoring the optical properties of epitaxially grown biaxial ZnO/Ge, and coaxial ZnO/Ge/ZnO and Ge/ZnO/Ge heterostructures. *Adv Funct Mater* 17:270–276
49. Gong NW et al (2008) Au(Si)-filled β -Ga₂O₃ nanotubes as wide range high temperature nanothermometers. *Appl Phys Lett* 92(7):073101–073103
50. Vomiero A et al (2007) Preparation of radial and longitudinal nanosized heterostructures of In₂O₃ and SnO₂. *Nano Lett* 7(12):3553–3558
51. Dong A et al (2007) Solution-liquid-solid (SLS) growth of ZnSe-ZnTe quantum wires having axial heterojunctions. *Nano Lett* 7(5):1308–1313

Nanomaterials Produced by Electrocrystallization Method

6

Maria Trzaska and Zdzislaw Trzaska

Contents

Introduction.....	136
Fundamentals of Electrocrystallization Processes.....	138
Electrocrystallization of Nanostructured Copper.....	141
Control of Nanocrystalline Copper by Current Waveforms.....	141
Control of Nanocrystalline Copper Structures by Compositions of Electrolyte Solutions.....	144
Electrocrystallization of Nanostructured Nickel.....	151
Electrocrystallization of Nanostructured Composites.....	154
Nanocrystalline Composites with Nickel Matrix.....	155
Nanocrystalline Composites with Nickel Matrix and Disperse Phases Built from Carbon.....	159
Nanocrystalline Composites with Copper Matrix.....	163
Summary and Conclusions.....	165
References.....	166

Abstract

This chapter presents the possibility of forming nanocrystalline structure and design properties of materials by electrocrystallization method. The basis of the electrocrystallization process and factors determining the result of the processes under considerations are presented. The electrocrystallization method was used for producing metal materials Cu and Ni and nanocrystalline structure of the nanocrystalline composite materials with matrix Cu, Ni, and nanosized particles

M. Trzaska (✉)

Institute of Precision Mechanics, Warsaw, Poland

e-mail: maria.trzaska@imp.edu.pl; matrz@inmat.pw.edu.pl

Z. Trzaska

University of Ecology and Management, Warsaw, Poland

e-mail: zdzislaw.trzaska@netlandia.pl

© Springer International Publishing Switzerland 2016

M. Aliofkhaezei, A.S.H. Makhlof (eds.), *Handbook of Nanoelectrochemistry*,

DOI 10.1007/978-3-319-15266-0_16

135

of the disperse phase in the form of Al_2O_3 , Si_3N_4 , and CNTs. Methods of X-ray diffraction (XRD), scanning electron microscopy (SEM), and transmission electron microscopy (TEM) were applied for the complete characterizations of the dispersion phases and the structure of the produced materials. The results of these studies are presented in the form of the corresponding images and graphs.

Keywords

Electrocrystallization • Nanomaterials • Nanocrystalline composites • Nanocrystalline surface layers • Doped graphene nanocrystalline layers

Introduction

The rapid development of technology and the increasing requirements of the final products force researchers not only to new designs of appliance's structures but also to the search for new materials with improved performance characteristics. Tasks posed for materials used presently in the practice are becoming more and more expressive in terms of better adapting them to the special technological characteristics and reducing their wear and tear. Thus, the basis for rapid technological progress are intensive studies aimed on the development of new materials, which should be characterized by much better performance parameters compared with those being currently in use. Progress in science and engineering at the nanoscale appears now as a critical factor for society's security, prosperity of the economy, and enhancement of the quality of life. Nanotechnology is focusing on the formation of purposeful materials, devices, and systems through the management of matter on the nanometer scale and the utilization of new occurrences and attributes at that scale. Rapid and continued advancement in the field of nanotechnology has accelerated the demand for specific professional knowledge and skill. Recently determined research and development for targeted nanoscience and nanotechnology have resulted in discovery and application now culminating in marketable products and new commercial applications, among other things, graphene. Because such products, for instance, sunscreens, cosmetics, clothing, upholstery, paint, bodywork of vehicles, and computer components, utilize nanotechnologies, it is not strange at present as well as in the near future that nanotechnology will infiltrate consumer products holistically.

The enormous potential for use in the development of new properties of the material lies in the possibility of conscious control of its structure at the nanometric scale. Presently, it is well known, that material properties, both mechanical, electrical, thermal, and chemical, are the result of the phenomena occurring in structures of nanometric size. Nanometric structure materials have particularly advantageous properties and are an effective alternative to conventional materials. Material engineers have just started to produce complex nanomaterials, and there is still a long way to go to reach the natural "best practice" examples in terms of precision, functionality, and efficiency of production. Therefore, a solution-based approach to

innovation in material research seems to be more rewarding and beneficial, for the companies as well as for the scientists and engineers who develop and produce such materials on the prototype level. Diverse range of nanomaterials is extensive and includes, among other things, functional materials, hierarchical materials, functional gradient materials, responsive materials, materials with an expiration date (i.e., they only work for a certain amount of time), and biodegradable materials [14]. A short summary of previous works in the subject is given in Table 1.

An efficient method of preparation of nanocrystalline materials is the electrochemical method using electrocrystallization processes stemming from reactions of oxidation and electrochemical reduction. Electrocrystallization method gives the ability to control the structure of the gauge area, which is a great potential for use in the development of new material properties [15]. This method is exceptionally suitable for preparations of specific materials, mainly the protective layers, and in the near future may be more effective than previously involved methods in surface

Table 1 Topics in electrochemical manufacturing at the nanoscale

Topics	Area of study	References
Nanostructures in electrochemistry	Metal clusters, wires, functionalized layers	[1, 2]
Electrocrystallization technology	Processes stemming from reactions of oxidation and electrochemical reduction, development of new material properties, preparations of specific materials, conscious control of the structures in the nanometric areas, expensive equipment not required	[3–6]
Precision through electrochemistry	Precision sensing and ultrasensitive sensors, control at nanoscale, transparent electronics	[7–9]
Nanoartifacts	Fuel cells, batteries, photovoltaic generation, electronic and computing devices, lighter parts for transport vehicles	[2, 10, 11]
Scanning electron microscopy techniques	Characterization of local structures and properties of surfaces and interfaces, modification on the micro- to subnanoscale	[1, 6, 12, 13]
Potentiometric investigations	Light-addressable potentiometric sensors, cytosensor microphysiometers, integrated biosensors, potential Donnan sensors	[14, 15, 28]
Biomedical applications	Fluorescent biological labels, drug and gene delivery, biodetection of pathogens, cancer therapy, detection of proteins, probing of DNA structure, phagokinetic studies	[15, 16]
Modeling and computer simulations	Large molecules of technological interest, supramolecular structures in interaction or adsorbed at surfaces, and bulk systems for which nanostructural units can be clearly identified, self-assembly and self-recognition of nanoscale objects, understand and characterize the behavior of nanostructures	[17, 18, 29, 31]

modification technologies of known materials, as well as newly produced materials.

These layers can be used together with their grounds or separated from them. Taking into account the specificity of materials electrolytically produced, it is possible that the formation of such a structure of the material and its properties cannot be obtained by other technologies. The possibility of conscious control of the structures in the nanometric areas leads to the production of useful materials with new properties and overcomes previously insurmountable barriers to the development of technology. Understanding of biological processes on the nanoscale level is a strong driving force behind the development of nanotechnology.

This chapter aims at mapping new frontiers in emerging and developing technology areas in nanomaterial research and innovation. Section “[Fundamentals of Electrocrystallization Processes](#)” is devoted to the presentation of fundamentals of electrocrystallization processes and parameters influenced by the final quality of the resulting products. In section “[Electrocrystallization of Nanostructured Copper](#),” essential problems concerning the electrocrystallization process of nanostructured copper products are presented. Section “[Electrocrystallization of Nanostructured Nickel](#)” is aimed on descriptions of electrocrystallization processes of nanostructured nickel products. Problems involving the application of the electrocrystallization method for producing nanostructured composites are included in section “[Electrocrystallization of Nanostructured Composites](#).” Conclusions and final remarks are presented in section “[Summary and Conclusions](#).”

Fundamentals of Electrocrystallization Processes

Electrocrystallization method offers ample opportunities to shape the structure and properties of materials so produced (Table 1). It is currently the most efficient method of producing nanocrystalline materials. The attractiveness of the method for the electrocrystallization of materials is, among other things, in the fact that it does not require expensive equipment. It eliminates a dilemma, whether to master technologies of materials using expensive and complicated equipment or cheap, not demanding financial outlays, but only appropriate knowledge of the physical and chemical processes. Recently, much interest in electrocrystallization of nanocrystalline materials has evolved due to (i) the low temperatures involved; (ii) the ability to coat geometrically complex or non-line-of-sight surfaces of porous products; (iii) the ability to control the thickness, composition, and microstructure of the final product; (iv) the possible improvement of the substrate/coating bond strength; and (v) the availability and low cost of equipments [3].

A simplified scheme of appliances being widely applied as electrochemical reactors and automated nanostructured materials' processing equipments is presented in Fig. 1. Charged electrodes being able to carry out chemical reactions are in use for realizations of electrocrystallization processes [13].

Current directions of research conducted on the process for producing nanostructured materials by crystallization concentrate on the manufacture of materials with

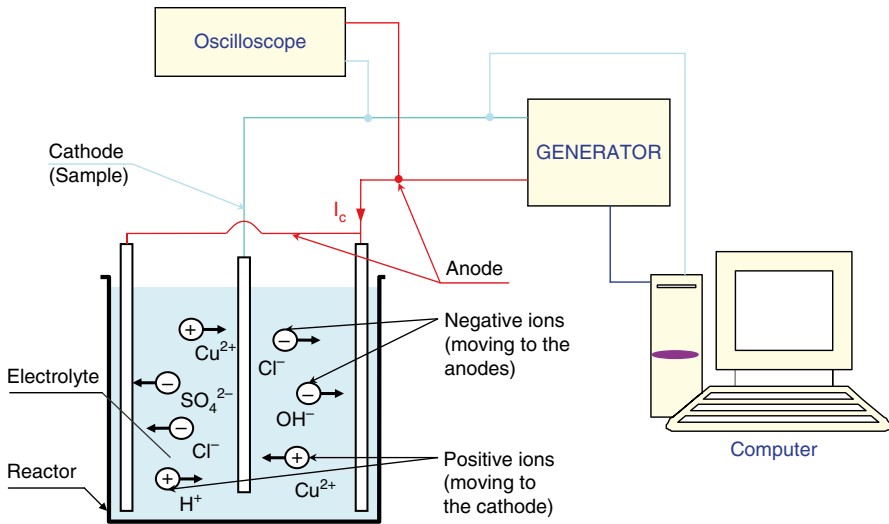


Fig. 1 Simplified scheme of appliances for electrocrystallization of nanocrystalline materials

different chemical and phase compositions and different structures which provide adjustment of their properties to the high demands on working conditions. By choosing the type and composition of the electrolyte solution, and the process parameters such as type and density of the current, temperature, and time duration of the process, can be designed a variety of materials meeting the features in the art.

Several application-specific types of electrocrystallization processing systems, each with its own specific requirements, have been produced up to date. Various waveforms of the current supplying the electrocrystallization reactor are shown in Fig. 2. All major process studies concentrate currently around the PPRC electrodeposition technology and the general metal finishing products (Fig. 2b–e). Pulse current electrocrystallization is able to produce layers with more uniform particle distribution and better surface morphology than those obtained under direct current [9].

By electrocrystallization method can be prepared a variety of metals, metal alloys, and composite materials. Especially great potential resides in shaping the properties of composite materials. Composite materials prepared by this method can be formed with a metal matrix, and a disperse phase may be constituted by different materials, for example, other metal (W), ceramics (Al_2O_3 , Cr_2O_3 , Si_3N_4), polymer (PFE), or carbon (graphite, nanotubes, graphene). The combination of two different materials, disperse phase and matrix metal, allows the control of produced material properties in a fairly wide range, which enables the formation of a material satisfying efficiently various functions in practice [5, 10, 19].

Realization's efficiency of simultaneous deposition of metal and nonmetallic disperse phase in the same process and the electrochemical reduction of the quality of the material will depend on such factors such as the nature and composition of the electrolyte solution, the process parameters (concentration, pH, temperature,

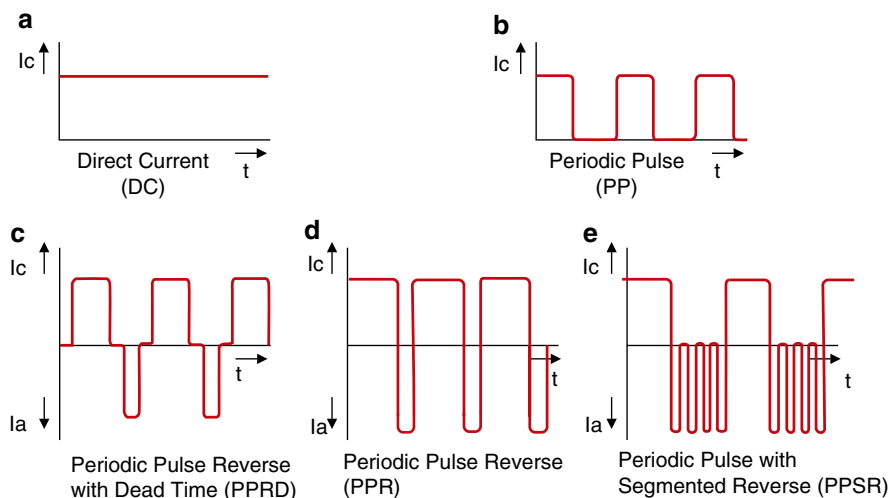


Fig. 2 Current waveforms for electrocrystallization processing

stirring, current conditions), and the chemical nature of the grain structure built in nonmetallic disperse phase, chemical nature, and content of various additives, as well as the quality of the substrate material and the condition of its surface. The low processing temperatures minimizes crystallite interdiffusion, while the high selectivity of electrocrystallization process allows uniform modification of surfaces and structures with complicated profiles. All of these factors must be taken into account when designing a composite material to be properly (i.e., as expected) working under determined conditions. Such a large number of parameters, which influenced the control of electrocrystallization processes and affected the quality of the manufactured material, give on one hand a great flexibility in its ability to modify constituted material but on the other hand present a big challenge for the proper and optimal choice of their selection. This requires a thorough diagnosis of the mechanisms of these complex processes, as well as their practical implementation of parameters. So, the set of the parameters of the implementation of such processes in the production environment and the relationships between these parameters and the structure and properties of the produced nanocrystalline material requires complex experimental research and in-depth analysis [1, 4, 20].

The parameters of the current supplying electrochemical reactor and its density limit the electrode redox processes on the surface of the electrodes. In contrast, the composition of the electrolyte solution can control the rates of the two competing processes of forming a new phase resulting from the electrocrystallization and decides on the size of grains of the deposited material.

While the applications of nanocrystalline materials are beginning to play a greater role not only on quantitative considerations as quality, electrocrystallization method could be competitive in relation to other methods. So far, the main obstacle in the application of electrocrystallization technology for receiving materials on a larger

scale was undoubtedly the complexity and synergistic influence of the preparation of raw materials in accord to the desired properties of final products. It seems, however, that in the era of modern techniques of analysis of processes during the material production, including electrocrystallization process, it will be possible to know precisely than ever the relationship between structure and properties of materials and their resulting parameters [7]. Applying the electrocrystallization method nanocrystalline materials from pure metals Cu, Ni, and Co and composite materials nanocrystalline Ni/Al₂O₃ and Ni/Si₃N₄ were prepared. Appropriate chemical composition of electrolyte solutions and process parameters of electrocrystallization process capable of producing nanocrystalline materials were established. Produced nanocrystalline materials exhibited crystallites with sizes ranging from 10 to 50 nm, depending on the nature and chemical composition of the electrolyte solution, temperature, degree of agitation, if used, and other parameters of electrocrystallization processes. Taking into account potential applications of nanocrystalline materials, the pursuit of deposit *uniformity*, especially thickness uniformity, has been a technical imperative for suitable controlling every produced nanocrystalline material [21, 27].

Studies of the properties of the produced materials including corrosion resistance and microhardness were performed using the mathematical modeling and scanning electron microscopy (SEM), atomic force microscopy (AFM), X-ray diffraction (XRD), and transmission electron microscopy (TEM).

For comparative purposes, tests were also subjected to the same kind of materials with microcrystalline structure produced also by electrocrystallization method.

Electrocrystallization of Nanostructured Copper

In the present section, an effort has been made to examine various modes of nucleation and growth of nanostructured copper electrocrystallization with direct and pulse periodic currents. The performed studies focus on nanocrystalline bulk copper deposits and composite surface layers with grain sizes smaller than 100 nm because such materials attract presently high technological and scientific interests due to their improved electrochemical, mechanical, and physical properties being useful for extensive applications. The attention is focused on nanocrystalline structures, surface roughness, hardness, and process parameters leading to major differences in final products.

Control of Nanocrystalline Copper by Current Waveforms

As we have already shown previously [13] copper electrocrystallization on high-end thin layers and on other product in cutting-edge technologies was at the very limit of what DC processes could achieve, and it turned out PPR technology could go beyond that. By varying the duty cycle, that is, on time/on time + off time, changes in electrocrystallized structure, mainly crystallite size, can be achieved, because of forced nucleation during each new cathodic pulse. In an acid solution, the cation Cu²⁺

associates with the anion SO_4^{2-} to form copper sulfate. At the cathode, the Cu^{2+} is reduced to metallic Cu by gaining two electrons. The result is the effective transfer of Cu from the anode source to a cathode plate. Current densities, cathodic (on time) and anodic (reverse on) times, as well as solution concentration and temperature can be varied independently, forming a fivefold parameter space [9].

The pulse current density, i_p , is divided into the capacitive current density, i_C , and the faradaic current density, i_F , as follows:

$$i_p(t) = i_C(t) + i_F(t) \quad (1)$$

The capacitive current density is related to the double layer potential by

$$i_C(t) = C_{dl} \frac{dv_1(t)}{dt} \quad (2)$$

where $v_1(t)$ is the potential drop within the double layer and C_{dl} is the capacitance of double layer. Since the applied current density is low, the relationship between faradaic current and overpotential can be assumed in the form

$$i_F(t) = \frac{v_1(t)}{R_{ct}} \quad (3)$$

where R_{ct} denotes the charge transfer resistance.

Combining Eqs. 1, 2, and 3 gives

$$C_{dl} \frac{dv_1(t)}{dt} + \frac{v_1(t)}{R_{ct}} = i_p(t) \quad (4)$$

The copper ions are firstly adsorbed on the electrode and reduced to copper adatoms in two steps. The first term on the left of Eq. 4 represents the reaction of copper ions disproportionation, and the second describes the dissolution of metal. Similarly to $v_1(t)$, the response of the potential drop $v_2(t)$, corresponding to metal dissolution, is given by

$$C_{psd} \frac{dv_2(t)}{dt} + \frac{v_2(t)}{R_{sd}} = i_p(t) \quad (5)$$

where C_{psd} and R_{sd} denote the dissolution capacitance and resistance, respectively.

In this way the total surface overpotential $v(t)$ is determined by

$$v(t) = v_1(t) + v_2(t) \quad (6)$$

Early treatments correctly predicted that since the peak current densities in pulse electrocrystallization were higher than the time-average-equivalent DC current densities, the nonuniformity would be larger, according to

$$W_t = \frac{2.303RTk}{jZfL} = \frac{R_t}{R_e} \quad (7)$$

were R_t and R_e denote the charge transfer resistance and the ohmic resistance, respectively, with k as solution conductivity and L as length.

Under influence of PPR electric current, the following changes of ion concentrations take place:

During the current on interval, we have

$$c(t) = c_0 + c_j \left[1 - 8\pi^2 \sum_{m=1}^{\infty} A_m \right], \quad (8a)$$

with

$$A_m = \frac{1}{(2m-1)^2} \exp \left[\frac{\pi^2}{4} (2m-1)^2 a (t-PT) \right] K, \quad (8b)$$

$$K = \frac{1 - \exp \left[-\frac{\pi^2 a}{4} (2m-1)^2 \tau \right]}{1 - \exp \left[-\frac{\pi^2 a}{4} (2m-1)^2 T \right]}. \quad (8c)$$

where c_0 is the concentration of the electrolyte solution; c_j the parameter dependent on current amplitude I_p , diffusion layer thickness d , Faraday constant F , rate n of ion oxidation, and diffusion coefficient D ; P the number of current cycles; and T the absolute temperature.

During the current off interval, we obtain

$$c_p(t) = c_0 + c_j \left[8\pi^2 \sum_{m=1}^{\infty} A_{mp} \right] \quad (9a)$$

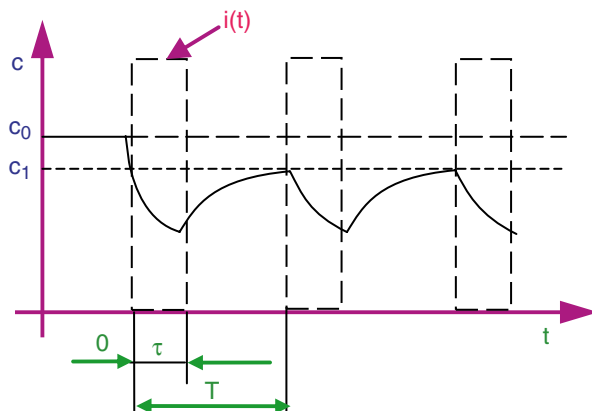
with

$$A_{mp} = \frac{1}{(2m-1)^2} \exp \left[\frac{\pi^2}{4} (2m-1)^2 a (t-PT) \right] K_p, \quad (9b)$$

$$K_p = \frac{1 - \exp \left[-\frac{\pi^2 a}{4} (2m-1)^2 (T-\tau) \right]}{1 - \exp \left[-\frac{\pi^2 a}{4} (2m-1)^2 T \right]} \quad (9c)$$

The above result indicates that the current amplitude I_p and the coefficient α of the current rate as well as frequency $f=1/T$ have significant influence on the quality of deposited copper layers. Applications of PPR current give relatively easy control of the microstructure, thickness, and useful properties of the nanocrystalline copper layers. The time-varying current and ion concentration in the diffusion layer during the copper electrocrystallization are demonstrated in Fig. 3.

Fig. 3 Variations of the current and ion concentration in the diffusion layer



It should be emphasized that the electrodeposition of Cu is strongly dependent on the structure of the substrate, supplying current and concentration of Cu^{2+} ions in the precursor electrolyte solution. Since the effect of increasing current density is to increase the electrode surface reaction, a faster surface reaction makes Cu^{2+} under-supplied from the electrolyte solution. Hence, the polarization is higher, and smoother film morphology is observed. Nevertheless, when the applied current density is greater than the limiting current density, it is impossible for the electrode to gain any Cu ions from the electrolyte solution, thereby leading to an increase in the Cu film surface roughness [8, 13].

Control of Nanocrystalline Copper Structures by Compositions of Electrolyte Solutions

Components of electrolyte solutions for Cu electrocrystallizations may vary widely depending on the substrate and the type of Cu deposit desired. The electrolytic solutions include acid solutions and alkaline solutions as well as some additives used to provide desired surface finishes for the Cu structure and to initiate bottom-up adhesion of surface layers. Successful PPR applications include the optimization of the electrolyte composition, additive package, solution agitation, and electrochemical reactor design. We have previously shown [13] that pure and other electrolyte solutions prepared at contents of appropriate additives are represented by Cu1, Cu2, ..., Cu8, respectively, and correspond to specifications given in Table 2. Organic additives are adsorbed on the surface of the substrates and slow down the diffusion of the chemicals in the electrolyte solution to the surface of the substrate. They are not incorporated into the deposit. Copper is unique in that at least one additive such as PEG (polyethylene glycol) is required to suppress the electrocrystallization rate in order to obtain smooth, dense nanocrystalline materials. The higher current densities used in PPR electrocrystallization force developing additives that can guarantee more stability at higher currents. Thus, the additive system must be designed to work at high current densities.

Table 2 Compositions of Co per electrocrystallization solution

Symbol	Additive substance	Content [g/dm ³]
<i>Cu1</i>	–	–
<i>Cu2</i>	HCl	0.01
<i>Cu3</i>	H ₂ N-CS-NH ₂	0.20
<i>Cu4</i>	HCl H ₂ N-CS-NH ₂	0.01 0.20
<i>Cu5</i>	C ₇ H ₅ NO ₃ S C ₁₂ H ₂₅ NaO ₄ S	0.20 0.44
<i>Cu6</i>	HCl C ₁₂ H ₂₅ NaO ₄ S C ₇ H ₅ NO ₃ S	0.01 0.44 0.20
<i>Cu7</i>	HCl Cu-189	0.01 6 ml
<i>Cu8</i>	HCl C ₁₂ H ₂₅ NaO ₄ S H ₂ N-CS-NH ₂	0.01 0.44 0.20

Important benefits in copper electrocrystallizations can be delivered by using appropriate acid copper electrolyte in combination with pulse period reversal current. Surface microstructures of Cu thin layer electrodeposits produced in different solutions are presented in Fig. 4. Their counterparts with nanosize grains are shown in Fig. 5. These images indicate that the electrocrystallization process appears as an easy way for surface modification of known materials, as well as newly received ones.

The produced micro- and nanocrystalline copper structures consist of agglomerates of copper grains being a function of the current density of the electrocrystallization process. Nanosized dimensions of copper grains are achieved by increasing the current density to the allowable higher level. The higher the current density, the finer the grains and the faster the electrocrystallization rate will be, although there is a practical limit enforced by poor adhesion and quality when the rate is too high.

It is worth noticing that in Cu nanomaterials, a non-negligible fraction of the atoms is on or close to the surface of the material. These surface atoms are surrounded partially by the material and partially by vacuum. The density distributions viewed from these atoms differ from those viewed from the deeply buried atoms.

Influences of electrolyte solution composition on the hardness of copper thin layer produced by DC process are presented in Fig. 6. The diagram shows that the highest hardness of copper electrocrystalline bulk material can be obtained at bathes Cu4 and Cu5 at current density 5 A/dm².

The performed studies lead to the statement that the hardness and tensile strength are inversely proportional to the grain size – so a pulse supplying current produces harder copper electrocrystallites than switch mode current or DC in the absence of additives [11].

Exceptional technological features consist in the relatively low processing temperature and the high selectivity. The low processing temperatures minimize interdiffusion, whereas the high selectivity of electrocrystallization processes allows uniform modification of surfaces and structures with complicated profiles.

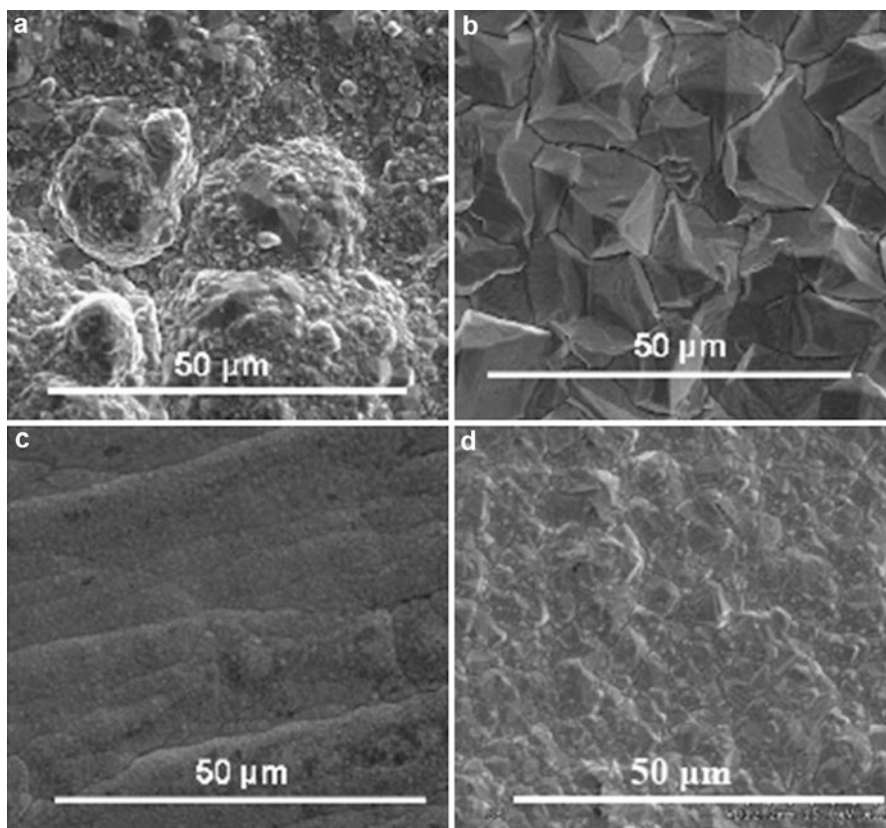


Fig. 4 Surface microstructures of Cu thin layer electrodeposits produced with $J = 5 \text{ Adm}^{-2}$ in different solutions: (a) microcryst., CuSO_4 and H_2SO_4 ; (b) microcryst., CuSO_4 , H_2SO_4 , and HCl ; (c) nanocryst., CuSO_4 and additive D1; (d) nanocryst., CuSO_4 , H_2SO_4 , and HCl ; and organic additive D1

Simultaneous influences of the current density and kinds of the electrolyte solution on the surface morphology of microcrystalline copper are illustrated in Fig. 7.

Applications of PPR current give relatively easy control of the microstructure, thickness, and useful properties of the deposited copper layers. Differences in the surface morphologies of microstructure electrocrystallized copper are shown in Fig. 8a–c for various current waves in absolute values of positive and negative current pulses during the symmetric semi-periods, respectively.

We have observed significant growth of selected grains in a polycrystalline interconnect, which subsequently become more susceptible to surface offset formation with further cycling (Fig. 9).

These materials can be used together with the substrate or separated from it. Apart from the known uses for protecting the substrate material in corrosive conditions or to improve the mechanical properties surface, they can extend the life of the tool and ensure its longer life. This is particularly important if, in these operating

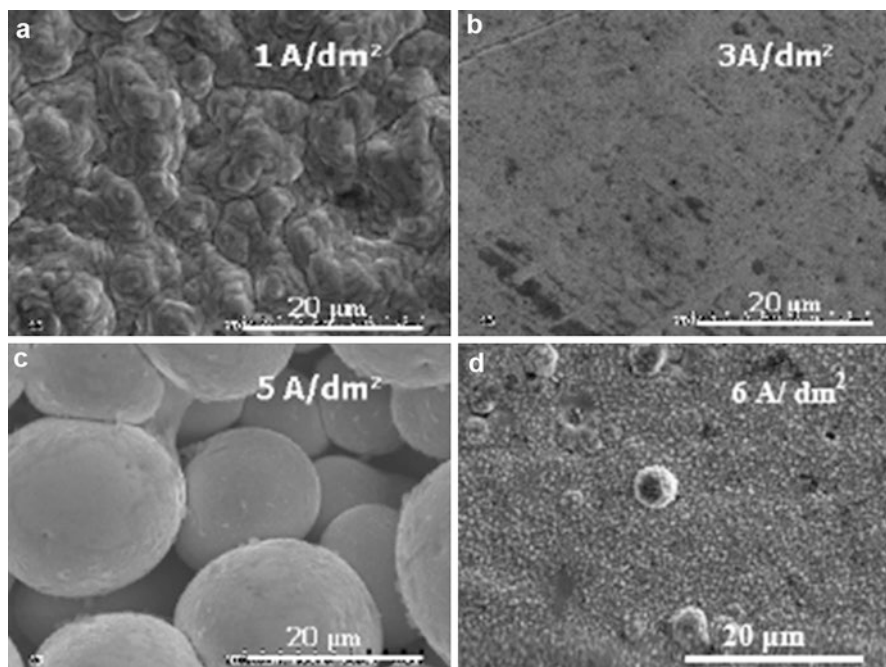


Fig. 5 Surface of Cu nanocrystalline thin layer electrodeposits produced with different current densities in CuSO₄, H₂SO₄, HCl, and organic additive D1 solution

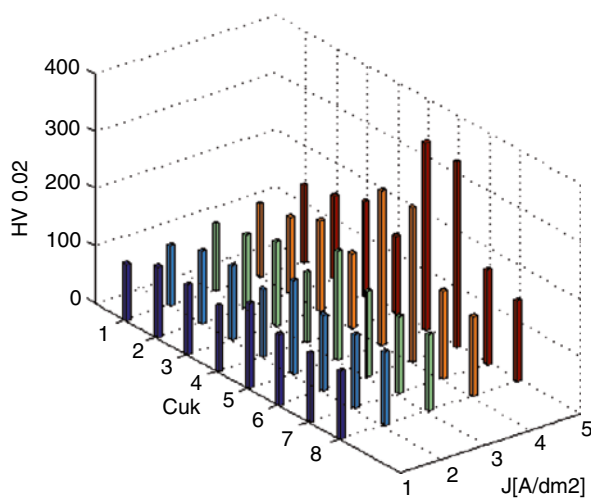


Fig. 6 Hardness of the copper deposits versus DC current density and bath composition

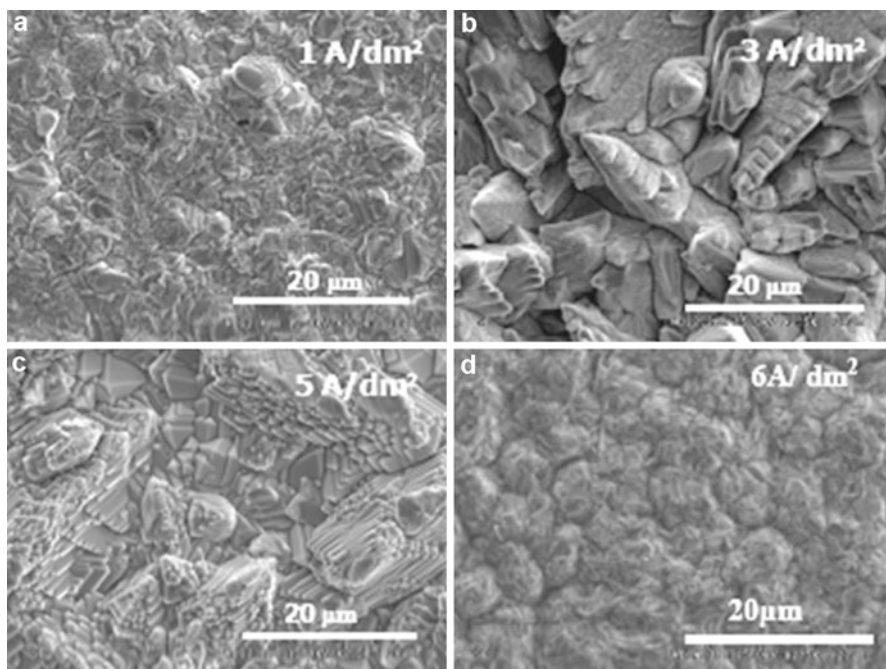


Fig. 7 Microcrystalline structure of Cu thin layer electrodeposits produced with different current densities in CuSO_4 , H_2SO_4 , and H_2NCSNH_2 solution: (a) 1 A/dm^2 and HCl, (b) 3 A/dm^2 , (c) 5 A/dm^2 and an organic substance, (d) 6 A/dm^2

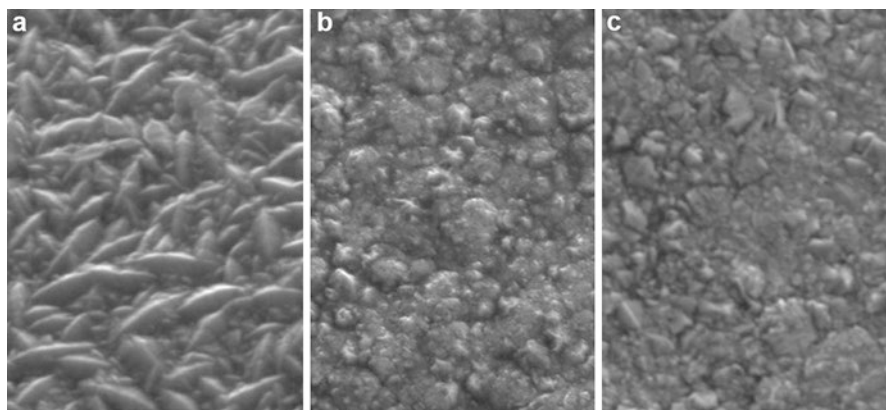


Fig. 8 Surface morphology of copper electrodeposits produced with $J=1.1 \text{ A}/\text{dm}^2$: (a) DC, (b) PC at $f=0.5 \text{ kHz}$, (c) PC at $f=10 \text{ kHz}$

Fig. 9 Influence of the PPC frequency on crystallite dimensions

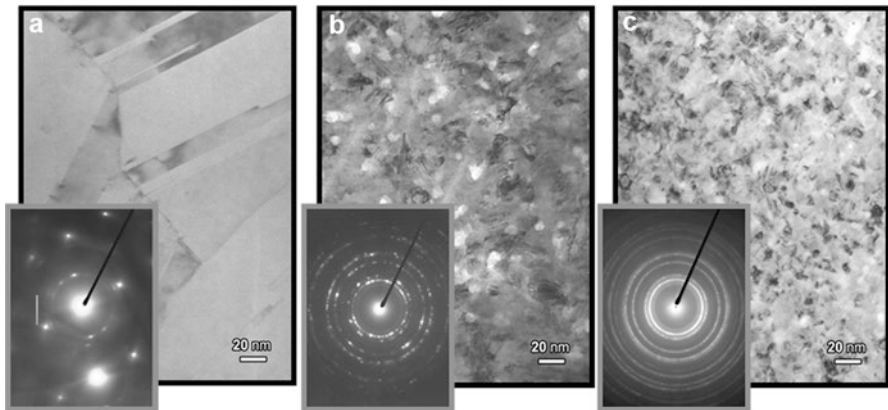
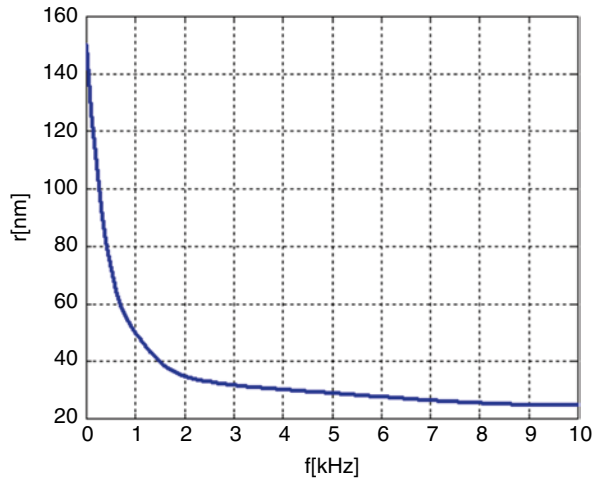


Fig. 10 The images of internal nanostructure of produced copper: (a) without additives, (b) additive D1, (c) additive D2

conditions, it is not possible to select a material resistant to providing differentiated factors (corrosion resistance, good mechanical properties, or the specific physical characteristics). In this case, the substrate may provide one kind of properties, the coating surface layer excites others.

The benefits of reverse pulse current plating are evident because it allows a precise control of the deposited material, including its composition, crystallographic structure, and texture and grain size. The higher the current density, the finer the grain. Hardness and tensile strength are inversely proportional to the grain size – so a pulse supply will produce harder deposits than switch mode or DC in the absence of additives (Fig. 10).

Effects of the electrocrystallization process of producing nanocrystalline copperware depend in a clear manner on chemical composition of the used electrolyte solution. Some organic additives denoted by D1 and D2 being supplements to the basic solution (CuSO_4 , H_2SO_4) play important roles in shaping internal structure of the produced nanocrystalline material. Figure 10 demonstrates diversity of the internal structure of nanocrystalline copper caused by appropriate additives in the electrolyte solution [22].

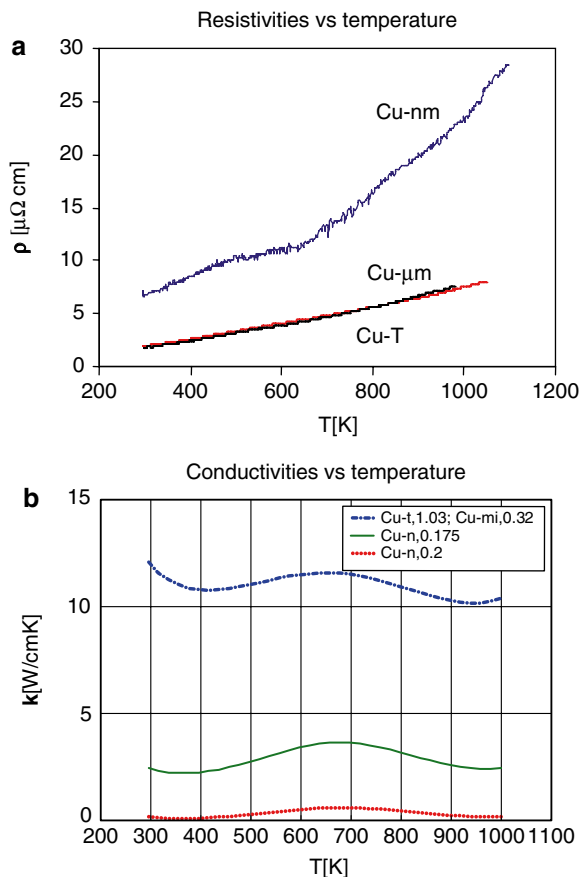
Although electrodeposition has been one of the methods for nanocrystalline material manufacturing, properties of nanocrystalline copper electrodeposits are less evaluated, especially for tribological applications or potential applications in very large scale of integration devices such as micro- and nano-electro-mechanical systems.

The SEM micrographs illustrating the morphology of copper deposits formed under current constant density and various electrocrystallization times clearly suggest the case of instantaneous nucleation of crystallites. Instantaneous nucleation corresponds to a slow growth of nuclei on a small number of active sites, all activated at the same time. It can be noted that in most of the samples, the nuclei may be formed almost simultaneously, as confirmed by their similar size. In other words, i.e., at high nucleation rates (instantaneous nucleation), all nuclei are formed immediately after imposition of the current and grow at the same rate. As a result, they are all of the same age, and their number remains constant. As nucleation progresses, the nuclei begin to overlap. Each nucleus is defined by its own diffusion zone through which copper diffuses, thus representing the mass supply mechanism for continuation of growth. Progressive nucleation corresponds to fast growth of nuclei on many active sites all activated during the course of electroreduction.

Electrical and thermal properties of nanocrystalline copper are very sensitive to the inner structure of a material, so theoretical prediction of these properties is a difficult task [6]. Defects of crystalline structure influence useful properties of the electrocrystallized copper. Moreover, in layers of thickness comparable or smaller than the characteristic lengths of carriers, new physical phenomena occur, and in this case theoretical models describing a copper layer as a continuum medium cannot be used for the description of its thermal properties. Figure 11 shows selected diagrams of electrical resistivity and thermal conductivity for various kinds of the copper.

The given plots exhibit an important decrease of the electric and thermal conductivities of nanocrystalline copper thin layers when comparing them with that of bulk copper being widely up to date used in the practice (Cu-T). In polycrystalline copper layers, the scattering on grain boundaries dominates over scatterings on layer boundaries and causes an additional reduction of the electrical and thermal conductivity. The observations obtained in this investigation reveal that the thermal conductivity of nanocrystalline copper thin layers takes maximal values in the temperature range of 600–700 K. However, the layer thickness has an additional influence on the thermal conductivity of copper surface electrodeposits.

Fig. 11 Electrical and thermal properties of crystalline copper: (a) electrical resistivity, (b) thermal conductivity



Electrocrystallization of Nanostructured Nickel

In the completed studies, nickel layers were produced by the electrochemical reduction method in multiple electrolyte solution of a Watts type. An equal width of cathodic surface periodic pulse current of 3 A/dm^2 and carry out ratio $\alpha = 10 \%$ was used in the processes for producing nanocrystalline nickel layers. The current frequency was varied in the range of 0–10 kHz.

The structure of the produced nickel was studied by X-ray diffraction (X) and by scanning electron microscopy (SEM) approaches. The influence of the current type and the frequency of pulsed current on the topography and morphology of the surface of the produced nickel are illustrated in Fig. 12.

The structure of electrocrystallized nickel produced in the basic electrolytic solution (Watts bath) without organic additives is characterized by a large grain size and develops a rough and dull surface (Fig. 13a). In contrast, the surface of nanoelectrolytic nickel formed in a solution of nickel modified with organic additives D1 and

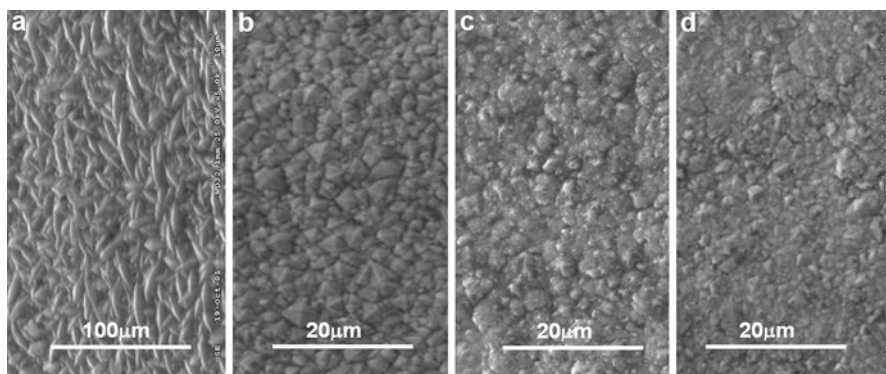


Fig. 12 The topology and morphology of the surface of the deposited nickel layers: (a) microcrystalline, by DC; (b–d) nanocrystalline, by PPR with the frequency 0.5, 5, and 10 kHz, respectively

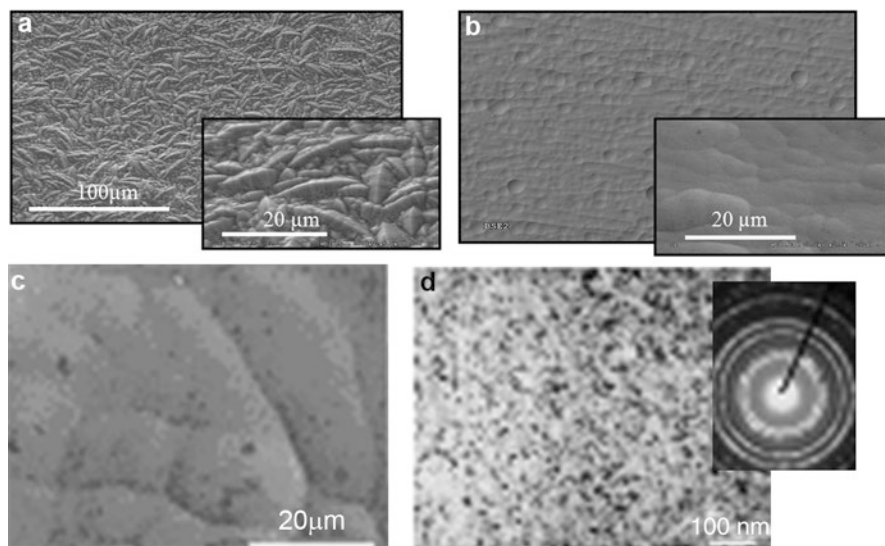


Fig. 13 Morphology of produced nickel deposits examined by using SEM and TEM: (a) microcrystalline, (b, c, d) nanocrystalline

D2 (Fig. 13b–d) is smooth, glossy, and less developed than that of layers of microcrystalline material [20].

Differences in the topographies and structures of such materials appear as an effect of different atomic arrangements within the material volume and on the layer surface. The presented, selected area, diffraction pattern (Fig. 13d) of the nanocrystalline Ni exhibits a variation in the grain size that is visible both on the material surface and within the material volume. Moreover, the diffraction patterns of such

materials with spots situated on the ring circumferences indicate nanocrystalline textured structures.

The internal structure of the material has a decisive influence on its properties. Comparison of abrasive wear of nickel materials produced electrochemically by applying the DC and periodic pulse current is illustrated by the graphs shown in Fig. 14. The materials formed by periodic pulse currents, which are composed of nanocrystallites, exhibit a lower degree of wear [28].

All produced nanonickel materials are characterized by a compact structure. Both the type of supplying current and the frequency, in the case of pulsed current, affect the topography of the material surface and the size, diversity, and shape of crystallites. Selected results of research carried out on the surface of nanocrystalline nickel are shown in Fig. 15. The fine grain material deposited here exhibits layered structure. Each layer, being parallel to the substrate surface, is made of spherical nanocrystalline agglomerates. Increased refinement of grain structure increases the hardness and stress resistance of the material and thereby reduces its plasticity. Grain boundaries may strengthen the structure and prevent deformations or may facilitate grain sliding along the boundaries and lead to formation of intergrain cracks.

Dimensions of the nickel crystallites depend on the chemical composition of the electrolytic solution used for process realization, as well as on process parameters such as density and the type of supplying current and temperature of the solution. The addition of organic matter D1 and D2 inhibits crystal growth processes and promotes the formation of new crystal nuclei, leading to crystal structures of nanometer grain size. The produced nanocrystalline nickel exhibited grain size of the order of 25 nm.

Diversity of the intensity of diffraction peaks at various diffraction patterns provides a significantly textured material. Diffraction line profiles indicate that the nickel layers formed in the basic electrolytic solution are characterized by a greater primary grain size and the special crystallographic direction $\langle 200 \rangle$.

In the case of nanocrystalline nickel which has been formed in the solution modified with organic additives, preferred crystal growth orientation takes the direction of

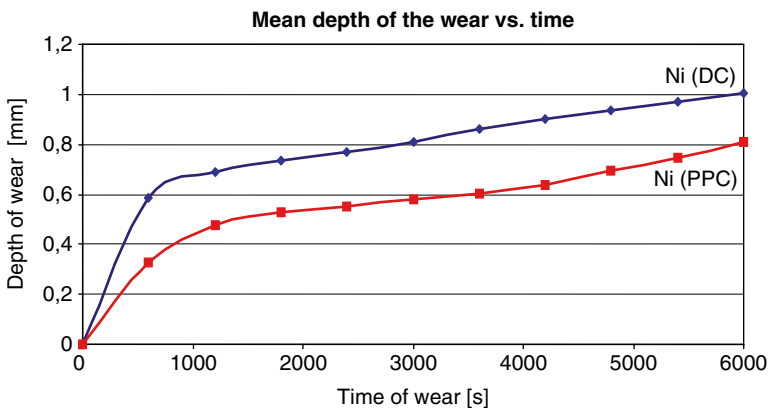


Fig. 14 Abrasive wear of the nickel surface produced by applying: DC-Ni (DC), PPC-Ni (PPC)

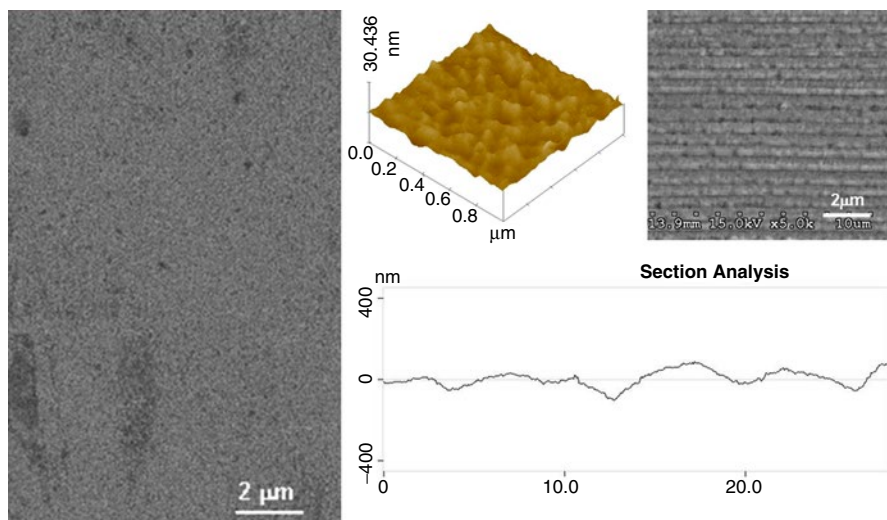


Fig. 15 Topography and surface geometric profile and layer cross section of nanocrystalline nickel

$\langle 111 \rangle$, and the increased width of the reflections indicates the nanosized dimension of the produced crystallites. From the set of diffraction patterns based on the broadening of X-ray reflections and using the Scherrer relationship in the following form:

$$\beta_k = K \lambda / D_{hkl} \cos(\theta_{hkl}) \quad (10)$$

where

β_k – reflex width depending on the size of the crystallites [rad]

K – Scherrer constant close to unity

λ – wavelength of X-rays [Å]

D_{hkl} – average crystallite size in a direction perpendicular to the planes (hkl)

θ_{hkl} – angle reflections, the size was determined of crystallites occurring in the nickel material formed as the nanocrystalline structure [18].

The electrocrystallization process is suitable for producing surface nanostructured nickel layers. In addition to the compact construction and a good adhesion to the material of the substrate, the surface nanocrystalline nickel layers significantly increase the performance of the products in which they are embedded. It was observed a significant increase in the corrosion resistance as well as impact properties, such as hardness, or resistance to tribological wear.

Electrocrystallization of Nanostructured Composites

Advanced composites are already extremely important to the defense industry and will be more critical in the near future because they offer the greatest strength and stiffness-to-weight ratio among engineering materials. Composites are expected to

be a key enabler in the development of light and more mobile not only military force but also cars, planes, buildings, and so on. They also offer the simplest route for embedded sensors, actuators, and other elements, thus providing much sought-after multifunctionality. Revolutionary advances in composites result from the use of nanotechnology, wireless technology, and self-healing mechanisms. Provided that the cost of composite manufacturing continues to decline, composites could displace steel and aluminum as the primary materials in manufacturing, transportation, and construction. In electronics, carbon-based nanocomposites could potentially replace silicon as the basic building blocks for chips and circuit boards.

It is interesting to note that due to the charge transfer effect, the electrical conductivity of the composite can be higher than the conductivity of both of the components considered separately. Moreover, preparation of a nanocrystalline composite can be achieved with commercially available low-cost reagents, which enable large-scale production. Hence, there are significant challenges in developing nanostructured composite materials for a large displacement of classic materials and a rapid response to the needs of highly advanced technology as well as in developing compatible fabrication methods. The extraordinary mechanical, optical, and electrical properties of nanostructured composites are implementable into working devices [12, 23].

Nanocrystalline Composites with Nickel Matrix

Nanocrystalline composites with nickel matrix create a good potential for designing and producing materials proving favorable properties. One of the possibilities in this domain appears to be nanocrystalline nickel layer composed of pure metal Ni and modified by disperse phase in the form of ceramic silicon carbide SiC, silicon nitride Si₃N₄, or molybdenum disulfide MoS₂. Introduction of the disperse phase to the metal matrix appears as an efficient way to increase the hardness and resistance to frictional wear of the resulting material while maintaining the corrosion resistance of the matrix material. Selected disperse phase in the nickel modifies significantly the surface properties of the composite material. Silicon carbide SiC is a ceramic material, characterized by a favorable physicochemical properties, such as high hardness and thermal as well as chemical resistances and good thermal and electrical conductivities. In contrast molybdenum sulfide MoS₂, as a material with strong ionic bonds and the layered crystal structure, has low hardness and good mechanical and chemical resistances and lubricating properties.

The combination of nickel nanocrystalline material as the matrix and the disperse phases in the form of SiC or MoS₂ creates the possibility of forming high potential output properties of the produced composite material. Combinations of two such different materials allow completion of their measurable characteristics, while the interactions between these different phases of such a modification induce these properties. For the disperse phase, by selection of particle size and their content in the matrix material, it is possible to design the respective properties of the composite material produced by electrocrystallization processes. This type of

nanocomposite surface layers can perform optimally a variety of functions in the art, and above all where the products and devices are placed particularly as high technical requirements.

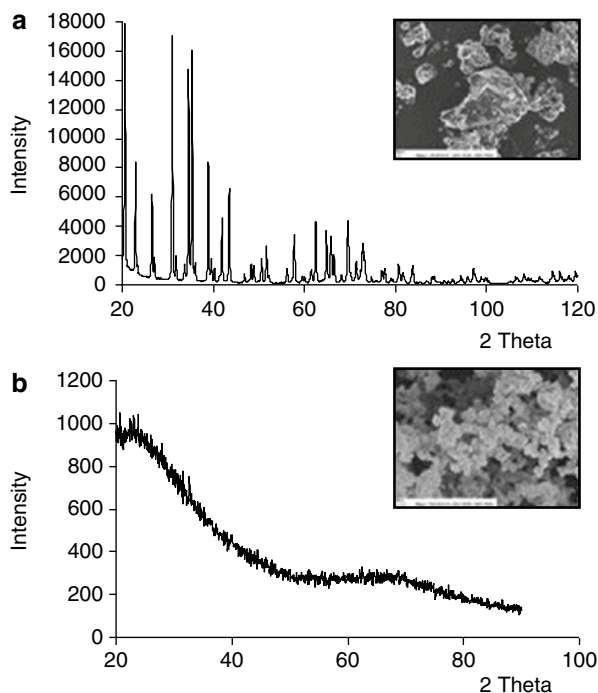
Disperse ceramic phase was used for the production of composite layers Ni/Si₃N₄, constituted by the microcrystalline structure of polydisperse Si₃N₄ powder containing both crystalline forms α and β of the hexagonal structure and a large variety of grain size (Fig. 16a), while for the production of composite layers of Ni/Si₃N₄ having nanometric structure, an amorphous silicon nitride powder (Fig. 16b), with an average grain size of 15 nm, was applied.

The topography of the nickel and composite layers (Fig. 17), the diversity of their morphology and their internal structures and thickness, and the distribution of particles of the ceramic phase in a volume of the composite material were determined by using a scanning electron microscope Hitachi S-3500 N equipped with an EDS spectrometer (Norman Vantage). The content of the disperse ceramic phase Si₃N₄ in the composite material of the layers was determined by quantitative metallography methods and computer image analysis.

Measurements of microhardness within the cross sections of the material layers were performed by the Vickers method at a load of 20G (HV 0.02) using a microscope NEOPHOT-1 with the Hanemann attachment.

The volume fraction of the disperse phase in layers containing micrometer Si₃N₄ powder was reduced from 18 % vol. in layers produced by DC to 14 % in layers produced by periodic pulsed current, and in the case of nanometric layers with Si₃N₄

Fig. 16 Diffractograms and SEM images of Si₃N₄ powders: (a) crystalline, (b) amorphous



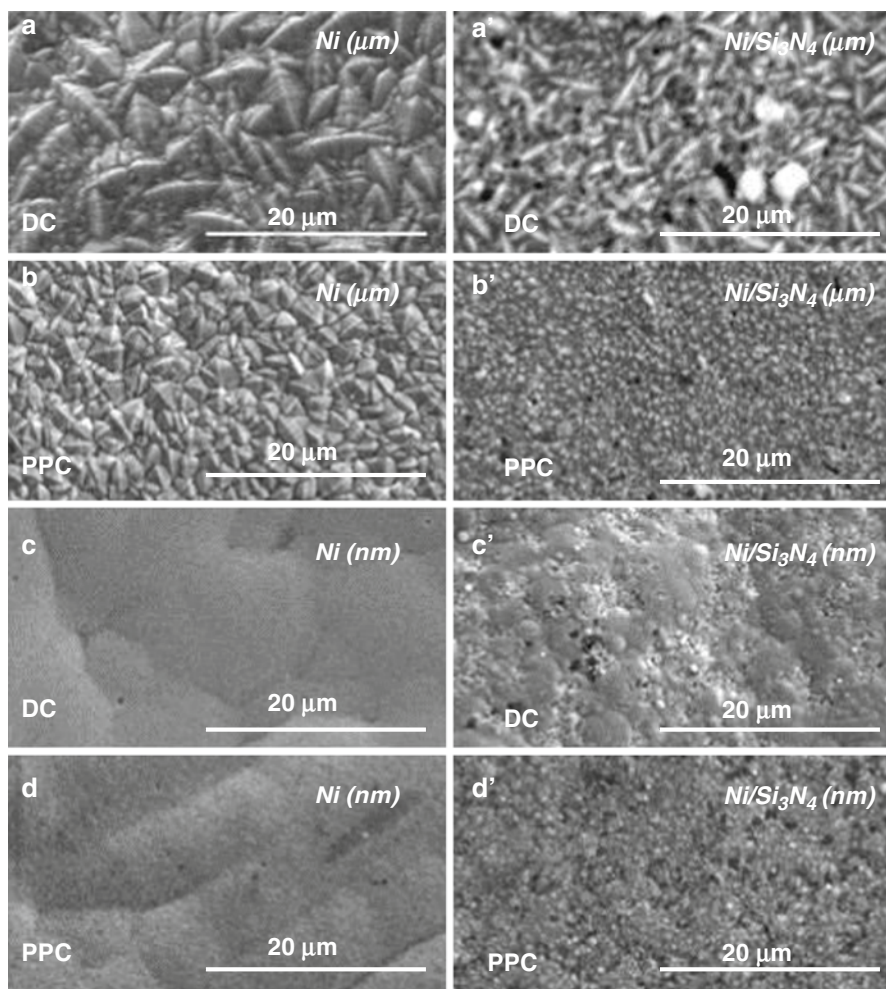


Fig. 17 Morphologies of produced nickel and composite layers: (a, a', c, c'), direct current (DC); (b, b', d, d'), periodic pulse current (PPC)

powder, the decrease corresponds from 8 % vol. up to 5 % vol. (Fig. 18), respectively.

The decrease in the volume fraction of the ceramic phase in the layer of Si_3N_4 formed a nickel by pulsed current with respect to their counterparts produced by DC reduces the microhardness of the layers of composite as shown in Fig. 19.

The use of the periodic pulse current instead of direct current leads to the production of layers with a lower surface development and smaller grain size of nickel and also affects the amount of ceramic phase embedded in the matrix material. In this way, it is possible to improve the hardness and corrosion resistance of the $\text{Ni}/\text{Si}_3\text{N}_4$ surface layers.

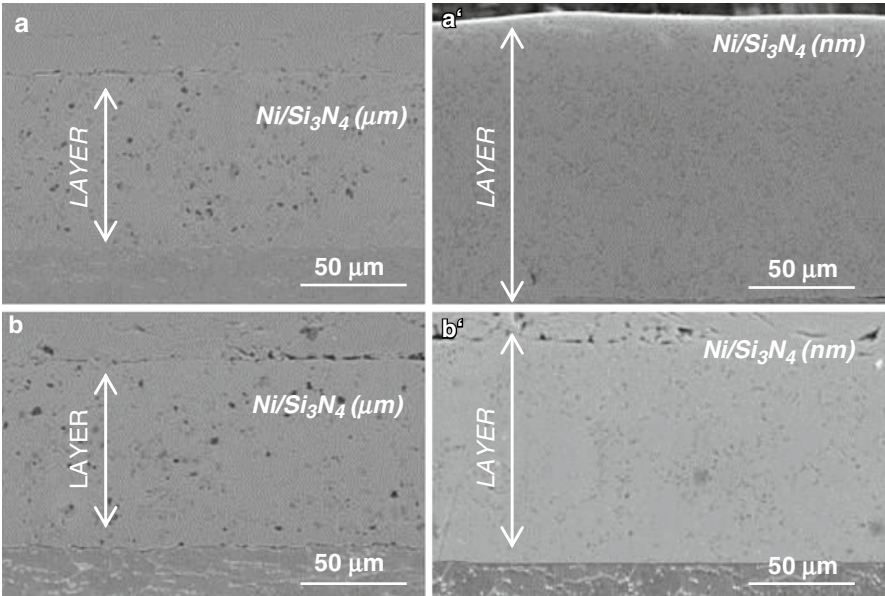
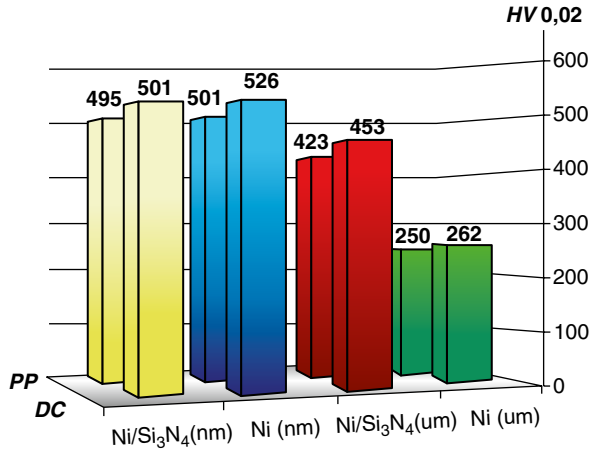


Fig. 18 The distribution of the ceramic phase Si_3N_4 within the volume of composite layers: (a, a'), direct current (DC); (b, b'), periodic pulse current (PPC)

Fig. 19 Hardness of the Ni and $\text{Ni/Si}_3\text{N}_4$ layers produced by direct and pulse periodic currents



Recently, there has been an explosion of interest directed toward depositions of nickel-nanostructured composite thin layers containing ceramic Al_2O_3 disperse phase. By decreasing the particle size of composite constituents, one can obtain nanocomposite layers with considerably better properties compared to those of its previous classic equivalent. Such type of nanocomposite materials also exhibits differences in the structure of the matrix and in the sizes and shapes of the disperse phase [30, 31].

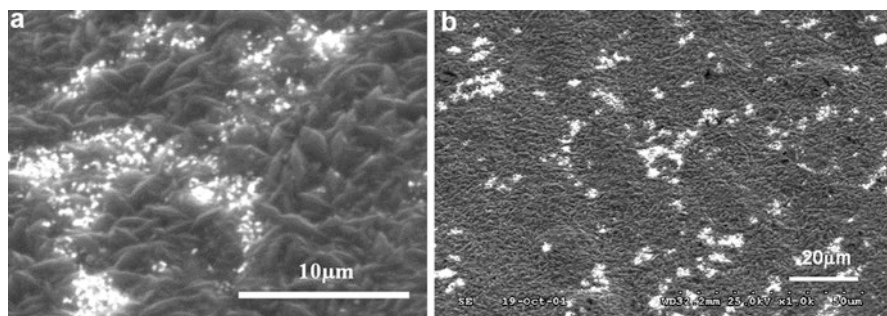


Fig. 20 Ni/Al₂O₃ composite layers: (a) coarse grain powder, (b) fine grain powder

The SEM pictures of the surface of the composite Ni/Al₂O₃ layers produced by the electrochemical method with a matrix formed by microcrystalline nickel and ceramic phase characterized by different grain sizes are presented in Fig. 20. They reveal that on the surface of the composite layers, agglomerates of nanometric (Fig. 20a) and reasonably homogeneously distributed (Fig. 20b) Al₂O₃ powder particles are seen. Increased refinement of grain structure amplifies the stress resistance and hardness of the material and thereby reduces its ductility.

Nanocrystalline Composites with Nickel Matrix and Disperse Phases Built from Carbon

Carbon, as one of the widely known and used chemical elements for many decades, was considered as the elementary component of both diamond and graphite. Since then, more allotropes of carbon have been reported, and a large scientific community has been passionate about deciphering the properties of this element that can adopt many structures ranging from diamond and graphite (3D), graphene (2D), nanotubes (1D), or fullerenes (0D) as illustrated in Fig. 21. With the exception of diamond, it is possible to think of fullerenes, nanotubes, and graphite as different structures built from the same hexagonal array of sp² carbon atoms, namely, graphene. Indeed, fullerenes and nanotubes can be mentally visualized as a graphene sheet rolled into a spherical and cylindrical shape, respectively, and graphite can be described as a stack of alternately shifted graphene sheets. The rapid adoption of graphene as a material of interest lies in its actual availability by the range of techniques and methods well known and also because monolayer and few layer graphene and graphene oxide exhibit a diverse set of exceptional properties. Graphene is, according to many experts, the electronics material of the future [24, 26].

Graphene, graphite, diamond, and nanotubes attest each set built of their own data in terms of mechanical robustness, be it hardness or strength modulus. However, the mechanical behavior of graphene has been much less investigated than its electronic and optical properties. It has to be emphasized that graphene possesses a

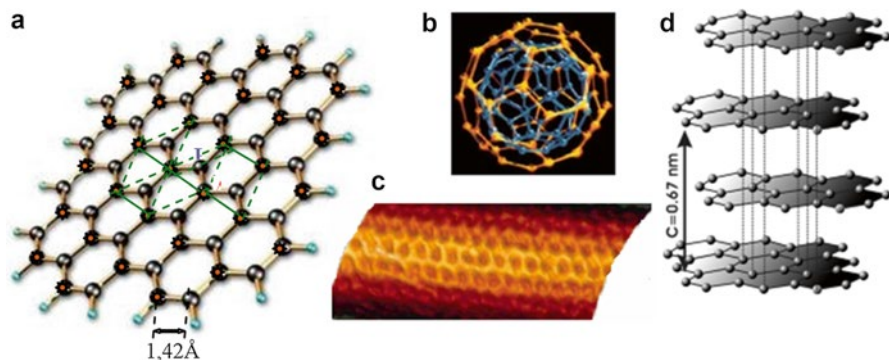


Fig. 21 The crystalline structure of carbon: (a) 2D (graphene) (b) 0D (fullerene), (c) 1D (nanotube), (d) graphite

combination of special properties which come out against answers for several limitations of currently known materials and systems.

Graphene, a single sp^2 -bonded carbon atomic sheet, has great potential for microelectronics applications, including conventional components such as high-frequency analog devices, and devices in emerging fields such as spintronics, terahertz oscillators, and single-molecule gas sensors. More recently, graphene has been the focus of considerable attention, due to its unusual density of states.

During the past decade, several outstanding advancements in graphene growth technology have been achieved. Novoselov et al. demonstrated mechanical exfoliation of graphene from graphite, permitting the first observations of some of the highly. The growth of graphene by thermal desorption of Si from SiC (sublimated epitaxial graphene: S-EG) was developed by Berger et al. [25]. Attractive and novel physical properties of graphene follow the early experiments of Van Bommel et al. Further improvements in the quality of S-EG were realized by sublimating Si at elevated temperatures in argon (Ar) atmosphere rather than in vacuum. However, vacuum sublimation is still successfully applied with a Si vapor pressure control system.

The most important physical properties of graphene are (i) a two-dimensional lattice $a=0.142$ nm, (ii) the greatest surface-to-volume ratio, (iii) very good heat conductivity (4800–5300 W/mK), (iv) low electrical resistance, (v) very high electron mobility $\mu=20,000$ cm^2/Vs , (vi) very high electron velocity $v=10^8$ $\text{m}\cdot\text{s}^{-1}$, (vii) almost complete optical transparency, (viii) molecular opacity for transmission, (ix) extremely high mechanical strength $\gamma\approx 1$ Tpa, and (x) quantum Hall effect.

One of the effective technologies is producing graphene film epitaxy by growth on a substrate with a 6H-Si(C). Image of the surface of graphene produced using such a method is presented in Fig. 22.

Theoretical analysis of doped graphene layers and research experiments suggest that they exhibit potential applications, among others, in transparent electrodes, photodetectors, touch screens, lighting elements, photovoltaic elements, optical filters, optical power limiters, and elements of terahertz systems.

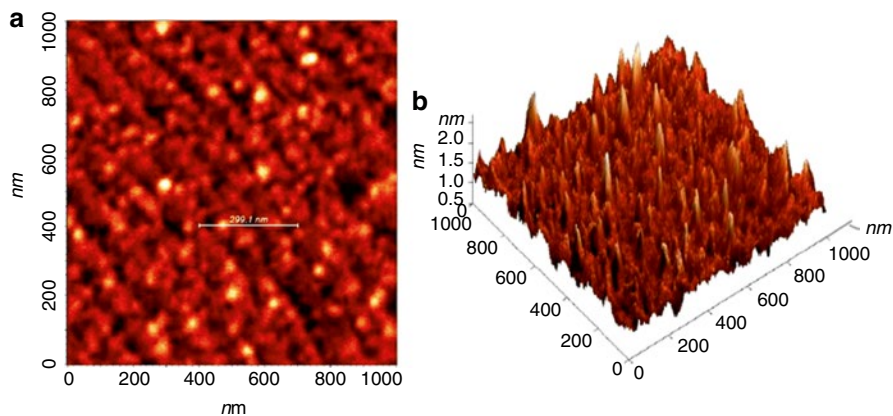


Fig. 22 AFM surface images of 2D graphene produced on 6H-Si(C) substrate: (a) topography, (b) morphology

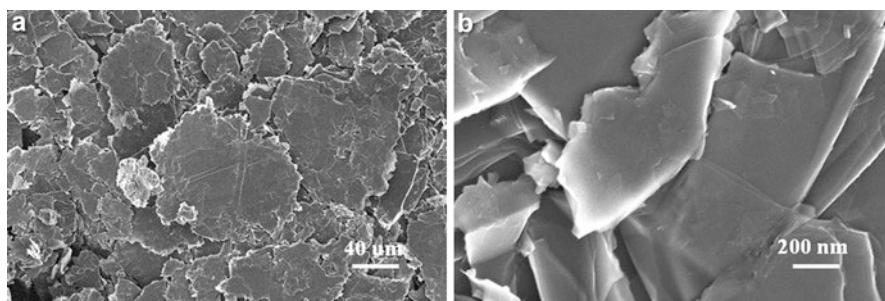


Fig. 23 Images with different magnifications of graphene structure applied in the study

Layered composite Ni/graphene was prepared by the electrocrystallization process on the substrate of carbon steel S235JR in the bath composed of sulfate (VI) nickel (II) chloride, nickel (II), boric acid, organic compound additives, wetting, and graphene as a dispersed phase in the 0.5 g/dm³ bath. Electrodeposition process was carried out in the bath at a temperature of 45 °C at a current density equal to 3 Adm⁻²; the process time was chosen to give a layer thickness of about 30 μm. A mixing agitator 50 rpm./min was used.

Graphene in the form of flakes with dimensions for thickness of 5–8 nm, diameter of 5 μm, and the area of 120–150 m²/g was used as a disperse phase (Fig. 23). SEM images of the produced nanostructured Ni/C_{graph} are presented in Fig. 24.

For the production of composite layers of Ni/CNTs, we used carbon nanotubes (CNTs) having a tendency to agglomerate in an aqueous medium as a dry suspension. Images of carbon nanotubes of polyhedral structure (MWCNTs) made up of several layers of graphene spaced at the same distance which were used as disperse phase in the manufacturing of nickel-based composite are shown in Fig. 25.

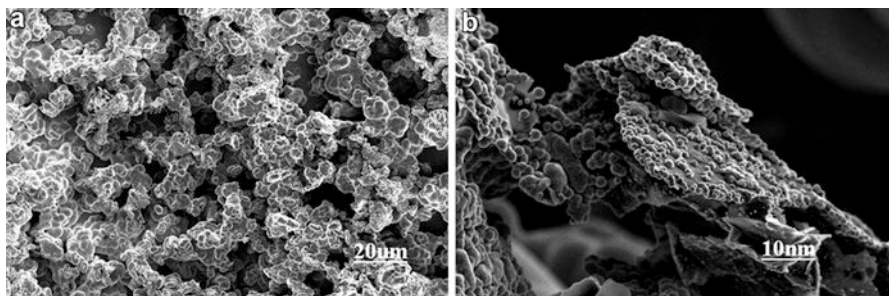


Fig. 24 SEM images of produced Ni/Cgraph nanocomposite: (a) topography, (b) morphology

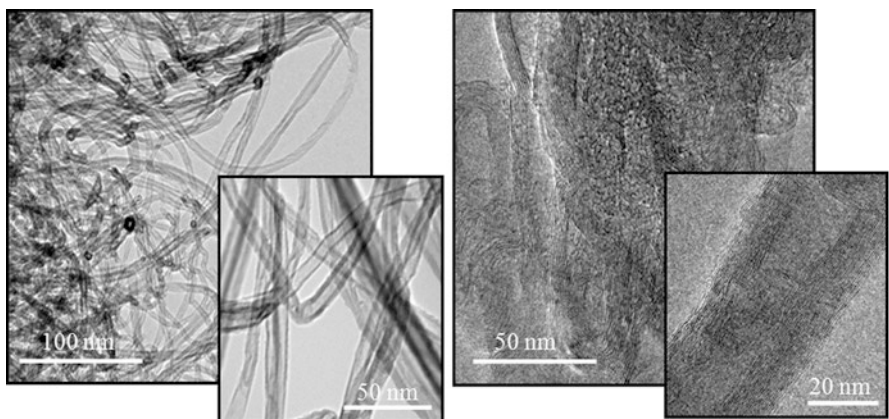


Fig. 25 TEM images of MWCNTs at different reinforcements

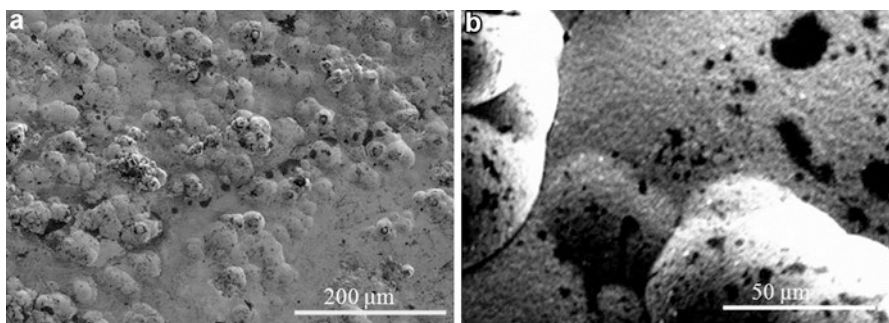


Fig. 26 Morphology of Ni/CNTs composites at different reinforcements

The resulting nanocomposite layer Ni/CNTs (Fig. 26) have a more developed surface as compared with the layers of nanocrystalline nickel (Fig. 10). On the surface of the composite layers are visible agglomerates CNTs that are not completely enclosed by the deposited nickel [16].

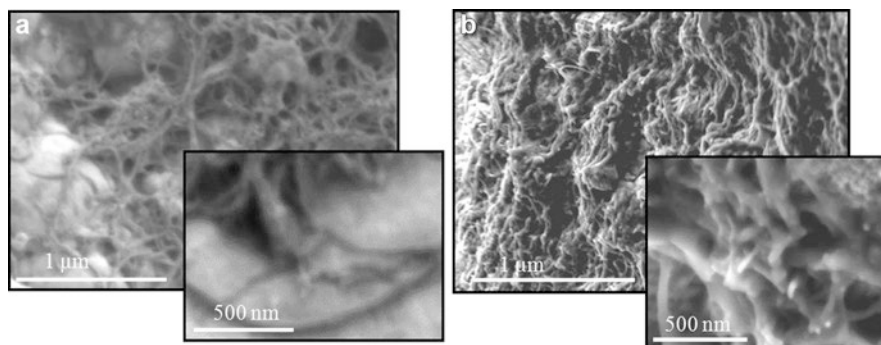


Fig. 27 Nanocrystalline Ni-P/CNTs composite: (a) surface, (b) cross section

The distribution of CNTs built-in nickel matrix within the whole composite material is illustrated in Fig. 27. Dispersed carbon nanotubes due to their nanometric dimensions pose some difficulties in their identification in a matrix of nanocrystalline nickel. One of the most effective methods for identification and characterization of CNTs is the Raman spectroscopy. Characteristic elements of the Raman spectra of carbon nanotubes are D and G mods. Mod G allows to determine the purity of CNTs, while mod D indicates the presence of functional groups or defects on the surface of carbon nanotubes.

Plots of the Raman spectra of a nanocrystalline materials related to Ni/CNTs composite are shown in Fig. 28. Comparing these spectra, it is easy to show that the D and G characteristic modes of CNTs (Fig. 28a) are also present in the produced Ni/CNT nanocomposites (Fig. 28c).

Nanocrystalline Composites with Copper Matrix

To modify the properties of copper products and in particular their surface layers produced by the electrocrystallization method, disperse phases were applied in the forms of graphite powder and carbon nanotubes. Graphite, built as the disperse phase, is characterized by good lubricating properties, low hardness in one direction, and electrical and thermal conductivities similar to those of most metals. Soft graphite particles embedded in the metal layer create a wide possibility for improving the lubricity and increase the electrical and thermal conductivities of the surface layer.

Carbon nanotubes as the disperse phase, because of its unique mechanical properties; chemical, electronic, optical, and magnetic recording; and unique structure (high ratio of length to diameter), allow to improve the mechanical, tribological, corrosion, and thermal and electrical conductivity of the surface layers of the material.

Composite layers with copper matrix were prepared by electrochemical reduction in the Watts bath of the following composition: CuSO_4 , H_2SO_4 (conc). This bath was modified with both organic substance and a disperse phase in the form of

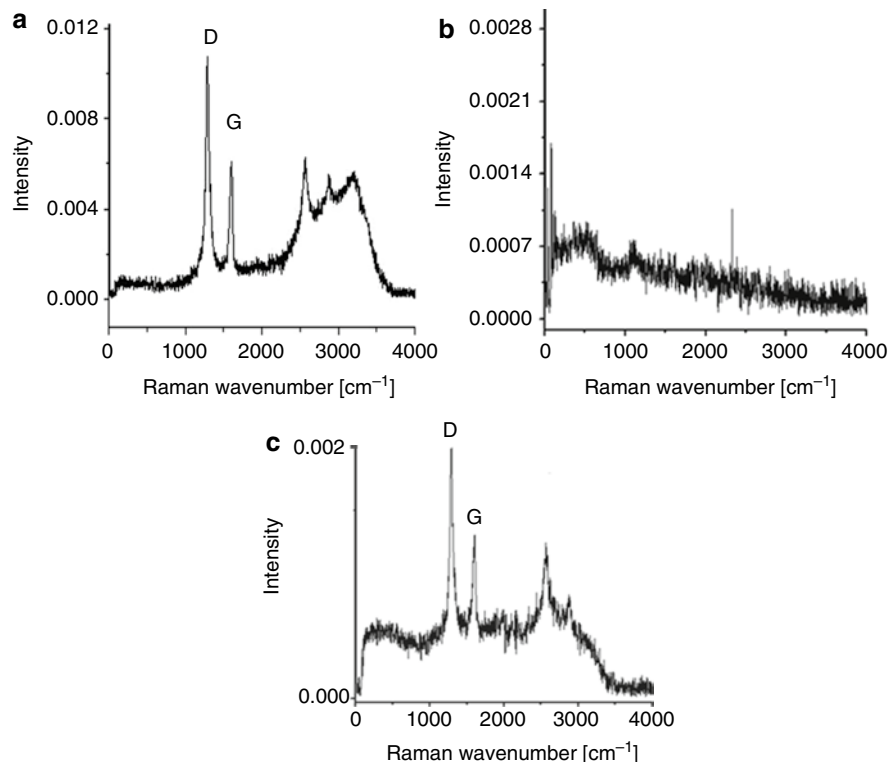


Fig. 28 Plots of Raman spectra for nanocrystalline materials: (a) CNTs, (b) Ni, (c) Ni/CNTs composite

graphite powder or carbon nanotubes. In addition, to make possible the fragmentation of the structure, some organic additives were used. The suspension of both graphite and CNTs in the solution was mixed in advance by ultrasounds, and during the process realization, a mechanical stirrer was used in order to prevent reagglomeration of CNTs and graphite powder.

Introduction of graphite particles or carbon nanotubes into Cu layer results in changes in the structure of the material layer. The composite layers are more developed, and on their surfaces, there are particles of graphite or CNTs completely encased by copper. CNTs are incorporated in the composite layers as individual particles or in the forms of different clusters. Images illustrating the composite layers with a copper matrix are presented in Fig. 29.

CNTs due to their nanometric dimensions make it difficult to identify them in the copper layers produced by electrocrystallization method. Their existence in the copper composite layers was confirmed by Raman spectroscopy exhibiting in the spectra of peaks with characteristic values for CNTs.

The results of performed studies revealed that the incorporation of graphite in the Cu layer reduces its microhardness and thus improves the lubricating properties and

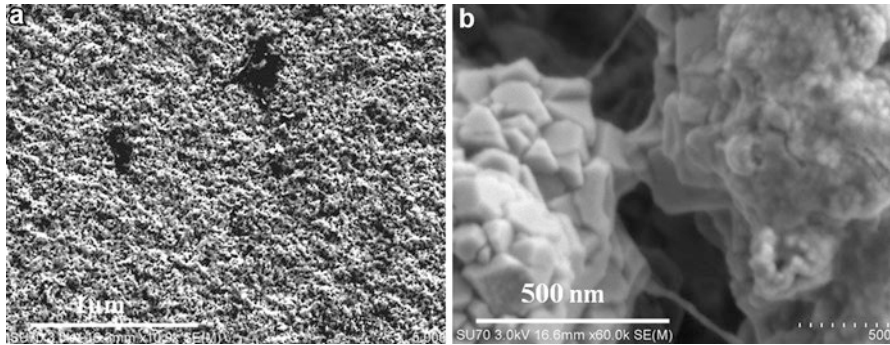


Fig. 29 Nanocrystalline layers produced by electrochemical reduction: (a) Cu/C_{grafite}, (b) Cu/CNTs

tribological properties of the material. In contrast, introducing CNTs into the copper composite layers produced by electrochemical reduction method greatly increases the microhardness of these layers. Moreover, the growth of microcomposite layers affects not only the CNTs presence but also the additions of organic substances into the electrolyte solution.

Summary and Conclusions

In this chapter, an attempt has been put on the description of a new method for electrocrystallization process realizations which take into account the activation energy and mass transfer effects. It is based on non-sinusoidal periodic excitations of the electrolytic reactor and controls of the measured response waveforms. This is done through the use of time-pulse periodic currents of suitable amplitudes and frequencies, and it is not recommended to introduce a DC for supplying the reactor, because it may induce disadvantageous electrochemical activities. Emphasis has been placed on nanocrystalline copper electrodepositions and manufacture of surface thin layers because these are the most important of the electrochemical cutting-edge industries in terms of quality improvements and possible energy savings.

This chapter presented results of studies focused on electrocrystallization on nanostructured materials that enable the production of nanocrystalline Ni and nanocomposite Ni/CNTs. Both nanocrystalline materials exhibited uniform structures and good adhesion to the substrate. Incorporation of carbon nanotubes in the nickel matrix has a significant impact on the structure, morphology, and topography of the resultant material and improves its mechanical properties.

It has been experimentally observed that most of the enhancement in the performance of materials thus far achieved has been due to lowering of the thermal conductivity.

Here, we showed that using two types of ceramic powder grains introduces another strategy to enhance the performance of the bulk material through enhancing the power factor in addition to reducing the thermal conductivity.

Therefore the electrocrystallization can be considered as an enabling technology by which existing materials, virtually all man-made materials, can acquire novel properties and functionalities making them suitable for numerous novel applications varying from structural and functional to advanced biomedical in vivo and in vitro applications. Moreover, the advantages of the electrocrystallization method can be pointed out including the possibility of synthesizing materials in an automatic regime under mild conditions at temperature below 100 °C on substrates of complex shape by using simple apparatus.

Electrodeposition allows a precise control of the material, including its composition and its crystallographic structure, texture, and grain size. Temperature- and corrosion-resistant materials will be in demand for the automotive and aerospace sectors of the industrial market, while silicon and various thin films will be the leaders in photovoltaic and microelectronics industry.

In summary, we have demonstrated that using the modulation-doping approach, one can enhance significantly the power factor of electrocrystallized materials.

References

1. Work Programme: Nanotechnology and nanoscience knowledge-based multifunctional materials and new production processes and devices (2006) <http://www.cordis.lu/nmp/home.html>
2. Trzaska M (2007) Chemically and electrochemically deposited thin layer materials. *Annales de Chimie Science des Matériaux* 32:325–344
3. Chen SY, Lin K-L, Mohanty US (2012) Chapter 8: Nanoscale electrodeposition of copper on an AFM tip and its morphological investigations. In: Hashim A (ed) *Smart nanoparticles technology*. InTech, Rijeka, pp 173–194
4. Paunovic M, Schlesinger M (2006) *Fundamentals of electrochemical deposition*. Wiley-Interscience, New York
5. Trzaska M (2007a) Nanocrystalline materials' production by electrocrystallization method. In: Mazurkiewicz A (ed) *Nanoscience and nanotechnology. Present state and development perspectives*. Institute of Technology Exploitation, Radom, pp 540–541
6. Wang ZL (2011) Picoscale science and nanoscale engineering by electron microscopy. *J Electron Microsc* 60(Suppl 1):S269–S278. doi:10.1093/jmicro/dfr027
7. Salzemann C, Lisiecki I, Brioude A, Urban J, Pileni M-P (2004) Collections of copper nanocrystals characterized by different sizes and shapes: optical response of these nanoobjects. *J Phys Chem B* 108:13242–13248
8. Trzaska M (2005) Structure and hardness of Ni, Cu and Co surface layers produced by electrochemical method. *Mater Eng* 147:698–700
9. Trzaska M, Trzaska Z (2007b) Control of copper thin-layer coatings with electrochemical impedance spectroscopy. In: *Proceedings of ACC'07, New York*, pp 2837–2843
10. Powell C, Webster P (2011) *Copper alloys for marine environments*. Copper development association, New York, 260 madison Avenue. CDA Publication No 206, pp 1–33
11. Trzaska M (2005b) Electromagnetic properties of nanocrystalline copper conductors. In: *Proceedings of XIII international symposium on theoretical electrical engineering, Lvov*, 4–7 July, pp 101–102
12. Trzaska M (2010) Studies of the structure and properties of Ni-P and Ni-P/Si surface layers deposited on aluminum by the electroless method. *J Achiev Mater Manufact Eng (JAMME)* 43:269–275
13. Trzaska M, Trzaska Z (2008) Control of nano- and micro-crystalline copper electrodeposits. In: *2008 American control conference Westin Seattle Hotel, Seattle*, 11–13 June, pp 2196–2201, ThA12.5, doi:10.1109/ACC.2008.4586818

14. Salata OV (2004) Applications of nanoparticles in biology and medicine. *J Nanobiotechnol* 2:1–6
15. Schmuki P, Virtanen S (2009) *Electrochemistry at the nanoscale*. Springer, New York
16. Trzaska M, Gostomska M (2009) The composite layers of Ni/Cgrafit produced by electrochemical method. *Composites* 9:84–88
17. Trzaska M, Kowalewska M (2005) Structure and properties of nanocrystalline Ni/Si₃N₄ composite layers produced by periodic pulse current. *Electronics* 7:45–49
18. Trzaska M, Trzaska Z (2006) Model development of high-frequency phenomena in nanocrystalline copper conductors. In: *Proceedings of the IASTED international conference on modeling, identification, and control MIC 2006, Lanzarote, 6–8 Feb*, pp 332–337
19. Rasool HI, Kaner RB, Song EB, Wang KL, Allen MJ, Weiller BH, Wassei JK, Gimzewski JK (2011) Continuity of graphene on polycrystalline copper. *Nano Lett* 11:251–256
20. Trzaska M, Trzaska Z (2007) Straightforward energetic approach to studies of the corrosion behavior of nano-copper thin-layers coatings. *J Appl Electrochem* 37:1009–1014
21. Trzaska M, Kowalewska M (2004) Nanocrystalline composite layers of Ni-Al₂O₃ – preparation and structures. *Composites* 4:99–103
22. Trzaska M, Trzaska Z (2012) Nonlinear circuit model of bipolar pulse process of electrocrystallization. *Material Engineering* 6:705–711
23. Trzaska M, Kucharska B (2009) Surface properties of Ni/PTFE composite layers. *Composites* 9:363–368
24. Strupinski W, Grodecki K, Wysmolek A, Stepniewski R, Szkopek T, Gaskell PE, Grüneis A, Haberer D, Bozek R, Krupka J, Baranowski JM (2011) Graphene epitaxy by chemical vapor deposition on SiC. *Nano Lett* 11:1786–1791
25. Zhu Y, Murali S, Cai W, Li X, Suk JW, Potts JR, Ruoff RS (2010) Graphene and graphene oxide: synthesis, properties, and applications. *Adv Mater* 22:3906–3924
26. Novoselov KS, Geim AK et al (2004) Electric field effect in atomically thin carbon films. *Science* 306:666–669
27. Trzaska M, Kowalewska M, Wyszynska A (2004) Electrolytic composite nickel layers with nano-sized Si₃N₄ disperse phase. *Rev Adv Mater Sci* 8:195–200
28. Trzaska M, Trzaska Z (2010) *Electrochemical impedance spectroscopy in materials science*. Publishing Office of the Warsaw University of Technology, Warsaw
29. Trzaska M, Trzaska Z (2011) Energetic process modelling of thin-layer electrocrystallization. *Electr Rev* 87:173–175
30. Trzaska M, Trzaska Z (2011) Chaotic oscillations in fractional-order nonlinear circuit models of bipolar pulsed electroplatings. In: *IEEE 20th European conference on circuit theory and design (ECCTD)*, 978-1-4577-0616-5/11/\$26.00 ©2011 I.E. Linköping, 29–31 Aug, pp 165–168
31. Trzaska M, Trzaska Z (2010) Modelling of energetic processes in thin-layer electroplating. In: *Xth international workshop. Computational problems of electrical engineering*, Laznie Kynžvart, Czech Republic, 13–16 Sept

Formation and Characterization of Bimetallic Nanoparticles in Electrochemistry

7

Chun-Jern Pan, Loka Subramanyam Sarma,
and Bing-Joe Hwang

Contents

Introduction.....	170
Bimetallic Nanoparticles.....	173
Synergistic, Electronic, and Geometric Effects.....	174
Electrochemical Aspects of Bimetallic Nanoparticles.....	175
Architectures of Bimetallic Nanoparticles.....	177
Alloy-Structured Bimetallic Nanoparticles.....	177
Core-Shell Bimetallic Nanoparticles.....	178
Hollow-Structured Bimetallic Nanoparticles.....	179
Formation of Bimetallic Nanoparticles.....	181
Structure-Controllable Synthesis Methodologies.....	181
Formation Mechanism Studies.....	183
Characterization of Bimetallic Nanoparticles.....	191
Physical Characterization.....	192
Electrochemical Characterization.....	203

C.-J. Pan

Nanoelectrochemistry Laboratory, Department of Chemical Engineering,
National Taiwan University of Science and Technology, Taipei, Taiwan
e-mail: pom9106054@gmail.com

L.S. Sarma

Department of Chemistry, Yogi Vemana University, Kadapa, Andhra Pradesh, India
e-mail: sarma7@yogivemanauniversity.ac.in

B.-J. Hwang (✉)

Nanoelectrochemistry Laboratory, Department of Chemical Engineering,
National Taiwan University of Science and Technology, Taipei, Taiwan

National Synchrotron Radiation Research Center, Hsinchu, Taiwan
e-mail: bjh@mail.ntust.edu.tw

Electrocatalytic Applications: Electrochemical Studies	
of Fuel Cell Reactions on Bimetallic Nanoparticles	217
Decisive Factors Influencing Electrocatalytic Activity	217
Hydrogen Fuel Cells	221
Methanol Fuel Cells	223
Electrochemical Oxidation of Formic Acid	224
Conclusions and Future Perspective	225
References	225

Abstract

Bimetallic nanoparticles have revolutionized nanomaterial-linked advances in science and technology. The key to their success, in many applications, relies largely on the superior chemical and physical properties endowed to them through synergistic effects between the two metallic constituents. Thorough studies on the formation and characterization of bimetallic nanoparticles are crucial to understand the viability of these systems in many technological applications. In this chapter, we present recent advances in the formation and characterization of bimetallic nanoparticles, especially with respect to electrochemical applications including our own efforts targeted in this direction. At first, we will outline the recent progress achieved in developing diverse structure-controllable synthesis strategies for bimetallic nanoparticles and promising characterization techniques that can provide information on atomic distribution, composition, morphology, and nanostructure. Later, emphasis will be focused on composition–activity and structure–catalytic activity relationships of bimetallic nanoparticles for specified electrochemical reactions generally involved in clean energy production. Finally, possibilities for future developments and challenges in bimetallic nanoparticle research will be discussed.

Keywords

Bimetallic nanoparticles • Formation and characterization • Electrochemistry

Introduction

Nanoscale metallic particles have attracted a great deal of attention as they afford myriad of opportunities in nanotechnology and nano-biotechnological applications. The rush toward the development of materials with smaller dimensions is due to the fact that nanoparticles exhibit unusual chemical and physical properties that are different to those of their bulk analogues as a result of surface and quantum size effects [1, 2]. The surface effect is related to the lower stabilization of atoms thereby forming more unsaturated bonds at the surface than the bulk region, thus making the nanoparticle more reactive. The quantum size effect is involved when the de Broglie wavelength of electron at the Fermi energy is comparable to the size of metallic particle itself and as a result particles behave electronically as zero-dimensional

quantum dots relevant to quantum mechanical rules [3, 4]. Today many nanotechnological applications largely rely on the effective use of nanosized effects in fine-tuning the materials properties.

Heterogeneous catalysis is an area where development of nanomaterials is crucial. Utilization of nanomaterials as nanocatalysts and corresponding nanocatalyst-linked advances in catalysis can have a positive economic as well as environmental impact. In particular, deployment of bimetallic nanoparticles for catalyzing electrochemical reactions is gaining momentum as they play a vital role in promising technologies related to both environmental and energy-related applications such as polymer electrolyte membrane fuel cells (PEMFC) and direct methanol fuel cells (DMFC). In order to harness the potentiality of bimetallic electrocatalysts, a thorough understanding of the origin of their enhanced performance is needed. The electrocatalytic activities of nanoparticles employed in fuel cells are generally dependent on numerous factors such as particle size and particle size distribution [5–8], morphology(shape), atomic distribution (intra- and interparticle distribution) [9], composition [10, 11], and in particular surface composition, oxidation state, support, and microstructure [11–21] (Table 1).

In the synthesis of bimetallic nanoparticles, special emphasis has been given to the achievement of a high level of control over the particle's size, morphology, atomic distribution, and dispersion over supports by means of reproducible, low cost, and scalable synthetic approaches [22, 23]. Further, rigorous characterization techniques which can provide information about the above-described nanoscale properties are required. For example, parameters such as surface structure, atomic distribution, and composition are dominant nanostructural properties that require both control and careful characterization.

Further, success in either particle design or scale-up requires a detailed knowledge of the particle's formation mechanism and will greatly benefit the development of structure-controllable synthesis pathways for bimetallic nanoparticles. The recent advent of high-intensity tunable sources of X-rays, now available at synchrotron facilities worldwide, has made X-ray absorption spectroscopy (XAS) as a powerful tool to examine the nucleation and growth process during the formation of nanoparticles. We have recently made some significant contributions that highlight the applicability of XAS technique to study the nanoparticle formation mechanism [23–31]. The information obtained from XAS studies on local structural changes during early stages of nanoparticle formation can be utilized to control the size, shape, and surface morphology of the nanoparticles.

Certainly, understanding the formation mechanism and thorough characterization of bimetallic nanoparticles are two aspects that warrant important consideration in nanoscience and nanotechnology research. This chapter provides a comprehensive review of the recent advances in the field of bimetallic nanoparticles research pertaining to the formation and characterization of bimetallic nanoparticles and their corresponding applications toward electrocatalytic reactions. Furthermore, this chapter also examines decisive factors that are presently believed to play significant role in the electrocatalytic reactivity of bimetallic nanoparticles with a specific emphasis on understanding the relationship between the structure, chemical

Table 1 Properties of nanoparticles which influence catalytic activities

Property	System	Catalytic reactivity	References
Size	Dendrimer-encapsulated Pt ₁₂ @3 (d = 0.9 nm), Pt ₂₈ (d = 1.0 nm), Pt ₆₀ (d = 1.2 nm), Pt/C (d = 2.5)	Pt ₁₂ @3 with a particle size of 0.9 nm exhibits three orders of efficiency toward oxygen reduction reaction (ORR) compared to Pt ₆₀ @3 particles	[5]
Shape	Tetrahexahedral Pt nanocrystals (THH Pt NCs) Polyhedral, truncated cubic and cubic-Pt nanoparticles 3D Urchin-like-shaped AuPt NPs	THH Pt nanocrystals with high-index facets exhibit 2–4 times efficiency per unit surface area for ethanol oxidation compared to Pt/C nanoparticles with low-index facets Cubic-Pt nanoparticles have dominant (100) facets and exhibit higher ORR activity High catalytic activity toward oxygen reduction reaction	[19] [14] [18]
Composition	Pt–Co/C (3:1, 1:1, 1:3) Pt–Cr/C (90:10, 80:20, 70:30)	Highest ORR activity for Pt–Co/C (1:1) Highest ORR activity for Pt–Cr/C 80:20 compared to Pt/C	[10] [11]
Support	PtAu/graphene, PtAu/C	PtAu/graphene exhibits 37 % higher activity toward formic acid oxidation compared to PtAu/C	[17]
Structure	Pd _{Core} –Pt _{Shell} nanowire arrays Spherical Ru _{Core} –Pt _{Shell} NPs PtC _{OCore} –Pt _{Shell} nanoparticles	Possess more electrochemical active surface area (ECASA). High activity toward methanol oxidation reaction (MOR) Higher catalytic activity than alloyed PtRu nanoparticles toward MOR Threefold efficiency toward ORR activity when compared to Pt nanoparticles	[13] [16, 12] [14, 15]
Alloying extent	Pt ₇₅ Ru ₂₅ /C (J _{Pr} , 57 %; J _{Ru} , 85 %) Pt ₅₀ Ru ₅₀ /C (J _{Pr} , 41 %; J _{Ru} , 57 %) Pt ₂₅ Ru ₇₅ /C (J _{Pr} , 36 %; J _{Ru} , 50 %)	Pt ₇₅ Ru ₂₅ /C catalyst with a higher extent of Pt alloying (J _{Pr}) exhibits threefold efficiency toward methanol oxidation reaction compared to Pt ₂₅ Ru ₇₅ /C which possesses lower extent of Pt alloying	[9]

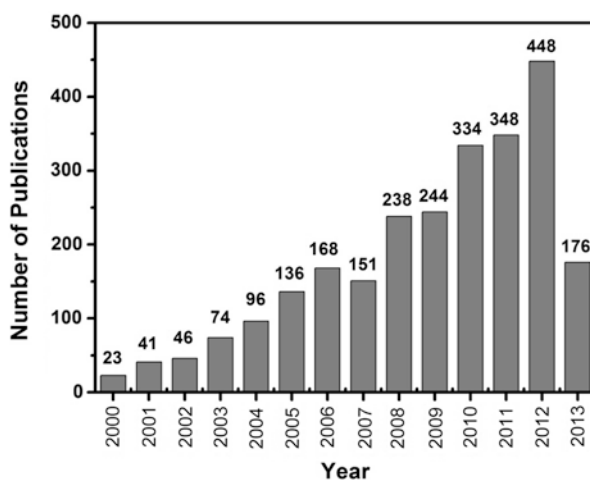
composition, surface composition, atomic distribution, and reactivity of bimetallic nanoparticles especially toward electrocatalytic reactions involved in PEMFCs.

Bimetallic Nanoparticles

Bimetallic nanoparticles constituted as the combination of two different metals show multiple functionalities, enhanced selectivity, catalytic activity, and stability when compared to monometallic nanoparticles [32–36]. During the past few decades, much research has been directed toward the design and synthesis of bimetallic nanoparticles due to their promising activity in catalyzing clean energy conversion reactions. Figure 1 illustrates the recent growth in the number of papers published on the formation and characterization of bimetallic nanoparticles.

Platinum-based bimetallic nanoparticles are widely utilized for both anodic and cathodic reactions in fuel cells. Some excellent reviews of the progress made in Pt-based fuel cell catalyst development for stationary and mobile applications have been written from both an academic and industrial perspective [37–41]. Very recently, Debe has critically reviewed the electrocatalyst approaches and challenges for automotive fuel cells [42]. The phenomenal interest in Pt-based bimetallic nanoparticles largely stems from their ability in offering the favorable electronic and geometric structures needed to catalyze small reactant molecules in fuel cells [43–47]. The use of Pt alone as an anode catalyst is detrimental to the performance of either H₂ or CH₃OH-fed PEMFC. For example, in the case of H₂-fed PEMFC, the carbon monoxide, even when present in trace quantities, competes with H₂ adsorption and poisons the Pt-active surface [48]. Similarly, in

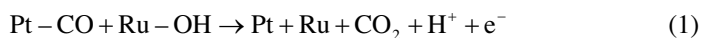
Fig. 1 Research articles published per year for bimetallic nanoparticles during the period 2000 to April 2013 (Search made through SciFinder Scholar Database)



the case of the electrooxidation of CH_3OH in DMFC, the CO formed as one of the intermediates covers the Pt-active surface and impedes the catalytic performance for methanol oxidation [49]. The oxygen reduction reaction (ORR) involved in PEMFC is a multi-electron reaction, and depending on the experimental conditions, it is known to take place through two different reaction pathways: the direct four-electron pathway in which O_2 is reduced directly to water and the two-electron pathway in which O_2 is reduced to hydrogen peroxide, followed by decomposition, or further reduction, to water [50–52]. Platinum has long been the best electrocatalyst for ORR. However, OH species formed from water decomposition on Pt electrodes inhibit oxygen reduction by blocking active surface sites which may lead to cathodic overpotentials. To overcome the difficulties associated with the use of monometallic Pt nanoparticles as electrocatalysts in PEMFC, Pt-based bimetallic nanoparticles are being extensively investigated and deployed for fuel cell applications. Several explanations have been given for the superior performance of Pt-based bimetallic nanoparticles based on structural variations caused by the presence of the second metal and will be discussed in the following sections.

Synergistic, Electronic, and Geometric Effects

Three explanations have been put forward for the higher activity offered by Pt-based bimetallic nanoparticles over Pt-alone nanoparticles: these include (i) bifunctional (or) ligand effect, (ii) electronic effect, and (iii) geometric (ensemble) effect. According to the bifunctional effect, in bimetallic nanoparticles, each metal component could promote different elementary reaction steps. For example, in the case of PtRu bimetallic nanoparticles, the intermediate CO species formed during CH_3OH electrooxidation is strongly adsorbed on Pt sites. When Pt is alloyed with Ru, water dissociation occurs on Ru sites to produce Ru–OH groups at (0.2–0.3 V vs. RHE), i.e., at less positive potentials than on pure Pt surface (0.7 V vs. RHE) [53], and the Ru–OH groups react with the neighboring CO adsorbed on Pt to give carbon dioxide through the bifunctional mechanism (Eq. 1) [53–56].



Secondly, the ensemble effect (or geometric effect) largely deals with specific groupings of surface atoms that serve as active sites in the presence of secondary metal component [57]. The third explanation is based on the electronic effect. According to this effect, interactions between two metal components could improve the reactivity. In PtRu bimetallic interactions, the presence of Ru can alter the electronic state of the Pt (variations in Pt d-band vacancies) leading to the weakening of the Pt–CO bond facilitating CO oxidation. The enhancement of ORR kinetics on bimetallic nanoparticles is also explained by electronic effect [58–61]. It was reported that PtNi and Pt₃Fe bimetallic systems which contain a quasi-complete Pt surface layer with more, or less, Ni or Fe in the sublayers show strong electronic

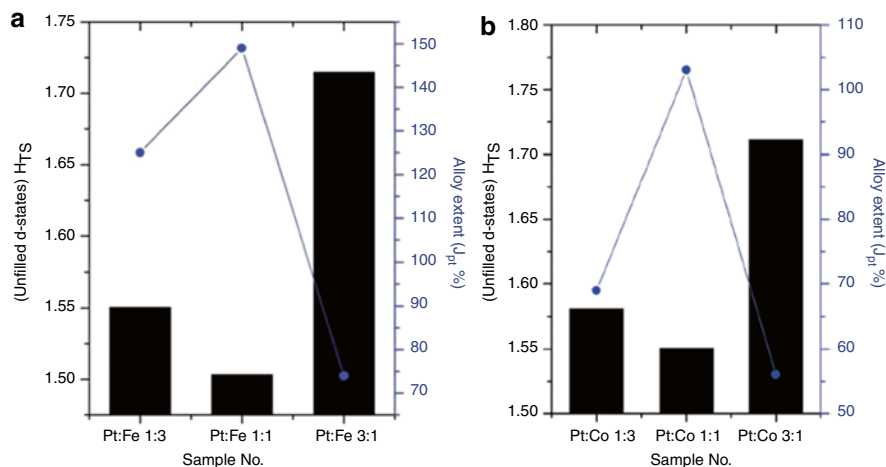


Fig. 2 The variations in Pt-unfilled d-states and extent of platinum alloying in bimetallic (a) PtFe/C with various Pt-to-Fe ratios and (b) PtCo/C with various Pt-to-Co ratios (panel (a) and (b) of Fig. 2 were reproduced with permission from ref. [63], © 2010 Royal Society of Chemistry and Ref. [10] © 2009, American Chemical Society), respectively

modifications. The presence of an alloying component-rich second layer increases the d-electron vacancies of the thin Pt layer and improves the chemisorptive properties and corresponding electrocatalytic performances [47, 62]. In our recent X-ray absorption spectroscopic investigations, it was found that the alloying of Co¹⁰ and Fe⁶³ with Pt induces variations in unfilled d-states (Fig. 2) which in turn significantly influences the catalyst's electrochemical performance toward the ORR.

The variations in Pt-unfilled d-states in Pt-based bimetallic nanoparticles suggest that charge transfer from one element to the other modifies the local electronic properties of pure platinum particles and makes bimetallic nanoparticles more attractive catalyst candidates. It is suggested that charge localization or transfer within a nanoparticle is strongly correlated with its structure, composition, and size. Therefore, it becomes crucial, during synthesis, to have complete size, composition, and structural control over the nanoparticles [64].

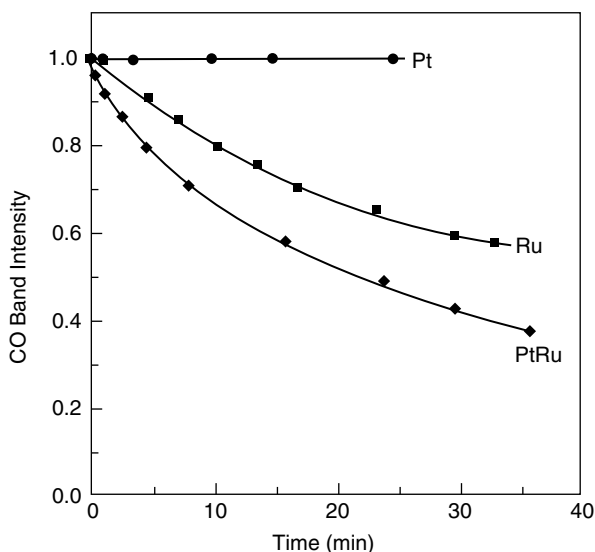
Electrochemical Aspects of Bimetallic Nanoparticles

Electrocatalytic reactions play a decisive role in emerging technologies related to environmental and energy-related applications, such as fuel cells. The efficiency and selectivity of electrocatalytic processes can be substantially improved by replacing monometallic with bimetallic nanoparticle-based catalysts. Recently, Gasteiger et al. have studied the electrooxidation of CO, formic acid, and methanol on well-characterized PtRu alloys. The authors claim that a PtRu alloy having a 50:50 surface composition presents the highest catalytic activity for CO oxidation [45, 65–67].

In another interesting work, Lin et al. [68] have made a comparative study of CO electrooxidation on different catalysts using in situ FTIR spectroscopy. From their results, it was found that, compared to Pt, the onset of CO₂ formation at PtRu and Ru is shifted by about -0.1 and -0.05 V, respectively. Further, the authors noticed a faster increase of the CO₂ band intensity for PtRu than for the other materials. At 0.5 V, the CO₂ band intensity reaches already 97 % of its maximum value at the alloy and only 23 % and 5 % of the maximum at Ru and Pt, respectively, indicating the potentiality of bimetallic surfaces in removing the poisoning CO intermediate. From the CO band intensities versus time plots, the authors found that the CO band intensity at platinum does not change, since the onset potential for oxidation on this metal lies above 0.4 V. For the other materials, the authors observed the oxidative removal of CO: the rate being higher at PtRu than at pure Ru. It is noteworthy that the same experiments performed at 0.35 V showed CO₂ formation at PtRu after 3 min, while no oxidation was observed at pure Ru even after 10 min; the authors thus concluded that the onset of oxidation is fastest on the alloy (Fig. 3).

Park et al. carried out electrochemical infrared reflection absorption spectroscopy (EC-IRAS) for carbon monoxide (CO) adlayers formed by partial CO dosing on various ruthenium-decorated platinum nanoparticles [69]. The observed promotion in CO electrooxidation by the existence of a Ru-island on Pt nanoparticles, of interest to fuel cell catalysts, showed a strong relationship with Ru surface concentrations, consistent with previous studies on single-crystal or polycrystalline bimetallic surfaces. Based on the attenuation of H₂-upd peak with an increase in charge in the double-layer region as the amount of Ru increases on platinum, the authors suggested that at more negative potentials, the formation of oxygen-like species takes place on bimetallic surfaces (Gasteiger et al.) [58]. The authors observed that

Fig. 3 Change of band intensity for adsorbed CO on Pt, Ru, and PtRu during CO stripping at a constant potential of 0.4 V; spectra (50 scans) were collected each 15 s. The respective surface was saturated with CO at 0.3 V after which CO was eliminated from the electrolyte by nitrogen bubbling (Reproduced with permission from Ref. [68], © 1999 American Chemical Society)



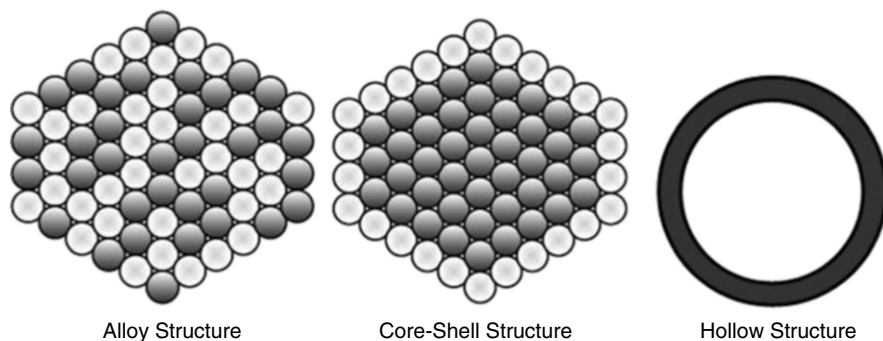
Ru-decorated Pt nanoparticles with a composition of PtRu-48 % lower the CO stripping peak down to 0.3 V when compared to the Pt-black nanoparticles which showed a CO stripping peak at 0.45 V. However, the authors claim that if the surface Ru concentration was increased to 66 %, then the CO oxidation peak shifts positively to be centered at 0.37 V. The results show that the presence of PtRu boundaries in PtRu catalysts plays an important role in lowering the potential of irreversible CO electrooxidation.

Architectures of Bimetallic Nanoparticles

Bimetallic nanoparticles assume various types of architectures based on the conditions employed during the synthesis (Scheme 1). For example, during the simultaneous reduction process, if the standard reduction potentials of two distinct metals used are different, then the two kinds of metals thermodynamically prefer to nucleate and grow separately to generate core-shell-structured particles. By utilizing strong reducing agents which are capable of reducing simultaneously all metal precursors at optimized rates, alloyed structures can be fabricated. In another approach, by properly adjusting the redox potentials of two metals through specific adsorption or coordination by the use of selected surfactants and counterions, two distinct metal ions can be simultaneously reduced to produce alloyed nanoparticles.

Alloy-Structured Bimetallic Nanoparticles

Bimetallic nanoparticles are formed as alloy nanoparticles when the two metals are mixed at the atomic level. Co-reduction of two different metal ions with a strong reducing agent is a widely employed method for the generation of alloy-structured bimetallic nanoparticles. Alloying Pt with suitable noble metals such as Ru, Rh, Pd, Ir, Os, Ag, and Au or non-noble transition metals such as Cu, Fe, Co, or Ni has been

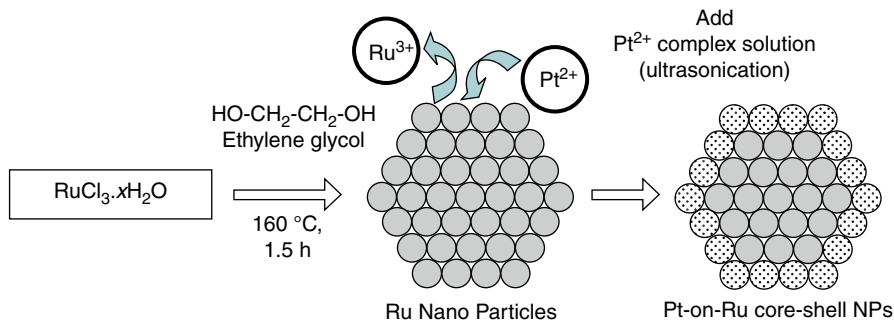


Scheme 1 Various structures of bimetallic nanoparticles

proved to be effective in electrocatalysis of fuel cell reactions, such as the methanol oxidation reaction and the oxygen reduction reaction [35, 70–74]. It was reported that the catalytic activity and long-term stability of Pt-based alloyed structures are dependent both on composition and structure. For example, the stability of fct-FePt NPs is much better compared to fcc-FePt NPs toward ORR activity in acidic environments. Superior intermetallic stacking of Fe and Pt obtained under temperature alloying coupled with well-order structures was proposed as a reason for the enhanced catalytic activities of the fct-FePt versus fcc-FePt [75]. Among the various alloyed Pt-based catalysts studied, the PtRu alloy has been identified to be the most effective for MOR. The degree of alloying in bimetallic PtRu nanoparticles plays a crucial role in determining the CO oxidation and methanol oxidation rates. Recently, Lee et al. demonstrated that CO oxidation and methanol oxidation were enhanced as the PtRu alloying degree became higher [76].

Core–Shell Bimetallic Nanoparticles

Core–shell-structured bimetallic nanoparticles are particularly attractive for electrocatalysis in view of atom economy, which refers to the possibility to substitute the use of noble metals with other less expensive materials. A number of synthesis strategies have already been used for the production of core–shell bimetallic nanoparticles, such as redox-transmetalation [25, 77–79], ethylene glycol-assisted polyol method [80], co-reduction [81], and seed-mediated growth method [82]. In seed-mediated growth, a pair of metallic precursors is selected which differs in reduction potentials. When a reducing agent is introduced into the synthetic system containing metallic precursors, the metal cations with the highest redox potential will be reduced first by forming seeds, while the second metal will reduce and grow on the preformed metal seeds [83]. In recent years, the redox-transmetalation method has been widely used to fabricate core–shell-type nanoparticles [78]. It is an advanced process compared with the conventional reduction methodologies available for the bimetallic nanoparticles. In this method, a first core component is generated by reducing its corresponding metal ion. Later, a metal precursor solution intended for shell component will be added to the solution containing core component. When the shell-forming metal salts come into contact with the metallic core surface, they are reduced by the sacrificial oxidation of surface atoms of the metal core and deposited on the surface of the core by redox-transmetalation (Scheme 2). By properly understanding the redox chemistry, wide varieties of bimetallic nanostructures can be generated through redox-transmetalation. When compared to traditional successive reduction strategies, the redox-transmetalation process has several advantages. For example, the self-nucleation of the added second metal, which usually occurs in conventional successive reduction methods, can be avoided in redox-transmetalation, as it allows spontaneous shell layer deposition on the surface of the core nanoparticle. Various bimetallic core–shell nanoparticles, e.g., PtAu [84], PtRu [12, 85], and Pt–Co [78, 79], fabricated by redox-transmetalation are reported in the literature.



Scheme 2 Schematic of a polyol-assisted redox-transmetalation strategy to fabricate Pt-on-Ru nanoparticles

Recently, we described the fabrication of well-defined bimetallic core-shell-structured nanoparticles using a kinetically controlled autocatalytic chemical process [23]. In this work, under kinetically controlled conditions, we carried out autocatalytic deposition of a sacrificial Cu ultrathin layer on a dimensionally stable palladium-metal core, which is later displaced to form an active ultrathin platinum-layered shell by redox-transmetalation (Fig. 4a). As can be seen from panels a and b of Fig. 4, an ultrathin Pt layer was deposited on spherical and cubic Pd nanoparticles, respectively. The striking advantages of the fabricated $\text{Pd}_{\text{core}}\text{Pt}_{\text{ultrathin-shell}}$ nanoparticles are enhanced platinum surface-to-volume ratio and superior catalytic activities.

Adzic et al. [86] and Zhang et al. [87] synthesized Pt monolayers on various core structures in an effort to stabilize Pt and Pt group metals. In their experiments, either carbon-supported Pt or a noble single-crystal metal was used as the core component [88, 89]. Later, a monolayer of another noble metal was deposited on top of the core component to generate core-shell-structured nanocatalysts. These catalytic platinum monolayers on various core structures were tested for ORR activity and stability. By properly tuning the compositions of the core and monolayer components, the authors achieved remarkable ORR activity on monolayer catalysts. For example, in rotating ring-disk (RRDE) experiments in 0.1 M HClO_4 supporting electrolyte solutions, the observed Pt mass-specific activities for the ORR of $\text{Pt}_{\text{ML}}/\text{Pd}/\text{C}$ catalyst, with a typical loading of $3.4\text{ }\mu\text{gPt}/\text{cm}^2$, were 5–8 times higher than that of Pt/C. Oxygen reduction followed a four-electron reduction pathway O_2 to H_2O , with the first-charge transfer as the rate-determining step.

Hollow-Structured Bimetallic Nanoparticles

In recent years, there has been a growing interest in the fabrication of hollow-structured bimetallic nanoparticles for catalytic applications because of their unique void structure, increased surface areas, and reduced densities [90–92]. The interior voids that are usually present in hollow-structured bimetallic NPs play a dual role by serving both as a tiny container for encapsulating multifunctional active materials

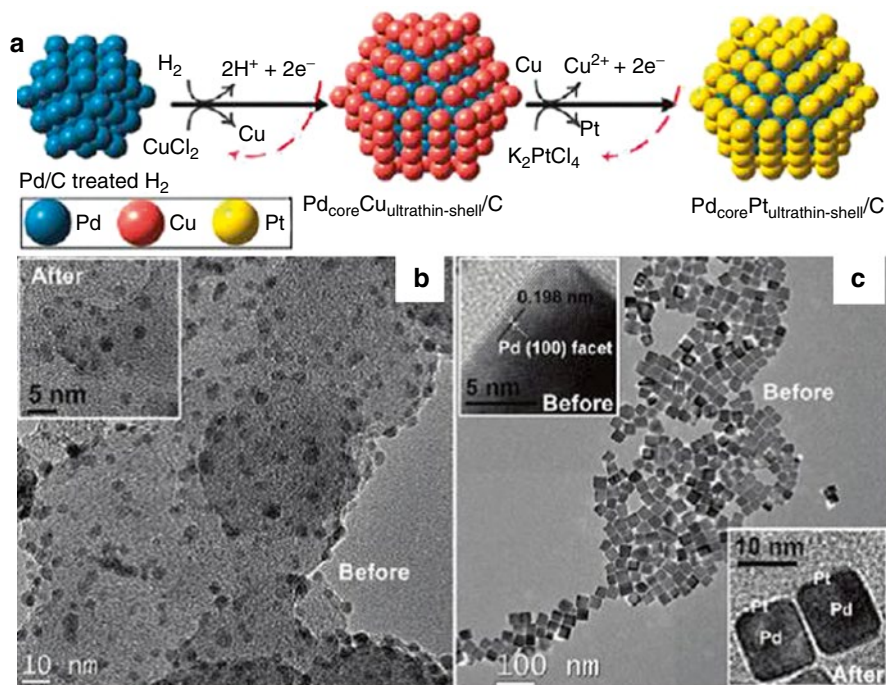


Fig. 4 Schematic of architecture of Pd_{core}-Pt_{ultrathin-shell}/C nanoparticles (a), TEM images of different morphologies (b and c), and corresponding Pd@Pt nanocrystals (*insets*) (Reproduced with permission from ref. [23], © 2011 American Chemical Society)

and as a nanoreactor. Many synthesis strategies including hard-templating, soft-templating, and sacrificial templating approaches have been developed for the synthesis of hollow-structured bimetallic nanoparticles. Silica colloids [93–95], selenium colloids [96], polystyrene colloids [97], and Ag nanoparticles [98] are some of the commonly utilized templates for the fabrication of hollow structures. Au–Pt and Au–Pd bimetallic hollow structures have been conveniently prepared by utilizing silica colloidal templates [96]. Zhang et al. emphasized a facial colloidal templating method to monodisperse hollow Ag and Ag/Au submicrometer spheres by using silica colloidal templates [99]. Xia and coworkers have proposed a galvanic replacement reaction for the fabrication of various noble metal-based NPs [90–92, 100]. In this process, a Ag-based sacrificial template reacts with a precursor compound of the desired metal such as Au, Pd, and Pt. It has been demonstrated that by tuning the synthesis conditions and structures of starting Ag nanoparticle templates, different end products can be made [100, 101]. The Kirkendall effect which deals with the creation of “Kirkendall voids” close to the interface of a bimetallic couple has been used as a new fabrication route to designed new hollow nano-objects [102]. Puentes and coworkers [36] demonstrated fabrication of bimetallic Au–Ag hollow nanoparticles by the simultaneous or sequential action of galvanic replacement and the Kirkendall effect using a silver template and $\text{HAuCl}_4 \cdot 4\text{H}_2\text{O}$ as an oxidizing agent. Li and coworkers demonstrated a one-pot synthesis for bimetallic

Pt/Cu [103] and Pd/Sn [104] hollow nanostructures with large surface areas that potentially open up new opportunities for catalytic applications.

Formation of Bimetallic Nanoparticles

Structure-Controllable Synthesis Methodologies

The performance of the fuel cell is dependent on how robust the electrocatalyst is for each electrode. The electrocatalyst must exhibit high activity and durability while being cost-effective. Regardless of being an anode or cathode, the electrocatalyst's activity is surface atom sensitive only, which means that a high surface area-to-volume ratio must be achieved. Therefore, the ability to manipulate the size and shape of the nanocatalyst is crucial to achieving high activity without losing durability. However, the challenge still lies in fabricating highly active and durable catalysts while also having homogeneity in size and good particle dispersion.

Various methods have been employed for the preparation of bimetallic nanocatalysts, based on colloidal chemistry [105, 106], reverse micelles [107, 108], microwave irradiation, [109] and alcohol reduction [74, 110]: a brief summary of each is given below. No single method is universally superior; thus depending on the situation, the reader is advised to consider the intrinsic advantages and disadvantages of each approach when deciding which method to employ.

Colloidal Chemistry Methods

The colloidal methods, which offer a good capability for structural control, are widely used for the preparation of metal nanoparticles. The starting material, or precursor, is a metallic salt solution mixed with protective agents, which are usually surfactant molecules. The metal precursors are chemically reduced by the addition of reducing agents to form metal nanoparticles. A narrow size distribution can be achieved by the colloidal metal nanoparticles stabilized by stereo-hindrance effects or electrostatic charge.

The major drawback is the presence of protecting ligands (stereo-hindrance) such as NR_4^+ , PPh_3 , PVP, PNI, PAAm, and PVA, which may also block the catalytic active sites of the nanoparticles. Therefore, the removal of the protecting shells is necessary and important for realistic applications. The protecting shells can be removed by washing in an appropriate solvent or by decomposition at high temperature in an inert atmosphere. However, these processes result in unpredictable phenomena such as the surface segregation or cluster growth due to sintering effects during decomposition.

It is preferable to use an alternative route to prepare colloidal metal nanoparticles without protecting agents. The synthesis of bimetallic nanoparticles by this approach was shown to be effective; see Christina et al. [111]: they proved that size-selected PtRu bimetallic nanoparticles can be synthesized by reducing Pt^{4+} and Ru^{3+} ions in ethylene glycol (EG) without a need for protection agents. The size of nanoparticles can be easily manipulated by varying the pH value of EG solvent. Shape-controlled synthesis of nanocrystals can also be achieved by the colloidal route.

Reverse Micelles Methods

Metal nanoclusters can be prepared by reverse micelle methods with oil, water, and surfactant. The inverse micelle solution is used to solubilize the metal salt and provide a microreactor for the nucleation, growth, and stabilization of the nanometer-sized clusters. For example, the oil component (n-heptane) and surfactant ((2-ethylhexyl) sulfosuccinate (AOT)) are first well-mixed, and an aqueous solution containing metal ions is subsequently added to form well-defined microemulsion phase with the metallic complex in the “water pool.”

An important parameter in characterizing the microemulsion is the water-to-surfactant molar ratio, $W_0 = [\text{water}]/[\text{surfactant}]$, which plays a crucial role in controlling the equilibrium state of phase in a microemulsion system. The microemulsion of the same composition of oil, water, and the surfactant that contained the reducing agent was also prepared. An appropriate amount of reducing agents containing microemulsion was then gradually added to the microemulsion containing metal ions, reducing them to metal nanoparticles. For a binary system, the final composition of the bimetallic nanoparticles can be easily controlled by the molar ratio of the metal precursors [25, 29–31]. Therefore, the materials synthesized from micellar solutions of surfactants, which combine the advantages of both high specific surface area and uniform particle size distribution, are of great interest for applications in catalysis and fuel cells. However, the disadvantage of this method is its cost since the surfactant and oil used are expensive. Additionally, both surfactant and oil have negative environmental impacts, and the removal of the surfactants is also necessary for further catalytic applications.

Microwave Irradiation Methods

Microwaves are electromagnetic waves. Dielectric materials in a microwave field will be heated by the amount $\tan\delta$, the dielectric loss tangent, to define the ability of a material to convert electromagnetic energy into heat energy at a given frequency. The major advantage of microwave irradiation is that it can heat a substance uniformly through a glass or plastic reaction container, leading to a more homogeneous nucleation and shorter crystallization time compared to those obtained from conventional heating.

Conductive heating is often used, but microwave dielectric loss heating may be a better synthesis approach in view of its energy efficiency, speed, uniformity, and implementation simplicity; hence, the microwave-assisted method is beneficial to the formation of metal colloids. Liu et al. [112] have prepared the PtRu nanoparticles supported on Vulcan XC-72 carbon and carbon nanotubes by a microwave-assisted polyol process. An ethylene glycol solution containing Pt and Ru salts was heated in a household microwave oven for several seconds. The resulting suspension was filtered, and the residue was washed with acetone and dried at 100 °C overnight in a vacuum oven. It was found that the PtRu nanoparticles (2–6 nm in diameter) were uniformly dispersed on carbon. It was also found that both PtRu/C catalysts exhibited higher electrocatalytic activities for methanol oxidation than a comparative Pt/C catalyst.

Alcohol-Reduction Methods

The alcohol-reduction method has been developed for the preparation of metal colloids for both homogeneous and heterogeneous catalysis. In both cases, well monodispersed metal colloids can be formed and stabilized in aqueous solution

with the existence of polymers. The successful application of the alcohol-reduction method for the preparation of supported Pt and PtRu catalysts for fuel cell applications has been reported by Hsing et al. [110].

The prepared metal colloids were stabilized with a surfactant (SB12) without influencing the deposition of the colloids on the carbon support during the reduction process. Hwang et al. [74] have synthesized a nanosized PtRu/C catalyst using a modified alcohol-reduction method by incorporating small amount of Nafion in the preparation step. The addition of Nafion eliminates the use of stabilizers, which are commonly used to prevent cluster agglomeration. Even though the addition of stabilizers prevents agglomeration and coalescence of the metal particles on the supports, their removal prior to the electrochemical measurements requires complex procedures. However, the addition of Nafion in the present investigation serves a dual role. It disperses the catalyst particles on the carbon support and controls the size of the PtRu particles. Additionally, it is found that the Nafion addition into the catalytic layer can enhance the activity of PtRu catalyst for the electrooxidation of methanol by acting as a dispersing agent while increasing the ionic conductivity.

Electrochemical Deposition

Electrochemical deposition can be utilized to deposit a variety of metal nanoparticles, such as Pt and Cu, onto various substrates. The deposition system consists of an electric conductive working electrode, counter electrode, and a reference electrode. A metal salt was dissolved in the electrolyte, by applying suitable potential on the substrate, upon which metal salts can be deposited to form metal nanoparticles.

The 2-D or 3-D growth of metal can be controlled by the selection of applied potentials. 2-D growth can be fabricated by using underpotential deposition (UPD), in which the potential used for depositing the metal is higher than its reversible thermodynamic potential. For 3-D growth, overpotential deposition (OPD) can be used for bulk-like metal film. Adzic et al. [87, 113, 114] has utilized the UPD method to fabrication a variety of core-shell nanocatalysts. For example, they deposited Cu onto the substrate of Pd nanoparticles using an UPD method, in which a thin layer of Cu was formed on the surface the Pd substrate. By using redox-transmetalation, Pt metal can be deposited onto the surface of Pd nanoparticles to fabricate the Pd_{core}-Pt_{shell} nanocatalyst. Fabrication of nanocatalysts by using electrochemical method may not be as attractive as chemical methods in which the large-scale synthesis of catalyst can be achieved. Fabrication of nanocatalysts using electrochemical methods may not be attractive as chemical methods in which the large-scale synthesis of catalyst can be achieved.

Formation Mechanism Studies

Understanding structural variations during the nucleation and growth process, especially in the early stages of nanoparticle formation, are extremely important to achieve structural as well as size control of the nanoparticles. For metal nanoparticles,

X-ray absorption spectroscopy (XAS) has proved to be one of the most suitable methods for investigating structural evolution, and in many cases structural properties of metal particles can be probed in situ during the different preparation steps [20, 115–118]. Other techniques such as X-ray diffraction (XRD) and transmission electron microscopy (TEM) [119] are difficult to employ in situ because the nanoparticle's structure changes during preparation of the sample or due to the lack of long-range ordering [120]. UV–Vis spectroscopy has also been utilized for probing the nanoparticle formation mechanism [121–125]. By following the shift in the absorbance band and accompanying changes in the intensity in absorbance, information about the formation of nanoparticles can be obtained.

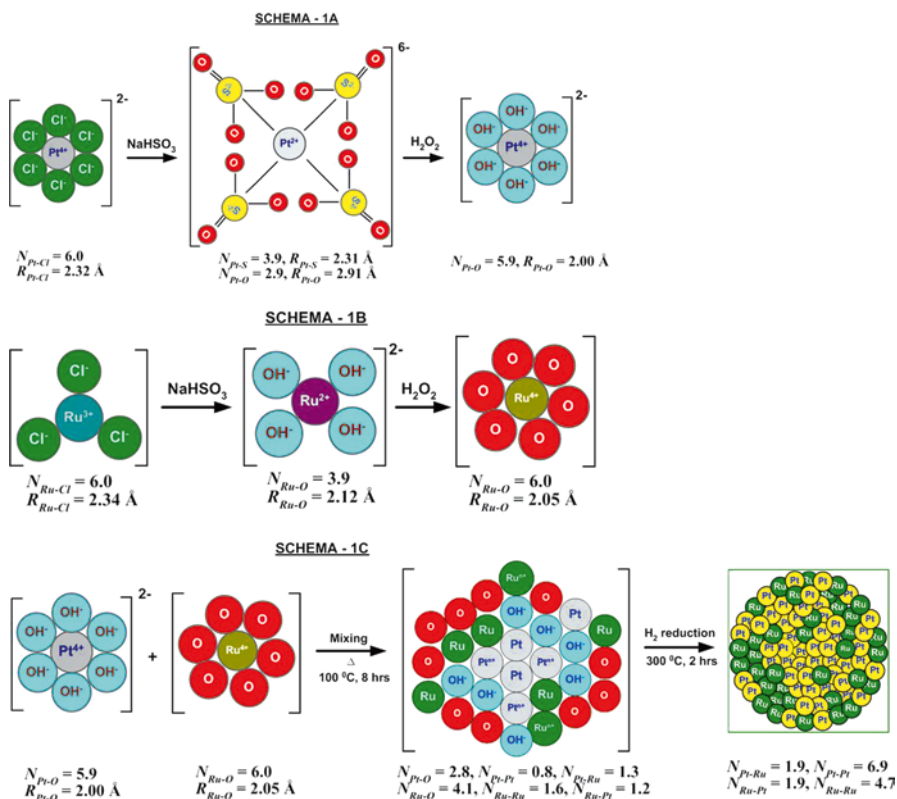
X-ray Absorption Spectroscopy

It has been shown in the literature that the study at the X-ray absorption near-edge spectroscopy (XANES) region (conventionally from below the edge up to $\sim 30 - 50$ eV) provides information about the oxidation state, fractional d-electron density, and electronic environment of the absorbing atom. Spectra obtained from the region extending from the XANES region to as high as 2 keV above the edge are known as the extended X-ray absorption fine structure (EXAFS) and are primarily due to the scattering of the photoelectron by near-neighbor atoms. The amplitude of the EXAFS function $\chi(k)$, where k is the wave vector, is proportional to the number of nearest neighbors, and the change of phase with the wavelength of the photoelectron depends on the distance between the emitter and the backscattering atom. The backscattering strength also depends on the type or atomic number of atoms evolved in the backscattering process. Thus, an analysis of EXAFS data yields structural details about the absorbing atom and its local environment. In recent years, XAS studies have been explored on bimetallic nanoparticles. In our group, we explored XAS methodologies to understand the formation of bimetallic nanoparticles.

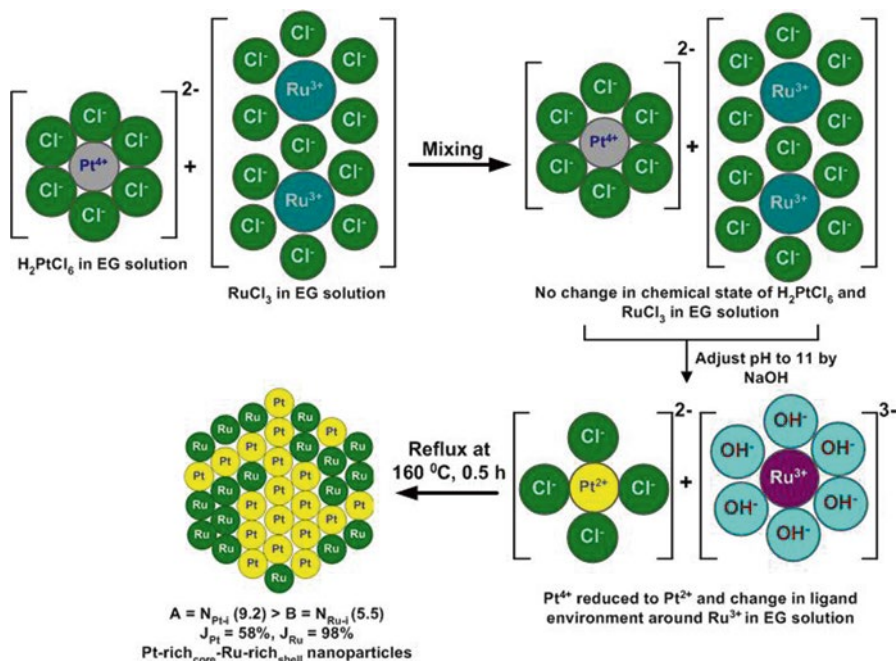
Formation mechanism of PtRu/C bimetallic nanoparticles synthesized by a modified Watanabe's method: We reported the formation mechanism of carbon-supported bimetallic PtRu nanoparticles by performing XAS measurements at each stage of synthesis [27]. The synthesis process involves adjustment of the pH of equimolar aqueous H_2PtCl_6 and RuCl_3 followed by reduction with NaHSO_3 to their corresponding intermediate compounds. Later, to each compound, hydrogen peroxide was added, and again the pH was adjusted to 5 using 1 M NaOH. These two solutions were then mixed, and the pH was maintained at 5. Later, an appropriate amount of Vulcan XC-72R carbon was mixed in, and the mixture was heated at 100°C for 8 h. The resulting colloidal product was then washed with ultrapure water and dried. Hydrogen reduction was performed on the colloidal product at 300°C for 2 h to achieve carbon-supported PtRu bimetallic NPs.

Based on the XAS parameters, formation mechanism of bimetallic PtRu/C NPs was proposed. From Pt L_{III} -edge XAS, we observed that, for the beginning compound H_2PtCl_6 , the coordination number of Pt, i.e., $N_{\text{Pt-Cl}}$, is 6.0 showing that Pt^{4+} ion is surrounded by six chloride ions. Upon addition of NaHSO_3 , we observed the change in Pt neighbors with sulfur contribution around Pt ($N_{\text{Pt-S}}$, 3.9). From the EXAFS results, we confirmed that the species formed at this stage is in the form of $[\text{Pt}(\text{SO}_3)_4]^{6-}$ in which Pt^{2+}

ion is surrounded by four SO_3^{2-} ionic groups. The addition of H_2O_2 to these species increases $N_{\text{Pt-O}}$ coordination to 5.9 with a bond length of 2.00 Å which is comparable with that of the Pt–OH bond length indicating that Pt^{2+} ions are oxidized to Pt^{4+} and surrounded by six hydroxide ions. Ru K-edge XAS analysis reveals that $N_{\text{Ru-Cl}}$ coordination is 6.0 for RuCl_3 , and after the addition of NaHSO_3 , the contribution from Ru–O coordination with $N_{\text{Ru-O}}$ is 3.9 similar to the $[\text{Ru}(\text{OH})_4]^{2-}$ species, while upon addition of H_2O_2 , the Ru–O coordination with $N_{\text{Ru-O}}$ is 6.0 similar to the RuO_2 species. Later, when we mixed the RuO_2 species with the $\text{H}_2\text{Pt}(\text{OH})_6$ and heated this mixture at 100 °C for about 8 h, it produced Ru and Pt coordination values of around Ru as 1.6 and 1.2, respectively. Similarly, Pt and Ru coordination around Pt is found to be 0.8 and 1.3, respectively. The oxygen contribution around Pt and Ru is found to be 2.8 and 4.1, respectively. After hydrogen reduction, the $N_{\text{Ru-Pt}}$ is increased to 1.9, and N_{PtRu} is increased to 1.9 revealing the formation of PtRu bimetallic NPs. From the compilation of XAS data, a schematic of PtRu formation process was proposed as shown in Scheme 3.



Scheme 3 Schematic of formation of carbon-supported bimetallic PtRu nanoparticles synthesized by a modified Watanabe's method (Reproduced with permission from ref. [27], © 2006 American Chemical Society)



Scheme 4 Formation of PtRu bimetallic NPs in EG solutions (Reproduced with permission from ref. [26], © 2007 American Chemical Society)

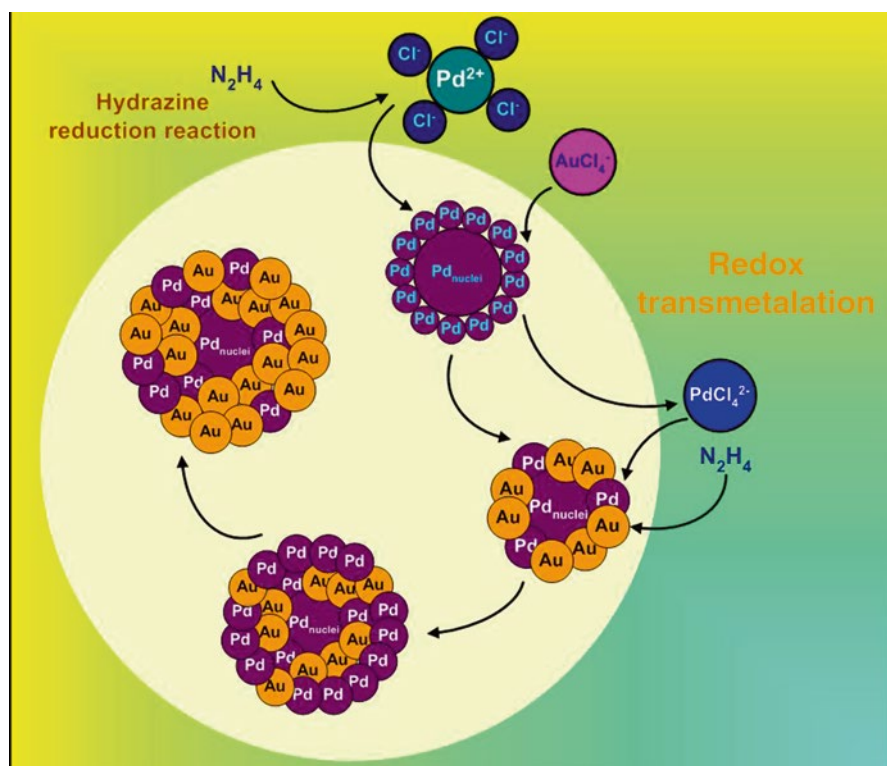
XAS results of this study revealed that the mixing of Pt^{4+} ions with a ligand environment of OH^- groups and Ru^{4+} surrounded by oxygen groups at a reaction temperature of $100\text{ }^\circ\text{C}$ for 8 h prior to H_2 reduction initiated the reduction reaction as evidenced by the presence of Pt and Ru bimetallic and ionic contributions that enhance the atomic distribution and dispersion in PtRu bimetallic nanoparticles.

Formation of PtRu/C bimetallic nanoparticles in ethylene glycol solutions: Very recently, by using XAS, we deduced the formation process of PtRu nanoparticles in ethylene glycol solutions [26]. The reduction of Pt^{4+} and Ru^{3+} metallic ions was performed in ethylene glycol solutions at $160\text{ }^\circ\text{C}$ for four time periods, i.e., 0.5, 1, 2, and 4 h. After reflux at each time period, the reaction mixture was cooled to room temperature and was taken for the XAS measurements.

By comparing the FT-EXAFS spectra and fitting results of both Pt L_{III} -edge and Ru K-edge, the formation mechanism of PtRu nanoparticles in EG solutions was understood (Scheme 4). From the Pt L_{III} -edge XAS and Ru K-edge XAS, we observed that upon mixing H_2PtCl_6 with RuCl_3 in EG solution, the coordination numbers $N_{\text{Pt-Cl}}$ and $N_{\text{Ru-Cl}}$ were found to be 5.6 and 6.0, respectively. However, after controlling the pH at 11, the $N_{\text{Pt-Cl}}$ are found to be 3.8 with a Pt–Cl distance of 2.311 Å related to anionic PtCl_4^{2-} ions, respectively. However, at the same step, around Ru, a contribution from OH^- appeared ($N_{\text{Ru-O}} = 4.9$) and the contribution from Cl – is largely decreased ($N_{\text{Ru-Cl}} = 0.5$).

Hence, higher OH^- coordination around Ru indicated that the species produced at this stage are in the form of $[\text{Ru}(\text{OH})_6]^{3-}$. Later refluxing the mixture containing PtCl_4^{2-} and $[\text{Ru}(\text{OH})_6]^{3-}$ ions at 160°C for 0.5 h produces Pt and Ru coordination around Pt of 6.5 and 2.7, respectively. Similarly, the Ru and Pt coordinations around Ru are 2.8 and 2.7, respectively. No change in coordination numbers and interatomic distances were found after increasing the reflux time, i.e., to 1, 2, and 4 h, indicating good stability of PtRu NPs formed in EG solutions.

Formation of Pd–Au/C bimetallic nanoparticles in AOT reverse micelles: We have recently demonstrated the unique application of XAS as a fundamental characterization tool to help in designing and controlling the architecture of Pd–Au bimetallic nanoparticles within a water-in-oil microemulsion system of water/sodium bis(2-ethylhexyl)sulfosuccinate (AOT)/n-heptane [25]. By properly performing hydrazine reduction and redox-transmetalation reactions sequentially within water-in-oil microemulsions, we have generated Pd–Au bimetallic clusters with various Pd–Au atomic stackings. At first by performing a redox-transmetalation reaction between $\text{Pd}_{\text{nuclei}}$ NPs and the Au^{3+} ions, $\text{Pd}_{\text{nuclei}}\text{--Au}_{\text{stack-1}}$ NPs were generated. By following hydrazine reduction reaction, Pd^{2+} ions were reduced on the preformed $\text{Pd}_{\text{nuclei}}\text{--Au}_{\text{stack-1}}$ NPs in order to fabricate $(\text{Pd}_{\text{nuclei}}\text{--Au}_{\text{stack-1}})\text{--Pd}_{\text{surf}}$ NPs (Scheme 5).



Scheme 5 Schematic of architecture of Pd–Au bimetallic NPs as investigated by X-ray absorption spectroscopy (Modified and reproduced with the permission from the original figure of ref. [29], © 2007 American Chemical Society)

Both the redox-transmetalation and hydrazine reduction reactions were repeated to manipulate the Pd–Au stacking until we reach (Pd_{nuclei}–Au_{stack-3})–Pd_{surf} NPs.

From the XAS structural parameters, the degree of alloying and extent of atomic distribution were evaluated. In the case of (Pd_{nuclei}–Au_{stack-1})–Pd_{surf}-stacked Pd–Au bimetallic NPs formed during the second hydrazine reduction reaction, the $N_{\text{Au–Au}}$ and $N_{\text{Au–Pd}}$ were determined as 8.17 and 1.37, respectively, giving the total coordination number of Au and Pd around Au ($\sum N_{\text{Au–i}} = N_{\text{Au–Au}} + N_{\text{Au–Pd}}$) as 9.54. Similarly, the $N_{\text{Pd–Pd}}$ and $N_{\text{Pd–Au}}$ are determined as 6.37 and 0.87, respectively, providing the total coordination number of Pd and Au around Pd ($\sum N_{\text{Pd–i}} = N_{\text{Pd–Pd}} + N_{\text{Pd–Au}}$) as 7.24. From these values, the structural parameters $P_{\text{observed}} (= N_{\text{Au–Pd}} / \sum N_{\text{Au–i}})$ and $R_{\text{observed}} (= N_{\text{Pd–Au}} / \sum N_{\text{Pd–i}})$ are calculated as 0.14 and 0.12, respectively. From the calculated degree of alloying of Au and Pd, i. e., J_{Au} (22.9 %) and J_{Pd} (30.8 %), by our developed methodology, low J_{Au} and J_{Pd} indicated that both Pd and Au atoms are segregated in the cluster. Thus, XAS can be conveniently utilized to characterize the segregation in nanomaterials once we properly extract the coordination number parameters.

Nashner et al. have studied the formation process of carbon-supported PtRu5 bimetallic nanoparticles synthesized from molecular cluster precursors, i.e., PtRu5C(CO)₁₆ [117, 126]. By following in situ EXAFS studies, scanning transmission electron microscopy, the authors have understood the atomic distribution and surface segregation phenomena. Authors have shown that during the nucleation and growth process, while the metallic character increases, the bond between the CO ligands and metals should gradually break. Further, it was demonstrated that Pt exhibits a marked preference for segregation to the particle's surfaces under an ambient H₂ atm. However, in the presence of O₂, the authors observed the formation of a metal oxide surface over a metal core which can revert back to the initial metal core structure on exposure to H₂.

The examples discussed above indicate that XAS can be conveniently employed to understand the early stage formation of bimetallic nanoparticles. The information obtained from XAS can be utilized to develop structure-controllable synthesis strategies for a wide variety of bimetallic nanoparticles.

UV–Vis Absorbance Spectroscopy

The characteristic surface plasmon absorption of metallic species is a convenient tool for following the formation of nanoparticles and their reaction kinetics. In addition, when following the simultaneous reduction of two metal systems, UV–Vis spectroscopy offers information whether the resultant system is a bimetal, an alloy, or a physical mixture [127, 128]. Torigoe et al. studied the formation of Ag–Pt alloy colloidal nanoparticles with optical absorption spectra [123]. The Ag–Pt alloy colloidal nanoparticles were prepared by step-by-step reduction of Ag₂[Pt(C₂O₄)₂] by dropwise addition of NaBH₄ in ethylene glycol solution. The authors recorded optical spectra of Ag₂[Pt(C₂O₄)₂] at various stages of the reduction (Fig. 5). The authors pointed out that the reduction reaction is composed of at least three stages. In the first stage (a–c), colloidal Ag particles were formed as evidenced by the growth of the absorption band at 407 nm with increasing concentrations of the reductant and lower extent of shift in the λ_{max} (less than 3 nm). In the second stage (d–f), the

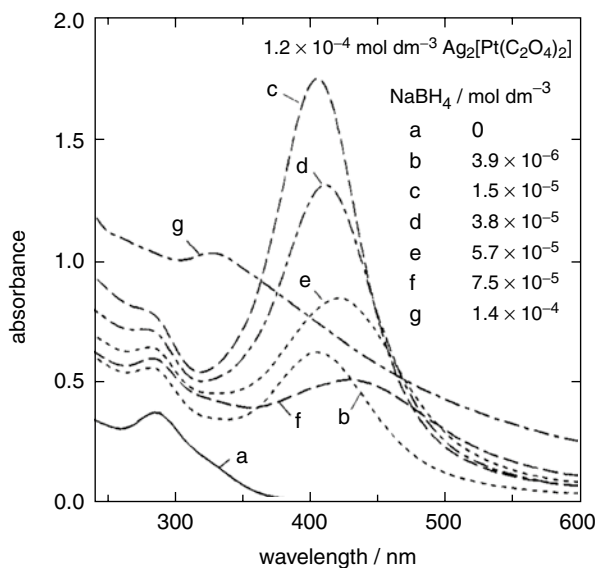


Fig. 5 Optical spectra of Ag₂[Pt(C₂O₄)₂] at various reduction stages with NaBH₄. (Reproduced with permission from ref. [123], © 1993 American Chemical Society)

authors observed a red shift of the plasmon band and an accompanying decrease in the absorbance. The authors opined that this is probably due to the hole injection and the accompanying decrease in the density of conduction electron. In the final stage (g), the plasmon band abruptly reestablishes at further shorter wavelengths than the initial position, i.e., at 340 nm, with a long tail toward longer wavelengths. At this stage, the plasmon band has only one peak, with a bandwidth broader than that of the silver colloid observed in the first stage. This observation was taken as evidence for the formation of Ag–Pt alloy colloid.

In another interesting study, M. A. El-Sayed and coworkers followed the formation of bimetallic gold–silver alloy nanoparticles with UV–Vis spectroscopy [121]. The authors prepared Au–Ag bimetallic nanoparticles by the co-reduction of chloroauric acid (HAuCl₄) and silver nitrate (AgNO₃) with sodium citrate. From the UV–Vis absorption spectra (Fig. 6), the authors noticed that the plasmon maximum blue-shifts linearly with increasing silver content. Further, as the optical absorption spectra of their solutions shows only one plasmon absorption, the authors concluded that co-reduction of chloroauric acid and silver nitrate with sodium citrate leads to a homogeneous formation of alloy nanoparticles.

Zhang et al. followed the evolution of Ag@AgAu metal core–alloy shell bimetallic nanoparticles by UV–Vis spectroscopy [129]. The authors prepared Ag@AgAu metal core–alloy shell bimetallic nanoparticles by a replacement reaction between Ag nanoparticles and HAuCl₄. The authors recorded absorption spectra at various stages of nanoparticle formation (Fig. 7). The surface plasmon resonance

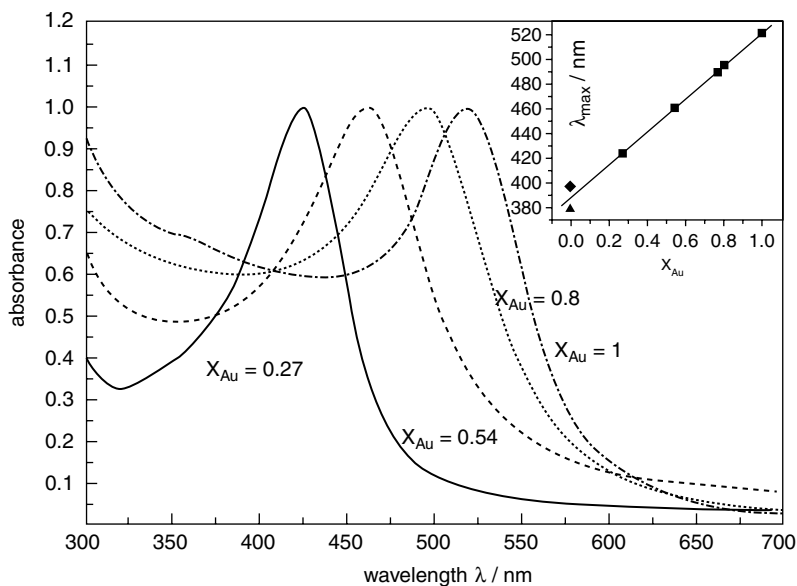
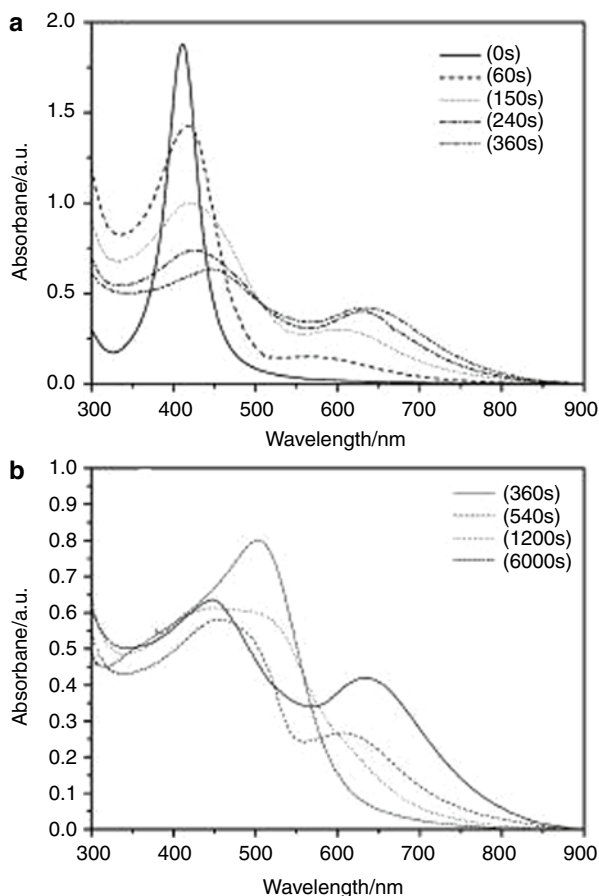


Fig. 6 UV-Vis absorption spectra of gold and gold-silver alloy nanoparticles with varying gold mole fractions x_{Au} . The inset shows how the absorption maximum of the plasmon band depends on the composition (Reprinted with permission from Ref. [121], © 1999 American Chemical Society)

peak appeared at 409 nm for the initial Ag nanoparticles was slightly red shifted with a decrease in peak intensity. At the same time the authors noticed the appearance of a new peak at 565 nm which began to red shift with reaction time (panel A of Fig. 6). The authors pointed out that the position of the peak at 565 nm was a significant red shift from the SPR of non-alloyed Ag@Au core-shell nanoparticles which normally exhibit a SPR peak at 530 nm. From this observation, the authors surmise that Au atom deposition and Ag atom dissolution were not uniform across the nanoparticle's surface. By comparing the locations of two peaks with the theoretical calculations derived from plasmon hybridization theory, the intermediate bimetallic nanoparticle was a hybrid of a Ag nanosphere and a hexapod-like branched particle. The authors also noticed that the position of the second peak did not change 4 to 6 min after the HAuCl_4 addition, while the first peak underwent a red shift (spectrum 360 s in Fig. 6a). This observation was related to the deposition of Au atoms and alloying with the underlying Ag atoms. The authors observed a blue shift of the second peak 9 min after the addition of HAuCl_4 (spectrum 540 s, Fig. 6b) and pointed out that this happened due to the atomic rearrangement by Ostwald ripening. Finally, the red shifting of the first peak and the blue shifting of second peak finally collapsed into a common peak (spectrum 1200s and 6000 s in Fig. 6b), signaling the complete formation of Ag@AgAu bimetallic nanoparticles.

Fig. 7 Evolution of the absorption spectra of bimetallic nanoparticles (Reproduced with permission from ref. [129], © 2008 Wiley-VCH)



Characterization of Bimetallic Nanoparticles

Electrochemical energy conversion for technical applications relies largely on the high catalytic reactivity of electrocatalysts. The optimum catalytic activity is strongly dependent on various factors such as atomic distribution of catalytic metal sites in the catalyst matrix [20, 111, 130, 131], as well as the surface structure, composition, and particle size distribution of the nanocatalysts. In order to select the proper electrocatalyst materials for energy applications, characterization methods play an important role in energy-related research. Ideally, the characteristics of the electrocatalyst materials should be used as selection criteria, and they should allow researchers to forecast the corresponding PEMFCs performance. The physical characterization and electrochemical characterization will be introduced and discussed in this section.

Physical Characterization

Several experimental techniques, including microscopy, diffraction, and numerous spectroscopies, have been successfully applied to deduce the structural aspects of bimetallic nanoparticles. Size distribution, morphology, segregation, alloying extent, atomic distribution, degree of alloying, and surface composition are some of the key properties given considerable attention in the characterization of bimetallic alloy or core-shell-structured electrocatalysts.

X-Ray Diffraction (XRD)

XRD has been widely employed to study supported and unsupported electrocatalyst nanoparticles to gather information on structure, crystallinity, lattice spacing, and grain size. In practice, the average particle size of PtRu-based electrocatalysts is calculated from the broadening of the (220) peak using the Scherrer equation [132], as shown in Eq. 2.

$$d = \frac{0.94 \lambda_{k\alpha 1}}{B_{(2\theta)} \cos \theta_B} \quad (2)$$

where d is the average particle diameter, $\lambda_{k\alpha 1}$ is the wavelength of X-ray radiation, θ_B is the angle of the (220) peak, and $B_{(2\theta)}$ is the width in radians of the diffraction peak at half-height. The determination of average particle diameter using (220) peak broadening in $2\theta \sim 67^\circ$ is particularly reliable for carbon-supported PtRu electrocatalysts, since in this region there are no reflection signals associated with the carbon support. By careful XRD measurements, several authors have followed the changes in the lattice constant caused by alloying in electrocatalysts in order to obtain information about the alloying degree [133–136]. Antolini and coworkers have proposed an equation for determining the alloying degree of a PtRu catalyst which is defined as the Ru atomic fraction (x_{Ru}) through Eq. 3 [137, 138]:

$$a = a_0 - 0.124 x_{Ru} \quad (3)$$

where a_0 is the lattice constant of pure Pt. For unsupported pure Pt, a_0 has the value of 0.39231 nm, whereas for supported pure Pt, $a_0 = 0.39155$ nm reported for Pt/C catalyst of E-TEK [137]. Radmilović and coworkers also proposed a similar type of relationship for single-phase PtRu bulk alloys: $a = 0.39262 - 0.124 x_{Ru}$ (or $a = 0.38013 + 0.1249 x_{Pt}$) [132]. Antolini and Cardellini utilized the peak height ratio of the Pt[111] crystal face and the C[0015] reflection of the carbon in order to evaluate the thermal crystallization considered as a crystallinity degree index of PtRu/C nanoparticles [138]. In some cases, XRD has been also used to calculate the surface area of the catalyst if the shape of the catalyst particles is spherical by using Eq. 4:

$$S = \frac{6000}{\rho d} \quad (4)$$

where S is the surface area ($\text{m}^2 \text{g}^{-1}$), d is the average particle size (nm), and ρ is the Pt density (21.4 g cm^{-3}). Information on chemical composition can be obtained first by constructing a calibration graph of lattice parameter versus atomic fraction and later by quantifying a composition based on the measured lattice parameter. Gasteiger et al. carried out detailed studies on the correlation of the lattice parameter with the alloy composition in the binary PtRu system [58] and found a linear dependence, according to the Vegard's law. These studies allowed the authors to establish the relationship between the electrode composition and electrocatalytic activity. However, XRD is a bulk method and reveals information on the bulk structure of the catalyst, and its support and its application to the interpretation of nano-sized particles are rather difficult. By using simulation calculations, *Debye function analysis* (DFA) offers a convenient approach to determine the size distribution and structure of small clusters [139]. In contrast to the analysis restricted to the limited regions such as the integral intensities of single *Bragg* peaks, the DFA provides detailed structural information in a range of dispersion (approx. > 40 %). In a typical DFA analysis, the measured diffraction curves are fitted by a set of *Debye* functions for clusters with the "magic" numbers $N = 13, 55, 147, \dots$ (for cuboctahedra and icosahedra) and $N = 54, 181$ (for decahedra) and $N = 13, 57, 154$ (for hexagonal close-packed clusters) [140]. A histogram plotting the mass fraction of specific structural units present within the sample against their average size can then be constructed through the evaluation of the full pattern. By carrying out the systematic numerical simulations using *Debye* functions, Vogel et al. obtained the intrinsic structure including the average lattice constant and the size distribution of surfactant-stabilized PtRu catalysts and silica-supported PtRu colloids in the as-synthesized state and after several heat treatments under various atmospheres [106].

Transmission Electron Microscopy (TEM)

TEM in which the electrons pass through the sample generally requires the electrocatalyst particles to be dispersed onto an electron-transparent substrate such as a thin carbon film-coated copper microgrid. TEM is particularly useful because of the high contrast between the metal atoms (especially heavy metals) and gives information about the size, size distribution, dispersion, and even the morphology of various shapes of particles. In general, for fuel cell catalysts, microscopic investigation is combined with other spectroscopic and diffraction techniques to obtain a comprehensive understanding on real structure. Radmilovic et al. [132] reported a detailed study of carbon-supported nanoparticles by TEM and XRD. The focus of their work was put on the characterization of a commercially available carbon-supported PtRu (1:1) catalyst in terms of both particle size and completeness of alloy formation. In the authors' opinion, many of the difficulties of XRD can be addressed by TEM. Especially, the lattice structure can be studied by high-resolution electron microscopy (HRTEM), including the presence of defects such as dislocations, twins, etc. HRTEM presents an interesting tool in catalyst characterization, as it can be used to determine the geometric shape of faceting planes, the presence of surface steps, the surface roughness, as well as the size and distribution of electrocatalyst nanoparticles. HRTEM offers resolution down to the Ångstrom level and enables

information to be obtained on the structure (atomic packing) rather than just morphology of the nanoparticles. Zhang and Chan presented TEM images along with the selected area electron diffraction patterns of PtRu nanoparticles synthesized by a two-microemulsion route in which the metal precursors and reducing agent formed two individual microemulsion systems [141]. Based on the presence of only diffractions from the face-centered cubic (fcc) in the electron diffraction pattern of PtRu nanoparticles, authors have concluded the formation of binary PtRu alloy with the fcc structure. Further evidence of the formation of fcc-structured PtRu binary alloy was given through the established linear relationship of the root of the sum of squares of the lattice coordinates versus the radius of the concentric rings with the lattices (111), (200), (220), (311), and (222). The authors have indicated that the calculated lattice cell constant through such a relationship is 3.862 Å which is in between those of platinum and ruthenium and is in agreement with that of a 1:1 PtRu alloy. Once the particle size distributions were obtained through TEM images, the mean particle size d_m can be calculated with the following formula (5) [142]:

$$d_m = \frac{\sum n_i d_i}{\sum n_i} \quad (5)$$

where n_i is the number of particles with diameter d_i . It is also possible to estimate the dispersion (ratio of surface atoms to total number of atoms) of the spherically shaped PtRu clusters through the information of cluster composition and particle size distribution.

Scanning Electron Microscopy (SEM)

In SEM, the surface of the sample is scanned in a raster pattern with a beam of energetic electrons. The SEM image is produced due to secondary electrons emitted by the sample surface following excitation by the primary electron beam [143]. Bi and Lu utilized SEM to follow the growth process and morphological control of platinum nanostructure, nanofiber, and nanotube junction structures [144]. These Pt nanostructures with various anisotropies were obtained by the galvanic replacement reaction between Ag nanowires and platinum salt solution in the presence of CTAB solution. From SEM observations, the authors have found that the platinum nanostructure growth follows three steps; at first, platinum nanoparticles will grow on the surface of Ag nanowire, and then Ag–Pt composite nanowires will be formed, and finally the Pt nanofibers and nanotubes will grow. From the field-emission SEM images, the authors were able to determine the length and the inner and outer diameters of the platinum nanotubes. Additionally, information related to Pt nanotube uniformity was conveniently obtained from the SEM images. Kawaguchi et al. studied the process of particle growth for Pt, Ru, and binary PtRu supported on carbon as a function of pyrolysis time [145]. The catalyst nanoparticles were prepared by an impregnation-reductive pyrolysis method at various temperatures. The authors have discussed the particle growth behavior from high-resolution SEM images. Although SEM images have lower resolution than TEM, SEM offers better three-dimensional images of the electrocatalysts [146, 147].

Atomic Force Microscopy (AFM)

AFM is a nondestructive method for investigating the microscopic surface topography of nanostructures. In this method, a probe scans the surface of a material with a sharp tip in order to clearly image the features of a sample and senses the small (approximately 1 nN) repulsive force between the probe tip and the surface. Rodríguez-Nieto et al. utilized AFM in order to obtain morphological and microscopic surface characterization of PtRu electrodeposits produced on activated highly ordered pyrolytic graphite (HOPG) substrates [148]. The authors were able to deduce the surface roughness of PtRu electrodeposits in nanometer scale from AFM images. Schmidt et al. employed UHV-AFM to determine the particle size distribution and corresponding dispersion of PtRu nanoparticles from height measurements of the imaged PtRu nanoparticles [149].

X-ray Absorption Spectroscopy (XAS)

In order to understand the structure of either alloy or core-shell-structured bimetallic electrocatalysts, especially in the sub-nm 2–3 nm range, combinations of characterization techniques are required. In general, the X-ray absorption spectrum of a sample can be divided into two regions: the near-edge region (XANES, 0–50 eV above the absorption edge) and the oscillatory part of the spectrum (EXAFS, > 50 eV above the absorption edge). The capability of tuning the X-ray energy to the absorption edge of each participating metal in bimetallic systems makes EXAFS as an attractive technique to elucidate the local structure and provide information on the environment about a particular atom. By analyzing the EXAFS spectrum of each metal in bimetallic nanocatalysts concurrently, valuable structural and chemical information (e.g., interatomic distance, coordination number, oxidation state of chemical species) about the nanostructure can be conveniently obtained, and this information can supplement the microscopy data. From XANES measurements, information about oxidation states, valence states, valence bond vacancies, and adsorption geometries of molecules at the surface can be obtained. However, as the evaluation of the spectra is quite complex, due to multiple scattering processes, EXAFS analysis is generally preferred. Several researchers have successfully used EXAFS to study the bonding, geometry, and surface structure of many electrocatalysts nanoparticles (e.g., PtRu, Pt-Co, and PtMo.), from which the shape, size, and short-range order in atomic distributions occurring within the particles can be reliably obtained [126, 150–154]. Recently, Russell and Rose thoroughly reviewed the capabilities of XAS with respect to the analysis of structural aspects of low-temperature fuel cell catalysts [118].

By collecting the XAS data at the absorption edges corresponding to each element in the bimetallic nanocatalysts under investigation, the extent of intermixing (alloying extent) and homogeneity (atomic distribution) of bimetallic nanocatalysts may be assessed [20, 155]. In general one can assess the alloyed or core-shell structure of nanomaterials simply from the coordination numbers of participating elements in core-shell materials. For a homogeneous bimetallic system of $A_{\text{core}}-B_{\text{shell}}$ cluster in which the core of the cluster is composed of N atoms of A (N_A) and the surface is made of N atoms of B (N_B), the total coordination number ($N_{AA} + N_{AB}$) for

the A atom will be greater than the total coordination number ($N_{\text{BB}} + N_{\text{BA}}$) for the B atom [156, 157]. If bimetallic nanocatalysts possess a random alloyed structure, the ratios of coordination number of A and B coordination, $N_{\text{AA}}/N_{\text{AB}}$ and $N_{\text{BA}}/N_{\text{BB}}$, should be consistent with the ratio of atomic fraction $x_{\text{A}}/x_{\text{B}}$.

The alloy or core-shell-type structure of metallic nanostructures from XAS measurements can be better understood if we can obtain knowledge about the atomic distribution and alloying extent of the participating elements. This is particularly important since, among the various structural aspects, it is most important to control the homogeneity, dispersion, and alloying extent as they have profound influence on the surface properties which affect the activity and stability of the bimetallic NPs. Hence, methods to gain more insights into structural aspects are highly needed. Even though alloying is a well-known phenomenon, detailed studies on the quantitative assessment of alloying extent in bimetallic NPs have been lacking so far. In our research group, by deriving the structural parameters from X-ray absorption spectroscopy (XAS) analysis, a general methodology to estimate the alloying extent or atomic distribution in bimetallic NPs has been developed.

By estimating the ratio of the coordination number (CN) of A around B and also the CN of B around A to the total CNs, one can conveniently estimate the alloying extent of A (J_{A}) and B (J_{B}) in A-B bimetallic NPs. The parameters that are needed to derive the extent of alloying are represented as P_{observed} , R_{observed} , P_{random} , and R_{random} . The parameter P_{observed} can be defined as a ratio of the scattering atoms “B” CN around absorbing “A” atoms ($N_{\text{A-B}}$) to the total CN of absorbing atoms ($\sum N_{\text{A-i}}$), ($P_{\text{observed}} = N_{\text{A-B}} / \sum N_{\text{A-i}}$). Similarly, R_{observed} can be defined as a ratio of the scattering atoms “A” CN around absorbing “B” atoms ($N_{\text{B-A}}$) to the total CNs of absorbing atoms ($\sum N_{\text{B-i}}$), ($R_{\text{observed}} = N_{\text{B-A}} / \sum N_{\text{B-i}}$), whereas P_{random} and R_{random} can be taken as 0.5 for perfect alloyed bimetallic NPs if the atomic ratio of “A” and “B” is 1:1. The J_{A} and J_{B} for 1:1 A-B bimetallic NPs can then be estimated by using Eqs. 6 and 7, respectively.

$$J_{\text{A}} = \left(\frac{P_{\text{observed}}}{P_{\text{random}}} \right) \times 100 \% \quad (6)$$

$$J_{\text{B}} = \left(\frac{R_{\text{observed}}}{R_{\text{random}}} \right) \times 100 \% \quad (7)$$

Based on $\sum N_{\text{A-i}}$, $\sum N_{\text{B-i}}$, J_{A} , and J_{B} , it is possible to develop structural models of NPs. For example, if $\sum N_{\text{A-i}} > \sum N_{\text{B-i}}$, the core is rich in “A” atoms and shell is rich in “B” atoms. In this case if both $J_{\text{A}} < J_{\text{B}}$, then the bimetallic NPs structure is almost pure $\text{A}_{\text{core}}\text{-B}_{\text{shell}}$ (case 1, Fig. 8). However, if $J_{\text{B}} > J_{\text{A}}$ with a coordination parameter relationship $\sum N_{\text{A-i}} > \sum N_{\text{B-i}}$, then the bimetallic NPs possess an “A” rich in core-“B” rich in shell structure (case 2, Fig. 8). If $\sum N_{\text{A-i}} = \sum N_{\text{B-i}}$ and J_{A} and $J_{\text{B}} \approx 100\%$, then bimetallic NPs adopt an alloy structure (case 3, Fig. 8).

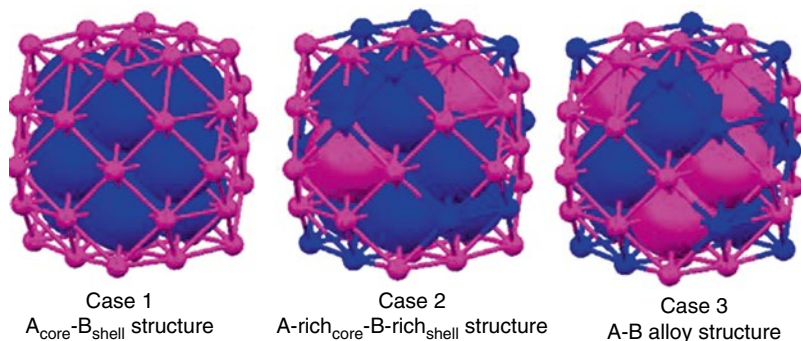


Fig. 8 Structural models of bimetallic nanoparticles with core–shell and alloy structures deduced from XAS structural parameters (key: *blue*, A; *pink*, B)

It is possible to construct structural models emphasizing the atomic distribution in the bimetallic NPs with knowledge of the $\sum N_{A-i}$, $\sum N_{B-i}$, J_A , and J_B values derived from XAS. With the help of alloying extent values and structural parameters extracted from EXAFS, it is possible to generate structural models for PtRu/C catalysts. We have calculated the alloying extent of Pt (J_{Pt}) and Ru (J_{Ru}) for commercial 30 wt% PtRu/C catalysts.

In the case of JM 30 catalyst, the coordination numbers of Pt and Ru atoms around the Pt atom are found to be 5.6 ± 0.3 and 1.4 ± 0.1 , respectively, and the total coordination number $\sum N_{\text{Pt}-i}$ is 7.0. The coordination numbers of Ru and Pt atoms around the Ru atom were determined as 3.4 ± 0.2 and 2.2 ± 0.3 , respectively, and the total coordination number $\sum N_{\text{Ru}-i}$ is calculated as 5.6. From these values, P_{observed} and R_{observed} are determined as 0.20 and 0.39, respectively, and J_{Pt} and J_{Ru} values are calculated as 40 and 78 %, respectively. For E-TEK 30 catalyst, we have calculated the coordination numbers of Pt and Ru atoms around the Pt atom as 6.2 ± 0.3 and 0.9 ± 0.1 , respectively, and $\sum N_{\text{Pt}-i}$ as 7.1; the coordination numbers of Ru and Pt atoms around the Ru atom are determined as 3.7 ± 0.2 and 1.2 ± 0.2 , respectively, and the $\sum N_{\text{Ru}-i}$ as 4.9. The other two structural parameters P_{observed} and R_{observed} in the case of E-TEK 30 are calculated as 0.13 and 0.24, respectively, and the J_{Pt} and J_{Ru} values are calculated as 26 and 48 %, respectively. It is clear from the structural coordination parameter values of both the catalysts that $\sum N_{\text{Pt}-i} > \sum N_{\text{Ru}-i}$ and $J_{\text{Ru}} > J_{\text{Pt}}$ and indicates that the catalysts adopt a Pt rich in core and Ru rich in shell structure.

From the quantitative extent of alloying values, we can see that in both the catalysts, a considerable amount of Ru is segregated on the shell layer, but the extent of segregation of Ru is higher in E-TEK 30 when compared to the JM 30. The increased value of J_{Ru} in JM 30 catalyst indicated that most of the Ru is involved in alloying and hence less segregation of Ru in the shell, whereas in the case of E-TEK 30 catalyst, lesser extent of Ru is involved in the alloying and considerable extent of segregation of Ru can be expected in the shell region. The segregation of Ru in the case of E-TEK 30 may in part be responsible for its lower methanol oxidation activity

compared to JM 30. Recent infrared measurements on the PtRu alloy particle electrodes indicate that two modes of adsorbed CO vibrations related to both Pt and Ru domains present on the surface support the surface segregation of Ru in commercial catalysts [69]. The XAS results support the Pt-rich core and Ru-rich shell structure for commercial carbon-supported PtRu catalysts. Increase in J_{Pt} and J_{Ru} values in JM 30 compared to E-TEK 30 indicates that the atomic distribution of Pt and Ru atoms are much facilitated, while an increase in atomic distribution can be taken as a measure for enhanced homogeneity.

Lin et al. investigated the commercial and in-house prepared PtRu catalysts by ex situ EXAFS [158]. From the observed EXAFS parameters, the authors have proposed that the two catalysts differed in the degree of PtRu alloying. The EXAFS data of the in-house prepared catalyst indicated the signatures of PtRu bonds, whereas no significant contributions were found in the commercial catalyst. These observations lead the authors to conclude that the catalyst synthesized in-house was at least partially alloyed, while the commercial catalyst system seemed to contain mixed phases of Pt and RuO_x . Greeger and Lytle demonstrated the feasibility of EXAFS technique for measuring the size and shape of small metal particles [159]. This methodology relies on developing a two-region model for various geometrical shapes like spheres, cubes, and disks and calculating the EXAFS average coordination number for first, second, and third coordination spheres as a function of cluster size. Nuzzo and coworkers have also elaborated the modeling nanoparticle size and shape with EXAFS [116]. They considered two model particles characterized by a common average first-shell coordination number (a value of ~ 8 for a 92 atom hemispherical and a 55 atom spherical cubooctahedral cluster). The authors have emphasized that the geometry of these two clusters is significantly different with different sizes, shapes, or lattice symmetries, so each cluster can generate a unique sequence of average coordination numbers in the first few nearest-neighbor shells. Once such a sequence is obtained experimentally, then the corresponding cluster size, shape, and symmetry may be conveniently determined. Several authors have studied the effect of particle size on the XANES region of the XAS spectra for Pt/C catalysts [116, 160, 161]. In their potential-dependent XANES studies on Pt/C catalyst particles with a 3.7 and ≤ 1.0 nm in diameter, Yoshitake et al. have observed that the white line intensity was increased for both particle sizes as the potential increased. In general the white line at the Pt L_{III} -edge is an absorption threshold resonance, attributed to electronic transitions from $2p_{3/2}$ to unoccupied states above the Fermi level and is sensitive to changes in electron occupancy in the valence orbitals of the absorber [162]. Hence, changes in the white line intensity have been directly related to the density of unoccupied d -states and indicate the changes in the oxidation state of the Pt absorber. In general, if the white line intensity decreases, lower the density of unoccupied d -states and lower the oxidation state of Pt. The lower white line intensity observed at negative potentials thus corresponds to a more metallic state. Mansour and coworkers [163] have proposed that by comparing the white line intensities of Pt L_3 and Pt L_2 edges of a sample with those of a reference metal foil, one can determine the fractional d -electron occupancy (f_d) of the absorber atoms in the sample by the following formula (8):

$$f_d = \frac{(\Delta A_3 + 1.11 \Delta A_2)}{(A_{3,r} + 1.11 A_{2,r})} \quad (8)$$

where $A_{3,r}$ and $A_{2,r}$ represent the areas under the white line at the L_{III} -edge and L_{II} -edge, respectively, of the reference foil spectrum.

$$\Delta A_x = A_{x,s} - A_{x,r} \quad (9)$$

with $x = 2$ or 3 and $A_{x,s}$ the area under the white line at the L_x edge of the sample spectrum.

f_d can then be used to calculate the total number of unoccupied d -states per Pt atom in the samples:

$$(h_j)_{t,s} = (1.0 + f_d) (h_j)_{t,r} \quad (10)$$

where $(h_j)_{t,r}$, t = total for Pt has been shown to be 0.3 [164]. A large $(h_j)_{t,s}$ value thus indicates a smaller d -electron density and an increased d -band vacancy as compared to those for bulk Pt.

Further, Mukerjee et al. [165] and Min et al. [166] studied detailed particle size effects in several binary anode and cathode electrocatalysts. Mukerjee et al. calculated the values for Pt/C particles with four different diameters at potentials corresponding to the hydrogen adsorption (0.0 V vs. RHE), the double layer (0.54 vs. RHE), and the oxide formation (0.84 V vs. RHE) regions. With the decreasing particle size, authors have observed an increased widening of the white line. The authors observed an increase in Pt L_{III} white line intensity at 0.84 V vs. RHE due to the adsorption of OH species at higher potentials, whereas the broadening of the white line at 0 V vs. RHE is related to adsorbed hydrogen. It has been shown that with increasing particle size, the d -band vacancy decreases, indicating that the electronic effects due to adsorption of H and OH are more pronounced for smaller particles. The authors have proposed that as the adsorption strength of H, OH, and CO is increased with decreasing particle size, however, below a certain size, there is a reduction methanol oxidation activity. It has been proposed that the intrinsic activity of Pt-based electrocatalysts for ORR in acidic solutions depends on both the shape, size of the particles, and the adsorption strength of oxygen intermediates [167]. Min and coworkers carried out detailed investigations on the particle size and alloying effects in Pt-based Pt–Co, Pt–Ni, and Pt–Cr catalysts [166]. From the XANES region of the spectra, the authors observed a decrease of the d -band vacancy with increasing particle size which is in agreement with Mukerjee et al. This observation suggests lowered adsorption strength of adsorbed oxygen species, thus facilitating the ORR reaction at larger particles.

Nashner and coworkers reported X-ray absorption spectroscopy characterization of carbon-supported PtRu nanoparticles with exceptionally narrow size and compositional distributions synthesized from the molecular cluster precursor $\text{PtRu}_5\text{C}(\text{CO})_{16}$ [126]. The authors have deduced structural variations in the PtRu nanoparticles exposed to different gaseous atmospheres such as hydrogen and oxygen on the basis of ex situ EXAFS measurements in combination with transmission electron

microscopy. In case of PtRu nanoparticles exposed to H₂ atm, the authors found that the ratio of PtRu bonds to Ru–M ($N_{\text{Ru-Pt}}/N_{\text{Ru-M}}$) as well as PtRu bonds to Pt–M ($N_{\text{PtRu}}/N_{\text{Pt-M}}$) obtained from experimental EXAFS data is always lower than the statistically predicted ratios indicating stronger weighting of the homometallic coordination in nanoparticles. The authors proposed that Pt shows a pronounced preference for segregation to the particle surfaces based on the fact that $N_{\text{PtRu}}/N_{\text{Pt-M}} > N_{\text{Ru-Pt}}/N_{\text{Ru-M}}$. Upon chemisorption of oxygen, the authors found an increase in the disorder in the first-shell metal bond lengths accompanied by the average bonding of two oxygens to both Pt and Ru with bond distances similar to those found in structures with binding oxygen atoms. In another interesting study, Nuzzo and coworkers utilized XAS to follow core–shell inversion in PtRu nanoparticles during hydrogen treatment at various temperatures [117]. Based on XAS structural parameters, the authors found that the incipient PtRu nanoparticles initially formed a disordered structure at 473 K in which Pt is found preferentially at the core of condensing particle. After exposure to high-temperature treatment to 673 K, the nanoparticle undergoes a core–shell inversion leading to the migration of Pt to the equilibrated bimetallic nanoparticle.

Very recently, by utilizing the XAS, we examined heat-induced changes in the surface population of Pt and Ru in PtRu/C catalyst NPs and correlated them with the electrocatalytic activity [168]. In this study, the thermal treatment procedure was designed in such a way that the particle size of initial NPs was not altered upon thermal treatment but can change only the surface population of Pt and Ru allowing us to deduce the structural information independent of particle size effect. We utilized X-ray absorption spectroscopy (XAS) to deduce the structural parameters that can provide information on atomic distribution (or) alloying extent as well as surface population of Pt and Ru in PtRu/C NPs. The PtRu/C catalyst sample obtained from Johnson Matthey was subjected to heat treatment in two environments. At first the as-received catalyst was reduced in 2 % H₂ and 98 % Ar gas mixture at 300 °C for 4 h (PtRu/C as-reduced). Later this sample was subjected to either oxygen (PtRu/C-O₂-300) or hydrogen thermal treatment (PtRu/C-H₂-350). XAS results reveal that when the as-reduced PtRu/C catalyst was exposed to the O₂ thermal treatment strategy, considerable amount of Ru was moved to the catalyst surface. In contrast, H₂ thermal treatment strategy led to the higher population of Pt on the PtRu/C surface. Characterization of the heat-treated PtRu/C samples by XRD and TEM reveals that there are no significant changes in the particle size of thermal-treated samples when compared to the as-received PtRu/C sample. Both XAS and electrochemical CO_{ads} stripping voltammetry results suggested that the PtRu/C-H₂-350 sample exhibits significant enhancement in reactivity toward CO oxidation as a result of the increased surface population of the Pt when compared to the PtRu/C-O₂-300 and PtRu/C as-reduced samples.

X-ray Photoelectron Spectroscopy (XPS)

XPS analyses are commonly used in the characterization of fuel cell electrocatalysts. XPS works based on the photoelectric effect where the energy of X-ray beam is sufficient to overcome the binding energy of electron of the analyte atom,

molecule, or solid/surface, allowing the electrons to be ejected. In general, both valence and core electrons can be ejected by X-ray radiation. The composition of materials can be determined using the peak areas under the binding energy curves of the core electron which is characteristic of each element present in the sample [34]. Further, information on chemical bonding can also be conveniently obtained through XPS since the peak shape and binding energy are sensitive to the oxidation and chemical state of the emitting atom [169, 170]. XPS is also particularly useful in determining the particle size effects in fuel cell catalysts. In their studies, Kao et al. observed a 0.3 eV increase of the Pt 4f binding energy when compared to bulk systems [171]. Eberhard et al. also found a continuous increase of the Pt 4f binding energy with decreasing particle size [172]. Zhang and Chan presented XPS analyses of PtRu nanoparticles prepared in water-in-oil reverse microemulsion [173]. The Pt 4f_{7/2} and Pt 4f_{5/2} lines that appeared at 71.30 eV and 74.57 eV, respectively, were attributed to metallic Pt⁰. The peaks that appeared at 72.49 eV and 75.88 eV were assigned to Pt^{II} in PtO and Pt(OH)₂, respectively. Based on the relative height of the peaks, the authors suggested that metallic Pt⁰ is the predominant species in the nanoparticles. The authors observed three components with binding energies of 461.32, 463.41, and 465.72 eV in the corresponding Ru 3p_{3/2} spectrum corresponding to the Ru⁰ metal, Ru^{IV} (e.g., RuO₂), and Ru^{VI} (in RuO₃), respectively. From these results, the authors concluded that the surface of nanoparticles contains metal and Ru oxides species.

Although XPS is suitable for obtaining the chemical state and bonding in electrocatalysts, its application toward the determination of surface composition is limited. For particle size < 3 nm, not less than half of the atoms in the cluster belong to the surface. Hence, the surface-specific XPS with the escaping depth of an electron of about 3 nm becomes a bulk method for small particles [174]. Recently, the work done by Tao et al. demonstrated that using a synchrotron-based X-ray light source with tunable incident X-ray energy allows for investigation of the composition of bimetallic nanoparticles [34, 175].

Auger Electron Spectroscopy (AES)

AES is a powerful tool for determining the composition of the top few layers of a surface. In AES, the sample of interest is irradiated with a high-energy (2 – 10 keV) primary electron beam. This bombardment results in the emission of backscattered, secondary, and Auger electrons that can be detected and analyzed. The backscattered and the secondary electrons are used for imaging purposes similar to that in scanning electron microscopy (SEM). The Auger electrons are emitted at discrete energies that are characteristic of the elements present on the sample surface. When analyzed as a function of energy, the peak positions are used to identify the elements and the chemical states present. AES is widely employed on electrocatalysts to realize the surface structure. Stamenkovic et al. investigated the surface structure of PtM (M = Co, Ni, Fe) polycrystalline alloys with the combination of AES, low energy ion scattering (LEIS) and ultraviolet photoemission spectroscopy (UPS) [176]. By careful modeling of emission from several subsurface layers with dynamic scattering of the outgoing Auger electron, the authors have observed that the Co₇₇₅/Pt₂₃₇

AES peak ratio for Pt₃Co sample is different on sputtered and annealed surface indicating that the concentration profile of Pt and Co atoms in the surface region may depend on the respective UHV treatment of the alloy sample. From the combination of spectroscopic results, the authors found that in the case of annealed Pt₃Co sample at 1,000 K, a completely Pt-skin surface was formed, and due to complete segregation of Pt atoms, the surface composition of Pt is calculated as 100 at.%. In the case of ion-sputtered Pt₃Co sample, the surface composition corresponds to the ratio of alloying elements in the bulk, i.e., 75 at.% Pt and 25 % Co. In another interesting study, Tremiliosi-Filho et al. utilized AES as a primary characterization technique to investigate the ruthenium coverage on Pt (111) surface [177]. The authors have calculated the amount of Ru monolayers formed on Pt(111) surface from the intensity of AES peak observed at 274 eV as a result of Pt(111) exposure to RuCl₃ solution. With the increasing concentration of RuCl₃ solution, the intensity of AES peak was found to be increased, and the corresponding amount of Ru monolayer coverage on Pt(111) was calculated to be higher.

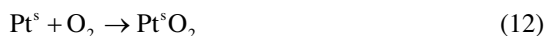
Electrochemical Nuclear Magnetic Resonance (EC-NMR) Spectroscopy

Electrochemical nuclear magnetic resonance (EC-NMR) spectroscopy which combines both solid state NMR and electrochemistry has emerged as a powerful technique to elucidate the electronic properties of metal surfaces [178]. In particular, EC-NMR provides an electronic level description based on the Fermi level local density of states (E_F -LDOS) [179]. The Wieckowski group carried out detailed EC-NMR studies in order to explore the structure of electrocatalyst nanoparticles, to estimate various E_F -LDOS that are involved in construction of the metal-adsorbate bonds, and to examine the diffusional behavior of CO on PtRu bimetallic catalysts as well as interesting relationship between electrochemical current generation and the E_F -LDOS of CO on Pt [180, 181]. ¹³C and ¹⁹⁵Pt are particularly useful nuclei for investigating electrochemical interfaces. Quantitative information about the E_F -LDOS of both 5 σ and 2 π^* orbitals of the chemisorbed CO on Pt nanoparticles can be conveniently achieved by the ¹³C EC-NMR. This analysis is particularly based on metal and ligand Knight shifts and spin–lattice relaxation rates, and it is important since the variation of these E_F -LDOS reflects the changes in Pt–CO chemisorption bonds. Similarly, from the ¹⁹⁵Pt EC-NMR, the 6 s and 5d E_F -LDOS of Pt surfaces can be obtained. The electronic alterations of the metal surfaces can be understood through variations in E_F -LDOS. In elegant work, Wieckowski and coworkers carried out thorough ¹⁹⁵Pt EC-NMR measurements on commercial PtRu alloy nanoparticles and ¹³C EC-NMR for CO chemisorbed on these catalysts [180]. The authors showed ¹⁹⁵Pt EC-NMR spectra of a Pt-black sample (with an average particle diameter of 2.8 nm) and PtRu nanoparticles (with an average particle diameter of 2–3 nm). The authors found that for the Pt-black sample, the Pt NMR spectrum extends from 1.095 to 1.14 G/kHz, whereas for PtRu nanoparticles, a much narrower NMR signal extending only from 1.095 to 1.115 G/kHz was found. Based on the observation that the whole spectrum is shifted toward lower Knight shifts, the authors arrived to a conclusion that there are no Pt atoms whose electronic properties resemble those of bulk

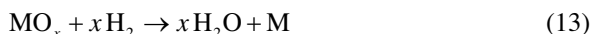
Pt. The authors have suggested that if the nanoparticle retains a homogeneous composition, then the corresponding NMR spectra of bimetallic catalysts can be expected to show broad, layer-like structures. For example, the ^{195}Pt NMR spectrum of a 2.5 nm-sized PtPd bimetallic catalyst extended from 1.09 to 1.13 G/kHz [182]. In contrast, the presence of relatively narrow peak can be found if there is a surface segregation of one component in bimetallic catalysts. Based on the fact that the ^{195}Pt NMR spectrum of PtRu nanoparticles exhibited a relatively narrow peak centered at about 1.104 G/kHz, the authors have suggested that there is a major surface enrichment of Pt atoms in the PtRu alloy nanoparticles. From the spin–lattice relaxation measurements, the authors have found significant reduction in $E_{\text{r}}\text{-LDOS}$ at Pt sites and also on the C-sites of adsorbed CO due to Ru addition, indicating a decrease in the total DOS at E_{F} for the Pt atoms. Thus EC-NMR is useful to evaluate the electronic effects in bimetallic electrocatalysts and for investigating electrochemical interfaces.

Temperature-Programmed Reduction (TPR)

Temperature-programmed reduction (TPR) has been successfully explored to evaluate the surface composition of bimetallic PtRu/C catalysts [183–185]. In their work, the authors suggested that upon calcination, surface platinum (Pt^{s}) on reduced Pt crystallites is oxidized to $\text{Pt}^{\text{s}}\text{O}$ and $\text{Pt}^{\text{s}}\text{O}_2$ as shown in Eqs. 11 and 12:



After calcinations, the state of $\text{Pt}^{\text{s}}\text{O}_x$ can easily be characterized with the TPR technique by reducing the calcined catalysts by flowing H_2 as shown in Eq. 13:



Similarly, the state of Ru also can be characterized by calcinations followed by the reduction. The authors found that oxygen chemisorbed on Ru exhibited a higher reduction temperature ($T_{\text{r}} = 300 \text{ K}$) than that chemisorbed on Pt ($T_{\text{r}} = 250 \text{ K}$). In case of bimetallic PtRu alloy nanoparticles, the experimental results suggested that T_{r} varies with PtRu surface composition [183]. For example, a Pt-rich surface displays a lower T_{r} ($\sim 300 \text{ K}$) when compared to Ru-rich surface ($T_{\text{r}} = 320 \text{ K}$). Based on these observations, the authors evaluated the surface enrichment in bimetallic PtRu catalysts.

Electrochemical Characterization

Characterizing the electrocatalytic activity of bimetallic nanocatalysts is an important step en route to performance optimization that requires several electrochemical methods. For instance, cyclic voltammetry (potential cycling), linear scan

voltammetry (LSV), rotating disk electrode (RDE), rotating ring-disk electrode (RRDE), and CO stripping voltammetry are widely employed to get structural as well as electrocatalytic activity information about electrocatalysts. An electrochemical reaction generally involves sequence of steps: it usually starts with the transport and adsorption of the reactants on the surface of the electrode/catalyst, followed by charge transfer related to either oxidation or reduction on the surface of the electrode/catalyst, and finishing with the transport of product(s) from the surface of the electrode/catalyst.

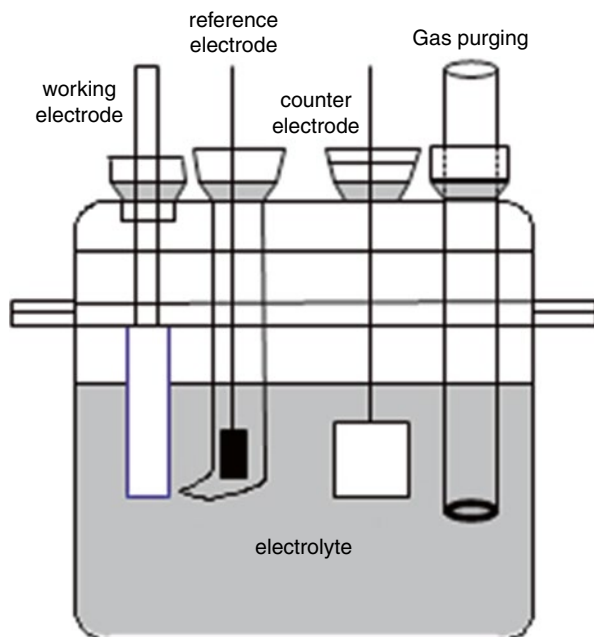
In this section, we attempt to cover several electrochemical techniques commonly employed in evaluating the electrochemical properties of bimetallic nanoparticles, with emphasis on applied aspects. We have also considered the following aspects: the electrochemical cell and its instrumentation in order to obtain valid results of the characterization and evaluation of the electrocatalyst activity will be presented where appropriate but not described in detail.

Cyclic Voltammetry (CV)

CV is a type of potentiodynamic electrochemical measurement and generally used to study the basic characteristics of the studied system regarding mainly the mechanism of electrode reactions and their kinetic parameters. It offers a rapid determination of redox potentials of electroactive species. CV is characterized by the linear sweep of a working electrode potential from one starting potential to high (or low) limit and back to low (or high) limit. In that case, the current at the working electrode is plotted versus the applied potential to give the cyclic voltammogram trace [186].

In general, the trace or feature of cyclic voltammogram is contributed from the sequence of electrochemical process steps, which can be described as follows. First, when the potential goes higher (or lower) enough to cause the oxidation (or reduction) of an electrochemically active species, we may observe an appearance of anodic (or cathodic) current. An increase in anodic (or cathodic) current as the potential goes higher (or lower) is because of the reaction kinetics becoming faster. Second, the concentrations of the oxidized and the reduced forms of electrochemically active species become equal on the surface of the electrode when the potential reaches the standard reduction potential. The highest anodic (or cathodic) current is obtained when the potential reaches a value at which all the reduced (or oxidized) form of the electrochemically active species at the electrode surface is consumed. At this particular moment, the highest anodic (or cathodic) current is obtained because the mass transport rate of the electrochemically active species reaches a maximum rate, which is driven by the largest concentration gradient between the bulk and surface concentration of the electrochemically active species. Third, when the potential goes higher (or lower) beyond this point, the current starts to fall off because the diffusion thickness increases, resulting in a less steep concentration gradient of the electrochemically active species. Therefore, an anodic (or a cathodic) peak develops. Finally, when the potential reaches the set high (or low) limit, it reverses direction and scans toward the set low limit. During this reverse potential scan, the oxidized (or reduced) form of the electrochemically active species reacts and develops a cathodic (or anodic) peak. The cathodic (anodic) peak is located at a

Fig. 9 The schematic diagram of the structure of a three-electrode cell



slightly lower (higher) potential than the anodic (cathodic) peak. If the redox couple is reversible, the cathodic and anodic peaks are of equal height (or equal area), and their peak positions do not change with the potential scan rate. In order to characterize electrocatalysts through CV, three-electrode electrochemical cells are widely used. The schematic diagram of a typical three-electrode electrochemical cell is presented in Fig. 9.

Materials with good electronic conductivity can be used as the working electrode, such as glassy carbon, gold, or platinum. The surfaces of these materials are exposed to the electrolyte, and the other parts are usually covered by an inert material, such as Teflon. The reference electrode is an electrode which has a stable and well-known electrode potential, is typically placed in the Luggin capillary, and is constructed in a way that its fine tip can reach the surface of working electrode in order to minimize the influence of the uncompensated electrolyte resistance, without hindering the electrochemical reaction on the surface of working electrode. The most common reference electrodes are Pt/H₂/H⁺ (standard/normal/dynamic hydrogen electrode), Ag/AgCl/Cl⁻ (silver/silver chloride electrode), and Hg/Hg₂Cl₂/Cl⁻ (calomel electrode). A counter electrode in three-electrode system often has a surface area much larger than that of the working electrode. For example, Pt was chosen as the counter electrode in the DMFCs field when the Pt-based catalysts were under characterization [186–189].

A catalyst is usually made in the form of a slurry before it is applied on the surface of the electrode. A catalyst is first well-mixed with other components:

solvent and additives, through ultrasonication. A solvent could be typically water and short chain alcohols such as ethanol. Naturally, the catalyst particles adhere to the surface of working electrode. However, in order to increase the adhesion, a typical additive, e.g., DuPont's perfluorinated ionomers (Nafion), may be used. Nafion can also be used as a binding material between each catalyst particles, which may lead to higher catalyst utilization. The dispersion of the catalyst particles is also crucial regarding with the optimum catalyst utilization; therefore, it is important to find the optimum loading of the metal: we found that an optimum Pt loading for the working electrode preparation was 0.22 mg-Pt/cm² [190]. The working electrode was made of unsupported or supported Pt-based catalysts immobilized on glassy carbon (GC) electrode surface (0.1964 cm²). The procedure for electrode fabrication involved three steps: first, the preparation of a clear suspension by sonication of a known amount of catalyst powder dispersed in 0.5 % Nafion; second, placing an aliquot of the suspension (7 μ L of 6.2 μ g-Pt mL⁻¹ of the catalyst) on the GCE disk; and third, air-drying about 5 min at room temperature and then at 80 °C to yield a uniform thin film of the catalyst [24, 168, 188, 191].

Typically, dilute aqueous acid solutions, such as sulfuric acid (H₂SO₄) and perchloric acid (HClO₄), are usually applied as an electrolyte in the study of DMFCs. However, it is also important to carefully choose a proper electrolyte in the fuel cell system. Although, sulfuric acid has been commonly used in the experiments, their sulfate anions (SO₄²⁻) can be absorbed on the surface of Pt catalyst. That situation is completely different from perchloric anion (ClO₄⁻), where this anion will not be absorbed onto the surface of Pt catalyst and will not influence the reaction kinetics.

Linear Sweep Voltammetry (LSV)

As mentioned in the previous section, it is appropriate to continue our discussion on linear scan voltammetry (LSV) experiment performed on a RDE to study the intrinsic kinetics of the catalyst [105, 192–194]. The knowledge of the velocities in radial and vertical direction, which can be obtained via the Navier–Stokes equations, allows the calculations of the mass transport to the disk surface through a diffusion layer with the thickness of δ according to Eq. 14:

$$\delta = 1.61 \cdot \nu^{1/6} \cdot D^{1/3} \cdot \omega^{-1/2} \quad (14)$$

where ν represents the kinematic viscosity of the electrolyte. As mentioned earlier, according to Eq. 14, the thickness of the diffusion layer of a chosen system strongly depends on the rotation rate. The potential of the working electrode in the LSV experiment is scanned from a potential in which no reaction occurs to a potential that leads to the occurrence of a reaction. Furthermore, when the overpotential is high enough, the reaction rate will be determined by the diffusion of the reactant at a given electrode rotation rate. In this condition, a diffusion-limiting current is achieved and can be described as a function of the diffusion layer thickness as shown in Eq. 15, by assuming that Fick's law can be applied.

$$i_d = nFAC \frac{D}{\delta} \quad (15)$$

n , A , and F are the number of electrons involved, geometric electrode area, and Faraday constant, respectively. The combination of Eqs. 14 and 15 results in *Levich's equation* for the diffusion-limited current on a RDE. The diffusion-limited current is for a given system only determined by the rotation rate with B being the *Levich constant*: [187, 189]

$$i_d = 0.62nFACD^{2/3} \nu^{-1/6} \omega^{1/2} = BC\omega^{1/2} \quad (16)$$

It is clearly seen in Eq. 16 that a linear relationship exists in the plotting of i_d versus $\omega^{1/2}$ and goes through the (0, 0) origin. Indeed, we also found a same linear relationship in part of our recent result as can be observed in Fig. 10b. It is of interest to

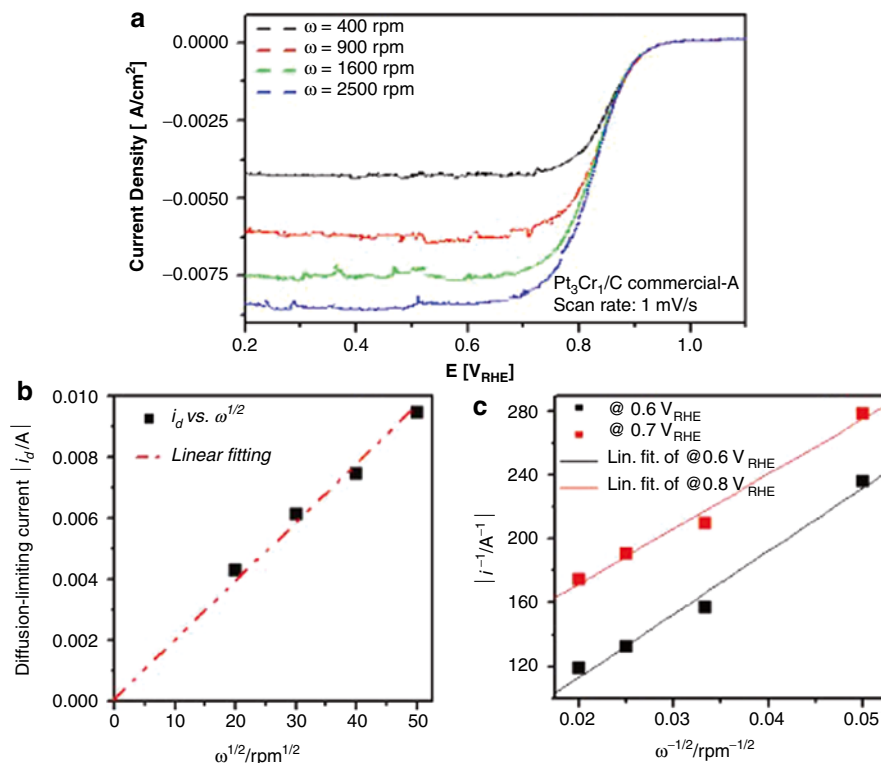


Fig. 10 Evaluation of intrinsic kinetics activity toward oxygen reduction reaction for commercial carbon-supported Pt₃-Cr₁ catalyst. (a) LSV recorder at 1 mV/s under various rotation rates in oxygen-saturated 0.5 M sulfuric acid at 25 °C. (b) Plot of i_d versus $\omega^{1/2}$. (c) Koutecky–Levich plots at various potentials

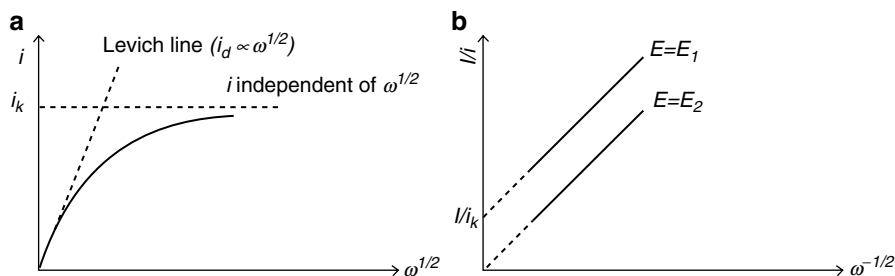


Fig. 11 (a) Variation of i with $\omega^{1/2}$ in the RDE experiment under a constant E_D for the slow reaction on the electrode. (b) Koutecky–Levich plots at potential E_1 , where the rate of electron transfer is sufficiently slow to act as limiting factor, and at E_2 , where electron transfer is rapid

point out that at the onset potential, the current is controlled mainly by reaction kinetics rather than mass transport rate and is expressed in Eq. 17 [186, 189].

$$i_k = nFk_\eta C \quad (17)$$

where k_η is the rate constant and is a function of overpotential (η). Furthermore, i_k is the current that would flow under the kinetic limitation if the mass transfer was efficient enough to keep the concentration at the electrode's surface equal to the bulk value, regardless of the electrode reaction.

In an entire potential scan range, the overall current (i) in Eq. 18 is described by the *Koutecky–Levich* equation, as the partition of the overall current in a kinetically determined and a diffusion determined part as shown below[186, 189, 195]:

$$\frac{1}{i} = \frac{1}{i_k} + \frac{1}{i_d} = \frac{1}{i_k} + \frac{1}{BC\omega^{1/2}} \quad (18)$$

It is clearly seen in Eq. 18 that $\frac{1}{\omega^{1/2}C}$ is a constant only when i_k is very large.

Otherwise, a plot of i versus $\omega^{1/2}$ will be curved and tend toward the limit $i = i_k$ as $\omega^{1/2} \rightarrow \infty$ (Fig. 10a). The plot of i^{-1} versus $\omega^{-1/2}$ as observed in Figs. 10c and 11b will yield a straight line, where its slope can be used to determine *Levich constant* of B , from which the number of electrons involved in the reaction can be calculated using known values of solubility and the diffusion of particular reactant in the medium under investigation. The intercept of the plot on the ordinate axis at $\omega^{1/2} = 0$ gives the values of i_k^{-1} , which can be used for further determination of the kinetic parameter k_η according to Eq. 18.

The combination of LSV and RDE methods can be utilized to obtain several intrinsic catalyst parameters, such as kinetic parameters of the Tafel slope, mass activity, and specific activity which together define the catalyst's activity. Figure 12 shows a sequence of steps for evaluating the activity of carbon-supported Pt and Pt–Co catalysts toward oxygen reduction reaction (ORR) [80].

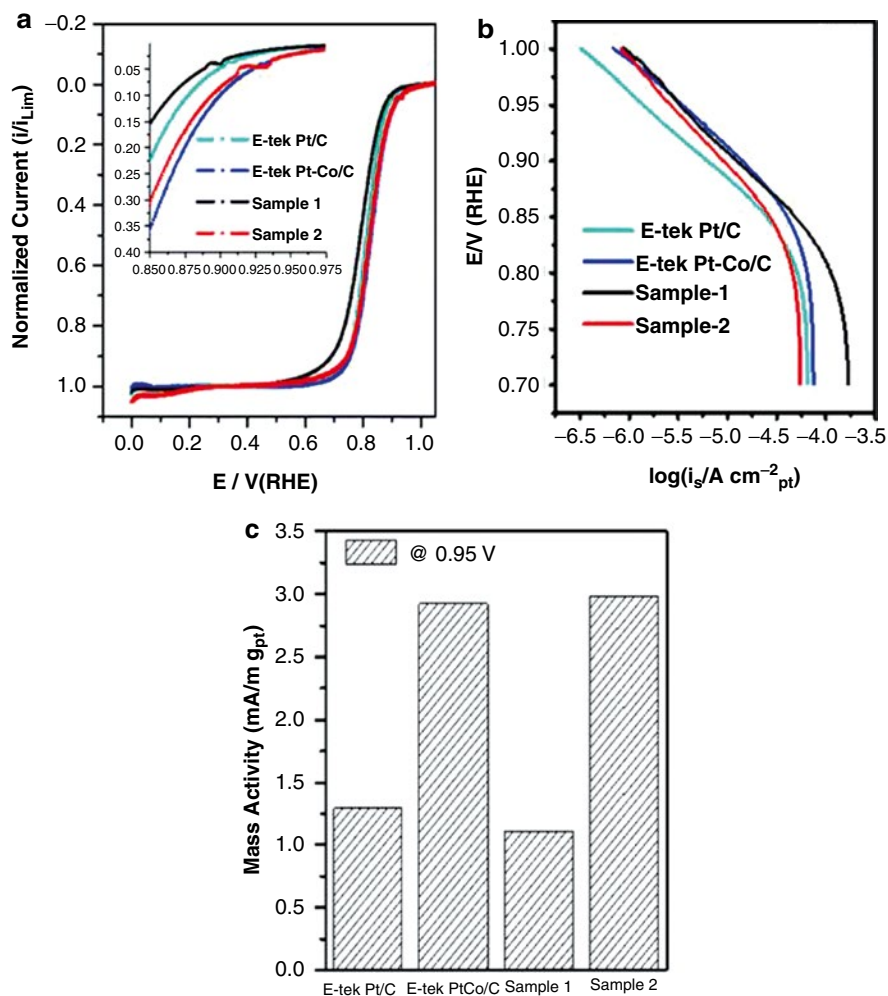


Fig. 12 Evaluation of electroactivity toward oxygen reduction reaction for various carbon-supported Pt and Pt–Co catalysts. **(a)** LSV recorder at 1 mV/s under rotation rate of 2,500 rpm in oxygen-saturated 0.5 M sulfuric acid at 25 °C. **(b)** Tafel plots. Currents are per gram of Pt used in the electrode preparation. **(c)** Mass activity measured at 0.95 V_{RHE} (Reprinted from ref. [191], © 2007 American Association for the Advancement Science)

It is possible to take an advantage of these observed phenomena: one can measure the value of diffusion-limited current by linearizing the observed current of the LSV region 0–0.7 V. Between 0 and 0.7 V, the observed current commonly shows almost a constant value, thus one can easily make a linearization of that observed current. The result of the linearization is known as the diffusion-limited current and is denoted as i_d . We believe that the normalized current in Fig. 12a is more appropriate for qualitative comparisons of the catalysts ORR activity. The normalized current is obtained by simply dividing the measured currents with the obtained i_d . In the Tafel region (higher than 0.85 V) and the mixed potential region, the ORR activities show a

significant difference in their magnitudes. It can be visualized from the inset of Fig. 12a that E-tek Pt-Co/C and sample-2 show a drastically enhanced activity in raising a portion of the curves compared to that for E-tek Pt/C. On the other hand, sample-1 displays comparatively poor activity toward ORR.

Adsorptive CO Stripping Voltammetry ($\text{CO}_{\text{ads}}\text{-SV}$)

The second electrochemical method for the estimation of $ECSA$ is CO stripping voltammetry [105, 196–201]. Figure 13a shows two CVs obtained on the bimetallic homemade PtRu catalyst with a CO-adsorbed adlayer. CO can be strongly adsorbed onto the surface of Pt to form a monolayer; however, this irreversible monolayer of

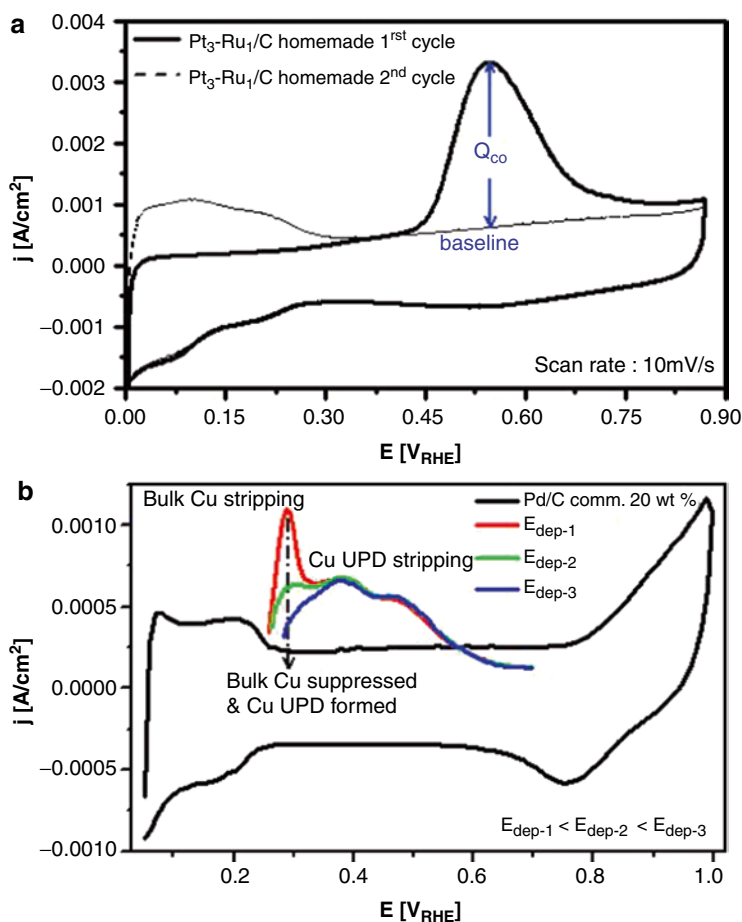
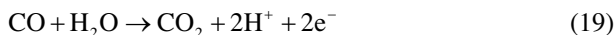


Fig. 13 (a) CO stripping voltammograms for the homemade Pt₃-Ru₁/C catalysts in N₂-saturated 0.5 M sulfuric acid electrolyte at a scan rate of 10 mV/s and 25 ± 1 °C. (b) Cu deposition in N₂-saturated 0.5 M sulfuric acid and in the presence of 32 mM CuSO₄ on commercial carbon-supported Pd (20 wt%)/GC electrode under various deposition potentials for 120 s at 30 ± 1 °C. Scan rate for Pd/C in the absence of CuSO₄ solution was 20 mV/s, while the Cu deposition was scanned at 10 mV/s. Note: $E_{\text{dep-1}} < E_{\text{dep-2}} < E_{\text{dep-3}}$

CO will be removed quickly and completely by electrochemical oxidation at a high enough potential in the first cycle of CV.

During the first forward step, the peak characteristics of hydrogen/desorption ($H_{ads/des}$) were suppressed due to the presence of adsorbed CO. Moreover, the observed peaks at 0.45–0.50 V correspond to oxidative stripping of the adsorbed CO layer. On the second sweep after electrooxidation of CO, the voltammograms return to those observed in the absence of adsorbed CO. The calculated charge under the CO oxidation peak (Q_{CO}) is related to the following oxidation process converts CO to CO₂:



CO oxidation to CO₂ involves 2 electrons as shown in Eq. 19. Therefore, if one CO molecule bonded with one Pt atom in a linear adsorption configuration (Pt–CO_{ad}), then the charge required to oxidize a monolayer of CO adsorbed on Pt is equal to 420 μC/cm². ECSA can then be calculated by using Eq. 20:

$$\text{ECSA}_{CO} (\text{m}^2 / \text{g}) = \frac{Q_{CO} (\text{C})}{420 (\mu\text{C} / \text{cm}^2) \cdot w_{Pt} (\text{g})} \times 100 \quad (20)$$

However, a bridge adsorption configuration (2Pt–CO_{ad}) may happen if 1 CO molecule occupies 2 Pt atoms. In that case, the charge required to oxidize a monolayer CO adsorbed on Pt is equal to 210 μC/cm². Those two CO adsorption configurations are strongly affected by the applied potential. A linear adsorption may dominate if the CO adsorption occurs at a potential close to 0 V, as shown in a recent study [202].

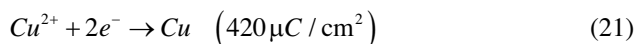
Pozio et al. [203] have suggested that ECSA calculated by means of CO adsorption seems not to be dependent on the platinum loading. This may be due to the stripping mechanism being dominated by the electronic conduction of the oxidation reaction involving the hydroxyl group from water (the electronic conduction is not to be influenced by the Nafion layer resistance in the catalyst). In this study of bimetallic PtRu, the CO stripping method basically gives a separate determination of platinum and second metal (Ru) in Pt-based alloy catalysts to bring a true ECSA, as desorption of CO from “Pt” and “Ru” usually takes place at different potentials [105, 200, 201].

Underpotential Deposition (UPD)

Up to now, we have described two typical electrochemical methods which are used for the estimation of ECSA. However, other studies have reported an alternative electrochemical method based on foreign-applied metal ad-atoms, such as copper (Cu) [196, 198, 204–207], silver (Ag) [208, 209], lead (Pb) [210], and antimony (Sb) [211]. This technique, the so-called underpotential deposition (UPD) of metal is extremely useful for carbon-supported catalysts as the ad-atoms can only be formed on metallic portion in the complex surface. In that case, an advantage of this method over $H_{ads/des}$ methods is that there is no spillover effect. Indeed, in a very

recent study, Green and Kucernak [206, 207] showed the viability of underpotential deposition of copper (Cu-UPD) to characterize supported and unsupported Pt, Ru, and PtRu catalysts. In their particular study of Pt, Ru, and PtRu catalysts, the choice of Cu ad-atoms as a probe was motivated by the close atomic radii of Cu (0.128 nm), Ru (0.134 nm), and Pt (0.138 nm) and a suitable potential region of Cu desorption at relatively low potential. This can introduce a correction for double-layer charging and oxygen adsorption. Furthermore, they also showed that it is also possible to determine the surface composition of PtRu catalyst using a Cu-UPD method due to the difference in adsorption energies for Cu on either Pt or Ru. The UPD studies have been performed using a variety of metals that include Cu, Pb, Sn, and Fe deposited on particular Pt catalyst [212].

The phenomenon of UPD itself refers to the deposition of metals on foreign metal substrates at the potentials more positive than that predicted by the Nernst equation for bulk deposition. This implies that the depositing ad-atoms are more strongly bonded to the foreign metal electrode [213–215]. In the case of Cu-UPD, the metal deposition processes at the electrode surface can be represented by Eq. 21:



The Nernst equation was applied in order to predict the equilibrium potential (E_{eq}) at which the deposition and dissolution of the bulk-metal phase happens:

$$E_{eq} = E^0 + \frac{RT}{2F} \ln \frac{a_{\text{Cu}^{2+}}}{a_{\text{Cu}}} \cong 0.34 V_{RHE} \quad \text{for Cu} \quad (22)$$

where E^0 is the standard potential and a is the activity. R , T , and F are the molar gas constant, temperature, and Faraday constant, respectively. The formation of the first monolayer is inferred from the pronounced current peaks at the potential $E > E_{eq}$, while the bulk deposition occurs at $E < E_{eq}$. Taking an example of Cu on Au system, UPD Cu on Au occurs at ~ 0.46 V, while bulk deposition occurs at ~ 0.25 V.

The cyclic voltammogram of platinum in solution composed of H_2SO_4 and CuSO_4 at wide scan range of 0–1.5 V commonly exhibited four main peaks related to different mechanisms. The CV is dominated by the deposition and stripping of both bulk and underpotential-deposited copper. In a forward anodic scan, one may find a distinct sharpened peak that represents the bulk copper stripping, while in the backward cathodic scan, the bulk copper deposition occurs at almost similar potential with bulk copper deposition. From detailed observations, bulk copper deposition occurs at around 0.25 V, which is a slightly lower potential than its bulk copper stripping. At the platinum double-layer region, we may able to observe several peaks associated with the UPD processes of copper on platinum. It is indicating that the Cu stripped from different sites, which has different adsorption energies, on the surface of platinum. In a forward anodic scan, UPD of copper stripping occurs at much positive potentials compared to that of bulk copper stripping. Furthermore, UPD of copper deposition is also shifted to much positive potentials compared to the deposition of bulk copper. In addition, the hydrogen adsorption region is

suppressed due to the presence of copper, and the oxide reduction is distorted due to the onset of copper UPD [206].

It is worth mentioning that Green and Kucernak used the plot of the ratio of copper stripping charge to hydrogen charge ($Q_{\text{Cu-UPD}}/Q_{\text{H-des}}$) as a function of deposition potential on platinum electrode in order to obtain an optimum condition for the formation of well-ordered monolayer of UPD copper without the possibility of a three-dimensional growth of bulk copper [206]. The charge of $420 \mu\text{C}/\text{cm}^2$ in the copper metal deposition reaction is used in the calculation of $Q_{\text{Cu-UPD}}$, while $Q_{\text{Cu-UPD}}$ itself is obtained after subtracting the total measured UPD copper stripping charges with the platinum background. The ratio of $Q_{\text{Cu-UPD}}/Q_{\text{H-des}}$ is to be expected 2, where a copper atoms adsorbs on platinum surface at the same sites with hydrogen to form a completely UPD copper layer. Their results showed that $Q_{\text{Cu-UPD}}/Q_{\text{H-des}} \approx 2$ was achieved when the deposition potential is in the range of 0.25–0.3 V. When E_{dep} is lower than 0.25 V, the deposition of bulk copper occurs, and when higher than 0.3 V, the UPD layer does not form completely. This technique can be also widely applied in finding an optimum deposition time of UPD copper.

In our recent results which are shown in Fig. 13b, we also found a similar trend, where the UPD of Cu occurs at the potentials more positive than that of bulk Cu deposition. The bulk copper deposition on commercial Pd/C occurs at the deposition potential of $E_{\text{dep.-1}}$. In a detailed observation, an increase in deposition potentials at $E_{\text{dep.-2}}$ and $E_{\text{dep.-3}}$ is followed by a decrease in current density corresponding to bulk copper stripping while the UPD copper starts to grow, as is shown with black arrow.

In any study of Pt-based catalysts, the method used for the determination of ECSA from Cu-UPD should consider: (i) applied deposition potential and time for the formation of UPD copper, (ii) applied potential scan range for both Pt background and UPD copper stripping, and (iii) a correction for double-layer charging, oxygen adsorption, and further possibility of adsorbed anion. In our earlier discussion, we mentioned that an optimum condition for the formation of well-ordered monolayers of UPD copper can be achieved when the ratio of $Q_{\text{Cu-UPD}}/Q_{\text{H-des}}$ is nearly equal to 2, as suggested by Green and Kucernak [206]. Thus, for the first important aspect, the plot between $Q_{\text{Cu-UPD}}/Q_{\text{H-des}}$ versus potential and (or) time deposition should be made in order to find out which potential and (or) time deposition region shows a value of $Q_{\text{Cu-UPD}}/Q_{\text{H-des}} \approx 2$. In the second aspect, the CV for bare Pt (as background) should be scanned from 0.05 to 0.85 V. The end potential in forward scan was chosen to be 0.85 V, at the point where oxide growth commonly starts on platinum, and thus only a very small oxide reduction peak was expected to occur at the backward scan. The linear potential scan for the Cu-UPD stripping should be also scanned until the end potential of 0.85 V. In case of PtRu catalyst, the linear potential scan for Cu-UPD stripping could be started from 0.3 V to 0.85 V. An applied potential at 0.3 V was chosen as the starting point of the scan due to a completion of monolayer of UPD copper while 0.85 V as the end potential which was due to a completion of oxidative removal of UPD copper layer and also a suppression of oxide adsorption/desorption. Once the oxide adsorption/desorption mechanism was suppressed, we may consider it as an advantage for the calculation

of Q_{Cu-UPD} as a very small correction would be expected and will be discussed in the following third aspect.

In the third aspect, the charge of Q_{Cu-UPD} should result after subtracting the total measured charge from experiment (Q_{exp}) with the charge due to the charging of double-layer capacitance (Q_{DL}), the charge due to the growth of any oxide and (or) oxygenated species (Q_{ox}), and the charge due to adsorption/desorption of any adsorbed anion (Q_{anion}) as shown in Eq. 23 [207]:

$$Q_{Cu-UPD} = Q_{exp} - Q_{DL} - Q_{ox} - Q_{anion} \quad (23)$$

Therefore, it is important to include the CV for bare platinum as a background for the matter of correction to Q_{Cu-UPD} . ECSA can be calculated by assuming that a charge required to oxidize a monolayer of Cu adsorbed on each metal surface is equal to $420 \mu\text{C}/\text{cm}^2$ as shown in the following equation [207]:

$$ECSA_{Cu-UPD} (\text{m}^2 / \text{g}) = \frac{Q_{Cu-UPD} (\text{C})}{420 (\mu\text{C} / \text{cm}^2) \cdot w_{Pt} (\text{g})} \times 100 \quad (24)$$

Once the ECSA was obtained either from H-UPD, CO stripping, and Cu-UPD methods, it was possible to determine the average particle size (d) by assuming that the shape of the catalyst particle is spherical, as shown below:

$$d (\text{nm}) = \frac{6,000}{ECSA (\text{m}^2 / \text{g}) \cdot \rho (\text{g} / \text{cm}^3)} \quad (25)$$

where ρ is the average particle density, and it was $21.4 \text{ g}/\text{cm}^3$ for Pt. However for the bimetallic system, the average particle density could be obtained by using the following relationship:

$$\rho_{Pt-M} = x_{Pt}^{bulk} \rho_{Pt} + x_M^{bulk} \rho_M \quad (26)$$

where x_{Pt}^{bulk} and x_M^{bulk} are the bulk compositions of Pt and second metal ‘‘M,’’ respectively, while ρ_M is the average particle density of second metal ‘‘M.’’

Surface composition of Pt-based catalysts through the Cu-UPD method. It is of interest to describe the feature for the stripping of Cu-UPD layer formed on particularly dispersed bimetallic PtRu catalyst. Commonly, a peak at low potential around 0.42 V is accompanied by a shoulder that continues to a much higher potential. The first peak at around 0.42 V was due to the oxidative removal of adsorbed Cu-UPD layer, while the shoulder was the removal from the Pt sites. This information strongly supports the differing adsorption energies for Cu on either Pt or Ru that could be used to quantify the Ru metal surface content of PtRu catalyst. Further deconvolution of linear anodic stripping of Cu-UPD should be made to separate a charges contributed by Ru and Pt sites by assuming that the feature of CU-UPD has a Gaussian line shape. The Ru coverage on the surface of bimetallic PtRu catalyst

(x_{Ru}^s) can be quantified from the ratio of charge in first peak contributed by Ru (Q_{Ru}^{Cu-UPD}) to Q_{Cu-UPD} as shown below [207]:

$$x_{Ru}^s = \frac{Q_{Ru}^{Cu-UPD}}{Q_{Cu-UPD}} \quad (27)$$

Rotating Disk Electrode (RDE) Method

It is well known that the steady-state current generated by cyclic voltammetry is mainly determined by the diffusion of substrate around the electrode's surface when immersed in a stagnant/unstirred electrolyte solution. A minor natural convection from the impact of environmental fluctuation in some cases may appear, but its effect can be neglected. It is possible to increase the mass transport by introducing a forced convection in which the analyte solution flows relative to a working electrode. A popular method for creating such a relative movement is by rotating the working electrode. Such a method is called a rotating disk electrode (RDE). Therefore, RDE could also be called as a hydrodynamic working electrode, where the steady-state current is determined by solution flow rather than diffusion [186, 188].

In common three-electrode cells, when a working electrode spins, the reactant in the solution is dragged to the surface of the working electrode, and the resulting centrifugal flings the product away from it. However, one should notice that there is still a stagnant reaction layer covering that surface of the working electrode and the reactants transport through this layer by diffusion. There is a strong dependency of thickness of diffusion layer (δ) with applied rotation rate (ω) of working electrode as shown in Eq. 14. An increase in rotation rate will lead to a thinner diffusion layer. A rotation rate between 5 and 10,000 rpm can control the flow of the reactant through the surface of working electrode that follows a laminar pattern. Figure 14 shows a schematic diagram of RDE setup. The working electrode was connected to the electrode rotator that has very fine control of the electrode's rotation rate.

The flow pattern under the rotating disk electrode was obtained by numerically solving the Navier–Stokes equation and continuity equation under the following conditions:

- (i) The radius of the disk on the working electrode is large enough compared to that of boundary layer thickness, and thus the small distortion of flow pattern at the center and edge can be neglected.
- (ii) The roughness of the disk surface of the working electrode is small enough compared to that of the boundary layer thickness.
- (iii) The radius of the electrochemical cell is large enough compared to that of the disk on the working electrode, and thus the reflection of the flow at the vessel of electrochemical cell's wall does not affect the flow pattern under the disk.
- (iv) The rotation speed is sufficiently greater than the lower critical value in which the effect of natural convection is negligible. Furthermore, the rotating speed is also smaller than that of the higher critical value in which the flow gets to be turbulent.

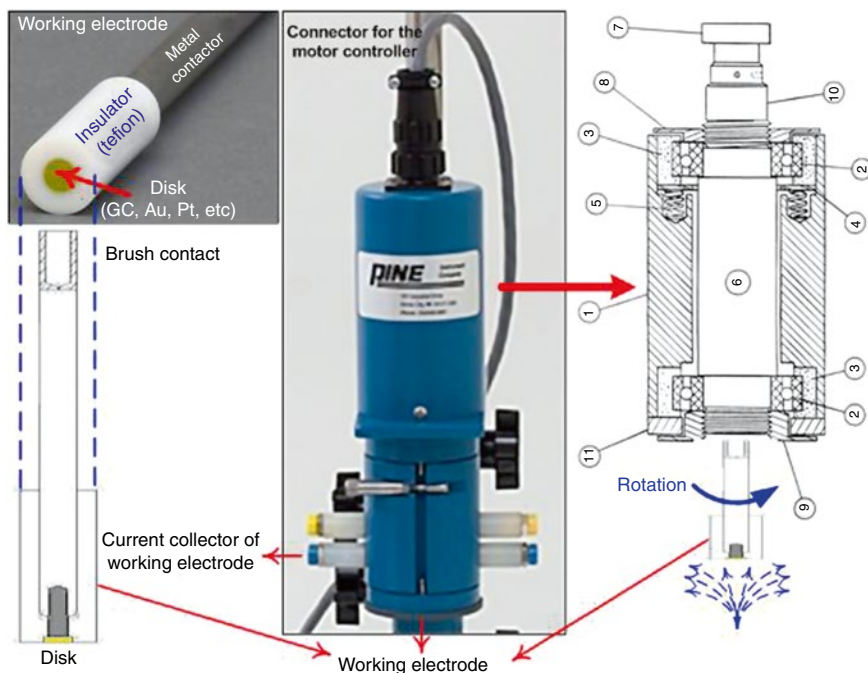


Fig. 14 The RDE setup of Pine instrument and its schematic diagram. 1 Rotator body; 2 bearing, 2; 3 rubber housing, 2; 4 washer; 5 spring, 4; 6 spindle for electrode; 7 pulley; 8 top lock nut; 9 bottom lock nut; 10 bushing/brush contact; and 11 retainer

The solution of the Navier–Stokes equation and continuity equation under those mentioned conditions may bring two possibilities of the net mass transport rate of a reactant to the surface of the working electrode. The first net mass transport is the convection which can control the thickness of the diffusion layer, while the second one is the diffusion which can control the reactant through the diffusion layer. The flux normal to the electrode surface due to diffusion is given by $D\left(\frac{\partial^2 C}{\partial x^2}\right)$ and that due to convection is given by $v_x\left(\frac{\partial C}{\partial x}\right)$, where D is the diffusion coefficient of the species, C is the bulk concentration of the species, and v_x is the solution velocity in the x direction, which is normal to the electrode surface [186, 189].

The rotating disk electrode is becoming one of the most powerful methods for studying both the diffusion in electrolytic solutions and the kinetics of moderately fast electrode reaction because the hydrodynamics and the mass-transfer characteristics are well understood and the current density on the disk electrode is supposed to be uniform. V. G. Levich [195] solved the family of equations and provided an empirical relationship between diffusion-limiting current (i_d) and rotation rate (ω) as shown in Eq. 15. In particular application in fuel cells, the empirical relationship which is given by Levich is also applicable in linear scan voltammetry (LSV) experiment performed on a RDE to study the intrinsic kinetics of the catalyst [105, 192].

Electrocatalytic Applications: Electrochemical Studies of Fuel Cell Reactions on Bimetallic Nanoparticles

Success in fuel cell technology largely relies on electrocatalysts. Electrocatalysts employed for fuel cell reactions are required to possess well-controlled structures, dispersions, and compositional homogeneities. Further, in order to realize fuel cells as viable future power-generating technology, electrocatalysts must meet performance, durability, and cost targets. Recently, Mark K. Debe critically reviewed electrocatalytic approaches and challenges for automotive fuel cells [42]. The author pointed out that a clear understanding of electrocatalyst surface area and activity loss mechanisms and insights into durability issues associated with externally and internally generated impurities should significantly assist the development of fuel cell technology. Critical factors that are presently believed to play significant role in the electrocatalysts need to be thoroughly understood in order to develop newer catalyst system that can meet the targeted performance and durability.

Decisive Factors Influencing Electrocatalytic Activity

Structural Effects

With regard to electrocatalysts, structure-dependent catalytic activity toward methanol oxidation reaction (MOR) [12, 216–218], formic acid oxidation reaction (FAOR) [17, 219], and oxygen reduction reaction (ORR) [220–222] have been observed. Maillard et al. studied the influence of the catalyst's structure on the reactivity of electrooxidation of methanol [218]. The authors noticed that the electrocatalytic activity of a PtRu catalyst with a Ru-decorated Pt surface was two orders of magnitude higher when compared to the commercial Johnson Matthey PtRu black (Pt:Ru = 1:1)-alloyed structured catalyst. In our recent investigations, we found that Pt-decorated Ru catalyst exhibited higher mass activity for MOR than commercial Johnson Matthey PtRu black (Pt:Ru = 1:1)-alloyed structured catalyst [12]. From the X-ray absorption spectroscopy measurements, we observed more Pt d-band vacancies in the case of Pt-on-Ru nanoparticles causing weaker CO adsorption on the synthesized catalyst surface. Zeng et al. showed that a core-shell-structured Ag@Pt/C bimetallic nanoparticle exhibits enhanced specific activity in methanol electrooxidation when compared to similarly prepared bimetallic Ag-Pt catalyst. The authors attributed the observed activity enhancement to the presence of Au underneath a very thin Pt shell where electron exchange between Au and Pt had promoted the formation of active oxygen species on Pt, which facilitated the removal of inhibiting CO-like reaction intermediates [84]. The core-shell-structured bimetallic nanoparticles available for MOR reveal that the core material influences the outer shell layer and optimizes its surface electronic and structural properties thereby exhibiting improved catalytic activities. Zhang et al. studied the formic acid electrooxidation on Pt-around-Au nanocomposite structures [223]. From the electrochemical measurements in supporting electrolyte containing formic acid solutions, the authors found that formic acid oxidation on Pt-around-Au/C

nanocomposites was about 3.0 times than on Pt/C catalyst. Based on cyclic voltammetric analyses, the authors concluded that the possible reason for the unexpected high activity for HCOOH oxidation on the Pt-around-Au nanocomposite is due to the efficient spillover of HCOO from Au to the surrounding Pt nanoparticles where HCOO is further oxidized to CO₂. Based on voltammetric studies, the authors found that the specific activity of Pt atoms increased with the decrease of Pt surface coverage. Authors found a 3 % Pt-covered-Au/C surface that showed 17.0- and 23.9-folds more activity toward formic acid oxidation compared to 75 % and 100 % Pt-covered surfaces, respectively. In the case of oxygen reduction reaction, Pt-based bimetallic nanoparticles with various structures have been studied. Several efforts have been made to improve the dispersion and stability of Pt-based ORR catalysts, e.g., by creating a near-surface region with a Pt-skin structure in Pt-alloys via acid treatment [176, 224] and by forming core-shell structures [87]. In a recent study, Stamenkovic et al. showed that the Pt₃Ni(111) surface is about 90 times more active than the state-of-the-art Pt/C catalysts for ORR [21]. In another interesting study, Chen et al. [225] demonstrated that by creating a percolated structure with Pt-rich and Pt-poor regions within individual Pt₃Co nanoparticles through acid treatment, their ORR activity could be increased by up to two orders of magnitude when compared to Pt nanoparticles. These results clearly indicate that significant improvements in electrocatalytic activity can be achieved by properly fine-tuning the structure of bimetallic nanoparticles.

Composition/Surface Composition Effects

The composition of bimetallic nanoparticles in either bulk or surface need to be properly controlled during the fabrication process as the bulk/surface composition strongly influences the electrocatalytic activity. Further, variations in composition are very important in modifying the surface structure of bimetallic nanoparticles. Ball et al. studied the effect of atomic ratio of Pt-M/C (M = Co, Cr, Fe, Ni, and Mn) catalysts on the fuel cell activity and stability [226]. The authors found that bimetallic Pt-M/C catalysts with Pt-to-M ratio 3:1 showed higher electrocatalytic activities. Very recently, in our group Pt_xRu_{100-x}/C with various alloy compositions was prepared by a microwave-assisted ethylene glycol method [9]. Among the Pt_xRu_{100-x}/C with various Pt:Ru atomic ratios ($x = 25, 50, \text{ and } 75$), the Pt₇₅Ru₂₅/C NPs were shown to be superior in MOR activity on account of their favorable alloying extent, Pt *d*-band vacancy, and Pt electrochemical active surface area (ECASA). In another work, we also studied ORR on Pt_x-Fe_{1-x} nanoparticles with various Pt:Fe atomic compositions (3:1, 1:1, and 1:3) and found that Pt₁Fe₁ nanocatalyst showed a greater enhancement in ORR than Pt/C. The higher alloying extent of platinum coupled with promising electronic structure offered by the lower Pt *d*-band vacancies was given as the reason for the enhanced ORR activity [63]. Stamenkovic et al. observed that the arrangement of surface atoms in the near-surface region of a Pt₃Ni (111) surface drastically improves its catalytic activity toward ORR [21]. From the crystal truncation rod (CTR) experiments, they showed that the first layer entirely consists of Pt, whereas the second layer was Ni-rich with 52 % Ni and the third layer is Pt-enriched with a Pt content of 87 %. With this surface configuration, the Pt₃Ni(111)

surface exhibited 10 times higher mass activity toward ORR when compared to Pt(111) surfaces and 90 times higher ORR activity than the current state-of-the-art Pt/C catalysts in 0.1 M HClO₄ solutions. Further the authors showed that different low-index Pt₃Ni surfaces exhibited different ORR activities with the order, Pt₃Ni(100)-skin < Pt₃Ni(110)-skin < Pt₃Ni(111)-skin [21]. The authors pointed out that the observed differences in the ORR activities of three low-indexed planes of Pt₃Ni were attributable to the variations in *d*-band center and surface atomic arrangement of platinum and decreased coverage of nonreactive oxygenated species (OH_{ads}), due to the incorporation of Ni atoms. These results suggested that surface engineering strategies offer a big help in fine-tuning the electrocatalytic activity of bimetallic nanoparticles.

Morphological Effects

In recent years, morphology-controlled synthesis of various Pt-based catalysts with shapes such as nanodendrites, polyhedral, hollow structures, and core-shell has been explored for fuel cell reactions. It was reported that different crystallographic facets stabilized on particles with different shapes exhibit different reactivities and selectivities [227, 228]. Commonly found low-index planes or facets on single-crystal surfaces of bulk Pt appear to possess lower reactivity than the high-index planes. Armed with high density of atomic steps, ledges, and kinks, which usually serve as active sites for breaking chemical bonds, the high-index planes exhibit much higher catalytic activity. Sun and coworkers developed a novel electrochemical approach to prepare tetrahedral (THH) Pt nanocrystals (NCs) with high-index facets on glass carbon substrates [19]. The THH Pt nanocrystals developed in this study exhibited much enhanced catalytic activity per unit surface compared to the other Pt morphologies like Pt-nanospheres and commercial Pt/C catalysts for the oxidation of formic acid and ethanol which are considered to be promising alternative fuels for direct fuel cells. The enhanced catalytic activity was attributed to the higher extent of stepped atoms on the surface of THH Pt NCs. In a recent study, Kim et al. reported the synthesis protocol for heterogeneous bimetallic nanocrystals consisting of Pt multibranches on Au nanocrystal cores with well-defined morphologies (cubes, rods, and octahedral) [229]. The authors showed the TEM and HRTEM images of the formation of Pt-islands on various Au morphologies (Fig. 15). The ORR activity of Au@Pt heteronanostructures with various morphologies recorded in O₂-saturated 0.1 M HClO₄ solutions showed that at 0.8 V versus RHE, the mass activities follows the order: Au_{cube}@Pt < Au_{rod}@Pt < Au_{octahedron}@Pt. The higher electrocatalytic activity observed in the case of Au_{octahedron}@Pt was attributed to its (111)-orientation-rich Pt surface. The above examples illustrate that specific facets of metallic component along with its shape play a crucial role in determining the electrocatalytic activity.

Size Effects

Substantial efforts have been directed to the investigation of the influence of particle size on the catalytic activity after the breakthrough experiments of Haruta et al. on Au nanoparticles [230]. Park et al. [231] demonstrated the electrooxidation of

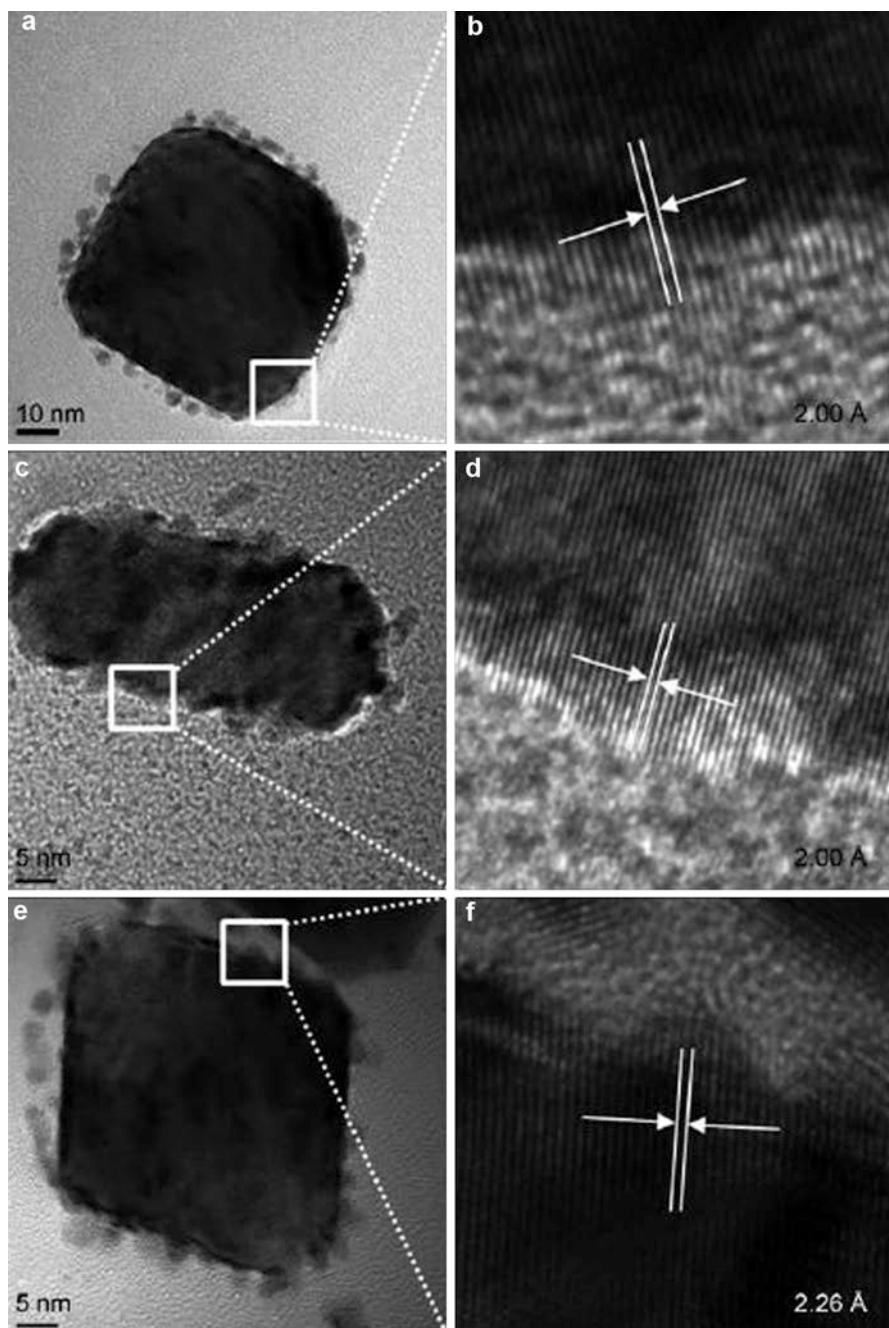


Fig. 15 Left and right panels features low- and high-magnification TEM images, respectively, of (a, b) Au_{cube}@Pt, (c, d) Au_{rod}@Pt, and (e, f) Au_{octahedron}@Pt nanoparticles (Reproduced with permission from ref. [229], © 2010 Wiley – VCH Verlag GmbH & Co. KGaA)

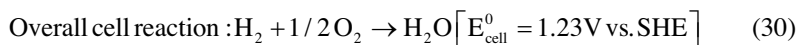
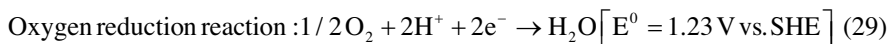
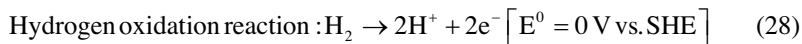
formic acid, formaldehyde, and methanol in acidic environment on Pt/C nanoparticles with the varying particle diameters in the range of 2–9 nm. Authors carried out electrooxidation of formic acid, formaldehyde, and methanol in acidic electrolyte on Pt/C nanoparticles with varying particle diameters in the range of 2–9 nm. From the voltammetry and infrared spectroscopy measurements, the authors found size-dependent chemisorption of CO formed from three reactants. The observed rates of methanol electrooxidation decrease for Pt nanoparticle diameters below 4 nm. In contrast, the rate of formic acid electrooxidation increases for Pt nanoparticle diameters above 4 nm. Different roles played by Pt ensemble effect were given as the reason for the observed size-dependent CO chemisorptions and corresponding CO₂ production. The rate of formaldehyde electrooxidation found little sensitivity to the Pt size. Yamamoto and coworkers investigated size-specific catalytic activity of Pt clusters synthesized in G-3 dendrimers toward oxygen reduction reaction [5]. Three kinds of Pt_n@3 (n = 12, 28, 60) clusters, viz., Pt₁₂@3 (particle size = 0.9 ± 0.1 nm), Pt₂₈@3 (particle size = 1.0 ± 0.1 nm), and Pt₆₀@3 (particle size = 1.2 ± 0.1 nm) were synthesized. Authors found smallest cluster Pt₁₂@3 exhibited 13 times higher ORR activity than that of commercial Pt/C catalyst. Sun's group studied the particle size and catalytic activity relationship of Co₆₀Pd₄₀ nanoparticles toward formic acid oxidation [232]. The authors observed that the catalytic activity of Co₆₀Pd₄₀ nanoparticles for formic acid oxidation increases with the decrease in particle size.

Atomic Distribution/Alloying Extent

In bimetallic nanoparticles, the atomic distribution between two different metals and the degree of alloying play significant role in catalyst activity [10, 20, 24, 63, 233]. In our group, X-ray absorption spectroscopy methods were developed to determine the atomic distribution in bimetallic nanoparticles [20]. By collecting the XAS data at the Pt and Ru absorption edges of two commercial PtRu catalysts, the extent of intermixing of Pt and Ru (alloying extent) and Pt and Ru atom distribution was determined. The extent of both Pt and Ru alloying was found to be higher in commercial Johnson Matthey PtRu catalyst than with commercial E-TEK PtRu catalyst, which was reflected in higher methanol electrooxidation activity. In another study, we observed enhanced ORR activities in bimetallic PtFe catalysts with higher extent of platinum and iron alloying [63].

Hydrogen Fuel Cells

Proton exchange membrane fuel cells (PEMFCs) powered by hydrogen from secure and renewable sources are considered to be a promising energy source for various applications [234–237]. In a typical H₂-fed PEMFC, hydrogen is oxidized on an anode leaving protons and electrons. The protons generated at anode travel through the proton exchange membrane to the cathode where they react with oxygen to form water. The overall electrochemical reaction between hydrogen and oxygen to form water gives a theoretical potential of 1.23 V versus SHE at room temperature. The principal reactions are shown in Eqs. 28, 29, and 30:



Pt is the best-known material for the hydrogen oxidation. However, CO present even in trace quantities will impede hydrogen adsorption on Pt surfaces and decreases its rate of oxidation popularly known as CO-poisoning effect. Experiments illustrate that CO oxidation on bimetallic Pt–M-based electrodes, where M is a promoter metal (e.g., Ru), occurs at potentials lower than that of a pure Pt electrode [238]. The enhanced CO oxidation on such Pt–M formulations may be achieved by two metals working synergistically as explained by the so-called bifunctional (or) reactant pair mechanism. Higher PEMFC performance was reported on PtRu bimetallic nanoparticles for fuel streams containing CO [239, 240]. The development of bimetallic electrocatalysts helps in the reduction of Pt loadings as well as CO tolerance of the anode. In the case of bimetallic catalysts, strong interaction of participating components is required. It was reported that the catalytic performance of PtRu nanoparticles is strongly dependent on the distribution of Pt and Ru sites at the atomic level and believed to be sensitive to the particle's shape and size and to the nature of the support. In the past few years, our research group has actively worked on developing suitable electrocatalysts for both CO oxidation and oxygen reduction reactions for fuel cell applications by focusing on size, structure, and atomic distribution manipulation strategies [24, 26, 27, 130, 168, 241, 242]. In a recent study by studying the stepwise formation mechanism employing X-ray absorption spectroscopy, we established a structure-controllable synthesis strategy based on a modified Watanabe's process for bimetallic PtRu/C nanoparticles [27]. With this methodology, PtRu/C NPs with a particle size of about 2.9 nm were conveniently achieved.

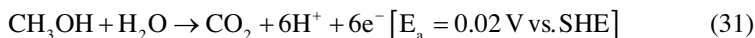
Many other bimetallic electrocatalysts such as PtMo [154, 243–248], PtSn [249, 250] PtPd [251–253], and Pt–Co [254] have been successfully explored for CO-tolerant HOR. In most cases, electrocatalyst particles were dispersed on conductive supports of high surface area. The support for the catalyst nanoparticles turns out to be a major factor in influencing their dispersion and stability. Characteristics such as electrical conductivity, surface area, hydrophobicity, morphology, porosity, and corrosion resistance are most considered in the choice of a good catalyst support. Based on these considerations, carbon is the best catalyst support material for PEMFC electrocatalysts. Carbon black and activated carbons have been extensively studied as catalyst supports, with Vulcan 72 being the most representative. In the last decade, a number of new synthetic carbons with various mesostructures and nanostructures have been reported. These include carbon nanotubes [254], aerogel carbon [255, 256], and meso-carbon [257] with or without a high degree of order. With the developments in attaining high performance bimetallic electrocatalysts and high

surface area carbon supports, bottlenecks such as higher catalyst loadings and costs associated with fuel cell technology were nearly resolved.

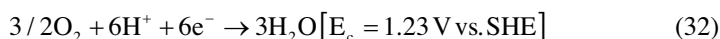
Methanol Fuel Cells

Direct methanol fuel cells (DMFCs) are advantageous over H₂-fed PEMFCs due to easy fuel transportation, energy storage, and high-energy conversion efficiency and are found as promising power sources for electric vehicles and portable devices [258, 259]. In a typical DMFC, methanol and water molecules are simultaneously electro-oxidized at the anode to produce CO₂, electrons, and protons called as methanol oxidation reaction (MOR). Protons generated at the anode pass through the proton exchange membrane to cathode where they combine with electrons and the oxidant air or oxygen simultaneously reducing to water called as oxygen reduction reaction (ORR). The principal reactions involved in DMFCs are show in Eqs. 31, 32, and 33:

Methanol oxidation reaction:



Oxygen reduction reaction:



Overall cell reaction:



Pt is the best material for the adsorption and dehydrogenation of methanol. However, the formation of intermediate species such as CO, formic acid, and formaldehyde poisons the platinum anode and critically lowers the performance. During methanol oxidation, the efficient catalyst should allow a complete oxidation to CO₂. Presently, carbon-supported PtRu catalysts have been shown to be the best candidates for electrochemical oxidation of methanol [74, 260]. Many studies confirm that Ru could produce OH_{ads} species at lower potential to react with adsorbed intermediates on neighboring Pt sites [260–263]. Furthermore, the presence of Ru can induce variations in the electronic structure of Pt. This electronic or ligand effect enhances methanol dehydrogenation on Pt and facilitates weakening of Pt–CO bond, and thus an easy removal of poisoned CO on Pt is expected.

Many other bimetallic Pt-based nanocatalysts have been explored as low cost alternatives to PtRu catalysts for MOR. For example, alloys of Pt with Fe [264], Ni [265], Co [266], Mo [154, 247], Sn [267, 268], Pb [269], V [270], or Ir [271] show promise in generating OH_{ads} at lower potentials than Pt with improved activity toward MOR. In most cases, catalytic nanoparticles were dispersed on high surface carbon structures. The advantage of using a supported metal catalyst lies in the possibility to reduce the metal loadings drastically. The development in highly

CO-resistant Pt-based bimetallic nanoparticles as electrocatalysts for MOR is a big help in making DMFC a viable power-generating technology. However, significant improvements are still required in increasing the durability of bimetallic Pt-based catalysts for the widespread implementation of DMFCs.

Electrochemical Oxidation of Formic Acid

Formic acid-based direct formic acid fuel cells (DFAFCs) are another attractive power source for portable electronic applications due to their promising energy densities, power system simplicities, and the convenient storage and transport of liquid formic acid [272, 273]. Further, DFAFCs claim lower fuel crossover than DMFCs due to the repulsive nature of formate ions with sulfuric acid groups of the Nafion membrane so that higher concentrations of formic acid can be used to get the higher energy density of the cell [274]. On conventional platinum surfaces, formic acid is electrooxidized directly to produce CO₂ (dehydrogenation path), or it may leave adsorbed CO species (dehydration pathway) as shown below:



Although pure Pt can be easily poisoned by adsorbed CO species, one tactic to improve its activity is to form bimetallic Pt-based catalysts. Many efforts have been made to enhance the oxidation rates of formic acid by developing PtAu [223, 274–277], PtPd [278, 279], PtFe [280], PtBi [273, 281, 282], PtAg [283], Pt–Co [284], and PtSb [285] bimetallic catalysts. Pt-based bimetallic catalysts display improved catalytic activity toward formic acid as a result of the ensemble effect. According to this, at least two ensembling binding Pt sites are required for the dissociative adsorption of formic acid to CO. However, the direct oxidation of formic acid via dehydration pathway does not require the same Pt atom ensemble [231, 286].

In recent years, much interest has been focused on the development of PtAu bimetallic nanoparticles as electrocatalysts for formic acid electrooxidation. The addition of Au to Pt promises the enhancement of formic acid oxidation kinetics by operating a combined ensemble and electronic effect which helps in diminishing the CO_{ads} formation and increasing the intrinsic activity, respectively [219]. Further, Au is believed to promote the first electron transfer during the direct dehydrogenation process of formic acid oxidation which generates HCOO_{ads} species on Au [287–289]. If Pt is around Au, efficient spillover of HCOO_{ads} from Au to the neighboring Pt occurs, which is further oxidized to CO₂ [223]. Various carbon-based supports have been utilized for the purpose of depositing Pt-based bimetallic nanoparticles, including carbon [290], carbon nanotubes [291], carbon nanofibers [276], and graphene [275], which have led to improved kinetics during formic acid electrooxidation. It was widely demonstrated that the use of formic acid as a fuel is more

advantageous than hydrogen and methanol due to its low-temperature operation, storage, and convenient transport.

Conclusions and Future Perspective

In conclusion, the content reviewed here underscores the importance of understanding the formation of bimetallic nanoparticles in particle design and in establishing structure-controllable synthesis methodologies and scaling-up processes. X-ray absorption spectroscopy has a striking advantage in revealing the underlying chemistry involved in the nucleation and growth process of bimetallic nanoparticles. Further, XAS can be utilized to follow the formation of alloy and core-shell structures which are believed to influence bimetallic nanoparticles electrocatalytic activities toward fuel cell reactions. In addition, the capabilities of XAS can be used to provide atomic level information on alloying extent and atomic distribution. So far, significant developments have been made in the bimetallic nanoparticle synthesis with achievements such as synthesizing more complicated structures with an easy control over composition, size, and morphology. The relationship between the catalytic activity and the selectivity of bimetallic nanoparticles with their structural characteristics in fuel cell reactions such as the methanol oxidation reaction, oxygen reduction reaction, and formic acid oxidation reactions has been discussed. Key influencing factors including surface structure, composition, size, and morphology have been investigated by many researchers. These studies strengthen our fundamental understanding of bimetallic catalysis and the rational selection of novel materials for power-generating devices such as fuel cells. Although great progress has been made in bimetallic nanoparticle research, the common challenges of achieving long-lasting, highly active, selective, and environmentally benign bimetallic nanoparticles are still remain. A promising hope is that by systematically minimizing the experimental trial-and-error strategies by integrating theoretical and practical approaches, great strides in the development bimetallic nanoparticle-linked catalysis can be expected.

Acknowledgments Financial support from the National Science Council (NSC) (101-3113-E-011-002, 101-2923-E-011-001-MY3, 100-2221-E-011-105-MY3), the Ministry of Economic Affairs (MOEA) (101-EC-17-A-08-S1-183), and the Top University Projects of Ministry of Education (MOE) (100H451401) and the facilities' supports from the National Taiwan University of Science and Technology (NTUST) and the National Synchrotron Radiation Research Center (NSRRC) are gratefully acknowledged.

References

1. Roduner E (2006) Size matters: why nanomaterials are different. *Chem Soc Rev* 35(7):583–592
2. Jortner J (1992) Cluster size effects. *Z Phys D: At Mol Clusters* 24(3):247–275
3. Valden M, Lai X, Goodman DW (1998) Onset of catalytic activity of gold clusters on Titania with the appearance of nonmetallic properties. *Science* 281(5383):1647–1650
4. Valden M, Pak S, Lai X, Goodman DW (1998) Structure sensitivity of CO oxidation over model Au/TiO₂ 2 catalysts. *Catal Lett* 56(1):7–10

5. Yamamoto K, Imaoka T, Chun W-J, Enoki O, Katoh H, Takenaga M, Sonoi A (2009) Size-specific catalytic activity of platinum clusters enhances oxygen reduction reactions. *Nat Chem* 1(5):397–402
6. Saida T, Ogiwara N, Takasu Y, Sugimoto W (2010) Titanium oxide nanosheet modified PtRu/C electrocatalyst for direct methanol fuel cell anodes. *J Phys Chem C* 114(31):13390–13396
7. Cherstiouk OV, Simonov PA, Savinova ER (2003) Model approach to evaluate particle size effects in electrocatalysis: preparation and properties of Pt nanoparticles supported on GC and HOPG. *Electrochim Acta* 48(25–26):3851–3860
8. Mukerjee S, McBreen J (1998) Effect of particle size on the electrocatalysis by carbon-supported Pt electrocatalysts: an in situ XAS investigation I. *J Electroanal Chem* 448(2):163–171
9. Taufany F, Pan C-J, Rick J, Chou H-L, Tsai M-C, Hwang B-J, Liu D-G, Lee J-F, Tang M-T, Lee Y-C, Chen C-I (2011) Kinetically controlled autocatalytic chemical process for bulk production of bimetallic core-shell structured nanoparticles. *ACS Nano* 5(12):9370–9381
10. Lai F-J, Sarma LS, Chou H-L, Liu D-G, Hsieh C-A, Lee J-F, Hwang B-J (2009) Architecture of bimetallic Pt_xCo_{1-x} electrocatalysts for oxygen reduction reaction as investigated by X-ray absorption spectroscopy. *J Phys Chem C* 113(29):12674–12681
11. Koffi RC, Coutanceau C, Garnier E, Léger JM, Lamy C (2005) Synthesis, characterization and electrocatalytic behaviour of non-alloyed PtCr methanol tolerant nanoelectrocatalysts for the oxygen reduction reaction (ORR). *Electrochim Acta* 50(20):4117–4127
12. Chen C-H, Sarma LS, Wang D-Y, Lai F-J, AlAndra C-C, Chang S-H, Liu D-G, Chen C-C, Lee J-F, Hwang B-J (2010) Platinum-decorated ruthenium nanoparticles for enhanced methanol electrooxidation. *ChemCatChem* 2(2):159–166
13. Xu CW, Wang H, Shen PK, Jiang SP (2007) Highly ordered Pd nanowire arrays as effective electrocatalysts for ethanol oxidation in direct alcohol fuel cells. *Adv Mater* 19(23):4256–4259
14. Wang C, Daimon H, Onodera T, Koda T, Sun S (2008) A general approach to the size- and shape-controlled synthesis of platinum nanoparticles and their catalytic reduction of oxygen. *Angew Chem Int Ed* 47(19):3588–3591
15. Mayrhofer KJJ, Juhart V, Hartl K, Hanzlik M, Arenz M (2009) Adsorbate-induced surface segregation for core-shell nanocatalysts. *Angew Chem Int Ed* 48(19):3529–3531
16. Cheng F, Wang H, Sun Z, Ning M, Cai Z, Zhang M (2008) Electrodeposited fabrication of highly ordered Pd nanowire arrays for alcohol electrooxidation. *Electrochem Commun* 10(5):798–801
17. Zhang S, Shao Y, Liao H-G, Liu J, Aksay IA, Yin G, Lin Y (2011) Graphene decorated with PtAu alloy nanoparticles: facile synthesis and promising application for formic acid oxidation. *Chem Mater* 23(5):1079–1081
18. Sun S, Zhang G, Geng D, Chen Y, Li R, Cai M, Sun X (2011) A highly durable platinum nanocatalyst for proton exchange membrane fuel cells: multiarmed starlike nanowire single crystal. *Angew Chem Int Ed* 50(2):422–426
19. Tian N, Zhou Z-Y, Sun S-G, Ding Y, Wang ZL (2007) Synthesis of tetrahedral platinum nanocrystals with high-index facets and high electro-oxidation activity. *Science* 316(5825):732–735
20. Hwang B-J, Sarma LS, Chen J-M, Chen C-H, Shih S-C, Wang G-R, Liu D-G, Lee J-F, Tang M-T (2005) Structural models and atomic distribution of bimetallic nanoparticles as investigated by X-ray absorption spectroscopy. *J Am Chem Soc* 127(31):11140–11145
21. Stamenkovic VR, Fowler B, Mun BS, Wang G, Ross PN, Lucas CA, Marković NM (2007) Improved oxygen reduction activity on Pt₃Ni(111) via increased surface site availability. *Science* 315(5811):493–497
22. Cuenya BR (2010) Synthesis and catalytic properties of metal nanoparticles: size, shape, support, composition, and oxidation state effects. *Thin Solid Films* 518(12):3127–3150
23. Taufany F, Pan C-J, Rick J, Chou H-L, Tsai M-C, Hwang B-J, Liu D-G, Lee J-F, Tang M-T, Lee Y-C, Chen C-I (2011) Kinetically controlled autocatalytic chemical process for bulk production of bimetallic core-shell structured nanoparticles. *ACS Nano* 5(12):9370–9381

24. Hwang BJ, Senthil Kumar SM, Chen C-H, Chang R-W, Liu D-G, Lee J-F (2008) Size and alloying extent dependent physicochemical properties of Pt–Ag/C nanoparticles synthesized by the ethylene glycol method. *J Phys Chem C* 112(7):2370–2377
25. Chen C-H, Sarma LS, Chen J-M, Shih S-C, Wang G-R, Liu D-G, Tang M-T, Lee J-F, Hwang B-J (2007) Architecture of Pd–Au bimetallic nanoparticles in sodium bis(2-ethylhexyl)sulfosuccinate reverse micelles as investigated by X-ray absorption spectroscopy. *ACS Nano* 1(2):114–125
26. Sarma LS, Chen C-H, Kumar SMS, Wang G-R, Yen S-C, Liu D-G, Sheu H-S, Yu K-L, Tang M-T, Lee J-F, Bock C, Chen K-H, Hwang B-J (2007) Formation of Pt–Ru nanoparticles in ethylene glycol solution: an in situ X-ray absorption spectroscopy study. *Langmuir* 23(10):5802–5809
27. Hwang BJ, Chen C-H, Sarma LS, Chen J-M, Wang G-R, Tang M-T, Liu D-G, Lee J-F (2006) Probing the formation mechanism and chemical states of carbon-supported Pt–Ru nanoparticles by in situ X-ray absorption spectroscopy. *J Phys Chem B* 110(13):6475–6482
28. Chen C-H, Sarma LS, Wang G-R, Chen J-M, Shih S-C, Tang M-T, Liu D-G, Lee J-F, Chen J-M, Hwang B-J (2006) Formation of bimetallic Ag–Pd nanoclusters via the reaction between Ag nanoclusters and Pd²⁺ ions. *J Phys Chem B* 110(21):10287–10295
29. Chen C-H, Hwang B-J, Wang G-R, Sarma LS, Tang M-T, Liu D-G, Lee J-F (2005) Nucleation and growth mechanism of Pd/Pt bimetallic clusters in sodium bis(2-ethylhexyl)sulfosuccinate (AOT) reverse micelles as studied by in situ X-ray absorption spectroscopy. *J Phys Chem B* 109(46):21566–21575
30. Tsai YW, Tseng YL, Sarma LS, Liu DG, Lee JF, Hwang BJ (2004) Genesis of Pt clusters in reverse micelles investigated by in situ X-ray absorption spectroscopy. *J Phys Chem B* 108(24):8148–8152
31. Hwang B-J, Tsai Y-W, Sarma LS, Tseng Y-L, Liu D-G, Lee J-F (2004) Genesis of bimetallic Pt–Cu clusters in reverse micelles investigated by in situ X-ray absorption spectroscopy. *J Phys Chem B* 108(52):20427–20434
32. Yu W, Porosoff MD, Chen JG (2012) Review of Pt-based bimetallic catalysis: from model surfaces to supported catalysts. *Chem Rev* 112(11):5780–5817
33. Liu X, Li X, Wang D, Yu R, Cui Y, Peng Q, Li Y (2012) Palladium/tin bimetallic single-crystalline hollow nanospheres. *Chem Commun* 48(11):1683–1685
34. Tao F, Grass ME, Zhang Y, Butcher DR, Renzas JR, Liu Z, Chung JY, Mun BS, Salmeron M, Somorjai GA (2008) Reaction-driven restructuring of Rh-Pd and Pt-Pd core-shell nanoparticles. *Science* 322(5903):932–934
35. Lim B, Jiang M, Camargo PHC, Cho EC, Tao J, Lu X, Zhu Y, Xia Y (2009) Pd-Pt bimetallic nanodendrites with high activity for oxygen reduction. *Science* 324(5932):1302–1305
36. González E, Arbiol J, Puntes VF (2011) Carving at the nanoscale: sequential galvanic exchange and Kirkendall growth at room temperature. *Science* 334(6061):1377–1380
37. Gasteiger HA, Kocha SS, Sompalli B, Wagner FT (2005) Activity benchmarks and requirements for Pt, Pt-alloy, and non-Pt oxygen reduction catalysts for PEMFCs. *Appl Catal B Environ* 56(1–2):9–35
38. Norskov JK, Bligaard T, Rossmeisl J, Christensen CH (2009) Towards the computational design of solid catalysts. *Nat Chem* 1(1):37–46
39. Wagner FT, Lakshmanan B, Mathias MF (2010) Electrochemistry and the future of the automobile. *J Phys Chem Lett* 1(14):2204–2219
40. Greeley J, Stephens IEL, Bondarenko AS, Johansson TP, Hansen HA, Jaramillo TF, Rossmeisl J, Chorkendorff I, Nørskov JK (2009) Alloys of platinum and early transition metals as oxygen reduction electrocatalysts. *Nat Chem* 1(7):552–556
41. Chen A, Holt-Hindle P (2010) Platinum-based nanostructured materials: synthesis, properties, and applications. *Chem Rev* 110(6):3767–3804
42. Debe MK (2012) Electrocatalyst approaches and challenges for automotive fuel cells. *Nature* 486(7401):43–51
43. Lamy C, Lima A, LeRhun V, Delime F, Coutanceau C, Léger J-M (2002) Recent advances in the development of direct alcohol fuel cells (DAFC). *J Power Sources* 105(2):283–296
44. Marković NM, Schmidt TJ, Stamenković V, Ross PN (2001) Oxygen reduction reaction on Pt and Pt bimetallic surfaces: a selective review. *Fuel Cells* 1(2):105–116

45. Gasteiger HA, Markovic N, Ross PN, Cairns E (1994) *J Electrochim Acta* 39:1825
46. Marković NM, Ross PN Jr (2002) Surface science studies of model fuel cell electrocatalysts. *Surf Sci Rep* 45(4–6):117–229
47. Toda T, Igarashi H, Uchida H, Watanabe M (1999) Enhancement of the electroreduction of oxygen on Pt alloys with Fe, Ni, and Co. *J Electrochem Soc* 146(10):3750–3756
48. Oetjen HF, Schmidt VM, Stimming U, Trila F (1996) Performance data of a proton exchange membrane fuel cell using H₂/CO as fuel gas. *J Electrochem Soc* 143(12):3838–3842
49. Beden BLC, Leger J-M (1992) *Modern aspects of electrochemistry*. Plenum Press, New York, 97
50. Adžić RR, Wang JX (1998) Configuration and site of O₂ adsorption on the Pt(111) electrode surface. *J Phys Chem B* 102(45):8988–8993
51. Shukla AK, Raman RK (2003) Methanol-resistant oxygen-reduction catalysts for direct methanol fuel cells. *Annu Rev Mater Res* 33(1):155–168
52. Damjanovic A, Brusic V (1967) Electrode kinetics of oxygen reduction on oxide-free platinum electrodes. *Electrochim Acta* 12(6):615–628
53. Ticanelli E, Beery JG, Paffett MT, Gottesfeld S (1989) An electrochemical, ellipsometric, and surface science investigation of the PtRu bulk alloy surface. *J Electroanal Chem Interfacial Electrochem* 258(1):61–77
54. Frelink T, Visscher W, van Veen JAR (1995) On the role of Ru and Sn as promoters of methanol electro-oxidation over Pt. *Surf Sci* 335:353–360
55. Watanabe M, Motoo S (1975) Electrocatalysis by ad-atoms: part II. Enhancement of the oxidation of methanol on platinum by ruthenium ad-atoms. *J Electroanal Chem Interfacial Electrochem* 60(3):267–273
56. Davies JC, Hayden BE, Pegg DJ (1998) The electrooxidation of carbon monoxide on ruthenium modified Pt(110). *Electrochim Acta* 44(6–7):1181–1190
57. Maroun F, Ozanam F, Magnussen OM, Behm RJ (2001) The role of atomic ensembles in the reactivity of bimetallic electrocatalysts. *Science* 293(5536):1811–1814
58. Gasteiger HA, Markovic N, Ross PN, Cairns EJ (1993) Methanol electrooxidation on well-characterized platinum-ruthenium bulk alloys. *J Phys Chem* 97(46):12020–12029
59. Jiang X, Parmeter JE, Estrada CA, Goodman DW (1991) The adsorption and decomposition of methanol on copper overlayers on the Rh(100) surface. *Surf Sci* 249(1–3):44–60
60. Goodenough JB, Manoharan R, Shukla AK, Ramesh KV (1989) Intraalloy electron transfer and catalyst performance: a spectroscopic and electrochemical study. *Chem Mater* 1(4):391–398
61. Goodenough JB, Hamnett A, Kennedy BJ, Manoharan R, Weeks SA (1988) Methanol oxidation on unsupported and carbon supported Pt + Ru anodes. *J Electroanal Chem Interfacial Electrochem* 240(1–2):133–145
62. Bertolini JC (1996) Local order at the surface of binary alloys in relation to their chemical reactivity. *Surf Rev Lett* 03(05n06):1857–1868
63. Lai F-J, Chou H-L, Sarma LS, Wang D-Y, Lin Y-C, Lee J-F, Hwang B-J, Chen C-C (2010) Tunable properties of Pt_xFe_{1-x} electrocatalysts and their catalytic activity towards the oxygen reduction reaction. *Nanoscale* 2(4):573–581
64. Lisiecki I (2005) Size, shape, and structural control of metallic nanocrystals. *J Phys Chem B* 109(25):12231–12244
65. Gasteiger HA, Markovic N, Ross PN, Cairns EJ (1994) Carbon monoxide electrooxidation on well-characterized platinum-ruthenium alloys. *J Phys Chem* 98(2):617–625
66. Markovic NM, Gasteiger HA, Ross PN (1995) Oxygen reduction on platinum low-index single-crystal surfaces in sulfuric acid Solution: rotating ring-Pt(hkl) disk studies. *J Phys Chem* 99(11):3411–3415
67. Alexandridis P, Holzwarth JF, Hatton TA (1995) Thermodynamics of droplet clustering in percolating AOT water-in-oil microemulsions. *J Phys Chem* 99(20):8222–8232
68. Lin WF, Iwasita T, Vielstich W (1999) Catalysis of CO electrooxidation at Pt, Ru, and PtRu alloy. An in situ FTIR study. *J Phys Chem B* 103(16):3250–3257

69. Park S, Wieckowski A, Weaver MJ (2003) Electrochemical infrared characterization of CO domains on ruthenium-decorated platinum nanoparticles. *J Am Chem Soc* 125(8): 2282–2290
70. Paulus UA, Wokaun A, Scherer GG, Schmidt TJ, Stamenkovic V, Radmilovic V, Markovic NM, Ross PN (2002) Oxygen reduction on carbon-supported Pt–Ni and Pt–Co alloy catalysts. *J Phys Chem B* 106(16):4181–4191
71. Stamenković V, Schmidt TJ, Ross PN, Marković NM (2003) Surface segregation effects in electrocatalysis: kinetics of oxygen reduction reaction on polycrystalline Pt₃Ni alloy surfaces. *J Electroanal Chem* 554–555:191–199
72. Gupta G, Slanac DA, Kumar P, Wiggins-Camacho JD, Wang X, Swinnea S, More KL, Dai S, Stevenson KJ, Johnston KP (2009) Highly stable and active Pt–Cu oxygen reduction electrocatalysts based on mesoporous graphitic carbon supports. *Chem Mater* 21(19):4515–4526
73. Peng Z, Yang H (2009) Synthesis and oxygen reduction electrocatalytic property of Pt-on-Pd bimetallic heteronanostructures. *J Am Chem Soc* 131(22):7542–7543
74. Sarma LS, Lin TD, Tsai Y-W, Chen JM, Hwang BJ (2005) Carbon-supported Pt–Ru catalysts prepared by the Nafion stabilized alcohol-reduction method for application in direct methanol fuel cells. *J Power Sources* 139(1–2):44–54
75. Kim J, Lee Y, Sun S (2010) Structurally ordered FePt nanoparticles and their enhanced catalysis for oxygen reduction reaction. *J Am Chem Soc* 132(14):4996–4997
76. Lee K-S, Jeon T-Y, Yoo SJ, Park I-S, Cho Y-H, Kang SH, Choi KH, Sung Y-E (2011) Effect of PtRu alloying degree on electrocatalytic activities and stabilities. *Appl Catal B Environ* 102(1–2):334–342
77. Lee W-R, Kim MG, Choi J-R, Park J-I, Ko SJ, Oh SJ, Cheon J (2005) Redox–transmetalation process as a generalized synthetic strategy for core–shell magnetic nanoparticles. *J Am Chem Soc* 127(46):16090–16097
78. Park J-I, Kim MG, Jun Y-W, Lee JS, Lee W-R, Cheon J (2004) Characterization of superparamagnetic “core–shell” nanoparticles and monitoring their anisotropic phase transition to ferromagnetic “solid solution” nanoalloys. *J Am Chem Soc* 126(29):9072–9078
79. Park J-I, Cheon J (2001) Synthesis of “solid solution” and “core–shell” type cobalt–platinum magnetic nanoparticles via transmetalation reactions. *J Am Chem Soc* 123(24):5743–5746
80. Harpeness R, Gedanken A (2004) Microwave synthesis of core–shell gold/palladium bimetallic nanoparticles. *Langmuir* 20(8):3431–3434
81. Nath S, Praharaj S, Panigrahi S, Ghosh SK, Kundu S, Basu S, Pal T (2005) Synthesis and characterization of N,N-dimethyldodecylamine-capped Au core-Pd shell nanoparticles in toluene. *Langmuir* 21(23):10405–10408
82. Srnová-Šloufová I, Vlčková B, Bastl Z, Hasslett TL (2004) Bimetallic (Ag)Au nanoparticles prepared by the seed growth method: two-dimensional assembling, characterization by energy dispersive X-ray analysis, X-ray photoelectron spectroscopy, and surface enhanced raman spectroscopy, and proposed mechanism of growth. *Langmuir* 20(8):3407–3415
83. Huang X, Tang S, Liu B, Ren B, Zheng N (2011) Enhancing the photothermal stability of plasmonic metal nanoplates by a core-shell architecture. *Adv Mater* 23(30):3420–3425
84. Zeng J, Yang J, Lee JY, Zhou W (2006) Preparation of carbon-supported core–shell Au–Pt nanoparticles for methanol oxidation reaction: the promotional effect of the Au core. *J Phys Chem B* 110(48):24606–24611
85. Hwang B-J, Sarma LS, Chen C-H, Bock C, Lai F-J, Chang S-H, Yen S-C, Liu D-G, Sheu H-S, Lee J-F (2008) Controlled synthesis and characterization of Ru core–Pt shell bimetallic nanoparticles. *J Phys Chem C* 112(50):19922–19929
86. Adzic RR, Zhang J, Sasaki K, Vukmirovic MB, Shao M, Wang JX, Nilekar AU, Mavrikakis M, Valerio JA, Uribe F (2007) *Top Catal* 46:249
87. Zhang J, Lima FHB, Shao MH, Sasaki K, Wang JX, Hanson J, Adzic RR (2005) Platinum monolayer on nonnoble metal–noble metal core–shell nanoparticle electrocatalysts for O₂ reduction. *J Phys Chem B* 109(48):22701–22704

88. Zhang J, Vukmirovic MB, Xu Y, Mavrikakis M, Adzic RR (2005) Controlling the catalytic activity of platinum-monolayer electrocatalysts for oxygen reduction with different substrates. *Angew Chem Int Ed* 44(14):2132–2135
89. Zhang J, Mo Y, Vukmirovic MB, Klie R, Sasaki K, Adzic RR (2004) Platinum monolayer electrocatalysts for O₂ reduction: Pt monolayer on Pd(111) and on carbon-supported Pd nanoparticles. *J Phys Chem B* 108(30):10955–10964
90. Sun Y, Xia Y (2004) Mechanistic study on the replacement reaction between silver nanostructures and chloroauric acid in aqueous medium. *J Am Chem Soc* 126(12):3892–3901
91. Chen J, Wiley B, McLellan J, Xiong Y, Li Z-Y, Xia Y (2005) Optical properties of Pd–Ag and Pt–Ag nanoboxes synthesized via galvanic replacement reactions. *Nano Lett* 5(10):2058–2062
92. Chen J, McLellan JM, Siekkinen A, Xiong Y, Li Z-Y, Xia Y (2006) Facile synthesis of gold–silver nanocages with controllable pores on the surface. *J Am Chem Soc* 128(46):14776–14777
93. Graf C, van Blaaderen A (2001) Metallo-dielectric colloidal core–shell particles for photonic applications. *Langmuir* 18(2):524–534
94. Lu L, Sun G, Xi S, Wang H, Zhang H, Wang T, Zhou X (2003) A colloidal templating method to hollow bimetallic nanostructures. *Langmuir* 19(7):3074–3077
95. Kim S-W, Kim M, Lee WY, Hyeon T (2002) Fabrication of hollow palladium spheres and their successful application to the recyclable heterogeneous catalyst for Suzuki coupling reactions. *J Am Chem Soc* 124(26):7642–7643
96. Mayers B, Jiang X, Sunderland D, Cattle B, Xia Y (2003) Hollow nanostructures of platinum with controllable dimensions can be synthesized by templating against selenium nanowires and colloids. *J Am Chem Soc* 125(44):13364–13365
97. Chen Z, Zhan P, Wang ZL, Zhang JH, Zhang WY, Ming NB, Chan CT, Sheng P (2004) Two- and three-dimensional ordered structures of hollow silver spheres prepared by colloidal crystal templating. *Adv Mater* 16(5):417–422
98. Sun Y, Mayers BT, Xia Y (2002) Template-engaged replacement reaction: a one-step approach to the large-scale synthesis of metal nanostructures with hollow interiors. *Nano Lett* 2(5):481–485
99. Zhang J, Zhan P, Liu H, Wang Z, Ming N (2006) A facile colloidal templating method to monodisperse hollow Ag and Ag/Au submicrometer spheres. *Mater Lett* 60(2):280–283
100. Lu X, Tuan H-Y, Chen J, Li Z-Y, Korgel BA, Xia Y (2007) Mechanistic studies on the galvanic replacement reaction between multiply twinned particles of Ag and HAuCl₄ in an organic medium. *J Am Chem Soc* 129(6):1733–1742
101. Qingbo Z, Jim Yang L, Jun Y, Chris B, Jixuan Z (2007) Size and composition tunable Ag–Au alloy nanoparticles by replacement reactions. *Nanotechnology* 18(24):245605
102. Fan HJ, Gösele U, Zacharias M (2007) Formation of nanotubes and hollow nanoparticles based on Kirkendall and diffusion processes: a review. *Small* 3(10):1660–1671
103. Yu X, Wang D, Peng Q, Li Y (2011) High performance electrocatalyst: Pt–Cu hollow nanocrystals. *Chem Commun* 47(28):8094–8096
104. Liu X, Wang D, Li Y (2012) Synthesis and catalytic properties of bimetallic nanomaterials with various architectures. *Nano Today* 7(5):448–466
105. Schmidt TJ, Noeske M, Gasteiger HA, Behm RJ, Britz P, Bönemann H (1997) Electrocatalytic activity of PtRu alloy colloids for CO and CO/H₂ electrooxidation: stripping voltammetry and rotating disk measurements. *Langmuir* 13(10):2591–2595
106. Vogel W, Britz P, Bönemann H, Rothe J, Hormes J (1997) Structure and chemical composition of surfactant-stabilized PtRu alloy colloids. *J Phys Chem B* 101(51):11029–11036
107. Zhang X, Chan K-Y (2002) Water-in-oil microemulsion synthesis of platinum–ruthenium nanoparticles, their characterization and electrocatalytic properties. *Chem Mater* 15(2):451–459
108. Liu Y, Qiu X, Chen Z, Zhu W (2002) A new supported catalyst for methanol oxidation prepared by a reverse micelles method. *Electrochem Commun* 4(7):550–553

109. Boxall DL, Deluga GA, Kenik EA, King WD, Lukehart CM (2001) Rapid synthesis of a Pt1Ru1/carbon nanocomposite using microwave irradiation: a DMFC anode catalyst of high relative performance. *Chem Mater* 13(3):891–900
110. Wang X, Hsing IM (2002) Surfactant stabilized Pt and Pt alloy electrocatalyst for polymer electrolyte fuel cells. *Electrochim Acta* 47(18):2981–2987
111. Bock C, Paquet C, Couillard M, Botton GA, MacDougall BR (2004) Size-selected synthesis of PtRu nano-catalysts: reaction and size control mechanism. *J Am Chem Soc* 126(25):8028–8037
112. Liu Z, Lee JY, Chen W, Han M, Gan LM (2003) Physical and electrochemical characterizations of microwave-assisted polyol preparation of carbon-supported PtRu nanoparticles. *Langmuir* 20(1):181–187
113. Knupp S, Vukmirovic M, Haldar P, Herron J, Mavrikakis M, Adzic R (2010) Platinum monolayer electrocatalysts for O₂ reduction: Pt monolayer on carbon-supported PdIr nanoparticles. *Electrocatalysis* 1(4):213–223
114. Koenigsman C, Santulli AC, Gong K, Vukmirovic MB, Zhou W-P, Sutter E, Wong SS, Adzic RR (2011) Enhanced electrocatalytic performance of processed, ultrathin, supported Pd–Pt core–shell nanowire catalysts for the oxygen reduction reaction. *J Am Chem Soc* 133(25):9783–9795
115. Frenkel AI, Yevick A, Cooper C, Vasic R (2011) Modeling the structure and composition of nanoparticles by extended X-ray absorption fine-structure spectroscopy. *Annu Rev Anal Chem* 4(1):23–39
116. Frenkel AI, Hills CW, Nuzzo RG (2001) A view from the inside: complexity in the atomic scale ordering of supported metal nanoparticles. *J Phys Chem B* 105(51):12689–12703
117. Nashner MS, Frenkel AI, Somerville D, Hills CW, Shapley JR, Nuzzo RG (1998) Core shell inversion during nucleation and growth of bimetallic Pt/Ru nanoparticles. *J Am Chem Soc* 120(32):8093–8101
118. Russell AE, Rose A (2004) X-ray absorption spectroscopy of low temperature fuel cell catalysts. *Chem Rev* 104(10):4613–4636
119. Ashcroft AT, Cheetham AK, Harris PJF, Jones RH, Natarajan S, Sankar G, Stedman NJ, Thomas JM (1994) Particle size studies of supported metal catalysts: a comparative study by X-ray diffraction, EXAFS and electron microscopy. *Catal Lett* 24(1–2):47–57
120. Cao D, Bergens SH (2004) Pt–Ru atoms nanoparticles as anode catalysts for direct methanol fuel cells. *J Power Sources* 134(2):170–180
121. Link S, Wang ZL, El-Sayed MA (1999) Alloy formation of gold–silver nanoparticles and the dependence of the plasmon absorption on their composition. *J Phys Chem B* 103(18):3529–3533
122. Torigoe K, Esumi K (1993) Preparation of bimetallic silver-palladium colloids from silver(I) bis(oxalato)palladate(II). *Langmuir* 9(7):1664–1667
123. Torigoe K, Nakajima Y, Esumi K (1993) Preparation and characterization of colloidal silver-platinum alloys. *J Phys Chem* 97(31):8304–8309
124. Zhao D, Xu B-Q (2006) Enhancement of Pt utilization in electrocatalysts by using gold nanoparticles. *Angew Chem Int Ed* 45(30):4955–4959
125. Henglein A (2000) Preparation and optical absorption spectra of Au core Pt shell and Pt core Au shell colloidal nanoparticles in aqueous solution. *J Phys Chem B* 104(10):2201–2203
126. Nashner MS, Frenkel AI, Adler DL, Shapley JR, Nuzzo RG (1997) Structural characterization of carbon-supported platinum–ruthenium nanoparticles from the molecular cluster precursor PtRu₅C(CO)₁₆. *J Am Chem Soc* 119(33):7760–7771
127. Mulvaney P (1996) Surface plasmon spectroscopy of nanosized metal particles. *Langmuir* 12(3):788–800
128. D’Souza L, Bera P, Sampath S (2002) Silver-palladium nanodispersions in silicate matrices: highly uniform, stable, bimetallic structures. *J Colloid Interface Sci* 246(1):92–99

129. Zhang Q, Xie J, Lee JY, Zhang J, Boothroyd C (2008) Synthesis of Ag@AgAu metal core/ alloy shell bimetallic nanoparticles with tunable shell compositions by a galvanic replacement reaction. *Small* 4(8):1067–1071
130. Chen J-M, Sarma LS, Chen C-H, Cheng M-Y, Shih S-C, Wang G-R, Liu D-G, Lee J-F, Tang M-T, Hwang B-J (2006) Multi-scale dispersion in fuel cell anode catalysts: role of TiO₂ towards achieving nanostructured materials. *J Power Sources* 159(1):29–33
131. Iwasita T, Hoster H, John-Anacker A, Lin WF, Vielstich W (1999) Methanol oxidation on PtRu electrodes. influence of surface structure and Pt–Ru atom distribution. *Langmuir* 16(2):522–529
132. Radmilovic V, Gasteiger HA, Ross PN (1995) Structure and chemical composition of a supported Pt–Ru electrocatalyst for methanol oxidation. *J Catal* 154(1):98–106
133. Wang D, Zhuang L, Lu J (2007) An alloying-degree-controlling step in the impregnation synthesis of PtRu/C catalysts. *J Phys Chem C* 111(44):16416–16422
134. Aricò AS, Creti P, Modica E, Monforte G, Baglio V, Antonucci V (2000) Investigation of direct methanol fuel cells based on unsupported Pt–Ru anode catalysts with different chemical properties. *Electrochim Acta* 45(25–26):4319–4328
135. Rolison DR, Hagans PL, Swider KE, Long JW (1999) Role of hydrous ruthenium oxide in Pt–Ru direct methanol fuel cell anode electrocatalysts: the importance of mixed electron/proton conductivity. *Langmuir* 15(3):774–779
136. Gurau B, Viswanathan R, Liu R, Lafrenz TJ, Ley KL, Smotkin ES, Reddington E, Sapienza A, Chan BC, Mallouk TE, Sarangapani S (1998) Structural and electrochemical characterization of binary, ternary, and quaternary platinum alloy catalysts for methanol electro-oxidation I. *J Phys Chem B* 102(49):9997–10003
137. Antolini E, Cardellini F, Giorgi L, Passalacqua E (2000) Effect of Me (Pt+Ru) content in Me/C catalysts on PtRu alloy formation: an XRD analysis. *J Mater Sci Lett* 19(23):2099–2103
138. Antolini E, Cardellini F (2001) Formation of carbon supported PtRu alloys: an XRD analysis. *J Alloys Compd* 315(1–2):118–122
139. Gnutzmann V, Vogel W (1990) Structural sensitivity of the standard platinum/silica catalyst EuroPt-1 to hydrogen and oxygen exposure by in situ x-ray diffraction. *J Phys Chem* 94(12):4991–4997
140. Vogel W, Rosner B, Tesche B (1993) Structural investigations of gold (Au55) organometallic complexes by x-ray powder diffraction and transmission electron microscopy. *J Phys Chem* 97(45):11611–11616
141. Bommarius AS, Holzwarth JF, Wang DIC, Hatton TA (1990) Coalescence and solubilize exchange in a cationic four-component reversed micellar system. *J Phys Chem* 94(18):7232–7239
142. Dobrosz I, Jiratova K, Pitchon V, Rynkowski JM (2005) Effect of the preparation of supported gold particles on the catalytic activity in CO oxidation reaction. *J Mol Catal A Chem* 234(1–2):187–197
143. Ferrando R, Jellinek J, Johnston RL (2008) Nanoalloys: from theory to applications of alloy clusters and nanoparticles. *Chem Rev* 108(3):845–910
144. Bi Y, Lu G (2008) Facile synthesis of platinum nanofiber/nanotube junction structures at room temperature. *Chem Mater* 20(4):1224–1226
145. Kawaguchi T, Sugimoto W, Murakami Y, Takasu Y (2005) Particle growth behavior of carbon-supported Pt, Ru, PtRu catalysts prepared by an impregnation reductive-pyrolysis method for direct methanol fuel cell anodes. *J Catal* 229(1):176–184
146. Bauer A, Gyenge EL, Oloman CW (2006) Electrodeposition of Pt–Ru nanoparticles on fibrous carbon substrates in the presence of nonionic surfactant: application for methanol oxidation. *Electrochim Acta* 51(25):5356–5364
147. Park K-W, Sung Y-E, Han S, Yun Y, Hyeon T (2004) Origin of the enhanced catalytic activity of carbon nanocoil-supported PtRu alloy electrocatalysts. *J Phys Chem B* 108(3):939–944

148. Rodriguez-Nieto FJ, Morante-Catacora TY, Cabrera CR (2004) Sequential and simultaneous electrodeposition of Pt–Ru electrocatalysts on a HOPG substrate and the electro-oxidation of methanol in aqueous sulfuric acid. *J Electroanal Chem* 571(1):15–26
149. Schmidt TJ, Noeske M, Gasteiger HA, Behm RJ, Britz P, Bönnemann H (1998) PtRu alloy colloids as precursors for fuel cell catalysts: a combined XPS, AFM, HRTEM, and RDE study. *J Electrochem Soc* 145(3):925–931
150. Liu D-G, Lee J-F, Tang M-T (2005) Characterization of Pt-Ru/C catalysts by X-ray absorption spectroscopy and temperature-programmed surface reaction. *J Mol Catal A Chem* 240(1–2):197–206
151. Russell AE, Maniguet S, Mathew RJ, Yao J, Roberts MA, Thompsett D (2001) In situ X-ray absorption spectroscopy and X-ray diffraction of fuel cell electrocatalysts. *J Power Sources* 96(1):226–232
152. O’Grady WE, Hagans PL, Pandya KI, Maricle DL (2001) Structure of Pt/Ru catalysts using X-ray absorption near edge structure studies. *Langmuir* 17(10):3047–3050
153. Harada M, Toshima N, Yoshida K, Isoda S (2005) Aggregated structure analysis of polymer-protected platinum/ruthenium colloidal dispersions using EXAFS, HRTEM, and electron diffraction measurements. *J Colloid Interface Sci* 283(1):64–78
154. Mukerjee S, Urian RC (2002) Bifunctionality in Pt alloy nanocluster electrocatalysts for enhanced methanol oxidation and CO tolerance in PEM fuel cells: electrochemical and in situ synchrotron spectroscopy. *Electrochim Acta* 47(19):3219–3231
155. Frenkel AI (2012) Applications of extended X-ray absorption fine-structure spectroscopy to studies of bimetallic nanoparticle catalysts. *Chem Soc Rev* 41(24):8163–8178
156. Bazin DC, Sayers DA, Rehr JJ (1997) Comparison between X-ray absorption spectroscopy, anomalous wide angle X-ray scattering, anomalous small angle X-ray scattering, and diffraction anomalous fine structure Techniques applied to nanometer-scale metallic clusters. *J Phys Chem B* 101(51):11040–11050
157. Via GH, Sinfelt JH (1996) X-ray absorption fine structure for catalysts and surfaces (ed: Iwasawa Y). World Scientific, London
158. Lin SD, Hsiao T-C, Chang J-R, Lin AS (1999) Morphology of carbon supported Pt–Ru electrocatalyst and the CO tolerance of anodes for PEM fuel cells. *J Phys Chem B* 103(1):97–103
159. Greggor RB, Lytle FW (1980) Morphology of supported metal clusters: determination by EXAFS and chemisorption. *J Catal* 63(2):476–486
160. Yoshitake H, Yamazaki O, Ota K (1994) In situ X-ray absorption fine structure study on structure transformation and electronic state of various Pt particles on carbon electrode. *J Electrochem Soc* 141(9):2516–2521
161. Siepen K, Bönnemann H, Brijoux W, Rothe J, Hormes J (2000) EXAFS/XANES, chemisorption and IR investigations of colloidal Pt/Rh bimetallic catalysts. *Appl Organomet Chem* 14(10):549–556
162. Horsley JA (1982) Relationship between the area of L_{2,3}X-ray absorption edge resonances and the d orbital occupancy in compounds of platinum and iridium. *J Chem Phys* 76(3):1451–1458
163. Mansour AN, Sayers DE, Cook JW, Short DR, Shannon RD, Katzer JR (1984) X-ray absorption studies of some platinum oxides. *J Phys Chem* 88(9):1778–1781
164. Brown M, Peierls RE, Stern EA (1977) White lines in x-ray absorption. *Phys Rev B* 15(2):738–744
165. Mukerjee S, Srinivasan S, Soriaga MP, McBreen J (1995) Role of structural and electronic properties of Pt and Pt alloys on electrocatalysis of oxygen reduction: an in situ XANES and EXAFS investigation. *J Electrochem Soc* 142(5):1409–1422
166. Min M-K, Cho J, Cho K, Kim H (2000) Particle size and alloying effects of Pt-based alloy catalysts for fuel cell applications. *Electrochim Acta* 45(25–26):4211–4217
167. Markovic N, Gasteiger H, Ross PN (1997) Kinetics of oxygen reduction on Pt(hkl) electrodes: implications for the crystallite size effect with supported Pt electrocatalysts. *J Electrochem Soc* 144(5):1591–1597

168. Hwang B-J, Sarma LS, Wang G-R, Chen C-H, Liu D-G, Sheu H-S, Lee J-F (2007) Heat-induced alterations in the surface population of metal sites in bimetallic nanoparticles. *Chem Eur J* 13(21):6255–6264
169. Reetz MT, Lopez M, Grünert W, Vogel W, Mahlendorf F (2003) Preparation of colloidal nanoparticles of mixed metal oxides containing platinum, ruthenium, osmium, and iridium and their use as electrocatalysts. *J Phys Chem B* 107(30):7414–7419
170. Park K-W, Choi J-H, Sung Y-E (2003) Structural, chemical, and electronic properties of Pt/Ni thin film electrodes for methanol electrooxidation. *J Phys Chem B* 107(24):5851–5856
171. Kao CC, Tsai SC, Bahl MK, Chung YW, Lo WJ (1980) Electronic properties, structure and temperature-dependent composition of nickel deposited on rutile titanium dioxide (110) surfaces. *Surf Sci* 95(1):1–14
172. Eberhardt W, Fayet P, Cox DM, Fu Z, Kaldor A, Sherwood R, Sondericker D (1990) Photoemission from mass-selected monodispersed Pt clusters. *Phys Rev Lett* 64(7):780–783
173. Zhang X, Chan K-Y (2003) Water-in-oil microemulsion synthesis of platinum–ruthenium nanoparticles, their characterization and electrocatalytic properties. *Chem Mater* 15(2):451–459
174. Phung X, Groza J, Stach EA, Williams LN, Ritchey SB (2003) Surface characterization of metal nanoparticles. *Mater Sci Eng A* 359(1–2):261–268
175. Tao F, Grass ME, Zhang Y, Butcher DR, Aksoy F, Aloni S, Altoe V, Alayoglu S, Renzas JR, Tsung C-K, Zhu Z, Liu Z, Salmeron M, Somorjai GA (2010) Evolution of structure and chemistry of bimetallic nanoparticle catalysts under reaction conditions. *J Am Chem Soc* 132(25):8697–8703
176. Stamenkovic VR, Mun BS, Mayrhofer KJJ, Ross PN, Markovic NM (2006) Effect of surface composition on electronic structure, stability, and electrocatalytic properties of Pt-transition metal alloys: Pt-skin versus Pt-skeleton surfaces. *J Am Chem Soc* 128(27):8813–8819
177. Tremiliosi-Filho G, Kim H, Chrzanowski W, Wieckowski A, Grzybowska B, Kulesza P (1999) Reactivity and activation parameters in methanol oxidation on platinum single crystal electrodes ‘decorated’ by ruthenium adlayers. *J Electroanal Chem* 467(1–2):143–156
178. Tong Y, Oldfield E, Wieckowski A (1998) Peer reviewed: exploring electrochemical interfaces with solid-state NMR. *Anal Chem* 70(15):518A–527A
179. Babu PK, Tong YY, Kim HS, Wieckowski A (2002) Nanostructured electrode surfaces studied by electrochemical NMR. *J Electroanal Chem* 524–525:157–167
180. Babu PK, Kim HS, Oldfield E, Wieckowski A (2003) Electronic alterations caused by ruthenium in Pt–Ru alloy nanoparticles as revealed by electrochemical NMR. *J Phys Chem B* 107(31):7595–7600
181. Lu C, Rice C, Masel RI, Babu PK, Waszczuk P, Kim HS, Oldfield E, Wieckowski A (2002) UHV, electrochemical NMR, and electrochemical studies of platinum/ruthenium fuel cell catalysts. *J Phys Chem B* 106(37):9581–9589
182. Tong YY, Yonezawa T, Toshima N, van der Klink JJ (1996) 195Pt NMR of polymer-protected Pt/Pd bimetallic catalysts. *J Phys Chem* 100(2):730–733
183. Huang S-Y, Chang S-M, Yeh C-T (2005) Characterization of surface composition of platinum and ruthenium nanoalloys dispersed on active carbon. *J Phys Chem B* 110(1):234–239
184. Huang S-Y, Chang S-M, Lin C-L, Chen C-H, Yeh C-T (2006) Promotion of the electrochemical activity of a bimetallic platinum–ruthenium catalyst by oxidation-induced segregation. *J Phys Chem B* 110(46):23300–23305
185. Wang K-W, Huang S-Y, Yeh C-T (2007) Promotion of carbon-supported platinum–ruthenium catalyst for electrodecomposition of methanol. *J Phys Chem C* 111(13):5096–5100
186. Bard AJ, Faulkner LR (2000) *Electrochemical methods: fundamentals and applications*, 2nd edn. Wiley, New York
187. Zoski CG (2006) *Handbook of electrochemistry*, 1st edn. Elsevier
188. Sawyer DT, Roberts JL (1974) *Experimental electrochemistry for chemist*. Wiley, New York
189. Rieger PH (1994) *Electrochemistry*, 2nd edn. Prentice-Hall

190. Pan C-J, Su W-N, Kumar SMS, Al Andra CC, Yang S-J, Chen H-Y, Hwang BJ (2012) An electrochemical approach for estimation of intrinsic active area and activation of Pt/C nanocatalysts. *J Chin Chem Soc* 59(10):1303–1312
191. Hwang BJ, Kumar SMS, Chen C-H, Monalisa XX, Cheng M-Y, Liu D-G, Lee J-F (2007) An investigation of structure–catalytic activity relationship for Pt–Co/C bimetallic nanoparticles toward the oxygen reduction reaction. *J Phys Chem C* 111(42):15267–15276
192. Schmidt TJ, Gasteiger HA, Stäb GD, Urban PM, Kolb DM, Behm RJ (1998) Characterization of high-surface-area electrocatalysts using a rotating disk electrode configuration. *J Electrochem Soc* 145(7):2354–2358
193. Mayrhofer KJJ, Strmcnik D, Blizanac BB, Stamenkovic V, Arenz M, Markovic NM (2008) Measurement of oxygen reduction activities via the rotating disc electrode method: from Pt model surfaces to carbon-supported high surface area catalysts. *Electrochim Acta* 53(7):3181–3188
194. Wang JX, Markovic NM, Adzic RR (2004) Kinetic analysis of oxygen reduction on Pt(111) in acid solutions: intrinsic kinetic parameters and anion adsorption effects. *J Phys Chem B* 108(13):4127–4133
195. Levich VG (1962) *Physical hydrodynamics*. Prentice-Hall, Englewood Cliffs
196. Watt-Smith MJ, Friedrich JM, Rigby SP, Ralph TR, Walsh FC (2008) Determination of the electrochemically active surface area of Pt/C PEM fuel cell electrodes using different adsorbates. *J Phys D Appl Phys* 41(17):174004
197. Vidaković T, Christov M, Sundmacher K (2007) The use of CO stripping for in situ fuel cell catalyst characterization. *Electrochim Acta* 52(18):5606–5613
198. Nagel T, Bogolowski N, Baltruschat H (2006) Towards a determination of the active surface area of polycrystalline and nanoparticle electrodes by Cu upd and CO oxidation. *J Appl Electrochem* 36(11):1297–1306
199. Jusys Z, Kaiser J, Behm RJ (2002) Composition and activity of high surface area PtRu catalysts towards adsorbed CO and methanol electrooxidation: a DEMS study. *Electrochim Acta* 47(22–23):3693–3706
200. Dinh HN, Ren X, Garzon FH, Piotr Z, Gottesfeld S (2000) Electrocatalysis in direct methanol fuel cells: in-situ probing of PtRu anode catalyst surfaces. *J Electroanal Chem* 491(1–2):222–233
201. Paseka I (2007) Adsorption of CO on Ru and Pt blacks and catalysts and the possibility of its utilization for the determination of the ruthenium-free surface. *J Solid State Electrochem* 11(1):52–58
202. Rush BM, Reimer JA, Cairns EJ (2001) Nuclear magnetic resonance and voltammetry studies of carbon monoxide adsorption and oxidation on a carbon-supported platinum fuel cell electrocatalyst. *J Electrochem Soc* 148(2):A137–A148
203. Pozio A, De Francesco M, Cemmi A, Cardellini F, Giorgi L (2002) Comparison of high surface Pt/C catalysts by cyclic voltammetry. *J Power Sources* 105(1):13–19
204. Thiel KO, Hintze M, Vollmer A, Donner C (2008) A new approach on the Cu UPD on Ag surfaces. *J Electroanal Chem* 621(1):7–12
205. Hernandez F, Baltruschat H (2007) Hydrogen evolution and Cu UPD at stepped gold single crystals modified with Pd. *J Solid State Electrochem* 11(7):877–885
206. Green CL, Kucernak A (2002) Determination of the platinum and ruthenium surface areas in platinum–ruthenium alloy electrocatalysts by underpotential deposition of copper. I. Unsupported catalysts. *J Phys Chem B* 106(5):1036–1047
207. Green CL, Kucernak A (2002) Determination of the platinum and ruthenium surface areas in platinum–ruthenium electrocatalysts by underpotential deposition of copper. 2. Effect of surface composition on activity. *J Phys Chem B* 106(44):11446–11456
208. Mascaro LH, Santos MC, Machado SAS, Avaca LA (1997) Underpotential deposition of silver on polycrystalline platinum studied by cyclic voltammetry and rotating ring-disc techniques. *J Chem Soc Faraday Trans* 93(22):3999–4003
209. Takakusagi S, Kitamura K, Uosaki K (2008) In situ real-time monitoring of electrochemical Ag deposition on a reconstructed Au(111) surface studied by scanning tunneling microscopy. *J Phys Chem C* 112(8):3073–3077

210. Uhm S, Chung ST, Lee J (2007) Activity of Pt anode catalyst modified by underpotential deposited Pb in a direct formic acid fuel cell. *Electrochem Commun* 9(8):2027–2031
211. Lee JK, Jeon H, Uhm S, Lee J (2008) Influence of underpotentially deposited Sb onto Pt anode surface on the performance of direct formic acid fuel cells. *Electrochim Acta* 53(21):6089–6092
212. Lamy-Pitara E, Barbier J (1997) Platinum modified by electrochemical deposition of adatoms. *Appl Catal A Gen* 149(1):49–87
213. Kolb DM, Przasnyski M, Gerischer H (1974) Underpotential deposition of metals and work function differences. *J Electroanal Chem Interfacial Electrochem* 54(1):25–38
214. Kolb DM (1978) *Advances in electrochemistry and electrochemical engineering*, vol 11. John Wiley Interscience, New York, p 125
215. Aramata A (1997) *Underpotential deposition on single-crystal metals, modern aspects of electrochemistry*, vol 31. Plenum Press, New York, p 181
216. Kaplan D, Alon M, Burstein L, Rosenberg Y, Peled E (2011) Study of core–shell platinum-based catalyst for methanol and ethylene glycol oxidation. *J Power Sources* 196(3):1078–1083
217. Jiang X, Gür TM, Prinz FB, Bent SF (2010) Atomic layer deposition (ALD) co-deposited Pt–Ru binary and Pt skin catalysts for concentrated methanol oxidation. *Chem Mater* 22(10):3024–3032
218. Maillard F, Lu GQ, Wieckowski A, Stimming U (2005) Ru-decorated Pt surfaces as model fuel cell electrocatalysts for CO electrooxidation. *J Phys Chem B* 109(34):16230–16243
219. Kristian N, Yu Y, Gunawan P, Xu R, Deng W, Liu X, Wang X (2009) Controlled synthesis of Pt-decorated Au nanostructure and its promoted activity toward formic acid electro-oxidation. *Electrochim Acta* 54(21):4916–4924
220. Ramirez-Caballero GE, Balbuena PB (2008) Surface segregation of core atoms in core–shell structures. *Chem Phys Lett* 456(1–3):64–67
221. Zhang J, Vukmirovic MB, Sasaki K, Nilekar AU, Mavrikakis M, Adzic RR (2005) Mixed-metal Pt monolayer electrocatalysts for enhanced oxygen reduction kinetics. *J Am Chem Soc* 127(36):12480–12481
222. Zhang J, Sasaki K, Sutter E, Adzic RR (2007) Stabilization of platinum oxygen-reduction electrocatalysts using gold clusters. *Science* 315(5809):220–222
223. Zhang S, Shao Y, Yin G, Lin Y (2010) Electrostatic self-assembly of a Pt-around-Au nanocomposite with high activity towards formic acid oxidation. *Angew Chem Int Ed* 49(12):2211–2214
224. Stamenkovic VR, Mun BS, Arenz M, Mayrhofer KJJ, Lucas CA, Wang G, Ross PN, Markovic NM (2007) Trends in electrocatalysis on extended and nanoscale Pt-bimetallic alloy surfaces. *Nat Mater* 6(3):241–247
225. Chen S, Sheng W, Yabuuchi N, Ferreira PJ, Allard LF, Shao-Horn Y (2008) Origin of oxygen reduction reaction activity on “Pt₃Co” nanoparticles: atomically resolved chemical compositions and structures. *J Phys Chem C* 113(3):1109–1125
226. Ball SC, Hudson SL, Leung JH, Russell AE, Thompsett D, Theobald BR (2007) Mechanisms of activity loss in PtCo alloy systems. *ECS Trans* 11(1):1247–1257
227. Narayanan R, El-Sayed MA (2004) Effect of nanocatalysis in colloidal solution on the tetrahedral and cubic nanoparticle SHAPE: electron-transfer reaction catalyzed by platinum nanoparticles. *J Phys Chem B* 108(18):5726–5733
228. Narayanan R, El-Sayed MA (2004) Shape-dependent catalytic activity of platinum nanoparticles in colloidal solution. *Nano Lett* 4(7):1343–1348
229. Kim Y, Hong JW, Lee YW, Kim M, Kim D, Yun WS, Han SW (2010) Synthesis of AuPt heteronanostructures with enhanced electrocatalytic activity toward oxygen reduction. *Angew Chem Int Ed* 49(52):10197–10201
230. Masatake H (1997) Size- and support-dependency in the catalysis of gold. *Catal Today* 36(1):153–166

231. Park S, Xie Y, Weaver MJ (2002) Electrocatalytic pathways on carbon-supported platinum nanoparticles: comparison of particle-size-dependent rates of methanol, formic acid, and formaldehyde electrooxidation. *Langmuir* 18(15):5792–5798
232. Mazumder V, Chi M, Mankin MN, Liu Y, Metin Ö, Sun D, More KL, Sun S (2012) A facile synthesis of MPd (M = Co, Cu) nanoparticles and their catalysis for formic acid oxidation. *Nano Lett* 12(2):1102–1106
233. Chang S-H, Su W-N, Yeh M-H, Pan C-J, Yu K-L, Liu D-G, Lee J-F, Hwang B-J (2010) Structural and electronic effects of carbon-supported Pt_xPd_{1-x} nanoparticles on the electrocatalytic activity of the oxygen-reduction reaction and on methanol tolerance. *Chem Eur J* 16(36):11064–11071
234. Steele BCH, Heinzel A (2001) Materials for fuel-cell technologies. *Nature* 414(6861):345–352
235. Faur Ghenciu A (2002) Review of fuel processing catalysts for hydrogen production in PEM fuel cell systems. *Curr Opin Solid State Mater Sci* 6(5):389–399
236. Costamagna P, Srinivasan S (2001) Quantum jumps in the PEMFC science and technology from the 1960s to the year 2000: part II. Engineering, technology development and application aspects. *J Power Sources* 102(1–2):253–269
237. Costamagna P, Srinivasan S (2001) Quantum jumps in the PEMFC science and technology from the 1960s to the year 2000: part I. Fundamental scientific aspects. *J Power Sources* 102(1–2):242–252
238. Ianniello R, Schmidt VM, Stimming U, Stumper J, Wallau A (1994) CO adsorption and oxidation on Pt and Pt-Ru alloys: dependence on substrate composition. *Electrochim Acta* 39(11–12):1863–1869
239. Castro Luna AM, Camara GA, Paganin VA, Ticianelli EA, Gonzalez ER (2000) Effect of thermal treatment on the performance of CO-tolerant anodes for polymer electrolyte fuel cells. *Electrochem Commun* 2(4):222–225
240. Divisek J, Oetjen HF, Peinecke V, Schmidt VM, Stimming U (1998) Components for PEM fuel cell systems using hydrogen and CO containing fuels. *Electrochim Acta* 43(24):3811–3815
241. Hwang BJ, Sarma LS, Chen CH, Tang MT, Liu DG, Lee JF (2007) Depth profile of alloying extent and composition in bimetallic nanoparticles investigated by in situ x-ray absorption spectroscopy. *Appl Phys Lett* 91(2):023108
242. Sarma LS, Chen C-H, Wang G-R, Hsueh K-L, Huang C-P, Sheu H-S, Liu D-G, Lee J-F, Hwang B-J (2007) Investigations of direct methanol fuel cell (DMFC) fading mechanisms. *J Power Sources* 167(2):358–365
243. Janssen GJM, de Heer MP, Papageorgopoulos DC (2004) Bilayer anodes for improved reformate tolerance of PEM fuel cells. *Fuel Cells* 4(3):169–174
244. Grgr BN, Markovic NM, Ross PN (1999) The electro-oxidation of H₂ and H₂/CO mixtures on carbon-supported Pt x Mo y alloy catalysts. *J Electrochem Soc* 146(5):1613–1619
245. Lebedeva NP, Janssen GJM (2005) On the preparation and stability of bimetallic PtMo/C anodes for proton-exchange membrane fuel cells. *Electrochim Acta* 51(1):29–40
246. Ball S, Hodgkinson A, Hoogers G, Maniguet S, Thompsett D, Wong B (2002) The proton exchange membrane fuel cell performance of a carbon supported PtMo catalyst operating on reformate. *Electrochem Solid-State Lett* 5(2):A31–A34
247. Götz M, Wendt H (1998) Binary and ternary anode catalyst formulations including the elements W, Sn and Mo for PEMFCs operated on methanol or reformate gas. *Electrochim Acta* 43(24):3637–3644
248. Santiago EI, Camara GA, Ticianelli EA (2003) CO tolerance on PtMo/C electrocatalysts prepared by the formic acid method. *Electrochim Acta* 48(23):3527–3534
249. Lee SJ, Mukerjee S, Ticianelli EA, McBreen J (1999) Electrocatalysis of CO tolerance in hydrogen oxidation reaction in PEM fuel cells. *Electrochim Acta* 44(19):3283–3293
250. Gasteiger HA, Markovic NM, Ross PN (1995) Electrooxidation of CO and H₂/CO mixtures on a well-characterized Pt₃Sn electrode surface. *J Phys Chem* 99(22):8945–8949

251. Wee J-H, Lee K-Y (2006) Overview of the development of CO-tolerant anode electrocatalysts for proton-exchange membrane fuel cells. *J Power Sources* 157(1):128–135
252. Garcia AC, Paganin VA, Ticianelli EA (2008) CO tolerance of PdPt/C and PdPtRu/C anodes for PEMFC. *Electrochim Acta* 53(12):4309–4315
253. Stonehart P (1984) Electrocatalyst advances for hydrogen oxidation in phosphoric acid fuel cells. *Int J Hydrog Energy* 9(11):921–928
254. Uchida H, Izumi K, Aoki K, Watanabe M (1771–1779) Temperature-dependence of hydrogen oxidation reaction rates and CO-tolerance at carbon-supported Pt, Pt-Co, and Pt-Ru catalysts. *Phys Chem Chem Phys* 2009:11(11)
255. Guilminot E, Fischer F, Chatenet M, Rigacci A, Berthon-Fabry S, Achard P, Chainet E (2007) Use of cellulose-based carbon aerogels as catalyst support for PEM fuel cell electrodes: electrochemical characterization. *J Power Sources* 166(1):104–111
256. Marie J, Berthon-Fabry S, Achard P, Chatenet M, Pradourat A, Chainet E (2004) Highly dispersed platinum on carbon aerogels as supported catalysts for PEM fuel cell-electrodes: comparison of two different synthesis paths. *J Non-Cryst Solids* 350:88–96
257. Zhou J-H, He J-P, Ji Y-J, Dang W-J, Liu X-L, Zhao G-W, Zhang C-X, Zhao J-S, Fu Q-B, Hu H-P (2007) CTAB assisted microwave synthesis of ordered mesoporous carbon supported Pt nanoparticles for hydrogen electro-oxidation. *Electrochim Acta* 52(14):4691–4695
258. Hwan Jung D, Hyeong Lee C, Soo Kim C, Ryul Shin D (1998) Performance of a direct methanol polymer electrolyte fuel cell. *J Power Sources* 71(1–2):169–173
259. McNicol BD, Rand DAJ, Williams KR (1999) Direct methanol–air fuel cells for road transportation. *J Power Sources* 83(1–2):15–31
260. Herrero E, Franaszczuk K, Wiecowski A (1993) A voltammetric identification of the surface redox couple effective in methanol oxidation on a ruthenium-covered platinum (110) electrode. *J Electroanal Chem* 361(1–2):269–273
261. Ma L, Liu C, Liao J, Lu T, Xing W, Zhang J (2009) High activity PtRu/C catalysts synthesized by a modified impregnation method for methanol electro-oxidation. *Electrochim Acta* 54(28):7274–7279
262. Watanabe M, Motoo S (1975) Electrocatalysis by ad-atoms: part III. Enhancement of the oxidation of carbon monoxide on platinum by ruthenium ad-atoms. *J Electroanal Chem Interfacial Electrochem* 60(3):275–283
263. Watanabe M, Motoo S (1975) Electrocatalysis by ad-atoms: part II. Enhancement of the oxidation of methanol on platinum by ruthenium ad-atoms. *J Electroanal Chem Interfacial Electrochem* 60(3):267–273
264. Hsieh C-T, Lin J-Y (2009) Fabrication of bimetallic Pt–M (M=Fe, Co, and Ni) nanoparticle/carbon nanotube electrocatalysts for direct methanol fuel cells. *J Power Sources* 188(2):347–352
265. Jiang Q-Z, Wu X, Shen M, Ma Z-F, Zhu X-Y (2008) Low-Pt content carbon-supported Pt–Ni–TiO₂ nanotube electrocatalyst for direct methanol fuel cells. *Catal Lett* 124(3–4):434–438
266. Page T, Johnson R, Hormes J, Noding S, Rambabu B (2000) A study of methanol electro-oxidation reactions in carbon membrane electrodes and structural properties of Pt alloy electro-catalysts by EXAFS. *J Electroanal Chem* 485(1):34–41
267. Shubina TE, Koper MTM (2002) Quantum-chemical calculations of CO and OH interacting with bimetallic surfaces. *Electrochim Acta* 47(22–23):3621–3628
268. Dupont C, Jugnet Y, Loffreda D (2006) Theoretical evidence of PtSn alloy efficiency for CO oxidation. *J Am Chem Soc* 128(28):9129–9136
269. Ghosh T, Matsumoto F, McInnis J, Weiss M, Abruña H, DiSalvo F (2009) PtPb nanoparticle electrocatalysts: control of activity through synthetic methods. *J Nanoparticle Res* 11(4):965–980
270. Justin P, Rao GR (2009) Enhanced activity of methanol electro-oxidation on Pt–V₂O₅/C catalysts. *Catal Today* 141(1–2):138–143

271. Wang J, Holt-Hindle P, MacDonald D, Thomas DF, Chen A (2008) Synthesis and electrochemical study of Pt-based nanoporous materials. *Electrochim Acta* 53(23):6944–6952
272. Yu X, Pickup PG (2008) Recent advances in direct formic acid fuel cells (DFAFC). *J Power Sources* 182(1):124–132
273. Uhm S, Lee HJ, Kwon Y, Lee J (2008) A stable and cost-effective anode catalyst structure for formic acid fuel cells. *Angew Chem Int Ed* 47(52):10163–10166
274. Zhang S, Shao Y, Yin G, Lin Y (2010) Facile synthesis of PtAu alloy nanoparticles with high activity for formic acid oxidation. *J Power Sources* 195(4):1103–1106
275. Wang S, Wang X, Jiang SP (2011) Self-assembly of mixed Pt and Au nanoparticles on PDDA-functionalized graphene as effective electrocatalysts for formic acid oxidation of fuel cells. *Phys Chem Chem Phys* 13(15):6883–6891
276. Huang J, Hou H, You T (2009) Highly efficient electrocatalytic oxidation of formic acid by electrospun carbon nanofiber-supported Pt_xAu_{100-x} bimetallic electrocatalyst. *Electrochem Commun* 11(6):1281–1284
277. Yu Y, Hu Y, Liu X, Deng W, Wang X (2009) The study of Pt@Au electrocatalyst based on Cu underpotential deposition and Pt redox replacement. *Electrochim Acta* 54(11):3092–3097
278. Liu B, Li HY, Die L, Zhang XH, Fan Z, Chen JH (2009) Carbon nanotubes supported PtPd hollow nanospheres for formic acid electrooxidation. *J Power Sources* 186(1):62–66
279. Lee H, Habas SE, Somorjai GA, Yang P (2008) Localized Pd overgrowth on cubic Pt nanocrystals for enhanced electrocatalytic oxidation of formic acid. *J Am Chem Soc* 130(16):5406–5407
280. Hu C, Zhao Y, Cheng H, Hu Y, Shi G, Dai L, Qu L (2012) Ternary Pd₂/PtFe networks supported by 3D graphene for efficient and durable electrooxidation of formic acid. *Chem Commun* 48(97):11865–11867
281. Casado-Rivera E, Volpe DJ, Alden L, Lind C, Downie C, Vázquez-Alvarez T, Angelo ACD, DiSalvo FJ, Abruña HD (2004) Electrocatalytic activity of ordered intermetallic phases for fuel cell applications. *J Am Chem Soc* 126(12):4043–4049
282. Tripković AV, Popović KD, Stevanović RM, Socha R, Kowal A (2006) Activity of a PtBi alloy in the electrochemical oxidation of formic acid. *Electrochem Commun* 8(9):1492–1498
283. Xu JB, Zhao TS, Liang ZX (2008) Synthesis of active platinum–silver alloy electrocatalyst toward the formic acid oxidation reaction. *J Phys Chem C* 112(44):17362–17367
284. Chi N, Chan K-Y, Phillips D (2001) Electrocatalytic oxidation of formic acid by Pt/Co nanoparticles. *Catal Lett* 71(1–2):21–26
285. Yang Y-Y, Sun S-G, Gu Y-J, Zhou Z-Y, Zhen C-H (2001) Surface modification and electrocatalytic properties of Pt(100), Pt(110), Pt(320) and Pt(331) electrodes with Sb towards HCOOH oxidation. *Electrochim Acta* 46(28):4339–4348
286. Kristian N, Yan Y, Wang X (2008) Highly efficient submonolayer Pt-decorated Au nanocatalysts for formic acid oxidation. *Chem Commun* 3:353–355
287. Zhao D, Wang Y-H, Xu B-Q (2009) Pt flecks on colloidal Au (Pt^δAu) as nanostructured anode catalysts for electrooxidation of formic acid. *J Phys Chem C* 113(49):20903–20911
288. Ojeda M, Iglesia E (2009) Formic acid dehydrogenation on Au-based catalysts at near-ambient temperatures. *Angew Chem Int Ed* 48(26):4800–4803
289. Xiang J, Wu B-L, Chen S-L (2001) Investigation of the mechanism of the electrochemical oxidation of formic acid at a gold electrode in sulfuric acid solution. *J Electroanal Chem* 517(1–2):95–100
290. Wang J, Yin G, Wang G, Wang Z, Gao Y (2008) A novel Pt/Au/C cathode catalyst for direct methanol fuel cells with simultaneous methanol tolerance and oxygen promotion. *Electrochem Commun* 10(6):831–834
291. Wang J, Yin G, Liu H, Li R, Flemming RL, Sun X (2009) Carbon nanotubes supported Pt–Au catalysts for methanol-tolerant oxygen reduction reaction: a comparison between Pt/Au and PtAu nanoparticles. *J Power Sources* 194(2):668–673

Synthesis, Modification, and Characterization of Nanocarbon Electrodes for Determination of Nucleic Acids

David Hynek, Katerina Tmejova, Jiri Kudr, Ondrej Zitka,
Lukas NejdI, Pavel Kopel, Branislav Ruttkay-Nedecky,
Jindrich Kynicky, Jaromir Hubalek, Rene Kizek,
and Vojtech Adam

Contents

Introduction.....	242
Carbon Materials for Electroanalysis.....	243
Carbon Nanotubes.....	244
Graphene.....	250
Fullerene.....	252
Electroanalysis of Nucleic Acids on Carbon-Based Electrodes.....	253
Carbon as an Electrode Material for NA Detection.....	253
Electroanalysis of Nucleic Acid: Short Historical Overview.....	255
Modification of Electrode Surface.....	256
Carbon Paste Electrodes.....	257
Glassy Carbon Electrodes.....	257
Carbon Nanotubes.....	258
Graphene.....	260

D. Hynek • K. Tmejova • J. Kudr • O. Zitka • P. Kopel • B. Ruttkay-Nedecky
J. Hubalek • R. Kizek • V. Adam (✉)

Department of Chemistry and Biochemistry, Faculty of Agronomy,
Mendel University in Brno, Brno, Czech Republic, European Union

Central European Institute of Technology, Brno University of Technology,
Brno, Czech Republic, European Union

e-mail: d.hynek@email.cz; severo@centrum.cz; george.kudr@centrum.cz;
zitkao@seznam.cz; paulko@centrum.cz; brano.ruttkay@seznam.cz;
hubalek@feec.vutbr.cz; kizek@sci.muni.cz; vojtech.adam@mendelu.cz

L. NejdI

Department of Chemistry and Biochemistry, Faculty of Agronomy,
Mendel University in Brno, Brno, Czech Republic, European Union
e-mail: lukasnejdl@gmail.com

J. Kynicky

Central European Institute of Technology, Brno University of Technology,
Brno, Czech Republic, European Union

Diamond.....	261
Fullerene	261
Electrochemical Determination of Nucleic Acid on Modified Carbon Electrodes.....	262
Carbon Paste Electrodes	262
Glassy Carbon.....	262
Carbon Nanotubes.....	264
Graphene.....	266
Diamond.....	268
Fullerene	269
Conclusions.....	270
References.....	270

Abstract

Unique mechanical, electronic, chemical, optical, and electrochemical properties of nanosized carbon materials predestine them for numerous potential applications including photocatalysis, electrochemistry, electronics, and optoelectronics. Carbon nanotubes and graphene are some of the most intensively explored carbon allotropes in materials science. The possibility to translate the individual properties of these monodimensional (carbon nanotubes SWCN, MWCN) and bidimensional (graphene) building units into two-dimensional free-standing thick and thin films has paved the way to use these allotropes in a number of the mentioned applications. Moreover, the possibility to conjugate carbon nanomaterials with biomolecules has received particular attention with respect to the design of chemical sensors and biosensors. In this paper, we reviewed types, structure, and especially different methods of synthesis (preparation) of carbon nanomaterials including arc discharge, laser ablation, and chemical vapor deposition. Moreover, we mentioned some rarely used ways of arc discharge deposition, which involves arc discharge in liquid solutions in contrary to standard used deposition in a gas atmosphere. Besides synthesis, modifications of carbon nanomaterials with biologically important molecules for biosensing of DNA and RNA are discussed.

Keywords

Carbon • Nanoelectrode • Synthesis • Modification • Biochemistry • Nucleic acid • Adenine • Cytosine • Guanine • Thymine

Introduction

Electroanalytical techniques have been widely used for the determination of nucleic acids. These analyses can be divided according to many parameters, including the type of material of a working electrode (mercury, carbon, gold) or applied electrochemical method and/or structure of a detected system (presence or absence of biocompound(s)). Electrochemical determination of nucleic acid(s) on carbon electrodes can be divided into the two basic groups as follows: (i) hybridization-based

techniques and (ii) oxidation of DNA bases. Application of hybridization reaction is very widespread due to the specificity of determination and low limit of detection. The other way, oxidation of DNA bases is presented too. Improvement of physico-chemical properties of carbon electrodes is possible via a modification of its surface. The modification of surface is possible, in general, by chemical entities or biocompounds according to the suggested detection system. The following text is focused on the electroanalytical determination of nucleic acids by direct detection (mainly by oxidation of DNA bases) using chemically modified carbon electrodes.

Carbon Materials for Electroanalysis

Carbon nanostructures have been in the center of research activities since the discovery of fullerene in 1985. Interest in carbon and its importance can be demonstrated by Nobel Prize obtained by Andre Geim and Kostya Novoselov in 2010 for their research on unexpected properties of one atom thick layer of graphene. Various carbon nanostructures (Fig. 1) like carbon nanotubes (CNTs), graphene, and fullerene are the most studied ones as promising materials with applications in different technologies and in biology and medicine [1].

Carbon nanotubes can be described as rolled-up graphene sheets with no overlapping edges, and the ends are capped with half fullerene balls. Their diameters

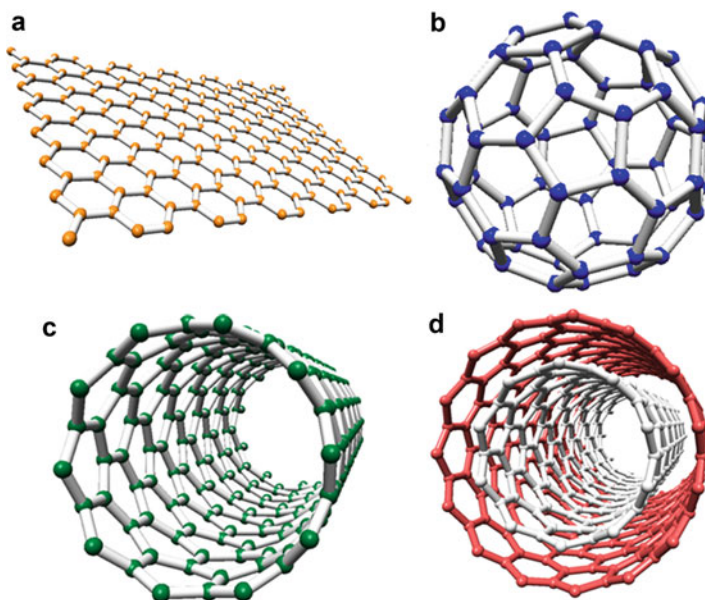


Fig. 1 Nanoallotropes of carbon. (a) Graphene, (b) fullerene C₆₀, (c) single-walled carbon nanotube, (d) multiwalled carbon nanotube

typically vary from 1 to 100 nm, and their lengths can be several orders of magnitude larger, up to millimeters and even centimeters long. This is, in the fact, the minimum energy conformation of a graphite layer of finite size. The properties of the nanotubes depend on the arrangement of the graphene sheets, the diameter and length of the tubes. The multiwalled nanotubes (MWNTs) consist of a coaxial assembly of several single-walled nanotubes (SWNTs), separated from one another by ~ 0.34 nm, which is slightly more than the interlayer distance in single-crystal graphite. Double-walled carbon nanotubes (DWNNTs), which consist of two graphene layers only, represent another form of nanotubes.

The graphene honeycomb lattice is composed of two equivalent sublattices of carbon atoms bonded together with σ bonds. Each carbon atom in the lattice has a π orbital that contributes to a delocalized network of electrons. Graphene possess 1D structure, and monolayer or few-layer graphene is known. Graphite oxide is also planar, but there are also oxygen atoms involved in the structure.

Fullerenes are composed of carbon, such as C_{60} and C_{70} , which may carry additional functional groups. Fullerenes are spherical molecules containing aromatic moieties, but despite their extensive conjugation, they behave chemically and physically as electron-poor alkenes rather than electron-rich aromatic systems. Fullerene is a rigid substance with 12 pentagons and 20 hexagons constituting a single C_{60} molecule with a hybridization of sp^2 for all the carbon atoms and a length of C–C bond of 1.46 Å. It follows the Euler theorem of spherical network closure where the pentagons are responsible for the formation of curvature in the fullerene structure. The most stable is C_{60} followed by C_{70} , C_{76} , C_{78} , C_{80} , C_{82} , and C_{84} . In terms of addition reactions, it shows some similarity to olefins. Especially, the purely carbon-based fullerenes exhibit very low solubility in water. However, fullerenes have the ability to form stable aggregate clusters with nanoscale dimensions upon contact with water [1].

Carbon Nanotubes

Iijima et al. in 1991 used arc discharge method [2] to prepare CNTs. CNTs are produced between two graphite water-cooled electrodes at high temperatures (above 1700 °C) in a chamber with helium atmosphere at subatmospheric pressure. Thus prepared CNTs have less structural defects in comparison with other techniques. Vertically aligned CNTs were prepared by hydrogen arc discharge using pure graphite powder as a source of carbon without catalysts added. The activation of hydrogen radicals, the heating effect of the arc, and the electric field surrounding the arc column area are considered to play important roles for the non-catalyst growth of the CNTs [3].

Another method (Fig. 2a) used especially for the preparation of high-purity SWCNTs is laser ablation utilizing Nd:YAG and CO_2 lasers, where the laser energy for graphite target evaporation is used. Laser ablation of Ni or Fe is used to create nanoparticles within a reactive flame environment to catalyze in situ generation [4]. Ablation of Fe in a CO-enriched flame produces single-walled nanotubes, whereas

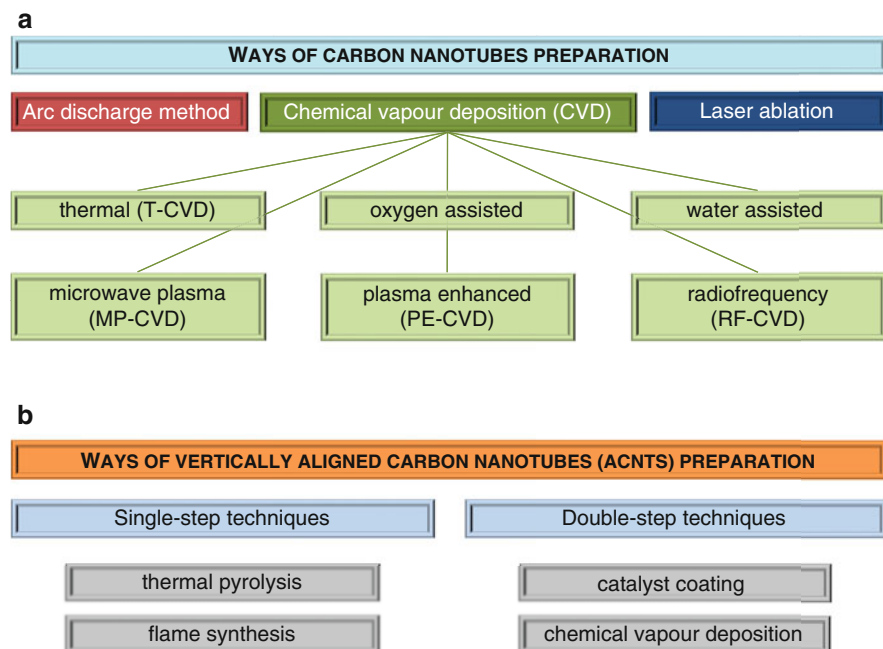


Fig. 2 (a) Scheme of subdividing ways of carbon nanotubes preparation. (b) Scheme of subdividing ways of vertically aligned carbon nanotubes preparation

ablation of Ni in an acetylene-enriched flame produces carbon nanofibers. Moreover, SWNTs and nanofibers can be synthesized within very short timescales, of the order of tens of milliseconds.

Nowadays, mostly low-temperature chemical vapor deposition (CVD) technique is applied in the field CNTs synthesis, because growth, alignment, length, diameter, purity, and density of CNTs can be better controlled. CO or hydrocarbons as a carbon source are heated to 800–1000 °C with a transition metal catalyst to promote growth of nanotubes [5]. The CVD is a suitable method with well-controlled reaction conditions for production of pure CNT (Table 1). Catalysts are often necessary [6]. Thermal [10], plasma-enhanced (PE), water-assisted [8, 9, 11], and oxygen-assisted CVD [7], microwave plasma (MP-CVD) [12, 13], or radiofrequency CVD (RF-CVD) [14] methods have been developed (Fig. 2a).

The most frequently used catalysts in the CVD are transition metals Fe, Co, and Ni [15], whereas substrates are Ni, Si, SiO₂, Cu, Cu/Ti/Si, steel, graphite and tungsten foil [16, 17], mesoporous silica [18, 19], and zeolites [20]. An influence of the composition and the morphology of the catalyst nanoparticles on growth of CNTs by the CVD has been summarized in the review paper [21]. Millimeter-long vertically aligned CNTs were grown after 12 h of deposition by adjusting the growth parameters for making the catalyst active for a long time (Table 2). The direct dependence of the number of walls of mm-long CNTs on the Fe catalyst thickness was observed.

Table 1 Carbon nanotube preparation with low-temperature chemical vapor deposition (CVD) technique

Carbon nanotube growth by PECVD: a review	[5]
The effect of nickel content of composite catalysts synthesized by hydrothermal method on the preparation of carbon nanotubes	[6]
A synthesis of high-purity single-walled carbon nanotubes from small diameters of cobalt nanoparticles by using oxygen-assisted chemical vapor deposition process	[7]
Optimization of water-assisted chemical vapor deposition parameters for super growth of carbon nanotubes	[8]
Synthesis and mechanical properties of carbon nanotubes produced by the water-assisted CVD process	[9]
Nanoscale zirconia as a nonmetallic catalyst for graphitization of carbon and growth of single- and multiwalled carbon nanotubes	[10]
Ink-jet printing of ferritin as method for selective catalyst patterning and growth of multiwalled carbon nanotubes	[11]
Direct growth of carbon nanotubes with a catalyst of nickel nanoparticle-coated alumina powders	[12]
Growth of vertically aligned bamboo-like carbon nanotubes from ammonia/methane precursors using a platinum catalyst	[13]
Chirality-enriched semiconducting carbon nanotubes synthesized on high surface area MgO-supported catalyst	[14]

Table 2 Carbon nanotube preparation with low-temperature chemical vapor deposition (CVD) technique connected with various catalysts

Selective synthesis of double-walled carbon nanotubes by CCVD of acetylene using zeolite supports	[20]
A catalytic chemical vapor deposition synthesis of double-walled carbon nanotubes over metal catalysts supported on a mesoporous material	[18]
Selective chemical vapor deposition synthesis of double-walled carbon nanotubes on mesoporous silica	[19]
Number of walls controlled synthesis of millimeter-long vertically aligned brushlike carbon nanotubes	[22]
Rhenium-catalyzed growth carbon nanotubes	[23]
Effects of temperature and catalysts on the synthesis of carbon nanotubes by chemical vapor deposition	[15]
Synthesis methods of carbon nanotubes and related materials	[21]
Synthesis and purification of bimetallic catalyzed carbon nanotubes in a horizontal CVD reactor	[16]
Large-area synthesis of conical carbon nanotube arrays on graphite and tungsten foil substrates	[17]
Control of dense carbon nanotube arrays via hierarchical multilayer catalyst	[24]
3-Orders-of-magnitude density control of single-walled carbon nanotube networks by maximizing catalyst activation and dosing carbon supply	[25]
Controlled synthesis of a large fraction of metallic single-walled carbon nanotube and semiconducting carbon nanowire networks	[26]

The successful syntheses of SWNTs, DWNT, and MWNTs with high percentages of yield (similar to 80 %) were achieved by varying in the thickness of catalyst layer. The effect of Al_2O_3 layer was found to be critical for this controlled synthesis [22]. Controlled synthesis of SWNTs and carbon nanowire networks using Fe/ Al_2O_3 catalyst by altering the hydrogenation and temperature conditions is demonstrated. The growth mechanism is based on the catalyst nanoisland analysis by AFM. The results are important to achieve the ultimate control of chirality, structure, and conductivity of one-dimensional all-carbon networks [25]. In addition, preparation of DWNTs over the Fe and Co catalyst on mesoporous silica was observed [18]. Ramesh et al. reported high-yield selective synthesis of DWNTs over Fe/Co-loaded high-temperature stable mesoporous silica [19]. Hiraoka et al. used zeolites as a substrate and acetylene over well-dispersed metal particles (Co/Fe binary system) at temperatures above 900 °C for selective synthesis of DWNTs [20].

Rhenium is a suitable catalyst for the synthesis of SWCNTs, DWCNTs, and MWCNTs with uniform diameter and defined numbers of shells (Table 2). Scanning and transmission electron microscopy investigations, Raman spectroscopy, and magnetic measurements show the tubular structure, the high crystallinity, and the diamagnetic character of the grown nanotubes. The growth mechanism of the re-catalyzed nanotubes was compared with the growth behavior supported by the conventional catalyst metals iron, cobalt, and nickel [23]. The effective control of dense, high-quality carbon nanotube arrays using hierarchical multilayer catalyst patterns was demonstrated. Scanning/transmission electron microscopy, atomic force microscopy, Raman spectroscopy, and numerical simulations show that by changing the secondary and tertiary layers, one can control the properties of the nanotube arrays. The arrays with the highest surface density of vertically aligned nanotubes are produced using a hierarchical stack of iron nanoparticles and alumina and silica layers differing in thickness by one order of magnitude from one another. The results are explained in the terms of the effect of catalyst structure on carbon diffusivity [24]. Han et al. reported on a simple and effective method to maximize the number of nanoparticles as active catalyst. By modulating short pulses of acetylene into a methane-based CVD growth process, the density of SWCNTs is dramatically increased by up to three orders of magnitude without increasing the catalyst density and degrading the nanotube quality [26].

For the preparation of CNTs, hydrocarbons such as methane [27], ethane [28], ethylene [29], acetylene [30], xylene [31, 32], their mixtures [33], isobutane [34], or ethanol [35, 36] belong to the carbon sources. Resources for CNTs preparation are summarized in Table 3. In the case of gaseous carbon source, growth of CNTs strongly depends on the reactivity and concentration of gas-phase intermediates produced together with reactive species and free radicals as a result of hydrocarbon decomposition. Thus, it can be expected that the most efficient intermediates, which have the potential of chemisorption or physical sorption on the catalyst surface to initiate CNT growth, should be produced in the gas phase [42]. Thus, Zhang et al. prepared MWNTs with diameter of 40–60 nm by the catalytic decomposition of

Table 3 Resources for carbon nanotube preparation

High-quality double-walled carbon nanotubes produced by catalytic decomposition of benzene	[37]
Preparation and modification of carbon nanotubes	[38]
Preparation and desalination performance of multiwalled carbon nanotubes	[39]
Preparation of carbon nanotubes by pyrolysis of dimethyl sulfide	[40]
Catalytic decomposition of hydrocarbons on cobalt, nickel, and iron catalysts to obtain carbon nanomaterials	[29]
Chemical kinetics of catalytic chemical vapor deposition of an acetylene/xylene mixture for improved carbon nanotube production	[33]
Synthesis of carbon nanotubes in graphite microchannels in gas-flow and submerged-in-liquid reactors	[41]
Calibration of reaction parameters for the improvement of thermal stability and crystalline quality of multiwalled carbon nanotubes	[34]
Interdependency of gas-phase intermediates and chemical vapor deposition growth of single-walled carbon nanotubes	[42]
Prospective growth region for chemical vapor deposition synthesis of carbon nanotube on C–H–O ternary diagram	[28]
Nickel catalyst-assisted vertical growth of dense carbon nanotube forests on bulk copper	[32]
Growth of carbon nanotubes in six orthogonal directions on spherical alumina microparticles	[30]
Decomposition of ethanol and dimethyl ether during chemical vapor deposition synthesis of single-walled carbon nanotubes	[35]
Investigation of Fe/MgO catalyst support precursors for the chemical vapor deposition growth of carbon nanotubes	[27]
Effects of different carbon precursors on synthesis of multiwalled carbon nanotubes: purification and functionalization	[31]
Synthesis of heterostructured helical carbon nanotubes by iron-catalyzed ethanol decomposition	[36]

methane at 680 °C for 120 min, using nickel oxide–silica binary aerogels as the catalyst [38, 39]. Sano et al. evaluated two systems of metallic catalyst/carbon source for CNTs growth: ethanol/Co and benzene/Fe. Moreover, the authors investigated an effect of two different reactors (gas-flow reactor and a submerged-in-liquid reactor) on quality of CNTs [41]. Lyu et al. produced high-quality and high-purity DWNTs by a catalytic decomposition of benzene as an ideal carbon source and Fe–Mo/Al₂O₃ as catalyst at 900 °C. They obtained DWNTs bundles free of amorphous carbon covering on the surface and of a low defect level in the atomic carbon structure [37]. Du et al. synthesized CNTs by Co/MgO catalyzed pyrolysis of dimethyl sulfide at 1000 °C, which is rarely used as a carbon source. The presence of sulfur can promote the growth of long SWNTs or branched CNTs. The authors found that the concentration of dimethyl sulfide vapor as well as flow rate in the reaction chamber determines the quality of the product [40].

The growth of vertically aligned carbon nanotubes (ACNTs) is very often studied because it is a method giving the highest yields in CNTs growth [43]. Vertically aligned carbon nanotubes are bundles of carbon nanotubes oriented perpendicular to a substrate, and horizontally aligned CNTs are parallel to the substrate. The methods of synthesis of ACNTs can be classified into single-step and double-step

Table 4 Various ways of vertically aligned carbon nanotubes preparation

Size-selective growth of double-walled carbon nanotube forests from engineered iron catalysts	[44]
Growth of vertically aligned arrays of carbon nanotubes for high field emission	[45]
Aligned synthesis of multiwalled carbon nanotubes with high purity by aerosol-assisted chemical vapor deposition: effect of water vapor	[46]
Synthesis of vertically aligned carbon nanotubes on stainless steel by water-assisted chemical vapor deposition and characterization of their electrochemical properties	[47]
Wet-chemical catalyst deposition for scalable synthesis of vertically aligned carbon nanotubes on metal substrates	[48]
Tailoring the microstructure and mechanical properties of arrays of aligned multiwalled carbon nanotubes by utilizing different hydrogen concentrations during synthesis	[49]
Synthesis of aligned carbon nanotubes	[50]
Origin of periodic rippling during chemical vapor deposition growth of carbon nanotube forests	[43]
Plasma-enabled, catalyst-free growth of carbon nanotubes on mechanically written Si features with arbitrary shape	[51]
Synthesis of tall carpets of vertically aligned carbon nanotubes by in situ generation of water vapor through preheating of added oxygen	[52]
Synthesis and field emission properties of vertically aligned carbon nanotube arrays on copper	[53]

techniques (Fig. 2b). Thermal pyrolysis and flame synthesis are the most common single-step methods (Table 4). The double-step methods, including catalyst coating and chemical vapor deposition (Table 4), provide more control over the catalyst morphology [50]. Nanolithography is used to create pattern of catalyst on the surface on which CNTs are formed using the CVD methods. Kim et al. used Si as a substrate and Ni as a catalyst deposited on a diffusion barrier from Ni/Ti. Ni dots catalyst of 1.6 μm and about 200 nm was patterned using UV and e-beam lithography, respectively. The method of CNTs formation uses the reactor with gas ratio $\text{C}_2\text{H}_2/(\text{H}_2 \text{ or } \text{NH}_3)$ at 620 $^\circ\text{C}$. The diameter of created CNTs depended on Ni dots size [45]. Yamada et al. used high efficiency water-assisted CVD synthesis of vertically aligned DWNTs forests with heights of up to 2.2 μm using Fe catalyst. They achieved CNTs with a carbon purity of 99.95 % [44]. Aligned MWCNTs with high purity and bulk yield were achieved on a silicon substrate by an aerosol-assisted chemical vapor deposition. The introduction of specific amounts of water vapor played a key role in in situ controlling the purity and surface defects of the nanotubes. However, excessive water vapor would inhibit the MWCNTs growth with a poor surface quality. In addition, it has been found that the surface morphology of the CNTs can be modified intentionally through producing some surface defects by tuning the amount of the water vapor, which may offer more nucleation sites on the chemically inert surface of CNTs for various applications such as a catalyst support [46]. Kim et al. demonstrated synthesis of carbon nanotubes on stainless steel by a water-assisted chemical vapor deposition using an Al/Fe bimetallic catalyst. A forest of vertically oriented carbon nanotubes with a length of a few hundreds of micrometers were grown on the substrates. Electrical measurement confirmed that the CNTs were electrically connected to the stainless steel [47]. A scalable process for growth of CNTs on metallic substrates was developed. This process includes

dip-coating steps for a wet-chemical catalyst and cocatalyst layer deposition and a subsequent chemical vapor deposition step. Organic metal salt/2-propanol solutions were applied as precursors for alumina cocatalyst thin films and the actual Fe (Co, Mo) catalyst layer. Vertically aligned CNTs were obtained on catalyst-coated nickel foil at atmospheric pressure and 730 °C using ethene as a carbon source. The influence of the catalyst composition on growth rate, density, and structure of CNT films was showed [48]. Raney et al. synthesized vertically aligned CNTs in a chemical vapor deposition system with a floating catalyst, using different concentrations of hydrogen in the gas feedstock. The effect of different concentrations of hydrogen on the microstructure and mechanical properties of the resulting material is given [49]. Neupane et al. reported the synthesis of periodic arrays of CNTs with different densities on a copper substrate by employing nanosphere lithography and plasma-enhanced chemical vapor deposition. At a growth pressure of 8 Torr and temperature of 520 °C, vertically aligned bamboo-like CNTs were formed with a catalyst particle on the tip [53]. Dense millimeter-tall carpets of vertically aligned CNTs were grown using the thermal CVD from ethylene and hydrogen gases with two or three independently controlled hot zones while introducing controlled flows of oxygen. Through preheating, oxygen and hydrogen reacted through a multistep reaction to form water, enabling the growth of tall CNT carpets. The simplicity of this CVD process provides a simpler alternative to direct the addition of water vapor for manufacturing tall carpets of ACNTs with a high level of control [52]. Simple, rapid, catalyst-free synthesis of complex patterns of long, vertically aligned MWCNTs strictly confined within mechanically written features on a Si(100) surface has been reported. It is shown that dense arrays of the nanotubes can nucleate and fully fill the features when the low-temperature microwave plasma is in a direct contact with the surface [51]. More information about CNTs can be found, for example, in the following papers and reviews [54–59].

Graphene

Preparation of graphene by the CVD growth on epitaxially matched metal surfaces was firstly reported by May [60]. Blakely et al. published many papers on growth of monolayer and bilayer graphite on Ni [61–63]. Growth on SiC wafer surfaces by high temperature (1300 °C) evaporation of Si in ultrahigh vacuum [64, 65] or atmospheric pressure [66] is a method to prepare wafer-size graphene [67]. Large-area monolayer or multilayer graphene was prepared on copper by deposition of carbon [68–70].

Ruoff et al. published numerous papers on micromechanical exfoliation for preparation of graphene [71, 72]. Micromechanical exfoliation can be used to prepare graphene of high quality that is electrically isolated for fundamental studies of transport physics and other properties but does not appear to be scalable to large area. It typically produces graphene particles with lateral dimensions in the order from tens to hundreds of micrometers.

Exfoliation of graphite in solvents was also reported as another method to make dispersions of graphite in various organic solvents like dimethylformamide (DMF) or *N*-methylpyrrolidone (NMP) in an ultrasonic bath. Unfortunately, the yield of

graphene prepared by this method is relatively low. Graphene dispersions with concentrations up to 0.01 mg/ml were produced by dispersion and exfoliation of graphite in NMP. This is possible because the energy required to exfoliate graphene is balanced by the solvent graphene interaction for solvents whose surface energies match that of graphene. Individual graphene sheets were confirmed by Raman spectroscopy, TEM, and electron diffraction. This method results in a monolayer yield of 1 %, which could potentially be improved to 7–12 % with further processing. Semitransparent conducting films and conducting composites can be also produced [73].

Substrate-free synthesis of graphene in a microwave plasma reactor was demonstrated, too [74]. Graphene sheets in the gas phase were prepared using a substrate-free way in atmospheric pressure microwave plasma reactor. Graphene sheets were synthesized by passing liquid ethanol droplets into argon plasma. The graphene sheets were characterized by TEM, electron energy loss spectroscopy, Raman spectroscopy, and electron diffraction. Graphene can be created without three-dimensional materials or substrates.

Arc discharge synthesis of multilayered graphene has also been reported [75]. N-doped multilayered graphene sheets were synthesized in large scale by the method of direct current arc discharge between pure graphite rods. For the use of NH_3 as one of the buffer gas, the multilayered graphene sheets were doped with N without the addition of other nitrogen source. The graphene sheets were mainly of two to six layers and their sizes of about 100–200 nm. The multilayered graphene sheets can be purified by a simple heat treatment process. The content of N atoms in the multilayered graphene sheets can be tuned by simply changing the proportion of NH_3 in the atmosphere. Arc discharge between graphite electrodes under a relatively high pressure of hydrogen yields graphene flakes that generally contain two to four layers in the inner wall region of the arc chamber. The method is eminently suited to dope graphene with boron and nitrogen by carrying out arc discharge in the presence of diborane and pyridine, respectively [76].

Graphene can be obtained by chemical reduction of graphite oxide colloidal dispersions with reducing agents, such as hydrazine [77], hydroquinone [78], sodium borohydride [79], or ascorbic acid [80]. Reduction by a thermal treatment [81, 82] has been reported to be an efficient and low-cost method [83, 84]. Graphite oxide (GO) is mostly prepared by the Hummers method [85]. It involves oxidation of graphite with potassium permanganate and sulfuric acid. Graphite salts made by intercalating graphite with strong acids such as sulfuric acid, nitric acid, or perchlorate acid have also been used as precursors for the subsequent oxidation to GO [86].

A green and facile method for the preparation of gelatin-functionalized graphene nanosheets (gelatin–GNS) was reported by using gelatin as a reducing reagent. Meanwhile, gelatin also played an important role as a functionalized reagent to prevent an aggregation of the graphene nanosheets. The obtained biocompatible gelatin–GNS exhibited excellent stability in water and various physiological fluids including cellular growth media as well as serum, which were critical prerequisites for biomedicine application of graphene [87]. More information can be found in reviews [88, 89]. The summary of methods used for this purpose is shown in Table 5.

Table 5 Various ways of graphene preparation and characterization

Preparation of graphitic oxide	[85]
Untersuchungen am graphitoxid. 5. Über den bildungsmechanismus des graphitoxids	[86]
A mechanism for surface reconstruction at room temperature	[60]
Equilibrium segregation of carbon to a nickel (111) surface – surface phase transition	[61]
Carbon monolayer phase condensation on Ni (111)	[63]
Carbon interaction with nickel surfaces – monolayer formation and structural stability	[62]
Tailoring graphite with the goal of achieving single sheets	[71]
Three-dimensional manipulation of carbon nanotubes under a scanning electron microscope	[72]
Ultrathin epitaxial graphite: 2D electron gas properties and a route toward graphene-based nanoelectronics	[64]
Electronic confinement and coherence in patterned epitaxial graphene	[65]
Functionalized single graphene sheets derived from splitting graphite oxide	[82]
Single sheet functionalized graphene by oxidation and thermal expansion of graphite	[81]
Synthesis of graphene-based nanosheets via chemical reduction of exfoliated graphite oxide	[77]
Substrate-free gas-phase synthesis of graphene sheets	[74]
High-yield production of graphene by liquid-phase exfoliation of graphite	[73]
Bottom-up growth of epitaxial graphene on 6H-SiC(0001)	[67]
Synthesis of water-soluble graphene	[79]
Facile synthesis and characterization of graphene nanosheets	[78]
Toward wafer-size graphene layers by atmospheric pressure graphitization of silicon carbide	[66]
Large-area synthesis of high-quality and uniform graphene films on copper foils	[68]
Evolution of graphene growth on Ni and Cu by carbon isotope labeling	[69]
Transfer of large-area graphene films for high-performance transparent conductive electrodes	[70]
Chemical methods for the production of graphenes	[84]
Simple method of preparing graphene flakes by an arc discharge method	[76]
The chemistry of graphene oxide	[83]
All-organic vapor sensor using ink-jet-printed reduced graphene oxide	[80]
Synthesis of graphene and its applications: a review	[88]
Large-scale synthesis of N-doped multilayered graphene sheets by simple arc discharge method	[75]
Chemical preparation of graphene-based nanomaterials and their applications in chemical and biological sensors	[89]
Green and facile synthesis of highly biocompatible graphene nanosheets and its application for cellular imaging and drug delivery	[87]

Fullerene

Fullerenes are molecules with minimum of 60 atoms of carbon with a spherical molecular structure where the carbon atoms are positioned at the vertices of a regular truncated icosahedron structure (for Buckminsterfullerene C_{60}) [90]. There are also higher mass fullerenes with different geometric structures, such as C_{70} , C_{76} , C_{78} , and C_{80} [91]. However, the C_{60} is the most widely studied molecule. The method of production based on the use of an arc discharge between graphite electrodes in 200 Torr of helium gas is still the most used method for preparation of fullerenes [92].

Table 6 Various ways of fullerene preparation and characterization

C-60 – Buckminsterfullerene	[90]
Solid C-60 – a new form of carbon	[92]
Improved chromatographic separation and purification of C-60 and C-70 fullerenes	[93]
NMR characterization of isomers of C-78, C-82, and C-84 fullerenes	[91]
High-performance liquid-chromatographic separation of fullerenes (C-60 and C-70) using chemically bonded gamma-cyclodextrin as stationary phase	[94]
Chromatographic separation of fullerenes	[95]
Fullerene-derivatized amino acids: synthesis, characterization, antioxidant properties, and solid-phase peptide synthesis	[96]

Fullerenes are generated through the heat produced at the contact point between the electrodes. The evaporation of the carbon at this point promotes the formation of soot, which contains approximately 15 % of fullerenes (13 % of C₆₀ and 2 % of C₇₀). Generally, the mixture of fullerenes is separated by using liquid chromatography [93–95]. Applications of fullerenes in biomedicine were summarized by Yang et al. [96]. The summary of methods used for this purpose is shown in Table 6.

Electroanalysis of Nucleic Acids on Carbon-Based Electrodes

Electrochemical analysis is a widely used technique for the determination of nucleic acid (NA) [97–102]. In the general view, we can distinguish several approaches in DNA electroanalysis. The simplest approach is a direct detection of oxidizable or reducible components of DNA (bases, nucleosides, nucleotides). While mercury electrodes are suitable for studies including NA base reduction, solid electrodes, especially carbon electrodes, are used for oxidation processes. The other way is focused on an application of hybridization of nucleic acid in combination with the detection of electroactive labels or intercalators [103–106]. This chapter is focused only on the direct detection of oxidizable parts of NA on the carbon electrodes.

Carbon as an Electrode Material for NA Detection

Carbon as an electrode material has some unique properties, which are extremely important in terms of electrochemistry. It is especially its ability to bind a variety of functional groups that paved the way for a large number of electrode surface modification [103, 107–109]. Carbon materials have one important property, great adsorption potential. Adsorption of nucleic acids was firstly demonstrated by Brabec et al. [110]. Because of a hydrophilic nature of the carbon surface (reached by an oxidative pretreatment), NAs are adsorbed via phosphate backbone, leaving bases accessible for hybridization. If the carbon electrode is positively charged, electrostatic attraction of negatively charged backbone makes the adsorption even stronger [97]. It is obvious that the physicochemical conditions (ionic strength or a type of the background electrolyte) influence the adsorption phenomenon.

To carbon materials, which are used in electrochemistry, glassy carbon (GC), pyrolytic graphite (PG), amorphous carbon, carbon paste (CP), and carbon nanomaterials (highly conducting diamond films, graphene, carbon nanotubes (CNTs)) belong. These materials are used to manufacture a glassy carbon electrode (GCE), carbon paste electrode (CPE), carbon microelectrode (CME), electrodes with carbon composites (CCE), and carbon screen-printed electrodes (CSPE) that are sometimes called thick-film graphite-containing electrodes (TFGE). As the electrode it is also possible to use ordinary pencil graphite [111]. In some studies the suitability of carbon electrodes for electrochemical analysis of nucleic acids was compared [111, 112]. Carbon electrodes are probably the most frequently employed electrodes in studies of oxidation of NA bases and their nucleotides or nucleosides.

Carbon electrodes create the wide potential window, which allows the direct oxidation of guanine (G), adenine (A), thymine (T), and cytosine (C) [97]. Detected signals of bases start at around +0.7 V versus SCE for guanine and increase in the order of the abovementioned bases (Fig. 3; [113]). Binding of bases to the ribose and/or deoxyribose does not change the electrochemical behavior significantly. Therefore, nucleotides and oligonucleotides can be accumulated and directly oxidized [114]. It was shown that A is oxidized in a process involving a total of

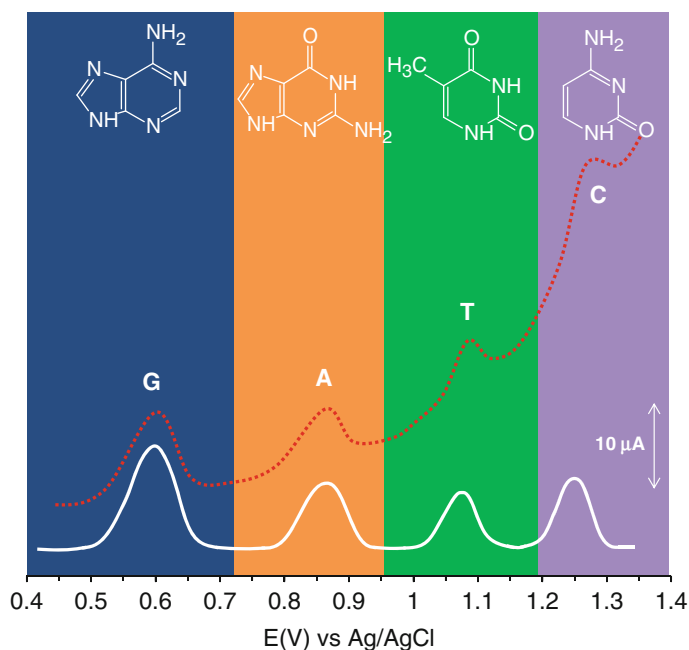


Fig. 3 Differential pulse voltammogram obtained with a 3 mm diameter GCE electrode for the mixture of 2×10^{-5} M guanine (G) and adenine (A), 2×10^{-4} M thymine (T), and cytosine (C) in 0.1 M phosphate buffer (pH 7.4) as a supporting electrolyte. *Pointed curve* is real measured voltammogram; *solid curve* is baseline-corrected voltammogram

six electrons per single A molecule [115]. G is oxidized electrochemically in a four electron process to give an unstable intermediate, followed by further reactions yielding either parabanic acid or oxalylguanine [116]. Although purine bases were focused in most of studies, T and C were also shown to produce oxidation signals [117]. While the detection of signals of individual bases was mentioned above, the simultaneous determination of all four DNA monophosphate nucleosides by differential pulse voltammetry (DPV) at GCE has been reported [118]. The limit of detection was shown to be less than 1 μM for each nucleotide.

Electroanalysis of Nucleic Acid: Short Historical Overview

In the early electrochemical studies of nucleic acids, the technique of polarography was used [119]. In polarography, reduction signals of electroactive components of nucleic acids are analyzed using hanging mercury drop electrode. History of detection of components of nucleic acids on carbon electrodes began at the end of 1970s, when the first voltammograms of residues of oxidation of purine bases (guanine and adenine) in denatured DNA and RNA were recorded by DPV on a pyrolytic graphite electrode [98, 110]. A few years later simultaneous oxidation of both purine bases in dsDNA was reported [98]. It has been found that both purine bases provide oxidative signals over a wide pH range from 0 to 12.5 [115, 116]. At the end of the 1990s, in contrast with previous studies, electroactivity of pyrimidine bases and later the corresponding nucleosides and nucleotides were proved [117, 118]. In this decade, the existence of new carbon materials was discovered.

Carbon electrodes challenged the mercury electrodes in terms of sensitivity only after the application of constant current chronopotentiometric stripping (CPS) analysis or square wave voltammetry (SWV) with baseline correction, enabling determination of submicromolar oligonucleotide (ODN) concentrations (in the order of ng/ml) [112, 120]. CPS combines an electrochemical oxidation pretreatment of carbon electrode or more precisely its surface and preconcentration of an analyte. Pretreatment is based on application of a constant potential on a pretreated electrode. The aim of pretreatment is to improve electrode surface properties and increase the amount of analyte adsorbed on the electrode during preconcentration step. Suitable pretreatment includes a series of polishing, sonication, scanning in electrolyte, electrochemical activation (application of constant potential), and cycling in new electrolyte for GCE [121]. Then the accumulated NA is oxidized by a constant anodic current, and the dependence of potential on time is recorded. While this method is quite sensitive, high potentials are need to oxidize DNA directly, and consequently high background currents are an issue [122].

The application of CNTs in the electrochemistry of NA was started several years ago. A contribution of CNTs lies mainly in their unique electric, thermal, chemical, mechanical, and 3-D spatial properties [123]. Besides the most common applications of CNTs lie in the construction of NA biosensors (single strand probe attached to the surface of CNT), some applications in direct NA detection, mainly direct oxidation of DNA G residues, have been published [124, 125]. The principle of

detection relies on the enhancement of the G oxidation due to the large specific surface of the CNTs, which results in an increased number of detected molecules of NA. Graphene as another promising carbon material was used for the electrochemical detection of NA. Oxidation signals of DNA bases were detected by Zhou et al. [126]. They used chemically reduced graphene oxide on a GCE to determine all four DNA bases at physiological pH.

Modification of Electrode Surface

The functionality of electrode materials is limited through the available potential window. In electrochemical measurements, the analytes can be monitored if they are electroactive, and their electrochemical response is within the operational potential range. The reactivity of individual compounds is closely connected with the electrochemical transformations on the surface of electrode (electron transfer). The other important phenomena, which influenced the obtained results, are sorption effects on the electrode surface.

The primary purpose of the modification of the electrode surface is to improve its analytical performance either by increasing its sensitivity and selectivity or by protecting the surface from unwanted reactions. In general, four main reasons for modifying the electrodes involving typical modifier–substrate interactions, which increase the analytical qualities of the electrodes, may be defined:

- Preconcentration of components of the analyte
- Exploitation of catalytic electrochemical responses
- Immobilization of molecules involved in electrochemical reactions
- Change of the physical properties of the electrode surface

The abovementioned information could be understood in general; it means that is valid for both basic groups of electrode modifiers (biomodifiers and non-biomodifiers). Our chapter is focused on non-biomodifiers. From this reason it could be said that the chemically modified electrodes (CMEs, understood as electrodes, which do not contain the bio component) are the main object of our interest. CMEs are, in general, understood as electrodes that possess chemical reactivity besides their ability to transfer the electrons to/from the analyte. This is possible by the presence of reactive groups or substances on the electrode surface [127].

The electrochemical performance of carbon materials is determined basically by the electronic properties and, given by its interfacial character, the surface structure and surface chemistry (i.e., surface terminal functional groups or adsorption processes) [128]. Such features would affect the electrode kinetics, potential limits, background currents, and the interaction with molecules in solution. Carbon materials are interesting because of the presence of different allotropes and their electronic and electrochemical properties. According to their structure, they are divided into graphene, diamond, diamond-like carbon, carbon, graphite, and fullerene. Due to abovementioned facts, each material is modified in another way, and therefore the next part of the text is divided according to individual types of carbon structures.

Carbon Paste Electrodes

Historically, carbon paste electrodes were the first modified carbon electrodes. The concept of modified electrode appeared in the 1970s for the first time and was strongly propagated by Murry [129, 130] and later by Wang [131]. Modification of carbon paste electrodes can be divided according to various criteria as follows: method of modification, type, and/or modifier location. Basically, the modifications can be separated to *intrinsic* (components that create the paste are modified by functional groups) and *extrinsic* (modifiers are added to the electrode components as a further components) modification.

The *intrinsic modification* is usually done directly via the pasting liquid or particles. The first step of covalent modification with reactive groups is oxidation of the carbon surface by strong oxidizing reagent (nitric acid), which produces the oxygen-containing groups on the surface. Reduction of carbonyl groups that can be chemically reduced to phenols or alcohols and can be subsequently used (or used as anchoring groups for modifier) could be the next step of modification. Modifier molecules can be bound via spacers or directly in dependence on chemical structure of modifiers [127].

Extrinsic modifications should be further subdivided according to the placement of the modifying agent, particularly distinction of the surface or bulk modifications [127]. The surface modification is characterized by the presence of modifier just on the electrode surface (thin layer, film, or membrane). These surface modifications contain submonolayers (modifier is spread fortuitously over the electrode in an amount that is necessary to create monolayer [132]), monolayers (modifier molecules cover the surface of electrode to create single layer normally achieved as self-assembled monolayers [133] or Langmuir–Blodgett films [134]), and polylayers (many layers of the modifier that can be homogenous/heterogeneous, e.g., conductive organic polymers [135], or redox polymers [136]). In the case of bulk modification, a modifier can be added directly to the carbon paste [137], or a modifier can be mixed or adsorbed on the powder during the preparation of carbon paste [138].

Glassy Carbon Electrodes

Glassy carbon was the further carbon material which historically creates the next step of “evolution.” This material seems to be very suitable for the modification procedures (especially due to its surface properties). In general, the modification of glassy carbon electrodes can be divided into several points (directions). The first one includes physical modification through the applied voltage, duration, and pH value of electrolyte. This direction is presented by Wang et al. [139]. Opposite this the chemical modifications represent the next way of modification. Gautier et al. [140] modified glassy carbon electrodes by an acetonitrile solution containing 0.1 M Bu_4NPF_6 as a support salt and 1 mM 4-chloromethylphenyl diazonium tetrafluoroborate. The combination of both the abovementioned approaches is presented by the linkage of carbon nanotubes to the surface of glassy carbon. One example of such a

procedure was published in [141], where glassy carbon electrode was modified by dispersing CoNP/MWCNT (cobalt-immobilized MWCNT).

Although graphite, carbon nanotubes (CNTs), and fullerene are built from the same basic element, the chemical reactivity is substantially different among them [128]. The chemical reactivity is higher for CNTs than for graphene layer, but lower if compared with fullerene [142–144]. Such behavior can be closely related to curvature of the surface of the carbon structure.

Graphite could be modified through the number of edge plane sites present on the electrode surface. According to this, carbon-based material can be divided into several groups: highly pyrolytic graphite (HOPG), edge plane pyrolytic graphite (EPPG), and basal plane pyrolytic graphite (BPPG). From the work of Li et al. [145], it follows that there are two main factors that influence voltammetry: (a) the density of edge plane sites for electrooxidation of the electrolyte and (b) the density of basal plane sites available for adsorption. It is clear that the morphology of surface plays a critical role. Modification of graphite electrodes by SWCNT is another possibility. Disposable graphite electrodes modified by SWCNT (SWCNT–PGEs) were prepared by Erdem et al. [146]. According to this protocol: at the first step, the SWCNT solution was prepared – the amount of SWCNT was suspended in DMF and subsequently sonicated for 1 h at room temperature. The second step involves the preparation of SWCNT–PGEs – each pencil lead was submerged into the 110 μl of SWCNTs solution 1 h to form a thin SWCNTs layer on the electrode surface. Then electrodes were washed out with solution consisting of 0.5 M acetate buffer with 20 mM NaCl (pH 4.8) for 10 s and allowed to dry for 15 min at upside down position.

Carbon Nanotubes

Carbon nanotubes (CNTs) have been studied for their excellent specific properties for many years. From the view of possible modifications, it must be remembered that ends of CNTs exhibit higher chemical reactivity than the walls. In addition, the presence of local defects on the walls also constitutes efficient reactive sites [147]. For instance, when CNTs are subjected to oxidative acid treatment, the local creation of carboxylic, ketone, alcohol, and ester groups represents introduction of active sites that can be profited for molecular anchoring [128, 148].

The strategies for modifying the surface of CNTs can be divided into three general areas:

- Covalent binding (chemisorption) of the modifier to the CNTs through the chemical or electrochemical activation
- Physical adsorption of the modifier onto the CNT surface
- Miscellaneous methods of modification (incorporation of CNTs into film-modified electrodes and intercalation of the modifier into the CNTs)

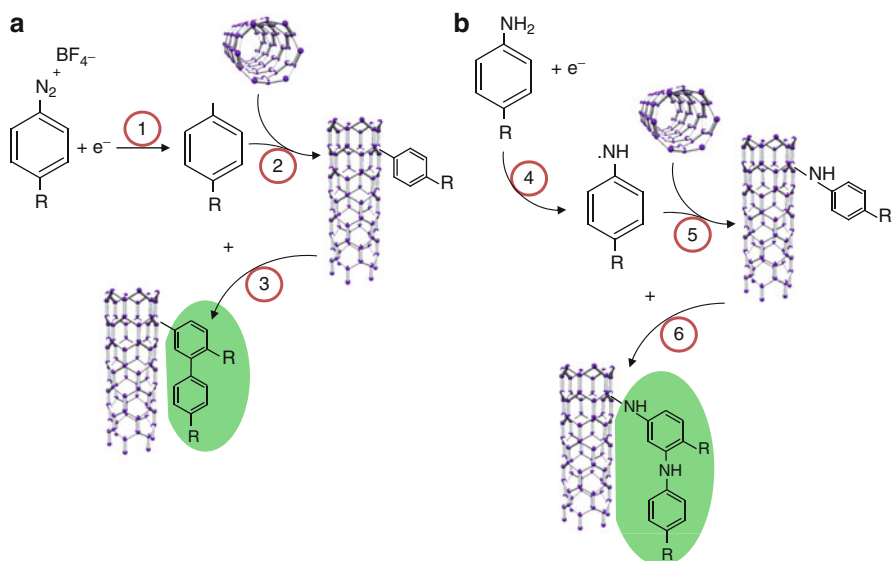


Fig. 4 The scheme of derivatization mechanism of CNTs via the electrochemical reduction of (a) aryldiazonium salts and (b) via subsequent further electropolymerization. The reaction (1) is one-electron cathodic reduction and consists in release of molecule of nitrogen. Second reaction (2) accumulates product of reaction (1) on the sidewall of SWCNT. Step (3) presents a few individual reaction steps as H abstraction, radical propagation, and polymerization. Another product of reaction 1 is bounded to the modified SWCNT. The reaction (4) is one-electron anodic oxidation that results in release of hydrogen proton. Reaction (5) is the adsorption of radical intermediate of reaction 4 on the sidewall of SWCNT. Step (6) presents a few individual reaction steps as H abstraction, radical propagation, and polymerization. Another molecule (radical intermediate) of reaction 4 is bounded to the modified SWCNT. The modifier group R could be for (a) as it follows: R=Br, NO₂, SO₃H, COOH, CH₂Cl, and for (b) R=Cl, F, ⁿBu, CO₂Me, ⁿC₁₄H₂₉, and (–O–CH₂–CH₂)₃–OMe (Adapted and modified according to the [147])

The first way of modification represented by the covalent binding of modifiers can be further subdivided into two main parts related to the functional groups as it follows: modifications using diazonium salts and modifications using carboxyl groups. The first way, an application of diazonium salts, is based on the action of free radical species generated by the electrochemical oxidation or reduction of a solution-phase compound (Fig. 4). For this purpose aryldiazonium salts are commonly used [149–152]. The process is initiated by a one-electron reduction yielding dinitrogen, and free radical species are electrogenerated. They are subsequently attached covalently onto the surface of SWCNTs. A wide range of 4-substituted aryldiazonium salts have been employed, and a variety of behaviors have been illustrated by the modified CNTs [147]. Polymerization of the radical species on the surface of CNTs has been demonstrated for R=NO₂, Br, CH₂Cl, SO₃H, and COOH. The process results in a creation of polymer that is based on aryl chains.

The thickness of the deposited coating may be controlled effectively by the magnitude and direction of the applied potential [147]. One of the main issues of the electrochemically activated modification is the fact that the quantities of derived CNTs produced are rather limited and the modified CNTs are often difficult to remove from the surface of the electrode. Therefore, alternative bulk derivatization methods have been suggested [128, 147]. CNTs can also be modified in bulk (gram) quantities with aryldiazonium salts through thermolysis, photolysis, or chemical reduction of the diazonium moiety to form radical or cationic reactive intermediates, which can then attack the surface of the CNTs to form covalent bonds [125, 153–156].

Carboxylated CNTs are located on the border line between the modified and native CNTs. CNTs have some oxygen-containing functional groups located on the edge of the graphite sheets that make up the tube walls, particularly hydroxyl, quinonyl, and carboxyl moieties [128, 147]. The number of such groups is often used in any significant modification process. Simple stirring the CNTs in concentrated nitric acid is the most widely used method for preparation of carboxylated CNTs. This strong oxidizing agent introduces carboxyl groups at the ends of CNTs. The range of chemical species that can be coupled to carboxylated CNTs (e.g., through amide linkages or esterification) is often limited only by the chemical route available to create covalent bond in the target molecule.

The way of physical adsorption as modification process is very often connected with biocompounds as the applied modifier. Therefore this chapter is defined as a non-biomodification; this area of research will not be further discussed. Opposite this, an application of nanoparticles is presented. The physical adsorption of a large number of CdS nanoparticles onto the surface of SWCNTs through hydrophobic interactions, a process that is activated by first adsorbing acetone onto the SWCNT surface, has been described by Wang et al. [157].

The example of the third group that represents miscellaneous methods is the derivatization method of MWCNTs based on the partial intercalation of 4-nitrobenzylamine (4-NBA) molecules into both graphite powder and MWCNTs [158]. This procedure is able to process upon stirring the MWCNTs with a solution of 4-NBA in acetonitrile and is the first such example of an organic molecule partially intercalating into a graphitic material. Partial intercalation differs from full intercalation processes, which are well known for graphite and MWCNTs, in that the 4-NBA molecules only penetrate a small distance into the interlaminal spacing between the graphite sheets.

Graphene

Graphene is due to its excellent mechanical, chemical, thermodynamic, and electronic properties studied as a new suitable material for the preparation of electrodes. Graphene has edge plane structure, and this induces high electrode activity to various analytes [159]. The effect of edge plane defects on heterogeneous charge transfer kinetics and capacitive noise was studied on epitaxial graphene with the use of

inner-sphere and outer-sphere redox mediators. It was observed that anodic epitaxial graphene is a suitable material for the detection of nucleic, uric, and ascorbic acids and dopamine [160]. By reducing graphene oxide, it is possible to modify electrode for reaching a good electron transfer rate for the detection of specific biomolecules including DNA bases [159].

Diamond

Sp³-bonded diamond is an insulator; however, it is also used in biochemistry. One possibility how to modify the conductivity is a *boron-doped diamond* (BDD) substrate surface. Zhou et al. [161] prepared BDD film by a microwave plasma-assisted chemical vapor deposition and hot-filament chemical vapor deposition. By this way it is possible to modify surface of different substrates with various crystal sizes. According to this fact, BDD surface is possible to divide into nanocrystalline (grain size smaller than 100 nm) and polycrystalline films (grain in μm). Next to this fact, BDD has excellent properties, such as (a) low and stable capacitive background, (b) long-term response stability and high response reproducibility, (c) wide electrochemical potential window in aqueous electrolyte solutions, and (d) good biocompatibility due to carbon materials [162, 163]. The preparation of BDD has been described in [164] and more details are available in [165]. Shortly, BDD films grew on Si substrates by a microwave-assisted plasma chemical vapor deposition technique. B₂O₃ was dissolved in the acetone–methanol mixture. A thickness of a film (~40 μm) was achieved after 10 h deposition. The description of the whole area of the possible modifications of diamond surfaces was appropriately described by Wenmackers et al. [166].

Fullerene

The idea of introducing a *fullerene* (C₆₀) chemically modified electrode to the electrochemical research was firstly presented by Compton et al. [167]. In this work, CMEs were prepared by immobilizing C₆₀ films by drop coating onto surfaces of the noble metal electrodes, which were then coated with the Nafion protecting films.

Fullerene-based CMEs may be prepared in several different ways. The most common, simplest, and efficient procedure involves the electrode drop coating by using a fullerene solution of a volatile solvent, such as dichloromethane or chloroform [168, 169]. However, like this prepared small crystalline films are usually nonuniform and porous. Morphology of these films depends on the rate of solvent evaporation, concentration of the casting solution, nature of the solvent, and roughness of the electrode surface [148]. Hernandez et al. studied properties of new fullerene-doped carbon black-paste electrodes, exactly SWCNTs and C₆₀ [170]. The amount (yield) of fullerene was about 10 wt%. Electrochemical stability was studied for composites of *n*-type fullerene C₆₀–Pd polymers and MWCNTs [171].

Electrochemical Determination of Nucleic Acid on Modified Carbon Electrodes

Carbon Paste Electrodes

The parallel evolution of carbon materials and the electrochemistry of nucleic acid here met just in a point of direct detection of DNA bases. The carbon paste electrodes are over other connected with non-biomodification of electrode surface in detection of DNA bases. In principle, the electrode modification through the physical processes is possible. Preanodization and electrochemical pretreatment in adenine/DNA detection have been presented [172]. The chemical modification of carbon paste is more widespread. Broad spectrum of modifiers were used, for example, Na-montmorillonite [173], hexacyanoferrate [174, 175], *N*-butylpyridiniumtetrafluoroborate [176], clay mineral [177], or tris(2,2'-bipyridyl)dichloro-ruthenium(II)/Nafion [178].

Application of the modified carbon paste electrodes for the detection of the nucleic acid and/or its components leads to the use of nanoparticles. Their application appears in literature in the last years. The guanine determination is connected with the modification of TiO₂ nanoparticles by bis[bis(salicylidene-1,4-phenylenediamine)molybdenum(VI)] [179]. Arvand et al. published the simultaneous determination and direct electrooxidation behavior of guanine, adenine, and thymine on a TiO₂ nanoparticle–magnesium-doped zeolite Y-modified carbon paste electrode (TiO₂NPs–MgY/ZMCPE) [180]. Such modified electrode exhibited potent and persistent electrooxidation behavior followed by well-separated oxidation signals toward G, A, and T with increasing the oxidation current. Under the selected conditions, the signals of oxidation currents were proportional to the concentration of guanine, adenine, and thymine within the concentration range from 0.1 to 100 μM, 0.1 to 100 μM, and 8 to 1000 μM, respectively, with the detection limit 0.013, 0.02, and 0.878 μM, respectively.

Glassy Carbon

Glassy carbon electrodes are, according to the list of applications, probably the most applied electrodes in modifications. In general, the usage of glassy carbon electrodes to the detection of nucleic acid may be separated into several groups.

The first one could be named as a glassy carbon electrode modified through the physical processes. Electrochemically modified glassy carbon electrode (GCE) was used to study the electrochemical oxidation and detection of denatured single-stranded DNA by means of adsorptive stripping voltammetry [139]. The modification of GCE by electrochemical oxidation at +1.75 V (vs. SCE) for 10 min and cyclic sweep between +0.3 V and +1.3 V for 20 cycles in pH 5.0 phosphate buffer resulted in 100-fold improvement in sensitivity for detection of ssDNA.

The second group is characterized by the modification of GC surface by carbon nanotubes and graphene. This group of systems lies in the borderline between modifiers and modified surfaces. We decided to divide the whole text in accordance with

the material that is modified. Therefore, this part is placed here, because the materials that are modified in these cases are just GC and carbon nanotubes, and graphene are modifiers. The most common connection of glassy carbon with the other carbon material as a solid conductive material is its widely applied connection with CNTs. Several interesting constructions will be presented in the next paragraphs.

Abdullin et al. [181] present the glassy carbon electrodes modified with preoxidized MWCNTs. Guanine and deoxyguanosine monophosphate are strongly adsorbed on GCE/CNT and oxidized at +0.69 and +0.93 V (pH 7.0), respectively. The oxidation current of guanine DNA nucleotides adsorbed on a GCE/CNT is significantly higher for the thermally denatured biopolymer than for the native one.

Thangaraj et al. [182] prepared a graphitized mesoporous carbon-modified glassy carbon electrode (GCE/GMC) for simultaneous electrochemical oxidation of guanine (G) and adenine (A) at oxidation potentials +0.60 and +0.85 V, respectively, using DPV. Interestingly, the GCE/GMC showed highly efficient, stable, and well-defined voltammetric signals. Signal of thymine oxidation noticed discretely at +1.15 V versus Ag/AgCl on the GCE/GMC was not influenced for the simultaneous determination of G and A. In another study, Jalit et al. [183] reported the advantages of the adsorption and electrooxidation of oligonucleotides on glassy carbon electrodes (GCE) modified with a dispersion of MWCNT in poly-L-lysine (Plys) (GCE/MWCNT-Plys). Important enhancement in the oxidation signal of guanine was obtained by adsorptive stripping voltammetry (AdSV) due to a most favorable interaction between the negatively charged DNA molecules and the positively charged Plys that supports the MWCNT [183].

Construction of modification films on the surface of glassy carbon was presented too [184, 185]. The first case was showed by Wang et al. [184]. They suggested an efficient electrochemical approach for the evaluation of the level of DNA methylation according to the oxidation signal of DNA bases at an overoxidized polypyrrole (PPyox)-directed MWNTs film-modified glassy carbon electrode (GCE). As a result, all purine and pyrimidine bases, guanine (G), adenine (A), thymine (T), cytosine (C), and 5-methylcytosine (5-mC), exhibited well-identified oxidation signals on the PPyox/MWNTs/GCE. The direct potential resolution between 5-mC and C was determined to be +0.18 V, which was enough for the recognition of the signal and the accurate detection in a mixture [184]. The second example was presented by Tang et al. [185]. The authors prepared a composite film (MWCNT-PNF), which contained MWCNTs together with the incorporation of poly(new fuchsin) (PNF). It was synthesized on a glassy carbon electrode (GCE) by potentiostatic methods. The modification of GCE increases the electron transfer rate constant to approximately 350 %.

As it was mentioned above, graphene is the other popular carbon modifier of a surface of GCE. The graphene structure is considered as a basic structure of CNT structures. Several approaches related to this concept will be further described below. The basic concept was presented by Wang et al. [186] who investigated the electrochemistry of double-stranded DNA (dsDNA) on a graphene-modified glassy carbon electrode (GR/GCE). Electrochemical characterization showed that GR on GCE surface enhanced significantly the specific surface area and electrical conductivity of the sensing platform. On GR/GCE, the electrooxidation signal of guanine

residues in dsDNA was enhanced obviously, and the potential of signal was lowered significantly as compared to bare GCE. Under the optimal conditions, the detection limit of $0.35 \mu\text{g mL}^{-1}$ was estimated.

A functionalization of graphene by carboxylic groups (graphene-COOH) was prepared and used for a simultaneous detection of adenine and guanine by Huang et al. [187]. The obtained measurements indicated that both adenine and guanine showed the increase of the current of oxidation signal with the negative shift of the potentials in contrast to that on a bare glassy carbon electrode. The detection limit for individual determination of guanine and adenine was 5.0×10^{-8} M and 2.5×10^{-8} M, respectively. Usage of graphene oxide instead of graphene in similar concept was published by Zhou et al. [126]. They reported a chemically reduced graphene oxide (CR-GO)-modified GC electrode that exhibits a good electron transfer rate for certain biomolecules including DNA bases. The oxidation potentials of four free DNA bases ($10 \mu\text{g mL}^{-1}$) on the CR-GO shifted negatively with enhanced signal currents compared with GC and graphite-based electrodes.

The creation of graphene films on the surface of a GC electrode is shown by two various approaches. The first one was presented by Vin et al. [188], where the electrochemical behavior of guanine and adenine on the graphene and a Nafion composite film-modified glassy carbon electrode was investigated by DPV. Based on this, a novel electrochemical method was suggested and developed to simultaneously determine guanine and adenine with the detection limits of 0.58 (guanine) and 0.75 (adenine) μM . The second way is presented by Ba et al. [189] who prepared a poly(alizarin red)/graphene composite film-modified glassy carbon electrode (PAR/graphene/GCE) for simultaneous determination of four DNA bases (guanine, adenine, thymine, and cytosine) in 0.1 M phosphate buffer solution (pH 7.4).

The last group of modifiers is represented by nanoparticles. This area of research has been developed in last few years. We describe here one system presented by Ghavami et al. [190] for simultaneous detection of DNA bases (guanine, adenine, thymine, and cytosine) without any pretreatment or separation processes. This system is based on a glassy carbon electrode modified with silicon carbide nanoparticles (SiCNP/GC). The modified electrode shows an excellent electrocatalytic activity toward guanine, adenine, thymine, and cytosine. As it was showed in the work, this sensor can be used for nano- and micromolar detection of different DNA bases simultaneously or individually.

Carbon Nanotubes

Application of carbon nanotubes in electrochemical detection of nucleic acid is widely used. However, the most widely used constructions of electrode material (including modifications) lead to the development of biosensors. These biosensors utilize mostly immobilization and hybridization effects of nucleic acids. The connection of CNTs with other modifiers for detection of NAs is very infrequent. Such way of development is presented mainly by the modification of CNTs by nanoparticles. Several examples of such constructions are presented below.

Development of carbon materials led to the creation of CNTs as a new material with better physicochemical and electrochemical properties. Therefore, the direct detection of NAs on CNTs was presented before application of a modifier. Serpi et al. [191] investigated the performance of three types of multiwalled carbon nanotube paste electrodes (MWCNTPEs) in combination with adsorptive transfer stripping voltammetry for the determination of calf thymus dsDNA. The results indicated that the electroactivity inherent to carbon nanotube paste electrodes allows enhancing an oxidation signal of the guanine substantially in comparison with that obtained on the conventional carbon paste electrodes (CPEs). Based on the signal of guanine under optimal conditions, very low levels of dsDNA can be detected. The authors described short accumulation times for all three types of MWCNTPEs with detection limits of 2.64, 2.02, and 1.46 mg/L, respectively.

The next developmental stage of CNTs for electrochemical detection of nucleic acid is based on the application of nanoparticles, as was mentioned above. Several examples of such constructions are presented below.

Zhang et al. [192] prepared multiwalled carbon nanotube–gold (MWCNT–Au) nanocomposite-modified electrodes by using a one-step method, where gold nanoparticles were deposited on the sidewall of MWCNTs directly and orderly. The modification of gold electrode with these nanocomposites enhanced the electrochemical response of DNA bases and extended the application of relevant electrodes (Fig. 5). It is noted that the selective enhancement of electrochemical

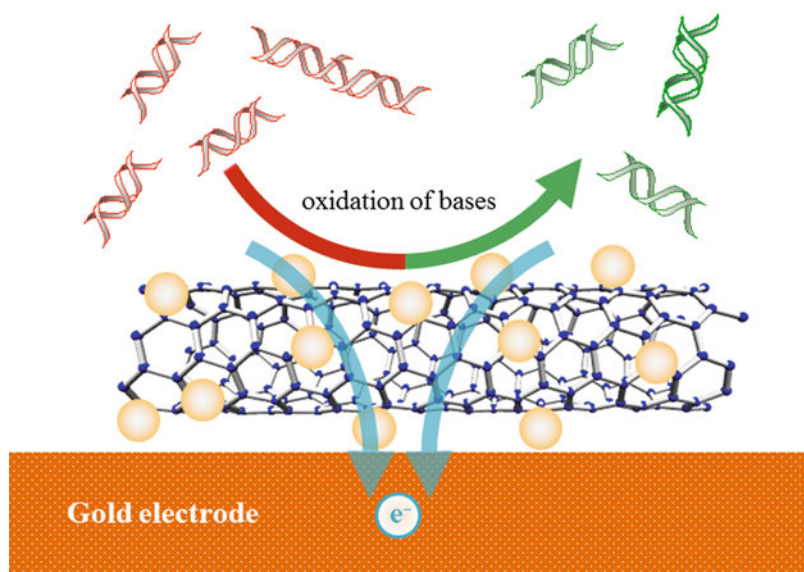


Fig. 5 Scheme of electrochemical detection of DNA bases based on MWCNT–Au nanocomposites modified gold electrode. Gold nanoparticles have been readily attached on the sidewall of MWCNT with homogenous size, and the size distribution was between 20 and 24 nm with average diameter of 22 nm

response of individual DNA bases was related to the special interactions of bases with the nanointerface and the large effective surface area of this modified electrode. Especially, the signal of pyrimidine bases was enhanced for several times on the MWCNT–Au nanocomposite-modified electrodes than that of the carbon nanotube-modified electrodes.

Another approach to the modifications by CNTs was presented by Fang et al. [193]. The authors used carbon nanotube (CNTs)/lanthanum hydroxide ($\text{La}(\text{OH})_3$) nanocomposite as electrode material for the determination of guanine and adenine. Cyclic voltammetry was used to characterize the modified electrode. The result demonstrated that the CNTs/ $\text{La}(\text{OH})_3$ -modified electrode provides an effective way on how to make the determination of adenine and guanine more effective. Detection limits were 0.22 and 0.26 μM , respectively.

Ensaifi et al. [194] developed an electrochemical sensor for the detection of guanine and adenine. They designed the modification of MWCNTs with NiFe_2O_4 magnetic nanoparticles; the whole complex was located on the surface of a glassy carbon electrode (Fig. 6). Incorporation of MWCNT/ NiFe_2O_4 nanohybrid onto the surface of the electrode increased the current of oxidation signals significantly; however, it reduces the potential of signals for guanine and adenine. The modified electrode was employed for detecting purine bases using linear sweep voltammetry. The signal currents exhibited linear dependence on concentration in the concentration range of 0.05–3.0 μM for guanine and in the concentration range of 0.1–4.0 μM for adenine. The limit of detection was found to be 0.006 and 0.01 μM for guanine and adenine, respectively.

The last example of modification of CNTs is based on the application of CeO_2 nanoparticles (CeO_2 -decorated multiwalled carbon nanotubes). This procedure was developed by Wei et al. [195] for electrochemical determination of guanine and adenine. Cyclic voltammetry (CV) and DPV were used to study the electrochemical oxidation of guanine and adenine. The detection limit for adenine and guanine was found to be 20 and 10 nM, respectively.

Graphene

Usage of graphene in the detection of NAs via direct electrochemical oxidation of bases is possible to divide, in the point of view of modification processes, into two groups related to the fact if the modification is located on a GC electrode or not. The GC electrodes are mentioned here as the most applied type of conducting surface connected with graphene (in this area of research). The group of detection systems connected with the presence of GC and graphene (here as a modifier) was mentioned above (see section “[Glassy Carbon](#)”). The other systems (graphene+modifier) will be described in the text below.

Graphene is characterized by the high electron transfer of DNA molecules [160] by electrochemical detection. Although DNA bases generally exhibit higher sensitivity under acidic conditions, graphene-based materials made it possible to measure all of the free DNA bases, even under neutral pH conditions [113]. This fact is

probably caused by the surface stacking effect between graphene and the target molecules that exhibit high electron transfer rates.

The comparison of graphene with the edge plane pyrolytic graphite (EPPG), basal plane pyrolytic graphite (BPPG), and electrodes modified by graphite was studied by Randviir et al. [196], who monitored electrochemical oxidation of adenine and guanine. The application of graphene led to a decrease of voltammetric response of adenine and guanine, respectively. Unfortunately, graphene has low density of edge plane sites, which account for the reduced voltammetric response. Therefore, the modification of the surface of the electrode by graphene was found to be analytically unacceptable.

On the other hand, modification of the graphene material has brought better results. Ambrosi et al. [197] showed stacked graphene nanofibers (SGNFs), which demonstrate superior electrochemical performance for oxidation of DNA bases.

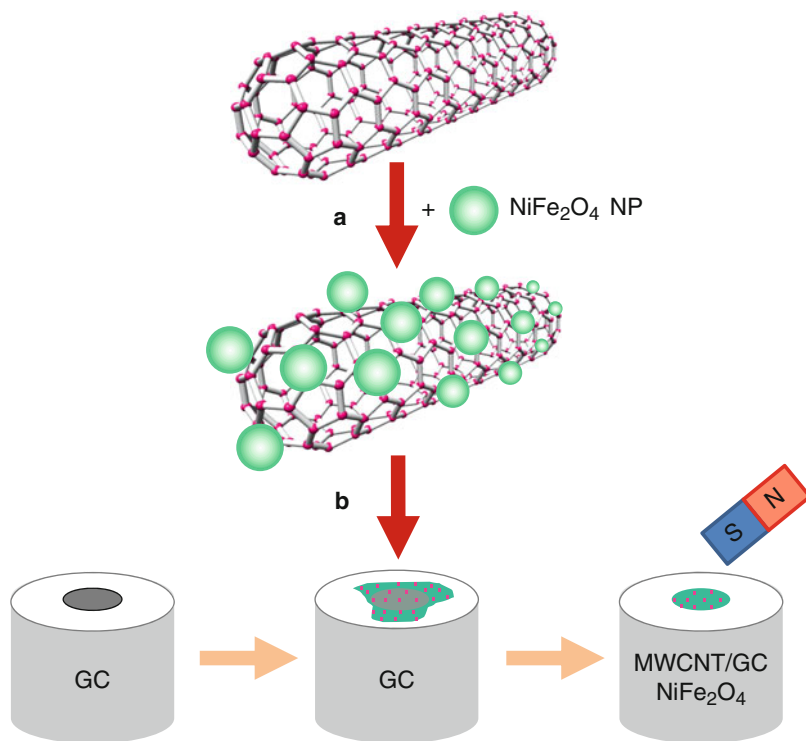


Fig. 6 Schematic draw of (a) modification of SWCNT by NiFe_2O_4 nanoparticles by sol-gel method and (b) the preparation of the modified GC electrode. Portion of MWCNT/GC NiFe_2O_4 was dispersed in 1.0 mL ethanol and homogenized ultrasonically. 10 μL of this solution was deposited on the freshly prepared GCE surface. In order to homogenize the modifier on the surface of the electrode, a magnetic field (magnet) was used above the surface electrode until the solvent evaporated (Adapted and modified according to the [194])

This is caused by an exceptionally high number of accessible graphene sheet edges on the surface of the nanofibers when compared to carbon nanotubes. The oxidation signals of adenine, guanine, cytosine, and thymine exhibited from two to four time higher currents than that on CNT-based electrodes. SGNFs also exhibited higher (better) sensitivity compared to edge plane pyrolytic graphite (EPPG), GC, or graphite microparticle-based electrodes.

Niu et al. and Sun et al. suggested very interesting way of application of graphene material in the detection of DNA bases [198, 199]. Both authors based their detection systems on carbon ionic liquid electrode (CILE) modified by chitosan (CTS) and graphene (GR). Both experiments differ in the way of the preparation of CILE. Due to the synergistic effects of GR and CILE and the interaction of GR with IL on the surface of the electrode, the electrochemical performance of CTS/GR/CILE was enhanced greatly. Electrochemical behavior of adenine on the modified electrode was investigated with a single well-defined oxidation signal that appeared. The electrochemical reaction of adenine was an adsorption-controlled irreversible process.

The modification of graphene with nanoparticles is available too. As an example, the work of Biris et al. may be presented [200]. It is based on few-layer graphene sheets embedded with various amounts of gold nanoparticles (Gr-Au-x) over an Au-x/MgO catalytic system (where $x=1, 2, \text{ or } 3 \text{ wt\%}$). The number of layers within the sheets varied from two to seven. The sample with the highest percentage of gold nanoparticles embedded within the graphitic layers (Gr-Au-3) showed the highest degree of crystallinity. The Gr-Au-x composites were used to modify platinum substrates. For the bare electrode, no oxidation signal was recorded. In contrast, all of the modified electrodes showed a strong electrocatalytic effect, and a clear signal for adenine oxidation was recorded at approximately +1.05 V. The highest increase in the electrochemical signal was obtained using a platinum/Gr-Au-3-modified electrode.

Diamond

In direct electrochemistry of nucleic acid, diamond is usually applied in the form of boron-doped diamond (BDD). From the viewpoint of possible modifications, it is possible to consider it to be a modification of carbon material (diamond). The as-deposited diamond surface is terminated by hydrogen, because the films are grown under hydrogen plasma or in a hydrogen atmosphere. Such hydrogen-terminated diamond surfaces are known to be remarkably stable, but the oxygen-terminated surface can easily be formed by exposing the surface to oxygen plasma, boiling in strong acids, or applying high oxidizing potentials [201]. The surface activation by applying high oxidizing potentials leads to the oxidation of surface groups into hydroxyl and carbonyl terminations. Such change of the chemical termination can affect the electrochemical properties of the diamond electrode (allow to increase anodically its working potential window).

The effect of boron-doped diamond (BDD) surface termination immediately after cathodic and anodic electrochemical pretreatment and the influence of the

pretreatment in different supporting electrolytes on potentials of the electrochemical oxidation of dsDNA were studied by Oliveira et al. [202]. DNA bases, nucleotides, and homopolynucleotides were investigated using differential pulse voltammetry in aqueous media at different pH. The anodic and cathodic BDD surface pretreatments were performed in three different solutions as follows: 0.1 M acetate buffer (pH 4.5), 0.1 M phosphate buffer (pH 7.0), and 0.5 M sulfuric acid (pH 0.55). The electrochemical response on the BDD surface varied as a function of the potential applied in the pretreatment of the surface and also in dependence on the electrolyte used. Presented results showed that the electrochemical properties of the BDD electrode highly depend on the state of the surface termination due to oxygen and hydrogen terminations. Concerning the compounds being studied, a better response was obtained when the BDD surface was pretreated cathodically. The interaction and adsorption of the electrochemical species by the surface pretreated cathodically were facilitated due to a higher conductivity of the BDD electrode surface. On the other hand, after anodic pretreatment, a wider potential window of BDD surface was obtained. It enabled the detection of the pyrimidine bases. However, the hydroxyl radicals produced on the surface of BDD during the anodic pretreatment are highly reactive, and consequently the BDD surface is not completely inert. These conclusions resulted in the statement that the BDD is a promising material for electroanalytical chemistry mainly due to its chemical stability, high electrical conductivity, and large amplitude of its electroactive window in aqueous media.

The investigation of the direct electroanalytical detection of nucleic acids on BDD is possible to observe in various ways. The basic studies were done by Fortin et al. [203] who focused on the study of direct oxidation of the two electroactive nucleosides, guanosine and adenosine. The authors studied the electrochemical behavior of oxidizable bases guanosine (+1.2 V vs. Ag/AgCl) and adenosine (+1.5 V vs. Ag/AgCl), respectively. Ivandini et al. [204] studied the electrochemical oxidation of underivatized nucleic acids in terms of single-stranded and double-stranded DNA by cyclic voltammetry and square wave voltammetry. Two well-defined voltammetric signals (for guanine and adenine) were observed for both types of DNA. For single-stranded DNA, a third peak related to the pyrimidine group oxidation appeared. The influence of native and denatured DNA on electrochemical signals detected on the BDD was investigated by Apilux et al. [205]. The mixture of acetic acid and sodium acetate solution (0.2 M) was used as a supporting electrolyte. Two oxidation peaks were observed at about +1.1 V and +1.3 V at pH 4.6 for thermally denatured fish DNA. In contrast, the native fish DNA showed well-defined peaks at +1.1 V.

Fullerene

Fullerenes as the newest carbon material applied in analytical electrochemistry is connected only with the construction of DNA biosensors based on the hybridization

process [206, 207]. The application of fullerenes in the direct detection of nucleic acid has not been presented yet.

Conclusions

New carbon materials have shifted the electrochemical properties of carbon materials to the new lines, especially the usable potential window. This improvement allows expanding the applications in the field of electrochemical determination of nucleic acids. Carbon material-based electrodes allow detecting nucleic acids directly, mainly via the direct electrochemical oxidation of bases. We briefly reviewed the history, types, structure, and especially modifications of carbon materials for direct detection of nucleic acids.

Acknowledgment Financial support from CEITEC CZ.1.05/1.1.00/02.0068 is highly acknowledged.

References

1. Roy N, Sengupta R, Bhowmick AK (2012) Modifications of carbon for polymer composites and nanocomposites. *Prog Polym Sci* 37(6):781–819. doi:10.1016/j.progpolymsci.2012.02.002
2. Iijima S (1991) Helical microtubules of graphitic carbon. *Nature* 354(6348):56–58
3. Cai XK, Cong HT, Liu C (2012) Synthesis of vertically-aligned carbon nanotubes without a catalyst by hydrogen arc discharge. *Carbon* 50(8):2726–2730. doi:10.1016/j.carbon.2012.02.031
4. Vander Wal RL, Berger GM, Tichich TM (2003) Carbon nanotube synthesis in a flame using laser ablation for in situ catalyst generation. *Appl Phys A Mater Sci Process* 77(7):885–889. doi:10.1007/s00339-003-2196-3
5. Meyyappan M, Delzeit L, Cassell A, Hash D (2003) Carbon nanotube growth by PECVD: a review. *Plasma Sources Sci Technol* 12(2):205–216. doi:10.1088/0963-0252/12/2/312
6. Zhu YJ, Lin TJ, Liu QX, Chen YL, Zhang GF, Xiong HF, Zhang HY (2006) The effect of nickel content of composite catalysts synthesized by hydrothermal method on the preparation of carbon nanotubes. *Mater Sci Eng B Solid State Mater Adv Technol* 127(2–3):198–202. doi:10.1016/j.mseb.2005.10.030
7. Byon HR, Lim H, Song HJ, Choi HC (2007) A synthesis of high purity single-walled carbon nanotubes from small diameters of cobalt nanoparticles by using oxygen-assisted chemical vapor deposition process. *Bull Kor Chem Soc* 28(11):2056–2060
8. Patole SP, Alegaonkar PS, Lee HC, Yoo JB (2008) Optimization of water assisted chemical vapor deposition parameters for super growth of carbon nanotubes. *Carbon* 46(14):1987–1993. doi:10.1016/j.carbon.2008.08.009
9. Smajda R, Andresen JC, Duchamp M, Meunier R, Casimirius S, Hernadi K, Forro L, Magrez A (2009) Synthesis and mechanical properties of carbon nanotubes produced by the water assisted CVD process. *Phys Status Solidi B Basic Solid State Phys* 246(11–12):2457–2460. doi:10.1002/pssb.200982269
10. Steiner SA, Baumann TF, Bayer BC, Blume R, Worsley MA, MoberlyChan WJ, Shaw EL, Schlögl R, Hart AJ, Hofmann S, Wardle BL (2009) Nanoscale zirconia as a nonmetallic catalyst for graphitization of carbon and growth of single- and multiwall carbon nanotubes. *J Am Chem Soc* 131(34):12144–12154. doi:10.1021/ja902913r

11. Tempel H, Joshi R, Schneider JJ (2010) Ink jet printing of ferritin as method for selective catalyst patterning and growth of multiwalled carbon nanotubes. *Mater Chem Phys* 121(1–2): 178–183. doi:10.1016/j.matchemphys.2010.01.029
12. Kim HD, Lee JH, Choi WS (2011) Direct growth of carbon nanotubes with a catalyst of nickel nanoparticle-coated alumina powders. *J Korean Phys Soc* 58(1):112–115. doi:10.3938/jkps.58.112
13. Brown B, Parker CB, Stoner BR, Glass JT (2011) Growth of vertically aligned bamboo-like carbon nanotubes from ammonia/methane precursors using a platinum catalyst. *Carbon* 49(1):266–274. doi:10.1016/j.carbon.2010.09.018
14. Xu Y, Dervishi E, Biris AR, Biris AS (2011) Chirality-enriched semiconducting carbon nanotubes synthesized on high surface area MgO-supported catalyst. *Mater Lett* 65(12): 1878–1881. doi:10.1016/j.matlet.2011.03.040
15. Lee O, Jung J, Doo S, Kim SS, Noh TH, Kim KI, Lim YS (2010) Effects of temperature and catalysts on the synthesis of carbon nanotubes by chemical vapor deposition. *Met Mater Int* 16(4):663–667. doi:10.1007/s12540-010-0822-0
16. Afolabi AS, Abdulkareem AS, Mhlanga SD, Iyuke SE (2011) Synthesis and purification of bimetallic catalysed carbon nanotubes in a horizontal CVD reactor. *J Exp Nanosci* 6(3): 248–262. doi:10.1080/17458080.2010.497941
17. Dumpala S, Jasinski JB, Sumanasekera GU, Sunkara MK (2011) Large area synthesis of conical carbon nanotube arrays on graphite and tungsten foil substrates. *Carbon* 49(8): 2725–2734. doi:10.1016/j.carbon.2011.02.065
18. Zhu J, Yudasaka M, Iijima S (2003) A catalytic chemical vapor deposition synthesis of double-walled carbon nanotubes over metal catalysts supported on a mesoporous material. *Chem Phys Lett* 380(5–6):496–502. doi:10.1016/j.cplett.2003.09.049
19. Ramesh P, Okazaki T, Taniguchi R, Kimura J, Sugai T, Sato K, Ozeki Y, Shinohara H (2005) Selective chemical vapor deposition synthesis of double-wall carbon nanotubes on mesoporous silica. *J Phys Chem B* 109(3):1141–1147. doi:10.1021/jp0465736
20. Hiraoka T, Kawakubo T, Kimura J, Taniguchi R, Okamoto A, Okazaki T, Sugai T, Ozeki Y, Yoshikawa M, Shinohara H (2003) Selective synthesis of double-wall carbon nanotubes by CCVD of acetylene using zeolite supports. *Chem Phys Lett* 382(5–6):679–685. doi:10.1016/j.cplett.2003.10.123
21. Szabo A, Perri C, Csato A, Giordano G, Vuono D, Nagy JB (2010) Synthesis methods of carbon nanotubes and related materials. *Materials* 3:3092–3140
22. Chakrabarti S, Kume H, Pan LJ, Nagasaka T, Nakayama Y (2007) Number of walls controlled synthesis of millimeter-long vertically aligned brushlike carbon nanotubes. *J Phys Chem C* 111(5):1929–1934. doi:10.1021/jp0666986
23. Ritschel M, Leonhardt A, Elefant D, Oswald S, Buchner B (2007) Rhenium-catalyzed growth carbon nanotubes. *J Phys Chem C* 111(24):8414–8417. doi:10.1021/jp070467x
24. Fisher C, Han ZJ, Levchenko I, Ostrikov K (2011) Control of dense carbon nanotube arrays via hierarchical multilayer catalyst. *Appl Phys Lett* 99(14):1–5. doi:10.1063/1.3645625. 143104
25. Han ZJ, Levchenko I, Yick S, Ostrikov K (2011) 3-Orders-of-magnitude density control of single-walled carbon nanotube networks by maximizing catalyst activation and dosing carbon supply. *Nanoscale* 3(11):4848–4853. doi:10.1039/c1nr10765h
26. Han ZJ, Yick S, Levchenko I, Tam E, Yajadda MMA, Kumar S, Martin PJ, Furman S, Ostrikov K (2011) Controlled synthesis of a large fraction of metallic single-walled carbon nanotube and semiconducting carbon nanowire networks. *Nanoscale* 3(8):3214–3220. doi:10.1039/c1nr10327j
27. Palizdar M, Ahgababazadeh R, Mirhabibi A, Brydson R, Pilehvari S (2011) Investigation of Fe/MgO catalyst support precursors for the chemical vapour deposition growth of carbon nanotubes. *J Nanosci Nanotechnol* 11(6):5345–5351. doi:10.1166/jnn.2011.3787
28. Tomie T, Inoue S, Kohno M, Matsumura Y (2010) Prospective growth region for chemical vapor deposition synthesis of carbon nanotube on C–H–O ternary diagram. *Diamond Relat Mater* 19(11):1401–1404. doi:10.1016/j.diamond.2010.08.005

29. Narkiewicz U, Podsiadly M, Jedrzejewski R, Pelech I (2010) Catalytic decomposition of hydrocarbons on cobalt, nickel and iron catalysts to obtain carbon nanomaterials. *Appl Catal A Gen* 384(1–2):27–35. doi:10.1016/j.apcata.2010.05.050
30. He DL, Li H, Li WL, Haghi-Ashtiani P, Lejay P, Bai JB (2011) Growth of carbon nanotubes in six orthogonal directions on spherical alumina microparticles. *Carbon* 49(7):2273–2286. doi:10.1016/j.carbon.2011.01.060
31. Shirazi Y, Tofighy MA, Mohammadi T, Pak A (2011) Effects of different carbon precursors on synthesis of multiwall carbon nanotubes: purification and functionalization. *Appl Surf Sci* 257(16):7359–7367. doi:10.1016/j.apsusc.2011.03.146
32. Atthipalli G, Epur R, Kumta PN, Yang MJ, Lee JK, Gray JL (2011) Nickel catalyst-assisted vertical growth of dense carbon nanotube forests on bulk copper. *J Phys Chem C* 115(9):3534–3538. doi:10.1021/jp108624n
33. Li H, He DL, Li TH, Genestoux M, Bai JB (2010) Chemical kinetics of catalytic chemical vapor deposition of an acetylene/xylene mixture for improved carbon nanotube production. *Carbon* 48(15):4330–4342. doi:10.1016/j.carbon.2010.07.046
34. Santangelo S, Messina G, Faggio G, Lanza M, Pistone A, Milone C (2010) Calibration of reaction parameters for the improvement of thermal stability and crystalline quality of multi-walled carbon nanotubes. *J Mater Sci* 45(3):783–792. doi:10.1007/s10853-009-4001-y
35. Hou B, Xiang R, Inoue T, Einarsson E, Chiashi S, Shiomi J, Miyoshi A, Maruyama S (2011) Decomposition of ethanol and dimethyl ether during chemical vapor deposition synthesis of single-walled carbon nanotubes. *Jpn J Appl Phys* 50(6):1–4. doi:10.1143/jjap.50.065101
36. Yong Z, Fang L, Zhi-hua Z (2011) Synthesis of heterostructured helical carbon nanotubes by iron-catalyzed ethanol decomposition. *Micron* 42(6):547–552. doi:10.1016/j.micron.2011.01.007
37. Lyu SC, Liu BC, Lee CJ, Kang HK, Yang CW, Park CY (2003) High-quality double-walled carbon nanotubes produced by catalytic decomposition of benzene. *Chem Mater* 15(20):3951–3954. doi:10.1021/cm030309s
38. Zhang DS, Shi LY, Fang JH, Li XK, Dai K (2005) Preparation and modification of carbon nanotubes. *Mater Lett* 59(29–30):4044–4047. doi:10.1016/j.matlet.2005.07.081
39. Zhang DS, Shi LY, Fang JH, Dai K, Li XK (2006) Preparation and desalination performance of multiwall carbon nanotubes. *Mater Chem Phys* 97(2–3):415–419. doi:10.1016/j.matchemphys.2005.08.036
40. Du GH, Zhou YS, Xu BS (2010) Preparation of carbon nanotubes by pyrolysis of dimethyl sulfide. *Mater Charact* 61(4):427–432. doi:10.1016/j.matchar.2010.01.009
41. Sano N, Ishimaru S, Tamaon H (2010) Synthesis of carbon nanotubes in graphite microchannels in gas-flow and submerged-in-liquid reactors. *Mater Chem Phys* 122(2–3):474–479. doi:10.1016/j.matchemphys.2010.03.029
42. Skukla B, Saito T, Ohmori S, Koshi M, Yumura M, Iijima S (2010) Interdependency of gas phase intermediates and chemical vapor deposition growth of single wall carbon nanotubes. *Chem Mater* 22(22):6035–6043. doi:10.1021/cm1005746
43. Vinten P, Bond J, Marshall P, Lefebvre J, Finnie P (2011) Origin of periodic rippling during chemical vapor deposition growth of carbon nanotube forests. *Carbon* 49(15):4972–4981. doi:10.1016/j.carbon.2011.02.017
44. Yamada T, Namai T, Hata K, Futaba DN, Mizuno K, Fan J, Yudasaka M, Yumura M, Iijima S (2006) Size-selective growth of double-walled carbon nanotube forests from engineered iron catalysts. *Nat Nanotechnol* 1(2):131–136. doi:10.1038/nnano.2006.95
45. Kim D, Lim SH, Guilley AJ, Cojocar C, Bouree JE, Vila L, Ryu JH, Park KC, Jang J (2008) Growth of vertically aligned arrays of carbon nanotubes for high field emission. *Thin Solid Films* 516(5):706–709. doi:10.1016/j.tsf.2007.06.089
46. Liu H, Zhang Y, Li RY, Sun XL, Wang FP, Ding ZF, Merel P, Desilets S (2010) Aligned synthesis of multi-walled carbon nanotubes with high purity by aerosol assisted chemical vapor deposition: effect of water vapor. *Appl Surf Sci* 256(14):4692–4696. doi:10.1016/j.apsusc.2010.02.074
47. Kim B, Chung H, Chu KS, Yoon HG, Lee CJ, Kim W (2010) Synthesis of vertically-aligned carbon nanotubes on stainless steel by water-assisted chemical vapor deposition and charac-

- terization of their electrochemical properties. *Synth Met* 160(7–8):584–587. doi:10.1016/j.synthmet.2009.12.008
48. Dorfler S, Meier A, Thieme S, Nemeth P, Althues H, Kaskel S (2011) Wet-chemical catalyst deposition for scalable synthesis of vertical aligned carbon nanotubes on metal substrates. *Chem Phys Lett* 511(4–6):288–293. doi:10.1016/j.cplett.2011.06.027
 49. Raney JR, Misra A, Daraio C (2011) Tailoring the microstructure and mechanical properties of arrays of aligned multiwall carbon nanotubes by utilizing different hydrogen concentrations during synthesis. *Carbon* 49(11):3631–3638. doi:10.1016/j.carbon.2011.04.066
 50. Seah CM, Chai SP, Mohamed AR (2011) Synthesis of aligned carbon nanotubes. *Carbon* 49(14):4613–4635. doi:10.1016/j.carbon.2011.06.090
 51. Kumar S, Levchenko I, Ostrikov K, McLaughlin JA (2012) Plasma-enabled, catalyst-free growth of carbon nanotubes on mechanically-written Si features with arbitrary shape. *Carbon* 50(1):325–329. doi:10.1016/j.carbon.2011.07.060
 52. Nessim GD, Al-Obeidi A, Grisaru H, Polsen ES, Oliver CR, Zimrin T, Hart AJ, Aurbach D, Thompson CV (2012) Synthesis of tall carpets of vertically aligned carbon nanotubes by in situ generation of water vapor through preheating of added oxygen. *Carbon* 50(11):4002–4009. doi:10.1016/j.carbon.2012.04.043
 53. Neupane S, Lastres M, Chiarella M, Li WZ, Su QM, Du GH (2012) Synthesis and field emission properties of vertically aligned carbon nanotube arrays on copper. *Carbon* 50(7):2641–2650. doi:10.1016/j.carbon.2012.02.024
 54. Zhou WW, Ding L, Yang S, Liu J (2011) Synthesis of high-density, large-diameter, and aligned single-walled carbon nanotubes by multiple-cycle growth methods. *ACS Nano* 5(5):3849–3857. doi:10.1021/nn200198b
 55. Merkoci A (2006) Carbon nanotubes in analytical sciences. *Microchim Acta* 152(3–4):157–174. doi:10.1007/s00604-005-0439-z
 56. Kim SN, Rusling JF, Papadimitrakopoulos F (2007) Carbon nanotubes for electronic and electrochemical detection of biomolecules. *Adv Mater* 19(20):3214–3228. doi:10.1002/adma.200700665
 57. Valcarcel M, Cardenas S, Simonet BM (2007) Role of carbon nanotubes in analytical science. *Anal Chem* 79(13):4788–4797. doi:10.1021/ac070196m
 58. Komatsu N, Wang F (2010) A comprehensive review on separation methods and techniques for single-walled carbon nanotubes. *Materials* 3(7):3818–3844. doi:10.3390/ma3073818
 59. Perez-Lopez B, Merkoci A (2012) Carbon nanotubes and graphene in analytical sciences. *Microchim Acta* 179(1–2):1–16. doi:10.1007/s00604-012-0871-9
 60. May JW (1969) A mechanism for surface reconstruction at room temperature. *Surf Sci* 18(2):431–436. doi:10.1016/0039-6028(69)90184-8
 61. Shelton JC, Patil HR, Blakely JM (1974) Equilibrium segregation of carbon to a nickel (111) surface – surface phase-transition. *Surf Sci* 43(2):493–520. doi:10.1016/0039-6028(74)90272-6
 62. Eizenberg M, Blakely JM (1979) Carbon interaction with nickel surfaces – monolayer formation and structural stability. *J Chem Phys* 71(8):3467–3477. doi:10.1063/1.438736
 63. Eizenberg M, Blakely JM (1979) Carbon monolayer phase condensation on ni(111). *Surf Sci* 82(1):228–236. doi:10.1016/0039-6028(79)90330-3
 64. Berger C, Li TB, Li XB, Ogbazghi AY, Feng R, Dai ZT, Marchenkov AN, Conrad EH, First PN, de Heer WA (2004) Ultrathin epitaxial graphite: 2D electron gas properties and a route toward graphene-based nanoelectronics. *J Phys Chem B* 108(52):19912–19916. doi:10.1021/jp040650f
 65. Berger C, Song ZM, Li XB, Wu XS, Brown N, Naud C, Mayou D, Li TB, Hass J, Marchenkov AN, Conrad EH, First PN, de Heer WA (2006) Electronic confinement and coherence in patterned epitaxial graphene. *Science* 312(5777):1191–1196. doi:10.1126/science.1125925
 66. Emtsev KV, Bostwick A, Horn K, Jobst J, Kellogg GL, Ley L, McChesney JL, Ohta T, Reshanov SA, Rohrl J, Rotenberg E, Schmid AK, Waldmann D, Weber HB, Seyller T (2009) Towards wafer-size graphene layers by atmospheric pressure graphitization of silicon carbide. *Nat Mater* 8(3):203–207. doi:10.1038/nmat2382

67. Huang H, Chen W, Chen S, Wee ATS (2008) Bottom-up growth of epitaxial graphene on 6H-SiC(0001). *ACS Nano* 2(12):2513–2518. doi:10.1021/nn800711v
68. Li XS, Cai WW, An JH, Kim S, Nah J, Yang DX, Piner R, Velamakanni A, Jung I, Tutuc E, Banerjee SK, Colombo L, Ruoff RS (2009) Large-area synthesis of high-quality and uniform graphene films on copper foils. *Science* 324(5932):1312–1314. doi:10.1126/science.1171245
69. Li XS, Cai WW, Colombo L, Ruoff RS (2009) Evolution of graphene growth on Ni and Cu by carbon isotope labeling. *Nano Lett* 9(12):4268–4272. doi:10.1021/nl902515k
70. Li XS, Zhu YW, Cai WW, Borysiak M, Han BY, Chen D, Piner RD, Colombo L, Ruoff RS (2009) Transfer of large-area graphene films for high-performance transparent conductive electrodes. *Nano Lett* 9(12):4359–4363. doi:10.1021/nl902623y
71. Lu XK, Yu MF, Huang H, Ruoff RS (1999) Tailoring graphite with the goal of achieving single sheets. *Nanotechnology* 10(3):269–272. doi:10.1088/0957-4484/10/3/308
72. Yu MF, Dyer MJ, Skidmore GD, Rohrs HW, Lu XK, Ausman KD, Von Ehr JR, Ruoff RS (1999) Three-dimensional manipulation of carbon nanotubes under a scanning electron microscope. *Nanotechnology* 10(3):244–252. doi:10.1088/0957-4484/10/3/304
73. Hernandez Y, Nicolosi V, Lotya M, Blighe FM, Sun ZY, De S, McGovern IT, Holland B, Byrne M, Gun'ko YK, Boland JJ, Niraj P, Duesberg G, Krishnamurthy S, Goodhue R, Hutchison J, Scardaci V, Ferrari AC, Coleman JN (2008) High-yield production of graphene by liquid-phase exfoliation of graphite. *Nat Nanotechnol* 3(9):563–568. doi:10.1038/nnano.2008.215
74. Dato A, Radmilovic V, Lee Z, Phillips J, Frenklach M (2008) Substrate-free gas-phase synthesis of graphene sheets. *Nano Lett* 8(7):2012–2016. doi:10.1021/nl8011566
75. Li N, Wang ZY, Zhao KK, Shi ZJ, Gu ZN, Xu SK (2010) Large scale synthesis of N-doped multi-layered graphene sheets by simple arc-discharge method. *Carbon* 48(1):255–259. doi:10.1016/j.carbon.2009.09.013
76. Subrahmanyam KS, Panchakarla LS, Govindaraj A, Rao CNR (2009) Simple method of preparing graphene flakes by an arc-discharge method. *J Phys Chem C* 113(11):4257–4259. doi:10.1021/jp900791y
77. Stankovich S, Dikin DA, Piner RD, Kohlhaas KA, Kleinhammes A, Jia Y, Wu Y, Nguyen ST, Ruoff RS (2007) Synthesis of graphene-based nanosheets via chemical reduction of exfoliated graphite oxide. *Carbon* 45(7):1558–1565. doi:10.1016/j.carbon.2007.02.034
78. Wang GX, Yang J, Park J, Gou XL, Wang B, Liu H, Yao J (2008) Facile synthesis and characterization of graphene nanosheets. *J Phys Chem C* 112(22):8192–8195. doi:10.1021/jp710931h
79. Si Y, Samulski ET (2008) Synthesis of water soluble graphene. *Nano Lett* 8(6):1679–1682. doi:10.1021/nl080604h
80. Dua V, Surwade SP, Ammu S, Agnihotra SR, Jain S, Roberts KE, Park S, Ruoff RS, Manohar SK (2010) All-organic vapor sensor using inkjet-printed reduced graphene oxide. *Angew Chem Int Ed* 49(12):2154–2157. doi:10.1002/anie.200905089
81. McAllister MJ, Li JL, Adamson DH, Schniepp HC, Abdala AA, Liu J, Herrera-Alonso M, Milius DL, Car R, Prud'homme RK, Aksay IA (2007) Single sheet functionalized graphene by oxidation and thermal expansion of graphite. *Chem Mater* 19(18):4396–4404. doi:10.1021/cm0630800
82. Schniepp HC, Li JL, McAllister MJ, Sai H, Herrera-Alonso M, Adamson DH, Prud'homme RK, Car R, Saville DA, Aksay IA (2006) Functionalized single graphene sheets derived from splitting graphite oxide. *J Phys Chem B* 110(17):8535–8539. doi:10.1021/jp060936f
83. Dreyer DR, Park S, Bielawski CW, Ruoff RS (2010) The chemistry of graphene oxide. *Chem Soc Rev* 39(1):228–240. doi:10.1039/b917103g
84. Park S, Ruoff RS (2009) Chemical methods for the production of graphenes. *Nat Nanotechnol* 4(4):217–224. doi:10.1038/nnano.2009.58
85. Hummers WS, Offeman RE (1958) Preparation of graphitic oxide. *J Am Chem Soc* 80(6):1339–1339. doi:10.1021/ja01539a017
86. Boehm HP, Eckel M, Scholz W (1967) Untersuchungen am graphitoxid. 5. Über den bildungsmechanismus des graphitoxids. *Z Anorg Allg Chem* 353(5–6):236–242. doi:10.1002/zaac.19673530503

87. Liu KP, Zhang JJ, Cheng FF, Zheng TT, Wang CM, Zhu JJ (2011) Green and facile synthesis of highly biocompatible graphene nanosheets and its application for cellular imaging and drug delivery. *J Mater Chem* 21(32):12034–12040. doi:10.1039/c1jm10749f
88. Choi W, Lahiri I, Seelaboyina R, Kang YS (2010) Synthesis of graphene and its applications: a review. *Crit Rev Solid State Mater Sci* 35(1):52–71. doi:10.1080/10408430903505036
89. Jiang HJ (2011) Chemical preparation of graphene-based nanomaterials and their applications in chemical and biological sensors. *Small* 7(17):2413–2427. doi:10.1002/sml.201002352
90. Kroto HW, Heath JR, O'Brien SC, Curl RF, Smalley RE (1985) C-60 – Buckminsterfullerene. *Nature* 318(6042):162–163. doi:10.1038/318162a0
91. Kikuchi K, Nakahara N, Wakabayashi T, Suzuki S, Shiromaru H, Miyake Y, Saito K, Ikemoto I, Kainosho M, Achiba Y (1992) NMR characterization of isomers of C-78, C-82 and C-84 fullerenes. *Nature* 357(6374):142–145. doi:10.1038/357142a0
92. Kratschmer W, Lamb LD, Fostiropoulos K, Huffman DR (1990) Solid C-60 – a new form of carbon. *Nature* 347(6291):354–358. doi:10.1038/347354a0
93. Bhyrappa P, Penicaud A, Kawamoto M, Reed CA (1992) Improved chromatographic-separation and purification of C-60 and C-70 fullerenes. *J Chem Soc Chem Commun* 1992(13):936–938. doi:10.1039/c39920000936
94. Cabrera K, Wieland G, Schafer M (1993) High-performance liquid-chromatographic separation of fullerenes (C-60 and C-70) using chemically bonded gamma-cyclodextrin as stationary-phase. *J Chromatogr* 644(2):396–399. doi:10.1016/0021-9673(93)80725-n
95. Saito Y, Ohta H, Jinno K (2004) Chromatographic separation of fullerenes. *Anal Chem* 76(15):266A–272A. doi:10.1021/ac041599e
96. Yang JZ, Alemany LB, Driver J, Hartgerink JD, Barron AR (2007) Fullerene-derivatized amino acids: synthesis, characterization, antioxidant properties, and solid-phase peptide synthesis. *Chem Eur J* 13(9):2530–2545. doi:10.1002/chem.200601186
97. Palecek E, Bartosik M (2012) Electrochemistry of nucleic acids. *Chem Rev* 112(6):3427–3481. doi:10.1021/cr200303p
98. Brabec V (1981) Nucleic-acid analysis by voltammetry at carbon electrodes. *Bioelectrochem Bioenerg* 8(4):437–449. doi:10.1016/0302-4598(81)80005-0
99. Palecek E (1996) From polarography of DNA to microanalysis with nucleic acid-modified electrodes. *Electroanalysis* 8(1):7–14
100. Palecek E (2002) Past, present and future of nucleic acids electrochemistry. *Talanta* 56(5):809–819
101. Palecek E (2009) Fifty years of nucleic acid electrochemistry. *Electroanalysis* 21(3–5):239–251. doi:10.1002/elan.200804416
102. Wang J (2002) Electrochemical nucleic acid biosensors. *Anal Chim Acta* 469(1):63–71
103. Tanaka H, Aramata A (1997) Aminopyridyl cation radical method for bridging between metal complex and glassy carbon: cobalt(II) tetraphenylporphyrin bonded on glassy carbon for enhancement of CO₂ electroreduction. *J Electroanal Chem* 437(1–2):29–35. doi:10.1016/s0022-0728(97)00080-6
104. Millan KM, Saraullo A, Mikkelsen SR (1994) Voltammetric DNA biosensor for cystic-fibrosis based on a modified carbon-paste electrode. *Anal Chem* 66(18):2943–2948. doi:10.1021/ac00090a023
105. Meller A, Nivon L, Branton D (2001) Voltage-driven DNA translocations through a nanopore. *Phys Rev Lett* 86(15):3435–3438. doi:10.1103/PhysRevLett.86.3435
106. Storm AJ, Storm C, Chen JH, Zandbergen H, Joanny JF, Dekker C (2005) Fast DNA translocation through a solid-state nanopore. *Nano Lett* 5(7):1193–1197. doi:10.1021/nl048030d
107. Dequaire M, Degrand C, Limoges B (1999) Biotinylation of screen-printed carbon electrodes through the electrochemical reduction of the diazonium salt of *p*-aminobenzoyl biocytin. *J Am Chem Soc* 121(29):6946–6947. doi:10.1021/ja990920l
108. Guo B, Anzai J, Osa T (1996) Modification of a glassy carbon electrode with diols for the suppression of electrode fouling in biological fluids. *Chem Pharm Bull* 44(4):860–862
109. Dong HF, Zhu Z, Ju HX, Yan F (2012) Triplex signal amplification for electrochemical DNA biosensing by coupling probe-gold nanoparticles-graphene modified electrode with enzyme

- functionalized carbon sphere as tracer. *Biosens Bioelectron* 33(1):228–232. doi:10.1016/j.bios.2012.01.006
110. Brabec V, Dryhurst G (1978) Electrochemical behavior of natural and biosynthetic polynucleotides at pyrolytic-graphite electrode a new probe for studies of polynucleotide structure and reactions. *J Electroanal Chem* 89(1):161–173. doi:10.1016/s0022-0728(78)80041-2
 111. Wang J, Kawde AN, Sahlin E (2000) Renewable pencil electrodes for highly sensitive stripping potentiometric measurements of DNA and RNA. *Analyst* 125(1):5–7. doi:10.1039/a907364g
 112. Cai XH, Rivas G, Farias PAM, Shiraishi H, Wang J, Palecek E (1996) Evaluation of different carbon electrodes for adsorptive stripping analysis of nucleic acids. *Electroanalysis* 8(8–9):753–758. doi:10.1002/elan.1140080809
 113. Kato D, Niwa O (2013) Carbon-based electrode materials for DNA electroanalysis. *Anal Sci* 29(4):385–392
 114. Stempkowska I, Liga M, Jasnowska J, Langer J, Filipiak M (2007) Electrochemical response of oligonucleotides on carbon paste electrode. *Bioelectrochemistry* 70(2):488–494. doi:10.1016/j.bioelechem.2006.07.012
 115. Dryhurst G, Elving PJ (1968) Electrochemical oxidation of adenine – reaction products and mechanisms. *J Electrochem Soc* 115(10):1014–1020. doi:10.1149/1.2410847
 116. Dryhurst G, Pace GF (1970) Electrochemical oxidation of guanine at pyrolytic graphite electrode. *J Electrochem Soc* 117(10):1259–1264. doi:10.1149/1.2407283
 117. Brett AMO, Matysik FM (1997) Voltammetric and sonovoltammetric studies on the oxidation of thymine and cytosine at a glassy carbon electrode. *J Electroanal Chem* 429(1–2):95–99
 118. Oliveira-Brett AM, Piedade JAP, Silva LA, Diculescu VC (2004) Voltammetric determination of all DNA nucleotides. *Anal Biochem* 332(2):321–329. doi:10.1016/j.ab.2004.06.021
 119. Heath JC (1946) Polarographic behaviour of adenine. *Nature* 158(4001):23–23. doi:10.1038/158023a0
 120. Wang J, Cai XH, Wang JY, Jonsson C, Palecek E (1995) Trace measurements of RNA by potentiometric stripping analysis at carbon-paste electrodes. *Anal Chem* 67(22):4065–4070. doi:10.1021/ac00118a006
 121. Oliveira-Brett AM, Diculescu VC (2004) Electrochemical study of quercetin-DNA interactions – part II. In situ sensing with DNA biosensors. *Bioelectrochemistry* 64(2):143–150. doi:10.1016/j.bioelechem.2004.05.002
 122. Drummond TG, Hill MG, Barton JK (2003) Electrochemical DNA sensors. *Nat Biotechnol* 21(10):1192–1199. doi:10.1038/nbt873
 123. Wang J, Lin YH (2008) Functionalized carbon nanotubes and nanofibers for biosensing applications. *TrAc Trends Anal Chem* 27(7):619–626. doi:10.1016/j.trac.2008.05.009
 124. Wang J, Kawde AN, Jan MR (2004) Carbon-nanotube-modified electrodes for amplified enzyme-based electrical detection of DNA hybridization. *Biosens Bioelectron* 20(5):995–1000. doi:10.1016/j.bios.2004.06.016
 125. Wang J, Liu GD, Jan MR (2004) Ultrasensitive electrical biosensing of proteins and DNA: carbon-nanotube derived amplification of the recognition and transduction events. *J Am Chem Soc* 126(10):3010–3011. doi:10.1021/ja031723w
 126. Zhou M, Zhai YM, Dong SJ (2009) Electrochemical sensing and biosensing platform based on chemically reduced graphene oxide. *Anal Chem* 81(14):5603–5613. doi:10.1021/ac900136z
 127. Svancara I, Kachler K, Walcarius A, Vytras K (2012) *Electroanalysis with carbon paste electrodes. Analytical chemistry series, CRC Press, Taylor&Francis Group, Boca Raton, FL, USA*
 128. Alkire RC, Kolb DM, Lipkowski J, Ross PN (2011) *Advances in electrochemical science and engineering, vol 11, Chemically modified electrodes. Wiley-VCH Verlag GmbH & Co. KGaA, Weinheim*
 129. Murray RW (1984) Chemically modified electrodes. *Electroanal Chem* 13:191–368

130. Murray RW, Ewing AG, Durst RA (1987) Chemically modified electrodes – molecular design for electroanalysis. *Anal Chem* 59(5):A379. doi:10.1021/ac00132a001
131. Wang J (1990) Voltammetry following nonelectrolytic preconcentration. *Electroanal Chem* 16:1–88
132. Berek J, Peckova K, Vyskocil V (2008) Adsorptive stripping voltammetry of environmental carcinogens. *Curr Anal Chem* 4(3):242–249. doi:10.2174/157341108784911325
133. Xu GY, Jiao K, Fan JS, Zhang B (2007) Immobilizing DNA on cetyltrimethyl ammonium bromide cationic membrane for the detection of specific gene related to NPT II. *Asian J Chem* 19(6):4161–4172
134. Arrieta A, Rodriguez-Mendez ML, de Saja JA (2003) Langmuir-Blodgett film and carbon paste electrodes based on phthalocyanines as sensing units for taste. *Sens Actuators B Chem* 95(1–3):357–365. doi:10.1016/s0925-4005(03)00438-6
135. Bobacka J, Ivaska A, Lewenstam A (2003) Potentiometric ion sensors based on conducting polymers. *Electroanalysis* 15(5–6):366–374. doi:10.1002/elan.200390042
136. Mullor SG, SanchezCabezudo M, Ordieres AJM, Ruiz BL (1996) Alcohol biosensor based on alcohol dehydrogenase and Meldola blue immobilized into a carbon paste electrode. *Talanta* 43(5):779–784
137. Ravichandran K, Baldwin RP (1981) Chemically modified carbon paste electrodes. *J Electroanal Chem* 126(1–3):293–300. doi:10.1016/0368-1874(81)87209-7
138. Kalcher K (1986) Voltammetric behavior of gold at a dithizone-modified carbon-paste electrode. *Fres Zeitschrift Anal Chem* 325(2):181–185. doi:10.1007/bf00468886
139. Wang HS, Ju HX, Chen HY (2002) Adsorptive stripping voltammetric detection of single-stranded DNA at electrochemically modified glassy carbon electrode. *Electroanalysis* 14(23):1615–1620. doi:10.1002/elan.200290001
140. Gautier C, Ghodbane O, Wayner DDM, Belanger D (2009) Modification of glassy carbon electrodes by 4-chloromethylphenyl units and D-glucosaminic acid. *Electrochim Acta* 54(26):6327–6334. doi:10.1016/j.electacta.2009.05.072
141. Shahrokhian S, Ghalkhani M, Adeli M, Amini MK (2009) Multi-walled carbon nanotubes with immobilised cobalt nanoparticle for modification of glassy carbon electrode: application to sensitive voltammetric determination of thioridazine. *Biosens Bioelectron* 24(11):3235–3241. doi:10.1016/j.bios.2009.04.004
142. Sondaghuethorst JAM, Vanhelleputte HRJ, Fokkink LGJ (1994) Generation of electrochemically deposited metal patterns by means of electron-beam (nano)lithography of self-assembled monolayer resists. *Appl Phys Lett* 64(3):285–287. doi:10.1063/1.111182
143. Shalaev VM (2007) Optical negative-index metamaterials. *Nat Photonics* 1(1):41–48. doi:10.1038/nphoton.2006.49
144. Barnes WL, Dereux A, Ebbesen TW (2003) Surface plasmon subwavelength optics. *Nature* 424(6950):824–830. doi:10.1038/nature01937
145. Li Q, Batchelor-McAuley C, Compton RG (2010) Electrochemical oxidation of guanine: electrode reaction mechanism and tailoring carbon electrode surfaces to switch between adsorptive and diffusional responses. *J Phys Chem B* 114(21):7423–7428. doi:10.1021/jp1021196
146. Erdem A, Karadeniz H, Caliskan A (2009) Single-walled carbon nanotubes modified graphite electrodes for electrochemical monitoring of nucleic acids and biomolecular interactions. *Electroanalysis* 21(3–5):464–471. doi:10.1002/elan.200804422
147. Wildgoose GG, Banks CE, Leventis HC, Compton RG (2006) Chemically modified carbon nanotubes for use in electroanalysis. *Microchim Acta* 152(3–4):187–214. doi:10.1007/s00604-005-0449-x
148. Sherigara BS, Kutner W, D'Souza F (2003) Electrocatalytic properties and sensor applications of fullerenes and carbon nanotubes. *Electroanalysis* 15(9):753–772. doi:10.1002/elan.200390094

149. Marcoux PR, Hapiot P, Batail P, Pinson J (2004) Electrochemical functionalization of nanotube films: growth of aryl chains on single-walled carbon nanotubes. *New J Chem* 28(2):302–307. doi:10.1039/b309509f
150. Burghard M, Kooi S, Schlecht U, Balasubramanian K, Kern K (2002) Electrochemical functionalization of individual single-wall carbon nanotubes. In: Kuzmany H, Fink J, Mehring M, Roth S (eds) *Structural and electronic properties of molecular nanostructures*, vol 633, AIP conference proceedings. Amer Inst Physics, Melville, pp 77–81
151. Knez M, Sumser M, Bittner AM, Wege C, Jeske H, Kooi S, Burghard M, Kern K (2002) Electrochemical modification of individual nano-objects. *J Electroanal Chem* 522(1):70–74. doi:10.1016/s0022-0728(01)00728-8
152. Kooi SE, Schlecht U, Burghard M, Kern K (2002) Electrochemical modification of single carbon nanotubes. *Angew Chem Int Ed* 41(8):1353–1355. doi:10.1002/1521-3773(20020415)41:8<1353::aid-anie1353>3.0.co;2-i
153. Yang WR, Thordarson P, Gooding JJ, Ringer SP, Braet F (2007) Carbon nanotubes for biological and biomedical applications. *Nanotechnology* 18(41):1–6. doi:10.1088/0957-4484/18/41/412001
154. Wang J (2005) Carbon-nanotube based electrochemical biosensors: a review. *Electroanalysis* 17(1):7–14. doi:10.1002/elan.200403113
155. Balasubramanian K, Burghard M (2005) Chemically functionalized carbon nanotubes. *Small* 1(2):180–192. doi:10.1002/sml.200400118
156. Agui L, Yanez-Sedeno P, Pingarron JM (2008) Role of carbon nanotubes in electroanalytical chemistry – a review. *Anal Chim Acta* 622(1–2):11–47. doi:10.1016/j.aca.2008.05.070
157. Wang J, Liu GD, Jan MR, Zhu QY (2003) Electrochemical detection of DNA hybridization based on carbon-nanotubes loaded with CdS tags. *Electrochem Commun* 5(12):1000–1004. doi:10.1016/j.elecom.2003.09.010
158. Wildgoose GG, Wilkins SJ, Williams GR, France RR, Carnahan DL, Jiang L, Jones TGJ, Compton RG (2005) Graphite powder and multiwalled carbon nanotubes chemically modified with 4-nitrobenzylamine. *ChemPhysChem* 6(2):352–362. doi:10.1002/cphc.200400403
159. Shan CS, Yang HF, Song JF, Han DX, Ivaska A, Niu L (2009) Direct electrochemistry of glucose oxidase and biosensing for glucose based on graphene. *Anal Chem* 81(6):2378–2382. doi:10.1021/ac802193c
160. Lim CX, Hoh HY, Ang PK, Loh KP (2010) Direct voltammetric detection of DNA and pH sensing on epitaxial graphene: an insight into the role of oxygenated defects. *Anal Chem* 82(17):7387–7393. doi:10.1021/ac101519v
161. Zhou YL, Zhi JF (2009) The application of boron-doped diamond electrodes in amperometric biosensors. *Talanta* 79(5):1189–1196. doi:10.1016/j.talanta.2009.05.026
162. Chailapakul O, Siangproh W, Tryk DA (2006) Boron-doped diamond-based sensors: a review. *Sens Lett* 4(2):99–119. doi:10.1166/sl.2006.008
163. Granger MC, Witek M, Xu JS, Wang J, Hupert M, Hanks A, Koppang MD, Butler JE, Lucazeau G, Mermoux M, Strojek JW, Swain GM (2000) Standard electrochemical behavior of high-quality, boron-doped polycrystalline diamond thin-film electrodes. *Anal Chem* 72(16):3793–3804. doi:10.1021/ac0000675
164. Ivandini TA, Honda K, Rao TN, Fujishima A, Einaga Y (2007) Simultaneous detection of purine and pyrimidine at highly boron-doped diamond electrodes by using liquid chromatography. *Talanta* 71(2):648–655. doi:10.1016/j.talanta.2006.05.009
165. Ivandini TA, Sarada BV, Terashima C, Rao TN, Tryk DA, Ishiguro H, Kubota Y, Fujishima A (2002) Electrochemical detection of tricyclic antidepressant drugs by HPLC using highly boron-doped diamond electrodes. *J Electroanal Chem* 521(1–2):117–126. doi:10.1016/s0022-0728(02)00666-6
166. Wenmackers S, Vermeeren V, van de Ven M, Ameloot M, Bijnens N, Haenen K, Michiels L, Wagner P (2009) Diamond-based DNA sensors: surface functionalization and read-out strategies. *Phys Status Solidi A Appl Mater* 206(3):391–408. doi:10.1002/pssa.200880486

167. Compton RG, Spackman RA, Wellington RG, Green MLH, Turner J (1992) A C-60 modified electrode – electrochemical formation of tetrabutylammonium salts of C-60 anions. *J Electroanal Chem* 327(1–2):337–341. doi:10.1016/0022-0728(92)80159-2
168. Jehoulet C, Obeng YS, Kim YT, Zhou FM, Bard AJ (1992) Electrochemistry and langmuir trough studies of C-60 and C-70 films. *J Am Chem Soc* 114(11):4237–4247. doi:10.1021/ja00037a030
169. Compton RG, Spackman RA, Riley DJ, Wellington RG, Eklund JC, Fisher AC, Green MLH, Douthwaite RE, Stephens AHH, Turner J (1993) Voltammetry at C-60-modified electrodes. *J Electroanal Chem* 344(1–2):235–247. doi:10.1016/0022-0728(93)80058-p
170. Miranda-Hernandez A, Gonzdzlez I (2005) Characterization of carbon-fullerene-silicone oil composite paste electrodes. *Carbon* 43(9):1961–1967. doi:10.1016/j.carbon.2005.03.004
171. Gradzka E, Winkler K, Borowska M, Plonska-Brzezinska ME, Echegoyen L (2013) Comparison of the electrochemical properties of thin films of MWCNTs/C-60-Pd, SWCNTs/C-60-Pd and ox-CNOs/C-60-Pd. *Electrochim Acta* 96:274–284. doi:10.1016/j.electacta.2013.02.035
172. Cai XH, Ogorevc B, Kalcher K (1995) Synergistic electrochemical and chemical modification of carbon paste electrodes for open-circuit preconcentration and voltammetric determination of trace adenine. *Electroanalysis* 7(12):1126–1131. doi:10.1002/elan.1140071206
173. Huang W, Zhang S, Wu Y (2006) Electrochemical behavior and detection of guanine using a sodium montmorillonite-modified carbon paste electrode. *Russ J Electrochem* 42(2):153–156. doi:10.1134/s1023193506020078
174. Zen JM, Kumar AS, Chen HW (2000) Electrochemical formation of Prussian blue in natural iron-intercalated clay and cinder matrixes. *Electroanalysis* 12(7):542–545. doi:10.1002/(sici)1521-4109(200005)12:7<542::aid-elan542>3.0.co;2-5
175. Abbaspour A, Mehrgardi MA (2004) Electrocatalytic oxidation of guanine and DNA on a carbon paste electrode modified by cobalt hexacyanoferrate films. *Anal Chem* 76(19):5690–5696. doi:10.1021/ac049421f
176. Sun W, Duan YY, Li YZ, Gao HW, Jiao K (2009) Electrochemical behaviors of guanosine on carbon ionic liquid electrode and its determination. *Talanta* 78(3):695–699. doi:10.1016/j.talanta.2008.12.034
177. Xu GY, Fan JS, Jiao K (2008) Immobilizing DNA on clay mineral modified carbon paste electrodes. *Appl Clay Sci* 40(1–4):119–123. doi:10.1016/j.clay.2007.11.002
178. El-Maali NA, Wang J (2001) Tris(2,2'-bipyridyl)dichloro-ruthenium(II) modified carbon paste electrodes for electrocatalytic detection of DNA. *Sens Actuators B* 76(1–3):211–214. doi:10.1016/s0925-4005(01)00643-8
179. Mazloum-Ardakani M, Taleat Z, Beitollahi H, Salavati-Niasari M, Mirjalili BBF, Taghavinia N (2008) Electrocatalytic oxidation and nanomolar determination of guanine at the surface of a molybdenum (VI) complex-TiO₂ nanoparticle modified carbon paste electrode. *J Electroanal Chem* 624(1–2):73–78. doi:10.1016/j.jelechem.2008.07.027
180. Arvand M, Mazhabi RM, Niazi A (2013) Simultaneous determination of guanine, adenine and thymine using a modified carbon paste electrode by TiO₂ nanoparticles-magnesium(II) doped natrolite zeolite. *Electrochim Acta* 89:669–679. doi:10.1016/j.electacta.2012.11.014
181. Abdullin TI, Nikitina II, Ishmukhametova DG, Budnikov GK, Konovalova OA, Salakhov MK (2007) Carbon nanotube-modified electrodes for electrochemical DNA-sensors. *J Anal Chem* 62(6):599–603. doi:10.1134/s1061934807060184
182. Thangaraj R, Kumar AS (2013) Simultaneous detection of guanine and adenine in DNA and meat samples using graphitized mesoporous carbon modified electrode. *J Solid State Electrochem* 17(3):583–590. doi:10.1007/s10008-012-1895-0
183. Jalit Y, Moreno M, Gutierrez FA, Arribas AS, Chicharro M, Bermejo E, Zapardiel A, Parrado C, Rivas GA, Rodriguez MC (2013) Adsorption and electrooxidation of nucleic acids at glassy carbon electrodes modified with multiwalled carbon nanotubes dispersed in polylysine. *Electroanalysis* 25(5):1116–1121. doi:10.1002/elan.201200622

184. Wang P, Chen HB, Tian JY, Dai Z, Zou XY (2013) Electrochemical evaluation of DNA methylation level based on the stoichiometric relationship between purine and pyrimidine bases. *Biosens Bioelectron* 45:34–39. doi:10.1016/j.bios.2013.01.057
185. Tang C, Yogeswaran U, Chen SM (2009) Simultaneous determination of adenine guanine and thymine at multi-walled carbon nanotubes incorporated with poly(new fuchsin) composite film. *Anal Chim Acta* 636(1):19–27. doi:10.1016/j.aca.2009.01.055
186. Wang QX, Zheng MX, Shi JL, Gao F (2011) Electrochemical oxidation of native double-stranded DNA on a graphene-modified glassy carbon electrode. *Electroanalysis* 23(4):915–920. doi:10.1002/elan.201000713
187. Huang KJ, Niu DJ, Sun JY, Han CH, Wu ZW, Li YL, Xiong XQ (2011) Novel electrochemical sensor based on functionalized graphene for simultaneous determination of adenine and guanine in DNA. *Colloid Surf B Biointerfaces* 82(2):543–549. doi:10.1016/j.colsurfb.2010.10.014
188. Yin HS, Zhou YL, Ma QA, Ai SY, Ju P, Zhu LS, Lu LN (2010) Electrochemical oxidation behavior of guanine and adenine on graphene-Nafion composite film modified glassy carbon electrode and the simultaneous determination. *Process Biochem* 45(10):1707–1712. doi:10.1016/j.procbio.2010.07.004
189. Ba X, Luo LQ, Ding YP, Zhang Z, Chu YL, Wang BJ, Ouyang XQ (2012) Poly(alizarin red)/graphene modified glassy carbon electrode for simultaneous determination of purine and pyrimidine. *Anal Chim Acta* 752:94–100. doi:10.1016/j.aca.2012.09.031
190. Ghavami R, Salimi A, Navaee A (2011) SiC nanoparticles-modified glassy carbon electrodes for simultaneous determination of purine and pyrimidine DNA bases. *Biosens Bioelectron* 26(9):3864–3869. doi:10.1016/j.bios.2011.02.048
191. Serpi C, Voulgaropoulos A, Girousi S (2013) Electrochemical study of dsDNA on carbon nanotubes paste electrodes applying cyclic and differential pulse voltammetry. *Cent Eur J Chem* 11(3):413–423. doi:10.2478/s11532-012-0180-5
192. Zhang RY, Wang XM (2010) Selective enhanced electrochemical response of DNA bases on carbon nanotube-gold nanocomposites modified gold electrode. *Phys Status Solidi A Appl Mater* 207(10):2263–2268. doi:10.1002/pssa.201026094
193. Fang B, Zhang W, Wang GF, Liu HY, Wei SP (2008) Microwave-assisted preparation of a carbon nanotube/La(OH)(3) nanocomposite, and its application to electrochemical determination of adenine and guanine. *Microchim Acta* 162(1–2):175–180. doi:10.1007/s00604-007-0901-1
194. Ensafi AA, Jafari-Asl M, Rezaei B, Allafchian AR (2013) Simultaneous determination of guanine and adenine in DNA based on NiFe₂O₄ magnetic nanoparticles decorated MWCNTs as a novel electrochemical sensor using adsorptive stripping voltammetry. *Sens Actuators B* 177:634–642. doi:10.1016/j.snb.2012.11.028
195. Wei Y, Huang QA, Li MG, Huang XJ, Fang B, Wang L (2011) CeO₂ nanoparticles decorated multi-walled carbon nanotubes for electrochemical determination of guanine and adenine. *Electrochim Acta* 56(24):8571–8575. doi:10.1016/j.electacta.2011.07.048
196. Randviir EP, Banks CE (2012) Electrochemical measurement of the DNA bases adenine and guanine at surfactant-free graphene modified electrodes. *RSC Adv* 2(13):5800–5805. doi:10.1039/c2ra20173a
197. Ambrosi A, Pumera M (2010) Stacked graphene nanofibers for electrochemical oxidation of DNA bases. *Phys Chem Chem Phys* 12(31):8944–8948. doi:10.1039/c0cp00213e
198. Niu XL, Yang W, Ren J, Guo H, Long SJ, Chen JJ, Gao JZ (2012) Electrochemical behaviors and simultaneous determination of guanine and adenine based on graphene-ionic liquid-chitosan composite film modified glassy carbon electrode. *Electrochim Acta* 80:346–353. doi:10.1016/j.electacta.2012.07.041

199. Sun W, Liu J, Ju XM, Zhang L, Qi XW, Hui N (2013) Highly sensitive electrochemical detection of adenine on a graphene-modified carbon ionic liquid electrode. *Ionics* 19(4):657–663. doi:10.1007/s11581-012-0789-6
200. Biris AR, Pruneanu S, Pogacean F, Lazar MD, Borodi G, Ardelean S, Dervishi E, Watanabe F, Biris AS (2013) Few-layer graphene sheets with embedded gold nanoparticles for electrochemical analysis of adenine. *Int J Nanomedicine* 8:1429–1438. doi:10.2147/ijn.s42613
201. Hayashi K, Yamanaka S, Watanabe H, Sekiguchi T, Okushi H, Kajimura K (1997) Investigation of the effect of hydrogen on electrical and optical properties in chemical vapor deposited on homoepitaxial diamond films. *J Appl Phys* 81(2):744–753. doi:10.1063/1.364299
202. Oliveira SCB, Oliveira-Brett AM (2010) Boron doped diamond electrode pre-treatments effect on the electrochemical oxidation of dsDNA, DNA bases, nucleotides, homopolynucleotides and biomarker 8-oxoguanine. *J Electroanal Chem* 648(1):60–66. doi:10.1016/j.jelechem.2010.06.020
203. Fortin E, Chane-Tune J, Mailley P, Szunerits S, Marcus B, Petit JP, Mermoux M, Vieil E (2004) Nucleosides and ODN electrochemical detection onto boron doped diamond electrodes. *Bioelectrochemistry* 63(1–2):303–306. doi:10.1016/j.bioelechem.2003.10.027
204. Ivandini TA, Sarada BV, Rao TN, Fujishima A (2003) Electrochemical oxidation of underivatized-nucleic acids at highly boron-doped diamond electrodes. *Analyst* 128(7):924–929. doi:10.1039/b301483e
205. Apilux A, Tabata M, Chailapakul O (2007) Electrochemical behaviors of native and thermally denatured fish DNA in the presence of cytosine derivatives and porphyrin by cyclic voltammetry using boron-doped diamond electrode. *Bioelectrochemistry* 70(2):435–439. doi:10.1016/j.bioelechem.2006.07.001
206. Shiraishi H, Itoh T, Hayashi H, Takagi K, Sakane M, Mori T, Wang J (2007) Electrochemical detection of *E. coli* 16S rDNA sequence using air-plasma-activated fullerene-impregnated screen printed electrodes. *Bioelectrochemistry* 70(2):481–487. doi:10.1016/j.bioelechem.2006.07.011
207. Zhang XZ, Qu YT, Piao GZ, Zhao JA, Jiao K (2010) Reduced working electrode based on fullerene C60 nanotubes@DNA: characterization and application. *Mater Sci Eng B Adv Funct Solid State Mater* 175(2):159–163. doi:10.1016/j.mseb.2010.07.020

Suchikova Yana

Contents

Introduction.....	284
Technology for Production of Porous Structures.....	286
Electrochemical Etching.....	286
Getting the Initial Pore Growth.....	287
The Structure of Porous Layers.....	288
Obtaining Low-Dimensional Structures on the Surface of Indium Phosphide.....	289
Physicochemical Regularities of the Porous Layer of Indium Phosphide.....	291
Effect of the Type of Electrolyte Anion on the Porous InP Morphology Obtained by the Electrochemical Etching.....	291
Influence of the Carrier Concentration of Indium Phosphide on the Porous Layer Formation.....	298
Influence of Dislocations on the Process of Pore Formation in n-InP (111) Single Crystals.....	300
Texturing of the Indium Phosphide Surface.....	302
Conclusion.....	303
References.....	304

Abstract

Porous semiconductors attract the attention of many researchers due to the relatively simple technology of obtaining them and possibility of controlling the geometry parameters of the pores (from nanometer- to micrometer-scale objects), as well as prospects of manufacturing of combined optoelectronic devices, in which information is processed not only in an electronic but also in an optical form. In this work the analysis of the dependence of the porous InP morphology

S. Yana (✉)

Berdiansk State Pedagogical University, Berdiansk, Zaporizhia Oblast, Ukraine
e-mail: yanasuchikova@mail.ru

on the type of reacting anion is presented. It is shown that nanoporous InP layers are obtained through certain conditions of electrochemical etching. The observation results of InP-layered heterogeneity are discussed and explained in terms of the features of the growing process of heavily doped crystals.

Using scanning electron microscopy, the influence of dislocations on the mechanism of pore formation during electrolytic etching of single-crystal InP is shown. In this work the photoelectrochemical method for texturing the monocrystal InP surface is proposed. By means of the scanning electron microscopy the optimal formation conditions of the samples with developed morphology and uniform cluster distribution over InP surface are established.

Keywords

The porous indium phosphide • Electrochemical etching • Semiconductor • Surface Nanostructures

Introduction

Needs of modern society in processing and transfer of the growing information content led to the formation of the super-high-speed optoelectronic integrated circuits based on silicon and binary semiconductors. Integration of transistor structures into very large-scale integrated circuits is technologically limited by the physical boundaries of the microregion size and the low charge mobility in semiconductors. The solution of this problem is in the increase in the functionality of the elements.

Recently, scientific interest is directed to the formation of nanostructures considered as a promising material for the creation of photon devices. The electrochemical process, which is unique due to its simplicity, low process temperature, and low cost, stands out against different formation techniques of semiconductor nanostructures. The most well-known application of the electrochemical methods is the formation of a porous layer on the surface of semiconductor plate by anode etching. For the first time such structures were obtained on silicon. Lately it was established that porous layers can be also obtained on binary compounds, such as GaAs, GaP, and InP.

Porous semiconductors attract the attention of many researchers due to the relatively simple technology of obtaining them and possibility of controlling the geometry parameters of the pores (from nanometer- to micrometer-scale objects), as well as prospects of manufacturing of combined optoelectronic devices, in which information is processed not only in an electronic but also in an optical form. The recently attained progress in studying the properties of porous silicon stimulated similar studies for the III–V compounds. Particularly, the most promising in this aspect is porous InP, since the energy parameters of its single crystals are very close to the parameters of single-crystal silicon and devices of integrated optoelectronics

compatible with silicon, particularly resistive and diode optopairs, can be easily fabricated based on it.

Indium phosphide (InP) has great prospects of wide industrial production. Field-effect transistors and other microwave devices are manufactured based on InP. Monocrystalline InP plates are used as substrates for the growth of different heterostructures, which are the basis of effective radiation sources (injection lasers, light-emitting diodes) and high-speed photodetectors for the systems of fiber-optic communication lines. InP is promising for the development of super-high-speed integrated circuits. Presently InP is the most probable material for the mass production of integrated circuits. It is impossible not to mention about the growing interest in porous InP, which has unusual optical and electrical properties in comparison with the monocrystalline InP.

It is established that different factors, namely, the composition and concentration of electrolyte, current density, and etching time, influence the formation of porous layer. Behavior of the semiconductor under electrochemical treatment also depends on the type and concentration of majority carriers. Here one should keep in mind that electrochemical process is accompanied by a number of coupled chemical reactions, and the final result of the electrochemical treatment of semiconductor depends on the ratio of the reaction rates.

It is possible to use the halogenide, sulfate, phosphate, nitrate aqueous, and anhydrous solutions of alkalis at considerable current densities as electrolyte for obtaining the porous III–V materials (particularly InP), Table 1. In most cases, for the electrolytic etching of binary III–V compounds, solutions of HCl in ethanol or water are used.

The interest in investigation of defects in the crystals and their influence on the formation of porous layers of semiconductors increased because of the requirements, each deviation from which leads to the emergence of defects. External conditions are the determining factor, due to which the surface of the crystal during etching varies its shape and morphology, which is expressed on the faces in the form

Table 1 Electrolytes and regimes of anodic etching

Electrolyte	Current, voltage	Time	The type of pore
HCl	$J=4-4.2 \text{ mA/cm}^2$	120	Crysto
	$J=4-100 \text{ mA/cm}^2$	10–60	Curro
	$U=0.8-5 \text{ V}$	1–3	Crysto
	$U=4-9 \text{ V}$	1–3	Curro
HCl + HNO ₃	$U=4-9 \text{ V}$	1–3	Curro
	$U=1-3 \text{ V}$	–	Crysto
HCl + HF	$J=50 \text{ mA/cm}^2$	1	Crysto
HCl + NH ₄ Cl	$U=7-10 \text{ V}$	0.3–0.4	Curro
NaCl	$U=5 \text{ V}$	1.5	Curro
KBr + HBr	$U=7-10 \text{ V}$	0.3–0.4	Curro

of hatching, figures of etching, etc. Thus, a defect brings information about the events that took place with this crystal and about the factors determining the behavior of the crystal during the anodic etching.

Thus, the questions associated with the methods of obtaining the porous structures of InP, mechanisms of their formation, and dependence of conditions of pore formation on internal defects and imperfections of crystals remain unresolved. In this article, we consider the procedure of obtaining the porous layers on the (111) surface of indium phosphide of *n*-type of conductivity as well as the influence of defects and dislocations on the configuration and structure of porous layers obtained during this process.

Technology for Production of Porous Structures

There are several physical and chemical technologies for obtaining porous structures: the colloidal deposition, MOCVD, spark discharge, plasma etching, hydrothermal synthesis, sol-gel methods, vapor deposition, and chemical and electrolytic deposition.

Electrochemical Etching

Electrochemical etching has the following features: low-temperature process, minor surface damage, easy, and low cost. This method does not require high-tech equipment and is fast (2–30 min). Electrochemical methods allow for a high density of pores, which is unattainable using other methods.

Electrochemical etching can be divided into two different processes:

- Chemical etching (electroless etching)
- Anodic etching

Note that in both cases there is electrochemical etching of charge exchange at the border of the semiconductor and electrolyte.

Chemical etching is usually a process of electrochemical oxidation without external potential. The performance of this type of etching requires strong enough reagents that can form/rip holes and electrons to/from the valence band of the semiconductor. Thus, the redox coupled with high positive standard electrode potential is required for efficient etching. Electronic energy distribution function oxidants exceed the energy level of the valence band in solid.

The mechanism of electrochemical oxidation is usually divided into two partial reactions:

- Injection of holes in the valence band (release of electrons).
- Broken bonds will be occupied by molecules such as OH, which leads to the dissolution of the material.

These two steps of chemical etching split apart in time. Because of this, you can stop the progress of the first phase and the second stage (dissolution) will also be stopped.

When applying an electrical displacement that causes electrons to move from the solution to the electrode, the process is called anodic etching (holes move to the buffer zone).

On the other hand, if they are moved from the electrode into the solution, the process is called cathode etching (holes are removed from the buffer zone). Anode etching, like chemical etching, requires hole for the process. A large number of holes on the surface will induce a bond failure. Similar to the chemical etching, broken bonds will react with nucleophilic molecules (such as OH^-) in the electrolyte. If all the bonds of atoms of the solid will be replaced by bonds with nucleophilic molecules, this will form new compounds that consist of atoms of the solid and nucleophilic molecules. New compound will have only a small portion of the solid bonds or will not have them at all. If this compound is dissolved in the electrolyte, it can dissolve chemically pure, and thus, the surface of the sample will be free and ready for the next interaction with nucleophilic molecules of the etchant.

Otherwise, i.e., if the newly created compound is dissolved in the electrolyte, a thin oxide layer on the surface of the electrode will form which will prevent electrochemical attack. For this reason, suitable for electrochemical etching, electrolytes contain two main components:

- Nucleophilic (i.e., decelerating) components
- Components that dissolve oxides

In general, for *n*-type semiconductors required for etching, holes can be generated by the avalanche breakdown mechanism that can be achieved by a high positive potential on the electrode or whether this effect can be achieved with a semiconductor light photons with energies greater than the energy gap of the semiconductor.

Getting the Initial Pore Growth

Getting the initial pore growth can be realized in two main areas:

- Providing certain places of origin of pores, i.e., lithographs – “seeding pore formation.”
- Pore formation is going its own way – “random pore formation.”

Seeding origin has a practical significance only for macropores because micropores or mesopores, by definition, require very small structures. The easiest way to ensure this process is the use of standard lithography to transmit the desired pattern on the photoresist. The template can be referred to as the “mask.”

After macropore growth is finished and if stable pore growth conditions prevail, the mask is no longer needed. Thus, it does not matter if the mask dissolves during a long process of etching.

Applying a template can be realized by other methods:

- Electron beam lithography: expensive and slow way, but still used and necessary for small sizes.
- Imprinting the appropriate template.
- Laser interferometry: standing waves, which are formed from the impact of several lasers, can produce periodic structures in photoresist. The method is a bit limited, but relatively easily repeated.
- Overlaying masks with template. For example, here can be used a two-dimensional crystals from latex or have any mask.

There are several aspects that must be considered for the process of seed pore formation:

- Pores may arise in the given nodes, but not for everyone. They can also arise out of nodes elsewhere – in particular, if the mask is not too stable and homogeneous.
- Even if the pore formation was properly, receiving pores may move at further etching and not grow steadily, so the target structure is disrupted with increasing of depth. This is an inevitable process, if the external length scale imposed on the porous structure is too different from the scale of the internal process.
- However, the pores can emerge and grow steadily, but their form is far from ideal.

Emergence of random pores takes place on unstructured but nevertheless uniform and clean surface. The concept of “clean surface” is obviously relative. But, as it is obvious, “dirty” heterogeneous surfaces (e.g., polished surface with a locally damaged area) will somehow influence the pore formation. Random pore growth can be quite different on the polished or “rough” surface. The characteristic feature of most semiconductors is the stable structure of their pores by random pore formation. In other words, the average pore diameter and the distance between them have their own values with relatively small standard deviation.

The Structure of Porous Layers

According to the recommendations of the International Union of Pure and Applied Chemistry (IUPAC), pore sizes are divided into:

- Macropores (pore width greater than 50 nm)
- Mesopores (pore width of 2–50 nm)
- Micropores (pore width less than 2 nm)

Pores in A3B5 compounds exhibit a variety of forms. Therefore, it is convenient to classify them in the direction of growth:

- Pores are oriented along the crystallographic directions (crysto).
- Pores are oriented on current (curro).
- Pores have no definite direction.

This shows the anisotropy of etching crystals.

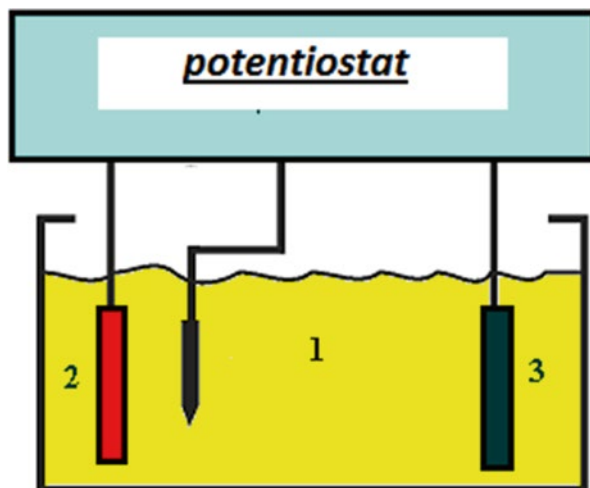
Anisotropic etching is important for the structuring of semiconductors and is mainly related to the differences in the rate of etching low-indexed surfaces of crystals. The reasons for this behavior are not yet fully understood. Typically, we investigate low-indexed crystal surface – orientations (111) (100) (110). Each set of planes has its own different behavior in solution. One of the reasons may be the density of atoms in the crystallographic planes (high density = low dissolution rate). However, this is not the only factor that determines the anisotropy. In III–V compounds, there are several additional factors that contribute to the anisotropy; this is due to different chemical properties of atoms in the third and fifth groups of the periodic table of elements. For example, along the surface with the orientation $\langle 111 \rangle$, atomic planes are occupied by atoms of the third and fifth groups, forming double layers, i.e., there are small and large gaps between the planes $\{111\}$, which alternate. Each atom has three bonds within a double layer and one bond outside the double layer. Surfaces limited by atoms of In are called $\{111\}A$, while surfaces limited by atoms of P $\{111\}B$. It is important to note that almost all surface oxidation processes such as $\{111\}$ have a slower dissolution rate. This can be explained by the assumption that three bonds (within the same double layer) are much harder to break from A than from B, due to the fact that the electronic cloud of a bond is polarized in the direction of B atom (more electronegative).

If we assume that in order to break the bond by atom B, we need the average time t_1 , whereas for A, it takes time $t_2 \gg t_1$. So to eliminate the double layer of B, we must spend time $(3t_1 + t_2)$, whereas for A, it is equal to the total time $(3t_2 + t_1)$. It is easy to see that $(3t_2 + t_1) \gg (3t_1 + t_2)$. As a result, the etching of B (along the $\langle 111 \rangle B$) is much faster than A (along the direction $\langle 111 \rangle A$). Besides, along the directions of atomic planes $\langle 100 \rangle$, space is also alternately occupied by atoms of the third and fifth groups. However the atomic planes are equidistant and symmetrically related to each atom with atoms of neighboring layers. Thus, the time required for etching of two layers from A side is $(2t_2 + 2t_1)$ and from B $(2t_2 + 2t_1)$. As a result, in this case there is no difference on what surface is etched, because the average time is the same.

Obtaining Low-Dimensional Structures on the Surface of Indium Phosphide

Indium phosphide monocrystals were produced in the research laboratory of Molecular Technology GmbH company (Berlin). Thickness of the samples was

Fig. 1 Plant for the semiconductor etching



1 mkm. Plates were cut out perpendicular to the growth axis and polished on both sides.

InP samples with different surface orientations of the *n*- and *p*-types and with different charge carrier concentrations were chosen for the experiment. Electrochemical etching was performed using the standard plant in the electrolytic cell with the platinum cathode. The plant scheme is presented in Fig. 1.

Solutions of hydrofluoric and hydrochloric acids with different concentrations were taken as the electrolytes. Etchants based on HF and HCl with added iodides (KOH), ethanol, and nitric acid were also used. The experiment was carried out at room temperature.

Samples were thoroughly purified before the experiment. The following are the purification steps:

1. Degreasing in hot (75–80 °C) peroxide-ammonia solution
2. Treatment in hot (90–100 °C) concentrated nitric acid (metal ion removal)
3. Washing in distilled water
4. Drying of the plates using centrifuge in the purified dry air

After experiment the samples were purified in acetone and isopropanol, washed in distilled water, and dried in extra pure hydrogen, whereupon they were undergoing natural aging during 3 days.

Morphology of the obtained porous structures was investigated using the scanning electron microscope JSM-6490. Chemical composition was studied with the EDAX method, and the diffractometric investigations were carried out using the diffractometer DRON-3 M.

Physicochemical Regularities of the Porous Layer of Indium Phosphide

Effect of the Type of Electrolyte Anion on the Porous InP Morphology Obtained by the Electrochemical Etching

The processes that form at the junction of the semiconductor and electrolyte should lead to the establishment of thermodynamic equilibrium between the electronic subsystem of the semiconductor and hydrogen redox system solution, as well as the establishment of local chemical equilibrium at the interface which minimizes its free energy. Setting electrochemical equilibrium between aqueous electrolyte and semiconductor *n*-type is provided by the transition of electrons from the conduction band to the hydronium cations. As a result, semiconductor is positively charged, and the electric double layer arises in solution with excess anionic concentration at the border of the crystal.

Let us consider the surface of InP as a free crystal surface. Depending on the crystallographic orientation of this surface, the atoms that go into it may have one or two broken bonds. In the volume-surface equilibrium, one orbital of the broken bonds of the indium atom should be vacant, and phosphorus atoms occupied by the unshared pair of electrons. Then during the adsorption of at least one atom in the anion of the indium, full heat of adsorption should be the same with the heat on the electrophilic center. At the same time for P atoms, conversion of the filled orbitals of broken bond into the electrophilic center requires energy, which, in general, exceeds the energy released in the act of adsorption. Therefore, in the absence of an electric shift, only a small part of the surface atoms of phosphorus may be associated with halogen adatoms. On the surface of indium phosphide *n*-type, a thin dense layer of particles is formed, in which the negative charge of the semiconductor is concentrated – Helmholtz layer. As the anodic shift increases, gradual convergence of the energy of levels takes place, filled states in the Helmholtz layer and vacant states in the crystal. As a result of the convergence, channels of tunneling electron transfer in the crystal from components of this layer arise. As the deviation from the initial equilibrium conditions, the growth of several processes may take place, the complete oxidation of the material, electrode oxidation of solvated anions, and the emergence and growth of pores; pore formation in this sense is the nature of an avalanche breakdown.

Morphology analysis of the tested samples obtained using the scanning electron microscopy (SEM) showed that almost in all cases the active pore formation was observed (Table 2 and 3). In the conditions when pore formation is the dominant electrochemical process, which takes place at the given value of the polarizing voltage on the monocrystal semiconductor anode, the steady-state configuration of the porous layer surface is formed by the time of the maximum current density attainment.

Under equal conditions (identical crystals, equal charge and anion concentration in the solution), the electrolytic reaction rate depends on the type of reacting anion. Depending on the degree of dissociation into ions, electrolytes can be classified as

Table 2 Conditions for obtaining of various classes of nanostructures on the surface of indium phosphide

Low-dimension structures	Electrolyte	Current density, mA/cm ²	Etching time, min	Additional conditions
Porous layers <i>n</i> -type <i>p</i> -type	HF HCl	50–250	3–30	For etching of <i>p</i> -type tungsten lighting lamps of 200 W
Surface textured	HBr	130–170	6–10	Tungsten lighting lamps of 200 W
Superlattices	HF	80–150	25–35	Pulsating voltage: etching at a voltage of 5 V (1 min), etching without voltage (simple chemical etching) – 2 min
Nanoclusters	HF+ C ₂ H ₅ OH	70–130	10–15	After digestion – aging for 3 days in the open air
Zero-dimensional structures	HF+ HNO ₃	180	4–6	Influence of pulse magnetic field by a series of symmetrical triangular impulses amplitude B=0.5 T with a frequency f=50 Hz

Table 3 Types of nanostructures on the surface InP

Low-dimensional structures	Structure type	Unit size	Structure features
Porous layers	Pore	Pore diameter 7–300 nm	The form depends on the orientation of the surface: for the (111) oriented crystal pores have a triangular shape for the (100) – close to square
Textured surfaces	Pyramidal clusters	The height of the pyramid from 0.7 to 1.1 μm	The angle of inclination of faces 64°–85°
Superlattices	Periodic layers of porous and single-crystal indium phosphide	Width of porous and single-crystal bands 20–25 nm and 30–35 nm, respectively	Superlattice is formed across the sample thickness. Monocrystalline layer also has pores, but they are few; they are located mainly at the interface of two layers and have ordered nature
Nanoclusters	Crystalline indium oxide	Cluster size of 10–200 μm	Flower-crystal structures
Zero-dimensional structures	Clusters of the indium quantum dots type	From 3 to 40 nm	The clusters are distributed uniformly over the surface of the crystal; some clusters are combined in a massive accumulation

strong and weak ones. Their behavior on dissolving is different. Some molecules of weak electrolytes dissociate into ions under solvation. Their dissociation is the reversible process since ions are easily associated in collisions; therefore, in solutions of weak electrolytes, the dynamic equilibrium between ions and undissociated molecules is attained. When strong electrolytes dissolve, the dissociation occurs almost completely, and ionic crystals or molecules dissociate with the formation of aquated (solvated) ions.

Some of the most important acids, namely, HNO_3 , H_2SO_4 , HClO_4 , HCl , and HBr , belong to strong electrolytes. Most of weak electrolytes are inorganic compounds, such as H_2CO_3 , H_2S , HCN , and HF .

HF-Based Etchants

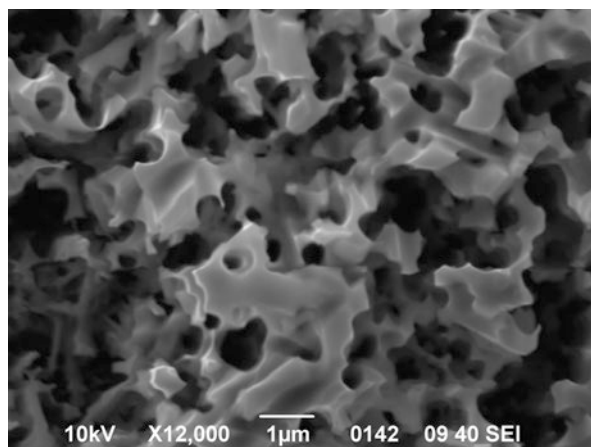
Small size of F atom substantially influences the fluoride properties. F atom in chemical compounds practically always is negatively charged. F is the most active oxidant among the elementary substances; it reacts with almost all substances. The feature of fluorine chemistry is the presence of stable hydrogen bonds HF. The average degree of association of HF molecules in a liquid state is closed to 6. Etching acid is considered to be the half-strength acid (the dissociation constant is 6.8×10^{-4}). Electronegativity of F^- atoms in the series F^- , Cl^- , and Br^- is the largest and is equal to 4 on the Pauling scale.

In the halogenide-ion series, the minimum voltage value of the formation initiation always corresponds to fluorine anion. Morphology of the porous samples obtained using etching acid demonstrates the net of meso- and macropores.

Formation of such pores is often connected with the displacement of defects and dislocations on the crystal surface. In this case the substantial overetching of the surface is observed (Fig. 2).

In Fig. 2 it is possible to see clearly the etched regions that imply about very “harsh” etching conditions. Porous surface demonstrates the developed morphology with the formed large etching pits. Such surface has a huge effective area in

Fig. 2 Morphology of porous n-InP (111); electrolyte $\text{HF}:\text{H}_2\text{O}=1:1$, $j=80 \text{ mA/cm}^2$, $t=10 \text{ min}$



comparison with the monocrystal one, but it is imperfect enough for use as the substrate for heterostructure production. In this case, in order to decrease the electrolyte effect on the porous structure formation, it is reasonable to change the etching regimes (time, current density) for the more soft ones or use more dilute etchant solution.

When adding ethanol to this solution, the value of threshold voltage of the pore-formation initiation substantially increases, and here porous layer has more qualitative structure that has appeared in the decrease in the pore size (Fig. 3).

In general, ethyl alcohol is an organic diluent of electrolyte. When adding it to the aqueous solution of etching acid (the component ratio is $\text{HF}:\text{H}_2\text{O}:\text{C}_2\text{H}_5\text{OH} = 1:1:2$), the electrolytic reaction rate slows down, and therefore, more time is needed to obtain the porous structures.

Ethyl alcohol is used for the improvement of HF penetration into pores. In our case this leads to the formation of the denser of anisotropically propagating pores along the directions $\langle 111 \rangle_A$ and $\langle 111 \rangle_B$ (Fig. 4). The degree of porosity is about 30 % of the total area of the sample.

In Fig. 5 we present the cleavage of porous $n\text{-InP}$ (111) obtained in the HF-based etchant. Irritated area, the appearance of which can be caused by the dislocation displacement, is clearly observed under the crystal surface.

The following fact is found to be interesting: the crystal surface is not so irritated as an area under it. This implies about the pore formation inside the crystal as well, where pores can be combined due to the thinning of the walls and their accumulation around defects.

HCl-Based Etchants

Hydrochloric acid is the aqueous solution of hydrogen chloride; it is strong monatomic acid. The maximum concentration of such solution at 200 °C is 38 % and the density is 1.19 g/cm³. HCl is most often used during the electrochemical

Fig. 3 Morphology of porous $n\text{-InP}$ (111); electrolyte $\text{HF}:\text{H}_2\text{O}:\text{C}_2\text{H}_5\text{OH} = 1:1:2$, $j = 40 \text{ mA/cm}^2$, $t = 15 \text{ min}$

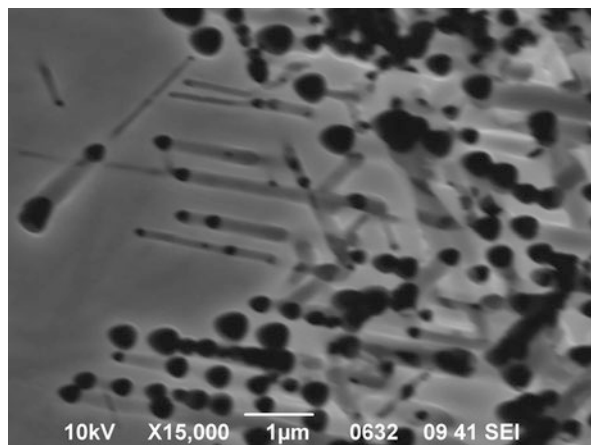
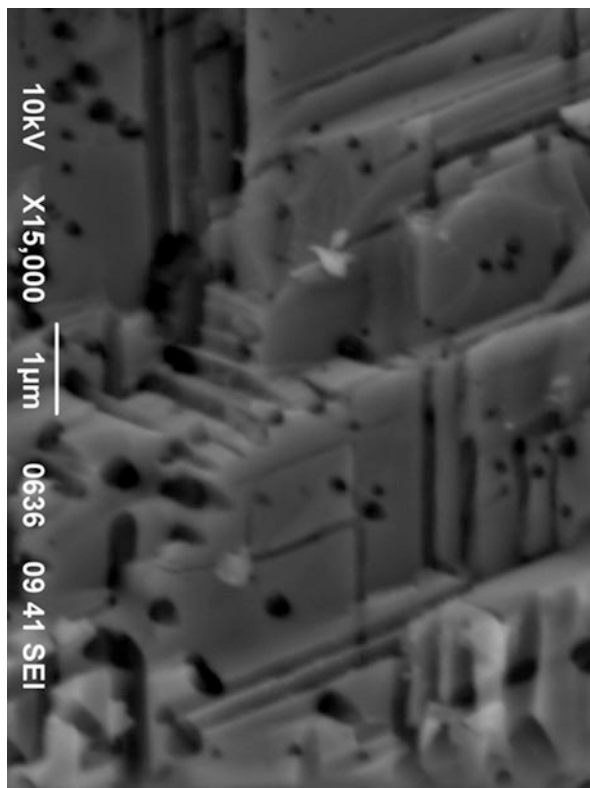


Fig. 4 Anisotropic pore propagation along the directions $\langle 111 \rangle$ A and $\langle 111 \rangle$ B



etching of the crystals that is explained by the possibility of this acid to easily dissociate into ions.

HCl-based etchants allow to obtain the layer composed of the nanopores mainly. Figure 6 demonstrates the ordered assembly of pores formed on the monocrystal InP substrate during the etching in 5 % hydrochloric acid solution. Pores appeared all over the sample surface. The average pore size is 40 nm that implies about the nanodimensionality of the given structure. The wall size between pores is in the range (5–10) nm. Such a result is important technologically, since the quality of porous films is determined by the nanostructure sizes, degree of porosity, and uniformity of the pore distribution over the sample surface. The smaller the pore size and the larger porosity percent, the more qualitative porous structure is. The degree of porosity is about 60 % of the total area of the sample.

In Fig. 7 we present the cleavage of the porous sample obtained in 5 % hydrochloric acid solution. This figure demonstrates the long parallel pore channels placed strictly perpendicular to the crystal surface. Such pores are directed along the lines of flow and reach the depth of 60 µm inside the sample.

Fig. 5 Cleavage of porous n-InP (111), electrolyte HF:H₂O:C₂H₅OH = 1:1:2, J = 50 mA/cm², t = 10 min

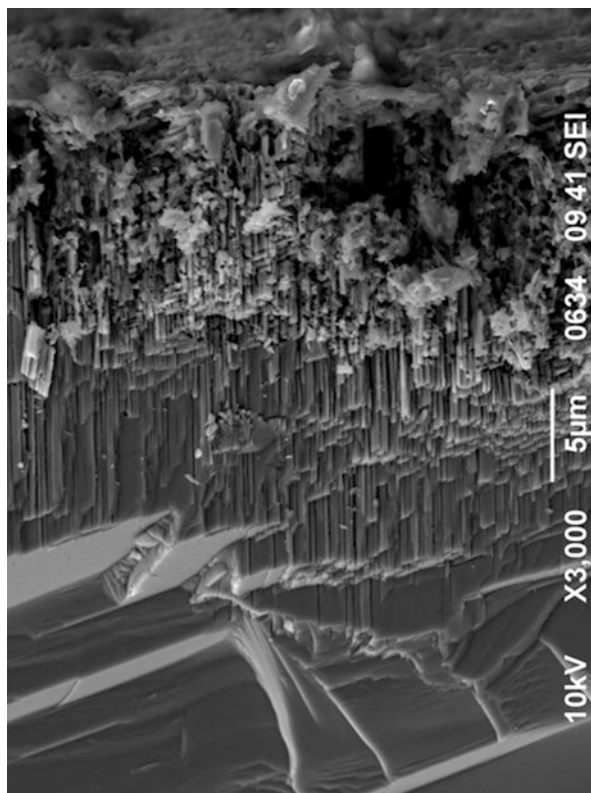


Fig. 6 Morphology of porous n-InP (100) obtained by the electrochemical etching in 5 % HCl solution, t = 5 min

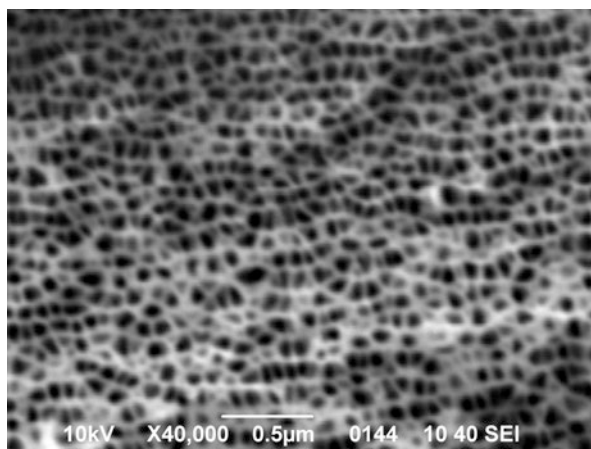
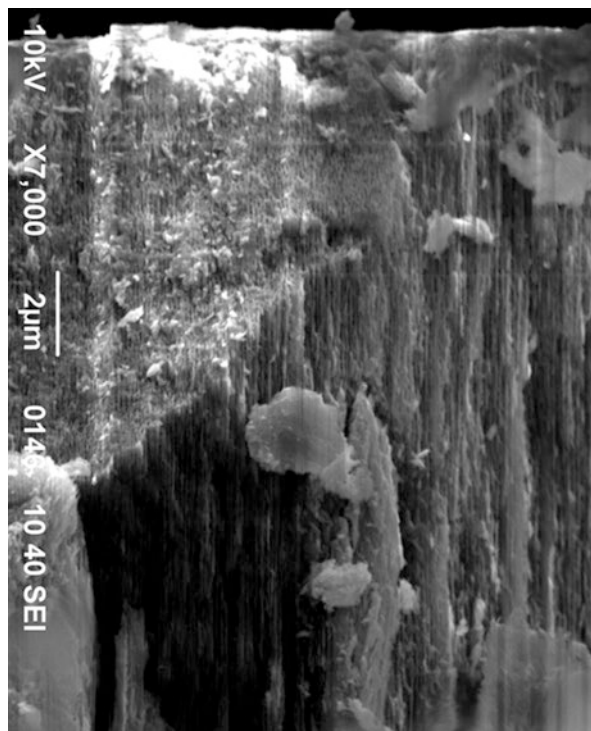


Fig. 7 Cleavage of porous n-InP (100) obtained by the electrochemical etching in 5 % HCl solution, $t=5$ min



Salts and Acids Addition to the Electrolyte Solution

Iodide addition to the fluoride solution essentially influences the pore-formation process. When adding KI (potassium iodide) to 50 % etching acid solution, the pore-formation process slows down somewhat what the current-voltage characteristics taken during anodization imply about. Morphology of the samples obtained in such solution demonstrates the decrease of the pore inlets (the degree of porosity is about 15 %). However, the branching of the pore channels under the crystal surface increases. Here the irregular layer preceding the long mutually parallel pores widens up to 2 mkm (in comparison with the irregular pore layer formed in the aqueous fluoride solution, which in this case is 0.5–1 mkm).

Nitric acid in addition to the chloride solutions accelerates the electrolytic reaction rate and allows to obtain the porous surfaces with the more densely packed pores (the degree of porosity is 60–70 %). However, as in the case of iodides, nitric acid influences the thickness of irregular porous layer. In this case the given value is about 1.8 mkm (in the absence of nitric acid, it is 0.4–0.7 mkm).

Influence of the Carrier Concentration of Indium Phosphide on the Porous Layer Formation

Additional doping of the monocrystalline InP surface is a sufficiently interesting, to our opinion, way to obtain pores of the specified shape and provide the necessary quality of the *por*-InP – monocrystalline InP boundary. This circumstance allows, firstly, to form pores of the required shape, which makes further cleaving of the basic plate easier, and, secondly, to provide the necessary quality of the cleavage surface.

Rate of a chemical reaction essentially depends on the doping level of the semiconductor. Threshold voltage of the pore formation decreases with the increase in the volume concentration of free electrons. Moreover, increase in the doping level leads to the reduction of the dislocation density but simultaneously is accompanied by the generation of microdefects (stacking faults, small prism dislocation loops, dispersed second-phase release). As known, the pore growth occurs along preferential directions, which the given defects of the crystal surface are. Figure 8 illustrates

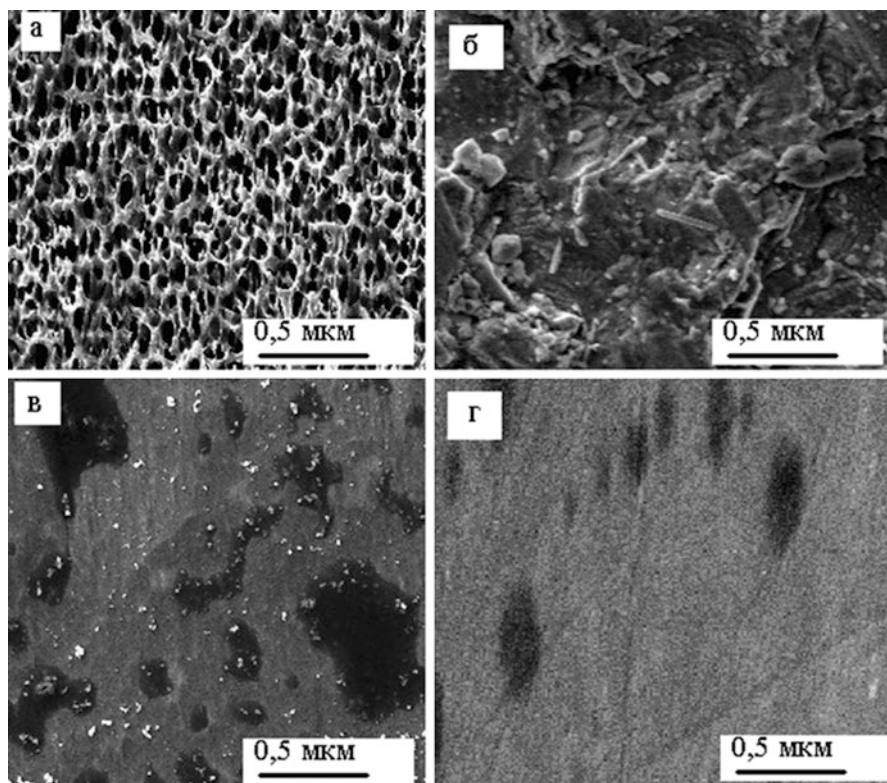


Fig. 8 SEM image of the (001) InP porous surface, $j=100 \text{ mA/cm}^2$, $t=10 \text{ min}$. Concentration of impurity charge carriers: $2.3 \times 10^{18} \text{ cm}^{-3}$ (a), $3 \times 10^{19} \text{ cm}^{-3}$ (b), $2 \times 10^{17} \text{ cm}^{-3}$ (c), $1.8 \times 10^{16} \text{ cm}^{-3}$ (d)

the morphology of the InP porous surface with different charge carrier concentration.

A porous layer with low pore density is formed during the etching of the semiconductor with the concentration of impurity charge carriers of the order of $1.8 \times 10^{16} \text{ cm}^{-3}$. However, in this case the obtained pores are sufficiently small (20–50 nm) and demonstrate a certain order and uniform distribution over the ingot surface. Moreover, the coarse etched areas, which appear due to the dislocation outcrop, can be observed on the sample surface. With the increase in the number of charge carriers, one can observe a completely different scenario for the pore distribution over the sample surface. Pores with different diameters (from 100 nm to 3 μm) appear under electrochemical treatment of the samples, which are doped with sulfur up to the concentration $2 \times 10^{17} \text{ cm}^{-3}$. Appearance of crystallites, which can indicate the formation of oxide islands on the upper porous semiconductor layer, is possible in this case. Another situation takes place during electrochemical treatment of the heavily doped InP crystals (about $2.3 \times 10^{18} \text{ cm}^{-3}$). Such concentration of impurity charge carriers is the most favorable for the formation of a qualitative porous layer on the surface of monocrystalline InP that is expressed in a high pore density and their uniform distribution over the plate surface. Pores, which are formed in this case, have a size of the order of tens of nanometers; the degree of porosity is 60 %. Varying other etching conditions (current density, etching time), it is possible to obtain porous structures with different parameters (pore diameter, porosity, depth of the porous layer). However, while using materials for crystal etching with higher impurity concentration ($3 \times 10^{19} \text{ cm}^{-3}$), the surface etching without pore formation is observed, that is, the upper crystal layers just break off along certain planes. Such structures cannot be used as effectively as porous ones due to the fact that the surface layer is strongly disturbed. Thus, the given experiment demonstrates the role of the charge carrier concentration for the pore formation on the semiconductor surface.

However, one should take into account that additional doping leads to the impurity segregation, which appears during the crystal growth. Elastic long-range stresses can impede the formation of continuous splicing surface. The regions of compositional and structural inhomogeneities, namely, the bands of impurity segregation and crystalline defect clusters, are the sources of these stresses. Microfluctuations of the growth rate on the boundary of the solid and liquid phases lead to the formation of the sulfur segregation bands (growth bands). Denser pore clusters in the central segregation lines with respect to the peripheral ones indicate the increase in the sulfur concentration along the direction from the center to the InP crystal periphery. Moreover, sulfur distribution in InP crystals can be nonuniform not only along but also across the growth axis. In this case, change in the lattice parameter of the solid solution excites elastic stresses.

Moreover, significant etching of the crystal surface is observed in the areas of dense pore clusters. This can be connected with the outcrop of the secondary pores, as well as with the coalescence of small pores into bulk holes.

Generation of the bulk etching holes can be explained from the point of view of the impurity influence on the defect formation in the crystal. Doping with donor

impurities up to the high concentrations is accompanied by the appearance of microdefects but leads to the decrease in the dislocation density. Intrinsic point defects play the main role in the microdefect formation. At high doping levels, decomposition of supersaturated solid solution of the doping impurity influences the formation of microdefects. The main production problems during InP crystal growth are the following: tendency to twinning, formation of dislocation clusters, and segregation phenomena conditioned by high impurity content in semi-insulating crystals. Impurity concentration, which is the function of the crystal growth rate, has periodicity and excites the so-called doping streakiness. This is partly explained by the fact that the crystal growth rate on the microscopic level is not the same, but cyclic.

Appearance of nanoregions with different element concentrations can lead to the qualitative change in the InP properties. Imperfection of the crystals connected with the striate growth structure influences the semiconductor properties of the crystals. The presence of the domain (the twin) structure is an undesirable factor from the point of view of using the given materials in optical devices and sensors. Therefore, investigation of the mentioned phenomenon is of a great importance from the point of view of both the crystal production technique and research of the properties connected with nonuniformity of the element distribution, which enter into the composition of the grown crystals.

Influence of Dislocations on the Process of Pore Formation in *n*-InP (111) Single Crystals

The chemical composition was analyzed with the use of the procedure of energy dispersive X-ray analysis (EDAX). The component composition was analyzed for four arbitrarily selected points at the surface.

It is evident that the results of analysis of oxygen and fluorine on the sample surface are associated with random processes correlating with the etching process. The excess of indium atoms indicates that they are situated not only in the associated state (in the form of the In-P clusters) but also in the free state (due to their accumulation along the crystallographic axis [111] of *n*-InP), which is promoted by the production process of single-crystal growth.

In a microphotograph of the surface (Fig. 9), the nonuniformity of the distribution of the pores over the crystal surface is observed. After the electrolytic etching, dark and light bands emerge on the surface of the samples; these bands are detected visually. Using scanning electron microscopy, we managed to establish that the dark bands are places of more dense accumulation of the pores, i.e., etch pits. Etching locally took place precisely in the region of the defects of the crystal structure.

The width of each band was ~100 μm . Dark bands have clear external boundaries, while the boundaries directed inside the crystal are more spread. The striation nonuniformity in the distribution of the components is a very widespread phenomenon during growing the single crystals by the Czochralski method. We can also observe an increase in the concentration of input orifices of the pores along the

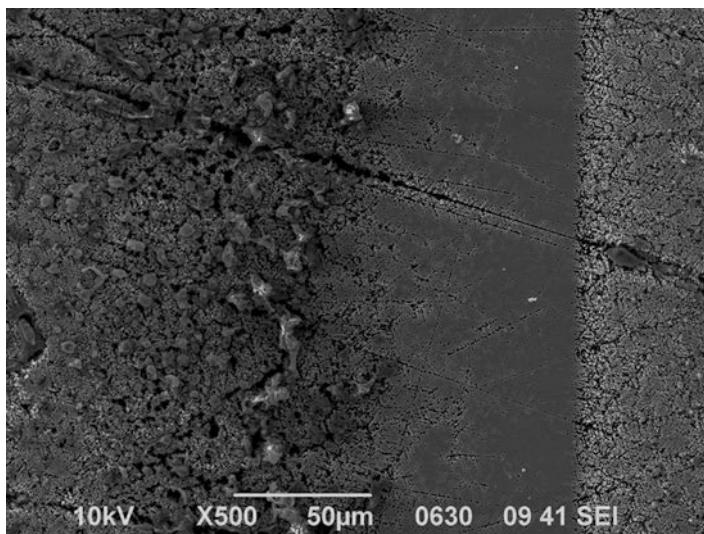


Fig. 9 Surface morphology of the porous n-InP

direction from the center to the periphery of the crystals. The formation of the continuous overgrowth boundary can be prevented by the elastic long-range stresses. The sources of these stresses are the regions of the compositional and structural nonuniformity or the bands of segregation of the impurity and accumulation of the defects of the crystal structure.

In this case, each fragment is a region of increased impurity concentration. Such a region can be considered as the inclusion possessing the intrinsic deformation caused by the lattice mismatch and discrepancy in coefficients of thermal expansion of segregation bands and the surrounding material. As the ingot cools, the elastic stresses of such inclusion decrease and the shift components of residual elastic stresses can cause plastic deformation.

Figures 3 and 4 represent the image of the fragment of the surface of the *n*-InP sample, on which the location of formation of pore cores is clearly seen. The edges of pores are somewhat extended along the (111) plane. Comparison with the known published data indicates that the anions (the F^- ions) play the decisive role in the formation of the pores (their shape, diameter, and location). The diameter of the most of pores is in the range from 100 to 600 nm. We can also notice that, both in the plane of the (111) surface and to the depth of the sample, the pores practically have no specific growth direction, which largely manifests itself during etching of the (111)V surface, the formation of pores in the plane of which is energetically more favorable.

The pore depth depends on the imperfection of the material in the places of their formation. The seeds of the pores are the dislocations, which are the sources of elastic stresses and generate elastic deformations around them. Elastic interactions of starting dislocations with point defects of the crystal structure lead to an increase

in the concentration of residual defects near the dislocation axis and to the formation of the Cottrell cloud. During etching of the *n*-InP single crystals, the tendency is observed to grouping the pores into symmetrical agglomerations near the seed pores, which emerged previously and are associated with the outcrop of dislocations and microcracks on the (111) surface.

In some cases, the impurity atoms of the crystal act electrochemically on the dissolution processes in the region of the dislocation outcrop on the surface since the preferential localization of impurity is often performed in the region of dislocation lines. The symmetry and periodicity of the ensemble of pores repeat the symmetry and periodicity of the defect structure of InP, which emerges in the surface layer of semiconductor.

The number of etch pits in this case is considered as the measure of dislocation density. The calculation of the average dislocation density N_D is performed by the formula

$$N_D = n_{av} / S,$$

where n_{av} is the average number of etch pits and S is the area of the field of view.

The calculation of the dislocation density in the places of the increased impurity concentration (dark bands) yields the value $2 \times 10^6 \text{ cm}^{-2}$. In the regions less filled with pores, the dislocation density is $\sim 10^4 \text{ cm}^{-2}$. This result agrees well with the manufacturer's data of the samples obtained from the producing company – namely, the dislocation density is 10^6 – 10^7 and 10^4 in the places of accumulation of the impurity and in the regions where the impurity concentration is lower, respectively.

It should be also noted that, in InP, the pores in the (111) plane emerge over the entire range of electric potentials of formation of the pores corresponding to the conditions of pore formation in all fluoride electrolytes.

Texturing of the Indium Phosphide Surface

While submerging the semiconductor InP plate in the etchant solution, its molecules are adsorbed on the plate surface. With direct current passing through the electrolyte, adsorbed molecules detach from the surface of the plate. In this case the phosphorus atoms adsorb easier with the hydrogen ions that provide faster etching of the phosphorus sublattice. Stoichiometry of the sample is violated toward the increase in the concentration of indium atoms. As a result the set of pyramidal clusters is formed on the plate surface. Slope of the cluster edges provides the obtaining of a rather low reflection coefficient and the tenfold increase in the active area of the plate in comparison with the monocrystalline sample.

The optimal concentration of the electrolyte, current density, and etching time were established experimentally in order to obtain the most uniform in height and shape texture. Thus, the optimal conditions for the obtaining of qualitative texturing *p*-InP surface are given below: the etchant composition is HBr:H₂O 1:1; the current density is 150 mA/cm²; the etching time is 8 min; the power of the tungsten lamp is 200 W.

Figure 10 demonstrates the morphology of the textured InP plate. As seen from this figure, the dense system of pyramidal growths with the slope connected with

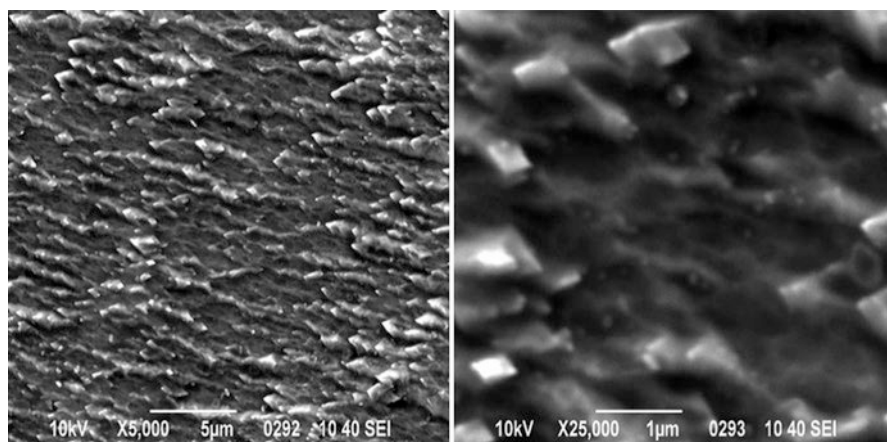


Fig. 10 p-InP textured structure

the crystal anisotropy and current direction is formed on the monocrystal surface. The pyramid height varies from 0.7 to 1.1 μm. Under the assumption that the abovementioned conditions are not executed, the semiconductor behavior during the anodization has some peculiarities. Thus, with the increase in the etching time up to 15 min, the pore grooves start to grow deep into the substrate that is accompanied by the plate surface failure. While etching takes less than 8 min, the incomplete surface texturing is observed, i.e., some surface regions stay with the conserved monocrystallinity and surface orientation.

If the current density is more than 150–170 mA/cm², the etching of InP layer of the thickness of about 8–10 μm is observed. At current densities less than the mentioned values, the pyramids have insufficiently pronounced shape and height (less than 0.5 μm). At higher acid concentrations in the electrolyte solution, the insoluble films composed of the adsorbed by the semiconductor surface bromine atoms are formed. At low acid concentrations the figure formation on the InP surface does not take place at all. Illumination of the plates is the necessary condition as well. This provides high density of the pyramid distribution over the surface of the sample (density is about five pyramids per 1 μm).

We have to note that solutions of other acids also do not provide sufficient level of the surface texturing. Moreover, *n*-InP monocrystals demonstrate an inability to texture. The fact is that while anodizing in the acid solutions, the plates with electron conductivity are easily etched forming the porous layers.

Conclusion

The large and well-developed porous semiconductor surface puts on the agenda the study of the fundamental characteristics of matter that lies in the relationship and mutual influence of the surface and volumetric properties. The research can lead to answer

the question: What determines the properties of porous indium phosphide – extensive surface or decrease in the volume? In any case, the modification of the morphology of space essentially creates a new interesting object, in which different classes of phenomena both physical and chemical nature are closely intertwined; besides the surface and volumetric properties in this sense are difficultly separated. In this connection, it opens the prospect of further study of the presence of fractal properties of the phenomena associated with the formation of porous space. The possibility of forming porous spaces with regular distribution of pores and diverse correct form of the intersection allows quite easily to create photonic crystals.

Etching indium phosphide in fluorinated and chlorinated etchants, along with epitaxy and lithography techniques, is included in the arsenal of modern microelectronics that allows us to create objects with reduced dimensionality. Types of porous indium phosphide (por-InP), which constitute a new class of substances, have different physicochemical properties: photo- and electroluminescence, adsorption sensitivity, properties of photonic crystals, etc. The presence of photo- and electroluminescence properties is directly associated with decreasing of the output dimension of the semiconductor crystal. Adsorption sensitivity is caused by the fact that substances from the environment are well adsorbed by the porous bodies.

Approaching the limits of miniaturization of classical microelectronic devices enhances the interest in devices capable of providing of the further progress of electronics. One possible way of such progress is the development and creation of devices, in which moving of certain number of electrons is controlled.

A more complete understanding of the relationship of process parameters with the characteristics of porous indium phosphide will determine the conditions for the formation of the material with strictly specified, reproducible properties that enhance its applied potential and will develop the theoretical understanding of the mechanism of pore formation in semiconductors. In addition, por-InP is a good model to study the subject of quantum size effects, fractal phenomena of self-organization, and the fundamental problems of nanoelectronics.

References

1. Suchikova Y (2010) Influence of the carrier concentration of indium phosphide on the porous layer formation. *J Nano Electron Phys* 4:142–147
2. Suchikova Y, Kidalov V, Balan O (2010) Texturing of the indium phosphide surface. *J Nano Electron Phys* 2:52–53
3. Suchikova Y, Kidalov V, Sukach G (2009) Effect of the type of electrolyte anion on the porous InP morphology obtained by the electrochemical etching. *J Nano Electron Phys* 4:111–118
4. Suchikova Y (2010) Influence of dislocations on the process of pore formation in *n*-InP (111) single crystals. *Semiconductors* 45(1):121–124
5. Suchikova Y, V K, Sukach G (2010) Morphology of porous *n*-InP (100) obtained by electrochemical etching in HCl solution. *Funct Mater* 17(1):1–4
6. Langa S, Carstensen J, Christophersen M, Föll H, Tiginyanu I (2001) Observation of crossing pores in anodically etched *n*-GaAs. *Appl Phys Lett* 78(8):1074–1076
7. Langa S, Carstensen J, Christophersen M, Föll H (2002) Formation of tetrahedron-like pores during anodic etching of (100) oriented *n*-GaAs. *Electrochem Solid-State Lett* 5(1):1–4

8. Langa S, Carstensen J, Christophersen M, Steen K, Frey S, Tiginyanu I, Föll H (2005) Uniform and nonuniform nucleation of pores during the anodization of Si, Ge, and III-V semiconductors. *J Electrochem Soc* 152(8):C525–C531
9. Schmuki P, Lockwood D, Labbe H, Fraser J (1996) Visible photoluminescence from porous GaAs. *Appl Phys Lett* 69(11):1620–1622
10. Zeng A, Zheng M, Ma L, Shen W (2006) Etching temperature dependence of optical properties of the electrochemically etched n-GaAs. *Appl Phys A* 84:317–321
11. Schmuki P, Erickson L, Lockwood D, Fraser J, Champion G, Labbe H (1998) Formation of visible light emitting porous GaAs micropatterns. *Appl Phys Lett* 72(9):1039–1041
12. Finnie C, Bohn P (1999) Near-field photoluminescence of microcrystalline arsenic oxides produced in anodically processed gallium arsenide. *Appl Phys Lett* 74(8):1096–1098
13. Tondare VN, Naddaf M, Bhise AB, Bhoraskar SV, Joag DS, Mandale AB, Sainkar SR (2002) Stability of field emission current from porous n-GaAs (110). *Appl Phys Lett* 80(6):1085–1087
14. Dmitruk N, Kutovyi S, Dmitruk I, Simkiene I, Sabataityte J (2005) Atomic force microscopy, Raman scattering and optical reflectance of porous GaAs films. In: Proceedings of the first international workshop on semiconductor nanocrystals, SEMINANO, pp 399–403
15. Ben Jomaa TR, Beji L, Ltaief A, Bouazizi A (2006) The current–voltage characteristics of heterostructures formed by MEH-PPV spin-coated on *n*-type GaAs and *n*-type porous GaAs. *Mater Sci Eng* 26(2–3):530–533
16. Ręza A, Šimkienė I, Babonas GJ, Sabataitytė J (2003) Spectroscopic ellipsometry of porous n-GaAs. *Mater Sci* 9(4):441–446
17. Zangoie S, Woollam JA (2000) Ellipsometric characterization of thin porous GaAs layers formed in HF solutions. *J Mater Sci Lett* 19:2171–2173
18. Dmitruk N, Kutovyi S, Dmitruk I, Simkiene I, Sabataityte J, Berezovska N (2007) Morphology, Raman scattering and photoluminescence of porous GaAs layers. *Sens Actuators B* 126(1):294–300
19. Simkiene I, Sabataityte J, Kinduryš A, Treideris M (2008) Formation of porous n-A3B5 compounds. *Acta Phys Polon A* 113(3):1085–1090
20. Tiginyanu IM, Irmer G, Monecke J, Vogt A, Hartnagel HL (1997) Porosity-induced modification of the phonon spectrum of n-GaAs. *Semicond Sci Technol* 12:491–493
21. Meijerink A, Bol AA, Kelly JJ (1996) The origin of blue and ultraviolet emission from porous GaP. *Appl Phys Lett* 69(19):2801–2803
22. Kuriyama K, Ushiyama K, Ohbora K, Miyamoto Y, Kakeda S (1998) Characterization of porous GaP by photoacoustic spectroscopy: the relation between band-gap widening and visible photoluminescence. *Phys Rev B* 58(3):1103–1105
23. Tomioka K, Adachi S (2005) Structural and photoluminescence properties of porous GaP formed by electrochemical etching. *J Appl Phys* 98(7):073511–073611–7
24. Sarua A, Tiginyanu IM, Ursaki VV, Irmer G, Monecke J, Hartnagel HL (1999) Charge carrier distribution in freestanding porous GaP membranes studied by Raman spectroscopy. *Solid State Commun* 112:581–585
25. Ichizli V, Hatnagel HL, Mimura H, Shimawaki H, Yokoo K (2001) Field emission from porous (100) GaP with modified morphology. *Appl Phys Lett* 79(24):4016–4018
26. Stevens-Kalceff MA, Langa S, Tiginyanu IM, Carstensen J, Christophersen M, Föll H (2000) Comparative SEM and cathodoluminescence microanalysis of porous GaP structures. In: MRS conference proceedings, vol 638, p F5.31
27. Schuurmans FJP, Vanmaekelbergh D, Lagemaat J, Lagendijk A (1999) Strongly photonic macroporous gallium phosphide networks. *Science* 284(5411):141–143
28. Karavanski VA, Lomov AA, Sutyryn AG, Imamov RM, Dravin VI, Mel’nik NN, Zavaritskaya TN (2003) Influence of defects on the formation of thin porous GaP(001) films. *Crystallogr Rep* 48(5):851–859
29. Melnikov VA, Golovan LA, Konorov SO, Muzychenko DA, Fedotov AB, Zheltikov AM, Timoshenko VY, Kashkarov PK (2004) Second-harmonic generation in strongly scattering porous gallium phosphide. *Appl Phys B* 79(2):225–228

Part II

Synthesis and Fabrication of Nanostructured Coatings and Thin Films

Recent Approaches for Designing Nanomaterials-Based Coatings for Corrosion Protection

10

Nedal Abu-Thabit and Abdel Salam Hamdy Makhlouf

Contents

Introduction	310
Microcapsule-Based Self-healing Coatings	312
Definition and Limitations	312
Synthesis and Preparation	312
Nanocontainer-Based Self-healing Coatings	314
Halloysite Nanocontainers	314
Mesoporous Silica Nanocontainers (MSNs)	317
Layered Double Hydroxides (LDHs)	318
Hydroxyapatite (HAP) Microparticles	319
Layer-by-Layer Approach for Designing Self-healing Coatings	320
Electrically Conductive Polymers for Self-healing Coatings	323
Conclusions and Future Remarks	326
References	327

Abstract

Nanotechnology-based coatings have shown remarkable growth in recent years in many strategic industries such as automotive, aerospace, petroleum, electronics, etc. The unique characteristics that can be offered from nanotechnology are one

N. Abu-Thabit (✉)

Department of Chemical and Process Engineering Technology,
Jubail Industrial College, Jubail, Saudi Arabia
e-mail: abuthabit_nidal@yahoo.com

A.S.H. Makhlouf

Manufacturing Engineering Department, College of Engineering
and Computer Science, University of Texas Pan-American, Edinburg, TX, USA
e-mail: abdel.makhlouf@utrgv.edu

of the main driving forces for the sharp innovation in coatings technology nowadays. Nanocoatings have recently been proposed to add functionalities to the materials to be coated such as anticorrosion self-healing, anti-icing, self-cleaning, etc. Different types of nanomaterials have been incorporated in anticorrosion coatings by adopting various approaches. The basic approach utilizes incorporation of inorganic nanomaterials with the traditional organic coatings to enhance certain functionality of the formulated nanocomposite coating. However, one of the recent trends in nanotechnology is to design nanomaterial-based coatings of multifunctionality. These include stimuli-responsive/smart coatings, self-healing coatings, organic/inorganic hybrid coatings, and electroactive coatings. This chapter highlights these emerging nanotechnologies and presents the most recent achievements in this area.

Keywords

Nanotechnology • Self-healing • Nanocoatings • Smart coatings • Corrosion protection

Introduction

Protective polymeric coatings are the most widespread approach for corrosion protection of metallic structures. They act as barrier to prevent or impede the interaction of corrosive species with the metallic substrates. However, there are some factors affecting the protection performance of the polymer such as temperature, humidity, and the presence of aggressive salts which result in the degradation of the polymer and deteriorate their barrier effect (Fig. 1a, b). Therefore, there is an increased demand for designing coatings with self-healing functionalities to provide long-term protection.

The sharp innovation in nanotechnology is one of the main reasons for the development of “smart” functional coatings which can be used for a variety of applications including antifogging [1] and anti-icing coatings [2–4], scratch-resistant coatings [5–7], anti-stain coatings [8, 9], moisture-resistant coatings [10–12], oil-repellent coatings [13, 14], self-cleaning coatings [15–17], antimicrobial coatings [18–22], UV protection coatings [23, 24], adhesive coatings [25], and anticorrosive self-healing coatings [26–37].

Self-healing coatings can be constructed by the adsorption of stimuli-responsive polymers on solid support materials. The stimuli-responsive polymers can be classified into two categories: (1) intrinsic polymers that are able to heal the cracks by themselves and (2) extrinsic polymers in which the healing agent has to be pre-embedded [38]. For example, thermally responsive reversible cross-linked polymers represent an important class of intrinsic self-healing polymers [39–41]. The mechanism of self-healing is based on Diels-Alder and *retro*-Diels-Alder reactions. However, in the case of extrinsic self-healing, the healing agent is encapsulated within a reservoir [42, 43]. The encapsulated healing agent contains liquid monomer that is able to polymerize at room temperature with the help of a

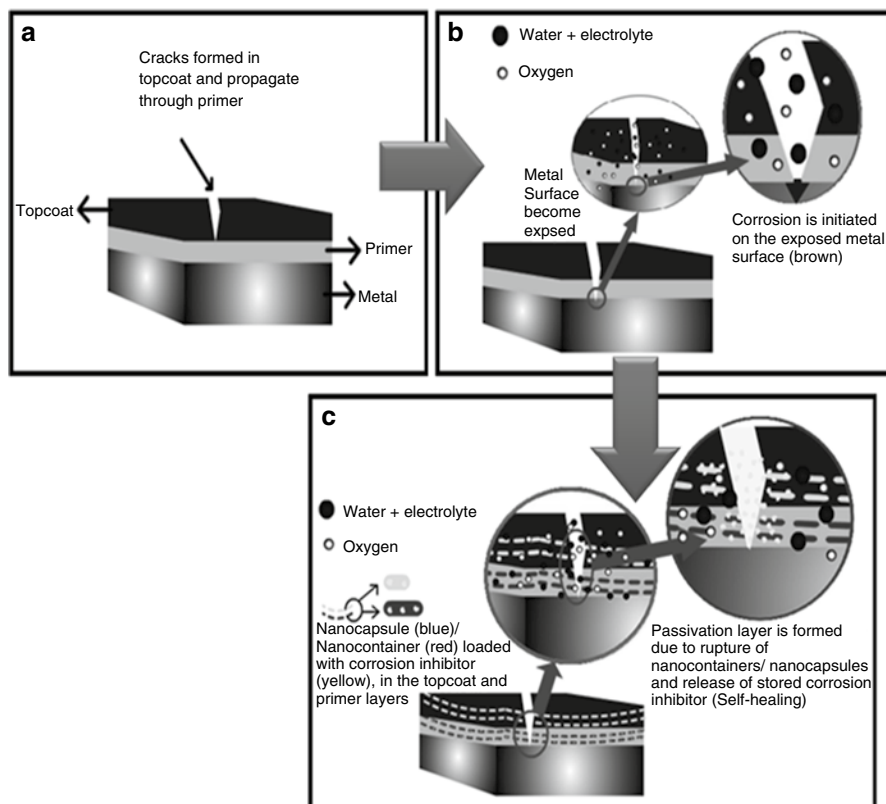
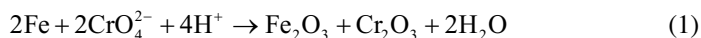


Fig. 1 Schematic illustration of self-healing anticorrosion coating (a) corrosion initiation at the topcoat layer, (b) corrosion penetrates to the metal surface, and (c) self-healing through the release of the encapsulated inhibitor that is embedded in the coating matrix

catalyst present in the composite matrix [44, 45]. However, there are some cases that the self-healing agent can polymerize without any catalytic support [46].

Smart self-healing coatings are designed to interact with the surrounding environment by responding to external physical or chemical changes induced by external stimuli such as temperature, pH, ionic strength, pressure, corrosion products, or light. This switching of the physiochemical properties will lead to the rupture of the self-healing container/capsule and eventually the release of the encapsulated corrosion inhibitor. Figure 1c illustrates the concept of self-healing-protective coating with autorepair functionality. The effective release of stored corrosion inhibitor from the encapsulated container provides a real triggering mechanism for spontaneous repair of small defects in a similar fashion to the toxic chromate coatings which maintain a passive layer of protective metal oxide through the intelligent release of chromate anions as illustrated in Eq. 1:



This chapter discusses the recent approaches for the design and preparation of anticorrosive coatings of self-healing functionality. These approaches include encapsulation of corrosion inhibitors, embedding corrosion inhibitors into nanocontainers and various inorganic microparticles, application of polyelectrolyte multilayers, and utilization of electrically conductive polymers as potential self-healing anticorrosive coatings.

Microcapsule-Based Self-healing Coatings

Definition and Limitations

The encapsulation process is considered as a key step for obtaining effective and functional self-healing coatings. The designed containers must possess strong shell walls, for long life durability, and impermeability to corrosive species such as atmospheric oxygen and water. Also, the containers should be able to supply the stored active content on demand upon certain triggering mechanism and consequently provide self-healing response.

The encapsulation process enables the self-healing coatings to provide superior performance over their traditional coating counterparts. In traditional coating systems, where the corrosion inhibitor is incorporated by direct mixing, possible interactions with the formulated coating can result in loss of inhibitor efficiency, coating degradation, or both [47]. However, in the case of smart-responsive coatings, the corrosion inhibitor is encapsulated in a variety of micro- or nanostructured materials such as microcapsules, nanocapsules, nanocontainers, and nanoreservoirs. Thus, the encapsulating container acts as a “host” for the corrosion inhibitor and also prevents the direct contact between the inhibitor and the coating, allowing for the controlled release of the stored active content at the time of corrosion initiation.

Synthesis and Preparation

Microcapsules can be designed and prepared by using different techniques including pan coating, spray drying, centrifugal extrusion, and emulsion-based methods [48]. Emulsion methods include emulsion polymerization, layer-by-layer assembly, internal phase separation, and coacervation. The efficient trigger-release performance of the prepared capsule depends on parameters such as shell wall thickness, permeability, mechanical integrity, and chemical functionality of the capsule shell wall as well as the capsule size.

Emulsion Polymerization

Emulsion polymerization process can be utilized for the preparation of capsules as illustrated in Fig. 2a. Emulsion is created by strong agitation or sonication of biphasic liquid, typically oil in water (emulsion) or water in oil (inverse emulsion) [49, 50]. Stirring or sonication creates droplets which become the core material of

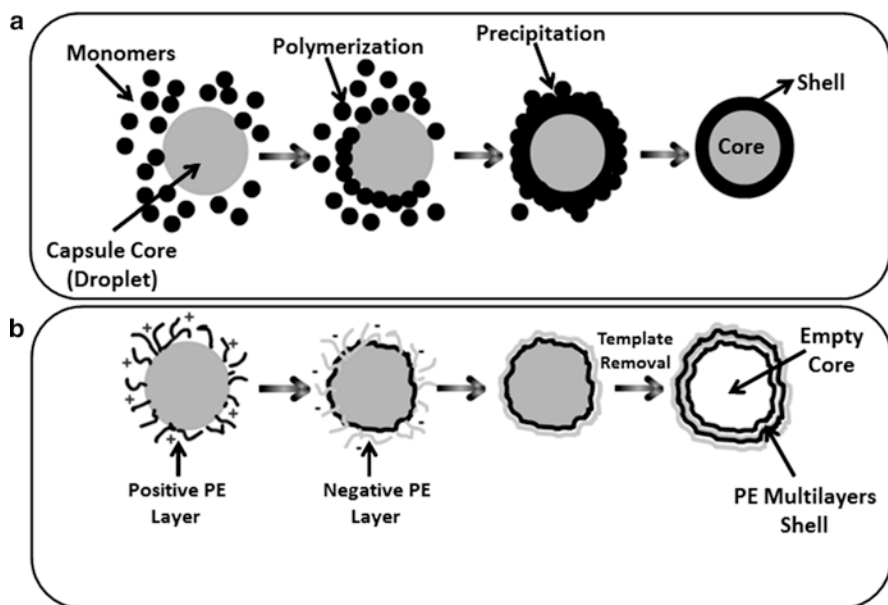


Fig. 2 Schematic illustration for microcapsule preparation (a) emulsion polymerization is used to create polymeric shell around the stabilized droplet, which become the core material, and (b) layer-by-layer deposition of polyelectrolytes onto metal oxide template, which is removed to create hollow and porous microcapsule

the capsule. The capsule shell wall is created by the polymerization at the aqueous/organic interface around these droplets. Polymers can be formed by condensation polymerization of two immiscible monomers at the aqueous/organic interface [44] or through in situ free radical polymerization reactions of vinyl monomers such as styrene, vinyl acetate, 1,3-butadiene, and isoprene [51].

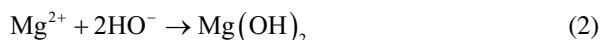
Layer-by-Layer Assembly

In layer-by-layer (LBL) assembly, polyelectrolyte layers with alternating positive and negative charges are deposited on the capsule shell wall [47, 52, 53]. The thickness of capsule shell wall can be controlled by the number of deposited layers. Since polyelectrolytes are pH-responsive macromolecules, the trigger and release mechanism depends on the stability of the polyelectrolyte layers, which in turn is governed by the pH of the surrounding environment. Thus, the selection of weak/strong, acidic/basic ionizable groups allows for the optimization of trigger and release mechanism to occur at certain pH range.

Capsule fabrication using LBL method can be achieved via three stages as illustrated in Fig. 2b. The first stage represents the selection of suitable capsule core material such as metal oxide particles. Then, polyelectrolytes with alternating positive and negative charges are deposited on the capsule shell wall. The final stage includes the removal of the metal oxide core by acid treatment, leaving behind hollow, porous, and semipermeable capsules.

The porosity of the capsule shell wall enables the capsule core to be loaded and exchanged with a variety of molecules after the preparation process. However, the main disadvantage of this technique is the weakness of the created capsule shell wall due to the weak integrity of the layered polyelectrolytes shell wall, which often results in capsules that resemble deflated balloons after being dried.

In another approach, inverse emulsion polymerization was used to prepare epoxy-amine microcapsules, with diameter of 10–240 μm , which was embedded with 10 wt% magnesium sulfate solution as inhibitor [54]. Magnesium ions (Mg^{2+}) can react with hydroxide ions in alkaline medium, at $\text{pH}=9.3$, to produce insoluble magnesium hydroxide as shown in the following equation:



Nanocontainer-Based Self-healing Coatings

Compared to microcapsules, thin tubular nanocontainers are more attractive as they exhibit superior aero- and hydrodynamic properties and hence better processability. The modification of the inner and outer surfaces of the nanocontainers with well-defined functionality allows for designing nanocontainers with fine-tuned properties, for example, for varying hydrophobicity.

Halloysite nanotubes, mesoporous silica containers, hydroxyapatite microparticles, and layered double hydroxides have been utilized as carriers and reservoirs for immobilization, storage, and controlled release of inhibitors that incorporated in self-healing anticorrosive coatings. In general, this can be achieved in three steps as illustrated in Fig. 3. The first step includes loading the organic or inorganic inhibitors into the target nanocontainer by the absorption of the inhibitor through the porous nanocontainers' structure, by encapsulation process utilizing emulsion polymerization, or by ion exchange with counter positive/negative ions in the corresponding nanocontainers. In the second step, the inhibitor-loaded nanocontainers are coated with pH-sensitive polyelectrolyte multilayers. Finally, the inhibitor-loaded nanocontainers are dispersed in suitable organic/inorganic polymeric matrix material.

Halloysite Nanocontainers

Nanocontainers can be made from different tubular materials such as carbon, polymeric, metal, and metal oxide nanotubes. Polymeric nanotubes can be templated by molecular sieves or cylindrical nanopores to form tubular structures [55]. Metal and metal oxide nanotubes are synthesized by employing polymeric or inorganic nanorods as scaffold template. The shortcoming of these types of nanotubes is the employment of template that needs to be prepared separately and requires extra post-synthesis removal steps, which is time-consuming and a costly process.

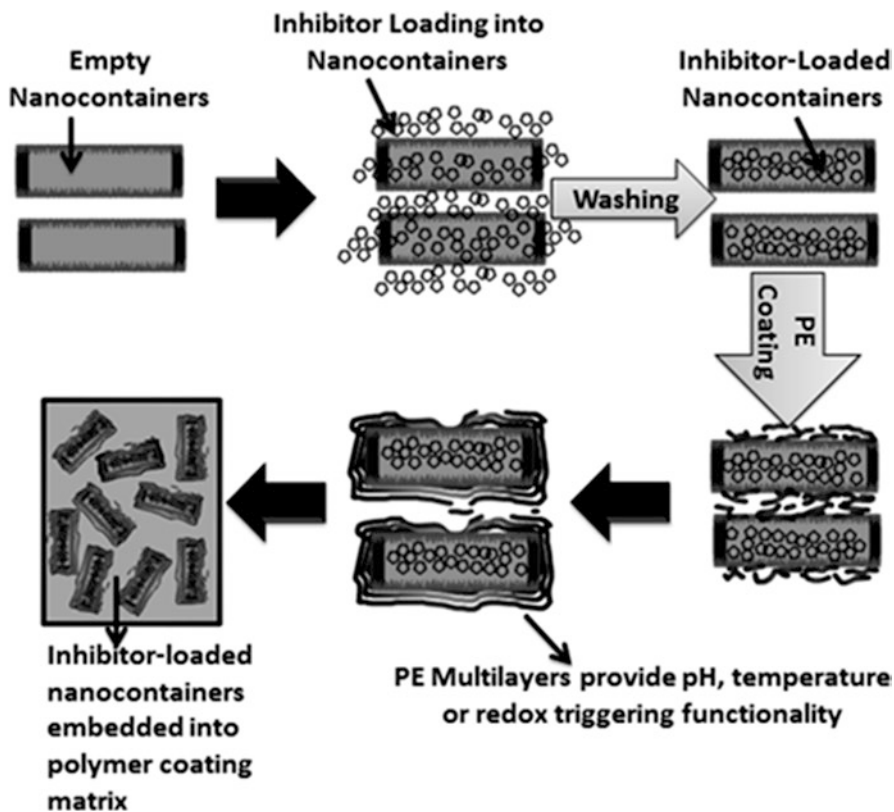


Fig. 3 Schematic illustration for preparation of inhibitor-loaded nanocontainers and their incorporation into coating matrix

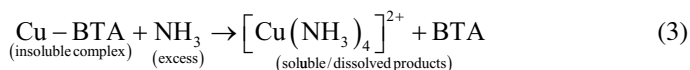
One of the future prospective containers that can be industrially applicable is halloysite nanotubes. In comparison to the carbon nanotubes, halloysite is biocompatible and inexpensive nanocontainer (\$4/Kg with annual production of 50,000 t per year) that can be used for a variety of applications including microencapsulation of biologically active molecules.

Halloysite is defined as a two-layered aluminosilicate with hollow tubular structure in the submicrometer range [56]. The adjacent alumina and silica layers create a packing disorder causing them to curve. The size of halloysite particles varies within 1–15 μm in length and 10–150 nm in inner diameter depending on the deposits. Thus, a variety of active agents such as drugs, corrosion inhibitors, and marine biocides can be entrapped within the halloysite inner lumen as well as within void spaces in the multilayered aluminosilicate shell. The entrapped and stored active agents are retained and released in a controlled manner for specific application. Both hydrophilic and hydrophobic agents can be entrapped after suitable pretreatment and conditioning of the halloysite [57–61].

A hybrid sol-gel film doped with halloysite nanotubes for controlled release of entrapped corrosion inhibitor on aluminum substrate has been proposed [62]. Initially, the halloysite nanocontainers were doped with 5 wt% 2-mercaptobenzothiazole inhibitor. In order to prevent the leakage of the doped inhibitor, the surface of the inhibitor-doped halloysite nanocontainers was coated with several alternating polyelectrolyte multilayers of (poly(styrene sulfonate)/poly(allylamine hydrochloride)). This step was essential to close the edges of the nanocontainers as well as to enable the controlled release of the doped 2-mercaptobenzothiazole inhibitor to the surrounding environment upon pH change. In a separate step, the organically modified hybrid sol-gel was prepared by using zirconium (IV) *n*-propoxide (TPOZ) and 3-glycidoxypropyltrimethoxysilane (GPTMS) precursors. Finally, the inhibitor-doped halloysite nanocontainers suspension was incorporated into the sol-gel solution prior to the dip coating of the AA2024-T3 samples. The prepared sol-gel films with the halloysite nanocontainers provided long-term corrosion protection in comparison with the undoped sol-gel film.

Abdullayev et al. reported an enhanced and strong anticorrosion self-healing effect caused by the sol-gel coating embedded with benzotriazole-doped halloysite nanocontainers in the cracked area of 2024 alloy [63]. In the same study, the corrosion protection performance of the industrial oil-based paint coating (ECS-34 True-Test) embedded with/without benzotriazole-doped halloysite nanotubes was investigated on scratched copper strips. After 10 days, immersion in highly corrosive environment, there was no evidence of visible rust in the scratched area, and the elemental analysis of the reacted corrosive solution did not show any copper content, whereas samples without halloysite nanocontainers were rusted, and their reacted corrosive solution was found to contain 128 ppm Cu(II) ions. These results demonstrate the self-healing functionality of the coating prepared by incorporation of the benzotriazole-loaded halloysite nanocontainers. The release rate of the benzotriazole was controlled by adapting two methods: (1) tube stopper formation and (2) layer-by-layer polyelectrolyte encapsulation for the inhibitor-embedded halloysite nanotubes. In the first method, the complexation reaction between loaded benzotriazole and transition metal ions was employed for the formation of stoppers at the tube ends. The best results were obtained when Cu(II) ions were employed for complex formation. It was found that the concentration of the Cu(II) ions has a direct and reverse effect on the release rate of the entrapped benzotriazole. In contrast, the polyelectrolyte multilayer shell (second method) did not slow down benzotriazole release from the encapsulated tubes. This finding was attributed to the low molecular weight of the benzotriazole inhibitor, which makes the diffusion through the polyelectrolyte multilayers more difficult to control.

In a later study, Abdullayev et al. [64] investigated the decrease in the release rate of the benzotriazole (BTA) through Cu-BTA complex at the tube ends based on the following reaction:



When ammonia solution was injected, a switch of the release rate of benzotriazole was observed, as was evident from the sharp increase in the concentration of both copper and benzotriazole in the treated solution. This result demonstrates that the stoppers can be diluted and the release rate can be restored with ammonia treatment.

Mesoporous Silica Nanocontainers (MSNs)

Monodisperse, mesoporous silica nanoparticles were loaded with organic corrosion inhibitor benzotriazole (BTZ) and embedded in hybrid sol-gel coating for corrosion protection of aluminum alloy AA2024 [65]. The reported mesoporous silica-BTZ system exhibited a number of interesting properties: (1) high surface area ($\approx 1000 \text{ m}^2 \text{ g}^{-1}$), (2) narrow pore size distribution ($d \approx 3 \text{ nm}$), large pore volume (1 mL g^{-1}), and high loading capacity of BTZ (41 wt%). The BTZ-doped silica nanocontainers were embedded in the sol-gel hybrid coating without further encapsulation steps (i.e., without using additional polyelectrolyte multilayer coating), which means that the trigger-release mechanism was entirely based on the corrosion process, providing a self-healing effect.

Li et al. investigated the synthesis and preparation of silica/polymer double wall hybrid nanotubes and their applications as stimuli-responsive nanocontainers in self-healing coatings [66]. The synthesis procedure started with the preparation of nickel hydrazine/silica core-shell rod templates, which were then surface modified by grafting methodology, using 3-(trimethoxysilyl) propyl methacrylate, for introducing carbon-carbon double bonds on silica surface. The thickness of the polymer coating was controlled by varying the feed ratio between monomer and nickel hydrazine/silica templates. Three different polymers were grafted on the surface of the silica: (1) the pH-responsive poly(methacrylic acid) (PMAA), (2) the temperature-responsive poly(N-isopropylacrylamide) (PNIPAM), and (3) the redox-responsive poly(poly(ethylene glycol)methacrylate) (PPEGMA). The final synthetic step was the selective etching of the nickel hydrazine/silica/polymer core-double shell rods in HCl solution. Then, the corrosion inhibitor benzotriazole (BTA) was encapsulated into the prepared $\text{SiO}_2/\text{polymer}$ hybrid nanotubes, with 6–7 wt% loading capacity. The self-healing coating was prepared by dispersing BTA-loaded nanotube containers into $\text{SiO}_x/\text{ZrO}_y$ hybrid films at room temperature. The anticorrosion agent BTA encapsulated in the hybrid nanotubes can be controlled to be released in the absence or presence of external stimuli. Silica/PMMA hybrid nanotubes showed pH-dependent release of BTA corrosion inhibitor, which was attributed to the swelling (at $\text{pH} = 12$) and shrinkage (at $\text{pH} = 2$) behavior of the grafted weak carboxylic acid moieties. Silica/PNIPAM hybrid nanotubes showed temperature-dependent release of BTA inhibitor due to the swelling and shrinkage of the PNIPAM outer wall at 25 and 50 °C, respectively. BTA-Silica/PPEGMA hybrid nanocontainers exhibited redox-dependent release of corrosion inhibitor due to the presence of the disulfide bonds in the grafted PPEGMA polymer networks.

Maia et al. reported one-stage process for the synthesis of porous silica nanocapsules (SiNC) loaded with 2-mercaptobenzothiazole (MBT) inhibitor for corrosion protection application [67]. The synthesized SiNCs have regular shape and a diameter in the range of 100–150 nm, with gradual mesoporosity. The encapsulation efficiency was 68 %, with MBT loading content of 10 wt%. Two samples were investigated for their corrosion protection performance. In the first sample, MBT-SiNCs were incorporated (2 wt%) in water-based epoxy coating, which was subsequently used to coat AA2024 plates with a film of 30 μm thickness. The second sample was prepared with empty SiNC, and the MBT inhibitor was incorporated in the formulated coating matrix by direct addition. The active protection of MBT-SiNC was assessed by the introduction of two circular defects (spots) in each sample. The MBT release was triggered by changes in pH and concentration of chloride anion. The self-healing functionality of the MBT-SiNC was evident from the high value of the electrochemical impedance measurements and visual inspection after 30 days of immersion in aggressive solution. In comparison to coating prepared by direct dispersion of MBT inhibitor, the coating with MBT-encapsulated SiNCs exhibited better and controlled inhibitor release for longer periods.

Layered Double Hydroxides (LDHs)

Layered double hydroxides (LDHs), also known as anionic clays or hydrotalcite-like compounds, are anion exchange materials consisting of stacks of positively charged, mixed metal hydroxide layers between which anionic species and solvent molecules are intercalated [68, 69]. Due to their low toxicity, biocompatibility, and their ability to release active species in a controlled way, LDHs have been employed as nanocarriers for drug-delivery applications at cellular level [70–73]. Therefore, LDHs can be thought of as suitable nanocarrier substrates for immobilization and encapsulation corrosion inhibitor molecules. LDHs can be incorporated in corrosion-protective organic coatings to provide self-healing protection functionality through the release of the stored inhibitors. The anion exchange property of the LDHs is important for two reasons: (1) it allows the immobilization of negatively charged organic/inorganic inhibitor, and (2) it allows the entrapment of the corrosive anions such as, chloride and sulfate anions [74–78].

Poznyak et al. reported the preparation of nanocrystalline LDHs, with platelike morphology, as novel inorganic host materials intercalated with guest organic inhibitors for anticorrosion applications [79]. Two different organic inhibitors were used, 2-mercaptobenzothiazolate (MBT) and quinaldate (QA). The anion exchange reaction of the nitrate-loaded LDHs precursors was utilized for creation of organic inhibitor containers. The release of the negatively charged organic inhibitors was found to occur by an exchange mechanism (i.e., release of inhibitor and entrapment of the aggressive anions) and sequential release of the anions, providing active feedback for corrosion protection control. The corrosion protection performance of the prepared LDHs was investigated by electrochemical impedance spectroscopy (EIS)

technique on a bare AA2024 aluminum alloy for two weeks. The AA2024 samples were placed in contact with LDH suspensions in a 0.05 M NaCl solution. After 24 h immersion time, EIS showed a small anticorrosion activity of these systems. This observation was attributed to the local alkalization of the solution in the presence of hydroxide-rich LDHs particles, which causes a decrease in the inhibition efficiency of MBT and QA inhibitors. However, the corrosion process was inhibited after long immersion times due to the formation of a protective film, with enhanced performance in case of MBT inhibitor.

Tedim et al. utilized the anion exchange reaction to prepare Zn-Al LDHs intercalated with phosphate, vanadate, and 2-mercaptobenzothiazolate inhibitors [80]. The corrosion protection assessment was performed on AA2024 substrate. The AA2024 samples were treated with a thin layer (2 μm) of hybrid sol-gel, followed by overpainting with non-inhibited water-based epoxy primer (25 μm), and finally, a 30 μm topcoat layer was introduced. Both primer and sol-gel formulations were loaded with 10 wt% LDHs nanocontainers in dry paint film. The developed coating showed well-defined active corrosion protection toward AA2024 substrates. The best results were obtained with a combination of sol-gel film (pretreatment layer) doped with LDH-MBT and primer doped with LDH-VO_x. It was concluded that the MBT anions were available in a very short time scale for protection of the interface layer between the aluminum substrate and the sol-gel film, whereas the long-term protection was conferred by vanadate anions released from LDH nanocontainers added to the primer. The results proved that the combination of different types of nanocontainers in the same or in different functional coating layers is an effective way to design active corrosion protection systems with enhanced and superior performance.

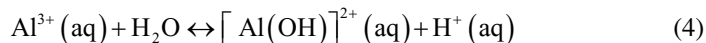
Guo et al. proposed a simple one-step hydrothermal synthesis method for the direct fabrication of zinc-aluminum layered double hydroxide (ZnAl-LDH)/alumina bilayer film on an aluminum substrate [81]. The resulted film was found to exhibit strong, compact, and uniform adhesion to the aluminum substrate. Coated aluminum substrates were immersed in 3.5 % NaCl aqueous solution for the assessment of the corrosion protection performance. Polarization measurements showed that the bilayer film was able to provide an effective corrosion protection for the coated substrates, as revealed from the low corrosion current density value (10^{-8} A/cm²). EIS showed that the impedance of the bilayer was as high as 16 M Ω , which means that the film was able to provide a protective passive layer with high charge transfer resistance.

Hydroxyapatite (HAP) Microparticles

Hydroxyapatite (HAP) microparticles, which is a calcium phosphate-based clay ($\text{Ca}_{10}(\text{PO}_4)_6(\text{OH})_2$), possess a number of features that make them suitable carriers for corrosion inhibitors. These features include crystallinity, insolubility in water, submicrometer size, high surface area, and chemical dissolution at acidic pH range. The dissolution of HAP microparticles in the acidic medium provides a

pH-dependent triggering mechanism for the release of stored inhibitors, whereas their high surface area enables a high loading capacity.

Snihirova et al. investigated the incorporation of inhibitor-doped HAP microparticles into a hybrid sol-gel coating as new feedback-active anticorrosion system [82]. Cerium (Ce^{3+}) and lanthanum (La^{3+}) cations, salicylaldehyde (Sal), and 8-hydroxyquinoline (8HQ) were used as the dopants in the HAP microparticles. Inorganic cationic inhibitors were incorporated by cation exchange with Ca^{2+} , and the organic inhibitors were adsorbed on the surface of HAP microparticles. This resulted in 22, 20, 9.3, and 0.54 wt% loadings for (Ce^{3+}), (La^{3+}), (8HQ), and (Sal), respectively. AA2024-T3 was coated with thin films of the formulated coating that contains 0.2 wt% inhibitor-doped HAP microparticles, by employing dip coating technique. The release of doped inhibitors occurred at pH below 6, with an acceleration of Ce^{3+} and La^{3+} release when the pH falls below 3.1. The local acidification down to $\text{pH}=3.65$ was attributed to the anodic dissolution of Al (Eq. 4), as revealed from localized pH measurements that was conducted using pH-selective microelectrodes.



Thus, the HAP microparticles were able to sense the corrosion onset (local acidification) and release the stored inhibitors on demand. Also, the dissolution of HAP microparticles contributed to corrosion protection by pH buffering mechanism, as conferred from the delayed corrosion of the AA2404-treated substrates with sol-gel coating embedded with blank HAP microparticles (i.e., undoped with inhibitor).

Layer-by-Layer Approach for Designing Self-healing Coatings

Polyelectrolytes multilayers with alternating charges can be deposited on metal substrate, and the low molecular weight corrosion inhibitors can be embedded between the deposited polyelectrolyte layers as shown in Fig. 4. The key parameters for controlling the growth of the multilayers are the pH and the ionic strength (degree of ionization/dissociation) of certain polyelectrolyte. These factors affect the conformations of the deposited polyelectrolytes and, consequently, the thickness of the multilayers [83–90]. The conformation of the polyelectrolytes can be altered by changing the pH or by the addition of salt. The presence of salt in the deposited layers allows for polymeric chains to collapse and converts the expanded chains into the coil conformation. Deposition of the weak polyelectrolytes can be easily affected by the pH of the polymeric solution. At certain pH range, the polyelectrolyte is completely dissociated, and, as a result, the maximum charge density can be achieved at that pH range.

Layer-by-layer (LBL) deposition can be achieved by three different methods: spraying, spin coating, and dip coating. The dip coating technique includes the following steps: (1) the substrates are immersed in the dipping solution, (2) equilibrium time of 10–20 min, and (3) washing the substrate with suitable solvent to

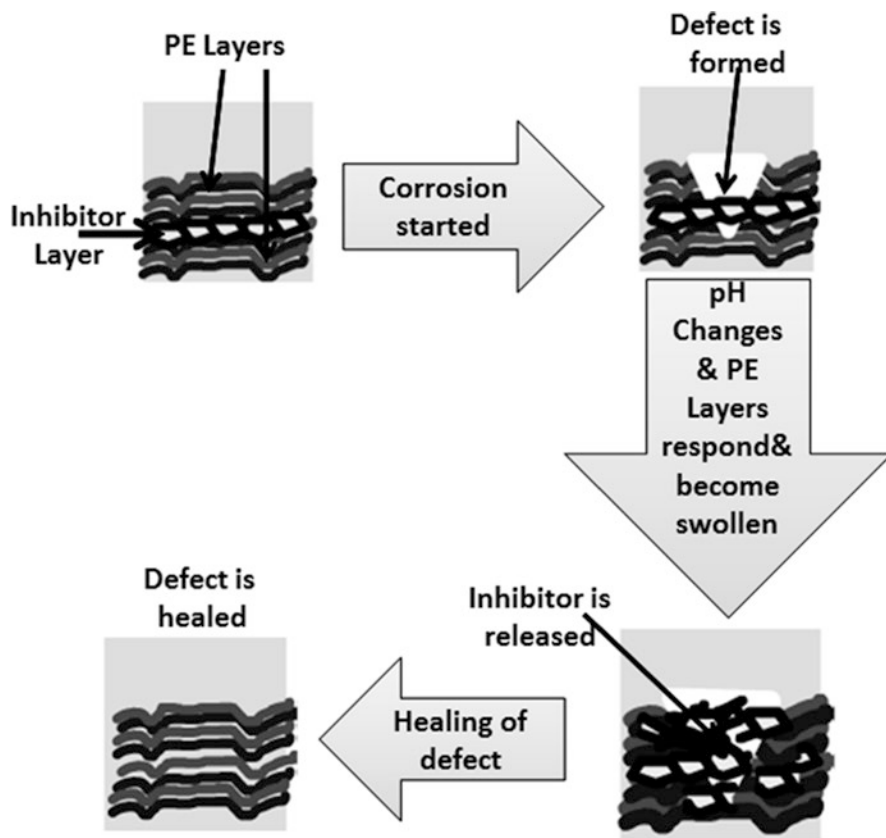


Fig. 4 Schematic illustration for using polyelectrolyte multilayers, embedded with corrosion inhibitor layer, for preparation of self-healing coating

remove the excess polyelectrolyte. This method is time-consuming and requires relatively large amount of material for each deposition. However, this is the only method that can be used for the formation of polyelectrolyte capsules and deposition of LBL films on spheres, microcapsules, and nanocontainers, as discussed previously in Sections 2 and 3.

In case of spraying technique, the procedure involves the following steps: (1) two spraying sequences per single layer, (2) waiting time interval for the removal of excess polyelectrolyte solution, (3) spraying with the rinsing solution, and (4) another waiting time interval for the removal of the excess rinsing solution. The key advantage of the spraying technique is the time reduction for the multilayers formation.

Spin coating technique requires excess polyelectrolyte solution to be applied to the metal substrate before spinning. Next, the solvent is expelled from the substrate surface, and the dissolved component forms a layer. The spinning time and rate can

be varied for particular system. This technique is very fast and does not require equilibration time. However, this technique can be only applied to planar surfaces.

The thickness and roughness of the prepared layer-by-layer films depend on the used coating technique. The self-healing ability of the deposited polyelectrolyte layers is strongly affected by the ionic strength of the used polyelectrolytes. For example, when the scratched metal substrate was coated with two weak polyelectrolytes, polyethylenimine (PEI) and poly(acrylic acid) (PAA), and immersed in 0.1 M NaCl solution, the (PEI/PAA) system was able to stop the initiation of the corrosion [52]. The self-healing mechanism was attributed to the high mobility of the nanolayers that facilitate the water penetration through the polyelectrolyte multilayers and trigger the release of the embedded inhibitor. In comparison with the above “weak-weak” polyelectrolytes, the two strong polyelectrolytes, poly(diallyldimethylammonium) chloride (PDADMAC) and polystyrene sulfonate (PSS), did not show self-healing property. In this case, the high charge density of the two strong polyelectrolytes cannot be altered by pH change.

Grigoriev and coworkers prepared a series of polyelectrolyte/inhibitor complexes by employing different LBL deposition procedures [91]. The polyelectrolyte/inhibitor complexes have two main advantages: (1) they will help to build up more thick and protective multilayers and, thus, reduce the permeability of polyelectrolyte multilayers that may lead to the undesired fast release of the stored inhibitor and (2) the polyelectrolyte/inhibitor complex is formed through interlayer bonds that enable the coating to respond more effectively to the aggressive factors. The thickness of the multilayers formed between polyethylene imine (PEI), poly(allylamine hydrochloride) (PAH), and 2-(benzothiazole-2-ylsulfanyl) succinic acid inhibitor (BYS), PEI(BYS/PAH)₁₀, showed a pH dependence, with a distinct maximum at pH 7. At acidic or basic conditions, the thickness of the multilayers decreases, allowing for partial release of the bonded inhibitor and hence providing the self-healing functionality of the coating. Similarly, the protective coating with embedded 8-hydroxyquinoline (8HQ) in the PSS/(8HQ/PSS)_n multilayers demonstrated a very effective mechanism for corrosion suppression. Thus, the inhibitor release provided an active feedback for effective termination of corrosion.

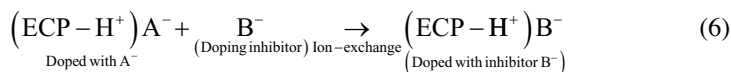
In addition, the above study [91] reported the utilization of SiO₂ mesoporous microcontainers filled with benzotriazole (BTA) inhibitor and plugged by the (PSS/BTA) complex into a sol-gel coating for protection of aluminum alloy AA2024. The stiff inorganic SiO₂ carriers provided the integrity for the microcontainers, and their charged shells improve their dispersion in the coating matrix. The results of the scanning vibrating electrode (SVET) for the anticorrosion efficiency in 0.1 M NaCl revealed that the protective coating with incorporated nanocarriers exhibited an excellent self-healing performance. Anodic activity was developed after 42 h of the total immersion time. However, after another 18 h (i.e., after 60 h of the total immersion time in NaCl solution), almost complete suppression of the corrosion process was detected, with anodic activity less than 2 μA cm⁻², demonstrating the self-healing response of the coating for the corrosion process.

Electrically Conductive Polymers for Self-healing Coatings

Electrically conductive polymers (ECPs) belong to those classes of polymers which have π conjugation along the polymer backbone such as polyaniline (PANi), polypyrrole (PPy), and polythiophene (PTh), as shown in Fig. 5. ECPs are known for their ability to undergo oxidation-reduction reactions by gaining or losing electrons from the surrounding environment. Due to this interesting property, ECPs have been utilized as novel corrosion-protective coatings for a variety of metals and alloys [92–94].

ECPs function as corrosion-protective coatings by one or more of the following three mechanisms [95]. First, ECPs can provide barrier protection by isolating the metal surface from the surrounding environment. This can be achieved by using the ECPs as primers or as a component of the barrier layer [96–101]. Second, ECPs can provide anodic protection through the formation of passive layer of metal oxide (enobling mechanism) [102, 103]. In this case, ECPs act as oxidizing agent for the leached metal ions, maintaining the metal in the passive domain by providing a thin layer of metal oxide.

In the third protection mechanism, Kendig [104] proposed that ECPs can provide self-healing functionality for the coated metal substrates through storage and immobilization of the doped corrosion inhibitor anions as illustrated in Fig. 6 [105]. The release of the stored inhibitor anions to the corroded areas is triggered by the electrochemical reduction of the ECP. Different organic/inorganic dopants (Fig. 7) can be immobilized on the polymeric backbone of ECPs [106–114]. This can be achieved during polymerization process of the ECP, through doping process (Eq. 5), or by ion exchange reaction with negatively charged inhibitor anions (Eq. 6).



Polyaniline doped with 2,5-dimercapto-1,3,4-thiadiazole (DMcT) was tested, in solvent-borne epoxy, as anticorrosion coating for aluminum alloys (AA2024-T3 and 7075-T6) [115]. The results showed that DMcT-doped PANi epoxy primer

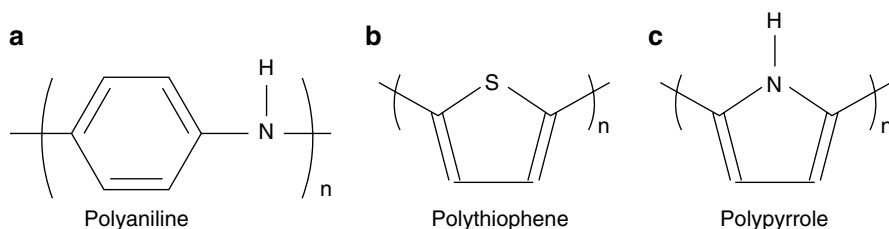


Fig. 5 Chemical structure of common electrically conductive polymers

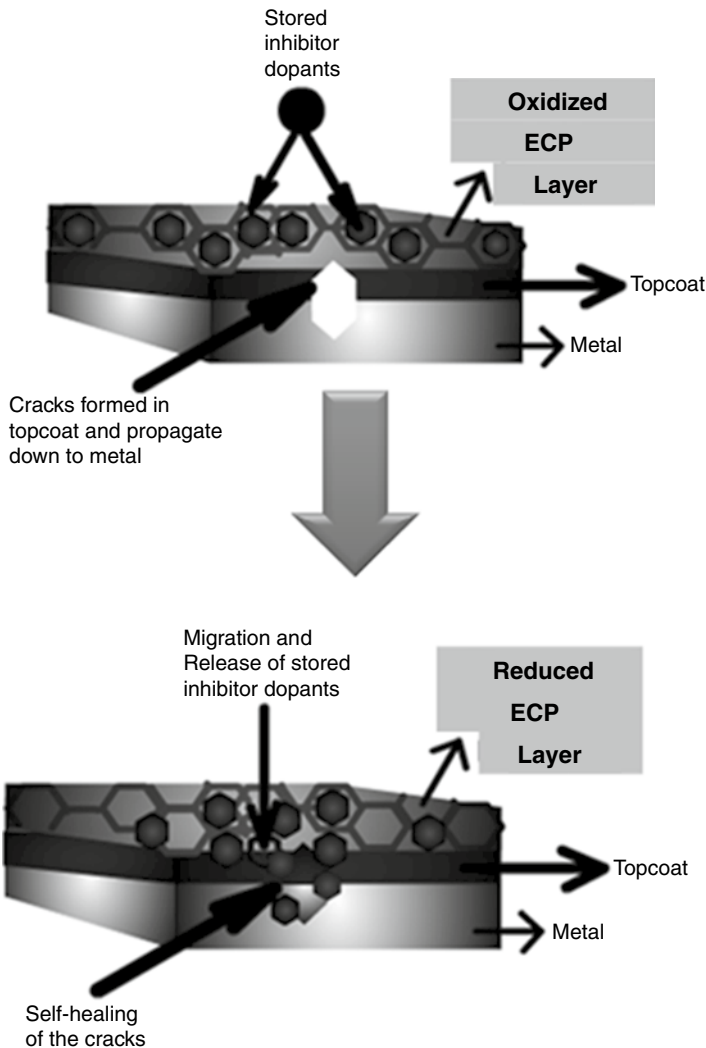


Fig. 6 Schematic illustration of self-healing functionality of an electrically conductive polymer (ECP)

coating was able to provide similar protection performance to that of strontium chromate coating for a period of 2,000 h in corrosive media. The enhanced anticorrosion performance was attributed to the effective release of the anionic organic inhibitor (DMcT) from the reduced polyaniline which suppresses the oxygen reduction reactions and consequently delayed the corrosion process.

Inorganic inhibitors such as MoO_4^{2-} , PO_4^{3-} , and WO_4^{2-} can be immobilized and stored as dopant anions into the ECP matrix. Molybdate-doped polyaniline was investigated as self-healing anticorrosive coating [116]. PANi– MoO_4^{2-} film was

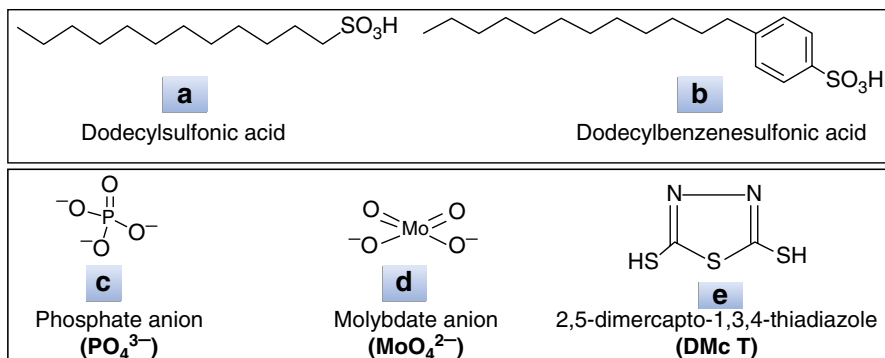
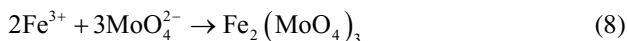


Fig. 7 Chemical structure of organic doping acids (a and b), inorganic inhibitor dopants (c and d), and organic inhibitor dopant (e)

deposited on mild steel substrate by in situ electrochemical polymerization in the presence of oxalic acid solution. PANi – MoO₄²⁻ coating system showed superior anticorrosion performance to that of pure PANi due to the formation of iron-molybdate complex along with the passive film as shown in the following equations:



Steel substrates coated with molybdate-doped polypyrrole film were protected in chloride-containing solution even when the coating has defects [117]. This was attributed to the migration of molybdate anions through the polypyrrole film in a short time and subsequent formation of passive layer at the defected sites.

Polypyrrole doped with larger molecular size phosphomolybdate anion [PMo₁₂O₄₀]³⁻ has also been investigated and showed significant self-healing corrosion protection performance [118, 119]. Responsive release of the inhibitor [PMo₁₂O₄₀]³⁻ occurs only when the potential at the metal-polymer interface decreases at an active defects.

Kowalski et al. investigated bilayered polypyrrole coating composed of molybdate-doped internal layer and dodecyl sulfate-doped external layer [120]. The immobile and bulky counter anion (dodecyl sulfate) prevents the penetration of small aggressive anions through anion exchange reaction, whereas the internal layer provides the self-healing functionality through the controlled release of the molybdate anions. The above duplex coating was applied to steel substrate and provided corrosion protection for 190 h in chloride-containing solution. However, steel substrate coated with similar thickness of dodecyl sulfate-doped polypyrrole monolayer was able to provide corrosion protection for only 10 h. It was concluded that the molybdate-doped internal layer was able to maintain the metal substrate in the passive domain for longer period, which is attributed to the formation of salt layer of ferric molybdate complex at the defect site [121].

Chen et al. prepared polyaniline (PANI)-containing coating for waterborne corrosion protection applications by using oxidative dispersion polymerization of aniline monomer in the presence of partially phosphorylated polyvinyl alcohol (P-PVA) [122]. The resulted PANi nanoparticles were stabilized by P-PVA with uniform diameters in the range of 60–100 nm. The coating was prepared by using waterborne epoxy resin as matrix, with a dry film thickness of $\approx 90 \mu\text{m}$. Mild steel samples were dip coated with the waterborne PANi/P-PVA-containing coating and exposed to 3.0 wt% NaCl solution. The corrosion protection performance was evaluated by the measurement of OCP versus time of exposure and EIS. After 30 days of salt spray tests, samples coated with 2.5 wt% PANi/P-PVA content, the measured impedance values were higher than $1 \times 10^7 \Omega \text{ cm}^2$, which showed that the PANi/P-PVA coating was able to provide superior corrosion protection for long period.

Conclusions and Future Remarks

Development of self-healing coatings for corrosion protection applications can be considered as one of the future emerging nanotechnology fields. Nowadays, there is a lot of scientific research interest in this fast growing area. The main advantage of self-healing coatings is their autoresponse to the corrosion phenomena. The *responsive* self-healing coatings are characterized by their ability to provide instantaneous feedback upon corrosion initiation. The criterion for automatic feedback depends on the design of the self-healing coating as well as the surrounding environment.

Different materials with nano and microscale dimensions have been utilized for the preparation of self-healing agents prior to their embedding and incorporation into the polymeric coating matrix. The selection and design of specific self-healing agent can provide specific triggering mechanism for the effective release of the encapsulated active corrosion inhibitor molecules. Since corrosion is an electrochemical process accompanied with pH change, *redox*-dependent and *pH-dependent* triggering mechanisms are suitable for providing active feedback in case of corrosion initiation.

Different approaches have been investigated for the design, synthesis, and preparation of self-healing coatings. The first approach employs different types of inorganic *nanocontainers* and microparticles as carriers/reservoirs for storage and immobilization of corrosion inhibitor molecules. These carriers include halloysite nanotubes, mesoporous silica nanotubes, hydroxyapatite microparticles, and layered double hydroxides nanotubes. Corrosion inhibitors are incorporated by simple adsorption or by cationic/anionic exchange with unbound cations/anions, like in the case of hydroxyapatite and layered double hydroxide microparticles.

The second approach utilized layer-by-layer polyelectrolyte assembly for the preparation of thin-responsive coating films. Corrosion inhibitor layers are sandwiched between the alternating positive and negative polyelectrolyte multilayers. The effective release of the corrosion inhibitor and the self-healing functionality of the polyelectrolyte multilayer depend on the type of the used polyelectrolytes

(weak/strong), the ionic strength of the polyelectrolyte solution, and the conformation of the polyelectrolyte multilayers (coiled/expanded).

The third approach utilized the electrically conductive polymers (ECPs) as potential class of the self-healing anticorrosive polymeric coatings. ECPs are redox-active polymers and have the ability to sense the corrosion process by the accompanied oxidation-reduction reactions. ECPs can immobilize the anionic corrosion inhibitors through doping/de-doping process. When corrosion is initiated, the metal substrate is oxidized at the defected site, and consequently, the ECP gains the released electrons and became the reduced state. As a result, the stored anionic inhibitor migrates to the defected site and provides a self-healing action.

Properties of certain self-healing coatings can be designed and fine-tuned by using a combination of the above discussed approaches. However, the development in the area of nanomaterial-based anticorrosive self-healing coatings is still in its early stage, and multidisciplinary collaboration is required to overcome both economic and technical challenges for commercialization of this type of coatings. The applicable environmental conditions and the cost are very important criteria for marketing self-healing coatings. The technical challenges such as mechanical properties, adhesion, durability, and coating lifetime are essential factors for future investigation and improvement in this area.

References

1. Xiong J et al (2010) A multifunctional nanoporous layer created on glass through a simple alkali corrosion process. *J Mater Chem* 20(45):10246–10252
2. Wang Y et al (2013) Verification of icephobic/anti-icing properties of a superhydrophobic surface. *ACS Appl Mater Interfaces* 5(8):3370–3381
3. Li H, Zhao Y, Yuan X (2013) Facile preparation of superhydrophobic coating by spraying a fluorinated acrylic random copolymer micelle solution. *Soft Matter* 9(4):1005–1009
4. Chen J et al (2013) Robust prototypical anti-icing coatings with a self-lubricating liquid water layer between Ice and substrate. *ACS Appl Mater Interfaces* 5(10):4026–4030
5. Xin C et al (2013) A novel route to prepare weather resistant, durable antireflective films for solar glass. *Solar Energy* 93:121–126
6. Sangermano M et al (2013) Multifunctional antistatic and scratch resistant UV-cured acrylic coatings. *Prog Org Coat* 76:1191–1196
7. Lioni K et al (2013) Hybrid silica coatings on polycarbonate: enhanced properties. *J Sol-Gel Sci Technol* 65:52–60
8. Nagappan S et al. (2013) Polymethylhydrosiloxane-based organic–inorganic hybrids for amphiphobic coatings. *Compos Interfaces* 20:33–43
9. Nagappan S et al (2013) Highly transparent, hydrophobic fluorinated polymethylsiloxane/silica organic–inorganic hybrids for anti-stain coating. *Macromol Res* 21:669–680
10. Vu CHT, Won K (2013) Novel water-resistant UV-activated oxygen indicator for intelligent food packaging. *Food Chem* 140(1-2):52–56
11. Vu CHT, Won K (2013) Bioinspired molecular adhesive for water-resistant oxygen indicator films. *Biotechnol Prog* 29(2):513–519
12. Triftaridou AI et al (2013) Water-resistant, hydrophobic UVB-shielding films from water-borne nanostructured latexes. *Polym Chem* 4:2125–2131

13. Zhu L et al (2013) Ice-phobic coatings based on silicon oil infused polydimethylsiloxane. *ACS Appl Mater Interfaces* 5(10):4053–4062
14. Xu L-P et al (2013) An ion-induced low-oil-adhesion organic/inorganic hybrid film for stable superoleophobicity in seawater. *Adv Mater* 25(4):606–611
15. Parkin IP et al (2013) The combinatorial APCVD of graded TiO₂-VO₂ mixed-phase composites and their dual functional property as self-cleaning and photochromic window coatings. *ACS Comb Sci* 15(6):309–319
16. Li X, He J (2013) Synthesis of raspberry-Like SiO₂-TiO₂ nanoparticles toward antireflective and self-cleaning coatings. *ACS Appl Mater Interfaces* 5(11):5282–5290
17. Ganesh VA et al (2011) A review on self-cleaning coatings. *J Mater Chem* 21(41):16304–16322
18. Nikkola J et al (2013) Surface modification of thin film composite RO membrane for enhanced anti-biofouling performance. *J Membr Sci* 444:192–200
19. Hui F, Debiemme-Chouvy C (2013) Antimicrobial N-halamine polymers and coatings: a review of their synthesis, characterisation and applications. *Biomacromolecules* 14(3):585–601
20. Forbes S et al (2013) Comparative surface antimicrobial properties of synthetic biocides and novel human apolipoprotein E derived antimicrobial peptides. *Biomaterials* 34(22):5453–5464
21. Cloete W, Verwey L, Klumperman B (2013) Permanently antimicrobial waterborne coatings based on the dual role of modified poly (styrene-co-maleic anhydride). *Eur Polym J* 49(5):1080–1088
22. Andre R et al (2013) Self-cleaning antimicrobial surfaces by SnO₂ coatings on glass deposited with surface-bound spermine. *Nanoscale* 5(8):3447–3456
23. Broasca G et al (2013) Characterization of ZnO coated polyester fabrics for UV protection. *Appl Surf Sci* 279(15):272–278
24. Dispinar T, Colard CAL, Du Prez FE (2013) Polyurea microcapsules with a photocleavable shell: UV-triggered release. *Polym Chem* 4(3):763–772
25. Ershad-Langroudi A et al (2013) Adhesion enhancement of 316L stainless steel to acrylic bone cement through nanocomposite sol-gel coating system. *Plast Rubber Compos* 42(3):101–107
26. Borisova D, Moehwald H, Shchukin D (2012) Influence of embedded nanocontainers on the efficiency of active anticorrosive coatings for aluminum alloys part II: influence of nanocontainer position. *ACS Appl Mater Interfaces* 5(1):80–87
27. Hamdy AS, Butt D (2013) Novel smart stannate based coatings of self-healing functionality for AZ91D magnesium alloys. *Electrochim Acta* 97:296–303
28. Hamdy AS, Doench I, Möhwald H (2011) Smart self-healing anti-corrosion vanadia coating for magnesium alloys. *Prog Org Coat* 72(3):387–393
29. Hamdy AS, Doench I, Möhwald H (2011) Intelligent self-healing corrosion resistant vanadia coating for AA2024. *Thin Solid Films* 520(5):1668–1678
30. Hamdy AS, Doench I, Möhwald H (2011) Assessment of a one-step intelligent self-healing vanadia protective coatings for magnesium alloys in corrosive media. *Electrochim Acta* 56(5):2493–2502
31. Hamdy A (2010) The role of nanotechnology in designing high performance nano-ceramic coatings. *Int Rev Chem Eng* 2(2):256–262
32. Hamdy AS (2015) Intelligent stannate based coatings of self-healing functionality for magnesium alloys. In: Tiwari A, Rawlins JW, Hihara LH (eds) *Intelligent coatings for corrosion control*. Elsevier Publication, USA, ISBN: 9780124114678, chapter 15, pp 537–555
33. Hamdy AS (2010) Corrosion protection performance via nano-coatings. *J Recent Patents Mater Sci* 2:258–267
34. Hamdy AS (2008) A novel approach in designing chrome-free chemical conversion coatings for automotive and aerospace materials. *Eur Coatings J* 86(3):43–50
35. Hamdy Makhoulouf AS, Tiginyanu I (eds) (2011) *Nanocoatings and ultra thin-films: technologies and applications*. Woodhead Publishing Limited, Cambridge, UK, ISBN: 978-1-84569-812-6, 2011, 428 p

36. Hamdy Makhlof AS (eds) (2010) High performance coatings for automotive and aerospace Industries. Nova Science Publishers, New York, ISBN: 978-1-60876-579-9, 2010, 415 p
37. Hamdy Makhlof AS (ed) (2014) Handbook of smart coatings for materials protection. Woodhead Publishing Limited, Cambridge, UK, ISBN: 978-0-85709-680-7, 2014, 608 p
38. Yuan YC et al (2008) Self healing in polymers and polymer composites. Concepts, realization and outlook: a review. *Expr Polym Lett* 2(4):238–250
39. Chen X et al (2002) A thermally re-mendable cross-linked polymeric material. *Science* 295(5560):1698–1702
40. Chen X et al (2003) New thermally remendable highly cross-linked polymeric materials. *Macromolecules* 36(6):1802–1807
41. Szalai ML et al (2007) Dendrimers based on thermally reversible furan-maleimide Diels-Alder adducts. *Macromolecules* 40(4):818–823
42. Toohey KS et al (2007) Self-healing materials with microvascular networks. *Nat Mater* 6(8):581–585
43. Hansen CJ et al (2009) Self-healing materials with interpenetrating microvascular networks. *Adv Mater* 21(41):4143–4147
44. White SR et al (2001) Autonomic healing of polymer composites. *Nature* 409(6822):794–797
45. White SR et al (2002) Correction: autonomic healing of polymer composites. *Nature* 415(6873):817–817
46. Yang J et al (2008) Microencapsulation of isocyanates for self-healing polymers. *Macromolecules* 41(24):9650–9655
47. Shchukin DG et al (2006) Layer-by-layer assembled nanocontainers for self-healing corrosion protection. *Adv Mater* 18(13):1672–1678
48. Yow HN, Routh AF (2006) Formation of liquid core-polymer shell microcapsules. *Soft Matter* 2(11):940–949
49. Grigoriev DO et al (2008) New method for fabrication of loaded micro- and nanocontainers: emulsion encapsulation by polyelectrolyte layer-by-layer deposition on the liquid core. *Langmuir* 24(3):999–1004
50. Grigoriev DO et al (2012) Emulsion route in fabrication of micro and nanocontainers for biomimetic self-healing and self-protecting functional coatings. *Bioinspired Biomim Nanobiomater* 1(2):101–116
51. Berg J, Sundberg D, Kronberg B (1989) Microencapsulation of emulsified oil droplets by in-situ vinyl polymerization. *J Microencapsul* 6(3):327–337
52. Andreeva DV, Skorb EV, Shchukin DG (2010) Layer-by-layer polyelectrolyte/inhibitor nanostructures for metal corrosion protection. *ACS Appl Mater Interfaces* 2(7):1954–1962
53. Zhuk A, Sukhishvili SA (2013) Stimuli-responsive layer-by-layer nanocomposites. *Soft Matter* 9:5149–5154
54. Sauvant-Moynot V, Gonzalez S, Kittel J (2008) Self-healing coatings: an alternative route for anticorrosion protection. *Prog Org Coat* 63(3):307–315
55. Iyoda M, Hasegawa M, Enozawa H (2007) Self-assembly and nanostructure formation of multi-functional organic-donors. *Chem Lett* 36(12):1402–1407
56. Levis SR, Deasy PB (2002) Characterisation of halloysite for use as a microtubular drug delivery system. *Int J Pharm* 243(1–2):125–134
57. Luca V, Thomson S (2000) Intercalation and polymerisation of aniline within a tubular aluminosilicate. *J Mater Chem* 10(9):2121–2126
58. Abdullayev E, Lvov YM (2013) Halloysite clay nanotubes as ceramic “Skeleton” for functional biopolymer composites with sustained drug release. *J Mater Chem B* 1:2894–2903
59. Yuan P et al (2012) Organosilane functionalization of halloysite nanotubes for enhanced loading and controlled release. *Nanotechnology* 23(37):375705
60. Yah WO et al (2012) Biomimetic dopamine derivative for selective polymer modification of halloysite nanotube lumen. *J Am Chem Soc* 134(29):12134–12137
61. Yah WO, Takahara A, Lvov YM (2012) Selective modification of halloysite lumen with octadecylphosphonic acid: new inorganic tubular micelle. *J Am Chem Soc* 134(3):1853–1859

62. Shchukin DG et al (2008) Active anticorrosion coatings with halloysite nanocontainers. *J Phys Chem C* 112(4):958–964
63. Abdullayev E et al (2009) Halloysite tubes as nanocontainers for anticorrosion coating with benzotriazole. *ACS Appl Mater Interfaces* 1(7):1437–1443
64. Abdullayev E, Lvov Y (2010) Clay nanotubes for corrosion inhibitor encapsulation: release control with end stoppers. *J Mater Chem* 20(32):6681–6687
65. Borisova D, Möhwald H, Shchukin DG (2011) Mesoporous silica nanoparticles for active corrosion protection. *ACS Nano* 5(3):1939–1946
66. Li GL et al (2013) Silica/polymer double-walled hybrid nanotubes: synthesis and application as stimuli-responsive nano-containers in self-healing coatings. *ACS Nano* 7(8):2470–2478
67. Maia F et al (2012) Silica nanocontainers for active corrosion protection. *Nanoscale* 4(4):1287–1298
68. Newman S (1998) Synthesis, characterization and applications of layered double hydroxides containing organic guests. *New J Chem* 22(2):105–115
69. Shao M et al (2013) Hierarchical structures based on functionalized magnetic cores and layered double-hydroxide shells: concept, controlled synthesis, and applications. *Chem-A Eur J* 19(13):4100–4108
70. Choy J-H et al (2004) Layered double hydroxide as an efficient drug reservoir for folate derivatives. *Biomaterials* 25(15):3059–3064
71. Choy J-H et al (2007) Clay minerals and layered double hydroxides for novel biological applications. *Appl Clay Sci* 36(1):122–132
72. Hennous M et al (2013) Lignosulfonate interleaved layered double hydroxide: a novel green organoclay for bio-related polymer. *Appl Clay Sci* 71:42–48
73. Xu F-J et al (2013) Functionalized layered double hydroxide nanoparticles conjugated with disulfide-linked polycation brushes for advanced gene delivery. *Bioconjug Chem* 24(6):968–978
74. Buchheit RG et al (2003) Active corrosion protection and corrosion sensing in chromate-free organic coatings. *Prog Org Coat* 47(3–4):174–182
75. Liu Z et al (2006) Synthesis, anion exchange, and delamination of Co-Al layered double hydroxide: assembly of the exfoliated nanosheet/polyanion composite films and magneto-optical studies. *J Am Chem Soc* 128(14):4872–4880
76. Chico B et al (2008) Anticorrosive behaviour of alkyd paints formulated with ion-exchange pigments. *Prog Org Coat* 61(2–4):283–290
77. Zhang F et al (2008) Corrosion resistance of superhydrophobic layered double hydroxide films on aluminum. *Angew Chem Int Ed* 47(13):2466–2469
78. Zheludkevich M et al (2010) Active protection coatings with layered double hydroxide nanocontainers of corrosion inhibitor. *Corros Sci* 52(2):602–611
79. Poznyak SK et al (2009) Novel inorganic host layered double hydroxides intercalated with guest organic inhibitors for anticorrosion applications. *ACS Appl Mater Interfaces* 1(10):2353–2362
80. Tedim J et al (2010) Enhancement of active corrosion protection via combination of inhibitor-loaded nanocontainers. *ACS Appl Mater Interfaces* 2(5):1528–1535
81. Guo X et al (2009) One-step hydrothermal crystallization of a layered double hydroxide/alumina bilayer film on aluminum and its corrosion resistance properties. *Langmuir* 25(17):9894–9897
82. Snihirova D et al (2010) Hydroxyapatite microparticles as feedback-active reservoirs of corrosion inhibitors. *ACS Appl Mater Interfaces* 2(11):3011–3022
83. Ferreira M, Rubner MF (1995) Molecular-level processing of conjugated polymers. 1. Layer-by-layer manipulation of conjugated polyions. *Macromolecules* 28(21):7107–7114
84. Dubas ST, Schlenoff JB (1999) Factors controlling the growth of polyelectrolyte multilayers. *Macromolecules* 32(24):8153–8160
85. Shiratori SS, Rubner MF (2000) pH-Dependent thickness behavior of sequentially adsorbed layers of weak polyelectrolytes. *Macromolecules* 33(11):4213–4219

86. Dubas ST, Schlenoff JB (2001) Polyelectrolyte multilayers containing a weak polyacid: construction and deconstruction. *Macromolecules* 34(11):3736–3740
87. Dubas ST, Schlenoff JB (2001) Swelling and smoothing of polyelectrolyte multilayers by salt. *Langmuir* 17(25):7725–7727
88. Choi J, Rubner MF (2004) Influence of the degree of ionization on weak polyelectrolyte multilayer assembly. *Macromolecules* 38(1):116–124
89. El Haitami AE et al (2009) Effect of the supporting electrolyte anion on the thickness of PSS/PAH multilayer films and on their permeability to an electroactive probe. *Langmuir* 25(4):2282–2289
90. Lundin M et al (2011) Layer-by-layer assemblies of chitosan and heparin: effect of solution ionic strength and pH. *Langmuir* 27(12):7537–7548
91. Grigoriev DO et al (2009) Polyelectrolyte complexes as a “smart” depot for self-healing anticorrosion coatings. *Soft Matter* 5:1426–1432
92. Subathira A, Meyyappan RM (2010) Inhibition of corrosion of steel alloy using polyaniline conducting polymer coatings. *Int J Chem Sci* 8(4):2563–2574
93. Saji VS (2010) A review on recent patents in corrosion inhibitors. *Recent Patents Corros Sci* 2:6–12
94. Rohwerder M (2009) Conducting polymers for corrosion protection: a review. *Int J Mater Res* 100(10):1331–1342
95. Shabani-Nooshabadi M, Ghoreishi SM, Behpour M (2011) Direct electrosynthesis of polyaniline-montmorillonite nanocomposite coatings on aluminum alloy 3004 and their corrosion protection performance. *Corros Sci* 53(9):3035–3042
96. Gözen Bereket EH (2009) The corrosion protection of mild steel by single layered polypyrrole and multilayered polypyrrole/poly(5-amino-1-naphthol) coatings. *Prog Org Coat* 65:116–124
97. Redondo MI et al (2009) Poly(N-methylpyrrole) electrodeposited on copper: corrosion protection properties. *Prog Org Coat* 65(3):386–391
98. Akbarinezhad E et al (2011) Synthesis and evaluating corrosion protection effects of emeraldine base PANi/clay nanocomposite as a barrier pigment in zinc-rich ethyl silicate primer. *Prog Org Coat* 70(1):39–44
99. Armelin E, Aleman C, Iribarren JI (2009) Anticorrosion performances of epoxy coatings modified with polyaniline: a comparison between the emeraldine base and salt forms. *Prog Org Coat* 65(1):88–93
100. Radhakrishnan S, Sonawane N, Siju CR (2009) Epoxy powder coatings containing polyaniline for enhanced corrosion protection. *Prog Org Coat* 64(4):383–386
101. Cheng Yue G, Xiao Gang Y, Bao Rong H (2012) Synthesis of polyaniline nanofiber and anti-corrosion property of polyaniline-epoxy composite coating for Q235 steel. *J Coat Technol Res* 9(1):59–69
102. Wessling B (1994) Passivation of metals by coating with polyaniline: corrosion potential shift and morphological changes. *Adv Mater (Weinheim Ger)* 6:226–228
103. Wessling B (1997) Scientific and commercial breakthrough for organic metals. *Synth Met* 85:1313–1318
104. Kendig M, Hon M, Warren L (2003) ‘Smart’ corrosion inhibiting coatings. *Prog Org Coat* 47(3-4):183–189
105. Mçhwald DGS (2007) Self-Repairing Coatings Containing Active Nanoreservoirs. *Small* 3:926–943
106. Pereira DSJE, Cordoba DTSI, Torresi RM (2007) Polyaniline/poly(methylmethacrylate) blends for corrosion protection: The effect of passivating dopants on different metals. *Prog Org Coat* 58:33–39
107. Qi K et al (2012) Corrosion of conductive polypyrrole: effects of environmental factors, electrochemical stimulation, and doping anions. *Corros Sci* 60:50–58
108. Hien NTL et al (2005) Role of doping ions in the corrosion protection of iron by polypyrrole films. *Electrochim Acta* 50(7–8):1747–1755

109. Riaz U et al (2009) Effect of dopant on the corrosion protective performance of environmentally benign nanostructured conducting composite coatings. *Prog Org Coat* 65(3):405–409
110. Williams G et al (2006) Dopant effects in polyaniline inhibition of corrosion-driven organic coating cathodic delamination on iron. *J Electrochem Soc* 153:B425–B433
111. Wallace GG et al (2003) Factors influencing the performance of inherently conducting polymers as corrosion inhibitors: the dopant. *ACS Symp Ser* 843:103–123
112. Dominis AJ, Spinks GM, Wallace GG (2003) Comparison of polyaniline primers prepared with different dopants for corrosion protection of steel. *Prog Org Coat* 48:43–49
113. Chowdhury P et al (2007) Effect of acrylic acid doping on the properties of chemically synthesized polyaniline. *J Indian Chem Soc* 84:176–180
114. Gabriel A et al (2006) Inhibition by polyaniline of corrosion-driven coating delamination on carbon steel: aspects regarding the role of the counter-anion. *ECS Trans* 1:37–46
115. Kinlen PJ, Graham CR, Ding Y (2004) Corrosion protection of aluminum alloys by controlled release of inhibitors from inherently conductive polymer coatings. *Polym Prepr (Am Chem Soc Div Polym Chem)* 45:146–147
116. Karpakam V et al (2011) Electrosynthesis of polyaniline-molybdate coating on steel and its corrosion protection performance. *Electrochim Acta* 56(5):2165–2173
117. Rammelt U, Duc LM, Plieth W (2005) Improvement of protection performance of polypyrrole by dopant anions. *J Appl Electrochem* 35(12):1225–1230
118. Łapkowski M, Bidan G, Fournier M (1991) Synthesis of polypyrrole and polythiophene in aqueous solution of Keggin-type structure heteropolyanions. *Synth Met* 41(1–2):407–410
119. Kulesza PJ et al (2002) Polyoxometallates as inorganic templates for monolayers and multilayers of ultrathin polyaniline. *Electrochem Commun* 4(6):510–515
120. Kowalski D, Ueda M, Ohtsuka T (2008) The effect of ultrasonic irradiation during electropolymerization of polypyrrole on corrosion prevention of the coated steel. *Corros Sci* 50:286–291
121. Kowalski D, Ueda M, Ohtsuka T (2010) Self-healing ion-permselective conducting polymer coating. *J Mater Chem* 20(36):7630–7633
122. Liu P, Chen F (2011) Conducting Polyaniline Nanoparticles and Their Dispersion for Waterborne Corrosion Protection Coatings. *ACS Appl Mater Interfaces* 3:2694–2702

Electrodeposited Zn-Nanoparticles Composite Coatings for Corrosion Protection of Steel

11

Liana Maria Muresan

Contents

Introduction.....	334
Obtaining Methods.....	335
Drawbacks and Difficulties.....	336
Mechanism of Co-deposition.....	337
Factors Influencing the Electrolytic Co-deposition.....	338
Characteristics of the Plating Solution.....	338
Operating Conditions.....	341
Properties of Nanocomposite Deposits.....	342
Corrosion Resistance.....	342
Microhardness.....	342
Wear Resistance.....	343
Zinc-Nanoparticle Composite Coatings Obtained by Electrodeposition.....	343
Zn-TiO ₂	343
Zn-SiO ₂	347
Zn-PTFE.....	348
Zn-ZrO ₂	348
Zn-CeO ₂	348
Conclusions.....	349
References.....	349

Abstract

In the field of galvanic plating, one of the ways to obtain metallic coatings with improved mechanic and anti-corrosion properties consists in the electrolytic entrapment of inert nanoparticles (e.g., oxides, carbides, carbon nanotubes, polytetrafluoroethylene etc.) in the metallic matrix. The particles confer to the

L.M. Muresan (✉)

Department of Chemical Engineering, Babes-Bolyai University, Cluj-Napoca, Romania

e-mail: lianamuresan2002@yahoo.com

© Springer International Publishing Switzerland 2016

M. Aliofkhazraei, A.S.H. Makhlof (eds.), *Handbook of Nanoelectrochemistry*,

DOI 10.1007/978-3-319-15266-0_34

333

resulting composite layers improved corrosion and wear resistance, increased hardness, superior tribologic properties, better subsequent adhesion of paintings and increased lifetime. Due to the fact that the nanosized particles possess special properties which could be transferred to the composite layers, there is a lot of research directions to be investigated, beginning with the exceptional properties of deposited layers and finishing with the incompletely elucidated electro-deposition mechanism. In this context, recent advances in electro-deposition of metal-matrix composite coatings will be reviewed with emphasis on electrolytic co-deposition of Zn with nanoparticles of TiO_2 , CeO_2 , ZrO_2 etc. The factors influencing the co-deposition and the properties of the resulting composite coatings are also briefly discussed.

Keywords

Composite coatings • Electrodeposition • Nanoparticles • Zinc

Introduction

Metal matrix composites (MMCs) are innovative multifunctional materials obtained by dispersion of a reinforcing material into a metal matrix. They can replace conventional materials by offering a unique balance of mechanical and physical properties: increased hardness and wear resistance, low coefficients of thermal expansion, dry lubrication properties, and better corrosion resistance than pure metals [1]. Different shapes (fibers, filaments, spherical particles, etc.) as well as various types of reinforcing materials can be used, conferring to composites an easiness to be tailored that is unusual in materials engineering.

There is a large number of useful metal/particle combinations, including on one side metals like copper, nickel, silver, zinc, and many others and on the other side inert materials such as oxides, carbides, graphite, PTFE, etc., which are successfully used in many practical applications such as advanced surface finishing, electronic industry, automotive engineering, aerospace industry [2], etc. Some of the most common metal-nanoparticle composites are summarized in Table 1.

The reinforcement material used most frequently is SiC by a significant margin, followed by Al_2O_3 [28], but TiO_2 , WC, Cr_2O_3 , V_2O_5 , Si_3N_4 , or SiO_2 particles are used as well for different practical purposes. Several physical and chemical properties of the particles are transferred to the resulting composite and an improvement in the specific properties of materials can result, offering possibilities of extending their application area and optimizing materials properties. For example, the inclusion of Al_2O_3 , TiO_2 , WC, and SiC in the metallic matrix results in enhanced hardness and wear resistance [3, 5, 7, 22, 29]; increased corrosion resistance is reached when Cr_2O_3 , V_2O_5 , and CeO_2 are used [23, 24, 27], while graphite, PTFE, or MoS_2 particles confer lubricant properties to the deposits in which they are embedded [14].

Table 1 Some metal-nanoparticle composites used in practical applications

Metal	Nanoparticles	References
Copper	Al ₂ O ₃	[3]
	Ti ₂ SnC	[4]
	SiC	[5, 6]
Nickel	Al ₂ O ₃	[7–11]
	SiO ₂	[12, 13]
	SiC	[12, 14]
	Boron nitride (BN)	[14]
	PTFE	[14]
Silver	TiO ₂	[15]
	SiO ₂	[16]
	Cu, Ag, and Au clusters	[17]
Zinc	SiO ₂	[18, 19]
	C (graphite)	[20]
	PTFE	[21]
	TiO ₂	[22]
	CeO ₂	[23]
	V ₂ O ₅	[24]
Bronze	PTFE	[25]
Various metals	C (graphite)	[26]
Steel	Cr ₂ O ₃	[27]

Moreover, the catalytic properties of several metals are amplified in the presence of included particles [30], this leading to materials with excellent catalytic activity or photoactivity for batteries and electrochemical cells or for pollutant degradation [31].

By coating metals with a composite layer of various natures, they can be protected not only against corrosion but also against abrasion and erosion. MMC coatings are especially important in surface finishing and automotive industry, as corrosion-protective coatings exhibiting superior tribologic properties, better subsequent adhesion of paintings, and increased lifetime. The thickness of the coatings is usually of tens of μm and can be rigorously controlled (e.g., by monitoring the electrical charge consumed during the electrodeposition process).

Obtaining Methods

The methods generally used to obtain composite metallic coatings include thermal methods (spray, internal oxidation) [32–35], hot dip coating [36], radio-frequency magnetron co-sputtering [18, 37], or electrolytic co-deposition, in direct or pulsed current [38].

Among these methods, electrolytic co-deposition is intensely used, the tendency being to replace the microparticles (used in the 1990s) with nanoparticles, which confer improved properties to metallic coatings. The different electrodeposition techniques (galvanostatic or potentiostatic) allow the obtaining of various types of nanostructured materials, ranging from single metal to alloy nanocomposites and from monolayers to multilayered deposits.

Electrolytic co-deposition presents some advantages over other methods [38]: the possibility of rigorous control of the deposited layer thickness, the control of deposition speed, the work at room temperature, and the use of accessible equipments. Moreover, electrodeposition is a single-step method, without secondary treatment, allowing the obtaining of nanostructured materials and of nonuniform films on substrates with complex shapes.

Direct current (DC) electrodeposition has most commonly been used to obtain metal-nanoparticle composite coatings. The deposition mechanism involves the reduction of the metallic ions simultaneously with the nanoparticle incorporation [38]. Generally, the particles are suspended in the plating solution before and are embedded in the growing metallic deposit. Sometimes, the co-deposited particles are produced during the plating process (e.g., during high-speed zinc plating by co-deposition of Ti, Al, and Cr hydroxides by means of nitrate reduction at the cathode [39]).

Other electrodeposition techniques are pulse current (PC) and pulse reversed current (PRC) electrodeposition. The first one is based on alternative applying of two or more direct cathodic currents during various deposition times. During the PRC electrodeposition, a cathodic current is imposed during the “on” time and an anodic current during the “off” time [40]. Working with PRC leads to a higher nanoparticle content in the deposit. According to Low et al. [38], the nanoparticles are entrapped in higher amount due to the partial dissolution of the metallic deposit during the anodic impulse. Pulse electrodeposition is more advantageous than DC electrodeposition because it offers more controllable parameters and it can use much higher instantaneous current densities [41], improving throwing power and enabling the incorporation of higher concentrations of particles. In the same time, it can lead to wider range of deposit compositions [38]. Other deposits characteristics which are affected during pulse plating are grain size, texture, porosity, hardness, and corrosion resistance [39].

Drawbacks and Difficulties

Several problems were identified as critical in the electrodeposition of metal matrix composites: (i) the low degree of particle incorporation (frequently < 1 %), (ii) the agglomeration of the particles in the plating bath, and consequently (iii) the difficulty to ensure a uniform distribution of the particles in the coating.

The particle agglomeration in the electrodeposition bath occurs even at low concentrations because of the compression of the diffuse double layer surrounding the particles by the high ionic strength of the electrolyte solution [42]. Smaller particles

agglomerate easier than bigger ones and are incorporated more difficultly in the deposit [43]. When hydrophilic materials are co-deposited with metals, additional difficulties appear. Thus, a destruction of the aqueous film existing between the particles and the interface is necessary, in order to allow the capturing of particles in the metallic deposit [44].

Some of these problems can be partially solved by tuning the surface properties of the particles (e.g., making the particles more hydrophobic), by introducing organic agents in the plating bath, and by controlling the process parameters (agitation, current density, etc.). The dispersion degree of the nanoparticles can be enhanced by combining high-speed mechanical stirring method and the chemical surface modification of the particles. This method was used successfully to achieve the dispersion and suspension stabilization of nanoparticles in the solution to give Ni/SiO₂ composites [8].

Another possibility to decrease the interface energy between the hydrophilic particles and the aqueous electrolyte providing a driving force for the incorporation of the particles in the metallic matrix consists in modifying the particles with functional groups that have strong affinity toward the metallic matrix. In the case of Zn-SiO₂ electrodeposition, best incorporation was achieved for SiO₂ particles modified with thiols, dithiooxamide, or cysteamine [45].

As it can be seen, some practical issues have been overcome, including compatibility between inert particles and metal, reinforcement distribution and control of interfacial properties, etc. Nevertheless, there are still many aspects to be elucidated concerning the effects of incorporated particles on the quality of composites, i.e., on their mechanical, electrical, and corrosion properties, and the co-deposition mechanism.

Mechanism of Co-deposition

The kinetics of particle incorporation in the metallic matrix was described by several models that take into account the forces involved in the process (gravitational, hydrodynamic, etc.), the particle characteristics (size, concentration, diffusion coefficient, etc.), as well as the electrode geometry, electrode rotation rate, etc. However, the co-deposition mechanism is still not completely understood.

An excellent review of the theoretical models used to describe the behavior of metal electrodeposition from an electrolyte containing particles belongs to Low et al [38]. These models take into consideration the mass transport [46, 47], the trajectories of the particles [5, 44], the gravitational and hydrodynamic forces [7], and the adsorption phenomena [48, 49]. The colloidal forces (van der Waals, electrostatic attraction/repulsion, and hydrophobic/hydrophilic interaction forces) involved in the electrodeposition process play an important role especially in the case of small particles.

It is generally accepted that the reduction of adsorbed ions is the determining factor for particle deposition. Thus, several consecutive steps are involved in the co-deposition process [50]: (1) formation of surface charge on the suspended

particles, (2) convection toward the cathode surface, (3) diffusion through a hydrodynamic boundary layer, (4) diffusion through a concentration boundary layer, and finally (5) adsorption at the cathode followed by particle incorporation into the metallic matrix.

The adsorption of the particles is loose at the beginning and becomes stronger after destruction of the ionic cloud round the particles. The rate-determining step of the electrodeposition process is, in many cases, the strong adsorption, which takes place more difficultly than the loose adsorption.

Factors Influencing the Electrolytic Co-deposition

A lot of experimental parameters strongly influence the properties of the electrodeposited composite coatings. These factors can be divided into three categories [51]:

- Characteristics of the plating solution (concentration of metallic ions being deposited, of particles and additives, particle properties and concentration, pH, etc.)
- Experimental conditions (current density, temperature, hydrodynamic conditions, shape of applied current (i.e., constant, pulsating, reversing etc.))
- Other parameters (geometry of the cell, shape of the cathode, deposit thickness, substrate nature, etc.)

It is worth mentioning that some of the factors act in opposite way, and the final result should be an acceptable compromise between all their actions. For example, increasing metal ion concentration, temperature, and stirring results in larger grain dimensions of the deposits, while the presence of addition agents, an increase of current density, and polarization enhancement stimulate grain refinement. On the other hand, generally the particle volume fraction in the coatings increases with increasing stirring rate and decreases with the increasing deposition current density [47].

Characteristics of the Plating Solution

Particle Characteristics

It was observed that the nature, concentration, shape, size, and charge of the particles strongly influence the properties of the composite deposits in which they are incorporated [29]. Thus, it was reported that, in the same experimental conditions, the incorporation degree of particles in the metallic matrix depends on the particle nature and, for the same particles, on their crystallographic phase. For example, TiO_2 incorporates three times more than Al_2O_3 in a copper matrix, and $\gamma\text{-Al}_2\text{O}_3$ is much less embedded than $\alpha\text{-Al}_2\text{O}_3$ [12, 29]. An explanation for this behavior could be the different way in which adsorption phenomena take place on $\gamma\text{-Al}_2\text{O}_3$ and $\alpha\text{-Al}_2\text{O}_3$ [52].

The concentration of particles suspended in the plating bath is variable, ranging between 2 and 200 g/l leading to composites with typically 1–10 vol.% of incorporated particles [53]. Generally, an increase of particle concentration in the solution and a decrease of their dimensions stimulate their incorporation [5]. However, it was established in many cases [22] that an optimal concentration of particles in the plating bath should be used in order to attain the desired mechanical properties and corrosion resistance of the coatings. It is possible that, in some cases, especially when the concentration of particles in the plating bath is high, a disturbance of the metallic matrix structure takes place because of the embedded particles which co-deposit with the metallic ions. This may result in crystalline defects (cracks, pores, internal stresses, etc.), especially at the interface, increasing the probability of occurrence of problems such as local and stress corrosion and brittleness of the coating [9].

One of the key factors playing a role in particle incorporation as well as in suspension stability is the particle charge. The surface charge of the particles depends on the nature of the particle and its surrounding medium: dissociation of acidic groups on the surface, ionization of basic groups, adsorption of charged species (ions and ionic surfactants), etc. An electrical double layer is formed round each particle, determining the appearance of a potential difference between the dispersion medium and the stationary layer of liquid attached to the dispersed particle, namely, the zeta potential. The zeta potential (ζ) of small particles depends on many factors, such as their preparation and stabilization methods, the presence of surfactants, the electrolyte concentration, the particle morphology and dimensions, the pH of the plating solution, and the degree of hydration [54].

It is common knowledge that the boundary line between stable and unstable suspensions is generally taken as +30 or –30 mV, with particles having zeta potentials outside of these limits normally considered stable due to a larger electrostatic repulsion between particles. The positive charge can be acquired by adsorption of H^+ and M^{2+} ions on the particle surface. The negative charge is due to a preferential adsorption of anions present in the plating solution. Ions adsorbed onto oxide particles influence their behavior in the vicinity of the cathode, but are not the determining factor for achieving an irreversible incorporation of the particles in the metallic matrix [55].

Generally, positively charged particles incorporate better than negatively charged ones [29]. However, in some particular cases, negatively charged particles are easier incorporated than positively charged ones. After the attraction of the negatively charged particles by the double layer of the metallic substrate, the hull of anions adsorbed on the particles is stripped off, allowing them to incorporate in the growing metallic deposit (e.g., Al_2O_3 incorporation in Cu from a pyrophosphate electrolyte) [3].

Hydrophilic particles (e.g., SiO_2) incorporate less than hydrophobic ones (e.g., SiC, Si_3N_4 , graphite, etc.). Studies carried out in this direction led to the conclusion that, even when adsorbed on the electrode surface, hydrophilic particles are separated from the electrode by a film of liquid that is thicker than the width of the double layer. Consequently, a destruction of the film is necessary in order to get an embedding of the particles in the growing metallic matrix [12, 55].

Additives and Surfactants

In the presence of organic additives in an electrodeposition bath containing particles in suspension, the suspensions' properties, as well as the structure and the morphology of the cathodic deposits, can change, sometimes dramatically. Thus, the leveling and brightening agents used in electrodeposition processes can play an essential role in modifying simultaneously the particle interfacial properties and the electrodeposition mechanism [56].

Cationic surfactants (e.g., CTAB) are adsorbed on the inert particle surfaces, increasing thus the suspension stability and reducing particle agglomeration, which results in larger incorporation fraction and more uniform distribution of the particles in the coating [10]. In other cases, the additives increase the particles' hydrophobicity [3], which leads also to a higher incorporation fraction. On the other side, the adsorption of surfactants on the particles increases the adhesion force to the cathode, allowing large particles to be embedded. This was confirmed in the case of SiC incorporation in Ni coatings in the presence of CTAB [57].

Surprisingly, there are cases in which a negatively charged surfactant increases the content of incorporated inert particles in the metallic coating [3]. The negative charge induced by the surfactant on the suspended particles determines, in a first step, their attraction by the positively charged electric double layer of the substrate. In a subsequent step, the double layer of the particles is deformed, the hull of anions adsorbed on the particles is stripped off, and the particles may be embedded in the metallic deposit. This type of mechanism suggests the fact that the co-electrodeposition process is not entirely decided by electrostatic forces.

Among the disadvantages exhibited by the surfactants used for increasing the degree of incorporation of inert particles in a metallic coating, one can count a change of mechanical properties of the deposit (e.g., internal tensions, fragility, etc.) when these compounds are not used in appropriate concentration.

Some inorganic additives can be also used in order to improve the properties of the composite electrodeposits. For example, the addition of small amounts of monovalent cations, like Tl^+ , Cs^+ , Rb^+ , and NH_4^+ , promotes the co-deposition of particles [58].

pH

As the charge of the suspended particles strongly depends on pH, it is obvious that the incorporation degree, as well as the electrodeposition mechanism depends on pH of the plating solution. Thus, it is recommended to investigate how the pH affects the zeta potential of the particles and to choose the value that ensures a good stability of the suspension ($|\zeta| > 30$ mV).

For example, in the case of Ni–Al₂O₃ electrodeposition from a Watt's-type nickel electrolyte, no influence of pH above 2 and a sharp decrease in occluded particles below this value was noticed [59].

The pH can affect the deposit texture. For example, the Zn–TiO₂ composites prepared at pH2 exhibit a (002) preferential orientation, while at pH4, the deposit loses the preferred *c*-axis orientation, and in addition a higher incorporation degree of TiO₂ particles is observed [60]. Nevertheless, a change in electrodeposited zinc

structure as a function of pH of the plating bath was noticed even in the absence of nanoparticles. This effect was explained by a change in nucleation mode as a function of solution pH: at pH2, instantaneous nucleation was predominant, whereas at pH4, a progressive one was noticed [61].

Operating Conditions

Current Density

The current density influences in various ways the incorporation degree of the particles in the composite coating. In some cases, it seems that the increase of current density has no influence on the incorporation fraction, while in other cases a dependence with minima and maxima is noticed [19]. In the case of various metal composites with Al_2O_3 , it was reported that the maximum amount of incorporated particles can be correlated with a change in the slope of polarization curves that corresponds to the minimum in the double-layer capacity of the electrode [53]. The regions wherein the incorporation degree is influenced by the current density are sensitive to particle size, to crystallographic phase, and to other particle properties.

The relationship between the current density and the fraction of embedded particles is a complex one, and it is influenced by the agitation rate of the electrolyte. For example, in the case of Ni-TiO₂, it was reported that the maxima are shifted to higher current densities when the agitation rate increases [62]. This is why a detailed study of the incorporation degree – current density dependence in correlation with all experimental parameters – should be carried out for each particular case of electrocodeposition.

Hydrodynamic Regime

Agitation serves to keep particles in suspension and ensures the transport of the active species toward the electrode surface. In accordance with the mechanism proposed by Fransaer for particle incorporation, it is accepted that the particles which are attached to the surface are submitted to forces which act in opposite ways: adhesion forces and frictional forces exerted by the electrode surface and stagnation and shear forces determined by the fluid flow [44]. If the shear force is larger than the sum of the adhesion force and the stagnation force, the attached particle is rejected [5]. This is why the hydrodynamic regime has a great importance, as it influences the incorporation mechanism of the particles in the cathodic deposit by controlling the rate, direction, and force with which the suspended particles contact the electrode surface [53].

It is worth mentioning that the agitation enhancement generally helps particles to incorporate, but if the agitation is too intense, the time spent by the particles at the electrode surface becomes insufficient, and they can be swept away before they can be incorporated into the growing metal deposit [53]. Consequently, from practical point of view, it is necessary to control the hydrodynamic regime to get a uniform and compact coating [5]. This control is relatively easy at small scale (i.e., by RDE, ultrasonication, magnetic stirring, etc.) but more difficult in industrial conditions, where bubbling or electrolyte recirculation is used for mass transport control.

Temperature

The temperature effect is not the same in different composite electrodeposition processes. In some cases the temperature has no effect on the particle incorporation degree [59], while in other cases it determines an increase [63] or a decrease [64] of the amount of embedded particles. Sometimes, a maximum can be reached at a certain temperature, as in the case of Ni–V₂O₅, at 50 °C [65].

Properties of Nanocomposite Deposits

As already mentioned, the metal-nanoparticle coatings have remarkable properties, some of them being detailed below.

Corrosion Resistance

One of the reasons of producing metal matrix composite coatings is due to their increased corrosion resistance as compared to pure metals. There are different explanations for this phenomenon. On one side, the structure of the coating becomes finer, and this grain refining improves its anticorrosion properties [5, 66]. On the other side, the particles of an inert electrically nonconducting substance dispersed in the metallic coating have a screening effect by reducing the contact area between the metal matrix and the surrounding corrosive medium. Nevertheless, other explanations could be taken into consideration, since the embedded nanoparticles fill in crevices, gaps, and micron holes on the surface of the metallic deposit giving birth to a physical barrier [67] or improving self-passivation of substrates by providing better barrier properties at localized defects [68].

Microhardness

The microhardness of coatings is beneficially influenced by the presence of nanoparticles exhibiting good mechanical properties such as SiC, ZrO₂, TiO₂, etc. Generally, metal matrix composite coatings possess higher hardness than pure metal coatings, due to finer-grained structure and to disperse particles which may obstruct the easy movement dislocations [67]. The dispersive strengthening effect becomes stronger with increase in particle loading, as reported by various investigators [69]. However, sometimes the microhardness reaches a constant value at a certain particle concentration in the plating bath [70] due to agglomeration of the particles in the coating and to the loss of any dispersion hardening effect due to their large size. It should be also mentioned that in the case of soft particles such as MoS₂, C, etc., a decrease of microhardness takes place, instead of an increase, as in the case of abrasive particles [71].

Wear Resistance

Wear is related to contact between opposite surfaces. Due to mechanical interactions, the removal and deformation of material on the surface in contact take place [72]. Generally, composite coatings possess lower wear rate than pure metals. For example, a good sliding wear resistance was obtained when Ni–SiC composite coatings containing 4–5 vol.% submicron SiC particles were prepared [73]. A possible explanation of this behavior could be the fact that the embedded nanoparticles hinder the growth of the metallic grains and the plastic deformation of the metal under load [67].

Zinc-Nanoparticle Composite Coatings Obtained by Electrodeposition

Zinc has found widespread use as protective coating against corrosion for ferrous substrates. Compared to pure zinc, zinc matrix composite coatings provide better mechanical and tribologic properties, enhanced sacrificial protection to steel, and improved paint ability than the pure metal [1].

Using electrodeposition in DC or pulsed current, a whole range of nanosized particles, having diameters from 4 to 800 nm, has been successfully incorporated into zinc deposits. A survey of literature data is summarized in Table 2.

Generally, the characteristic features of metal matrix composites are encountered also in the case of Zn-nanoparticle composites. However, some particularities of the latter deserve to be presented in more details below.

Zn–TiO₂

Among the nanomaterials used for the preparation of composite zinc coatings on steel, TiO₂ is often preferred, due to the fact that it can improve corrosion and wear resistance of the coatings, in parallel with their mechanical properties [67]. Micro- or nano-TiO₂ particles can be co-deposited with Zn using a classical zinc electroplating bath containing TiO₂ particles in suspension [74, 75, 83].

As in other cases of MMCs coatings, the incorporated TiO₂ nanoparticles modify the morphology and the structure of the Zn layer by providing more nucleation sites and retarding the crystal growth. This effect depends on the particle loading in the plating bath, and an optimal concentration of TiO₂ should be used in order to obtain coatings with structures granting enhanced corrosion resistance. In the case of Zn–TiO₂ composites prepared from a chloride-based electrolyte, the optimal nanoparticle loading was 5 g/l [22]. If the TiO₂ concentration in the plating bath increases, the interactions between the particles become more intense, and, due to their high surface energy, the nanoparticles showed a pronounced tendency to form conglomerates, leading to nonuniform deposits.

Table 2 Zn-nanoparticle coatings obtained by electrodeposition

Plating bath	Particle characteristics	Particle loading	Current density/temperature	References
350 g/l ZnSO ₄ , + 30 g/l (NH ₄) ₂ SO ₄ pH4	TiO ₂ anatase, 6 nm	0–200 g/l	4–20 A/dm ² 45 °C	[74]
350 g/l ZnSO ₄ , 7 H ₂ O + 26.4 g/l (NH ₄) ₂ SO ₄ , pH4	TiO ₂ aerogel-specific area 305 m ² /g	20 g/l	100 mA/cm ² 25 °C	[75]
0.6 M ZnSO ₄ , 7 H ₂ O + 0.1 M (NH ₄) ₂ SO ₄ , CTAB 1 mM, pH2–4	TiO ₂ Degussa P25, 25 nm	0.1 M	Pulse crt. density – 125 mA/cm ² ; on-time 4 ms off-time 40 ms	[60]
200 g/l ZnSO ₄ + 80 g/l Na ₂ SO ₄ + 40 g/l NaCl + 16 g/l H ₃ BO ₃ , + 2 g/l CTAB	TiO ₂ 100–200 nm	5 g/l	3.5 A/dm ² 27 °C	[67]
240 g/l ZnSO ₄ , 7 H ₂ O + 40 g/l Na ₂ SO ₄ , 6H ₂ O + 10 g/l H ₃ BO ₃ + (NH ₄)VO ₃ + 0.5 g/l CTAB (pH3.5)	V ₂ O ₅	1 g/l	4 A/dm ² 25 °C	[24]
75 g/l ZnCl ₂ , 230 g/l KCl, 20 g/L H ₃ BO ₃ , + brightening agents (pH5.9)	TiO ₂ Degussa (21 nm, rutile-anatase); Alfa Aesar (32 nm, anatase)	3, 5 and 10 g/l	i = 20 mA cm ² 25 ± 2 °C	[22]
1.4 M ZnSO ₄ + 0.53 M Na ₂ SO ₄ + 2.81 mM Sn ²⁺ (pH2)	SiO ₂ , Nissan 50 nm	0.3 g/l	3,000 A/m ² 50 °C	[76]
250 g/l ZnSO ₄ , 7 H ₂ O + 80 g/l Na ₂ SO ₄ + N,N-dimethyl-dodecylamine (pH2–2.5)	SiO ₂ Alfa Aesar 20–2,000 nm		1–30 A/dm ² 50 °C	[19]
200 g/l ZnSO ₄ , + 50 g/l Na ₂ SO ₄ + 40 g/l NaCl + 1.5 g/l CTAB (pH2–2.5)	C black 5–10 nm	2 g/l	3.5 A/dm ² 27 °C	[77]
200 g/l ZnSO ₄ , 6 H ₂ O + 80 g/l Na ₂ SO ₄ + 40 g/l NaCl + 4 g/l CTAB (pH3)	CNTs multiwalled 10–15 μm	1 g/l	4 A/dm ² 35 °C	[78]
180 g/l ZnSO ₄ , 7 H ₂ O + 30 g/l Na ₂ SO ₄ + 10 g/l NaCl + 0.5 mM CTAB (pH2.5)	CeO ₂ Sigma-Aldrich <25 nm	0.5–2.5 g/l	4 A/dm ² 25 °C	[79]

150 g/l ZnSO ₄ , 7 H ₂ O + 20 g/l Na ₂ SO ₄ + 20 g/l H ₃ BO ₃ + 0.5 g/l SDS (pH3.5)	ZnO 280 nm	0.5–5 g/l	4 A/dm ² 25 °C	[69]
201.3 g/l ZnSO ₄ , 7 H ₂ O + 35.2 g/l Na ₂ SO ₄ + 15.7 g/l NaCl + 0.5–6 g/l gelatin (pH3–5)	Yttria-stabilized zirconia surface area 7 m ² /g	2–15 g/l	20 mA/cm ² room temperature	[70]
75 g/l ZnCl ₂ , 230 g/l KCl, 20 g/l H ₃ BO ₃ , + brightening agents (pH5.9)	TiO ₂ (Degussa 99.5 % 21 nm, rutile-anatase); CeO ₂ Sigma-Aldrich, <25 nm); TiO ₂ /CeO ₂ binary oxide (80:20)	1.25 g/L	20 mA/cm ² 21 ± 2 °C	[66]
57 g/l ZnSO ₄ , 7 H ₂ O + 40.6 g/l NaCl + 39 g/l citric acid + 0.08 g/l benzalacetone + 2 g/l gelatin (pH4.5)	Mica 1–15 µm; SiO ₂ flakes 10–50 µm	50 g/l	2.25–2.5 A/dm ²	[81]
1.5 M ZnSO ₄ + 0.5 M H ₃ BO ₃ + 0.05 M Al ₂ (SO ₄) ₃ cetylpyridinium chloride (pH3)	Polystyrene 80 µm		50–100 A/dm ² 45 °C	[82]
ZnCl ₂ , 50 g/l; H ₃ BO ₃ , 20 g/l; Al(SO ₄) ₃ 0–100 g/l; KNO ₃ 0–0.1 g/l	Al(OH) ₃		0.4–14 A/dm ² 25–50 °C	[39]
ZnSO ₄ · 7H ₂ O 125 g/l; (NH ₄) ₂ SO ₄ 5–25 g/l; CrK(SO ₄) ₂ · 12H ₂ O 0.5–3 g/l; KNO ₃ 0.05–0.75 g/l	Cr(OH) ₃		10 A/dm ² 40–60 °C	

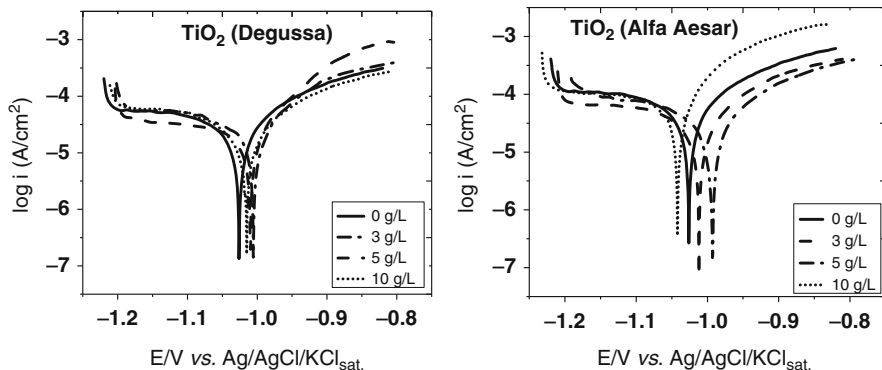


Fig. 1 Polarization curves recorded after 1 h immersion in 0.2 g/l $(\text{NH}_4)_2\text{SO}_4$ (pH3) on pure zinc deposit and on the composite coatings: (a) Zn-TiO₂ (Degussa); (b) Zn-TiO₂ (Alfa Aesar) recorded [22]

Even if the incorporation degree of nanosized TiO₂ in electrodeposited zinc is small, the nanoparticles confer an enhanced resistance against corrosion [80] acting as uniform passive sites that diminish the corrosion propensity of the coating. The polarization curves of pure zinc and Zn-TiO₂ coatings immersed in Na₂SO₄ (pH3) corrosive media (Fig. 1) indicate clearly that the Zn-TiO₂ coatings are less active than pure zinc. i_{corr} is minimal, and R_p is maximal at 5 g/l TiO₂, suggesting once again the existence of an optimal TiO₂ concentration. Due to the existence of defects, dislocations, or chemical heterogeneities generated in the metallic coating by the incorporated particles at higher concentrations, an acceleration of the corrosion process takes place.

The corrosion behavior of the composite layers is influenced by the particles origin and concentration and by the presence of additives in the plating bath.

The origin of the particles and their crystalline structure are of great importance. It was demonstrated that same concentrations of TiO₂ nanoparticles having various crystalline structures and origins introduced in the plating bath produce composites with different properties. Thus, the polarization curves of the composite Zn-TiO₂ coatings (Fig. 1) and the kinetic parameters estimated during their corrosion process were different when two different TiO₂ nanopowders (Degussa, Alfa Aesar) were used in the plating bath [22]. This was attributed to the different crystalline structure of TiO₂ (TiO₂ Degussa is a mixture of anatase-rutile, while TiO₂ Alfa Aesar consists only of anatase). It is also possible that the different surface properties of the nanoparticles (charge, hydrophobicity, previous treatments, etc.) play a role in their incorporation mechanism and may influence the corrosion resistance of the resulting coatings. The lowest corrosion current density corresponds, as expected, to the optimal concentration of TiO₂ detected from SEM-EDX analysis of the deposits.

The additives used in composite electrodeposition should be carefully selected. It was reported that the presence of benzyl triethanol ammonium ethoxylate [84] and CTAB [67] in a ZnSO₄-based plating bath led to a decrease in the metallic grain dimensions. Inorganic additives, such as NH₄NO₃ added in a ZnSO₄-based plating

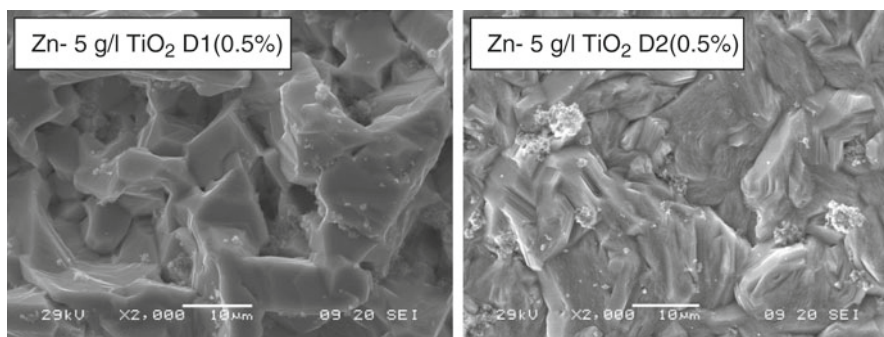


Fig. 2 SEM micrographs of Zn–TiO₂ films prepared with 5 g/l TiO₂ (Degussa P25) from a ZnCl₂-based electrolyte with dispersants (D1, D2, Coatex, France) [94]

bath, increase significantly the uptake and average size of the TiO₂ aggregates in a Zn film deposited on steel [74]. Apparently, TiO₂ particles were incorporated into the holes generated by the NH₄NO₃ addition.

In order to improve the stability of the suspensions used for the electrodeposition, different dispersants can be added to the electrodeposition bath. They influence also the deposit quality, in terms of morphology and structure, and may favor the TiO₂ incorporation. The SEM micrographs of two Zn–TiO₂ coatings obtained with different polymeric dispersants (Fig. 2) show the different morphologies and repartitions of TiO₂ nanoparticles inside these.

Zn–SiO₂

Zinc composite electrodeposits with SiO₂ are known to show good corrosion resistance and paint ability [76]. Due to the fact that SiO₂ is hydrophilic, to enhance its incorporation degree, it is strongly recommended to modify the particle surface properties. One suggested way is to exploit the interaction between cationic head groups of a surfactant and silanol groups [55, 86]. The modification of SiO₂ particles surface with functional groups that can strongly interact with zinc (e.g., SiO₂–SH, dithiooxamide, or cysteamine) led to better incorporation silica into the metal matrix [45]. Contrarily, other modifications of the silica particles (e.g., SiO₂–NH₃⁺, SiO₂–Cl, and *N,N*-dimethyldodecylamine) didn't lead to their incorporation, but to adsorption and entrapment only.

Mesoporous silica particles can be loaded with corrosion inhibitors, by encapsulation [85], and then could be incorporated in a zinc matrix. When the composite zinc coating is exposed to a corrosive medium, the particles are released to the steel surface, which plays the role of cathode. There, the cathodic polarization would produce a pH change to alkaline values, which determines the release of the stored inhibitor. The thickness of the outer silica shell can be adjusted in order to control the delay time for the inhibitor release. This approach is very promising for the preparation of self-repairing material systems.

The SiO₂ contents in the composite coatings increase with nanoparticle concentration in the bath; however, a too high concentration (>100 g/l) reduces bath stability, causes agglomeration of the particles, and diminishes the service life of the plating bath [19].

Zn-PTFE

Zinc composite coatings containing PTFE can be also prepared by electrodeposition and were largely studied because of their very useful properties such as wear resistance, self-lubrication, etc.

Previously electroplated composite Zn-PTFE coating was obtained, both in alkaline [87] and low acidic [88] zinc bath with high operation reliability and low operation costs.

In alkaline baths containing 125 g/l NaOH, PTFE particles were dispersed uniformly and deposited along with Zn at 3 A/dm² [87]. PTFE particles embedded in the composite coatings determined increased lubrication properties to Zn coatings offering possibilities to surface protection against erosion and abrasion.

In low acidic baths, the most suitable current density was identified within the range of 1.5–2 A.dm⁻²; the time of electroplating should not exceed 20 min, and the pH should range between 4.8 and 5.5 [88]. A coating with homogenous distribution of PTFE particles of high concentrations was deposited at the temperature of 21.5 °C, electroplating process duration 10 min, current density 1.5 A.dm⁻², and bath pH value 5.51.

Zn-ZrO₂

Zirconium oxides are resistant to wear, corrosion, and heat, being in the same time biocompatible and adherent to metallic surfaces [89]. Common routes to prepare ZrO₂ coatings with improved mechanical properties for anticorrosion purposes are chemical vapor deposition, electrophoretic deposition, and sol-gel deposition by dip coating technique. Zn-ZrO₂ composite coatings were successfully produced by electrodeposition from sulfate baths. During the electrodeposition process, the hydrogen evolution reaction is blocked by addition of ZrO₂ to the plating solution [69]. On the other side, ZrO₂ particles hinder the Zn²⁺ reduction. The resulting coatings present improved anticorrosive properties, higher hardness due to ZrO₂ inclusion, and changed morphology as compared to pure Zn coatings.

Zn-CeO₂

Cerium oxides and hydroxides are generally known as effective cathodic corrosion inhibitors being recommended for the protection of metals from corrosion and for improving different properties such as wear, temperature oxidation resistance,

microhardness, etc. The antioxidant and thermal barrier properties of nanocerium have been previously reported [90, 91]. Cerium compounds, either as coatings or as inhibitors, are known to hinder the cathodic corrosion reaction, thereby slowing down oxidation of substrates, by enhancing the barrier protection of the interior layers of zinc coatings [92]. Moreover, embedded CeO₂ nanoparticles diminish the grain size of metallic deposits obtained by electrodeposition by stimulating nucleation [66]. The deposits prepared from a bath containing CTAB showed higher corrosion resistance compared to those obtained without surfactant [81] as in other cases [93].

Conclusions

- (i) In the field of galvanic plating, the electrolytic entrapment of inert nanoparticles in the metallic matrix is a successful way to obtain coatings with better mechanic and anticorrosion properties than pure metal deposits. The resulting composite layers exhibit improved corrosion and wear resistance, increased hardness, superior tribologic properties, better subsequent adhesion of paintings, and increased lifetime.
- (ii) In spite of their low incorporation fraction (frequently <1 %), the embedded particles induce significant changes in the morphology and structure of the deposits. The general tendency is to induce smaller grain size and an oriented crystalline structure.
- (iii) Under identical experimental conditions, certain types of nanoparticles incorporate in higher amount and confer better corrosion protection to the coatings than other. The particle nature and dimensions could be the reasons of this behavior, but not the only ones.
- (iv) The existence of an optimal concentration of nanoparticles in the plating bath was proved in most cases and could be attributed to the existence of two contrary effects: a beneficial one (the embedded particles reduce the active surface in contact with the corrosive medium) and a harmful one (they generate dislocations and defects in the metallic matrix disturbing the nucleation and growth of the deposit, thus favoring the corrosion process).
- (v) As the co-deposition process is a complex one, involving heterogeneous multicomponent systems and combining interfacial electron transfer with mass transport, a rigorous control of the experimental parameters in the plating baths is required in order to obtain coatings with desired properties.

References

1. Musiani M (2000) Electrodeposition of composites: an expanding subject in electrochemical materials science. *Electrochim Acta* 45:3397–3402
2. Rittner MN (2002) Market analysis of nanostructured materials. *Am Ceram Soc Bull* 81(3):33–36

3. Bund A, Thieming D (2007) Influence of bath composition and pH on the electrodeposition of alumina nanoparticles and copper. *J Appl Electrochem* 37:345–351
4. Wu JY et al (2006) Tribological behavior of Ti₂SnC particulate reinforced copper matrix composites. *Mater Sci Eng A* 422:266–271
5. Maurin G, Lavanant A (1995) Electrodeposition of nickel/silicon carbide composite coatings on a rotating disc electrode. *J Appl Electrochem* 25:1113–1121
6. Zhu J et al (2006) Microstructure and performance of electroformed Cu/nano-SiC composite. *Mater Des* 28:1958–1962
7. Vereecken PM et al (2000) Particle codeposition in nanocomposite films. *J Electrochem Soc* 147(7):2572–2575
8. Bin-shi X et al (2005) Electrodepositing nickel silica nano-composites coatings. *Electrochem Commun* 7:572–575
9. Szczygiel B, Kolodziej M (2005) Composite Ni/Al₂O₃ coatings and their corrosion resistance. *Electrochim Acta* 50:4188–4195
10. Chen L et al (2006) Effect of surfactant on the electrodeposition and wear resistance of Ni–Al₂O₃ composite coatings. *Mater Sci Eng* 434:319–325
11. Chen L et al (2006) Influence of pulse frequency on the microstructure and wear resistance of electrodeposited Ni–Al₂O₃ composite coatings. *Surf Coat Technol* 201:599–605
12. Nowak P et al (2000) Electrochemical investigation of the codeposition of SiC and SiO₂ particles with nickel. *J Appl Electrochem* 30:429–437
13. Tu W et al (2006) Electrocatalytic action of nano-SiO₂ with electrodeposited nickel matrix. *Mater Lett* 60:1247–1250
14. Ploof L (2008) Electroless nickel composite coatings. *Adv Mater Process* 166:36–38
15. Boskovic I et al (2006) Electrochemical behavior of an Ag/TiO₂ composite surfaces. *Electrochim Acta* 51:2793–2799
16. Banerjee S, Chakravorty D (1999) Electrical resistivity of silver–silica nanocomposites. *J Appl Phys* 85:3623–3625
17. Armelao L et al (2006) Recent trends on nanocomposites based on Cu, Ag and Au clusters: a closer look. *Coord Chem Rev* 250:1294–1314
18. Shi L et al (2006) Synthesis of bamboo-leaf-shaped ZnO nanostructures by oxidation of Zn/SiO₂ composite films deposited with radio frequency magnetron co-sputtering. *Appl Surf Sci* 252:2853–2857
19. Tuaweri TJ, Wilcox GD (2006) Behaviour of Zn–SiO₂ electrodeposition in the presence of N, N-dimethyldodecylamine. *Surf Coat Technol* 200:5921–5930
20. Sharma SC et al (1996) Drillability of zinc/graphite metal matrix composites. *NML Tech J* 38:127–131
21. Drasnar P et al (2011) The properties of electrolytically deposited composite Zn–PTFE coatings. *MM Sci J* 7:248–249
22. Vlasa A et al (2010) Electrodeposited Zn–TiO₂ nanocomposite coatings and their corrosion behavior. *J Appl Electrochem* 40(8):1519–1527
23. Hamlaoui Y et al (2010) Electrodeposition of ceria-based layers on zinc electroplated steel. *Corros Sci* 52:1020–1025
24. Bindiya S et al (2011) Electrodeposition and corrosion properties of Zn–V₂O₅ composite coatings. *J Mater Eng Perform*. doi:10.1007/s11665-011-0099-6
25. Balaji R et al (2006) Electrodeposition of bronze–PTFE composite coatings and study on their tribological characteristics. *Surf Coat Technol* 201:3205–3211
26. Rohatgi PK et al (1992) Tribological properties of metal matrix-graphite particle composites. *Int Mater Rev* 37:129–152
27. Tanaka M et al (1993) Ceramic metal-composite coated piston ring and cylinder liner of marine low speed diesel engine. *Bull MESJ* 21(2):77–85
28. Rittner MN (2000) Metal matrix composites in the 21st century: markets and opportunities. BCC, Inc., Norwalk, CT
29. Hovestad R, Janssen LJJ (1995) Electrochemical codeposition of inert particles in a metallic matrix. *J Appl Electrochem* 25:519–527

30. Keddam M et al (1994) Composite electrode for studying powdered electroactive materials – preparation and performance. *J Appl Electrochem* 24:1037–1043
31. Deguchi T et al (2000) Photocatalytically highly active nanocomposite films consisting of TiO₂ particles and ZnO whiskers formed on steel plates. *J Electrochem Soc* 147(6):2263–2267
32. Kang H-K (2005) Microstructure and electrical conductivity of high volume Al₂O₃-reinforced copper matrix composites produced by plasma spray. *Surf Coat Technol* 190:448–452
33. Tian B et al (2006) Microstructure and properties at elevated temperature of a nano-Al₂O₃ particles dispersion-strengthened copper base composite. *Mater Sci Eng A* 435–436:705–710
34. Shi Z, Yan M (1998) The preparation of Al₂O₃-Cu composite by internal oxidation. *Appl Surf Sci* 134:103–106
35. Guobin L et al (2005) Fabrication of the nanometer Al₂O₃/Cu composite by internal oxidation. *J Mater Process Technol* 170:336–340
36. Shibli SMA et al (2006) Incorporation of TiO₂ in hot dip zinc coating for efficient resistance to biogrowth. *Surf Coat Technol* 200:4791–4796
37. Battaglin G et al (2004) RF magnetron co-sputtering deposition of Cu-based nanocomposite silica films for optical applications. *Appl Surf Sci* 226:52–56
38. Low CTJ et al (2006) Electrodeposition of composite coatings containing nanoparticles in a metal deposit. *Surf Coat Technol* 201:371–383
39. Fontenay F et al (2001) Electroplating and characterization of zinc composite coatings. *Galvanotechnik* 92:928–939
40. Chandrasekar MS, Pushpavanam M (2008) Pulse and pulse reverse plating- Conceptual, advantages and applications. *Electrochim Acta* 53:3313–3322
41. Wang W et al (2005) Fabrication and characterization of Ni-ZrO₂ composite nano-coatings by pulse electrodeposition. *Scr Mater* 53:613–618
42. Franssaer JP et al (2002) Aluminium composite coatings containing micrometre and nanometre-sized particles electroplated from a non-aqueous electrolyte. *J Appl Electrochem* 32:123–128
43. Wang SC, Wei WC-J (2003) Kinetics of electroplating process of nano-sized ceramic particle/Ni composite. *Mater Chem Phys* 78:574–580
44. Franssaer J et al (1992) Analysis of the electrolytic codeposition of non-brownian particles with metals. *J Electrochem Soc* 139:413–425
45. Khan TR et al (2011) Electrodeposition of zinc silica composite coatings: challenges in incorporation of functionalized silica particles within the zinc metal matrix. *Sci Technol Adv Mater* 12:055005
46. Celis JP et al (1987) A mathematical model for the electrolytic codeposition of particles with a metallic matrix. *J Electrochem Soc* 134(6):1402–1408
47. Shao I et al (2002) Kinetics of particle codeposition of nanocomposites. *J Electrochem Soc* 149:C610–C614
48. Guglielmi N (1972) Kinetics of the deposition inert particles from electrolytic baths. *J Electrochem Soc* 119:1009–1012
49. Bercot P et al (2002) Electrolyte composite Ni-PTFE coatings: an adaptation of Guglielmi's model of the phenomena of incorporation. *Surf Coat Technol* 157:282–289
50. Roos JR et al (1990) The development of composite plating for advanced materials. *J Met* 42:60–63
51. Popov KI et al (2002) *Fundamental aspects of electrometallurgy*. Kluwer Academic Publishers, New York
52. Lee CC, Wan CC (1988) A study of the composite electrodeposition of copper with alumina powder. *J Electrochem Soc* 135:1930–1933
53. Stojak JL et al (2001) Review of electrocodeposition. In (Alkire RC and Kolb DM (eds). *Adv Electrochem Sci Eng* 7:193–222
54. Hovestad A, Janssen LJJ (2005) Electroplating of metal matrix composites by codeposition of suspended particles. In: Conway BE (ed) *Modern aspects of electrochemistry*, vol 38. Kluwer Academic/Plenum Publishers, New York
55. Franssaer J, Celis JP (2001) New insights into the mechanism of composite plating. *Galvanotechnik* 92:1544–1550

56. Mureşan LM, Varvara SC (2005) Leveling and brightening mechanisms in metal electrodeposition. In: Nunez M (ed) Metal electrodeposition. Novascience Publishers, New York. ISBN 1-59454-330-5
57. Gerr M-D (2004) Electrochemical deposition of nickel/SiC composites in the presence of surfactants. *Mater Chem Phys* 87:67–74
58. Tomaszewski TW et al (1969) Codeposition of finely dispersed particles with metal. *Plating* 56:1234–1239
59. Sautter FK (1963) Electrodeposition of dispersion hardened nickel Al₂O₃ alloys. *J Electrochem Soc* 110:557–560
60. Gomes A et al (2005) Zn–TiO₂ composite films prepared by pulsed electrodeposition. *J Solid State Electrochem* 9:190–196
61. Raeissi K et al (2003) Effect of nucleation mode on the morphology and texture of electrodeposited zinc. *J Appl Electrochem* 33:635–642
62. Celis JP, Roos JR (1977) Kinetics of the deposition of alumina particles from copper sulfate plating baths. *J Electrochem Soc* 124:1508–1511
63. Narayan R, Narayana BH (1981) Electrodeposited composite metal coatings. *J Electrochem Soc* 128:1704–1708
64. Narayan R, Chattopadhyay S (1982) Electrodeposited Cr–Al₂O₃ composite coatings. *Surf Technol* 16:227–234
65. Ramesh Babu GNK, Mohammed Yusuf M (1993) Electrodeposition of nickel-vanadium pentoxide composite and its corrosion behaviour. *Mater Chem Phys* 36:134–138
66. Nemeş PI et al (2013) Initial corrosion behavior of composite coatings obtained by co-electrodeposition of zinc with nanoparticles of Ti and Ce oxides. *J Solid State Electrochem* 17:511–518
67. Praveen BM, Venkatesha TV (2008) Electrodeposition and properties of Zn-nanosized TiO₂ composite coatings. *Appl Surf Sci* 254:2418–2424
68. Montemor et al (2008) The synergistic combination of bis-silane and CeO₂/ZrO₂ nanoparticles on the electrochemical behaviour of galvanised steel in NaCl solutions. *Electrochim Acta* 53:5913–5922
69. Vathsala K, Venkatesha TV (2011) Zn–ZrO₂ nanocomposite coatings: electrodeposition and evaluation of corrosion resistance. *Appl Surf Sci* 257:8929–8936
70. Xia X et al (2009) Electrodeposition of zinc and composite zinc-yttria stabilized zirconia coatings. *J Mater Process Technol* 209:2632–2640
71. Stankovic VD, Gojo M (1996) Electrodeposited composite coatings of copper with inert, semiconductive and conductive particles. *Surf Coat Technol* 81:225–232
72. Rabinowicz E (1995) Friction and wear of materials. Wiley, New York
73. Garcia I et al (2001) Electrodeposition and sliding wear resistance of nickel composite coatings containing micron and submicron SiC particles. *Surf Coat Technol* 148:171–178
74. Deguchi T et al (2001) Rapid electroplating of photocatalytically highly active TiO₂-Zn nanocomposite films on steel. *J Mater Sci* 36:4723–4729
75. Muresan L et al (2007) Corrosion behavior of electrochemically deposited Zn–TiO₂ nanocomposite coatings. *Studia Universitatis Babeş-Bolyai Chemia LII*:97–104
76. Kondo K et al (2000) Electrodeposition of zinc-SiO₂ composite. *J Electrochem Soc* 147:2611–2613
77. Praveen BM, Venkatesha TV (2009) Generation and corrosion behavior of Zn-nano sized carbon black composite coating. *Int J Electrochem Sci* 4:258–266
78. Praveen BM et al (2007) Corrosion studies of carbon nanotubes-Zn composite coating. *K Surf Coat Technol* 201:5836–5842
79. Ranganatha S et al (2012) Electrochemical studies on Zn/nano-CeO₂ electrodeposited composite coatings. *Surf Coat Technol* 208:64–72
80. Fustes J et al (2008) Electrodeposition of Zn–TiO₂ nanocomposite films-effect of bath composition. *J Solid State Electrochem* 12:1435–1443
81. Azizi M et al (2005) Electrolytic co-deposition of silicate and mica particles with zinc. *J Solid State Electrochem* 9:429–437

82. Hovestad A et al (1999) Electrochemical deposition of zinc-polystyrene composites in the presence of surfactants. *J Appl Electrochem* 29:331–338
83. Praveen BM et al (2007) Corrosion behavior of Zn–TiO₂ composite coating. *Synth React in Inorg Metal-Organic and Nano-Metal Chem* 37:461–465
84. Abdel Hamid Z (2001) Thermodynamic parameters of electrodeposition of Zn–Co–TiO₂ composite coatings. *Anti-Corros Methods Mater* 48:235–241
85. Stempniewicz M, Rohwerder M, Marlow F (2007) Release from silica SBA-3-like mesoporous fibers: cross-wall transport and external diffusion barrier. *Chem Phys Chem* 8:188
86. Terzieva V et al (2000) Codeposition of hydrophilic and hydrophobic silica with copper from acid copper sulfate baths. *J Electrochem Soc* 147:198–202
87. Pazderova M et al (2010) Qualitative. Analysis of composite Zn–PTFE coatings. *MM Sci J* 11:208–209
88. Drasnar P et al (2010) Composition analysis of composite electrolytic coatings containing PTFE. *Proceedings of international conference on innovative technologies, Prague, 14–16 Sept* 619–623
89. Yen SK et al (2001) Characterization of electrolytic ZrO₂ coating on Co–Cr–Mo implant alloys of hip prosthesis. *Biomaterials* 22:125–133
90. Ivanov VK et al (2009) Antioxidant activity of nanocrystalline ceria to anthocyanins. *Russian J Inorg Chem* 54:1522–1527
91. Cao XQ, Vassen Stoeve RD (2004) Ceramic materials for thermal barrier coatings. *J Eur Ceram Soc* 24:1–10
92. Shibli SMA, Chacko F (2008) Development of nano-CeO₂-incorporated high performance hot-dip zinc coating. *Surf Coat Technol* 202:4971–4975
93. Satoshi O et al (2002) Electrodeposition of Zn–Al₂O₃ composite from non-suspended solution containing quaternary ammonium salt. *J Surf Finish Soc Japan* 53:920–925
94. Vlása A (2010) Revêtements composites obtenus par voie électrochimique. Ph.D. thesis, Babes-Bolyai University Cluj-Napoca

Paul McCloskey, Terence O'Donnell, Brice Jamieson,
Donald Gardner, Michael A. Morris, and Saibal Roy

Contents

Introduction	356
Electrodeposition	358
Magnetic Property Overview	361
State of the Art for Electroplated Soft Magnetic Alloys.....	366
Early Work on Electrodeposited Co-P	367
DC Plated Co-P	367
Pulse Reverse Plated Co-P	368
Pulse Plated Co-P	370
Electrodeposited Co-P With Higher Saturation Magnetization	371
Background	371
Experimental	372
Results and Discussion	373
Electrodeposited Co-P with Improved Temperature Stability	379
Background	379
Experimental	379
Results and Discussion.....	380
Conclusions.....	385
References.....	385

P. McCloskey (✉)
Tyndall National Institute, University College Cork, Cork, Ireland
e-mail: paul.mccloskey@tyndall.ie

T. O'Donnell
University College Dublin, Dublin, Ireland
e-mail: terence.odonnell@ucd.ie

B. Jamieson
ELIX Wireless Charging Systems, Vancouver, Canada
e-mail: brice.jamieson@gmail.com

D. Gardner
Intel Corporation, Santa Clara, USA
e-mail: d.s.gardner@intel.com

Abstract

The fabrication of multi-nanolayer structures can in some cases be achieved electrochemically if, for example, the plating current density has a significant effect on the deposit composition or if reverse plating changes the composition. Moreover, the realization of a multi-nanolayer structure can also crucially affect the properties of the material. This chapter will look at one material system in which both of the above apply, namely, amorphous Co-P.

When produced using conventional DC plating, amorphous Co-P tends to exhibit perpendicular magnetic anisotropy and hence very low permeability and somewhat high coercivity. This limits the usefulness of the material as a magnetic core for power conversion applications which require low coercivity, high saturation magnetization, high permeability, high anisotropy field, and high resistivity. Riveiro et al. used pulse reverse plating to fabricate multilayers of alternate magnetic and nonmagnetic materials. With the thickness of the magnetic layers at around 30 nm, they were able to achieve in-plane anisotropy and low coercivity 8 A m^{-1} .

This chapter will describe the early work and a selection of subsequent research on multi-nanolayers of amorphous Co-P, e.g., Perez et al., who used pulse plating, and McCloskey et al., who improved the saturation magnetization and thermal stability of the material.

Keywords

Electrochemical • High frequency soft magnetic material • Integrated inductor • Multi-nanolayer • Nanotechnology • Thermal stability Co-P

Introduction

The last 30 years have seen a revolution in the area of materials science centered around the development of solid structures with at least one dimension below 100 nm. These can be 3D materials with all dimensions below 100 nm (known as nanoparticles), 2D materials (essentially thin films), 1D materials (nanowires), and 0D materials with all dimensions below 10 nm, and often described as quantum dots [1]. It also encompasses materials which are nanostructured such as mesoporous or microporous substances that have structure arrangements of small pores [2]. The use of these materials in various fields is known as nanotechnology [3, 4], and while

M.A. Morris
University College, Cork, Ireland
e-mail: m.morris@ucc.ie

S. Roy
Tyndall National Institute, Cork, Ireland
e-mail: saibal.roy@tyndall.ie

Table 1 Summary of key nanotechnology references

Summary	Author/References
An overview of nanoparticle preparation and science	Karkare [1]
Details of nanoporous materials used as nanoparticle hosts	Hanrahane et al. [2]
Introduction to the theory of nanoscience and applications	Mansoori [3]
Basic introduction to nanotechnology and potential applications	Wilson et al. [4]
Perspective on the development of nanoscience	Lacaze [5]
Landmark paper detailing scaling development in microelectronics and Moore's Law	Moore [6]
Scaling and miniaturization in microelectronics	Roco and Gargini [7]
Roadmap for data storage requirements	Information Storage Industry Consortium [8]
Review of the emerging area of Spintronics for novel devices	Wolf et al. [9]

it is normally associated with hi-tech applications such as in the information and communications area, nanotechnology spans areas as diverse as biomedicine, transistors, and separation media. While there are many potential architects of the nanorevolution including Davy, Feynman, and Drexler [5], there is no doubt that the main driver of nanotechnology has been the microelectronics industry and the development of ultrasmall transistor devices. Scaling in the device industry (and, thus, our control of substrate features below 100 nm dimension) has been precipitated by an observation by Gordon Moore where he noted that the number of devices on a semiconductor chip doubled every 18–24 months [6]. Key references in nanotechnology are summarized in Table 1 below.

As dimensions have shrunk, miniaturization has not only been applied to silicon but also to a series of other materials including interconnects, vias, dielectrics, and photolithographic masks/resists [7]. One of the areas that have been as aggressively scaled as the silicon devices has been memory storage, which has needed to maintain commensurability because of the need to store an ever-increasing amount of information in both volatile and permanent formats [8]. Typical targets include 64 Tb storage capacities by around 2020 and magnetic feature volumes of less than 1500 nm³ (although it is worth noting that dimension cannot be wholly stripped from the fundamental magnetic properties of the materials such as coercivity).

The global market for nanomagnetic materials and devices is growing markedly with sales expected to reach \$9 billion by 2017. The data storage sector alone had sales of \$6.9 billion in 2012, but markets are rapidly developing nanomagnet-based applications in sensors, biosensors, and bioassay platforms and should reach nearly \$8.4 billion in 2017 while markets for sensors, biosensors, bioassay products, and giant magnetoresistance (GMR) readers are expected to develop quickly. Indeed, limitations in silicon technologies may precipitate the development of novel spintronic-based switches as devices [9]. Other markets for magnetic materials include soft magnetic cores, ferrofluids, catalysts, and environmental remediation products. It is worth stressing that there is no universal material for all these applications and any potential technology will be based around development of novel optimized systems that are likely to be unique for each application.

Electrodeposition

Electrodeposition can be applied to the fabrication of multi-nanolayers in which the composition is modulated. Such multilayer structures are of interest in relation to GMR [10], mechanical properties [11], and in some cases the improvement in soft magnetic properties [12, 13].

Modulation of composition can be achieved by either depositing the different components from separate electrolytes or by using voltage or current modulation to enable deposition from a single bath. A disadvantage with the former method is that it requires physical transport between electrolytes following the deposition of each layer. Whether or not it is possible to achieve composition modulation from a single bath depends on the particular properties of the electrochemical system being considered, and the circumstances in which it is possible will now be discussed.

The electrodeposition of a metal involves the reduction of metal ions in an electrolyte at a negatively charged cathode. As per Faraday's law, the amount of metal deposited is directly related to the quantity of charge transferred at the cathode and hence the current flowing. In the case of alloy plating, the amount of each component deposited will be proportional to the amount of charge transfer at the electrode, which is related to the deposition of each individual component of the alloy. Consequently, the composition of an alloy will be altered if the fraction of the overall current density related to a particular component is changed. Current flow in an electrodeposition process is driven by the voltage supplied, and hence it is necessary to consider the relationship between current and potential in an electrochemical electrode.

When a metal electrode is placed in a solution containing ions of the metal, an exchange equilibrium arises in which the number of metal atoms dissolving into the solution is equal to the number of metallic ions discharging and depositing on the electrode. As a result of this exchange, the electrode is at an equilibrium potential E relative to the solution. In order to drive the system away from equilibrium so that current can flow and metal will be deposited, the potential has to be changed to a new value $E(I)$, and the difference between these potentials is termed the "overpotential,"

$$\eta = E(I) - E \quad (1)$$

Electrodeposition always entails a number of steps, which include

- "Charge transfer," in which metal ions are neutralized and adsorbed
- "Mass transport," in which metal ions diffuse through a "stagnant" layer of electrolyte to the electrode surface
- "Incorporation," in which the adsorbed atom is incorporated into the growing lattice

The slowest step in the overall electrode reaction is rate determining. However, several of the steps can have low reaction rates and hence can contribute to the

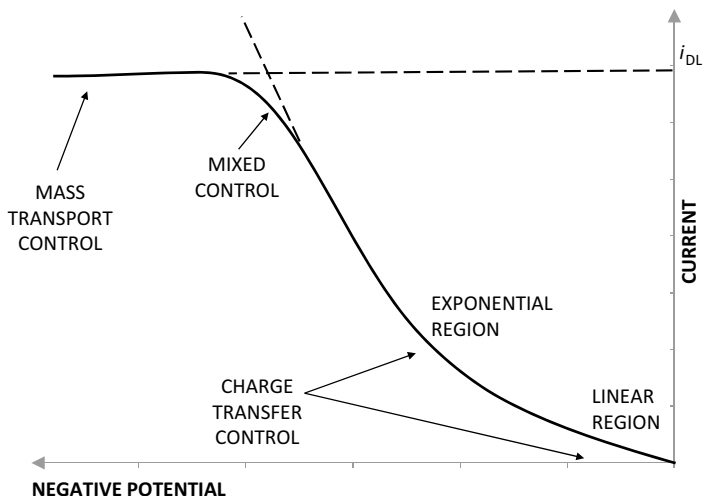


Fig. 1 Schematic of current density versus potential for electrodeposition

overall electrode reaction rate. The only stage that is directly affected by the electrode potential is charge transfer. The relationship between current density and potential for electrodeposition is illustrated schematically in Fig. 1.

It can be seen that initially potential has a strong influence on the linear and exponential regions in which the deposition is under “charge transfer” control. However, as the potential is increased further, “mass transport” begins to influence and eventually dominate the reaction rate, at which point the potential has no influence on current density. The exponential region applies to large values of overpotential, e.g., for a cathodic process, $\eta > -100$ mV [14]. By taking logarithms, this region can be represented by the linear Tafel relationship for reduction shown below:

$$\eta = a - b \log |i| \quad (2)$$

The effect of changing the overpotential on the composition of an alloy can be understood by considering the Tafel plots for a two-component alloy x-y shown in Fig. 2.

The logarithm of the ratio of the current densities for each component is a measure of the alloy composition, and for an overpotential η , this is given by

$$\ln(i_x / i_y) = \ln(i_x) - \ln(i_y) \quad (3)$$

with

$$\ln(i_x) = a_x + b_x \eta \quad (4)$$

and

$$\ln(i_y) = a_y + b_y \eta \quad (5)$$

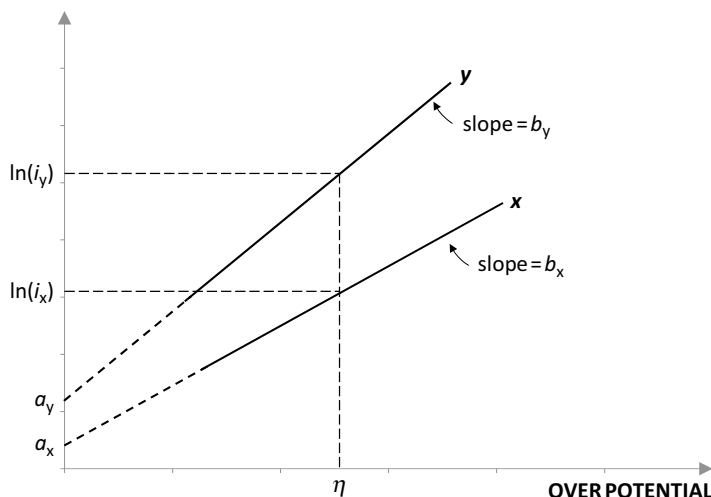


Fig. 2 Schematic Tafel plots for deposition of alloy x-y

Hence, substituting into Eq. 3, we obtain

$$\ln(i_x / i_y) = (b_x - b_y)\eta + a_x - a_y \quad (6)$$

It can be seen from Eq. 6 that the composition of the alloy will be unchanged by changes in overpotential (η) if the Tafel slopes of each component are identical ($b_x = b_y$).

The above argument applies to a situation in which the reaction rate for both components is under charge transfer control. However, if one of the components is under mass transfer control, then changing the value of overpotential will change the composition. Formulating the electrolyte to contain a low concentration of a more noble metal and a high concentration of a less noble metal can create this situation. Ions of the more noble metal will be quickly depleted at the cathode, and consequently its deposition will be under mass transport control. Composition modulation is achieved by varying the overpotential between a value at which only the more noble metal deposits and a value in which both metals deposit with the less noble metal being deposited under charge transfer control. The layers thus produced will alternate between pure noble metal and a low concentration of noble metal. This approach has been applied to the fabrication of multilayers of Cu-Ni [15], Ni-Fe-Cu/Cu [16], and Co/Cu [17].

An implicit assumption in the use of Tafel plots to determine the effect of overpotential on alloy composition is that the deposition of one component is unaffected by the presence of other alloy components. Often this is not the case, a situation described by Landolt [18] as “charge transfer coupled,” i.e., the partial currents are not independent of each other. Landolt [18] further categorized such systems as either “inhibited codeposition” or “catalyzed codeposition.”

One of the situations in which this arises is the electrodeposition of amorphous alloys based on iron group metals (Fe, Co, Ni). Amorphous alloys of these metals

can be produced by the codeposition of P or B. In aqueous solution, P and B cannot be deposited alone but can readily be deposited in the presence of iron group metals, a phenomenon usually termed “induced codeposition.” The overpotential does often seem to affect the composition, as many studies have indicated a tendency for the deposited alloy to become more rich in the iron group metal as the current density is increased; e.g., this was the case for Ni-P, Co-P and Ni-Co-P [19], Co-P [13], and high phosphorous bath content Ni-P [20]. Perez et al. [13] used this dependency of composition on current density to produce modulated Co-P films with alternate high and low P contents.

Pulse reverse plating involves reversing the polarity of the cathode and anode during part of the plating cycle. During the “reverse” period, material previously deposited will dissolve back into solution. In the case of an alloy, pulse reverse plating can be used to produce composition modulation if one of the alloy components has a greater tendency to dissolve than other components. This is the case for Co-P plating as the Co tends to dissolve more quickly than P during current reversal. Riveiro and Riveiro [12] used this effect to produce nanolayered deposits.

Magnetic Property Overview

Fundamentally, magnetism is defined by both the spin and orbital momentum of electrons, and since most solid materials contain many electrons within an effectively continuous band structure, permanent magnetism is actually rather rare [21, 22]. However, all bulk or molecular materials can be magnetically categorized according to a limited number of forms. These are summarized in Fig. 3.

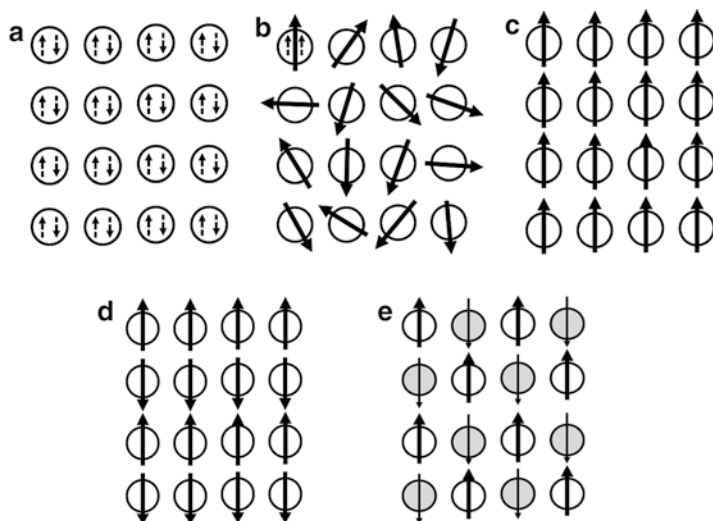


Fig. 3 Types of magnetism illustrated schematically. Electrons spins are indicated as dashed arrows and magnetic moment of individual atoms as a large arrow

Diamagnetism (Fig. 3a) is exhibited in materials where all of the electrons are paired and the total magnetic moment is essentially zero (at all temperatures above 0 K). Paramagnetic materials contain atoms, molecules, or ions that have unpaired electrons, but within the solid and in the absence of a magnetic field, these individual entities behave independently and show no tendency for the magnetic moments to align (Fig. 3b). In an applied field, a net magnetic moment will develop because of field-imposed alignment. In a few special cases, alignment of the individual magnetic moments spontaneously occurs, and a ferromagnet results (Fig. 3c). In iron, e.g., this occurs because the band structure is such that spatial minimization of electron–electron repulsions is more significant than the energy decrease defined by electron pairing. In the vast majority of examples, neighboring atoms/molecules containing unpaired electrons will antiferromagnetically align (maximizing attractive north–south low-energy arrangements, minimizing the repulsive arrangements). These are called antiferromagnets and have close to zero magnetic moment (Fig. 3d). A few special cases exist where even though the system is antiferromagnetically arranged, because of the presence of heteroatoms of differing magnetic moment, the total magnetic moment is nonzero, and these materials are called ferrimagnetic (Fig. 3e).

In Fig. 3e, heteroatoms are shown as filled circles, and these carry a smaller net moment indicated by the thinner arrow.

Bulk ferromagnets and ferrimagnets are characterized by strong magnetic moments below a critical temperature known as the Curie temperature for ferromagnets and the Néel temperature for ferrimagnets. Above these temperatures, the materials are paramagnetic because of thermal randomization of electron spins.

When a ferromagnetic material is placed in a magnetic field, H (the magnetizing field), an extra field is induced within the magnetic material as the unpaired electrons in the material align in response to H . This field, B , is referred to as the magnetic induction or, more commonly, the magnetic flux density and arises from the properties of the material itself. In SI units, the relationship between these fields is usually expressed as

$$B = \mu_0 (H + M) \quad (7)$$

where $\mu_0 = 4\pi \times 10^{-7} \text{ H m}^{-1}$, B is in teslas, H and M are both in A m^{-1} , and B , H , and M are all vector quantities.

This expression shows that the B field induced in the material is proportional to the sum of the magnetizing field H and a magnetization, M , arising from the material itself. The constant of proportionality is the permeability of free space.

Alternatively, the B field is often expressed in a direct relationship to the magnetizing field H as

$$B = \mu_0 \mu_r H \quad (8)$$

where μ_r is the relative permeability, a value representing the strength of the response of a magnetic material to an applied field. Materials with a higher permeability will respond more strongly to a given field than materials with a low permeability.

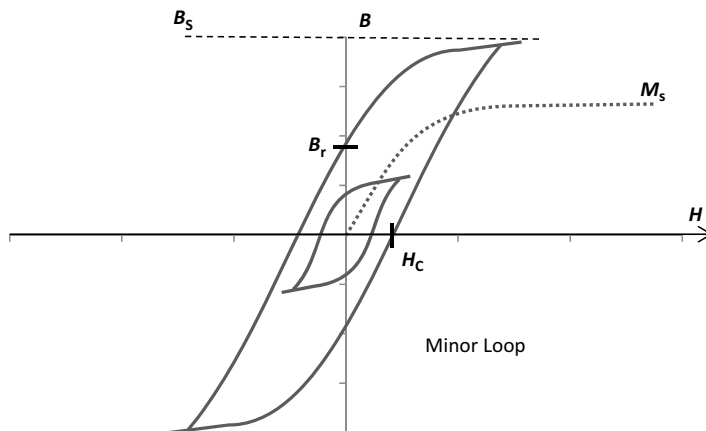


Fig. 4 Typical B - H curve for a ferromagnetic material

In general, the relationship between B and H in a ferromagnetic material is highly nonlinear and hysteretic, taking the form of a B - H curve. A typical example of such a curve is shown in Fig. 4. Moreover, the exact value of B arising within a magnetic material from application of an H field is dependent on the previous history of magnetization of the material.

The magnetization curve for any material is typically characterized in terms of the parameters shown in the figure, i.e., the saturation flux density, B_s , the remnant flux density, B_r , and the coercivity, H_c . In soft magnetic materials, the slope of the B - H curve, i.e., the permeability, can be an important consideration. A specific application of magnetic materials might demand B - H curves of a specific shape, and therefore material development efforts usually focus tailoring the shape of the B - H curve using different alloy compositions, production, or processing techniques. In order to appreciate the cobalt phosphorus material development described later in this chapter, it is important to explain some of the underlying processes which give rise to the shape of the B - H curve.

The magnetization curve of ferromagnetic materials is understood in terms of the “molecular field” theory advanced by Pierre Weiss in 1906 [23]. Weiss postulated that a ferromagnet in an unmagnetized state is spontaneously divided into a number of small regions called “domains.” Each domain is spontaneously magnetized to the saturation value M_s , but the directions of magnetization of the domains are all different such that in a large collection they cancel and the sample has no overall magnetization. Consequently, the process of magnetization may be understood as changing the specimen from a situation in which there are many misaligned domains to a situation where all the domains are aligned with the direction of the external applied magnetic field H . At this point, the sample has reached its saturation value, M_s or B_s .

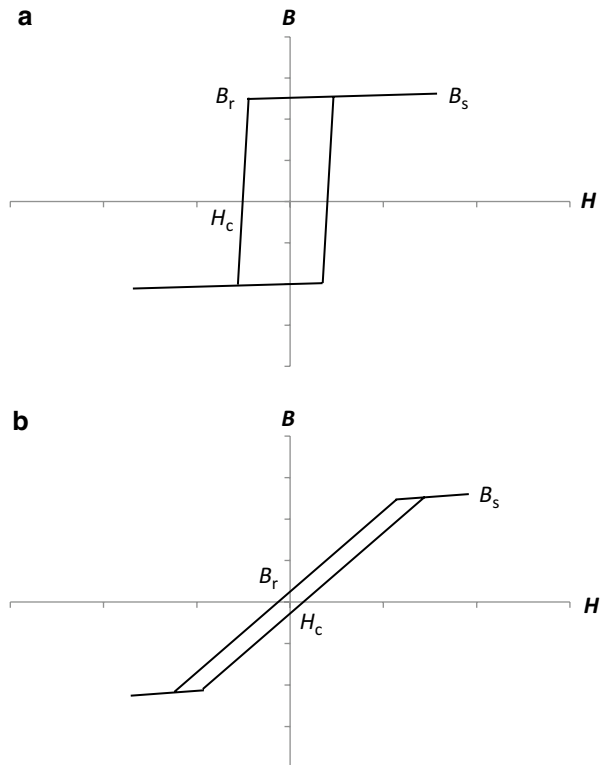
This transformation from misaligned domains to fully aligned domains takes place by two mechanisms, namely, domain wall motion and domain rotation.

Domain wall motion allows domains that are favorably aligned with the external field to grow in size. This process can involve both reversible and irreversible steps. Domain walls can be pinned or impeded from moving by nonmagnetic inclusions in the materials. When a domain wall becomes unpinned, it advances in a sudden step known as a “Barkhausen jump.” Such events are irreversible and are a cause of hysteresis and consequently energy loss. Nevertheless, domain wall motion typically requires less energy than domain rotation and so tends to dominate the magnetization process at low fields where the magnetization curve has the steepest slope; i.e., a small change in field produces a large change in magnetization. At higher fields, the slope of the magnetization curve is reduced (and hence a relatively large change in field is required to produce a small change in M). This is generally the point at which there are few favorably aligned domains left to grow in size and so further magnetization takes place by domain rotation where the magnetization of unaligned domains rotates to align with the magnetic field.

Magnetic materials may be anisotropic, in which there is an easy-axis direction in which it is “easy” to magnetize the material and a hard-axis direction in which it is “hard” to magnetize – see Fig. 5 for schematic B-H loops of an anisotropic material.

The direction and strength of the anisotropy will be determined by various contributions to anisotropy which can arise from a number of sources, namely, the

Fig. 5 Schematic B-H loops of anisotropic material, (a) Easy axis, (b) Hard axis



magnetocrystalline anisotropy, the magnetoelastic anisotropy, the shape anisotropy, and the induced anisotropy. Of these, only the magnetocrystalline anisotropy is intrinsic to the material. It acts as a force that tends to hold the magnetization in certain equivalent crystallographic directions and is mainly due to spin-orbit interactions [24]. The magnetoelastic anisotropy results from stress in the film. Shape anisotropy arises from the fact that for a nonspherical open magnetic circuit specimen, a demagnetizing field will arise from induced magnetic poles at the surfaces of the sample, the strength of which is inversely proportional to the length of the axis. On the shortest axis of a sample, the demagnetizing factor is the strongest. Thus, shape anisotropy will favor the formation of an easy axis along the longest axis of a material sample and will generally force the easy axis to lie in the plane of a thin film as opposed to perpendicular to the film. In the plane of a finite film as well, the shape anisotropy will push the easy axis to lie along the longest possible axis.

The easy axis is the direction in which the material can be brought to saturation with the lowest applied field, which also implies that the slope of the B - H (and hence the relative permeability) is highest in this direction as can be seen illustrated in Fig. 5a. Conversely, as shown in Fig. 5b, the permeability would be expected to be lowest in the hard-axis direction.

As previously mentioned, domain wall movement entails energy loss through irreversible Barkhausen jumps. In addition, such jumps dissipate energy due to the formation of microscopic eddy currents in the region of the domain wall. As a result, magnetization through domain wall movement tends to be effective only up to moderate frequencies, e.g., 10–100 kHz [25], and indeed permeability in the easy axis typically decreases rapidly with frequency.

In contrast, magnetization through rotation, especially if domains are oriented perpendicular to the applied field, occurs gradually and uniformly throughout the material and can be almost lossless. As a result, although the permeability in the hard axis is lower, it remains more stable with frequency. This is the primary reason why anisotropy is often deliberately induced in the magnetic core of magnetic devices designed for high-frequency operation.

It should be pointed out that for conductive magnetic materials, used in the hard axis, there will still be macroscopic eddy currents induced by the flux changes, as would be expected from any conductor experiencing a time-changing magnetic field. Such macroscopic eddy current loss is a major loss mechanism in magnetic materials at high frequencies and provides the main motivation for the development of higher-resistivity materials.

As mentioned above, shape anisotropy would generally dictate that for thin films the easy axis would lie in the plane of the film. However, in some materials, with, for example, strong crystal anisotropies, it may be energetically favorable for the easy axis to lie perpendicular to the plane of the film. Such films are said to have perpendicular anisotropy, which can lead to the formation of “stripe domains,” which consist of alternate antiparallel domains, leading to poor in-plane soft magnetic properties, i.e., very low permeability and the requirement for high external fields ($>800 \text{ A m}^{-1}$) to reach saturation [26].

The above describes the magnetic properties largely in terms of the macroscopic perspective of magnetic domain interaction. However, when dealing with materials on the nanoscale, it is also necessary to realize that the fundamental magnetic properties of a material can change dramatically with dimension. Since magnetic properties derive from correlated movements of electronic charge, changes in electronic band structure, crystallography, the contribution of surface states and morphological variation can cause dramatic changes in magnetism with dimension.

For example, groundbreaking work by Louise Néel [27] led to the identification of a new form of magnetization (superparamagnetism) which appears when the size of the particles is such that a single domain exists in the whole solid [28]. Effectively, this is at particle dimensions of less than 50 nm dependent on the material. Usually, nanoparticles have a preferred direction for magnetic alignment (called uniaxial anisotropy); however, the magnetic alignment direction will periodically “flip” or rotate due to thermal motion. When the particles are flipping rapidly, within a real time, the net magnetic moment of the nanoparticle is effectively zero. This is said to be the superparamagnetic state. In this state, an external magnetic field is able to “magnetize” the nanoparticles via spin rotation similar to the magnetization of a collection of paramagnetic molecules. However, their magnetic susceptibility is much larger than a conventional paramagnet.

State of the Art for Electroplated Soft Magnetic Alloys

There has been a significant level of research interest, mainly driven by the demand in various microelectronic applications, in developing high-performance soft magnetic alloys that exhibit good properties, i.e., the coercivity (H_c) should be minimized, especially in the hard axis, the saturation flux density (B_s) should be maximized, as should resistivity (ρ) so as to minimize eddy current loss.

One of the first significant developments in this area introduced by IBM in 1979 [29, 30] was the electrodeposition of permalloy ($\text{Ni}_{81}\text{Fe}_{19}$) ($B_s = 1.0$ T, $\rho = 2.8 \times 10^{-7}$ Ωm and $H_c = 72$ Am^{-1}), for application as the core material of a thin-film inductive head to increase magnetic recording density. The introduction of magnetoresistive read head by IBM in 1991 resulted in the need of high-speed writing head with a very narrow writing track width and the capability of recording in a highly coercive recording media to achieve a higher density of recording. This has led to the advent of newer permalloy compositions such $\text{Ni}_{45}\text{Fe}_{55}$ [31, 32] with better soft magnetic properties ($B_s = 1.4$ – 1.6 T, $\rho = 4.0$ – 4.5×10^{-7} Ωm and $HC = 103$ Am^{-1}). However, $\text{Ni}_{45}\text{Fe}_{55}$ films were particularly sensitive to residual stresses, whereas $\text{Ni}_{80}\text{Fe}_{20}$ films were not, due to its ultralow magnetostriction ($<1 \times 10^{-6}$) value.

Osaka [33] produced electroplated films of CoNiFe with sulfur-containing additives such as saccharin and thiourea. It was found that with sulfur content at 0.9 % the resistivity had increased to 5.1×10^{-7} Ωm with a reasonable saturation flux density of 1.7 T, low coercivity of 72 Am^{-1} , and permeability retained up to 30 MHz frequency.

Electrodeposited amorphous Co-P alloys have reported values of coercivity that are extremely low, i.e., $H_c < 24 \text{ A m}^{-1}$, even at high values of resistivity, i.e., $\rho = 1.9 \times 10^{-6} \Omega \text{ m}$ [34]. However, Co-P has a strong tendency to form an out-of-plane, perpendicular anisotropy, and electrodeposition techniques must be employed that prevent this by producing a multi-nanolayer structure.

Such electrodeposited magnetic materials are an attractive possibility in the integration of on-chip inductors into silicon process technology, which has been a major challenge in the development of monolithic solutions for wireless communications, RF ICs, radar, power delivery, and EMI noise reduction [35]. The use of such materials has the potential to considerably reduce the footprint required but requires a material with low losses at high frequency.

Early Work on Electrodeposited Co-P

DC Plated Co-P

Riveiro and Sanchez-Trjillo [26] investigated the anisotropy behavior of electrodeposited amorphous Co-P films. They used a plating bath which was based on those described by Brenner et al. [20], which for a “high” phosphorous deposit of 9–11 % had a bath composition and conditions as shown in Table 2.

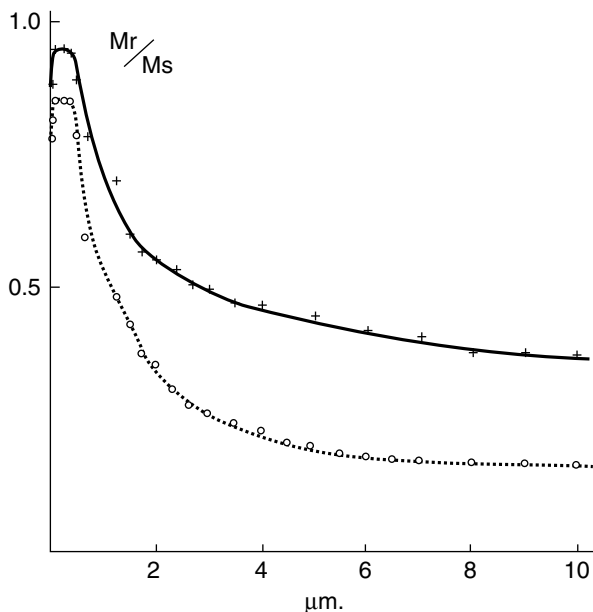
As a substrate for plating, Riveiro and Sanchez-Trjillo [26] used smoothed polycrystalline copper. M - H hysteresis loops of the samples thus produced were obtained using two methods, the integrating fluxmeter and the transverse magneto-optic Kerr effect (MOKE). The ratio of remnant magnetization to saturation magnetization M_r/M_s as obtained by these methods is shown plotted against deposit thickness in Fig. 6.

It can be seen that for samples with a thickness below 400 nm the value of M_r/M_s is high (which implies a high permeability) but as the thickness is increased the value of M_r/M_s decreases (which implies a low permeability). Riveiro and Sanchez-Trjillo [26] interpreted these results as indicating that an in-plane anisotropy is present for samples with a thickness below 400 nm but as the thickness is increased above 500 nm the anisotropy develops an out-of-plane direction eventually becoming perpendicular at approximately 10 μm .

Table 2 Plating bath composition and conditions

Component	Amount (g l^{-1})
H_3PO_3	40
Co CO_3	~15 (sufficient to achieve desired pH)
$\text{CoCl}_2 \cdot 6\text{H}_2\text{O}$	180
H_3PO_4	50
Temperature ($^\circ\text{C}$)	75–95
Current Density (A m^{-2})	500–4000
PH	0.5–1.0
Anode	Co

Fig. 6 Ratio of M_r/M_s , versus sample thickness with; “0” indicating “Integrating fluxmeter” and “+” indicating “Kerr effect” (Reproduced from Riveiro and Sanchez-Trujillo [26])



This phenomenon was explained based on the theory presented by Chi and Cargill [36] that the anisotropy is due to the formation of a “columnar structure” which arises due to fluctuations in the composition. However, a detailed study by Ruythooren et al. [37] of DC-plated Co-P films using transmission electron spectroscopy (TEM) failed to find evidence of a columnar microstructure.

Pulse Reverse Plated Co-P

Riveiro and coworkers investigated the use of pulse reverse plating to produce composition-modulated films and hence interrupt the “presumed” columnar growth. Initially, this was achieved by adding a 5 Hz sinusoidal current to the conventional DC electrodeposition current [34]. Subsequently, Riveiro and Riveiro [12] used a square wave with current reversal – see Fig. 7.

They used the following settings:

- Forward current density, $CD_{\text{forward}} = 5000 \text{ A m}^{-2}$
- Reverse current density, $CD_{\text{reverse}} = 2000 \text{ A m}^{-2}$
- Forward on-time $t_{\text{forward}} = 90\text{--}500 \text{ ms}$
- Reverse on-time $t_{\text{reverse}} = 50 \text{ ms}$

The plating bath composition was very similar to that shown in Table 2 except that the H_3PO_3 was higher at 65 g l^{-1} .

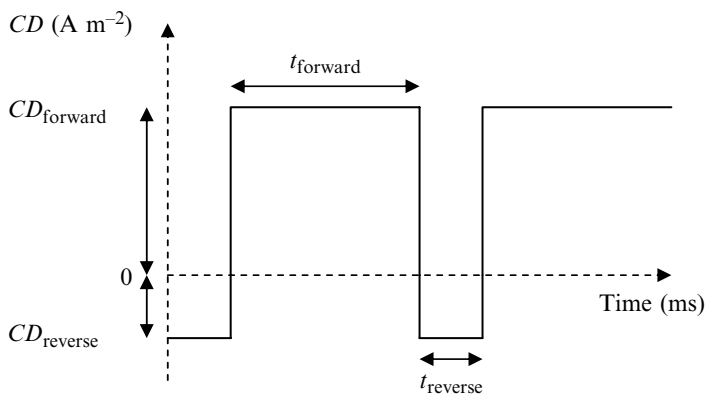


Fig. 7 Pulse Reverse Waveform used by Riviero et al. [12]

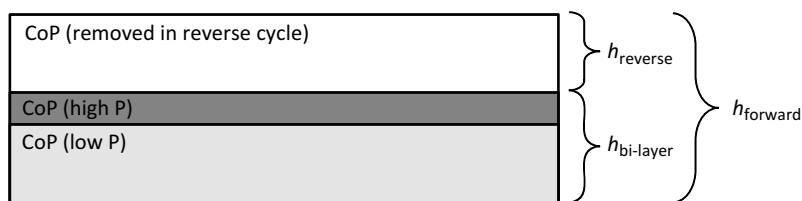


Fig. 8 Effect of Pulse Reverse waveform

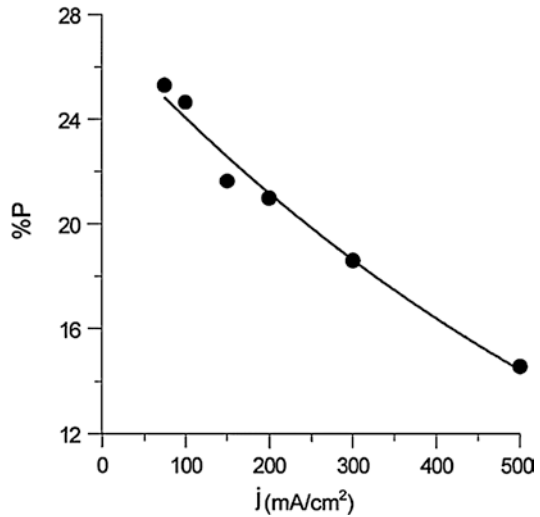
It was supposed by Riveiro et al. [12] that during the forward on time, t_{forward} , Co-P is deposited (with a thickness of h_{forward}) while during the reverse time, t_{reverse} , Co-P is removed (with a thickness of h_{reverse}). During the reverse cycle, Co is removed preferentially, and hence the upper part of the remaining layer is enriched in P.

Consequently, a bilayer structure is created, which is represented in Fig. 8.

Using this approach Riveiro and Riveiro [12] fabricated multilayers of alternate magnetic and nonmagnetic materials. The magnetic layers had a composition of $\text{Co}_{76}\text{P}_{24}$ while the nonmagnetic layers had a composition of $\text{Co}_{67}\text{P}_{33}$ (thickness 2–5 nm).

Holding the thickness of nonmagnetic layers constant, they varied the thickness of the magnetic layers. They found that the H_c initially fell from 40 A m^{-1} (at a magnetic layer thickness of 3 nm) to 8 A m^{-1} (at a magnetic layer thickness of 30 nm). Above this thickness, the H_c started to rise again, and “stripe domains” were observed when the magnetic layer thickness was greater than 150 nm. Riveiro et al. [40] made a thorough study of magnetic domains in multilayered amorphous Co-P alloys produced by pulse reverse plating.

Fig. 9 Co-P composition versus electrolytic current density (Reproduced from Perez et al. [13])



Pulse Plated Co-P

The effect of DC plating current density on the deposit composition of Co-P was investigated [13]. It was found that the composition is strongly dependent on current density as is shown in Fig. 9.

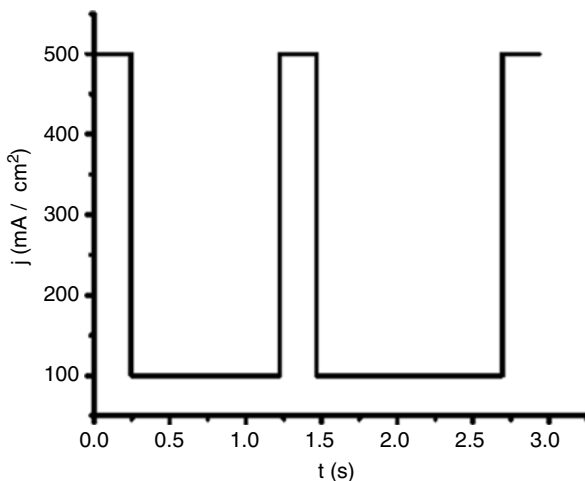
Perez et al. [13] went on to exploit this effect by using square wave pulse plating at different current densities to produce multilayer structures in which both layers were ferromagnetic and where the composition of the first layer was $\text{Co}_{83}\text{P}_{17}$, the composition of the second was $\text{Co}_{78}\text{P}_{22}$, and the double layer thickness was in the range 10 nm to 30 μm . These layers were replicated in order to produce a stack of layers with alternating composition. Perez et al. [13] did not quote the exact plating conditions used in this study but in subsequent work aimed at fabricating a fluxgate sensor with an electrodeposited amorphous Co-P core [38], described using [39] a single electrolyte and current densities of 5000 and 1000 A m^{-2} to modulate the composition of the layers. The plating waveform utilized is shown in Fig. 10.

In their initial study, Perez et al. [13] experimented by varying the bilayer thickness while keeping a constant total deposit thickness of 30 μm . They found that they could reduce the normalized perpendicular anisotropy of the film from 1 (bilayer thickness of 30 μm) to 0.38 (bilayer thickness of 10 nm).

Subsequently, Perez et al. [13] tried keeping the number of bilayers constant at 1000 while varying the composition of the layers. They found that the perpendicular anisotropy could be related to the difference between the B_s of the two layers that form a bilayer. With a difference in B_s smaller than 0.3 $\mu_B \text{ atom}^{-1}$ (resulting from a difference in current density smaller than 3000 A m^{-2}), the normalized perpendicular anisotropy was reduced from 1 to 0.25.

The bilayer films were characterized, and it was found that they exhibited the magnetic properties, $H_c = 3\text{--}10 \text{ A m}^{-1}$, $B_s = 0.6 \text{ T}$, and permeability, $\mu = 10^4$.

Fig. 10 Plating waveform used to fabricate multilayer Co-P core for fluxgate sensor (Reproduced from Perez et al. [38])



Bitter domain pattern analysis was carried out, and it was found that domain walls were present and that these were associated with more than one layer, thus indicating exchange coupling between layers. Perez et al. [13] contrasted this with a similar bitter analysis of magnetic/nonmagnetic layers carried out by Riveiro et al. [39], in which Neel and Cross-Tie walls were observed, indicating that there was no exchange coupling between the ferromagnetic layers. Based on this difference, Perez et al. [13] suggested that the presence of exchange interaction between the ferromagnetic bilayers was the reason for the lower coercivity values exhibited.

Electrodeposited Co-P With Higher Saturation Magnetization

Background

As discussed earlier, Riveiro and Riveiro [12] produced thick films of amorphous Co-P with low coercivity using pulse reverse plating to fabricate multi-nanolayers of alternate magnetic and nonmagnetic material. The value of saturation magnetization B_s was not reported, but considering the composition and thickness of the magnetic layers it would be expected that the films would have saturation below 0.5 T.

As also discussed previously, Perez et al. [13] produced multi-nanolayers of amorphous Co-P using square wave pulse plating at two current densities. They produced multilayer structures which exhibited coercivity $H_c = 3\text{--}10 \text{ A m}^{-1}$, saturation magnetization $B_s = 0.6 \text{ T}$, and relative permeability $\mu_r = 10,000$.

However, one of the key requirements for a material to be suitable for integrated inductors in a power delivery application is to have a high saturation magnetization coupled with a relatively high anisotropy field. In order to obtain a material with a higher saturation and high anisotropy field, it was decided to investigate the use of

a bath with lower phosphorous acid content than that used by Riveiro and Riveiro [12] and to optimize the plating waveform in order to obtain the best properties with the lower phosphorous bath.

Experimental

A bath was prepared with a composition similar to that shown in Table 2. The bath composition was identical to the bath used by Riveiro and Riveiro [12] except that the quantity of H_3PO_3 was reduced from 65 g l^{-1} to 30 g l^{-1} .

The cathode for the plating experiments was a silicon wafer with a top layer of 500 nm of silicon oxide and a conductive seed layer consisting of 20 nm titanium and 200 nm copper. All samples were plated in the presence of a uniaxial magnetic field of around 16 kA m^{-1} , which was provided using two large permanent magnets ($140 \times 100 \times 100 \text{ mm}$) that were separated by a distance of 220 mm. The magnetic field was oriented to be parallel to the surface of the cathode. Cobalt metal pieces, in close contact with an inert Pt/Ti mesh, were used as the anode.

The film resistance was measured using the four-probe method in the central area of the wafer before and after plating. After dicing to the appropriate sample sizes, DC magnetic characterization was obtained using an ShB Instruments MESA-200 Magnetic Measurement System, and complex permeability spectra were measured using a Ryowa PMM9G1 permeameter. Compositional analysis was obtained using EDX.

The Brenner [39] bath does not work well if the pH is too high because under these conditions a powdery nonmetallic film is deposited. Moreover, the pH tends to rise with use, and hence, a low pH value is usually maintained with the addition of H_3PO_3 . However, as this is the main phosphorus source and the aim was to reduce the phosphorus content, it was decided that HCl would be used to acidify the bath.

The trial consisted of two separate experimental runs, Run A and Run B.

Run A had a starting pH (i.e., no HCl added) of 1.7 while Run B had a starting pH of 1.4. Within each run, two sets of samples were produced. For the first set, the pulse parameters were kept constant and the pH of the bath was lowered by the addition of HCl. A pulse reverse waveform as shown in Fig. 11 was used. Apart from the presence of an off-time t_{off} , this waveform is very similar to that used by Riveiro and Riveiro [12] as shown in Fig. 7.

For the first set of samples, the pulse parameters were maintained as follows:

- Forward on time, $t_{\text{forward}} = 870 \text{ ms}$
- Forward current density, $CD_{\text{forward}} = 1700 \text{ A m}^{-2}$
- Reverse on time, $t_{\text{reverse}} = 54 \text{ ms}$
- Reverse current density, $CD_{\text{reverse}} = 670 \text{ A m}^{-2}$
- Off time, $t_{\text{off}} = 72 \text{ ms}$

In the second set of samples, the pH was maintained at a constant value of around 0.88 and the forward on time t_{forward} was varied between 96 ms and 5000 ms with the other pulse parameters kept as constant as possible.

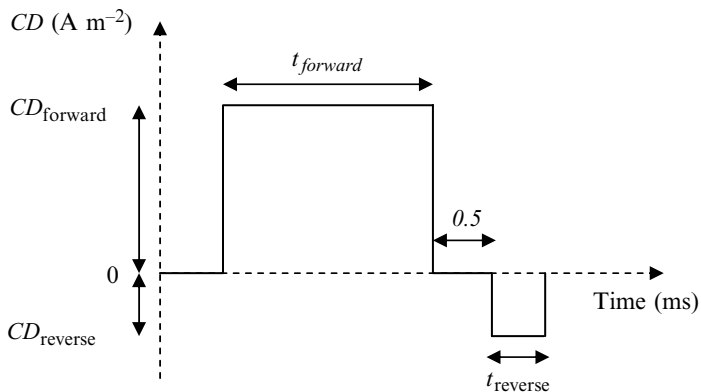


Fig. 11 Pulse Reverse Waveform used by McCloskey et al. [41]

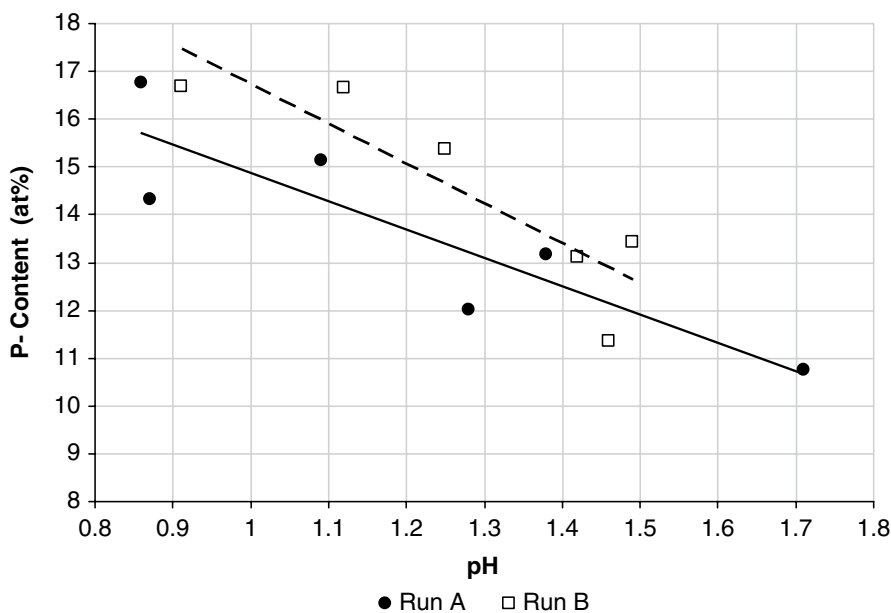


Fig. 12 Effect of pH on at.% P in deposit (Reproduced from McCloskey et al. [41])

Results and Discussion

Effect of pH (With Pulse Parameters Kept Constant)

At higher pH values (1.7–1.3), a “powdery” nonmetallic material was deposited particularly at the edges of the wafer. The size of the area affected by the nonmetallic deposit decreased dramatically as the pH was reduced and disappeared completely for pH values below about 1. The starting pH value influenced the phosphorus content of the deposit as is shown in Fig. 12.

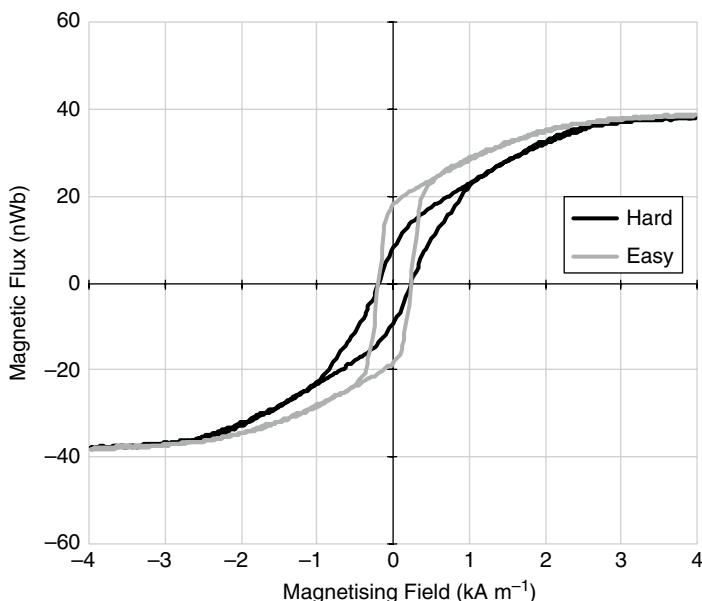


Fig. 13 Magnetisation loop of sample from Run A, Set 1 with $\text{pH} = 1.7$

Magnetization loops showed the samples to be magnetically soft with low values of H_c (i.e., below 40 A m^{-1}) for all samples except the starting sample of Run A – Set 1 ($H_c = 263 \text{ A m}^{-1}$). This sample had the largest nonmetallic deposit. The magnetization plot for the starting sample of Run A is shown in Fig. 13. This loop shows three distinct regions that are characteristic of perpendicular anisotropy. That is, at applied fields below $\sim 0.3 \text{ kA m}^{-1}$, the loop exhibits a large hysteresis (i.e., wide coercivity) followed by a region in which the magnetization is changed by the applied field but with little or no hysteresis and finally a region in which the magnetization is not changed by the applied field, i.e., the magnetization has reached saturation. Furthermore, the sample shows only rather small in-plane anisotropy. The easy axis, which exhibits the highest slope, i.e., a high permeability, was obtained at the orientation of the sample relative to the magnetic field applied during electrodeposition. The hard axis, which exhibits a lower slope, i.e., a lower permeability, was obtained at an orientation perpendicular to the easy axis.

An example of the much-improved magnetization loops obtained for samples plated at a lower pH is shown in Fig. 14. The magnetization plot consists of only two regions, i.e., a low-hysteresis region, in which the magnetization is changed by an applied field, and a further region in which the magnetization is unchanged by the applied field, i.e., the magnetization has reached saturation. This type of loop is typical for in-plane anisotropy.

Furthermore, the magnetization loop shows a pronounced anisotropy with a clear difference between the easy and hard axis.

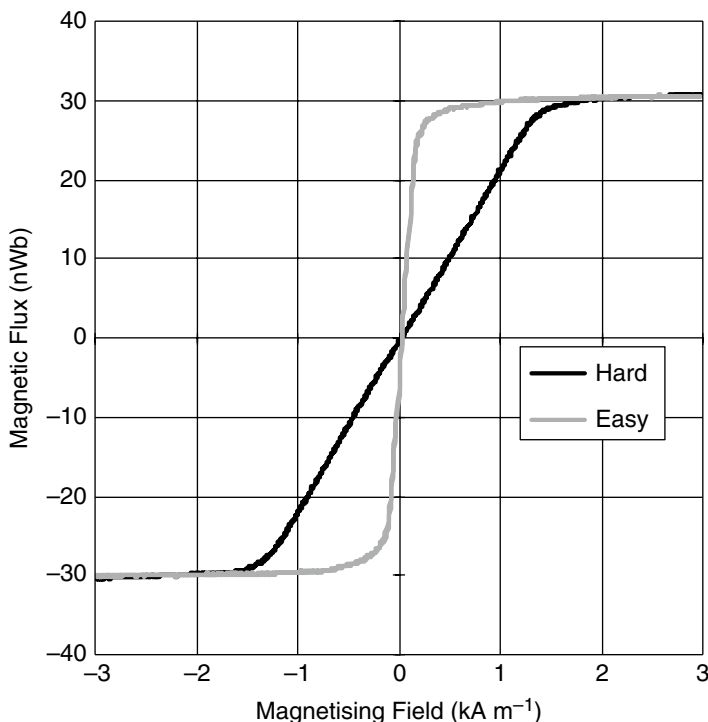


Fig. 14 Magnetisation loop of sample from Run A, Set 1 with pH = 1.28

The field required to rotate the magnetic orientation of the sample from the easy to hard axis orientation is known as the anisotropy field, H_k . On a B-H loop, it is the nonzero field at which the extrapolated hard axis loop intersects the easy axis loop. From Fig. 14, it can be seen that $H_k \sim 1.4 \text{ kA m}^{-1}$.

The hard axis coercivity is plotted against pH for both Run A and Run B (excluding the results for samples produced with pH = 1.7) in Fig. 15. It may be seen that for both Run A and Run B, the H_c shows a downward trend with increasing pH.

It should be noted that for a given pH Run A has a lower % P but a higher H_c and hence the correlation of H_c with pH is not explained as simply a dependence on P content.

The saturation magnetization B_s is plotted against phosphorus content in Fig. 16 for both Run A and Run B. This is with the pulse plating parameters held constant and pH varied.

It can be seen that as anticipated the B_s increases with decreasing phosphorus content for both experimental runs, varying from 0.9 to 1.2 T.

Effect of Forward on Time (With pH Kept Constant)

As discussed earlier, Riveiro and Riveiro [12] used pulse reverse plating to create a bilayer structure of alternate compositions (see Fig. 8) and supposed that during the

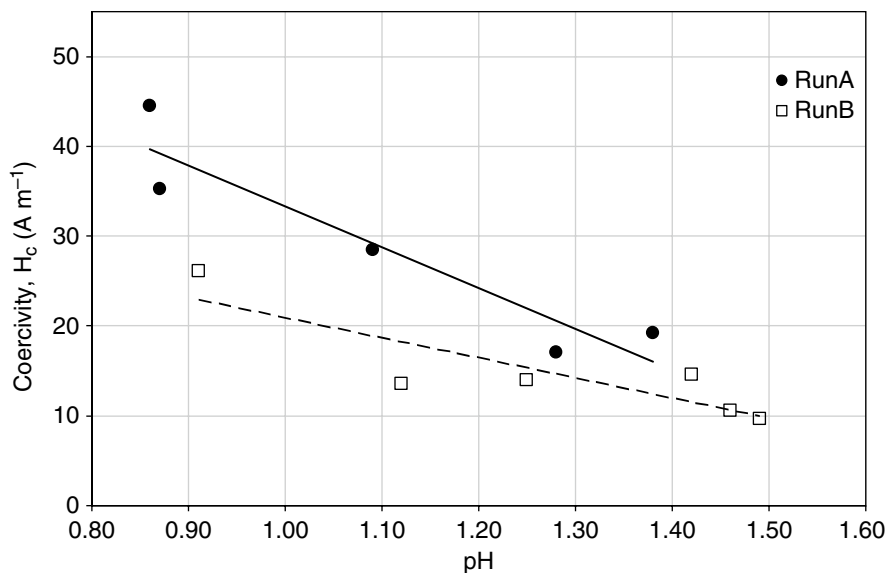


Fig. 15 Hard axis H_c versus pH for Set 1 samples (Reproduced from McCloskey et al. [41])

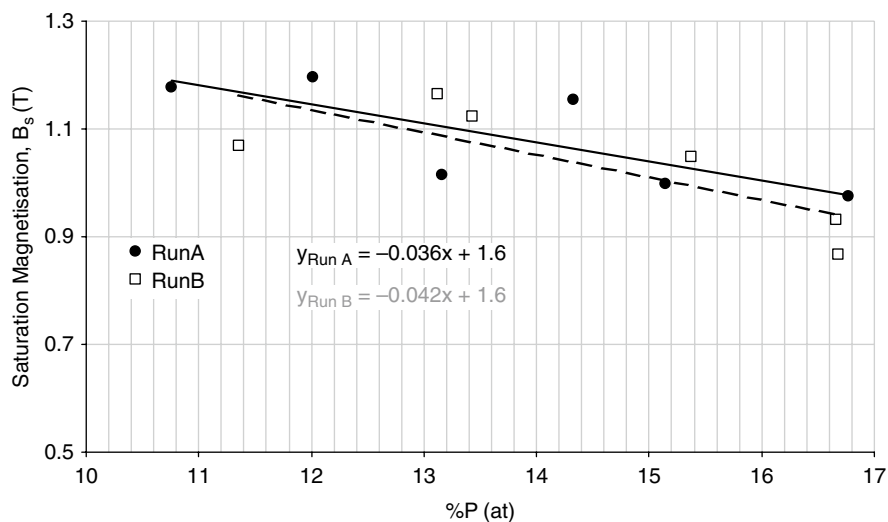


Fig. 16 Saturation magnetization B_s versus phosphorous content (Reproduced from McCloskey et al. [41])

reverse time $t_{reverse}$ is removed preferentially and hence the upper part of the deposit is enriched in P.

In a treatment similar to that in Riveiro and Riveiro [12] for a constant forward current density $CD_{forward}$, reverse current density $CD_{reverse}$, and reverse time $t_{reverse}$, the thickness of the bilayer is given by

$$h_{\text{bi-layer}} = kt_{\text{forward}} - h_{\text{reverse}} \quad (9)$$

where t_{forward} = forward on time and k is a constant. This thickness may be readily determined since it is also given by

$$h_{\text{bi-layer}} = \left(t_{\text{cycle}} / t_{\text{plating}} \right) h_{\text{sample}} \quad (10)$$

where t_{cycle} = total cycle time, t_{plating} = total plating time, and h_{sample} = sample thickness.

When the bilayer thickness is plotted against forward on time for each experimental run, a straight line with a negative intercept is obtained as shown in Fig. 17. The plots would show a zero intercept if no material was removed during the reverse cycle, and the value of the intercept is the average thickness of material removed during each reverse cycle. It will be noted that the intercept values are similar for both experimental runs (A and B).

The $B-H$ loops obtained for the samples showed that the hard axis H_c was strongly influenced by t_{forward} (see Fig. 18). It can be seen that the $B-H$ loops for the DC-plated sample and the sample plated with $t_{\text{forward}} = 3760$ ms are very similar, i.e., both have a high coercivity and consist of three regions, which, as previously mentioned, is typical of out-of-plane anisotropy.

The $B-H$ loop for the sample-plated $t_{\text{forward}} = 1200$ ms is radically different with a very low coercivity, a two-region $B-H$ loop, and a pronounced in-plane anisotropy.

Figure 19 shows the coercivity plotted against the forward on time for the two experimental runs.

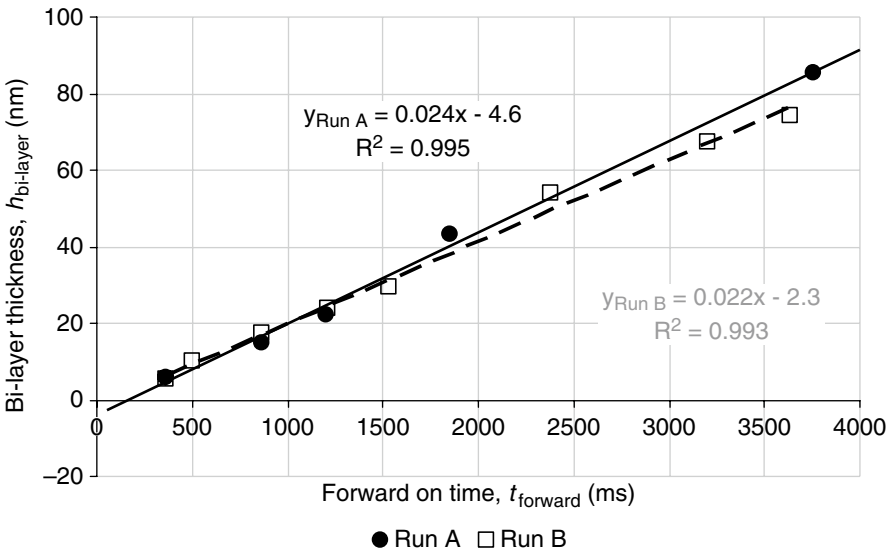


Fig. 17 Bi-layer thickness versus forward on time (Reproduced from McCloskey et al. [41])

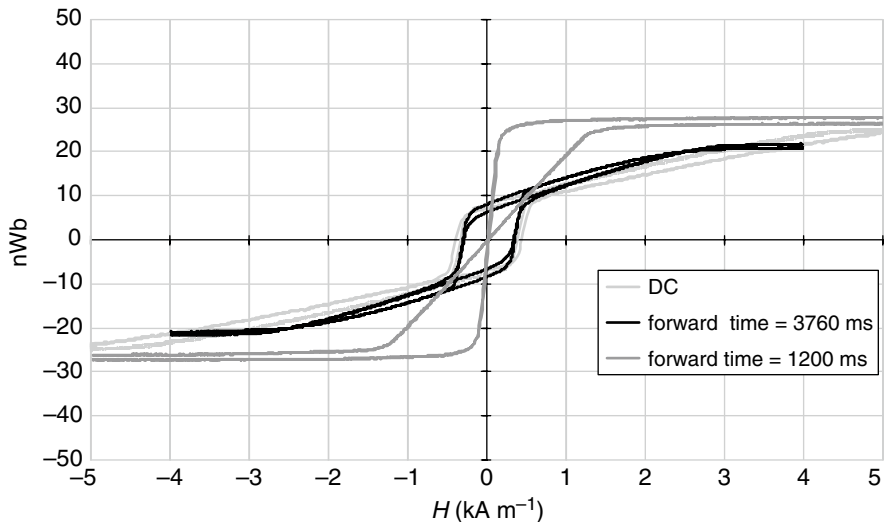


Fig. 18 Magnetisation plot for various values of forward on time

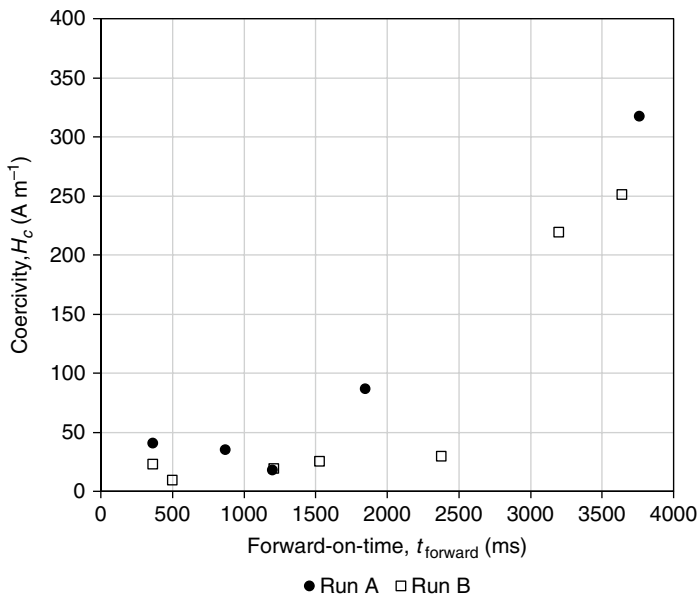


Fig. 19 Coercivity, H_c versus Forward On-Time, $t_{forward}$ (Reproduced from McCloskey et al. [41])

Thus, for good soft magnetic properties, it is essential to use forward on times of 1530 ms or less. From Fig. 17, it can be seen that this corresponds to a bilayer thickness of 29 nm or less.

The relative permeability of the samples was found to be approximately 700 and was found to retain 90 % of its initial value to frequencies of up to 103 MHz. The anisotropy field was found to vary between 1.2 and 1.5 kA m⁻¹ with the higher values being obtained at lower phosphorus contents.

The resistivity of the samples varied between $1.16 \times 10^{-6} \Omega \text{ m}$ at 13 at.% P and $1.36 \times 10^{-6} \Omega \text{ m}$ at 17 at.% P.

Electrodeposited Co-P with Improved Temperature Stability

Background

Electrodeposited amorphous Co-P is an attractive material for use in the integration of on-chip inductors into silicon process technology because of its high resistivity and advantageous magnetic properties. However, as it is an amorphous material, the properties of Co-P are dramatically changed upon crystallization. The stability of magnetic properties with respect to temperature is important since in fabricating an integrated inductor the magnetic core is likely to be exposed to processes such as the thermal cure of polymeric photoresist used to provide electrical insulation. A good candidate material is the Cyclotene 3000 series from Dow, which is derived from B-staged bisbenzocyclobutene (BCB) monomers. These materials use a soft cure temperature of 210 °C and hard cure temperatures of 250 °C and 300 °C [42].

This section concerns work undertaken to evaluate the inclusion of rhenium in a cobalt–phosphorus amorphous alloy in order to improve its thermal stability.

Oda et al. [43] used small additions of tungsten to improve crystallization temperature of amorphous Fe-Co-P alloys. Tungsten has a large atomic weight of 183.8 g mol⁻¹ and it is thought that its large atomic radii play a role in bringing about an increase in crystallization temperature. However, despite extensive experimental trials, it was found that Co-P electroplating baths containing tungsten were found to have a considerable tendency to be unstable and a reliable plating bath for the deposition of Co-P-W was not identified.

Rhenium also has a large atomic weight of 186.2, and Brenner [39] describes how it can be readily codeposited with iron group metals. Hence, it was decided to determine if the inclusion of rhenium in Co-P was feasible and if its presence did in fact improve the thermal stability of the new composition. Finally, the effect of including Re on properties other than thermal stability was also investigated.

Experimental

A plating bath was prepared with a composition (see Table 3) very similar to that used by Riveiro and Riveiro [12], apart from the addition of KReO₄, which was used as the source of Re.

A glass beaker was used as the plating cell with a total solution volume of 1 l and agitation provided by mechanical stirring. The electrodes were horizontally

Table 3 Plating bath composition for Co-P-Re (Reproduced from McCloskey et al. [44])

Component	Amount (g l ⁻¹)
H ₃ PO ₃	65
Co CO ₃	39.4
CoCl ₂ .6 H ₂ O	181
H ₃ PO ₄	50
KReO ₄	0–6

opposed, and the cathode-to-anode separation was 65 mm. The temperature of the solution was maintained at 72 °C using a hotplate and the plating carried out in “the presence of a uniaxial magnetic field of around 16 kA m⁻¹ oriented to be parallel to the surface of the cathode. Cobalt metal pieces, in close contact with an inert Pt/Ti mesh, were used as the anode.

Copper foil with a thickness of 10 µm was used as a cathode to provide samples for annealing and DSC experiments. Silicon wafers with a top layer of 500 nm of oxide and a conductive sputtered seed layer consisting of 20 nm titanium and 200 nm copper was used as a substrate to provide samples for resistivity, permeability, and saturation magnetization measurement.

In all cases, the pulse reverse plating was used with parameters at values found to be optimal for Co-P plating [41]:

- Forward on time $t_{\text{forward}} = 860$ ms
- Forward current density $CD_{\text{forward}} = 1520$ A m⁻²
- Reverse on time $t_{\text{reverse}} = 52$ ms
- Reverse current density $CD_{\text{reverse}} = 620$ A m⁻²
- Off time $t_{\text{off}} = 80$ ms

As described earlier, the control of pH is very important in the plating of Co-P alloys since at higher values of pH, plating of nonmetallic deposits can occur with an adverse effect on the coercivity of the as-deposited film. Furthermore (and described in detail later), it was found that the temperature stability of the deposit is adversely affected by low pH conditions. Consequently, the pH was adjusted by addition of either HCl or NaOH.

DSC analysis using a Perkin Elmer Pyris 1 instrument was carried out on free-standing samples that were produced by dissolving the underlying copper foil. An aqueous 30 g l⁻¹ ammonium persulfate, (NH₄)₂S₂O₈ at 40 °C was used as the etchant to remove the Cu foil.

Results and Discussion

Composition Analysis

The composition of Co-P and Co-P-Re samples plated on Cu foil is shown in Fig. 20.

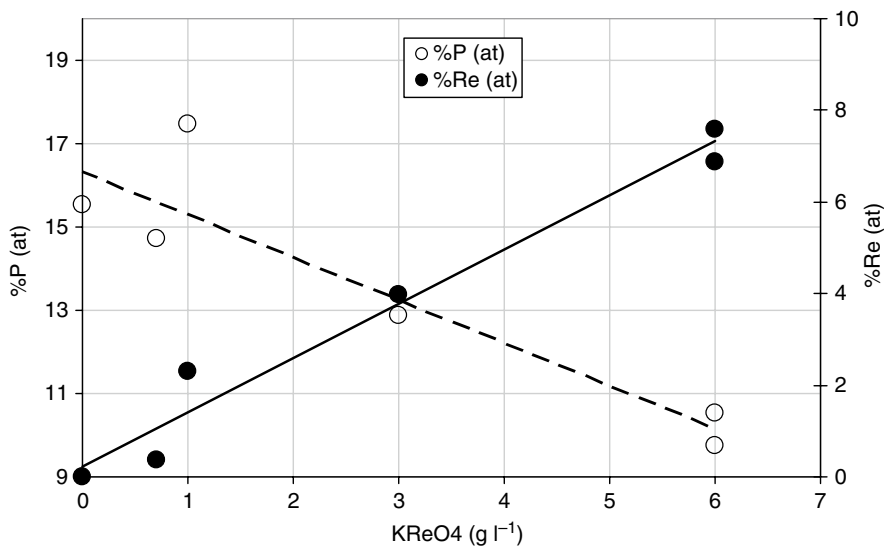


Fig. 20 Composition of Co-P and Co-P-Re samples (Reproduced from McCloskey et al. [44])

It can be seen that as expected increasing the amount of KReO_4 led to an increase in the amount of Re in the plated film. However, increasing the amount of KReO_4 in the bath also led to a dramatic reduction in the amount of P in the plated film.

Thermal Annealing

Thermal annealing experiments were carried out under vacuum and consisted of a 15 min ramp, a 30 min dwell at the peak temperature of 298 °C, and approximately 20 min cooling. Prior to the annealing, all the samples showed coercivity $H_c < 120 \text{ A m}^{-1}$.

The coercivity of samples after a thermal annealing at 298 °C for 30 min plotted against pH is shown in Fig. 21.

It can be observed that the pH of the bath had a very strong effect on the coercivity values obtained after annealing. However, the coercivity of the Co-P samples produced at higher pH values was still very high.

Figure 22 shows hard axis hysteresis loops obtained before (as plated) and after a 298 °C anneal for a Co-P sample produced with a pH value of 0.79. The dramatic affect of the 298 °C annealing on the B-H loop of the sample can be seen with the coercivity increasing from 80 A m^{-1} to 1.9 kA m^{-1} .

In contrast, as can be seen in Fig. 21, the samples produced with a KReO_4 addition all had coercivity values after annealing that were significantly lower than similar Co-P samples. Furthermore, very low coercivity values $H_c < 80 \text{ A m}^{-1}$ were obtained for samples with an addition of 3 g l^{-1} or more of KReO_4 .

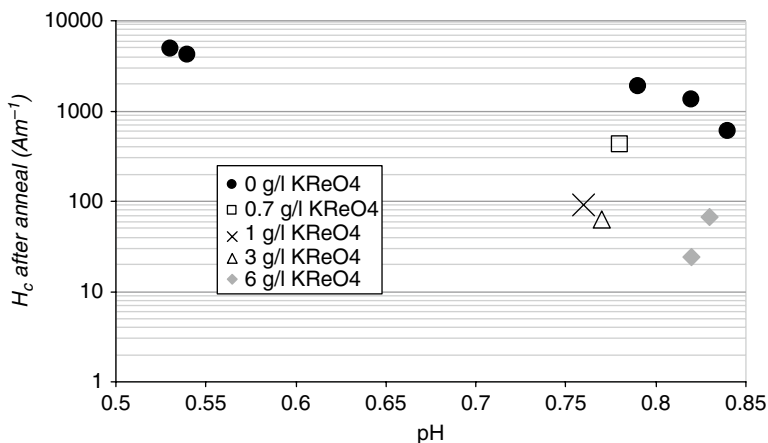


Fig. 21 Coercivity after thermal annealing at 298 °C for 30 min plotted against pH

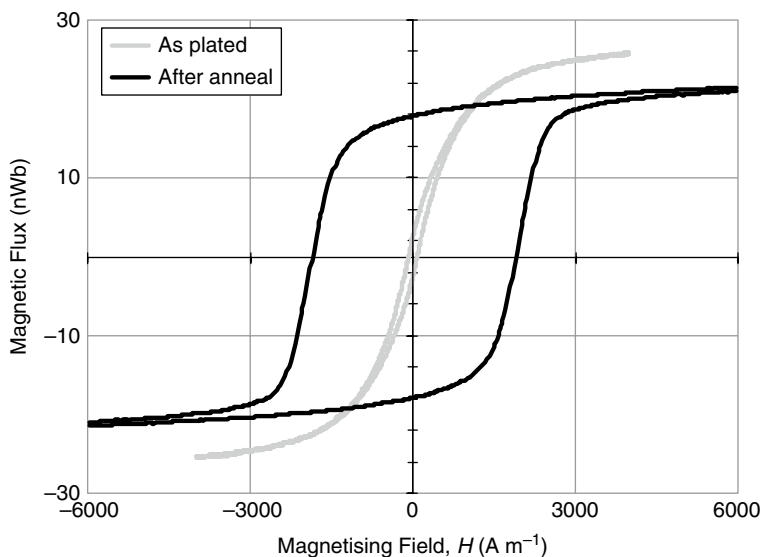


Fig. 22 Hysteresis loops before and after a 298 °C anneal for a Co-P sample produced with a pH value of 0.79 (Reproduced from McCloskey et al. [44])

The hard-axis hysteresis loops obtained before (as plated) and after 298 °C annealing for a Co-P-Re sample produced with 1 g l⁻¹ KReO₄ and at a pH value of 0.76 are shown in Fig. 23.

It can be seen that the B-H loop for the Co-P-Re sample is largely unaffected by the 298 °C anneal with the coercivity $H_c < 80 \text{ Am}^{-1}$ after annealing.

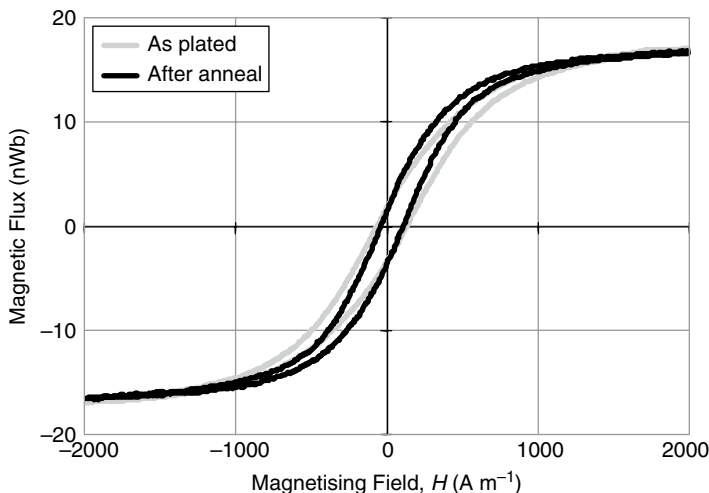


Fig. 23 Hysteresis loops before and after a 298 °C anneal for a Co-P-Re sample (Reproduced from McCloskey et al. [44])

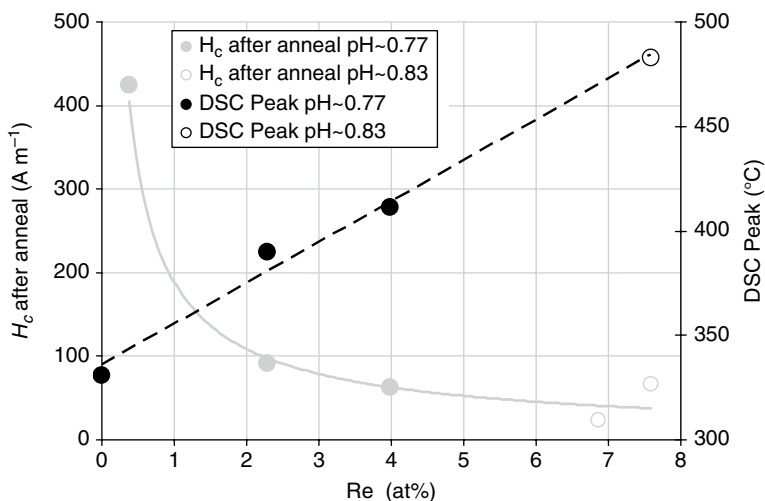


Fig. 24 DSC Peak and Coercivity (H_c) for Co-P-Re after 298 °C annealing for 30 min

Differential Scanning Calorimetry (DSC) analysis

The DSC analysis was carried out using a Perkin Elmer Pyris 1 instrument with a scan rate of 10 °C/min. The phase change peak from the DSC analysis and the coercivity after a 298 °C anneal for the a-Co-P-Re samples are shown in Fig. 24.

The pH of the bath was maintained in the range 0.76–0.83, and in fact four of the samples were produced at a pH ~ 0.77 while two were produced at a pH ~ 0.83.

Separate plots of H_c and DSC peak versus at.% Re are shown for each of these pH values. Again as discussed previously, prior to annealing, $H_c < 120 \text{ A m}^{-1}$ for all the samples, and it can be seen that for all the samples with $\text{Re} > 2 \text{ at.}\%$, the coercivity after thermal treatment remains very low. It can also be seen that the trend line for H_c after annealing is the same for both pH values and hence it appears that the effect of the higher pH is effectively eliminated at the higher at.% Re values.

It can also be observed that the DSC peak increases sharply with increasing at.% Re. Again, it can be seen that the trend line is the same for both values of pH and hence pH had little effect.

Saturation Magnetization and Resistivity

The saturation magnetization (B_s) and resistivity (ρ) for Co-P and Co-P-Re samples plated on a silicon substrate are shown in Figs. 25 and 26 respectively.

It can be seen that apart from one sample (with $\text{Co} = 82.4 \text{ at.}\%$) the B_s values obtained for higher values of Re ($\text{Re} > 3 \text{ at.}\%$) are reasonably consistent with those obtained for lower values ($\text{Re} < 3 \text{ at.}\%$). Moreover, the sample with $82.4 \text{ at.}\%$ Co had a Re content of $3.1 \text{ at.}\%$, and hence it does not appear that the lower-than-expected value of B_s obtained arose from its Re content.

It would be expected that the resistivity value obtained should be lower at lower values of P content. However, the dependence of P content on the Re content shown in Fig. 20 means that samples with a high Re content ($\text{Re} > 3 \text{ at.}\%$) also tended to have lower levels of P than those with a low Re content ($\text{Re} < 3 \text{ at.}\%$). Contrary to this, the resistivity of the samples does not seem to have been dramatically affected by the level of Re. This is probably due to the difference in the value of resistivity between Re ($\rho = 18 \times 10^{-8} \Omega \text{ m}$) and Co ($\rho = 6 \times 10^{-8} \Omega \text{ m}$).

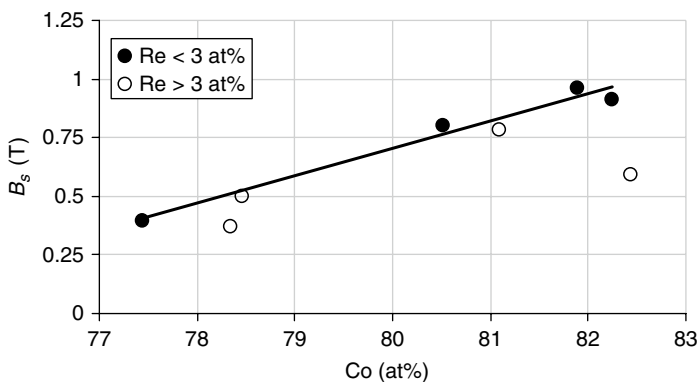


Fig. 25 Saturation Magnetisation (B_s) for as plated Co-P and Co-P-Re (Reproduced from McCloskey et al. [44])

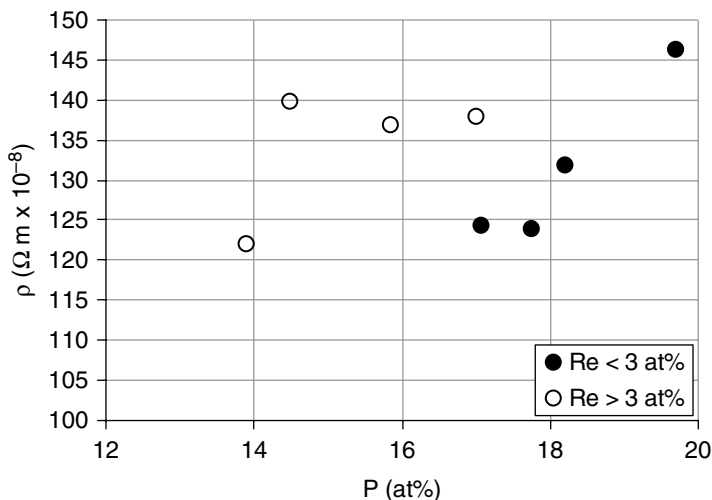


Fig. 26 Resistivity for as plated Co-P and Co-P-Re (Reproduced from McCloskey et al. [44])

Conclusions

Plated multi-nanolayer Co-P films were produced that show a higher saturation magnetization B_s in the range of 0.9–1.2 T and good soft magnetic properties, typically $H_c < 40 \text{ A m}^{-1}$ with a minimum value of 8 A m^{-1} . The films had an anisotropy field between 1.2 and 1.5 kA m^{-1} and resistivity in the range of 1.16×10^{-6} to $1.36 \times 10^{-6} \text{ } \Omega \text{ m}$.

An electrodeposited magnetic alloy, Co-P-Re, was obtained that shows a significantly improved thermal performance in comparison to Co-P, retaining $H_c < 120 \text{ A m}^{-1}$ after a thermal annealing under vacuum at $298 \text{ }^\circ\text{C}$ for 30 min. These results were obtained for alloys with a composition of $\text{Co}_{100-x-y}\text{P}_x\text{Re}_y$, where $9.7 \text{ at.}\% < x < 17.5 \text{ at.}\%$ and $2.3 \text{ at.}\% < y < 7.6 \text{ at.}\%$. It was found that other important properties, i.e., B_s and ρ , were largely unaffected by the addition of Re.

References

1. Karkare M (2008) Nanotechnology: fundamentals and applications. I. K International, New Delhi
2. Hanrahan JP, Copley MP, Ziegler KJ, Spalding TR, Morris MA, Steytler DC, Heenan RK, Schweins R, Holmes JD (2005) Pore size engineering in mesoporous silicas using supercritical CO_2 . *Langmuir* 21:4163
3. Mansoori G (2005) Principles of nanotechnology. World Scientific, Hackensack
4. Wilson M, Kannangara K, Smith G, Simmons M, Raguse B (2002) Nanotechnology: basic science and emerging technologies. CRC Press LLC, Boca Raton, Florida

5. Lacaze PC (2013) *Nanotechnologies: concepts, processing and applications*. Wiley, Hoboken
6. Moore GE (1965) Cramming more components onto integrated circuits. *Electronics* 114–117
7. Roco MC, Gargini P (2011) *Nanoelectronics: an international perspective*. *Proc IEEE* 99:751
8. Information Storage Industry Consortium (2011) *International magnetic tape storage roadmap*, © Information Storage Industry Consortium, <http://www.insic.org/news/A&S%20Roadmap.pdf>
9. Wolf SA, Awschalom DD, Buhrman RA, Daughton JM, von Molnár S, Roukes ML, Chtchelkanova AY, Treger DM (2001) Spintronics: a spin-based electronics vision for the future. *Science* 294:1488–1495
10. Bird KD, Schlesinger M (1995) Giant magnetoresistance in electrodeposited Ni/Cu and Co/Cu multilayers. *J Electrochem Soc* 142:L65–L66
11. Simunovich D, Schlesinger M, Snyder D (1994) Electrochemically layered copper-nickel nanocomposites with enhanced hardness electrochemical society letters. *J Electrochem Soc* 141(1): L10–L11, doi:10.1149/1.2054717
12. Riveiro JM, Riveiro G (1981) Multilayered magnetic amorphous Co-P films. *IEEE Trans Magn MAG* 17(6):3082
13. Pérez L, de Abril O, Sánchez MC, Aroca C, López E, Sánchez P (2000) Electrodeposited amorphous CoP multilayers with high permeability. *J Magn Magn Mater* 215–216:337–339
14. Paunovic M, Schlesinger M, Snyder DD, Paunovic M (2010) Chapter 1, “Fundamental considerations”. In: Schlesinger M, Paunovic M (eds) *Modern electroplating*, 5th edn. Wiley
15. Alper M, Aplin PS, Attenborough K, Dingley DJ, Hart R, Lane SJ, Lashmore DS, Schwarzacher W (1993) Growth and characterization of electrodeposited Cu/Cu-Ni-Co alloy superlattices. *J Magn Magn Mater* 126(1–3):8–11
16. Yahalom A, Tessier DF, Timsit RM, Rosenfeld AM, Mitchel DF, Robinson PT (1989) *J Mater Res* 4/4:755
17. Attenborough K, Hart R, Lane SJ, Alper M, Schwarzacher W (1995) Magnetoresistance in electrodeposited Ni-Fe-Cu/Cu multilayers. *J Magn Magn Mater* 148:335–336
18. Landolt D (1994) Electrochemical and materials science aspects of alloy deposition. *Electrochimica Acta* 39(8/9):1075–1090
19. Djokic SS (1999) Electrodeposition of Amorphous Alloys Based on the Iron Group of Metals 146(5):1824–1828
20. Brenner A, Couch DE, Williams EK (1950) Electrodeposition of alloys of phosphorous with nickel or cobalt. *J Res Natl Bur Stand* 44:109
21. Dekker AJ (1957) *Solid state physics*. Prentice-Hall, Englewood
22. Cullity BD (1972) *Magnetic materials*. CRC Press LLC, Boca Raton, Florida
23. Weiss P (1906) La variation du ferromagnetisme du temperature. *Compte Rendu* 143: 1136–1139
24. Cuillity BD, Graham CD (2009) *Introduction to magnetic materials*, 2nd edn. Wiley, IEEE Press
25. Roozeboom F, Bloemen PJH, Klaassens W, Van De Riet’ EGJ, Donkers JJTM (1998) Soft-magnetic fluxguide materials. *Philips J Res* 51:59–91
26. Riveiro JM, Sanchez-Trjillo MC (1980) Magnetic anisotropy of electrodeposited Co-P amorphous alloys. *IEEE Trans Magn MAG-16(6):1426–1428*
27. Néel L (1949) Théorie du tramage magnetique desferromagnetiques engrains fins avec applications aux terres cuites 5:99
28. Papaefthymiou GC (2009) Nanoparticle Magnetism. *Nano Today* 4:438
29. Jones RE Jr (1990) *IBM Disk Storage Tech* 3:6
30. Tsang C, Chon M-M, Yogi T, Ju K (1990) Gigabit density recording using dual-element MR/ inductive heads on thin-film disks. *IEEE Trans Magn MAG-26:1689*
31. Robertson N, Hu HL, Tsang C (1997) High performance write head using NiFe 45/55. *IEEE Trans Magn* 33:2818
32. Harada K, Takahashi F (1997) *Nikkei Electron* 691:91
33. Osaka T, Takai M, Tachibana H (2000) US Patent 6,063,512
34. Riveiro JM, Sanchez MC, Riveiro G (1981) Electrodeposited Co-P alloys with variable magnetic anisotropy. *IEEE Trans Magn MAG* 17(3):1282–1285

35. Gardner DS et al (2006) IEEE International Electron Device Meeting (IEDM), San Francisco, pp 11–13
36. Chi GC, Cargill GS III (1975) Structural anisotropy of amorphous cobalt-phosphorus alloys. *AIP Conf Proc* 29:147
37. Ruythooren W, De Boeck J, Celis JP (2004) Microstructural investigation of Co-P by TEM. *J Electrochem Soc* 151(5):C315–C317
38. Perez L, Aroca C, Sánchez P, López E, Sánchez MC (2004) Planar fluxgate sensor with an electrodeposited amorphous core. *Sens Actuators A* 109:208–211
39. Brenner A (1963) *Electrodeposition of alloys*. Academic, London
40. Riveiro JM, Guijarro MS, Rivero G, Sánchez MC (1982) Magnetic domains in multilayered amorphous Co-P alloys. *Phys Rev D* 15:145
41. McCloskey P, Jamieson B, O'Donnell T, Gardner D, Morris MA, Roy S (2008) High-frequency nanostructured magnetic materials for integrated inductors. *J Magn Magn Mater* 320(20): 2509–2512
42. Wang H, Yi X, Chen S, He S, Xiaochao F, Ma H (2006) Planarization of CMOS ROIC dies for uncooled detectors. *Infrared Phys Technol* 47:251–256
43. Oda M, Ohashi H, Kamadu K (1995) US Patent 5,435,903
44. McCloskey P, Jamieson B, O'Donnell T, Gardner D, Morris MA, Roy S (2010) Electrodeposited amorphous Co-P based alloy with improved thermal stability. *J Magn Magn Mater* 322(9–12): 1536–1539

Electroless Nanocomposite Coatings: Synthesis, Characteristics, and Applications

13

Sankara Narayanan T.S.N., Seshadri S.K., Il Song Park, and Min Ho Lee

Contents

Introduction.....	390
EL Ni–P Nanocomposite Coatings.....	391
Preparation of EL Ni–P Nanocomposite Coatings by Conventional Method.....	391
Challenges and Issues on Particle Incorporation in EL Ni–P Nanocomposite Coatings Prepared by the Conventional Method.....	392
Alternate Methods of Preparation of EL Ni–P Nanocomposite Coatings.....	399
Influence of Incorporation of Nanoparticles on the Characteristics of EL Ni–P Nanocomposite Coatings.....	401
Nucleation, Plating Rate, and Adhesion.....	401
Surface Appearance and Roughness.....	403
Level of Incorporation of Nanoparticles and Their Distribution in the EL Ni–P Matrix.....	404
Structure and Composition.....	405
Hardness.....	407
Tribological Characteristics.....	407
Corrosion Resistance.....	409
Applications of EL Ni–P Nanocomposite Coatings.....	411
Summary and Concluding Remarks.....	412
References.....	414

Sankara Narayanan T.S.N. (✉) • M.H. Lee
Department of Dental Biomaterials and Institute of Biodegradable Materials,
Institute of Oral Bioscience and BK21 Plus Program, School of Dentistry,
Chonbuk National University, Jeonju, Republic of Korea
e-mail: tsnsn@rediffmail.com; lmh@jbnu.ac.kr

Seshadri S.K.
Department of Metallurgical and Materials Engineering,
Indian Institute of Technology Madras, Chennai, India

I.S. Park
Division of Advanced Materials Engineering and Institute of Biodegradable Materials,
Chonbuk National University, Jeonju, Republic of Korea

Abstract

This chapter presents an overview of electroless (EL) Ni–P nanocomposite coatings, focusing on their preparation, challenges, and issues on particle incorporation in the metal matrix in terms of dispersibility of nanoparticles in the plating bath, interaction between the nanoparticles and the EL Ni–P matrix during deposition, influence of incorporation of nanoparticles on the characteristics of EL Ni–P nanocomposite coatings, and applications of EL Ni–P nanocomposite coatings.

Keywords

Electroless plating • Nanocomposite coating • Codeposition • Hardness • Wear resistance • Corrosion resistance

Introduction

Electroless (EL) plating was an accidental discovery by Brenner and Riddell, way back in 1946, in which they have identified that sodium hypophosphite has the ability to supply the electrons necessary for the reduction of metal ions from aqueous solution [1]. Among the variety of metals that can be plated, Ni has assumed significance due to its ability to offer a high hardness, excellent wear resistance, and good corrosion resistance. Unlike electrodeposited Ni, EL Ni is uniform regardless of the substrate geometry, and it is a metal–metalloid alloy (Ni–P or Ni–B) coating in which alloying of P or B provides it with unique characteristics [1]. The mechanism of deposition of EL Ni–P coating is governed by mixed potential theory. Accordingly, at the mixed potential, the rate of anodic oxidation of the reducing agent (hypophosphite) and cathodic reduction of Ni²⁺ ions becomes equal, and both of them occur simultaneously [2].

The idea of codepositing various second phase particles in a metal matrix by EL plating and thereby taking advantage of their desirable qualities such as hardness, wear and abrasion resistance, corrosion resistance, etc., has led to the development of EL composite coatings [3–5]. The essential requirements of particles that can be codeposited in a metal or alloy matrix are the following: (i) they should be effectively dispersed in the plating bath; and (ii) they should be chemically inert. In recent years, the use of nanomaterials has received considerable attention in a variety of applications, and EL composite coatings are not an exception to this. The basic requirements for preparing EL composite coatings with the addition of nanoparticles are quite similar to those prepared using micron-sized particles. Following this, synthesis of EL nanocomposite coatings using a variety of nanoparticles such as carbon nanotubes (CNTs), multi-walled carbon nanotubes (MWCNTs), SiC, Al₂O₃, ZrO₂, Si₃N₄, SiO₂, TiO₂, TiC, B₄C, diamond, WC, TiN, carbon black (CB), graphite, MoS₂, WS₂, halloysite nanotubes (HNT), hydroxyapatite (HA), etc., has been explored. Nevertheless, the deposition of EL

nanocomposite coatings possess serious challenges in terms of dispersibility of the nanoparticles in the EL plating bath and in achieving uniform distribution of nanoparticles in the metal/alloy matrix.

EL Ni–P Nanocomposite Coatings

Preparation of EL Ni–P Nanocomposite Coatings by Conventional Method

EL nanocomposite coatings are prepared by dispersing the nanoparticles in the plating bath. An acidic hypophosphite-reduced EL Ni plating bath is commonly used to prepare the EL nanocomposite coatings. This is due to the ability of the EL Ni–P matrix to offer a high hardness, excellent wear resistance, and good corrosion resistance besides providing a suitable base for the incorporation of nanoparticles in them. Upon addition of nanoparticles in the plating bath, they will be covered by an ionic cloud (Fig. 1a). Most of the nanoparticles are likely to be in the form of clusters following their agglomeration in the plating bath (Fig. 1b). The mechanical agitation employed during EL plating to assist dispersion of the nanoparticles helps the ion-adsorbed nanoparticle clusters to transport toward the electrode surface by means of convection and diffusion. Once the ion-adsorbed nanoparticle clusters are reduced, in a similar way as that of the Ni^{2+} ions, they get incorporated and subsequently engulfed by the growing EL Ni–P matrix. A pictorial representation of the various stages involved in the formation of EL nanocomposite coatings is shown in Fig. 2.

There is no molecular bonding between the nanoparticles and the EL Ni–P matrix. Unlike the micron-sized particles, incorporation of nanoparticles in the EL

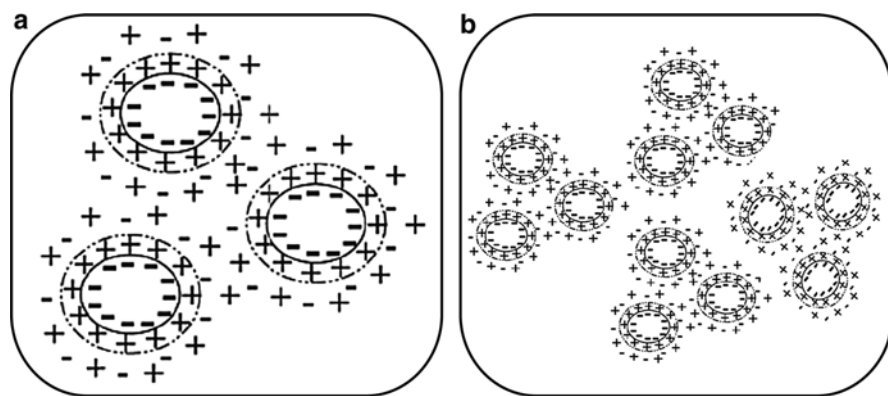


Fig. 1 Schematic representation of (a) formation of an ionic cloud surrounding the nanoparticles and (b) agglomeration of the nanoparticles in the form of clusters after dispersing them in electroless nickel plating solution having a pH of 4.0–5.5 (Reprinted from *Journal of Colloid and Interface Science*, Vol. 314, B.S. Necula, I. Apachitei, L.E. Fratila-Apachitei, C. Teodosiu, J. Duszczuk, Stability of nano-/micro-sized particles in deionized water and electroless nickel solutions, pp. 514–522 (2007), with permission from Elsevier)

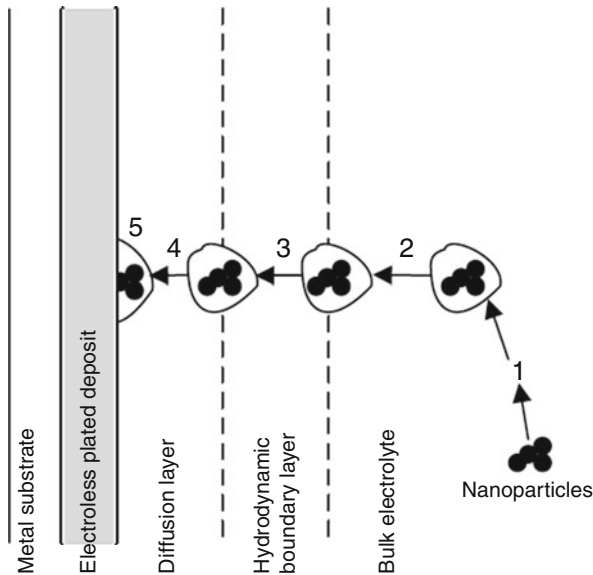


Fig. 2 Pictorial representation of the various stages involved in the formation of electroless nanocomposite coatings: (1) formation of an ionic cloud, (2) transport by means of convection, (3) transport by diffusion, (4) reduction, and (5) adsorption and incorporation in the growing electroless deposited metal matrix (Reprinted from *Progress in Natural Science*, Vol. 21, Wei-wei CHEN, Wei GAO, Microstructures and properties of sol-enhanced nanostructured metal-oxide composite coatings, pp. 355–362 (2011), with permission from Elsevier)

Ni–P matrix occurs not only at the borders and edges but also on the inside of the nickel crystals. Hence, the embedding mechanism of the nanoparticles can be characterized as “intercrystalline.” Based on the mechanism of formation of EL Ni–P nanocomposite coatings (Fig. 2), it appears that the formation of these coatings is quite simple as long as the nanoparticles are kept in suspension. However, the agglomeration of nanoparticles affects the homogeneity and weakens the mechanical properties of the resultant coatings. Hence, the benefits of incorporating nanoparticles in the EL Ni–P matrix could not be fully realized, and it calls for a thorough understanding of the means of achieving an effective dispersion of nanoparticles in the plating bath for the development of EL Ni–P nanocomposite coatings with the desired characteristics.

Challenges and Issues on Particle Incorporation in EL Ni–P Nanocomposite Coatings Prepared by the Conventional Method

Dispersibility of Particles in the Electroless Plating Bath

One of the prime requirements of preparing nanocomposite coatings by EL deposition is the effective dispersion of nanoparticles in the plating bath. Since the nanoparticles possess high surface energy, the attractive energy between them will

be much higher than the repulsive energy, which promotes their agglomeration. This makes the effective dispersion of nanoparticles in the plating bath really challenging. Since a variety of nanoparticles are available and each one of them is unique in its characteristics, many protocols were evolved for dispersing them in the plating bath.

Unlike other nanoparticles, dispersion of CNTs and MWCNTs assumes significance since their length to diameter ratio poses a major problem in dispersing them in the plating bath. In addition, impurities such as silica and amorphous carbon should be removed. Mostly, an acidic solution is recommended for the pretreatment of CNTs/MWCNTs, and it eliminates these impurities [6–12]. In addition, it helps to introduce carboxyl, aldehyde, and other oxygen-containing functional groups on the surface of the CNTs/MWCNTs [7, 8]. However, acid treatment alone is not considered as sufficient since even after acid treatment, the length of the CNTs/MWCNTs is reasonably longer, and most of them are entwined with each other [7]. Ball milling is suggested as an option to decrease the length of the CNTs/MWCNTs. Ball milling using hardened steel balls (~12 mm \varnothing) as the milling medium, with a weight ratio of the steel balls to CNTs/MWCNTs as 50:1, at 200–500 rpm for 10–20 h makes the CNTs/MWCNTs shorter and straighter [7, 10, 12]. The TEM images of MWNTs after acid treatment and subsequent ball milling are shown in Fig. 3a, b, respectively. After acid treatment, the MWNTs were much longer in length than in their diameter, and most of MWNTs were entwined with each other (Fig. 3a), which would have a negative effect on dispersing them in the electroless plating bath. In

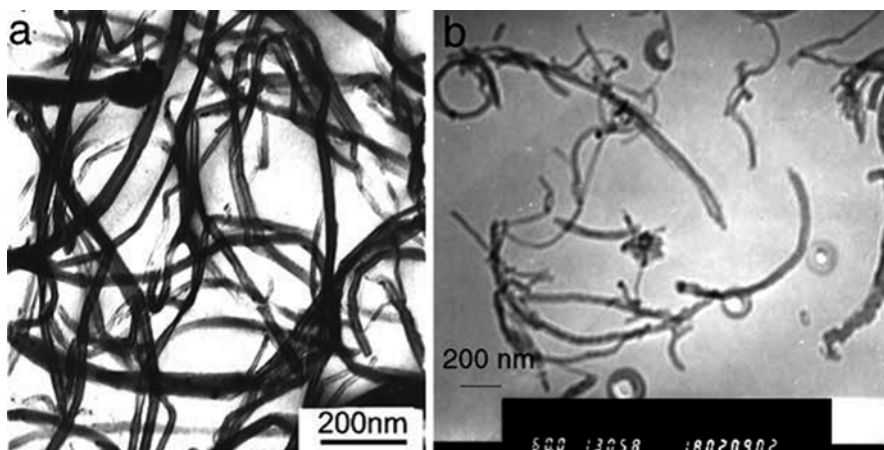


Fig. 3 TEM images of MWNTs (a) after acid treatment using a 3:1 mixture of concentrated H_2SO_4 and HNO_3 , refluxed for 30 min at boiling conditions, followed by refluxing in 5 M HCl for 2 h at boiling condition, washing with deionized water, and drying at 80 °C, and (b) after ball milling for 20 h under nitrogen at a rotating speed of 257 rpm, with a weight ratio of steel balls to purified MWNTs at 50:1 (Reprinted from *Diamond and Related Materials*, Vol. 15, Chuan-sheng Chen, Xiao-hua Chen, ZhiYang, Wen-hua Li, Long-shan Xu, Bin Yi, Effect of multi-walled carbon nanotubes as reinforced fibres on tribological behaviour of Ni-P electroless coatings, pp. 151–156 (2006), with permission from Elsevier)

contrast, after ball milling for a duration of 20 h, the MWNTs were shortened and straightened and were distributed in the form of isolated tube (Fig. 3b), which would be beneficial to improve their dispersion ability in the electroless plating bath. It has been reported that removal of impurities by acid treatment and decrease in length by ball milling have enabled a better dispersion of CNTs/MWCNTs in the plating bath [7, 10–12]. The decrease in length of the CNTs/MWCNTs also helped them to accommodate easily in the Ni–P matrix [6]. In a recent study, Alishahi et al. [12] have described a protocol for preparing CNTs, which sequentially involves ball milling to reduce the length of the CNTs, immersion in 70 % HNO₃ for 1 h to remove the impurities, immersion in 1:3 mixture of HNO₃ and H₂SO₄ for 3 h to exfoliate the CNTs, and addition of a small quantity of HCl to impart carboxyl function groups.

Unlike the CNTs/MWCNTs, pretreatment of other types of nanoparticles is relatively less complex. In general, the nanoparticles are added to a small portion of the EL plating bath along with a suitable surfactant (the choice is based on the type of nanoparticles used), and the suspension is stirred by a magnetic stirrer for 12–24 h followed by ultrasonic agitation for 20–30 min. Subsequently, the nanoparticle suspension is added to the EL plating bath. This procedure is widely used for many types of nanoparticles, viz., SiC [13, 14], WC [15], TiO₂ [16], Al₂O₃ [17], halloysite nanotubes [18], ZrO₂ [19], WS₂ [20] TiN [21], TiC [22] Si₃N₄ [23] diamond [24], etc. Besides CNTs, ball milling is also considered as a pretreatment for other nanoparticles. Li et al. [25] have milled a suspension containing 30 wt% Al₂O₃ nanoparticles along with a polymeric surfactant using ZrO₂ beads (bead size: 0.4–0.5 mm) at 2500 rpm for 12 h. Subsequently, the suspension is dried by *n*-butanol azeotropic distillation process. This methodology leads to significant reduction in particle size of Al₂O₃ nanoparticles from 500 to 12 nm.

The deposition of nanocomposite coatings using EL plating is usually performed for 2–3 h. Hence, the use of some form of agitation, which includes mechanical agitation, circulation by pumping, purging of air, oxygen and nitrogen, plate-pumping technique, and ultrasonic agitation, is necessary to ensure dispersion of the nanoparticles. A schematic representation of the various strategies adopted for bath agitation in industrial applications and laboratory investigations are shown in Fig. 4. It is important to note that in spite of the pretreatments, implementation of some form of agitation is indispensable to achieve an effective dispersion of nanoparticles in the plating bath. Among the various methods of agitation, ultrasonic agitation is considered to be effective. The propagation of ultrasonic waves in the plating bath leads to the generation of cavitation bubbles and its subsequent destruction. This in turn generates a giant pressure (reaching thousands of pressure atmospheres), causing a mammoth stress that destroys the binding energy of the inter-particles and decreases their agglomeration [26].

Surfactants play a vital role in preventing agglomeration and in achieving an effective dispersion of nanoparticles. Various types of surfactants, namely, anionic, cationic, and nonionic, are used for this purpose. The most commonly used surfactants are cetyltrimethylammonium bromide (CTAB), dodecyltrimethylammonium bromide (DTAB), hexadecyltrimethylammonium bromide (HTAB), sodium dodecyl

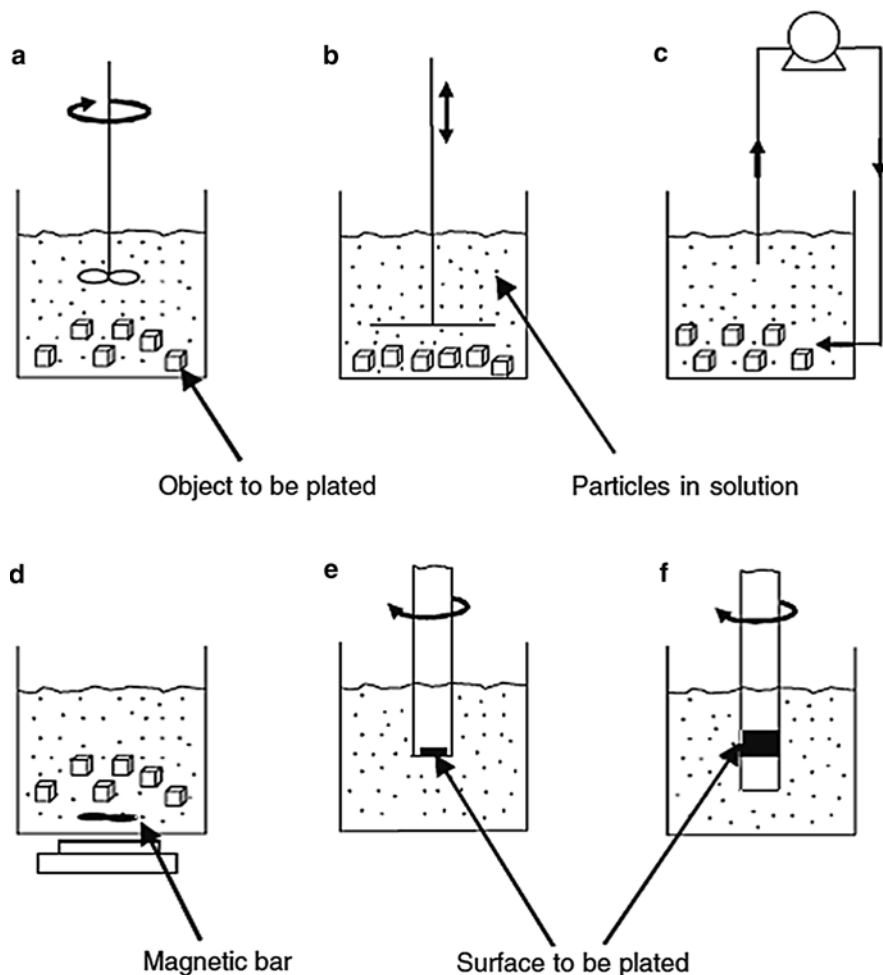


Fig. 4 Schematic representation of the various strategies adopted for bath agitation in industrial applications (a–c) and laboratory investigations (d–f): (a) overhead blade stirrer, (b) reciprocating plate plunger, (c) pumped electrolyte, (d) magnetic stirrer, (e) rotating disk, and (f) rotating cylinder electrodes (Reprinted from *Surface and Coatings Technology*, Vol. 201, C.T.J. Low, R.G.A. Wills, F.C. Walsh, Electrodeposition of composite coatings containing nanoparticles in a metal deposit, pp. 371–383 (2006), with permission from Elsevier)

sulfate (SDS), 1,3-toloyltriethanolammonium chloride (TTAC), tetraethyleneglycol dodecyl ether (Brij 30), polyethylene glycol (PEG), and fluorosurfactants [6, 11, 14, 16, 17, 27–30]. It is important to understand the role of surfactants and its interaction with the nanoparticles so that an effective dispersion of nanoparticles could be achieved in the plating bath. Adsorption of surfactants (by their heads) on the surface of the nanoparticles imparts a charge on the particles. Meanwhile, the tail (usually the long hydrophobic one) of the surfactants provides a steric hindrance, which is helpful

in improving the stability of the nanoparticle suspension. Moreover, surfactants could reduce the surface tension between the hydrogen bubbles and the metal substrate as well as between the metal substrate and the nanoparticles, thus favoring their removal.

The right choice of the surfactant and its concentration, however, is very critical. According to Amell et al. [27], the level of incorporation of SiC nanoparticle in EL Ni–P matrix from a surfactant-free bath is about 2.7 wt%. Addition of lower concentration of fluorosurfactants (0.2 mg/g for cationic and anionic, 1 mg/g for nonionic), regardless of their chemical nature, enabled an increase in level of incorporation (6.0, 5.8, 4.5 wt% for nonionic, cationic, and anionic, respectively). However, at higher concentrations (1 mg/g for cationic and anionic, 2 mg/g for nonionic), the level of incorporation is drastically decreased (3.0, 1.0, and 1.5 wt% for nonionic, cationic, and anionic, respectively). According to Zielinska et al. [28], a higher level of incorporation of ZrO₂ nanoparticles in the EL Ni–P matrix is achieved with the addition of DTAB (cationic surfactant), whereas addition of SDS (anionic surfactant) and Brij 30 (nonionic surfactant) tends to destabilize the plating bath in about 20 min. This is mainly due to the change in surface charge on the ZrO₂ nanoparticles following the adsorption of these surfactants (Table 1). Addition of lower concentration of DTAB (0.50 × cmc) enabled an increase in the level of incorporation of ZrO₂ nanoparticles from 8.11 wt% (from surfactant-free bath) to 12.44 wt%. At higher DTAB concentrations (equal to or above the critical micelle concentration), an enhanced transport of the ZrO₂ nanoparticles is observed, and the level of incorporation is more or less doubled. However, when the DTAB concentration becomes equal to or above the critical micelle concentration, there observed to be a decrease in the Ni and P content of the EL Ni–P matrix. It has been reported that surfactants exhibit a strong interaction with ionic species having an opposite charge and could retain them within the micelles [31]. If the hypophosphite ions are surrounded by the surfactant molecules, then the reduction of Ni and P could be

Table 1 Zeta potential (ζ) values of ZrO₂ nanoparticle in the EL plating bath in the presence of different types of surfactants (measurements made at 25 °C) [28]

Type of surfactant	Critical micelle concentration (cmc) (mol/dm ³)	Concentration used	Zeta potential (ζ) (mV)
No surfactant addition	–	–	–11.6 ± 1.0
Anionic surfactant Sodium dodecyl sulfate (SDS)	0.25 × 10 ⁻³	0.25 × cmc	–46.9 ± 6.0
		0.50 × cmc	–42.5 ± 6.3
		1.00 × cmc	–75.9 ± 5.0
		2.00 × cmc	–35.4 ± 2.1
Cationic surfactant Dodecyltrimethyl-ammonium bromide (DTAB)	14.1 × 10 ⁻³	0.25 × cmc	1.6 ± 0.4
		0.50 × cmc	11.6 ± 0.4
		1.00 × cmc	13.0 ± 1.4
		2.00 × cmc	7.7 ± 0.9
Nonionic surfactant Polyethylene glycol dodecyl ether (Brij 30)	2.3 × 10 ⁻⁵	0.25 × cmc	–6.7 ± 0.6
		0.50 × cmc	–7.5 ± 2.7
		1.00 × cmc	–12.2 ± 0.8
		2.00 × cmc	–11.0 ± 1.6

hampered. This will have other implications in terms of the characteristics of the coating in which the contribution from the matrix will be decreased. Hence, it is very clear that the choice of the surfactant and its concentration should be made judiciously.

Ionic strength of the plating bath is an important factor in achieving effective particle dispersion. It has been reported that the average diameter of agglomerated nanosized (80 nm) Al_2O_3 particles is 183 nm in deionized water, whereas it is increased to 1,109 nm when a considerable amount of nickel ions (1.73 M as Ni^{2+} ions) are present in the solution [32]. A similar trend could also be expected when nanoparticles are added to the electroless plating bath. The use of ultrasonic agitation could reduce the average diameter of the agglomerated Al_2O_3 particles from 1,109 to 280 nm while addition of surfactants could reduce it to 448 nm. The average diameter of the agglomerated Al_2O_3 particles could be reduced to 178 nm only when the concentration of Ni^{2+} ions is decreased to 0.20 M. However, decreasing the concentration of the Ni^{2+} ions is not practically feasible since it will affect the formation of a uniform and pore-free coating.

The charge on the particles also influences their dispersibility. Adsorption of Ni^{2+} ions and/or surfactants could change the surface charge, resulting in either a beneficial or detrimental influence on the dispersibility of the nanoparticles. Measurement of Zeta potential will be a useful guideline in this perspective. However, the higher concentration of Ni^{2+} ions present in the bath poses a serious limitation on the measurement of Zeta potential. Diluting the plating solution may not reflect the reality. The different components present in EL Ni plating bath could influence the Zeta potential to varying degrees [33]. It has been reported that particles which remain stable at room temperature for several weeks could flocculate rapidly when the temperature approaches $\sim 65^\circ\text{C}$, resulting in destabilization of particle suspension [34]. Since majority of the EL plating baths require a very high operating temperature of the order of $85\text{--}95^\circ\text{C}$, achieving a good stability of the particle suspension in the EL plating bath still remains challenging.

Interaction Between the Nanoparticles and the EL Ni-P Matrix During Deposition

The particle flux at the electrode/solution interface is important in determining the interaction between the nanoparticles and the EL Ni-P matrix. The particle flux at the interface depends on the concentration of the nanoparticles, charge on the particle, type and concentration of surfactants, and the mode and speed of agitation. In general, an increase in concentration of nanoparticles will increase the particle flux. However, beyond a threshold value, grouping or agglomeration of nanoparticles becomes predominant, resulting in their settlement rather than increasing the flux. Unlike micron-sized particles, the concentration of nanoparticles used in the plating bath is relatively low. Though an increase in concentration would help to increase the particle flux, it could pose other challenges. An increase in concentration beyond a threshold level could lead to lack of cohesion of between the nanoparticles and the EL Ni-P matrix [6].

Upon addition of nanoparticles to the plating bath, adsorption of metal ions and formation of an ionic cloud over them will occur (Fig. 1). The conditions employed

during EL plating are conducive enough that the nanoparticles could also be plated. The higher surface area, the adsorption of metal ions, and the ability of EL plating baths to coat a variety of substrates make the conditions amenable for plating of the nanoparticles. Studies have convincingly proved that nanoparticles incorporated in EL Ni–P matrix are coated with the corresponding metal ions in the plating bath [6, 10]. Plating of nanoparticles is beneficial to establish a better interaction with the growing metal matrix. However, due to the higher surface area, the nanoparticles might compete with the metal surface during plating that would lead to destabilization of the plating bath. It is important to remember that EL plating baths are highly susceptible for decomposition in the presence of impurities and by all practical means the nanoparticles could also be considered as impurities. The conductivity of the nanoparticles also plays a vital role in this perspective. The chance of plating would be higher for conducting particles than the nonconducting ones. Hence, it appears that for nanoparticles with better conductivity, a relatively lower concentration should be used to ensure process safety.

Another factor that determines the interaction between the nanoparticles and EL Ni–P matrix is the flow conditions (agitation) employed during deposition. Under laminar flow conditions, the particle flux in the vicinity of the electrode surface would be low, and this limits the chances of interaction. In contrast, under turbulent flow conditions, the rate of mass transport of nanoparticles would much be higher that the nanoparticles will be blown away from the electrode surface and collide with the incoming ones. In addition, under turbulent flow conditions, the generation of a shearing force could dislodge the loosely adsorbed nanoparticles from the electrode surface. These conditions could drastically affect the level of incorporation of nanoparticles [26]. Similarly, ultrasonic agitation could also lead to dislodge of nanoparticles if they are not firmly adsorbed to the electrode surface. In general, the laminar-to-turbulent transition region is considered as the most effective agitation condition to achieve higher level of particle incorporation. However, it is important to note that for nanoparticles the laminar-to-turbulent transition occurs at a much lower agitation speed than those experienced by the micron-sized ones [26].

The extent of hydrogen evolution is yet another factor that would limit the residency time of the nanoparticles on the surfaces of the electrode and decrease their chances of incorporation in the matrix. Excessive hydrogen evolution during plating from an alkaline borohydride-reduced EL Ni plating bath has limited the level of incorporation of micron-sized Si_3N_4 particles to a mere 2 wt% [35]. However, the hydrogen evolution during plating has been shown to be very effective in dispersing CNTs during the deposition of EL Ni–P–CNT nanocomposite coating on Mg powders [36].

In the case of micron-sized particles, a particle is considered to be completely incorporated into the metal matrix only when the deposit reaches a certain thickness. Hence, the time required for the complete incorporation of particles is a function of their size and the rate of deposition of the metal matrix. Fortunately, for nanoparticles, their smaller size and the narrow size distribution help them to firmly hold on to the EL Ni–P matrix and ensure a better integrity between them and the matrix.

Alternate Methods of Preparation of EL Ni–P Nanocomposite Coatings

The difficulties encountered in achieving an effective dispersion of nanoparticles in the plating bath as well as in the metal matrix have led to development of two alternate methods of deposition of EL Ni–P nanocomposite coatings. One of the methods explored a combination of sol–gel and EL plating to prepare EL Ni–P–TiO₂ and EL Ni–P–ZrO₂ nanocomposite coatings [37–39]. In this methodology, instead of nanoparticles, the corresponding sol is added to the plating bath at a controlled rate (0.3–0.4 ml/min). The unique feature of this methodology is the in situ formation of nanoparticles, which get incorporated in the growing EL Ni–P matrix. Since the sol is continuously added at a controlled rate, the problems due to agglomeration of nanoparticles are largely eliminated. Unlike the conventional method, no clusters of nanoparticles could be seen on the resultant coatings. Instead, the nanoparticles formed in situ (~15 nm) are uniformly dispersed in the matrix. The morphological features of the EL Ni–P–TiO₂ nanocomposite coatings prepared by the sol–gel and EL plating method in comparison with those prepared by the conventional method (Fig. 5) confirm these attributes. In spite of the addition of the sol, the use

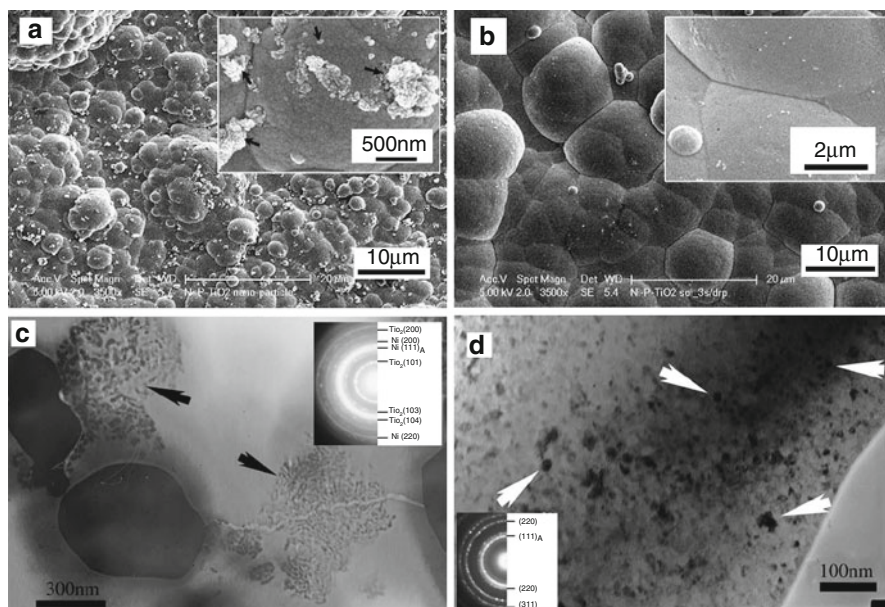


Fig. 5 Scanning (a, b) and transmission electron (c, d) micrographs of EL Ni–P–TiO₂ nanocomposite coatings prepared by conventional electroless plating method (a, c) and the combined sol–gel electroless plating method (Arrows in a, c, and d indicate TiO₂ nanoparticles; insets in a and b indicate extent of agglomeration of TiO₂ nanoparticles; and insets in c and d are the electron diffraction patterns of the coating) (Reprinted from *Surface & Coatings Technology*, Vol. 204, W. Chen, W. Gao, Y. He, A novel electroless plating of Ni–P–TiO₂ nanocomposite coatings, pp. 2493–2498 (2010), with permission from Elsevier)

of mechanical agitation is still required for an effective dispersion of the sol in the plating bath. The decrease in P content of the coating could be a matter of concern in terms of the corrosion resistance.

Zhao et al. [40] have explored a mechanical attrition (MA)-assisted EL plating method to prepared EL Ni–P–CNT nanocomposite coatings. In this method, the CNTs (0.5, 1 and 2 g/l) are added to the EL plating bath along with a large number of 2 mm \varnothing glass balls (1600 g/l), and the substrate is subjected to mechanical attrition during plating. The schematic diagram of the MA-assisted EL deposition of nanocomposite coatings is shown in Fig. 6. The use of MA during plating decreases the concentration gradient, minimizes the depletion layer thickness, and forces the CNTs to distribute uniformly. This condition not only enables a higher level of incorporation of CNTs (59 wt% against 22 wt% by the conventional method) but also ensures their firm attachment in the matrix. The morphological features of the EL Ni–P–CNT nanocomposite coatings prepared by MA-assisted EL plating in comparison with those obtained by the conventional method (Fig. 7) confirm these attributes. The level of incorporation of CNTs is increased with its increase in concentration from 0.5 to 2 g/l. However, coatings prepared using 2 g/l of CNTs have resulted in the formation of a porous coating with a higher surface roughness and exhibit a decrease in hardness. The applicability of this methodology for preparing other types of EL Ni–P nanocomposite coatings is yet to be explored.

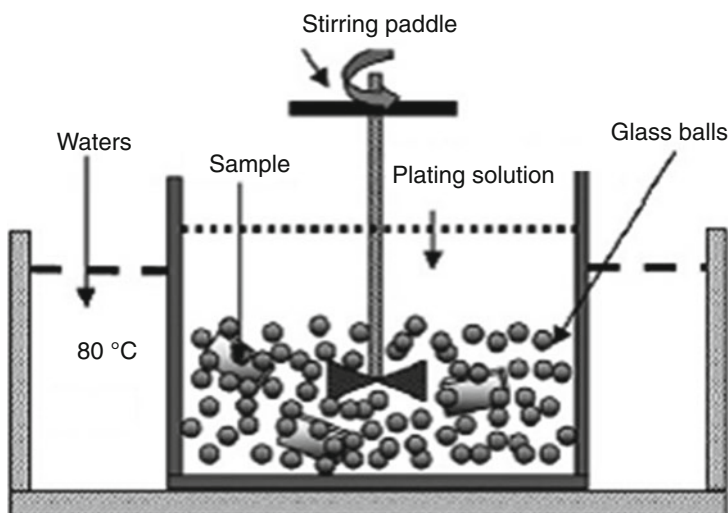


Fig. 6 Schematic diagram of the mechanical attrition-assisted electroless deposition of nanocomposite coatings (Reprinted from *Surface & Coatings Technology*, Vol. 206, G. Zhao, C. Ren, Y. He, Ni–P–multiwalled carbon nanotubes composite coatings prepared by mechanical attrition (MA)-assisted electroless plating, pp. 2774–2779 (2012), with permission from Elsevier)

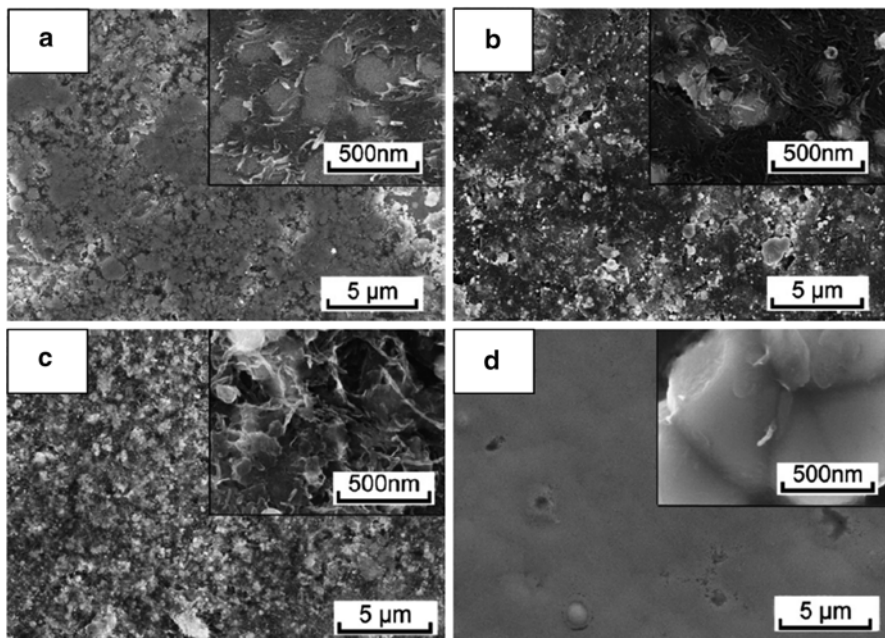


Fig. 7 Surface morphologies of EL Ni–P–CNT nanocomposite coatings prepared by mechanical attrition-assisted (a–c) and conventional electroless plating method (d) using (a) 0.5 g/l CNTs, (b) 1 g/l CNTs, and (c, d) 2 g/l CNTs (insets: higher magnification image of selected regions showing the distribution of CNTs) (Reprinted from *Surface & Coatings Technology*, Vol. 206, G. Zhao, C. Ren, Y. He, Ni–P–multiwalled carbon nanotubes composite coatings prepared by mechanical attrition (MA)-assisted electroless plating, pp. 2774–2779 (2012), with permission from Elsevier)

Influence of Incorporation of Nanoparticles on the Characteristics of EL Ni–P Nanocomposite Coatings

Nucleation, Plating Rate, and Adhesion

Codeposition of nanoparticles in the EL Ni–P matrix influences the nucleation of the metal crystallites. During deposition, adsorption of nanoparticles promotes the number of nucleation sites and reduces nodule formation. Momenzadeh and Sanjabi [16] have shown that the nodular feature which is quite common for particle-free EL Ni–P coating are considerably reduced with the incorporation of TiO₂ nanoparticles. An increase in concentration of TiO₂ nanoparticles in the bath from 3 to 5 g/l leads to the formation of numerous submicron nodules. When the concentration of TiO₂ nanoparticles is increased from 7 to 9 g/l, the shape of the nodules is decreased further. The formation of EL Ni–P–TiC nanocomposite coatings using varying concentrations of TiC nanoparticles was studied by Afroukhteh et al. [22]. Particle-free EL Ni–P coatings exhibit cauliflower-like nodules, which are typical of amorphous

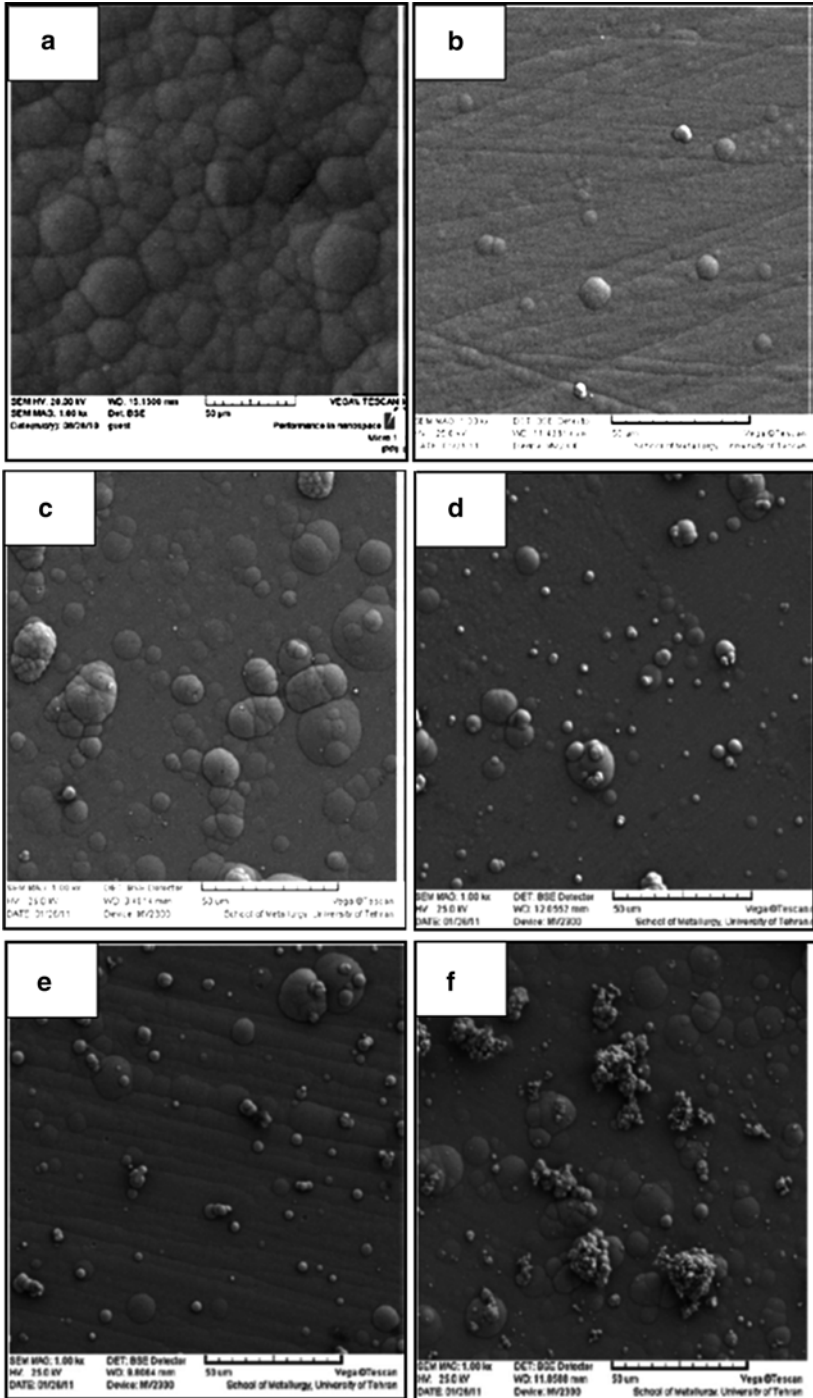


Fig.8 (continued)

material (Fig. 8a). Addition of lower concentrations of TiC nanoparticles (0.01, 0.03, and 0.1 g/l) enables the formation of a smooth coating with few visible nodules (Fig. 8b, c). The average size of the nodules is decreased from 12 to 2 μm . Coatings prepared with the addition of 0.3 and 0.5 g/l of TiC nanoparticles indicate that at locations where the TiC nanoparticles are trapped, another nodular mechanism is initiated (Fig. 8e, f). Lower concentrations of TiC nanoparticles of the order of 0.01, 0.03, and 0.1 g/l may not be sufficient enough to get trapped in the matrix (Fig. 8b, c, d), while the effect becomes dominant at 0.3 and 0.5 g/l of TiC nanoparticles (Fig. 8e, f). These inferences confirm that the nucleation of EL Ni–P nanocomposite coating is influenced by the addition of nanoparticles in the plating bath.

If nanoparticles could act as nucleation sites, then one would expect an increase in the rate of deposition. Hu et al. [23] have reported that addition of Si_3N_4 nanoparticles to EL Ni–Co alloy plating bath has increased the number of catalytic active sites and increased the rate of deposition from 4.2 to 5.6 μm . Addition of TiN nanoparticles, however, has caused a decrease in the deposition rate from 11 to 5 μm [21]. A careful analysis reveals that it is due to the adsorption of surfactant and TiN nanoparticles, which covers the electrode surface and impedes the diffusion of the Ni^{2+} ions toward the interface, thus hindering the rate of deposition. The quench test performed on EL Ni–P–SiC nanocomposite coatings did not show any blisters or delamination of the coating, which suggests that incorporation of nanoparticles in the EL Ni–P matrix will not have any deleterious influence on the adhesion of the coating to the metal substrate [13].

Surface Appearance and Roughness

Codeposition of nanoparticles decreases the metallic luster of the EL Ni–P matrix. The entrapment of particles in EL Ni–P matrix is likely to influence the roughness of the resultant coating. Incorporation of Si_3N_4 nanoparticles in EL Ni–Co–P matrix has increased the average surface roughness from 0.235 μm (for particle-free EL Ni–Co–P coating) to 0.658 μm [23]. However, incorporation of CNTs in the EL Ni–P matrix has led to a decrease in the average roughness from 192 to 129 nm (assessed using atomic force microscopy at a $14\ \mu\text{m} \times 14\ \mu\text{m}$ scale) [12]. The evolution of surface roughness of EL Ni–P nanocomposite coatings depends upon many factors which include (i) growth of EL Ni–P matrix on top of the nanoparticles, (ii) increase in nucleation rate of newer crystals on the surface of the nanoparticles before they are covered by the growing metallic layer, (iii) agglomeration of nanoparticles in the EL Ni–P matrix, and (iv) sticking/protrusion of the nanoparticles out of the EL Ni–P matrix. The addition of surfactants in the EL plating bath could also influence the surface roughness of the resultant nanocomposite coatings [16].



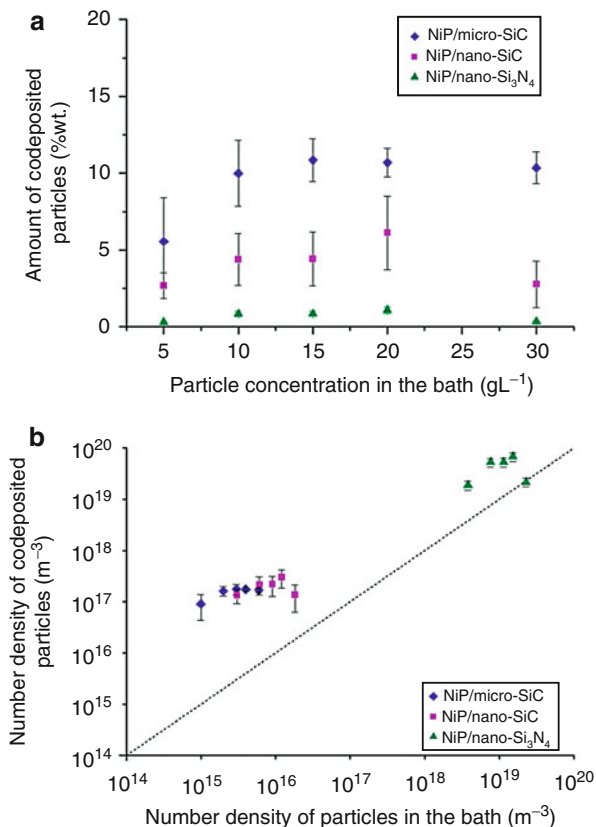
Fig. 8 Surface morphology of particle-free EL Ni–P coating (a) and EL Ni–P–TiC nanocomposite coatings (b–f) prepared using different concentrations of TiC nanoparticles: (a) 0 g/l, (b) 0.01 g/l, (c) 0.03 g/l, (d) 0.1 g/l, (e) 0.3 g/l, and (f) 0.5 g/l (Reprinted from *Applied Surface Science*, Vol. 258, S. Afroukhteh, C. Dehghanian, M. Emamy Preparation of the Ni–P composite coating co-deposited by nano TiC particles and evaluation of its corrosion property, pp. 2597–2601 (2012), with permission from Elsevier)

Level of Incorporation of Nanoparticles and Their Distribution in the EL Ni–P Matrix

The level of incorporation of nanoparticles in EL Ni–P matrix increases with increase in its concentration in the bath up to a threshold value, beyond which it is either saturated or decreased slightly [10, 18, 24]. The increase in level of incorporation of nanoparticles with its concentration can be ascribed to the increased particle flux adjacent to the electrode surface. However, when the concentration is increased beyond a threshold level, there is a possibility of grouping or agglomeration of nanoparticles due to the decrease in the mean distance between them that results in settlement of these particles. Such an effect will lead to a leveling off in the particle flux, causing either saturation or a slight decrease in the level of incorporation. The other reason suggested for the decrease in the level of incorporation at higher concentrations is the increased level of adsorption which deactivates some of the active spots on the electrode surface [10]. In case of CNTs, the threshold level at which saturation or decrease in the extent of incorporation of nanoparticles occurs also depends upon its length. If the length of the CNTs is longer, then its tendency for agglomeration will be higher, and it could exhibit the threshold level at a much lower concentration [8]. The extent of incorporation of nanoparticles in the EL Ni–P matrix should preferably be expressed in terms of number density of the particles [41] although the conventional means of expressing it in terms of volume or weight percentage is still in use. A comparison of the amount of particles codeposited in the metal matrix measured as a function its concentration in the plating bath plotted in terms of both weight percent as well as number density of particles explains the logic behind this (Fig. 9).

Distribution of nanoparticles in the EL Ni–P matrix is an important requirement since the characteristic properties of nanocomposite coatings such as hardness, corrosion resistance, and wear resistance will be decided based on this factor. Studies have shown that the distribution of nanoparticles is uniform as long as the concentration of particles is lesser than the threshold level and they are thoroughly dispersed in the plating bath. If such conditions are maintained, then uniform distribution of nanoparticles could be achieved throughout the thickness of the coating. The surface and cross-sectional morphology of EL Ni–P–Al₂O₃ nanocomposite coatings prepared using varying concentrations of Al₂O₃ nanoparticles (Fig. 10) confirm this attribute. Protrusion of particles outside the matrix is also observed in EL Ni–P nanocomposite coatings, and this possibility is very high for CNTs. Fortunately, due to their smaller size, the nanoparticles are held firmly in the matrix, and they exhibit better integrity with the matrix than their micron-sized counterparts. In spite of the numerous efforts taken, agglomeration of nanoparticles in the plating bath is evitable, and its reflection could be observed in the EL Ni–P nanocomposite coatings in the form of clusters of nanoparticles.

Fig. 9 Comparison of the amount of codeposited particles in the metal matrix as a function of its concentration in the plating bath in terms of (a) weight percent and (b) number density of particles (*Dotted line*: codeposition efficiency, defined as the ratio between the number density of particles in the coating and in the bath = 1) (Reprinted from *Surface & Coatings Technology*, Vol. 205, A. Amell, C. Muller, M. Sarret, Influence of fluorosurfactants on the codeposition of ceramic nanoparticles and the morphology of electroless NiP coatings, pp. 356–362 (2010), with permission from Elsevier)



Structure and Composition

The structure of the EL Ni–P nanocomposite coating is mainly a function of its chemical composition. Coatings prepared from an acidic hypophosphite-reduced EL Ni plating bath depending on the type of additives and operating conditions could contain about 8–11 wt% P, and it is amorphous in nature. Incorporation of nanoparticles in such a matrix is not likely to have much influence on the structural characteristics. However, studies have shown that there is some variation in the P content of the EL Ni–P matrix following the incorporation of nanoparticles. Alishahi et al. [12] have reported that with the incorporation of CNTs, the P content of the EL Ni–P matrix is decreased from 8.2 to 6.4 wt%. Similarly, incorporation of 3.1 wt% of TiN nanoparticles has decreased the P content from 9.4 to 8.9 wt% [21]. Ranganatha et al. [18] have also observed a decrease in P content from 10.4 to 8.6 wt% with the incorporation of 7.8 wt% of HNT in the EL Ni–P matrix.

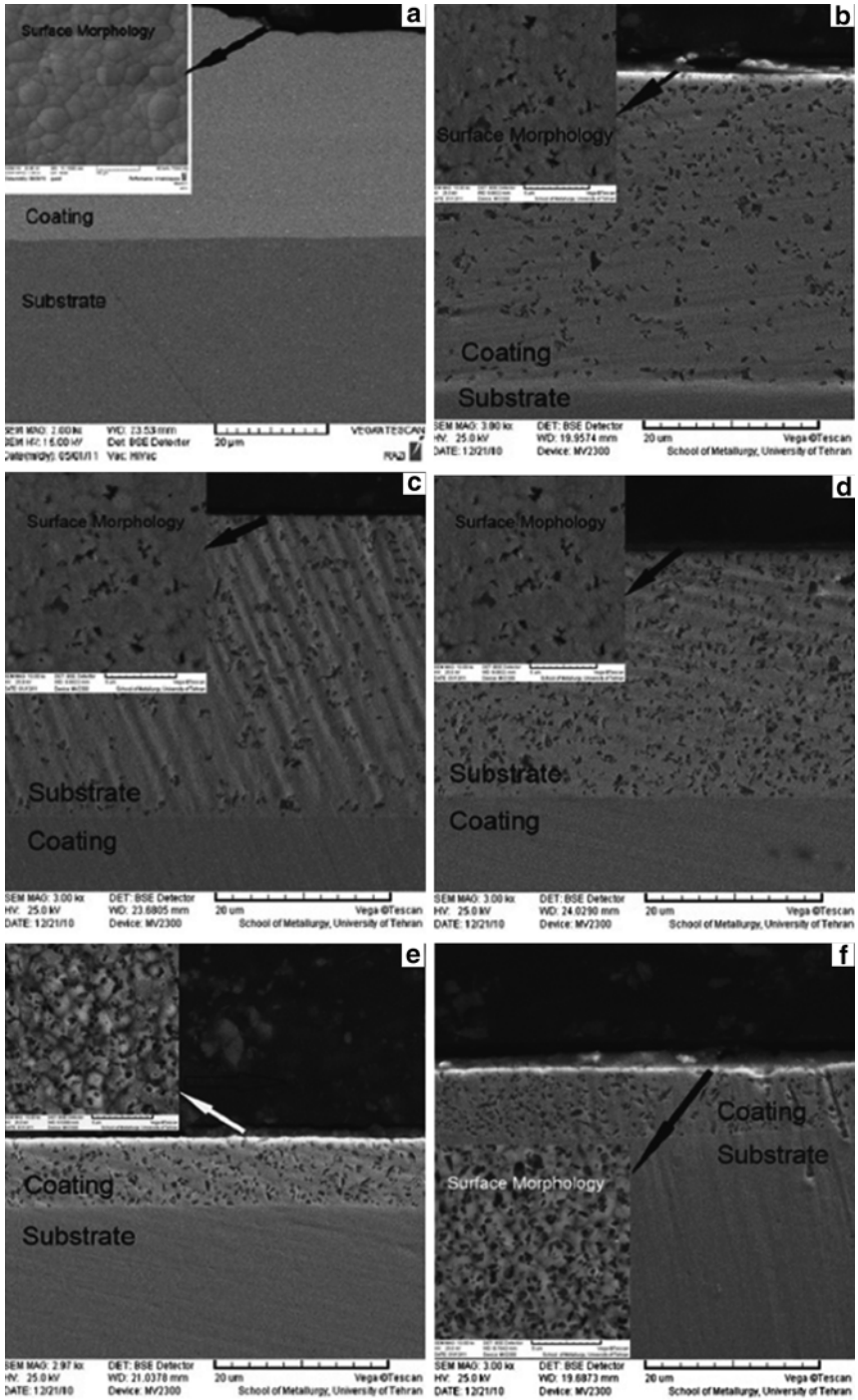


Fig. 10 (continued)

Hardness

EL Ni–P nanocomposite coatings exhibit a higher hardness when compared to their particle-free counterparts. This is due to the combination of grain refinement (Hall–Petch strengthening) and dispersion strengthening (Orowan strengthening) following the incorporation of nanoparticles in the EL Ni–P matrix. The extent of increase in hardness is largely a function of the level of incorporation, distribution, and interparticle spacing between the nanoparticles in the Ni–P matrix. In addition, the alloying elements of the metal matrix and heat treatment determine the overall hardness of EL Ni–P nanocomposite coatings. A higher level of incorporation and uniform distribution of nanoparticles in the Ni–P matrix are likely to increase the hardness.

Tribological Characteristics

EL Ni–P nanocomposite coatings offer a better wear resistance when compared to their particle-free counterparts. The improvement in wear resistance is due to the increase in hardness and load-bearing capacity of the Ni–P matrix following incorporation of nanoparticles, which reduces the extent of plastic deformation and adhesive wear between the mating surfaces. Heat treatment at 400 °C for 1 h enables the formation of hard nickel phosphide intermetallic phases and increases the wear resistance further. To achieve a better wear resistance, it is necessary to ensure (i) a high number density of nanoparticles, (ii) uniform distribution, (iii) better integrity between the nanoparticles and the Ni–P matrix, and (iv) heat treatment to impart a high hardness and to present an incompatible surface for the counterface material during wear. The tribological performance of EL Ni–P nanocomposite coatings incorporated with CNTs/MWCNTs [6–8, 12], Si₃N₄ [23], SiO₂ [42], Al₂O₃ [25], HNT [18], WS₂ [20], and WC [15] nanoparticles confirms the above attributes.

EL Ni–P nanocomposite coatings incorporated with CNTs/MWCNTs assume significance due to its self-lubrication property and unique antifriction structure. The elastic buckling property of CNTs makes them as exceedingly tough materials. The improved mechanical characteristics, unique topological structure of the central hollow nanotubes, uniform distribution of CNTs in the EL Ni–P matrix, and ability of CNTs with its netlike structure to assist in load-bearing ability, to enhance the stiffness and toughness of EL Ni–P matrix, and to continuously release the CNTs that could serve as spacers between the mating surfaces are considered responsible for the improved tribological behavior of EL Ni–P–CNT nanocomposite coatings [6–8, 12]. A comparison of the wear track patterns and the wear morphology of



Fig. 10 Surface and cross-sectional morphology of EL Ni–P–Al₂O₃ nanocomposite coatings prepared using varying concentrations of Al₂O₃ nanoparticles: (a) 0 g/l, (b) 3 g/l, (c) 5 g/l, (d) 10 g/l, (e) 20 g/l, and (f) 30 g/l (Reprinted from *Progress in Natural Science: Materials International*, Vol. 22, S. Afroukhteh, C. Dehghanian, M. Emamy, Preparation of electroless Ni–P composite coatings containing nanoscattered alumina in presence of polymeric surfactant, pp. 318–326 (2012), with permission from Elsevier)

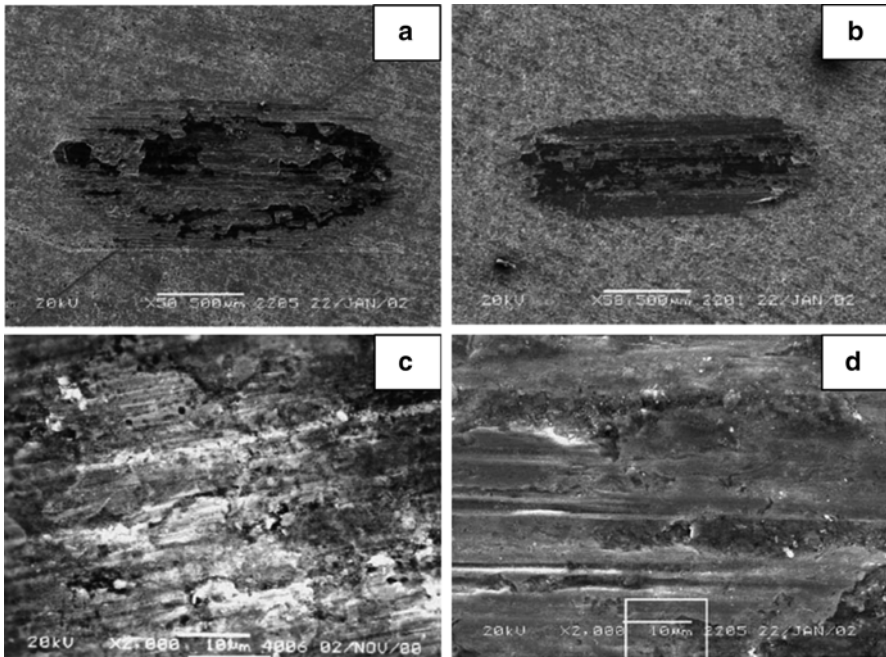


Fig. 11 Scanning electron micrographs of the wear tracks (a, b) and wear morphology (c, d) at specific location in the wear tracks of particle-free EL Ni–P coatings (a, c) and electroless Ni–P–CNT nanocomposite coatings (Reprinted from *Tribology International*, Vol. 39, X.H. Chen, C.S. Chen, H.N. Xiao, H.B. Liu, L.P. Zhou, S.L. Li, G. Zhang, Dry friction and wear characteristics of nickel/carbon nanotube electroless composite deposits, pp. 22–28 (2006), with permission from Elsevier)

particle-free EL Ni–P coating and EL Ni–P–CNT nanocomposite coatings (Fig. 11) confirms these attributes. EL Ni–P nanocomposite coatings incorporated with HNT and WS_2 also exhibit similar characteristics [18, 20].

Hu et al. [23] have reported that the worn tracks of EL Ni–Co–P exhibit signs of serious adhesion, scuffing, and plastic deformation. Conversely, for EL Ni–Co–P– Si_3N_4 nanocomposite coatings, the extent of adhesion is decreased significantly following the increase in hardness and load-bearing capacity of the matrix with the incorporation of Si_3N_4 nanoparticles. In this case, the incorporation of Si_3N_4 nanoparticles in the EL Ni–P matrix does not change the wear mechanism; rather, it barely decreased the extent of damage. A similar behavior is also expected for other types of nanocomposite coatings. It is important that the nanoparticles should establish a good integrity with the EL Ni–P matrix and get engulfed in it. Otherwise, during wear, the nanoparticles could be pulled out of the matrix. Protrusion of hard nanoparticles could cause wear of the mating surface. This is particularly critical for nanoparticles like WC, which under such conditions change the wear mechanism from sliding friction to rolling friction, resulting in abrasive wear [15]. In spite of its ability to serve as spacer between mating surfaces, integrity with the EL Ni–P

matrix is also important for CNTs. Incorporation of higher concentration of CNT beyond a threshold level could lead to lack of cohesion between them and EL Ni–P matrix, which would adversely influence the wear resistance [6].

Corrosion Resistance

Corrosion resistance of EL Ni–P nanocomposite coatings has been a debatable issue. Incorporation of certain types of nanoparticles in the Ni–P matrix enables an increase in corrosion resistance, while a reversal in trend is observed for others. EL Ni–P nanocomposite coatings incorporated with CNTs [12], WS₂ [20], TiO₂ [16], SiC [13], and SiO₂ [43] have increased the corrosion resistance, while those built-in with TiN [21], B₄C [44], and α -Al₂O₃ [25] exhibit a decrease in corrosion resistance when compared to their particle-free counterparts. A variety of reasons is suggested to account for this behavior. Decrease in effective metallic surface area, decrease in porosity, sealing of defects and cracks due to accommodation of nanoparticles, ability of the codeposited nanoparticles to act as barriers for the growth of corrosion paths, formation of a compact layer, and decrease in chemical reactivity at the nanocomposite coating/corrosive electrolyte interface, promotion of homogeneous or uniform corrosion rather than the localized corrosion attack are considered as the major reasons for the observed improvement in corrosion resistance. Conversely, an increase in surface roughness and porosity of the coating, lower electrical resistivity of the nanoparticles, and formation of galvanic cells are accountable for the decrease in corrosion resistance.

In a certain type of nanocomposite coatings, an improvement in corrosion resistance is observed for coatings prepared using lower concentration of nanoparticles in the plating bath, whereas a reversal in trend is observed if the concentration of nanoparticles is increased beyond a threshold level (Table 2). EL Ni–P nanocomposite coatings incorporated with SiC, ZrO₂, HNT, and diamond nanoparticles exhibit such dependence [14, 18, 19]. This decrease in corrosion resistance observed in these instances is due to the formation of cracks in the coating due to the buildup of stress with a higher level of incorporation of nanoparticles [14] and due to the poor adhesion of nanoparticles in the Ni–P matrix [18]. The findings of Farzaneh et al. [14] and Ranganatha et al. [18, 19] indicate that decrease in effective metallic

Table 2 Corrosion parameters of EL Ni–P–SiC nanocomposite coatings in 3.5 % NaCl, evaluated by potentiodynamic polarization studies [14]

Type of coating/concentration of SiC nanoparticles	Corrosion potential E_{corr} (mV vs. SCE)	Corrosion current density i_{corr} ($\mu\text{A}/\text{cm}^2$)	Polarization resistance R_p ($\Omega \text{ cm}^2$)
EL Ni–P (0 g/l SiC)	–662	2.51	9,123
EL Ni–P–SiC (2 g/l SiC)	–512	0.56	41,070
EL Ni–P–SiC (4 g/l SiC)	–537	0.93	24,730
EL Ni–P–SiC (8 g/l SiC)	–618	1.27	18,110

surface area though a possible reason for the improvement in corrosion resistance of nanocomposite coatings, but it could not be the main reason. In addition, it is clear that the ability of EL Ni–P nanocomposite coatings to offer a better corrosion resistance is not dependent on the type of nanoparticles incorporated in the matrix; rather, it is a function of the quality of the coating in terms of its uniformity and compactness.

Another interesting aspect of the corrosion resistance of EL Ni–P nanocomposite coatings is the role of the metal matrix. During corrosion, at open circuit conditions, preferential dissolution of nickel enables an enrichment of phosphorus on the surface layer, which upon reaction with water leads to the formation of a layer of adsorbed hypophosphite anions (H_2PO_2^-). This layer in turn blocks the supply of water to the electrode surface, thereby preventing the hydration of nickel, which is considered to be the first step to form either soluble Ni^{2+} species or a passive nickel film [45, 46]. If the P content of the EL Ni–P nanocomposite coatings is decreased with the incorporation of nanoparticles, then the ability of the matrix to form the protective layer by hypophosphite anions could be decreased. The findings of Afroukhteh et al. [22] help to understand this phenomenon. The EL Ni–P–TiC nanocomposite coatings prepared using 0.01 and 0.03 g/l of TiC fail to show a reasonable level of incorporation of TiC nanoparticles and decreased the P content of the coating. The corrosion resistance offered by these coatings is much lower than their particle-free counterparts. Coatings prepared using 0.3 and 0.5 g/l of TiC have also led to a decrease in P content. However, incorporation of a reasonable level of TiC nanoparticles ($\sim 1.7 \pm 0.2$ wt%) has enabled an increase in corrosion resistance. Hence, it can be inferred that a decrease in P content could cause a deleterious influence, whereas an increase in level of incorporation of nanoparticles is likely to offer a beneficial influence, and the net effect between these factors will dictate the corrosion behavior of EL Ni–P nanocomposite coatings. According to Ashassi-Sorkhabi and Es'haghi [47], the typical cauliflower-like morphological features of EL Ni–P coating provide a suitable path for the corrosion process. However, the codeposited diamond nanoparticles (DNP) act as barriers for the growth of corrosion paths. In addition, the corrosion paths become less straight when the level of incorporation of DNP in the EL Ni–P matrix becomes higher. The schematic of the possible corrosion paths that could occur in EL Ni–P and EL Ni–P–diamond nanoparticle (DNP) composite coatings are shown in Fig. 12.

Heat treatment of EL Ni–P nanocomposite coatings is performed at 400 °C for 1 h to improve their hardness and wear resistance. However, heat treatment at such conditions leads to structural changes and contraction/shrinkage of the EL Ni–P matrix. In spite of its even distribution in the EL Ni–P matrix, it will be difficult for the nanoparticles to accommodate these structural changes. This would result in formation of fissures/cracks, which originate at the nanoparticles and drastically affect the corrosion resistance of the EL Ni–P nanocomposite coatings. In addition, it would also change the mode of corrosion attack from general and uniform corrosion to the localized one. Since heat treatment is considered necessary to improve the hardness and wear resistance, it is recommended to perform the heat treatment at 200 °C for a relatively longer duration of time and/or to employ a duplex coating

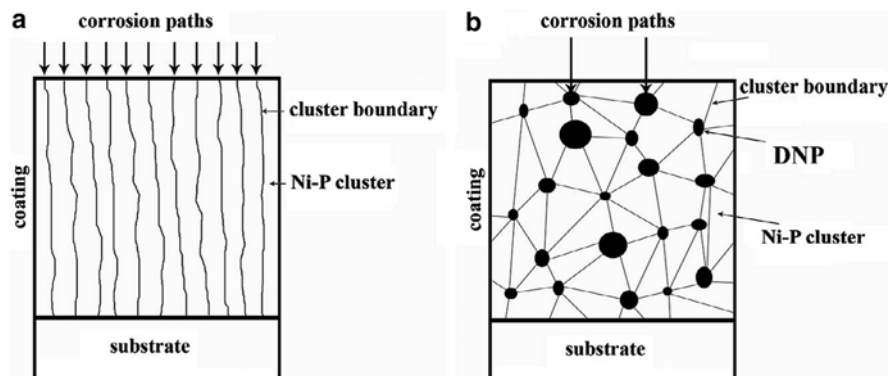


Fig. 12 Schematic of the possible corrosion paths in (a) EL Ni-P and (b) EL Ni-P–diamond nanoparticle (DNP) composite coatings (Reprinted from *Corrosion Science*, Vol. 77, Habib Ashassi-Sorkhabi, Moosa Es’haghi, Corrosion resistance enhancement of electroless Ni–P coating by incorporation of ultrasonically dispersed diamond nanoparticles, pp. 185–193 (2013), with permission from Elsevier)

consisting of an initial EL Ni–P coating followed by EL Ni–P nanocomposite coating. This combination would provide a better corrosion protection by barrier-layer effect. Allahkaram et al. [13] have employed this duplex coating methodology to improve the corrosion resistance of X70 steel in oil and gas industry environments containing CO_2 along with dissolved acetic acid.

Applications of EL Ni–P Nanocomposite Coatings

EL Ni–P nanocomposite coatings incorporated with CNTs/MWCNTs, WS_2 , and HNT provide a low coefficient of friction. Hence, these coatings could be used in molds for rubber and plastic, pumps, ball and butterfly valves, fasteners, aluminum air cylinders, carburetor choke shafts, etc. Similarly, EL Ni–P–SiC and other similar nanocomposite coatings due to their high hardness, excellent wear resistance, and better corrosion resistance could be considered as an effective replacement for hard chrome plating.

EL Ni–Cu–P–graphite nanocomposite coatings deposited on anodized 5083 Al alloy have decreased the in-plane electrical resistivity and through-plane resistance, increased the corrosion resistance in 0.5 M H_2SO_4 + 2 ppm NaF at 80 °C, and offered an improved long-term stability in such aggressive conditions [48]. The ability of these coatings to meet the electrical property and corrosion resistance requirements of the US Department of Energy (DOE) 2020 technical targets for bipolar plates used in PEMFCs suggests that they could be utilized for such applications.

Deposition of EL Ni–P– TiO_2 nanocomposite coatings on 316 L stainless steel (316 L SS) followed by UV irradiation for 2 h has reduced the adhesion of *Pseudomonas fluorescens* (freshwater bacteria) and *Cobetia marina* 4741 and

Vibrio alginolyticus 2171 (marine bacteria) by about 75 % [49]. The microbiocidal property of the TiO₂ nanoparticles along with the UV treatment enables a decrease in water contact angle and an increase in electron donor surface energy. These types of coatings could be used in heat exchangers, ship hulls, pipelines, etc., where bio-fouling is a major problem.

EL Ni–P–TiO₂ nanocomposite-coated carbon electrodes incorporated with 1.4, 4.5, and 5.1 wt% of TiO₂ nanoparticles exhibit an increase in efficiency toward electrochemical oxidation of organic compounds such as methanol, formaldehyde, and glucose when compared to their particle-free counterpart [50]. The decrease in grain size and increase in surface area following the incorporation of TiO₂ nanoparticles enabled an increase in the number of active sites for the oxidation. These attributes enhanced the formation of Ni redox couple (Ni³⁺/Ni²⁺), which decides the rate of oxidation of these organic compounds. The EL Ni–P–TiO₂ nanocomposite-coated carbon electrodes could find application in environmental treatment.

Deposition of EL Ni–P–CB nanocomposite coating on ABS plastic has led to an abrupt decrease in infrared emissivity from 0.956 to 0.303 at a wavelength of 8–14 μm [51]. Moreover, it also improved the electrical conductivity. These attributes indicate that EL Ni–P–CB nanocomposite coating could be used as an ideal low-infrared emissivity material. EL Ni–P–HA nanocomposite coating deposited on 316 L SS improved corrosion resistance in simulated body fluid. It also served as an intermediate layer for subsequent electrochemical deposition of HA, with improved adhesion [52]. These coatings could be explored for biomedical applications. EL Ni–P–CNT-coated magnesium powder could be used as the feedstock for production of bulk magnesium nanocomposites through casting or powder metallurgy routes [36]. In addition to the applications described above, EL Ni–P nanocomposite coatings have also received considerable attention for a variety of other applications, some of which are compiled in Table 3.

Summary and Concluding Remarks

Deposition of EL Ni–P nanocomposite coatings appears to be simple as it calls for a mere dispersion of the nanoparticles in the plating bath and incorporating them in the metal matrix. However, due to their high surface energy, nanoparticles tend to agglomerate in the plating bath, which makes the process complex. The protocols recommended for pretreatment and dispersion, though effective to varying degrees, are far from success in achieving an effective dispersion of nanoparticles. The use of surfactants is beneficial in many ways as it imparts a surface charge on the particle and it reduces the surface tension between the hydrogen bubbles and the metal substrate as well as between the metal substrate and the nanoparticles. However, the right choice of the surfactant and its concentration becomes very critical. Considering the options of reducing the concentration of metal ions and/or performing the plating process at lower temperatures, the window of opportunity available to manipulate these parameters is rather limited. The level of incorporation of nanoparticles in the metal matrix exhibits a linear dependence with the concentration of particles in

Table 3 Choice of electroless nanocomposite coatings for various types of applications [4]

Intended application	Type of composite coatings
To provide friction and dry lubrication	EL Ni-P-PTFE EL Ni-P-MoS ₂ EL Ni-P-PTFE-MoS ₂ EL Ni-P-PTFE-SiC
To increase the wear resistance	EL Ni-P-diamond EL Ni-P-h BN
To increase in life of molds for plastics, rubber, butterfly valves, etc.	EL Ni-P-CNT EL Ni-P-MWCNTs EL Ni-P-WS ₂ EL Ni-P-HNT
To reduce the wear and enable an easy release of sand cores	EL Ni-P-SiC
To prevent the pickup and galling from arising during forming and drawing operations	EL Ni-P-SiC EL Ni-P-PTFE
To prevent buildup of gummy deposits	EL Ni-P-PTFE
To achieve high accuracy microfinishing	EL Ni-P-diamond
To prevent accelerated corrosion of molds	EL Ni-P-SiC EL Ni-P-PTFE
To increase the corrosion resistance of carbon steel	EL Ni-P-Al ₂ O ₃ EL Ni-P-PTFE EL Ni-P-Si ₃ N ₄ EL Ni-P-CeO ₂ EL Ni-P-TiO ₂ EL Ni-B-Si ₃ N ₄ EL Cu-P-SiC
To develop electrothermal actuators for micro and nano electromechanical (MEMS/NEMS) systems	EL Ni-P-diamond EL Ni-P-CNT
Electrocatalytic electrode materials for hydrogen evolution reaction	EL Ni-P-TiO ₂ EL Ni-P-TiO ₂ -supported RuO ₂ EL Ni-P-TiO ₂ -supported IrO ₂
To develop smart coating and to identify genuine OEM parts as an indicator	EL Ni-P-europium-doped yttrium vanadate
To develop a sensor for sensing ethanol	EL Ni-P-TiO ₂ -supported nano-RuO ₂
To decrease infrared emissivity	EL Ni-P-carbon black
To increase microwave absorption	EL Ni-P-X nanocomposite coating (X = BaZn _{2-y} Co _y Fe ₁₆ O ₂₇ , where y = 0, 0.4, 0.8, 1.2, 1.6, 2.0)
To increase electrocatalytic and photocatalytic degradation of organic compounds	EL Ni-P-TiO ₂

the bath up to a threshold level. However, even at concentrations much below the threshold level, other problems such as plating of the particles becomes dominant. Plating of nanoparticles though beneficial in terms of a better interaction with the metal matrix could destabilize the bath. The alternate methods of preparing EL Ni-P nanocomposite coatings could handle the issues of particle dispersion with

some degree of success. However, these methods have their own limitations, and the applicability of these methods for incorporating a variety of nanoparticles is yet to be explored. The nanoparticles could act as nucleation sites and promote the rate of deposition. They have the ability to decrease the nodule formation and/or the size of the nodules. Since the concentration of nanoparticles in the plating bath and their level of incorporation in the metal matrix are limited, no change in structural characteristics is expected. However, the decrease in P content observed with some particles especially at higher level of incorporation could be a matter of concern in terms of corrosion resistance. The EL Ni–P nanocomposite coatings offer a high hardness and excellent wear resistance. Improvement in corrosion resistance is also observed with the incorporation of nanoparticles as long as they do not create any pores and/or cracks in the coatings, increase the surface roughness, and decrease the P content to a large extent, and they are electrically nonconducting. Certain types of EL Ni–P nanocomposite coatings find applications in critical areas such as fuel cells, environmental degradation, biomedical applications, preventing biofouling, etc. In spite of the numerous research efforts made in the field of EL Ni–P nanocomposite coatings, achieving an effective dispersion of nanoparticles in the EL plating bath still remains a challenging issue, and the quest for an effective solution continues.

References

1. Riedel W (1991) Electroless plating. ASM International, Ohio
2. Ohno I (1991) Electrochemistry of electroless plating. *Mater Sci Eng A* 146:33–49
3. Balaraju JN, Sankara Narayanan TSN, Seshadri SK (2003) Electroless Ni–P composite coatings. *J Appl Electrochem* 33:807–816
4. Sankara Narayanan TSN, Seshadri SK (2012) Electro- and electroless deposited composite coatings: preparation, characteristics, and applications. In: Wiley encyclopaedia of composites, John Wiley & Sons, Inc., New Jersey, pp 1–17
5. Sudagar J, Lian JS, Sha W (2013) Electroless nickel, alloy, composite and nano coatings – a critical review. *J Alloy Compd* 571:183–204
6. Chen WX, Tu JP, Gan HY, Xu ZD, Wang QG, Lee JY, Liu ZL, Zhang XB (2002) Electroless preparation and tribological properties of Ni–P–Carbon nanotube composite coatings under lubricated condition. *Surf Coat Technol* 160:68–73
7. Chen CS, Chen XH, Yang Z, Li WH, Xu LS, Yi B (2006) Effect of multi-walled carbon nanotubes as reinforced fibres on tribological behaviour of Ni–P electroless coatings. *Diam Relat Mater* 15:151–156
8. Chen XH, Chen CS, Xiao HN, Liu HB, Zhou LP, Li SL, Zhang G (2006) Dry friction and wear characteristics of nickel/carbon nanotube electroless composite deposits. *Tribol Int* 39:22–28
9. Li ZH, Wang XQ, Wang M, Wang FF, Ge HL (2006) Preparation and tribological properties of the carbon nanotubes–Ni–P composite coating. *Tribol Int* 39:953–957
10. Yucheng W, Rong R, Fengtao W, Zaoshi Y, Tugen W, Xiaoye H (2008) Preparation and characterization of Ni–Cu–P/CNTs quaternary electroless composite coating. *Mater Res Bull* 43:3425–3432
11. Zarebidaki A, Allahkaram SR (2011) Effect of surfactant on the fabrication and characterization of Ni–P–CNT composite coatings. *J Alloy Compd* 509:1836–1840
12. Alishahi M, Monirvaghefi SM, Saatchi A, Hosseini SM (2012) The effect of carbon nanotubes on the corrosion and tribological behavior of electroless Ni–P–CNT composite coating. *Appl Surf Sci* 258:2439–2446

13. Allahkaram SR, Honarvar Nazari M, Mamaghani S, Zarebidaki A (2011) Characterization and corrosion behavior of electroless Ni-P/nano-SiC coating inside the CO₂ containing media in the presence of acetic acid. *Mater Design* 32:750–755
14. Farzaneh A, Mohammadi M, Ehteshamzadeh M (2013) Electrochemical and structural properties of electroless Ni-P-SiC nanocomposite coatings. *Appl Surf Sci* 276:697–704
15. Liu YY, Yu J, Huang H, Xu BH, Liu XL, Gao Y, Dong XL (2007) Synthesis and tribological behavior of electroless Ni-P-WC nanocomposite coatings. *Surf Coat Technol* 201:7246–7251
16. Momenzadeh M, Sanjabi S (2012) The effect of TiO₂ nanoparticle codeposition on microstructure and corrosion resistance of electroless Ni-P coating. *Mater Corros* 63:614–619
17. Alirezaei S, Monirvaghefi SM, Saatchi A, Urgan M (2013) Novel investigation on tribological properties of Ni-P-Ag-Al₂O₃ hybrid nanocomposite coatings. *Tribol Int* 62:110–116
18. Ranganatha S, Venkatesha TV, Vathsala K (2012) Development of high performance electroless Ni-P-HNT composite coatings. *Appl Surf Sci* 263:149–156
19. Ranganatha S, Venkatesha TV, Vathsala K (2012) Process and properties of electroless Ni-Cu-P-ZrO₂ nanocomposite coatings. *Mater Res Bull* 47:635–645
20. Ranganatha S, Venkatesha TV, Vathsala K (2012) Electroless Ni-W-P coating and its nano-WS₂ composite: Preparation and properties. *Ind Eng Chem Res* 51:7932–7940
21. Mafi IR, Dehghanian C (2011) Studying the effects of the addition of TiN nanoparticles to Ni-P electroless coatings. *Appl Surf Sci* 258:1876–1880
22. Afroukhteh S, Dehghanian C, Emamy M (2012) Preparation of the Ni-P composite coating co-deposited by nano TiC particles and evaluation of its corrosion property. *Appl Surf Sci* 258:2597–2601
23. Hu J, Fang L, Zhong P, Tang A, Yin B, Li Y (2012) Preparation and properties of Ni-Co-P/nano-sized Si₃N₄ electroless composite coatings. *Surf Interf Anal* 44:450–455
24. Mazaheri H, Allahkaram SR (2012) Deposition, characterization and electrochemical evaluation of Ni-P nano diamond composite coatings. *Appl Surf Sci* 258:4574–4580
25. Li C, Wang Y, Pan Z (2013) Wear resistance enhancement of electroless nanocomposite coatings via incorporation of alumina nanoparticles prepared by milling. *Mater Design* 47:443–448
26. Lajevardi SA, Shahrabi T, Hasannaemi V (2011) Synthesis and mechanical properties of nickel-titania composite coatings. *Mater Corros* 62:29–34
27. Amell A, Muller C, Sarret M (2010) Influence of fluorosurfactants on the codeposition of ceramic nanoparticles and the morphology of electroless NiP coatings. *Surf Coat Technol* 205:356–362
28. Zielinska K, Stankiewicz A, Szczygieł I (2012) Electroless deposition of Ni-P-nano-ZrO₂ composite coatings in the presence of various types of surfactants. *J Colloid Interf Sci* 377:362–367
29. Afroukhteh S, Dehghanian C, Emamy M (2012) Corrosion behavior of Ni-P/nano-TiC composite coating prepared in electroless baths containing different types of surfactant. *Prog Nat Sci Mater Int* 22:480–487
30. Afroukhteh S, Dehghanian C, Emamy M (2012) Preparation of electroless Ni-P composite coatings containing nano-scattered alumina in presence of polymeric surfactant. *Prog Nat Sci Mater Int* 22:318–325
31. Ogihara H, Hara A, Miyamoto K, Shrestha NK, Kaneda T, Ito S, Saji T (2010) Synthesis of super hard Ni-B/diamond composite coatings by wet processes. *Chem Commun* 46:442–444
32. Erler F, Jakob C, Romanus H, Spiess L, Wielage B, Lampke T, Steinhäuser S (2003) Interface behaviour in nickel composite coatings with nano-particles of oxidic ceramic. *Electrochim Acta* 48:3063–3070
33. de Hazan Y, Reuter T, Werner D, Clasen R, Graule T (2008) Interactions and dispersion stability of aluminum oxide colloidal particles in electroless nickel solutions in the presence of comb polyelectrolytes. *J Colloid Interf Sci* 323:293–300
34. de Hazan Y, Werner D, Z'graggen M, Groteklaes M, Graule T (2008) Homogeneous Ni-P/Al₂O₃ nanocomposite coatings from stable dispersions in electroless nickel baths. *J Colloid Interf Sci* 328:103–109

35. Krishnaveni K, Sankara Narayanan TSN, Seshadri SK (2012) Electroless Ni-B-Si₃N₄ composite coating: Deposition and evaluation of its characteristic properties. *Synth React Inorg Metal* 42:920–927
36. Firoozbakht M, Monirvaghefi SM, Niroumand B (2011) Electroless composite coating of Ni-P-carbon nanotubes on magnesium powder. *J Alloy Compd* 509:S496–S502
37. Chen W, Gao W, He Y (2010) A novel electroless plating of Ni-P-TiO₂ nano-composite coatings. *Surf Coat Technol* 204:2493–2498
38. Yang Y, Chen W, Zhou C, Xu H, Gao W (2011) Fabrication and characterization of electroless Ni-P-ZrO₂ nano-composite coatings. *Appl Nanosci* 1:19–26
39. Chen W, Gao W (2011) Microstructures and properties of sol-enhanced nanostructured metal-oxide composite coatings. *Prog Nat Mater Mater Int* 21:355–362
40. Zhao G, Ren C, He Y (2012) Ni-P-multiwalled carbon nanotubes composite coatings prepared by mechanical attrition (MA)-assisted electroless plating. *Surf Coat Technol* 206:2774–2779
41. Sarret M, Muller C, Amell A (2006) Electroless NiP micro- and nano-composite coatings. *Surf Coat Technol* 201:389–395
42. de Hazan Y, Zimmermann D, Z'graggen M, Roos S, Aneziris C (2010) Homogeneous electroless Ni-P/SiO₂ nanocomposite coatings with improved wear resistance and modified wear behavior. *Surf Coat Technol* 204:3464–3470
43. Rabizadeh T, Allahkaram SR (2011) Corrosion resistance enhancement of Ni-P electroless coatings by incorporation of nano-SiO₂ particles. *Mater Design* 32:133–138
44. Araghi A, Paydar MH (2013) Electroless deposition of Ni-W-P-B₄C nanocomposite coating on AZ91D magnesium alloy and investigation on its properties. *Vacuum* 89:67–70
45. Balaraju JN, Sankara Narayanan TSN, Seshadri SK (2001) Evaluation of the corrosion resistance of electroless Ni-P and Ni-P composite coatings by electrochemical impedance spectroscopy. *J Solid State Electrochem* 5:334–338
46. Sankara Narayanan TSN, Baskaran I, Krishnaveni K, Parthiban S (2006) Deposition of electroless Ni-P graded coatings and evaluation of their corrosion resistance. *Surf Coat Technol* 200:3438–3445
47. Ashassi-Sorkhabi H, Es'haghi M (2013) Corrosion resistance enhancement of electroless Ni-P coating by incorporation of ultrasonically dispersed diamond nanoparticles. *Corros Sci* 77:185–193
48. Lee CK (2012) Electroless Ni-Cu-P/nano-graphite composite coatings for bipolar plates of proton exchange membrane fuel cells. *J Power Sources* 220:130–137
49. Zhao Q, Liu C, Su X, Zhang S, Song W, Wang S, Ning G (2013) Antibacterial characteristics of electroless plating Ni-P-TiO₂ coatings. *Appl Surf Sci* 274:101–104
50. Abdel Aal A, Hassan HB, Abdel Rahim MA (2008) Nanostructured Ni-P-TiO₂ composite coatings for electrocatalytic oxidation of small organic molecules. *J Electroanal Chem* 620:17–25
51. Liu X, Wu C, Wang X (2010) Synthesis, characterization, and infrared-emissivity study of Ni-P-CB nanocomposite coatings by electroless process. *J Coat Technol Res* 7:659–664
52. Shibli SMA, Jayalekshmi AC (2009) A novel nano hydroxyapatite-incorporated Ni-P coating as an effective inter layer for biological applications. *J Mater Sci Mater Med* 20:711–718

Self-Assembled Monolayers on Nanostructured Composites for Electrochemical Sensing Applications

14

Nada F. Atta, Ekram H. El-Ads, and Ahmed Galal

Contents

General Introduction	418
Sensor	418
Nanostructured Hybrids for Electrochemical Sensing Applications.....	419
Nanostructured Metallic Particles on Polymers.....	419
General Introduction	419
Different Routes of Formation of Polymer/Metal Nanocomposite Hybrid	420
Characterization of Nanometallic Particles/Polymer Composite	422
Sensing Applications.....	428
Self-Assembled Monolayer of Surfactant on Polymers and Hybrid Nanostructures	437
Surfactants and Self-Assembly in Solution.....	437
Micelles in Aqueous Medium	437
Surfactants Self-Assembly at Solid/Liquid Interface.....	438
Modes of Surface Modification by Surfactants.....	438
Sensor Applications of Surfactant SAM on Polymers.....	442
SAM of Surfactant on Polymers/Nanometallic Structures	451
Self-Assembled Monolayer of S-Containing Compounds on Nanostructures	454
Self-Assembled Monolayer.....	455
Methods of SAM Preparation	456
SAM-Modified Nanostructured Electrodes.....	457
Desorption of SAM	458
Sensing Applications of SAM-Modified Nanostructures.....	460
Conclusions.....	470
References.....	471

N.F. Atta • E.H. El-Ads • A. Galal (✉)

Chemistry Department, Faculty of Science, Cairo University, Giza, Egypt

e-mail: galal@sci.cu.edu.eg

© Springer International Publishing Switzerland 2016

M. Aliofkhaezrai, A.S.H. Makhlof (eds.), *Handbook of Nanoelectrochemistry*,

DOI 10.1007/978-3-319-15266-0_38

417

Abstract

Self-assembled monolayer (SAM) represents one of the methods to precisely modify surface structures in the nanoscale dimension. It has opened up a new era of exploration and has a profound impact on sensors and biosensors due to its unique properties. Different self-assemblies will be considered in this chapter: SAM of metallic nanoparticles on polymeric film, SAM of surfactant on polymeric film, and SAM of S-containing compounds on nanometallic films. The main goal of this chapter is to present comprehensive collection of the recent achievements in this area. Several issues will be discussed including the morphology, sensitivity, selectivity, stability, and electrochemical properties of the sensor.

Keywords

Nanostructured composites • Self-assembled monolayer • Conducting polymers • Metal nanoparticles • Surfactants • Sensors

General Introduction

Sensor

A sensor can be described as a device capable of converting the different types of signals. Systems generate signals due to physical, chemical, biological, and several other changes that are normally transformed into electrical signals. A typical sensor responds with selectivity and specificity to the target analyte without interference (Fig. 1). The main components of the sensor are transducer and detector devices. Signals are collected, amplified, and displayed using signal processor. A biosensor is a specific type of sensor that should include a biological component in its sensing element; an example is blood glucose biosensor. On the other hand, a chemical sensor can convert the chemical information that results from a chemical reaction including the analyte itself or from a physical property of the system under investigation into an analytically representative signal. This chemical information may be ranged from the concentration of a specific component to the analysis of the total composition of the sample. Selectivity, anti-interference ability, linear dynamic

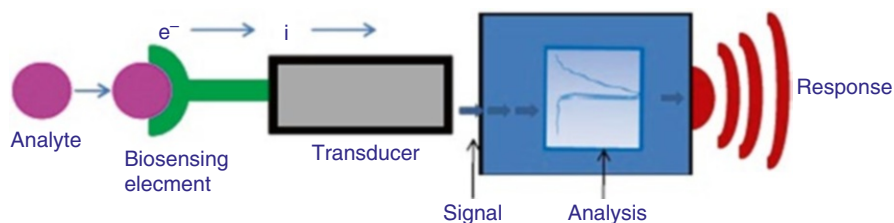


Fig. 1 A schematic of an electrochemical biosensor with electrochemical transducer (Reprinted from [1], Copyright (2013), with permission from Elsevier)

ranges, limit of detection, sensitivity, and precision of response can be used to experimentally evaluate the performance of any biosensor. Other parameters can be taken into consideration like portability, ease of use, stability, and time of response. A typical sensing surface should be renewable so that several repetitive measurements can be made [1].

Nanostructured Hybrids for Electrochemical Sensing Applications

Self-assembled monolayer (SAM), a fashionable approach to electrically orient and address a molecular component of interest, represents one of the methods that precisely modify the surface structure in the nanoscale dimension. It has opened up a new era of exploration and has a profound impact on sensors and biosensors due to its unique properties. SAM may be nanometallic film, surfactant film, or SAM of S-containing compounds, particularly cysteine over modified or bare substrates. This chapter will give a brief review of SAM of metallic nanoparticles (Pd, Pt, etc.) over different polymeric films (poly(3-methylthiophene), polypyrrole, polyfuran, etc.) showing the enhanced catalytic activity of these hybrid nanocomposites and its biosensing applications. Moreover, it will show the SAM of different surfactants over polymeric film of poly(3,4-ethylenedioxythiophene) PEDOT and over the hybrid nanocomposite of PEDOT/gold nanoparticles. It will show its biosensing applications toward different neurotransmitters and drugs. On the other hand, this chapter will explain the effect of formation of SAM of S-containing compounds on different substrates: macro- and nanoelectrode (bare electrodes and metallic nanoparticle-modified electrodes). It will display the sensing applications of gold nanoparticles electrode modified with self-assembled monolayers of cysteine and surfactants. It will explain the role of SAM of surfactant and that of cysteine in the enhancement of the catalytic activity and improvement of the stability of the proposed electrodes toward sensing applications.

Nanostructured Metallic Particles on Polymers

General Introduction

The physicochemical characteristics of bare electrodes can be improved using electrode modifiers such as conducting polymers. Conducting polymers can significantly improve the analytical detection by enhancing the sensitivity and selectivity and lowering the detection limit; therefore, they are utilized as redox mediators for several analytes. Moreover, they exhibit an anti-interference ability which resulted in electrochemical responses with excellent repeatability. On the other hand, the catalytic electrode processes can be activated using mediating agent that can be used in the solution containing the analyte, and this was the first developed system suitable for this purpose. On the other hand, the mediating agent can be immobilized directly on the electrode surface through electrochemical polymerization resulting in chemically modified electrode. The electrochemical polymerization can

be achieved via galvanostatic, potentiostatic, or potential sweeping techniques. As a result, these modified electrodes exhibited several advantages such as reduced matrix effect, fast regeneration of the catalyst, anti-contamination of the solution by the redox mediator, and improved performance of the redox mediator [2]. Due to their combination of useful electrochemical, electrochromic, and electrocatalytic properties [3]; antifouling, mechanical, optical, and electronic properties; as well as their high sensitivities and low detection limits [4], conducting polymers have been widely used for a variety of sensors, biosensors [5], and actuators to improve the response time, sensitivity, reliability, and versatility of different sensors and biosensors [6].

On the other hand, it is well known that metal nanoparticles exhibited unique electronic, physical, and chemical characteristics besides their small size (1–100 nm) and flexibility. As a result, they have obvious applications in electrochemical sensing and catalysis. Metal nanoparticles are described as “electron wires” that enhance the kinetics of electron transfer between the redox centers of the target molecules and the electrode surface [1]. It is well known that the catalytic activity of metal nanoparticles is affected by their dispersion and surface properties. Conducting polymers exhibited metallike conductivity reaching a range as high as 10^3 – 10^5 S cm^{-1} and long π -conjugation length; therefore, they are considered as useful matrices for metal nanoparticles immobilization [7]. In addition, the high porosity of the conducting polymer structure generates additional electrocatalytic sites by allowing the dispersion of metal nanoparticles into the polymer matrix. As well, the facilitation of the charge transfer kinetics between the substrate and the dispersed metal nanoparticles is more obvious in the conducting polymer matrix. Also, metal nanoparticles’ incorporation to conducting polymers enhances the performance for both the “host” and the “guest” leading to various physical characteristics and potential applications in electrochemical capacitors and protective coatings against corrosion [8], magnetic devices, biomaterial separation membranes [9], electronics, sensors, nanoelectronic sensor devices, biosensors, and catalysis.

Conducting polymer-incorporated metallic nanoparticles, or the so-called nanocomposites [8], exhibited synergistic unique physical and chemical characteristics based on the porous polymer and the dispersed metal [10–14]. The combination of the porous structure and high efficient electronic charge flow of the conducting polymers with the high reactive surface area presented by noble metal nanoparticles resulted in interesting electrocatalytic properties [15]. As well, the development of the composite material aims to enhance the electrocatalytic properties of the simple polymeric electrode coating [16]. Various hybrid nanocomposites were fabricated for different applications which are summarized in Table 1.

Different Routes of Formation of Polymer/Metal Nanocomposite Hybrid

There are different routes for the growing of metal nanoparticles inside the polymer matrix: chemical routes [8, 9, 20, 21], electrochemical deposition of metal

Table 1 Summary of various hybrid nanocomposites and their applications

Hybrid nanocomposites	Application	References
Pt nanoparticles' dispersed poly(3-methylthiophene)	DNA biosensor	[17]
Pd and Pt nanoclusters' modified poly(3-methylthiophene) (PMT), poly(<i>N</i> -methylpyrrole) (PMPy), and polyfuran	Sensors for simultaneous determination of catecholamine neurotransmitters and acetaminophen in the presence of uric acid and ascorbic acid	[10–13]
Gold nanoclusters' modified insulating overoxidized polypyrrole	Electrochemical biosensor for dopamine and serotonin	[18]
PEDOT/Pd composite	Electrochemical sensor for simultaneous determination of dopamine and uric acid	[19]

Table 2 Summary of the different routes of formation of polymer/metal nanocomposite hybrid

Routes of formation of polymer/metal nanocomposite	Example	References
Chemical routes for the growth of metal nanoparticles inside the polymer matrix	Chemical preparation of gold-incorporated PEDOT nanocomposite via reverse emulsion polymerization method [8] Spontaneous deposition of Au and Pt nanoparticles on polymers containing sulfur by the immersion of the polymer into the metal nanoparticle suspension (colloidal methods; citrate or borohydride reduction in the presence of citrate capping agent) [15, 17]	[8, 9, 15, 17, 20, 21]
Electrodeposition of polymer and metal nanoparticles simultaneously	PEDOT including Au nanoparticles by constant current method on ITO glass in aqueous medium [26]	[14, 24–26]
Electrodeposition of metal nanoparticles on the spin-coated polymer		[22]
Electrochemical deposition of metal nanoparticles on the electropolymerized polymer	Electrodeposited Au nanoparticles by bulk electrolysis BE method (at -400 mV for 400 S) over the electrochemically prepared PEDOT film by BE at 1400 mV for 30 S [27] Nano-Au/PPy _{ox} composite by electrochemical polymerization of pyrrole by cycling the potential from -0.35 to 0.85 V for 3 cycles. Then, Au nanoclusters were electrochemically deposited on the PPy _{ox} /GCE by cycling the potential between 0.2 and -1.0 V in HAuCl ₄ solution for 15 cycles [18]	[7, 18, 19, 23, 27, 28]

nanoparticles on the polymer matrix that was prepared by spin coating [22] or electrochemical methods [23], and electrodeposition of polymer and metal nanoparticles simultaneously [14, 24, 25]. Summary of the different routes of formation of polymer/metal nanocomposite hybrid is given in Table 2.

Characterization of Nanometallic Particles/Polymer Composite

Surface and Chemical Characterization

Scanning electron microscope (SEM) is an electrochemical tool which gives an image for the different studied surfaces explaining their morphology in relation to electrocatalytic activity. Pd nanoparticles electrodeposited on poly(3-methylthiophene) (PMT) film-modified Pt electrode was utilized as novel electrochemical biosensor. The electrocatalytic activity of the obtained nanocomposite is affected to a great extent by the polymerization method of the polymer (bulk electrolysis BE, cyclic voltammetry CV) and the deposition method of Pd nanoparticles. Pt/PMT (BE), Pt/PMT(CV), Pt/PMT(BE)/Pd(BE), and Pt/PMT(BE)/Pd(CV) showed great difference in their electrocatalytic response which can be explained in terms of their morphology analyses (Fig. 2a–e). Pt/PMT(BE) exhibited a compact morphology with low porosity but Pt/PMT(CV) showed fluffy surface with high porosity. On the other hand, Pd nanoparticles are larger with dendrite forms at Pt/PMT(BE)/Pd(BE), while smaller Pd particles with homogenous distribution are observed at Pt/PMT(BE)/Pd(CV). In a conclusion, the electrocatalytic activity of the modified electrodes is highly affected by the size and homogeneity of the deposited nanoparticles [11].

Furthermore, the loading of the metal nanoparticles on the polymer matrix can be confirmed using energy dispersive X-ray analysis (EDX). Atta et al. constructed a novel biosensor by the electrodeposition of Pt or Pd nanoparticles into poly(3-methylthiophene) (PMT) matrix. BE technique was used to prepare PMT film at 1800 mV for 30 s. Then, metal nanoparticles were electrodeposited by double potential step (BE) method. The formed electrode can be represented as Pt/PMT(240 or 360 nm)/M, M: Pt or Pd particles. EXD analysis was performed to investigate the ratio of the loaded Pd/Pt over the polymer film corresponding to its value in the deposition solution and to confirm the immobilization of metal nanoparticles over the polymer matrix. The deposition solution contained equimolar amounts of PdCl₂ and PtCl₂. Figure 3 showed the EDX analysis explaining the atomic percentages of 47.22 and 52.78 corresponding to Pd and Pt, respectively, which is very close to their ratio in the deposition solution [11].

XRD

XRD was used to confirm the formation of polymer incorporating metal nanoparticles. Gold nanoparticles are dispersed in the PEDOT backbone that was polymerized in a linear fashion. The XRD patterns of PEDOT and Au-incorporated PEDOT nanoparticles are shown in Fig. 4. No characteristic peaks are observed in case of PEDOT, except the low angle peak at ~25° which is characteristic to the amorphous nature of the polymeric material. On the other hand, the diffraction characteristic peaks for PEDOT–Au nanocomposite appeared at 2θ 38.20°, 44.41°, 64.54°, 77.50°, and 81.68° corresponding to (111), (200), (220), (311), and (222) planes of the standard cubic phase of Au, respectively [8, 9, 28]. The broadening of XRD peaks suggests the formation of nanocrystallites. The average particle size of Au nanoparticles was ~50 nm based on Scherrer equation [8].

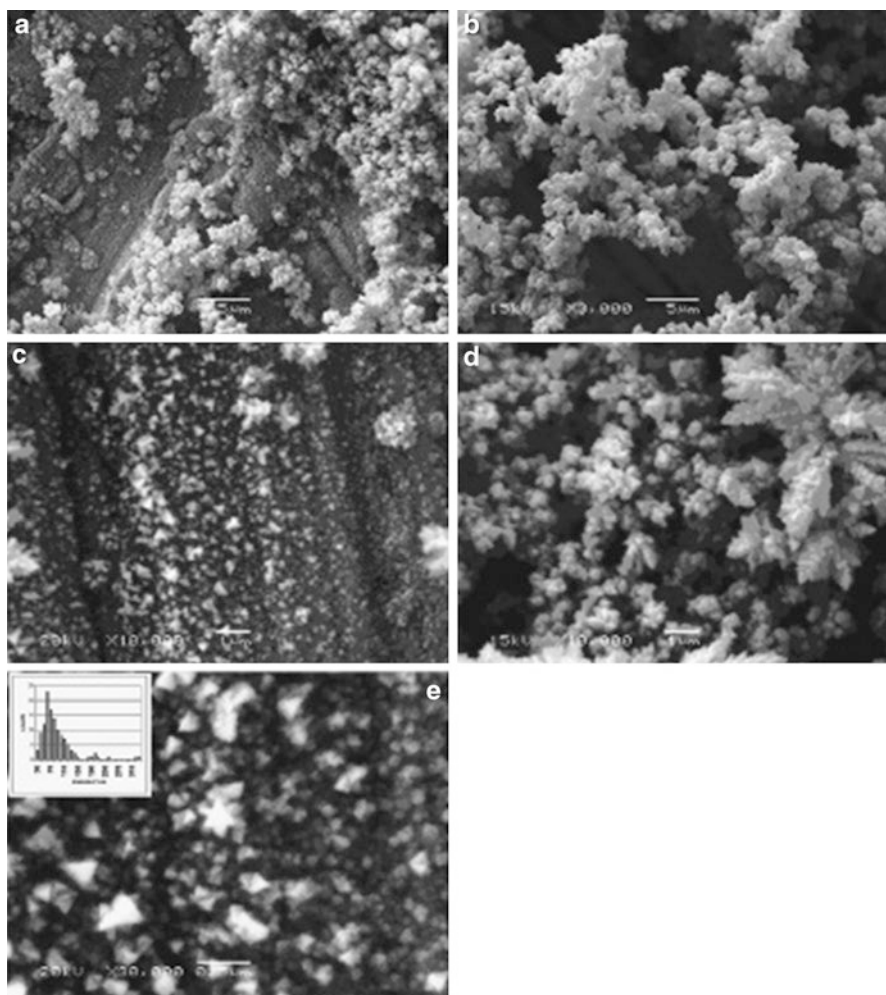


Fig. 2 Scanning electron micrographs for (a) Pt/PMT(BE), (b) Pt/PMT(CV), (c) Pt/PMT(BE)/Pd(BE), and (d, e) Pt/PMT(BE)/Pd(CV). *Inset*: histogram showing the Pd particle size distribution; average size is around 60 nm (Reprinted from [11], Copyright (2010), with permission from Elsevier)

AFM

Topography and properties of different surfaces can be measured using atomic force microscope. Figure 5a, b shows the AFM 3D images of Au/PEDOT and Au/PEDOT–Au_{nano} electrodes by the noncontact mode, respectively [27].

XPS

X-ray photoelectron spectra (XPS) can be used to confirm the incorporation of metal nanoparticles on the polymer film. Y. Lee prepared PEDOT/Au nanocomposite using a redox cycle system. Two strong signals of Au 4f_{5/2} and 4f_{7/2} energy levels

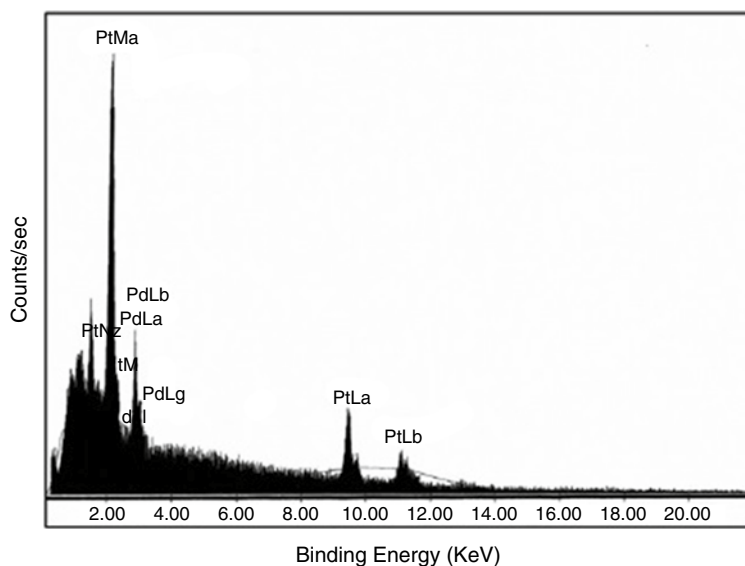


Fig. 3 Energy dispersive analysis by X-ray, EDAX, for Pt/PMT/(Pd+Pt) electrode. Pd and Pt were deposited by the double potential step method from a solution of 2.5 mM PdCl₂+2.5 mM PtCl₂/0.1 M HClO₄ (Reprinted from [11], Copyright (2010), with permission from Elsevier)

were centered at 84.4 and 88.0 eV, respectively, indicating the presence of metallic gold [21] (Fig. 6). Moreover, Ce Wang utilized Pt/polypyrrole (PPy) hybrid hollow microspheres as electrocatalysts for hydrogen peroxide reduction. Pt/polypyrrole was prepared by wet chemical method via Fe₃O₄ template. Figure 7 showed the XPS patterns of Pt/polypyrrole composites showing a significant Pt4f signal due to the binding energy of metallic Pt (Fig. 7a), a C1s signal due to the binding energy of C (Fig. 7b) and a N1s signal corresponding to the binding energy of N (Fig. 7c). Therefore, XPS can be used to confirm the formation of Pt/PPy hybrid hollow spheres by the wet chemical method using Fe₃O₄ template [29].

FTIR

FTIR can be used to illustrate the molecular structure of nanocomposites. FTIR spectroscopy was used to characterize the molecular structure of the Pt/PPy hybrid hollow spheres. Figure 8 investigated the characteristic bands of the Pt/PPy hybrid hollow spheres which are the pyrrole ring fundamental vibrations. The characteristic bands appeared at 1564 cm⁻¹ (C=C stretching), 1456 cm⁻¹ (C-C stretching), 1338 cm⁻¹ (C-N stretching vibration in the ring), 1068 cm⁻¹ (C-H deformation vibration), 1132 cm⁻¹ (C-C breathing), 3461 cm⁻¹ (N-H stretching mode), and 846 cm⁻¹ (C-H out of plane vibration). The FTIR spectra of Pt/PPy hybrid hollow spheres and Fe₃O₄/PPy spheres showed no obvious difference indicating that no chemical bonds exist between Pt nanoparticles and PPy shell [29].

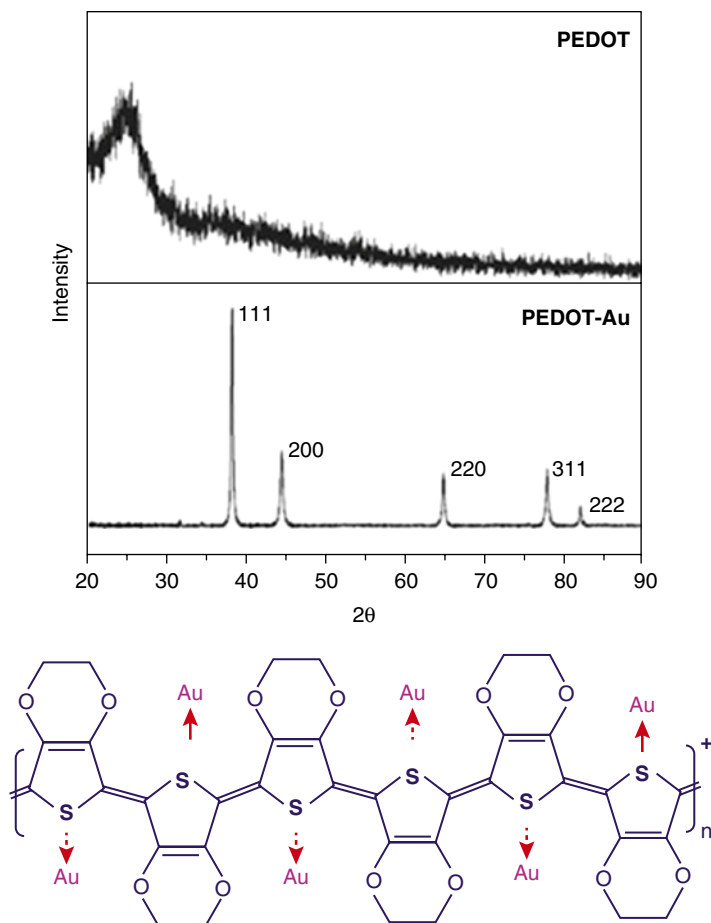


Fig. 4 XRD pattern of nanoparticles of PEDOT and Au–PEDOT nanocomposite and schematic diagram showing Au nanoparticles incorporated within the polymer backbone (Reprinted from [8], Copyright (2007), with permission from Elsevier)

On the other hand, the FTIR spectrum of the PEDOT film and monomer is shown in Fig. 9. The formation of PEDOT chains with α , $\acute{\alpha}$ -coupling can be demonstrated by the disappearance of the strong band at 890 cm^{-1} (C–H bending mode) in the polymer spectrum compared to the monomer spectrum. Thiophene ring exhibited vibrations at 1518 , 1483 , and 1339 cm^{-1} due to C=C and C–C stretching modes. C–S bond vibration modes in the thiophene ring appeared at 978 , 842 , and 691 cm^{-1} . The stretching modes of ethylenedioxy group appeared at 1213 and 1093 cm^{-1} . The band around 920 cm^{-1} is attributed to the ethylenedioxy ring deformation mode. On the other hand, the doped state of PEDOT usually shows an absorption peak at 1722 cm^{-1} . The intensity increases in the case of Au-incorporated polymer matrix as a result of Au_{nano} doping within the polymer matrix [8].

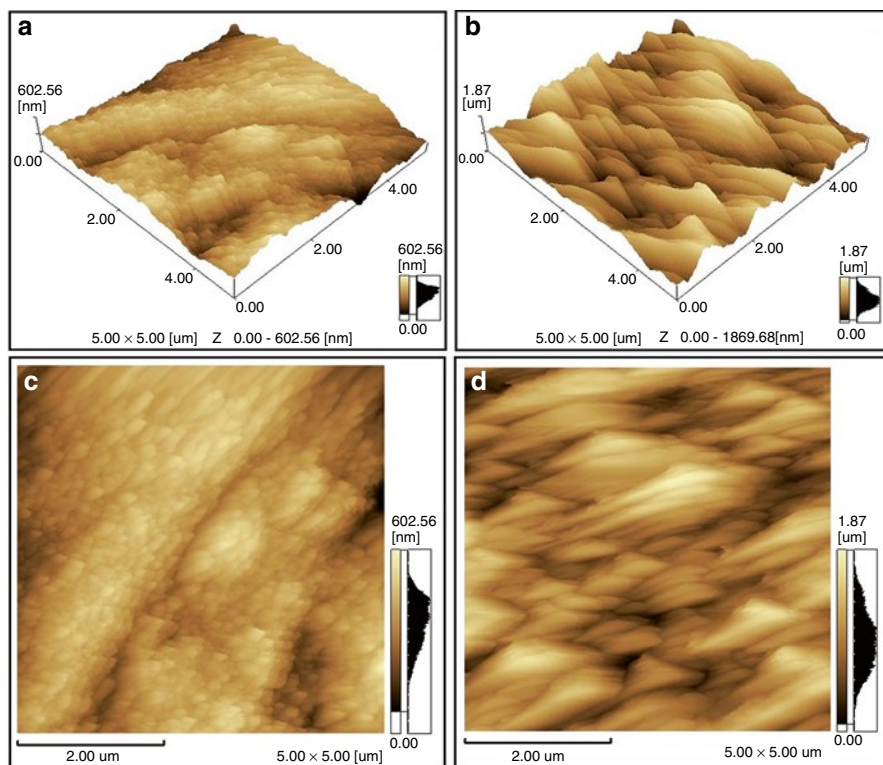


Fig. 5 3D AFM images of Au/PEDOT (a) and Au/PEDOT–Au_{nano} (b) electrodes by noncontact mode. 2D AFM images by noncontact mode of Au/PEDOT (c) and Au/PEDOT–Au_{nano} (d) electrodes (Reprinted from [27], Copyright (2012), with permission from Elsevier)

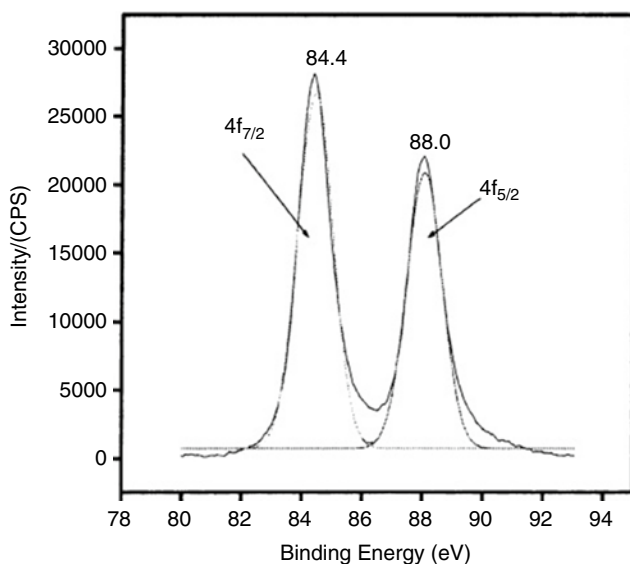


Fig. 6 XPS spectrum of PEDOT/Au composite film (Reprinted from [21], Copyright (2005), with permission from Elsevier)

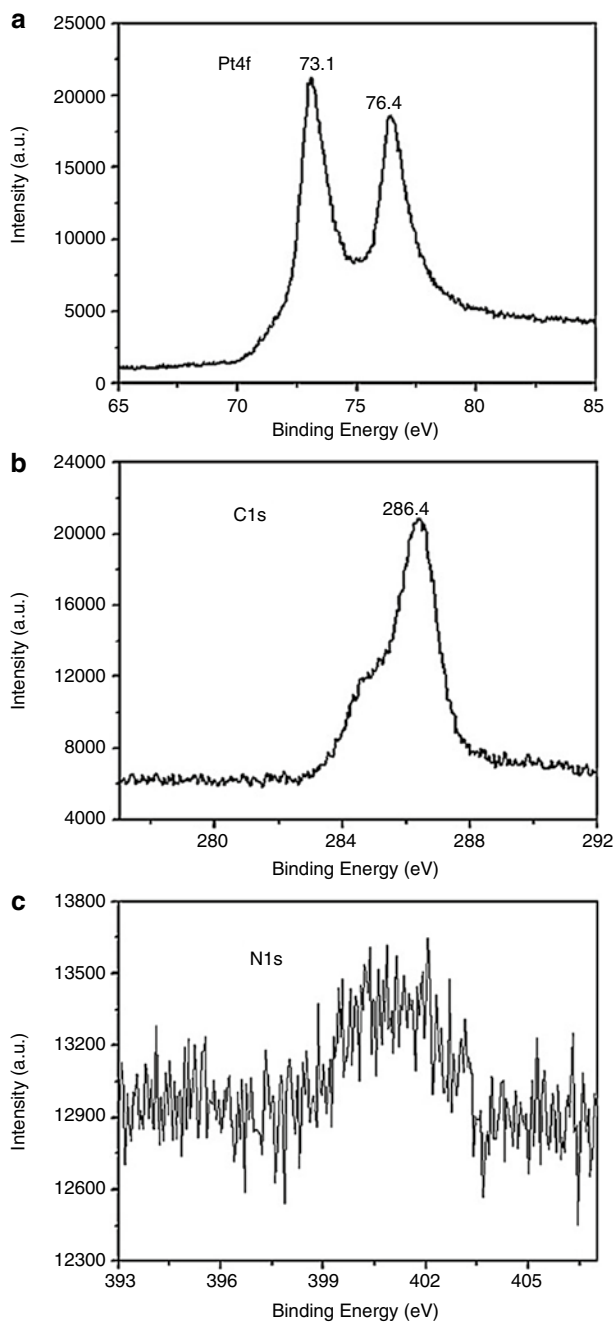


Fig. 7 XPS patterns of the Pt/PPy hybrid hollow spheres: (a) Pt 4f; (b) C 1 s; (c) N 1 s (Reprinted from [29], Copyright (2010), with permission from Elsevier)

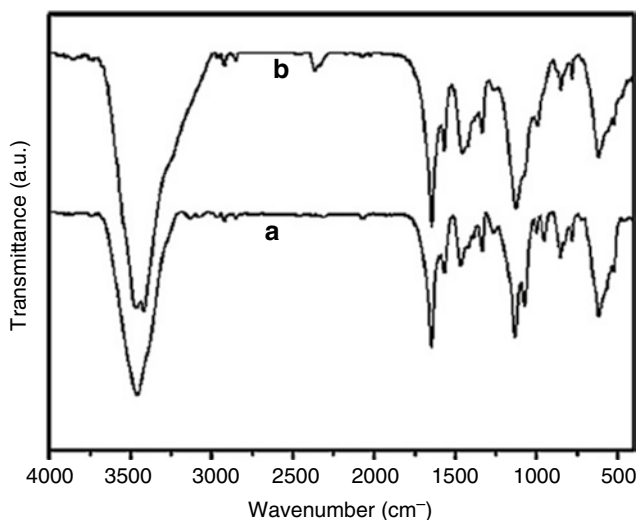


Fig. 8 FTIR images of (a) $\text{Fe}_3\text{O}_4/\text{PPy}$ composites and (b) Pt/PPy hybrid hollow microspheres (Reprinted from [29], Copyright (2010), with permission from Elsevier)

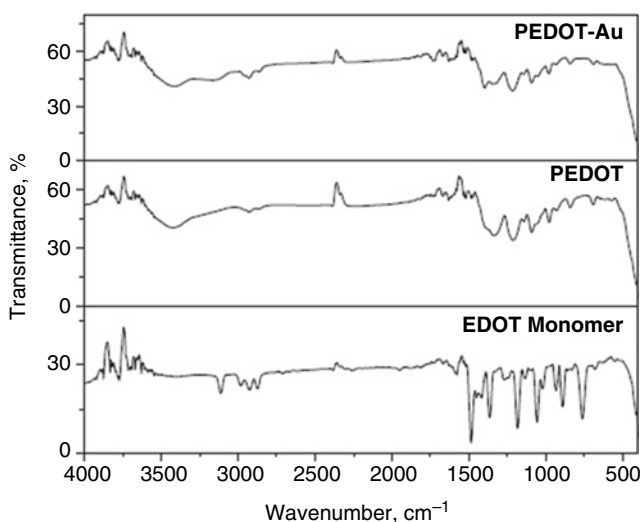


Fig. 9 FTIR spectrum of EDOT monomer, PEDOT, and Au–PEDOT nanocomposite (Reprinted from [8], Copyright (2007), with permission from Elsevier)

Sensing Applications

Polymer/metal nanocomposites have been widely utilized as sensor and biosensors. Pd nanoparticles distributed into conductive polymer matrix of poly(3-methylthiophene) (PMT), poly(*N*-methylpyrrole) (PMPy), or polyfuran (PF) film-coated Pt electrode were utilized as biosensors for neurotransmitters and

acetaminophen. Different parameters were studied because they have a great effect on the electrocatalytic activity of the resulting nanocomposite such as polymer film thickness, its polymerization method, type of deposited metal nanoparticles, metal nanoparticles deposition method, deposition voltage, and its amount. The resulting hybrid nanocomposite combined the perfect properties of the polymer matrix and metal nanoparticles. This combination resulted in dramatic enhancement in the electrocatalytic activity of the modified electrodes toward the studied compounds. In addition, the interference of ascorbic and uric acids (AA and UA, respectively) and other interferents with the studied analyte was eliminated at the surface of these modified electrodes showing perfect selectivity and anti-interference ability [10–13].

The enhanced electrocatalytic effect of Pt/PMT/Pd nanocomposites was highly affected by the method of formation of polymer film (bulk electrolysis (BE), cyclic voltammetry (CV)) (Fig. 10a). Cyclic voltammetry technique was used to test the resulting Pd-modified PMT electrodes in 5 mM hydroquinone (HQ). Pt/PMT(BE)/Pd(CV) nanocomposite exhibited higher electrocatalytic activity compared to Pt/PMT(CV)/Pd(CV) electrode as it exhibited higher oxidation current, lower oxidation potential, and smaller peak separation.

Another factor that affects the electrocatalytic activity of polymer/metal nanocomposite is the conducting polymers' doping level. After the formation of PMT polymer with BE method, the film was washed with acetonitrile and dedoped in a solution free from the monomer (0.05 M $\text{Bu}_4\text{NPF}_6/\text{CH}_3\text{CN}$) for 1 min at -0.2 mV. Then, Pd nanoparticles were electrodeposited using CV over the dedoped polymer film (Scheme 1). Pt/PMT(dedoped) exhibited lower current response, larger peak separation, and broader oxidation peak compared to the doped one (Fig. 10b). The inclusion (doping) and expulsion (dedoping) of the given anion resulted in reorganization of polymer chains which resulted in further conformational changes and structural differences leading to broader oxidation peaks at the dedoped films. In a conclusion, the electroactivity of the Pt/PMT and Pt/PMT/Pd electrodes toward HQ electrooxidation is greatly affected by the doping level of the PMT film [11, 12].

As well, the electrocatalytic activity of the resulting hybrid nanocomposite is highly affected by the method of deposition of Pd particles (BE and CV). The electrochemistry of bare Pt, Pt/PMT(BE), Pt/PMT(BE)/Pd(BE), and Pt/PMT(BE)/Pd(CV) electrodes toward 5 mM HQ was shown in Fig. 11. The current response was enhanced by 3.88- and 6.18-fold at Pt/PMT(BE)/Pd(BE) and Pt/PMT(BE)/Pd(CV) electrodes, respectively, compared to bare Pt. Also, the oxidation potential was shifted to less positive potential by 119 and 107 mV at the same electrodes. Pt/PMT(BE)/Pd(CV) electrode can catalyze the electrooxidation of HQ greatly due to the enhancement of peak current and the decrease in the oxidation potential. On the other hand, the effect of interference from UA on the simultaneous determination of DA and AA was investigated at Pt/PMT(BE)/Pd(CV) electrode. Three well-resolved peaks were defined at the modified electrode at -128 mV, $+113$ mV, and $+400$ mV for AA, DA, and UA, respectively. As a result of this good separation, the simultaneous determination of the three components can be achieved well at this modified electrode. Also, glucose and other interferents did not show any interference with

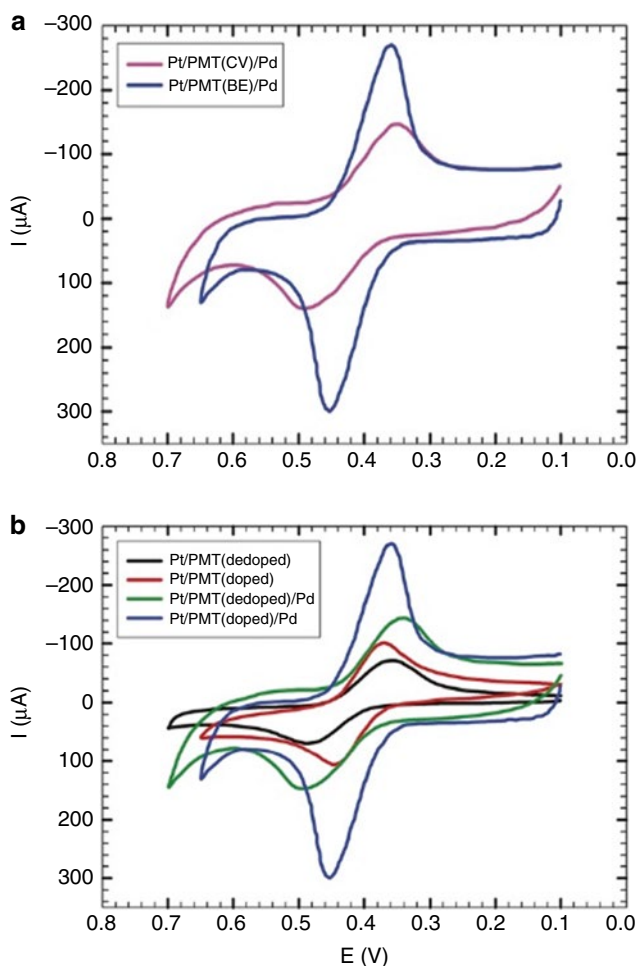
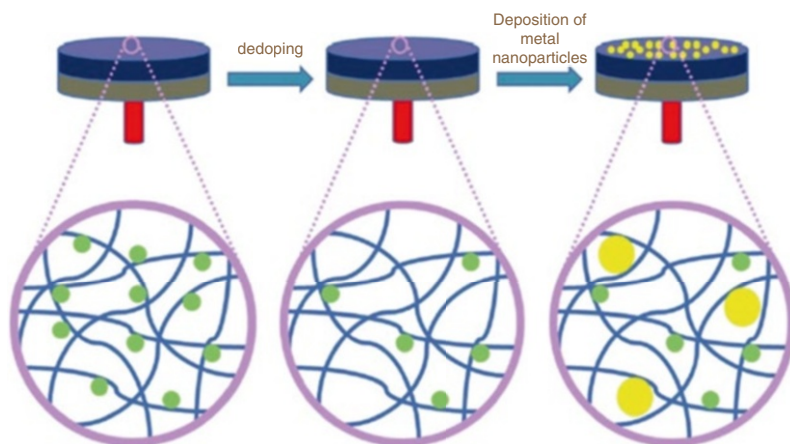


Fig. 10 Effect of the method of PMT formation (a) and doping level of PMT films (b) on the electroactivity of the produced PMT–Pd hybrid. The electrodes are tested in 5 mM HQ/0.1 M H_2SO_4 at a scan rate of 50 mV s^{-1} (Reprinted from [11], Copyright (2010), with permission from Elsevier)

the studied species [11, 12]. On the other hand, the simultaneous determination of a quaternary mixture containing AA, HQ, DA, and acetaminophen (APAP) in $0.1 \text{ mol L}^{-1} \text{ H}_2\text{SO}_4$ was achieved at Pt/PMT(BE)/Pd (CV) electrode. Four well-defined peaks were obtained at Pt/PMT(BE)/Pd (CV) electrode: 264, 408, 504, and 656 mV for AA, HQ, DA, and APAP, respectively [12].

Randles–Sevcik equation was used to calculate the apparent diffusion coefficient D_{app} for DA at Pt/PMPy(BE), Pt/PMPy(CV), Pt/PMPy(BE)/Pd_{nano}(BE) (I), and Pt/PMPy(BE)/Pd_{nano}(CV) (II). The order of the increase of D_{app} values was Pt/PMPy(BE) ~ Pt/PMPy(CV) < Pt/PMPy(BE)/Pd_{nano} (I) < Pt/PMPy(BE)/Pd_{nano} (II).



Scheme 1 Schematic diagram showing the mechanism of undoping and loading of nanoparticles into the polymer matrix (Reprinted from [11], Copyright (2010), with permission from Elsevier)

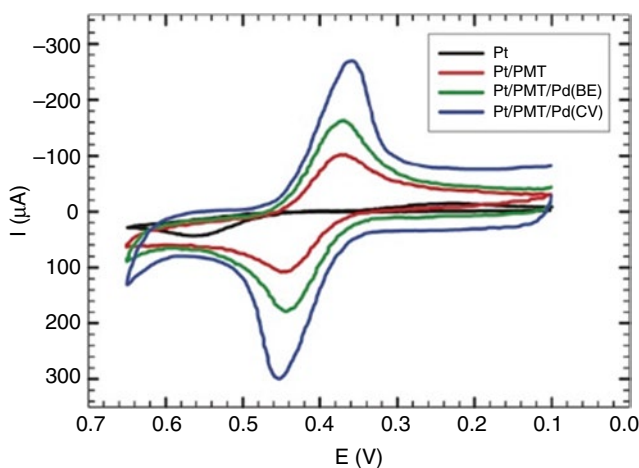


Fig. 11 Comparison between the different electrodes formed by the electrodeposition of Pd on PMT films. Cyclic voltammograms obtained by testing the electrodes in 5 mM HQ/0.1 M H₂SO₄ solution at a scan rate of 50 mV s⁻¹ (Reprinted from [11], Copyright (2010), with permission from Elsevier)

The analyte diffusion increased due to the inclusion of Pd nanoparticles in the polymer matrix; the D_{app} values calculated at Pt/PMPy(BE)/Pd_{nano} (II) for some analytes are 100 times greater than that at Pt/PMPy electrodes. D_{app} values obtained at Pt/PMPy(BE)/Pd_{nano} (II) are close to those found in aqueous solution (10^{-5} cm² s⁻¹) because of the fast mass transfer of the analyte species from bulk solutions toward electrode surface and/or fast electron transfer process of analyte electrochemical

oxidation at the electrode surface/solution interface. In addition, the analyte redox reaction occurs at the electrode surface controlled with the molecules diffusion from the solution bulk to the electrode surface. The analyte redox reaction does not occur within the polymer/Pd_{nano} matrix. As the DA molecule reaches the Pt/PMPy/Pd_{nano} surface, it simultaneously undergoes oxidation due to the greater number of active sites on this surface. On the other hand, DA diffuses on the Pt/PMPy surface until it finds the active site for oxidation. The previous results showed that the electrodeposited Pd_{nano} has a great electrocatalytic effect on the electrochemistry of the studied species [10].

Figure 12 showed the differential pulse voltammograms (DPV) of different micromolar concentrations of DA and UA at Pt/PMPy(BE)/Pd_{nano}(II) and different millimolar concentrations of AA. The oxidation peak currents of DA, UA, and AA increased with the increase in their concentrations in the working concentration range. For AA, the linear dynamic range was 0.05–1 mM with 0.9993 correlation coefficient and 0.0056 $\mu\text{A}/\mu\text{M}$ sensitivity. For DA, the linear dynamic range was 0.1–10 μM with 0.9995 correlation coefficient and 0.71 $\mu\text{A}/\mu\text{M}$ sensitivity. For UA, the linear dynamic range was 0.5–20 μM with 0.9991 correlation coefficient and 0.28 $\mu\text{A}/\mu\text{M}$ sensitivity. The potential peak separations were large enough for the individual and simultaneous determination of DA, UA, and AA. The obtained

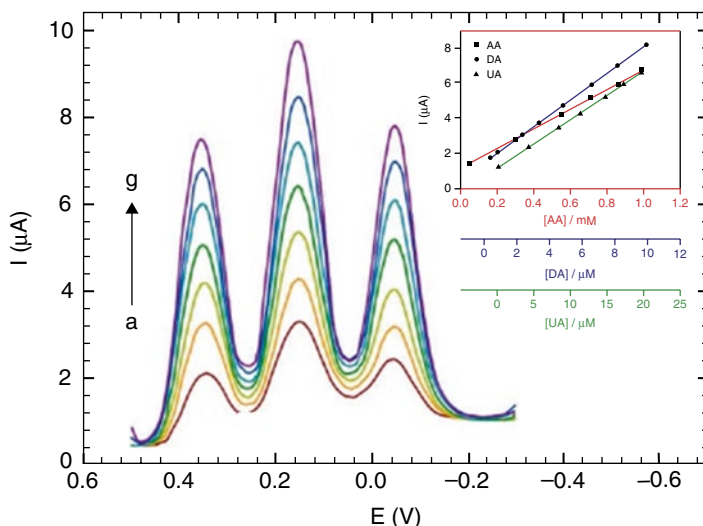
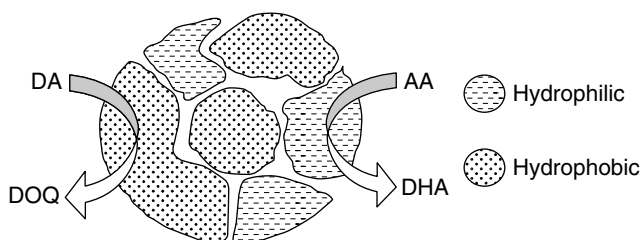


Fig. 12 Simultaneous determination of AA, DA, and UA. Differential pulse voltammograms of AA, DA, and UA were obtained at Pt/PMPy(BE)/Pd_{nano}(II) in 0.1 M PBS (pH 7.4). Concentrations of the three compounds (a–g): AA (0.05, 0.2, 0.34, 0.55, 0.72, 0.87, and 1.0 mM), DA (0.1, 1.7, 3.2, 4.8, 6.4, 8.0, and 10.0 μM), and UA (0.5, 5.0, 8.5, 11.5, 15.3, 18.0, and 20.0 μM). *Inset*: the peak current of AA, DA, and UA increases linearly over a concentration range typical of physiological conditions. Interestingly, the difference between peak potentials does not change with the concentration of the three species in the mixture (Reprinted from [10], Copyright (2010), with permission from Elsevier)

values of detection limit (signal/noise [S/N]=3) at Pt/PMPy(BE)/Pd_{nano}(II) were 12 nM, 27 nM, and 7 μM for DA, UA, and AA, respectively. Also, the detection limits of DA were not affected by the absence and presence of UA and AA (14 and 12 nM, in the absence and presence of AA and UA, respectively). These results confirmed the independent oxidation processes of AA, DA, and UA and their independent simultaneous determination [10].

Furthermore, Atta et al. studied the simultaneous determination of AA, DA, and acetaminophen ACOP at bare Pt, Pt/PF(BE), and Pt/PF(BE)/Pd(CV) in 0.1 M H₂SO₄. The voltammetric signals of AA, DA, and ACOP were not resolved at bare Pt and Pt/PF(BE). On the other hand, three well-resolved voltammetric signals were resolved at Pt/PF(BE)/Pd(CV) at 246, 508, and 673 mV for AA, DA, and ACOP, respectively. The presence of AA affected the determination of the actual concentration of DA as the dopamine-*o*-quinone “DA oxidation product” reacts catalytically with AA and regenerates DA again by the reduction of dopamine-*o*-quinone. At Pt/PF(BE)/Pd(CV), AA is oxidized before DA, and large potential separation (262 mV) between AA and DA was achieved. As a result, the interference from the oxidation product of DA was minimized. In a conclusion, the synergistic presence of PF and Pd in the new composite affected greatly the simultaneous determination of AA, DA, and ACOP [13].

On the other hand, PEDOT-incorporated gold nanoparticles were prepared by J. Mathiyarasu via chemical and electrochemical routes and were utilized for DA and UA sensing in presence of excess AA. A distribution of reduced (hydrophobic) and oxidized (hydrophilic) regions was present in the PEDOT matrix. Au_{nano} has the tendency to reside within the “hydrophobic regions” of PEDOT. DA is considered one of the hydrophobic analytes; therefore, DA interacts with the hydrophobic regions. On the other hand, the hydrophilic analytes like AA interact with hydrophilic regions of PEDOT (Scheme 2) [14, 25]. Figure 13 showed the electrochemistry of DA and UA in the presence of excess of AA at Au_{nano}-PEDOT nanocomposite. Au_{nano}-PEDOT nanocomposite exhibited more efficient response toward DA and UA. The detection limit of DA/UA in the presence of 0.5 mM of AA was 2 nM. The PEDOT matrix allowed perfect peak potential separation for the studied species exhibiting excellent selectivity. The gold nanoparticles allowed the nanomolar



Scheme 2 Depiction of hydrophobic and hydrophilic regions on the conducting polymer film; *DOQ* dopamine-*o*-quinone, *DHA* dehydroascorbate (Reprinted from [25], Copyright (2005), with permission from Elsevier)

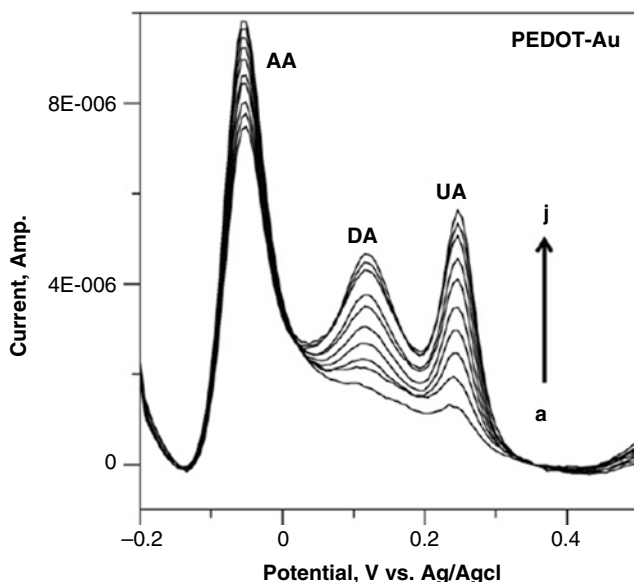


Fig. 13 Differential pulse voltammograms of Au–PEDOT-coated electrode in phosphate buffer solution (pH 7.4) containing 0.5 mM AA with different concentrations of DA and UA (*a–j* correspond to mixed solutions of 2, 4, 6, 8, 10, 12, 14, 16, 18, and 20 nM) (Reprinted from [14], Copyright (2008), with permission from Elsevier)

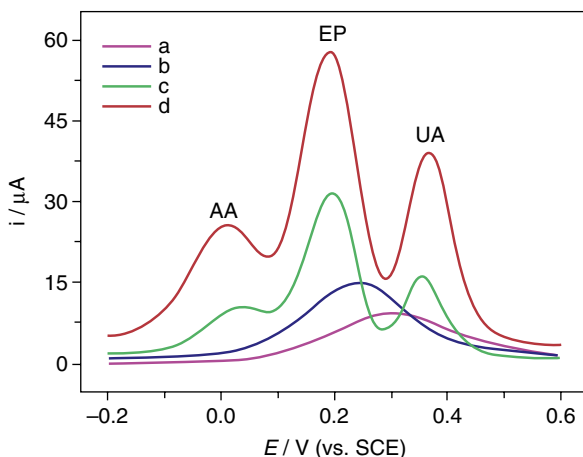
determination of these species exhibiting high sensitivity [14]. Therefore, Au_{nano}–PEDOT nanocomposite can detect DA and UA sensitively and selectively in the presence of AA.

Moreover, Pd/PEDOT/GCE enhanced the current response and the reversibility of DA in comparison with bare GCE and PEDOT/GCE. The DA oxidation process at the nanocomposite does not cause any fouling of the electrode surface. Also, simultaneous determination of DA and UA in the presence of AA was achieved at Pd/PEDOT/GCE. Good peak potential separations of 190 and 320 mV were achieved between DA–AA and UA–AA, respectively [19]. Moreover, poly(4-aminothiophenol) (PAT)–Au_{nano} was utilized for the simultaneous determination of AA and DA showing two well-resolved anodic peaks at 75 and 400 mV for AA and DA, respectively. The nanocomposite exhibited good selectivity and high sensitivity without fouling by AA or DA oxidation products. Also, PAT–Au_{nano} was utilized for the real determination of DA in human blood serum. No interference from AA, UA, albumin, and glucose was observed (Table 3) showing an applicable selective and sensitive DA sensor in real samples. In addition, long-term stability was observed for DA electrochemical response (>15 days) [28].

On the other hand, Nano-Au/PPy_{ox} composite-coated GCE was developed by Xiangqin Lin as an electrochemical biosensor for DA and serotonin 5-HT,

Table 3 Determination of DA in human blood serum ($n=5$) (Reprinted from [28], Copyright (2007), with permission from Elsevier)

Samples	Added ($\mu\text{mol L}^{-1}$)	Found ($\mu\text{mol L}^{-1}$)	Recovery (%)	R.S.D %
1	0.3	0.32	101	2.3
2	0.6	0.57	98	2.4
3	0.9	0.89	96	2.0

Fig. 14 DPVs of 1.0×10^{-5} M EP and 2.5×10^{-5} M UA in pH 7.0 PBS containing 5.0×10^{-3} M AA at bare GCE (a), nano-Au/GCE (b), PPyox/GCE (c), and nano-Au/PPyox/GCE (d) (Reprinted from [30], Copyright (2007), with permission from Elsevier)

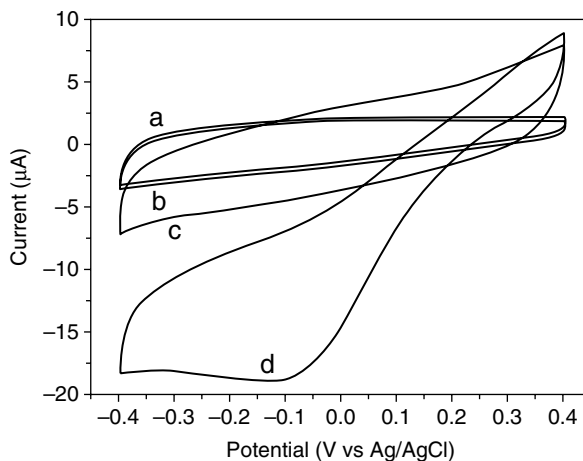
exhibiting stable and sensitive current responses toward their oxidation. Gold nanoclusters were electrochemically deposited on ultrathin overoxidized polypyrrole (PPy_{ox}) film. There is a remarkable enhancement in the DA and 5-HT oxidation response current and a lowering of overpotential due to the synergistic effect of the utilized composite. An enlarged template for the growth of Au nanoclusters was provided by the nanoporous PPy_{ox} film on the GCE, resulting in an array of nano-Au electrodes, enlargement in the effective surface area, and enhancement in the electronic conductivity of the composite. Therefore, the sandwiched Au nanoclusters can facilitate the mass and electronic transportation rates of the reactions of DA and 5-HT. The overlapping anodic peaks of 5-HT, DA, and AA (1000-fold) were simultaneously resolved at the modified electrode into three well-defined voltammetric peaks at 370, 200, and 10 mV (vs. SCE), respectively. The oxidation process of DA and 5-HT was adsorption-controlled as investigated by scan rate effect. A linear response was obtained in the range of 7.0×10^{-9} to 2.2×10^{-6} M with a detection limit of 1.0×10^{-9} M for 5-HT and in the range of 7.5×10^{-8} to 2.0×10^{-5} M with a detection limit of 1.5×10^{-8} M for DA ($s/n=3$), respectively [18]. Moreover, this novel biosensor (nano-Au/PPy_{ox}/GCE) exhibited strong catalytic activity toward the oxidation of epinephrine (EP), UA, and AA with three well-defined peaks with a large anodic peak difference. Figure 14 shows the DPV curves of 1.0×10^{-5} M EP and 2.5×10^{-5} M UA solution containing 5.0×10^{-3} M AA at

different electrodes. A broad small anodic peak at 0.31 V was obtained at bare GC electrode (curve a). Moreover, only one broad anodic peak at 0.25 V was obtained at nano-Au/GCE (curve b). However, three well-defined peaks were resolved at both PPy_{ox}/GCE (curve c) and nano-Au/PPy_{ox}/GCE (curve d). An enhancement in the oxidation currents of EP, AA, and UA was obtained at nano-Au/PPy_{ox}/GCE than that at PPy_{ox}/GCE, indicating that the nanocomposite has a strongly electrocatalytic activity toward EP, UA, and AA oxidation. In addition, the sensor exhibited excellent sensitivity, selectivity, and stability and has been applied for determination of EP in epinephrine hydrochloride injection and UA in urine samples with satisfactory results [30].

Moreover, a hybrid nanocomposite of PEDOT and Au-NPs is fabricated electrochemically onto a screen-printed carbon electrode (SPCE). SPCE/PEDOT/Au-NPs-modified electrode exhibited great catalytic activity for the oxidation of cysteine in various pH buffer solutions (pH 2.0–8.0). The selectivity of the method is demonstrated by the separation of the oxidation peaks at up to 240 mV for cysteine and glutathione in pH 6.0 buffer solutions. Flow-injection amperometry is performed for 0.5–200 μM of cysteine in pH 4.0 buffer solutions, and a linear calibration plot with a slope of 0.115 $\mu\text{A}/\mu\text{M}$ is obtained with detection limit ($S/N=3$) 0.05 μM . Additionally, the proposed methods obtain satisfactory results in the detection of cysteine-containing medicine samples [23].

Moreover, Pt/polypyrrole (PPy) hybrid hollow microspheres were utilized by Ce Wang as enzymeless electroactive H₂O₂ biosensor. At bare GCE, no H₂O₂ reduction peak was obtained, but a H₂O₂ reduction peak appeared at -100 mV at the proposed sensor (Fig. 15) because of the high electrocatalytic activity of the ultrahigh-density Pt nanoparticles with the mean diameters of around 4.1 nm deposited on PPy shell. The proposed composite showed some advantages such as fast response of less than 2 s with linear range of 1.0–8.0 mM, sensitivity of 80.4 mA M⁻¹ cm⁻², and a relatively low detection limit of 1.2 μM ($S/N=3$) [29].

Fig. 15 CVs of H₂O₂ reduction at the bare GCE (a and b) and GCE modified by Pt/PPy hybrid microspheres (c and d) in a 0.1 M PBS in the absence (a and c) and presence of 1.0 mM H₂O₂ (b and d). The scan rate is 100 mV/s (Reprinted from [29], Copyright (2010), with permission from Elsevier)



Self-Assembled Monolayer of Surfactant on Polymers and Hybrid Nanostructures

Surfactants and Self-Assembly in Solution

Surfactants, surface active agents, are chemical compounds that have the ability to affect the interfacial relationship between two dissimilar substances such as oil and water.

Surfactants have the ability to reduce the free energy of the system by reducing the contact between the hydrophobic group and the aqueous surrounding. Surfactants are considered as amphiphilic molecules which have a hydrophilic polar head on one side and a long hydrophobic nonpolar tail on the other. They have wide potential applications in electrochemistry [31, 32]. The polar head group is characteristic with the presence of heteroatoms like N, P, S, or O. These heteroatoms are present in functional groups like alcohol, thiol, ether, ester, acid, sulfate, sulfonate, phosphate, amine, amide, etc. A hydrocarbon chain of alkyl or alkylbenzene type represented the nonpolar tail group. The unique solution and interfacial characteristics of the surfactant that resulted in enhanced electrode/solution interface property are attributed to the polar–nonpolar duality nature of the surfactants [33]. Moreover, surfactants can reduce oil–water contact by the accumulation at various interfaces or the formation of different self-assembled structures in the solution. Thus, the hydrophobic domains of surfactant molecules can associate to form various structures achieving segregation of the hydrophobic parts from water [34, 35]. Formation of a specific self-assembled structure in solution depends on the type of surfactant (the size of the hydrophobic tail group, the nature, and size of the polar head group) and the solution conditions (temperature, salt concentration, pH, etc.).

Micelles in Aqueous Medium

At low concentration surfactants form true solutions where they are dispersed as individual molecules or ions and do not associate themselves to form micelles. With increasing the concentration, spontaneous self-association in solution takes place and the surfactant molecules form micelles due to the split personality structure nature of such amphiphilic substances leads their spontaneous self-association in solution resulting in the formation of micelles [35, 36]. Aggregates of long-chain surfactant molecules or ions which are formed spontaneously in their solution at definite concentration are known as micelles which possess regions of hydrophilic and hydrophobic character. This concentration was found to be dependent on the size of the hydrophobic moiety, the nature of polar head group, the nature of counter ions (for charged surfactants), the salt concentration, pH, temperature, and presence of co-solutes. In water, the charged polar head groups are oriented toward the water, and the hydrocarbon chains are oriented

away from the water to face the interior of the micelles. Micelles are characterized by aggregation number (N) and critical micelle concentration (CMC). N is the number of molecules or monomers in the micelle determining the size and geometry of the micelle, and it ranges between 10 and 100 in aqueous solution [36]. The CMC of the amphiphile can be defined as the narrow concentration range at which the micelles first become detectable. Also, it can be defined as the concentration at which an abrupt change in physical properties like surface tension and conductivity takes place [34, 36]. Each surfactant has a characteristic CMC value where dynamic aggregates are formed. The CMC values for most surfactants are in the range of 10^{-4} to 10^{-2} mol L $^{-1}$ [36].

Surfactants Self-Assembly at Solid/Liquid Interface

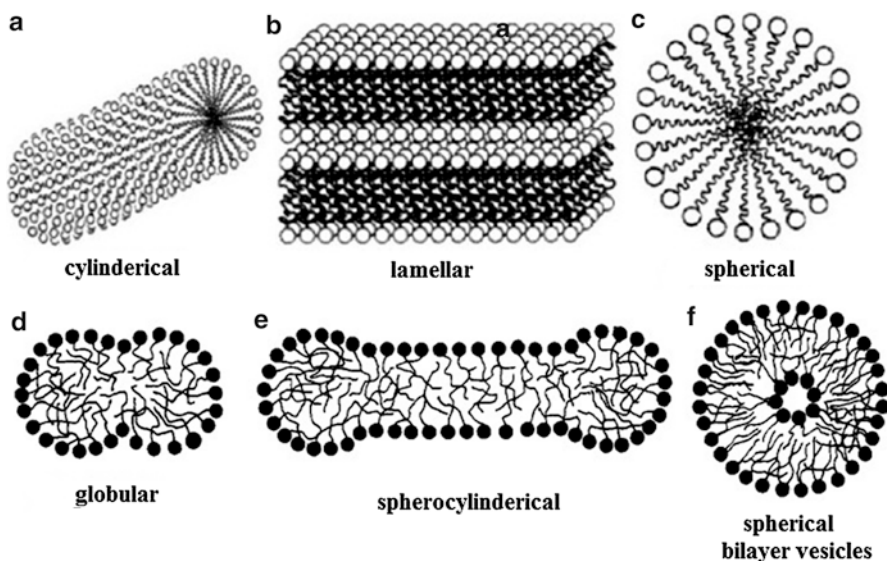
The formation of micelles in solution starts to occur upon reaching the CMC [35, 36]. At concentration less than the CMC, the cooperative hydrophobic forces are not sufficient to form micelles or any self-assembled structures in solution. As a result, surfactant molecules or ions pass out into the surface layer at the interface of the surfactant with the other phases (we will focus on solid–liquid interface), thus reducing the oil–water contact and hence lowering the free energy of the system [35]. Soon, the surface layer becomes saturated and with further increase in the surfactant concentration, the system expels the hydrophobic chains from the water into the liquid “pseudo phase” – a micelle. The adsorption of surfactants at solid substrate not only occurs before CMC but also occurs above CMC [37–41]. The adsorbed surfactant films on the surface of solid substrates exhibited different molecular structures in the form of monolayer [42–46], bilayer [47–49], multilayer (especially at extreme potentials of opposite sign for that of surfactant head group) [50–53], and surface micelles or hemimicelle (full sphere, full cylinder, or half cylinder) [54–57].

The formation of specific self-assembled structure on the solid substrate surface depends on the hydrophobicity and morphology of the substrate [58–60], the nature of the electrolyte and counter ions [61, 62], the applied potential and the charge of the substrate [63–67], the surfactant concentration [68–73], the structure and type of surfactant, and the pH of the solution from which adsorption occurs. Typical surfactant aggregate structures are shown in Scheme 3 [33, 74].

Modes of Surface Modification by Surfactants

Two important modes of modification of the electrode surface by surfactants:

1. **Surface modification**, in which spontaneous adsorption or self-assembly of surfactants occurs on the electrode surface
2. **Bulk modification**, in which surfactants (modifiers) are mixed intimately with the electrode material such as carbon paste



Scheme 3 Typical surfactant aggregates: (a) cylindrical, (b) lamellar, (c) spherical, (d) globular, (e) spherocylindrical micelles, and (f) spherical bilayer vesicles (Reprinted from [33, 74], Copyright (1991, 2011), with permission from Elsevier)

Surface Modification by Surfactants

Amphiphilic compounds can be used to control the electrochemistry at the modified electrode surface [75]. The adsorption of these amphiphilic compounds on the electrode surface can be achieved via different approaches [76–78]. One approach is based on the physico-chemisorption of highly ordered self-assembled monolayers (SAMs) [79]. Different self-assembled structures of surfactants were formed through the spontaneous physisorption of surfactant molecules at the electrode surface. This was achieved via the exposure of a clean electrode surface to a dilute solution of surfactants either by dipping or by the application of a drop of solution followed by spinning to evaporate the solvent (spin coating).

Effect of the Surfactants on the Electrochemical Kinetics of the Electrode Reaction

Dimensions, polarities, and molecular structures of surfactant aggregates on the electrode and the position of the electroactive species within them must be known to predict the effect of surfactants on the electrochemical kinetics of the electrode reaction [80]. Moreover, to observe the influences of the adsorbed surfactant films on the discharge of electroactive solutes on the electrode surface, it is necessary to investigate the adsorption of surfactants from aqueous solution onto the electrode surface. The most important influences of the adsorbed surfactant films on the electron transfer rates include (1) blocking by surfactants and (2) electrostatic interactions between electroactive solutes and the adsorbed surfactant films [80, 81].

The surfactant films may physically block the partial or full access of the electroactive species to the electrode surface inhibiting the electron transfer process [81]. The unfavorable entrance of hydrophilic species through the hydrophobic region of the adsorbed surfactant film or the coulombic repulsion between the charged head group of the surfactant and similar charged electroactive species was the origin of this blocking effect [82, 83]. As a result, the adsorbed surfactant film acts as a barrier between the electrode surface and the electroactive species.

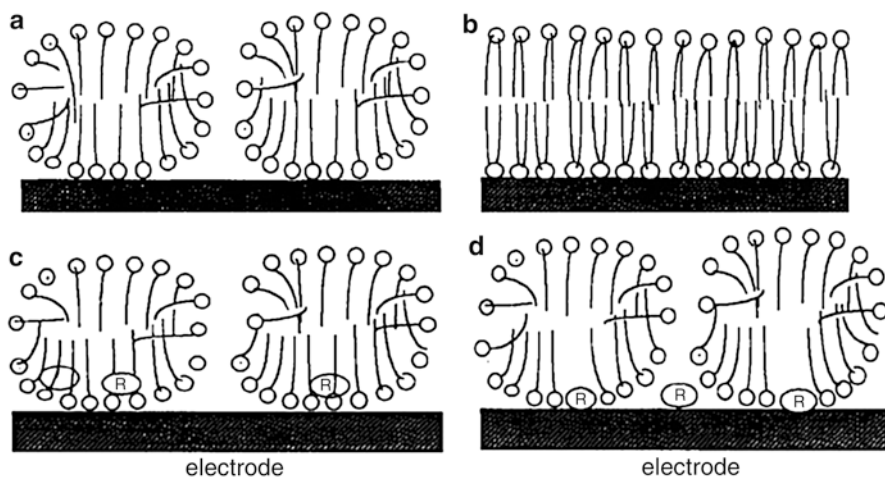
On the other hand, mild kinetic enhancement for the electrode reaction may be observed due to the adsorbed surfactant film on the electrode. This enhancement depends on the preconcentration process (the accumulation of the electroactive species through or into the adsorbed surfactant film). The coulombic attraction forces as well as the hydrophobic interactions between the electroactive species and the adsorbed surfactant layers are the main driving forces for the preconcentration process [82–84]. Moreover, incorporation of electroactive species within the adsorbed surfactant films will introduce different distances between the electroactive species and the electrode surface. Thus, the rate of the electron transfer will decrease with increasing the distance between the electroactive species and the electrode surface within the adsorbed surfactant film [85–87]. This is in accordance with the electron transfer theory [88], which predicts the exponential decrease of the electron transfer rate with increasing the distance between the electroactive species and the electrode surface.

When electroactive species presents in micellar system, it may bind to the micelles present in the aqueous medium or partitioned between micelles and aqueous media [89]. Electroactive ions which are oppositely charged to the ionic micelles can bind at the micelle–water interface, whereas nonpolar electroactive species can bind in hydrophobic regions of the micelles just below this interface [90]. Electroactive species solubilized in micelles or bonded to micelles can undergo electron transfer reactions in which the current is controlled by diffusional mass transport of micelles containing the electroactive species.

Surfactant Adsorption

Surfactants have a specific amphiphilic structure which enables them to be adsorbed at the surface/interface in an oriented form [91, 92]. The adsorption of the surfactant involves the transfer of the surfactant molecules from the solution bulk to the electrode/solution interface. This adsorption process of surfactant at the solid/liquid interface plays a crucial role in many applications. There are various mechanisms by which the surfactant molecules can be adsorbed onto the solid substrates from aqueous solutions. The adsorption involves single ions rather than micelles [92].

- (I) **Ion exchange** takes place through the substitution of counterions adsorbed onto the substrate from the solution by surfactant ions with similar charges.
- (II) **Ion pairing** takes place through adsorption of surfactant ions from solution onto sites which are oppositely charged and unoccupied by counterions.
- (III) **Hydrophobic bonding** takes place through the electrostatic attraction between a hydrophobic group of adsorbed molecule and a molecule present in the solution.



Scheme 4 Conceptual drawings of interfacial region on hydrophilic electrode in micellar solutions: (a) side view of surface micelles or cylinders, (b) side view of a bilayer, (c) position of reactants R which are dissolved in the surface aggregates, (d) position of reactants R which are specifically adsorbed to the electrode (Reprinted from [80], Copyright (1997), with permission from Elsevier)

- (IV) **Adsorption by polarization of n electrons** takes place through the attraction between the electron-rich aromatic nuclei of the adsorbate “surfactant” and the positive sites on the solid adsorbent.
- (V) **Adsorption by dispersion forces** takes place through the adsorption by London van der Waals force between adsorbate “surfactant” and solid adsorbent [92].

Electron Transfer Modes in Micellar Solutions

Electron transfer kinetics of electrode reaction process can be controlled by the surfactant aggregates on the electrode surface or inside the solution. Aggregates in the form of bilayers, cylinders, or surface micelles have the tendency to be adsorbed onto the electrode surface in solutions with surfactant concentration above the CMC. On hydrophilic electrodes, head-down orientations of surfactants are preferred (Scheme 4a, b) [80].

We will start by talking about the mechanism of discharge of electroactive species binding to the adsorbed dynamic surfactant film. The electron transfer process will take place when the electroactive species approaches to the vicinity of the electrode surface. Two main possibilities allow the charge transfer; the first is the displacement of the adsorbed surfactant by the reactant, thus, the reactant approaches the electrode closely (Scheme 4c), and the second is the approach of the reactant to the electrode surface within one head group diameters of adsorbed surfactant moieties (Scheme 4d). Different possibilities have been suggested for the molecular interpretation of electron transfer between a micelle-solubilized electroactive species and the electrode.

One possibility is the dissociation of solute bound to the micelle followed by its entry into the adsorbed surfactant film, then its orientation near the surface, and finally electron transfer occurs. The entry into the films and orientation are expected to occur on a millisecond time scale. Another possibility is the joining of the micelle in solution with the aggregates on the electrode surface, bringing the reactant close enough to the electrode for electron transfer [80].

The Role of Surfactants in Electrochemistry

The importance of surfactants to electrochemistry is based on the following points [93]:

- (a) Surfactants in aqueous solution will affect the double layer structure, the redox potential, the charge transfer, and the diffusion coefficient of the electrode processes [91, 93].
- (b) Surfactants can stabilize radicals or intermediate reaction products.
- (c) Surfactants can easily dissolve hydrophobic substances.

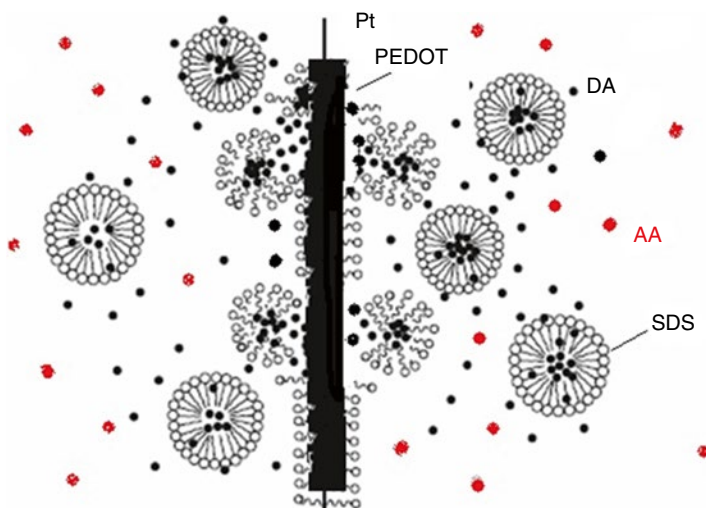
Surfactants can endow the electrode/solution interface with different electrical properties and change the electrochemical process. For example, the adsorption of ionic surfactants can form charged surfactant layers on the electrode surface, which have a strong accumulation capacity toward the oppositely charged analytes and an electrostatic repulsion ability toward the same charged analytes. Similarly, surfactants can form loose hydrophobic layers on the electrode surface by their hydrophobic tails exhibiting a strong accumulation capacity toward hydrophobic analytes. Moreover, the formation of surfactant layers on the electrode surfaces can also avoid the direct contact of the analyte with the electrode surface enhancing the antifouling capacity of the electrodes [94, 95]. On the other hand, surfactants play a very important role in electrode reactions, not only in solubilizing organic compounds but also by providing specific orientation of the molecules at the electrode interface. Surfactants are effective excipients in many drug formulations via improving dissolution rate and increasing drug solubility. The ability of surfactants to reduce interfacial tension and contact angle between solid particles and aqueous media leads to improving the drug wettability and increasing the surface availability for the drug dissolution [96]. Accordingly, surfactants were found to have several applications in electrochemistry, polarography, corrosion, batteries, fuel cells, electrometallurgy, electroorganic chemistry, photoelectrochemistry, electrocatalysis, and electroanalysis [36]. Surfactants are very effective to be used in the electroanalysis of organic compounds, biologically important compounds, drugs, some important inorganic ions, and metals [97–99]. Moreover, micelles have also been employed as selective masking agents to improve selectivity and sensitivity of electrochemical analysis [100].

Sensor Applications of Surfactant SAM on Polymers

A promising biosensor based on poly(3,4-ethylenedioxythiophene)-modified Pt electrode (Pt/PEDOT) was constructed for DA determination in the presence of SDS. There are electrostatic interactions between the positively charged DA and the

negatively charged SDS which resulted in enhanced accumulation of protonated DA at the polymeric electrode surface, improved electrochemical response of DA, and increased current response by one and a half folds. Surfactant aggregates can be formed on the electrode surface in the form of bilayers, cylinders, or surface micelles (at higher SDS concentration), and these aggregates can explain the enhanced current response. The process of electron transfer starts when the electroactive analytes come close to the vicinity of electrode surface. The charge transfer mediation is attributed to the space of one to two head groups of adsorbed surfactant moieties extended from the surface of the electrode. On the other hand, ion pair of the protonated DA and the charged surfactant may be formed and adhered on the electrode surface via the hydrophobic parts in both sides [32]. On the other hand, three well-resolved oxidation peaks for DA, AA, and UA were defined at PEDOT/Pt in the presence of SDS. By the addition of SDS, the peak current signal of DA increases, and the peak current signals of AA and UA disappear. These observations are attributed to the electrostatic attractions between the negatively charged surfactant film and the positively charged DA which enables DA to reach the electrode surface faster. In the case of AA and UA, there are electrostatic repulsion between the anionic surfactant and the negatively charged species resulting in slower electron transfer kinetics (Scheme 5) [32].

The morphology of PEDOT matrix in the absence and presence of SDS showed a great difference (Fig. 16). In the absence of SDS, PEDOT exhibited the globular shape, and the surface appeared to be rough because of Pt substrate (Fig. 16a). In the presence of SDS, the PEDOT matrix becomes spongy and cotton-like because of the anionic tails of the surfactant (Fig. 16b). SDS aggregates have the ability to accumulate over the polymer surface and affect greatly the film conductivity [32].



Scheme 5 Electrostatic interaction between DA cation and the PEDOT in the presence of SDS and AA (Reprinted from (Reprinted from [32], Copyright (2011), with permission from Elsevier)

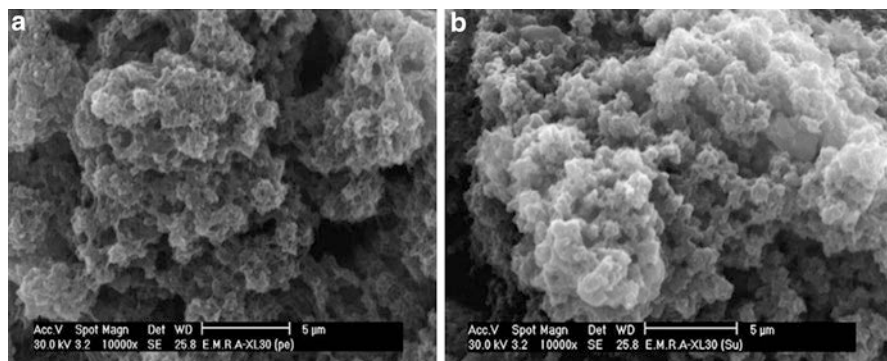


Fig. 16 SEM image of the PEDOT layers deposited on Pt wire from 0.01 mol L^{-1} EDOT in 0.1 mol L^{-1} LiClO_4 in acetonitrile (10 cycles) (magnification $10,000\times$, 30 kV), (a) in the absence of SDS, (b) in the presence of $150 \mu\text{L}$ 0.1 mol L^{-1} SDS (Reprinted from [32], Copyright (2011), with permission from Elsevier)

Furthermore, PEDOT/Pt in the presence of SDS was utilized for the determination of catecholamine compounds, namely, epinephrine, L-norepinephrine, and L-DOPA, as well as serotonin (ST). The electrochemical data for the oxidation of catecholamines, serotonin, tryptophan, acetaminophen, and some interfering compounds such as UA and AA were collected from the cyclic voltammograms at PEDOT/Pt electrode in the absence and presence of $150 \mu\text{L}$ SDS. For cationic catecholamines, an increase in the anodic and cathodic peak current values was observed upon the addition of SDS due to the electrostatic interaction between the anionic surfactant film adsorbed on the electrode and the cationic catecholamine. For anionic compounds, the oxidation current response decreases in the presence of SDS. Tryptophan, AA, and UA, which are in the anionic form at $\text{pH}=7.4$, establish an electrostatic repulsion with anionic surfactant SDS resulting in a large decrease in the peak current value in micellar medium. L-DOPA and ACOP are neutral species at physiological pH ($\text{pH}=7.4$), thus SDS would not affect the kinetic of these compounds. The adsorption of the surfactant molecules onto the surface of the electrode resulted in changing the oxidation current values for positively and negatively charged species, altering the electrode overpotential and affecting the kinetics of the electron transfer. Also, the micellar aggregates may influence the mass transport of the electroactive analytes toward the electrode surface [101].

On the other hand, the electrochemical response of ST in the presence of UA, AA, and glucose was investigated. The presence of more than 1000-fold excess of AA and 100-fold excess of glucose did not interfere with the response of ST. The presence of SDS in the medium plays a key role in the electrostatic attraction of ST toward the polymeric surface and causes repulsion toward the interfering species. Furthermore, both DA and ST coexist in a biological system, and they affect each other in their respective releasing. So, it was interesting to study the interaction of both compounds with SDS (Fig. 17). At PEDOT/Pt electrode, DA and ST yielded two well-defined oxidation peaks at 0.20 and 0.35 V , respectively. The current

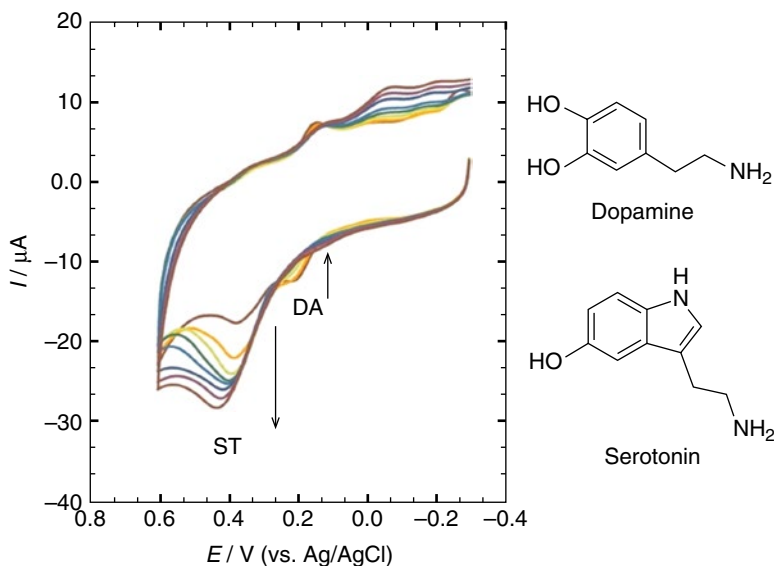


Fig. 17 Cyclic voltammograms of equimolar solution 0.5 mmol l^{-1} of both DA and ST in B-R (0.1 mol l^{-1}), scan rate 50 mV s^{-1} at PEDOT/Pt electrode pH 7.4 with successive additions of $10 \mu\text{l}$ 0.1 mol l^{-1} SDS (0–150 μl) (Reprinted from [101], Copyright (2011), with permission from Elsevier)

response of ST increased, while DA response decreased with successive additions of $150 \mu\text{L}$ SDS in 0.1 mol l^{-1} B-R pH=7.4. This is due to the competitive interaction of DA and ST with the PEDOT/Pt film that is more pronounced in the case of ST. This is due to the large conjugated structure of ST which has the possibility to intercalate into the interior of PEDOT/Pt film. Another reason is the presence of $-\text{NH}_2$ and $-\text{NH}$ groups in ST which increases the positive charge density on ST enhancing its interaction with the anionic surfactant SDS, thus facilitating its diffusion to the polymeric film [101].

Interaction of anionic SDS with ST and DA in aqueous B-R buffer solutions was followed by UV–Vis spectroscopy. Figure 18a, b shows the effect of successive additions of SDS on the absorption spectrum of each of ST and DA. The anionic SDS showed no absorption background. A band is identified at 274 nm , and a shoulder is present at 296 nm for ST due to the different possible sites of protonation in the case of indole nucleus having various constituent groups.

It was assumed that protonation on nitrogen always occurs first and then takes place in other places (Fig. 18a). The absorbance of these bands decreased from 1.31 to 0.95 with five SDS additions. On the other hand, a sharp band was formed at 279 nm for DA (Fig. 18b); its absorbance decreased from 1.27 to 0.97 with five SDS additions. The anionic character of SDS favors coulombic attraction forces with the compounds and leads to the formation of aggregates in the solution phase. The aggregation in aromatic systems could be attributed to the formation of larger units (possibly due to the formation of longer repeat unit chains). This “oligomerization”

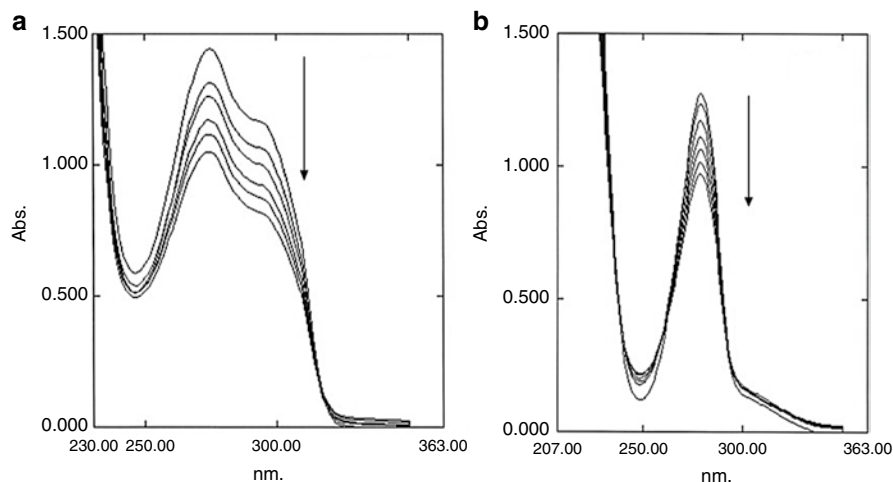


Fig. 18 Absorption spectra of five successive aliquots of 0.2 ml of 0.01 mol l⁻¹ SDS added to 4.0 ml of (a) 2.5 × 10⁻⁴ mol l⁻¹ serotonin, (b) 5 × 10⁻⁴ mol l⁻¹ for DA (Reprinted from [101], Copyright (2011), with permission from Elsevier)

was due to the London–Margenau attractive forces between the π -electrons that are counterbalanced by the columbic and Lennard-Jones repulsive forces. This should be accompanied with a blue shift or a red shift in the corresponding spectra that was not observed in the present case for ST and DA. Thus, the charge interaction of the compound with SDS is the main contribution to the association that resulted in the decrease in the absorption spectra. Also, it was noticed from the results that the decrease in absorbance in the case of ST was larger than in the case of DA showing that there is more charge interaction of ST with SDS than in the case of DA. So, the spectrophotometry data are in good agreement with what we obtained from the voltammetry experiments [101].

On the other hand, drug analysis is an important branch of chemistry which plays an important role in drug quality control. Therefore, the development of sensitive, simple, rapid, and reliable method for the determination of active ingredient is very important [102]. Surfactants have proven effective to be used in different occasions for the electroanalysis of drugs [97–99]. Improvement of drug analysis using surfactants was found to be concentrated in two important points:

1. The ability of surfactant systems to dissolve hydrophobic (insoluble) drugs
2. The preferential accumulation of drug molecules on the electrode surface via electrostatic and hydrophobic interactions [103–108]

Atta et al. employed PEDOT/Pt for morphine (MO) determination in the presence of SDS. MO is used as a relief from severe pain. The anionic surfactant SDS facilitates the arrival of MO molecules to the electrode surface faster, improves its

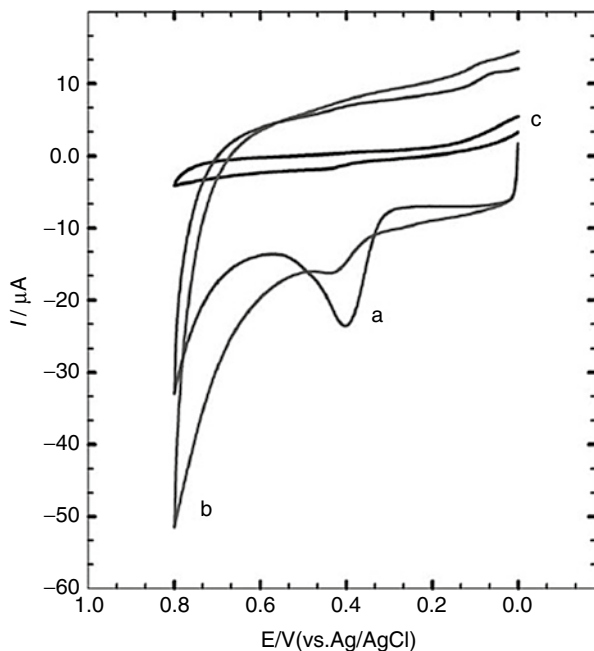


Fig. 19 Cyclic voltammograms of 5.0×10^{-4} mol L $^{-1}$ morphine/ 0.1 mol L $^{-1}$ BR, pH 7.4, at (a) PEDOT/Pt electrode in the presence of SDS, (b) PEDOT/Pt electrode (c) Pt electrode at scan rates 50 mV s $^{-1}$ (Reprinted from [109], Copyright (2011), with permission from Elsevier)

reaction rate, and enhances greatly its anodic peak current (Fig. 19). PEDOT/Pt in the presence of SDS exhibited perfect electrocatalytic activity toward MO as it lowers its oxidation potential, enhances its current response, and improves its electron transfer kinetics. D_{app} (cm 2 s $^{-1}$) value for MO at PEDOT/Pt is 2.6×10^{-4} in the presence of SDS which is higher than the corresponding value in the absence of SDS 1.1×10^{-4} . The diffusion component of the charge transfer at the electrode surface is greatly affected by the anionic surfactant SDS [109].

On the other hand, DA is considered one of the most common interferents for MO in urine or blood. Two well-resolved peaks for DA and MO were obtained at 220 and 410 mV at PEDOT/Pt in the presence of SDS, respectively. The proposed sensor can determine MO in the presence of DA with high sensitivity and excellent peak potential separation (190 mV). Moreover, the simultaneous sensitive determination of MO and epinephrine EP was achieved well at the proposed sensor. Therefore, this promising sensor can be used to selectively and sensitively discriminate MO from neurotransmitters. Also, the simultaneous determination of MO, AA, and UA proved excellent at the proposed sensor. By the addition of SDS, the MO oxidation current increased, and the AA and UA oxidation current disappeared. This is attributed to the electrostatic attractions between the positively charged MO and negatively charged SDS and the electrostatic repulsion between the negatively charged AA and UA and anionic SDS [109]. On the other hand, MO can be discriminated

from codeine that is very close to MO in structure at the surface of the proposed sensor. Codeine usually interferes with MO and affects the MO determination because of the competitive adsorption between them. At the surface of the proposed sensor, no interference was detected from codeine in a solution containing equimolar amounts of MO and codeine in the presence of SDS. Only an oxidation peak for MO was detected at 550 mV. As a result, PEDOT/Pt in the presence of SDS can be used to detect MO in opium poppy in the presence of high concentration of codeine (ten-fold) [109].

As well, electrochemical impedance spectroscopy (EIS) is a characteristic tool that can be used to examine the electrode/solution interface properties. It also can be used to examine the type of interaction of MO at the proposed sensor in the absence and presence of SDS. The diameter of the semicircle in the Nyquist plot resembles the resistance of the electron transfer. In the absence of SDS, a semicircle with larger diameter was observed which is diminished obviously by SDS addition. As a result, the resistance of electron transfer of MO electrooxidation decreases, and electron transfer kinetics is improved. The fitting values calculated from the equivalent circuit for the impedance data were summarized in Table 4. R_u is the solution resistance, R_p is the polarization resistance, CPE is the predominant diffusion influence on the charge transfer process, and n is its corresponding exponent ($n < 1$). C_f is the capacitance of the double layer. W is the Warburg impedance due to diffusion. The capacitive component values are higher at PEDOT/Pt in the presence of SDS compared to the case of the absence of SDS because of the ionic adsorption at the electrode surface, the charge transfer process, and the conducting character of the surface. In selective electrostatic interactions between MO and SDS, the accelerated electron transfer kinetics resulted in the obvious decrease in the interfacial electron transfer resistance [109].

Also, the voltammetric behavior of isoniazid (an antituberculous drug, INH) was investigated at PEDOT/Pt in the presence and absence of SDS and CTAB. INH exhibited a very weak electrochemical response at bare Pt electrode which was markedly enhanced in the presence of SDS achieving an improved response of INH in pH 2.3 (INH is positively charged in this pH). Two well-defined irreversible anodic peaks of INH were obtained at 630 mV and 820 mV (Fig. 20a) that resulted to form an irreversible oxidation of INH. In the absence of SDS, no peaks were obtained for INH due to electrostatic repulsion between the positively charged INH

Table 4 Summary of the data obtained from EIS in the determination of MO using PEDOT/Pt electrode in the absence and presence of SDS at the oxidation potential (Reprinted from [109], Copyright (2011), with permission from Elsevier)

Electrode PEDOT/Pt	E (mV)	R_p (k Ω cm ²)	R_u (k Ω cm ²)	C_f (μ F cm ⁻²)	W (K Ω ⁻¹ cm ⁻²)	C_{CPE} (μ F cm ⁻²)	n
In the absence of SDS	420	122	0.39	45	2.49	75	0.88
In the presence of SDS	420	52	0.5	50	2.38	279.8	0.7

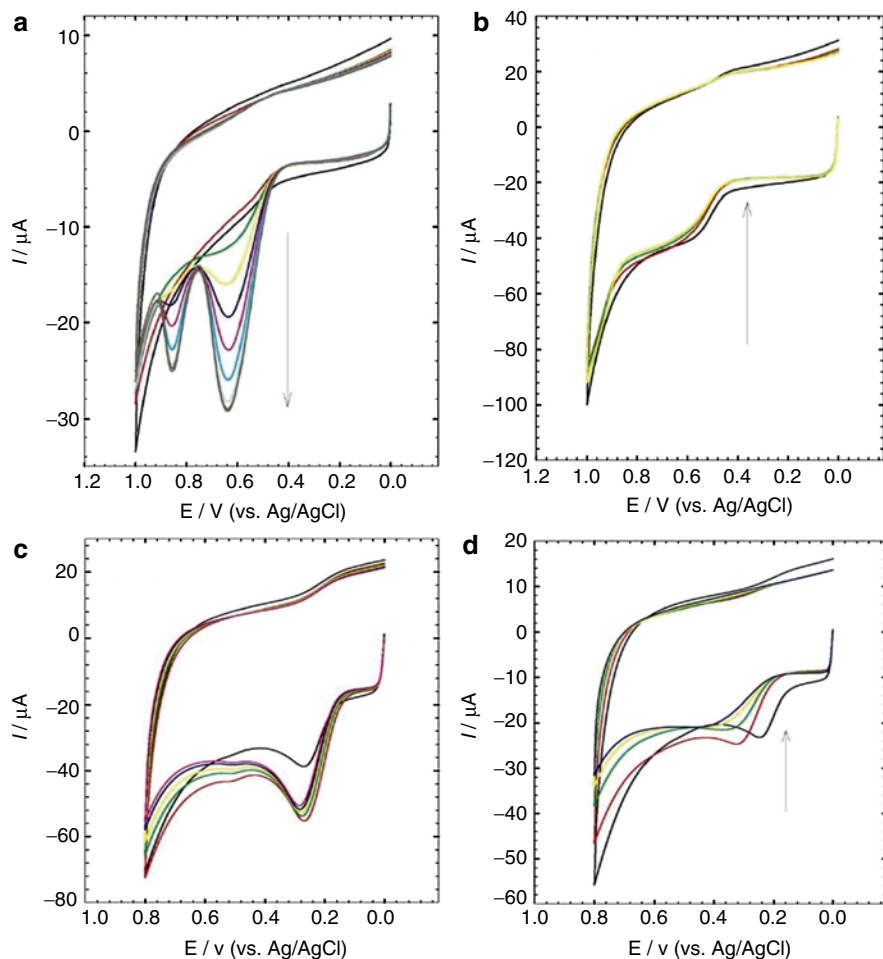


Fig. 20 Cyclic voltammograms of 5.0×10^{-4} mol L INH/0.1 mol L⁻¹ L B-R, scan rate 50 mV s^{-1} at PEDOT/Pt electrode at pH 2.3 with successive additions (0–150 μL) of 0.1 mol L⁻¹ (a) SDS, (b) CTAB and at pH 7.4 with successive additions (0–150 μL) of 0.1 mol L⁻¹ (c) CTAB and (d) SDS (Reprinted from [110], Copyright (2011), with permission from Elsevier)

and positive charge density of PEDOT. SDS improves the oxidation current of INH and mediates the electron transfer kinetics as it facilitates the arrival of cationic INH to the electrode surface faster. Also, PEDOT/Pt in the presence of SDS exhibited high electrocatalytic activity toward INH showing lower oxidation potential and higher oxidation current [110]. On the other hand, a weak broad peak is observed at PEDOT/Pt in the presence of CTAB for INH solution/pH 2.3. By the addition of CTAB, the INH oxidation current decreases (Fig. 20b) due to the electrostatic repulsion between the cationic CTAB and the positively charged INH resulting in a retarded diffusion.

On the other hand, the electrochemical response of INH at pH 7.4 was studied at PEDOT/Pt in the presence of SDS and CTAB. INH becomes neutral at pH 7.4 according to its pK_a value resulting in different types of interaction of INH with the polymer film and surfactant molecules. At PEDOT/Pt, one oxidation peak for INH appeared at 260 mV with a current value of 38 μ A because INH becomes neutral and diffuses easier toward the cationic polymer. By CTAB additions, the INH oxidation current increases to 55 μ A then becomes stable (Fig. 20c). There are electrostatic force between INH molecules and CTAB resulting in enhanced oxidation current as the INH approaches the electrode surface faster and the reaction becomes easier. Figure 20d showed the opposite manner by the addition of anionic SDS; the INH oxidation current decreases because of the electrostatic force between INH and SDS resulting in difficult diffusion of INH to electrode surface [110]. Moreover, it is necessary to examine the simultaneous determination of INH, AA, and UA. At PEDOT/Pt in the presence of SDS, the selective determination of INH, AA, and UA at pH 2.3 proved excellent. This is attributed to the electrostatic attractions between anionic SDS and positively charged INH and electrostatic repulsions between SDS and anionic AA and UA. Also, the simultaneous determination of IHN, AA, and UA at pH 7.4 achieved well at PEDOT/Pt in presence of CTAB. Two oxidation peaks for AA and UA were observed at 100 and 486 mV, respectively, as a result of electrostatic attractions between cationic CTAB and anionic AA and UA. The oxidation current of INH is firstly observed at 700 mV and increased by the addition of CTAB as a result of INH neutral structure which improves its diffusion toward the polymeric film by CTAB. One can say that the presence of surfactant molecules plays a crucial role in the electrostatic interactions of INH toward the polymeric film in different pH values [110].

On the other hand, the electrochemical response of 0.3 mM atropine in 0.1 M B-R/ pH 7.4 was examined at PEDOT/Pt in SDS. One well-resolved irreversible peak was observed at 670 mV for atropine at PEDOT/Pt in the presence of SDS which was four and eight times higher than that observed at PEDOT/Pt and Pt electrodes, respectively. The oxidation current of atropine was markedly enhanced by the anionic SDS which mediates the approaching of atropine molecules to the electrode surface and facilitates the reaction. Higher current response, lower oxidation potential, and low detection limit of 34 nM were remarkable characteristics of the electrocatalytic activity of PEDOT/Pt toward atropine in the presence of SDS.

Also, an electroanalytical method was developed for the sensitive determination of flutamide in pharmaceutical formulations at polyglutamic acid polymer-modified carbon paste electrode in the presence of CTAB. The reduction current of flutamide increases by the addition of CTAB exhibiting a maximum 1 % CTAB and after that decreases continuously. The adsorption manner changes at 1 % CTAB from monomer adsorption to monolayer adsorption with an increase in CTAB concentration at the electrode surface. After 1 % CTAB, the reduction current decreases because of the retardation of electron transfer rate by micelle aggregates. Therefore, 1.0 % CTAB is selected as the optimum concentration. The proposed sensor showed perfect electrocatalytic activity toward flutamide determination, good sensitivity, excellent stability, and applicability with wide concentration range [111].

SAM of Surfactant on Polymers/Nanometallic Structures

Chunya Li et al. utilized gold nanoparticle-modified glassy carbon electrode (Au-NPs/GCE) for the determination of tryptophan (Trp) in the presence of sodium dodecylbenzenesulfonate (SDBS). The oxidation peak potential of Trp at Au-NPs/GCE showed a negative shift of 50 mV, and the peak current was improved in the presence of SDBS indicating that the electron transfer between the electrode and the bulk of solution was facilitated. Surfactants can be adsorbed on hydrophobic surface to form surfactant film altering the overvoltage of the electrode and influencing the rate of electron transfer [112]. In the presence of SDBS, a hydrophilic film with negative charge was formed through the interaction of Au-NPs and sulfonic group of SDBS. This hydrophilic layer improves the accumulation of Trp at the electrode surface through electrostatic interaction, thus the electron transfer of Trp was facilitated, its oxidation overpotential decreased, and its current response was enhanced [112]. Moreover, Gong-Jun Yang studied the electrochemistry of ethamsylate (ESL), a homeostatic agent that appears to maintain the stability of capillary walls and correct abnormal platelet adhesion, at hydrophobic gold nanoparticle-modified GCE ($C_{18}NH_2$ -capped Nano-Au/GCE) in the presence and absence of cationic surfactant CTAB. A significant negative shift of the oxidation potential and increase of the anodic peak current were observed in the presence of CTAB indicating the role of CTAB in the oxidation of ESL. Sulfo acid group in ESL is ionized and negatively charged in the weak acid solution. In the presence of CTAB, a positively charged hydrophilic film of CTAB was formed on the modified surface. The hydrophobic interaction between ESL and hydrophobic chain of CTAB was more dominant than the static interaction with the polar head group, thus the overvoltage was reduced and the electron transfer rate was enhanced. Therefore, the electrochemical oxidation of ESL was facilitated in the presence of cationic surfactant CTAB, and very low detection limit was obtained, 3.5 nM [113].

Furthermore, the electrochemical response of DA was examined at Au/PEDOT-Au_{nano}/SDS (gold nanoparticle-modified PEDOT-modified gold electrode in the presence of SDS). This promising sensor combined the effective properties of PEDOT matrix to lower the DA oxidation potential and the catalytic properties of gold nanoparticles and SDS to facilitate the electron transfer kinetics (Fig. 21). The SDS addition improves the preconcentration-accumulation of hydrophobic positively charged DA, facilitates its diffusion through the modified electrode, and mediates the electrostatic transfer rate as a result of electrostatic interactions between cationic DA and anionic SDS leading to enhanced DA current signal at the proposed surface. The utilized sensor showed the effective synergism between PEDOT, Au_{nano}, and SDS to selectively and sensitively determine DA [27]. The previous results may be explained as follows: PEDOT matrix involves a distribution of reduced (hydrophobic) and oxidized (hydrophilic) regions, and positively charged DA tends to interact with the more reduced regions. In addition, PEDOT film acts as an electron facilitator as it contains a rich electron cloud. Furthermore, gold nanoparticles act as a mediator to facilitate the electrochemical reaction and mediate the electron transfer rate. Also, DA cations tend to be weakly adsorbed at

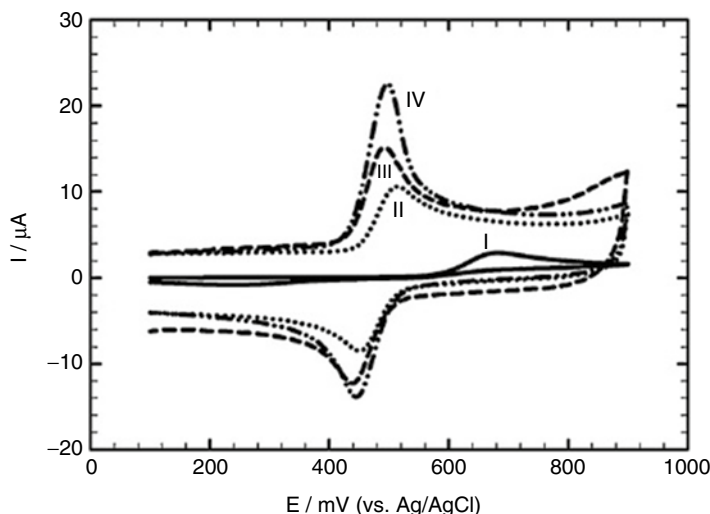


Fig. 21 CVs of 1 mmol L^{-1} DA/ 0.1 mol L^{-1} PBS/pH 2.58 at (I) bare Au, (II) Au/PEDOT, (III) Au/PEDOT–Au_{nano}, and (IV) Au/PEDOT–Au_{nano}/SDS-modified electrodes; scan rate 50 mV s^{-1} (Reprinted from [27], Copyright (2012), with permission from Elsevier)

Au/PEDOT–Au_{nano} as DA has the ability to form self-assembled monolayer on Au via the interaction NH_2 group of DA with Au. As mentioned before, SDS improves the preconcentration–accumulation of the positively charged DA at the surface of the modified electrode and enhances its diffusion through the modified electrode [27]. On the other hand, the simultaneous determination of AA, DA, and APAP ($0.1 \text{ M PBS/ pH } 2.58$) achieved well at Au/PEDOT–Au_{nano} electrode. Three well-resolved peaks appeared at 0.235, 0.499, and 0.678 V for AA, DA, and APAP, respectively. By SDS addition, the anodic current of DA increased, the anodic current of AA diminishes, and the anodic current of APAP decreases slightly. The negative charge density of SDS film and the hydrophobic property of this film will act to enhance the preconcentration–accumulation of the hydrophobic DA⁺ cations at the electrode surface and repel hydrophilic AA molecules away from the electrode surface. The anodic current of APAP decreased slightly by SDS addition because of its neutral structure in this pH resulting in slow diffusion toward electrode surface and retarded interaction with SDS. Furthermore, this promising sensor is used for the simultaneous determination of DA in the presence of AA and UA ($0.1 \text{ M PBS/ pH } 7.40$). The oxidation peaks for UA, DA, and AA appeared at Au/PEDOT–Au_{nano} at 349 mV, 217 mV, and 19 mV, respectively, with large peak potential separation (Fig. 22, Scheme 6). By addition of SDS, the anodic current of DA increases, and the anodic current of AA and UA diminished. This is attributed to the electrostatic attraction between cationic DA and anionic SDS and electrostatic repulsion between anionic UA and AA and anionic SDS [27].

Au/PEDOT–Au_{nano}/SDS showed excellent stability which was examined through repeated cycles up to 50 cycles. Perfect stability was obtained at Au/PEDOT–Au_{nano}/

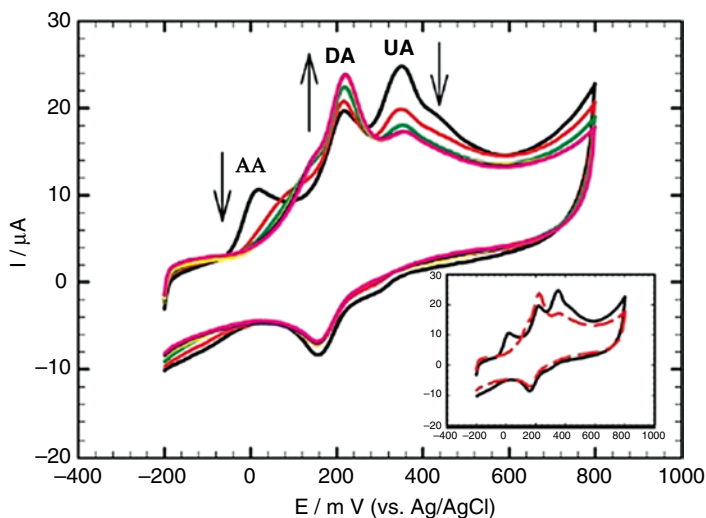
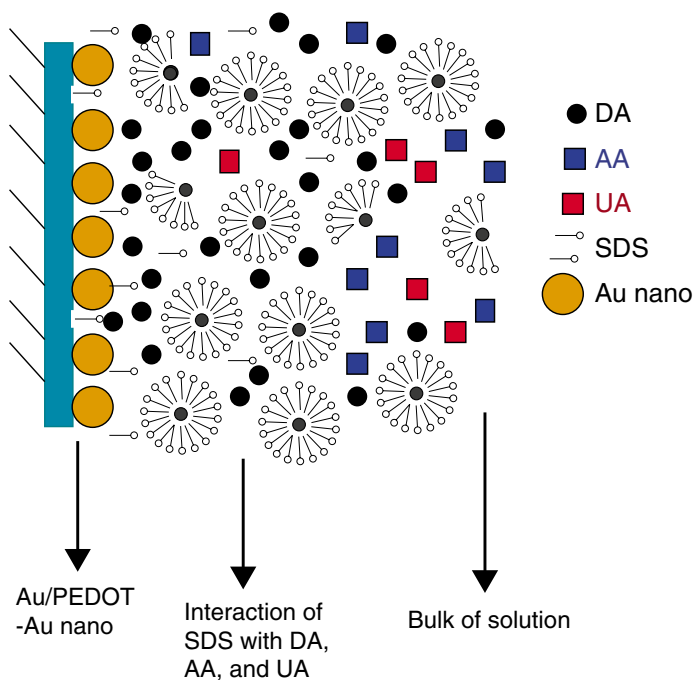


Fig. 22 CVs of tertiary mixture of 1 mmol L^{-1} AA, 0.5 mmol L^{-1} DA, and 0.5 mmol L^{-1} UA in 0.1 mol L^{-1} PBS/pH 7.40 at Au/PEDOT–Au_{nano}-modified electrode with successive additions of (0–200 μL) of 0.1 mol L^{-1} SDS; *inset* represents the initial (in the absence of SDS) and final (in the presence of 200 μL SDS) CVs; scan rate 50 mV s^{-1} (Reprinted from [27], Copyright (2012), with permission from Elsevier)



Scheme 6 Schematic diagram of interaction of DA, AA, and UA at Au/PEDOT/Au_{nano} in the presence of SDS

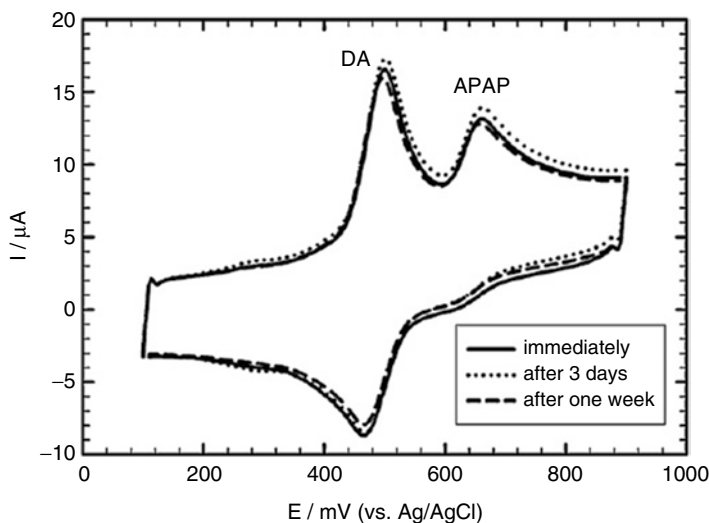


Fig. 23 CVs of the comparison of 50th cycle of long-term stability of Au/PEDOT–Au_{nano}-SDS for tertiary mixture (1 mmol L⁻¹ AA, 1 mmol L⁻¹ DA, and 1 mmol L⁻¹ APAP/0.1 mol L⁻¹ PBS/pH 2.58) separation immediately, after 3 days and 1 week of storage; scan rate 50 mV s⁻¹ (Reprinted from [27], Copyright (2012), with permission from Elsevier)

SDS in 1 mmol L⁻¹ DA/0.1 mol L⁻¹ PBS/pH 2.58, and no decrease in the current response was observed. Furthermore, a very small peak separation was observed, nearly zero or 15 mV peak separation, which indicated the unusual reversibility obtained by repeated cycles. Moreover, long-term stability for the separation of a tertiary mixture of 1 mmol L⁻¹ AA, 1 mmol L⁻¹ DA, and 1 mmol L⁻¹ APAP/0.1 mol L⁻¹ PBS/pH 2.58 was examined at Au/PEDOT–Au_{nano}/SDS up to 1 week. The electrode is kept in 0.1 mol L⁻¹ PBS/pH 2.58 in the refrigerator after each measurement. The CVs of the 50th cycle of repeated cycles of Au/PEDOT–Au_{nano}/SDS for tertiary mixture of AA, DA, and UA immediately after 3 days and 1 week of storage were shown in Fig. 23. The decrease of I_{pa} of DA and APAP was 6.7 % and 1.2 %, respectively, after 1 week of storage. Therefore, better stability via repeated cycles and long-term stability were obtained at Au/PEDOT–Au_{nano}/SDS not only for one component detection (DA) but also for tertiary mixture components separation [27].

Self-Assembled Monolayer of S-Containing Compounds on Nanostructures

SAMs formed by S-containing compounds, namely, thiols on gold–nanogold electrodes, are well-ordered, stable, and densely packed monolayers. They exhibit great characteristics like small overpotential, good sensitivity, perfect selectivity, reproducibility, and short response time in the electrocatalytic reactions. Moreover, the immobilized amount of S-functionalized compounds can be greatly increased by

their modifications with gold nanoparticles which further resulted in enhanced Au–S bond and enhancement of the SAMs stability. On the other hand, the sensory applications at SAM-modified metallic nanoparticle surface, namely, gold nanoparticles, in the presence of surfactants proved excellent and will be addressed in details.

Self-Assembled Monolayer

The design of electrodes with well-defined function and controllable surface properties can be effectively achieved by employing self-assembled monolayers (SAMs) of few nm to several hundred nm thickness [114, 115] of organic molecules (both aliphatic and aromatic) containing free anchor groups such as thiols, disulfides, amines, silanes, or acids [116, 117]. The advantages of SAMs include simplicity of preparation, versatility [118], extraordinary thermodynamic stability [119, 120], reproducibility, and the possibility of introducing different chemical functionalities with high level of order on a molecular dimension [121–127] providing an elegant approach to design tailored surfaces with controlled physical and chemical properties [128, 129]. In addition, several applications were allowed using SAM based on their terminal hydrophilic or hydrophobic functionality or by changing the chain length [115]. SAMs proved excellent in the immobilization of sensing elements like enzymes [118] and DNA. Also, they are very efficient in the electron transfer and capacitance control of an electrode [115]. SAMs can be described as an elegant method by which we can address electrically a molecular component [126, 127]. The method by which the SAMs were formed is the spontaneous adsorption of self-assembled molecules on metals like Au, Ag, Cu, Zn, Fe, Ni, glass, or Pt [130–132]. As well, highly organized [133], stable, and tightly packed compact monolayers can be formed on the electrode surface through the strong interchain and hydrophobic interactions (van der Waals interactions). As a result, various applications can be achieved like chemical sensing, protective coatings [128], lubricants [122], corrosion protection [128], patterning, semiconductor passivation, and optical second-order harmonic generation [134]. There are several reasons for the attractive features that SAMs are offering in biosensing applications:

- (i) Miniaturization is very easy as SAMs utilize the bare minimum resources (a monolayer consisting of 10^{-7} mol/cm² or 10^{13} molecules/cm²) [114].
- (ii) The long-chain alkane thiols of SAMs that showed high degree of ordered and dense nature [114, 120] resulted in a microenvironment membrane which is efficient for the biological molecule immobilization.
- (iii) The good chemical stability of SAMs even after its coupling with the immobilizing molecules for biological sensing makes SAMs efficient as biosensors and immunosensors [114].

Organosulfur compounds can form SAMs on metal substrate [116, 129] especially gold and the formed SAMs [135, 136]. This method is considered an effective method to prepare chemical interfaces that exhibited perfect features and

well-organized, structurally, well-defined, and stable resulting in SAMs having controllable thickness [137] and favorable function [118]. Organothiols lose the hydrogen of the thiol group [130] as molecular hydrogen H_2 upon chemisorption [138–143] on gold surface resulting in the formation of covalent, strong, and thermodynamically favored S–Au bond [144–146]. Thiols have great affinity to be adsorbed on gold due to the following:

- (i) Inertness of gold; therefore, it does not form stable oxides on its surface.
- (ii) The strong specific interaction of gold with sulfur resulting in stable monolayer formation [130, 131, 147] in a short time [141] and in a very reproducible way [131].

SAMs of thiols formed on gold electrodes are well-ordered, stable, and densely packed monolayers [131, 133]. They exhibit great characteristics like small overpotential, good sensitivity, perfect selectivity, reproducibility, and short response time in the electrocatalytic reactions [136, 148].

The electrochemical response at the SAM-modified electrode depends on the monolayer thickness. The “thick” monolayer (e.g., monolayers of long-chain alkanethiols) would passivate the electrode surface, and it slows down the electron transfer [137]. Also, the monolayer having hydrophilic functional groups can favor the permeation of ions in solution into the electrode surface, if any specific interaction exists at the monolayer solution interface. The SAMs having –COOH and –NH₂ functional groups are extensively used for electrochemical sensing applications and served as a platform for the fabrication of biosensors [134]. In recent years, more and more attention has been focused on L-cysteine (Cys) SAM-modified electrochemical sensors due to their good stability and highly characterized structures of the Cys SAM [149].

Methods of SAM Preparation

SAM can be prepared via two methods: immersion and electrochemical growth [114, 149]. The immersion growth is a common method for SAMs’ formation through which the metal electrode is soaked in the required solution for a certain time then the electrode was washed with the same solvent and dried [114]. The substrate nature and roughness, type of solvent, adsorbate nature, adsorbate concentration, and temperature greatly affected the packing density and formation of SAMs. Very dilute solution gives ordered SAMs, while high concentration and long time (6 days) resulted in the formation of multilayer. Highly pure solvents such as water, ethanol, acetonitrile, and hexane are used to prepare solutions of thiol, sulfide, and disulfide [114]. The electrochemical growth was developed by Ying Zhuo et al. They reported that the immersion growth suffered from the competitive adsorption from other ions, for example, supporting electrolytes. In addition, the assemblies formed by immersion growth sometimes were subjected to nonuniform layer growth. The electrochemical method was free of the above drawbacks and more advantageous than immersion growth such as controllable and selective [149].

SAM-Modified Nanostructured Electrodes

SAM procedure opens a new avenue for the fabrication of electrodes having an electrocatalytic activity toward many electrochemical reactions superior to that of unmodified electrodes [150]. SAM-modified electrodes are very promising for the construction of electrochemical biosensors because they can enhance the electron transfer rate, selectivity, and sensitivity, improve the response time, and decrease the overpotential [151–153]. The SAM plays three important roles in the biosensing applications: (i) it forms thin monolayer, (ii) it forms weak hydrogen-bonding interactions, and (iii) it prevents fouling of the electrode surface by the oxidation products [137]. SAMs of thiol molecules on a metal surface provide a useful means of immobilizing electrode surfaces to attach various functional groups, such as nanoparticles and redox-active species [136].

Gold nanoparticles that are conjugated to globular protein, bovine serum albumin, through S–Au bond showed more surface area for strong interaction with the external species [154]. Furthermore, the modification using gold nanoparticles could greatly improve the S-functionalized compounds' immobilized amount, affect the SAM structure [155], enhance the Au–S bond, and improve the SAMs' layer stability [147]. The high surface energy of nanoparticles resulted in their instability; therefore, they need suitable surface modifications to be stabilized against aggregation. Cyano (CN), amino (NH₂), and mercapto (SH) are functional groups that exhibited great affinity toward gold. Hak Yong Kim identified the interaction of cysteine and gold nanoparticles and indicated that the cysteine thiol moiety is an effective site for gold interaction resulting in the formation of stable cysteine-capped gold nanoparticles. Gold nanoparticles were stabilized by cysteine molecules through S–Au interaction [45]. Figure 24a displayed the TEM image of spherical gold nanoparticles with a corona of cysteine ligand. Moreover, the TEM confirmed the gold

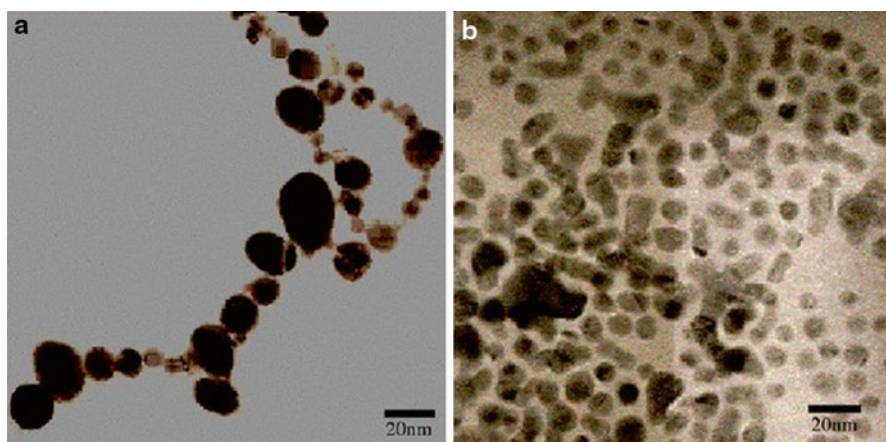


Fig. 24 TEM images of (a) cysteine-capped gold nanoparticles and (b) gold nanoparticles in gold hydrosol (Reprinted from [154], Copyright (2006), with permission from Elsevier)

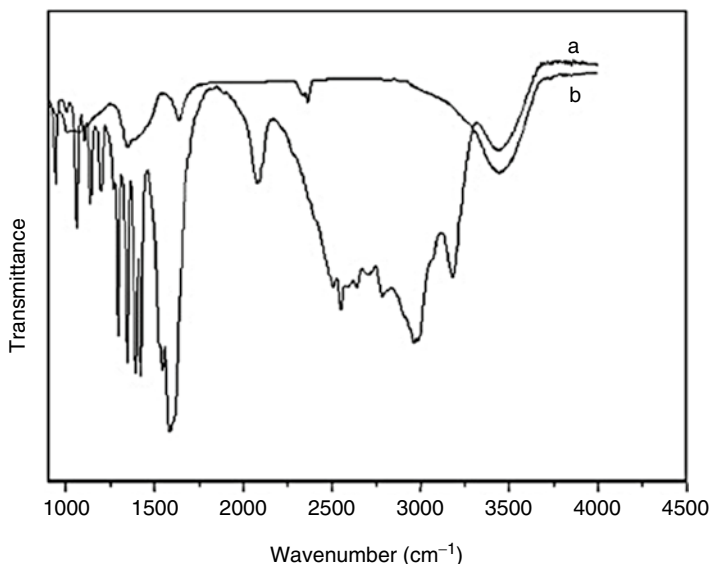


Fig. 25 Infrared spectra of cysteine (*spectrum a*) and cysteine-capped gold nanoparticles (*spectrum b*) (Reprinted from [154], Copyright (2006), with permission from Elsevier)

nanoparticles' stabilization because of their interaction with cysteine. Figure 24b showed the TEM image of the clusters of gold nanoparticles that are formed by NaBH_4 reduction. Moreover, the characteristic bands of cysteine moiety after gold nanoparticles' conjugation were detected through the application of FTIR spectra. Amino acids exhibit spectra characteristic of both carboxylate and primary amine salts as they can be described as zwitterions. The FTIR spectra of Cys and Cys/gold nanoparticles were shown in Fig. 25. The characteristics bands in Cys (spectrum a) appeared at 1600, 1390 cm^{-1} for the asymmetric and symmetric stretching of COO^- , at 1532 cm^{-1} for N-H bending, the broad 3000–3500 cm^{-1} range for stretching NH_3^+ , and near 2550 cm^{-1} for S-H group in the cysteine molecule. These results are very close to IR spectra of cysteine. The spectra of Cys/gold nanoparticles (spectrum b) showed slight changes. A slight shift in COO^- and NH_3^+ stretching positions occurs because of the change in their dipole moment as a result of cysteine binding on the high electron density metal surface. Significantly, the S-H band was not observed in the spectra of Cys/gold confirming the Au-S bond [154].

Desorption of SAM

The formation of SAM of alkanethiols on bare gold and gold nanoparticle-modified electrode through the S-Au bond can be confirmed using the electrochemical desorption experiment. Alkanethiol monolayers on gold electrodes undergo oxidative and reductive desorption. The oxidative desorption of Au-Cys (a) and

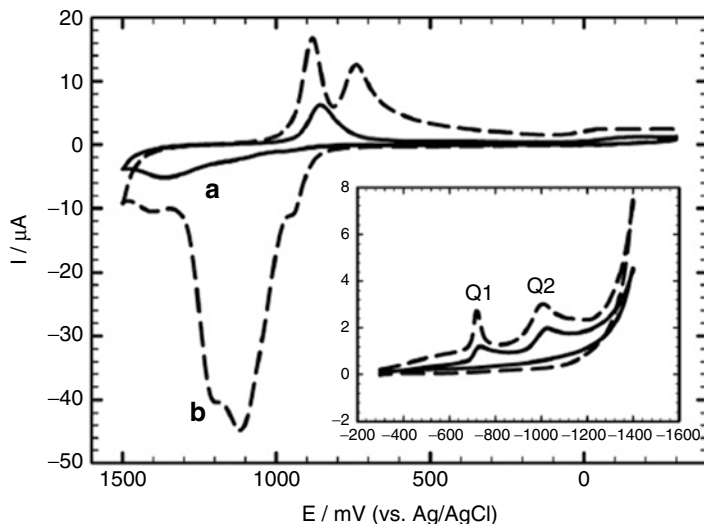
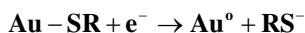


Fig. 26 CVs of the oxidative desorption of Au–Cys (a) and Au/Au_{nano}–Cys (b) in 0.1 mol L⁻¹ PBS/pH 2.58, *inset*; CVs of the reductive desorption of Au–Cys (solid line) and Au/Au_{nano}–Cys (dash line) in 0.5 mol L⁻¹ KOH; scan rate 50 mV s⁻¹ (Reprinted from [31], Copyright (2012), with permission from Elsevier)

Au/Au_{nano}–Cys (b) electrodes in 0.1 mol L⁻¹ PBS/pH 2.58 was shown in Fig. 26. From this figure, we can deduce that gold nanoparticles increase the assembly amount of cysteine and affect the SAM structure and stability. On the other hand, thiols undergo reductive desorption in alkaline solutions via a one-electron reduction reaction:



The amount of the charge consumed during the reductive desorption can be used to determine the surface concentration of the thiolates. The reductive desorption of Au–Cys (solid line) and Au/Au_{nano}–Cys (dash line) in 0.5 mol L⁻¹ KOH was shown in the inset of Fig. 26. At bare gold electrode, two cathodic peaks are observed at -736 mV and -1027 mV, and at gold nanoparticle-modified electrode, cathodic peaks are at -720 mV and -1008 mV. As a result of gold nanoparticles' deposition, the desorption peak current increased largely. Wenrong Yang et al. indicated that the first peak (Q1) is attributed to the Au–S bond cleavage (having a shape characteristic of an adsorbed species), and the second peak (Q2) is attributed to a similar field-induced rearrangement of cysteine clusters which would occur within the electrical double layer (having more diffusion-like character). Therefore, the area under the first peak (Q1) can be used to determine the surface coverage of cysteine. The estimated surface coverage of cysteine SAM is 2.64×10^{-9} mol cm⁻² and 4.43×10^{-9} mol cm⁻² on bare gold- and gold nanoparticle-modified electrode, respectively. As a result, modification using gold nanoparticle can markedly improve the immobilization amount of cysteine and enhance the Au–S bond and stability of cysteine SAM [31, 155].

Sensing Applications of SAM-Modified Nanostructures

Binary SAM of 3-mercaptopropionic acid (MPA, $\text{HS}-(\text{CH}_2)_2-\text{COOH}$) and 1-tetradecanethiol (TDT, $\text{HS}-(\text{CH}_2)_{13}\text{CH}_3$) was formed on 2D bare gold (Au) and 3D Au-NP-modified electrode by Dong-Shik Kim. Electron transfer rate (k_{et}), charge transfer resistance (R_p), Warburg element (W_0), double layer capacitance (C_{dl}), and time constant exhibited significant changes of the binary SAM and uni-SAM formation on the bare gold and Au-NP surfaces. Greater k_{et} and C_{dl} were obtained in the case of a binary SAM of MPA and TDT on the Au-NP compared to that on the binary SAM on planar bare gold surface. This is due to the less ordering of binary SAM structure on the Au-NP than that on the planar Au electrode resulting in a reduced interaction between the SAM molecules on the Au-NP than that on the planar Au electrode. Moreover, the functional group affinity, COOH and CH_3 , chain-chain interaction, hydrogen bonding, and Au-NPs surface curvature affect the stability and surface coverage of the SAM [115]. Moreover, gold electrodes modified with gold nanoparticles, cysteamine (CA) and 3-mercaptopropionic acid (MPA), was utilized for simultaneous determination of epinephrine EP, AA, and UA. The electron transfer rate of EP on the modified electrodes was enhanced compared to the bare electrode. The voltammetric response of EP at 2D- and 3D-modified gold templates, Au/MPA, Au/MPA/CA/Au-NPs, Au/Au-NPs, Au/Au-NPs/MPA, and Au/Au-NPs/MPA/CA/Au-NPs, respectively, were compared and showed in Fig. 27. Lower oxidation potential, higher oxidation current, and greater catalytic effect were achieved for EP at modified electrodes prepared on 3D template compared to that on 2D gold template. The 3D layer may provide better curvature and therefore better penetration of EP through the alkane chains on nanoparticle surface compared to the 2D layers. As a result, the electron transfer kinetics of EP and the electrode surface is better on 3D MPA layers compared to 2D MPA layers [147]. On the other hand, a promising electrochemical sensor of Au/Au_{nano}-Cys/SDS for DA [156] and EP [31] was constructed through the formation of SAM of cysteine on gold nanoparticle-modified gold electrode. The electrochemistry of DA at different modified electrodes (Au/Au_{nano}, Au/Au_{nano}/SDS, Au/Au_{nano}-Cys, and Au/Au_{nano}-Cys/SDS) was displayed in Fig. 28 and Table 3. The electrochemistry of DA at Au/Au_{nano} (Au electrode modified with gold nanoparticles) showed a great current response ($I_{\text{pa}}=5.6 \mu\text{A}$), low oxidation potential ($E_{\text{pa}}=516 \text{ mV}$), and enhanced reversibility ($\Delta E_p=45 \text{ mV}$) Fig. 28 (I). These observations are attributed to the catalytic effect of Au_{nano} that act as a facilitator to improve the electron transfer rate and enhance the electrochemical reaction. By the addition of 160 μL of SDS at Au/Au_{nano}, the oxidation current of 1 mmol L^{-1} DA in 0.1 mol L^{-1} PBS/pH 2.58 decreased from 5.6 μA at Au/Au_{nano} to 4.2 μA at Au/Au_{nano}/SDS Fig. 28 (II). There is an interaction between Au_{nano} and SDS through SDS hydrophobic long carbon chain that resulted in the blocking of the binding sites on gold nanoparticles. This SDS layer acts as an insulating layer rather than enhancing the charge transfer, thus the oxidation current of DA decreases in the presence of SDS. On the other hand, the CV of DA at Au/Au_{nano}-Cys (cysteine SAM-modified Au_{nano}-modified gold electrode) was shown in Fig. 28 (III). The oxidation current of DA decreased from 5.6 μA to 3 μA ,

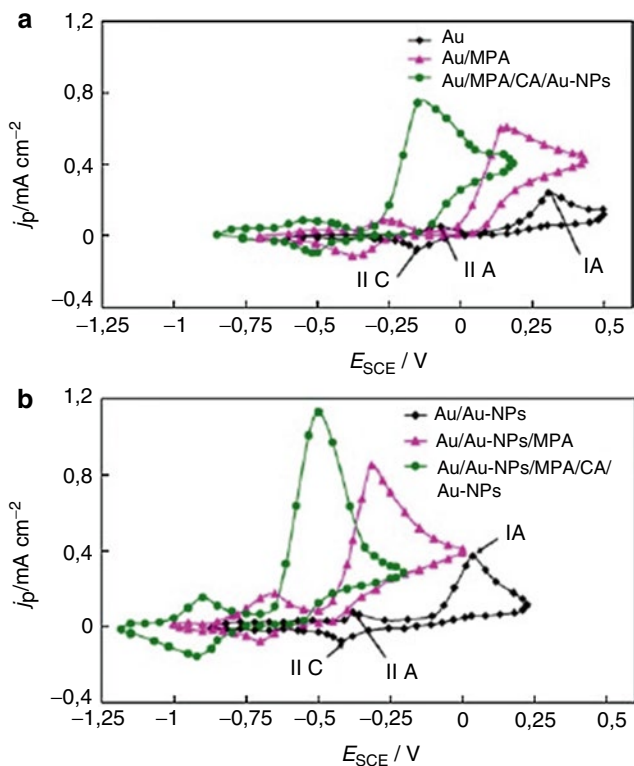


Fig. 27 (a) Cyclic voltammograms of the Au electrode, Au/MPA, and Au/MPA/CA/Au-NP-modified gold electrodes and (b) cyclic voltammograms of the Au-NPs, Au/Au-NPs/MPA, Au/Au-NPs/MPA/CA/Au-NP-modified gold electrodes in 60 mM phosphate buffer (pH 7) with 500 μM epinephrine. $v=0.1 \text{ Vs}^{-1}$ (Reprinted from [147], Copyright (2009), with permission from Elsevier)

the oxidation potential was shifted from 516 mV to 586 mV, and the peak separation increased from 45 mV to 148 mV by the modification with Cys SAM. These observations were attributed to the (i) cysteine molecules' disorganization on gold nanoparticles resulting in the inhibition of hydrogen bond formation between DA and cysteine and (ii) electrostatic repulsion between the positively charged cysteine (it is a zwitterionic amino acid and its isoelectric point is 5.06; if the pH of electrolyte is lower than 5.06, the amino group of cysteine is protonated and cysteine is positively charged) and the cationic DA resulting in the hindrance of DA molecules from reaching the electrode surface, decrease of the oxidation current, and increase of the potential peak separation.

The electrochemistry of DA at cysteine SAM-modified Au_{nano} -modified gold electrode in the presence of 40 μL SDS was shown in Fig. 28 (IV) ($\text{Au}/\text{Au}_{\text{nano}}\text{-Cys}/\text{SDS}$). In the presence of 40 μL SDS, the oxidation current increased from 3 μA to 4.3 μA , the oxidation potential was shifted from 586 mV to 504 mV, and the peak separation

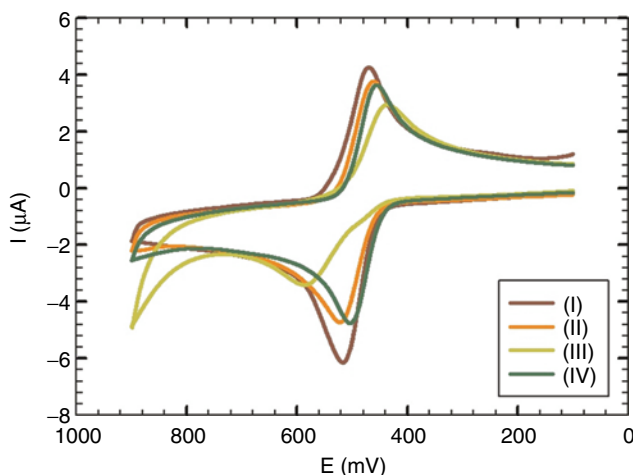
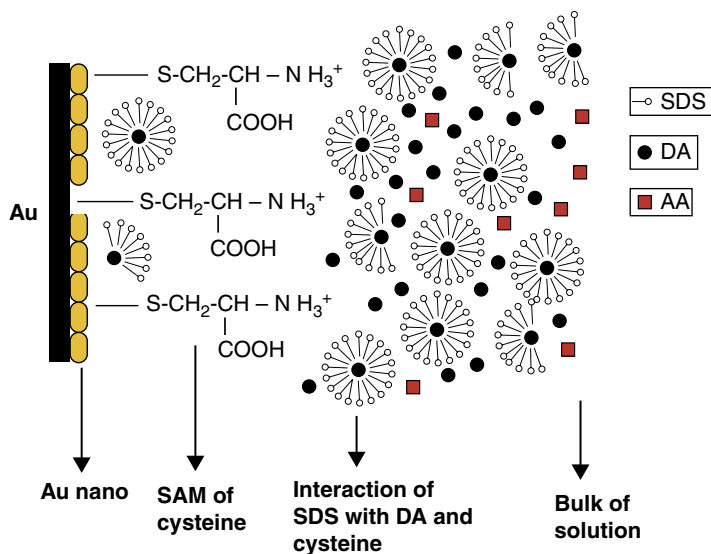


Fig. 28 CVs of 1 mmol L⁻¹ DA at (I) Au/Au_{nano}, (II) Au/Au_{nano}/SDS, (III) Au/Au_{nano}-Cys, and (IV) Au/Au_{nano}-Cys/SDS-modified electrodes; scan rate 50 mV s⁻¹ (Reprinted from [156], Copyright (2012), with permission from Elsevier)

decreased from 148 mV to 47 mV. As mentioned before, there is an electrostatic repulsion between cationic DA and cationic cysteine layer. The addition of SDS (an anionic surfactant) improves the DA diffusion through the cationic cysteine layer because of the electrostatic attractions between the anionic SDS and cationic DA (Scheme 7). Moreover, there is an electrostatic attraction between anionic SDS and the positively charged cysteine SAM which allows cysteine molecules' reorganization on gold nanoparticles, improving the formation of the hydrogen bond between DA and cysteine and promoting faster the rate of the electron transfer. An increase of the oxidation current, higher electron transfer rate, smaller peak separation, and better reversibility were observed for DA [156] and EP at Au/Au_{nano}-Cys/SDS. Table 5 showed the CVs of DA at Au-Cys and Au/Au_{nano}-Cys, we can deduce that the cysteine effect on the polycrystalline bare Au response is more pronounced than that on gold nanoparticles and its effect on gold nanoparticles is enhanced by using SDS. SDS promotes the cysteine reorganization on gold nanoparticles resulting in enhanced oxidation current, small peak separation, and better reversibility. The peak potential separation ($\Delta E_p \sim 45$ mV) was the same in the cases of Au/Au_{nano} and Au/Au_{nano}-Cys/SDS indicating the high reversibility and the strong adsorption of the electroactive species at the electrode surface. Au/Au_{nano} displays a little higher current response, but Au/Au_{nano}-Cys/SDS shows, besides the high current response, better stability through repeated cycles and long-term stability.

In addition, the diffusion coefficient (D_{app}) values for DA and EP were 5.00×10^{-6} and 1.24×10^{-5} cm² s⁻¹ at Au/Au_{nano}-Cys and 1.06×10^{-5} and 3.86×10^{-5} cm² s⁻¹ at Au/Au_{nano}-Cys/SDS, respectively. The charge transfer diffusion component at Au/Au_{nano}-Cys was affected markedly by the anionic SDS. The D_{app} values showed that



Scheme 7 Schematic model of Au/Au_{nano}-Cys/SDS-modified electrode in the presence of DA cations and AA (Reprinted from [156], Copyright (2012), with permission from Elsevier)

Table 5 CV results for the redox reaction of 1 mmol L⁻¹ DA/0.1 mol L⁻¹ PBS/pH 2.58 at different modified electrodes (Au, Au-Cys, Au/Au_{nano}, Au/Au_{nano}/SDS, Au/Au_{nano}-Cys, and Au/Au_{nano}-Cys/SDS (Reprinted from [156], Copyright (2012), with permission from Elsevier)

Electrode	E _{pa} (mV)	I _{pa} (μA)	E _{pc} (mV)	I _{pc} (μA)	ΔE _p (mV)
Au	683	2.82	235	0.478	448
Au-Cys	636	2.55	379	2.14	257
Au/Au _{nano}	516	5.57	471	4.56	45
Au/Au _{nano} /SDS	522	4.20	462	4.24	60
Au/Au _{nano} -Cys	586	2.99	438	3.24	148
Au/Au _{nano} -Cys /SDS	504	4.35	457	3.99	47

DA and EP diffusion on Au/Au_{nano}-Cys was improved in the presence of SDS rather than in the absence of it [31, 156]. On the other hand, simultaneous determination of tertiary mixture of AA, DA [156] or EP [31], and APAP was examined at this modified electrode. The DPVs of tertiary mixture of 1 mmol L⁻¹ AA, 1 mmol L⁻¹ DA, and 1 mmol L⁻¹ APAP in 0.1 mol L⁻¹ PBS/pH 2.58 at Au/Au_{nano}-Cys with successive additions of 0–40 μL of 0.1 mol L⁻¹ SDS was shown in Fig. 29. At Au/Au_{nano}-Cys, three well-resolved oxidation peaks appeared at 300, 468, and 648 mV for AA, DA and APAP, respectively. By SDS addition, the DA and APAP oxidation current increases, while the AA oxidation current diminishes. The negatively charged SDS film besides the hydrophobic character of the interior of this film resulted in the repulsion of the hydrophilic AA molecules away from the electrode

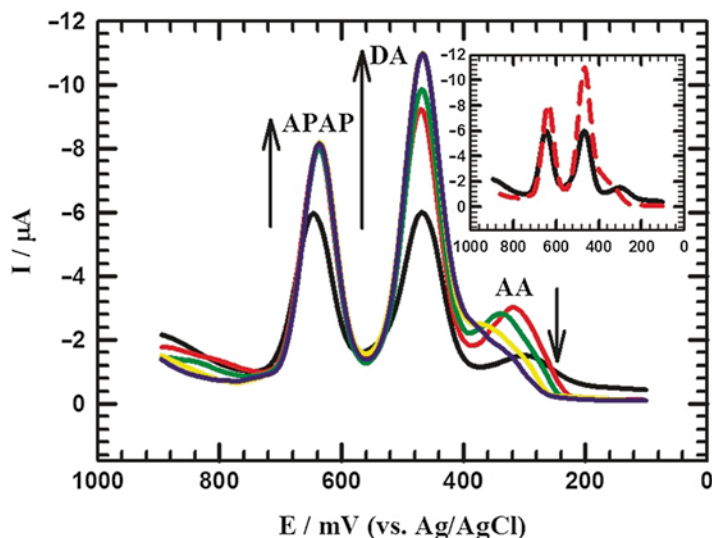


Fig. 29 Differential pulse voltammograms for 1 mmol L^{-1} AA, 1 mmol L^{-1} DA, and 1 mmol L^{-1} APAP in PBS (0.1 mol L^{-1}) at Au/Au_{nano}-Cys with successive additions of (0–40 μL) of 0.1 mol L^{-1} SDS at pH 2.58; the *inset* represents the initial (in the absence of SDS) and final (in the presence of 40 μL SDS) DPVs (Reprinted from [156], Copyright (2012), with permission from Elsevier)

surface while enhancing the preconcentration–accumulation of hydrophobic cations of DA and APAP. The negatively charged SDS that adsorbed onto the electrode surface has the ability to control the electrode reactions of AA, DA or EP, and APAP that differ in their net charge [31, 156]. Furthermore, Au/Au_{nano}-Cys/SDS was utilized for the simultaneous determination of binary mixture of EP and APAP (0.1 M PBS/pH 7.40) (inset of Fig. 30). Two well-defined peaks appeared at 222 mV and 431 mV for EP and APAP at Au/Au_{nano}-Cys, respectively. By SDS addition, EP oxidation peak current increased as a result of electrostatic interaction of the anionic SDS with the cationic EP, while the oxidation current of APAP decreased due to its neutral structure [31]. Also, Au/Au_{nano}-Cys/SDS can selectively determine EP in the presence of a large amount of UA and glucose (PBS/pH 7.40) (Fig. 30). No interference was observed from glucose at the modified electrode. At Au/Au_{nano}-Cys, two well-defined peaks appeared: 212 mV and 418 mV for EP and UA, respectively. By SDS addition, EP oxidation peak current increased, and UA oxidation peak current decreased due to the electrostatic interactions (attraction and repulsion, respectively) with anionic SDS. Furthermore, low detection limit of $0.294 \text{ nmol L}^{-1}$ and quantification limit of $0.981 \text{ nmol L}^{-1}$ for EP were obtained at Au/Au_{nano}-Cys/SDS [31]. Moreover, the physical morphology of the surface can be used to explain the electrochemical responses of different sensors. Figure 31a showed the SEM image of gold nanoparticles which are located at different elevations and homogeneously distributed exhibiting large surface area. Figure 31d showed the SEM image of gold nanoparticles modified with SDS; the nanoparticles have dendritic shape with different sizes and are randomly distributed on the surface. Also, a

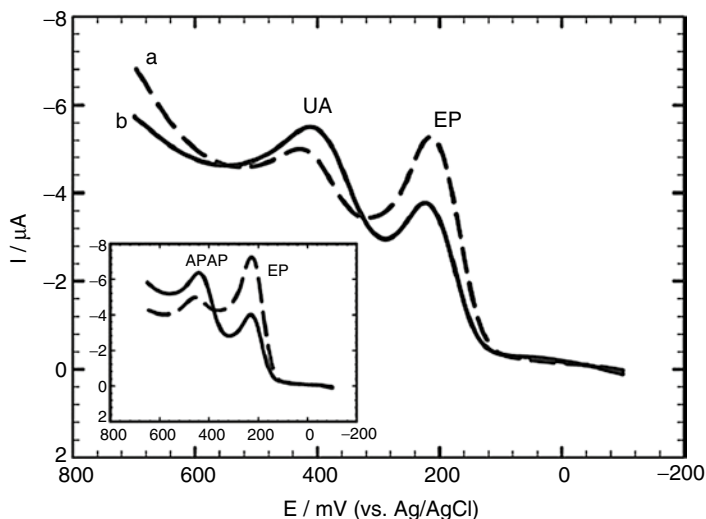


Fig. 30 Linear sweep voltammograms (LSVs) of 0.5 mmol L^{-1} EP, 1 mmol L^{-1} UA in the presence of 5 mmol L^{-1} glucose in 0.1 mol L^{-1} PBS/pH 7.40 at (a) Au/Au_{nano}-Cys and (b) Au/Au_{nano}-Cys/SDS, *inset*; LSVs of 1 mmol L^{-1} EP, 1 mmol L^{-1} APAP/ 0.1 mol L^{-1} PBS/pH 7.40 at Au/Au_{nano}-Cys (solid line) and Au/Au_{nano}-Cys/SDS (dash line); scan rate 50 mV s^{-1} (Reprinted from [31], Copyright (2012), with permission from Elsevier)

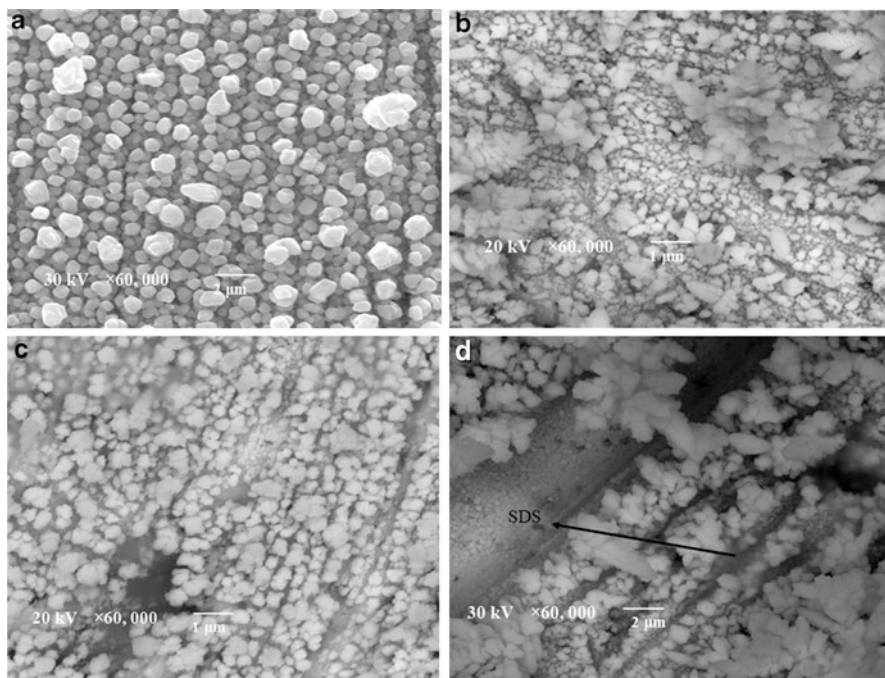


Fig. 31 SEM images of (a) Au/Au_{nano}, (b) Au/Au_{nano}-Cys, (c) Au/Au_{nano}-Cys/SDS, and Au/Au_{nano}/SDS electrodes (Reprinted from [31], Copyright (2012), with permission from Elsevier)

Table 6 CV results for the 1st, 25th, and 50th cycles of the repeated cycle stability of Au/Au_{nano}-Cys electrode in 1 mmol L⁻¹ DA/0.1 mol L⁻¹ PBS/pH 2.58

Cycle	I _{pa} (μA)	E _{pa} (mV)	I _{pc} (μA)	E _{pc} (mV)	ΔE _p (mV)
1st	2.46	585	2.63	465	120
25th	3.87	480	3.16	480	zero
50th	3.84	480	3.13	480	zero

spongy film is observed due to the surfactant film on the surface acting as an insulating layer rather than enhancing the charge transfer, thus, the oxidation current of DA at gold nanoparticles surface decreases in the presence of SDS. Figure 31b showed the SEM image of gold nanoparticles modified with cysteine SAM; the nanoparticles have dendritic shape with different sizes and are randomly distributed on the surface. Figure 31c showed the SEM image of gold nanoparticles modified with cysteine SAM and further modified with SDS; the nanoparticles are better dispersed, highly packed, and homogeneously distributed on the surface. Reorganization and redispersion of gold nanoparticles occur as a result of the electrostatic attraction between the anionic SDS and cationic cysteine. A spongy film is observed in Fig. 31c due to the surfactant film on the surface [31, 156]. Furthermore, the stability of the different modified electrodes was studied via repeated cycles up to 50 cycles. Au/Au_{nano}, Au/Au_{nano}/SDS, Au/Au_{nano}-Cys, and Au/Au_{nano}-Cys/SDS electrodes in 1 mmol L⁻¹ DA/0.1 mol L⁻¹ PBS/pH 2.58 exhibited excellent stability with no current response decrease. These modified electrodes exhibited good reproducibility and do not suffer from surface fouling during the repetitive voltammetric measurement. The bare Au electrode exhibited bad stability because of the electrode fouling. On the other hand, very small peak potential separation (~ zero or 15 mV) was obtained indicating unusual high reversibility at the surface of these modified electrodes. From the CV that compared the 1st, 25th, and 50th cycles of repeated cycles stability of Au/Au_{nano}-Cys electrode, it was found that I_{pa} increased from 2.5 μA in the 1st cycle up to 3.8 μA in the 25th and 50th cycles and the peak separation decreased from 120 mV in the 1st cycle to ~0 mV in the 25th and 50th cycles (Table 6). These observations indicate that cysteine molecules undergo reorganization on gold nanoparticles resulting in mediation of DA diffusion through the electrode surface and enhancement of the hydrogen bonding between the hydrogen in hydroxyl-phenol of DA and the nitrogen in the L-Cys which enhances the electron transfer rate of DA molecules. Therefore, cysteine molecules undergo reorganization on gold nanoparticles by repeated cycles or by SDS addition (instantaneous reorganization).

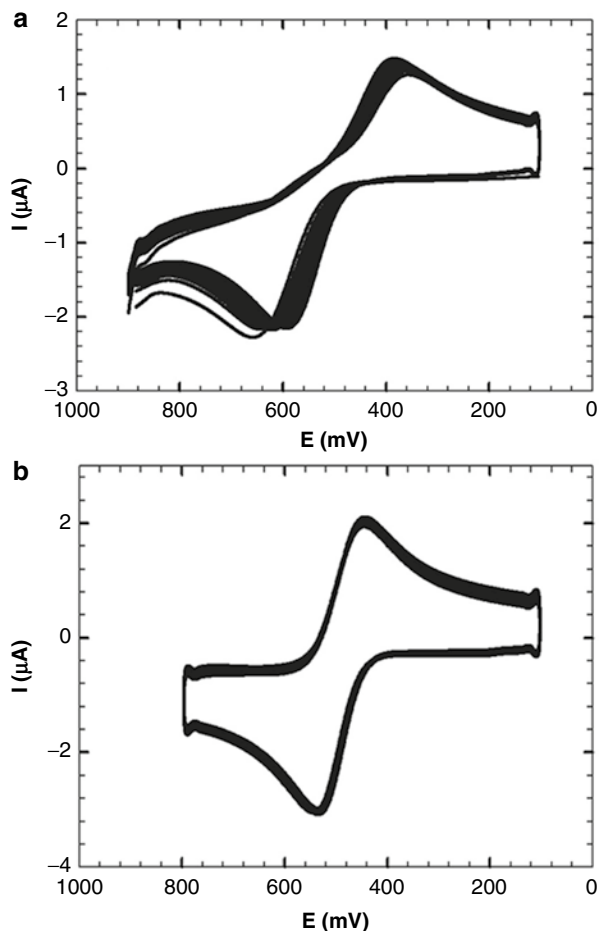
Moreover, the long-term stability of Au/Au_{nano}, Au/Au_{nano}-Cys, and Au/Au_{nano}-Cys/SDS electrodes was studied up to 1 week (Tables 7 and 8). The electrode is kept in 0.1 mol L⁻¹ PBS/pH 2.58 in the refrigerator after each measurement. The repeated cycles of Au/Au_{nano} and Au/Au_{nano}-Cys/SDS electrodes after 1 week of storage were shown in Fig. 32a, b, respectively. I_{pa} of the 50th cycle decreased by 26 % and 44 %, and the peak separation increased to 120 mV and 180 mV after 3 days and 1 week of storage, respectively, in the case of Au/Au_{nano} electrode. In addition, I_{pa} of the 50th cycle decreased by 23.6 % and 35.6 %, and the peak separation was zero and 15 mV after the same periods of storage, respectively, in

Table 7 CV results for the 50th cycle of the repeated cycle stability of Au/Au_{nano}, Au/Au_{nano}-Cys, and Au/Au_{nano}-Cys/SDS electrodes in 1 mmol L⁻¹ DA/0.1 mol L⁻¹ PBS/pH 2.58 immediately

Electrode	E _{pa} (mV)	I _{pa} (μA)	E _{pc} (mV)	I _{pc} (μA)	ΔE _p (mV)
Au/Au _{nano}	480	3.54	480	3.14	zero
Au/Au _{nano} -Cys	480	3.84	480	3.13	zero
Au/Au _{nano} -Cys/SDS	495	3.53	480	3.07	15

Table 8 CV results for the 50th cycle of the repeated cycle stability of Au/Au_{nano}, Au/Au_{nano}-Cys, and Au/Au_{nano}-Cys/SDS electrodes in 1 mmol L⁻¹ DA/0.1 mol L⁻¹ PBS/pH 2.58 after 1 week of storage

Electrode	E _{pa} (mV)	I _{pa} (μA)	E _{pc} (mV)	I _{pc} (μA)	ΔE _p (mV)
Au/Au _{nano}	585	1.97	405	1.51	180
Au/Au _{nano} -Cys	495	2.47	480	2.40	15
Au/Au _{nano} -Cys/SDS	525	2.69	465	2.57	60

Fig. 32 Long-term stability of (a) Au/Au_{nano} and (b) Au/Au_{nano}-Cys/SDS (40 μL) after 1 week, 50 repeated cycles, 50 mV s⁻¹ scan rate (Reprinted from [156], Copyright (2012), with permission from Elsevier)

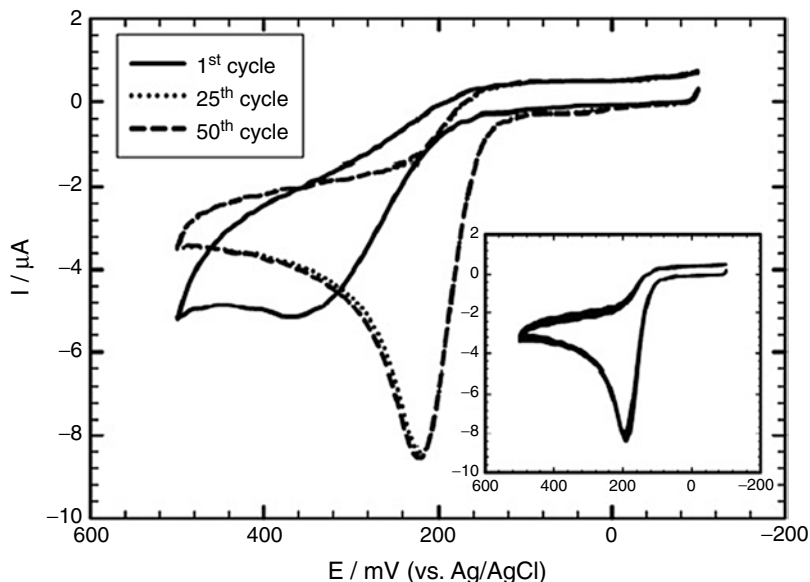


Fig. 33 Comparison of 1st, 25th, and 50th cycles of repeated cycle stability of Au/Au_{nano}-Cys electrode in 1 mmol L⁻¹ EP/0.1 mol L⁻¹ PBS/pH 7.40. *Inset*: CV of repeated cycles stability of Au/Au_{nano}-Cys/SDS-modified electrode in 1 mmol L⁻¹ EP; scan rate 50 mV s⁻¹ (Reprinted from [31], Copyright (2012), with permission from Elsevier)

the case of Au/Au_{nano}-Cys electrode. Also, I_{pa} decreased by 24 %, and the peak separation was 15 and 60 mV after 3 days and 1 week of storage, respectively, in the case of Au/Au_{nano}-Cys/SDS electrode (Tables 7 and 8).

These results confirmed that the presence of cysteine SAM on gold nanoparticles improved the reversibility and the long-term stability of Au/Au_{nano}-Cys and Au/Au_{nano}-Cys/SDS electrodes due to the formation of strong Au-S bond [156].

On the other hand, excellent stability of Au/Au_{nano}-Cys electrode for mixture separation (AA, DA, and APAP) in the presence of SDS was achieved via repeated cycling up to 50 cycles. As well, the long-term stability for the separation of AA, DA, and APAP tertiary mixture on Au/Au_{nano}-Cys electrode was studied in the presence of SDS. I_{pa} of DA decreased by 14 % and 17 % and I_{pa} of APAP decreased by 15 % and 28 % after 3 days and 1 week of storage, respectively. In addition, the long-term stability for the separation of the same mixture at Au/Au_{nano} electrode was studied. I_{pa} of DA decreased by 34 % and 44 % and I_{pa} of APAP decreased by 9 % and 33 % after 3 days and 1 week of storage, respectively. Therefore, Au/Au_{nano}-Cys in the presence of SDS exhibited a better stability via repeated cycles and longer-term stability not only for one component detection but also for tertiary mixture separation [156].

Furthermore, the same study was utilized in EP at the different modified electrodes via repeated cycles up to 50 cycles. The repeated cycle stability of the Au/Au_{nano}-Cys/SDS-modified electrode was shown in the inset of Fig. 33. Au/Au_{nano}-Cys and

Au/Au_{nano}-Cys/SDS-modified electrodes in 1 mmol L⁻¹ EP/0.1 mol L⁻¹ PBS/pH 7.40 showed better stability compared to the Au/Au_{nano} electrode indicating that these modified electrodes have good reproducibility and do not suffer from surface fouling during repetitive voltammetric measurement due to Au-S bond formation.

Figure 33 showed the CV comparing the 1st, 25th, and 50th cycles of repeated cycles stability of Au/Au_{nano}-Cys electrode, I_{pa} increased from 4.9 μ A in the 1st cycle up to 8.2 μ A in the 25th and 50th cycles, and the oxidation peak potential shifted from 363 mV in the 1st cycle to 220 mV in the 25th and 50th cycles. This result confirms the reorganization of cysteine molecules on gold nanoparticles by repeated cycles resulting in enhanced hydrogen bond formation between EP and cysteine and improved electron transfer rate. Also, the long-term stability of Au/Au_{nano} and Au/Au_{nano}-Cys/SDS electrodes was studied for up to 1 week. I_{pa} of EP decreased by 20 % and 30 % after 3 days and 1 week of storage, respectively, in the case of Au/Au_{nano} electrode. I_{pa} decreased by 9 % and 16 % after the same periods of storage, respectively, in the case of Au/Au_{nano}-Cys/SDS electrode. These results indicate that cysteine SAM organized on gold nanoparticles enhances the long-term stability of Au/Au_{nano}-Cys/SDS electrode due to Au-S bond formation. Therefore, Au/Au_{nano}-Cys/SDS electrode showed better stability via repeated cycles and long-term stability compared to the Au/Au_{nano} electrode [31]. In conclusion, the synergistic effect between cysteine SAM-modified gold nanoparticles and surfactant enhances the use of surfactant-modified electrodes as nanosensors with excellent reproducibility, high sensitivity, and unique selectivity.

On the other hand, Gan Yang prepared a hemoglobin (Hb)/gold colloid (nano-Au)/L-cysteine (L-cys)/nano-Au/nanoparticles Pt (nano-Pt)-chitosan (CHIT) composite film-modified Pt disk electrode as a biosensor for the determination of H₂O₂. Figure 34 compares the response of different modified electrodes toward H₂O₂. The current increased upon adsorption of L-cys on the nano-Au/nano-Pt-CHIT surface, and maximal current is obtained at the modified electrode. L-cys molecules were assembled on the nano-Au-modified electrode, and the interfacial resistance decreased as obtained from EIS study suggesting that L-cys promotes the electron transfer rate [157]. Furthermore, Guoli Shen prepared L-cysteine-gold particle nanocomposite (CGN) by a self-assembly process to involving L-cysteine on gold nanoparticles providing a general method to realize the direct electrochemistry of enzymes [138]. A new electrode interface was constructed by using CGN to be immobilized in the network of a Nafion membrane on a glassy carbon (GC) electrode (GC/NCGN). GC/NCGN was utilized to fabricate the third-generation horseradish peroxidase biosensor exhibiting good response to H₂O₂ and displayed the remarkable sensitivity and repeatability. The effect of the amount of L-cysteine on the response of the GC/NCGN was investigated. The response was rather small when only a small amount or even no L-cysteine was added to prepare the nanocomposites. This may be attributed to the formation of a rather small amount of CGN during the assembly of L-cysteine on gold nanoparticles. A maximum response was obtained when 5 μ L of 10⁻³ M of L-cysteine was used, and the response decreased again when more than 5 μ L of 10⁻³ M of L-cysteine was added. The optimum amount was 5 μ L of 10⁻³ M of L-cysteine [138].

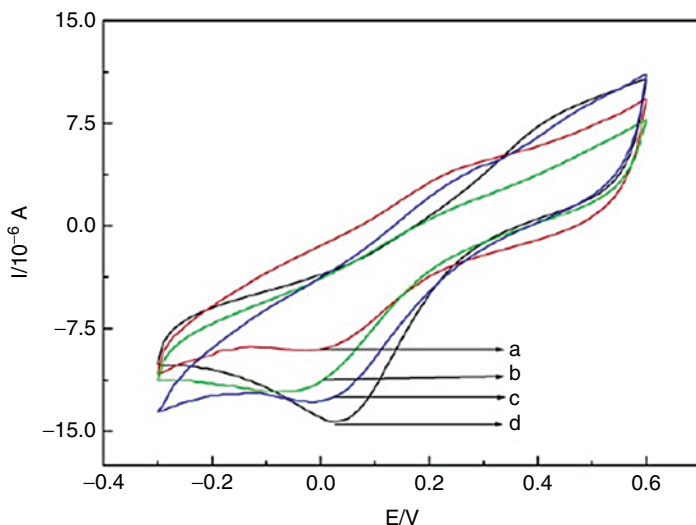


Fig. 34 Cyclic voltammograms of the different electrodes in 0.1 M pH 7.0 PBS containing 3.5×10^{-4} M H_2O_2 . (a) Hb/n-Pt-CHIT composite film-modified Pt electrode, (b) Hb/n-Au/n-Pt-CHIT composite film-modified Pt electrode, (c) Hb/L-cys/n-Au/n-Pt-CHIT composite film-modified Pt electrode, (d) modified electrode (Reprinted from [157], Copyright (2008), with permission from Elsevier)

Conclusions

Self-assembled monolayer has opened up new era of exploration and has a profound impact on sensors and biosensors due to its unique properties. SAM-modified electrodes have been utilized as nanosensors with excellent reproducibility, high sensitivity, unique selectivity, and exceptional stability. Different self-assemblies were considered in this chapter: SAM of metallic nanoparticles on polymeric film, SAM of surfactant on polymeric film, and SAM of S-containing compounds on nanometallic films. Simplicity, cheapness, and fastness are the main advantages of the proposed methods utilizing SAM-modified electrodes when compared with other determination methods of different studied compounds. Furthermore, these methods are highly sensitive so that the studied analytes can be determined under physiological conditions in real urine samples with good accuracy, excellent selectivity, and sub-nanomolar concentration detection.

Acknowledgment The authors would like to recognize the Cairo University financial support that was achieved through the vice president of research funds' office.

References

1. Prakash S, Chakrabarty T, Singh AK, Shahi VK et al (2013) Polymer thin films embedded with metal nanoparticles for electrochemical biosensors applications. *Biosens Bioelectron* 41:43–53
2. Bello A, Giannetto M, Mori G, Seeber R, Terzi F, Zanardi C et al (2007) Optimization of the DPV potential waveform for determination of ascorbic acid on PEDOT-modified electrodes. *Sens Actuators B* 121:430–435
3. Lupu S (2011) In situ electrochemical preparation and characterization of PEDOT–Prussian blue composite materials. *Synth Met* 161:384–390
4. Pigani L, Foca G, Ionescu K, Martina V, Ulrici A, Terzi F, Vignali M, Zanardi C, Seeber R et al (2008) Amperometric sensors based on poly(3,4-ethylenedioxythiophene)-modified electrodes: discrimination of white wines. *Anal Chim Acta* 614:213–222
5. Istamboulie G, Sikora T, Jubete E, Ochoteco E, Marty J, Noguier T et al (2010) Screen-printed poly(3,4-ethylenedioxythiophene) (PEDOT): a new electrochemical mediator for acetylcholinesterase-based biosensors. *Talanta* 82:957–961
6. Ricardo A, Alves G, Ghica ME, Brett CMA et al (2011) Preparation and characterisation of poly(3,4-ethylenedioxythiophene) and poly(3,4-ethylenedioxythiophene)/poly(neutral red) modified carbon film electrodes, and application as sensors for hydrogen peroxide. *Electrochim Acta* 56:3685–3692
7. Atta NF, Galal A, Khalifa F et al (2007) Electrodeposited metals at conducting polymer electrodes I – effect of particle size and film thickness on electrochemical response. *Appl Surf Sci* 253:4273–4282
8. Selvaganesh SV, Mathiyarasu J, Phani KLN, Yegnaraman V et al (2007) Chemical synthesis of PEDOT–Au nanocomposite. *Nanoscale Res Lett* 2:546–549
9. Harish S, Mathiyarasu J, Phani KLN et al (2009) Generation of gold–PEDOT nanostructures at an interface between two immiscible solvents. *Mater Res Bull* 44:1828–1833
10. Atta NF, El-Kady MF, Galal A et al (2010) Simultaneous determination of catecholamines, uric acid and ascorbic acid at physiological levels using poly(N methylpyrrole)/Pd-nanoclusters sensor. *Anal Biochem* 400:78–88
11. Atta NF, El-Kady MF (2010) Novel poly(3-methylthiophene)/Pd, Pt nanoparticle sensor: synthesis, characterization and its application to the simultaneous analysis of dopamine and ascorbic acid in biological fluids. *Sens Actuators B* 145:299–310
12. Atta NF, El-Kady MF (2009) Poly(3-methylthiophene)/palladium sub-micro-modified sensor electrode. Part II: voltammetric and EIS studies, and analysis of catecholamine neurotransmitters, ascorbic acid and acetaminophen. *Talanta* 79:639–647
13. Atta NF, El-Kady MF, Galal A et al (2009) Palladium nanoclusters-coated polyfuran as a novel sensor for catecholamine neurotransmitters and paracetamol. *Sens Actuators B* 141:566–574
14. Mathiyarasu J, Senthilkumar S, Phani KLN, Yegnaraman V et al (2008) PEDOT–Au nanocomposite film for electrochemical sensing. *Mater Lett* 62:571–573
15. Ferreira VC, Melato AI, Silva AF, Abrantes LM et al (2011) Attachment of noble metal nanoparticles to conducting polymers containing sulphur – preparation conditions for enhanced electrocatalytic activity. *Electrochim Acta* 56:3567–3574
16. Galal A, Atta NF, Darwish SA, Ali SM et al (2008) Electrodeposited metals at conducting polymer electrodes. II: study of the oxidation of methanol at poly(3-methylthiophene) modified with Pt–Pd Co-catalyst. *Top Catal* 47:73–83
17. Ferreira VC, Melato AI, Silva AF, Abrantes LM et al (2011) Conducting polymers with attached platinum nanoparticles towards the development of DNA biosensors. *Electrochem Commun* 13:993–996

18. Li J, Lin X (2007) Simultaneous determination of dopamine and serotonin on gold nanocluster/overoxidized-polypyrrole composite modified glassy carbon electrode. *Sens Actuators B* 124:486–493
19. Harish S, Mathiyarasu J, Phani KLN, Yegnaraman V et al (2008) PEDOT/palladium composite material: synthesis, characterization and application to simultaneous determination of dopamine and uric acid. *J Appl Electrochem* 38:1583–1588
20. Namboothiry MAG, Zimmerman T, Coldren FM, Liu J, Kim K, Carroll DL et al (2007) Electrochromic properties of conducting polymer metal nanoparticles composites. *Synth Met* 157:580–584
21. Kim BY, Cho MS, Kim YS, Son Y, Lee Y et al (2005) Fabrication and characterization of poly(3,4-ethylenedioxythiophene)/gold nanocomposite via in-situ redox cycle system. *Synth Met* 153:149–152
22. Manesh KM, Santhosh P, Gopalan A, Lee KP et al (2008) Electrocatalytic oxidation of NADH at gold nanoparticles loaded poly(3,4-ethylenedioxythiophene)–poly(styrene sulfonic acid) film modified electrode and integration of alcohol dehydrogenase for alcohol sensing. *Talanta* 75:1307–1314
23. Hsiao Y, Su W, Cheng J, Cheng S et al (2011) Electrochemical determination of cysteine based on conducting polymers/gold nanoparticles hybrid nanocomposites. *Electrochim Acta* 56:6887–6895
24. Zanardi C, Terzi F, Seeber R et al (2010) Composite electrode coatings in amperometric sensors. Effects of differently encapsulated gold nanoparticles in poly(3,4-ethylenedioxythiophene) system. *Sens Actuators B* 148:277–282
25. Kumar SS, Mathiyarasu J, Phani KL et al (2005) Exploration of synergism between a polymer matrix and gold nanoparticles for selective determination of dopamine. *J Electroanal Chem* 578:95–103
26. Zanardi C, Terzi F, Pigani L, Heras A, Colina A, Lopez-Palacios J, Seeber R et al (2008) Development and characterisation of a novel composite electrode material consisting of poly(3,4-ethylenedioxythiophene) including Au nanoparticles. *Electrochim Acta* 53:3916–3923
27. Atta NF, Galal A, El-Ads EH et al (2012) Gold nanoparticles-coated poly(3,4-ethylenedioxythiophene) for the selective determination of sub-nano concentrations of dopamine in presence of sodium dodecyl sulfate. *Electrochim Acta* 69:102–111
28. Gopalan AI, Lee K, Manesha KM, Santhosh P, Kim JH, Kang JS et al (2007) Electrochemical determination of dopamine and ascorbic acid at a novel gold nanoparticles distributed poly(4-aminothiophenol) modified electrode. *Talanta* 71:1774–1781
29. Bian X, Lu X, Jin E, Kong L, Zhang W, Wang C et al (2010) Fabrication of Pt/polypyrrole hybrid hollow microspheres and their application in electrochemical biosensing towards hydrogen peroxide. *Talanta* 81:813–818
30. Li J, Lin X (2007) Electrodeposition of gold nanoclusters on overoxidized polypyrrole film modified glassy carbon electrode and its application for the simultaneous determination of epinephrine and uric acid under coexistence of ascorbic acid. *Anal Chim Acta* 596:222–230
31. Atta NF, Galal A, El-Ads EH et al (2012) A novel sensor of cysteine self-assembled monolayers over gold nanoparticles for the selective determination of epinephrine in presence of sodium dodecyl sulfate. *Analyst* 137:2658–2668
32. Atta NF, Galal A, Ahmed RA et al (2011) Poly(3,4-ethylene-dioxythiophene) electrode for the selective determination of dopamine in presence of sodium dodecyl sulfate. *Bioelectrochemistry* 80:132–141
33. Nagarajan R, Ruckenstein E (1991) Theory of surfactant self-assembly: a predictive molecular thermodynamic approach. *Langmuir* 7:2934–2969
34. Malmsten M (2002) Surfactant and polymer in drug delivery. Marcel Dekker, New York
35. Fridrikhsberg DA (1986) A course in colloid chemistry. Mir Publishers, Moscow
36. Vittal R, Gomathi H, Kim K et al (2006) Beneficial role of surfactants in electrochemistry and in the modification of electrodes. *Adv Colloid Interface Sci* 119:55–68

37. Rosen MJ (1989) Surfactants and interfacial phenomena, 2nd edn. Wiley-Inter-Science, New York
38. Rusling JF (1991) Controlling electrochemical catalysis with surfactant microstructures. *Acc Chem Res* 24:75–81
39. Rusling JF (1994) Reactions and synthesis in surfactant systems. In: Bard AJ (ed) *Electroanalytical chemistry*, vol 18. Marcel Dekker, New York, p 267
40. Franklin TC, Mathew S (1989) Surfactants in solution. In: Mittal KL (ed) vol 2. Plenum, New York 267–286
41. Shinozuka N, Hayano S (1979) Solution chemistry of surfactants. In: Mittal KL (ed) vol 2. Plenum, New York
42. Diaz A, Kaifer AZ (1988) Self-assembled surfactant monolayers on electrode surfaces: the formation of surfactant viologen monolayers on Au and Pt. *J Electroanal Chem* 249: 333–338
43. Widrig CA, Majda M (1989) Self-assembly of ordered monolayers and bilayers of *N-methyl-N'-octadecylviologen* amphiphile on gold surfaces in aqueous solutions. *Langmuir* 5:639
44. Long HCD, Donohue JJ, Buttry DA et al (1991) Ionic interactions in electroactive self-assembled monolayers of ferrocene species. *Langmuir* 7:2196–2202
45. Grant LM, Ducker WA (1997) Effect of substrate hydrophobicity on surface–aggregate geometry: zwitterionic and nonionic surfactants. *Phys Chem B* 101:5337–5345
46. Grant LM, Tiberg F, Duker WA et al (1998) Nanometer-scale organization of ethylene oxide surfactants on graphite, hydrophilic silica, and hydrophobic silica. *J Phys Chem B* 102:4288
47. Rennie AR, Lee EM, Simister EA, Thomas RK et al (1990) Structure of a cationic surfactant layer at the silica-water interface. *Langmuir* 6:1031–1034
48. Manne S, Gaub HE (1995) Molecular organization of surfactants at solid–liquid interfaces. *Science* 270:1480–1482
49. Schulz JC, Warr GG, Bulter PD, Hamilton WA et al (2001) Adsorbed layer structure of cationic surfactants on quartz. *Phys Rev E* 63:041604–041608
50. Facci JS (1987) *Langmuir* 3:525–529
51. Rusling JF, Shi CN, Gosser DK, Shukla SS et al (1988) Electrocatalytic reactions in organized assemblies I. Reduction of 4-bromobiphenyl in cationic and nonionic micelles. *J Electroanal Chem* 240:201–216
52. Rusling JF (1988) Electrocatalytic systems organized by micelles. *Trends Anal Chem* 7:266–269
53. Boussaad S, Tao NJ (1999) Electron transfer and adsorption of myoglobin on self-assembled surfactant films: an electrochemical tapping-mode AFM study. *J Am Chem Soc* 121: 4510–4515
54. Liu JF, Min G, Duker WA et al (2001) AFM study of adsorption of cationic surfactants and cationic polyelectrolytes at the silica–water interface. *Langmuir* 17:4895
55. Retter U, Avranas A (2001) On anion-induced formation of hemicylindrical and hemispherical surface micelles of amphiphiles at the metal/electrolyte interface. *Langmuir* 17:5039–5044
56. Schulz JC, Warr GG (2002) Adsorbed layer structure of cationic and anionic surfactants on mineral oxide surfaces. *Langmuir* 18:3191–3197
57. Petri M, Kolb DM (2002) Nanostructuring of a sodium dodecyl sulfate-covered Au(111) electrode. *Phys Chem* 4:1211–1216
58. Wanless EJ, Duker WA (1996) Organization of sodium dodecyl sulfate at the graphite-solution interface. *J Phys Chem* 100:3207
59. Duker WA, Grant LM (1996) Effect of substrate hydrophobicity on surfactant surface–aggregate geometry. *J Phys Chem* 100:11507–11511
60. Wolgemuth JL, Workman RK, Manne S et al (2000) Surfactant aggregates at a flat, isotropic hydrophobic surface. *Langmuir* 16:3077–3081
61. Wanless EJ, Duker WA (1997) Weak influence of divalent ions on anionic surfactant surface-aggregation. *Langmuir* 13:1463–1474

62. Subramanian V, Duker WA (2000) Counterion effects on adsorbed micellar shape: experimental study of the role of polarizability and charge. *Langmuir* 16:4447–4454
63. Burgess I, Jeffrey CA, Cai X, Szymanski G, Lipkowski J et al (1999) Direct visualization of the potential controlled transformation of hemimicellar aggregates of dodecyl sulfate into a condensed monolayer at the electrode surface. *Langmuir* 15:2607–2616
64. Burgess I, Zamlyny V, Szymanski G, Lipkowski J et al (2001) Electrochemical and neutron reflectivity characterization of dodecyl sulfate adsorption and aggregation at the gold-water interface. *Langmuir* 17:3355–3367
65. Cholewa E, Burgess I, Kunze J et al (2004) Adsorption of *N*-dodecyl-*N*, *N*-dimethyl-3-ammonio-1-propanesulfonate (DDAPS), a model zwitterionic surfactant, on the Au(111) electrode surface. *J Solid State Electrochem* 8:693–705
66. Chandar P, Somasundaram P, Turro NJ et al (1987) Fluorescence probe studies on the structure of the adsorbed layer of dodecyl sulfate at the alumina – water interface. *Colloid Interface Sci* 117:31–46
67. Manne S (1997) Visualizing self-assembly: force microscopy of ionic surfactant aggregates at solid–liquid interfaces. *Progr Colloid Polym Sci* 103:226–233
68. Gao Y, Du J, Gu T et al (1987) Hemimicelle formation of cationic surfactants at silica gel–water interface. *Chem Soc Faraday Trans* 1:2671–2679
69. Fan A, Somasundaram P, Turro N et al (1997) Adsorption of alkyltrimethylammonium bromides on negatively charged alumina. *Langmuir* 13:506–510
70. Sharma BJ, Basu S, Sharma MM et al (1996) Characterization of adsorbed ionic surfactants on a mica substrate. *Langmuir* 12:6506–6512
71. Singh PK, Adler JJ, Rabinovich YI, Moudgil BM et al (2001) Investigation of self-assembled surfactant structures at the solid–liquid interface using FT-IR/ATR. *Langmuir* 17(2): 468–473
72. Li H, Tripp CP (2002) Spectroscopic identification and dynamics of adsorbed cetyltrimethylammonium bromide structures on TiO₂ surfaces. *Langmuir* 18:9441–9446
73. Atkin R, Craig VSJ, Wanless EJ, Biggs S et al (2003) Mechanism of cationic surfactant adsorption at the solid–aqueous interface. *Adv Colloid Interface Sci* 103:219–304
74. Gonzalez-Macia L, Smyth MR, Morrinh A, Killard AJ et al (2011) Enhanced electrochemical reduction of hydrogen peroxide at metallic electrodes modified with surfactant and salt. *Electrochim Acta* 58:562–570
75. Muray RW (1992) Molecular design of electrode surfaces, vol 22. Wiley, New York, p 18
76. Goldenberg M (1997) Use of electrochemical techniques to study the Langmuir–Blodgett films of redox active materials. *Russ Chem Rev* 66:1033–1052
77. Gomez M, Li J, Kaifer AE et al (1991) Surfactant monolayers on electrode surfaces: self-assembly of a series of amphiphilic viologens on gold and tin oxide. *Langmuir* 7:1797–1806
78. Ulman A (1991) An introduction to ultrathin organic films from Langmuir–Blodgett to self-assembly. Academic, San Diego
79. Kaifer A, Kaifer MG (1999) Supramolecular electrochemistry. Wiley-VCH, Weinheim, New York, Chichester, Brisbane, Singapore, Toronto
80. Rusling JF (1997) Molecular aspects of electron transfer at electrodes in micellar solutions. *Colloids Surf* 123:81–88
81. Mackay RA (1994) Electrochemistry in association colloids. *Colloids Surf A* 82:1–28
82. Rusling JF, Zhang H, Willis WS et al (1990) Properties of octadecylsilyl-coated electrodes in ionic micellar media. *Anal Chim Acta* 235:307–315
83. Guidelli R, Foresti ML (1977) The inhibitory effect of neutral organic surfactants upon simple electrode reactions. *Electroanal Chem* 77:73
84. Marino A, Brajter-Toth A (1993) Ionic surfactants as molecular spacers at graphite electrodes. *Anal Chem* 65:370–374
85. Lee KAB (1990) Electron transfer into self-assembling monolayers on gold electrodes. *Langmuir* 6:709–712
86. Chidsey CED (1991) Free energy and temperature dependence of electron transfer at the metal–electrolyte interface. *Science* 251:919–922

87. Abbott AP, Gounili G, Bobbitt JM, Rusling JF, Kumosinski TF et al (1992) Electron transfer between amphiphilic ferrocenes and electrodes in cationic micellar solution. *J Phys Chem* 96:11091–11095
88. Marcus RA (1964) Chemical and electrochemical electron-transfer theory. *Annu Rev Phys Chem* 15:155–196
89. Georges J, Desmettre S (1984) Electrochemistry of ferrocene in anionic, cationic and non-ionic micellar solutions. Effect of the micelle solubilization of the half-wave potentials. *Electrochim Acta* 29:521–525
90. Fendler JH (1982) *Membrane mimetic chemistry*. Wiley, New York
91. Hosseinzadeh R, Sabzi RE, Ghasemlu K et al (2009) Effect of cetyltrimethyl ammonium bromide (CTAB) in determination of dopamine and ascorbic acid using carbon paste electrode modified with tin hexacyanoferrate. *Colloids Surf B* 68:213–217
92. Paria S, Khilar KC (2004) A review on experimental studies of surfactant adsorption at the hydrophilic solid–water interface. *Adv Colloid Interface Sci* 110:75–95
93. Love LJC, Habarta JG, Dorsey JG et al (1984) The micelle-analytical chemistry interface. *Anal Chem* 56:1132A–1148A
94. Yang C, Sang Q, Zhang S, Huang W et al (2009) Voltammetric determination of estrone based on the enhancement effect of surfactant and a MWNT film electrode. *Mater Sci Eng C* 29:1741–1745
95. Hu C, Yang C, Hu S et al (2007) Hydrophobic adsorption of surfactants on water-soluble carbon nanotubes: a simple approach to improve sensitivity and antifouling capacity of carbon nanotubes-based electrochemical sensors. *Electrochem Commun* 9:128–134
96. Jain R, Mishra R, Dwivedi A et al (2009) Effect of surfactant on voltammetric behaviour of ornidazole. *Colloids Surf A* 337:74–79
97. Liu S, Li J, Zhang S, Zhao J et al (2005) Study on the adsorptive stripping voltammetric determination of trace cerium at a carbon paste electrode modified in situ with cetyltrimethylammonium bromide. *Appl Surf Sci* 252:2078
98. Svancara I, Foret P, Vytras K et al (2004) A study on the determination of chromium as chromate at a carbon paste electrode modified with surfactants. *Talanta* 64:844–852
99. Hoyer B, Jensen N (2004) Use of sodium dodecyl sulfate as an antifouling and homogenizing agent in the direct determination of heavy metals by anodic stripping voltammetry. *Analyst* 129:751–754
100. Dar RA, Brahma PK, Tiwari S, Pitre KS et al (2012) Electrochemical studies of quinine in surfactant media using hanging mercury drop electrode: a cyclic voltammetric study. *Colloids Surf B* 98:72–79
101. Atta NF, Galal A, Ahmed RA et al (2011) Simultaneous determination of catecholamines and serotonin on poly(3,4-ethylene dioxathiophene) modified Pt electrode in presence of sodium dodecyl sulfate. *J Electrochem Soc* 158(4):F52–F60
102. Atta NF, Galal A, Abu-Attia FM, Azab SM et al (2011) Characterization and electrochemical investigations of micellar/drug interactions. *Electrochim Acta* 56:2510–2517
103. Castilho M, Almeida LE, Tabak M, Mazo LH et al (2000) The electrochemical oxidation of the antioxidant drug dipyrindamole at glassy carbon and graphite electrodes in micellar solutions. *Electrochim Acta* 46:67–75
104. Goyal RN, Jain N, Gurnani V et al (2001) Electrooxidation of chlorpromazine in aqueous and micellar media and spectroscopic studies of the derived cationic free radical and dication species. *Monatsh Chem* 132:575–585
105. Wang LH, Tseng SW (2001) Direct determination of D-panthenol and salt of pantothenic acid in cosmetic and pharmaceutical preparations by differential pulse voltammetry. *Anal Chim Acta* 432:39–48
106. Zhang S, Wu K, Hu S et al (2002) Voltammetric determination of diethylstilbestrol at carbon paste electrode using cetylpyridine bromide as medium. *Talanta* 58:747–754
107. Zhang S, Wu K, Hu S et al (2002) Carbon paste electrode based on surface activation for trace adriamycin determination by a preconcentration and voltammetric method. *Anal Sci* 18:1089–1092

108. Fernandez SG, Lopez MCB, Castanon MJL, Ordieres AJM, Blanco PT et al (2004) Adsorptive stripping voltammetry of rifamycins at unmodified and surfactant-modified carbon paste electrodes. *Electroanalysis* 16:1660–1666
109. Atta NF, Galal A, Ahmed RA et al (2011) Direct and simple electrochemical determination of morphine at PEDOT modified Pt electrode. *Electroanalysis* 23(3):737–746
110. Atta NF, Galal A, Ahmed RA et al (2011) Voltammetric behavior and determination of isoniazid using PEDOT electrode in presence of surface active agents. *Int J Electrochem Sci* 6:5097–5113
111. Brahman PK, Dar RA, Tiwari S, Pitre KS et al (2012) Voltammetric determination of anticancer drug flutamide in surfactant media at polymer film modified carbon paste electrode. *Colloids Surf A* 396:8–15
112. Li C, Ya Y, Zhan G et al (2010) Electrochemical investigation of tryptophan at gold nanoparticles modified electrode in the presence of sodium dodecylbenzene sulfonate. *Colloids Surf B* 76:340–345
113. Yang G, Qu X, Shen M, Wang C, Qu Q, Hu X et al (2007) Preparation of glassy carbon electrode modified by hydrophobic gold nanoparticles and its application for the determination of ethamsylate in the presence of cetyltrimethylammonium bromide. *Sens Actuators B* 128:258–265
114. Chaki NK, Vijayamohan K (2002) Self-assembled monolayers as a tunable platform for biosensor applications. *Biosens Bioelectron* 17:1–12
115. Park B, Yoon D, Kim D et al (2011) Formation and modification of a binary self-assembled monolayer on a nano-structured gold electrode and its structural characterization by electrochemical impedance spectroscopy. *J Electroanal Chem* 661(2):329–335
116. Goldmann M, Davidovits JV, Silberzan P et al (1998) Kinetics of self-assembled silane monolayers at various temperatures: evidence of 2D foam. *Thin Solid Films* 327–329:166–171
117. Maksymovych P, Voznyy O, Dougherty DB, Sorescu DC, Yates JT Jr et al (2010) Gold adatom as a key structural component in self-assembled monolayers of organosulfur molecules on Au(111). *Prog Surf Sci* 85:206–240
118. Campuzano S, Pedrero M, Montemayor C, Fatàs E, Pingarrón JM et al (2006) Characterization of alkanethiol-self-assembled monolayers-modified gold electrodes by electrochemical impedance spectroscopy. *J Electroanal Chem* 586:112–121
119. Ozoemena KI, Nyokong T (2006) Comparative electrochemistry and electrocatalytic activities of cobalt, iron and manganese phthalocyanine complexes axially co-ordinated to mercaptopyridine self-assembled monolayer at gold electrodes. *Electrochim Acta* 51:2669–2677
120. Xian Y, Wang H, Zhou Y, Pan D, Liu F, Jin L et al (2004) Preparation of L-Cys–Au colloid self-assembled nanoarray electrode based on the microporous aluminium anodic oxide film and its application to the measurement of dopamine. *Electrochem Commun* 6:1270–1275
121. Freire RS, Kubota LT (2004) Application of self-assembled monolayer-based electrode for voltammetric determination of copper. *Electrochim Acta* 49:3795–3800
122. Wang T, Bai Y, Luo H, Yan X, Zheng W et al (2011) Electrochemical characteristic of selenocysteine self-assembled monolayers at Au electrode. *J Electroanal Chem* 657:74–78
123. Desikan R, Lee I, Thundat T et al (2006) Effect of nanometer surface morphology on surface stress and adsorption kinetics of alkanethiol self-assembled monolayers. *Ultramicroscopy* 106:795–799
124. Krysiński P, Brzostowska-Smolka M (1998) Capacitance characteristics of self-assembled monolayers on gold electrode. *Bioelectrochem Bioenerg* 44:163–168
125. Sun J, Xu J, Fang H, Chen H et al (1997) Electrocatalytic oxidation of NADH with dopamine covalently bound to self-assembled cysteamine monolayers on gold electrode. *Bioelectrochem Bioenerg* 44:45–50
126. Zhao YQ, Luo HQ, Li NB et al (2009) Electrochemical characterization of in situ functionalized gold *p*-aminothiophenol self-assembled monolayer with 4-formylphenylboronic acid for recognition of sugars. *Sens Actuators B* 137:722–726

127. Kühnle A (2009) Self-assembly of organic molecules at metal surfaces. *Curr Opin Colloid Interface Sci* 14:157–168
128. Lang P, Nogues C (2008) Self-assembled alkanethiol monolayers on a Zn substrate: interface studied by XPS. *Surf Sci* 602:2137–2147
129. Zhang H, Li N, Zhu Z et al (2000) Electrocatalytic response of dopamine at a DL-HOMOCYSTEINE self-assembled gold electrode. *Microchem J* 64:277–282
130. Duwez A (2004) Exploiting electron spectroscopies to probe the structure and organization of self-assembled monolayers: a review. *J Electron Spectrosc Relat Phenom* 134:97–138
131. Briand E, Salmain M, Compère C, Pradier C et al (2006) Immobilization of protein a on SAMs for the elaboration of immunosensors. *Colloids Surf B* 53:215–224
132. Arezki B, Delcorte A, Bertrand P et al (2004) Emission processes of molecule–metal cluster ions from self-assembled monolayers of octanethiols on gold and silver. *Appl Surf Sci* 231:122–126
133. Saga Y, Tamiaki H (2004) Facile synthesis of chlorophyll analog possessing a disulfide bond and formation of self-assembled monolayer on gold surface. *J Photochem Photobiol B* 73:29–34
134. Behera S, Raj CR (2007) Self-assembled monolayers of thio-substituted nucleobases on gold electrode for the electroanalysis of NADH, ethanol and uric acid. *Sens Actuators B* 128: 31–38
135. Zhang X, Wang S (2005) Determination of ethamsylate in the presence of catecholamines using 4-amino-2-mercaptopyrimidine self-assembled monolayer gold electrode. *Sens Actuators B* 104:29–34
136. Zhong X, Yuan R, Chai Y, Liu Y, Dai J, Tang D et al (2005) Glucose biosensor based on self-assembled gold nanoparticles and double-layer 2d-network (3-mercaptopropyl)-trimethoxysilane polymer onto gold substrate. *Sens Actuators B* 104:191–198
137. Raj CR, Ohsaka T (2003) Voltammetric detection of uric acid in the presence of ascorbic acid at a gold electrode modified with a self-assembled monolayer of heteroaromatic thiol. *J Electroanal Chem* 540:69–77
138. Li X, Wu J, Gao N, Shen G, Yu R et al (2006) Electrochemical performance of L-cysteine–gold particle nanocomposite electrode interface as applied to preparation of mediator-free enzymatic biosensors. *Sens Actuators B* 117:35–42
139. Liu Z, He Q, Xiao P, Liang B, Tan J, He N, Lu Z et al (2003) Self-assembly monolayer of mercaptopropyltrimethoxysilane for electrodeless deposition of Ag. *Mater Chem Phys* 82:301–305
140. Hoffmann H, Mayer U, Brunner H, Krischanitz A et al (1995) Reflection-absorption infrared spectroscopy of self-assembled monolayers on gold and silicon surfaces. *Vib Spectrosc* 8: 151–157
141. Wang S, Du D (2002) Studies on the electrochemical behaviour of hydroquinone at L-cysteine self-assembled monolayers modified gold electrode. *Sensors* 2:41–49
142. Giz MJ, Duong B, Tao NJ et al (1999) In situ STM study of self-assembled mercaptopropionic acid monolayers for electrochemical detection of dopamine. *J Electroanal Chem* 465:72–79
143. Dodero G, Michieli LD, Cavalleri O, Rolandi R, Oliveri L, Daccà A, Parodi R et al (2000) L-Cysteine chemisorption on gold: an XPS and STM study. *Colloids Surf A* 175:121–128
144. Wang Q, Dong D, Li N et al (2001) Electrochemical response of dopamine at a penicillamine self-assembled gold electrode. *Bioelectrochemistry* 54:169–175
145. Wang Q, Jiang N, Li N et al (2001) Electrocatalytic response of dopamine at a thiolactic acid self-assembled gold electrode. *Microchem J* 68:77–85
146. Li J, Cheng G, Dong S et al (1997) Electrochemical study of the interfacial characteristics of redox-active viologen thiol self-assembled monolayers. *Thin Solid Films* 293:200–205
147. Łuczak T (2009) Comparison of electrochemical oxidation of epinephrine in the presence of interfering ascorbic and uric acids on gold electrodes modified with S-functionalized compounds and gold nanoparticles. *Electrochim Acta* 54:5863–5870
148. Shervedani RK, Bagherzadeh M, Mozaffari SA et al (2006) Determination of dopamine in the presence of high concentration of ascorbic acid by using gold cysteamine self-assembled monolayers as a nanosensor. *Sens Actuators B* 115:614–621

149. Zhuo Y, Yu R, Yuan R, Chai Y, Hong C et al (2009) Enhancement of carcinoembryonic antibody immobilization on gold electrode modified by gold nanoparticles and SiO₂/Thionine nanocomposite. *J Electroanal Chem* 628:90–96
150. El-Deab MS, Ohsaka T (2003) Quasi-reversible two-electron reduction of oxygen at gold electrodes modified with a self-assembled submonolayer of cysteine. *Electrochem Commun* 5:214–219
151. Raj CR, Ohsaka T (2001) Electroanalysis of ascorbate and dopamine at a gold electrode modified with a positively charged self-assembled monolayer. *J Electroanal Chem* 496:44–49
152. Liu T, Li M, Li Q et al (2004) Electroanalysis of dopamine at a gold electrode modified with *N*-acetylcysteine self-assembled monolayer. *Talanta* 63:1053–1059
153. Dalmia A, Liu CC, Savinell RF et al (1997) Electrochemical behavior of gold electrodes modified with self-assembled monolayers with an acidic end group for selective determination of dopamine. *J Electroanal Chem* 430:205–214
154. Aryal S, Dharmaraj N, Bhattarai N, Kim CH, Kim HY et al (2006) Spectroscopic identification of S Au interaction in cysteine capped gold nanoparticles. *Spectrochim Acta A* 63:160–163
155. Liu S, Li X, Li Y, Li Y, Li J, Jiang L et al (2005) The influence of gold nanoparticle modified electrode on the structure of mercaptopropionic acid self-assembly monolayer. *Electrochim Acta* 51:427–431
156. Galal A, Atta NF, El-Ads EH et al (2012) Probing cysteine self-assembled monolayers over gold nanoparticles – towards selective electrochemical sensors. *Talanta* 93:264–273
157. Yang G, Yuan R, Chai Y et al (2008) A high-sensitive amperometric hydrogen peroxide biosensor based on the immobilization of hemoglobin on gold colloid/*L*-cysteine/gold colloid/nanoparticles Pt–chitosan composite film-modified platinum disk electrode. *Colloids Surf B* 61:93–100

Nanostructured Hybrid Graphene-Conducting Polymers for Electrochemical Supercapacitor Electrodes

15

Punya A. Basnayaka, Manoj K. Ram, Elias K. Stefanakos,
and Ashok Kumar

Contents

Introduction.....	480
Working Principle of ES	482
Electrolytes	484
Methods.....	486
Synthesis of Novel G-CPs.....	486
Synthesis of G-CPs Nanocomposites.....	486
Results and Discussion	488
Conclusions.....	498
References.....	499

P.A. Basnayaka (✉)

Department of Mechanical Engineering and Clean Energy Research Center,
University of South Florida, Tampa, FL, USA

Department of Engineering and Engineering Technology,
Cuyahoga Community College, Cleveland, OH, USA

e-mail: pbasnaya@mail.usf.edu

M.K. Ram

Clean Energy Research Center, University of South Florida, Tampa, FL, USA

Nanotechnology Research and Education Center, University of South Florida,
Tampa, FL, USA

e-mail: mkram@usf.edu

E.K. Stefanakos

Clean Energy Research Center, University of South Florida, Tampa, FL, USA

e-mail: stefanak@eng.usf.edu

A. Kumar

Department of Mechanical Engineering, University of South Florida, Tampa, FL, USA

Clean Energy Research Center, University of South Florida, Tampa, FL, USA

e-mail: kumar@usf.edu

Abstract

Recently, advanced nanohybrid electrodes based on graphene-conducting polymers have shown a rapid growth in electrochemical energy storage (EES) systems, such as fuel cells, batteries, and supercapacitors. The supercapacitors are unique among the EES systems due to their long cycle life, high power density, and environmental compatibility. The mitigation of the drawbacks of electrode materials for supercapacitor applications, such as low energy density and fast self-discharge due to leakage current, is the focus of extensive research at the present time. Transition metal oxides (ruthenium oxides, manganese oxide, etc.) and conducting polymers (polyaniline, polypyrrole, and polythiophene) have been studied extensively with carbon-based materials as nanocomposites to address some of these issues related to supercapacitors. In the manuscript, we present the applications of (G)-CPs nanocomposite materials, such as G-polyanilines (G-PANIs), G-poly(pyrrole) (G-PPY), G-poly(hexylthiophene) (G-PHTh), and G-poly(3–4 ethylenedioxythiophene) (G-PEDOT), as supercapacitor electrodes. The G-PANIs, G-PPY, G-PHTh, and G-PEDOT electrode materials were synthesized chemically using the oxidative polymerization method and characterized by using scanning electron microscope (SEM), transmission electron microscope (TEM), Fourier transform infrared spectroscopy (FTIR), thermo gravimetric analysis (TGA), and Raman spectroscopy techniques. The electrochemical behavior of various G-CP electrode materials for supercapacitor applications have been understood using cyclic voltammetry, charging–discharging, and electrochemical impedance spectroscopy techniques. The studied G-CP-based nanocomposite electrode-based supercapacitors hold great promise for the use in future commercial applications.

Keywords

Nanocomposites • Conducting polymers • Electrolytes • Electrochemical analysis

Introduction

Recently, the US Department of Energy (USDOE) has revealed that electrochemical supercapacitors (ES) could be important and possibly used together with batteries in the future development of efficient, clean, and sustainable energy storage systems due to rapid development of global economy. The batteries, fuel cells, and ESs are practical electrochemical energy storage technologies; moreover, supercapacitors are very important because of their high power density ($>10^3$ W/kg) and long life cycle ($>10^5$ cycles) [1–3]. Further, supercapacitors bridge the power/energy requirements between dielectric capacitors with high power density and batteries having high energy density. Today, supercapacitors find applications in the areas of transportation, portable electronics, and stationary power storage [4, 5]. The supercapacitor technology became popular in the mid-1990s and drew attention for its

potential use in hybrid electric vehicles. Further, technological developments of ES enable them to act as backup power supplies by complimenting batteries or fuel cells in mitigating power disruption in the most consumer electronic devices.

The low energy density, high production cost, and leakage currents are identified as the main challenges for future technical developments of supercapacitors [1]. The development of novel electrode materials and suitable electrolytes to surpass the problem of low energy density has been given major emphasis in recent reach [6–8]. The use of most viable industrial carbon-based electrode materials are limited because of the limited number of pores that can allow mobility of charges/ions and therefore, resulting in smaller active surface areas. The capacitance of carbon-based supercapacitor ranges between 75 and 200 F/g. The supercapacitors of carbon-based materials are called electrical double-layer supercapacitors (EDLSs) or electrostatic capacitors [6].

The EDLS capacitors are limited by low energy density and capacitance. The second type of capacitors are called pseudocapacitors, which composed of either transition metal oxides or conducting polymer as electrode active material. The transition metal oxides (ruthenium oxides, manganese oxide, nickel oxides, and vanadium oxides) are limited by their high cost, whereas the CPs (PANI, PPy, and PTh) are limited by their low stability [9–11]. As a result, hybrid materials have been synthesized to overcome the low energy density and specific capacitance of the carbon-based supercapacitor [12–15]. It has been found that hybrid materials contain both EDL-type materials and pseudocapacitive-type material that has a higher specific capacitance and energy density than EDLS. The transition metal oxides and their nanocomposites, especially nanocomposites of ruthenium oxide, produce high capacitance and energy/power density but are commercially limited due to their higher cost.

Even though the higher crystallinity gives rise to higher conductivity, the loss of surface area reduces the specific capacitance. Therefore, attempts are made to synthesize the materials of larger surface area. The MnO_2 , low cost metal oxide, having a theoretical specific capacitance value of 1370 F/g, has been identified of being a competitive material to RuO_2 . However, experimentally observed specific capacitance for MnO_2 is lower by ~ 2 to 3 orders of magnitude than theoretically calculated value due to poor electrical conductivity ($\sim 10^{-6} \text{ S cm}^{-1}$). Table 1 shows the capacitance ranges for major material categories, carbon-based materials, CPs, and transition metal oxides discussed above.

The hybridization of carbon-based materials with transition metal oxides for supercapacitor electrode materials is limited by the availability of pristine transition metal oxides. Therefore, this manuscript focuses on graphene (G)-CP nanocomposites and their applications in ES electrodes. Recently, we have synthesized G-PPy, G-PANI, and G-PTh and G-polyethylenedioxythiophene (PEDOT)-conducting nanocomposite materials and studied extensively the supercapacitive behavior of nanocomposite materials [20, 28, 39, 41, 44]. The new G-CP nanocomposite materials have shown higher conductivity throughout the various redox processes during charging–discharging cycles and have offered higher specific capacitance than their pristine materials.

Table 1 Performance of major electrode material categories for supercapacitors

Material category	Capacitance	Advantage/disadvantage	References
Activated carbon, carbon nanotube, graphene	75–200 F/g	Stable, low capacitance, not expensive	[6, 8, 16]
Conducting polymers(PANI, PPy, PEDOT)	100–500 F/g	Not stable, not expensive, high capacitance	[2, 17] (Basnayaka et al. 2013)
Transition metal oxide (MnO ₂ , RuO ₂ , etc.)	100–1000 F/g	Stable, expensive, high capacitance	[2, 18, 19]

The objectives of this chapter are to present and discuss novel supercapacitor electrode materials for supercapacitor applications. First, we discussed the fundamentals of supercapacitors with respect to our synthesized materials as electrode materials. The G-CPs were synthesized and characterized by several techniques (SEM TEM, X-ray diffraction FTIR, UV–vis, Raman spectroscopy, CV, charging–discharging, and impedance measurements) to establish that the electrode material could be used in the supercapacitor applications. Finally, the impedance measurements were performed to determine the time constants for the G-CP-based nanocomposites applied to symmetric supercapacitors. The G-CP supercapacitor technology could be viable and surpass existing properties when our material synthesis approach and multicapacitor fabrication techniques could be employed and exploited.

Working Principle of ES

The design and manufacturing of ES devices are similar to that of fabrication of battery. An ES cell consists of two electrodes, a separator (separating two electrodes electrically), an electrolyte, and current collectors. The electrode material mostly stores charges at the electrode/electrolyte interface and consists of large area nanostructure and high porosity materials. The electrochemical double-layer capacitors, pseudocapacitors, and hybrid capacitors are based on the types of the electrode materials. These types of ES have unique mechanism for storing the charges.

The electrostatic type capacitor consists of two parallel plates separated by vacuum or a dielectric material, while the electrolytic capacitor uses solid or liquid electrolytes instead of vacuum or dielectric materials [1]. In the presence of the applied electric field, the dielectric material inside the two plates polarizes and arranges the charges (dipole alignment) to assure charge neutrality on the electrode plates as illustrated in Fig. 1a.

The charge accumulation in linear capacitors is independent on the capacitance. The capacitance depends on the area of the charged plates (A), the distance between two charged parallel plates (d), and the dielectric constant of the dielectric material

between the two plates (ϵ). The relationship of these parameters to the capacitance is shown in Eq. 1 [1].

$$C = \epsilon_0 \epsilon_r A / d \quad (1)$$

A typical charging and discharging schematic of an EDL is shown in Fig. 1b. The separator prevents the short circuiting of the two conducting plates and allows ions to be exchanged between the two electrodes. There is no electron transfer across the interface. Complete double-layer capacitors consist of positive and negative electrodes as shown in Fig. 1b. In addition to the double layer, a supercapacitor can also contain pseudocapacitance in the presence of certain electrode materials. The pseudocapacitance is developed by means of three processes, that is, the electrochemical adsorption, faradaic redox reactions, and the doping/dedoping at the surfaces and the bulk material. A simple resistor–capacitor (RC) equivalent circuit represents the constant current charging–discharging measurements as shown in Fig. 2 for the basic operation of a single-cell supercapacitor [21].

The time constant (τ) of the self-discharge of the anode or cathode is equal to the product of R_{Leakage} and C . The Gibb's free energy (E); ($E = \int dw = V \times dq$), stored by the applied voltage (V) to the capacitor, is given in Eq. 2, where C is the total capacitance of the cell [21].

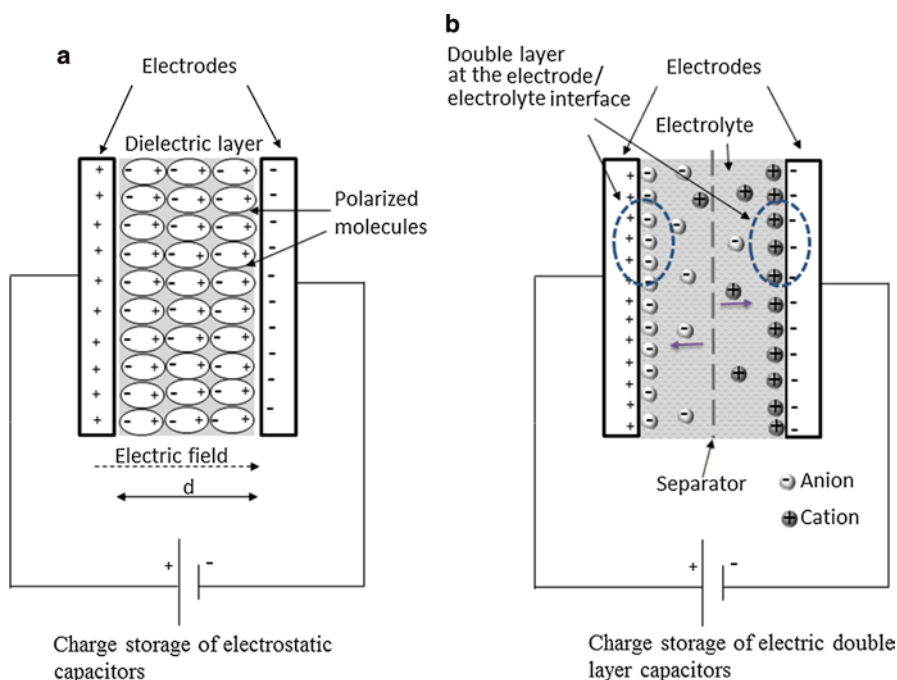
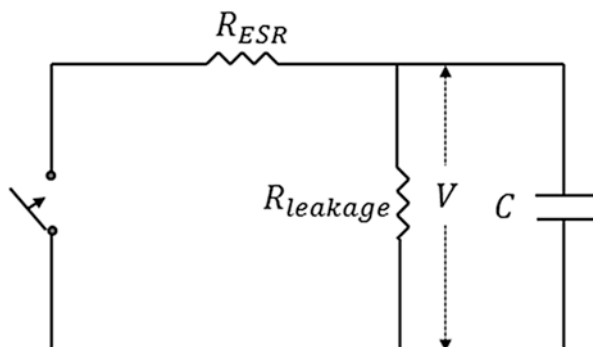


Fig. 1 Charging schematics of (a) electrostatic capacitor and (b) electrochemical double-layer capacitor

Fig. 2 Equivalent circuit of charging and discharging of supercapacitors at constant current



$$E = 1/2 CV^2 \quad (2)$$

The maximum energy P_{\max} delivered is presented in Eq. 3 based on constant current discharge measurements [21].

$$P_{\max} = V^2 / (4 \times R_{\text{ESR}}) \quad (3)$$

where ESR is the internal resistance.

The performance of carbon-based materials and CP nanocomposites reported in the literature is summarized in Table 2. The cyclic voltammetry (CV) and constant current charging–discharging techniques are employed in most of the supercapacitor performance evaluation in two- or three-electrode configuration cells (3E or 2E).

Electrolytes

The electrolytes used in supercapacitor cells are as significant as the electrode materials, because they define the performance of supercapacitors, especially the working potential. There are three major types of electrolytes called aqueous, organic, and ionic liquid (IL) electrolytes [32–35]. Presently, most of the available capacitors are made up of organic and aqueous electrolytes. The properties of electrolyte have substantial effect on internal resistance and breakdown voltage of the supercapacitor.

There are two factors which affect the conductivity of any electrolytes, namely, the concentration of free charge carriers and the ionic mobility per dissociation ion in the electrolytes [36]. Other secondary factors include the solubility, salt concentration, temperature, viscosity, and dielectric constant of the solvent. Acetonitrile propylene carbonate and water are the most widely used solvents of the electrolytes with dielectric constants of 36.64, 66.14, and 88 at room temperature [6]. Further, it is also necessary for the solvent to be chemically stable for many hundreds or thousands of charge–discharge cycles. Table 3 summarizes the ionic diameters of widely used electrolytic ions [6].

Table 2 Performance of some composite electrode-based supercapacitors

Material	Capacitance	Energy/power density	Remarks	References
G-activated carbon composite	122 F/g 2E(KOH)	52.2 Wh/kg	798 m ² /g	[22]
G-carbon nanotube composite	290.6 F/g and 201.0 F/g 2E Con cell (KCl, 1 M) TEABF ₄ /PC	62.8 Wh/kg 58.5 kW/kg	NA	[23]
SWNT/PPy	200 F/g 3E(1 M NaPF ₆) CV at 10 mV/s	NA	33 wt.% SWNT/PPy	[24]
PANI/CNT composites	597.82 F/g 3E(1 M H ₂ SO ₄) CV at 2 mV/s	NA	NA	[25]
G-PANI/NF composites	480 F/g 3E(2 M H ₂ SO ₄) galvanostatic at a current density of 0.1 A/g	NA	BET surface 20.2 m ² /g	[26]
G-PANI [27]	1126 F/g 3E(1 M H ₂ SO ₄)	37.9 Wh kg ⁻¹ at 141.1 Wkg ⁻¹	NA	[27]
Graphene-PEDOT	374 F/g 3E(2 M HCl)	NA	NA	[28]
G-PPy nanocomposite	417 F/g (2 M H ₂ SO ₄) CV at 10 mV/s	94.93 W h kg ⁻¹ and 3797.2 Wkg ⁻¹	98.62 m ² g ⁻¹	[29]
G-PPy	424 F/g 3E(H ₂ SO ₄) galvanostatic at a current density of 1 A/g Three-electrode	NA	NA	[30]
G-MnO ₂	256 F/g (0.5 M Na ₂ SO ₄) galvanostatic at current density of 0.1 mA/cm ²	NA	NA	[31]

Table 3 Ionic radius of some common electrolytes

Electrolytes	Ionic diameter (nm)	
	Cation	Anion
H ₂ SO ₄	0.26	0.533
HCl	0.26	
Na ₂ SO ₄	0.36	0.533
KOH	0.26	
LiClO ₄	0.152	0.474
LiPF ₆	0.152	0.508
TEABF ₄	0.686	0.458
TBABF ₄	0.830	0.458

In general, the use of nonaqueous electrolytes gives higher energy than aqueous electrolytes, because of the higher operating voltage due to the larger decomposition limit of such electrolyte solutions [33]. The aqueous-based electrolyte reveals less viscosity, better conductivity, and superior kinetics to ions leading to efficient charging and discharging rates in supercapacitor. The gel polymer electrolytes are another type of electrolyte used in supercapacitors [37]. They are composed of two phases called ionic conducting medium and host polymer matrix [38].

Methods

Synthesis of Novel G-CPs

Materials

The monomers, pyrrole (98 %), aniline (99.5 %), *o*-anisidine (99.5 %), *o*-toluidine (99.5 %) thiophene (99 %), ethylenedioxythiophene (98 %) monomers, poly(sodium 4-styrenesulfonate) (Na-PSS), ammonium per sulfate (APS), ferric chloride (FeCl₃), hydrochloric acid (HCl), ethanol, and methanol are all A.C.S. grade and purchased from Sigma-Aldrich (USA). Graphene platelets (less than 10 nm in thickness) were purchased from Angstrom Materials (USA). All the chemicals and materials were employed as purchased without any modifications unless indicated in the manuscript.

Synthesis of G-CPs Nanocomposites

The G-CP nanocomposites are prepared by chemical oxidative polymerization involving monomer and graphene nanosheets in acidic media (1 M HCl). The molar ratios of monomer, HCl, and oxidant (APs/FeCl₃/Na-PSS) are kept at 1:1:1 ratio for all nanocomposite material synthesis processes. The graphene to monomer weight ratio was kept at 1:1 for all the G-CP nanocomposite synthesis. Initially, the

monomer is added to 0.2 M HCl solution and stirred for 30 min before adding the graphene to the resulting solution. The graphene is added slowly and stirred for another 45 min. A mixture of concentrated HCl and oxidant is slowly added dropwise to the monomer solution under stirring in a 4–5 °C ice bath. The system is kept stirred vigorously for 24 h.

The prepared nanocomposite is filtered and rinsed with methanol and deionized water. Finally, the G-CP nanocomposites are dried at 60 °C in an oven. Figure 3 shows a schematic of the synthesis of G-PPy nanocomposite materials. Since thiophene derivatives studied do not dissolve in an aqueous solvent due to the rigid polymer backbone structure, the monomers has been mixed in ethanol first and then by a similar procedure is followed to synthesize the G-PTh and the G-PEDOT nanocomposite materials (Basnayaka et al. 2013, 2013; [28]; Basnayaka et al. 2013).

Characterization of the G-Conducting Polymer

The SEM, TEM, XRD, UV–vis, Raman, and FTIR spectroscopes were used to characterize the G-CPs. SEM and TEM images were produced using Hitachi S-800 SEM and the Tecnai F20 TEM to investigate the morphology of the surface of the G-CP nanocomposites. TEM samples were prepared by adding a small amount of dry powder to ethanol, and a small drop of the solution was dropped on 300 mesh copper TEM grids. UV–vis measurements were obtained by a Jasco V-530 for G-PANI solution in *N*-methyl 2- pyrrolidinone (NMP), which is the common organic solvent for the base form of PANI. FTIR spectra of G-CPS nanocomposites were measured using a PerkinElmer spectrometer. TGA analysis was performed from SDT Q600 thermal analysis instrument.

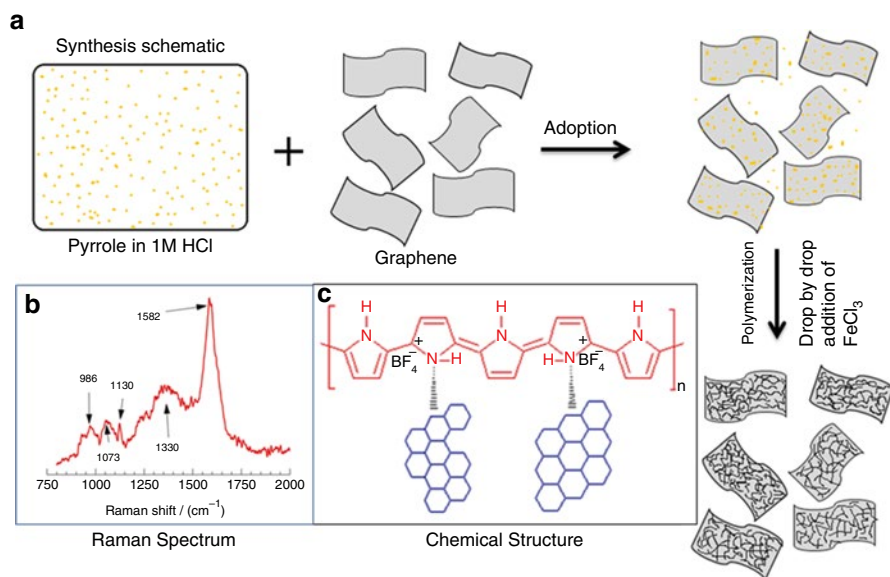


Fig. 3 Synthesis schematic of G-PPy [48]

Preparation of Electrodes

The G-PANI electrodes were fabricated by dissolving the emeraldine base form of PANI using *N*-methyl 2-pyrrolidinione (NMP), and the solution mixture is deposited on graphite. Then the electrodes are dried under vacuum at 100 °C for 12 h. The other test electrodes (G-PPy, G-PEDOT, and G-PTh) are prepared by mixing G-CPs in nafion solution. All electrochemical experiments are carried out using a two-electrode system in different electrolytes (1 M HCl and 0.2 M LiClO₄).

Electrochemical Characterizations

The electrochemical performance of G-CP was investigated through cyclic voltammetry (CV), charging–discharging, and impedance measurements using VoltaLab instrument. The CVs were recorded at different scan rates (100, 50, 25, 10, and 5 mV/s) to understand the redox processes and to evaluate the supercapacitor performance of the G-CP nanocomposites. The impedance measurements were made in the frequency range between 100 mHz and 100 kHz to understand the internal resistance and the equivalent circuit model of the supercapacitors. A comparative study of the specific capacitance was carried out for different electrolytes using CV curves.

Results and Discussion

An extended study was carried out on G-poly(*o*-anisidine) POA, a derivative of aniline with methoxy group (OCH₃ functional group attached to ortho position of aniline) nanocomposites with different compositions of graphene and *o*-anisidine. The presence of graphene in the POA polymer chain improves the conductivity of the nanocomposite material as shown in Fig. 4. The conductivity of the G-POA50

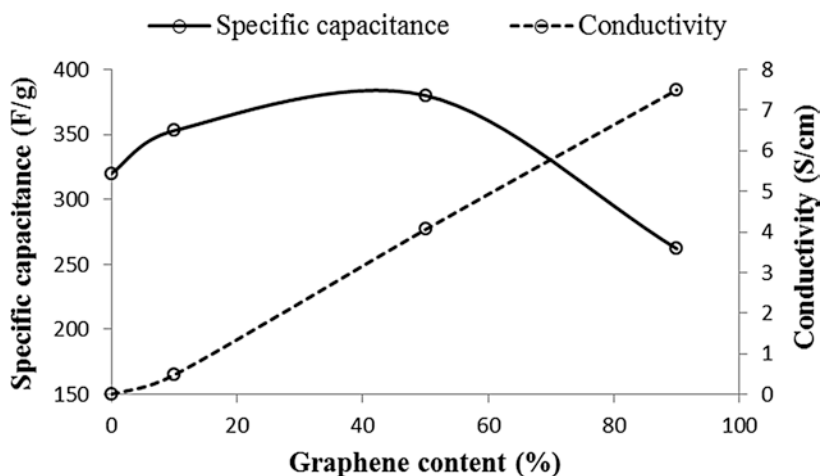


Fig. 4 Specific capacity and conductivity dependence with composition of graphene [48]

nanocomposite is 4.06 S/cm, which is about 1000 times higher than the conductivity of the POA (3.7×10^{-3} S/cm) [39]. The conductivity of the G-PANI nanofiber composite containing 44 % graphene has been found to be 5.51 S/cm, which is about 10 times higher than that of the pristine PANI-NFs (0.5 S/cm). It is clear that the graphene filler is more effective in increasing the conductivity of POA and POT than the PANI.

The electrode materials were characterized using SEM and TEM techniques to understand the morphology of the G-CPs, and the results are shown in Figs. 5 and 6, respectively. The G-PPy and G-PEDOT exhibit a cauliflower-like structure with

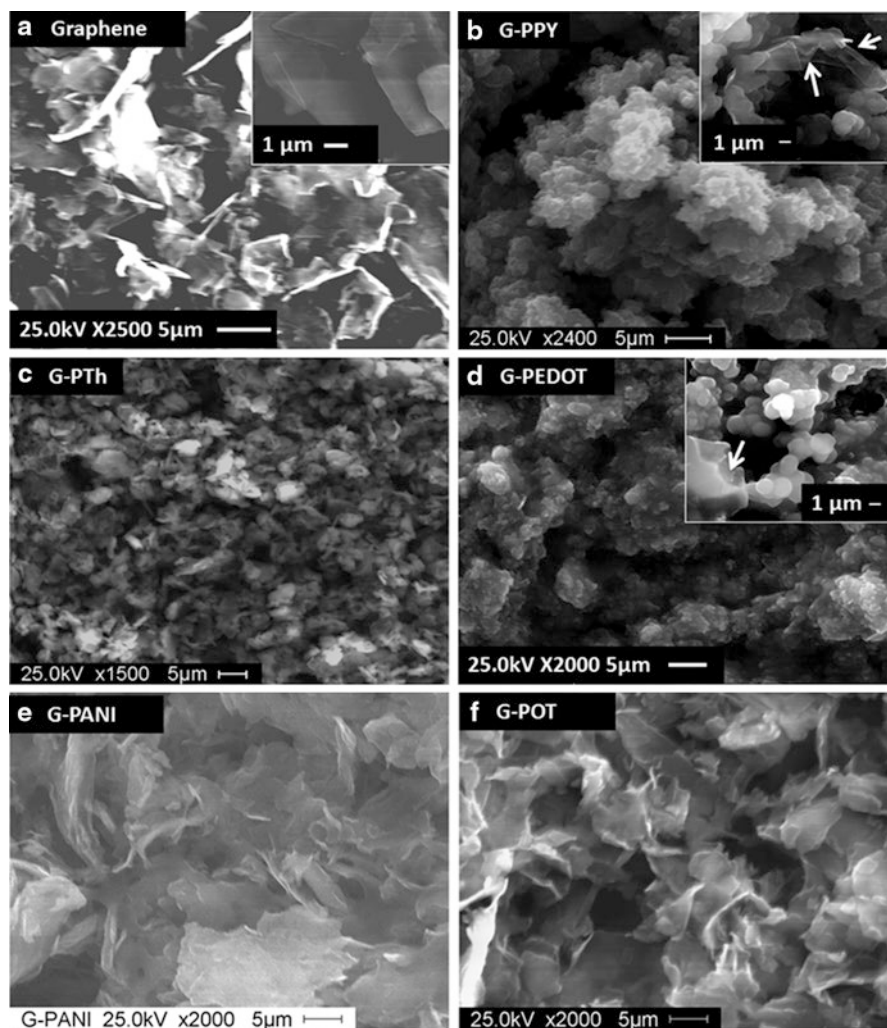


Fig. 5 SEM images of (a) graphene, (b) G-PPy, (c) G-PTh, (d) G-PEDOT, (e) G-PANI, and (f) G-POT nanocomposites

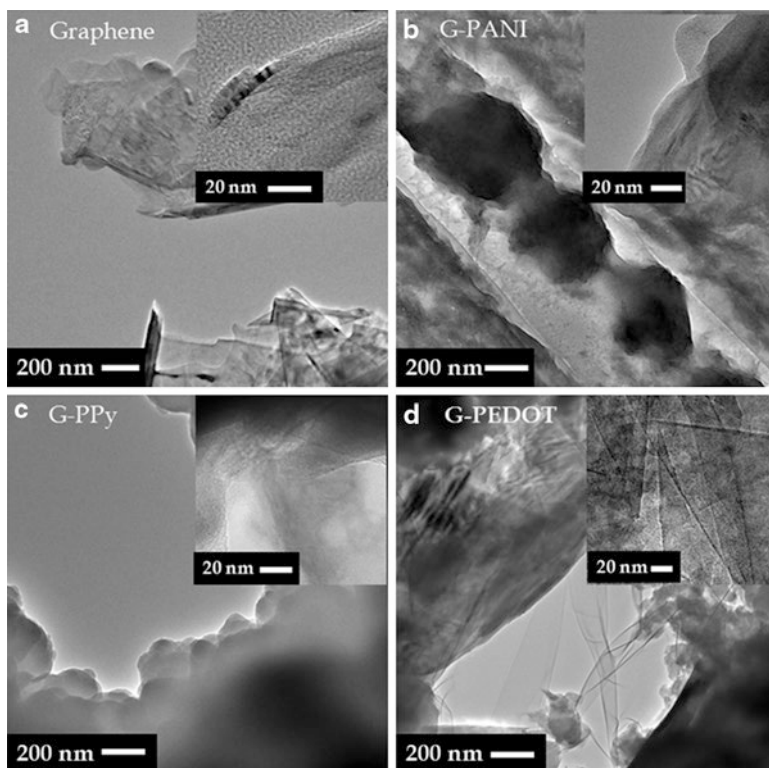


Fig. 6 TEM images of (a) graphene, (b) G-PANI, (c) G-PPy, and (d) G-PEDOT nanocomposites

some pores throughout the film as evident from the SEM pictures in Fig. 5a, b. The inset shows how graphene platelets agglomerate in PPy and PEDOT polymer. The G-PTh, G-PANI, and G-POT shows differently orientated graphene plates in the composites exhibiting small pores as compared to the G-PPy or the G-PEDOT.

Figure 6a shows graphene platelets in different orientations and composed of a few layers. Figure 4b reveals the G-PANI and graphene structure with magnification of 200 nm. The TEM pictures of G-PPy shows the evidence of graphene agglomeration in PPy as shown in Fig. 4c. Sphere-like structure could be seen in the low magnification of the TEM images (figure not shown). G-PEDOT exhibits an interesting structure combined with graphene even in a lower magnification (200 nm). The conducting channels of polymers are also evidenced from Fig. 4. TEM studies confirm that multiple graphene sheets are stacked for all the G-CPs composites.

The FTIR spectra of the G-PPy, G-PANI, G-PTh, and G-PEDOT are shown in Fig. 7. As indicated by the blue line, the characteristic PPy peaks are located at 1547 cm^{-1} and 1445 cm^{-1} , and they are due to the antisymmetric and symmetric ring-stretching vibrational modes. The sharp peaks near 1145 cm^{-1} and 887 cm^{-1} indicate the doping states of the G-PPy nanocomposite. The broadband at

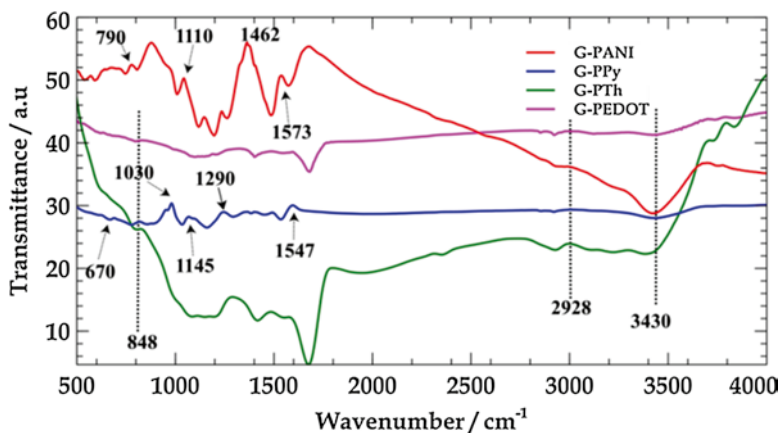


Fig. 7 FTIR spectra of G-CPs

3000–3500 cm^{-1} is assigned to N–H and C–H stretching vibrations of PPY- and PANI-based CP nanocomposite with graphene. The band at 848 cm^{-1} is ascribed to the vibration mode of C–S bond in the thiophene ring in the G-PTh and G-PEDOT nanocomposites (Alvi et al. 2011). The curves related to G-PTh and G-PEDOT show a (C–H) stretching vibration peak at 2928 cm^{-1} . The main peak bands at 1547 and 1462 cm^{-1} are assigned to the stretching vibrations of quinone and benzene rings for all G-CPs in Fig. 7. The band peak at 1290 cm^{-1} is corresponding to the C–N stretching vibration of G-PPy and G-PANI [40, 41]. The in-plane bending of C–H is reflected in the 1110 cm^{-1} peak. The peak at 790 cm^{-1} is attributed to the out-of-plane bending of C–H. All of the above peaks are related to G-CPs films, showing that CPs are in the composite film.

Figure 8 depicts the TGA curves of graphene, G-PANI, G-PEDOT, and G-PPy nanocomposites. Graphene shows a highly stable (only 4 % weight loss) behavior with no decomposition over the entire operating temperature. The G-CP nanocomposites show three weight loss steps. A 10 % sudden decrease in mass below 100 °C is due to the water absorbed in the sample or due to the volatilization of the solvent. The sudden decrease in temperature around 200–250 °C could be due to the decomposition of the dopant in CPs [42]. The significant weight reduction in the third region is due to the full-scale polymer degradation [39]. Based on the TGA study, it can be concluded that the nanocomposites are thermally more stable than the pristine CPs. The CP polymer backbone structure and graphene provide a pathway for free charge through the polymer backbone chain via a sequential delocalization with π -bonds (hopping) under an applied electric field.

Finally, the materials are tested in electrode for supercapacitors in a two-electrode system with the presence of 2 M H_2SO_4 electrolyte. When G-PANI is considered, initial electrodes were made of the emeraldine salt form of PANI in a nanocomposite [43]. During oxidation and reduction of PANI, the nanocomposite is oxidized

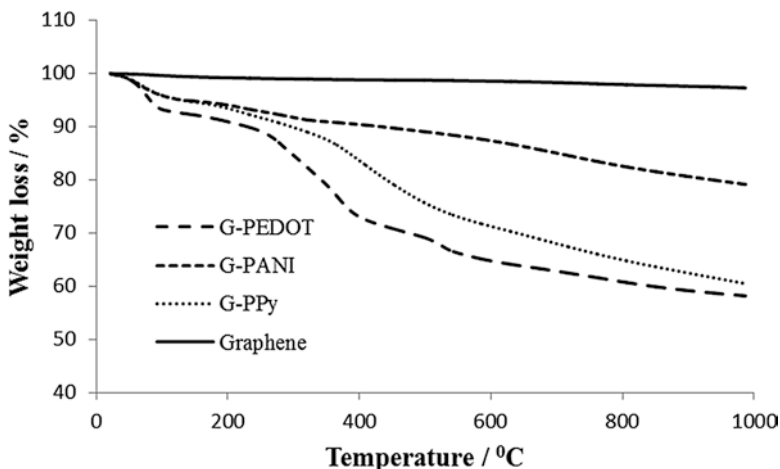


Fig. 8 TGA curves of graphene, G-PANI, G-PPy, and G-PEDOT

into pernigraniline at the positive electrode and reduced to leucoemeraldine at the negative electrode. Figure 9 shows the change in chemical structure during the charging process of G-PANI. Figure 9 shows the electrochemical activations that could take place during charging–discharging of the electrode cell (anode) on G-PANI in HCl electrolyte.

Electroneutrality within the CP film is essential during the reversible redox reaction of CPs and is facilitated by the movement of the ions between the electrode and the electrolyte solution (process 2 in Fig. 10). This process includes electron transfer at the electrode–film interface (process 1) and electron and counterion transport in the G-CP film (process 2, e.g., H^+ and Cl^- ions when the electrolyte used is a 2 M HCl solution). The processes that can occur in the electroactive G-CP film and electrolyte system can be summarized as follows: (a) heterogeneous electron transfer due to oxidation and reduction inside the film as well as film/solution interface, (b) ionic diffusion of H^+/Cl^- from the solution into the film to maintain electroneutrality, and (c) ionic transfer (conduction) of H^+/Cl^- within the film.

Figure 11 shows the CV characteristic curves for G-PANI, G-PEDOT, G-PPy, and G-PTh at different scan rates in 2 M HCl. The G-CP (G-PANI, G-PPy, and G-PTh) nanocomposites exhibit pseudocapacitive-type behavior, whereas simple capacitive behavior is observed in the G-PEDOT nanocomposite-based supercapacitor. The oxidation and reduction peaks that appear which can be observed in CVs in Fig. 10 are the characteristic redox peaks for CPs in the nanocomposite. The G-PANI has a larger potential window for redox potential in Fig. 10. The prominent redox peak at 0.5 V clearly indicates the presence of an oxidized state in the G-PANI nanocomposite.

Figure 12a depicts the charging–discharging behavior of the G-PANI nanocomposite in 1 M HCl at charging–discharging current (5 mA). The G-CP-based supercapacitors exhibit similar characteristic as indicated in Fig. 12 with an operating

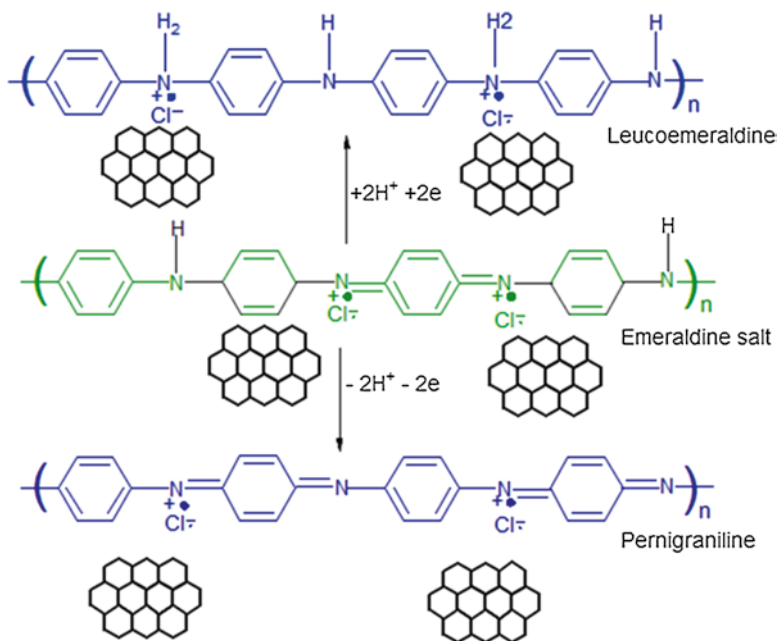


Fig. 9 Chemical structures of charging and discharging states of G-PANI nanocomposite electrodes

potential of 1 V in 1 M H_2SO_4 [45]. The pseudocapacitive behavior of its charging–discharging is similar to the charging–discharging characteristic of a rechargeable battery.

The employment of various electrolytes strongly influences the properties of supercapacitors. The drawback of the aqueous electrolyte-based supercapacitor is also obvious mainly due to the narrow cell voltage range and therefore low energy density, as observed in Fig. 12. Therefore, electrochemical characteristics were investigated in the presence of 0.2 M LiClO_4 electrolytes, and charging–discharging behavior is shown in Fig. 12. However, the increased operating voltage (2.5 V) is observed in organic electrolyte (0.2 M LiClO_4), and the power density has increased in 0.2 M LiClO_4 -based supercapacitors. This shows the advantage of organic electrolyte use in the G-CPs supercapacitors.

The specific capacitances of G-CPs are calculated at different scan rates using CV plots in 2 M H_2SO_4 . Figure 13 observes the specific capacitance of G-CP-based supercapacitors by using the equation given below.

$$C = I / ((dV / dt) \times m) \quad (4)$$

where C (F/g) is the specific capacitance, I is the current, dV/dt is the scan rate, and m is the mass of the electrode material.

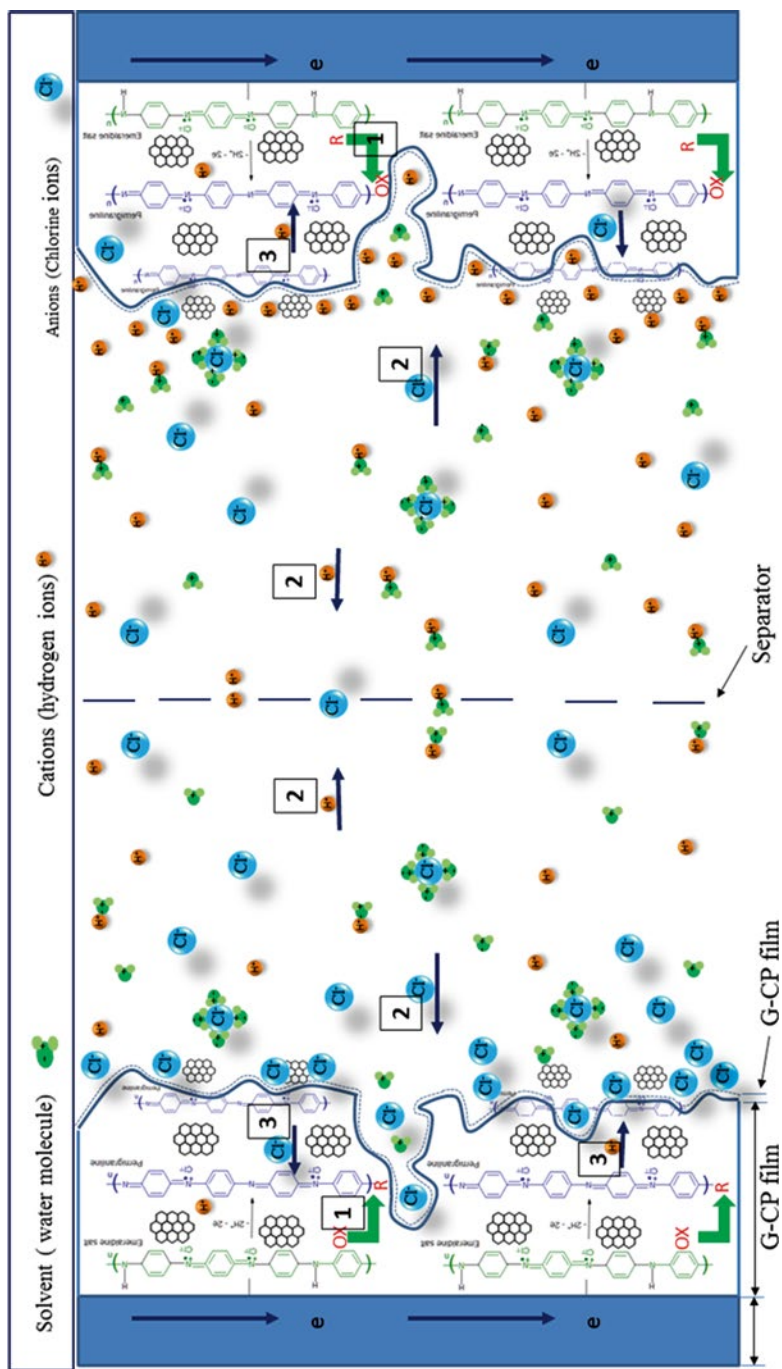


Fig. 10 Charge storage mechanism of G-PANI supercapacitor [48]

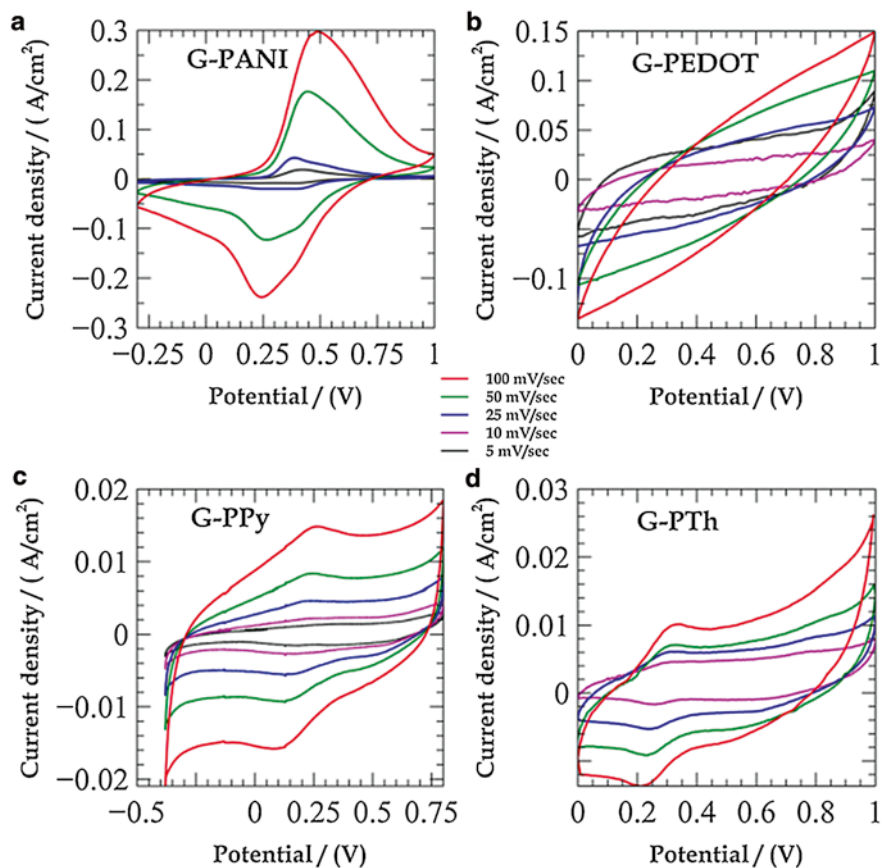


Fig. 11 CV characteristics of (a) G-PANI, (b) G-PEDOT, (c) G-PPy, and (d) G-PTh

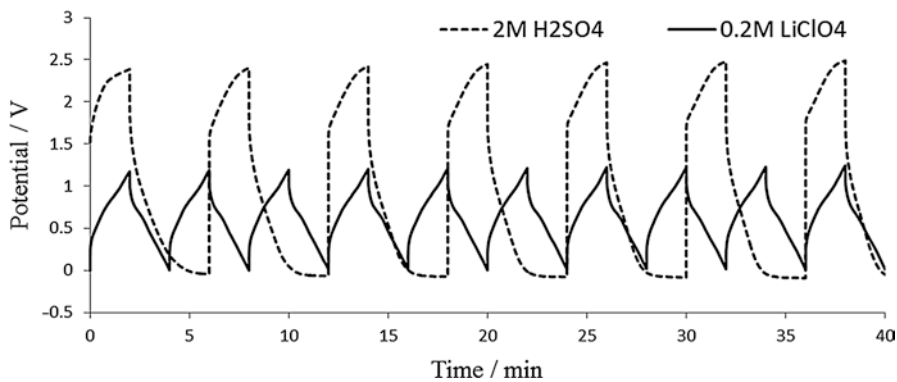


Fig. 12 Charging-discharging cycles of G-PANI at 40 mA of charging current and different discharging currents in 2 M H₂SO₄ and charging-discharging characteristic of G-PANI at 20 mA charging-discharging current in 0.2 M LiClO₄

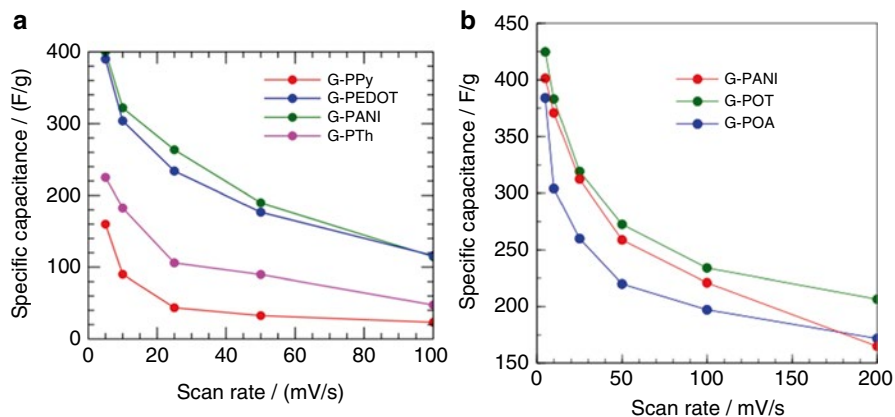


Fig. 13 Specific capacitance comparison in 2 M H_2SO_4 for (a) G-CPs and (b) G-PANI derivatives

The highest capacitance value is shown for G-PANI in Fig. 13. The specific capacitance of G-PEDOT has been found to be four times greater than the pristine graphene or polyaniline. The lowest specific capacitance is obtained from G-PPy due to the limited access to the electrolytes to react with bulk of the material [46]. The TEM of G-PPy shows the graphene platelets which are covered by PPy and limit the capacitance. We understand that the use of surfactant could overcome the low specific capacitance.

Impedance measurements are important to understand the conductivity of the electrolyte and electrode interface of the supercapacitors. The measurements are carried out to analyze the response including information about the interface, its structure, and reaction times in G-CPs nanocomposite-based supercapacitors. The small semicircle in the Nyquist plot indicates that there is charge transfer resistance in the electrochemical system in Fig. 14. The internal resistance of the system increases twice in magnitude in the electrolyte, 2 M H_2SO_4 , than in electrolyte, 0.2 M LiClO_4 . The reduction in capacitance value is the disadvantage of using organic electrolytes in supercapacitor, but it has better stability than the aqueous-based electrolytic system in supercapacitor application.

Figure 14 shows the measured impedance spectra of a G-PPy-based supercapacitor in 2 M H_2SO_4 for 100 mHz to 100 kHz frequency range.

EIS is a powerful tool to evaluate the frequency behavior and ESR of supercapacitor. It is possible to define a complex model of a capacitance as in Eqs. 5, 6, and 7 [47].

$$C(\omega) = C'(\omega) - jC''(\omega) \quad (5)$$

where $C'(\omega)$ is the real part of the cell capacitance and $C''(\omega)$ is the imaginary part of the cell capacitance. $C''(\omega)$ is corresponding to the energy losses in an

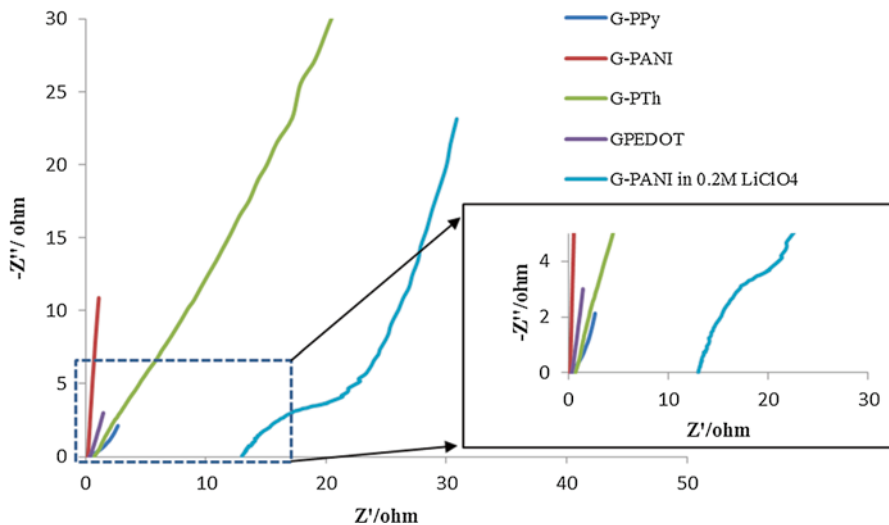


Fig. 14 Impedance of G-CP supercapacitors in 2 M H₂SO₄

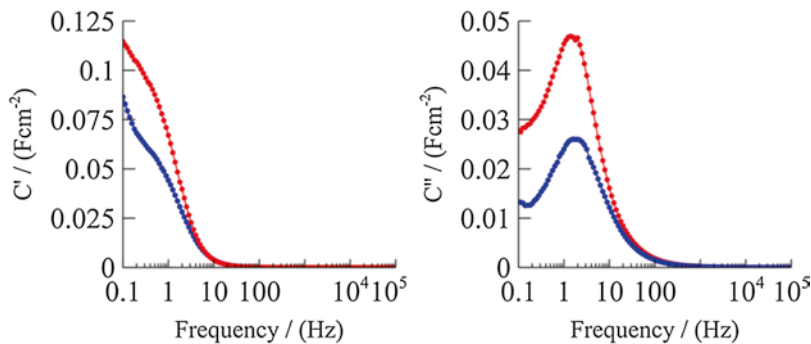


Fig. 15 Imaginary and real capacitance over frequency for G-PPy-based supercapacitor in 2 M H₂SO₄ electrolytes

irreversible process. The two components of the capacitance can be written as follows:

$$C'(\omega) = -Z''(\omega) / (\omega |Z(\omega)|^2) \tag{6}$$

$$C''(\omega) = Z'(\omega) / (\omega |Z(\omega)|^2) \tag{7}$$

The imaginary part of capacitance goes through a maximum at a frequency, f_0 , which defines a time constant as $t_0 = 1/f_0$ as seen in Fig. 15. The time constant is described as a characteristic relaxation time of the whole system (the minimum time

Table 4 Time constants of G-CP supercapacitors in 2 M H₂SO₄ electrolytes

Material	Experimental time constant (s)
G-PANI	2.5
G-POA	5
G-POT	0.6
G-PPy	0.3
G-PEDOT	2.3
G-PTh	4.2

to discharge all the energy from the device with an efficiency of greater than 50 %). Thus, such smaller value is indicative of high rate capability in supercapacitor's many applications. Table 4 indicates the experimentally calculated time constants for G-CP supercapacitors. The lower time constants of G-CP supercapacitors compared with time constants of carbon-based supercapacitors (~10 s) reveals the excellent rate capability of G-CP supercapacitors.

Conclusions

The G-CPs nanocomposites were synthesized by oxidative polymerization method. The physical characterizations of the G-CPs nanocomposites were investigated by SEM, TEM, FTIR, and TGA spectroscopy techniques. The SEM study on G-CPs reveals that the electrode materials are porous with higher surface areas. Successful investigation on capacitive performances carried out using electrochemical characterization and EIS study proved short diffusion paths and low ionic resistance for diffusion of counter ions in studied supercapacitors. This fast electrochemical reaction enables to achieve the higher power density in H₂SO₄ electrolyte. The highest specific capacitance value of 400 F/g is estimated for G-PANI, and G-PEDOT also gives the better specific capacitance value. A comparative study on G-PANI derivative observed a higher capacitance of 425 F/g in G-POT due to strong electron donating group of CH₃. Also, all G-PANI derivatives observed higher operating voltage in organic-based electrolytes. Time constants of G-CP supercapacitors in 2 M H₂SO₄ electrolytes are less than 5 s, which is an indication of fast charging and discharging characteristic of G-CPs supercapacitors. Our study has provided the fundamental understanding of synthesis, characterization, and application of electrodes based on G-CP nanocomposites for supercapacitor applications.

Acknowledgments The authors would like to acknowledge the support from the Nanotechnology Research and Education Center (NREC) and Clean Energy Research Center (CERC) at the University of South Florida in the characterization of the G-CP nanocomposites. The internal grant (USF01 TPA 18326 211200 000000 0080042) from the Office of Research, University of South Florida, is also gratefully acknowledged.

References

1. Conway BE (1999) *Electrochemical supercapacitors: scientific fundamentals and technological applications*. New York Kluwer Academic/Plenum Publishers
2. Wang G, Zhang L, Zhang J (2012) A review of electrode materials for electrochemical supercapacitors. *Chem Soc Rev* 41:797–828
3. Kötz R, Carlen M (2000) Principles and applications of electrochemical capacitors. *Electrochim Acta* 45:2483–2498
4. Burke AF (2007) Batteries and ultracapacitors for electric, hybrid, and fuel cell vehicles. *Proc IEEE* 95:806–820
5. Prashanth J, Manivannan A, Kumta PN (2010) Advancing the supercapacitor materials and technology frontier for improving power quality. *Electrochem Soc Interface* 57–62
6. Inagaki M, Konno H, Tanaike O (2010) Carbon materials for electrochemical capacitors. *J Power Sources* 195:7880–7903
7. Rolison DR, Nazar LF (2011) Electrochemical energy storage to power the 21st century. *MRS Bull* 36:486–493
8. Stoller MD, Park S, Zhu Y, An J, Ruoff RS (2008) Graphene-based ultracapacitors. *Nano Lett* 8:3498–3502
9. Jayalakshmi M, Balasubramanian K (2008) Simple capacitors to supercapacitors – an overview. *Int J Electrochem Sci* 3:1196–1217
10. Arbizzani C, Mastragostino M, Soavi F (2001) New trends in electrochemical supercapacitors. *J Power Sources* 100:164–170
11. Huang Y, Liang J, Chen Y (2012) An overview of the applications of graphene-based materials in supercapacitors. *Small* 8:1805–1834
12. Algharaibeh Z, Liu X, Pickup PG (2009) An asymmetric anthraquinone-modified carbon/ruthenium oxide supercapacitor. *J Power Sources* 187:640–643
13. Zhang D, Zhang X, Chen Y, Yu P, Wang C, Ma Y (2011) Enhanced capacitance and rate capability of graphene/polypyrrole composite as electrode material for supercapacitors. *J Power Sources* 196:5990–5996
14. Da-Wei Wang, Feng Li, Jinping Zhao, Wencai Ren, Zhi-Gang Chen, Jun Tan, Zhong-Shuai Wu, Ian Gentle, Gao Qing Lu, Hui-Ming Cheng (2009) Fabrication of graphene/polyaniline composite paper via in situ anodic electropolymerization for high-performance flexible electrode. *ACS Nano* 3:1745–1752
15. Kumar NA, Choi H-J, Shin YR, Chang DW, Dai L, Baek J-B (2012) Polyaniline-grafted reduced graphene oxide for efficient electrochemical supercapacitors. *ACS Nano* 6:1715–1723
16. Aaron D, Yu A (2011) Material advancements in supercapacitors: from activated carbon to carbon nanotube and graphene. *Can J Chem Eng* 89:1342–1357
17. Snook GA, Kao P, Best AS (2011) Conducting-polymer-based supercapacitor devices and electrodes. *J Power Sources* 196:1–12
18. Xia H, Shirley Y, Meng B, Guoliang Y, Chong Cui, Li Luc (2012) A symmetric RuO₂/RuO₂ supercapacitor operating at 1.6 V by using a neutral aqueous electrolyte. *Electrochem Solid-State Lett* 15:A60–A63
19. Wei W, Cui X, Chen W, Ivey DG (2011) Manganese oxide-based materials as electrochemical supercapacitor electrodes. *Chem Soc Rev* 40:1697–1721
20. Gómez H, Ram MK, Alvi F, Villalba P, Stefanakos EL, Kumar A (2011) Graphene-conducting polymer nanocomposite as novel electrode for supercapacitors. *J Power Sources* 196:4102–4108
21. Yu A, Chabot V, Zhang J (2013) *Electrochemical supercapacitors for energy storage and delivery: fundamentals and applications*, 1st edn, Electrochemical energy storage and conversion. CRC Press, Boca Raton

22. Chen Y, Zhang X, Zhang H, Sun X, Zhang D, Ma Y (2012) High-performance supercapacitors based on a graphene-activated carbon composite prepared by chemical activation. *RSC Adv* 2:7747–7753
23. Cheng Q, Tang J, Ma J, Zhang H, Shinya N, Qin L-C (2011) Graphene & CNT composite electrodes for supercapacitors with ultra-high energy density. *Phys Chem Chem Phys* 13: 17615–17624
24. Oh J, Kozlov ME, Novitski DM, Baughman RH (2010) Preparation and characterization of electrochemical supercapacitors based on SWNT/PPy nanocomposites. In: 2010 10th IEEE conference on nanotechnology (IEEE-NANO). Presented at the 2010 10th IEEE conference on nanotechnology (IEEE-NANO), pp 499–502. Seoul, Korea
25. Sharma AK 1, Sharma Y, Malhotra R, Sharma JK (2012) Solvent tuned PANI-CNT composites as advanced electrode materials for supercapacitor application. *Adv Materials Lett* 3:82–86
26. Zhang K, Zhang LL, Zhao XS, Wu J (2010) Graphene/polyaniline nanofiber composites as supercapacitor electrodes. *Chem Mater* 22:1392–1401
27. Wang H, Hao Q, Yang X, Lu L, Wang X (2010) A nanostructured graphene/polyaniline hybrid material for supercapacitors. *Nanoscale* 2:2164–2170
28. Alvi F, Ram MK, Basnayaka PA, Stefanakos E, Goswami Y, Kumar A (2011) Graphene-polyethylenedioxythiophene conducting polymer nanocomposite based supercapacitor. *Electrochim Acta* 56:9406–9412
29. Bose S, Kim NH, Kuila T, Lau K, Lee JH (2011) Electrochemical performance of a graphene-polypyrrole nanocomposite as a supercapacitor electrode. *Nanotechnology* 22:295202
30. Chang H-H, Chang C-K, Tsai Y-C, Liao C-S (2012) Electrochemically synthesized graphene/polypyrrole composites and their use in supercapacitor. *Carbon* 50:2331–2336
31. Zhangpeng Li ab, Yongjuan Mi ab, Xiaohong Liu a, Sheng Liu ab, Shengrong Yang, Jinqing Wang (2011) Flexible graphene /MnO₂ composite papers for supercapacitor electrodes. *J Mater Chem* 21:14706–14711
32. Khomenko V, Raymundo-Piñero E, Frackowiak E, Béguin F (2006) High-voltage asymmetric supercapacitors operating in aqueous electrolyte. *Appl Phys A* 82:567–573
33. Kurzweil P, Chwistek M (2008) Electrochemical stability of organic electrolytes in supercapacitors: spectroscopy and gas analysis of decomposition products. *J Power Sources* 176: 555–567
34. Ruiz V, Huynh T, Sivakumar SR, Pandolfo AG (2012) Ionic liquid-solvent mixtures as supercapacitor electrolytes for extreme temperature operation. *RSC Adv* 2:5591–5598
35. Balducci A, Dugas R, Taberna PL, Simon P, Plée D, Mastragostino M, Passerini S (2007) High temperature carbon-carbon supercapacitor using ionic liquid as electrolyte. *J Power Sources* 165:922–927
36. Noorden ZA, Sugawara S, Matsumoto S (2012) Electrical properties of hydrocarbon-derived electrolytes for supercapacitors. *IEEJ Trans Electr Electron Eng* 7:S25–S31
37. Yang X, Zhang F, Zhang L, Zhang T, Huang Y, Chen Y (2013) A high-performance graphene oxide-doped ion gel as gel polymer electrolyte for all-solid-state supercapacitor applications. *Adv Funct Mater* 23:3353–3360
38. Sivaraman P, Thakur A, Kushwaha RK, Ratna D, Samui AB (2006) Poly(3-methyl thiophene)-activated carbon hybrid supercapacitor based on gel polymer electrolyte. *Electrochem Solid-State Lett* 9:A435–A438
39. Basnayaka PA, Ram MK, Stefanakos L, Kumar A (2013) High performance graphene-poly (*o*-anisidine) nanocomposite for supercapacitor applications. *Mater Chem Phys* 141:263–271
40. Hasik M, Drelinkiewicz A, Wenda E, Paluszkiwicz C, Quillard S (2001) FTIR spectroscopic investigations of polyaniline derivatives-palladium systems. *J Mol Struct* 596:89–99
41. Basnayaka PA, Ram MK, Stefanakos EK, Kumar A (2013) Supercapacitors based on graphene-polyaniline derivative nanocomposite electrode materials. *Electrochim Acta* 92:376–382
42. Wei Y, Hsueh KF (1989) Thermal analysis of chemically synthesized polyaniline and effects of thermal aging on conductivity. *J Polymer Sci Part A Polymer Chem* 27:4351–4363

43. Yue J, Epstein AJ (1990) Synthesis of self-doped conducting polyaniline. *J Am Chem Soc* 112:2800–2801
44. Alvi F, Ram MK, Basnayaka P, Stefanakos E, Goswami Y, Hoff A, Kumar A (2011) Electrochemical supercapacitors based on graphene-conducting polythiophenes nanocomposite. *ECS Trans* 35:167–174
45. Liu S, Liu X, Li Z, Yang S, Wang J (2011) Fabrication of free-standing graphene/polyaniline nanofibers composite paper via electrostatic adsorption for electrochemical supercapacitors. *New J Chem* 35:369–374
46. Basnayaka PA, Ram MK, Stefanakos L, Kumar A (2013) Graphene/polypyrrole nanocomposite as electrochemical supercapacitor electrode: electrochemical impedance studies. *Graphene* 2:81–87
47. Daniel V (1967) *Dielectric Relaxation*, Academic Press, London and New York
48. Basnayaka PA (2013) Development of nanostructured graphene/Conducting polymer composite materials for supercapacitor applications, graduate theses and dissertations

Emanuela Gatto, M. Caruso, and M. Venanzi

Contents

Introduction.....	504
Peptide Electron-Transfer Theory.....	505
Electrochemical Techniques.....	510
Cyclic Voltammetry.....	510
Chronoamperometry.....	517
AC Voltammetry.....	519
Electrochemical Impedance Spectroscopy.....	522
Photocurrent Generation Measurements.....	527
Peptide-Based SAMs.....	529
Electrochemistry of Peptide-Based SAMs.....	530
Photocurrent Generation Measurements.....	545
Conclusions.....	555
References.....	556

Abstract

The self-assembly ability of molecules is of fundamental importance in modern science and technology, making possible to produce nanostructures with a precision that is not achievable with classical lithographic miniaturization techniques. In particular, self-assembled monolayers (SAMs) formed by helical oligopeptides are very promising materials, used as archetypal systems in various fields of current nanoscience research, materials science, molecular biology, and

E. Gatto (✉) • M. Caruso • M. Venanzi
Department of Chemical Sciences and Technologies, University of Rome “Tor Vergata”,
Rome, Italy
e-mail: emanuela.gatto@uniroma2.it; mario.caruso@uniroma2.it; venanzi@uniroma2.it

surface science, and with potential application as molecular sensors and optoelectronic devices. The motivation for fabricating polypeptide SAMs is to exploit the unique features of polypeptide primary and secondary structures: it is possible to create a designed peptide sequence (a sequence of side chains with specified functionality) that in turn would be manifested in the corresponding SAM as spatially resolved, chemically distinct functionalities localized in a series of strata coplanar with the substrate. Moreover, the macrodipole moment associated with the vector sum of the individual peptide dipoles in an α -helical secondary structure gives rise to an intrinsically polar SAM, which favors electron-transfer in one precise direction and facilitates light-induced electron-hole separation, for appropriately placed chromophores. In this chapter we review the electrochemical properties of peptide SAMs, both in their fundamental and excited electronic states, focusing on their characterization and on their charge-transport properties.

Keywords

Peptides • Self-assembled monolayers • Electron transfer • Electrochemistry

Introduction

The rational design and preparation of materials for a wide range of applications, such as information storage and processing, requires protocols for the assembly of molecular units into supramolecular array. For example, optical switches based on second-order nonlinear effects [1] or optoelectronic devices require materials with unidirectional alignment. Several techniques for the alignment of organic materials have been investigated, making use of single-crystal materials, liquid crystals, Langmuir–Blodgett films, and host–guest inclusion complexes. However, none of these techniques have provided long-term stability of the system to both heat and light. In 1983 Nuzzo and Allara [2] first reported on the formation of ordered self-assembled monolayers (SAMs) by the spontaneous adsorption of dialkyl disulfides on gold by covalent Au–S linkage. Since then, many reports have appeared in the literature about SAMs having different thicknesses (chain lengths) and exterior surface functionalities [3, 4].

In one of the first contributions to the field, Enriquez and coworkers showed that also α -helical oligopeptides containing a disulfide moiety are promising self-assembly materials [5]. In fact, in nature, the three-dimensional structure of protein is driven by a number of non-covalent interactions, among them the aggregation of helical segments into a more specific spatial conformation. The key advantage of helical peptides over alkyl chains is their larger efficiency in long-range electron-transfer processes [6] and their rectifying properties due to the effect of the helical macrodipole on the electron-transfer processes. In fact, in

biological systems, electron-transfer (ET) reactions efficiently occur along a sequential array of redox moieties embedded in polypeptide matrices [7, 8]. These polypeptide matrices are generally believed to act not only as scaffolds to fix the three-dimensional location of the redox moieties but also as mediators to facilitate electron-transfer. α -Helix is the most frequently secondary structure observed in such polypeptide matrices and is considered to play an important role in the mediation of electron-transfer.

To study the nature of peptide-mediated electron-transfer processes, radiolysis [9, 10] and photoinduced electron-transfer [11] studies in solution (donor–peptide–acceptor) have been performed, together with theoretical calculations [12–14]. These studies have shown that the efficiency of the coupling between redox centers is determined by the 3D structure of the intervening peptide matrix, the length of the peptide, the nature of the scaffold, and the amino acid sequence [15–18]. The presence of hydrogen bonding also influences the electron-transfer rates [14, 19, 20]. Furthermore, in the case of α -helical peptides, the ET may be strongly affected by the molecular dipole of the helix. It is well known that helical peptides have large dipole moments oriented along the molecular axis. When the direction of the electron transfer is aligned with the field generated by the dipole, the ET rates are usually faster than the ET rates in the against-dipole direction, as proved by time-resolved fluorescence measurements for dichromophoric α -helical peptides [21, 22]. It was also observed that the molecular dipole of a 3_{10} -helical secondary structure is minor than that of an α -helix, because of the hydrogen bond distortion along the helix in the former structure [12, 87].

Beyond all these results, SAMs functionalized with redox-active species have contributed powerfully to characterize ET processes at the nanoscale. The two-dimensional organization of peptide SAMs minimizes the conformational freedom of the single peptide sequence. In this chapter we will focus on electrochemical studies of peptides immobilized on gold electrodes, which led to fundamental achievements in the comprehension of charge transfer across biological systems. Electrochemical techniques, such as cyclic voltammetry (CV), chronoamperometry (CA), and electrochemical impedance spectroscopy (EIS), have been used extensively to study the ET kinetics across peptide SAMs immobilized on gold surfaces. In the next section, the basic theory of electron-transfer (section “[Peptide Electron-Transfer Theory](#)”) and behind each electrochemical method (section “[Electrochemical Techniques](#)”) will be described.

Peptide Electron-Transfer Theory

To introduce the basic theory of models used to explain ET across peptide matrices, it is possible to refer to a D–B–A system, where D and A are, respectively, an electron donor and electron acceptor group, while B represents a linear peptide chain. One of the mechanisms for peptide ET is *bridge-assisted superexchange* [16, 23, 24], where the bridge is only a medium and electrons (or holes) never stay on the bridge. Superexchange (SE) is a coherent tunneling process, which is mediated by

virtual states associated to electron (D^+-B^--A) or hole ($D-B^+-A^-$) transfer. In the absence of stepping zones, ET is limited to a maximum distance of about 20 Å. In the Marcus–Hush theory of ET reactions [25, 26], the ET rate constant is given by

$$k_{\text{ET}} = \left(\frac{1}{\hbar^2 \lambda kT} \right)^{\frac{1}{2}} H_{\text{DA}}^2 \exp \left[-\frac{(\lambda + \Delta G^\circ)^2}{4\lambda RT} \right] \quad (1)$$

where H_{DA}^2 is the electronic coupling matrix, which is the probability that an electron tunnels through the D–A potential barrier; ΔG° is the driving force of the ET reaction, i.e., the difference in the oxidation potentials of the D–A pair; and λ is the reorganization energy, i.e., the energy needed to bring the nuclei from the position of the reactants to the position of the products.

These parameters may be determined by spectroscopic studies of charge-transfer band intensities and energies (H_{DA} , λ), structural and vibrational frequency differences (λ), and electrochemical or other thermodynamic measurements (ΔG°). The reorganization energy λ is in general factorized in two contributions: an outer contribution, which takes into account the reorganization of solvent modes around a charge-separated (CS) state, and an inner contribution, which takes into account the nuclear (vibrational) reorganization of the D–A pair, i.e., $\lambda = \lambda_{\text{in}} + \lambda_{\text{out}}$.

In a description of ET based on quantum theory, Eq. 1 can be written as [25]

$$k_{\text{ET}} = \frac{1}{\hbar^2} H_{\text{DA}}^2 (\text{FCWD}) \quad (2)$$

where FCWD is the Franck–Condon-weighted density of vibronic states, i.e.,

$$\text{FCWD} = \left(\frac{1}{4\pi\lambda kT} \right)^{\frac{1}{2}} \exp \left[-\frac{(\lambda + \Delta G^\circ)^2}{4\lambda RT} \right] \quad (3)$$

In the case of a molecular bridge composed of n bridge units (n amino acids of a peptide chain), the D–A coupling matrix can be factorized in terms of the electronic coupling between the donor and the first bridging unit (H_{D1}), the inter-site coupling matrix G_{in} , and the coupling matrix between the terminal bridging unit and the electron acceptor group (H_{nA}):

$$H_{\text{DA}} = H_{\text{D1}} G_{\text{in}} H_{\text{nA}} \quad (4)$$

G_{in} is usually expressed as a product of the Green function, calculated at the energy state of the donor. Therefore, SE may be considered as a coherent tunneling process through molecular orbitals mediated by D^+-B^--A (electron-transfer) or $D-B^+-A^-$ (hole transfer) virtual states (Fig. 1).

Within this scheme, the electronic coupling matrix decreases exponentially with the distance between the donor–acceptor pair r_{DA} [27, 28]:

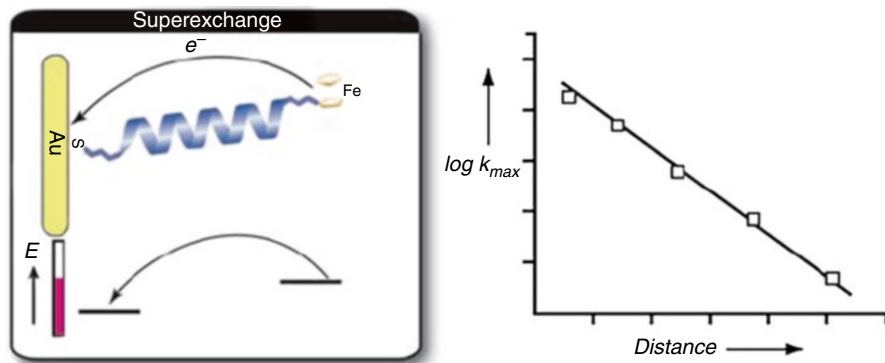


Fig. 1 Scheme of the superexchange mechanism through a helical peptide immobilized on gold surface. The exponential relationship of the electron-transfer rate constant vs. the D–A separation is also illustrated (Reprinted with permission from Long et al. [23]. Copyright (2005) Wiley)

$$H_{\text{DA}} = H_{\text{DA}}^0 \exp[-\beta(r_{\text{DA}} - r_0)] \quad (5)$$

where H_{DA}^0 is the value of the electronic coupling matrix at the donor–acceptor contact distance r_0 and β is the coupling strength parameter, which is found to be

$$\beta = \frac{2}{l} \ln \left(\frac{E_{\text{D}} - E_{\text{B}}}{H_{\text{BB}}} \right) \quad (6)$$

from perturbation theory calculations [26], and where l is the length of the bridging unit. For long-range ET, β is small and is favored by a strong coupling between the bridging units (so a big H_{BB}) and a small energy difference between the donor and the virtual states (a small $E_{\text{D}} - E_{\text{B}}$). In the case of resonant tunneling (where there is no energy gap), distance independence or little decrease of rates with distance is expected, introducing to the concept of molecular wires.

So, following the SE model, the ET rate constant would decrease in an exponential way with the donor–acceptor distance:

$$k_{\text{ET}} = k_{\text{tun}} = k_{\text{ET}}^0 e^{-\beta r_{\text{DA}}} \quad (7)$$

This exponential decrease has been observed in a series of donor–acceptor systems, in which the β values are found to be typical of the different molecular spacers. In peptide systems, definitely small decay constants have been reported at long distances: 0.18 \AA^{-1} for helical oligoproline [29], $0.02\text{--}0.04 \text{ \AA}^{-1}$ for helical peptides [30, 31], and 0.05 \AA^{-1} for collagen-like triple helices [32].

The other mechanism reported in the literature is the *electron hopping*, where an electron is injected from the donor to the peptide bridge and then it hops through the peptide bridge to reach the acceptor moiety. This is a thermally activated process, involving nuclear motion and electron hopping over the barrier.

The ET rate constant is described by

$$k_{\text{ET}} = k_{\text{ET}}^0 \exp\left(-\frac{E_a}{kT}\right) \quad (8)$$

In the limit of diffusive hopping, the electronic conduction is typical of ohmic ET, and the ET rate constant is inversely proportional to the D–A separation [33]:

$$k_{\text{ET}} = k_{\text{hop}} \propto \frac{1}{N} \exp\left(-\frac{\Delta E_{\text{DB}}}{RT}\right) \quad (9)$$

where N is the number of hopping sites and ΔE_{DB} is the energy difference between the donor and the bridging unit. The electron-transfer rate constant shows an exponential decay by increasing the distance in the tunneling, while it is inversely proportional to the distance in the hopping (Fig. 2). However, both mechanisms are always present in each electron-transfer reaction, but the dominant may change, depending on the electron-transfer distance and the reaction driving force. In the hopping mechanism the driving force is the difference in the redox potentials of the donor and acceptor (in the case of a metal, its Fermi level). The tunneling prevails when the driving force is large or the ET distance is short.

The hopping mechanism has attracted growing attention in explaining the efficient long-range electron transfer in biological systems such as double strands of DNA, in which the charge propagates with the assistance of the π -stacked bases. This mechanism is still controversial for peptides, mainly because peptides do not have specific “hopping sites,” even if it has been suggested that amide groups, or specific amino acids, such as tyrosine or tryptophan, may exploit this function,

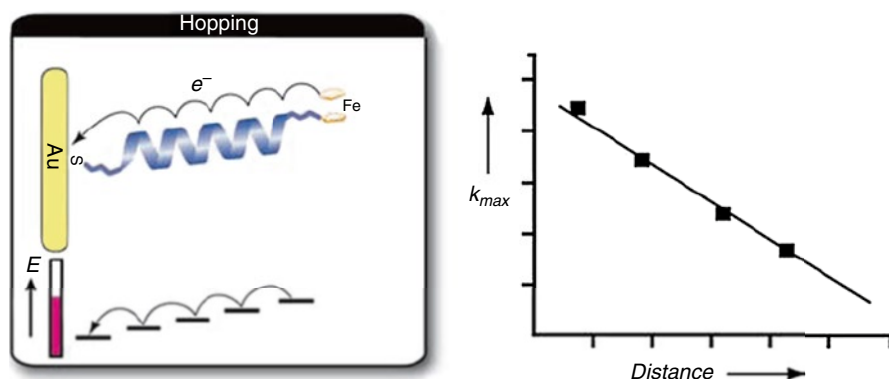


Fig. 2 Scheme of the hopping mechanism through a helical peptide immobilized on gold surface. The linear relationship of the electron-transfer rate constant vs. the D–A separation is also illustrated (Reprinted with permission from Long et al. [23]. Copyright (2005) Wiley)

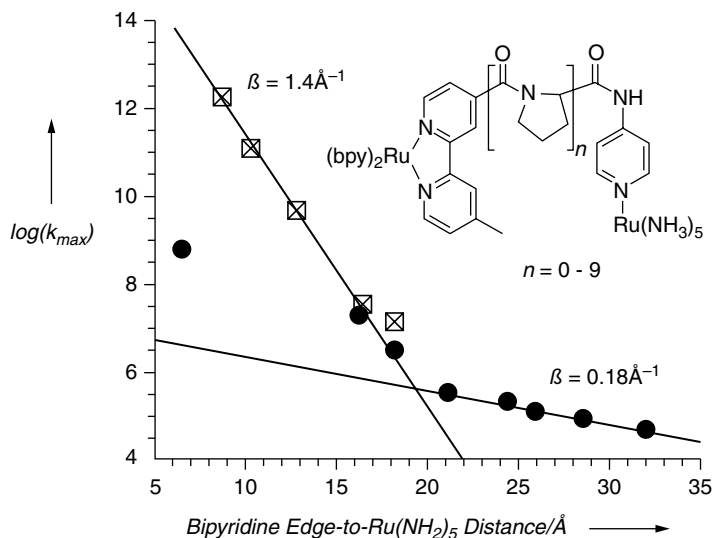


Fig. 3 Plot of $\log k_{\max}$ (radiolysis ● and photolysis ☒) versus edge-to-edge D–A distance for Isied's oligoproline conjugates (Reprinted with permission from Malak et al. [29]. Copyright (2004) American Chemical Society)

through aromatic groups. It is now generally accepted that SE and hopping mechanisms can operate in a parallel and competitive way [34], i.e.,

$$k_{\text{ET}} = k_{\text{SE}} + k_{\text{hop}} \quad (10)$$

The main results obtained in solution, studying a diruthenium system bridged by a oligoproline spacer of different length, showed a transition from a predominant superexchange mechanism to a predominant electron hopping mechanism at a D–A distance of 20 Å [29] (Fig. 3). These results were supported by theoretical calculations carried out by Petrov and May [13].

Experimental results obtained for oligopeptides containing α -aminoisobutyric acid (Aib) units by Maran and coworkers did not confirm electron tunneling contributions to the ET rate [35]. The authors supposed that the unusually smooth distance dependence of the rate constants observed in their experiments resulted from the increase of electronic coupling due to the lowering of the energy of the bridge in the presence of hydrogen bonds (Fig. 4). This effect counteracted the exponential decrease of the rate constant expected for a superexchange mechanism.

As matter of fact, the β values of different peptide chains span the full range from saturated to unsaturated hydrocarbon chains. This confirms what is already known about ET processes in proteins, where only a *multiple pathway approach* could explain their long-distance character and their efficiency values [36]. Through this approach, several mechanisms are taken into account: through-bond ET

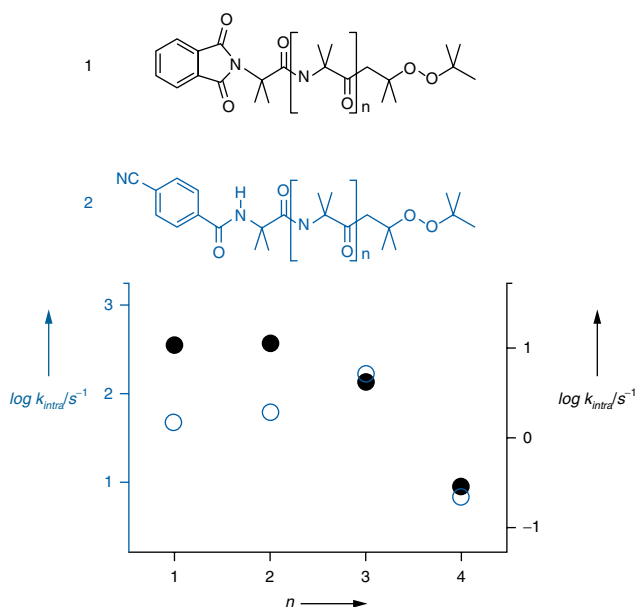


Fig. 4 Dependence of the intramolecular ET rate constants for p-cyanobenzamide-substituted oligopeptides (white, left scale) and phthalimide-substituted oligopeptides (black, right scale) on the number of intramolecular hydrogen bonds (Reprinted with permission from Antonello et al. [35]. Copyright (2003) American Chemical Society)

(comprising through-space tunneling), hopping between aromatic side chains, and hydrogen bond (HB)-assisted electron-transfer. Therefore, the matrix element for the electronic coupling, H_{DA} , should be evaluated by the product of the coupling terms for jumps along a σ bond and jumps across the space, eventually mediated by aromatic groups or HB shortcuts. The pathway that gives the largest product is taken as the optimum one. The agreement with experimental data has been recently improved, by taking protein dynamics into account [37, 38].

Electrochemical Techniques

In this section, the most widely used electrochemical techniques and their basic theory will be described (Table 1).

Cyclic Voltammetry

The most widely used electrochemical technique for SAM characterization is cyclic voltammetry (CV). CV is a potential sweep method where the potential of an electrode, which is immersed in an unstirred solution, is varied and the corresponding

Table 1 Scheme summarizing the most commonly used electrochemical techniques to study peptide SAMs

Electrochemical technique	Kind of experiment	Information given	Description
Cyclic voltammetry (CV)	<i>Blocking experiment</i> In this kind of measurement, the SAM-coated gold electrode is used as working electrode and immersed in a solution of a standard redox couple, such as $K_4[Fe(CN)_6]/K_3[Fe(CN)_6]$	Confirm of the SAM formation	In the absence of the layer, the electrochemical signal corresponding to the oxidation and reduction species is present. After the SAM formation, in general, there is a decrease of the reversible redox peaks, which is proportional to the SAM packing
	<i>Cyclic voltammetry of electrochemically active molecules</i>	Determination of the surface coverage, k_{ET} , λ , and H_{AB}	Measurement of the current from the electroactive molecule to gold, through the peptide film, as a function of the applied potential Measurement changing the scan rate is generally performed The peak shape is diagnostic of the homogeneity of the monolayer
	<i>Desorption measurements</i> The potential is swept to sufficiently negative values. A reductive desorption peak of the sulfur-containing molecules from the electrode surface is observed	Determination of the surface coverage	This experiment is based on the voltammetric measurement of the charge passed for the electron reductive desorption of the gold-bound thiolate layer in an alkaline solution: $Au(s) - S - R + ne \rightarrow Au(s) + R(S^-)_n$

(continued)

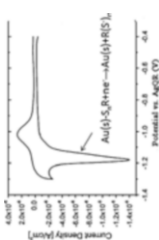
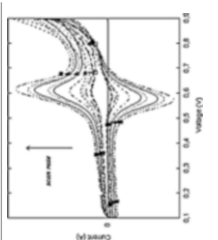
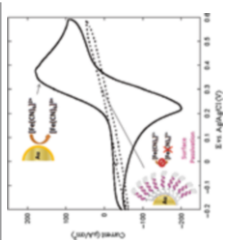
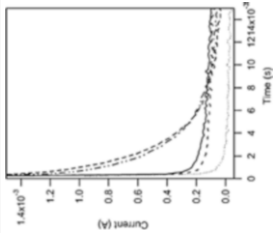
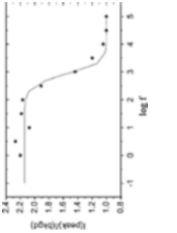
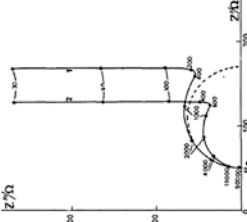
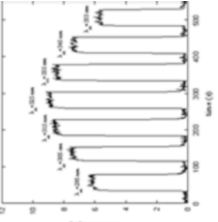


Table 1 (continued)

Electrochemical technique	Kind of experiment	Information given	Description	
Chronoamperometry	<p>Potential step method</p> <p>An overpotential (compared to the formal potential of the redox center) is applied to the working electrode, and the current decay is immediately measured as a function of time</p>	<p>Determination of the electron-transfer rate constant</p>	<p>In general, following the capacitive response, a linear relationship between $\ln(i)$ and t is obtained, from which it is possible to determine the electron-transfer rate constant</p>	
Alternating current (AC) voltammetry	<p>Potential sweep method, where starting potential and ending potential are specified, and in addition, a sinusoidally oscillating AC wave is superimposed on the potential waveform</p>	<p>Determination of the electron-transfer rate constant</p>	<p>Plotting the ratio of the AC voltammetric peak current (i_p) to the background current (i_b) as a function of the logarithm of frequency and fitting the plot using the complex nonlinear least-squares (CNLS) method, the electron-transfer rate constant may be obtained</p>	

Electrochemical impedance spectroscopy (EIS)	The impedance is a measure of the ability of a circuit to resist the flow of electrical current, and it is usually measured by applying a small AC signal over a range of frequencies at a specified potential to an electrochemical cell and then measuring the current through the cell	Determination of the k_{ET} and film capacitance in peptide SAMs	Measuring impedances over a wide range of frequencies allows the value of each individual element of the Randles circuit to be determined	
Photocurrent generation (PG) measurements	The experiment consists in the measurement of the current generated after illumination of the SAM-covered working electrode with a high-power lamp	Capability of the system to give rise to photoinduced electron-transfer reactions	Generally, in the presence of an electron donor in solution, an electron-transfer (ET) process from the photoexcited chromophore to the gold surface is observed. On the other hand, in the presence of an electron acceptor in solution, the direction of the current is reversed, and ET from the gold surface to the chromophore occurs	

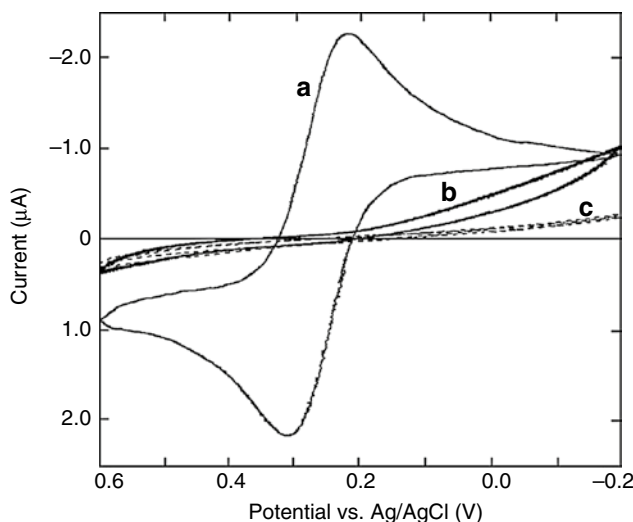


Fig. 5 Cyclic voltammetry experiments in a 0.50 mM $K_3[Fe(CN)_6]$ aqueous solution: (a) bare gold electrode, (b) gold electrode modified by a helical peptide SAM, and (c) gold electrode modified by an undecanethiol SAM. Sweep rate: $50 \text{ mV} \cdot \text{s}^{-1}$ (Reprinted with permission from Gatto et al. [44]. Copyright (2007) Elsevier)

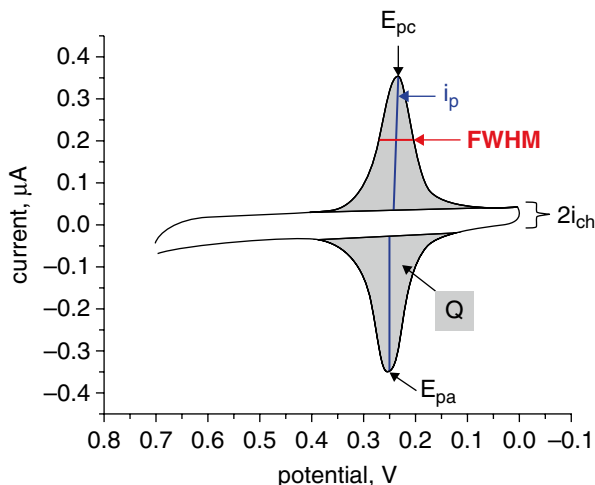
current is measured [46, 39, 40]. The potential of this working electrode is controlled versus a reference electrode, such as saturated calomel electrode (SCE) or silver/silver chloride electrode (Ag/AgCl). This technique does not require expensive or sophisticated instrumentation, and it is therefore widely available.

The most used CV experiment reported in the literature concerns the verification of the SAM formation, through blocking experiments [41–43].

In this kind of measurement, the SAM-coated gold electrode is used as working electrode and immersed in a solution of a standard redox couple, such as $K_4[Fe(CN)_6]/K_3[Fe(CN)_6]$ or $[Ru(NH_3)_6Cl_3]/[Ru(NH_3)_5Cl_3]$. The advantage of this kind of experiment is that also electrochemically inactive SAMs may be analyzed. In the absence of the layer, the electrochemical signals corresponding to the oxidation and reduction species are present. After the SAM formation, in general, there is a decrease of the reversible redox peaks, which is proportional to the SAM packing (Fig. 5) [44].

For peptide SAMs functionalized with redox species, CV can be used to determine k_{ET} , λ , and H_{AB} from the electroactive molecule to gold, through the peptide film. The values of background and peak currents and the peak potentials may be used to determine the rate constant of ET reactions. However, the integrity of the monolayer is of great importance in determining the value of the k_{ET} , because the redox centers should be ideally isolated from one another and local molecular environments homogeneous. Some SAM disorder can disperse the value of the measured rate constants. In Fig. 6 the relevant parameters that can be determined from CV data are reported.

Fig. 6 Relevant parameters of a CV of a surface-bound redox species. Parameters include E_{pc} , E_{pa} , i_{ch} , i_p , Q , and FWHM (Reprinted with permission from Eckermann et al. [45]. Copyright (2010) Elsevier)



The background current (also defined as charging or capacitive current, i_{ch}) may be associated with the thickness of the SAMs (Fig. 6). In order to compare different values, the double-layer capacitance, C_{DL} , is often normalized to the surface area, A [45]:

$$\frac{i_{ch}}{A} = \frac{C_{DL}}{A} \nu \quad (11)$$

As the faradic current peak (i_p) is directly proportional to the scan rate, ν , as described by Eq. 12 [46], the number of the redox-active sites on the surface may be determined from the slope of i_p versus ν :

$$i_p(\nu) = \frac{N \cdot n^2 \cdot F^2}{4 \cdot R \cdot T} \nu \quad (12)$$

where i_p is the peak current (anodic or cathodic), ν the voltage scan rate, N the number of redox-active sites on the surface, n the number of electron transferred, F the Faraday constant, R the gas constant, and T the temperature. The surface coverage Γ can be determined dividing N by A . This value is often compared to a theoretical maximum based on the molecular surface area of the peptide. In particular, for helical peptides, this value depends on the cross-sectional area of the helix (which is 0.69 nm^2 for a 3_{10} -helix and 0.92 nm^2 for an α -helix) and on the steric hindrance of the electrochemical probe used. By assuming a tilt angle with respect to the surface normal of 0° and a close hexagonal packing of the helical peptides, a surface density of $21.7 \cdot 10^{-11} \text{ mol/cm}^2$ and $16.5 \cdot 10^{-11} \text{ mol/cm}^2$ may be obtained, respectively, for a 3_{10} -helix and α -helix [30]. However, it is generally found that the peptide SAMs are never perpendicularly oriented and their axis has a tilt angle of 30 – 60° with respect to the surface normal [30, 47]. As a consequence, the surface density value is

reduced, and in order to know the real surface density, the theoretical value should be multiplied by the cosine of the tilt angle that the peptide helical axis forms with respect to the normal to the gold surface. Also the integration of the background-subtracted anodic or cathodic peak in a slow scan rate voltammetry experiment may be used to determine the surface coverage [48]:

$$\Gamma = \frac{Q}{nFA} \quad (13)$$

where Q is the amount of charge passed during exhaustive electrolysis of the assembly, which may be correlated to the number of the redox molecules.

The peak width is diagnostic of the homogeneity of the monolayer and can be evaluated by the full width at half of the peak maximum height (FWHM; Fig. 6, Eq. 14). Values of FWHM that are different from the theoretical one ($90.6/n$ mV) have been attributed to electrostatic effects incurred by neighboring charged species:

$$\text{FWHM} = 3.53 \frac{RT}{nF} = \frac{90.6}{n} \text{ mV} (25^\circ\text{C}) \quad (14)$$

The redox potential, E_0 , is the average value of the anodic and cathodic peak potentials, $(E_{pa} + E_{pc})/2$, while the peak separation, E_p , is $E_{pa} - E_{pc}$. In general, when the redox species are adsorbed onto the electrode and at low scan rates, the diffusion does not play a role, so the peak separation is 0. By increasing the scan rate, the peak separation increases [46].

The overpotential η is defined according to Eq. 15 as the difference between peak potential E_p and the formal potential of the complex:

$$\eta = E_p - E^0 \quad (15)$$

For each scan rate, $k_s(\eta)$, the rate constant for electron-transfer at a particular overpotential can be determined. At any point of the voltammogram, the instantaneous faradic current is given by [49]:

$$i_f = nFA(k_a \Gamma_{\text{red-}} - k_c \Gamma_{\text{ox}}) \quad (16)$$

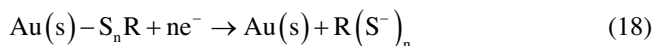
where n is the number of electrons, F is the Faraday constant, A is the area of the electrode, k_a and k_c are the rate constants of anodic and cathodic processes, and Γ_{red} and Γ_{ox} are the surface concentrations of the redox centers in the reduced and oxidized state. If the potential is at least 60 mV beyond the formal potential of the redox couple, the equation given above reduces to [49]

$$i_f = kQ(t) \quad (17)$$

where $k = k_a$ for oxidation and $k = k_c$ for reduction and $Q(t)$ is the charge corresponding to the quantity of unreacted redox sites in the electrode. The rate at given overpotential can be calculated by dividing the instantaneous faradic current by $Q(t)$ for

that potential. A plot of η vs. $\log k_s(\eta)$ is known as a Tafel plot and, importantly, can be used to determine k_{ET}^0 .

In the case of non-electrochemically active molecules, to determine the surface coverage, desorption measurements in a 0.5 M KOH aqueous solution may be performed. This experiment is based on the voltammetric measurement of the charge passed for the electron reductive desorption of the gold-bound thiolate layer in an alkaline solution:



In this equation, n represents the degree of charge transferred between the sulfur atom and the surface (for lipoic acid $n=2$, while for alkanethiols $n=1$).

The surface coverage due to gold-bound peptides may be estimated from the charge corresponding to the reductive desorption of the thiol linker from the gold surface. A typical CV curve obtained from this experiment is shown in Fig. 7 [50]. When the potential is swept to sufficiently negative values, a reduction peak appears, which corresponds to the reductive desorption of the sulfur-containing molecules from the electrode surface [50, 51]. The surface coverage of the electrode can be calculated from the peak area (i.e., the charge associated with the reduction process).

Chronoamperometry

Chronoamperometry is a basic potential step method [46]. In a potential step experiment, an overpotential is applied to the working electrode and the current is recorded as a function of time. In a double potential-step experiment, the potential is applied

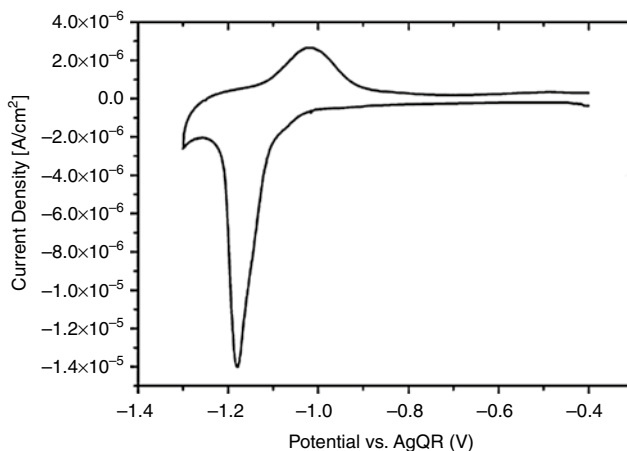
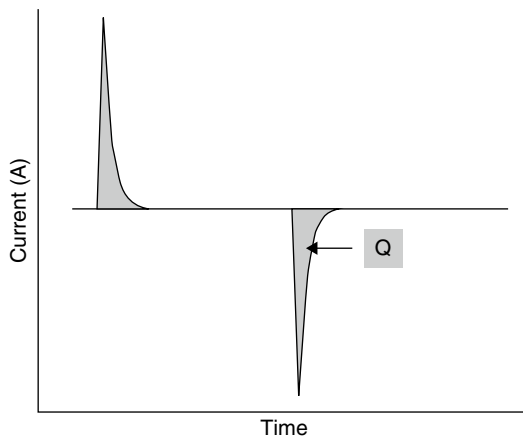


Fig. 7 Electrochemical desorption of the monolayer of nonelectroactive polyalanine. The curve was recorded in 1 M KOH (Reprinted with permission from Sek et al. [50]. Copyright (2005) American Chemical Society)

Fig. 8 Example of chronoamperometric data from a double-step experiment. After a potential step, the current decays with time. Q represents the total charge that has passed to fully oxidize or reduce the surface species (Reprinted with permission from Eckermann et al. [45]. Copyright (2010) Elsevier)



symmetrically around the formal potential of the redox center (Fig. 8). For example, if the E^0 of the redox center is 0.4 V, the first and second applied potentials would be +0.45V and 0.35 V. The potential limits of the electrolyte and electrode must be taken into account when setting the potential limits. Importantly, the initial potential should be chosen such that all redox centers are in the same oxidation state.

An important aspect is the delay of time between potential steps, which must allow for the measurement of the complete current decay. For accurate measurements, the time must be long enough for the faradic current to be separated from the charging current (the initial current spike). High charging currents are generated initially and decay with time and can therefore be temporally separated from the faradic response as long as the time constant for the charging current is smaller than the rate constant for the faradic current. Large potential steps can lead to charging currents much larger than the faradic currents, complicating data analysis. The appropriate time must be determined experimentally by observing the time it takes for the current to return to baseline levels.

The measured current and applied potential vs. time are required data for rate analysis. The overpotential (η) should be corrected for i_R drop. The solution resistance, R_s , can be determined using electrochemical impedance spectroscopy (section “[Electrochemical Impedance Spectroscopy](#)”):

$$\eta(t) = E(t) - E_0 - i(t)R_s \quad (19)$$

The total current i_T is the sum of the faradic and the charging current (i_f and i_{ch} , Eq. 20). The charging current i_{ch} can be determined as in Eq. 21. C_{DL} can be determined using electrochemical impedance spectroscopy (section “[Electrochemical Impedance Spectroscopy](#)”):

$$i_T(t) = i_f(t) + i_{ch}(t) \quad (20)$$

$$i_{\text{ch}}(t) = C_{\text{DL}} \left(\frac{\Delta\eta}{\Delta t} \right) \quad (21)$$

The total charge passed, Q_{T} , can be obtained by integrating the faradic current over the total time as in Eq. 22:

$$Q_{\text{T}} = \int i_{\text{f}}(t) dt \quad (22)$$

The charge remaining at any given time t is derived from Eq. 23:

$$Q(t) = Q_{\text{T}} - \int_0^t i_{\text{f}}(t) dt \quad (23)$$

Finally, the apparent rate constant at a given time k_{APP} is calculated as shown in Eq. 24:

$$k_{\text{APP}}(t) = \frac{i_{\text{f}}(t)}{Q(t)} \quad (24)$$

The rate as a function of time, $k_{\text{APP}}(t)$, may be used rather than rate as a function of overpotential, $k(\eta)$, due to kinetic heterogeneity. A simple way to determine if a distribution of kinetic sites is present is to plot $\ln(i)$ vs. time. If this plot is curved rather than linear, then kinetic heterogeneity must be considered [52]. An experimental Tafel plot can be generated by plotting each overpotential against the measured $k_{\text{APP}}(t)$.

Another method to analyze CA measurements is described by Finklea [53]. In interfacial electron-transfer reactions between the surface-bound redox group and the metal, the current i decays exponentially with time following the equation:

$$i = i_0 \exp(-k_{\text{ET}}t) \quad (25)$$

Where i_0 and k_{ET} represent the current at $t=0$ and the electron-transfer rate constant. In general, following the capacitive response, a linear relationship between $\ln(i)$ and t may be obtained, from which it is possible to determine the electron-transfer rate constant [54]. By plotting the ET rate constants vs. positive and negative overpotentials, a Tafel plot may be obtained, from which the k_{ET}^0 value may be determined. Furthermore, asymmetry in the Tafel plot may be an indication of the helical macrodipole effect on the ET rate constants, for peptides in helical conformation [86, 50, 54] (Fig. 9).

AC Voltammetry

Alternating current (AC) voltammetry is similar to cyclic voltammetry, meaning that it is a potential sweep method [46]. A starting potential and ending potential are selected, and the corresponding current is measured. In addition to that, a sinusoidal component AC (the frequency of which can be varied) of about 5 mV peak-to-peak amplitude is superimposed on the potential waveform (Fig. 10a). The measured

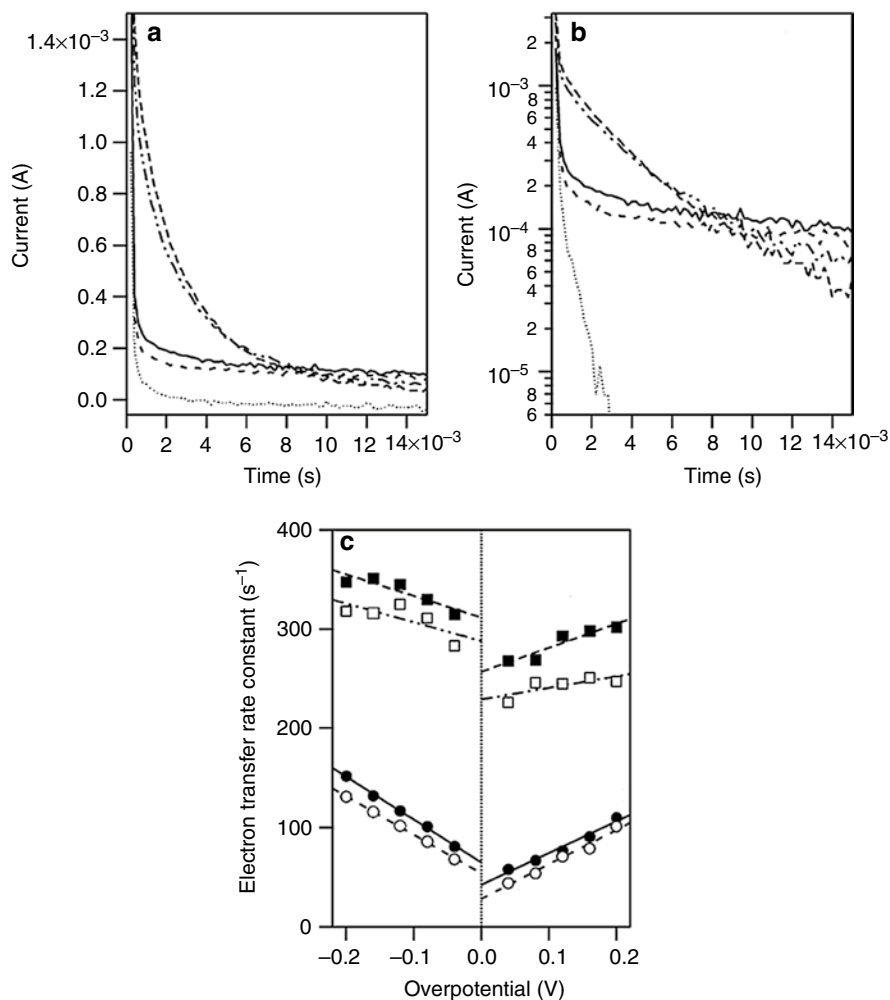
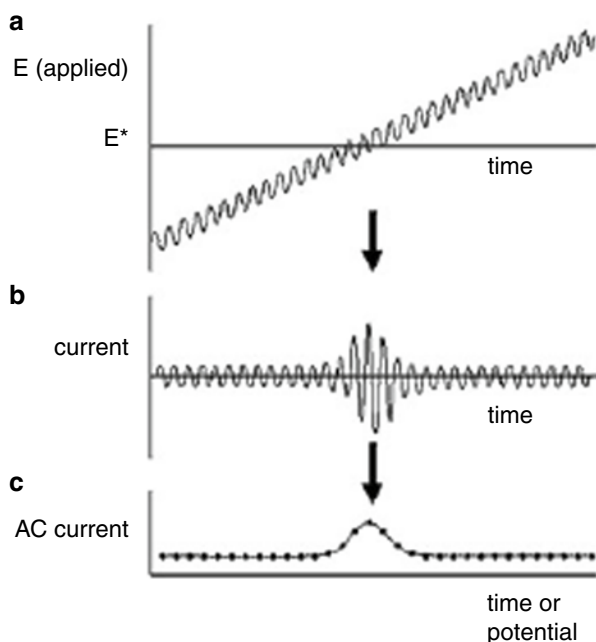


Fig. 9 Results in chronoamperometry of several ferrocene-containing helical peptide SAMs: (a) i - t curves of the helical peptide SAMs at an overpotential of 0.04 V, (b) its semilog plots, and (c) dependence of electron-transfer rate constants on overpotentials for the electron-transfer between the ferrocene moiety and gold in helical peptide SAMs. Also the capacitive response of a ferrocene devoid peptide is reported for comparison (Reprinted with permission from Watanabe et al. [54]. Copyright (2005) American Chemical Society)

response is the resulting alternating current (Fig. 10b), but the electrochemical response appears as a single peak, since a lock-in amplifier or frequency response analyzer allows the component of the current (which is varying sinusoidally) to be separated from the dc signal. Passing the signal above through the lock-in amplifier provides the magnitude of the change over each cycle, as shown in Fig. 10c.

The electron-transfer rate constants (k_0) for immobilized redox centers may be obtained using the treatment proposed by Creager and Wooster [55]. This method

Fig. 10 (a) AC voltammetry wave form showing the oscillating component of the potential sweep (E vs. time), (b) the measured current signal vs. time, and (c) the data representation, AC current vs. potential (Reprinted with permission from Eckermann et al. [45]. Copyright (2010) Elsevier)



involves plotting the ratio of the AC voltammetric peak current (i_p) to the background current (i_b) as a function of the logarithm of frequency (Fig. 11) and then fitting the plot using the complex nonlinear least-squares (CNLS) method of MacDonald and Potter [57].

The magnitudes of the fitted circuit elements may be used to calculate the ET rate constant using the Randles equivalent circuit model [56]. This circuit (Fig. 11) is one of the simplest models for describing ET of a redox species attached to a monolayer. It includes a solution resistance (R_s), a double-layer capacitance (C_{DL}), a charge-transfer resistance (R_{CT}), and an adsorption pseudocapacitance (C_{AD}). The double-layer capacity is in parallel with the impedance, due to the charge-transfer reaction, and C_{DL} reflects the order of the monolayer and its permeability toward electrolyte ions and solvent molecules [58].

The only variables needed for determining k_{ET} are the double-layer capacitance (C_{DL}), the charge-transfer resistance (R_{CT}), electrode surface area (A), and surface coverage Γ . Γ is measured independently using Eq. 13. The four parameters in the Randles circuit are given by Eqs. 26–29:

$$C_{DL} = \left(\frac{C}{A} \right) A \quad (26)$$

$$C_{AD} = \frac{\Gamma A F^2}{4RT} \quad (27)$$

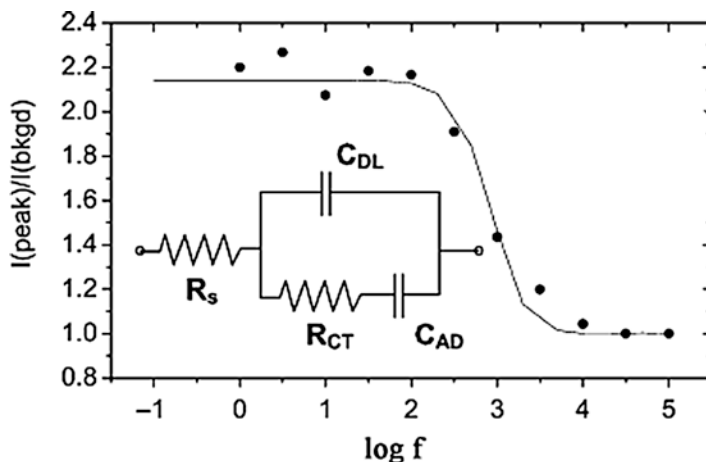


Fig. 11 Plot of I_p/I_b vs. $\log(\text{frequency})$ for a mixed monolayer consisting of a ferrocene-labeled peptide and $\text{CH}_3(\text{CH}_2)_8\text{-SH}$. Points represent experimental data. The solid line is calculated using the Randles equivalent circuit model shown above. C_{DL} is the double-layer capacitance, C_{AD} is the adsorption pseudocapacitance, R_s is the solution resistance, and R_{CT} is the charge-transfer resistance expressed as $R_{CT} = (2RT)/(F^2\Gamma k_{ET})$. (Reprinted with permission from [56] Sek et al. [56]. Copyright (2004) American Chemical Society)

$$R_s = \frac{1}{4\pi \cdot r_0 k} \quad (28)$$

$$R_{CT} = \frac{4RT}{F^2 A \Gamma k_{ET}} \quad (29)$$

Different articles have appeared that take advantage of this approach to measure k_{ET} in peptide SAMs [47, 56, 59, 60]. There are several advantages of using this method to determine k_{ET} . First, the input variables (C_{DL} , Γ , A , R_s) are easily obtained from impedance spectroscopy or cyclic voltammetry measurements. Second, due to the high sensitivity of the AC voltammetry method, very low surface coverages can be probed. The disadvantage of this approach is that only k_{ET} can be obtained; no information regarding electronic coupling or reorganization energy can be obtained.

Electrochemical Impedance Spectroscopy

Electrochemical Impedance Spectroscopy (EIS) measures the frequency response of a system by measuring impedance, Z [46]. The impedance is a measure of the ability of a circuit to resist the flow of electrical current, and it is usually measured by applying a small alternated current signal over a range of frequencies at a specified potential to an electrochemical cell and then measuring the current through the cell.

By applying a sinusoidal potential excitation, the corresponding current response is an AC signal. Electrochemical impedance spectroscopy is in general measured using a small excitation signal, so that the cell's response is pseudo-linear. In that case, the current response is a sinusoid at the same frequency, but shifted in phase (see Fig. 12).

The excitation signal, expressed as a function of time, has the form

$$E_t = E^0 \sin(\omega t) \quad (30)$$

where E_t is the potential at time t , E^0 is the amplitude of the signal, and ω is the radial frequency. In a linear system, the response signal, I_t , is shifted in phase (ϕ) and has a different amplitude, I^0 :

$$I_t = I^0 \sin(\omega t + \phi) \quad (31)$$

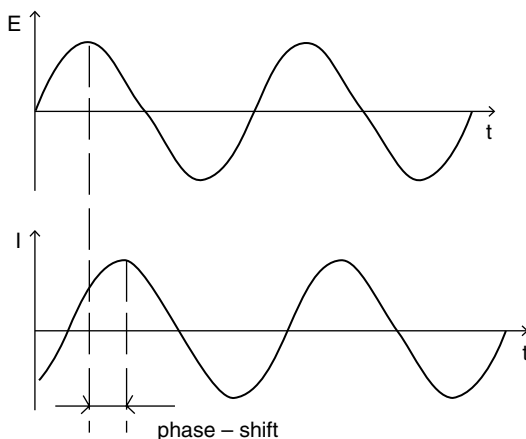
An expression analogous to Ohm's law allows to calculate the impedance of the system as

$$Z = \frac{E_t}{I_t} = \frac{E_0 \cos(\omega t)}{I_0 \cos(\omega t - \phi)} = Z_0 \frac{\cos(\omega t)}{\cos(\omega t - \phi)} \quad (32)$$

The impedance is therefore expressed in terms of a magnitude, Z_0 , and a phase shift, ϕ , and it may be expressed as a complex function, where ω is the angular frequency of the AC signal:

$$Z(\omega) = Z_0 (\cos(\omega t) + i \sin(\omega t)) = Z_{\text{Re}} - iZ_{\text{Im}} \quad (33)$$

Fig. 12 Sinusoidal current response in a linear system



A variation in the frequency value changes the relative contribution of each of the elements in the Randles circuit to the overall impedance. For that reason the impedance values are measured over a wide range of frequencies, in order to determine the value of each individual element of the Randles circuit.

R_S and R_{CT} only contribute to the real component of impedance (Z_{Re}). A resistor has no effect on the phase, ϕ , between the voltage and current, so across R_S and R_{CT} , voltage and current remain in phase (Fig. 13). As shown in Fig. 13, the voltage lags the current by 90° across a capacitor, so the voltage and current are out-of-phase across C_{DL} and C_{AD} . As such, C_{DL} and C_{AD} contribute to the out-of-phase or imaginary component of impedance (Z_{Im}) [46].

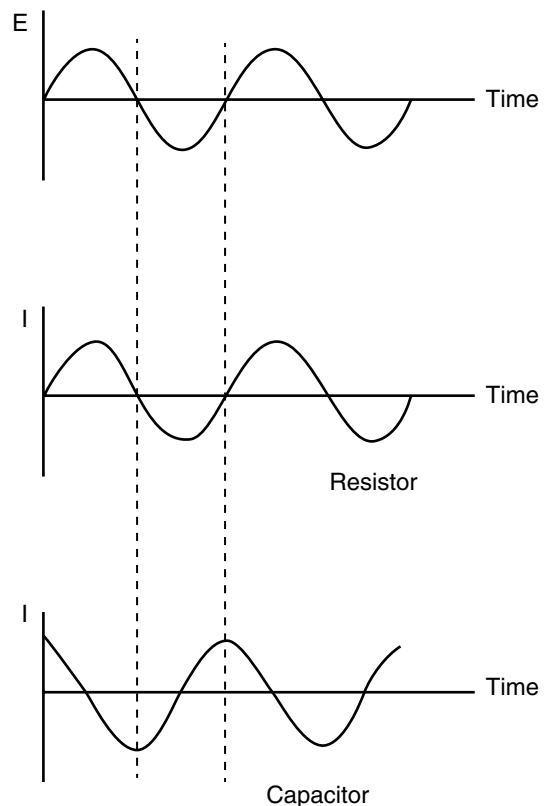
In general, the amount of the impedance (Z) in complex form is given by Eq. 34:

$$Z = \sqrt{Z_{Re}^2 + Z_{Im}^2} \quad (34)$$

The phase of the impedance (ϕ) in complex form is given by Eq. 35:

$$\phi = \tan^{-1} \left(\frac{Z_{Im}}{Z_{Re}} \right) \quad (35)$$

Fig. 13 Scheme showing the effect of a resistor and a capacitor on the phase (ϕ) of an alternating current (I) with respect to the voltage (E). For a resistor, current and voltage are in phase. For a capacitor, voltage lags current by 90° (Reprinted with permission from Eckermann et al. [45]. Copyright (2010) Elsevier)



Electrochemical impedance spectroscopy data are generally plotted in one of two ways: a Bode plot or a Nyquist plot [46]. In Bode plots, $\log |Z|$ (from Eq. 34) and ϕ (from Eq. 35) are both plotted vs. $\log(\omega)$ [46]. In Nyquist plots (also defined as complex-plane impedance plots), the imaginary axis, Z_{Im} , is plotted vs. the real axis, Z_{Re} , for different values of ω . Each point of the plot is the impedance at one frequency. For data analysis, Nyquist plots are much more frequently used than Bode plots.

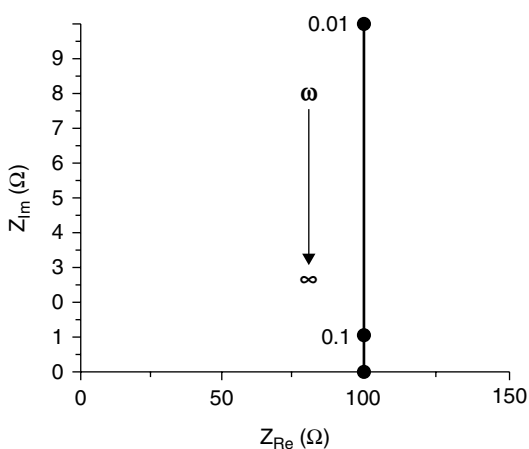
When a potential is chosen so that no ET occurs (i.e., away from the E^0 of the redox species of the monolayer), the faradic component of the Randles circuit would not be considered [55]. Only R_S and C_{DL} , connected in series, are considered, and the impedances are additive. At high frequencies ($\omega \rightarrow \infty$) there is no time for C_{DL} to charge, and the curve approaches the Z_{Re} axis at R_S . As the frequency decreases there is more time for C_{DL} to charge, and, at low frequencies ($\omega \rightarrow 0$), the main contribution to the impedance is from C_{DL} . In this case the Nyquist plot appears with a vertical line, because the impedance contribution from R_S is not affected by the frequency (Fig. 14).

When a potential where ET occurs is chosen (i.e., at or near the E^0 of the redox species inserted into the monolayer), the entire Randles circuit is considered. The additional R_{CT} and C_{AD} contributions to the impedance complicate the equation representing the Nyquist plot. At high frequencies, the plot has the shape of an ellipse [55, 61]. As $\omega \rightarrow \infty$ there is no time for ET to occur (R_{CT} and C_{AD} become negligible), and there is no time for C_{DL} to charge. Thus, as $\omega \rightarrow \infty$ the high-frequency portion of the ellipse approaches the R_S value at the Z_{Re} axis.

Equation 36 shows which is the center of the ellipse situated on the real axis:

$$\text{Ellipse}_{\text{center}(Z_{\text{Re}})} = R_S + \frac{R_{\text{CT}}}{2 \cdot \left(1 + \frac{C_{\text{DL}}}{C_{\text{AD}}}\right)^2} \quad (36)$$

Fig. 14 Example of a Nyquist plot for a series circuit containing only R_S (100 Ω) and C_{DL} . The vertical line on the right approaches the Z_{Re} axis at R_S as $\omega \rightarrow \infty$ (indicated by the arrow). For reference, points are shown at $\omega=0.01$ and 0.1 (Reprinted with permission from Eckermann et al. [45]. Copyright (2010) Elsevier)



Equation 37 shows the maximum of the ellipse on the Z_{Im} axis is

$$\text{Ellipse}_{\max(Z_{\text{Im}})} = \frac{R_{\text{CT}}}{2 \cdot \left(1 + \frac{C_{\text{DL}}}{C_{\text{AD}}}\right)} \quad (37)$$

As shown in Eq. 38, the point at which the ellipse would cross the Z_{Re} axis at low frequency ($\omega \rightarrow 0$) is

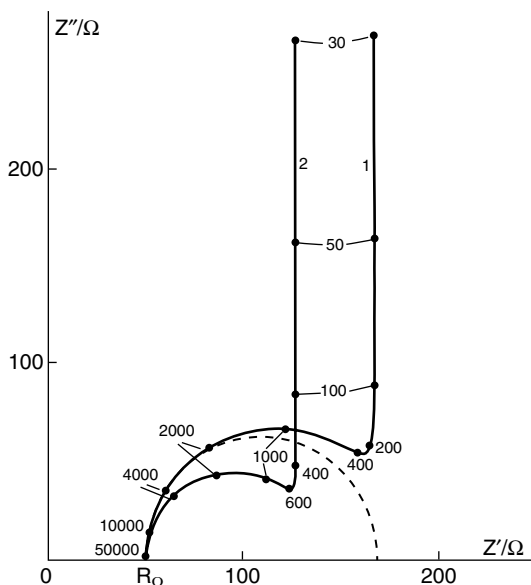
$$\text{Ellipse}_{\text{Low}(\omega)(Z_{\text{Re}})} = R_{\text{S}} + \frac{R_{\text{CT}}}{\left(1 + \frac{C_{\text{DL}}}{C_{\text{AD}}}\right)^2} \quad (38)$$

However, at low frequencies, the Nyquist plot ellipse never approaches the Z_{Re} axis. Instead, the plot becomes a vertical line with an increasingly large Z_{Im} component, as the C_{DL} and C_{AD} contributions dominate the impedance. If the vertical line continues to the Z_{Re} axis, the intercept would be at the same point where the ellipse would cross the Z_{Re} axis as $\omega \rightarrow 0$ (Eq. 38, Fig. 15).

In this case, R_{S} can be directly measured, but fitting programs, typically supplied with the potentiostat software, are typically used to determine the values of C_{DL} , C_{AD} , and R_{CT} . Once these parameters are known, k_{ET} can be determined using Eq. 39:

$$k_{\text{ET}} = \frac{1}{R_{\text{CT}} \cdot C_{\text{AD}}} \quad (39)$$

Fig. 15 Examples of a Nyquist plots for a Randles circuit for a redox species integrated into a monolayer. $R_{\Omega} = R_{\text{S}}$, $Z' = Z_{\text{Re}}$, $Z'' = Z_{\text{Im}}$, R_{S} is 50Ω , C_{DL} is $1 \mu\text{F}$, C_{AD} is $18.8 \mu\text{F}$, and R_{CT} is for (1) 133Ω and (2) 88.8Ω . The dashed line is the limiting ellipse for (1); this is what the plot would look like if C_{AD} were $0 \mu\text{F}$. See the text for descriptions of the partial ellipses and the vertical portion of the plots (Reprinted with permission from Laviron [61]. Copyright (1979) Elsevier)



A number of articles have appeared that take advantage of using EIS to measure k_{ET} in peptide SAMs [30, 59, 60, 62–64]. Electrochemical impedance spectroscopy experiments are very useful, as it is possible to measure several different parameters in one experiment. However, the nonideal behavior of the system under study may cause some problem. For example, nonideal behavior can dramatically modify the values obtained from analysis based on the Randles circuit model. In this case, in order to obtain accurate data, these non-idealities must be addressed. One way to do this is the use of additional circuit elements. For peptide SAMs, in general, a constant phase element (CPE) is added, which acts as a nonlinear capacitor and accounts for the inhomogeneity on the electrode surface [60, 62]. The lesser the film capacitance, the higher the film thickness or compactness. Higher-frequency power (n) indicates more order. The diameter of the semicircle in a Nyquist plot is the measure of the charge-transfer resistance (R_{CT}), which is inversely proportional to the ET rate. R_{SOL} is the interfacial resistance through the SAM, and although its correct nature is unknown, it has been a consequence of the orientation of the dipoles in the SAM structure [65].

Photocurrent Generation Measurements

Photocurrent generation (PG) measurements of peptide SAMs are in general carried out in an aqueous solution of Na_2SO_4 (0.1 M) containing an electron donor (in general triethanolamine, TEOA) or acceptor (in general methyl viologen (MV^{2+})), using the same three-electrode setup described in the other electrochemical measurements. The experiment consists in the measurement of the current generated after illumination of the SAM-covered working electrode with a high-power lamp (in general a xenon lamp). The lamp should be equipped with a monochromator, in order to select the excitation wavelength (Fig. 16). Generally, in the presence of an electron donor in solution, an electron-transfer (ET) process from the photoexcited chromophore to the gold surface is observed. If an electron acceptor is present in solution, the current direction is reversed, and the electron-transfer process occurs from the gold surface to the chromophore.

A typical time course of photocurrent upon photoirradiation of the peptide SAM at different wavelengths (15 nm bandwidth) in the presence of TEOA is shown in Fig. 17, where repeated on–off cycles of photoexcitation, each one 30 s long, are reported. To confirm that the chromophore inserted into the peptide is responsible of the current measured, in general, the action spectrum, i.e., the photocurrent response *vs.* the excitation wavelength, of the SAM is compared to the chromophore absorption spectrum. If they overlap, this demonstrates that the chromophore (chr) used is the photosensitizing species.

The mechanism of photoactivated generation of a cathodic current in an electrochemical cell with an electron acceptor in solution (methyl viologen (MV^{2+})) proceeds through the following steps (Fig. 18). Upon photoexcitation of the chromophore ($\text{chr} \rightarrow \text{chr}^*$), ET from the singlet excited state to MV^{2+} readily occurs (step I), followed by ET from gold to the chromophore radical cation (step II). The reduced viologen diffuses to the auxiliary electrode, and the transferred electron closes the circuit, giving rise to a net electronic current (step III).

Fig. 16 Schematic representation of the experimental setup for photocurrent generation experiments

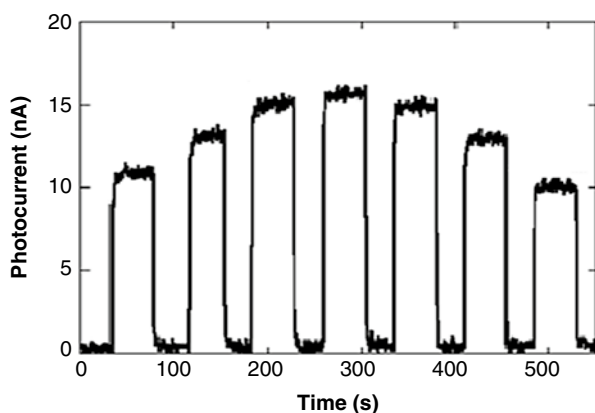
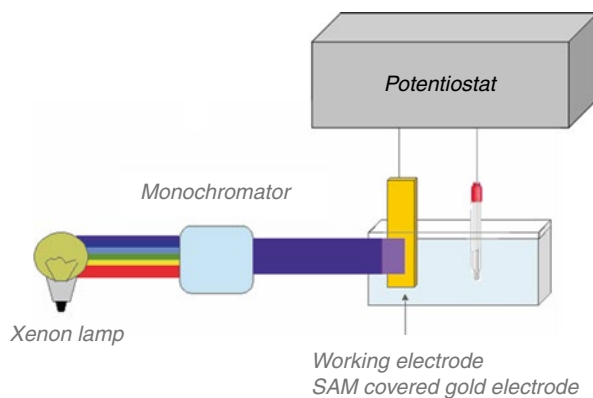


Fig. 17 Time course of the photocurrent of a bicomponent peptide SAM in an aqueous TEOA solution at 0 V vs. Ag/AgCl upon photoirradiation at different wavelengths (every 10 nm from 295 to 355 nm) (Reprinted with permission from Gatto et al. [51]. Copyright (2012) American Chemical Society)

In the presence of an electron acceptor in solution (TEOA 50 mM), an anodic current is measured, as a result of a $\text{chr}^* \rightarrow \text{Au}$ ET, followed by $\text{TEOA} \rightarrow \text{chr}^{2+}$ ET (Fig. 19).

The second step in cathodic and the first step in anodic condition most likely represent the rate-limiting steps of photocurrent generation, because of the long distance between the gold surface and the photoactive probe. In general the anodic photocurrent intensity decreases by decreasing the bias to the gold electrode, reaching a value of zero at a certain potential (zero current potential, zcp). A bias decrease reduces the energy gap between the oxidation potential of chr^* and the Fermi level of gold, resulting in a lower anodic photocurrent.

The efficiency of the process may be determined by the incident photon-to-current efficiency (IPCE), described by the following equation:

$$\text{IPCE}(\%) = \frac{100 \cdot i(\text{A} / \text{cm}^2) \cdot 1240}{I(\text{W} / \text{cm}^2) \cdot \lambda(\text{nm})} \quad (40)$$

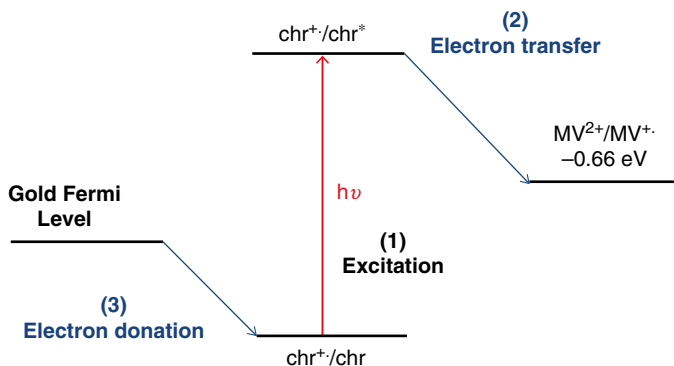
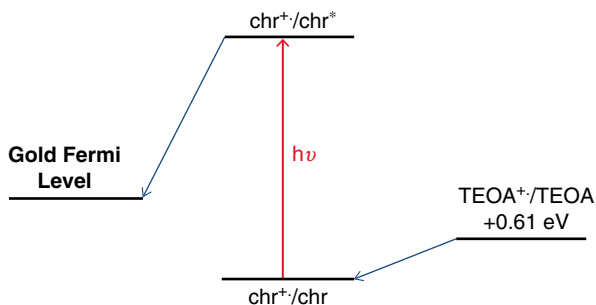


Fig. 18 Schematic illustration of cathodic photocurrent generation by a chromophore-containing peptide SAM in the presence of MV^{2+} . MV^{2+} reduction potential is referred to an Ag/AgCl reference electrode

Fig. 19 Schematic illustration of anodic photocurrent generation by a chromophore-containing peptide SAM in the presence of TEOA. TEOA oxidation potential is referred to an Ag/AgCl reference electrode



where i is the measured photocurrent, I is the incident light power density, and λ is the incident wavelength. The intensity of the incident light may be measured using a power meter or evaluated by azobenzene actinometry [66].

Peptide-Based SAMs

In general, peptides form tightly packed SAMs depending on their length and 3D structure. Typically, short peptides are very flexible; they populate several conformations, rapidly interconverting between the different conformers. For this reason, they form poorly packed films that show a large degree of inhomogeneity and have up to 15 % vacant gold sites [23]. On the contrary, longer helical peptides form ordered and densely packed films. However, not only the length of the peptide primary sequence but also the type of secondary structure attained by the peptide chains and the presence of aromatic groups in the molecules influence the order and packing of the corresponding SAM. We have recently demonstrated that also six-residue-long peptides possess very good self-assembly properties if they are folded in 3_{10} -helical

conformation, and that if they are functionalized with properly arranged aromatic chromophores, these properties can be extremely improved [44, 67, 68]. A marked restriction on the available ϕ , ψ space, constraining short peptides to populate helical conformations, may be imposed by using C $^{\alpha}$ -tetrasubstituted amino acids [69], thus conferring stability to peptide 3D structures and, consequently, making helical peptides good candidates as building blocks for the construction of self-assembled nanostructures. The most extensively used and investigated residue of this group is the α -aminoisobutyric acid (Aib, also known as 2-methylalanine).

Furthermore, it is well known that helical peptides have a large macrodipole moment (3.5 D per residue, [70]) which is oriented parallel to the molecular axis (directed from the C- to the N-terminus). In protein organization and function, where helical segments aggregate to populate supramolecular structures, this can have a great impact. For this reason, also the SAM package can be influenced by the direction of the molecular dipole moment. Furthermore, it has been demonstrated that the direction of the electron-transfer processes is influenced by this parameter. Indeed, several papers demonstrated that electron-transfer (ET) processes occur more rapidly from the C- to N-terminus direction than along the opposite direction, both in solution [21, 22, 87] and on surface [50, 71, 84]. Moreover Miura et al. [72] reported important surface potentials for oriented polypeptide SAMs.

Electrochemistry of Peptide-Based SAMs

Electrochemical techniques have been widely used to investigate the kinetics of electron-transfer through self-assembled monolayers (SAMs) of molecules linked to gold surfaces through a gold–thiolate bond [45]. SAMs can serve as useful model systems for studying the kinetics of mediated electron-transfer. In particular conformationally constrained peptides are ideal candidates for ET studies, since they possess a well-defined rigid secondary structure and can serve as starting point for a comprehensive study of the influence of peptide secondary structure on ET rates.

The first report in this field appeared in 2002 [73], where Galka and Kraatz synthesized and characterized a series of ferrocenoyl–oligoproline–cystamines [Fc–Pro $_n$ –CSA] $_2$ ($n=0-6$) in order to study the influence of peptide secondary structure on ET rates. Oligoprolines are good candidates to do that, since they possess a defined secondary structure (polyproline II, 3.1 Å per proline residue). They immobilized these systems on gold microelectrodes and characterized them by cyclic voltammetry. Each peptide SAM exhibited a well-defined and fully reversible one-electron oxidation. The linear relationship between the peak currents and the sweep rates indicated that the Fc-peptides were surface bound, while from the integration of the oxidative peaks they evaluated the mean molecular area.

They obtained ET rates from the cyclic voltammograms at variable scan rates by the Butler–Volmer formalism. These values are reported in Fig. 20, as a function of the length of the peptide spacer. Although they observed an exponential decrease with increasing number of proline residues, the decrease was less pronounced than expected for the Marcus through-space electron-transfer mechanism, suggesting a through-bond mechanism.

Fig. 20 Dependence of the electron-transfer rate on the length of the oligoproline spacer. Curve fit: $k_{ET} = 15.8886 \exp(-0.1175x)$ for k_{ET} [$=10^{-3} \text{ s}^{-1}$] and d (\AA), correlation $R^2=0.9994$ (Reprinted with permission from Galka and Kraatz [73]. Copyright (2002) Wiley)

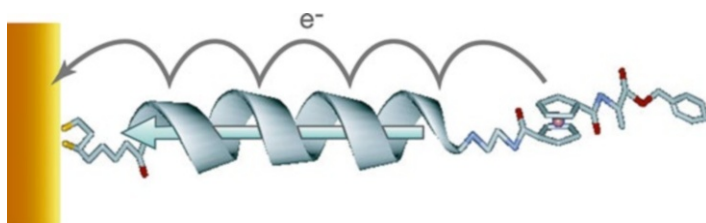
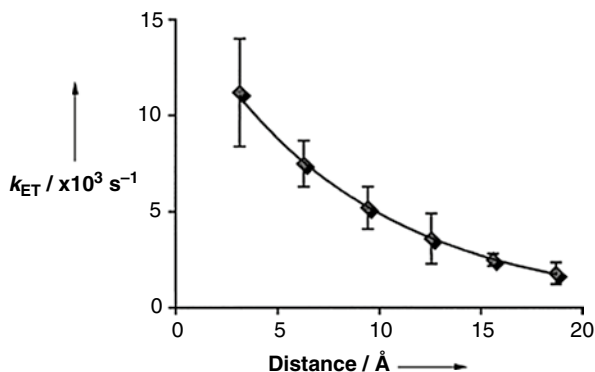


Fig. 21 Schematic illustration of the helical peptide on gold surface, studied by [74] (Reprinted with permission from Morita and Kimura [74]. Copyright (2003) American Chemical Society)

The experimental β value was 0.12 \AA^{-1} , which was much lower than the one estimated for proteins in this secondary structure, but very similar to the one obtained for a very similar proline-based peptide systems by pulse radiolysis, where a combined through-space and through-bond mechanism was proposed.

One year after, Kimura and Morita studied 16-residue-long helical peptides [74]. The peptides were composed of eight (Leu-Aib) repeating unit, with a lipoic acid to bind gold surfaces and a ferrocene electrochemical probe at the C-terminus (SSL16Fc) and N-terminus (FcL16SS), to evaluate the effect of the peptide macro-dipole on the electron-transfer process. Cyclic voltammetry experiments showed that the ferrocene was able to transfer one electron through the peptide bridge, even at a distance of more than 4 nm (Fig. 21).

Furthermore, by chronoamperometry measurements, they have been able to determine the electron-transfer rate constants for this process, the standard values being 0.68 s^{-1} for the FcL16SS and 2.0 s^{-1} for the SSL16Fc. These values were much larger than the calculated value of 0.003 s^{-1} , obtained by assuming a pure superexchange mechanism. The calculation was carried out using an exponential decay as function of the peptide length:

$$k_{ET} = k_{ET}^0 \exp(-\beta_A n_A - \beta_B n_B - \beta'_C d'_C)$$

k_{ET}^0 represents the preexponential factor, β_A and β_B are the tunneling constants per atom number, and n_A and n_B are, respectively, the atom number of the methylene chain and amide group not involved in the peptide chain. k_{ET}^0 , β_A , and β_B were taken to be $3 \cdot 10^8 \text{ s}^{-1}$, 1.2, and 0.5, respectively [75]. β'_C is the tunneling constant per length for the helical peptide chain, and it was reported to be 6.6 nm^{-1} [11], $n_A=7$, $n_B=2$, and $d_C=2.4 \text{ nm}$ (0.15 nm for each residue in helical conformation). Furthermore, the difference found for the standard electron-transfer rates in the N- or C-terminal ferrocene-bound peptides suggested that the positive partial charge at the N-terminal of the helical peptide in the SSL16Fc should have lowered the barrier height at the interface between the gold and the peptide layers. The same asymmetry of electron transmission through helical peptides monolayers on gold surfaces was found by Bilewicz and coworkers [50]. They studied the electrochemical properties of monolayer-modified electrodes by cyclic voltammetry and impedance spectroscopy. In particular, they have studied a polyaniline peptide, containing a cysteamine linker and a ferrocene electrochemical probe. For electrochemical measurements, they have prepared a two-component electroactive SAM, containing 0.05 mM of peptide diluted into 0.95 mM of octadecanethiol. From cyclic voltammetry measurements performed in HClO_4 supporting electrolyte, the signal corresponding to the one-electron redox process of the Fc/Fc^+ couple was clearly visible. They found a linear relationship between the peak current and the scan rates, indicating that the electron-transfer process originates from the surface-bound redox center. From the area of the cyclic voltammetric peak corresponding to the oxidation of ferrocene centers, they found a surface coverage of poly(L-alanine) peptide of $7.4 \cdot 10^{-12} \text{ mol}/\text{cm}^2$. As the maximum coverage for this peptide was estimated to be $3.1 \cdot 10^{-10} \text{ mol}/\text{cm}^2$, the electroactive component within the monolayer was calculated to be 2 %.

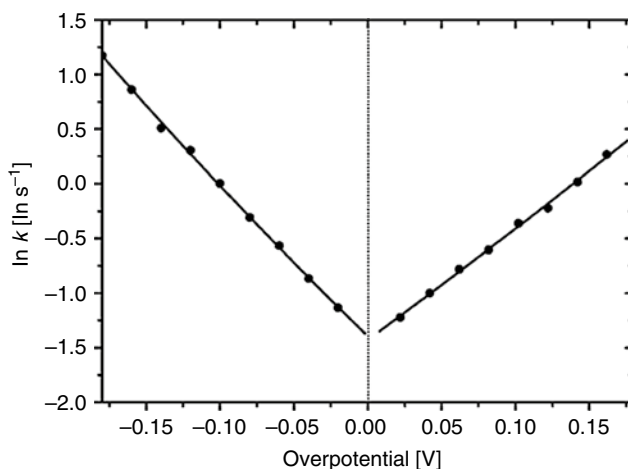


Fig. 22 Tafel plot at low overpotentials obtained for mixed SAMs of electroactive polyaniline and *n*-octadecanethiol (Reprinted with permission from Sek et al. [50]. Copyright (2005) American Chemical Society)

From cyclic voltammetry they also determined the electron-transfer rate constants by the Butler–Volmer formalism, from which they built a Tafel plot (Fig. 22). By extrapolating of $\ln k$ to zero overpotential, the standard rate constant for electron-transfer through poly(L-alanine) was found to be $k^0 = 0.30 \pm 0.08 \text{ s}^{-1}$. From this value, by knowing the peptide length (28.5 Å), they calculated a tunneling coefficient of $0.73 \pm 0.01 \text{ Å}^{-1}$.

The asymmetry of the Tafel plot, where at a given absolute value of overpotential the k_c were higher than the k_a , was ascribed to the helical macrodipole, which favored the reduction process (negative overpotentials), where the electron-transfer direction was from the C-terminal to the N-terminal (see Fig. 23).

The average ratio of cathodic and anodic rate constants k_c/k_a was 1.43 ± 0.07 . This value was not as large as that observed in solution by time-resolved measurements for dichromophoric α -helical peptides ([21, 22] in this case the ratio ranged from 5 to 27).

The same result was obtained by us some years after [86], studying a hexapeptide, in a 3_{10} -helical conformation. The system studied was composed of three Aib, two Ala, and a 2,2,6,6-tetramethylpiperidine-1-oxyl-4-amino-4-carboxylic acid (TOAC) residues. TOAC is characterized by a nitroxide group, a stable radical species that endow the molecule with peculiar redox activity. For this reason, TOAC has been extensively used as a probe in electron spin resonance and fluorescence studies. Cyclic voltammetry experiments performed at various sweep rates (Fig. 24a) showed that the oxidative peak current, as obtained by subtraction of background current from the oxidative peak current, linearly increased with the scan rate (Fig. 24b). This result supported the idea that the observed redox peak arose from the surface-bound TOAC moiety, because according to Fick's law, for a diffusion-limited process, a dependence on the square root of the scan rate would have been observed. Some diffusion of the peptide TOAC moiety to the gold surface by bending motions of the peptide chain was also ruled out, because conformationally constrained helical peptides have a rigid cylindrical structure in a well-packed monolayer. The measured standard potential (0.60 V vs. SCE) was very similar to that determined in solution, suggesting that the peptide layer caused only a

Fig. 23 Scheme illustrating directional dependence of electron-transfer through polyaniline derivative (Reprinted with permission from Sek et al. [50]. Copyright (2005) American Chemical Society)

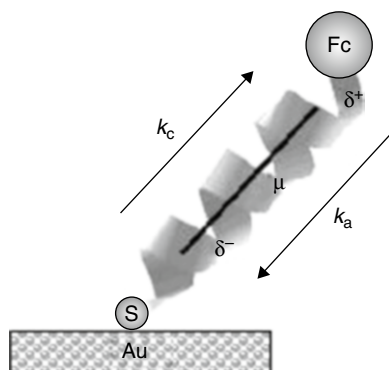
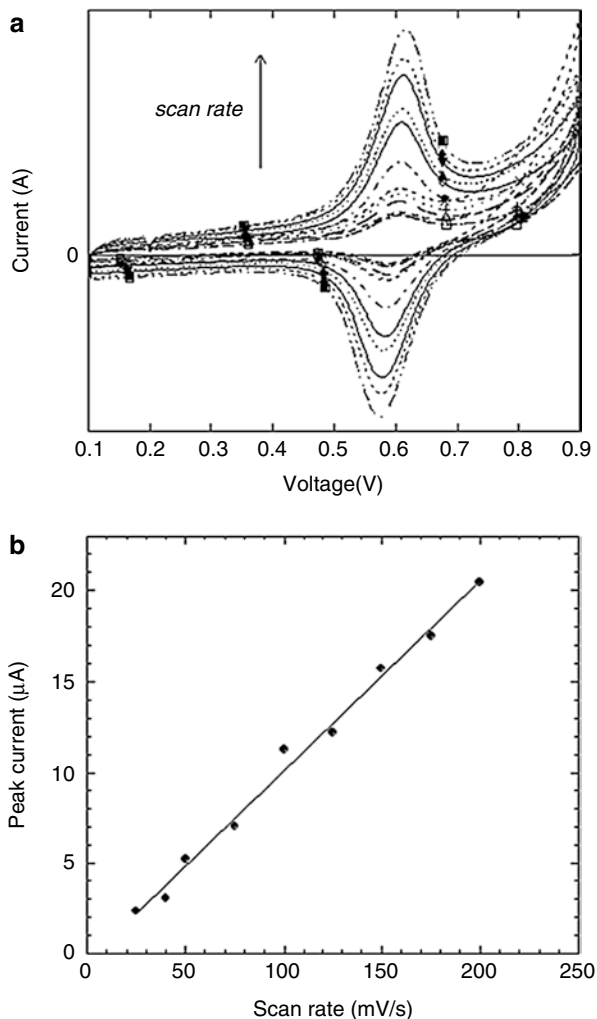


Fig. 24 (a) Cyclic voltammograms of the helical peptide SAM reported by [87], in a 0.2 M NaClO₄ ethanolic solution at a range of sweep rates. (b) Linear dependence of the oxidative peak currents on scan rates in the same helical peptide SAM



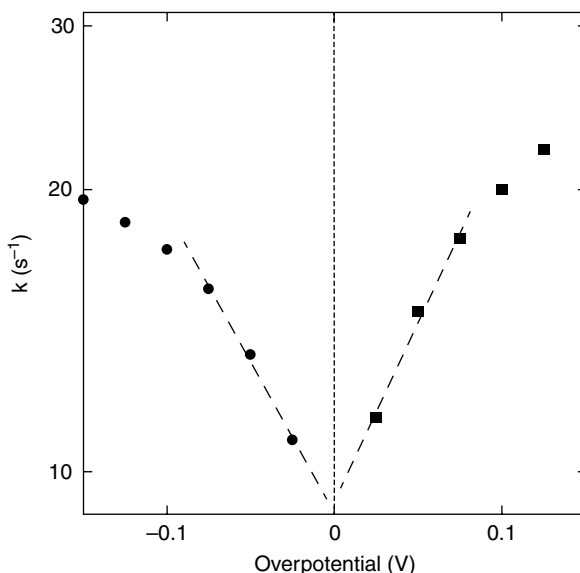
relatively small interfacial potential drop. At sufficiently slow scan rates, i.e., under reversible condition, typically 0.1 V/s or slower, the cyclic voltammograms of the monolayer were ideal: peak splittings (ΔE_p) were very small (0 V within experimental uncertainty ± 4 mV) and the peak half-width was 90 mV. This meant that all the redox centers were in a rather uniform environment, as that provided by an ordered film, even for a so short peptide. A disordered electroactive monolayer should have exhibited a set of formal potentials due to the varying dielectric constant around the redox centers.

From the slope of I_p vs. v , a surface coverage of $14.4 \cdot 10^{-11}$ mol/cm² was obtained, in good agreement with that estimated by assuming closely packed 3_{10} -helical peptide, not vertically oriented. In order to characterize the electron-transfer process from TOAC to the gold electrode, chronoamperometry experiments were carried out. The through-space distance from the electrochemical probe to the gold surface was estimated to be around 17 Å. This value was obtained by considering the lipoic acid in all-trans conformation and the peptide as a rigid 3_{10} -helix (2.0 Å rise per residue) tilted with respect to the normal surface by 40°, as suggested by IR-RAS measurements. Experimental I-t, i.e., current intensity vs. time, curves in the 2–200 μs time region were collected at positive (TOAC oxidation) and negative (TOAC⁺ reduction) overpotentials, as shown in the Tafel plot reported in Fig. 25.

Interestingly, also in this case, the corresponding Tafel plot showed that the k_{ET} values obtained in oxidative (anodic, k_a) conditions were always bigger than those obtained in reductive (cathodic, k_c) conditions. The electron-transfer standard rate constant extrapolated at zero overpotentials was $k_{ET}^0 = 9.2 \pm 0.1$ s⁻¹. This effect was attributed to the electrostatic field associated to the helix dipole, which favored anodic ET to the gold surface (in this case the peptide was bound at the N-terminal). Nevertheless, the ratio between the anodic and cathodic rate constants ($k_a/k_c = 1.19 \pm 0.05$) was found to be definitely smaller than that observed in α -helical peptides, probably because of the distorted H-bond pattern of 3_{10} -helix with respect to α -helix, giving a smaller molecular dipole, as theoretically supposed by Shin and coworkers [12].

The dipole moment effect on the electron-transfer rate constant was investigated by electrochemical methods also by Watanabe and coworkers [54]. They studied a

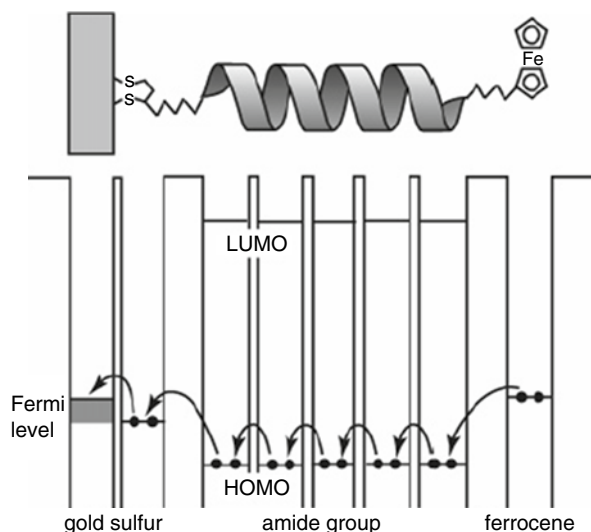
Fig. 25 Dependence of the ET rate constant on the applied overpotential (V) for TOAC oxidation (filled squares) and TOAC⁺ reduction (filled circles) at the gold electrode through the SSA4TA SAM (Reprinted with permission from Gatto et al. [86]. Copyright (2008) Wiley)



series of octadecapeptides carrying a ferrocene moiety and a sulfur-containing group at the respective terminals, in order to study the effect of dipole moment, linkers, and chromophores at the side chains, on long-range electron-transfer rate constants. An alternating sequence of *L*-alanine and α -aminoisobutyric acid in the main chain was interrupted by insertion of *L*-glutamic acid derivatives at two positions (5 and 14). To evaluate the effect of the first parameter (dipole moment), two peptides, differing only for the position of the ferrocene–lipic acid groups along the helix dipole, were studied: the SS18Fc peptide, with the disulfide group at the N-terminal, and the Fc18SS with the same group at the C-terminal. This caused the opposite direction of the dipole moment, when the peptides were immobilized on gold. By cyclic voltammetry and chronoamperometry experiments, they found that long-range electron-transfer over 40 Å occurred and that the ferrocene standard redox potential was independent of the dipole direction. Also in this case the electrostatic field of the helix dipole was found to affect the ET process ($k_{\text{ET}}=42 \text{ s}^{-1}$ for the peptide functionalized with ferrocenyl at the C-terminus, to compare with $k_{\text{ET}}=28 \text{ s}^{-1}$ for the N-terminus derivative).

Furthermore, a very weak dependence of the ET rates on the applied overpotential was found. This was again explained by a hopping mechanism through the amide groups in the helical backbone. Accordingly, they calculated the ET rate constants by assuming a pure SE mechanism (see section “Peptide Electron-Transfer Theory”), and they found that these values were order of magnitudes lower than those obtained by experimental data (i.e., 42 s^{-1} and 28 s^{-1} vs. 0.0005 s^{-1} for the two octadecapeptides investigated). Also in this case, the plausible hopping sites were suggested to be the amide groups, because of their regular arrangement and proximity (they are strongly electronically coupled). The carrier was considered to be a hole because the amide LUMO (-1.2 V) is so high that electron

Fig. 26 Energy diagram for the long-range electron-transfer from the ferrocene moiety to gold through the helical peptide through a hopping mechanism. The amide groups were suggested to be the hopping sites (Reprinted with permission from Watanabe et al. [54]. Copyright (2005) American Chemical Society)



injection from the HOMO (-5.1 eV) of ferrocene to the amide group was supposed to be very unlikely (Fig. 26).

Therefore, the overall ET was composed of three steps: from the ferrocene moiety to the nearest amide group (-6.5 eV), electron hopping among the amide groups, and electron-transfer to gold from the nearest amide group. This last process can be further divided into two processes: i) ET from the amide HOMO level (-6.5 eV) to the S-atom (-5.5 eV) and ii) ET from the S-atom to gold (-5.1 eV). To investigate the effect of the linker on the ET rates, two peptides having different linkers to connect the helical peptides to gold were analyzed. The substitution of a phenylene spacer to a methylene group fastened the ET rate constant from 42 s $^{-1}$ to 257 s $^{-1}$, suggesting the electron-transfer between the sulfur atom and the molecular terminal of the helical peptide to be the rate-determining step. As matter of fact, the same peptide system, but having two pyrenyl groups linked to the side chains of the glutamic acid residues, did not show an appreciable increase of the ET rate constants. This was explained considering that even if the two pyrenyl groups could facilitate electron-transfer through the peptide part, the rate-determining step was not electron hopping among the amide groups, but the electron-transfer localized near the gold surface. Based on these results, the authors predicted that the elongation of the peptide chain would not have severely reduced the electron-transfer rate. They demonstrate this finding some years after, with α -helical peptide self-assembled monolayers of 100 – 120 Å length [63, 64]. The peptide building blocks studied were composed of 4, 8, 16, 24, 32, and 40 consecutive Ala-Aib dyads, a lipico group at the N-terminus for immobilization on gold and a redox-active ferrocene unit at the C-terminus. They found that the tilt angle of the helices from the surface normal decreased as the chain was elongated, suggesting the helices to be more vertical (Fig. 27).

Blocking experiments performed in a ferrocyanide solution confirmed the well-packed properties of all the monolayers. Cyclic voltammetry experiments showed a reversible peak associated to the ferrocenium/ferrocene redox pair with a formal potential of 0.45 V for all the SAM analyzed, clearly demonstrating that ET across the peptide SAM over such long distances was possible, even for the longest peptide [64]. Standard ET rate constants were determined by EIS measurements. By plotting the $\log k_{ET}^0$ versus the film thickness determined by ellipsometric measurements, a nonlinear relationship was obtained, indicating that the electron-transfer was not solely governed by electron tunneling (Fig. 28a). They found instead a linear relationship between the inverse of the square root of k_{ET}^0 versus the film thickness (Fig. 28b), suggesting a hopping mechanism to be operative [76].

Theoretical calculation on the standard ET rate constants, able to perfectly reproduce the experimental data, showed that the hopping mechanism was dominant in all the SAMs, even for the shortest one. As far as the longest peptide was concerned, they found a wide variation in the k_{ET}^0 values over 2 orders of magnitude (0.1 – 10 s $^{-1}$). However, considering a pure superexchange tunneling mechanism, the ET rate constants should have had insignificant values (10^{-21} – 10^{-47} s $^{-1}$). For this reason this finding was taken as a strong evidence of a predominant hopping mechanism, where it is supposed that an electron was transferred from the N-terminal amide group to

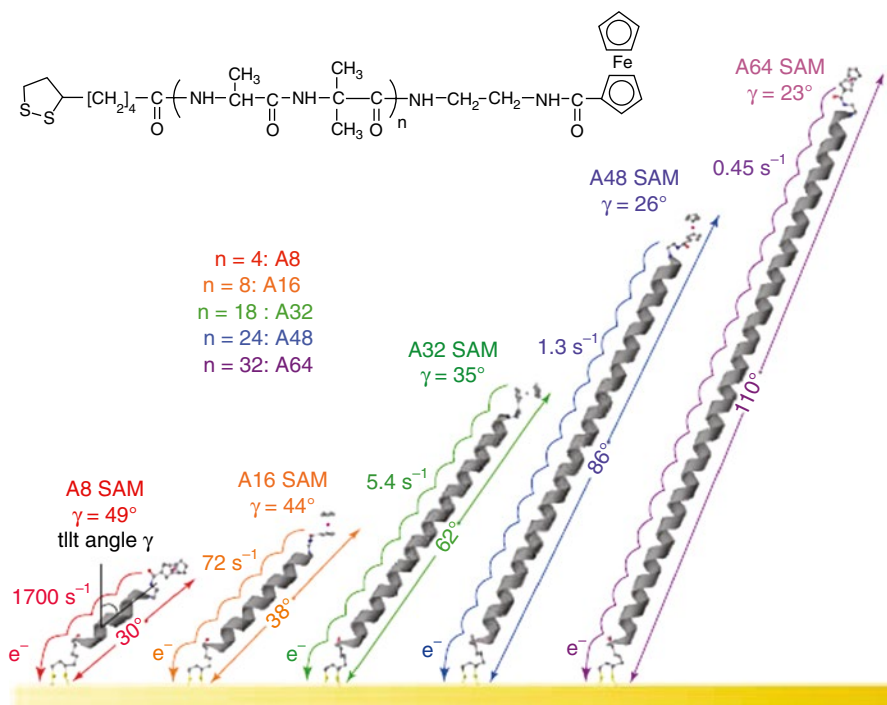
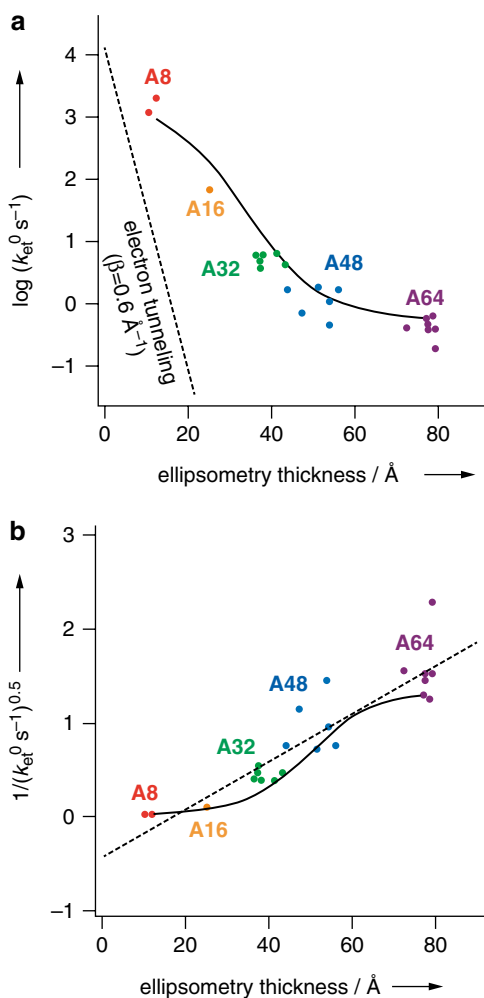


Fig. 27 Chemical structures and schematic illustration of the helical peptides studied by [63]. The helices represented as ribbons, and the other atoms are shown in a ball-and-stick format (Reprinted with permission from Arikuma et al. [63]. Copyright (2010) Wiley)

the gold surface, generating an amide cation radical (hole) that hopped through the amide groups to reach the C-terminus, which was at the end reduced from the ferrocene unit. Also temperature-dependent EIS measurements allowed to determine the k_{ET}^0 at different temperatures, from which it has been possible to determine the ET activation energies ($E_a=0.45\text{--}0.73$ eV). These values compared very well with the theoretical value of $E_a=0.63$ eV obtained supposing a hopping mechanism, while the value reported for the tunneling mechanism was 0.2 eV. The predominant mechanism was thought to be the intramolecular pathway, which is characterized by the hopping process across the amide sites of a single peptide chain. However, also other pathways, such as through-space intermolecular mechanism and HB-mediated ET, should have been considered. Interestingly, electrochemical impedance spectroscopy experiments indicated that as the capacitance increased, ET was accelerated, showing saturation at high capacitances. This finding suggested that the loose packing of the monolayer, due to the dynamics of some peptide chains, could positively affect the ET rate (*activated hopping* mechanism). The effect of structural fluctuations on the electron-transfer processes was firstly proposed by Kraatz and Mandal in 2006 [62]. In this contribution they have studied three

Fig. 28 Distance dependence of k_{et}^0 on the monolayer thickness. a) Plot of the logarithm of k_{et}^0 against the monolayer thickness (determined by ellipsometry). The filled circles represent the experimental data, the dotted line is the curve of electron tunneling considering a decay constant of 0.6 \AA^{-1} , while the solid line shows the result of calculations upon taking into consideration both the tunneling and hopping mechanisms. b) Plot of $(1/\sqrt{k_{\text{et}}^0})$ versus the monolayer thickness. The dashed line is the linear fit, and the solid line shows the result of calculations upon taking into consideration the tunneling and hopping mechanisms (Reprinted with permission from Arikuma et al. [63]. Copyright (2010) Wiley)



18-residue-containing peptides, all equipped with a cysteine sulfhydryl group to bind gold surfaces, one of them containing a ferrocene probe at the C-terminal (Fc18L). The other two peptides differed for the position of the Cys residue: Ac18L had it at the C-terminal, while 18Lac at the N-terminal. They prepared two kinds of films: one consisting of Fc18L and Ac18L (5:95), where the dipole moment of all the peptides was aligned parallel (SAM1), while the other (SAM2) was composed of Fc18L, Ac18L, and 18Lac (5:45:50), where the peptide dipole moment was antiparallely aligned (Fig. 29).

By IR-RAS measurements, they found that the SAM2 had a lower tilt angle, consistently with a more compact packing of the peptides, due to the antiparallel arrangement of intermolecular macrodipoles. Using cyclic voltammetry and

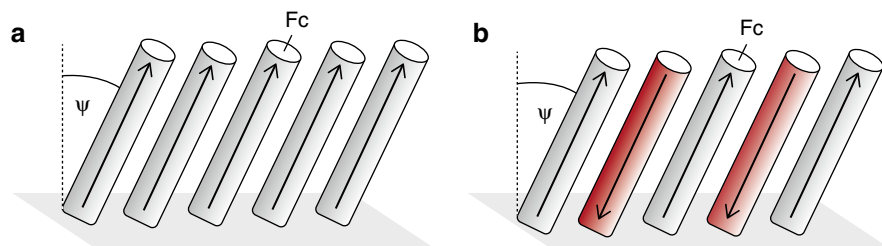


Fig. 29 Schematic depiction of peptide monolayers on gold surfaces, indicating the direction of the peptide dipole moments. (a) SAM1 and (b) SAM2 (Reprinted with permission from Wain et al. [77]. Copyright (2008) American Chemical Society)

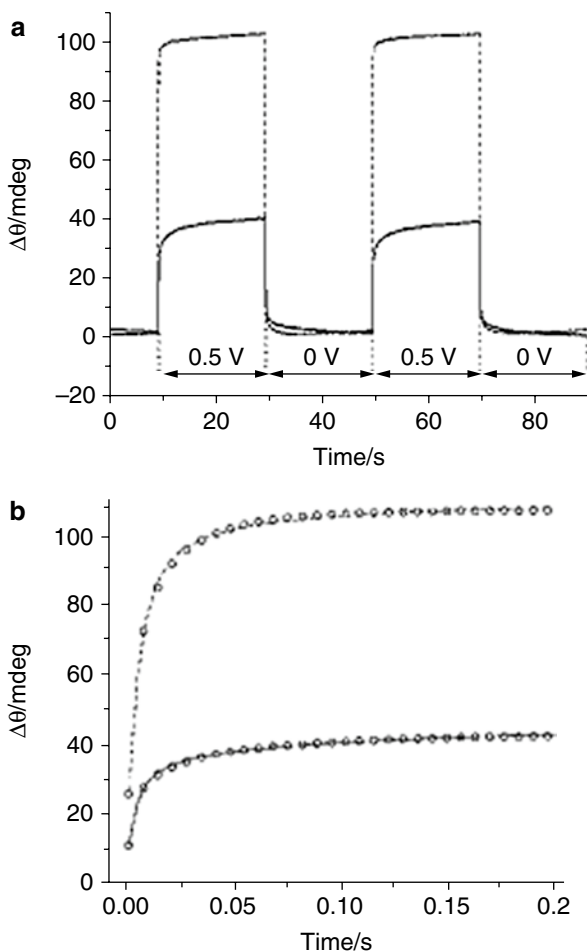
electrochemical impedance spectroscopy, it was found that ET kinetics were slower in the antiparallel (SAM2, $k_{\text{ET}} = 1.2 \cdot 10^{-3} \text{ s}^{-1}$) than in the parallel (SAM1, $k_{\text{ET}} = 1.5 \cdot 10^{-2} \text{ s}^{-1}$) dipole arrangement, which was ascribed to a more restricted motion due to stronger intermolecular interactions between opposing dipoles. EIS experiments confirmed this hypothesis, giving a R_{CT} and R_{SOL} values higher for the SAM2 if compared to one obtained with the SAM1. Thus, a gated ET mechanism was proposed, on the basis that the parallel dipole arrangement facilitates the ET between the gold surface and the Fc label.

Interestingly, the CPE value, which accounts for the film thickness, was lower for the SAM2, indicating higher film thickness or more compactness. The same group found some year after, by electrochemical surface plasmon resonance, that after ferrocene oxidation, SAM2 gave rise to a great change in the peptide film thickness due to the electrostatic repulsion between the electrogenerated ferrocenium moiety and the positively charged gold surface, while the greater permeability of SAM1 to electrolyte anions appeared to effectively neutralize this electrostatic repulsion [77]. Furthermore, by measuring SPR angular changes concomitant with potential steps, they have been able to determine the time scale for the redox-induced film reorganization event, estimating the time constants for the anodic process to be 16 and 6 ms for SAM1 and SAM2 (Fig. 30). These values indicated that the SAM thickness changes were fast.

In the same year, after the introduction of molecular motion-assisted ET mechanism, Takeda and coworkers proposed the occurrence of a molecular motion-assisted hopping mechanism [60].

By electrochemical techniques, they investigated the effects of different constituent amino acids, molecular packing, and molecular orientation, on long-range ET through helical peptide monolayers. In particular, they used helical peptides with a thiophenyl group at the N-terminus and a redox-active ferrocene moiety at the C-terminus, immobilized on gold electrodes. They studied two hexadecamer peptides, the primary sequence being composed of eight L-Leu-Aib and L-Ala-Aib repeats. ET rate dependence on the peptide sequence was studied by investigating ET from ferrocene to gold. The isobutyl side chain of Leu is much more bulky than the methyl, making the peptide backbone separation in the Leu-Aib SAM larger

Fig. 30 Time-resolved SPR response of SAM1 (solid line) and SAM2 (dashed line) during potential steps between 0 and 0.5 V vs. Ag/AgCl. **(a)** 20 s anodic and cathodic pulses. **(b)** Initial (0–200 ms) anodic response with data simulated using Eq. 1 and the parameters listed in Table 2 (circles) (Reprinted with permission from Wain et al. [77]. Copyright (2008) American Chemical Society)



than the separation obtained in the Ala-Aib SAM. However, the Leu-Aib peptide formed a tightly packed monolayer through interdigitation among the Leu side chains. CV, CA, and EIS measurements showed that ET was definitely slower in the Leu-Aib peptide SAM than in the Ala-Aib peptide SAM. The standard ET rate constants obtained from EIS experiments were $46 \pm 5 \text{ s}^{-1}$ vs. $603 \pm 289 \text{ s}^{-1}$, while those from CA experiments were $50 \pm 6 \text{ s}^{-1}$ vs. $889 \pm 300 \text{ s}^{-1}$. They prepared and characterized also three mixed monolayers wherein one component was the ferrocene-labeled Ala-Aib peptide and the others were three different peptides, having different lengths (8mer, 12mer, and 16mer) and lacking the ferrocene moiety. The bicomponent SAMs had opposite dipole moments when immobilized on gold (Fig. 31). The same electrochemical experiments, performed on the bicomponent Ala-Aib SAMs, suggested also that ET was accelerated as the monolayer became less packed. The monolayer regularity in terms of molecular orientation and packing was higher

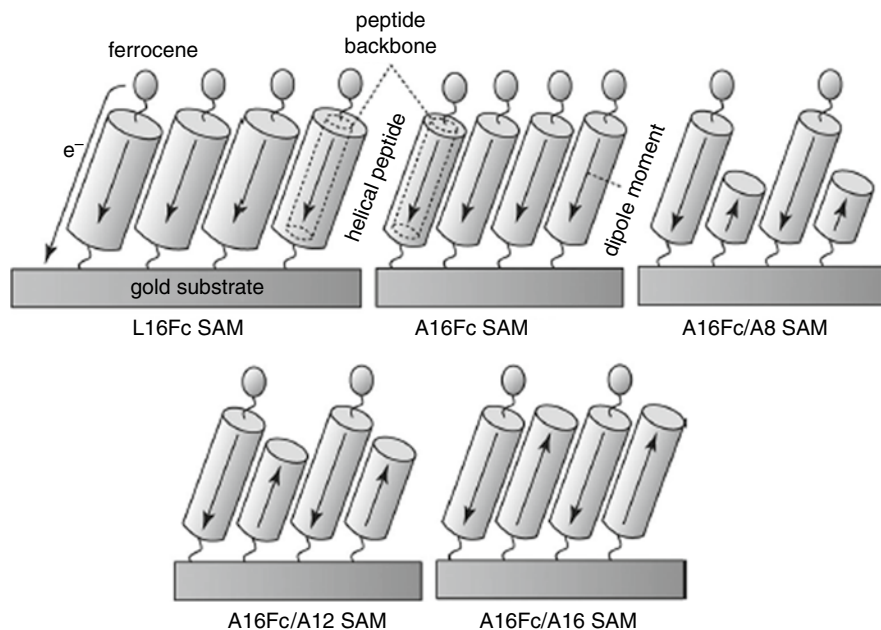


Fig. 31 Schematic illustration of the helical peptide SAMs studied by [60] (Reprinted with permission from Takeda et al. [60]. Copyright (2008) American Chemical Society)

roughly in the order of the monolayers mixed with 16mer > 12mer > no additive > 8mer, but the electron-transfer became faster in the opposite order.

A general conclusion was that more vertical orientation and tighter packing suppressed the electron transfer. Furthermore, the observed ET appeared to occur intermolecularly. In the case of the Leu-Aib peptides, the slower ET rates were interpreted as the result of the larger separation among the peptide chains, giving rise to less probable electron tunneling or suppression of interchain hole hopping among the amide groups. A tight molecular packing could have been also responsible for dynamical effects, i.e., restricted molecular motions lowering the ET process in a tight monolayer.

In the case of the bicomponent SAMs, three mechanisms were proposed to explain this molecular dynamic effect: electron tunneling gated by global helix motion, electron tunneling coupled to helix conversion from α -helix to 3_{10} -helix, and hole hopping assisted by local motion of the peptide chain (Fig. 32).

The first mechanism hypothesizes that collective vibrations of the C–C and C–N bonds of the peptide backbone generate global motions such as stretching, contraction, bending, and other deformation of the helix. During these global motions, a specific conformation enabling a strong electronic coupling through the peptide bridge is formed, when an electron instantly tunnels to the bridge. However, the authors excluded the global bending of the helix (Fig. 10a, right). In the second mechanism, the electrostatic repulsion between the oxidized ferrocene cation and

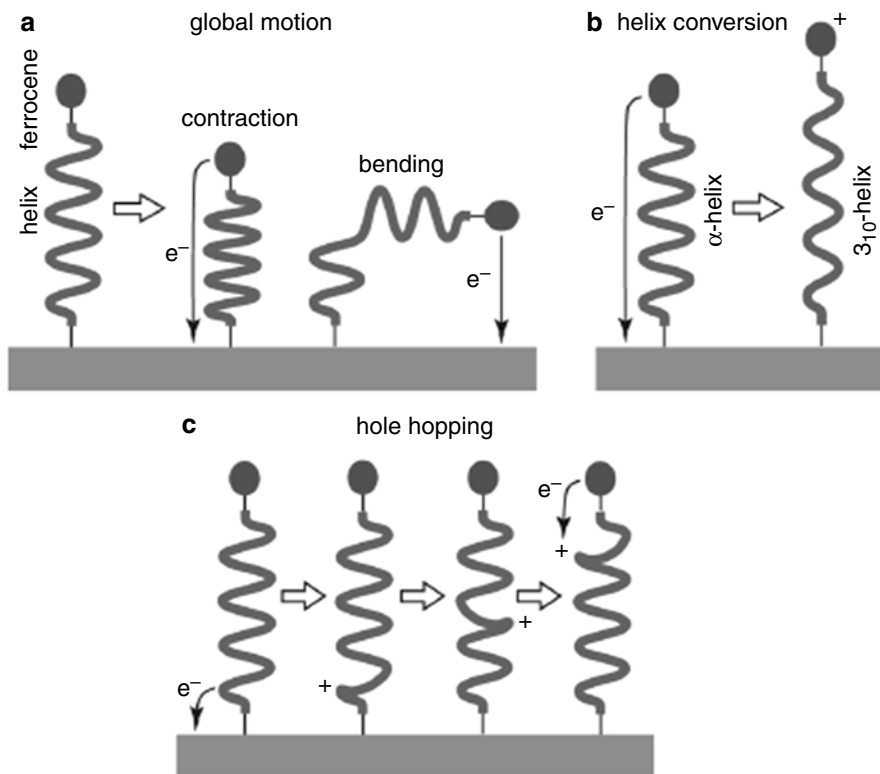


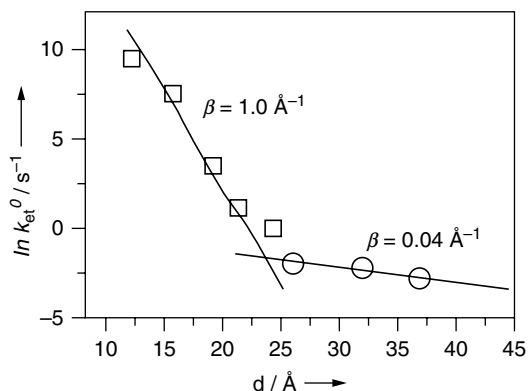
Fig. 32 Proposed mechanisms for the molecular dynamic effect on the electron-transfer, (a) global motion-gated electron tunneling, (b) electron tunneling coupled with helix conversion from α -helix to 3_{10} -helix, and (c) hole hopping among the amide groups assisted by a local backbone motion (Reprinted with permission from Takeda et al. [60]. Copyright (2008) American Chemical Society)

the positively biased metal surface should stretch the α -helix to 3_{10} -helix. The third proposed mechanism was that, following ET from the nearest amide group to gold via the sulfur atom to form a cation radical of the amide group (hole), the hole hopped among the amide groups until it reached the ferrocene moiety. This was the most probable mechanism, as confirmed by these groups in later publications. [63, 64]. Interestingly, Schlag and coworkers [78] demonstrated by theoretical calculations that when a hole was transferred from one amide group to the other, the dihedral angles of the peptide backbone notably changed to an active conformation. In this conformation, there was a strong electronic coupling between the neutral and cationic radical of amide groups, producing an almost negligible activation barrier. Tight molecular packing of the monolayer might hinder local vibrational motions at the interface and along the peptide backbone and reduce the hole hopping process, thus lowering the overall ET rate.

One year after the same group indicated that the hole hopping was the most probable mechanism in helical peptide SAMs, investigating the effect of the linker molecule on monolayer formation and long-range ET. The linker structure was found to influence the monolayer orientation, packing, and dynamics. Furthermore, by changing the linker, the ET rate through the SAM/metal junction may be modified, because of the different electronic coupling between the redox unit and the electrode. In this work, helical peptides composed of sixteen residues, formed by alternated sequences of L-Leu and Aib, and functionalized by a ferrocenyl redox unit at the C-terminus and three different linkers at the N-terminus for immobilization on gold were synthesized. The linkers were 4-thiobenzoic acid (NL), 3-fluoro-4-thiobenzoic acid (FL), and 2-methoxy-4-thiobenzoic acid (ML) in the acetyl-protected form. The ET rate constants were determined by CA and EIS. Comparable values were obtained for the three different SAMs, i.e., $k_{ET}^0 = 11.3 \pm 1.9 \text{ s}^{-1}$ (NL), $12.0 \pm 2.0 \text{ s}^{-1}$ (FL), and $14.4 \pm 0.8 \text{ s}^{-1}$ (ML). They supposed that since the HOMOs of both the linkers and the amide groups are closer to the gold Fermi level than their LUMOs, the ET process is thought to proceed via hole charge carriers. Their theoretical calculations demonstrated that the hopping mechanism was more probable than electron tunneling. After that, this group always supported hole hopping mechanism in peptide SAMs, even for an eight-residue peptide [63], even if never excluding the potential influence of molecular dynamics in this hopping process.

In 2004, also a series of oligoglycine derivatives (with two to six residues) functionalized at the N-terminal with a Fc unit and at the C-terminal with a cysteamine linker were self-assembled on gold in the presence of selected alkanethiols in order to form mixed monolayers [56]. The properties and electron-transfer behavior of the monolayer assemblies were investigated using electrochemical methods. It was found that the rates of electron-transfer through oligoglycine bridges, determined by dc cyclic voltammetry and AC voltammetry experiments, decreased rapidly with distance only for short-chain derivatives (two–four amino acid residues), while for the longer bridges (five and six amino acid residues), the distance dependence was weaker, and the rates were faster than expected on the basis of extrapolation of the rates for the shorter oligoglycines. Differences in the secondary structure of the peptide bridges (from polyproline I to polyproline II) and the change of the electron-transfer mechanism (from superexchange to hopping) were considered as possible reasons of the increase of the rate constants observed for longer peptide chains. The first interpretation was supported by theoretical investigations reported by Shin and coworkers [12], while the second one by theoretical investigations of Petrov and May [13]. Interestingly, some year after, Mandal and Kraatz studied a set of SAMs of leucine-rich ferrocene-labeled helical peptides diluted in a ferrocene devoid peptide and compared their results with the one obtained by Sek and coworkers on the oligoglycine SAMs [31]. By CV and EIS they determined the k_{ET}^0 values, and by plotting these values vs. the peptide spacer length, they found a very weak distance dependence. This has been interpreted as a result of a dynamically controlled tunneling mechanism. Furthermore, by combining their results with the one obtained

Fig. 33 ET rate constant versus the D–A distance for several oligoglycine Fc-labeled peptides (\square) and the series of peptides Fc10L, Fc14L, and Fc18L (\circ) (Reprinted with permission from Mandal and Kraatz [31]. Copyright (2012) American Chemical Society)



by Sek and coworkers [56], they obtained the graph reported in Fig. 33, where two different ET regimes are clearly evident.

Similar observations were already reported and rationalized as a transition from tunneling to hopping mechanism [29] following theoretical predictions [79, 80]. Herein, the authors ruled out the occurrence of a hopping mechanism, due to the absence of reduction and oxidation CV signals of the peptide bridges, as already observed by Kimura and coworkers [63]. They explained their results as a structural change (from random to stable helices) with the increase in the length of the peptide. Furthermore, they explained the low β value obtained (0.04 Å^{-1}) in the helical conformation as an effect due to the presence of several H-bond network in this conformation, as suggested by Maran and coworkers [35]. However, the β values reported in the literature for helical peptides in solution were higher ($\beta = 0.5\text{--}1.3$). The authors gave two different explanations for this experimental result: one is the hypothesis of a slower equilibrium between the α - and 3_{10} -helical conformers in the SAM if compared to the one in solution, the rate of formation of the more conductive 3_{10} -helical conformer being related to the ET transfer observed, and the other is the decrease of motion, due to the more limited MD in the longer helical peptides (because of their larger van der Waals interactions) which reduced the ET rate constants.

Despite the big efforts made in this field, the picture appears still confusing. Anyway, the main conclusions obtained at this point from electrochemical studies on peptide SAMs are similar to the one obtained in solution: when the electron-transfer distance is short and the driving force is large, tunneling prevails. On the other hand, when a peptide bridge is long and the driving force is small, a hopping mechanism should take over tunneling. However, independently of the mechanism, in the last years, the importance of molecular dynamics has been emphasized, which can strongly influence the ET rate constants. For this reason also on surface the *multiple pathway approach* which takes into account peptide dynamics seems to be the more appropriate approach to explain experimental results.

Photocurrent Generation Measurements

Photoinduced electron-transfer experiments on peptide SAMs covalently linked to gold electrodes via Au–S linkages have been extensively investigated by Kimura and coworkers.

In a first report to this field, they synthesized a tridecapeptide, composed of only Ala-Aib dyad, functionalized at the N-terminus with an N-ethylcarbazolyl (ECz) group and at the C-terminus with a disulfide group [81]. The primary sequence was chosen for the high propensity of Ala-Aib to attain helical secondary structures, the disulfide group (introduced as lipoic acid) for covalent linking to the Au electrode and the N-ethylcarbazolyl as a photosensitizer group. The same peptide scaffold was synthesized, inverting the position of the ECz and lipoic acid groups, in order to investigate the effect of the electrostatic field associated to the helical macrodipole, on the PG efficiency and SAM packing. They found that when the peptide SAM was linked to gold through the N-terminus, the coverage of the gold electrode was larger. This is because the Au⁺–S⁻ linkage is stabilized, when the electrostatic field of the helical macrodipole is directed from the C-terminus (negative) to the N-terminus (positive).

A standard three-electrode configuration has been used to perform PG measurements, with the gold-coated substrate acting as the working electrode, Ag/AgCl as the reference electrode, and a Pt wire as the auxiliary electrode. In solution, an electron donor (MV²⁺) or acceptor (TEOA) has been used. They found that with the electron donor in solution, the PG efficiency was higher when the peptide helix dipole pointed to the aqueous phase, so to accelerate the gold → ECz ET, while with an electron acceptor, the contrary happened. The second step in cathodic and the first step in anodic conditions most likely represent the rate-limiting steps of photocurrent generation because of the long distance between the gold surface and the photoactive probe (experimental section “[Photocurrent Generation Measurements](#)”). The decrease of anodic photocurrent was observed reducing the bias to the gold electrode, reaching an apparent zero current status at certain negative potential. The origin of this decrease has been already explained in section “[Photocurrent Generation Measurements](#)”. Interestingly, at applied potentials more negative than ζ_{cp} , a reverse in the current direction was observed (cathodic current), indicating that ζ_{cp} corresponds to a balance situation between cathodic and anodic currents.

The β values experimentally obtained for the two peptide SAMs were lower (0.58–0.60 Å⁻¹) compared to those obtained with alkanethiol SAMs of comparable thickness (0.9–1.1 Å⁻¹).

The same authors published also on PG experiments carried out on 3₁₀-helical nonapeptide SAMs having as chromophore the photoactive naphthyl units [82]. They synthesized four different peptides, all composed of three Ala-Aib-Aib triads and differing only in the number of Ala residues functionalized with a naphthyl unit: none in the reference compound (SSA3B), one at the N-terminus in SSNA2B, one at the C-terminus in SSA2NB, and three in SSN3B. They observed a significant photocurrent value only in the case of the SSN3B SAM (2.1 % efficiency) where the three naphthyl groups are spaced in a linear array along the helical axis with face-to-face

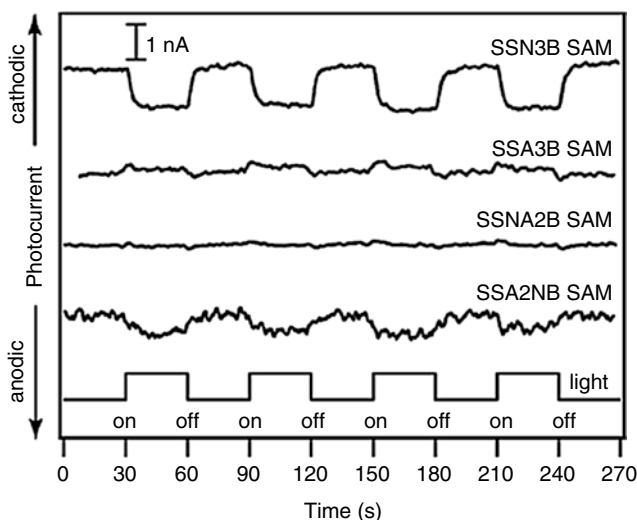


Fig. 34 Photocurrent generation upon light irradiation at 280 nm (0 V applied potential) in 50 mM TEOA solution (Reprinted with permission from Morita et al. [81]. Copyright (2000) American Chemical Society)

orientation. No anodic photocurrent was generated by the SSA3B or SSNA2B SAMs, while only a weak value was detected for the SSA2NB SAM (Fig. 34).

These results evidently assess the role of the naphthyl group and its position in the photoinduced ET process. In fact, the SSNA2B peptide formed a densely packed SAM, not able to generate a photocurrent signal. This is because the naphthyl group at the N-terminus could not be reached by the TEOA electron donor through its diffusion across the SAM. The high photocurrent efficiency obtained with the SSN3B SAM, instead, supported the idea that the ET process was speeded up by the electron hopping between the linearly arranged naphthyl groups. Furthermore, additional electrostatic dipole effects and HB pathways of the helical conformation should have promoted this kind of ET mechanism (Fig. 35).

In the same year Yasutomi et al. designed a molecular photodiode system, able to switch the current direction from anodic to cathodic, by choosing the excitation wavelength [71]. The SAM was composed of two types of helical peptides on a gold surface, carrying two different photoactive chromophores that could be selectively excited. As already shown in the previous paragraph, helical peptides having a chromophore can act as a molecular photodiode, controlling the direction of the induced photocurrent through the electrostatic field generated by the helix dipole. Figure 36 shows the chemical structures of the two hexadecapeptides used: they were composed of alternating sequences of L- or D-leucines and Aib residues. L- and D-LEUCINES were chosen in order to favor phase separation in their mixed SAMs, so to reduce photoinduced ET between the ECz and Ru groups. The first peptide, SSL16ECz, carried an ethylcarbazoyl (ECz) group at the C-terminus and a

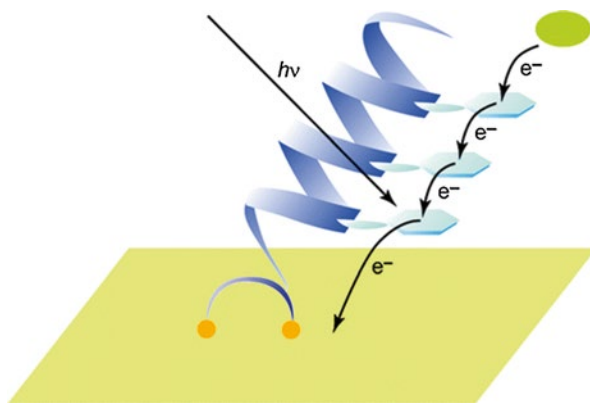


Fig. 35 Schematic representation for anodic photocurrent generation by the SSN3B SAM in the case that the naphthyl group at the site nearest to gold is excited by photoirradiation (Reprinted with permission from Yanagisawa et al. [82]. Copyright (2004) American Chemical Society)

disulfide group at the N-terminus, while the second one, Ru116SS, carried a disulfide group at the C-terminus and a tris(2,2'-bipyridine)ruthenium(II) complex (Ru) at the N-terminus. In this mixed SAM, the dipole moment of Ru116SS pointed from the gold to the monolayer surface, while that of SSL16ECz was directed in the opposite direction. As already discussed, ET along the dipole moment in a helical peptide is more rapid than that against the dipole moment. Therefore, the excitation of the ECz group in the SSL16ECz peptide produced an anodic photocurrent (the ET direction is from the SAM outer surface to gold), while the excitation of the Ru group in the Ru116SS peptide produced cathodic photocurrent (the ET direction is from gold to the monolayer surface) (Fig. 36).

In both cases, the rate-determining step was ET between the chromophore and gold that was evaluated to be of the order of 10^6 s^{-1} , which was much lower (about 5 orders of magnitude) than that for the diffusion-controlled reaction between the chromophore and the redox species in solution. Inset a of Fig. 36 shows the time course of PG with alternating photoirradiation of ECz (at 351 nm, anodic current) and Ru groups (at 459 nm, cathodic current). The action spectrum, shown in inset b of Fig. 36, was clearly determined by the overlap of the absorption spectra of ECz (from 310 to 400 nm) and Ru (from 400 to 520 nm).

Yasutomi et al. [71] showed that the photocurrent direction could be also reversibly switched between cathodic and anodic, by changing the pH of the solution. To do that, they synthesized a helical hexadecapeptide, composed of eight sequences of L-Leu-Aib dyads, and functionalized at the C-terminus with a L-3-(3-N-ethylcarbazolyl)alanine group and at the N-terminus with a disulfide group. Working at low pH, upon photoexcitation of ECz, in an aqueous solution containing TEOA, they observed anodic photocurrent. The photoinduced ET from ECz* to gold was accelerated by the electrostatic field associated to the helix dipole. Working at high

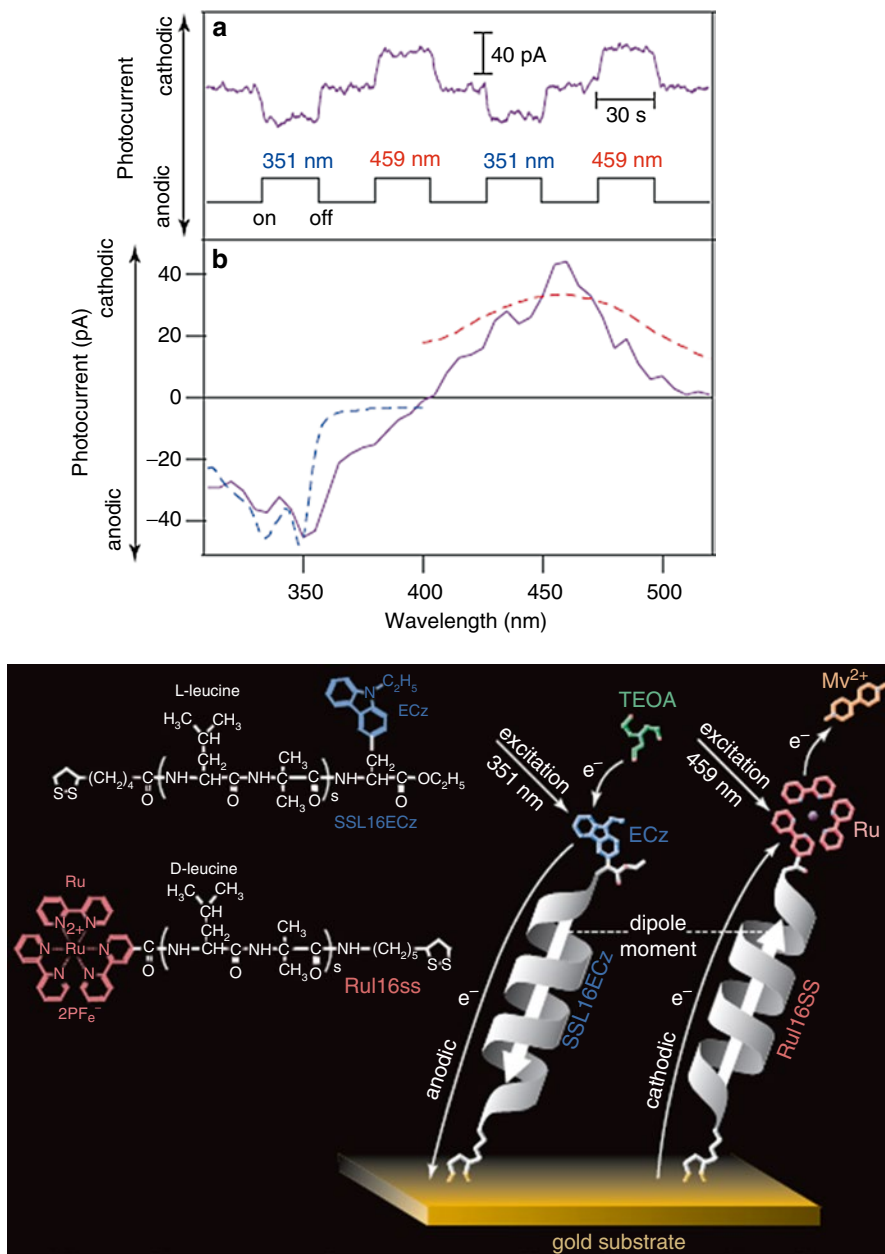


Fig. 36 Molecular structures of the SSL16ECz and Ru16SS peptides and schematic illustration of the photocurrent switch with the bicomponent SAM. *Inset:* (a) time course of photocurrent generated by the bicomponent SSL16ECz/Ru16SS SAM upon alternating photoirradiation of Ru (459 nm) and ECz (351 nm) and (b) action spectra (purple solid line) compared with the absorption spectra of SSL16ECz (blue dashed line) and Ru16SS (red dashed line) (Adapted with permission from Yasutomi et al. [71])

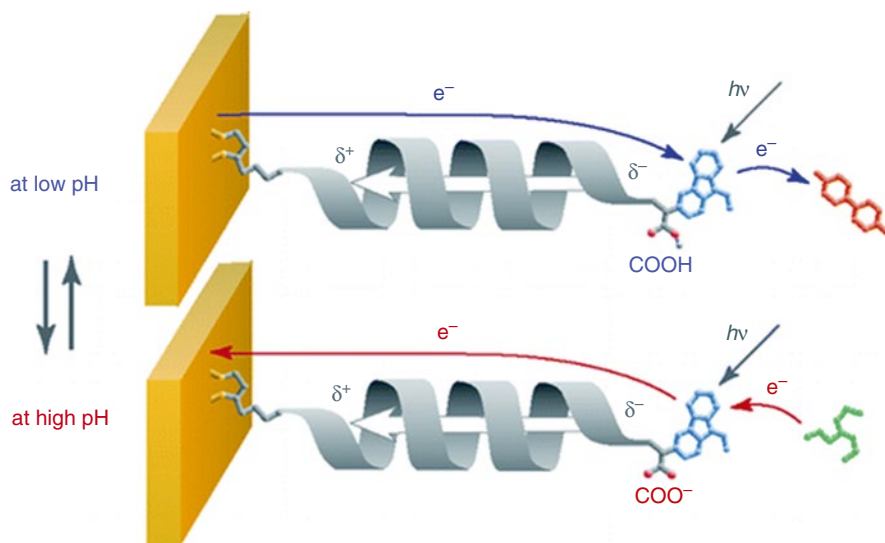
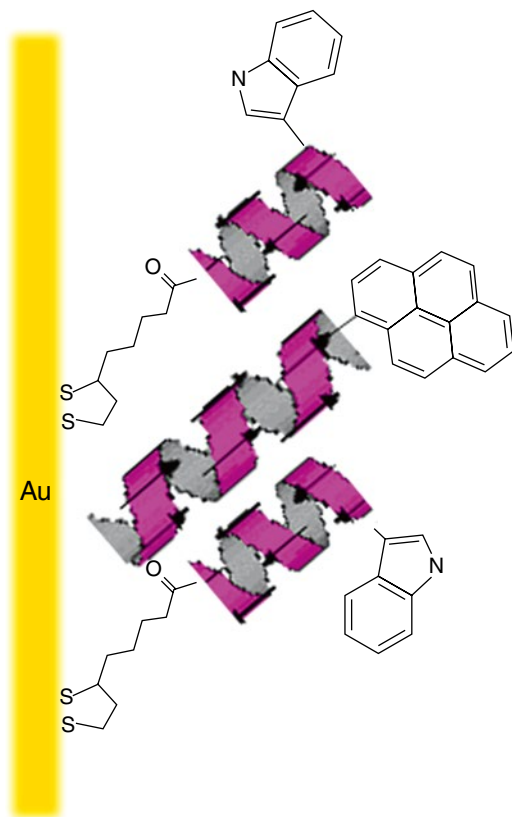


Fig. 37 Chemical structure of the ECzCOOH peptide and schematic illustration of the photocurrent switching due to the solution pH change, in the self-assembled monolayer composed of the ECzCOOH molecules (Reprinted with permission from Yasutomi et al. [88]. Copyright (2005) American Chemical Society)

pH they observed an enhancement of this effect, due to the negative charge attained by the terminal carboxylate group. The IPCE values found at pH=10 were 2.0 % and 0.07 % for the carboxylate and esterified ($-\text{COOEt}$) peptide SAMs, respectively (Fig. 37). The pH-induced switch of photocurrent direction was completely reversible.

One year after, Kraatz and coworkers showed that significant photocurrent signals and pH switching could be generated even in the absence of peptide films or antenna probes by using a laser excitation source [83]. They explained these results by ascribing most of the measured photocurrent to a simple photothermal effect, i.e., a potential drop caused by heating of the diffusion layer at the electrode interface upon illumination. Indeed, in their experiments, they were able to demonstrate that a photocurrent signal could be obtained by irradiating a bare gold electrode with a laser. They also claimed that the enhanced photocurrent signal measured in the presence of a chromophore-containing peptide could be correlated to the increase in temperature due to UV absorption of the chromophore. Our group significantly contributed to this debate, by studying photocurrent generation properties of a peptide-based self-assembled monolayer composed of two helical peptides [51]. Specifically, a pyrene-containing octapeptide, devoid of any sulfur atom (A8Pyr), and an hexapeptide, functionalized at the N-terminus with (*S,R*) lipoic acid, for binding to gold substrates (SSA4WA) via an Au-S linkage, were employed. Both peptides investigated attained a helical structure, because they were almost exclusively formed by strongly folding inducer C^α -tetrasubstituted α -amino acids. We demonstrated that the two peptides generated a stable supramolecular nanostructure (a densely packed bicomponent

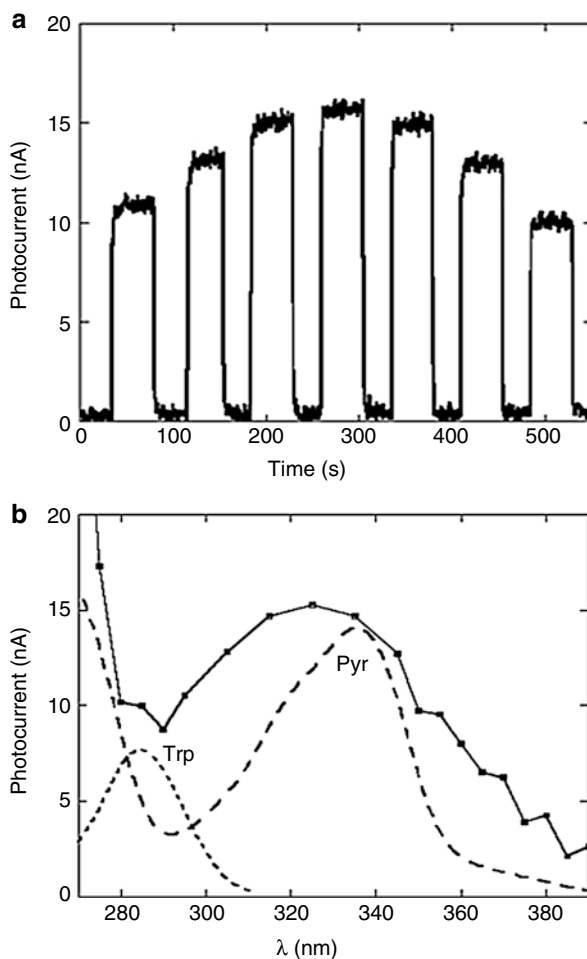
Fig. 38 Schematic representation of the bicomponent SAM. The SSA4WA peptide was immobilized onto a gold surface by the N-terminal liponic acid, while the A8Pyr was embedded into the SSA4WA palisade in an antiparallel orientation



peptide monolayer), where the A8Pyr was incorporated into the SSA4WA palisade by exploiting helix···helix macrodipole interactions (Fig. 38).

To demonstrate the presence of the A8Pyr peptide into the SAM, we performed photocurrent generation measurements in the Pyr absorption region using as electrolyte an aqueous solution of TEOA. Upon illumination, an intense anodic current was measured (Fig. 39a). Remarkably, the action spectrum, i.e., the photocurrent response *vs.* the excitation wavelength, of the mixed SAM almost perfectly overlapped the excitation spectra of Pyr and Trp measured in ethanol solution using the same slit opening conditions (15 nm) (Fig. 39b). It is worth noting that both the bare gold electrode and the electrode modified by a peptide SAM devoid of the Pyr antenna group (SSA6) generated just a very small photocurrent signal under the same experimental conditions. Interestingly, the IPCE% value for the bicomponent A8Pyr/SSA4WA SAM at $\lambda = 340$ nm (Pyr absorption maximum) was found to be 0.02 %, while the SSA6-modified electrode showed a value ten times lower. We described our results by ascribing to photothermal effect only the very weak signal measured in the case of the bare gold electrode and the peptide film without Pyr (SSA6). In the case of the bicomponent SAM, instead, a very high photocurrent signal in correspondence of the Pyr absorption spectrum was obtained, although in our experiment,

Fig. 39 (a) Time course of the photocurrent of the bicomponent SAM in an aqueous TEOA solution at 0 V vs. Ag/AgCl upon photoirradiation at different wavelengths (every 10 nm from 295 to 355 nm) at room temperature. (b) Photocurrent action spectrum of the gold electrode modified by deposition of the bicomponent A8Pyr/SSA4WA SAM in ethanol (solid line with black dots), as compared to the excitation (---) (15 nm slit width) spectra of the isolated Pyr(——) and Trp(---) chromophores (Reprinted with permission from Gatto et al. [51]. Copyright (2012) American Chemical Society)



excitation was achieved by using a Xe lamp instead of a laser source. To clarify the origin of this signal, we performed photocurrent generation measurements at the potential at which SSA6 had a zero current response (-0.15 V). This potential value corresponded to the maximum entropy of formation of the double layer and where the photothermal effect should have been zero [83]. Under these conditions, a high photocurrent signal was also obtained, which indicated that the photothermal effect could be safely considered only as a minor contribution to the whole photocurrent. Moreover, by a combination of electrochemical and spectroscopic techniques, we have determined the composition of the bicomponent SAM on the surface. In particular, the amount of Au-S linkages from the sulfur-containing peptides was quantified from reductive desorption of the peptide-based SAM, while the amount of A8Pyr was estimated by fluorescence spectroscopy after electrochemical desorption. The SAM stoichiometry was found to be SSA4WA/A8Pyr 2:1. Since the initial concentration ratio of the deposition solution was 1:1, we would have expected the same surface stoichiometry. But the formation of a SAM is a dynamical process, which

requires quite a long time (18 h). Rearrangement and favorite linkage of the thiol-functionalized peptide probably would lead the final composition to 2:1, as a result of the balance between the quite strong Au–S bond (35 kcal/mol) and the weaker electrostatically driven peptide–peptide interactions.

We also studied the photocurrent generation properties of the monocomponent SSA4WA peptide [44, 85] and of an Aib-based hexapeptide functionalized with a pyrene chromophore at the C-terminal and a lipoic acid at the N-terminal [84]. Interestingly, despite the shortness of the primary chain, these peptides were able to form a tightly packed SAM, where the quite short distance between the chromophore and the gold surface allowed an efficient electron-transfer. The introduction of Aib residues in the peptide chain was responsible for the rigid 3_{10} -helical structure attained by the hexapeptides, making it possible for us to modulate the separation distance between the gold surface and the photoactive group. Both the Trp (W) amino acid and the pyrene chromophore were used as photoactive molecules for photocurrent generation measurements. The photoexcitation of the sensitizer gave rise to a photoinduced current (*antenna effect*), when a gold electrode coated by the

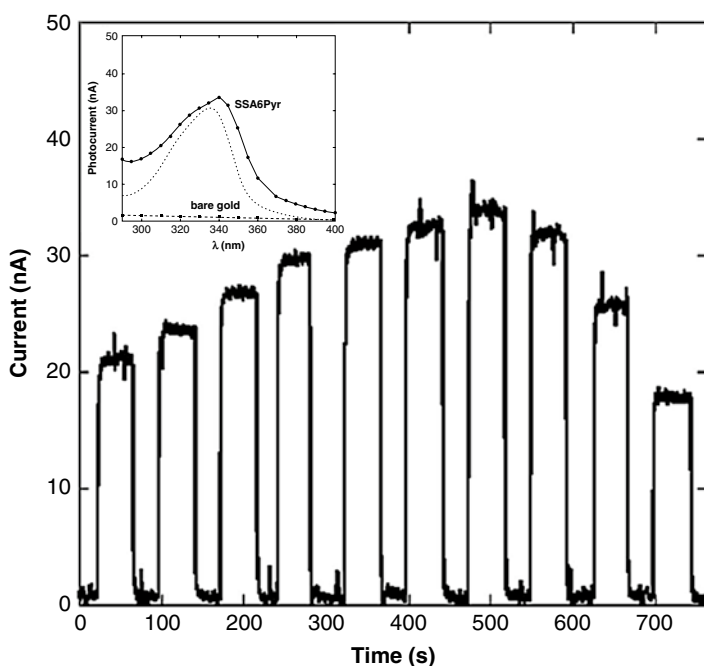


Fig. 40 On–off cycles of electronic current upon photoexcitation of the Py unit in SSA6Py at different excitation wavelengths ($\lambda_{\text{max}} = 340$ nm). The electronic current intensities depend on the pyrene absorption spectrum, as shown by the excitation spectrum of SSA6Py reported in the *inset*. *Inset*: photocurrent action spectrum and excitation spectrum of SSA6Py in the same experimental conditions (slit width = 15 nm). For comparison, the photocurrent action spectrum of the bare gold electrode is also reported (Reprinted with permission from Gatto et al. [85]. Copyright (2011) Wiley)

chemisorbed peptide layer was immersed in an electrolytic solution containing TEOA or methyl viologen. However, the recorded anodic photocurrent values were in both cases higher than the cathodic one. We explained this result as the effect of the electric field generated by the helical macrodipole on the ET process.

The anodic current generated upon photoexcitation of the SSA6Pyr at different excitation wavelengths in the presence of an electron donor (TEOA) in solution is shown in Fig. 40. The photocurrent efficiency was found to be equal to 0.05 % (at $\lambda_{\text{ex}} = 340$ nm).

In the inset of Fig. 40, the action spectrum of SSA6Pyr, which closely overlapped the pyrene absorption spectrum recorded under the same experimental conditions (slit width = 15 nm), was also reported.

We played a lot with peptides, comparing the PG efficiency of several mono- and bicomponent peptide SAMs on gold substrates [85].

The antenna effect of the pyrene sensitizer in different peptide systems was verified by measuring PG for a series of bicomponent peptide SAMs (1:10 SSA6Pyr/SSA6, 1:1 A8Pyr/SSA4WA, 1:1 A8Pyr/SSA6). Interestingly, the IPCE% measured upon excitation of the pyrene group is definitely higher for the chemisorbed SSA6Pyr SAM with respect to the SAMs containing the adsorbed A8Pyr peptide. To investigate in detail the role of the peptide/gold junction in determining the efficiency of the ET process, the dependence of the anodic photocurrent on the applied

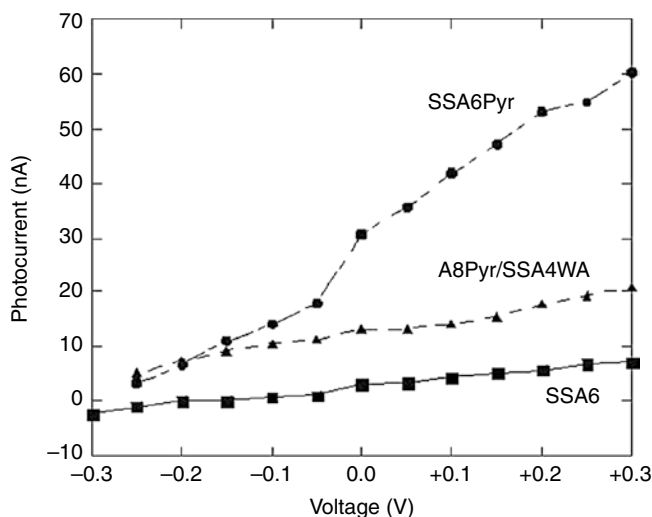


Fig. 41 Photocurrent generated by SSA6Pyr (full circles), A8Pyr/SSA4WA (full triangles), or SSA6 (full squares) peptide SAMs by excitation at 340 nm as a function of the applied bias potential (Reprinted with permission from Gatto et al. [85]. Copyright (2011) Wiley)

potential was analyzed at the pyrene maximum excitation wavelength ($\lambda = 340$ nm) for the SSA6Pyr and the A8Pyr/SSA4WA peptide SAMs (Fig. 41). As control experiment, the same analysis was also carried out for the SAM formed by the pyrene-lacking peptide SSA6.

The slope of the photocurrent/voltage (P/V) graph depends on the coupling between the electronic state density of the metal and the HOMO/LUMO orbitals of the antenna chromophore, mediated by the peptide bridge. Unfortunately, the observed linear dependence of the photocurrent on the applied potential does not allow to distinguish between a diffusive hopping mechanism and a coherent tunneling SE, because both ET models should show this linear dependence at low voltages.

Figure 41 shows that the slope of the P/V curve measured for the SSA6Pyr SAM was definitely steeper than that measured in the PyA8/SSA4WA SAM, a finding ascribable to the different types of contacts established by the two SAMs at the peptide/gold interface (*junction effect*). The Au^{δ+}-S^{δ-} junction allowed a through-bond ET pathway, with a relatively low ET activation barrier at the gold-peptide interface. This pathway was not operative for the A8Pyr peptide, which lacked the disulfide group. In the latter case, a direct Pyr* → Au ET across the A8Pyr peptide backbone would have necessarily required a through-space step from the peptide N-terminus to the gold surface, an event characterized by high activation energy. Furthermore, the helix dipole of A8Pyr in the bicomponent SAM pointed to the SAM outer surface, so to reduce ET in that direction. A possible alternative pathway may have proceeded through initial intermolecular ET from the excited Pyr to Trp (Pyr* + Trp → Pyr⁺ + Trp⁻) or to the amide site of a nearby peptide chain, followed by ET across the Au-S linked peptide chain from Trp⁻ or the amide radical anion to gold. This second step should have been also favored by the electrostatic field generated by the peptide helix. In agreement with this idea, the photocurrent efficiency of the A8Pyr/SSA6 SAM (ICPE=0.006 %) was found to be definitely lower than that one measured for the A8Pyr/SSA4WA SAM (IPCE=0.02 %), suggesting a predominant contribution of the Trp group to the intermolecular ET process. In any case, the photocurrents generated by both A8Pyr/SSA6 and A8Pyr/SSA4WA SAMs were definitely greater than that measured for the SSA6 SAM (IPCE=0.002 %), emphasizing the role of pyrene as photosensitizer even in the case of a peptide not covalently linked to the gold surface.

Conclusions

In this chapter, the most used electrochemical methods for the study of peptide SAMs are described and analyzed, together with the experimental results on the studies of these systems. Also a brief description of basic theoretical models of ET across peptide matrices is provided, in order to better understand the discussion in the experimental section. Most of the researchers agree that peptides are very good electron mediator matrix, enabling electron-transfer over long distances. However, ET parameters depend on several factors, such as the peptide secondary structure and length, the molecular dynamics of the system, and the presence of hydrogen

bonds. Herein, we have focused our attention especially on helical peptides, due to their good self-assembly and rectification properties, which enables ET over long distances. There are two mechanisms proposed: one is electron tunneling, which prevails when the ET distances are short, and the other prevails at longer distances, beyond a critical molecular length, and is characterized by a very shallow distance dependence. For this last feature, two mechanisms have been proposed: a hopping mechanism with the amide groups as hopping sites and molecular dynamics-associated electron tunneling. Probably both mechanisms are present.

Although the tunneling factor of helical peptides is larger than those of phenylene ethynylene or phenylene vinylene oligomers, which are intensively studied at the present moment as molecular wires, helical peptides have several advantages for the development of practical molecular electronic components in terms of well-specified molecular structure, facile molecular design and arrangement of functional groups along the molecule, and peculiar self-assembling properties to be suitably exploited in the building up of nanostructures.

References

1. Eaton DF (1991) Nonlinear optical materials. *Science* 253:281–287
2. Nuzzo RG, Allara DL (1983) Adsorption of bifunctional organic disulfides on gold surfaces. *J Am Chem Soc* 105:4481–4483
3. Ulman A (1996) Formation and structure of self-assembled monolayers. *Chem Rev* 96:1533–1554
4. Love JC, Estroff LA, Kriebel JK, Nuzzo RG, Whitesides GM (2005) Self-assembled monolayers of thiolates on metals as a form of nanotechnology. *Chem Rev* 105:1103–1169
5. Enriquez EP, Gray CH, Guarisco VF, Linton RV, Mar DK, Samulski ET (1992) Behavior of rigid macromolecules in self-assembly at an interface. *J Vacc Sci Technol* 10:2775–2782
6. Beratan DN, Onuchic JN, Winkler JR, Gray HB (1992) Electron-tunneling pathways in proteins. *Science* 258:1740–1741
7. Page CC, Moser CC, Chen X, Dutton PL (1999) Natural engineering principles of electron tunneling in biological oxidation-reduction. *Nature* 402:47–52
8. Wasielewski MR (1992) Photoinduced electron transfer in supramolecular systems for artificial photosynthesis. *Chem Rev* 92:435–461
9. Vassilian A, Wishart JF, Vanhemelryck B, Schwarz H, Isied SS (1991) Electron-transfer across polypeptides. 6. Long-range electron transfer in osmium-ruthenium binuclear complexes bridged with oligoproline peptides. *J Am Chem Soc* 112:7278–7286
10. Ogawa MY, Wishart JF, Young ZY, Miller JR, Isied SS (1993) Distance dependence of intramolecular electron-transfer across oligoprolines in $[(\text{BPy})_2\text{Ru}^{\text{II}}\text{L}(\text{pro})_n\text{-Co}^{\text{III}}(\text{NH}_3)_2]^{3+}$, $n = 1-6$: different effects for helical and nonhelical polyproline-ii structures. *J Phys Chem* 97:11456–11463
11. Sisido M, Hoshino S, Kusano H, Kuragaki M, Makino M, Sasaki H, Smith TA, Ghiggino KP (2001) Distance dependence of photoinduced electron transfer along α -helical polypeptides. *J Phys Chem B* 105:10407–10415
12. Shin YK, Newton MD, Isied SS (2003) Distance dependence of electron transfer across peptides with different secondary structures: the role of peptide energetic and electronic coupling. *J Am Chem Soc* 125:3722–3732
13. Petrov EG, May V (2001) A unified description of superexchange and sequential donor-acceptor electron transfer mediated by a molecular bridge. *J Phys Chem A* 105:10176–10186
14. Skourtis SS, Beratan DN (1997) High and low resolution theories of protein electron transfer. *J Biol Inorg Chem* 2:378–386

15. Giese B, Napp M, Jacques O, Boudebous H, Taylor AM, Wirz J (2005) Multistep electron transfer in oligopeptides: direct observation of radical cation intermediates. *Angew Chem* 44:4073–4075
16. Isied SS, Ogawa MY, Wishart JF (1992) Peptide-mediated intramolecular electron transfer: long-range distance dependence. *Chem Rev* 92:381–394
17. Sisido M, Tanaka R, Inai Y, Imanishi Y (1989) Photoinduced electron transfer on a single α -helical polypeptide chain. *J Am Chem Soc* 111:6790–6796
18. Inai Y, Sisido M, Imanishi Y (1991) Photoinduced electron transfer on a single α -helical polypeptide chain. Evidence of a through-space mechanism. *J Phys Chem* 95:3847–3851
19. Zheng YJ, Case MA, Wishart JF, McLendon GL (2003) Do main chain hydrogen bonds create dominant electron transfer pathways? An investigation in designed proteins. *J Phys Chem B* 107:7288–7292
20. De Rege PJF, Williams SA, Therien MJ (1995) Direct evaluation of electronic coupling mediated by hydrogen bonds: implications for biological electron transfer. *Science* 269:1409–1413
21. Fox MA, Galoppini E (1997) Electric field effect on electron transfer rates in dichromophoric peptides: the effect of helix unfolding. *J Am Chem Soc* 119:5277–5285
22. Galoppini E, Fox MA (1996) Effect of the electric field generated by the helix dipole on photoinduced intramolecular electron transfer in dichromophoric α -helical peptides. *J Am Chem Soc* 118:2299–2300
23. Long YT, Abu-Irhayem E, Kraatz HB (2005) Peptide electron transfer: more questions than answers. *Chem Eur J* 11:5186–5194
24. Cordes M, Giese B (2009) Electron transfer in peptides and proteins. *Chem Soc Rev* 38:892–901
25. Bolton JR, Archer MD (1991) Basic electron transfer theory. In: *Electron Transfer in Inorganic, Organic and Biological Systems*, vol 228, Adv. Chem. Ser. American Chemical Society, Washington, DC, pp 7–23
26. Newton MD (1991) Quantum chemical probes of electron transfer kinetics: the nature of donor-acceptor interactions. *Chem Rev* 91:767–792
27. McConnell HM (1961) Intramolecular charge-transfer in aromatic free radicals. *J Chem Phys* 35:508–515
28. Hopfield JJ (1974) Electron transfer between biological molecules by thermally activated tunneling. *Proc Natl Acad Sci U S A* 71:3640–3644
29. Malak RA, Gao Z, Wishart JF, Isied SS (2004) Long-range electron transfer across peptide bridges: the transition from electron superexchange to hopping. *J Am Chem Soc* 126:13888–13889
30. Kai M, Takeda K, Morita T, Kimura S (2008) Distance dependence of long-range electron transfer through helical peptides. *J Pept Sci* 14:192–202
31. Mandal HS, Kraatz HB (2012) Electron transfer mechanism in helical peptides. *J Phys Chem Lett* 3:709–713
32. Dey SK, Long YT, Chowdhury S, Sutherland TC, Mandal HS, Kraatz HB (2007) Study of electron transfer in ferrocene-labeled collagen-like peptides. *Langmuir* 23:6475–6477
33. Aviram A, Ratner MA (1974) Molecular rectifiers. *Chem Phys Lett* 29:277–283
34. Adams DM, Brus L, Chidsey CE, Creager S, Creutz C, Kagan CR, Kamat PV, Lieberman M, Lindsay S, Marcus RA, Metzger RM, Michel-Beyerle ME, Miller JR, Newton MD, Rolison DR, Sankey O, Schanze KS, Yardley J, Zhu X (2003) Charge transfer on the nanoscale: current status. *J Phys Chem B* 107:6668–6697
35. Antonello S, Formaggio F, Moretto A, Toniolo C, Maran F (2003) Anomalous distance dependence of electron transfer across peptide bridges. *J Am Chem Soc* 125:2874–2875
36. Onuchic JN, Beratan DN, Winkler JR, Gray HB (1992) Pathway analysis of protein electron transfer reactions. *Annu Rev Biophys Biomol Struct* 21:349–377
37. Kourtis SS, Balabin IA, Kawatsu T, Beratan DN (2005) Protein dynamics and electron transfer. Electronic decoherence and non-Condon effects. *Proc Natl Acad Sci USA* 102:3552–3557

38. Prytkova TR, Kurnokov IV, Beratan DN (2007) Coupling coherence distinguishes structure sensitivity in protein electron transfer. *Science* 315:622–625
39. Mabbott GA (1983) An introduction to cyclic voltammetry. *J Chem Educ* 60:697–702
40. Kissinger PT, Heineman WR (1983) Cyclic voltammetry. *J Chem Educ* 60:702–706
41. Finklea HO, Snider DA, Fedyk J (1993) Characterization of octadecanethiol-coated gold electrodes as microarray electrodes by cyclic voltammetry and ac impedance spectroscopy. *Langmuir* 9:3660–3667
42. Diao P, Jiang D, Cui X, Gu D, Tong R, Zhong B (1999) Studies of structural disorder of self-assembled thiol monolayers on gold by cyclic voltammetry and ac impedance. *J Electroanal Chem* 464:61–67
43. Kryszinski P, Smolska BN (1997) Three-probe voltammetric characterisation of octadecanethiol self-assembled monolayer integrity on gold electrodes. *J Electroanal Chem* 424:61–67
44. Gatto E, Venanzi M, Palleschi A, Stella L, Pispisa B, Lorenzelli L, Toniolo C, Formaggio F, Marletta G (2007) Self-assembled peptide monolayers on interdigitated gold microelectrodes. *Mater Sci Eng C* 27:1309–1312
45. Eckermann AL, Feld DJ, Shaw JA, Meade TJ (2010) Electrochemistry of redox-active self-assembled monolayers. *Coord Chem Rev* 254:1769–1802
46. Bard AJ, Faulkner RL (2001) *Electrochemical Methods: Fundamental and Applications*, 2nd edn. John Wiley and Sons, Inc, New York
47. Okamoto S, Morita T, Kimura S (2009) Electron transfer through a self-assembled monolayer of a double-helix peptide with linking the terminals by ferrocene. *Langmuir* 25:3297–3307
48. Forster J, Keyes TE, Vos JG (2003) *Interfacial Supramolecular Assemblies*. Wiley, England
49. Finklea HO (1996) Electrochemistry of Organized Monolayers of Thiols and Related Molecules on Electrodes. In: Bard AJ, Rubinstein I (eds) *Electroanalytical Chemistry*. Dekker, New York, pp 109–335
50. Sek S, Tolak A, Misicka A, Palys B, Bilewicz R (2005) Asymmetry of electron transmission through monolayers of helical polyalanine adsorbed on gold surfaces. *J Phys Chem B* 109:18433–18438
51. Gatto E, Porchetta A, Scarselli M, De Crescenzi M, Formaggio F, Toniolo C, Venanzi M (2012) Playing with peptides: how to build a supramolecular peptide nanostructure by exploiting helix \cdots helix macrodipole interaction. *Langmuir* 28:2817–2826
52. Ravenscroft MS, Finklea HO (1994) Kinetics of electron transfer to attached redox centers on gold electrodes in nonaqueous electrolytes. *J Phys Chem* 98:3843–3850
53. Finklea HO, Hanshew DD (1992) Electron-transfer kinetics in organized Thiol monolayers with attached pentaammine(pyridine)ruthenium redox centers. *J Am Chem Soc* 114:3173–3181
54. Watanabe J, Morita T, Kimura S (2005) Effects of dipole moment, linkers and chromophores at side chains on long-range electron transfer through helical peptides. *J Phys Chem B* 109:14416–14425
55. Creager SE, Wooster TT (1998) A new way of using ac voltammetry to study redox kinetics in electroactive monolayers. *Anal Chem* 70:4257–4263
56. Sek S, Sepiol A, Tolak A, Misicka A, Bilewicz R (2004) Distance dependence of the electron transfer rate through oligoglycine spacers introduced into self-assembled monolayers. *J Phys Chem B* 108:8102–8105
57. Mc Donald JS, Potter LD (1987) A flexible procedure for analyzing impedance spectroscopy results: description and illustrations. *Solid State Ion* 23:61–79
58. Janek RP, Fawcett WR, Ulman A (1997) Impedance spectroscopy of self-assembled monolayers on Au(111): evidence for complex double-layer structure in aqueous NaClO₄ at the potential of zero charge. *J Phys Chem B* 101:8550–8558
59. Arikuma Y, Takeda K, Morita T, Ohmae M, Kimura S (2009) Linker effects on monolayer formation and long-range electron transfer in helical peptide monolayers. *J Phys Chem B* 113:6256–6266

60. Takeda K, Morita T, Kimura S (2008) Effects of monolayer structures on long-range electron transfer in helical peptide monolayer. *J Phys Chem B* 112:12840–12850
61. Laviron E (1979) A. C. polarography and faradaic impedance of strongly adsorbed electroactive species. Part III: theoretical complex plane analysis for a surface redox reaction. *J Electroanal Chem Interfacial Electrochem* 105:35–42
62. Mandal HS, Kraatz HB (2006) Electron transfer across α -helical peptides: potential influence of molecular dynamics. *Chem Phys* 326:246–251
63. Arikuma Y, Nakayama H, Morita T, Kimura S (2010) Electron hopping over 100 Å along an α -helix. *Angew Chem Int Ed* 49:1800–1804
64. Arikuma Y, Nakayama H, Morita T, Kimura S (2011) Ultra-long-range electron transfer through a self-assembled monolayer on gold composed of 120 Å-long α -helices. *Langmuir* 27:1530–1535
65. Janek RP, Fawcett WR, Ulman A (1998) Impedance spectroscopy of self-assembled monolayers on Au (111). *Langmuir* 14:3011–3018
66. Kuhn JH, Braslavsky SE, Schmidt R (1989) Chemical actinometry. *Pure Appl Chem* 61:187–210
67. Venanzi M, Pace G, Palleschi A, Stella L, Castrucci P, Scarselli M, De Crescenzi M, Formaggio F, Toniolo C, Marletta G (2006) Densely-packed self-assembled monolayers on gold surfaces from a conformationally constrained helical hexapeptide. *Surface Sci* 600:409–416
68. Pace G, Venanzi M, Castrucci P, Scarselli M, De Crescenzi M, Palleschi A, Stella L, Formaggio F, Toniolo C, Marletta G (2006) Static and dynamic features of a helical hexapeptide chemisorbed on a gold surface. *Mater Sci Eng C* 26:918–923
69. Toniolo C, Crisma M, Formaggio F, Peggion C (2001) Control of peptide conformation by the Thorpe-Ingold effect (C^{α} -tetrasubstitution). *Biopolymers (Pept Sci)* 60:396–419
70. Wada A (1976) The alpha-helix as an electric macro-dipole. *Adv Biophys* 9:1–63
71. Yasutomi S, Morita T, Imanishi Y, Kimura S (2004) A molecular photodiode system that can switch photocurrent direction. *Science* 304:1944–1947
72. Miura Y, Kimura S, Kobayashi S, Iwamoto M, Imanishi Y, Umemura U (1999) Negative surface potential produced by self-assembled monolayers of helix peptides oriented vertically to a surface. *Chem Phys Lett* 315:1–6
73. Galka MM, Kraatz HB (2002) Electron transfer studies on self assembled monolayers of helical ferrocenoyl-oligoproline cystamine bound to gold. *ChemPhysChem* 3:356–359
74. Morita T, Kimura S (2003) Long-range electron transfer over 4 nm governed by an inelastic hopping mechanism in self-assembled monolayers of helical peptides. *J Am Chem Soc* 125:8732–8733
75. Sek S, Palys B, Bilewicz R (2002) Contribution of intermolecular interactions to electron transfer through monolayers of alkanethiols containing amide groups. *J Phys Chem B* 106:5907–5914
76. Berlin YA, Ratner MA (2005) Intra-molecular electron transfer and electric conductance via sequential hopping: unified theoretical description. *Radiat Phys Chem* 74:124–131
77. Wain AJ, Do HNL, Mandal HS, Kraatz HB, Zhou F (2008) Influence of molecular dipole moment on the redox-induced reorganization of α -helical peptide self-assembled monolayers: an electrochemical SPR investigation. *J Phys Chem C* 112:14513–14519
78. Schlag EW, Scheu SY, Yang DY, Selzle HL, Lin SH (2000) Charge conductivity in peptides: dynamic simulations of a bifunctional model supporting experimental data. *Proc Natl Acad Sci U S A* 97:1068–1072
79. Petrov EG, Shevchenko V, Teslenko VI, May V (2001) Nonadiabatic donor-acceptor electron transfer mediated by a molecular bridge: a unified theoretical description of the superexchange and hopping mechanism. *J Chem Phys* 115:7107–7122
80. Bixon M, Jortner J (1997) Electron transfer via bridges. *J Chem Phys* 107:5154–5170
81. Morita T, Kimura S, Kobayashi S (2000) Photocurrent generation under a large dipole moment formed by self-assembled monolayers of helical peptides having an N-Ethylcarbazolyl group. *J Am Chem Soc* 122:2850–2859

82. Yanagisawa K, Morita T, Kimura S (2004) Efficient photocurrent generation by self-assembled monolayers composed of 3_{10} -helical peptides carrying linearly spaced Naphthyl groups at the side chains. *J Am Chem Soc* 126:12780–12781
83. Mandal HS, Burgess IJ, Kraatz HB (2006) Investigation of laser induced photocurrent generation experiments. *Chem Comm* 4802–4804
84. Gatto E, Stella L, Baldini C, Venanzi M, Toniolo C, Formaggio F (2009) Photocurrent generation in peptide-based self-assembled monolayers on gold electrodes. *Superlatt Microstruct* 46:34–39
85. Gatto E, Caruso M, Porchetta A, Toniolo C, Formaggio F, Crisma M, Venanzi M (2011) Photocurrent generation through peptide-based self-assembled monolayers on a gold surface: antenna and junction effects. *J Pept Sci* 17:124–131
86. Gatto E, Stella L, Formaggio F, Toniolo C, Lorenzelli L, Venanzi M (2008) Electroconductive and photocurrent generation properties of self-assembled monolayers formed by functionalized, conformationally constrained peptides on gold electrodes. *J Pept Sci* 14:184–191
87. Gatto E, Porchetta A, Stella L, Guryanov I, Formaggio F, Toniolo C, Kaptein B, Broxterman QB, Venanzi M (2008) Conformational effects on the electron-transfer efficiency in peptide foldamers based on α , α -disubstituted glycyl residues. *Chem Biodivers* 5:1263–1278
88. Yasutomi S, Morita T, Kimura S (2005) pH-controlled switching of photocurrent detection by self-assembled monolayer of helical peptides. *J Am Chem Soc* 127:14564–14565

Electrophoretic Deposition (EPD): Fundamentals and Applications from Nano- to Microscale Structures

17

Pouya Amrollahi, Jerzy S. Krasinski, Ranji Vaidyanathan,
Lobat Tayebi, and Daryoosh Vashaee

Contents

Introduction.....	562
Mechanisms of EPD	566
Process Variables	568
Suspension Parameters.....	568
Process Parameters.....	569
Applications	570
Oriented Ceramic Materials.....	570
Multilayered Composites.....	572
Thermoelectric Thick Films.....	573

P. Amrollahi • R. Vaidyanathan
Helmerich Advanced Technology Research Center, School of Material Science
and Engineering, Oklahoma State University, Tulsa, OK, USA
e-mail: pouya.amrollahi@okstate.edu; vaidyan@okstate.edu

J.S. Krasinski
Helmerich Advanced Technology Research Center, School of Electrical
and Computer Engineering, Oklahoma State University, Tulsa, OK, USA
e-mail: krasins@okstate.edu

L. Tayebi (✉)
Helmerich Advanced Technology Research Center, School of Material Science
and Engineering, Oklahoma State University, Tulsa, OK, USA
Department of Developmental Sciences, Marquette University School of Dentistry,
Milwaukee, WI, USA
e-mail: lobat.tayebi@marquette.edu

D. Vashaee (✉)
Helmerich Advanced Technology Research Center, School of Electrical
and Computer Engineering, Oklahoma State University, Tulsa, OK, USA
Electrical and Computer Engineering Department, North Carolina State University,
Raleigh, NC, USA
e-mail: dvashae@ncsu.edu

Particle Size Separation	574
Deposition of Nanotubes.....	574
Dye Sensitized Solar Cells.....	575
SiC Fiber Reinforced Composites	575
Thick Film Optical Modulators	575
Batteries and Electrochemical Capacitors	576
Solid Oxide Fuel Cells (SOFCs).....	576
Corrosion-Resistant Coatings	578
Catalyst Support and Molecular Sieves	578
Sensors	579
Piezoelectric Actuators	580
Biomedical Applications.....	582
Conclusion	585
References.....	586

Abstract

EPD is a technique where charged particles in a stable colloidal suspension are moved through the liquid due to electric field and deposited on an oppositely charged conductive substrate, forming the intended material or device. EPD enables fabrication of a wide range of structures from traditional to advanced materials, from nanometric thin films to a fraction of 1 mm thick films, and from porous scaffolds to highly compact coatings. These structures include different compositions with complex shapes and structures which can be formed in a relatively short experimentation time by simple apparatus. This review presents the fundamentals, mechanisms, and characteristics of EPD along with its past and recent applications.

Keywords

Electrophoretic deposition (EPD) • Ceramic materials • Biomedical materials • Thermoelectric materials • Materials fabrication

Introduction

Electrophoretic deposition (EPD) is a material processing technique using deposition of charged particles in a stable colloidal suspension on a conductive substrate, acting as one of the two oppositely charged electrodes in the EPD cell. The deposited particles form the intended material or device [1]. Both alternating current (AC) and direct current (DC) electrical fields have been applied in EPD process, although DC fields are more common [1–3]. Highly versatile application, simple apparatus and equipment, short processing time, cost effectiveness, facile modification, desirable dense packing of particles in the final piece, high quality of the microstructures produced, easy production of geometrically complicated shapes and simple control of the thickness and morphology have made EPD an interesting technique both in academia and industry [1, 4]. In EPD, the state of particles in suspension and their evolution during the process can be controlled and manipulated. Moreover, appropriate and accurate choice of processing variables could enable production of dense

and homogeneous or porous microstructures. A combustible substrate that can be removed by further heating in sintering process is used for fabricating complicated shapes. But for coatings, the operator needs to be very cautious about possible cracks due to drying and sintering. These thermally derived cracks are the intractable nature of the technique and the quality of the final surface depends on overcoming this problem.

This process was discovered by Bose in a liquid-siphon experiment during the 1740s [5] and has been known since Ruess observed the movement of clay particles in water under an electrical field [6]. The first practical use of this technique was done by Harsanyi [7] in 1927 in order to deposit thoria (thorium (IV) oxide) and tungsten on a platinum cathode as an emitter for electron tube applications. The first large-scale application of EPD dates back to early 1950s, when the scientists used this method to make insulating Al_2O_3 layers on cathode heaters in vacuum tubes [8].

An EPD cell contains four different parts: working electrodes (substrate and counter electrode), colloidal suspension, and power supply (AC or DC).

Despite the fact that many mechanisms have been proposed for EPD, there are several unquestionable characteristics to distinguish EPD from other similar deposition-based techniques. As it can be seen in Fig. 1, (a) colloidal particles are well dispersed and able to move freely and independently in solvent suspension, (b) electrochemical equilibrium of the solvent is responsible for particles' surface charge, (c) particles move electrophoretically in the bulk of the suspension to the oppositely charged electrode (substrate), and (d) the substrate is covered by a neutralized, firmly deposited layer of particles. Therefore, EPD is a technique where moving species are solid particles, required conductance of the liquid medium is low, and the organic liquids are preferred. In EPD, the liquid stays motionless while particles and ions move under the electrostatic force [4].

Like in any other system, it is absolutely essential to avoid contamination or impurity that can unfavorably influence the properties of the process and/or resulting materials. As the characteristics of the resulting materials are highly dependent on stability of suspension and control on surface charge, powder washing multiple times before preparation of a particulate suspension is mandatory in order to eliminate the residual impurities caused by the powder preparation procedure [9].

Generally, it is preferred to use organic liquids as the suspending medium in an EPD cell even though they are dangerous, expensive, and unfriendly to the environment. However, in aqueous EPD, one needs much lower voltage, we have more control on temperature, and deposition takes place faster. Also, water is much more environmental friendly. Unfortunately, electrolysis of water generates gas bubbles that drastically compromise the quality of the deposited layer. It has been reported that application of short voltage pulses in an aqueous EPD system can suppress the bubble incorporation [10, 11]. Figure 2 demonstrates complete suppression of bubbles during aqueous electrophoresis of α -alumina thin film, deposited on stainless steel (316 L) substrate by applying periodically pulsed voltage. As can be seen, bubble-free deposits were obtained at pulses equal to or shorter than 5 m. It has also been reported that constant current rather than constant voltage depositions are more efficient and can provide better control over the EPD process.

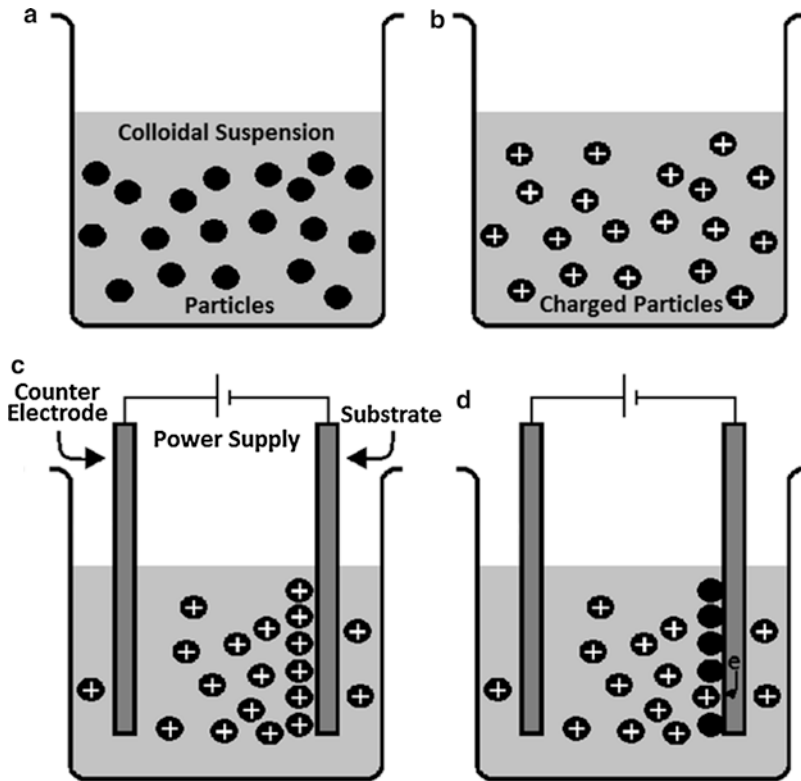


Fig. 1 Four steps of EPD; (a) dispersion, (b) electrochemical charging, (c) electrophoresis and (d) deposition

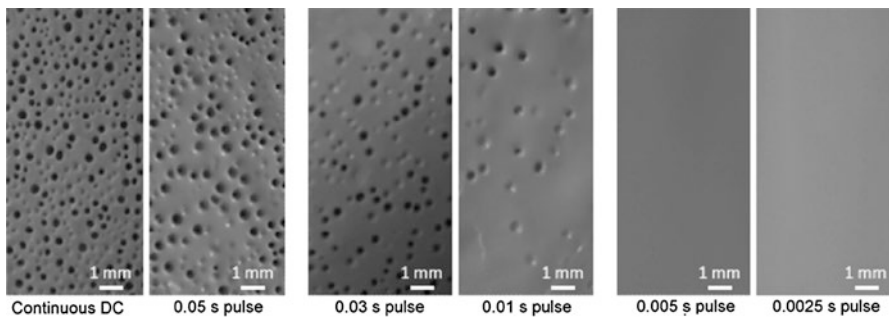


Fig. 2 Suppression of bubbles by applying constant current pulses (α -alumina deposited on stainless steel substrates) (Reprinted from Besra et al. [11], Copyright (2009), with permission from Elsevier)

Table 1 Applications of EPD

No.	Category	Application	References
1	Oriented ceramic materials	Fabricating crystalline oriented thick films	[6, 12, 13]
		Textured TiO ₂	[14–16]
		Textured alumina	[17, 18]
2	Multilayered composites	Multilayered alumina	[19]
		Fabricating functionally gradient, multi-layer composites and sandwich structures	[20–22]
3	Thermoelectric thick films	Si-Ge thick films	[23]
4	Particle size separation	SnO ₂ particles	[24]
5	Deposition of nanotubes	Graphene synthesis	[25–27]
		SiO ₂ /CNT composites	[28]
		CNT/TiO ₂ composites	[29, 30]
		MnO ₂ /CNT composites	[31]
		Fe ₃ O ₄ /CNT composites	[32]
		Hydroxyapatite/CNT composites	[33–35]
		Bioactive glass/CNT composites	[36, 37]
6	Solar cells	Dye sensitized solar cells	[38, 39]
7	Reinforced composites	SiC fiber reinforced composites	[40]
8	Thick film optical modulators	WO ₃ nanorods	[41]
		ZnO thin films	[42]
9	Batteries and electrochemical capacitors	Lithium ion batteries	[43]
		Super-capacitors	[44]
10	Solid oxide fuel cells	Y ₂ O ₃ -stabilized ZrO ₂	[45–48]
		Perovskite structures	[49]
		CeO ₂ films	[50]
		Gd ₂ O ₃	[51]
11	Corrosion-resistant coatings	Silica hybrid coatings	[52]
12	Catalyst support and molecular sieves	PPy coated tubes	[53]
13	Sensors	Gas sensors	[54–57]
14	Piezoelectric materials	PZT actuators	[58, 59]
15	Biomedical materials	Forming biocompatible layers	[60–69]
		Porous scaffolds	[35]
		Bacteria	[70]
		Corrosion protection of implants	[71]

Table 1 lists selected significant applications of EPD in various fields.

EPD process involves four steps. First, a stable suspension of particles is needed. Since the particles only need to be stable within the time frame between dispersing to depositing processes, which can be as short as a few minutes, various stabilization techniques may be utilized such as low concentration, proper charging of the particles, polymer depletion, polyelectrolyte, block copolymer, and homopolymer adsorption [72]. In electrostatic technique, creation of an energy barrier between 10 and 15 kT prevents the particles from attaching to each other. In polymer depletion,

a concentration of soluble polymer which cannot be adsorbed to the particle surfaces is used to prevent them from sticking together. Other polymeric stabilization methods necessitate a polymer where one side of it can be attached to the particle, while the other side is dissolved in the solvent [72]. As the second step, a solvent able to enable ionic charge is required where adsorption/dissolution equilibria for a positive and negative ion are different. The next step is electrophoretic migration of particles under the influence of electric field. During electrochemical charging of particles, the solvent must be able to dissolve ions; because a solvent with no or a minute concentration of dissolved ions drastically increase the required voltage across the cell. Electrochemical reactions at the electrodes guarantee the change in the valence of ions in order to prevent ions from screening the electric field at the electrode surface. Moreover, absence of these reactions would lead to fast migration of ions to oppositely charged electrodes after applying a voltage. The last step is deposition of particles on one of the electrodes. As there are various mechanisms for both stabilizing and destabilizing of the particles (in the first and fourth steps), there is no single mechanism for EPD.

Mechanisms of EPD

There are several mechanisms by which the particles come together and form a rigid solid structure. Combining them with the abovementioned dispersing techniques leads to different EPD mechanisms although the exact mechanisms which allow deposition of particles on the substrate are still not completely understood.

It has been suggested that EPD should be considered as a two-step process, where particles first migrate to the substrate due to the applied electric field (the particles lose their charge at the electrode surface) and then after complex electrochemical reactions and aggregation the deposited layer is formed.

Electrophoretic motion of the particles is stopped by the substrate and the density of the particles will keep increasing there, due to accumulation. If those particles agglomerate, a low-density deposit may form which is difficult to dry without cracking. In this mechanism, there is no guarantee that the thickness of the layer remains uniform all over the substrate; since the nonuniformity of the electric field can lead to a very nonuniform deposit.

If the applied electric field is powerful enough (around several hundred volts per cm), it is also possible that deposition takes place via suppressing the electrostatic repulsion with the electric field. In this mechanism, the electrical force gradient has to be low in order to make an even deposit [73, 74], although some irregularities may occur due to strong electroconvection.

The next approach is flocculation of the particles by electro sedimentation [72]. It was found that a stable suspension can produce strongly adhering sediment. Sediment is formed in the innermost layer of the particles due to gravitation plus the pressure made by electrically induced flow of particles to the substrate. Although the density of the deposited layer is very good, the charge of the layer confronts the

electrochemical charge of the solvent and acts as the driving force reducing the electrophoretic force in the layer. This instability can cause convection within the layer of particles before they are deposited on the substrate [75, 76].

Decrease in total ionic concentration around the substrate can raise the voltage gradient and, by quelling the convection, conduction occurs between unbalanced ions as a consequence. This effect results in raising the voltage gradient to mega volts per meter. These layers are very convectively unstable. Preservation of the surface charge of the particles results in a very strong compacting force that can make a powerful leveling effect when it is accompanied by high voltage gradient. This mechanism leads to forming very even thin layer [77].

On the contrary, it has also been reported that an increase in ionic concentration at the substrate makes the electrostatic boundary layer of particles thinner and thinner until they become unstable and the deposit is formed [78].

The particles may lose their charge and neutralize after contacting the substrate and make a thin deposit. This mechanism continues until the deposited layer gets thick, the particle–substrate interactions are stopped, or the pH level changes around the substrate [72].

It has been reported that repulsive forces between the particles can be reduced only when the electrode reactions generate $(OH)^-$ ions [4]. The calculated amount of ionic strength around the substrate was sufficient for flocculation of the suspension. Interparticle repulsion decreases when near-substrate electrolyte concentration is increased. Consequently, the zeta potential is lowered and flocculation of particles is induced.

In the case of polymers, it has been reported that when electrophoretic force brings the particles together, branches of a copolymer can be detached from one particle and attach to a neighbor particle and make a polymer bridge that holds these particles together [72]. Another deposition mechanism for polymers is called “squeezing out,” where a constant stable electrophoretic force brings two polymers into contact and deposit. Furthermore, in some cases, changing the solvent ionic composition leads to an alteration in particle surface potential and polymer particles can be stabilized [72]. Table 2 summarizes the mechanisms through which (a) particles stabilize at the substrate and (b) EPD takes place.

Table 2 Different mechanisms of EPD [72]

(a) Particle stabilization at substrate	(b) EPD layer formation mechanisms
Low number density	Densification
Electrostatic	Direct electrostatic force
Polymer depletion	Electrosedimentary
Homo-polymer adsorption	Ion depletion enhanced electrostatic
Poly-electrolyte	Desorption of neutral/charged polymer
Block co-polymer	Charge reduction/neutralization
	Squeezing out
	Bridging flocculation

Process Variables

There are two sets of parameters which can affect both EPD process and the resulting specimen: first, parameters that control the status and quality of suspension, and then the parameters which qualify the whole process, such as electrical parameters. When the first group is fixed, the latter can be manipulated for gaining favorable deposition. Table 3 summarizes the possible parameters that can be manipulated in order to get the desired properties and quality in the deposited film.

Suspension Parameters

Particle Size

Uniformity of the deposited layer is tightly tied to whether or not the particles remain stable and dispersed throughout the whole process, because, motionless and accumulated particles lead to the formation of gradient in deposition. In case of larger particles, there is always a competition between the gravity and electrophoresis forces. The first one result in sedimentation of the powder while the latter deposits the particles on the substrate. In this situation, when EPD is completed, surface charge is highly increased and/or the electrical double layer region is thickened.

Dielectric Constant, Conductivity, and Viscosity of Suspension

It has been reported that the dielectric constant of the liquids must be in the range of 12–25 for deposition to happen [1]. In liquids with dielectric constants less than 12, lack of dissociative power stalls the deposition, while in liquids with dielectric constants higher than 25, electrophoresis is halted by the reduction in size of the double layer region, caused by high ionic concentration.

Impurities can also change the conductivity of the suspension. Moreover, the method used for preparing the suspension also affects the conductivity drastically. A highly resistive suspension leads to instability because electronically originated charge forms in the particles. On the other hand, proper adjustment of temperature and dispersant concentration can raise the conductivity. Research has shown that, for each exact dispersant concentration and each temperature, there is a narrow conductivity range which enhances the deposition process [79]. Generally, an ideal suspension has high dielectric constant, low conductivity and low viscosity. Table 4 shows viscosity and relative dielectric constant of some popular solvents [80],

Table 3 Parameters governing EPD

Suspension parameters	Process parameters
Particle size	Applied electric field
Dielectric constant, conductivity and viscosity	Deposition time
Zeta potential	Conductivity of the substrate
Stability	
Concentration of solids	

Table 4 Physical properties of solvents

Solvents	Viscosity (cP) = $10^{-3} N.s.m^{-2}$	Relative dielectric constant
Acetone	0.3087	20.7
Methanol	0.557	32.63
Water	0.890	78.2
Ethanol	1.0885	24.55
Acetylacetone	1.09	25.7
<i>n</i> -Propanol	1.9365	20.33
Iso-propanol	2.0439	19.92
<i>n</i> -Butanol	2.5875	17.51
Ethylene glycol	16.265	37.7

ordered from best to worst. Methanol and acetone are the first two best solvents. However, comparing these two, methanol has higher dielectric constant while acetone has a viscosity of almost half of methanol. Therefore, acetone can be considered as the best solvent for making an ideal suspension.

Zeta Potential

Zeta potential governs several key parameters in EPD, such as the density of the deposit, particle direction and speed, and the repulsive interactions between the particles which determine the stability of the suspension. Generally, a high surface charge is needed not only to avoid particle agglomeration but also to enable formation of a dense highly packed deposit. Zeta potential manipulation is done through addition of acids, bases, and adsorbed ions.

Stability of Suspension

Finding the best state of stability of the suspension is a matter of compromise. When the suspension is stable, flocculation does not happen and a thick adherent material deposits at the bottom of the cell due to sedimentation. Too much stability disables EPD, because a high electric field is needed to defeat the repulsive forces between particles. Conversely, a flocculating suspension just forms thin nonadhering deposits.

Concentration of Solids in Suspension

High concentrations of solids in suspension enable uniform and even deposition rates, while low concentrations lead to deposition rates proportional to electrophoretic mobility of each particle [81].

Process Parameters

Effect of Applied Electric Field

As there are both intended particles and free ions in the suspension, a portion of the electric field, which is the driving force of EPD, is carried by the free ions and the field efficiency is compromised. However, when we cannot limit the presence of

free ions, the amount of current carried by them is insignificant. Ideally, the applied electric field must be totally spent on advancement of the electrophoresis in a stable-current manner, because the deposition increases in direct relation with raising the applied potential. While too low fields are not capable of triggering the electrophoresis, with too high applied electrical fields, the quality of the deposits is sacrificed. It has been suggested that the best quality of deposits are gained at moderate applied fields. Moreover, a high electric field can cause turbulence in the suspension, which compromises the quality of the resulting deposit. Also, it increases the speed of the particles and consequently they cannot have the chance to be seated in the best position, which makes the formation of a dense close-packed structure impossible [82].

Effect of Deposition Time

In EPD, the deposition rate starts with a linear relationship to time and then it lowers as time goes on, until the deposit is thick enough to interrupt the conductance and the deposition rate reaches plateau at high deposition times.

Conductivity of Substrate

In EPD, the quality of the deposited film is strongly dependent on the conductivity of the substrate. Low conductivity of the substrate leads to both slow deposition and nonuniformity of the deposit [47].

Applications

Oriented Ceramic Materials

EPD has been given special attention as the leading ceramic electrodeposition technique in the last decades [13, 83]. This technique has revolutionized advanced ceramic materials processing both in academia and industry. In ceramic industries, thin ceramic films can be achieved from colloidal suspensions. In recent years, the attractive characteristics of EPD have made it a potential alternative approach for many purposes in several fields. For example, EPD has been reported as a promising technique for fabricating crystalline oriented thick films [6, 12, 13, 16]. Titanium oxide, which has three crystallographic polymorphs (anatase, rutile, and brookite), has been widely used in different areas due to its remarkable optical characteristics. In another study [14], it has been shown that EPD in a strong magnetic field enables taking advantage of magnetic anisotropy of materials with asymmetric crystalline structures to produce layers of aligned crystalline magnetic particles. The crystal anisotropy produces the driving force (ΔF) of this magnetic alignment and it is described by Eq. 1 [15],

$$\Delta F = \Delta\chi V B^2 / 2\mu_0 \quad (1)$$

where $\Delta\chi$ is the difference between susceptibilities parallel and perpendicular to the magnetic principal axis, V is the volume of the material, B is the applied magnetic field, and μ_0 is the permeability in a vacuum. Figure 3 depicts a schematic view of the EPD cell in this investigation.

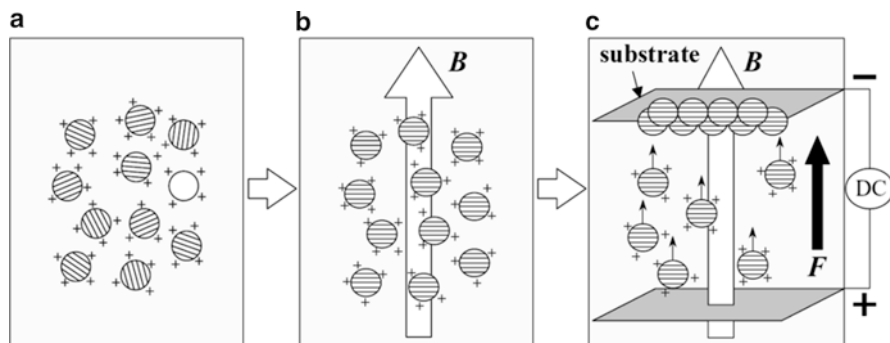
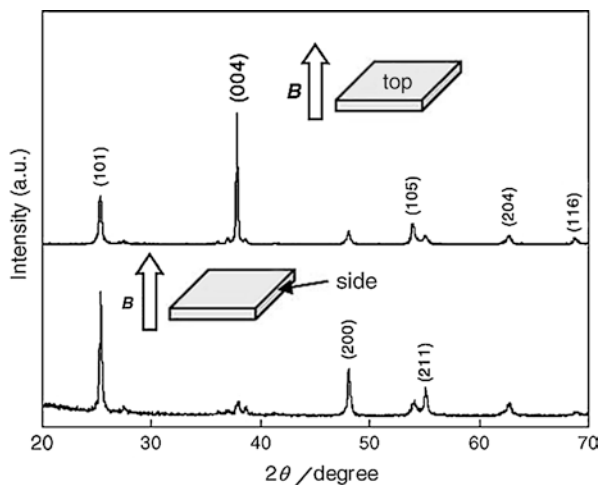


Fig. 3 Schematic view of EPD under high magnetic field; (a) suspension, (b) magnetic orientation and (c) preferred deposition (Reprinted from Uchikoshi et al. [16], Copyright (2004), with permission from Elsevier)

Fig. 4 XRD pattern of the top and side planes of deposited anatase (Reprinted from Uchikoshi et al. [14], Copyright (2006), with permission from Elsevier)



TiO₂ powder was sonicated in distilled water at pH 5.5, and then polyethylenimine (PEI) was added to improve stability of the suspension. PEI modified the zeta potential of the powder. The EPD was done in presence of magnetic field at current density of 2.7 mA/cm². As a result, the magnetic field fixes the orientation of each particle and the crystalline structure of polycrystalline TiO₂ can be controlled [14]. Figure 4 shows the XRD pattern of the top and side planes of the deposited anatase.

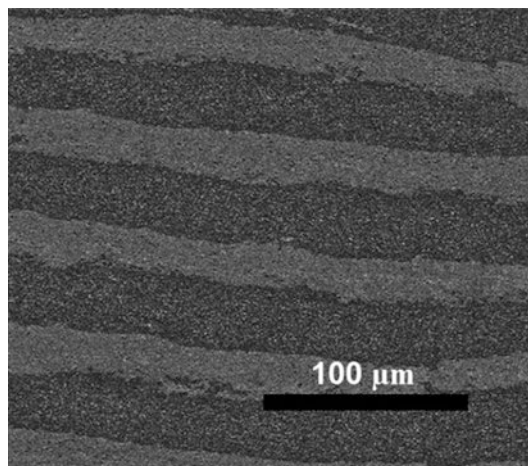
α-alumina is an interesting engineering material [17]. Possibility of fabrication of textured alumina by EPD was also investigated [18]. High purity fine α-alumina and hexagonal alumina platelets as matrix powder and template were used.

The matrix powder was milled for 24 h in ethanol and 0.5 vol% de-ionized water. Platelets were then added to the suspension with n-butylamine and Dolapix Ce-64 (Dolapix is an anionic polyelectrolyte dispersant that contains ammonium salt of polymethacrylic acid [84]) in order to negatively charge and disperse the particles. The pH of the suspension was at 11.5 for the whole 450-s duration of the procedure. As a result, (001) alumina texture was obtained.

Multilayered Composites

Another group reported enhanced mechanical properties in textured, multilayered alumina produced via EPD [19]. It has also been reported that EPD is capable of fabricating functionally gradient and multilayer composites and sandwich structures [20–22]. Functionally graded materials are advanced composite materials which consist of different layers with different mechanical properties and are able to alleviate problems associated with interfaces of different materials [85, 86]. Polycrystalline diamond has wide applications in for cutting and grinding in machining, mining and oil industries. Researchers have been successful in electrophoresis of diamond powder which was first acid washed and then boiled and rinsed in HCl solution and distilled water. Figure 5 shows a SEM image of diamond/diamond laminates formed by electrophoretic deposition of diamond powders with different concentrations in HCl solution. Direct-current EPD on tungsten carbide substrates was conducted at a constant voltage of 1.5 for 7.5 min for each layer [22]. Due to the high accuracy of EPD [1], sandwich-structured materials can be fabricated after several steps in both single-bath and multi-baths experiments [22].

Fig. 5 SEM image of cross-section of diamond/diamond laminates (Reprinted from Dzepina et al. [22], Copyright (2013), with permission from Elsevier)



Thermoelectric Thick Films

Recently our research group has been successful in improving the thermoelectric power factor of SiGe thick films through electrophoresis of elemental Si and Ge powders [23]. For a highly efficient thermoelectric device, the resistance of the ohmic contact must be much smaller than the resistance of the thermoelectric element. Therefore, the length of the device must be bigger than the ratio of the specific ohmic contact resistance to the resistivity of the thermoelectric material. Computational simulation studies show that a thickness of more than a few tens of micrometers is needed to satisfy this criterion [87]. The small heights of the thermoelectric legs introduce complexity for making simultaneous electrical contacts to the entire thermoelectric array. Even a small height variation in one leg can lead to open circuit failure of the whole module. EPD has shown great capabilities in making films with thicknesses from submicron to hundreds of micron, while maintaining the composition of the starting materials with stoichiometric ratios. In that project, our group prepared $\text{Si}_{80}\text{Ge}_{20}$ powder via milling and then sonicated the resulting material in acetone for 2 h in order to avoid any agglomeration and achieve a homogeneously dispersed colloidal solution. Silicon wafer was used as the substrate and it was etched in buffered oxide etch solution for 2 min, and then washed with deionized water to remove the native SiO_2 . The process was carried out in a custom-made cell under a constant voltage of 30 V at room temperature. After that, the sample was dried at room temperature and then cold pressed under 30 MPa pressure. Afterward, the coated substrate was sintered for 3 h at 1200 °C in nitrogen atmosphere. Figure 6 shows a SEM image and a photograph of $\text{Si}_{80}\text{Ge}_{20}$ layered on silicon substrate. Formation of dense and uniform layers of $\text{Si}_{80}\text{Ge}_{20}$ can be seen in Fig. 6a, while Fig. 6b shows the overall uniformity of the thick films. Seebeck coefficient and electrical conductivity measurements from the room temperature to 950 °C showed that the thermoelectric power factor of $\text{Si}_{80}\text{Ge}_{20}$ thick film is approximately $1.9 \times 10^{-3} \text{ W}\cdot\text{m}^{-1}\cdot\text{K}^{-2}$, which is an order of magnitude larger than the previously achieved values for thin films of this material.

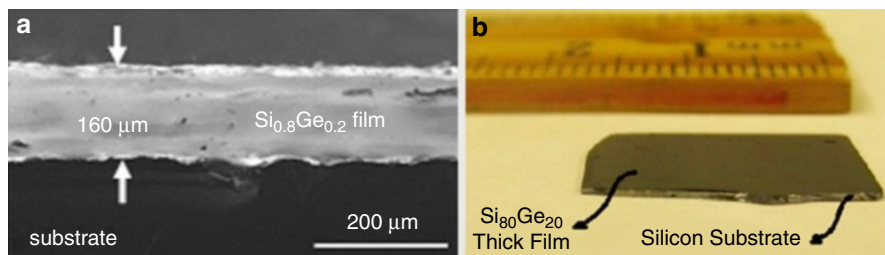


Fig. 6 (a) SEM image and (b) photograph of $\text{Si}_{80}\text{Ge}_{20}$ EPD coating sintered on silicon substrate (Reprinted from Nozariasbmarz et al. [23], Copyright (2013), with permission from Elsevier)

Particle Size Separation

Particle size separation is another capacity of EPD [24]. In one investigation, two parallel nonconductive electrodes were attached to borosilicate glass by gold paste. SnO_2 particles were dispersed in pure acetone and alternating-current EPD was done at 40 V for 10 min. It has been shown that increasing the frequency of the AC field leads to narrowing of the size distribution curve [24].

Deposition of Nanotubes

EPD has been used to improve carbon nanotubes (CNTs), to make CNT-composites, and for graphene synthesis [25–27]. Various composites including SiO_2/CNT [28], CNT/TiO_2 [29, 30], MnO_2/CNT [31], $\text{Fe}_3\text{O}_4/\text{CNT}$ [32], hydroxyapatite/CNT [33–35], and bioactive glass/CNT composites [36, 37] have been made using homogeneous dispersion of CNTs in an appropriate solvent. Fibers coated with single-walled CNTs, which can be used for extracting phenols from aqueous solutions, have also been prepared by electrophoresis of a suspension of CNTs in dimethylformamide at a constant voltage of 40 V for 10 s [88].

Figure 7 shows different outcomes of EPD made CNT/ceramic nanocomposites. Depending on the conditions sometimes ceramic or metallic particles are deposited on CNTs, in other cases CNTs are coagulated onto particles, and it is also possible to achieve simultaneous deposition of CNTs and particles.

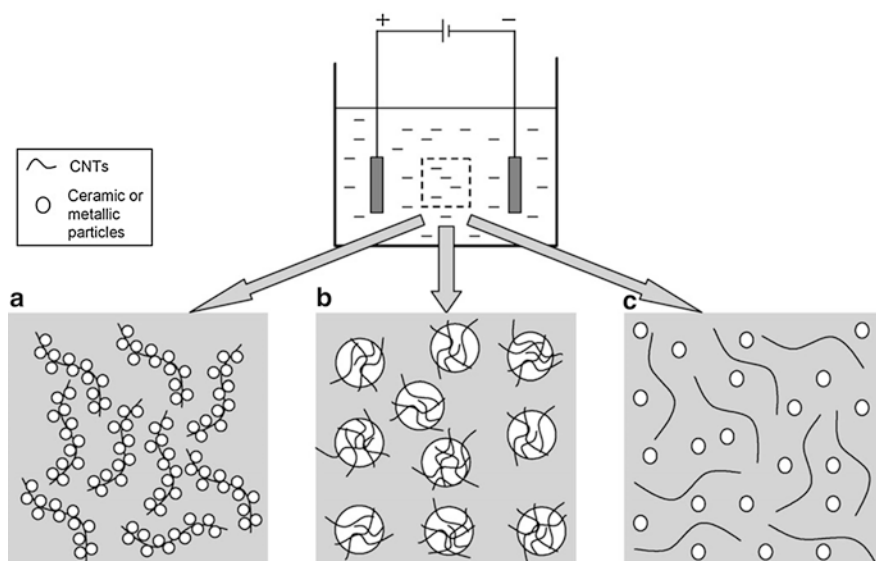


Fig. 7 Deposition of (a) particles on CNTs, (b) CNTs on particles, and (c) co-deposition of CNTs and particles (Reprinted from Boccacini et al. [25], Copyright (2010), with permission from Elsevier)

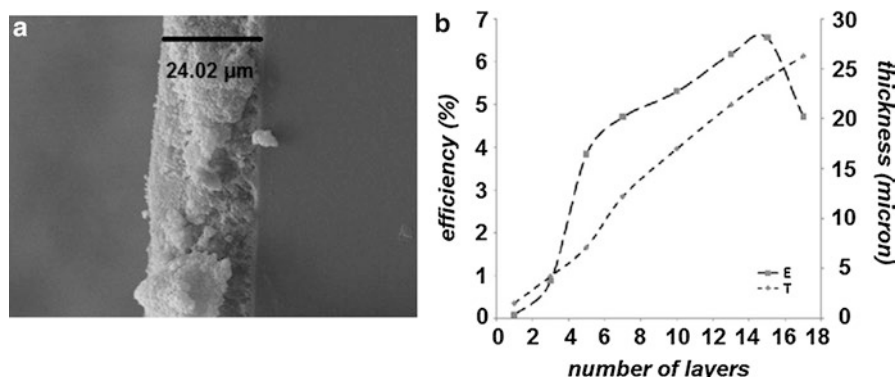


Fig. 8 (a) SEM image of cross-section of fabricated DSSC after annealing at 500 °C, (b) the effect of number of layers on thickness (T) and efficiency (E) of EPD fabricated DSSCs (Reprinted from Hamadani et al. [39], Copyright (2013), with permission from Elsevier)

Dye Sensitized Solar Cells

Efficient dye sensitized solar cells (DSSCs) can be made through multiple EPDs [38, 39]. DSSCs are photovoltaic devices with high conversion efficiency [89] and their properties were modified after EPD at constant voltage of 10 V for 20–15 cycles at 25 °C and further annealing (Fig. 8a). Figure 8b shows the enhanced efficiency of these cells by increasing the number of the layers.

SiC Fiber Reinforced Composites

SiC-fiber-reinforced composites have a great potential to be used for fusion reactors due to their remarkable resistance against neutron flux [90, 91]. EPD production of these composites [40] led to the idea that the quality and density obtained in this procedure is highly correlated with the zeta potential of the charged particles. The experiment was conducted at constant voltage of 60 V for 5 min under DC electrical field. It has also been demonstrated that addition of both cationic deflocculant and Dolapix (a common deflocculant and dispersant in ceramic industry) and adjusting the pH around 9 improved the resulting properties.

Thick Film Optical Modulators

WO₃ is used for optical modulation due to its electrochromic color [92]. Although hydrothermal process is the most popular technique for the synthesis of tungsten oxide [93], it needs several additional steps to complete the procedure; EPD has the significant advantage of having control over the whole process via manipulating pH level, process duration, and electrical power [41]. In the experiment, nanorods of

WO₃ were dispersed in deionized water with a pH level of around 6.77. Indium tin oxide glass (ITO-glass is a transparent conductive solid solution of In₂O₃ and SnO₂) was used as the working electrode with positive charge, and the process was done at a constant current of 0.8 mA/cm². Successful EPD of transparent ZnO thin films has also been reported recently [42].

Batteries and Electrochemical Capacitors

The ability of producing thick films by EPD has made it interesting for application in lithium batteries [43] which currently are the most favorable portable energy source in electronic devices [94]. High power and long life cycle of electrochemical capacitors, which operate via taking advantage of the double layer formed at the interface of electrode and electrolyte [95], have made them a promising choice for energy storage applications [96, 97]. The supercapacitor performance was significantly improved through EPD of hydrous ruthenium oxide particles with polytetrafluoroethylene (PTFE is a highly hydrophobic synthetic polymer) [44]. A schematic sketch of electrophoresis of these to particles can be seen in Fig. 9a; while Fig. 9b shows the increase in specific capacitance of electrodes coated with these materials as a function of loading weight for hydrous ruthenium oxide electrodes.

Manganese oxide coatings for supercapacitor applications were also produced by electrophoresis [98]. The experiment was carried out under DC electrical field at a constant voltage of 100 V for 20 min. Manganese oxide particles were dispersed in ethanol suspension by sonication and graphite electrodes were utilized.

Solid Oxide Fuel Cells (SOFCs)

Solid oxide fuel cells (SOFCs) have played a crucial leading role in power generation. Many scientists believe that SOFCs can revolutionize the future of science and technology due to the cells clean operation and efficiency. As it can be understood from the name, the difference between a SOFC and a conventional fuel cell is that the first one uses a solid ion conductive ceramic as the electrolyte, while the latter works with liquid electrolytes [99]. The electronic conductivity of the dense electrolyte of a SOFC at the working temperature of approximately 600–1000 °C should be low [100]. Generally, in SOFCs, the cathode is exposed to open air or oxygen and oxygen is reduced to an oxygen anion. Then the oxygen anions travel through the electrolyte to the anode where hydrogen molecules or hydrocarbons are oxidized at the operating temperatures [101]. Lanthanum strontium gallium magnesium oxides (LSGMs), Lanthanum strontium cobalt ferrites (LSCFs), yttria stabilized zirconia (YSZ), and ceria gadolinium oxides (CGOs) which have remarkable long-term stability and strong mechanical properties are the most popular materials for electrolyte, while lanthanum strontium manganite (LSM), Ni foil, Ni/ZrO₂ cermet, and Ni/YSZ substrates are used as cathodes and anodes [102, 103]. There are several challenges in fabrication of SOFCs such as their high operating temperatures and high

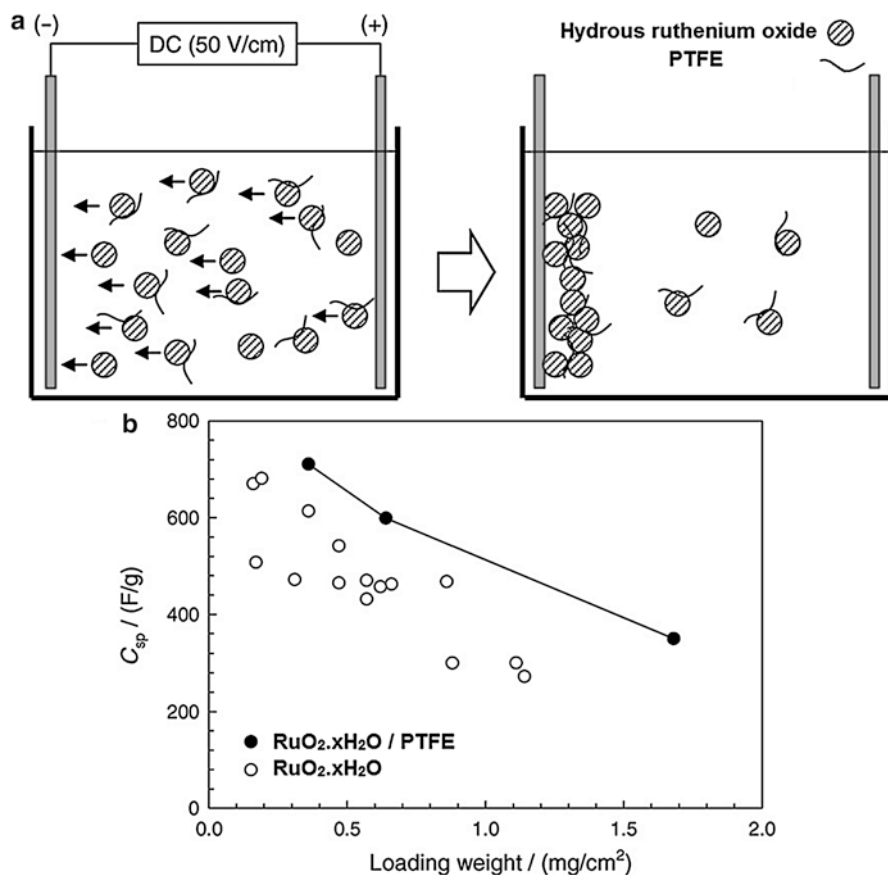


Fig. 9 (a) EPD by adding PTFE, (b) specific capacitance versus loading weight (Reprinted from Jang et al. [44], Copyright (2006), with permission from Elsevier)

layer thickness [104]. There are two possible approaches to solve these issues. First, as the operating temperature is completely dependent on the nature of the electrolyte material, there is always a possibility to find better materials with higher ion conductivity at lowered temperatures (500–800 °C) [105]. Second, it is known that reducing the thickness of the film can also lower the operating temperatures [106]. EPD has been widely exploited to fabricate SOFCs in the last two decades [45, 46, 49–51]. EPD is able to fabricate complex shapes, prepare both dense and porous films, and allows codeposition of different source materials. Figure 10 shows the SEM images of the surface and the cross section of a positive electrolyte negative cell [48].

Preparation of YSZ on LSM and LSM/YSZ substrates through EPD was carried out by a constant-voltage method [107]. Another research group successfully produced well-distributed LSGM films with good adhesion to platinum substrate from a suspension in a mixture of acetone and ethanol [108]. The right selection of solvent, dispersant, and binder is of great importance in electrophoresis of ceramic

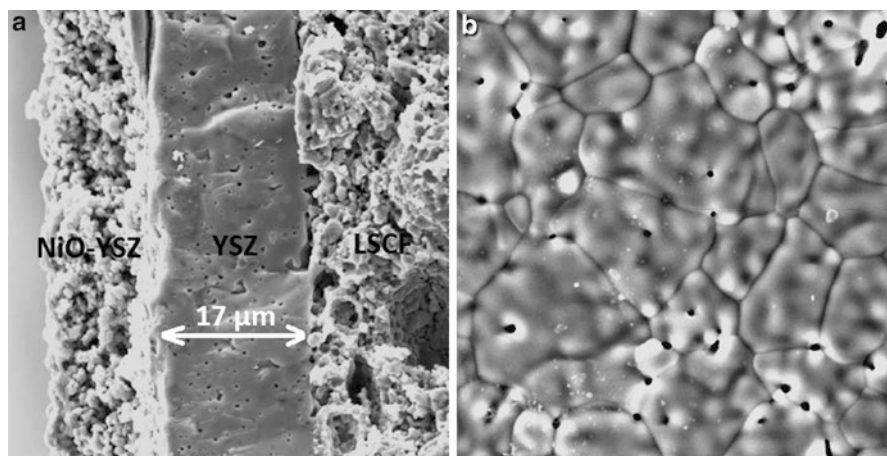


Fig. 10 SEM image of the sintered EPD films of positive-electrolyte-negative (NiO-YSZ/YSZ/LSCF) in a SOFC; (a) cross-section and (b) surface (Reprinted from Jia et al. [48], Copyright (2006), with permission from Elsevier)

laminates to be used in SOFCs. In one experiment, they found the best properties using ternary selection of ethyl alcohol, phosphate ester, and polyvinyl butyral as solvent, dispersant, and binder, respectively [109].

Corrosion-Resistant Coatings

EPD is one of the most promising techniques for fabricating thick films, which may be applied to increase the corrosion resistance of metals. Corrosion-resistant coatings have been used for protecting different substrates that suffer from weak corrosion resistance [110–112]. Silica hybrid coatings have provided both excellent mechanical and corrosion resistance properties, they have drawn much attention in the last decade and EPD was commonly used to make corrosion protective coatings [52, 113–115]. One study compared corrosion behavior of silica hybrid coatings made by dipping with these made by EPD [52]. Stainless steel and graphite electrodes were used as the substrate and counter electrode, respectively. Temperature was maintained at 5 °C during the whole procedure. EPD coatings were thicker than dipped coatings and had more enhanced corrosion resistance.

Catalyst Support and Molecular Sieves

Porous ceramics are used as catalyst supports and molecular sieves due to their corrosion resistance and high temperature stability. In order to broaden and modify the range of their application, coatings are applied all over the outer and inner surface of these ceramics. Pore size and surface functionality must be controlled too in order

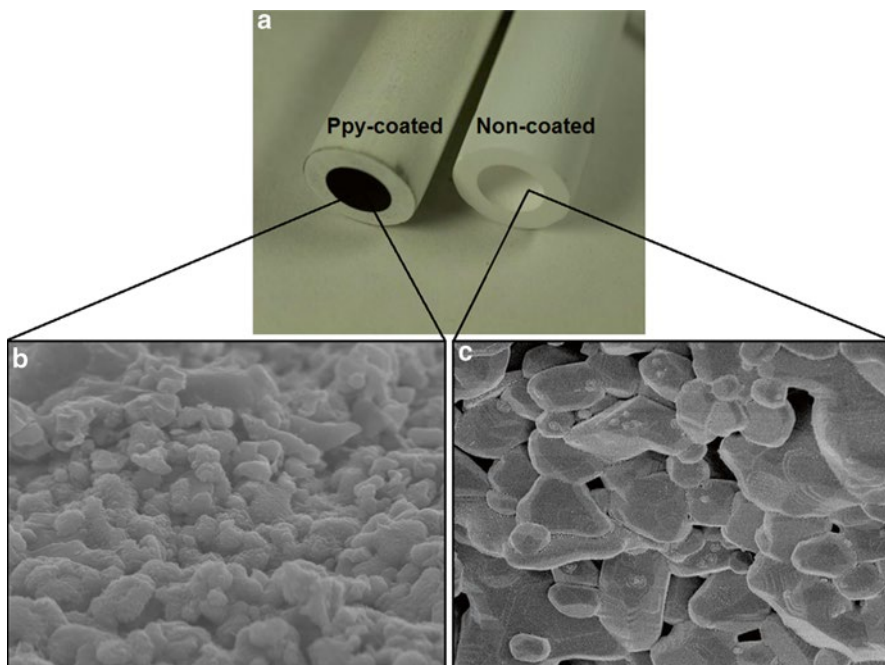


Fig. 11 (a) Porous alumina tubes, and SEM images of the inner wall of (b) Ppy-coated and (c) noncoated tubes (Reprinted from Kreethawate et al. [53], Copyright (2010), with permission from Elsevier)

to improve their properties. EPD makes possible embedding strong and uniform coatings on complex-shaped materials [116, 117], such as coating the inner surface of porous foams and tubes. Near-200 μm layer of alumina particles was deposited onto the inner surface of porous alumina tube via electrophoresis at a constant voltage of 100 V under DC electrical field, using polypyrrole-coated glass and stainless steel as the substrate and the counter electrode, respectively [53]. Figure 11 shows SEM images of the inner wall of the noncoated and Ppy-coated tubes.

Sensors

Gas sensors, with high sensitivity, capability of real-time detection, and economic efficiency, are widely used in industry [118]. EPD has greatly contributed in generating both new original and modified production routes for production of common gas sensor films [54]. Figure 12 depicts a schematic sketch of the process of fabricating a gas sensor with anodic aluminum oxide (AAO)/Al substrate and SEM image of gas sensors fabricated with a current density of 90 mAcm^{-2} . It is noteworthy that an insulator support has to be used between the gas sensing film and the conductive substrate, in order to avoid of a short circuiting between these two layers [55].

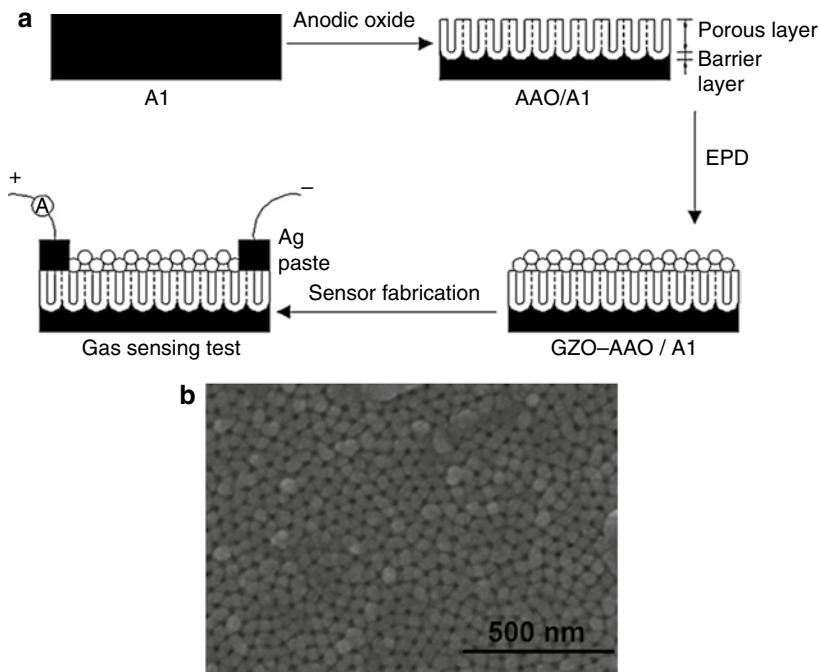


Fig. 12 Schematic sketch of fabricating gas sensor via EPD (Reprinted from Han et al. [57], Copyright (2010), with permission from Elsevier)

Al-Cr-Fe conductive substrate was electrophoretically coated by zinc oxide in construction of one of the sensors [56]. Another sensor was constructed using aqueous electrophoretic deposition of aluminum oxide on aluminum substrate [57].

Piezoelectric Actuators

Piezoelectric actuators (PAs) use voltage-induced size changes of ferroelectrics for highly accurate mechanical actuators. A good PA provides high forces at low voltages. In addition, low sintering temperature and high Curie temperature and high piezoelectric constant are very important [119, 120]. PAs are utilized in a wide range of applications, from optical to aerospace industries [121–123]. PAs suffer from weak mechanical properties at both low and high temperatures and their efficiency is highly dependent on the continuity and uniformity of their structures. EPD has been proven to successfully solve these shortcomings due to its intrinsic properties. Two versions of piezoelectric actuators based on Pb-Zr-Ti-Bi-Fe-Ba-Cu-W oxides (PZT1 and PZT in Fig. 17) were tested in functionally graded structures with silver coated electrodes (Fig. 13) [58]. The results confirmed formation of a piezoelectric actuator.

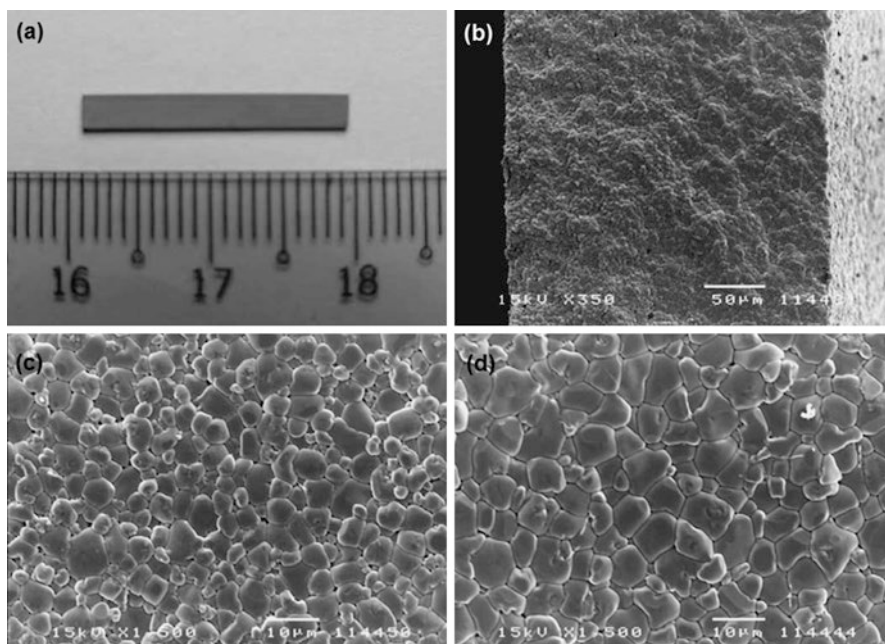
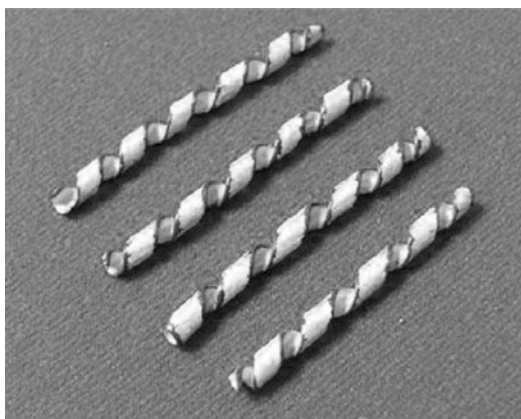


Fig. 13 Microstructure of piezoelectric functionally graded monomorph actuator; (a) plate, (b) cross-section, (c) PZT surface, and (d) PZT1 surface (Reprinted from Chen et al. [58], Copyright (2004), with permission from Elsevier)

Fig. 14 Image of piezoelectric actuators made by deposition on graphite rods (Reprinted from Chen et al. [59], Copyright (2008), with permission from Elsevier)



In another investigation, EPD was used to deposit piezoelectric layer on a graphite rod from a suspension containing doped piezoelectric material (Fig. 14) [59]. The graphite rods were removed from the spiral shape, resulting in complex shape PA actuators that would be very difficult to make using traditional methods. The studies showed that EPD is a promising method in production of PAs.

Biomedical Applications

EPD has many interesting characteristics for biomedical applications, such as simplicity, cost efficiency, high production rate, low processing temperature, full controllability, ability to form complex shapes and structures, and low processing temperature [13].

Forming Biocompatible Layers

In general, metallic biomaterials which are widely used as prosthesis and implants have one important shortcoming which is their bioinert nature [62]. Overcoming this problem, EPD can form bioactive ceramic coatings [124]. Amongst all, electrophoresis of hydroxyapatite (HA) and bioactive glass (BG) has been vastly investigated by scientists [60–62, 125, 126].

HA ($\text{Ca}_{10}(\text{PO}_4)_6(\text{OH})_2$) is a crystalline mineral that has very similar chemical composition to bone and teeth tissue and as it has excellent biocompatibility, osteoconductivity, and bioactivity; it is widely used as hip replacements and dental implants [63–65, 127]. Processing HA via a powder route has many difficulties, for example, sintering must be done at relatively high temperatures, which may sacrifice the biocompatibility and decompose the favorable HA structure [66]. It was demonstrated that electrophoresis of thermal-sprayed HA powders in ethanol suspension at a pH of 5, using graphite and stainless steel electrodes, leads to successful preparation of porous hydroxyapatite scaffold (Fig. 15a) [35]. In comparison to salt leaching and microsphere burn out, which are the two popular routes for fabrication of porous scaffolds, EPD has the advantages of needing no additives or binders and being a simpler process, although the costs of preparing large components are higher. As HA has poor mechanical properties, its applications are mostly in coating and composites with metallic substrates and matrices. Deposition of submicron HA in the form of a thick coating by EPD has been reported (Fig. 15b) [128]. Ethanol suspension and ultrasonic agitation was used in order to disperse the thermal-plasma-sprayed HA particles. EPD process was carried out at pH value of 3–5 and under current density of 0.05–1.5 mA/cm² for 90 s. Carbon rod and stainless steel

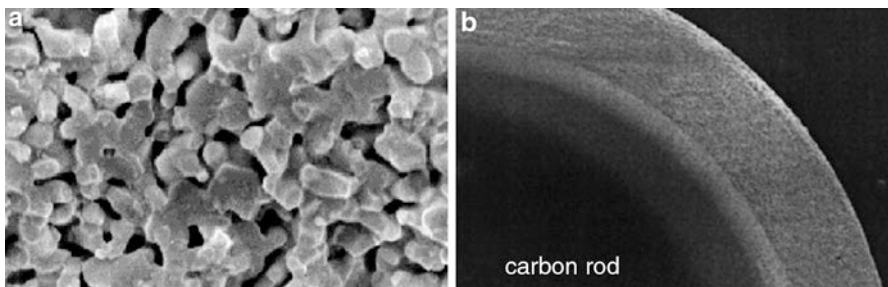


Fig. 15 (a) Interconnectivity of porous HA scaffold fabricated (Reprinted from Ma et al. [35], Copyright (2003), with permission from Elsevier), (b) dense, uniform and crack-free HA tube both prepared by EPD (Reprinted from Wang et al. [128], Copyright (2002), with permission from Elsevier)

cylinder were used as the substrate and the counterelectrode, respectively. Recently, another group has studied the formation of HA nanocomposite coatings in alcohols [129]. In their investigation, two 316 L stainless steel plates were used as electrodes and the experiment was carried out at voltages of 20 and 60 V/cm for up to 10 min. The quality of HA-chitosan nanocomposites were tested in alcoholic suspensions using methanol, ethanol, and isopropanol. Results revealed that the adsorption of chitosan on HA nanoparticles showed its highest and lowest levels, in isopropanol and methanol, respectively.

BG (FDA approved composition of a mixture of SiO_2 , CaO , Na_2O , and P_2O_5) is a surface reactive glass biomaterial with a very good biocompatibility [130]. The deficiencies of both BG and some metallic implants (which are low corrosion resistance and low biocompatibility [131],) were eliminated by coating BG on the metallic implants. Figure 16 shows deposited BG composite on Ti wire. In one study, BG was electrophoretically deposited on 316 L stainless steel substrate in a mixture of ethanol and triethanolamine as the suspension at constant voltages of 30, 60, and 90 V/cm^2 . They have also reported that the layer acts as a barrier layer in artificial saliva [69]. In another study, EPD of BG/polymer composite coatings were made at a constant voltage range of 10–30 V and a pH level of 11 [68].

Moreover, EPD has helped to develop novel bioactive composites. For example, wollastonite (CaSiO_3) particles were deposited into porous alumina and porous ultrahigh molecular weight polyethylene in a suspension of iodine and acetone at a constant voltage of 1000 V for 60 min. In the procedure, accumulation of wollastonite particles occurred near the cathode surface [67].

EPD of Bacteria

In addition, EPD of bacterial cells was carried out and the interesting results of the investigation have opened new windows to electrophoresis of inorganic materials [70]. In that investigation, a mixture of demineralized water and sucrose ($\text{C}_{12}\text{H}_{22}\text{O}_{11}$)

Fig. 16 Alginate/BG composite deposited on Ti wire (Reprinted from Zhitomirsky et al. [68], Copyright (2009), with permission from Elsevier)

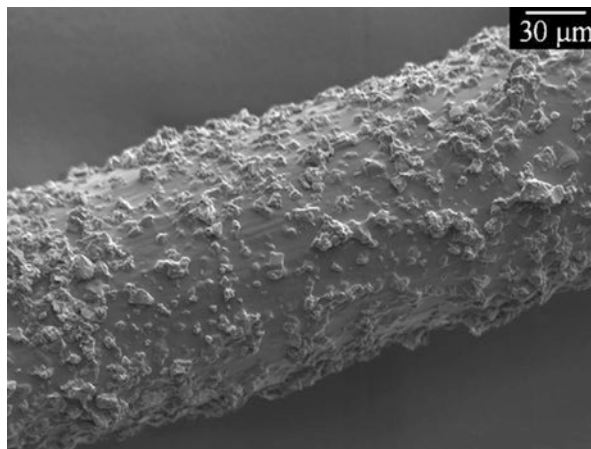
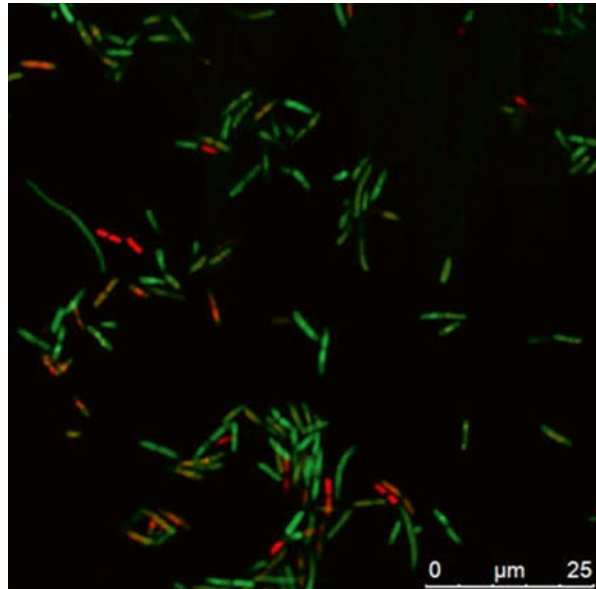


Fig. 17 Confocal laser scanning microscope image of electrophoretically deposited bacteria after 2400 s (Reprinted from Neirinck et al. [70], Copyright (2009), with permission from Elsevier)

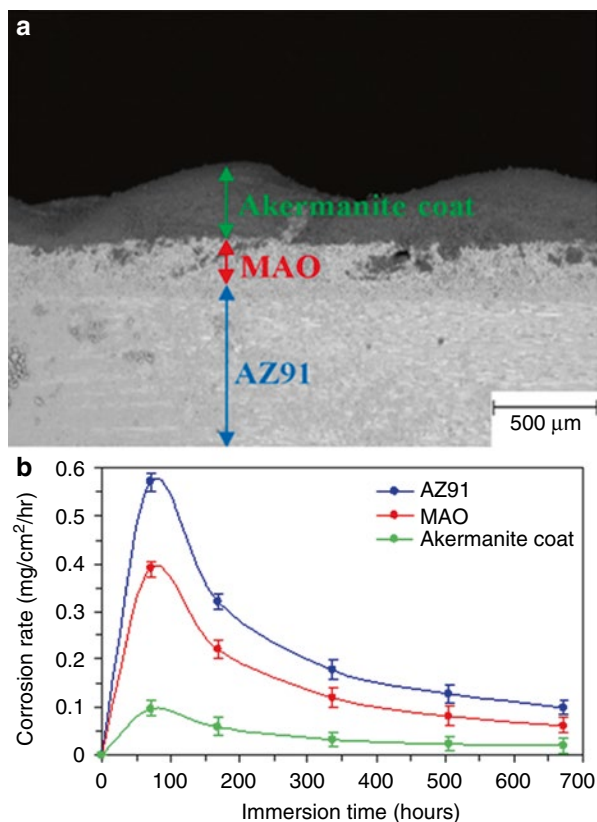


was used as. The experiment was done under AC field at a constant voltage of 100 V and a frequency of 25 Hz for 10 min. Confocal laser scanning microscope image (Fig. 17) demonstrated that both live Gram-positive and Gram-negative bacteria were successfully deposited; however, the viability of the bacteria cells was compromised after the deposition.

Corrosion Protection of Implants

Magnesium alloys have an outstanding strength to weight ratio, suitable biodegradability and nontoxicity which make them appropriate candidates for implants. The major drawback for these alloys is their low corrosion resistance in the body. EPD has been shown to be useful in forming corrosion resistant coatings on magnesium bio implants [71]. AZ91 Mg alloy bioimplants were coated by nanostructured akermanite ($\text{Ca}_2\text{MgSi}_2\text{O}_7$) to improve the corrosion resistance of these implants. Akermanite nano powders were suspended and then ultrasonically dispersed in methanol and immediately deposited electrophoretically on micro arc oxidized (MAOed) AZ91 Mg alloy substrates. EPD process was carried out at constant voltage of 100 V for 3 min. The resulting samples were then immersed in simulated body fluid (SBF) to study the corrosion rate. Figure 18a shows SEM morphology of AZ91 after MAO and coating with akermanite; Fig. 18b demonstrates the comparative results of the immersion test for studying the corrosion behavior of AZ91 before and after being assisted by MAO and coating. As can be seen, the corrosion rate has been significantly reduced after applying MAO and akermanite coating. It is noteworthy that the porous coating has been made intentionally in order to enhance biological fixations of the living tissue to the implant.

Fig. 18 (a) Cross-section view of the SEM morphology of final sample. (b) Corrosion rate of AZ91, MAO and akermanite coated samples immersed in SBF (Reprinted from Razavi et al. [71], Copyright (2014), with permission from Elsevier)



Conclusion

Electrophoretic deposition (EPD) is a versatile processing technique, with remarkable characteristics such as cost effectiveness, simple equipment, offering relatively short processing time and easy modification. EPD was proven to be useful for production of geometrically complicated shapes, and full controllability of the thickness and morphology, and it has gained considerable attention in the last few decades. Deep understanding of EPD mechanisms along with appropriate process variables can lead to efficient fabrication of the intended piece. This technique is capable of fabricating both micro- and nanostructured ceramics, which can be used in a wide range of applications such as biomedical, optical, and corrosion protection. It has also found applications in production of carbon nano tubes, fuel cells, sensors, and actuators. Although EPD has been studied for more than 50 years, there are still opportunities for novel applications and material advancements based on EPD due to its exceptional characteristics.

Acknowledgment This study is partially based upon work supported by Air Force Office of Scientific Research (AFOSR) High Temperature Materials program under grant no. FA9550-10-1-0010, Oklahoma Center for Advancement of Science and Technology (grant no. AR131-054 8161 and grant no. AR131-049) and the National Science Foundation (NSF) under grant no. 0933763.

References

1. Besra L, Liu M (2007) A review on fundamentals and applications of electrophoretic deposition (EPD). *Prog Mater Sci* 52:1–61
2. Yoshioka T, Chávez-Valdez A, Roether J, Schubert D, Boccaccini A (2013) AC electrophoretic deposition of organic–inorganic composite coatings. *J Colloid Interface Sci* 392:167–171
3. Gardeshzadeh A, Raissi B, Marzbanrad E (2008) Electrophoretic deposition of SnO₂ nanoparticles using low frequency AC electric fields. *Mater Lett* 62(10–11):1697–1699
4. P Sarkar, D De, T Uchikochi, L Besra (2012) Electrophoretic deposition (EPD): fundamentals and novel applications in fabrication of advanced ceramic microstructures. In: *Electrophoretic deposition of nanomaterials*. Springer, New York, pp 181–215
5. Pickard W (1933) Remarks on the theory of electrophoretic deposition. *J Electrochem Soc* 115:105–108
6. Sarkar P, Nicholson P (1996) Electrophoretic deposition (EPD): mechanism, kinetics and application to ceramics. *J Am Ceram Soc* 79:1987–2002
7. E Harsanyi (1933) Method of coating radiant bodies. US Patent 1,897,902, 14 Feb 1933
8. T Blickwedel, W Rhyne (1958) Cathoretically coated heater insulator assembly. US Patent 2,831,140, 15 Apr 1958
9. Tang F, Sakka Y, Uchikoshi T (2002) Electrophoretic deposition of aqueous nano-sized zinc oxide suspensions on a zinc electrode. *J Am Ceram Soc* 85:2161–2165
10. Besra L, Uchikoshi T, Suzuki T, Sakka Y (2008) Bubble-free aqueous electrophoretic deposition (EPD) by pulse potential application. *J Am Ceram Soc* 91:3154–3159
11. Besra L, Uchikoshi T, Suzuki T, Sakka Y (2009) Application of constant current pulse to suppress bubble incorporation and control deposit morphology during aqueous electrophoretic deposition (EPD). *J Eur Ceram Soc* 29:1837–1845
12. Biest OVD, Vandepierre L (1999) Electrophoretic deposition of materials. *Annu Rev Mater Sci* 29:327–352
13. Boccaccini A, Zhitomirsky I (2002) Application of electrophoretic and electrolytic deposition techniques in ceramic processing. *Curr Opin Solid State Mater Sci* 6:251–260
14. Uchikoshi T, Suzuki T, Imura S, Tang F, Sakka Y (2006) Control of crystalline texture in polycrystalline TiO₂ (anatase) by electrophoretic deposition in a strong magnetic field. *J Eur Ceram Soc* 26:559–563
15. Rango PD, Lees M, Lejay P, Sulpice A, Tournier R, Ingold M, Germi P, Pernet M (1991) Texturing of magnetic materials at high temperature by solidification in a magnetic field. *Nature* 349:770–772
16. Uchikoshi T, Suzuki T, Tang F, Okuyama H, Sakka Y (2004) Crystalline-oriented TiO₂ fabricated by the electrophoretic deposition in a strong magnetic field. *Ceram Int* 30:1975–1978
17. Uchikoshi T, Suzuki T, Sakka Y (2006) Crystalline orientation of alumina ceramics prepared by electrophoretic deposition under a high magnetic field. *J Mater Sci* 41:8074–8078
18. Zhang L, Vleugels J, Biest OVD (2010) Fabrication of textured alumina by orienting template particles during electrophoretic deposition. *J Eur Ceram Soc* 30:1195–1202
19. Suzuki T, Uchikoshi T, Okuyama H, Sakka Y, Hiraga K (2006) Mechanical properties of textured, multilayered alumina produced using electrophoretic deposition in a strong magnetic field. *J Eur Ceram Soc* 26:661–665
20. Askaria E, Mehralib M, Metselaara I, Kadrib N, Rahmana M (2012) Fabrication and mechanical properties of Al₂O₃/SiC/ZrO₂ functionally graded material by electrophoretic deposition. *J Mech Behav Biomed Mater* 12:144–150

21. Ferrari B, Bartret A, Baudín C (2009) Sandwich materials formed by thick alumina tapes and thin-layered alumina–aluminium titanate structures shaped by EPD. *J Eur Ceram Soc* 29:1083–1092
22. Dzepina B, Sigalas I, Herrmann M, Nilen R (2013) The aqueous electrophoretic deposition (EPD) of diamond–diamond laminates. *Int J Refract Met Hard Mater* 36:126–129
23. Nozariasmarz A, Tahmasbi Rad A, Zamanipour Z, Krasinski JS, Tayebi L, Vashae D (2013) Enhancement of thermoelectric power factor of silicon germanium films grown by electrophoresis deposition. *Scr Mater*. doi:10.1016/j.scriptamat.2013.06.025
24. Raissi B, Marzbanrad E, Gardeshzadeh A (2009) Particle size separation by alternating electrophoretic deposition. *J Eur Ceram Soc* 29:3289–3291
25. Boccaccini A, Cho J, Subhani T, Kaya C, Kaya F (2010) Electrophoretic deposition of carbon nanotube–ceramic nanocomposites. *J Eur Ceram Soc* 30:1115–1129
26. Wang L, Chen Y, Chen T, Que W, Sun Z (2007) Optimization of field emission properties of carbon nanotubes cathodes by electrophoretic deposition. *Mater Lett* 61:1265–1269
27. Ata M, Sun Y, Li X, Zhitomirsky I (2012) Electrophoretic deposition of graphene, carbon nanotubes and composites using aluminum as charging and film forming agent. *Colloids Surf A Physicochem Eng Asp* 398:9–16
28. Chicatun F, Cho J, Schaab S, Brusatin G, Colombo P, Roether J (2007) Carbon nanotube deposits and CNT/SiO₂ composite coatings by electrophoretic deposition. *Adv Appl Ceram* 106:186–195
29. Lee S, Sigmund W (2003) Formation of anatase TiO₂ nanoparticles on carbon nanotubes. *Chem Commun* 6:780–781
30. Jitianu A, Cacciaguerra T, Benoit R, Delpeux S, Béguin F, Bonnamy S (2004) Synthesis and characterization of carbon nanotubes–TiO₂ nanocomposites. *Carbon* 42:1147–1151
31. Li J, Zhitomirsky I (2009) Electrophoretic deposition of manganese dioxide–carbon nanotube composites. *J Mater Process Technol* 209:3452–3459
32. Mahajan S, Hasan S, Cho J, Shaffer M, Boccaccini A (2008) Carbon nanotube–nanocrystal heterostructures fabricated by electrophoretic deposition. *Nanotechnology* 19:195301 (8pp)
33. White A, Best S (2007) Hydroxyapatite–carbon nanotube composites for biomedical applications: a review. *Int J Appl Ceram Technol* 4:1–13
34. Chen Y, Zhang Y, Zhang T, Gan C, Zheng C, Yu G (2006) Carbon nanotube reinforced hydroxyapatite composite coatings produced through laser surface alloying. *Carbon* 44:37–45
35. Ma J, Wang C, Peng K (2003) Electrophoretic deposition of porous hydroxyapatite scaffold. *Biomaterials* 24:3505–3510
36. Boccaccini A, Chicatun F, Cho J, Bretcanu O, Roether J, Novak S, Chen Q (2007) Carbon nanotube coatings on bioglass-based tissue engineering scaffolds. *Adv Funct Mater* 17:2815–2822
37. Harrison B, Atala A (2007) Carbon nanotube applications for tissue engineering. *Biomaterials* 28:344–353
38. Chiu W, Lee K, Hsieh W (2011) High efficiency flexible dye-sensitized solar cells by multiple electrophoretic depositions. *J Power Sources* 196:3683–3687
39. Hamadani M, Gravand A, Jabbari V (2013) High performance dye-sensitized solar cells (DSSCs) achieved via electrophoretic technique by optimizing of photoelectrode properties. *Mater Sci Semicond Process* 16(5):1352–1359
40. Novak S, Rade K, König K, Boccaccini A (2008) Electrophoretic deposition in the production of SiC/SiC composites for fusion reactor applications. *J Eur Ceram Soc* 28:2801–2807
41. Khoo E, Lee P, Ma J (2010) Electrophoretic deposition (EPD) of WO₃ nanorods for electrochromic application. *J Eur Ceram Soc* 30:1139–1144
42. Verde M, Peiteado M, Caballero A, Villegas M, Ferrari B (2012) Electrophoretic deposition of transparent ZnO thin films from highly stabilized colloidal suspensions. *J Colloid Interface Sci* 373:27–33
43. Ferrari B, Moreno R, Hernan L, Melero M, Morales J, Caballero A (2007) EPD of thick films for their application in lithium batteries. *J Eur Ceram Soc* 27:3823–3827
44. Jang J, Machida K, Kim Y, Naoi K (2006) Electrophoretic deposition (EPD) of hydrous ruthenium oxides with PTFE and their supercapacitor performances. *Electrochim Acta* 52:1733–1741

45. Ishihara T, Sato K, Takita Y (1996) Electrophoretic deposition of Y_2O_3 -stabilized ZrO_2 electrolyte films in solid oxide fuel cells. *J Am Ceram Soc* 79(4):913–919
46. Ishihara T, Sato K, Mizuhara Y, Takita Y (1992) Preparation of yttria-stabilized zirconia films for solid oxide fuel cells by electrophoretic deposition method. *Chem Lett* 21:943–946
47. Ishihara T, Shimise K, Kudo T, Nishiguchi H, Akbay T, Takita Y (2000) Preparation of Yttria-stabilised zirconia thin-films on strontium doped $LaMnO_3$ cathode substrate via Electrophoretic. *J Am Ceram Soc* 83:1921–1927
48. Jia L, Lü Z, Huang X, Liu Z, Chen K, Sha X, Li G, Su W (2006) Preparation of YSZ film by EPD and its application in SOFCs. *J Alloys Compd* 424:299–303
49. Konno H, Tokita M, Furusaki A, Furuichi R (1992) Electrochemical formation of a-site substituted perovskite structure $La_{1-x}M_xCrO_3$ oxide coatings. *Electrochim Acta* 37(13): 2421–2426
50. Zhitomirsky I, Petric A (1999) Electrolytic and electrophoretic deposition of CeO_2 films. *Mater Lett* 40:263–268
51. Zhitomirsky I, Petric A (2000) Electrolytic deposition of Gd_2O_3 and organoceramic composite. *Mater Lett* 42:273–279
52. Castro Y, Ferrari B, Moreno R, Durán A (2005) Corrosion behaviour of silica hybrid coatings produced from basic catalysed particulate sols by dipping and EPD. *Surf Coat Technol* 191:228–235
53. Kreethawate L, Larpiattaworn S, Jiemsirilers S, Besra L, Uchikoshi T (2010) Application of electrophoretic deposition for inner surface coating of porous ceramic tubes. *Surf Coat Technol* 205:1922–1928
54. Dougami N, Takada T (2003) Modification of metal oxide semiconductor gas sensor by electrophoretic deposition. *Sens Actuators B* 93:316–320
55. Korotcenkov G (2005) Gas response control through structural and chemical modification of metal oxide films: state of the art and approaches. *Sens Actuators B* 107:209–232
56. Hossein-Babaei F, Taghibakhsh F (2001) Electrophoretically deposited zinc oxide thick-film gas sensors. *Electron Lett* 36:1815–1816
57. Han N, Deng P, Chen J, Chai L, Gao H, Chen Y (2010) Electrophoretic deposition of metal oxide films aimed for gas sensors application: the role of anodic aluminum oxide (AAO)/Al composite structure. *Sens Actuators B* 144:267–273
58. Chen Y, Ma J, Li T (2004) Electrophoretic deposition and characterization of a piezoelectric FGM monomorph actuator. *Ceram Int* 30:1807–1809
59. Chen Y, Boey T, Li F, Ma J (2008) Electrophoretic deposition and characterization of helical piezoelectric actuator. *Ceram Int* 34:1–6
60. Zhitomirsky I, Gal-Or L (1997) Electrophoretic deposition of hydroxyapatite. *J Mater Sci Mater Med* 8:213–219
61. Roether J, Boccaccini A, Hench L, Maquet V, Gautier S, Jerome R (2002) Development and in vitro characterization of novel bioresorbable and bioactive composite materials based on polylactide foams and Bioglass® for tissue engineering applications. *Biomaterials* 23:3871–3878
62. Stojanovic D, Jokic B, Veljovic D, Petrovic R, Uskokovic P, Janackovic D (2007) Bioactive glass-apatite composite coating for titanium implant synthesized by electrophoretic deposition. *J Eur Ceram Soc* 27:1595–1599
63. Javid M, Javadpour S, Bahrololoom M (2008) Electrophoretic deposition of natural hydroxyapatite on medical grade 316L stainless steel. *Mater Sci Eng C* 28:1509–1515
64. Pang X, Zhitomirsky I (2005) Electrodeposition of composite hydroxyapatite–chitosan films. *Mater Chem Phys* 94:245–251
65. Ducheyne P, Radin S, Heughebaert M, Heughebaert J (1990) Calcium phosphate ceramic coatings on porous titanium: effects of structure and composition on electrophoretic deposition. *Biomaterials* 11:244–254
66. Wei M, Ruys A, Milthorpe B, Sorrel C (1999) Solution ripening of hydroxyapatite nanoparticles: effects on electrophoretic deposition. *J Biomed Mater Res* 45:11–19

67. Yamaguchi S, Yabutsuka T, Hibino M, Yao T (2009) Development of novel bioactive composites by electrophoretic deposition. *Mater Sci Eng C* 29:1584–1588
68. Zhitomirsky D, Roether J, Boccaccini A, Zhitomirsky I (2009) Electrophoretic deposition of bioactive glass/polymer composite coatings with and without HA nanoparticle inclusions for biomedical applications. *J Mater Process Technol* 209:1853–1860
69. Mehdipour M, Afshar A, Mohebbali M (2012) Electrophoretic deposition of bioactive glass coating on 316L stainless steel and electrochemical behavior study. *Appl Surf Sci* 258:9832–9839
70. Neirincq B, Mellaert LV, Fransaeer J, Biest OVD, Anné J, Vleugels J (2009) Electrophoretic deposition of bacterial cells. *Electrochem Commun* 11:1842–1845
71. Razavi M, Fathi M, Savabi O, Razavi S, Hashemi Beni B, Vashae D, Tayebi L (2014) Controlling the degradation rate of bioactive magnesium implants by electrophoretic deposition of akermanite coating. *Ceram Int* 40(3):3865–3872. doi:10.1016/j.ceramint.2013.08.027
72. Tassel JV, Randall C (2006) Mechanisms of electrophoretic deposition. *Key Eng Mater* 314:167–174
73. Tassel JV, Randall C (1999) Electrophoretic deposition and sintering of thin/thick PZT films. *J Eur Ceram Soc* 19:955–958
74. Tassel JV, Randall C (2004) Potential for integration of electrophoretic deposition into electronic device manufacture; demonstrations using silver/palladium. *J Mater Sci* 39:867–880
75. Hamaker H (1940) Formation of deposition by electrophoresis. *Trans Faraday Soc* 36:279–287
76. Hamaker H, Verwey E (1940) Colloid stability: the role of the forces between the particles in the electrodeposition and other phenomena. *Trans Faraday Soc* 36:180–185
77. Sarkar P, Huang X, Nicholson P (1993) Electrophoretic deposition and its use to synthesize YSZ/Al_2O_3 micro laminate ceramic/ceramic composites. *Ceram Eng Sci Proc* 14:707–726
78. Koelmans H, Overbeek J (1954) Stability and electrophoretic deposition of suspensions in non-aqueous media. *Discuss Faraday Soc* 18:52–63
79. Ferrari B, Moreno R (1996) The conductivity of aqueous Al_2O_3 slips for electrophoretic deposition. *Mater Lett* 28:353–355
80. Negishi H, Yanagishita H, Yokokawa H (2002) Electrophoretic deposition of solid oxide fuel cell material powders. In: *Proceedings of the electrochemical society on electrophoretic deposition: fundamentals and applications*, vol 21, New Jersey, pp 214–221
81. Vandeperre L, Biest OVD, Clegg W (1997) Silicon carbide laminates with carbon interlayers by electrophoretic deposition. *Key Eng Mater* 1:127–131
82. Basu R, Randall C, Mayo M (2001) Fabrication of dense zirconia electrolyte films for tubular solid oxide fuel cells by electrophoretic deposition. *J Am Ceram Soc* 84:33–40
83. Gani MSJ (1994) Electrophoretic deposition: a review. *Ind Ceram* 14:163–174
84. Sarraf H, Škarpová L, Louda P (2007) Influence of different anionic polyelectrolyte dispersants on the rheological and electrokinetic properties of carbon nanotubes. *Ann Trans Nordic Rheol Soc* 15:1–4
85. Suresh S, Mortensen A (1997) Functionally graded metals and metal–ceramic composites: part 2 thermomechanical behaviour. *Int Mater Rev* 42:85–116
86. Bueno S, Baudín C (2007) Layered materials with high strength and flaw tolerance based on alumina and aluminium titanate. *J Eur Ceram Soc* 27(2–3):1455–1462
87. Vashae D, Christofferson J, Zhang Y, Shakouri A, Zeng G, LaBounty C, Fan X, Bowers JE, Croke E (2005) Modeling and optimization of single-element bulk SiGe thin-film coolers. *Microscale Thermophys Eng* 9:99–118
88. Li Q, Wang X, Yuan D (2009) Preparation of solid-phase microextraction fiber coated with single-walled carbon nanotubes by electrophoretic deposition and its application in extracting phenols from aqueous samples. *J Chromatogr A* 1216:1305–1311
89. Chen C, Wang M, Li J, Pootrakulchote N, Alibabaei L, Ngoc-le C, Decoppet J, Tsai J, Gratzel C, Wu C, Zakeeruddin S, Gratzel M (2009) Highly efficient light-harvesting ruthenium sensitizer for thin-film dye-sensitized solar cells. *ACS Nano* 3:3103–3109

90. Muroga T, Gasparotto M, Zinkle S (2002) Overview of materials research for fusion reactors. *Fusion Eng Des* 61–62:13–25
91. Tavassoli A (2002) Present limits and improvements of structural materials for fusion reactors – a review. *J Nucl Mater* 302:73–88
92. Niklasson G, Granqvist C (2007) Electrochromics for smart windows: thin films of tungsten oxide and nickel oxide, and devices based on these. *J Mater Chem* 17:127–156
93. Subrahmanyam A, Karuppusamy A (2007) Optical and electrochromic properties of oxygen sputtered tungsten oxide (WO₃) thin films. *Sol Energy Mater Sol Cells* 91:266–274
94. Souquet J, Duclot M (2002) Thin film lithium batteries. *Solid State Ion* 148:375–379
95. Miller J, Burke A (2008) Electrochemical capacitors: challenges and opportunities for real-world applications. *Electrochem Soc Interface* 17:53–57
96. Sharma P, Bhatti T (2010) A review on electrochemical double-layer capacitors. *Energy Convers Manag* 51:2901–2912
97. Deng L, Hao Z, Wang J, Zhu G, Kang L, Liu Z, Yang Z, Wang Z (2013) Preparation and capacitance of graphene/multiwall carbon nanotubes/MnO₂ hybrid material for high-performance asymmetrical electrochemical capacitor. *Electrochim Acta* 89:191–198
98. Chen C, Wang S, Lin C, Chen F, Lin C (2009) Electrophoretically deposited manganese oxide coatings for supercapacitor application. *Ceram Int* 35:3469–3474
99. Minh N (1993) Ceramic fuel cells. *J Am Ceram Soc* 76(3):563–588
100. Huijsmans J (2001) Ceramics in solid oxide fuel cells. *Curr Opin Solid State Mater Sci* 5:317–323
101. Minh N (2004) Solid oxide fuel cell technology – features and applications. *Solid State Ion* 174:271–277
102. Sun C, Stimming U (2007) Recent anode advances in solid oxide fuel cells. *J Power Sources* 171:247–260
103. Badwal S, Foger K (1996) Solid oxide electrolyte fuel cell review. *Ceram Int* 22(3):257–265
104. Yokokawa H, Tu H, Iwanschitz B, Mai A (2008) Fundamental mechanisms limiting solid oxide fuel cell durability. *J Power Sources* 182:400–412
105. Zhu B (2003) Functional ceria–salt-composite materials for advanced ITSOFC applications. *J Power Sources* 114(1):1–9
106. Talebi T, Raissi B, Haji M, Maghsoudipour A (2010) The role of electrical conductivity of substrate on the YSZ film formed by EPD for solid oxide fuel cell applications. *Int J Hydrog Energy* 35:9405–9410
107. Chen F, Liu M (2001) Preparation of yttria-stabilized zirconia (YSZ) films on La_{0.85}Sr_{0.15}MnO₃ (LSM) and LSM–YSZ substrates using an electrophoretic deposition (EPD) process. *J Eur Ceram Soc* 21:127–134
108. Sora I, Pelosato R, Simone A, Montanaro L, Maglia F, Chiodelli G (2006) Characterization of LSGM films obtained by electrophoretic deposition (EPD). *Solid State Ion* 177:1985–1989
109. Zhitomirsky I, Petric A (2000) Electrophoretic deposition of ceramic materials for fuel cell applications. *J Eur Ceram Soc* 20:2055–2061
110. Priyantha N, Jayaweera P, Sanjurjo A, Lau K, Lu F, Krist K (2003) Corrosion-resistant metallic coatings for applications in highly aggressive environments. *Surf Coat Technol* 163–164:31–36
111. El-Sharif M, Su Y, Chisholm C, Watson A (1993) Corrosion resistance of electrodeposited zinc-chromium alloy coatings. *Corros Sci* 35:1259–1265
112. O'Donnell P (1967) Beryllium fluoride coating as a corrosion retardant for beryllium. *Corros Sci* 7(10):717–718
113. Pepe A, Aparicio M, Ceré S, Durán A (2005) Synthesis of hybrid silica sol–gel coatings containing Zn particles on carbon steel and Al/Zn coated carbon steel. *Mater Lett* 59:3937–3940

114. Pepe A, Galliano P, Ceré S, Aparicio M, Durán A (2005) Hybrid silica sol–gel coatings on Austempered Ductile Iron (ADI). *Mater Lett* 59:2219–2222
115. Lu H, Hu Y, Gu M, Tang S, Lu H, Meng X (2009) Synthesis and characterization of silica–acrylic–epoxy hybrid coatings on 430 stainless steel. *Surf Coat Technol* 204:91–98
116. Kanamura K, Hamagami J (2004) Innovation of novel functional material processing technique by using electrophoretic deposition process. *Solid State Ion* 172:303–308
117. Boccaccini A, Schindler U, Krüger H (2001) Ceramic coatings on carbon and metallic fibres by electrophoretic deposition. *Mater Lett* 51(3):225–230
118. Franchini RDA, Souza CD, Colombara R, Matos MC, Matos R (2007) Rapid determination of hydrogen peroxide using peroxidase immobilized on Amberlite IRA-743 and minerals in honey. *J Agric Food Chem* 55:6885–6890
119. King T, Preston M, Murphy B, Cannell D (1990) Piezoelectric ceramic actuators: a review of machinery applications. *Precis Eng* 12(3):131–136
120. Crawley E, Luis JD (1987) Use of piezoelectric actuators as elements of intelligent structures. *Am Inst Aeronaut Astronaut J* 25:1373–1385
121. Chao X, Yang Z, Li G, Cheng Y (2008) Fabrication and characterization of low temperature sintering PMN–PZN–PZT step-down multilayer piezoelectric transformer. *Sens Actuat A* 144:117–123
122. Trolier-McKinstry S, Muralt P (2004) Thin film piezoelectrics for MEMS. *J Electroceram* 12:7–17
123. Dong W, Sun L, Du Z (2007) Design of a precision compliant parallel positioner driven by dual piezoelectric actuators. *Sens Actuat A* 135:250–256
124. Boccaccini A, Keim S, Ma R, Li Y, Zhitomirsky I (2010) Electrophoretic deposition of biomaterials. *J R Soc Interface* 7:S581–S613
125. Hench L (2006) The story of bioglass. *J Mater Sci Mater Med* 17:967–978
126. Kim H (2003) Ceramic bioactivity and related biomimetic strategy. *Curr Opin Solid State Mater Sci* 7:289–299
127. Wang P, Li C, Gong H, Jiang X, Wang H, Li K (2010) Effects of synthesis conditions on the morphology of hydroxyapatite nanoparticles produced by wet chemical process. *Powder Technol* 203:315–321
128. Wang C, Ma J, Cheng W, Zhang R (2002) Thick hydroxyapatite coatings by electrophoretic deposition. *Mater Lett* 57:99–105
129. Mahmoodi S, Sorkhi L, Farrokhi-Rad M, Shahrabi T (2013) Electrophoretic deposition of hydroxyapatite–chitosan nanocomposite coatings in different alcohols. *Surf Coat Technol* 216:106–114
130. Jones J (2013) Review of bioactive glass: from Hench to hybrids. *Acta Biomater* 9:4457–4486
131. Hench L (1998) Bioceramics. *J Am Ceram Soc* 81:1705–1728

Nanoporous Anodic Aluminum Oxide: Fabrication, Characterization, and Applications

18

Wojciech J. Stępniewski and Zbigniew Bojar

Contents

Introduction.....	594
Formation of Anodic Aluminum Oxide.....	594
Influence of Operating Conditions on Nanopores' Geometry.....	602
Influence of Operating Conditions on Anodic Alumina Arrangement.....	605
Luminescent Properties of Anodic Aluminum Oxide.....	609
Applications of Anodic Aluminum Oxide.....	611
Anodization of Aluminum Alloys.....	630
Summary.....	630
References.....	631

Abstract

Anodic aluminum oxide (AAO) consists of parallel pores arranged in a honeycomb-like array. Since a two-step self-organized approach in anodic alumina fabrication was invented, tremendous attention was paid to this material. Structural features of anodic alumina, like pore diameter, interpore distance, and nanoporous oxide thickness, can be fully controlled by operating conditions, including type, concentration and temperature of the electrolyte, applied voltage, and duration of the anodization process. Moreover, these operating conditions have also a major impact on the nanoporous array arrangement. Quantitative arrangement analysis methods employing fast Fourier transforms have been developed to assess the nanopores' arrangement. The most frequent application of the anodic aluminum oxide is a template-assisted fabrication of nanostructures.

W.J. Stępniewski (✉) • Z. Bojar

Department of Advanced Materials and Technologies, Faculty of Advanced Technologies and Chemistry, Military University of Technology, Warszawa, Poland
e-mail: wojciech.stepniowski@wat.edu.pl; zbigniew.bojar@wat.edu.pl

Templates made of the AAO are being successfully applied in fabrication of nanowires, nanotubes, and nanodots by using diversity of techniques, including electrochemical deposition, physical and chemical vapor deposition, sol-gel techniques, etc. Due to the size of obtained nanostructures, magnetic, electric, piezoelectric, luminescent, and catalytic properties of the deposited materials can be significantly improved. Thus, control of the nanopores' structural features and arrangement is crucial for AAO applications in nanotechnology.

Keywords

Anodizing • Anodic Aluminum Oxide • AAO • Self-organization • Template-assisted nanofabrication • Nanostructures • Nanopores

Introduction

Anodic aluminum oxide (AAO) is one of the most frequently nanostructured materials obtained by electrochemical technique. Nanoporous anodic alumina consists of the parallel, periodically arranged capillars, in which geometrical features and arrangement strongly depend on the experimental conditions. Due to the controllable synthesis of the anodic alumina, one can obtain templates for nanofabrication with desired geometrical features. Therefore, diversity of nanowires, nanotubes, and nanodots has been obtained with electrochemical, physical, and chemical methods of deposition into anodic alumina nanopores. It allows to enhance magnetic, electric, catalytic, optical, and sensing properties of the deposited materials due to the small size and high-aspect ratio of the obtained nanostructures. Thus, numerous developments in nanotechnology, electronics, catalysis, memory storage systems, energy storage and harvesting systems, magnetic materials, catalysis, photonics, and sensor systems have been achieved. Moreover, anodic alumina itself poses numerous interesting properties like surface chemistry or luminescence.

In this chapter, a review on the anodic alumina fabrication and characterization is presented. Moreover, properties of the AAO resulting from phenomena occurring during the oxide growth are described. Additionally, applications of the AAO, including the most recent ones, have also been reviewed in details.

Formation of Anodic Aluminum Oxide

There are two types of anodic oxides formed on aluminum. At pH range 5–7 nonporous, adherent, compact oxide layers are being formed [245]. In more acidic electrolytes, nanoporous oxides are being formed with hexagonally arranged nanopores [245]. Scheme of a typical hexagonally arranged nanoporous oxide is shown in Fig. 1. One can distinguish hexagonal cells with pores in their centers (Figs. 1a and 2a). On a cross-sectional view, one can see that the pores are parallel capillars ended with hemispherical barrier layer at their bottoms at the metal-oxide interface (Figs. 1b and 2b–d). Typical quantities characterizing anodic aluminum oxide are pore diameter, interpore distance (equal to the cell diagonal), and thickness of the oxide layer.

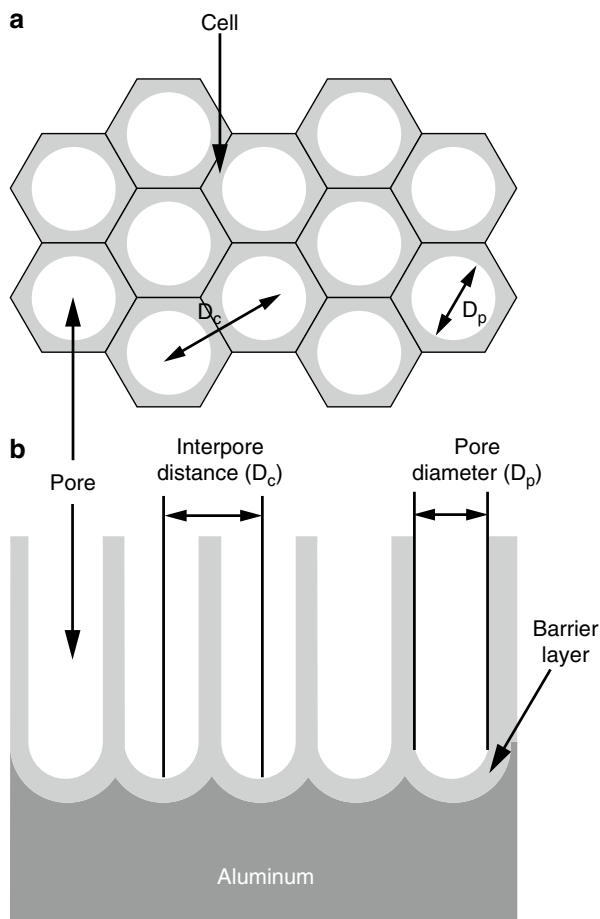


Fig. 1 A scheme of ideally arranged nanopores: top view (a) and cross section (b)

On the FE-SEM images, one can see hexagonally arranged nanopores, but these are organized into defect-free domains, with numerous defects at the domain boundaries (Fig. 2a). Randon et al.'s [213] approach brings some explanation in this matter. According to the presented model, first, pores appear as an effect of electric field spatial distribution inhomogeneities (Fig. 3a). These pores are singular and randomly distributed at the anode surface. Next, during anodization process, other pores are growing with hexagonal symmetry around the first pores (Fig. 3b). Therefore, randomly distributed defect-free domains are presented on the anode surface. Subsequently, population of pores increases and the defect-free domains expand by the growth of the next hexagonally arranged pores (Fig. 3c). Finally, the defect-free domains are expanding till the whole surface of the anode is covered with pores. Then, one can observe highly ordered domains with hexagonally arranged nanopores with numerous defects at the domains boundaries (compare Fig. 2a to Fig. 3d).

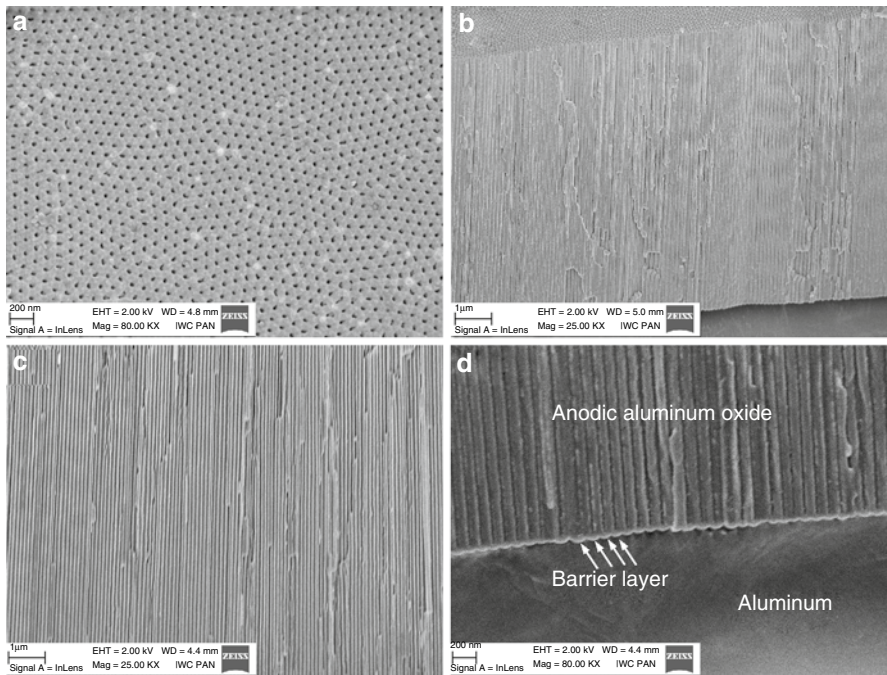


Fig. 2 Top view (a) and cross-sectional view (b–d) of anodic aluminum oxide formed by a two-step self-organized 15 min long (a–b) and 120 min long (c–d) anodization in 0.3 M oxalic acid at 40 V

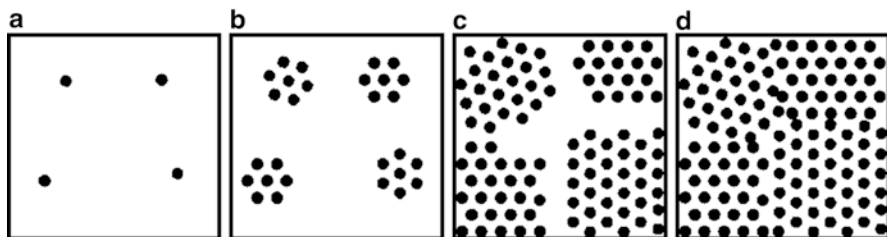


Fig. 3 A model of defect-free domains expansions (Based on Randon et al. [213])

According to Parkhutik and Shershulsky [196] one can obtain valuable information about phenomena occurring at the anode during anodic oxide growth from current density – time or voltage – time curves. At the beginning of the anodization process, one can observe a voltage increase (galvanostatic anodization, Fig. 4a) corresponding to a rapid drop of current density (potentiostatic anodization, Fig. 4b). This is acknowledged to the formation of compact, adherent nonporous oxide layer on the aluminum (Fig. 4 stage I). Next, one can observe decrease of the voltage raise and current density decrease rate, what is caused by the appearance of microcracks in the oxide surface (Fig. 4 stage II). Next nanopores appear what decreases voltage and increases current density (Fig. 4 stage III). Finally, both current density and voltage reach plateau corresponding to the steady pore growth and array of

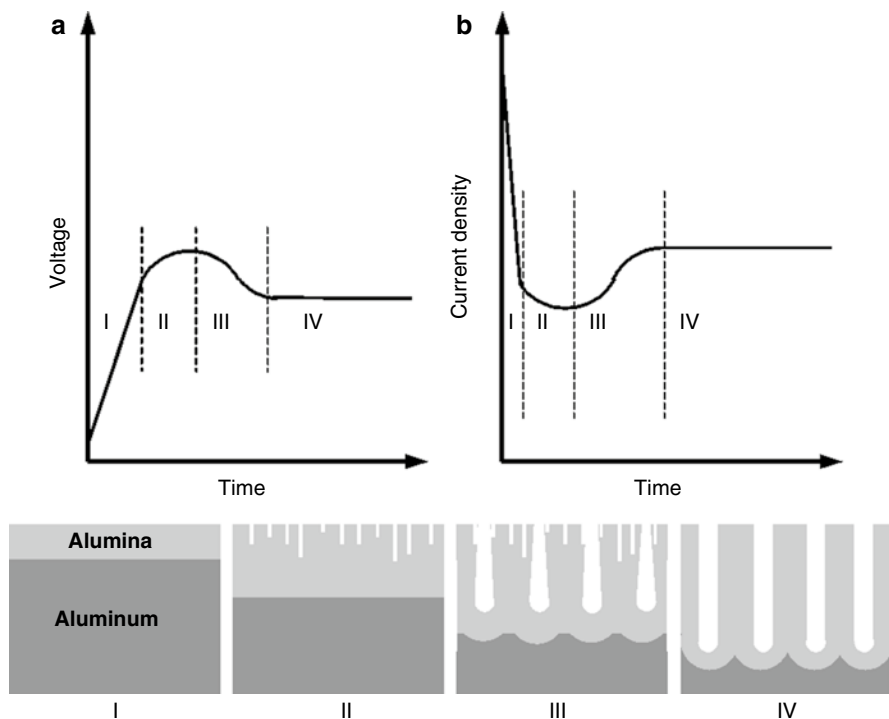


Fig. 4 A model of nanoporous oxide growth stages (I–IV) with corresponding voltage–time (a) and current density–time (b) curves (Based on Parkhutik and Shershuls [196])

hexagonally arranged cylindrical nanopores are being formed (Fig. 4 stage IV). Distribution of electric field lines in this situation is radial – almost all charge flows through the pores’ bottom and barrier layer. For too high values of voltages, the barrier layer may not be formed, or the high-density current can break through the barrier layer, and then one can observe samples “burning” accompanied with local temperature increase at the anode [11].

According to Thompson and Wood [255], the formation of anodic aluminum oxide is an effect of two opposite phenomena: on the one hand Al^{3+} , OH^- , and O^{2-} are forming the oxide, but on the other hand, the growing oxide is all the time in contact with acidic electrolyte and reacts, so the oxide is being partly etched then. Due to the alumina reaction with acidic electrolyte, dissolved Al^{3+} cation can again react with O^{2-} anions and again form the oxide. Simultaneously, both water and electrolyte molecules are being adsorbed on the oxide surface. Electrolyte’s molecules attract hydrogen atoms from the water particles, and OH^- as well as O^{2-} species are being formed [245]. Meanwhile, the adsorbed electrolytes’ anions are being absorbed by the growing oxide bulk. The mentioned surface reaction is responsible for electrolyte’s anions’ incorporation into the anodic alumina [60].

In nanotechnology, high-quality arrangement and periodicity of the elements are demanded to obtain materials with new or enhanced properties owed to their dimensions. To obtain highly ordered monodomain alumina with uniform

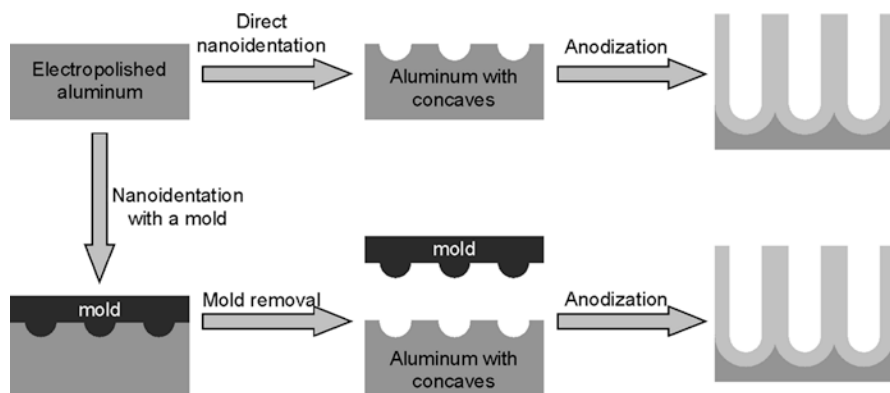


Fig. 5 Two various routes of aluminum nanoindentation before anodization

nanopores, two major approaches based on the aluminum pretexturation have been developed. After electropolishing, aluminum can be nanoindented with techniques such as fast ion bombardment [145, 146, 150, 202], atomic force microscopy [97], or scanning probe microscopy [167] (Fig. 5). After the nanoindentation, the aluminum with obtained concaves is being anodized, and highly ordered arrays of the nanopores are then formed. Unfortunately there are few limitations of the direct nanoindentation: surface area is strongly limited to few mm^2 , and time-consuming techniques are employed. Thus, other indentation techniques have been worked out. With the use of lithographic techniques, molds made of hard materials like SiC [9, 10, 160, 168, 278, 279], Si_3N_4 [39, 44, 45], or Ni [169, 284, 285] with highly ordered arrays of nanopillars are being fabricated. Next, electropolished aluminum is being indented with the mold, and an array of concaves on aluminum is being obtained (Fig. 5). After anodization, highly ordered array of nanopores is obtained. Nanopores with various geometries, including typical hexagonal arrangement with cylindrical pores (Fig. 6a), but also square arrays of cylindrical pores (Fig. 6b) as well as triangular pores (Fig. 6c) and square-shaped pores (Fig. 6d), can be obtained with this approach. Nevertheless, this method requires employment of sophisticated and expensive lithographic techniques.

To overcome disadvantages linked to aluminum nanoindentation, a self-organized two-step anodization has been developed (Fig. 7). After the first step of anodization, disordered nanopores are being obtained (Fig. 8). After chemical oxide removal, one receives highly ordered concaves on aluminum. These concaves serve as the pore nucleation sites during the re-anodization (second step of anodization carried out – which is very important – in the same experimental conditions as the first step of the process). In this case, one can get highly ordered arrays of the nanopores at large surfaces, up to few dm^2 [72]. With this approach, formed anodic alumina is made of highly ordered domains with common defects at the domains' boundaries (Figs. 1a, 8)

According to Nielsch et al. [183], for every applied electrolyte, there is a certain voltage where one can achieve the best arrangement of the nanopores. The best nanopore arrangement, depending on the electrolyte type, was found at 25, 40, and 195 V for 0.3 M sulfuric acid, 0.3 M oxalic acid, and 0.1 M phosphoric acid, respectively.

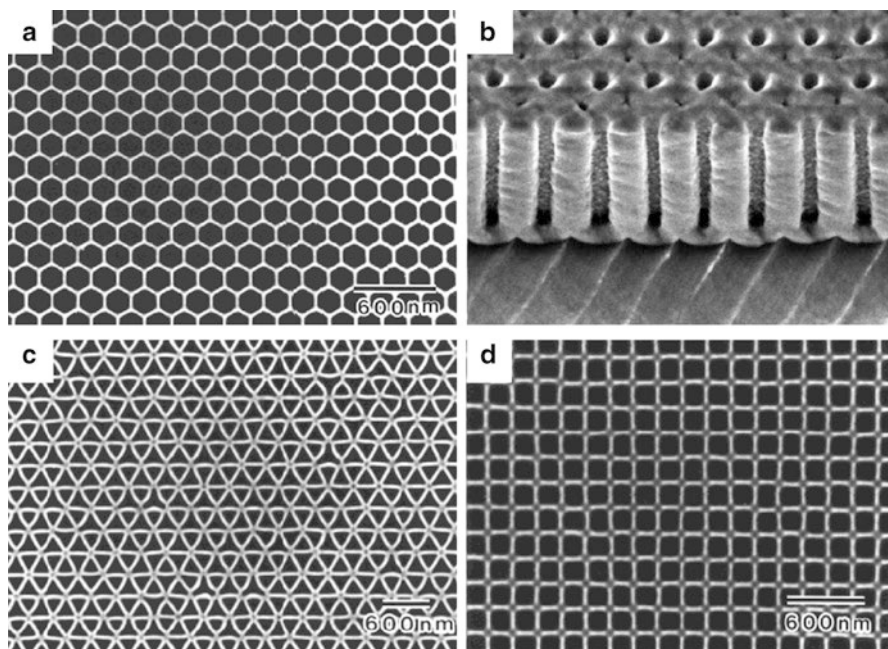


Fig. 6 FE-SEM images of anodic aluminum oxide with various pore shapes and arrangement grown on pre-textured aluminum (Reprinted with permission from Masuda et al. [164], (a, c, d) and Asoh et al. [10])

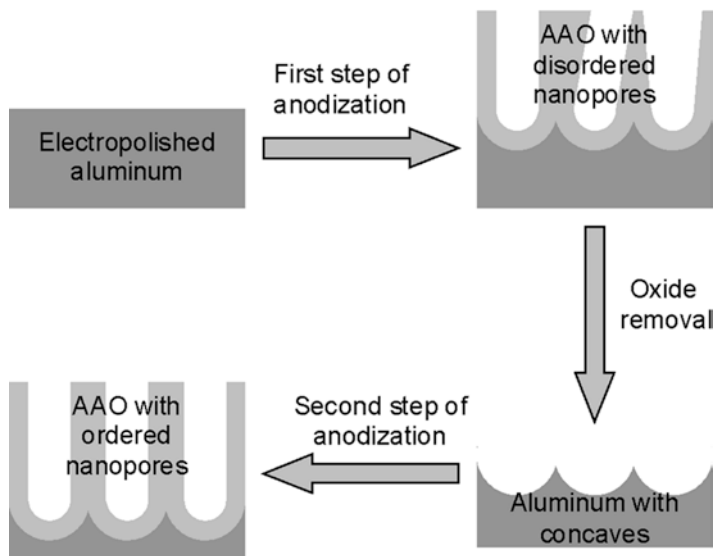


Fig. 7 The experimental procedure for a two-step self-organized anodization

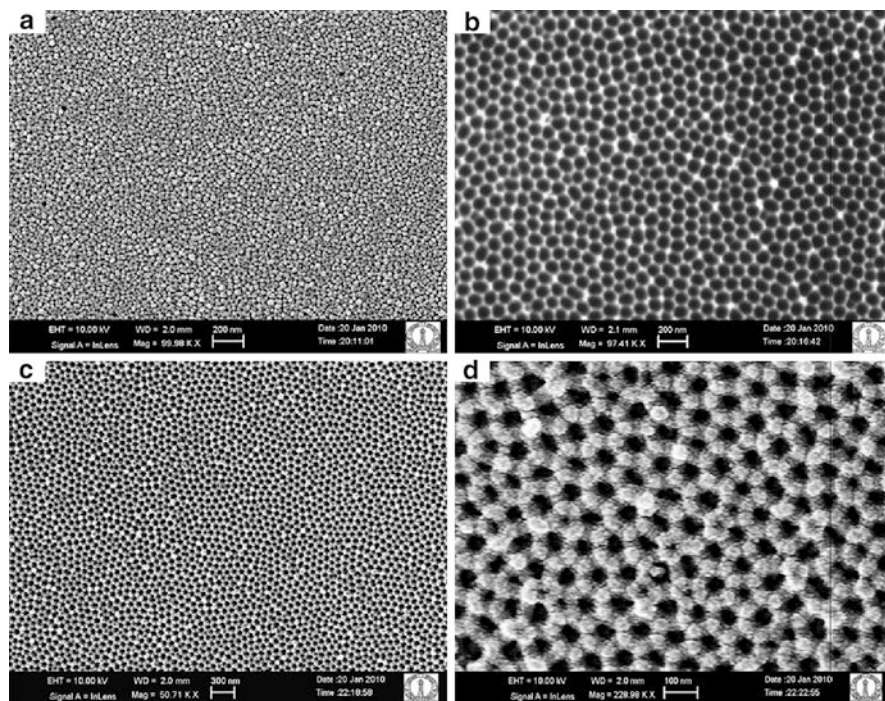


Fig. 8 FE-SEM images of the samples prepared by anodization in 0.3 M oxalic acid at 40 V. Top view of the surface after the first step of anodization (a), alumina removal (b), and second step of anodization providing high-quality arrangement of the pores (c–d) (Reprinted from Choudhari et al. [47])

To improve nanopore arrangement and enhance the rate of the oxide growth, hard anodization is employed. Opposite to typical anodization conditions (called mild anodization (MA)), hard anodization (HA) is conducted at much greater values of voltage. Namely, aluminum is usually anodized in sulfuric acid at voltages ranging from 15 to 25 V (MA) [244] and results in interpore distance ranging from 50 to 60 nm [169]. Above 25 V anodic dissolution of aluminum occurs. Hard anodization is conducted for sulfuric acid at voltage ranging from 40 to 70 V and results in interpore distance ranging from 90 to 140 nm. The major benefit from the application of HA is fast oxide growth rate and high quality of the nanopores' arrangement. For example, anodic alumina grows in 0.3 M oxalic acid at 1 °C and 40 V (MA) with a rate of 2.0 $\mu\text{m}/\text{h}$. While the HA procedure is applied (0.3 M oxalic acid, 1 °C, 110–150 V), oxide growth rate increases up to 70 $\mu\text{m}/\text{h}$ (Lee et al. 2006).

Additionally, mild anodization and hard anodization can be used alternately during the oxide growth. Then, multisegment nanopores with a rapidly changing diameter are obtained. So obtained, periodically modulated alumina nanoporous arrays are in demand in nanofabrication (Lee et al. 2006 [248]).

Due to the rapid voltage changes, Y-branched nanopores can be also obtained. For example, Zaraska et al. [295] reported fabrication of Y-branched AAO formed in oxalic acid. After the first step of anodization and oxide removal, the second step

of anodization was initiated with a voltage of 60 V (Fig. 9d). After certain time, voltage was reduced to 42 V that implied the growth of AAO with narrower pores (Fig. 9e). Another voltage decrease, to 30 V, causes that one can distinguish three

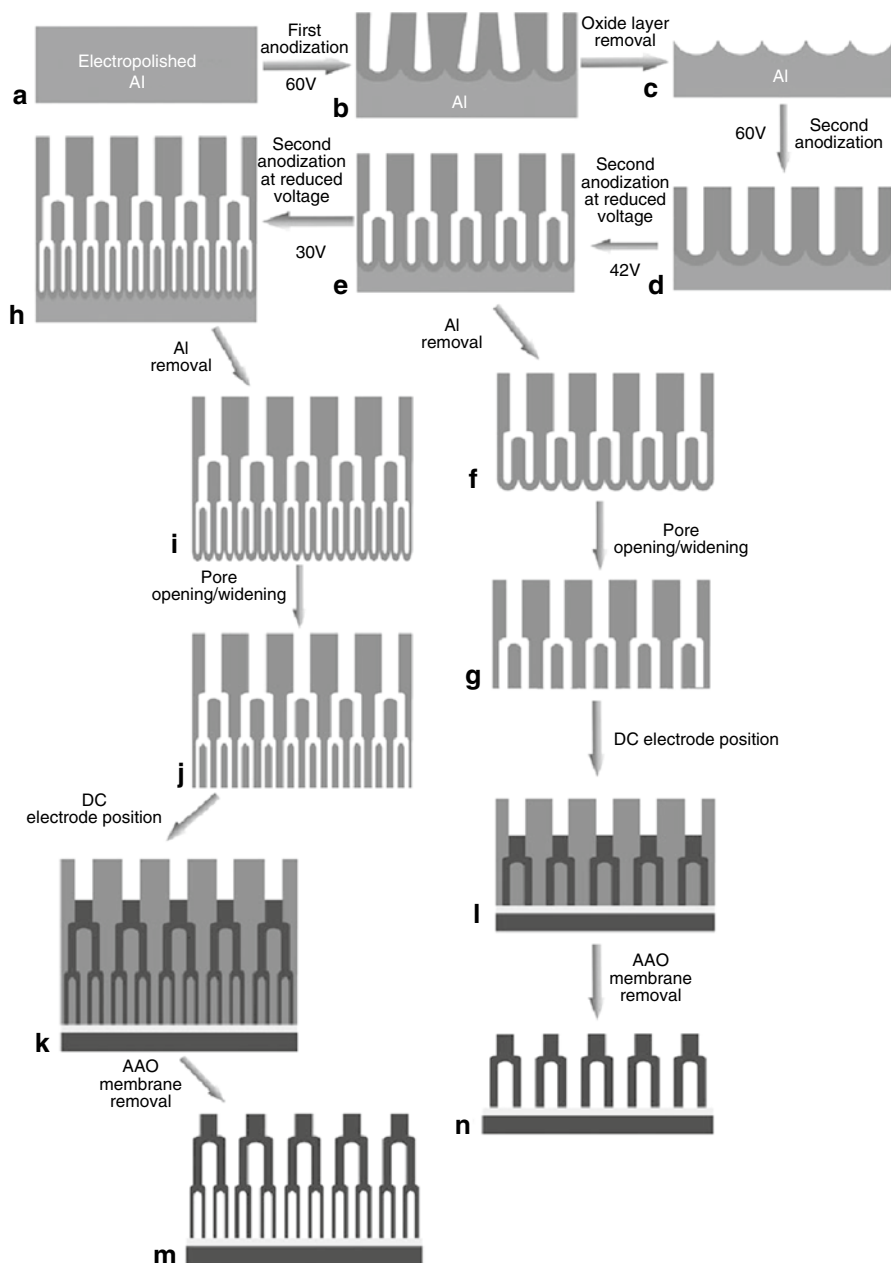


Fig. 9 Schematic representation of Y-branched anodic alumina synthesis and its application in synthesis of nanowires with electrochemical deposition (Reprinted from Zaraska et al. [295])

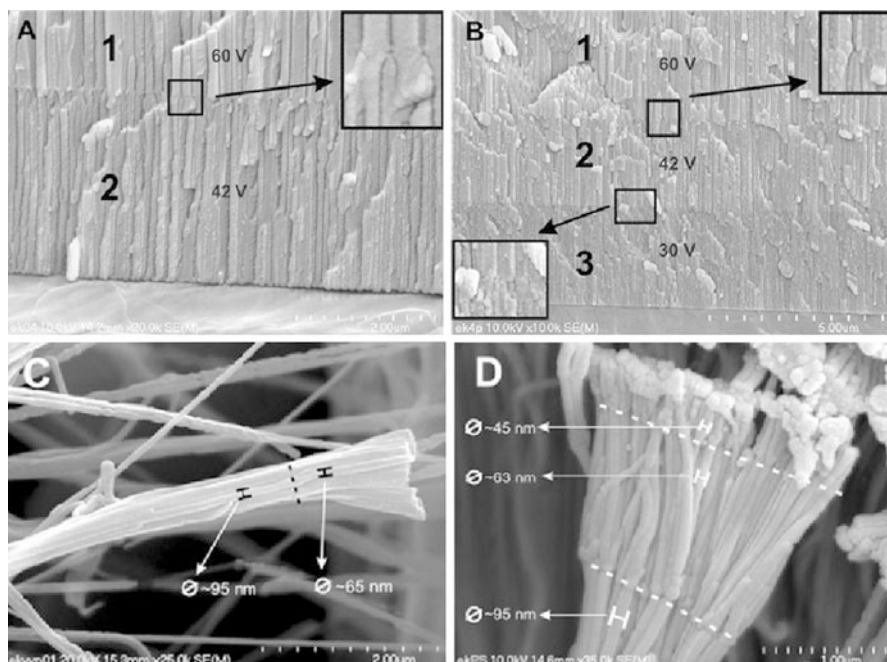


Fig. 10 Anodic alumina with Y-branched pores (a–b) and gold nanowires obtained by direct current electrodeposition into the AAO template with branched pores (c–d) (Reprinted from Zaraska et al. [295], Springer)

segments of AAO with different pore diameters (Figs. 9h, 10a–b). Moreover, direct current electrodeposition of gold into a AAO template with branched pores resulted in Y-branched gold nanowires, with structures being very attractive for sophisticated microelectronics (Fig. 10c–d). According to Santos et al. [221] Y-branched anodic alumina nanopores can also be obtained with the use of mild anodization and hard anodization. After mild anodization, rapid voltage increase to the value from HA range results in nanoporous alumina with relatively large pores at the bottom (HA) and narrower ones on top (MA).

Influence of Operating Conditions on Nanopores' Geometry

Anodic alumina is typically anodized in one of three electrolytes: sulfuric acid, oxalic acid, or phosphoric acid [245]. Researchers have paid a lot of attention to investigate quantitatively the influence of operating conditions on the nanopores' geometry. Geometry control, for desirable nanopores' dimensions, is demanded in the nanofabrication. For most of the electrolytes, operating conditions like the type and concentration of the electrolyte, anodizing voltage, and temperature and

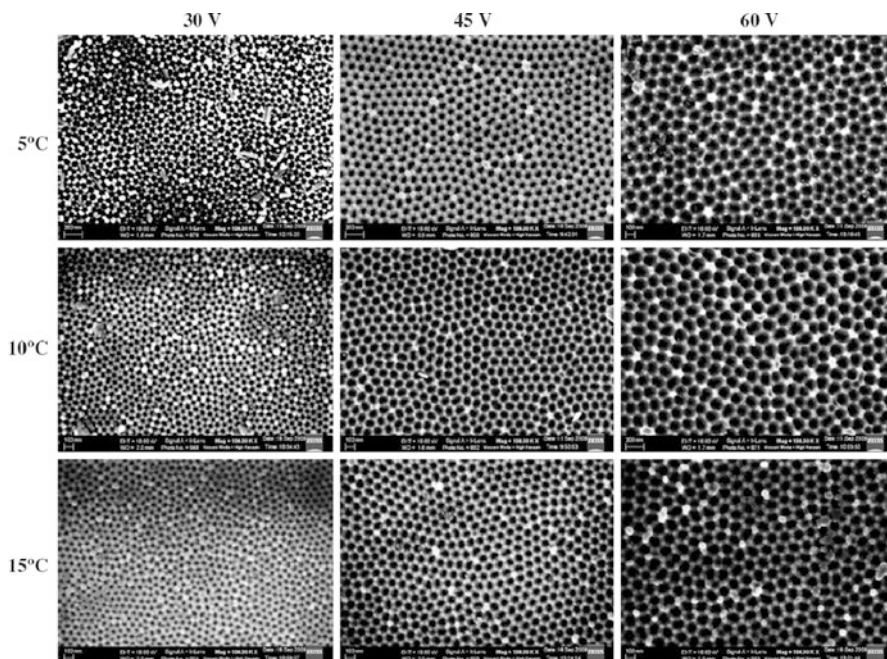


Fig. 11 Top view FE-SEM images of anodic alumina formed in 0.3 M oxalic acid at various voltages and temperatures (Reprinted from Chowdhury et al. [48]1), Springer)

duration of the second step of anodization influence the geometry of anodic alumina, including pore diameter, interpore distance, thickness of the anodic alumina porous film, porosity, barrier layer thickness, and wall thickness. Certain voltage ranges are being applied for certain electrolytes. For example, anodization in sulfuric acid results in nanoporous oxide formation at voltage ranging from 15 to 25 V [243]. For greater voltages, anodic dissolution of aluminum occurs, while for lower voltages no porous structure can be obtained. To conduct successful anodization at greater voltages, oxalic acid has to be applied as the electrolyte. Then aluminum can be anodized at voltage ranging from 20 to 100 V [47, 48, 82, 94, 177, 234, 246, 290, 296, 297]. Phosphoric acid is applied for the voltage up to 195 V [183, 291]. Already, direct observation of FE-SEM images shows that operating conditions have major impact on the nanopores' geometry (Fig. 11). One can notice that the greater the anodizing voltage, the greater the pore diameter and interpore distance. Figure 12 shows pore diameter versus voltage (A) and interpore distance versus voltage (B) dependencies gathered from numerous publications for three most frequently used electrolytes. Pore diameter and interpore distance increase linearly with the applied voltage. The smallest pore diameter (about 20 nm) and interpore distance (about 43 nm) are for anodic alumina formed in 20 % wt sulfuric acid at 15 V [243]. The greatest value of pore diameter (about 158 nm) and interpore distance

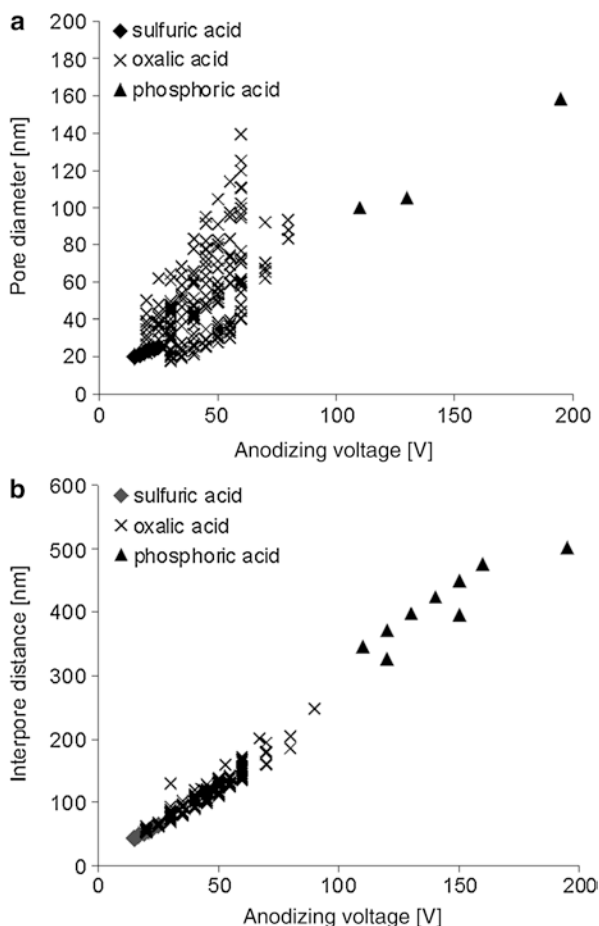


Fig. 12 Influence of anodizing voltage on pore diameter (a) and interpore distance (b) (Data from Sulka and Parko [243], Stępniewski and Boj [234], Yuan et al. [290], Sulka and Stępniewski [246], Zaraska et al. [296, 297], Montero-Moreno et al. [177], Chowdhury et al. [48], Huang et al. [82], Choudhari et al. [47, 291], Nielsch et al. [183] were used)

(about 500 nm) is for alumina formed in 0.1 M phosphoric acid at 195 V [183]. Moreover, electrolyte's temperature and duration of the second step of the self-organized anodization have also a major impact on the nanopores' geometry. Only anodizing voltage influences the interpore distance. It is a well-recognized fact. But, the greater the temperature, or the longer second step of anodization, the wider the pores being obtained (Fig. 12b). This is related with the fact that the growth of the anodic oxide is an effect of two opposite phenomena: oxide growth and oxide dissolution in contact with acidic electrolyte. Thus, the greater the temperature of the electrolyte, the faster the reaction of the oxide with the electrolyte. Moreover, the longer the second step of anodization, the greater the quantity of oxide being consumed, which results into a pore diameter increase [246, 234].

Thus, for nanopores obtained by anodization in oxalic acid, a strong increase of pore diameter with electrolyte's temperature and duration of the second step of anodization is observed (Fig. 12a). Such an effect is not observed for the values of interpore distance; hence, the greater the electrolyte's temperature, or the longer the anodization, the greater the porosity of the anodic alumina (Fig. 12b) [246, 234]. For an ideal hexagonal pore arrangement, porosity (α) can be estimated from the following equation [245, 246]:

$$\alpha = 0.907 \left(\frac{D_p}{D_c} \right)^2 \quad (1)$$

where D_p and D_c are pore diameter and interpore distance, respectively. Therefore, when the pore diameter increases at constant value of the interpore distance, porosity increases. On the one hand, it provides wider pores, but on the other hand, a better close packaging is obtained. Temperature increase assures also thinner walls (W) and thinner barrier layer (B). These quantities are also strongly related to the pore diameter and interpore distance (2) [245]:

$$W = \frac{D_c - D_p}{2} = 0.71 \cdot B \quad (2)$$

Another quantity strongly influenced by the operating conditions is thickness of the anodic oxide layer. Anodic oxide growth is a typical faradic process [245]. As one could expect, the greater the charge flows through the anode, the greater the quantity of the anodic oxide being formed. Hence, all the quantities influencing the current density are influencing nanoporous oxide growth rate in the same way. For example, both oxide growth rate and current density increase exponentially with anodic voltage (Fig. 13). Here, electrolyte's temperature increase is also beneficial. Temperature increase increases ionic mobility, which enhances the electrolyte's conductivity. The greater the conductivity, the greater the current density and oxide growth rate. Due to the temperature increase, anodic alumina can be obtained via anodization in oxalic acid with the rate of even 55.6 $\mu\text{m/h}$ at current density of about 21.8 mA/cm^2 (onefold greater than for low temperature anodization) [177, 246].

Thus, geometry of the nanopores can be successfully steered by the application of appropriate experimental conditions during the anodization process, which assures fabrication of high-aspect ratio nanomaterial fabricated with the use of self-organized electrochemical method.

Influence of Operating Conditions on Anodic Alumina Arrangement

Not only dimensions but also quality of the individual arrangement and ideality of their periodicity are very often crucial in nanotechnology. For this reason, several approaches for quantitative description of arrangement of the nanopores have been developed by the researchers.

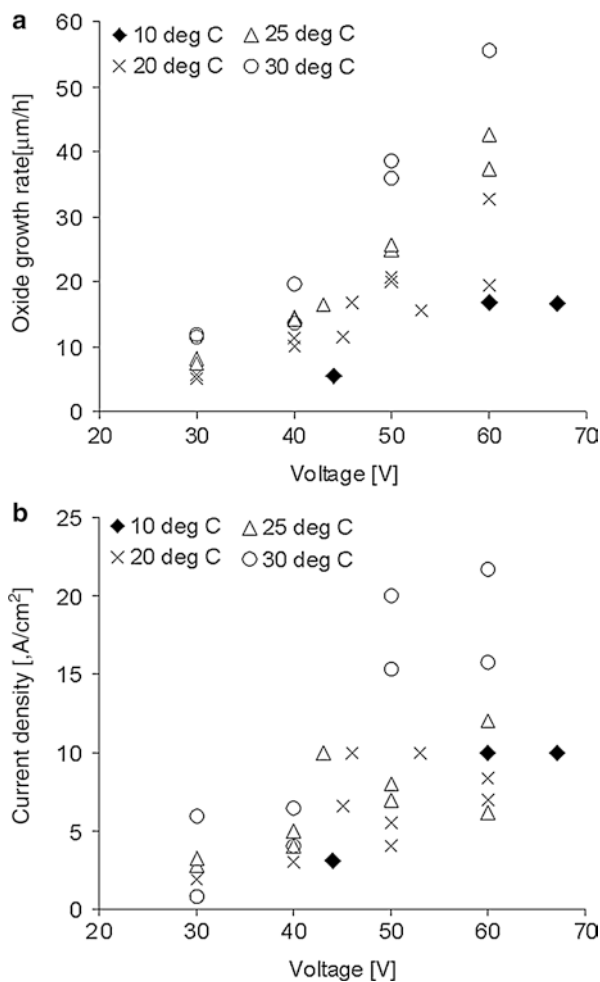


Fig. 13 Influence of anodic voltage on the oxide growth rate (a) and current density (b) (Data from Sulka and Stępniewski [246] and Montero-Moreno et al. [177])

One of the most popular groups of the analysis method is based on the fast Fourier transforms (FFT). With the use of dedicated software, the FE-SEM image is transformed into the FFT image. Qualitatively, the nanopores are quite well-arranged if the FFT image is not blurred. For high-quality arrangement, the FFT image consists of six distinct dots in the corners of the hexagon. While the arrangement of the nanopores is poor, the FFT image is a blurred, thick ring. To perform FFT-based quantitative arrangement analyses of the nanopores' arrangement, intensity profiles have to be conducted through the FFT image (Fig. 14). Maximum height of the intensity profile (I) and width of the intensity profile's peak at half of its height (σ) are quantities involving information about the nanopores' regularity (Fig. 14c).

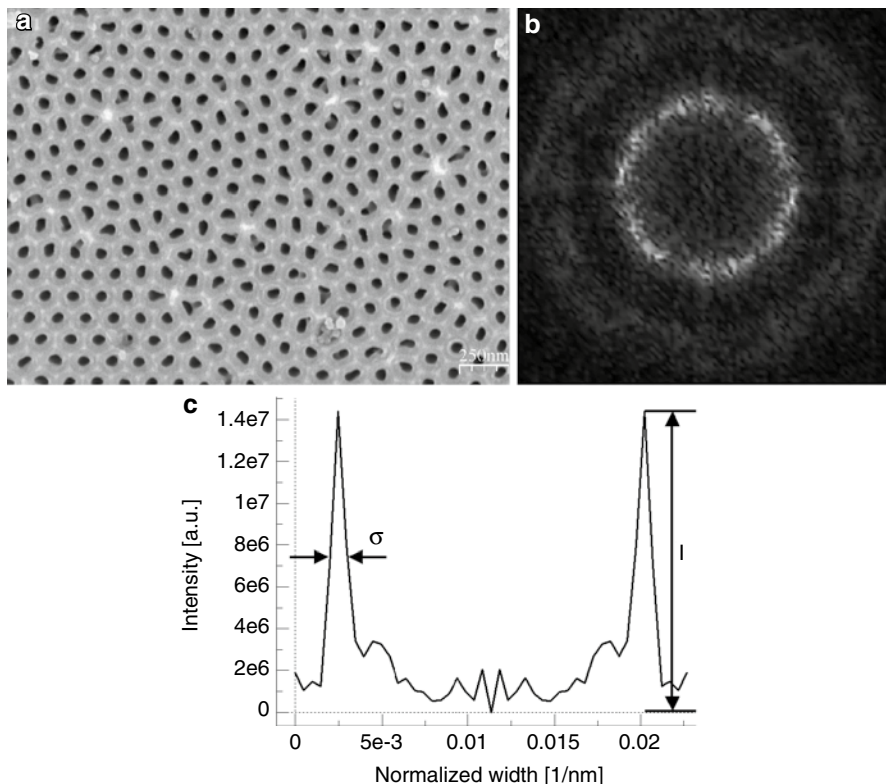


Fig. 14 FE-SEM image (a), its fast Fourier transform (FFT) (b), and one of the intensity profiles (c) of anodic alumina formed in 0.3 M oxalic acid

The arrangement of nanopores is hexagonal, thus three intensity profiles are obtained from each FFT images. According to Shingubara et al. [229, 230], Almasi Kashi and Ramazani [4, 5], Almasi Kashi et al. [6], Sulka and Parkoła [244] and Zaraska et al. (2013), the intensity (I) of the profile to width of the intensity profile's peak at half of its height (σ) ratio brings information about the AAO regularity (3):

$$R = \frac{I}{\sigma} \quad (3)$$

The greater the regularity ratio being estimated in this approach, the better the arrangement of the nanopores. For the nanopores formed in sulfuric acid, regularity ratio increases linearly with applied voltage, and its greatest value is for AAO formed at 25 V [244]. This result is in agreement with Nielsch's findings [183]. According to Zaraska et al. (2013), anodization in oxalic acid at 40 V results in the best arrangement of the nanopores. This finding is in agreement with results obtained by Nielsch et al. [183] and Shingubara et al. [4, 229]. Almasi Kashi et al. (2007) and Shingubara et al. [229] have also investigated regularity ratio of the nanopores

fabricated in mixtures of sulfuric and oxalic acid. It was found, that the greater the addition of sulfuric acid, the greater the regularity ratio for AAO formed at voltage range dedicated to oxalic acid. However, for various sulfuric acid additives, there are various optimal voltages providing the best arrangements – the greater the sulfuric acid content, the lower the optimal voltage (Almasi Kashi et al. 2007).

The presented approach in the quantitative arrangement analysis of the nanopores is beneficial; nevertheless, it has few major drawbacks. First of all, fast Fourier transform consists of periodic functions in the case of analysis of periodic structures images. Thus, the greater the number of nanopores, the greater the estimated regularity ratio independently from the real spatial ideality. Thus, such an error should be taken into account during the regularity ratio estimations. Recently, such an approach has been developed [237]. Numerous simulations have been performed with various numbers of pores (n), sizes of analyzed model (S), and porosities (α) with fixed other values. After numerous calculations, it was found that reliable regularity ratio, linked only to the arrangement of the nanopores, can be estimated with the following equation:

$$R = \frac{(nS)^{\frac{3}{2}}}{\alpha^2} \cdot \frac{I}{\sigma} \quad (4)$$

It was found that there is no significant temperature effect on the nanopores' arrangement. Despite the fact, obtained results are in agreement with results obtained with previous approach that the best regularity is for AAO formed in 0.3 M oxalic acid at voltage of 40 V.

Another approach due to which one can estimate quantitatively nanopores' arrangement is performance of the Delaunay maps. There, a pore neighboring with a number of pores different than six is a defect. Percentage of defects is influenced by the operating conditions. According to Sulka and Jaskuła [242], the lowest percentage of defects in the nanoporous array obtained by anodization in sulfuric acid can be achieved at a voltage of 25 V (about 9.5 %). According to Stępniewski et al. [235], the lowest percentage of defects in the AAO formed in oxalic acid can be achieved at 40 V, when the first step of the anodization is extended (10.3 %). These results correspond with the regularity ratio obtained with FFT. Moreover, for other voltages than these two, percentage of defects is significantly greater (Fig. 15).

There are few other approaches in quantitative arrangement analysis of the nanopores, based on the nanopores' geometry. Hillebrand et al. [87] proposed two approaches derived from angle and interpore distance deviations. For ideal hexagonal arrangement, the angle between the lines linking the pores centers should be 60°. The more the counts close to the value, the better the pore arrangement and the greater the regularity ratio being derived from angle distribution function (ADF) (Zaraska et al. 2013). Pair distribution function (PDF)-based regularity ratio has the greatest value, translated into the best nanopores' arrangement, for uniform interpore distances. For anodic alumina formed in oxalic acid, the greatest values of ADF- and PDF-derived regularity ratio are for AAO formed at 40 V. The results are in agreement with findings derived from arrangement analyses performed with

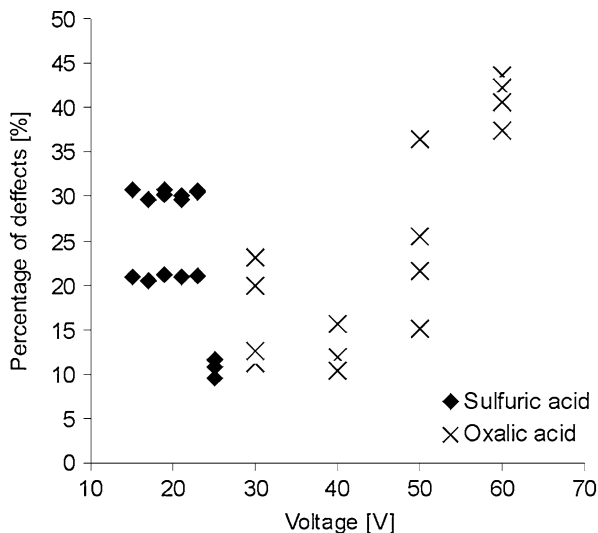


Fig. 15 Percentage of defects versus voltage (Data from Sulka and Jaskuła [242], Stępniewski et al. [235])

other methods. Except for the PDF and ADF regularity ratio, there are also few other similar arrangement analysis methods based on the investigation of the inter-pore distance and angle distribution like the ones reported by Borba et al. [19] or Mátéfi-Tempfli et al. [171].

There are also approaches based on the investigation of the defect-free domain size (the greater the defect-free domain, the better the arrangement) [207, 1] or even on the nanopores' circularity ([235], Zaraska et al. 2010).

In total, quantitative arrangement analysis methods described above give a coherent view on the anodic alumina nanopores' arrangement. With the use of these methods, experimental procedures can be optimized to obtain almost ideally arranged arrays of the nanopores.

Luminescent Properties of Anodic Aluminum Oxide

As it was mentioned above, during anodic oxide growth, positively polarized anode attracts negatively charged anions. Next, the anions are being adsorbed on the oxide's surface and then incorporated into the AAO walls. Thus, anodic alumina poses anionic impurities in its walls. According to the results reported by Le Coz et al. [124], the oxide walls possess incorporated electrolyte's anions; however, the AAO skeleton is made of pure alumina (Fig. 16). It was also found that due to the anions incorporation and presence of F-centers in the formed oxide, AAO has luminescent properties. For example, anodization of aluminum in oxalic acid provides photoluminescent (PL) emission bands ranging from 429 to 480 nm, depending on the excitation wavelength (Table 1 [30, 136]). Photoluminescence can be also caused

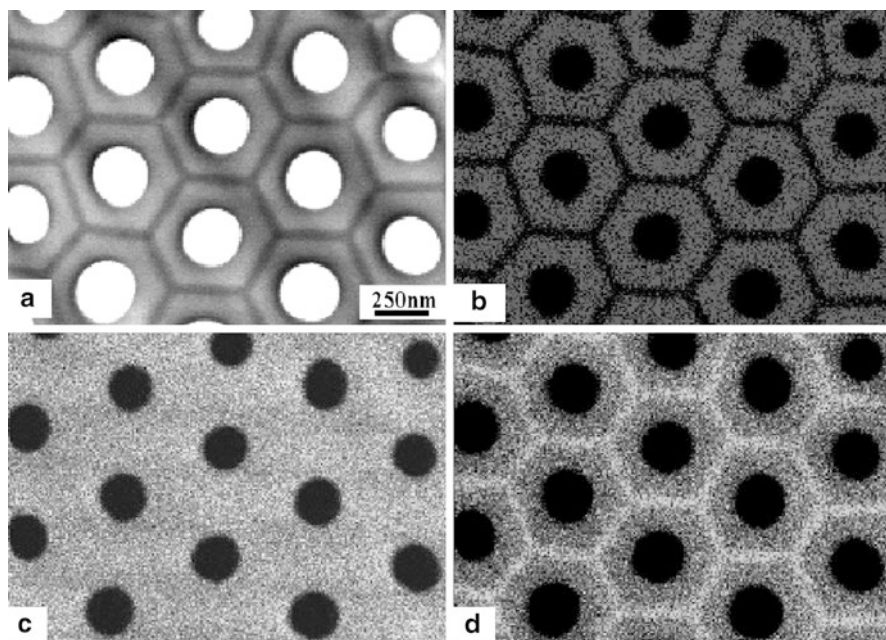


Fig. 16 TEM top view image (a) and corresponding X-ray elemental maps of phosphorus (b), oxygen (c), and aluminum (d) of AAO formed in phosphoric acid (Reprinted with permission from Le Coz et al. [124])

Table 1 Photoluminescence of anodic alumina prepared in various electrolytes

Source of luminescence	Excitation wavelength [nm]	Emission wavelength maximum or band [nm]	References
F ⁺ centers	355	450	Rauf et al. [214]
F-centers	395	500	
Oxalate anions	360–370	429–460	Li and Huang [136]
F-centers	305	461	Komarov et al. [116]
Sulfate and oxalate anions	265 and 340	420–520	[135]
F-centers	265 and 340	440	
F ⁺ centers	325	390	Mukhurov et al. [178]
Oxalate anions	325	435, 470–480	
Sulfate anions	325	400	
F ⁺ centers	440	443	Chen et al. (2006)
Oxalate anions	440	470	
Chromate anions	255 and 350	310–510	Stępniewski et al. [236]

by the incorporation of sulfate and chromate anions. The excitation spectrum of nanoporous anodic alumina formed in 0.3 M chromic acid is the same as the absorption spectrum of the electrolyte, which translates into a successful incorporation of chromate anions into the AAO [236].

There are also PL bands originating from F-type centers (oxygen vacancies with various numbers of electrons). The peaks of the PL emission caused by the presence of the F-centers have their maxima at wavelengths ranging from 390 to 500 nm (Table 1 [214, 116, 135, 178], Chen et al. 2006). These bands, together with the ones originating from incorporated anionic species, form broad PL bands. According to Li et al. [135], PL bands originating from the incorporated electrolyte's anions can be distinguished from the ones that originate from F-centers. The F-centers PL lifetime is shorter than 7 ns, while PL originating from the anions has much longer lifetime. Moreover, the smaller the pores, the longer the PL lifetime. Thus, the PL lifetime can be controlled by the nanopores' morphology.

According to Rauf et al. [214], intensity of PL originating from F-centers can be also controlled. The worse the nanopores' arrangement, the more the defects, like F-centers present in the AAO walls. Therefore, the worse the nanopores' arrangement, the more intensive the PL from the F-centers.

Both pore diameter and nanoporous array arrangement influence the PL of the AAO. Simultaneously, morphology and arrangement of the nanopores and chemical composition of the AAO walls are controlled by the operating conditions during the anodization process. Hence, luminescent properties of AAO can be steered by the operating conditions.

Applications of Anodic Aluminum Oxide

Anodic aluminum oxide is a widely applied template material for nanofabrication. To prepare a suitable template, a posttreatment of AAO formed after the second step of anodization is required. Firstly, the remaining, unoxidized aluminum has to be removed (Fig. 17). The most frequent mixtures for aluminum removal are saturated aqueous solution of HgCl_2 [294] or CuCl_2 [52] and aqueous solution of CuSO_4 [154] or CuCl_2 [143] in HCl . Then alumina with closed pores at their bottoms is obtained. Gao et al. [68] reported a new approach in the remaining alumina detachment with the use of an electrochemical method. Anodic alumina with remaining aluminum was working as an anode in a $\text{HClO}_4:\text{CH}_3\text{OH}$ (1:1) solution with the addition of polyglycol. Application of voltage ranging from 15 to 25 V for 5–15 s allowed to obtain AAO totally detached from unoxidized aluminum. The next step of a through-hole anodic alumina membrane preparation is pore opening. One can distinguish



Fig. 17 Fabrication of anodic alumina templates for nanofabrication. Obtained AAO has to be detached from remaining Al, and next the pores' bottoms have to be opened (Adapted from Zaraska et al. [294])

chemical, electrochemical, and physical methods of pore opening (barrier layer removal). Typically, for chemical approach, 5 % wt H_3PO_4 is being used ([52], Liu et al. 2011 [294]). However, during pore opening, usually whole alumina is reacting with the acid. Therefore, barrier layer removal (pores' opening) is accompanied with pore widening on the membrane top, and as a result, one obtains AAO membrane with narrower pores at the bottom and wider pores on the top [294]. To avoid this issue, Cui et al. [52] developed a new approach in pore opening. The AAO with closed pores is gently placed on the H_3PO_4 aqueous solution with closed pores down. Initially, surface tension keeps the membrane on the surface, and only the pores' bottom reacts with the acid (and the pores are not being widened on the top). Finally, when all the barrier layers are consumed due to the chemical reaction, the whole membrane dips into the solution. Due to this approach, AAO membranes with uniform diameters in whole depth are obtained. The uniformity of the AAO membranes is very often a crucial factor in nanofabrication. Lillo and Losic [143] have developed an electrochemical method of the nanopore opening. They placed AAO with closed pores in the hole in the middle of the two-half permeation cell (AAO is sandwiched between the half-cells). A typical etching solution (5 % H_3PO_4) was placed on the barrier layer's side, and 0.2 M KCl was placed on the AAO's top side (to provide electric conductivity). Between two platinum electrodes (each on every side of the AAO), a voltage of 1.5–2.0 V was applied. Current measurements were indicating progress of pore opening. While the current approaches the plateau, barrier layer removal was done. Lillo and Losic [143] have also developed a physical method of barrier layer removal. A Ga^+ focused ion beam (FIB) can also successfully open the pores' bottoms. Another approach in pore opening is an electrochemical barrier layer thinning [67]. Here, after the final step of anodization, the voltage is being exponentially decreased. The most important is current transient control – a steady-state pore growth stadium during voltage decrease cannot be achieved. As a result pores with significantly thinned or even removed barrier layer are obtained.

When the AAO template is thick enough, it can be directly transferred on the desired substrate, and nanofabrication with the template can be easily performed. Nevertheless, while the template is thinner than about 1 μm (ultrathin aluminum membrane (UTAM)), it is hard to directly transfer it on the substrate (template rolls, cracks, and even breaks). To overcome issues linked to the thickness, an intermediate is material essential. For example, Liu et al. (2011) reported the use of black wax. After the second step of anodization, the pores are coated with black wax. Next, the remaining aluminum is removed, and pores are opened. Next, the AAO is placed onto the desired substrate, and finally the black wax coating is removed.

After AAO template transfer onto desired substrate, the top-down nanofabrication can be done with the use of numerous techniques, resulting in materials with new or enhanced properties owed to the small dimensions.

Metallic nanowires, nanotubes, and nanodots as 1D and 0D individuals attract attention of the researchers mainly due to their electric, magnetic, and catalytic properties. Fabrication of nanowires, nanotubes, and nanodots made of metals is strongly linked with electrochemical methods. Usually, anodic alumina serves as an insulating mask for conductive support, and electrodeposited metal crystallizes only at the pore bottoms at the support/AAO interface. To form metallic nanodots, short

electrodeposition time is required [117]. Further deposition leads to formation of nanorods, nanowires, or nanotubes. To form nanorods and nanopillars, the deposition time has to be longer than for nanodots.

To form nanowires (high-aspect ratio 1D nanostructures), AAO template has to be thick enough and experimental procedure has to provide relatively large charge during the electrodeposition (Table 2). DC electrodeposition, AC electrodeposition, and pulse electrodeposition are used to obtain highly ordered arrays of nanowires made of Al, Ag, Ag–Au, Au, Bi, Co, and its alloys, Cu, Fe, and its alloys, Ni, and its alloys, Sn, Pd, and Pt (Fig. 18, Table 2). Among electrochemical fabrication methods, also deposition from nonaqueous solution is applied [25]. So formed Al nanowires serve as a support for TiO₂ deposited with atomic layer deposition. Fabricated high surface area electrode provides greater currents and longer viability of the battery. Magnetic properties of nanowires made of ferromagnetic materials are intensively researched [193, 210, 239, 23, 284, 65, 259, 38, 258, 216, 12, 64, 275, 83, 61, 191, 180, 81]. Also optical properties [56, 95, 102, 283], as well as catalytic properties [148, 307], attract the attention of the researchers. Template-assisted formation of metallic nanowires employs mainly electrochemical methods. However, one can find barely few others like surface redox reaction (cementation) [197], vacuum evaporation (DC sputtering) [153], solid state reduction [63], or pressure casting [16].

To form metallic nanotubes via electrochemical methods, firstly conductive layer has to be sputtered onto the AAO nanopores' walls, or surface redox reaction providing precipitation of conductive materials on the AAO inner walls surface has to be conducted. Then, electrodeposited metal crystallizes not only at the templates' bottom but also on the walls [126]. With this approach one can obtain uniform metallic nanotubes made from Au [126, 127], Co [13, 22, 66, 138], Fe [22, 276], Ni [22, 264, 286], and Pt [66] (Table 3). Here, also the electrochemical methods are majority. However, methods like vacuum sputtering (Au [80]), surface redox reaction (Au [289]), wet impregnation with precursor decomposition (Au–C [75], Co/PS, [184, 185]), sol–gel technique (Pd [233]), or physical vapor deposition (Pd [188]) are applied. Metallic nanotubes are useful in applications where high surface electrodes are required, including catalysis (Au [289], Ni [286]) and energy storage (Pd [188]). Also magnetic properties of metallic nanotubes made of Co [13, 138], Cd [184, 185], and Ni [264] are extensively researched.

Arrays of nanodots with the use of anodic alumina templates are formed with the use of diversity techniques (Table 4), including pulse laser deposition (Ag, Ni, Zn [179]), vacuum sputtering (Ag, Au [162]), electron beam evaporation (Ag [28, 155], Au [118–120]), electron beam epitaxy (Fe [149]), AC electrodeposition (Au [117]), and pulse electrodeposition (Cu–Ni [79]). Electronic, optical, and magnetic properties of the obtained nanodots were investigated in details. For example, plasmonic Ag nanodots were formed with the use of electron beam epitaxy (Fig. 19 [28]). It was found that the geometry of the nanodots is strongly related to the plasmonic resonance wavelength of the electrons.

Nanowires, nanotubes, and nanodots made of metalloids and inorganic compounds are fabricated with the use of various techniques. Due to their properties, nanowires made of metalloids and inorganic compounds attract the attention of the researchers. Here, also electrochemical methods are often in use (Table 5).

Table 2 Set of nanowires made of metals with their deposition techniques and investigated properties

Metal or alloy	Deposition technique	Investigated properties/applications/remarks	References
Al	Pulse electrodeposition	Fabrication of high surface area electrodes for energy storage systems	Cheah et al. [25]
Al	Surface redox reaction (cementation)	Zn NW were immersed in AlCl_3 -containing replacement solution, and Al NW were formed due to the redox reaction	Pang et al. [197]
Ag	DC electrodeposition	–	Sulka et al. [247], Choi et al. [40], Zaraska et al. [291], Pang et al. (2003)
Ag	AC electrodeposition	Antibacterial properties	Chi et al. [36]
Ag	AC electrodeposition	–	[304]
Ag	AC electrodeposition	Plasmonic properties were strongly related to the NW diameter	[95]
Ag	DC electrodeposition	Diameter-modulated NWs	Sulka et al. [248]
Ag	Solid state reduction	–	Feliciano and Martínez-Iñesta [63]
Ag–Au	AC electrodeposition	UV–vis absorption spectra	Yasui et al. [283]
Au	DC electrodeposition	Optical properties	Evans et al. [56]
Au	AC electrodeposition	DNA arranging on the Au NWs surface	Matsumoto et al. [170]
Au	DC electrodeposition	–	Zaraska et al. [291]
Au	AC and subsequent DC electrodeposition	–	Wu et al. [271]
Au	DC electrodeposition	Diameter-modulated porous NWs	Sulka et al. [248]
Au	DC electrodeposition	Y-branched NWs	Zaraska et al. [295]
Au	DC sputtering	–	Losic et al. [153]
Bi	DC electrodeposition	Optical properties	Jin et al. [102]
Bi	Pressure casting	–	Black et al. [16]
Bi	AC electrodeposition	Various experimental procedures were studied	Yin et al. [287]
Co	DC electrodeposition	–	Fu et al. [66]

Co	DC electrodeposition	Magnetic properties	Ohgai et al. [193], Qin et al. [210], Strikers et al. [239], Cattaneo et al. [23]
Co	AC electrodeposition	Magnetic properties	Yasui et al. [284]
Co	Pulse electrodeposition	Magnetic properties	Foyet et al. [65]
Co	DC electrodeposition	Magnetic properties	Vivas et al. [259]
Co-Cu	AC electrodeposition	Magnetic properties	Ohgai et al. [193]
Co-Cu	Pulse electrodeposition	Magnetic properties	Cho et al. [38]
Co _x Ni _{1-x}	DC electrodeposition	Magnetic properties	Vega et al. [258]
Co-Ni	Pulse electrodeposition	Magnetic properties	Rosa et al. [216]
Co _{0.2} Ni _{0.64} Fe _{0.24}	DC electrodeposition	Magnetic properties	Atalay et al. [12]
Co _{0.45} Fe _{0.55}	AC electrodeposition	Magnetic properties	Fodor et al. [64]
CoPt	DC electrodeposition	–	Chu et al. [50], Fu et al. [66]
CoPt	DC electrodeposition	Magnetic properties for high-density memory storage systems	Cagnon et al. [21]
Co _{1-x} Zn _x	AC electrodeposition	Magnetic properties	Xu et al. [275]
Cu	DC electrodeposition	–	Riveros et al. [215]
Cu	AC electrodeposition	Wave shape and pulse polarity influence on AAO pore filling were investigated	Gerain and Haber [73]
Cu	DC electrodeposition	Multigram synthesis of the Cu NWs	Gelves et al. [72]
Cu	DC electrodeposition	Cu NWs were grown on NiTi shape memory alloy thin film	Bayat et al. [14]
Cu	DC electrodeposition	Y-branched NW	Gao et al. [69]
Cu	Solid state reduction	–	Feliciano and Martínez-Iñesta [63]
Fe	DC electrodeposition	Magnetic properties	Haehnel et al. [83], Qin et al. [210]
Fe-Pd	AC electrodeposition	Magnetic properties	Fei et al. [61]
FePt	DC electrodeposition	–	Chu et al. [50]
FePt	DC electrodeposition	Magnetic properties for high-density memory storage systems	Cagnon et al. [21], Inoue et al. [96]
Ni	DC electrodeposition	Electric resistance of singular NWs	Choi et al. [46]
Ni	DC electrodeposition	Optical properties	Evans et al. [56]

(continued)

Table 2 (continued)

Ni	DC electrodeposition	Diameter-modulated NWs	Sulka et al. [248]
Ni	DC electrodeposition	Magnetic properties	Ohgai et al. [193], Qin et al. [210], Oh et al. [191], Napolskii et al. [180]
Ni	DC electrodeposition	–	Han et al. [84], Meng et al. [172], Chu et al. [49]
Ni	Pulse electrodeposition	–	Nielsen et al. [182]
Ni	AC electrodeposition	Various experimental procedures were studied	Yin et al. [287]
Ni	DC electrodeposition	Magnetic properties of Y-branched NWs	Guo et al. [81]
Ni	DC electrodeposition	Ni NW were investigated as a fluorescent material	Feizi et al. [62]
Ni	Pulse electrodeposition	Y-branched NWs were obtained	Montero-Moreno et al. [176]
Ni	DC electrodeposition	–	Proenca et al. [208]
Ni ₄ Fe _{1-x}	Pulse electrodeposition	Composition and size of NWs influence their magnetic properties	Salem et al. [220]
Ni _{1/2} -Fe ₂ O ₃	DC electrodeposition and impregnation with [Fe(NH ₂) ₄] ³⁺	Core (Ni)-shell (γ -Fe ₂ O ₃) nanostructures were formed	Chen et al. [30]
NiPt	DC electrodeposition	–	Chu et al. [50]
Sn	DC electrodeposition	–	Sulka et al. [247], Zaraska et al. [291]
Sn	AC electrodeposition	–	Kolmakov et al. [115]
Pd	Solid state reduction	–	Feliciano and Martínez-Iñesta [63]
Pt	DC electrodeposition	Magnetic properties	Evans et al. [57]
Pt	DC electrodeposition	–	Fu et al. [66], Holubowitch et al. [90]
Pt	DC electrodeposition	High surface area for electrocatalytic methanol decomposition	Zhao et al. [307]
Pt-Co	DC electrodeposition	High surface area electrocatalytic material made of porous NW obtained via dealloying	Liu et al. [148]
Zn	DC electrodeposition	Extensive lattice parameters expansion of bulk and NW	Wang et al. [262]

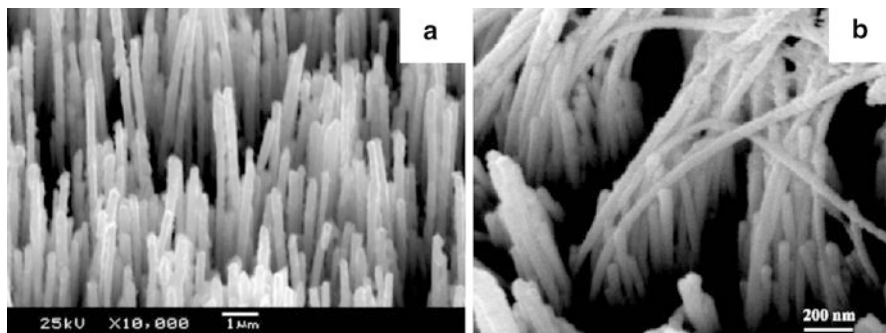


Fig. 18 Copper (a) and silver (b) nanowires obtained by AAO template-assisted electrodeposition (Reprinted from Riveros et al. [215] and Pang et al. [197])

Table 3 Set of nanotubes made of metals with their deposition techniques and investigated properties

Metal or alloy	Deposition technique	Investigated properties/ applications/remarks	References
Au	DC electrodeposition	Fabrication of high surface area electrodes	Lee et al. (2005)
Au	Sputtering	–	Guo et al. [80]
Au	Redox reaction on the pores' inner surface	Catalytic properties	Yu et al. [289]
Au–C	Impregnation of AAO walls with acetone and HAuCl ₄ followed by annealing at 200 °C	Au–C composite NTs were obtained	Göring et al. [75]
Au–Ni	DC electrodeposition	Multisegment NTs	Lee et al. [126]
Co	DC electrodeposition	Magnetic properties	Bao et al. [13]
Co	DC electrodeposition	–	Cao et al. [22], Fu et al. [66]
Co	DC electrodeposition	Co nanorings (short tubes) were formed; magnetic properties	Li et al. [138]
Co–Pt	DC electrodeposition	–	Fu et al. [66]
Co/PS	Co precursor decomposition inside the polystyrene containing	Magnetic properties	Niensch et al. [184, 185]
Fe	DC electrodeposition	–	Cao et al. [22]
Fe	DC electrodeposition	–	Xu et al. [276]
Ni	DC electrodeposition	–	Cao et al. [22]
Ni	DC electrodeposition	Magnetic properties	Wang et al. [264]
Ni	DC electrodeposition	High surface area of Ni catalyst for water decomposition	Yi et al. [286]
Pd	Sol–gel	–	Steinhart et al. [233]
Pd	Physical vapor deposition	Mg-decorated Pd NT served as a material for hydrogen storage	Norek et al. [188]
Pt	DC electrodeposition	–	Fu et al. [66]

Table 4 Set of nanodots made of metals with their deposition techniques and investigated properties

Metal or alloy	Deposition technique	Investigated properties/ applications/remarks	References
Ag	Pulse laser deposition	–	Nam et al. [179]
Ag	Sputtering	Multiple arrays of ND were formed	Masuda et al. [162]
Ag	Electron beam evaporation	The greater aspect ratio, the longer wavelength of the plasmon resonance maximum	Chen et al. [28]
Ag	Electron beam evaporation	Ag NDs on GaAs substrate were deposited	Liu et al. [155]
Au	Sputtering	Multiple arrays of ND were formed	Masuda et al. [162]
Au	AC electrodeposition	Fabrication of Au ND 3D arrays	Kondo et al. [117]
Au–Al ₂ O ₃	Electron beam evaporation	Multilayer ND were formed for Surface enhanced Raman spectroscopy	Kondo et al. [118, 120]
Cu	Atomic layer deposition	70 nm uniform Cu NDs were formed in AAO with greater pores (up to 200 nm)	Johansson et al. [104]
Cu–Ni	Pulse electrodeposition + ultrasonication	Multisegment NW were obtained; after sonication, these fell apart into ND	Guo et al. [79]
Fe	Electron beam epitaxy	Magnetic properties	Liu et al. [149]
Ni	Pulse laser deposition	–	Nam et al. [179]
Pd	Plasma-enhanced chemical vapor deposition	Small NDs were formed on the inner walls of AAO	Kim et al. [111]
Pd	Atomic layer deposition	Pd ND-based hydrogen sensor	Elam et al. [54]
W	Electron beam-induced deposition	–	Xie et al. [272]
Zn	Pulse laser deposition	–	Nam et al. [179]

For example, nanowires made of Ag₂S [141], CdS ([108, 2, 71], Liu et al. 2011), CdTe [306], CoSb [282], Cu₂O [112], Cu₂S [141], In₂S₃ [225], NiHCF [218], Se [299], PbS [270], or ZnO (Fig. 20) [74, 194] were formed with DC electrodeposition. To form nanowires made of oxides or salts, deposition from nonaqueous solutions is also applied (i.e., CdS [152, 154], ZnO [74] deposited compounds from DMSO solutions). Numerous nanowires made of inorganic compounds are formed also due to the ease of fabrication with inexpensive chemical methods, like precipitation in pores or template wetting. With these methods, variety of nanowires including AgI [261, 203, 204], Ag₂S [204], Ag₂Se [204], CdS [175], Cu₂S [204], CuS [204], CuSe [204], CsHSO₄ [17] was fabricated. Due to the high-aspect ratio and two confined dimensions, numerous properties of deposited materials are enhanced or modified. Therefore, thermoelectric (Bi₂Te_{2.7}Se_{0.3} [137]), optical (CdS [108, 2, 71, 175], Liu et al. 2011; Cu₂O [112]; In₂O₃ [70]; In₂S₃ [225]; Si [159]; SnO₂ [70]; PbS [270]; ZnO [37, 189]), magnetic (CoFeB [226]), or piezoelectric properties (ZnO [59]) are investigated. With the use of nanowires made of

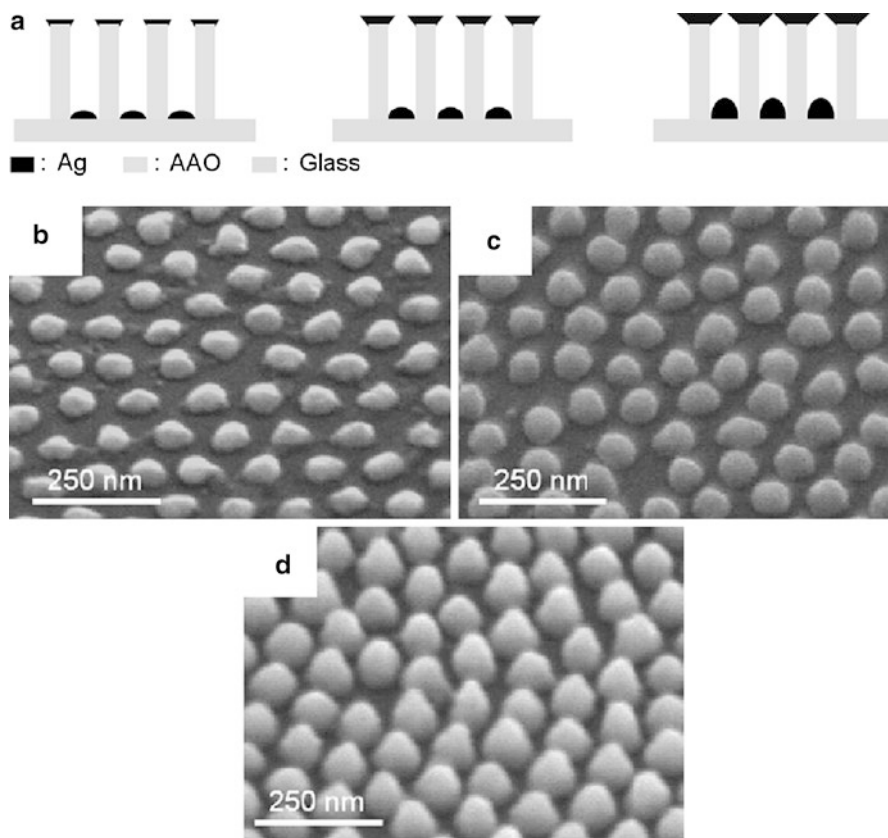


Fig. 19 Silver plasmonic nanodots obtained via electron beam evaporation (Reprinted from Chen et al. [28], doi:10.1007/s00339-012-7404-6)

semiconducting materials, advances in energy harvesting and storage systems can be achieved. According to Liu et al. (2011), with the use of CdS nanowires, photovoltaic cells with efficiency of 17 % were manufactured. Moreover, nanowires made of LiCoO_2 [142] and CoSb [282] are promising materials for high surface area electrodes for batteries. Moreover, Bocchetta et al. [17] reported fabrication of nanowires made of CsHSO_4 , which can serve as a protonic conductor in fuel cells. Additionally, with the use of sol-gel technique, superconducting nanowires made of YBCO were formed [100].

Nanotubes made of oxides and semiconductors are beneficial in all the applications, where developed surface area is demanded, including catalysis (TiO_2 , V_2O_5 , ZnO [205]), high surface electrodes for energy harvesting [18] and storage (LiMn_2O_4 [186]), and sensors (CuCo_2O_4 , NiCo_2O_4 , ZnCo_2O_4 [299]; NiHCF [218]; ZnFe_2O_4 [301]) (Table 6). Optical (InGaAs [27], In_2O_3 [228], MoS_2 [288]) and magnetic (Fe_2O_3 [240], $\text{Fe}_3\text{O}_4/\text{ZrO}_2/\text{Fe}_3\text{O}_4$ [206]) properties of the nanotubes are also researched. Numerous nanotubes are formed with classical chemical methods including reaction in pores (CdS [204], Fe_2O_3 [240], LiMn_2O_4 [186]) and template

Table 5 Set of nanowires made of inorganic compounds and metalloids with their deposition techniques and investigated properties

Compound or element	Deposition technique	Investigated properties/applications/remarks	References
AgI	Precipitation in AAO pores	Ionic conductance	Wang et al. [261], Piao and Kim [203] Piao et al. [204]
Ag ₂ S	Precipitation in AAO pores	–	Piao et al. [204]
Ag ₂ S	DC electrodeposition of Ag and DC electrochemical sulfurization of Ag NW	Ag/Ag ₂ S segment heterowires were obtained	Liang et al. [141]
Ag ₂ Se	Precipitation in AAO pores	–	Piao et al. [204]
AlN	Reaction of Al and NH ₃ at 1100 °C	–	Wu et al. [269]
Bi ₂ Te ₃ /PANI	Galvanostatic polymerization of aniline and DC electrodeposition of Bi ₂ Te ₃	Core (Bi ₂ Te ₃)–shell (PANI) NWs were obtained	Xu et al. [273]
Bi ₂ Te _{2.7} Se _{0.3}	DC electrodeposition	High-aspect ratio NWs made of thermoelectric materials were formed	Li et al. [137]
CdS	DC electrodeposition	Optical properties for photovoltaics	Kang and Kim [108], Aguilera et al. [2]
CdS	DC electrodeposition	Optical properties	Gavrilo et al. [71]
CdS	AC electrodeposition	–	Routkevitch et al. [217]
CdS	Precipitation in AAO pores	Optical properties	Mondal et al. [175]
CdS	DC electrodeposition and sulfurization at 300 °C in Ar atmosphere	–	Fan et al. [58]
CdS	Physical vapor deposition (PVD)	–	Wu and Tao [268]
CdS	DC electrodeposition (DMMSO)	Optical properties; photovoltaic applications (17 % of current efficiency)	Liu et al. (2011)
CdTe	DC electrodeposition	–	Zhao et al. [306]
CoFeB	AC electrodeposition	Magnetic properties	Sharif et al. [226]
Cu ₂ O	DC electrodeposition	Optical properties	Ko et al. [112]

Cu ₂ S	Precipitation in AAO pores	–	Piao et al. [204]
Cu ₂ S	DC electrodeposition of Cu and DC electrochemical sulfuration of Cu NW	Cu/Cu ₂ S segment heterowires were obtained	Liang et al. [141]
CuS	Precipitation in AAO pores	–	Piao et al. [204]
CuSe	Precipitation in AAO pores	–	Piao et al. [204]
CsHSO ₄	Filling AAO with liquid solution of CsHSO ₄	Protonic conductor for fuel cells	Bocchetta et al. [17]
CoSb	DC electrodeposition	Prospective material for lithium-ion batteries	Yang et al. [282]
GaN	Reaction between Ga ₂ O and NH ₃ at 1,000 °C	Vapor liquid–solid mechanism with application of indium catalyst	Cheng et al. [33]
In ₂ O ₃	Sol–gel	Optical properties; NWs were doped with rare earth metals	Gaponenko et al. [70]
In ₂ O ₃	Magnetron sputtering	–	Zhang et al. [302, 303]
In ₂ S ₃	DC electrodeposition and heat treatment	Optical properties	Shi et al. [225]
LiCoO ₂	Radio frequency magnetron sputtering	High surface area materials for lithium-ion batteries	Liao et al. [142]
NiHCF	DC electrodeposition	Biosensing	Sabzi et al. [218]
Se	DC electrodeposition	–	Zhang et al. [300]
Si	Chemical vapor deposition	Optical properties	Márquez et al. [159]
Si	Chemical vapor deposition	–	Lefevvre et al. [132]
SnO ₂	Sol–gel	Optical properties; NWs were doped with rare earth metals	Gaponenko et al. [70]
SnO ₂	AC electrodeposition and heat treatment	–	Kolmakov et al. [115]
Pbs	DC electrodeposition	Optical properties	Wu et al. [270]
YBa ₂ Cu ₃ O _{7-δ} (YBCO)	Sol–gel	Monocrystalline superconducting NWs	Jian et al. [100]
ZnO	Metal–organic chemical vapor deposition	Piezoelectric NWs	Fan et al. [59]
ZnO	Vapor liquid–solid	Optical properties	Chik et al. [37]
ZnO	Atomic layer deposition	Optical properties	Norek et al. [189]
ZnO	DC electrodeposition	Electrodeposition mechanism from DMSO solution with and without KCl was investigated	Gomez et al. [74]
ZnO	DC electrodeposition	Electrodeposition from aqueous solution of Zn(NO ₃) ₂	Öztürk et al. [194]

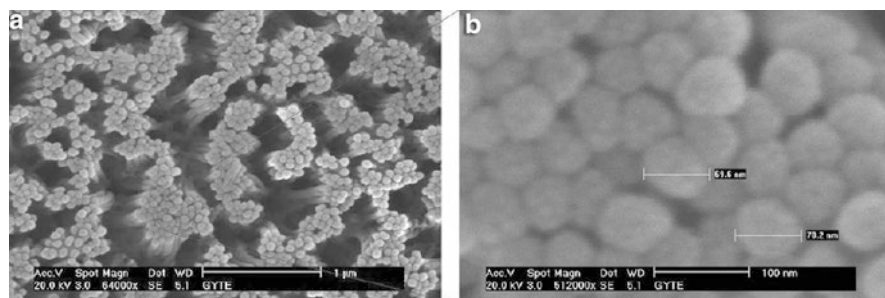


Fig. 20 ZnO nanowires obtained by DC electrodeposition into anodic alumina template (Reprinted from Öztürk et al. [194])

wetting ($\text{Bi}_{1.25}\text{La}_{0.75}\text{Ti}_3\text{O}_{12}$ [224]; CuCo_2O_4 , NiCo_2O_4 , ZnCo_2O_4 [299]; ZnFe_2O_4 [301]). Sol-gel technique, chemical vapor deposition, and atomic layer deposition are also in use (Table 6).

Hexagonally arranged arrays of nanodots made of semiconductors and oxides are being formed with anodic alumina templates mainly due to their optical properties related to their dimensions (Table 7). With the use of anodic alumina templates, arrays of nanodots made of CdTe [106, 107], GaAs [140], GaN [32], In_2O_3 [133, 134], InAs [8], NiHCF [218], $\text{Si}_{1-x}\text{Ge}_x$ [92], Si [93], TiO_2 [29], and ZnS [257] were fabricated. Variety of techniques is applied to form these nanodots, including molecular beam epitaxy (Jung et al. 2006, [140, 8]), reaction in pores [32], thermal sputtering and evaporation [133, 134, 257], direct current electrodeposition [218], or plasma-enhanced chemical vapor deposition (Hu and He 2006).

Also carbon nanotubes are formed with the use of anodic alumina templates. Carbon nanotubes are usually fabricated by chemical vapor deposition (CVD) inside the AAO template pores, even without a catalyst [223, 51, 157] (Table 8). To conduct carbon nanotubes synthesis in the AAO pores, very often catalysts are being deposited on the pores' bottoms via various techniques, including DC electrodeposition [298, 78, 85], AC electrodeposition [91, 105, 266, 267, 279], dip coating [173], and thermal evaporation [121]. The most commonly applied catalysts are Co ([26, 91, 105, 241], Wen et al. 2006, [279, 298]), Fe [173], and Ni [78, 85, 121]. Carbon nanotubes formed with AAO template technique are attractive due to their electric properties ([223, 51, 26, 105], Wen et al. 2006). Much effort has been put into investigation of the carbon nanotubes' highly ordered arrays as electrochemical double layer capacitors ([105], Wen et al. 2006). Additionally, carbon nanotubes formed inside the AAO templates are also researched as NH_3 and NO_2 sensors [157].

Anodic aluminum oxide is also applied as a template for fabrication of arranged nanowires made of organic compounds (Table 9). These are often formed via template dipping or wetting [3, 94, 98, 99, 114, 174, 187, 190, 192, 251]. Optical properties of organic and polymeric nanowires are very often researched [3, 98, 99, 101, 125, 192, 174, 273]. Electric properties of conductive organic nanowires are also in the focus of investigations (polypyrrole [277], polythiophene [190]). Additionally, nanowires made of triglycine sulfate possess pyroelectric properties, which were investigated by Nitzani and Berger [187]. Moreover, copper

Table 6 Set of nanotubes made of inorganic compounds and metalloids with their deposition techniques and investigated properties

Compound or element	Deposition technique	Investigated properties/applications/remarks	References
BiFeO ₃	Sol-gel	-	Park et al. [201]
Bi _{1.35} La _{0.75} Ti ₃ O ₁₂	Template wetting	-	Seo et al. [224]
CdS	Precipitation in AAO pores	-	Piao et al. [204]
CdS	Microwave-assisted template wetting	-	Ni et al. [181]
CdSe	Cyclovoltammetric electrodeposition	Photocurrents of NTs were measured	Bocchetta et al. [18]
CuCo ₂ O ₄	Template wetting	CH ₃ COOH, SO ₂ , C ₂ H ₅ OH, CO, Cl ₂ , NO ₂ sensor	Zhang et al. [299]
Fe ₂ O ₃	Precipitation in AAO pores and sol-gel	Magnetic properties	Suber et al. [240]
Fe ₃ O ₄ /ZrO ₂ /Fe ₃ O ₄	Atomic layer deposition	Magnetic properties of multilayer Fe ₃ O ₄ /ZrO ₂ /Fe ₃ O ₄ NT	Pitzschel et al. [206]
Ga ₂ O ₃	Sol-gel	-	Cheng and Samulski [34]
InGaAs	Metal-organic chemical vapor deposition	Optical properties	Chen et al. [27]
In ₂ O ₃	Sol-gel	-	Cheng and Samulski [34]
In ₂ O ₃	Chemical vapor deposition	Optical properties	Shen et al. [228]
LiMn ₂ O ₄	Reaction in pores	Material for high surface area electrodes for lithium batteries	Nishizawa et al. [186]
MoS ₂	Thermal decomposition of (NH ₄) ₂ MoS ₄	Optical properties	Yu et al. [288]
NiCo ₂ O ₄	Template wetting	CH ₃ COOH, SO ₂ , C ₂ H ₅ OH, CO, Cl ₂ , NO ₂ sensor	Zhang et al. [299]
NiHCF	DC electrodeposition	Biosensing	Sabzi et al. [218]
TiO ₂	Sol-gel	-	Chu et al. [49]
TiO ₂	Atomic layer deposition	Catalytic decomposition of cyclohexane	Pellin et al. [205]
TiO ₂ -RuO ₂	DC electrodeposition	-	Chu et al. [49]
V ₂ O ₅	Atomic layer deposition	Catalytic decomposition of cyclohexane	Pellin et al. [205]
ZnO	Atomic layer deposition	Catalytic decomposition of cyclohexane	Pellin et al. [205]
ZnCo ₂ O ₄	Template wetting	CH ₃ COOH, SO ₂ , C ₂ H ₅ OH, CO, Cl ₂ , NO ₂ sensor	Zhang et al. [299]
ZnFe ₂ O ₄	Template wetting	C ₂ H ₅ OH, CH ₃ OH, (H ₃ C) ₂ CO, HCHO sensor	Zhang et al. [301]

Table 7 Set of nanodots made of inorganic compounds and metalloids with their deposition techniques and investigated properties

Compound or element	Deposition technique	Investigated properties/ applications/remarks	References
CdTe	Molecular beam epitaxy	Promising UV–vis optoelectronic material	[107]
CdTe/GaAs	Molecular beam epitaxy	–	[106]
GaAs	Molecular beam epitaxy	–	[140]
GaN	Reaction between Ga ₂ O and NH ₃ at 900 °C	Optical properties	[32]
In/In ₂ O ₃	Thermal sputtering	Optical properties	[133]
In ₂ O ₃	Thermal sputtering	–	[134]
InAs	Molecular beam epitaxy	–	[8]
NiHCF	DC electrodeposition	Biosensing	[218]
Si _{1-x} Ge _x	Plasma-enhanced chemical vapor deposition	Optical properties	[92]
Si	Plasma-enhanced chemical vapor deposition	Optical properties	[92]
TiO ₂	Anodization of aluminum with sputtered TiN on the backside	-	[29]
ZnS	Thermal evaporation	Optical properties	[257]

phthalocyanine was investigated as a material for photodetectors, due to its semi-conducting properties [273]. PMMA poly(methyl methacrylate) nanowire arrays were investigated as a drug-releasing platform by Kokonou et al. [114]. Bioinspired materials are also formed with the use of anodic alumina template approach. Lee et al. [131] reported fabrication of hierarchically branched nanowires made of polystyrene (PS), inspired by gecko's feet. Polystyrene was simply melted into the branched pores, and these nanostructures with sophisticated shape were formed, providing relatively high values of friction coefficient.

Majority of organic nanotubes are formed with the anodic alumina template dipping or wetting methods (Table 10). Hexagonally arranged organic nanotubes are being investigated due to their optical (poly(methyl methacrylate) [174], polynorbornene [192], poly(vinyl pyrrolidone) [209]), pyroelectric (triglycine sulfate [187]), and piezoelectric properties (poly(vinylidene fluoride) [139]).

Nanodots made of organic compounds are rarely fabricated. PS nanodots were, i.e., applied as corks, closing the nanotubes inside the AAO. After template removal, nano-test tubes were obtained [88]. Also polymer nanoporous arrays made of polymers are formed. For example, Yanagashita et al. [280] reported fabrication of through-hole membranes made of PMMA. The PMMA membranes were formed with a two-step replication technique. Firstly, nickel nanowires were electrodeposited into the AAO membrane. After AAO removal, arrays of Ni nanowires were dipped into the methyl methacrylate solution. After polymerization, Ni nanowires were chemically removed with HCl and HNO₃, and PMMA through-hole membrane was formed (Fig. 21).

Due to the nanofabrication employing anodic aluminum oxide templates, various devices are fabricated. Due to the high surface area provided by nanopores, nanowires, and nanotubes, these structures are being investigated as active materials for sensing (Table 11). Even anodic alumina itself is being applied as a humidity [147, 7, 86],

Table 8 Set of fabrication methods, investigated properties of carbon nanotubes formed with AAO template technique

Deposition technique	Investigated properties/applications/remarks	Catalyst	Catalyst deposition technique	References
Chemical vapor deposition	Electrical conductivity	None	-	[223]
Chemical vapor deposition	Electrical conductivity	None	-	[51]
Chemical vapor deposition	NH ₃ and NO ₂ sensing	None	-	[157]
Chemical vapor deposition	Electrochemical properties	Co	Reduction of cobalt acetate inside the pores	[26]
Flame method	-	Co	AC electrodeposition	[91]
Chemical vapor deposition	CNTs investigated as electrochemical double layer capacitors	Co	AC electrodeposition	[105]
Precursor pyrolysis	-	Co	Co precursor reduction with CO gas	[241]
Chemical vapor deposition	CNTs investigated as electrochemical double layer capacitors	Co	AC electrodeposition	[267]
Chemical vapor deposition	CNTs investigated as electrochemical double layer capacitors	Co	AC electrodeposition	[266]
Chemical vapor deposition	CNTs with triangular cross section were formed	Co	AC electrodeposition	[279]
Precursor pyrolysis	-	Co	DC electrodeposition	[298]
Chemical vapor deposition	Various experimental procedures were studied	Fe	Fe(NO ₃) ₃ dip coating or ferrocene as a floating catalyst	[173]
Plasma-enhanced chemical vapor deposition	Template synthesis of CNTs array on Si substrate was conducted	Ni	DC electrodeposition	[78]
Chemical vapor deposition	-	Ni	DC electrodeposition	[85]
Plasma-enhanced chemical vapor deposition	Highly ordered CNT arrays were formed in 300 mm wafer scale on silicon substrate	Ni	Thermal evaporation	[121]

Table 9 Set of nanowires made of organic compounds and polymers with their deposition techniques and investigated properties

Compound	Deposition technique	Investigated properties/applications/remarks	References
Albumen	Dipping	Optical properties	[98]
1,4-Bis[2-(5-fenylsazotil)] benzene	Sublimation into the pores	Optical properties	[125]
2,7-Di-tert-butylpyrene	Dipping	Optical properties	[3]
Copper phthalocyanine	Electrophoresis	Promising material for photodetectors (organic semiconductor)	[273]
8-Hydroxy quinoline	Dipping	Optical properties	[94]
Morin	Dipping	Optical properties	[98, 99]
Polyaniline	DC electrodeposition	Optical properties	[101]
Poly(3-hexylthiophene)	Template wetting (dipping)	Various synthesis approaches were researched	[114]
Poly(methyl methacrylate)	Vacuum infiltration	–	[195]
Poly(methyl methacrylate)	Template wetting (dipping)	Various synthesis approaches were researched; PMMA NWs were tested as drug-releasing platform	[114]
Polynorbomene	Template wetting (dipping)	Optical properties of PNB NW with CdSe/ZnS core–shell nanodots	[192]
Polypyrrole	Polymerization in pores after dipping	–	[35]
Polypyrrole	Electrosynthesis (DC electrodeposition and polymerization in pores)	Electric properties and field emission behavior	[277]
Polypyrrole	Electropolymerization	–	[89]
Polystyrene	Melting into the pores	High friction material, inspired by gecko's feet (hierarchical nanowires)	[131]
Polystyrene–poly(methyl methacrylate)	Melting and dipping	Core–shell nanowires were obtained	[251]
Polythiophene	Template wetting (dipping)	Electric conductivity	[190]
Triglycine sulfate	Dipping with the presence of electric field	Pyroelectric properties	[187]
Tris (8-quinolinolato)-aluminum (III)	Dipping	Optical properties	[174]
Trypsin	Dipping	Optical properties	[99]

Table 10 Set of nanotubes made of organic compounds and polymers with their deposition techniques and investigated properties

Compound	Deposition technique	Investigated properties/ applications/remarks	References
Ethylene vinyl acetate	Dipping	Various experimental techniques were studied	[227]
Poly(methyl methacrylate)	Dipping	–	[232]
Poly(methyl methacrylate)	Dipping	Optical properties	[174]
Polynorbornene	Template wetting (dipping)	Optical properties of PNB NW with CdSe/ZnS core-shell nanodots	[192]
Polystyrene	Dipping	–	[232]
Polypyrrole	Polymerization in pores after dipping	–	[35]
Polytetrafluoroethylene	Dipping	–	[232]
Poly(vinyl pyrrolidone)	Dipping and annealing	Optical properties	[209]
Poly(vinylidene fluoride)	Dipping and annealing	Piezoelectric properties	[139]
Triglycine sulfate	Dipping with the presence of electric field	Pyroelectric properties	[187]

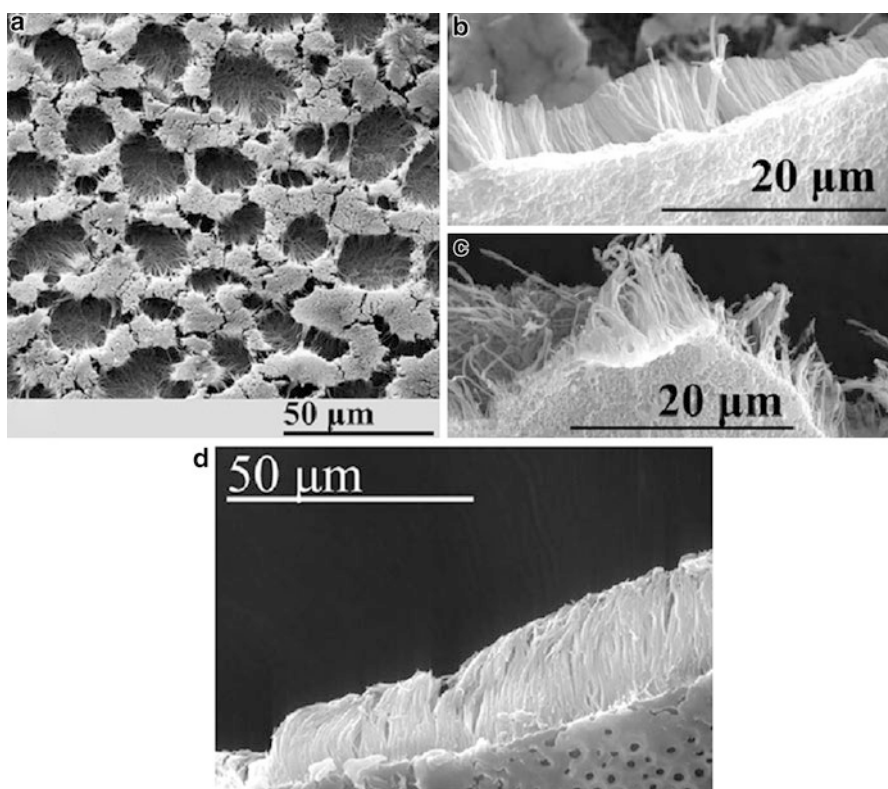
**Fig. 21** Poly(methyl methacrylate) (a–c) and poly(3-hexylthiophene) (d) nanowire arrays (Reprinted from Kokonou et al. [114])

Table 11 Nanostructured sensors formed with anodic alumina template technique (NW, nanowires; NT, nanotubes)

Active material	Fabrication technique	Detected compound	Sensing method	References
AAO	–	Methane	Voltage changes (Wheatstone bridge circuit)	[110]
AAO	Sputtered gold electrode on both surfaces of AAO	Water (humidity)	Electrochemical impedance spectroscopy	[147]
AAO	–	Water (humidity)	Electric capacity	[7]
AAO	–	Water (humidity)	Electric capacity	[86]
AAO	–	Polychlorinated biphenyls (PCBs)	Electric capacity	[103]
Ag NW	DC electrodeposition	H ₂ O ₂	Cyclic voltammetry	[122]
Antibodies on the functionalized AAO surface	Surface chemical reactions	<i>E. coli</i> O157:H7 (one of the most harmful food pathogens)	Electrochemical impedance spectroscopy	[24]
Anti-glucose oxidase (immunoglobulin G)	Surface chemical reactions	Glucose oxidase	Cyclic voltammetry	[113]
Aptamer attached to the AAO inner walls	Surface chemical reactions	Thrombin	Voltammetry	[55]
Au NW	DC electrodeposition	Glucose	Cyclic voltammetry	[265]
Au NW	Two-step electrodeposition technique	Specifically hybridized DNA	Differential pulse voltammetry	[212]
CuCo ₂ O ₄ NT	Template wetting	CH ₃ COOH, SO ₂ , C ₂ H ₅ OH, CO, Cl ₂ , NO ₂	Electric resistance measurements	[299]

DNA	Surface chemical reactions	Complementary DNA	Pulse voltammetry and electrochemical impedance spectroscopy	[211]
DNA	Surface chemical reactions	DNA	Electrochemical impedance spectroscopy	[263]
DNA	Surface chemical reactions	DNA	Electrochemical impedance spectroscopy	[260]
Lipid bilayers	Surface chemical reactions	Triton X-100 (surface active agent)	Cyclic voltammetry	[123]
NiCo ₂ O ₄ NT	Template wetting	CH ₃ COOH, SO ₂ , C ₂ H ₅ OH, CO, Cl ₂ , NO ₂	Electric resistance measurements	[299]
Polypyrrole NW	Electropolymerization	Ammonia	Optical	[302]
Polypyrrole with incorporated glucose oxidase	Electrochemical co-deposition of pyrrole and glucose oxidase and electropolymerization	Glucose	Cyclic voltammetry	[151]
Polypyrrole doped with hydroquinone monosulfonate	Potentiostatic electropolymerization	pH	Potentiometry	[250]
Selective antibody	Surface chemical reactions	Ara h1 peanut protein	Electrochemical impedance spectroscopy	[231]
Trypsin	Surface chemical reactions	Trypsin	Photoluminescence	[222]
Urease immobilized on the AAO	Surface chemical reactions	Urea	Electrode-separated piezoelectric sensor (ESPS)	[281]
ZnCo ₂ O ₄ NT	Template wetting	CH ₃ COOH, SO ₂ , C ₂ H ₅ OH, CO, Cl ₂ , NO ₂	Electric resistance measurements	[299]
ZnFe ₂ O ₄ NT	Template wetting	C ₂ H ₅ OH, CH ₃ OH, (H ₃ C) ₂ CO, HCHO,	Electric resistance measurements	[301]

methane [110], and polychlorinated biphenyl [103] sensor. Due to the surface chemistry of anodic alumina, the pore walls are being functionalized, and numerous sensors are being formed. The detection of glucose oxidase [113], thrombin [55], DNA [211, 260, 263], surface active agents [123], Ara h1 peanut protein [231], trypsin [222], and urea [281] is enabled. Moreover, application of various nanofabrication techniques, including electrochemical deposition and electropolymerization, allows to form Ag [122], Au [212, 265], and polypyrrole [151, 250, 302] nanowire-based sensors. Also nanotubes fabricated with anodic alumina template employing techniques are being applied as sensors [299, 301]. It is worth to note that majority of the sensing techniques is based on electrochemical methods like voltammetry and electrochemical impedance spectroscopy (Table 11).

With the use of anodic alumina, light polarizers are being assembled. AC and DC electrodeposition techniques are being employed to deposit Ag [199], Co [254], Cu [198], and Ni [219] to form parallel nanowire arrays serving as polarizers. Nanowire-AAO composite polarizers are attractive devices for infrared wavelengths. Recently anodic alumina also finds applications in electronics and optoelectronics [158, 249, 53], photonics [161, 162, 39, 42, 305], integration of living cells with electronics [76, 77, 20], cells culture and tissue engineering [252, 130, 109], and drug-releasing platforms [253].

Anodization of Aluminum Alloys

Anodic alumina is also being formed on technical purity aluminum, containing various alloying elements and on the aluminum alloys. Anodization of technical purity aluminum provides poor arrangement of the nanopores due to the substrate chemical inhomogeneities [156, 292]. Nevertheless, various approaches are being undertaken to conduct successful anodization of aluminum-containing alloys. Zhou et al. [308] reported anodization of zinc-containing aluminum alloy. Three main various anodic layers have been distinguished. The upper layer was made of pure alumina, middle one was made of alumina with incorporated zinc ions, and the bottom layer was made of unoxidized zinc nanopillars. Additionally, Kondo et al. [119] reported anodization of purple gold, AuAl₂ intermetallic alloy. After anodic alumina removal, there were hexagonally arranged hemispherical gold nanodots with diameter of about 30 nm. Anodic nanoporous oxides were also formed on such an intermetallic alloys like Ni₃Al [237], TiAl₃, TiAl, and Ti₃Al [15, 256]. Despite worse arrangement of the nanopores, anodization of aluminum-containing alloys provides functional surface on the substrate which can be advantageous during exploitation of the alloys.

Summary

Nanoporous anodic aluminum oxide morphology and arrangement can be controlled by the operating conditions. For this reason, anodic alumina is a very suitable material in nanofabrication. Moreover, due to the ions incorporation, luminescent

properties of anodic alumina can be tuned. Additionally, self-organized anodization is cost-effective, which makes it attractive for high-tech industries.

With the use of diverse techniques, including electrochemical ones, sophisticated materials with unusual properties are obtained by researchers. Anodic alumina templates allow to obtain hexagonally arranged arrays of nanowires, nanotubes, and nanodots made of various materials, which translate into unlimited possibilities of materials' nanofabrication with new or enhanced properties. It implies assembly of devices with better performance and efficiency.

References

1. Abdollahifard MJ, Faez K, Pourfard M, Abdollahic M (2012) A histogram-based segmentation method for characterization of self-assembled hexagonal lattices. *Appl Surf Sci* 257:10443–10450
2. Aguilera A, Jayaraman V, Sanagapalli S, Suresh Singh R, Jayaraman V, Sampson K, Singh VP (2006) Porous alumina templates and nanostructured CdS for thin film solar cell applications. *Sol Energy Mat Sol Cell* 90:713–726
3. Al-Kaysi RO, Bardeen CJ (2006) General method for the synthesis of crystalline organic nanorods using porous alumina templates. *Chem Commun* 2006:1224–1226
4. Almasi Kashi M, Ramazani A (2005) The effect of temperature and concentration on the self-organized pore formation in anodic alumina. *J Phys Appl Phys* 38:2396–2399
5. Almasi Kashi M, Ramazani A, Noormohammadi M, Zarei M, Marashi P (2007) Optimum self-ordered nanopore arrays with 130–270 nm interpore distances formed by hard anodization in sulfuric/oxalic acid mixtures. *J Phys Appl Phys* 40:7032–7040
6. Almasi Kashi M, Ramazani A, Rahmandoust M, Noormohammadi M (2007) The effect of pH and composition of sulfuric–oxalic acid mixture on the self-ordering configuration of high porosity alumina nanohole arrays. *J Phys Appl Phys* 40:4625–4630
7. Almasi Kashi M, Ramazani A, Abbasian H, Khayyatian A (2012) Capacitive humidity sensors based on large diameter porous alumina prepared by high current anodization. *Sens Actuators A* 174:69–74
8. Alonso-Gonzalez P, Martyn-Gonzalez MS, Martín-Sanchez J, Gonzalez Y, Gonzalez L (2006) Ordered InAs QDs using prepatterned substrates by monolithically integrated porous alumina. *J Cryst Growth* 294:168–173
9. Asoh H, Nishio K, Nakao M, Tamamura T, Masuda H (2001) Conditions for fabrication of ideally ordered anodic porous alumina using pretextured Al. *J Electrochem Soc* 148:B152–B156
10. Asoh H, Ono S, Hirose T, Nakao M, Masuda H (2003) Growth of anodic porous alumina with square cells. *Electrochim Acta* 48:3171–3174
11. Asoh H, Ono S (2007) Fabrication of ordered anodic nanoporous alumina layers and their application to nanotechnology. In: Staikov G (ed) *Electrocrystallization in nanotechnology*. Wiley, Weinheim
12. Atalay S, Kaya H, Atalay FE, Aydogmus E (2013) Magnetoimpedance effects in a CoNiFe nanowire array. *J Alloys Comp* 561:71–75
13. Bao J, Xu Z, Hong J, Ma X, Lu Z (2004) Fabrication of cobalt nanostructures with different shapes in alumina template. *Scripta Mater* 50:19–23
14. Bayat N, Sanjabi S, Barber ZH (2012) Growth of copper nanowire arrays on NiTi shape memory alloy thin film. *Surf Coat Technol* 206:4075–4078
15. Berger S, Tsuchiya H, Schmuki P (2008) Transition from nanopores to nanotubes: self-ordered anodic oxide structures on titanium/aluminides. *Chem Mater* 20:3245–3247
16. Black MR, Padi M, Cronin SB, Lin YM, Rabin O, McClure T, Dresselhaus G, Hagelestein PL, Dresselhaus MS (2002) Intersubband transitions in bismuth nanowires. *Appl Phys Lett* 77:4142–4144

17. Bocchetta P, Chiavarotti G, Masi R, Sunseri C, Di Quarto F (2004) Nanoporous alumina membranes filled with solid acid for thin film fuel cells at intermediate temperatures. *Electrochem Commun* 6:923–928
18. Bocchetta P, Santamaria M, Di Quarto F (2013) One-step electrochemical synthesis and physico-chemical characterization of CdSe nanotubes. *Electrochim Acta* 88:340–346
19. Borba JR, Brito C, Migowski P, Vale TB, Stariolo DA, Teixeira SR, Feil AF (2013) Quantitative characterization of hexagonal packings in nanoporous alumina arrays: a case study. *J Phys Chem C* 117:246–251
20. Brüggemann D, Wolfrum B, Maybeck V, Mourzina Y, Jansen M, Offenhäuser A (2011) Nanostructured gold microelectrodes for extracellular recording from electrogenic cells. *Nanotechnology* 22:265104
21. Cagnon L, Dahmane Y, Voiron J, Pairis S, Baci M, Ortega L, Benbrahim N, Kadri A (2007) Electrodeposited CoPt and FePt alloys nanowires. *J Magn Magn Mater* 310:2428–2430
22. Cao H, Wang L, Qiu Y, Wu Q, Wang G, Zhang L, Liu X (2006) Generation and growth mechanism of metal (Fe, Co, Ni) nanotube arrays. *Chem Phys Chem* 7:1500–1504
23. Cattaneo L, Franz S, Albertini F, Ranzieri P, Vincenzo A, Bestetti M, Cavallotti PL (2012) Electrodeposition of hexagonal Co nanowires with large magnetocrystalline anisotropy. *Electrochim Acta* 85:57–65
24. Chan KY, Ye WW, Zhang Y, Xiao LD, Leung PHM, Li Y, Yang M (2013) Ultra sensitive detection of *E. coli* O157:H7 with biofunctional magnetic bead concentration via nanoporous membrane based electrochemical immunosensor. *Biosens Bioelectron* 41:532–537
25. Cheah SK, Perre E, Rooth M, Fondell M, Hårsta A, Nyholm L, Boman M, Gustafsson T, Lu J, Simon P, Edström K (2009) Self-supported three-dimensional nanoelectrodes for microbattery applications. *Nano Lett* 9:3230–3233
26. Chen QL, Xue KH, Shen W, Tao FF, Yin SY, Xu W (2004) Fabrication and electrochemical properties of carbon nanotube array electrode for supercapacitors. *Electrochim Acta* 49:4157–4161
27. Chen P, Chua SJ, Wang YD, Sander MD, Fosta CG (2005) InGaN nanorings and nanodots by selective area epitaxy. *Appl Phys Lett* 87:143111–143113
28. Chen IC, Chen YH, Wang YC, Shih MH (2012) Plasmon resonance properties of silver-patterned glass substrates fabricated by anodic alumina oxide templates. *Appl Phys A* 112:381–386. doi:10.1007/s00339-012-7404-6
29. Chen PL, Kuo CT, Tsai TG, Wu BW, Hsu CC, Pana FM (2003) Self-organized titanium oxide nanodot arrays by electrochemical anodization. *Appl Phys Lett* 82:2796–2798
30. Chen JH, Huang CP, Chao CG, Chen TM (2006) The investigation of photoluminescence centers in porous alumina membranes. *Appl Phys A* 84:297–300
31. Chen Y, Yan H, Li XH, Li W, Zhang JW, Zhang XY (2006) Assembly of Ni/ γ -Fe₂O₃ shell/core nanowires. *Mater Lett* 60:245–247
32. Cheng GS, Zhang LD, Zhu XG, Chen SH, Li Y, Zhu Y, Fei GT (1999) Synthesis of orderly nanostructure of crystalline GaN nanoparticles on anodic porous alumina membrane. *Nanostruct Mater* 11:421–426
33. Cheng GS, Chen SH, Zhu XG, Mao YQ, Zhang LD (2000) Highly ordered nanostructures of single crystalline GaN nanowires in anodic alumina membranes. *Mat Sci Eng A* 286:165–168
34. Cheng B, Samulski ET (2001) Fabrication and characterization of nanotubular semiconductor oxides In₂O₃ and Ga₂O₃. *J Mater Chem* 11:2901–2902
35. Cheng FL, Zhang ML, Wang H (2005) Fabrication of polypyrrole nanowire and nanotube arrays. *Sensors* 5:245–249
36. Chi GJ, Yao SW, Fan J, Zhang WG, Wang HZ (2002) Antibacterial activity of anodized aluminum with deposited silver. *Surf Coat Technol* 157:162–165
37. Chik H, Liang J, Cloutier SG, Kouklin N, Xu JM (2004) Periodic array of uniform ZnO nanorods by second-order self-assembly. *Appl Phys Lett* 84:3376–3378
38. Cho JU, Wu JH, Min JH, Lee JH, Liu HL, Kim YK (2007) Effect of field deposition and pore size on Co/Cu barcode nanowires by electrodeposition. *J Magn Magn Mater* 310:2420–2422

39. Choi J, Schilling J, Nielsch K, Hillebrand R, Reiche M, Wehrspohn RB, Gösele U (2002) Large-area porous alumina photonic crystals via imprint method. *Mat Res Soc Symp Proc* 722:L5.2.1–L5.2.6
40. Choi J, Nielsch K, Reiche M, Wehrspohn RB, Gösele U (2003) Fabrication of monodomain alumina pore arrays with an interpore distance smaller than the lattice constant of the imprint stamp. *J Vac Sci Technol B* 21:763–766
41. Choi J, Sauer G, Nielsch K, Wehrspohn RB, Gösele U (2003) Hexagonally arranged monodisperse silver nanowires with adjustable diameter and high aspect ratio. *Chem Mater* 15:7767–7779
42. Choi J, Sauer G, Göring P, Nielsch K, Wehrspohn RB, Gösele U (2003) Monodisperse metal nanowire arrays on Si by integration of template synthesis with silicon technology. *J Mater Chem* 13:1100–1103
43. Choi J, Luo Y, Wehrspohn RB, Hillebrand R, Schilling J, Gösele U (2003) Perfect two-dimensional porous alumina photonic crystals with duplex oxide layers. *J Appl Phys* 94:4757–4762
44. Choi JH, Kim TH, Seo J, Kuka Y, Suh MS (2004) In situ fabrication of single-crystal Fe nanomagnet arrays. *Appl Phys Lett* 85:3235–3237
45. Choi J, Wehrspohn RB, Gösele U (2005) Mechanism of guided self-organization producing quasi-monodomain porous alumina. *Electrochim Acta* 50:2591–2595
46. Choi DS, Rheem Y, Yoo B, Myung NV, Kim YK (2010) I-V characteristics of a vertical single Ni nanowire by voltage-applied atomic force microscopy. *Curr Appl Phys* 10:1037–1040
47. Choudhari KS, Sudheendra P, Udayashankar NK (2012) Fabrication and high-temperature structural characterization study of porous anodic alumina membranes. *J Porous Mat* 19:1053–1062
48. Chowdhury P, Raghuvaram M, Krishnan M, Barshilia HC, Rajam KS (2011) Effect of process parameters on growth rate and diameter of nano-porous alumina templates. *Bull Mater Sci* 34:423–427
49. Chu SZ, Wada K, Inoue S, Todoroki S (2003) Fabrication and characteristics of nanostructures on glass by Al anodization and electrodeposition. *Electrochim Acta* 48:3147–3153
50. Chu SZ, Inoue S, Wada K, Kurashima K (2005) Fabrication of integrated arrays of ultrahigh density magnetic nanowires on glass by anodization and electrodeposition. *Electrochim Acta* 51:820–826
51. Ciambelli P, Arurault L, Sarno M, Fontorbes S, Leone C, Datas L, Sannino D, Lenormand P, Le Blond Du Plouy S (2011) Controlled growth of CNT in mesoporous AAO through optimised conditions for membrane preparation and CVD operation. *Nanotechnology* 22:265613
52. Cui J, Wu Y, Wang Y, Zheng H, Xu G, Zhang X (2012) A facile and efficient approach for pore-opening detection of anodic aluminium oxide membranes. *Appl Surf Sci* 258:5305–5311
53. Davydov DN, Sattari PA, AlMawlawi D, Osika A, Haslett TL, Moskovits M (1999) *J Appl Phys* 86:3983–3987
54. Elam JW, Zinovev A, Han CY, Wang HH, Welp U, Hryn JN, Pellin MJ (2006) Atomic layer deposition of palladium films on Al₂O₃ surfaces. *Thin Solid Films* 515:1664–1673
55. Escosura-Muniz A, Chunglok W, Surareungchai W, Merkoci A (2013) Nanochannels for diagnostic of thrombin-related diseases in human blood. *Biosens Bioelectron* 40:24–31
56. Evans P, Hendren WR, Atkinson R, Wurtz GA, Dickson W, Zayats AV, Pollard RJ (2006) Growth and properties of gold and nickel nanorods in thin film alumina. *Nanotechnology* 17:5746–5753
57. Evans PR, Zhu XH, Baxter P, McMillen M, McPhillips J, Morrison FD, Scott JF, Pollard RJ, Bowman RM, Gregg JM (2007) Toward self-assembled ferroelectric random access memories: hard-wired switching capacitor arrays with almost Tb/in² densities. *Nano Lett* 7:1134–1137
58. Fan J, Gao T, Meng G, Wang Y, Liu X, Zhang L (2002) Synthesis of CdS nanowires by sulfurization. *Mater Lett* 57:656–659

59. Fan HJ, Lee W, Scholz R, Dadgar A, Krost A, Nielsch K, Zacharias M (2005) Arrays of vertically aligned and hexagonally arranged ZnO nanowires: a new template-directed approach. *Nanotechnology* 16:913–917
60. Fan DH, Ding GQ, Shen WZ, Zheng MJ (2007) Anion impurities in porous alumina membranes: existence and functionality. *Micropor Mesopor Mat* 100:154–159
61. Fei XL, Tang SL, Wang RL, Su HL, Du YW (2007) Fabrication and magnetic properties of Fe–Pd nanowire arrays. *Solid State Commun* 141:25–28
62. Feizi E, Scott K, Baxendale M, Pal C, Ray AK, Wang W, Pang Y, Hodgson SNB (2012) Synthesis and characterisation of nickel nanorods for cold cathode fluorescent lamps. *Mat Chem Phys* 135:832–836
63. Feliciano J, Martínez-Iñesta MM (2012) Synthesis and characterization of Pd, Cu, and Ag nanowires in anodic alumina membranes using solid state reduction. *Mat Lett* 82:211–213
64. Fodor PS, Tsoi GM, Wenger LE (2003) Zero magnetization states in electrodeposited Co_{0.45}Fe_{0.55} nanowire arrays. *J Appl Phys* 93:7035–7037
65. Foyet A, Hauser A, Schäfer W (2007) Electrochemical deposition of the cobalt nanostructure by double template and pulse current methods. *Mat Sci Eng C* 27:100–104
66. Fu J, Cherevko S, Chung CW (2008) Electroplating of metal nanotubes and nanowires in a high aspect-ratio nanotemplate. *Electrochem Commun* 10:514–518
67. Furneaux RC, Rigby WR, Davidson AP (1989) The formation of controlled-porosity membranes from anodically oxidized aluminium. *Nature* 337:147–149
68. Gao L, Wang P, Wu X, Yang S, Song X (2008) A new method detaching porous anodic alumina films from aluminum substrates. *J Electroceram* 21:791–794
69. Gao T, Meng G, Zhang J, Sun S, Zhang L (2002) Template synthesis of Y-junction metal nanowires. *Appl Phys A* 74:403–406
70. Gaponenko NV, Molchan IS, Tsyrukunov DA, Maliarevich GK, Aegerter M, Puetz J, Al-Dahoudi N, Misiewicz J, Kudrawiec R, Lambertini V, Li Pira N, Repetto P (2005) Optical and structural properties of sol–gel derived materials embedded in porous anodic alumina. *Microelectron Eng* 81:255–261
71. Gavrilo SA, Gusev VV, Dneprovski VS, Zhukov EA, Syrnikov AN, Muljarov EA (1999) Optical properties of excitons in CdS semiconductor–insulator quantum wires. *JETP Lett* 70:216–221
72. Gelves GA, Murakami ZTM, Krantz MJ, Haber JA (2006) Multigram synthesis of copper nanowires using ac electrodeposition into porous aluminium oxide templates. *J Mater Chem* 16:3075–3083
73. Gerein NJ, Haber JA (2005) Effect of ac electrodeposition conditions on the growth of high aspect ratio copper nanowires in porous aluminum oxide templates. *J Phys Chem B* 109:17372–17385
74. Gomez H, Riveros G, Ramirez D, Henriquez R, Schrebler R, Marotti R, Dalchiale E (2012) Growth and characterization of ZnO nanowire arrays electrodeposited into anodic alumina templates in DMSO solution. *Appl Phys A* 16:197–204
75. Göring P, Pippel E, Hofmeister H, Wehrspohn RB, Steinhart M, Gösele U (2004) Gold/carbon composite tubes and gold nanowires by impregnating templates with hydrogen tetrachloroaurate/acetone solutions. *Nano Lett* 6:1121–1125
76. Graham AHD, Bowen CR, Robbins J, Taylor J (2009) Formation of a porous alumina electrode as a low-cost CMOS neuronal interface. *Sens Actuators B* 138:296–303
77. Graham AHD, Bowen CR, Robbins J, Lalev G, Marken F, Taylor J (2010) Nanostructured electrodes for biocompatible CMOS integrated circuits. *Sens Actuators B* 147:697–706
78. Gras R, Duvaill JL, Mine T, Dubosc M, Tessier PY, Cagnon L, Coronel P, Torres J (2006) Template synthesis of carbon nanotubes from porous alumina matrix on silicon. *Microelectron Eng* 83:2432–2436
79. Guo YG, Wan LJ, Gong JR, Bai CL (2002) Preparation and dispersion of Ni–Cu composite nanoparticles. *Phys Chem Chem Phys* 4:3422–3424
80. Guo YG, Zhang HM, Hu JS, Wan LJ, Bai CL (2005) Nanoarchitected metal film electrodes with high electroactive surface areas. *Thin Solid Films* 484:341–345

81. Guo Q, Qin L, Zhao J, Hao Y, Yan Z, Mu F, Chen P (2012) Structural analysis and angle-dependent magnetic properties of Y-branched Ni nanowires. *Physica E* 44:1988–1991
82. Huang GS, Wu XL, Yang LW, Shao XF, Siu GG, Chu PK (2005) Dependence of blue-emitting property on nanopore geometrical structure in Al-based porous anodic alumina membranes. *Appl Phys A* 81:1345–1349
83. Haehnel V, Fahler S, Schaaf P, Miglierini M, Mickel C, Schultz L, Schlörb H (2010) Towards smooth and pure iron nanowires grown by electrodeposition in self-organized alumina membranes. *Acta Mater* 58:2330–2337
84. Han S, Chen HY, Chen CC, Yuan TN, Shih HC (2007) Characterization of Ni nanowires after annealing. *Mat Lett* 61:1105–1108
85. Hashishin T, Tono Y, Tamaki J (2006) Guide growth of carbon nanotube arrays using anodic porous alumina with Ni catalyst. *Jpn J Appl Phys* 45:333–337
86. He Z, Yao L, Zheng M, Ma L, He S, Shen W (2010) Enhanced humidity sensitivity of nanoporous alumina films by controlling the concentration and type of impurity in pore wall. *Physica E* 43:366–371
87. Hillebrand R, Müller F, Schwirn K, Lee W, Steinhart M (2008) Quantitative analysis of the grain morphology in self-assembled hexagonal lattices. *ACS Nano* 5:913–920
88. Hillebrenner H, Buyukserin F, Kang M, Mota MO, Stewart JD, Martin CR (2006) Corking nano test tubes by chemical self-assembly. *J Am Chem Soc* 128:4236–4237
89. Hnida K, Brzózka A, Jaskuła M (2012) Electrochemical method of preparing metallic, polymeric and organic–inorganic hybrid nanowires inside porous anodic alumina templates. *Jordan J Phys* 5:1–7
90. Holubowitch N, Nagle LC, Rohan JF (2012) Porous alumina thin films on conductive substrates for templated 1-dimensional nanostructuring. *Solid State Ion* 216:110–113
91. Hu W, Yuan L, Chen Z, Gong D, Saito K (2002) Fabrication and characterization of vertically aligned carbon nanotubes on silicon substrates using porous alumina nanotemplates. *J Nanosci Nanotech* 2:203–207
92. Hu H, He D (2006) The properties of $\text{Si}_{1-x}\text{Ge}_x$ nanodot arrays prepared by plasma-enhanced CVD on porous alumina templates. *Chem Vap Deposition* 12:751–754
93. Hu H, He D (2006) Fabrication of Si nanodot arrays by plasma enhanced CVD using porous alumina templates. *Mat Lett* 60:1019–1022
94. Huang GS, Wu XL, Xie Y, Kong F, Zhang ZY, Siu GG, Chu PK (2005) Photoluminescence from 8-hydroxy quinoline aluminum embedded in porous anodic alumina membrane. *Appl Phys Lett* 87:151910
95. Huang CH, Lin HY, Tzeng Y, Fan CH, Liu CY, Li CY, Huang CW, Chen NK, Chui HC (2012) Optical characteristics of pore size on porous anodic aluminium oxide films with embedded silver nanoparticles. *Sensors Actuators A* 180:49–54
96. Inoue S, Chu SZ, Wada K, Kanke Y (2003) Preparation of Fe-Pt nanowires through anodic oxidation of sputtered aluminum on glass surface. *Mat Res Soc Symp Proc* 788:L8.4.1–L8.4.5
97. Jaafar M, Navas D, Hernández-Vélez M, Baldonado JL, Vázquez M, Asenjo A (2009) Nanoporous alumina membrane prepared by nanoindentation and anodic oxidation. *Surf Sci* 603:3155–3159
98. Jia RP, Shen Y, Luo HQ, Chen XG, Hu ZD, Xue DS (2003) Photoluminescence spectra of human serum albumen and morin embedded in porous alumina membranes with ordered pore arrays. *J Phys Condens Mater* 15:8271–8279
99. Jia RP, Shen Y, Luo HQ, Chen XG, Hu ZD, Xue DS (2004) Enhanced photoluminescence properties of morin and trypsin absorbed on porous alumina films with ordered pores array. *Solid State Commun* 130:367–372
100. Jian X, Xiaohe L, Yadong L (2004) Single crystalline $\text{YBa}_2\text{Cu}_3\text{O}_{7-x}$ nanowires from a template-directed sol–gel route. *Mat Chem Phys* 86:409–413
101. Jiang L, Cui Z (2006) One-step synthesis of oriented polyaniline nanorods through electrochemical deposition. *Polym Bull* 56:529–537
102. Jin GC, Jiang GW, Liu WF, Cai WL, Yao LZ, Yao Z, Li XG (2003) Fabrication of large-area single crystal bismuth nanowire arrays. *J Mater Chem* 13:1743–1746

103. Jin Z, Meng F, Liu J, Li M, Kong L, Liu J (2011) A novel porous anodic alumina based capacitive sensor towards trace detection of PCBs. *Sens Actuators B* 157:641–646
104. Johansson A, Törndahl T, Ottosson LM, Boman M, Carlsson JO (2003) Copper nanoparticles deposited inside the pores of anodized aluminium oxide using atomic layer deposition. *Mater Sci Eng C* 23:823–826
105. Jung M, Kim HG, Lee JK, Joo OS, Mho S (2004) EDLC characteristics of CNTs grown on nanoporous alumina templates. *Electrochim Acta* 50:857–862
106. Jung M, Lee HS, Park HL, Lim H, Mho S (2006) Fabrication of the uniform CdTe quantum dot array on GaAs substrate utilizing nanoporous alumina masks. *Curr Appl Phys* 6:1016–1019
107. Jung M, Lee HS, Park HL, Mho S (2006) Fabrication of high density CdTe/GaAs nanodot arrays using nanoporous alumina masks. *Curr Appl Phys* 6S1:e187–e191
108. Kang Y, Kim D (2006) Well-aligned CdS nanorod/conjugated polymer solar cells. *Sol Energy Mater Sol Cell* 90:166–174
109. Karlsson M, Palsgard E, Wilshaw PR, Di Silvio L (2003) Initial in vitro interaction of osteoblasts with nano-porous alumina. *Biomater* 24:3039–3046
110. Karpov EE, Karpov EF, Suchkov A, Mironov S, Baranov A, Sleptsov V, Calliari L (2013) Energy efficient planar catalytic sensor for methane measurement. *Sens Actuators A* 194:176–180
111. Kim YS, Godbole VP, Cho JH, Khang G, Shin HS (2006) Plasma enhanced chemical vapor deposition of palladium in anodic aluminum oxide template. *Curr Appl Phys* 681:e58–e61
112. Ko E, Choi J, Okamoto K, Tak Y, Lee J (2006) Cu₂O nanowires in an alumina template: electrochemical conditions for the synthesis and photoluminescence characteristics. *Chem Phys Chem* 7:1505–1509
113. Koh G, Agarwal S, Cheow PS, Toh CS (2007) Development of a membrane-based electrochemical immunosensor. *Electrochim Acta* 53:803–810
114. Kokonou M, Ioannou G, Rebholz C, Doumanidis CC (2013) Polymeric nanowires and nanopillars fabricated by template wetting. *J Nanopart Res* 15:1552
115. Kolmakov A, Zhang Y, Moskovits M (2003) Topotactic thermal oxidation of Sn nanowires: intermediate suboxides and core-shell metastable structures. *Nano Lett* 8:1125–1129
116. Komarov FF, Mudryi AV, Vlasukova LA, Mukhurov NI, Ivanyukovich AV (2008) Intense blue luminescence of anodic aluminum oxide. *Opt Spectros* 104:235–237
117. Kondo T, Tanji M, Nishio K, Masuda H (2006) Cross-striped ordered arrays of Au nanoparticles in anodic porous alumina matrix. *Electrochem Solid-State Lett* 12:C189–C191
118. Kondo T, Nishio K, Masuda H (2009) Surface-enhanced Raman scattering in multilayered Au nanoparticles in anodic porous alumina matrix. *Appl Phys Express* 2:032001
119. Kondo T, Nishio K, Masuda H (2009) Fabrication of Au fine structures of nanoparticles by anodization of purple gold (AuAl₂). *Chem Lett* 38:1148–1149
120. Kondo T, Miyazaki H, Nishio K, Masuda H (2011) Surface-enhanced Raman scattering on multilayered nanodot arrays obtained using anodic porous alumina mask. *J Photochem Photobiol A* 221:199–203
121. Krishnan R, Nguyen HQ, Thompson CV, Choi WK, Foo YL (2005) Wafer-level ordered arrays of aligned carbon nanotubes with controlled size and spacing on silicon. *Nanotechnology* 16:841–845
122. Kurowska E, Brzózka A, Jarosz M, Sulka GD, Jaskuła M (2013) Silver nanowire array sensor for sensitive and rapid detection of H₂O₂. *Electrochim Acta* 104:439
123. Lagueze JB, El Kirat K, Morandat S (2010) Preparation of an electrochemical biosensor based on lipid membranes in nanoporous alumina. *Colloids Surf B* 79:33–40
124. Le Coz F, Arurault L, Datas L (2010) Chemical analysis of a single basic cell of porous anodic aluminium oxide templates. *Mater Character* 61:283–288
125. Lee JK, Koh WK, Chae WS, Kim YR (2002) Novel synthesis of organic nanowires and their optical properties. *Chem Commun* 2002:138–139
126. Lee W, Alexe M, Nielsch K, Gösele U (2005) Metal membranes with hierarchically organized nanotube arrays. *Chem Mater* 17:3325–3327

127. Lee W, Scholz R, Nielsch K, Gösele U (2005) A template-based electrochemical method for the synthesis of multisegmented metallic nanotubes. *Angew Chem Int Ed* 44:6050–6054
128. Lee W, Ji R, Ross CA, Gösele U, Nielsch K (2006) Wafer-Scale Ni imprint stamps for porous alumina membranes based on interference lithography. *Small* 2:978–982
129. Lee W, Ji R, Gösele U, Nielsch K (2006) Fast fabrication of long-range ordered porous alumina membranes by hard anodization. *Nat Mater* 5:741–747
130. Lee JH, Kim DN, Park S, Lee Y, Koh WG (2011) Micropatterning of a nanoporous alumina membrane with poly(ethylene glycol) hydrogel to create cellular micropatterns on nanotopographic substrates. *Acta Biomater* 7:1281–1289
131. Lee DY, Lee DH, Lee SG, Cho K (2012) Hierarchical gecko-inspired nanohairs with a high aspect ratio induced by nanoyielding. *Soft Mater* 8:4905–4910
132. Lefeuvre E, Kim KH, He ZB, Maurice JL, Châtelet M, Pribat D, Cojocaru CS (2011) Optimization of organized silicon nanowires growth inside porous anodic alumina template using hot wire chemical vapor deposition process. *Thin Solid Films* 519:4603–4608
133. Lei Y, Chim WK (2005) Highly ordered arrays of metal/semiconductor core-shell nanoparticles with tunable nanostructures and photoluminescence. *J Am Chem Soc* 127:1487–1492
134. Lei Y, Chim WK, Weissmüller J, Wilde G, Sun HP, Pan XQ (2005) Ordered arrays of highly oriented single-crystal semiconductor nanoparticles on silicon substrates. *Nanotechnology* 16:1892–1898
135. Li GH, Zhang Y, Wu YC, Zhang LD (2005) Photoluminescence of anodic alumina membranes: pore size dependence. *Appl Phys A* 81:627–629
136. Li Z, Huang K (2007) Optical properties of alumina membranes prepared by anodic oxidation process. *J Luminescence* 127:435–440
137. Li XL, Cai KF, Li H, Yu DH, Wang X, Wang HF (2010) Alumina template-assisted electrodeposition of Bi₂Te₂:7Se₀:3 nanowire arrays. *Superlatt Microstruct* 47:710–713
138. Li YL, Tang SL, Xia WB, Chen LY, Wang Y, Tang T, Du YW (2012) Large area Co nanoring arrays fabricated on silicon substrate by anodic aluminum oxide template-assisted electrodeposition. *Appl Phys Lett* 100:183101
139. Li X, Lim YF, Yao K, Tay FEH, Seah KH (2013) Ferroelectric poly(vinylidene fluoride) homopolymer nanotubes derived from solution in anodic alumina membrane template. *Chem Mater* 25:524–529
140. Liang J, Luo H, Beresford R, Xu J (2004) A growth pathway for highly ordered quantum dot arrays. *Appl Phys Lett* 85:5974–5976
141. Liang C, Terabe K, Hasegawa T, Aono M (2006) Template synthesis of M/M₂S (M=Ag, Cu) hetero-nanowires by electrochemical technique. *Solid State Ion* 177:2527–2531
142. Liao CL, Wu MT, Yen JH, Leu IC, Fung KZ (2006) Preparation of RF-sputtered lithium cobalt oxide nanorods by using porous anodic alumina (PAA) template. *J Alloys Comp* 414:302–309
143. Lillo M, Losic D (2009) Pore opening detection for controlled dissolution of barrier oxide layer and fabrication of nanoporous alumina with through-hole morphology. *J Memb Sci* 327:11–17
144. Lillo M, Losic D (2009) Ion-beam pore opening of porous anodic alumina: the formation of single nanopore and nanopore arrays. *Mater Lett* 63:457–460
145. Lin MN, Lin MT, Liu CY, Lai MY, Liu NW, Peng CY, Wang HH, Wang YL (2005) Long-range ordered nanoaperture array with uniform diameter and interpore spacing. *Appl Phys Lett* 87:173116
146. Lin MN, Liu CY, Liu NW, Lai MY, Peng CY, Wang HH, Wang YL, Lin MT (2006) Fabrication of an ordered nanoparticle array with a nanoaperture membrane used as a contact-mask. *Nanotechnology* 17:315–319
147. Ling ZY, Chen SS, Wang JC, Li Y (2008) Fabrication and properties of anodic alumina humidity sensor with through-hole structure. *Chin Sci Bull* 53:183–187
148. Liu L, Pippel E, Scholz R, Gösele U (2009) Nanoporous Pt-Co alloy nanowires: fabrication, characterization, and electrocatalytic properties. *Nano Lett* 12:4352–4358
149. Liu K, Nogue J, Leighton C, Masuda H, Nishio K, Roshchin IV, Schuller IK (2002) Fabrication and thermal stability of arrays of Fe nanodots. *Appl Phys Lett* 81:4434–4436

150. Liu CY, Datta A, Wang YL (2001) Ordered anodic alumina nanochannels on focused-ion-beam-prepatterned aluminum surfaces. *Appl Phys Lett* 78:120–122
151. Liu L, Jia N, Zhou Q, Yan M, Jiang Z (2007) Electrochemically fabricated nanoelectrode ensembles for glucose biosensors. *Mat Sci Eng C* 27:57–60
152. Liu P, Singh VP, Jarro CA, Rajaputra S (2011) Cadmium sulfide nanowires for the window semiconductor layer in thin film CdS–CdTe solar cells. *Nanotechnology* 22:145304
153. Losic D, Shapter JG, Mitchell JG, Voelcker NH (2006) Fabrication of gold nanorod arrays by templating from porous alumina. *Nanotechnology* 16:2275–2281
154. Liu HF, Lim ES, Tung PKH, Xiang N (2011) Fabrication and transfer of nanoporous alumina thin films for templating applications: Metal dots array deposition and porous ZnO film growth. *Thin Solid Films* 519:3050–3054
155. Liu W, Wang X, Xu R, Wang X, Cheng K, Ma H, Yang F, Li J (2013) Long-range-ordered Ag nanodots arrays grown on GaAs substrate using nanoporous alumina mask. *Mat Sci Semicond Proces* 16:160–164
156. Lo D, Budiman RA (2007) Fabrication and characterization of porous anodic alumina films from impure aluminum foils. *J Electrochem Soc* 154:C60–C66
157. Mangu R, Rajaputra S, Clore P, Qian D, Andrews R, Singh VP (2010) Ammonia sensing properties of multiwalled carbon nanotubes embedded in porous alumina templates. *Mat Sci Eng B* 174:2–8
158. Mardare AI, Kaltenbrunner M, Sariciftci NS, Bauer S, Hassel AW (2012) Ultra-thin anodic alumina capacitor films for plastic electronics. *Phys Status Solidi A* 209:813–818
159. Márquez F, Morant C, López V, Zamora F, Campo T, Elizalde E (2011) An alternative route for the synthesis of silicon nanowires via porous anodic alumina masks. *Nanoscale Res Lett* 6:495
160. Masuda H, Yamada H, Satoh M, Asoh H, Nakao M, Tamamura T (1997) Highly ordered nanochannel-array architecture in anodic alumina. *Appl Phys Lett* 71:2770–2772
161. Masuda H, Ohya M, Nishio K, Asoh H, Nakao M, Nohtomi M, Tamamura T (1999) Photonic crystal using anodic porous alumina. *Jpn J Appl Phys* 38:L1403–L1405
162. Masuda H, Yasui K, Nishio K (2000) Fabrication of ordered arrays of multiple nanodots using anodic porous alumina as an evaporation mask. *Adv Mater* 14:1031–1033
163. Masuda H, Ohya M, Nishio K, Asoh H, Nakao M, Nohtomi M, Yokoo A, Tamamura T (2000) Photonic band gap in anodic porous alumina with extremely high aspect ratio formed in phosphoric acid solution. *Jpn J Appl Phys* 39:L1039–L1041
164. Masuda H, Asoh H, Watanabe M, Nishio K, Nakao M, Tamamura T (2001) Square and triangular nanohole array architectures in anodic alumina. *Adv Mater* 13:189–192
165. Masuda H, Yasui K, Sakamoto Y, Nakao M, Tamamura T, Nishio K (2001) Ideally ordered anodic porous alumina mask prepared by imprinting of vacuum-evaporated Al on Si. *Jpn J Appl Phys* 40:L1267–L1269
166. Masuda H, Yotsuya M, Asano M, Nishio K (2001) Self-repair of ordered pattern of nanometer dimensions based on self-compensation properties of anodic porous alumina. *Appl Phys Lett* 78:826–828
167. Masuda H, Kanezawa K, Nishio K (2002) Fabrication of ideally ordered nanohole arrays in anodic porous alumina based on nanoindentation using scanning probe microscope. *Chem Lett* 31:1218–1219
168. Masuda H, Abe A, Nakao M, Yokoo A, Tamamura T, Nishio K (2003) Ordered mosaic nanocomposites in anodic porous alumina. *Adv Mater* 15:161–164
169. Matsui Y, Nishio K, Masuda H (2005) Highly ordered anodic porous alumina by imprinting using Ni molds prepared from ordered array of polystyrene particles. *Jpn J Appl Phys* 44:7726–7728
170. Matsumoto F, Kamiyama M, Nishio K, Masuda H (2005) Highly ordered nanopatterning of DNA with 40nm diameter using anodic porous alumina substrate. *Jpn J Appl Phys* 44:L355–L358
171. Mátéfi-Tempfli S, Mátéfi-Tempfli M, Piraux L (2008) Characterization of nanopores ordering in anodic alumina. *Thin Solid Films* 516:3735–3740

172. Meng G, Cao A, Cheng JY, Vijayaraghavan A, Jung YJ, Shima M, Ajayan PM (2005) Ordered Ni nanowire tip arrays sticking out of the anodic aluminum oxide template. *J Appl Phys* 97:064303
173. Mi W, Lin JYS, Li Y, Zhang B (2005) Synthesis of vertically aligned carbon nanotube films on macroporous alumina substrates. *Micropor Mesopor Mater* 81:185–189
174. Miura I, Okada Y, Kudoh S, Nakata M (2004) Organic electroluminescence in porous alumina. *Jpn J Appl Phys* 43:7552–7553
175. Mondal SP, Das K, Dhar A, Ray SK (2007) Characteristics of CdS nanowires grown in a porous alumina template using a two-cell method. *Nanotechnology* 18:095606
176. Montero-Moreno JM, Belenguer M, Sarret M, Müller CM (2009) Production of alumina templates suitable for electrodeposition of nanostructures using stepped techniques. *Electrochim Acta* 54:2529–2535
177. Montero-Moreno JM, Sarret M, Müller C (2010) Self-ordered porous alumina by two-step anodizing at constant current: behaviour and evolution of the structure. *Micropor Mesopor Mater* 136:68–74
178. Mukhurov NI, Zhvavyi SP, Terekhov SN, Panarin AY, Kotova IF, Pershukevich PP, Khodasevich IA, Gasenkova IV, Orlovich VA (2008) Photoluminescence of F-centers in films of anodic alumina. *J Appl Spectros* 75:214–218
179. Nam W, Seo H, Park SC, Bae CH, Nam SH, Park SM, Ha JS (2004) Fabrication of nanodot arrays on Si by pulsed laser deposition using anodic aluminum oxide nanopore membrane as mask. *Jpn J Appl Phys* 43:7793–7797
180. Napolskii KS, Eliseev AA, Yesin NV, Lukashin AV, Tretyakov YD, Grigoriev NA, Grigoriev SV, Eckerleb H (2007) Ordered arrays of Ni magnetic nanowires: synthesis and investigation. *Physica E* 37:178–183
181. Ni Y, Ma X, Hong J, Xu Z (2004) Microwave-assisted template synthesis of an array of CdS nanotubes. *Mat Lett* 58:2754–2756
182. Nielsch K, Müller F, Li AP, Gösele U (2000) Uniform nickel deposition into ordered alumina pores by pulsed electrodeposition. *Adv Mater* 12:582–586
183. Nielsch K, Choi J, Schwirn K, Wehrspohn RB, Gösele U (2002) Self-ordering regimes of porous alumina: 10%-porosity rule. *Nano Lett* 7:677–680
184. Nielsch K, Castaño FJ, Matthias S, Lee W, Ross CA (2005) Synthesis of cobalt/polymer multilayer nanotubes. *Adv Eng Mater* 7:217–221
185. Nielsch K, Castaño FJ, Ross CA, Krishnan R (2005) Magnetic properties of template-synthesized cobalt/polymer composite nanotubes. *J Appl Phys* 98:034318
186. Nishizawa M, Mukai K, Kuwabata S, Martin CR, Yoneyama H, Nishizawa M, Mukai K, Kuwabata S, Martin CR, Yoneyama H (1997) Template synthesis of polypyrrole-coated spinel LiMn_2O_4 nanotubules and their properties as cathode active materials for lithium batteries. *J Electrochem Soc* 144:1923–1927
187. Nitzani M, Berger S (2007) Pyroelectric nano-rods grown inside alumina nano-pores. *Physica E* 37:260–264
188. Norek M, Stepniowski WJ, Zasada D, Karczewski K, Bystrzycki J, Bojar Z (2012) H_2 absorption at ambient conditions by anodized aluminum oxide (AAO) pattern-transferred Pd nanotubes occluded by Mg nanoparticles. *Mat Chem Phys* 133:376–382
189. Norek M, Łuka G, Godlewski M, Płociński T, Michalska-Domańska M, Stepniowski WJ (2013) Plasmonic enhancement of blue emission from ZnO nanorods grown on the anodic aluminum oxide (AAO) template. *Appl Phys A* 111:265–271
190. O'Brien GA, Quinn AJ, Iacopino D, Pauget N, Redmond G (2006) Polythiophene mesowires: synthesis by template wetting and local electrical characterisation of single wires. *J Mater Chem* 16:3237–3241
191. Oh SL, Kim YR, Malkinski L, Vovk A, Whittenburg SL, Kim EM, Jung JS (2007) Magnetic properties of nickel nanostructures grown in AAO membrane. *J Magn Magn Mater* 310:e827–e829
192. Oh S, Cho YH, Char K (2009) Luminescent Polynorbornene/Quantum Dot Composite Nanorods and Nanotubes Prepared from AAO Membrane Templates. *Macromol Res* 17:995–1002

193. Ohgai T, Hoffer X, Fabian A, Gravier L, Ansermet JP (2003) Electrochemical synthesis and magnetoresistance properties of Ni, Co and Co/Cu nanowires in a nanoporous anodic oxide layer on metallic aluminium. *J Mater Chem* 13:2530–2534
194. Öztürk S, Tasaltın N, Kılınc N, Yüzer H, Öztürk ZZ (2010) Fabrication of ZnO nanowires at room temperature by cathodically induced sol–gel method. *Appl Phys A* 99:73–78
195. Palacios R, Formentín P, Ferré-Borrull J, Pallarés J, Marsal LF (2009) Polymer nanopillars using self-ordered nanoporous alumina templates. *Phys Status Solidi C* 6:1584–1586
196. Parkhutik VP, Shershulsky VI (1992) Theoretical modelling of porous oxide growth on aluminium. *J Phys D Appl Phys* 25:1258–1263
197. Pang YT, Meng GW, Shan WJ, Zhang LD, Gao XY, Zhao AW, Mao YQ (2003) Arrays of ordered Ag nanowires with different diameters in different areas embedded in one piece of anodic alumina membrane. *Appl Phys A* 77:717–720
198. Pang YT, Meng GW, Zhang LD, Shan WJ, Zhang C, Gao XY, Zhao AW (2003) Synthesis of ordered Al nanowire arrays. *Solid State Sci* 5:1063–1067
199. Pang YT, Meng GW, Zhang Y, Fang Q, Zhang LD (2003) Copper nanowire arrays for infrared polarizer. *Appl Phys A* 76:533–536
200. Pang YT, Meng GW, Fang Q, Zhang LD (2003) Silver nanowire array infrared polarizers. *Nanotechnology* 14:20–24
201. Park TJ, Mao Y, Wong SS (2004) Synthesis and characterization of multiferroic BiFeO₃ nanotubes. *Chem Commun* 23:2708–2709
202. Peng CY, Liu CY, Liu NW, Wang HH, Datta A, Wang YL (2005) Ideally ordered 10 nm channel arrays grown by anodization of focused-ion-beam patterned aluminum. *J Vac Sci Technol B* 23:559–562
203. Piao Y, Kim H (2003) Paired cell for the preparation of AgI nanowires using nanoporous alumina membrane templates. *Chem Commun* 23:2898–2899
204. Piao Y, Lima H, Chang JY, Lee WY, Kim H (2005) Nanostructured materials prepared by use of ordered porous alumina membranes. *Electrochim Acta* 50:2997–3013
205. Pellin MJ, Stair PC, Xiong G, Elam JW, Birrell J, Curtiss L, George SM, Han CY, Iton L, Kung H, Kung M, Wang HH (2005) Mesoporous catalytic membranes: synthetic control of pore size and wall composition. *Cat Lett* 102:127–130
206. Pitzschel K, Bachmann J, Montero-Moreno JM, Escrig J, Görlitz D, Nielsch K (2012) Reversal modes and magnetostatic interactions in Fe₃O₄/ZrO₂/Fe₃O₄ multilayer nanotubes. *Nanotechnology* 23:495718
207. Pourfard M, Faez K (2012) A statistical approach for the characterization of self-assembled hexagonal lattices. *Appl Surf Sci* 259:124–134
208. Proenca MP, Sousa CT, Ventura J, Vazquez M, Araujo JP (2012) Ni growth inside ordered arrays of alumina nanopores: Enhancing the deposition rate. *Electrochim Acta* 72: 215–221
209. Qiao J, Zhang X, Meng X, Zhou S, Wu S, Lee ST (2005) Morphology-controllable preparation of 1D poly(vinyl pyrrolidone) nanostructured arrays. *Nanotechnology* 16:433–436
210. Qin J, Nogue J, Mikhaylova M, Roig A, Munoz JS, Muhammed M (2005) Differences in the magnetic properties of Co, Fe, and Ni 250–300 nm wide nanowires electrodeposited in amorphous anodized alumina templates. *Chem Mater* 17:1829–1834
211. Rai V, Deng J, Toh CS (2012) Electrochemical nanoporous alumina membrane –based label – free DNA biosensor for the detection of Legionella sp. *Talanta* 98:112–117
212. Ramulu TS, Venu R, Sinha B, Lim B, Jeon SJ, Yoon SS, Kim CG (2013) Nanowires array modified electrode for enhanced electrochemical detection of nucleic acid. *Biosens Bioelectron* 40:258–264
213. Randon J, Mardilovich PP, Govyadinov AN, Paterson R (1995) Computer simulation of inorganic membrane morphology part III: anodic alumina films and membranes. *J Colloid Interface Sci* 169:335–341
214. Rauf A, Mehmood M, Ahmed M, ul Hasan M, Aslam M (2010) Effects of ordering quality of the pores on the photoluminescence of porous anodic alumina prepared in oxalic acid. *J Luminescence* 130:792–800

215. Riveros G, Gomez H, Cortes A, Marotti RE, Dalchiele EA (2005) Crystallographically-oriented single-crystalline copper nanowire arrays electrochemically grown into nanoporous anodic alumina templates. *Appl Phys A* 81:17–24
216. Rosa WO, Vivas LG, Pirola KR, Asenjo A, Vazquez M (2012) Influence of aspect ratio and anisotropy distribution in ordered CoNi nanowires arrays. *J Magn Magn Mater* 324:3679–3682
217. Routkevitch D, Bigioni T, Moskovits M, Xu JM (1996) Electrochemical fabrication of CdS nanowire arrays in porous anodic aluminum oxide templates. *J Phys Chem* 100:14037–14047
218. Sabzi RE, Kant K, Losic D (2010) Electrochemical synthesis of nickel hexacyanoferrate nanoarrays with dots, rods and nanotubes morphology using a porous alumina template. *Electrochim Acta* 55:1829–1835
219. Saito M, Kiriwara M, Taniguchi T, Miyagi M (1989) Micropolarizer made of the anodized alumina film. *Appl Phys Lett* 55:607–609
220. Salem MS, Sergelius P, Zierold R, Montero Moreno JM, Górlitz D, Nielsch K (2012) Magnetic characterization of nickel-rich NiFe nanowires grown by pulsed Electrodeposition. *J Mater Chem* 22:8549–8557
221. Santos A, Montero-Moreno JM, Bachmann J, Nielsch K, Formentín P, Ferre-Borrull J, Pallares J, Marsal LF (2011) Understanding pore rearrangement during mild to hard transition in bilayered porous anodic alumina membranes. *ACS Appl Mater Interfaces* 3:1925–1932
222. Santos A, Macías G, Ferré-Borrull J, Pallarès J, Marsal LF (2012) Photoluminescent enzymatic sensor based on nanoporous anodic alumina. *ACS Appl Mater Interfaces* 4:3584–3588
223. Sarno M, Tamburrano A, Arurault L, Fontorbes S, Pantani R, Datas L, Ciambelli P, Sarto MS (2013) Electrical conductivity of carbon nanotubes grown inside a mesoporous anodic aluminum oxide membrane. *Carbon* 55:10–22
224. Seo BI, Shaislamov UA, Lee SJ, Kim SW, Kim IS, Hong SK, Yang B (2006) Growth of ferroelectric BLT and Pt nanotubes for semiconductor memories. *J Cryst Growth* 292:315–319
225. Shi JB, Chen CJ, Lin YT, Hsu WC, Chen YC, Wu PF (2009) Anodic aluminum oxide membrane-assisted fabrication of β - In_2S_3 nanowires. *Nanoscale Res Lett* 4:1059–1063
226. Sharif R, Zhang XQ, Shamaila S, Riaz S, Jiang LX, Han XF (2007) Magnetic and magnetization properties of CoFeB nanowires. *J Magn Magn Mater* 310:e830–e832
227. She X, Song G, Jiang F, Yang S, Yang C, Zhou D (2009) Preparation of ethylene vinyl acetate (EVA) copolymer nanotubes by wetting of anodic alumina oxide (AAO) method. *J Porous Mater* 16:267–271
228. Shen XP, Liu HJ, Fan X, Jiang Y, Hong JM, Xu Z (2005) Construction and photoluminescence of In_2O_3 nanotube array by CVD-template method. *J Cryst Growth* 276:471–477
229. Shingubara S, Morimoto K, Sakaue H, Takahagi T (2004) Self-organization of a porous alumina nanohole array using a sulfuric/oxalic acid mixture as electrolyte. *Electrochem Solid State Lett* 7:E15–E17
230. Shingubara S, Maruo S, Yamashita T, Nakao M, Shimizu T (2010) Reduction of pitch of nanohole array by self-organizing anodic oxidation after nanoimprinting. *Microelectronic Eng* 87:1451–1454
231. Singh R, Sharma PP, Baltus RE, Suni II (2010) Nanopore immunosensor for peanut protein Ara h1. *Sens Actuators B* 145:98–103
232. Steinhart M, Wendorff JH, Greiner A, Wehrspohn RB, Nielsch K, Schilling J, Choi J, Gösele U (2002) Polymer nanotubes by wetting of ordered porous templates. *Science* 296:1997
233. Steinhart M, Jia Z, Schaper AK, Wehrspohn RB, Gösele U, Wendorff JH (2003) Palladium nanotubes with tailored wall morphologies. *Adv Mater* 15:706–709
234. Stępniewski WJ, Bojar Z (2011) Synthesis of anodic aluminum oxide (AAO) at relatively high temperatures. Study of the influence of anodization conditions on the alumina structural features. *Surf Coat Technol* 206:265–272
235. Stępniewski WJ, Zasada D, Bojar Z (2011) First step of anodization influences the final nanopore arrangement in anodized alumina. *Surf Coat Technol* 206:1416–1422
236. Stępniewski WJ, Norek M, Michalska-Domańska M, Bombalska A, Nowak-Stepniowska A, Kwaśny M, Bojar Z (2012) Fabrication of anodic aluminum oxide with incorporated chromate ions. *Appl Surf Sci* 259:324–330

237. Stępniewski WJ, Nowak-Stepniowska A, Bojar Z (2013) Quantitative arrangement analysis of anodic alumina formed by short anodizations in oxalic acid. *Mater Character* 78:79–86
238. Stępniewski WJ, Cieślak G, Norek M, Karczewski K, Michalska-Domańska M, Zasada D, Polkowski W, Jóźwik P, Bojar Z (2013) Nanoporous alumina formed by self-organized two-step anodization of Ni₃Al intermetallic alloy in citric acid. *Appl Surf Sci* 264:605–610
239. Strikers GJ, Dalderop HJ, Broeksteeg MAA, Swagten HJM, de Jonge WJM (1999) Structure and magnetization of arrays of electrodeposited Co wires in anodic alumina. *J Appl Phys* 86:5141–5145
240. Suber L, Imperatori P, Ausanio G, Fabbri F, Hofmeister H (2005) Synthesis, morphology, and magnetic characterization of iron oxide nanowires and nanotubes. *J Phys Chem B* 109:7103–7109
241. Suh JS, Lee JS (1999) Highly ordered two-dimensional carbon nanotube arrays. *Appl Phys Lett* 75:2047–2049
242. Sulka GD, Jaskuła M (2006) Defects analysis in self-organized nanopore arrays formed by anodization of aluminium at various temperatures. *J Nanosci Nanotech* 6:3803–3811
243. Sulka GD, Parkoła KG (2006) Anodising potential influence on well-ordered nanostructures formed by anodisation of aluminium in sulphuric acid. *Thins Solid Films* 515:338–345
244. Sulka GD, Parkoła KG (2007) Temperature influence on well-ordered nanopore structures grown by anodization of aluminium in sulphuric acid. *Electrochim Acta* 52:1880–1888
245. Sulka GD (2008) Highly ordered anodic porous alumina formation by self-organized anodizing. In: Eftekhari A (ed) *Nanostructured materials in electrochemistry*. Wiley-VCH, Weinheim, p 1
246. Sulka GD, Stępniewski WJ (2009) Structural features of self-organized nanopore arrays formed by anodization of aluminum in oxalic acid at relatively high temperatures. *Electrochim Acta* 54:3683–3691
247. Sulka GD, Brzózka A, Zaraska L, Jaskuła M (2010) Through-hole membranes of nanoporous alumina formed by anodizing in oxalic acid and their applications in fabrication of nanowire arrays. *Electrochim Acta* 55:4368–4376
248. Sulka GD, Brzózka A, Liu L (2011) Fabrication of diameter-modulated and ultrathin porous nanowires in anodic aluminum oxide templates. *Electrochim Acta* 56:4972–4979
249. Sulka GD, Hnida K (2012) Distributed Bragg reflector based on porous anodic alumina fabricated by pulse anodization. *Nanotechnology* 23:075303
250. Sulka GD, Hnida K, Brzózka A (2013) pH sensors based on polypyrrole nanowire arrays. *Electrochim Acta* 104:536–541. doi:10.1016/j.electacta.2012.12.064
251. Sun Y, Steinhart M, Zschech D, Adhikari R, Michler GH, Gösele U (2005) Diameter-dependence of the morphology of PS-b-PMMA nanorods confined within ordered porous alumina templates. *Macromol Rapid Commun* 26:369–375
252. Swan EEL, Popat KC, Desai TA (2005) Peptide-immobilized nanoporous alumina membranes for enhanced osteoblast adhesion. *Biomater* 26:1969–1976
253. Szuwarzyński M, Zaraska L, Sulka GD, Zapotoczny S (2013) Pulsatile releasing platform of nanocontainers equipped with thermally responsive polymeric nanovalves. *Chem Mater* 25:514–520
254. Tang HJ, Wu FQ, Zhang S (2006) Optical properties of Co/Al₂O₃ nano-array composite structure. *Appl Phys A* 85:29–32
255. Thompson GE, Wood GC (1983) Anodic films on aluminum, corrosion: aqueous processes and passive films. In: Scully JC (ed) *Corrosion: aqueous processes and passive films*. Academic Press Inc., New York, Chapter 5, pp. 205–329
256. Tsuchiya H, Berger S, Macak JM, Ghicov A, Schmuki P (2007) A new route for the formation of self-organized anodic porous alumina in neutral electrolytes. *Electrochem Commun* 9:545–550
257. Valeev R, Romanov E, Beltukov A, Mukhgalin V, Roslyakov I, Eliseev A (2012) Structure and luminescence characteristics of ZnS nanodot array in porous anodic aluminum oxide. *Phys Status Sol C* 9:1462–1465

258. Vega V, Böhnert T, Martens S, Waleczek M, Montero-Moreno JM, Görlitz D, Prida VM, Nielsch K (2012) Tuning the magnetic anisotropy of Co–Ni nanowires: comparison between single nanowires and nanowire arrays in hard-anodic aluminum oxide membranes. *Nanotechnology* 23:465709
259. Vivas LG, Ivanov YP, Trabada DG, Proenca MP, Chubykalo-Fesenko O, Vazquez M (2013) Magnetic properties of Co nanopillar arrays prepared from alumina templates. *Nanotechnology* 24:105703
260. Vlasiouk I, Takmakov P, Smirnov S (2005) Sensing DNA hybridization via ionic conductance through a nanoporous electrode. *Langmuir* 21:4776–4778
261. Wang Y, Ye C, Wang G, Zhang L, Liu Y, Zhao Z (2003) In situ x-ray diffraction study on AgI nanowire arrays. *Appl Phys Lett* 82:4253–4255
262. Wang Y, Zhao H, Hu Y, Ye C, Zhang L (2007) Thermal expansion behavior of hexagonal Zn nanowires. *J Cryst Growth* 305:8–11
263. Wang X, Smirnov S (2009) Label-free DNA sensor based on surface charge modulated ionic conductance. *ACS Nano* 4:1004–1110
264. Wang XW, Yuan ZH, Fang BC (2011) Template-based synthesis and magnetic properties of Ni nanotube arrays with different diameters. *Mat Chem Phys* 125:1–4
265. Wang Q, Min F, Zhu J (2013) Preparation of gold nanowires and its application in glucose biosensing. *Mat Lett* 91:9–11
266. Wen S, Jung M, Joo OS, Mho S (2006) EDLC characteristics with high specific capacitance of the CNT electrodes grown on nanoporous alumina templates. *Curr Appl Phys* 6:1012–1015
267. Wen S, Mho S, Yeo IH (2006) Improved electrochemical capacitive characteristics of the carbon nanotubes grown on the alumina templates with high pore density. *J Power Sources* 163:304–308
268. Wu XC, Tao YR (2002) Growth of CdS nanowires by physical vapor deposition. *J Cryst Growth* 242:309–312
269. Wu Q, Hu Z, Wang X, Hu Y, Tian Y, Chen Y (2004) A simple route to aligned AlN nanowires. *Diamond Relat Mater* 13:38–41
270. Wu C, Shi JB, Chen CJ, Lin JY (2006) Synthesis and optical properties of ordered 30 nm PbS nanowire arrays fabricated into sulfuric anodic alumina membrane. *Mat Lett* 60:3618–3621
271. Wu Z, Zhang Y, Du K (2013) A simple and efficient combined AC–DC electrodeposition method for fabrication of highly ordered Au nanowires in AAO template. *Appl Surf Sci* 265:149–156
272. Xie GQ, Song M, Mitsuishi K, Furuya K (2004) Selective tungsten deposition into ordered nanohole arrays of anodic porous alumina by electron-beam-induced deposition. *Appl Phys A* 79:1843–1846
273. Xu X, Chen L, Wang C, Yao Q, Feng C (2005) Template synthesis of heterostructured polyaniline/Bi₂Te₃ nanowires. *J Solid State Chem* 178:2163–2166
274. Xu HB, Chen HZ, Xu WJ, Wang M (2005) Fabrication of organic copper phthalocyanine nanowire arrays via a simple AAO template-based electrophoretic deposition. *Chem Phys Lett* 412:294–298
275. Xu Y, Fu JL, Gao DQ, Xue DS (2010) The fabrication and characteristic properties of amorphous Co_{1-x}Zn_x alloy nanowires arrays. *J Alloy Comp* 495:450–452
276. Xu X, Huang J, Shao M, Wang P (2012) Synthetic control of large-area, ordered Fe nanotubes and their nanotube-core/alumina-sheath nanocables. *Mat Chem Phys* 135:6–9
277. Yan H, Zhang L, Shen J, Chen Z, Shi G, Zhang B (2006) Synthesis, property and field-emission behaviour of amorphous polypyrrole nanowires. *Nanotechnology* 17:3446–3450
278. Yanagishita T, Nishio K, Nakao M, Fujishima A, Masuda H (2002) Synthesis of diamond cylinders with triangular and square cross sections using anodic porous alumina templates. *Chem Lett* 31:976–977
279. Yanagishita T, Sasaki M, Nishio K, Masuda H (2004) Carbon nanotubes with a triangular cross-section, fabricated using anodic porous alumina as the template. *Adv Mater* 16:429–432

280. Yanagashita T, Nishio K, Masuda H (2006) Polymer through-hole membranes with high aspect ratios from anodic porous alumina templates. *Jpn J Appl Phys* 45:L1133–L1135
281. Yang Z, Si S, Dai H, Zhang C (2007) Piezoelectric urea biosensor based on immobilization of urease onto nanoporous alumina membranes. *Biosens Bioelectron* 22:3283–3287
282. Yang Y, Liu F, Li T, Chen Y, Wu Y, Kong M (2012) Electrochemical performance of template-synthesized CoSb nanowires array as an anode material for lithium ion batteries. *Scripta Mater* 66:495–498
283. Yasui A, Iwasaki M, Kawahara T, Tada H, Ito S (2006) Color properties of gold–silver alternate nanowires electrochemically grown in the pores of aluminum anodic oxidation film. *J Colloid Interface Sci* 293:443–448
284. Yasui K, Nishio K, Nunokawa H, Masuda H (2005) Ideally ordered anodic porous alumina with Sub-50 nm hole intervals based on imprinting using metal molds. *J Vac Sci Technol B* 23:L9–L12
285. Yasui K, Morikawa T, Nishio K, Masuda H (2005) Patterned magnetic recording media using anodic porous alumina with single domain hole configurations of 63nm hole interval. *Jpn J Appl Phys* 44:L 469–L 471
286. Yi Y, Lee JK, Lee HJ, Uhm S, Nam SC, Lee J (2009) A single-step approach to create nanopottery structures for efficient water electrocatalysis. *Electrochem Commun* 11:2121–2124
287. Yin AJ, Li J, Jian W, Bennet AJ, Xu JM (2001) Fabrication of highly ordered metallic nanowire arrays by electrodeposition. *Appl Phys Lett* 79:1039–1041
288. Yu D, Feng Y, Zhu Y, Zhang X, Li B, Liu H (2011) Template synthesis and characterization of molybdenum disulfide nanotubules. *Mater Res Bull* 46:1504–1509
289. Yu Y, Kant K, Shapter JG, Addai-Mensah J, Losic D (2012) Gold nanotube membranes have catalytic properties. *Micropor Mesopor Mater* 153:131–136
290. Yuan ZH, Sun SQ, Duan YQ, Wang DJ (2009) Fabrication of densely packed AlN nanowires by a chemical conversion of Al₂O₃ nanowires based on porous anodic alumina film. *Nanoscale Res Lett* 4:1126–1129
291. Zaraska L, Sulka GD, Jaskuła M (2010) The effect of n-alcohols on porous anodic alumina formed by self-organized two-step anodizing of aluminum in phosphoric acid. *Surf Coat Technol* 204:1729–1737
292. Zaraska L, Sulka GD, Jaskuła M (2010) Porous anodic alumina membranes formed by anodization of AA1050 alloy as templates for fabrication of metallic nanowire arrays. *Surf Coat Technol* 205:2432–2437
293. Zaraska L, Sulka GD, Szeremeta J, Jaskuła M (2010) Porous anodic alumina formed by anodization of aluminum alloy (AA1050) and high purity aluminium. *Electrochim Acta* 55:4377–4386
294. Zaraska L, Sulka GD, Jaskuła M (2011) Anodic alumina membranes with defined pore diameters and thicknesses obtained by adjusting the anodizing duration and pore opening/widening time. *J Solid State Electrochem* 15:2427–2436
295. Zaraska L, Kurowska E, Sulka GD, Jaskuła M (2012) Porous alumina membranes with branched nanopores as templates for fabrication of Y-shaped nanowire arrays. *J Solid State Electrochem* 16:3611–3619
296. Zaraska L, Stepniowski WJ, Sulka GD, Ciepela E, Jaskuła M (2013) Analysis of nanopore arrangement and structural features of anodic alumina layers formed by two-step anodizing in oxalic acid using the dedicated executable software. *Appl Phys A* 114(2):571–577
297. Zaraska L, Stepniowski WJ, Sulka GD, Ciepela E (2013) The effect of anodizing temperature on structural features and hexagonal arrangement of nanopores in alumina synthesized by two-step anodizing in oxalic acid. *Thin Solid Films* 534:155–161
298. Zhang XY, Zhang LD, Zheng MJ, Li GH, Zhao LX (2001) Template synthesis of high-density carbon nanotube arrays. *J Cryst Growth* 223:306–310
299. Zhang XY, Xu LH, Dai JY, Cai Y, Wang N (2006) Synthesis and characterization of single crystalline selenium nanowire arrays. *Mat Res Bull* 41:1729–1734
300. Zhang GY, Guo B, Chen J (2006) MCo₂O₄ (M = Ni, Cu, Zn) nanotubes: template synthesis and application in gas sensors. *Sens Actuator B* 114:402–409

301. Zhang G, Li C, Cheng F, Chen J (2007) ZnFe₂O₄ tubes: synthesis and application to gas sensors with high sensitivity and low-energy consumption. *Sens Actuator B* 120:403–410
302. Zhang R, Jiang KM, Chen DL, Ding GQ (2009) Indium oxide nanorods and nanowires on porous anodic alumina. *Mat Lett* 63:1044–1046
303. Zhang L, Meng F, Chen Y, Liu J, Sun Y, Luo T, Li M, Liu J (2009) A novel ammonia sensor based on high density, small diameter polypyrrole nanowire arrays. *Sens Actuators B* 142:204–209
304. Zhang J, Kielbasa JE, Carroll DL (2010) Controllable fabrication of porous alumina templates for nanostructures synthesis. *Mater Chem Phys* 122:295–300
305. Zhang Y, Son SJ, Ju H (2012) Anodized aluminum oxide membranes of tunable porosity with platinum nanoscale-coating for photonic application. *Curr Appl Phys* 12:1561–1565
306. Zhao AW, Meng GW, Zhang LD, Gao T, Sun SH, Pang YT (2003) Electrochemical synthesis of ordered CdTe nanowire arrays. *Appl Phys A* 76:537–539
307. Zhao GY, Xu CL, Guo DJ, Li H, Li HL (2007) Template preparation of Pt nanowire array electrode on Ti/Si substrate for methanol electro-oxidation. *Appl Surf Sci* 253:3242–3246
308. Zhou X, Habazaki H, Shimizu K, Skeldon P, Thompson GE, Wood GC (1996) Enrichment-dependent anodic oxidation of zinc in Al–Zn alloys. *Corros Sci* 38:1563–1577

Electrodeposition of ZnO Nanostructures: Growth, Doping, and Physical Properties

19

M. Allan Thomas and Jingbiao Cui

Contents

Introduction.....	648
ZnO Basics.....	648
Growth Techniques.....	648
Electrochemical Growth in Aqueous Solution.....	649
ECD ZnO: Methods, Materials, and Properties.....	650
Electrochemical Growth of ZnO: A History.....	650
ECD ZnO: Dissolved Oxygen Method.....	651
ECD ZnO: Zinc Nitrate Method.....	653
Optical and Electrical Properties: Growth Conditions and Annealing.....	663
ECD ZnO: Doping for Device Applications.....	668
Electrochemical Doping of ZnO.....	668
Summary and Outlook.....	675
References.....	675

Abstract

ZnO is one of the most promising semiconductors for low-cost optoelectronics and can be obtained from a variety of deposition techniques. Among them, electrochemical growth in aqueous solution has become an important approach for ZnO deposition with abundant morphologies and doping capabilities. This chapter summarizes the current achievements in electrodeposition of ZnO and also

M.A. Thomas (✉)

Department of Physics and Astronomy, University of Arkansas at Little Rock, Little Rock, AR, USA

e-mail: mathomas1@ualr.edu

J. Cui

Department of Physics, University of Memphis, Memphis, TN, USA

e-mail: jcui@memphis.edu

discusses the challenges and extensive potential in this research area. The effects of electrochemical growth conditions, annealing, and doping on the structural, optical, and electrical properties of ZnO thin films and nanowires are presented in detail. Electrical characterization using electrochemical impedance spectroscopy and photoelectrochemical cell measurements are also included. *n*-Type and *p*-type semiconductor nanowires are achieved by electrochemical doping of ZnO with various elements such as Cl and Ag and are discussed as nanoscale building blocks in advanced optoelectronics. Electrochemical deposition of highly uniform ZnO thin films and oriented ZnO nanowire arrays with desired physical properties opens up possibilities for large-scale and economic fabrication of advanced optoelectronic devices.

Keywords

ZnO • Electrodeposition • Doping • Optoelectronics • Nanomaterials

Introduction

ZnO Basics

ZnO is a semiconductor with a direct bandgap of 3.37 eV (368 nm) at room temperature. ZnO is therefore transparent to visible light, yet still a semiconductor. Such a combination of properties is rare and enables ZnO to be considered for a much wider span of device applications. ZnO also possesses an exciton binding energy of 60 meV [1], which is significantly larger than its comparable materials GaN (25 meV) and ZnSe (22 meV). Excitonic processes in ZnO, such as those associated with light-emitting diode (LED), laser diode, and solar cell operation, will be significantly more efficient and effective as compared to other wide bandgap semiconductors. Optical processes involving excitons in ZnO also produce a rich variety of interesting physics and behavior, making ZnO an attractive material not only for devices but also for fundamental research.

Growth Techniques

The available growth techniques for ZnO are practically endless. Nearly every deposition method for materials has been exploited to obtain ZnO in bulk, thin film, or nanostructure form [2]. Many of the common growth techniques for ZnO are associated with relatively high temperatures and vacuum environments, such as molecular beam epitaxy (MBE) [3], chemical vapor deposition (CVD) [4], pulsed laser deposition (PLD) [5, 6], thermal evaporation [7], and sputtering [8]. Bulk ZnO single crystals can be formed in hydrothermal [9], chemical vapor transport [10], and pressurized melt-growth processes [11]. ZnO materials from these high-temperature growth methods are often of very high quality and serve as the stepping stone for

ZnO's breakthrough into the device application market. But perhaps the most interesting distinction for ZnO among other semiconductors is its amenability to be deposited at low growth temperatures (<200 °C) and in aqueous solution.

Electrochemical Growth in Aqueous Solution

The device application potential of ZnO in the areas of electronics and optoelectronics relies on achieving large-scale and homogeneous materials at low cost as well as controlling ZnO's fundamental physical properties. As mentioned above, a wide variety of growth techniques has been explored to accomplish these goals and obtain ZnO materials for potential use in device applications. In particular, low-temperature growth processes for ZnO materials are becoming increasingly studied due to their low cost and scale-up potential [12, 13]. Solution-based techniques for depositing ZnO include electrochemical deposition (ECD), hydrothermal and/or chemical bath deposition methods, sol-gel processes, and spray pyrolysis, just to name a few. For a thorough and enlightening review of solution-based techniques for ZnO deposition, see Ref. [12]. The various growth techniques and materials that can be deposited for ZnO are summarized in Table 1.

This chapter is focused on ECD growth processes for ZnO, and therefore they receive most of the attention here. The current achievements, challenges, and extensive potential in the area of ZnO ECD are summarized. The effects of electrochemical growth conditions, annealing, and doping on the structural, optical, and electrical properties of ZnO nanowires and thin films are presented in detail. Recent work on utilizing ECD ZnO nanowires as nanoscale building blocks for advanced

Table 1 Growth techniques and materials available for ZnO

ZnO materials and growth methods			
<i>High temperature (>100 °C)</i>			
Method	Environment	Structure types	References
MBE	High vacuum	Thin films, 3D nano	[3]
CVD	Moderate vacuum	Thin films, 3D nano	[4]
PLD	High vacuum	Thin films, 3D nano	[5, 6]
Evaporation	High vacuum	Thin films	[7]
Sputtering	High vacuum	Thin films, 3D nano	[8]
Hydrothermal	Ionic solution	Single crystal	[9]
CVT	Moderate vacuum	Single crystal	[10]
PMG	High pressure	Single crystal	[11]
<i>Low temperature (<100 °C)</i>			
CBD	Aqueous	Thin films, 3D nano	[12, 13, 21–24]
ECD	Aqueous	Thin films, 3D nano	[12, 14, 15, 25]

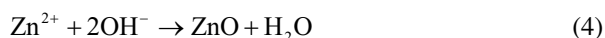
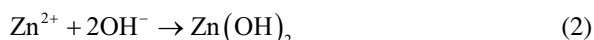
Abbreviations: *MBE* molecular beam epitaxy, *CVD* chemical vapor deposition, *PLD* pulsed laser deposition, *CVT* chemical vapor transport, *PMG* pressurized melt growth, *CBD* chemical bath deposition, *ECD* electrochemical deposition, *Nano* nanostructures

optoelectronic devices is also highlighted. ECD of highly uniform ZnO thin films and oriented ZnO nanowire arrays with desired physical properties opens up possibilities for large-scale and economic fabrication of advanced optoelectronic devices.

ECD ZnO: Methods, Materials, and Properties

Electrochemical Growth of ZnO: A History

In 1996, two alternative methods for ECD of ZnO were introduced: (1) the dissolved oxygen method developed by Peulon and Lincot [14] and (2) the zinc nitrate method developed by Izaki and Omi [15]. The amount of research activity associated with similar low-cost and low-temperature growth methods for ZnO materials has increased tremendously since then. The basic scheme to produce ZnO in ECD processes is as follows:



The first requirement is the production of hydroxide ions (OH^-) in the growth solution, and typically this step is accomplished by an electrochemical reduction reaction (Eq. 1). In the zinc nitrate method, the ion species in Eq. 1 is NO_3^- , while in the dissolved oxygen method, it is O_2 gas bubbled into the growth solution. Once produced, the OH^- ions react with zinc ions (Zn^{2+}) also present in the solution to eventually form ZnO. Zn^{2+} ions are already present in the zinc nitrate method, but in the dissolved oxygen method, they must come from a secondary source such as zinc chloride, perchlorate, acetate, or sulfate. Many studies of solution-based processes in the literature list Eqs. 2 and 3 as the eventual pathway for ZnO crystallization, which involves an intermediary $\text{Zn}(\text{OH})_2$ phase [12, 16, 17]. However, recent investigations have provided strong support for the idea that Eq. 4 is the route for ZnO formation – a direct crystallization from Zn^{2+} and OH^- ions that does not involve any intermediate hydroxide phase [18]. If $\text{Zn}(\text{OH})_2$ is an intermediate to eventual ZnO formation, only under appropriate conditions of pH, temperature, and concentrations will it decompose to produce ZnO and water (Eq. 3) [12].

Among the various options for ECD ZnO, there is not a single method that possesses all of the desirable traits for ease of use and process flexibility. While the zinc nitrate method is likely the simplest in that only one source material is needed and it is not necessary to make dissolved oxygen solutions, it possesses the smallest ZnO (instead of Zn) deposition potential window due to the reduction potential of

the nitrate reduction reaction [15]. Meanwhile, both the dissolved oxygen and hydrogen peroxide processes [19, 20] require a secondary source material to obtain Zn^{2+} ions, creating an immediate situation of unwanted and potentially contaminant species in the growth solution. Regarding the viability of process scalability, in principle only the dissolved oxygen method is limited due to the low solubility of O_2 gas in water which creates an upper boundary on the growth rate of ZnO materials by this method.

In addition to ECD, there are many similar techniques for depositing ZnO materials in solution. Another low-temperature deposition method for ZnO materials that has experienced a seemingly exponential increase in growth since its beginnings in 2001 [12] is the so-called hydrothermal or chemical bath deposition [21–24]. This method is actually quite similar to ECD of ZnO in aqueous solution in that chemical species are mixed in water and a reaction between Zn^{2+} and OH^- ions eventually produces ZnO [12]. Only substrates with specific properties and of certain materials can be utilized in the hydrothermal growth processes, however, due to limited initial ZnO nucleation.

Based on the difficulty in facilitating ZnO nucleation in chemical bath deposition and hydrothermal processes [21–24], Cui and Gibson developed a new ECD method for ZnO in 2005 which is a modified version of the most common hydrothermal growth process (zinc nitrate and hexamine, [21]) [25]. This method exploits the benefits and overcomes the limitations of both the zinc nitrate ECD process and the zinc nitrate plus hexamine hydrothermal process by combining them together. By applying a potential during growth, it becomes possible to significantly increase the nucleation density and growth rate of ZnO as compared to strictly hydrothermal processes. This allows for the deposition of ZnO directly onto conducting or semi-conducting substrates (e.g., polished Si) without the need for a ZnO seed layer. In addition, the electrochemical growth of ZnO in a solution that contains zinc nitrate as well as hexamine immediately provides the ability to obtain controlled 3D nanowire structures [25]. While both the zinc nitrate and dissolved oxygen ECD methods for ZnO were initially developed for thin film deposition, work on both processes over the years has enabled modifications, such as the zinc nitrate plus hexamine method [25], that allow for significant tunability of the ZnO structures to include 3D nanowires and other useful morphologies. The growth conditions and structural properties for a wide range of ECD ZnO materials and methods are summarized in Table 2 and then discussed at length and in detail below.

ECD ZnO: Dissolved Oxygen Method

Much like any other deposition method for ZnO, the specific growth conditions in the ECD process maintain a strong effect on the eventual physical properties of the materials. Since all ECD methods for depositing ZnO eventually involve the reaction of Zn^{2+} ions with OH^- ions to make ZnO, the relative concentration of these two species near the electrode/growing crystal surface is expected to play a dominant role in governing the properties of the ZnO materials obtained. Even though the

Table 2 Growth conditions and structural properties for ECD ZnO materials

ECD ZnO: growth conditions and structural properties			
Dissolved oxygen method			
Main conditions	Substrate/special condition	Structural	References
0.5 mM [Zn ²⁺], 0.1 M KCl	FTO	Nanowires	[14, 26]
5 mM [Zn ²⁺], 0.1 M KCl	FTO	Dense films	[14, 27]
0.5 mM [Zn ²⁺], 0.1 M KCl	FTO; Cl ⁻ , SO ₄ ⁻ , acetate ions added	Nanowires (various aspect ratios)	[29]
Zinc nitrate method			
[Zn(NO ₃) ₂]	Substrate/special condition	Structural	References
0.1 M	ITO; low potential	3D nano	[15]
0.1 M	ITO; high potential	Dense films	[15]
8–10 mM	Si, poly Au, ITO; hexamine added	Nanowires	[25]
0.5–3 mM	ITO	Nanowires	[29]
0.05 M	Poly Au; galvanostatic, low current	Dense films	[31]
0.05 M	Poly Au; galvanostatic, high current	Nanowires	[31]
0.05–0.1 mM	ZnO seed; [NO ₃ ⁻] source: 0.1 M NaNO ₃	Nanowires (various aspect ratios)	[35]
0.05 M	Poly Au	Nanowires	[36]
0.05 M	Poly Au; 30–70 % methanol electrolyte	Dense films	[36, 41]
0.05 M	Poly Au; 70–100 % methanol electrolyte	Nanosheets, nanowalls	[41]
0.08 M	ITO; 25 % ethanol electrolyte	Dense films	[37]

Abbreviations: *FTO* fluorine-doped tin oxide, *ITO* indium tin oxide, *Nano* nanostructures, *poly* polycrystalline

eventual ZnO formation mechanism is the same in all ECD ZnO processes, many factors related to the particular ECD method and growth conditions used will affect the [Zn²⁺]/[OH⁻] ratio.

In the dissolved oxygen method, precursor concentration limits are very much set by the low solubility of O₂ gas in solution. As a result, the concentrations of the reactant species used to deposit ZnO are typically very low, and a supporting electrolyte such as KCl or KClO₄ is used to establish a growth solution conductivity that is amenable to ECD processes. The initial [Zn²⁺] and [O₂] are quite small, even below the mM range [14, 26], resulting in a strong effect of [Zn²⁺] as it is increased to higher concentrations. At low zinc concentrations, e.g., 0.5 mM, 3D nanowire-type structures can be deposited (Fig. 1) [14, 26], while at slightly higher [Zn²⁺], such as 5 mM, more dense and 2D type thin film structures are obtained (Fig. 2) [14, 27]. An even finer tuning of [Zn²⁺] in the 3D nanowire regime enables control of the nanowire diameter from 25 to 80 nm [28].

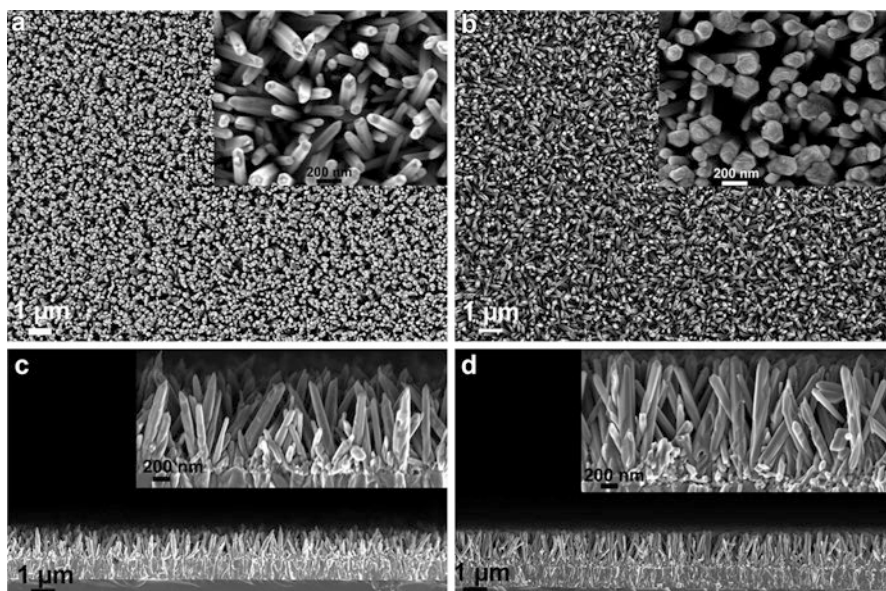


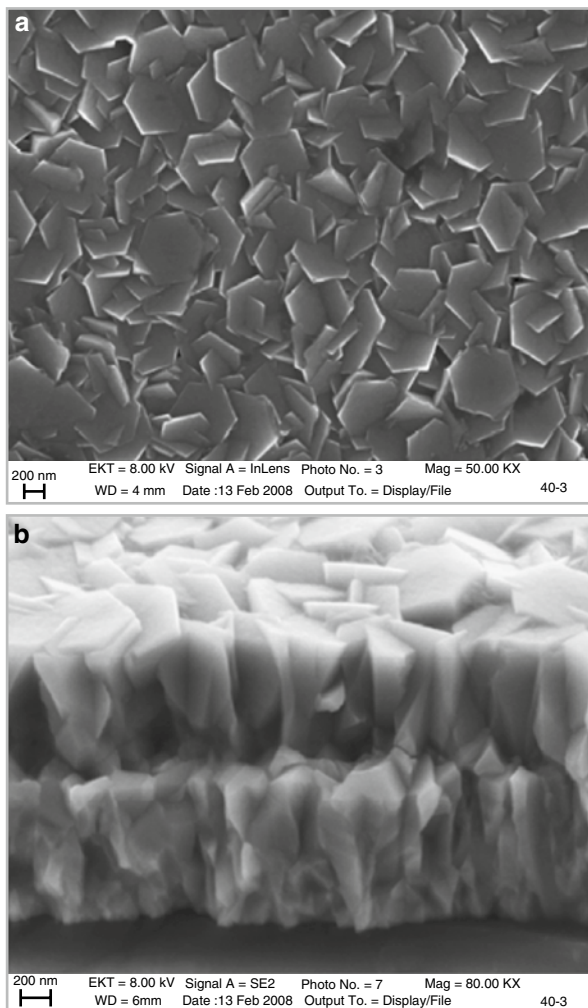
Fig. 1 SEM images of 3D ZnO nanowires obtained from the dissolved oxygen method with $[\text{Zn}^{2+}] = 0.5 \text{ mM}$ (Reproduced with permission from Tena-Zaera et al. [26]. Copyright (2008) American Chemical Society)

Other chemical species can be used to modify the ZnO growth process in the dissolved oxygen ECD method. Various additives such as Cl^- , acetate, and SO_4^{2-} can control the ZnO nanowire aspect ratio [29]. While additional Cl^- leads to thicker and shorter nanowires, i.e., a low aspect ratio (Fig. 3a, b), acetate ions enable the growth of longer and thinner nanowires to significantly increase their aspect ratio (Fig. 3e, f). Cyclic voltammetry (CV) studies indicate the various ion species preferentially adsorb onto the growing ZnO crystal surface in different ways and also affect the electrochemical reduction of O_2 [29]. Both of these factors change the local ZnO growth environment and in turn modify the rate and type of ZnO deposition.

ECD ZnO: Zinc Nitrate Method

While the zinc nitrate ECD method utilizes a similar reaction pathway for depositing ZnO, it is certainly distinct from the dissolved oxygen process in several ways. Perhaps most importantly, zinc nitrate is the only necessary precursor material – it serves as the Zn^{2+} source and the OH^- source (via reduction of nitrate). Furthermore, zinc nitrate is highly soluble in water; therefore, much larger precursor concentrations can be used. This situation is quite different from the dissolved oxygen method, suggesting that ECD of ZnO with the zinc nitrate method will lead to unique

Fig. 2 SEM images of 2D ZnO thin films obtained from the dissolved oxygen method with $[\text{Zn}^{2+}] = 5 \text{ mM}$ (Adapted with permission from Rousset et al. [27]. Copyright (2009) American Chemical Society)



conditions for crystal growth and in turn physical properties of the ZnO materials are obtained. Various growth conditions such as $[\text{Zn}^{2+}]$, $[\text{NO}_3^-]$, temperature, applied potential, and electrolyte additives in the zinc nitrate method have been tested thoroughly in the literature.

Growth Conditions and Structural Properties

In the original work on the zinc nitrate ECD method, it was shown that the applied potential during growth affects the structural properties of the ZnO materials significantly [15]. More defined and 3D-type structures are formed at lower potentials

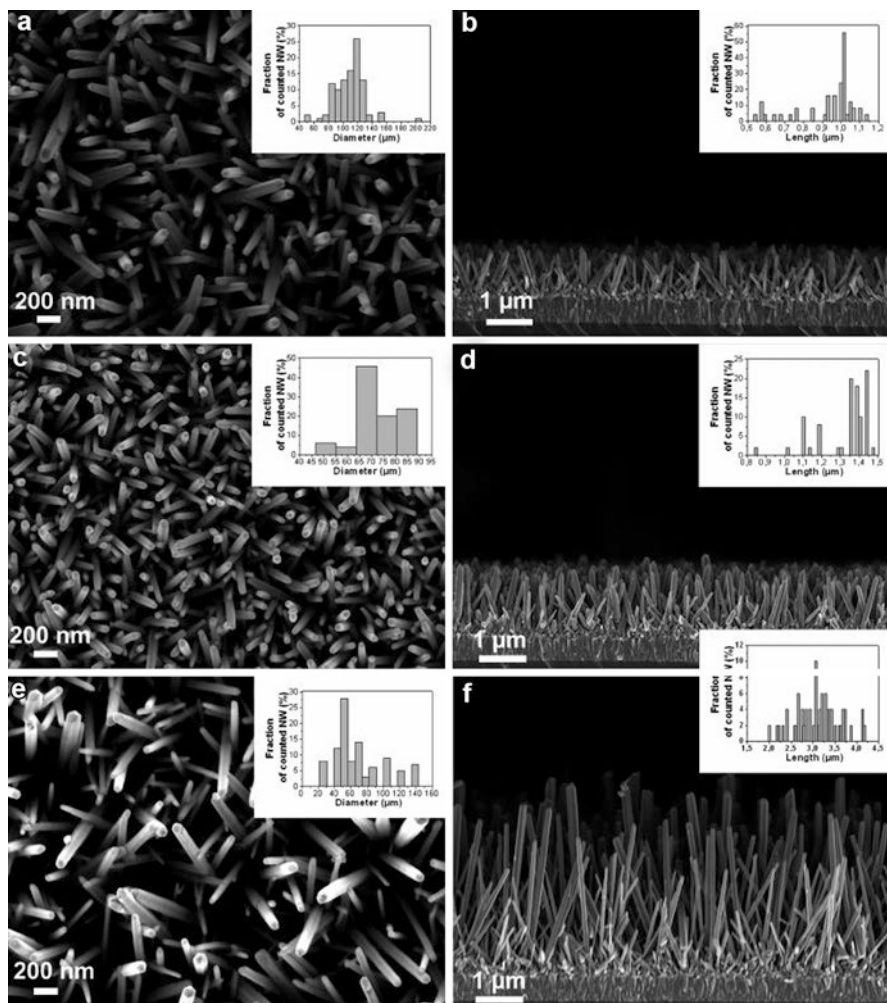


Fig. 3 SEM images of ZnO nanowires from the dissolved oxygen method with the addition of (a, b) Cl^- , (c, d) SO_4^{2-} , and (e, f) acetate ions. Diameter and length distributions are shown in the insets of each figure (Reproduced with permission from Elias et al. [29]. Copyright (2008) American Chemical Society)

(near the limit for reduction of nitrate to occur), while more dense and 2D film structures are obtained at more negative potentials well into the overpotential regime (Fig. 4). As expected, the ZnO growth rate is also strongly affected by the growth potential with a significant increase for more negative potentials [15].

More recent work associated with growth conditions in the zinc nitrate ECD method showed that, much like in the dissolved oxygen process, a lower $[\text{Zn}^{2+}]$ during growth leads to truly 3D nanowire structures [30]. In the same work, the authors also concluded that an increased negative growth potential in fact leads to denser and more

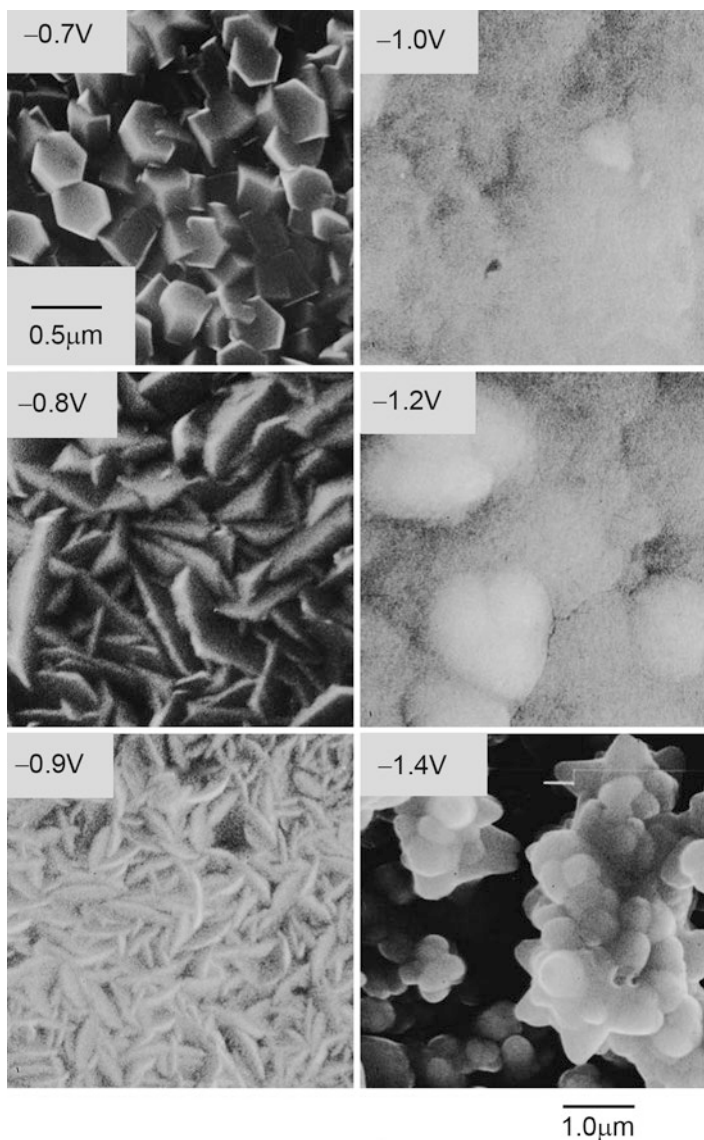
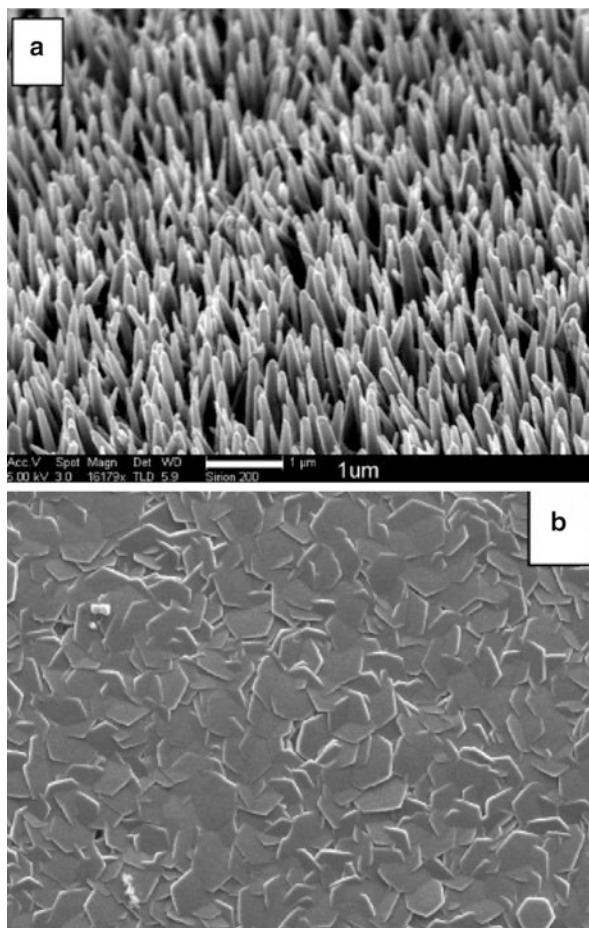


Fig. 4 SEM images of ZnO materials obtained by the zinc nitrate method. The applied potentials as measured relative to an Ag/AgCl reference electrode are shown in the figures (Reproduced with permission from Izaki and Omi [15]. Copyright (1996) American Institute of Physics)

filmlike structures, perhaps due to the increased growth rate. Interestingly, in a different study where the deposition was galvanostatic (constant current rather than constant potential), a lower current during growth led to well-formed 2D films, while an increased current produced very well-defined 3D nanowires structures (Fig. 5) [31].

Fig. 5 SEM images of ZnO materials obtained by the zinc nitrate galvanostatic method: (a) higher deposition current, (d) lower deposition current (Adapted with permission from Cao et al. [31]. Copyright (2006) American Chemical Society)



These ideas were confirmed later in another work on galvanostatic deposition using zinc nitrate when the most uniform and 2D film structures were obtained at quite low deposition currents [32].

Zn²⁺ as a Catalyst for Nitrate Reduction

It would appear as though the zinc nitrate method showcases some inconsistencies and difficulties in obtaining repeatable structures based on certain growth conditions. Recent investigations of the electrochemical growth mechanism in the zinc nitrate method aid in understanding these difficulties.

As discussed already, perhaps the most important aspect of the growth mechanism for ZnO in ECD processes is the local $[\text{Zn}^{2+}]/[\text{OH}^-]$ ratio at the electrode. Whereas the dissolved oxygen method allows for a broader control of this ratio, in the zinc nitrate method, $[\text{Zn}^{2+}]$ and $[\text{OH}^-]$ are more difficult to separate. If zinc nitrate is the only source material in the electrolyte, $[\text{Zn}^{2+}]$ and $[\text{NO}_3^-]$ are

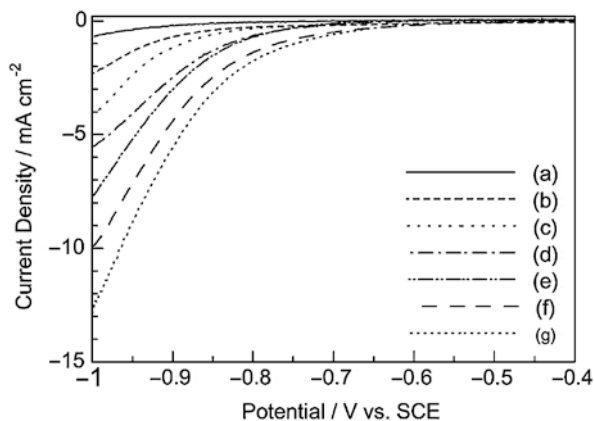


Fig. 6 I - V curves measured at a ZnO-coated Pt disk-rotating electrode (500 rev/min) in aqueous mixed solutions of zinc nitrate and potassium nitrate for which the concentration of NO_3^- was fixed at 200 mM while that of Zn^{2+} was varied as (a) 0, (b) 0.5, (c) 2, (d) 4, (e) 10, (f) 20, and (g) 100 mM. Potential sweep rate = 5 mV/s (Reproduced with permission from Yoshida et al. [16]. Copyright (2004) Elsevier B.V)

essentially predetermined: it is not immediately possible to independently control $[\text{Zn}^{2+}]$, a very important ECD growth parameter. It was discussed in section “[ECD ZnO: Dissolved Oxygen Method](#)” that certain ion species affect the electrochemical reduction reaction that governs ZnO deposition in ECD growth processes. The same is true in the zinc nitrate method. It has been very well established that metallic ion species in solution catalyze the nitrate reduction reaction [33, 34]. In fact, without Zn^{2+} present in the zinc nitrate method, the reduction of nitrate electrochemical reaction will not even occur (Fig. 6) [16]. So it becomes clear that while both Zn^{2+} and OH^- are needed to deposit ZnO by ECD, in the zinc nitrate method, these separate ion species are very much interconnected by the catalyst nature of Zn^{2+} . Understandably, this complicates the zinc nitrate method to a certain degree in comparison to the dissolved oxygen process.

Separate NO_3^- Source in the Zinc Nitrate Method

One strategy developed to overcome this limitation is to utilize a separate source for NO_3^- ions in the zinc nitrate method [35]. By using sodium nitrate as the main electrolyte precursor, the nitrate concentration can be held constant while the zinc nitrate concentration is changed. What was found in this study was that the zinc nitrate process can become very much like the dissolved oxygen method: low $[\text{Zn}^{2+}]$ leads to strongly diffusion-limited growth of ZnO, and high aspect ratio 3D nanowires are obtained. Here, the limited diffusion of Zn^{2+} ions not only minimizes the availability of Zn^{2+} for the reaction with OH^- to produce ZnO but also the catalytic effect for the nitrate reduction reaction to *produce* OH^- ions in the first place. The end result is a very strongly limited growth regime in which the lateral growth of the ZnO structures is completely suppressed, and highly uniform in diameter ZnO

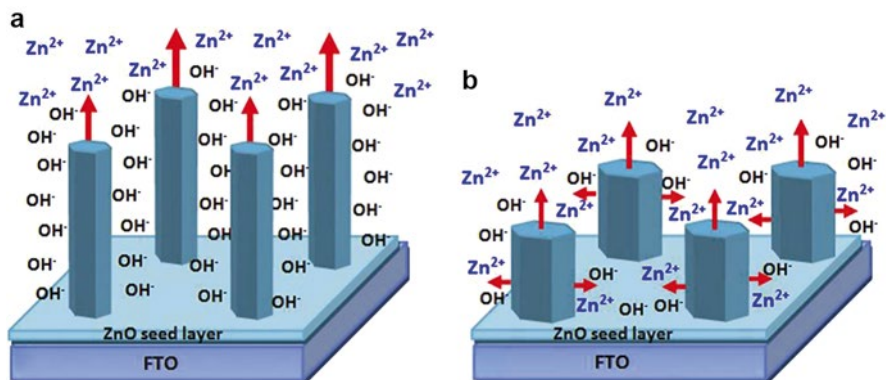


Fig. 7 Schematic view of the growth of ZnO nanowires from nitrate-based solutions. (a) The Zn^{2+} diffusion is significantly slower than the OH^- generation rate, and (b) the OH^- generation rate and Zn^{2+} diffusion are in the same order (Reproduced with permission from Khajavi et al. [35]. Copyright (2012) Elsevier B.V)

nanowires are obtained (Fig. 7) [35]. By tuning $[\text{Zn}^{2+}]$ while keeping other growth conditions constant, it is possible to increase their lateral growth and in turn control the aspect ratio of the ECD ZnO nanowires [35].

Mixed Water/Methanol Electrolytes for Zinc Nitrate ECD

Another strategy related to controlling the availability of Zn^{2+} and OH^- in the zinc nitrate method involves the use of a mixed water/alcohol electrolyte. In this technique, zinc nitrate remains the only source material but instead of a water-only electrolyte, various vol.% of an appropriate cosolvent are added (such as ethanol or methanol) [36, 37]. This technique has been shown to effectively produce very consistent and uniform 2D film structures using the zinc nitrate method across a wide range of other growth conditions [36].

Structural Properties

As is typically found in the literature, when utilizing a water-only deposition solution in the zinc nitrate method, it is difficult to prepare samples with a consistent morphology and homogeneity. Often, scattered and spotty 3D nanorod-type structures that do not eventually form a continuous and hole-/defect-free film are formed [15, 38–41]. An example of the morphologies obtained using a water-only solution is shown in the scanning electron microscopy (SEM) image in Fig. 8a. On the other hand, by simply adding 50 % by volume methanol to the deposition solution, the ZnO morphology is remarkably changed such that a 2D coalesced film made up of compact, hexagonal grains is formed (Figs. 8b, c). Figure 8c is a lower magnification image to showcase the uniformity of and lack of defects in the ZnO film obtained with 50 % methanol.

Furthermore, some of the specific properties of the ZnO films can be controlled with various growth parameters such as applied potential, current density, and

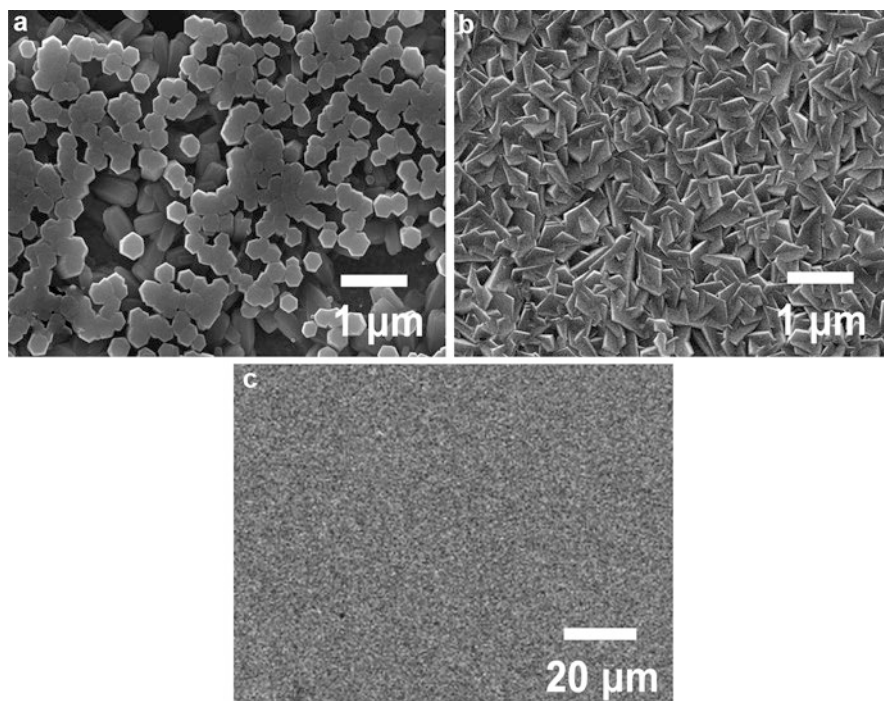


Fig. 8 SEM images of ZnO samples deposited in 0.05 M zinc nitrate solutions: (a) 100 % water; (b, c) 50 % water/50 % methanol (Reproduced with permission from Thomas and Cui [36]. Copyright (2013) The Electrochemical Society)

methanol concentration. Figure 9 shows some of the ZnO films obtained under different growth conditions to modify the specific crystal and film morphology. An increased current density during growth leads to a larger ZnO growth rate and therefore larger crystal grains (Fig. 9a), while a more controlled current density produces smaller and more complete grains (Fig. 9b). The cross section in Fig. 9c shows that the films are very uniform and dense.

Growth Mechanism: CV Analysis and Effects of Methanol

In the combined water/methanol zinc nitrate ECD method, the availability of Zn^{2+} for the deposition of ZnO is quite constant because it comes directly from zinc nitrate and is present at a relatively high concentration (0.05 M). On the other hand, the availability of OH^- is not immediate but instead relies on the reduction of nitrate ions and therefore is dependent on the electrochemical growth conditions.

Figure 10 illustrates CV scans of growth solutions with varying amounts of methanol. Methanol addition does not cause a drastic change in the CV scans; however, the most distinct change visible is the increased current density in the range of potentials used for the deposition of ZnO (highlighted area: -2.4 to -2.6 V). For example, at a potential of -2.5 V, the current density is increased by ~ 50 %

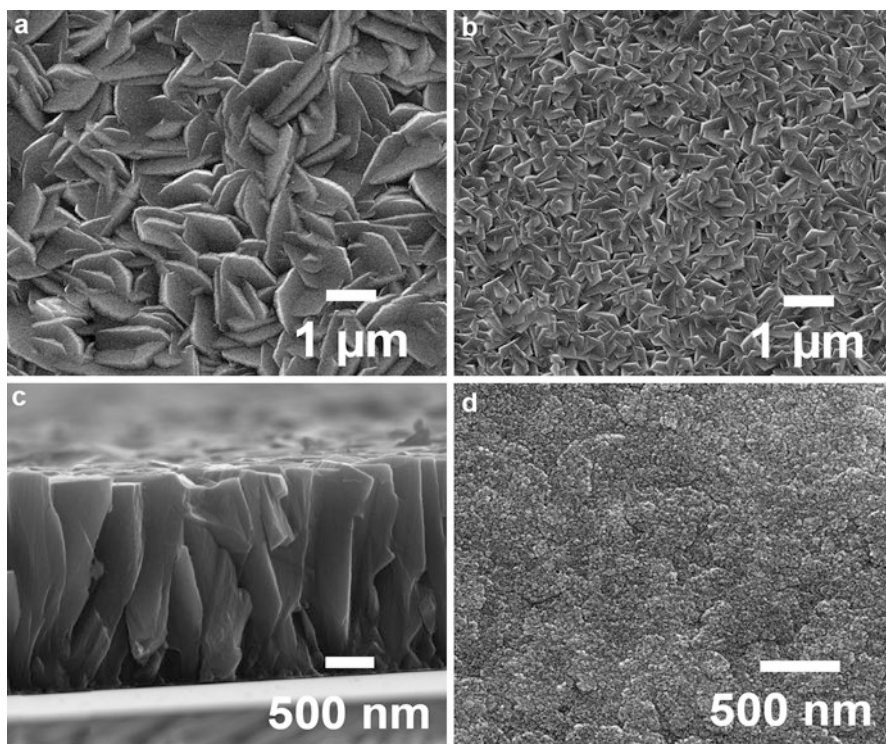


Fig. 9 SEM images of ZnO thin films obtained in a water/methanol zinc nitrate solution: (a) -2.5 V, large current density, 50 % methanol; (b) -2.5 V, small current density, 50 % methanol; (c) cross section of (a) $2.2 \mu\text{m}$ thick film; (d) -2.5 V, 25 % methanol (Reproduced with permission from Thomas and Cui [36]. Copyright (2013) The Electrochemical Society)

for the electrolytes with methanol added as compared to the water-only solution. Because the current density should be mostly associated with the nitrate reduction reaction, the CV scans indicate that adding methanol to the ZnO growth solution enhances the nitrate reduction reaction, increasing the production of OH^- ions [36]. Growth solutions with methanol also create a much faster nucleation process, as well as a faster time to coalescence and uniform film growth in general [36]. This likely plays a role in establishing more 2D and uniform film growth dynamics rather than “spotty” growth of 3D nanostructures.

OH^- Ion Production and Thermodynamic Equilibrium

A secondary, yet related, explanation for the improvement in the ZnO film morphology upon methanol addition is an increase in the availability of OH^- ions. When the supply of OH^- ions is slow and steady, a near equilibrium crystallization process for ZnO likely dominates. Recent work on the crystallization of ZnO in solution processes showed that the most important factor for obtaining ZnO nanowire-/nanorod-type structures, i.e., a strongly dominant [0001] crystallization scheme, is the slow and

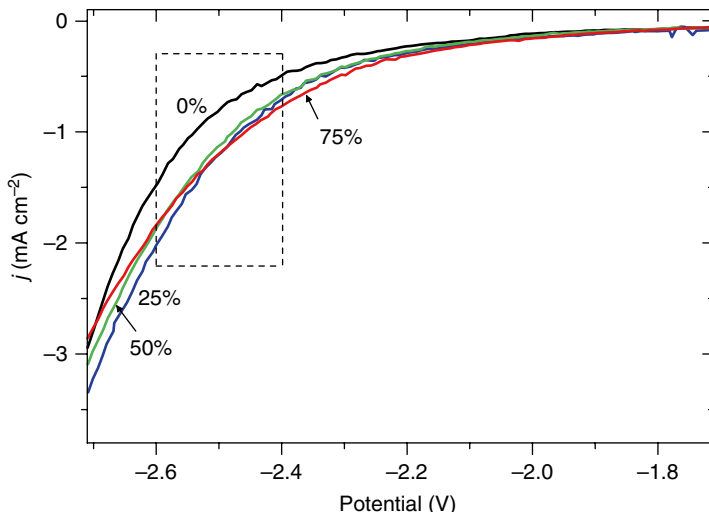


Fig. 10 CV scans of different electrolytes used for ZnO thin film growth. Only the forward scans (0 to -2.7 V) are shown for clarity. The % methanol in the electrolyte is indicated in the figure. Note that all scans were performed at a rate of 20 mV/s on Au substrates (1 cm²) after a thin layer of ZnO was deposited (5 min growth time) using the respective solution. Only the first scans are shown as no significant change was observed for repeating scans (Reproduced with permission from Thomas and Cui [36]. Copyright (2013) The Electrochemical Society)

steady “release” or availability of OH^- ions to react with Zn^{2+} and make ZnO [42]. This is similar to the minimized availability of Zn^{2+} in the dissolved oxygen method and separate NO_3^- method due to their use of a low $[\text{Zn}^{2+}]$.

As a result, it becomes easier to see why ZnO grows preferentially along the [0001] direction and forms nanorod or columnar structures in water-only deposition solutions. The availability of OH^- ions is minimal, producing a growth process that is very much limited by diffusion and thermodynamic equilibrium. However, if the availability of OH^- ions is increased and conditions are shifted outside the realm of equilibrium and diffusion limits, other crystallization schemes can contribute more strongly and the anisotropic [0001] dominated growth may be overcome. This enables more lateral crystal growth and eventually dense, 2D film structures, as outlined in Fig. 7 in section “Separate NO_3^- Source in the Zinc Nitrate Method.”

Chemical Effects of OH^- and Methanol

The chemical effects specific to methanol should also be considered because various ion species were shown to affect the growth of ZnO in the dissolved oxygen method [29]. OH^- ions may also become preferentially associated with the polar (0001) face of the ZnO crystal once their availability is higher. This would be similar to NO_3^- ions as suggested in other work on ECD of ZnO using zinc nitrate in methanol [41] and citrate ions in the hydrothermal growth of ZnO films [43]. Such adsorption of ion species on the polar ZnO crystal faces could drive the growth of

the *nonpolar* crystal faces and produce a more 2D film structure. In fact, methanol can be used at even higher concentrations in the zinc nitrate method to produce more elaborate structures such as ZnO nanowalls and ZnO nanosheets [41]. This suggests that methanol indeed plays a strong role in the various crystallization schemes for ZnO when used in the zinc nitrate ECD method.

Optical and Electrical Properties: Growth Conditions and Annealing

Optical Properties

The rich optical properties of ZnO materials are very important for their use in advanced optoelectronics. The wide bandgap and large exciton binding energy nature of ZnO leads to strong ultraviolet (UV) luminescence at room temperature as well as the possibility for a range of optical emissions in the visible range.

Optical Quality and Luminescence

In one of the few studies on the effects of growth potential in the dissolved oxygen ECD ZnO method [44], it was established that a lower growth potential, i.e., one that is very close to the limit for O₂ reduction to occur, produces ZnO materials of a higher optical quality. Furthermore, a higher deposition temperature and growth conditions that produce more 3D nanowire-type structures as compared to 2D films also lead to ZnO with an intense UV photoluminescence (PL) emission and very little defect PL emissions. Finally, the use of a Cl⁻ electrolyte support also benefits the optical properties of ZnO deposited by the dissolved oxygen method [44]. In the zinc nitrate plus hexamine ECD method, it was also shown that the ZnO crystal quality, and in turn optical quality, of ZnO nanowires could be modified by growth conditions such as the applied potential and relative hexamine concentration during growth [45]. More negative growth potentials and a larger relative hexamine concentration lead to ZnO nanowires with a stronger UV emission and very little defects. Much like in the dissolved oxygen method, the addition of Cl⁻ to the electrolyte in the zinc nitrate plus hexamine process enables filling of native defects with Cl impurities and the removal of defect PL emissions [46].

Bandgap Tuning

Another key parameter with regard to ZnO's optical properties is its bandgap energy. Because ZnO maintains such a wide bandgap, the ability to modulate the bandgap even further into the UV as well as into the visible region becomes highly desirable. Interestingly, several studies have shown that the bandgap of ECD ZnO materials is highly tunable with specific growth conditions as well as doping. The results on doped ZnO will be discussed at length further in the chapter, but even undoped ECD ZnO can show a range of bandgaps by changing the applied potential during growth [47]. The ZnO bandgap is tunable within a range of about 0.2 eV with wider bandgaps being associated with more negative growth potentials.

Electrical Properties and Electrical Characterization Techniques

A sound understanding of the electrical properties of ECD ZnO materials is paramount to their eventual application in advanced devices. Unfortunately, ECD processes demand the use of a conductive substrate, stifling the ability to perform standard semiconductor electrical characterization without complications and errors.

Thin Film Transfer

Efforts have been made in the past to isolate semiconductor thin films obtained by ECD methods from their conductive substrate, most notably on solar cell materials such as CdTe [48], CdS [48], CIS [49], and Cu₂O [50]. Upon successful film transfer, resistivity and Hall effect measurements can be carried out as with any other semiconductor material. Only very recently have such methods been demonstrated with regard to ECD ZnO, and finally there are viable data available for the electrical properties of ZnO materials obtained by electrochemical methods [36, 51, 52].

Electrochemistry-Based Characterization Techniques

Another approach is associated with electrochemical impedance spectroscopy (EIS) and Mott–Schottky analysis (MS) in which the conductive growth substrate required for ECD processes is actually utilized in the electrical measurement. A wide variety of ZnO thin films and even 3D nanowire structures have been characterized by such EIS and MS methods [26, 27, 36, 38, 41, 53, 54]. For more details regarding the theory and practice of EIS and MS analysis, see Refs. [27, 36, 38, 53].

The final technique for characterizing the electrical properties of ECD materials is a photoelectrochemical cell (PEC) measurement [55–57]. This method cannot provide any detailed quantitative information regarding charge carrier concentration or mobility, but it can give qualitative insight into the conductivity type and relative magnitude of carriers. A PEC measurement involves a semiconductor and an electrolyte interface, and the charge transfer between the two is monitored upon illumination of the semiconductor with an external light source. A schematic of a typical PEC setup is shown in Fig. 11. A positive change in potential signifies *p*-type behavior, while a negative voltage change indicates *n*-type properties. Both ZnO thin films [58, 59] and nanowires [57] have been characterized by PEC measurements in order to gain information regarding their conductivity type and capability.

Specific Results on Various ECD ZnO Materials

While the available work on the electrical properties of ECD ZnO is somewhat minimal, certain trends and consistencies are beginning to develop. Highly uniform and dense 2D films grown by the dissolved oxygen method have shown electron concentrations close to the 10²⁰ cm⁻³ range when highly doped with Cl [27]. Meanwhile, the same study found that films deposited by the zinc nitrate method were also *n*-type, but had electron concentrations nearly two orders of magnitude lower than those obtained in the standard dissolved oxygen process [27].

The electrical properties of ZnO nanowires obtained by the dissolved oxygen method have also been explored with EIS and MS. It is necessary to modify the

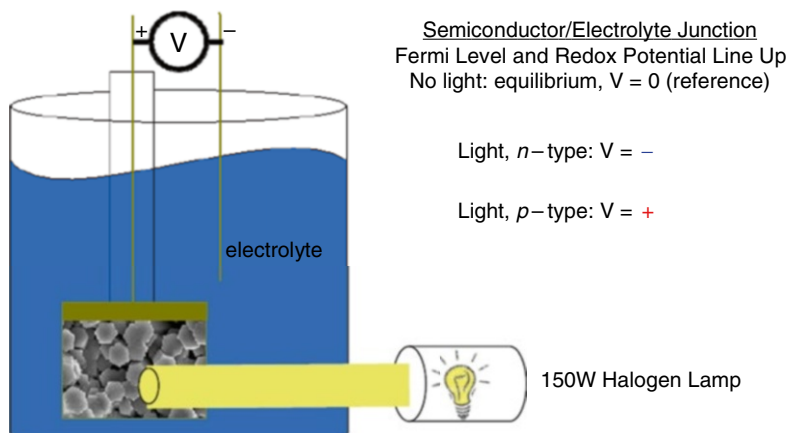


Fig. 11 Schematic of the PEC measurement setup and basic principles

analysis in order to compensate for the 3D geometry of the nanowires [53], but very consistent data has been obtained by a variety of groups [26, 53, 54]. As-grown ZnO nanowires by the dissolved oxygen method are typically highly n -type, with carrier concentrations at least in the 10^{19} cm^{-3} range [26, 53, 54]. This may stem from the fact that Cl doping takes place due to the Cl^- supporting electrolyte. Similar experiments have been performed on ZnO nanowires obtained by the zinc nitrate plus hexamine method, and they show that undoped nanowires have carrier concentrations in the mid- 10^{17} cm^{-3} range [60]. Then, purposeful Cl doping can be utilized to increase their electron concentration to the mid- 10^{20} cm^{-3} range [60]. It seems Cl doping is very much a part of the electrical properties of ECD ZnO nanowires, whether it is desired or not. In related studies [26], it was shown that Cl^- ions in particular inhibit the O_2 reduction reaction, which lowers the production of OH^- ions and alters the $[\text{Zn}^{2+}]/[\text{OH}^-]$ ratio during growth. The increased availability of Zn^{2+} in comparison to OH^- leads to more “Zn heavy” ZnO nanowires with an increased electron concentration due to zinc interstitial and oxygen vacancy defects [26].

The electrical properties of ZnO materials obtained by the zinc nitrate method have also been investigated. In this case, both MS and Hall effect measurements have been used so a more complete picture of the electrical properties can be seen. The applied potential during growth has been shown to be a very strong factor in determining the electrical properties of ECD ZnO obtained by nitrate reduction. Figure 12 displays the calculated carrier concentration values obtained from MS analysis for several ZnO films as a function of the applied potential used during growth (zinc nitrate in 50 % methanol). Three different films all deposited at -2.4 V are included in the data to show that the samples have reasonably consistent carrier concentrations for a given applied potential (-2.4 V ranges from 9.6×10^{15} to $2.9 \times 10^{16} \text{ cm}^{-3}$). A lower applied potential, which also corresponds to a lower current density and growth rate, produces ZnO films with higher carrier concentrations. Meanwhile, a more negative growth potential leads to a faster ZnO growth rate as well as lower carrier concentrations.

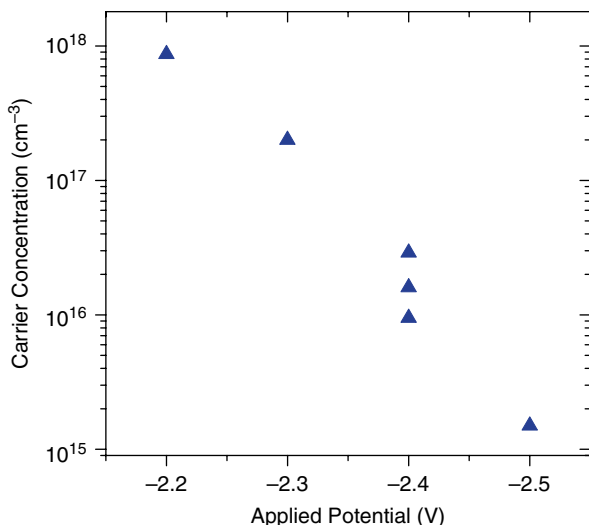


Fig. 12 Carrier concentration data calculated from MS plots of ZnO films deposited by the zinc nitrate plus methanol method as a function of applied potential during growth (Reproduced with permission from Thomas and Cui [36]. Copyright (2013) The Electrochemical Society)

The range of carrier concentrations for growth potentials from -2.2 to -2.5 V extends through nearly three orders of magnitude [36].

Other works on ZnO films obtained by nitrate reduction found highly similar results when the effects of current density on electrical properties were tested: a lower current density during growth produces ZnO films with higher carrier concentrations as measured by the Hall effect [52]. Changes in the current density alone enabled a similar three orders of magnitude control of the electron concentration of the ZnO films (Fig. 13) [52]. Previous work on ZnO by nitrate reduction using MS analysis has also shown that more negative growth potentials produce lower carrier concentrations with a three orders of magnitude range controlled by the potential [38].

A likely explanation for the observed carrier concentration changes is the growth conditions for ZnO associated with an increased current density and/or more negative growth potentials. Such conditions are related to an increased availability of OH^- ions from an enhanced nitrate reduction process. More OH^- ions may shift the ZnO growth conditions toward a more even Zn/O ratio in that there is plenty of the oxygen source (OH^-) available for stoichiometric ZnO crystallization.

Annealing Effects

Because of their very-low-temperature deposition, moderate annealing has been shown to affect the various properties of ECD ZnO materials as well. MS analysis of ZnO films from the zinc nitrate in 50 % methanol method annealed at 200°C in air reveals that they possess carrier concentrations as much as two orders of

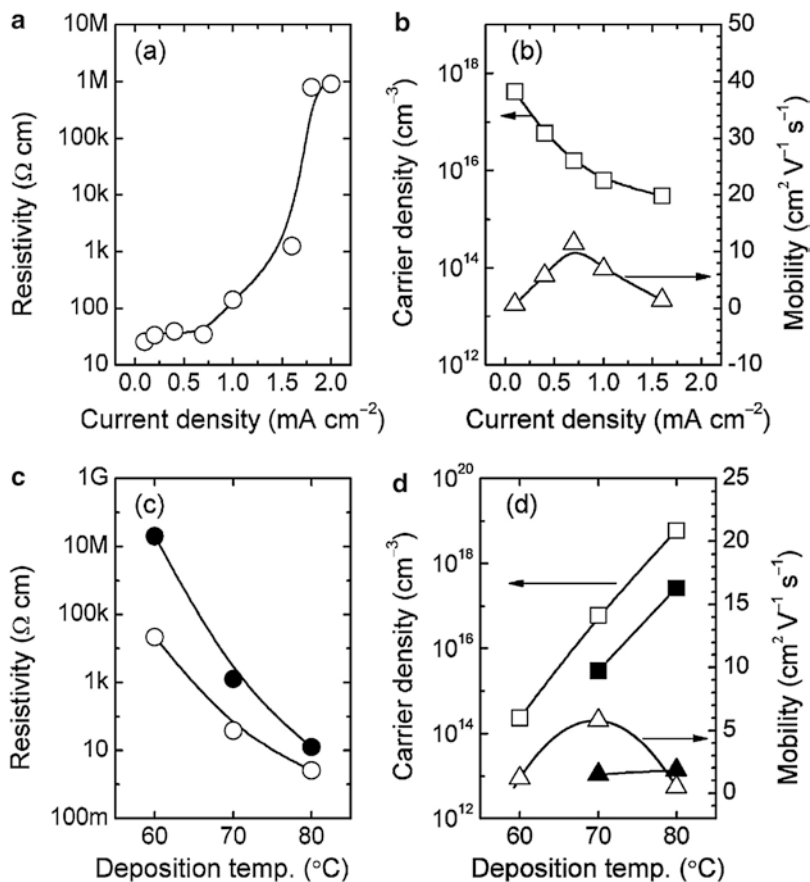
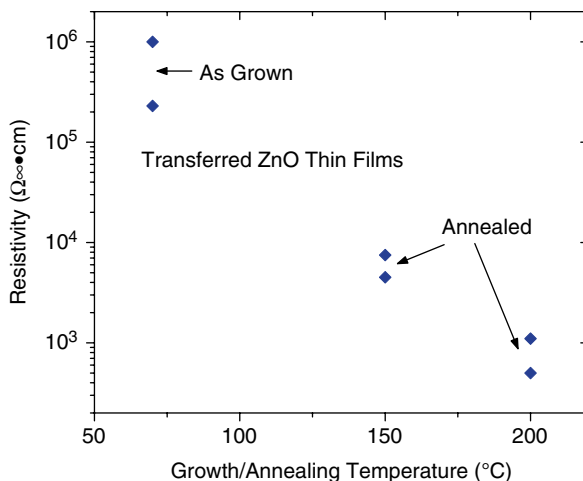


Fig. 13 Variation of electrical properties of electrodeposited ZnO films as a function of (a, b) current density and (c, d) deposition temperature (Reproduced with permission from Shinagawa et al. [52]. Copyright (2012) American Chemical Society)

magnitude higher than the as-grown films (annealed in air: high 10^{17} to low 10^{18} cm^{-3}) [36]. The increase in free carriers is partially dependent on the films' as-grown properties – those samples with lower as-grown carrier concentrations experience the most drastic increase in carrier concentration upon annealing.

Hall effect analysis from the same study indicates similar trends: some of the typical resistivities measured for such ZnO thin films are shown in Fig. 14. It is clear that as-grown films are highly resistive, while moderate annealing in air can improve their conductivity. Some other works on ZnO thin films by nitrate reduction have indicated a similar increase in conductivity after moderate annealing [51, 52], but the opposite seems to be true for ZnO nanowires obtained by ECD and then annealed in air [26, 53, 54]. It is interesting that as-grown nanowires by ECD have high electron concentrations and annealing can make them more “intrinsic,” in fact lowering their carrier density by as much as three orders of magnitude. Meanwhile, as-grown

Fig. 14 Measured resistivity values for as-grown and annealed ZnO thin films after the thin film transfer process. All films were deposited at either -2.4 or -2.5 V in 50 % methanol solutions (Reproduced with permission from Thomas and Cui [36]. Copyright (2013) The Electrochemical Society)



films by ECD are often highly resistive, but moderate annealing improves their conductivity. It is clear that the growth conditions leading to either 3D nanowires or 2D film structures also affect the electrical properties of ECD ZnO.

ECD ZnO: Doping for Device Applications

Electrochemical Doping of ZnO

The idea to dope ZnO utilizing low-temperature, electrochemical growth methods is certainly not new. Once the original methods for obtaining nominally undoped ZnO by ECD were established, work on doping ZnO by similar processes soon followed. To date, more than 17 dopants have been tested by various ECD growth processes for ZnO. In most cases, the purpose of the doping is to modulate the optical and/or electrical properties of the ZnO materials. For example, dopants such as Al [61, 62], Ga [61], In [62, 63], B [64], Cl [26, 27, 60, 65], and Y [66] were all expected to enhance the native *n*-type conductivity of ZnO. Dopants like Cd, Mg, and Eu have been shown to modify the optical properties of ZnO by changing its bandgap (Cd, Mg) [67–70] or utilizing excited state transitions of the dopant (Eu) [70]. In addition, a few particular dopants such as Ni [71], Co [71, 72], Fe [73], and Mn [74] were focused on introducing ferromagnetic properties into the ZnO materials for the purpose of creating dilute magnetic semiconductors (DMS).

There has been less work on *p*-type doping of ZnO by electrochemical methods, with only Ag-doped ZnO being tested recently [57, 75, 76]. Other low-temperature solution methods (hydrothermal) have been explored more in this regard, with Sb as the most common dopant [77, 78]. Others such as K [79], P [80], Ag [78], and Li [81] have been investigated as well. Some of the more thorough and enhanced work on electrochemical doping of ZnO is summarized here with focus on *n*-type and *p*-type dopants.

***n*-Type Doping with Cl**

While *n*-type doping of ZnO using ECD methods has been explored significantly, the most successful and consistent results are associated with Cl doping. In particular, the dissolved oxygen ECD method has been used to dope both ZnO thin films [27] and nanowires [26] with Cl, in part because Cl⁻ or ClO₄⁻ ions are naturally present in the supporting electrolyte. In fact, when a chlorine-containing electrolyte is used in the dissolved oxygen method, it is essentially impossible to avoid Cl doping in the ECD growth process. Naturally, such ECD ZnO materials become highly *n*-type with enhanced electron concentrations [26]. Upon further addition of Cl to the growth process, carrier concentrations as high as $9 \times 10^{19} \text{ cm}^{-3}$ for 2D films [27] and $4 \times 10^{20} \text{ cm}^{-3}$ for 3D nanowires [26] can be achieved. Such materials are excellent candidates for transparent conductor applications in solar cells and LEDs. In fact, Cl-doped ZnO films by ECD have been utilized as a top contact layer in solar cells [65]. Cl doping also widens the bandgap of both ZnO thin films [27] and nanowires [46, 60].

***p*-Type Doping with Ag**

Among various potential dopant materials, Ag has demonstrated its suitability for *p*-type doping of ZnO. So far, Ag-doped ZnO nanostructures and thin films have been explored by many techniques, but very few were low-temperature and/or solution-based methods [78, 82]. In many cases of the high-temperature methods, the Ag-doped materials showed *p*-type conductivity [83–85]; however, there is certainly not a guarantee that successful Ag doping of ZnO will lead to *p*-type behavior [86]. Achieving *p*-type ZnO via solution-based methods at lower deposition temperatures has proven to be more difficult.

In the past several years strides have been made in *p*-type doping of ZnO by ECD processes with Ag doping in the zinc nitrate plus hexamine process [57, 75, 76]. As was mentioned above, the zinc nitrate plus hexamine process tends to produce ZnO nanowires, and in the undoped case their background electron concentrations are not too high ($\sim 10^{17} \text{ cm}^{-3}$) [60]. Therefore, the zinc nitrate plus hexamine method provides an excellent starting point for *p*-type doping.

Effects of Ag⁺ on ECD Growth Process

Ag⁺ maintains a much stronger influence on the ECD growth process than many other additive ions have shown in previous work. Whereas Cl⁻, ClO₄⁻, SO₄²⁻, and acetate ions can all be added to the ECD growth solution to relatively high concentrations (0.1 M) [26–28], the addition of Ag⁺ must be much more closely monitored and controlled. Basically, even at concentrations of only 1–5 % relative to Zn²⁺, Ag⁺ disrupts the normal ZnO nanowire growth process, making the deposition of highly uniform Ag-doped ZnO materials difficult [87]. Investigations with CV analysis show that Ag⁺ catalyzes the nitrate reduction electrochemical reaction much like Zn²⁺, perhaps even more so [76].

Figure 15 shows CV scans of various zinc nitrate plus hexamine electrolytes with different amounts of Ag⁺ added. It is clear that even at a very low relative concentration of 0.05 %, Ag⁺ strongly affects the nitrate reduction reaction, enhancing the cathodic current significantly [76]. Figure 16 displays the measured deposition

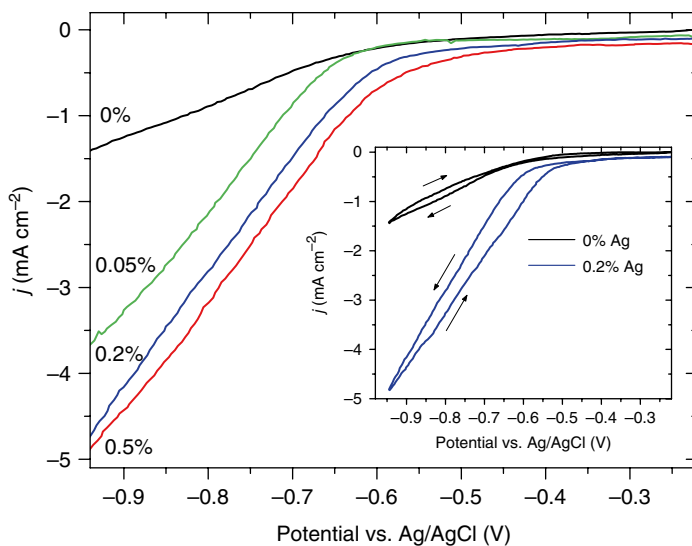


Fig. 15 CV scans of the electrolytes used for undoped and Ag-doped ZnO nanowire growth. The mol.% of Ag in the growth solution is indicated in the figure. Only the forward scans (0 → -0.95 V) are shown for clarity. The inset shows full CV scans for the 0 and 0.2 % Ag solutions (Reproduced with permission from Thomas et al. [76]. Copyright (2012) American Chemical Society)

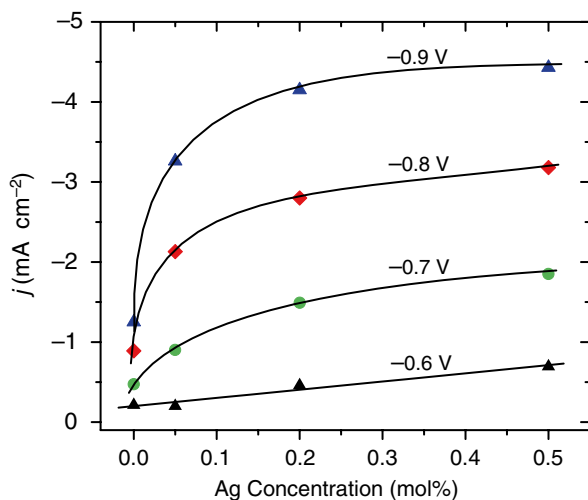


Fig. 16 Current density versus Ag concentration in the ZnO nanowire growth solution at different applied potentials. The data are taken from the CV scans in Fig. 17. The solid lines are simply guides for the eye (Reproduced with permission from [76]. Copyright (2012) American Chemical Society)

currents at various applied potentials along with the effects of Ag^+ at different concentrations. At larger negative potentials, the influence of Ag^+ is even more pronounced at the lowest concentration, indicating its true nature as a catalyst for nitrate reduction [76].

Structure and Morphology

The overall result of the catalyst nature of Ag^+ is simply that growth conditions such as $[\text{Ag}^+]$ and the applied potential must be well optimized for efficient doping of Ag into ZnO nanowires. The well-controlled and uniform growth of ZnO nanowires needs to be maintained, yet sufficient Ag doping must also occur in order to obtain *p*-type properties. Such conditions include a low Ag concentration in the growth solution (0.05–0.5 %) as well as a minimized current density.

Figure 17 shows representative SEM images of the undoped and Ag-doped nanowire arrays obtained by ECD under more controlled growth conditions. The nanowires have diameters of 100–200 nm and lengths ranging from 0.7 to 2.5 μm depending on the specific growth parameters. Under these milder growth conditions, the ZnO nanowire morphologies are not significantly affected by Ag doping. However, as discussed above, it is possible to drastically modify the morphologies of the Ag-doped ZnO nanomaterials by using higher Ag concentrations and potentials [87].

Ag Doping Levels: ECD Growth Conditions

An approximately linear increase in the Ag content of the nanowires is observed as the Ag concentration is increased in the electrolyte (Fig. 18). The actual Ag content in the doped nanowires is much larger than the Ag concentration in the growth solution, indicating Ag is readily incorporated into the ZnO nanowires even at a very low concentration relative to Zn in the electrolyte. The enhanced catalytic role of Ag^+ in the electrochemical growth process may help to explain this observation: much like Zn^{2+} , Ag^+ is adsorbed onto the electrode (ZnO nanowire) surface where it acts as a catalyst for the reduction of nitrate [76]. The CV analysis suggests Ag^+ is a more efficient catalyst than Zn^{2+} for nitrate reduction; therefore, it may be more easily incorporated into ZnO than Zn despite its very low concentration relative to Zn.

Because of the very low concentration of Ag relative to Zn, Ag incorporation is also highly limited by diffusion. As a result, the nanowire growth rate affects the final Ag content because faster ZnO deposition limits the possibility for Ag incorporation. This likely explains the trend of lower Ag contents in the samples deposited at more negative potentials but the same Ag concentration (Fig. 18). ZnO doped with other materials by ECD methods has shown similar behavior [62–64], suggesting the electrochemical doping process in ZnO maintains universal traits.

Optical and Electrical Properties: Evidence for *p*-Type Doping

The PL properties of ECD Ag-doped ZnO have also been investigated [57, 75]. Samples grown at increased applied potentials were very different from undoped ZnO with respect to their defect emission in the visible and near-band edge (NBE) emission in the near-UV range. These changes indicate that Ag doping enhances

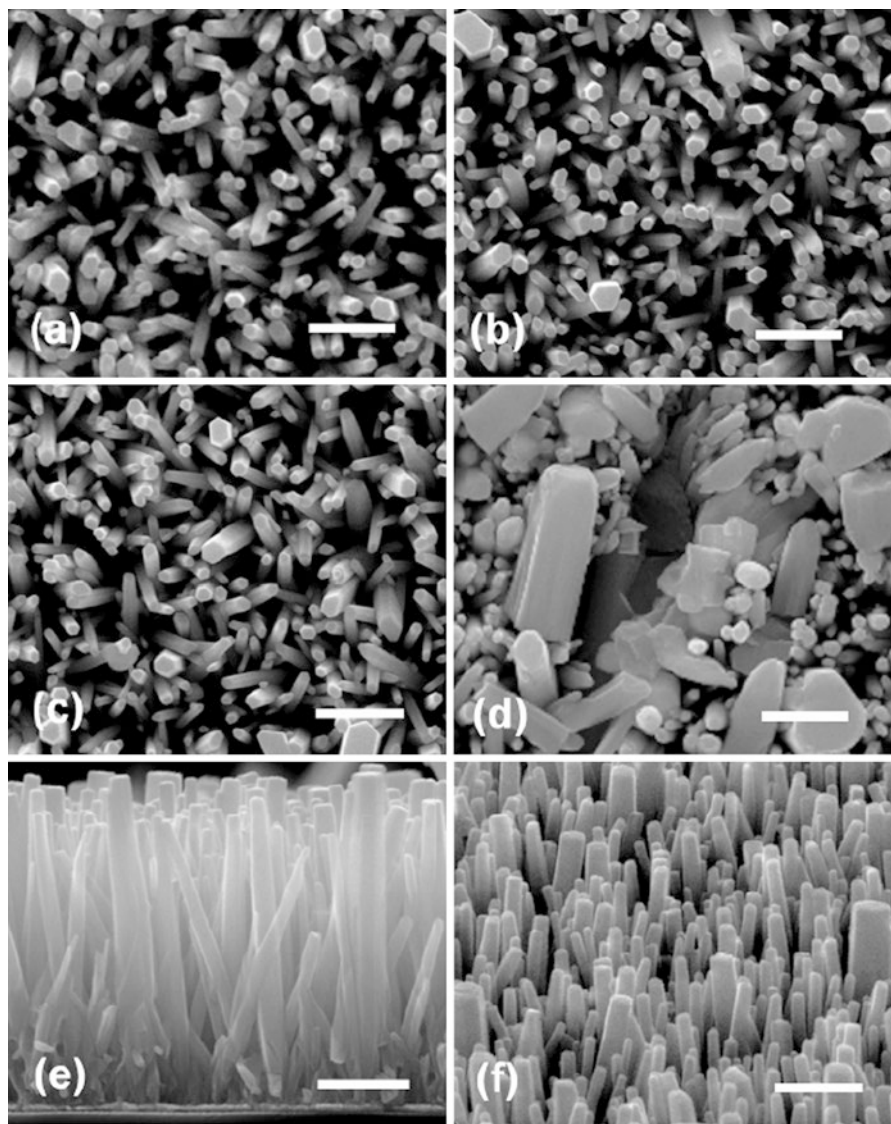
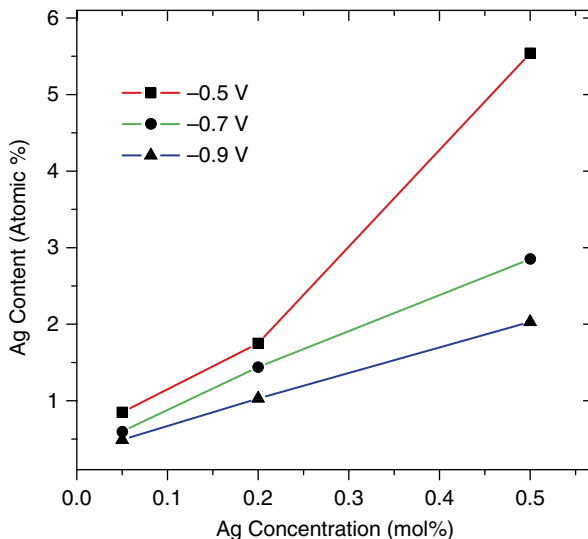


Fig. 17 SEM images of (a) undoped and (b–f) Ag-doped ZnO nanowires. The growth conditions are as follows: (a) -0.7 V, 0 % Ag; (b) -0.7 V, 0.05 % Ag; (c) -0.7 V, 0.2 % Ag; (d) -0.8 V, 1 % Ag. (e, f) are a cross section and tilted view of the sample in (c). The scale bar in each figure is 500 nm. Note that all deposition potentials are reported relative to an Ag/AgCl reference electrode (Adapted with permission from Thomas and Cui [57]. Copyright (2010) American Chemical Society)

the concentration of native defects during the nanowire growth process and also may establish a reduced bandgap in ZnO [57, 75]. Intense emissions at low temperature of a free electron to neutral acceptor transition at 3.323 eV were present in Ag-doped samples grown at more negative potentials, while a donor-bound

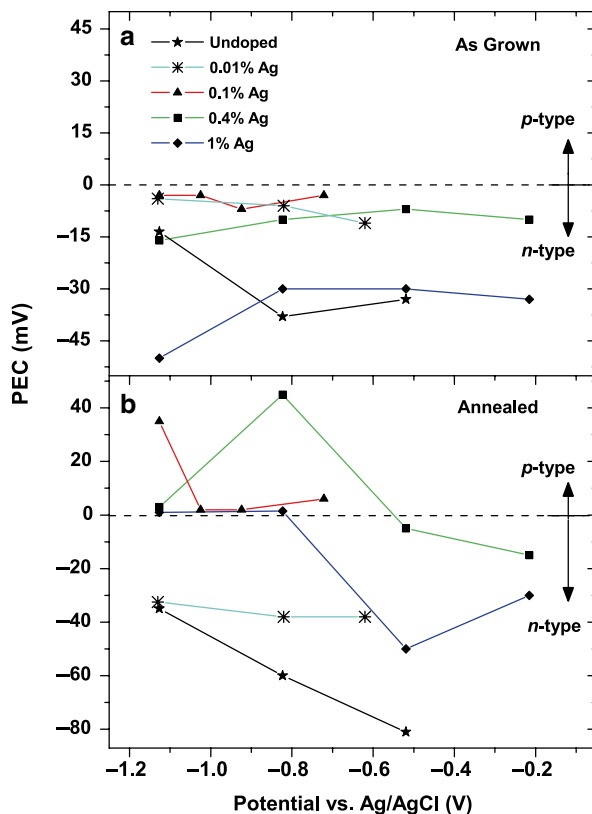
Fig. 18 Ag content measured by energy dispersive x-ray spectroscopy in the doped ZnO nanowires as a function of Ag concentration in the growth solution (Reproduced with permission from Thomas et al. [76]. Copyright (2012) American Chemical Society)



exciton emission dominated the band edge emission for undoped ZnO [75]. Temperature-dependent PL measurements allowed for the calculation of a binding energy of 117 meV for the acceptor involved in the transition at 3.323 eV [75]. The incorporation of Ag into ZnO enhanced the acceptor-related emission, although it is not clear whether this enhancement directly results from Ag impurities or native defects. The optical properties' results provide evidence that Ag is a potential *p*-type dopant for ZnO.

The electrical properties of the undoped and Ag-doped ZnO nanowires were also explored with a solution-based PEC technique. Both as-grown-doped and undoped nanowires have negative PEC responses upon illumination (*n*-type conductivity, Fig. 19). However, the doped samples tend to show a smaller magnitude of the negative PEC signal, indicating a possible decrease in donors and increase in acceptors in these samples due to Ag doping. The annealed Ag-doped nanowires display significant changes in their PEC responses depending on their growth conditions. Much like the PL results, Ag-doped samples grown at more negative applied potentials were distinct from undoped and other Ag-doped nanowires. These samples showed positive PEC responses, a strong indicator of *p*-type electrical properties [57]. Ag-doped samples grown at more negative growth potentials and annealed at moderate temperatures in air (350 °C) showed the most enhanced *p*-type properties [76]. The *p*-type properties of the nanowires were very repeatable under appropriate growth conditions and were also stable over long periods of sample storage. The key factors in producing Ag-doped ZnO with strong evidence of *p*-type properties from both optical and electrical characterization included sufficient Ag doping, improved crystalline quality from moderate annealing, and minimized effects of Ag⁺ on the ECD growth process [57, 76].

Fig. 19 PEC responses for (a) as-grown and (b) annealed (600 °C) samples. The mol.% of Ag in the growth solution is indicated in the figure (Reproduced with permission from Thomas and Cui [57]. Copyright (2010) American Chemical Society)



p-Type Doping Mechanism

It is possible that electrochemical growth parameters such as the applied potential and presence of Ag^+ can modulate the deposition conditions for ZnO, favoring either Zn-rich or O-rich environments. Certainly, as the deposition proceeds and ZnO is formed, some of the Zn is used up, in principle lowering the $[\text{Zn}^{2+}]/[\text{OH}^-]$ ratio. This should be true especially for larger growth rates. At larger negative potentials and with Ag^+ present, the ZnO growth rate is the highest, leading to the fastest use of the available Zn. The availability of OH^- from the electrochemical reduction of nitrate ions is also highly dependent on the applied potential, and from the CV analysis for Ag-doped growth solutions (Fig. 17), it is clear that the presence of Ag^+ creates a similar increase in the rate of nitrate reduction. Therefore, as the applied potential is increased negatively and Ag^+ is added to the electrolyte, the production of OH^- ions is substantially increased, and the $[\text{Zn}^{2+}]/[\text{OH}^-]$ ratio may decrease considerably. These combined effects shift the growth conditions toward an O-rich environment, in turn altering the native defect and Ag impurity formation mechanisms in the nanowires [76]. O-rich conditions are expected to minimize the formation of native donor defects (Zn_i, V_o) [88, 89] while also lowering the formation energy for native acceptor defects ($\text{V}_{\text{Zn}}, \text{O}^i$) [88, 89] and Ag impurities [90–92].

These ideas could help to explain the results discussed above where Ag-doped nanowires with *p*-type properties were mainly obtained at a potential more negative than -0.65 V [57], and the optimal *p*-type properties were associated with a larger negative potential (-0.9 V) and moderate annealing temperature of 350 °C [76]. Similarly, even in undoped ZnO nanowires, their PEC responses indicated reduced *n*-type character at more negative growth potentials, which fits well with the discussion here and in section “[Electrical Properties and Electrical Characterization Techniques](#).”

Summary and Outlook

From their humble beginnings almost 20 years ago, ECD processes for ZnO have become an increasingly important choice among the various techniques for fabricating ZnO materials. The low cost and low-temperature nature of ECD, along with its amenability to large-scale production, suggests it will only continue to gain interest in the future. The electrochemical growth mechanisms associated with ECD ZnO processes are now very well understood. Regardless of the specific ECD method used, the local ZnO growth environment, specifically the $[\text{Zn}^{2+}]/[\text{OH}^-]$ ratio, has been demonstrated to be the single most important parameter for governing the properties of ECD ZnO materials. Many strategies can be used to alter these conditions, such as changing the growth potential, adjusting initial precursor concentrations, and including additives with the standard ECD electrolyte. As a result of these modifications, it has become possible to control the structural, optical, and electrical properties of ZnO for use in a range of advanced device applications. ECD ZnO materials have been integrated into solar cells [65, 93–95], LEDs [68, 96], photonics [97], and DMS applications [71, 72], just to name a few.

The future of ECD ZnO is bright, with new opportunities to further improve the quality and variety of ZnO structures, sharpen controlled fabrication methods for tunable 1D and 2D arrays, and modulate the electrical properties of thin films and nanomaterials for use in low-cost optoelectronics.

References

1. Reynolds DC, Look DC, Jogai B, Jones RL, Litton CW, Harsch W, Cantwell G (1999) Optical properties of ZnO crystals containing internal strains. *J Lumin* 82:173
2. Ozgur U, Alivov YI, Liu C, Teke A, Reshchikov MA, Dogan S, Avrutin V, Cho SJ, Morkoc H (2005) A comprehensive review of ZnO materials and devices. *J Appl Phys* 98:103
3. Look DC, Reynolds DC, Litton CW, Jones RL, Eason DB, Cantwell G (2002) Characterization of homepitaxial *p*-type ZnO grown by molecular beam epitaxy. *Appl Phys Lett* 81:1830
4. Wu JJ, Liu SC (2002) Low-temperature growth of well-aligned ZnO nanorods by chemical vapor deposition. *Adv Mater* 14:215
5. Sun XW, Kwok HS (1999) Optical properties of epitaxially grown zinc oxide films on sapphire by pulsed laser deposition. *J Appl Phys* 86:408
6. Kaidashev EM, Lorenz M, von Wenckstern H, Rahm A, Semmelhack HC, Han KH, Benndorf G, Bundesmann C, Hochmuth H, Grundmann M (2003) High electron mobility of epitaxial

- ZnO thin films on c-plane sapphire grown by multistep pulsed-laser deposition. *Appl Phys Lett* 82:3901
7. Pan ZW, Dai ZR, Wang ZL (2001) Nanobelts of semiconducting oxides. *Science* 291:1947
 8. Lin BX, Fu ZX, Jia YB (2001) Green luminescent center in undoped zinc oxide films deposited on silicon substrates. *Appl Phys Lett* 79:943
 9. Ohshima E, Ogino H, Niikura I, Maeda K, Sato M, Ito M, Fukuda T (2004) *J Cryst Growth* 260:166
 10. Triboulet R, Munoz-Sanjose V, Tena-Zaera R, Martinez-Thomas MC, Hassani S (2005) In: Nickel NH, Terukov E (eds) Zinc oxide – a material for micro- and optoelectronic applications. NATO science series II, vol 194. Springer, Berlin, pp 3–14
 11. Reynolds DC, Litton CW, Look DC, Hoelscher JE, Claffin B, Collins TC, Nause J, Nemeth B (2004) High-quality, melt-grown ZnO single crystals. *J Appl Phys* 95:4802
 12. Lincot D (2010) Solution growth of functional zinc oxide films and nanostructures. *MRS Bull* 35:778
 13. Schmidt-Mende L, MacManus-Driscoll JL (2007) ZnO – nanostructures, defects, and devices. *Mater Today* 10:40
 14. Peulon S, Lincot D (1996) Cathodic electrodeposition from aqueous solution of dense or open-structured zinc oxide films. *Adv Mater* 8:166
 15. Izaki M, Omi T (1996) Transparent zinc oxide films prepared by electrochemical reaction. *Appl Phys Lett* 68:2439
 16. Yoshida T, Komatsu D, Shimokawa N, Minoura H (2004) Mechanism of cathodic electrodeposition of zinc oxide thin films from aqueous zinc nitrate baths. *Thin Solid Films* 451:166
 17. Ashfold MNR, Doherty RP, Ndifor-Angwafor NG, Riley DJ, Sun Y (2007) The kinetics of the hydrothermal growth of ZnO nanostructures. *Thin Solid Films* 515:8679
 18. McPeak KM, Becker MA, Britton NG, Majidi H, Bunker BA, Baxter JB (2010) In situ X-ray absorption near-edge structure spectroscopy of ZnO nanowire growth during chemical bath deposition. *Chem Mater* 22:6162
 19. Pauporte T, Lincot D (2001) Hydrogen peroxide oxygen precursor for zinc oxide electrodeposition I. Deposition in perchlorate medium. *J Electrochem Soc* 148:C310
 20. Pauporte T, Lincot D (2001) Hydrogen peroxide oxygen precursor for zinc oxide electrodeposition II – Mechanistic aspects. *J Electroanal Chem* 517:54
 21. Vayssieres L (2003) Growth of arrayed nanorods and nanowires of ZnO from aqueous solutions. *Adv Mater* 15:464
 22. Vayssieres L, Keis K, Hagfeldt A, Lindquist SE (2001) Three-dimensional array of highly oriented crystalline ZnO microtubes. *Chem Mater* 13:4395
 23. Vayssieres L, Keis K, Lindquist SE, Hagfeldt A (2001) Purpose-built anisotropic metal oxide material: 3D highly oriented microrod array of ZnO. *J Phys Chem B* 105:3350
 24. Greene LE, Law M, Goldberger J, Kim F, Johnson JC, Zhang YF, Saykally RJ, Yang PD (2003) Low-temperature wafer-scale production of ZnO nanowire arrays. *Angew Chem Int Ed* 42:3031
 25. Cui JB, Gibson UJ (2005) Enhanced nucleation, growth rate, and dopant incorporation in ZnO nanowires. *J Phys Chem B* 109:22074
 26. Tena-Zaera R, Elias J, Levy-Clement C, Bekeny C, Voss T, Mora-Sero I, Bisquert J (2008) Influence of the potassium chloride concentration on the physical properties of electrodeposited ZnO nanowire arrays. *J Phys Chem C* 112:16318
 27. Rousset J, Saucedo E, Lincot D (2009) Extrinsic doping of electrodeposited zinc oxide films by chlorine for transparent conductive oxide applications. *Chem Mater* 21:534
 28. Elias J, Tena-Zaera R, Levy-Clement C (2008) Electrochemical deposition of ZnO nanowire arrays with tailored dimensions. *J Electroanal Chem* 621:171
 29. Elias J, Tena-Zaera R, Levy-Clement C (2008) Effect of the chemical nature of the anions on the electrodeposition of ZnO nanowire arrays. *J Phys Chem C* 112:5736
 30. Xu F, Lu YN, Xia LL, Xie Y, Dai M, Liu YF (2009) Seed layer-free electrodeposition of well-aligned ZnO submicron rod arrays via a simple aqueous electrolyte. *MRS Bull* 44:1700

31. Cao BQ, Li Y, Duan GT, Cai WP (2006) Growth of ZnO nanoneedle arrays with strong ultraviolet emissions by an electrochemical deposition method. *Cryst Growth Des* 6:1091
32. Ashida A, Fujita A, Shim YG, Wakita K, Nakahira A (2008) ZnO thin films epitaxially grown by electrochemical deposition method with constant current. *Thin Solid Films* 517:1461
33. Cox JA, Brajter A (1979) Mechanisms of ZR(IV) and LA(III) catalysis of the reduction of nitrate at mercury. *Electrochim Acta* 24:517
34. Ogawa N, Ikeda S (1991) On the electrochemical reduction of nitrate ion in the presence of various metal ions. *Anal Sci* 7(Suppl):1681
35. Khajavi MR, Blackwood DJ, Cabanero G, Tena-Zaera R (2012) New insight into growth mechanism of ZnO nanowires electrodeposited from nitrate-based solutions. *Electrochim Acta* 69:181
36. Thomas MA, Cui JB (2013) Highly Uniform 2D Growth, Substrate Transfer, and Electrical Characterization of Electrodeposited ZnO Thin Films. *J Electrochem Soc* 160:D218
37. Musselman KP, Gershon T, Schmidt-Mende L, MacManus-Driscoll JL (2011) Macroscopically uniform electrodeposited ZnO films on conducting glass by surface tension modification and consequent demonstration of significantly improved p-n heterojunctions. *Electrochim Acta* 56:3758
38. Chatman S, Emberley L, Poduska KM (2009) Significant carrier concentration changes in native electrodeposited ZnO. *ACS Appl Mater Interfaces* 1:2348
39. Izaki M (1999) Preparation of transparent and conductive zinc oxide films by optimization of the two-step electrolysis technique. *J Electrochem Soc* 146:4517
40. Zhang LS, Chen ZG, Tang YW, Jia ZJ (2005) Low temperature cathodic electrodeposition of nanocrystalline zinc oxide thin films. *Thin Solid Films* 492:24
41. Wu KY, Sun ZQ, Cui JB (2012) Unique approach toward ZnO growth with tunable properties: influence of methanol in an electrochemical process. *Cryst Growth Des* 12:2864
42. McPeak KM, Le TP, Britton NG, Nicholov ZS, Elabd YA, Baxter JB (2011) Chemical bath deposition of ZnO nanowires at near-neutral pH conditions without hexamethylenetetramine (HMTA): understanding the role of HMTA in ZnO nanowire growth. *Langmuir* 27:3672
43. Andeen D, Kim JH, Lange FF, Goh GKL, Tripathy S (2006) Lateral epitaxial overgrowth of ZnO in water at 90 degrees C. *Adv Funct Mater* 16:799
44. Pauporte T, Jouanno E, Pelle F, Viana B, Aschehoug P (2009) Key growth parameters for the electrodeposition of ZnO films with an intense UV-light emission at room temperature. *J Phys Chem C* 113:10422
45. Cui JB (2008) Defect control and its influence on the exciton emission of electrodeposited ZnO nanorods. *J Phys Chem C* 112:10385
46. Cui JB, Soo YC, Chen TP, Gibson UJ (2008) Low-temperature growth and characterization of Cl-doped ZnO nanowire arrays. *J Phys Chem C* 112:4475
47. Ren T, Baker HR, Poduska KM (2007) Optical absorption edge shifts in electrodeposited ZnO thin films. *Thin Solid Films* 515:7976
48. von Windheim JA, Wynands H, Cocivera M (1991) Removal and preparation of electrodeposited semiconductors for high impedance hall-effect measurements. *J Electrochem Soc* 138:3435
49. Guillemoles JF, Cowache P, Lusson A, Fezzaa K, Boisivon F, Vidal J, Lincot D (1996) One step electrodeposition of CuInSe₂: improved structural, electronic, and photovoltaic properties by annealing under high selenium pressure. *J Appl Phys* 79:7293
50. Mizuno K, Izaki M, Murase K, Shinagawa T, Chigane M, Inaba M, Tasaka A, Awakura Y (2005) Structural and electrical characterizations of electrodeposited p-type semiconductor Cu₂O films. *J Electrochem Soc* 152:C179
51. Yoon S, Huh I, Lim JH, Yoo B (2012) Annealing effects on electrical and optical properties of ZnO thin films synthesized by the electrochemical method. *Curr Appl Phys* 12:784
52. Shinagawa T, Chigane M, Murase K, Izaki M (2012) Drastic change in electrical properties of electrodeposited ZnO: systematic study by hall effect measurements. *J Phys Chem C* 116:15925

53. Mora-Sero I, Fabregat-Santiago F, Denier B, Bisquert J, Tena-Zaera R, Elias J, Levy-Clement C (2006) Determination of carrier density of ZnO nanowires by electrochemical techniques. *Appl Phys Lett* 89:203117
54. Voss T, Bekeny C, Gutowski J, Tena-Zaera R, Elias J, Levy-Clement C, Mora-Sero I, Bisquert J (2009) Localized versus delocalized states: photoluminescence from electrochemically synthesized ZnO nanowires. *J Appl Phys* 106:054304
55. Samantilleke AP, Boyle MH, Young J, Dharmadasa IM (1998) Electrodeposition of n-type and p-type ZnSe thin films for applications in large area optoelectronic devices. *J Mater Sci Mater Electron* 9:289
56. Samantilleke AP, Boyle MH, Young J, Dharmadasa IM (1998) Growth of n-type and p-type ZnSe thin films using an electrochemical technique for applications in large area optoelectronic devices. *J Mater Sci Mater Electron* 9:231
57. Thomas MA, Cui JB (2010) Electrochemical route to p-type doping of ZnO nanowires. *J Phys Chem Lett* 1:1090
58. Wellings JS, Chaure NB, Heavens SN, Dharmadasa IM (2008) Growth and characterisation of electrodeposited ZnO thin films. *Thin Solid Films* 516:3893
59. Ahn KS, Deutsch T, Yan YF, Jiang CS, Perkins CL, Turner J, Al-Jassim MM (2007) Synthesis of band-gap-reduced p-type ZnO films by Cu incorporation. *J Appl Phys* 02:023517
60. Fan JD, Shavel A, Zamani R, Fabrega C, Rousset J, Haller S, Guell F, Carrete A, Andreu T, Arbiol J, Morante JR, Cabot A (2011) Control of the doping concentration, morphology and optoelectronic properties of vertically aligned chlorine-doped ZnO nanowires. *Acta Mater* 59:6790
61. Han XF, Han K, Tao M (2010) Electrodeposition of group-IIIa doped ZnO as a transparent conductive oxide. *ECS Trans* 15:93
62. Kemell M, Dartigues F, Ritala M, Leskela M (2003) Electrochemical preparation of In and Al doped ZnO thin films for CuInSe₂ solar cells. *Thin Solid Films* 434:20
63. Machado G, Guerra DN, Leinen D, Ramos-Barrado JR, Marotti RE, Dalchiale EA (2005) Indium doped zinc oxide thin films obtained by electrodeposition. *Thin Solid Films* 490:124
64. Ishizaki H, Imaizumi M, Matsuda S, Izaki M, Ito T (2002) Incorporation of boron in ZnO film from an aqueous solution containing zinc nitrate and dimethylamine-borane by electrochemical reaction. *Thin Solid Films* 411:65
65. Rousset J, Donsanti F, Genevee P, Renou G, Lincot D (2011) High efficiency cadmium free Cu(In,Ga)Se₂ thin film solar cells terminated by an electrodeposited front contact. *Sol Energy Mater Sol Cells* 95:1544
66. Han XF, Han K, Tao M (2010) Low resistivity yttrium-doped zinc oxide by electrochemical deposition. *J Electrochem Soc* 157:H593
67. Li GR, Zhao WX, Bu Q, Tong YX (2009) A novel electrochemical deposition route for the preparation of Zn_{1-x}Cd_xO nanorods with controllable optical properties. *Electrochem Commun* 11:282
68. Lupan O, Pauporte T, Bahers TL, Ciofini I, Viana B (2011) High aspect ratio ternary Zn_{1-x}Cd_xO nanowires by electrodeposition for light-emitting diode applications. *J Phys Chem C* 115:14548
69. Ishizaki H, Yamada N (2006) Preparation of Zn_{1-x}Mg_xO film by electrochemical reaction. *Electrochem Solid State Lett* 9:C178
70. Li GR, Dawa CR, Lu XH, Yu XL, Tong YX (2009) Use of additives in the electrodeposition of nanostructured Eu₃₊/ZnO films for photoluminescent devices. *Langmuir* 25:2378
71. Cui JB, Gibson UJ (2005) Electrodeposition and room temperature ferromagnetic anisotropy of Co and Ni-doped ZnO nanowire arrays. *Appl Phys Lett* 87
72. Cui JB, Zeng Q, Gibson UJ (2006) Synthesis and magnetic properties of Co-doped ZnO nanowires. *J Appl Phys* 99
73. Lipinski BB, Mosca DH, Mattoso N, Schreiner WH, de Oliveira AJA (2004) Electrodeposition of ZnO-Fe granular films. *Electrochem Solid State Lett* 7:C115
74. Li GR, Qu DL, Zhao WX, Tong YX (2007) Electrochemical deposition of (Mn, Co)-codoped ZnO nanorod arrays without any template. *Electrochem Commun* 9:1661

75. Thomas MA, Cui JB (2009) Investigations of acceptor related photoluminescence from electrodeposited Ag-doped ZnO. *J Appl Phys* 105:093533
76. Thomas MA, Sun WW, Cui JB (2012) Mechanism of Ag doping in ZnO nanowires by electrodeposition: experimental and theoretical insights. *J Phys Chem C* 116:6383
77. Briscoe J, Gallardo DE, Dunn S (2009) In situ antimony doping of solution-grown ZnO nanorods. *Chem Commun* 10:1273
78. Lupan O, Chow L, Ono LK, Cuenya BR, Chai GY, Khallaf H, Park SH, Schulte A (2010) Synthesis and characterization of Ag- or Sb-doped ZnO nanorods by a facile hydrothermal route. *J Phys Chem C* 114:12401
79. Tay CB, Chua SJ, Loh KP (2010) Stable p-type doping of ZnO film in aqueous solution at low temperatures. *J Phys Chem C* 114:9981
80. Fang X, Li JH, Zhao DX, Shen DZ, Li BH, Wang XH (2009) Phosphorus-doped p-type ZnO nanorods and ZnO nanorod p-n homojunction LED fabricated by hydrothermal method. *J Phys Chem C* 113:21208
81. Lee J, Cha S, Kim J, Nam H, Lee S, Ko W, Wang KL, Park J, Hong J (2011) p-type conduction characteristics of lithium-doped ZnO nanowires. *Adv Mater* 23:4183
82. Jin YX, Cui QL, Wang K, Hao JA, Wang QS, Zhang JA (2011) Investigation of photoluminescence in undoped and Ag-doped ZnO flowerlike nanocrystals. *J Appl Phys* 109:053521
83. Wang GP, Chu S, Zhan N, Zhou HM, Liu JL (2011) Synthesis and characterization of Ag-doped p-type ZnO nanowires. *Appl Phys A Mater Sci Process* 103:951
84. Fang F, Zhao DX, Fang X, Li JH, Wei ZP, Wang SZ, Wu JL, Wang XH (2011) Optical and electrical properties of individual p-type ZnO microbelts with Ag dopant. *J Mater Chem* 21:14979
85. Kang HS, Ahn BD, Kim JH, Kim GH, Lim SH, Chang HW, Lee SY (2006) Structural, electrical, and optical properties of p-type ZnO thin films with Ag dopant. *Appl Phys Lett* 88:202108
86. Chai J, Mendelsberg RJ, Reeves RJ, Kennedy J, von Wenckstern H, Schmidt M, Grundmann M, Doyle K, Myers TH, Durbin SM (2010) Identification of a deep acceptor level in ZnO due to silver doping. *J Electron Mater* 39:577
87. Thomas MA, Cui JB (2009) Electrochemical growth and characterization of Ag-doped ZnO nanostructures. *J Vac Sci Technol B* 27:1673
88. Kohan AF, Ceder G, Morgan D, Van de Walle CG (2000) First-principles study of native point defects in ZnO. *Phys Rev B* 61:15019
89. Zhang SB, Wei SH, Zunger A (2001) Intrinsic n-type versus p-type doping asymmetry and the defect physics of ZnO. *Phys Rev B* 63:075205
90. Yan YF, Al-Jassim MM, Wei SH (2006) Doping of ZnO by group-IB elements. *Appl Phys Lett* 89:181912
91. Volnianska O, Boguslawski P, Kaczkowski J, Jakubas P, Jezierski A, Kaminska E (2009) Theory of doping properties of Ag acceptors in ZnO. *Phys Rev B* 80:245212
92. Li YL, Zhao XA, Fan WL (2011) Structural, electronic, and optical properties of Ag-doped ZnO nanowires: first principles study. *J Phys Chem C* 115:3552
93. O'Regan B, Schwartz DT, Zakeeruddin SM, Gratzel M (2000) Electrodeposited nanocomposite n-p heterojunctions for solid-state dye-sensitized photovoltaics. *Adv Mater* 12:1263
94. Levy-Clement C, Tena-Zaera R, Ryan MA, Katty A, Hodes G (2005) CdSe-sensitized p-CuSCN/nanowire n-ZnO heterojunctions. *Adv Mater* 17:1512
95. Karuppuchamu S, Nonomura K, Yoshida T, Sugiura T, Minoura H (2002) Cathodic electrodeposition of oxide semiconductor thin films and their application to dye-sensitized solar cells. *Solid State Ion* 151:19
96. Lupan O, Pauporte T, Viana B (2010) Low-voltage UV-electroluminescence from ZnO-nanowire array/p-GaN light-emitting diodes. *Adv Mater* 22:3298
97. Cui JB, Gibson UJ (2007) Low-temperature fabrication of single-crystal ZnO nanopillar photonic bandgap structures. *Nanotechnology* 18:155302

Nanostructured Transition Metal Oxides Produced by Electrodeposition for Application as Redox Electrodes for Supercapacitors

20

M. Fátima Montemor, S. Eugénio, N. Tuyen, R.P. Silva, T.M. Silva, and M.J. Carmezim

Contents

Introduction.....	682
Electrodeposition for the Fabrication of Nanostructured Materials	685
Electrodeposition of Nanostructured Metal Oxide Electrodes for Supercapacitors	687
Current Materials.....	687
2D and 3D Doped MnO ₂ Nanostructures.....	689
Metallic Foams.....	695
Fabrication of 3D Hyperbranched Dendritic Structures	702
Fabrication of Composites Carbon and Metal Oxides	707
Conclusions and Outlook.....	709
References.....	710

M.F. Montemor (✉) • S. Eugénio • N. Tuyen • R.P. Silva
Centro de Química Estrutural, Instituto Superior Técnico, Universidade de Lisboa,
Avenida Rovisco Pais, Lisbon, Portugal
e-mail: mfmontemor@ist.utl.pt; s.eugenio@tecnico.ulisboa.pt;
nguyen.tuyen@tecnico.ulisboa.pt; rui.pedro.silva@tecnico.ulisboa.pt

T.M. Silva
Centro de Química Estrutural, Instituto Superior Técnico, Universidade de Lisboa,
Avenida Rovisco Pais, Lisbon, Portugal

Department of Mechanical Engineering, GI-MOSM,
Instituto Superior de Engenharia de Lisboa (ISEL), Lisbon, Portugal
e-mail: msilva@dem.isel.ipl.pt

M.J. Carmezim
Centro de Química Estrutural, Instituto Superior Técnico, Universidade de Lisboa,
Avenida Rovisco Pais, Lisbon, Portugal

ESTSetúbal, Instituto Politécnico de Setúbal, Setúbal, Portugal
e-mail: maria.carmezim@estsetubal.ips.pt

Abstract

The increasing demand for energy and the need of cleaner production technologies have turned energy storage into a hot research topic. Development of more efficient energy storage devices, such as batteries and supercapacitors, is the key to boost renewable energy production and the use of electric/hybrid vehicles. Electrochemistry is one of the sciences behind these challenging technologies. The performance of these devices relies on the nature of the electrodes they use. 2D and 3D nanostructured architectures composed of transition metal oxides, or their composites with carbon, have recently emerged as new materials with high potential as electrodes for supercapacitors due to their pseudocapacitive contribution and high theoretical capacitances.

For application in supercapacitors, the electrodes must present high porosity and surface area. These are necessary properties to enhance charge-transfer and redox reactions at the film/electrolyte interface. One of the most promising techniques to produce transition metal films with such characteristics is electrodeposition because of its versatility and it is easy to do. Electrodeposition is a widespread cheap and clean one-step technique for the fabrication of metals, metal oxides, polymers, and composite coatings. By combining optimized deposition parameters with the required electrolyte composition, the morphology and the chemical composition of the deposited film can be tailored to achieve nanostructured architectures.

In this chapter, recent advances in 2D and 3D nanostructured architectures of transition metal oxide films produced by electrodeposition and their application as electrodes for electrochemical pseudo supercapacitors, including their electrochemical performance, are reviewed, and recent trends and results are highlighted.

Keywords

Supercapacitors • Electrodeposition • Transition metal oxides

Introduction

Energy storage became the key to implement the production of energy from green/renewable sources. The increasing production/consumption from renewable sources (e.g., wind and photovoltaic) is demanding more reliable solutions for energy storage. On the other side, the extraordinary growth of hybrid and electric vehicles is also imposing new solutions for more efficient energy storage devices of very fast response. Moreover, the numerous applications in electronic devices, including mobile communications and various electronic tools, opened a new array for the development of energy storage devices with different sizes and functionalities. Indeed, new hi-tech applications, related with microsized devices for electronic

circuits or for biomedical applications, raised new challenges where materials science and electrochemistry play a major role.

Nowadays, the basic needs on energy storage are covered by the use of batteries, with supercapacitors playing a minor role. The recent generations of Li-ion batteries can answer several demands in what concerns energy storage needs, but there are still numerous drawbacks to overcome. Although the most recent generation of batteries clearly outperforms the conventional capacitors in terms of energy density, they are still very limited in what concerns power density. This drawback limits the application of batteries when this property becomes a requirement. On the other hand, the charge/discharge processes of batteries are slow, limiting its application in fast storage/demand cycles. To overcome these drawbacks, supercapacitors are the ideal solution for energy storage applications, which require higher power density and fast charge/discharge as well as long-term cycling ability. Supercapacitors can deliver much higher power densities, when compared to batteries, and can supply high currents in very short times. Another major advantage is the robust performance in what concerns charge/discharge cycles. Supercapacitors can sustain up to millions of cycles, without deterioration of the basic properties, whereas a battery sustains a much lower number of cycles (at least three orders of magnitude lower). However, the most important factor limiting a wider application of supercapacitors is still the lower energy density when compared to the most recent batteries. Table 1 [1] provides a snapshot of the most important properties of common batteries and supercapacitors.

Nowadays, despite the technology advances, commercial supercapacitors are still unable to combine, simultaneously, high power with high energy densities. The energy density is normally 5–10 times lower than that of the most recent generations Li or Ni batteries. Therefore, the key issue is to increase the energy density while keeping the other properties (power density, fast response, and efficiency) as high as possible. These requirements can only be achieved by designing appropriate electrode materials and by selecting appropriate electrolytes. Nowadays, the scientific challenge is to design materials for electrodes that can fulfill these requirements.

Supercapacitors can be classified into two main categories: the electrochemical double layer (EDL) supercapacitors that are based on carbon-based electrodes and the redox pseudocapacitors that make use of metallic oxide or inherent conductive polymer electrodes.

Table 1 Comparison between the most important properties of batteries and supercapacitors (Adapted from Ref. [1])

Parameter	Battery	Supercapacitor
Energy density (Wh kg⁻¹)	20–100	1–10
Power density (W kg⁻¹)	50–200	1000–2000
Charge time	0.3–3 h	1–30 s
Discharge time	1–5 h	1–30 s
Life cycle	500–2000	>100 000
Charge/discharge efficiency (%)	70–85	90–95

The most well-characterized and widely used supercapacitor device makes use of two identical electrodes, in which a high surface area carbon material is linked by organic binders, being then used to coat a current collector, made, for example, of thin stainless steel or aluminum foil. The energy storage process is based on reversible electrostatic accumulation of ions on the surface of the electrode, by a double layer mechanism.

Various forms of carbon, such as mesoporous powders, single- and multiwalled carbon nanotubes, carbon fibers and clothes, aerogels, and graphene, including graphene oxides, are being intensively studied for EDL supercapacitors. Some of these materials are not expensive, easily available, and free of environmental concerns. Others, such as graphene or carbon aerogels, are expensive and can be affordable only for hi-tech applications. Thus, several carbon-based materials can be used to fabricate electrodes, because of their low cost and availability, nontoxic nature, and stability/robustness in a wide range of environments. Existing commercial solutions rely on EDL supercapacitors using carbon-based electrodes, requiring the use of binders and organic electrolytes, which can operate in a voltage window of 2.5–3.0 V. Despite the higher energy densities, some of these electrolytes have poor stability in air and are very sensitive to alterations due to moisture. On the other hand, the size of the solvated ions becomes much larger than that of the protons, resulting in decreased specific capacitance values. However, the major disadvantages rely on the toxicity of some of these electrolytes (like acetonitrile) and the need of using binders and “inert” additives that may also raise environmental concerns. For improved adhesion to the current collector, the amount of binder can be increased, but at expenses of the electrolyte conductivity [2]. Nevertheless, carbon-based electrodes have a widespread use and many new insights are reported every day [3, 4]. The specific capacitance depends on the pore size and surface area available for the double layer formation and typical values fall in the range 100–300 Fg^{-1} [4].

More recently, graphene was introduced as material for SC electrodes due to its increased electroactivity and conductivity, well-developed surface area, and theoretical capacity while allowing a wide range of 3D nanoarchitectures [5, 6]. Graphene has also been used as a support for the growth of metal oxides providing additional electric conductivity and electrochemical activity [7]; however, agglomeration and sticking of graphene sheets are hard to overcome. Recently, flexible macroscopic 3D graphene foams became commercially available and are an attractive substrate for the formation of high surface area electrodes but only for very specific hi-tech applications because of its price. Co-electrodeposition has also been reported as a simple method to obtain of graphene–metal composites in one single step, resulting in materials with enhanced properties when compared to single materials [8].

Carbon structures can display good energy density, in a wide potential window, providing that organic electrolytes are used. However, most of them are not compliant with health, safety, and environmental regulations, and there is a need to find cleaner and more environmentally friendly solutions.

In order to overcome the drawbacks of organic electrolytes, there have been important developments concerning aqueous electrolytes. Literature reports that

some electrolytes, such as alkali or sulfates, allow extending the working window up to 2 V because of the highest overpotential for H₂ evolution. Furthermore, interesting results have been observed because faradaic contributions may contribute to increased capacitance [9]. The pseudocapacitive contribution relies on reversible and fast faradaic reactions between the electrode materials and the ions present in the electrolyte and provides an additional contribution for charge storage [10].

Thus, it has been shown that additional faradaic processes, occurring in the electrode, can result in a significant increase in the specific capacitance. This opens a new array of possibilities in what concerns the study of metallic oxides, especially the ones possessing multiple valence states. Current examples are manganese, ruthenium, nickel, cobalt, and vanadium oxides. Several routes can be used to fabricate these materials. However, for a wider use of these materials, there is a need for flexible and cheap routes able to fabricate versatile combinations and architectures. One of these routes is based on the electrodeposition technology.

Electrodeposition for the Fabrication of Nanostructured Materials

Electrochemistry is the science behind the working principles of batteries and supercapacitors, but it can also be used to fabricate tailored materials for more efficient electrodes, presenting improved performance. Electrodeposition has been known for years, being a well-established technique, versatile, and “easy to do.” Furthermore, scale-up and mass production are affordable and implementable, as electrodeposition lines are currently used to coat many materials in industrial applications.

Electrodeposition of metals and alloys has been performed for more than a century, allowing the production of a coating, usually metallic, on a surface by the action of electric current. This technique is based on simple redox process where the surface to be coated is made of a cathode of an electrolytic cell containing a salt of the metal to be deposited as electrolyte.

By the effect of the flowing current, the metallic cations migrate towards the negatively charged substrate where they undergo a reduction reaction, leading to the formation of a metallic deposit. This process allows the deposition of a wide variety of metals on different types of substrates. Deposition of alloys is also possible, providing that two (or more) metallic cations are present in the plating bath and that their deposition potentials are similar or can be made similar (by changing the relative concentration of the metallic ions in the electrolyte).

Various process parameters are critical in the electrodeposition process, namely, applied current density, overpotential, electrolyte composition, temperature, and agitation, among others. Adequate tuning of these parameters allows at accurately controlling the thickness, composition, and morphology of the deposited films. The flexibility of the electrodeposition process enables the production of surfaces in very different architectures, ranging from homogeneous dense layers to more rough or porous deposits and, more recently, to nanostructured compounds.

Nowadays, the vast majority of the coatings that are produced industrially are used for decorative or protective purposes, and for that reason, dense, uniform, and adherent films are desirable. However, in certain applications, such as in energy storage or materials for catalysis, high surface areas are required which can be achieved by the development of 3D nanostructured materials.

Recent investigations [11, 12] have shown that electrodeposition can be an attractive method for the preparation of such nanostructured materials and for the design of functional materials. The processing route employs traditional electroplating equipment provided that the suitable processing parameters are used. The obtained deposits show a remarkable degree of reproducibility which is related to the fact that their morphologies are consequence of the fabrication method, rather than those obtained in additional posttreatments.

The morphology of electrodeposited metals is determined by the interaction of various phenomena occurring during electrodeposition, in particular the type of control that is established during deposit growth, which is a function of the deposition parameters, namely, the applied potential (or current density). In the case of low overpotentials, i.e., when the applied potential is similar to the reduction potential of the species to be plated, deposits presenting large grains with generally well-defined crystallite shapes are obtained [13, 14]. Under such conditions, since the deposition rate is slow, charge-transfer control dominates the process. On the contrary, when the threshold overvoltage is exceeded [15], a dendritic structure develops, displaying a well-organized morphology, which develops and grows branches in various 3D well-defined directions. The 3D-branched structures are nanosized dimensions. In this case the deposition rate is high and the diffusion of metallic cations towards the cathode plays a significant role. Dendritic growth can therefore be explained as a protrusion formed under charge-transfer-controlled mechanisms. On the other hand, on the remaining electrode, the cathodic process develops under diffusion control [16, 17]. Accordingly, the formation of the 3D dendritic structure is favored by decreasing the concentration of the ions that are electrodeposited, temperature, and stirring or by increasing the concentration of the supporting electrolyte and the viscosity of the bath.

For overpotentials higher or, at least, located on the limiting diffusion current plateau, the formation of powders occurs. In this case, vigorous hydrogen evolution at the electrode surface takes place and, as a consequence, the hydrodynamic conditions change. In this way, powdered deposits basically represent dendritic electrodeposits which are disrupted by mechanical action or spontaneously fall apart during growth. Ultimately, this approach is used to produce a variety of powders for various technological applications.

Finally it should be mentioned that functional layers with highly porous morphologies can be synthesized through electrodeposition, using the surface of the cathode as a template. One example is a preparation method based on a template-driven synthesis. In this process the hard template is only used during electrodeposition and at the end of the process. After it is removed by etching or by combustion allowing to obtain a material, which replicates the morphology and structural effects of the initial disposable template [18]. Different templates, displaying tunable pore

sizes and structures, have been proposed. More recently, a different approach was proposed, where hydrogen bubbles, released during the electrodeposition process, when sufficiently high overpotentials are applied, act as a dynamic template allowing the fabrication of metallic 3D self-supporting foams [19].

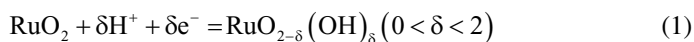
Electrochemistry is thus a powerful tool in the field of materials design and surface functionalization, suitable for application in various domains. Electrodeposition of various species such as metals, alloys, foams, graphene oxide, and inherent conductive polymers plays a key role in the fabrication of innovative materials with application in the energy storage domain, in particular effective electrodes for supercapacitors and batteries.

Electrodeposition of Nanostructured Metal Oxide Electrodes for Supercapacitors

Current Materials

Metallic assemblies based on interpenetrated or vertically aligned wirelike, tubular, and other 3D porous topologies offer low diffusion barrier and high density of active surface sites, being promising solutions for redox electrodes. Traditionally ruthenium oxides have been used because of their high theoretical capacitance, reversible behavior, chemical stability, and electric conductivity that can attain 10^5 S cm^{-1} [20, 21].

In the presence of protons, the ruthenium oxide can undergo the following reaction:



which is responsible for the high theoretical capacitance of RuO_2 (close to 2000 Fg^{-1}) [20]. However, in current applications the values are much lower (close to 700 Fg^{-1}). This difference has been attributed to changes that occur in the crystalline structure, irreversible reactions, low electron–proton transport, agglomeration of oxide particles, and conductivity decrease. To overcome some of these drawbacks, and also because ruthenium is quite expensive, many attempts have been done combining it with other materials such as carbon nanotubes or graphene [22–24]. The main goal is to increase the conductivity of the electrode, to increase the active surface area, and to combine the high double layer capacitance response of carbon materials with the high faradaic capacitance of RuO_2 . Other strategies include the fabrication by electroplating of composites made of RuO_2 and nanoporous gold substrates [20]. Although the increased energy densities and specific capacitances can be achieved, the cost of the materials limits very much such application, and RuO_2 -based electrodes are being replaced by other metallic oxides.

RuO_2 has been replaced primarily by MnO_2 , a material that can deliver practical specific capacitances close to 700 Fg^{-1} . Nowadays, several commercial systems are based on MnO_2 or MnO_2 and carbon composites. The pseudocapacitive contribution of manganese oxide is based on surface reactions or very-thin active surface layers and depends upon several factors such as structure of the oxides, porosity, and

valence of the species. One of the major drawbacks of MnO_2 , limiting its wider application, is the increased resistivity during continuous cycling, arising from non-reversible reactions. Many attempts have been made to increase the specific capacitance and its stability over time. The manipulation of the crystalline structure, pore size, and surface area through various additives and doping of the structure demonstrated effective results [25, 26], including increased capacitance and decreased electrode aging under repeated cycling.

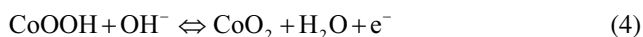
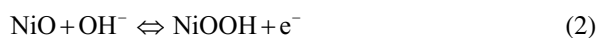
As in the case of RuO_2 , the charge storage mechanism of MnO_2 is mainly associated with highly reversible redox reactions within the film, in which the oxidation state of Mn centers changes between III and IV. Simultaneously to the oxidation process, there is a process of ion transfer between the electrolyte and the oxide, which maintains the electroneutrality of the metallic oxide. Two possible mechanisms [27] have been proposed:

- Adsorption/desorption of protons (H^+) or other alkali cations present in the electrolyte on the surface of the MnO_2 ; this mechanism seems predominant on amorphous oxides.
- Intercalation/de-intercalation of H^+ or alkali cations from the electrolyte in the bulk oxide particles constituent of the film and simultaneous oxidation/reduction of Mn cations; this mechanism seems predominant in crystalline systems.

The specific capacitance of MnO_2 can be increased when it is used in composites with carbon or conductive polymers. These include the use of carbon nanotubes as support for MnO_2 [27] for fabricating high-performance flexible supercapacitors or composites combining MnO_2 , carbon nanotubes, and graphene nanosheets for higher energy density (43 Whkg^{-1}) [28]. Composites made of polyaniline fibers (PANI) and MnO_2 have displayed capacitances above 400 Fg^{-1} , and the procedure could be extended to other inherent conductive polymers [29]. In carbon composites, MnO_2 loading is an approach that still requires further optimization in order to increase both the specific capacitance and cycling performance without detrimental increase in the charge-transfer resistance or undesired blocking of the electrode and therefore of the electrolyte transport [30].

MnO_2 can also be combined with other oxides, such as Co_3O_4 , to increase cycling life, specific capacitance, and energy density [31].

Alternatives to MnO_2 include transition metal oxides such as NiO_x , Co_3O_4 , and V_2O_5 , among others, possessing multiple oxidation states, which enable reversible redox reactions for increased pseudocapacitance response [21, 32]. NiO_x and Co_3O_4 can display theoretical capacitances of 2584 and 3560 Fg^{-1} , respectively, in KOH or NaOH electrolytes. The following reactions can explain the pseudocapacitive behavior of these oxides [21, 32]:



Ni oxides and hydroxides have been explored for hybrid SC, delivering specific capacitances above 1700 Fg^{-1} [33]. 2D layered Co_3O_4 flakes with high surface area and porosity were synthesized by precipitation processes, showing capacitances around 900 Fg^{-1} [34].

At the present moment, there are several new alternatives arising as very promising ones. A requisite for wider use of these alternatives is price. Therefore, to mitigate the impact of material price, it is of key relevance to address the cheapest routes for the fabrication of the novel electrodes. Electrodeposition is definitely the technology in the forefront to pursue this objective. Table 2 summarizes the fabrication method and characteristics of various metal oxide-based materials for application as electrodes for supercapacitors.

2D and 3D Doped MnO_2 Nanostructures

As referred, manganese oxide has been one of the most studied materials for the development of metallic oxide-based supercapacitors electrodes due to its reduced cost, environmental friendliness, and abundance in nature. Manganese oxide displays a theoretical specific capacitance of 1370 Fg^{-1} , making it very attractive for charge storage. However, electrode-based manganese oxides face two main drawbacks: decreased electronic conductivity and low ion diffusion through the bulk of the materials leading to lowering of the capacitive performance of the electrode.

Several approaches have been proposed in order to improve the pseudocapacitive performance of manganese oxide-based electrodes. One of the most successful consists on the deposition of MnO_2 over a porous current collector. This strategy results in (i) improvement of the capacitive response, due to a facile transport of electrolyte through the porous current collector framework; (ii) shortened ionic diffusion through the bulk; and (iii) increased surface area of the electroactive material compared to flat conducting current collectors. Nickel foams [35], carbon fibers and papers [36], nanoporous dealloyed gold [51], and nickel dendrites [37] are widely used as porous current collectors. For example, MnO_2 nanowires electrodeposited on nickel foam, within $\text{LiClO}_4\text{-OZO}$ quasi-ionic liquid electrolyte, present a working voltage extended up to 2.5 V and a very high energy density of 304 W h kg^{-1} [36]. Using nanoporous dealloyed gold as the current collector, the specific capacitance normalized to MnO_2 of about 1145 Fg^{-1} , almost reaching its theoretical value [37].

Design of electroactive electrodes, with improved cycling performance and high specific capacitance can also be done by creating hierarchical structures fabricated by various routes such as electrodeposition. Duay et al. [38] prepared MnO_2 nanowire arrays via template-assisted electrodeposition. These nanowires present a hierarchical structure that increases the electroactive area, improving ion accessibility as result of the smaller diameter of the nanowire, thus contributing for a higher specific capacitance. Furthermore, the vertical structure aligned with the electric field has proved to enhance effectively the ionic transport of electrolyte through the

Table 2 Fabrication method and characteristics of metal oxide-based films for application as electrodes for supercapacitors

Deposition method	Film morphology/ electrode configuration	Testing electrolyte	Specific capacitance	Capacitance retention (%)	Rate capability (%)	References
Cyclic electrodeposition	RuO ₂ /nanoporous gold	0.5 M H ₂ SO ₄	1500 Fg ⁻¹ (10 mV s ⁻¹)	n.d.	73.3 % (10–1000 mV s ⁻¹)	[20]
Anodic electrodeposition	Fibrous morphology of different MnO ₂ phases	0.5 M Na ₂ SO ₄	190 Fg ⁻¹ (2 mV s ⁻¹)	n.d.	57.9 % (2–1000 mV s ⁻¹)	[30]
Pulsed cathodic electrodeposition	NiOx/CNT electrode	1 M KOH	1701 (30 mV s ⁻¹)	n.d.	96.2 % (10–100 mV s ⁻¹)	[33]
Anodic electrodeposition	MnO ₂ nanowires on Ni foam	LiClO ₄ -OZO quasi-ionic liquid	350 Fg ⁻¹ (1.5 Ag ⁻¹)	96.1 % (1000 cycles)	n.d.	[35]
Cyclic electrodeposition	MnO ₂ onto carbon nanotube (CNT) paper	0.1 M Na ₂ SO ₄	167.5 Fg ⁻¹ (77 mA g ⁻¹)	88 % (3000 cycles)	64.4 % (77–770 mA g ⁻¹)	[36]
Anodic electrodeposition	MnO ₂ nanowires on hollow Ni dendrites	1 M Na ₂ SO ₄	1097 Fg ⁻¹ (12.5 Ag ⁻¹)	>90 % (>1000 cycles)	69.8 % (12.5–100 Ag ⁻¹)	[37]
Anodic deposition and electrochemical treatment	MnO ₂ nanofibril/ nanowire	1 M LiClO ₄ in water	377 Fg ⁻¹ (50 mV s ⁻¹)	82.5 % (1000 cycles)	87.3 % (50–250 mV s ⁻¹)	[38]
Anodic electrodeposition	MnO ₂ /nanoporous gold/MnO ₂	2 M Li ₂ SO ₄	841 Fg ⁻¹ (5 mV s ⁻¹)	97.1 % (3000 cycles)	60.6 % (5–100 mV s ⁻¹)	[39]
Cathodic electrodeposition and post-thermal annealing	MnO ₂ /Mn/MnO ₂ sandwich-like nanotube arrays	1 M Na ₂ SO ₄	937 Fg ⁻¹ (1.5 Ag ⁻¹)	98.5 % (3000 cycles)	70.4 % (1.5–24 Ag ⁻¹)	[40]

Anodic electrodeposition	Binary 80Mn–20Co oxides	2 M KCl	148 Fg ⁻¹ (2 mA cm ⁻²)	95 % (500 cycles)	n.d.	[41]
Anodic electrodeposition	Na _x MnO ₂ nanoflakes	1 M Na ₂ SO ₄	1237 Fg ⁻¹ (0.17 mA cm ⁻²)	99.9 % (1000 cycles)	<10 % (0.17–10 mA cm ⁻²)	[42]
Cathodic electrodeposition with post-thermal annealing	NiO nanoparticles/ Ni foam	1 M KOH	2558 Fg ⁻¹ (2 Ag ⁻¹)	74 % (1000 cycles)	70 % (2–40 Ag ⁻¹)	[43]
Cathodic electrodeposition	Co(OH) ₂ nanoflakes on Ni 3D nanofoam	2 M KOH	2028 Fg ⁻¹ (2 Ag ⁻¹)	94.7 % (2000 cycles)	94.6 % (2–40 Ag ⁻¹)	[44]
Cathodic electrodeposition	Ni–Cu nanofoam	1 M KOH	105 Fg ⁻¹ (1 mA · cm ⁻²)	90 % (10,000 cycles)	n.d.	[45]
Cyclic deposition	Manganese oxide nanoflower/carbon nanotube array	1 M Na ₂ SO ₄	199 Fg ⁻¹ (low current)	97 % (20,000 cycles)	50.8 % (low current to 77 Ag ⁻¹)	[46]
Cyclic electrodeposition	MnO _x /CNT sheet	0.1 M Na ₂ SO ₄	1250 Fg ⁻¹ (1 Ag ⁻¹)	95.5 % (500 cycles)	76.8 % (1–10 Ag ⁻¹)	[47]
Cyclic electrodeposition	V ₂ O ₅ /PAN nanofibers	2 M KCl	1308 Fg ⁻¹ (2 mV s ⁻¹)	80 % (1000 cycles)	<70 % (2–50 mV s ⁻¹)	[48]
Electrophoretic deposition	NiO-attached graphene oxide	0.5 M KOH	569 Fg ⁻¹ (5 Ag ⁻¹)	>80 % (3000 cycles)	59.5 % (5–30 Ag ⁻¹)	[49]
Drop casting	NiO nanoparticles/ graphene oxide	1 M KOH	890 Fg ⁻¹ (5 mV s ⁻¹)	n.d.	n.d.	[50]

Note: *n.d.* not determined in reference

electrodes, thereby improving its specific capacitance and rate capability. The previous work also reports the deposition of $\text{Mn}(\text{OH})_2$ nanofibrils in a second electrodeposition step, which also involves changes of the oxidation states of manganese. The core/shell nanowires/nanofibrils structure shows not only a significant improvement of the specific capacitance but also increased rate capability.

Electrodeposition of manganese oxide on the two sides of nanoporous gold substrates created a novel sandwich-like structure, which results in specific capacitances of about 916 Fg^{-1} with enhanced rate capability and increased stability under cycling; with 97.1 % of the maximum capacitance still observed after 3000 cycles. The high super capacitive performance of this type of electrode is consequence of the smart sandwich-designed structure, in which the nanoporous gold acting as support and current collector enhances both the electron/ion conductivity of the electroactive material and allows fast electrolyte transport through the open porous structure [39]. The combined sandwich/array structure has also been studied by Li et al. and once more [40] an enhanced capacitive performance was achieved.

Another promising alternative consists in doping of the MnO_2 structure with other metallic species via electrodeposition, providing a powerful alternative that in one single step allows at varying surface morphology and improving electronic conductivity and ionic diffusion through the bulk part of the electrode.

Hu et al. [52] reported an approach in which Mn–Ni oxides are anodically electrodeposited on graphite substrates. As the growing rate of manganese is faster than that of nickel, the authors used a an electrolyte with a $\text{Ni}^{2+}/\text{Mn}^{2+}$ ratio of 10, in order to get a high nickel content in the mixed oxide film. Results demonstrated an enhanced capacitive behavior in 0.1 M Na_2SO_4 with pH of 10.1 adjusted by NaOH compared with 0.1 M Na_2SO_4 . However, no comparison between pure manganese oxide electrodes and mixed electrode in the same electrolyte has been pointed out.

Potentiostatic anodic co-electrodeposition was used to prepare Mn–Co oxide films [53]. The co-deposition resulted in important changes of the surface morphology of the deposits. It was also determined that the rate capability was increased after doping with Co. The cycling stability of the doped electrode showed a great enhancement compared to the non-doped one. The incorporation of Co into the electrodeposited film contributes for a stable capacitance. On the other hand, a high content of Co (>10 at.%) reduces the surface area of the electrodes and so the specific capacitance. The authors further clarify chemical states of doped oxides, in which the doping Co species include Co_2O_3 , CoOOH , and $\text{Co}(\text{OH})_2$ [41]. The introduction of Co into the birnessite framework of manganese oxide, by electrodeposition, at temperatures of 70 °C resulted in better performance, higher specific capacitance, and enhanced rate capability when compared to non-doped ones [54]. Co doped manganese oxide nanorods were prepared by the template-free electrodeposition [55]. Cobalt addition led to a reduction of the specific density by approx. 11 % by an increase in ion transport ability and capacitance. The performance was further improved by coating the electrode with PEDOT shells.

Surfactants (SDS, CTAB) have also been used to assist the cathodic electrodeposition of MnO_2 and doping with silver. This approach resulted in deposited films with highly porous morphology [56]. The use of surfactants promotes the formation of foam-type and dendrite-like morphologies, which facilitate the ion transport. Moreover, doping with Ag increases the electron conductivity, thereby enhancing the performance of supercapacitors. Ag-doped MnO_2 has also been prepared by cathodic electrodeposition from electrolytes containing KMnO_4 with AgNO_3 [57]. These films showed a specific capacitance of 770 Fg^{-1} at a scan rate of 2 mVs^{-1} in $0.5 \text{ M Na}_2\text{SO}_4$. Through electrochemical impedance spectroscopy, the authors proved that doping with Ag reduces charge-transfer resistance. Although Ag is not an active material, it lowers the resistance of the electrode, hence improving its capacitive behavior.

Recently, electrodeposition combined with physical vapor deposition has been proposed for non-equilibrium-free electron metal doping of atomic gold in the structure of manganese oxide [58]. The Au dopant has a strong atomic interaction with the MnO_2 host and improves hydration of the electrode. Density functional theory calculations showed that Au doping creates localized states in the MnO_2 bandgap, enhancing electron conductivity. The specific capacitance increases with Au content doping, reaches the highest value at 9.9 at.% of Au, and then decreases with further Au additions. Moreover, doping shows a great capacitive stability with an enhancement of 7 % over 15,000 cycles, while the capacitance of pure MnO_2 decreased by 34 % over the same cycle number. However, the use of gold as dopant increases the cost of the supercapacitors. Therefore, other highly conductive metals can be utilized as a dopant. Besides, pulse-reversed electrodeposition can be employed as simply one-step approaches for preparing doped electrodes, further reducing the cost of the electrodes.

Atomic doping leads to a significant increase in capacitive performance of manganese oxide electrodes because it increases electronic conductivity. However, not only electron conductivity plays a crucial role in enhancing pseudocapacitive performance of manganese oxide electrodes, but also ion diffusion of electrolyte into the bulk of the active material is a key factor. Many efforts have been made to reduce bulk-ion diffusion path via nanosizing and micro-/nanodesigning as discussed above, but the problem is basically unsolved. Sodium can be incorporated within manganese oxide layer structure via conventional anodic electrodeposition by simply changing the concentration ratio of sodium sulfate buffer with a metal salt precursor ($\text{Na}^+:\text{Mn}^{2+} = 100:1$), resulting in an electrode with remarkably accelerated ion diffusion and thereby greatly enhanced capacitive performance and excellent cycling performance (99.9 % of initial capacitance after 1000 cycles) [42]. During electrodeposition, high amounts of Na^+ intercalate into the MnO_2 interlayers. Interestingly, a redox reaction of manganese oxide with sodium sulfate (Na_2SO_4), which is usually not evidenced as a peak in the cyclic voltammetry curve of manganese electrodes in Na_2SO_4 electrolyte, has also been observed, proving the redox mechanism and its contribution for the resulting capacitance.

Recently we have prepared nickel-doped manganese oxide electrodes by electrodeposition in the cathodic region and oxidation by potential cycling. The scanning

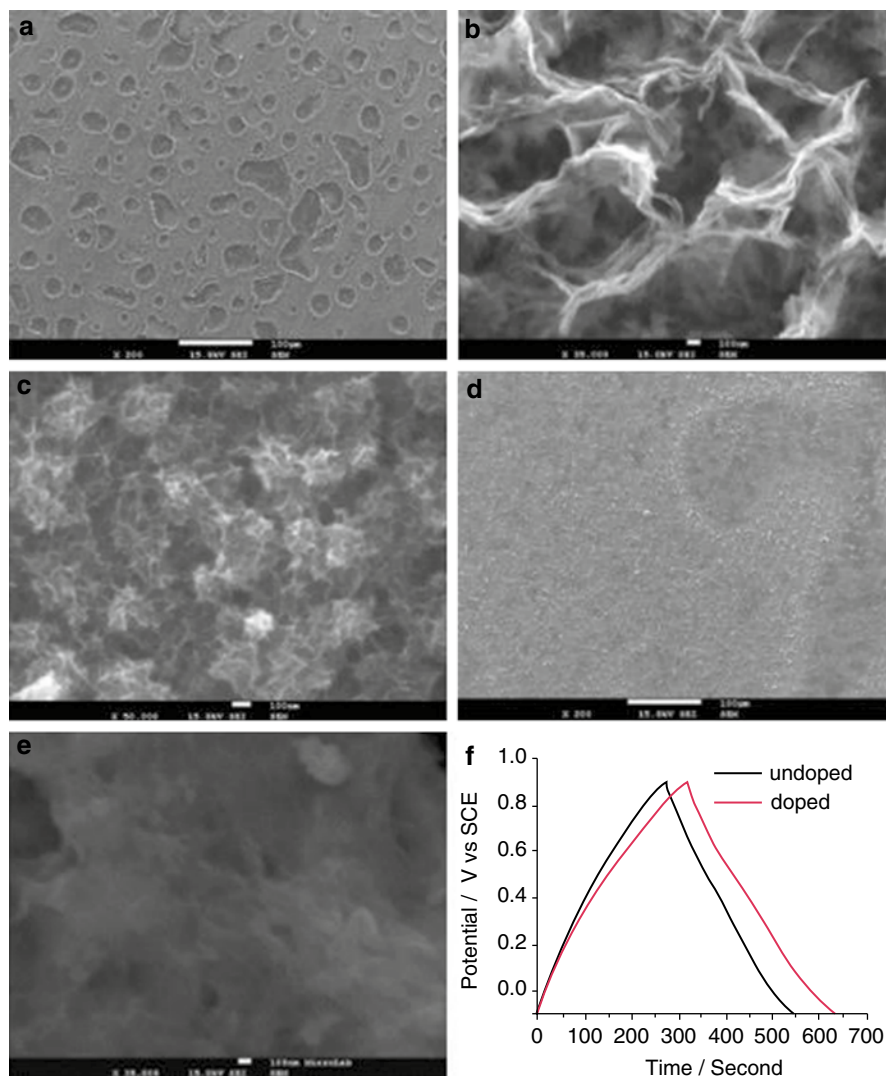


Fig. 1 SEM images of low-doped (a–c), high-doped electrode (d, e) with different magnifications and charge/discharge curve of doped and undoped electrode (f)

electron microscope (SEM) micrographs with low magnification (Fig. 1a) show that low-doped electrode presents a microporous structure with a lot of micro holes. Higher-magnification images (Fig. 1b, c) reveal a flake-like structure (Fig. 1b) formed outside the holes and a wirelike structure inside the holes (Fig. 1c). This type of structure may facilitate ion transport into the electrode.

The low-Ni-doped manganese oxide electrode shows an increase in specific capacitance in 1 M Na_2SO_4 solution when compared to the undoped electrode (Fig. 1f).

This difference arises from the enhanced electron conductivity owing to the contribution of Ni. Electrodes with a higher dopant content present a smooth surface (Fig. 1d, e), which leads to a decrease in the electrode specific capacitance due to its lower surface area.

The most recent developments in doped manganese oxide for supercapacitors evidence that doping via electrodeposition provides a facile and cheap way to control, optimize, and shape surface morphology, electronic conductivity, and ionic diffusion of manganese oxide electrodes for supercapacitors. Results show that doped manganese electrodes not only have high specific capacitance, being a possible electrode for supercapacitors. Still, there are several approaches to be investigated regarding the species to be used as dopants, such as its long-term stability. Further studies in this direction will result in new promising electrodes for supercapacitors.

Metallic Foams

Nanoporous metallic foams (NMFs) have been considered in the search for very high surface area conductive materials. NMFs are of particular interest for applications such as catalysis, sensors, and electrodes for energy storage devices [59], inviting a wide array of innovative technological solutions. NMFs are 3D structures of interconnected pores with nanoramified walls formed of metallic particles, filaments, or other morphologies. These materials usually exhibit porosities above 50 % and a wide pore size distribution that contributes to its specific surface area. They display properties characteristic of metals, such as good electric and thermal conductivities and excellent ductility and malleability with the extreme properties that are characteristic of more advanced nanoarchitectures, like aerogels, which include increased surface area and decreased density, making NMFs a topmost choice for porous electrodes for today's SC.

Metallic foams can be tailored to optimize the wetting properties while simultaneously providing faradaic capacitance if composed of multivalent transition metal species [59]. For example, nickel foams, which have a very high theoretical capacitance, can be used as the positive electrode in supercapacitors, being one of few materials that can display high theoretical specific capacitances. NiO–Ni foam electrodes evidence specific capacitance of approximately 2558 Fg^{-1} , enhanced rate capability, energy density of 90 Wh kg^{-1} , and power density of 10 kW kg^{-1} with slow and fast charge/discharge rates, respectively [43].

Common methods for the fabrication of highly porous networks are dealloying of metal alloys, where one of the metals is preferentially removed, and hard-template processes, where metal is deposited in the free spaces of the template followed by the template removal (chemical dissolution or burning) [59]. In addition to these methods, electrodeposition provides a one-step, low-cost method for the fabrication of NMFs by taking advantage of the dynamic template formed by hydrogen bubbling that often occurs simultaneously to metal deposition. In this way, self-supported nanoramified foam structures with properly tailored architectures can be

designed, enhancing mass and charge-transfer processes. Furthermore, electrodeposited NMFs are typically formed on metallic substrates of high electronic conductivity, which constitutes an advantage for fabrication of SC electrodes since the active material is directly applied on the current collector.

Hydrogen evolution is an intrinsic phenomenon in electrodeposition from aqueous solutions, in particular during deposition of transition metals. Application of sufficiently negative potentials results in hydrogen gas bubble formation and release from the substrate and/or incorporation of hydrogen in the deposit and/or the substrate (hydrogenation). This is considered detrimental for the fabrication of dense deposits because it decreases of current efficiency of the process and may lead, for example, to hydrogen embrittlement, cracking, and blistering, which insert defects and deteriorate the mechanical properties and surface quality of the deposited film [60]. However, Shin et al. [61, 62] showed that simultaneous metal electrodeposition and hydrogen evolution was a simple method for the production of high porous metallic foams, where hydrogen bubbles act as a negative dynamic template. The earlier papers on this subject concerned copper and tin metallic foams [61, 62], and a thorough study of the phenomenology of copper NMFs was carried out in a series of papers by Nikolic et al. [63–65]. NMFs are deposited from highly acidic electrolytes containing a salt of the metal to be deposited, in a current (or potential) range for which hydrogen evolution occurs, usually between 1 and 3 Acm^{-2} during short times (20–180 s) [63, 61, 62].

The morphology of electrodeposited NMFs is closely related to the nucleation and evolution of hydrogen bubbles that occurs simultaneously with nucleation and growth of the metal during deposition. In the early stages of the deposition process, both hydrogen bubbles and metal nuclei are formed at active sites at the electrode surface. The active sites shielded by hydrogen bubbles will be isolated, preventing the deposition of metal in those sites and concentrating the current lines around them and on the formed metal nuclei. Hence, metal growth will proceed in interstices between the hydrogen bubbles and at metal nuclei, forming metal agglomerates. As deposition proceeds, both hydrogen bubbles and metal nucleation will preferentially occur at the top of such metal agglomerates. Furthermore, the diffusion of metal ions to the electrode will be disrupted by continuous gas evolution and metal growth forced to occur between the gas bubbles (assuming that the metal growth is diffusion controlled). In this way, hydrogen bubbles act as a negative dynamic template around which metal grows, thus forming a foam structure with a pore network throughout the deposited film. A simplified scheme of this process is shown in Fig. 2.

Deposition parameters and electrolyte composition also have a significant influence on the morphology of electrodeposited NMFs [66]. In the case of copper foams, parameters that increase hydrogen evolution such as increasing the overpotential, decreasing the Cu(II) concentration, and increasing the concentration of H_2SO_4 in solution will decrease the pore size and increase pore density. Porosity can also be controlled by additives in the electrolyte that suppress the coalescence of the bubbles or have catalytic effect on the Cu deposition (such as Cl^- ions) leading to a decrease the size of the branches that are observed in the foam wall [67].

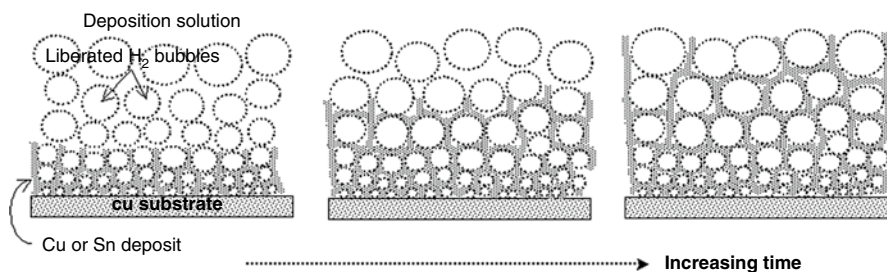


Fig. 2 Simplified scheme of the formation of NMFs using the hydrogen bubble template (Reprinted with permission from Ref. [61], Copyright 2013 Wiley and Sons)

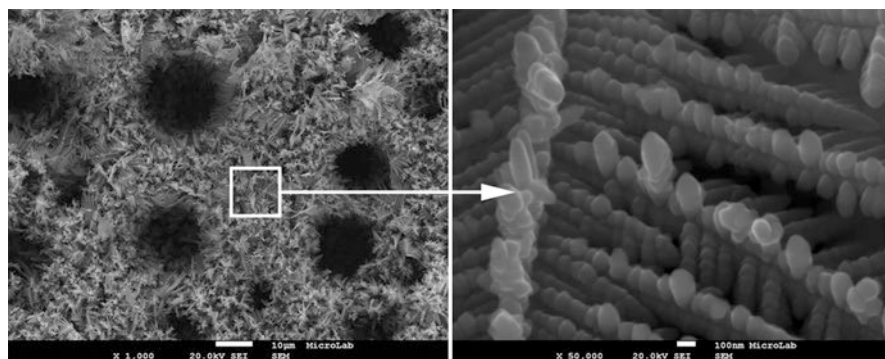


Fig. 3 SEM images of Ni–Cu foams deposited at 1.8 A cm^{-2} for 90 s (Reprinted with permission from Ref. [45], Copyright 2013 Springer)

As stated previously, copper NMFs have been the most studied materials [65, 61], but NMFs of tin [61], silver [68], palladium [69], and gold [70] have also been fabricated by electrodeposition using the dynamic hydrogen template method. On the other hand, few papers have discussed the fabrication of NMFs containing transition metals such as nickel and cobalt, which have an increased importance as low-cost alternatives to noble metals for high reactive surface applications. Choi et al. [71] reported the fabrication of nickel NMFs by electrodeposition of nickel–copper NMFs on copper-coated alumina and subsequent electrochemical etching of copper. As for pure copper foams, the deposits show a foamlike structure with nanoramified walls.

In our recent work [45], we have studied the influence of the deposition parameters on nanoporous Ni–Cu foams electrodeposited using hydrogen bubble template on stainless steel substrates and evaluated their application as electrodes for SCs.

Typical Ni–Cu NMFs (Fig. 3) present an array of randomly distributed nearly circular pores whose walls are a network of interconnected dendrites. The variation of the Ni–Cu NMF morphology with the deposition time is presented in Fig. 4. For a deposition time of 30 s (Fig. 4a), intertwined dendrites are formed around circular areas of the substrate, where a film formed of angular grains is visible.

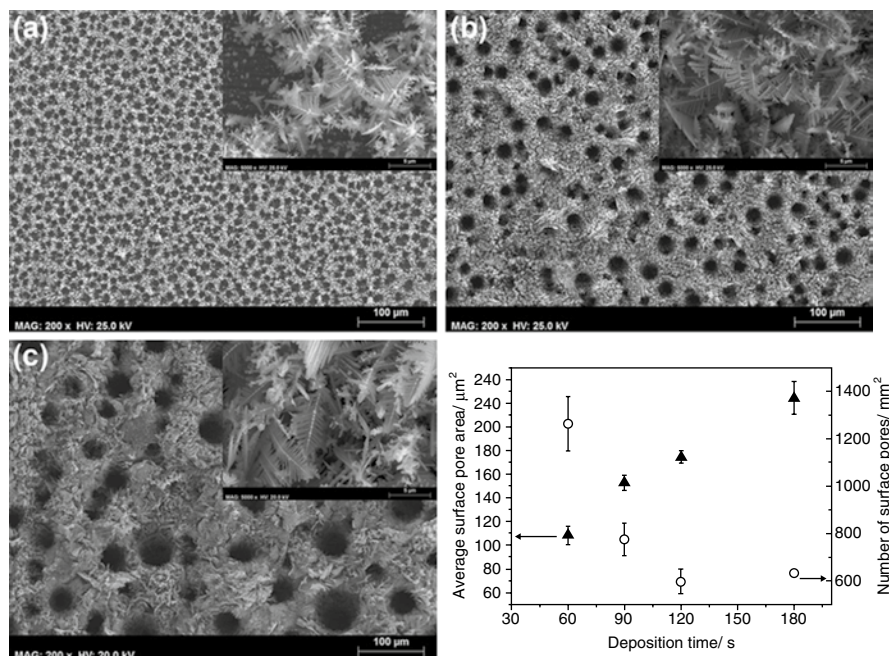


Fig. 4 SEM images of Ni–Cu foams deposited at 1.8 A cm^{-2} for with different deposition times (a) 30, (b) 90, and (c) 180 s. Images insets show higher magnifications (Reprinted with permission from Ref. [45], Copyright 2013 Springer)

As deposition time increases (Fig. 4b, c), a three-dimensional foam-type film is formed. The dendrites that form the pore walls do not present any preferential growth direction (in relation to the substrate), being randomly oriented. As deposition time increases, dendrites assume a fernlike structure with secondary and tertiary branching (inset of Fig. 4c). The surface pore size in the Ni–Cu foams increases with the deposition time, and at the same time, the density of surface pores decreases (Fig. 4d). This variation is in accordance with published works on Ni–Cu foams electrodeposited on an alumina substrate [71]. The average surface pore area varies between $108 \mu\text{m}^2$ in Ni–Cu foams deposited at 30 s and $225 \mu\text{m}^2$ for a deposition time of 180 s. If we consider that the surface pores are nearly circular, these values correspond to pore diameters between 12 and $17 \mu\text{m}$. As can be seen in Figs. 3 and 4, the surface area of Ni–Cu NMFs is enhanced not only by the surface pores but also by the empty spaces in the non-compact dendritic pore walls.

As expected the main elements detected in electrodeposited Ni–Cu foams, as determined by EDS, were nickel and copper. However, and in accordance with the literature [71], the copper content in the NMFs is much higher than that in the deposition electrolyte. In solution, copper represents only 2 at.% of the metallic ions in solution (the other 98 at.% are Ni), but it reaches up to approximately 40 at.% in metallic foams deposited for 180 s. This can be explained by the large difference between the reduction potentials of copper and nickel (about 0.6 V) so that Cu,

being the most noble metal, will deposit preferentially to Ni and the ratio of Cu in the foam will be higher than in solution. Accordingly, this process can be classified as preferential deposition as defined by Brenner [72]. This is actually the reason why most studies on the deposition of Ni–Cu alloys are performed on solutions containing complexing agents such as citrate, pyrophosphate, and not simple metal solutions [72].

X-ray diffractograms of Ni–Cu NMFs depict well-defined diffraction peaks (Fig. 5) indicating a crystalline nature. Nickel and copper have a full mutual solubility, and it is well known that Ni–Cu alloys form solid solutions with face-centered cubic (fcc) structure. The peaks at approximately 44.6° , 51.9° , and 76.5° are nearly coincident with fcc nickel (ICDD 00-04-0850) and present a slight shift to higher two theta angles. The peaks at 43.7° , 50.8° , and 74.7° are closer to the position of fcc copper (ICDD 01-070-3039), presenting a shift to higher 2 theta angles. These results indicate the formation of inhomogeneous alloys that contain segregated copper-rich and nickel-rich phases, a common effect in electrodeposited nickel–copper alloys [73].

The average lattice parameter (a) values calculated for the Ni-phase are actually the same as for fcc nickel ($a=3.5239$ Å, ICDD 00-04-0850) which indicates the presence of a pure nickel phase. The average a values calculated for the copper phase are lower than fcc copper ($a=3.6148$ Å, ICDD 01-070-3039) suggesting the presence of Ni in solid solution. It is also important to refer that no pure copper phase was detected in the diffractograms and that, although the copper content in

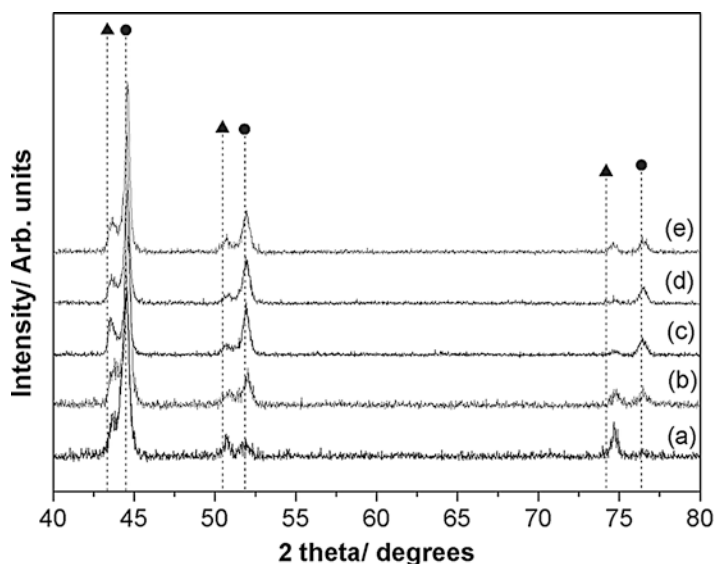


Fig. 5 X-ray diffractograms of Ni–Cu foams deposited at 1.8 A cm^{-2} for (a) 30, (b) 60, (c) 90, (d) 120, and (e) 180 s. Vertical lines represent diffraction peaks position for Cu (▲, ICDD 01–070–3039) and nickel (●, ICDD 00–04–0850) (Reprinted with permission from Ref. [45], Copyright 2013 Springer)

the films increases with the deposition time, the lattice parameters of its crystalline phases do not change significantly, indicating that the phases is the same, independently of deposition time.

The electrochemical behavior of Ni–Cu foams was evaluated in 1 M KOH solution by cyclic voltammetry and chronopotentiometry (galvanostatic charge/discharge) after potential cycling activation. The specific capacitance of the Ni–Cu foams was determined from chronoamperometry data. Figure 6 shows representative cyclic voltammograms of Ni–Cu foams. It is clearly seen that the shape of the voltammograms is distinct from those of materials exhibiting an electric double layer capacitance, which induces nearly rectangular curves [1]. In this case, voltammograms of Ni–Cu foams have a couple redox peaks in the potential window between -0.2 V and $+0.8$ V. The anodic peak can be assigned to the oxidation of $\text{Ni}(\text{OH})_2$ to a higher valence of oxyhydroxide (NiOOH). On the other hand, the cathodic peak can be assigned to the corresponding reduction reaction, following Eq. 2 [74].

Although the Ni–Cu foams have not suffered any oxidation pretreatment, their voltammetric response is in accordance with the reports in the literature for Ni oxides in alkaline solutions [75], suggesting that the Ni–Cu foam is oxidized upon its immersion on the KOH solution and potential cycling. It should also be noted

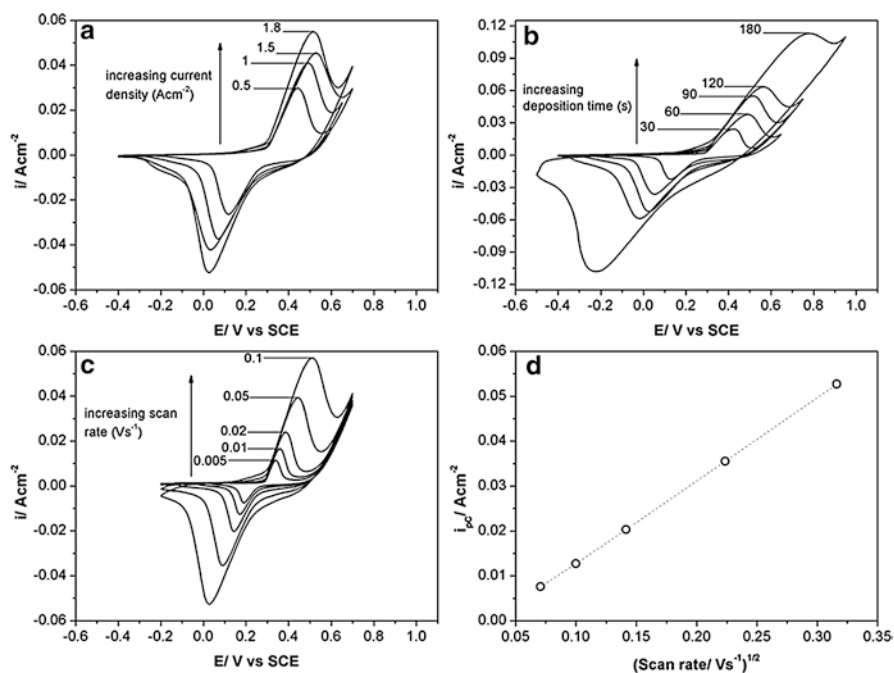


Fig. 6 Cyclic voltammograms of 1 M KOH solution on Ni–Cu foams (a) deposited during 90 s at different current densities (scan rate 100 mVs^{-1}) (b) deposited at 1.8 A cm^{-2} with different deposition times (scan rate 100 mVs^{-1}) and (c) deposited at 1.8 A cm^{-2} for 90 s with increasing scan rates (Reprinted with permission from Ref. [45], Copyright 2013 Springer)

that, in this potential range, copper undergoes a redox reaction Cu(II)/Cu(III) involving CuO surface species [76]. However, no peaks in the voltammograms could be attributed to these reactions, which can be explained by the fact that in Ni–Cu alloys copper oxidation reactions are hindered due to the formation of a protective nickel hydroxide film [77, 78].

The increase in applied current density and deposition time both lead to an increase in the current density and charge measured by cyclic voltammetry (Fig. 6a, b) having therefore a beneficial effect on the electrochemical activity of the films.

The influence of the potential scan rate on the voltammetric response of Ni–Cu foam deposited at 1.8 A cm^{-2} for 90 s is presented in Fig. 6c. The cathodic current density of the cathodic wave (i_{pC}) varies linearly with the square root of the scan rate (Fig. 6d), indicating that the redox reaction is diffusion controlled. On the other hand, the potentials corresponding to the anodic peak and cathodic peak are not independent of the scan rate (Fig. 6d), and peak separation is larger than that typically found for reversible reactions (0.059 V at 298 K) [79]. This indicates that the redox reaction is not completely reversible.

The galvanostatic charge/discharge curves of Ni–Cu NMFs are presented in Fig. 7. As expected, the curves are not triangular in shape and present charge and discharge plateaus resulting from the redox reactions occurring in this potential range. This confirms the pseudocapacitance behavior of the Ni–Cu in agreement with the cyclic voltammetry results. The specific capacitance of the Ni–Cu foams was calculated from charge/discharge data. Ni–Cu foams deposited for 180 s presented the highest specific capacitance value, 105 Fg^{-1} at 1 mA cm^{-2} maintaining 75 % of capacitance the charge/discharge rate changes from 1 to 10 mA cm^{-2} . These capacitance values are lower than those reported in the literature for Ni oxide materials [32]. This can be explained by the fact that the Ni–Cu NMFs have not suffered any oxidation treatment prior to testing so that the active material (Ni oxides/hydroxides) is formed only as a superficial layer, accounting for a small fraction of the deposited mass, for which the specific capacitance was calculated.

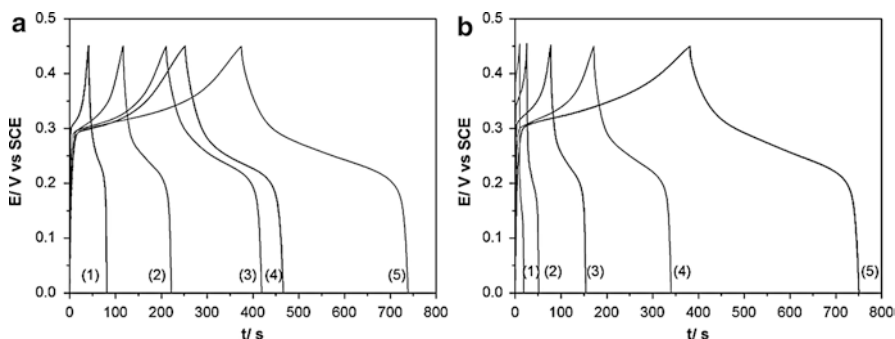


Fig. 7 Galvanostatic charge/discharge curves of Ni–Cu foam deposited at 1.8 A cm^{-2} (a) for (1) 30, (2) 60, (3) 90, (4) 120 and (5) 180 s at 1 mA cm^{-2} and (b) for 180 s at different current densities (1) 20, (2) 10, (3) 4, (4) 2 and (5) 1 mA cm^{-2} (Reprinted with permission from Ref. [45], Copyright 2013 Springer)

Fabrication of 3D Hyperbranched Dendritic Structures

3D branched dendritic structures have been used for various applications for the fabrication of electrode supercapacitors. These powders can be fabricated by wet chemical routes or by electrodeposition.

The Ni–Co powders, electrodeposited from electrolytes containing ammonium sulfate [80] and ammonium sulfate–boric acid [81], reveal a dependence of the morphology on the Ni to Co concentration and on the applied current. A composite 3D structure, showing improved performance, was obtained by a two-step process [44], the first step being associated with a nano-Ni film deposition and the second one related with $\text{Co}(\text{OH})_2$ flake deposition. However, in this work, due to the high cathodic current densities used to obtain such porous dendritic film (-0.4 A cm^{-2}), the deposition efficiency is low, about 30 %, which was attributed to simultaneous and intense hydrogen evolution.

The electrodeposition of Ni–Co alloys, in the cathodic domain, on stainless steel current collectors is a very interesting way to fabricate dendritic structures of high porosity and surface area. However, the process reveals a typical anomalous behavior as reported in literature, cobalt, the more active metal, being preferentially deposited [72]. Moreover, it has been reported that this anomalous behavior changes into normal at critical transition current. This fact can be explained by the diffusion-controlled kinetics that is established at high cathodic current densities, leading to the depletion of Co ions in the cathode diffusion layer.

Scarce literature can be found regarding fabrication of dendritic structures by electrodeposition for supercapacitor applications. A recent work reports the preparation of porous hydrous ruthenium oxides via electrodeposition. The 3D porous hydrous ruthenium oxide exhibits capacitances of 809 Fg^{-1} at 1.5 Ag^{-1} , high energy density (112 Wh kg^{-1}), and excellent capacitance retention under continuous charge/discharge cycling [82].

Very recently we proposed an approach for the fabrication of Ni–Co dendritic structures, targeted for supercapacitor electrodes [83]. One of the major advantages of this method is the fact that the films are self-supported on the current collector and the anomalous deposition behavior has been overcome by controlling the cathodic deposition current, using a pulsed route as described elsewhere [83]. When the more negative applied current varies between -20 and -50 mA cm^{-2} , the atomic Ni–Co ratio in the dendritic layer becomes identical to that of the electrolyte, which accounts for a normal electrodeposition behavior. Consequentially, when a sufficiently negative current density is applied ($< -20 \text{ mA.cm}^{-2}$), the cobalt content in the film decreases.

The SEM images depicted in Fig. 8 show the morphology of various Ni–Co films deposited at different cathodic current densities in the lower plateau of the applied pulse. As it can be seen, the morphology of the electrodeposited films is very dependent on the more negative current densities of the applied pulse, pointing to different growth type regimes. In fact, for values less negative than -15 mA cm^{-2} , (Fig. 8a, b), the electrodeposited Ni–Co films are quite smooth, displaying homogeneous micrometric grains, which grow with decreasing current densities of the lower pulse. For currents lower than -15 mA cm^{-2} , a 3D dendritic morphology is already

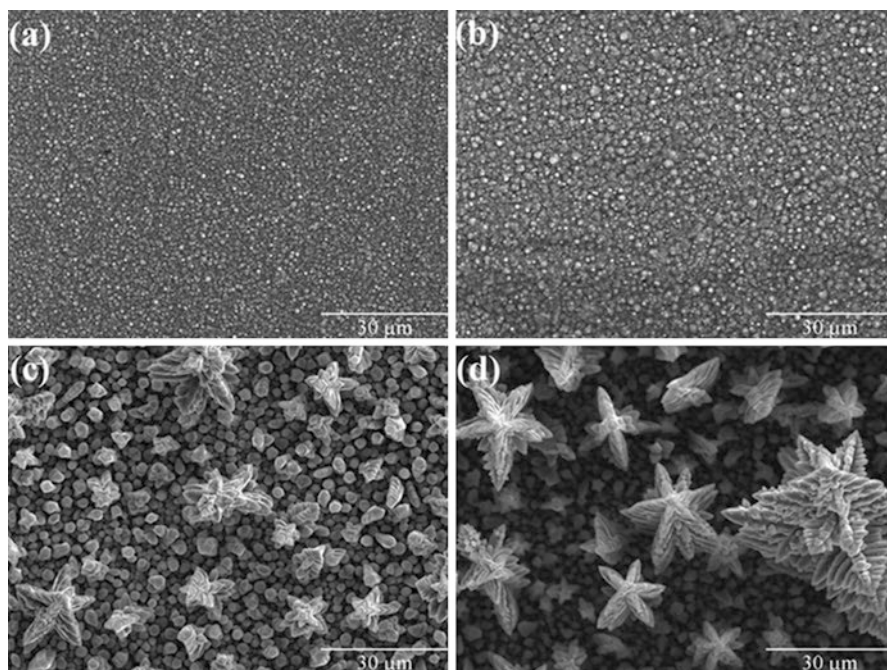


Fig. 8 SEM images of Ni–Co films formed by electrodeposition under various current densities of the lower pulse limit: -5 (a), -10 (b), -15 (c), and -20 mA cm $^{-2}$ (d) (Reprinted with permission from Ref. [83], Copyright 2012 American Chemical Society)

evident (Fig. 8c). This structure further develops as the applied current becomes more negative (Fig. 8d), starting to show longitudinal and transversal growth. This leads to the development of secondary branching, each dendrite being constituted by several hierarchical assemblies, which expand from a central pillar. At the end the structure is characterized by several interconnected secondary branches with different widths and lengths.

The films deposited in the most negative current density range (-30 and -45 mA cm $^{-2}$, Fig. 9) present larger dendrites evidencing more branches. A more heterogeneous morphology is observed probably because the existing structure cannot support the new branches and mechanically fractures. Moreover, circular spots are formed corresponding to H $_2$ evolution sites (see marked areas in Fig. 9b–d).

The cross section of the Ni–Co films deposited using a current density in the lower limit pulse of -20 mA cm $^{-2}$ shows the presence of an inner compact layer, with a thickness between 1 and 2 μ m (Fig. 10a). The 3D dendrites grow over this compact layer. It is possible to observe various morphologies:

- (i) Smaller dendrites (~ 2 – 3 μ m height) without additional branches
- (ii) 15 μ m high dendrites showing primary sets of branches (Fig. 10b)
- (iii) Completely formed dendrites with well-developed secondary branches growing up to 100 μ m

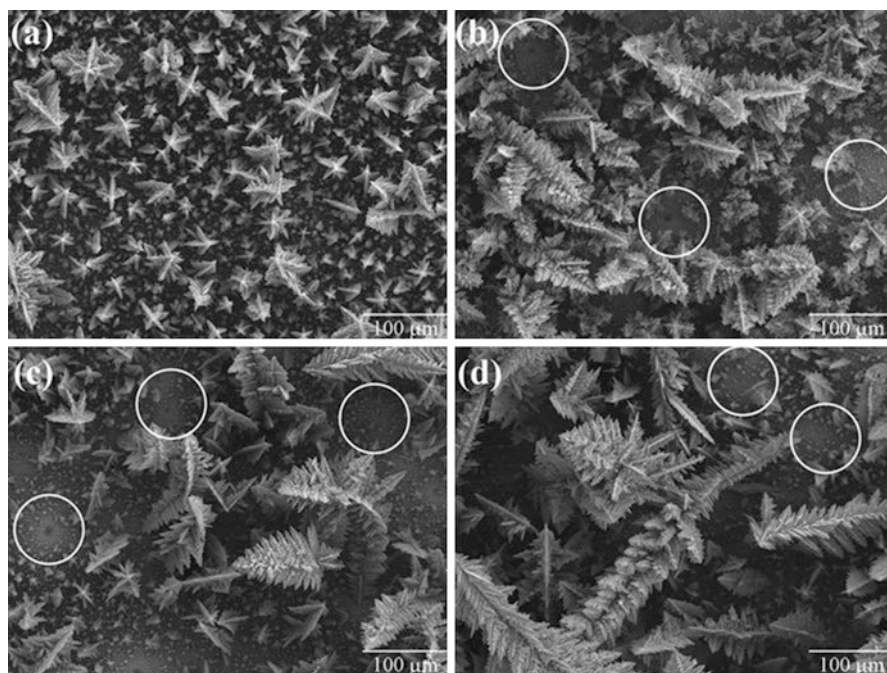


Fig. 9 SEM images of Ni-Co films formed under various current densities in the lower pulse limit: -25 (a), -30 (b), -35 (c), and -40 mA cm^{-2} (d) (Reprinted with permission from Ref. [83]. Copyright 2012 American Chemical Society)

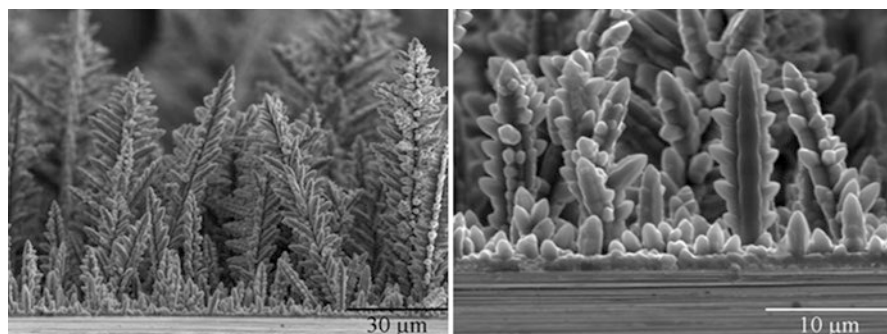


Fig. 10 Cross-sectional SEM images of Ni-Co film formed at lower pulse limit of -20 mA cm^{-2} (Reprinted with permission from Ref. [83], Copyright 2012 American Chemical Society)

This 3D dendritic morphology can be associated with distinct development stages. Previous work [84] reports that the interfacial compact structure, from where the dendritic structure evolves, is likely to be grown in the more positive plateau of the applied pulse.

The results of our previous work [85] highlight that the development of the 3D dendritic structures occurs at the same critical current density at which the change

from anomalous to normal electrodeposition occurs. These findings show that when the more negative current density is sufficient to guarantee that diffusional control is established, Ni and Co deposition will be proportional to their concentrations in the electrolyte, providing that both elements present similar diffusion coefficients and diffusion layer thicknesses [85].

The electrochemical behavior of 3D dendritic films deposited applying the pulse route described above with -20 mA cm^{-2} for the lower current plateau, from electrolytes containing different Ni–Co cation ratios, was studied by cyclic voltammetry in 1 M KOH. Comparing the voltammograms obtained for the electrodeposited films and for pure Ni and Co metals (Fig. 11), some important conclusions can be depicted:

- (i) The main anodic and cathodic peaks are broader compared to the peaks observed for the metallic electrodes. This behavior suggests that there are overlapped responses from cobalt and nickel present in the electrodeposited film, as addressed somewhere [86]. Moreover, the full width at half maximum of these redox waves is superior, implying a deconvolution in two peaks. Those can be associated with the redox couples Co(II)/Co(III) and Ni(II)/Ni(III), respectively, at +0.28 V and +0.37 V; this is further supported by the fact that the film presenting higher Co content shows wider redox waves. This behavior leads to a larger potential window that is highly beneficial for enhanced supercapacitor performance.
- (ii) The associated charge storage capacity (which can be evaluated by the area under the voltammograms) is much higher in the case of Ni–Co-electrodeposited films. This should be related with the contribution of both Ni and Co centers to the overall charge storage process which, as referred above, leads to an increase in the potential window where the materials are electroactive and also with the higher surface area that dendritic morphologies allow. In fact, this kind of structure enhances the contact of the electrolyte with an increased number of active sites through the 3D porous network.

Fig. 11 Voltammograms obtained for films formed in electrolytes containing different Ni–Co ratios at an imposed current density of -20 mA cm^{-2} in the lower pulse limit

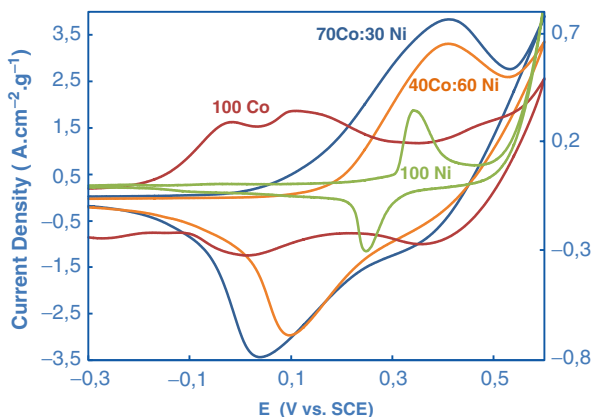
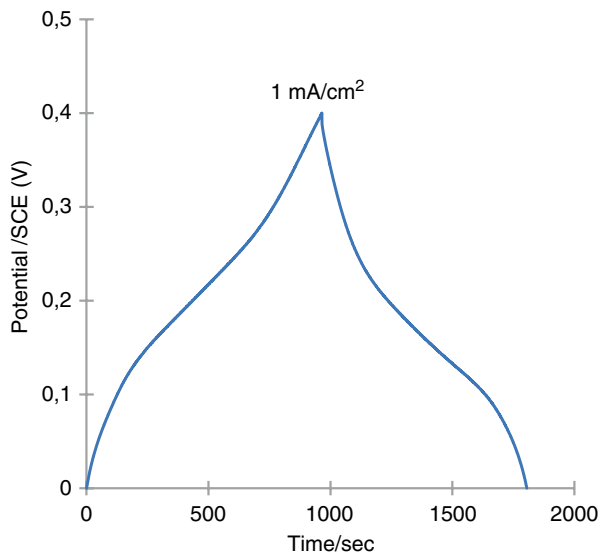


Fig. 12 Charge/discharge curve of an electrode made of 3D branched dendritic tested in 1 M KOH



The optimization of the electrodeposition parameters (applied current densities, metallic cation ratio in the electrolyte, pH and additives) led to the fabrication of structures with optimized response, displaying specific capacities between 500 and 600 Fg^{-1} as determined from consecutive charge/discharge curves (Fig. 12).

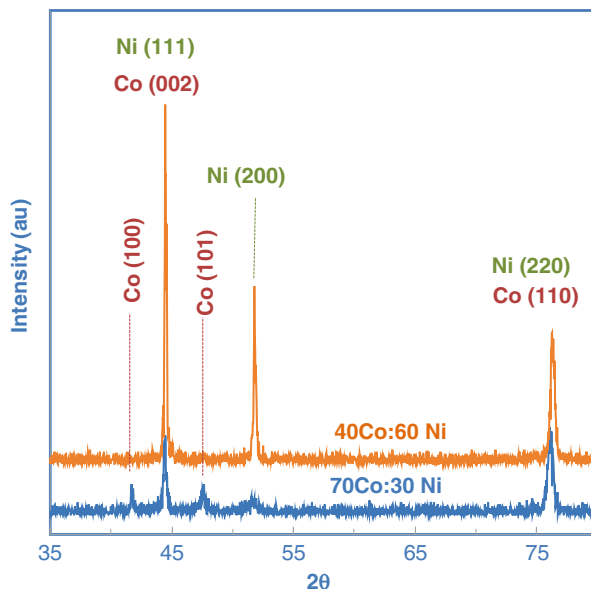
The XRD patterns of films with Ni–Co ratio composition similar to those from electrolytes (70Co:30Ni and 40Co:60Ni) are depicted in Fig. 13.

In the picture three peaks at 44.5° , 51.8° , and 76.4° can be identified, corresponding, respectively, to the (111), (200), and (220) planes of Ni face-centered cubic (fcc) crystallographic structure. The formation of a single phase is expected due to the total solubility of nickel and cobalt at this concentration. However, the diffractogram of films with 70Co:30Ni shows additional diffraction peaks associated with the cobalt hexagonal compact phase (hcp). This result points out that with increasing cobalt concentration, the crystal structure changes from fcc to hcp, in accordance with Ni–Co phase diagram.

Fabrication of Composites Carbon and Metal Oxides

In an attempt to combine the double layer charge storage mechanism of carbon and the faradaic contribution of metallic oxides, there has been an intense research work towards the electrodeposition of metals on carbon substrates. These include mesoporous carbon, carbon nanotubes, fullerene, carbon aerogels, graphene and graphene oxide nanosheets, carbon fibers, and carbon clothes. There are several methods to prepare these composites of metallic oxides and carbon materials. These

Fig. 13 XRD patterns of films formed on electrolytes containing different Ni–Co ratios



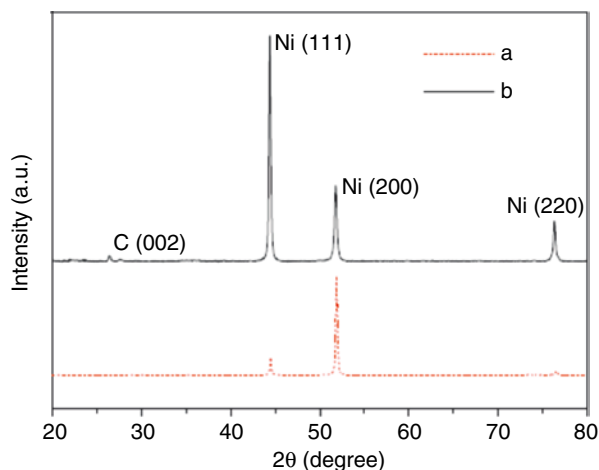
include chemical routes, carbonization, chemical vapor deposition (CVD), photolithography, and others. Interesting combinations have been reported such as the use of carbon nanotubes (CNTs) on which MnO_2 nanoflakes of high surface area are used as spacers in graphene nanosheets (GNs). These are further used to coat flexible substrates of carbon cloth. The incorporation of $\alpha\text{-MnO}_2$ /CNTs over GNs promotes electrolyte–electrode accessibility and improves the conductivity of the electrode through decreasing GNs agglomeration [28].

Another interesting approach relies on the electrodeposition of graphene oxide (GO) and its reduction to graphene at the working electrode. This occurs through two distinct steps: migration of GO sheets towards the electrode followed by their reduction [87].

Composites of Ni/graphene were formed by electrochemical reduction of GO sheets and Ni cations. Analysis by Raman and EDS clearly demonstrated the presence of reduced graphene oxide, a process that occurs during the electrodeposition process (Fig. 14). In this picture a peak appearing at 2θ degrees of 26.32° can be observed. This peak can be associated with the (002) plane of reduced graphene with a lattice fringe of 0.34 nm [88].

Composites of various metal oxides, such as SnO_2 , RuO_2 , and MnO_2 , chemically anchored on graphene oxide and carbon substrates display energy densities that can attain 50 Whkg^{-1} . Compared to single graphene electrodes, the improved properties were attributed to (i) increased specific area of the produced Ni/graphene composite, induced by a spacer effect of nano-metal oxides, and (ii) graphene electrochemical double layer that is the major contribution to the overall capacitance, the metal oxide nanoparticles' pseudocapacitive response being negligible [89].

Fig. 14 XRD patterns of (a) Ni coating, (b) Ni/graphene composite (Reprinted from Ref. [88], Copyright 2013, with permission from Elsevier)



The fabrication of graphene (and graphene oxide) and metal composites was extensively reviewed by Huang et al. [90]. Among the possible methods used to combine these classes of materials, there has been very little focus on electrodeposition. However, this can be one of the most suitable and non-expensive techniques to fabricate these composites.

Zhang et al. reported the fabrication of composites made of MnO_2 nanoflowers and carbon nanotube array (CNTA) electrodes by electrodeposition on vertically aligned CNTA framework [46]. These binder-free electrodes exhibited good rate capability and good specific capacitance. An identical approach was used to fabricate MnO nanoflowers on carbon nanotubes displaying capacitances above 500 Fg^{-1} [8]. Other oxides, such as V_2O_5 , were also successfully deposited on carbon substrates, achieving specific capacities as high as 1300 Fg^{-1} [48] in a 2 M KCl electrolytes.

Electrodeposition of Ni porous oxides and NiO_x particles was done on GO with improved conductive properties [49].

Kim et al. proposed the co-electrodeposition of graphene oxide treated with poly(ethyleneimine) and Co^{2+} ions from nitrate solutions in a one-step route. The electrochemical activity of the produced composite, used as anode, was improved comparatively to that of single materials [8]. Three-dimensional nickel oxide nanoparticles can be synthesized on the surface graphene oxide deposited on glassy carbon by electrochemical routes. The composite (NiONPs/GO/GC) electrode exhibited high electrochemical capacitance. It is reported that the graphene oxide has a major role in the growth of the 3D – NiONPs, creating a synergistic effect [50].

Du et al. reports the formation of 3D vertical structure of aligned carbon nanotube and graphene. These architectures are formed by intercalating carbon nanotubes into well-organized structures of pyrolytic graphite. These structures

combined with electrodeposited nickel hydroxide, which introduces additional pseudocapacitance, demonstrated increased capacitance values and very good rate capability, outperforming many electrode materials currently used [91].

Metallic oxides displaying a pseudocapacitive behavior, combined with carbon-based materials, especially graphene, are on the edge of the state of art of composite materials for supercapacitor electrodes. The wide array of combinations and available materials paves the avenue to solve most of the actual barriers limiting the application of supercapacitors.

Conclusions and Outlook

The development of different architectures, involving nano- and microstructured materials at different dimensions and its fabrication via electrodeposition will undoubtedly boost the supercapacitor market and will play a major role in the next generation of energy storage devices displaying much better performances.

In detail, the introduction of species, such as metallic transition oxides, became extremely attractive because of the faradaic contribution of these species. The combination of metals displaying high theoretical capacitances, such as manganese, nickel, and cobalt oxides, is one of the most promising routes to fabricate new typologies of electrodes. The careful design of oxides and its modification by doping with others is an extremely attractive strategy. When it comes to morphology of these materials, 1D, 2D, and 3D architectures such as nanosheets, vertically aligned nanotubes, hyperbranched dendrites, and metallic foams lead to a very large active surface area. This contributes to enhance the electrochemical behavior of these materials.

On the other hand, the combination of different classes of materials such as the wide array of carbon-based structures (nanotubes, fullerenes, graphene, mesoporous carbons, etc.) that guarantee a capacitance generated by its double layer, with the pseudocapacitive response of metallic oxides, is attracting large interest. Graphene is in the forefront of these materials because of its high promise of energy density. The number of possible combinations of carbon-based materials and metallic oxides and the resulting architectures opens such a wide range of possibilities that, undoubtedly, supercapacitors will be in the forefront of the energy storage.

The fabrication of these single or composite materials must be simple, flexible, easy to scale up, and, preferably, done in a one-step process. Moreover, by using the correct approach, the electrodes can be fabricated directly over the current collectors, thus eliminating steps in the assembling process. This strategy definitely contributes to decreasing the production costs of the electrodes, thus lowering price and boosting the market. By using routes based on electrodeposition and co-electrodeposition, it is possible to tune the electrode morphology, surface area, conductivity, and crystallinity towards more efficient materials. This facility enables the fabrication of new electrodes, displaying much higher energy density and specific capacitances as well as longer-term cycle ability. Moreover, these materials

are able to work at fast charge/discharge rates fulfilling all the requirements for high-power applications.

The key for the success of these devices resides on the joint effort of different sciences: materials, chemistry, physics, and electrochemistry to drive the design, development, testing, and understanding of novel electrode materials and architectures with unprecedented energy densities and specific capacitances as well as experts in electronics and integration of these electrodes in practical and safe devices. This demands a multidisciplinary approach in which various branches of science intersect their competences to boost a new class of energy storage devices.

Acknowledgments The authors would like to acknowledge FCT for financial support under the projects PEst-OE/QUI/UI0100/2013 and PTDC/CTM-MET/119411/2010 “Electrodeposition of oxide spinel films on stainless steel substrates for the development of new electrodes for supercapacitors” and the COST Action MP 1004 “Hybrid Energy Storage Devices and Systems for Mobile and Stationary Applications.”

References

1. Conway BE (1999) *Electrochemical supercapacitors: scientific fundamentals and technological applications*. Kluwer/Plenum, New York
2. Wu M-S, Lin K-H (2010) One-step electrophoretic deposition of Ni-decorated activated-carbon film as an electrode material for supercapacitors. *J Phys Chem C* 114:6190–6196
3. Bondavalli P, Delfaure C, Legagneux P, Pribat D (2013) Supercapacitor electrode based on mixtures of graphite and carbon nanotubes deposited using a dynamic air-brush deposition technique. *J Electrochem Soc* 160:A601–A606
4. Ghosh A, Lee YH (2012) Carbon-based electrochemical capacitors. *ChemSusChem* 5:480–499
5. Choi H-J, Jung S-M, Seo J-M, Chang DW, Dai L, Baek J-B (2012) Graphene for energy conversion and storage in fuel cells and supercapacitors. *Nano Energy* 1:534–551
6. Wang Y, Shi Z, Huang Y, Ma Y, Wang C, Chen M, Chen Y (2009) Supercapacitor devices based on graphene materials. *J Phys Chem C* 113:13103–13107
7. Wu Z-S, Zhou G, Yin L-C, Ren W, Li F, Cheng H-M (2012) Graphene/metal oxide composite electrode materials for energy storage. *Nano Energy* 1:107–131
8. Kim G-P, Nam I, Kim ND, Park J, Park S, Yi J (2012) A synthesis of graphene/Co₃O₄ thin films for lithium ion battery anodes by coelectrodeposition. *Electrochem Commun* 22:93–96
9. Frackowiak E, Abbas Q, Béguin F (2013) Carbon/carbon supercapacitors. *J Energy Chem* 22:226–240
10. Liu C, Li F, Ma L-P, Cheng H-M (2010) Advanced materials for energy storage. *Adv Mater* 22:E28–E62
11. Bicelli LP, Bozzini B, Mele C, D’Urzo L (2008) A review of nanostructural aspects of metal electrodeposition. *Int J Electrochem Sci* 3:356–408
12. Gurrappa I, Binder L (2008) Electrodeposition of nanostructured coatings and their characterization – a review. *Sci Technol Adv Mater* 9:043001
13. Allongue P, Maroun F (2006) Metal electrodeposition on single crystal metal surfaces mechanisms, structure and applications. *Curr Opin Solid State Mater Sci* 10:173–181
14. Siegfried MJ, Choi K-S (2005) Directing the architecture of cuprous oxide crystals during electrochemical growth. *Angew Chem* 117:3282–3287
15. Despic A, Popov K (1972) Transport Controlled Deposition and Dissolution of Metals. In: Conway B, Bockris JM (eds) *Modern aspects of electrochemistry*, vol 7. Plenum, New York
16. Diggle JW, Despic AR, Bockris JOM (1969) The mechanism of the dendritic electrocrystallization of zinc. *J Electrochem Soc* 116:1503–1514

17. Popov KI, Čekerevac MI (1989) Dendritic electrocrystallization of cadmium from acid sulphate solution II: the effect of the geometry of dendrite precursors on the shape of dendrites. *Surf Coat Technol* 37:435–440
18. Li Y, Jia W-Z, Song Y-Y, Xia X-H (2007) Superhydrophobicity of 3D porous copper films prepared using the hydrogen bubble dynamic template. *Chem Mater* 19:5758–5764
19. Hsu P-C, Seol S-K, Lo T-N, Liu C-J, Wang C-L, Lin C-S, Hwu Y, Chen CH, Chang L-W, Je JH, Margaritondo G (2008) Hydrogen bubbles and the growth morphology of ramified zinc by electrodeposition. *J Electrochem Soc* 155:D400–D407
20. Chen LY, Hou Y, Kang JL, Hirata A, Fujita T, Chen MW (2013) Toward the theoretical capacitance of RuO₂ reinforced by highly conductive nanoporous gold. *Adv Energy Mater* 3:851–856
21. Lokhande CD, Dubal DP, Joo O-S (2011) Metal oxide thin film based supercapacitors. *Curr Appl Phys* 11:255–270
22. Das RK, Liu B, Reynolds JR, Rinzler AG (2009) Engineered macroporosity in single-wall carbon nanotube films. *Nano Lett* 9:677–683
23. Soin N, Roy SS, Mitra SK, Thundat T, McLaughlin JA (2012) Nanocrystalline ruthenium oxide dispersed few layered graphene (FLG) nanoflakes as supercapacitor electrodes. *J Mater Chem* 22:14944–14950
24. Wu Z-S, Wang D-W, Ren W, Zhao J, Zhou G, Li F, Cheng H-M (2010) Anchoring hydrous RuO₂ on graphene sheets for high-performance electrochemical capacitors. *Adv Funct Mater* 20:3595–3602
25. Ragupathy P, Park DH, Campet G, Vasan HN, Hwang S-J, Choy J-H, Munichandraiah N (2009) Remarkable capacity retention of nanostructured manganese oxide upon cycling as an electrode material for supercapacitor. *J Phys Chem C* 113:6303–6309
26. Wang Y-T, Lu A-H, Zhang H-L, Li W-C (2011) Synthesis of nanostructured mesoporous manganese oxides with three-dimensional frameworks and their application in supercapacitors. *J Phys Chem C* 115:5413–5421
27. Kang YJ, Chung H, Kim W (2013) 1.8-V flexible supercapacitors with asymmetric configuration based on manganese oxide, carbon nanotubes, and a gel electrolyte. *Synth Met* 166:40–44
28. Rakhi RB, Chen W, Cha D, Alshareef HN (2012) Nanostructured ternary electrodes for energy-storage applications. *Adv Energy Mater* 2:381–389
29. Han J, Li L, Fang P, Guo R (2012) Ultrathin MnO₂ nanorods on conducting polymer nanofibers as a new class of hierarchical nanostructures for high-performance supercapacitors. *J Phys Chem C* 116:15900–15907
30. Wei W, Cui X, Chen W, Ivey DG (2008) Phase-controlled synthesis of MnO₂ nanocrystals by anodic electrodeposition: implications for high-rate capability electrochemical supercapacitors. *J Phys Chem C* 112:15075–15083
31. Liu J, Jiang J, Cheng C, Li H, Zhang J, Gong H, Fan HJ (2011) Co₃O₄ nanowire@MnO₂ ultrathin nanosheet core/shell arrays: a new class of high-performance pseudocapacitive materials. *Adv Mater* 23:2076–2081
32. Wang G, Zhang L, Zhang J (2012) A review of electrode materials for electrochemical supercapacitors. *Chem Soc Rev* 41:797–828
33. Nam K-W, Kim K-H, Lee E-S, Yoon W-S, Yang X-Q, Kim K-B (2008) Pseudocapacitive properties of electrochemically prepared nickel oxides on 3-dimensional carbon nanotube film substrates. *J Power Sources* 182:642–652
34. Meher SK, Rao GR (2011) Ultralayered Co₃O₄ for high-performance supercapacitor applications. *J Phys Chem C* 115:15646–15654
35. Deng M-J, Chang J-K, Wang C-C, Chen K-W, Lin C-M, Tang M-T, Chen J-M, Lu K-T (2011) High-performance electrochemical pseudo-capacitor based on MnO₂ nanowires/Ni foam as electrode with a novel Li-ion quasi-ionic liquid as electrolyte. *Energy Environ Sci* 4:3942–3946
36. Chou S-L, Wang J-Z, Chew S-Y, Liu H-K, Dou S-X (2008) Electrodeposition of MnO₂ nanowires on carbon nanotube paper as free-standing, flexible electrode for supercapacitors. *Electrochem Commun* 10:1724–1727

37. Sun Z, Firdoz S, Ying-Xuan Yap E, Li L, Lu X (2013) Hierarchically structured MnO₂ nanowires supported on hollow Ni dendrites for high-performance supercapacitors. *Nanoscale* 5:4379–4387
38. Duay J, Sherrill SA, Gui Z, Gillette E, Lee SB (2013) Self-limiting electrodeposition of hierarchical MnO₂ and M(OH)₂/MnO₂ nanofibril/nanowires: mechanism and supercapacitor properties. *ACS Nano* 7:1200–1214
39. Kang J, Chen L, Hou Y, Li C, Fujita T, Lang X, Hirata A, Chen M (2013) Electroplated thick manganese oxide films with ultrahigh capacitance. *Adv Energy Mater* 3:857–863
40. Li Q, Wang Z-L, Li G-R, Guo R, Ding L-X, Tong Y-X (2012) Design and synthesis of MnO₂/Mn/MnO₂ sandwich-structured nanotube arrays with high supercapacitive performance for electrochemical energy storage. *Nano Lett* 12:3803–3807
41. Chang J-K, Lee M-T, Huang C-H, Tsai W-T (2008) Physicochemical properties and electrochemical behavior of binary manganese – cobalt oxide electrodes for supercapacitor applications. *Mater Chem Phys* 108:124–131
42. Mai L, Li H, Zhao Y, Xu L, Xu X, Luo Y, Zhang Z, Ke W, Niu C, Zhang Q (2013) Fast ionic diffusion-enabled nanoflake electrode by spontaneous electrochemical pre-intercalation for high-performance supercapacitor. *Sci Rep* 3:1–8
43. Wang H, Yi H, Chen X, Wang X (2013) Facile synthesis of a nano-structured nickel oxide electrode with outstanding pseudocapacitive properties. *Electrochim Acta* 105:353–361
44. Xia XH, Tu JP, Zhang YQ, Mai YJ, Wang XL, Gu CD, Zhao XB (2011) Three-dimensional porous nano-Ni/Co(OH)₂ nanoflake composite film: a pseudocapacitive material with superior performance. *J Phys Chem C* 115:22662–22668
45. Eugénio S, Silva TM, Carmezim MJ, Duarte RG, Montemor MF (2014) Electrodeposition and characterization of nickel–copper metallic foams for application as electrodes for supercapacitors. *J Appl Electrochem* 44:455–465
46. Zhang H, Cao G, Wang Z, Yang Y, Shi Z, Gu Z (2008) Growth of manganese oxide nanoflowers on vertically-aligned carbon nanotube arrays for high-rate electrochemical capacitive energy storage. *Nano Lett* 8:2664–2668
47. Kim J-H, Lee KH, Overzet LJ, Lee GS (2011) Synthesis and electrochemical properties of spin-capable carbon nanotube sheet/mnox composites for high-performance energy storage devices. *Nano Lett* 11:2611–2617
48. Ghosh A, Ra EJ, Jin M, Jeong H-K, Kim TH, Biswas C, Lee YH (2011) High pseudocapacitance from ultrathin V₂O₅ films electrodeposited on self-standing carbon-nanofiber paper. *Adv Funct Mater* 21:2541–2547
49. Wu M-S, Lin Y-P, Lin C-H, Lee J-T (2012) Formation of nano-scaled crevices and spacers in NiO-attached graphene oxide nanosheets for supercapacitors. *J Mater Chem* 22:2442–2448
50. Yuan B, Xu C, Deng D, Xing Y, Liu L, Pang H, Zhang D (2013) Graphene oxide/nickel oxide modified glassy carbon electrode for supercapacitor and nonenzymatic glucose sensor. *Electrochim Acta* 88:708–712
51. Lang X, Hirata A, Fujita T, Chen M (2011) Nanoporous metal/oxide hybrid electrodes for electrochemical supercapacitors. *Nat Nanotechnol* 6:232–236
52. Chen Y-S, Hu C-C (2003) Capacitive characteristics of binary manganese-nickel oxides prepared by anodic deposition. *Electrochem Solid-State Lett* 6:A210–A213
53. Chang J-K, Hsieh W-C, Tsai W-T (2008) Effects of the Co content in the material characteristics and supercapacitive performance of binary Mn–Co oxide electrodes. *J Alloys Compd* 461:667–674
54. Nakayama M, Suzuki K, Okamura K, Inoue R, Athouël L, Crosnier O, Brousse T (2010) Doping of cobalt into multilayered manganese oxide for improved pseudocapacitive properties. *J Electrochem Soc* 157:A1067–A1072
55. Babakhani B, Ivey DG (2011) Investigation of electrochemical behavior of Mn–Co doped oxide electrodes for electrochemical capacitors. *Electrochim Acta* 56:4753–4762
56. Sawangphruk M, Pinitsoontorn S, Limtrakul J (2012) Surfactant-assisted electrodeposition and improved electrochemical capacitance of silver-doped manganese oxide pseudocapacitor electrodes. *J Solid State Electrochem* 16:2623–2629

57. Wang Y, Zhitomirsky I (2011) Cathodic electrodeposition of Ag-doped manganese dioxide films for electrodes of electrochemical supercapacitors. *Mater Lett* 65:1759–1761
58. Kang J, Hirata A, Kang L, Zhang X, Hou Y, Chen L, Li C, Fujita T, Akagi K, Chen M (2013) Enhanced supercapacitor performance of MnO_2 by atomic doping. *Angew Chem Int Ed* 52:1664–1667
59. Tappan BC, Steiner SA, Luther EP (2010) Nanoporous metal foams. *Angew Chem Int Ed* 49:4544–4565
60. Paunovic M, Schlesinger M, Snyder DD (2010) Fundamental considerations, ch1. In: *Modern electroplating*. Wiley, Hoboken, pp 1–32. doi:10.1002/9780470602638
61. Shin HC, Dong J, Liu M (2003) Nanoporous structures prepared by an electrochemical deposition process. *Adv Mater* 15:1610–1614
62. Shin H-C, Liu M (2004) Copper foam structures with highly porous nanostructured walls. *Chem Mater* 16:5460–5464
63. Nikolić ND, Branković G, Pavlović MG, Popov KI (2008) The effect of hydrogen co-deposition on the morphology of copper electrodeposits. II. Correlation between the properties of electrolytic solutions and the quantity of evolved hydrogen. *J Electroanal Chem* 621:13–21
64. Nikolić ND, Popov KI, Lj JP, Pavlović MG (2006) Phenomenology of a formation of a honeycomb-like structure during copper electrodeposition. *J Solid State Electrochem* 11:667–675
65. Nikolić ND, Popov KI, Lj JP, Pavlović MG (2006) Morphologies of copper deposits obtained by the electrodeposition at high overpotentials. *Surf Coat Technol* 201:560–566
66. Nikolić N (2010) Fundamental aspects of copper electrodeposition in the hydrogen co-deposition range. *Zaštita Materijala* 51:197–203
67. Soares DM, Wasle S, Weil KG, Doblhofer K (2002) Copper ion reduction catalyzed by chloride ions. *J Electroanal Chem* 532:353–358
68. Cherevko S, Xing X, Chung C-H (2010) Electrodeposition of three-dimensional porous silver foams. *Electrochem Commun* 12:467–470
69. Yang G-M, Chen X, Li J, Guo Z, Liu J-H, Huang X-J (2011) Bubble dynamic templated deposition of three-dimensional palladium nanostructure catalysts: approach to oxygen reduction using macro-, micro-, and nano-architectures on electrode surfaces. *Electrochim Acta* 56:6771–6778
70. Cherevko S, Chung C-H (2011) Direct electrodeposition of nanoporous gold with controlled multimodal pore size distribution. *Electrochem Commun* 13:16–19
71. Choi W-S, Jung H-R, Kwon S-H, Lee J-W, Liu M, Shin H-C (2012) Nanostructured metallic foam electrodeposits on a nonconductive substrate. *J Mater Chem* 22:1028–1032
72. Brenner A (1963) *Electrodeposition of alloys: principles and practice*, vol 1. Academic, New York
73. Chang JK, Hsu SH, Sun IW, Tsai WT (2008) Formation of nanoporous nickel by selective anodic etching of the nobler copper component from electrodeposited nickel-copper alloys. *J Phys Chem C* 112:1371–1376
74. Yau S-L, Fan F-RF, Moffat TP, Bard AJ (1994) In situ scanning tunneling microscopy of Ni (100) in 1 M NaOH. *J Phys Chem* 98:5493–5499
75. Hu C-C, Chang K-H, Hsu T-Y (2008) The synergistic influences of OH^- concentration and electrolyte conductivity on the redox behavior of $\text{Ni}(\text{OH})_2/\text{NiOOH}$. *J Electrochem Soc* 155:F196–F200
76. De Medina AMCL, Marciano SL, Arvia AJ (1978) The potentiodynamic behaviour of copper in NaOH solutions. *J Appl Electrochem* 8:121–134
77. Ismail K, Fathi A, Badawy W (2004) The influence of Ni content on the stability of copper-nickel alloys in alkaline sulphate solutions. *J Appl Electrochem* 34:823–831
78. Zaky AM, Assaf FH (2002) Cyclic voltammetric behaviour of copper-nickel alloys in alkaline media. *Br Corros J* 37:48–55
79. Bard AJ, Faulkner LR (2001) *Electrochemical methods: fundamentals and applications*. Wiley, New York
80. Jović VD, Jović BM, Pavlović MG (2006) Electrodeposition of Ni, Co and Ni–Co alloy powders. *Electrochim Acta* 51:5468–5477

81. Maksimović VM, Lačnjevac UČ, Stoiljković MM, Pavlović MG, Jović VD (2011) Morphology and composition of Ni–Co electrodeposited powders. *Mater Charact* 62:1173–1179
82. Jeong M-G, Zhuo K, Cherevko S, Kim W-J, Chung C-H (2013) Facile preparation of three-dimensional porous hydrous ruthenium oxide electrode for supercapacitors. *J Power Sources* 244:806–811
83. Silva RP, Eugénio S, Silva TM, Carmezim MJ, Montemor MF (2012) Fabrication of three-dimensional dendritic Ni–Co films by electrodeposition on stainless steel substrates. *J Phys Chem C* 116:22425–22431
84. Guo L, Searson PC (2010) On the influence of the nucleation overpotential on island growth in electrodeposition. *Electrochim Acta* 55:4086–4091
85. Fan C, Piron DL (1996) Study of anomalous nickel-cobalt electrodeposition with different electrolytes and current densities. *Electrochim Acta* 41:1713–1719
86. Fan Z, Chen J, Cui K, Sun F, Xu Y, Kuang Y (2007) Preparation and capacitive properties of cobalt–nickel oxides/carbon nanotube composites. *Electrochim Acta* 52:2959–2965
87. Niu Z, Zhang L, Liu L, Zhu B, Dong H, Chen X (2013) All-solid-state flexible ultrathin micro-supercapacitors based on graphene. *Adv Mater* 25:4035–4042
88. Kuang D, Xu L, Liu L, Hu W, Wu Y (2013) Graphene–nickel composites. *Appl Surf Sci* 273:484–490
89. Rakhi RB, Chen W, Cha D, Alshareef HN (2011) High performance supercapacitors using metal oxide anchored graphene nanosheet electrodes. *J Mater Chem* 21:16197–16204
90. Huang Y, Liang J, Chen Y (2012) An overview of the applications of graphene-based materials in supercapacitors. *Small* 8:1805–1834
91. Du F, Yu D, Dai L, Ganguli S, Varshney V, Roy AK (2011) Preparation of tunable 3D pillared carbon nanotube – graphene networks for high-performance capacitance. *Chem Mater* 23:4810–4816

Nanoscale Electrodeposition of Metals and Semiconductors from Ionic Liquids Probed by Scanning Tunneling Microscopy

21

Hong-Dan Peng, Yu Zhao, and Ge-Bo Pan

Contents

Introduction.....	716
Technological Point of STM for ILs.....	719
Adsorption of Anions and Cations.....	720
Anion Adsorption.....	720
Cation Adsorption.....	722
Electrodeposition of Metals.....	723
Reactive Metals (Al, Zn, Li).....	723
Magnetic Metals (Fe, Co, Ni).....	725
Semimetal Elements (Sb, Bi).....	727
Rare Metals (Ga, Ti, Ta).....	729
Other Metals (Cd, Pb).....	731
Electrodeposition of Semiconductors.....	732
Elemental Semiconductors (Ge, Si).....	732
Compound Semiconductors (AlSb, ZnSb).....	734
Conclusion.....	735
References.....	735

Abstract

In this chapter, we have reviewed the current state of the knowledge of the nanoscale electrodeposition of metals and semiconductors on single-crystal electrodes from ionic liquids (ILs), which might be vital for both basic and applied researches. Emphasis has been placed on the atomic- or submolecular-level characterization of the respective nucleation and growth by in situ scanning tunneling microscopy (STM), whose studies are still in its infancy. Firstly, technological

H.-D. Peng • Y. Zhao • G.-B. Pan (✉)

Division of Interdisciplinary Research, Suzhou Institute of Nano-tech and Nano-bionics (sinano), Chinese Academy of Sciences, Suzhou, China

e-mail: hdpeng2102@sinano.ac.cn; yzhao2012@sinano.ac.cn; gspan2008@sinano.ac.cn

© Springer International Publishing Switzerland 2016

M. Aliofkhaezai, A.S.H. Makhlof (eds.), *Handbook of Nanoelectrochemistry*,

DOI 10.1007/978-3-319-15266-0_21

715

point of STM for ILs has been briefly discussed as well as the adsorption behavior of anions and cations of ILs. Secondly, in situ STM studies on the metal electro-deposition in ILs are reviewed. For simplicity, the discussion will be categorized into reactive (e.g., Al, Zn, Li), magnetic (e.g., Fe, Co, Ni), semimetal (e.g., Sb, Bi), coinage (e.g., Cu, Ag, Au), and rare metals (e.g., Ga, Ti, Ta). Thirdly, in situ STM studies on the electrocrystallization of elemental (e.g., Si, Ge) and compound semiconductors (e.g., AlSb, ZnSb) are briefly reviewed. We conclude this chapter with our personal perspectives on future research in this field.

Keywords

Electrodeposition • Ionic liquid • Metal • Semiconductor • STM

Introduction

Ionic liquids (ILs) have been well-known for nearly 100 years; however, a tremendous explosion on this diverse class of solvents started only in the past decade [1, 2]. ILs are composed of organic cations and organic or inorganic anions and have a melting point typically lower than 100 °C, sometimes even below room temperature. They are credited with a number of unusual properties that are remarkably different from water and conventional organic solvents. For instance, they exhibit almost zero pressure of saturated vapor, extended temperature range, nonflammability, high conductivity, good chemical and thermal stability, and wide electrochemical window (even up to ~6 V) [3–5]. In particular, the properties of ILs are adjustable by selecting specific cations and anions, which can be independently modified. That is, ILs can be considered as a unique architectural platform, which enables tunable solubility and much synthetic flexibility in designing new functional solvents or materials. These favorable properties make ILs very promising to improve the durability and safety of electrochemical devices, extend the range of operating temperature, and increase the power and energy density [1, 6]. Therefore, ILs are considered as novel electrolyte candidates for electrochemical devices, including electric double layer capacitors, fuel cells, lithium batteries, and solar cells. To date, a variety of cations and anions have been combined to form ILs. Figure 1 shows a variety of cations and anions, which are used for the currently favored ILs. The commonly used cations include imidazolium, pyridinium, tetraalkylammonium, tetraalkylphosphonium, and pyrrolidinium, and the anions include tetrafluoroborate and hexafluorophosphate, trifluoromethanesulfonate, bis(trifluoromethanesulfonyl) amide, *p*-toluenesulfonate, and dicyanamide [2].

On the other hand, electrochemical deposition is very powerful tool for preparing novel nanostructured materials, in particular for transition metals and semiconductors. In comparison with other methods such as chemical vapor deposition, physical vapor deposition, and sputtering, electrochemical deposition is demonstrated to be least expensive, highly productive, and readily adoptable. Meanwhile, it benefits a facile control of potential and numerous electrolyte compositions of solvents and precursors of metals and semiconductors [7]. The development of ILs, in particular

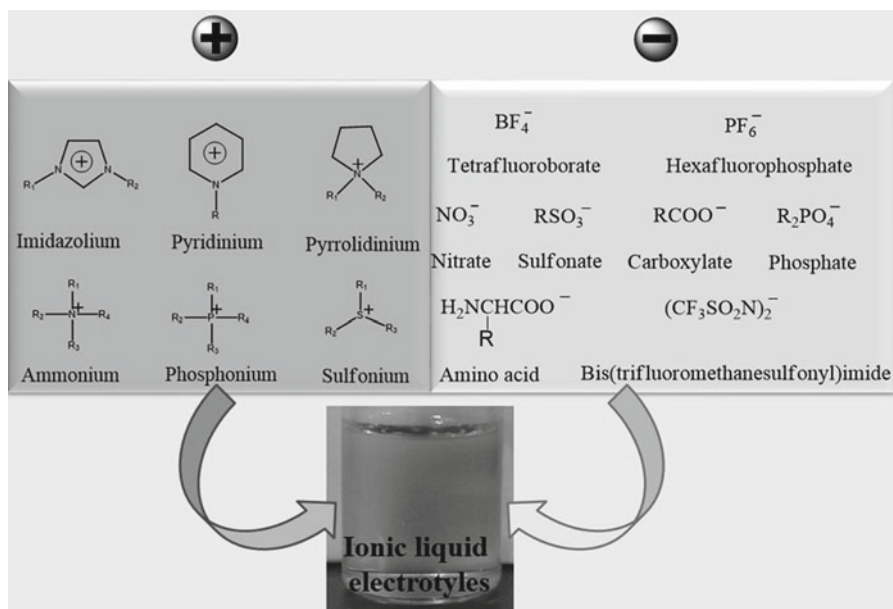


Fig. 1 A variety of commonly used cations and anions of ionic liquids

air and water stable ILs, has paved the way for the electrodeposition of metals and semiconductors [8]. As a sustainable and green media, ILs are capable to revolutionize traditional electroplating industry. Firstly, metals and alloys formerly accessible only in molten salts at high temperature can be deposited in ILs at room temperature. Secondly, by using ILs, electrolytes make it possible to electrodeposit active materials, such as aluminum, magnesium, and lithium, that can't be obtained in water-based baths. This is mainly because hydrogen evolution does not occur in ILs. More importantly, by designing and synthesizing task-specific ILs, toxicity of reagents and low efficiencies occurred with aqueous or organic processing can be overcome. In particular, it is able to control redox potentials and therefore to deposit novel alloys. These benefits have turned electrochemical deposition on the nanoscale from ILs into a fast-growing area of research [9].

However, the limited understanding of the IL/electrode interfaces severely hinders the applications of ILs in electrochemistry field. In comparison to those of molecular solvents, the IL/electrode interfaces are much more complicated and generally consist of three distinct zones: interfacial (innermost) layer, bulk phase, and transition zone [10, 11]. Recent efforts reveal that ILs form strongly adherent interfacial layers on electrode surfaces, which varies with the composition of ILs and the applied electrode potential. The unusual bulk and interfacial properties induced by the intrinsic strong interactions in ILs have an important influence on the structure and electrochemical processes at the IL/solid interfaces. Thus, it is highly desired to study the interfacial systems, in particular, to obtain either atomic- or molecular-level perspective. To obtain images of the IL/solid interfaces with atomic or

Table 1 A list of deposited metals and semiconductors from ionic liquids

Deposits		ILs	References
Metals	Reactive metals	Al AlCl ₃ /MEImCl, AlCl ₃ /[BMIm]Cl, AlCl ₃ /[EMIm]Cl, AlCl ₃ /[Py _{1,4}]Tf ₂ N, AlCl ₃ /[EMIm]Tf ₂ N, AlCl ₃ /[Py _{1,4}]Cl, AlCl ₃ /[Py _{1,4}]TfO, AlCl ₃ /[EMIm]TfO, AlCl ₃ /[Py _{1,4}]TfSA, AlCl ₃ /[EMIm]TfSA, AlCl ₃ /[MoeMIm]	[26–28] and references therein
	Zn	ZnCl ₂ /[MBI]Cl, ZnCl ₂ /[BMIm]BF ₄ , ZnCl ₂ /[EMIm]Cl, Zn(TfO) ₂ /[Py _{1,4}]TfO, Zn(TfO) ₂ /[EMIm]TfO, Zn(II)/AlCl ₃ -MBIC, ZnCl ₂ /AlCl ₃ -[EMIm]Cl	[29–31] and references therein
Magnetic metals	Li	LiTfSA/[Py _{1,4}]TfSA	[32]
	Fe	Fe(II)/AlCl ₃ -[MBIm]Cl, FeCl ₃ /[BMIm]BF ₄	[34–37]
	Co	CoCl ₂ /AlCl ₃ -[BMIm]BF ₄ , Co(BE ₂) ₂ /[BMIm]BF ₄ , Co(TfSA) ₂ /BMP/TfSA, CoCl ₂ /AlCl ₃ -[MBIm]Cl	[38, 39] and references therein
	Ni	Ni(TfSA) ₂ /EMITfSA, Ni(TfSA) ₂ /BMP/TfSA, Ni(II)/AlCl ₃ -[C ₄ mim]Cl, NiCl ₂ /ChCl-urea, NiCl ₂ /[BMIm]Cl-AlCl ₃	[40, 41] and references therein
Semimetal elements	Sb	SbCl ₃ /AlCl ₃ -[C ₄ mim]Cl, SbCl ₃ /[BMIm]BF ₄ , SbCl ₃ /MBIC-AlCl ₃ , SbCl ₃ /[BMIm]Cl-AlCl ₃	[42–45] and references therein
	Bi	Bi(NO ₃) ₃ /ChCl-Oxá, BiCl ₃ /MBIC-AlCl ₃ , BiCl ₃ /[BMIm]BF ₄	[46] and references therein
Coinage metals	Cu	Cu(II)/[BMP]Tf ₂ N, CuCl ₂ /AlCl ₃ -BMIC, CuCl ₂ /ChCl-urea	[47, 48] and references therein
	Ag	AgNO ₃ /[BMIm]BF ₄ , AgNO ₃ /[C ₄ mPyrr]TfSI, AgCl/AlCl ₃ -BMICl, AgTfSA/[BMP]TfSA, AgOTf/BMIOTf	[49, 50] and references therein
Rare metals	Ru	RuCl ₃ /[BMIm]DCA	[51]
	Ga	GaCl ₃ /[Py _{1,4}]Tf ₂ N, GaCl ₃ /[Py _{1,4}]TfSA, GaCl ₃ /AlCl ₃ -[C ₄ mim]Cl, GaCl ₃ /[BMIm]Cl, GaCl ₃ /[BMIm]Cl-AlCl ₃	[22, 52] and references therein
Others	Ti	TiCl ₄ /AlCl ₃ -EtImImCl, TiCl ₄ /[BMIm]BTA, TiCl ₄ /[BMIm]Tf ₂ N, TiX ₄ (Cl, Br, F)/[EMIm]Tf ₂ N, TiX ₄ (Cl, Br, F)/[BMP]Tf ₂ N, TiX ₄ (Cl, Br, F)/[P _{14,6,6,6}]Tf ₂ N	[53–55] and references therein
	Ta	TaCl ₅ /[EMIm]Cl, TaF ₅ /[BMP]Tf ₂ N, TaF ₅ /[Py _{1,4}]TfSA, TaF ₅ /[EMIm]TfSA, TaF ₅ /[PMIm]TfSA, TaF ₅ /AlCl ₃ -MBIC, CdCl ₂ /ZnCl ₂ -EMIC, CdCl ₂ /[EMIm]BF ₄	[56, 57] and references therein
	Cd	CdCl ₂ /AlCl ₃ -MBIC, CdCl ₂ /ZnCl ₂ -EMIC, CdCl ₂ /[EMIm]BF ₄	[58] and references therein
Elemental semiconductors	Pb	PbCl ₂ /AlCl ₃ -MBIC	[59]
	Ge	GeX ₄ (Cl, Br, I)/[BMIm]PF ₆ , GeCl ₄ /[Py _{1,4}]Tf ₂ N, GeCl ₄ /[EMIm]Tf ₂ N, GeCl ₄ /[HMIm]FAP	[60–62] and references therein
Compound semiconductors	Si	SiCl ₄ /[BMP]Tf ₂ N, SiCl ₄ /[BMIm]PF ₆ , SiCl ₄ /[Py _{1,4}]Tf ₂ N, SiCl ₄ /[EMIm]Tf ₂ N	[63–65] and references therein
	AlSb	SbCl ₃ /AlCl ₃ -[C ₄ mim]Cl, SbCl ₃ /[BMIm]Cl-AlCl ₃	[44, 45]
	ZnSb	SbCl ₃ /ZnCl ₂ -[C ₄ mim]Cl, SbCl ₃ /ZnCl ₂ -MBIC	[21, 66]

submolecular resolution, the most promising approach is use of scanning probe microscopies. In the past decade, scanning tunneling microscopy (STM) has proven to be a remarkable tool for direct observing the spatial arrangement of the adsorbed molecules and ions at the surface of metallic and semiconducting electrodes. More importantly, it is capable of providing direct information on the dynamic processes of molecule and structural defect in situ [12–14]. Combining with the conventional electrochemical methods, the mechanism of the electrodeposition of metals and semiconductors can be revealed on an atomic or molecular level, and the details of nucleation, growth, and phase can be observed in real space.

In this chapter, we have reviewed the current state of the knowledge of the nanoscale electrodeposition of metals and semiconductors from ILs (Table 1), which is of both fundamental and technological importance. Emphasis has been placed on atomic- or submolecular-level characterization by STM. Classical electrochemical methods such as cyclic voltammetry or potential step experiments often give only an overall insight into the deposition process. Firstly, technological point of STM for ILs has been briefly discussed as well as the adsorption behavior of anions and cations of ILs. Secondly, STM studies on the electrodeposition of metals in ILs are reviewed. For simplicity, the discussion will be categorized into reactive, magnetic, semimetal, coinage, and rare metals and so on. Thirdly, STM studies on electrodeposition of elemental and compound semiconductors are reviewed. We conclude this chapter with our personal perspectives on future research in this field.

Technological Point of STM for ILs

STM images the solid surface in real space and with high resolution by utilizing the ability of precise spatial localization and specific tip-sample interactions. By detecting the tunneling current, which is exponentially varying with the tip-sample distance, it is capable of probing the surfaces with spatial resolution down to the atomic or submolecular scale. Moreover, the rapid development of STM has also enabled the study of the electrolyte/electrode interfaces with atomic or submolecular resolution since 1990 and advanced surface electrochemistry since 1990. However, it is noted that most of STM application is performed in aqueous solution.

In 1997, Freyland et al. performed the first STM experiment in a chloroaluminate IL and observed in situ the growth of Ag nanostructures on a highly oriented pyrolytic graphite (HOPG) substrate [15]. In 2003, Mao et al. observed the reconstruction and restructuring process of Au(111) in a neat non-chloroaluminate IL [16]. The above works represent the initial efforts of in situ STM study of the IL/electrode interfaces. It is exciting that atomic or submolecular resolution images have been obtained for some specific systems in spite of its difficulties in obtaining high-resolution STM images in ILs.

Note that in situ STM experiments performed in ILs are more difficult than those in organic and aqueous solutions. In general, all the systems are required to be put into an inert container. This is because trace oxygen and water can affect significantly the physicochemical properties of ILs. Moreover, the reference and counter

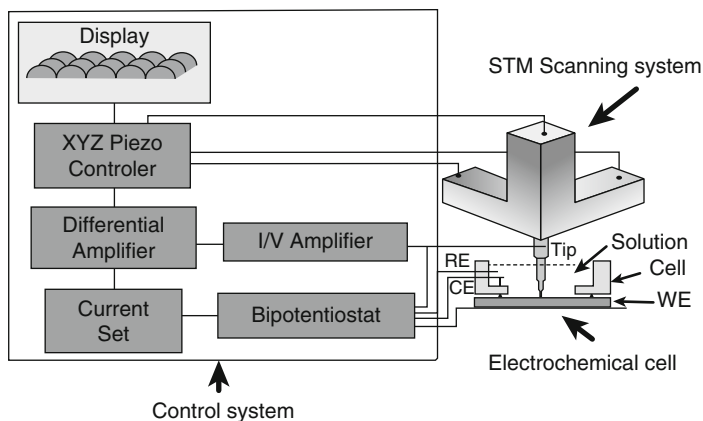


Fig. 2 Apparatus of in situ STM with the standard four-electrode arrangement

electrodes needed to be carefully selected, to avoid the effect of potential shift. Figure 2 shows a schematic of the STM apparatus with the standard four-electrode arrangement. By using a bipotentiostat, the electrode potentials of the working electrode (WE_1) and the tunneling tip (WE_2) can be controlled independently with respect to a reference electrode (RE).

Adsorption of Anions and Cations

STMs can provide atomic and submolecular resolution images of adsorbed targets and are widely used in investigating the electrolyte-electrode interface. In comparison to aqueous or conventional organic solutions, ILs form strongly adhering solvation layers that vary with and the composition of ILs and the applied electrode potential, which in turn alter the tunneling conditions during the STM imaging. Therefore, it remains a great challenge to obtaining STM images with high resolution in ILs. To date, relatively limited STM studies using well-defined single-crystalline metal electrodes have reached atomic or submolecular resolution in ILs. The potential-dependent long-range restructuring of electrode surfaces has also been studied with submolecular resolution as well as the formation of anion/cation layers.

Anion Adsorption

We have investigated for the first time the adsorption of PF_6^- anions on Au(111) in 1-butyl-3-methylimidazolium hexafluorophosphate ([BMI]PF₆). As shown in Fig. 3, the adlayers show a potential-dependent two-dimensional (2D) phase transition from a Moiré-like pattern structure to a $(\sqrt{3} \times \sqrt{3})$ phase upon cathodic excursion [17]. The formation of well-ordered adlayers is possibly because the PF_6^- anions have different solvation energies in [BMI]PF₆ from that in aqueous solution.

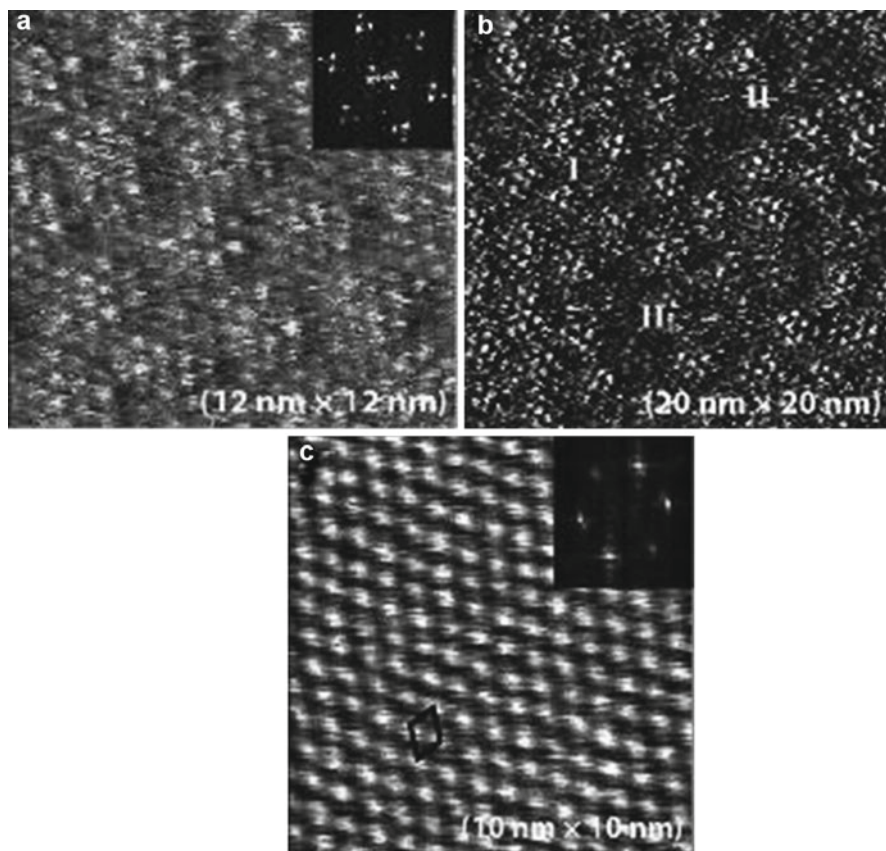


Fig. 3 STM images of Au(111) in [BMI]PF₆, revealing the adsorption layer of PF₆⁻. The applied potentials were (a) E=0.5 V; (b) E=0.0 V; and (c) E=-0.25 V versus Pt/Pt(II). The insets are the FFT analysis of Fig. 2a, c (Reprinted with permission from Pan and Freyland [17]. Copyright 2006 Elsevier)

Moreover, a marked structural difference of Au(111) surface exists at potentials positive and negative of the potential of zero charge (PZC) [18]. Similarly, the adsorption of BF₄⁻ anions has also been observed on Au(100) in 1-butyl-3-methylimidazolium tetrafluoroborate ([BMI]BF₄) [19].

The combination of quaternary ammonium chloride salts and metal chlorides has produced a number of ILs, leading to the formation of metal chloride anions such as AlCl₄⁻, ZnCl₃⁻, and GaCl₄⁻. These anions also adsorb on metal electrode and forming ordered adlayers. In situ STM studies have revealed an ordered ($2\sqrt{3} \times 2\sqrt{3}$) structure of AlCl₄⁻ anions on Au(111) before the occurrence of the underpotential deposition (UPD) process [20]. ZnCl₃⁻ anions adsorb on Au(111) at open-circuit potential (OCP) or under potential control and formed the Moiré-like patterns, which coexist with a disordered region. This phenomenon is comparable to the adsorption of PF₆⁻ anions [21]. Similarly, GaCl₄⁻ anions can adsorb and form ordered adlayer on Au(111) in an acidic chlorogallate melt [22].

Cation Adsorption

Similar to anion adsorption, the adsorption of cations has been investigated in neat ILs. High-resolution STM images, as shown in Fig. 4 have revealed ordered strip structures of BMI⁺ cations on Au(100) in [BMI]PF₆ and [BMI]BF₄ [19]. Each row of the strip consists of aligned BMI⁺ cations. The bright spots are imidazolium groups, while the less intense parts are butyl side chains. The BMI⁺ cations are assumed to lie flatly on Au(100) surface, which are stabilized by π - π interactions between the aromatic ring systems [23]. The length of the strips can vary from 3 to 30 nm. The adsorption of BMI⁺ cations shows a potential-induced transition from disorder to order phase. However, it is important to point out that the adsorption of BMI⁺ cations doesn't appear on Au(111). The results imply that the structural commensurability of the adsorbed BMI⁺ cations with the surface plays a key role in such a selective and ordered adsorption of BMI⁺ cations on Au(100).

In contrast to the cases with imidazolium-based [BMI]PF₆ and [BMI]BF₄, in which well-ordered patterns are formed on metal electrodes, no order adlayers of the cations are observed at negative potentials in hexaalkyl-substituted guanidinium-based ILs [24]. The two possible reasons are as follows: Firstly, the absence of aromatic π units leads to the weak cation-cation and cation-electrode interaction. Secondly, there is a larger sterical hindrance between the six alkyl chains of guanidinium cation and electrode surface than that of the imidazolium cation. Consequently, it prevents the charged core being close to the surface.

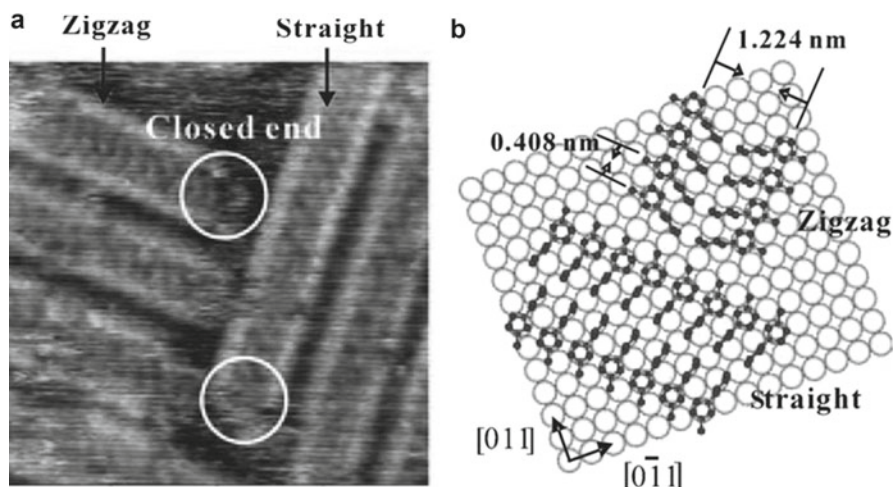


Fig. 4 (a) STM image of BMI⁺ adsorption from [BMI]PF₆ on Au(100) at -1.0 V. Scan size: 8×8 nm². (b) Structural model of BMI⁺ adsorption structure (Reprinted with permission from Su et al. [19]. Copyright 2009 WILEY-VCH Verlag GmbH & Co. KGaA, Weinheim)

Electrodeposition of Metals

Since the initial work in 1970s, a large number of studies are carried out for the electrochemical deposition in ILs, especially for metals and semiconductors that are impossible to be obtained in aqueous solutions. Several excellent review articles have addressed the achievements in this direction [8, 11, 25]. However, relatively little attention has been paid toward the initial stage of electrodeposition in ILs. In this section, recent progress of metal electrodeposition in both underpotential deposition (UPD) and overpotential deposition (OPD) ranges are summarized. For simplicity, the discussions have been categorized into reactive, magnetic, semi-metal, coinage, and rare metals and so on.

Reactive Metals (Al, Zn, Li)

Aluminum (Al) plays an important role in modern industries, e.g., automotives and planes, due to its high corrosion resistance. Electrodeposition of Al from ionic liquids, especially from those based on organic halides and anhydrous AlCl_3 , has been widely studied. In a Lewis acidic melt of 1-butyl-3-methylimidazolium chloride-aluminum chloride ($[\text{MBI}]\text{Cl}-\text{AlCl}_3$), STM images have revealed two UPD processes on Au(111) [26]. First, nanoscale clusters appear all over the Au surface and later become more preferential along the step edges. The growth of Al nanoclusters is up to 8 nm in diameter. In comparison, neither UPD process nor preferential nucleation is observed for the Al electrodeposition on Si(111):H. The growth of Al on Si(111):H follows a classical Volmer-Weber growth mode, which results in forming large islands spread all over the Si(111):H surface [27] (Fig. 5).

It is noted that chloroaluminate ILs can only be handled under inert-gas atmosphere due to their quite hygroscopic nature of AlCl_3 . To overcome this disadvantage, air and water stable ILs, which often have 1,3-dialkylimidazolium or 1,1-dialkylpyrrolidinium cation and more hydrophobic anions such as bis(trifluoromethylsulfonyl)amide, have been developed. In 1-ethyl-3-methylimidazolium bis(trifluoromethylsulfonyl)amide ($[\text{EMI}]\text{Tf}_2\text{N}$), the Al islands with single atomic height are firstly grown and coalesce to form a monolayer. Then, the second Al layer starts to grow and 2D Al islands are formed on top of the first monolayer. In contrast, no clear evidence is found for the Al UPD on Au(111) in 1-butyl-1-methylpyrrolidinium bis(trifluoromethylsulfonyl)amide ($[\text{Py}_{1,4}]\text{Tf}_2\text{N}$). Moreover, the Al deposition in $[\text{Py}_{1,4}]\text{Tf}_2\text{N}$ has the low reversibility. The above observations demonstrate that cations and/or anions have a great influence on the Al nucleation and crystallization in ILs [28].

Similar to the Al, electrodeposition of zinc (Zn) on metals is also used extensively in corrosion protective coatings and energy storage devices. In $[\text{MBI}]\text{Cl}-\text{ZnCl}_2$, STM characterization in the UPD range has resolved three successive Zn monolayers. This layer-by-layer growth mode continues into the bulk deposition regime. The thickness of the Zn layers extracted from STM images is $2.4 \pm 0.2 \text{ \AA}$ in the UPD and OPD range.

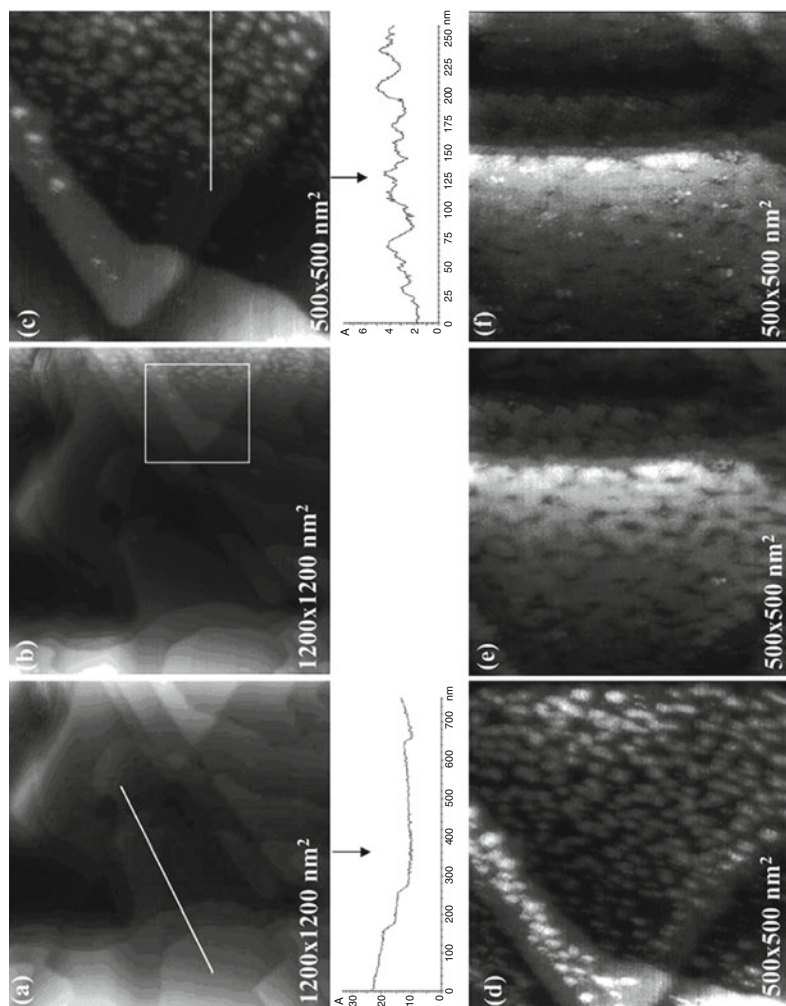


Fig. 5 STM of the Al UPD process on Au(111) from a mixture of $\text{AlCl}_3/\text{EMITTe}_2\text{N}$. (a) monatomic terraces on Au (111) recorded at $E=0.7$ V, (b) Al islands formed at $E=0.6$ V, (c) 500x500 nm² area from (b), (d) $E=0.4$ V, (e) $E=0.5$ V, (f) $E=0.3$ V (Reprinted with permission from Moustafa et al. [28]. Copyright 2007 American Chemical Society)

However, there is an exception that the thickness of the first UPD Zn is 2.2 ± 0.2 Å. Via potential jumping in the UPD range, 2D spinodal structures are observed both in deposition and in dissolution processes. The structural evolution may be described by a continuum model [29, 30]. The quasi-layer-by-layer growth is also observed for the Zn UPD on Au(111) in [BMI]BF₄. A compact layer is obtained just before the potentials where the second Zn UPD is started. The same growth feature is observed for the third layer on the second one and the bulk on the third layer. More importantly, the patterns as well as the large-scale arrays of Zn nanoclusters have been produced in [BMI]BF₄, which testified the feasibility of nanostructuring a new category of solvent systems that have been impossible in aqueous solution. Together with surface engineering, the STM tip-induced nanostructuring in ILs would pave the way for the investigation of nanoscopic effects in various aspects [31].

The electrochemical process of lithium (Li) is of practical significance regarding its wide application in lithium batteries. In situ STM studies demonstrate that the Li UPD on Au(111) in [Py_{1,4}]Tf₂N begins at potentials positive to the electrode potential of bulk deposition. Moreover, the deposition follows a layer-by-layer mechanism and at least two layers can be formed. This behavior is possibly attributed to the solvation of the Li⁺ in ILs that is different from in conventional organic solvents. Moreover, evidence of alloying between Li and Au has been observed when the potential reaches the region where the alloy dissolution takes place [32, 33].

Magnetic Metals (Fe, Co, Ni)

The electrodeposition of magnetic materials, including Fe, Co and Ni, is widely used to functionalize solid surfaces for anti-corrosion, electrocatalysis, data storage, and magnetic sensors, which generally requires a better control of the morphologies of the deposits. However, the hydrogen evolution reaction, which occurs during the electrodeposition in aqueous solutions, often leads to the low current efficiency and worse quality of deposits. In contrast, the use of ILs can avoid the hydrogen evolution reaction. Therefore, it provides a possibility to grow magnetic thin films, which can't be obtained in aqueous solutions. Meanwhile, the unique properties of ILs can change dramatically the growth mechanism of magnetic metals.

In situ STM studies have revealed that monodispersed Fe nanocrystals can be electrodeposited on Au(111) from a Lewis acidic [BMI]Cl-AlCl₃ [34]. In the initial stage, Fe islands grew two- and three-dimensionally on Au(111) to several monolayer thicknesses. In the later stage, Fe nanocrystals of with defined shape are formed and some of nanocrystals are aligned in boomerang shapes with an angle of 120–140°. This result is similar to the self-ordered Fe nanostructures on Si(111), indicating that the morphologies of electrodeposited Fe thin films are closely related to their magnetic properties [35]. Fe can also be electrodeposited from [BMI]BF₄ by using FeCl₃ as the precursor. Different from that in [BMI]Cl-AlCl₃, unusual shape-ordered, namely, pseudo-rods and pseudo-square rings are observed on Au(111) and Au(100) in STM images, respectively (Fig. 6). The same nanostructures are observed on Pt(111) and Pt(100). The above interesting nanoarchitectures are resulted from the

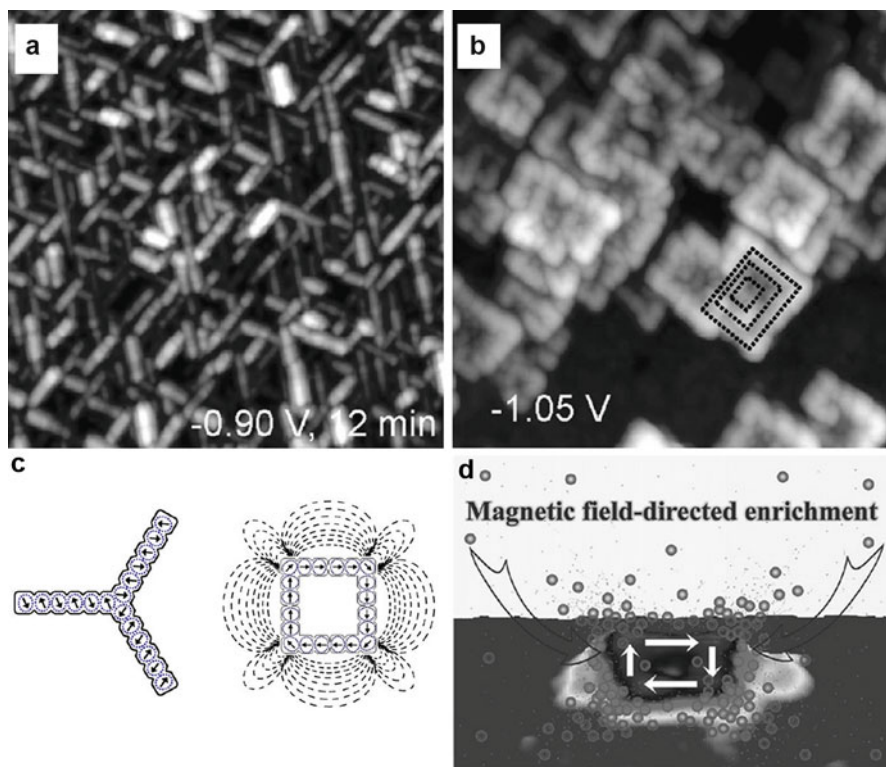


Fig. 6 STM images of (a) 3D pseudo-rods on Au(111) and (b) pseudo-square rings on Au(100). (c) Schematic illustration of magnetization of grains in the pseudo-rods on Au(111) and pseudo-square rings on Au(100). (d) Magnetic field-directed enrichment of magnetic reactants. The lower part is a real STM image of one pseudo-square ring presented in a 3D view (Reprinted with permission from Wei et al. [36]. Copyright 2010 American Chemical Society)

magnetostatic interactions under crystallographic constraints. The shape ordering of the Fe thin film serves as a paradigm of magnetostatic coupling, in which the roles of IL as surfactant and magnetic media may not be underestimated [36, 37].

The electrodeposition of Co on Au(111) is investigated in [BMI]Cl-AlCl₃. The 2D phase is formed at slightly cathodic potentials. The Co islands are mono-atomically high, with a radius of 2–3 nm and a narrow size distribution. When the potentials are negative of -0.2 V, a fast 3D growth of Co clusters is observed [38]. It is noted that the presence of AlCl₃ may restrict the cathodic potential limit. In order to avoid Al co-deposition, the initial stage of Co electrodeposition on Au(111) is carried out in [BMI]BF₄ [39]. It is interesting that the form of precursor has a substantially influence on the Co electrodeposition in [BMI]BF₄. When CoCl₂ is used as the Co source, the deposition starts at very negative potential at structure imperfections of reconstructed Au(111) surface. When Co(BF₄)₂ is used as the Co source, the deposition takes place at a much less negative potential without preference in nucleation sites.

The electrochemical phase formation and growth of Ni on Au(111) has been carried out in an acidic melt of [BMI]Cl-AlCl₃ (42: 58) [40, 41]. In the UPD range, 2D Ni

phase formation sets in and a complete monolayer grows over a period of ~ 800 s. In the OPD range, different morphologies of Ni nanoclusters are obtained when a different procedure of potential decreasing is followed. If jumping the potential directly from the OCP into the OPD region, large nearly spherical Ni clusters with diameters of ~ 10 nm first nucleate at the step edges of the Au(111) substrate and spread with time all over the surface. However, decreasing the potential through the Ni UPD stage, the elongated Ni clusters nucleate and grow instantaneously. Most interesting, they are all oriented in one direction, suggesting magnetic interaction between the Ni clusters.

Semimetal Elements (Sb, Bi)

Among the variety of UPD systems, the semimetal class of elements including Sb and Bi has received the enormous attention because of their interesting properties in forming bimetal alloys or compound semiconductors. Systematic investigation of the UPD of Sb and Bi on single-crystalline Au electrodes has revealed an obvious “solvent effect” from ILs. In [BMI]BF₄, the initial stage of Sb UPD proceeds with the formation of similar short atomic strips composed of Sb on both Au(111) and Au(100) shown by STM measurements. However, in the later stage of Sb UPD, dramatically different behaviors are observed: a multilevel feature with a small quantity of Sb aggregates on Au(111) and a distinct second layer with islands of ~ 4 nm on Au(100) [42]. These features contrast significantly from those observed in aqueous solutions and reveals strong medium effects on the Sb UPD.

Undoubtedly, it is expected that special solvation properties of ILs are particularly prominent in the UPD of Sb. In acidic [BMI]Cl-AlCl₃, the UPD of Sb has several different processes: formation of an ordered structure of SbCl₂⁺, further compression into a Moiré-like pattern, and a sudden smoothing of surface. In the later stage, the nucleation process begins to occur and the 2D-nanostripe architectures are formed. The number and the length of Sb increase remarkably with time, while the width keeps almost constant [43]. Moreover, different processes of Sb UPD are observed in the neutral and basic melt of [BMI]Cl-AlCl₃. The results imply that the acidity of ILs plays an important role in the electrodeposition of Sb [44, 45].

The solvent also played an important role in the electrodeposition of Bi. In a Lewis acidic [BMI]Cl-AlCl₃, STM images have revealed two different UPD processes of Bi on Au(111): multiple domain structures and uniaxially commensurate monolayer [46]. Moreover, for the first time some metastable intermediate superstructures have been resolved by high-resolution STM images (Fig. 7). They are possibly resulted from either a loosely packed Bi adlayer or a coadsorption of Bi and AlCl₄⁻, which are predominant anions in [BMI]Cl-AlCl₃. In the OPD range, the needlelike structures and ultrathin films have been formed through the different procedures of potential decreasing. On the other hand, the Bi UPD proceeds with the formation of a (7 × 7) structure, which further transforms into a unique “zipper-like” double-chain pattern with a (5 × 25√3/3) structure in [BMI]BF₄. The adlayers are composed of the well-aligned Bi trigonal clusters consisting of six Bi atoms. These features contrast significantly with those in aqueous solutions and chloroaluminate melt, but are comparable to those of the Sb UPD in [BMI]BF₄.

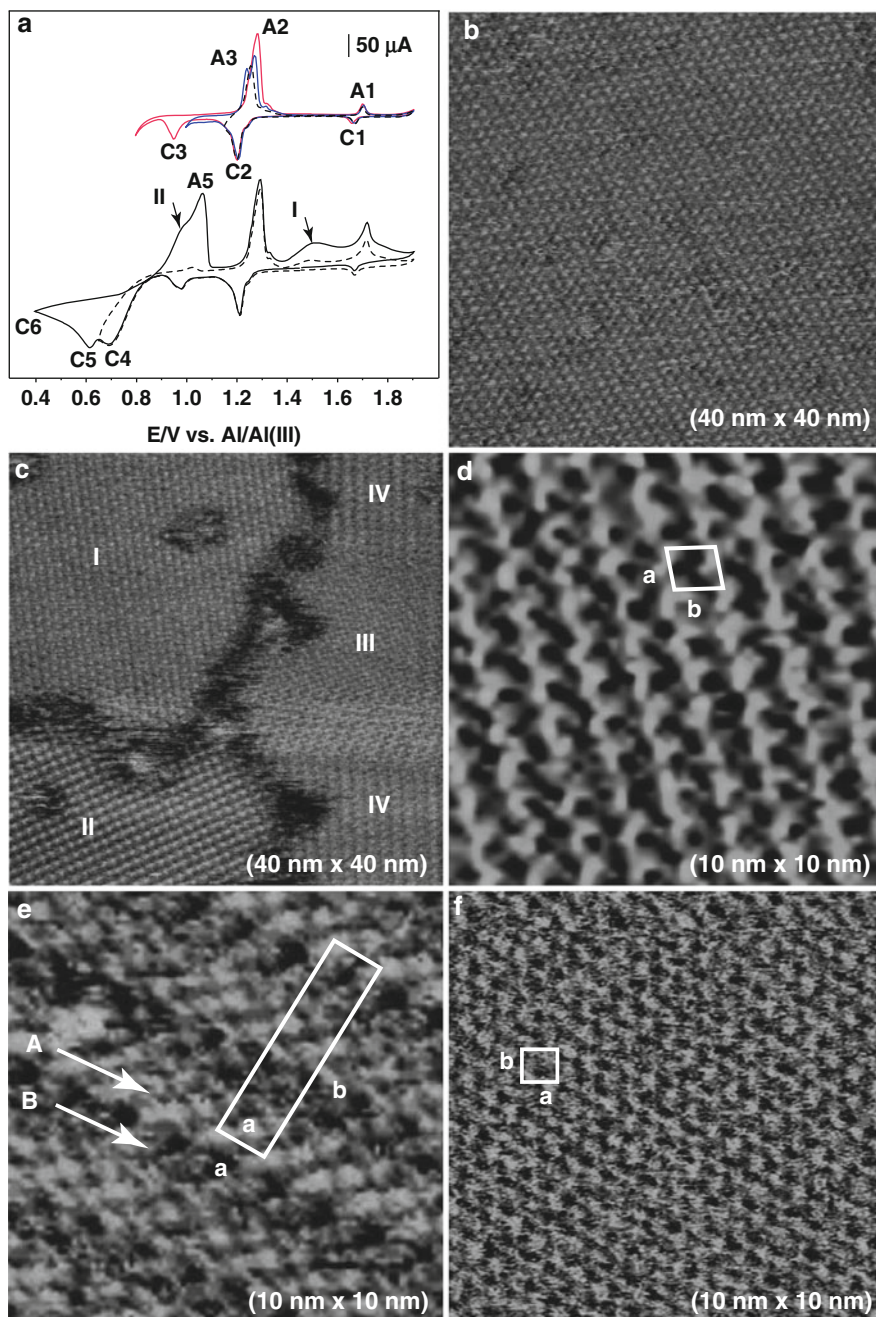


Fig. 7 (a) Cyclic voltammograms of Au(111) in MBIC-AlCl₃ (42:58) + 5 mM BiCl₃. The scan rate was 50 mV/s. (b–f) A set of STM images of the Bi UPD on Au(111) recorded at the different electrode potential: (b) E = 1.3 V, (c) E = 1.2 V, (d) E = 1.1 V, (e) E = 1.0 V, (f) E = 0.9 V (Reprinted with permission from Pan and Freyland [46]. Copyright 2007 Elsevier)

Coinage and *sp* Metals (Cu, Ag, Ru)

For noble metal, high-quality deposits with nanocrystals are desired, which often fail to be achieved in aqueous solutions. In a Lewis acidic [BMI]Cl-AlCl₃, Cu forms initially island structures on Au(111) [47]. On the Cu island, a Moiré-like pattern with (8 × 8) superstructure has been discerned. This is due to the anion coadsorption. The structure is different from the ($\sqrt{3} \times \sqrt{3}$) coadsorption structure of sulfate observed in sulfuric acid solution [48]. The different behaviors of Cu UPD in the two media can be contributed to the different existing forms of the Cu precursor as well as the nature of the solvent anions.

The electrodeposition of silver on highly oriented pyrolytic graphite (HOPG) from [BMI]Cl-AlCl₃ represents the first STM experiment in ILs [49]. Ag growth changes from 3D progressive nucleation at a finite number of active sites to 3D instantaneous nucleation with the increase of overpotential. In the far overpotential range, the deposition of Ag mainly takes place at steps and defects. Different from HOPG, the Ag UPD on Au(111) is adsorption controlled, whereas the Ag OPD on Au(111) is diffusion controlled in the same IL [50]. In the UPD range, the 2D Ag islands start to form and later merge into a uniform Ag monolayer. When the potential is further reduced, a second monolayer grows. In the OPD range, a layer-by-layer growth of Ag clusters occurs and is diffusion controlled.

Ruthenium can be electrodeposited on Au(111) from 1-butyl-3-methylimidazolium dicyanamide ([BMI]DCA), which shows a relatively high solubility of RuCl₃ and has a relatively low viscosity. It is important to point out that the formation of Ru(IV) complex is a prerequisite for Ru electrodeposition. With a very slow growth rate of 0.1 nm min⁻¹, thin Ru films with the average thickness of ~5 nm and with a relatively homogeneous morphology can be grown on Au(111) [51].

Rare Metals (Ga, Ti, Ta)

The electrodeposition of Ga on Au(111) has been investigated in [Py_{1,4}][Tf₂N] [52]. STM imaging shows that the first layer of the Ga deposit is composed of islands. The average width of islands is 10–30 nm in width and the height is several nanometers. This is a result of an electroless deposition at the OCP. Further reducing the potential, the bulk deposition of Ga occurs. To clarify the evolution of the Ga nanostructures from UPD to bulk OPD deposition, the electrocrystallization of Ga on Au(111) in two different ILs has been investigated. In [BMI]Cl-GaCl₃, the UPD leads to surface alloying, whereby a Ga-Au surface layer is formed on top of Au(111), while in [BMI]Cl-AlCl₃, 2D phase formation is driven by the conventional nucleation and growth of 2D Ga islands (Fig. 8) [22]. At potentials negative of the UPD, 3D Ga clusters are formed. On the basis of their shape and the coexistence of small and large clusters in contact, it is concluded that the clusters in the size range 5–30 nm are solid. Taking into account that the temperatures during electrodeposition ranged up to 313 K – above the melting point of R-Ga of 303 K – this observation is remarkable.

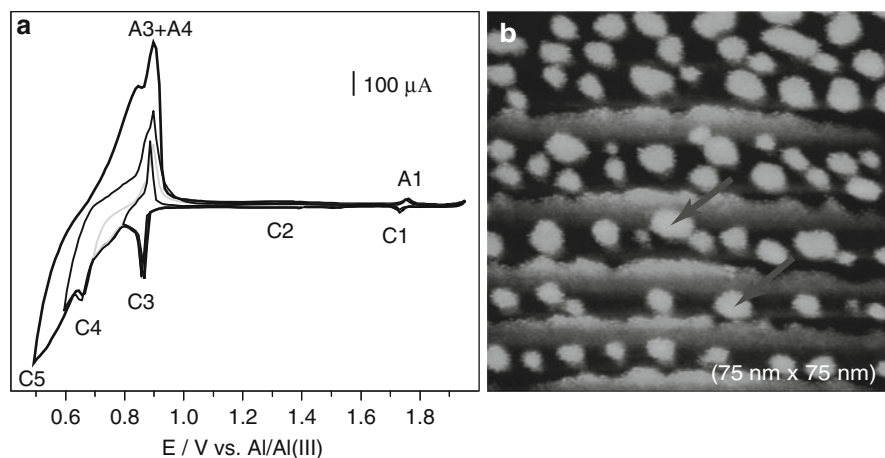


Fig. 8 (a) Cyclic voltammograms of a Au(111) electrode in AlCl_3 -[BMI]Cl (58:42)+5 mM GaCl_3 . The scan rate was 50 mV s^{-1} and the temperature was 298 K. (b) STM images of the Ga UPD on Au(111) at $E=0.7 \text{ V}$ versus Al/Al(III) (Reprinted with permission from Pan et al. [22]. Copyright 2011 American Chemical Society)

The ability to electrodeposit titanium is a breakthrough for making corrosion resistant layers on a variety of technically important materials. The electrodeposition of Ti has been firstly performed on HOPG in [BMI]Tf₂N and an unusual phenomenon, namely, a cooperative nucleation process has been observed [53]. At the initial stage, the first Ti nanowire is formed at the step edge of HOPG; subsequent straight and highly aligned nanowires grow in parallel to the first. Up to six nanowires with a narrow width distribution grow at constant potential over a period of about 20 min. The width of nanowires is $10 \pm 2 \text{ nm}$ and the length is more than 100 nm. Differently, 2D clusters presumably of TiCl₃ precipitates, which is subsequently reduced to metallic Ti, grow and coalesce in [BMI]Cl-AlCl₃ [54]. Ti can also be electrodeposited from its halides (TiCl₄, TiF₄, TiI₄) in [EMIm]Tf₂N, [BMP]Tf₂N, and [P_{14,6,6,6}]Tf₂N. In the best case, an ultrathin layer of Ti or TiCl_x with thickness below 1 nm has been obtained [55].

Tantalum (Ta) is another important coating material, which is capable of resisting high temperature, wear, and severe chemical environments. In [BMP]Tf₂N, a rough layer of Ta forms rapidly on Au(111); some triangularly shaped islands grow above the deposited layer and finally merge to a thick layer [56]. Ta can also be electrodeposited from [Py_{1,4}]Tf₂N. Different from the deposition in [BMP]Tf₂N, small 2D islands are grown on Au(111) and their number increases very slowly with time, and a complete layer is formed in more than 1 h. The deposit consists of 5–30 nm wide islands with an average diameter of 10–15 nm and an overall height of 1–2 nm. Decreasing the potential, the next layers start growing, 3D growth sets in, and some triangularly shaped islands with heights of several nanometers rapidly grow above the deposited layers. These islands grow vertically and laterally and finally merge to an ordered layer [57].

Other Metals (Cd, Pb)

The electrodeposition and anodic dissolution of Cd on Au(111) have been studied in [BMI]Cl-AlCl₃ (42:58) [58]. Prior to the first Cd UPD, STM imaging reveals an ordered adlayer of AlCl₄⁻ anions at potentials positive of 1.0 V versus Al/Al(III). Further reducing the potential, desorption of AlCl₄⁻ anions starts and a ($\sqrt{3} \times \sqrt{19}$) superstructure is formed at 0.95 V. This is presumably due to the coadsorption of Cd-AlCl₄⁻. At lower potentials of 0.45 V, surface alloying of Cd and Au occurs. This is evidenced by typical spinodal structures (Fig. 9), which are revealed both during deposition and dissolution of surface alloy layer. The formation of a complete surface alloy layer is relatively slow and takes about half an hour. At still lower potentials, a layer-by-layer growth of bulk Cd sets in and the layer has a hexagonal structure.

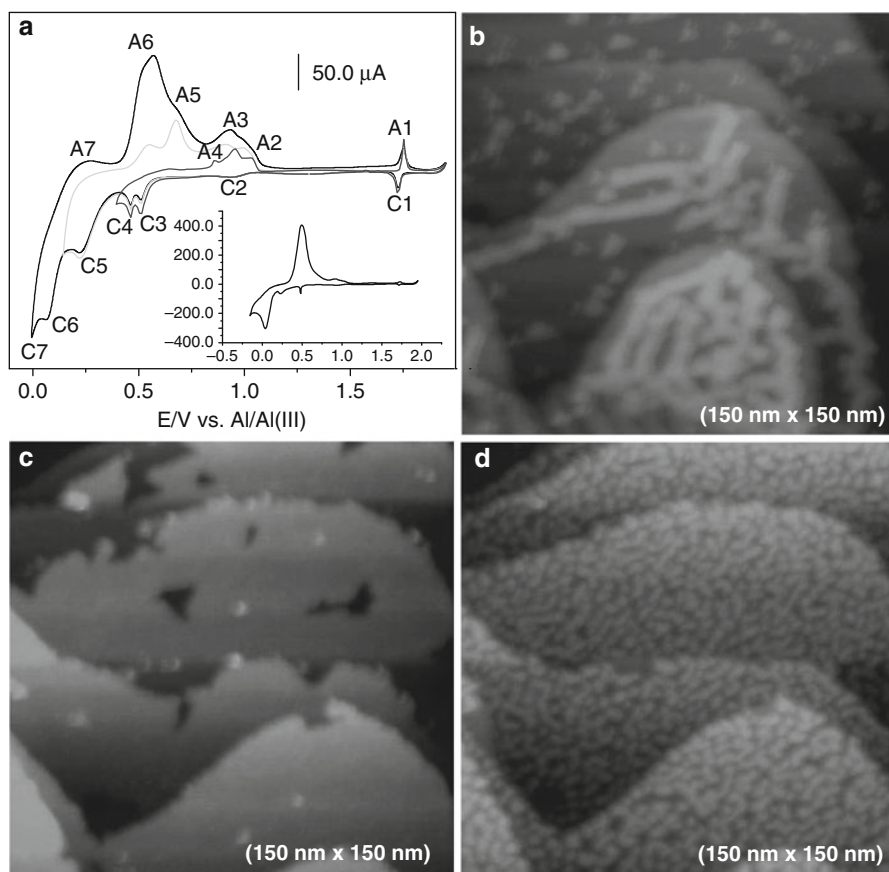


Fig. 9 (a) Cyclic voltammograms of Au(111) in MBIC-AlCl₃+5 mM CdCl₂. The inset is a cyclic voltammogram containing 20 mM CdCl₂. The scan rates are 50 mV/s. (b) STM images of Cd-Au surface alloy layer on Au(111) at E=0.45 V; (c) 30 min after (b); (d) dissolution of Cd-Au surface alloy layer at E=0.85 V (Reprinted with permission from Pan and Freyland [58]. Copyright 2007 Royal Society of Chemistry)

Lead (Pb) can be electrodeposited on Au(111) from [BMI]Cl-AlCl₃ (42:58) [59]. In the UPD range, high-resolution STM images reveal three sequential processes: terrace expansion at 0.8 V, island growth at 0.73 V, and monolayer formation with triangular vacancies at 0.5 V. In the monolayer, a Moiré-like pattern of Pb adatoms is resolved. Moreover, a smooth surface without triangular vacancy is formed when potentials are changed progressively. In this case, a quasi-equilibrium process can be expected. These results indicate that the Pb UPD is diffusion controlled. In the OPD range, the nucleation of 3D Pb crystal starts.

Electrodeposition of Semiconductors

Electrodeposition of semiconductors is advantageous over vapor deposition: (1) the preparation is carried out typically at room temperature, (2) the amount of deposited material is substantially dependent on the charge passed, and (3) the geometrical and electronic structures of the deposits can be directly characterized in situ. However, in comparison with the electrodeposition of metals, in situ STM studies on the electrodeposition of semiconductors are relative limited. One possible reason is that the electrodeposition of semiconductors, in particular element semiconductors of Ge and Si, seems to fail from a variety of ILs.

Elemental Semiconductors (Ge, Si)

The electrodeposition of germanium (Ge) on Au(111) has been successfully carried out in [BMI]PF₆ saturated with GeX₄ (X = Cl, Br or I). In the [BMI]PF₆ + GeI₄, STM images show the formation of 2D islands, which is about 230–270 pm in height [60]. However, stable nanoclusters or thick layers could not be obtained due to the low solubility of GeI₄ in [BMI]PF₆. Thus, other Ge compounds that can dissolve better in [BMI]PF₆ have been investigated. In the [BMI]PF₆ + GeBr₄, a thin rough layer with metallic behavior forms on Au(111) surface (Fig. 10) [61]. The bulk growth begins with the formation of nanoclusters, and 200 nm thick layers show a symmetrical band gap of 0.7 ± 0.1 eV, comparable to intrinsic bulk germanium. Moreover, the most reversible behavior has been observed in [BMI]PF₆ + GeCl₄. Ge deposition starts with the decoration of Au(111) steps in the UPD regime; then small islands of about 150 pm in height grow. This finally leads to a rough thin layer. Similar to the GeB₄, the thin film shows metallic behavior [62]. The variation of the electronic structures of the Ge deposits, going from very thin to thick films, is also investigated by in situ STM on Au (111) and Si(111):H. The interesting results show that a transition from metal to non-metal phase occurs with the increase of film thickness. Moreover, it is indicated that the thin Ge films are probably far from equilibrium and the metallic-like behavior reflects a metastable glass state.

Silicon has been firstly electrodeposited on HOPG in [BMP]Tf₂N saturated with SiCl₄ [63]. STM images reveal a silicon layer with a thickness of 100 nm. However, it is difficult to perform STM on HOPG because only a weak interaction exists

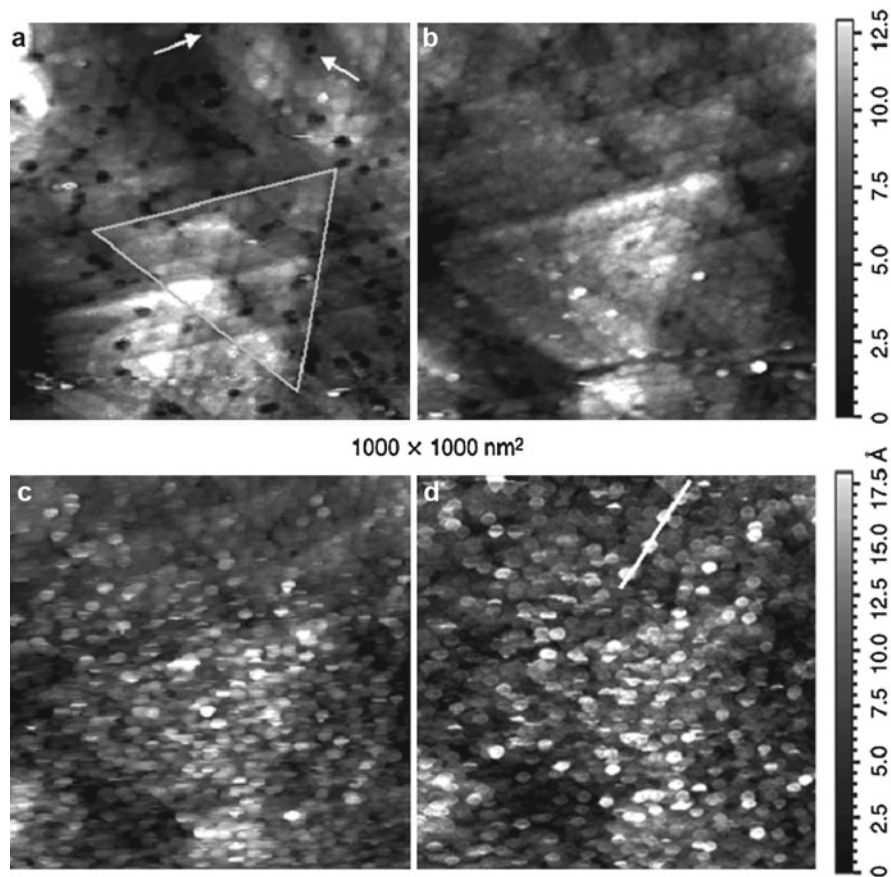


Fig. 10 A set of STM images recorded at different potentials: (a) OCP; (b) swept from +500 mV (*top*) to +50 mV (*bottom*); (c) swept from +50 mV (*top*) to -250 mV (*bottom*); and (d) held at -250 mV. The scan rate was 1 mV s^{-1} (Reprinted with permission from Endres and El Abedin [61]. Copyright 2007 Royal Society of Chemistry)

between HOPG and silicon deposit. From this point of view, Au(111) is a much better substrate. Si deposition starts on the terraces of a reconstructed Au(111) surface. Initially, small Si islands with the height of 0.15–0.45 nm are formed. Then, the islands grow slowly and cover the whole Au(111) after a while. The thickness of the layer is a few nanometers, and this layer has a band gap of $1.1 \pm 0.2 \text{ eV}$, typical for the bulk silicon [64]. It is clear that elemental, intrinsic semiconducting silicon was electrochemically deposited from the $[\text{BMP}]\text{Tf}_2\text{N}$ ionic liquid.

Based on the above results, i.e., electrodeposition of Ge and Si separately, it can be predicted that “SiGe” might be electrodeposited from ILs. $[\text{BMP}]\text{Tf}_2\text{N}$ with large electrochemical window (roughly 6 V for a gold electrode) has been proved favorable for this purpose. Interestingly, the $\text{Si}_x\text{Ge}_{1-x}$ deposit exhibits an obvious color change (from red to blue) during electrodeposition. This is possibly attributed to a

quantum size effect. The as-observed colors are indicative of band gaps between at least 1.5 and 3.2 eV. Therefore, the potential of ILs in $\text{Si}_x\text{Ge}_{1-x}$ electrodeposition is well demonstrated [65].

Compound Semiconductors (AlSb, ZnSb)

Compound semiconductors, such as CdTe, ZnTe, AlSb, and ZnSb, are of potentials in electronic and optoelectronic devices and can be electrodeposited from ILs. The first attempt has been made in the [BMI]Cl-AlCl₃ (45:55) [44]. 3D clusters of Al_xSb_y have been electrodeposited and characterized by in situ STM and scanning tunneling spectroscopy (STS). The results indicate that the Al_xSb_y cluster of ~ 20 nm in size exhibits semiconductor behavior with a band gap of 0.92 ± 0.2 eV. The stoichiometric AlSb has also been electrodeposited successfully from [BMI]Cl-AlCl₃ (1:1) and the corresponding STM images are shown in Fig. 11 [45]. The deposition potential for AlSb is well separated from those for pure Al and Sb. The obtained AlSb clusters

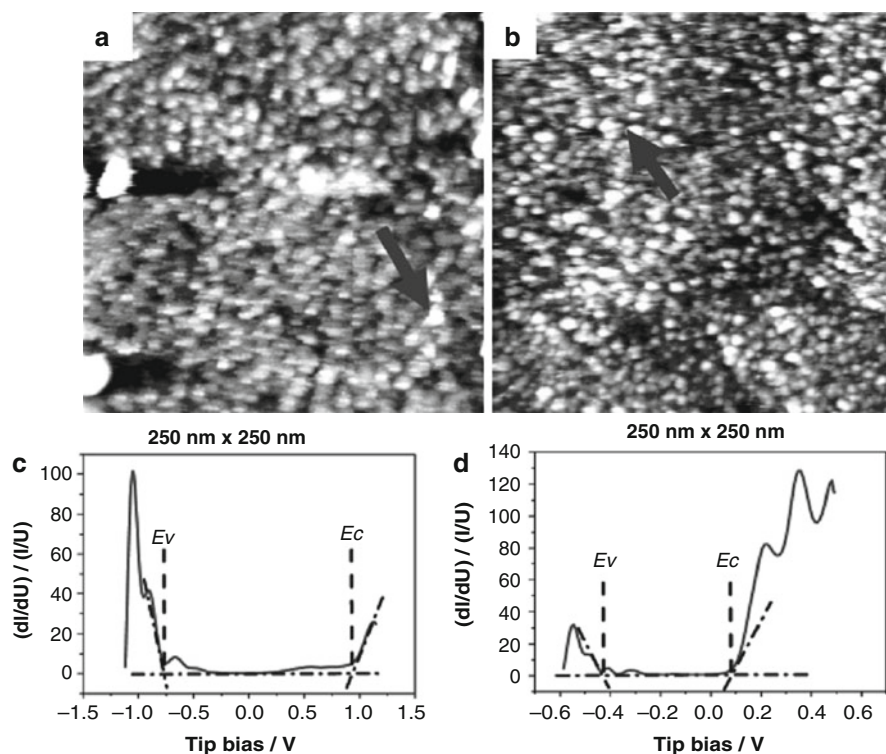


Fig. 11 Typical STM image of $\text{Al}_x\text{Sb}_{1-x}$ alloy formed at -0.9 V (a) and -1.5 V (b). (c, d) Normalized differential conductivity spectra of the clusters marked by arrows in (a, b). Current/voltage curves have been broadened with a one-pole Fourier low-pass filter (Reprinted with permission from Mann et al. [45]. Copyright 2006 American Chemical Society)

are with diameters of ~ 20 nm and exhibit a band gap of 2.0 ± 0.2 eV, the main features of the electronic structure of the bulk semiconductor AlSb.

Recently, compound semiconductor of ZnSb has been successfully electrodeposited from $\text{SbCl}_3\text{-ZnCl}_2\text{-[C}_4\text{mim]Cl}$ and [MBI]Cl-ZnCl_2 [21, 66]. The smallest energy gap in ZnSb is an indirect one with a value of 0.53 eV in the bulk. Near the deposition potential of ZnSb, clusters with the spherical shape are formed and homogeneously distributed. The average diameter of clusters is up to 15 nm. The STS curves of the clusters exhibit an obvious semiconducting behavior with a band gap of -0.6 ± 0.2 eV. More importantly, the corresponding normalized conductance spectra of the deposits, which are grown either on the Sb-rich or Zn-rich side relative to the ZnSb deposition potential, reveal an obvious doping effect.

Conclusion

With the growing demand for nanostructured materials, the interest in fabrication and characterization of low-dimensional systems is continuous strong. Focusing here on electrochemical applications, ILs have proven to be particularly attractive for nanoscale electrodeposition of metals and semiconductors under environment-friendly conditions. In particular, the application of in situ STM has enabled completely new insight into various processes of electrodeposition and comprehensive understanding of the growth mechanism of the deposits. However, the investigations on controlling the various deposition parameters precisely and designing the strategy for deposition of metal, alloy, and semiconductor nanostructure are still urgent and challenging. For example, the deposition parameters such as types of ILs, temperature, potential, and current density substantially affect the deposition process and the morphology of the deposits. We believe that the future work of electrochemical deposition from ILs should focus on the detailed elucidation of the elemental steps of electrochemical phase formation, which includes the nucleation and growth mechanism, the definition of the stability ranges of low-dimensional (1D and 2D) structures forming in UPD region, the influence of substrates, the occurrence of surface alloying, and finally the nucleation kinetics. More importantly, methods based on scanning probe microscopy (e.g., electrochemical STM and AFM) represent one of the most powerful tools, which can be successfully applied at the electrified IL/solid interfaces.

Acknowledgment This work was financially supported by the National Basic Research Program of China (No. 2010CB934100), the National Natural Science Foundation of China (No. 21273272), and the Chinese Academy of Sciences.

References

1. Hapiot P, Lagrost C (2008) Electrochemical reactivity in room-temperature ionic liquids. *Chem Rev* 108:2238–2264
2. Dean PM, Pringle JM, MacFarlane DR (2010) Structural analysis of low melting organic salts: perspectives on ionic liquids. *Phys Chem Chem Phys* 12:9144–9153

3. Ma Z, Yu JH, Dai S (2010) Preparation of inorganic materials using ionic liquids. *Adv Mater* 22:261–285
4. Hayes R, Warr GG, Atkin R (2010) At the interface: solvation and designing ionic liquids. *Phys Chem Chem Phys* 12:1709–1723
5. Torimoto T, Tsuda T, Okazaki KI, Kuwabata S (2010) New frontiers in materials science opened by ionic liquids. *Adv Mater* 22:1196–1221
6. Fujita K, Murata K, Masuda M, Nakamura N, Ohno H (2012) Ionic liquids designed for advanced applications in bioelectrochemistry. *RSC Adv* 2:4018–4030
7. He P, Liu HT, Li ZY, Liu Y, Xu XD, Li JH (2004) Electrochemical deposition of silver in room-temperature ionic liquids and its surface-enhanced raman scattering effect. *Langmuir* 20:10260–10267
8. Abbott AP, Mckenzie KJ (2006) Application of ionic liquids to the electrodeposition of metals. *Phys Chem Chem Phys* 8:4265–4279
9. Armand M, Endres F, MacFarlane DR, Ohno H, Scrosati B (2009) Ionic-liquid materials for the electrochemical challenges of the future. *Nat Mater* 8:621–629.
10. Su YZ, Fu YC, Wei YM, Yan JW, Mao BW (2010) The electrode/ionic liquid interface electric double layer and metal electrodeposition. *ChemPhysChem* 11:2764–2778
11. Abedin SZE, Endres F (2006) Electrodeposition of metals and semiconductors in air- and water-stable ionic liquids. *ChemPhysChem* 7:58–61
12. Binnig G, Rohrer H, Gerber C, Weibel E (1982) Tunneling through a controllable vacuum gap. *Appl Phys Lett* 40:178–180
13. Enderes F (2002) Ionic liquids: Solvents for the electrodeposition of metals and semiconductors. *ChemPhysChem* 3:144–154
14. Kolb DM (2001) Electrochemical surface science. *Angew Chem Int Ed* 40:1162–1181
15. Endres F, Freyland W, Gilbert B (1997) Electrochemical scanning tunnelling microscopy (ECSTM) study of silver electrodeposition from a room temperature molten salt. *Ber Bunsen-Ges* 101:1075–1077
16. Lin LG, Wang Y, Yan JW, Yuan YZ, Xiang J, Mao BW (2003) An in situ STM study on the long-range surface restructuring of Au (111) in a non-chloroaluminated ionic liquid. *Electrochem Commun* 5:995–999
17. Pan GB, Freyland W (2006) 2D phase transition of PF₆ adlayers at the electrified ionic liquid/Au (111) interface. *Chem Phys Lett* 427:96–100
18. Gnahn M, Pajkossy T, Kolb DM (2010) The interface between Au (111) and an ionic liquid. *Electrochim Acta* 55:6212–6217
19. Su YZ, Fu YC, Yan JW, Chen ZB, Mao BW (2009) Double layer of Au (100)/ionic liquid interface and its stability in imidazolium-based ionic liquids. *Angew Chem Int Ed* 48:5148–5151
20. Borissov D, Aravinda CL, Freyland W, (2005) Comparative investigation of underpotential deposition of Ag from aqueous and ionic electrolytes: an electrochemical and in situ STM study. *J Phys Chem B* 109:11606–11615
21. Mann O, Freyland W (2007) Mechanism of formation and electronic structure of semiconducting ZnSb nanoclusters electrodeposited from an ionic liquid. *Electrochim Acta* 53:518–524
22. Pan GB, Mann O, Freyland W, Phys J (2011) Nanoscale electrodeposition of Ga on Au (111) from ionic liquids. *Chem C* 115:7656–7659
23. Gnahn M, Müller C, Répánszki R, Pajkossy T, Kolb DM (2011) The interface between Au (100) and 1-butyl-3-methyl-imidazolium-hexafluorophosphate. *Phys Chem Chem Phys* 13:11627–11633
24. Gnahn M, Berger C, Arkhipova M, Kunkel H, Pajkossy T, Maas G, Kolb DM (2012) The interfaces of Au (111) and Au (100) in a hexaalkyl-substituted guanidinium ionic liquid: an electrochemical and in situ STM study. *Phys Chem Chem Phys* 14:10647–10652
25. Simka W, Puszczczyk D, Nawrat G (2009) Electrodeposition of metals from non-aqueous solutions. *Electrochim Acta* 54:5307–5319
26. Aravinda CL, Mukhopadhyay I, Freyland W (2004) Electrochemical in situ STM study of Al and Ti–Al alloy electrodeposition on Au (111) from a room temperature molten salt electrolyte. *Phys Chem Chem Phys* 6:5225–5231

27. Aravinda CL, Burger B, Freyland W (2007) Nanoscale electrodeposition of Al on n-Si (111): H from an ionic liquid. *Chem Phys Lett* 434:271–275
28. Moustafa EM, El Abedin SZ, Shkurankov A, Zschippang E, Saad AY, Bund A, Endres F, (2007) Electrodeposition of Al in 1-butyl-1-methylpyrrolidinium- bis(trifluoromethylsulfonyl) amide and 1-Ethyl-3-methylimidazolium bis(trifluoromethylsulfonyl)amide Ionic Liquids: in situ STM and EQCM studies. *J Phys Chem B* 111:4693–4704
29. Dogel J, Freyland W (2003) Layer-by-layer growth of zinc during electrodeposition on Au (111) from a room temperature molten salt. *Phys Chem Chem Phys* 5:2484–2487
30. Dogel J, Tsekov R, Freyland W (2005) Two-dimensional connective nanostructures of electrodeposited Zn on Au (111) induced by spinodal decomposition. *J Chem Phys* 122:094703
31. Wang JG, Tang J, Fu YC, Wei YM, Chen ZB, Mao BW (2007) STM tip-induced nanostructuring of Zn in an ionic liquid on Au (111) electrode surfaces. *Electrochem Commun* 9:633–638
32. Gasparotto LHS, Borisenko N, Bocchi N, El Abedinab SZ, Endres F (2009) In situ STM investigation of the lithium underpotential deposition on Au(111) in the air- and water-stable ionic liquid 1-butyl-1-methylpyrrolidinium bis(trifluoromethylsulfonyl)amide. *Phys Chem Chem Phys* 11:11140–11145
33. Endres F, El Abedin SZ, Borissenko N (2006) Probing lithium and alumina impurities in air- and water stable ionic liquids by cyclic voltammetry and in situ scanning tunneling microscopy. *Z Phys Chem* 220:1377–1394
34. Aravinda CL, Freyland W (2004) Electrodeposition of monodispersed Fe nanocrystals from an ionic liquid. *Chem Commun* 2754–2755
35. dos Santos MC, Geshev J, Silva DK, Schmidt JE, Pereira LG, Huber R, Allongue P (2003) Strong dependence of the Fe thin-film magnetic anisotropy on the Si (111) substrate preparation. *J Appl Phys* 23:1490–1494
36. Wei YM, Fu YC, Yan JW, Sun CF, Shi Z, Xie ZX, Wu DY, Mao BW (2010) Growth and shape-ordering of iron nanostructures on Au single crystalline electrodes in an ionic liquid: a paradigm of magnetostatic coupling. *J Am Chem Soc* 132:8152–8157
37. Wei YM, Zhou XS, Wang JG, Tang J, Mao BW, Kolb DM (2008) The creation of nanostructures on an Au (111) electrode by tip-induced iron deposition from an ionic liquid. *Small* 4:1355–1358
38. Zell CA, Freyland W (2003) In situ STM and STS study of Co and Co-Al alloy electrodeposition from an ionic liquid. *Langmuir* 19:7445–7450
39. Lin LG, Yan JW, Wang Y, Fu YC, Mao BW (2006) An in situ STM study of cobalt electrodeposition on Au (111) in BMIBF₄ ionic liquid. *J Exp Nanosci* 1:269–278
40. Zell CA, Freyland W (2002) STM study of 2D and 3D phase formation of Ni and Ni-Al-Alloys during electrodeposition from a chloroaluminate molten salt. *Molten Salts XIII* 19:660–670
41. Mann O, Freyland W, Phys J (2007) Electrocrystallization of distinct Ni nanostructures at the ionic liquid/Au (111) interface: An electrochemical and in-situ STM investigation. *Chem C* 111:9832–9838
42. Fu YC, Yan JW, Wang Y, Tian JH, Zhang HM, Xie ZX, Mao BW, (2007) In situ STM studies on the underpotential deposition of antimony on Au (111) and Au (100) in a BMIBF₄ ionic liquid. *J Phys Chem C* 111:10467–10477
43. Wang FX, Pan GB, Liu YD, Xiao Y, (2010) Electrodeposition of Sb on Au (111) from an acidic chloroaluminate ionic liquid: an in situ STM study. *J Phys Chem C* 114:4576–4579
44. Aravinda CL, Freyland W (1703–1705) Nanoscale electrocrystallisation of Sb and the compound semiconductor AlSb from an ionic liquid. *Chem Commun* 2006
45. Mann O, Aravinda CL, Freyland W, (2006) Microscopic and electronic structure of semimetallic Sb and semiconducting AlSb fabricated by nanoscale electrodeposition: An in situ scanning probe investigation. *J Phys Chem B* 110:21521–21527
46. Pan GB, Freyland W (2007) Electrocrystallization of Bi on Au (111) in an acidic chloroaluminate ionic liquid. *Electrochim Acta* 52:7254–7261
47. Endres F, Schweizer A (2000) The electrodeposition of copper on Au(111) and on HOPG from the 66/34 mol% aluminium chloride/1-butyl-3-methylimidazolium chloride room temperature molten salt: an EC-STM study. *Phys Chem Chem Phys* 2:5455–5462

48. Toney MF, Howard JN, Richer J, Borges GL, Gordon JG, Melroy OR, Yee D, Sorensen LB (1995) Electrochemical deposition of copper on a gold electrode in sulfuric acid: resolution of the interfacial structure. *Phys Rev Lett* 75:4472–4475
49. Endres F, Freyland W, (1998) Electrochemical scanning tunneling microscopy investigation of HOPG and silver electrodeposition on HOPG from the acid room-temperature molten salt aluminum chloride–1-methyl-3-butyl-imidazolium chloride. *J Phys Chem B* 102:10229–10233
50. Zell CA, Endres F, Freyland W (1999) . Electrochemical in situ STM study of phase formation during Ag and Al electrodeposition on Au (111) from a room temperature molten salt. *Phys Chem Chem Phys* 1:697–704
51. Mann O, Freyland W, Raz O, Ein-Eli Y (2008) Electrochemical deposition of ultrathin ruthenium films on Au (111) from an ionic liquid. *Chem Phys Lett* 460:178–181
52. Gasparotto LHS, Borisenko N, Höfft O, Al-Salman R, Maus-Friedrichs W, Bocchi N, Zein El Abedin S, Endres F (2009) In situ STM studies of Ga electrodeposition from GaCl₃ in the air- and water-stable ionic liquid 1-butyl-1-methylpyrrolidinium bis(trifluoromethylsulfonyl) amide. *Electrochim Acta* 55:218–226
53. Mukhopadhyay I, Freyland W (2003) Electrodeposition of Ti nanowires on highly oriented pyrolytic graphite from an ionic liquid at room temperature. *Langmuir* 19:1951–1953
54. Mukhopadhyay I, Aravinda CL, Borisso D, Freyland W (2005) Electrodeposition of Ti from TiCl₄ in the ionic liquid 1-methyl-3-butyl-imidazolium bis (trifluoro methyl sulfone) imide at room temperature: study on phase formation by in situ electrochemical scanning tunneling microscopy. *Electrochim Acta* 50:1275–1281
55. Endres F, El Abedin SZ, Saad AY, Moustafa EM, Borissenko N, Price WE, Wallace GG, MacFarlane DR, Newmanc PJ, Bund A (2008) On the electrodeposition of titanium in ionic liquids. *Phys Chem Chem Phys* 10:2189–2199
56. El Abedin SZ, Farag HK, Moustafa EM, Welz-Biermann U, Endres F (2005) Electroreduction of tantalum fluoride in a room temperature ionic liquid at variable temperatures. *Phys Chem Chem Phys* 7:2333–2339
57. Borisenko N, Ispas A, Zschippang E, Liu Q, Zein El Abedin S, Bund A, Endres F (2009) In situ STM and EQCM studies of tantalum electrodeposition from TaF₅ in the air- and water-stable ionic liquid 1-butyl-1-methylpyrrolidinium bis(trifluoromethylsulfonyl)amide. *Electrochim Acta* 54:519–528
58. Pan G-B, Freyland W (2007) In situ STM investigation of spinodal decomposition and surface alloying during underpotential deposition of Cd on Au (111) from an ionic liquid. *Phys Chem Chem Phys* 9:3286–3290
59. Wang FX, Pan GB, Liu YD, Xiao Y (2010) Pb deposition onto Au (111) from acidic chloroaluminate ionic liquid. *Chem Phys Lett* 488:112–115
60. Endres F, Schrod C (2000) In situ STM studies on germanium tetraiodide electroreduction on Au (111) in the room temperature molten salt 1-butyl-3-methylimidazolium hexafluorophosphate. *Phys Chem Chem Phys* 2:5517–5520
61. Endres F, El Abedin SZ (2002) Nanoscale electrodeposition of germanium on Au(111) from an ionic liquid: an in situ STM study of phase formation Part I. *Phys Chem Chem Phys* 4:1640–1648
62. Endres F, El Abedin SZ (2002) Nanoscale electrodeposition of germanium on Au(111) from an ionic liquid: an in situ STM study of phase formation Part II. *Phys Chem Chem Phys* 4:1649–1657
63. El Abedin SZ, Borissenko N, Endres F (2004) Electrodeposition of nanoscale silicon in a room temperature ionic liquid. *Electrochem Commun* 6:510–514
64. Borisenko N, El Abedin SZ (2006) Endres F In situ STM investigation of gold reconstruction and of silicon electrodeposition on Au(111) in the room temperature ionic liquid 1-butyl-1-methylpyrrolidinium bis(trifluoromethylsulfonyl)imide. *J Phys Chem B* 110:6250–6256
65. Al-Salman R, El Abedin SZ, Endres F (2008) Electrodeposition of Ge, Si and Si_xGe_{1-x} from an air- and water-stable ionic liquid. *Phys Chem Chem Phys* 10:4650–4657
66. Mann O, Pan GB, Freyland W (2009) Nanoscale electrodeposition of metals and compound semiconductors from ionic liquids. *Electrochim Acta* 54:2487–2490

Part III

**Electrochemical Properties
and Characterization of Nanostructured
Materials**

Giorgia Greco

Contents

Introduction.....	742
Experimental Techniques: Theory.....	743
X-ray Absorption Spectroscopy.....	743
X-ray Diffraction Techniques.....	748
X-ray Fluorescence.....	749
Imaging Methods.....	750
Experimental Techniques: Setups and Analysis Results.....	752
TEM Imaging.....	752
X-ray Diffraction and X-ray Fluorescence.....	753
X-ray Absorption Measurements.....	757
Conclusions.....	762
Appendix.....	762
Design and Performances of the XAS PEM Fuel Cell.....	762
Sample Preparation.....	763
In Situ Experimental Setups.....	764
References.....	766

Abstract

Establishing new protocol for nanomaterial characterization of functional materials is an important step in our knowledge for understanding the correlation between atomic changes and electrochemical performances. We propose a combination of different state-of-the-art techniques as a robust approach for nanomaterial characterization, which is suitable in structural refinements of nanocrystalline active systems. This technique of studying microscopic properties of nanomaterials includes XAS (X-ray absorption spectroscopy) ex situ

G. Greco (✉)

Department of Science, University of Roma Tre, Rome, Italy

e-mail: giorgiagreco80@gmail.com

and in situ, XRD (X-ray diffraction), high-resolution TEM (transmission electron microscopy), and XRF (X-ray fluorescence). In particular, we are using the site-selective XAS (performed at international synchrotron radiation facilities) that is sensible to the local structure (up to 5–10 Å around photoabsorbing sites) for characterization of the nanomaterials with singular accuracy. An investigation of the local structure and chemical disorder dynamics of a commercial Pt-Co alloy nanocatalyst, used as electrode material in proton exchange membrane fuel cells (PEMFC), will be presented and discussed.

Keywords

Absorption spectra, clusters • EXAFS in condensed matter • Nanocrystalline materials in electrochemistry • Structure of nanocrystalline materials

Introduction

The study of alternative energy sources is one of the main research subjects. In particular, the nanomaterials developing for applications of energy devices are of great interest today. This interest is driven by physical properties and environmental advantages offered by the nanomaterial technology. For example, nanoparticles of platinum (Pt) used as catalyst in the polymer electrolyte membrane (PEM) fuel cells (FCs) exhibit significantly higher oxygen reduction reaction (ORR) electrocatalytic activities than the same bulk material. In fact, the active catalytic sites are on the surface of the active material (Pt active sites); the nanoscale dimensions increase considerably the ratio of *surface atoms/bulk atoms* so that a high increase in active area and a strong reduction of Pt amount (very expensive material) are obtained. So nanosize can strongly influence the mechanical and electrochemical properties of an active material.

However, a deep structural characterization of nanomaterials is not simple because of the sample nanoscale size; in fact, the nanomaterials are made by only few atoms, and more common characterization techniques could be not achievable. So new protocols for nanomaterial characterization for understanding the correlation between changes in the atomic ordering, changes, and (degradation of) performances are important to be established. This chapter is organized as:

- Section “[Experimental Techniques: Theory](#)” presents the main theoretical aspects of the experimental techniques used in the characterization protocol, namely, X-ray absorption spectroscopy (XAS), X-ray diffraction (XRD), X-ray fluorescence (XRF), and transmission electrons microscopy (TEM).
- Section “[Experimental Techniques: Setups and Analysis Results](#)” presents the details of the experimental setups allowing characterization of the nanomaterials.
- Section “[EXAFS Analysis and Effect of Chemical Disorder](#)” reports about the methodology used to perform Co-Pt nanomaterial atomic structure characterization.

Full characterization of the pristine material Pt-Co sample is discussed in light of results obtained combining experimental data with theoretical calculations.

- Appendix shows experimental setup allowing characterization of the samples and performance of experiments under in situ conditions. Experiments were performed at synchrotron ESRF (Grenoble).

Experimental Techniques: Theory

In this section, the main characteristics of those techniques, such as XAS, XRD, XRF and TEM will be presented. The combination of all of these techniques represents a powerful atomic structure characterization methodology of active nanomaterials. In Table 1, the main informations obtained by the characterization techniques presented are shown.

X-ray Absorption Spectroscopy

One of the most powerful structural techniques that allows to investigate the neighborhood of a photo-absorber atom in a condensed medium is X-ray absorption spectroscopy (XAS) [1–4]. The absorption cross section above a deep core level excitation threshold presents oscillation characteristic of the compound being examined, due to interference effects in the transition matrix element, which in turn are related to a suitably projected density of the unoccupied electronic states. The development for XAS theory has been since the early 1970s, because of the rapid experimental advances obtained by the advent of synchrotron radiation, in particular for the extended X-ray absorption fine structure (EXAFS) [44–46]. The structural signal of EXAFS is defined as the relative oscillation with respect to a smooth total atomic cross section σ_0^t normalized to the atomic cross section of

Table 1 Summary of the main results that can be obtained with the characterization techniques presented in this chapter

Technique	Probe	Information about atomic structure	Results
XRD	X-rays	Long range order	Crystalline structure, primitive cell parameter, phase homogeneity, particle dimension
XAS	X-rays	Local structure	R = distances N = coordination number, σ^2 = Debye-Waller parameter
XRF	X-rays	Chemical components	Presence of impurities not detectable with other techniques
TEM	Electrons	Morphology and long range order	Crystalline structure, morphology of a particle, particle distribution, particle dimension

the edge under consideration σ_0 , i.e., $\chi(k) = [\sigma(E) - \sigma'_0(E)] / \sigma_0(E)$ where $k = \sqrt{2m(E - E_e)}$ is the modulus of the wave vector of photoelectron (E_e being the threshold energy). The contribution to $\chi(k)$ of each atom at a given distance R with is represented by an oscillating signal $A(k) \sin[2kR + \phi(k)]$.

This signal suggested the use of a Fourier transform technique [5–7]; in this way, the contributions from the coordination shells can be isolated. $A(k)$ is the amplitude and is characteristic of the backscattering atom. The dephasing term $\phi(k)$, which can be approximated with a linear function of k , is the sum of two independent functions associated with photo-absorber and backscatterer atoms, respectively, called “amplitude and phase transferability” [8]; this is at the basis of the standard method of EXAFS data analysis [1–4].

The photo-absorption process can be summarized as follows: a primary probe (a high-energy X-ray photon) interacts with a selected atom built in a certain structure. The photon excites a deep core electron that generates a free photoelectron that acts as a secondary probe. The photoelectron is in the continuum state with a defined energy; its wave function diffuses from the excited atom that strongly interacts (Coulomb interaction) with the surrounding atoms. The presence of neighboring atoms causes an effect in the absorption cross section. This can be calculated starting from the isolated atom in a perturbative scattering scheme. It is not possible to limit the expansion to single-scattering terms due to the strong electron-atom coupling, but multiple-scattering (MS) terms of the higher order should be included.

The presence of several atoms around the photo absorber can be probed by MS terms, so they probe the distribution functions of n particle. MS dominant effects are in the low kinetic energy region that corresponds to the X-ray absorption near edge structure (XANES). The MS contributions allow us to perform EXAFS data analysis based on theoretical calculations, GNXAS package [9].

Multiple-Scattering Expansion

For a model cluster, we can consider the problem of calculating the $\chi(k)$ which is relevant to the structure under investigation. The total many-body absorption cross section $\sigma_{tot}(\omega)$ under general conditions can be written in the following way:

$$\sigma_{tot}(\omega) = \int_0^{\infty} \sigma(\omega - \omega') A_c(\omega') d\omega' = \sigma(\omega) |S(\omega)|^2 \quad (1)$$

For transitions to a dipole sorted final state of angular momentum l_0 polarization averaged [10, 11], the XAS cross section is

$$\sigma(\omega) = \sigma_0 \left[\mathcal{J} \frac{1}{\mathcal{J}(l_0)} \frac{1}{2l_0 + 1} \sum_{m_0} \left[T(I - GT)^{-1} \right]_{0,0}^{l_0, l_0} \right] \quad (2)$$

With good approximation, this equation is valid for complex potentials, while for real potentials, it is exact. A complete discussion is referred to Ref. [12].

T and G are the atomic scattering and propagator matrices in a local basis and σ_0 is the atomic cross section. One element of these matrices is identified by the indices

i and j overrunning the several atomic centers in the matter and by angular momenta set L, L' (where $L=l, m$). Every atomic index couple locates an “atomic” block of the matrices. So the T matrix is diagonal block ($T_{i,j}=t_i\delta_{ij}$), and for the atom at center i , the scattering matrix is diagonal in the L indices ($t_i^{L,L'}=t_i^L\delta_{L,L'}$) in the MT approximation, since in the scattering from a single site, the angular momentum is conserved. In terms of the l th potential phase shift δ_i^l at site i , one has $t_i^l = \exp(i\delta_i^l)\sin(\delta_i^l)$. By solving the Schrödinger equation, these quantities can be calculated.

The matrices G_{ij} contain geometrical information on the atoms i and j dispositions regardless of their scattering power. In fact, looking at Eq. 1, the G matrix appears in an inverse expression $(I-GT)^{-1}$; for this reason, the effects of different structural dispositions on the cross section can be decoupled.

Assumed that the norm of the GT matrix (maximum modulus of its eigenvalues) is less than one, $\|GT\|<1$; in this case, the formal matrix expansion $T(I-GT)^{-1}=T(I+GT+GTGT+GTGTGT+\dots)$ is convergent and gives rise to the familiar MS series [11]. The series include χ_n terms defined for each order of scattering n according to the number of propagators G contained in each term of the series.

The χ_n represents the oscillating signals related to the scattering path that starts and ends at the origin with the constraint that successive sites must be distinct:

$$\chi_n(k) = A(k, R)\sin[kR_p + \phi(k, R)] \quad (3)$$

where A and ϕ are smooth functions of k and of the geometrical parameters R . The pertinent signal frequency is determined by the path length R_p .

So XAS cross sections of cluster of N atoms are possible to be calculated. Given the photo absorber “0” and the surrounding atoms i, j, k, \dots , let us skip some steps (details in Ref. [13]); total cross section expansion in the n -body cross sections is useful as

$$\begin{aligned} \sigma(0, i, j, \dots, n) &= \sigma_0 + \sum_i \sigma^{(2)}(0, i) + \\ &+ \sum_{(i,j)} \sigma^{(3)}(0, i, j) + \sum_{(i,j,k)} \sigma^{(4)}(0, i, j, k) + \dots \\ &+ \sigma^{(n)}(0, i, j, \dots, n) \end{aligned} \quad (4)$$

Let us introduce the dimensionless quantities $\gamma^{(n)} = \sigma^{(n)}/\sigma_0$, which represent the irreducible n -body contributions to the EXAFS, Eq. 5 reduces for the dimensionless experimental structural signal to an equivalent expansion χ :

$$\begin{aligned} \chi(0, i, j, \dots, n) &= \gamma_0 + \sum_i \gamma^{(2)}(0, i) + \\ &+ \sum_{(i,j)} \gamma^{(3)}(0, i, j) + \sum_{i,j,k} \gamma^{(4)}(0, i, j, k) + \dots \\ &+ \gamma^{(n)}(0, i, j, \dots, n) \end{aligned} \quad (5)$$

So we obtain a linear relationship between structure (in terms of 2, 3, 4, ... n-body distributions) and signal.

If the system is a cluster (finite), Eq. 6 contains a finite number of terms becoming a series only in the case of a system with an infinite number of atoms.

In this case, it is expected anyway, due to mean-free-path effects, that the higher-order n-body terms are smaller than the lower-order ones and that the series has very good convergence properties.

In GNXAS package, the equation solution of structural problem 1 used is based on the MS calculations for the $\gamma(n)$, substituting in equations

$$\gamma^{(2)}(0,i) = \sigma(0,i) / \sigma_0 - 1 \quad (6)$$

and

$$\gamma^{(3)}(0,i,j) = \sigma(0,i,j) / \sigma_0 - \sigma(0,j) / \sigma_0 - \sigma(0,i) / \sigma_0 - 1 \quad (7)$$

the respective series of MS. Because of the matrices structure in two blocks, for the two-body term 6, solely TG even powers give a contribution, and the matrix expression is

$$\left(\begin{Bmatrix} t_0 & 0 \\ 0 & t_i \end{Bmatrix} \sum_{n=1}^{\infty} \left[\begin{Bmatrix} 0 & G_{0,i} \\ G_{i,0} & 0 \end{Bmatrix} \begin{Bmatrix} 0 & G_{0,i} \\ G_{i,0} & 0 \end{Bmatrix} \right]^n \right)^{0,0} \quad (8)$$

$$= t_0 G_{0i} t_i G_{i,0} t_0 + t_0 G_{0i} t_i G_{i,0} t_0 G_{0i} t_i G_{i,0} t_0 + \dots$$

The MS expansion, pictorially represented in Fig. 1a, results

$$\gamma^{(2)}(0,i) = \chi_2^{(0i0)} + \chi_4^{(0i0i0)} + \chi_6^{(0i0i0i0)} + \dots \quad (9)$$

The necessary number of MS terms depends on bond distance, atomic numbers, and k range involved.

In the region of EXAFS signal, terms up to χ_6 for short bonds are found important while χ_4 is usually sufficient for longer bonds. The configurational average is even efficacious in the damping of MS higher-order signals. Moreover, the MS

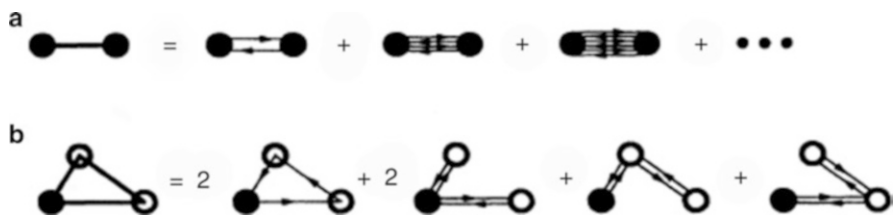


Fig. 1 (a) Schematic view of the expansion MS for $\gamma^{(2)}$ signals that include terms up to χ_6 . The $\gamma^{(2)}$ signals regard for an infinite number of MS paths. (b) Schematic view of the MS expansion for $\gamma^{(3)}$ signals that include terms up to χ_4 . The $\gamma^{(3)}$ signals regard for an infinite number of MS paths (From reference [13])

expansion is peculiar for $\gamma^{(2)}$, the following terms have main frequencies multiple of $2R$, R that is the distance between atoms 0 and i . As a result, there is a big difference of frequency between the main term χ_2 and the next order correction χ_4 .

Starting from Eq. 7, the MS succession for $\gamma^{(3)}(0, i, j)$ can be derived but is more complex (see Ref. [13]). By carrying out the products of matrix, for three-body part, we can obtain terms of any order in the scattering that contain all three atoms 0, i , and j or simply 0 and i or 0 and j .

These two contributions are exactly compensated by the terms resulting from the $\gamma^{(2)}$ signals that appear with negative sign. So in this way, $\gamma_{0,i,j}^{(3)}$ is equal to the sum of all possible MS signals that involve “all and only” 0, i , and j in any possible sequence. The terms with lowest order are the χ_3 signals that correspond to the sequences $O-i-j-O$ and $O-j-i-O$. Due to symmetry of time reversal, the two signals coincide and only one of them can be considered with double degeneracy. This happens for all the paths. When the paths are reversed, they generate a different sequence. These symmetric sequences under inversion happen conversely only once (single degeneracy). In Fig. 1b, $\gamma^{(3)}$ signal is depicted. So not taking into account the triangle geometry, for the χ_n terms successive starting from $R_{O_i} + R_{ij} + R_{j_0}$, the possible paths are multiple and bring a continuous distribution of dominant frequencies. As results, $\gamma^{(3)}$ presents a regular oscillation in k space. Examples of the importance of χ_5 and χ_6 terms have been reported [14]. In general in the low- k range, these higher-order terms contribute producing a total signal modification.

Configurational Average of the Signal

Now, there are different approaches for calculating the MS contribution configurational damping. Reproduce the signal intensity correctly is not simple and is crucial. In particular, GNXAS package uses the algorithm based on an advanced theory, which takes into account the related configurations of vibration of N atom [11] and spherical wave effects. In the small disorder case, the effect of configurational disorder and/or thermal vibrations can be calculated easily. In fact it has represented by an isolated and well-defined peak and the distribution function does not need Gaussian. Also the thermal broadening of crystalline and molecular peaks are included such as the case of low structural disorder. In case of a larger disorder the peaks are not well defined, but are broaden and overlapped. For both of these cases the signal can be reproduced and written in terms of an amplitude and a phase. Synthesists and skipping some steps the theoretical signal can be written in a more general case as a combination of terms for N neighboring atoms, and with thermal and static disorder of σ^2 (mean-square disorder in R). Then, considering a real system, we will have the different types of neighboring atoms at different distances:

$$\chi(k) = \sum_i \frac{N_i A_i(k) e^{-2k^2 \sigma_i^2}}{k R_i^2} \sin[2k R_i + \delta_i(k)] \quad (10)$$

Considering a damped wave function (photoelectron mean free path that includes core-hole lifetime) and amplitude reduction term S_0^2 which takes into

account the relaxation of all the other electrons, we obtain an equation modeling and interpreting EXAFS:

$$\chi(k) = \sum_i \frac{N_i S_0^2 A_i(k) e^{-2R_i/\lambda(k)} e^{-2k^2\sigma_i^2}}{kR_i^2} \sin[2kR_i + \delta_i(k)] \quad (11)$$

If we know $A(k)$, $\delta(k)$, and the mean free path $\lambda(k)$ by EXAFS analysis, we can determine:

1. R distance to neighboring atom
2. N coordination number of neighboring atom
3. σ^2 mean-square disorder of neighbor distance

X-ray Diffraction Techniques

The elastic scattering of X-rays from structures that have long range order is the base on X-ray diffraction (XRD) techniques. The most comprehensive description of scattering from crystals is given by the dynamical theory of diffraction [15].

- XRD of a single crystal is a technique used to determine the complete structure of crystalline materials, such as simple inorganic solids and complex macromolecules (proteins).
- Powder diffraction is a characterization technique used for establishing the crystal structure, crystallite size (grain size), and preferred orientation in polycrystalline or powdered solid samples. Powder diffraction is frequently used to identify substances, by comparing diffraction data against a database maintained by the International Center for Diffraction Data. P

Scherrer Equation

The effects of size and strain can be often separated in the powder diffraction technique, in particular when the size broadening is independent of q ($K=1/d$), strain broadening increases with increasing q -values. But frequently, there will be both size and strain broadening. By combining the two equations, it is possible to separate these with the Hall-Williamson method:

$$B \cdot \cos(\theta) = \frac{K\lambda}{D} + \eta \cdot \sin(\theta) \quad (12)$$

Therefore, when we plot $B \cdot \cos(\theta)$ vs. $\sin(\theta)$, we obtain a straight line with slope η and intercept $\frac{K\lambda}{D}$. This expression is the combination of the Scherrer equation [16] for size broadening and the Stokes and Wilson expression for strain broadening. The η value is the strain in the crystal structure and the D value features the size of the crystallites. K is constant typically ranges from 0.8 to 1.39.

X-ray diffraction and crystallography use a shape factor to correlate in a solid the size of sub-micrometer particles or crystallites to the peak broadening in a diffraction pattern: the Scherrer equation,

$$D = \frac{K\lambda}{\beta \cos \theta} \quad (13)$$

where K is the shape factor, λ is the X-ray wavelength (typically $\sim 1 \text{ \AA}$), β is the line broadening at half the maximum intensity (FWHM) in radians, and θ is the Bragg angle; D is the crystalline mean size (ordered) domains that may be equal to or smaller than the grain size. The shape factor is dimensionless and has a typical value of ~ 0.9 , but it can vary with the real crystallite shape. It is important to know that the Scherrer equation is limited to the particles in nanoscale. It cannot be applicable to particles larger than about $0.1 \text{ }\mu\text{m}$ (the Scherrer formula can calculate only a lower bound on the particle size; in fact, the broadening of the diffraction peak can include a variety of factors; one most important of these is inhomogeneous strain and instrumental effects).

X-ray Fluorescence

Bombarding a material with high-energy X-rays, it will emit a characteristic “secondary” X-ray, which is called X-ray fluorescence (XRF) (or fluorescent). This phenomenon is largely used for elemental and chemical analysis, particularly in the investigation of solid materials like glass, metals, building materials, and ceramics.

X-ray fluorescence spectroscopy is useful for knowing what chemical components are present in a sample, even if those components are in small quantities and in amorphous phase.

The electronic orbital has a characteristic energy for each element. After inner electron excitation in the continuum by an energetic photon given by a primary radiation source, an electron from an outer shell drops into its place. The ways in which this can happen are limited. The main transitions are the following: an $L \rightarrow K$ transition is traditionally called K_{α} , an $M \rightarrow K$ transition is called K_{β} , an $M \rightarrow L$ transition is called L_{α} , and so on. Any transition produces a fluorescent photon with a characteristic energy equal to the difference in energy of the initial and final orbital. The wavelength of this fluorescent radiation can be calculated from Planck’s Law:

$$\lambda = h \cdot c / E \quad (14)$$

This radiation can be analyzed in two ways: first by sorting the energies of the photons (energy-dispersive analysis) and second by separating the wavelengths of the radiation (wavelength-dispersive analysis). Once classified, the intensity of each radiation is related to the amount of each element in the material. This is a powerful technique widely used in analytical chemistry.

Imaging Methods

Transmission electron microscopy (TEM) utilizes imaging methods based on information that are contained in the electron waves exiting from the sample forming an image. The used lenses permit the correct electron wave distribution onto the viewing system. The image intensity, I , can be considered proportional to the time-averaged amplitude of the electron wave function, where the exiting wave forming the exit beam is called Ψ [17]:

$$I(x) = \frac{k}{t_1 - t_0} \int_{t_0}^{t_1} \Psi \Psi^* dt \quad (15)$$

Thus, there are different imaging methods trying to simplify the exiting electron waves in a useful form to obtain information regarding the sample or beam itself. The previous equation evidences that the observed image depends not only on the amplitude of beam but also on the electron phase, while at lower magnifications, phase effects can be ignored. But imaging at higher resolution requires higher energies of incident electrons and thinner samples. Hence, Beer's law effect [18] cannot be applicable at the sample longer, rather it is possible to model the sample as an object which does not change the incoming electron wave function amplitude but the phase of the incoming wave; for sufficiently thin samples, the phase effects dominate and this model is known as a pure phase object [17, 19].

High-Resolution Imaging

When an imaging formation process occurs [20], running the electron beam run through the microscope and different phenomena can be resulting, they can be distinguished (see Fig. 2a):

- In the plane of object, diffraction phenomena
- The image formation in the objective lens back focal plane
- The interference of diffracted beam in the image plane of the objective lens

Due to the Huygens' principle, the electron wave function $\phi_{ex}(r)$ at the exit face of the object can be considered a planar source of spherical waves. In the reciprocal vector \mathbf{g} direction, the amplitude of diffracted wave is given by objected function Fourier transformation:

$$\psi(g) = J_g \psi(r) \quad (16)$$

In the diffraction pattern, the intensity of the distribution is given by $|\psi(g)|^2$ in the objective lens back focal plane.

$$|\psi(g)|^2 = |J_g \psi(r)|^2 \quad (17)$$

If the objective is periodic, the diffraction pattern, the square of the FT of object function, will consist of sharp spots. In the second stage of the imaging process,

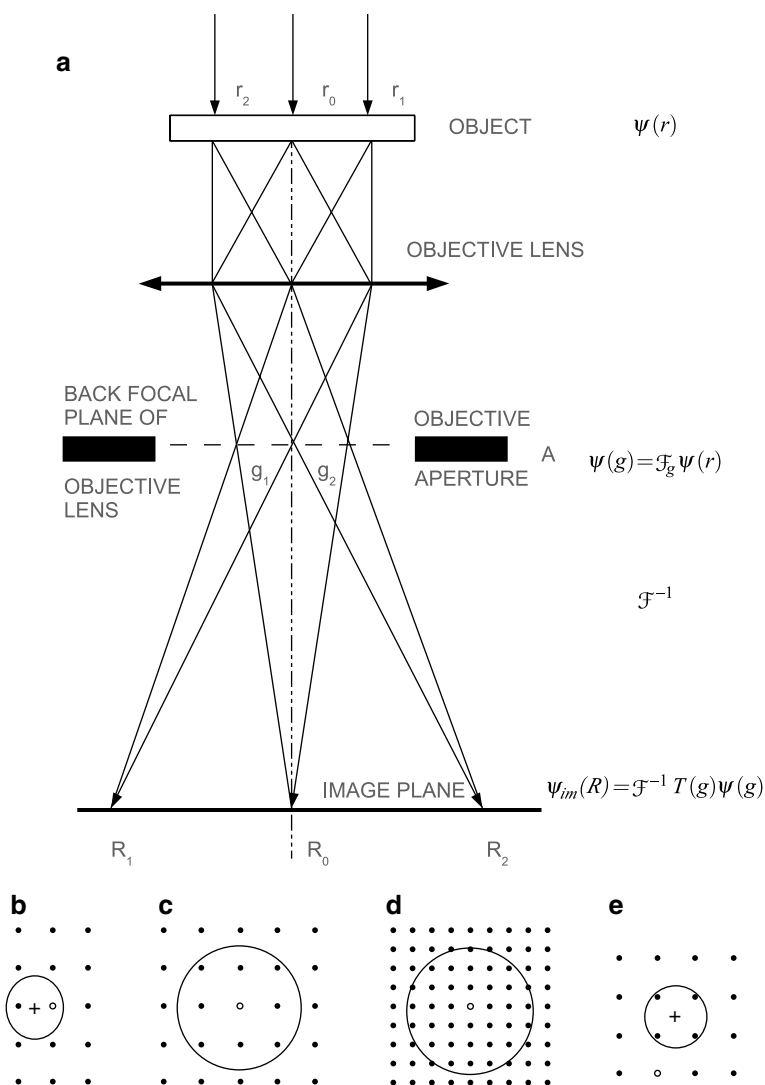


Fig. 2 (a) Image formation in a electron microscope; (b–e) scheme of diffraction patterns and aperture configurations; +, optical axis; o, undiffracted beam; O, objective aperture A as placed in (a) (Adapted from reference [21])

considered a system of lenses the back focal plane acts as a sequence of Huygens' spherical wave sources which interfere in the image plane. Inverse Fourier transform describes this stage in the imaging process that makes an enlarged object function $\psi(R)$. Finally, in the image plane, the intensity is given by $|\psi(R)|^2$. In the second step during the image formation, described by the inverse Fourier transform, the electron beam suffers phase shift $\chi(g)$ with respect to the central beam. This phase shift is

due to spherical aberration and defocus and damped by incoherent damping function $D(\alpha, \Delta, g)$, so at the image plane, the wave function $\psi_{im}(R)$ is obtained as

$$\psi_{im}(R) = J^{-1}T(g)\psi(g) \quad (18)$$

where $T(g)$ is the contrast transfer function (CTF) of thin phase object. $T(g)$ includes damping envelop $D(\alpha, \Delta, g)$ and phase shift $\chi(g)$:

$$\chi(g) = \pi\epsilon\lambda g^2 + \pi C_s \lambda^3 g^4 / 2 \quad T(g) = D(\alpha, \Delta, g) \exp[i\chi(g)]$$

where α is the convergent angle of the incident electron beam and Δ is the half width of the defocus spread ϵ due to chromatic aberration. For the details, consult references [21–23].

The main experimental techniques in common use at present in the field of conventional high-resolution electron microscopy, in phase contrast, are given in Fig. 2b–e [20]. The different imaging modes are determined by the size and geometrical position of the objective aperture in the focal plane back of the objective lens. An image of a lattice fringe is obtained, if only one (or a few) diffracted beams interfere with the unscattered beam (aperture like type b). The period of the fringes corresponds to the interplanar spacing of exited beam. Using aperture type c, many beam images will be observed. For thin crystal having large unit cell parameters under experimental conditions, obtained using type d, the “structure image” could be obtained if the micrograph is directly interpreted in terms of projected atomic arrangement of the crystal structure. If particular diffracted beam of interest interferes and all other beams are excluded, a dark-field lattice image is formed, aperture type e (see Fig. 2).

Experimental Techniques: Setups and Analysis Results

In this section, some important technical and scientific details about the experimental devices used for microstructure characterization of the nano-nanomaterial under various conditions will be discussed.

Some experiments performed on a nanocatalyst sample in different laboratories such as at synchrotron radiation (SR) facilities will be shown as examples.

The order in which the experimental techniques are presented reflects the ideal sequence of material science characterization technique used for nanoparticle analysis.

TEM Imaging

The first important characterization regards the knowledge of mean nanoparticle size, their distribution, if they are well dispersed and have a homogeneous crystal-line structure. This information can be obtained from HRTEM images (transmission high-resolution electron microscopy), looking at the individual particle shape and structure. Here, we would like to show an example: the nanocatalyst under

consideration is composed of Pt-Co alloy metal nanoparticles dispersed on a matrix of Vulcan. HRTEM images have been collected using a JOEL JEM-2100F at the Institute of Mineralogy and Physics of Condensed Matter (IMPMC) of UPMC University, Paris.

Given the size of nanoparticles, we have chosen to perform TEM measurements by JOEL JEM-2100F. In particular by the obtained images, we are able not only to calculate the average particle diameter but also to observe the crystal structure and calculate the distance between crystalline planes, information which allows us to observe possible phase separations. The JEM-2100F is equipped also with other techniques such as scanning transmission electron microscopy (STEM) and energy-dispersive X-ray spectroscopy (EXD) from which we did the elemental analysis and chemical characterization of the samples.

For TEM experiments, sample preparation is a complex procedure. In fact, TEM specimens have to be at most hundreds of nanometers thick, because of the electron beam that interacts quickly with the sample, and this effect increases in first approximation with atomic number squared (z^2) [18].

Quickly preparation by the deposition of a dilute sample containing the specimen onto support grids can be used for such nanomaterials, such as powders like Pt-Co/C nanocatalysts or nanotubes, that have dimensions small enough to be electron transparent.

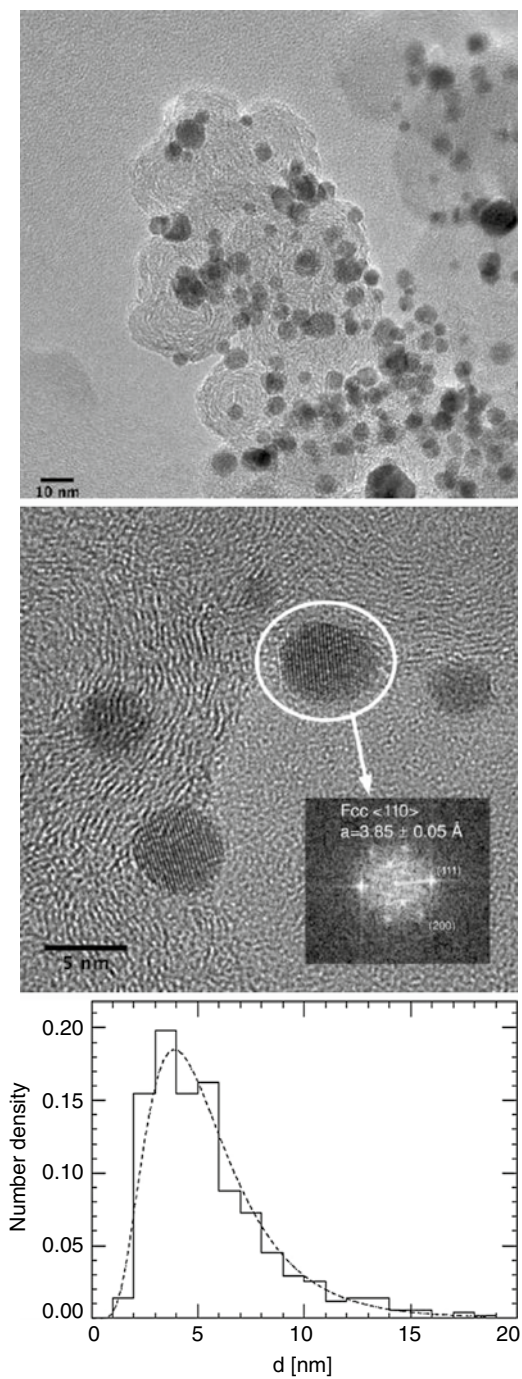
An example of particle size distribution, on the basis of TEM image analysis, using the ImageJ program, (ImageJ, Version 1.38x, Wayne Rasband, National Institutes of Health, USA) has been obtained and presented. The profiles of 500 randomly selected quasi-spherical particles have been taken under a consideration. A typical TEM image of Pt-Co nanoparticles with almost a spherical shape is shown in Fig. 3a–c presenting their size distribution, which is asymmetric and shows a tail extended to large-sized nanoparticles. A log-normal model can be reproduced quite accurately in this size distribution.

The fast Fourier transforms (FFTs) of high-resolution TEM (HRTEM) images [25, 26] calculated by ImageJ program were compared with simulated electron diffraction patterns of ordered Pt₃Co (space group $Pm\bar{3}m$) and ordered Pt-Co (space group $P4/mmm$) [27]. In the FFT images, each spot of diffraction pattern represents a set of equal spacing planes whose direction is normal and corresponds to the straight line connecting this diffraction spot with the transmitted one. This straight length line is proportional to the reciprocal of the interplanar distance. ImageJ program allows the calculation from FFT images of the interplanar distance and the angle between atomic planes that permits in the HRTEM images indexing of lattice fringes (see Fig. 3 in the inset).

X-ray Diffraction and X-ray Fluorescence

From X-ray diffraction technique, information on mean crystalline structure, multiple phases, mean nanocrystals size, and alloy stoichiometry can be obtained. Unlike the TEM results, the obtained informations from XRD are averaged all

Fig. 3 (Top) TEM and (middle) HRTEM images of platinum cobalt nanoparticles supported on Vulcan (E-TEK™). In the inset, lattice reflections are shown at fast Fourier transform (FFT) of the HRTEM image of nanoparticle. (Bottom) Metallic nanoparticle size distribution obtained by TEM image analysis (From reference [24])



over the sample. In fact, the alloys can crystallize in different phases (depending on the alloy composition), such as in ordered and substitutionally disordered form. Furthermore, it is difficult to obtain single phase nanoalloy crystals. So before EXAFS analysis, it is necessary to obtain a preliminary accurate morphological investigation and structural characterization.

Powder diffractometer is the instrument which performs powder diffraction measurements. Two measurement configurations in the diffractometers can be operated: in transmission (Debye-Scherrer configuration) and in reflection mode. The more common is the reflection one. It is based on filling the powder sample in a small container disk and its surface carefully leveled. The disk is putted on one diffractometer axis and tilted by an angle θ ; in the meantime, a detector (scintillation counter) rotates around it on an arm at twice this angle. This is the Bragg-Brentano configuration. Theta-theta configuration represents another diffraction geometry consisting in a stationary position of the sample, while the X-ray tube and the detector are rotated around it. The angle formed between the tube and the detector is 2θ .

For example, in Fig. 4a, typical X-ray diffraction pattern is shown. The peaks represent the Bragg planes with Miller indexes (111) for the first peak, (200), (220), (311), and (222) of the Pt-Co nanomaterial. Peaks are smoother due to the nanosize of the sample. By identifying their position as a function of θ , it is possible to identify the crystalline structure and calculate the cell parameter of the sample.

XRD data analysis has been performed using the PEAKFIT and EDXRD programs that are part of the GNXAS package [9, 13, 28] for XAS/XRD analysis.

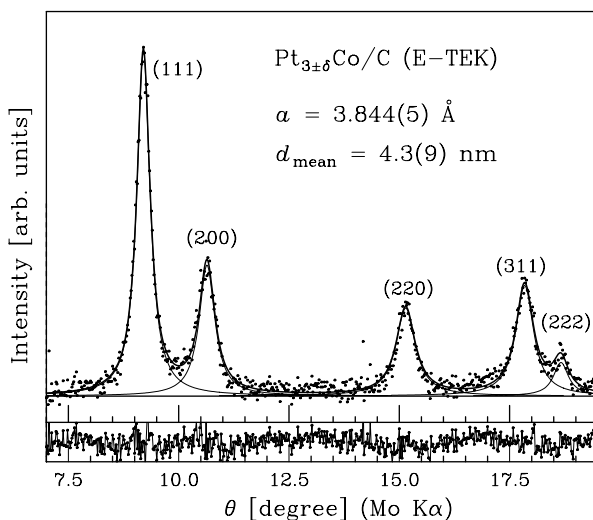


Fig. 4 X-ray diffraction pattern of platinum cobalt nanoparticle powder supported on Vulcan (E-TEK™). The calculated pattern was modeled using Voigt functions (*solid lines*), and experimental data (*points*) are compared. Residual diffraction pattern curve is shown below

Many factors determine the width B of a diffraction peak, including:

1. The presence of defects in the lattice
2. Instrumental factors
3. The crystallites size (peak width, Scherrer equation 13)
4. Strain differences in different grains

Pt-Co nanometric sample shows peaks' position characteristic of fcc structure nanoparticles. The crystalline phase is typical of a single phase because no additional peaks or shoulders are observed in the diffraction pattern.

From the cell parameter obtained can be evaluated also the Co atomic fraction, f_{Co} , by Vegard's law [29–31]:

$$f_{Co} = \frac{a - a_0}{a_s - a_0} f_s, \quad (19)$$

where a_0 and a_s are the lattice parameters of pure Pt (0.3925 nm) and Pt-Co alloy (0.375 nm [32]), respectively. f_s is the reference Co alloy atomic fraction in Pt-Co ($f_s=0.5$) [29, 33].

X-ray fluorescence spectroscopy is useful to know what chemical components that are present in a sample. The typical form of a fluorescence peak is sharp (shown in Fig. 5), and the spectral lines, shown in Fig. 5, are obtained by the wavelength-dispersive method (see Moseley's law).

Energy-dispersive analysis means that the fluorescent X-rays emitted are conducted from the material sample into a solid-state detector which yields a “continuous” distribution of pulses, whose voltages are proportional to the incoming photon energies. A multichannel analyzer (MCA) can process this signal producing a digital spectrum which can be converted to analytical data.

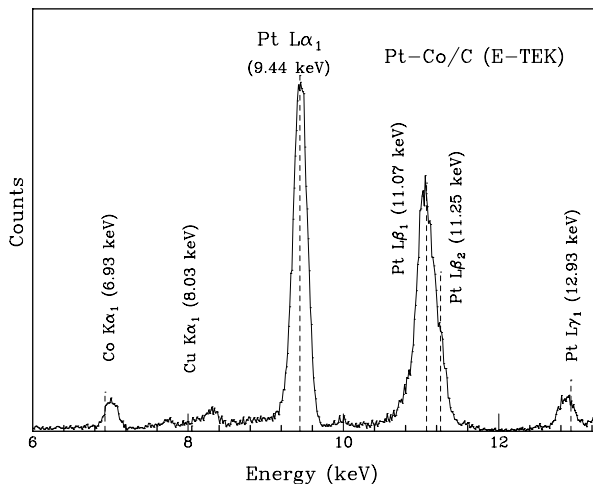


Fig. 5 Typical energy-dispersive XRF spectrum: spectra of Pt-Co powder (E-TEK™)

X-ray Absorption Measurements

XAS spectra could be acquired in two different modes: transmission and fluorescence modes. The X-ray absorption coefficient $\mu(E)$ of a material as a function of energy is measured by XAS. The sample is hit by X-rays. The incident and transmitted X-ray intensity is recorded when the incident X-ray energy is incremented. The transmitted number of X-ray photons through a sample (I_t) is equal to the number of X-ray photons irradiated on the sample (I_0) multiplied by a decreasing exponential depending on the atom type embedded in the sample structure, the absorption coefficient μ , and the thickness of the sample x : $I_t = I_0 e^{-\mu x}$. The log ratio of the incident X-ray intensity to the transmitted X-ray intensity represents the absorption coefficient

$$\mu x = \log(I_0 / I_t) \quad (20)$$

In performing XAS, measurements in transmission mode are necessary to prepare pellets by slightly grinding sample hand mixing the powdered material with graphite in given proportions calculated with specific software (XASAM). Optimizing the absorption jump, the bulk absorption effects were minimized, improving the display of pre- and post-edge details. For example, the values obtained for a 30 % of Pt-Co and 70 % of Vulcan pellet with a diameter about 13 and 2 mm of thickness are shown in Table 2. Typical XAS signals obtained in transmission mode are shown in Fig. 6.

When the amount of the sample is very low, fluorescence XAS measurements are necessary, for example, during the in situ experiments, when the sample is not the pristine material as a powder but is an electrode.

Fluorescence mode means to measure fluorescence emitted by secondary electron falling to core level. In order to obtain reliable measurements in fluorescence mode, the amount of tested material in the sample has to be very low.

Table 2 XASAM program output: Information obtained for an optimal XAS jump, J is the jump obtained using the $\rho(\text{mg}/\text{cm}^2)$ value in 30 % Pt-Co and 70 % of Vulcan (E-TEK) sample. The pellet has a surface area of approximately 1.32 cm^2 . Multiplying the pellet area to ρ the result is the number of milligrams of the sample that have to be put in a mixture with high-purity graphite (Alfa Aesar)

Edge	E(eV)	$\sigma \left(\frac{\text{cm}^2}{\text{g}} \right)$ –	$\sigma \left(\frac{\text{cm}^2}{\text{g}} \right)$ +	J	$\rho \left(\frac{\text{mg}}{\text{cm}^2} \right)$	Opt. sam. size d(μm)
Pt L ₁ -edge	13,892	50.64	57.64	0.17	24.1	241.0
Pt L ₂ -edge	13,273	41.76	56.51	0.36	24.6	245.8
Pt L ₃ -edge	11,564	26.65	58.92	0.76	23.6	235.7
Co K-edge	7,709	67.25	77.41	0.18	17.9	179.4

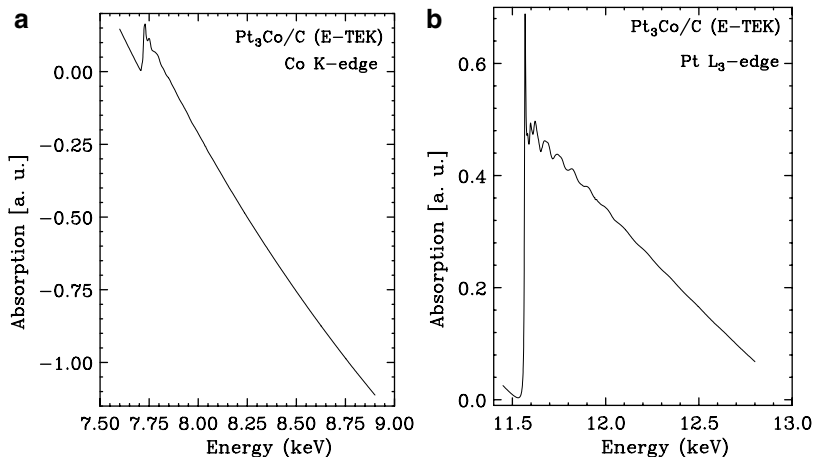


Fig. 6 30 % Pt-Co/C (E-TEK) X-ray absorption spectra measured at ELETTRA (Trieste); (a) Co K-edge, (b) Pt L_3 -edge

In fact, the intensity measured by an X-ray fluorescence detector, $I_f(E)$, is related to the intensity of the incoming X-ray beam, $I_0(E)$, and the “X” atomic species absorption coefficient $\mu_X(E)$ is linear Refs. [34–36]:

$$I_f = \frac{I_0(E)(\Omega/4\pi)\varepsilon_X\mu_X(E)}{\mu_{tot}(E) + \mu_{tot}(E_f)} \frac{\sin\phi}{\sin\theta} \left[1 - e^{-\left[\frac{\mu_{tot}(E)}{\sin\phi} + \frac{\mu_{tot}(E_f)}{\sin\theta} \right] d} \right] \quad (21)$$

where $\mu_{tot} = \mu_X + \mu_{oth}$ indicates the total linear absorption coefficient (μ_{oth} associated with other atoms within the sample), ε_X is the fluorescence produced by the photoabsorbing atom X, and $\Omega/4\pi$ is the solid angle with the detector (angles ϕ and θ are defined in Fig. 11b). In our experiments, μ_{tot} is associated with electrodes of very low catalyst loading. In this way, the transmission of the small thickness approximation can be applied to our case [1–3]. Within this limit, the exponential in Eq. 21 reduces to

$$1 - \exp\left[\left(\frac{\mu_{tot}(E)}{\sin\phi} + \frac{\mu_{tot}(E-f)}{\sin\phi} \right) d \right] \approx \left(\frac{\mu_{tot}(E)}{\sin\phi} + \frac{\mu_{tot}(E-f)}{\sin\phi} \right) d \quad (22)$$

Taking into account the approximation in Eq. 22 and the geometry used in this experiment ($\sin\phi = \sin\theta = \sqrt{2}/2$), Eq. 21 becomes

$$\begin{aligned}
 I_f(E) &= I_0(E) \frac{\Omega}{4\pi} \varepsilon_x \mu_x(E) \sqrt{2d} \\
 \Rightarrow \mu_x(E) &\propto \frac{I_f(E)}{I_0(E)}
 \end{aligned}
 \tag{23}$$

The interpretation of the raw XAS data in relation with the catalytic layer is simplified by result in Eq. 23 without ulterior theoretical corrections. But, when there are high-absorbing catalyst supports and/or excessive catalyst loading, this approximation in Eq. 23 can fail. Working in fluorescence mode can be an advantage for the small thickness approximation; in fact, inhomogeneities of the sample do not severely affect the XAS measurements as in the transmission mode.

EXAFS Analysis and Effect of Chemical Disorder

This section presents an example of a detailed XAS structural investigation of nanocrystalline Pt-Co supported on Vulcan (E-TEK™, 30 % of metal and 70 % of an amorphous and porous phase of carbon called Vulcan), used as a catalyst material in fuel cell applications in order to show and explain the characterization method. Results obtained by TEM and XRD demonstrate that the Pt-Co/C sample can be treated as constituted by a homogeneous ensemble of Pt_{3±δ}Co fcc nanocrystalline particles with a mean diameter of ~5 nm. Moreover, the average local structure of Pt-Co/C can be assumed very similar to the bulk crystalline Pt₃Co (as for Pt nanoparticles [37]) confirmed by XAS, TEM, and XRD results.

The Pt₃Co alloy has an *L1*₂ structure (Cu₃Au-like) [32]. In this structure, Pt atoms are substituted by Co atoms at the corners of the crystal structure of the face-centered cubic (fcc). Using theoretical calculations of the X-ray absorption cross section with GNXAS method, the experimental EXAFS data have been analyzed [13, 28]. The theoretical XAS signal for various two-body and three-body configurations of a typical fcc *L1*₂ structure has been calculated, and the details are listed in [24].

In crystalline alloys of platinum cobalt chemical, disorder is present and the disorder degree depends on the thermal treatment and preparation procedures. A simple methodology to reproduce the effect of substitutional disorder was used to calculate the coordination numbers (CNs) and multiplicities of the multiple-scattering signals contributing to the EXAFS spectra.

Chemical disorder affects the CNs components (Pt-Co, Co-Pt, Co-Co and Pt-Pt first and farther neighbor). So with a simple computer simulation scheme, the multiplicities of the main local two-body and three-body fcc *L1*₂ configurations as a function of the degree of chemical disorder (see also Ref. [38]) have been calculated. This was obtained by introducing the occupation probabilities of the lattice sites. We have considered a 6×6×6 supercell containing 216 fcc units (*a*=3.385 Å) for a total number of 864 atoms in order to minimize the effects of the finite size of our calculations.

By introducing a finite probability $0 \leq p \leq 1$ for the occupancy of selected lattice sites with Co atoms, substitutional disorder is simulated. In detail, *p* is taken as the probability that a Co atom occupies the site at the corner of the fcc cell ((0, 0, 0) position in each fcc unit, see Fig. 7a). While $(1-p)/3$ is the Co occupation probability

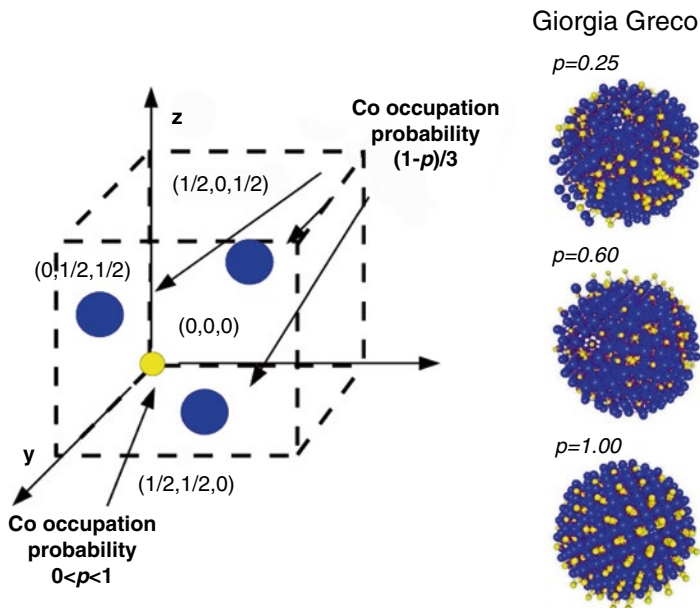


Fig. 7 (Left side) $L1_2$ primitive cell, the arrows indicate the Co occupation probability for every site. (Right side) Three different spherical nanocrystals with an fcc $L1_2$ structure and with a different degree of chemical disorder (From reference [24])

of any of the three other sites of the fcc unit ($(1/2, 1/2, 0)$, $(0, 1/2, 1/2)$, $(1/2, 0, 1/2)$ positions). In this way for a great number of crystalline sites, the stoichiometry in the thermodynamic limit is preserved.

The range $0.25 < p < 1$ is considered in the calculation that includes from a completely ordered structure ($p=1$) to a completely disordered one ($p=0.25$, for which no preferential position can be defined for Co). Three examples of spherical clusters in Fig. 7b (obtained using selected cutoff radii for the supercells) and different chemical ordering p are shown. It has to be underlined that the model does not reproduce a real atomic structure and dynamics in nanocrystalline materials including grain boundaries.

We found that CNs and degeneracy associated with the amplitude of the MS XAS signals are deep influenced by the chemical disorder. In fact, some CNs drop to zero for the fully ordered structure, while most CNs and degeneracy are slowly varying for p lower than 0.4. An appropriate order parameter is defined as

$$s \frac{p - C_a}{1 - C_a}, \quad (24)$$

where p is the occupation probability defined above and C_a is the atomic concentration of the selected chemical species ($1/4$ for Pt_3Co). In this way, $s=0$ indicates random occupancy ($p=1/4$) and $s=1$ perfect order.

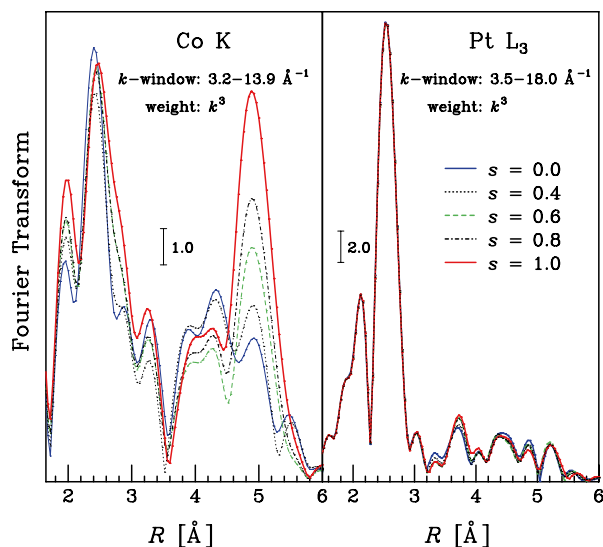


Fig. 8 (Colors online) Fourier transforms of the Pt L_3 and Co K theoretical XAS signals calculated for different values of the disorder parameter s (structural parameters optimized for the $Pt_{3\pm 0}Co$ nanoalloy) (From reference [24])

The most evident changes are founded in the CNs/degeneracy of the fourth-shell atoms (180° configurations) that can be considered as flags for chemical ordering in these alloys (along with the presence of Co-Co first neighbors). Figure 8 shows the Fourier transforms (FTs) of the Pt L_3 - and Co K-edge theoretical XAS signals calculated for different values of the disorder parameter s .

It has to be underlined that chemical disorder affects in particular the Co K-edge FT modifying the intensity of the FT peak around 5 \AA that is associated with collinear configuration changes of a factor of 3 between the limiting cases $s=0$ and $s=1$. Moreover, nanoparticle size affects also the total CNs, so reduction (first neighbor CN is ~ 11 instead of 12 for particles with a mean size about 5 nm) due to the finite size effect is taken into account using other simulations performed for fcc nanoparticles [37]. All of these constraints guarantee a robust structural refinement for double-edge EXAFS data analysis of the nanocrystalline $Pt_{3\pm 0}Co/C$ sample, using a total of 15 structural parameters over around 1000 experimental points and including all of the MS signals up to the fourth coordination shell [24].

Concluding and combining all results, the nanoparticle chemical disordering was found to be measurable with high accuracy. Moreover, compared to Pt, Co local structure is characterized by a higher level of structural disorder, verified also by the higher variances in interatomic distances.

This approach based on combining different state-of-the-art techniques allows us to conclude that it is robust and successful for nanomaterial characterization and is also appropriate for applications in structural refinements of any nanocrystalline active system. The mentioned above data analysis methodology is now applied for analyzing changes in local structure under in-operandi condition in a real fuel cell and during ageing process [39].

Conclusions

This chapter describes different characterization techniques such as TEM (transmission electron microscopy), XRD (X-ray diffraction), and in particular the site-selective XAS (X-ray absorption spectroscopy) that, when combined together in the correct way, represent a robust method for nanomaterial characterization. In this chapter, also a brief theoretical base of these techniques is presented. Particular evidence is given to XAS technique that permits not only a deep nanomaterial characterization (e.g., alloy chemical ordering identification) but also in situ characterization. An application of this method and this statement to Pt-Co nanomaterial used as catalyst in proton exchange membrane fuel cell is also presented.

Appendix

Design and Performances of the XAS PEM Fuel Cell

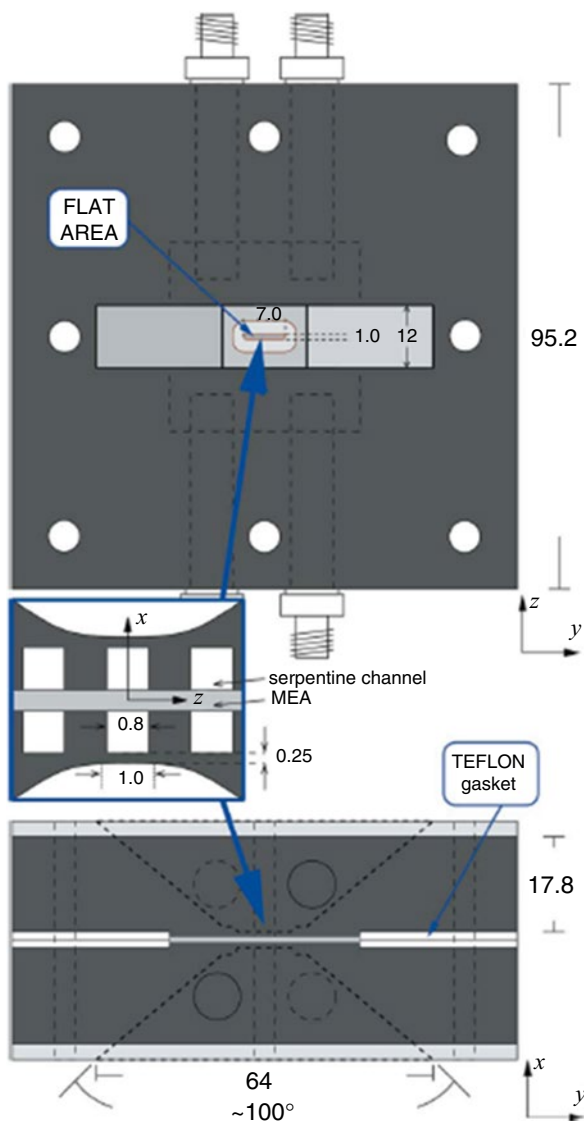
This section describes the experimental setup used to perform in cell measurements. For optimizing in situ XAS measurements on the catalyst during original electrochemical activity, a standard pemmican has been modified ad hoc [40]. In situ X-ray investigations of active materials first need to reduce the background absorption due to the various components of the cells. The thickness of the electrodes and membrane cell components has to be severely restricted if we would like to probe the valence and structure of metals participating in the catalytic process.

Due to this restriction, standard PEM fuel cells must be modified; the body of the cell was modified designing suitable windows for X-ray investigations. For obtaining XAS measurements in transmission mode with low noise, an EFC-05-02 (Electrochem) fuel cell was modified to achieve high transmission rates for photon energies in energy range about 515 keV, where the materials used as catalyst have most of the core levels.

The commercial fuel cell is made by two isotropic graphite separator plates, a 5 cm² active area (serpentine flow pattern) and two gold-plated current collectors. Eight screws keep together the plates of graphite; in this way, a high enough compression on the membrane electrode assembly (MEA) is induced providing a good electrical contact. In order to obtain maximum X-ray transmittance, two thin graphite windows (light and gas tight) are hollowed in the EFC-05-02 cells. The total graphite thickness obtained up to 0.25 mm, over a flat 1 mm × 7 mm area, providing a double window for XAS in transmission mode and possible X-ray fluorescence and X-ray diffraction measurements owing to the wide angular acceptance (~100° on the beam plane, ~5 % covered solid angle), as shown in Fig. 9. The X-ray window is positioned to be parallel (y) and in correspondence (z) with the serpentine channels (width 0.8 mm) in order to minimize absorption.

This modified cell allows standard condition XAS measurements at EXAFS beamlines with a typical beam size of ~0.4 mm × 5 mm. The cell position can be easily modified during the experiment in respect of beam, allowing the best geometry for the experimental technique in use. More details are listed in [40].

Fig. 9 Schematic view of the modified fuel cell optimized for in situ X-ray absorption measurements (front and side views, dimensions given in mm). The front view shows the drilling of the electrode of graphite in order to reduce the X-ray absorption saving space for the fuel channels (hydrogen and oxygen). Each graphite plate has a minimal thickness about 0.25 mm, thus minimizing the absorption along the X-ray path (x , see *inset*). The side view shows the wide angular aperture allowing for possible X-ray diffraction and X-ray fluorescence measurements; the cell MEA positioning is also shown (From reference [40])



Sample Preparation

Electrochemical and structural measurements were performed on electrodes. The catalytic layers were prepared using E-TEK 30 % Pt₃Co supported on Vulcan XC-72 powder (with total metal loading of about 1.0 mg/cm²).

The metal loading was counted from the weight. Membrane electrode assemblies (MEAs) used to perform cathode catalyst degradation were composed of

Nafion® N-112R as a proton conductive membrane and Pd (30%Pd/Vulcan XC-72 powder, Pd loading 1.0 mg cm^{-2}) as an anode catalyst.

In the X-ray beam window region, a Pd counter electrode [41] was used in order to prevent perturbations of the electrical field on the catalyst under consideration [42, 43]. Before XAS measurements, each new MEA was subjected to conditioning process at a voltage of $\sim 0.5 \text{ V}$ for 15 min, and then Rapid Check cell performances by electrochemical cycles were done.

In Situ Experimental Setups

A typical setup for in situ XAS experiments in transmission mode at the BM29 (ESRF) or XAFS 11.1 (ELETTRA) beamlines is shown in Fig. 10. In those beamlines, the XAS fuel cell described before has been tested.

In a standard transmission configuration, the fuel cell has been positioned and aligned along the beam with motorized translation stages. The reference sample has been included for a more precise energy calibration. The cell channels for oxygen and hydrogen gas were connected to their lines working at 1.2 bar (the gas flow was set to $\sim 100 \text{ ml min}^{-1}$). During XAS measurements, the voltage output was remotely controlled by a computer-driven potentiostat/galvanostat and continuously stored.

Figure 11 shows the setup, which allows measurements both in transmission and in fluorescence modes. Looking at Fig. 11, the fuel cell has been installed between the ionization chambers I_0 and I_1 at the X-ray spectrometer BM29 (ESRF) close to a 13-channel Ge X-ray detector (I_f). Figure 10 shows the setup schematic view, and it is possible to identify the fuel cell, the gas lines (humidified O_2 and H_2), the electrical connections necessary to operate the cell, and the X-ray fluorescence detector located on the left side. The pressure of the gases has been set to 1 atm; the gas flux

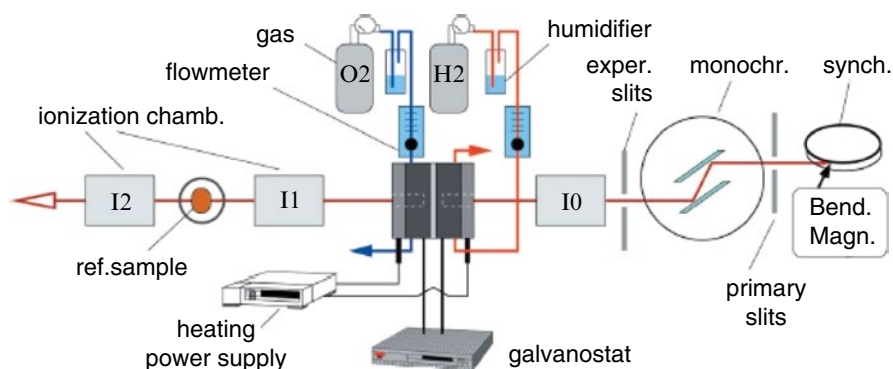
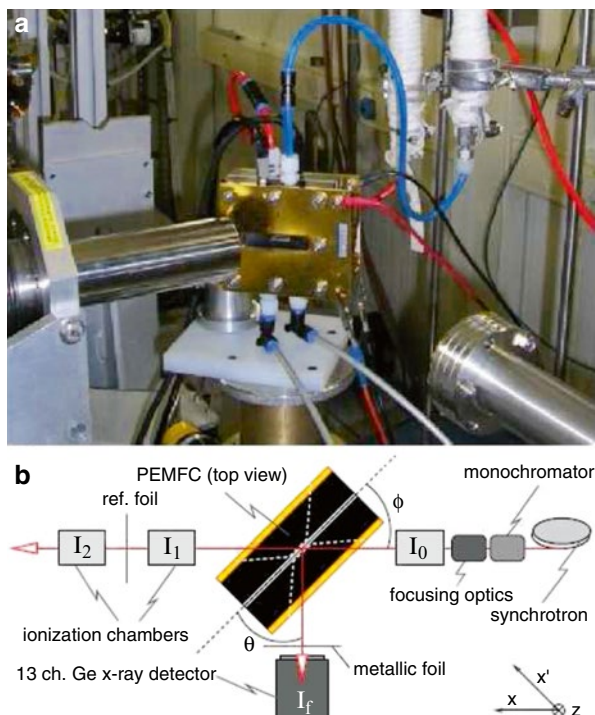


Fig. 10 Typical setup for XAS experiments on fuel cells under operating conditions (From reference [40])

Fig. 11 (a) Picture taken at the BM29 beamline (ESRF) that shows the modified fuel cell positioned close to the 13-channel Ge X-ray detector (on the *left*) on the beam direction. (b) The schematic experimental setup top view $\theta = \phi = 45^\circ$. The absorption coefficient $\mu(E)$ of selected atomic species embedded inside the electrode can be measured both in transmission mode ($\mu(E) = \ln(I_0/I_1)$) and in fluorescence mode ($\mu(E) \propto I_f/I_0$). The absorption coefficient of a reference sample is measured ($\mu(E) = \ln(I_1/I_2)$) at the same time



was about 100 ml min^{-1} . The fuel cell has been located with an angle of 45° with respect to the X-ray beam direction. In order to maximize the recovered solid angle, the multichannel detector has been positioned close to the cell at 90° to the incident beam in the synchrotron (horizontal) plane.

Taking advantage of this geometry and the twofold wide aperture machined on both sides of the cell, simultaneous XAS measurements in transmission and energy-dispersive fluorescence (EDXRF) mode can be carried out (see Fig. 11) without further alignment.

So make the most of this geometry simultaneous XAS measurements in transmission and energy-dispersive fluorescence (EDXRF) mode can be carried out (see Fig. 11) without further alignment. The quality of the carried-out signals is really good as shown in Fig. 12 where extracted EXAFS signals of Pt-Co nanocatalyst at different potentials are presented for both ages. It has also to be underlined that the Co quantity in the electrode is very few (0.1 mg/cm^2) in spite of the quality of the signal being more than satisfactory

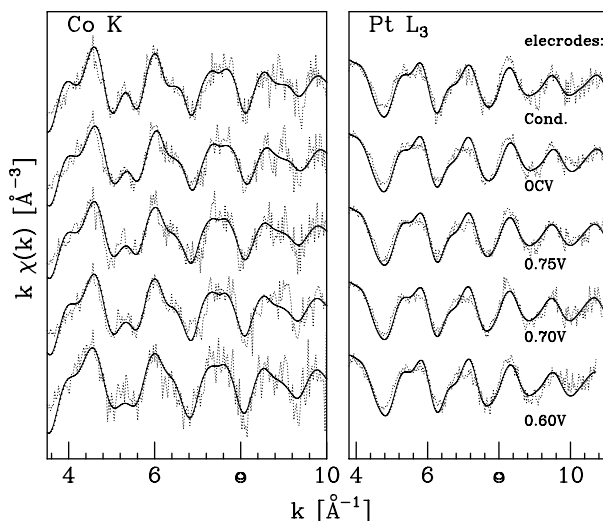


Fig. 12 30 % Pt-Co/C electrode in situ EXAFS signals at different potentials. Starting from the top of the figures: electrode conditioned, at OCV, 0.75, 0.70, and 0.60 V. Dotted lines represent the experimental signals and the solid lines the theoretical ones

References

1. Lee PA, Citrin P, Eisenberger P, Kincaid B (1981) Extended x-ray absorption fine structure—its strengths and limitations as a structural tool. *Rev Mod Phys* 53:769
2. Teo BK, Joy DC (1981) EXAFS spectroscopy, techniques and applications. Plenum, New York
3. Hayes TM, Boyce JB (1982) EXAFS spectroscopy. In: Eherenreich H, Seitz F, Turnbull D (eds) *Solid state physics advances in research and applications*, vol 37. Academic, New York, p 173
4. Koningsberger DC, Prins R (eds) (1988) X-ray absorption: principles, applications, techniques of EXAFS, SEXAFS, and XANES. Wiley, New York
5. Sayers DE, Stern EA, Lytle FW (1971) New technique for investigating noncrystalline structure: fourier analysis of the EXAFS. *Phys Rev Lett* 27:1204
6. Stern EA, Sayers DE, Dash JG, Shechter H, Bunker B (1977) Adsorbate and substrate characterization using extended X-ray absorption fine structure. *Phys Rev Lett* 38:767
7. Stern EA, Heald SM, Bunker B (1979) Amplitude of the extended-X-ray-absorption fine structure in bromine molecules. *Phys Rev Lett* 42:1372
8. Citrin H, Eisenberger P, Kincaid BM (1976) Transferability of phase shifts in EXAFS. *Phys Rev Lett* 36:1346
9. GNXAS (2009) In: Di Cicco A (ed) *Extended suite of programs for advanced X-ray absorption data-analysis: methodology and practice*. TASK Publishing, Scientific Bulletin of Academic Computer Center in Gdansk, Poland. ISBN 978-83-908112-8-4
10. Benfatto M, Natoli CR, Bianconi A, Garcia J, Marcelli A, Fanfoni M, Davoli I (1986) Multiple-scattering regime and higher-order correlations in x-ray-absorption spectra of liquid solutions. *Phys Rev B* 34:5774
11. Natoli R, Benfatto M (1986) A unifying scheme of interpretation of X-ray absorption spectra based on the multiple scattering theory. *J Phys (Paris) Colloq* 47:C8–C11

12. Tyson TA, Hodgson KO, Natoli CR, Benfatto M (1992) General multiple-scattering scheme for the computation and interpretation of x-ray absorption fine structure in atomic clusters with applications to SF₆, GeCl₄, and Br₂ molecules. *Phys Rev B* 46:5997
13. Filippini A, Di Cicco A (1995) X-ray absorption spectroscopy and n-body distribution functions in condensed matter ({I}): theory. *Phys Rev B* 52:15122
14. Filippini A, Di Cicco A, Natoli CR (1995) Multiple-scattering analysis of the X-ray absorption spectrum of Os 3 (CO) 12 carbonyl cluster. *Phys Rev B* 52:15135
15. Azroff LV, Kaplow R, Kato N, Weiss RJ, Wilson AJC, Young RA (1974) X-ray diffraction. McGraw-Hill, New York, US
16. Langford J, Wilson A (1978) Scherrer after sixty years: a survey and some new results in the determination of crystallite size. *J Appl Cryst* 11:102–113
17. Cowley JM (1995) Diffraction physics. Elsevier Science BV, Amsterdam, The Netherlands
18. Fultz B, Hove J (2007) Transmission electron microscopy and diffractometry of materials. Springer, Berlin, Germany
19. Kirkland E (1998) Advanced computing in electron microscopy. Springer, New York, US
20. Neumann W, Hillebrand R, Werner P (1897) Electron microscopy in solid state physics. Elsevier, Amsterdam
21. Zou XD (1995) Electron crystallography of inorganic structures. Theory and practice. PhD thesis, Stockholm University
22. Cowley JM (1993) Electron diffraction technique, high resolution imaging. International Union Crystallography. Oxford University Press, Oxford, pp 131–169
23. Kilhborg L (1995) Phase contrast and high resolution electron microscopy. Department of Inorganic Chemistry, Stockholm University, Sweden
24. Greco G, Witkowska A, Principi E, Minicucci M, Di Cicco A (2011) Local ordering of nanostructured Pt-Co probed by multiple-scattering XAFS. *Phys Rev B* 83(13):134103
25. Gontard LC, Chang LY, Hetherington CJD, Kirkland AI, Ozkaya D, Dunin-Borkowski RE (2007) Aberration-corrected imaging of active sites on industrial catalyst nanoparticles. *Angew Chem* 46:3683
26. Chen S, Sheng W, Yabuuchi N, Ferreira PJ, Allard LF, Shao-Horn Y (2009) Enhanced activity for oxygen reduction reaction on “Pt₃Co” nanoparticles: direct evidence of percolated and sandwich-segregation structures. *J Phys Chem C* 113(3):1109–1125
27. Menguy N (2007) Microscopes électroniques. Online transparencies <http://www.imPMC.jussieu.fr/menguy/Cours.html>
28. Filippini A, Di Cicco A, Zanoni R, Bellatreccia M, Sessa V, Dossi C, Psaro R (1991) X-ray absorption spectroscopy and n-body distribution functions in condensed matter ({II}): data-analysis and applications. *Chem Phys Lett* 184:485
29. Vegard L (1921) Die konstitution der mischkristalle und die raumfüllung der atome. *Z Phys* 5(1):17
30. Denton AR, Ashcroft NW (1991) Vegard’s law. *Phys Rev A* 43(6):3161
31. Urusov VS (1992) A geometric model of deviations from Vegard’s rule. *J Struct Chem* 33:68–79
32. Hansen M (1958) Constitution of binary alloys. McGraw-Hill, New York
33. Zignani SC, Antolini E, Gonzalez ER (2008) Evaluation of the stability and durability of Pt and Pt–Co/C catalysts for polymer electrolyte membrane fuel cells. *J Power Sources* 182:83
34. Pfalzer P, Urbach J-P, Klemm M, Horn S, DenBoer ML, Frenkel AI, Kirkland JP (1999) Elimination of self-absorption in fluorescence hard-x-ray absorption spectra. *Phys Rev B* 60:9335
35. Tröger L, Arvanitis D, Baberschke K, Michaelis H, Grimm U, Zschech E (1992) Full correction of the self-absorption in soft-fluorescence extended x-ray-absorption fine structure. *Phys Rev B* 46:3283
36. Eisebitt S, Boske T, Rubensson J-E, Eberhardt W (1993) Determination of absorption coefficients for concentrated samples by fluorescence detection. *Phys Rev B* 47:14103
37. Witkowska A, Di Cicco A, Principi E (2007) Local ordering of nanostructured Pt probed by multiple-scattering XAFS. *Phys Rev B* 76:104–110

38. Lu ZW, Wei S-H, Zunger A (1992) Electronic structure of ordered and disordered Cu_3Au and Cu_3Pd . *Phys Rev B* 45:10314
39. Greco G, Witkowska A, Minicucci M, Olivi L, Principi E, Dsoke S, Moretti A, Marassi R, Di Cicco A (2012) Local ordering changes in Pt–Co nanocatalyst induced by fuel cell working conditions. *J Phys Chem C* 116(23):12791–12802
40. Principi E, Di Cicco A, Witkowska A, Marassi R (2007) Performance of a fuel cell optimized for in situ X-ray absorption experiments. *J Synch Rad* 14:276–281
41. Viswanathan R, Hou G, Liu R, Bare S, Modica F, Mickelson G, Segre C, Leyarovska N, Smotkin E (2002) In-situ XANES of carbon-supported Pt-Ru anode electrocatalyst for reformat-air polymer electrolyte fuel cells. *J Phys Chem B* 106:3458–3465
42. Roth C, Martz N, Buhrmester T, Scherer J, Fuess H (2002) In-situ XAFS fuel cell measurements of a carbon-supported Pt–Ru anode electrocatalyst in hydrogen and direct methanol operation. *Phys Chem Chem Phys* 4:3555–3557
43. Roth C, Benker N, Buhrmester T, Mazurek M, Loster M, Fuess H, Koningsberger D, Ramaker D (2005) Determination of O[H] and CO coverage and adsorption sites on PtRu electrodes in an operating PEM fuel cell. *J Am Chem Soc* 127:14607–14615
44. Durham J, Pendry JB, Hodges CH (1981) XANES: Determination of bond angles and multi-atom correlations in order and disordered systems. *Solid State Commun* 38:159
45. Durham J (1988) X-ray absorption: principles, applications, techniques of EXAFS, SEXAFS, and XANES (Ref. 2), p 53
46. Kizler P (1991) Three-body correlations in the metallic glass $\text{Ni}_{81}\text{B}_{19}$ probed by x-ray-absorption near-edge-structure spectroscopy. *Phys Rev Lett* 67:3555

Electrochemical Control of the Core-Shell Cobalt-Platinum Nanoparticles

23

S. Grau, E. Gómez, J.M. Feliu, and E. Vallés

Contents

Introduction.....	770
Nanoparticle Preparation.....	772
Results and Discussion.....	772
Conclusions.....	781
References.....	781

Abstract

Electrodeposition technique allows depositing nanoparticles of metals and alloys with variable size as a function of the deposition conditions, the deposition charge, and the nature of the substrate. In this work, the possibility of obtaining electrochemically core-shell submicrometric particles with a platinum shell has been tested; in order to design a preparation method of particles of different size, the general purpose is to approach the surface properties of platinum but with lower amounts than those in a massive platinum particle. Cobalt nanoparticles in the range 100–600 nm of diameter have been electrodeposited on vitreous carbon. The size of the particles and the average distance between them varies as a function of the deposition potential and the transferred charge. Low overpotentials have been selected to obtain isolated cobalt particles

S. Grau • E. Gómez • E. Vallés (✉)
Ge-CPN, Departament de Química Física, Institut de Nanociència i Nanotecnologia (IN2UB),
Universitat de Barcelona, Barcelona, Spain
e-mail: serxga@gmail.com; e.gomez@ub.edu; e.valles@ub.edu

J.M. Feliu
Departamento de Química Física, Instituto de Electroquímica,
Universidad de Alicante, Alicante, Spain
e-mail: juan.feliu@ua.es

of similar size (around 140 nm). These particles have been covered with a skin layer of platinum by galvanic displacement reaction by immersion in a platinum-containing solution. The control of the total recovery of the particles (to obtain core-shell cobalt-platinum particles) has been performed electrochemically by recording the voltammetric profile of the samples in a blank solution. The electrocatalytic activity of the prepared particles for methanol oxidation has been tested.

Keywords

Electrodeposition • Co nanoparticles • Core-shell particles • Platinum • Electrocatalytic properties

Introduction

During the last years, nanotechnology has been consolidated in very different fields of application from therapeutic application to computer science. One of the interests of nanotechnology is the preparation of different materials in submicrometric dimensions due to its special catalytic or magnetic properties (Table 1). Between the different methods of preparation of micro/nanostructures, electrochemical methods have been revealed as useful techniques to obtain small nanostructures of metals, alloys, and oxides [1–3]. Although electrodeposition is not the best method to prepare metallic nanoparticles in the range of few nanometers (usually prepared by chemical reduction [4–6]), its results are very adequate to prepare nanopowders, nanowires, nanotubes, or particles in the range of tens of nanometers. The method is simple and economic, but it requires a strict control of the deposition charges to allow the growth of metallic structures at nano/submicrometric level.

Different types of templates have been used to grow nanostructures electrochemically [3, 7–11]. Polymeric or alumina templates have been used to electrodeposit nanowires and nanotubes of metals and alloys with diameters from few nanometers to tens of nanometers and lengths from tens of nanometers to several microns. Recently, the possibility of using microemulsions as templates has been tested [12, 13]. Another method to control the size of the growing nanostructures by means of electrodeposition is the strict control of the surface of the conductive substrate used and both the deposition rate and the transferred charge.

In this work, the possibility of preparing particles of controlled size by means of electrodeposition and recovering them with a shell of platinum metal is tested. The objective is the use of this kind of particles as catalytic objects, in substitution of pure platinum particles of the same size. Cobalt particles will be tested, in the manner that both cobalt and superficial cobalt oxides spontaneously formed can react with a solution containing platinum species, leading to Co-Pt core-shell particles of tailored size. Co-Pt nanoparticles, but of very small size, have been previously prepared from chemical reduction in water-in-oil (w/o) microemulsions [14].

Table 1 Resume of some previous nanostructures synthesis

Structure	Material	Growth technique	References	Authors
Metal nanoparticles	Ni	Electrodeposition (ED) in microemulsion	[12]	H. Zhou, C. Peng, S. Jiao, W. Zeng, J. Chen, Y. Kuang
Alloy nanoparticles	PtRuNi	Reduction in microemulsion	[5]	X. Zhang, F. Zhang, R. Guan, K. Chan
	PtPd	Reduction in microemulsion	[6]	J. Solla-Gullon, V. Montiel, A. Aldaz, J. Clavilier
Oxides nanoparticles	Ferrites, manganites	Reduction in reverse micelles	[4]	V. Uskokovic, M. Drogenik
Core-shell nanoparticles	Co-Pt	Reduction in microemulsion	[14]	J. Solla-Gullón, E. Gómez, E. Vallés, A. Aldaz, J.M. Feliu
Nanowires	Bi,Co,Fe,Cu, Cu/Cu	ED	[1]	M.S. Dresselhaus, Y-M. Lin, O. Rabin, M.R. Black, J. Kong, G. Dresselhaus
	CoPt	ED	[2]	S. Shamaila, R. Sharif, S. Riaz, M. Khaleequr-Rahman, X.F. Han
	Co, Pt, CoPt	ED	[3]	J. Fu, S. Cherevko, C.H. Chung
	Co	ED	[7]	Y. Yang, Y. Chen, Y. Wu, X. Chen, M. Kong
			[11]	V.R. Caffarena, A.P. Guimarães, W.S.D. Folly, E.M. Silva, J.L. Capitaneo
	Segmented CoNi	ED	[8]	S. Talapatra, X. Tang, M. Padi, T. Kim, R. Vajtai, G.V.S. Sastry, M. Shima, S.C. Deevi, P.M. Ajayan
	CoNi	ED	[9]	A. Ghahremani Nezhad, A. Dolati
Nanotubes	Ni	ED	[10]	X.W. Wang, Z.H. Yuan, S.Q. Sun, Y.Q. Duan, L.J. Bie
Porous nanofilms	CoNi	ED in microemulsion	[13]	A. Serrà, E. Gómez, G. Calderó, J. Esquena, C. Solans, E. Vallés

The work described here implies (1) the definition of the best conditions to prepare cobalt particles of different size over the surface of a conductive substrate by means of electrodeposition, (2) the test of the formation of a superficial platinum layer on the freshly prepared cobalt particles by immersion in a platinum-containing solution, (3) the electrochemical characterization of these coated particles, and (4) the test of the catalytic properties of the core-shell particles using the methanol oxidation as electrocatalytic reaction. The possibility of substituting pure platinum particles of different size by Co-Pt ones (containing less platinum amount) for catalytic purposes will be tested. Moreover, as platinum particles are not free from poisoning of adsorbed intermediates, there is increasing interest in the search of more active and less expensive catalysts than Pt and in the development of structures of Pt with other metals.

Nanoparticle Preparation

CoCl₂ 0.5 M solution was used to prepare the cobalt nanoparticles over vitreous carbon electrodes by means of electrodeposition. The pH was adjusted to 4 in order to simultaneously avoid hydroxide precipitation and minimize hydrogen evolution during the electrochemical reduction process. A Na₂PtCl₆ 1 mM solution was used to induce the formation of the platinum skin on the cobalt nanoparticles. NaOH 0.1 M solution was used to analyze the electrochemical behavior of the different prepared particles. All the reagents were of analytical grade. Solutions were prepared with distilled water further treated with a Millipore Milli-Q system.

The electrochemical study of the electrodeposition process and the preparation of the deposits was performed using a thermostated cell with Ag/AgCl(s)/KCl (3 M) as electrode of reference, a large platinum wire spiral as counter electrode, and vitreous carbon, with exposed area of 0.0314 cm², as working electrode. The deposition temperature was maintained at 28 °C. The vitreous carbon electrode was polished with alumina of 3.75 and 1.87 μm to obtain a mirror finish, and it was rinsed with Milli-Q water in an ultrasonic bath. The solution was deaerated by argon bubbling before and maintained under argon atmosphere during each experiment. For the study of the electrochemical behavior of the prepared particles, Ag/AgCl(s)/NaCl (1 M)/NaOH 0.5 M was used as reference electrode. Electrochemical experiments were carried out using a microcomputer-controlled potentiostat/galvanostat Autolab PGSTAT30 with GPES software.

A Hitachi H-4100FE was used for the observation of the different samples.

Results and Discussion

A voltammetric study of the cobalt electrodeposition process in the selected solution was performed to define the suitable potential range to prepare cobalt particles with low interference of hydrogen evolution. A 50 mV s⁻¹ scan rate was selected, with a starting potential at which no redox process takes place (-0.3 V), scanning

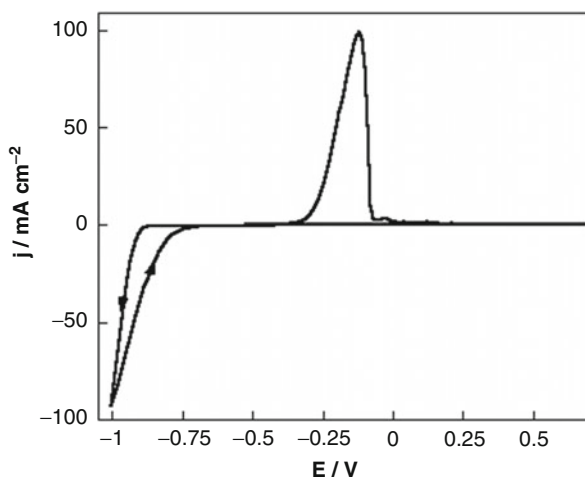


Fig. 1 Voltammetric curve of the CoCl_2 0.5 M solution, pH 4, on vitreous carbon electrode. Starting potential: -0.3 V. Cathodic limit: -1.0 V. $\nu = 50$ mV s^{-1}

first to negative potentials. The voltammetric curves show, for moderate cathodic limits, the typical nucleation and growth loop characteristic of the electrodeposition processes (Fig. 1 – all figures are ours and previously unpublished). Reduction current was detected from around -0.9 V at the selected scan rate. A single oxidation peak, centered at -0.2 V, was recorded, reflecting the oxidation of only the deposited cobalt and the absence of cobalt oxides or hydroxides in the substrate under these preparation conditions.

From the voltammetric results, different potentials were selected to prepare cobalt submicrometric particles. The potentiostatic technique was used, and the deposition charge was adjusted to very small values to avoid the formation of cobalt films. The equilibrium potential observed from the voltammetric curve was around -700 mV, and deposition potentials in the -750 to -850 mV range were selected to favor slow growth of the deposits, taking into account the crystallization overpotential. Figure 2 shows the chronoamperometric curves corresponding to cobalt deposition at different potentials, maintaining in all cases a deposition charge of 95 mC cm^{-2} (0.5 $\mu\text{mol Co cm}^{-2}$). The j - t slope (and therefore the deposition rate) varied drastically with the applied potential. At -750 mV, very slow process occurred, and 1400 s of deposition were necessary to attain the desired charge. However, only 70 s were required at -850 mV to transfer the same charge.

The reproducibility of the deposition process can be observed in Fig. 3, in which the same j - t transient was obtained at the same potential using different vitreous carbon rods to obtain deposits of different charge.

The deposits of low charge (95 mC cm^{-2}) obtained through the described potentiostatic curves were observed by FE-SEM (Fig. 4).

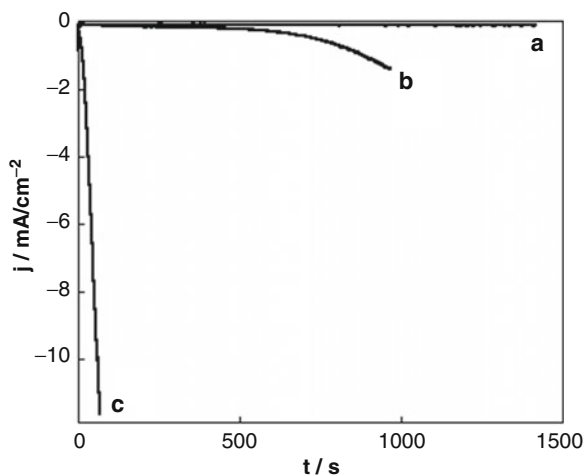


Fig. 2 Cronoamperometric curves of cobalt deposition on vitreous carbon substrate at (a) -750 , (b) -800 , (c) -850 mV

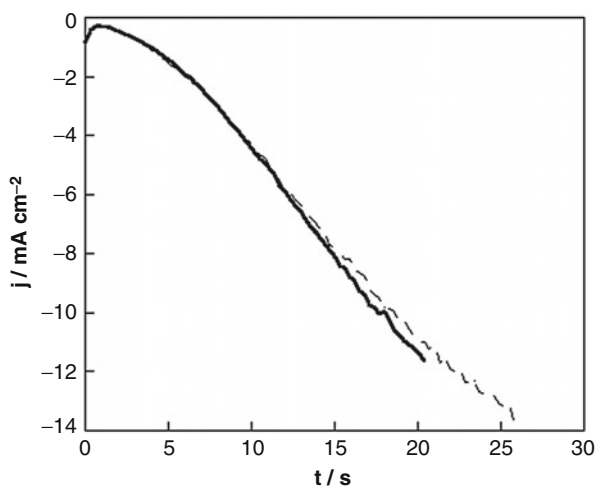


Fig. 3 Cronoamperometric curves of cobalt deposition on two different vitreous carbon substrates at -850 mV and two deposition times. $Q = 95$ mC cm⁻² (solid line) and $Q = 160$ mC cm⁻² (dashed line)

At very low deposition potential (-750 mV), monodisperse cobalt particles homogeneously distributed on the substrate were obtained with an average size of 140 nm for the applied deposition charge (detail in Fig. 5).

By decreasing the deposition potential to -800 mV, particles of different sizes were obtained, revealing the progressive nucleation and simultaneous growth and aggregation of the particles. The greater ones present a star-like morphology (Fig. 5) as corresponds to an hcp crystalline structure of the cobalt particles, and they range between 250 and 600 nm. For more negative deposition potentials (-850 mV), a

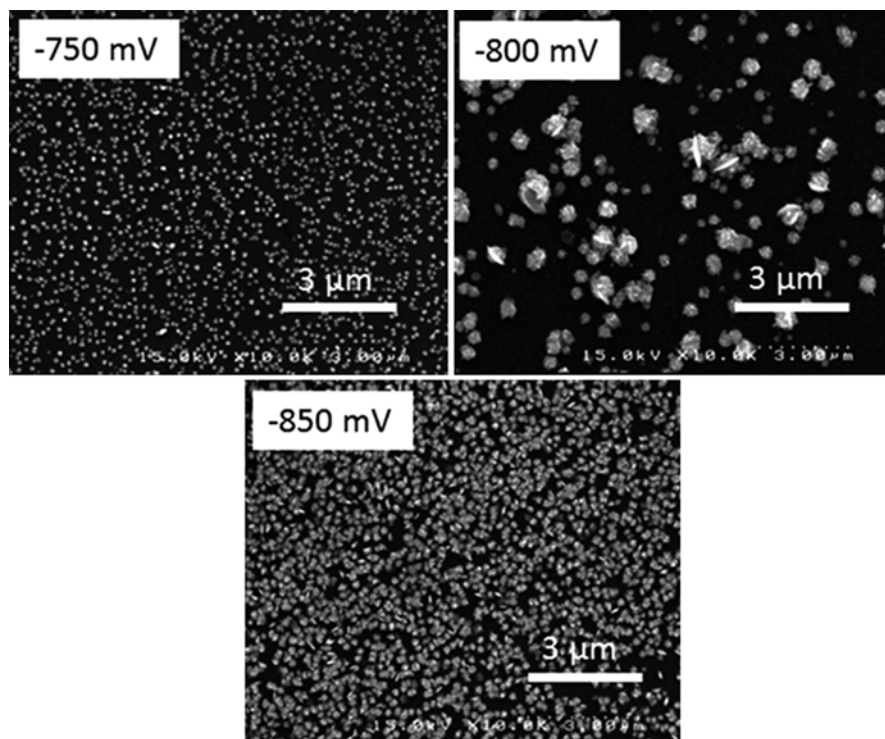


Fig. 4 Co particles electrodeposited from a CoCl_2 0.5 M solution, $\text{pH}=4$, over vitreous carbon substrates at different potentials. Final coverage is $0.5 \mu\text{mol Co cm}^{-2}$

high quantity of cobalt particles of similar size (around 200 nm) were observed; the increase of the overpotential leads to instantaneous nucleation and growth and, consequently, to particles of similar size. However, coalescence between the star-shaped particles was observed, favored by raising the deposition charge. The increase of the deposition charge leads to define clearly the cobalt nanostructures (Fig. 6). The *desert rose* shape observed is the typically one almost universally detected for electrodeposited hcp cobalt [15].

From these results, very low deposition potentials and low charges were required to obtain isolated cobalt particles, homogeneous in size. A potential of -750 mV was selected to prepare cobalt particles of around 150 nm.

Different vitreous carbon/Co particle replicas were further immersed in a Na_2PtCl_6 1 mM solution for different times between 10 and 120 s. For each sample, after treatment with the platinum solution, an electrochemical test of the particle's behavior in NaOH 0.1 M solution was performed to detect partial or total recovery of the cobalt particle by a platinum layer. This electrochemical detection of Pt would involve underpotential deposition of oxygen and hydrogen within the potential range of stability of water. Figure 7 shows the voltammetric profiles, at 50 mV s^{-1} , for the vitreous carbon/Co-Pt particle samples. As reference, the voltammetric profile of both electrodeposited pure cobalt particles (Fig. 7a) and platinum wire (Fig. 7d) were recorded.

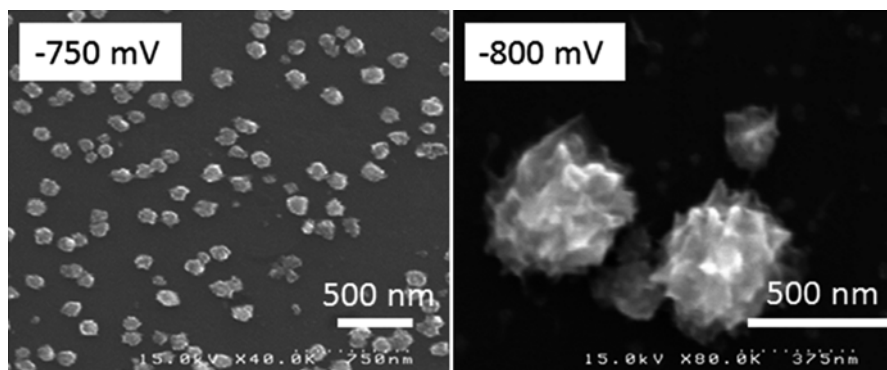


Fig. 5 Detail of the Co electrodeposited particles of Fig. 4

Fig. 6 Coalesced Co particles electrodeposited from a CoCl_2 0.5 M solution, pH=4, over vitreous carbon substrates at -850 mV and $Q=160$ mC cm^{-2}

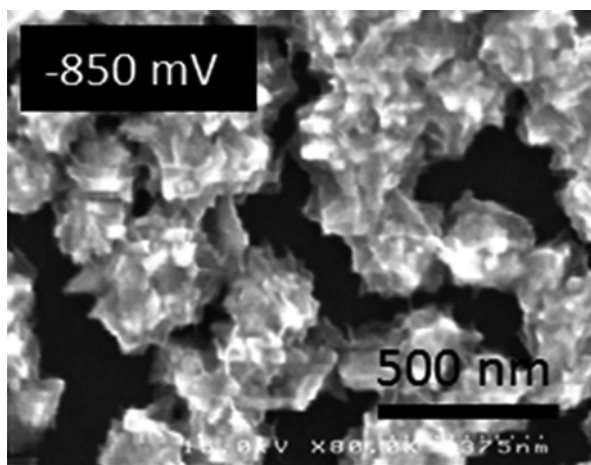


Figure 7b shows that after only 10 s of immersion in the platinum solution, some characteristic features of pure platinum can be just detected: those corresponding to superficial platinum oxidation and reduction of the superficial oxides. However, the characteristic peaks of hydrogen adsorption were not clearly pointed out at this stage. By increasing the immersion time, both the superficial platinum oxidation peaks and hydrogen adsorption current were detected (Fig. 7c), which reveals higher coverage of the particles. The similar voltammetric profile of the particles immersed in platinum solution at 60 and 120 s demonstrates the total coverage of the cobalt particles by the platinum layer after 60 s of immersion, i.e., the formation of Co-Pt core-shell particles of submicrometric size.

Therefore, it is worth to note that the recording of the voltammetric profile of the samples in a blank solution is a good tool to in situ follow the formation of a shell of platinum on the cobalt particles.

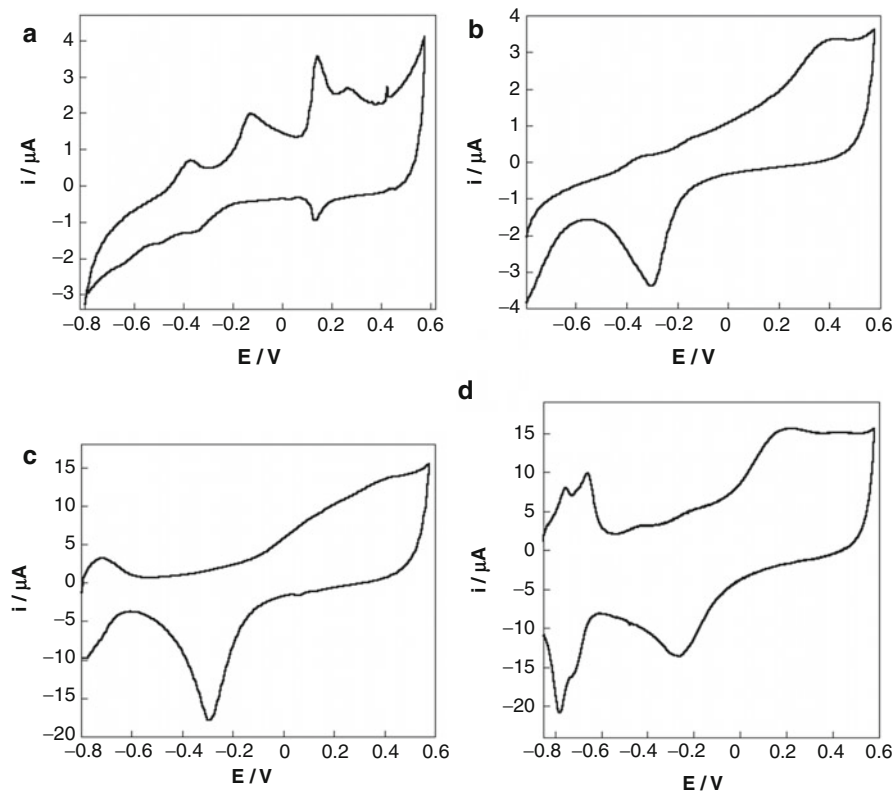
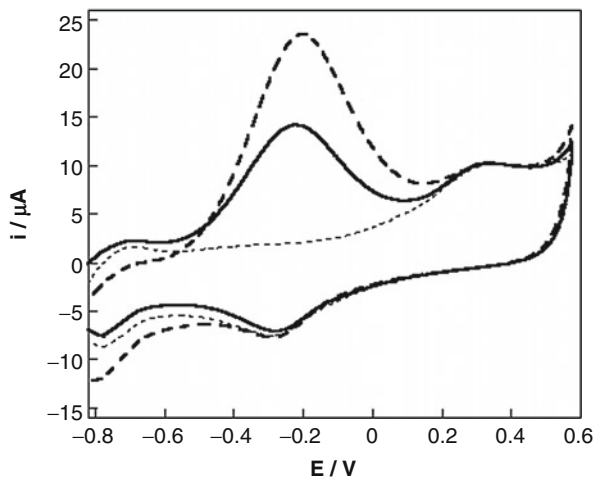


Fig. 7 Voltammetric curves in NaOH 0.1 M solution of (a) vitreous carbon/Co particles obtained at -750 mV , (b) vitreous carbon/Co particles immersed 10 s in Na_2PtCl_6 1 mM, (c) vitreous carbon/Co particles immersed 60 s in Na_2PtCl_6 1 mM, (d) platinum wire of 0.2 cm^2 . $v=50 \text{ mV s}^{-1}$

Electrochemical experiments demonstrate that platinum can easily substitute both the superficial cobalt of the electrodeposited particles and the native cobalt oxides. The applicability of the covered particles in catalytic purposes was tested. It has been reported that the catalytic activity of Pt can be enhanced by alloying it with nonprecious metals such as Fe, Co, or Ni [16]. Also, it has been reported that the spontaneous formation of a Pt skin layer, which presents a modified electronic structure on the metal surface, results in the increase of the ORR activity [17]. The Pt skin maintains the durability of the particle, keeping the stable structure of the catalyst particle, particle size, and dispersed state.

In this respect, the possible electrocatalytic properties of the prepared Co-Pt particles were analyzed by testing, in this case, their reactivity for methanol oxidation. Two different concentrations of methanol in NaOH 0.1 M were studied. The voltammetric curves in the presence of methanol in solution were recorded and compared with the profiles of the same particles in the NaOH solution. A defined oxidation peak corresponding to methanol oxidation is clearly observed previous

Fig. 8 Voltammetric curves of vitreous carbon/Co-Pt particles in NaOH 0.1 M solution (*dotted curve*), NaOH 0.1 M + Methanol 0.4 M solution (*solid line*) and NaOH (0.1 M) + Methanol 0.8 M solution (*dashed line*). $v = 50 \text{ mV s}^{-1}$



to the surface oxidation current of the platinum shell (Fig. 8). By comparing the position of the methanol oxidation peak with that recorded with a pure platinum wire (Fig. 9), significant increase in the oxidation rate is detected at lower potentials. This demonstrates that the cobalt particles totally coated with a platinum shell were more catalytic for this particular reaction, as corresponds to a new structure that differs from the conventional bulk platinum surface. A modification of the cell parameter of the platinum of the shell with respect to that of pure Pt fcc phase is possible, when it is incorporated in the crystalline cell of the cobalt. The influence of the Pt-Pt distance in platinum alloys or platinum layers over the catalytic properties of this metal has been previously demonstrated [18].

In order to test if the advancement of the methanol oxidation over Co-Pt nanoparticles with respect to the process on Pt wire is due to the specific properties of the platinum layer over the cobalt core or to the size of the particles, pure platinum nanoparticles were prepared on vitreous carbon substrate and its effect on the methanol oxidation process tested.

A 1.2 mM $\text{Na}_2\text{PtCl}_6 + 0.1 \text{ M NH}_4\text{Cl} + 0.16 \text{ M boric acid}$, pH=4.5 solution was prepared to perform the platinum deposition. A voltammetric study of this solution on vitreous carbon substrate was carried out to detect the potential value at which platinum begins to deposit. The appearance of the superficial platinum oxidation peak in the anodic scan was defined as a criterion to detect the formation of platinum deposit (Fig. 10). It was necessary to scan up to a minimum potential of -265 mV to induce the reduction of hexachloro platinate to platinum.

Platinum deposits on vitreous carbon were prepared potentiostatically. A potential of -285 mV was selected to induce the formation of platinum particles, avoiding the coalescence between them. Simultaneously, the deposition charge was fixed to very low value (190 mC cm^{-2} corresponding to $0.5 \text{ μmol Pt cm}^{-2}$). Figure 11 shows the morphology of the vitreous carbon/platinum substrates.

Fig. 9 Voltammetric curves of a platinum wire of 0.2 cm^2 in NaOH 0.1 M + Methanol 0.4 M solution (*continuous line*) and NaOH (0.1 M) + Methanol 0.8 M solution (*dashed line*). $\nu = 50 \text{ mV s}^{-1}$

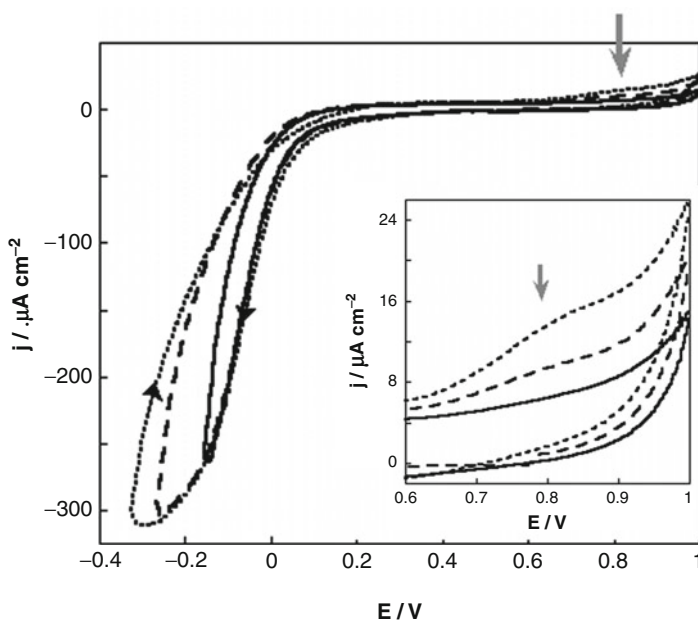
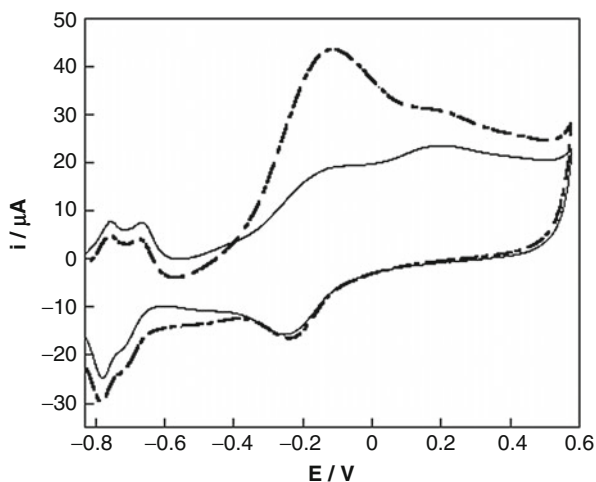


Fig. 10 Voltammetric curves of a vitreous carbon substrate in a $1.2 \text{ mM Na}_2\text{PtCl}_6 + 0.1 \text{ M NH}_4\text{Cl} + 0.16 \text{ M boric acid}$ solution, $\text{pH}=4.5$, $24 \text{ }^\circ\text{C}$. Starting potential: 500 mV . Cathodic limits: -165 mV (*solid line*), -265 mV (*dashed line*), -325 mV (*pointed line*). $\nu = 50 \text{ mV s}^{-1}$. *Inset*: detail of the voltammetric curves in the $600\text{--}1000 \text{ mV}$ range

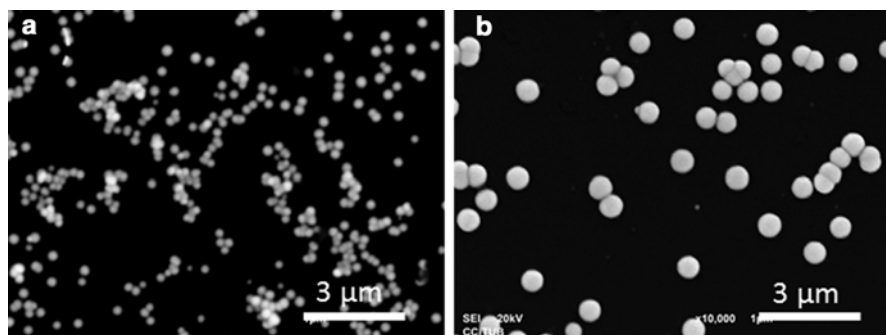
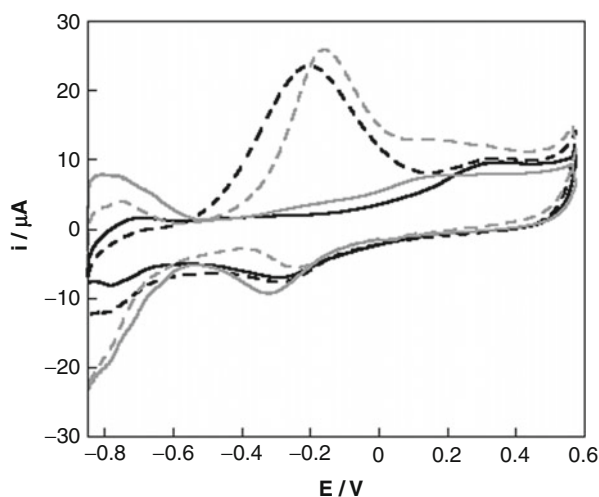


Fig. 11 Pt particles electrodeposited from a 1.2 mM Na_2PtCl_6 +0.1 M NH_4Cl +0.16 M boric acid solution, pH=4.5, over vitreous carbon substrates at -265 mV. $0.5 \mu\text{mol cm}^{-2}$

Fig. 12 Voltammetric curves of vitreous carbon/Co-Pt particles in 0.1 M NaOH (solid black line), vitreous carbon/Pt NPs in 0.1 M NaOH (solid gray line), vitreous carbon/Co-Pt particles in NaOH 0.1 M + methanol 0.64 M solution (dashed black line), vitreous carbon/Pt deposit in NaOH 0.1 M + methanol 0.64 M solution (dashed gray line). 24°C , $v = 50 \text{ mV s}^{-1}$



The applied potential allows the formation of rounded platinum nanoparticles (NPs), both in stirring (A) and in stationary (B) conditions. The size of the nanoparticles in each case is very homogeneous. Stirring of solution during platinum deposition favors the nucleation on the vitreous carbon leading to small particles (around 200 nm). For the same deposition charge and potential, nonstirring conditions lead to the formation of less particles of larger size.

The *vitreous carbon/Pt NP* substrates (Fig. 11a) were tested in the NaOH solution, resulting in a similar profile to that obtained with the platinum wire, although the region of hydrogen adsorption/desorption potentials is less defined (Fig. 12, solid gray line). When methanol was added to the NaOH solution, the onset of the methanol oxidation process on *vitreous carbon/Pt NPs* substrate coincides with the value observed over the platinum wire. On the other hand, when the voltammetric profiles of *vitreous carbon/Co-Pt particles* and *vitreous carbon/Pt NPs* substrates in

NaOH-methanol solution were compared, a clear advancement of the oxidation was observed for the Pt-covered cobalt particles, which corroborates the better catalytic properties of the platinum layer in the recovered cobalt particles.

Conclusions

The electrodeposition process using potentiostatic techniques allows preparing cobalt particles of tailored size as a function of the applied potential and deposition charge. Vitreous carbon substrate and very low overpotentials were necessary to attain low nucleation and very slow deposition growth. In this way, monodisperse isolated particles of around 100–150 nm can be formed over the carbon substrate. Both potential and time must be strictly controlled to avoid either the coalescence of the particles or the formation of particles of different size.

Superficial substitution of cobalt and probably native cobalt oxides by platinum takes place easily by means of a galvanic displacement reaction when substrates are immersed in a Pt(IV)-containing solution. The detection of the coverage of the Co particles and the further formation of Co-Pt has been tested voltammetrically. The comparison of the profiles of the recorded voltammograms, after the immersion of the Co particles in the solution containing Pt(IV), in an NaOH test solution, allows to establish the formation of a continuous layer of platinum.

The test of the behavior of the obtained particles with respect to the methanol oxidation reaction demonstrates that it is possible to substitute pure cobalt particles by particles with better surface properties like those of platinum. These particles contain a core of the nonprecious metal and the catalytic reactivity something better than that obtained using pure platinum. This method could be extended to other metallic cores following a similar procedure. A probable modification of the Pt-Pt distance in the shell with respect to that of pure platinum can justify the modification of its catalytic properties.

Acknowledgments This work was supported by contract CQT2010-20726 from MINECO. The authors wish to thank the Centres Científics i Tecnològics de la Universitat de Barcelona (CCITUB) for allowing us to use their SEM equipment.

References

1. Dresselhaus MS, Lin Y-M, Rabin O, Black MR, Kong J, Dresselhaus G (2010) In: Bhushan B (ed) Springer handbook of nanotechnology, 3rd edn. Springer, Berlin, pp 123–124, Chap 4
2. Shamaila S, Sharif R, Riaz S, Khaleeq-ur-Rahman M, Han XF (2008) Fabrication and magnetic characterization of $\text{Co}_x\text{Pt}_{1-x}$ nanowire arrays. *Appl Phys A Mater* 92:687–691
3. Fu J, Cherevko S, Chung CH (2008) Electroplating of metal nanotubes and nanowires in a high aspect-ratio nanotemplate. *Electrochem Commun* 10:514–518
4. Uskokovic V, Drogenik M (2007) Reverse micelles: Inert nano-reactors or physico-chemically active guides of the capped reactions. *Adv Colloid Interface Sci* 133:23–34
5. Zhang X, Zhang F, Guan R, Chan K (2007) Preparation of Pt-Ru-Ni ternary nanoparticles by microemulsion and electrocatalytic activity for methanol oxidation. *Mater Res Bull* 42:327–333

6. Solla-Gullon J, Montiel V, Aldaz A, Clavilier J (2003) Synthesis and electrochemical decontamination of platinum-palladium nanoparticles prepared by water-in-oil microemulsion. *J Electrochem Soc* 150:E104–E109
7. Yang Y, Chen Y, Wu Y, Chen X, Kong M (2010) Diameter-controllable magnetic properties of Co nanowire arrays by pulsed electrodeposition. *J Nanomater* Article ID 793854, 4 pages
8. Talapatra S, Tang X, Padi M, Kim T, Vajtai R, Sastry GVS, Shima M, Deevi SC, Ajayan PM (2009) Synthesis and characterization of cobalt–nickel alloy nanowires. *J Mater Sci* 44: 2271–2275
9. Ghahremani N, Ninezhad A, Dolati A (2009) A study on electrochemical growth behavior of the Co–Ni alloy nanowires in anodic aluminum oxide template. *J Alloy Compd* 480:275–278
10. Wanga XW, Yuana ZH, Suna SQ, Duana YQ, Biea LJ (2008) Electrochemically synthesis and magnetic properties of Ni nanotube arrays with small diameter. *Mater Chem Phys* 112: 329–332
11. Caffarena WR, Guimaraes AP, Folly WSD, Silva EM, Capitaneo JL (2008) Magnetic behavior of electrodeposited cobalt nanowires using different electrolytic bath acidities. *Mater Chem Phys* 107:297–304
12. Zhou H, Peng C, Jiao S, Zeng W, Chen J, Kuang Y (2006) Electrodeposition of nanoscaled nickel in a reverse microemulsion. *Electrochem Commun* 8:1142–1146
13. Serrà A, Gómez E, Calderó G, Esquena J, Solans C, Vallés E (2013) Microemulsions for obtaining nanostructures by means of electrodeposition method. *Electrochem Commun* 27:14–18
14. Solla-Gullón J, Gómez E, Vallés E, Aldaz A, Feliu JM (2010) Synthesis and structural, magnetic and electrochemical characterization of PtCo nanoparticles prepared by water-in-oil microemulsion. *J Nanopart Res* 12:1149–1159
15. Gómez E, Vallés E (2002) Thick cobalt coatings obtained by electrodeposition. *J Appl Electrochem* 32:693–700
16. Toda T, Igarashi H, Uchida H, Watanabe M (1999) Enhancement of the Electroreduction of Oxygen on Pt Alloys with Fe, Ni, and Co. *J Electrochem Soc* 146:3750–3756
17. Stamenković V, Schmidt TJ, Ross PN, Marković NM (2003) Surface segregation effects in electrocatalysis: kinetics of oxygen reduction reaction on polycrystalline Pt₃Ni alloy surfaces. *J Electroanal Chem* 554:191–199
18. Shubina TE, Koper MTM (2002) Quantum-chemical calculations of CO and OH interacting with bimetallic surfaces. *Electrochim Acta* 47:3621–3628

Pawel Jerzy Wojcik, Luis Pereira, Rodrigo Martins,
and Elvira Fortunato

Contents

Introduction.....	784
Electrochemically Active Nanocrystalline Films	787
Morphology of Printed Films.....	787
Required Functionality.....	789
Influence of Chemical and Crystallographic Structure on Electrochemical Performance	790
Nanoparticle Engineering	791
Size–Shape Impact: From Small Clusters to Massive Agglomerates	791
Fluid Control of Printable Dispersions.....	799
Design Rule Outline.....	801
Case Study: Ink-Jet-Printed Dual-Phase Electrochromic Film.....	802
Structure and Morphology of Synthesized Products.....	802
Shape Impact.....	803
Ink Formulation and Printability	805
Film Forming.....	807
Electrochromic Response.....	807
Prototypes of Printed Electrochromic Devices	810
Summary	813
References.....	814

Abstract

Engineering procedures governing the selection or development of printable nanostructured metal oxide nanoparticles for chromic, photovoltaic, photocatalytic, sensing, electrolyte-gated TFTs, and power storage applications are established

P.J. Wojcik (✉) • L. Pereira • R. Martins • E. Fortunato (✉)
CENIMAT/I3N, Departamento de Ciência dos Materiais, Faculdade de Ciências e
Tecnologia, FCT, Universidade Nova de Lisboa (UNL), Caparica, Portugal
e-mail: p.wojcik@campus.fct.unl.pt; lmnp@fct.unl.pt; rm@uninova.pt; emf@fct.unl.pt

in this chapter. The main focus is given on how to perform the material selection and formulation of printable dispersion in order to develop functional films for electrochemical applications.

This chapter is divided into four main parts. Firstly, a brief introduction on electrochemically active nanocrystalline metal oxide films developed via printing techniques is given. This is followed by the description of the film morphology, structure, and required functionality. A theoretical approach to understand the impact of size and shape of nanoparticles on an ink formulation and electrochemical performance being the subject of the third section provides a greater control over the material selection. We attempt to describe these properties and show that for a given material, geometry and size of the nanoparticles have a major influence on the electrochemical reactivity and response time. This gives the ability to tune the performance of the film simply by varying the morphology of incorporated nanostructures. This section is completed by the recommendations on each major step of an ink formulation, together with imposed critical constraints concerning the fluid control. Finally, the performance of the ink-jet-printed dual-phase electrochromic films is discussed as a case study.

By providing such a rather systematic survey, we aim to stress the importance of proper design strategy that would result in both improved physicochemical properties of nanoparticle-loaded inks and enhanced electrochemical performance of printed functional films.

Keywords

Electrochromic device • Ink-jet-printing • Metal oxide • Nanoparticle engineering • Printed electronics

Introduction

One of the most active trends in applied electrochemistry is the development of metal oxide (MO_x) nanoparticles (NPs) with structural, electrical, and optical properties tailored to the specific application such as chromic devices [1–3], photovoltaic cells [4], photocatalytic systems [5–8], energy storage devices [9–13], electrolyte-gated TFTs [14, 15], gas sensors [16–18], and electrocatalytic biosensors [19, 20] (see Table 1). Features of those nanostructures are equally as important as their processability, enabling thin-film formation with desired functionality [21, 22]. The combination of these two requirements implies a need for a set of engineering rules combining selection/synthesis of the nanocrystalline material and technologically oriented aspects of printing methods into one consistent theory.

Many attempts have been made to deposit previously synthesized MO_x NPs in order to form an electrochemically active nanocrystalline film via drop-casting [2], dip-coating [23], or electrophoretic deposition [24, 25]. In other studies, MO_x

Table 1 Examples of an electrochemically active MO_x NPs with corresponding deposition technique and application

Material	Deposition technique	Application	Reference
WO_3 nanoplates	Hydrothermal growth using spin-coated seeds	Electrochromic	[1]
WO_3 nanorods	Drop casting	Electrochromic	[2]
$\text{WO}_3 \cdot n\text{H}_2\text{O}$	Drop casting	Photochromic	[3]
ZnO nanowires	Bath growth using dip-coated seeds	Dye-sensitized solar cells	[4]
TiO_2 nanorods	Particulate suspension	Photocatalysis	[5]
WO_3	Particulate suspension/doctor blade	Photocatalysis	[6]
WO_3	Doctor blade	Photocatalysis	[7]
$\alpha\text{-Fe}_2\text{O}_3$	Spray pyrolysis	Photocatalysis	[8]
TiO_2 nanosheets and nano-octahedra		Charge storage	[9]
WO_3 nanorods	Compressing to pellets	Charge storage	[10]
MnO_2	Plating into gold nanopores	Charge storage	[11]
In_2O_3	Ink-jet printing	Electrolyte-gated TFTs	[14]
$\text{In}_2\text{O}_3/\text{SnO}_2$ (ITO)	Spin coating	Electrolyte-gated TFTs	[15]
WO_3	Drop casting	Gas sensing	[16]
WO_3 nanoplates	Drop casting	Gas sensing	[17]
3D WO_3 nanowall	Drop casting	Gas sensing	[18]
MnO_2 -based colloid	Drop casting/electrodeposition	Electrocatalytic biosensors	[19]
Hierarchical $\text{WO}_3 \cdot 0.33\text{H}_2\text{O}$	Dip coating		[23]
WO_3 nanorods	Electrophoretic deposition	Electrochromic	[24]
V_2O_5	Electrophoretic deposition	Electrochromic	[25]
Hierarchical WO_3	Hydrothermal growth using crystal seeds		[26]
TiO_2	Ink-jet printing	Dye-sensitized solar cells	[27]
a- $\text{WO}_3/\text{TiO}_2/\text{WO}_x$	Ink-jet printing	Electrochromic	[28, 29]

nanostructures were grown directly on TCO (transparent conductive oxide)-coated glass substrate by crystal-seed-assisted hydrothermal synthesis [1, 26]. However, obtaining a uniform nanocrystalline film with good adhesion to the substrate and desired functionality still remains a challenge. As it was previously reported by our group [27, 28], the advent of printing deposition techniques has led to new possibilities in a field of thin solid films based on MO_x NPs. Printing techniques, apart from being widely used in graphics, are promising and attractive fabrication methods for a cost-efficient “low-end” electronics. An innovative and dynamic research in

this area results in new materials and devices, demonstrating their potential to cope with ever-changing requirements and challenges of the electronic market. It was demonstrated that the application of ink-jet printing for deposition of MO_x dispersion provides an excellent method for the production of inorganic thin films with controlled composition and microstructure for electrochemical devices such as dye-synthesized solar cells (DSCs) [27] and electrochromic (EC) windows/displays [28, 29]. The use of printing techniques is particularly promising for electrochemically active film development, because of its merits of low processing energy, precise patterning with reduced raw material waste, high throughput, and flexibility in deposited film composition.

To make genuine progress in the development of printed electrochemical devices, it is necessary to take the time to study the problem for which an engineering solution is desired in a broad and interdisciplinary context. In order to define a strategy for MO_x NP-based printed devices, one must consider the requirements and characteristics of electrochemically active material. Previous studies have shown that MO_x NP content strongly influences the final performance of ink-jet-printed electrochemically active films [28, 29], underlying the demand to understand the role of the NP properties, along all stages of their development and processing. Therefore, the selected strategy is based on a correlation between NP properties and further technological steps that lead to the development of a functional film for an electrochemical device. These technologically oriented aspects of printing methods consist of the following:

- (a) Formulation of the MO_x NP dispersion according to the objectives related to chemical composition and fluid flow aspects
- (b) Film deposition with regard to the fluid properties, selected printing technique, and substrate
- (c) Posttreatment process in which printed layer is subjected to external factors (usually highly energetic process), in order to set the required functionality
- (d) Film validation in terms of physical aspects and electrochemical performance

In this chapter, we attempt to show a general view on how we can perform both the MO_x NP selection and formulation of printable dispersions in order to develop functional films for electrochemical applications. The grain size, shape, crystallinity, and stoichiometry of MO_x NPs incorporated into the printed film are dependent only on the origin of those crystals and are defined at ink/paste formulation stage [28, 29]. This flexibility in material selection not only endows printed electrochemical devices with a better chemical stability but is also responsible for the superior performance, e.g., shorter response time or higher reactivity. Therefore, the versatility of this method makes it an ideal tool for creating materials with predictable and controlled properties, while maintaining their good processability via printing techniques.

To assure the desired electrochemical performance and processability, the criteria for MO_x NP size, shape, crystallinity, as well as the uniformity and agglomeration mechanism are going to be established in following subsections.

Electrochemically Active Nanocrystalline Films

Morphology of Printed Films

Nanocrystalline film is a special category assigned to polycrystalline layers of NPs. Furthermore, the NPs forming the film can be either sintered (mesoporous) or embedded in an amorphous matrix (dual phase). Figure 1 gives a generalized overview presenting both kinds of NP-loaded printed films for electrochemical applications.

From the broad range of available film morphologies used typically in electrochemical applications [30], only these two are so far feasible in a printing process. Due to the technological limitations, development of, e.g., vertically aligned

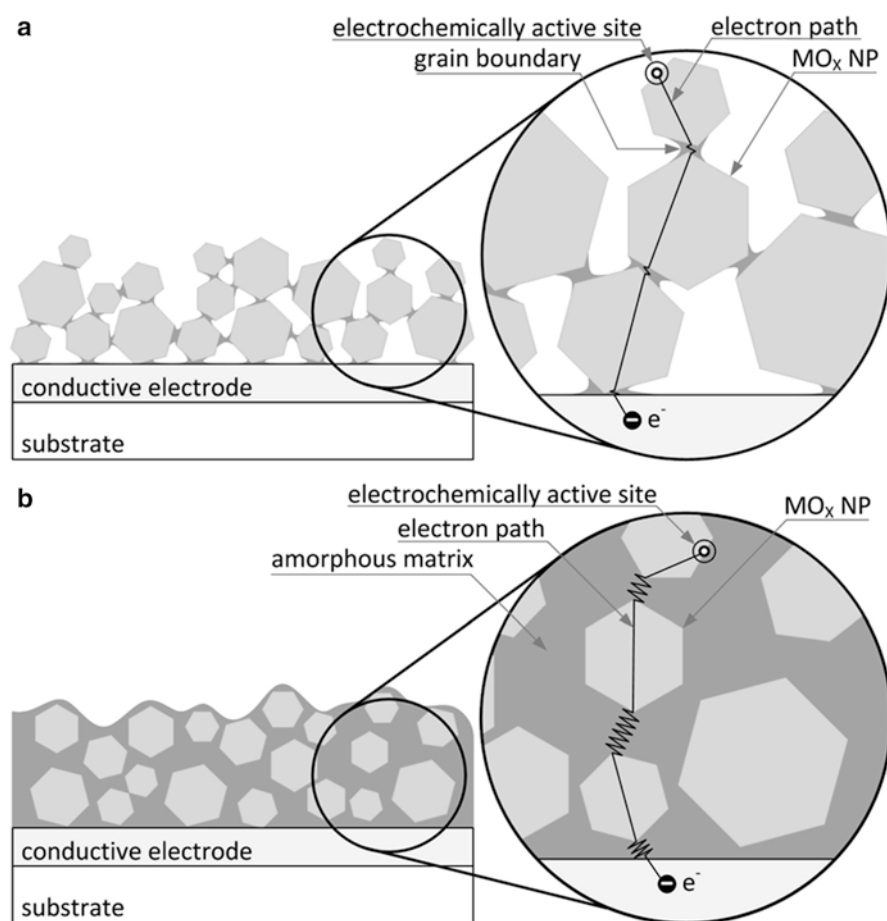


Fig. 1 Schematically presented nanocrystalline material for electrochemical applications as (a) mesoporous and (b) dual-phase films; the electron paths were drawn with respect to their electrical transport properties

ordered nanostructures or nanoarrays is not possible via printing process. Printed mesoporous film shown in Fig. 1a is developed using NP-loaded dispersion, usually stabilized by polymeric additives. Once the dispersion is deposited on a substrate, its liquid components, i.e., solvents, NP stabilizers, thickeners, wetting agents, and surfactants, are no longer needed. Unfortunately, additives typically used to stabilize dispersions of MO_x NPs in a liquid medium are long-chain molecules with high evaporation temperatures, which are difficult to eliminate and usually require high energy to be applied. Such additives may deteriorate or even inhibit electrochemical reaction. The posttreatment process which may include application of elevated temperature or more specific techniques such as photonic pulse curing or UV irradiation is performed in order to form and dry the film, organic burnout or sintering of NPs. On the other hand, high temperature may affect morphology and microstructure of NPs, due to their thermal instability [31].

As an alternative to energy requiring methods, a dual-phase composition of the film shown in Fig. 1b can be induced by mixing NPs with liquid sol-gel precursor or overprinting the NP film by sol-gel precursor. Resulting film contains randomly dispersed nanocrystals in a continuous amorphous matrix of the same MO_x , which provides conductive medium for electrons and ions and physically bonds the NPs to the surface of the substrate. This approach was successfully applied in the development of printed EC films based on sol-gel precursor and NPs of WO_3 [28]. The sol-gel precursor of WO_3 formulated from peroxopolytungstic acid requires relatively low temperature of 120 °C for 1 h in order to condensate and densify, resulting in a non-soluble film [32]. However, formation of other metal oxides, such as ternary $\text{M}_x^1\text{M}_y^2\text{O}_z$ films (where M^1 and M^2 are metals such as In, Ga, Sn, or Zn), by standard sol-gel route requires an annealing step at relatively high temperature (>250 °C) [33]. In order to overcome this issue, a photochemical activation by deep UV irradiation at low temperature should be applied to provide an amorphous MO_x matrix [34]. In this method, photo-induced condensation and densification of the wet gel film resulted in device with excellent electronic performance.

The main difference between mesoporous and dual-phase film microstructure lies in the character of interconnections between NPs. Randomly oriented NPs are separated by grain boundaries in case of nanocrystalline films or interfacial amorphous regions in dual-phase counterpart. Also the thickness of the printed nanocrystalline electrodes depends on the film morphology. Too thick mesoporous electrode leads to the higher resistance and thus reduction in the efficiency of electrochemical process (e.g., conversion efficiency of DSC). In case of dual-phase morphology used in EC devices, two thick films prevent EC action to take place. The optimum thickness is typically around 10 μm in mesoporous TiO_2 film in DSCs and 1 μm in dual-phase $a\text{-WO}_3/\text{WO}_x$ film in EC devices.

This generalized overview shows nanocrystalline material with length scale in all three dimensions which corresponds to quasi-spherical NPs. However, restriction of nanocrystalline regions to one or two dimensions (rod-shaped or layered NPs, respectively) results in an anisotropic charge transport, which is beneficial from electrochemical point of view. Electron transport in elongated shape NPs is much faster than percolation through a network of quasi-spherical crystals [4].

Another aspect is related to the disorder at the interface between neighboring NPs. Regardless of the film morphology, one particular weakness is the presence of a massive number of interfacial boundaries acting as trap sites for electron transport. Such trap-limited diffusion lowers overall efficiency of electrochemical device. Grain boundaries in mesoporous films have smaller disorder when comparing with amorphous interface in dual-phase film. However, in the second variant, by reducing the NP size and increasing solid content, the volume fraction of interfacial regions can be significantly reduced.

Required Functionality

Printed nanocrystalline films described previously can be used interchangeably, unless a technological step exists in a device development which is not compatible with a given film morphology. A typical example is dye molecules anchoring on a surface of MO_x NPs, as an integral step in DSC development. The mesoporous structure can be easily penetrated by a solution of dye, while in the case of dual-phase film, the dye is able to anchor only on the surface of the amorphous layer. Similarly, in electrocatalytic biosensors, immobilization of enzymes on the specific surface area requires proper wetting of the mesoporous structure. Therefore, the application of dual-phase film in DSCs and catalytic biosensors is very limited. In other electrochemical devices based on MO_x films such as electrolyte-gated TFTs, EC displays/windows, or energy storage devices, the application of dual-phase films seems to be less restricted.

Another aspect is related to the posttreatment of the mesoporous film, which is necessary in order to sinter NPs and provide electron percolation paths. The application of elevated temperature to sinter nanocrystalline film deposited on flexible substrates is limited due to the heat sensitivity of those materials. Maximum processing temperature is 90 °C for regular paper, 130 °C for polyethylene terephthalate (PET), 160 °C for polyethylene naphthalate (PEN), and 250 °C for polyimide (PI), which irrespectively of the NP size is not sufficient to sinter most of MO_x materials.

As a summary of this section, we can point out some basic requirements, which should be fulfilled in order to obtain well performing nanocrystalline film. From the electrochemical point of view, the film must:

- (a) Provide high surface area for electrochemical reaction (e.g., large surface area for dye absorption in DSC)
- (b) Allow effective diffusion of electrolyte ions into the interface/surface
- (c) Provide sufficient electronic conductivity (e.g., fast charge compensation in EC device, low recombination rates in DSC)
- (d) Be mechanically stable having good adhesion to the substrate
- (e) Assure negligible deviation from the reversibility according to the application requirements

- (f) Provide other specific functionalities if required, such as high transparency in a visible range (in the case of, i.e., EC and DSC)
- (g) Be compatible with device processing (e.g., enables dye absorption on MO_x NPs, low processing temperature for film deposited on heat-sensitive substrates)

Influence of Chemical and Crystallographic Structure on Electrochemical Performance

The nature of electrochemical reaction depends on a distinct mechanism governing the interaction between MO_x and ions. In some materials (e.g., SnO_2 or PbO_2), alloying/dealloying processes are responsible for reversible reaction with ions [35]. In other MO_x (e.g., TiO_2 or WO_x), ions are inserted/deinserted into/out of the crystal network [36]. In transition, MO_x (e.g., Fe_xO_y , Ni_xO_y , Co_xO_y , RuO_2 , IrO_2 , or MoO_3) reaction with ions is conducted through an unusual conversion reaction [37]. In many other MO_x (e.g., ZnO , In_2O_3 , or ternary and quaternary oxide systems such as indium zinc oxide (IZO), zinc tin oxide (ZTO), indium zinc thin oxide (IZTO), or indium gallium zinc oxide IGZO)), the reaction with ions is surface limited, inducing field effect in the NP volume [14].

Ion-intercalation reaction is strongly dependent on chemical and crystallographic structure of MO_x , while ion diffusion coefficient and the length of diffusion path depend on NP microstructure [38, 39]. High electronic conductivity of crystalline phase leads to the enhancement in lithium ion diffusion rate. As an example, the electronic conductivity of stable WO_x NPs was reported to be the highest for orthorhombic hydrate (*ortho*- $\text{WO}_3 \cdot 0.33\text{H}_2\text{O}$) and gradually smaller for sub-stoichiometric (WO_{3-y} where $0 \leq y \leq 3$), monoclinic (*m*- WO_3), and hexagonal (*h*- WO_3) structure, respectively [40]. The high charge carrier concentration in anhydrate WO_{3-y} ($0 \leq y \leq 3$) is explained by non-stoichiometry, where the free electrons are balanced by much less mobile oxygen vacancies. Better electron transport is also a product of an internal electric field which separates the electrons from the surrounding electrolyte and sweeps them toward the collection electrode (e.g., in DSCs) or active site (e.g., in EC device). However, in order to support such radial electric field (depletion layer), the minor axis width of the 1D or 2D NP should be big enough (higher than Debye–Hückel screening length) in regard to carrier concentration in a given MO_x .

Fast insertion/extraction of ions in EC and energy storage devices may be achieved by short diffusion length typical for 1D or 2D shapes and NPs of small size. The smaller NP dimensions, the shorter diffusion path length. In case of storage devices such as thin-film batteries or super capacitors, the charge–discharge capacity was found to be inversely proportional to the NP size [13]. The insertion/extraction dynamics is related to the energy barrier for diffusion (preferred crystallographic orientation of the facets exposed to the electrolyte) [9]. Electrochemical properties of the MO_x NPs are particularly sensitive to atomic surface structure also in other devices. As an example, anatase TiO_2 has been proved to show the highest photo-electrochemical performance among all possible crystallographic phases of

this MO_x [41]. Moreover, the crystallographic orientation of exposed facets has been demonstrated to play the major role in defining its intrinsic properties and thus its catalytic activity [5, 9]. The wide bandgap semiconductors such as TiO_2 become one of the best choices to form mesoporous layer in DSCs. However, ZnO was found to be a promising alternative to TiO_2 , mainly due to the much higher electronic mobility [42–46], which improves the electron transport and reduces recombination losses [47, 48].

These conduction phenomena assure efficient charge compensation during the redox process and hence improve the response time of the films in EC devices and electron collection in DSCs. When the size of NPs dispersed in a film decreases, the trapping and scattering effect of free charge carriers on grain boundaries result in increased film resistivity. If the size of NPs is smaller than electron mean free path, the scattering on grain boundaries dominates, and the advantage of nanocrystalline composition is becoming negligible. Design of NPs with proper dimensions while maintaining optimal crystallographic structure leads to fast response kinetics and enhanced overall performance.

Nanoparticle Engineering

Size–Shape Impact: From Small Clusters to Massive Agglomerates

When the dimensions of a material system are reduced below a certain length, typically tens of nanometers, the physical properties, which are associated with this length, may drastically change. Then, material properties are no longer solely given by its chemical composition, but also by the size and shape of its nanoscale constituents [49, 50]. In the following section, we attempt to describe these properties and show that for a given material, geometry (shape) and particle size have a major influence on the overall electrochemical properties of a printed film. The size, as well as the shape, of the NPs determines physical and chemical properties of the material. The laws of quantum chemistry govern the smallest particles with sizes ranging from less than a nanometer up to several nanometers. For particles with sizes higher than tens of nanometers, the laws of solid-state physics hold. For the intermediate sizes ranging from several to tens of nanometers, chemical and physical properties do not comply strictly with any of those theories [51]. In the following section, we attempt to correlate electrochemical performance of NP-loaded films such as reactivity and response time with geometrical properties of NPs.

In the large range between molecules and massive agglomerates of particles, three size–shape regimes can be distinguished in which electrochemical properties are mainly related to distribution of atoms on the surface and in the bulk (regime I), geometry of nanocrystals (regime II), and agglomeration process (regime III). In order to transform the shape into mathematical form that still would contain its geometrical description, let us use the aspect ratio (AR). This parameter is defined as the length of the major axis (b) divided by the width of the minor axis (a) [52]. Using size–shape coordinate system, all three regimes can be schematically

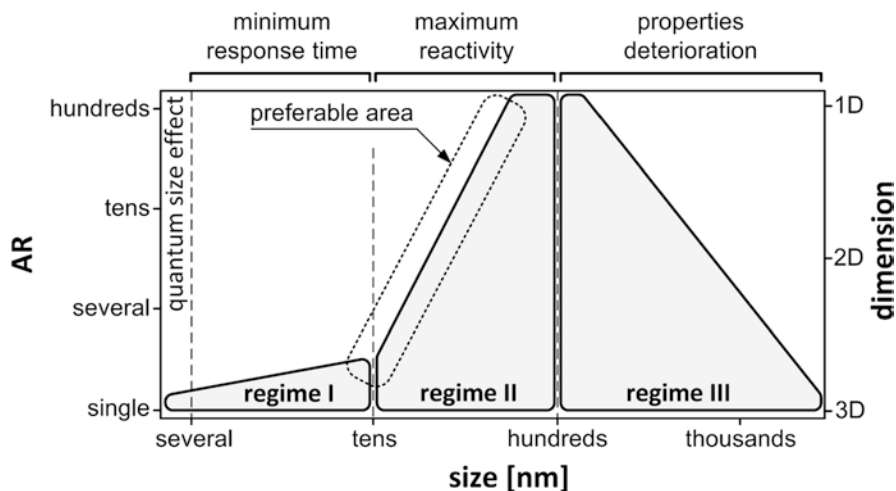


Fig. 2 Electrochemical properties of MO_x NPs in the size–shape coordinating system

presented as it is shown in Fig. 2. The highest values of AR correspond to 1D morphologies such as nanowires and nanorods. Medium values are typical for 2D morphologies such as nanolamellas, nanoplates, and nanodisks, while the lowest values are the domain of 3D morphologies such as nanocubes or nanospheres.

In the following subsections, we provide deeper considerations on size–shape impact on electrochemical performance of MO_x NPs. We deduce that the minimum response time of those nanostructured systems can be achieved in a first regime of the size–shape space. On the other hand, the electrochemical reactivity is attributed mainly to the shape of the NPs and can be maximized in the second regime with increase in active surface area. When the NPs are becoming larger entering the third regime, the agglomeration process caused the properties' deterioration and hence lowered the electrochemical performance of the material.

Small Clusters

Irrespective of the size, an important factor for electrochemical reactivity, that is, the rate at which the electrochemical reaction will proceed, is the area/volume ratio of the nanosized object. In the first size regime, in which NPs are larger than molecules and smaller than tens of nanometers, electrochemical properties are strongly dependent on surface-to-volume atomic ratio ($\text{SA:V}^{(a)}$), defined as the number of surface atoms to the number of bulk atoms [53, 54]. It should be noted that by the number of atoms in case of MO_x , we understand the number of electrochemically active sites, which means the number of metal atoms. Therefore, let us consider spherical WO_3 cluster in which each tungsten atom serves as potential electrochemically active center changing from transparent state to a colored state. A schematic drawing of the cross section of monoclinic WO_3 spherical cluster with diameter of 5 nm is presented in Fig. 3.

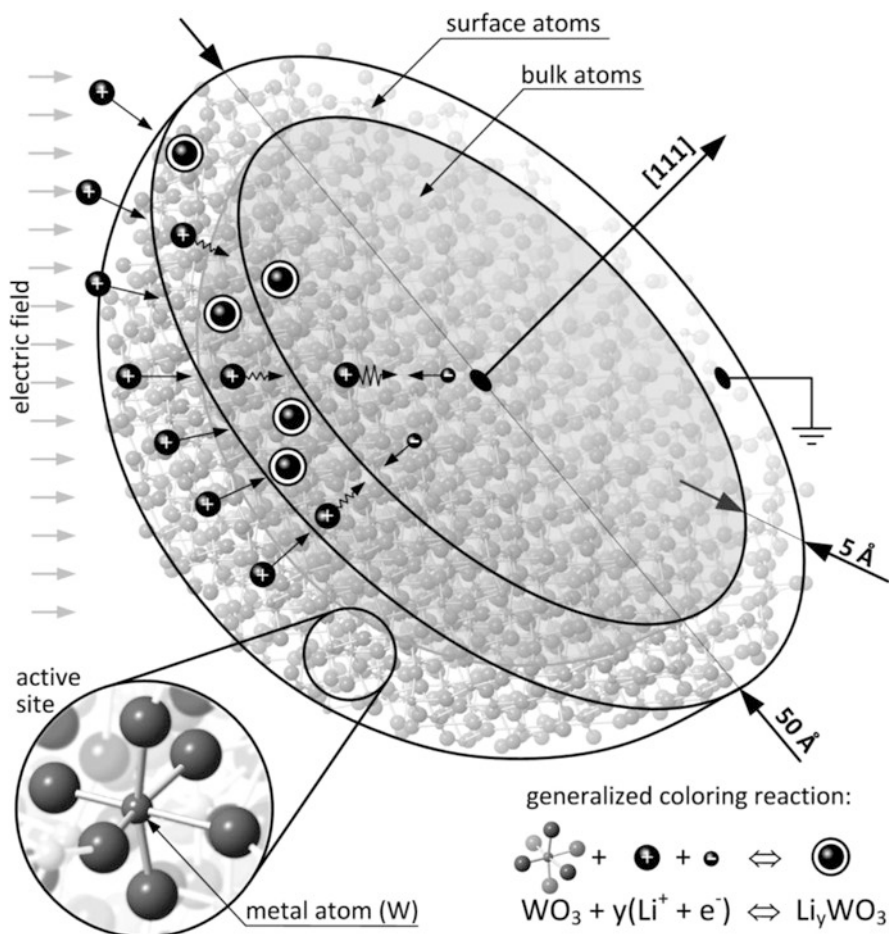


Fig. 3 Schematic drawing of the cross section (along [111] plane) of monoclinic WO_3 spherical cluster with diameter of 5 nm; in this case, tungsten atoms are distributed equally, 50 % in the surface hollow sphere and 50 % in the bulk ball which gives $\text{SA}:\text{V}^{(a)}=1$; an equation represents generalized mechanism of electrochemical reaction for coloring action

According to calculations for such cluster (see Fig. 4), high percentage of electrochemically active sites at the surface of NP (let us assume a hollow sphere with thickness of 0.5 nm), being in contact with electrolyte, is a characteristic for nanostructures with mean particle size ranging in the first regime. In the cluster of around 2 nm in diameter, 85 % of tungsten atoms are located on the surface ($\text{SA}:\text{V}^{(a)}=5.7$), while in cluster of 5 nm in diameter, tungsten atoms are distributed equally in the surface and bulk ($\text{SA}:\text{V}^{(a)}=1$).

According to the electrochromism theory, the mechanism of optical modulation is different in crystalline and amorphous phase. In nanocrystalline, WO_x

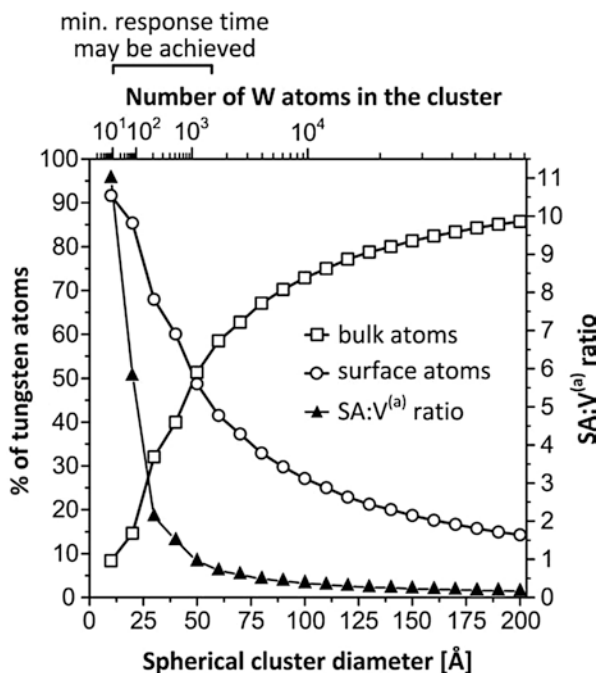


Fig. 4 Relative numbers of tungsten surface/bulk atoms and SA:V^(a) ratio as a function of spherical cluster diameter calculated for monoclinic tungsten oxide (ICSD: 98-009-1587)

electrochromism arises due to the increasing Drude-type (metallic) reflection, observed especially in IR region with increasing free electron/lithium injection [55]. On the other hand, in amorphous phase, the most widely accepted model assumes that the optical modulation upon the double injection occurs through increasing absorption arising from the transfer of localized electrons between W⁵⁺ and W⁶⁺ sites, the so-called small polaron absorption [56–58]. Figure 3 presents generalized mechanism of electrochemical reaction of coloring in EC NP. It is assumed that WO₃ NP in transparent state can be switched reversibly to a colored state by both insertion of ions and electrons to form tungsten bronze (*a*-Li_yWO₃, where *y* is the fractional number of sites filled in the WO₃ lattice). Although being an obvious oversimplification, presented schema provides a very convenient background for further discussion. In considered situation, WO₃ NP is in contact with ion (Li⁺) conductor, which also serves as ion storage, and electron (e⁻) conductor as negative charge collector/source. An electric field shuttles ions into and out of the NP causing coloring (Li_yWO₃) and bleaching (WO₃) action. A hollow sphere representing surface atoms is more conductive for ions and less conductive for electrons when comparing with NP's interior made of bulk atoms. Therefore, the probability of electrochemical reaction (redox) is the highest at the interface between surface and bulk volume, where electrons meet ions leading to the formation of Li_yWO₃.

Moreover, high SA:V^(a) ratio drastically reduces response time due to the fast charge compensation during the redox process [59].

In the MO_x-based electrolyte-gated TFT, external voltage applied to semiconductor/electrolyte interface causes creation of space-charge regions which consists of charged immobile donors or acceptors or by mobile electrons or holes from the conduction and valence bands, respectively. High amount of surface atoms and low sizes result in grains wholly filled with space-charge region, improving current switching characteristics. In those NPs, the electrical conduction is no longer controlled by the grain boundaries, but by the grain itself.

Similarly, in MOX-based chemical gas sensors, the space-charge region extended to the whole NP volume causes significant improvement in the sensitivity. Additionally, much higher concentration of surface defects leads to a higher surface reactivity, when comparing to their hundred nanometer-sized counterparts. Thus, the use of materials with the mean particle size ranging in the first regime significantly improves the gas-sensing properties [60, 61]. The large active surface area enhances the material sensitivity, while the faster response is related to short diffusion paths and rapid grain boundary diffusion.

Shaped Nanocrystals

In the second regime of size–shape coordinating system, which comprises NPs higher than tens and lower than several hundreds of nanometers, electrochemical properties are dependent rather on geometric shape than size. Electrochemical properties in this size range are strongly dependent on surface-to-volume ratio (SA:V) defined by means of geometric surface area to the volume of the object. Let us use the aspect ratio (AR) to analyze various NPs with primary and regular shapes drawn in Fig. 5. Please note that presented considerations are valid as

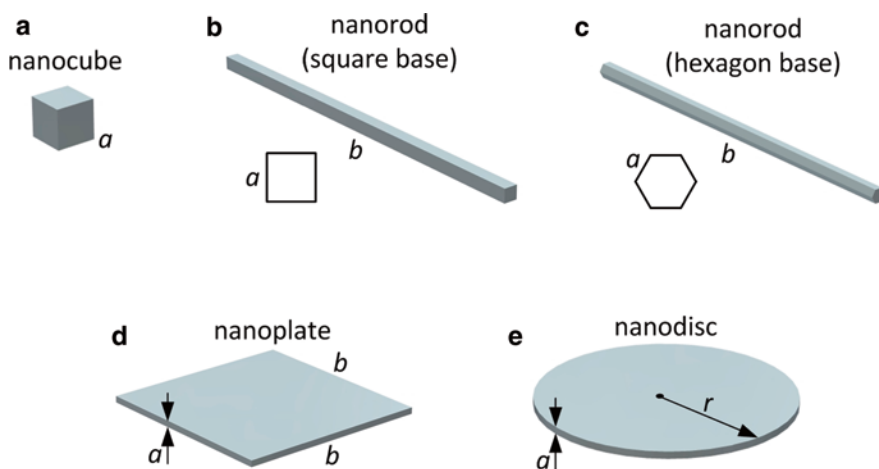
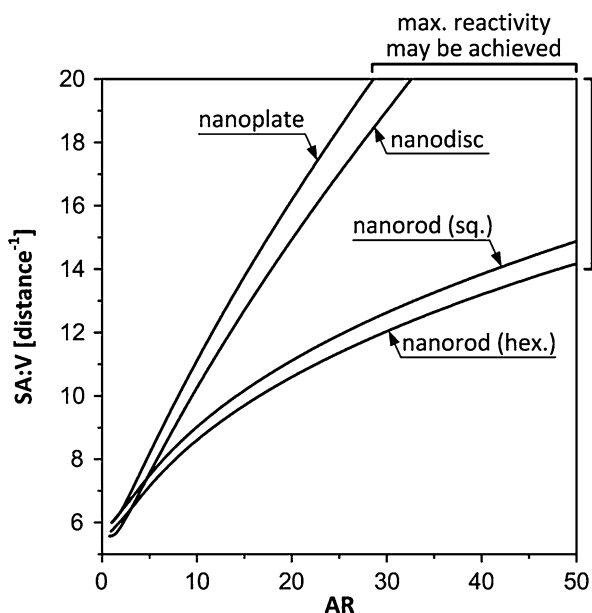


Fig. 5 Theoretical examples of various regular shaped NPs: (a) nanocube (3D), (b) square base nanorod (1D), (c) hexagon base nanorod (1D), (d) nanoplate (2D), and (e) nanodisk (2D)

Table 2 Relations between AR and SA:V derived from various regular shaped NPs

Shape	AR	SA : V = $f(AR)$
Nanorod (square base)	$\frac{b}{a}$	$\frac{2a}{b^2} AR + \frac{4}{b} AR$
Nanorod (hexagon base)	$\frac{b}{a\sqrt{3}}$	$\frac{2a\sqrt{3}}{b^2} AR + \frac{4}{b} AR$
Nanoplate	$\frac{b}{a}$	$\frac{2}{b} AR + \frac{4a}{b^2} AR$
Nanodisk	$\frac{2r}{a}$	$\frac{1}{r} AR + \frac{a}{r^2} AR$

Fig. 6 Simulation of SA:V as a function of AR for various regular shaped NPs. Variables a and b were selected according to the simple assumption that the volume of all individual particles is equal



long as ideal dispersion of NPs is concerned. This means that we consider the products of a synthesis which consists of separated nanocrystals with equal volume and shape.

Accordingly, sphere and cube are characterized by $AR=1$. The SA:V parameter for other regular shaped NPs can be calculated using equations presented in Table 2. Although it is very rare in practice to synthesize such ideal shaped nanostructures, by plotting SA:V in a function of AR, we can get an idea of how those regular shape may influence electrochemical reactivity.

Plots presented in Fig. 6 indicate that nanoplates and nanodisks are the most preferable shapes of NPs in terms of SA:V value. Along with enhanced anisotropy of NPs, and thus higher AR value (conventionally for $AR > 20$), nanoplates, nanodisks, and nanorods transform into nanoribbons, nanomembranes, and nanowires, respectively.

Nanostructured MO_x NPs with high SA:V and high AR enhance electrochemical performance of printed nanocrystalline films in two different ways: firstly, in terms of electrochemical reactivity manifested differently depending on the device functionality. Higher values of optical modulation in EC devices are obtained by increased interaction with lithium ions due to the larger interface between NPs and amorphous coating or NPs and electrolyte. The EC reaction occurs in electrochemically active sites, and so it will be favored as the number of active sites available at the interface increases. High AR of NPs results in high roughness factor of the film defined as the total film area per unit substrate area [4]. Due to high roughness of the film, it is possible to increase the dye and enzyme loading in DSC and electrocatalytic biosensors, respectively. In DSC, high SA:V of MO_x nanocrystalline electrode indicates high area exposed to the sensitizer during the dye absorption and thus higher number of light-sensitive active sites. The sensitivity and response time of electrochemical gas sensors are also highly dependent on the SA:V [62]. Moreover, large surface area is beneficial when placing of selective catalytic dopants is concerned.

Secondly, electronically conductive network of elongated nanostructures enhances conductivity of the film thanks to the anisotropic diffusion of electrons, helping the electrochemical reaction to be completed faster (e.g., efficient carrier collection in DSCs or decreased switching time in EC devices) [28]. Additionally, semiconducting electrode form of elongated nanostructures provides a more direct path, with less trap sites for electron transport to the collection electrode, and, thus, reduces electron percolation deficiency [63]. The application of 1D-shaped NPs may also introduce an internal electric field to provide additional driving force and enhance electrochemical reaction.

Agglomerates

An unfavorable aspect associated with MO_x NPs from the third regime of size–shape coordinating system is agglomeration which leads to the formation of massive blocks, significantly reducing SA:V. The relation between SA:V and the number of agglomerated particles using a simple agglomeration model (see Fig. 7) is presented in Fig. 8. NPs of various shapes are described with simple assumption that the volume of all individual particles is equal. Particles presented in such simulation have primary and regular shapes with unit volume.

When considering the ideal dispersion of NPs in which agglomeration does not occur, nanoplates and nanodisks are the most preferable in terms of SA:V value. For agglomerated NPs, high values of SA:V are obtained for agglomerates of nanorods (agglomerates consisting of more than three NPs), although their individual specific surface area is not the highest among shapes under consideration. The least

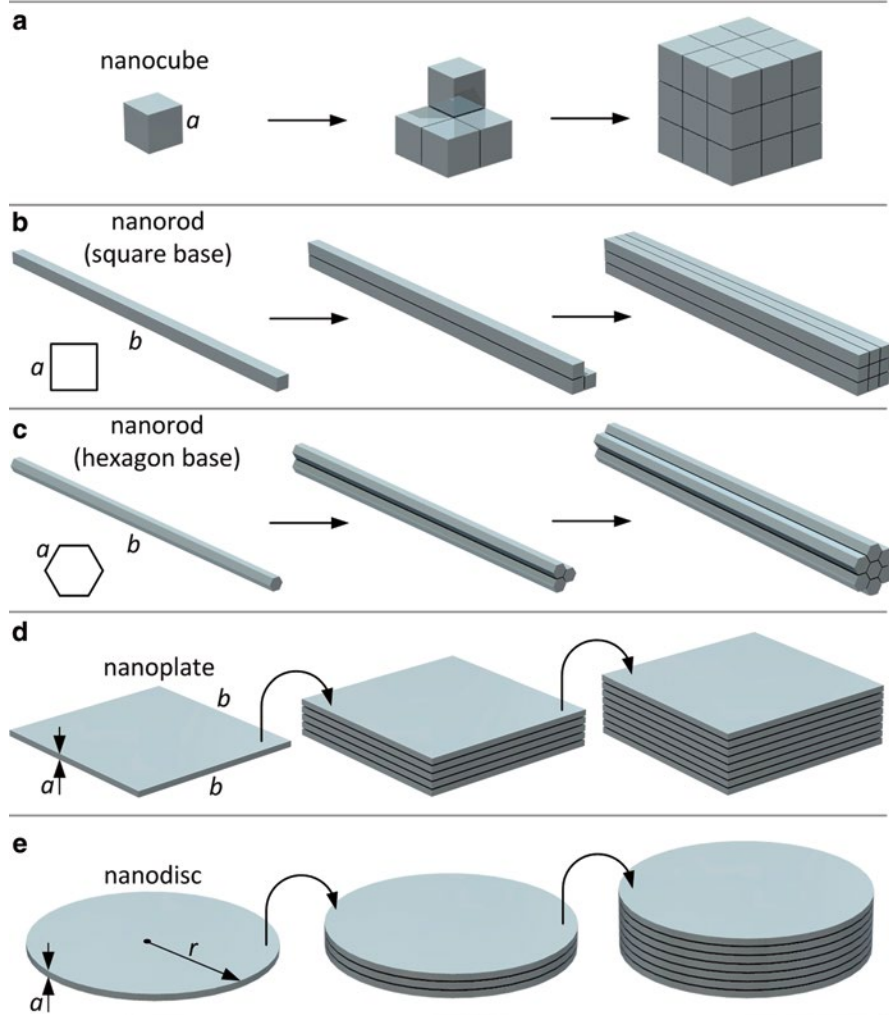


Fig. 7 Basic agglomeration model for various regular shaped NPs: (a) nanocubes (3D), (b) square base nanorods (1D), (c) hexagon base nanorods (1D), (d) nanoplates (2D), and (e) nanodisks (2D)

favorable seem to be nanocubes in the case of which SA:V is small for fine dispersions and significantly drops down with increased number of agglomerated particles. As it is very rare in practice to synthesize not agglomerated NPs, it may be assumed that 1D nanorods are the most desirable products of synthesis as long as their electrochemical application is concerned.

In contrast to the agglomerated NPs, hollow and hierarchical nanostructures assembled in a highly periodic and porous manner generally exhibit much higher SA:V [64, 65]. The van der Waals attraction between hierarchical structures is

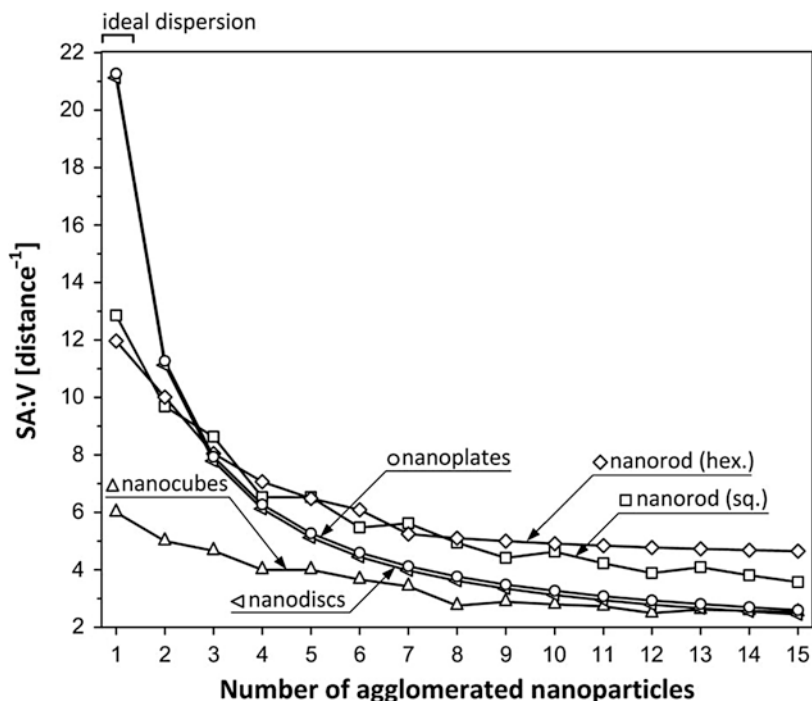


Fig. 8 Model of agglomeration for various regular shaped NPs; the volume of all individual particles is equal to 1; the term “ideal dispersion” refers to the situation in which agglomeration does not occur

relatively weak due to larger size, which makes them more advantageous in dispersions when comparing to anisotropic NPs. However, the large size of such particles restricts their application in printable dispersions. The synthesis of highly porous, hierarchical MO_x nanostructures with sub-micrometer dimensions, although very promising, is still a challenging issue.

Fluid Control of Printable Dispersions

The development of printable functional MO_x dispersion is strictly reliant on the development of NPs. Thereby, the key issue is to select product with morphology tailored to assure desired physical properties of its dispersion [66]. In this section, we attempt to provide basic recommendations on each major step of an ink formulation and impose critical constraints. The requirements for MO_x NP-loaded ink/paste in the area of printed electronics are the following:

- The dispersion must ensure reliable print under deposition conditions.
- Chemical and physical stability of the dispersion must be provided.

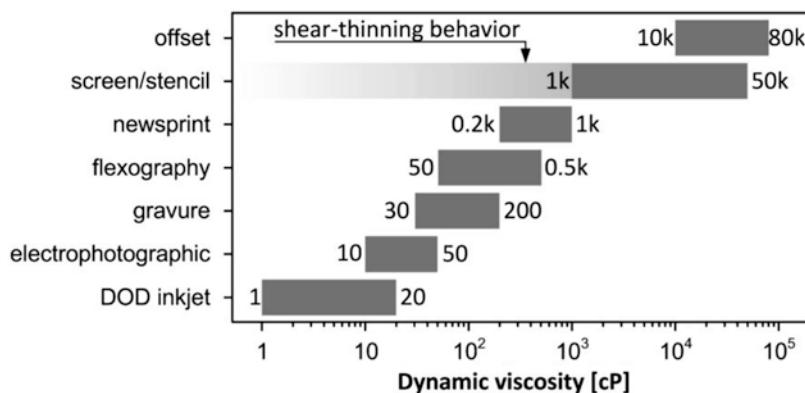


Fig. 9 Dynamic viscosity values of MO_x NP dispersions for various printing techniques

- (c) Printable formulation is not hazardous.
 (d) Printed film must display required functional performance.

In general, printable MO_x dispersions are two phase fluids consisting of a dispersion of NPs in a liquid carrier (aqueous or organic), the so-called vehicle. The viscosity of such dispersion varies between 1 and 10^5 cP depending mainly on the vehicle composition and is tailored for a specific printed technique. However, NP volume fraction, their shape as well as particle orientation in a fluidic flow, may imply critical consequences on viscosity especially when the drop-on-demand (DOD) ink-jet-printing process is concerned [66]. Typical viscosities of NP dispersion for basic printing techniques are presented in Fig. 9.

The viscosity of the dispersion can be easily increased to the acceptable level without substantially modifying its other properties, by addition of thickening agents. For inorganic solid/liquid mixtures, it can be a low boiling point, viscous, and miscible with the vehicle organic solvent or soluble polymer, e.g., (for aqueous ink) polyethylene glycol (PEG) or polyvinyl alcohol (PVA). However, there is another aspect related to fluid viscoelasticity, which makes NP-loaded fluid control much more complicated [67, 68]. Newtonian character of pure liquid is changing radically with the addition of NPs, due to the increased viscoelasticity of the dispersion [69, 70]. The most drastic consequence may be observed in the case of ink-jet printing, where the formation of the fluid drops from the nozzle is disrupted leading to the formation of satellite drops, which deteriorate pattern quality. Nonlinear character of the shear stress in a function of shear rate affects also the droplet behavior on a substrate surface in the moment of impact (deposition, splashing, or rebound) and spreading (pattern size) [71]. In a roll-to-roll processing (R2R) of creating electronic devices on a flexible substrate, the viscoelasticity of dispersion may significantly limit the printing speed. Therefore, the viscosity of the dispersion should not change with shear stress applied in a broad range of values (10^{-2} – 10^2 Pa), which

means that Newtonian behavior of the fluid is expected [66]. In order to fulfill this requirement, a solid content of the ink should be in a relatively low range of 0.01–1 wt%. Additionally, an agglomeration phenomenon among NPs is not desirable, especially in the case of low viscosity dispersion, in which stability is the main issue. Therefore, a narrow particle size distribution is recommended.

An exception among printing techniques under consideration is screen printing in which shear-thinning behavior (viscosity decreases with applied shear stress) is necessary to transfer the NP-loaded paste through printing mesh.

The surface tension value for typical low viscosity inks is between 30 and 40 mN m⁻¹. In order to adjust this parameter to acceptable range, the nonionic surfactant such as, e.g., Triton X-100 or Triton X-45 can be added in the amount of 0.1–0.5 wt%. It is worth mentioning that the spontaneous movement of NPs toward the ink/air interface may affect the surface tension. However, imposed changes usually do not affect the printing process significantly, as long as proper ink rheology is maintained.

In order to effectively disperse nanomaterial powder in a vehicle, breaking of NP agglomerates and stabilization by pH modification, additions of surfactants or polymers are required. However, liquid medium complexity may significantly deteriorate electrical performance of final printed films. Therefore, in a perfect situation, NPs are dispersed in a pure water or aqueous alcoholic solution with no other organic additives, which allows for low posttreatment temperature. Moreover, it is crucial that the ink components are chemically compatible with the substrate they will be printed on.

Selected or synthesized NPs must comply with important size limitation in order to allow its usage in printing system. The most drastic restrictions are applied in formulation of ink-jet-printable ink. It can be assumed (with some exceptions, e.g., nanorods alignment in a microfluidic flow [72, 73]) that the maximum particle size should be at least 50 times smaller than nozzle diameter. If NPs are too large, the nozzle may clog, and printing will simply stop. Moreover, larger NPs also increase probability that the dispersion will suffer from particle precipitation and agglomeration, unless the mixture is constantly agitated or special additives are included to the large particles in dispersion.

Design Rule Outline

Engineering rules presented in Fig. 10 have been developed as a summary of the previous section existing in this chapter. In order to determine preferable regime for printed electrochemical applications, each alternative was studied until the choice is clear, rational, and optimal according to existing knowledge and common practice. By following the diagram, one can formulate MO_x NP-loaded ink which assures good printing processability and enhancement in electrochemical performance. Such design rule outline is an approach to proper arrangement of various factors including structural, morphological, electrical, and rheological properties while

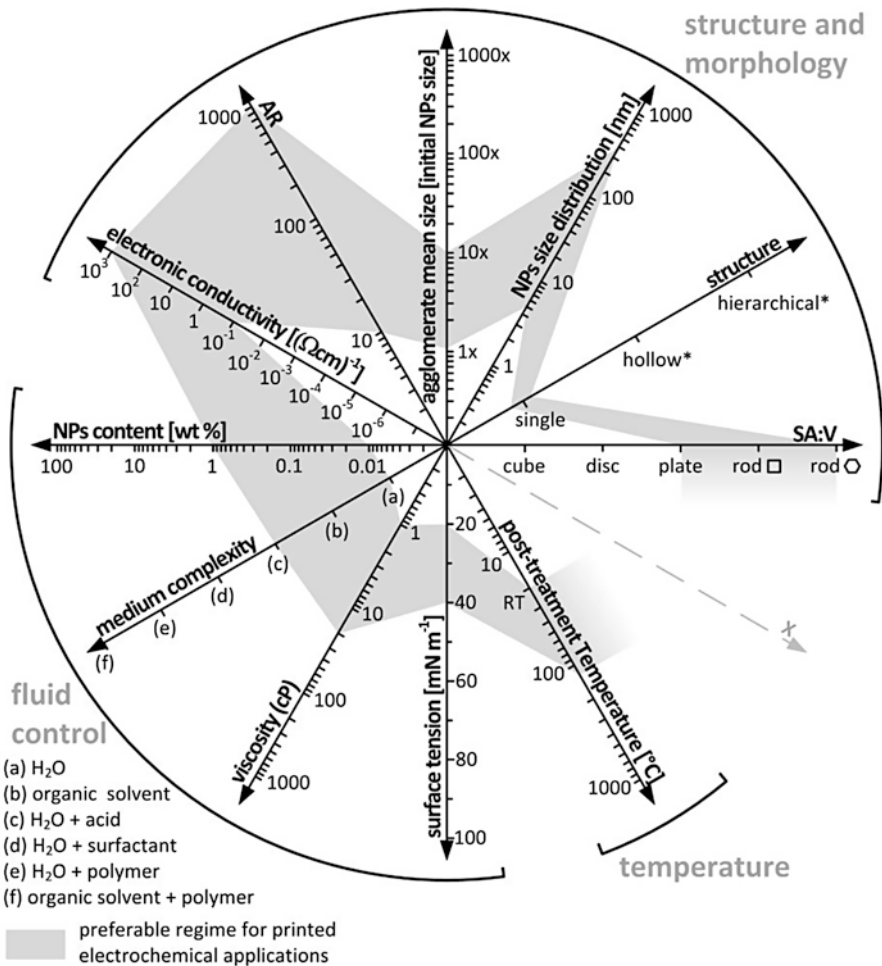


Fig. 10 The design rule outline for the formulation of MO_x NP-loaded printable dispersions for the development of electrochemically active films; preferable regime for electrochemical applications based on ink-jet-printed inorganic film is indicated

taking into account posttreatment conditions. However, those eleven parameters do not restrict the scope of research in this area. Many other factors may be considered as relevant, depending on the studies complexity.

As presented here, engineering rules for NP selection and ink formulation have, to a large extent, a universal character and may be implemented to create a variety of new ink-jet-printable nanostructured MO_x materials for chromic, photovoltaic, photo- and electro catalytic, sensing, power storage, and basic electronic devices. It can be also expanded to other printing techniques by establishing appropriate physical and chemical constrains.

Case Study: Ink-Jet-Printed Dual-Phase Electrochromic Film

Structure and Morphology of Synthesized Products

We have already used the size–shape coordinate system in order to illustrate specific topics on MO_x NP selection. We also presented the graphical design rule outline which is intended to resume basic requirements for a dispersion formulation and facilitate printing experiment. We will now consider this task in a more detailed way so that the reader can appreciate the application of the several topics that were previously described in a complete worked-out case study.

Taking under account existing state-of-the-art and our own observations, it is expected that the incorporation of WO_x NPs synthesized in external process into the amorphous matrix of the same MO_x would enhance performance of printed EC films. Accordingly, in the present work, WO_x NPs with known structure and morphology were synthesized and tested in a dual-phase EC device.

Among many wet chemical syntheses, hydrothermal treatment was selected to synthesize WO_x NPs as it seems to be the most facile, cost-effective, and well-studied technique, which additionally offers flexibility in possible nanomorphologies [6, 16–18, 74–77]. An aqueous solution of peroxopolytungstic acid (PTA) [78, 79] with controlled acidity [2] (addition of HCl) was used as a source of tungsten. Selected precursor was then subjected to hydrothermal conditions in Teflon-lined stainless-steel autoclave, which imply elevated temperature (180 °C) and high vapor pressure (~1.1 MPa) for a certain period of time enabling nucleation and growth of crystallites. The products of syntheses are presented in Fig. 11. Product obtained from non-acetified precursor solution indicates the coexistence of two WO_x polymorphs, namely, monoclinic (*m*- WO_3 , ICSD: 98-009-1587) and orthorhombic tungsten oxide hydrate (*ortho*- $\text{WO}_3 \cdot 0.33\text{H}_2\text{O}$, ICSD: 98-003-7822) in a shape of nanoplates and nanorods, respectively. Lowering acidity of precursor by dissolving PTA in 0.3 M HCl and 3 M HCl causes phase unification to *ortho*- $\text{WO}_3 \cdot 0.33\text{H}_2\text{O}$ (ICSD: 98-003-7822) nanowires and *m*- WO_3 (ICSD: 98-009-1587) nanoplates, respectively.

The enhancement in lithium ion diffusion rate, and hence faster electrochemical response, is expected for films containing orthorhombic hydrate (*ortho*- $\text{WO}_3 \cdot 0.33\text{H}_2\text{O}$) NPs due to the higher electronic conductivity of this phase when comparing to monoclinic (*m*- WO_3) nanocrystals [40]. Therefore, the products of synthesis from PTA dissolved in non-acidified and 0.3 M HCl seem to be the most desirable, as long as the crystallinity is concerned.

The *ortho*- $\text{WO}_3 \cdot 0.33\text{H}_2\text{O}$ nanorods synthesized from non-acetified precursor solution are 116 ± 48 nm long, ~40 nm wide, and ~20 nm thick ($\text{AR} = 5.8 \pm 2.4$). Rectangular *m*- WO_3 nanoslab fraction of the same product has uniform thickness of ~12 nm, while length varies in size of 223 ± 85 nm ($\text{AR} = 18.6 \pm 7.1$). The *ortho*- $\text{WO}_3 \cdot 0.33\text{H}_2\text{O}$ nanowires prepared from PTA dissolved in 0.3 M HCl are 187 ± 46 nm long, having well-defined square cross section with a side length of ~12 nm ($\text{AR} = 15.6 \pm 3.8$). The *m*- WO_3 cubic structures prepared from PTA dissolved in 3 M HCl are agglomerates of rectangular nanoslabs with

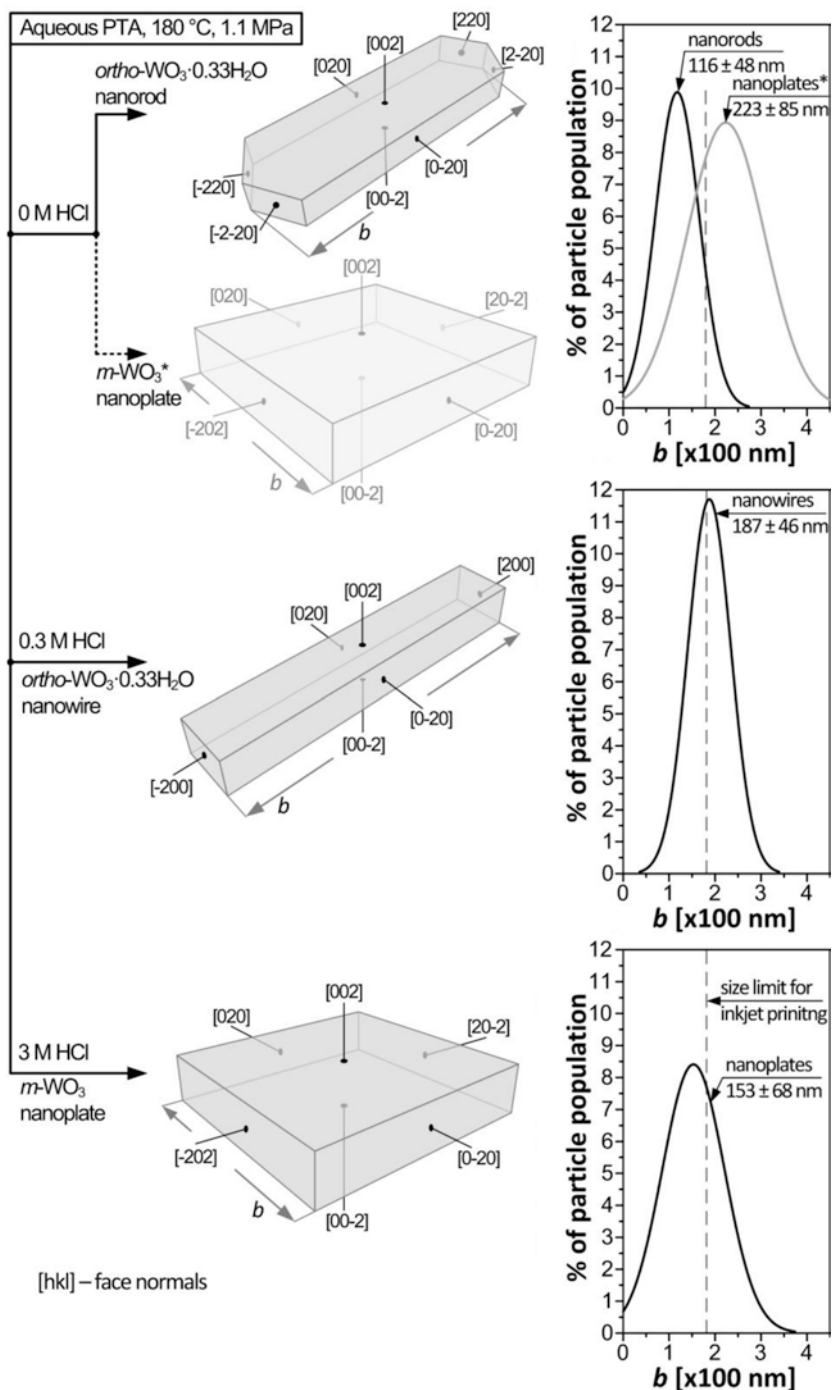
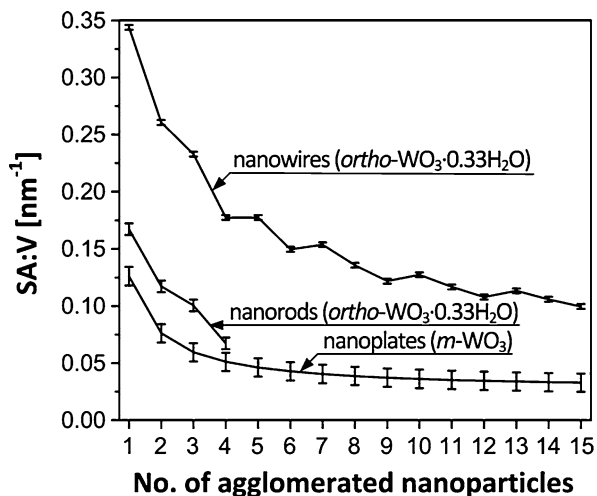


Fig. 11 The products obtained via hydrothermal syntheses with corresponding continuous (Gaussian) particle size distributions; models (isometric projections) of NPs were developed based on quantitative information concerning the preferential crystalline orientation (texture coefficient) and SEM observations; *synthesized product does not comply with size limitation for ink-jet-printing method

Fig. 12 Estimation of SA:V as a function of agglomerate size, based on particle size distribution and basic agglomeration model; y-axis error bars reflect standard deviation of a mean particle size; *agglomerates of nanorods (synthesized from PTA dissolved in 0 M HCl) with number of NPs higher than four were not observed



uniform thickness of ~ 20 nm, while the length varies in size of 153 ± 68 nm ($AR = 7.7 \pm 3.4$).

Shape Impact

Size distributions of synthesized products were used also to estimate SA:V as a function of agglomerate size, shown in Fig. 12. The highest values of SA:V were obtained for agglomerates of *ortho*-WO₃·0.33H₂O nanowires prepared from PTA dissolved in 0.3 M HCl. Their individual specific surface area is also the highest among synthesized products. The least favorable in terms of SA:V are *m*-WO₃ nanoplates synthesized from PTA dissolved in 3 M HCl, irrespectively of the agglomerate size.

Obtained estimations of SA:V stay in agreement with theoretical considerations which results were plotted in Fig. 8 (see section “[Shaped Nanocrystals](#)”). Therefore, synthesized *ortho*-WO₃·0.33H₂O nanowires are the most desirable products in terms of SA:V, as long as their electrochemical application is concerned.

Ink Formulation and Printability

According to the printhead specification (Canon Thermal DOD FINE™) used in Canon PIXMA iP4850 printer, the nozzle diameter is 9 μ m. Therefore, not all nanostructured products obtained in experiments comply with size limitations (space diagonal ≤ 180 nm; see section “[Fluid Control of Printable Dispersions](#)”), even when assuming that agglomeration does not occur. Based on particle size distributions and the simple model of agglomeration presented in section

“Agglomerates” (under assumption of uniform size distribution of agglomerates and agglomerate block not exceeding 15 NPs), it is possible to estimate that nanorods synthesized from non-acidified are printable in 100 %, while the fraction of nanoplates is not printable at all. Nanowires synthesized from PTA dissolved in 0.3 M HCl are printable in 48 %. Only 17 % of nanoplates synthesized from PTA dissolved in 3 M HCl are capable to pass the printing nozzle. Therefore, the presented example shows that NP agglomeration has dramatic influence on NP printability. The major concern is associated with the nanoplates, as they are relatively large in size and tend to agglomerate significantly exceeding size limitation for this particular Canon printing system.

Irrespective of the complexity of an ink vehicle, controllable and reproducible deposition of NP-loaded inks encompasses some challenges. In standard desktop printers, such as CANON PIXMA iP4850 used in present studies, the jetting parameters can be controlled only by proper adjustment of ink fluid parameters, as there is no direct access to the printhead’s driver. To assure proper droplet formulation, the custom ink should have similar rheology to the genuine CANON inks (indicated in Fig. 13).

At the same time, it should be water-based ink as most of the organic solvents may dissolve the structure of the printhead. Such water-based ink offers the following advantages when comparing with organic solvent-based counterparts:

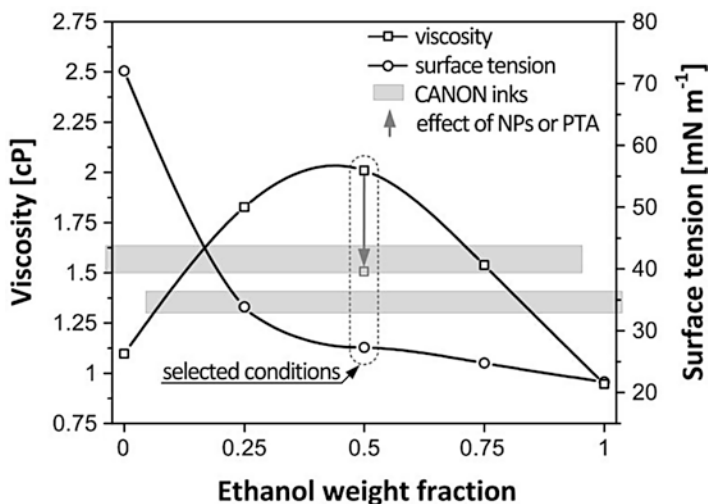


Fig. 13 The viscosity and surface tension of an alcohol aqueous ink vehicle as a function of alcohol (*ethanol*) weight fraction, the adjustment of fluid parameters to the acceptable range via the addition of NPs or PTA precursor, as well as the regime of genuine CANON inks (CLI-526 cyan, magenta, and yellow) are indicated

- (a) Reduces volatility
- (b) Assures low reactivity with the substrate and printhead elements
- (c) Imposes fewer restrictions in terms of safe handling

In order to adjust the viscosity and surface tension to the range within which the printer operates, the ethanol weight fraction of vehicle was selected as 0.5, according to the plot shown in a Fig. 13, resulting in values of 2 cP and 27 mN m⁻¹, respectively. The viscosity of obtained vehicle is too high when comparing with genuine CANON inks, but addition of NPs in the amount of 0.03 wt% (in the case of NP dispersion ink) or 8.7 wt% of PTA (in the case of amorphous coating) transfers the value of viscosity into CANON ink regime. Thus, the viscosity and the surface tension of both NP dispersion and WO₃ sol assure expected printability.

Film Forming

The fabrication of ink-jet-printed dual-phase EC films was performed via two separate depositions. Firstly, printable WO_x NP dispersion was deposited on the substrate and dried. Secondly, such mesoporous-like film was coated with printable sol, containing precursor of WO₃, resulting in dual-phase *a*-WO₃/WO_x film. All films were dried at room temperature for 24 h and annealed in air at 120 °C for 1 h. Depending on the type of the NPs incorporated to the dispersion in the first deposition step, the following compositions of films were obtained:

- (a) Dual-phase *a*-WO₃/*ortho*-WO₃·0.33H₂O (nanorods)
- (b) Dual-phase *a*-WO₃/*ortho*-WO₃·0.33H₂O (nanowires)
- (c) Dual-phase *a*-WO₃/*m*-WO₃ (nanoplates)
- (d) Amorphous *a*-WO₃ for reference purposes (no NPs incorporated)

The existence of amorphous phase (*a*-WO₃) in each film under investigation provides compact mechanical structure of the film and guarantees EC effect, by allowing electronic conduction to take place in the structure processed at low temperature. The use of PTA as the precursor for NP synthesis and *a*-WO₃ coating shows convergence of the technologies. A uniform coverage of nanocrystals by amorphous coating was confirmed by SEM examination. Revealed film microstructure shows randomly dispersed NPs embedded in continuous amorphous film.

Electrochromic Response

Quantitative EC response analysis is based on chronoabsorptometry (CA) technique which is a square-wave potential step method coupled with optical spectroscopy used for analysis of switching kinetics and contrast of the film. The electrochemical

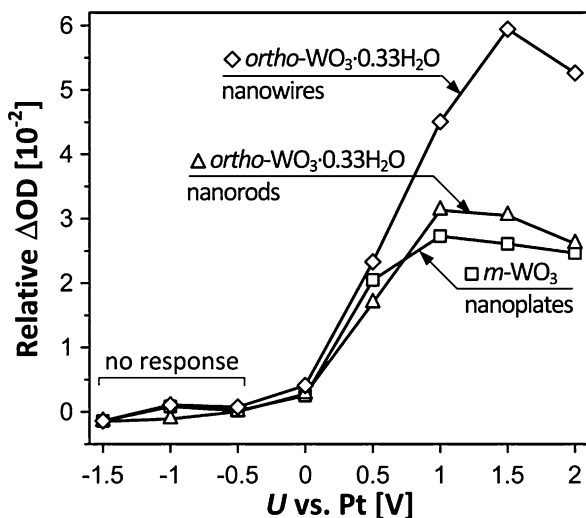
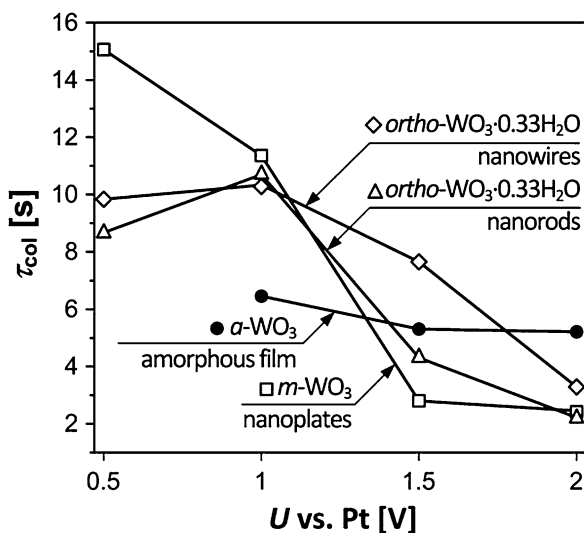


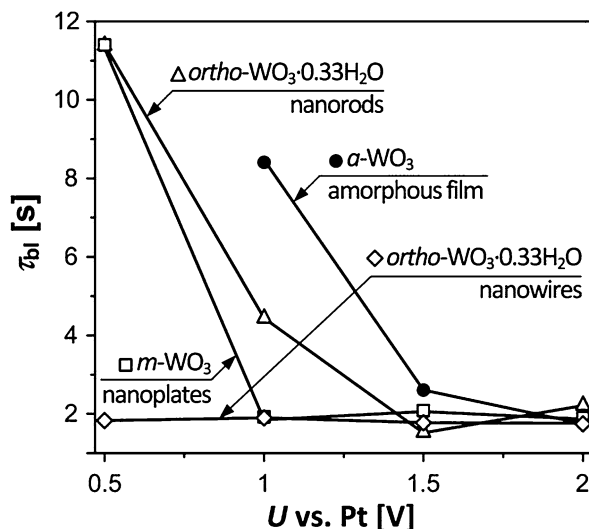
Fig. 14 Change in optical density (ΔOD) as a function of operating voltage for dual-phase ink-jet-printed films containing different types of NPs; relative values represent the difference between ΔOD of dual-phase film and ΔOD of pure amorphous analog (reference)

Fig. 15 Variation in coloring time as a function of operating voltage for dual-phase ink-jet-printed films containing different types of NPs; amorphous film is presented for comparison



cell consisting of working electrode (printed film on indium tin oxide (ITO) PET substrate) and platinum wire used as counter electrode was filled with lithium-based gel electrolyte prepared according to the recipe described elsewhere [80]. Resulting cell was driven by power supply in order to induce EC action in a linear stair pulse mode (from -2 V up to 2 V in a 0.5 V step, -2 V of bias, and 30 s per pulse). Spectra

Fig. 16 Variation in bleaching time for dual-phase ink-jet-printed films containing different types of NPs; bleached state was restored by supplying -2 V, after coloring under operational voltage (an abscissa); amorphous film is presented for comparison



were recorded in reference to the uncoated substrate under equal conditions. The main output is confined to the basic performance indicators consisting of:

- Change in optical modulation defined as $\Delta OD = \log_{10}(T_{bl}/T_{col})$, where T_{bl} and T_{col} stand for bleaching and coloring transmittance, respectively, measured at $\lambda = 800$ nm (see Fig. 14)
- Coloration time denoted as τ_{col} (see Fig. 15)
- Bleaching time denoted as τ_{bl} (see Fig. 16), both determined using transmittance modulation trace at $\lambda = 800$ nm induced by linear stair pulse signal, and defined as the requisite time for the transmittance change by 80 % of the total difference between final states

Comparison between corresponding changes in optical densities of dual-phase films in reference to the response of pure amorphous film is shown in Fig. 14. Such presentation of the optical modulation provides the information regarding the role of NP content selectively, in EC mechanism.

Films, which contain either $ortho\text{-WO}_3 \cdot 0.33\text{H}_2\text{O}$ or $m\text{-WO}_3$ NPs, outperform their amorphous analogs in terms of optical modulation. It is a consequence of dual-phase microstructure which provides large interfaces between dual-phase film and gel electrolyte, as well as between amorphous and nanocrystalline phases itself. Such microstructure promotes ion diffusion through the porous film. The highest ΔOD values were recorded for film containing $ortho\text{-WO}_3 \cdot 0.33\text{H}_2\text{O}$ nanowires, which is a direct repercussion of the highest value of SA:V for those NPs, even in spite of progressing agglomeration.

Differences in switching dynamics of dual-phase and amorphous films shown in Figs. 15 and 16 provide an information regarding the role of NPs in the dynamics of the EC reaction. Low potentials applied between electrodes (0.5 V and 1 V) cause

slow but apparent transition between bleached and colored state. However, the rate of the electrochemical reaction is lower when comparing with pure amorphous phase (see Fig. 15). Operation with the higher voltage level (1.5 V and 2 V) results in improved coloration time (<3 s for 2 V) of all films containing NPs in comparison with pure amorphous film (~5 s).

The application of a reverse potential (−2 V) restores the film to its bleached state over a short period of time denoted as τ_{bl} . The switching dynamics from colored to bleached state depends on the voltage level at which coloration was induced. According to Fig. 16, when restoring the pure amorphous film after coloration at low potential (1 V), the optical change proceeds very slowly (~8.5 s). However, bleaching period is much shorter in case of dual-phase films. Films containing *ortho*-WO₃·0.33H₂O nanowires bleach within time lower than 1.9 s, irrespectively of the level of the operational voltage which induced coloring state, owed to high electronic conductivity of those nanostructures. For other films, NP content is beneficial especially when low voltage levels are used to supply the device.

The coloration kinetics is observed to be slower than bleaching kinetics for all the films under investigation, which stays in agreement with the well-defined, but different, mechanism governing the two processes. While the exchange of the current density at the EC film–electrolyte interface controls coloration kinetics, the space-charge-limited Li⁺ ion diffusion current governs the bleaching time [57].

Presented case study clearly shows beneficial impact of WO_x NPs on electrochromic performance of printed films, reflected in 2.5 times higher optical modulation, and 2 times faster coloration time, when comparing with pure amorphous film. Such improvement is mainly attributed to higher interface between amorphous and nanocrystalline phase, as well as between MO_x layer and ion conductor.

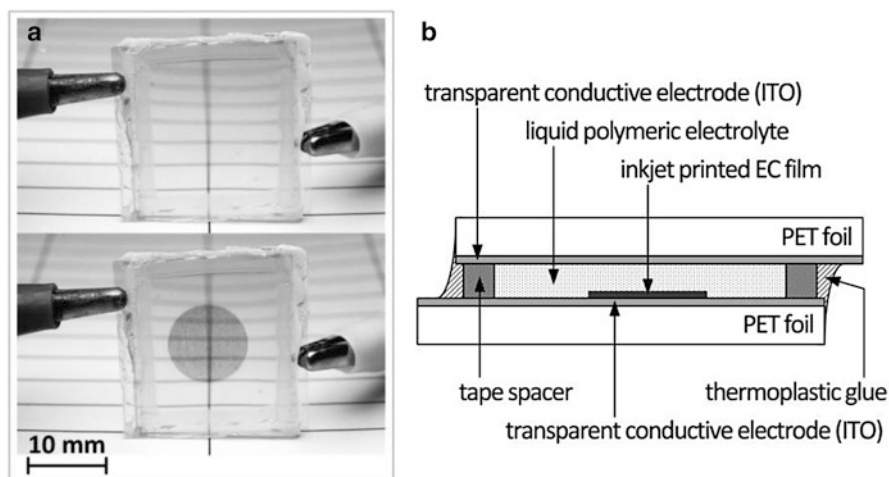


Fig. 17 Lab-testing EC pixel based on ink-jet-printed dual-phase *a*-WO₃/WO_x/TiO₂ film on ITO PET substrate and liquid electrolyte: (a) picture in a bleached and colored state and (b) schematic cross section of the device

Prototypes of Printed Electrochromic Devices

The potential of the electrochemical applications as the practical devices is supported by the commercial interest in early market prototypes of printed EC displays (e.g., Acreo Swedish ICT AB, Sweden; NTERA Inc., USA; Aveso Inc., USA). Niche applications in smart cards, smart packaging, and automotive displays have already been identified. However, new applications are being announced regularly as this is still an emerging technology area. In this section, we present some examples of EC displays demonstrated by our group over the years 2010–2013, which incorporate printed dual-phase MO_x films.

The preliminary evaluation of the printed dual-phase films was performed using a lab-testing transparent EC device presented in Fig. 17a, developed in 2010 [28]. The device was assembled using sandwich structure (see Fig. 17b), which consists of an ink-jet-printed $\alpha\text{-WO}_3/\text{WO}_x/\text{TiO}_2$ EC film, a liquid electrolyte for ion storage [80] and two transparent ITO-coated PET foil substrates separated by double-sided 1 mm thick tape spacer.

When applying an operational voltage to the electrodes, the ions are driven from the electrolyte into EC film, where they are intercalated causing the chromatic effect. Reversing the voltage returns them to the electrolyte resulting in pixel bleaching. Sealing with thermoplastic glue ensures integrity of the device and allows carrying out the necessary measurements in order to evaluate performance of printed EC film. However, this lab-testing EC device uses liquid electrolyte based on volatile organic solvents which significantly reduces its lifetime (typically up to several days).

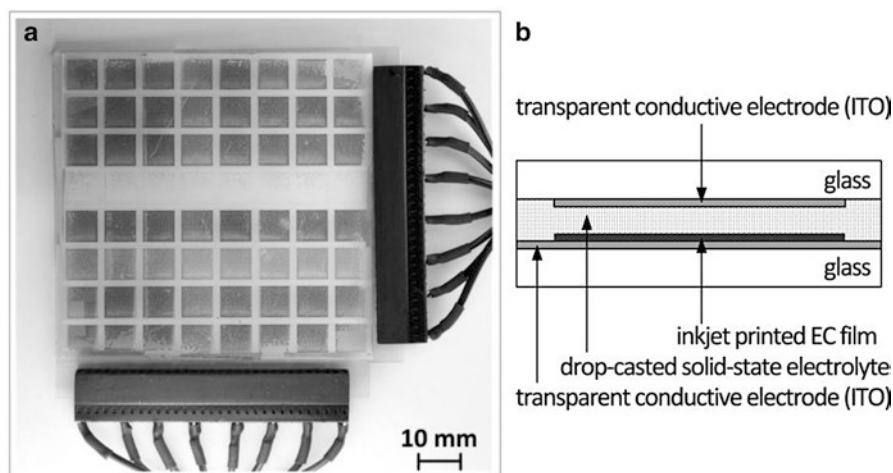


Fig. 18 Prototype of the 64 pixel passive EC matrix with ink-jet-printed $\alpha\text{-WO}_3/\text{WO}_x$ film on ITO glass substrate with thermosetting solid-state electrolyte drop-casted and UV-cured in situ: (a) picture of the opaque display operating under driving signal and (b) schematic cross section of an individual pixel

In order to overcome those limitations, in 2011, we have developed EC display, which has the advantage of high overall stability ensured by an all-solid-state structure. An 8×8 EC passive matrix consisting of two 100 mm by 90 mm glass substrates with 64 pixels, 1 cm^2 each, is shown in Fig. 18a. Prototype of this non-transparent display was fabricated by selective ITO etching, ink-jet printing of optically active film ($\alpha\text{-WO}_3/\text{WO}_x$), and drop casting of the TiO_2 -loaded thermo-setting composite solid-state electrolyte (TCSE). The prepolymer of the opaque electrolyte was then uniformly distributed by squeezing with upper glass substrate and UV curing in situ at ambient conditions (see Fig. 18b). No additional encapsulation is required, as the cured TCSE provides perfect sealing of the structure itself.

Each pixel of the developed EC matrix can be operated separately by applying a voltage between selected pair of electrodes. Rigid structure provided by glass substrates together with a strong adhesion of the TCSE assures excellent mechanical strength. Although the long-time stability investigation of prototype was not carried out according to standard methodology, the matrix was operated every ones in a while within 21 months till present, functioning with no apparent performance deterioration. Furthermore, no delamination was observed, which proves that this configuration of materials and processes results in excellent durability.

While the abovementioned sandwich structure is used in the great majority of the state-of-the-art prototypes of EC devices, it does not represent the only possibility. A fully printed EC display with a thin-film structure shown in Fig. 19a has been developed in our group in 2013. Flexible EC thin-film passive display was built up on a single ITO PET foil substrate according to the stack structure shown in Fig. 19b. Active display area was defined as 15.5 mm by 15.5 mm. The transparent conductive tracks were chemically etched using screen-printed polymer mask pattern, defining 64 pixels with dimensions of 1.65 mm by 1.65 mm each. In the consecutive

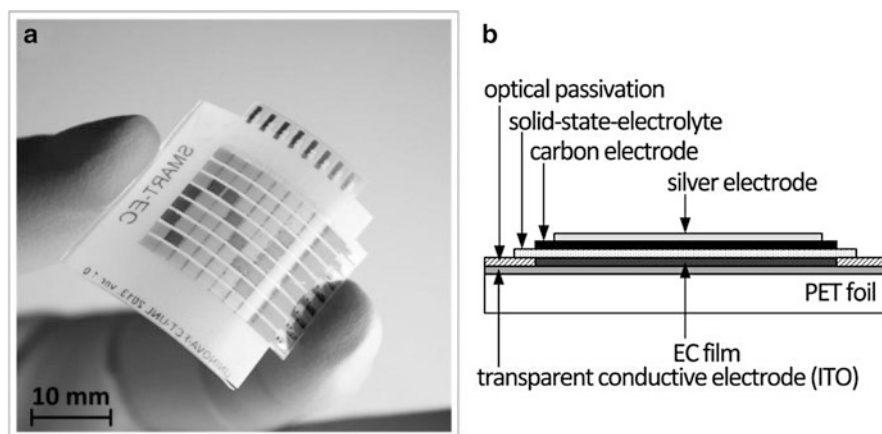


Fig. 19 Prototype of a fully screen-printed 64 pixel passive EC matrix based on $\alpha\text{-WO}_3/\text{WO}_x$ film developed on a single ITO PET foil substrate: (a) picture of the device displaying the pattern due to the memory effect and (b) schematic cross section of an individual pixel

printing steps, the following materials optimized for screen-printing processing were deposited:

- (a) TiO_2 -loaded UV-curable resin as optical passivation
- (b) WO_x NP-loaded PTA paste to form α - WO_3/WO_x EC film
- (c) TiO_2 -loaded UV-curable TCSE
- (d) Carbon counter electrode
- (e) Silver electrode

Although, the performance measurements of the thin-film EC display were not carried out according to classical electrochemical methodology, it is evident that the matrix exhibits high optical contrast, while the switching time is comparable with the fastest lab-testing EC devices developed using liquid electrolyte (<3 s for coloring and <2.5 s for bleaching).

There are two key reasons why this type of approach is thought to be the most suitable for end-user devices. First, the consumer demands are oriented toward reliable operation assured by all-solid-state structure of the EC device. Second, the development of the EC devices using solely printing techniques facilitates scale-up process from a pilot plant operation to the production at commercial levels using R2R facilities.

Summary

Nowadays, printable films based on MO_x NPs attract growing attention as convenient and scalable to mass production way of producing electrochemically active thin films. The process has developed as means of depositing light and easily ion-penetrable films from the dispersions on NPs on a variety of substrates, including flexible and heat-sensitive materials such as plastic foil (PET, PEN, PI) or paper.

The reasonable theoretical explanation of the dependence between morphology of NPs and electrochemical performance, i.e., response time and reactivity, has been provided in this chapter. We have deduced that the minimum response time can be achieved when small (several nanometers) NPs are incorporated to the printed film. On the other hand, the electrochemical reactivity can be enhanced by selection of NPs with high aspect ratio and thus high specific surface area. We have also considered agglomeration phenomenon which causes lowering of electrochemical performance. Basic simulations have shown that an effective way to limit the deterioration of material properties via agglomeration is to select 1D morphologies such as nanowires and nanorods.

We have also developed basic rules governing selection or development of a variety of nanostructured MO_x -based materials for ink-jet-printed electrochemical applications. Proposed engineering rules can be expanded to other printing techniques by establishing appropriate physical and chemical constrains. The versatility of this outline makes it a useful guide not only in the selection of MO_x NPs for high

performance applications but also meets the challenges encountered when using those materials in a printing process.

In the presented case study, the morphology evolution of tungsten oxide nanostructures has been successfully controlled by acidity level of sol-gel precursor under hydrothermal conditions. In order to evaluate EC properties of developed NPs, dual-phase films deposited via ink-jet printing have been investigated showing higher values of transmission modulation over the visible and solar regions as compared to the EC performance of pure amorphous films. Films containing synthesized NPs exhibit change in optical modulation up to 2.5 times higher than amorphous counterparts. Such improvement is mainly attributed to higher interface between amorphous and nanocrystalline phase, as well as between MO_x layer and ion conductor. Moreover, the presence of orthorhombic hydrate improves kinetics of intercalation and deintercalation mechanisms due to the increased hydration of the structure. The conductive network of interconnected WO_x NPs facilitates charge transport in the EC layer and increases significantly the active surface area of the amorphous matrix. Therefore, the impact of synthesized NP morphology and structure on EC performance has been identified as crucial.

Presented prototypes demonstrate that a combination of printing techniques with controlled synthesis of NPs provides an excellent method for the production of inorganic dual-phase electrochemically active films. Flexibility in the material selection and simplicity of the processing give a control over the film composition at low temperature in a direct-write fabrication.

Acknowledgments This work was funded by the Portuguese Science Foundation (FCT-MEC) through project Electra, PTDC/CTM/099124/2008, ERA-MNT/0005/2009, Strategic Project PEst-C/CTM/LA0025/2011, and the PhD grant SFRH/BD/45224/2008 given to P. J. Wojcik. Moreover, this work was also supported by E. Fortunato's ERC 2008 Advanced Grant (INVISIBLE contract number 228144), "A3PLE" FP7-NMP-2010-SME/262782-2, "SMART-EC" FP7-ICT-2009.3.9/258203, and "POINTS" FP7-NMP-263042.

References

1. Jiao Z, Sun XW, Wang J, Ke L, Demir HV (2010) Hydrothermally grown nanostructured WO_3 films and their electrochromic characteristics. *J Phys D Appl Phys* 43:285501
2. Wang J, Khoo E, Lee PS, Ma J (2009) Controlled synthesis of WO_3 nanorods and their electrochromic properties in H_2SO_4 electrolyte. *J Phys Chem C* 113:9655–9658
3. Songara S, Gupta V, Kumar Patra M, Singh J, Saini L, Siddaramana Gowd G, Raj Vadera S, Kumar N (2012) Tuning of crystal phase structure in hydrated WO_3 nanoparticles under wet chemical conditions and studies on their photochromic properties. *J Phys Chem Solid* 73: 851–857
4. Law M, Greene LE, Johnson JC, Saykally R, Yang P (2005) Nanowire dye-sensitized solar cells. *Nat Mater* 4:455–459
5. Li J, Xu D (2010) Tetragonal faceted-nanorods of anatase TiO_2 single crystals with a large percentage of active {100} facets. *Chem Commun (Camb)* 46:2301–2303
6. Hong SJ, Jun H, Borse PH, Lee JS (2009) Size effects of WO_3 nanocrystals for photooxidation of water in particulate suspension and photoelectrochemical film systems. *Int J Hydrogen Energy* 34:3234–3242

7. Wang H, Lindgren T, He J, Hagfeldt A, Lindquist S (2000) Photoelectrochemistry of nanostructured WO_3 thin film electrodes for water oxidation: mechanism of electron transport. *J Phys Chem B* 104:5686–5696
8. Sartoretti JC, Alexander BD, Solarska R, Rutkowska I, Augustynski J, Cerny R (2005) Photoelectrochemical oxidation of water at transparent ferric oxide film electrodes. *J Phys Chem B* 109:13685–13692
9. Sun CH, Yang XH, Chen JS, Li Z, Lou XW, Li C, Smith SC, Lu GQM, Yang HG (2010) Higher charge/discharge rates of lithium-ions across engineered TiO_2 surfaces leads to enhanced battery performance. *Chem Commun (Camb)* 46:6129–6131
10. Huang K, Pan Q, Yang F, Ni S, Wei X, He D (2008) Controllable synthesis of hexagonal WO_3 nanostructures and their application in lithium batteries. *J Phys D Appl Phys* 41:155417
11. Lang X, Hirata A, Fujita T, Chen M (2011) Nanoporous metal/oxide hybrid electrodes for electrochemical supercapacitors. *Nat Nanotechnol* 6:232–236
12. Deng W, Ji X, Chen Q, Banks CE (2011) Electrochemical capacitors utilising transition metal oxides: an update of recent developments. *RSC Adv* 1:1171
13. Bruce PG, Scrosati B, Tarascon J-M (2008) Nanomaterials for rechargeable lithium batteries. *Angew Chem Int Ed Engl* 47:2930–2946
14. Dasgupta S, Kruk R, Mechau N, Hahn H (2011) Inkjet printed, high mobility inorganic-oxide field effect transistors processed at room temperature. *ACS Nano* 5:9628–9638
15. Dasgupta S, Gottschalk S, Kruk R, Hahn H (2008) A nanoparticulate indium tin oxide field-effect transistor with solid electrolyte gating. *Nanotechnology* 19:435203
16. Zhang H, Liu T, Huang L, Guo W, Liu D, Zeng W (2012) Hydrothermal synthesis of assembled sphere-like WO_3 architectures and their gas-sensing properties. *Physica E* 44:1467
17. Liu S, Zhang F, Li H, Chen T, Wang Y (2012) Acetone detection properties of single crystalline tungsten oxide plates synthesized by hydrothermal method using cetyltrimethyl ammonium bromide supermolecular template. *Sens Actuators B* 162:259–268
18. Yan A, Xie C, Zeng D, Cai S, Li H (2010) Synthesis, formation mechanism and illuminated sensing properties of 3D WO_3 nanowall. *J Alloys Compd* 495:88–92
19. Wang K, Xu J-J, Chen H-Y (2006) Biocomposite of cobalt phthalocyanine and lactate oxidase for lactate biosensing with MnO_2 nanoparticles as an eliminator of ascorbic acid interference. *Sens Actuators B* 114:1052–1058
20. Ansari A, Alhoshan M, Alsalmi M, Aldwayyan A (2010) Nanostructured metal oxides based enzymatic electrochemical biosensors. In: Serra PA (ed) *Biosensors*. INTECH, Croatia, pp 23–46
21. Goesmann H, Feldmann C (2010) Nanoparticulate functional materials. *Angew Chem Int Ed Engl* 49:1362–1395
22. Bisquert J (2007) Photovoltaic, photoelectronic, and electrochemical devices based on metal-oxide nanoparticles and nanostructures. In: Rodríguez JA, Fernández-García M (eds) *Synthesis, properties, and applications of oxide nanomaterials*. Wiley, Hoboken, pp 451–490
23. Zhou L, Zou J, Yu M, Lu P, Wei J, Qian Y, Wang Y, Yu C (2008) Green synthesis of hexagonal-shaped $\text{WO}_3 \cdot 0.33\text{H}_2\text{O}$ nanodiscs composed of nanosheets. *Cryst Growth Des* 8:3993–3998
24. Khoo E, Lee PS, Ma J (2010) Electrophoretic deposition (EPD) of WO_3 nanorods for electrochromic application. *J Eur Ceram Soc* 30:1139–1144
25. Takahashi K, Wang Y, Cao G (2005) Growth and electrochromic properties of single-crystal V_2O_5 nanorod arrays. *Appl Phys Lett* 86:053102
26. Wang J, Lee PS, Ma J (2009) One-pot synthesis of hierarchically assembled tungsten oxide (hydrates) nano/microstructures by a crystal-seed-assisted hydrothermal process. *Cryst Growth Des* 9:2293–2299
27. Bernacka-Wojcik I, Senadeera R, Wojcik PJ, Silva LB, Doria G, Baptista P, Aguas H, Fortunato E, Martins R (2010) Inkjet printed and “doctor blade” TiO_2 photodetectors for DNA biosensors. *Biosens Bioelectron* 25:1229–1234
28. Wojcik PJ, Cruz AS, Santos L, Pereira L, Martins R, Fortunato E (2012) Microstructure control of dual-phase inkjet-printed a- $\text{WO}_3/\text{TiO}_2/\text{WO}_x$ films for high-performance electrochromic applications. *J Mater Chem* 22:13268

29. Wojcik PJ, Pereira L, Martins R, Fortunato E (2014) Statistical mixture design and multivariate analysis of inkjet printed a-WO₃/TiO₂/WO_x electrochromic films. *ACS Comb Sci* 16:5–16
30. Jiang J, Li Y, Liu J, Huang X, Yuan C, Lou XWD (2012) Recent advances in metal oxide-based electrode architecture design for electrochemical energy storage. *Adv Mater* 24:5166–5180
31. Woodward PM, Sleight AW, Vogt T (1997) Ferroelectric tungsten trioxide. *J Solid State Chem* 131:9–17
32. Yamanaka K, Oakamoto H, Kidou H, Kudo T (1986) Peroxotungstic acid coated films for electrochromic display devices. *Jpn J Appl Phys* 25:1420–1426
33. Frenzer G, Maier WF (2006) Amorphous porous mixed oxides: sol–gel ways to a highly versatile class of materials and catalysts. *Annu Rev Mater Res* 36:281–331
34. Kim Y-H, Heo J-S, Kim T-H, Park S, Yoon M-H, Kim J, Oh MS, Yi G-R, Noh Y-Y, Park SK (2012) Flexible metal-oxide devices made by room-temperature photochemical activation of sol–gel films. *Nature* 489:128–132
35. Sandu I, Brousse T, Santos-Pena J (2002) Comparison of the electrochemical behaviour of SnO₂ and PbO₂ negative electrodes for lithium ion batteries. *Ionics (Kiel)* 8:27–35
36. Granqvist CG (1993) Electrochromic materials: microstructure, electronic bands, and optical properties. *Appl Phys A Solids Surf* 57:3–12
37. Poizot P, Laruelle S, Grugeon S, Dupont L, Tarascon JM (2000) Nano-sized transition-metal oxides as negative-electrode materials for lithium-ion batteries. *Nature* 407:496–499
38. Yebka B, Pecquenard B, Julien C, Livage J (1997) Electrochemical Li+ insertion in WO₃ – xTiO₂ mixed oxides. *Solid State Ion* 104:169–175
39. Pyun S-I, Bae J-S (1996) Lithium ion transport in r.f.-magnetron sputtered WO₃ film as a function of lithium content. *J Alloys Compd* 245:L1–L4
40. Mohammad A (2009) Al: synthesis, separation and electrical properties of WO_{3-x} nanopowders via partial pressure high energy ball-milling. *Acta Phys Pol A* 116:240–244
41. Karunakaran C, Dhanalakshmi R, Manikandan G, Gomathisankar P (2011) Photodegradation of carboxylic acids on Al₂O₃ and SiO₂ nanoparticles. *Indian J Chem* 50A:163–170
42. Nunes P, Fortunato E, Tonello P, Fernandes FB, Vilarinho P (2002) Effect of different dopant elements on the properties of ZnO thin films. *Vacuum* 64:281–285
43. Nunes P, Costa D, Fortunato E, Martins R (2002) Performances presented by zinc oxide thin films deposited by r.f. magnetron sputtering. *Vacuum* 64:293–297
44. Nunes PU, Fortunato E, Martins R (2001) Influence of the post-treatment on the properties of ZnO thin films. *Thin Solid Films* 383:277–280
45. Assuncao V, Ferreira I, Martins R, Fortunato E, Marques A, Aguas H (2003) Influence of the deposition pressure on the properties of transparent and conductive ZnO Ga thin-film produced by r.f. sputtering at room temperature. *Thin Solid Films* 427:401–405
46. Fortunato E, Pimentel A, Gonçalves A, Marques A, Martins R (2006) High mobility amorphous/nanocrystalline indium zinc oxide deposited at room temperature. *Thin Solid Films* 502:104–107
47. Zhang Q, Chou TP, Russo B, Jenekhe SA, Cao G (2008) Aggregation of ZnO nanocrystallites for high conversion efficiency in dye-sensitized solar cells. *Angew Chem Int Ed Engl* 47:2402–2406
48. Zhang Q, Dandeneau CS, Zhou X, Cao G (2009) ZnO nanostructures for dye-sensitized solar cells. *Adv Mater* 21:4087–4108
49. Jolivet J-P, Cassaignon S, Chanéac C, Chiche D, Durupthy O, Portehault D (2010) Design of metal oxide nanoparticles: control of size, shape, crystalline structure and functionalization by aqueous chemistry. *C R Chim* 13:40–51
50. Navrotsky A (2003) Energetics of nanoparticle oxides: interplay between surface energy and polymorphism. *Geochem Trans* 4:34
51. Klabunde K, Richards RM (2001) *Nanoscale materials in chemistry*. Wiley, New York
52. Murphy CJ, Jana NR (2002) Controlling the aspect ratio of inorganic nanorods and nanowires. *Adv Mater* 14:80–82

53. Jayalakshmi M, Rao MM, Kim K (2006) Effect of particle size on the electrochemical capacitance of α -Ni(OH)₂ in alkali solutions. *Int J Electrochem Sci* 1:324–333
54. Klabunde KJ, Stark J, Koper O, Mohs C, Park DG, Decker S, Jiang Y, Lagadic I, Zhang D (1996) Nanocrystals as stoichiometric reagents with unique surface chemistry. *J Phys Chem* 100:12142–12153
55. Granqvist CG (2000) Electrochromic tungsten oxide films: review of progress 1993–1998. *Sol Energy Mater Sol Cells* 60:201–262
56. Krasnov Y (2004) Electrochromism and reversible changes in the position of fundamental absorption edge in cathodically deposited amorphous WO₃. *Electrochim Acta* 49:2425–2433
57. Faughnan BW, Crandall RS, Lampert MA (1975) Model for the bleaching of WO₃ electrochromic films by an electric field. *Appl Phys Lett* 27:275–277
58. Kadam PM, Tarwal NL, Shinde PS, Mali SS, Patil RS, Bhosale AK, Deshmukh HP, Patil PS (2011) Enhanced optical modulation due to SPR in gold nanoparticles embedded WO₃ thin films. *J Alloys Compd* 509:1729–1733
59. Vidotti M, Torresi SICD (2008) Nanochromics: old materials, new structures and architectures for high performance devices. *J Braz Chem Soc* 19:1248–1257
60. Baraton M-I, Merhari L (2001) Influence of the particle size on the surface reactivity and gas sensing properties of SnO₂ nanopowders. *Mater Trans* 42:1616–1622
61. Franke ME, Koplin TJ, Simon U (2006) Metal and metal oxide nanoparticles in chemiresistors: does the nanoscale matter? *Small* 2:36–50
62. Liu J, Guo Z, Zhu K, Wang W, Zhang C, Chen X (2011) Highly porous metal oxide polycrystalline nanowire films with superior performance in gas sensors. *J Mater Chem* 21:11412
63. Hagfeldt A, Boschloo G, Sun L, Kloo L, Pettersson H (2010) Dye-sensitized solar cells. *Chem Rev* 110:6595–6663
64. Lee J-H (2009) Gas sensors using hierarchical and hollow oxide nanostructures: overview. *Sens Actuators B Chem* 140:319–336
65. Gu Z, Zhai T, Gao B, Sheng X, Wang Y, Fu H (2006) Controllable assembly of WO₃ nanorods/nanowires into hierarchical nanostructures. *J Phys Chem B* 110:23829–23836
66. Mueller S, Llewellyn EW, Mader HM (2009) The rheology of suspensions of solid particles. *Proc R Soc A* 466:1201–1228
67. Duan F, Kwek D, Crivoi A (2011) Viscosity affected by nanoparticle aggregation in Al₂O₃-water nanofluids. *Nanoscale Res Lett* 6:248
68. Pastoriza-Gallego MJ, Casanova C, Páramo R, Barbés B, Legido JL, Piñeiro MM (2009) A study on stability and thermophysical properties (density and viscosity) of Al₂O₃ in water nanofluid. *J Appl Phys* 106:064301
69. Cooper-White JJ, Fagan JE, Tirtaatmadja V, Lester DR, Boger DV (2002) Drop formation dynamics of constant low-viscosity, elastic fluids. *J Nonnewton Fluid Mech* 106:29–59
70. Furbank RJ, Morris JF (2004) An experimental study of particle effects on drop formation. *Phys Fluids* 16:1777
71. Tuladhar TR, Mackley MR (2008) Filament stretching rheometry and break-up behaviour of low viscosity polymer solutions and inkjet fluids. *J Nonnewton Fluid Mech* 148:97–108
72. Khoo HS, Lin C, Huang S-H, Tseng F-G (2011) Self-assembly in micro- and nanofluidic devices: a review of recent efforts. *Micromachines* 2:17–48
73. Huang Y, Duan X, Wei Q, Lieber CM (2001) Directed assembly of one-dimensional nanostructures into functional networks. *Science* 291:630–633
74. Yayapao O, Thongtem T, Phuruangrat A, Thongtem S (2011) CTAB-assisted hydrothermal synthesis of tungsten oxide microflowers. *J Alloys Compd* 509:2294–2299
75. Huang R, Shen Y, Zhao L, Yan M (2012) Effect of hydrothermal temperature on structure and photochromic properties of WO₃ powder. *Adv Powder Technol* 23:211–214
76. Sungpanich J, Thongtem T, Thongtem S (2012) Large-scale synthesis of WO₃ nanoplates by a microwave-hydrothermal method. *Ceram Int* 38:1051–1055
77. Huirache-Acuña R, Paraguay-Delgado F, Albiter MA, Lara-Romero J, Martínez-Sánchez R (2009) Synthesis and characterization of WO₃ nanostructures prepared by an aged-hydrothermal method. *Mater Charact* 60:932–937

78. Jiayin L, Jianfeng H, Jianpeng W, Liyun C, Yanagisawa K (2012) Morphology-controlled synthesis of tungsten oxide hydrates crystallites via a facile, additive-free hydrothermal process. *Ceram Int* 38:4495–4500
79. Wang J, Lee P, Ma J (2009) Synthesis, growth mechanism and room-temperature blue luminescence emission of uniform WO_3 nanosheets with W as starting material. *J Cryst Growth* 311:316–319
80. Barbosa PC, Rodrigues LC, Silva MM, Smith MJ, Valente PB, Gonçalves A, Fortunato E (2011) Characterization of polyether-poly(methyl methacrylate)-lithium perchlorate blend electrolytes. *Polym Adv Technol* 22:1753–1759

Mirosław M. Bućko

Contents

Introduction.....	820
Preparation of Zirconia Solid Solutions of Varying Microstructure.....	826
Structural Properties of Zirconia Solid Solutions with Varying Microstructure.....	829
Microstructural Differentiation of Zirconia Solid Solutions.....	831
Ionic Conductivity of Zirconia Solid Solutions with Different Microstructures.....	835
Conclusions.....	845
References.....	845

Abstract

Zirconia solid solutions have been actively intensively investigated as an oxide ion conductor in solid oxide fuel cells (SOFC), oxygen sensors, or electrochemical oxygen pumps. The importance of grain size and density of grain boundaries in such materials for their properties is obvious. It is generally believed that a formation of nanomaterials with high density of grain boundaries can lead to their much improved electrical properties [1]. A possibility to modify the ion conductor conductive properties by means of changes in its microstructure was shown for the first time, as the explanation of a significant difference in the conductivity values of zirconium dioxide solid solutions, obtained in different conditions [2]. However, a distinct determination the effect of microstructure on the ion conductive properties is not easy, if at all possible. The information on the impact of various elements of the microstructure on the ionic conductivity is scattered and fragmented and practically no systematic studies exist. In the case of zirconium dioxide solid solutions, an additional complication is a strong

M.M. Bućko (✉)

Faculty of Materials Science and Ceramics, University of Science and Technology,
Krakow, Poland

e-mail: bucko@agh.edu.pl

connection between material microstructural changes with variations in the chemical and phase composition. Describing the effect of microstructure on the conductivity level, the influence of each factor forming the microstructure should be determined separately, i.e., porosity, average particle size, as well as their size distribution, associated with the amount of grain boundaries, and their condition.

Keywords

Ionic conductivity • Nanomaterials • Stabilized zirconia

Introduction

Zirconia solid solutions have been actively intensively investigated as an oxide ion conductor in solid oxide fuel cells (SOFC), oxygen sensors, or electrochemical oxygen pumps. The importance of grain size and density of grain boundaries in such materials for their properties is obvious. It is generally believed that a formation of nanomaterials with high density of grain boundaries can lead to their much improved electrical properties [1]. A possibility to modify the ion conductor conductive properties by means of changes in its microstructure was shown for the first time, as the explanation of a significant difference in the conductivity values of zirconium dioxide solid solutions, obtained in different conditions [2]. However, a distinct determination the effect of microstructure on the ion conductive properties is not easy, if at all possible. The information on the impact of various elements of the microstructure on the ionic conductivity is scattered and fragmented and practically no systematic studies exist. In the case of zirconium dioxide solid solutions, an additional complication is a strong connection between material microstructural changes with variations in the chemical and phase composition. Describing the effect of microstructure on the conductivity level, the influence of each factor forming the microstructure should be determined separately, i.e., porosity, average particle size, as well as their size distribution, associated with the amount of grain boundaries, and their condition.

The most commonly used microstructure model for the description of the ionic conductivity in solid solutions of zirconium dioxide is a brick layer model [3, 4]. In this model, the ion conductor is made up of particles of cubic shapes separated by thin, flat grain boundaries. In this model it is assumed that the grain size, expressed as a length of the cube side d_g , is many times larger than the thickness of the grain boundary d_{gb} . Another assumption is the one-dimensional current flow and neglecting the curvature at the cube's corners. The model considered two extreme situations arising from the grain interior conductivity values (σ_b) and grain boundaries' conductivity (σ_{gb}). When $\sigma_b \gg \sigma_{gb}$, the flow of electric charges is carried out mainly by volume of the particles and across grain boundaries and in the opposite situation along the boundaries. Assuming that the grain boundaries' conductivity is significantly lower than the conductivity of the interior of grains, which

actually exist in the zirconia solid solutions, it is possible to provide a relation connecting the measured values of the material electrical parameters with the parameters describing the microstructure:

$$C_{gb} \cdot \frac{L}{A} = \varepsilon_{gb} \cdot \frac{d_g}{d_{gb}} \quad (1)$$

where C_{gb} is the capacity of grain boundaries; ε_b and ε_{gb} are the dielectric permittivity of grains and grain boundaries, respectively; L , A are geometric dimensions of the sample associated with the measurement conditions; A is the area of the parallel electrodes; and L is the distance between them.

This equation is derived on the assumption that the measured capacitance value grain boundaries, C_{gb} , are the sum of all the individual boundaries' capacity perpendicular to the direction of the applied electric field [4]. The values of capacitance, C_b and C_{gb} , as well as resistance, R_b and R_{gb} , can be directly measured by impedance spectroscopy. In determining the conductivity inside the grains, taking the sum of their total volume as an equal volume of the sample does not lead to significant errors.

Slightly different is the case of conductivity at the grain boundaries. The determination of the value of the conductivity from the formula:

$$\sigma_{gb} = \frac{L}{A} \cdot \frac{1}{R_{gb}}, \quad (2)$$

gives only a magnitude described as an apparent value. By means of the stereological analysis of microscopic images of the material microstructure, it is possible to determine both the thickness of the borders and their total length, but this is a tedious procedure and an uncertain process of achieving fully reliable results. The application of the brick layer model the size of σ_{gb} with sufficiently high accuracy is to be determined. Assuming that the interior volume of the grain may be treated as the whole sample volume capacity, it results from the described above model that

$$\frac{d_{gb}}{d_g} = \frac{C_b}{d_{gb}} \cdot \frac{\varepsilon_{gb}}{\varepsilon_b} \quad (3)$$

Defining the "real" value of the grain boundaries' conductivity, σ_{gb}^* , also referred to as the microscopic conductivity at the grain boundaries, in the form of:

$$\sigma_{gb}^* = \frac{d_{gb}}{d_g} \cdot \sigma_{gb} \quad (4)$$

based on a combination of relations (2) and (3), and assuming that the volume of the dielectric properties of grains and boundaries between them are not significantly different ($\varepsilon_b \approx \varepsilon_{gb}$), we obtain

$$\sigma_{gb}^* \approx \frac{C_g}{C_{gb}} \cdot \sigma_{gb} \quad (5)$$

The conductivity of the grain boundaries in zirconia solid solutions depends mainly on two partially connected to each other factors, the space charge creation and the phenomenon of segregation of impurities and stabilizing cations. Structurally, the grain boundary is the crystallographic mismatch area of two monocrystalline regions and has a thickness of several interatomic distances, which is usually equal to about 1 nm. This boundary is typically enriched in ions, native or foreign, giving it a certain electric charge in opposition to the volume of grain. This charge is compensated by ions of opposite signs gathered near the border in the area described as the space charge region (space charge layer). In a perfectly clean material, the nature of this space charge is dependent on the free enthalpy of point defect formation, specific to the type of compound. In the real material the main factor is the presence of additives with different valences and impurities.

The theory of the space charge and its applications are widely described in the literature [5–7]. Due to the charge at the boundary, the point defect concentration in the space charge area may even differ considerably from the corresponding concentration in the interior of the grain. This effect strongly influenced the properties of ion conductors [8]. The size of the space charge region is a consequence of an overall solution to the Poisson equation describing the impact on the border of two phases with different electrical properties, for example, between a conductor and insulator. In this equation, a quantity describing the size of electrostatic interaction area at the phase interface appears, defined as the Debye length L_D :

$$L_D = \frac{\varepsilon \cdot \varepsilon_0 \cdot R \cdot T}{2 \cdot z_i^2 \cdot F^2 \cdot c_{i\infty}} \quad (6)$$

which, in turn, is a measure of thickness of the double layer, λ :

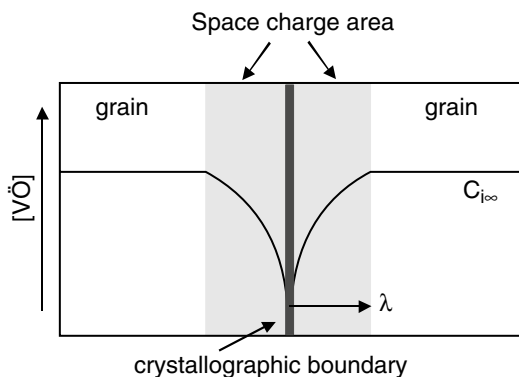
$$\lambda = 2 \cdot L_D \cdot \sqrt{\frac{e \cdot \Delta\Phi(0)}{k \cdot T}} \quad (7)$$

where $\varepsilon \cdot \varepsilon_0$ is permittivity, R is gas constant, T is absolute temperature, F is Faraday constant, z is defect charge, $c_{i\infty}$ is molar concentration of defects in the grain volume, e is electron charge, and $\Delta\Phi(0)$ is electrostatic potential at the phase interface (in this case at the grain boundary).

As it can be seen, the volume of the space charge region depends on both the electrical properties of the ion conductor ($\varepsilon \cdot \varepsilon_0$, $c_{i\infty}$) and the structure of the grain boundaries $\Delta\Phi(0)$. Presented description, from a mathematical point of view, is the model equivalent to a double Schottky barrier. Structurally, the space charge region is a part of the grain's interiors, but from the point of view of transport properties, it belongs to the grain boundary. In this case, the concept of "electric" grain boundary can be introduced consisting of the crystallographic area mismatches and space charge regions. The thickness of such a border, corresponding to the double size of the space charge region, is many times larger than the thickness of the structural border and even exceeds 100 nm.

The segregation of foreign cations, both admixtures and impurities in the grain boundaries' area, is a phenomenon that occurs spontaneously. In the case of solid

Fig. 1 Distribution of oxygen vacancies' concentration in the grain boundary area



solutions stabilized by tri- or divalent cations, the grain boundaries are enriched with defects which have a negative charge, e.g., Y_{Zr}^{\bullet} or Ca_{Zr}^{\bullet} . In the presence in the lattice of zirconia pentavalent cations, no segregation was observed, such as a positively charged defects Nb_{Zr}^{\bullet} or Ta_{Zr}^{\bullet} type. This indicates the existence of positive charge in the crystallographic grain boundary [9]. It is assumed that the reason for this is the presence of incomplete oxygen octahedra in grain boundaries acting as fixed oxygen vacancies, resulting from the lattice stress compensation [10, 11]. Negatively charged cationic defects form, in turn, stable complexes with the “fixed” oxygen vacancies, which effectively reduce the concentration of the “normal” anionic vacancies in this area. The concentration distribution of oxygen vacancies in the grain boundary area is presented in Fig. 1.

It is assumed that the above-described phenomenon of the space charge depletion in oxygen vacancies is a major, although not the only, cause of extremely low conductivity in grain boundaries in zirconia solid solutions [3]. This conductivity is at least two orders of magnitude lower than the conductivity of the grain interiors, which is the basis for determination of the grain boundaries' blocking nature [12–14]. This situation takes place at temperatures not higher than a certain characteristic temperature; in the case of zirconia it is about 1000 °C, and after exceeding the size of the space charge region, it is comparable with the Debye length, which in these circumstances may be even less than 0.1 nm. This effect causes a relatively rapid decrease in grain boundaries' resistivity with temperature increase. The space charge model has become a good basis for a series of quantitative descriptions of conductivity at the grain boundaries [13, 15–17]. It can be observed from the descriptions of these results, among others, that the blocking nature of grain boundaries disappears with the increasing concentration of stabilizer in the solid solution, whose immediate cause is a decrease of the Schottky barrier.

Another very important factor deteriorating grain boundaries' conductive properties is the presence of impurities such as alkali and transition metal oxides or compounds mainly silica-rich silicon dioxide. During sintering, these substances, accumulated on the grain boundaries, react with each other forming various forms of amorphous or crystalline phases. The presence of silica compounds border grain, and their destructive effects on the ionic conductivity in solid solutions of zirconium

dioxide have been repeatedly confirmed [18–22]. These phases, depending on the level of impurities and sintering conditions, are very diverse in terms of phase and chemical compositions, location in the microstructure, and such properties as viscosity or wettability.

The morphology of the grain boundary siliceous phase can be described by models in two ways. In the first one it is assumed that the silica phase continuously covers all the grains of the conductive phase. In this case, the transport of ions from one grain to the other must take place through a layer of the said phase, and consequently the activation energy of the ionic conductivity of the process must vary with the chemical composition and conductive properties. The second model assumes that the silica phase occurs only in certain specific areas in the sintered microstructure resulting in a reduction in the surface area contact between individual grains. Taking into account that the silica phase is more an insulator than electrical conductor, this means that the level of ionic conductivity is dependent only on the amount of the phase and its characteristic properties, such as wettability. This model also shows that the value of the conductivity activation energy should not be dependent on either the number or the type of silica phase, which is confirmed by numerous experiments [23–25]. As it was often frequently documented, microscopic observations using transmission electron microscopy also confirmed the second model of siliceous phase distribution in the microstructure of the zirconia solid solution [12, 13, 23–26].

Summing up the impact of grain boundaries on the ionic conductivity of zirconia solid solutions, it can be stated that in the case of high-purity materials, the decrease of the concentration of oxygen vacancies in the border areas leads to a significant decrease in the grain boundary conductivity and its activation energy is dependent on the height of the Schottky barrier. In the case of materials with “normal” purity, the dominant influence on the conductivity of the grain boundaries is exerted by the presence of a silica phase on them.

The particle size effect of on the ionic conductivity of zirconia solid solutions is directly related to the density of grain boundaries, resulting directly from the grain size and the state of boundaries. Experimental results indicate that in the case of solid solutions containing 3 mol% yttrium oxide in which the grain size ranges from about 40 nm to 1.5 μm , the conductivity of the grain interiors is increased several times with the increasing grain size [14]. The effect of the weaker lattice conductivity of materials with smaller grain has been attributed to a decrease of stabilizing cation concentration in the interior of grains, resulting from the stronger segregation of these cations in the case of materials with a better surface grain boundaries' development. A similar volume conductivity dependence on the particle size was also observed in the case of a solid solution of zirconia containing 8 mol% yttrium oxide [3], but in the case of materials containing 15 mol% calcium oxide, the trend is reversed – the conductivity drops with the grain size increase [12].

The conductivity of grain boundaries, regardless of the chemical and phase composition of the material, decreases with increasing particle size. The use of the previously described space charge models to explain this phenomenon indicates that in each case the concentration of oxygen vacancies in the area boundary power decreases with the increasing particle size and thus increases the Schottky barrier height.

The microstructural aspect of ionic conductivity takes on a new dimension in the case where the grain size in the material becomes comparable to the width of the space charge region. The areas of the spatial charge are then superimposed on each other, and the concentration of defects, either in these areas and within the grains, undergoes significant changes. Ionic conductivity of the material in which the grain size is comparable with the Debye length may vary up to several orders from ionic conductivity of the material with a grain size of hundreds of nanometers or more. This phenomenon has been forecast theoretically by J. Maier [8, 27] and has been confirmed in some cationic and anionic conductors, usually obtained in the form of thin films [28, 29]. The model calculations show that in the case of zirconia solid solutions, the nanometric particle size effect on the ionic conductivity would be noticeable only for the grains, according to the source, from 10 to 100 nm [30]. The comparison of this size range with the minimum size of crystallites (approximately 5 nm) present in the powders of zirconia obtained by unconventional methods [31] and the knowledge of the fact that the temperature of at least 1200 °C is recognized to obtain a dense material with this type of powder indicate restriction on the ability to obtain dense nanometric zirconia microstructure. Hence, the studies of the conductive properties of materials with nanozirconia grains are extremely rare.

In [12] the effect of particle size on the ionic conductivity of the solid solution of zirconia containing 15 mol% calcium oxide was investigated. The grain size in the sintered material varied from about 100 nm to more than 10 μm . It was observed that the conductivity of the grain boundaries falls rapidly, approximately six times, with a minimal increase in particle size, and stabilizes the grain size of about 4 μm . It is noteworthy that the observed effects are attributed rather to the changes in the distribution of the silica phase with a change in particle size than to the impacts of the space charge area. In another work on the zirconia solid solution containing 16 mol%, an increase in calcium oxide ion conductivity at temperatures below 800 °C was observed, associated with a decrease in particle size [32]. Sintered bodies with smaller grains were characterized by a lower activation energy for bulk conductivity and higher activation energy for conduction at the grain boundaries.

Sintering the powder obtained by the condensation from the gas phase made it possible to obtain dense tetragonal zirconia, containing to 3 mol% yttrium oxide with a grain size of 25–50 nm and a density from 82 % to 93 % of the theoretical density [33]. Despite its small particle size, both the activation energy of conductivity and conductivity values of the materials were not significantly different from other similar results obtained by other researchers for sintering of submicron grains. The authors of [34] obtained similar results. They sintered a powder at temperatures from 1200 °C to 1400 °C obtained by decomposition of the metal nitrate mixture, obtaining a material having a density up to 95 % of a theoretical value and a grain size below 200 nm. And also in this case the level of the conductivity and its activation energy were comparable with the corresponding values characterizing the materials with micron and submicron grains.

Somewhat different is the situation in the case of zirconia solid solutions obtained in the form of thin films [35, 36]. The nanocrystalline material containing 8 mol% Y_2O_3 , obtained from the organometallic polymeric precursor on an alumina substrate,

was characterized by conductivity two orders of magnitude higher as compared to the polycrystalline material with the same chemical composition as well as a slightly smaller conductivity activation energy [35]. Similarly, the stabilized ZrO_2 thin films with 8 mol% yttrium oxide or scandium oxide obtained by the sol-gel have the tenfold increase in conductivity in relation to the bulk material [36]. In both cases, the observed effects are attributed to the changes occurring in the grain boundaries, yet not directly to the size of the grains. It is worth noting that even in the comments of the literature, the difficulties in unambiguous interpretation of the results and the need to take into account the specificity of thin-film materials are stressed [37].

The presented relations clearly confirm the influence of the zirconia solid solutions' microstructure on their conductive properties. On the other hand, the range of microstructure parameters' variation is limited by both the morphology of the used powder and the conditions of the process compaction. In this context, the main reason for undertaking the work described in the next chapter was to investigate the possible influence on the ionic conductivity of zirconia solid solutions by modifying their microstructure. Microstructural changes of these materials due to differences in the conditions of preparation are also considered in the context of chemical and phase composition of appropriate materials. The subject of studies on the effect of microstructure on the conductive properties of the solid solutions is sintered zirconium dioxide containing yttrium oxide in an amount from 5 to 10 mol%. A major motivation to undertake such studies was the lack of systematic experiment description in the literature, whose results would allow a correlation between microstructure and conductive properties of zirconia solid solutions to be evaluated as well as the limits of their modification to be determined.

The hereinafter described preparation was aimed at obtaining sintered zirconia, stabilized with yttria with the maximum variation in grain sizes. While the problem of obtaining sintered grains comprising sizes of 10 μm is relatively easily solvable by choosing a suitable combination of temperature and sintering time, to produce enough material having an extremely small grain requires the use of both ZrO_2 nanopowder and a special way of its formation.

Preparation of Zirconia Solid Solutions of Varying Microstructure

In the course of studies of the microstructure influence of the zirconia solid solution, containing from 5 to 10 mol% yttrium oxide, pressureless sintering of nanopowders was applied for the conductive properties. The zirconia nanopowders were prepared by means of hydrothermal treatment of hydrous zirconium oxide coprecipitated with amorphous yttrium hydroxide. Regardless of the chemical composition of the powder, the process was performed in the environment of distilled water at 240 °C for 2 h. The obtained powders consisted of isometric-shape crystallites (Fig. 2) whose size depends on the chemical composition. The changes in the size of crystallites in the powders determined on the basis of the observed half-width of the (111)

Fig. 2 Morphology of the powder of zirconia solid solution containing 8 mol% Y_2O_3 obtained by hydrothermal method

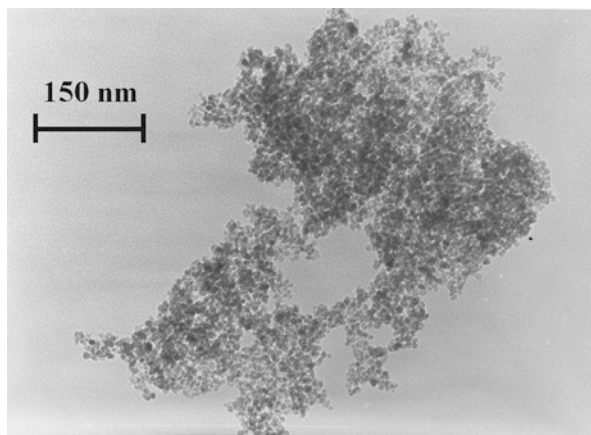
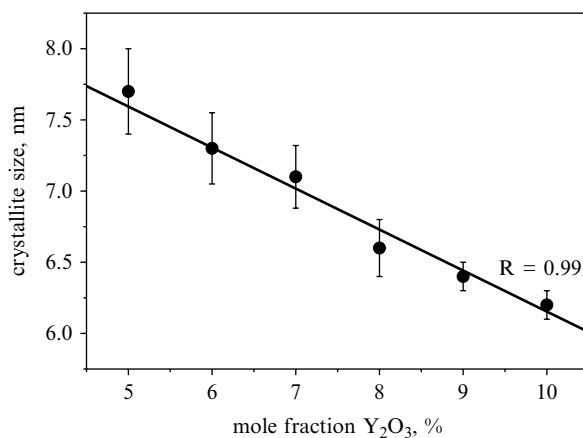


Fig. 3 Changes in crystallite size determined by X-ray diffraction in the powders of zirconia solid solutions obtained by hydrothermal method



line of zirconia cubic phase were presented in Fig. 3. A linear decrease in the crystallite size with the increasing yttria content in the solid solution is observed.

The X-ray phase analysis showed that the powders, regardless of their chemical composition, were consisting solely of cubic ZrO_2 . The linear dependence of the unit cell volume with increasing amounts of Y_2O_3 confirms the quantitative incorporation of yttria into the structure of the cubic zirconia phase.

Zirconia powders containing from 5 to 10 mol% yttrium oxide were used to prepare the two series of sintered samples. In the first one, the powders dried at 70 °C after addition of 5 % solution of the wax emulsion as a lubricant were pressed uniaxially at the pressure of about 100 MPa and then isostatically at 250 MPa and finally pressureless sintered at 1300 °C for 2 h. The need to carry out the sintering process at a relatively high temperature is mainly due to the complex composition and poor compressibility of dried nanoparticles, which in turn causes the formation of retaining areas of varying density [38, 39]. The consequence of this is that the

differential sintering phenomenon leads to a very rapid shrinkage of the material in the areas of higher density, for example, it can be the inside of aggregates and agglomerates, and very slow densification in the less packed areas, e.g., between agglomerate zones. A prerequisite to eliminate the large pores generated during this process is grain growth [40], which makes it practically impossible to obtain a dense material at relatively low temperatures. In this case the applied treatment led to the materials with a density of not lower than 98 % of the theoretical value.

A solution to this situation is the use of special methods of nanoparticle forming that provide appropriate density and a high degree of homogeneity of the material before sintering. One of such methods is filter pressing, which has been used to produce the second series of samples. The first step of this method is suspending the nanopowder, usually in an aqueous medium, with a relatively high proportion of the solid phase. In this case, suspensions of nanoparticles were obtained directly as a product of the hydrothermal reaction, using a sedimentation process, and finally only liquid excess was removed to obtain the solid phase of about 20 % volume. These suspensions were placed in the filter of the pressing device, followed by gradual raising of the pressure for the water excess removal. The drained materials were gently dried in a desiccator over anhydrous calcium chloride and then sintered at 1200 °C for 1 h.

The behavior of the filter-pressed materials during sintering is illustrated by dilatometric curves in Fig. 4. When compared to the commercial submicron 8 mol% yttria-stabilized powder of Tosoh company, the filter-pressed nanopowders start sintering at temperatures of at least 500 °C lower, without showing the initial stage of the expansion of the sample. Achieving the maximum density in the case of materials made of nanoparticles takes place at lower temperatures at least of about 200 °C. Also visible is the effect of chemical composition on sinterability of the powder.

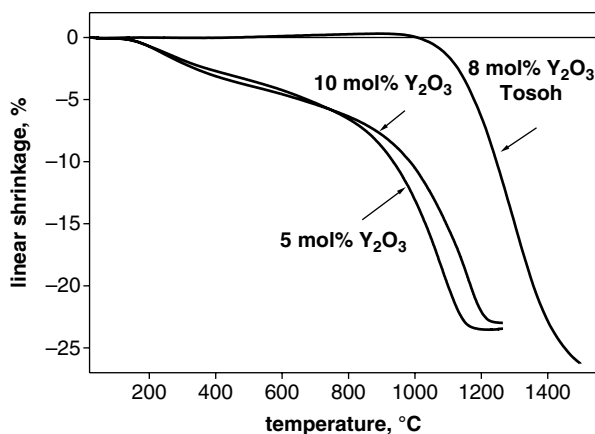


Fig. 4 Dilatometric curves of the filter-pressed zirconia nanopowders with 5 and 10 mol% Y_2O_3 and uniaxially pressed submicron powder from Tosoh company with 8 mol% Y_2O_3

The powder with the stabilizer content equal to 10 mol%, despite the greater shrinkage at lower temperatures, ultimately reaches a maximum density at temperatures higher than 5 mol% of Y_2O_3 powder. This effect is probably related to the diversity of compaction mechanisms depending on the temperature. Due to the fact that at lower temperatures surface effects dominate, the surface is more defected for the nanocrystallite powder with 10 mol% yttrium oxide as a consequence of both the higher concentration of vacancies and the intensive process of segregation, and they influence more strongly transport processes, for example, on the rearrangement of the grains. At higher temperatures, where the volume transport is predominant, higher quality and diversity of order-diffusing elements slows down the process of compaction. The filter-pressing method as well as behavior during sintering of compacts obtained by this method is described in detail in [41]. The use of the filter pressing contributed to obtaining materials which in the process of sintering for 1 h at 1200 °C have been densified to over 99 % of the theoretical density.

In the further part of the text, the materials obtained by sintering the powders synthesized under hydrothermal conditions and isostatically pressed are marked as IP and filter-pressed as FP.

Structural Properties of Zirconia Solid Solutions with Varying Microstructure

Sintered bodies obtained from the powders prepared in a hydrothermal environment, series IP and FP, consisted of a tetragonal and/or cubic phase. Quantitative phase compositions of both series are listed in Table 1.

As it can be seen, from the materials sintered at 1200 °C for 1 h, the series of FP, only the one containing 7 mol% yttrium oxide is biphasic. The sintered samples with lower content of Y_2O_3 are fully tetragonal, while those with the higher consist solely of the cubic phase. The increase in the sintering temperature to 1300 °C and extending the time to 2 h, IP series, causes the appearance of the cubic phase in the sintered materials with the lower stabilizer content. This effect is a direct result of the phase diagram form.

Table 1 Phase composition of the sintered material derived from hydrothermally synthesized powders

Molar fraction Y_2O_3 , %						
Weight fraction, %	5	6	7	8	9	10
IP series, 1300 °C, 2 h						
Tetragonal phase	76.7	65.3	16.5	0	0	0
Cubic phase	23.3	44.7	83.5	100	100	100
FP series, 1200 °C, 1 h						
Tetragonal phase	100	100	23.2	0	0	0
Cubic phase	0	0	76.8	100	100	100

Fig. 5 A part of the phase diagram of the $\text{ZrO}_2\text{-Y}_2\text{O}_3$ system. The marked points correspond to compositions and sintering temperatures of the tested materials. The lines dividing the field come from the cited works

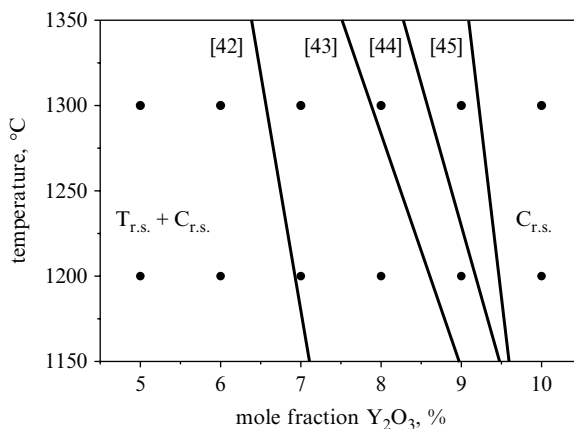


Figure 5 shows a part of the phase diagram of the studied system with marked points corresponding to compositions and sintering temperatures of individual materials. In the diagram, the lines are borders between areas of existence of the cubic phase ($C_{s.s.}$) and its mixture with the tetragonal phase ($T_{s.s.}$). These lines come from the selected phase diagrams [42–45]. It can be concluded that depending on the diagram used for the sake of comparison, the particular materials strive to achieve different phase compositions. Nevertheless, it can be assumed that the solid solutions containing minor amounts of stabilizer, regardless of sintering temperature, should consist of both regular and tetragonal zirconia forms. On the one hand this is due to the sintered materials at the temperatures at which ZrO_2 coexist in two forms and on the other, due to the possibility of tetragonal phase crystallization upon cooling. This process involves the diffusion of the stabilizer from one grain to another, which corresponds to a partitioning effect, until it reaches such a concentration gradient, which gives rise to a tetragonal phase.

The changeability of lattice parameters of particular phases is expressed as the volume of unit cells and it is shown in Fig. 6; the tetragonal cell volume has been calculated for the wall-centered lattice. In the case of filter-pressed materials sintered at 1200 °C (FP), the volume of the unit cells exhibit a linear dependence on the concentration of yttria in solid solution. Elementary cell volumes of the two phases in the material containing 7 mol% Y_2O_3 are very similar, which indicates that even their chemical compositions are similar. In a series of isostatically pressed materials sintered at 1300 °C (IP), the appearance of the cubic phase causes a segregation of Y_2O_3 between the two phases. In the solid solutions nominally containing from 5 to 7 mol% Y_2O_3 , the content of this oxide in the cubic phase is approximately constant and is about 7 mol%, while in the tetragonal phase it is lower than the nominal from about 1 to 0.2 mol%, depending on the nominal value. Similarly as in the FP series, also here the cubic phase elementary cell volume is a linear function of the chemical composition.

The presented graph also shows the differences in the volume of the unit cells in powders and sintered materials increasing with the amount of stabilizer. Because the chemical composition of powders and sintered materials are the same, the only

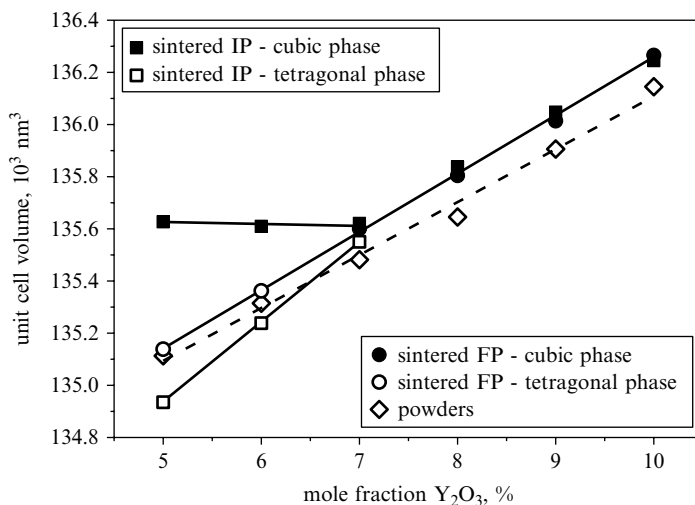


Fig. 6 Changes in the unit cell volume of the respective ZrO_2 phases in the powders and in the sintered materials. Standard deviations are less than 50 nm^3

explanation for this phenomenon is an error in the evaluation of lattice parameters in the case of powders. This error is related to the deformation of the crystal lattice resulting from the nanometric size of the crystallites in the powders. In such a case, the hydrostatic pressure, due to surface tension, creates a compressive stress in crystallite, causing an apparent decrease in the size of the unit cell. The smaller the particle size of the crystallites the stronger this effect. It is confirmed for both material series prepared from the hydrothermally synthesized powders.

This effect of changing the size of the lattice parameters with the crystallites size was also observed in other substances [46]. In such a case, it is proposed to use the term of “apparent lattice parameter.”

Microstructural Differentiation of Zirconia Solid Solutions

Microscopic (SEM) observations showed that all sintered materials from powders synthesized under hydrothermal conditions are homogeneous and consist of particles of isometric forms, as evidenced by particle size distribution and shape factors, determined from numerical analysis of SEM images. The collected SEM micrographs were analyzed on the basis of the selected parameters of the microstructure, such as area and circumference of a grain, Feret diameters in two mutually perpendicular, randomly selected directions, and also grain diameter and aspect ratio. The grain diameter was defined as the diameter of the circle of area equal to the measured surface of the grain while aspect ratio as a ratio of the measured grain circumference to the circle circumference, which would have a circle of the same area as the measured area of this grain. Figure 7 shows selected photomicrographs illustrating the variation of the microstructure of these materials.

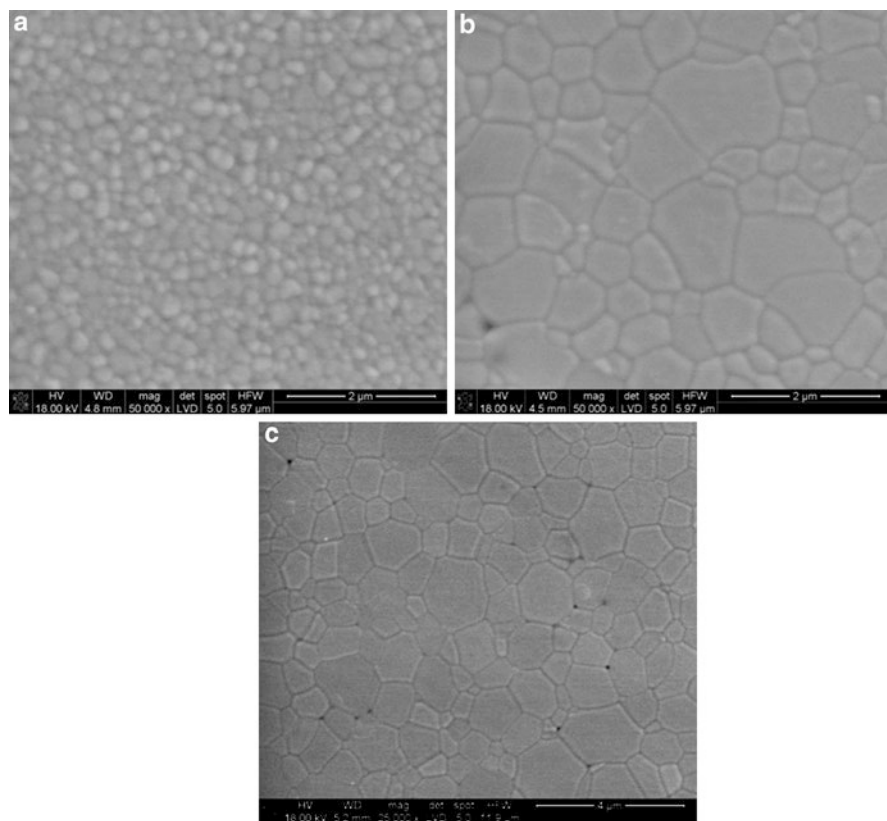


Fig. 7 The microstructures of the materials of IP series

Figure 8 shows several examples of particle size distributions in the selected sinters from IP and FP series, while Fig. 9 cumulative curves of these distributions. These distributions are in each case unimodal. In the series of powders isostatically pressed and then sintered at 1300 °C (series IP) a shift of the mode values toward larger grains can be observed. This effect is also evident in the presented micrographs (Fig. 7c) where, surrounded by smaller grains, there are grains even several times larger. The appearance of the large-grain population is a direct result of increasing the cubic phase amount with the sintering temperature; these phase grains have a much stronger tendency to grain growth than the tetragonal phase. It is worth noting that in the sinter bodies obtained from the filter-pressed powders, FP series, especially for materials having lower yttrium oxide content, a significant particle population of size less than 100 nm is observed.

In the case of particle size distribution in tested materials, due to rather large differences in average particle sizes of individual sintered series, the standard deviation of the distribution state, as a measure of the dispersion, could lead to errors in the assessment. The n parameter value was implemented as a degree of this particle

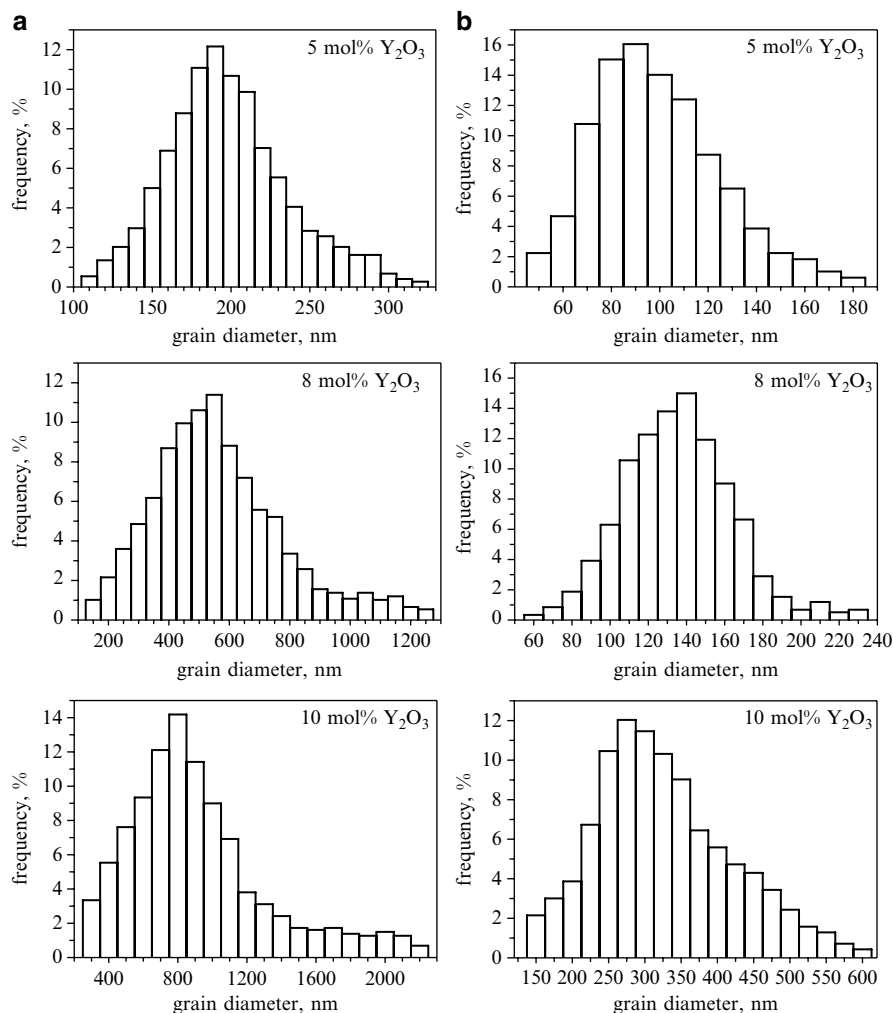


Fig. 8 Grain size distributions in the selected materials of the (a) IP and (b) FP series

size dispersion, which is one of the constants in the Rosin–Rammler expression for grain size distribution [47]:

$$W(d) = e^{-b \cdot d^n} \quad (7)$$

where $W(d)$ is the residue, d is the grain size, and b and n are constants. Constant n value describes a distribution width; the n is the larger the more the particle size are placed in a narrower size range.

The formation of large grains, correlated with an increase in the stabilizing oxide content, is reflected in the values of the parameter n of Rosin–Rammler distribution shown in Fig. 10. In the case of IP series, particle size distributions are becoming

Fig. 9 Cumulative curves of grain size distributions of the (a) IP and (b) FP series

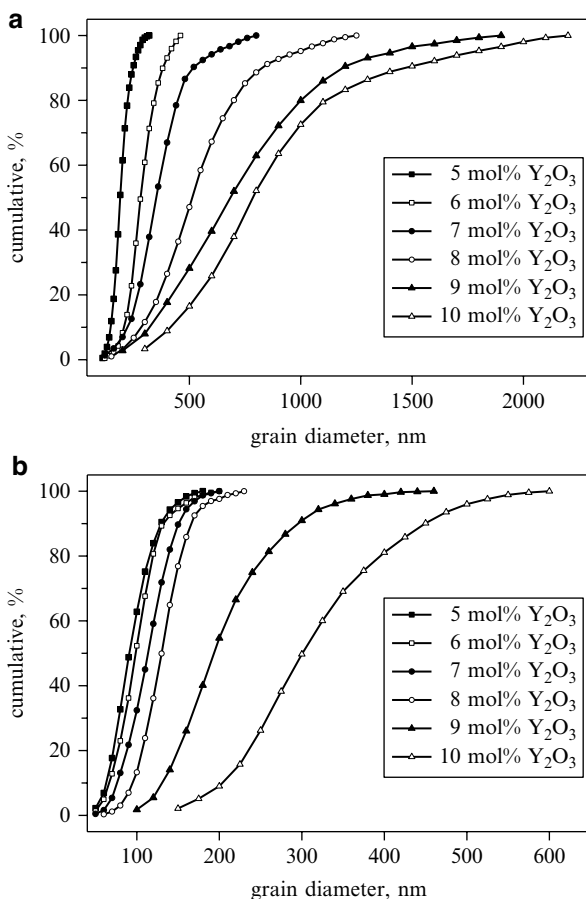


Fig. 10 Changes in the grain size distribution of the n parameter in the Rosin–Rammler expression of all sintered materials

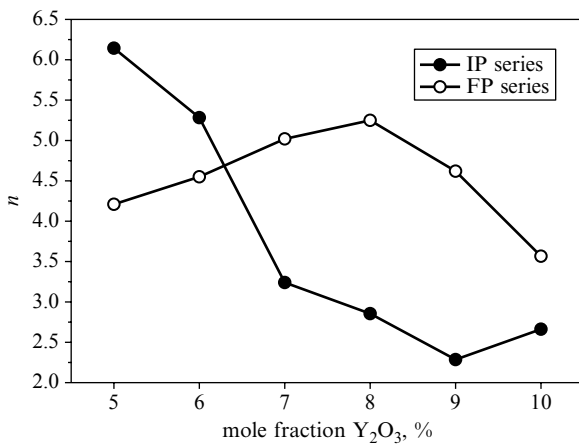
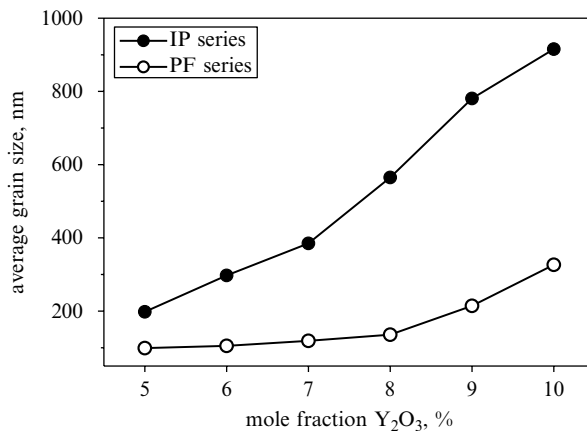


Fig. 11 Average grain size of the sintered IP and FP series



wider and wider together with the simultaneous increase in the content of yttrium oxide and the cubic zirconia phase. Only in the sample with the highest Y₂O₃ content, this trend is reversed. In the sintered materials of the FP series containing up to 8 mol% yttrium oxide, an increase in the value of parameter n is visible and particle size distributions are becoming narrower. This effect is due to several factors, such as a very narrow particle size distribution of the powder, a small tendency for growth of tetragonal phase grains, or a relatively low sintering temperature. In the materials containing higher amounts of stabilizing oxide, a population of larger grains appears, which leads to their distribution expansion. It can be seen also in this case, grain growth is intrinsically linked to the existence of the cubic phase.

The changes in average grain size of the IP and FP sample series related to the change in the chemical composition are shown in Fig. 11. The increase of the yttria content leads to the increase in the average grain size, and the main reason is tendency to grain growth of the cubic phase. A stronger effect of grain growth for IP series is probably due to the higher sintering temperature.

It results from the values of the parameters describing the grain shapes, that all the received materials consist of isometric particles. This is proved both by the similarity of Feret diameters, measured in two mutually perpendicular directions (no statistically significant differences between them), and the values of shape coefficients which do not differ significantly from unity.

Ionic Conductivity of Zirconia Solid Solutions with Different Microstructures

Conductive properties of all samples were determined according to the measurements made by impedance spectroscopy. The measurements were carried out in the frequency range from 1 Hz to 1 MHz, using a set consisting of an impedance meter FRA 1260 and 1294 dielectric interface (Solartron). The parallel surfaces of the test specimens were covered with porous platinum electrodes. Measurements were made

in the range of 250–400 °C. In every case, the measurement points on the graph of impedance ($Z' = f(Z'')$) were arranged in two clearly separated semicircles (or their fragments) and the straight line. It is assumed that the equivalent circuit describing this effect is composed of serially connected three parallel circuits, a resistor-fixed phase-angle element (CPE). The values of resistance, retrieved from matching the auxiliary circuit to measuring points, and sample geometrical dimensions allowed the bulk conductivity, σ_b , and conductivity of the grain boundaries, σ_{gb} , to be determined. In the case of the grain boundary conductivity, the calculations were performed using Eq. 5.

The presentation of the obtained results in the Arrhenius system ($\sigma \cdot T = f(T^{-1})$) in each case gave a statistically significant linear fit, which in turn allowed for conductivity activation energy, E , and pre-exponential factor values, σ_b^0 and σ_{gb}^0 , to be determined, respectively.

Figure 12 shows the dependence of the bulk conductivity activation energy, E_b , both sample series from their chemical composition. In the materials containing from 5 to 7 mol% Y_2O_3 , which corresponds to the area of the tetragonal phase or of two-phase coexistence, a relatively small increase in the value of E_b is observed. The increase in the stabilizing oxide content and interconnected presence of the cubic phase result in a significant increase in the activation energy of bulk conductivity. The presented dependences of E_b on the chemical composition of the material are in good agreement with the model description of ionic conductivity in compounds with fluorite structure [48].

It is also evident that the lowest values of the bulk conductivity activation energy characterized materials prepared from the hydrothermally synthesized and then filter-pressed powders (FP series). This effect is probably due to two reasons. The first one is the difference in phase composition of materials with the same chemical constitution. Sintered materials of FP series with 5 mol% Y_2O_3 consist solely of a tetragonal phase, while the IP series samples, having the same chemical composition, contain over 23 wt% of the cubic phase. Assuming that the cubic ZrO_2 phase

Fig. 12 Changes in the activation energy of bulk conductivity in the IP and FP series depending on their chemical composition. The E_b standard deviations do not exceed 0.01 eV

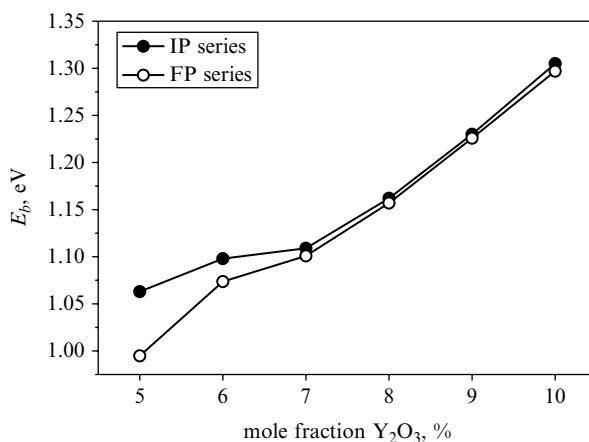


Fig. 13 The correlation between the weight percentage of the tetragonal phase and the bulk conductivity activation energy in the materials containing 5 and 6 mol% yttria

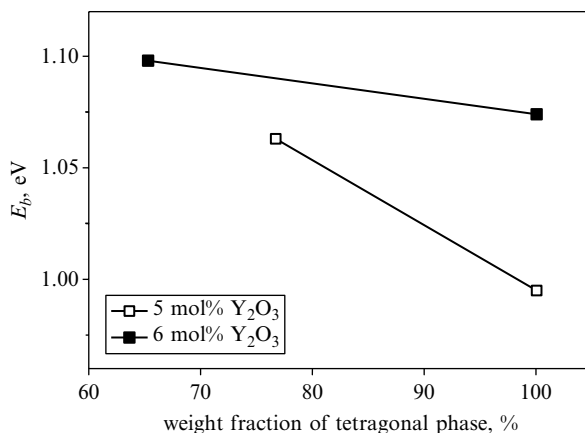
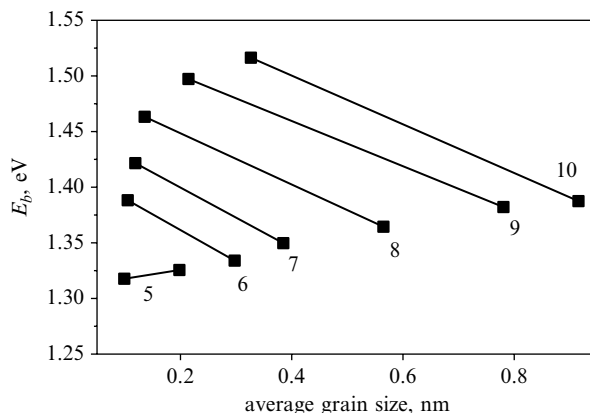


Fig. 14 The correlation between average grain size and the activation energy of bulk conductivity in both series. Numbers indicate content of yttria in the zirconia solid solutions

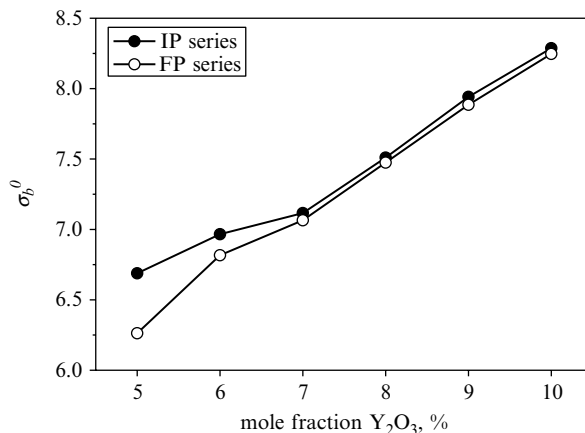


has a higher activation energy of conductivity than the tetragonal one, the observed effect is in line with expectations.

Figure 13 shows the relationship between the percentage of tetragonal phase and the activation energy for bulk conductivity in the samples containing 5 and 6 mol% yttrium oxide. In both cases, a correlation can be seen between these values and the difference between the directional coefficients of both straight lines results from changes in chemical composition of the tetragonal phase in individual sintered materials.

Another factor which may have an impact on the value of the activation energy is the size of the grains. Figure 14 shows the correlation between the average grain size in a sintered material and bulk conductivity activation energy depending on the chemical composition of materials. In most cases, the E_b “dependences” on particle size are quite small and rather resulting from the already described structural changes. Only in the materials, in which a large number of grains have a size

Fig. 15 The values of the pre-exponential factor of bulk conductivity in the IP and FP series. σ_b^0 standard deviation does not exceed 0.05



substantially smaller than 100 nm, in particular in FP series with 5 and 6 mol% Y₂O₃, large differences are shown in the described correlation. It can be therefore assumed that such a significant decrease in the bulk conductivity activation energy in these materials is due to the phenomena associated with the nanometric grain sizes. The effects of these usually include forming of tensile stresses near the grain boundary, increased solid solution components' segregation within the grain boundary and in the surrounding areas, or overlapping of space charge areas.

A similar change character as the bulk conductivity activation energy IP series and the FP is altered by the exponential factor changes (Fig. 15). Again in this case, the initial growth of the σ_b^0 in the tetragonal and two-phase region is distinctly smaller than that observed in the materials consisting solely cubic ZrO₂.

The σ_b values for the FP materials are smaller than in the case of the IP series. These differences in materials, in which the content of yttrium oxide exceeds 6 mol%, are practically in the margin of error. For the materials with 5 and 6 mol% Y₂O₃ the differences are significant and the larger the differences in average grain sizes the larger differences in respective pre-exponential factors.

Figure 16a–d shows changes in the bulk conductivity of sintered materials of FP and IP series depending on their chemical composition, in several selected temperatures. The draws for temperatures 300 °C and 400 °C have been prepared on the basis of measured values and those for 600 °C and 800 °C have been extrapolated according to the known quantities of E_b and σ_b^0 .

Low bulk conductivity activation energy values in solid solutions containing 5 and 6 % mol yttria caused the highest bulk conductivity to have the material of FP series containing 5 mol% Y₂O₃ at 300 °C. As the temperature rises, the maximum conductivity shifts toward solid solutions of the increasing conductivity activation energy and hence contains increasing amounts of Y₂O₃. In general, the materials of both series obtained from the hydrothermally synthesized powders are characterized by similar bulk conductance. The only higher differences are observed at the lowest temperatures in the samples with a minimum content of yttrium oxide.

An interesting correlation with bulk conductivity is shown by the n coefficient values that describe a constant phase element (CPE), which is an equivalent circuit

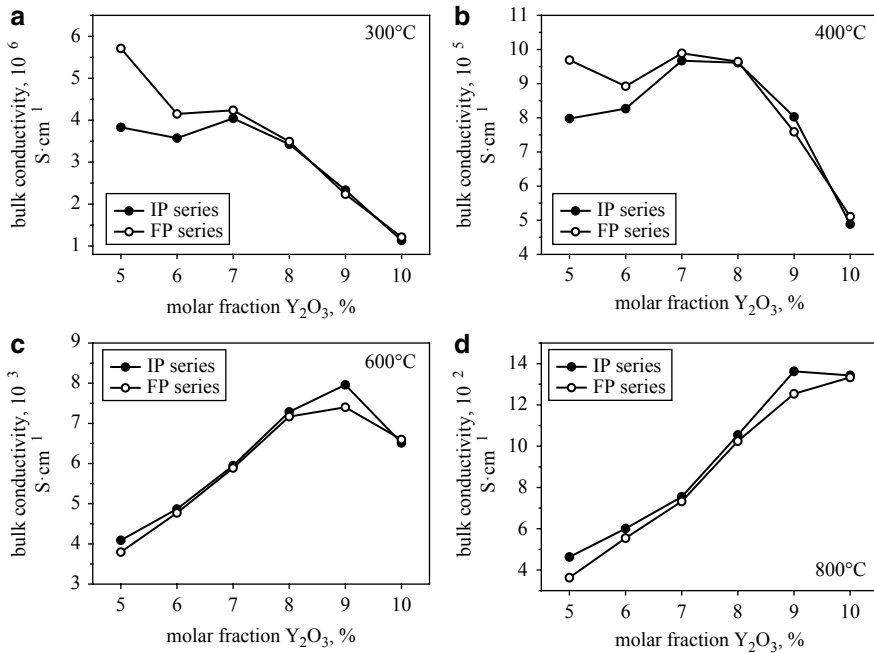


Fig. 16 Changes in the bulk conductivity of the IP and FP series depending on their chemical composition and temperature

element, simulating electrical characteristics of the grain interior. Admittance element of constant phase angle, also referred to as a capacitor of no Debye type, describes the relationship [49]:

$$Y(\omega) = A(j\omega)^n \quad (8)$$

where ω is current frequency, j is the imaginary unit, and A and n are constants ($0 < n < 1$).

Impedance spectra, characterizing the conductive properties of real materials, especially sintered polycrystalline, almost always are assigned to alternative circuits containing CPE elements. Their presence is associated with a number of phenomena that occur in both the electrode and the interior of the material. In the latter case, the most important cause of no Debye capacity creation is inhomogeneity of conducting properties. This feature can be a result of the statistical distribution of grains of a different chemical composition or phase, which promotes the path's creation with a clearly higher conductivity.

There is an evident relationship between the parameter n and bulk conductivity. Figure 17 shows the formal changes of parameter n , dependent on the chemical composition of materials. It can be seen that the lowest values of this parameter are characterized by the tetragonal and two-phase materials with relatively broad particle size distributions (IP series of 5 and 6 % mol Y_2O_3) and therefore those in

Fig. 17 Changes in the parameter n of Eq. 8 depending on the chemical composition of IP and FP series and the measurement temperature

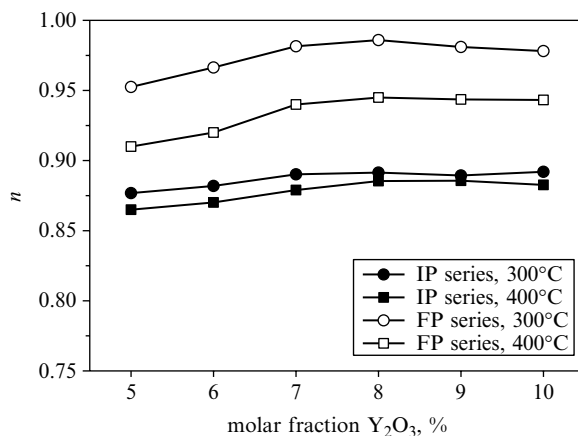
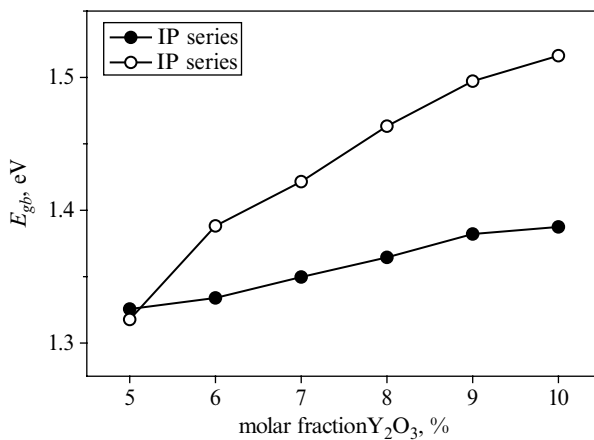


Fig. 18 Changes in the activation energy of the grain boundary conductivity in the IP and FP series depending on their chemical composition. The E_{gb} standard deviations do not exceed the value of 0.01 eV



which one can expect major heterogeneity. In the FP series materials exhibiting the highest homogeneity, both structural and microstructural, the nature of the grain interior capacity is close the Debye type. The increase of temperature leads to a decrease in n value; this drop is significantly higher in the FP series. A comparison of phase compositions and microstructural parameters of both series suggests that the cause of this phenomenon is associated rather with the phase composition than the microstructure of sintered materials. The temperature-increasing differences in the phase conductivity, i.e., tetragonal and regular, lead to an increase in the material heterogeneity from the point of view of ionic conductivity.

Changes in the activation energy of the grain boundary conductivity in all sample series, depending on their chemical composition, are presented in Fig. 18. With the

increase in the content of yttria in solid solution, based on the method of material compacting, larger (FP) or smaller (IP) increase in the activation energy of the grain boundary conductivity is observed.

It is obvious that this is not the chemical composition or even material phase which is a directly controlling factor of changes in E_{gb} . The nature of the presented changes suggests that these alterations will depend largely on the microstructural factors such as grain size and the associated surface development of grain boundaries as well as the strength and nature of the segregation phenomenon. The correlations between the grain boundaries' conductivity activation energy and the average grain size shown in Fig. 19 are partial confirmations of these findings.

Only in the case of materials containing 5 mol% yttrium oxide the change in the average grain size does not cause significant changes in E_{gb} ; in other cases, the decline in the grain size "induces" the increase of activation energy of the grain boundary conductivity. Moreover, this relationship, defined as a slope of the respective lines, is generally the weaker the higher is Y_2O_3 content in the solid solution. It can be assumed that this effect is associated primarily with the segregation of yttrium to grain boundaries, which, understood as the relative increase in the concentration of yttrium on the grain boundary, will be the smaller, and yttrium oxide content is higher in solid solution [9, 12]. However, since the increase in Y_2O_3 leads to an increase in the value of E_{gb} only for the materials with the smallest grains and sintered at relatively low temperatures, it can be assumed that there are other factors that control this value. The correlation with sintering temperature suggests that this factor may be, for example, even a small amount of silica-containing impurities. At lower temperatures, these impurities can block the transport of ions along the grain boundaries, while, at higher temperatures, they can spontaneously accumulate at three-grain contact points or dissolve in the volume of the grains.

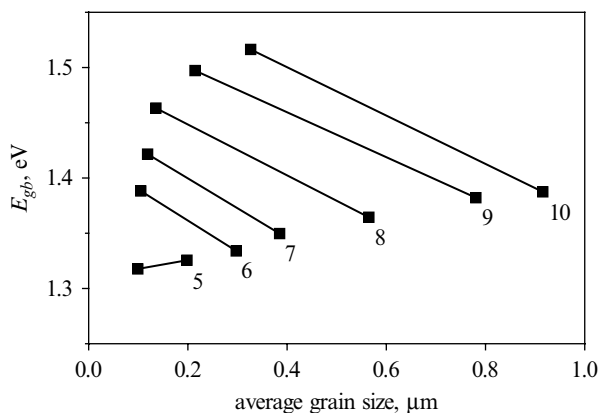
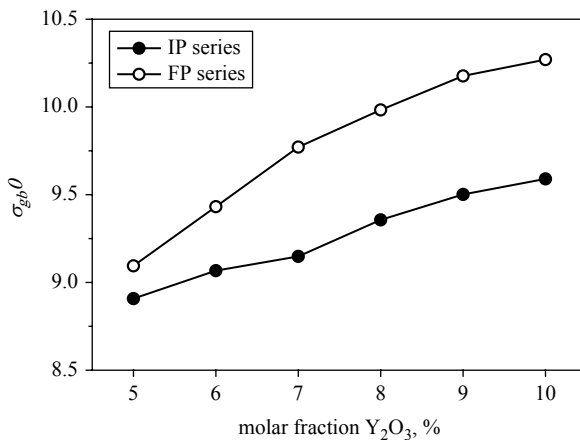


Fig. 19 The correlation between average grain size and the activation energy of grain boundary conductivity in IP and FP the series

Fig. 20 The values of the pre-exponential factor of the grain boundary conduction of the IP and FP series. The σ_{gb}^0 standard deviation does not exceed 0.05



Increasing Y₂O₃ concentration increases the grain size and thus effectively reduces the density of grain boundaries, which may be one of the elements affecting the value of the pre-exponential factor, σ_{gb}^0 . Changes in σ_{gb}^0 , shown in Fig. 20, are similar in nature to E_{gb} change, and an increase in the amount of yttrium oxide causes its growth in the IP and FP series.

The changes in grain boundary conductivity of the sintered materials of both series at selected temperatures depending on their chemical composition were shown in Fig. 21a–d. The charts for temperatures 300 °C and 400 °C have been prepared on the basis of the measured values and those for 600 °C and 800 °C, calculated on the basis of the appropriate E_{gb} and σ_{gb}^0 values.

The presented dependences have shown two trends that are direct consequences of the E_{gb} and σ_{gb}^0 values. The first one is a change in the conductivity nature of each material with temperature increase. At 300 °C in the materials of IP series, the conductivity of the grain boundaries decreases with increasing amount of yttrium oxide in the solid solution. At the higher temperatures, 600 °C and 800 °C, an increase in the grain boundary conductivity is visible. The increase of the yttrium content in the solid solutions and increase of temperature cause higher increase of the grain boundary conductivity. In the case of the FP series, a decrease of σ_{gb}^0 at 300 °C and 400 °C is associated with increasing amounts of yttrium oxide, and at elevated temperatures a significant increase in the conductivity of the grain boundaries appears. The consequence of these effects is the fact that the higher the temperature, the more conductive are grain boundaries in sintered materials with lower yttrium oxide content.

The second trend is due to the mutual relationship between the grain boundaries' conductivity values of individual sintered series. At low temperatures, the best ionic conductivity is exhibited by coarse sintered materials. The temperature increase slightly reduces the differences, wherein the effect is also dependent on the chemical composition of materials. It should be noted that a relationship to the chemical composition has only formal character. The actual correlation exists in relation to

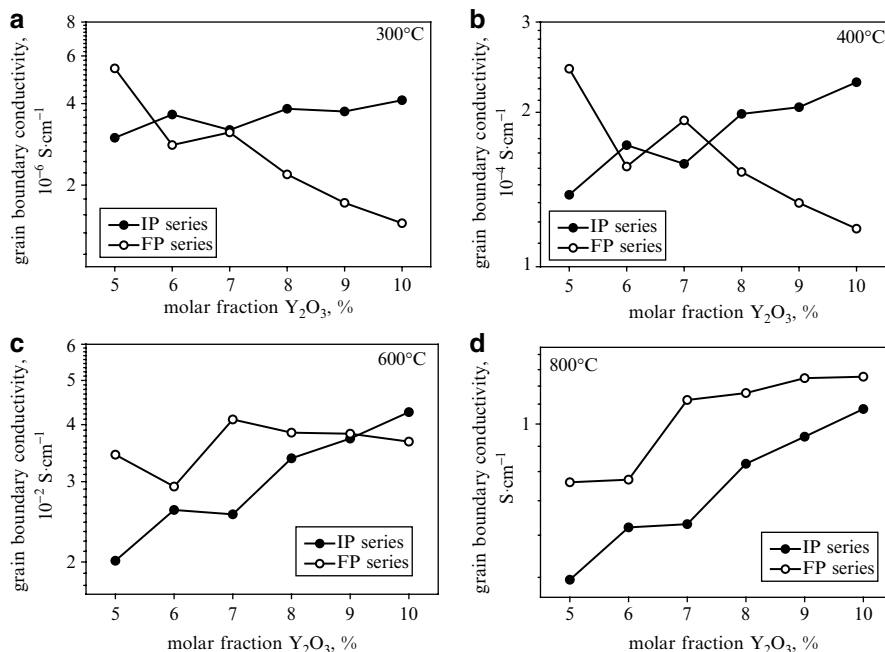
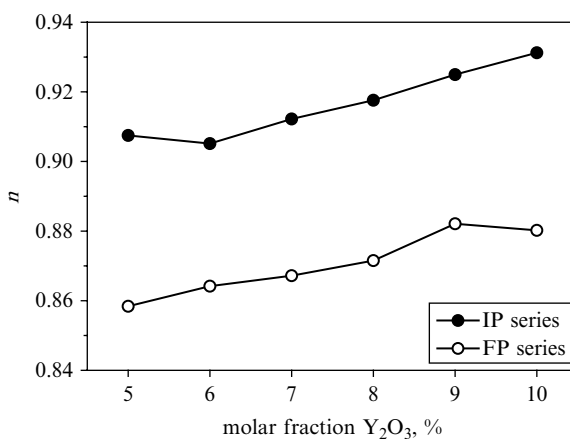


Fig. 21 Changes in the grain boundaries' conductivity in the IP and FP series depending on their chemical composition and temperature

Fig. 22 Changes of the n parameter (see Eq. 8) measured at 300 °C, depending on the chemical composition of the IP and FP series



the phenomena of induced changes in the amount of Y_2O_3 in the investigated solid solution, such as a number or grain boundaries' structure.

The changes in the nature of the grain boundaries' capacity correlated to the chemical composition of the materials are similar as in the case of bulk capacity variation (Fig. 22). With the increase of the yttrium oxide content in parallel with

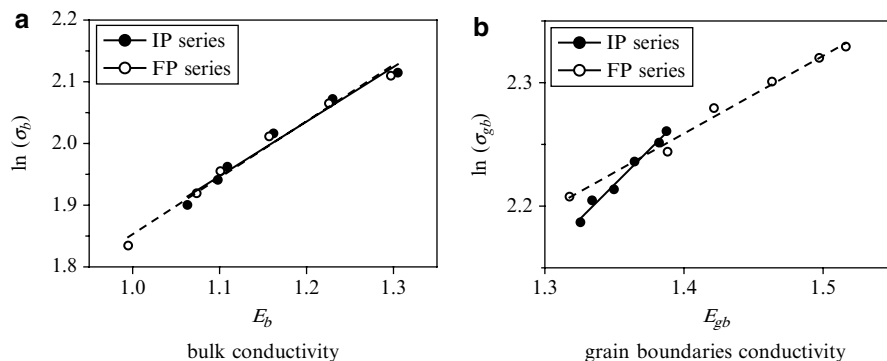


Fig. 23 Applicability of the Meyer–Neldel rule in zirconia solid solutions with different microstructures in the case of (a) bulk conductivity and (b) the grain boundaries' conductivity. The correlation coefficients higher than 0.96 (a) and 0.98 (b)

Table 2 The values of T_0 characteristic temperature calculated from the Meyer–Neldel rule

Material	T_0 , °C	
	Bulk conductivity	Grain boundary conductivity
IP	858	1315
FP	819	615

the sintering temperature and therefore generally with the decrease in the grain boundaries' density, the value of parameter n from Eq. 8 increases, and electric capacity is more of the Debye capacitor character. It appears that the relatively large differences between the values of the parameter n in the case of IP and FP series cannot be attributed solely to the differences in grain sizes. It may indicate arranging of the grain boundary caused e.g., by chemical homogenization of the material or less intensive segregation process.

The values of the activation energy and the pre-exponential factors calculated on the basis of temperature conductivity allow us to check the applicability of the compensation rules (the Meyer–Neldel rule) for the obtained materials [50]. Figure 23 shows the correlation between E_b and σ_b as well as E_{gb} and σ_{gb} for all series of materials. It was found that in each case the relationship between these two parameters, the activation energy and the natural logarithm of the pre-exponential factor, has a linear character.

Directional coefficients of fitted lines constitute a measure of the characteristic temperature, T_0 , whose values are collected in Table 2. Because each of individual material series consisted of the solid solutions obtained under the same conditions but with a different chemical composition, it can be assumed that T_0 is the temperature at which the chemical composition has no effect on the value of conductivity. This corresponds to such a situation as a total dissociation of the all complex defects. In the case of bulk conductivity, characteristic temperatures of all the series do not vary significantly from each other as it was confirmed by a small influence of

microstructure on the type and number of defects. The values of T_0 in the case of grain boundaries' conductivity are clearly linked to the microstructural properties of the individual series of sintered materials. However, there is no simple correlation such as the average grain size which could lead to the assumption that in this case also other factors must be taken into account, affecting the structure of the grain boundaries such as the sintering temperature or the impurity level resulting from the method of powder preparation.

Conclusions

The research results presented in this paper of the influence of the microstructure of the zirconia solid solutions on their ionic conductivity can be a good basis for evaluating the application of nanomaterials, meant as the solid electrolyte. As it was shown, the limitation of the grain size to the nanoscale particles results in a significant decrease in bulk conductivity activation energy and in the increase in the value of this conductivity at relatively low temperatures. The E_b decline, however, is similarly accompanied by the pre-exponential factor depreciation, which results in a relative decrease in bulk conductivity with increasing temperature, with respect to the materials of submicron microstructure. This factor increases with increasing yttria content in the solid solution; thus, a natural way to increase the conductivity values would be to obtain a material with the nanometric microstructure and containing a larger amount of Y_2O_3 . A restriction and possibly even impossibility of achieving this project is related to the fact that the increase in the amount of yttrium oxide in the solid solution promotes grains coarsening during sintering. As it follows from the presented investigations, sintering at 1200 °C of powders consisting of crystallites of dimensions approximately 7 nm and containing 7 or 8 mol% Y_2O_3 results in materials in which the vast majority of the particles has a size larger than 100 nm. Lowering the sintering temperature, whose consequence would be effective, particle size reduction without the use of such a hot pressing does not seem possible. More hope would rather be associated with a reduction in the size of crystallites, although the minimum size of them is about 4 nm, and the development of a new method of compaction. In the latter case, a natural obstacle is constituted by the surface effects forming a natural barrier in obtaining relatively dense nanoparticle systems.

References

1. Knauth P (2006) Ionic and electronic conduction in nanostructured solids: concepts and concerns, consensus and controversies. *Solid State Ion* 177:2495–2502
2. Bauerle JE (1969) Study of solid electrolyte polarization by a complex admittance method. *J Phys Chem Solid* 30:2657–2670
3. Verkerk MJ, Middelhuis BJ, Burggraaf AJ (1982) Effect of grain boundaries on the conductivity of high-purity ZrO_2 - Y_2O_3 ceramics. *Solid State Ion* 6:159–170
4. van Dijk T, Burggraaf AJ (1981) Grain boundary effects on ionic conductivity in ceramic $Gd_xZr_{1-x}O_{2-(x/2)}$ solid solutions. *Phys Status Solidi A* 63:229–240

5. Guo X, Waser R (2006) Electrical properties of the grain boundaries of oxygen ion conductors: acceptor-doped zirconia and ceria. *Prog Mater Sci* 51:151–210
6. Yan MF, Cannon RM, Bowen HK (1983) Space charge, elastic field, and dipole contributions to equilibrium solute segregation at interfaces. *J Appl Phys* 54:764–778
7. Maier J (1985) Space charge regions in solid two-phase systems and their conduction contribution – I. Conductance enhancement in the system ionic conductor-“inert” phase and application on AgCl:Al₂O₃ and AgCl:SiO₂. *J Phys Chem Solid* 46:309–320
8. Maier J (1995) Ionic conduction in space charge regions. *Prog Solid State Chem* 23:171–263
9. Hwang S-L, Chen I-W (1990) Grain size control of tetragonal zirconia polycrystals using the space charge concept. *J Am Ceram Soc* 73:3269–3277
10. Browning ND, Buban JP, Moltaji HO, Pennycook SJ, Duscher G, Johnson KD, Rodrigues RP, Dravid VP (1999) The influence of atomic structure on the formation of electrical barriers at grain boundaries in SrTiO₃. *Appl Phys Lett* 74:2638–2640
11. Fisher CAJ, Matsubara H (1999) Molecular dynamics investigations of grain boundary phenomena in cubic zirconia. *Comput Mater Sci* 14:177–184
12. Aoki M, Chiang Y-M, Kosacki I, Lee LJ-R, Tuller H, Liu Y (1996) Solute segregation and grain-boundary impedance in high-purity stabilized zirconia. *J Am Ceram Soc* 79:1169–1180
13. Guo X, Sigle W, Fleig J, Maier J (2002) Role of space charge in the grain boundary blocking effect in doped zirconia. *Solid State Ion* 154–155:555–561
14. Guo X, Zhang Z (2003) Grain size dependent grain boundary defect structure: case of doped zirconia. *Acta Mater* 51:2539–2547
15. Bingham D, Tasker PW, Cormack AN (1989) Simulated grain-boundary structures and ionic conductivity in tetragonal zirconia. *Philos Mag* A60:1–14
16. Kliewer KL, Koehler JS (1965) Space charge in ionic crystals. I. General approach with application to NaCl. *Phys Rev* A140:A1226–A1240
17. Guo X, Maier J (2001) Grain boundary blocking effect in zirconia: a Schottky barrier analysis. *J Electrochem Soc* 148:E121–E126
18. Badwal SPS (1992) Zirconia-based solid electrolytes: microstructure, stability and ionic conductivity. *Solid State Ion* 52:23–32
19. Hughes AE, Badwal SPS (1990) Impurity segregation study at the surface of yttria-zirconia electrolytes by XPS. *Solid State Ion* 40–41:312–315
20. Kleitz M, Dessemond L, Steil MC (1995) Model for ion-blocking at internal interfaces in zirconias. *Solid State Ion* 75:107–115
21. Martin MC, Mecartney ML (2003) Grain boundary ionic conductivity of yttrium stabilized zirconia as a function of silica content and grain size. *Solid State Ion* 161:67–79
22. Jung Y-S, Lee J-H, Lee JH, Kim D-Y (2003) Liquid-phase redistribution during sintering of 8 mol% yttria-stabilized zirconia. *J Eur Ceram Soc* 23:499–503
23. Badwal SPS, Hughes AE (1992) The effects of sintering atmosphere on impurity phase formation and grain boundary resistivity in Y₂O₃-fully stabilized ZrO₂. *J Eur Ceram Soc* 10:115–122
24. Badwal SPS (1995) Grain boundary resistivity in zirconia-based materials: effect of sintering temperatures and impurities. *Solid State Ion* 76:67–80
25. Gödicke-meier M, Michel B, Orliukas A, Bohac P, Sasaki K, Gauckler L, Heinrich H, Schwander P, Kosterz G, Hofmann H, Frei O (1994) Effect of intergranular glass films on the electrical conductivity of 3Y-TZP. *J Mater Res* 9:1228–1240
26. Gremillard L, Epicier T, Chevalier J, Fantozzi G (2000) Microstructural study of silica-doped zirconia ceramics. *Acta Mater* 48:4647–4652
27. Maier J (1987) Defect chemistry and ionic conductivity in thin films. *Solid State Ion* 23:59–67
28. Sata N, Eberman K, Eberl K, Maier J (2000) Mesoscopic fast ion conduction in nanometre-scale planar heterostructures. *Nature* 408:946–949
29. Maier J (1987) Composite electrolytes. *Mater Chem Phys* 17:485–498
30. Hui S, Roller J, Yick S, Zhang X, Dec’es-Petit C, Xie Y, Maric R, Ghosh D (2007) A brief review of the ionic conductivity enhancement for selected oxide electrolytes. *J Power Sources* 172:493–502

31. Bučko MM, Haberko K, Faryna M (1995) Crystallization of zirconia under hydrothermal conditions. *J Am Ceram Soc* 78:3397–3440
32. Tien TY (1964) Grain boundary conductivity of $Zr_{0.84}Ca_{0.16}O_{1.84}$ ceramics. *J Appl Phys* 35:122–124
33. Mondal P, Klein A, Jaegermann W, Hahn H (1999) Enhanced specific grain boundary conductivity in nanocrystalline Y_2O_3 -stabilized zirconia. *Solid State Ion* 118:331–339
34. Jiang S, Schulze WA, Amarakoon VRW, Stangle GC (1997) Electrical properties of ultrafine-grained yttria-stabilized zirconia ceramics. *J Mater Res* 12:2374–2380
35. Kosacki I, Suzuki T, Petrovsky V, Anderson HU (2000) Electrical conductivity of nanocrystalline ceria and zirconia thin films. *Solid State Ion* 136–137:1225–1233
36. Zhang YW, Jin S, Yang Y, Li GB, Tian SJ, Jia JT, Liao CS, Yan CH (2000) Electrical conductivity enhancement in nanocrystalline $(RE_2O_3)_{0.08}(ZrO_2)_{0.92}$ ($RE = Sc, Y$) thin films. *App Phys Lett* 77:3409–3411
37. Tuller HL (2000) Ionic conduction in nanocrystalline materials. *Solid State Ion* 131:143–157
38. Mayo MJ (1996) Processing of nanocrystalline ceramics from ultrafine particles. *Int Mater Rev* 41:85–115
39. Groza JR (1999) Sintering of nanocrystalline powders. *Int J Powder Metall* 35:59–66
40. Kellett BJ, Lang FF (1989) Thermodynamics of densification: II, grain growth in porous compacts and relation to densification. *J Am Ceram Soc* 72:735–741
41. Zych Ł, Haberko K (2003) Zirconia nanopowder – its shaping and sintering. *Solid State Phenom* 94:157–164
42. Scott HG (1975) Phase relationships in the zirconia-yttria system. *J Mater Sci* 10:1527–1535
43. Suzuki Y (1995) Phase transition temperature of fluorite-type ZrO_2 - Y_2O_3 solid solutions containing 8–44 mol.% Y_2O_3 . *Solid State Ion* 81(3–4):211–216
44. Yokokawa H, Sakai N, Kawada T, Dokiya M (1993) Phase diagram calculations for ZrO_2 based ceramics: thermodynamic regularities in zirconate formation and solubilities of transition metal oxides. In: Badwal SPS, Bannister MJ, Hannink RHJ (eds) *Science and technology of zirconia*. Technomic Publishing, Lancaster, pp 59–68
45. Du Y, Jin ZP, Huang PY (1991) Thermodynamic assessment of ZrO_2 - $YO_{1.5}$ system. *J Am Ceram Soc* 74:1569–1577
46. Nowotny J (1988) Surface segregation of defects in oxide ceramic materials. *Solid State Ion* 28–30:1235–1243
47. Rosin P, Rammler E (1933) The laws governing the fineness of powdered coal. *J Inst Fuel* 7:29–36
48. Kilner JA, Steel BCH (1981) Mass transport in anion-deficient fluorite oxides. In: Sørensen OT (ed) *Non-stoichiometric oxides*. Academic, New York, pp 233–269
49. Macdonald JR (1987) In: Macdonald JR (ed) *Impedance spectroscopy – emphasizing solid materials and systems*. Wiley, New York
50. Almond DP, West AR (1986) Entropy effects in ionic conductivity. *Solid State Ion* 18–19: 1105–1109

Wet Chemical Approaches for Chemical Functionalization of Silicon and Titanium Nanomaterials

26

Kerrilee A. Stewart and Harinder Pal Singh Missan

Contents

Introduction.....	850
Wet Chemical Functionalization of Silicon.....	851
H-Termination.....	852
Metal Complex Catalyzed Reactions.....	852
Radical Induced Hydrosilylation Reactions.....	854
Thermally Induced Hydrosilylation.....	854
Electrochemical Methods.....	855
Applications.....	857
Wet Chemical Functionalization of Titanium Dioxide.....	859
Acid Functionalization of Titanium Dioxide.....	859
Conclusion.....	863
References.....	864

Abstract

Since the advent of nanomaterials, 1D nanotubes of varying materials have attracted attention for their unique physical and chemical properties. Whilst the utilization of these structures has become a reality today, many of its potential applications remain a far-off dream. One of the ways to move this dream closer to a reality is through the functionalization of the nanotubes. Carbon nanotubes are one the most exciting nanostructures discovered to date and still generate much interest due to their extraordinary thermal conductivity, mechanical, and electrical properties. Silicon nanomaterials are also particularly useful as they form crucial part of the electronic developer's desire to make technological devices smaller and smarter. Titanium generates much interest as a biomaterial and for its good conductivity,

K.A. Stewart • H.P.S. Missan (✉)
Fuel Cell Materials Research Lab, Department of Physics, University of the West Indies,
Trinidad and Tobago, West Indies
e-mail: Harinder.Missan@sta.uwi.edu

chemical durability, high melting point, and wide applicability. Chemical functionalization allows for the alteration of the electronic properties whilst effecting new functions through the chemical tailoring of the surface to suit the particular application. Wet chemistry techniques are one of the more popular ways of accomplishing these functionalizations. In this chapter, wet chemistry approaches to the chemical functionalization of titanium and silicon nanomaterials are explored.

Introduction

The advent of nanotechnology has the potential to change every part of our lives as it is the foundation of recent and major technological advances. It has the potential to change our approach of manufacturing, technology, electronics, bio materials, polymers, and ceramics. Besides the creation of novel materials using nanotechnology, it also allows one to harness properties that would have previously been inaccessible in known materials, creating ultraprecise structures with the potential for vastly improved mechanical, chemical, and electrical properties.

The functionalization of nanomaterials presents a way in which nanomaterials can be specifically tailored to fulfill a specific objective. The aim is to improve specific properties to suit the application required. Its electronic properties and selective reactivity are some of the properties that are most often tailed. There are many different methods used to functionalize nanomaterials with wet chemistry techniques being one of the more popular methods.

Wet chemistry allows for the functionalization to take place using typical bench top chemistry methods, therefore reducing the cost of equipment required and allowing for greater control of the reaction conditions. The most popular functionalized nanomaterial lies with porous silicon surfaces due to its relative cheapness and wide usage. Titanium dioxide and carbon nanomaterials have also been the subject of functionalization techniques to improve their already attractive properties, although the reported research findings/data for them is much smaller than that available for the functionalization of porous silicon.

The Advent of the Wet Chemical Functionalization of Silicon Surfaces happened when:

- In 1956, the discovery was made by Uhlir that during the electropolishing of crystalline Silicon, the upper surface did not dissolve [1].
- It was first noted in 1971, that rather than dissolution, brownish layers of fine holes are produced [3].
- Silanization was then the first method utilized to graft organics to SiO₂. This method however, suffers from low OH-content on the surface.
- T-BAG- Tethering by aggregation and Growth was then used to improve on the silanization technique first used. In this process phosphonate molecules are grafted onto SiO₂.

Functionalization could then occur once an H-terminated surface was obtained.

Wet Chemical Functionalization of Silicon

In 1956 Uhlir observed that during the electropolishing of crystalline silicon that the silicon substrate did not dissolve under the appropriate conditions but rather, as Watanabe et al. later reported, produced a brownish layer of fine holes [1–3]. Since then, silicon has been the forerunner in microelectronic technology for the past few decades owing to its abundance and its relative cheapness. Because its interface is chemically and electrically stable with its oxide it can be produced with high purity [4]. As the size condenses into the nanoscale and beyond, its surface properties play an ever-increasing role. The low concentration of the electrical defect states at the Si/SiO₂ interface is, in fact, the main driving factor behind its use in photovoltaic and electrical biosensors [5]. Precise tailoring of its interfacial and surface properties becomes necessary in order for it to be effectively used in the abovementioned applications. The modification of the surface properties of Si/SiO₂ carried out by the grafting of molecules using OH groups has been the subject of many investigations. There are several disadvantages one has to face when attempting to modify the SiO₂ surface. Firstly, there is poor chemical stability of the Si–O–Si bond at the organic layer and SiO₂ interface. This is due to the ease with which hydrolysis occurs at basic and even neutral pH conditions. Secondly, the activation energy required for the reaction with OH groups on the surface is high. It is particularly high when considering the grafting of phosphonic acid groups onto the surface [6, 7].

There are two main methods that are currently used for the wet chemical functionalization of silicon nanostructures:

(i) Silanization:

It is a self-assembly process whereby the surface is covered with organofunctional alkoxysilane molecules [8]. During this process the –OH group “attacks” and displaces the alkoxy group on the silane thereby leading to the formation of a covalent –Si–O–Si– bond. There are several drawbacks when utilizing this method. For example, this method suffers from low OH group content of the Silicon surface oxide [7, 9]. In addition to it, the structural order is difficult to attain while the silicon surface coverage is obtained using amorphous siloxane polymerization whose degree of polymerization is heavily dependent on the water content of the deposition solvent [10, 11].

(ii) Tethering by aggregation and growth (T-BAG):

It is used where phosphonate molecules are grafted onto SiO₂. In this process, a phosphonic solution is weakly physisorbed onto the oxide substrate and then chemisorbed using heat. A well-ordered layer can be easily formed because of the interaction of the phosphonate groups with adjacent molecules. Any remaining physisorbed groups are easily removed by rinsing [10]. This process has two main advantages over the more popular silanization. Firstly, it is not restricted to specific environmental conditions, and secondly, this method is simple and highly reliable. However, it does have some disadvantages especially that the chemisorption process can be very long and can take upwards of 48 h. This particular disadvantage has recently been reported as one that can be

minimized by controlling the humidity under which the reaction occurs [12]. The $-\text{Si}-\text{O}-\text{P}-$ bond which is formed during this process is very easily hydrolyzed and the sample must be heated in order to transition from the physisorbed phosphonic acid to the chemisorbed phosphonate.

Because of the disadvantages outlined, a driving force has led to a flurry of research into obtaining oxide-free surfaces through a process known as H-termination of the Si surface. Functionalization can now therefore occur through the transformation of H-terminated Si surfaces using metal complex catalyzed reactions [13], radical induced hydrosilylation reactions [14, 15], thermal hydrosilylation, electrochemical methods [16], and/or reactions with lithium or Grignard reagents [17]. Recently advances have also been made through the immersion of N-terminated Si (111) in neat, anhydrous CH_3OH at 65°C which leads to the slow formation of oxide free methoxy terminated surfaces. In the compound formed, each methoxy center is surrounded by six $\text{Si}-\text{H}$ surface molecules [18, 19].

H-Termination

Due to the instability of the $\text{Si}-\text{O}$ native surface, H-termination is necessary as it not only provides us with the necessary relative stability, but also the selective reactivity required for functionalization. $\text{Si}-\text{H}$ is easily prepared using an HF-based solution, usually HF/EtOH , under various chemical, electrochemical and photoelectrochemical conditions in order to suit the crystallography and type of Si surface to be treated. A solution of dilute (1–2 %) $\text{HF}_{(\text{aq})}$ is used to treat Si (100) surface yielding dihydride i.e., SiH_2 (100); whereas a treatment with a solution of 40 % $\text{NH}_4\text{F}_{(\text{aq})}$ of Si (111) yields the flat monohydride $=\text{SiH}$ [20]. Originally, the understanding of this process proved a challenge as the SiF ($\sim 5\text{ eV}$) bond was traditionally thought to be more stable than the SiH ($\sim 3.5\text{ eV}$) bond [21]. The $\text{Si}-\text{Si}$ bond is strongly polarized because of the high electronegativity of the F- atom. This makes the $\text{Si}-\text{Si}$ bond unstable leading to the easy removal of a surface Si atom in the form of SiF_x as has been proposed by Uhara and colleagues [21] and later confirmed by experimental reports [22]. A proposed reaction scheme is shown in Fig. 1.

Because Si has a relatively low electronegativity, H-termination partially oxidizes its surface and leads to the formation of a partial positive charge. This is particularly advantageous because of the ability of this H-atom to act as a Lewis base [23].

Metal Complex Catalyzed Reactions

Traditionally, lower transition metals such as platinum, palladium, and rhodium were utilized in the hydrosilylation of alkenes and alkynes on H-terminated Si surfaces [24]. However, many reports and publications to date find that the use of these

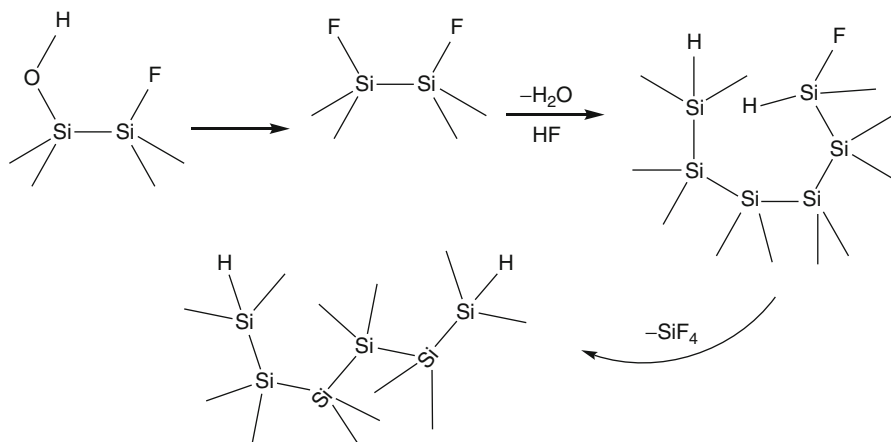


Fig. 1 A proposed reaction mechanism for H-termination

transition metals as metal complex catalysts in hydrosilylation reactions do not yield the desired reaction pathway. For example, Ito et al. reported that when the reaction was executed using $\text{RhCl}(\text{PPh}_3)_3$, or Wilkinson's reagent, and $\text{PdCl}_2(\text{Pet}_3)_2$ or the more common $\text{Pd}(\text{OAc})_2/1,1,2,3\text{-tetramethylbutylisocyanide}$ for functionalization with alkynes, the experiment yielded metal deposition and substantial oxidation [25].

Some breakthroughs in the use of lower transition metals have however been made. One group of researchers has shown that Karstedt's catalyst ($\text{O}[\text{Si}(\text{CH}_3)_2\text{CH}=\text{CH}_2]_2\text{Pt}$) does in fact produce the desired result. They have also noted that oxygen is necessary in order for hydrosilylation to take place as it plays a role in the stabilization of Pt colloids [26].

Lewis acids also represent a good alternative to traditional transition metals as a catalyst in hydrosilylation reactions due to their mild reactivity and high selectivity. AlCl_3 , poses a solubility challenge as it is insoluble in nonpolar solvents. This problem is easily rectified through the use of EtAlCl_2 , which would prevent multiphasic reactions from also occurring at the same time [27]. A reaction scheme for the use of EtAlCl_2 in hydrosilylation is shown in Fig. 2. An excess of EtAlCl_2 can be utilized in these functionalization reactions in order to add alkynes with ester, hydroxyl, or cyano groups.

One example of a reaction employing this technique is the reaction of 1.0 M solution of EtAlCl_2 in hexane with H-terminated Si surfaces. Upon addition of 1-dodecyne, dodecyl groups are found to have been successfully added to the surface.

The efficiency of these reactions depends directly on the chemistry and stereochemistry of the starting reagents used. 1-alkenes tend to produce the best efficiencies at 28 % leaving approximately 70 % of the H-terminated surface bonds undisturbed. Cis alkenes are also more efficient than trans alkenes [28].

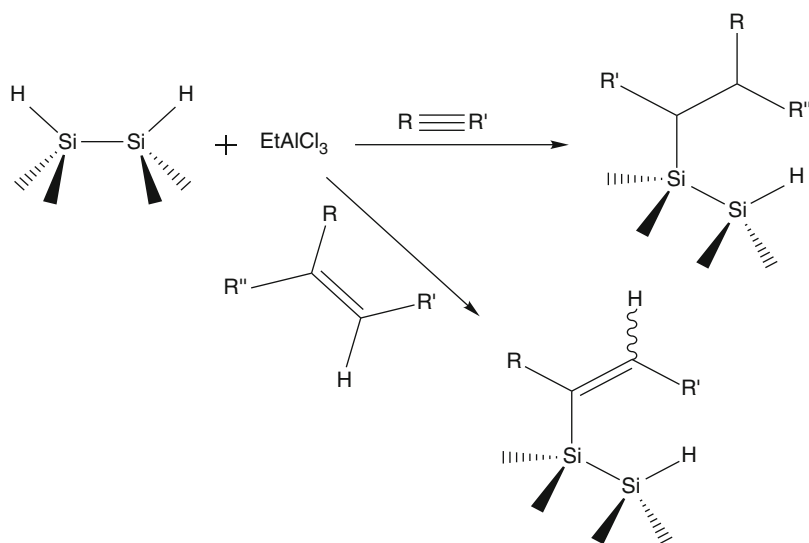


Fig. 2 A reaction scheme for the use of EtAlCl_2 in hydrosilylation

Radical Induced Hydrosilylation Reactions

During hydrosilylation, a saturated bond is inserted into the Si–H groups on the surface. The use of a radical initiator gives us one method of achieving this. The surface structures produced using this method are relatively stable, with the ability to withstand extended boiling in aerated chloroform, acidic conditions (2.5 M H_2SO_4 in 90 % dioxane v/v), and basic conditions (1 M $\text{NH}_4\text{OH}_{(\text{aq})}$) [29].

A mechanism was proposed and has been confirmed upon by several research groups [30–32] and is shown in Fig. 3.

Thermally Induced Hydrosilylation

Organic functionalization of H-terminated Si surfaces was first carried out by Bateman et al. in the 1990s [33]. Thermal hydrosilylation was initially avoided as a viable option because it was thought that thermally treating a compound would lead to activation of the functional groups. This activation of the functional groups would cause them to then react with the H-terminated Si instead of forming the unsaturated alkene terminals. The theory has been disproven since then with many successful attempts at thermally induced hydrosilylation [34–37].

In this process, the H-terminated Si surface is immersed in a solution of the desired alkene at temperatures of approximately 150–200 °C, for 18–20 h. This slow reaction time is one of the major disadvantages as it makes the reaction sensitive to infiltration by impurities. However, operating at these moderately high

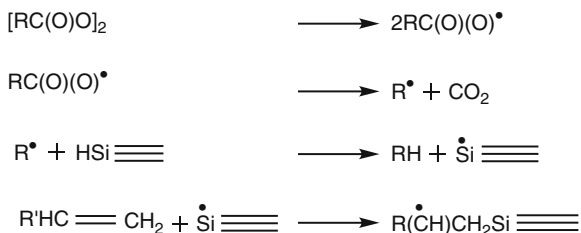


Fig. 3 A proposed mechanism for radical induced hydrosilylation reactions

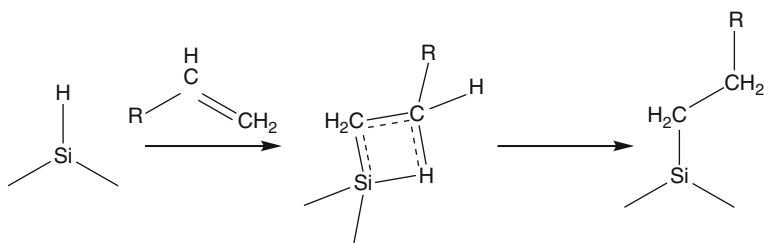


Fig. 4 A reaction mechanism showing thermally induced hydrosilylation

temperatures provides the advantage of a reduced risk of surface oxidation due to the elimination of water from the reaction sphere [38], in the process degradation being suppressed and ordering of the layer being promoted.

In the 1990s when the process was developed by Bateman et al., it was thought to be as a result of the presence of surface radicals [33] but now it is thought to be inaccurate and is actually due to the unlikelyhood of homolytic cleavage of the relatively strong H–Si bond (3.6 eV) occurring at such moderate temperatures. A more likely mechanism based on classical approaches was then proposed [28, 39] and is shown in Fig. 4.

Electrochemical Methods

Reduction of alkyl iodides and bromides and benzyl bromides can be done electrochemically to produce covalently bonded Si-functionalized surfaces. Several mechanisms have been proposed for this alteration using electrochemical methods. One suggests the reduction of alkyl and benzyl halides in order to produce their radicals which may then react with surface Si–H bonds (as shown in Fig. 5).

Functionalization can now take place via the reaction between the Si radical and the alkyl or benzyl radical. A proposed reaction is shown in Fig. 6.

Another functionalization option involves the reduction of the Si radical which can then be subject to nucleophilic attack. This process is illustrated in Fig. 7.

Another option also includes the in situ reduction of alkyl and benzyl radical to carbanions in a manner similar to the reaction of Grignard reagents. A reactive mechanism for this process is shown in Fig. 8.

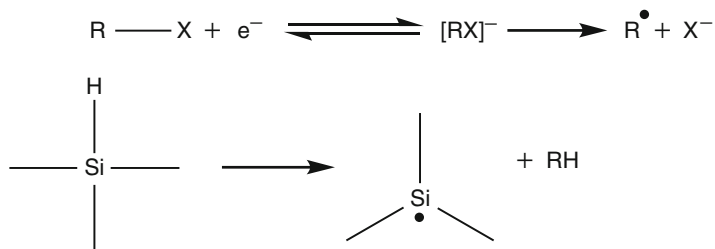


Fig. 5 One possible mechanism for the electrochemical reduction of alkyl iodides and bromides and benzyl bromides

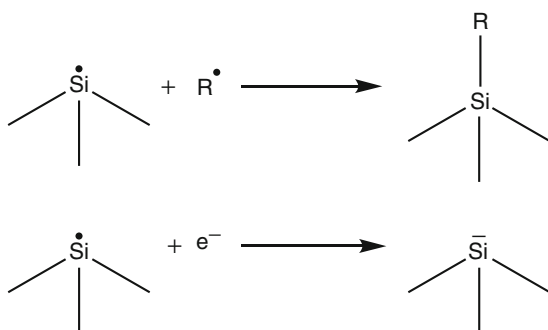


Fig. 6 Functionalization via reaction between the Si radical and the alkyl or benzyl radical

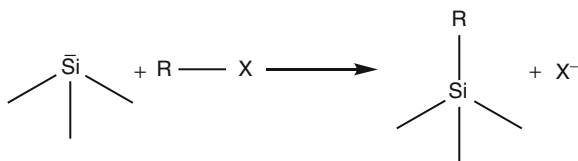


Fig. 7 Functionalization involving the reduction of the Si radical

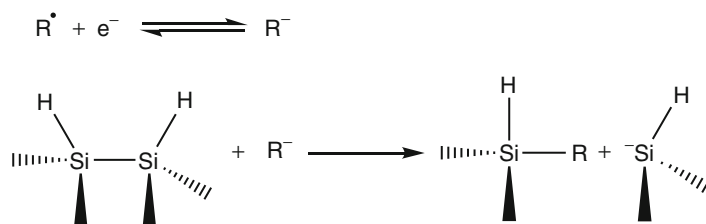


Fig. 8 In situ reaction of alkyl and benzyl radicals to carbanions

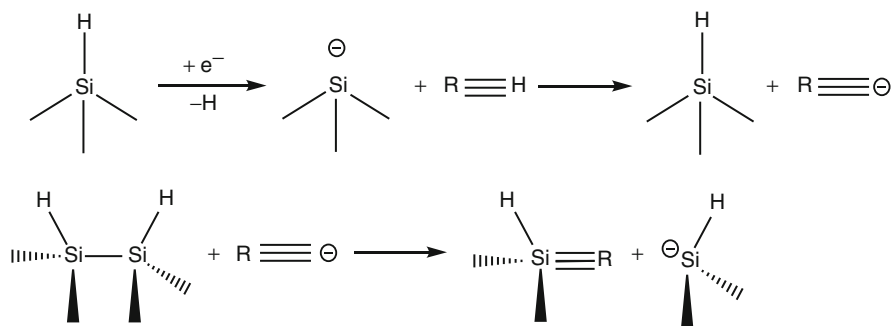


Fig. 9 Reaction mechanism for the cathodic electrografting process

The reduction can be done using $R-X$ ($X = \text{Br}, \text{I}$) in a mixture of acetonitrile and tetrahydrofuran containing 0.2 M LiBF_4 . A cathodic current of 10 mA/cm^2 is applied for approximately 2 min in order to execute the process. The process results in surfaces that have been reported to be very stable when compared with hydride terminated Si surfaces, sometimes referred to as 1-step process surfaces [40–42]. The surfaces were subjected to dimethylsulfoxide, aqueous Cu^{2+} , 10 % ethanol in phosphate solution having a pH of 7.4, and $\text{Na}_2\text{CO}_3/\text{NaHCO}_3$ in ethanol-water; has shown greater promise than hydride terminated Si surfaces under these conditions.

Using anodic electrografting (AEG) and cathodic electrografting (CEG), alkynes can be grafted onto H terminated Si surfaces [43]. Several authors [44, 45] have reported a mechanism for the cathodic electrografting process that includes the formation of a Si^- intermediate via a reduction process which is then protonated [28]. This mechanism is highlighted in Fig. 9. Anodic electrografting may occur via the nucleophilic attack of positively charged Si surfaces followed by hydride termination.

Mattei and Valentini, in recent years, reported in situ functionalization of Si surfaces during its electrochemical formation process via the dissolution of alkenes and alkynes within the H–F solution utilized. This process is reported to be 50–60 % efficient, relatively stable and quick and is shown in Fig. 10 [46].

Applications

(i) Surface Passivation.

Canham et al. were among the first group of researchers to demonstrate the promise of the use of microporous surfaces such as silicon in biotechnological advances [47]. In one reported application, functionalized Silicon which was derived through the use of a Lewis acid to mediate hydrosilylation of 1-dodecyne, was incubated at $37 \text{ }^\circ\text{C}$ in simulated bodily fluids (Fig. 11).

The functionalized surface suffered layer dissolution of less than 25 nm whilst, the unfunctionalised portion, $\sim 250 \text{ nm}$, was almost totally dissolved in under 70 h. The researchers reported a decrease in the corrosion rate of

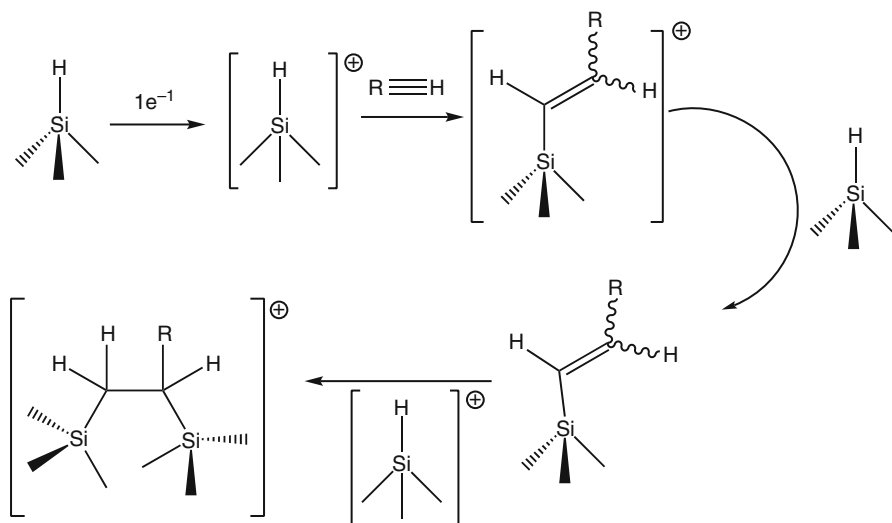


Fig. 10 In situ functionalization of Silicon surfaces

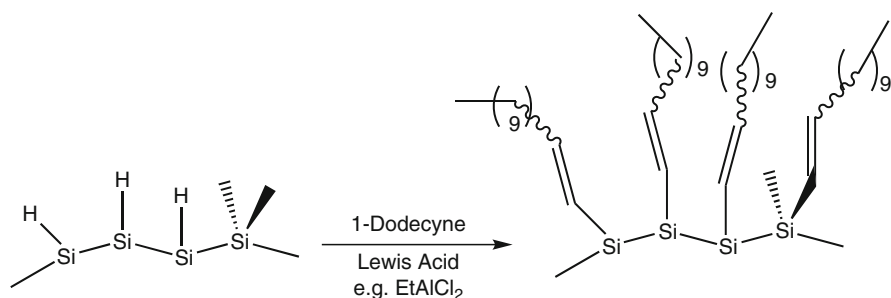


Fig. 11 Surface passivation of Silicon

approximately by 100 due to functionalization [48]. This serves to highlight the ability to utilize functionalized Si surfaces to direct selective bioreactivity in the fields of biosensors and biomedical research.

(ii) Electroluminescence Stabilization.

This phenomenon was investigated by Buriak et al. using cathodic electrografting, anodic electrografting and hydrosilylation via Lewis acids to functionalize the Si surfaces. Alkyl terminated surfaces showed bright emissions with its functionalized surfaces exhibiting recharging under cathodic conditions [28].

(iii) Desorption/Ionization on Silicon (DIOS).

Buriak and Siuzdak are widely known to be the pioneers for the use of porous silicon in desorption/ionization mass spectroscopy. The porous silicon replaces the traditional classical matrix assisted mechanism required allowing

for reliable analysis of low molecular weight molecules which is particularly useful in drug synthesis. The mechanism by which ionization occurs is not fully understood, although the influence of various parameters such as pore size and depth has been reported [20].

Wet Chemical Functionalization of Titanium Dioxide

Inorganic oxide nanotubes (titania nanotubes) were first developed by Kasuga et al. [49] and later evolved by Chen et al. These nanoparticles are appealing because of their crystalline and scroll structure and can be easily assembled by treating crystalline titanium dioxide (TiO_2) with highly concentrated sodium hydroxide (NaOH) [50]. The inclusion of hydroscopic oxide, for example, silicon dioxide (SiO_2) or titanium dioxide (TiO_2) increases water retention at high temperatures and composite membranes synthesized with this component exhibit appreciable conductivity up to 140 °C [51].

Acid Functionalization of Titanium Dioxide

TiO_2 nanotubes were prepared using a hydrothermal method by the hydrothermal alkali treatment of crystalline TiO_2 [49]. Five grams of titanium dioxide (TiO_2) powder and 200 ml of 10 M sodium hydroxide (NaOH) solution was prepared and the mixture was refluxed for 5 days in a nitrogen atmosphere at 100 °C. The obtained product was then washed with 0.1 M hydrochloric acid (HCl) and deionized water until a neutral pH was obtained. The solution was then filtered and dried at 70 °C for 24 h in a vacuum oven. Titania nanotubes of average length 100–200 nm and 15–20 nm width were obtained using TEM shown in Fig. 12. The nanotubular titania synthesized were then acid functionalized. Acid functionalization is the process whereby the surface groups which are attached to the nanotube can be changed into an acidic moiety to aid in the electrical properties of the materials. Acid functionalization was achieved via the mechanism shown in Fig. 13. The process starts with 0.5 g of nanotubular titania being dissolved in tetrahydrofuran (THF) and 5–10 ml of 1 M potassium tert-butoxide [$(\text{CH}_3)_3\text{COK}$] in THF added to the solution. The solution reacted for 3–4 h under reflux in nitrogen atmosphere at 80 °C with continuous stirring. The addition of 3 ml of 1,3-propane sultone was done and the solution was allowed to react under the same conditions for 24 h. Five milliliters of perchloric acid (HClO_4) (oxo-acid) was then added and the solution reacted under the same conditions for 3–4 h. Acid functionalized nanotubular titania was obtained with the centrifugation of the product followed by three wash cycles with THF and drying in oven at 80 °C.

$^1\text{H-NMR}$ studies obtained for unfunctionalized nanotubular titania and nanotubular titania functionalized with 1,3-propane sultone showed doublet peaks at 3.53 ppm, the triplet at 3.41 ppm, and the multiplet at 2.04 ppm. In functionalized nanotubes, a change in the structure of the unfunctionalized nanotubular titania is has been observed.

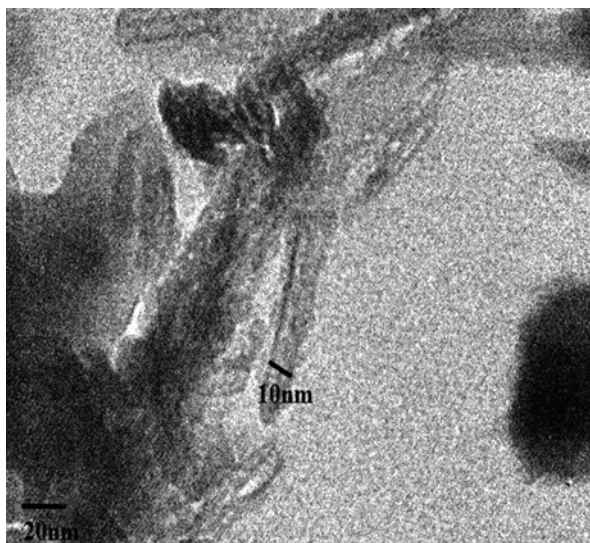


Fig. 12 TEM of nanotubular titania

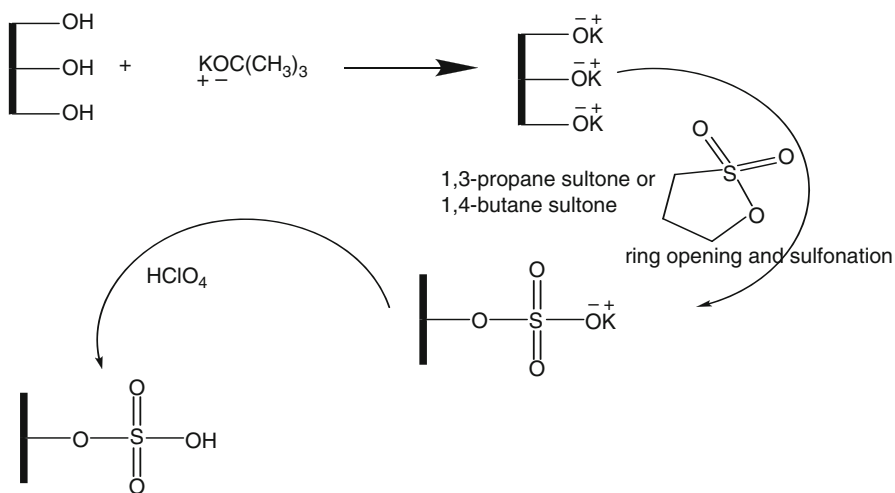


Fig. 13 Reaction showing the functionalization of titania nanotubes

The peaks present in the unfunctionalized nanotubes were observed more dispersed as well as broader around the chemical shift values of 3.53, 3.41, and 1.61 ppm. The broader peaks imply the presence of an increased number of protons whilst the fact that the position of the peaks remains the same implies that the same structure is maintained.

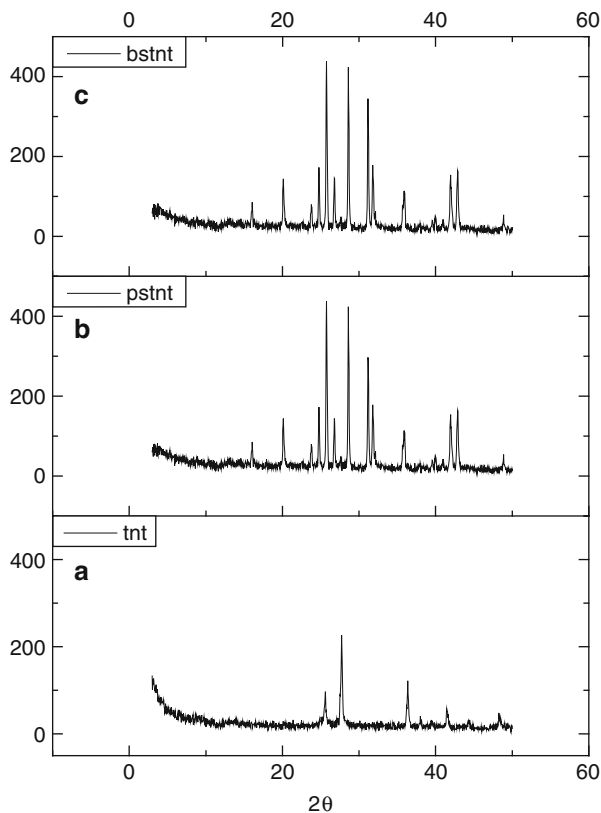


Fig. 14 Diffractograms for (a) nonfunctionalized titania nanotubes and acid-functionalized nanotubular titania using (b) 1,3-propane sulfone and (c) 1,4-butane sulfone

Acid functionalization confirmed using X-ray diffraction (XRD) and Fig. 14 shows the diffractograms for the sulfonated nanotubular titanium dioxide synthesized using different chain lengths of sulfonated chain. Diffractograms shown is for (a) nonfunctionalized titania nanotubes and acid functionalized nanotubular titania using (b) 1,3-propane sulfone and (c) 1,4-butane sulfone.

Same characteristic peaks of titania nanotubes were observed in the titania nanotubes that were acid functionalized by both 1,3-propane sulfone and 1,4-butane sulfone. TEM studies were conducted on the acid functionalized titania in order to determine if they retained their nanotubular structure. The TEM images micrographs are shown in Fig. 15 for 1,3-propane sulfone nanotubular titania (left hand figure) and for 1,4-butane sulfone nanotubular titania (right hand figure) functionalized titanium nanotubes. Although the acid functionalized titania showed an even greater propensity to coagulate than unfunctionalized titania the presence of nanotubular structures was still observed.

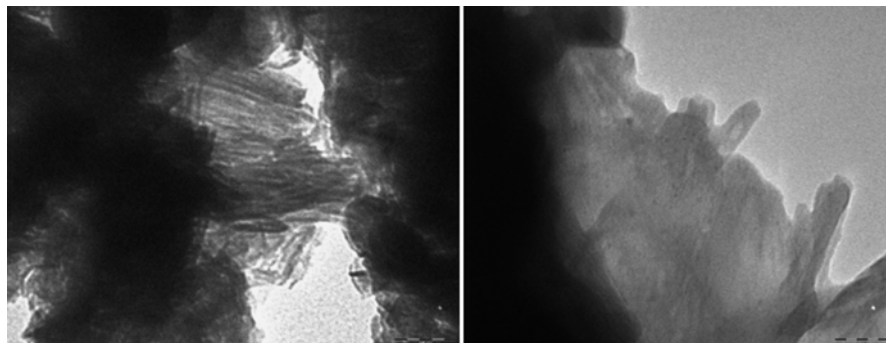


Fig. 15 TEM micrographs for 1,3-propane sultone nanotubular titania (*left hand figure*) and for 1,4-butane sultone nanotubular titania (*right hand figure*) functionalized titanium nanotubes

Table 1

Sample	IEC (Mequiv)
TiO ₂ nanotubes	0.09
1,3-propane sultone TiO ₂ nanotubes	0.49
1,4-butane sultone TiO ₂ nanotubes	0.165

Different properties have been found to be effected by changing the functionalized side chain length including ion exchange capacity (IEC), electrical conductivity, etc. The ion exchange capacity (IEC) of the unfunctionalized and functionalized titania nanotubes carried to determine in order to establish whether after acid functionalization there were more ions available for conduction which would indicate the ability of the acid functionalized nanotubes to be used to contribute to the proton conductivity. The ion exchange capacities (IEC) values for unfunctionalized and functionalized nanotubular titania obtained are shown in Table 1.

The samples acid functionalized showed a marked increase in IEC value over acid functionalized nanotubular titania. The 1,3-propane sultone acid functionalized nanotubular titania had an IEC value approximately three times higher than that for 1,4-butane sultone. This could be due to the fact that the additional chain length in the 1,4-butane sultone nanotubular titania causes entanglement and does not as readily allow for the passage of ions.

Conductivity studies shown for these acid functionalized systems showed improvement over the non functionalized nanotubular titania. Figure 16 shows conductivity variation of ionic conductivity as a function of temperature for unfunctionalized and acid-functionalized nanotubular titania.

The acid functionalized nanotubular titania functionalized with 1,3-propane sultone showed high conductivity values with maximum conductivity at 5.04×10^{-3} S/cm. The highest conductivity obtained for 1,4-butane sultone was 1.94×10^{-3} S/cm. Unfunctionalized nanotubular titania had its highest conductivity at 4.71×10^{-4} S/cm. As temperature increased past 100 °C, the conductivity of the unfunctionalized titania began to show a marked decrease and this continued as the sample was run past 160 °C. This may be due to loss of hydroxide groups along the surface in the form of condensation. This effect was not noticed in the acid functionalized titania samples.

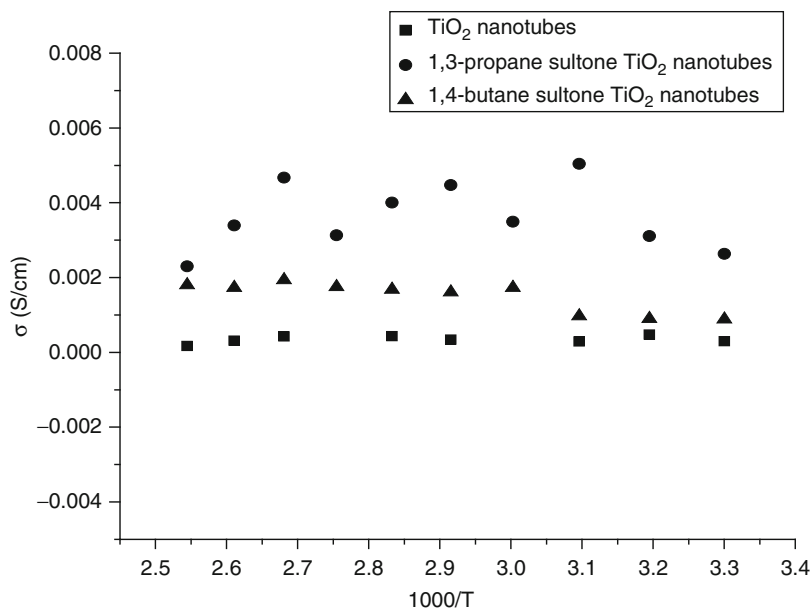


Fig. 16 Ionic conductivity as a function of temperature for unfunctionalized and acid-functionalized nanotubular titania

Conclusion

In this chapter, wet chemical techniques for the functionalization of Silicon and titanium nanocomposites are explored with Silicon being the more popular semiconductor in the research community. Two main methods were investigated for preparation for functionalization of Silicon nanocomposite surfaces: Silanization and Tethering by Aggregation and Growth (TBAG). Functionalization can then occur on H-terminated Silicon surfaces via metal complex catalyzed reactions, radical induced hydrosilylation reactions, thermal hydrosilylation, electrochemical methods, and/or reactions with lithium or Grignard reagents.

Advantages of wet chemical functionalization of H-terminated Si includes (1) the preservation of the nanostructure, (2) the compatibility if Si H-terminated bonds with the main organic and organometallic reactions and the organic functional groups, and (3) the use of well-established methods for the integration of chemical and biofunctionality. The major limitation lies in the high number of H-terminated surface bonds remaining unsubstituted due steric hindrance from surrounding bonds. These unsubstituted bonds left behind are not protected from oxidation and may hinder chemical and biofunctionality.

Acid functionalized titania nanocomposites occur when the nanotube surface groups are modified to an acidic moiety in order to change and enhance the electronic properties of the material. In the process outlined, 1,3-propane sultone and 1,4-butane sultone are utilized as the reacting agents to add sulfonic acid groups and

confirmed using $^1\text{H-NMR}$, XRD, and TEM studies. Electrochemical impedance studies done revealed that the shorter the chain length of the acid chain attached to the nanotubular surface, the higher the conductivity obtained whilst all samples demonstrated good amorphous characteristics.

This field of wet chemical functionalization will remain one of the most widely pursued aspects of semiconductor nanomaterials being mainly driven by their many applications in surface passivation and stabilization, biosensors, Polymer electrolyte membrane fuel cells, and battery technology.

References

1. Uhlir A (1956) *Bell Syst Tech J* 35:333
2. Watanabe Y, Sakai T (1971) *Rev Electron Commun Lab* 19:899
3. Watanabe Y, Arita Y, Yohoyana T, Igarasu Y (1975) *J Electrochem Soc* 122:1351
4. Helms CR, Poindexter EH (1994) *Rep Prog Phys* 57:791
5. Sze SM (1981) *Physics of semiconductor devices*, vol 2. Wiley-Interscience, New York
6. Miller JB, Schwartz J, Bernasek SL (1993) *J Am Chem Soc* 115:8239
7. Rye RR, Nelson GC, Dugger MT (1997) *Langmuir* 13:2965
8. Rozlosnik N, Gerstenberg MC, Larsen NB (2003) *Langmuir* 19:1182
9. Muller JB, Schwartz J, Bernasek SL (1993) *J Am Chem Soc* 115:8239
10. Hanson EL, Schwartz J, Niekel B, Kock H, Danisman MF (2003) *J Am Chem Soc* 125:16074
11. Wang YL, Lieberman M (2003) *Langmuir* 19:1159
12. Vega A, Thissen P, Chabal YJ (2012) *Langmuir* 28:8046
13. Buriak JM (2002) *Chem Rev* 102:1271
14. Ciero RL, Linford MR, Chidsey CED (2000) *Langmuir* 16:5688
15. Sieval AB, Linke R, Zuilof H, Sudhover EJ (2000) *Adv Mater* 12:1457
16. deVilleneuve CH, Pinson J, Bernard MC, Allongue P (1997) *J Phys Chem B* 101:2415
17. Kim NY, Laibinis PE (1999) *J Am Chem Soc* 121:7162
18. Michalak DJ, Amy SR, Esteve A, Chabal YJ (2008) *J Phys Chem C* 112:11907
19. Michalak DJ, Amy SR, Aureau D, Dai M, Esteve A, Chabal YJ (2010) *Nat Mater* 9:266
20. Alimpiev S, Nikiforov S, Karavanskii VA, Minton T, Sunner J (2001) *J Chem Phys* 115:1891
21. Chabal YJ, Higashi GS, Raghavachari K, Burrows VA (1989) *J Vac Sci Technol A* 7:2104
22. Imura T, Mogi K, Hiraki A, Nakashima S, Mitsuishi A (1981) *Solid State Commun* 40:161
23. Himpfel FJ, Heimann P, Chiang TC, Eastman DE (1980) *Phys Rev Lett* 45:1112
24. Holland JM, Stewart MP, Allen MJ, Buriak JM (1999) *J Solid State Chem* 45:251
25. Marciniak B, Gulinski J (1993) *J Organomet Chem* 446:15
26. Saghatelian A, Buriak JM, Lin VS-Y, Ghadiri MR (2001) *Tetrahedron* 57:5131
27. Buriak JM, Allen MJ (1998) *J Am Chem Soc* 120:1339
28. Boukherroub R, Szunerits S (2009) In: Schmuki P, Virtanen S (eds) *Electrochemistry at the nanoscale*. Springer, New York, pp 183–248
29. Buriak JM (1999) *Chem Commun*:1051
30. Linford MR, Chidsey CED (1993) *J Am Chem Soc* 115:12631
31. Chatgililoglu C (1992) *Acc Chem Res* 25:188
32. Linford MR, Fenter P, Eisenberger PM, Chidsey CED (1995) *J Am Chem Soc* 117:3145
33. Bateman JE, Horrocks BR, Houlton A (1997) *J Chem Soc Faraday Trans* 93:2427
34. Fan HJ, Kuok MH, Ng SC, Boukherroub R, Lockwood DJ (2002) *Semicond Sci Technol* 17:692
35. Fan HJ, Kuok MH, Ng SC, Lim HS, Liu NN, Boukherroub R, Lockwood DJ (2003) *J Appl Phys* 94:1243
36. Muller F, H'erino R, Ligeon M, Gaspard F, Romenstain R, Vial JC, Bsiesy A (1993) *J Lumin* 57:283

37. Vial JC, Bsiesy A, Gaspard F, H'erin R, Ligeon M, Muller F, Romenstain R, Macfarlane RM (1992) *Phys Rev B* 45:14171
38. Demierry P, Ballutaud D, Aucouturier M, Etcheberry AJ (1990) *Electrochem Soc* 137:2966
39. Coletti C, Marrone A, Giorgi G, Sgamellotti A, Cerofolini G, Re N (2006) *Langmuir* 22:9949
40. Coulthard I, Jiang DT, Lorimer JW, Sham TK, Feng X-H (1993) *Langmuir* 9:3441
41. Andsager D, Hillard J, Nayfeh MH (1994) *Appl Phys Lett* 64:1141
42. Andsager D, Hillard J, Hetrick JM, AbuHassan LH, Plisch M, Nayfeh MH (1993) *J Appl Phys* 74:4783
43. Robins EG, Stewart MP, Buriak JM (1999) *Chem Commun*:2479
44. Jouikov V, Salaheev G (1996) *Electrochim Acta* 41:2623
45. Jouikov V (1997) *Russ Chem Rev* 66:509
46. Mattei G, Valentini V (2003) *J Am Chem Soc* 125:9608
47. Canham LT (1995) *Adv Mater* 7:1033
48. Canham LT, Reeves CL, Newey JP, Houlton MR, Cox TI, Buriak JM, Stewart MP (1999) *Adv Mater* 11:1505
49. Kasuga T (2006) *Thin Solid Films* 496:141
50. Thorne A, Angela K, Tunstall D, Irvine JTS, Zhou W (2005) *J Phys Chem B* 109:5439
51. O'Hayre J, Cha S, Colella W, Prinz FB (2009) *Fuel cell fundamentals*. Wiley, New York

Part IV

Electrochemical Properties and Characterization of Nanostructured Coatings and Thin Films

Krzysztof Winkler and Emilia Grądzka

Contents

Introduction.....	870
Quantum Effects in Electrochemistry of Nanoparticles	871
Electrochemical Properties of Nanoparticles in the Solid State	877
Metallic Nanoparticles	877
Charge Transfer in Thin Films Composed of Carbon Nanomaterials.....	893
Nanoparticle Material Thin Films in Charge Storage Devices	904
General Characteristics of Supercapacitors.....	904
Double-Layer Capacitors Based on the Carbon Nanoparticles.....	906
Supercapacitors Containing Conductive Polymer and Metal Oxide Nanoparticles.....	914
Composites of Conducting Polymers or Metal Oxides and Carbon Nanostructures	917
Conclusion	925
References.....	926

Abstract

This review is focused on the fundamental developments in the charge transfer processes and charge storage properties of different kinds of nanoparticles. Special attention is paid to metallic nanoparticles and nanostructured carbon materials. Behavior related to the discrete electron levels distribution is emphasized. Depending on the nanoparticle size, the electrochemistry is systemized in three regimes: bulk-continuum electrochemistry, electrochemical behavior reflective of quantized double-layer charging, and molecule-like behavior. Recent progress in understanding charge transfer process in two- and three-dimensional films of metallic nanoparticles based on electron-hopping model is discussed. A conductivity of carbon nanostructures, nanotubes, nano-onions, and graphene is briefly described in terms of their electronic structure.

K. Winkler (✉) • E. Grądzka

Institute of Chemistry, University of Białystok, Białystok, Poland

e-mail: winkler@uwb.edu.pl; emilia@uwb.edu.pl

© Springer International Publishing Switzerland 2016

M. Aliofkhaezai, A.S.H. Makhlof (eds.), *Handbook of Nanoelectrochemistry*,

DOI 10.1007/978-3-319-15266-0_37

869

The exemplary results of nanoparticles thin film conductivity determination are presented. The review is concluded with an outlook on the technological potential of nanoparticles in charge storage devices. Principles of double-layer and faradaic electrochemical supercapacitors are given. Double-layer capacitance performances of carbon nanostructure that involved materials are summarized. Pseudocapacitance properties of polymeric nanoparticles that involved thin films are also discussed. Finally, electrochemical supercapacitors based on the nanocomposites containing carbon nanostructures are described.

Keywords

Metallic nanoparticles • Carbon nanostructures • Charge transfer process • Thin films of nanoparticles • Capacitance and conductivity of nanoparticles

Introduction

For more than two decades, the investigation of nanoscale phenomena has dominated many domains of science. A vast number of synthesis methods have been performed in order to reach nanostructured materials with designed and improved structures and properties. They have been mainly focused on the formation of stable and size-controlled monolayer-protected metallic clusters. Spectacular progress in the synthesis of carbon nanostructures has been also observed. This carbon family of nanomaterials has opened a large area of study for theoretical and practical investigation. Recently, nanoparticles of transition metal and nonmetal oxides have been synthesized due to their perspective application in charge storage and photochemical and photoelectrochemical devices.

Years spent studying nanoparticles revealed the potential and limitations of these materials in pure and applied science. The properties of materials on the nanoscopic scale are determined by a material's chemical nature, size, and shape. In most cases, stable nanoparticles are formed under the protection of layered organic compounds or ions to prevent aggregation. This protective layer may also influence the properties of the core material. Due to their size, the nanoparticles exhibit properties different from those of both the individual molecules and the bulk material. These features promise extensive and unique applications of nanoparticles and nanomaterials.

The conductivity and capacitance properties of nanoscopic particles or materials composed of nanoparticles are particularly important because these materials are used in nano- and microsize electronic devices, charge storage materials, light-converting systems, and chemical detectors based on electrocatalytic processes. The electronic structure and therefore the electric and electrochemical properties of nanoparticles depend upon the size and shape of the nanoparticles. Relatively large nanoparticles have an electronic structure similar to that of the bulk material. As the size of the nanoparticles decreases, quantum effects begin to dominate. Finally, very small particles have electronic structures similar to those of individual molecules. Their large surface area-to-volume ratio makes these nanoparticles suitable to use in charge storage devices.

A number of reviews have covered the electrochemical properties and electro-technological applications of nanomaterials [1–19]. The early electrochemical studies of monolayer-protected metallic clusters have been summarized by Murray and coworkers [1]. Two other reviews by Murray that reported different aspects of nanoelectrochemistry [2, 3] are particularly important. These articles address the problems encountered while fabricating nanoparticle materials for electrochemical study and examining the electrochemical properties of these materials, as well as nanoelectrodes and electrochemistry in nanopores. Gold nanoclusters receive special attention in these reviews. Chen gives a brief overview of the recent research concerning discrete charge transfer processes in nanoparticle solid films [4]. Many reviews detail the electrical properties of carbon nanomaterials [5–11]. Selected aspects of the synthesis and practical applications of polymeric nanoparticles were reviewed by Hanemann and Szabo [12]. Nanoparticles have been frequently used in charge storage devices, and many reviews have reported the problems encountered during these applications, especially for devices using carbon nanomaterials [13–19].

The subject of this review is too large to present a comprehensive summary in the space available. We have thus selected areas to highlight. First, we have mainly focused on two major types of nanoparticles: organic monolayer-protected metallic nanoparticles and carbon nanoparticles. These are the most important and the most intensely studied nanoparticles. The first section of this chapter discusses the conductivity and electrochemical properties of these nanomaterials. The effect of size, shape, and composition of nanoparticles is emphasized. The second part of this section is concerned with the practical application of nanomaterials in charge storage devices.

Quantum Effects in Electrochemistry of Nanoparticles

Metallic nanoparticles have two essential components: a metal core and a core-stabilizing organic monolayer (Fig. 1). The organic monolayer may be additionally covalently functionalized with redox-active groups, such as ferrocene, anthraquinone, and viologen. These nanoparticles form stable colloidal solutions and may be directly studied using potentiodynamic electrochemical techniques.

The electrochemical activity of these types of nanoparticles may be related to the following: (i) faradaic processes of the metallic core, (ii) faradaic process of the protective organic layer, and (iii) capacitive charging of the nanoparticle surface. Therefore, the electrochemical properties of metallic nanoparticles depend on (i) the core material, (ii) the nanoparticle size and shape, (iii) the composition of protective organic layer and its thickness, and (iv) the composition of the solution.

The capacitance of nanoparticles greatly influences the electrochemical behavior of nanoparticles and their technological applications. The change in electrochemical potential (ΔV) is related to the double-layer capacitance of the individual metal cluster (C_{CLU}) through the equation [1]:

$$\Delta V = \frac{ze}{C_{CLU}} \quad (1)$$

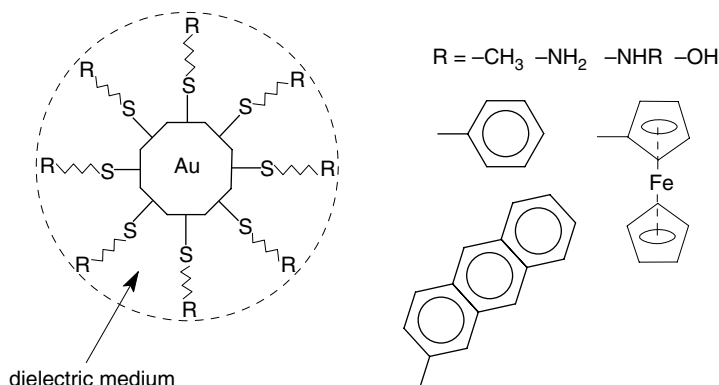


Fig. 1 Cartoon of organic monolayer-stabilized metallic nanoparticles

where z is the number of electrons transferred and e is the electron charge. The value of ΔV must be considered relative to the Boltzmann thermal energy distribution factor [2]. When $\Delta V \ll k_B T$ ($k_B T = 25.7$ meV in room temperature), the system can be treated as a metallic bulk material, and a nanoparticle's potential can be expected to continuously change. If ΔV is higher than 25.7 meV, then a stepwise change in the nanoparticle's potential is expected. The value of ΔV may be treated as an electrochemical or optical HOMO–LUMO energy gap. The changes in ΔV for gold nanoparticles protected by an organothiolate ligand layer relative to core size are illustrated in Fig. 2 [2]. The range of particle sizes can be divided into three types: metallic quantum dot-like behavior for large nanoparticles and bulk material, metal-like quantized behavior for the intermediate size, and molecule-like behavior for small nanoparticles (less than 100 gold atoms in the metallic core). Sufficiently low double-layer capacitance in the nanoparticles (Eq. 1) should also change the energy of the metallic core's electronic levels and consequently force metallike quantized behavior to occur.

The steady-state voltammetric responses of the quantized capacitance-charging ability of metallic particles were simulated utilizing different core sizes, core size dispersity, and the properties of the protective organic layer [20]. The charging energetics are easily described using the simple electrostatic relationships via the following equation for microelectrode current response (i) [20]:

$$i_{\text{Nor}} = 4nr_{\text{el}}F \int_{r_{\text{low}}}^{r_{\text{high}}} f(r) \left[\sum_{-1}^0 \frac{-1}{1 + \alpha_z} + \sum_1^N \frac{\alpha_z}{1 + \alpha_z} \right] \frac{k_B T}{6\pi\eta(r+d)} C_{\text{CLU}}^* dr \quad (2)$$

where k_B is the Boltzmann constant, r is the core radius, d is the thickness of the protective monolayer, r_{low} and r_{high} are the lower and upper limit of core radius in dispersion, r_{el} is the microelectrode radius, η is the solvent viscosity, C_{CLU}^* is the

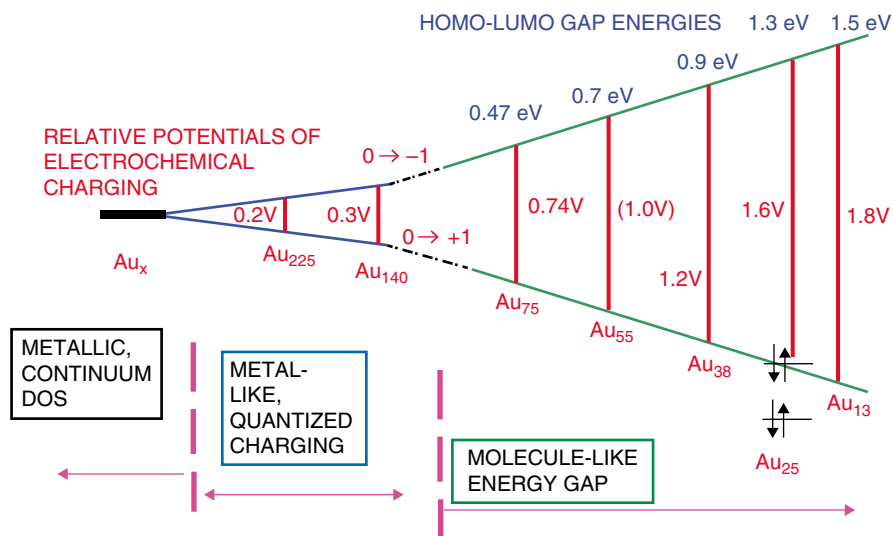


Fig. 2 Estimated HOMO–LUMO energy gap and electrochemical energy gap as a function of core size of gold nanoparticles (Reproduced from Ref. [2] with permission from American Chemical Society)

nanoparticle bulk concentration, and d is the thickness of protective dielectric monolayer. The α_z parameter is described by Eq. 3:

$$\alpha_z = \frac{N_z}{N_{z-1}} = \exp \left[\frac{e}{k_B T} \left(E_{APP} - E_{PZC} - \frac{\left(z - \frac{1}{2} \right) e}{C_{CLU}} \right) \right] \quad (3)$$

where N_z and N_{z-1} are the Boltzmann population of particles having charges z and $z-1$, E_{APP} is the potential applied to the working electrode, and E_{PZC} is the nanoparticle zero charge potential. This equation can be expressed in the following Nernst equation form:

$$E = E_{PZC} + \frac{\left(z - \frac{1}{2} \right) e}{C_{CLU}} + \frac{k_B T}{e} \ln \frac{N_z}{N_{z-1}} \quad (4)$$

where $E_{PZC} + [(z-0.5)e]/C_{CLU}$ represents formal potential of the MNP^z/MNP^{z-1} pair. This equation also predicts a series of equally separated waves at positive and negative potentials relative to the zero charge potential of the nanoparticle.

Figure 3a displays the effect of the core size on the steady-state voltammetric response [19]. The charging steps are easily observed for the nanoparticles with cores smaller than approximately 1 nm. The spacing decreases with increasing core

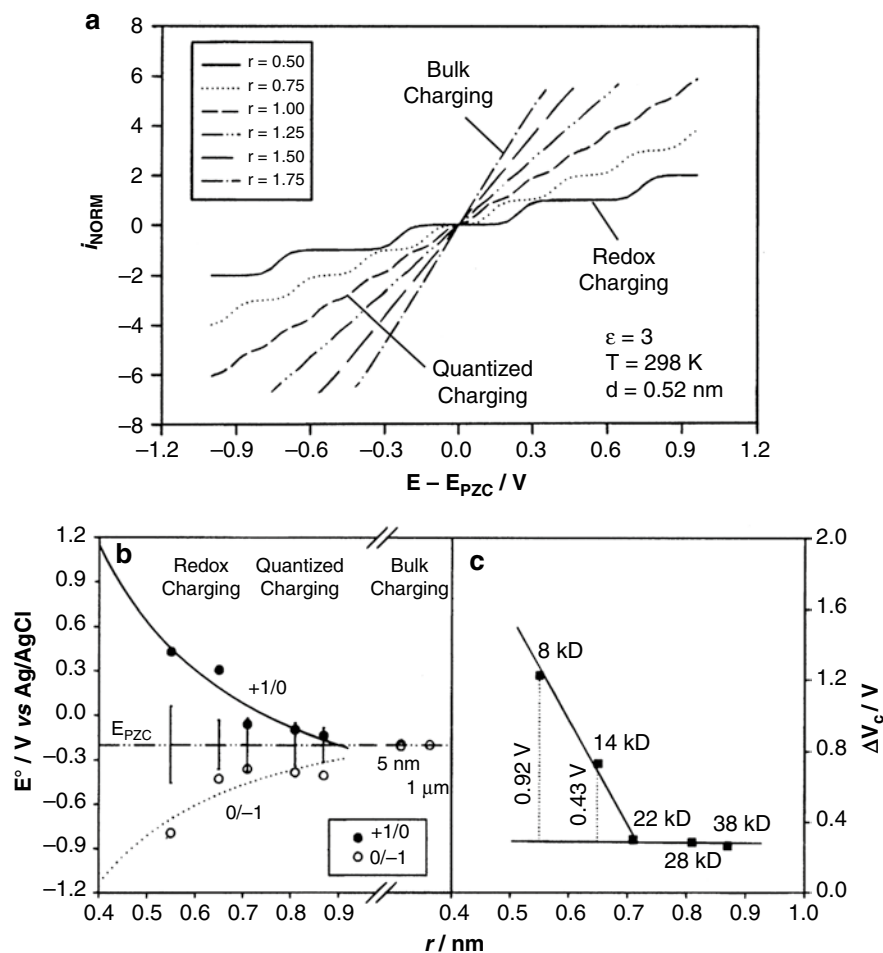


Fig. 3 (a) Steady-state microelectrode voltammetry simulations for monodisperse organic layer-stabilized metallic nanoparticles with various core sizes. (b) Formal potentials and (c) peak spacing between the $z = \pm 1/0$ peaks of AuSC6 nanoparticles with various core sizes (Reproduced from Ref. [20] with permission from American Chemical Society)

size according to Eqs. 2 and 3 because the capacitance C_{CLU} depends on the nanoparticle's size. The theoretical difference in the formal redox potentials of the $0/+$ and $0/-$ steps, in addition to the theoretical prediction of ΔV as a function of nanoparticle size, is displayed in Fig. 3b and c, respectively.

Experimentally, the electrochemical behavior expected for bulk materials was observed for relatively large metallic nanoparticles [21–25]. Figure 4 presents examples of current-potential curves recorded on rotating disk electrodes in acetonitrile containing Au_{310} stabilized by $\text{C}_8/\text{C}_8\text{Fc}$ (C_8 – octanethiol, C_8Fc – ferrocenyloctanethiol) particles [21]. The voltammetric wave is related to the faradaic current generated

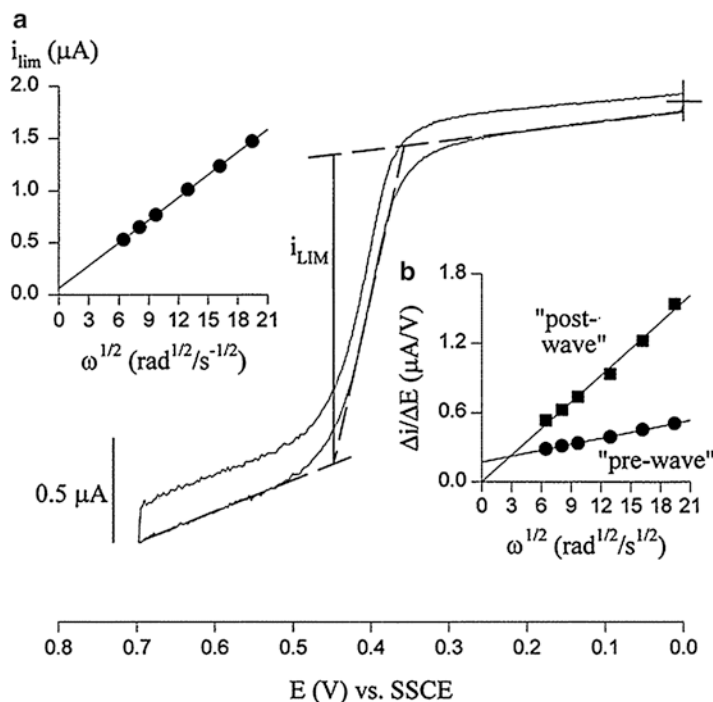


Fig. 4 Voltammogram at GC rotating disk electrode ($v=10$ mV/s, $\omega=3600$ rpm) in CH_2Cl_2 containing 1 mM $\text{Au}_{310}\text{SC}_8/\text{SC}_8\text{Fc}$ (1:5.5) and 0.1 M $(n\text{-Bt})_4\text{NClO}_4$. Inset (a) shows the dependence of the limiting current on the square root of the electrode rotation ($\omega^{1/2}$) and inset (b) shows the dependence of pre-wave and post-wave slopes on the $\omega^{1/2}$ (Reproduced from Ref. [21] with permission from American Chemical Society)

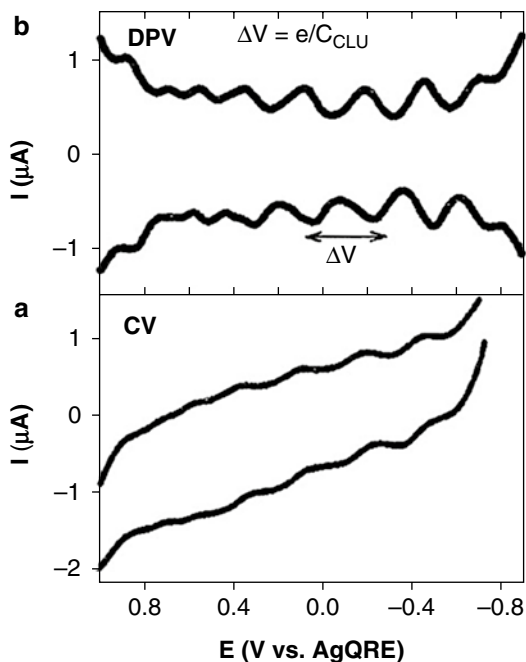
by the ferrocene groups' oxidation. The changes in the current of the pre- and the post-wave potential ranges are related to the gold cluster molecules charged after being transported to the electrode surface due to their double-layer capacitance properties. The slopes of the pre- and post-wave potential ranges are different.

In the pre-wave region, the capacitance is related to the capacitance of the octanethiol/ferrocenyloctanethiol monolayer. The values obtained for the nanoclusters are remarkably close to the capacitance obtained for the self-assembled monolayers of the n -alkanethiols on the polycrystalline gold electrode [26]. The oxidation of the ferrocenyl group sharply increases the clusters' capacitance. This effect is related to the charging of protecting $\text{C}_8/\text{C}_8\text{Fc}$ layer analogously to the adsorption of ions on the electrode/electrolyte interface. For spherical nanoparticles, the capacitance per unit area of metal can be expressed in the following way:

$$C = \frac{\varepsilon_r \varepsilon_0}{d} \frac{r+d}{r} \quad (5)$$

where ε_r is the relative dielectric of the monolayer, ε_0 is the permittivity of the free space, and d is the organic monolayer thickness.

Fig. 5 (a) Cyclic voltammogram at 10 mV/s and (b) differential pulse voltammogram at 10 mV/s and 25 mV pulse of $\text{Au}_{145}(\text{SC6})_{50}$ in CH_2Cl_2 at 1.6 mm diameter Au electrode (Reproduced from Ref. [1] with permission from American Chemical Society)



When the single-electron transfer causes the change of nanoparticle potential greater than the ambient thermal voltage ($k_B T$), the quantized double-layer charging is observed [27–31]. Such behavior observed for $\text{Au}_{145}(\text{S}(\text{CH}_2)_5\text{CH}_3)_{50}$ particles in CH_2Cl_2 solution is shown in Fig. 5 [1]. The sequence of the voltammetric peaks relates to the single-electron transfer processes occurring in the potential intervals e/C_{np} . An even peak spacing signifies that a metallic core that displays electrostatically controlled charging is present. Similar behavior was observed during the charging processes of nanoparticles immobilized on the electrode surface [32–35].

Molecule-like electrochemical behavior is observed for small A_{25} [36–39], Au_{38} [29], and Au_{55} [40] nanoparticles. Voltammograms obtained for $\text{A}_{25}(\text{SCH}_2\text{CH}_2\text{Ph})_{18}$ nanoparticles are shown in Fig. 6. The potential separation between first oxidation step at about +0.10 V vs. Ag/Ag+ and first reduction process at -1.5 V (Fig. 6) approximately corresponds to a 1.3 eV energy gap. The two oxidation steps at +0.10 and +0.39 V are related to the $\text{A}_{25}(\text{SCH}_2\text{CH}_2\text{Ph})_{18}^{-1/0}$ and $\text{A}_{25}(\text{SCH}_2\text{CH}_2\text{Ph})_{18}^{0/+1}$ charging processes, respectively. This first pair of oxidation peaks is followed by second pair of current peaks at more positive potentials. This is a typical behavior of electron transfer processes of gold molecular species which reflects the presence of doubly occupied molecular orbitals [38].

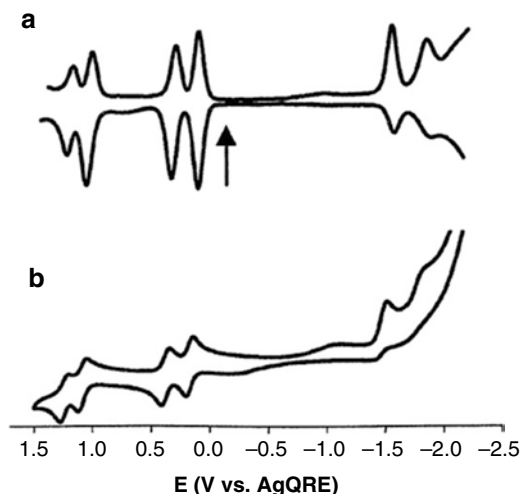


Fig. 6 (a) Cyclic voltammogram at 0.1 V/s and (b) differential pulse voltammogram at 10 mV/s and 25 mV pulse of $\text{Au}_{25}(\text{SC}_2\text{Ph})_{24}$ in CH_2Cl_2 containing $(n\text{-Bt})_4\text{NPF}_6$ at 0.4 mm diameter Pt electrode. Temperature was 70 °C (Adopted from Ref. [38] with permission from American Chemical Society)

Electrochemical Properties of Nanoparticles in the Solid State

The charge transfer processes of mono- or multilayers of nanoparticles include the following: (i) the electron transfer between the electrode and nanoparticle material, (ii) the electron transfer within the nanoparticle, (iii) the electron hopping between nanoparticles, and (iv) the transport of counterions between the solution and solid phases. This process depends on the following: (i) the contact between the electrode and the nanoparticles, (ii) the nanoparticle material's chemical nature, (iii) the nanoparticles' size and shape, (iv) the protective monolayer which stabilize nanoparticles, (v) the interactions between the nanoparticles, (vi) the distance between the nanoparticles within the material, and (vii) the solvent and supporting electrolytes surrounding the nanoparticle material.

The nanoparticle ensembles that produce the one-, two-, or three-dimensional structures are schematically presented in Fig. 7. Single separated nanoparticles are considered 0-dimensional systems.

Metallic Nanoparticles

Electrochemical Behavior of Single Metallic Nanoparticles

Determining the redox properties of zero-dimensional phase is quite challenging when studying the electrochemistry of nanoparticles. During the electrochemical studies of single nanoparticles, a highly amplified signal current is required.

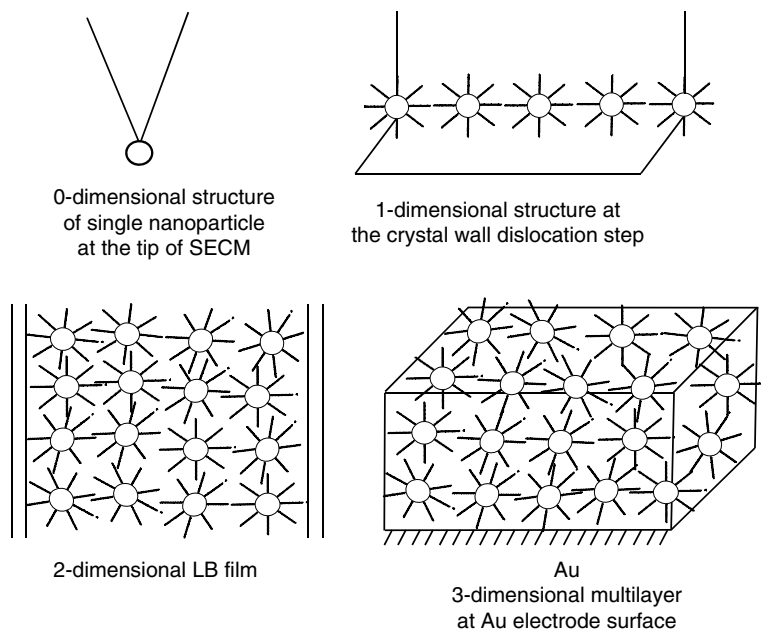


Fig. 7 Schematic presentation of zero-, one-, two-, and three-dimensional structures of organic monolayer-stabilized metallic nanoparticles

The preparation and isolation of individual nanoparticles is also challenging. However, these studies remain advantageous. Unlike surfaces covered with multiple species, single nanoparticles have no size or shape distribution. Their electrochemical responses are also unaffected by any interparticle charge transfer process. The effects of material density and the distance between nanoparticles can also be omitted. The nanoparticle's electrochemical properties are determined with a reversible redox probe. The transport to a nanoparticle's surface is described by the equation used for spherical diffusion under potentiostatic steady-state conditions because the nanoparticle is spherical. The limiting current is expressed by the following equation:

$$i_{\text{lim}} = \frac{nFA_{\text{CLU}}DC^*}{r} \quad (6)$$

where D is diffusion coefficient of the reactant, C^* is the reactant concentration in solution, A_{CLU} is the nanoparticle's surface area, and r is the nanoparticle's radius.

Tel-Vered and Bard proposed three approaches for generating a single nanoparticle on a large support [41], as illustrated in Fig. 8. For controlled deposition of nanoparticles with a low surface density (Fig. 8a), the following procedures can be applied [41]: (i) nanoparticle deposition on a surface with minimal defects, (ii) nanoparticle formation from a dilute solution, and (iii) deposition in a diffusion-controlled overpotential region to increase the effect of the nucleation exclusion zones around the growing nucleation sites.

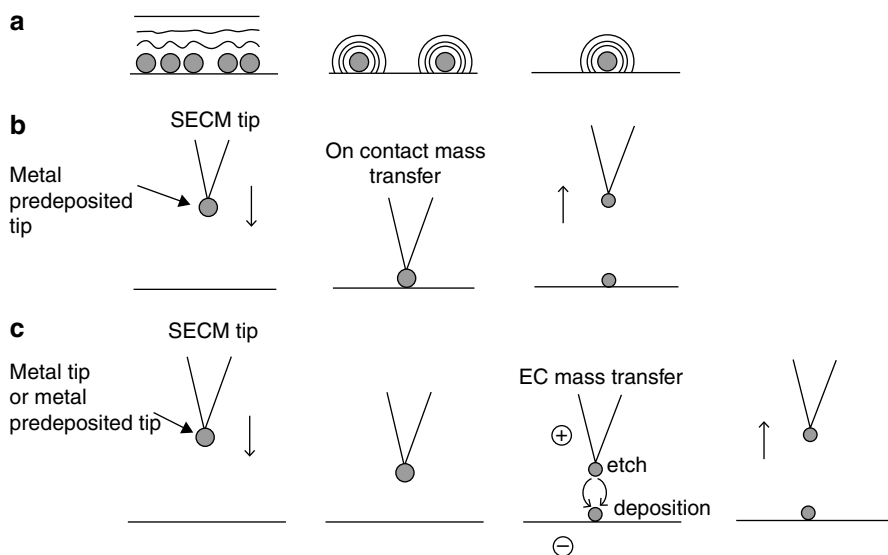


Fig. 8 Schematic presentation of different techniques of (a) well-spaced nanoparticles at HOPG and (b and c) single nanoparticles at the SECM tip (Reproduced from Ref. [41] with permission from American Chemical Society)

All of these approaches require a very short deposition time. The time needed to transition from spherical to planar diffusion (t_d) is given by the following equation [41]:

$$t_d = \frac{R^2}{2D} \quad (7)$$

where R is half the distance between the closest neighboring nanoparticles and D is the diffusion coefficient of the redox reactant (mediator species in the case of SECM) in solution.

In the approaches presented in Fig. 8b and c, a SECM tip with extra material deposited on the end was used to form single nanoparticles. During the contact procedure, the substrate was mechanically crushed by the sharp microtip, generating small nanoparticles. During the procedure to anodize the material on the tip (Fig. 8c), the problematic multinanoparticle deposition was reduced by closing the electrode gap between the tip and the substrate or using smaller tips. This method is particularly favorable for metals that undergo electrochemical etching rapidly. Figure 9 displays the SEM image of a tip with nickel nanoparticles that have radii of 60 ± 10 nm produced via potentiostatic pulse deposition from a Ni (II) solution [41]. A similar method was applied to produce palladium nanoparticles.

The electrochemical detection of single nanoparticles has several prerequisites [41]. Tiny particles require electrocatalytic processes for detection to amplify the current signal. Under these conditions, the nanoparticle should be stable. The catalytic current from a single platinum nanoparticle was tested during hydrogen evolution, oxygen reduction, and $\text{Fe}^{2+}/\text{Fe}^{3+}$ redox processes. The gas evolution reactions

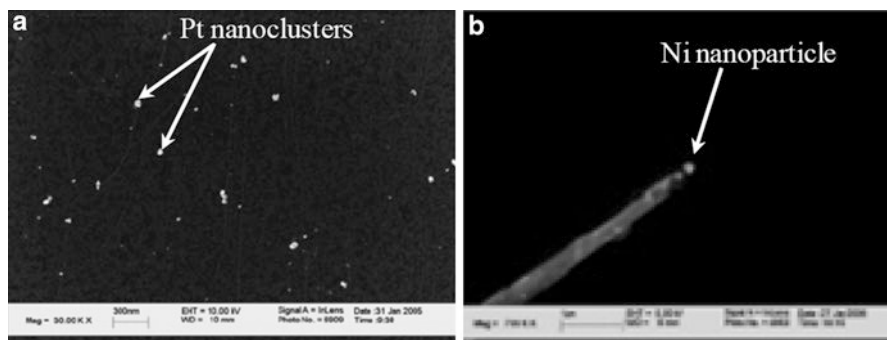


Fig. 9 (a) SEM image of well-separated nickel nanoparticles at HOPG and (b) TEM image of single nickel nanoparticle 60 nm in diameter at carbon fiber electrode tip (Adopted from Ref. [41] with permission from American Chemical Society)

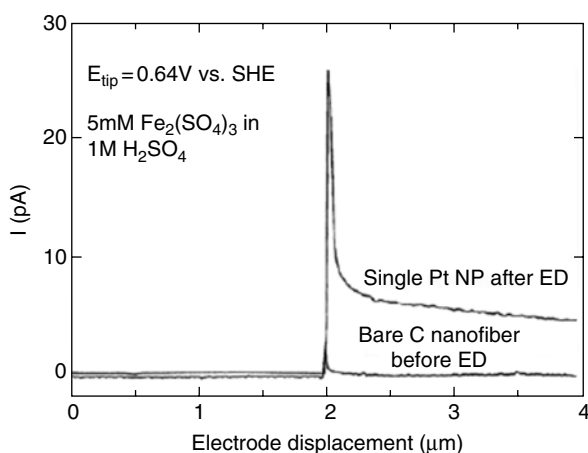


Fig. 10 Approach from air curves for carbon fiber electrode tip moving from air to solution of Fe^{3+} in H_2SO_4 before and after the deposition of a single Pt nanoparticle 60 nm in diameter (Reproduced from Ref. [41] with permission from American Chemical Society)

cause the rapid detachment of the nanoparticle from the tip. The current associated with oxygen reduction is similar to that of the other processes, such as underpotential metal deposition or hydrogen reduction, and is too small to use for measuring the nanoparticle's electrochemical properties. Fe^{3+} reduction was successfully used to detect single nanoparticles [41]. Figure 10 displays the amperometric response for the Fe^{3+} reduction at a carbon tip attached to a 60 nm single platinum nanoparticle. Significant magnification of the current is observed for the nanoparticle.

Single metallic nanoparticle charge transfer processes may also be examined using SECM of the nanoparticle monolayer deposited on a solid phase [42, 43]. In Fig. 11a, the tunneling current at an STM tip addresses individual gold Au_{146} core nanoparticles deposited on the mica substrate under ultrahigh vacuum [42].

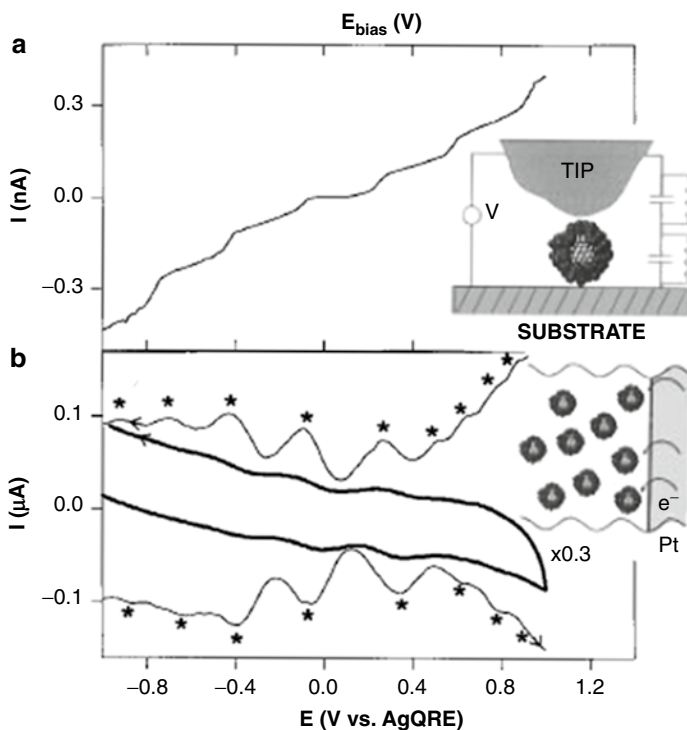


Fig. 11 (a) Schematic picture of STM tip addressing a single Au cluster (28 kDa) adsorbed on mica substrate and Coulomb staircase I–V response at 83 K. (b) Cyclic voltammetry at 100 mV/s and differential pulse voltammogram at 10 mV/s and 25 mV pulse for negative (*top*) and positive (*bottom*) scan recorded in acetonitrile/toluene (2:1) containing 0.1 mM 28 kDa Au clusters and 0.5 M (*n*-Hx)₄NClO₄ (Reproduced from Ref. [42] with permission from American Chemical Society)

The current steps separated at regular intervals of 0.34 V, representing single-electron changes in the metallic core. Based on the equivalent circuit presented in Fig. 11a, a capacitance of 0.59 and 0.48 aF was calculated for the tip/nanoparticle and nanoparticle/substrate junctions, respectively. Quantized charging voltammograms (CV and DPV) of Au nanoparticles with 2.2 nm cores stabilized with hexanethiolate/ ω -ferrocenylhexanethiolate groups were dispersed in toluene/acetonitrile (2:1) and are shown in Fig. 11b. The DPVs qualitatively mirror the I–V response of the STM experiment. The 0.40 V peak-to-peak potential separation corresponds to the 0.40 aF/cluster capacitance. This value is similar to the capacitance obtained from the STM measurements.

Quantized Effects in the Nanoparticles Thin Films Charging Processes

Similar to the electrochemical behavior of metallic nanoparticles in solution, the quantized electron exchange effect may be observed for processes involving two- and three-dimensional films of metallic nanoparticles [32–35, 44–50]. The voltammetric behavior of the self-assembled alkenethiolate-protected gold nanoparticle monolayer on a gold electrode is presented in Fig. 12 [49].

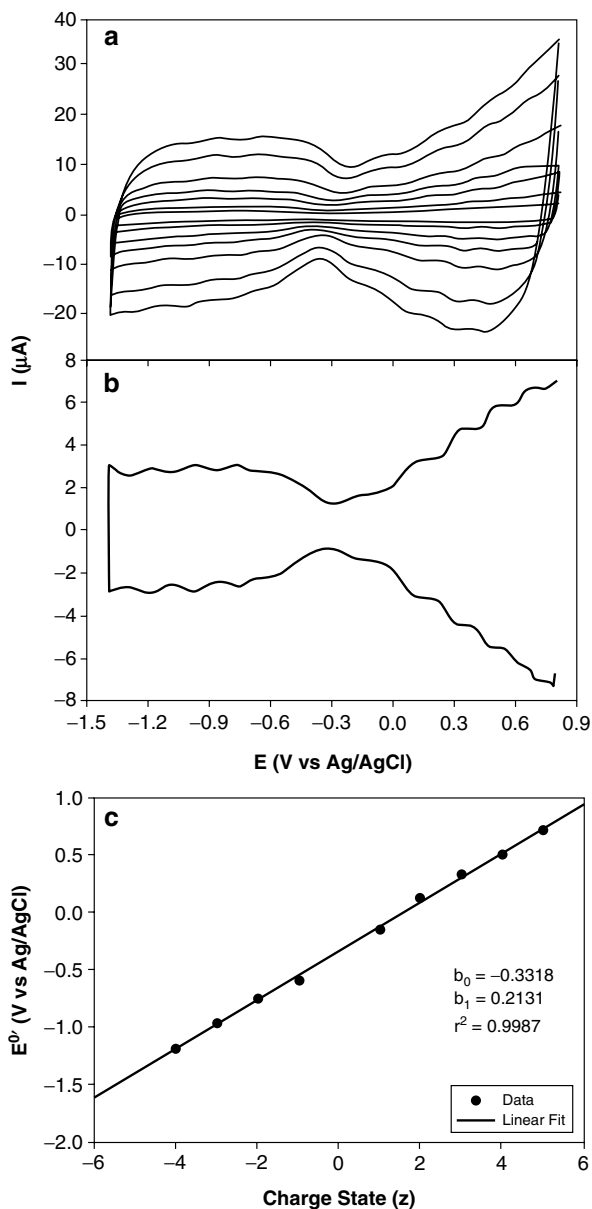


Fig. 12 (a) Cyclic voltammograms at scan rate changed from 0.1 to 2 V/s and (b) differential pulse voltammograms at 10 mV/s and 50 mV pulse amplitude of AuSC₆ self-assembled monolayer at gold electrode surface in CH₂Cl₂ containing 0.1 M (*n*-Bt)₄NClO₄. (c) Dependence of the charging formal potentials on the nanocluster charge state (Reproduced from Ref. [49] with permission from American Chemical Society)

Many well-defined DPV peaks are observed within the studied potential range. Each Coulombic step represents the average charge on a nanoparticle generated by one electron. The formal redox potential (Eq. 4) is linearly dependent upon the particle's charge. From the slope and intercept of this function, the capacitance of the metallic particle and the zero charge potential can be estimated.

Pradhan and coworkers [43] studied the temperature's effect on single-electron transfer processes in $\text{Au}_{314}(\text{C}_6)_{91}$ monolayers. They observed that quantized charging occurs within a small temperature range. At temperatures below 280 K, the monolayer conductance decreases approximately four times. The temperature where this abrupt change occurs coincides with the AuC_6 nanoparticle solids' phase-transition temperature [43]. Below 280 K, the conductivity exhibits almost no temperature dependence, indicating that the monolayer is highly insulating.

Conductivity of a Thin Layer Formed from a Ligand-Stabilized Metal Nanoclusters

In nanoparticle-based solids, the conductivity depends on (i) the disorder caused by different particle cores' sizes and shapes, (ii) the distance between particles in the solid state, (iii) the degree of coupling between adjacent particles, and (iv) the Coulombic repulsion between electrons in each cluster. Highly disordered particle ensembles with large separations between particles protected by an organic layer diminish the interparticle electronic coupling. Consequently, the electronic wave function is localized on each individual nanoparticle, generating a large Coulombic barrier for charge migration.

Two-dimensional nanoparticle structures can be formed using the Langmuir-Blodgett technique. The electrochemical properties of these systems can be probed using scanning electrochemical microscopy [51–53]. In a condensed system composed of organic monolayer-stabilized metallic nanoparticles, a tunneling electron hops through a conductivity barrier formed by the organic monolayer. The SECM tip is immersed in a solution containing an electroactive mediator (Fig. 13). When the tip approaches the nanoparticle film, the current increases or decreases are observed, depending on the film's conductivity. Figure 14 presents the current changes during the approach toward a film of hexanethiol-encased silver nanoparticles at different surface pressures [52]. At low pressures (large distances between nanoparticles), the film behaves as an insulator (negative feedback) due to the large Coulombic gap. After compression, the interparticle distance decreases until the Coulombic gap is closed, generating a conductive film (positive feedback). The collective electronic wave function of the individual nanocrystals overlaps and hybridizes with the wave function of neighboring nanoparticles. The critical distance (δ) can be established from the equation:

$$\delta = \frac{D}{zr} \quad (8)$$

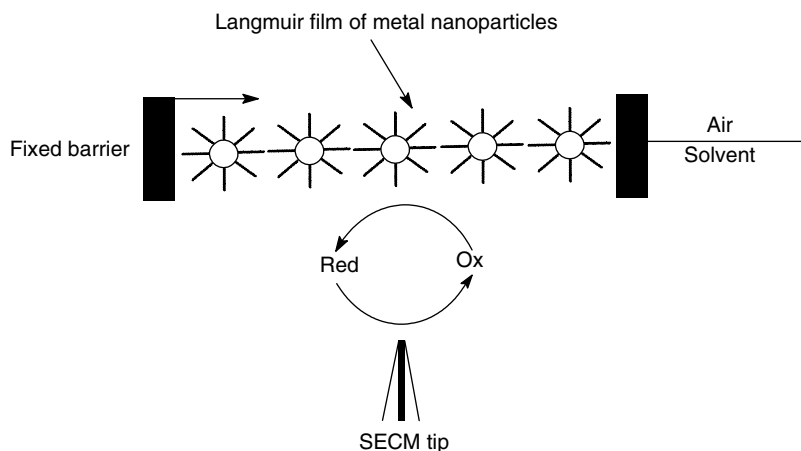


Fig. 13 Schematic presentation of conductivity measurements at an inverted SECM tip on compressing Langmuir film of metallic nanoparticles

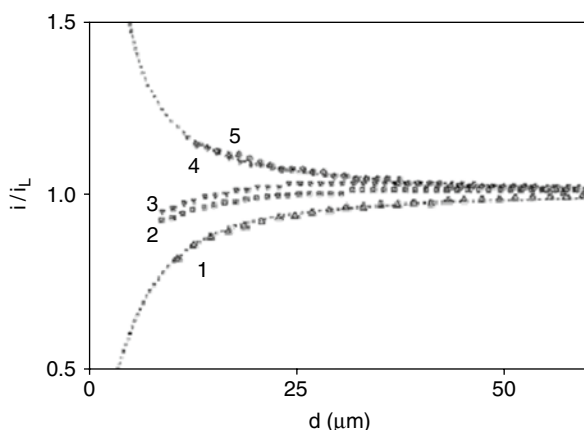


Fig. 14 SECM approach curves to the Ag nanoparticles film at various compressions: (1) open barrier position -0 mN/m, (2) 11 mN/m, (3) 22 mN/m, (4) 42 mN/m, and (5) 56 mN/m. Dotted lines represent the theoretical approach curves to an insulator (lower) and conductor (upper) (Reproduced from Ref. [52] with permission from American Chemical Society)

Similar measurements were performed on gold nanoparticle monolayers deposited on silanized glass slides [51]. The effects of core size, thickness, and the density of the protective alkynethiolate layer were examined. The influence of these parameters on the two-dimensional film conductivity is displayed in Fig. 15. The conductivity decreases with decreases in nanoparticle size. The films of particles protected with longer alkyl chains exhibit lower conductivity.

When studying the conductivity of three-dimensional structures, interdigitated array electrodes are usually used (Fig. 16) [50, 54–56]; nanoparticle films are

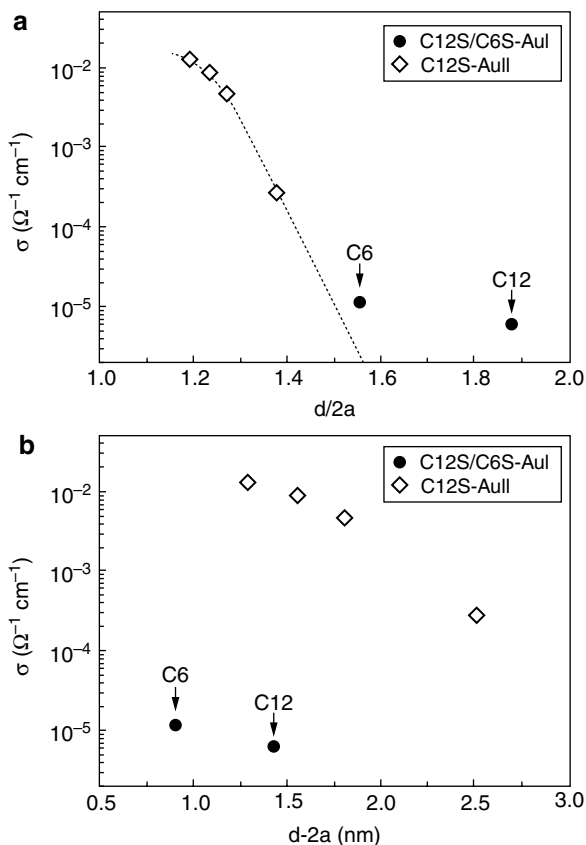


Fig. 15 Conductivity of AuSC6/SC12 and AuSC12 nanoparticles films as a function of (a) the center-to-center distance, d , scaled by the particle diameter $2a$ and (b) the core-to-core distance, $d-2a$ (Reproduced from Ref. [51] with permission from American Chemical Society)

deposited between the interdigitated arrays. Low current and voltage probes are connected to one pad of the interdigitated electrode, while high current and voltage probes are connected to the other pad. The nanocrystal array electronic conductivity (σ_{EL}) is expressed as follows:

$$\sigma_{EL} = \frac{\Delta i}{A \Delta E} \quad (9)$$

where ΔE is the difference in applied potential and Δi is the current flowing between electrodes.

Doty et al. [54] used interdigitated microelectrode arrays to study the conductivity of silver nanocrystals. Two types of nanoparticles were used: size-polydispersed and size-monodispersed samples with different particle diameters. There is a striking qualitative difference between the conductivity temperature dependencies for size-polydisperse and size-monodisperse nanocrystals (Fig. 17).

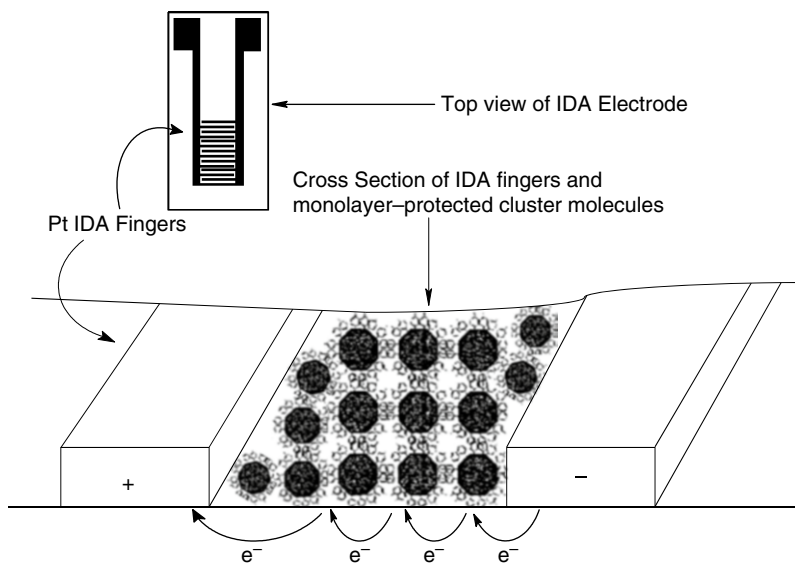


Fig. 16 Schematic presentation of conductivity of metallic nanoparticles film with an interdigitated arrays (IDA) electrode

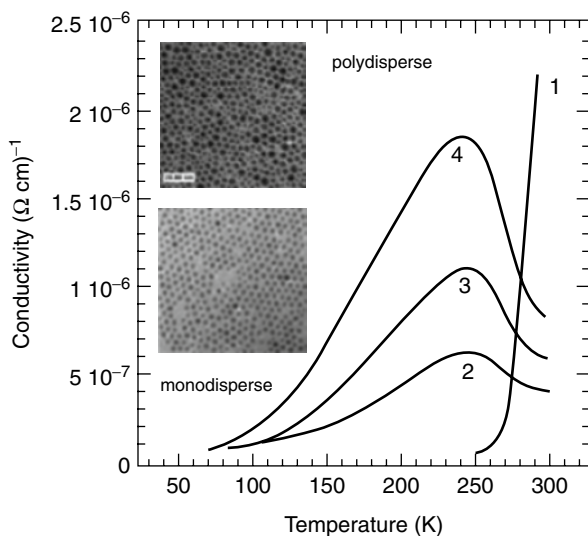


Fig. 17 Dependence of the conductivity on the silver nanocrystals size: (1) size-polydisperse sample, (2) 5.5 nm monodisperse sample, (3) 4.8 nm monodisperse sample, and (4) 4.5 nm monodisperse sample (Adopted from Ref. [54] with permission from American Chemical Society)

Table 1 Conductivity parameters the metal–insulator transition temperature for polydisperse and monodisperse silver crystals with different core sizes (Adopted from Ref. [54] with permission from American Chemical Society)

Nanocrystals	Diameter	T_{MI}	σ_{RL} at T_{MI}	Conductance exponent, ν	Activation energy, E_a
	nm	K	$10^{-6}\Omega^{-1}$		eV
Polydisperse					1.5
	7.7	225	0.47	0.67	0.038
	5.5	241	1.8	1.22	0.069
Monodisperse	4.8	244.5	1.1	1.34	0.079
	4.2	245	0.63	1.35	0.080
	3.5	245	0.98	1.34	0.098

The size-polydisperse crystals behave as typical insulators. The conductivity drops off abruptly with decreasing temperature. The amount of disorder in the system causes the width of the energy barrier to increase. The site-to-site function also causes an absence of translational order in the polydisperse nanocrystal arrays, providing additional perturbation in electron transfer. For size-monodisperse samples, simple transition between metal and insulator behavior at temperature T_{MI} (Fig. 17) is observed. However, the conductivity values of the silver macrocrystals are several times lower relative to the silver nanocrystals. The exchange coupling between nanocrystals is not sufficient for true metallic behavior. The polarons formed during the electron–proton coupling are responsible for the metal–insulator transition at temperature T_{MI} . Below T_{MI} , the carrier concentration is lower than what is required for polaron gas formation, causing the insulator behavior. Above T_{MI} , the polarons form gas and can be transported through the nanocrystal lattice. Lattice vibrations are responsible for the increased polaron mobility and higher conductivity. In larger particles with lower Coulombic blockade energies, the carriers are more easily promoted and T_{MI} decreases. In Table 1, the conductivity parameters of polydisperse and monodisperse films of different sizes are compared.

Figure 18 shows the alkanethiolate chain length affecting the electronic conductivity of the $\text{Au}_{309}(\text{C}_n)_{92}$ particles via Arrhenius plots. These plots are described by the following relationship [55]:

$$\sigma_{EL}(n, T) = \sigma_0 \exp[-n\beta_n] \exp\left[-\frac{E_a}{RT}\right] \quad (10)$$

where n is the number of carbon atoms in alkanethiol chain, β_n – the electronic coupling term, E_a is the activation energy of conductivity, and $\sigma_0 \exp(-n\beta_n)$ is the electric conductivity at an infinite temperature. The linear relationships between the logarithm of conductivity and the number of carbon atoms in the alkanethiol obtained at different temperatures are presented in Fig. 19. In Table 2, the E_a values calculated from the slope of the $\log \sigma_{EL} - 1/T$ functions for different alkanethiol ligands are collected.

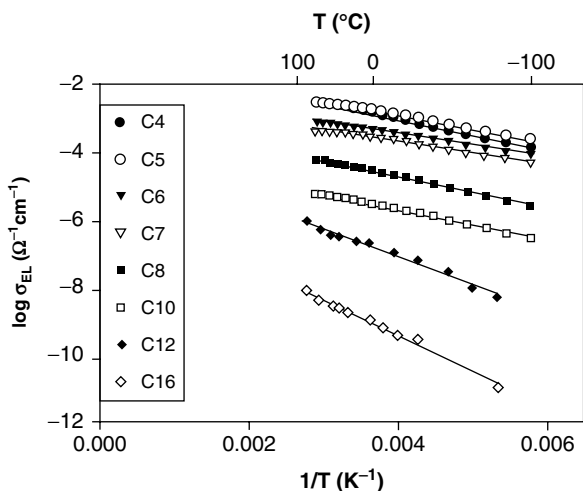


Fig. 18 Arrhenius plots of electric conductivity of series of $\text{Au}_{309}(\text{SCn})_{92}$ nanoparticle films with varying alkanethiolate chain lengths (Reproduced from Ref. [55] with permission from American Chemical Society)

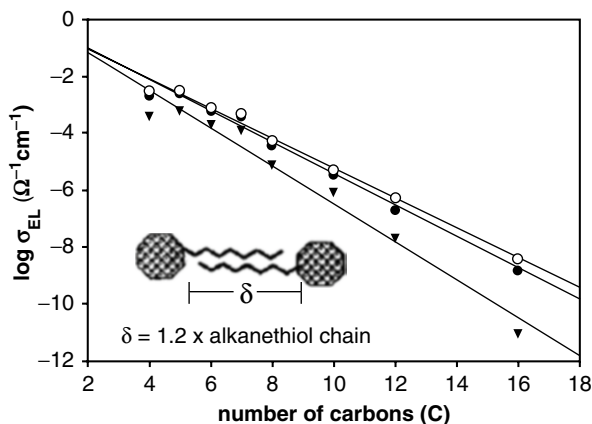


Fig. 19 Plots of conductivity versus number of carbon atoms in the alkanethiolate chains of $\text{Au}_{309}(\text{SCn})_{92}$ nanoparticle films at (1) 70 °C, (2) 30 °C, and (3) -60 °C. The inset is a schematic describing interdigitation of monolayer chains in the solid-state nanoparticle films (Reproduced from Ref. [55] with permission from American Chemical Society)

The activation energy can be predicted based on Marcus theory [57, 58]. The free energy of activation for the electron exchange between two neighboring gold clusters can be calculated according to the following equation:

$$\Delta G^* = \frac{1}{\lambda} = \frac{e^2}{16\pi\epsilon_0} \left(\frac{1}{2r_{\text{CLU}}^1} + \frac{1}{2r_{\text{CLU}}^2} - \frac{1}{\delta^*} \right) \left(\frac{1}{\epsilon_{0p}} - \frac{1}{\epsilon_s} \right) \quad (11)$$

Table 2 Activation energies for conductivity of Au₃₀₉(SCn)₉₂ thin films (Adopted from Ref. [55] with permission from American Chemical Society)

Au ₃₀₉ (Cn) ₉₂ alkanethiolate (carbon units)	E _A , Arrhenius plots	Caled E _A , Marcus theory	Caled E _{A GM} granular model
	kJ/mol ^a	kJ/mol ^b	kJ/mol ^c
C16	19.0	5.4	14.6
C12	16.0	5.2	13.2
C10	8.8	5.0	12.3
C8	9.1	4.8	11.1
C7	6.6	4.7	10.4
C6	6.5	4.6	9.6
C5	7.5	4.5	8.8
C4	9.2	4.4	7.7

^aActivation energy from Arrhenius plots (ln σ_{EL} vs 1/T)

^bCalculated by Eq. 11. Chain lengths used for alkanethiolate ligands were calculated by HyperChem software. C16=2.02 nm, C12=1.52 nm, C10=1.27 nm, C8=1.02 nm, C7=0.90 nm, C6=0.77 nm, C5=0.65 nm, and C4=0.52 nm. Chain interdigitation was taken into account for all calculations

^cCalculated by Eq. 12

where λ is the outer-sphere reorganization energy, r_{CLU}^1 and r_{CLU}^2 are the radii of two neighboring metal nanoparticles, δ^* is the center-to-center distance, and ϵ_{op} and ϵ_s are the solvent optical and static dielectric constants, respectively. For symmetrical self-exchange reactions, the entropic activation factor equals zero and ΔG^* equals E_a .

The conductivity of metal nanoparticles may also be described using the granular metal conductivity model [59, 60]. In this model, the activation energy of conductivity is described by the following equation:

$$E_a = -\frac{e^2 \left[\frac{1}{r} - \frac{1}{r + \delta} \right]}{4\pi\epsilon_0\epsilon} \quad (12)$$

where δ is the core-to-core distance (Fig. 19) and ϵ is the dielectric constant of the intervening medium.

Theoretical activation energy values for the conductivity of Au₃₀₉(C_n)₉₂ three-dimensional films are presented in Table 3. Marcus theory predicts slightly lower E_a values than observed experimentally. Values calculated based on the granular metal conductivity model are larger and closer to the experimentally obtained E_a values. However, a large discrepancy between the theoretical or experimental values is still observed.

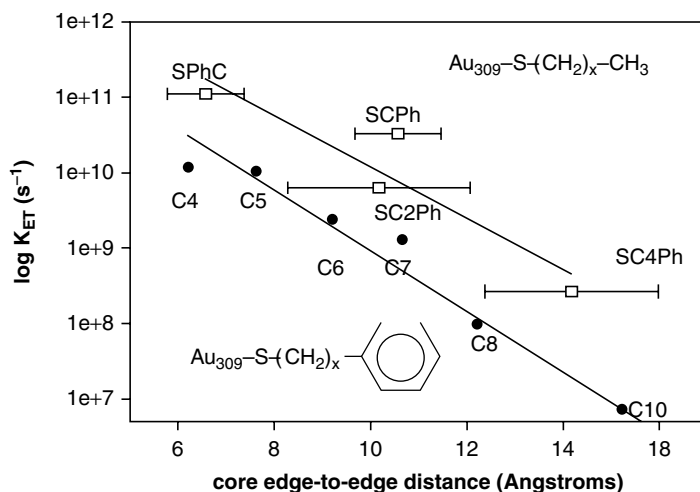
Charge Transfer in Two- and Three-Dimensional Layer of Nanoparticles

The electronic mixed-valence hypothesis may explain the charge transfer process in metallic nanoparticle (MNP) networks. For uncharged nanoparticle films, the charge carriers are generated thermally through a disproportionation reaction:



Table 3 Activation energy and conductivity data arenethiolate protected Au nanoparticle films (Adopted from Ref. [61] with permission from American Chemical Society)

	E_A , Arrhenius	E_A , calcd	σ_{EL} (30 °C)	k_{ET} -cubic lattice
CLU	kJ/mol	kJ/mol ^a ($\epsilon_s = 3.9$)	$\Omega^{-1} \text{ cm}^{-1}$	s^{-1} ^b
$\text{Au}_{309}(\text{S}(\text{CH}_2)_4\text{C}_6\text{H}_5)_{143}$	4.1 ± 0.4	4.1	1.5×10^{-4}	$2.6(\pm 0.3) \times 10^8$
$\text{Au}_{309}(\text{S}(\text{CH}_2)_2\text{C}_6\text{H}_5)_{98}$	8.8 ± 0.2	3.9	2.6×10^{-3}	$6.1(\pm 1.1) \times 10^9$
$\text{Au}_{976}(\text{SCH}_2\text{C}_6\text{H}_5)_{363}$	6.2 ± 0.6	2.7	7.2×10^{-3}	$3.3(\pm 0.3) \times 10^{10}$
$\text{Au}_{309}(\text{SC}_6\text{H}_4\text{CH}_3)_{363}$	5.7 ± 0.2	2.6	1.3×10^{-2}	$1.1(\pm 0.1) \times 10^{11}$

^aCalculated from Eq. 11^bCalculated from Eq. 15 using the σ_{EL} value**Fig. 20** Dependence of electron exchange rate constant, k_{ET} , on the core-to-core distance for arenethiolate and alkanethiolate Au_{309} nanoparticle films (Reproduced from Ref. [61] with permission from American Chemical Society)

The charge is transferred between nanoparticles according to the self-exchange reaction:



The protecting thiolate monolayer forms the potential barrier for the electron transfer. First-order electron-hopping rate constant (k_{ET}) is related to the conductivity through the equation [61]:

$$k_{ET} = \frac{6RT\sigma_{EL}}{10^{-3} F^2 \delta^2 C_{exp}} \quad (15)$$

The linear correlation between $\ln k_{ET}$ and the core-to-core distance is presented in Fig. 20 [61]. In Fig. 21, the linear relationships of $\ln k_{ET} - n'$ and $\lg \delta - n'$ (n' is the number of carbon units between the aromatic components and the thiolate center) are

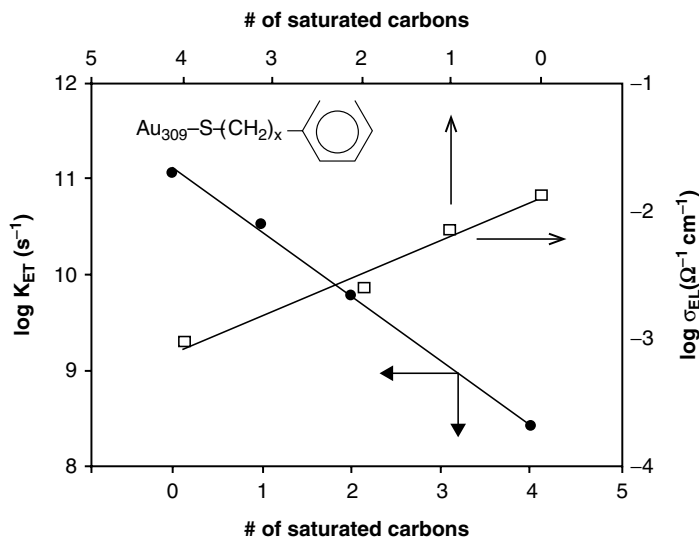


Fig. 21 Dependence of electron exchange rate constant, k_{ET} , and the conductivity, σ , on the number of saturated carbon units between the aromatic component and the thiolate center for Au_{309} nanoparticle films (Reproduced from Ref. [61] with permission from American Chemical Society)

displayed [61]. The conductivity values and kinetic parameters of the electron hopping between gold alkanethiolate-protected nanoparticles are collected in Table 3.

The rate of electron exchange depends on the nanoparticle size. For example, the conductivity of a $\text{Au}_{25}(\text{SC}_2\text{Ph})_{18}$ nanoparticle film is 10^{-3} -fold in lower relative to the alkanethiolate-protected Au_{140} . This behavior may be because the inner-sphere energy barrier controls the electron transfer processes due to the structural changes in $\text{Au}-\text{SC}_2\text{Ph}$.

Charge transfer processes within three-dimensional metallic nanoparticle film may also be investigated in solutions containing redox pairs (Fig. 22). Nanoparticles in these films may remain unlinked [33, 47, 48, 62, 63] or linked together [34, 44, 64] with covalent or electrostatic interactions, as illustrated in Fig. 22b. In these systems, the electron-hopping mechanism also describes the charge transfer process. The changed electrode potentials alter the Fermi level potentials of the nanoparticles, corresponding to the metallic core's charge state. The charge carriers (electron or holes) propagate from the electrode–nanoparticle interface into the bulk of the metallic nanoparticle film until the entire film equilibrates with the applied potential. The film charging process may force the electron exchange reaction to occur with the redox couple in solution or by supporting the transfer of electrolyte ions into the layer, balancing the film's charge.

In Fig. 23, the voltammetric behavior of a $\text{Au}_{140}(\text{MUA})_{20}(\text{C}_6)_{33}$ multilayer with $(n\text{-Bu})_4\text{NPF}_6$ in dichloromethane is illustrated [44]. The gold nanoparticles are bound together via carboxylate–zinc (II) ion–carboxylate bridges. The sequence of the voltammetric peaks corresponds to the successive charging of the gold

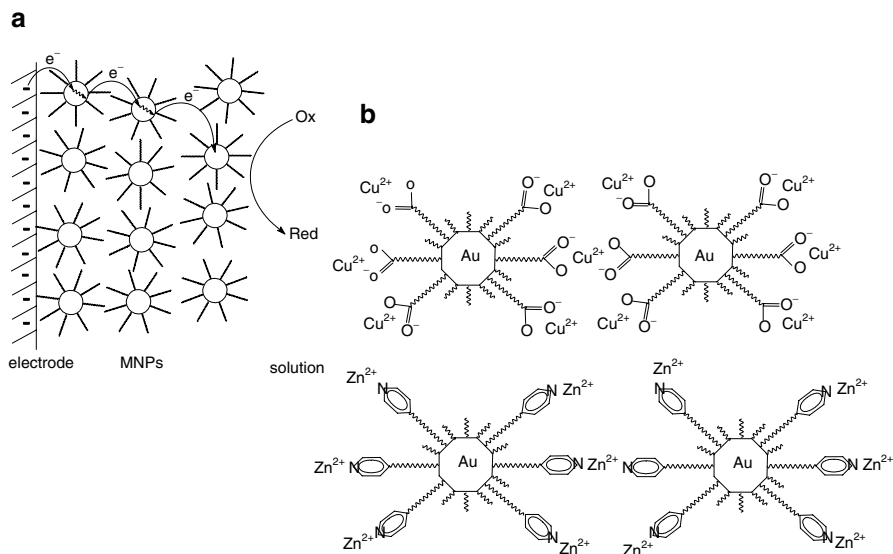


Fig. 22 (a) Schematic presentation of electron transfer through thin film of metallic nanoparticles in solution containing redox couple and (b) examples of nanoparticles bounding in the film

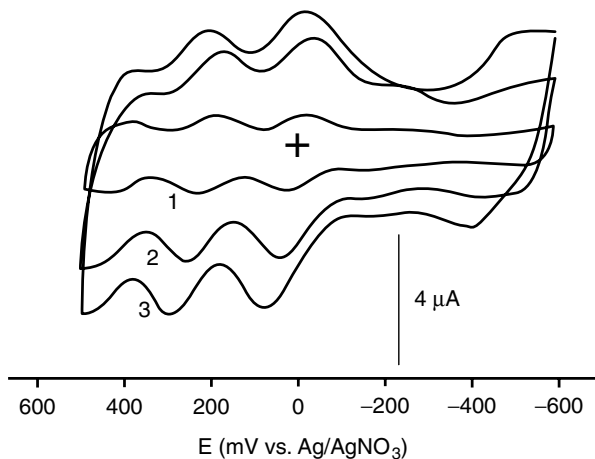


Fig. 23 Cyclic voltammograms of Au₁₄₀(MUA)₂₀(SC6)₃₃ film of different thicknesses of (1) 16 monolayers, (2) 31 monolayers, and (3) 55 monolayers in CH₂Cl₂ containing 0.1 M (*n*-Bt)₄NPF₆ at 50 mV/s (Reproduced from Ref. [44] with permission from American Chemical Society)

nanoparticle film. For gold nanoparticles with a cubic lattice, the rate constant for electron hopping is expressed as a first- (k_{HOP}) or second-order process (k_{ex}); the reaction order is determined using the electron diffusion coefficient D_E :

$$D_E = \frac{k_{\text{HOP}}\delta^2}{6} = \frac{k_{\text{ex}}\delta^2 C_{np}}{\delta} \quad (16)$$

where C is the concentration of nanoparticles in the film. A k_{HOP} value near 10^6 s^{-1} was obtained from chronoamperometric measurements. This value significantly exceeded the rapid electron-hopping rate that would have been measured for redox polymerization [65] or ferrocene-to-metal electron transfer reactions measured in gold nanoclusters stabilized by ferrocene alkanethiolates [66, 67].

Charge Transfer in Thin Films Composed of Carbon Nanomaterials

Carbon nanostructures form a relatively large structural family. Graphene is the youngest member of this family and is the basic unit of all other members. The most important structures are the carbon nano-onions and nanotubes displayed in Fig. 24 [68]. Other less important structures include bamboo-shaped nanotubes, nanohorns, nanorods, nanocones, nanocups, nanoribbons, and others.

Capacitance and Charge Transfer Properties of Carbon Nanotubes

Carbon nanotubes exist as single-wall (SWCNTs) and multiwall (MWCNTs) nanotubes. MWCNTs are composed of coaxial nanotube cylinders of different helicities typically spaced ca. 0.34 nm apart. These adjacent layers exhibit usually different chirality properties and a very small interlayer electronic interaction. In these structures, charge transfers occur through the outer nanotube cylinder under flowing current [69] with only a minor contribution from inter-tube coupling [70]. Therefore, MWCNTs are pseudo-1D-conductors [5].

The electronic structure and conductivity properties of SWCNTs depend on the atoms arranged in the hexagonal lattice [7, 71–73]. Carbon atoms covalently bonded to three neighbor carbons via sp^2 molecular orbitals form graphene sheets. A carbon nanotube is a rolled-up graphene sheet that forms a concentric cylinder. The chiral vector is expressed as follows (Fig. 25a):

$$C_h = na_1 + ma_2 \quad (17)$$

This expression describes how graphene is wrapped to form a nanotube. The n and m integrals in Eq. 17 indicate the number of steps along the zigzag carbon atoms in the hexagonal lattice, while a_1 and a_2 are the unit vectors. The electrical properties of CNTs are structurally related and depend on how the graphene sheet is rolled [7, 71–73]. When $n-m=3z$ (where z is integer) or $n=m$ (the armchair structure), the CNT exhibits metallic properties. In all other cases, the CNT demonstrates nonmetallic/semiconducting behavior. In Fig. 25b and c, the density state

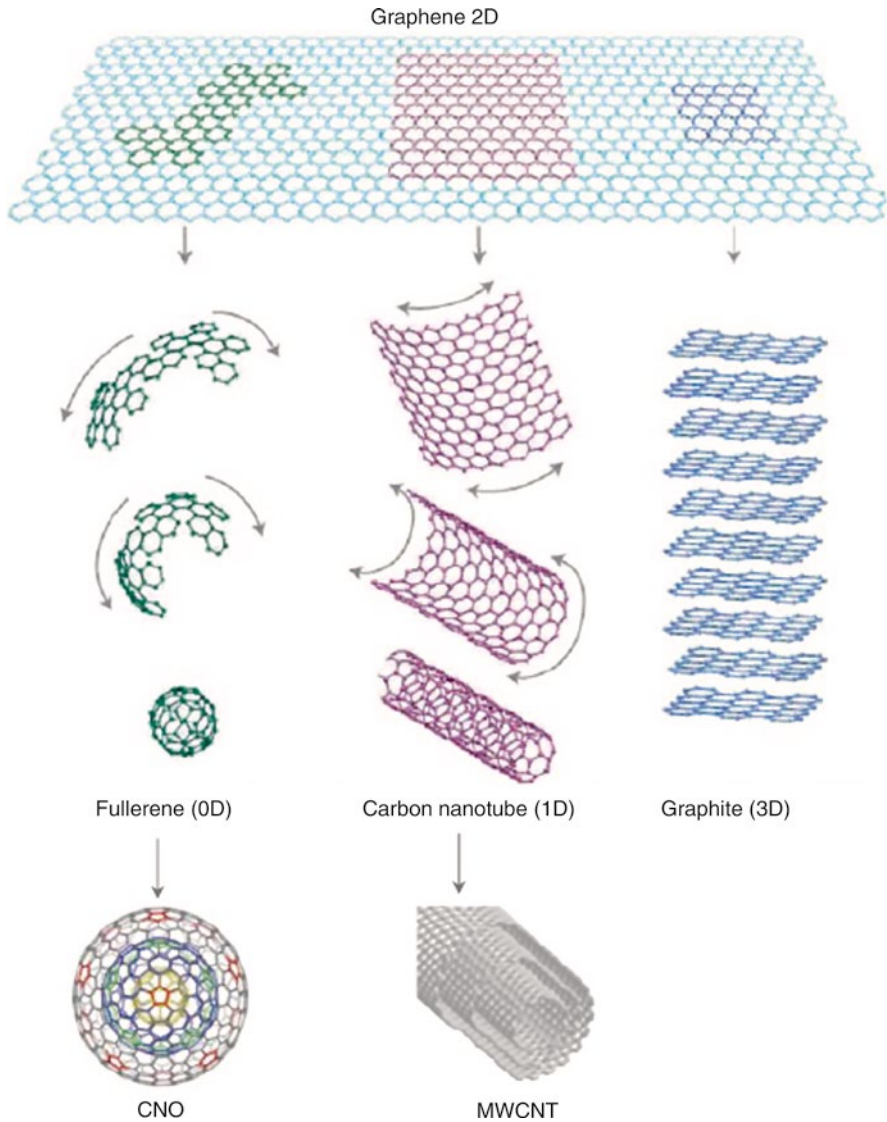


Fig. 24 Graphene as the basic unit of fullerenes, single- and multiwalled carbon nanotubes, nano-onions, and graphite (Adopted from Ref. [68] with permission from Nature Publishing Group)

distribution as a fraction of energy is shown for armchair (5, 5) and zigzag (7, 0) nanotubes. In the first case, there is finite value for the charge carriers at the Fermi energy level at zero. No charge carriers are expected at the Fermi energy level for a zigzag (7, 0) single-wall nanotube.

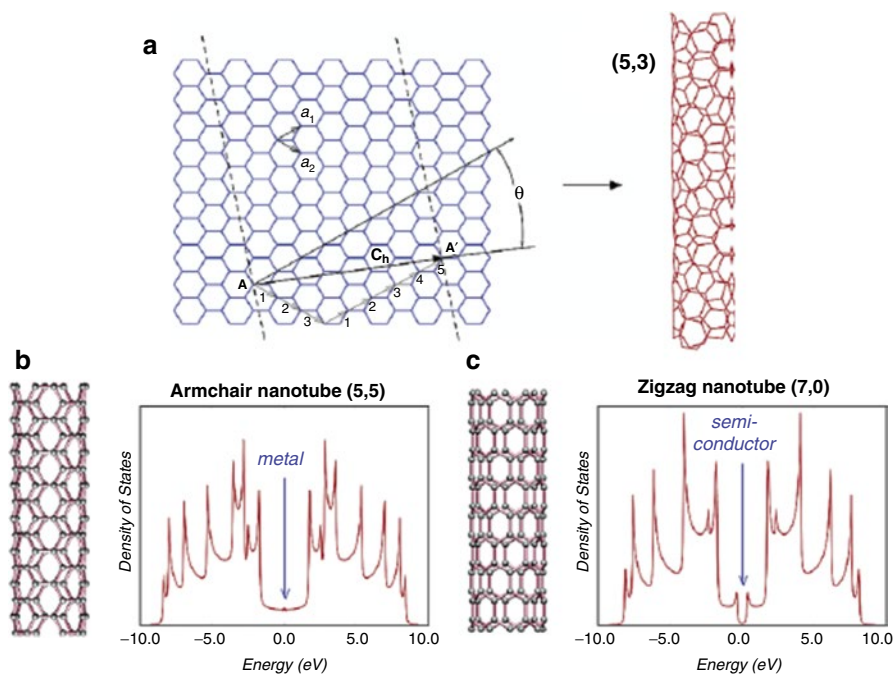


Fig. 25 (a) Schematic diagram showing the possible wrapping of two-dimensional graphene sheet into tubular form. In this example, a (5, 3) nanotube is under construction, and the resulting tube is illustrated on the right. (b) Electronic structure of metallic *armchair* (5, 5) nanotube. (c) Electronic structure of semiconducting *zigzag* (7, 0) nanotube (Reproduced from Ref. [7] with permission from American Chemical Society)

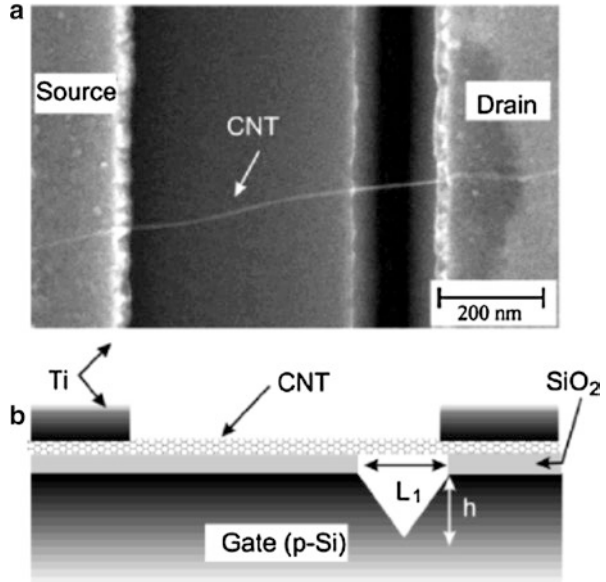
The energy gap between the conducting and valence levels depends on the nanotube diameter:

$$E_{\text{gap}} = \frac{2\gamma_0 a_{c-c}}{d} \quad (18)$$

where γ_0 denotes the tight C–C binding overlap energy (2.45 eV), a_{c-c} is the nearest neighboring C–C distance (~ 1.42 Å), and d is the diameter of the nanotube.

Since 1997, when the first charge transfer measurements were reported for nanotubes devices [74–77], many papers have been published on the conductivity and charge transfer behaviors of CNTs [78–85]. The simple three-terminal device present in Fig. 26 was used most frequently for these studies [76, 86–88]. The nanotube is aligned between two metallic electrodes (source and drain) on an oxidized silicon wafer. Subsequently, experiments are typically carried out with three terminals, utilizing a silicon wafer as a buck gate.

Fig. 26 (a) SEM image of gated CNT and (b) schematic of the device cross section (Reproduced from Ref. [86] with permission from American Chemical Society)



If the coherence effect is neglected, the total resistance is a sum of the nanotube resistance R_{CNT} and the resistance of a metal–CNT connection:

$$R = R_{CNT} + R_{contact} \tag{19}$$

Intrinsic nanotube resistance can be expressed using the following equation:

$$R_{CNT} = \frac{h}{4e^2} \frac{L}{l} \tag{20}$$

where L is the tube length and l is the electron mean-free path for momentum relaxation ($L \gg l$). The contact resistance depends on the Schottky behavior at the metal/nanotube interface.

In Fig. 27 the current–voltage curves generated as a function of the gate voltage V_{gate} are presented. The carrier mobility (μ) is related to the measured conductance (G) [89]:

$$G = \frac{C_{g'}(V_g - V_{go})\mu}{L} \tag{21}$$

where $C_{g'}$ is the capacitance of the CNT per length L and V_{go} is the trans hold voltage.

At low temperatures, the nonlinear transport behavior related to a quantized effect can be observed. This behavior is similar to the behavior of metallic

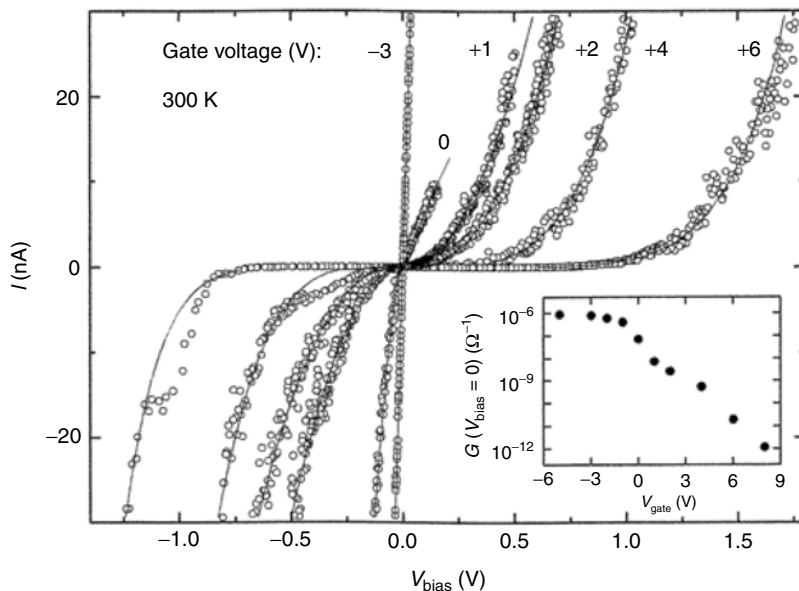


Fig. 27 Room temperature current–voltage traces measured in vacuum for a nanotube device at a series of gate voltages (V_g). *Inset* shows small-signal conductance (s) vs. V_g (Adopted from Ref. [76] with permission from Nature Publishing Group)

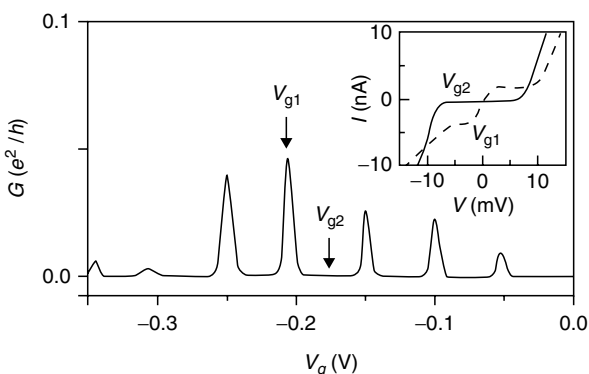


Fig. 28 Conductivity–gate voltage trace for nanotube transistor device at 4.2 K showing a series of Coulomb blockade peaks. *Inset* shows current–voltage characteristics taken at the center of CB peak (V_{g1}) and in between peaks (V_{g2}) (Reproduced from Ref. [90] with permission from Springer-Verlag)

nanoparticles when $k_B T < E_F$. The addition of each electron to the array exhibits a very small capacitance ($\sim 10^{-18}$ F), resulting in a large increase in charging energy ($e^2/2C$). The conductance peaks that correspond to the addition of each electron to the CNT are observed as a function of the gate voltage (Fig. 28) [90].

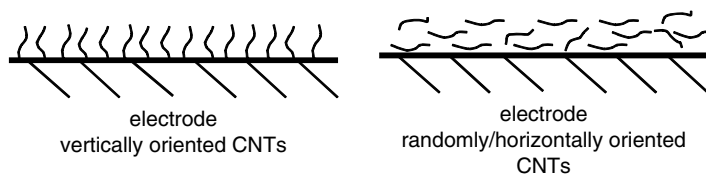


Fig. 29 Schematic representation of nanotubes orientation at the electrode surface

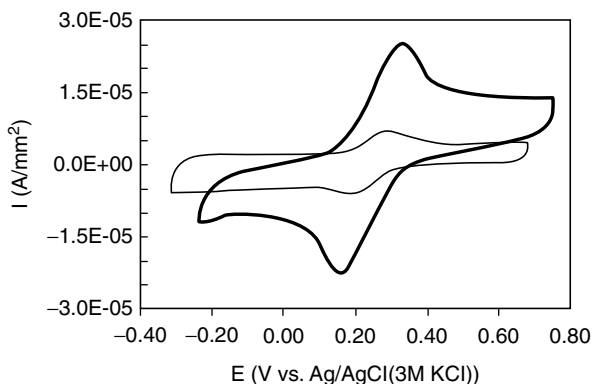


Fig. 30 Cyclic voltammograms of $\text{Fe}(\text{CN})_6^{3-} / \text{Fe}(\text{CN})_6^{4-}$ redox couple at a multiwalled (thick line) and single-walled (thin line) carbon nanotube-modified electrode in aqueous solution containing 5 mM $\text{K}_3\text{Fe}(\text{CN})_6$ and 0.1 M KCl at 20 mV/s. Current was normalized to the geometric surface area (Reproduced from Ref. [91] with permission from American Chemical Society)

The electrochemical properties of carbon nanotubes may be studied in the different configurations [91–96]. Two of the most common orientations are displayed schematically in Fig. 29. The vertical orientation (Fig. 30b) was achieved using specially designed substrates for nanotube deposition [97–100], gas flow [101], or dc-current electric field [102, 103].

The redox pair in solution may also be used to benchmark the electron transfer properties of the nanotube films [91–96, 104]. Representative results obtained for a $\text{Fe}(\text{CN})_6^{3-/4-}$ redox couple at a GC electrode modified with SWCNTs and MWCNTs are displayed in Fig. 30 [91]. The normalized faradaic current increased for the $\text{Fe}(\text{CN})_6^{3-} / \text{Fe}(\text{CN})_6^{4-}$ redox couple due to the increased coverage of the electrode by the nanotubes. The separation between the cathodic and anodic peak current indicates that the electron transfer rate through the films of nanotubes is higher for SWCNTs than MWCNTs.

The voltammetric response of a redox pair also depends on the orientation of the carbon nanotubes at the electrode surface [92]. Figure 31 displays the voltammograms from $\text{Fe}(\text{CN})_6^{4-}$ oxidations on silicon wafers covered with vertically or randomly/horizontally oriented MWCNTs. The voltammetric response of the $\text{Fe}(\text{CN})_6^{3-/4-}$ redox process over the vo-CNTs layer is much more reversible than the process over the r/h-CNTs film.

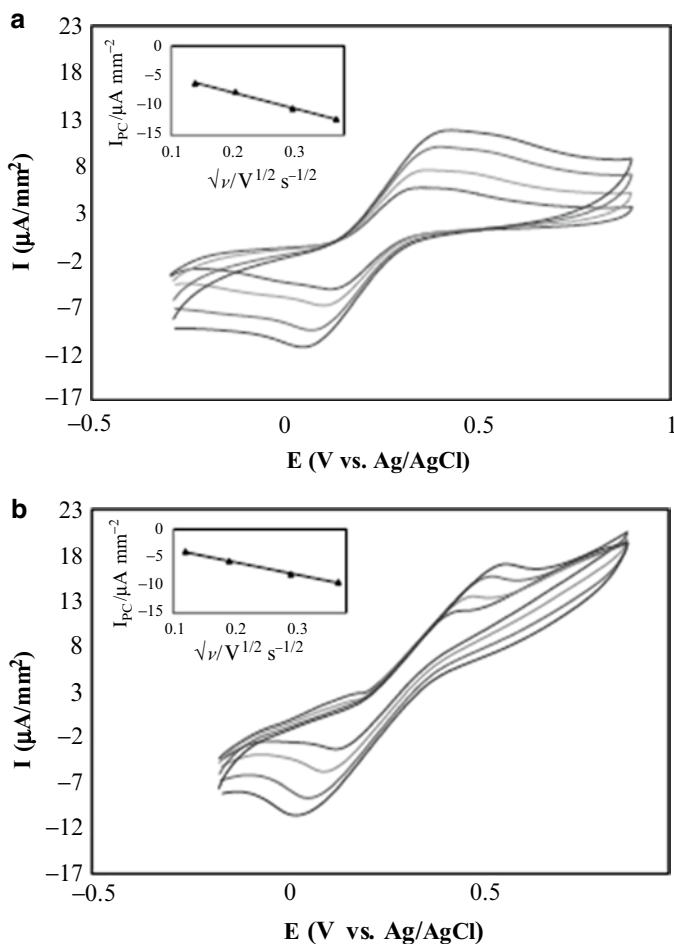


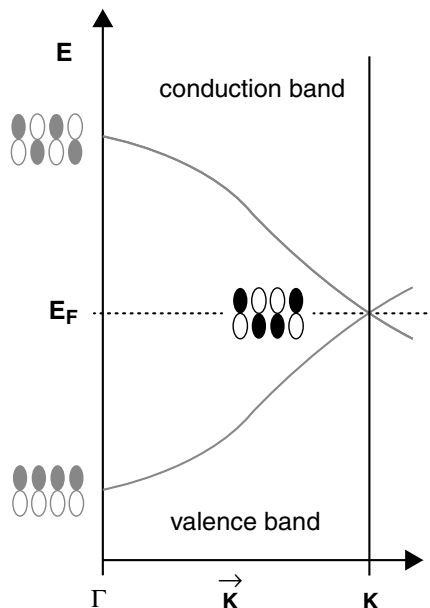
Fig. 31 Cyclic voltammograms of $\text{Fe}(\text{CN})_6^{3-}/\text{Fe}(\text{CN})_6^{4-}$ redox couple at a (a) vertically aligned and (b) horizontally randomly oriented multiwalled carbon nanotube-modified electrode in aqueous solution containing 5 mM $\text{K}_3\text{Fe}(\text{CN})_6$ and 0.01 M PSB at sweep rates 25, 50, 100, and 150 mV/s (Reproduced from Ref. [92] with permission from Elsevier)

Capacitance and Charge Transfer Properties of Graphene

Graphene is a two-dimensional planar sheet composed of sp^2 hybridized carbon atoms. These graphene sheets (between two and ten) may be stacked to form three-dimensional graphene nanoplates. A single graphene nanosheet is equivalent to a SWCNT, and graphene nanoplates are equivalent to MWCNTs.

A schematic representation of a graphene sheet's band structure is presented in Fig. 32 [105]. The unit cell for graphene consists of two carbon atoms generating two π bands, a π -band of delocalized electrons and a π^* -band. These bands overlap at the K-point within the hexagonal first-Brillouin zone at Fermi energy level. The close carbon-carbon distance in graphene leads to interatomic overlap that

Fig. 32 A schematic representation of the band structure in graphene (Reproduced from Ref. [68] with permission from Nature Publishing Group)



spreads these bands over a wide energy range, resulting in the large velocity of electrons. Graphene may be either a semimetallic or a zero-gap semiconductor that combines metallic and semiconducting properties. Graphene conductivity can be determined using a system similar to the one used to measure the conductivity of carbon nanotubes [106–108]. According to the theoretical predictions, the minimum conductivity of a graphene sheet depends on its geometry and the microscopic details of its edges to approach $4e^2/\pi h$ for large width-to-length (W/L) ratios [108]. The theoretical models also predict that the electrical conductivity in perfect graphene occurs via tunneling between the electrical contacts while at the Dirac point. For samples that are not perfect, the conductivity is affected by scattering centers, such as impurities, defects, and phonons [109]. These theoretical predictions are confirmed by experimental results [110, 111].

Capacitance properties of a single layer of graphene can be measured using the setup displayed in Fig. 33a [112]. Total capacitance consists of two components: the interfacial capacitance arising from the double layer formed by the ions at the graphene/solution interface and the quantum capacitance of graphene. These components are connected in series, and the smaller of the two contributors dominates the total capacitance. The changes in the total capacitance and the quantum component in ionic liquid solutions relative to the gate potential are shown in Fig. 33b [112]. The quantum capacitance has a nonzero minimum at the Dirac point related to the charged impurities present within the graphene sheet.

The electrochemical properties of graphene films deposited at an electrode surface were also studied in a solution containing different redox couples [113–115].

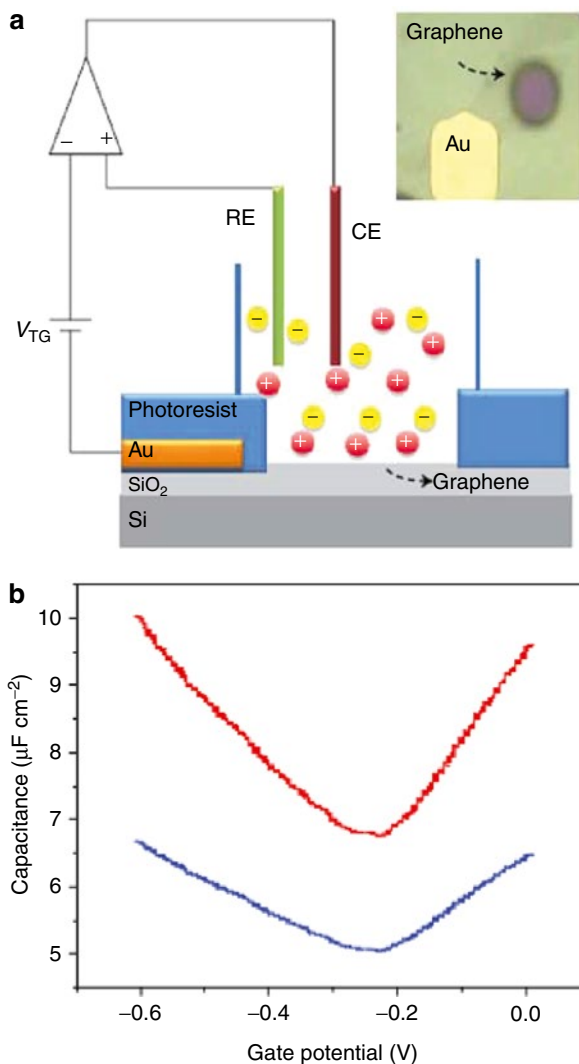
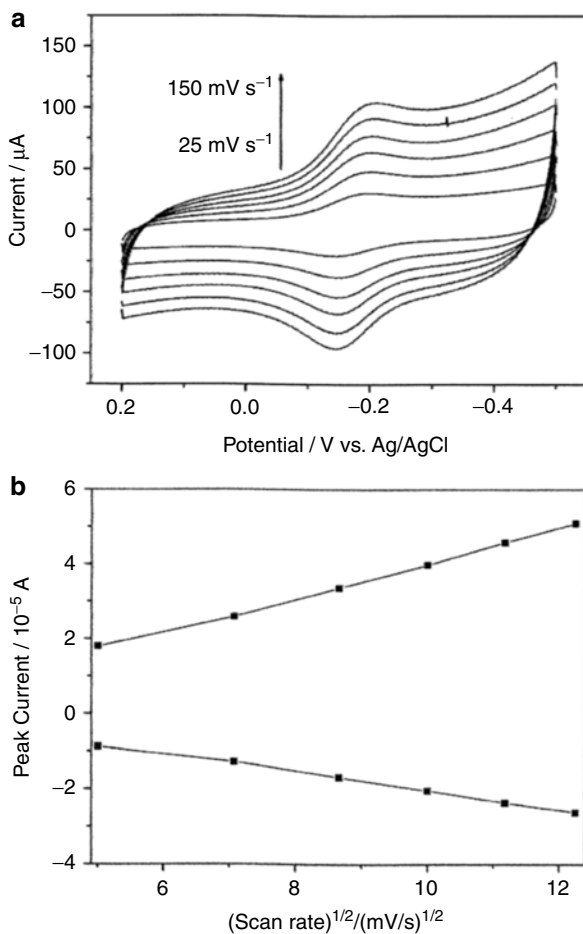


Fig. 33 (a) Single-layer graphene device used for quantum capacitance measurement. The edge of graphene sheet is covered with an insulation layer so the top surface is exposed to an ionic liquid electrolyte. The inset is an optical micrograph of the graphene device. (b) Total capacitance (a) and quantum capacitance (b) of graphene measured in ionic liquid BMIM-PF₆ as a function of gate potential (Reproduced from Ref. [112] with permission from Nature Publishing Group)

The model results obtained for GC modified with reduced graphene sheet films in a water solution containing KCl as the supporting electrolyte and $\text{Ru}(\text{NH}_3)_6^{2+/3+}$ as the redox pair are shown in Fig. 34 [113]. The large increase in the capacitance current depends on the observed increases in surface area.

The parameters of the charge transfer processes on the GC covered with a graphene film are collected in Table 4. The electron exchange processes significantly speed up at the surface of graphene [113].

Fig. 34 (a) Cyclic voltammograms of $\text{Ru}(\text{NH}_3)_6^{3+} / \text{Ru}(\text{NH}_3)_6^{2+}$ redox couple at a glassy carbon electrode coated with graphene in 1 M aqueous solution of KCl at various scan rates. (b) Dependences of peak currents on the square root of scan rate (Reproduced from Ref. [113] with permission from WILEY-VCH Verlag GmbH & Co.)



Carbon Nano-onions

Carbon nano-onions are quasi-spherical nanoparticles consisting of concentric graphitic shells. These structures are essentially multiwalled fullerenes. Knowledge about the electronic structure of these materials is limited. Pudlak and Pincak [116] calculated the HOMO and LUMO level energies for C_{60} and C_{240} nano-onions consisting of two carbon spheres. They observed a decrease in the HOMO–LUMO energy gap for the nano-onion relative to that of C_{60} . The C 1 s core excitation spectra and electron-energy-loss spectra of nano-onions 4–8 nm in diameter indicate that the electronic structure and conducting properties of nano-onions are strongly governed by the band structure of graphite for particles as small as 4 nm in diameter [116].

Table 4 Comparison of cyclic voltammetry data and electron transfer rate constant for selected redox couples at bare glassy carbon electrode (GC) and glassy carbon covered with graphene sheet films (GSF) (Adopted from Ref. [113] with permission from WILEY-VCH Verlag GmbH & Co.)

Parameter	Redox system					
	$\text{Fe}(\text{CN})_6^{3-/4-}$		$\text{Ru}(\text{NH}_3)_6^{2+/3+}$		Dopamine ^{0/+}	
ΔE_p (mV)	68 ^{GC}	65 ^{GSF}	64 ^{GC}	61 ^{GSF}	73 ^{GC}	60 ^{GSF}
$E_{1/2}$ (mV)	259 ^{GC}	266 ^{GSF}	-157 ^{GC}	-178 ^{GSF}	532 ^{GC}	585 ^{GSF}
i_p^{ox} ($\mu\text{A}/\text{cm}^2$)	117 ^{GC}	128 ^{GSF}	221 ^{GC}	248 ^{GSF}	328 ^{GC}	886 ^{GSF}
k_{app}^o (cm/s)	0.029 ^{GC}	0.049 ^{GSF}	0.055 ^{GC}	0.18 ^{GSF}	0.024 ^{GC}	0.25 ^{GSF}
α	0.5		0.5		0.35	

ΔE_p – difference in cathodic and anodic peak potentials, $E_{1/2}$ – half wave potential, i_p^{ox} – oxidation peak current, k_{app}^o – heterogenous standard rate constant, α – charge transfer coefficient. The supporting electrolyte for $\text{Fe}(\text{CN})_6^{3-/4-}$ and $\text{Ru}(\text{NH}_3)_6^{2+/3+}$ was 1 M KCl and for dopamine was 1 M HClO_4 . Scan rate was 100 mV/s

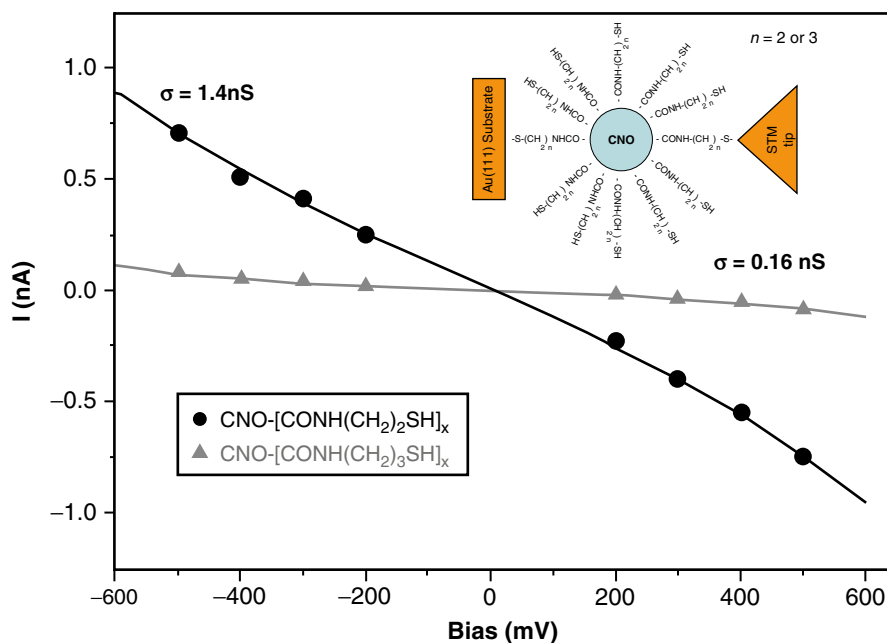


Fig. 35 Current–voltage characteristics obtained on the basis of current–distance curves recorded at different bias voltages for CNO functionalized with $-\text{CONH}(\text{CH}_2)_x\text{-SH}$ ($x=2$ and 3) (Reproduced from Ref. [118] with permission from WILEY-VCH Verlag GmbH & Co.)

The nano-onion agglomerates produced by nanodiamond annealing demonstrate variable range hopping conductivity [117]. The conductivity depends on the annealing temperature, size of nano-onions, and degree of their interaction in agglomerates.

The conductivity of individual carbon nano-onions functionalized with thiols was investigated using STEM [118]. Figure 35 depicts the current–voltage

characteristics obtained based on the current–distance curves. The current–voltage curves are symmetric and display a sigmoid slope. From the slope of these curves, conductivity values of 1.4 ± 0.1 and 0.16 ± 0.05 nS were found for CNO-(CONH-(CH₃)₂SH)_x and CNO-(CONH-(CH₃)₃SH)_x nanoparticles, respectively. The overall electron transmission through the CNOs is affected by the alkanethiol chains that determine the tunneling behavior. The intrinsic conductivity of CNO was calculated to be ~ 72 μ S [118].

Nanoparticle Material Thin Films in Charge Storage Devices

General Characteristics of Supercapacitors

Supercapacitors are also known as electrochemical capacitors, ultracapacitors, electrical double-layer capacitors, pseudocapacitors, gold capacitors, or power caches; these devices are energy storage devices that accumulate energy as charge on the electrode surface or subsurface layer [119, 120]. The stored electrical charge can be converted to electric current. Typical supercapacitors consist of two electrodes, one positive and one negative, separated by a dielectric material. The total capacitance, C , is expressed by the following equation:

$$C = \frac{\epsilon A}{d} \quad (22)$$

where A is the total area of the electrode surface, d is the distance between two electrodes, and ϵ is a dielectric constant. These electrodes are charged by the external potential, consequently storing energy. The maximum energy storage of a supercapacitor is proportional to the capacitance and to the voltage squared (V^2):

$$E = \frac{1}{2} CV^2 \quad (23)$$

The total power (P) of supercapacitor is given by the following equation:

$$P = \frac{V^2}{4R} \quad (24)$$

where R is the internal resistance of the capacitor [16].

The charge storage mechanism of electrochemical capacitors is controlled by two principle mechanisms: (i) an electrostatic interaction called electric double-layer capacitance (EDLC) and (ii) an electrochemical reaction named pseudocapacitance. Pure carbon materials, such as carbon aerogels, single- or multiwall carbon nanotubes, carbon nano-onions, and graphene, store charges electrostatically [17, 19, 120–140]. However, carbon materials modified with metal oxides, conducting polymers, or metallic nanoparticles store charge both electrostatically and through a redox reaction [14, 120, 123–125, 141–161]. Conductive polymers and metal oxides are competent pseudocapacitors that accumulate charge from chemical processes [16, 162–177].

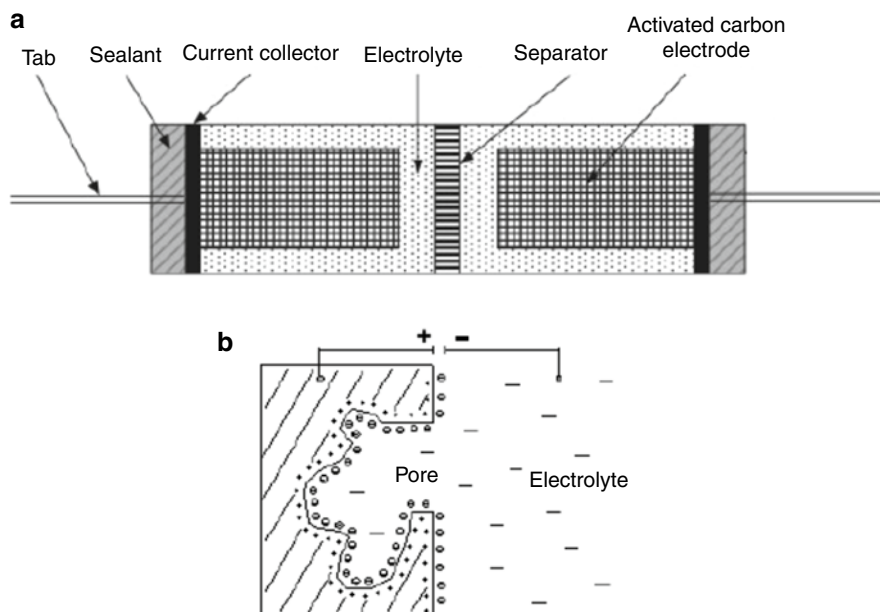


Fig. 36 Schematic representation of (a) double-layer capacitor based on activated carbon and (b) charge transfer distribution in pore of carbon electrode active layer

The electrodes in double-layer capacitors consist of highly porous carbon materials and therefore possess a large surface area-to-volume ratio. In these systems, the electric charge accumulates at the carbon electrode/electrolyte interface. Figure 36 displays the schematic representation of an EDLC consisting of two carbon electrodes. The mechanism of the surface charge formation occurs as three processes: surface dissociation, ion adsorption, and crystal lattice defects [120]. The small charge separation in the double-layer, high surface area of the electrode material, and high field strength generate the high energy density in EDLCs [178].

In the pseudocapacitive system, the fast and reversible oxidation and reduction processes in the electrode material drive the charging process [120, 122]. Figure 37 illustrates a charging process that utilizes conductive polymer chains during redox reactions. Conductive polymers exhibit two different electrochemical behaviors. *P*-type conductive polymers are electroactive in the positive potential range and are able to donate electrons; this system is the most common. During electrochemical reactions, *p*-type polymer chains are oxidized and doped with the anion from the electrolyte solution (Fig. 37a). The *n*-type polymers exhibit electron-accepting behavior. These polymeric chains have a negative charge and are subsequently doped with cations (Fig. 37b).

Mixed capacitors may be constructed using nanoporous carbon materials and redox systems. These supercapacitors characteristically have a higher capacitance and energy density than the EDLCs and redox capacitors because they can accumulate charge on both the conducting material/solution interface and within the bulk electrode material [119].

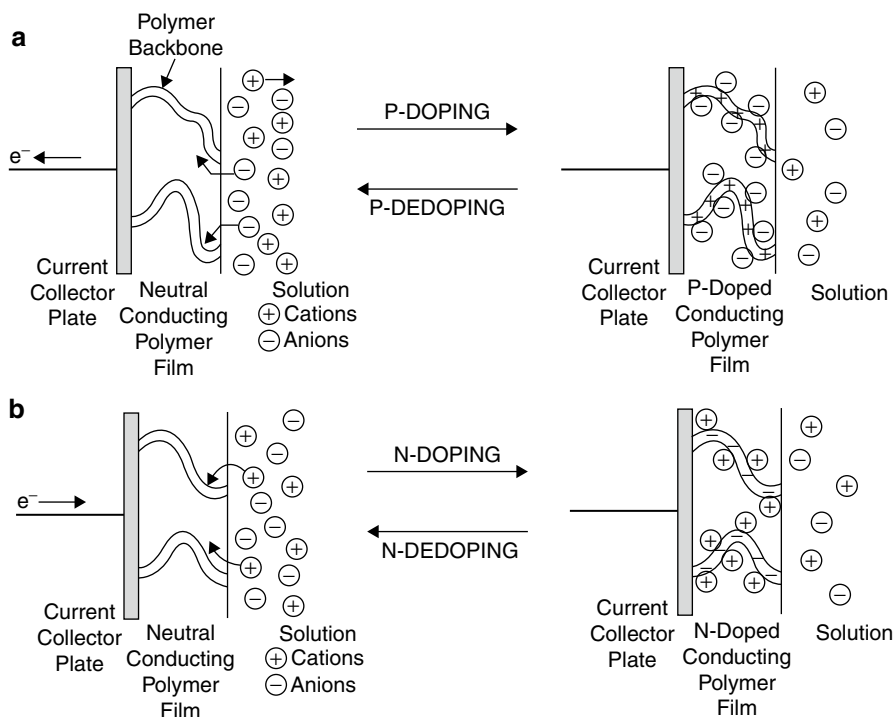


Fig. 37 Schematic representation of charging process of conducting polymer chains during reduction oxidation reactions (Reproduced from Ref. [168] with permission from Springer-Verlag)

Double-Layer Capacitors Based on the Carbon Nanoparticles

Carbon materials have a long history of use in energy storage devices as electroconductive additives, supports for active materials, electron transfer mediators, intercalation hosts, and capacitors [120, 123, 130, 138, 140, 179–185]. Due to their porous structures and high surface area, they are able to accumulate large amounts of charge in the double layer formed at the interphase between the carbon and the electrolyte solution. To improve capacitance, the structure of carbon materials may be modified using heat during chemical treatment [186–191].

In the last two decades, research has focused on the capacitance properties of materials composed of carbon nanostructures, such as carbon nanotubes, nano-onions, and graphene [17, 119, 121, 124–129, 131–137, 139, 192]. Carbon nanostructures exhibit unique morphology, relatively good electrical conductivity, exceptional mechanical properties, and large surface areas. These properties make the nanostructures attractive as components of electrochemical capacitors. The preparation of nanostructured carbon thin films is quite complicated. The general procedures to generate systems with CNTs are displayed schematically in Fig. 38. Functionalized nanotube surfaces can be generated in solution (Fig. 38) or by using material deposited on an electrode's surface. Two types of carbon nanotube

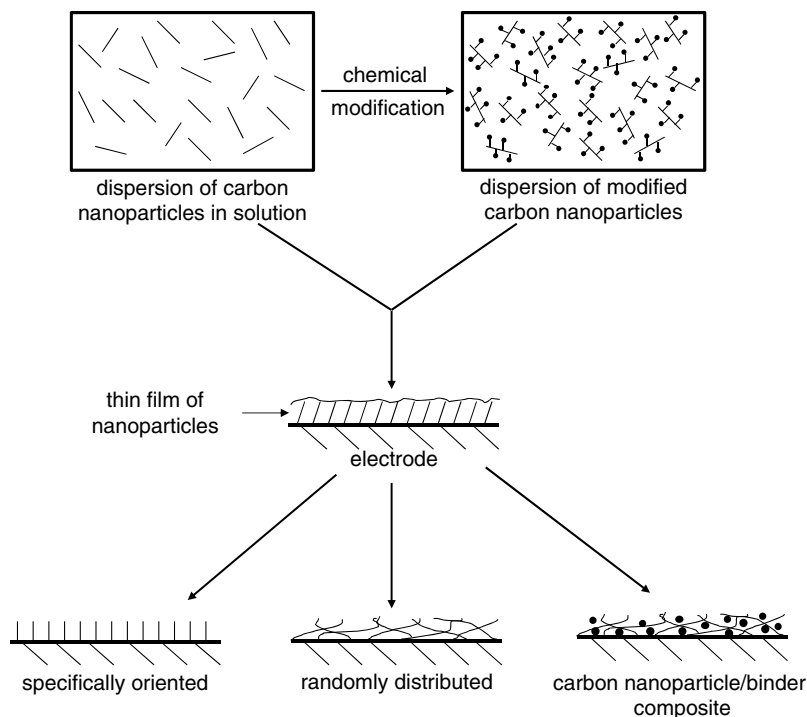
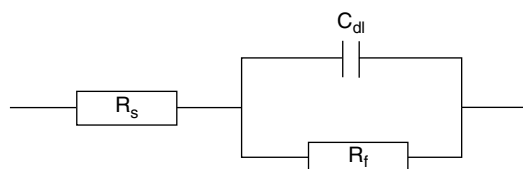


Fig. 38 Schematic representation of thin film of the carbon nanoparticles (CNTs) formation at the electrode surface

electrodes can be developed: binder free [127, 193–195] and binder enriched [128]. In the binder-free electrodes, the carbon nanotubes are mechanically loose. The electrical contact is limited between the carbon nanostructures. The binder introduction can solve these problems. However, binders might introduce contaminants to the electroactive material and therefore reduce capacitance performance. The surface morphologies of thin films of SWCNTs, graphene, and CNOs are presented in Fig. 39.

The capacitance properties of carbon nanoparticle-based materials are collected in Table 5. These materials all exhibit typical double-layer responses under voltammetric conditions (Fig. 40a). Rectangle-shaped cyclic voltammograms were obtained over a wide range of scan rates within a large potential window. For the unmodified carbon nanoparticles, the double-layer charging at the carbon nanoparticle film/electrolyte solution interface can be represented by a simple equivalent circuit:



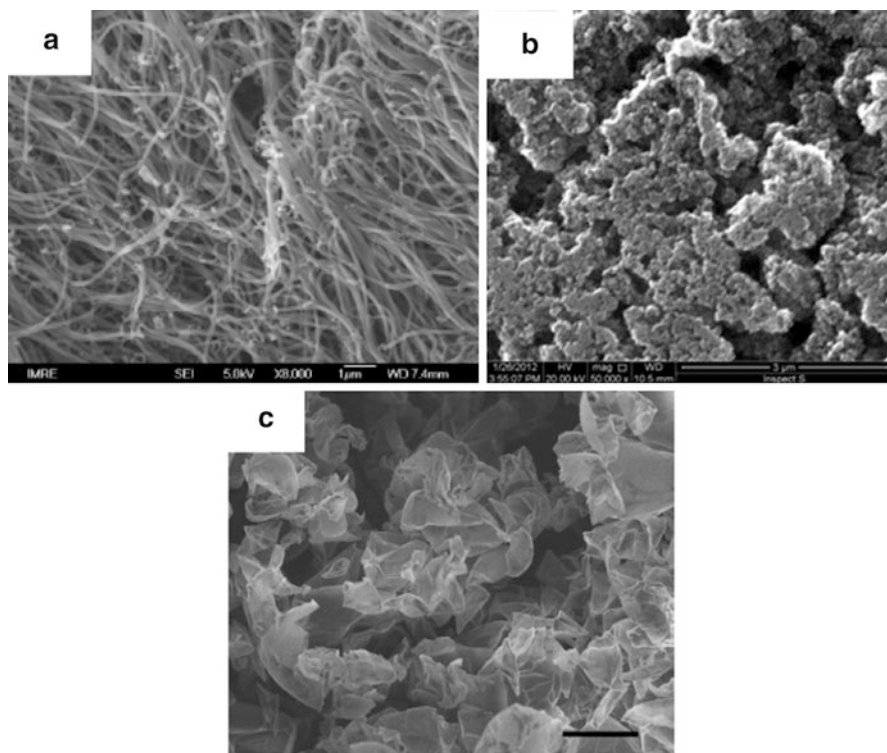


Fig. 39 SEM images of surface morphology of (a) SWCNTs (Reproduced from Ref. [196] with permission from Elsevier Ltd.), (b) CNOs, (Reproduced from Ref. [197] with permission from Elsevier Ltd.), and (c) graphene (Reproduced from Ref. [133] with permission from American Chemical Society)

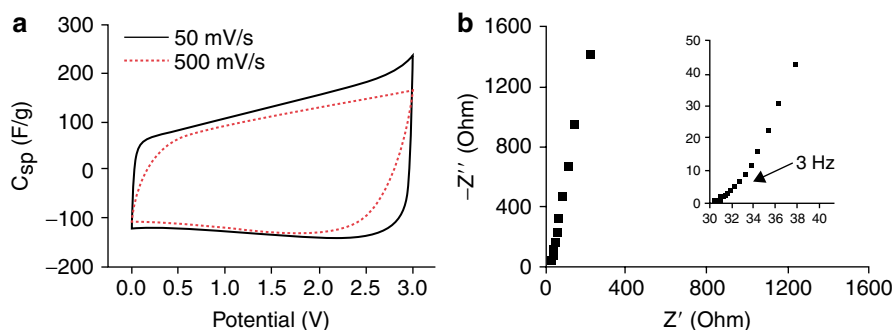
where R_s and R_f represent internal and self-discharge resistance, respectively, and C is the capacitance. Figure 40b displays the representative impedance spectra obtained from thin films of CNT/paper electrode.

Wide ranges of specific capacitances have been reported for each type of carbon nanoparticle (Table 5). The electrochemical properties of these materials depend on the procedures for their formation, the particle size, the solvent and supporting electrolyte, and the method used to prepare the nanostructured thin film. Despite the large surface areas observed for carbon nano-onions, the specific capacitances reported for these nanoparticles are relatively low [134, 139, 206, 207]. CNOs that agglomerate at the electrode surface are dense materials with low porosity, as illustrated in Fig. 39b. These structures explain the CNOs' relatively poor capacitance properties. Additionally, CNO inner shells do not participate in the charge storage process. Therefore, the specific capacitances are lower. Similar behavior is expected for nanostructured films composed of MWCNTs.

Graphene is an outstanding candidate for double-layer capacitor construction. [113, 126, 132, 137, 192, 203–205, 208, 209]. It exhibits exceptionally high specific

Table 5 Selected values of specific capacitances obtained for thin films of unoxidized and oxidized carbon nanostructures

Carbon nanostructure	C _s of carbon nanostructure	Condition of modification	C _s of oxidized carbon nanostructure
	F g ⁻¹		F g ⁻¹
SWCNTs	45 [198]	Humid air at 225 °C	65 [198]
	20 [199]	6 M KOH	56 [199]
	18 [145]		
	40 [145]		
	64 [126]		
MWCNTs	12 [200]	H ₂ SO ₄ +HNO ₃ (3:1)	33.5 [200]
	80 [148]	HNO ₃ , T= 80 °C	137 [148]
	33 [196]	Electrooxidation in 0.2 M HNO ₃	335 [196]
	36 [148]		
	62 [148]		
CNOs	14 [126]		
	34 [201]	H ₂ SO ₄ +HN ₃ (3:1), T= 80 °C,	70 [201]
Grapheme	10 [139]	3 M HNO ₃	7 [139]
	187 [200]	Electrooxidation in 1 M H ₂ SO ₄	297 [202]
	26 [202]		
	118 [203]		
	233 [204]	KMnO ₄ in H ₂ SO ₄	211 [205]

**Fig. 40** (a) Cyclic voltammograms and (b) Nyquist plot of CNT/paper capacitor in 1-ethyl-3-methylimidazolium bis(trifluoromethylsulfonyl)imide gel electrolyte (Reproduced from Ref. [121] with permission from IOP Publishing Ltd.)

surface area up to 2675 m²g⁻¹. The intrinsic capacitance of graphene is 21 μF g⁻¹ [112], setting the upper limit for the double-layer capacitance of carbon-based materials. Graphene has a 200 F g⁻¹ specific capacitance in ionic liquids [101, 210]. The capacitance behavior of graphene materials depends on the graphene preparation procedure, as well as the material used for synthesis [126, 143]. In Fig. 41, structures of graphene sheets obtained from graphitic oxide and nanodiamond are compared. The capacitance behavior of these films differs significantly, as demonstrated in Fig. 42 [126].

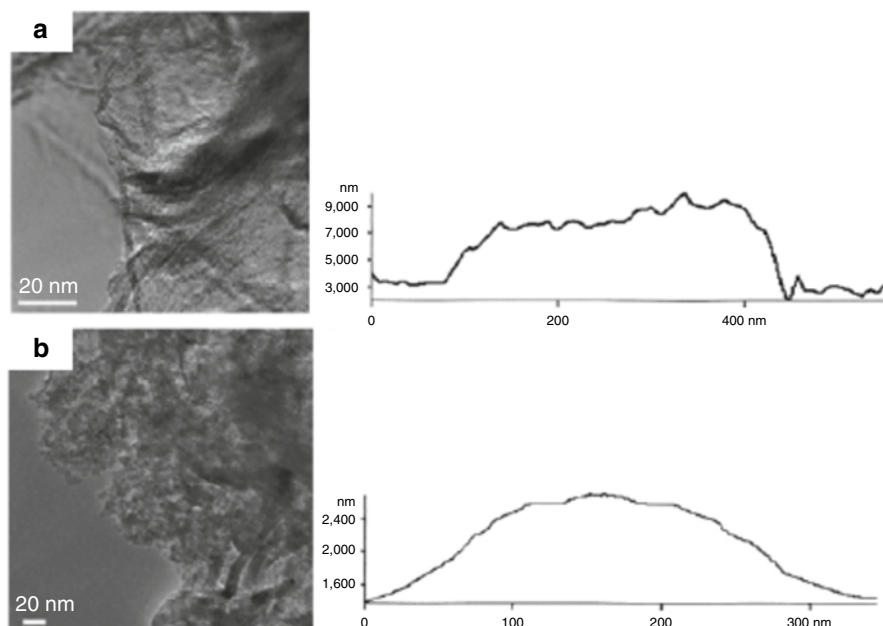
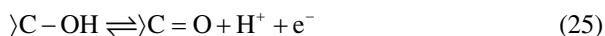


Fig. 41 TEM images and AFM height profiles of (a) graphene obtained by the thermal exfoliation of graphitic oxide (EG) and (b) thermal conversion of nanodiamond (DG) (Reproduced from Ref. [126] with permission from Springer-Verlag)

To enhance the capacitance performance of carbon-based nanostructured materials, a nanoparticle surface is modified with electrochemically active functional groups that contribute to the pseudocapacitance of the materials [127, 131, 137, 139]. Nitrogen-containing functional groups may enhance the capacitance through the interaction between the protons and electron-donating nitrogens [211]. Oxygen atoms also improve charge storage performance by participating in electron transfer reactions. Oxygen-containing functional groups may also enhance the operating voltage and the energy density. Carbon nanoparticles can be modified chemically [198, 200–202, 212–220], photochemically [221, 222], electrochemically [196, 199], or using plasma-induced technique [223, 224]. The chemical modifications are usually performed in concentrated nitric acid or in the mixture of nitric and sulfuric acids. Schematically, the chemical modification of a carbon nanotube surface is described in Fig. 43. The hydroxyl, carbonyl, and carboxylic groups formed on the surface of nanotubes can participate in the following electrochemical reactions:



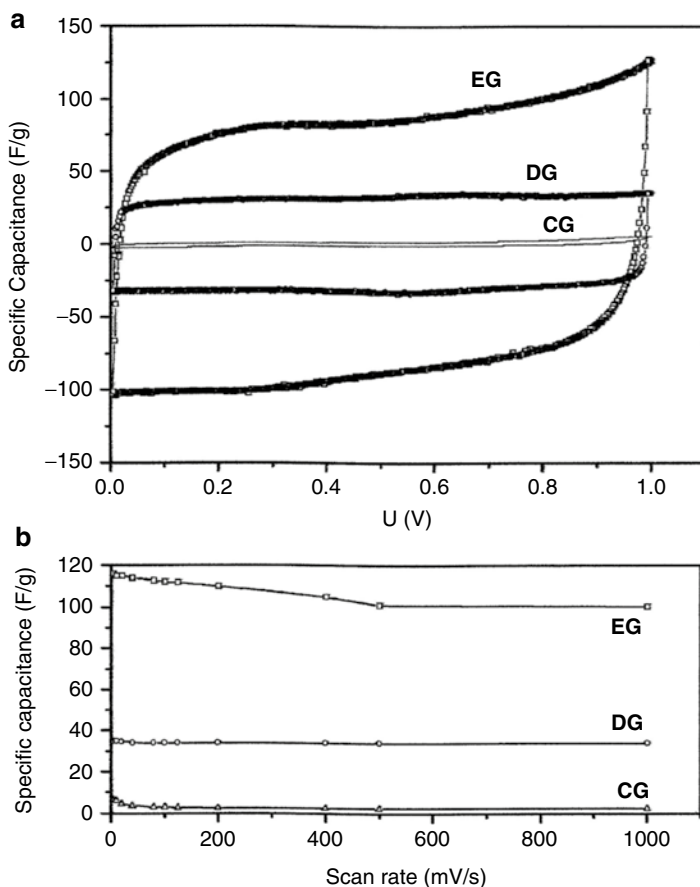


Fig. 42 (a) Voltammetric characteristic of a capacitors built from graphene (EG and DG) electrodes at a scan rate of 100 mV/s in 1 M H₂SO₄. (b) Specific capacitance as a function of scan rate (Reproduced from Ref. [126] with permission Springer-Verlag)

Because carboxylate reductions are irreversible, higher ratios of hydroxyl and carbonyl groups to carboxylate groups should generate better capacitive performance. The distribution of oxygen-containing functional groups depends on the oxidant (Fig. 44) [225]. These results suggest that better capacitance performance can be expected for materials oxidized by weak oxidants, such as H₂O₂.

The electrochemical oxidation of carbon nanostructures are performed under potentiostatic or voltammetric conditions at positive potentials [196]. For SWCNTs, electrooxidation takes place at the nanotubes' caps to form open-end structures modified with oxygen functional groups.

The equivalent circuit for the carbon nanotubes chemically modified with redox-active groups is shown bellow. It additionally considers pseudocapacitive component (C_p) and resistance R_f ' representing faradaic reaction.

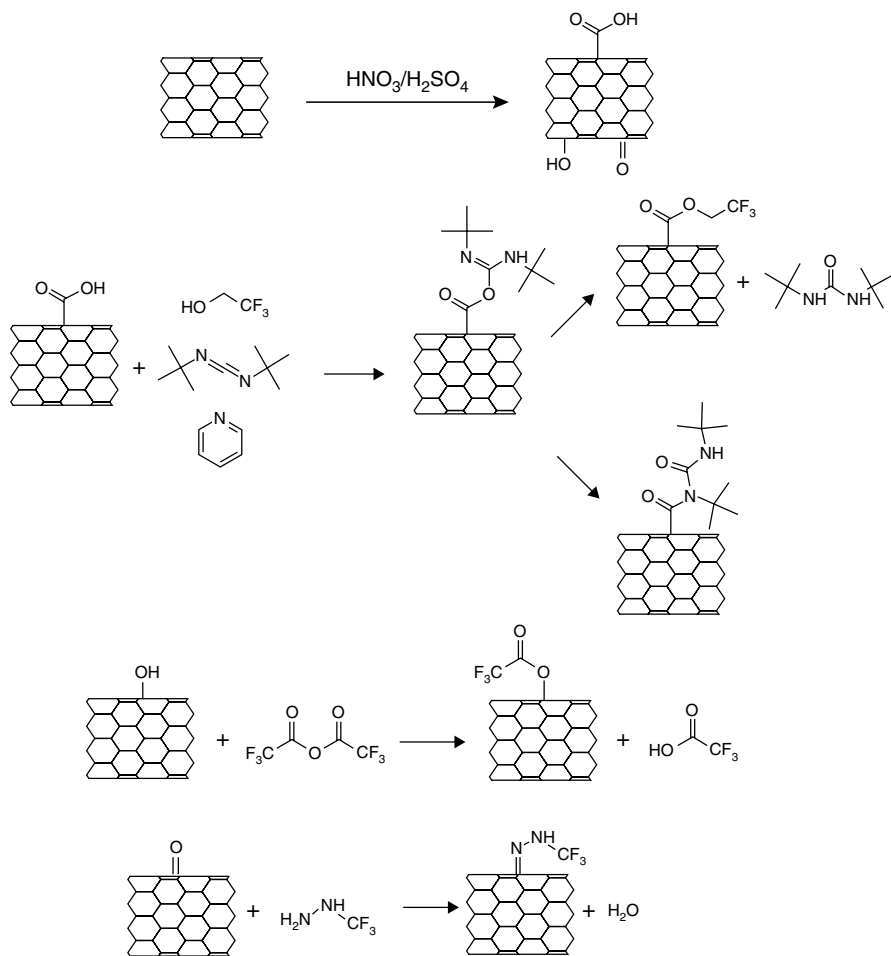
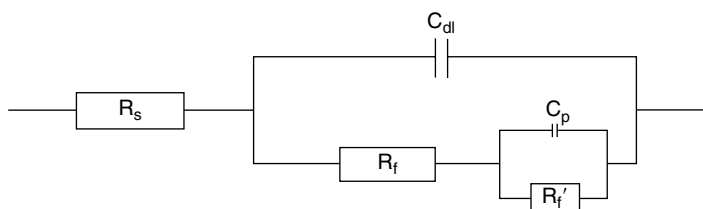


Fig. 43 Schematic illustration of examples of CNT surface chemical modification (Adopted from Ref. [225] with permission from Elsevier Ltd.)



The representative voltammetric responses of the unmodified and electrochemically oxidized MWCNTs are compared in Fig. 45. The oxidized MWCNTs exhibit pseudocapacitive behavior with well-developed faradaic current peaks from the electron transfer reactions of the oxygen-containing functional groups ($-\text{OH}$, $-\text{C=O}$, $-\text{CHO}$).

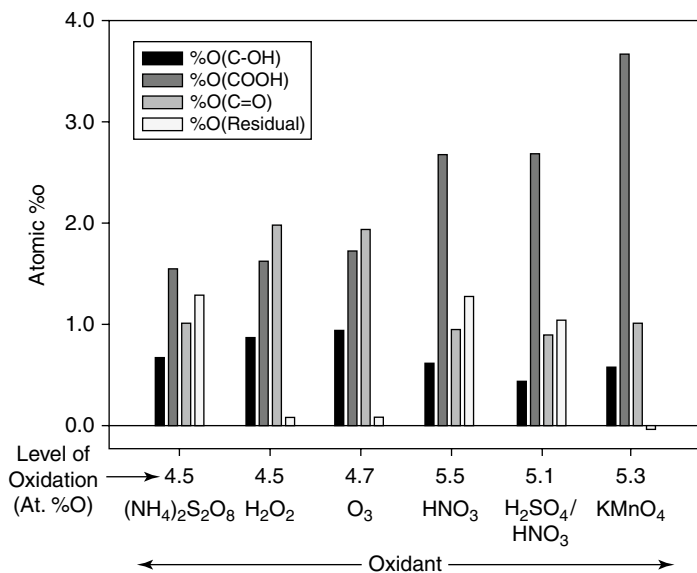


Fig. 44 Influence of the oxidant on the distribution of oxygen-containing functional groups on MWCNT (Reproduced from Ref. [225] with permission from Elsevier Ltd.)

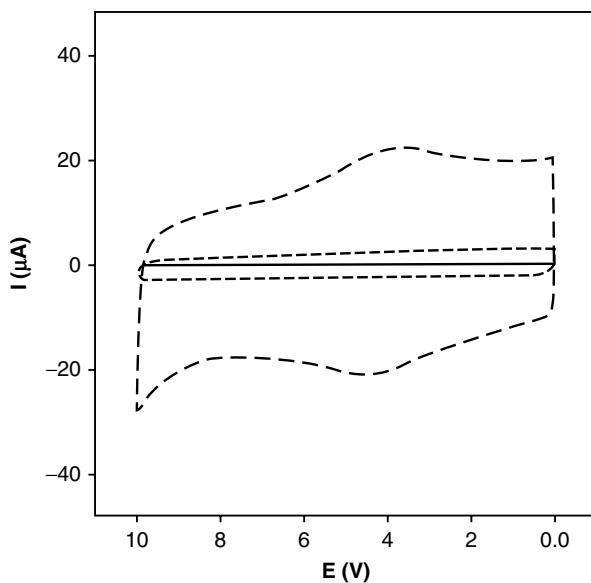


Fig. 45 Cyclic voltammogram of a glassy carbon electrode (solid line), unmodified MWCNTs electrode (dash line), and electrochemically oxidized MWCNTs electrode (dotted line) at 50 mV/s in 1 M H_2SO_4 (Adopted from Ref. [196] with permission from Elsevier Ltd.)

Table 6 Ranges of specific capacitances reported for selected metal oxides and conductive polymer bulk materials

Material	Range of C_s F g ⁻¹
Polypyrrole (PPy)	78–1000
Polyaniline (PANI)	400–1300
Polythiophene (PTh)	25–240
Poly(3,4-ethylenedioxythiophene) (PEDOT)	90–110
RuO ₂	220–1300
MnO ₂	145–720
NiO	85–840

Table 5 compares the capacitance properties of unmodified and chemically modified carbon nanoparticle thin films. In all cases, a significant improvement in capacitance performance was reported.

Supercapacitors Containing Conductive Polymer and Metal Oxide Nanoparticles

Conducting polymers [172, 176, 226–228] and transition metal oxides [229–231] are considered promising materials for supercapacitors because they have a high specific capacitance, highly reversible charge transfer processes, redox reactions with wide potential windows, and stable behavior during discharge/charge steps. The specific capacitances of selected transition metal oxides and conductive polymer bulk materials are collected in Table 6. The electrochemical performance of these materials was enhanced when nanostructured materials were used [161–165, 170, 171, 232–238]. The smaller particle size and high surface-to-volume ratio strongly influence the capacitance properties of these materials. However, the conductivity of nanoparticle-derived material is usually lower than the conductivity of the bulk material because the resistance toward electron transfer is higher between nanoparticles.

The conductivity properties of the nanoparticle-derived materials depend on the type of polymer and the preparation conditions. The conductivity of these nanostructured materials may be tuned with the degree of doping, the oxidation state of the electroactive material, the particle morphology and size, the crystallinity of the material, the effective conjugation length, and the amount of stabilizer on the particle surface. Usually, increasing the amount of nanoparticle stabilizer causes a decrease in a nanostructured material's conductivity [238–242]. However, if the stabilizer works as a counterion during the polymeric nanoparticle formation, the conductivity of nanoparticles may be enhanced. For *p*-doped polyaniline and polypyrrole nanoparticles, the anionic surfactant stabilizers enhance the nanoparticles conductivity [243–246] when compared to similar materials prepared without anionic surfactant or with cationic surfactant.

The generation of polymeric nanoparticles is often performed in microemulsions [247–251]. Nanoparticles formed under these conditions exhibit higher crystallinity and highly ordered polymeric chain structures. These factors enhance the

polymeric nanoparticles' conductivity. For example, 4 nm polyaniline nanoparticles synthesized in a low temperature microemulsion using cationic surfactants displayed conductivity as high as 85 S cm^{-1} [251].

The particle size also influences the capacitive properties of nanostructured materials. This effect was observed in material formed from a two-component C_{60} -Pd polymer [233]. This polymer may be formed electrochemically [252–256] or chemically [257, 258]. Electrochemical polymerization generates relatively uniform and compact material at the electrode surface. Good capacitance performance is observed for this material. A capacitance of ca. 200 F g^{-1} was reported for a C_{60} -Pd polymer in acetonitrile containing tetra (*n*-butyl) ammonium perchlorate [259]. Chemical polymerization performed in a benzene solution between fullerene and a zero-valent palladium complex generated large, irregular, and superficial cubic crystalline structures with size ranging from 20 to $80 \mu\text{m}$. The electrochemical behavior of films formed from these crystalline structures is much less reversible because the resistance is higher and the specific capacitance is much lower [258]. The cubic structures formed during the chemical synthesis of C_{60} -Pd may be easily disintegrated to furnish spherical nanoparticles using high energy ultrasound. The capacitance properties of the films formed from these nanoparticles depend on the particle size. The specific capacitance increased when a decrease in nanoparticle diameter was observed [233]. Additionally, the voltammetric response becomes more reversible for material composed of smaller polymeric nanoparticles. The capacitance properties of C_{60} -Pd polymer-derived nanostructured material are demonstrated in Fig. 46, and the specific capacitance values for different C_{60} -Pd

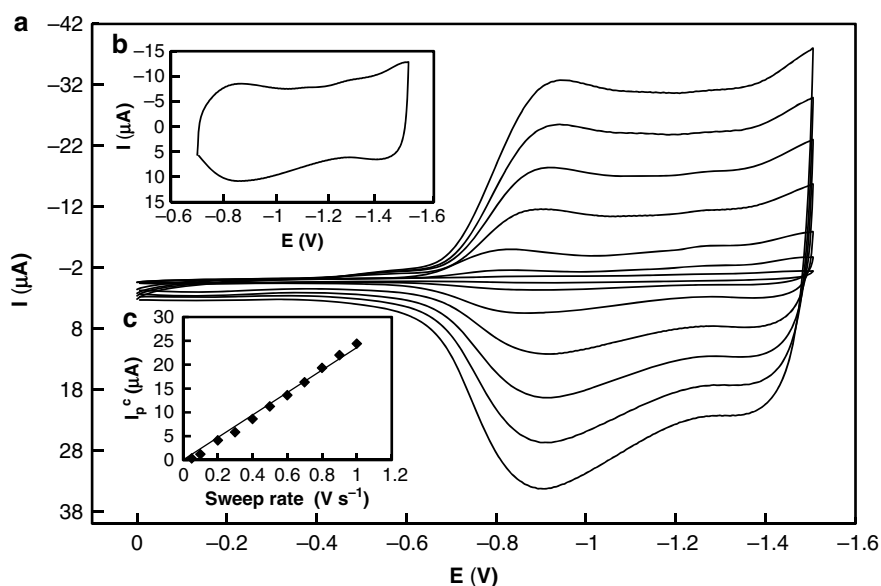


Fig. 46 (a) Voltammetric responses of C_{60}Pd_3 polymer at scan rates changed in the range from 20 to 500 mV/s in acetonitrile containing 0.1 M $(n\text{-C}_4\text{H}_9)_4\text{NClO}_4$. (b) Voltammetric response in the polymer reduction potential range at 200 mV/s. (c) Dependence of the capacitance current on the scan rate

Table 7 Specific capacitance and conductivity of C₆₀-Pd films formed under different conditions in acetonitrile containing 0.1 M (n-C₄H₉)₄NClO₄

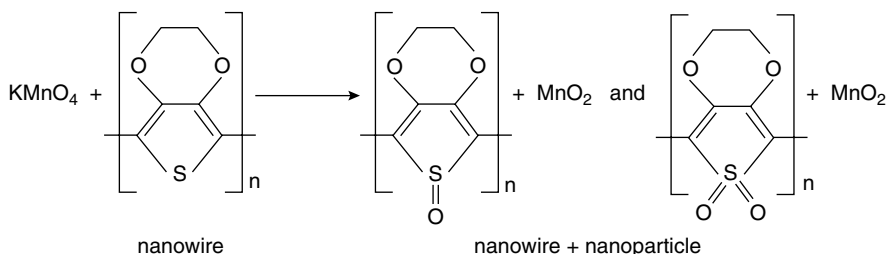
Polymeric film	Specific capacitance (F g ⁻¹)	Conductivity (μS)
C ₆₀ -Pd synthesized electrochemically ^a	200	44
C ₆₀ -Pd ₃ large cubic crystalline structures ^b	30	–
C ₆₀ -Pd nanoparticles (ca. 65 nm) ^c	180	35
C ₆₀ -Pd ₂ nanoparticles (ca. 125 nm) ^c	120	31
C ₆₀ -Pd ₃ nanoparticles (ca. 180 nm) ^c	95	28

^aRef. [259]^bRef. [258]^cRef. [233]

materials are collected in Table 7. Similar behavior was observed for the stabilizer-free polypyrrole nanoparticles synthesized in glycerol [235].

The particle size effects were also observed for nanostructured transition metal oxide materials [161–163, 236, 237]. RuO₂ electrodes were prepared using electrostatic spray deposition of ruthenium oxide on a glassy carbon electrode [162]. The film was composed of large agglomerated particles that were 100–200 nm in diameter (Fig. 47a). The electrochemical lithiation/delithiation process produces nanostructured material with 2–5 nm particles. The porosity of the material also increases (Fig. 47b). Figure 47c displays representative cyclic voltammograms of both materials, as well as the relationship between the specific capacitance and the scan rate [162]. The nanostructured RuO₂ film that was prepared by electrochemical lithiation/delithiation exhibited much a specific capacitance of ca. 650 F g⁻¹; this capacitance was higher than the capacitance of the as-prepared material (250 F g⁻¹).

To combine the properties of conductive polymers and transition metal oxides, nanocomposites of these materials were synthesized, and their electrochemical properties were investigated [260–263]. For nanostructured materials composed of polyaniline and ZnO or CdO, the conductivity of the composites increased relative to the conductivity of the polyaniline [262, 263]. Composites of PEDOT nanowires and MnO₂ nanoparticles demonstrate better capacitance performance than PEDOT alone [260]. The nanocomposite formed during the oxidation of the PEDOT nanowire with KMnO₄ occurs according to the following reaction:



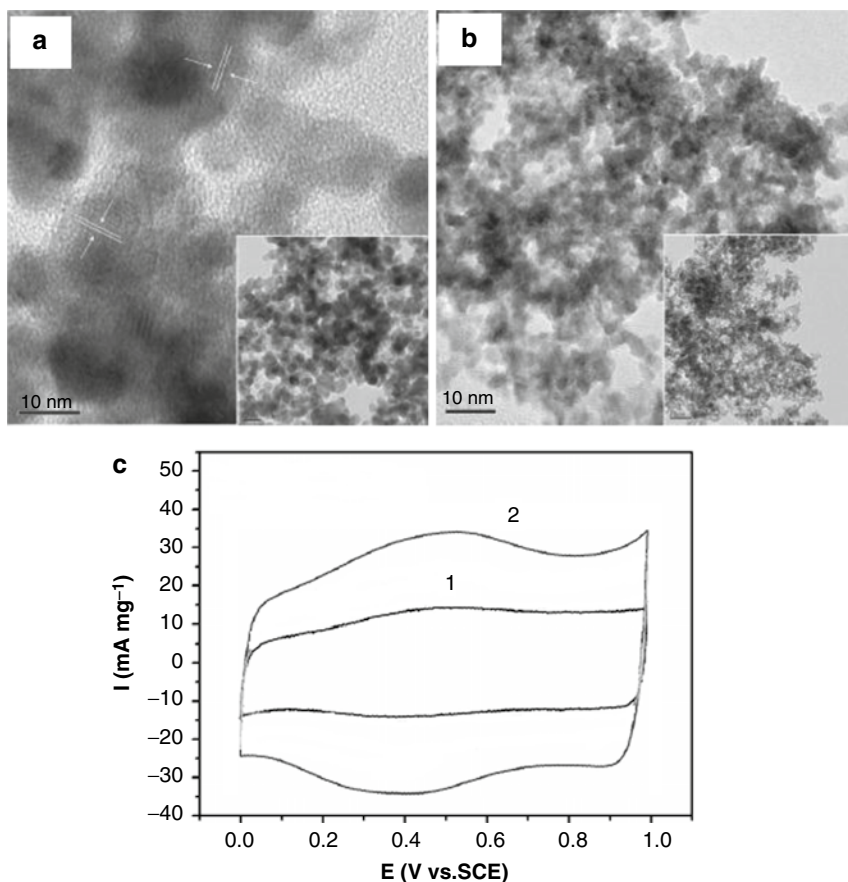


Fig. 47 HRTEM images of (a) as-prepared RuO₂ thin film and (b) nanostructured RuO₂ thin film after lithiation/delithiation. (c) Cyclic voltammety of the as-prepared RuO₂ thin film (1) and nanostructured RuO₂ thin film (2) (Reproduced from Ref. [162] with permission from WILEY-VCH Verlag)

The voltammetric curves for the PEDOT nanowires and the PEDOT/MnO₂ nanocomposites are compared in Fig. 48. Galvanostatic charge/discharge measurements also revealed the superior capacitive performance of the nanocomposite material.

Composites of Conducting Polymers or Metal Oxides and Carbon Nanostructures

Combining carbon nanomaterials with redox-active systems, such as conductive polymers or metal oxides, generates highly effective charge storage composites [14, 16–18, 119, 124, 131, 141–147, 149–153, 155–161, 197, 264–273]. In these systems, the power and energy density are both significantly enhanced due to the

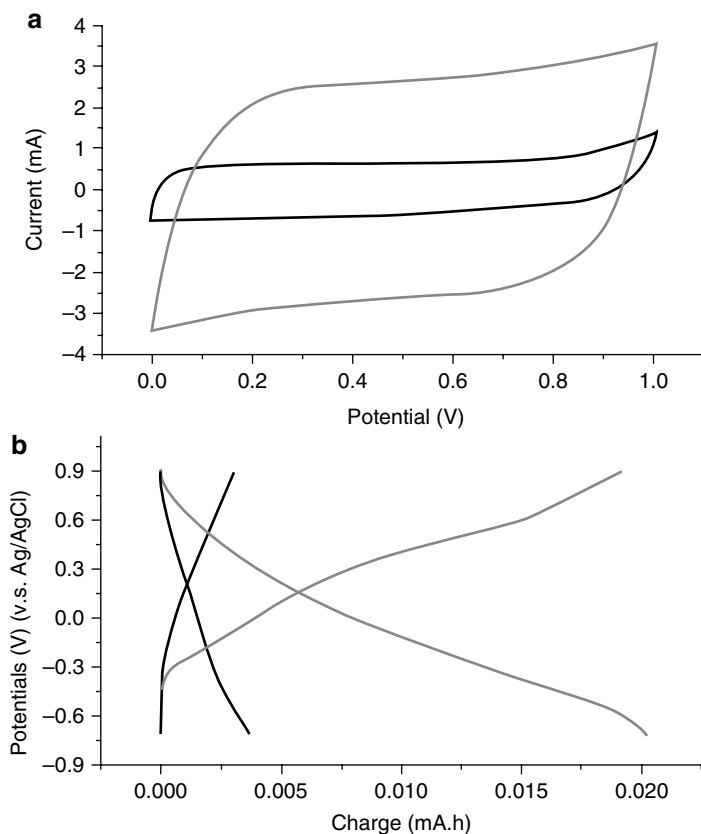
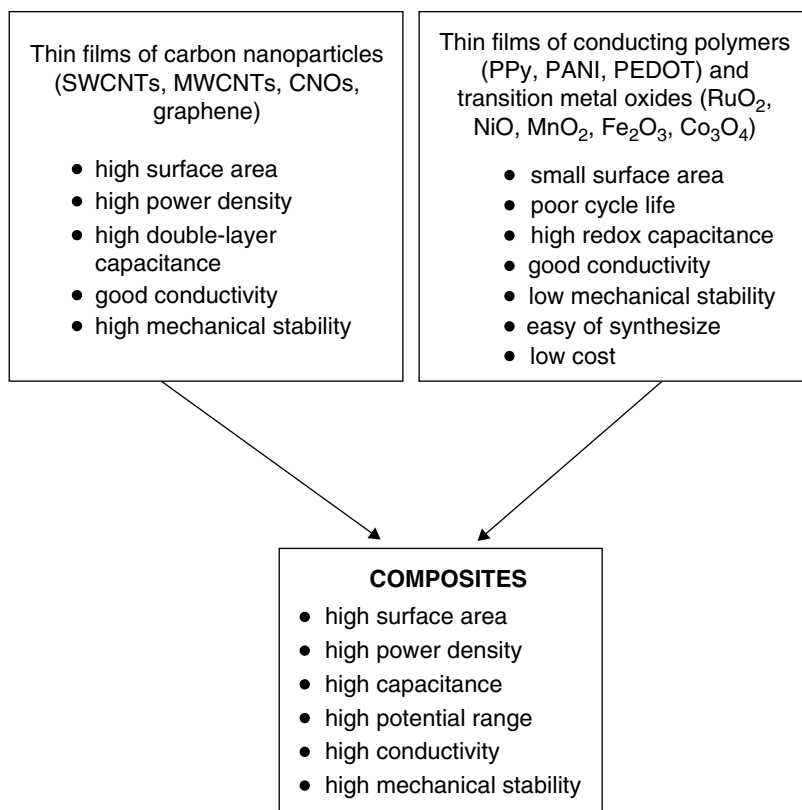


Fig. 48 (a) Cyclic voltammogram of (1) PEDOT nanowires and (2) PEDOT–MnO₂ nanocomposite at 100 mV/s in 1 M LiClO₄ water solution. (b) Galvanostatic charge/discharge curves of (1) PEDOT nanowires and (2) PEDOT–MnO₂ nanocomposite at current density of 1.25 mA/cm² 1 M LiClO₄ water solution (Reproduced from Ref. [260] with permission from American Chemical Society)

redox-active materials' faradaic processes. They possess novel properties and better characteristics than either of the individual components [14, 172, 271–273]. Scheme 1 compares the properties of carbon nanostructures, redox systems, and the composite materials.

Three general procedures are used to form nanocomposites containing carbon nanoparticles: (i) in situ chemical polymerization, (ii) chemical polymerization of monomers attached to carbon nanostructure, and (iii) electrochemical polymerization carried out on an electrode surface modified with carbon nanostructures (Fig. 49). In most cases [269, 274–276], electrochemical synthesis provides homogeneous films. However, the chemical polymerization generates polymers with a more porous morphology [149, 269]. Additionally, the morphology of the composites depends on the polymeric material [149]. Figure 50 displays the SEM images of carbon nanotubes composited with three types of conducting polymers using



Scheme 1 Properties of separate components (carbon nanostructures, conducting polymers, metal oxides) and their composites

chemical methods. In contrast to the MWCNTs/PPy and MWCNTs/PEDOT composites, the polyaniline nanocomposite is very homogenous.

The electrochemical properties of carbon nanostructure-derived composites are usually studied using cyclic voltammetry and electrochemical impedance spectroscopy. The electrochemical behavior of MWCNTs, polyaniline (PANI), and a PANI/MWCNT composite is compared in Fig. 51 [270]. The cyclic voltammogram obtained for the MWCNTs is typical of the double-layer capacitors, displaying the ideal symmetric response relative to the zero current line. For PANI and PANI/MWCNT, the current's response to the change of potential scan is slower. The current obtained for the PANI/MWCNT composite is larger than the current obtained for pure PANI. The high surface area and low resistivity of the MWCNTs improved the contact between the PANI matrices. Well-coated MWCNTs exhibit porous three-dimensional composite networks that have a large surface area; these materials are also highly susceptible to doping by the electrolyte ions, and charge storage is efficient in three-dimensional systems. The PANI/MWCNTs composite has more available

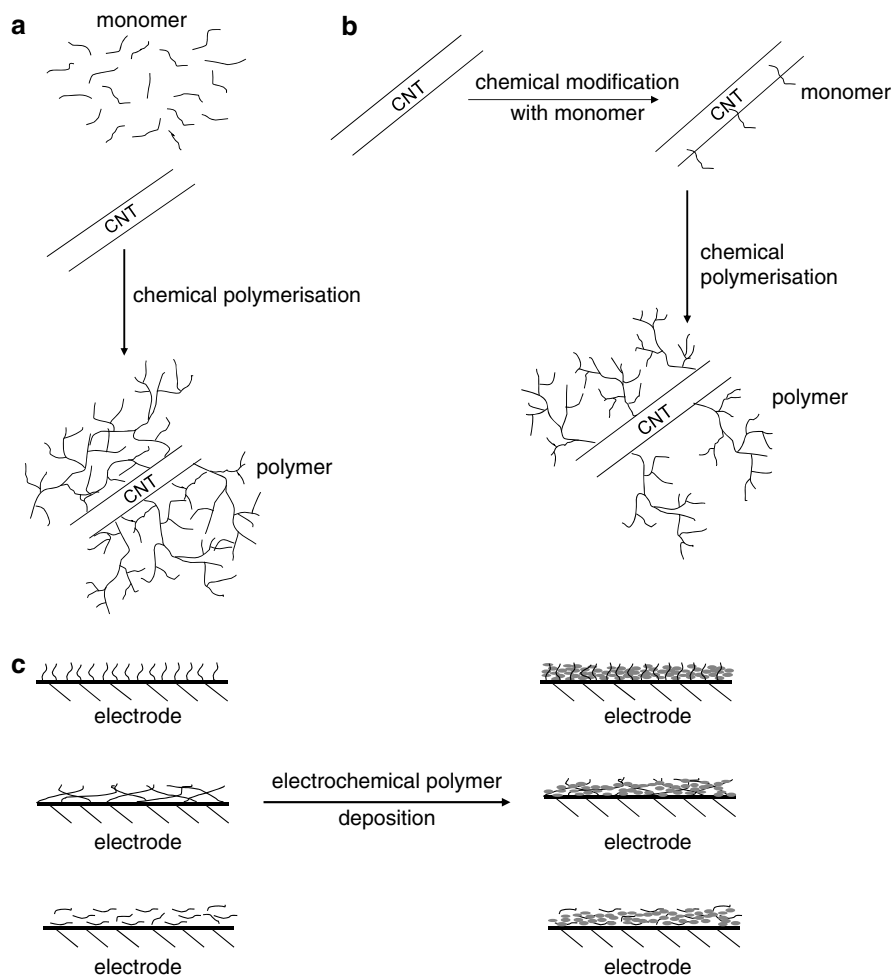


Fig. 49 A schematic representation of different procedures of nanocomposites formation for electrochemical measurements. (a) In situ chemical polymerization, (b) chemical polymerization of monomers attached to carbon nanostructure, and (c) electrochemical polymerization carried out on an electrode surface modified with carbon nanostructures

active sites for faradaic reactions and a larger specific capacitance compared to the pure PANI film. The specific capacitance obtained for PANI/MWCNTs is 328 F g^{-1} , which is significantly higher than the capacitance of PANI (193 F g^{-1}) [270].

The impedance spectra obtained for the PANI and PANI/MWCNT composite are displayed in Fig. 51b. Both plots are similar. The semicircle obtained in the high-frequency region is due to the faradaic process of PANI oxidation. The linear capacitive response in the low frequency region is accompanied by a diffusion-controlled

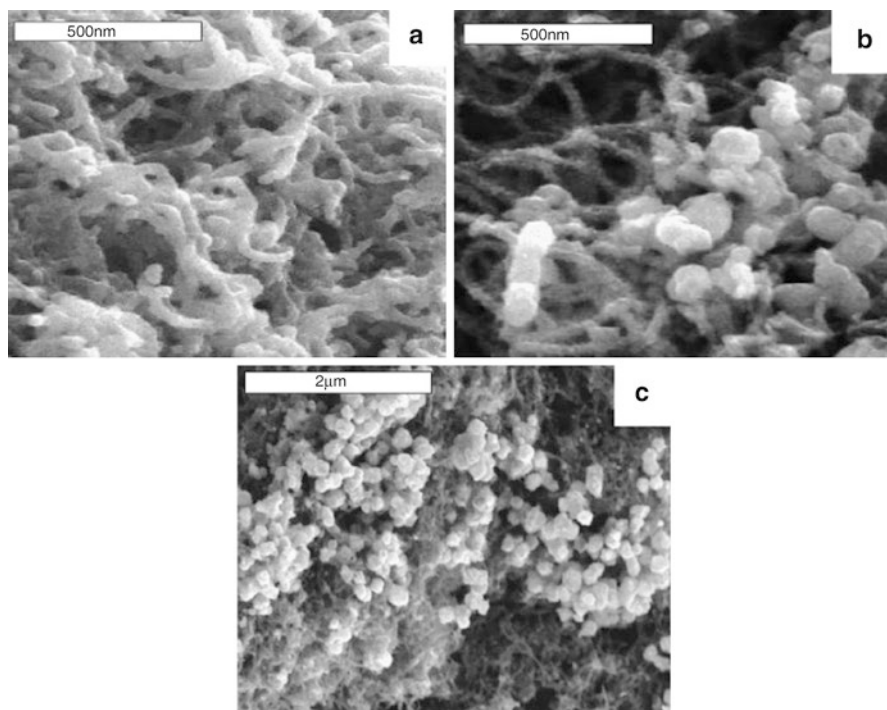


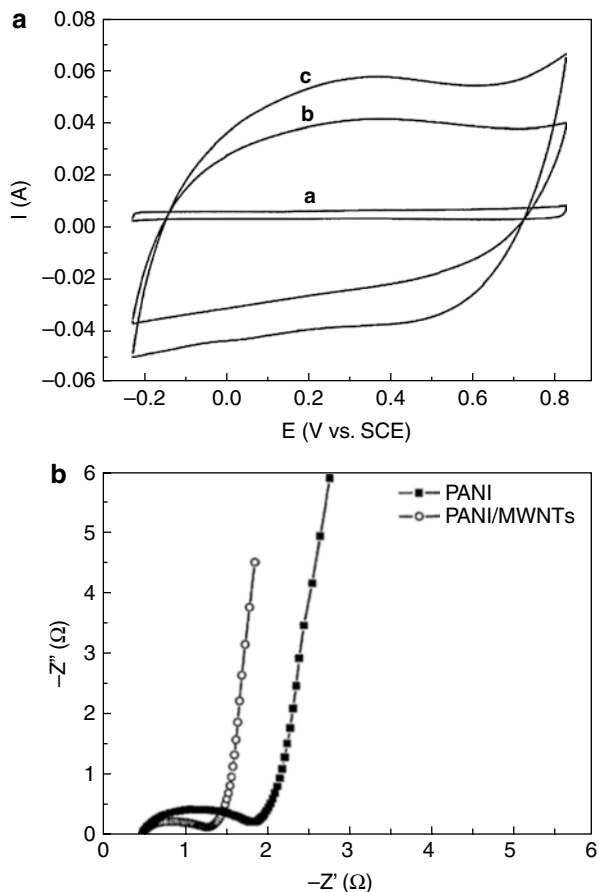
Fig. 50 SEM images of (a) MWCNT/polyaniline, (b) MWCNT/polypyrrole, and (c) MWCNT/PEDOT composite (Reproduced from Ref. [149] with permission from Elsevier Ltd.)

doping process caused by Warburg behavior. The charge transfer resistance of the PANI/MWCNTs composites is much smaller than the resistance of pure PANI.

The MWCNTs/PANI composite also exhibits better capacitance properties at higher current densities (Fig. 52). The decrease in the specific capacitance of PANI/MWCNTs with increased current density is lower relative to that of pure PANI [270].

Two-component C_{60} -Pd polymers are *n*-doped materials. The capacitance properties of pure C_{60} -Pd and its composites with different carbon nanostructures (SWCNTs, MWCNTs, CNOs) have been studied [197]. The C_{60} -Pd polymer demonstrates pseudocapacitance behavior due to the faradaic reduction of C_{60} in the negative potential range; at potentials lower than this threshold, the material exhibits very high resistance. Composites of C_{60} -Pd and carbon nanomaterials demonstrate capacitive properties in a larger potential range (Fig. 53). At positive potentials, behavior typical of double-layer capacitors is observed. Porous carbon nanostructures are responsible for these properties. At negative potentials, pseudocapacitive behavior is observed. The capacitance depends on the type of carbon nanomaterial because they have different porosities. The specific capacitances obtained for the composites are also significantly higher relative to the pure C_{60} -Pd film. The

Fig. 51 (a) Cyclic voltammograms of (a) MWCNTs, (b) PANI, and (c) PANI/MWCNTs composite electrodes in 1 mol/l NaNO_3 solution. The sweep rate was 10 mV s^{-1} . (b) Electrochemical impedance spectra of PANI and PANI/MWCNTs composite (Reproduced from Ref. [270] with permission from Elsevier Ltd.)



improvement in the specific capacitance is caused by the increased active surface area in the composites.

The capacitive properties of composites containing oxidized carbon nano-onions with covalently attached polyaniline [158, 159] and composites of carbon nano-onions and chitosan [206] were also investigated.

Very promising storage behavior was also reported for composites based on graphene and conductive polymers. For these systems, very high specific capacitances relative to the capacitance of a pure conductive polymer or graphene were reported. Representative specific capacitances obtained for graphene/PPy [153] and graphene nanosheets/PANI [152] are 1510 and 1046 F g^{-1} , respectively.

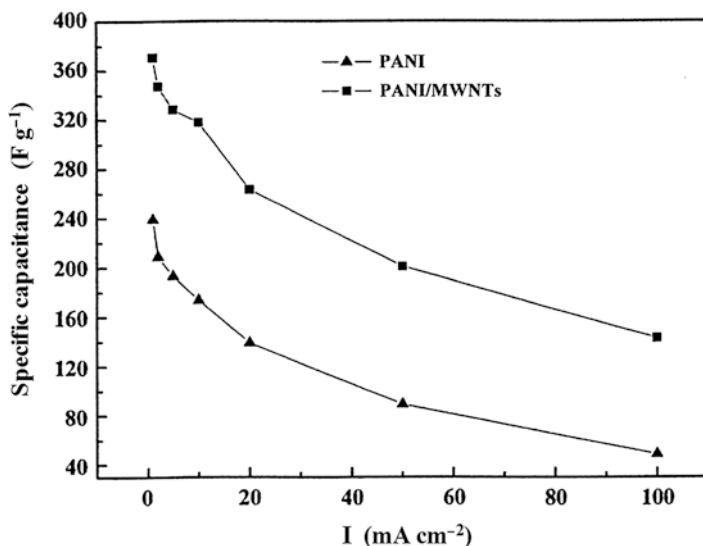


Fig. 52 Specific capacitance of PANI and PANI/MWNTs composite electrodes as a function of discharge current density (Reproduced from Ref. [270] with permission from Elsevier Ltd.)

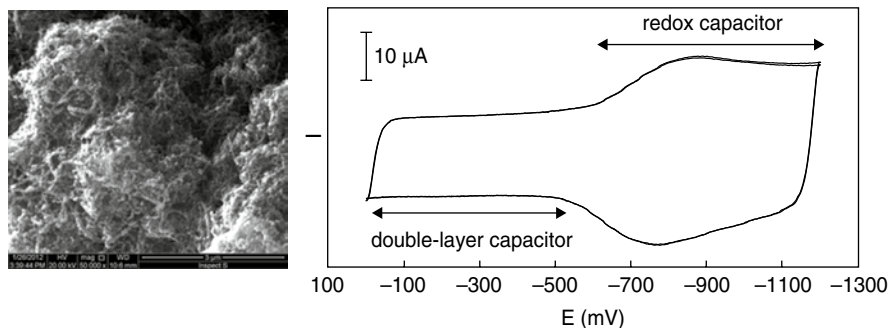


Fig. 53 SEM and cyclic voltammogram of MWCNT/C₆₀-Pd at 100 mV/s in acetonitrile containing 0.1 M $(n\text{-C}_4\text{H}_9)_4\text{NClO}_4$ (Adopted from Ref. [197] with permission from Elsevier Ltd.)

The composites utilizing carbon nanostructures with transition metal oxides, such as hydrous RuO_2 [141, 142, 160], NiO [277–279], MnO_2 [142, 266, 277], Fe_2O_3 [280], Co_3O_4 [155], and NiCo_2O_4 [281], that exhibit properties typical of redox capacitors were also prepared. The main goal was to improve the capacitance properties of these systems by depositing metal oxides on the porous surface of carbon nanotubes. Electrically conductive carbon nanotubes complement the high resistivity of the metal oxides. These systems also exhibit superior mechanical stability because of the carbon nanostructures. Of the transition metal oxides, MnO_2 has seen the most frequent use as an electroactive material in faradaic

Table 8 Capacitance properties of selected composites containing carbon nanostructure and conducting polymer or transition metal oxide

Carbon nanostructure	Composite	Specific capacitance F g ⁻¹
SWCNT	SWCNT/PANI	190 [146]
	SWCNT/PANI	247 [158]
	SWCNT/C ₆₀ -Pd	994 [197]
	SWCNT/NiC ₂ O ₄	1642 [281]
MWCNT	MWCNTs/PANI	670 [262]
	MWCNT/PPy	506 [262]
	MWCNT/C ₆₀ -Pd	758 [197]
	MWCNT/PEDOT	160 [150]
	MWCNT/NiO	523 [279]
CNO	CNO/PANI	496 [158]
	ox-CNO/C ₆₀ -Pd	284 [197]
	CNO/RuO ₂	151 [160]
Graphene	Graphene nanosheet/PANI	1046 [152]
	Graphene/PPy	1510 [153]
	Graphene nanosheet/RuO ₂	375 [142]
	Reduced graphene/NiO	770 [292]
	Graphene nanosheet/Mn ₃ O ₄	708 [155]

supercapacitors because it is inexpensive, readily available, and environmentally benign [14, 266]. The specific capacitance of this material is in the range of 200 Fg⁻¹ [282]. Compositing MnO₂·xH₂O with carbon nanomaterials generates superior capacitance properties. Specific capacitances of 580 Fg⁻¹ and 315 Fg⁻¹ were reported for MnO₂·xH₂O/MWCNTs [276] and MnO₂·xH₂O/graphene [283] composites, respectively. Additionally, improved electrochemical stability through repeated charge/discharge cycles was observed [266].

Hydrous ruthenium oxide (RuO₂·xH₂O) exhibits excellent capacitance properties (720 F g⁻¹ [284]), relatively high conductivity, and exceptional electrochemical reversibility. However, the high cost and toxicity limit its practical application [285]. To reduce the cost of this material and enhance its capacitance properties, composites containing carbon nanostructures and RuO₂ have been proposed [141, 142, 160].

In most studies, the metal oxide particles were deposited onto the CNTs' surface. It is also possible to encapsulate metal oxides with CNTs. The MnO₂@CNTs material exhibits a significantly higher specific capacitance compared to MnO₂ outside of the carbon nanotubes [286].

To improve the capacitance properties of metal oxides or conducting polymers, three component composites containing carbon nanoparticles, conductive polymer, and metal oxides were constructed [287–289].

Very promising properties were also reported for composites of conductive polymers or metal oxides based on activated carbon or carbon aerogel. For example,

specific capacitances as high as 771 F g^{-1} and 515 F g^{-1} were reported for PANI/activated carbon [290] and MnO_2 /carbon aerogel [291], respectively. The capacitance properties of selected composites of carbon nanoparticles and transition metal oxides are reported in Table 8.

Conclusion

Now a pool of synthetic methodologies are available for production of different material nanoparticles with controlled size, structure, and properties. These structures have been commonly used in basic and applied research. Nanoparticles not only have unique structures and physical and chemical properties but also provide a great opportunity to understand chemical and physical processes at the molecular level. The quantized electron transport in nanoparticles has played dominant role in these studies. The first section of this chapter is devoted to the nanoparticle involved in charge transfer phenomena. The proper description of this process in nanoscale material has been possible due to the progress in the development of computational/theoretical tools and experimental techniques, such as scanning probe microscopy/spectroscopy, particularly.

While many of the basic electron transfer phenomena are now understood, endless opportunities await the utilization of this unique nanoscale world. For example, high-frequency phenomena, such as quantized vibration moods, or plasmons, could be used to investigate the charge transport propagation in carbon nanostructures. The more attention should be focused on polymeric nanoparticles and transition metal oxide nanoparticles. These classes of material have been still waiting for progressive investigation in the field of quantized charge transfer process. They should be capable of stepwise single-electron charging similar to the behavior observed for metallic nanoclusters and carbon nanotubes. In the case of carbon nanostructures, more research has to be focused on the electron transfer phenomena in thin solid films. Such materials are particularly suitable to study the size and the intrinsic conductivity (SWCNTs chirality) effects in the interparticle electron exchange process.

Although nanoparticles can find applications in a number of fields, the significant part of this chapter mainly focuses on application involving charge storing materials. Conductivity and charging properties are particularly important for these applications. With a large ratio of surface area to volume, tuned porous structure, and surface chemistry, nanoparticle materials demonstrate excellent properties for charge storage applications. Despite of large number of experimental work done in this area, several important aspects have to be considered in future studies. Systematic investigation of capacitance properties of carbon nanomaterials sorted according to their size and chirality in the case of nanotubes should be performed. Atomic and electron level control of carbon nanostructures remains the main electrochemical challenge. More attention has to be also focused on the molecular architecture of materials used for the supercapacitors fabrication. Although, a number of prototypical nanoparticle-based charge storage devices have already been made, the massive production and integration of the nanoparticle components into

easily reproduced device structures is very challenging. Well-ordered multicomponent systems should exhibit more efficient charge storage properties and ability to tune their properties. The charge transfer processes in such systems and energy storage properties can be also easily theoretically described, what is particularly important in modeling of the capacitance behavior of these materials. This progress requires development of new techniques for all-nanoparticle composites synthesis. There is also a whole issue of practical aspects for careful consideration, such as mechanical, thermal, and electrochemical stability of nanostructured materials, voltage limit in which they can operate, solvent and electrolyte use for capacitor fabrication, and many others. Advancement in these areas should develop a new generation of nanostructured materials with finely tuned electronic properties.

References

1. Templeton AC, Wuelfing WP, Murray RW (2000) Monolayer-protected cluster molecules. *Acc Chem Res* 33:27–36
2. Murray RW (2008) Nanoelectrochemistry: metal nanoparticles, nanoelectrodes, and nanopores. *Chem Rev* 108:2688–2720
3. Sardar R, Funston AM, Mulvaney P, Murray RW (2009) Gold nanoparticles: past, present, and future. *Langmuir* 25(24):13840–13851
4. Chen S (2007) Discrete charge transfer in nanoparticle solid films. *J Mater Chem* 17:4115–4121
5. Bandaru PR (2007) Electrical properties and applications of carbon nanotube structures. *J Nanosci Nanotechnol* 7:1–29
6. Biercuk MJ, Ilani S, Marcus CM, McEuen PL (2008) Electrical transport in single-wall carbon nanotubes. In: Jorio A, Dresselhaus G, Dresselhaus MS (eds) *Carbon nanotubes, Topics in applied physics*. Springer, Berlin/Heidelberg, pp 455–493
7. Charlier J-C (2002) Defects in carbon nanotubes. *Acc Chem Res* 35:1063–1069
8. Wu YH, Yu T, Shen ZX (2010) Two-dimensional carbon nanostructures: fundamental properties, synthesis, characterization, and potential applications. *J Appl Phys* 108:071301-1–071301-38
9. Joselevich E (2004) Electronic structure and chemical reactivity of carbon nanotubes: a chemist's view. *ChemPhysChem* 5:619–624. doi:10.1002/cphc.200301049
10. Huang L, Wu B, Yu G, Liu Y (2011) Graphene: learning from carbon nanotubes. *J Mater Chem* 21:919–929
11. Brownson DAC, Banks CE (2010) Graphene electrochemistry: an overview of potential applications. *Analyst* 135:2768–2778
12. Hanemann T, Szabo DV (2010) Polymer-nanoparticle composites: from synthesis to modern applications. *Materials* 3:3468–3517
13. Frackowiak E (2007) Carbon materials for supercapacitor application. *Phys Chem Chem Phys* 9:1774–1785
14. Lota G, Fic K, Frackowiak E (2011) Carbon nanotubes and their composites in electrochemical applications. *Energy Environ Sci* 4:1592–1605
15. Frackowiak E, Beguin F (2002) Electrochemical storage of energy in carbon nanotubes and nanostructured carbons. *Carbon* 40:1775–1787
16. Ghosh A, Lee YH (2012) Carbon-based electrochemical capacitors. *ChemSusChem* 5:480–499
17. Candelaria SL, Shao Y, Zhou W, Li X, Xiao J, Zhang J-G, Wang Y, Liu J, Li J, Cao G (2012) Nanostructured carbon for energy storage and conversion. *Nano Energy* 1:195–220
18. Choi H-J, Jung S-M, Seo J-M, Chang DW, Dai L, Baek J-B (2012) Graphene for energy conversion and storage in fuel cells and supercapacitors. *Nano Energy* 1:534–551

19. Frackowiak E, Beguin F (2001) Carbon materials for the electrochemical storage of energy in capacitors. *Carbon* 39:937–950
20. Chen S, Murray RW, Feldberg SW (1998) Quantized capacitance charging of monolayer-protected Au clusters. *J Phys Chem B* 102:9898–9907
21. Green SJ, Stokes JJ, Hostetler MJ, Pietron J, Murray RW (1997) Three-dimensional monolayers: nanometer-sized electrodes of alkenethiolate-stabilized gold cluster molecules. *J Phys Chem B* 101:2663–2668
22. Chen S, Huang K (2000) Electrochemical studies of water-soluble palladium nanoparticles. *J Clust Sci* 11:405–421
23. Templeton AC, Cliffler DE, Murray RW (1999) Redox and fluorophore functionalization of water-soluble, tiopronin-protected gold clusters. *J Am Chem Soc* 121:7081–7089
24. Templeton AC, Hostetler MJ, Warmoth EK, Chen S, Hartshorn CM, Krishnamurthy VM, Forbes MDE, Murray RW (1998) Gateway, reactions to diverse, polyfunctional monolayer-protected gold clusters. *J Am Chem Soc* 120:4845–4849
25. Aoki K, Chen J, Yang N, Nagasawa H (2003) Charge-transfer reactions of silver stearate-coated nanoparticles in suspensions. *Langmuir* 19:9904–9909
26. Porter MD, Bright TB, Allara DL, Chidsey CED (1987) Spontaneously organized molecular assemblies. 4. Structural characterization of *n*-alkyl thiol monolayers on gold by optical ellipsometry, infrared spectroscopy, and electrochemistry. *J Am Chem Soc* 109:3559–3568
27. Peterson RR, Cliffler DE (2006) Scanning electrochemical microscopy determination of organic soluble MPC electron-transfer rates. *Langmuir* 22:10307–10314
28. Guo R, Georganopoulou D, Feldberg SW, Donkers R, Murray RW (2005) Supporting electrolyte and solvent effects on single-electron double layer capacitance charging of hexanethiolate-coated Au₁₄₀ nanoparticles. *Anal Chem* 77:2662–2669
29. Quinn B, Liljeroth P, Ruiz V, Laaksonen T, Kontturi K (2003) Electrochemical resolution of 15 oxidation states for monolayer protected gold nanoparticles. *J Am Chem Soc* 125:6644–6645
30. Hicks JF, Templeton AC, Chen S, Sheran KM, Jasti R, Murray RW, Debord J, Schaaff TG, Whetten RL (1999) The monolayer thickness dependence of quantized double-layer capacitances of monolayer-protected gold clusters. *Anal Chem* 71:3703–3711
31. Hicks JF, Miles DT, Murray RW (2002) Quantized double-layer charging of highly monodisperse metal nanoparticles. *J Am Chem Soc* 124:13322–13328
32. Jhaveri SD, Lowy DA, Foss EE, Snow AW, Ancona MG, Tender LM (2002) Ion-induced discrete charging of immobilized water-soluble gold nanoclusters. *Chem Commun* 1544–1545
33. Chen S, Pei R, Zhao T, Dyer DJ (2002) Gold nanoparticle assemblies by metal ion-pyridine complexation and their rectified quantized charging in aqueous solutions. *J Phys Chem B* 106:1903–1908
34. Zamborini FP, Hocks JF, Murray RW (2000) Quantized double layer charging of nanoparticle films assembled using carboxylate/(Cu²⁺ or Zn²⁺)/carboxylate bridges. *J Am Chem Soc* 122:4514–4515
35. Hicks JF, Zamborini FP, Murray RW (2002) Dynamics of electron transfer between electrodes and monolayers of nanoparticles. *J Phys Chem B* 106:7751–7757
36. Georganopoulou DG, Mirkin MV, Murray RW (2004) SECM measurement of the fast electron transfer dynamics between Au₃₈¹⁺ nanoparticles and aqueous redox species at a liquid/liquid interface. *Nano Lett* 4:1763–1767
37. Chen S, Ingram RS, Hostetler MJ, Pietron JJ, Murray RW, Schaaff TG, Khoury JT, Alvarez MM, Whetten RL (1998) Gold nanoelectrodes of varied size: transition to molecule like charging. *Science* 280:2098–2101
38. Lee D, Donkers RL, Wang G, Harper AS, Murray RW (2004) Electrochemistry and optical absorbance and luminescence of molecule-like Au₃₈ nanoparticles. *J Am Chem Soc* 126:6193–6199
39. Jimenez VL, Georganopoulou DG, White RJ, Harper AS, Mills AJ, Lee D, Murray RW (2004) Hexanethiolate monolayer protected 38 gold atom cluster. *Langmuir* 20:6864–6870

40. Balasubramanian R, Mills AL, Murray RW (2005) Reaction of $\text{Au}_{55}(\text{PPh}_3)_{12}\text{Cl}_6$ with thiols yields thiolate monolayer protected Au_{75} clusters. *J Am Chem Soc* 127:8126–8132
41. Tel-Vered R, Bard AJ (2006) Generation and detection of single metal nanoparticles using scanning electrochemical microscopy techniques. *J Phys Chem B* 110:25279–25287
42. Ingram RS, Hostetler MJ, Murray RW, Schaaff TG, Khoury JT, Whetten RL, Bigioni TP, Guthrie DK, First PN (1997) 28 kDa alkanethiolate-protected Au clusters give analogous solution electrochemistry and STM coulomb staircases. *J Am Chem Soc* 119:9279–9280
43. Pradhan S, Sun J, Deng F, Chen S (2006) Single-electron transfer in nanoparticle solids. *Adv Mater* 18:3279–3283
44. Hicks JF, Zamborini FP, Osisek AJ, Murray RW (2001) The dynamics of electron self-exchange between nanoparticles. *J Am Chem Soc* 123:7048–7053
45. Chen A, Pei R (2001) Ion-induced rectification of nanoparticle quantized capacitance charging in aqueous solutions. *J Am Chem Soc* 123:10607–10615
46. Chen S (2000) Nanoparticle assemblies: “rectified” quantized charging in aqueous media. *J Am Chem Soc* 122:7420–7421
47. Deng F, Chen S (2005) Self-assembled multilayers of gold nanoparticles: nitrate-induced rectification of quantized capacitance charging and effects of alkaline (earth) ions in aqueous solutions. *Phys Chem Chem Phys* 7:3375–3381
48. Deng F, Chen S (2007) Electrochemical quartz crystal microbalance studies of the rectified quantized charging of gold nanoparticle multilayers. *Langmuir* 23:936–941
49. Chen S (2000) Self-assembling of monolayer-protected gold nanoparticles. *J Phys Chem B* 104:663–667
50. Gittins DI, Bethell D, Nichols RJ, Schiffrin DI (1999) Redox-connected multilayers of discrete gold particles: a novel electroactive nanomaterial. *Adv Mater* 11:737–740
51. Liljeroth P, Vanmaekelbergh D, Ruiz V, Kontturi K, Jiang H, Kauppinen E, Quinn BM (2004) Electron transport in two-dimensional arrays of gold nanocrystals investigated by scanning electrochemical microscopy. *J Am Chem Soc* 126:7126–7132
52. Quinn BM, Prieto I, Haram SK, Bard AJ (2001) Electrochemical observation of a metal/insulator transition by scanning electrochemical microscopy. *J Phys Chem B* 105:7474–7476
53. Ahonen P, Ruiz V, Kontturi K, Liljeroth P, Quinn BM (2008) Electrochemical gating in scanning electrochemical microscopy. *J Phys Chem C* 112:2724–2728
54. Doty RC, Yu H, Shih CK, Korgel BA (2001) Temperature-dependent electron transport through silver nanocrystal superlattices. *J Phys Chem B* 105:8291–8296
55. Wuelfing WP, Green SJ, Pietron JJ, Cliffel DE, Murray RW (2000) Electronic conductivity of solid-state, mixed-valent, monolayer-protected Au clusters. *J Am Chem Soc* 122:11465–11472
56. Snow AW, Wohltjen H (1998) Size-induced metal to semiconductor transition in stabilized gold cluster ensemble. *Chem Mater* 10:947–949
57. Marcus RA (1993) Electron transfer reactions in chemistry: theory and experiment. *Angew Chem Int Ed Engl* 32:1111–1121
58. Marcus RA (1965) On the theory of electron-transfer reactions. VI. Unified treatment for homogenous and electrode reactions. *J Chem Phys* 43:679–701
59. Sheng P, Abeles B, Arie Y (1973) Hopping conductivity in granular metals. *Phys Rev Lett* 31:44–47
60. Likalter AA (1999) On hopping conductivity in granular metals. *J Non Cryst Solids* 250–252:771–775
61. Wuelfing WP, Murray RW (2002) Electron hopping through films of arenethiolate monolayer-protected gold clusters. *J Phys Chem B* 106:3139–3145
62. Ranganathan S, Guo R, Murray RW (2007) Nanoparticle films as electrodes: voltammetric sensitivity to the nanoparticle energy gap. *Langmuir* 23:7372–7377
63. Wang Y, Laborda E, Salter C, Crossley A, Compton RG (2012) Facile in situ characterization of gold nanoparticles on electrode surfaces by electrochemical techniques: average size, number density and morphology determination. *Analyst* 137:4693–4697

64. Uosaki K, Kondo T, Okamura M, Song W (2002) Electron and ion transfer through multilayers of gold nanoclusters covered by self-assembled monolayers of alkylthiols with various functional groups. *Faraday Discuss* 121:373–389
65. Facci JS, Schmehl RH, Murray RW (1982) Effect of redox site concentration on the rate of electron transport in a redox copolymer film. *J Am Chem Soc* 104:4959–4960
66. Chidsey CED (1991) Free energy and temperature dependence of electron transfer at the metal-electrolyte interface. *Science* 251:919–921
67. Smalley JF, Feldberg SW, Chidsey CED, Linford MR, Newton MD, Liu YP (1995) The kinetics of electron transfer through ferrocene-terminated alkanethiol monolayers on gold. *J Phys Chem* 99:13141–13149
68. Geim AK, Novoselov KS (2007) The rise of graphene. *Nat Mater* 6:183–191
69. Bachtold A, Strunk C, Salvetat JP, Bonard JM, Forro L, Nussbaumer T, Schonenberger C (1999) Aharonov-Bohm oscillations in carbon nanotubes. *Nature* 397:673–675
70. Saito R, Dresselhaus G, Dresselhaus MS (1993) Electronic structure of double-layer graphene tubes. *J Appl Phys* 73(2):494–500
71. Li TL, Ting JH (2010) Determination of the Fermi-level subband indices of single-walled carbon nanotubes. *Chin J Phys* 48:629–649
72. Chico L, Santos H, Ayuela A, Jaskólski W, Pelc M, Brey L (2010) Unzipped and defective nanotubes: rolling up graphene and unrolling tubes. *Acta Phys Polo A* 118:433–441
73. Wang X, Yang DP, Huang G, Hunag P, Shen G, Guo S, Mei Y, Cui D (2012) Rolling up graphene oxide sheets into micro/nan scrolls by nanoparticle aggregation. *J Mater Chem* 22:17441–17444
74. Tans SJ, Devoret MH, Dai H, Thess A, Smalley RE, Geerligs LJ, Dekker C (1997) Individual single-wall carbon nanotubes as quantum wires. *Nature* 386:474–477
75. Bockrath M, Cobden DH, McEuen PL, Chopra NG, Zettl A, Thess A, Smalley RE (1997) Single-electron transport in ropes of carbon nanotubes. *Science* 275:1922–1925
76. Tans SJ, Verschueren ARM, Dekker C (1998) Room-temperature transistor based on a single carbon nanotube. *Nature* 393:49–52
77. Martel R, Schmidt T, Shea HR, Hertel T, Avouris P (1998) Single- and multi-wall carbon nanotube field-effect transistors. *Appl Phys Lett* 73:2447–2449
78. Miao M (2011) Electrical conductivity of pure carbon nanotube yarns. *Carbon* 49:3755–3761
79. Mattia D, Rossi MP, Kim BM, Korneva G, Bau HH, Gogotsi Y (2006) Effect of graphitization on the wettability and electrical conductivity of CVD-Carbon nanotubes and films. *J Phys Chem B* 110:9850–9855
80. Li Q, Li Y, Zhang X, Chikkannanavar SB, Zhao Y, Dangelewicz AM, Zheng LZ, Doorn SK, Jia Q, Peterson DE, Arendt PN, Zhu Y (2007) Structure-dependent electrical properties of carbon nanotube. *Adv Mater* 19:3358–3363
81. Chen IWP, Liang R, Zhao H, Wang B, Zhang C (2011) Highly conductive carbon nanotube buckypapers with improved doping stability via conjugational cross-linking. *Nanotechnology* 22:1–7
82. Ryu Y, Yin L, Yu C (2012) Dramatic electrical conductivity improvement of carbon nanotube networks by simultaneous de-bundling and hole-doping with chlorosulfonic acid. *J Mater Chem* 22:6959–6964
83. Marinho B, Ghislandi M, Tkalya E, Koning CE, de With G (2012) Electrical conductivity of compacted graphene, multi-wall carbon nanotubes, carbon black, and graphite powder. *Powder Technol* 221:351–358
84. Tantang H, Ong JY, Loh CL, Dong X, Chen P, Chen Y, Hu X, Tan LP, Li LJ (2009) Using oxidation to increase the electrical conductivity of carbon nanotube electrodes. *Carbon* 47:1867–1885
85. Rezanian H (2012) Electrical conductivity of zigzag carbon nanotubes including Holstein polarons. *Eur Phys J B* 85:1–5
86. Lin YM, Appenzeller J, Avouris P (2004) Ambipolar-to-unipolar conversion of carbon nanotube transistors by gate structure engineering. *Nano Lett* 4:947–950

87. Yao Z, Dekker C, Avouris P (2001) Electrical transport through single-wall carbon nanotubes. In: Dresselhaus MS, Dresselhaus G, Avouris PH (eds) *Carbon nanotubes, Topics in applied physics*. Springer, Berlin/Heidelberg, pp 147–171
88. Ilani S, Donev LAK, Kindermann M, McEuen PL (2006) Measurement of the quantum capacitance of interacting electrons in carbon nanotubes. *Nat Phys* 2:687–691
89. McEuen PL, Park JY (2004) Electron transport in single-walled carbon nanotubes. *MRS Bull* 29:272–275
90. Nygard J, Cobden DH, Bockrath M, McEuen PL, Lindelof PE (1999) Electrical transport measurements on single-walled carbon nanotubes. *Appl Phys A* 69:297–304
91. Li J, Cassell A, Delzeit L, Han J, Meyyappan M (2002) Novel three-dimensional electrodes: electrochemical properties of carbon nanotube ensembles. *J Phys Chem B* 106:9299–9305
92. Taurino I, Carrara S, Giorelli M, Tagliaferro A, De Micheli G (2012) Comparison of two different carbon nanotube-based surfaces with respect to potassium ferricyanide electrochemistry. *Surf Sci* 606:156–160
93. Taurino I, Carrara S, Giorelli M, Tagliaferro A, De Micheli G (2011) Comparing sensitivities of differently oriented multi-walled carbon nanotubes integrated on silicon wafer for electrochemical biosensors. *Sensors Actuators B* 160:327–333
94. Yu J, Shapter J, Quinton J, Johnston M, Beattie D (2006) Preparation, characterization and electrochemistry of carbon nanotubes directly attached to Si(100) surface. In: *Abstracts of the international conference of nanoscience and nanotechnology ICONN 06, Brisbane, Qld, 3–7 July 2006*
95. Diao P, Liu Z (2005) Electrochemistry AT chemically assembler single-wall carbon nanotube arrays. *J Phys Chem B* 109:20906–20913
96. Chou A, Bocking T, Singh NK, Gooding JJ (2005) Demonstration of the importance of oxygenated species at the ends of carbon nanotubes for their favourable electrochemical properties. *Chem Commun* 842–844
97. Wang Y, Iqbal Z (2005) Vertically oriented single-wall carbon nanotube/enzyme on silicon as biosensor electrode. *JOM* 34:27–29
98. Wang D, Song P, Liu C, Wu W, Fan S (2008) Highly oriented carbon nanotube papers made of aligned carbon nanotubes. *Nanotechnology* 19:1–6
99. Cao A, Ajayan PM, Ramanath G, Baskaran R, Turner K (2004) Silicon oxide thickness-dependent growth of carbon nanotubes. *Appl Phys Lett* 84:109–111
100. Liu Z, Shen Z, Zhu T, Hou S, Ying L (2000) Organizing single-walled carbon nanotubes on gold using a wet chemical self-assembling technique. *Langmuir* 16:3569–3573
101. Xin H, Woolley AT (2004) Directional orientation of carbon nanotubes on surfaces using a gas flow cell. *Nano Lett* 4:1481–1484
102. Kamat PV, Thomas KG, Barazzouk S, Girishkumar G, Vinodgopal K, Meisel D (2004) Self-assembled linear bundles of single wall carbon nanotubes and their alignment and deposition as a film in a dc field. *J Am Chem Soc* 126:10757–10762
103. Mazurenko I, Etienne M, Tananaiko O, Urbanova V, Zaitsev V, Walcarius A (2013) Electrophoretic deposition of macroporous carbon nanotube assemblies for electrochemical applications. *Carbon* 53:302–312
104. Schanmugam S, Gedanken A (2006) Electrochemical properties of bamboo-shaped multi-walled nanotubes generated by solid state pyrolysis. *Electrochem Commun* 8:1099–1105
105. Burghard M, Klauk H, Kern K (2009) Carbon-based field-effect transistors for nanoelectronics. *Adv Mater* 21:2586–2600
106. Mao S, Yu K, Chang J, Steeber DA, Ocola LE, Chen J (2013) Direct growth of vertically-oriented graphene for field-effect transistor biosensor. *Sci Rep* 3:1–6
107. Wang X, Li X, Zhang L, Yoon Y, Weber PK, Wang H, Guo J, Dai H (2009) N-doping of graphene through electrothermal reactions with ammonia. *Science* 234:768–771
108. Tworzydło J, Trauzettel B, Titov M, Rycerz A, Beenakker CWJ (2006) Sub-poissonian shot noise in graphene. *Phys Rev Lett* 96:246802-1–246802-4
109. Schaffique A, Hwang EH, Galitski VM, Das Sarma S (2007) A self-consistent theory for graphene transport. *Proc Natl Acad Sci U S A* 104:18392–18397

110. Martin J, Akerman N, Ulbricht G, Lohmann T, Smet JH, von Klitzing K, Yacoby A (2008) Observation of electron-hole puddles in graphene using a scanning single-electron transistor. *Nat Phys* 4:144–148
111. Zhang H, Liu CX, Qi XL, Dai X, Fang Z, Zhang SC (2009) Topological insulators in Bi_2Se_3 , Bi_2Te_3 and Sb_2Te_3 with a single Dirac cone on the surface. *Nat Phys* 5:438–442
112. Xia J, Chen F, Li J, Tao N (2009) Measurement of the quantum capacitance of graphene. *Nat Nanotechnol* 4:505–509
113. Tang L, Wang Y, Li Y, Feng H, Lu J, Li J (2009) Preparation, structure, and electrochemical properties of reduced graphene sheet films. *Adv Funct Mater* 19:2782–2789
114. Kang X, Wang J, Wu H, Liu J, Aksay IA, Lin Y (2010) A graphene-based electrochemical sensor for sensitive detection of paracetamol. *Talanta* 81:754–759
115. Alvarappan S, Erdem A, Liu C, Li CZ (2009) Probing the electrochemical properties of graphene nanosheets for biosensing applications. *J Phys Chem C* 113:8853–8857
116. Pudlak M, Pincak R (2009) Energy gap between highest occupied molecular orbital and lowest unoccupied molecular orbital in multiwalled fullerenes. *Phys Rev A* 79:033202-1–033202-5
117. Kuznetsov V, Moseenkov S, Ischenko A, Romanenko A, Buryakov T, Anikeeva O, Maksimenko S, Kuzhir P, Bychanok D, Gusinski A, Ruhavets O, Shenderova O, Lambin P (2008) Controllable electromagnetic response of onion-like carbon based materials. *Phys State Solidi B* 245:2051–2054
118. Sek S, Breczko J, Plonska-Brzezinska ME, Wilczewska AZ, Echegoyen L (2013) STM-based molecular junction of carbon nano-onion. *Chem Phys Chem* 14:96–100
119. Yang Z (2012) Application of nanocomposites for supercapacitors: characteristics and properties. In: Ebrahimi F (ed) *Nanocomposites – new trends and developments*. Nanotechnology and nanomaterials. INTECH, Rijeka, Croatia, 299–327
120. Zhang Y, Feng H, Wu X, Wang L, Zhang A, Xia T, Dong H, Li X, Zhang L (2009) Progress of electrochemical capacitor electrode materials: a review. *Int J Hydrog Energy* 34:4889–4899
121. Kang YJ, Chung H, Han CH, Kim W (2012) All-solid-state flexible supercapacitors based on papers coated with carbon nanotubes and ionic-liquid-based gel electrolytes. *Nanotechnology* 23:065401
122. Chandra A (2012) Supercapacitors: an alternate technology for energy storage. *Proc Natl Acad Sci Sect A Phys Sci* 82(1):79–90
123. Simon P, Gogotsi Y (2008) Materials for electrochemical capacitors. *Nat Mater* 7:845–854
124. Bose S, Kuila T, Mishra AK, Rajasekar R, Kim NH, Lee JH (2012) Carbon-based nanostructured materials and their composites as supercapacitor electrodes. *J Mater Chem* 22:767–784
125. Suppiger D, Busato S, Ermanni P, Motta M, Windle A (2009) Electromechanical actuation of macroscopic carbon nanotube structures: mats and aligned ribbons. *Phys Chem Chem Phys* 11:5180–5185
126. Vivekchand SRC, Rout CS, Subrahmanyam KS, Govindaraj A, Rao CNR (2008) Graphene-based electrochemical supercapacitors. *J Chem Sci* 120:9–13
127. Chen JH, Li WZ, Wang DZ, Yang SX, Wen JG, Ren ZF (2002) Electrochemical characterization of carbon nanotubes as electrode in electrochemical double-layer capacitors. *Carbon* 40:1193–1197
128. Portret C, Taberna PL, Simon P, Flahaut E, Laberty-Robert C (2005) High power density electrodes for carbon supercapacitor applications. *Electrochim Acta* 50:4174–4181
129. Show Y (2012) Electric double-layer capacitor fabricated with addition of carbon nanotube to polarizable electrode. *J Nanomater* 2012:1–8
130. Qu D, Shi H (1998) Studies of activated carbons used in double-layer capacitors. *J Power Sources* 74:99–107
131. Pan H, Li J, Feng YP (2010) Carbon nanotubes for supercapacitor. *Nanoscale Res Lett* 5:654–668
132. Stoller MD, Park S, Zhu Y, An J, Ruoff RS (2008) Graphene-based ultracapacitors. *Nano Lett* 8:3498–3502

133. Liu C, Yu Z, Neff D, Zhamu A, Jang BZ (2010) Graphene-based supercapacitor with an ultrahigh energy density. *Nano Lett* 10:4863–4868
134. Pech D, Brunet M, Durou H, Huang P, Mochslin V, Gogotsi Y, Taberna PL, Simon P (2010) Ultrahigh-power micrometer-sized supercapacitors based on onion-like carbon. *Nat Nanotechnol* 5:651–654
135. Al-zubaidi A, Inoue T, Matsushita T, Ishii Y, Hashimoto T, Kawaski S (2012) Cyclic voltammogram profile of single-walled carbon nanotube electric double-layer capacitor electrode reveals dumbbell shape. *J Phys Chem C* 116:7681–7686
136. Sharma P, Bhatti TS (2010) A review on electrochemical double-layer capacitors. *Energy Convers Manage* 51:2901–2912
137. Miller JR, Outlaw A, Holloway BC (2010) Graphene double-layer capacitor with ac line-filtering performance. *Science* 329:1637–1639
138. Zhang LL, Zhao XS (2009) Carbon-based materials as supercapacitor electrodes. *Chem Soc Rev* 38:2520–2531
139. Plonska-Brzezinska ME, Palkar A, Winkler K, Echegoyen L (2010) Electrochemical properties of small carbon nano-onion films. *Electrochem Solid State Lett* 13(4):K35–K38
140. Lee YJ, Jung JC, Yi J, Baek SH, Yoon JR, Song IK (2010) Preparation of carbon aerogel in ambient conditions for electrical double-layer capacitor. *Curr Appl Phys* 10:682–686
141. Arable G, Wagh D, Kulkarni M, Mulla IS, Vernekar SP, Vijayamohan K, Rao AM (2003) Enhanced supercapacitance of multiwalled carbon nanotubes functionalized with ruthenium oxide. *Chem Phys Lett* 376:207–213
142. Rakhi RB, Chen W, Cha D, Alshareef HN (2011) High performance supercapacitors using metal oxide anchored graphene nanosheet electrodes. *J Mater Chem* 21:16197–16204
143. Hughes M, Chen GZ, Shaffer MSP, Fray DJ, Windle AH (2002) Electrochemical capacitance of a nanoporous composite of carbon nanotubes and polypyrrole. *Chem Mater* 14:1610–1613
144. Zhou Y, Qin ZY, Zhang Y, Wei YL, Wang LF, Zhu MF (2010) Polyaniline/multi-walled carbon nanotube composites with core-shell structures as supercapacitor electrode material. *Electrochim Acta* 55:3904–3908
145. Gajendran P, Saraswathi R (2008) Polyaniline-carbon nanotube composite. *Pure Appl Chem* 80:2377–2395
146. Zhou YK, He BL, Zhou WJ, Huang J, Li XH, Wu B, Li HL (2004) Electrochemical capacitance of well-coated single-walled carbon nanotube with polyaniline composites. *Electrochim Acta* 49:257–262
147. Sivakkumar SR, Kim WJ, Choi JA, MacFarlane DR, Forsyth M, Kim DW (2007) Electrochemical performance of polyaniline nanofibres and polyaniline/multi-walled carbon nanotube composite as an electrode material for aqueous redox supercapacitors. *J Power Sources* 171:1062–1068
148. Frackowiak E, Jurewicz K, Delpeux S, Beguin F (2001) Nanotubular materials for supercapacitors. *J Power Sources* 97–98:822–825
149. Frackowiak E, Khomenko V, Jurewicz K, Lota K, Beguin F (2006) Supercapacitors based on conducting polymers/nanotubes composites. *J Power Sources* 153:413–418
150. Lota K, Khomenko V, Frackowiak E (2004) Capacitance properties of poly(3,4-ethylenedioxythiophene)/carbon nanotubes composites. *J Phys Chem Solid* 65:295–301
151. Wu Q, Xu Y, Liu A, Shi G (2010) Supercapacitors based on flexible graphene/polyaniline nanofiber composite films. *ACS Nano* 4:1963–1970
152. Yan J, Wei T, Shao B, Fan Z, Qian W, Zhang M, Wei F (2010) Preparation of a graphene nanosheet/polyaniline composite with high specific capacitance. *Carbon* 48:487–493
153. Mini PA, Balakrishnan A, Nair SV, Subramanian RV (2011) Highly super capacitive electrodes made of graphene/poly(pyrrole). *Chem Commun* 47:5753–5755
154. Park MS, Needham SA, Wang GX, Kang YM, Park JS, Dou SX, Liu HK (2007) Nanostructured SnSb/carbon nanotube composites synthesized by reductive precipitation for lithium-ion batteries. *Chem Mater* 19:2406–2410

155. Zhang W, Liu F, Li Q, Shou Q, Cheng J, Zhang L, Nelson BJ, Zhang X (2012) Transition metal oxide and graphene nanocomposites for high-performance electrochemical capacitors. *Phys Chem Chem Phys* 14:16331–16337
156. Khomeenko V, Raymundo-Pinero E, Beguin F (2006) Optimisation of an asymmetric manganese oxide/activated carbon capacitor working at 2 V in aqueous medium. *J Power Sources* 153:183–190
157. Bleda-Martinez MJ, Peng C, Zhang S, Chen GZ, Morallon E, Cazorla-Amaros D (2008) Electrochemical methods to enhance the capacitance of activated carbon/polyaniline composites. *J Electrochem Soc* 155(10):A672–A678
158. Plonska-Brzezinska ME, Brezczko J, Palys B, Echegoyen L (2013) The electrochemical properties of nanocomposite films obtained by chemical in situ polymerization of aniline and carbon nanostructures. *ChemPhysChem* 14:116–124
159. Plonska-Brzezinska ME, Mazurczyk J, Palys B, Brezczko J, Lapinski A, Dubis AT, Echegoyen L (2012) Preparation and characterization of composites that contain small carbon nanoions and conducting polyaniline. *Chem Eur J* 18:2600–2608
160. Borgohain R, Li J, Selegue JP, Cheng YT (2012) Electrochemical study of functionalized carbon nano-ions for high-performance supercapacitor electrodes. *J Phys Chem C* 116:15068–15075
161. Gujar TP, Kim WY, Puspitasari I, Jung KD, Joo OS (2007) Electrochemically deposited nanograin ruthenium oxide as a pseudocapacitive electrode. *Int J Electrochem Sci* 2:666–673
162. Park SH, Kim JY, Kim KB (2010) Pseudocapacitive properties of nanostructured anhydrous ruthenium oxide thin film prepared by electrostatic spray deposition and electrochemical lithiation/delithiation. *Fuel Cells* 10:865–872
163. Zhang J, Ma J, Zhang LL, Guo P, Jiang J, Zhao XS (2010) Template synthesis of tubular ruthenium oxides for supercapacitor applications. *J Phys Chem C* 114:13608–13613
164. Peng H, Lu Q, Zhang Y, Li Y, Gao F (2010) Selective synthesis of nickel oxide nanowires and length effect on their electrochemical properties. *Nanoscale* 2:920–922
165. Cho HW, Nam JH, Park JH, Kim KM, Ko JM (2012) Supercapacitive properties of Co-Ni mixed oxide electrode adopting the nickel foam as a current collector. *Bull Korean Chem Soc* 33:3993–3997
166. Ahn YR, Song MY, Jo SM, Park CR, Kim DY (2006) Electrochemical capacitors based on electrodeposited ruthenium oxide on nanofibre substrates. *Nanotechnology* 17:2865–2869
167. Inamdar AI, Kim YS, Sohn JS, Im H (2011) Supercapacitive characteristics of electrodeposited polyaniline thin films grown on indium-doped tin-oxide substrates. *J Korean Phys Soc* 59:145–149
168. Conway E (1999) Capacitance behavior of films of conducting, electrochemically reactive polymers. In: *Electrochemical supercapacitors*. Springer Science, New York, pp 299–333
169. Radhakrishnan S, Muthukannan R, Kamatchi U, Rao CRK, Vijayan M (2011) Performance of phosphoric acid doped polyaniline as electrode material for aqueous redox supercapacitor. *Indian J Chem* 50A:970–978
170. Peng C, Hu D, Chen GZ (2011) Theoretical specific capacitance based on charge storage mechanisms of conducting polymers: comment on “vertically oriented arrays of polyaniline nanorods and their super electrochemical properties”. *Chem Commun* 47:4105–4107
171. Pan L, Qiu H, Li Y, Pu L, Xu J, Shi Y (2010) Conducting polymer nanostructures: template synthesis and applications energy storage. *Int J Mol Sci* 11:2636–2657
172. Snook GA, Kao P, Best AS (2011) Conducting-polymer-based supercapacitor devices and electrodes. *J Power Sources* 196:1–12
173. Snook GA, Best AS (2009) Co-deposition of conducting polymers in a room temperature ionic liquid. *J Mater Chem* 19:4248–4254
174. Ryu KS, Kim KM, Park NG, Park YJ, Chang SH (2002) Symmetric redox supercapacitor with conducting polyaniline electrodes. *J Power Sources* 103:305–309
175. Kim MS, Moon JH, Yoo PJ, Park JH (2012) Hollow polypyrrole films: applications for energy storage devices. *J Electrochem Soc* 159(7):A1052–A1056

176. Guranthan K, Murugan AV, Marimuthu R, Mulik UP, Amalnerker DP (1999) Electrochemically synthesized conducting polymeric materials for applications towards technology in electronics, optoelectronics and energy storage devices. *Mater Chem Phys* 61:173–191
177. Kim BC, Ko JM, Wallace GG (2008) A novel capacitor material based on Nafion-doped polypyrrole. *J Power Sources* 177:665–668
178. Signorelli R, De K, Kassakian JG, Schindall JE (2009) Electrochemical double layer capacitors using carbon nanotube electrode structures. *Proc IEEE* 97:1837–1847
179. Park TR, Rhee SS (2001) Multilayer model of interlayer spacing in graphite intercalation compounds. *Appl Phys A* 72:367–372
180. Li CZ, Liu G, Prabhulkar S (2009) Comparison of kinetics of hemoglobin electron transfer in solution and immobilized on electrode surface. *Am J Biomed Sci* 1(4):303–311
181. Jain A, Connolly JO, Woolley R, Krishnamurthy S, Marsili E (2013) Extracellular electron transfer mechanism in *Shewanella loihica* PV-4 biofilms formed at indium tin oxide and graphite electrodes. *Int J Electrochem* 8:1778–1793
182. Hoshino T, Sekiguchi SI, Muguruma H (2012) Amperometric biosensor based on multilayer containing carbon nanotube, plasma-polymerized film, electron transfer mediator phenothiazine, and glucose dehydrogenase. *Bioelectrochemistry* 84:1–5
183. Duo I, Fujishima A, Comminellis C (2003) Electron transfer kinetics on composite diamond (sp³) – graphite (sp²) electrodes. *Electrochem Commun* 5:695–700
184. Maluangnont T, Sirisaksoontorn W, Lerner MM (2012) A comparative structural study of ternary graphite intercalation compounds containing alkali metals and linear or branched amines. *Carbon* 50:597–602
185. Matsumoto R, Akuzawa N, Takahashi Y (2006) Thermoelectric properties of cesium-graphite intercalation compounds. *Mater Trans* 47:1458–1463
186. Kumar NA, Choi HJ, Bund A, Baek JB, Jeong YT (2012) Electrochemical supercapacitors based on a novel graphene/conjugated polymer composite system. *J Mater Chem* 22:12268–12274
187. Wang CC, Hu CC (2004) The capacitive performance of activated carbon-ruthenium oxide composites for supercapacitors: effects of ultrasonic treatment in NaOH and annealing in air. *Mater Chem Phys* 83:289–297
188. Yuan GH, Jiang ZH, Aramata A, Gao YZ (2005) Electrochemical behavior of activated-carbon capacitor material loaded with nickel oxide. *Carbon* 43:2913–2917
189. Nian YR, Teng H (2002) Nitric acid modification of activated carbon electrodes for improvement of electrochemical capacitance. *J Electrochem Soc* 149:A1008–A1014
190. Tian Y, Song Y, Tang Z, Guo Q, Liu L (2008) Influence of high treatment of porous carbon on the electrochemical performance in supercapacitor. *J Power Sources* 184:675–681
191. Sun GW, Wang C, Zhan L, Qiao WM, Liang XY, Ling LC (2008) Influence of high temperature treatment of activated carbon on performance of supercapacitors. *J Mater Sci Eng* 2:41–47
192. Pumera M (2009) Electrochemistry of graphene: new horizons for sensing and energy storage. *Chem Rec* 9:211–223
193. Azam MA, Fujiwara A, Shimoda T (2013) Significant capacitance performance of vertically aligned single-walled nanotube supercapacitor by varying potassium hydroxide concentration. *Int J Electrochem Sci* 8:3902–3911
194. Du C, Pan N (2006) High power density supercapacitor electrodes of carbon nanotube films by electrophoretic deposition. *Nanotechnology* 17:5314–5318
195. Tzeng Y, Chen Y, Liu C (2003) Electrical contacts between carbon-nanotube coated electrodes. *Diamond Relat Mater* 12:774–779
196. Ye JS, Liu X, Cui HF, Zhang WD, Sheu FS, Lim TM (2005) Electrochemical oxidation of multi-walled carbon nanotubes and its application to electrochemical double layer capacitors. *Electrochem Commun* 7:249–255
197. Grądzka E, Winkler K, Borowska M, Plonska-Brzezinska ME, Echegoyen L (2013) Comparison of the electrochemical properties of thin films of MWCNTs/C₆₀-Pd, SWCNTs/C₆₀-Pd and ox-CNOs/C₆₀-Pd. *Electrochim Acta* 96:274–284

198. Shiraishi S, Kurihara H, Okabe K, Hulicova D, Oya A (2002) Electric double layer capacitance of highly pure single-walled carbon nanotubes (HiPco™ Byckytubes™) in propylene carbonate electrolytes. *Electrochem Commun* 4:593–598
199. Liu CG, Fang HT, Li F, Liu M, Cheng HM (2006) Single-walled carbon nanotubes modified by electrochemical treatment for application in electrochemical capacitors. *J Power Sources* 160:758–761
200. Liu F, Xue D (2013) An electrochemical route to quantitative oxidation of graphene frameworks with controllable C/O ratios and added pseudocapacitances. *Chem Eur J*. doi:10.1002/chem.201300679
201. Gu W, Peters N, Yushin G (2013) Functionalized carbon onions, detonation nanodiamond and mesoporous carbon as cathodes in Li-ion electrochemical energy storage. *Carbon* 53:292–301
202. Buglione L, Chng ELK, Ambrosi A, Sofer Z, Pumera M (2012) Graphene materials preparation methods have dramatic influence upon their capacitance. *Electrochem Commun* 14:5–8
203. Fu C, Kuang Y, Huang Z, Wang X, Yin Y, Chen J, Zhou H (2011) Supercapacitor based on graphene and ionic liquid electrolyte. *J Solid State Electrochem* 15:2581–2585
204. Wang Y, Sun H, Zhang R, Yu S, Kong J (2013) Large scale template synthesis of single-layered graphene with a high electrical capacitance. *Carbon* 53:245–251
205. Hsieh CT, Hsu SM, Lin JY (2012) Fabrication of graphene-based electrochemical capacitors. *Jpn J Appl Phys* 51:01AH06-1–01AH06-7
206. Brezcko J, Winkler K, Plonska-Brzezinska ME, Villalta-Cerdas A, Echegoyen L (2010) Electrochemical properties of composites containing small carbon nano-onions and solid polyelectrolytes. *J Mater Chem* 20:7761–7768
207. Bushueva EG, Galkin PS, Okotrub AV, Bulusheva LG, Gavrilov NN, Kuznetsov VL, Molisekov SI (2008) Double layer supercapacitor properties of onion-like carbon materials. *Phys Status Solidi B* 245:2296–2299
208. Zhu Y, Murati S, Stoller MD, Ganesh KJ, Cai W, Ferreira PJ, Pirkle A, Wallace RM, Cychosz KA, Thommes M, Su D, Stach EA, Ruoff RS (2011) Carbon-based supercapacitors produced by activation of graphene. *Science* 332:1537–1541
209. Kim TY, Lee HW, Stoller M, Dreyer DR, Bielawski CW, Ruoff RS, Suh KS (2011) High-performance supercapacitors based on poly(ionic liquid)-modified graphene electrodes. *ACS Nano* 25(1):436–442
210. Li X, Zhu Y, Cai W, Borysiak M, Han B, Chen D, Piner RD, Colombo L, Ruoff RS (2009) Transfer of large-area graphene films for high-performance transparent conductive electrodes. *Nano Lett* 9:4359–4363
211. Yun YS, Park HH, Jin HJ (2012) Pseudocapacitive effects of *N*-doped carbon nanotube electrodes in supercapacitors. *Materials* 5:1258–1266
212. Smith B, Wepasnick K, Schrote KE, Bertele AR, Ball WP, O'melia C, Fairbrother H (2009) Colloidal properties of aqueous suspensions of acid-treated multi-walled carbon nanotubes. *Environ Sci Technol* 43:819–825
213. Smith B, Wepasnick K, Schrote KE, Cho HH, Ball WP, Fairbrother DH (2009) Influence of surface oxides on the colloidal stability of multi-walled carbon nanotubes: a structure-property relationship. *Langmuir* 25(17):9767–9776
214. Hu CC, Su JH, WEn TC (2007) Modification of multi-walled carbon nanotubes for electric double-layer capacitors: tube opening and surface functionalization. *J Phys Chem Solids* 68:2353–2362
215. Esteve W, Budzinski H, Villenave E (2004) Relative rate constants for the heterogeneous reactions of OH, NO₂ and NO radicals with polycyclic aromatic hydrocarbons adsorbed on carbonaceous particles. Part 1: PAHs adsorbed on 1-2 μm calibrated graphite particles. *Atmos Environ* 38:6063–6072
216. Zhang J, Zou H, Qing Q, Yang Y, Li Q, Liu Z, Guo X, Du Z (2003) Effect of chemical oxidation on the structure of single-walled carbon nanotubes. *J Phys Chem B* 107:3712–3718
217. Datsyuk V, Kalyva M, Papagelis K, Parthenios J, Tasis D, Siokou A, Kallisis I, Galiotis C (2008) Chemical oxidation of multiwalled carbon nanotubes. *Carbon* 46:833–840

218. Li M, Boggs M, Beebe TP, Huang CP (2008) Oxidation of single-walled carbon nanotubes in dilute aqueous solutions by ozone as affected by ultrasound. *Carbon* 48:466–475
219. Krishnamoorthy K, Veerapandian M, Yun K, Kim SJ (2013) The chemical and structural analysis of graphene oxide with different degrees of oxidation. *Carbon* 56:38–49
220. Dreyer DR, Park S, Bielawski CW, Ruoff RS (2010) The chemistry of graphene oxide. *Chem Soc Rev* 39:228–240
221. Savage T, Bhattacharaya S, Sadanadan B, Gaillard J, Tritt TM, Sun YP, Wu Y, Nayak S, Car R, Marzari N, Ajayan PM, Rao AM (2003) Photoinduced oxidation of carbon nanotubes. *J Phys Condens Matter* 15:5915–5921
222. Vione D, Maurino V, Minero C, Pelizzetti E, Harrison MAJ, Olariu RI, Arsene C (2006) Photochemical reactions in the tropospheric aqueous phase and on particulate matter. *Chem Soc Rev* 35:441–453
223. Yang DQ, Sacher E (2008) Strongly enhanced interaction between evaporated Pt nanoparticles and functionalized multiwalled carbon nanotubes via plasma surface modifications: effects of physical and chemical defects. *J Phys Chem C* 112:4075–4082
224. Zschoerper NP, Katzenmaier V, Vohrer U, Haupt M, Oehr C, Hirth T (2009) Analytical investigation of the composition of plasma-induced functional groups on carbon nanotube sheets. *Carbon* 47:2174–2185
225. Wepasnick KA, Smith BA, Schrote KE, Wilson HK, Diegelmann SR, Fairbrother DH (2011) Surface and structural characterization of multi-walled carbon nanotubes following different oxidative treatments. *Carbon* 49:24–36
226. Mastragostino M, Arbizzani C, Soavi F (2002) Conducting polymers as electrode materials in supercapacitors. *Solid State Ion* 148:493–498
227. Khomenko V, Frackowiak E, Beguin F (2006) Development of supercapacitors based on conducting polymers. In: Barsukov IV, Johnson CS, Doninger JE, Barsukov VZ (eds) *New carbon based materials for electrochemical energy storage systems*. Springer, Netherlands, pp 41–50
228. Conte S, Rodriguez-Calero GG, Burkhardt SE, Lowe MA, Abruna HD (2013) Designing conducting polymer films for electrochemical energy storage technologies. *RSC Adv* 3:1957–1964
229. Lokhande CD, Dubal DP, Joo OS (2011) Metal oxide thin film based supercapacitors. *Curr Appl Phys* 11:255–270
230. Deng W, Ji X, Chen Q, Banks CE (2011) Electrochemical capacitors utilizing transition metal oxides: an update of recent developments. *RSC Adv* 1:1171–1178
231. Cottineau T, Toupin M, Delahaye T, Brousse T, Belanger D (2006) Nanostructured transition metal oxides for aqueous hybrid electrochemical supercapacitors. *Appl Phys A* 82:599–606
232. Pecher J, Mecking S (2010) Nanoparticles of conjugated polymers. *Chem Rev* 110:6260–6279
233. Brancewicz E, Grądzka E, Basa A, Winkler K (2014) Chemical synthesis and characterization of the C60-Pd polymer spherical nanoparticles. Submitted to *Electrochim Acta* 128:91–101
234. Li N, Xiao Y, Xu C, Li H, Yang X (2013) Facile preparation of polyaniline nanoparticles via electrodeposition for supercapacitors. *Int J Electrochem Sci* 8:1181–1188
235. Kwon WJ, Suh DH, Chin BD, Yu JW (2008) Preparation of polypyrrole nanoparticles in mixed surfactants system. *J Appl Polym Sci* 110:1324–1329
236. Channu VSR, Holze R, Wicker SA Sr, Walker EH Jr, Williams QL, Kalluru RR (2011) Synthesis and characterization of (Ru-Sn)O₂ nanoparticles for supercapacitors. *Mater Sci Appl* 2:1175–1179
237. Thiagarajan S, Tsai TH, Chen SM (2011) Electrochemical fabrication of nano manganese oxide modified electrode for the detection of H₂O₂. *Int J Electrochem* 6:2235–2245
238. Bjorklund RB, Liedberg B (1986) Electrically conducting composites of colloidal polypyrrole and methylcellulose. *J Chem Soc Chem Commun* 1293–1295
239. Armes SP, Miller JF, Vincent B (1987) Aqueous dispersions of electrically conducting monodisperse polypyrrole particles. *J Colloid Interface Sci* 118(2):410–416
240. Lee ES, Park JH, Wallace GG, Bae YH (2004) In situ formed processable polypyrrole nanoparticle/amphiphilic elastomer composites and their properties. *Polym Int* 53:400–405

241. Digar ML, Bhattacharyya SN, Mandal BM (1994) Dispersion polymerization of pyrrole using poly(vinyl methyl ether) as stabilizer. *Polymer* 35(2):377–382
242. Xia H, Wang Q (2001) Synthesis and characterization of conductive polyaniline nanoparticles through ultrasonic assisted inverse microemulsion polymerization. *J Nanopart Res* 3:401–411
243. Stejskal J, Omastova M, Fedorova S, Prokes J, Trchova M (2003) Polyaniline and polypyrrole prepared in the presence of surfactants: a comparative conductivity study. *Polymer* 44:1353–1358
244. Omastova M, Trchova M, Kovarova J, Stejskal J (2003) Synthesis and structural study of polypyrroles prepared in the presence of surfactants. *Synth Met* 138:447–455
245. Kim BJ, Oh SG, Han MG, Im SS (2000) Preparation of polyaniline nanoparticles in micellar solutions as polymerization medium. *Langmuir* 16:5841–5845
246. Han MG, Cho SK, Oh SG, Im SS (2002) Preparation and characterization of polyaniline nanoparticles synthesized from DBSA micellar solution. *Synth Met* 126:53–60
247. Yan F, Xue G (1999) Synthesis and characterization of electrically conducting polyaniline in water-oil microemulsion. *J Mater Chem* 9:3035–3039
248. Selvan ST, Mani A, Anthinaarayanamy K, Phani KLN, Pitchumani S (1995) Synthesis of crystalline polyaniline. *Mater Res Bull* 30:699–705
249. Zhou Q, Wang J, Ma Y, Cong C, Wang F (2007) The relationship of conductivity to the morphology and crystallinity of polyaniline controlled by water content via reverse microemulsion. *Colloid Polym Sci* 285:405–411
250. Marie E, Rothe R, Antonietti M, Landfester D (2003) Synthesis of polyaniline particles via inverse and direct miniemulsion. *Macromolecules* 36:3967–3973
251. Jang J, Ha J, Kim S (2007) fabrication of polyaniline nanoparticles using microemulsion polymerization. *Macromol Res* 15:154–159
252. Winkler K, Balch AL (2006) Electrochemically formed two-component films comprised of fullerene and transition-metal components. *CR Chimie* 9:928–943
253. Balch AL, Costa DA, Winkler K (1998) Formation of redox-active, two-component films by electrochemical reduction of C₆₀ and transition metal complexes. *J Am Chem Soc* 120:9614–9620
254. Winkler K, de Bettencourt-Dias A, Balch AL (2000) Electrochemical studies of C₆₀/Pd films formed by the reduction of C₆₀ in the presence of palladium (II) acetate trimer. Effects of varying C₆₀/Pd (II) ratios in the precursor solutions. *Chem Mater* 12:1386–1392
255. Winkler K, Noworyta K, de Bettencourt-Dias A, Sobczak W, Wu CT, Chen LC, Kutner W, Balch AL (2003) Structure and properties of C₆₀-Pd films formed by electroreduction of C₆₀ and palladium (II) acetate trimer: evidence for the presence of palladium nanoparticles. *J Mater Chem* 13:518–525
256. Grodzka E, Grabowska J, Wysocka-Zolopa M, Winkler K (2008) Electrochemical formation and properties of two-component films of transition metal complexes and C₆₀ or C₇₀. *J Solid State Electrochem* 12:1267–1278
257. Nagashima H, Nakaoka A, Saito Y, Kato M, Kawanishi T, Itoh K (1992) C₆₀Pd_n: The first organometallic polymer of buckminsterfullerene. *J Chem Soc* 4:377–379
258. Brancewicz E, Grądzka E, Winkler K (2013) Comparison of electrochemical properties of two-component C₆₀-Pd polymers formed under electrochemical conditions and by chemical synthesis. *J Solid State Electrochem* 17:1233–1245
259. Winkler K, Grodzka E, D'Souza F, Balch AL (2007) Two-component films of fullerene and palladium as materials for electrochemical capacitors. *J Electrochem Soc* 154(4):K1–K10
260. Liu R, Duay J, Lee SB (2010) Redox exchange induced MnO₂ nanoparticle enrichment in poly(3,4-ethylenedioxythiophene) nanowires for electrochemical energy storage. *ACS Nano* 4:4299–4307
261. Bedre MD, Deshpande R, Salimath B, Abbaraju V (2012) Preparation and characterization of polyaniline-Co₃O₄ nanocomposites via interfacial polymerization. *Am J Mater Sci* 2(3):39–43
262. Kondawar SB, Bompilwar SD, Khatri VS, Thakre SR, Tabhane VA, Burghate DK (2010) Characterizations of zinc oxide nanoparticles reinforced conducting polyaniline composites. *Arch Appl Sci Res* 2(1):247–253

263. Kondawar S, Mahore R, Dahegaonkar A, Agrawal S (2011) Electrical conductivity of cadmium oxide nanoparticles embedded polyaniline nanocomposites. *Adv Appl Sci Res* 2(4):401–406
264. Tao L, Zai J, Wang K, Zhang H, Xu M, Shen J, Su Y, Qian X (2012) Co₃O₄ nanorods/graphene nanosheets nanocomposites for lithium ion batteries with improved reversible capacity and cycle stability. *J Power Sources* 202:230–235
265. Khomenko V, Frackowiak E, Beguin F (2005) Determination of the specific capacitance of conducting polymer/nanotubes composite electrodes using different cell configuration. *Electrochim Acta* 50:2499–2506
266. Raymundo-Pinero E, Khomenko V, Frackowiak E, Beguin F (2005) Performance of manganese oxide/CNTs composite as electrode materials for electrochemical capacitors. *J Electrochem Soc* 152(1):A229–A235
267. Peng C, Zhang S, Jewell D, Chen GZ (2008) Carbon nanotube and conducting polymer composites for supercapacitors. *Prog Nat Sci* 18:777–788
268. Xu F, Jamal R, Ubul A, Shao W, Abdiryim T (2013) Characterization and electrochemical properties of poly(aniline-co-o-methoxyaniline)/multi-walled carbon nanotubes composites synthesized by solid-state method. *Fibers Polym* 14:8–15
269. Jurewicz K, Delpoux S, Bertagna V, Beguin F, Frackowiak E (2001) Supercapacitors from nanotubes/polypyrrole composites. *Chem Phys Lett* 347:36–40
270. Dong B, He BL, Xu CL, Li HL (2007) Preparation and electrochemical characterization of polyaniline/multi-walled carbon nanotubes composites for supercapacitors. *Mater Sci Eng B* 143:7–13
271. Xu Y, Zhuang SQ, Zhang XY, He PG, Gang YZ (2011) Configuration and capacitance properties of polypyrrole/aligned carbon nanotubes synthesized by electropolymerization. *Chin Sci Bull* 56:3823–3828
272. Bahrami A, Talib ZA, Shahriari E, Yunus WMM, Kasim A, Behzed K (2012) Characterization and electrosynthesized conjugated polymer-carbon nanotube composite: optical nonlinearity property. *Int J Mol Sci* 13:918–928
273. Zhang B, Xu Y, Zheng Y, Dai L, Zhang M, Yang J, Chen Y, Chen X, Zhou J (2011) A facile synthesis of polypyrrole/carbon nanotube composites with ultrathin, uniform and thickness-tunable polypyrrole shells. *Nanoscale Res Lett* 6(431):1–9
274. Moraes SR, Hurta-Vilca D, Motheo AJ (2004) Characteristics of polyaniline synthesized in phosphate buffer solution. *Eur Polym J* 40:2033–2041
275. Oh KW, Park HJ, Kim SH (2004) Electrical property and stability of electrochemically synthesized polypyrrole films. *J Appl Polym Sci* 91:3659–3666
276. Bazzaoui M, Martins L, Bazzaoui EA, Martins JI (2002) New single-step electrosynthesis process of homogeneous and strongly adherent polypyrrole films on iron electrodes in aqueous medium. *Electrochim Acta* 47:2953–2962
277. Ma SB, Nam KW, Yoon WS, Yang XQ, Ahn KY, Oh KH, Kim KB (2008) Electrochemical properties of manganese oxide coated onto carbon nanotubes for energy-storage applications. *J Power Sources* 178:483–489
278. Lin P, She Q, Hong B, Liu X, Shi Y, Zheng M, Dong Q (2010) The nickel oxide/CNT composites with high capacitance for supercapacitor. *J Electrochem Soc* 157(7):A818–A823
279. Gao B, Yuan CZ, Su LH, Chen L, Zhang XG (2009) Nickel oxide coated on ultrasonically pretreated carbon nanotubes for supercapacitor. *J Solid State Electrochem* 13:1251–1257
280. Wang D, Li Y, Wang Q, Wang T (2012) Nanostructured Fe₂O₃-graphene composite as a novel electrode material for supercapacitors. *J Solid State Electrochem* 16:2095–2102
281. Wang X, Han X, Lim M, Singh N, Gan CL, Jan M, Lee PS (2012) Nickel cobalt oxide-single wall carbon nanotubes composite material for superior cycling stability and high-performance supercapacitor application. *J Phys Chem C* 116:12448–12454

282. Zolfaghari A, Ataherian F, Ghaemi M, Gholami A (2007) Capacitive behavior of nanostructured MnO₂ prepared by sonochemistry method. *Electrochim Acta* 52:2806–2814
283. Yu G, Hu L, Vosgueritchian M, Wang H, Xie X, McDonough JR, Cui X, Cui Y, Bao Z (2011) Solution-processed graphene/MnO₂ nanostructured textiles for high-performance electrochemical capacitors. *Nano Lett* 11:2905–2911
284. Hu CC, Chen WC, Chang KH (2004) How to achieve maximum utilization of hydrous ruthenium oxide for supercapacitors. *J Electrochem Soc* 151(2):A281–A290
285. Li J, Wang X, Huang Q, Dai C, Gamboa S, Sebastian PJ (2007) Preparation and characterization of RuO₂·xH₂O/carbon aerogel composites for supercapacitors. *J Appl Electrochem* 37:1129–1135
286. Chen W, Fan Z, Gu L, Bao X, Wang C (2010) Enhanced capacitance of manganese oxide *via* confinement inside carbon nanotubes. *Chem Commun* 46:3905–3907
287. Hou Y, Cheng Y, Hobson T, Liu J (2010) Design and synthesis of hierarchical MnO₂ nanospheres/carbon nanotubes/conducting polymer ternary composite for high performance electrochemical electrodes. *Nano Lett* 10:2727–2733
288. Ko JM, Ryu KS, Kim S, Kim KM (2009) Supercapacitive properties of composite electrodes consisting of polyaniline, carbon nanotube, and RuO₂. *J Appl Electrochem* 39:1331–1337
289. Mirmohseni A, Dorraji MSS, Hosseini MG (2012) Influence of metal oxide nanoparticle on pseudocapacitive behavior of wet-spun polyaniline-multiwall carbon nanotube fibers. *Electrochim Acta* 70:182–192
290. Oh M, Kim S (2012) Preparation and electrochemical characterization of polyaniline/activated carbon composites as an electrode material for supercapacitors. *J Nanosci Nanotechnol* 12:519–524
291. Li GR, Feng ZP, Ou YN, Wu D, Fu R, Tong YX (2010) Mesoporous MnO₂/carbon aerogel composites as promising electrode materials for high-performance supercapacitors. *Langmuir* 16(4):2209–2213
292. Zhu X, Dai H, Hu J, Ding L, Jiang L (2012) Reduced graphene oxide-nickel oxide composite as high performance electrode materials for supercapacitors. *J Power Sources* 203:243–249

Electroforming and Electrodeposition on Complex 3D Geometries: Special Requirements and New Methods

28

Anne Jung, Martin Weinmann, and Harald Natter

Contents

Challenges and Problems in Nanostructuring of Nickel.....	942
Fundamentals of Electroforming.....	942
Advantages of Nanostructuring.....	944
Electrochemical Nanostructuring.....	946
Electroforming of Thick, Complex 3D Deposits.....	948
Problems of Electroforming.....	948
Special Requirements for Electroforming.....	950
Special Methods for the Filling of Notches.....	952
Leveling Agents and Suppressors.....	952
Magnetic Field-Assisted Electroplating.....	953
Continuous Fiber-Reinforced Metal Matrix Composites.....	957
State of the Art to Continuous Fiber-Reinforced MMCs.....	958
New Electroforming Method for the Production of Continuous Fiber-Reinforced MMCs.....	958
Coating of Metal Foams.....	961
Metal Foams: Basics.....	961
Coating of Metal Foams by Electrodeposition.....	961
A Special Method for the Production of Ni/Al Hybrid Metal Foams.....	964
Conclusion.....	965
References.....	967

A. Jung (✉)

Applied Mechanics, Saarland University, Saarbruecken, Germany
e-mail: anne.jung@mx.uni-saarland.de

M. Weinmann • H. Natter

Physical Chemistry, Saarland University, Saarbruecken, Germany
e-mail: m.weinmann@mx.uni-saarland.de; h.natter@mx.uni-saarland.de

Abstract

The chapter presents fields of electrodeposition where nanostructuring of nickel is challenging (electroforming, replication of fine-structured surfaces, filling of small- and large-scaled notches, e.g., in microsystem technology and for electroformed slush-tools for automotive of dashboards for automotive applications). It outlines the special requirements for the electroforming process of thick complex 3D-shaped deposits including bath analytics and stress measurements which are essential for the production of thick deposits, where the properties are hardly affected by impurities and internal stresses. Methods for the filling of the notches are presented. We further describe a new electrodeposition method to produce continuous fiber-reinforced metal matrix composites. Incorporating the fibers modifies the electrocrystallization and produces nanocrystalline structures around the fibers. As a hot special topic a new electrodeposition method is described to coat 3D porous structures as metal foams that there is an almost homogeneous coating thickness over the total cross section of the foams. The special experimental setup, special mass transport, and deposition mechanism in order to produce nanocrystalline nickel coatings around the foam struts are explained.

Keywords

Electroforming • Magnetic-field assisted electroplating • Fibre metal matrix composites • Hybrid metal foams

Challenges and Problems in Nanostructuring of Nickel

Fundamentals of Electroforming

The electroforming process is a widely spread technique for the formation of structures in different dimensions ranging from nanoscaled to macroscopic objects. The production of very complex product shapes (undercuts, high-aspect-ratio structures) and also a very good moulding behavior are features of this a further characteristic of this method. For this reason electroforming was used in different branches of production. An overview is given in Table 1.

Electroforming processes can be divided in five groups depending on the size, the shape, and the surface structure of the electroformed product:

1. Large-sized products (0.5×0.5 – 1×2 m²) with thick walls (several centimeters) and a functionalized or decorative surface; product shape is complex.
2. Large-sized products (0.2×0.2 – 1×1 m²) with a complex shape consisting of a sophisticated material.
3. Large-sized products (0.2×0.2 – 1×1 m²) with thin walls (sub-mm to mm range) with a very smooth or complex-shaped surface structure including foils or stripes manufactured by reel-to-reel plating.

Table 1 Applications of electroforming

Industry sector	Product feature	Products	Reference
Automotive	Molding of microstructures	Tools for slush molding process	[1–4]
Micromachining	Micron-sized structures	Microparts for machines	[5–7]
MEMS (microelectromechanical systems)	High-aspect-ratio microstructures or parallel side walls	Sensors, optical systems, replication of complex parts, absorber patterns for X-ray lithography, micro-actuators, micro-piezoelectronics	[8–10]
Medicine/dentistry	Complex shapes	Dental implants, coronal restorations, prosthesis parts	[11–13]
Energy	Complex shapes, special materials	Beam dump manufacturing, electroformed parts consisting of binary and ternary alloys, flow fields for fuel cells, molds for solar reflectors	[14–16]
Jewelry manufacturing	Complex designs of jewelries	Hollow, thin-walled jewelry manufacturing	[17, 18]
Optical	Parabolic, elliptical, and off-axis products	Reflectors, lighting products	[19]
Aerospace	Complex shapes, special materials	Combustion chambers, jets, concentrators	[20]

4. Small-sized products (1×1 – 10×10 cm²) with a complex shape or surface, massive, or hollow structures.
5. Supported or unsupported micro- or nanosized structures.

Depending on the products, the electroforming process has to be optimized according to plating rate, shape homogeneity, molding properties, and deposit composition. In all cases the formation of pores, voids, and inclusions has to be avoided because these faults lead to a decrease in strength and imprecise shapes of the final products. Most of the mentioned problems can be avoided by the use of suitable additives: surfactants (sodiumdodecylsulfate, alkyl polyglucoside [21]) reduce the adhesion of gas bubbles onto the deposit surface; anorganic additives and complex formers (arsenic acid, EDTA [22], citric acid [23]) reduce the overpotential of metal deposition; grain refiners (saccharin [24], butindiol) decrease the crystallite size; and stress relievers (cyanides [25]) reduce the microstrain and textures. The pH value is kept constant with buffer systems (boric acid, citric acid). Depending on the product type, electrolytes for electroforming purposes have more or less a complex composition. Especially, for thick-walled products like tools for injection molding or slush casting, only moderate and low plating rates are used. The complete production time takes several weeks. For these applications, the monitoring of the electrolyte and the product is very extensive. It can be reduced by minimizing the chemical components and by the use of mechanical devices (stirrer, linear motion tools).

Serious problems for the manufacturing of nano- and microformed products are gas bubble evolution, inclusion of dust or microparticles, and the inhomogeneous filling of parts with an extreme aspect ratio. The filling of extreme geometries like very sharp profiles, needlelike structures, micron-sized parallel walls, and parts with an elongated aspect ratio of 1:3 and above is also a challenge for electroforming procedures. For some electroformed products, the use of strong adsorbing agents could be a problem because the organic molecules were incorporated in the metal matrix. Depending on the amount of organic agents, the products embrittle at temperatures above 100 °C which leads to a mechanical failure.

As shown before electroforming is one of the most sophisticated electrochemical deposition techniques because all physical (bath temperature, hydrodynamic conditions) and chemical (bath composition, pH value, additives) parameters strongly depend on shape, surface structure, and the application of the electroformed product. For this reason it is very difficult to develop a procedure which is universally usable for a large number of products. In this chapter we show solutions for the formation of large-sized and thick-walled products with complex geometries that also consist of a nanosized structure.

Advantages of Nanostructuring

Many electroformed products were used in technical processes or built in mechanical, optical, or electronical devices. These parts were often used under very rough conditions, e.g., at high temperatures and under thermally or mechanically alternating loads. The dimensions of electroformed parts of electronic devices and microelectromechanical systems (MEMS) are very small (0.5–100 μm) and therefore fragile. Large electroformed molds and machine parts are very expensive. The production costs of tools for the manufacturing of polymer skins for vehicle interiors are in the range of 100.000 Euros. A cost reduction by long-term stability can only be achieved by a sufficient mechanical strength and corrosion stability. The nanostructuring of the material could be a solution for the mentioned problems. Table 2 shows that various mechanical properties of nanostructured Ni (crystallite sizes up to 10 nm), submicrocrystalline nickel (100 nm), and polycrystalline nickel

Table 2 Mechanical properties of nickel with different crystallite sizes

Property at 25 °C in air	Microcrystalline nickel 10 μm	Nanostructured 80–100 nm	Nickel 10 nm	Reference
Yield strength, MPa	103	690	>900	[26]
Ultimate tensile strength, MPa	403	1,100	>2,000	[27]
Tensile elongation, %	50	>15	1	[26, 27]
Young's modulus, GPa	207	214	204	[28]
Vickers hardness, kg/mm^2	140	300	650	[29, 30]
Fatigue strength, MPa (10^8 cycles)	241	275	–	[26]
Wear resistance (Taber Wear Index)	32	27	21	[30]

(crystallite size 10 μm) depend strongly on the crystallite size. In addition to the remarkable increases in hardness, yield strength, and ultimate tensile strength with decreasing grain size, it is interesting to note that the wear resistance increases by 40 % for nanostructured nickel with a crystallite size of 10 nm. The ductility of nickel decreases with decreasing grain size from 50 % elongation to failure for conventional material to 15 % at 100 nm grain size and about 1 % at 10 nm grain size. As a result of Hall–Petch strengthening, nanocrystalline materials display significant increases in hardness and strength relative to their coarse-grained counterparts due to their ultrafine grain size [30]. The literature [31] reports about the tensile properties of electrodeposited nanocrystalline cobalt which were compared with that of a coarse-grained polycrystalline counterpart. The greater than twofold increase in yield and tensile strength while maintaining considerable ductility is quite remarkable.

Materials with a very high hardness find extensive use in numerous industrial applications. They require a high intrinsic hardness (600–1,000 HV) and low friction coefficient (<0.20) in order to impart the desirable wear performance. It could be shown that it is possible to prepare nanocrystalline metals and alloys with these special properties by different electrodeposition techniques [32, 33]. The nanostructuring of electroformed free-standing microparts is extreme essentially for their mechanical stability [34, 35]. If the wall thickness of a structure is only 1 μm , the material should consist of crystallites with a size of at least 20 nm. In this case about 50 crystallites can be found along the cross section of the wall. If the structure of the metal is more coarse grained (e.g., 200 nm), the wall consists only of five grains. From the mechanically point of view, this bamboo-like structure is very fragile and tends to crack formation and mechanical failure.

In conclusion nanostructuring offers a lot of advantages, but also there are some disadvantages such as higher processing costs. Figure 1 summarizes the advantages and disadvantages of nanostructuring mentioned in this chapter. The many advantages leading to longer lifetime of nanostructured products in contrast to coarse-grained products prevail the few disadvantages.

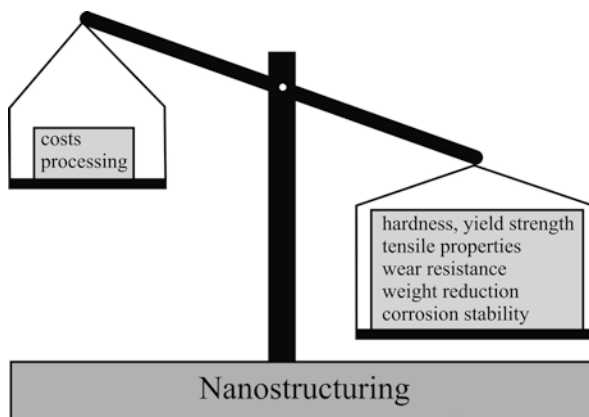


Fig. 1 Summary of disadvantages and advantages of nanostructuring

Electrochemical Nanostructuring

Nanostructuring by electrochemical methods is a well-established technique which enables the deposition of metals and alloys in crystallite sizes from several nm up to one micron. Electrochemical techniques have been developed for the synthesis of nanostructured materials for over twenty years. Several direct current (DC) [36, 37] and pulse techniques (PED) [38–40] offer the ability to synthesize a large number of metals, alloys, composite materials, and compounds in any size or shape. First routes for the production of nanostructures are different kinds of DC techniques using electrolytes with a relatively high amount of organic additives [41]. The process parameter of these techniques is limited to the current density and bath composition. In most cases organic grain refiners were used [42–44]. The amount and the molecular structure of the additive have to be optimized for each metal: specific additives are arsenic acid for gold deposition [45], saccharin for nickel deposition [40], and citric acid for copper deposition [23]. A crucial disadvantage of this method is the careful adjustment of the current density to the bath chemistry, and therefore the crystallite size can only be varied in a small range.

The pulsed electrodeposition technique (PED) is a more advanced method for the preparation of nanostructured metals and alloys. One prerequisite of the nanostructuring by PED is the formation of a high nuclei number onto the electrode surface combined with a very well-controlled nuclei growth. Effective parameters for a controlled nuclei formation and growth are the pulse parameters I_p , t_{on} , and t_{off} , whereas I_p denotes to the pulse current, t_{on} is the duration of the pulse, and t_{off} belongs to the t_{off} -time. According to the theory of nucleation [46], the size and the number of nuclei depend on the overvoltage (η):

$$r = \frac{2\sigma V}{ze_0 |\eta|} \quad (1)$$

In this electrochemical version of the Kelvin equation, r means the critical nucleation radius, σ the specific surface energy, V the atomic volume in the crystal, and z the number of elementary charges e_0 . A high nucleation density on the electrode surface can be achieved by a high overvoltage. This enormous overvoltage can only be applied for a few milliseconds because the metal ion concentration in the vicinity of the cathode decreases very strong, and therefore the process would become diffusion controlled. During the t_{off} -time, the metal ions diffuse from the bulk electrolyte to the cathode and compensate the metal ion depletion. Meanwhile Ostwald ripening sets in that means that the larger crystallites are the energetically more preferred growth on expense of the smaller crystallites. Figure 2 shows the crystallite sizes of different copper samples prepared with increasing t_{off} -times. For comparison reasons, the deposits were prepared with same charge during the pulse period – that means the I_p -values have to increase for long t_{off} -times. The number of nuclei increases with increasing current density resulting in a reduced crystallite size. Results shown in Fig. 2 are in accordance with the nucleation and growth theory presented above. The smallest crystallite size was observed for high deposition currents (I_p) and long t_{off} -times. With an eightfold increase of the t_{on} -time, the

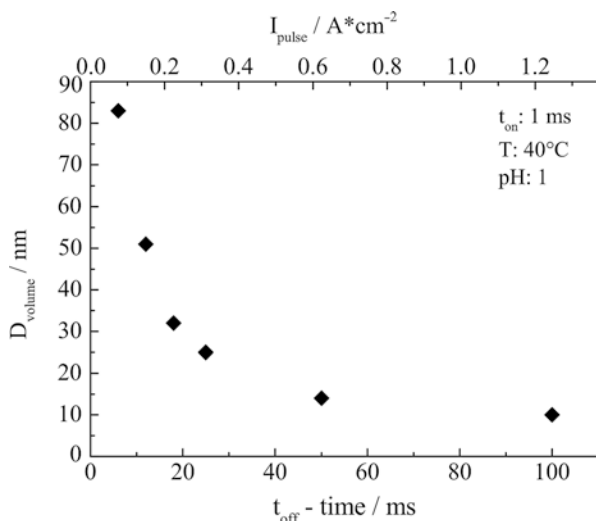


Fig. 2 Influence of the t_{off} -time on the crystallite size of copper deposits [23]. Electrolyte composition: $CuSO_4$ 28 g/l, $(NH_4)_2SO_4$ 50 g/l, citric acid 50 g/l. D_{volume} denotes the volume-weighted crystallite size

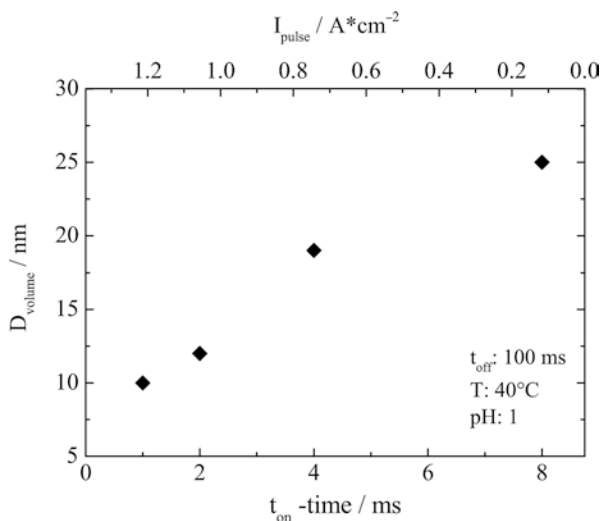


Fig. 3 Influence of the t_{on} -time on the crystallite size of copper deposits [23]. Electrolyte composition: $CuSO_4$ 28 g/l, $(NH_4)_2SO_4$ 50 g/l, citric acid 50 g/l

crystallite size increases the two-and-a-half fold up to 25 nm. The t_{on} -time has no strong influence on the electrocrystallization process, because during this state of deposition, nuclei were generated – at the observed time scale, the process is nearly time independent (Fig. 3).

The surface diffusion of the so-called adatoms can be influenced by the addition of substances which have a very weak interaction with the surface. If the interaction between the molecule and the surface is too strong, the additive is built in the metallic matrix. In the case of a moderate or weak interaction, the molecules are not bound to the surface and are able to desorb. The adsorption–desorption equilibrium depends on the chemical structure of the molecules and the temperature. At high temperatures, most surface active additives are inactive. Experimental results concerning this parameter are reported for gold [45] and copper [47]. The pulse electro-deposition is an economically viable method for the large-scale manufacture of near net-shape components, coatings, and foils and also for massive bulk products prepared in electroforming processes [48, 49]. This technique enables the preparation of a large number of metals, alloys, and composite materials in various forms. While production rates are significant, the capital investment required for electroplating lines remains modest. The existing infrastructure for electroplating and electroforming operations is a further benefit. Adjusting bath chemistry and pulse plating parameters provides significant flexibility in controlling grain size. The addition of particles to the plating bath yields nanometal matrix composites with properties tailored to desired applications. Tank plating processes are very suitable to fabricate nanostructured bulk materials or electroformed products [50].

Electroforming of Thick, Complex 3D Deposits

Problems of Electroforming

It is very difficult to transfer for complex 3D geometries and for deposition of thick-walled deposits experiences and plating parameter from galvanic coating techniques to electroforming processes. Based on the longer deposition times, effects are arising which are neglectable in the electrodeposition of thin deposits. Such effects are:

- 3D and rough surfaces. Based on the high current densities on edges and peaks, they lead to uncontrolled growth and bud formation and induce further roughness. Also co-deposited impurities are a source of roughness.
- Internal stresses. These may result in the spalling, blistering, or warping of the deposit.
- Formation of delamination layers. Delamination layers are formed by changes in the composition of the electrolyte, in the plating parameter, or geometrically in interior edges and corners. Such delamination planes lead to a mechanical weakening of the deposits.

Current Distribution and Coating Thickness Distribution

Based on the difference in the interdistance of anode and cathode for complex 3D-shaped cathodes, there is a lower electrolyte resistance at prominent edges and hence a higher local current density compared to notches and undercuts.

According to this there are different deposition thicknesses at edges and undercuts or planar regions on 3D-shaped cathodes. The metal layer is thicker at edges and peaks and thinner in undercuts and valleys. Also at rough surfaces, there are higher current densities on the peaks and lower ones in the valleys better recesses. Hence, in order to produce smooth deposits, it is necessary to guarantee particle-free and dust-free electrolytes to prevent the co-deposition of impurities which may arise, e.g., from insoluble components of the anodes.

Internal Stresses

Internal stresses establish in electrodeposits as tensile or compressive stresses and do strongly affect the mechanical properties of the deposits. Internal stresses result from the electrocrystallization process or by the incorporation of impurities like sulfur, hydrogen, and organic compounds. The electroformed tool can be compared with a spring. If the tool is free of internal stresses, the deposit is unwrapped and has the same angles as on the mandrel. Are there internal compression stresses in the tool, in analogy to a compressed spring, it tries to expand after the removal from the mandrel. Hence, in comparison to the mandrel, there are obtuse angles. At the appearance of tensile stresses like a spring under tension, the tool tries to contract. As a result of this contraction, the angles in the tool are flatter than in the mandrel. Thus in electroforming, internal stresses should not be neglected. In the case of coatings, there are much lower forces in the deposits, and mostly internal stresses can be neglected.

The common methods to measure the internal stresses are X-ray diffraction and the bent strip method. For routine in situ measurements during the deposition process, the bent strip method is best suitable. The stresses are measured by deposition on a thin strip that is isolated on the rear side. According to the nature of the stresses, the strips deforms by bending to the direction of the anode or away from it. The method is based on the beam theory. In the case of tensile stresses, the strip bends toward the anode; in the case of compressive stresses, it bends away from the anode. The degree of bending is a quantitative measure for the internal stresses. For evaluation of the internal stresses σ , the formula of Sykes and Rothwell is used [51].

$$\sigma = \frac{4F L}{3W T t} \quad (2)$$

whereas F belongs to the acting force on the strip; L , B , and T denotes for the length, width, and thickness of the strip; and t represents the thickness of the deposited layer.

Formation of Delamination Layers

The formation of delamination layers or interfacial layers leads to the weakening of the deposited components. There are several reasons for the formation. In the case of interior angles, growing metal layers from both edges of the angle collide and build an angle bisecting plane. If an electroformed tool is loaded under pressure, mostly it fails at such bisecting planes. Besides this geometrical reason, other layers arise from every change in the electrolyte composition or in the plating parameter. These include changes in the pH, metal content, content of additives or surfactants, and

also in the current density, electrolyte temperature, or hydrodynamic conditions. In order to prevent the layer formation, the whole composition of the electrolyte and all other plating parameter have to be maintained constant.

Special Requirements for Electroforming

According to the most complex 3D geometries and the high internal stresses, it is not possible to use very high pulse or average current densities. These would cause large bud formation, undesired roughness, and large internal stresses of the deposits. Hence, in order to produce nanocrystalline electroformed deposits, it is necessary to use grain-refining additives like the sodium salt of saccharine, the trisodium salt of naphthalene trisulfonic acid, or other organic molecules which absorb on the growing metallic grains during the electrodeposition process and act as inhibitors for the surface diffusion of the adatoms. Hence, the formation of new nucleation sites is for the adatoms energy to be more favorable than the surface diffusion to nucleation sites which are distant. By blocking the surface diffusion of the adatoms, the inhibitors increase the nucleation rate and reduce the growth rate. This leads to the production of very fine-grained nanocrystalline deposits (Fig. 4).

Besides the addition of organic additives, it is possible to use inorganic additives. The latter ones have a lot of advantages in comparison of organic additives:

- Easy analysis methods (e.g., ICP-OES)
- No decomposition products
- No embrittlement at higher temperatures

Unfavorably, there is only a slight effect on the grain size, and there are shifts in the deposition potential and the pH, and alloying might be possible. Alloying is mischievous because it needs very sophisticated control of the deposition

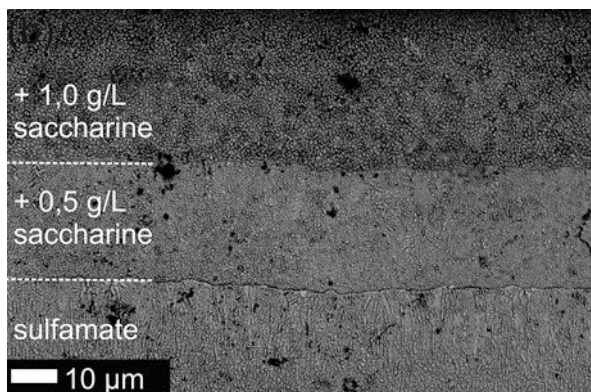


Fig. 4 SEM image of a cross section of a sample deposited at $j_m=20 \text{ mA/cm}^2$ under the addition of saccharin during the plating

conditions, and according to the changes in the local current density on complex geometries, it is not possible to guarantee a uniform composition of the alloy over the complete geometry.

In literature, there are only a few reports about the effect and the acting mechanism of inorganic additives. Possible inorganic additives are, e.g., magnesium chloride or manganese sulfate (for the case of nickel deposition). Magnesium chloride is a conducting salt and does not form any alloy with nickel. According to Makar'eva [52], the addition of magnesium chloride increases the hardness and brightness of the deposit by reducing the grain size. The effect makes itself felt only at very high concentrations of 4 mol/l and is independent of the choice of the counterion. Magnesium acts as electrolyte film inhibitor. It does not only increase the density and viscosity of the electrolyte, but it also acts by the formation of magnesium hydroxide in the diffusion layer on the diffusion velocity of the protons and nickel ions [53]. Hence, it increases the overall overvoltage, and according to equation 1, it leads to a nanostructuring of the deposit. A similar mechanism mechanism can be assumed for other metallic additives which do actively interfere in electrocrystallization.

A further inorganic additive for nickel electrodeposition is manganese sulfate. Compared to magnesium chloride it works in small amounts. Concentrations of 0.1 mol/l are enough for grain refinement into the nanoscale. The mechanism is totally different. Manganese has a deposition potential of -1.18 V and is up to now the most electronegative metal that could be electrochemically deposited from aqueous solutions [54]. It makes the formation of an alloy with nickel, but only up to 1.5 % of manganese can be alloyed with nickel [55–57]. Based on the less alloying tendency there is no complex control of the metal contents on the electrolyte needed. The manganese content decreases very slowly. By the addition of manganese sulfate to nickel electrolyte, it is possible to increase the hardness by grain refining of the deposit by 150 % [58].

Bath Analytics

Besides the purity of the electrolyte, in order to produce thick deposits which are from good quality and show homogeneous properties over the whole thickness without the formation of delamination layers, it is important to guarantee a constant composition of the electrolyte. That is the reason why in contrast to the deposition of coatings, the electroforming needs a lot of bath analytics. The following section describes the necessary analytics in the case of nickel plating with a nickel sulfate electrolyte which is the most common used electrolyte for electroforming.

For the electroforming of nanocrystalline nickel, it is important to monitor the following bath components:

- Metal content
- Additive content

For the deposition of metals and alloy it is important to determine the electrolyte's metal content. There are several spectroscopic methods applicable such as UV–VIS,

Raman, absorption, or emission spectroscopy. These methods are no absolute methods; hence, a calibration is necessary. The best methods for routine observation of the metal content are AAS (atomic absorption spectrometry) and ICP-OES (inductively coupled plasma optical emission spectrometry). The best method for the simultaneous determination of several metals is ICP-OES.

The electroforming of nanocrystalline deposits requires the addition of organic or inorganic additives. The concentration of these additives strongly affects the properties of the deposits. Most of the organic grain-refining additives can be determined by high-performance liquid chromatography (HPLC). The content of inorganic additives can be easily determined like the metal content by ICP-OES. The advantage of inorganic additives is that they can simultaneously be determined with the metal content of the depositing metal.

Special Methods for the Filling of Notches

The widespread application of electroplating leads to problems. It is not possible to use a standard procedure for all length scales, and so different methods for the replication of complex geometries have to be used. In the following we want to present a review of the methods to replicate sophisticated structures on different length scales.

Leveling Agents and Suppressors

An important field of electroforming is the production of strip conductors for electronic industries. Nowadays, the dimensions of computer components get smaller and smaller. For the upcoming generations of computer chips, size reduction is a real challenge [59]. A possible solution for this task is a 3D integration of computer chips and thereby the usage of through silicon vias (TSV).

The major difficulty in the production process is the superfilling of small notches [60–62] without voids, which leads to an enhanced electrical resistance, higher shifting times, and a reduced element lifetime. Several approaches to solve this problem are proposed in literature and partly established in industrial processes. Usually leveling agents (e.g., thiourea, benzotriazole, 1,4-butyne-1,3-diol) [63], suppressors (e.g., polyethylene glycol, polypropylene glycol) [64], a combination of both [65], or catalysts [61] are used to enhance the deposition process.

The mode of action for suppressors is to adsorb on free surfaces of the cathode. Due to its high molecular mass, the diffusion rate of these molecules is very low. Therefore, the smaller metal ions can diffuse faster into the cavities. On top of the surface, a passive layer of suppressors is formed. Inside the cavities, an electrical conductive surface enables to reduce the positively charged metal ions and creates a deposited metal film. So the deposition only takes place inside the notch, where no suppressor molecules are adsorbed on the walls and a filling of the notch can be realized.

But this approach can only be applied for small structures. If the width of the notch is too wide, the diffusion of large molecules is not hindered, and therefore a passivation of the whole cathodic surface takes place. So the notch filling is not enhanced, and the overall deposition rate is significantly reduced.

The second approach for additives in a plating bath is the so-called curvature-enhanced accelerator coverage (CEAC) model [61]. In this case, the electrolyte of the plating bath contains a catalytic active species which supports the deposition process.

Performing a deposition on a nonplanar surface, the plating process causes a change in the surface topography. Thus, locally, the curvature of the surface is changed. As a result of this change of curvature, the local density of adsorbed catalytic active species is changed. For a convex-curved surface, the density of catalyst molecules is lowered; for the concave case, it is enhanced. Due to a proportionality of deposition rate and the amount of catalyst on the surface, the deposition is favored on concave areas of the surface. In average the growth occurs parallel to the cathodic surface.

A very complex procedure is necessary to perform this process in an industrial scale. For bigger parts of systems that will be investigated in the following, this approach is not meaningful. Therefore, other ways for optimizing the deposition procedure have to be found.

In conclusion, additives are a promising way to enhance the plating process itself and the material properties of deposited layers. Some disadvantages arising for the use of additives. So a complex procedure for keeping the concentration of the additives in the electrolyte constant is required. In addition additives act on a global scale, and therefore negative effects like embrittlement due to their incorporation in the deposited layer can occur. Thus, other methods for enhancing the plating process have to be found. One promising approach is the superposition of a magnetic field during deposition process, which is described in the following.

Magnetic Field-Assisted Electroplating

There are many investigations on the influence of a magnetic field during electroplating in literature. Some review articles give a good survey of this topic [66–68].

There are two different ways in which magnetic fields influence the deposition process. On the one hand, the mass transport during electroplating can be enhanced, or on the other hand, reaction kinetics are influenced [69–71]. Therefore, an application of magnetic fields for enhancing the deposition rate inside a notch seems to be possible.

During the electrodeposition process, different forces are acting on the involved ions. There are three main forces that have to be considered:

- Convection
- Migration
- Diffusion

The above mentioned forces play an important role in every deposition process. For the special case of deposition with a superposed magnetic field, further resulting forces have to be regarded. In literature [66], three main forces, related to the magnetic field, are mentioned: a paramagnetic gradient force, a field gradient force, and the Lorentz force.

These forces have a different influence on the plating process. But they are all related to the magnetic properties. Important parameters are the molar susceptibility χ_m and the vacuum permeability μ_0 . Furthermore, the concentration of magnetic ions c and the magnetic field B influence the resulting forces.

At first we want to take a closer look on the paramagnetic gradient force F_p .

$$\mathbf{F}_p = \frac{\chi_m \mathbf{B}^2 \nabla c}{2\mu_0} \quad (3)$$

A gradient in the concentration of paramagnetic ions evokes a force leading ions to the electrode. Coey and coworkers [72] showed in simulations and experiments that this force has only to be considered for ferromagnetic solids and ferrofluids. For all other materials, the contribution of this force is negligible. For aqueous electrolytes like sulfamate electrolytes used for nickel deposition, the force can be assumed as zero. Therefore, this force is not considered in the following.

In contrast, a big influence on the plating process is proven for the field gradient force \mathbf{F}_B .

$$\mathbf{F}_B = \frac{\chi_m c \mathbf{B} \nabla B}{\mu_0} \quad (4)$$

Different authors showed [73–75] that a gradient in the magnetic field influences the electrochemical deposition if metal ions. This gradient results from inhomogeneities in the magnetic field, e.g., caused by different materials for cathode support.

Due to this gradient, a force is acting on the ions in front of the electrode. Depending on the magnetic properties of the ions, different magnetic effects can be distinguished. Paramagnetic ions are attracted to the magnetic field and diamagnetic ones are pushed off.

Tschulik and coworkers [76] showed that the field gradient force plays an important role for structuring surfaces by superposing a magnetic field. Comparing the deposition process of diamagnetic and paramagnetic ions, they could prove that the main influence results from the field gradient force. So it should be possible to locally influence the plating process by tailoring magnetic field gradients.

A further force that has to be considered is probably the best known one: the Lorentz force \mathbf{F}_L .

$$\mathbf{F}_L = q(\mathbf{v} \times \mathbf{B}) \quad (5)$$

This force acts on every moving charge carrier in a magnetic field. In contrast to the field gradient force, there is no need for a gradient in the magnetic field. Equally there is no significance of the magnetic properties of the electrode or the involved ionic species [75]. The Lorentz force acts in the case that the magnetic field and the

electrical field are not parallel. The force acting on the ions leads to a deviation of them. On a global view, this can be seen as a stirring of the electrolyte. In literature this effect is known as the magneto hydrodynamic effect (MHD effect) [77, 78].

It can be distinguished between two effects by observing different length scales. On a macroscale, there is the so-called macro-MHD effect. The Lorentz force leads to a global stirring of the electrolyte and enhances the mass transport to the electrode surface. Thereby the thickness of the diffusion layer is reduced [79].

On the other hand, there is a second effect of the Lorentz force. Even for macroscopically parallel magnetic and electrical fields, an influence of the Lorentz force can be observed. In this case, we talk about the micro-MHD effect [80]. Inhomogeneities of the surface topography evoke disturbances in the electrical field lines. So even for a macroscopically parallel magnetic field at special points, the magnetic and the electric field are not parallel and the Lorentz force is unequal to zero.

The magnetic field does not only affect the mass transport by the Lorentz force but also the surface morphology. A higher magnetic field is responsible for smoother surfaces of the deposited material [81, 82].

Bund and coworkers [69] showed that the current efficiency increases with increasing magnetic field. They explain it with the mass transport-limited hydrogen evolution reaction (HER) and a mixed-controlled deposition of nickel. They observed a shift of the deposition potential to more negative values with increasing magnetic field strength. Due to this potential decrease, the nickel deposition rate is enhanced; meanwhile, the hydrogen evolution reaction is not affected by the changes in deposition potential. A slight enhancement of HER can be observed due to the higher mass transport of protons evoked by the Lorentz force-induced stirring of the electrolyte.

This enhanced deposition rate of metals in a magnetic field can be used in industrial applications, e.g., for filling notches. Probably the most important effect on the filling process of a notch is the influence on the mass transport [83]. In the following, we want to present the main problems during the filling of notches with a low aspect ratio. The problem is schematically shown in Fig. 5.

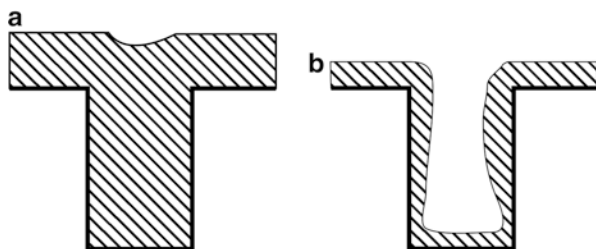


Fig. 5 Electrochemically notch filling. Due to an inhomogeneous distribution of the electrical field lines the deposit growth much faster at the edges of the notch (Fig. 5b). Fig. 5a shows a homogeneous notch filling process

Due to electrical shielding effects and a lowered mass transport to the ground of the notch, the deposition rate decreases. Additionally the deposition of ions is favored in upper parts of the notch. The wall-thickness at the upper rim of the notch is much thicker than at the bottom. So there are two different ways to enhance the deposition rate. The first one is to reduce the electrical shielding, e.g., by auxiliary anodes, and the second one is to enhance the mass transport into the notch. Using an auxiliary anode creates new positioning problems at complex geometries. So this approach is not suitable for industrial applications, and we will only consider the second approach in the following.

Basic experiments were performed to measure the influence of the magnetic field strength in the homogeneous field of an electromagnet. Cyclovoltammetric measurements, as shown in Fig. 6, were performed without a magnetic field and with field strengths of 250 mT and 500 mT. As reported in the literature [69] an influence of the magnetic field on the deposition process can be observed. Performing a cyclovoltammetric measurement, the amount of dissolved nickel in the anodic regime corresponds to the deposited nickel. With increasing magnetic field, a higher charge for the stripping peak can be observed. So we can conclude that with increasing magnetic field, the deposition rate of nickel increases.

But these investigations on basic principles of deposition in a magnetic field do not suffice to establish an industrial process. Therefore further examinations considering the deposition conditions for certain geometries are necessary. For investigating the influence of a magnetic field on the filling process of a real notch – e.g., for applications in automotive dashboards – various experiments with different resins

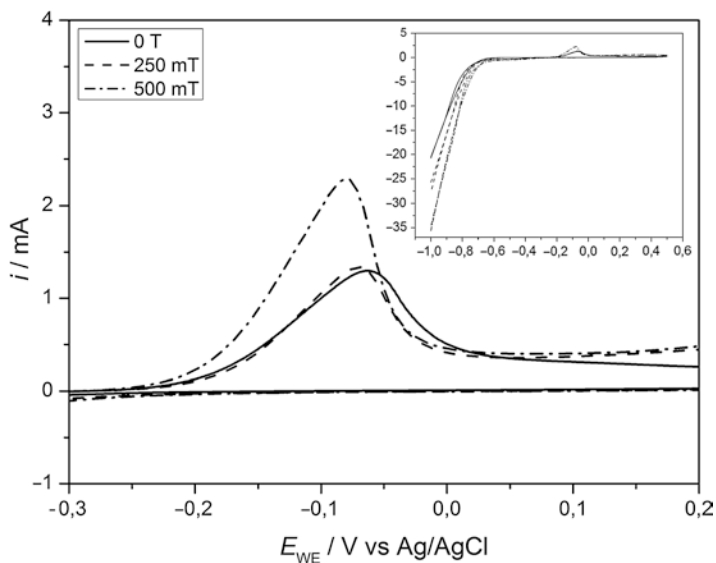


Fig. 6 Investigation of the influence of a magnetic field on the deposition of nickel by cyclovoltammetry

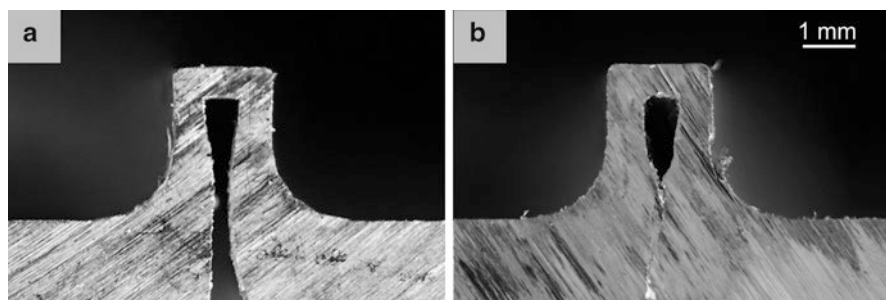


Fig. 7 Comparison of a notch filled (a) without and (b) with superposed magnetic field

Table 3 Development of grain size and hardness in dependence of the applied magnetic field during the deposition process [83]

Field strength (mT)	Crystallite size DV (nm)
0	107
250	78
500	56

for producing the cathode backing were performed. Permanent magnets were directly positioned behind the cathode backing in areas with notches. In contrast to additives in the electrolyte, the magnetic field only acts in a short range, and therefore the influence on the material behavior is limited to a small area and not affecting the whole part.

The superposition of a magnetic field in the range of 40 mT enhances the wall thickness in the notch area by 10–15 %. In Fig. 7 the filling of notches electroplated without and with a superposed magnetic field is compared. The enhancement in wall thickness is clearly visible.

Additionally the magnetic field also influences the material properties of deposited nickel [84]. The grain size is reduced, and therefore the hardness is increased according to the Hall–Petch relation [85, 86]. The development of grain sizes of a nickel deposit with increasing magnetic field is reported in Table 3.

Beside the higher lifetime due to thick walls of the elements, a finer grain structure also enhances a lifetime. Using cheap permanent magnets during plating process helps to improve the economic feasibility for deposited parts of system.

Continuous Fiber-Reinforced Metal Matrix Composites

Metal matrix composites (MMCs) consist of a continuous metallic matrix phase which is predominant in the composite in mass, volume, and thickness and of a reinforcing second phase which improves particular properties of the matrix phase or evokes new properties. Typical reinforcing phases are fibers, particles, or 3D phases that built up an interpenetration phase composite (IPC) with the matrix phase.

State of the Art to Continuous Fiber-Reinforced MMCs

The most common composites are particle- and fiber-reinforced composites. According to the length of the fibers, there are three types of fiber-reinforced MMCs: short fiber-, long fiber-, and continuous fiber-reinforced composites. Short fibers have a length of 0.1–1 mm, long fibers are of a length of 1–50 mm, and all fibers longer than 50 mm are called continuous fibers. Among the MMCs, continuous fiber-reinforced MMCs (CFR-MMCs) exhibit the highest strengths but are also very expensive in manufacturing [87]. Typical fields of application are space and aerospace industry as well as engine manufacturing industry. The composites show high ductility of the matrix combined with high temperature resistance. A further advantage is the better application of force between the matrix and the fiber according to the higher fracture strength of the matrix in comparison to ceramic an polymer matrix composites.

State-of-the-art methods for the synthesis of continuous fiber-reinforced MMCs are the dispersion bonding, infiltration processes, and powder metallurgical (PM) methods. At the dispersion bonding, the pre-oriented fibers are sprayed with the liquid matrix metal. The consolidated fibers are pressed to the resulting component under high temperature. Between the infiltration processes, there are two versions. Either the fiber mats are positioned in the mold and poured with the liquid matrix metal or the fiber mats are pulled through the liquid matrix metal. According to the mostly bad wetting of the molten metal, the bonding of the metal to the fibers causes some difficulties [87]. Using PM methods, fiber mats or fleeces are embedded into powdery matrix metal and solidified via sintering to the dense component. For all this production methods, only fibers with a higher melting point as the matrix are possible.

New Electroforming Method for the Production of Continuous Fiber-Reinforced MMCs

The present chapter outlines a new production method for CFR-MMCs by electroforming. We investigated the incorporation of glassy, carbon, and aramid fibers into a nickel matrix via the electrodeposition of nickel onto a bath model. A bath model is a 3D form mostly made of plastics that has been made conductible by coating with a conductive ink. Fiber mats known from the production of glassy fiber-reinforced plastic (GFRP) have been used. The electroforming method consists of three steps:

1. Deposition of a thin nickel layer on the bath model
2. Positioning of the fiber mats on the as-deposited nickel layer
3. Further deposition of nickel

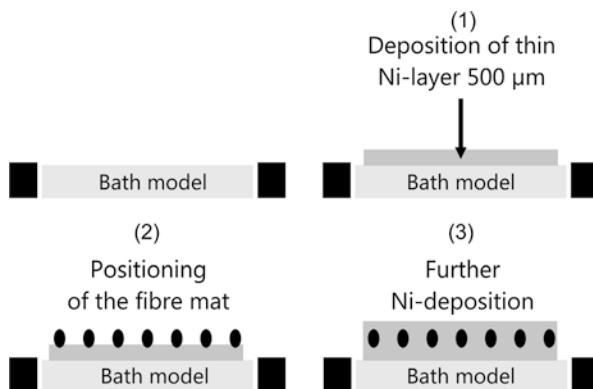


Fig. 8 Process steps for the electrochemical production of continuous fiber-reinforced MMCs

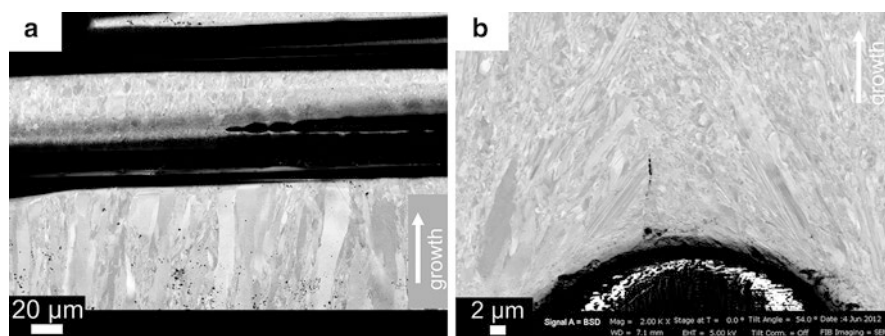


Fig. 9 SEM images of continuous fiber-reinforced MMCs, nanostructuring by fiber incorporation. (a) Cross section perpendicular to fiber direction, (b) cross section in fiber direction

Steps 2 and 3 can be repeated in order to produce 3D composites. The process is schematically outlined for a planar bath model in Fig. 8. Only nonconductive fibers or fibers with a nonconductive coating can be used. The usage of conductive fibers leads to the electrodeposition of the metal onto the fibers unless the interspaces have not been completely filled. Hence, there is a bad bonding between the metallic layers.

Figure 9a shows scanning electron microscopy (SEM) images of the microstructure of the resulting composite deposited from a nickel sulfamate electrolyte (Ltd. Candorchemie, Bochum, Germany) at a current density of 20 mA/cm². According to the considerations in sections “Challenges and Problems in Nanostructuring of Nickel” and “Electroforming of Thick, Complex 3D Deposits” under the fiber, there is a coarse, columnar microstructure. This structure forms due to the growth-dominated electrodeposition process, which is typical for sulfamate nickel. Over the fiber, there

is an untypical very fine-grained microstructure. That suggests a grain-refining effect of the fiber incorporation. Based on the fact that this grain refinement is also visible by using aramid fibers or glassy fibers with different coatings and it is more pronounced by the presence of more fibers, the grain refinement effect of fiber incorporation is independent of the fiber material and only belongs to the incorporation of new surfaces that disturbs the normal grain growth. A closer look (Fig. 9b) shows the very complex microstructure around a single fiber.

Impinge a growing grain on the fiber; it does not stop growing; instead, it grows around the fiber. Behind the fiber, the grain grows together in building up a rooflike structure over the fiber. These grains show the typical columnar structure of sulfamate nickel. Over and under these coalescing columnar grains, there are the very fine-grained regions. The grain refinement in these regions is based on heterogenous nucleation. In this early state of deposition at the fibers, there is a nucleation-dominated electrodeposition, if there are no more hindrances in grain growth direction. Sometimes later, the electrodeposition process will change already to the growth-dominated process in building up columnar microstructure, but by the incorporation of more fibers, e.g., in the form of mats, at every new surface, there is the disturbance of the growth-dominated deposition mechanism and the new formation of the nucleation-dominated mechanism. A further explanation of the grain refinement is given by Weibach [88]. According to him, fibers are able to fix grain boundaries during the formation of the matrix and therefore lead to a reduction in the grain size.

Hence, the incorporation of fibers is a method for the nanostructuring of metal matrixes by electrodeposition without the usage of organic additives and the disadvantages of these, like embrittlement and complex bath analytics. Figure 10 concludes schematically the observations of the microstructure in Fig. 9.

Advantages of this method for the production of CFR-MMCs are not only the relatively low process temperature of no more than 50 °C, the possible use of fibers with a lower melting point than the matrix and the flexibility in the forming of the composite components but also the nanostructuring of the metal matrix.

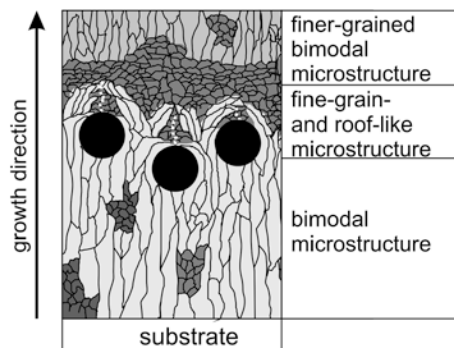


Fig. 10 Schematic structure evolution in nanostructuring by fiber incorporation

Coating of Metal Foams

Metal Foams: Basics

Metal foams are a very interesting class of materials for engineering and science. They are 3D porous structures which mimic the construction elements of large natural load-bearing materials as bones and wood. Open-cell foams consist of a 3D network of interconnected pores and are characterized by the so-called ppi-number, the number of pores per inch (Fig. 11).

The fields of application for metal foams are wide spread and range based on their high stiffness to weight ratio from lightweight construction materials over kinetic energy absorbers according to their special stress versus strain diagram up to functional applications like heat exchangers, sound absorbers, and catalyst supports, based on the large internal surface. But metal foams did not gain large attraction up to now, because they are quite expensive and have to compete with established materials. Hence, a breakthrough is only possible if one is able to create foams which are not only good in one of the three fields of application but also in two or even all three fields. Such foams would be ideal multifunctional materials. In order to create such multifunctional foams, there is the effort to improve the foam properties.

Coating of Metal Foams by Electrodeposition

A coating of metal foams could be done by electrodeposition to improve mechanical properties or for the production of catalysts. The deposition has to take place not only on the outer geometric surface but also on the inner surface.

The first efforts to coat open-cell metal foams via electrodeposition have been made in 2008 by Boonyongmaneerat et al. [89]. They coated aluminum foams with

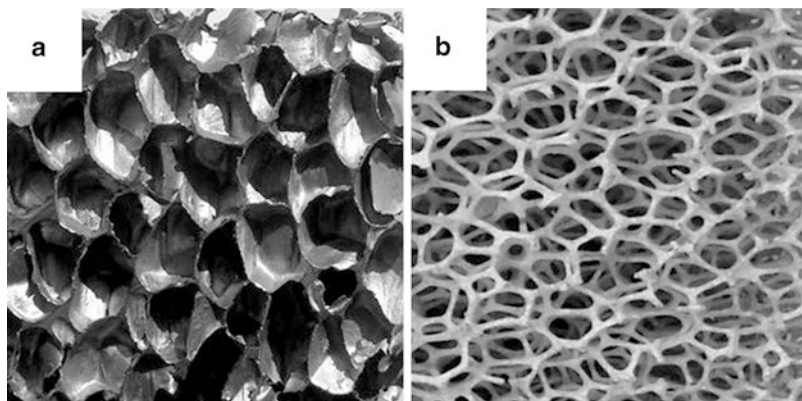


Fig. 11 Closed-cell metal foam (a), open-cell metal foam (b)

a NiW alloy. They were able to demonstrate that the coating enhances the stiffness, strength, and energy absorption capacity, but due to the parallel increase in mass, the positive effect of the coating was not reflected by the specific properties per mass or density of the coated foams. Further efforts have been done in 2009 by Bouwhuis et al. [90]. They performed electrodeposition of nanocrystalline nickel on aluminum foams. According to Boonyongmaneerat et al., there was an enhancement of the absolute mechanical properties but a degradation of the specific mechanical properties. The reason for the degradation is the bad coating homogeneity over the cross section of the foams. Arising from the 3D deposition process not only on the outer geometric surface but also on the inner surface, there are mass flow limitation problems [91, 92]. A further problem is the Faraday effect. The foam structure itself acts as a Faraday cage. This shielding prevents or impedes the plating of the foam center. Figure 12 outlines the prescribed situation. Regarding the concentration profile, in front of planar electrodes, there are two regimes for direct current plating and three for pulsed electrodeposition. In a large distance to the electrode surface, there is the constant concentration c_∞ of the bulk electrolyte. With decreasing distance to the electrode, the concentration in the electrolyte decreases according to the consumption of metal ions by the deposition process and the limited diffusion of the metal ions. If the deposition rate, expressed by the applied current density, is much larger than the diffusion rate, the current is called the limiting diffusion current (LDC) i_{lim} , and metal ion concentration at the cathode becomes zero. In the case of pulse plating, there is a second diffusion layer which oscillates in the concentration with the pulse frequency between the concentration of the abovementioned stationary diffusion layer according to direct current plating and the cathode surface concentration c_s .

For metal foams, the theory of the concentration profiles have to be extended into the porous structure of the foams, whereas each strut acts as a 2D planar electrode in the abovementioned manner. If no current is applied, the metal ions are homogeneously distributed all over in the electrolyte both in the porous electrolyte and in the bulk electrolyte (case 1). After a current is applied (case 2), all metal ions in the porous electrolyte and in the vicinity of the outer surface of the foam will be suddenly deposited. In order to maintain the deposition process (case 3a), metal ions have to diffuse from the bulk electrolyte up to the foam center. This diffusion process is superposed by the deposition process at every point in the foam, and this leads to a depletion of the electrolyte in the porous structure; only a small amount of metal ions reach the center part of the foam. As a result, there is an increasing concentration gradient from the outer geometric surface to the center of the foam. This is responsible for the inhomogeneous coating thickness (case 3b).

The usage of pulsed electrodeposition improves the coating homogeneity. Up to the end of the t_{on} -time, there is the same situation as for direct current plating. During the t_{on} -time, there is the buildup of the concentration gradient between the inner and the outer parts of the foam structure (case 2b). But in the following t_{off} -time, there is an unimpeded diffusion of metal ions to the foam center without

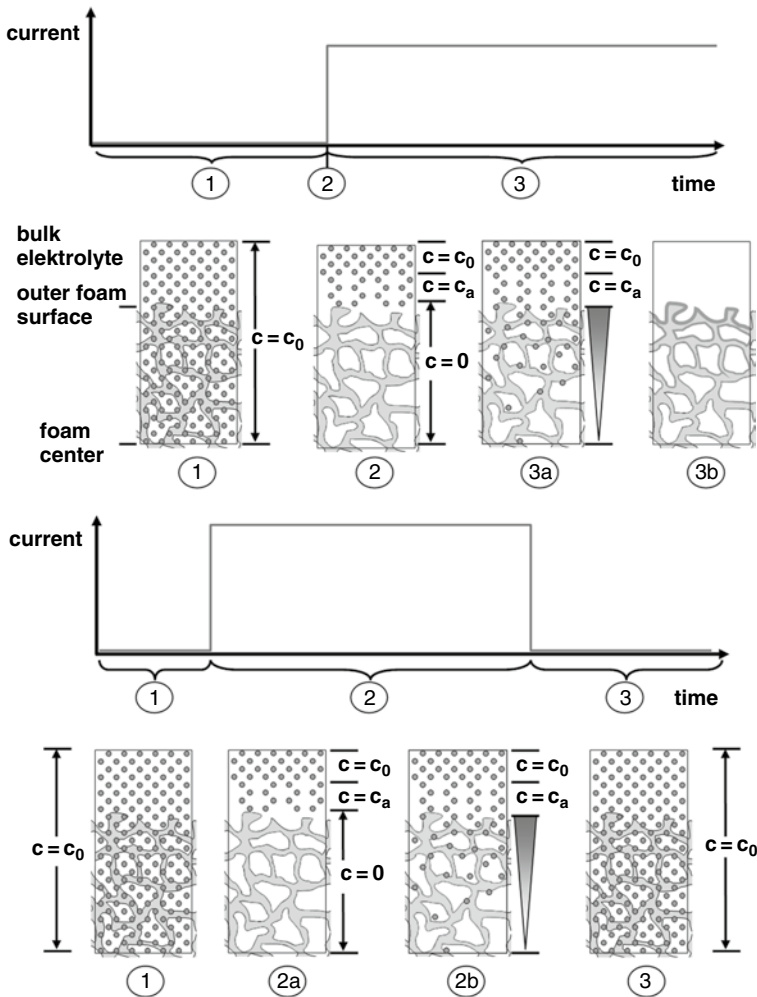


Fig. 12 Mass transport problems in plating of open-cell metal foams

superposed deposition. As a result of long t_{off} -time, the metal ion concentration in the porous electrolyte will be homogeneously distributed over the cross section of the foam and in the range of the bulk concentration (case 3). From this, there is a much homogeneous coating thickness distribution.

According to the strong mass transport limitations during the plating, the deposition is nucleation dominated; hence, the deposited metal has a nanocrystalline grain structure even in the case of direct current plating.

A Special Method for the Production of Ni/Al Hybrid Metal Foams

Cubic aluminum foams with an edge length of 40 mm and a pore size of 10 ppi (AlSi₇Mg_{0.3}, m-pore GmbH, Dresden, Germany) were coated by direct current plating with nanocrystalline nickel. Plating of aluminum needs special pretreatments. First there is an alkaline pickling followed by an acid pickling and an electroless coating of the aluminum foam in an alkaline zincate solution.

The electrodeposition process is carried out with a commercial nickel sulfamate electrolyte with a concentration of 110 g/l nickel (Enthone GmbH, Langenfeld, Germany). The electrolyte is maintained at 50 °C and pH of 3.8. As shown in section “Metal Foams: Basics,” the electrodeposition on metal foams is strongly governed by mass transport limitations. In order to simplify the mass transport, Jung et al. [91, 93] developed a special anode–cathode arrangement. The anode consists of a double-walled hollow cube filled with nickel pellets (A.M.P.E.R.E. GmbH, Dietzenbach, Germany) as sacrificial anode. The anode cage is shown in Fig. 13. The foams were coated with current densities of 0.5, 1.0, 2.0, 7.5, and 20 mA/cm², respectively. The crystallite size of the nickel coating has been determined by X-ray diffraction using a modified Warren–Averbach method. For all foams, the crystallite size was in the range of 43 ± 2 nm. Table 4 shows the relative coating thickness in a depth of 20 mm of the foams plated at the different current densities. The use of low current densities leads to the strong increase in the homogeneity of the coating.

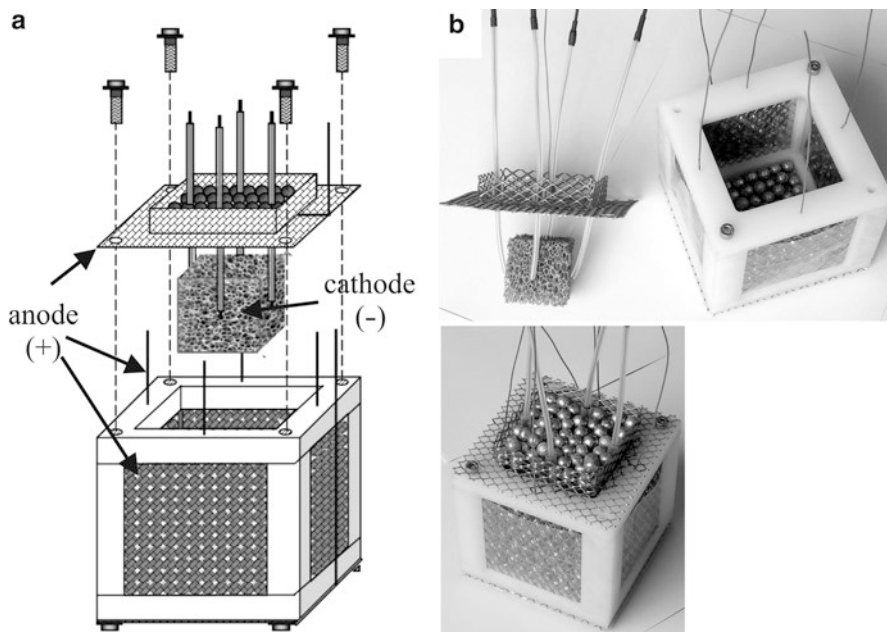
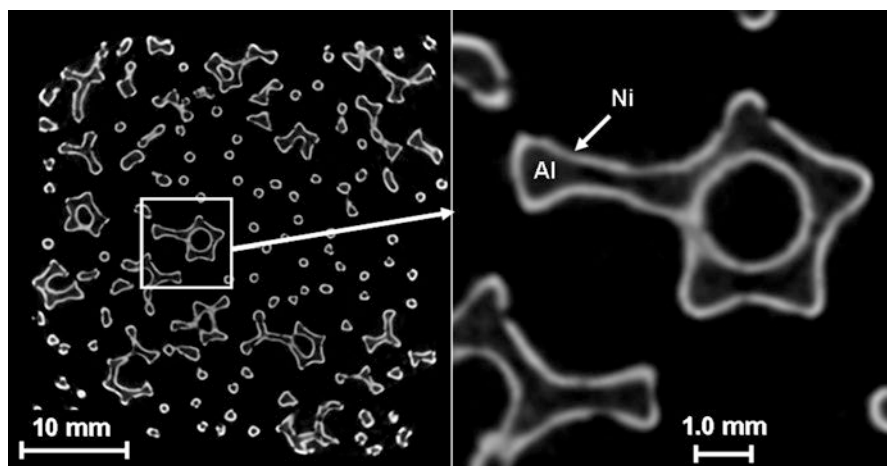


Fig. 13 Special anode–cathode arrangement for plating of open-cell metal foams

Table 4 Homogeneity of the coating as function of the applied current density

Current density mA/cm ²	Rel. coating thickness %
0.5	61
1.0	54
2.0	36
7.5	32
20.0	31

**Fig. 14** X-ray CT image of an 10 ppi Ni/Al hybrid foam, produced at a current density of 0.5 mA/cm²

For higher current densities, there is a strong decrease in the coating thickness. The reason for this is that the current exceeds the LDC for the foam center. For higher current densities, it exceeds also the local LDC for regimes which are closer to the outer geometric foam surface. Hence, most of the applied current is used to deposit nickel at the outer geometric surface. Figure 14 shows an X-ray computed tomography (CT) image of a 10ppi aluminum foam coated with nanocrystalline nickel at a current density of 0.5 mA/cm².

In order to achieve a very homogeneous coating over the complete cross section of porous substrates like metal foams, there must be the use of very low current densities. But according to the Faraday effect of such porous substrates, it is not possible to create coatings with a homogeneity of 100 %.

Conclusion

The present contribution shows how the mechanical properties of deposits and the formation of electroformed structures can be influenced by electrochemical nanostructuring. Furthermore, pulsed electrodeposition methods are used for the

electrodeposition of metal matrix composites and the filling of complex 3D structures. Electrodeposition is a powerful tool for the tailor-made nanostructuring of metals and alloys by the variation of the different chemical and physical process parameters. An efficient way to adjust the crystallite size is to influence the electrocrystallization by the current parameters, the temperature, and the addition of chemical additives. If no chemical additives were used, very small crystallite sizes and stress-free deposits are difficult to archive, but on the other hand these chemical molecules, like grain refiners and stress relievers, can be co-deposited, and therefore the mechanical properties are changed in a negative way. For this reason, a brief combination of the physical and chemical process parameters is necessary. The field of process parameters is more or less complex, but following the electrocrystallization theory, the crystallite size decreases with short t_{on} -times, moderate t_{off} -times, and high pulsed current densities. The identification of the active additives is not so easy because each metal is sensitive to a special molecule structure. The following rule of thumb is very helpful: functionalities with free electron pairs like amino-, carboxylic-, or carbonylic groups are potential additives. An effective identification of the right combination of process parameter can be found out with a combinative design of experiments.

It could be demonstrated that based on the thick deposition thickness, it is not possible simply to transfer experiences and plating parameter from galvanic coating technologies to electroforming. Problems are the highly complex current distribution for 3D substrates, internal stresses, and formation of delamination layers. Bath analytics is a very important fact in order to guarantee reproducible and high quality properties of the deposits.

A brief overview about the resulting forces during a magnetic field supported deposition was given. It could be shown that the problem of notch filling can be attenuated by the superposition of a magnetic field. The magnetic field affects the deposition and enhances the deposition rate locally. Different measurements could prove this phenomena, and the mode of action was discussed. The wall thickness of the regarded parts of the system could be enhanced by 10–15 %. Additionally the crystallite size is reduced, and according to the Hall-Petch relation, the strength of the material is enhanced. For this reason, the lifetime can be raised.

A new method for the synthesis of continuous fiber-reinforced metal matrix composites has been presented. The incorporation of electrically nonconducting fibers leads to the strengthening of the deposit not only by the production of a composite but also by grain refinement based on heterogenous nucleation at the fibers. Finally the electrochemical coating technology was expanded on very complex 3D substrates as metal foams where there is not only a coating of the outer geometric but also of the inner surface. For quite homogeneous coatings, very low current densities have to be used.

Acknowledgments Financial support from the Bayerische Forschungsförderung in the framework of the project “Galvano 21” and the Wirtschafts- und Wissenschaftsministerium des Saarlandes is gratefully acknowledged. We thank Prof. Dr. R. Hempelmann and Dr. M. R. Koblischka for stimulating discussions and Dipl.-Ing. M. Prell, Dipl.-Ing. S. Kuhn, and D. Münch for their experimental help.

References

1. Ellis TS, Kakarala N, Patel S (2006) Thermoplastic polyolefins (TPO) for slush molding of interior skins: materials and processing requirements. Society of Plastics Engineers, Automotive Thermoplastic Polyolefins (TPO) Global Conference 2005, pp 36–58
2. Hättig J, Kaufhold W (2001) Dashboards meet highest requirements: new market for slush-moulded skins made from TPU. *Kunststoffe Plast Eur* 91(3):16–17
3. Lohner A, Bojahr T (2011) Two colors with one stroke. *Kunststoffe Int* 101(3):55–57
4. Monzon M, Hernandez P, Benitez A, Marrero M, Alvarez M, Kearns M (2009) An innovative electroforming process for oil heated rotational moulding tools. Proceedings of the 9th Biennial Conference on Engineering Systems Design and Analysis, vol. 1, pp 185–191
5. Leoni NJ, Birecki H, Gila O, Lee MH, Hanson EG, Fotland R (2011) Small dot ion print-head. International Conference on Digital Printing Technologies, pp 50–53
6. Liu C, Li M, Shi W, Du L, Wang L (2011) New method for dimensional precision control of electroformed parts by using micro electroforming technique with SU-8 thick photoresist. *Jixie Gongcheng Xuebao/J Mech Eng* 47(3):179–185
7. Sun Kim J, Ki Min I, Deok Kim J (2012) Development of a selective electroforming process for micro-sized probe tips used in LCD inspection machines. *J Phys: Conf Ser* 379(1)
8. Gol'denberg BG, Reznikova EF, Lemzyakov AG, Pindyurin VF (2013) Microbeam x-ray lithography apparatus for direct production of deep LIGA structures. *Optoelectron Instrum Data Process* 49(1):81–86
9. Kuboyama Y, Nishida S, Noda D, Hattori T (2012) Fabrication of micro-capacitive inclination sensor using the LIGA process. *Key Eng Mater* 523–524:592–597
10. Zhixiang X, Fengjuan J (2013) Design and fabrication of micro-coil sensor array by using UV-LIGA process. *Appl Mech Mater* 300–301:585–588
11. Bayer S, Kraus D, Keilig L, Glz L, Stark H, Enkling N (2012) Changes in retention force with electroplated copings on conical crowns: a comparison of gold and zirconia primary crowns. *Int J Oral Maxillofac Implants* 27(3):577–585
12. Gorlach P (2003) Electroformed galvanic gold base for anatomically retained orbital prosthesis. *J Facial Somato Prosthet* 9(2):69–74
13. Watanabe M (1989) Application of electroforming for coronal restorations. Metal frame for porcelain fused to metal crowns. *Kanagawa Shigaku J Kanagawa Odontol Soc* 24(1):77–95
14. Arranz F, Brafias B, Busch M, Gonzalez M, Munoz A, Szcapaniak B, Castro L, Galan P, Iglesias D, Lapena J, Lopez D, Rucandio I, Plaza D, Garcia M, Gomez B (2011) Evaluation of the electroforming technique for IFMIF-EVEDA beam dump manufacturing. *Fusion Sci Technol* 60(2):538–543
15. Chen TY, Wang DC (2009) An experimental study on the electroforming of ternary Ni-Co-Mn alloy. *Int J Nucl Desal* 3(3):301–309
16. Lee SJ, Lee YM, Lee CY, Lai JJ, Kuan FH, Chuang CW (2007) The performance of miniature metallic PEM fuel cells. *J Power Sources* 171(1):148–154
17. Arnet E (2004) Electroforming of hollow jewellery – functionality and quality. *Galvanotechnik* 95(9):2156–2162, +VI
18. Kuhn AT, Lewis LV (1988) The electroforming of gold and its alloys. *Gold Bull* 21(1):17–23
19. Leuw DH (1991) Fabrication of special purpose optical components. Proceedings of SPIE - The International Society for Optical Engineering, vol. 1442, pp 31–41
20. Suchentrunk R, Tuscher O (1979) Electroforming in aerospace engineering. *Galvanotechnik* 70(12):1178–1184
21. Hanafi I, Daud AR, Radiman S, Ghani MHA, Budi S (2013) Surfactant assisted electrodeposition of nanostructured CoNiCu alloys. *J Phys Conf Ser* 431(1)
22. Natter H, Krajewski T, Hempelmann M (1996) Nanocrystalline palladium by pulsed electrodeposition. *Berichte der Bunsengesellschaft/Phys Chem Chem Phys* 100(1):55–64
23. Natter H, Hempelmann R (1996) Nanocrystalline copper by pulsed electrodeposition: the effects of organic additives, bath temperature, and pH. *J Phys Chem* 100(50):19,525–19,532

24. Rezaei-Sameti M, Nadali S, Falahatpisheh A, Rakhshi M (2013) The effects of sodium dodecyl sulfate and sodium saccharin on morphology, hardness and wear behavior of Cr-Wc nano composite coatings. *Solid State Commun* 159:18–21
25. Durney LJ (ed) (1984) *Graham's electroplating engineering handbook*, 4th edn. Chapman & Hall, London
26. Tomantschger K, Palumbo G, Gonzalez F, Natter H, Hempelmann R, Endres F, Erb U, Aust KT (2004) Electrochemical synthesis of nanocrystalline materials. Eugen G. Leuze, Bad Saulgau
27. Zimmerman AF, Palumbo G, Aust KT, Erb U (2002) Mechanical properties of nickel silicon carbide nanocomposites. *Mater Sci Eng A* 328(1):137–146
28. Giallonardo JD, Erb U, Aust KT, Palumbo G (2011) The influence of grain size and texture on the young's modulus of nanocrystalline nickel and nickel-iron alloys. *Philos Mag* 91(36): 4594–4605
29. El-Sherik AM, Erb U, Palumbo G, Aust KT (1992) Deviations from Hall–Petch behaviour in as-prepared nanocrystalline nickel. *Scr Metall Mater* 27(9):1185–1188
30. Jeong DH, Gonzalez F, Palumbo G, Aust KT, Erb U (2001) The effect of grain size on the wear properties of electrodeposited nanocrystalline nickel coatings. *Scr Mater* 44(3):493–499
31. Karimpoor AA, Erb U, Aust KT, Wang Z, Palumbo G (2002) Tensile properties of bulk nanocrystalline hexagonal cobalt electrodeposits. *Mater Sci Forum* 386–388:415–420
32. Alanazi N, Abdelmounan HK, Sherik AM (2012) Wear performance of electroplated nanocrystalline Ni-P alloy coatings. *Mater Perform* 51(10):36–39
33. Brooks I, Lin P, Palumbo G, Hibbard GD, Erb U (2008) Analysis of hardness-tensile strength relationships for electroformed nanocrystalline materials. *Mater Sci Eng A* 491(1–2):412–419
34. Guo Y, Wang Y, Xie L (2011) Micro electroformed Ni-P alloy parts by extended UV-LIGA technology. *Adv Mater Res* 317–319:1635–1639
35. Suresha SJ, Haj-Taieb M, Bade K, Aktaa J, Hemker KJ (2010) The influence of tungsten on the thermal stability and mechanical behavior of electrodeposited nickel MEMS structures. *Scr Mater* 63(12):1141–1144
36. Cui X, Chen W (2008) Saccharin effects on direct-current electroplating nanocrystalline Ni-Cu alloys. *J Electrochem Soc* 155(9):K133–K139
37. See SH, Seet HL, Li XP, Lee JY, Lee KYT, Teoh SH, Lim CT (2003) Effect of nanocrystalline electroplating of NiFe on the material permeability. *Mater Sci Forum* 437–438:53–56
38. Erb U, El-Sherik AM, Palumbo G, Aust KT (1993) Synthesis, structure and properties of electrodeposited nanocrystalline materials. *Nanostruct Mater* 2(4):383–390
39. Natter H, Hempelmann R (2003) Tailor-made nanomaterials designed by electrochemical methods. *Electrochim Acta* 49(1):51–61
40. Natter H, Schmelzer M, Hempelmann R (1998) Nanocrystalline nickel and nickel-copper alloys: synthesis, characterization, and thermal stability. *J Mater Res* 13(5):1186–1197
41. Shen X, Lian J, Jiang Z, Jiang Q (2008) The optimal grain sized nanocrystalline Ni with high strength and good ductility fabricated by a direct current electrodeposition. *Adv Eng Mater* 10(6):539–546
42. Ashiru OA (1995) Gelatin inhibition of a silver plating process. *Plating Surf Finish* 82(4): 76–82
43. Georgiev G, Kamenova I, Georgieva V, Kamenska E, Hempelmann R, Natter H (2006) Poly(dimethylaminoethylmethacryloylpropanesulfonate)-suitable polymer additive for pulsed electrodeposition of nanocrystalline nickel. *J Appl Polym Sci* 102(3):2967–2971
44. Lee JW, Ju JB, Kim JD (2007) Electrodeposition of palladium on the copper lead frame: electrode reaction characteristics and the effects of primary additives. *Korean J Chem Eng* 24(6):960–964
45. Yevtushenko O, Natter H, Hempelmann R (2006) Grain-growth kinetics of nanostructured gold. *Thin Solid Films* 515(1):353–356
46. Kashchiev D (2000) *Nucleation basic theory with applications*. Butterworth-Heinemann, Oxford
47. Natter H, Hempelmann R (2008) Nanocrystalline metals prepared by electrodeposition. *Z Phys Chem* 222(2–3):319–354

48. Majumdar S (2001) Structural analysis of electrosleeved tubes under severe accident transients. *Nucl Eng Des* 208(2):167–179
49. Palumbo G, Gonzalez F, Brennenstuhl AM, Erb U, Shmayda W, Lichtenberger PC (1997) In-situ nuclear steam generator repair using electrodeposited nanocrystalline nickel. *Nanostruct Mater* 9(1–8):737–746
50. Yang B, Leu MC (2000) Rapid electroforming tooling. *Materials Research Society Symposium - Proceedings*, vol. 625, pp 57–66
51. Sykes JM, Rothwell GP (1971) Relaxation of internal stresses in electrodeposits during stress measurement by null-deflection methods. *J Electrochem Soc* 118:91–93
52. Makar'eva S (1938) *Bull Acad Sci U.S.S.R., Classe Sci Math Nat, Ser Chim* :1211–1223
53. Geneidy A, Koehler WA, Machu W (1959) The effect of magnesium salts on nickel plating baths. *J Electrochem Soc* 106:394–403
54. Brenner A (1963) *Electrodeposition of alloys – principles and practice*, vols 1 and 2. Academic, New York/London
55. Atanassov N, Mitreva V (1996) Electrodeposition and properties of nickel-manganese layers. *Surf Coat Technol* 78(1–3):144–149
56. Atanassov N, Schils H (1996) Deposition of Ni-based alloys with addition of manganese and sulfur. *Plating Surf Finish* 83(7):49–53
57. Srivastava M, Grips VKW, Rajam KS (2010) Influence of cobalt on manganese incorporation in Ni-Co coatings. *J Appl Electrochem* 40(4):777–782
58. Yang NYC, Headley TJ, Kelly JJ, Hrubby JM (2004) Metallurgy of high strength Ni-Mn microsystems fabricated by electrodeposition. *Scr Mater* 51(8):761–766
59. Bernstein K, Andry P, Cann J, Emma P, Greenberg D, Haensch W, Ignatowski M, Koester S, Magerlein J, Puri R, Young A (2007) Interconnects in the third dimension: design challenges for 3D ICs. In: *Proceedings of the 44th annual design automation conference, DAC'07*. ACM, New York, pp 562–567
60. Moffat T, Josell D (2012) Extreme bottom-up superfilling of through-silicon-vias by damascene processing: Suppressor disruption, positive feedback and Turing patterns. *J Electrochem Soc* 159(4):D208–D216
61. Moffat T, Wheeler D, Edelstein M, Josell D (2005) Superconformal film growth: mechanism and quantification. *IBM J Res Dev* 49(1):19–36
62. Vereecken PM, Binstead RA, Deligianni H, Andricacos PC (2005) The chemistry of additives in damascene copper plating. *IBM J Res Dev* 49:3–18
63. Kelly JJ, Tian C, West AC (1999) Leveling and microstructural effects of additives for copper electrodeposition. *J Electrochem Soc* 146(7):2540–2545
64. Moffat TP, Bonevich JE, Huber WH, Stanishevsky A, Kelly DR, Stafford GR, Josell D (2000) Superconformal electrodeposition of copper in 50090 nm features. *J Electrochem Soc* 147:4524–4535
65. Taephaisitphongse P, Cao Y, West AC (2001) Electrochemical and fill studies of a multicomponent additive package for copper deposition. *J Electrochem Soc* 148(7):C492–C497
66. Coey JMD, Hinds G (2001) Magnetic electrodeposition. *J Alloys Compd* 326(1–2):238–245
67. Fahidy TZ (1983) Reviews of applied electrochemistry. 8. Magneto-electrolysis. *J Appl Electrochem* 13(5):553–563
68. Fahidy TZ (2002) The effect of magnetic fields on electrochemical processes. In: Conway BE, Bockris JO, White RE (eds) *Modern aspects of electrochemistry*, vol 32. Springer US, New York, pp 333–354
69. Bund A, Ispas A (2005) Influence of a static magnetic field on nickel electrodeposition studied using an electrochemical quartz crystal microbalance, atomic force microscopy and vibrating sample magnetometry. *J Electroanal Chem* 575(2):221–228
70. Chia-Chien L, Chou TC (1995) Effects of magnetic field on the reaction kinetics of electroless nickel deposition. *Electrochim Acta* 40(8):965–970
71. Steiner UE, Ulrich T (1989) Magnetic field effects in chemical kinetics and related phenomena. *Chem Rev* 89:51–147

72. Coey J, Rhen F, Dunne P, McMurry S (2007) The magnetic concentration gradient force – is it real? *J Solid State Electrochem* 11:711–717
73. Hinds G, Coey JMD, Lyons MEG (2001) Influence of magnetic forces on electrochemical mass transport. *Electrochem Commun* 3(5):215–218
74. Mutschke G, Tschulik K, Weier T, Uhlemann M, Bund A, Frhlich J (2010) On the action of magnetic gradient forces in micro-structured copper deposition. *Electrochim Acta* 55(28):9060–9066
75. Pullins MD, Grant KM, White HS (2001) Microscale confinement of paramagnetic molecules in magnetic field gradients surrounding ferromagnetic microelectrodes. *J Phys Chem B* 105(37):8989–8994. doi:10.1021/jp012093s
76. Tschulik K, Koza JA, Uhlemann M, Gebert A, Schultz L (2009) Effects of well-defined magnetic field gradients on the electrodeposition of copper and bismuth. *Electrochem Commun* 11(11):2241–2244
77. Bund A, Koehler S, Kuehnlein HH, Plieth W (2003) Magnetic field effects in electrochemical reactions. *Electrochim Acta* 49(1):147–152
78. Devos O, Olivier A, Chopart J, Aaboubi O, Maurin G (1998) Magnetic field effects on nickel electrodeposition. *J Electrochem Soc* 145(2):401–405
79. Hinds G, Spada FE, Coey JMD, Mhochin TRN, Lyons MEG (2001) Magnetic field effects on copper electrolysis. *J Phys Chem B* 105:9487–9502
80. Matsushima H, Nohira T, Ito Y (2004) AFM observation for iron thin films electrodeposited in magnetic fields. *Electrochem Solid-State Lett* 7:C81–C83
81. Ispas A, Matsushima H, Plieth W, Bund A (2007) Influence of a magnetic field on the electrodeposition of nickel-iron alloys. *Electrochim Acta* 52(8):2785–2795
82. Matsushima H, Nohira T, Mogi I, Ito Y (2004) Effects of magnetic fields on iron electrodeposition. *Surf Coat Technol* 179(2–3):245–251
83. Weinmann M, Jung A, Natter H (2013) Magnetic field-assisted electroforming of complex geometries. *J Solid State Electrochem* 17(10):2721–2729. doi:10.1007/s10008-013-2172-6
84. Ganesh V, Vijayaraghavan D, Lakshminarayanan V (2005) Fine grain growth of nickel electrodeposit: effect of applied magnetic field during deposition. *Appl Surf Sci* 240(14):286–295
85. Hall EO (1951) The deformation and ageing of mild steel: III. Discussion of results. *Proc Phys Soc Sect B* 64(9):747
86. Petch NJ (1953) The cleavage strength of polycrystals. *J Iron Steel Inst* 174:25–28
87. Rösler J, Harders H, Bäker M (2006) *Mechanisches Verhalten der Werkstoffe, 2. durchgesehene und erweiterte Auflage*. Teubner, Wiesbaden
88. Weißbach W (2010) *Werkstoffkunde – Strukturen, Eigenschaften, Prüfung, 17. überarbeitete und aktualisierte Auflage*. Vieweg-Teubner-Verlag, Wiesbaden
89. Boonyongmaneerat Y, Schuh C, Dunand D (2008) Mechanical properties of reticulated aluminum foams with electrodeposited Ni-W coatings. *Scr Mater* 59(3):336–339. doi:10.1016/j.scriptamat.2008.03.035
90. Bouwhuis B, McCrea J, Palumbo G, Hibbard G (2009) Mechanical properties of hybrid nanocrystalline metal foams. *Acta Mater* 57(14):4046–4053
91. Jung A, Koblischka MR, Lach E, Diebels S, Natter H (2012) Hybrid metal foams: mechanical testing and determination of mass flow limitations during electroplating. *Int J Mater Sci* 2(4):97–107
92. Jung A, Natter H, Hempelmann R, Diebels S, Koblischka MR, Hartmann U, Lach E (2010) Electrodeposition of nanocrystalline metals on open cell metal foams: improved mechanical properties. *ECS Trans* 25(41):165–172
93. Jung A, Natter H, Diebels S, Lach E, Hempelmann R (2011) Nanonickel coated aluminum foam for enhanced impact energy absorption. *Adv Eng Mater* 13(1–2):2328. doi:10.1002/adem.201000190

O.A. Oviedo and E.P.M. Leiva

Contents

On the Nanoscale	972
On Nanoelectrochemistry	974
Physical Versus Electrochemical Control of Metal Surface Coverage	975
Selected Recent Experimental Work.....	976
Underpotential Deposition	978
Galvanic Replacement.....	982
Dendrimer-Encapsulated Nanoparticles.....	985
Nanothermodynamic Stability	988
Some Basic Considerations.....	988
Electrodeposition on Planar Surfaces.....	992
Straightforward Generation of Nanoparticles from Their Precursors.....	995
Nanoparticle Growth from Preexisting Seeds.....	999
<i>Upd-opd</i> Transition in the Nanoscale.....	1004
Conclusions and Perspectives in <i>Upd</i> Modeling.....	1006
References.....	1007

Abstract

In this chapter, we give an overview of selected experimental and computer simulation literature research on thermodynamic modeling applied to the understanding of metal electrodeposition on metallic nanostructures. A brief survey on underpotential deposition, galvanic replacement, and dendrimer-encapsulated nanoparticles is given first. Focus is made on applications related to size and shape control and the formation of hollow, core/shell, and reversed nanoparticles. Then, a nanothermodynamic model is proposed, providing understanding on the

O.A. Oviedo (✉) • E.P.M. Leiva (✉)
Instituto de Investigaciones en Físico-Química de Córdoba (INFIQC-CONICET),
Departamento de Matemática y Física, Facultad de Ciencias Químicas,
Universidad Nacional de Córdoba, Córdoba, Argentina
e-mail: o.a.oviedo@gmail.com; eleiva@fcq.unc.edu.ar

physics behind the electrodeposition problem. At the end of the chapter, we highlight the main conclusions drawn from the chapter and give some perspectives in advanced modeling of the present problem.

Keywords

Metal electrodeposition • Underpotential deposition • Nanothermodynamic • Nanoparticles • Galvanic replacement

On the Nanoscale

Nanoscience has been defined as the study of the fundamental principles of structures with at least one dimension roughly in the range between 1 and 100 nm [1]. Within this conception, we have in it the confluence of various branches of science, like chemistry, physics, biology, engineering, medicine, mathematics, psychology, etc. To address the topic given in the title, we will give a representative example. Let us think of a cubic piece of Au, containing Avogadro's number of atoms, $N = 6.022 \times 10^{23}$. The number of atoms on its surface, say, N^{surf} , will be of the order $N^{\text{surf}} \propto N^{2/3}$, that is, about $\sim 4 \times 10^{16}$, and corresponds to about $\sim 6 \times 10^{-6}\%$ of the total number of atoms. In this case, the relation area to volume is about $\sim 3 \times 10^{-7} \text{ nm}^{-1}$. In other words, the ratio of the number of atoms at the surface to the total number of atoms is under these conditions negligible. The question is at which size of the Au piece will this situation drastically change? To answer this, we show in Fig. 1 the

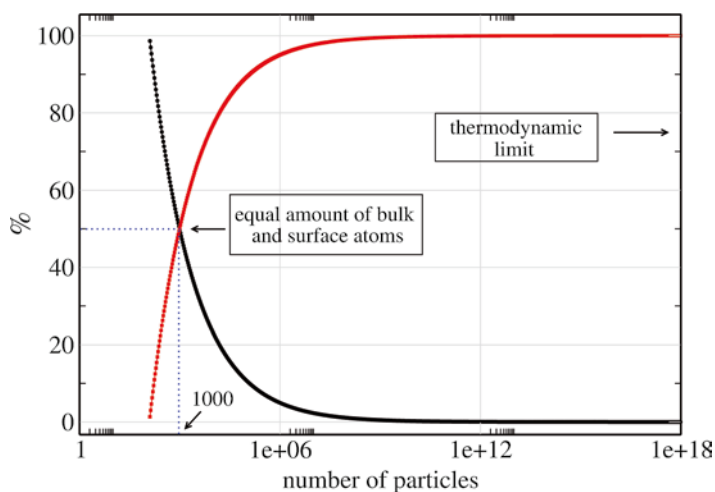


Fig. 1 Percentage of surface atoms (*black*) and bulk atoms (*red*) in a cubic piece of metal as a function of the total number of atoms in the cube

percentage of bulk and surface atoms of the Au piece as a function of the total number of atoms. It comes out that the number of surface atoms appears as negligible for metal pieces where $N > 10^6$. On the other hand, we see there that the number of total atoms of the NP at which the number of surface atoms is equal to the number of inner atoms is close to 1000, corresponding in the case of a Au cubic particle to an edge of about 3 nm. Under these conditions, no proper bulk or surface regions may be clearly defined. Thus, we can expect that when metallic particles are of the order of a hundred of nanometers or smaller, special properties may appear, becoming particularly remarkable in the region of a few nanometers.

The singular properties of nanobjects and their consequences for technological development may become manifest in different ways, as has been pointed out in extensive theoretical and experimental work (see Table 1).

Table 1 Some milestones of nanoscience and nanotechnology

1931	Invention of the transmission electron microscope by M. Knoll and E. Ruska
1942	Development of the scanning electron microscope by V. Zworykin
1952	L. V. Radushkevich and V. M. Lukyanovich show the first image of 50 nm carbon nanotubes
1959	The term “nanotechnology” is introduced for the first time in R. Feynman’s lecture: “There is a plenty of room at the bottom: an invitation to enter a new field of physics”
1963	T. L. Hill edits his book: “Thermodynamic of Small Particles.” Although the term “nano” is absent there, this work settled the theoretical basis for tackling nanothermodynamics
1965	G. E. Moore settles his first law, concerning the doubling of the number of transistors of integrated circuits every 2 years
1966	R. Young suggests the use of piezomotors for positioning
1981	G. Binnig and H. Röhrer develop the scanning tunneling microscope, making it possible to observe individual atoms
1981	Quantum dots are discovered by L. E. Brus, A. L. Efros and A. Ekimov
1985	R. Curl, H. Kroto and R. Smalley discover fullerene. Nanofabrication based on carbon begins
1986	G. Binnig, C. Gerber and C. Quate develop atomic force microscopy
1986	E. Drexler edits his book: “Engines of Creation,” one of the most popular books on nanobjects
1986	A. Ashkin invents “optical tweezers.” These make it possible manipulations on nanobjects through a laser beam
1987	J-M. Lehn introduces the “self-organization” and “self-assembly” terms
1990	D. Eigler writes “IBM” using 35 individual Xe atoms using STM
1991	Multiwalled carbon nanotubes are discovered by S. Ijima
1998	C. Dekker fabricates the first nanotransistor based on carbon nanotubes
2003	The sequence of the human genome is decoded
2003	Intel launches to the market the first processor in the nanoscale (90 nm)
2004	Synthesis of graphene
2008	The force required to move individual atoms on a surface is determined experimentally

From this table we see that the emergence of nanoscience is strongly linked to technological advance in the area. Reciprocally, increased understanding of phenomena at the nanoscale leads to technological progress.

On Nanoelectrochemistry

Electrochemistry is a mature science, whose origin dates back to the work of Galvani and Volta, at the end of the eighteenth and at the beginning of the nineteenth century [2]. Establishing the origin of the studies on nanometric electrochemical systems is a bit more difficult. Schmickler [2] has defined electrochemistry as the science that studies structures and processes at the interface between an electronic conductor (the electrode) and an ionic conductor (the electrolyte) or at the interface between two electrolytes. This statement, along with the definition of nanoscience given above and the fact that the electrochemical interphase typically extends over lengths of a few nanometers, would lead to the conclusion that the study of most electrochemical interfaces belongs to nanoelectrochemistry. While this could be in principle an alternative, we would be led to the conclusion that electrochemists have been already working in the field of nanoscience for centuries. To remain more specific and be in rule with other areas of science where the word “nano” denotes a particular approach in a given discipline, it is better not to base our definition on a certain dimension of the system but rather on the properties of the materials under study. To give an example, let us consider a bulky Pt electrode, which is set in contact with a given redox system (say, oxygen/water) and is polarized to study its potentiostatic behavior. Although, as previously stated, the electrochemical interphase in consideration has nanometric dimensions, all the concepts and formalisms used to describe this phenomenon do not come from concepts that emerged during the recent “nano” revolution. In a different example, let us think of a nanometer-sized Pt nanoparticle (NP) supported on a conductive but otherwise inert foreign surface. As this Pt NP is polarized at the same potential as the bulk Pt material and in contact with the same redox system, a very different behavior may be found from the previous one concerning the current measured per unit area [3]. Both electrocatalysts are made of the same type of atoms, and the redox system and the solution are the same, but the behavior may be radically different. Where is the difference? The point is that the electronic state and thus the reactivity of the NP and the bulk material may be different. Thus, nanoelectrochemistry may be more properly defined as that branch of electrochemistry that deals with the understanding and prediction of properties that cannot be understood by the sole presence of a surface, but have to do with the overall size scale where the processes occur. Curvature effects are in many cases responsible for the deviation of the behavior of nanomaterials from that of the bulk constituents, and they provide the reason why macroscopic thermodynamics fails to explain the behavior of these materials. It is clear that the smaller the size of the objects, the larger these contributions will be.

Physical Versus Electrochemical Control of Metal Surface Coverage

Adsorption from (desorption towards) the gas phase has provided for numerous experimental systems valuable information on adsorption equilibrium. We will shortly analyze here why this methodology is not practicable in most metallic systems and further show why electrochemistry provides an interesting alternative tool. Let us consider desorption of adatoms constituting an adlayer on a foreign metal surface. To take a straightforward example, let us think of a Ag monolayer deposited on a Au(100) surface, yielding a pseudomorphic monolayer. The binding energy of Ag on this surface is slightly larger than (but close to) the cohesive energy of Ag, $E_{\text{coh}}^{\text{Ag}} = 2.95$ eV, a moderate value for a metal. The potential energy curve for desorption of a Ag adatom from the surface is shown schematically in Fig. 2 in the black full line.

We can roughly estimate from $E_{\text{coh}}^{\text{Ag}}$ the average desorption time t_{des} of a Ag atom towards the gas phase using the transition state theory expression $t_{\text{des}}^{-1} = \nu \exp[-\beta E_{\text{des}}]$, where ν is an attempt frequency and E_{des} is the adatom desorption energy. Setting approximate values of $\nu = 10^{13}$ s⁻¹ and $E_{\text{des}} = E_{\text{coh}}^{\text{Ag}}$ in this equation, we get $t_{\text{des}} \approx 2 \times 10^{38}$ s at room temperature. This is a huge number, even compared with the age of the universe, $t_{\text{univ}} \approx 4 \times 10^{18}$ s. Even a time span of the latter order of magnitude would be needed to observe the desorption of a single

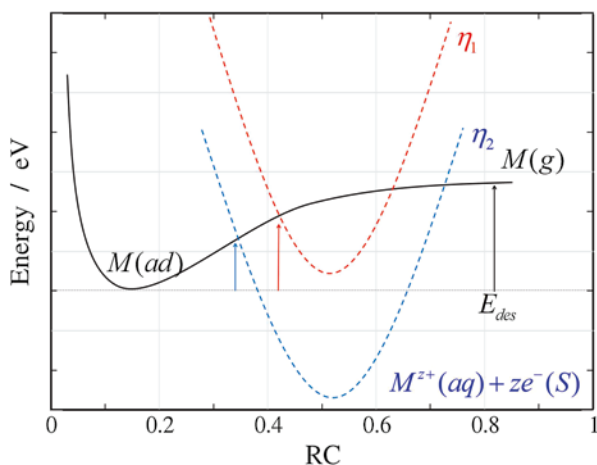


Fig. 2 Schematic comparison between the desorption of a metal adatom from a metal surface by physical detachment (*continuous line*) and electrochemical oxidation (*broken lines*). The full line illustrates the potential energy curve of the adatom as function of the distance from the surface (reaction coordinate (RC)). The *dotted lines* represent the potential energy of the cations in solution plus the electron located in the metal for two different overpotentials η , where $\eta_2 > \eta_1$. The *arrows* show the point where the potential energy of the adatom and the ion+electron systems meet. The heights of these arrows give an idea of the activation energy for the detachment process

atom from an ensemble of macroscopic size, say, 10^{20} atoms. It could be proposed to increase the temperature to get a faster desorption rate. However, to get the desorption of a single atom in 1 s, we need a temperature of the order of 1200 K. This is close to the melting point of Ag and not far from that of Au. Already well below this temperature, the increased mobility of substrate and adsorbate adatoms would allow diffusion of the former into the later, and the identity of the system (as adsorbate/substrate) would be lost. The introduction of the present system in an electrochemical environment provides an alternative path for the desorption of a Ag adatom: if the substrate is adequately polarized in an electrolyte with a large dielectric constant, a Ag^+ ion core may leave the surface, and its corresponding electron will be left on the electrode. The final energetic status of the Ag^+ ion is illustrated in broken lines for two different dissolution overpotentials (η_1 and η_2). The larger the overpotential (here η_2), the more stable the ion in solution will be, and the monolayer will become desorbed. A measure of the ability of the electrochemical system to exchange adatoms is the *exchange current density*. This is the current in the absence of net electrolysis and at zero overpotential, and in a redox reaction it reflects intrinsic rates of electron transfer between the analyte (in this case Ag^+ ions) and the electrode. For an electron to be left on the substrate according to the reaction $\text{Au}(100) - \text{Ag} \rightarrow \text{Ag}^+ + \text{Au}(100) - \text{e}^-$, a Ag^+ ion must be transferred, so the exchange current density measures here the rate of disappearance of Ag atoms from the surface at zero overpotential. To make an estimation of this rate for the electrochemical system, we consider the exchange current density reported for Ag adatoms on Ag(100) given in Ref. [23], of 0.06 A cm^{-2} . This corresponds to an exchange rate of $3.7 \times 10^{17} \text{ atoms s}^{-1} \text{ cm}^{-2}$. Assuming a surface density of $1.3 \times 10^{15} \text{ atoms cm}^{-2}$, we arrive to the conclusion that on the average all surface atoms are exchanged every 3 ms. Thus, measurement in the time scale of several seconds, as performed in voltammetry, may measure equilibrium properties, as long as care is taken to get rid of diffusional limitations.

Selected Recent Experimental Work

Metallic nanosystems such as clusters, nanoparticles, nanoalloys, nanocavities, etc., appear within the most promising materials in current engineering and materials science, because of the unique size-dependent properties of noble metals on the nanoscale [4–15]. These size- and shape-tailorable physical–chemical properties have potential applications in areas such as optics, spectroscopy, biological labeling, electronic, medicine, and catalysis just to mention some [16–22]. Several types of syntheses, which include thermal, photochemical, electrochemical, and template methods, have been used to achieve control over the size and shape of these nanomaterials [4, 5, 7, 11–16]. One of the main goals of current scientists is precisely the design (and synthesis) of nanomaterials with tailored shape, size, and composition. In this sense, electrochemical and particularly wet-electrochemical methods are favored for the cost-effective and large-scale production of such nanomaterials [4, 8, 12]. The main advantage of electrochemical nanostructuring methods with respect to physical ones, is that they allow the precise adjustment of under/oversaturation

conditions at the interface [4, 8, 11–13, 16, 23, 24], making them one of the best bottom-up methods (or approaches) with great prospects for the future.

Extensive experimental and theoretical investigations along with computer simulation of nanoelectrochemical systems have greatly enhanced our understanding on the nature of this cutting-edge topic. Because nanosystems contain a relatively small number of atoms, they exhibit a different behavior from the corresponding bulk materials, and even the macroscopic thermodynamic description may be insufficient to try to understand their thermodynamic behavior [25, 26]. This special behavior of nanomaterials was recognized in the 1960s by Terrell Hill [27], who described the basis of the thermodynamics that originally he called “of small systems.” Hill described in a visionary way how size could affect various thermodynamic properties of these systems. This formalism has recently been renamed by Hill as nanothermodynamics [28]. We redirect the interested reader to find some application of the formalism of Hill for the case of nanothermodynamic stability of nanomaterials in Chapter 10 of Ref [4].

Two electrochemical methods employed in the 1990s to modify flat surfaces, like underpotential deposition (*upd*) and galvanic replacement (*gr*), are today being successfully applied to the manipulation and modification of metallic nanoparticles (NPs) [4, 5, 8, 12, 29–34]. Figure 3 gives an overview of the topics addressed along the present section.

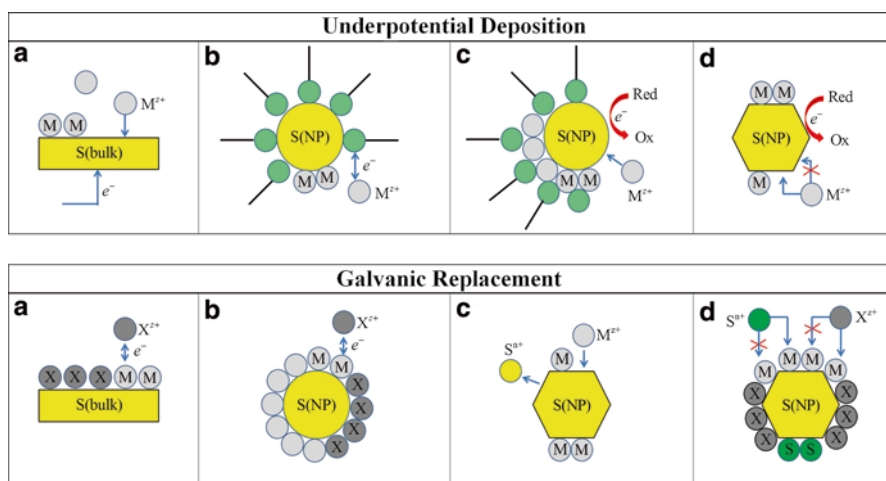


Fig. 3 Schematic representation of the different approaches used to synthesize nanoobjects: underpotential deposition (*upd*) and galvanic replacement (*gr*). The *upper sequence* of Figures shows the progress of *upd* techniques used as a tool: *upd* decoration of infinite planar surfaces (**a**), *upd* on nanoparticles limited by a given amount of adsorbed molecular species (**b**), *upd* on nanoparticles mediated by a redox couple dissolved in solution (**c**), selective decoration of facets of a nanoparticle by *upd* (**d**). For a detailed description see below section “Underpotential Deposition.” The *lower sequence* of Figures illustrates the progress of *gr* techniques used as a tool: *gr* on infinite planar surfaces (**a**), *gr* on nanoparticles previously decorated by *upd* (**b**), *gr* replacement at expenses of the less stable atoms of a preexisting nanoparticle (**c**), two-component *gr* at expenses of the less stable atoms of a preexisting nanoparticles (**d**). For a detailed description see below section “Galvanic Replacement”

In the next three sections, we describe some of the latest experimental developments, aimed at controlling the sizes and shapes and the formation of hollow, core/shell, and reversed NPs.

Underpotential Deposition

In the *upd* process, metal ions are deposited on a foreign substrate at potentials more positive than those predicted by the Nernst equation [4, 8, 29, 35–37]. This phenomenon is characteristic of systems (some selected metal couples) where the interaction of the adsorbate with the substrate is stronger than the interaction of the adsorbate with its bulk material. The *upd* monolayer is stable and has been widely characterized in electrochemical experiments since it may remain stable as long as diffusion of the adsorbate into the substrate is hindered by a kinetic barrier.

Fonticelli et al. [38] have proposed in 2007 an electrochemical method for the generation of bimetallic Au(core)/Ag(shell) NPs in solution. In this method, the deposition potential is controlled by means of a redox couple (*p*-benzoquinone + *p*-hydroquinone) and the *pH* of the solution. The method is based on two well-known electrochemical phenomena: *upd* and the ability of redox couples to control the potential at a given metallic interface. Figure 4 shows the voltamperogram for this system and the adsorption isotherms for *upd* of Ag on Au(111) obtained using electronic potentiostatic control and the redox couple, respectively, both in similar conditions. The coincidence of the resulting Ag coverages obtained by both methods shows that it could be possible to use *upd* for surface modification of free-standing NPs in solution, where the redox couple fixes the potential of the system in the same way as a potentiostat does.

Inspired by the former experimental results, Oviedo et al. [39] addressed theoretically in 2008 the topic of metal deposition on nanoparticles using a redox couple to set potential control. These studies were based on a nanothermodynamic formalism and computer simulations. These authors extended the theoretical concepts of *upd* to the case of NPs. Three important new aspects of *upd* emerged from this work:

1. The behavior of the free energy as a function of number of atoms in the nanostructure differs remarkably from that currently used to understand nucleation and growth phenomena.
2. The fact that *upd* phenomena may disappear.
3. Selective decoration of facets of NPs may be achieved in *upd* systems.

These studies showed that the *upd* phenomenon seems to vanish in the Au–Ag [40–43] and Pd–Au [44] systems when the size of the substrate (core) is reduced below 2 nm in diameter. Figure 5a shows the energy excess as a function of the numbers of Ag atoms deposited on Au octahedral truncated NPs of 201, 586, and 1289 atoms obtained from Grand Canonical Monte Carlo (GCMC) simulations at a zero overpotential (equivalently to $\mu = -2.77$ eV at 300 K). It can be seen on Fig. 5a

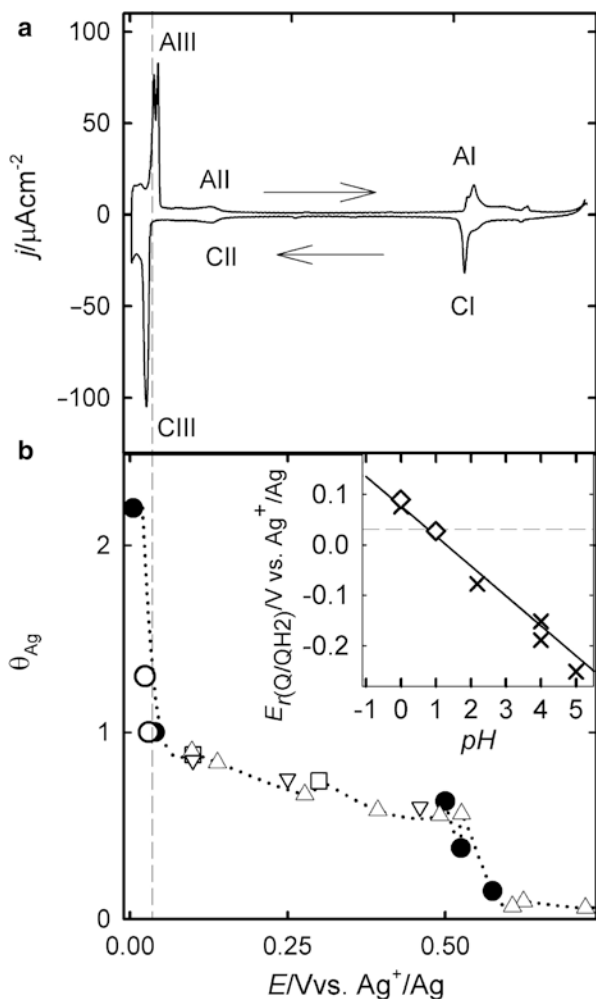


Fig. 4 (a) Current density (j) vs. potential (E) profile for Au(111) in 5×10^{-4} M $\text{Ag}_2\text{SO}_4 + 0.1$ M H_2SO_4 . Scan rate = 1×10^{-3} Vs^{-1} . (b) θ_{Ag} vs. E plot obtained from different data. Circles correspond to coverages obtained using the Q/QH₂ redox couple. Other data taken from the literature as reported in [38]. *Inset*: $E_{r(\text{Q}/\text{QH}_2)}$ vs. pH plot for the Q/QH₂ redox couple (concentration = 1×10^{-3} M). The horizontal dashed lines indicate the potential selected for depositing Ag by using the Q/QH₂ redox couple (Reprinted with permission from Ref. [38] Copyright 2007. American Chemical Society)

how the atoms deposited on Ag are considerably less stable on the 201 seed-NP than on the other two seeds. Deposition on the 586 seed-NP leads to some particular structures that appear to be energetically more stable than bulk Ag, as denoted by the presence of minima. In the case of the 1289 seed-NP, practically all simulated structures show lower energies than that corresponding to the bulk Ag material.

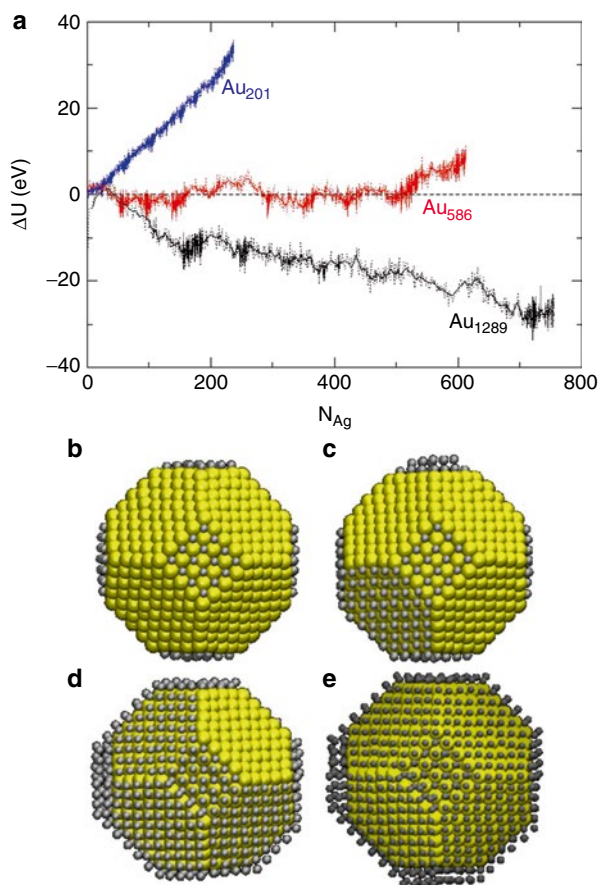


Fig. 5 (a) Excess energy ΔU as a function of the number of deposited Ag atoms for the three Au seed nanoparticles at zero over potential. Representative atomic configurations taken for Au(1289) at (b) $\mu_{Ag} = -2.99$ eV, (c) $\mu_{Ag} = -2.81$ eV, (d) $\mu_{Ag} = -2.79$ eV, and (e) $\mu_{Ag} = -2.77$ eV (Reprinted with permission from Ref. [42])

In the *upd* region ($\mu < -2.77$ eV) at 300 K, different structures may be obtained, some of them are shown in Fig. 5b–e.

Experiments by Compton and coworkers [31–33] have shown experimentally that the *upd* phenomenon in fact vanishes in the nanoscale. There, the *upd* of Pb and Cd on Ag NPs was analyzed at different NP sizes, with the remarkable finding that *upd* is absent for NPs smaller than 70 nm in diameter. On the other hand, Carino et al. [45] showed that NPs containing 55, 147, and 225 atoms of Pt, with size ranging between 1.5 and 2.0 nm, show Cu *upd* features. As we see, experimental and theoretical evidence shows that the occurrence of this phenomenon may reach a limit for very small NPs but is dependent on the metal couple used and the environmental variables. We go back to this issue in the section “*Upd–opd* Transition in the Nanoscale.”

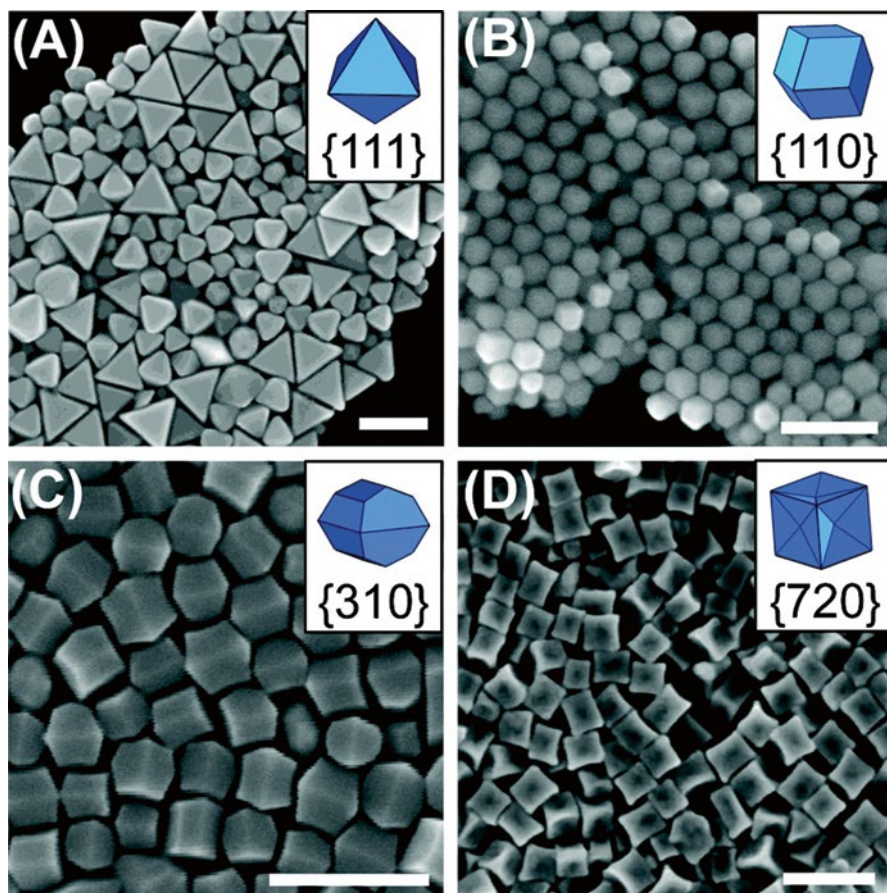


Fig. 6 Scanning Electron Microscopy (SEM) images of (a) octahedra, (b) rhombic dodecahedra, (c) truncated ditetragonal prisms, and (d) concave cubes synthesized from reaction solutions containing $\text{Ag}^+ / \text{Au}^{3+}$ ratios of 1:500, 1:50, 1:12.5, and 1:5, respectively. Scale bars: 200 nm (Reprinted with permission from Ref. [49])

Upd is currently being used for the generation of NPs with a predefined shell thickness, for their selective decoration, and for tuning their sizes and shapes. Recently, *upd* has been used to block selectively the growth of the material of which the NPs are made. By changing the concentration of the metal being deposited, it is possible to obtain NPs of different sizes and shapes. Mirkin and coworkers [46] have shown that a fine control of particle shape is possible using *Ag upd* to direct the growth of different Au NP morphologies: for example, octahedra with {111} facets, rhombic dodecahedra with {110} facets, truncated ditetragonal prisms with {310} facets, and concave cubes with {720} facets (see Fig. 6).

In a later work, Mirkin and coworkers [47] analyzed in detail the effect of including other additives like chloride, bromide, and iodide on NP growth under *Ag upd* control. These authors showed how different sets of NP shapes can be obtained via

kinetic control, surface passivation, or a combination of both. A number of important findings emerged from this work; some of them are the following:

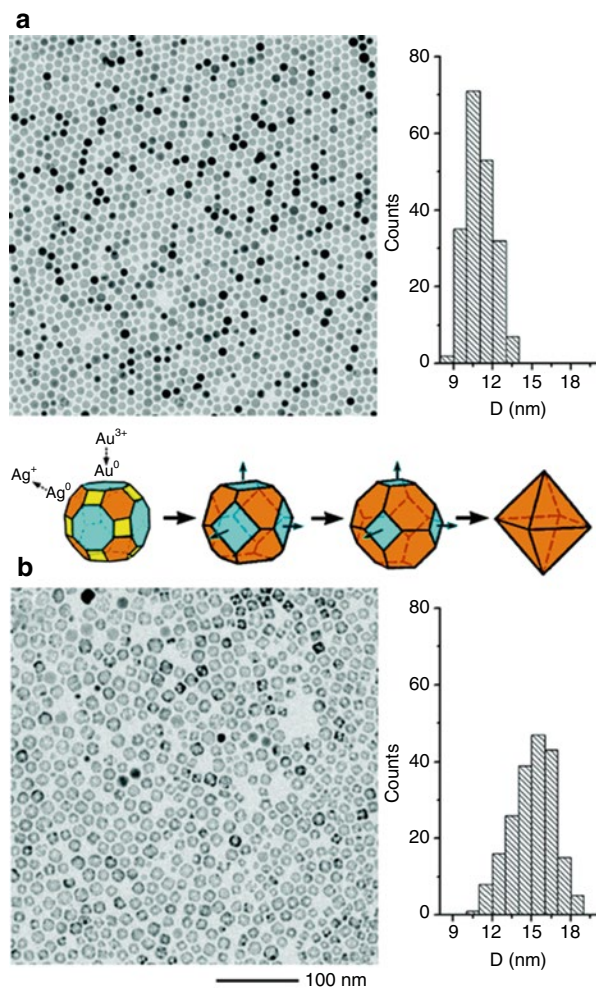
- (a) In the absence of bigger halides (bromide and iodide), increasing concentrations of silver ions stabilize particles with a larger number of exposed surface atoms per unit surface area, enabling the formation of high-index nanostructures.
- (b) In the presence of silver ions as a shape-directing additive, the addition of a large amount of the bigger halides (bromide and iodide) greatly decreases the stability of the Ag *upd* layer and blocks silver deposition, limiting the number of particle shapes that can form.
- (c) The enhanced stability of the Ag *upd* layer in the presence of chloride causes growing Au NPs to become kinetically “trapped” or “locked” into a particular facet structure early in their growth, enabling the formation of a wide variety of shapes as well as concave particles.

Galvanic Replacement

The main handicap for the application of the *upd* process to a wide number of systems is probably the fact that it is limited to the deposition of a less noble metal on a more noble one. A way to circumvent this problem has been found by Brankovic et al. [48], who produced the galvanic replacement (*gr*) of a sacrificial monolayer. The driving force of *gr* is the difference in electric potential between two metals. The deposition occurs as a spontaneous irreversible redox process in which a monolayer (eventually submonolayer), obtained via *upd* process, is oxidized by the ions of a more noble metal, which are reduced and simultaneously deposited. Nowadays, galvanic replacement is used to obtain reversed NPs, hollow particles, hollow nanorods, nanorattles, nanoboxes, alloys, and dealloys, among others [49–55]. Yin et al. [49] showed that Ag NPs with a spherical shape act, in the presence of Au³⁺, as precursors for formation of hollow Au nanocrystals with truncated octahedral shape. Figure 7a shows a transmission electron microscopy (TEM) image of a Ag NP before the galvanic replacement reaction. A replacement reaction between gold and silver removes silver atoms preferentially from (111) facets while depositing Au atoms selectively on the higher-energy facets such as (100) and (110). Figure 7b shows the TEM image of the Au NP after the *gr* reaction, resulting in a hollow NP of Au with truncated octahedron geometry. The exposure time and/or the Au³⁺ activity can be used as control variable to determine the percentage of Au and Ag in the hollow NP. It has been postulated that a possible mechanism may be that a large fraction of vacancies in the NP finally coalesce, producing a well-defined void in the center of each nanocrystal [56]. These pinholes were observed in other similar experiments with other NPs.

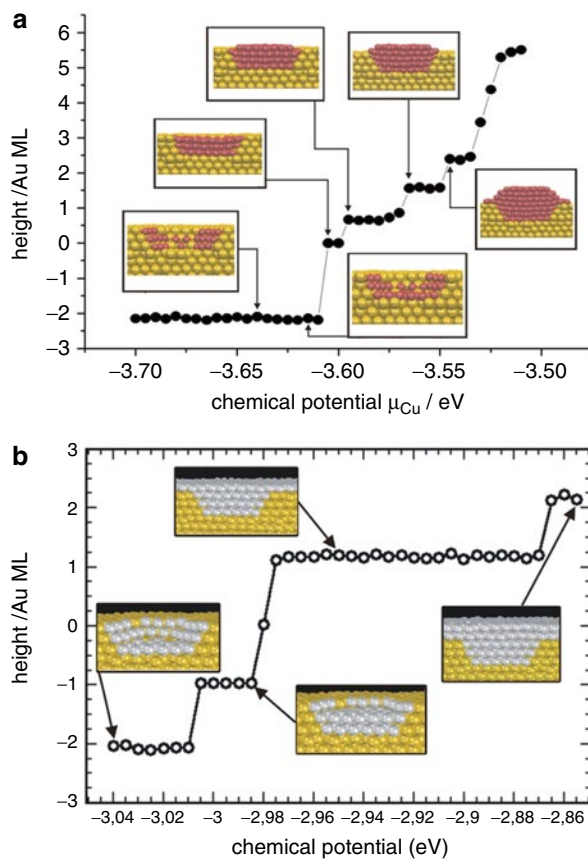
The study of pinholes or nanocavities was initially developed by Li et al. [57]. These authors managed to create a Ag nanostructure on a previously formed nanocavity on graphite. A double potential pulse of an electrochemical scanning

Fig. 7 Galvanic replacement on Ag nanoparticles by Au. **(a)** TEM image of silver nanocrystals and their diameter distribution before galvanic replacement. **(b)** TEM image and diameter distribution for gold hollow nanocrystals obtained by performing a replacement reaction on the silver nanocrystals shown in **(a)**. The schematic illustration between images **(a)** and **(b)** shows the mechanism proposed for the formation of gold truncated octahedra (Reprinted with permission from Ref. [49])



tunneling microscopy (ESTM) arrangement was used to create a pit on the surface of graphite and subsequently dissolve the Ag from the tip that deposited selectively into the newly created nanocavity. Further research on defect nanostructuring was undertaken by Xia et al. [58], who managed to create defects on a Au(111) surface by the application of ultrashort (10 ns) voltage pulses to the ESTM tip. This led to local confinement of the reactions and to the formation of nanostructures, so that for every pulse applied, just one nanohole was created directly under the tip. The nanoholes generated in this way were then filled with Cu by an accurate potentiostatic control. This technique has been also employed by Solomun and Kautek [59] to study the filling of nanocavities on Au(111) by Bi and Ag. In this last work, the behavior of Bi was contrasted with that of Ag. While the nanoholes are filled at underpotentials in the first case, the Au nanoholes are only filled by Ag during the

Fig. 8 Nanocavity filling in Au(111) with different adsorbates. Decoration of a Au(111) cavity with (a) Cu and (b) Ag atoms as a function of their chemical potential (Reprinted with permission from Ref. [60])



layer-by-layer growth of Ag at overpotentials. Computer simulations of this phenomenon were undertaken by Luque et al. [60] using the GCMC methodology. These studies showed that depending on the interaction between the adsorbate and the substrate as compared with the adsorbate–adsorbate interactions, the deposit may grow defining a cluster over the surface level, like Cu/Au(111), or heal the damage on the surface with the subsequent formation of a monolayer, like Ag/Au(111). In the former case, Cu deposition remains confined to the defects generated on the surface, since the formation of clusters on the Au(111) is disfavored. On the contrary, Ag deposition on the flat Au(111) surface occurs after the filling of the nanocavity. Figure 8 shows the confined and heal growth [60].

Going back to the problem of NPs, some experimental strategies are directed to minimize the amount of noble metal material used as a substrate, in order to lower economical costs. In this respect, Zhang et al. [61] have developed the strategy depicted in Fig. 9. A bimetallic NP made of a noble (Au or Pd) and a nonnoble material (Co or Ni) is synthesized with a certain amount of (controlled percentage) alloying. In a subsequent stage, noble metal segregation is driven by temperature,

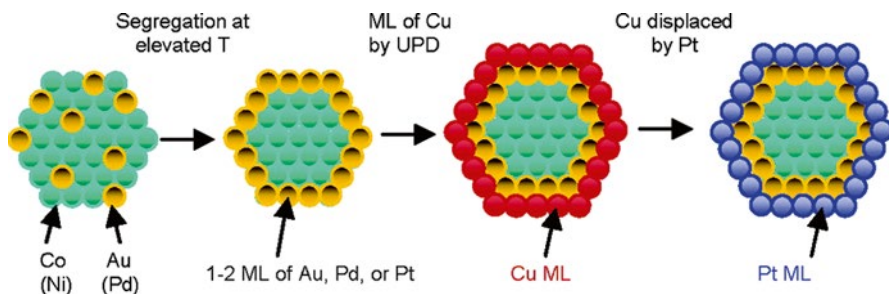


Fig. 9 Model for the synthesis of Pt monolayer catalysts on nonnoble metal–noble metal core/shell nanoparticles (Reprinted with permission from Ref. [61])

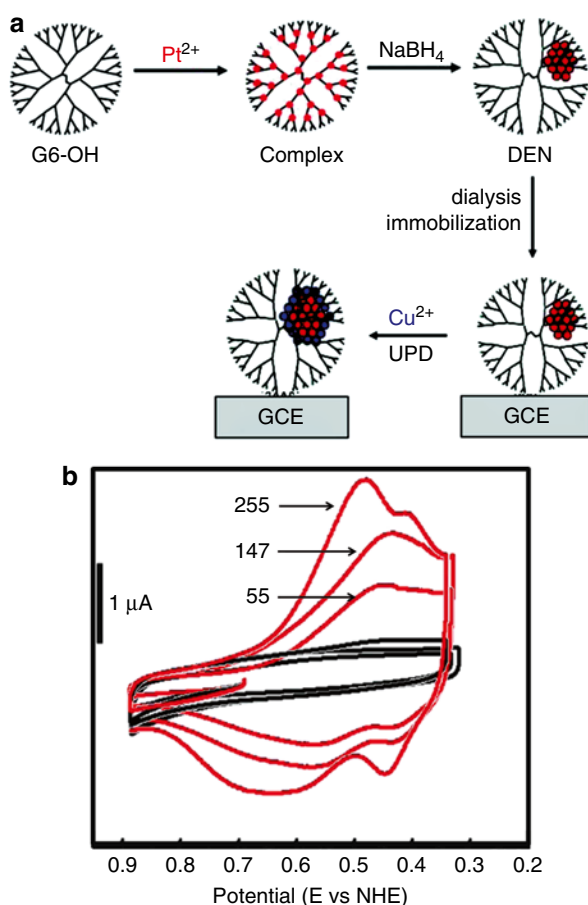
favoring the formation of a core/shell structure, where the most noble material migrates towards the surface of the NP. A Cu *upd* monolayer is then deposited on the noble metal, and subsequent irreversible *gr* by Pt leads to the final structure of the NP, an onion with an inner core of Co(or Ni), an intermediate shell of Au(or Pd), and an outer shell of Pt. Depending on the percentage of the initial alloy, different widths of the intermediate shell may occur.

Dendrimer-Encapsulated Nanoparticles

In the early 2000s, Crooks and coworkers developed a technique for the generation of metallic NPs, yielding the so-called dendrimer-encapsulated nanoparticles (DENs) [12, 62, 63]. An actual scheme of this procedure is shown in Fig. 10a. In the first step, S^{2+} cations are embedded into the dendrimer matrix, yielding a complex $[G6-OH(S^{2+})_n]$, where $G6-OH$ is sixth-generation, hydroxyl-terminated poly(amidoamine) (PAMAM) dendrimers and n is the number of ions encapsulated in the dendrimer. The driving force for encapsulation of metal ions within dendrimers is usually based on covalent bond formation, electrostatic interactions, complexation reactions, or a combination thereof [62]. In the second step the cations are completely reduced using borohydride, being obtained in this way metallic NPs within the cavities of the dendrimers. In a further step, a monolayer of less noble metal may be electrodeposited onto the DENs by *upd* to yield $[G6-OH(S_n @ Me_m)]$. Subsequent *gr* of the *upd* monolayer may yield different core/shell NPs. Carino et al. [45] have analyzed the voltammetric behavior of Cu deposition on 55, 147, and 255 Pt atoms NPs (see Fig. 10b). Their results indicate that a single atomic monolayer of Cu is deposited onto Pt DEN cores containing an average number of 147 and 225 atoms, while more than one monolayer deposits onto Pt DEN cores containing an average of 55 atoms. Two remarkable features emerge from the voltammetry of these systems:

- As NP size decreases, the peak potentials of anodic and cathodic processes show a shift towards lower potentials, that is, Cu *upd* weakens for relatively small NPs.
- Deposition and stripping peaks become split into two components.

Fig. 10 (a) Scheme of the method dendrimer-encapsulated nanoparticles. (b) Cyclic voltammograms obtained using G6-OH(Pt_n) DENs in aqueous electrolyte solutions containing 0.10 M H_2SO_4 + 0.010 M CuSO_4 . The scans started at 0.64 V and were initially swept in the positive direction at a rate of 10 mV/s (Adapted with permission from Ref. [45])



As we will see below, some of these features can be explained from the thermodynamic model mentioned in section “[Underpotential Deposition](#)” and will be described in more detail in section “[Upd-opd Transition in the Nanoscale](#).”

The development of NP synthesis by means of dendrimers presents two appealing aspects: on one side, it allows the generation of metallic NPs with a very sharp size distribution. On the other side, this method allows the generation of metal NPs with very small sizes, between 1 and 2 nm. These two factors allow correlating directly experimental results with theoretical predictions. In this respect, it is worth mentioning the work of Yancey et al. [64] and Carino et al. [45], who contrasted experimental results of electrochemical deposition with density functional (DFT) calculations for NP of similar sizes. In the last study, these authors showed that *upd* of Cu onto Pt NP(147) occurs in two steps: first onto the {100} facets (partial deposition) and then onto {111} facets (full deposition). The partial and full shell structures were characterized by voltammetry, and the experimental results were compared with computational models generated using DFT and molecular dynamics (MD) simulations. Figure 11a shows the different models

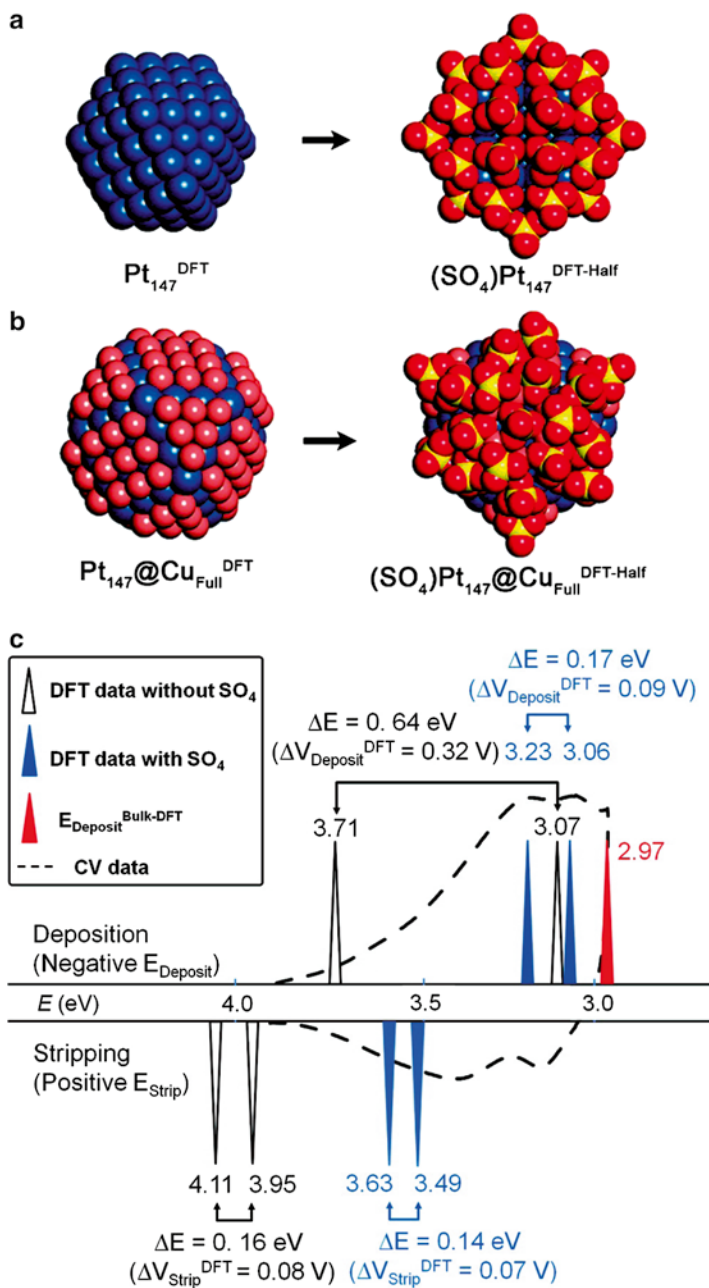


Fig. 11 Different models used to consider the adsorption of sulfate ions on (a) a Pt NP made of 147 atoms. (b) A core/shell NP Pt(147)/Cu(full). *Left* and *right* images show the NP without and with adsorbed SO_4 molecules, respectively, (c) DFT-calculated Cu deposition and stripping energies, as compared with the experimental voltammogram obtained for Cu *upd* on Pt NPs (*black dashed line*) (Reprinted with permission from Ref. [45])

used by Carino et al. [45] to emulate the Cu deposition phenomena. Binding energies were calculated using DFT for Cu adsorbed on Pt(100) and Pt(111) facets of a “solvated” NP, in which SO_4 ligands were adsorbed on the surface to mimic the solvent–surface interactions existing in the experiments. The calculated binding energies were found to correspond well with the peaks observed in the CVs of Cu *upd* onto Pt NPs(147) (see Fig. 11b). In contrast, the same calculations performed on a naked, SO_4 -free (solvent free) NP model did not fit the electrochemical data.

From the preceding discussion, it comes out that the understanding of the *upd* phenomenon may be of paramount importance for the synthesis of some metallic nanostructures. Hereafter, we will concentrate on aspects of metal electrode position at the nanoscale related to curvature effects. Therefore, we go deeper into the essential physical concepts of the electrodeposition problem. We will find how the formulation of a simple model that includes surface and curvatures terms allows rationalizing and understanding the occurrence of different sizes and shapes in nanoelectrodeposits.

Nanothermodynamic Stability

We will take now a first step towards the understanding of the thermodynamic stability of metallic systems by making some basic considerations. The effects of solvent, electric field, and ion adsorption will be left aside in the present approach.

Some Basic Considerations

One of the advantages of electrochemical methods (discussed in section “[Physical Versus Electrochemical Control of Metal Surface Coverage](#)”) with respect to physical ones is that the growth of the new phase may be achieved under a precise control of the over(under) saturation conditions of the interface. This is possible by means of a proper adjustment of the deposition potential, which results in the control of the electrochemical potential of the species being deposited [4, 8, 12, 29, 35–37]. As stated previously in section “[Underpotential Deposition](#),” this control may be achieved by a potentiostat or by selection of a proper redox couple [38, 39].

Most electrochemical methods start by the reduction of the metal ions, say, M^{z+} :



where z is the valence and e is the elemental charge. The thermodynamic stability of the metal adatoms (M) depends on the local morphology of the nanosystem. In this way, the binding energy of an adatom is not the same in a nanocavity as in a supported cluster. Figure 12 illustrates some possible arrangements for the formation of different adatom structures on a foreign substrate.

Depending on the chemical nature of the substrate, metal electrodeposition phenomena can be divided into two big groups: homoatomic and heteroatomic deposition. The first of these refers to phase growth on a substrate of the same chemical nature.

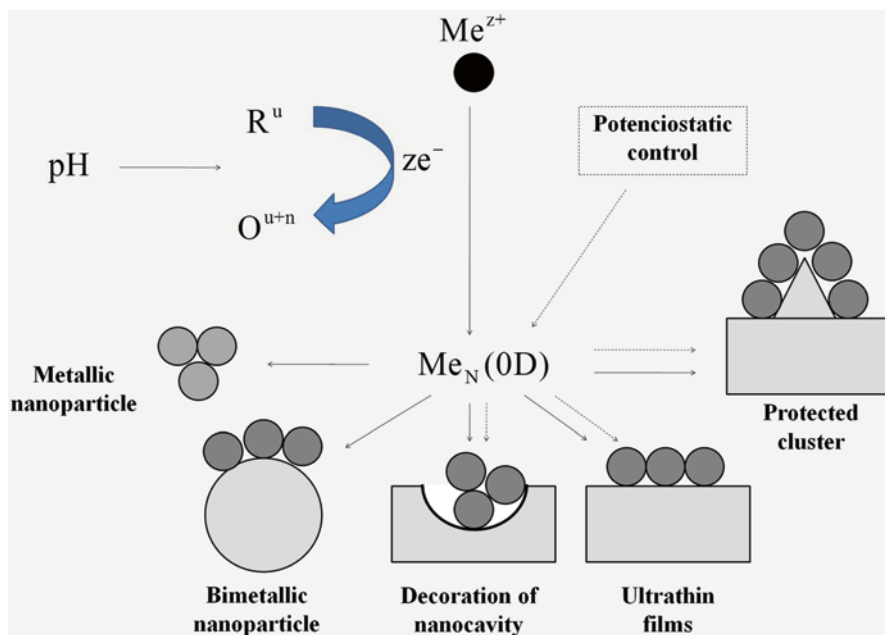


Fig. 12 Schematic representation of the early stages of the formation of a new phase at the nanoscale on different morphologies of a foreign substrate. Its growth may take place by potential control via a potentiostat (*dotted line*) or via a redox system (*full line*)

On the contrary, the second refers to deposition on a foreign substrate. The reduction reaction involved in the electrodeposition process may be generally rewritten as



where S represents the substrate. In the case of metal electrodeposition in the presence of a redox couple, electrons in Eq. 2 are provided by an oxidation reaction like



where we have assumed a single electron transfer for mathematical simplicity and we are omitting any other species that may participate in the process. If the oxidation reaction given in Eq. 3 is actually accompanied by other species (i.e., protons in the case of benzoquinone), then the concentration of these other species can be used to control the surface potential of the nanosystem (see Fig. 4). We will also assume that the activities of Red and Ox species are large enough to undergo a relatively small change upon reaction with M^{z+} to yield M. Thus, the electric potential at the surface of the NPs will be determined only by the Red/Ox ratio and will remain relatively unchanged throughout the process. Thus, we will consider a situation where electrodeposition takes places in an environment where the pressure (p), the temperature (T), the size of the nanoparticle (N_s), and the chemical

potentials of M, Ox, and Red (μ_M , μ_{Ox} , and μ_{Red}) are fixed. The thermodynamic potential that characterizes the representative statistical mechanical ensemble of this system is a modified free energy that we will denote with $\hat{G}(\mu_M, \mu_{Ox}, \mu_{Red}, N_S, p, T)$ and corresponds to an open system in M, Ox, and Red but closed in the S component. This system can be shown to be equivalent to another one with the thermodynamic potential $\hat{G}(\mu_M, \mu_{Ox}, \mu_{Red}, N_S, T)$ if we consider it as incompressible [4, 65]. Figure 13 shows a schematic view of the thermodynamic system required to analyze the present electrochemical problem. Four different reservoirs are connected to the system: a heat reservoir and three reservoirs with chemical species. These allow controlling the temperature and the chemical potential of the M, Ox, and Red species.

The driving force for metal electrodeposition is twofold:

- On one side, it is enforced by the electrochemical potential of the electrons in the redox couple (or potentiostat), in equilibrium with the electronic system of S.
- It is also promoted by the concentration (activity) of the M^{z+} ions in solution.

Let us denote with $\Phi(N_M, N_S, T)$ the excess of Gibbs free energy required to generate an S/M structure made of a nanophase containing N_M -type M atoms on a pre-formed structure having N_S atoms, starting from the bulk material M. Thus, Φ is given by

$$\Phi(N_M, N_S, T) = [G_{S/M}(N_M, N_S, T) - G_S(0, N_S, T)] - N_M \mu_M^{\text{bulk}} \quad (4)$$

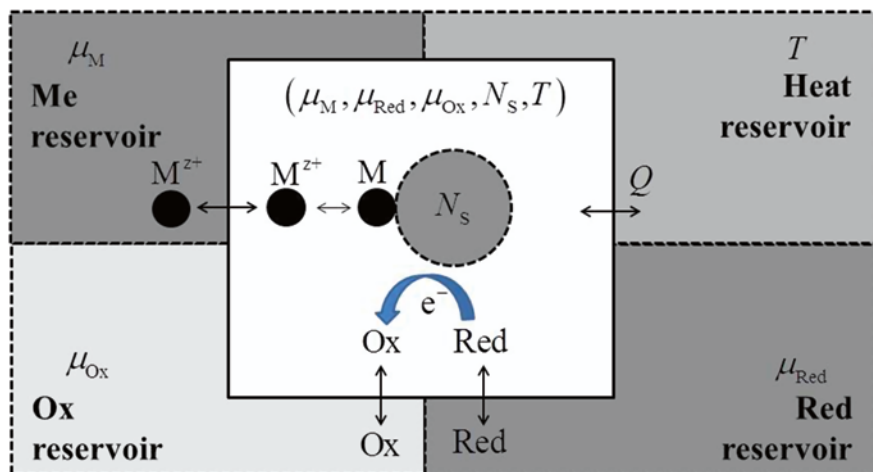


Fig. 13 Thermodynamic view of the present electrochemical system, consisting in a nanoparticle in contact with heat, M, Ox, and Red reservoirs, which serve to set the temperature and the chemical potentials of the different species involved

where $G_{S/M}$ is the Gibbs free energy of the nanostructure and G_S is the Gibbs free energy of the naked substrate. The work of shell formation for the electrochemical generation of the S/M system is given by

$$\Delta\hat{G}(\eta, N_M, N_S, T) = \Phi(N_M, N_S, T) + N_M z e \eta \quad (5)$$

The detailed derivation of this equation is given in Refs. [60, 66, 67]. η corresponds to the overpotential set by the redox couple with respect to the bulk deposition of metal M according to

$$\eta = \frac{(\mu_M^{\text{bulk}} - \mu_M)}{ze} \quad (6)$$

Usually η is worked out as a negative quantity, since bulk metal deposition always occurs at $\eta < 0$ due to kinetic hindrances. As we will see below, when considering metal deposition phenomena in the nanoscale, it is useful to consider both signs for η .

Going back to Eq. 5, it appears that the problem of predicting the thermodynamic stability of a nanostructure at different overpotentials from a theoretical–computational approach reduces to know Φ . However, important physical insight may be gained from a qualitative analysis of the different contributions involved in it. In the following section, we introduce some simplifying modeling with this purpose.

Electrodeposition on Planar Surfaces

We start the present analysis considering electrodeposition in a simple system: an infinite, planar surface. With this purpose, we use a model with three types of atoms with different free energy: a monolayer, a surface layer of the substrate, and its bulk. This is illustrated in Fig. 14.

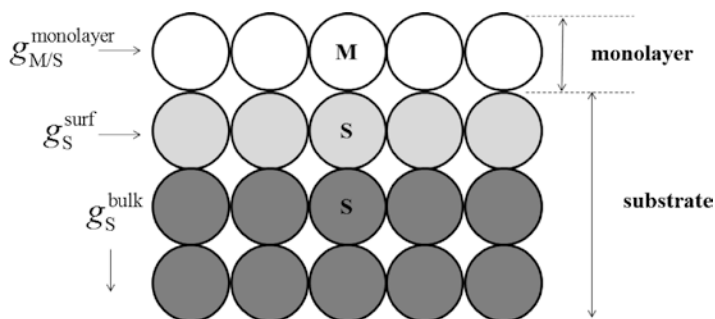


Fig. 14 Schematic representation of the three-component model, used to analyze the deposition on flat surfaces

M and S may be of the same or different chemical nature, so that the model may be applied to the study of homoatomic or heteroatomic systems. For the present system, the total Gibbs free energy is

$$G^{\text{system}} = G^{\text{substrate}} + G^{\text{monolayer}} = \left(N_S^{\text{bulk}} g_S^{\text{bulk}} + N_S^{\text{surf}} g_S^{\text{surf}} + N_{M/S}^{\text{monolayer}} g_{M/S}^{\text{monolayer}} \right) \quad (7)$$

where N_S^{bulk} and N_S^{surf} denote the number of substrate atoms in the bulk and in contact with the monolayer, respectively, and $N_{M/S}^{\text{monolayer}}$ is the number of atoms in the monolayer. g_S^{bulk} and $g_{M/S}^{\text{monolayer}}$ denote the average free energy per atom of the substrate and the monolayer, respectively, and g_S^{surf} is the free energy of the S atoms in contact with the monolayer. Note that $N_S^{\text{substrate}} = N_S^{\text{bulk}} + N_S^{\text{surf}}$ and $g_S^{\text{bulk}} = \mu_S^{\text{bulk}}$, where μ_S^{bulk} is the chemical potential of the bulk S species.

The free energy of the naked substrate is

$$G^{\text{substrate}} = N_S^{\text{bulk}} g_S^{\text{bulk}} + N_S^{\text{surf}} g_S^{\text{surf},0} \quad (8)$$

where $g_S^{\text{surf},0}$ now denotes the free energy per surface substrate atom when the monolayer is not present. Note that the monolayer adsorption may affect the energetic stability of the surface atoms of the substrate, so that $g_S^{\text{surf},0} \neq g_S^{\text{surf}}$.

Using Eq. 4, we obtain

$$\Phi = N_{M/S}^{\text{monolayer}} \left(g_{M/S}^{\text{monolayer}} - \mu_M^{\text{bulk}} \right) + N_S^{\text{surf}} \left(g_S^{\text{surf}} - g_S^{\text{surf},0} \right) \quad (9a)$$

Since N_S^{surf} and $N_{M/S}^{\text{monolayer}}$ are linearly related, say, by $N_S^{\text{surf}} = \alpha N_{M/S}^{\text{monolayer}}$, where α is a geometrical coefficient. We rewrite the previous equation as

$$\Phi = N_{M/S}^{\text{monolayer}} \left(g_{M/S}^{\text{monolayer,eff}} - \mu_M^{\text{bulk}} \right) \quad (9b)$$

where we have collected into $g_{M/S}^{\text{monolayer,eff}} = g_{M/S}^{\text{monolayer}} + \alpha \left(g_S^{\text{surf}} - g_S^{\text{surf},0} \right)$ terms corresponding to both the monolayer and the substrate.

According to Eq. 5, the work of monolayer formation from the bulk material at the overpotential η is given by

$$\Delta \bar{G} = N_{M/S}^{\text{monolayer}} \left(g_{M/S}^{\text{monolayer,eff}} - \mu_M^{\text{bulk}} + z e \eta \right) \quad (10)$$

Although Eq. 10 seems to contain variables only referred to the monolayer, it must be noted that the value of $g_{M/S}^{\text{monolayer,eff}}$ depends on the chemical nature of S as well as on its crystal orientation. The term $\left(g_{M/S}^{\text{monolayer,eff}} - \mu_M^{\text{bulk}} \right)$ corresponds to the free energy difference between an M-type atom on the surface of S and this atom in the bulk M material. Depending on the chemical nature of S and M, we can distinguish three different categories of systems:

- (a) Metal couples of the same chemical nature ($M=S$), $g_{M/M}^{\text{monolayer}} = \mu_M^{\text{bulk}}$
- (b) Metal couples of different chemical natures, with a relatively strong adsorbate-substrate interaction $g_{M/S}^{\text{monolayer,eff}} < \mu_M^{\text{bulk}}$
- (c) Metal couples of different chemical natures, with a relatively weak adsorbate-substrate interaction, $g_{M/S}^{\text{monolayer,eff}} > \mu_M^{\text{bulk}}$

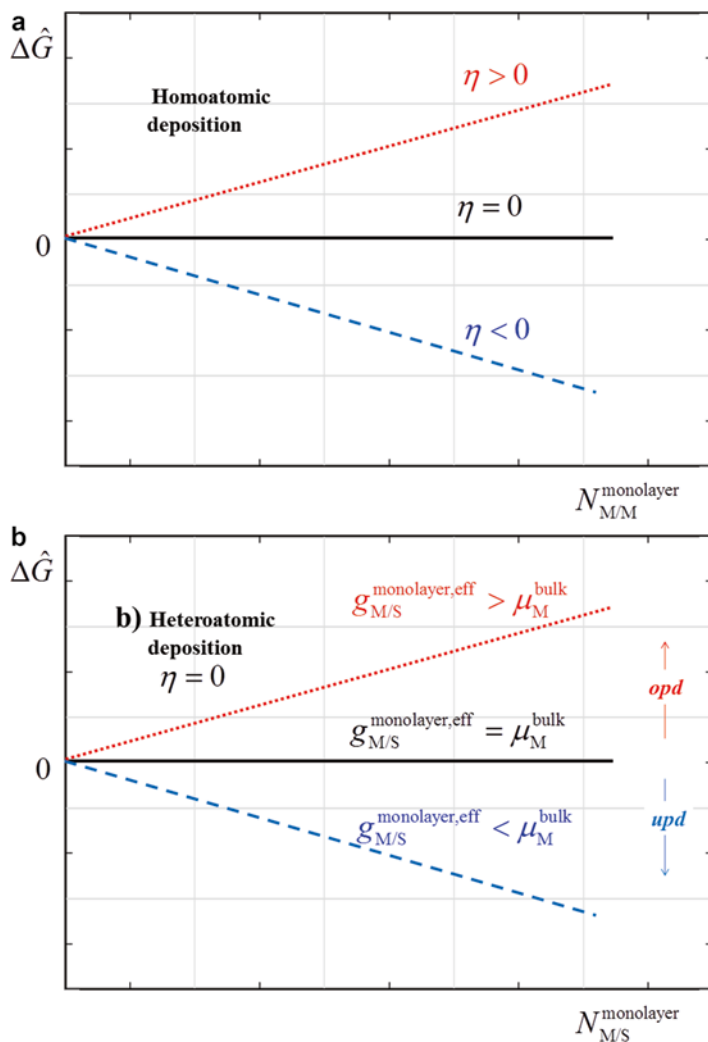


Fig. 15 (a) Schematic representation of $\Delta \hat{G}$ as a function of $N_{M/M}^{\text{monolayer}}$ at different overpotentials, for homoatomic deposition. (b) Schematic representation $\Delta \hat{G}$ as a function of $N_{M/S}^{\text{monolayer}}$ at zero overpotential, for heteroatomic deposition. See discussion in the text

The first category refers to homoatomic, while the second and the third refer to heteroatomic deposition.

In the first case, when $g_{M/M}^{\text{monolayer}} = \mu_M^{\text{bulk}}$, Eq. 10 reduces to

$$\Delta \hat{G} = ze\eta N_{M/M}^{\text{monolayer}} \quad (11)$$

Figure 15a shows a schematic picture of $\Delta \hat{G}$ vs. $N_{M/M}^{\text{monolayer}}$ for different overpotentials.

Equation 11 and Fig. 15a indicate that homoatomic metal deposition on planar surfaces only occurs upon application of a negative overpotential ($\eta < 0$).

In the case of heteroatomic systems, categories (b) and (c), the term $(g_{M/S}^{\text{monolayer,eff}} - \mu_M^{\text{bulk}})$ may be positive or negative, depending on the interaction between S and M. Figure 15b shows $\Delta\hat{G}$ vs. $N_{M/S}^{\text{monolayer}}$ for both cases at $\eta = 0$. The systems with a relatively strong S–M interaction should show the spontaneous formation of a monolayer ($\Delta\hat{G} < 0$) at zero overpotential, which should remain even at a certain range of positive overpotentials. The latter phenomenon, where a metal monolayer occurs at positive potentials with respect to that given by the Nernst equation, is the denominated underpotential deposition already defined in section “Underpotential Deposition.” The maximum potential at which the *upd* monolayer remains stable is given by

$$\Delta\phi^{\text{upd}} = \frac{\Delta\hat{G}}{N_{M/S}^{\text{monolayer}}} = (g_{M/S}^{\text{monolayer,eff}} - \mu_M^{\text{bulk}}) \quad (12)$$

$\Delta\phi^{\text{upd}}$ is known in the literature as underpotential shift and in the case of voltammetric profiles corresponds to the difference between the peak potential corresponding to the stripping of the *upd* phase and the Nernst reversible deposition potential [4, 8, 35–37]. In many systems more than one *upd* phase is found to exist, and it comes out that this phenomenon is affected by the adsorption of anions, solvent molecules, surfactants, and any other factor that may change the value of $g_{M/S}^{\text{monolayer,eff}}$. As an example, it has been observed that the $\Delta\phi^{\text{upd}}$ of the (1 × 1) monolayer of Ag on Au(111) electrodes is increased by the presence of chloride, while it is decreased by the presence of bromide and iodide anions [68–70]. This fact indicates that chlorides contributes favorably to $g_{M/S}^{\text{monolayer,eff}}$, while the opposite occurs with the other anions. Anions also seem to play a role in the formation of expanded monolayers. This is, for example, the case of the formation of overlayer domains with commensurate structures for Pb c(2 × 2) on Ag(100), Pb c(2 × 2) on Au(100), and Pb c(3√2 × √2) R45° on Au(100) [23, 24, 71].

Upd of Cu on Au(111) constituted for a long time some sort of paradox. While this system has been considered as an experimental *upd* paradigm, all energy calculations performed for the (1 × 1)Cu monolayer on Au(111) showed that it should be less stable than the bulk Cu material [23, 24]. This apparent contradiction was recently explained by Oviedo et al. [72], who showed that the extraordinary stability of the Cu(1 × 1) monolayer is due to the adsorption of sulfate anions.

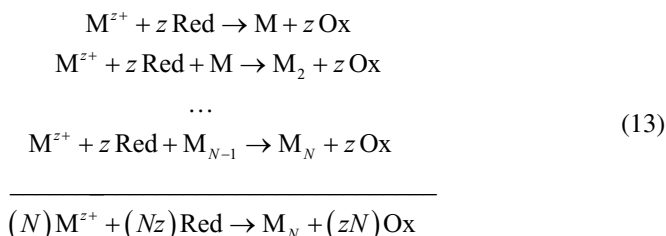
According to previous discussion, $g_{M/S}^{\text{monolayer,eff}}$ can be visualized as the average adsorption energy of a new species, say, X–M, where $X^{m-} = \text{Cl}^-, \text{Br}^-, \text{I}^-, \text{SO}_4^{2-}$, etc. These species may be considered as oriented perpendicular to the surface of the substrate in the case of coadsorption at full metal coverage or parallel to the surface of the substrate in the case of expanded structures. Within this reinterpretation of $g_{M/S}^{\text{monolayer,eff}}$, Eqs. 9–12 remain valid. However, the correct description of the problem requires consideration of the free energy of formation of the X–M bond from its precursors in solution (with activity $a_{M^{z+}}$ and $a_{X^{m-}}$) using a correct Legendre transform. The reader interested in this point is addressed to the work of Oviedo et al. [72].

Straightforward Generation of Nanoparticles from Their Precursors

In this section we focus on the electrochemical formation of homoatomic NPs from their precursors. The synthesis of NPs may lead to a variety of shapes, as shown in Figs. 6 and 7. It is even possible to get NPs with a diversity of forms, like stars, cylinders, etc., where control of kinetic factors plays the key role to reach the desired structure [4, 5, 7–9]. Such types of studies are out of the scope of the present chapter, and to the best of our knowledge, a comprehensive picture of this type of phenomena (kinetics of electrodeposition at the nanoscale) is still missing.

From a thermodynamic perspective, the most stable NP shapes do not differ strongly from the most compact ones [4, 65–67]: icosahedra, octahedra, cuboctahedra, etc. A first glance to these objects induces to classify the surface sites in two types: facet and border sites. A closer inspection reveals that in many cases the different facets present different crystalline orientations, as well as the existence of a different coordination of the particles at the vertices. In the present section and in order to emphasize on some key concepts on the electroformation of nanostructures, we will differentiate only two types of sites on the surface of the NP.

The electrochemical reaction associated with the formation of an NP made of N atoms may be represented as a sequence of N reactions, as those given above in Eqs. 1 and 3:



where Red corresponds to the chemical species that provide the electron for the reduction of the metal ions. As it was introduced in the previous paragraphs, we will consider a model of three types of atoms with different free energies: facets, borders, and bulk material. This is shown schematically in Fig. 16.

The free energy of this system may be written as

$$G^{\text{system}} = N_M^{\text{core}} \mu_M^{\text{bulk}} + N_M^{\text{facet}} g_M^{\text{facet}} + N_M^{\text{border}} g_M^{\text{border}} \tag{14}$$

where N_M^{facet} , N_M^{border} , and N_M^{core} correspond to the number of atoms at the facets, at the borders, and in the core, respectively. These quantities fulfill the following conditions: $N_M = N_M^{\text{core}} + N_M^{\text{facet}} + N_M^{\text{border}}$ and $N_M^{\text{surf}} = N_M^{\text{facet}} + N_M^{\text{border}}$.

The free energy of formation of a homoatomic NP from the bulk M material may be obtained using Eqs. 4 and 14, setting $G^{\text{substrate}} = 0$, since the NP is formed from its precursors:

$$\Phi = N_M^{\text{facet}} (g_M^{\text{facet}} - \mu_M^{\text{bulk}}) + N_M^{\text{border}} (g_M^{\text{border}} - \mu_M^{\text{bulk}}) \tag{15}$$

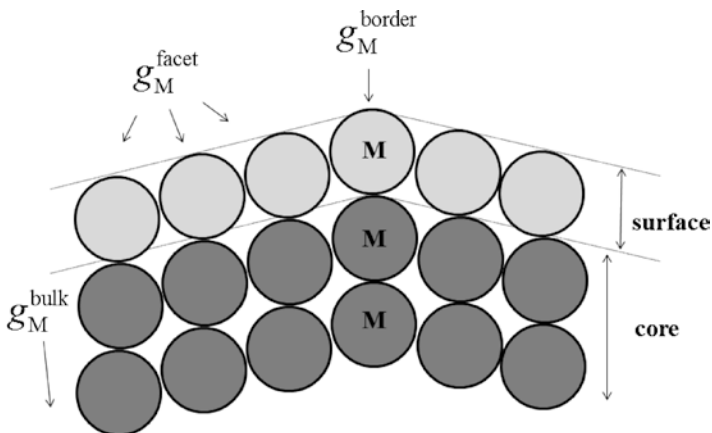


Fig. 16 Schematic representation of a portion of a homoatomic NP where the atoms may exist in three different types: facet and border atoms at the surface and core atoms inside

and the corresponding work of nanoparticle formation is

$$\Delta\hat{G} = N_M^{\text{facet}} \left(g_M^{\text{facet}} - \mu_M^{\text{bulk}} \right) + N_M^{\text{border}} \left(g_M^{\text{border}} - \mu_M^{\text{bulk}} \right) + N_M z e \eta \tag{16}$$

The first term on the *rhs* of Eq. 16 takes into account the free energy difference between an atom on the facet of the NP and another one in the bulk of the material, while the second term considers the free energy difference between a border atom and one in the bulk. Since the system is homoatomic, both terms are positive. Equation 16 may be written in terms of a single variable, say, N_M , if a relationship is given between N_M^{facet} , N_M^{border} , and N_M , that is, if a given geometry is assumed. In the case of a spherical NP, we can write

$$\begin{aligned} N_M^{\text{facet}} &= \alpha N_M^{2/3} \\ N_M^{\text{border}} &= \delta N_M^{1/3} \end{aligned} \tag{17}$$

where α and δ correspond to geometrical coefficients. Replacing (17) into (16), we get

$$\Delta\hat{G} = \alpha N_M^{2/3} \left(g_M^{\text{facet}} - \mu_M^{\text{bulk}} \right) + \delta N_M^{1/3} \left(g_M^{\text{border}} - \mu_M^{\text{bulk}} \right) + N_M z e \eta \tag{18}$$

Similar equations may be obtained by means of geometrical relationships applicable to icosahedra [41, 73], truncated octahedra [66, 67], and other geometries [73, 74].

We can see in Fig. 17 that the behavior of $\Delta\hat{G}$ is that of the classical nucleation and growth modeling. At zero or positive overpotentials ($\eta \geq 0$), the curve shows a monotonic growth, indicating that the generation of the NP is thermodynamically not spontaneous. At negative overpotentials, the curve exhibits a maximum, corresponding to the critical nucleus size (N_M^*). Clusters of size smaller than the critical one ($N_M < N_M^*$) will dissolve, while larger ones ($N_M > N_M^*$) will evolve towards the bulk state.

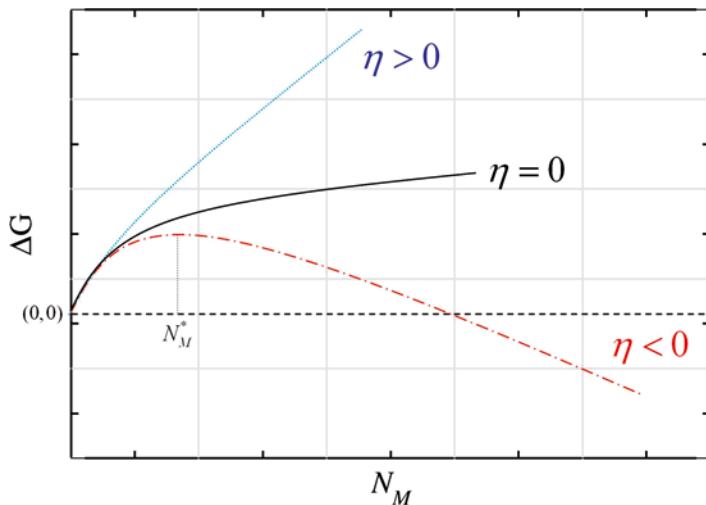


Fig. 17 Scheme of the work of nanoparticle formation $\Delta\hat{G}$ as a function of the number of deposited atoms N_M for the electrochemical formation of a metallic nanostructure at different overpotentials (Reprinted with permission from Ref. [42])

Generally speaking, for a given η , the work of nanoparticle formation is larger than the work of formation of a flat surface, due to curvature effects given by g_M^{border} . For NPs of intermediate sizes, such that border contributions are negligible, we can write

$$\Delta\hat{G} \approx \alpha N_M^{2/3} (g_M^{\text{facet}} - \mu_M^{\text{bulk}}) + N_M z e \eta \quad (19)$$

This is the typical form of the free energy equation for homoatomic nucleation and growth [23, 24]. At $\eta = 0$ we get the usual curve proportional to $N_M^{2/3}$ so that to get phase growth, we need $\eta < 0$.

For very large NPs, the first term on the *rhs* of Eq. 19 turns negligible as compared with the second term, yielding

$$\Delta\hat{G} \approx N_M z e \eta \quad (20)$$

which results similar to Eq. 11 for metal deposition on infinite flat homoatomic systems.

Figure 18a shows $\Delta\hat{G}$ as a function of particle size for the growth of an icosahedral Au NP, obtained by means of molecular dynamics annealing simulations using tight binding interaction potentials. The overall behavior is similar to that given previously in Fig. 17. However, the $\Delta\hat{G}$ vs. N_M curve is not smooth but presents a number of kinks and/or maxima and minima (see enlargement in the inset of Fig. 18a). This behavior is typical of small clusters, where the discrete character of the variable N_M becomes apparent. For $\eta < 0$, the largest $\Delta\hat{G}$ value observed at a given

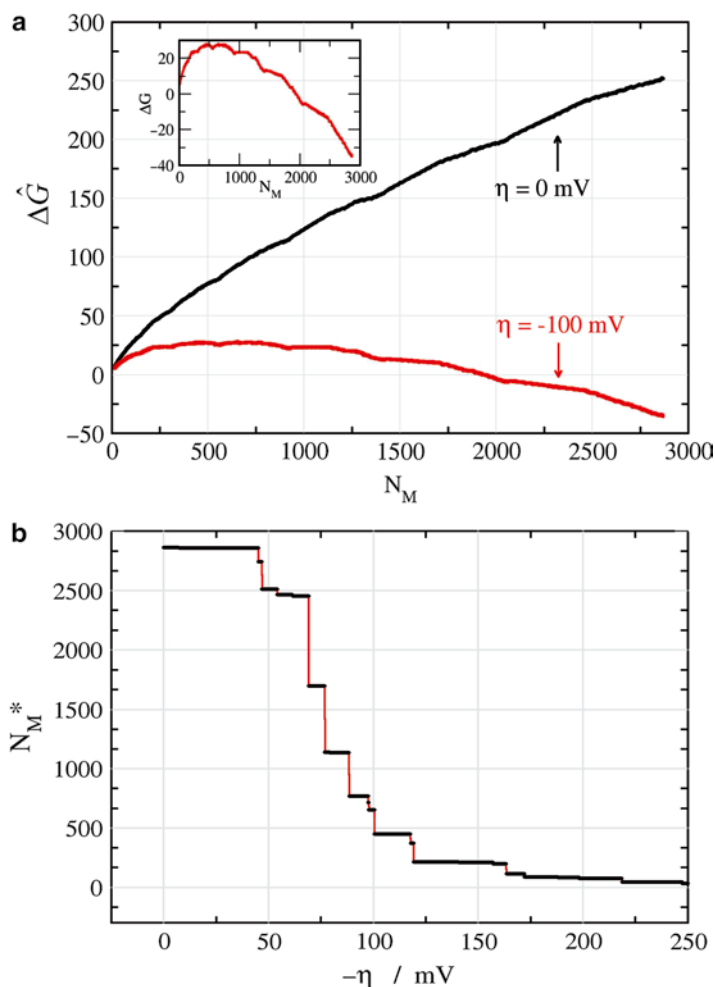


Fig. 18 (a) Work of nanoparticle formation $\Delta\hat{G}$ vs. number of metal atoms N_M curves corresponding to growth of a Au icosahedron at different overpotentials, (b) Critical cluster size as a function of applied overpotential for the same system as that of (a)

overpotential corresponds to the critical cluster size N_M^* , as described previously. The role of the discrete nature also becomes obvious in Fig. 18b, where N_M^* is plotted as a function of overpotential. At difference with the continuum modeling, in the atomistic approach, there are some overpotential ranges where one or more cluster sizes could become locally stable, leading to metastability.

As a final remark it must be noted that when border effects are considered, the whole $\Delta\hat{G}$ vs. N_M profile is shifted upward. This is a consequence of the fact that $g_M^{\text{facet}} < g_M^{\text{border}}$ and also due to the increase in N_M^{border} at expenses of N_M^{facet} . Thus, NPs with higher curvatures need larger overpotentials for their growth.

Nanoparticle Growth from Preexisting Seeds

In the present section, we analyze the electrochemical formation of NPs from preexisting seeds. We are here interested in describing the thermodynamic stability of NPs stemming from two types of experiments: on one side the growth of homoatomic NPs and on the other the formation of core/shell structures each from a preexisting NP.

Figure 19 shows a scheme of the simplified model we address here. We define three regions in the system: an inner part(inner), an intermediate part(intermediate), and an external part (monolayer). The former two belong to the preexisting seed and will build the core of a core/shell structure in the case of heteroatomic growth.

We will characterize the free energy of the inner atoms by the chemical potential of the bulk S atoms, μ_S^{bulk} , and define two types of atoms in the intermediate region: those located at the facets, characterized by the free energy g_S^{facet} , and those located at border sites, with the free energy g_S^{border} . In the case of the monolayer, we also differentiate between facet and border adatoms, with their free energies given by $g_{M/S}^{\text{facet}}$ and $g_{M/S}^{\text{border}}$, respectively:

$$G^{\text{substrate}} = N_S^{\text{core}} \mu_S^{\text{bulk}} + N_S^{\text{facet}} g_S^{\text{facet},0} + N_S^{\text{border}} g_S^{\text{border},0} \quad (22)$$

According to Eq. 4 the excess of free energy for the formation of the core/shell NP is given by

$$\begin{aligned} \Phi = & N_{M/S}^{\text{facet}} (g_{M/S}^{\text{facet}} - \mu_M^{\text{bulk}}) + N_{M/S}^{\text{border}} (g_{M/S}^{\text{border}} - \mu_M^{\text{bulk}}) \\ & + N_S^{\text{facet}} (g_S^{\text{facet}} - g_S^{\text{facet},0}) + N_S^{\text{border}} (g_S^{\text{border}} - g_S^{\text{border},0}) \end{aligned} \quad (23a)$$

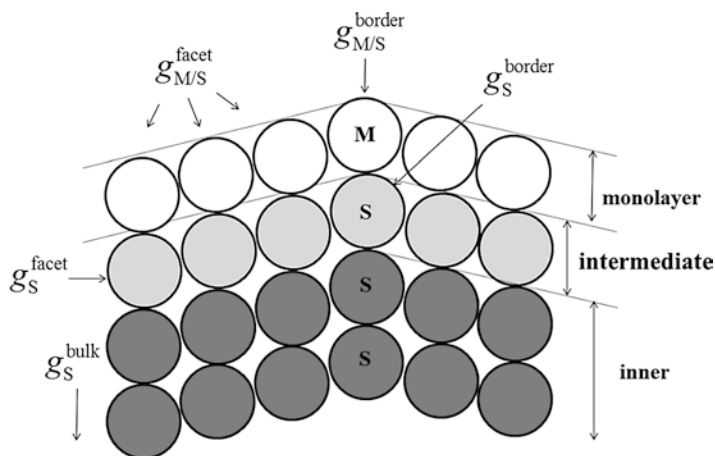


Fig. 19 Schematic representation of the NP model described in terms of five different atom types that we use to analyze the electroformation metal NP on preexisting metal seeds

where $g_S^{\text{facet},0}$ and $g_S^{\text{border},0}$ denote the free energy per atom of the facet and border site, where the shell is not present. As we did above (section “[Electrodeposition on Planar Surfaces](#)”) to switch from Eq. 9a to 9b, we can define quantities $g_{M/S}^{\text{facet,eff}}$ and $g_{M/S}^{\text{border,eff}}$, which embed substrate terms, to get

$$\Phi = N_{M/S}^{\text{facet}} \left(g_{M/S}^{\text{facet,eff}} - \mu_M^{\text{bulk}} \right) + N_{M/S}^{\text{border}} \left(g_{M/S}^{\text{border,eff}} - \mu_M^{\text{bulk}} \right) \quad (23b)$$

Using the previous equation, we get for the work of formation of the core/shell NP:

$$\Delta\hat{G} = N_{M/S}^{\text{facet}} \left(g_{M/S}^{\text{facet,eff}} - \mu_M^{\text{bulk}} + z\eta \right) + N_{M/S}^{\text{border}} \left(g_{M/S}^{\text{border,eff}} - \mu_M^{\text{bulk}} + z\eta \right) \quad (24)$$

where the first term on the *rhs* is a facet contribution and the second is a border contribution. There are two important differences between Eqs. 16 and 24 concerning the overpotential contribution. While in Eq. 16 the η term is proportional to all the atoms of the NP, in Eq. 24 the overpotential term is only proportional to the number of atoms of the monolayer (shell). We come back to this point below.

It is possible to distinguish among two growth cases for the present system, depending on the relative bond strengths:

Homoatomic systems ($M=S$) and heteroatomic ones with a relatively weak M–S interaction:

$$(a) \quad g_{M/S}^{\text{facet,eff}} > \mu_M^{\text{bulk}} \quad \text{and} \quad g_{M/S}^{\text{border,eff}} > \mu_M^{\text{bulk}}$$

Heteroatomic systems with a strong M–S interaction:

$$(b) \quad g_{M/S}^{\text{facet,eff}} < \mu_M^{\text{bulk}} \quad \text{and} \quad g_{M/S}^{\text{border,eff}} > \mu_M^{\text{bulk}} .$$

As was previously analyzed in section “[Electrodeposition on Planar Surfaces](#),” if a relationship between $N_{M/S}^{\text{facet}}$ and $N_{M/S}^{\text{border}}$ is known, it is possible to express Eq. 24 as a function of a single variable. In the case of a spherical NP, we have $N_{M/S}^{\text{border}} = \delta \left(N_{M/S}^{\text{facet}} \right)^{1/2}$.

The $\Delta\hat{G}$ vs. $N_{M/S}^{\text{facet}}$ behavior of case (a) may be generally represented in terms of Fig. 17, as previously discussed. Case (b) may be described in terms of Fig. 20.

Figure 20 shows the case where the M–S interaction is stronger than the M–M one. A relatively strong M–S interaction may generate a minimum, N_M^{min} , in the $\Delta\hat{G}$ vs. $N_{M/S}^{\text{facet}}$ curve, indicating the occurrence of thermodynamic stable structures. At zero or positive overpotentials ($\eta \geq 0$), the minimum of $\Delta\hat{G}$ at N_M^{min} shown in Fig. 20 is a global one, corresponding to a thermodynamically stable state. However, if this minimum is deep enough, it also may subsist at $\eta < 0$, yielding a metastable S/M system. In this case, the curve exhibits a maximum, corresponding to the critical nucleus size (N_M^*). At very negative overpotentials, $\eta \ll 0$, the system will be able to surmount the free energy barrier, $\Delta\hat{G}^*$, and will grow evolving towards the bulk structure.

If a metal atom deposited on a facet of S is more stable than in the bulk state, $g_{M/S}^{\text{facet,eff}}$ will be more negative than μ_M^{bulk} (case b) and we will have the inequality $\left(g_{M/S}^{\text{facet,eff}} - \mu_M^{\text{bulk}} \right) < 0$, which corresponds to the condition $\eta > 0$. Thus, the atoms

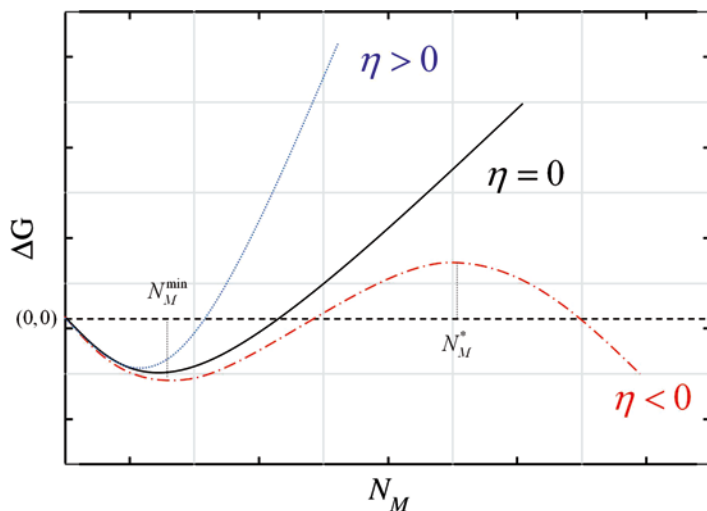


Fig. 20 Scheme of the work of shell formation $\Delta\hat{G}$ as a function of the number of deposited atoms $N_{M/S}^{\text{facet}}$ for the electrochemical formation of a metallic nanostructure at different overpotentials. In the present case, the interaction of the deposited atoms with the substrate is stronger than the interaction with each other (Reprinted with permission from Ref. [42])

will subsist on the surface of S at more positive potentials than the Nernst reversible potential for bulk M deposition. This reminds us the occurrence of the *upd* phenomenon on planar metal surfaces. The reverse situation will take place when $(g_{M/S}^{\text{facet,eff}} - \mu_M^{\text{bulk}}) > 0$ (case a), yielding $\eta < 0$, corresponding to overpotential deposition (*opd*). The latter is clearly an unsuitable condition for size and shape control of nanosystems, since when $\eta < 0$ the bulk deposit can be formed, so that the application of an overpotential allowing the deposition on S should inevitably drive it to M-bulk growth, at least from a thermodynamic viewpoint.

$\Delta\hat{G}$ atomistic calculations for different systems are given in Fig. 21. There, $\Delta\hat{G}$ is shown as a function of $N_{M/S}^{\text{monolayer}}$, for the systems Ag(core)/Au(shell) and Pt(core)/Au(shell) at zero overpotential [39]. The behavior of the first system is similar to that of the homogeneous systems shown in Figs. 17 and 18a. On the other hand, for the second system, the function $\Delta\hat{G}$ presents a minimum at $N_M^{\text{monolayer}} = 165$, which corresponds to a fraction of 0.8 of the first pseudomorphic shell on the surface of the Pt NP. On a perfect flat surface (infinite large NPs), the $\Delta\hat{G}$ vs. $N_M^{\text{monolayer}}$ curve would yield a linear decreasing curve (like Fig. 15b). However, in an NP there are sites with different adsorption energies that lead to the observed minimum. For instance, the borders where the facets merge present sites with a particularly high binding energy.

The number of particles at the minimum of the free energy curve observed for Pt(core)/Au(shell), say, N_M^{min} , may be shifted by the application of an overpotential. Figure 21b presents $\Delta\hat{G}$ vs. $N_M^{\text{monolayer}}$ curves for different overpotentials, while the inset shows how the value of N_M^{min} shifts with the overpotential applied. It is found that the Pt NP should become partially covered by Au at underpotentials. Note the similarity of the inset of Fig. 21b with the adsorption isotherm of Fig. 4.

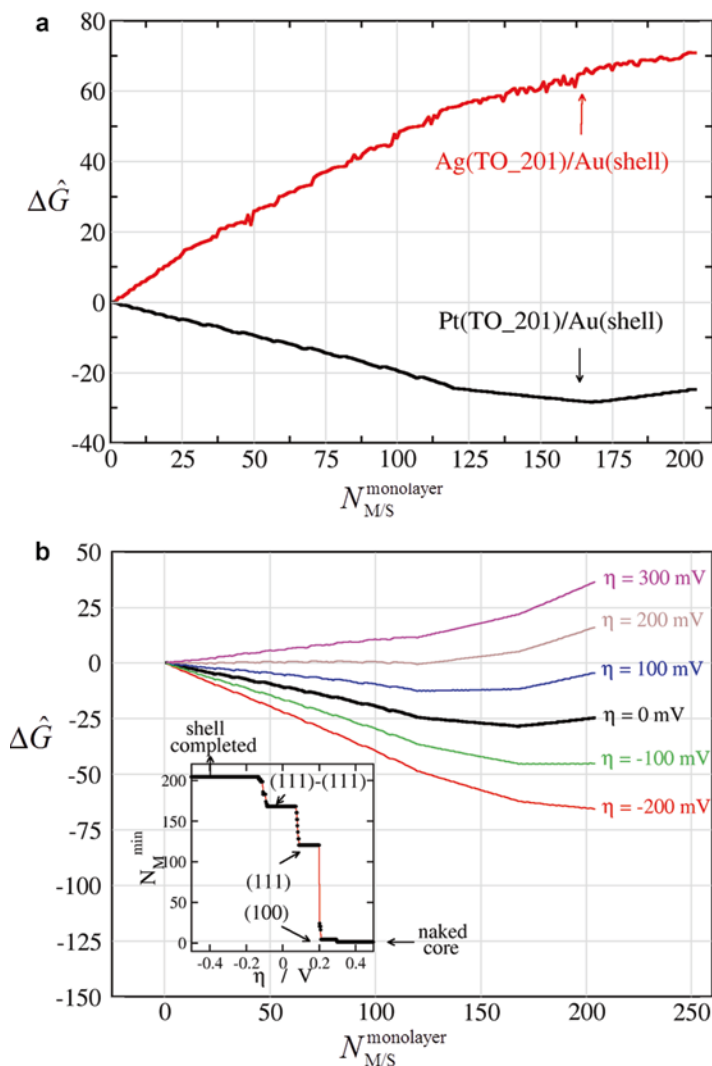


Fig. 21 (a) Work of shell formation profiles of Au deposition on Pt and Ag nanoparticles at $\eta = 0$. (b) Work of shell formation profiles for Au deposition on Pt nanoparticles at different overpotentials. The *inset* shows the number of particles at the minimum, $N_{M/S}^{\text{min}}$, as a function of overpotential. Note the possibility of decorating selectively different facets, as indicated by the arrows (Adapted from Ref. [39] with permission from the PCCP Owner Societies)

A straightforward and representative comparison between metal *upd* on nanoparticles and planar substrates may be observed in Fig. 22. We show there results from Grand Canonical Monte Carlo Lattice (GCMC-L) simulations using embedded atom potentials for Ag deposition on an octahedral Au NP, Au(111), and Au(100) planar surfaces. It is found that Ag deposition on Au(100) occurs at

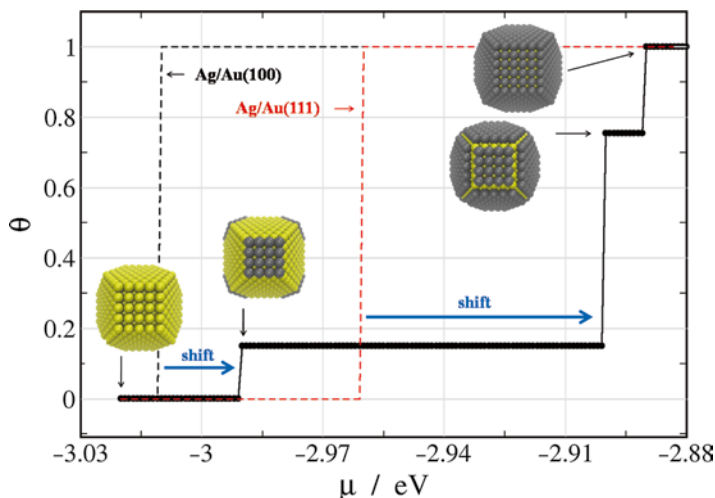


Fig. 22 Adsorption isotherms for Ag deposition on a Au truncated octahedral nanoparticle made of 1289 atoms, in comparison with Ag deposition on Au(100) (black dashes) and Au(111) (red dashes)

$\mu_{\text{Ag}/\text{Au}(100)} \approx -3,018$ eV, while on Au(111) it takes place at $\mu_{\text{Ag}/\text{Au}(111)} \approx -2,968$ eV. These values are represented with dashed lines. Nanoeffects are evident in the results for Ag deposition on the octahedral Au NP made of 1289 atoms. In this case, Ag deposition on the Au(100) facets takes place at $\mu_{\text{Ag}/\text{Au}(100_NP)} \approx -2,990$ eV, showing a shift of 28 meV towards the bulk deposition chemical potential. On its side, deposition on (111) facets occurs at $\mu_{\text{Ag}/\text{Au}(111_NP)} \approx -2,907$ eV, presenting a shift of 61 meV towards the bulk metal. These simulations clearly show the existence of a positive shift of metal deposition towards larger chemical potentials (more negative electrode potentials in the electrochemical system), thus weakening *upd*, as predicted qualitatively by Eq. 24.

Going back to homoatomic metal deposition on preexisting NPs, characterized by $g_{M/M}^{\text{facet}} > \mu_M^{\text{bulk}}$ and $g_{M/M}^{\text{border}} > \mu_M^{\text{bulk}}$, we note that for medium size NPs, surface effects predominate over border effects. In this limit the work of formation may be written as

$$\Delta \hat{G} \approx N_{M/M}^{\text{facet}} \left(g_{M/M}^{\text{facet}} - \mu_M^{\text{bulk}} + z e \eta \right) \quad (25)$$

In the case of very large nanoparticles, the facet term $g_{M/M}^{\text{facet}}$ approaches the bulk one, μ_M^{bulk} , the term $\left(g_{M/M}^{\text{facet}} - \mu_M^{\text{bulk}} \right)$ goes to zero, so that Eq. (25) yields the limits of Eq. (20).

It is well known that the redox potential delivered, for example, by citrate is not enough to generate nucleation and growth of new phases, but it is enough to generate growth on preexisting NPs [4, 7, 8, 12, 14–16]. We can note on the basis of Eq. 25 that the energy required per atom to build a homoatomic layer decreases as NP size increases.

Upd–opd Transition in the Nanoscale

The more the border (or curvature) effects become important, the smaller the NPs are [25, 26, 75, 76]. As a consequence of this, the *upd* phenomenon could disappear in the limit of small particles, thus defining an *upd–opd* transition. The particle size at which this transition occurs may be estimated assuming a given geometry and setting Eq. 24 equal to zero at $\eta = 0$ [41]. Thus, the number of particles of the facet at which the *upd–opd* transition occurs, say, $N_{M/S}^{\text{facet}(upd \rightarrow opd)}$, will be given by

$$N_{M/S}^{\text{facet}(upd \rightarrow opd)} = \left[-\delta \frac{\left(g_{M/S}^{\text{border,eff}} - \mu_M^{\text{bulk}} \right)}{\left(g_{M/S}^{\text{facet,eff}} - \mu_M^{\text{bulk}} \right)} \right]^2 \quad (26)$$

where we have assumed $N_{M/S}^{\text{border}} = \delta \left(N_{M/S}^{\text{facet}} \right)^{1/2}$ for the relationship between border and facet atoms. $\delta > 0$ is a geometrical factor that depends on the shape of the NP. Equation 26 shows that the stronger the border effects, given by $\left(g_{M/S}^{\text{border,eff}} - \mu_M^{\text{bulk}} \right)$, the larger the NP size at which the *upd–opd* transition occurs will be. On the opposite, systems with large *upd* shifts in planar surfaces (large $\left(g_{M/S}^{\text{facet,eff}} - \mu_M^{\text{bulk}} \right)$) will present the *upd–opd* transition at smaller NP sizes. According to computer simulations, *upd* has been predicted to disappear in the systems Au(core)/Ag(shell) [40–43] and Au(core)/Pd(shell) [44]. In the case of experiments, *upd* has been found to disappear for Pb and Cd deposition on Ag NPs [31–33]. Figure 5 in section “[Underpotential Deposition](#)” shows GCMC simulations for the system Au(core)/Ag(shell) where it is evident that the *upd* phenomenon disappears for cores smaller than 512 atoms.

As mentioned in section “[Dendrimer-Encapsulated Nanoparticles](#)” of the present chapter, the *upd–opd* transition is not evident for the system Pt(core)/Cu(Shell) as small as 1.3 nm. However, it must be noted in the experiments of Crooks and coworkers that the peak potential associated with Cu *upd* shifts towards larger positive potentials, as predicted by the present model (see Fig. 10).

In a similar way to what happens with NPs, an *upd–opd* transition may be found in nanocavities, but in the opposite direction, small enough cavities, with large negative curvatures, may present *upd*, even in those systems where *upd* is absent in planar surfaces. This phenomenon has been found in atomistic simulations using embedded atom potentials. The analytic formalism to predict such transitions is analogous to that developed in section “[Nanoparticle Growth from Preexisting Seeds](#)” for NPs, but considering a negative curvature. According to this, the size of the nanohole at which the *opd–upd* transition occurs, say, $N_{M/S}^{\text{facet,(opd} \rightarrow \text{upd)}}$, may be estimated from

$$N_{M/S}^{\text{facet}(opd \rightarrow upd)} = \left[-\kappa \frac{\left(g_{M/S}^{\text{border,eff}} - \mu_M^{\text{bulk}} \right)}{\left(g_{M/S}^{\text{facet,eff}} - \mu_M^{\text{bulk}} \right)} \right]^2 \quad (27)$$

which looks similar to Eq. 26 for the NP case.

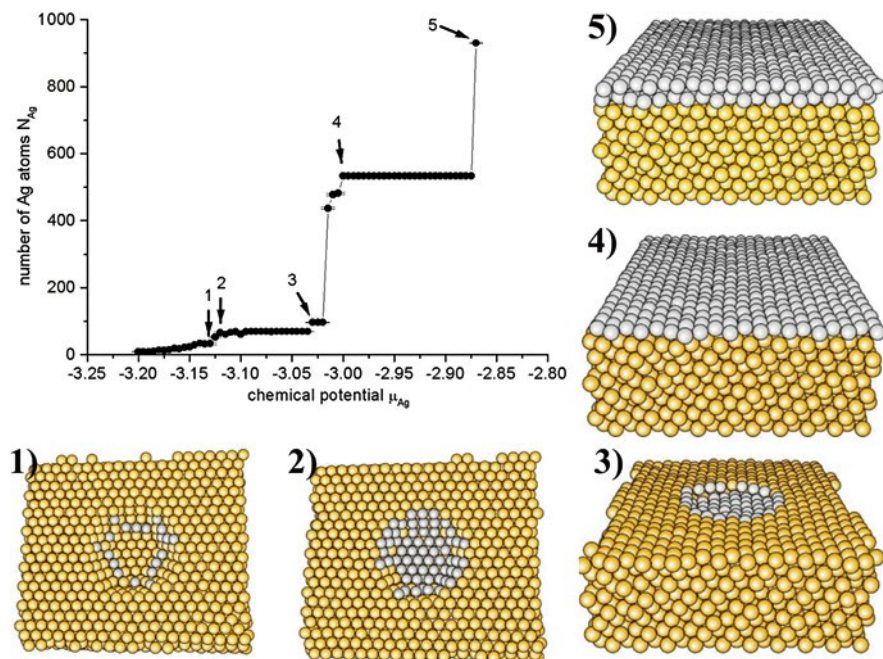


Fig. 23 (a) Number of deposited Ag atoms as a function of the chemical potential for decoration of a nanocavity on a Au(111) surface. (b) Snapshots of the simulation showing the different stages of nanohole decoration, corresponding to the numbers of part (a). The chemical potentials were $\mu_{Ag} = -3.155$ eV, $\mu_{Ag} = -3.12$ eV, $\mu_{Ag} = -3.03$ eV, $\mu_{Ag} = -3.00$ eV, and $\mu_{Ag} = -2.87$ eV (Reprinted with permission from Ref. [60])

Figure 23 shows the results from GCMC atomistic simulations for the decoration of nanocavities on Au(111) with Ag atoms. The decoration of the nanocavity starts at $\mu_{Ag} \approx -3.155$ eV at its bottom, being the first Ag atoms deposited on the border sites. The base of the nanocavity becomes completely covered at $\mu_{Ag} \approx -3.12$ eV and its filling occurs at $\mu_{Ag} \approx -3.03$ eV. All these processes take place at chemical potentials more negative than that corresponding to the bulk Ag metal, $\mu_{Ag} = -3.00$ eV. In this way, these atomistic simulations showed for the first time that negative curvatures allow metal deposition at more negative chemical potentials (more positive electrode potentials in the electrochemical scale) than those corresponding to *upd* on planar surfaces with the same crystal orientation, as predicted by Eq. 27.

Conclusions and Perspectives in *Upd* Modeling

The present chapter attempted to focus on some aspects of metal deposition that are relevant at the nanoscale. The approach was essentially nanothermodynamic, and some of the conclusions that were drawn may be summarized as follows:

- The use of electrochemical methods (by these we understand quite generally those methods where electron transfer is involved) appears as the most suited alternative to handle metal deposition at the nanoscale, especially concerning the thermodynamic control of the structures being formed on the substrate. The reason for this is that material exchange with the environment is greatly enhanced in the electrochemical systems.
- Underpotential deposition, combined with galvanic replacement, allows relatively simple control of metal deposition at the submonolayer level. These methods have been successfully employed to generate nanoparticles of different shapes and composition.
- Relatively simple modeling has been described here, based on experimental evidence and on results from atomistic simulations. The modeling is not only able to account for some aspects of experimental findings but also to make some remarkable predictions.
- One of the predictions emerging from the present modeling is the fact that underpotential deposition, depending on the strength of the substrate–adsorbate interaction, may vanish in the nanoscale. This underpotential–overpotential transition may be understood in terms of a curvature effect. The high curvature of very small nanoparticles results in a weaker binding of foreign adatoms to them. Conversely, the same modeling predicts that the filling of nanocavities may lead to an enhancement of underpotential deposition. Even systems showing no underpotential deposition on planar surfaces may yield underpotential deposition into small enough cavities.

It is desirable for the extension of the present modeling to include the following:

- The presence of capping agents on the nanoparticles that may contribute to their stabilization.
- The presence of other adsorbed species on the nanostructures, mainly anions.
- Electrostatic (electric double layer) effects.
- Kinetic effects in metal deposition at the nanoscale. A suitable option would be the application of kinetic Monte Carlo techniques.

Acknowledgments We acknowledge CONICET PIP: 112-200801-00983 and 112-201101-00992, SECyT 381 (Universidad Nacional de Córdoba), Program BID (PICT 382 2006 Nr 946, PICT 2010 Nr 123 and PICT 2012 Nr 2324), and PME: 2006–01581 383 for financial support.

References

1. Ratner M, Ratner D (2003) Nanotechnology, a gentle introduction to the next big idea. Prentice Hall, Professional Technical Reference, Upper Saddle River
2. Schmickler W (1996) Interfacial electrochemistry. Oxford University Press, New York
3. Shao M, Peles A, Shoemaker K (2011) Electrocatalysis on platinum nanoparticles: particle size effect on oxygen reduction reaction activity. *Nano Lett* 11:3714
4. Mariscal MM, Oviedo OA, Leiva EPM (2012) Metal clusters and nanoalloys: from modelling to applications. Springer, New York
5. Johnston RL, Wilcoxon J (2012) Metal nanoparticles and nanoalloys (Vol 3). Elsevier, Oxford.
6. Rieth M, Schommers W (2006) Handbook of theoretical and computational nanotechnology. American Scientific Publishers, Stevenson Ranch, CA, USA
7. Corain B, Schmid G, Toshima N (2008) Metal nanocluster in catalysis and materials science. Elsevier, The Netherlands
8. Mariscal MM, Dassie SA (2007) Recent advances in nanoscience. *Research Signpost, Trivandrum*
9. Ferrando R, Jellinek J, Johnston RL (2008) Nanoalloys: from theory to applications of alloy clusters and nanoparticles. *Chem Rev* 108:845
10. Boisseliera E, Astruc D (2009) Gold nanoparticles in nanomedicine: preparations, imaging, diagnostics, therapies and toxicity. *Chem Soc Rev* 38:1759
11. Epron F, Especel C, Lafaye G, Marécot P (2008) Multimetallic nanoparticles prepared by redox processes applied in catalysis. In: Astruc D (ed) *Nanoparticles and catalysis*. Wiley VCH, Weinheim
12. Crooks RM, Chechik V, Lemon BI III, Sun L, Yeung LK, Zhao M (2002) Synthesis, characterization, and applications of dendrimer-encapsulated metal and semiconductor nanoparticles. In: Feldheim DL, Foss CA Jr (eds) *Metal nanoparticles- synthesis, characterization, and applications*. Marcel Dekker, New York
13. Feldheim DL, Foss CA Jr (2002) *Metal nanoparticles- synthesis, characterization, and applications*. Marcel Dekker, New York
14. Schmid G (1994) *Clusters and colloids: from theory to applications*. VCH- Verlagsgesellschaft, Weinheim
15. Sugimoto T (2001) *Monodispersed particles*. Elsevier, Amsterdam
16. Zhang L, Fang X, Ye C (2007) *Controlled growth of nanomaterials*. World Scientific, Hackensack
17. Reza MM (2007) *Nanomaterials and nanosystems for biomedical applications*. Springer, Dordrecht
18. Varadan VK, Chen L, Xie J (2008) *Nanomedicine – design and applications of magnetic nanomaterials, nanosensors and nanosystems*. Wiley, Chichester
19. Desai T, Bhatia S (2006) *BioMEMS and biomedical nanotechnology: therapeutic micro/nanotechnology, vol III*. Springer, New York
20. De Micheli G, Leblebici Y, Gijs M, Vörös J (2009) *Nanosystems design and technology*. Springer, New York
21. Wieckowski A, Savinova ER, Vayenas CG (2003) *Catalysis and electrocatalysis at nanoparticles surfaces*. Marcel Dekker, New York
22. Liu XY, De Yoreo JJ (2004) *Nanoscale structure and assembly at solid–fluid interfaces: assembly in hybrid and biological system, vol. III*. Kluwer Academic Publishers, New York
23. Budevski E, Staikov G, Lorenz WJ (1996) *Electrochemical phase formation and growth – an introduction in the initial stages of metal deposition*. VCH, Weinheim
24. Staikov G, Lorenz WJ, Budevski E (1999) In: Ross PN, Lipkowski J (eds) *Imaging of surfaces and interfaces, vol 5, Frontiers of electrochemistry*. Wiley-VCH, New York
25. Tolman RCJ (1949) The effect of droplet size on surface tension. *Chem Phys* 17:333

26. Plieth WJJ (1982) Electrochemical properties of small clusters of metal atoms and their role in the surface enhanced Raman scattering. *Phys Chem* 86:3166
27. Hill TL (1994) Thermodynamics of small systems. Dover Publication, New York, Part I and II
28. Hill TL (2001) *Nano Lett* 1:273
29. Sudha V, Sangaranarayanan MVJ (2005) Underpotential deposition of metals—progress and prospects in Modeling. *Chem Sci* 117:207
30. Zhang J, Mo Y, Vukmirovic MB, Klie R, Sasaki K, Adzic RRJ (2004) Platinum Monolayer Electrocatalysts for O₂ Reduction: Pt Monolayer on Pd(111) and on Carbon-Supported Pd Nanoparticles. *Phys Chem B* 108:10955
31. Campbell FW, Zhou Y, Compton RG (2010) Thallium underpotential deposition on silver nanoparticles: size-dependent adsorption behaviour. *New J Chem* 34:187
32. Campbell FW, Compton RG (2010) Contrasting underpotential depositions of lead and cadmium on silver macroelectrodes and silver nanoparticle electrode arrays. *Int J Electrochem Sci* 5:407
33. Zhou Y, Rees NV, Compton RG (2011) Nanoparticle–electrode collision processes: the underpotential deposition of thallium on silver nanoparticles in aqueous solution. *Chem Phys Chem* 12:2085
34. Park S, Yang P, Corredor P, Weaver MJJ (2002) Transition metal-coated nanoparticle films: vibrational characterization with surface-enhanced Raman scattering. *Am Chem Soc* 124(11):2428
35. Kolb DM, Przasnyski M, Gerischer HJ (1974) Underpotential deposition of metals and work function differences. *Electroanal Chem* 54:25
36. Kolb DM (1978) In: Gerisher H, Tobias CW (eds) *Advances in electrochemistry and electrochemical engineering*, vol 11. Wiley, New York, p 125
37. Leiva EPM (1993) Current topics in electrochemistry. *Curr Top Electrochem* 2:269
38. Fonticelli MH, Corthey G, Benitez GA, Salvarezza RC, Giovanetti LJ, Requejo FG, Shon YS (2007) Preparation of ultrathin thiolate-covered bimetallic systems: from extended planar to nanoparticle surfaces. *J Phys Chem C* 26(111):9359
39. Oviedo OA, Leiva EPM, Mariscal MM (2008) Thermodynamic considerations and computer simulations on the formation of core-shell nanoparticles under electrochemical conditions. *Phys Chem Chem Phys* 10:3561
40. Mariscal MM, Oviedo OA, Leiva EPMJ (2012) On the selective decoration of facets in metallic nanoparticles. *Mater Res* 27:14
41. Oviedo OA, Reinaudi L, Leiva EPM (2012) The limits of underpotential deposition in the nanoscale. *Electrochem Comm* 21:14
42. Mariscal MM, Oviedo OA, Leiva EPM (2012) On the selective decoration of facets in metallic nanoparticles. *J Mater Res* 27:14
43. Oviedo OA, Negre CFA, Mariscal MM, Sánchez CG, Leiva EPM (2012) Underpotential deposition on free nanoparticles: Its meaning and measurement. *Electrochem Comm* 16:1
44. Oviedo OA, Reinaudi L, Mariscal MM, Leiva EPM (2012) Thermodynamic stability of electrochemically decorated Au-Pd core@shell nanoparticles. *Electrochem Acta* 76:424
45. Carino EV, Crooks RM (2011) Characterization of Pt@Cu core@shell dendrimer-encapsulated nanoparticles synthesized by Cu underpotential deposition. *Langmuir* 27:4227
46. Personick ML, Langille MR, Zhang J, Mirkin CA (2011) Shape control of gold nanoparticles by silver underpotential deposition. *Nano Lett* 11:3394
47. Langille MR, Personick ML, Zhang J, Mirkin CA (2012) Defining rules for the shape evolution of gold nanoparticles. *J Am Chem Soc* 134:14542
48. Brankovic SR, Wang JX, Adzic RR (2001) Metal monolayer deposition by replacement of metal adlayers on electrode surfaces. *Surf Sci* 474:L173
49. Yin Y, Erdonmez C, Aloni S, Alivisatos A (2006) Faceting of nanocrystals during chemical transformation: from solid silver spheres to hollow gold octahedra. *J Am Chem Soc* 128:12671
50. Seo D, Song H (2009) Asymmetric hollow nanorod formation through a partial galvanic replacement reaction. *J Am Chem Soc* 131:18210
51. Sun Y, Wiley B, Li ZY, Xia Y (2004) Synthesis and optical properties of nanorattles and multiple-walled nanoshells/nanotubes made of metal alloys. *J Am Chem Soc* 126:9399

52. Chen J, Wiley B, McLellan J, Xiong Y, Li ZY, Xia Y (2005) Optical properties of Pd–Ag and Pt–Ag nanoboxes synthesized via galvanic replacement reactions. *Nano Lett* 5:2058
53. Lu X, Au L, McLellan J, Li ZY, Marquez M, Xia Y (2007) Fabrication of cubic nanocages and nanoframes by dealloying Au/Ag Alloy nanoboxes with an aqueous etchant based on $\text{Fe}(\text{NO}_3)_3$ or NH_4OH . *Nano Lett* 7:1764
54. Hong X, Wang D, Cai S, Rong H, Li Y (2012) Single-crystalline octahedral Au–Ag nanoframes. *J Am Chem Soc* 134:18165
55. Wang Y, Wan D, Xie S, Xia X, Huang CZ, Xia Y (2013) Synthesis of silver octahedra with controlled sizes and optical properties via seed-mediated growth. *ACS Nano* 7:4586
56. Yin Y, Rioux RM, Erdonmez CK, Hughes S, Somorjai GA, Alivisatos AP (2004) Formation of hollow nanocrystals through the nanoscale Kirkendall effect. *Science* 304:711
57. Li W, Hsiao GS, Harris D, Nyffenegger RM, Virtanen JA, Penner RM (1996) Mechanistic study of silver nanoparticle deposition directed with the tip of a scanning tunneling microscope in an electrolytic environment. *J Phys Chem* 100:20103
58. Xia XH, Schuster R, Kirchner V, Ertl GJ (1999) The growth of size-determined Cu clusters in nanometer holes on Au(111) due to a balance between surface and electrochemical energy. *Electroanal Chem* 461:102
59. Solomun T, Kautek W (2001) Electrodeposition of bismuth and silver phases in nanometer-sized zero-dimensional STM-formed cavities on gold (111). *Electrochim Acta* 47:679
60. Luque NB, Reinaudi L, Serra P, Leiva EPM (2009) Electrochemical deposition on surface nanometric defects: Thermodynamics and grand canonical Monte Carlo simulations. *Electrochim Acta* 54:3011
61. Zhang J, Lima FHB, Shao MH, Sasaki K, Wang JX, Hanson J, Adzic RR (2005) Platinum monolayer on nonnoble Metal–Noble metal Core–Shell nanoparticle electrocatalysts for O_2 reduction. *J Phys Chem B* 109:22701
62. Crooks RM, Zhao M, Sun L, Chechik V, Yeung LK (2001) Dendrimer-encapsulated metal nanoparticles: synthesis, characterization, and applications to catalysis. *Acc Chem Res* 34:3
63. Scott RWJ, Wilson OM, Crooks RM (2005) Synthesis, characterization, and applications of dendrimer-encapsulated nanoparticles. *J Phys Chem B* 109:692
64. Yancey DF, Zhang L, Crooks RM, Henkelman G (2012) Au@Pt dendrimer encapsulated nanoparticles as model electrocatalysts for comparison of experiment and theory. *Chem Sci* 3:1033
65. Oviedo OA, Leiva EPM, Rojas M (2006) Energetic and entropic contributions to the underpotential/overpotential deposition shifts on single crystal surfaces from lattice dynamics. *J Electrochim Acta* 51:3526
66. Oviedo OA, Mariscal MM, Leiva EPM (2010) On the occurrence of stable and supersaturated metastable states in metallic core-shell nanoparticles. *Phys Chem Chem Phys* 12:4580
67. Oviedo OA, Mariscal MM, Leiva EPM (2010) Theoretical studies of preparation of core–shell nanoparticles by electrochemical metal deposition. *Electrochim Acta* 55:8244
68. Michalitsch R, Laibinis PE (2001) Adsorption-mediated electrochemical sensing of halides. *Angew Chem Int Ed* 40:941
69. Michalitsch R, Palmer BJ, Laibinis PE (2000) Formation of a more noble underpotentially deposited silver layer on gold by the adsorption of chloride. *Langmuir* 16:6533
70. Iski EV, El-Koued M, Calderon C, Wang F, Bellisario DO, Ye T, Sykes ECH (2011) The extraordinary stability imparted to silver monolayers by chloride. *Electrochim Acta* 56:1652
71. Schmidt U, Vinzelberg S, Staikov G (1996) Pb UPD on Ag(100) and Au(100) – 2D phase formation studied by in situ STM. *Surf Sci* 348:261
72. Oviedo OA, Vélez P, Macagno VA, Leiva EPM (2015) Underpotential deposition: from planar surfaces to nanoparticles. *Surf Sci* 631:23
73. Pinto OA, López de Mishima BA, Leiva EPM, Oviedo OA (2012) Computer simulation of adsorption on nanoparticles: the case of attractive interactions. *Phys Rev E* 86:061602
74. Wales D (2003) Energy landscapes: applications to clusters, biomolecules and glasses. Cambridge University Press, New York
75. Rusanov AI (1996) Thermodynamics of solid surfaces. *Surf Sci Report* 23:173
76. Rusanov AI (2006) On the material equilibrium of nanoparticles. *Nanotechnology* 17:575

Part V

New Properties

Plasmonic Nanostructured Supports for Spectro-Electrochemistry of Enzymes on Electrodes

30

Inez M. Weidinger

Contents

Introduction.....	1014
Nanostructured Multilayer Electrodes.....	1016
Roughened Silver Electrodes.....	1016
Silver-Gold and Silver-Platin Electrodes.....	1018
Spectro-Electrochemistry.....	1020
Silver-TiO ₂ Electrodes.....	1022
Calculation of Raman Enhancement Factors.....	1023
Determining Electron Transfer Pathways in Bio-Electrocatalysis.....	1025
Human Sulfite Oxidase (hSO).....	1027
The Membrane-Bound Hydrogenase (MBH).....	1028
Determination of Turnover Rates.....	1029
Conclusions.....	1029
References.....	1030

Abstract

Nanoscaled noble metals exhibit unique optical properties. One of these is the ability to create localised surface plasmon resonances upon light illumination, which makes it possible to study adsorbed molecules via surface enhanced spectroscopy. Silver and gold nanostructured electrodes with plasmonic properties can be created via electrochemical roughening or electro deposition methods. For studying enzyme/electrode systems the metal surface has to be functionalised with a biocompatible surface layer. Once the electrode is incorporated in an electrochemical cell the system can be studied by spectro-electrochemistry. With this combinational approach catalytic efficiency can be

I.M. Weidinger (✉)

Institut für Chemie, PC 14, Technische Universität Berlin, Berlin, Germany

e-mail: i.weidinger@mailbox.tu-berlin.de

tested via electrochemistry while the structural state of the enzyme is probed via surface enhanced Raman spectroscopy. Several techniques will be presented in this book chapter to create plasmonic electrode systems via electrochemical methods with defined optical and chemical properties. A focus will be given on the formation of hybrid electrode systems that make it possible to study enzyme/electrode interactions also on non plasmonic interfaces. Furthermore spectro-electrochemical investigations on several enzyme/electrode systems are discussed. It is shown how the combination of electrochemistry with spectroscopy can be used to get mechanistic insight into the functionality of enzymes on surfaces. This information can then be used for rational design of biosensors and biofuel cells.

Keywords

Biofuel cells • Enzymes • Nanostructured noble metals • Surface plasmon resonances • Surface enhanced Raman spectroscopy • Spectro-electrochemistry • Structure-function relationships

Introduction

Nanoscaled noble metals exhibit unique optical properties. One of them is the ability to create localized surface plasmon resonances upon light illumination [1]. Surface plasmon resonances are collective oscillations of the metal's free electron gas triggered by the oscillating electric field of incoming light. Depending on the nanostructure's size, geometry, and chemical composition, resonant coupling between light and electron gas is achieved for certain wavelengths of the incoming light. Under resonance conditions the surface plasmons create a strong local electric field enhancement at the metal/dielectric interface which can be used for spectroscopic analysis of surface-bound molecules. The most developed spectroscopic analytical method that makes use of plasmon-enhanced fields is surface-enhanced Raman (SER) spectroscopy that has an enormous abilities regarding molecular and structural identification of surface-bound analytes.

A variety of procedures are described in the literature to create plasmonic nanostructures with defined optical properties. However most of them are based on high-cost lithographic methods [2–4]. In contrast techniques based on electrochemical roughening or electrodeposition are much easier to apply and do not need high-cost equipment. Although they lack a much defined surface morphology, electrochemically created nanostructures do exhibit plasmonic enhancement sufficient for SER spectroscopy. Additionally these plasmonic supports can be used as working electrodes in an electrochemical cell allowing spectroscopic analysis of adsorbed molecules during a potential-induced redox reaction [5]. Special interest for plasmonic electrode systems lies in the field of biosensor and biofuel cell development. In biosensors the electrocatalytic response of an enzyme/electrode system in the presence of substrate is used for substrate identification [6], while in

biofuel cells enzyme/electrode complexes are employed for fuel generation or consumption [7]. Optimization of these systems requires a detailed knowledge about the structure-function relationship of the surface-bound enzymes. This can be gained by simultaneous use of electrochemical and spectroscopic methods. With such a combinational approach, catalytic efficiency can be tested via electrochemistry, while the structural state of the enzyme is probed via surface-enhanced Raman spectroscopy (SERS).

However, the choice of electrode material does have a great influence on the efficiency of enzyme/electrode systems. Standard materials in bio-electrocatalysis include noble metals like gold and platinum or metal oxides such as ITO or TiO₂ [8, 9]. On the other side the highest plasmonic field enhancement for excitation wavelengths in the visible region is given by silver, which is used as a standard support material in SER spectroscopy. Silver, however, plays only a minor role as a support material in bio-electrocatalysis. This makes the transformation of the results obtained from SER spectro-electrochemistry to real systems difficult. Several approaches to solve this problem are described in the following sections:

In section “[Nanostructured Multilayer Electrodes](#),” procedures are described to design plasmonic hybrid electrodes that contain silver as plasmonic amplifier but a different metal or metal oxide interface for enzyme adsorption. Here the small redox proteins cytochrome c (Cyt c) and cytochrome b5 (Cyt b5) are used as model enzymes. In section “[Calculation of Raman Enhancement Factors](#),” it is explained how the surface field enhancement can be calculated for these systems with the help of electrochemical methods.

Section “[Determining Electron Transfer Pathways in Bio-Electrocatalysis](#)” then describes how electrochemical and surface spectroscopic analysis can be combined on the example of two heme-containing enzymes, human sulfite oxidase (hSO) [10] and the membrane-bound hydrogenase trimer from *Ralstonia eutropha* (MBH) [11]. A summary of (spectro)-electrochemical investigations on the abovementioned enzyme/electrode systems is given in Table 1.

Table 1 Previous work in (spectro)-electrochemistry of the enzyme/support systems discussed in this book chapter

Enzyme	Electrode	Methods	References
Cyt c	Silver-SAM	SERRS	[14]
Y-Cyt c	Silver-SAM	SERRS	[38]
Cyt c	ITO	Electrochemistry SERRS	[39]
hSO/Cyt c	Gold-polymer	Electrochemistry	[34]
hSO	Silver-SAM	Electrochemistry SERRS	[35]
hSO	TiO ₂	Electrochemistry	[9]
MBH	Graphite	Electrochemistry	[36]
[NiFeSe] hydrogenase	TiO ₂	Electrochemistry	[8]
MBH	Silver-SAM	Electrochemistry SERRS	[37]

Table 2 SERR spectro-electrochemistry of proteins on multilayer electrodes

Enzyme	Electrode	Reference
Cyt c	Silver-gold	[20] [23] [22]
Cyt c	Silver-platin	[26]
Cyt b5	Silver-TiO ₂	[28]

Nanostructured Multilayer Electrodes

In this section the use of electrochemically roughened silver and silver containing multilayer electrodes will be discussed with respect to SERR spectro-electrochemistry of enzyme/electrode systems. A summary of the systems investigated is given in Table 2.

Roughened Silver Electrodes

Nanostructured silver and other noble metal electrodes can be fabricated via electrochemical surface roughening procedures. Hereby an oxidation-reduction cycle (ORC) is applied to a polished metal bulk electrode. Depending on the metal's oxidation-reduction potential, a time-dependent potential sequence is applied that leads to the formation of a nanostructured surface. Roughened silver electrodes exhibiting SERS activity can be easily created by ORC techniques. In Fig. 1b an SEM picture of an electrochemically roughened silver electrode can be seen, which shows a randomly, coral-like nanostructure. A detailed description on what sequences have to be applied to silver and other metals in order to achieve optimum SERS activity can be found in Tian et al. [12]. In comparison with highly ordered nanostructures made from lithographic methods, no clear resonance frequency can be determined for electrochemically roughened electrodes. This is especially true for roughened silver electrodes for which surface enhancement can be achieved in a wavelength range from 400 nm to near infrared [13]. While this very broad enhancement profile is clearly a disadvantage with respect to signal intensity of adsorbates, it gives more freedom to the choice of excitation line. Specifically for investigations of chromophores, the wavelength of the illuminating light has to be chosen with respect to the molecular absorption maximum of the analyte to make use of the resonance Raman (RR) effect. This analyte specific molecular absorption maximum will not necessarily match a specific surface plasmon resonance of the nanostructured electrode. The broad enhancement profile of roughened electrodes makes it much easier to combine the effect of surface enhancement and resonance Raman scattering in order to apply surface-enhanced resonance Raman spectroscopy (SERRS) for adsorbate analysis.

Next to silver also other noble metals such as gold and copper are able to create surface plasmon resonances in the red to near-infrared regime. However, silver

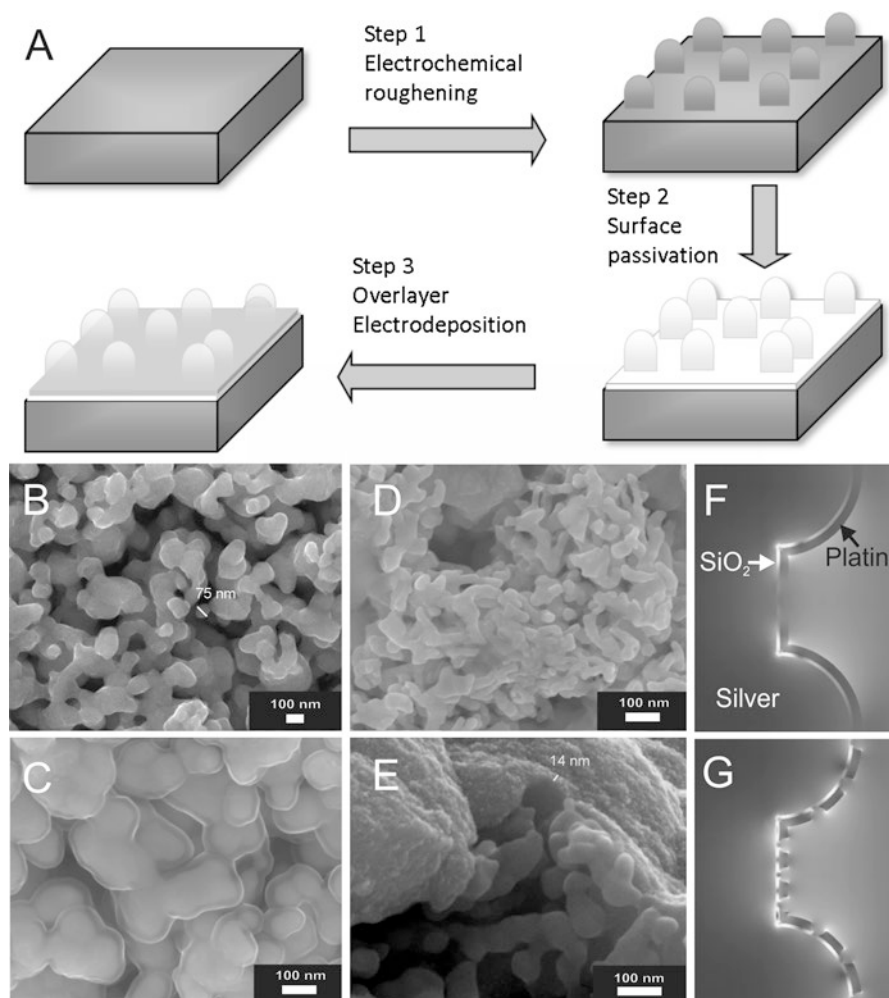


Fig. 1 (a) Preparation scheme of nanostructured multilayer electrodes. A bulk silver electrode is first electrochemical roughened (*Step 1*) and then passivated by coating with a dielectric spacer (*Step 2*). In the third step metal ions attached to the coated electrode are electrochemically reduced to create a thin overlayer film. In **b–e** SEM pictures of the silver electrodes are shown after the following steps: roughening (**b**), coating with SiO₂ (**c**), and overlayer deposition of platinum (**d**) or gold (**e**). (**f**, **g**) Electric field calculations of a silver-SiO₂-platin multilayer electrode geometry without (**f**) and with (**g**) defects. The introduction of defects into the platin film strongly promotes field enhancement at the platin/water interface (Adapted with permission from Feng et al. [20] Copyright 2009 American Chemical Society, Feng et al. [23] Copyright 2010 Wiley-VCH and Ly et al. [26] Copyright 2012 American Chemical Society)

remains the only material that can provide plasmonic field enhancement in the wavelength range from 500 to 400 nm. Many common protein cofactors such as hemes or flavins show strong molecular absorbance in this region. For SERR analysis of such biological systems, only silver can be used as support material.

Unfortunately for electrochemical investigations, silver is a second choice material, as the small potential range of silver electrodes limits their applicability, i.e., for development of sensors. Furthermore with respect to protein electrochemistry, the low biocompatibility of silver can have a harmful effect on the nativity of adsorbed proteins. The latter effect can partially be overcome by coating the silver surface with thin layers of self-assembled monolayers (SAMs) [14], SiO₂ [15], or polymers [16]. Any coating, however, increases the distance from the analyte to the plasmonic silver surface and thus reduces signal intensity of analytes. This effect is huge as dielectric coatings with a thickness of ca. 2 nm roughly result in a drop in SER intensity of one order of magnitude [17, 18].

The strong distance effect can be rationalized if one looks at the decay of the surface electric field into the dielectric medium. Localized surface plasmons can be considered as dipole oscillations. The electric field, generated by this oscillation, will decay with d^{-3} , d being the distance between dipole and analyte. The intensity of the electric field is given by the square of the absolute value of the electric field. One further has to take into consideration that also the Raman-scattered light, emitted from the analyte, will be enhanced. Therefore, the SER enhancement will roughly scale with the fourth power of the electric field enhancement. This leads in a first approximation to a distance dependence of the SER enhancement that is proportional to d^{-12} . In this estimation several assumptions were made: First it is stated that the enhancement of the Raman-scattered light is the same as for the incident light which might not be true for plasmonic materials with very defined surface plasmon resonance conditions. Second the surrounding environment has to consist of a dielectric medium with a homogeneous dielectric constant. These assumptions can be made for rough electrodes with a single dielectric coating layer. Consequently a d^{-12} distance behavior of SER enhancement could be demonstrated for analytes on electrodes coated with a single layer of different thickness [17, 19]. As a rule of thumb, this limits SERR spectroscopic investigations to analytes that are closer than 4 nm to the plasmonic surface.

Silver-Gold and Silver-Platin Electrodes

Strong deviations of the SER enhancement distance dependence are observed if the single dielectric coating is replaced by a multilayered structure with respective different dielectric properties. One example would be an alternating coating layer structure of a dielectric spacer and a thin metallic film. In such multilayer structures theoretical calculations predict enhanced electric fields at the outer interface at distances much larger than determined for systems with a single homogeneous layer of comparable thickness [20, 21].

Also experimentally unexpected high SER signals are observed for analytes on multilayer electrodes in which only the underlying support consists of a plasmonic material (i.e., silver). Such SERS-active multilayer electrodes can be constructed very simply by electrochemical deposition presented schematically in Fig. 1a. To build up these multilayer structures, first an electrochemically roughened silver

electrode is coated with a dielectric spacer consisting of either a SAM [20, 22] or a thin silica film [23]. Functionalization with a SAM can be achieved by incubating the electrode in a solution of alkanethiols with an appropriate functional group. The thickness of the spacer can hereby be tuned by choosing SAMs with different alkane chain lengths. However, with this method only coating layers with a thickness up to 2.5 nm can be built up. A much broader tuning of spacer thickness is possible using silica coatings, for which procedures are well established [24]. Hereby thin SiO₂ films are created via hydrolysis of precursor silicates (i.e., tetraethyl orthosilicate or sodium silicate). The thickness of the SiO₂ layer is controlled by the concentration of the precursor [25]. The resulting SiO₂ coating covers the silver electrode completely without changing its surface nanostructure, as shown exemplarily in Fig. 1c. The introduction of a spacer is needed to passivate the silver surface and to separate the silver from a second metal film. This second metal film is created by incubating the coated silver electrode in a solution containing the respective metal ion salt. Electrostatic attraction leads to adsorption of the metal ions on top of the dielectric spacer. The functionalization of the spacer layer has therefore to be made with respect of the metal ion's sign of charge. For negatively charged ions like AuCl₄⁻ or PtCl₄⁻, a silver electrode coated with an amino-terminated SAM would be preferable. In the case of silica coating, a final functionalization with aminopropyltriethoxysilane (APTES) has to be made. After the electrode has been incubated for several hours in the metal ion solution, it is put back into an electrochemical cell-containing buffer solution. Upon applying a negative potential, the adsorbed metal ions are reduced. This final step results in the formation of an overlayer metal island film on top of the coated silver electrode. The overlayer film shows a coral-like nanostructure that is quite different from the morphology of the underlying silver. Typical examples are shown in Fig. 1d, e [20, 26]. In general the grain sizes of the overlayer nanocorals are smaller and the film contains a lot of holes that allow the light going through the coating layers to interact with the plasmonic silver surface.

The existence of holes and defects in the overlayer film is very crucial as demonstrated by calculations of the electric field enhancement at the overlayer film/dielectric interface shown in Fig. 1f, g [26]. There the electric field enhancement is shown for a multilayer electrode-like geometry. The layers consist of silver as a solid support, SiO₂ as spacer layer, and platinum as overlayer metal. It can be clearly seen that a defect-containing platinum film promotes field enhancement at the platinum/water interface. Such defect-containing films are automatically created upon electrochemical deposition methods. In contrast other techniques such as film sputtering would create a closed film. While this clearly has other advantages with respect to surface chemistry, it will not work in favor of a high surface enhancement suitable for SER spectroscopy.

The high surface enhancement of multilayered electrodes is confirmed by SER(R) measurements of test proteins attached to the functionalized overlayer metal island film. The functionalization of the overlayer metal with either carboxyl- or amino-terminated SAMs is necessary to avoid protein denaturation. Suitable test molecules are heme-based redox proteins such as cytochrome c (Cyt c) or cytochrome b5 (Cyt b5). Due to the presence of the heme cofactor, strong SERR signals

are expected upon illumination with violet laser light, i.e., the 413 nm line of a krypton laser. Furthermore the redox properties of these proteins, which do mainly function as electron transfer units in biology, can be used to test the electrochemical properties of the system.

A SERR spectrum of Cyt c, attached to a functionalized platinum overlayer film, is shown exemplarily in Fig. 2a. In comparison to the spectra that are observed if the protein is directly attached to a functionalized silver electrode, only a very minor loss in Raman intensity is observed for multilayer electrode systems. For dielectric spacers with a thickness of ca. 2 nm, roughly a decrease by a factor 1.5–2 in SER intensity is observed if the analyte is exclusively bound to the overlayer film. From the SER signal intensity of the redox-active analyte, the enhancement factor of the Raman signal can be derived. A detailed description on the calculation procedure is given in section “[Calculation of Raman Enhancement Factors.](#)” Interestingly the choice of overlayer metal plays only a minor role for the Raman enhancement factor (REF). This can be rationalized if one assumes that the electric field enhancement is solely created by the plasmonic silver support. The overlayer film is not plasmonic active and only mirrors the dipole oscillation of the silver surface plasmons. The exclusive role of silver in the amplification of the SER signal is supported by the decreased Raman signals of analytes for increased spacer layer thickness, shown in Fig. 3. The thickness of the spacer layer, however, is not as crucial as one might expect having the d^{-12} dependency in mind. Even for a 20 nm silica spacer layer, the decrease in signal intensity is just one order of magnitude [23]. The choice of metal used as overlayer film again does not influence the observed distance dependence seen in Fig. 3.

Spectro-Electrochemistry

SERR spectro-electrochemistry can be used to probe the electric communication between redox protein and electrode in multilayer systems. Cyclo-voltammetric measurements of Cyt c attached to gold or platinum overlayer films show a fast redox response of the protein to a change in the applied potential. This is shown exemplarily for a silver-platinum electrode in Fig. 2c trace b. Comparing the amplitude of the cathodic and anodic peaks of Cyt c to its value on pure roughened silver (trace a), one can estimate that the amount of proteins in multilayer systems is increased by a factor 3–4. The protein's redox potential is identical in silver, silver-gold, and silver-platinum systems.

Redox-dependent changes of the heme cofactor can also be monitored very sensitive with SERRS as the resonance Raman spectra of hemes have been studied intensively [27]. The Raman spectra of oxidized and reduced heme cofactors show well-defined differences in the wavenumber region between 1300 and 1700 cm^{-1} such that a change in oxidation state can easily be detected. Analysing the SERR spectra of Cyt c attached to gold or platinum overlayer films at different potentials allows thus determining the molar ratio of reduced and oxidized protein for each applied potential. In Fig. 2a the spectra of Cyt c at an applied potential of -0.4 V and

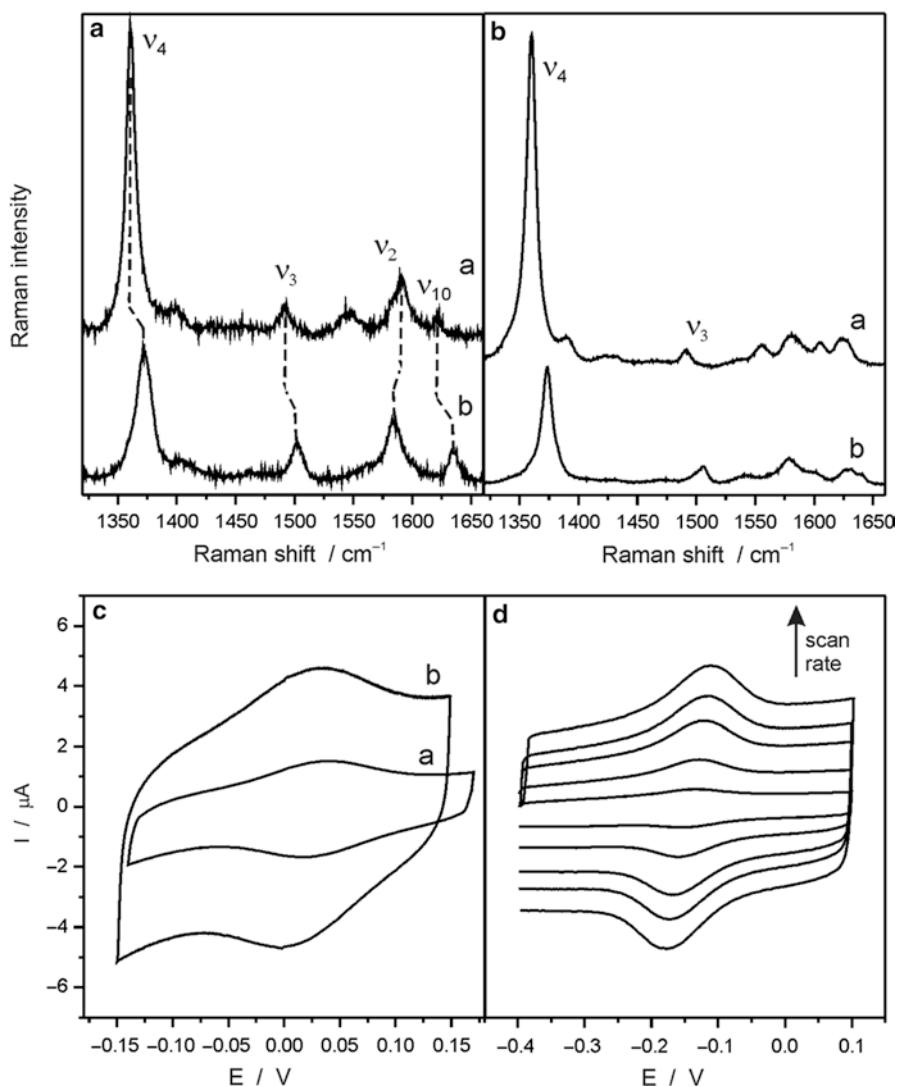
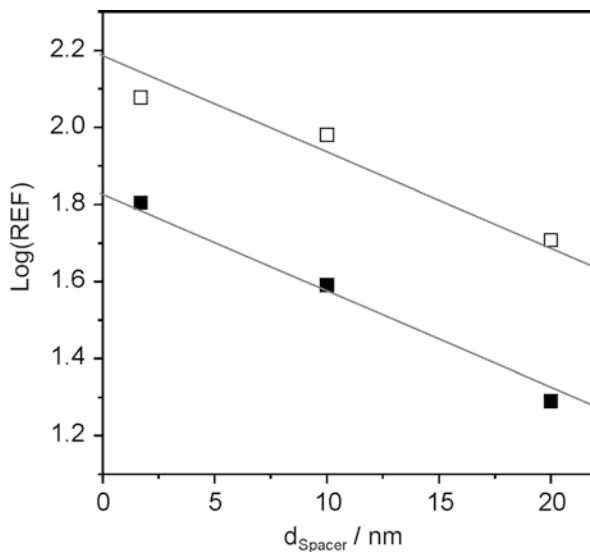


Fig. 2 (a) SERR spectra of the redox enzyme Cyt c adsorbed on functionalized silver-platin electrodes at an applied potential of -0.4 (top) and 0.15 V (bottom), respectively. (b) SERR spectra of Cyt b5 adsorbed on silver- TiO_2 electrodes at an applied potential of -0.3 (top) and 0.1 V (bottom), respectively. For both electrodes the vibrational marker bands show a complete reduction and oxidation of the protein. (c) Cyclic voltammogram of Cyt c on functionalized silver (trace a) and silver-platin (trace b) electrodes. The amount of redox-active species has increased on the silver-platin electrode. (d) Cyclic voltammogram of Cyt b5 on silver- TiO_2 electrodes for different scan rates (100, 300, 600, 800, and 1000 V/s) (Adapted with permission from Ly et al. [26] Copyright 2012, Sivanesan et al. [28] Copyright 2013 American Chemical Society)

Fig. 3 Raman enhancement factors (*REF*) at the metal/protein interface as a function of silica spacer thickness for silver-gold (*hollow squares*) and silver-platin (*solid squares*) electrodes (Reprinted with permission Ly et al. [26] Copyright 2012 American Chemical Society)



0.15 V (vs. Ag/AgCl) are shown. The redox-dependent shifts of the porphyrin ring vibrations (ν_4 , ν_3 , ν_2 , and ν_{10}) can be clearly seen and show that the protein can be completely reduced and oxidized at the respective potentials.

Silver-TiO₂ Electrodes

In principle one could rationalize the strong enhancement seen at the overlayer/analyte interface by an induced plasmon oscillation of the free electrons of the metal overlayer film. In this case the overlayer film itself is not able to enhance the electric field. However, if the field is already enhanced by the nearby silver, the overlayer film is capable to couple to this plasmon oscillation and to transport the electric field to the outer metal/analyte interface. Such an explanation is reasonable if the overlayer film consists of a metal. However, also strong Raman signals are observed if the metal oxide TiO₂ is used as overlayer film material [28].

Silver-TiO₂ multilayer electrodes are created very similar as the previously described silver-metal electrodes. The main difference lays in the coating of the silver as in this case carboxyl-functionalized SAMs are used as spacer layers. Attachment of TiO₂ is done using commercially available TiO₂ nanoparticles which are covalently bound to the carboxylate groups of the SAM under acidic conditions [29, 30]. With this procedure a TiO₂ overlayer island film is created that looks very similar to the metal films shown in Fig. 1d, e.

Due to its high biocompatibility, TiO₂ does not need further functionalization for protein attachment. Cytochrome *b5* (*Cytb5*) was used as test redox enzyme since it exhibits several carboxylic residues close to the heme which are expected to bind

covalently to the TiO₂ interface in the same way as the carboxylate groups of the SAM. With this setup SERR signals of Cytb5 are obtained (Fig. 2b) that under acidic conditions even exceed the signals of the protein directly attached to a functionalized silver electrode. To explain this high Raman signals by plasmon coupling is not as straightforward as in the case of metal overlayer films. TiO₂ is a semiconductor with no free electrons that could couple to an external oscillating field. Therefore, also geometrical effects have to play a role. This could be the case if, i.e., the TiO₂ layer is placed in the interspace between two silver corals. Interestingly the covalent attachment to silver also influences the electronic properties of the TiO₂ nanostructure. Cyclic voltammic measurements show a strong redox response and a fast electron transfer from the redox protein to the electrode as shown in Fig. 2d. This is unexpected as the conductivity of TiO₂ itself is rather poor. However, TiO₂ and silver are connected via a spacer layer and it might be that silver under these conditions injects electrons into the conducting band of TiO₂ [31]. Such a scenario would be able to explain the high conductivity of the system. Additionally the injected electrons could couple to plasmon oscillations supporting the observed high SERR signals.

In conclusion silver-TiO₂ electrodes exhibit very interesting properties. The underlying mechanism that is responsible for the high SERS activity and fast electron transfer, however, still needs to be further elucidated.

Calculation of Raman Enhancement Factors

The local electric field enhancement of a given nanostructure is a very important parameter, which, unfortunately, cannot be easily extracted from experiments. An experimentally accessible parameter is the SERS intensity of an analyte attached to the surface under investigation. From this intensity in principle, the Raman enhancement factor can be derived if the number of surface-bound analyte molecules is known.

Under the approximation that the Raman enhancement is equal to the forth power of the field enhancement, the latter can be calculated from REF values. In doing so one has always to be aware that the measured Raman intensities give average enhancement factors of all molecules that are probed within the laser spot. This average Raman enhancement factor can generally be derived by the following equation [3]:

$$\text{REF} = \frac{I_{\text{SERS}}}{I_{\text{R}}} \cdot \frac{N_{\text{R}}}{N_{\text{SERS}}} = \frac{I_{\text{SERS}}}{I_{\text{R}}} \cdot \frac{c_{\text{R}} \cdot V_{\text{L}}}{\Gamma_{\text{SERS}} \cdot A_{\text{L}}} \quad (1)$$

I_{R} and I_{SERS} are the Raman intensities of probe molecules in solution and adsorbed on the SERS-active surface, respectively. These intensities have to be normalized to the same accumulation time and laser intensity. N_{R} and N_{SERS} refer to the number of molecules that are in the focus of the laser beam. The latter quantities are related to the product of illuminated volume V_{L} and the bulk concentration c_{R} in the normal

Raman and to the product of the illuminated area A_L and the surface concentration Γ_{SERS} in the SER experiments. While some parameters like c_R, I_R and I_{SERS} can easily be measured, a precise determination of the surface coverage, the laser illuminated volume V_L and the surface area A_L is very difficult.

To determine A_L and V_L , one has to know very precisely the radius r_L of the laser beam. If r_L is known, the illuminated surface area of an ideally flat electrode is given by $A_L = \pi r_L^2$. However, as we look at nanostructured surfaces, a so far unknown roughness factor f has to be multiplied to this equation. V_L is standardly approximated by a cylinder with radius r_L and a height given by $h = 2r_L^2\pi/\lambda$, where λ is the wavelength of the laser light. Since the true laser spot has a shape of a Gaussian beam, it becomes clear that V_L gives the highest uncertainty in the calculation of the Raman enhancement factor.

An option for determination of the surface coverage Γ_{SERS} is the use of redox-active Raman probes in combination with electrochemical measurements. Integrating the peak area of the cathodic or anodic current I_a at a given scan rate ν yields the surface coverage of redox-active molecules Γ_a on the surface via the following equation [32]:

$$\Gamma_a = \frac{4 \cdot I_a \cdot R \cdot T}{A \cdot \nu \cdot n^2 \cdot F^2} \quad (2)$$

In this equation n is the number of transferred electrons. T, R, and F refer to temperature, gas and Faraday constant, respectively. The highest uncertainty in this equation is again given by the surface area A of the nanostructured electrode. To solve this problem, the electrode area is now also expressed by the product of its geometrical area A_0 (i.e., the area exposed to electrolyte solution of an ideally flat electrode) and its roughness factor f . If the SERS and the electrochemical experiment probe the same molecules, Γ_{SERS} in Eq. 1 can be substituted by Γ_a of Eq. 2 yielding the following equation for REF:

$$\text{REF} = \frac{I_{SERS}}{I_R} \cdot \frac{c_R \cdot \pi \cdot r_L^2 \cdot A_0 \cdot \nu \cdot n^2 \cdot F^2}{2 \cdot I_a \cdot R \cdot T \cdot \lambda} \quad (3)$$

Equation 3 now only contains experimental accessible parameters. However, two points have to be considered when applying Eq. 3. First this equation is only valid if all molecules that contribute to the SERS signal are also electro-active. Here again the advantage of using Cyt_c as model analyte becomes clear, since it exhibits, next to its high-resonance Raman intensity, almost full redox activity when adsorbed on carboxyl-functionalized electrode surfaces. However, even in a case when only a portion of the surface molecules is electro-active, SERS measurements can be used to determine the redox-inactive molar fraction. This fraction has then to be treated as a factor in the denominator of Eq. 3. Secondly it is assumed that all molecules in the area of the laser spot are actually seen in the SERS spectrum. This is not necessarily true, as, due to the nanostructured surface, some molecules might be shielded from the laser light. Therefore, in the given calculation, REF is possibly underestimated.

Determining Electron Transfer Pathways in Bio-Electrocatalysis

In section “[Nanostructured Multilayer Electrodes](#)” of this chapter, the redox chemistry between a protein and a nanostructured electrode was investigated by SERR spectro-electrochemistry. The same technique can also be applied to enzymatic systems in which electron transfer processes are coupled to a catalytic reaction. Understanding the interplay between catalytic substrate conversion and charge transfer in such enzyme/electrode complexes is of high interest for development of biosensors and biofuel cells. To get efficient substrate conversion, the enzyme has to be bound to a functionalized electrode surface in a way that first the catalytic reaction is not altered and second the electrons, which are produced or consumed in the catalytic reaction, are transported very fast from and to the electrode. This requires finding an appropriate electrode functionalization that prevents enzyme denaturation and that promotes a closed electron transfer pathway from the catalytic center to the electrode.

Although for each enzyme optimum conditions have to be found individually, certain immobilization strategies have shown great potential. One established procedure is done by covalent binding of the enzyme to the support via a specific single amino acid residue, such as a surface-exposed cysteine. While this immobilization strategy certainly gives the highest control over enzyme orientation, it strongly restricts its mobility on the surface. Alternatively electrostatic attraction can be used for immobilization if the enzyme exhibits a significant dipole moment. While this strategy lacks the defined orientation of the enzyme on the surface, it allows the enzyme to maintain some flexibility. This flexibility can work in favor of the charge transfer kinetic as the enzyme is capable of having different orientations on the surface over time.

Electrochemistry is a strong technique in order to determine electron transfer and catalytic turnover rates. It is however silent to inactive species on the surface. Furthermore structural information of the redox or catalytic center that would help to understand the mechanism of electron transfer and substrate conversion cannot be extracted by applying electrochemistry. This information is given by SER(R) spectroscopy, which on the other hand is not capable to determine overall catalytic efficiency. Therefore, only the combination of both methods allows drawing a comprehensive picture of the processes that take place at the electrode/enzyme interface.

Additional insight is given by time-resolved (TR)-SER spectroscopy. Hereby the Raman measurement is coupled to a trigger event like a change in applied potential or addition of substrate [33]. The schematic setup of such a TR-SERS measurement is drawn in Fig. 4a. As the time resolution is much smaller than the accumulation time needed to obtain one SER spectrum, the reaction has to be triggered repeatedly. In this case laser light accesses the probe only in a short time interval after a defined delay time to the trigger event.

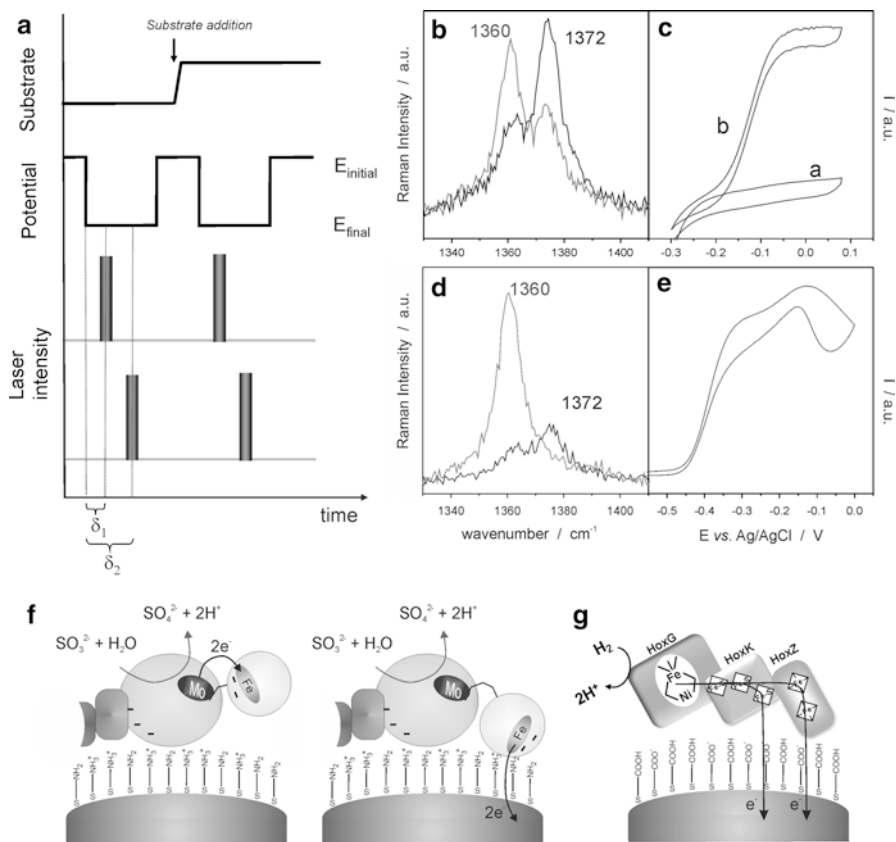


Fig. 4 (a) Schematic setup of a time-resolved SERR measurement conducted after a defined delay time with respect to substrate addition or change in potential. (b) SERR spectrum of hSO before and after addition of sulfite. (c) Cyclovoltammogram of hSO on amino-functionalized electrodes under low-(trace a) and high-(trace b) ionic-strength buffer conditions. (d) SERR spectrum of MBH before and after addition of H₂ which shows the reduction of the heme due to H₂ splitting. (e) Cyclovoltammogram of MBH on a functionalized electrode demonstrating catalytic activity of the immobilized enzyme. (f, g) Mechanistic schemes of the electron transfer pathway of hSO and MBH on electrodes. In the first case electron transfer via the heme is a requirement for catalytic activity; in the second case it is not (Adapted with permission from Sezer et al. [35], Copyright 2010 Royal Society of Chemistry and Sezer et al. [37], Copyright 2011 American Chemical Society)

Whether the catalytic center itself can be analyzed via SERRS depends strongly on its optical properties. While some cofactors such as flavins and hemes do have strong absorbance (and therefore high RR signal intensity) in the visible light region, many others such as Fe-Ni or molybdenum (Mo) catalytic centers do not. The latter ones are consequently not accessible by SERR spectroscopy.

However, catalytic activity strongly depends on fast supply and removal from electrons to and from the catalytic center. In many enzymes heme-containing subunits fulfill this task. For the majority of enzymes, the electron transfer pathway and kinetics are altered when immobilized on a solid electrode. As a consequence catalytic turnover of the enzyme might stop although the catalytic center is still intact. SERR spectro-electrochemistry can simultaneously probe catalytic turnover currents with structural changes of the heme cofactor and is thus able to determine electron transfer pathways on electrodes for complex enzyme systems. This will be demonstrated in the following on the two enzymes human sulfite oxidase (hSO) and the membrane-bound hydrogenase (MBH) trimer from *Ralstonia eutropha*. In both enzymes the electron transfer pathway goes via a heme subunit under physiological conditions. However, their behavior on electrodes is quite different.

Human Sulfite Oxidase (hSO)

Sulfite oxidases (SO) catalyze the oxidation of sulfite to sulfate and play an essential role in sulfite detoxification of living organisms. In biotechnology SO/electrode systems can be used as sensors for sulfite detection in food and wine [34]. The human sulfite oxidase (hSO) consists of three domains, one harboring a catalytic molybdenum (Moco) center and a second one that contains a heme cofactor. The third domain is used for dimerization. The Moco and heme domain are loosely connected via a flexible loop. This flexibility allows the heme domain to transiently bind to the Moco domain and to take up one of the electrons that are generated during sulfite oxidation. The domain then desorbs and binds, again transiently, to an external redox partner. This redox partner would be Cyt c under physiological conditions and a functionalized electrode in a biosensor. The process is then repeated for the second electron.

SERR spectroscopic investigations of hSO on amino-functionalized nanostructured silver electrodes show a strong Raman signal that exclusively depicts the vibrational fingerprint of the heme cofactor [35]. The strongest SERR intensity is obtained using a low-ionic-strength buffer solution (10 mMTris), which indicates that a high amount enzyme is immobilized on the surface under this condition. The electrochemical response, however, is weak as no catalytic currents can be observed in the presence of sulfite (Fig. 4c trace a). This observation suggests that the electron transfer pathway is at some point interrupted. Potential-dependent SERR spectroscopy shows that the heme can be fully oxidized and reduced as a function of applied electrode potential. Therefore, interruption of electron transfer does not occur between the heme and the electrode. On the other hand the heme is not reduced in the presence of sulfite under open-circuit conditions. This observation strongly indicates that the intramolecular electron transfer pathway between Moco and heme domain is not established once the enzyme is immobilized on the electrode surface.

The situation changes drastically if the ionic strength of the buffer solution is increased. Efficient catalytic turnover is then observed in the presence of sulfite (Fig. 4c trace b), concomitant with reduction of the heme under open-circuit potential measured with SERRS (Fig. 4b). Here the heme reduction can be identified by a shift of the ν_4 vibration from 1372 cm^{-1} (oxidized heme) to 1360 cm^{-1} (reduced heme). The overall SERR intensity is decreased but can be regained by going back to low ionic strength. This demonstrates that the enzyme is not desorbed at high ionic strength. However, the interaction between the heme domain and the electrode is weakened such that it is able to switch between a conformation close to the electrode and a conformation close to the Moco domain as illustrated in Fig. 4f. Only when this flexibility is maintained, a closed electron pathway from the catalytic center to the electrode is established.

The Membrane-Bound Hydrogenase (MBH)

Immobilization strategies cannot be easily generalized and adapted to other enzyme/electrode systems. A good example is in this respect the membrane-bound hydrogenase trimer from *Ralstonia eutropha* (MBH). This enzyme consists of three subunits. A large hydrogenase subunit harbors the catalytic bimetallic [NiFe] core. A second subunit contains three iron sulfur clusters acting as an electron relay unit. The third subunit anchors the enzyme to the membrane and ensures electron transfer between the hydrogenase dimer and the quinone pool of the respiratory chain via two separated heme cofactors. MBH/electrode complexes are very promising candidates for hydrogen biofuel cells especially since they are able to work in the presence of oxygen [36].

SERR spectra of the MBH trimer adsorbed on carboxyl-functionalized nanostructured silver electrodes exclusively display the vibrational fingerprint of the heme cofactor [37]. The high intensity of the SERR spectra suggests that the enzyme is bound to the electrode in an orientation where at least one of the hemes is close to the electrode surface. This is supported by a fast heterogeneous electron transfer between heme and electrode measured with time-resolved SERR spectroscopy.

Upon addition of H_2 electrochemical measurements reveal a good turnover signal as shown in Fig. 4e. Furthermore SERR measurements at open-circuit potential clearly indicate a reduction of the heme (Fig. 4d). Although this scenario looks similar as in the case of hSO, there are clear differences regarding the electron transfer pathway on electrodes. Using potential-dependent SERR spectroscopy, the redox potential of the hemes is determined to be at -0.3 V (vs. Ag/AgCl). If one takes a closer look at Fig. 4e, it can be seen that catalytic turnover starts already at a more negative potential. At this potential the hemes are still reduced and therefore not capable to participate in the electrocatalytic electron transfer pathway. This leads to the conclusion that for the immobilized MBH, the electron transfer pathway can either go via the heme cofactors or directly from the hydrogenase dimer to the electrode. The two pathways are illustrated in Fig. 4g.

Determination of Turnover Rates

Quantitative determination of catalytic turnover rates from cyclovoltammic current/voltage scans is derived by the following equation [32]:

$$k_{cat} = \frac{I_{lim}}{\Gamma_{cat} \cdot A \cdot n \cdot F} \quad (4)$$

I_{lim} refers to the maximum catalytic current obtained in an experiment where mass transport is not the rate limiting step. A is the surface area of the electrode as defined in section “Calculation of Raman Enhancement Factors.” As already mentioned determination of A is highly uncertain for nanostructured surfaces as the surface roughness factor f is not known. This problem can again be solved by concomitant measurements of the redox transition under nonturnover conditions and applying Eq. 2. By replacing Γ_{cat} with Γ_a from Eq. 2 the following equation is derived, in which all variables are experimentally accessible:

$$k_{cat} = \frac{I_{lim} \cdot v \cdot n \cdot F}{4 \cdot I_a \cdot R \cdot T} \quad (5)$$

The only requirement to make Eq. 5 valid is that all catalytic active molecules have to be also redox active. This assumption is not necessarily true, as demonstrated by the hSO measurements under low-ionic-strength conditions. It is however possible to extract this information directly from SERRS measurements as here the molar fraction of redox-inactive and catalytically inactive molecules can be determined, respectively.

Conclusions

In this chapter it was shown how electrochemical methods can be used to create unique nanostructured surfaces that are suitable platforms for SER spectro-electrochemistry. Upon designing multilayer silver-metal or silver-metal oxide electrodes, SER spectroscopic investigations of analytes on non-plasmonic supports become possible. At the same time the electrochemical response of redox proteins attached to the outer overlayer film is not altered with respect to single-layer silver electrodes.

By the combination of surface-enhanced Raman spectroscopy with electrochemical analysis, insight into the structure-function relation of enzyme/electrode systems can be given. The specific spectroscopic analysis of a heme cofactor in a complex enzyme system gives insight into the electron transfer pathway of enzymes on electrodes used for electrocatalytic applications. In the case of hSO/electrode systems, electron transfer over the heme domain is essential for its functionality as a biosensor. In contrary bio-electronic devices using the MBH trimer as biocatalyst also can establish an electron transfer on the electrode that shortcuts the pathway over the heme subunit.

Acknowledgments Financial support by the DFG (Cluster of Excellence UniCat) and the Fonds der Chemie is greatly acknowledged.

References

1. Maier SA (2007) Plasmonics: fundamentals and applications. Springer, New York
2. Haynes CL, Van Duyne RP (2001) Nanosphere lithography: a versatile nanofabrication tool for studies of size-dependent nanoparticle optics. *J Phys Chem B* 105:5599–5611
3. McFarland AD, Young MA, Dieringer JA, Van Duyne RP (2005) Wavelength-scanned surface-enhanced Raman excitation spectroscopy. *J Phys Chem B* 109:11279–11285
4. Wouters D, Schubert US (2004) Nanolithography and nanochemistry: probe-related patterning techniques and chemical modification for nanometer-sized devices. *Angew Chem Int Ed* 43:2480–2495
5. Siebert F, Hildebrandt P (2008) Vibrational spectroscopy in life science. Wiley-VCH, Weinheim
6. Scheller F, Lisdat F, Wollenberger U (2005) Application of electrically contacted enzymes for biosensors. In: Willner I, Katz E (eds) *Bioelectronics*. Wiley-VCH, Weinheim, pp 99–126
7. Cammack R, Frey M, Robson R (2001) Hydrogen as a fuel: learning from nature. Taylor & Francis, London
8. Reisner E, Fontecilla-Camps JC, Armstrong FA (2009) Catalytic electrochemistry of a [NiFeSe]-hydrogenase on TiO₂ and demonstration of its suitability for visible-light driven H₂ production. *Chem Commun* 2009:550–552
9. Sarauli D, Riedel M, Wettstein C, Hahn R, Stiba K, Wollenberger U, Leimkuhler S, Schmuki P, Lisdat F (2012) Semimetallic TiO₂ nanotubes: new interfaces for bioelectrochemical enzymatic catalysis. *J Mater Chem* 22:4615–4618
10. Garrett RM, Bellissimo DB, Rajagopalan KV (1995) Molecular-cloning of human liver sulfite oxidase. *Biochim Biophys Acta Gene Struct Expr* 1262:147–149
11. Frielingsdorf S, Schubert T, Pohlmann A, Lenz O, Friedrich B (2011) A trimeric supercomplex of the oxygen-tolerant membrane-bound [NiFe]-hydrogenase from *Ralstonia eutropha* H16. *Biochemistry* 50:10836–43. doi:10.1021/bi201594m
12. Tian ZQ, Ren B, Wu DY (2002) Surface-enhanced Raman scattering: from noble to transition metals and from rough surfaces to ordered nanostructures. *J Phys Chem B* 106:9463–9483
13. Sanchez-Gil JA, Garcia-Ramos JV (1998) Calculations of the direct electromagnetic enhancement in surface enhanced Raman scattering on random self-affine fractal metal surfaces. *J Chem Phys* 108:317–325
14. Murgida DH, Hildebrandt P (2001) Active-site structure and dynamics of cytochrome c immobilized on self-assembled monolayers – a time-resolved surface enhanced resonance Raman spectroscopic study. *Angew Chem Int Ed* 40:728–731
15. Sivanesan A, Kozuch J, Ly HK, Kalaivani G, Fischer A, Weidinger IM (2012) Tailored silica coated Ag nanoparticles for non-invasive surface enhanced Raman spectroscopy of biomolecular targets. *RSC Adv* 2:805–808
16. Sivanesan A, Kalaivani G, Fischer A, Stiba K, Leimkuhler S, Weidinger IM (2012) Complementary surface-enhanced resonance Raman spectroscopic biodetection of mixed protein solutions by Chitosan- and silica-coated plasmon-tuned silver nanoparticles. *Anal Chem* 84:5759–5764
17. Murgida DH, Hildebrandt P (2001) Heterogeneous electron transfer of cytochrome c on coated silver electrodes. Electric field effects on structure and redox potential. *J Phys Chem B* 105:1578–1586
18. Sivanesan A, Ly HK, Kozuch J, Sezer M, Kuhlmann U, Fischer A, Weidinger IM (2011) Functionalized Ag nanoparticles with tunable optical properties for selective protein analysis. *Chem Commun* 47:3553–3555
19. Compagnini G, Galati C, Pignataro S (1999) Distance dependence of surface enhanced Raman scattering probed by alkanethiol self-assembled monolayers. *Phys Chem Chem Phys* 1: 2351–2353

20. Feng JJ, Gernert U, Sezer M, Kuhlmann U, Murgida DH, David C, Richter M, Knorr A, Hildebrandt P, Weidinger IM (2009) Novel Au-Ag hybrid device for electrochemical SE(R)R spectroscopy in a wide potential and spectral range. *Nano Lett* 9:298–303
21. David C, Richter M, Knorr A, Weidinger IM, Hildebrandt P (2010) Image dipoles approach to the local field enhancement in nanostructured Ag-Au hybrid devices. *J Chem Phys* 132: 024712-1–024712-8
22. Sezer M, Feng JJ, Ly HK, Shen YF, Nakanishi T, Kuhlmann U, Hildebrandt P, Mohwald H, Weidinger IM (2010) Multi-layer electron transfer across nanostructured Ag-SAM-Au-SAM junctions probed by surface enhanced Raman spectroscopy. *Phys Chem Chem Phys* 12: 9822–9829
23. Feng JJ, Gernert U, Hildebrandt P, Weidinger IM (2010) Induced SER-activity in nanostructured Ag-Silica-Au supports via long-range plasmon coupling. *Adv Funct Mater* 20:1954–1961
24. Ung T, Liz-Marzan LM, Mulvaney P (1998) Controlled method for silica coating of silver colloids. Influence of coating on the rate of chemical reactions. *Langmuir* 14:3740–3748
25. Stober W, Fink A, Bohn E (1968) Controlled growth of monodisperse silica spheres in micron size range. *J Colloid Interface Sci* 26:62–69
26. Ly HK, Kohler C, Fischer A, Kabuss J, Schlosser F, Schoth M, Knorr A, Weidinger IM (2012) Induced surface enhancement in coral Pt island films attached to nanostructured Ag electrodes. *Langmuir* 28:5819–5825
27. Hu SZ, Morris IK, Singh JP, Smith KM, Spiro TG (1993) Complete assignment of cytochrome-C resonance Raman-spectra via enzymatic reconstitution with isotopically labeled hemes. *J Am Chem Soc* 115:12446–12458
28. Sivanesan A, Ly KH, Adamkiewicz W, Stiba K, Leimkuhler S, Weidinger IM (2013) Tunable electric field enhancement and redox chemistry on TiO₂ island films via covalent attachment to Ag or Au nanostructures. *J Phys Chem C* 117:11866–11872
29. Vittadini A, Selloni A, Rotzinger FP, Gratzel M (2000) Formic acid adsorption on dry and hydrated TiO₂ anatase (101) surfaces by DFT calculations. *J Phys Chem B* 104:1300–1306
30. Petrone L, McQuillan AJ (2011) Alginate ion adsorption on a TiO₂ particle film and interactions of adsorbed alginate with calcium ions investigated by Attenuated Total Reflection Infrared (ATR-IR) spectroscopy. *Appl Spectrosc* 65:1162–1169
31. Yang LB, Jiang X, Ruan WD, Yang JX, Zhao B, Xu WQ, Lombardi JR (2009) Charge-transfer-induced surface-enhanced Raman scattering on Ag-TiO₂ nanocomposites. *J Phys Chem C* 113:16226–16231
32. Promdromidis MI, Florou AB, Tzouwara-Karayanni SM, Karayannis MI (2000) The importance of surface coverage in the electrochemical study of chemically modified electrodes. *Electroanalysis* 12:1495
33. Wackerbarth H, Klar U, Gunther W, Hildebrandt P (1999) Novel time-resolved surface-enhanced (resonance) Raman spectroscopic technique for studying the dynamics of interfacial processes: application to the electron transfer reaction of cytochrome c at a silver electrode. *Appl Spectrosc* 53:283–291
34. Spricigo R, Dronov R, Lisdat F, Leimkuhler S, Scheller F, Wollenberger U (2009) Electroanalytic sulfite biosensor with human sulfite oxidase co-immobilized with cytochrome c in a polyelectrolyte-containing multilayer. *Anal Bioanal Chem* 393:225–233
35. Sezer M, Spricigo R, Utesch T, Millo D, Leimkuhler S, Mroginski MA, Wollenberger U, Hildebrandt P, Weidinger IM (2010) Redox properties and catalytic activity of surface-bound human sulfite oxidase studied by a combined surface enhanced resonance Raman spectroscopic and electrochemical approach. *Phys Chem Chem Phys* 12:7894–7903
36. Vincent KA, Cracknel JA, Lenz O, Zebger I, Friedrich B, Armstrong FA (2005) Electrocatalytic hydrogen oxidation by an enzyme at high carbon monoxide or oxygen levels. *Proc Natl Acad Sci U S A* 102:16951–16954

37. Sezer M, Frielingsdorf S, Millo D, Heidary N, Utesch T, Mroginski MA, Friedrich B, Hildebrandt P, Zebger I, Weidinger IM (2011) Role of the HoxZ subunit in the electron transfer pathway of the membrane-bound [NiFe]-hydrogenase from *Ralstonia eutropha* immobilized on electrodes. *J Phys Chem B* 115:10368–10374
38. Feng JJ, Murgida DH, Utesch T, Mroginski MA, Hildebrandt P, Weidinger IM (2008) Gated electron transfer of yeast Iso-1 Cytochrome c on SAM-coated electrodes. *J Phys Chem B* 112:15202–15211.
39. Frasca S, von Graberg T, Feng JJ, Thomas A, Smarsly BM, Weidinger IM, Scheller FW, Hildebrandt P, Wollenberger U (2010) Mesoporous Indium Tin Oxide as a novel platform for bioelectronics. *Chem Cat Chem* 2(7):839–845

Self-Organized Nano- and Microstructure of Electrochemical Materials by Design of Fabrication Approaches

31

Zhenyu Chu, Lei Shi, and Wanqin Jin

Contents

Introduction.....	1034
The Defect Analysis of Material Growth.....	1035
Rapid Reaction Rate of PB.....	1035
Overlarge Size of Ni(en) ₃ Ag ₂ I ₄	1037
The Strategies of Structure Control	1038
Reduction of PB Reaction Rate.....	1039
Partially Rapid Crystallization of PB	1040
Increase of the Ni(en) ₃ Ag ₂ I ₄ Crystal Nucleus	1040
Purposed Development of Novel Fabrication Method.....	1041
Aerosol Deposition Approach for Nanocubic PB Formation	1041
Electric Field-Induced Self-Assembly for Double Structures of PB Formation.....	1045
Interfacial Molecule-Induced Approach for Hybrid Film Formation	1049
Conclusions.....	1053
References.....	1054

Abstract

Introduction of nanostructure into electrochemistry has been widely confirmed to succeed in the performance enhancement. The morphology control of electrochemical material has become a key to the combination of electrochemistry and nanoscience. Normally, it is not easy to realize the regular structures in nanoscale by self-organization for all materials. This must rely on the well-understood properties of the desired material. The crucial control parameter of morphology should be recognized first. In this case, the design of fabrication approach can

Z. Chu • L. Shi • W. Jin (✉)

State Key Laboratory of Materials-Oriented Chemical Engineering,

Nanjing Tech University, Nanjing, People's Republic of China

e-mail: zhenyuchu0411@gmail.com; shileinjut@126.com; wqjin@njtech.edu.cn

fix a direction. For the electrochemical material, application normally requires the immobilization on electrode surface. Therefore, in situ formation methods are more appreciated. Here in this chapter, two different kinds of electrochemical materials – Prussian Blue, an inorganic complex compound, and Ni(en)₃Ag₂I₄, a hybrid material – served as examples to describe the nano/microstructure control of crystal growth by the targeted design of novel preparation approaches. Focusing on the different issues of structure control, different synthesis techniques have been developed to reach the goal. According to characterizations, these self-organized nanostructures can obviously increase the electrochemical performance of original materials which exhibits the meaningful and useful functions for the nanostructure self-organization that relied on this targeted design of fabrication approach.

Keywords

Self-organized structure • Fabrication design • Electrochemical materials • Performance enhancement

Introduction

As an important subject in chemistry, electrochemistry still keeps its activity in scientific development. Currently, one hot topic and strong tendency of electrochemistry is the knowledge cross with other fields [1, 2]. Optical [3], physical [4], magnetic [5], and structure chemistry [6] can all be employed in the new inspiration of electrochemistry development, while the basement of this big fusion should require the “powerful” materials, which own excellent performance, various abilities, and easy production. Of course, not all electrochemical materials can satisfy the above requirement with birth. According to recent researches in material science, morphology control, especially in nano/microscale, is an effective strategy for the performance improvement [7, 8]. Meanwhile, the introduction of nano/microstructure into electrochemistry has widely started to show its energy to push the advance of application [9, 10]. However, the structure control of electrochemical materials is always a challenge for the combination of electrochemistry and nanoscience. Lots of traditional techniques of material synthesis cannot satisfy the demands of microstructure creation; hence, the targeted design of novel preparation method for the structure control should generate with requirement.

Normally, new design of fabrication approach should follow the characters of materials. Not all materials can easily self-organize their regular structures in nano/microscale. Therefore, for the consideration of structure control, it must rely on the well study of the material which is aimed to synthesize. The crucial parameter of morphology control should be recognized first. In this case, the design direction of fabrication approach can be determined. For electrochemical materials, they are normally immobilized on electrode surface for usage [11].

Table 1 The common preparation methods of PB film

Prepared approach	Microstructure	Time consumption	References
Self-assembly	Round nanoparticle	Slow	[18]
Electrodeposition	Microparticle	Medium	[19]
Chemical deposition	Irregular	Rapid	[20]

Accordingly, in situ formation methods are often appreciated. Electrodeposition is a very common method in electrochemical material synthesis [12, 13]. Through the control of deposition current, potential, electric quantity, or electrolyte composition, some substances can self-form various nanoshapes. Like gold, the structures of nanoflower, nanosheet, and nanorod have already been obtained [14, 15]. But many materials are not suitable. Hence, new inspiration should be aroused.

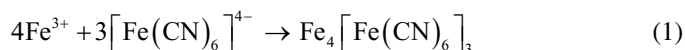
Surely, as abovementioned, innovation should follow the inherent principles of targeted materials. In this chapter, two different types of materials – Prussian Blue (PB), an inorganic complex compound [16], and Ni(en)₃Ag₂I₄, a hybrid material [17] – served as samples for analysis. Due to some reasons, both of them cannot easily in situ form regular structures on support surface in nano/microscale (shown in Table 1). Here, we provide a new design route to solve the above problems on the regular growth of these materials. Then the advantages of these novel approaches were demonstrated to exhibit the importance of approach design for self-organized nano-/microstructure. According to the success in structure control, these strategies are promising to be extended for morphology control and nano-/microsynthesis of electrochemical materials.

The Defect Analysis of Material Growth

Rapid Reaction Rate of PB

PB, iron hexacyanoferrate, was initially served as a dark blue pigment [21]. Its unit cell is a face-centered cubic structure. Only Fe, C, and N are the three elements that construct its cell structure (Fig. 1). In iron atoms located at the vertices of the cube, C and N construct the edges. Specially, the neighbor Fe atoms own different valences which can provide a natural electron transfer channel for electrocatalysis [22]. However, before a long time, it is just applied as a dark blue pigment. Till the 1980s, because of its high electrocatalytic ability and low operation potential, PB began to be used in the fabrication of modified electrode [23]. Compared with other electrode materials, its morphology is really hard to control which caused the rare self-formation of regular nano/microstructure. This has already become one obstruction for its performance development.

PB formation is mainly dependent on the reaction between Fe³⁺ and [Fe(CN)₆]⁴⁻. The related equation is shown as follows:



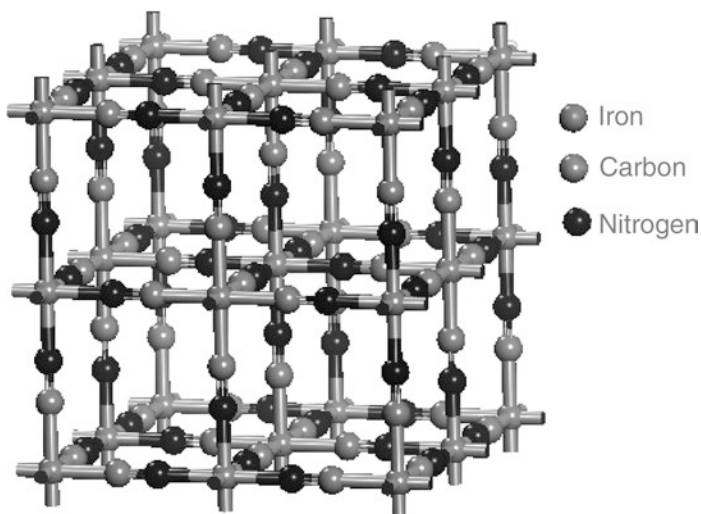


Fig. 1 Unit cell of PB

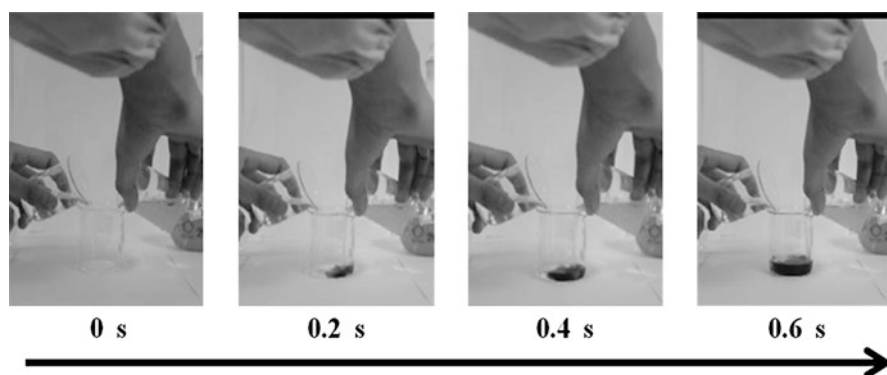


Fig. 2 The instantaneous reaction process between FeCl_3 and $\text{K}_4[\text{Fe}(\text{CN})_6]$ solutions

As shown in Fig. 2, this reaction rate is considerably rapid. Although the fast synthesis rate is benefited to the large-scale preparation, it will cause the difficult control of PB structure. Electrochemical materials, usually, should be modified on a substrate for application. Crystal growth on a support normally requires two steps [24]: one is the formation of crystal nucleus on some active sites; the other is the continuous growth around the formed nucleus. Commonly, the first step is more time consuming, belonging to the control step [25]. Meanwhile, it was also the basement for the further crystallization process. Therefore, its distribution and structure are essential to the final state of modified materials. Rapid growth could

produce two results: (1) abundant nucleuses rapidly and chockablock formed on the initial crystal growth and (2) tight growth space of crystal that can limit the adequate morphology growth which could lead to amorphous shapes. Therefore, according to the above description, two strategies can be designed:

1. If the whole PB formation rate can be reduced during the film preparation, the amount of PB nucleus will decrease to provide a free space for the regular crystallization.
2. If the crystallization behavior can occur only on some partial sites, it will also offer a relaxed environment and sufficient crystallization source for crystal growth.

Overlarge Size of $\text{Ni}(\text{en})_3\text{Ag}_2\text{I}_4$

$\text{Ni}(\text{en})_3\text{Ag}_2\text{I}_4$ is a hybrid material constructed by coordination center $\text{Ni}(\text{en})_3$ and ligand Ag_2I_4 . This substance is first synthesized in 2008 [17]. In its structure, AgI chains served as a cage to pack $\text{Ni}(\text{en})_3$ molecules (Fig. 3). Owing to the existence of AgI , this material is of semiconductive behaviors which can be prepared as an electrode material.

Different with PB, the free growth of $\text{Ni}(\text{en})_3\text{Ag}_2\text{I}_4$ will obtain the quite big crystal. Under the room temperature and normal pressure, the size of single crystal can reach millimeter (Fig. 4). As well known in electrocatalysis theory, surface area of one material is very important to determine the electrochemical performance [26].

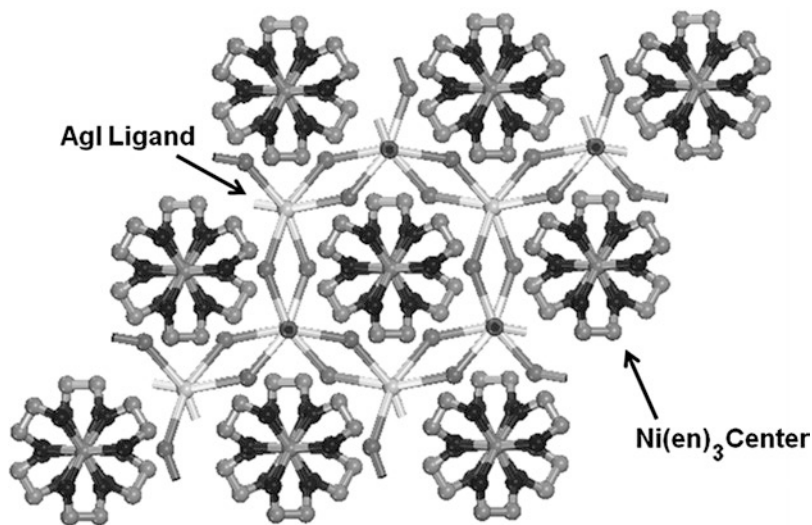


Fig. 3 Cell structure of $\text{Ni}(\text{en})_3\text{Ag}_2\text{I}_4$

Fig. 4 Digital photo of $\text{Ni}(\text{en})_3\text{Ag}_2\text{I}_4$ single crystal

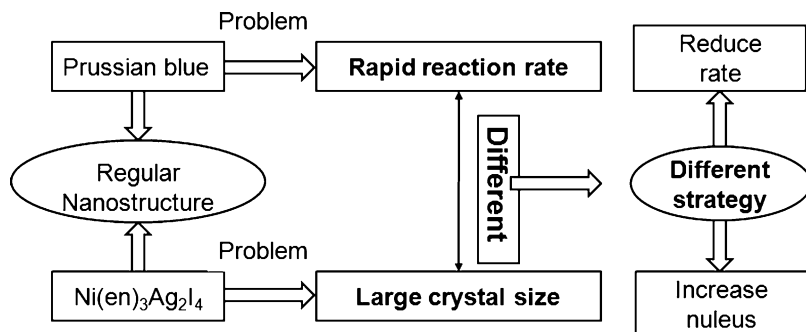
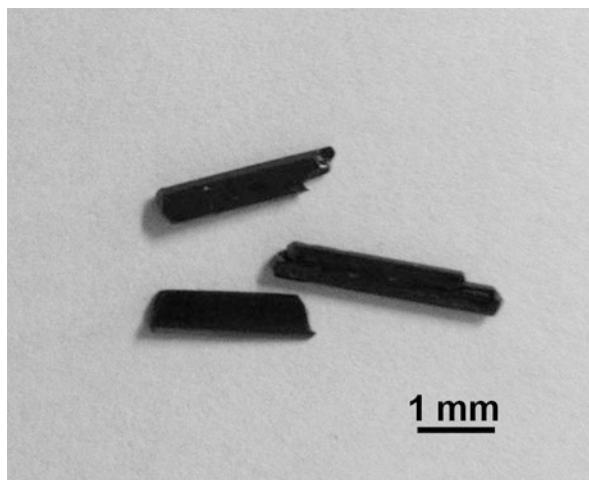


Fig. 5 The scheme of structure control design for PB and $\text{Ni}(\text{en})_3\text{Ag}_2\text{I}_4$

Too large size of single crystal will directly decrease the surface area of prepared film which leads to the lack of active sites for target reaction. Besides, the immobilization of material on support will also meet challenge if the size is too big. Therefore, if this material is expected to apply in electrochemistry, its size should be required to change smaller.

The Strategies of Structure Control

According to the abovementioned, both PB and $\text{Ni}(\text{en})_3\text{Ag}_2\text{I}_4$ encounter the same problem: how to control their structures to satisfy the requirements of electrochemical applications. However, due to the different types of these two materials, the solutions should be separately considered and designed as Fig. 5.

Reduction of PB Reaction Rate

As the above analysis, PB formation between reactive solutions is too rapid. To solve this problem, the principle of chemical reaction rate should be first comprehended. In the terms of reaction kinetics, the description of reaction rate has already been summarized by a classical equation [27]:

$$r = kC_A^{a_A}C_B^{a_B} \dots = k \prod_{i=1}^N C_i^{a_i} \quad (2)$$

where r represents one reaction rate; a_A and a_B represent the reaction order of components A and B, respectively; C_A and C_B are the concentrations of substances A and B, respectively; and k is the kinetic parameter of this reaction.

According to this equation, we can recognize that under the same reactive environment, the lesser the concentration of reactants, the slower the whole reaction rate. Now, the problem has altered to the reduction of the reactive concentration per unit time.

One common treatment is decrease of reactive solution concentration. Traditional PB preparation technologies, such as electrochemical deposition [28] and chemical deposition [29], both belong to rapid synthesis approaches. Although the reactive solution concentration can be reduced, the whole formation period is still very fast. Tremendous decrease may be possible, but not realistic. The concept of reactive concentration is description of the reactive molecule amount per volume. Therefore, from another understanding, decrease of the molecules per unit time to participate in this PB reaction process can also realize the goal.

If we presume the solution is a big collection of molecules, cutting half volume of original solution will obtain 50 % molecules. Ideally, through the continuous separation of solution volume, the satisfied amount can be harvested. Naturally, fog is consisted of numinous droplets with microsize to suspend in air [30]. Compared with rain, the size of fog droplet is much smaller. With this inspiration, if we change the reactive solution to “fog” in lab, the slow reaction rate may be expected.

Aerosol is a suspension of fine solid particles or liquid droplets in a gas [31]. It satisfies the requirement of the above hypothesis. Therefore, we designed to create the lab “fog” by aerosols for the formation of PB film-modified electrode. Ultrasonic vibration can be used to disperse the reactive liquids as microdroplets. $\text{Fe}(\text{CN})_6^{4-}$ and Fe^{3+} small aerosols with fewer molecules are then successively sprayed onto metal substrate for reaction. In this process, the aerosol volume can be greatly expanded, so the average amount of aerosol reached on electrode surface is very few. Moreover, due to the light weight of aerosols, they can suspend in the air which effectively avoids the influence of gravity for the uniform adsorption on substrate. Hence, it can eliminate the over-rapid formation of PB caused by the partially high concentration of reactive solution. According to the above characteristics of this method, the reaction rate is promising in realizing the reduction which is attributed by the fewer molecules in reaction per unit time.

Partially Rapid Crystallization of PB

Based on the description in the section of defect analysis, another way to realize the regular growth of PB is the control of partial crystallization. However, the common PB preparation methods, such as electrodeposition, chemical deposition, or self-assembly [32], are all uniform growth behaviors. The obtained film only exhibits a homogeneous state for every site of surface. Hence, if we want to break this uniform preparation, an extra force will be introduced to impel the crystal rapid accumulation on partial regions. It should be noticed that this force cannot be strong; otherwise, the whole film morphology will be totally changed instead of partial stimulation.

According to the reaction mechanism of PB which relies on the combination of cation Fe^{3+} and anion $[\text{Fe}(\text{CN})_6]^{4-}$, electric field may be an effective force to affect the common growth rule. The intensity should be weak to avoid the global influence. Besides the extra force, the selection of main synthesis approach must be carefully considered. Chemical reaction, electrodeposition, and self-assembly are the most applied preparation methods for PB-modified electrode. Ranking on the basis of particle size, self-assembly can obtain the smallest PB crystal to benefit the enhancement of performance. Moreover, due to the weak electric field intensity we adopted, if the reaction time is too rapid, the effects of external force may be hard to function. Consequently, we developed an electric field-assisted self-assembly to fulfill the PB preparation for its regular structure formation.

However, the amount of PB crystal nucleus prepared by self-assembly will still be huge. If all these cores keep the same distribution style at the beginning growth, the introduction of extra force will be useless for realization of partial rapid crystallization. Therefore, the key to success is how to produce different nucleus deposition environments on partial sites of substrate.

Increase of the $\text{Ni}(\text{en})_3\text{Ag}_2\text{I}_4$ Crystal Nucleus

The problems of crystal growth to PB and $\text{Ni}(\text{en})_3\text{Ag}_2\text{I}_4$ are opposite: with PB, we hope that its crystal can sufficiently grow on some sites; but to $\text{Ni}(\text{en})_3\text{Ag}_2\text{I}_4$, we prefer the limited and minified crystallization. Accordingly, strategies of preparation to these two materials should be distinguished.

At the beginning growth of crystal, nucleus formation is essential to donate the basement for the further crystallization. Normally, the size of completely grown crystal of electrode material is related to the amount of nucleus which initially formed on the substrate. More nucleuses can reduce the amount of accumulation source for each crystal to result in smaller size. However, this objective is not easy to be realized. Due to the newborn of this material, its preparation method is rare. According to literature reports, till now, only solvent thermal method can be applied to obtain the $\text{Ni}(\text{en})_3\text{Ag}_2\text{I}_4$ crystals. But this approach is mainly specific to powder synthesis instead of film; therefore, the amount and distribution of nucleus can hardly be adjusted during the whole process.

Since there is inability to minify crystal size through its free growth, an extra force can be also considered to introduce for the intervention of crystallization stage. As noted, electrochemical material is often immobilized on support electrode or other substrates for application. According to lots of researches, the surface state, such as roughness and element composition, is confirmed to be really important for the morphology, structure, and manner of crystal growth. Hence, maybe the surface modification method is possible to endow some functions of substrate for the in situ limited growth of $\text{Ni}(\text{en})_3\text{Ag}_2\text{I}_4$ crystals.

$\text{Ni}(\text{en})_3\text{Ag}_2\text{I}_4$ is composed by the complexation of $\text{Ni}(\text{en})_3^{2+}$ and AgI_2^- . Element Ni has already firmly combined with ethylenediamine (en); comparatively, Ag can more easily interact with some strongly electronegative group. Meanwhile, for a convenient application, formed crystal should be adhered on substrate surface. Accordingly, the modification agent can be selected to own both interaction abilities between substrate and Ag element. Normally, in the nano/microstructure control, metal substrate can make a promotion of the regular morphology formation [33, 34]. Here, the design scheme is clear: modifying an agent on metal support which owns the ability to strongly link metal and AgI_2^- . In the process of reaction between $\text{Ni}(\text{en})_3^{2+}$ and AgI_2^- , this agent can preferentially catch a large amount of AgI_2^- as a reactive site; then partial $\text{Ni}(\text{en})_3^{2+}$ will complex around these first arrived molecules. According to the adjustment of modified agent concentration, the nucleus quantity can be expected to be controlled.

Purposed Development of Novel Fabrication Method

Aerosol Deposition Approach for Nanocubic PB Formation

Methodology Process

On the basis of the above conception, the preparation scheme of aerosol preparation has been designed and illustrated in Fig. 6. Different with the direct reaction between $\text{K}_4\text{Fe}(\text{CN})_6$ and FeCl_3 solution of traditional preparation methods, developed aerosol deposition approach adds an extra step before reaction: transfer from reactive liquids to aerosols. 1.7 MHz frequency of ultrasonic vibration is implied to generate aerosols. In this experiment, we selected a bare platinum (Pt) electrode as a growth bed for aerosol adsorption. Due to the special interaction between Pt electrode and C atoms from $\text{K}_4\text{Fe}(\text{CN})_6$ molecules, $\text{K}_4\text{Fe}(\text{CN})_6$ was prior to be injected into an airtight container for free absorption on the substrate. Since the end of first injection, FeCl_3 aerosol was subsequently deposited to react with the already combined $\text{K}_4\text{Fe}(\text{CN})_6$ molecules. In this process, environment temperature and deposition time are control parameters of PB film synthesis. According to our previous study [35], deposition time is mainly affected by the amount of PB surface concentration and temperature determines the final structure of PB crystal. In this chapter, we mainly focus on the importance of new method design on purpose for the realization of self-organized nanostructure to electrochemical materials.

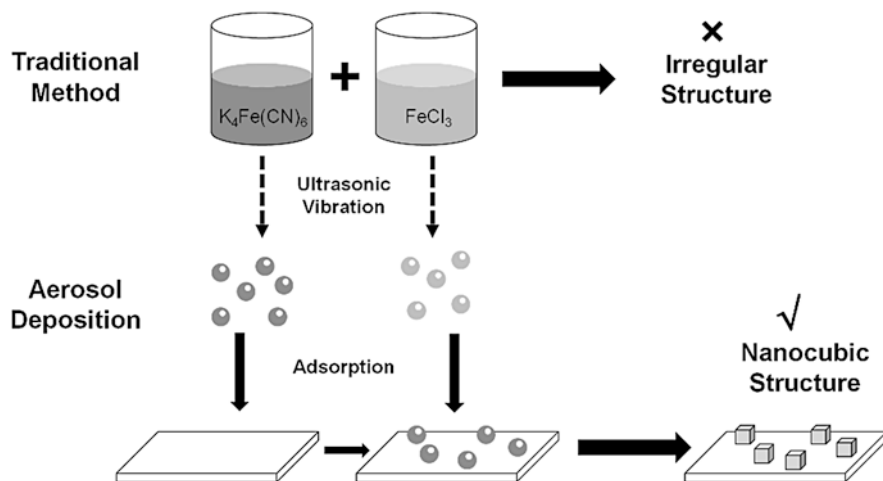


Fig. 6 Designed process of aerosol deposition approach for PB formation

Accordingly, the next contents are related to the comparisons of traditional and novel fabrication approaches on micromorphology and electrochemical properties dominated by nano/microstructure.

Nano/Microstructure Investigation

For convincing illustration, we selected electrodeposition approach which is mostly applied in PB film preparation as a contrasted method. In order to ensure the similar synthetic conditions, the following measures should be adopted:

1. Both preparations apply the same types and concentrations of reactive solutions.
2. The substrate electrodes are both bare Pt electrodes with the same pretreatment.
3. Both deposition temperatures should be kept the same.
4. The final surface concentrations of PB films prepared by two methods should be nearly same.

The process of electrodeposition is referred to Karyakin's work [36]. Pt electrode was dipped into the mixture solution of 0.1 M $K_4Fe(CN)_6$ and $FeCl_3$ with 0.01 M HCl. Cyclic voltammetry (CV) scanning between -0.2 and 0.4 V was implied for deposition. Since 300 cycles were fulfilled, the peak current value of PB film was nearly same with that prepared by aerosol deposition approach. The preparation parameters of aerosol deposition were set as 6 h, $35^\circ C$. According to the calculation of PB surface concentrations, electrodeposition and aerosol deposition can, respectively, form 6.54 and $6.82 \text{ nmol} \cdot \text{cm}^{-2}$ PB on Pt electrode surface. In this case, morphology comparison stands the equal altitude.

From the shapes of CV results (Fig. 7a), two PB electrodes prepared by different methods were different. The potential differences of redox peaks were 0.078 and

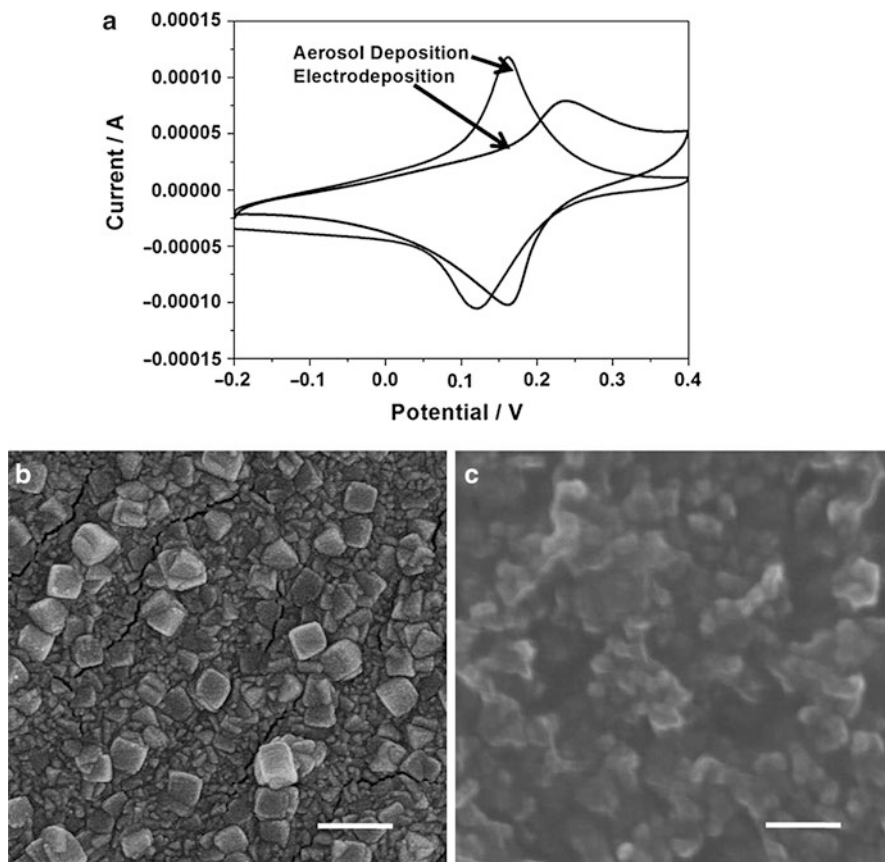


Fig. 7 CV diagrams (a) and FESEM images (b), (c) of PB-modified Pt electrodes, respectively, prepared by aerosol deposition [32] and electrodeposition

0.039 V for electrodeposition and aerosol deposition, respectively. This parameter can reveal the electron transfer rate of redox material, and the higher value illustrates stronger transfer resistance. Consequently, the result can be obtained that PB film prepared by aerosol deposition will own better ability for electrochemical signal transport. Due to the similar amounts of PB films, the difference of electrochemical performances should be attributed by the change of microstructures. Therefore, it is necessary to investigate the surface morphologies of two PB films.

As shown in Fig. 7b, c, although the synthesis solvents, material composition, and surface concentration are all the same, the morphologies of PB fabricated by different approaches caused absolute distinction. PB film synthesized by aerosol deposition can self-organize a cubic shape on Pt substrate, and the size of PB cube is ca. 250 nm. Besides some cubic crystals, other sites of film were composed of lots of edges which come from imperfect crystals. On the contrary, if

electrodeposition was adopted as the synthesis method, instead of regular structure, only nanoparticles can be observed on electrode surface. Moreover, the irregular aggregation behavior is more obvious. What causes these differences?

Compared with the preparation time of two methods, whole aerosol deposition should consume 6 h, and CV electrodeposition only required half an hour. In the terms of crystallography [24], rapid reaction will tend to harvest more crystal nucleuses. The application of rapid preparation method such as electrodeposition could lead to the tight distribution of nucleuses on substrate in the beginning. With the prolonging crystallization, each crystal obtains slow growth due to the average distribution of reacted formation onto lots of nucleuses. Therefore, the film surface is consisted of the accumulation of small-sized particles. But this is a difficult manner in realizing the regular structure which is mainly caused by the too many nucleuses at the first step. Differently, aerosol deposition initially provides a slow formation rate, which relies on the transformation of liquid to aerosol. Thus, the formation of PB nucleuses on substrate will be much fewer. Under the same prepared amount, the formed PB can assemble, surrounding only few cores. This can ensure abundant space and amount to crystallize for regular structure formation. Thereby, the above evidences can demonstrate the importance of targeted approach design to morphology construction.

Performance Characterization

In order to exhibit the advances of regular nanostructure, electrochemical performance was characterized. PB possesses a strong selectivity to and electrocatalysis abilities for hydrogen peroxide (H_2O_2) [37]; hence, it is widely named “artificial hydrogen peroxidase” by researchers [38]. Here, we also applied H_2O_2 as a target to evaluate the competences of PB films prepared by aerosol deposition and electrodeposition.

Electrocatalytic performances of PB films were tested by chronoamperometry technology. In this detection process, H_2O_2 solution of 0.01 mM concentration was continuously added in the phosphate buffer system at each 80 s. Electrochemical workstation can receive the current signal from PB-modified electrode by reduction of H_2O_2 . According to linear fitting of chronoamperometry data, the sensitivity which is an important parameter to represent the electrocatalytic ability can be calculated. As shown in Fig. 8, for each addition of H_2O_2 , the response strength of regular PB nanostructure based film is much higher than irregular PB film. For more clarity, the values of sensitivity were analyzed as 1309.8 and 535.5 $\mu\text{A} \cdot \text{mM} \cdot \text{cm}^{-2}$ for PB films synthesized by aerosol deposition and electrodeposition, respectively. Obviously, the performance of PB electrode fabricated by aerosol deposition owns more than two times of that prepared by electrodeposition. However, the amounts of PB formed on substrates were nearly same, but the electrocatalytic abilities were really different. This should be attributed to the structure differences. According to the mechanism analysis in H_2O_2 catalytic reaction, for nano- or micromaterials, the edges of their geometrical configurations can arouse stronger catalytic activity than other sites [39]. Compared with the morphologies of PB films in Fig. 6b, c, aerosol deposition can produce a film surface with abundant nanocubes. They own perfect

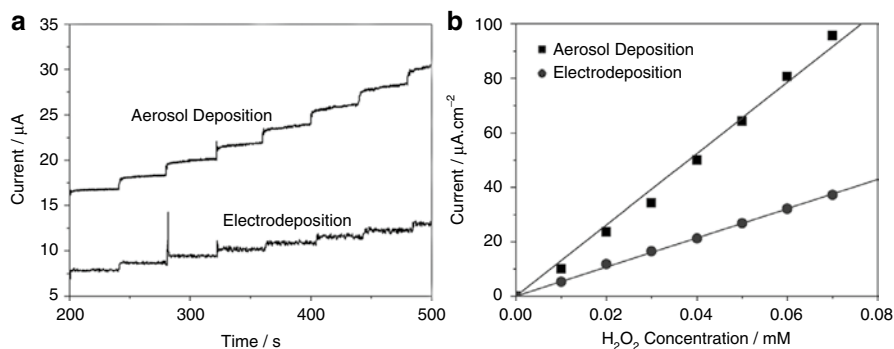


Fig. 8 (a) Chronoamperometry data of PB-modified electrodes prepared by aerosol deposition and electrodeposition; (b) linear fitted diagram to chronoamperometry results

and long edges to consist an ideally regular structure. Besides the cubes, the ground film is consisted of lots of broken crystals which can also provide edges. On the contrary, there are rare regular crystals with no edges for the film prepared by electrodeposition. Therefore, not only the actively catalytic sites decrease, but also the surface area is much less. Surely, the performances of PB films prepared by different approaches are quite different.

According to the above evidences, the advantages of performance enhancement by regular nanostructure formation have been shown.

Electric Field-Induced Self-Assembly for Double Structures of PB Formation

Methodology Process

With the purpose of rapid crystallization on partial sites, a novel PB preparation strategy – electric field-induced self-assembly – has been designed. The main synthesis process is similar as the traditional self-assembly method [40]. Two reactive solutions of $\text{K}_4[\text{Fe}(\text{CN})_6]$ and FeCl_3 were prepared as certain concentration and pH value, respectively. Deionized water was served as a cleaner to remove the redundant solutions after each dip-coating. The difference is the addition of electric field generation system [41]. Bare platinum foil electrodes were selected as the electric field producer. These two electrode surfaces are kept parallel to make the field line vertical (shown in Fig. 9). Hence, reactive ions can move along the field direction to arrive on electrode surface. The time of dip-coating in reactive solution was set to 60 s which referred to our previous investigation results [32]. Since electrodes finished the dipping following the orders $\text{K}_4[\text{Fe}(\text{CN})_6]$, deionized water, FeCl_3 , and deionized water, a cycle has ended (Fig. 9). Normally, a whole preparation process requires multiple cycles. The standard can be evaluated by the characterizations of electrochemistry and microscopy technologies.

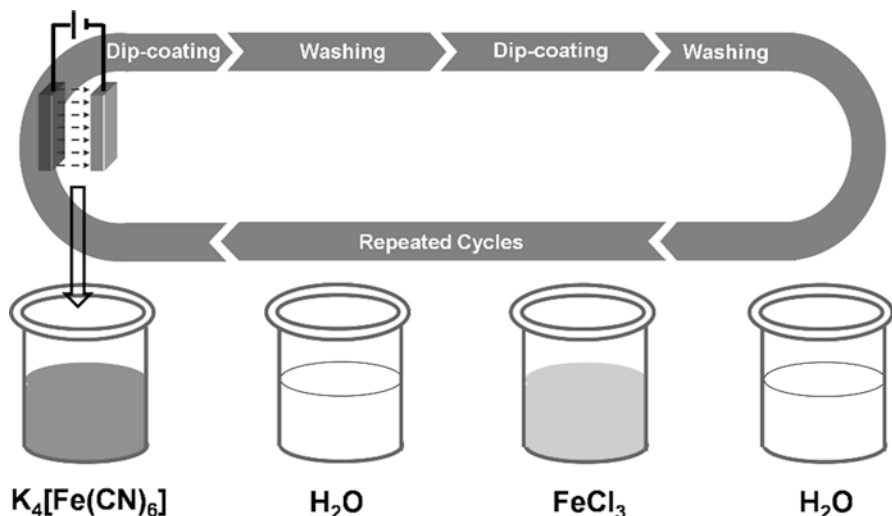


Fig. 9 Designed process of electric field-assisted self-assembly approach for PB formation

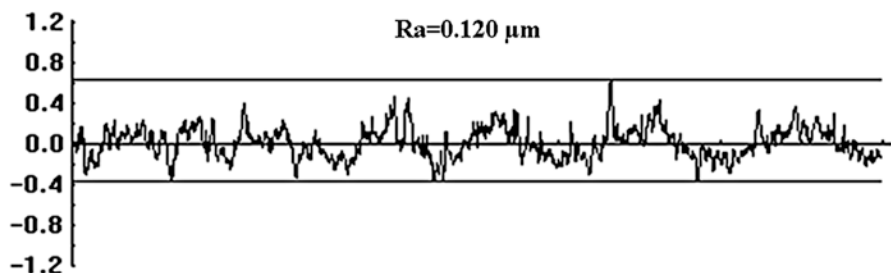


Fig. 10 The roughness characterization result of polished Pt electrode surface

Nano/Microstructure Investigation

In order to realize the heterogeneous growth, initially, the substrate should be pre-treated to provide the different environments for PB crystal nucleus formation. The Pt electrode was repeatedly polished by a metallographic abrasive paper which can cause a coarse surface for crystal deposition. As shown in Fig. 10, the roughness state of polished substrate can be monitored by surface roughness measuring instrument. Since the polishing finished, lots of “ravines” which will benefit the formation and accumulation of crystal nucleuses can be produced on metal surface. Meanwhile, in consideration of the regular distribution of formed crystals, a uniform distribution of cavities is also preferable. According to the illustration in Fig. 10, the average roughness of substrate surface is 0.12 μm . This depth is big enough to promote the rapidly together assembly of numerous cores at the initial PB formation. Oppositely, on the even sites, the formation of PB nucleus could be much slower and fewer. Therefore, at the beginning, the distinction of nucleus growth occurs due

to the different growth environments. Moreover, under the stimulation of electric field, this distinction will be widened with the prolonging deposition cycles. Electric field can arouse the travel of reactive ions. Crystal growth would like to stack on already formed nucleus. Bigger nucleus can offer more combination sites for further growth. Just like the snowball effect, the difference of crystal grown on coarse and even surface will be more and more obvious; hence, hierarchical growth has happened. In order to demonstrate the above deduction, self-assembled PB films induced by electric field or not were respectively characterized by FESEM. Here, the applied field was weak – only 125 V/m – and the assembled cycles were kept the same: 40 layers.

As shown in Fig. 10, introduction of electric field has brought a huge change of PB film. Just using self-assembly, it obtained a uniform and smooth film surface. This film is consisted of tight irregular particles with the size of ca. 50 nm. Moreover, the boundary of each particle was vague, and the whole surface looks like an integral plane instead of fluctuation. However, if a lasting electric field was implied on the preparation process, lots of regular cubes were observed on film surface, and the size of each cube was ca. 1.5 μm [41]. The distribution of PB cubes was considerably uniform. Every 5 μm distance, one cube was observed. During further magnification of scanning area, besides the well-defined cubic structure, the bottom film was very coarse. Small particles were aggregated toward the direction which was vertical to the film plane, shown as a mastoid-like shape. These behaviors can demonstrate that electric field owns an oriented force to push the crystal growth along its field direction. This external force can also enhance the hierarchical growth of PB crystals due to the coarse substrate by pretreatment. Surely, compared with the PB-modified electrode prepared by traditional self-assembly, performance must be changed because of this special film structure.

Performance Characterization

According to lots of literatures, the morphology of material surface owns essential effects on electrochemical performance [42, 43]. Therefore, firstly, CV method was also adopted to investigate the series of film properties. As shown in Fig. 12a, the redox peaks of PB prepared by electric field-induced self-assembly were much higher than that without electric field. This result illustrates that the introduction of extra force can obviously promote the formation of PB. Under the lasting function of electric field, reactive ions will crowd around the work electrode which leads to the sudden enhancement of partial solution concentration to accelerate its reaction. The potential differences of redox peaks which belonged to electric field addition or not were, respectively, calculated as 0.0919 and 0.0483 V. Only from the above data, it seems that using electric field excitation will cause an increase of electron transfer resistance. However, in consideration of the possible catalysis improvement due to the high PB amount, which preparation approach owns better performance should be further investigated.

The current responses to H_2O_2 additions for two types of PB films were characterized by chronoamperometry tests. Relevant results were linear fitted as the relations between current signals and H_2O_2 concentration (Fig. 12). For each addition of

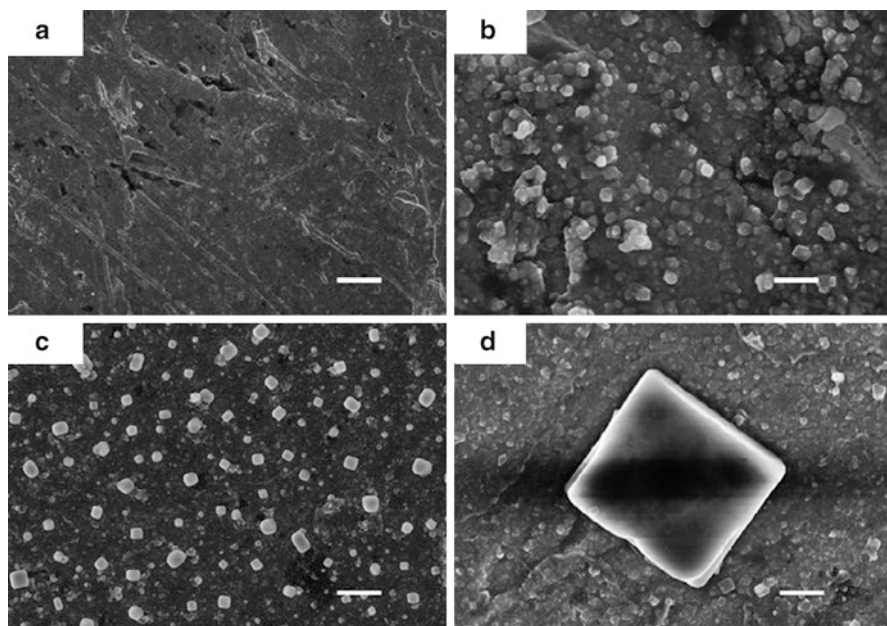
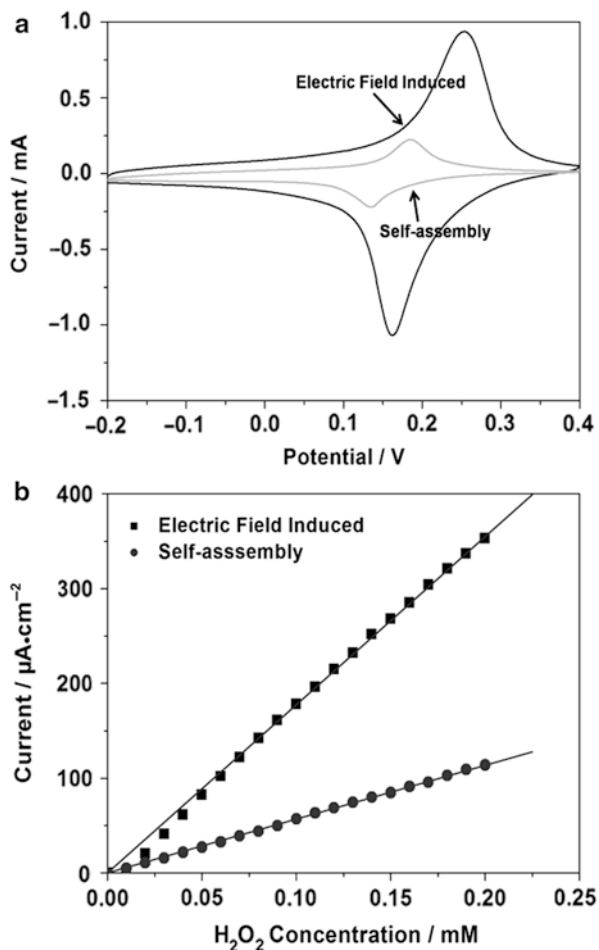


Fig. 11 FESEM images of PB films prepared by (a), (b) self-assembly and (c), (d) electric field (125 V/m)-induced self-assembly

H_2O_2 , the current change for electric field preparation was much higher than only self-assembly preparation. According to calculation, the sensitivities of PB films synthesized with electric field or not were 1774.3 and $568.2 \mu\text{A} \cdot \text{mM} \cdot \text{cm}^{-2}$, respectively. The performance has increased nearly two times since the assistance of electric field in preparation. It is mainly dependent on the special film structure in microscale. As in the analysis of film morphology in Fig. 11, the electric field-prepared film owns double different structures of PB: one is microcube and another is nanomastoid. The regular shape has been demonstrated to own strong catalytic ability because of the perfect edge supplement. These structure-based crystals can produce huge amount of catalytic electrons. Moreover, the isolate distribution style of each cube can also increase the contact area of H_2O_2 solution as the function collection of many microelectrodes obviously improve the total performance. It should be noted that the ground film was consisted of lots of nanomastoids which were of large surface area. In this case, the produced electrons can be rapidly transferred through this wide route. Although the electron transfer resistance of electric field-prepared film was stronger according to the above CV results, however, higher catalytic ability can not only offset this deficiency but also improve the performance effectively. Hence, the final H_2O_2 detection performance has obtained tremendous enhancement. Also, the targeted design of novel preparation approach has shown its effective and important function in the control of self-organized PB nano/microstructure.

Fig. 12 (a) CV diagrams of PB films prepared by electric field-induced self-assembly and just self-assembly; (b) chronoamperometry results of the above two PB films



Interfacial Molecule-Induced Approach for Hybrid Film Formation

Methodology Process

In order to realize the reduction in crystal size of $\text{Ni}(\text{en})_3\text{Ag}_2\text{I}_4$, different with the demand of PB structure controlling, novel synthesis strategy should be again designed.

The preparation of hybrid mother solution of $\text{Ni}(\text{en})_3\text{Ag}_2\text{I}_4$ was described in the literature [17]. As a brief, silver nitrate dissolving in DMF was firstly added to a saturated potassium iodide solution in DMF to yield a KAgI_2 solution. Subsequently, nickel nitrate was added to 1,2-ethylenediamine solution and then mixed with the as-prepared KAgI_2 solution. To realize the controllable regulation on the crystal

size, here special treatment toward the hybrid solution was needed. Firstly, the hybrid solution was heated to 80 °C and kept for 72 h and then 100 °C for 24 h and finally cooled slowly to the room temperature. This process was essential and critical during the synthesis of the desired hybrid crystals, during which more crystal nucleuses were prone to form in the mother solution and simultaneously the growth rate of the nuclei was improved, forming a facile method to regulate both the dimension and growth rate of the hybrid crystal.

Organic self-assembled monolayers (SAMs) were usually introduced to modify the various substrates for the growth of versatile films [44–51]. According to reported research [49–51], the interfacial SAMs might provide more binding sites for crystal nucleus formation and even induce the orientation growth of formed film, which was mainly dependent on the conformation of the adopted molecules. Here, a SAM of 1,4-benzenedithiol molecule was adopted on account of its interaction abilities with Ag and metal substrate [52–54]. One thiol group at the terminal of the SAM was anchored onto the gold substrate via the covalent bond of Au–S, while the other thiol group would bind with Ag ions in the hybrid crystal. Moreover, another advantage of this method should be noticed: because of the rigid backbone and relatively aligned monolayer, the thiol groups at the free terminal of SAM were deemed to orient along some special orientation [47, 48]; therefore, the binding of thiol groups with Ag⁺ may enable crystal growth only along this direction to give the highly oriented hybrid films, which is schematically illustrated in Fig. 13.

To get a satisfactory SAM on the substrate, prior to the modification of SAM, the gold substrate was polished with alumina slurry and then sonicated with water and electrochemically cleaned by cycling between –0.3 and 1.55 V versus Ag/AgCl in 0.5 M H₂SO₄ until a stable voltammogram was obtained [55]. The freshly cleaned gold substrate was immersed in the 1,4-benzenedithiol solution for different times (e.g., 2, 6 and 10 h) to form the SAM, which was followed by rinsing with sufficient ethanol.

Finally, after removing the sediment formed in the hybrid mother solution using the filter membrane, the SAM-modified gold substrate was dipped vertically into the hybrid filtrate and crystallized at 25 °C.

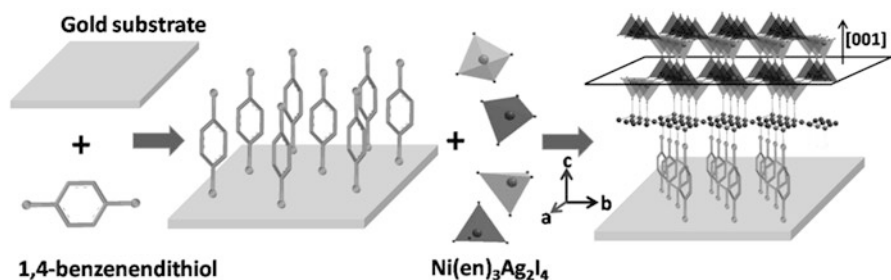


Fig. 13 Schematic illustration for the oriented growth of hybrid films on gold substrates modified with the SAM of 1,4-benzenedithiol. Hybrid crystals grow in some special direction

Nano-/microstructure Investigation

As shown in Fig. 14a, a highly integrated and uniform hybrid film, composing of the hexagonal prism-shaped crystals, was obtained on the gold substrate which was modified with 1,4-benzenedithiol SAM. For this oriented hybrid film, only two Bragg reflections indexed as (002) and (004) exhibited in the XRD profile (Fig. 14c), indicating that the fabricated hybrid film was highly oriented along the crystallographic [001] direction. In contrast, in the absence of 1,4-benzenedithiol SAM, bare gold substrate was also served for the growth of hybrid films. As shown in Fig. 14b, the hybrid film with disordered structure was obtained on the bare gold substrates. In this condition, it is noted that crystals with various sizes were obtained, and particularly the XRD showed no crystallographic orientation (Fig. 14d). It is obvious that the formed SAM induced the oriented and uniform growth of hybrid film on the gold substrate.

In addition, the effect of surface coverage of SAM molecules on the morphologies of hybrid film was explored. With the gold substrates immersing into the SAM solution for 2, 6, and 10 h, respectively, the density of hybrid films changed accordingly (Fig. 15). A sparse hybrid film was created when the assemble time was short (Fig. 15a), while a crowded film was harvested with a longer time (Fig. 15c).

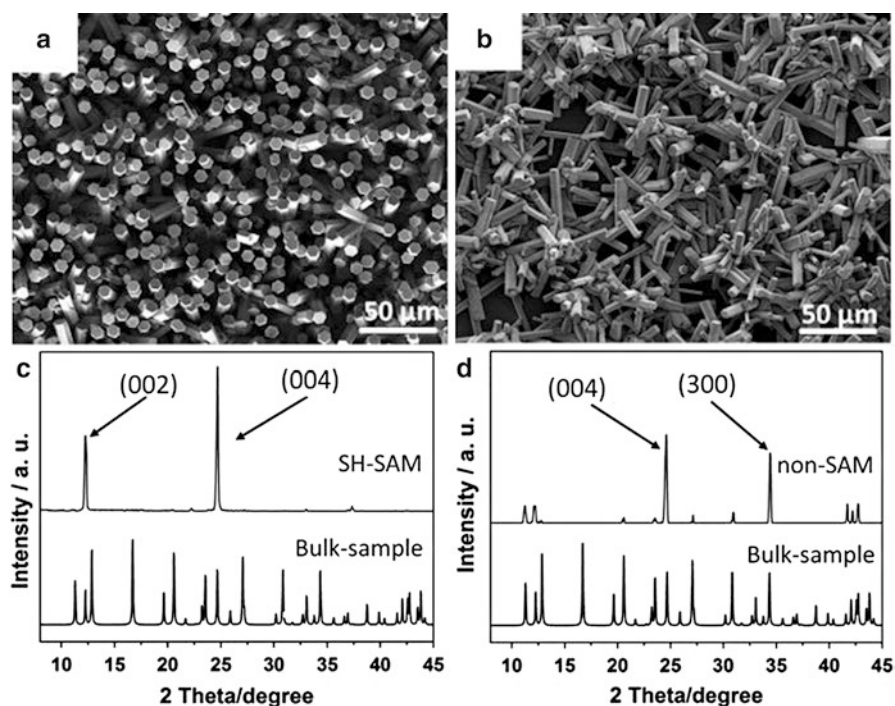


Fig. 14 (a), (b) FESEM images of hybrid films with distinct morphologies grown on the gold substrate modified with 1,4-benzenedithiol SAM and bare gold substrate, respectively. (c), (d) X-ray diffraction patterns corresponding to (a), (b)

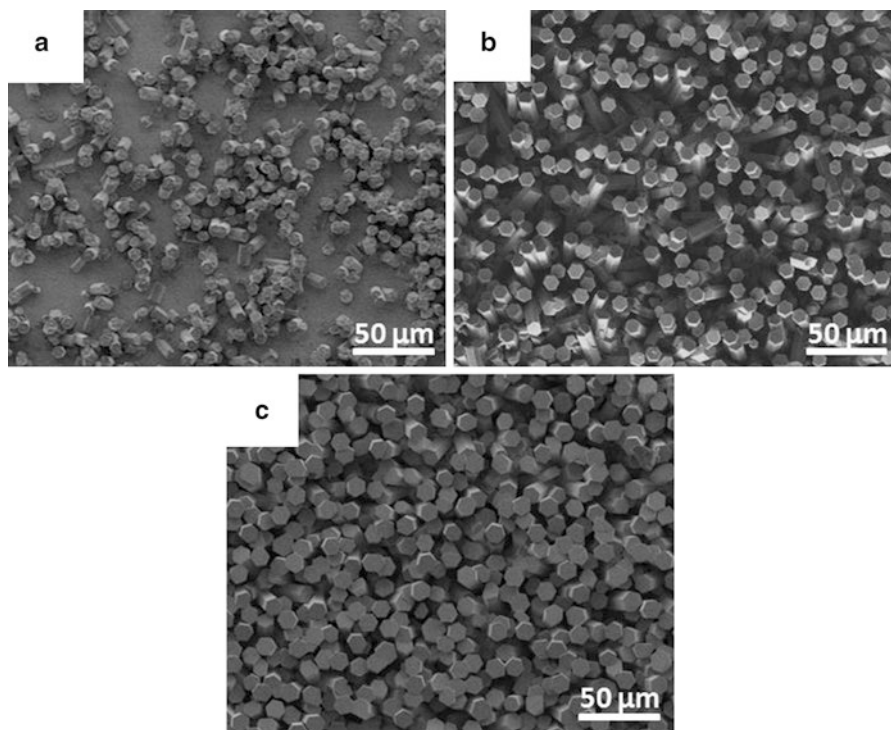


Fig. 15 Hybrid films with various distribution densities on the gold substrates modified with the 1,4-benzenedithiol solution for (a) 2 h, (b) 6 h, and (c) 10 h, respectively

With an appropriate assembled time of 6 h, homogenous film was prepared with each microcrystal separated at a proper distance (Fig. 15b).

In summary, as the thiol groups at the free terminal of 1,4-benzenedithiol SAM molecules are considered to orient along [001] [50, 51], the binding of thiol groups with Ag ions in hybrid crystals will enable crystal growth only along the [001] direction to produce the highly oriented hybrid film. Meanwhile, a higher coverage of the SAM would provide more binding sites, resulting in the formation of a more crowded hybrid film. In addition, because there was no agent on the bare gold substrates to induce the oriented growth of hybrid crystals, disordered hybrid films were obtained subsequently. Particularly, in the absence of the binding strength arising from the SAM, the obtained hybrid film was prone to peel from the gold surfaces.

Performance Characterization

Due to the unique framework of $[\text{Ag}_2\text{I}_4]^{2-}$, two novel properties of photons and electronics were observed on this hybrid material. One fascinating feature was a high chemical stability in a phosphate buffer saline (PBS, pH=6.8–7.8), and the other was a robust resistance to ambient illumination compared with silver iodide (AgI).

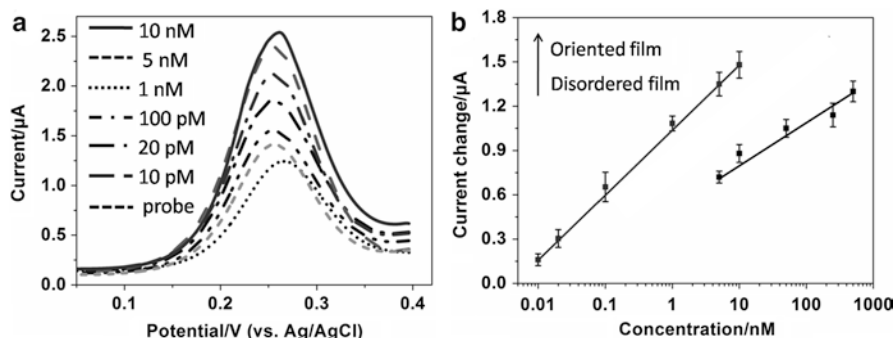


Fig. 16 (a) SWVs of 5 mM $K_3Fe(CN)_6$ at the oriented hybrid film after hybridization with complementary targets of various concentrations. (b) Calibration sensitivity curves based on hybrid films with different morphologies fabricated on bare gold substrates and SAM-modified gold substrates, respectively

Especially, due to regularly distributed Ag ions on the hybrid framework, the hybrid material could serve as a promising platform for the controllable immobilization of thiolated biomolecules through Ag–S bonds [56], which would facilitate the distribution of biomolecules.

Based on the proposed hybrid films, a label-free electrochemical DNA biosensor was prepared for the assay of an oligonucleotide fragment of the avian flu virus H_5N_1 . As expected, a significantly ultralow detection limit of 5 pM with a wide linear response from 10 pM to 10 nM, as well as excellent selectivity, good regeneration, and high stability, was observed on the highly oriented hybrid film (Fig. 16). As a comparison, in the condition of disordered hybrid film, a higher detection limit of 4 nM was obtained. It needs to be mentioned that the highly oriented hybrid film would improve immobilization sites for the DNA probes, provide more interfacial reaction positions, and make the molecules easily accessible to electrode surface. All these merits of the highly oriented hybrid film contribute to the ultrasensitive detection limit of 5 pM, which is significantly lower than that of disordered hybrid film. The above performance results exhibit the function promotion arising from microstructure adjustment through the approach design [57].

Conclusions

In this chapter, focused on the difficulties of traditional methods in nano/microstructure control for electrochemical materials, we have provided a strategy route to break this obstruction:

1. Investigating the main reasons of hard structure control of each electrochemical material
2. Searching the key parameters which strongly affect the structure establishment in material preparation

3. Designing a novel synthesis approach to control the above key parameters
4. Checking the nano/microstructure by microscopy techniques
5. Demonstrating whether the performance enhancement is related by the realization of self-organized regular structure

Based on the above route, two different types of electrochemical materials, PB and $\text{Ni}(\text{en})_3\text{Ag}_2\text{I}_4$, were served as samples to confirm the validity of this design thought. In consideration of the different challenges for each material on self-organized structure, different strategies were adopted. Two novel PB preparation techniques, aerosol deposition approach and electric field-induced self-assembly, both successfully realized the goals of structure control based on the principles of reduction of whole reaction rate and acceleration of partial crystallization rate, respectively. For $\text{Ni}(\text{en})_3\text{Ag}_2\text{I}_4$, we applied an interfacial molecule-induced approach to also obtain an oriented microarray structure with size minimization. All as-prepared PB or $\text{Ni}(\text{en})_3\text{Ag}_2\text{I}_4$ films of regular nano/microstructure exhibited a superior electrochemical performance which further confirmed the powerful advantage of this design concept in material structure control. We expect that the description of this chapter can give an assistance and inspiration in the microstructure design and synthesis approach development of materials.

Acknowledgment This work was supported by the Innovative Research Team Program by the Ministry of Education of China (No. IRT13070) and the Doctoral Fund of Ministry of Education of China (No. 20113221110001) and is a project funded by the Priority Academic Program Development of Jiangsu Higher Education Institutions (PAPD).

References

1. Meier J, Schiøtz J, Liu P et al (2004) Nano-scale effects in electrochemistry. *Chem Phys Lett* 390(4-6):440–444
2. Bockris JO'M (2000) *Modern electrochemistry 2B: electrocatalysis in chemistry, engineering, biology and environmental science*. Kluwer/Plenum, New York
3. O'Regan B, Grätzel M, Fitzmaurice D (1991) Optical electrochemistry I: steady-state spectroscopy of conduction-band electrons in a metal oxide semiconductor electrode. *Chem Phys Lett* 183(1-2):89–93
4. Trasatti S (1991) Physical electrochemistry of ceramic oxides. *Electrochim Acta* 36(2): 225–241
5. Schindler W, Kirschner J (1997) Ultrathin magnetic films: electrochemistry versus molecular-beam epitaxy. *Phys Rev B* 55(4):1989–1996
6. Ohzuku T, Ueda A, Nagayama M (1993) Electrochemistry and structural chemistry of LiNiO_2 ($R\bar{3}m$) for 4 volt secondary lithium cells. *J Electrochem Soc* 140(7):1862–1870
7. Stupp SI (2005) Introduction: functional nanostructures. *Chem Rev* 105(4):1023–1024
8. Guo Y, Hu Y, Sigle W et al (2007) Superior electrode performance of nanostructured mesoporous TiO_2 (anatase) through efficient hierarchical mixed conducting networks. *Adv Mater* 19(16):2087–2091
9. Yu A, Liang Z, Cho J et al (2003) Nanostructured electrochemical sensor based on dense gold nanoparticle films. *Nano Lett* 3(9):1203–1207
10. Bisquert J (2008) Physical electrochemistry of nanostructured devices. *Phys Chem Chem Phys* 10:49–72

11. Adams RN (1969) *Electrochemistry at solid electrodes*. Marcel Dekker, New York
12. Fulop GF, Taylor RM (1985) Electrodeposition of semiconductors. *Ann Rev Mater Sci* 15:197–210
13. Gurrappa I, Binder L (2008) Electrodeposition of nanostructured coatings and their characterization—a review. *Sci Technol Adv Mat* 9(4):43001–43011
14. Li Y, Shi G (2005) Electrochemical growth of two-dimensional gold nanostructures on a thin polypyrrole film modified ITO electrode. *J Phys Chem B* 109(50):23787–23793
15. Gou L, Murphy CJ (2005) Fine-tuning the shape of gold nanorods. *Chem Mater* 17(14):3668–3672
16. Chu Z, Liu Y, Jin W et al (2009) Facile fabrication of a Prussian blue film by direct aerosol deposition on a Pt electrode. *Chem Commun* 24:3566–3567
17. Jiang YS, Yao HG, Ji SH et al (2008) New framework iodoargentates: $M(en)_3Ag_2I_4$ ($M=Zn, Ni$) with tridymite topology. *Inorg Chem* 47(10):3922–3924
18. Razmi H, Mohammad-Rezaei R, Heidari H (2009) Self-assembled Prussian blue nanoparticles based electrochemical sensor for high sensitive determination of H_2O_2 in acidic media. *Electroanalysis* 21(21):2355–2362
19. Ricci F, Palleschi G, Yigzaw Y et al (2003) Investigation of the effect of different glassy carbon materials on the performance of Prussian blue based sensors for hydrogen peroxide. *Electroanalysis* 15(3):175–182
20. Haghghi B, Nikzad R (2009) Prussian blue modified carbon ionic liquid electrode: electrochemical characterization and its application for hydrogen peroxide and glucose measurements. *Electroanalysis* 21(16):1862–1868
21. Ludi A (1981) Prussian blue, an inorganic evergreen. *J Chem Educ* 58(12):1013
22. Robin MB (1962) The color and electronic configurations of Prussian blue. *Inorg Chem* 1(2):337–342
23. Itaya K, Akahoshi H, Toshima S (1982) Electrochemistry of Prussian blue modified electrodes: an electrochemical preparation method. *J Electrochem Soc* 129(7):1498–1500
24. Muller G, Metois J, Rudolph P (eds) (2004) *Crystal growth—from fundamentals to technology*. Elsevier, Amsterdam
25. Ulrich J, Strege C (2002) Some aspects of the importance of metastable zone width and nucleation in industrial crystallizers. *J Cryst Growth* 237–239(3):2130–2135
26. Debe MK (2012) Electrocatalyst approaches and challenges for automotive fuel cells. *Nature* 486:43–51
27. Laidler KJ (1979) *Theories of chemical reaction rates*. R. E. Krieger, Michigan
28. Itaya K, Uchida I, Neff VD (1986) Electrochemistry of polynuclear transition metal cyanides: Prussian blue and its analogues. *Acc Chem Res* 19(6):162–168
29. Ricci F, Palleschi G (2005) Sensor and biosensor preparation, optimisation and applications of Prussian blue modified electrodes. *Biosens Bioelectron* 21(3):389–407
30. Gulpepe I (ed) (2007) *Fog and boundary layer clouds: fog visibility and forecasting*. Springer, Berlin
31. Hinds WC (1999) *Aerosol technology: properties, behavior, and measurement of airborne particles*. Wiley, Hoboken
32. Liu Y, Chu Z, Jin W (2009) A sensitivity-controlled hydrogen peroxide sensor based on self-assembled Prussian blue modified electrode. *Electrochem Commun* 11(2):484–487
33. Zhang J, Huang M, Ma H et al (2007) High catalytic activity of nanostructured Pd thin films electrochemically deposited on polycrystalline Pt and Au substrates towards electro-oxidation of methanol. *Electrochem Commun* 9(6):1298–1304
34. Lao C, Liu J, Gao P et al (2006) ZnO nanobelt/nanowire schottky diodes formed by dielectrophoresis alignment across Au electrodes. *Nano Lett* 6(2):263–266
35. Chu Z, Zhang Y, Dong X et al (2010) Template-free growth of regular nano-structured Prussian blue on a platinum surface and its application in biosensors with high sensitivity. *J Mater Chem* 20:7815–7820
36. Karyakin A, Puganova E, Bolshakov I et al (2007) Electrochemical sensor with record performance characteristics. *Angew Chem Int Edit* 119(40):7822–7824

37. Karyakin A (2001) Prussian blue and its analogues: electrochemistry and analytical applications. *Electroanalysis* 13(10):813–819
38. Chu Z, Shi L, Liu Y et al (2013) In-situ growth of micro-cubic Prussian blue-TiO₂ composite film as a highly sensitive H₂O₂ sensor by aerosol co-deposition approach. *Biosens Bioelectron* 47(15):329–334
39. Zeis R, Lei T, Sieradzki K et al (2008) Catalytic reduction of oxygen and hydrogen peroxide by nanoporous gold. *J Catal* 253(1):132–138
40. Millward RC, Madden CE, Sutherland I et al (2001) Directed assembly of multilayers—the case of Prussian blue. *Chem Commun* 19:1994–1996
41. Chu Z, Shi L, Zhang Y et al (2011) Hierarchical self-assembly of double structured Prussian blue film for highly sensitive biosensors. *J Mater Chem* 21:11968–11972
42. Johansson A, Widenkvist E, Lu J et al (2005) Fabrication of high-aspect-ratio Prussian blue nanotubes using a porous alumina template. *Nano Lett* 5(8):1603–1606
43. Puganova E, Karyakin A (2005) New materials based on nanostructured Prussian blue for development of hydrogen peroxide sensors. *Sens Actuators B* 109(1):167–170
44. Pham T, Kim H, Yoon K (2011) Growth of uniformly oriented silica MFI and BEA zeolite films on substrates. *Science* 334:1533–1538
45. Shibata T, Fukuda K, Ebina Y, Kogure T, Sasaki T (2008) One-nanometer-thick seed layer of unilamellar nanosheets promotes oriented growth of oxide crystal films. *Adv Mater* 20(2):231–235
46. Hermes S, Schroder F, Chelmoski R, Wöll C, Fischer RA (2005) Selective nucleation and growth of metal-organic open framework thin films on patterned COOH/CF₃-terminated self-assembled monolayers on Au(111). *J Am Chem Soc* 127(40):13744–13745
47. Liu B, Shekha O, Arslan HK, Liu JX, Wöll C, Fischer RA (2012) Enantiopure metal–organic framework thin films: oriented SURMOF growth and enantioselective adsorption. *Angew Chem Int Ed* 51(3):807–810
48. Yusenko K, Meilikhov M, Zacher D, Wieland F, Sternemann C, Stammer X, Ladnorg T, Wöll C, Fischer RA (2010) Step-by-step growth of highly oriented and continuous seeding layers of [Cu₂(ndc)₂(dabco)] on bare oxide and nitride substrates. *Cryst Eng Comm* 12:2086–2090
49. Biemmi E, Scherb C, Bein T (2007) Oriented growth of the metal organic framework Cu₃(BTC)₂(H₂O)₃•xH₂O tunable with functionalized self-assembled monolayers. *J Am Chem Soc* 129(26):8054–8055
50. Schoedel A, Scherb C, Bein T (2010) Oriented nanoscale films of metal–organic frameworks by room–temperature gel-layer synthesis. *Angew Chem Int Ed* 49(40):7225–7228
51. Scherb C, Schoedel A, Bein T (2008) Directing the structure of metal–organic frameworks by oriented surface growth on an organic monolayer. *Angew Chem Int Ed* 47(31):5777–5779
52. Love JC, Estroff LA, Kriebel JK, Nuzzo RG, Whitesides GM (2005) Self-assembled monolayers of thiolates on metals as a form of nanotechnology. *Chem Rev* 105(4):1103–1169
53. Flink S, van Veggel FCJM, Reinhoudt DN (2000) Sensor functionalities in self-assembled monolayers. *Adv Mater* 12(18):1315–1328
54. Reed MA, Zhou C, Muller CJ, Burgin TP, Tour JM (1997) Conductance of a molecular junction. *Science* 278:252–254
55. Zhang J, Song SP, Wang LH, Pan D, Fan CH (2007) A gold nanoparticle-based chronocoulometric DNA sensor for amplified detection of DNA. *Nat Protoc* 2:888–8895
56. Peng HI, Strohsahl CM, Leach KE, Krauss TD, Miller BL (2009) Label-free DNA detection on nanostructured Ag surfaces. *ACS Nano* 3(8):2265–2273
57. Shi L, Chu Z, Dong X et al (2013) A highly oriented hybrid microarray modified electrode fabricated by a template-free method for ultrasensitive electrochemical DNA recognition. *Nanoscale* 5:10219–10225

Application of Two-Dimensional Heisenberg Model to Electrochemical Nucleation Theory

32

Serghei A. Baranov

Contents

Introduction.....	1058
Statistical Model of Heisenberg.....	1059
Thermodynamic Analyze.....	1062
Electrochemical Nucleation.....	1063
Kinetic of the Nucleation Process.....	1065
Conclusions.....	1066
Appendix A.....	1067
References.....	1067

Abstract

The kinetic model of electrochemical nucleation of micro- and nanoparticles is studied. The functional dependence of probability of the energy of the particle on the relative radius found earlier is used in nucleation in the statistical Heisenberg model. On the basis of the proposed theory, a simple ratio for calculation of probabilities of kinetic processes is obtained for the case of electrochemical nucleation.

Keywords

Electrochemistry nucleation • Cylindrical nanoparticles • Phase transitions • Phase transitions • Surface energy

S.A. Baranov (✉)
Institute of Applied Physics AS RM, Chisinau, Moldova
Dnester University, Tiraspol, Moldova
e-mail: baranov@phys.asm.md; sabaranov07@mail.ru

Introduction

The control of the dimensions of the particles and layers of particles in the electrochemical processes is one of the basic problems of the various forms of electrochemical technologies. The transition from macro- to micro- and nanotechnologies is one of the basic tendencies in the development of the modern electrochemical dimensional treatment methods. The nucleation phenomenon plays a dominant role in the nanotreatment processes.

The nucleation phenomenon, i.e., the formation of the nuclei, has long been studied in kinetic of phase transition.

Some stages in the development of nucleation theory are presented in this table:

Thermodynamic theory of nucleation	Gibbs-Thomson theory 1878: [1–4]
Phenomenological theory of phase transitions	[5, 6]
Kinetic methods for calculating the time of nucleation	[7, 8]
Spinodal decomposition in theory of nucleation	[9–13]
The statistical theory of nucleation	[14–18]
The modern theory of nucleation	[19–29]

Along with the particular technological problems of the resolution of the electrochemical questions are the general approaches to these problems, specifically the evaluation of the possible dimensions of the particles and their connection with the energetic parameters. The present article is devoted to this question. While the first part of the article is a critique of the conventional thermodynamic approach, in the second part we point out the place of this approach and find its applicability criterion.

The thermodynamic approach makes it possible to obtain simple relations for the radius of the resulting particle r_c (see, e.g., [2, 10, 19, 22]):

$$r_c \sim K\sigma / \mu, \quad (1)$$

where σ is the specific surface energy, μ is the change of the volume energy in the phase transition (i.e., upon nucleation), and K is the particle shape factor. The account for the fact that nucleation may take place on the surface of the macroscopic body (or in the pores) reduces in essence the change of the constants in Eq. 1 with account for the phenomenological interaction with the surface of the macroscopic material. The further generalization of the results of the thermodynamic relations to the evaluation of the kinetic phenomena reduces to the introduction of the equilibrium thermodynamic potential (with account for formula (1)) and the use of fluctuation theory. However, in this approach the connection between the thermodynamic concepts and the possible statistical model that is able to include the nucleation phenomenon is not a priori evident.

At the present time the computational methods are used for the statistical models, but in this case it is difficult to generalize the solution and compare it with the general thermodynamic relations.

Therefore, the analytic solutions are of interest particularly since – in our view – the solution of a similar problem has already been examined [14–16] where the

two-dimensional model that is not completely adequate for our problem was examined) and is not entirely suitable for the discussion of the physics on the subject phenomenon. Therefore, the first objective of the present work is to derive the analytic expression that is convenient for the discussion and to draw conclusions relating to the corresponding nucleation problem. We shall show that the division of the total system energy into the free surface energy and the bulk (corn) energy for the phenomenon of the nucleation of the micro- and nanoparticle – as was done in, e.g., [22] – is quite arbitrary. This division is easily realized for the systems with induced anisotropy.

The manuscript is structured as follows:

After the introductory (section “[Introduction](#)”), the first goal of the present work is to find an explicit form of the energy, which allows describing the nucleation phenomenon in a particle of cylindrical shape, taking into account the surface anisotropy effect. We find an analytical solution for the corresponding nonlinear differential equation of the nucleation phenomena for this kind of object (section “[Statistical Model of Heisenberg](#)”).

The theoretical model for thermodynamic description is developed in section “[Thermodynamic Analyze](#),” where the phase transition of the system is obtained. The results of the theory for the case of electrochemical nucleation were adapted in section “[Electrochemical Nucleation](#).”

The solutions of problems for the electrochemical kinetics are presented in section “[Kinetic of the Nucleation Process](#).”

Finally, the conclusions are summarized in section “[Conclusions](#).”

Connection for this theory with the well-known Cahn’s theory and theory of micro-magnetism is considered in “[Appendix A](#).”

Statistical Model of Heisenberg

The classic Heisenberg statistical model [31] for the two-dimensional space that is applicable for the study of the magnetization of the ferromagnetic material is examined in [15, 16]. It is known that the statistical sum and the thermodynamic functions are determined by the local energy minima. We shall use the variation minimum of the exchange energy (in the cylindrical coordinate system) that was proposed in [15, 16]. As in [14–18], we examine the low-temperature limit, when a single energy minimum is significant. Therefore, we replace the variation of the free energy by the variation of the energy of statistical model (we will discuss this approximation later):

$$\delta \int T(\rho) dV = 0, \quad (2)$$

where the integration is performed over the entire volume V of particulars, and

$$T(\rho) = A/2 \left\{ [\theta'(\rho)]^2 + \rho^{-2} [\sin \theta(\rho)]^2 \right\}, \quad (3)$$

where $\rho = r/r_c$ is the radial relative coordinate ($0 < \rho < 1$), $\theta(\rho)$ is the angle between the cylinder axis and the magnetization vector ($\pi < \theta(\rho) < \pi/2$), and A is the exchange interaction constant.

Next, let us analyze the energy form in cylindrical particle, and this is done by adding an anisotropy term; using the azimuthal symmetry, the energy in this case can be modeled as

$$E(\rho) = A/2 \left\{ [\theta'(\rho)]^2 + [a/\rho]^2 [\sin \theta(\rho)]^2 \right\}, \quad (3a)$$

$$a^2 = (B-1)/A, \quad (3b)$$

where B is anisotropy constant and a is anisotropy coefficient such that $a=1$ represents the previous case with no anisotropy [14, 17, 18].

We will examine the nucleation of cylindrical particle. The exchange energy $T(\rho)$ is the classic analog in the Heisenberg model for the two-dimensional space (see, e.g., [15, 16]). Then it follows from Eq. 2 and from Eqs. 3, 3a, and 3b the known nonlinear equation that was presented, specifically, in [14–18]:

$$\theta''(\rho) + \theta'(\rho)/\rho - [a/\rho]^2 \sin(\theta(\rho))\cos(\theta(\rho)) = 0. \quad (4)$$

To find the nonhomogeneous equation that physically describes the nucleation process, we specify the corresponding boundary conditions in the form

$$\theta(\rho) = \pi, \quad \rho = 0; \quad (5)$$

$$\theta(\rho) = \pi/2, \quad \rho = 1.$$

The analogous problem of determining the magnetization of the infinite cylinder was examined previously [14–18], for which was found the analytic relation:

$$tg\{\theta/2\} = 1/\rho^a. \quad (6)$$

We note that the mathematical solution (6) of Eq. 4 was also examined in [14–18]. This solution is termed the two-dimensional soliton (instanton) and is a rare example of the exact analytic solution of the nonlinear problem.

It is possible to obtain the analytic solution which corresponds only qualitatively to the real situation. We see that the obtained solution does not make it possible to clearly divide the system energy into the surface energy and the core energy. We can consider that this conclusion will remain valid with the increase of temperature. Consequently, the simplified model corresponds to the real physical problem. We shall examine the general case that corresponds to the exactly solvable model. This case makes it possible to find the criterion that determines when the expression (1) can be used adequately.

We should present calculation of change of the angle $\theta(\rho)$ from the beginning of coordinates (when $\rho=0$) of a cylindrical particle up to its surface (when $\rho=1$).

If $a=1$, there is no anisotropy in the system, and if $a>1$, the external anisotropy exceeds the exchange interaction in the system.

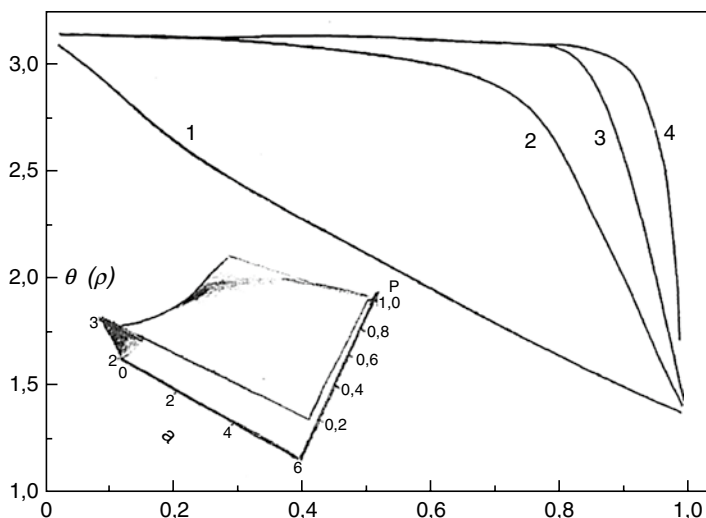


Fig. 1 Function $\theta(\rho)$ is the angle of an inclination to an axis of the cylinder (which characterizes energy of a particle in Heisenberg model from the given relative radius ρ coordinates of a particle). (Insets: 3D behavior of $\theta(\rho)$ as a function of a and ρ (See Ref. [32]))

To compare the results for the other cases, we present the calculated variation of the angle θ from the coordinate origin (where $\rho=0$) of the cylindrical particle to its surface (where $\rho=1$) (Fig. 1). At the same time (Fig. 1), let us limit our examination to the four extreme cases of the value of the parameter a :

- Curve 1 corresponds to the case $a=1$, which relates to the condition when microscopic anisotropy is absent.
- Curve 2 corresponds to the case $a=10$, which refers to the condition when microscopic anisotropy exists.
- Curve 3 corresponds to the case $a=50$.
- Curve 4 corresponds to the case $a=100$.

It is shown that, in the first case, it is difficult to isolate the volume of the cylinder that can be attributed to the surface energy, since the angle θ changes smoothly as a function of ρ . In the second case, when $a=10$, a range can be chosen whose volume amounts to the surface energy of the cylindrical particle. In the framework of our qualitative examination, we may conventionally assume, for example, that the surface layer is counted from the value $\rho \sim 0.8$. We make this choice using only the shape of curve 2, which sharply decreases for $\rho > 0.8$. The volume that defines the surface energy of the cylinder amounts to 30 % of the cylinder's volume in this case. When a increases further (e.g., by a factor of $a=100$), this volume will amount to less than 10 % of the cylinder's volume.

Thermodynamic Analyze

Formation of nanocrystalline structures often depends on the kinetics of nucleation, which includes the thermodynamics of the nucleation process only as an elementary step or event. Thus, the most probable dimensions of the particles in various physico-chemical processes are also determined from simple thermodynamic relationships involving thermodynamic functions. The nucleation is usually treated as a chain of sequential processes; that is, the N -atom nucleus is formed by addition of one atom to an $(N-1)$ -atom cluster or by a similar loss of atoms. Constructing a chain of Markov processes, one can obtain the Einstein-Fokker-Planck equation. It is worth noting that the kinetics of the nucleation process is simplified if the process of steady-state nucleation is examined. Therefore, we shall further evaluate the possible dimensions of the particles and their correlation with the energy parameters using the simple ideas and thermodynamic functions.

The further analysis of the kinetic phenomena reduces to description where the velocity of the steady-state stream of formation of the most probable nuclei is defined (see, e.g., [1, 4, 17, 18, 22]).

$$J \sim \exp\{-E_a / (kT)\}, \quad (7)$$

where E_a is the activation energy of formation of the nucleus. The solution of the problem further reduces to calculation of the magnitude of the activation energy.

Further, we assess how the free energy changes from the center of the particle to its surface. The layer-by-layer change of the free energy of the cylindrical particle is examined. The formula for the energy that was used to obtain the equation of motion has the form

$$\int E(\rho) dV \sim E_a, \quad (8)$$

the integration is performed over the entire volume V of particulars, and

$$E(\rho) = T + W, \quad (9)$$

where T is determined in Eq. 3 as exchange energy and W is determined as anisotropy energy in particle:

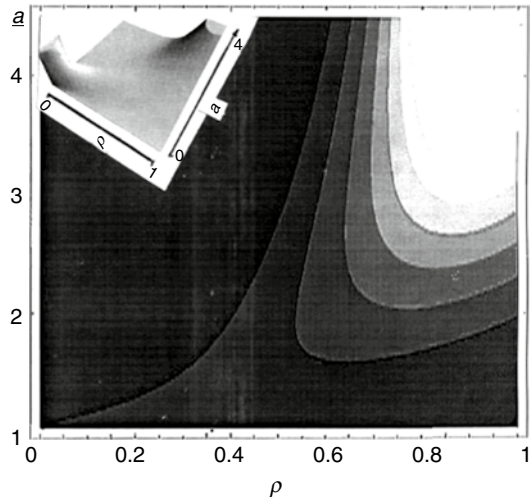
$$W = A(a^2 - 1)\sin^2 \theta(\rho) / 2\rho^2. \quad (10)$$

We use the solution (8) in Eq. 9, and we find:

$$T + W = \frac{4Aa^2 \rho^{2a}}{[\rho(1 + \rho^{2a})]^2}. \quad (11)$$

Let's analyze solution (11). In that specific case in the absence of anisotropy (when $a^2 = 1$), the energy of the surface of the cylinder (at $\rho^2 = 1$) goes to A . In a case when $a^2 > 1$, the energy on a surface of the cylinder goes to Aa^2 . It is possible to consider given parameter Aa^2 as the value of the surface energy.

Fig. 2 Density plot (diagram of levels) for the function of energy dependence $E(\rho)/A$ (see Eqs. 9 and 11) as a function of ρ (relative radius of a particle) and a (anisotropy coefficient) (See Ref. [32]) (Insets: 3D behavior of $E(\rho)/A$ as a function of a and ρ)



The energy inside a particle goes to a nonzero value if $a^2 = I$. On the other hand, the energy is equal to zero if $a^2 > 1$.

This characteristic for gap of the free energy can correspond to phase transition, when in the system is infinitesimal anisotropy. For example, such phase transition can give the result in jump of change of distribution of magnetization. The similar phase transitions are known. But in this case, it is received here as a result of the simple analytic solutions.

The energy T of particles, in a case $a^2 = I$, is equal A . With decrease of sizes of particles, the role of a thermodynamic condition of the surface is increasing. The given elementary model showed that in this case it becomes difficult to separate thermodynamic functions on the volumetric thermodynamic functions and the surface thermodynamic functions (Fig. 2). It is possible to do so using large parameter $a^2 > 10$.

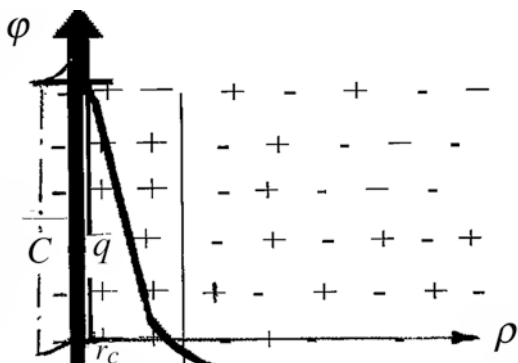
Electrochemical Nucleation

Then we shall investigate the physical nature of the examined anisotropy for the case of electrochemical nucleation. This anisotropy can be generated using the distribution of the electric field in the near-electrode layer, because the dimensions of the particles become comparable with the dimensions of the layer.

Let the surface energy change $d\sigma$ in the nucleation process according to the Lippmann equation (see, e.g., [33]).

$$-d\sigma = qd\varphi, \quad (12)$$

Fig. 3 Scheme of the physical process of nucleation for the case of electrochemical nucleation. The charge is q , and the potential is φ . The capacity of the double layer is C . The relative coordinates of the particle are ρ , and the radius of particle is r_c .



where q and φ are the charge and potential on the surface. In the approximation of the constant capacity of the double layer C , (Fig. 3)

$$q = C\varphi. \quad (13)$$

Note that the constant capacity C is defined as the specific amount, namely, the capacitance per unit area as the surface energy σ is defined as the amount of energy per unit area.

We obtain for the change in the surface energy σ

$$\sigma = C(\varphi)^2 / 2. \quad (14)$$

The change in the surface energy may be due to the anisotropy introduced above. Actually, if we assume that an asymptotic functional dependence occurs,

$$(\varphi)^2 \sim 1/\rho^2, \quad (15)$$

and then we finally obtain for the parameter a^2 [17]:

$$a^2 / r_c \sim C / 2, \quad (16)$$

where $r_c \sim 10^{-6}$ cm is the equilibrium value of the nanoparticle dimension.

For the evaluation, we take the specific capacity of a mercury electrode that is known to be on the order of

$$C / 2 \sim 10^7 (1/\text{cm}) \text{ (CGS)}. \quad (17)$$

If we confine ourselves to the upper limit of the r_c value, then we obtain for the evaluation of the dimensionless quantity a

$$a \sim 10. \quad (18)$$

Kinetic of the Nucleation Process

In the framework of the case where formula (7) is applicable, we obtain the formula for the velocity of the steady-state stream of formation of the most probable nuclei in the form (8)

$$J \sim \exp\left\{-\left(4 Aa^2 D(a)V\right) / \left(r_c kT^0\right)\right\}, \quad (19)$$

where V is the volume of the particle

$$D(a) = \int_0^1 \rho d\rho \frac{\rho^{2a}}{\left[\rho(1+\rho^{2a})\right]^2}. \quad (20)$$

Let us consider the physical meaning of formula (20).

The factor

$$A a^2 \sim B \quad (21)$$

represents the specific surface anisotropy having an electrochemical nature, and $D(a)$ is the fraction of the surface with the given energy. Thus, we come to formula (7), where E_a has the meaning of the surface energy of the nanoparticle (which dominates in the given case).

Let us discuss a possible variant of a high-temperature limit of the kinetic theory. With increasing temperature, the processes of growth of a stationary stream due to temperature transitions over the energy barrier of the instanton are possible. The energy height of the barrier (by analogy with magnetic problems) is defined in this case by the magnitude:

$$E(\rho) \sim (BA)^{1/2} / r_c. \quad (22)$$

For the potential energy of our topological model, we introduce instead of the usual time a complex time inversely proportional to the temperature (see, e.g., [35]). Then we obtain for the evaluation of the potential barrier

$$W \sim \left(1 - \exp\left\{-\left(BA\right)^{1/2} V / \left(r_c kT^0\right)\right\}\right). \quad (23)$$

The aforementioned effects will be significant only for temperatures

$$k T_c^0 \sim (BA)^{1/2} V / r_c. \quad (24)$$

Note that, precisely for such temperatures, the conditions of steady-state kinetics are violated. In this case, no activation processes that we do not examine here will define the kinetics of the process. Therefore, we shall consider the following expression to be the applicability criterion of Eq. 16:

$$T^0 < T_c^0. \quad (25)$$

It is clear from simple physical reasons that, when the temperature approaches the critical value T_c , the formed particles will begin to be destroyed owing to the effect of the temperature. To assess T_c , we assume that the volume of the particle V is on the order of 10^{-24} m^3 , and

$$E_a / V \sim E(\rho) \text{ varies from } 10^{-2} \text{ Jm}^{-3} \text{ to } 10^{-1} \text{ Jm}^{-3}. \quad (26)$$

Then we obtain for T_c^0 the range from 100^0 K to 1000^0 K .

Note that an increase in the energy of anisotropy also leads to an increase in the temperature limit at which the conditions of steady-state kinetics are not yet violated.

Conclusions

- With the decrease of the dimension of the particles, the thermodynamic state of its surface will play an ever-increasing role in describing its thermodynamic state. This article presents a very simple model that shows it becomes more and more difficult to separate the thermodynamic functions into the core and surface functions.
- The physical consequence of the examined model reduced to the fact that this separation into the core energy and the surface energy can be performed if the anisotropy in the system significantly exceeds the close order isotropic exchange interaction.
- The concept of the energy of anisotropy, introduced in theory, acquires the meaning of the electrostatic energy of a double electric layer. With the aim of creating equilibrium particles with nanodimensions, the electric capacitance of the system where such a particle is grown should be increased.
- For the velocity of the steady-state stream of motion of the most probable nuclei, we obtain a result that allows us to suggest that effective control is possible over the nucleation process by electrochemical methods.

In this research, as far as was possible, we did not examine the mathematical problems. For the mathematical problems discussed in other publication, see, e.g., [15, 16, 36–38]. Here, the greater attention was given to the application of these mathematical solutions to the problems of electrochemical nucleation.

A weakness of the examined model is that a cylindrical symmetry was used instead of a spherical symmetry. We had to examine only examples of very elongated nanoparticles whose geometrical properties can be well approximated by an infinite cylinder. Actually, such particles are often obtained by an electrochemical method. Synthesis of sphere-shaped particles is also interesting. However, in the case of spherical symmetry, it is not possible to obtain analytical solutions, but we put forward hope for the development of approximate numerical calculation methods.

Topological ideas applied, in particular, in the theory of field and elementary particles and later in the theory of magnetism have led to a number of new results in statistical physics as well. One of these results obtained in this article is a fundamental

solution in the form of instanton waves (see, e.g., [15, 36–38]), which are used to describe the physical behavior of magnetic materials (see, e.g., [14, 39]) and nematic liquids.

Acknowledgments This research received financial support from the NATO Science for Peace Program (2004) and RFFI – Moldova grant (2006–2007). The author was working with the senior scientific researcher (2009–2010) in Département de Génie Physique, École Polytechnique de Montréal, Université de Montréal.

Appendix A

Considered above theory is connected with the well-known theory of Cahn and Co. (see, e.g., [9, 10, 12, 13]).

As you can see, the free energy of the theory of Cahn represents the following form:

$$F(c) \sim B f(c) + A/2 \left[(c_x')^2 + (c_y')^2 + (c_z')^2 \right], \quad (27)$$

where c (meaning $c(x, y, z)$) is “concentration field,” as the generalized coordinate.

The variation $F(c)$ gives the well-known equation, which was studied in a one-dimensional

case (see, e.g., [11]).

$$Ac_x'' + \varphi(c) = 0, \quad (28)$$

where $\varphi(c) = B f_c'(c) - \mu$ (μ is a Lagrange multiplier).

That gives for phase boundary in the form of Landau-Lifshitz domain wall with energy gap ΔE , where ΔE is proportional: [38]

$$\Delta E \sim (BA)^{1/2} \quad (29)$$

(see also from Eq. 22).

The above problem is mathematically similar to the problem of thin cylinder micromagnetism (see, e.g., [14, 39]).

The problem of finding the free energy for the more complex models in the future will be decided by asymptotic methods (see, e.g., [11, 30]).

References

1. Becker R, Döring W (1935) Kinetische Behandlung der Keimbildung in übersättigten Dämpfen. Ann Phys 24:719
2. Frenkel JI (1955) Kinetic theory of liquids. Dover, New York
3. Gibbs JW (1928) Collected works. New Haven
4. Volmer M, Weber A (1926) Keimbildung in übersättigten Gebilden. Z Phys Chem (Leipzig) 119:277
5. Landau LD (1937) On the theory of phase transitions. Phys Zs Sowiet 11:26–36; 11:545–553
6. Landau LD, Lifshits EM (1964) Statistical physics. Nauka, Moscow, 567 p (in Russian)

7. Zeldovich JB (1943) On the theory of new phase formation; cavitation. *Acta Physicochim URSS* 18:1
8. Lifshits IM, Slezov VV (1961) The kinetics of precipitation from supersaturated solid solutions. *J Phys Chem Solids* 19:35
9. Cahn JW, Hilliard DJE (1958) Free energy of a nonuniform system. I. Interfacial free energy. *J Chem Phys* 28(2):258–267
10. Cahn JW, Larche'e FC (1982) Surface stress and the chemical equilibrium of single crystals II: solid particles imbedded in a solid matrix. *Acta Metall* 30:51–56
11. Khachatryan AG (1974) *Teoria fazovykh prevrashchenii i struktura tverdykh rastvorov* (Theory of structural transformations in solids). Nauka, Moscow, 384 p (in Russian)
12. Cahn JW, Hilliard DJE (1959) Free energy of a nonuniform system. II. Thermodynamic basis. *J Chem Phys* 30(5):1121–1124
13. Cahn JW, Hilliard DJE (1959) Free energy of a nonuniform system. III. Nucleation in two-component incompressible. *J Chem Phys* 30(5):688–699
14. Baranov SA, Laroze D, Vargas P, Vazquez M (2006) On micromagnetic theory of thin cast amorphous microwires. *Physica B* 372:320–323
15. Belavin AA, Polyakov AM (1975) Metastable states of a two-dimensional isotropic ferromagnetic. *Pis'ma Zh Eksp Teor Fiz (Sov Phys)* 22(10):503–506 (*JETP Lett* 22:245–248)
16. Woo G (1977) Pseudoparticle configurations in two-dimensional ferromagnets. *J Math Phys* 18:1264–1266
17. Baranov SA, Gamburg YD, Dikumar AI (2007) Kinetic model of electrochemical nucleation. *Surf Eng Appl Electrochem* 43(2):172–175
18. Baranov SA, Dikumar AI, Gamburg Yu D (2008) Microkinetic model of nucleation and its application in electrochemistry. *Surf Eng Appl Electrochem* 44(2):98–105
19. Abraham FF (1974) *Homogeneous nucleation theory*. Academic, New York/London
20. Binder K (1987) Theory of first-order phase transition. *Rep Prog Phys* 50:783
21. Gamburg Yu D (1997) *Elektrokhimicheskaya kristallizatsiya metallov i splavov* (Electrochemical crystallization of metals). Yanus K, Moscow, 384 p (in Russian)
22. Gunton JD, San Miguel M, Sahni PS (1983) The dynamics of first order phase transformations. In: Domb G, Lebowitz JL (eds) *Phase transition and critical phenomena*, vol 8. Academic, London/New York, p 267
23. Hill TL (2001) Perspective: nanothermodynamics. *Nano Lett* 1(3):111–112
24. Gunton JD, Droz M (1983) Introduction to the theory of metastable and unstable states vol 183, *Lecture notes in physics*. Springer, Berlin
25. Martin CR (1994) Nanomaterials: a membrane-based synthetic approach. *Science* 266:1961–1965
26. Penrose O (1997) The Becker-Döring equations at large times and their connection with the LSW theory of coarsening. *J Stat Phys* 89:305
27. Wagner C (1961) Theorie der Alterung von Niederschlägen durch Umlosen. *Z Electrochem* 65:581
28. Wu DT (1997) Nucleation theory. *Solid State Phys* 50:38
29. Martin CR, Mitchel DT (1999) Template-synthesized nanomaterials in electrochemistry. In: Bard AJ, Rubinstein I (eds) *Electroanalytical chemistry*. Marcel Dekker, New York, pp 1–74
30. Olemskoi AI (1998) Theory of stochastic systems with singular multiplicative noise. *UFN* 168(3):287–321
31. Heisenberg W (1928) Zur Theorie der Ferromagnetismus. *Z Phys* 49:619
32. Laroze D, Baranov SA, Vargas P, Vazquez M (2007) On the theory of nucleation in cylindrical magnetic nanoparticles. *Phys Stat Sol C* 4(11):4170–4173
33. Lippman G (1875) Relations entre les phenomenes electriques et capillaires. *Annales de Chimie et de Physique* 5 serie, t. V:494–520
34. Delahay P (1965) *Double layer and electrode kinetics*. Wiley-Interscience, New York
35. Feynman RP, Hibbs AR (1965) *Quantum mechanics and path integrals*. McGraw-Hill, New York
36. Perelomov AM (1981) Instanton – type solutions in chiral models. *UFN* 134(4 (8)):577–609

37. Rozhkov SS (1986) Topology, manifolds and homotopy; main concepts and applications to n – field models. *UFN* 149(2):259–273
38. Perelomov AM (1987) Chiral models: geometrical aspects. *Phys Rep* 146(3):135–213
39. Brown WF Jr (1963) *Micromagnetics*. Interscience Publishers: (a division of John Wiley & Sons), New York/London, 143p
40. Cahn JW, Larch'e FC (1982) Surface stress and the chemical equilibrium of single crystals II: solid particles imbedded in a solid matrix. *Acta Metall* 30:51–56
41. Larch'e FC, Cahn JW (1982) The effect of self-stress on diffusion in solids. *Acta Metall* 30:1835–1845
42. Khachatryan AG (1983) *Theory of structural transformations in solids*. Wiley, New York
43. Olemskoi AI, Kopyk IV (1995) Theory of spatiotemporal evolution of a nonequilibrium thermodynamic system. *UFN* 165(10):1105–1144
44. Kovarsky VA, Baranov SA (1976) Non-adiabatic frequency resonant radiation. *Zh Eksp Teor Fiz (Sov Phys)* 44(6):1067–1077 (*JETP* 44:245–248)
45. Binder K (1991) Spinodal decomposition. In: Haasen P (ed) *Phase transformation in materials*, vol 5, *Materials science and technology*. VCH, Weinheim, p 405
46. Cahn JW (1968) Spinodal decomposition. *Trans Metall Soc AIME* 242:166
47. Frenkel JI (1939) *Statistical theory of condensation phenomena*. *J Chem Phys* 7:200–201
48. Gunton JD, Droz M (1983) *Introduction to the theory of metastable and unstable states*, vol 183, *Lecture notes in physics*. Springer, Berlin

Part VI
Applications

Scanning Electrochemical Microscopy: A Multiplexing Tool for Electrochemical DNA Biosensing

33

Mohtashim Hassan Shamsi and Heinz-Bernhard Kraatz

Contents

Introduction.....	1074
History of SECM	1074
Principle of Feedback Mode of SECM.....	1075
Approach Curve and Tip Geometry	1077
DNA Films and Self-Assembled Monolayers (SAMs) on Gold Surface	1079
Multiplexed DNA Visualization of Hybridization and Mismatch Detection.....	1081
Conclusion	1088
References.....	1092

Abstract

Scanning electrochemical microscopy (SECM) translates the current generated by an electrochemical reaction occurring at a tip electrode scanned across a surface substrate into an image. SECM not only provides a simple electrochemical image of the conductive and/or insulating substrate but also provides kinetic information of the heterogeneous electron transfer reactions when the tip electrode approaches the surface. Applications including biosensing have been demonstrated. In this chapter, we will focus on recent advances in the application of SECM toward the label-free detection of base pair mismatches in DNA.

Despite having nanometer dimensions, the base pair mismatches along a DNA strand can be readily detected by SECM in an array format through exploiting the negative charge in the vicinity of self-assembled DNA films. The response can be amplified using metal ions to enhance the discrimination

M.H. Shamsi • H.-B. Kraatz (✉)

Department of Physical and Environmental Sciences, University of Toronto Scarborough,
Toronto, ON, Canada

Department of Chemistry, University of Toronto, Toronto, ON, Canada

e-mail: bernie.kraatz@utoronto.ca

© Springer International Publishing Switzerland 2016

M. Aliofkhaezaei, A.S.H. Makhlof (eds.), *Handbook of Nanoelectrochemistry*,
DOI 10.1007/978-3-319-15266-0_35

1073

between matched and mismatched DNA films. This simple strategy has been used to probe the position of a single nucleotide mismatch, the type of the mismatch, and hybridization position of complementary strand and even allows the identification of various animal species.

Keywords

Scanning electrochemical microscopy • Impedance spectroscopy • DNA • Mismatch • Surfaces • Biosensor

Introduction

Scanning electrochemical microscopy (SECM) is a surface probe microscopic (SPM) tool to study surfaces by electrochemical profiling of surfaces at submicron-level resolution. Electrochemical profiling is monitoring an electrochemical reaction between a biased tip and substrate in contrast to monitoring force in atomic force microscopy and tunneling current in scanning tunneling microscopy. SECM has been widely employed to study nonbiological and biological systems in research areas ranging from corrosion science, catalysis and fuel cells, self-assembled monolayers, polymer coatings, transport through membranes and biological tissue, enzymatic reactions, high-throughput DNA biosensing, studying cell metabolism, and monitoring immiscible interfaces such as gas/liquid interface. SECM also has potential to be coupled with other analytical techniques such as surface plasmon resonance [1] and atomic force microscopy [2]. This present chapter will provide a brief overview of the principles and feedback modes of SECM operation followed by a discussion of label-free DNA hybridization and mismatch detection by SECM. There are a number of excellent reviews available that cover the theory of SECM [3, 4] and its application to the study of biophysical and bioanalytical systems [5, 6], including the study of living cells and their metabolism [7].

History of SECM

In 1986, the fundamental experiments by Engstrom et al. [8] and Liu et al. [9] on using microelectrodes to probe diffusion layers and studying electrode surfaces by scanning electrochemical and tunneling ultramicroelectrode microscope in solution laid the foundation of scanning electrochemical microscopy. In 1989, Kwak and Bard [10] framed a quantitative detail of the diffusion-limited current at a UME as a function of the distance d above a macroscopic planar substrate providing a theoretical description of (a) how the Faradaic current measured at the tip can be a function of charge transfer properties of substrate, (b) the relationship between the Faradaic current obtained at the tip and the tip-substrate distance, and (c) the relationship between diffusion and homogeneous reaction kinetics in the gap between tip and substrate.

SECM imaging is carried out either in generation-collection mode (GC) or in feedback mode (FB). Because of the extensive use of feedback mode to study self-assembled DNA films, we will focus on the principle and theory of FB mode here.

Principle of Feedback Mode of SECM

Typically, a three-electrode assembly, consisting of a working, a counter, and a reference electrode, is used (Fig. 1a) in which a biased ultramicroelectrode tip approaches a substrate in presence of a redox-active mediator. The substrate can be conductive or insulating. The current is generated by a diffusion-limited redox reaction at the tip, i.e., $R \rightarrow O + ne^-$, thus generating a current. The current for a disk electrode can be given as

$$i_{\infty} = 4nFD C^o a \quad (1)$$

where n =number of electrons/redox couple, F =Faraday constant, D =diffusion coefficient of redox couple, C^o =concentration of redox mediator, a =radius of the disk electrode. The tip current (i_T) follows the relationship when away from substrate. When the tip approaches the substrate in micrometer steps using a piezoelectric positioner, the diffusion-limited tip current (i_T) either rises or falls, depending on the charge transfer property of the substrate as shown in Fig. 1b–d. If the substrate is insulating or electrochemically inert, the diffusion of the redox mediator to the tip from bulk solution is physically hindered, causing a decrease of the current, i.e., $i_T < i_{\infty}$. If the substrate is conducting, the rate of reaction Eq. 1 can be controlled by applying a suitable potential to the substrate. Otherwise, the potential of a conductive substrate E_s may be determined by the concentration of redox species in solution without an external bias. For example, if the solution contains only the reduced form of the redox species, most of the substrate surface, which is usually much larger than that of the tip, is exposed to solution of R. According to the Nernst equation

$$E_s = E^0 + RT / nF \ln(C_o / C_r) \quad (2)$$

considering, $C_o \sim 0$, and $E_s - E^0 \ll 0$, where E^0 =redox mediator standard potential, thus all oxidized species reaching the substrate get reduced at the surface.

Since regeneration is faster at the distance almost equal to the radius of the tip, between the tip and substrate, it causes a sharp increase in the current, i.e., $i_T > i_{\infty}$. This mode of SECM is called “feedback mode” where a positive feedback ($i_T > i_{\infty}$) is observed on conducting surfaces and a negative feedback ($i_T < i_{\infty}$) is observed on insulating surfaces. The rate of heterogeneous electron transfer on the tip electrode is the main parameter that can be extracted from these measurements. There may be one of three ways to regenerate a mediator, i.e., (a) electrochemical conversion of the mediator at the substrate, (b) an enzyme-catalyzed reaction with consumption of O and regeneration of R, or (c) local oxidation of the substrate by O.

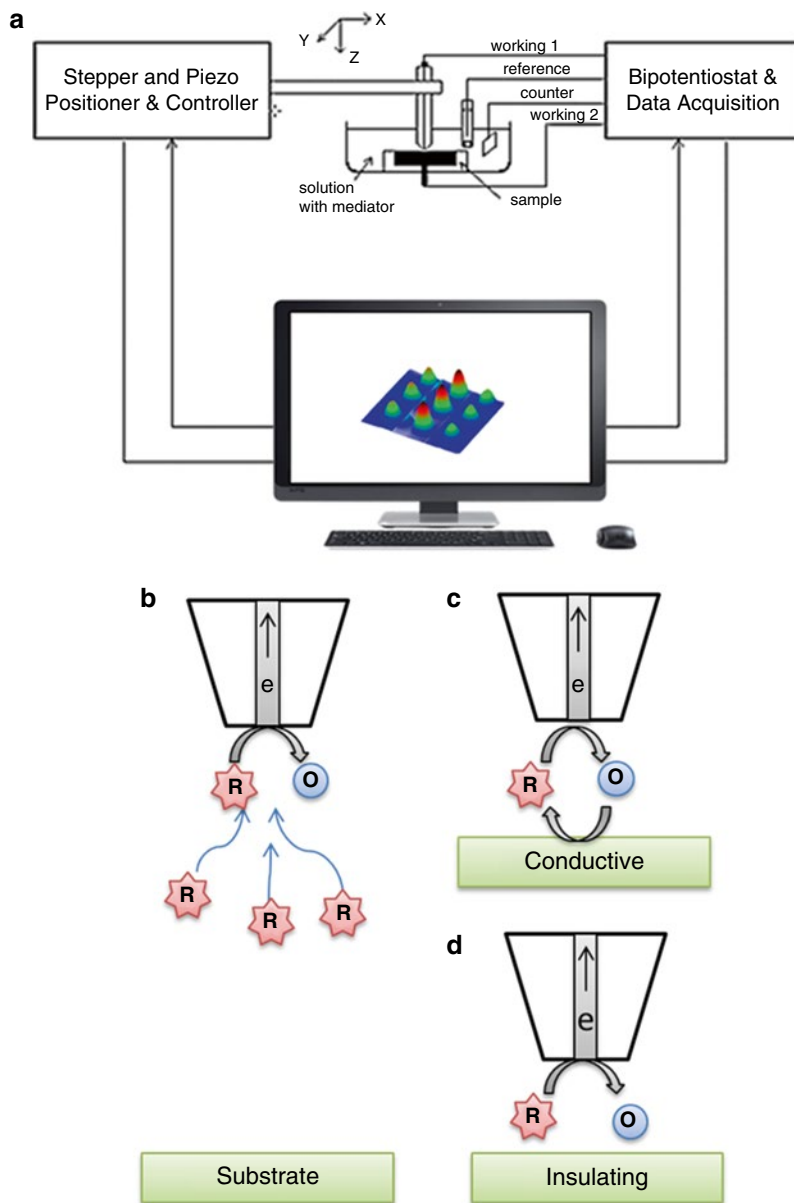


Fig. 1 (a) Block diagram of SECM cell connected to a stepper and piezoelectric controller and bipotentiostat. Piezoelectric positioning and applied potential can be controlled through software in PC. (b) SECM tip away from substrate in redox mediator solution. When a positive potential is applied, a reducing agent in solution diffuse to the UME tip and get oxidized. (c) When UME tip approaches close to a conductive substrate, the oxidized redox mediator is regenerated at the surface of substrate resulting in positive feedback. (d) When UME tip approaches close to a insulating substrate, the diffusion of the redox mediator is hindered due to a very small distance between the tip and substrate as well as oxidized redox mediator is not regenerated at the surface of substrate resulting in negative feedback

Approach Curve and Tip Geometry

When the tip is laterally – from the z -direction – brought to the surface with high accuracy of submicron steps, i_T is recorded versus lateral distance d and plotted as “approach curves” (Fig. 2a). The approach curves represent the normalized current $I_T = i_T/i_{T,\infty}$ as a function of the normalized distance $L = d/a$, where d is the distance in z -direction and a is the radius of disk electrode. The normalized approach curves are independent of the mediator concentration C^o , the diffusion coefficient D , and the tip radius a . The normalized tip current I_T depends only on L and the thickness of the insulating sheath forming thin-layer cell with the substrate. Simulations accounting for the amperometric response due to diffusion of the redox species around the corner of the insulating sheath for a wide range of tip-substrate distances over conducting and insulating substrates were performed for several RG ratios [11]. Diffusion around the edge of the insulating sheath was found to have a pronounced effect on the approach curves. The tip currents for conducting substrates were found significantly dependent on the tip geometry. The resolution of the image largely depends on the geometry and size of the ultramicroelectrode probe tip. Sharper tips (i.e., lower RG) produce a high-resolution image and a high feedback current. SECM also provides quantitative information about the electrochemical properties

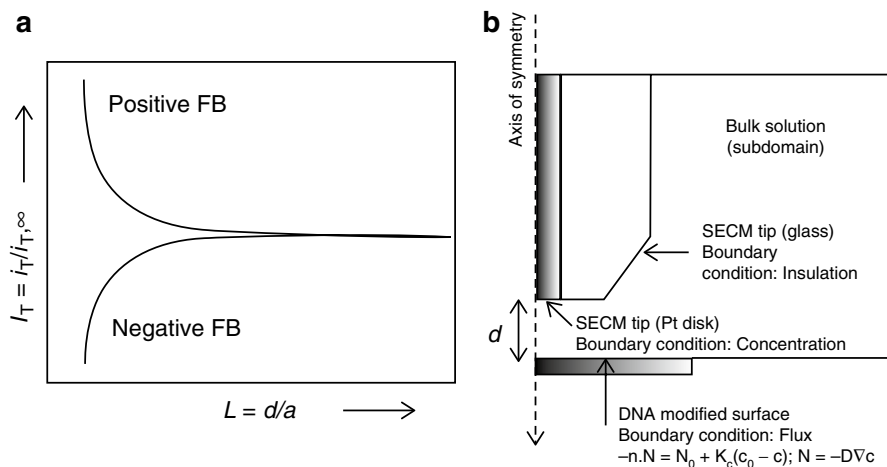


Fig. 2 (a) Approach curves (normalized tip current vs. normalized distance) recorded over the conductive substrate giving positive feedback current and an insulating substrate giving negative feedback current. (b) Sketch of numerical simulation to extract the reaction kinetics between the tip and substrate. Here, the steady-state diffusion problem for SECM geometry was solved numerically assuming irreversible substrate kinetics, in dimensionless form using the finite element method (COMSOL Multiphysics 3.5a software with Chemical Engineering Module) (Figure 2b has been taken from Diakowski P, Kraatz H-B (2011) Towards the electrochemical identification of species. Chem Comm 47:1431–1433 with permission from The Royal Society of Chemistry)

of a surface through numerical modeling. The simulations are useful to assess the SECM topographical sensitivity, i.e., the rate of change of tip current with respect to tip-substrate distance, and spatial resolution, i.e., the ability of the microdisk electrode to distinguish two conducting islands embedded in an insulating substrate. A system under investigation can be numerically modeled using the dimensions of the tip electrode, substrate, and the inter tip-substrate distance, which provides kinetics of the reaction under observation by simulations as shown in Fig. 2b. Theoretical approach curves can be obtained by setting the boundaries and varying d in numerical simulation. Recently, COMSOL Multiphysics 3.5a software with Chemical Engineering Module has been used to solve steady-state diffusion problems for SECM geometry by assuming irreversible substrate kinetics and using the finite element method in dimensionless form [12, 13].

Numerical simulation allowed the calculation of theoretical approach curves for different values of a dimensionless rate constant, Λ , which can be described as

$$\Lambda = k^0 a / D \quad (3)$$

where k^0 = apparent rate constant, a = radius of the tip, and D = diffusion coefficient of the redox mediator. In this case, the apparent rate constant accounts for the combined contributions of electron transfer across the film and penetration of the redox mediator into the film [14]. The diffusion coefficient for the redox mediator can be obtained from Eq. 1 $i_\infty = 4nFDC^o a$. Experimental data modeled on the above method allows evaluation of the apparent rate constants for electron transfer across DNA films.

The tips in the range 5–25 μm have been widely used for biophysical application along with the development toward submicron probes to study smallest possible areas with high resolution. Traditionally, the SECM tip is prepared by heat sealing of a metal wire having diameter in micron scale in a glass capillary under vacuum (Fig. 3) followed by connection with external copper wire using silver epoxy on the other side of the capillary. The size of the glass sheath surrounding the disk electrode is reduced through manual polishing with rotating polishing pads using 3.0 and 0.05 μm alumina particles to minimize the electrode RG. The obtained tip electrodes can be evaluated under microscope and tested electrochemically by performing cyclic voltammetry and SECM approach curves on conducting or insulating surfaces. Following procedures carefully may allow obtaining tip electrodes with RG value between 2 and 3. Nanometer- and submicron-sized tips can also be produced for the application of SECM-AFM by chemical etching of a metal wire followed by insulator coating leaving the apex exposed. Mirkin and coworkers studied the kinetics of fast heterogeneous ET reactions using flat Au nanoelectrodes by SECM [15]. The rate of mass transfer by diffusion was varied by changing the tip radius (a) and the tip-substrate distance (d); the kinetic parameters were found to be independent of both a and d . The reaction kinetics were found dependent on electrode material for some electroactive species, such as $[\text{Ru}(\text{NH}_3)_6]^{3+}$, and independent of electrode material for species such as ferrocene or ferrocenemethanol when compared to Pt nanoelectrodes [15].

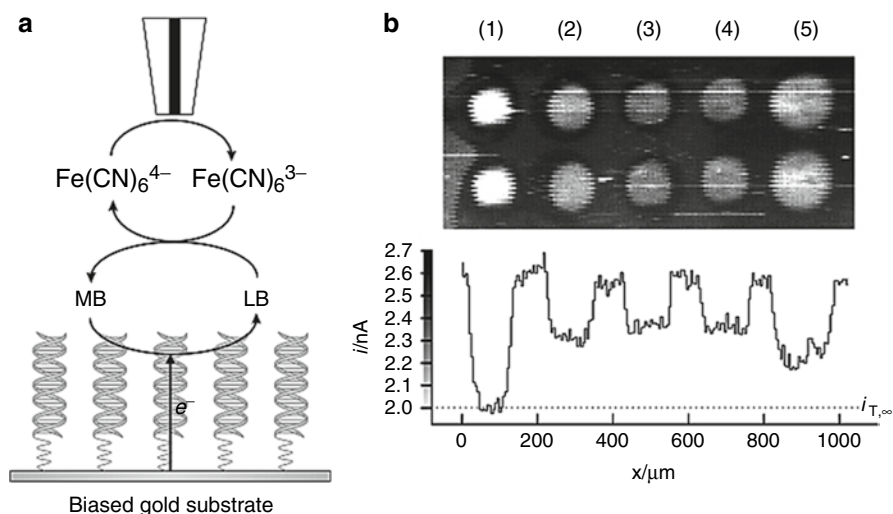


Fig. 3 (a) Schematic depicting the catalytic electron transfer between the biased gold substrate to the tip electrode through self-assembled DNA film via intercalated methylene blue and solution based ferro/ferricyanide. MB is reduced by the electron transfer from the biased gold substrate and then regenerated by donating electron to ferrocyanide which is reoxidized to ferricyanide on the tip electrode. (b) Multi-plexed SECM image and current profiles of a DNA microarray immobilized on a gold disk substrate biased at -0.4 V containing 2 mM $K_4Fe(CN)_6$ and 2 μ M MB. Both rows of spots correspond to (1) ss-DNA, (2) complementary ds-DNA, (3) one base mismatch ds-DNA, (4) two base mismatches ds-DNA, and (5) three base mismatches ds-DNA (Reprinted with permission from Wain A, Zhou F *Langmuir* 24:5155–5160. Copyright (2008) American Chemical Society)

DNA Films and Self-Assembled Monolayers (SAMs) on Gold Surface

After providing a brief introduction to SECM, we next want to redirect the discussion to the application of SECM for the study of thin films composed of deoxyribonucleic acid (DNA). DNA is a biological polymer composed of nucleotide monomeric blocks, which are linked through a phosphodiester linkage. There are two purine bases, adenine (A) and guanine (G), and two pyrimidine bases, thymine (T) and cytosine (C), which pair up in the Watson-Crick sense as A-T and G-C pairs, resulting in the formation of two antiparallel strands of DNA. Deoxyribonucleic acid has three different conformations, A, B, and Z. Under physiological conditions, the most common conformational form is B-DNA, which is a right-handed helix with a diameter of approximately 2.0 nm, a pitch of 10.5 base pairs (bp), and a separation of 0.34 nm between two successive bases. The separation of the sugar-phosphate backbone of the two antiparallel strands due to base pair stacks and repulsion between anionic phosphate groups give rise to a pair of grooves, the minor

and major grooves, that runs along the length of the duplex. These grooves facilitate base access for molecular recognition events. When DNA strands are immobilized on gold surfaces through Au-S linkages, the footprint area occupied by a ds-DNA strand on surface is about 3.14 nm², neglecting the hydrodynamic volume, while the length for a 30 base pair construct of ds-DNA is ~10.2 nm. A surface-immobilized single-stranded or double-stranded DNA not only physically passivates the surface but also makes the surface negatively charged due to poor shielding of the backbone charge by monovalent cations. The presence of base pair mismatches in ds-DNA can create significant distortions in the backbone structure. The presence of a mismatch destabilizes a duplex relatively by 1.7–10.0 kcal/mol depending upon position and type of mismatch as well as concentration of Na⁺ ions [16], consequently lowering the melting temperature T_m [17]. The important parameters of different conformers of double-stranded DNA are given in Table 1.

Self-assembly of DNA on gold surfaces is similar to organic self-assembled monolayers (SAMs), therefore it seems appropriate to discuss SAM behavior briefly in the light of SECM. Please note that DNA films lack the organization that is characteristic to alkythiols including the tight packing of molecules. Organic SAMs have been extensively studied by SECM. Steady-state measurements by SECM eliminate problems associated with double-layer charging as well as contributions due to oxide film formation and reduction. The small size of the tip and currents minimizes problems of iR drop and allows fast mass transport to occur, which is good for monitoring fast reactions [18]. Patterned SAMs on gold have been imaged through the local inhibition of electron transfer [19–21]. A well-packed nonconductive SAM covers the gold substrate and behaves like an insulator. Possible defects in the monolayer can be readily detected by SECM due to a lower i_T in the SAM-modified gold region and high i_T in the loosely packed areas or bare gold region. A sharper tip, having a lower RG, provides high-resolution details by providing a good contrast between SAM-covered areas and bare gold surfaces thus detecting

Table 1 Parameters of common conformers of double stranded DNA

Properties	Z-DNA	B-DNA	A-DNA
Helical turn	Left-handed	Right-handed	Right-handed
Length/residue (Å)	3.7	3.4	2.55
Pitch (residue/turn)	11.6	10.5	11
Rotation/residue	−60°/2 bp	36.0°	32.7°
Inclination of basepair towards axis	0.1°	2.8°	22.6°
Diameter (Å)		20	
Foot print area (Å ²)		314	
Destabilization due to single mismatch (kcal/mol)		1.7–10.0	

Parameter values adopted from P. Belmont, J.-F. Constant, M. Demeunynck, Chem. Soc. Rev. 30, 70 (2001); S. Neidle, Nucleic Acid Structure and Recognition, Oxford University Press, New York, 2002

the defects on the SAM-covered areas. The quality of the SAM can be evaluated by following the reaction kinetics using approach curves. SECM can differentiate the properties of terminally functionalized SAMs as a function of different chain length, amount of protonation, or complex formation [22, 23]. SAMs can be neutral or charged depending on the end groups, therefore a thoughtful selection of the redox mediator is required to address a specific question since if the SAM is negatively charged, then use of positively charged redox mediator will give an opposite response on measuring current in contrast to negatively charged redox mediator.

Multiplexed DNA Visualization of Hybridization and Mismatch Detection

Yamashita et al. [24] first time visualized DNA duplexes, poorly though, on gold surface in microarray format (DNA spot $\sim 300 \mu\text{m}$) by SECM in the electrolyte containing the intercalator ferrocenylnaphthalene diimide as a hybridization indicator. The idea was to discriminate ds-DNA containing base pair mismatches from a matched ds-DNA monitoring the difference in the amounts of intercalation between matched and mismatched duplexes. The study did not provide any quantitative information or clear discrimination between matched and mismatched ds-DNA.

Zhou and coworker [25] demonstrated the DNA hybridization detection by staining the DNA spots with silver particles. The higher feedback current due to regeneration of $[\text{Ru}(\text{NH}_3)_6]^{3+}$ redox mediator by silver particles confirmed the hybridization event. They claimed achieving detection limit of 30 mol of target per spot, however with poor imaging and significantly large microarray format $\sim 500 \mu\text{m}$ size/spot. They also demonstrated the DNA hybridization detection through tip-induced oxidation of guanine residues in the DNA molecules by generating $[\text{Ru}(\text{bpy})_3]^{2+}$ at the tip electrode. Imaging of DNA hybridization via guanine oxidation is a label-free approach. However, its oxidation is a destructive approach to discriminate between guanine-rich and guanine-poor DNA [26]. This strategy may not be an attractive way of detection for the samples lacking guanine bases. Subsequent studies employed methylene blue (MB) as a redox-active DNA intercalator and ferrocyanide as redox mediator in solution to image DNA microarrays fabricated on gold substrates (Fig. 4) [27]. The labeled approach involved catalytic regeneration of intercalated MB, by tip-generated ferricyanide, which was electrochemically reduced by electron transfer from the gold substrate. Subsequently, the feedback current is used to extract the heterogeneous electron transfer rate constant for the MB-intercalated DNA. In this work, they were able to discriminate between single-stranded and double-stranded oligomers as well as mismatched ds-DNA.

In contrast to Zhou and coworkers' insight of electron transfer through DNA film, there is another view, which involves electron transfer through the DNA π -stack from substrate to tip. It was postulated that the electrocatalytic cycle involving the oxidation of leucomethylene blue (LB) by tip-generated $[\text{Fe}(\text{CN})_6]^{3-}$ proceeds via long-range heterogeneous electron transfer mediated by the DNA π -stack.

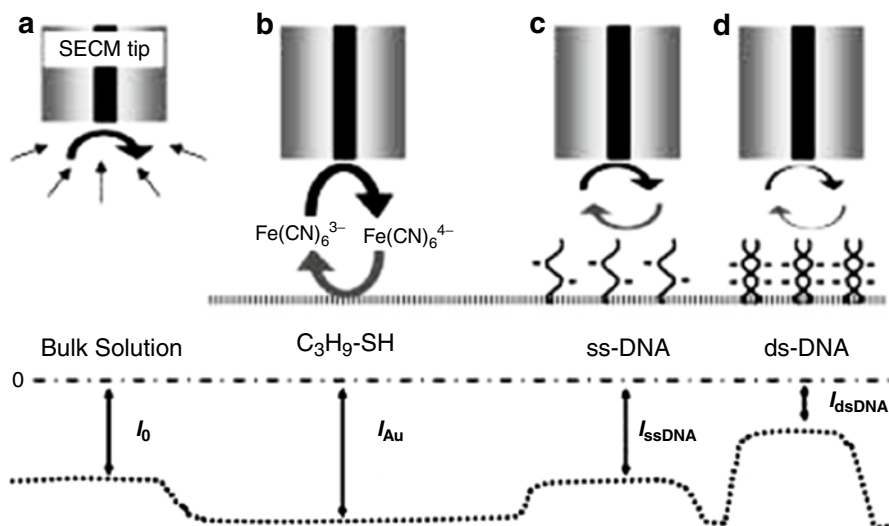


Fig. 4 Scheme depicting repelling-mode SECM. (a) A diffusion-limited steady state reduction current is recorded in $[\text{Fe}(\text{CN})_6]^{3-}$ solution at 0 mV (vs. Ag/AgCl) tip potential. (b) Recycling of tip-generated $[\text{Fe}(\text{CN})_6]^{4-}$ to $[\text{Fe}(\text{CN})_6]^{3-}$ occurs with the SECM tip close to a propane thiol-modified gold surface resulting in increase in tip current because of positive feedback redox cycling. (c) Above a ss-DNA, tip-generated $[\text{Fe}(\text{CN})_6]^{4-}$ experience charge repulsion with the oligonucleotide backbone causing a hindrance in diffusion of the mediator to the gold surface, thus modulating the diffusion rate which decreases tip current. (d) Hybridization increases the density of anionic phosphate groups leading to a further drop in tip current owing to enhanced repulsion of the redox mediator molecules (Extracted from Turcu F, Schulte A, Hartwich G, Schuhmann W *Angew. Chemie (Int. Ed. in English)* 43:3482–3485. John Wiley & Sons, Inc. (2004))

Disruptions in the DNA π -stack due to a single-base mismatch or a basic site disrupts the electrochemical catalytic cycle [28]. A similar approach was used in a study reported by Gorodetsky et al [29] to probe long-range charge transfer through the π -stack of DNA film containing the redox-active intercalator Nile blue (NB) covalently attached at discrete sites along the individual DNA helices. NB attached close to the solution side of the film is involved in the catalytic regeneration of ferrocyanide present in solution. It is important to note here that there is conflicting data, which will undoubtedly require further investigation of a possible DNA-mediated charge transfer between redox probes and the electrode surface. The impact of small defects in the SAMs as well as possible electronic conduction by hopping between differently located intercalated redox species by intra- and interstrand exchange need to be investigated. Since the biopolymer films are usually constructed of dense monolayers, one may query as how hopping and tunneling mechanisms would work, even though the redox signals measured are within a potential range where DNA bases are neither reduced nor oxidized [30].

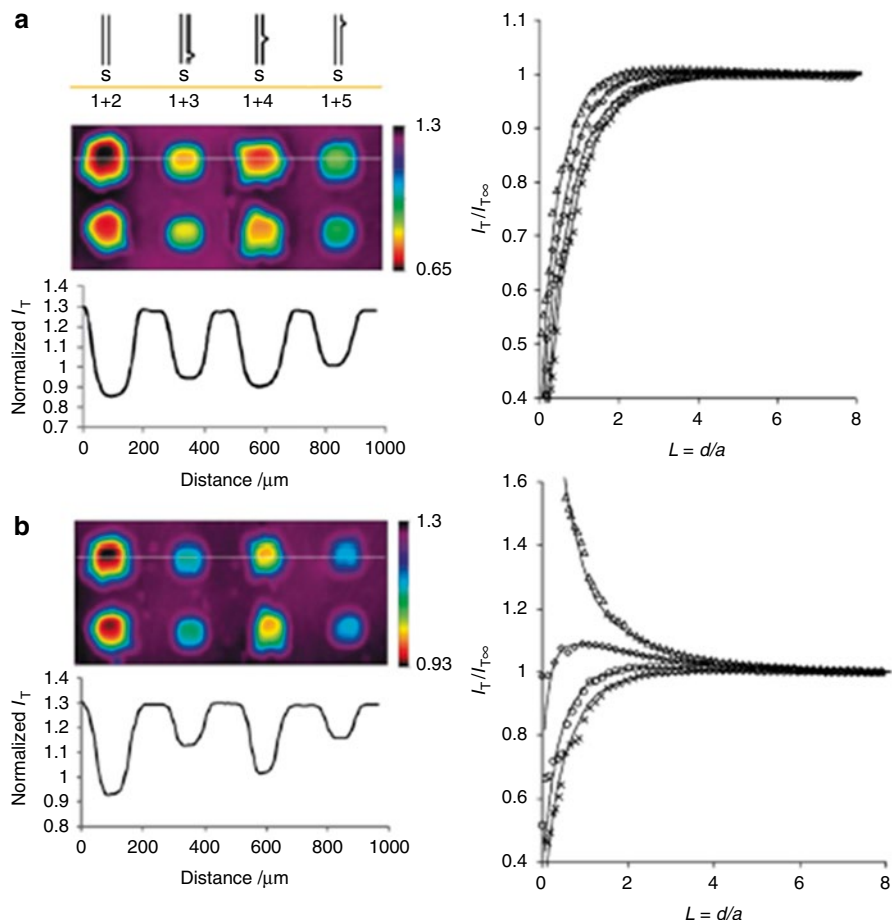


Fig. 5 Multiplexed charge repelling mode SECM images, current profiles and approach curves of ds-DNA microarrays in absence (a) and presence (b) of Zn^{2+} . 1 + 2 = fully matched, 1 + 3 = bottom mismatch, 1 + 4 = middle mismatch and 1 + 5 = top mismatch duplexes (Figure adapted from Diakowski P, Kraatz H-B (2009) Detection of single-nucleotide mismatches using scanning electrochemical microscopy. *Chem Comm* 45:1189–1191 with permission from The Royal Society of Chemistry)

Turcu et al. [31] introduced an electrostatic approach, exploiting charge repulsion, to visualize the surface-bound DNA hybridization process. The approach involves exploiting the Coulombic interactions between a negatively charged solution-based redox mediator, $[Fe(CN)_6]^{4-}$, and the backbone phosphodiester groups of the immobilized DNA strands as shown in Fig. 5. Electrostatic repulsion between phosphate groups of DNA and ferricyanide controls the diffusion transport properties of the dissolved mediator to the gold surface at DNA-modified regions. The increase in the density of the negative charge due to hybridization makes electrostatic repulsion a sensitive method to visualize hybridization. The effects of different factors including

probe and mediator concentrations, ionic strength, and tip-to-sample distance were studied in a separate study [32]. The feedback mode is particularly versatile in detecting hybridization events by exploiting biocatalytic reactions [33], signal amplification through enzymatic reaction by labeling capture or target strand [34, 35], and detecting surface-adsorbed matched and mismatched genomic DNA in a microarray format on polymer-coated carbon screen-printed electrodes [36].

Using the charge-repelling mode, Liu et al. [37] calculated the rate of electron transfer across self-assembled DNA duplexes on gold surfaces in absence and presence of Zn^{2+} . In absence of Zn^{2+} , the apparent rate constant for heterogeneous electron transfer from a dissolved redox probe, $[\text{Fe}(\text{CN})_6]^{3-/4-}$, to the gold surface through ds-DNA was $\sim 4.6 \times 10^{-7} \text{ cm s}^{-1}$, which increased to $\sim 5.0 \times 10^{-6} \text{ cm s}^{-1}$ in presence of the metal ion. The increase in rate constant was also observed with noncomplexing Ca^{2+} and Mg^{2+} ions, which inferred that the binding of these cations facilitated the penetration of DNA film by the negative probe mediator, thereby resulting in an increased redox signal. In contrast, cationic and neutral mediators were found to be unaffected by the ds-DNA film. In a combined SECM and impedance spectroscopy study in the presence of Zn^{2+} [38], Kraatz and coworkers addressed several interesting and legitimate questions in the area of DNA hybridization and mismatch detection. Diakowski and Kraatz [39] demonstrated that repelling-mode SECM can detect the presence and position of A-C single-nucleotide mismatches in unlabeled ds-DNA films, by monitoring change in the amperometric feedback current in the absence and presence of Zn^{2+} (Fig. 6).

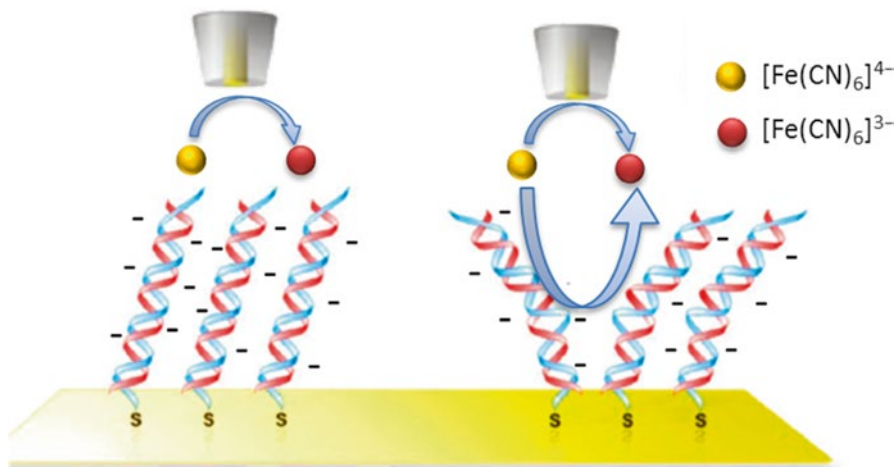


Fig. 6 Scheme depicting the self-assembled ds-DNA on gold surface through Au-S linkage. Well assembled and defect free layer resists the diffusion of the negative redox probe, by physical hindrance as well as negative charge repulsion, to reach the gold surface and get recycled, which ultimately decreases the feedback current on tip. Defects in ds-DNA layer allow the redox mediator to diffuse through the film and give higher feedback current (Adapted from Diakowski P, Kraatz H-B (2011) Towards the electrochemical identification of species. *Chem Comm* 47:431–1433 with permission from The Royal Society of Chemistry)

Table 2 Apparent electron transfer rate constants determined in the absence and presence of Zn^{2+} (Values extracted from Diakowski P, Kraatz H-B (2009) Detection of single-nucleotide mismatches using scanning electrochemical microscopy. Chem Comm 45:1189–1191)

Strand	$k^0/cm\ s^{-1}$ (No Zn^{2+})	$k^0/cm\ s^{-1}$ (Zn^{2+} present)
Fully matched	$3.52 \pm 0.24 \times 10^{-5}$	$7.03 \pm 0.3 \times 10^{-5}$
Bottom mismatch	$6.75 \pm 0.39 \times 10^{-5}$	$2.81 \pm 0.21 \times 10^{-4}$
Top mismatch	$9.98 \pm 0.47 \times 10^{-5}$	$1.26 \pm 0.28 \times 10^{-3}$

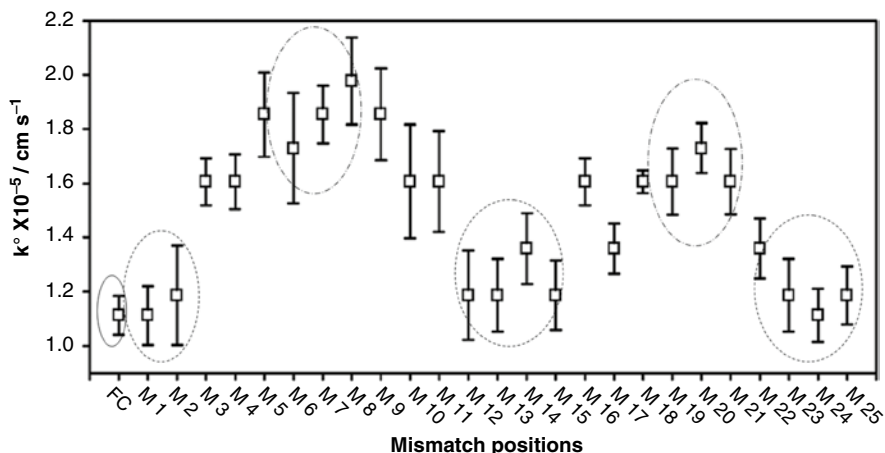


Fig. 7 Apparent rate constant (k^0) with respect to the position of mismatches in the presence of Zn^{2+} ds-DNA film. Error bars were calculated for at least three measurements. *Solid circle* (—) shows fully matched DNA, *dashed circle* (---) represents barely distinguishable single nucleotide mismatch positions and *dash eith dots* (-.-) represents highly distinguishable mismatch positions (Alam MN, Shamsi MH, Kraatz H-B (2012) Scanning positional variations in single-nucleotide polymorphism of DNA: an electrochemical study. Analyst 137:4220–4225 with permission from The Royal Society of Chemistry)

The heterogeneous electron transfer rates were obtained by finite element method to fit experimental approach curves to theoretical curves. The increase of the electron transfer rate constant (Table 2) in the presence of single-nucleotide mismatches was attributed to better penetration of the redox probe into the film. This is rationalized considering that the presence of a mismatch causes localized distortion in the backbone of the DNA, which ultimately gives rise to defects in the film (Fig. 7). The differences in feedback current and thus rate constants were amplified between matched and mismatched ds-DNA after the addition of Zn^{2+} . The discrimination of positions clearly demonstrates that ds-DNA films with single-nucleotide mismatch at different positions possess different electrochemical properties, presumably with respect to probe penetration. In a separate study based on impedance spectroscopy and SECM, Shamsi and Kraatz found that position of single-nucleotide mismatch is dominant over the type of mismatch.

This means that different mismatch types would give similar electrochemical film properties on surface with the exception of those located in the center of the DNA [40]. Most reported model studies involving mismatches involve the detection of one or two well-defined single-nucleotide mismatches at one or two positions. However, in a real sample, the analyst would be blind of the actual position or nature of the mismatch. Therefore, Kraatz's group decided to map out a single-nucleotide mismatch in all 25 positions of a 25-mer ds-DNA bound to a gold surface [41]. This systematic approach was expected to provide some insight as

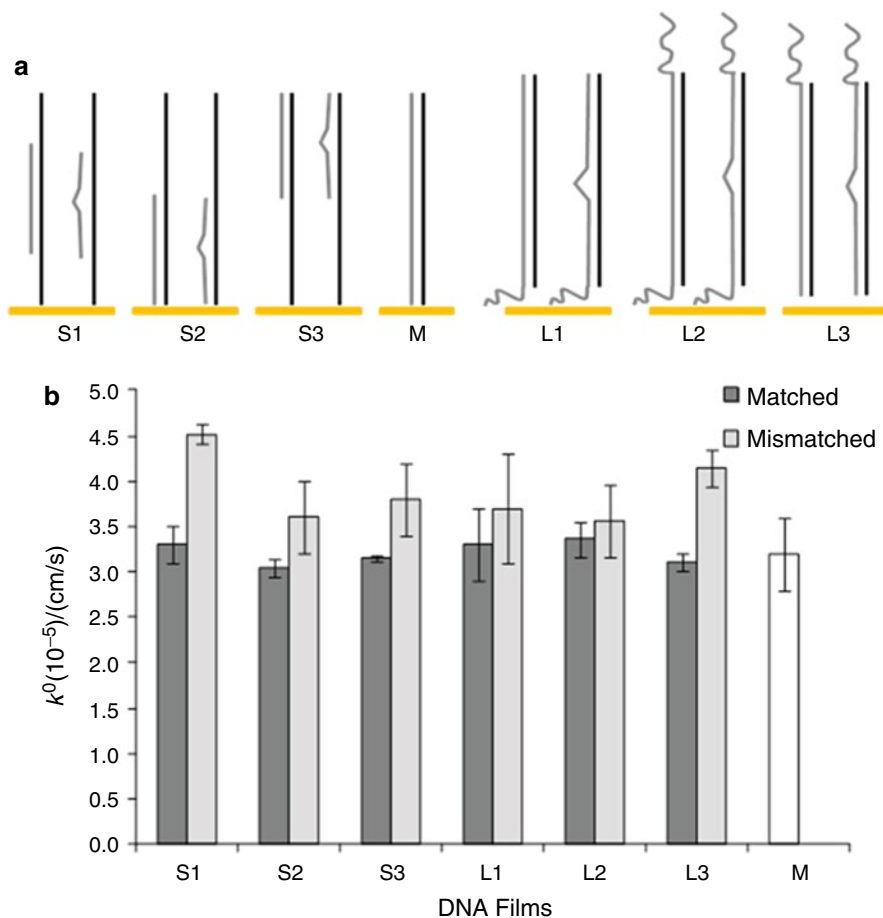


Fig. 8 (a and b) The ds-DNA films (matched and mismatched) with 25-mer short complementary strands (S1–S3), longer complementary strands (L1–L3), and exact size 51-mer fully matched (M). Estimated kinetic rate (k^0) constants for matched and mismatched duplexes in (a and b) (Adapted from Shamsi MH, Kraatz H-B (2013) Electrochemical signature of mismatch in overhang DNA films: a scanning electrochemical microscopic study. Analyst 138:3538–3543 with permission from The Royal Society of Chemistry)

to the specificity and sensitivity of this approach. The results showed that ds-DNA films containing single-nucleotide mismatch at the extreme positions along the strand (positions 1, 2, and 23–25) and in the middle of the strand (positions 12–15) show similar electrochemical properties and therefore are barely distinguishable from fully matched ds-DNA films. However, there are positions, which are moderately and highly distinguishable from fully matched duplex as shown in Fig. 8. Moreover, it is suggested that such highly distinguishable and barely distinguishable positions may differ with the length of the duplex. Another interesting issue, which was addressed by the group [42], was related to sample preparation and the inability to control the size of the target sequence. Can mismatches be detected in ds-DNA with unequal lengths of the probe and target strands, causing overhangs at the solution or electrode side of the film? Therefore, in order to study the potential impact of unmatched lengths of probe and target strands, the probe and target strands of unequal size were hybridized in absence and presence of single-nucleotide mismatches along the sequence. As a result of hybridization between unequal lengths of strands, the shorter target sequences formed overhangs in probe strand and longer target sequences formed overhangs in complementary strand. SECM images showed higher feedback current for all mismatched films regardless the length and the type of overhangs (Fig. 9). This is an important result, indicating that SECM is able to distinguish even nonideal

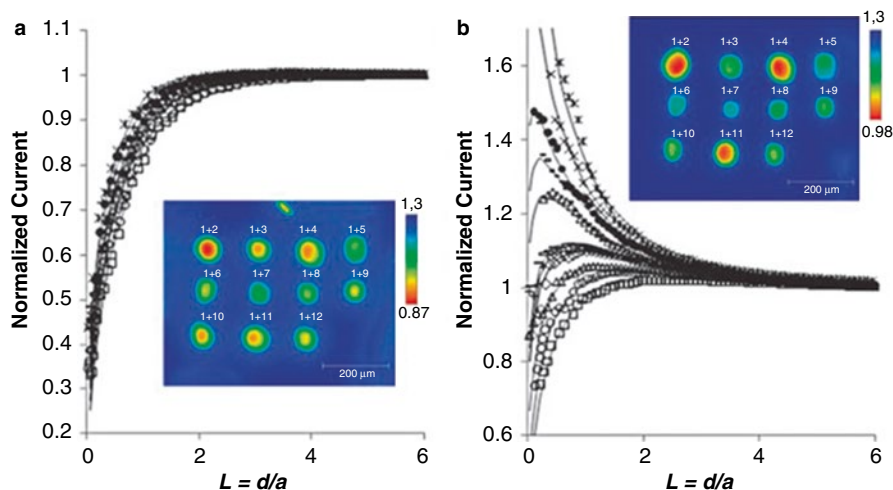


Fig. 9 Normalized approach curves with multiplexed SECM images observed above ds-DNA spots in the absence of Zn^{2+} (a) and in the presence of Zn^{2+} (b). *Solid lines* represent simulated approach curves. In this study bovine CYTbos1 primer sequence was hybridized with related sequences of animal species of different families which resulted in multiple mismatches along the sequence (Adapted from Diakowski P, Kraatz H-B (2011) Towards the electrochemical identification of species. Chem Comm 47:431–1433 with permission from The Royal Society of Chemistry)

length-mismatched ds-DNA. The kinetic rate constants monitored right above the ds-DNA films showed that hybridization position is critical for mismatch detection in short complementary stands, while mismatches are easily detectable in absence of bottom overhangs in longer complementary strands.

This detailed study on the variation in electrochemical response due to the presence of mismatch in ds-DNA films paved the way to exploit SECM for high-throughput discrimination of animal species. For this purpose, the bovine CYTbos1 primer sequence was hybridized with the related sequences of animal species of different families [13]. A fully matched ds-DNA SECM signature was obtained by hybridization with a bovine complement. Mismatched ds-DNA combinations containing various numbers of mismatches were obtained for pig, chicken, buffalo, deer, quail, and horse. The analysis of a microarray prepared of a range of ds-DNAs of different hybrids shows that different feedback currents are obtained. The magnitude of the feedback current is a function of the position and number of mismatches in the ds-DNA prepared from the CYT1bos1 primer and respective animal strands (Fig. 10). This barcoding approach to DNA testing, by exploiting the mitochondrial CO1 gene, was also effective to detect species from same family of Bovinae, i.e., dairy cattle, North American buffalo, and European buffalo [43]. Essentially, this approach allows the identification of minute quantities of DNA that are admixed to a matrix. This is of course of relevance given the most recent issue with food adulterations of beef and the discovery of nonbeef species in meat meant for human consumption. This clearly brings into focus one of the potential applications of SECM as a bioanalytical tool.

Conclusion

The electrochemical detection of DNA mismatches remains an attractive area of research. Initial studies exploiting voltammetric or amperometric measurements have led to a series of interesting controversies of the electron transfer properties of ds-DNA. More recent impedance spectroscopic studies have been more focused on the colligative properties of the ds-DNA, which has led to the development of label-free mismatch detection with ferri/ferrocyanide as a convenient electroactive probe. It was recognized that resistive differences are responsible for the impedance observations. This brings into focus the recent studies exploiting SECM for monitoring ds-DNA films. SECM allows convenient multiplexing of the measurement, while providing information on the electrochemical properties of the film. In this chapter, the value of SECM for the detection of single-nucleotide mismatches was the focus. Not only is it possible to distinguish any particular mismatch, but it is also possible to obtain information about the positional parameters of the mismatch. A simple application for the identification of animal species is an example for the versatility of SECM for bioanalysis. SECM as a laboratory-based bioanalytical method is undervalued but provides a promising alternative to other assays that make use of

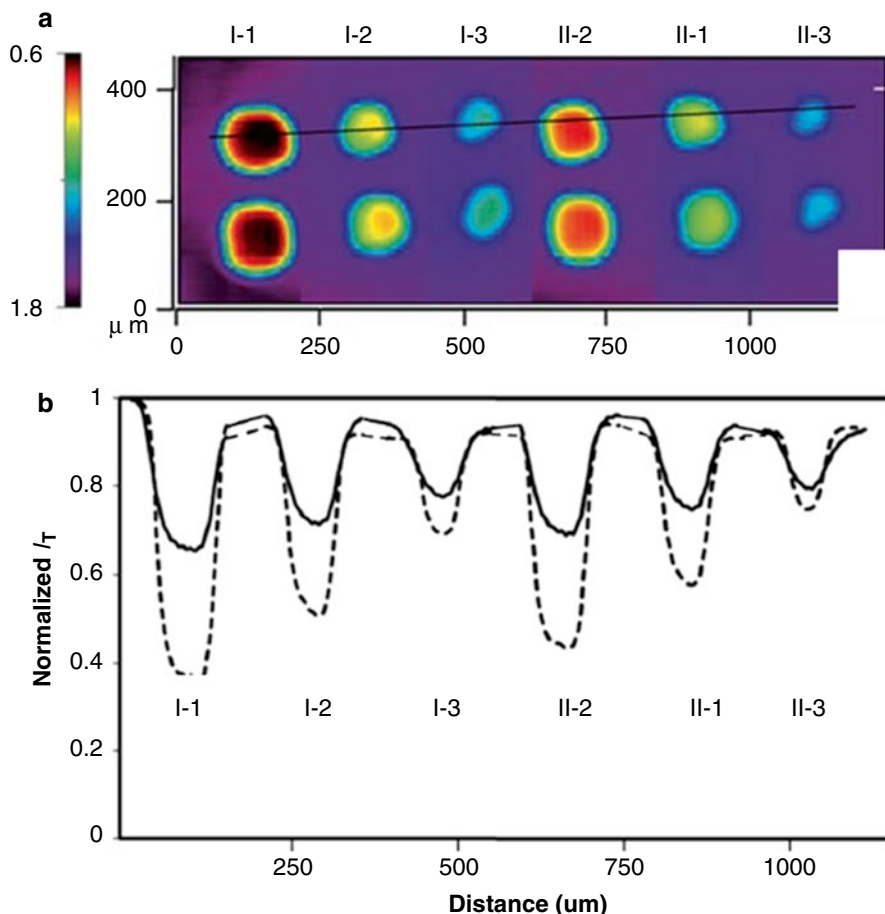


Fig. 10 (a) Multiplex detection of Bovine species by SECM images. (b) Current profile of DNA duplexes after hybridization of CO1 gene fragments of cow, NA buffalo and European buffalo before Zn^{2+} (solid line) and after Zn^{2+} (dashed line). I-1 and I-2 are fully matched ds-DNA of cow and North American buffalo respectively. I-2 and I-3 are the mismatched ds-DNA due to cross hybridization between cow CO1 gene with North American buffalo and European buffalo. II-1 and II-3 are the mismatched ds-DNA due to cross hybridization between North American buffalo CO1 gene with cow and European buffalo (Adapted from Shamsi MH, Kraatz H-B (2011) Electrochemical identification of artificial oligonucleotides related to bovine species. Potential for identification of species based on mismatches in the mitochondrial cytochrome C1 oxidase gene. Analyst 136:4724–4731 with permission from The Royal Society of Chemistry)

optical/spectroscopic detection, and one can expect to see significant results in this area over the next few years. Table 3 summarizes some of the key developments in the area of SECM and its application to the study of thin films with particular reference to the study of oligonucleotide films.

Table 3 Selected key references highlighting the development of scanning electrochemical microscopy and its applications

A new approach based on the combination of scanning electrochemical microscopy and surface plasmon resonance imaging (SECM/ SPR-i)	2005	Electroanalysis 17:495–503
Exploring the motional dynamics of end-grafted DNA oligonucleotides by in situ electrochemical atomic force microscopy	2007	J Phys Chem B 111:6051–6058
Scanning electrochemical microscopy for direct imaging of reaction rates	2006	Angew Chemie (Int Ed English) 46:1584–617
Scanning electrochemical microscopy in the 21st century	2007	Phys Chem Chem Phys 9:802–823
Scanning electrochemical microscopy: principles and applications to biophysical systems	2006	Physiol Meas 27:R63–R108
Advances in the application of scanning electrochemical microscopy to bioanalytical systems	2007	Biosens Bioelectron 23:301–318
Recent advances in high resolution scanning electrochemical microscopy of living cells – A review	2013	Analytica Chimica Acta 775:1–13
Measurements within the diffusion layer using a microelectrode probe	1986	Anal Chem 58:844–848
Scanning electrochemical and tunneling ultramicroelectrode microscope for high-resolution examination of electrode surfaces in solution	1986	J Am Chem Soc 108:3838–3839
Scanning electrochemical microscopy. Apparatus and two-dimensional scans of conductive and insulating substrates	1989	Anal Chem 61:1794–1799
Scanning electrochemical microscopy. Theory of the feedback mode	1989	Anal Chem 61:1221–1227
Scanning electrochemical microscopy (SECM): an investigation of the effects of tip geometry on amperometric tip response	1998	J Phys Chem B 102:9946–9951
Towards the electrochemical identification of species	2011	Chem Comm 47:431–1433
Analytical expressions for quantitative scanning electrochemical microscopy (SECM)	2010	ChemPhysChem 1:547–556
Scanning electrochemical microscopy. Effect of defects and structure on electron transfer through self-assembled monolayers	2008	Langmuir 24:2841–2849
Scanning electrochemical microscopy with gold nanotips: the effect of electrode material on electron transfer rates	2009	J Phys Chem C 113:459–464
Effect of base pair A/C and G/T mismatches on the thermal stabilities of DNA oligomers that form B-junctions	1997	Biochemistry 36:11419–11427
Single-base-pair discrimination of terminal mismatches by using oligonucleotide microarrays and neural network analyses	2002	Appl Environ Microbiol 68: 235–244
Electron transfer at self-assembled monolayers measured by scanning electrochemical microscopy	2004	J Am Chem Soc 126:1485–1492

(continued)

Table 3 (continued)

Patterned self-assembled alkanethiolate monolayers on gold. Patterning and imaging by means of scanning electrochemical microscopy	1997	Electroanalysis 9:746–750
Localized electrochemical desorption of gold alkanethiolate monolayers by means of scanning electrochemical microscopy (SECM)	2000	Microchim Acta 133:1–9
Scanning electrochemical microscope observation of defects in a hexadecanethiol monolayer on gold with shear force-based tip–substrate positioning	2006	Langmuir 22:7923–7927
Investigation of carboxylic-functionalized and n-alkanethiol self-assembled monolayers on gold and their application as pH-sensitive probes using scanning electrochemical microscopy	2005	Surf Sci 597:51–64
Studying the binding of Cd ²⁺ by ω-mercaptoalkanoic acid self-assembled monolayers by cyclic voltammetry and scanning electrochemical microscopy (SECM)	2005	J Electroanal Chem 581:310–319
Visualization of dna microarrays by scanning electrochemical microscopy (SECM)	2001	Analyst 126:1210–1211
Silver-enhanced imaging of dna hybridization at DNA microarrays with scanning electrochemical microscopy	2002	Langmuir 18:6653–6658
Scanning electrochemical microscopic imaging of surface-confined DNA probes and their hybridization via guanine oxidation	2002	J Electroanal Chem 537:95–102
Scanning electrochemical microscopy imaging of DNA microarrays using methylene blue as a redox-active intercalator	2008	Langmuir 24:5155–5160
Detection of DNA π-Stack lesions using scanning electrochemical microscopy	2009	ECS Transactions 166:55–62
Scanning electrochemical microscopy of DNA monolayers modified with Nile Blue	2008	Langmuir 24:14282–14288
Electron transfer in DNA and in DNA-related biological processes. Electrochemical insights	2008	Chem Rev 108:2622–2645
Label-free electrochemical recognition of DNA hybridization by means of modulation of the feedback current in SECM	2004	Angew Chemie (Int Ed English) 43:3482–3485
Imaging immobilised ssDNA and detecting DNA hybridisation by means of the repelling mode of scanning electrochemical microscopy (SECM)	2004	Biosens Bioelectron 20:925–932
Electrochemical imaging of localized sandwich DNA hybridization using scanning electrochemical microscopy	2007	Anal Chem 79:7206–7213
Optimization of an electrochemical DNA assay by using a 48-electrode array and redox amplification studies by means of scanning electrochemical microscopy	2009	Chem Bio Chem 10:1193–1199
Scanning electrochemical microscopy assay of DNA based on hairpin probe and enzymatic amplification biosensor	2010	Biosens Bioelectron 25:1953–1957

(continued)

Table 3 (continued)

Scanning electrochemical microscopy of genomic DNA microarrays study of adsorption and subsequent interactions	2009	Analyst 134:1302–1308
Scanning electrochemical microscopy. Studies of self-assembled monolayers of DNA in the absence and presence of metal ions	2005	J Phys Chem B 109: 5193–5198
Electrochemical detection of single-nucleotide mismatches using an electrode microarray	2006	Anal Chem 78:6096–6101
Detection of single-nucleotide mismatches using scanning electrochemical microscopy	2009	Chem Comm 45:1189–1191
Probing nucleobase mismatch variations by electrochemical techniques: exploring the effects of position and nature of the single-nucleotide mismatch	2010	Analyst 135:2280–2285
Scanning positional variations in single-nucleotide polymorphism of DNA: an electrochemical study	2012	Analyst 137:4220–4225
Electrochemical signature of mismatch in overhang DNA films: a scanning electrochemical microscopic study	2013	Analyst 138:3538–43
Electrochemical identification of artificial oligonucleotides related to bovine species. Potential for identification of species based on mismatches in the mitochondrial cytochrome C1 oxidase gene	2011	Analyst 136:4724–4731

References

1. Elodie F, Yann D, Pascal M, Thierry L, Sabine S (2005) Micro-imprinting of oligonucleotides and oligonucleotide gradients on gold surfaces: a new approach based on the combination of scanning electrochemical microscopy and surface plasmon resonance imaging (SECM/SPR-i). *Electroanalysis* 17:495–503
2. Wang K, Goyer C, Anne A, Demaille C (2007) Exploring the motional dynamics of end-grafted DNA oligonucleotides by in situ electrochemical atomic force microscopy. *J Phys Chem B* 111:6051–6058
3. Wittstock G, Burchardt M, Pust S, Shen Y, Zhao C (2006) Scanning electrochemical microscopy for direct imaging of reaction rates. *Angew Chem Int Ed Engl* 46:1584–1617
4. Sun P, Laforge F, Mirkin M (2007) Scanning electrochemical microscopy in the 21st century. *Phys Chem Chem Phys* 9:802–823
5. Edwards M, Martin S, Whitworth A, Macpherson J, Unwin P (2006) Scanning electrochemical microscopy: principles and applications to biophysical systems. *Physiol Meas* 27:R63–R108
6. Roberts WS, Lonsdale DJ, Griffiths J, Higson SPJ (2007) Advances in the application of scanning electrochemical microscopy to bioanalytical systems. *Biosens Bioelectron* 23:301–318
7. Bergner S, Vatsyayan P, Matsysik F-M (2013) Recent advances in high resolution scanning electrochemical microscopy of living cells – a review. *Anal Chim Acta* 775:1–13
8. Engstrom RC, Weber M, Wunder DJ, Burgess R, Winquist S (1986) Measurements within the diffusion layer using a microelectrode probe. *Anal Chem* 58:844–848
9. Liu H-Y, Fan F-RF, Lin CW, Bard AJ (1986) Scanning electrochemical and tunneling ultramicroelectrode microscope for high-resolution examination of electrode surfaces in solution. *J Am Chem Soc* 108:3838–3839
10. (a) Kwak J, Bard AJ (1989) Scanning electrochemical microscopy. Apparatus and two-dimensional scans of conductive and insulating substrates. *Anal Chem* 61:1794–1799; (b)

- Kwak J, Bard AJ (1989) Scanning electrochemical microscopy. Theory of the feedback mode. *Anal Chem* 6:1221–1227
11. Jonathan LA, Guy D (1998) Scanning electrochemical microscopy (SECM): an investigation of the effects of tip geometry on amperometric tip response. *J Phys Chem B* 102:9946–9951
 12. Diakowski P, Kraatz H-B (2011) Towards the electrochemical identification of species. *Chem Commun* 47:431–1433
 13. Lefrou C, Cornut R (2010) Analytical expressions for quantitative scanning electrochemical microscopy (SECM). *Chemphyschem* 1:547–556
 14. Kiani A, Alpuche-Aviles M-A, Eggers PK, Jones M, Gooding JJ, Paddon-Row M-N, Bard AJ (2008) Scanning electrochemical microscopy. 59. Effect of defects and structure on electron transfer through self-assembled monolayers. *Langmuir* 24:2841–2849
 15. Velmurugan J, Sun P, Mirkin MV (2009) Scanning electrochemical microscopy with gold nanotips: the effect of electrode material on electron transfer rates. *J Phys Chem C* 113: 459–464
 16. Otokiti E, Sheardy R (1997) Effect of base pair A/C and G/T mismatches on the thermal stabilities of DNA oligomers that form B-Z junctions. *Biochemistry* 36:11419–11427
 17. Urakawa H, Noble PA, El Fantroussi S, Kelly JJ, Stahl DA (2002) Single-base-pair discrimination of terminal mismatches by using oligonucleotide microarrays and neural network analyses. *Appl Environ Microbiol* 68:235–244
 18. Liu B, Bard AJ, Mirkin MV, Creager SE (2004) Electron transfer at self-assembled monolayers measured by scanning electrochemical microscopy. *J Am Chem Soc* 126:1485–1492
 19. Wittstock G, Hesse R, Schuhmann W (1997) Patterned self-assembled alkanethiolate monolayers on gold. Patterning and imaging by means of scanning electrochemical microscopy. *Electroanalysis* 9:746–750
 20. Wilhelm T, Wittstock G (2000) Localized electrochemical desorption of gold alkanethiolate monolayers by means of scanning electrochemical microscopy (SECM). *Microchim Acta* 133:1–9
 21. Yamada H, Ogata M, Koike T (2006) Scanning electrochemical microscope observation of defects in a hexadecanethiol monolayer on gold with shear force-based tip–substrate positioning. *Langmuir* 22:7923–7927
 22. Boldt F-M, Baltes N, Borgwarth K, Heinze J (2005) Investigation of carboxylic-functionalized and n-alkanethiol self-assembled monolayers on gold and their application as pH-sensitive probes using scanning electrochemical microscopy. *Surf Sci* 597:51–64
 23. Burshtain D, Mandler D (2005) Studying the binding of Cd²⁺ by ω-mercaptoalkanoic acid self assembled monolayers by cyclic voltammetry and scanning electrochemical microscopy (SECM). *J Electroanal Chem* 581:310–319
 24. Kenichi Y, Makoto T, Shigeori T, Kazuhiko U, Hiroki K (2001) Visualization of dna microarrays by scanning electrochemical microscopy (SECM). *Analyst* 126:1210–1211
 25. Jun W, Fayi S, Feimeng Z (2002) Silver-enhanced imaging of dna hybridization at DNA microarrays with scanning electrochemical microscopy. *Langmuir* 18:6653–6658
 26. Wang J, Zhou F (2002) Scanning electrochemical microscopic imaging of surface-confined DNA probes and their hybridization via guanine oxidation. *J Electroanal Chem* 537:95–102
 27. Wain A, Zhou F (2008) Scanning electrochemical microscopy imaging of DNA microarrays using methylene blue as a redox-active intercalator. *Langmuir* 24:5155–5160
 28. Hammonda WJ, Arndta J, Nguyena T, Slowinskaa KU, Jacksonb C, Burgoyneb HA, Hillb MG, Slowinskaa K (2009) Detection of DNA π-Stack lesions using scanning electrochemical microscopy. *ECS Trans* 166:55–62
 29. Gorodetsky A, Hammond W, Hill M, Slowinski K, Barton J (2008) Scanning electrochemical microscopy of DNA monolayers modified with Nile Blue. *Langmuir* 24:14282–14288
 30. Boussicault F, Robert M (2008) Electron transfer in DNA and in DNA-related biological processes. *Electrochemical insights. Chem Rev* 108:2622–2645
 31. Turcu F, Schulte A, Hartwich G, Schuhmann W (2004) Label-free electrochemical recognition of DNA hybridization by means of modulation of the feedback current in SECM. *Angew Chem Int Ed Engl* 43:3482–3485

32. Turcu F, Schulte A, Hartwich G, Schuhmann W (2004) Imaging immobilised ssDNA and detecting DNA hybridisation by means of the repelling mode of scanning electrochemical microscopy (SECM). *Biosens Bioelectron* 20:925–932
33. Palchetti I, Laschi S, Marrazza G, Mascini M (2007) Electrochemical imaging of localized sandwich DNA hybridization using scanning electrochemical microscopy. *Anal Chem* 79: 7206–7213
34. Neugebauer S, Zimdars A, Liepold P, Gebala M, Schuhmann W, Hartwich G (2009) Optimization of an electrochemical DNA assay by using a 48-electrode array and redox amplification studies by means of scanning electrochemical microscopy. *Chem Bio Chem* 10: 1193–1199
35. Zhang Z, Zhou J, Tang A, Wu Z, Shen G, Yu R (2010) Scanning electrochemical microscopy assay of DNA based on hairpin probe and enzymatic amplification biosensor. *Biosens Bioelectron* 25:1953–1957
36. Roberts W, Davis F, Higson S (2009) Scanning electrochemical microscopy of genomic DNA microarrays study of adsorption and subsequent interactions. *Analyst* 134:1302–1308
37. Liu B, Bard A, Li C-Z, Kraatz H-B (2005) Scanning electrochemical microscopy. 51. Studies of self-assembled monolayers of DNA in the absence and presence of metal ions. *J Phys Chem B* 109:5193–5198
38. Li X, Lee JS, Kraatz H-B (2006) Electrochemical detection of single-nucleotide mismatches using an electrode microarray. *Anal Chem* 78:6096–6101
39. Diakowski P, Kraatz H-B (2009) Detection of single-nucleotide mismatches using scanning electrochemical microscopy. *Chem Commun* 45:1189–1191
40. Shamsi MH, Kraatz H-B (2010) Probing nucleobase mismatch variations by electrochemical techniques: exploring the effects of position and nature of the single-nucleotide mismatch. *Analyst* 135:2280–2285
41. Alam MN, Shamsi MH, Kraatz H-B (2012) Scanning positional variations in single-nucleotide polymorphism of DNA: an electrochemical study. *Analyst* 137:4220–4225
42. Shamsi MH, Kraatz H-B (2013) Electrochemical signature of mismatch in overhang DNA films: a scanning electrochemical microscopic study. *Analyst* 138:3538–3543
43. Shamsi MH, Kraatz H-B (2011) Electrochemical identification of artificial oligonucleotides related to bovine species. Potential for identification of species based on mismatches in the mitochondrial cytochrome C1 oxidase gene. *Analyst* 136:4724–4731

Implementation of Nanostructured Catalysts in the Electrochemical Promotion of Catalysis

34

Holly A. E. Dole and Elena A. Baranova

Contents

Introduction.....	1096
Heterogeneous Catalysis: Nanoparticles, Promotion, and Metal–Support Interaction.....	1096
Electrochemical Promotion of Catalysis.....	1102
Application of Nanostructured Catalysts for EPOC.....	1107
Highly Dispersed Nanocatalyst Preparation.....	1107
Cell Configurations and Reactor Design.....	1109
Electrochemical Promotion of Nanostructured Catalysts.....	1112
Conclusion.....	1116
References.....	1117

Abstract

In the last 30 years, electrochemical promotion of catalysis (EPOC), also referred to as the non-Faradaic electrochemical modification of catalytic activity (NEMCA), has been extensively studied by research groups due to its ability to considerably enhance catalytic activity of heterogeneous catalysts. Application of a very small electrical stimulus to a catalyst-working electrode results in the modification of its electronic properties due to the controlled in situ addition or removal of the ionic species. Modification of the electronic properties alters the adsorption strength of the reaction components resulting in a distinct change in catalytic performance. Throughout the years, it has been shown that this phenomenon can be applied to various types of reactions, solid electrolytes, and conductive catalysts. Recent studies have been focused on developing these catalytic systems toward a more practical application. One aspect in regard to

H.A.E. Dole • E.A. Baranova (✉)

Department of Chemical and Biological Engineering, and Centre for Catalysis Research and Innovation, University of Ottawa, Ottawa, ON, Canada

e-mail: holly.dole@uottawa.ca; Elena.Baranova@uottawa.ca

this includes introducing nanostructured catalysts in the form of nanoparticles or nano-thin films as the working electrode to lower manufacturing costs or with the goal of applying EPOC to commercial highly dispersed catalysts. This involves the synthesis of new nanosized catalysts as well as altering the electrochemical cell design. A review of the current progress (from 2005 up to date) and challenges encountered in EPOC with nanoparticle catalysts using various ionic conducting ceramic and polymer supports will be discussed.

Keywords

Heterogeneous catalysis • Nanoparticles • Metal-support interaction • Electrochemical promotion of catalysis

Introduction

Heterogeneous Catalysis: Nanoparticles, Promotion, and Metal–Support Interaction

The form of catalysis where the reactants are in a different phase as the catalyst itself is referred to as heterogeneous catalysis [1]. The steps carried out during a heterogeneous catalytic reaction are first diffusion of the reactants to the catalyst surface then intraparticle diffusion of the reactants through the catalyst pores to the active sites. The reactants adsorb on the active sites and a surface reaction occurs. The products then desorb from the catalyst sites, intraparticle diffusion of the products occurs, and, finally, there is diffusion of the products away from the catalyst [1].

In heterogeneous catalysis, only the surface atoms are considered active for catalytic reactions; that is, for bulk material, most of the material is not being used (i.e., low volume-to-surface area ratio). The introduction of nanostructured catalysts changed the catalytic ability in heterogeneous catalysis research areas, giving an approach to optimize this volume-to-surface area ratio. To be considered “nano,” the catalyst is defined as having at least one dimension in the range of 1–100 nm. There are several methods that have been developed to prepare such nanostructured catalysts. For instance, nanofilms can be prepared through techniques such as physical vapor deposition [2, 3], chemical vapor deposition [4, 5], and atomic layer deposition [6, 7], while nanoparticles can be prepared by impregnation [8–13], deposition–precipitation [8, 14–18], coprecipitation [19–23], sol–gel [24–27], and polyol [28–40] as summarized in Table 1. The nanoparticle catalysts can be supported on two different types of supports, those considered non-active supports (i.e., γ - Al_2O_3 , SiO_2 , activated carbon) or active (i.e., TiO_2 , CeO_2 , YSZ, SDC).

An important factor related to the type of support is the dispersion of the catalyst which is defined as the ratio of the number of gas-exposed surface atoms to the total number of catalyst atoms. In general, dispersion increases with decreasing particle size and theoretically approaches 100 % for particles with diameter in the range of 1 nm. It has been shown that, typically, higher dispersion leads to higher catalytic activity due to the presence of more active sites [40, 41–43]. This trend has been

Table 1 Summary of preparation methods for nanoparticles

Method	Synthesized catalyst	Reference
Impregnation	Au/TiO ₂	[8]
	Fe ₂ O ₃ /SiO ₂	[9]
	Ru/SnO ₂ , Ru/CeO ₂ , Ru/ZrO ₂ , Ru/ γ -Al ₂ O ₃	[10]
	Pt/YSZ	[11, 12]
	Pt-Ir/TiO ₂ nanotubes	[13]
Deposition-precipitation	Au/TiO ₂	[8]
	Au/ γ -Al ₂ O ₃	[14]
	Au/TiO ₂ , Au/CeO ₂ , Au/Al ₂ O ₃ , Au/SiO ₂	[15]
	Au-Ag/TiO ₂	[16]
	Ag/SiO ₂	[17]
	Ag/TiO ₂ , Au-Ag/TiO ₂	[18]
Coprecipitation	Pd-doped CeO ₂	[19]
	Fe ₃ O ₄	[20]
	Pd/Al ₂ O ₃	[21]
	Co _{0.5-x} Mn _x Zn _{0.5} Fe ₂ O ₄	[22]
	LiFePO ₄ /C	[23]
Sol-gel	ZnO, CuO, Cu _{0.05} Zn _{0.95} O	[24]
	CoFe ₂ O ₄	[25]
	SnO ₂	[26]
	Ni _{0.7-x} Mg _x Cu _{0.3} Fe ₂ O ₄	[27]
Polyol	Pt	[31]
	Pt	[36–39]
	Ru	[40]
	PtRu	[29]
	PtRu	[34]
	Pt ₇ Sn ₃	[35]
	FePt	[28]
	Ru, Pt	[32, 38]
	Ag	[30]
Cu	[33]	

shown for the same support material (i.e., SiO₂) synthesized with different surface areas [41]. Moreover, the catalytic activity of supported metal or metal oxide nanoparticles can be further enhanced or stabilized by using catalyst promoters or through the metal-support interaction (MSI) phenomenon.

Enhancing the activity of a catalyst through the concept of promotion involves adding a chemical species, referred to as a promoter, during the catalyst preparation procedure to the catalyst in order to change its catalytic behavior. The discovery of this concept was first employed through what is referred to as chemical promotion [44–48]. The addition of such species can result in a change in the electronic and/or crystal structure of the catalyst which improves its catalytic performance, stability, and selectivity for the desired chemical reaction.

Table 2 Summary of the type and use of some electronic promoting species

Promoting species	Catalyst	Reaction	Reference
Potassium (K)	Fe(111), Fe(100)	Adsorption of N ₂	[50]
	Ru/ Zeolite-X (Ru-KX)	NH ₃ synthesis	[51]
	Fe ₃ O ₄ (111), α-Fe ₂ O ₃ (0001)	Dehydrogenation of ethylbenzene to styrene	[52]
	K-Fe (S6-20) BASF	Dehydrogenation of ethylbenzene to styrene	[53]
Sodium (Na)	Pd/YSZ	NO _x reduction by C ₃ H ₆	[54]
	Pt/γ-Al ₂ O ₃	NO _x reduction by C ₃ H ₆	[55]
	Pt/γ-Al ₂ O ₃	NO _x reduction by C ₃ H ₆ and CO	[56]
	Rh/YSZ	NO _x reduction by CO	[57]
	Pt/YSZ	C ₂ H ₄ oxidation	[58]
Cesium (Cs)	Ru/CsX	NH ₃ synthesis	[51]
Cesium (Cs), chlorine (Cl)	Ag ₂ O	Epoxidation of C ₂ H ₄	[59]
Barium (Ba)	Pt/γ-Al ₂ O ₃	NO _x reduction by C ₃ H ₆	[60]
Magnesium (Mg), barium (Ba)	Ru/BaX, Ru/MgX	NH ₃ synthesis	[51]
Magnesium (Mg), barium (Ba), calcium (Ca), strontium (Sr)	Au/Al ₂ O ₃	Partial oxidation of methanol to H ₂	[61]
Cobalt (Co), chromium (Cr), molybdenum (Mo)	VPO/TiO ₂ , VPO/γ-Al ₂ O ₃	Ammoxidation of 2-chloro benzaldehyde to 2-chloro benzonitrile	[62]
Carbon monoxide (CO)	Au(111)	Methanol oxidation	[63]

In general, promoters can be divided into two categories – structural and electronic promoters [46, 49]. Structural promoters (e.g., Al₂O₃) enhance and stabilize the active phase while not participating in the catalytic reaction itself. Contrary to this, electronic promoters (e.g., alkali metal atoms) have a role in the catalytic reaction; they enhance the catalytic properties of the active phase by altering its chemisorptive properties, with respect to bond strength, of the reactants and intermediate species. The focus of this discussion will be on electronic promoters since they are a common factor between chemical and electrochemical promotion, as will be discussed later. Table 2 summarizes some of the different types of electronic promoters and corresponding applications. The most commonly used electronic promoters include potassium [50–53] and sodium [54–58]. Other chemical promoters include other alkali metals (i.e., Cs) [51, 59], alkaline earth metals (i.e., Mg, Ba) [51, 60, 61], and some transition metals (i.e., Co, Cr, Mo) [62].

Potassium, as a chemical promoter, has been used for a variety of chemical reactions and fundamental chemistry studies [50, 51]. A fundamental study was done on a single crystal of Fe(111) and Fe(100) showing a pronounced electron transfer from K to the Fe surfaces; this is attributed to the lowering of the “local” work function near where the potassium atoms are adsorbed [50]. Bécue et al. [51] demonstrated the effect of K promoters on the surface of a zeolite-X-supported Ru catalyst (2 wt%) for the synthesis of ammonia. It was found that the presence of K promoters increases the activity by approximately 70 % for optimal potassium coverage.

For coverage higher than the optimal amount of potassium, it was observed that the activity did not increase; instead, a decrease in activity was attributed to the blocking of active sites due to excess potassium coverage.

More recently, chemical promotion has been shown using other alkali metals such as cesium or alkaline earth metals and transition metals. A recent review on the epoxidation of ethylene to ethylene oxide (EO) over a silver catalyst demonstrated the industrial application of using cesium and chlorine as promoters for the selectivity of EO [59]. It was found that the unpromoted metallic silver catalyst had an EO selectivity around 50 %, while, with the addition of the promoters, the selectivity was enhanced to as high as 90 %. It is proposed that the Cl blocks the nonselective sites and promotes the active oxygen, while Cs acts as a structural promoter. It is said that the Cl promoters weaken the Ag–O bond creating more reactive oxygen to enhance the EO isomerization. On the other hand, Cs interacts with the Ag₂O surface and subsurface oxygen resulting in CsO_x-type complexes.

The use of alkaline earth metals (i.e., Mg, Ca, Sr, Ba) as promoters was shown in one study to enhance both the activity and selectivity of supported gold catalysts (Au/Al₂O₃) in the partial oxidation of methanol to H₂ [61]. It was found that H₂ selectivity increased with increasing basicity of the promoting oxide species (i.e., unpromoted <MgO < CaO < SrO < BaO); however, the opposite trend was observed for the selectivity toward CO and CH₄. Similarly, the effect of transition metal additives on the catalytic properties of a vanadium phosphate (VPO) catalyst was studied for the selective ammoxidation of 2-chloro benzaldehyde to 2-chloro benzonitrile [62]. To observe the effect of such promoters, Co, Mo, and Cr were added to the VPO structure and supported on two different oxide supports – TiO₂ and γ-Al₂O₃. It was observed that a significant improvement in both selectivity and activity existed compared to the bulk VPO catalyst. More specifically, in the case of TiO₂-supported VPO, the addition of Cr exhibited the best performance followed by Mo. From these results, it was also found that the ability of the promoter appears to depend on the nature of the support and its interaction with the catalyst.

Furthermore, traditionally, it has been observed that electropositive species usually promote catalytic reactions, while electronegative species poison the catalyst surface. One electronegative species, CO, has been well known to act as a poison for many metal catalysts; however, recent studies have shown a promotional effect of this species [63, 64]. Rodriguez et al. [63] have demonstrated the promotional effect of adsorbed carbon monoxide for the oxidation of alcohols over a gold catalyst. It was proposed that neighboring adsorbed CO enhances the OH bond on the surface of the catalyst in addition to promoting the breaking of the C–H bond of the alcohol molecules, thus increasing catalytic activity.

A related phenomenon to the promotion of catalytic activity is referred to as metal–support interaction (MSI), where the support plays a key role in changing the properties of the catalyst due the interaction between the two materials, usually resulting in higher catalytic activity [65, 66]. It should be noted that despite the vast amount of MSI studies reported up-to-date, the mechanism and appearance of this effect are still under discussion. Both fundamental and catalytic reaction studies with regard to metal–support interaction are summarized in Table 3.

Table 3 Summary of metal–support interaction studies

Metal catalyst	Support	Reaction	Reference
Ru, Pd, Os, Ir, Pt	TiO ₂	H ₂ , CO sorption	[67]
Pt	YSZ	Not applicable (XPS study)	[39]
Pt	WO ₃ /C, TiO ₂ /C, C	Not applicable (XPS study)	[68]
Au	SiO ₂ , TiO ₂	CO oxidation	[41]
Pt	Al ₂ O ₃ , TiO ₂ (P25, rutile, anatase), CeO ₂ , SiO ₃ , MgO	CO oxidation	[43]
PdO	CeO ₂ , TiO ₂ , Co ₃ O ₄ , Mn ₂ O ₃ , SnO ₂	CO oxidation	[69]
Pt, Ni	YSZ, γ -Al ₂ O ₃ , TiO ₂ , CeO ₂	CO oxidation	[70]
Cu	YSZ, γ -Al ₂ O ₃	CO oxidation	[71–73]
Pt	YSZ, γ -Al ₂ O ₃ , C	CO oxidation	[74]
Pt	YSZ, CeO ₂ , Sm-doped CeO ₂ , C, γ -Al ₂ O ₃	CO oxidation, C ₂ H ₄ oxidation	[75]
Au	CeO ₂ /TiO ₂	CO oxidation, water–gas shift reaction	[76]
Pd	CeO ₂ /YSZ	CH ₄ oxidation	[77]
Pt	YSZ, RO ₂ , SiO ₂	C ₃ H ₈ oxidation	[12]
Pt	YSZ, γ -Al ₂ O ₃	Toluene oxidation	[78]

Overbury et al. [41] showed that for equally sized Au nanoparticles supported on SiO₂ (lower surface area) and TiO₂ (higher surface area), the catalytic activity was higher for the TiO₂-supported catalysts due to stronger metal–support interaction. Similarly, Kimura et al. [43] demonstrated that for the same loading of metal catalysts deposited on Al₂O₃ and TiO₂, a lower dispersion was obtained for the particles supported on Al₂O₃ compared to TiO₂ indicating aggregation of the metal particles. This was attributed as a stronger metal–support interaction between Pt and TiO₂ compared to Pt and Al₂O₃. It is especially noted that the smaller the nanoparticle, the stronger the interactions are with the support, therefore, increasing the effect of the support used [79].

A more specific term, strong metal–support interaction (SMSI), was first introduced in 1978 to describe the significant change in the chemisorptive properties of group VIII noble metals when they were supported on TiO₂ [67, 80]. It was shown that these metals, both unsupported and supported on common materials such as Al₂O₃, chemisorb one hydrogen atom per metal atom; however, in the case of TiO₂, the ability to chemisorb H₂ was either decreased or disappeared completely. It was suggested that SMSI is due to TiO_x migration to the catalyst surface. Among other theories, the possibility of d-orbital overlap between the Ti⁴⁺ cations and supported metal atoms was suggested [80]. More recently, Lewera et al. [68] carried out a study to further understand the change in electronic properties of nanosized metals when deposited on TiO₂ through the analysis of X-ray photoelectron spectroscopy (XPS) data. Pt nanoparticles with an average size of 2 nm were deposited on a composite of TiO₂/C. A downshift in binding energy of the Pt 4f_{7/2} peak was observed which indicated a local charge density change due to the interaction between the

metal and TiO_2 . In addition, the presence of an additional (O 1s) peak for the Pt/ TiO_2 /C spectrum, compared to Pt/C and TiO_2 /C, is attributed to oxygen bonded to Ti alloyed with Pt indicating the interaction between the two materials. The analysis of the Ti 2p peak also showed a downshift in binding energy for the supported Pt sample suggesting a new electronic state of Ti.

Similarly, Ntais et al. [39] conducted an XPS study for YSZ-supported Pt nanoparticles which also showed a downshift in the binding energy for smaller Pt nanoparticles indicating a stronger interaction with the support.

Several recent studies have studied the MSI phenomenon, not only using TiO_2 -supported metals but employing other ionic and mixed ionic–electronic conducting materials as well. High catalytic activity toward the water–gas shift reactions was shown for a Au/ $\text{CeO}_x/\text{TiO}_2(110)$ catalyst [76]. The high catalytic activity was attributed to the chemical properties of Ce_2O_3 , which was formed through the interaction with TiO_2 and its effect at the ceria–gold interfaces. Similarly, Jiménez-Borja et al. [77] demonstrated a strong interaction between Pd and CeO_2 for a Pd/ CeO_2 /YSZ catalyst for the oxidation of methane. It was observed that the presence of ceria caused a decrease in the size of Pd^0 particles (from 280 to 103 nm) and an increase in the size of PdO particles. This is attributed to the oxygen storage properties of CeO_2 which seems to play a key role in the formation of PdO. Higher catalytic activity was observed for the catalysts containing more PdO compared to Pd. Furthermore, Pd catalysts supported on highly ordered mesoporous metal oxides (i.e., CeO_2 , TiO_2 , Co_3O_4 , Mn_2O_3 , and SnO_2) for the oxidation of CO were carried out to demonstrate the interaction between the metal and metal oxide supports [69]. It was found from XPS results that the binding energy of the Pd $3d_{5/2}$ peak for Pd/meso- CeO_2 , Pd/meso- SnO_2 , and Pd/meso- TiO_2 catalysts shifted more than that for Pd/meso- Co_3O_4 and Pd/meso- Mn_2O_3 indicating that the former catalysts have more surface interactions with the Pd metal. From the catalytic experiments, the bare supports and supported Pd catalysts showed high catalytic activity in the order of $\text{Co}_3\text{O}_4 > \text{Mn}_2\text{O}_3 > \text{CeO}_2 > \text{SnO}_2 > \text{TiO}_2$; however, the increase in catalytic activity from bare support to supported Pd catalyst was the highest for the Pd/meso- CeO_2 , Pd/meso- SnO_2 , and Pd/meso- TiO_2 catalysts indicating the significant role of the support.

Ionically conductive supports or solid electrolytes have emerged as a class of very promising catalyst supports due to their high ionic conductivity, and chemical and mechanical stability [81]. For a material to be ionically conductive, it must possess the structure that allows for either ions to transfer through a series of interstitial sites (i.e., Frenkel defects) or ions to transfer through vacancies in the crystal structure (i.e., Schottky defects) [45, 82, 83]. Some examples include yttria-stabilized zirconia (YSZ) (O^{2-} conductor), K- $\beta\text{-Al}_2\text{O}_3$ (K^+ conductor), and Na- $\beta''\text{-Al}_2\text{O}_3$ (Na^+ conductor). As an extension, mixed ionic–electronic materials not only possess ionic conductive capabilities but electronic conductive properties as well [84, 85]. Ion transfer in such materials occurs through structure defects as discussed; however, electronic conductivity occurs through delocalized states in the conduction or valence band, or through localized states by a thermally assisted hopping mechanism. It should be noted that the reason for these properties is independent of each other – ion conductance depends on crystal structure, while electronic conductance

depends on electronic bandgap corresponding to the properties of the constituent ions [84]. Examples of mixed ionic–electronic conducting materials include ceria (CeO_2), titania (TiO_2), and perovskite-type materials in a form of $\text{La}_{1-x}\text{A}_x\text{Co}_{1-y}\text{B}_y\text{O}_{3-\delta}$ (where $\text{A} = \text{Sr}, \text{Ba}, \text{Ca}$, and $\text{B} = \text{Fe}, \text{Cu}, \text{Ni}$) [85, 86].

Initially, the concept of SMSI was attributed to electronic effect; however, further studies have shown an effect of oxygen vacancies in metal oxides as well. Metcalfe and Sundaresan [70] demonstrated this concept for CO oxidation over Pt and Ni catalysts supported on YSZ, $\gamma\text{-Al}_2\text{O}_3$, TiO_2 , and CeO_2 . It was found that catalytic activity for the Pt catalysts ranged from $\text{Pt}/\text{TiO}_2 > \text{Pt}/\text{YSZ} > \text{Pt}/\gamma\text{-Al}_2\text{O}_3$. The most interesting results are those for the Ni catalysts where Ni/TiO_2 , Ni/YSZ , TiO_2 , and YSZ showed significant catalytic activity, with the supported Ni catalyst showing higher activity than their corresponding pure supports. The difference in the activity of Ni/TiO_2 and pure TiO_2 could be attributed to only the electronic effects of TiO_2 ; however, after observing higher activity for Ni/YSZ compared to pure YSZ, it was proposed that oxygen ion transfer between the metal and support also plays a role in enhancing the catalytic activity. A similar conclusion was found for studies of a copper catalyst supported on $\gamma\text{-Al}_2\text{O}_3$ and YSZ [71–73]. The higher catalytic activity was attributed to the presence of Cu^+ due to the interaction between the copper oxide on the surface of the YSZ and the nearby oxygen vacancies. Vernoux et al. [87] also observed such migration of ionic species from the support to the surface of the nanocatalyst, referring to it as self-induced electrochemical promotion. This concept has been suggested as an explanation for higher catalytic activity for the oxidation of CO over YSZ-supported Pt nanoparticles [36, 74]. It was shown that the catalyst was active for a temperature as low as 40 °C. This high catalytic activity was attributed to the migration of O^{2-} species to the surface which may lead to alterations in the catalytic properties of the Pt nanoparticles. This phenomenon has also been observed for both propane oxidation [87] and toluene oxidation [78] over a Pt/YSZ catalyst. Most recently, Isaifan and Baranova [37, 38, 75] also demonstrated the role of ionic and mixed ionic–electronic supports and the mobility of O^{2-} from these supports for the oxidation of CO and C_2H_4 in an oxygen-free environment. It was found that Pt/YSZ, Pt/ CeO_2 , and Pt/Sm-doped CeO_2 (SDC) have high catalytic activity for CO and C_2H_4 oxidation while Pt/C and Pt/ $\gamma\text{-Al}_2\text{O}_3$ as well as the blank supports show no catalytic activity in the absence of gaseous O_2 . These results imply that O^{2-} from the support reacts with CO and C_2H_4 in an electrochemical reaction at the three phase boundary and the mechanism of nanogalvanic cells was proposed [37].

Electrochemical Promotion of Catalysis

Discovered in the 1980s [88], the phenomenon of electrochemical promotion of catalysis (EPOC), also referred to as non-Faradaic electrochemical modification of catalytic activity (NEMCA), demonstrated a new approach to enhancing the catalytic activity and opened up a new class of promoters previously unknown in heterogeneous catalysis (e.g., O^{2-} , H^+ , OH^- , H^+). By applying an electrical current or

potential between the catalyst-working electrode and a counter electrode deposited on a solid electrolyte, it was found that the catalytic activity and selectivity can be significantly altered due to modifications of the electronic properties of the catalyst. Consequently, the adsorption strength of the reaction components is altered resulting in a distinct change in catalytic performance [45]. Compared to chemical promotion, the addition of promoter species is done in situ and can be controlled depending on specified reaction conditions [44, 45, 89–98]. This also implies that promoters with short lifetimes can still effectively be utilized as its coverage on the catalyst surface can be fixed through the application of a current or potential. Therefore, it is said that there is an operational and not a functional difference between chemical and electrochemical promotions [45, 49, 57, 90, 99, 100]. Currently, EPOC has been studied for more than 100 catalytic systems and does not appear to be limited to any specific type of catalytic reaction, metal catalyst, or solid electrolyte. Since the discovery of EPOC, several comprehensive reviews [48, 94, 95, 100–113], book chapters [114–118], and a book [45] have been published to describe this phenomenon; the authors invite the reader to consult these works for comprehensive reading on the EPOC phenomenon. Here, a short overview of the principles, a common experimental setup and reactors, as well as some examples of EPOC with thick, low dispersion film catalysts will be discussed followed by recent studies using nanostructured catalysts.

The concept behind EPOC is that, initially, before current or potential is applied, the catalyst surface is covered by chemisorbed reactants (e.g., O_2 and C_2H_4) in an equilibrated state. Depending on the concentration of the species, there may be more or less of each species adsorbed on the catalyst surface. By applying a current or potential, ions (i.e., O^{2-} in the case of YSZ) from the solid electrolyte either back-spillover (i.e., move to the surface of the catalyst) or spillover (i.e., move from the surface of the catalysts) depending whether the electrochemical cell is positively or negatively polarized, respectively. In the case of back-spillover of the O^{2-} species, it is said that these species form a strong bond on the catalyst surface. The mechanism of this transformation can be seen in the following reaction (Eq. 1) [45]:



where $O^{\delta-}$ is the general form of the back-spillover species corresponding to its image charge $\delta+$, indicating that the back-spillover species is overall neutral. The formation of this layer is referred to as an effective double layer. Due to this back-spillover, the oxygen reactant from the gas phase is forced into a weakly bonded state resulting in a more reactive chemisorbed species. Therefore, it is observed that the catalytic rate increases until a new steady-state is reached through the equilibrium of the strongly and weakly bonded oxygen species [45]. The opposite effect is observed for the spillover of the O^{2-} species.

In general, the property of a solid surface that dictates its chemisorptive and catalytic properties is its work function (Φ). By definition, the work function is the minimum energy required for an electron to move from the Fermi level of the solid to an outer point, a few μm outside the surface [45, 119]. Depending on the type of species adsorbed or spilled over onto the catalyst surface, the work function can be

altered accordingly. An electron donor species (e.g., C_2H_4) will cause the work function to decrease, while an electron acceptor species (e.g., O_2) will cause the work function to increase. Four different types of reaction behaviors, in regard to the presence of these species, have been established to classify the relationship between work function and catalytic rate (r) for EPOC studies – electrophobic ($\delta r/\delta\Phi > 0$), electrophilic ($\delta r/\delta\Phi < 0$), volcano type (exhibits a minimum), and inverted volcano type (exhibits a maximum).

More specifically, to evaluate the performance of the catalyst in terms of electrochemical promotion, there are two main parameters that are calculated – rate enhancement ratio (ρ) and Faradaic efficiency (Λ) [45]. The rate enhancement ratio (Eq. 2) is defined as

$$\rho = r / r_0 \quad (2)$$

where r_0 is the open circuit oxidation rate of the reactant species ($\text{mol} \cdot \text{s}^{-1}$) and r is the oxidation rate ($\text{mol} \cdot \text{s}^{-1}$) for an applied current/potential. The Faradaic efficiency (Eq. 3), for an O^{2-} conducting system, is defined as the following:

$$\Lambda = (r - r_0) / (I / 2F) \quad (3)$$

where I is the current measured across the cell (A) and F is Faraday's constant ($96,485 \text{ C} \cdot \text{mol}^{-1}$). It should be noted that the enhancement is considered to be the effect of electrochemical promotion only when $|\Lambda| > 1$, which indicates non-Faradaic enhancement [45].

First discovered by Comninellis and coworkers [120], another important aspect that is considered in EPOC studies is what is referred to as “permanent” electrochemical promotion of catalysis (P-EPOC). It has been shown that the reversibility of EPOC strongly depends on the duration of polarization and magnitude of applied current or potential. With P-EPOC, after current interruption, the catalytic rate remains higher than the initial open circuit value. In the case of P-EPOC, the permanent rate enhancement can be evaluated using Eq. 4 [120]:

$$\gamma = r_p / r_0 \quad (4)$$

where γ is the permanent rate enhancement ratio and r_p is the catalytic rate ($\text{mol} \cdot \text{s}^{-1}$) at the new steady-state value after current interruption.

Two types of experimental reactors exist to carry out conventional EPOC studies – a fuel cell type reactor and single-chamber type reactor [45]. The fuel cell type reactor (Fig. 1a) consists of two chambers, one in which the catalyst-working electrode is exposed to the reactants and products, while the other chamber contains the counter and reference electrodes which are exposed to a reference gas only. Contrary to this, the single-chamber type reactor (cell configuration in Fig. 1b and typical experimental setup in Fig. 1c) consists of all electrodes exposed to the same reactants and products. The important consideration with this type of reactor is that the reference electrodes must be made of an inert material with respect to the reactants (in most cases, gold is used) to ensure no contribution to the catalytic rate. Conventional EPOC studies were carried out using metal

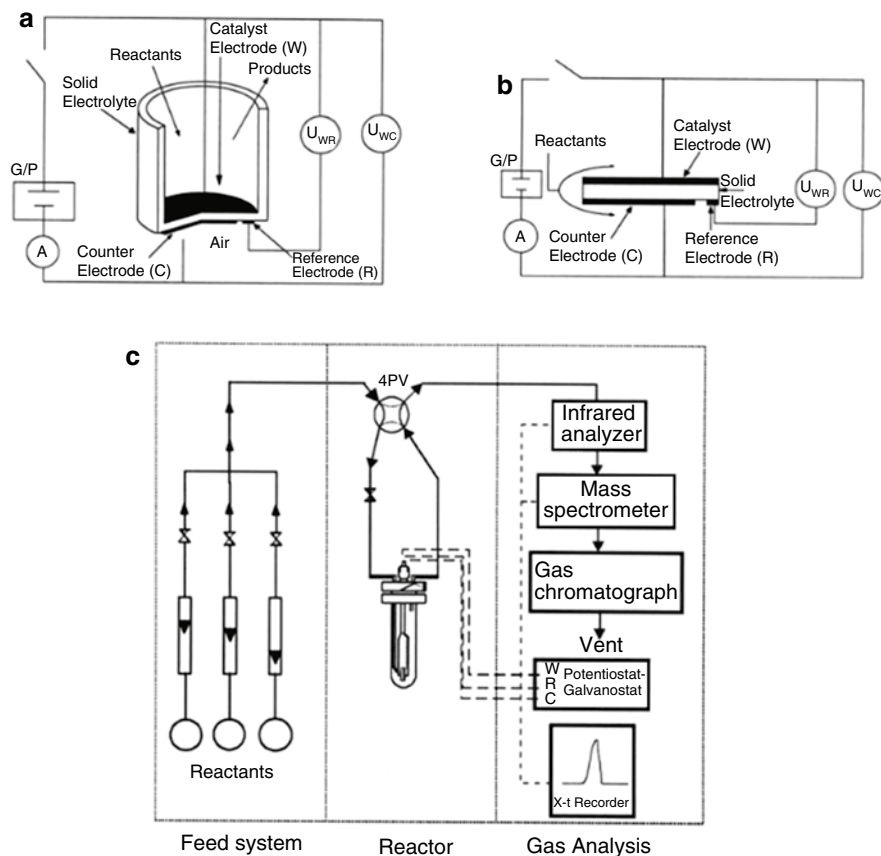


Fig. 1 Schematic of the (a) fuel cell type reactor, (b) single-chamber type reactor, and (c) typical gas flow experimental arrangement using the single-chamber type reactor (Reproduced from Vayenas et al. [45])

(deposited with metallic paste) catalyst films, typically, of a thickness in the range of 5–10 μm [90, 121] and a metal dispersion less than 0.1 % [122]. Typical solid electrolytes include YSZ (O^{2-} conductor), $\beta'\text{Al}_2\text{O}_3$ (Na^+ conductor), or $\beta''\text{Al}_2\text{O}_3$ (K^+ conductor).

The EPOC phenomenon has been shown to be effective for various reactions; however, the most common model reaction used in conventional EPOC studies is the complete oxidation of ethylene (Table 4) [88, 90, 94, 121–130]. This was the reaction under observation over a porous Ag film when it was first discovered that pumping and removing oxygen ions from the surface of the catalyst through an applied current can alter the catalytic rate and selectivity [88]. It was then later demonstrated that this effect is not specific to any type of reaction system, although the most significant enhancement (i.e., tenfold increase, Λ up to 15,000) was shown for the oxidation of C_2H_4 over a Pt catalyst [90, 121].

Table 4 Electrochemical promotion of ethylene oxidation for various catalytic systems

Catalyst	Solid electrolyte	Temperature (°C)	Promotion parameters		Reference
			ρ_{\max}	$\Lambda_{\max/\min}$	
Ag	YSZ	320–420	–	<300	[88]
Pt	YSZ	260–420	–	<15,000	[121]
Pt	YSZ	300–450	–	74,000	[90]
Pt	YSZ	375	300	289	[122]
Pt	YSZ	510	–	144	[123]
Rh	YSZ	320–450	1.4	123	[124]
IrO ₂	YSZ	380	–	200	[125]
IrO ₂	YSZ	380	13	~100	[126]
IrO ₂	YSZ	380	2.5	2000	[127]
Pd	YSZ, β'' -Al ₂ O ₃	300–400	–	3000	[128]
Pt	TiO ₂	500	21	1880	[128]
Pt	Gd-doped BaPrO ₃ Y-doped BaZrO ₃	400–600	1.3	–	[129]
Pt	La _{0.99} Sr _{0.01} NbO _{4.8}	350–450	1.4	–100	[130]

Enhancement in catalytic activity through this phenomenon for C₂H₄ oxidation has been shown over Pt catalysts supported on YSZ and TiO₂, O²⁻ conducting supports [128]. Further studies for IrO₂ film catalysts supported on YSZ electrolyte showed an enhancement in catalytic activity through an applied positive potential (i.e., oxygen ions migrate to the surface of the catalyst) [125–127]. Permanent promotion was also observed for this system which was attributed to the formation of a higher coordinated oxide at the catalyst/solid interface [126]. Moreover, Koutsodontis et al. [122] demonstrated that the catalyst film thickness for a Pt/YSZ cell is an important factor that affects the magnitude of electrochemical promotion as well, showing that the catalytic rate increases with the increase in film thickness. In addition to O²⁻ conducting electrolytes, positive ion (i.e., Na [128, 131–134], K [135], and H [128–130, 136]) conducting electrolytes have been employed. The electronic effect of these types of promoters are the opposite of that for oxygen ions; that is, by pumping positive ions to the catalyst surface, the work function decreases. In studies involving Na⁺ promoters, Na- β'' -Al₂O₃ is used as a solid electrolyte. In general, it has been found that catalytic activity, for CO [131] or C₂H₄ [128] oxidation and NO reduction by hydrocarbons [132–134], is increased with low Na coverage, while as Na coverage increases, this leads to poisoning of the catalyst surface. Similar observations were found in the case of potassium promoters from a K- β' -Al₂O₃ electrolyte for CO oxidation over a Pt catalyst [135]. With regard to the use of H⁺ promoters, several different electrolytes have been studied (e.g., Nafion [128, 136], Gd-doped BaPrO₃ [129], Y-doped BaZrO₃ [129], and La_{0.99}Sr_{0.01}NbO_{4.8} [130]). Compared to Na and K, H⁺ promoters do not seem to have a significant enhancement of the catalytic activity [129, 130]. In addition to a weak non-Faradaic effect [130].

Although much research has been performed regarding this technology, limitations have been identified that prevent its commercialization. These include eliminating the conventionally used thick film catalysts which have low surface areas and high material costs and moving from theoretical to more practical reactor designs [100]. Overall, the objective is to be able to apply the concept of EPOC to high dispersion heterogeneous catalysts.

Application of Nanostructured Catalysts for EPOC

Highly Dispersed Nanocatalyst Preparation

In heterogeneous catalysis, dispersion of a catalyst has been shown to be an important factor in terms of catalytic performance; the higher the dispersion, the more available the active sites, typically resulting in higher catalytic activity. Dispersion is one aspect of commonly used electrochemical promotion catalysts that has been recognized as an important factor that requires improvement in order to be competitive with the state-of-the-art commercial heterogeneous catalysts. To address the limitation of low metal dispersion found for the catalyst-working electrodes of conventional electrochemical promotion systems, several deposition techniques have been studied (Table 5).

Table 5 Preparation methods of highly dispersed nanocatalysts

Method	Catalyst	Dispersion/loading	Particle size	Film thickness	Reference
Impregnation	Pt	0.2 or higher	–	–	[137]
	Pt	34, 40, 42 %	3.5, 3.0 nm	–	[12]
	Pd	4.9 %	2.6 nm	–	[138]
	Ag	1 %	100 nm	–	[139]
	Ru	3 mg Ru	–	4 μm	[140]
	RuO ₂	1.72 g RuO ₂ /m ²	–	–	[141]
Metal sputtering	Pt	–	40 nm	–	[142,143]
	Pt	–	–	30, 90 nm	[144]
	Pt	2.2, 32 $\mu\text{g Pt/cm}^2$	–	2, 22 nm	[145]
	Pt	–	–	150 nm	[146]
	Pt	5 %	50 nm	–	[147,148]
	Pt	40 %	–	40 nm	[149]
	Rh	10 %	–	40 nm	[150]
	Rh, Pt	13–40 %	–	40 nm	[151]
	Rh, Pt	>10 %	–	40 nm	[152]
Rh–Pt	>15 %	–	40 nm	[153]	
Electroless deposition	Pd	5 mg Pd	–	–	[155]
Electrostatic spray deposition (ESD)	Pt	250 $\mu\text{g Pt}$	9 nm	65	[156]
		320 $\mu\text{g Pt}$	9 nm	85	
		420 $\mu\text{g Pt}$	23.2 nm	110	

The first technique that has been used in recent electrochemical promotion studies that results in near-nanometric or porous films is wet or dry impregnation [137–141]. In general, this type of technique employs a precursor salt of the desired metal dissolved in the solution. The solution is dried on the solid electrolyte, calcined, and reduced in H_2 . For example, Marwood and Vayenas [137] dissolved H_2PtCl_6 in water, dried at 80 °C (catalyst 1) and 90 °C (catalyst 2), calcined in air at 450 °C for 1 h, and reduced in 2 % H_2 in helium at 250 °C for 2 h. Using the CO titration technique [157] to determine dispersion, it was found that catalyst 2 had a dispersion of $D=21$ % while for catalyst 1, which had a similar mass as catalyst 2 but a surface area of a factor of 5 higher, the dispersion was estimated to be approximately $D \approx 100$ %. A similar procedure was carried out by Jiménez-Borja et al. [138] using a 0.1 M $Pd(NH_3)_4(NO_3)_2$ aqueous solution which resulted in a Pd metal dispersion of 4.9 % for 0.85 mg of Pd deposited. Even though not in the nanometric scale, other groups have demonstrated a decrease in metal required through porous micrometric films, as shown by Theleritis et al. [140] who deposited a porous film of thickness ~ 4 μm for a loading of approximately 3 mg of catalyst. In addition, Li and Gaillard [139] demonstrated the use of a less expensive metal, Ag, for working electrode films that was of a micrometric thickness of 1.8 and 3.9 μm , and an average crystallite size of approximately 100 nm.

Another common deposition technique that has been employed by many research groups [142–153] to increase catalyst dispersion is metal sputtering, in which the solid electrolyte substrate is placed inside a vacuum chamber in close proximity to the desired metal to be deposited. The desired metal is bombarded with ionized gas molecules in order to displace the metal in small quantities and slowly deposit a thin, nanometric layer on the substrate. This technique has been used by several groups to deposit Rh [150–152], Pt [12, 142–149], or Rh–Pt bimetallic [153] thin-film catalysts. Both Balomenou et al. [151, 152] and Baranova et al. [150, 158, 159] have achieved a film thickness of approximately 40 nm and a dispersion of approximately 13–40 % and 10 %, respectively. Other groups have also shown sputter deposition of Pt that achieves a thickness ranging from 30 to 150 nm, corresponding to dispersions from 5 % to 40 % [142–144, 146–149]. Uniquely, Karoum et al. [145] sputter deposited a thin layer of Pt (~ 2 nm) on an 80 nm LSM ($La_{0.7}Sr_{0.3}MnO_3$) interlayer where the Pt layer did not necessarily cover the entire surface; however, it was shown to be viable for electrochemical promotion and electronically conductive due to the LSM interlayer. Finally, co-deposition of both Rh and Pt (atomic ratio, 1:1) was performed by Koutsodontis et al. [153] which resulted in an approximate thickness of 40 nm and a total active metal surface area of 1.9×10^{-5} mol metal.

Other research groups have also employed alternative, less common techniques such as electroless deposition [155] and electrostatic spray deposition (ESD) [156]. Lintanf [156] describes the ESD method as using less material compared to conventionally used paste deposition and being fully reproducible. It was reported that three different types of films can be produced – reticulated, dense, and dense – with particles corresponding to film thicknesses of 110, 65, and 85 nm, respectively. The average crystallite size was found to be 23.2 nm for the reticulated film and 9.0 nm for both dense films. Also, an approximate dispersion of 40 % was reported.

Cell Configurations and Reactor Design

Another factor that has been identified and discussed in previous reviews [100, 109] which is preventing commercial application of electrochemical promotion from being achieved is the configuration of the cell and design of the reactor. In a recent comprehensive review, Tsiplakides and Balomenou [100] summarized the considerations taken to address the need for cell configurations that can accommodate thin films and nanoscale catalysts along with designing a more compact reactor that has efficient current collection. The development of electrocatalysts, new configurations such as bipolar or monolithic, and concept of “wireless” EPOC is discussed in this review.

As alluded to in the previous section, the simplest modification to the conventionally used electrochemical promotion cell is to deposit less metal for the working electrode. An important factor to consider, though, is that the metal deposited as a working electrode must remain electronically connected; otherwise, some of the film will not be polarized. Lintanf's [156] description includes a gold mesh on the working electrode side of the cell in order to ensure electronic connectivity for their thin (65–110 nm) Pt catalyst films deposited by ESD. These details are not indicated in other studies [138, 140, 146–148, 160]; however, electrochemical promotion using the conventional cell configuration was observed for catalyst films exhibiting dispersions ranging from 5 % to 80 % demonstrating the presence of at least some electrical connectivity. Similarly, another approach to establish electrical connectivity involves introducing a mixed ionic–electronic conductive (MIEC) interlayer between the nanostructured catalyst and solid electrolyte. Some examples of MIEC interlayer materials that have been used in recent studies include TiO_2 [144, 150, 159], LSM ($\text{La}_{0.7}\text{Sr}_{0.3}\text{MnO}_3$) [145], CeO_2 [161], and LSCF/GDC ($\text{La}_{0.6}\text{Sr}_{0.4}\text{Co}_{0.2}\text{Fe}_{0.8}\text{O}_{3.8}/\text{Ce}_{0.9}\text{Gd}_{0.1}\text{O}_{1.95}$) composite (30 % GDC) [162]. Several methods were used to introduce these interlayers. Baranova et al. [150, 159] deposit TiO_2 (~5 μm thickness) on a YSZ pellet by applying a solution of 20 % TiO_2 in EtOH:H₂O (1:1), evaporating at 60 °C for 10 min, and thermal treatment at 450 °C for 30 min in air; following this deposition, Rh is sputter deposited overlaying the TiO_2 . Alternatively, another study showed the use of sputter depositing for both the TiO_2 interlayers (~90 nm thickness) along with the deposition of Pt (~30 nm thickness) [144]. Figure 2 shows SEM micrographs of the deposited layers on the YSZ pellet. It was noted that the YSZ pellet is not fully covered by the TiO_2 interlayer (Fig. 2b).

Both interlayer (LSM) and Pt catalyst were also sputter deposited in a study performed by Karoum et al. [145]; however, interesting to note, the use of a CGO ($\text{Ce}_{0.9}\text{Gd}_{0.1}\text{O}_{2.8}$) pellet was shown to be an alternative to using YSZ. For a temperature range of 200–400 °C, the ionic conductivity of the CGO pellet was shown to be at least 10 times higher than that of the YSZ pellet. Finally, as described by Kambolis et al. [162], the electronic conductivity of the catalyst electrode in their EPOC cell was not ensured by the impregnated Pt nanoparticles but by the MIEC interlayer of LSCF/GDC which was deposited through screen printing on a GDC pellet.

The first step toward a modified cell configuration is shown in Fig. 3, proposed by Marwood [163] in the 1990s, in which the catalyst is not used as an electrode as in the conventional EPOC, but rather it is instead electronically isolated with current

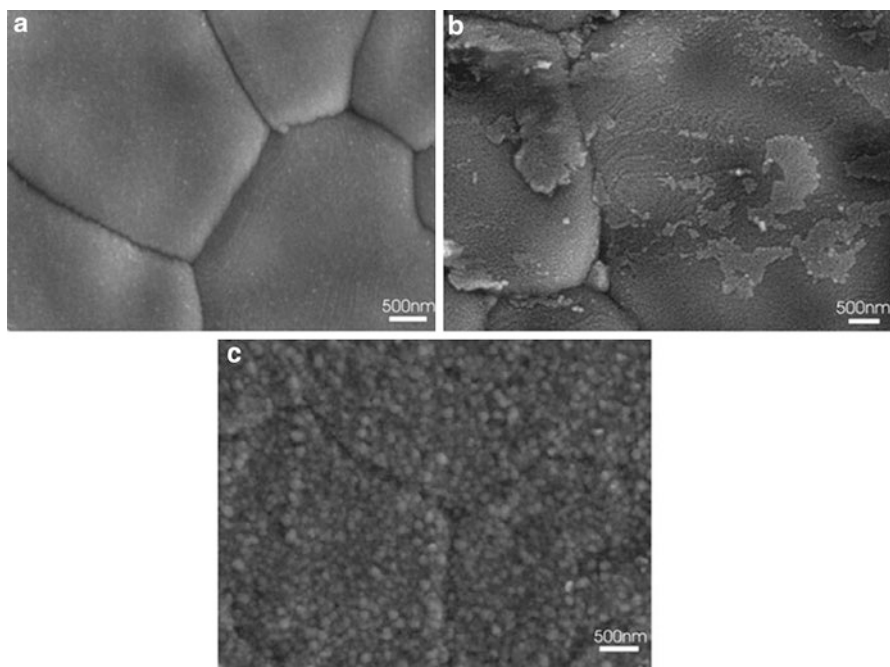


Fig. 2 SEM micrographs of (a) YSZ surface, (b) sputter-deposited TiO_2 on YSZ surface, and (c) sputter-deposited Pt on TiO_2/YSZ surface (Reproduced from Papaioannou et al. [144])

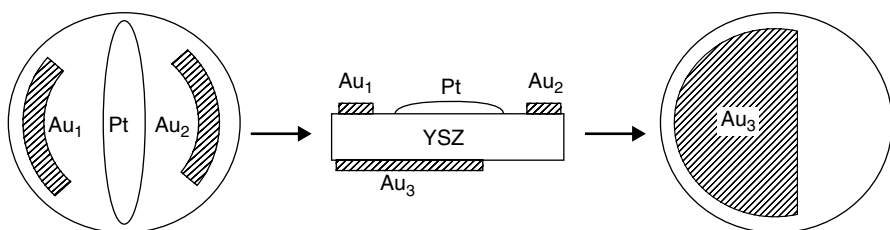


Fig. 3 Schematic of first proposed bipolar configuration, Pt catalyst and Au working (Au_1), counter (Au_2), and reference (Au_3) electrodes (Reproduced from Marwood [163])

passing between two gold electrodes. This pioneering work showed that Pt was deposited using the commonly used paste to determine whether a direct electrical connection between the catalyst and counter electrode was necessary to observe the effect of electrochemical promotion [163].

Similarly, a preceding study demonstrated the use of highly dispersed impregnated Pt (~ 5 nm) nanoparticles [137]; however, they were deposited on a gold working electrode. From this study, it was shown that direct contact between the catalyst and the solid electrolyte was not necessary as well. In addition, it was also not necessary for the catalyst to be continuous to observe the effects of electrochemical promotion.

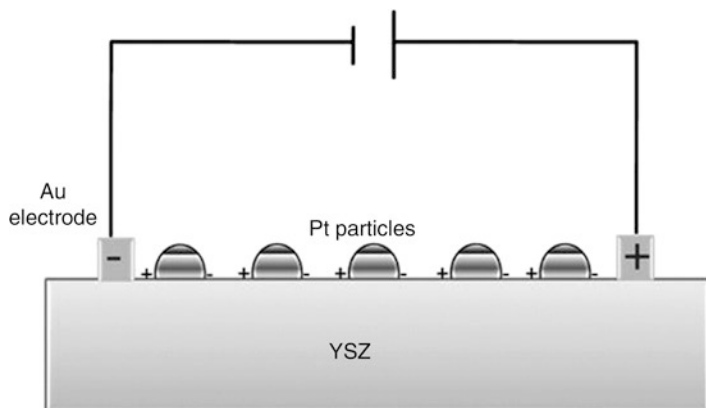


Fig. 4 Schematic of bipolar configuration of electrochemical cell, consisting of two Au electrodes and polarized Pt particles deposited on YSZ solid electrolyte (Reproduced from Xia et al. [143])

Various other cell designs have been proposed and tested by other research groups which fall under the bipolar configuration category. These include depositing Pt metal paste in the forms of stripes or dots between two gold electrodes [164], coating glass beads with Rh and placing them inside a YSZ tube that is coated with two gold electrodes on the outer surface [99], and sputtering Pt between the comb-like gold electrode structures (distance of 2 mm between electrodes) [142]. Figure 4 depicts a bipolar cell configuration presented by Xia et al. [143]. As shown in the figure, it was proposed that upon application of an electrical field, the dispersed Pt nanoparticles form partially or completely polarized galvanic cells, one side being positively polarized and the other negatively polarized.

Further cell modifications were first proposed by Wodiunig et al. [141] through the use of a cylindrical YSZ solid electrolyte monolith. A RuO_2 catalyst was deposited through thermal decomposition (i.e., impregnation) inside the channels of the monolith, while two gold electrodes were deposited symmetrically on the outside of the cylinder. A similar honeycomb monolith was used in a previous study where dispersed Pd particles were introduced into the channels by electroless deposition; however, instead of both electrodes deposited on the outside of the cylinder, a gold working electrode was deposited on the entire outside surface, while a continuous Pd film was deposited (as a counter electrode) on the center channel of the monolith [154]. Furthermore, using this concept of a monolithic reactor and in regard to both the desire for efficient current collection and a compact reactor design, the monolithic electrochemically promoted reactor (MEPR) was proposed by Balomenou et al. [151, 152]. Details of the design and construction of this reactor are well outlined, describing that the main advantage is that it can be assembled and dismantled easily and the plates can be replaced as necessary [151]. This type of reactor has also been employed by Koutsodontis et al. [153] who describe the design as a hybrid between the classical honeycomb monolith and a flat- or ribbed-plate solid oxide fuel cell; a feasible solution in order to minimize electrical connections.

More recently, as modified from the reactor in Fig. 1c, a single-chamber reactor (SCCR) was developed to accommodate highly-dispersed nanocatalysts [155].

A more recent concept that has been related to the electrochemical promotion phenomenon is that of self-induced electrochemical promotion. One of the main advantages of this type of catalytic cell is that there is no electrical contacts required which, in turn, means no external circuit. It has also been a suggestion in order to overcome the limitation of the electrical connectivity of nanocatalysts. This concept has been demonstrated for the oxidation of CO over YSZ-supported Pt nanoparticles [36, 74] as well as for propane oxidation [87] and toluene oxidation [78] over a Pt/YSZ catalyst.

Similarly, the concept of a wireless configuration has been studied as well which involves a concentration driving force that causes the migration of promoting ion species from the support toward the surface of the nanostructured catalyst [165–167]. These studies were also performed for a Pt catalyst deposited on a MIEC support (or membrane). The cell is placed inside a dual chamber reactor which consists of a reaction side (i.e., catalyst, reaction gases) and a sweep side (i.e., catalyst, sweep gas). In this case, open circuit conditions correspond to using the same reaction mixture on each side. To induce back-spillover (i.e., pushing oxygen toward the surface of the reaction side catalyst), oxygen was introduced on the sweep side. This creates an oxygen chemical potential difference across the membrane driving the oxygen toward the reaction side. Furthermore, spillover (i.e., removing oxygen from the surface of the reaction side catalyst) was induced by sweeping hydrogen on the sweep side creating a driving force in the opposite direction [165–167]. It should be noted that the same in situ control of catalytic activity as EPOC can be achieved with this type of wireless configuration by altering the oxygen concentration difference across the membrane.

Electrochemical Promotion of Nanostructured Catalysts

Several model reactions have been used to evaluate and investigate the viability of electrochemical promotion for the nanocatalyst systems (as shown in Table 6). These include complete oxidation of ethylene [40, 141, 144, 150, 151, 158, 159, 163, 164] and propane [12, 145, 146, 148, 162], combustion of CO [142, 143, 147] and natural gas [138, 154, 161], reduction of NO in the presence of hydrocarbons [99, 152, 153, 156, 160], and, more uniquely, SO₂ oxidation [149] and the reverse water–gas shift (RWGS) reaction [140]. Each study has shown promising results for electrochemical promotion over nanocatalysts for different cell configurations and reactor designs which prove to be furthering this technology toward commercialization.

In general, it has been concluded that the reaction rate of ethylene oxidation is significantly increased when a positive polarization is applied [141, 144, 150, 151, 158, 159, 163, 164]; however, a recent study showed an increase in catalytic rate when negative polarization is applied. This was attributed to partial reduction of CeO₂, the catalyst support, causing a stronger MSI of the Ru nanoparticles and CeO₂ [40]. The introduction of a MIEC interlayer, especially TiO₂, was shown to

Table 6 Electrochemical promotion of nanocatalytic systems

Reaction	Catalyst	Solid electrolyte	Temperature (°C)	Promotion parameters		Reference
				ρ_{\max}	$\Lambda_{\max/\min}$	
C ₂ H ₄ oxidation	Pt	YSZ	353	1.38	688	[163]
	Pt	YSZ	400	3.8	–	[164]
	Pt	YSZ TiO ₂ /YSZ	280	67 168	188 753	[144]
	Pt, Rh	YSZ	300–380	1.45	77	[151]
	Rh	YSZ TiO ₂ /YSZ	300–420	60 78	1400 1791	[150,158,159]
	Ru	YSZ	350–400	2.46	96	[40]
	RuO ₂	YSZ	360	–	90	[141]
C ₃ H ₈ oxidation	Pt	YSZ	350	5.6	330	[146]
	Pt	YSZ	150–500	22.4	480	[148]
	Pt	Ce _{0.9} Gd _{0.1} O ₂₋₆	170–250	1.3	6	[145]
	Pt	Ce _{0.9} Gd _{0.1} O _{0.95}	267–338	1.38	85	[161]
CO oxidation	Pt	YSZ	300	500	1.5	[142,143]
	Pt	YSZ	250	4	530	[147]
CH ₄ oxidation	Pd	YSZ	400	–	47	[130]
	Pd	YSZ	120–500	3.65	–	[138]
	Pd	CeO ₂ /YSZ	480	5.6	764	[160]
NO _x reduction	Pt	YSZ	300–510	2.3	48	[156]
	Pt, Rh	YSZ	290–305	14	900	[152]
	Pt–Rh	YSZ	335–380	6.46	13.75	[153]
	Rh	YSZ	275–450	6	5	[99]
	Rh	YSZ	370	220	1207	[160]
SO oxidation	Pt	YSZ	330–370	2	30	[149]
RWGS	Ru	YSZ	200–300	2.5	1000	[140]

enhance the catalytic activity even more [144, 150]. Baranova et al. [150] discuss that this enhancement due to the addition of the TiO₂ interlayer is attributed to the higher surface area of the catalyst deposited on TiO₂ compared to the catalyst deposited on the bare YSZ pellet. Further explanation of this behavior outlines that the TiO₂ layer, under polarization, acts as a catalyst in transforming the gaseous O₂ to promoter O²⁻ species at the Pt/gas interface [144]. Figure 5 shows a comparison of the catalytic performance of the Pt catalyst with and without the incorporation of a TiO₂ interlayer. Some of the observations discussed from these results include that there is an increase in U_{WR} for the Pt/TiO₂/YSZ catalyst which implies an increase in work function indicating a higher coverage of promoting O²⁻ species on the catalyst surface resulting in greater enhancement in activity; also, a new steady state, upon positive polarization, was achieved significantly faster for the Pt/TiO₂/YSZ catalyst compared to the Pt/YSZ catalyst.

Similar results were found using the bipolar configuration by both Marwood [163] and Balomenou et al. [164]; however, it was observed that the magnitude

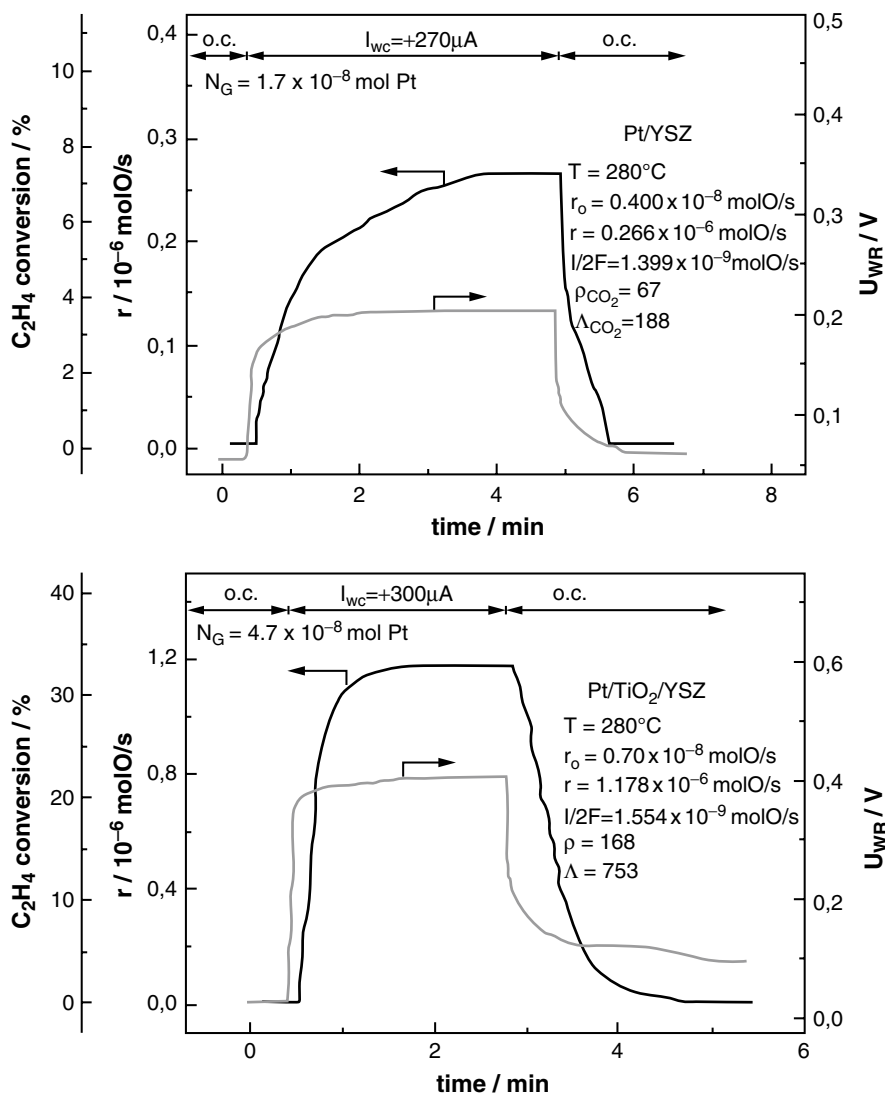


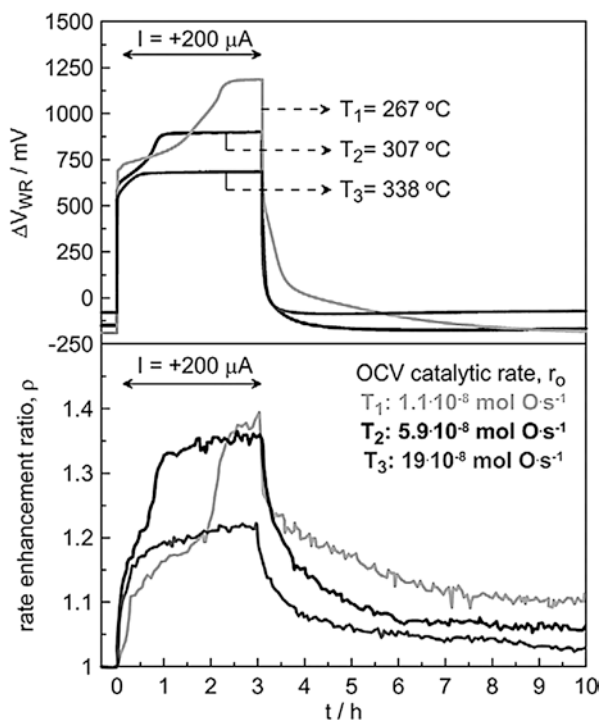
Fig. 5 Transient effect of applied constant current on the rate of C_2H_4 oxidation: (top) Pt/YSZ catalyst, (bottom) Pt/TiO₂/YSZ catalyst (Reproduced from Papaioannou et al. [144])

of electrochemical promotion (in terms of rate enhancement ratio and Faradaic efficiency) was factors lower than that observed for the conventional configuration. Both groups attributed this to two effects, current bypass and individual bipolar electrodes. Current bypass involves the possibility of current passing through the bulk of the YSZ without affecting the Pt catalyst. Some possible solutions in order to obtain similar catalytic performance include applying much larger currents, or using a thinner YSZ pellet or appropriate electrode geometry to lessen the loss of

current. The concept of individual bipolar electrodes means that each individual Pt nanoparticle catalyst behaves as a bipolar electrode; one side is positively charged, and the other side is negatively charged. This causes a nonuniform work function, contrary to that of a conventional electrode configuration; therefore, the resulting effect is a combination of catalytic activity due to both positive and negative polarizations. It has been suggested that this can be overcome by using this type of configuration for reactions that exhibit both electrophobic and electrophilic behavior.

A similar limitation (i.e., underestimation of promotion parameters) was found by Kambolis et al. [162] for the oxidation of propane over Pt/LSCF-GDC/GDC catalyst. It was stated that a minor part of the applied current between the LSCF/GDC electrode and the counter electrode passes over the Pt nanoparticles resulting in an underestimation of the Faradaic efficiency values. These results are shown in Fig. 6, summarizing the effect of positive polarization at three different temperatures. It can be seen that at 267 °C, a two-step increase of propane conversion was observed. This was attributed to the fact that the LSCF/GDC electrode conductivity is quite low at such a temperature indicating that the movement of oxygen ions requires some time to be delocalized from the bulk of the electrode; the opposite is observed when the current is interrupted [162].

Fig. 6 Transient effect of applied constant current on the rate of C_3H_8 oxidation for T_1 , 267 °C; T_2 , 307 °C; and T_3 , 338 °C (Reproduced from Kambolis et al. [162])



Xia et al. have attempted to quantify this difference in promotion parameters compared to the conventional equations, taking into account that when the catalyst is highly dispersed and not directly electronically connected, it acts as individual, isolated galvanic cells during polarization [143]. They proposed a new technique where a galvanostatic step is applied to a system in the presence of $C^{16}O$ and isotope $^{18}O_2$ under high vacuum conditions. The formation of $C^{18}O_2$ (Faradaic reaction; ^{16}O from YSZ) and $C^{16}O^{18}O$ (non-Faradaic reaction; ^{18}O from $^{18}O_2$) is observed, and the number of galvanic cells is quantified, thus, resulting in the following modified equation (Eq. 5) for rate enhancement ratio being proposed:

$$\rho = \frac{r_{C^{16}O_2} + r_{C^{16}O^{18}O}}{r_{C^{16}O^{18}O}^0} \quad (5)$$

where $r_{C^{16}O_2}$ is the rate of Faradaic formation of $C^{16}O_2$, $r_{C^{16}O^{18}O}$ is the rate of non-Faradaic formation of $C^{16}O^{18}O$, and $r_{C^{16}O^{18}O}^0$ is the initial open circuit catalytic rate. In addition, an adjustment to the equation (Eq. 6) for Faradaic efficiency was shown to be

$$\Lambda = \frac{r_{C^{16}O_2} + \Delta r_{C^{16}O^{18}O}}{r_{C^{16}O_2}} \quad (6)$$

or in the more conventional form (Eq. 7); however, accounting for the equivalent number of galvanic cells (n_{cell}),

$$\Lambda = \frac{2F}{I \cdot n_{\text{cell}}} \left(r_{C^{16}O_2} + \Delta r_{C^{16}O^{18}O} \right) \quad (7)$$

where $\Delta r_{C^{16}O^{18}O}$ is the enhancement of the catalytic rate of $C^{16}O^{18}O$ during polarization.

From this discussion, it is evident that some limitations still exist with regard to the application of nanostructured catalysts and the corresponding modified cell configurations and reactor designs; however, these have been identified and are being investigated for possible solutions and explanations. Further fundamental research with regard to these new designs would prove to be beneficial in the understanding of the behavior of these nanostructured catalysts compared to the commonly known systems. In addition, adjusting the reaction environment to more practical operation conditions would make it possible to evaluate the nanostructured catalysts for commercial applications.

Conclusion

Recent progress in the implementation of nanostructured catalysts to overcome the commercial limitations of conventional electrochemical promotion systems and to gain a better understanding of the related MSI phenomenon was presented. The limitations for practical application include the low metal dispersion, high metal

loading of expensive metals, and inefficient cell configuration and reactor design. It was shown that metal dispersion can be increased (by a factor of 10–100) through catalyst preparation techniques such as impregnation, sputter depositing, electroless deposition, and electrostatics spray deposition. In addition, adjustments to the cell configuration to accommodate these nanostructured catalysts, such as using the bipolar configuration or incorporating a mixed ionic–electronic conducting interlayer, have been studied along with new reactor designs, such as the monolithic electrochemical promotion reactor. These modifications have been shown to be the potential solutions to progressing toward commercial applications of electrochemical promotion. However, some of the limitations identified for these new designs include current bypass and individual bipolar electrodes, which cause an underestimation of conventional promotion parameters.

References

1. Dumesic JA, Huber GW, Boudart M (2008) Introduction. In: Ertl G (ed) Handbook of heterogeneous catalysis, 2nd edn. Wiley-VCH, Weinheim/Chichester, pp 1–15
2. Mattox DM (1998) Introduction. In: Handbook of physical vapor deposition, Film formation, adhesion, surface preparation and contamination control. Noyes Publications, Westwood, pp 29–55
3. Fee M, Ntais S, Weck A, Baranova EA (2014) Electrochemical behavior of silver thin films interfaced with yttria-stabilized zirconia. *J Solid State Electrochem* 18:2267–2277
4. Junes AC, Hitchman ML (2009) Chapter 1 Overview of Chemical Deposition Vapor Deposition In: Chemical vapour deposition precursors, processes and applications. Royal Society of Chemistry, Cambridge, UK, pp 1–36
5. Oh T, Haile SM (2015) Electrochemical behavior of thin-film Sm-doped ceria: insights from the point-contact configuration. *Phys Chem Chem Phys* 17:13501–13511
6. Pinna N, Knez M (2011) Atomic layer deposition of nanostructured materials. Wiley-VCH Verlag & Co, Weinheim, Germany
7. Mamun MA, Gu D, Baumgart H, Elmustafa AA (2015) Nanomechanical properties of platinum thin films synthesized by atomic layer deposition. *Sur Coat Tech* 265:185–190
8. Li W, Comotti M, Schuth F (2006) Highly reproducible syntheses of active Au/TiO₂ catalysts for CO oxidation by deposition–precipitation or impregnation. *J Catal* 237:190–196
9. Alcalá M, Real C (2006) Synthesis based on the wet impregnation method and characterization of iron and iron oxide-silica nanocomposites. *Solid State Ion* 177:955–960
10. Mitsui T, Tsutsui K, Matsui T et al (2008) Support effect on complete oxidation of volatile organic compounds over Ru catalysts. *Appl Catal B Environ* 81:56–63
11. Fortunato MA, Aubert D, Capdeillayre C et al (2011) Dispersion measurement of platinum supported on yttria-stabilised zirconia by pulse H₂ chemisorption. *Appl Catal A Gen* 403:18–24
12. Fortunato MA, Princiville A, Capdeillayre et al (2014) Role of Lattice Oxygen in the Propane Combustion Over Pt/Yttria-Stabilized Zirconia: Isotopic Studies. *Top Catal* 57:1277–1286
13. Toledo-Antonio JA, Ángeles-Chávez C, Cortés-Jácome MA et al (2012) Highly dispersed Pt–Ir nanoparticles on titania nanotubes. *Appl Catal A Gen* 437–438:155–165
14. Radnik J, Wilde L, Schneider M et al (2006) Influence of the precipitation agent in the deposition-precipitation on the formation and properties of Au nanoparticles supported on Al₂O₃. *J Phys Chem B* 110:23688–23693
15. Sandoval A, Gómez-Cortés A, Zanella R et al (2007) Gold nanoparticles: support effects for the WGS reaction. *J Mol Catal A Chem* 278:200–208

16. Sandoval A, Aguilar A, Louis C et al (2011) Bimetallic Au–Ag/TiO₂ catalyst prepared by deposition–precipitation: high activity and stability in CO oxidation. *J Catal* 281:40–49
17. Qian K, Luo L, Bao H et al (2013) Catalytically active structures of SiO₂-supported Au nanoparticles in low-temperature CO oxidation. *Catal Sci Technol* 3:679–687
18. Bokhimi X, Zanella R, Maturano V, Morales A (2013) Nanocrystalline Ag, and Au–Ag alloys supported on titania for CO oxidation reaction. *Mater Chem Phys* 138:490–499
19. Liang H, Raitano JM, He G et al (2011) Aqueous co-precipitation of Pd-doped cerium oxide nanoparticles: chemistry, structure, and particle growth. *J Mater Sci* 47:299–307
20. Petcharoen K, Sirivat A (2012) Synthesis and characterization of magnetite nanoparticles via the chemical co-precipitation method. *Mater Sci Eng B* 177:421–427
21. Kumar AP, Kumar BP, Kumar ABVK et al (2013) Preparation of palladium nanoparticles on alumina surface by chemical co-precipitation method and catalytic applications. *Appl Surf Sci* 265:500–509
22. Sharifi I, Shokrollahi H (2013) Structural, magnetic and mössbauer evaluation of Mn substituted Co–Zn ferrite nanoparticles synthesized by co-precipitation. *J Magn Magn Mater* 334:36–40
23. Wang S, Yang H, Feng L et al (2013) A simple and inexpensive synthesis route for LiFePO₄/C nanoparticles by co-precipitation. *J Power Sources* 233:43–46
24. Fernandes DM, Silva R, Hechenleitner AAW et al (2009) Synthesis and characterization of ZnO, CuO and a mixed Zn and Cu oxide. *Mater Chem Phys* 115:110–115
25. Gopalan EV, Joy PA, Al-Omari IA et al (2009) On the structural, magnetic and electrical properties of sol–gel derived nanosized cobalt ferrite. *J Alloys Compd* 485:711–717
26. Aziz M, Saber Abbas S, Wan Baharom WR (2013) Size-controlled synthesis of SnO₂ nanoparticles by sol–gel method. *Mater Lett* 91:31–34
27. Battoo KM, El-sadek M-SA (2013) Electrical and magnetic transport properties of Ni–Cu–Mg ferrite nanoparticles prepared by sol–gel method. *J Alloys Compd* 566:112–119
28. Liu C, Wu X, Klemmer T et al (2004) Polyol process synthesis of monodispersed FePt nanoparticles. *J Phys Chem B* 108:6121–6123
29. Bock C, Paquet C, Couillard M et al (2004) Size-selected synthesis of PtRu nano-catalysts: reaction and size control mechanism. *J Am Chem Soc* 126:8028–8037
30. Wiley B, Herricks T, Sun Y, Xia Y (2004) Polyol synthesis of silver nanoparticles: use of chloride and oxygen to promote the formation of single-crystal, truncated cubes and tetrahedrons. *Nano Lett* 4:1733–1739
31. Herricks T, Chen J, Xia Y (2004) Polyol synthesis of platinum nanoparticles: control of morphology with sodium nitrate. *Nano Lett* 4:2367–2371
32. Baranova EA, Bock C, Ilin D et al (2006) Infrared spectroscopy on size-controlled synthesized Pt-based nano-catalysts. *Surf Sci* 600:3502–3511
33. Park BK, Jeong S, Kim D et al (2007) Synthesis and size control of monodisperse copper nanoparticles by polyol method. *J Colloid Interface Sci* 311:417–424
34. Baranova EA, Le Page Y, Ilin D et al (2009) Size and composition for 1–5nm Ø PtRu alloy nano-particles from Cu K α X-ray patterns. *J Alloys Compd* 471:387–394
35. Baranova EA, Amir T, Mercier PHJ et al (2010) Single-step polyol synthesis of alloy Pt₇Sn₃ versus bi-phase Pt/SnO_x nano-catalysts of controlled size for ethanol electro-oxidation. *J Appl Electrochem* 40:1767–1777
36. Isaifan RJ, Dole HAE, Obeid E et al (2011) Catalytic CO oxidation over Pt nanoparticles prepared from the polyol reduction method supported on yttria-stabilized zirconia. *Electrocatal* 5, *ECS Trans* 35:43–57
37. Isaifan RJ, Ntais S, Couillard M, Baranova EA (2015) Size-dependent activity of Pt/yttria-stabilized zirconia catalyst for ethylene and carbon monoxide oxidation in oxygen-free gas environment. *J Catal* 324:32–40
38. Isaifan RJ, Baranova EA (2015) Effect of ionically conductive supports on the catalytic activity of platinum and ruthenium nanoparticles for ethylene complete oxidation. *Catal Today* 241:107–113
39. Ntais S, Isaifan RJ, Baranova EA (2014) An x-ray photoelectron spectroscopy study of platinum nanoparticles on yttria-stabilized zirconia ionic support: Insight into metal support interaction. *Mat Chem Phys* 148:673–679

40. Dole HAE, Safady LF, Ntais S et al (2014) Electrochemically enhanced metal-support interaction of highly-dispersed Ru nanoparticles with a CeO₂ support. *J Catal* 318:85–94
41. Overbury SH, Ortiz-soto L, Zhu H et al (2004) Comparison of Au catalysts supported on mesoporous titania and silica: investigation of Au particle size effects and metal-support interactions. *Catal Lett* 95:99–106
42. Wang Z, Li B, Chen M et al (2010) Size and support effects for CO oxidation on supported Pd catalysts. *Sci China Chem* 53:2047–2056
43. Kimura K, Einaga H, Teraoka Y (2011) Preparation of highly dispersed platinum catalysts on various oxides by using polymer-protected nanoparticles. *Catal Today* 164:88–91
44. Vayenas CG, Bebelis S, Ladas S (1990) Dependence of catalytic rates on catalyst work function. *Nature* 343:625–627
45. Vayenas CG, Bebelis S, Pliangos C et al (2001) Electrochemical activation of catalysis: promotion, electrochemical promotion, and metal-support interactions. Kluwer Academic/Plenum, New York
46. Vayenas C, Brosda S, Pliangos C (2001) Rules and mathematical modeling of electrochemical and chemical promotion 1. Reaction classification and promotional rules. *J Catal* 203:329–350
47. Brosda S, Vayenas CG (2002) Rules and mathematical modeling of electrochemical and classical promotion 2. Modeling. *J Catal* 208:38–53
48. Brosda S, Vayenas C, Wei J (2006) Rules of chemical promotion. *Appl Catal B Environ* 68:109–124
49. Van Santen RA (1991) Chemical basis of metal catalyst promotion. *Surf Sci* 251(252):6–11
50. Ertl G, Lee SB, Weiss M (1982) Adsorption of nitrogen on potassium promoted Fe(111) and (100) surfaces. *Surf Sci* 114:527–545
51. Bécue T, Davis RJ, Garces JM (1998) Effect of cationic promoters on the kinetics of ammonia synthesis catalyzed by ruthenium supported on zeolite X. *J Catal* 179:129–137
52. Shekhah O, Ranke W, Schlögl R (2004) Styrene synthesis: in situ characterization and reactivity studies of unpromoted and potassium-promoted iron oxide model catalysts. *J Catal* 225:56–68
53. Zhu XM, Schön M, Bartmann U et al (2004) The dehydrogenation of ethylbenzene to styrene over a potassium-promoted iron oxide-based catalyst: a transient kinetic study. *Appl Catal A Gen* 266:99–108
54. Yentekakis IV, Lambert RM, Tikhov MS et al (1998) Promotion by sodium in emission control catalysis: a kinetic and spectroscopic study of the Pd-catalyzed reduction of NO by propene. *J Catal* 176:82–92
55. Yentekakis I, Konsolakis M, Lambert R et al (1999) Extraordinarily effective promotion by sodium in emission control catalysis: NO reduction by propene over Na-promoted Pt/γ-Al₂O₃. *Appl Catal B Environ* 22:123–133
56. Konsolakis M, Macleod N, Isaac J et al (2000) Strong promotion by Na of Pt/γ-Al₂O₃ catalysts operated under simulated exhaust conditions. *J Catal* 193:330–337
57. Pliangos C, Raptis C, Badas T et al (2000) Electrochemical promotion of a classically promoted Rh catalyst for the reduction of NO. *Electrochim Acta* 46:331–339
58. Ibrahim N, Poulidi D, Metcalfe IS (2013) The role of sodium surface species on electrochemical promotion of catalysis in a Pt/YSZ system: the case of ethylene oxidation. *J Catal* 303:100–109
59. Özbek MO, van Santen RA (2013) The mechanism of ethylene epoxidation catalysis. *Catal Lett* 143:131–141
60. Konsolakis M, Yentekakis IV (2001) The reduction of NO by propene over Ba-promoted Pt/γ-Al₂O₃ catalysts. *J Catal* 198:142–150. doi:10.1006/jcat.2000.3123
61. Hereijgers BPC, Weckhuysen BM (2009) Selective oxidation of methanol to hydrogen over gold catalysts promoted by alkaline-earth-metal and lanthanum oxides. *ChemSusChem* 2:743–748
62. Nagaraju P, Lingaiah N, Sai Prasad PS et al (2008) Preparation, characterization and catalytic properties of promoted vanadium phosphate catalysts. *Catal Commun* 9:2449–2454
63. Rodriguez P, Kwon Y, Koper MTM (2012) The promoting effect of adsorbed carbon monoxide on the oxidation of alcohols on a gold catalyst. *Nat Chem* 4:177–182

64. Tong YJ (2012) Unconventional promoters of catalytic activity in electrocatalysis. *Chem Soc Rev* 41:8195–8209
65. Schwab GM, Block J, Muller W, Schultze D (1957) Zur Natur der katalytischen Verstärker-Wirkung. *Naturwissenschaften* 44:582–584
66. Schwab GM, Block J, Schultze D (1958) Kontaktkatalytische Verstärkung durch dotierte Träger. *Angew Chem* 71:101–104
67. Tauster SJ, Fung SC, Garten RL (1978) Strong metal-support interactions. Group 8 noble metals supported on titanium dioxide. *J Am Chem Soc* 100:170–175
68. Lewera A, Timperman L, Roguska A, Alonso-Vante N (2011) Metal-support interactions between nanosized Pt and metal oxides (WO_3 and TiO_2) studied using X-ray photoelectron spectroscopy. *J Phys Chem C* 115:20153–20159
69. Jin M, Park J-N, Shon JK et al (2012) Low temperature CO oxidation over Pd catalysts supported on highly ordered mesoporous metal oxides. *Catal Today* 185:183–190
70. Metcalfe IS, Sundaresan S (1988) Oxygen transfer between metals and oxygen-ion conducting supports. *AIChE J* 34:195–208
71. Dow W-P, Huang T-J (1994) Effects of oxygen vacancy of yttria-stabilized zirconia support on carbon monoxide oxidation over copper catalyst. *J Catal* 147:322–332
72. Dow W-P, Wang Y-P, Huang T-J (1996) Yttria-stabilized zirconia supported copper oxide catalyst I. Effect of oxygen vacancy of support on copper oxide reduction. *J Catal* 160:155–170
73. Dow W-P, Huang T-J (1996) Yttria-stabilized zirconia supported copper oxide catalyst II. Effect of oxygen vacancy of support on catalytic activity for CO oxidation. *J Catal* 160:171–182
74. Isaifan RJ, Dole HAE, Obeid E et al (2012) Metal-support interaction of Pt nanoparticles with ionically and non-ionically conductive supports for CO oxidation. *Electrochem Solid State Lett* 15:E14
75. Isaifan RJ, Baranova EA (2013) Catalytic electrooxidation of volatile organic compounds by oxygen-ion conducting ceramics in oxygen-free gas environment. *Electrochem Commun* 27:164–167
76. Park JB, Graciani J, Evans J et al (2009) High catalytic activity of $\text{Au/CeO}_x/\text{TiO}_2(110)$ controlled by the nature of the mixed-metal oxide at the nanometer level. *Proc Natl Acad Sci U S A* 106:4975–4980
77. Jiménez-Borja C, Matei F, Dorado F, Valverde JL (2012) Characterization of Pd catalyst-electrodes deposited on YSZ: influence of the preparation technique and the presence of a ceria interlayer. *Appl Surf Sci* 261:671–678
78. Dole HAE, Isaifan RJ, Sapountzi FM et al (2013) Low temperature toluene oxidation over Pt nanoparticles supported on yttria stabilized-zirconia. *Catal Lett* 143:996–1002
79. Toshima N (2010) Chapter 17: Inorganic nanoparticles for catalysis. In: Altavilla C, Ciliberto E (eds) *Inorganic nanoparticles: synthesis, applications, and perspectives*. CRC Press, Boca Raton, pp 475–505
80. Tauster SJ (1987) Strong metal-support interactions. *Acc Chem Res* 20:389–394
81. Vernoux P, Lizarraga L, Tsampas MN et al (2013) Ionically conducting ceramics as active catalyst supports. *Chem Rev* 113:8192–8260
82. Sato H (1977) Some theoretical aspects of solid electrolytes. In: Geller S (ed) *Solid electrolytes*. Springer, Berlin/Heidelberg, pp 3–39
83. Bagotsky VS (2006) Nonaqueous electrolytes. In: *Fundamentals of electrochemistry*, 2nd edn. Wiley, Hoboken, pp 127–137
84. Heyne L (1977) Electrochemistry of mixed ionic-electronic conductors. In: Geller S (ed) *Solid electrolytes*. Springer, Berlin/Heidelberg, pp 169–221
85. Stimming U, Hengyong T, Bagotsky VS (2006) Solid-state electrochemistry. In: *Fundamentals of electrochemistry*, 2nd edn. Wiley, Hoboken, pp 419–447
86. Chadwick AV, Savin SLP (2009) Ion-conducting nanocrystals: theory, methods, and applications. In: Kharton VV (ed) *Solid state electrochemistry I: fundamentals, materials and their applications*. Wiley-VCH Verlag GmbH/Betz-Druck GmbH, Weinheim, pp 79–132

87. Vernoux P, Guth M, Li X (2009) Ionically conducting ceramics as alternative catalyst supports. *Electrochem Solid State Lett* 12:E9–E11
88. Stoukides M, Vayenas C (1981) The effect of electrochemical oxygen pumping on the rate and selectivity of ethylene oxidation on polycrystalline. *J Catal* 70:137–146
89. Yentekakis IV, Vayenas CG (1988) The effect of electrochemical oxygen pumping on the steady-state and oscillatory behavior of CO oxidation on polycrystalline Pt. *J Catal* 111:170–188
90. Bebelis S, Vayenas CG (1989) Non-Faradaic electrochemical modification. *J Catal* 146:125–146
91. Cavalca CA, Larson G, Vayenas CG, Haller GL (1993) Electrochemical modification of CH₃OH oxidation selectivity and activity on a Pt single-pellet catalytic reactor. *J Phys Chem* 97:6115–6119
92. Neophytides SG, Vayenas CG (1995) TPD and cyclic voltammetric investigation of the origin of electrochemical promotion in catalysis. *J Phys Chem* 99:17063–17067
93. Pacchioni G, Illas F, Neophytides S, Vayenas CG (1996) Quantum-chemical study of electrochemical promotion in catalysis. *J Phys Chem* 100:16653–16661
94. Vayenas CG, Bebelis S (1999) Electrochemical promotion of heterogeneous catalysis. *Catal Today* 51:581–594
95. Vayenas C, Brosda S, Pliangos C (2003) The double-layer approach to promotion, electrocatalysis, electrochemical promotion, and metal–support interactions. *J Catal* 216:487–504
96. Piram A, Li X, Gaillard F et al (2005) Electrochemical promotion of environmental catalysis. *Ionics* 11:327–332
97. De Lucas-Consuegra A, Dorado F, Jiménez-Borja C, Valverde JL (2008) Electrochemical promotion of Pt impregnated catalyst for the treatment of automotive exhaust emissions. *J Appl Electrochem* 38:1151–1157
98. Toghan A, Rösken LM, Imbihl R (2010) The electrochemical promotion of ethylene oxidation at a Pt/YSZ catalyst. *Chemphyschem* 11:1452–1459
99. Pliangos C, Raptis C, Bolzonella I et al (2002) Electrochemical promotion of conventional and bipolar reactor configurations for NO reduction. *Ionics* 8:372–382
100. Tsiplakides D, Balomenou S (2009) Milestones and perspectives in electrochemically promoted catalysis. *Catal Today* 146:312–318
101. Vayenas CG, Ladas S, Bebelis S et al (1994) Electrochemical promotion in catalysis: non-Faradaic electrochemical modification of catalytic activity. *Electrochim Acta* 39:1849–1855
102. Vayenas CG, Yentekakis IV, Bebelis S, Neophytides SG (1995) In-situ controlled promotion of catalyst surfaces via solid electrolytes – the NEMCA effect. *Phys Chem Chem Phys* 99:1393–1401
103. Vayenas G, Bebelis SI (1997) Electrochemical promotion. *Solid State Ion* 94:267–277
104. Metcalfe I (2001) Electrochemical promotion of catalysis I: thermodynamic considerations. *J Catal* 199:247–258
105. Metcalfe I (2001) Electrochemical promotion of catalysis II: the role of a stable spillover species and prediction of reaction rate modification. *J Catal* 199:259–272
106. Katsaounis A (2008) Electrochemical promotion of catalysis (EPOC) perspectives for application to gas emissions treatment. *Glob Nest J* 10:226–236
107. Tsiplakides D, Balomenou S (2008) Electrochemical promoted catalysis: towards practical utilization. *Chem Ind Chem Eng Q* 14:97–105
108. Vayenas CG, Koutsodontis CG (2008) Non-Faradaic electrochemical activation of catalysis. *J Chem Phys* 128:182506
109. Anastasijevic NA (2009) NEMCA – from discovery to technology. *Catal Today* 146:308–311
110. Imbihl R (2010) Electrochemical promotion of catalytic reactions. *Prog Surf Sci* 85:241–278
111. Katsaounis A (2010) Recent developments and trends in the electrochemical promotion of catalysis (EPOC). *J Appl Electrochem* 40:885–902
112. Garagounis I, Kyriakou V, Anagnostou C et al (2011) Solid electrolytes: applications in heterogeneous catalysis and chemical cogeneration. *Indust Eng Chem Res* 50:431–472

113. Vayenas CG (2011) Bridging electrochemistry and heterogeneous catalysis. *J Solid State Electrochem* 15:1425–1435
114. Vayenas CG (1993) Electrochemical activation of catalysed reactions. In: Joyner RW, van Santen RA (eds) *Elementary reaction steps in heterogeneous catalysis*, 398th edn. Springer, Dordrecht, pp 73–92
115. Foti G, Bolzonella I, Comninellis C (2003) Electrochemical promotion of catalysis. In: Vayenas CG, Conway BE, White RE (eds) *Modern aspects of electrochemistry*, 36th edn. Plenum Press, New York, pp 191–254
116. Lambert RM (2003) Electrochemical and chemical promotion by alkalis with metal films and nanoparticles. In: Wieckowski A, Savinova ER, Vayenas CG (eds) *Catalysis and electrocatalysis at nanoparticle surfaces*. Marcel Dekker, New York, pp 583–612
117. Vayenas CG, Pliangos C, Brosda S, Tsiplakides D (2003) Promotion, electrochemical promotion, and metal-support interactions: the unifying role of spillover. In: Wieckowski AER, Savinova ER, Vayenas CG (eds) *Catalysis and electrocatalysis at nanoparticle surfaces*. Marcel Dekker, New York, pp 667–744
118. Jiménez-Borja C, de Lucas-Consuegra A, Valverde JL et al (2012) One of the recent discoveries in catalysis: the phenomenon of electrochemical promotion. In: Taylor JC (ed) *Advances in chemistry research*, 14th edn. Nova, New York, pp 99–132
119. Skriver HL, Rosengaard NM (1992) Surface energy and work function of elemental metals. *Phys Rev B* 46:7157–7168
120. Nicole J, Tsiplakides D, Wodiunig S, Comninellis C (1997) Activation of catalyst for gas-phase combustion by electrochemical pretreatment. *J Electrochem Soc* 144:L312–L314
121. Vayenas CG, Bebelis S, Neophytides S (1988) Non-Faradaic electrochemical modification of catalytic activity. *J Phys Chem* 92:5083–5085
122. Koutsodontis C, Katsaounis A, Figueroa JC et al (2006) The effect of catalyst film thickness on the electrochemical promotion of ethylene oxidation on Pt. *Top Catal* 39:97–100
123. Yentekakis IV, Bebelis S (1992) Study of the NEMCA effect in a single-pellet catalytic reactor. *J Catal* 137:278–283
124. Brosda S, Badas T, Vayenas CG (2011) Study of the mechanism of the electrochemical promotion of Rh/YSZ catalysts for C₂H₄ oxidation via AC impedance spectroscopy. *Top Catal* 54:708–717
125. Varkaraki E, Nicole J, Plattner E et al (1995) Electrochemical promotion of IrO₂ catalyst for the gas phase combustion of ethylene. *J Appl Electrochem* 25:978–981
126. Nicole J, Comninellis C (1998) Electrochemical promotion of IrO₂ catalyst activity for the gas phase combustion of ethylene. *J Appl Electrochem* 28:223–226
127. Tsiplakides D, Nicole J, Vayenas CG, Comninellis C (1998) Work function and catalytic activity measurements of an IrO₂ film deposited on YSZ subjected to in situ electrochemical promotion. *J Electrochem Soc* 145:905–908
128. Kaloyannis AC, Pliangos CA, Tsiplakides DT et al (1995) Electrochemical promotion of catalyst surfaces deposited on ionic and mixed conductors. *Ionics* 1:414–420
129. Poulidi D, Castillo-del-Rio MA, Salar R et al (2003) Electrochemical promotion of catalysis using solid-state proton-conducting membranes. *Solid State Ion* 162–163:305–311
130. Poulidi D, Mather GC, Tabacaru CN et al (2009) Electrochemical promotion of a platinum catalyst supported on the high-temperature proton conductor La_{0.99}Sr_{0.01}NbO_{4-δ}. *Catal Today* 146:279–284
131. Yentekakis IV, Moggridge G, Vayenas CG, Lambert RM (1994) In situ controlled promotion of catalyst surfaces via NEMCA: the effect of Na on the Pt-catalyzed CO oxidation. *J Catal* 146:292–305
132. Lambert RM, Harkness IR, Yentekakis IV, Vayenas CG (1995) Electrochemical promotion in emission control catalysis. *Ionics* 1:29–31
133. Dorado F, de Lucas-Consuegra A, Jiménez C, Valverde JL (2007) Influence of the reaction temperature on the electrochemical promoted catalytic behaviour of platinum impregnated catalysts for the reduction of nitrogen oxides under lean burn conditions. *Appl Catal A Gen* 321:86–92

134. Dorado F, de Lucas-Consuegra A, Vernoux P, Valverde JL (2007) Electrochemical promotion of platinum impregnated catalyst for the selective catalytic reduction of NO by propene in presence of oxygen. *Appl Catal B Environ* 73:42–50
135. De Lucas-Consuegra A, Dorado F, Valverde JL et al (2008) Electrochemical activation of Pt catalyst by potassium for low temperature CO deep oxidation. *Catal Commun* 9:17–20
136. Tsiplakides D, Neophytides SG, Enea O et al (1997) Nonfaradaic electrochemical modification of the catalytic activity of Pt-black electrodes deposited on nafion 117 solid polymer electrolytes. *J Electrochem Soc* 144:2072–2078
137. Marwood M, Vayenas CG (1998) Electrochemical promotion of a dispersed platinum catalyst. *J Catal* 178:429–440
138. Jiménez-Borja C, Delgado B, Díaz-Díaz LF et al (2012) Enhancing the combustion of natural gas by electrochemical promotion of catalysis. *Electrochem Commun* 23:9–12
139. Li N, Gaillard F (2009) Catalytic combustion of toluene over electrochemically promoted Ag catalyst. *Appl Catal B Environ* 88:152–159
140. Theleritis D, Souentie S, Siokou A et al (2012) Hydrogenation of CO₂ over Ru/YSZ electro-promoted catalysts. *ACS Catal* 2:770–780
141. Wodiunig S, Bokeloh F, Nicole J, Comninellis C (1999) Electrochemical promotion of RuO₂ catalyst dispersed on an yttria-stabilized zirconia monolith. *Electrochem Solid State Lett* 2:281–283
142. Xia C, Hugentobler M, Li Y et al (2010) Electrochemical promotion of CO combustion over non-percolated Pt particles supported on YSZ using a novel bipolar configuration. *Electrochem Commun* 13:99–101
143. Xia C, Hugentobler M, Comninellis C, Harbich W (2010) Quantifying electrochemical promotion of induced bipolar Pt particles supported on YSZ. *Electrochem Commun* 12:1551–1554
144. Papaioannou EI, Souentie S, Sapountzi FM et al (2010) The role of TiO₂ layers deposited on YSZ on the electrochemical promotion of C₂H₄ oxidation on Pt. *J Appl Electrochem* 40:1859–1865
145. Karoum R, Roche V, Pirovano C et al (2010) CGO-based electrochemical catalysts for low temperature combustion of propene. *J Appl Electrochem* 40:1867–1873
146. Souentie S, Lizarraga L, Papaioannou EI et al (2010) Permanent electrochemical promotion of C₃H₈ oxidation over thin sputtered Pt films. *Electrochem Commun* 12:1133–1135
147. Lizarraga L, Souentie S, Mazri L et al (2010) Investigation of the CO oxidation rate oscillations using electrochemical promotion of catalysis over sputtered-Pt films interfaced with YSZ. *Electrochem Commun* 12:1310–1313
148. Lizarraga L, Guth M, Billard A, Vernoux P (2010) Electrochemical catalysis for propane combustion using nanometric sputtered-deposited Pt films. *Catal Today* 157:61–65
149. Hammad A, Souentie S, Papaioannou EI et al (2011) Electrochemical promotion of the SO₂ oxidation over thin Pt films interfaced with YSZ in a monolithic electropromoted reactor. *Appl Catal B Environ* 103:336–342
150. Baranova EA, Thursfield A, Brosda S et al (2005) Electrochemical promotion of ethylene oxidation over Rh catalyst thin films sputtered on YSZ and TiO₂/YSZ supports. *J Electrochem Soc* 152:E40–E49
151. Balomenou S, Tsiplakides D, Katsaounis A et al (2004) Novel monolithic electrochemically promoted catalytic reactor for environmentally important reactions. *Appl Catal B Environ* 52:181–196
152. Balomenou S, Tsiplakides D, Katsaounis A et al (2006) Monolithic electrochemically promoted reactors: a step for the practical utilization of electrochemical promotion. *Solid State Ion* 177:2201–2204
153. Koutsodontis C, Hammad A, Lepage M et al (2008) Electrochemical promotion of NO reduction by C₂H₄ in excess O₂ using a monolithic electropromoted reactor and Pt–Rh sputtered electrodes. *Top Catal* 50:192–199
154. Roche V, Revel R, Vernoux P (2010) Electrochemical promotion of YSZ monolith honeycomb for deep oxidation of methane. *Catal Commun* 11:1076–1080

155. Dole HAE, Safady LF, Ntais S et al (2014) Improved catalytic reactor for electrochemical promotion of highly dispersed Ru nanoparticles with CeO₂ support. *ECS Trans* 61:65–74
156. Lintanf A (2008) Pt/YSZ electrochemical catalysts prepared by electrostatic spray deposition for selective catalytic reduction of NO by C₃H₆. *Solid State Ion* 178:1998–2008
157. Vayenas CG, Bebelis S, Yentekakis IV, Lintz H-G (1992) Non-Faradaic electrochemical modification of catalytic activity: a status report. *Catal Today* 11:303–442
158. Baranova EA, Thursfield A, Brosda S et al (2005) Electrochemically induced oscillations of C₂H₄ oxidation over thin sputtered Rh catalyst films. *Catal Lett* 105:15–21
159. Baranova EA, Fóti G, Jotterand H, Comninellis C (2007) Electrochemical modification of the catalytic activity of TiO₂/YSZ supported rhodium films. *Top Catal* 44:355–360
160. Constantinou I, Archonta D, Brosda S et al (2007) Electrochemical promotion of NO reduction by C₃H₆ on Rh catalyst-electrode films supported on YSZ and on dispersed Rh/YSZ catalysts. *J Catal* 251:400–409
161. Jiménez-Borja C, Dorado F, de L -Consuegra A et al (2011) Electrochemical promotion of CH₄ combustion over a Pd/CeO₂-YSZ catalyst. *Fuel Cells* 11:131–139
162. Kambolis A, Lizarraga L, Tsampas MN et al (2012) Electrochemical promotion of catalysis with highly dispersed Pt nanoparticles. *Electrochem Commun* 19:5–8
163. Marwood M (1997) Electrochemical promotion of electronically isolated Pt catalysts on stabilized zirconia. *J Catal* 168:538–542
164. Balomenou S, Pitselis G, Polydoros D et al (2000) Electrochemical promotion of Pd, Fe and distributed Pt. *Solid State Ion* 137:857–862
165. Poulidi D, Mather G, Metcalfe I (2007) Wireless electrochemical modification of catalytic activity on a mixed protonic–electronic conductor. *Solid State Ion* 178:675–680
166. Poulidi D, Thursfield A, Metcalfe IS (2007) Electrochemical promotion of catalysis controlled by chemical potential difference across a mixed ionic–electronic conducting ceramic membrane – an example of wireless NEMCA. *Top Catal* 44:435–449
167. Poulidi D, Metcalfe IS (2008) Comparative studies between classic and wireless electrochemical promotion of a Pt catalyst for ethylene oxidation. *J Appl Electrochem* 38: 1121–1126

Self-Assembled Peptide Nanostructures for the Development of Electrochemical Biosensors

35

Jaime Castillo-León, Kinga Zór, and Winnie E. Svendsen

Contents

Introduction.....	1126
Fabrication and Deposition of Self-Assembled Peptide Nanostructures on Transducers	1127
Functionalization of Self-Assembled Peptide Nanostructures	1132
Applications	1135
Biomedical Applications.....	1135
Environmental Applications.....	1137
Conclusions and Outlook.....	1138
References.....	1139

Abstract

Biological building blocks such as peptides or proteins are able to self-organize into nanostructures with particular properties. There are several possibilities for their use in varying applications such as drug delivery, biosensing, clean-room fabrication methods, and tissue engineering. These biological nanostructures have recently been utilized for bionanotechnological applications thanks to their easy and low-cost fabrication, their stability, and their facile functionalization. These features suggest the usage of self-assembled peptide nanostructures in the development of biosensing platforms, and the present chapter explores their

J. Castillo-León (✉)
Sol Voltaics AB, Lund, Sweden
e-mail: jcl@solvoltaics.com

K. Zór • W.E. Svendsen
DTU Nanotech, Technical University of Denmark, Kgs. Lyngby, Denmark
e-mail: kinzo@nanotech.dtu.dk; wisv@nanotech.dtu.dk

use for such purposes. Several immobilization strategies, mechanisms, and detected substrates are described. Moreover, different possibilities to functionalize and modify their structure toward utilization in sensing applications are also discussed.

Keywords

Self-assembly • Peptides • Biosensors • Amperometry • Biomedical analysis • Dielectrophoresis • Environmental analysis • Impedance • Cyclic voltammetry • Conductive polymers

Introduction

Traditionally, nanomaterials such as carbon nanotubes (CNTs), silicon nanowires, as well as gold, platinum, and silver nanowires or nanoparticles have been used in the development of electrochemical and optical biosensors due to their large surface area, mechanical stability, electrochemical properties, and advantages in terms of signal amplification (Table 1). However, issues involving fabrication costs, biocompatibility, and functionalization have directed much attention to finding alternatives to overcome these challenges.

Self-assembled peptides are natural molecular building blocks able to self-organize into structures such as nanofibers, nanotubes, or nanoparticles. Peptides, e.g., the short aromatic dipeptides diphenylalanine or diphenylglycine, octapeptides such as NSGAIITIG, or more complex linear peptides, have been reported to form nanotubes, nanofibers, or nanoparticles. These structures can, in most cases, be fabricated under very mild conditions: room temperature, aqueous media, and outside a clean room. Fabrication costs can thus be lowered as compared with the

Table 1 Nanostructures commonly used in the development of electrochemical biosensors

Nanostructure	Fabrication method	References
Metallic nanowires	Template assisted electrodeposition Electrochemical deposition Electroless deposition Template filling	[1]
Si nanowires	Reactive ion etching Photolithography	[2]
Carbon nanotubes	Chemical vapor deposition Arc discharge Laser ablation Gas-phase catalytic growth	[3–5]
Polymer nanowires	Electrochemical deposition Template filling Reactive ion etching	[1, 6]
Graphene nanostructures	Exfoliation Chemical vapor deposition Epitaxial growth	[7]

fabrication of CNTs or silicon nanowires. Due to these advantages and properties, self-assembled peptide nanostructures (SAPNs) have been used in several applications ranging from tissue engineering to microfabrication processes [8].

In addition to their easy fabrication, self-assembled peptide nanostructures have proven to be resistant to high temperatures and chemical attacks [9]. Moreover, SAPNs are easily functionalized through chemical modification with structures such as quantum dots, magnetic and metallic nanoparticles, or enzymes. This leads to new possibilities for their utilization in the development of ultrasensitive biosensing devices [10, 11].

Even though SAPNs are not yet mentioned in the literature review articles reporting the latest advances in the use of nanomaterials for electrochemical sensing [5, 12, 13], more and more reports are appearing, presenting the possibilities, advantages, and challenges to overcome when using SAPNs for the development of electrochemical sensing platforms [8, 14–22].

The use of SAPNs involves several challenges. Due to their biological origin, their conductivity is very low, and depending of the fabrication method, the control of the size of the final structure may prove to be difficult; the fabricated structure needs to be manipulated and immobilized in specific locations and some of the SAPNs are not stable in liquid environments [15]. These challenges need to be overcome in order to integrate them with transducers and accelerate their use in the fabrication of sensing devices.

The present chapter discusses these challenges and present various solutions for the use of SAPNs in the development of electrochemical biosensors, as well as methods to deposit these nanostructures on transducer surfaces and their decoration with functional molecules (such as enzymes, antibodies, conductive polymers) are listed and discussed.

Fabrication and Deposition of Self-Assembled Peptide Nanostructures on Transducers

As previously mentioned, one of the features that make SAPNs an attractive option for bionanotechnological applications is the easy fabrication under very mild conditions. Numerous techniques have been reported for the synthesis of nanotubes, nanofibers, and nanoparticles using SAPs as building blocks. These synthesis techniques include very simple steps ranging from the dilution and mixing of two liquids containing the precursor compounds in a small container or the controlled mixing in a microfluidic chip to the use of more complex instruments like in the case of physical vapor deposition of SAPNs [23–25]. Cyclic, linear, chemically modified linear peptides and short aromatic dipeptides have been used for the self-assembling of nanostructures using the fabrication techniques mentioned above.

One of the simplest methods to fabricate nanostructures through the self-assembly of peptides is by mixing a peptide stock solution with a solution that will promote the self-assembly of the peptide nanostructure. A very well-documented method is the self-assembly of the short aromatic dipeptide diphenylalanine. The dissolution of this peptide in 1,1,1,3,3,3-hexafluoro-2-propanol (HFIP) and further dilution with

water cause multiwall nanotubes to form in seconds at room temperature [25]. Another example of the fabrication of peptide nanotubes involves dissolving bis(*N*- α -amido-glycylglycine)-1-7-heptane dicarboxylate in water. In this case, the nanotubes were formed after 1 week at room temperature [26].

In both cases, the size of the obtained nanotubes differed both in diameter and length. In order to obtain nanostructures with more defined dimensions, various methods exist, such as on-chip fabrication, where a more controlled mixing of the precursor solutions is possible due to a laminar flow, or the use of templates that define the final diameter of the fabricated nanostructures [24, 27, 28].

A novel solid-phase method to grow vertically aligned crystalline peptide nanofibers in the absence of water and driven by aniline vapor was reported by Ryu and coworkers [29]. By using a μ -channeled polydimethylsiloxane (PDMS) mold, a micropattern of peptide nanofibers was fabricated. Figure 1 shows vertically aligned self-assembled peptide nanofibers prepared with the aniline vapor aging method.

Thanks to this method, it was possible to integrate these biological nanofibers in metallic electrodes for the development of a cell culture-biosensing platform for the

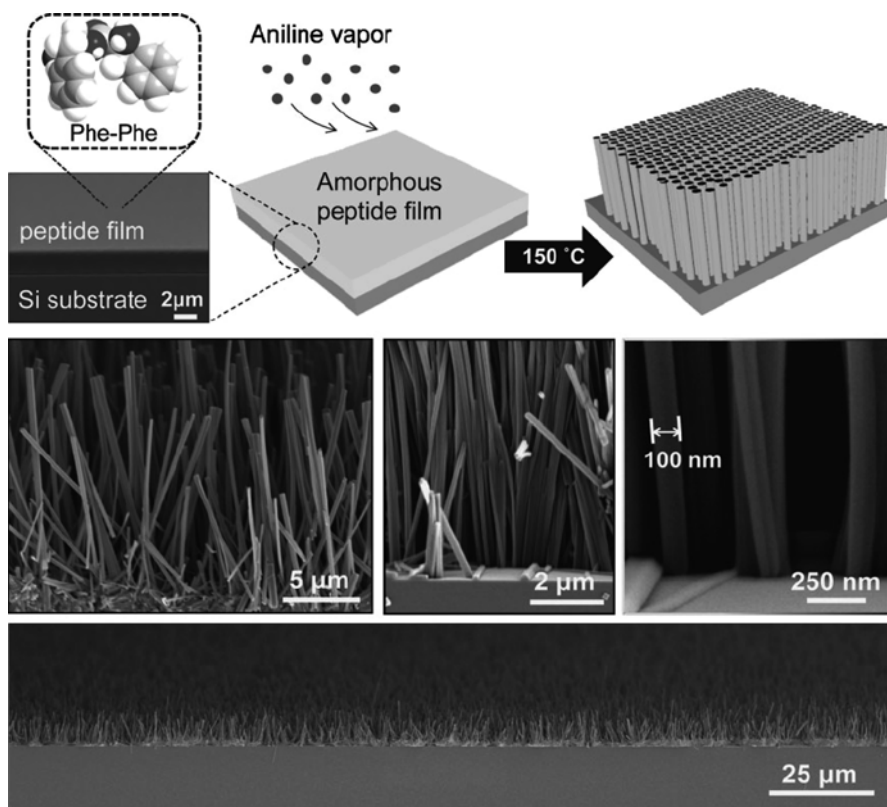


Fig. 1 Growth of vertically aligned nanofibers from an amorphous diphenylalanine thin film by high-temperature aniline vapor aging (Figure from Ryu and Park [29] with permission from John Wiley & Sons)

detection of neurotransmitters from cells [30]. This method requires temperatures around 140 °C but assures the synthesis of vertically well-aligned peptide nanofibers.

Physical vapor deposition was used for the controlled fabrication of dense and homogeneous peptide nanostructures to be used in microelectronics. The employed technique requires temperatures above 200 °C and the use of more specialized equipment, vacuum chambers, heating control systems, and thickness control systems among others, but enabled a controlled deposition of either nanotubes or nanofibers [23].

Another advantage of the last two preparation techniques is that the peptide nanostructures can – as they are being fabricated – be deposited on specific locations such as metallic electrodes or SiO₂ wafers for the development of biosensing devices.

Apart from these two methods that require temperatures over 120 °C, other deposition techniques can be used at room temperature for the controlled deposition of peptide nanostructures on top of transducers. The simplest method to immobilize peptide nanostructures on top of electrochemical transducers is the deposition of droplets of a solution containing the biological modified or unmodified nanostructures; once the solvent is evaporated, the nanostructures are physically immobilized on the transducer surface. Although this approach is both simple and rapid, it does not ensure a stable layer of nanostructures on the transducer surface: when the modified transducer is dipped in the sample to be measured, some of the nanostructures may become detached. In order to prevent this, an additional layer of polymer, e.g., poly(allylamine hydrochloride) (PAH), glutaraldehyde, or polyethyleneimine (PEI), is added to trap and keep the peptide nanostructures in the desired position [31, 32]. Figure 2 displays the use of glutaraldehyde as a cross-linker to immobilize glucose oxidase on peptide nanotubes and PEI to keep the functionalized peptide nanotubes on top of gold electrodes.

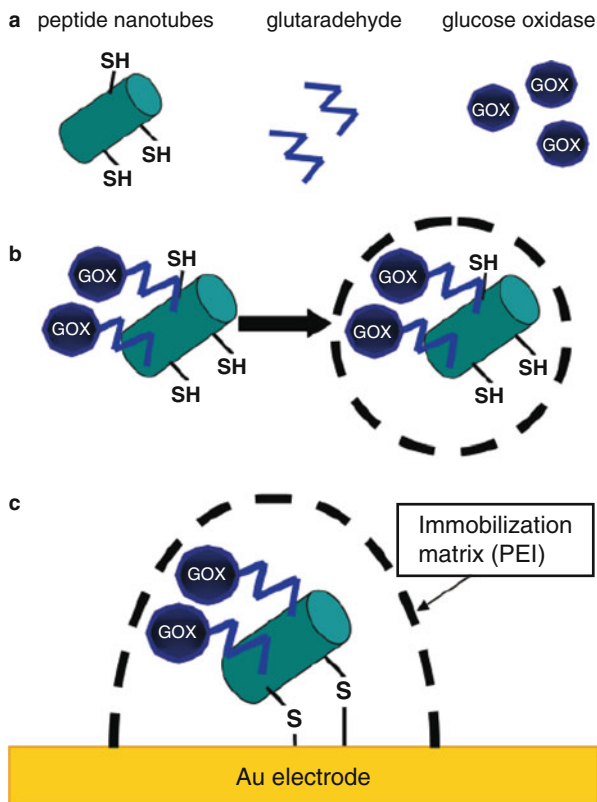
Dielectrophoresis is a technique where an inhomogeneous electric field is used to move a neutral but polarizable particle. It has been used for the controlled deposition of nanofibers and nanotubes on top of gold electrodes, as shown in Fig. 3. After deposition of the biological nanostructures on the electrodes, their electrical characterization and utilization as sensors were made possible, as previously reported. This deposition technique is a noncontact method ensuring that the peptide nanostructure does not become damaged during the manipulation step [33–35].

An inkjet printing technology was used for the deposition of peptide nanotubes and nanoparticles forming specific patterns on top of indium tin oxide electrodes, as shown in Fig. 4. This method was found to rapidly produce durable patterns at room temperature, making it very attractive for the deposition of peptide nanostructures at a high scale. However, challenges regarding clogging of the printing device need to be overcome [36].

Another way to immobilize peptide nanostructures on a transducer, both horizontally and vertically, involves the functionalization of peptide nanostructures with magnetic nanoparticles and then exposition of the modified tubes to an external magnetic field. With this technique, very highly organized peptide nanotube arrays were immobilized on siliconized glass [37].

A similar approach was used by Zhao and Matsui, in which case antibody-functionalized peptide nanotubes were accurately immobilized on protein-patterned arrays by optimizing their ligand-receptor interactions. In their work, peptide

Fig. 2 Immobilization of GOX-modified peptide nanotubes on Au electrodes using PEI as an immobilization matrix (Reprinted with permission from Yemini, M. et al. Peptide nanotube-modified electrodes for enzyme-biosensor applications. *Anal. Chem.* 77 (16): 5155–5159. Copyright (2005) American Chemical Society [32])



nanotubes self-assembled from bolaamphiphile peptide monomers were coated with antihuman-IgG antibody and immobilized on 150×600 nm trenches modified with human gamma immunoglobulin (IgG). Perfectly vertically aligned peptide nanotubes were deposited on the modified trenches with nearly 100 % efficiency [38, 39].

The direct transfer of octapeptide fiber arrays on gold surfaces was achieved using laser-induced forward transfer (LIFT). This immobilization technique involves a single pulse from a focused laser beam to transfer a peptide solution from a donor-coated surface to an acceptor surface [40]. The method provides the high-resolution, noncontact, direct, flexible, and parallel transfer of more than one type of material resulting in the deposition of peptide-based microarrays maintaining the biological functions of the nanostructures [41, 42]. As in the case of the physical vapor deposition method, this technique requires additional equipment such as laser systems, translation stage drivers, and microscopes.

In addition to the fabrication and manipulation-immobilization techniques mentioned in this section, there are a few others that could interest the reader. However, this chapter only presents techniques relevant for the development of electrochemical biosensors. The readers are thus invited to learn more about other methods to fabricate, manipulate, and immobilize SAPNs in some very good reviews and chapters focusing on these topics recently published [40, 43, 44].

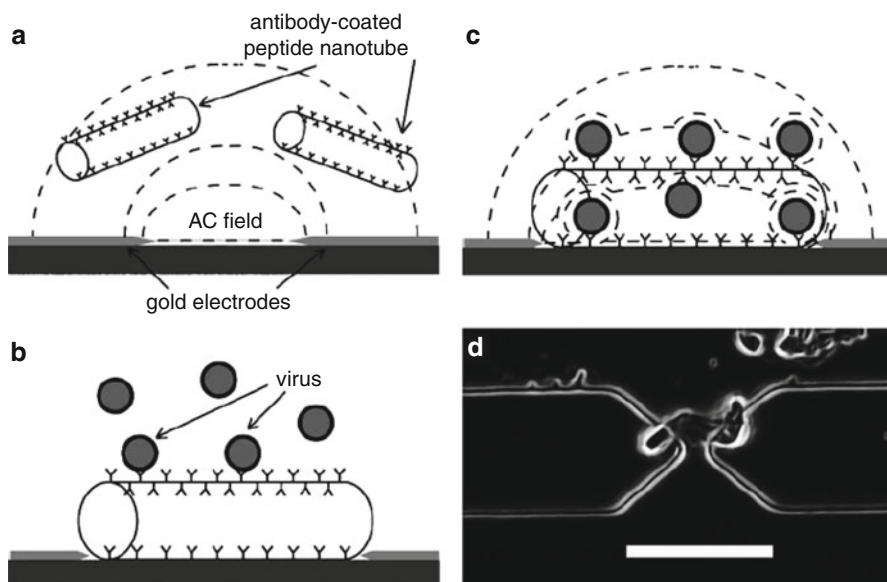


Fig. 3 Immobilization of antibody-coated peptide nanotubes using dielectrophoresis (Figure from de la Rica et al. [34] with permission from John Wiley & Sons)

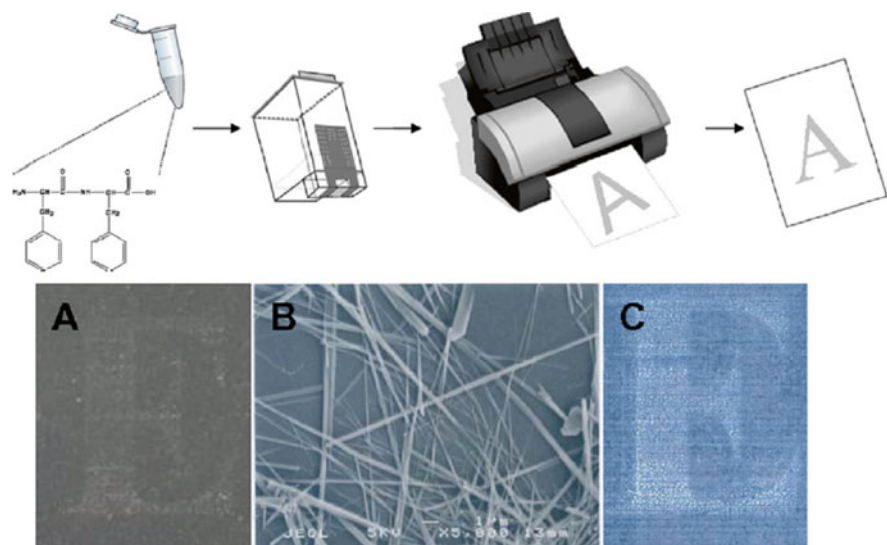


Fig. 4 Scheme of the inkjet printing deposition of self-assembled peptide nanotubes. (a) Image of a single printing cycle. (b) Scanning electron microscopy image of the printed area in (a). (c) Image of a 10-cycle print on transparent foil (Figure adapted from Adler-Abramovich and Gazit [36] with permission from John Wiley & Sons)

Functionalization of Self-Assembled Peptide Nanostructures

An important advantage of self-assembled peptide nanostructures, when compared with carbon nanotubes or silicon nanowires, is how easily these biological substrates can be decorated with functional compounds that increase the sensitivity and selectivity to the biosensing device. Thanks to the amino acids present on the structure of the self-assembled peptide, a variety of possible chemical interactions between the peptide nanostructure and the functional compound are available and have been utilized to decorate the surface of SAPNs.

If we focus only on the functionalization of SAPNs with the purpose of using them in electrochemical biosensing, we can find that these bionanostructures have been decorated with enzymes, antibodies, conductive polymers, metallic nanoparticles, and organic acids or integrated with inorganic nanomaterials, just to mention a few.

The manner in which SAPNs are functionalized varies depending of the type of peptide used to fabricate the nanostructure and the functional groups available on its surface. For instance, by taking advantage of the amino groups exposed on the external wall of diphenylalanine nanotubes, a biotinylation procedure was employed to decorate these nanotubes with gold nanoparticles, InGaP quantum dots, and a fluorescent labeling (Ato-610). The functionalization was performed through a rapid chemical reaction without any special requirements regarding equipment or temperature [45].

In a different study, antibodies were anchored via hydrogen bonding on the amide groups of self-assembled nanotubes of the bolaamphiphile peptide bis(N- α -amido-glycylglycine)-1,7-heptane dicarboxylate [38]. Using the same type of bolaamphiphile peptide nanotubes, *Candida rugosa* lipase – an enzyme previously used for the potentiometric detection of pesticides [46] – was encapsulated inside the nanotubes with a simple incubation process. The immobilization of the enzyme was possible via hydrogen bonding between amide groups present in the nanotube structure and the complementary functional groups of the enzyme [26]. This functionalization process required the incubation of the enzyme with the nanotubes during 1 week at 4 °C. A scheme of the functionalization process is shown in Fig. 5. This encapsulation process resulted in a catalytic activity of the enzyme which was 33 % higher than for a free-standing enzyme at room temperature.

Horseradish peroxidase and glucose oxidase, enzymes used for the electrochemical detection of hydrogen peroxide and glucose, were encapsulated within the internal cavity of diphenylalanine peptide nanotubes by capillary effect [47, 48]. The self-assembled nanotubes were incubated in the respective enzyme solutions at 5 °C during 1 week with constant shaking. The encapsulation of the enzymes inside the peptide nanostructures was confirmed by scanning transmission electron microscopy (STEM).

Kasotakis and coworkers presented a means to incorporate metallic nanoparticles at specific locations of nanofibers formed by self-assembly of the octapeptides: NSGAIITIG, NCGAIITIG, CNGAIITIG, and CSGAIITIG from the fiber protein of adenovirus [49]. The functionalization involved the mixing and incubation during 18 min of the peptide fibril solution with an aqueous solution of the metal salt

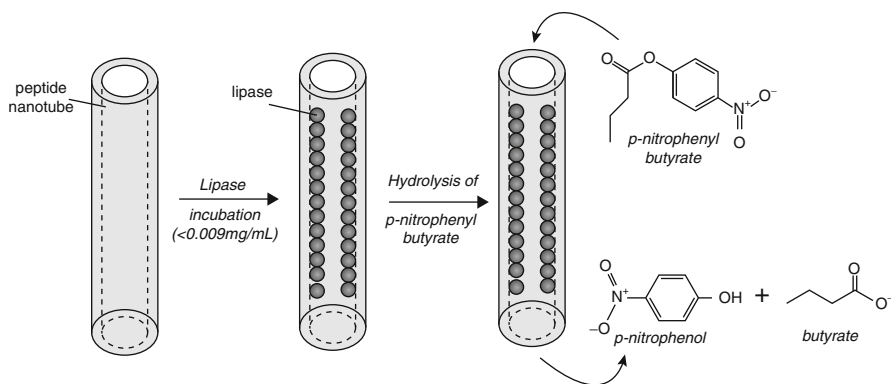


Fig. 5 Scheme of the immobilization of *Candida rugosa* lipase inside bolaamphiphile nanotubes (Reprinted with permission from Yu, L.T. et al. Fabrication and application enzyme-incorporated peptide nanotubes. *Bioconjugate Chem.* 16 (6): 1484–1487. Copyright (2005) American Chemical Society [26])

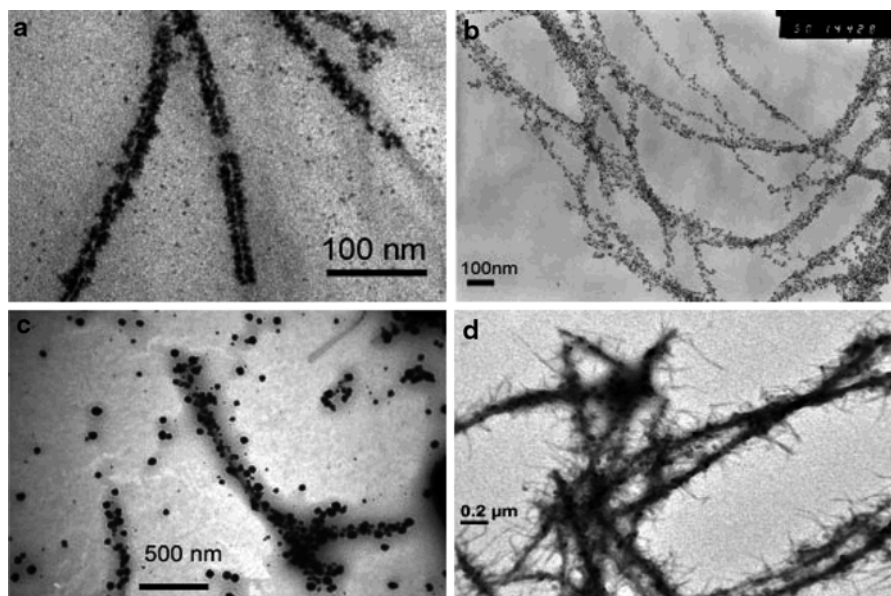


Fig. 6 Transmission electron microscopy images of the deposition of platinum on octapeptide nanofibrils. (a) Fibrils formed from the NSGAITIG peptide; (b) NCGAITIG peptide; (c) CNGAITIG peptide; (d) CSGAITIG peptide (Figure from Kasotakis et al. [49] with permission from John Wiley & Sons)

(AgNO_3 , $\text{HPtCl}_6 \cdot \text{H}_2\text{O}$, or $\text{HAuCl}_4 \cdot 3\text{H}_2\text{O}$). After the incubation, a reducing agent was added (1 % citric or ascorbic acid depending of the salt used). The mixed solution was then incubated during 1 h at room temperature. Figure 6 illustrates the NSGAITIG nanofibers after incubation with a platinum solution.

Glucose oxidase was covalently immobilized on the surface of EAK16-II nanofibers using 1-ethyl-3-(3-dimethylaminopropyl) carbodiimide hydrochloride (EDC)/N-hydroxysuccinimide (NHS) coupling. The functionalized EAK16-II nanofibers were deposited on highly ordered pyrolytic graphite for the amperometric detection of glucose. As in the case of the *Candida rugosa* lipase encapsulated on bolaamphiphile nanotubes, the activity and stability of the immobilized glucose oxidase were increased [50].

A recent study reported on the use of EDC as a linker agent between folic acid and diphenylalanine peptide nanotubes [51]. The functionalized peptide nanotubes were then deposited on a graphene electrode in order to capture cancer cells over-expressing folate receptors. The folic acid-functionalized self-assembled nanotubes were characterized using atomic force microscopy (AFM).

The templated polymerization of polyaniline (PANI), a conductive polymer, on the external wall of self-assembled peptide nanofibers was reported by Ryu [52]. For this, the formed nanofibers were immersed in a polymerizing solution of aniline for a desired time without stirring. The result was the formation of peptide nanofibers/PANI core/shell nanostructures, as shown in Fig. 7. Through doping/dedoping tests and electrochemical characterization, it was confirmed that the peptide/PANI nanofibers were electrochemically active.

Another example of the integration of SAPNs with conductive polymers was demonstrated by Hamedi and coworkers. Their work involved the decoration of amyloid fibrils synthesized from bovine insulin with poly(3,4-ethylenedioxythiophene)/poly(styrenesulfonate) (PEDOT/PSS). The PEDOT-functionalized amyloid fibrils were used to fabricate an electrochemical transistor device [53].

The same type of nanofibers was functionalized with Co_3O_4 nanostructures by treating the peptide nanofibers with 1 mM CoCl_2 solution in 10 mM Tris (pH 7.0)

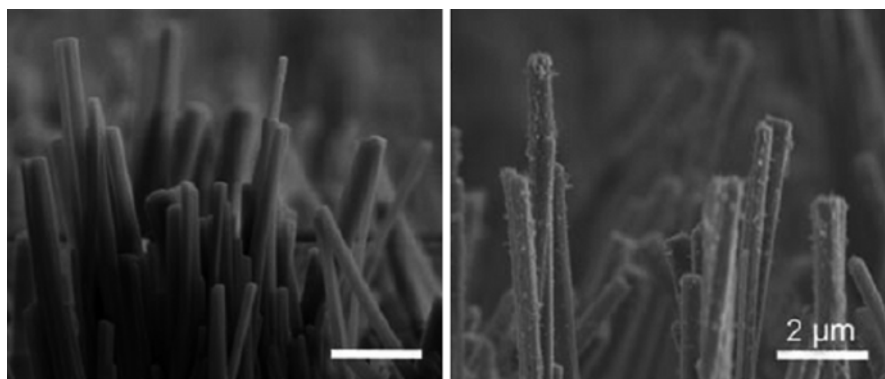


Fig. 7 Cross-sectional scanning electron microscope images of bare (*left image*) and PANI covered (*right image*) self-assembled peptide nanofibers (Figure from Ryu and Park [52] with permission from John Wiley & Sons)

overnight and reducing the adsorbed Co^{2+} ions with 5 mM NaBH_4 . The resultant peptide/ Co_3O_4 composite nanofibers were then subjected to structural and electrochemically characterizations [54].

Finally, an interesting example of the integration of SAPNs with carbon nanostructures was developed in order to fabricate peptide/graphene hybrid assemblies into core/shell nanowires by a single-step solution process. The prepared core/shell nanowires exhibited electroconductivity suggesting their use as a supercapacitor electrode [55].

As presented in the previous examples, there are many possibilities to functionalize SAPNs with a variety of functional molecules in order to improve the performance of the developed electrochemical sensing platform. These functionalization methods vary depending on the peptide used for the synthesis of the nanostructure and the target of the biosensing platform.

Applications

A majority of the electrochemical biosensing devices developed using SAPNs are used for the detection of relevant compounds in two main fields: biomedical and environmental applications. For the detection of these compounds, electrochemical techniques such as amperometry, cyclic voltammetry, and square wave voltammetry and impedance have been applied.

As mentioned before, SAPNs can be employed to encapsulate or support the biorecognition element in its structure. Additionally, SAPNs have been integrated with carbon nanomaterials such as graphene or carbon nanotubes in order to add extra functionalities.

Table 2 summarizes some of the electrochemical biosensors fabricated using SAPNs.

Biomedical Applications

Glucose and hydrogen peroxide are compounds of biomedical relevance that are connected with the diagnosis of diseases such as diabetes. The detection of glucose constitutes one of the biggest markets in the electrochemical biosensing industry [56, 57]. SAPNs offer a new alternative for the development of electrochemical biosensors aimed to follow changes in the concentrations of glucose, hydrogen peroxide, neurotransmitters, and metals involved in different pathologies.

Glucose oxidase was attached to peptide nanotubes through Traut's reagent for the electrochemical detection of glucose [32]. The modified nanotubes were then attached to a gold electrode using glutaraldehyde as a cross-linker as depicted in Fig. 2.

The electrochemical detection of tumor necrosis factor α (TNF- α) was reported using a biosensor combining ferrocene carboxylic acid-functionalized peptide nanofibers [58]. The sensor response was linear from 5 pg/mL to 10 ng/mL with a calculated detection limit of 2 pg/mL.

Table 2 Electrochemical biosensors fabricated using SAPNs

	Peptide	Immobilization method	Functionalization	Application	References
Biomedical	Boc-Phe-OH H-Phe-OMe	Physical adsorption	Gold nanoparticles Anti-TNF- α antibody	Detection of protein biomarker for tumor necrosis factor α	[58]
	(Cyclo[(Gln-D-Leu)4])	Physical adsorption	Antibody	Detection of <i>E. coli</i> cells	[63]
	Diphenylalanine	Physical adsorption	Horseradish peroxidase	Hydrogen peroxide	[64]
		Thiol modification and cross-linking with PEI	Glucose oxidase	Glucose and NADH	[26]
		Physical adsorption		Dopamine detection from PC12 cells	[30, 59]
		Physical adsorption	Folic acid	Cancer cells	[51]
Environmental		Cross-linking with glutaraldehyde		Ethanol and NADH	[65]
		EDC/NHS cross-linking	Glucose oxidase	Glucose	[48]
		Physical adsorption	Horseradish peroxidase	Hydrogen peroxide	[47]
	Octapeptides: NSGAIIG	Physical adsorption		Cu ion detection	[66]
	EAK16-II	Physical adsorption	Glucose oxidase	Glucose	[50]
	Bolaamphiphile	Dielectrophoresis	TAR-2-Asp	Pb ion detection	[61]
	Diphenylalanine	Physical adsorption	Tyrosinase	Phenol detection	[62]

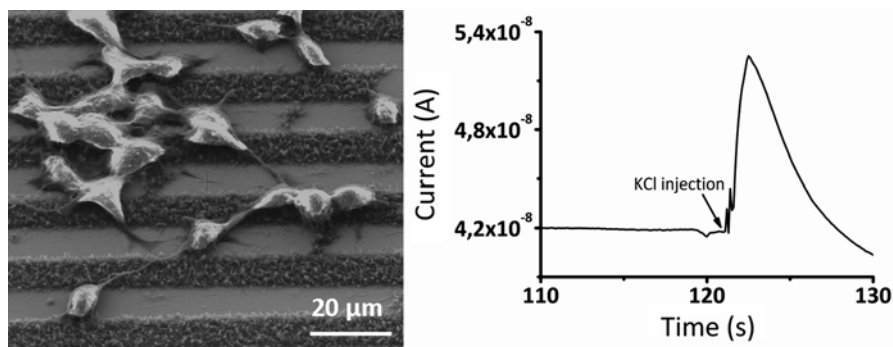


Fig. 8 Scanning electron microscope image of PC-12 cells on top of vertically aligned peptide nanofibers for the electrochemical detection of dopamine (*left*). Amperometric current-time curve corresponding to the dopamine release from PC12 cells triggered with KCl (*right*) (Reprinted with permission from Taskin, M. et al. Combined cell culture-biosensing platform using vertically aligned patterned peptide nanofibers for cellular studies. *ACS Appl. Mater. & Interf.* 5 (8): 3323–3328. Copyright (2013) American Chemical Society [30])

Vertically aligned self-assembled peptide nanofibers patterned on a microchip containing gold electrodes were used to fabricate a combined cell culture-biosensing platform for the detection of dopamine released from PC12 cells [30, 59]. The advantage of this combined platform was that it offered a 3D environment mimicking the situation experienced by cells *in vivo* and at the same time enabled the *in situ* detection of the neurotransmitter release upon stimulation with KCl, decreasing the loss of the signal due to the diffusion of the sample in the electrolyte.

Figure 8 shows PC12 cells grown on top of vertically aligned peptide nanofibers and the amperometric signal corresponding to the release of dopamine.

Folic acid, a ligand used for targeting cell membranes was deposited on the external wall of self-assembled peptide nanotubes; these functionalized nanotubes were then immobilized on graphene electrodes for the electrochemical detection of cancer cells over-expressing folate receptors [51]. A limit of detection of 250 cells/mL was obtained with the developed biosensor. This sensing platform could be used also with cells infected with parasites causing tropical disease such as leishmaniasis or Chagas disease over-expressing folate receptors.

Environmental Applications

Lead is a highly toxic heavy metal and environmental pollutant that can be poisonous at very low concentrations [60]. By taking advantage of the high affinity and specificity of some peptides to bind target metals, a Pb ion biosensor could be fabricated by integrating a gold transducer with self-assembled peptide nanotubes able to bind Pb ions and template the growth of Pb crystals via molecular recognition [61]. The biosensor was highly selective, displaying a linear response between 0 and 1 nM Pb^{II}, and the signal was not affected by the presence of other heavy metals such as Hg^{II}, Zn^{II}, Co^{II}, or Cu^{II} as shown in Fig. 9.

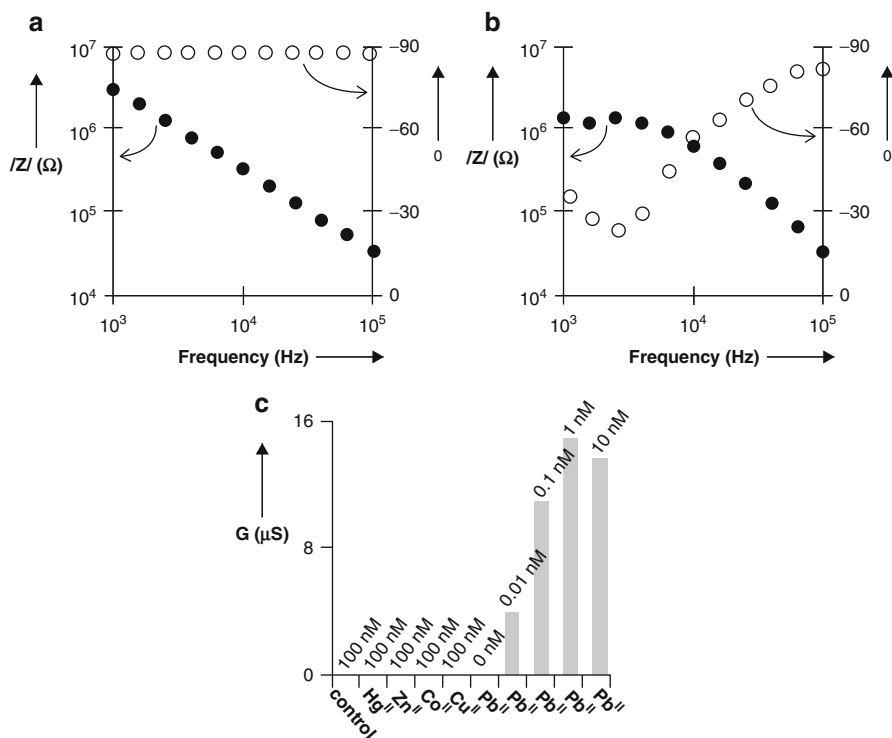


Fig. 9 Ultrasensitive detection of Pb (II) using an electrochemical biosensor with peptide nanotubes (a) in the absence of Pb (II) and (b) in the presence of 0.01 nM Pb (II); (c) conductance of the peptide nanotubes after incubation with different heavy metal ions (Figure from de la Rica et al. [61] with permission from John Wiley & Sons)

In a study aimed to detect phenol, a graphite electrode was coated with tyrosinase-functionalized diphenylalanine peptide nanotubes [62]. Phenol concentrations as low as 50 nM were recorded using the developed electrochemical biosensor. The deposition of the tyrosinase-functionalized nanotubes resulted in an increased surface area between 0.06 and 0.07 cm² compared with an unmodified graphite electrode.

Conclusions and Outlook

Due to its mild fabrication conditions, low-cost synthesis, and easy functionalization, self-assembled peptide nanostructures are being used in the development of electrochemical biosensors. SAPNs can be immobilized on electrochemical transducers using cross-linking agents, physical adsorption or deposited using dielectrophoresis. Different functional molecules are used to decorate the structure of SAPNs in order to improve the sensitivity and selectivity of the biosensing device.

Additionally, SAPNs were integrating with carbon materials (e.g., carbon nanotubes and graphene) and conductive polymers (e.g., PANI, PPY) in order to produce hybrid nanomaterials. Up to now electrochemical biosensors fabricated using SAPNs were applied for the detection of samples in two main areas: biomedical and environmental. Samples such as neurotransmitter metal, ions, and cancer cells among others are some of the compounds detected using this type of electrochemical sensors.

Studies evaluating the immunogenicity and toxicity of SAPNs could accelerate its use in implantable electrochemical biosensors. Additionally, new immobilization methods aiming to produce a more stable layer containing SAPNs together with the biorecognition element will improve the stability and reproducibility of the biosensing platforms and will expand its use in new application fields. Deposition methods such as inkjet print or airbrush will be convenient techniques for the industrial production of SAPNs paper-based electrochemical biosensors for point-of-care devices.

References

1. Garcia M, Batalla P, Escarpa A (2014) Metallic and polymeric nanowires for electrochemical sensing and biosensing. *Trends Anal Chem* 57:6–22
2. Choi Y, Moon D, Choi J, Ahn J (2014) Fabrication of nanowires and their applications. In: Kim DM, Jeong YH (eds) *Nanowire field effect transistors: principles and applications*. Springer, New York
3. Du F, Zhu L, Dai L (2013) Carbon nanotube-based electrochemical biosensors. In: Li J, Wu N (eds) *Biosensors based on nanomaterials and nanodevices*. CRC Press, Boca Raton
4. Guell AG, Meadows KE, Dudin PV, Ebejer N, Macpherson JV, Unwin PR (2014) Mapping nanoscale electrochemistry of individual single-walled carbon nanotubes. *Nano Lett* 14:220–224
5. Wanekaya AK, Chen W, Myung NV, Mulchandani A (2006) Nanowire-based electrochemical biosensors. *Electroanalysis* 18:533–550
6. Andersen KB, Christiansen NO, Castillo-León J, Rozlosnik N, Svendsen WE (2013) Fabrication and characterization of PEDOT nanowires based on self-assembled peptide nanotube lithography. *Organ Electron* 14:1370–1375
7. Guo CX, Ng SR, Li CM (2013) Graphene-based electrochemical biosensors. In: Li J, Wu N (eds) *Biosensors based on nanomaterials and nanodevices*. CRC Press, Boca Raton
8. de la Rica R, Matsui H (2010) Bioinspired target-specific crystallization on peptide nanotubes for ultrasensitive Pb ion detection. *Chem Soc Rev* 39:3499–3509
9. Ryu J, Park CB (2010) High stability of self-assembled peptide nanowires against thermal, chemical, and proteolytic attacks. *Biotechnol Bioeng* 105:221–230
10. Scanlon S, Aggeli A (2008) Self-assembling peptide nanotubes. *Nano Today* 3:22–30
11. Yan XH, Zhu PL, Li JB (2010) Self-assembly and application of diphenylalanine-based nanostructures. *Chem Soc Rev* 39:1877–1890
12. Chen AC, Chatterjee S (2013) Nanomaterials based electrochemical sensors for biomedical applications. *Chem Soc Rev* 42:5425–5438
13. Li HH, Liu SQ, Dai ZH, Bao JC, Yang XD (2009) Applications of nanomaterials in electrochemical enzyme biosensors. *Sensors* 9:8547–8561
14. Amit M, Cheng G, Hamley IW, Ashkenasy N (2012) Conductance of amyloid beta based peptide filaments: structure-function relations. *Soft Matter* 8:8690–8696
15. Andersen KB, Castillo-Leon J, Hedstrom M, Svendsen WE (2011) Stability of diphenylalanine peptide nanotubes in solution. *Nanoscale* 3:994–998

16. Beker P, Koren I, Amdursky N, Gazit E, Rosenman G (2010) Bioinspired peptide nanotubes as supercapacitor electrodes. *J Mater Sci* 45:6374–6378
17. Carny O, Shalev DE, Gazit E (2006) Fabrication of coaxial metal nanocables using a self-assembled peptide nanotube scaffold. *Nano Lett* 6:1594–1597
18. del Mercato LL, Pompa PP, Maruccio G, Della Torre A, Sabella S, Tamburro AM, Cingolani R, Rinaldi R (2007) Charge transport and intrinsic fluorescence in amyloid-like fibrils. *Proc Natl Acad Sci U S A* 104:18019–18024
19. Lakshmanan A, Zhang SG, Hauser CAE (2012) Short self-assembling peptides as building blocks for modern nanodevices. *Trends Biotechnol* 30:155–165
20. Scheibel T, Parthasarathy R, Sawicki G, Lin XM, Jaeger H, Lindquist SL (2003) Conducting nanowires built by controlled self-assembly of amyloid fibers and selective metal deposition. *Proc Natl Acad Sci U S A* 100:4527–4532
21. Takahashi R, Wang H, Lewis JP (2007) Electronic structures and conductivity in peptide nanotubes. *J Phys Chem B* 111:9093–9098
22. Xu HX, Das AK, Horie M, Shaik MS, Smith AM, Luo Y, Lu XF, Collins R, Liem SY, Song AM, Popelier PLA, Turner ML, Xiao P, Kinloch IA, Ulijn RV (2010) An investigation of the conductivity of peptide nanotube networks prepared by enzyme-triggered self-assembly. *Nanoscale* 2:960–966
23. Adler-Abramovich L, Aronov D, Beker P, Yevnin M, Stempler S, Buzhansky L, Rosenman G, Gazit E (2009) Self-assembled arrays of peptide nanotubes by vapour deposition. *Nat Nanotechnol* 4:849–854
24. Castillo-León J, Rodríguez-Trujillo R, Gauthier S, Jensen ACO, Svendsen WE (2011) Micro-“factory” for self-assembled peptide nanostructures. *Microelectron Eng* 88:1685–1688
25. Reches M, Gazit E (2003) Casting metal nanowires within discrete self-assembled peptide nanotubes. *Science* 300:625–627
26. Yu LT, Banerjee IA, Gao XY, Nuraje N, Matsui H (2005) Fabrication and application of enzyme-incorporated peptide nanotubes. *Bioconjugate Chem* 16:1484–1487
27. Porrata P, Goun E, Matsui H (2002) Size-controlled self-assembly of peptide nanotubes using polycarbonate membranes as templates. *Chem Mat* 14:4378–4381
28. Tarabout C, Roux S, Gobeaux F, Fay N, Pouget E, Meriadec C, Ligeti M, Thomas D, Ijsselstijn M, Besselièvre F, Buisson DA, Verbavatz JM, Petitjean M, Valery C, Perrin L, Rousseau B, Artzner F, Paternostre M, Cintrat JC (2011) Control of peptide nanotube diameter by chemical modifications of an aromatic residue involved in a single close contact. *Proc Natl Acad Sci U S A* 108:7679–7684
29. Ryu J, Park CB (2008) High-temperature self-assembly of peptides into vertically well-aligned nanowires by aniline vapor. *Adv Mater* 20:3754
30. Taskin MB, Sasso L, Dimaki M, Svendsen WE, Castillo-León J (2013) Combined cell culture-biosensing platform using vertically aligned patterned peptide nanofibers for cellular studies. *ACS Appl Mater Interfaces* 5:3323–3328
31. Cipriano TC, Takahashi PM, de Lima D, Oliveira VX, Souza JA, Martinho H, Alves WA (2010) Spatial organization of peptide nanotubes for electrochemical devices. *J Mater Sci* 45:5101–5108
32. Yemini M, Reches M, Gazit E, Rishpon J (2005) Peptide nanotube-modified electrodes for enzyme-biosensor applications. *Anal Chem* 77:5155–5159
33. Castillo J, Tanzi S, Dimaki M, Svendsen W (2008) Manipulation of self-assembly amyloid peptide nanotubes by dielectrophoresis. *Electrophoresis* 29:5026–5032
34. de la Rica R, Mendoza E, Lechuga LM and Matsui H (2008) Label-free pathogen detection with sensor chips assembled from peptide nanotubes. *Angew Chem-Int Edit* 47:9752–9755
35. Domigan L, Andersen KB, Sasso L, Dimaki M, Svendsen WE, Gerrard JA, Castillo-León J (2013) Dielectrophoretic manipulation and solubility of protein nanofibrils formed from crude crystallins. *Electrophoresis* 34:1105–1112
36. Adler-Abramovich L, Gazit E (2008) Controlled patterning of peptide nanotubes and nanospheres using inkjet printing technology. *J Pept Sci* 14:217–223

37. Reches M, Gazit E (2006) Controlled patterning of aligned self-assembled peptide nanotubes. *Nat Nanotechnol* 1:195–200
38. Zhao Z, Matsui H (2007) Accurate immobilization of antibody-functionalized peptide nanotubes on protein-patterned Arrays by optimizing their ligand-receptor interactions. *Small* 3: 1390–1393
39. Zhao ZY, Banerjee PA, Matsui H (2005) Simultaneous targeted immobilization of anti-human IgG-coated nanotubes and anti-mouse IgG-coated nanotubes on the complementary antigen-patterned surfaces via biological molecular recognition. *J Am Chem Soc* 127:8930–8931
40. Farsari M, Mitraki A (2011) Self-assembled peptide nanostructures and their controlled positioning on surfaces. In: Kumar C (ed) *Nanomaterials for the life sciences*, vol 10. Wiley-VCH, Weinham
41. Dinca V, Kasotakis E, Catherine J, Mourka A, Mitraki A, Popescu A, Dinescu M, Farsari M, Fotakis C (2007) Development of peptide-based patterns by laser transfer. *Appl Surf Sci* 254:1160–1163
42. Dinca V, Kasotakis E, Catherine J, Mourka A, Ranella A, Ovsianikov A, Chichkov BN, Farsari M, Mitraki A, Fotakis C (2008) Directed three-dimensional patterning of self-assembled peptide fibrils. *Nano Lett* 8:538–543
43. Castillo J, Dimaki M, Svendsen W (2011) *Micro and nano techniques for the handling of biological samples*. CRC Press, Boca Raton
44. Castillo J, Dimaki M, Svendsen WE (2009) Manipulation of biological samples using micro and nano techniques. *Integr Biol* 1:30–42
45. Reches M, Gazit E (2007) Biological and chemical decoration of peptide nanostructures via biotin-avidin interactions. *J Nanosci Nanotechnol* 7:2239–2245
46. Kartal F, Kilinc A, Timur S (2007) Lipase biosensor for tributyrin and pesticide detection. *Int J Environ Anal Chem* 87:715–722
47. Park BW, Yoon DY, Kim DS (2010) Encapsulation of enzymes inside peptide nanotube for hydrogen peroxide detection. ECS transactions, Las Vegas, NV, 2010
48. Park BW, Zheng R, Ko KA, Cameron BD, Yoon DY, Kim DS (2012) A novel glucose biosensor using bi-enzyme incorporated with peptide nanotubes. *Biosens Bioelectron* 38:295–301
49. Kasotakis E, Mossou E, Adler-Abramovich L, Mitchell EP, Forsyth VT, Gazit E, Mitraki A (2009) Design of metal-binding sites onto self-assembled peptide fibrils. *Biopolymers* 92:164–172
50. Yang H, Fung SY, Pritzker M, Chen P (2009) Ionic-complementary peptide matrix for enzyme immobilization and biomolecular sensing. *Langmuir* 25:7773–7777
51. Castillo JJ, Svendsen WE, Rozlosnik N, Escobar P, Martinez F, Castillo-Leon J (2013) Detection of cancer cells using a peptide nanotube-folic acid modified graphene electrode. *Analyst* 138:1026–1031
52. Ryu J, Park CB (2009) Synthesis of Diphenylalanine/Polyaniline Core/Shell Conducting Nanowires by Peptide Self-Assembly. *Angew Chem Int Ed* 48:4820–4823
53. Hamed M, Herland A, Karlsson RH, Inganas O (2008) Electrochemical devices made from conducting nanowire networks self-assembled from amyloid fibrils and alkoxy-sulfonate PEDOT. *Nano Lett* 8:1736–1740
54. Ryu J, Kim SW, Kang K, Park CB (2010) Mineralization of Self-assembled Peptide Nanofibers for Rechargeable Lithium Ion Batteries. *Adv Mater* 22:5537–5541
55. Han TH, Lee WJ, Lee DH, Kim JE, Choi EY, Kim SO (2010) Peptide/Graphene Hybrid Assembly into Core/Shell Nanowires. *Adv Mater* 22:2060
56. Turner A (2013) Biosensors: then and now. *Trends Biotechnol* 31:119–120
57. Turner APF (2013) Biosensors: sense and sensibility. *Chem Soc Rev* 42:3184–3196
58. Sun ZF, Deng L, Gan H, Shen RJ, Yang MH, Zhang Y (2012) Sensitive immunosensor for tumor necrosis factor alpha based on dual signal amplification of ferrocene modified self-assembled peptide nanowire and glucose oxidase functionalized gold nanorod. *Biosens Bioelectron* 39:215–219

59. Sasso L, Vedarethinam I, Emneus J, Svendsen WE, Castillo-Leon J (2012) Self-assembled Diphenylalanine nanowires for cellular studies and sensor applications. *J Nanosci Nanotechnol* 12:3077–3083
60. Brodtkin E, Copes R, Mattman A, Kennedy J, Kling R, Yassi A (2007) Lead and mercury exposures: interpretation and action. *Can Med Assoc J* 176:59–63
61. de la Rica R, Mendoza E, Matsui H (2010) Bioinspired target-specific crystallization on peptide nanotubes for ultrasensitive pb ion detection. *Small* 6:1753–1756
62. Adler-Abramovich L, Badihi-Mossberg M, Gazit E, Rishpon J (2010) Characterization of peptide-nanostructure-modified electrodes and their application for ultrasensitive environmental monitoring. *Small* 6:825–831
63. Cho EC, Choi JW, Lee MY, Koo KK (2008) Fabrication of an electrochemical immunosensor with self-assembled peptide nanotubes. *Colloid Surf A Physicochem Eng Asp* 313:95–99
64. Yemini M, Reches M, Rishpon J, Gazit E (2005) Novel electrochemical biosensing platform using self-assembled peptide nanotubes. *Nano Lett* 5:183–186
65. Yuan JH, Chen JR, Wu XH, Fang KM, Niu L (2011) A NADH biosensor based on diphenylalanine peptide/carbon nanotube nanocomposite. *J Electroanal Chem* 656:120–124
66. Viguier B, Zor K, Kasotakis E, Mitraki A, Clausen CH, Svendsen WE, Castillo-Leon J (2011) Development of an electrochemical meta-ion biosensor using self-assembled peptide nanofibrils. *ACS Appl Mater Interfaces* 3:1594–1600

Iuliana Moldoveanu, Raluca-Ioana Stefan-van Staden,
and Jacobus Frederick van Staden

Contents

Introduction.....	1144
Methods Used for Producing of Nanomaterials.....	1145
The Advantages of Using Nanomaterials	1146
Types of Sensors	1147
Classification of Sensors	1147
Sensors' Design	1149
Nanostructured Materials Used for Design of Sensors.....	1150
Surface Analysis	1153
Applications.....	1154
Conclusions.....	1155
References.....	1156

Abstract

Nanostructured materials became in the past years the materials of choice for the design of new electrochemical sensors. Enhanced electrocatalytic properties obtained due to the increase of active surface and the electrocatalytic activity of the nanostructured material were recorded for the amperometric sensors.

I. Moldoveanu • R.-I. Stefan-van Staden (✉)

Laboratory of Electrochemistry and PATLAB Bucharest, National Institute of Research for Electrochemistry and Condensed Matter, Bucharest, Romania

Faculty of Applied Chemistry and Materials Science,
Politehnica University of Bucharest, Bucharest, Romania
e-mail: iuli_0909@yahoo.com; ralucavanstaden@gmail.com

J.F. van Staden

Laboratory of Electrochemistry and PATLAB Bucharest, National Institute of Research for Electrochemistry and Condensed Matter, Bucharest, Romania
e-mail: koosvanstaden2012@yahoo.com

Stochastic sensors based on channel conductivity improved the quality and reliability of measurements especially when used in biomedical analysis. Design of sensors based on graphene, carbon nanotube, and carbon nanopowder will be discussed. Surface analysis is essential in the evaluation of the active area of the sensors. The most important applications of the sensors based on nanostructured materials will be shown.

Keywords

Electrochemical sensor • Nanostructured material • Carbon nanotube • Graphene

Introduction

The term “nanotechnology” in its evolution covers many applications in nanoscale electronics. At present, the term “nanotechnology” deals with particles or assemblies of particles which vary from a few nanometers to about 100 nm. New developments using nanoparticles or subassemblies of them are found in industry and research studies [37, 39].

The nanomaterials have extremely important applications due to the following characteristics: the materials (i) present a wide range of properties; (ii) usually present improved properties, e.g., conductivity and stiffness, and a broad range of fluorescent emissions in the case of quantum dots; (iii) can mix the best properties of classical and quantum behaviors; (iv) represent a bridge between classical and biological materials; and (v) offer improved methods for “materials by design.”

The well-known engineered nanostructures include to date the following materials: ceramics, nanostructured materials, and polymers. Nanocomponents such as coating materials and connectors and nanodevices such as sensors, switches, and reactors can also be engineered and synthesized accordingly with the needs.

The extremely small sizes of materials had as result improved properties such as significant enhancement of optical, mechanical, electrical, structural, and magnetic properties and extremely large specific surface area [39, 46].

Design of materials from building blocks was also possible using nanotechnology. It was proved several times that at the nanosize the theories of classical and quantum mechanics are changed, this being reflected also by the special properties of the designed materials. Few of the properties that are changing by downsizing are transparency, hydrophobicity, photoluminescence, toughness and hardness, chemical sensing, and bioavailability. The products obtained from these materials proved to have a high commercial value helping also in rapidly expanding markets.

The interest in nanotechnology and engineered nanostructured fields is from the design of nanomaterials up to applications, which attract the attention of materials developers [39] (Fig. 1).

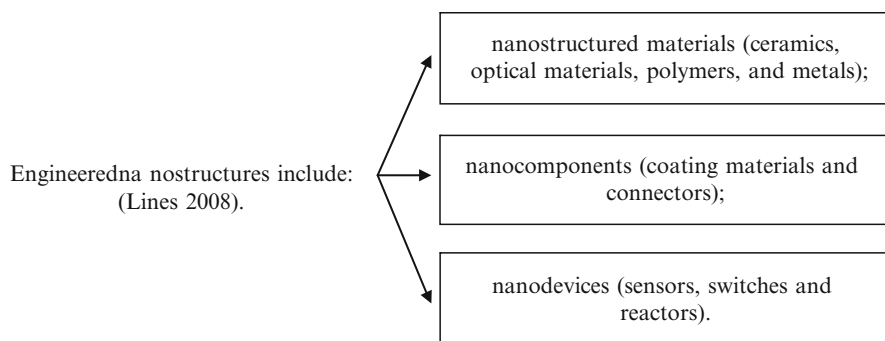


Fig. 1 Classification of engineered nanostructures

Methods Used for Producing of Nanomaterials

Development of new surface analysis techniques facilitated the study of nanostructured systems (nanotubes, nanowires, nanoparticles, nanoporous materials) fabricated using novel technologies. Therefore, the electrons may be confined strongly in any dimension, the materials' characteristics being improved versus the bulk material [66].

Besides direct atom manipulation, there were many methods developed to produce nanomaterials: plasma arcing (the very high temperatures associated with the formation of an arc or plasma are used to effectively separate the atomic species of feedstock), chemical vapor deposition (feed gases are reacted in a chamber and the resulting species attracted to a substrate), electrodeposition (involves a similar process; however the controlled coating is deposited from solution by the application of an electric field), sol-gel synthesis (uses chemical means to produce intimately mixed compounds that are hydrolyzed into gels, which decompose to leave a thin layer of the desired coating). Mechanochemical processing (MCP) technology developed by Advanced Nanotechnologies based in Perth is a new solid-state process for the manufacture of a wide range of nanopowders [39].

Two methods are commonly employed for fabrication of nanostructures:

- Bottom-up [22, 38] (by using the techniques of molecular synthesis [22], colloid chemistry [13], polymer science [43], and related areas to produce engineered nanostructures; these nanostructures produced in parallel are nearly identical, but with no long-range order when incorporated into extended materials).
- Top-down [76] (uses the lithography to pattern materials).

Materials needed an accessible strategy to bridge the two methods of formation. This strategy is self-assembly [76, 82] (synthesized bottom-up to organize themselves into regular patterns or structures by using local forces to find the lowest-energy configuration and to guide this self-assembly using templates fabricated top-down) (Table 1).

Table 1 Methods used to produce nanomaterials

No.	Method	References
1	Plasma arcing	[39]
2	Chemical vapor deposition	
3	Electrodeposition	
4	Sol-gel synthesis	
5	Mechanochemical processing (MCP) technology (a relatively new technique termed)	
6	Self-assembly layers	[76, 82]

The Advantages of Using Nanomaterials

During the last years, electrochemical sensors based on nanomaterials were very often used in chemical analysis due to their advantages: rapidity, simplicity, and low costs [60]. Utilization of nanomaterials and nanosensors improved the response characteristics of the sensors due to high surface area/volume ratios as well as enhanced optical properties (quantum dot fluorescence, gold nanoparticle quenching) [8, 10]. For example, nanoscale materials have a higher mechanical resistance compared with macroscopic samples of the same material. Substructures of the materials over a range of scales influenced the fracture strength and character, ductility/ flexibility, as well as various mechanical modules.

Downsizing of the materials used for sensor design influenced the properties of the materials with direct effects on sensor behavior and reliability. Few examples related to this point are as follows: materials at the nanometer scale have a lower melting point [6] and reduced lattice constant [18]. Nanomaterials may show different elastoplasticities compared with the macromaterials [9].

Functionalization of the nanostructured materials is essential in many cases for the design of new sensors and biosensors. Using these materials, new stable and reliable solid-state sensors and biosensors offering compatibility of inorganic materials with the chemical/biological agents were designed for reproducible screening of biological fluids [66].

Many processing methods have been developed for producing bulk nanostructured materials with a size less than 100 nm [51]. Typical sizes were known at electrochemical interfaces at the nanoscale. There are three aspects that deserve attention regarding the use of nanoscale materials in electrochemical field [25]:

- Downsizing of microelectrodes
- Utilization of materials with pores or surface roughness in nanometer range
- Utilization of materials with a large number of defects caused by extremely small-size crystallized amorphous-state or noncrystalline materials

The downsizing takes all the new instruments to new working conditions and optimized parameters, methods, and models. The size and the surface area/volume ratio play an essential role for the sensor behavior [25].

Types of Sensors

Electrochemical sensors had a fast progress in the term of electroactive materials, matrix materials, and size [3, 59]. Compared to the other instruments, electrochemical sensors are attractive due to screening capabilities, easy and reliable design, short time of analysis, and low cost. They are leaders among the other types of sensors. Some of them reached the commercial stage and found a wide range of important applications in the areas of clinical, industrial, food, and biomedical analyses [41]. Recent developments in nanomaterials used for the design of chemically modified sensors have opened new fields of applications such as screening of whole blood for early detection of diseases. The response of them converts chemical information in analytical signals and the chemical information can come from a chemical reaction of the target analyte or a physical property of the system investigated [27]. Optical sensors based on nanomaterials progressed due to utilization of nanomaterials in their design.

Classification of Sensors

Chemical sensors contain a receptor part and a transducer part. Some sensors need membranes attached to the active side to avoid its contamination. The role of the receptor part is to chemically transform the analyte in a measurable form by the transducer, and the transducer is capable of transforming the chemical information obtained from the receptor in a useful measurable analytical signal which is a physical property like electrode potential, intensity, or current. The transducer alone does not show selectivity; the selectivity may only be improved by the receptor part.

Chemical sensors are classified according to the type of the transducer – correlated with the result of the chemical reaction favored by the receptor in the following:

- Optical sensors: when the result of an interaction of the analyte with the receptor is an adsorption/emission, fluorescence, or chemiluminescence phenomenon.
- Electrochemical sensors: transform the effect of the interaction between analyte and electrode into a useful electrochemical signal, potential, intensity, or current. These effects may be stimulated electrically (an intensity or potential is applied) or may result in a spontaneous interaction at the zero-current condition. The following types of sensors are:
 1. Voltammetric sensors, including amperometric sensors:(current is measured in the continuous current or alternating current): examples are the sensors based on chemically inert electrodes, modified electrodes, and chemically active electrodes.
 2. Potentiometric sensors: the potential of the electrode (ion-selective electrode) is measured against a reference electrode, at zero current.
 3. Chemically sensitized field effect transistor (CHEMFET): the effect of the interaction between the analyte and the active coating is transformed into a change of the source–drain current.

- Mass-sensitive sensors.
- Magnetic sensors.
- Thermometric sensors.

Another way of sensor classification is accordingly with their applications, e.g., that are determining a given analyte (e.g., sensors for pH, for metal ions, or for determining oxygen or other gases), and with the type of application, e.g., sensors for in vivo analysis or sensors for process in vitro analysis [63].

Researchers developed platforms for multianalyte assay by combining sensors in sets, called in the 1990s multisensors [27].

The following electroanalytical methods are used: conductometric, potentiometric, and voltammetric/ampereometric methods. Conductometric method is versatile and is not selective but the principles of operation are very simple; measurement of solution resistance allows the deduction of the concentration of charge between two electrodes. The selectivity of this method can be improved by using it as detection method in high-performance liquid chromatography.

Potentiometric method. The equilibrium potential of an electrode is measured against a selected reference electrode at zero current. Ion-selective electrodes and enantioselective sensors can present a good selectivity for one analyte, especially if determined from a well-known matrix.

Ion-selective electrodes were developed since 1950. Glass membranes, solid-state homogeneous and heterogeneous membranes, and ion-exchange membranes and neutral carrier membranes were proposed for their design. Nernst equation was used for all quantitative measurements, one of the limitations being the interferences; therefore, the types of applications were limited later to pharmaceutical analysis. The limit of detection (often above 10^{-7} M), the response, and lifetime were acceptable for pharmaceutical analysis. The response time is particularly critical if the electrodes are placed in a flow system [5].

Voltammetric method. A current–voltage is recorded where the current is registered as a function of applied potential using a potentiostat, or potential is recorded as a function of applied current using a galvanostat. Amperometric sensors operate at fixed applied potential [5]. The first voltammetric device was the dropping mercury electrode proposed by Heyrovsky in 1922, for which he won the Nobel Prize in 1959 [23]. Later, electrode materials have been developed based on various forms of carbon [5].

In potentiometric analysis, the sensors are designed to be selective for a certain analyte in a certain matrix. In voltammetric analysis, the material of electrode, as well as the pH and composition of the solution, can influence the half-wave potential of species in mixtures, in this way enabling the separation of two similarly oxidizing or reducible species solving some interference problems. The choice the electrode material can lead to selectivity potentiometric and voltammetric sensors. An applied potential in voltammetric or amperometric sensors can lead to high selectivity [5].

Stochastic analysis is a novel technique and the most spectacular method developed so far in electrochemistry [20]; it is an approach based on observation of

individual events of target analyte. This class of sensors is based on pore/nanopore conductivity. Pores are promising elements for stochastic sensors, and they produce fluctuations simplistic in their binary manifestations, namely, τ_{on} and τ_{off} , representing response/ionic current through the pore [19].

Until now there have been built many sensors based on biological molecules (proteins, α -HL) and artificial pore with controlled size and shape. First occurrence of stochastic analyze was launched at a much larger scale. At the end of year 1940, Wallace H. Coulter has invented counters based on a resistive hole for the counting and classification by size of the blood cells [12].

The first biosensor based on an artificial nanopore was constructed from a cylindrical pore from gold nanotubes placed in a polymeric membrane, mechanically stable, by the group of researcher Charles Martin in 2005 [53].

The applications of these sensors are until now in the biomedical (e.g., DNA sequencing and analysis [24], enantioanalysis of pipercolic acid [58]), pharmaceutical, and environmental fields.

Sensors' Design

The design of the sensors influences the reliability of the analytical information. Matrix composition and ratio between electroactive materials used as matrix modifier influence the response characteristics of the electrode. Electroactive material has an essential role in the electrode response; therefore it will be attentive to choose according to selectivity, sensitivity, and detection limit. Another issue that must be considered in the construction of the sensors is the biocompatibility of the materials used for sensors' design [57].

Characteristics of the electrode can be adjusted by the appropriate designs and architectures.

New nanostructured materials were designed and used as modifier on different substrates like carbon or metal substrates. Carbon materials such as nanotubes and graphene, nanoparticles, and nanowires, and also conducting polymers engineered as nanowires, have been synthesized, characterized, and applied for the design of sensors. The use of nanomaterials increased the current intensity by increasing the active surface area with respect to a flat substrate where the sensor reaction can occur [5].

Solid-state electrodes based on noble metals and different forms of carbon have been used intensively in the past years. The electrodes based on carbon, platinum, gold, silver, nickel, and copper were used for many applications due to their characteristics like versatile potential window, low background current, low cost, and chemical inertness [60].

Chemically modified electrodes represent a modern approach in sensors' technology. Modification of the sensor surface is performed by incorporation of an appropriate surface modifier. By chemical modification of the active surface of sensors, the characteristics of the sensors may be improved. The interest for modified surfaces of sensors is motivated especially by the increase of selectivity and sensitivity for many potential applications.

Covering of the electrode surfaces with different films represents an easy and reliable method for surface modification; polymer films (most polymers are applied to electrode surfaces by a combination of adsorptive attraction and low solubility in the electrolyte solution) and inorganic films (metal oxide, clay, zeolite, metal ferrocyanide) are often used as modifiers [60].

There is significant progress in synthesis and characterization of nanostructured materials using surface characterization techniques which helped the evolution of the design and surface characterization of sensors. Special properties of carbon nanotubes (CNTs) modified with functional groups improved the properties of CNT and made possible its application in high-tech sensors' design [64, 65].

The sensors based on nanotube include also metal oxide-based tubes such as Co_3O_4 , Fe_2O_3 , SnO_2 , and TiO_2 and metal tubes such as Pt nanosensor. The sensors based on nanomaterials present improved sensitivity and selectivity, fast response, high recovery, and potential for integration in arrays on a massive scale. All these properties represent an improvement from classics sensors. These advantages are helping the detection of biomolecules at molecule level [26].

Nanostructured Materials Used for Design of Sensors

Carbon materials are preferred for the design of electrochemical sensors due to their high reliability, low residual current, wide potential window, readily renewable surface, and the large overpotential for O_2 reduction and H_2 evolution [72]. The carbon materials include zero-dimensional (e.g., fullerenes, nanodiamond), one-dimensional (carbon nanotubes), and two-dimensional carbon materials such as diamond and graphite [55].

Zero-Dimensional Nanostructures (Nanoparticles)

Nanoparticles (20–200 nm) include single crystals, polycrystalline, and amorphous materials with all possible morphologies, such as spheres, cubes, and platelets. The most used techniques used for their synthesis are top-down and bottom-up techniques. A very important issue of metal nanoparticles is that their optical properties depend on the size and shape of the nanoparticle. Magnetic nanoparticles have numerous applications which include targeted drug delivery, ultrasensitive disease detection, gene therapy, high-throughput genetic screening, biochemical sensing, and rapid toxicity cleansing [66].

One-Dimensional Nanostructures (Carbon Nanotubes)

Carbon nanotubes are 100 times stronger than steel, although they have only one-sixth the weight. Their conductivity is comparable with the one of copper or structures that act as semiconductors [39]. The discovery of carbon nanostructures in 1985 and the carbon nanotubes (CNTs) by Iijima in 1991 [28] made possible the faster evolution of nanotechnology. The progress in synthesis technologies favored the development of various nanostructured and advanced electronic materials with remarkable properties and unique applications. These materials show a high potential for the development of new electrochemical and optical devices and sensors [65].

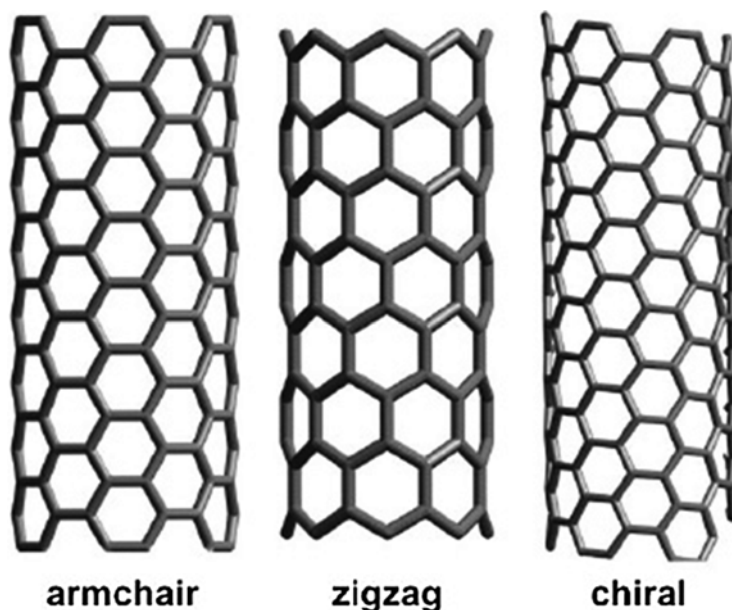


Fig. 2 Different types of nanotubes (Kind permission from Springer Science+Business Media B.V.)

CNTs can be presented as single- (SWNTs), double- (DWNTs), and multiwalled (MWNTs) structures. SWNTs consist of one single graphene sheet rolled up into a cylinder with internal diameters from 1 to 2 nm. MWNTs present essentially a number of concentric SWNTs presenting diameters between 2 and 100 nm. CNTs have excellent electrochemical properties presenting a large surface area [36].

Carbon-based nanostructures exhibit unique properties and morphological flexibility making them multifunctional and compatible with organic and inorganic systems [77]. The form is a tubelike structure that results from a special arrangement of carbon atoms. Also, they are fullerene-related structures consisting of graphene cylinders closed at either end with caps containing pentagonal rings, of the order of half a fullerene molecule [21, 56]. In Fig. 2 different arrangements of nanotube formation from the graphene sheet are presented.

The advantages of using CNTs as electrode materials were demonstrated for food, clinical, and environmental analysis. The sensors based on CNTs exhibited lower limits of detection and faster responses due to the signal enhancement provided by high surface area, lower overvoltage, and faster electrode kinetics if one compares these characteristics with those obtained for the same compounds with other electrochemical sensors. Other properties that made CNTs important for sensing applications are thermal conductivity, mechanically robustness, and chemical stability. Their high surface area/volume ratio is an important quality for the development of biosensing platforms for single-molecule detection [67]. It is advantageous to use them in the design of sensors due to their low cost, good electron transfer kinetics, and biocompatibility.

The sensors based on carbon nanotube exhibited higher sensitivities, lower limits of detection, and faster electron transfer kinetics compared with sensors based on other carbon materials, although performances of these sensors depend on the synthesis method of the nanotube, CNT surface modification, and the addition of electron mediators [29].

Two-Dimensional Nanostructures (Graphene)

Graphene can be wrapped up into fullerenes, stacked into graphite, and rolled into carbon nanotubes [52, 68] (Fig. 3). In 2004 the graphene was prepared by Novoselov and Geim [42].

Graphene has versatile properties, such as high electron mobility, large surface area, and robust mechanical strength. It provides the greatest sensing area per unit volume because each atom of graphene is a surface atom [48] and is categorized according to the number of stacked layers in single-layer, few-layer (2–10 layers), and multilayer or thin graphite [11]. To keep its distinct properties ideally, its use should be narrowed to single- or few-layer morphology. The number of layers needed for graphene's properties to completely match those of bulk graphite is over 100 [44].

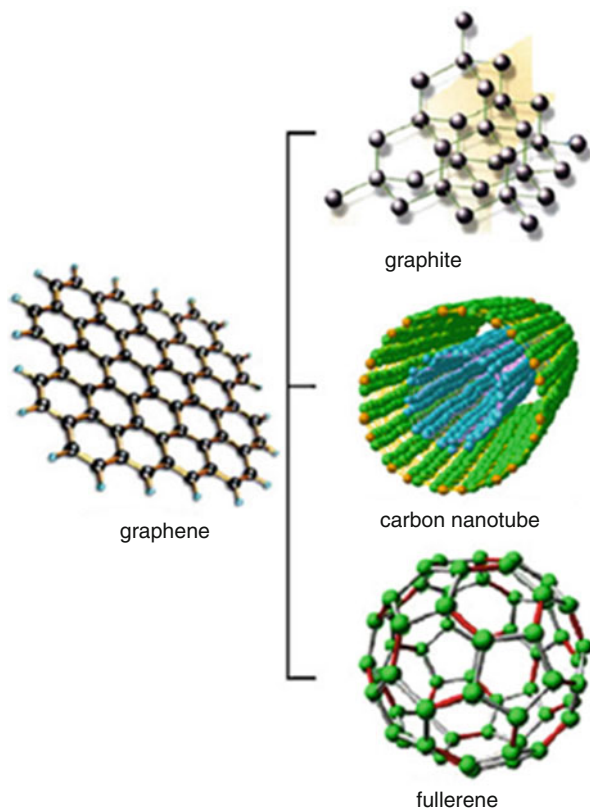


Fig. 3 The structures of graphene, graphite, carbon nanotube, and fullerene [16]

The electrochemical properties of graphene are wide electrochemical potential window, low charge resistance (compared with glassy carbon) [83], and well-defined redox peaks [62]. The sensors based on graphene exhibit high enzyme loading due to their high surface area, leading to increased catalytic activity and sensitivity [11].

Other properties that made graphene attractive for electrodes' design are low atomic thickness [79], flexibility, hardness (it is harder than diamond), electric conductivity at 25°, and higher catalytic activity than any other material [80]. Graphene represents the next-generation electronic material due to its remarkable electronic, optical, mechanical, thermal, and electrochemical properties [11]. The uniform distribution of electrochemically active sites compared with graphite [44] is making the active surface of sensors more reliable. Its 2D structure made the sensors efficient in detecting adsorbed molecules [11]. Molecular detection can be performed using this material, the sensors presenting low noise in electrochemical measurements [11].

Surface Analysis

The properties of nanomaterials are significantly different from those of atoms or bulk materials. The underlying theme of nanotechnology is downsizing. Many innovative methods for the synthesis of nanoparticles and nanotubes were developed [45].

The nanoscale morphology and topography can now be analyzed with innovative surface analysis techniques: atomic force microscopy (AFM), transmission electron microscopy (TEM), and scanning electron microscopy (SEM) [5]. These techniques are powerful tools for the study of nanostructures [45].

Some characteristics of the nanomaterial may cause several changes in the analytical performance of detection systems, e.g., limit of detection and sensitivity are closely associated with the transduction mechanism with morphological characteristics of sensors [7] being an important tool for the determination of reliability of techniques and devices [30]. Nanostructured polymers, ceramics, metals, semiconductors, and composite materials are used for sensors' design with high mechanical strength and heat resistance. The structural and chemical properties of these materials must be determined at the atomic level; therefore the surface analysis techniques are employed. High-resolution transmission electron microscopy (HRTEM) and analytical electron microscopy (AEM) are used for this purpose as well as for the correlation between microstructure/microchemistry on the one hand and materials properties on the other [49].

The combination between surface analysis and nanotechnology can lead to multiple questions, namely, what role does the analysis of surface in handling the properties of nanomaterials; how can the surface of materials for a better functionality change; how does it work mechanical surfaces and which are the means for characterizing nanostructured surfaces; how we can consolidate electrical, mechanical, and electronic properties in nanostructures; and what are the roles of these surface techniques? There are many things to be researched and studied in nanotechnology, and the most important key role in this research is the analysis of the surface [50].

Applications

Use of the nanomaterials such as graphene, carbon nanotube, carbon nanopowder, and others in sensors' design has been responsible for the development of a wide variety of nanoelectronic devices on environmental, food, and clinical applications, since such nanostructures display particular electrical, chemical, and transport properties [31].

Application areas of these nanostructures include pharmaceutical and chemical industry, electronic industry, metallurgical industry, biotechnology, food industry, optics, medicine, electronics, metrology, etc. Engineering of surface and handling of surfaces play an important role [31].

In the past years the graphene was proving to have excellent electrocatalytic material properties for the detection of variety of electroactive species; it can be used as matrix modifier for the design of different sensors, for example, for detection of glucose [32], dopamine ([40], [74], [75]), DNA base [4], H₂O₂ ([73]), 4 aminophenol [81], p-nitrophenol [2], catechol and hydroquinone ([15, 84]), paracetamol [33], and others.

Wang et al. [75] proposed a sensor based on modified graphene – doped with nitrogen. Nitrogen doping was realized by immobilizing the graphene in chitosan solution on a glassy carbon electrode. Peroxide was analyzed using this electrode in a linear range from 0.1 to 1.1 mM with a detection limit of 0.01 mM.

Xu et al. [80] developed a device with encapsulated hemoglobin (Hb) alongside graphene in a chitosan solution. The electrode showed a linear range from 6.5 to 230 μM and a detection limit of 5.1×10^{-7} M. The response time of this electrode changed with 19.9 % from initial response after 2 weeks of storage.

Another electrochemical sensor using graphene as modifier was studied by Majid Arvand and Mohsen Anvari for sensitive detection of quercetin in apple and onion [1]. The method used for quantification of quercetin in samples was differential pulse voltammetry. The accumulation potential was analyzed between -0.6 and 0.3 V, a maximum peak was achieved at 0.2 V, and the peak currents of DPV increased linearly with the quercetin concentration in the range from 0.006 to 10 and from 10 to 100 μmol L⁻¹ with a limit of detection 3.6 nmol L⁻¹.

Madeline Shuhua Goh and Martin Pumera have studied the electrochemical reduction of 2,4,6- trinitrotoluene (TNT), using single-, few-, and multilayer graphene nanoribbons and graphite microparticle-based electrodes. Few-layer graphene exhibits about 20 % enhanced signal for TNT after accumulation when compared to multilayer graphene nanoribbons. However, graphite microparticle-modified electrode provides higher sensitivity, and there was no significant difference in the performance of single-, few-, and multilayer graphene nanoribbons and graphite microparticles. The limit of detection of TNT in untreated seawater was 1 μg/mL [17].

Seul Ki Kim and her collaborators have synthesized different types of graphene nanosheet and have used them as electrocatalysts. The surface morphologies of the graphene nanosheets were determined using X-ray photoelectron spectroscopy (XPS) and field emission scanning electron microscopy (SEM). They have synthesized three kinds of RGO (reduced graphene oxide) using different reductants

(hydrazine together with ammonia solution (RGO1), only hydrazine (RGO2), and hydroxyl amine together with ammonia solution (RGO3)). The efficiency for the electrochemical detection of serotonin was also studied. Among the tested graphene-modified GCEs, RGO1 had the lowest detection limit, highest sensitivity, best selectivity, widest linear range, fastest response time, and best-defined peak of 5-HT. The oxidation mechanism of 5-HT demonstrated an irreversible diffusion-controlled electrode process [35].

A nanostructured film electrode, a multiwalled carbon nanotube (MWNT)-modified glassy carbon electrode (GCE), was designed and characterized by Kangbing Wu et al. The sensor was used for the simultaneous determination of guanine and adenine. The properties of the MWNT-modified GCE were determined using scanning electron microscopy (SEM) and cyclic voltammetry. The oxidation peak currents of guanine and adenine increased significantly at the MWNT-modified GCE in contrast to those at the bare GCE. The oxidation peak current of 5×10^{-7} mol L⁻¹ guanine was stable in the presence of adenine from 0 to 1×10^{-5} mol L⁻¹. Further increasing the adenine and guanine concentration caused a decrease in the peak current. The MWNT-modified GCE was also used for the measurement of native DNA. A detection limit of 30 ngmL⁻¹ with 2 min of open-circuit accumulation was obtained. Ten continuous measurements of 5 and 50 μ gmL⁻¹ calf thymus dsDNA show good reproducibility with a 4.1 % and 3.2 % RSD, respectively [78].

Insulin is an important protein hormone secreted by pancreatic islet cells. Detection of insulin is of high interest in research due to of the central role of insulin in diabetes. The first electrode based on CNT and metal oxides for direct amperometric determination of insulin was developed by Wang's group [71]. Cliffel and coauthors have also developed an electrochemical insulin sensor based on a composite of MWCNT and dihydropyran polymer [54]. The sensors based on CNT have great features for rapid detection of insulin [29].

The immunosensors/biosensors are capable of selectively detecting target analytes at very low concentration. The detection of cancer biomarkers in human serum and whole blood is essential for the early diagnosis of cancer. Accordingly, the development of highly sensitive detection devices for the point-of-care analysis of such biomarkers is a challenging task. The nanomaterials have been well exploited for the fabrication of sensing devices for cancer biomarkers [14]. Various CNT biosensors have been developed for prostate-specific antigen (PSA) [34, 47, 70] and carcinoembryonic antigen (CEA) [69] detection (Table 2).

Conclusions

Utilization of nanomaterials in sensors' design was a great challenge for the reliability of the analytical information as well as for applications of sensors in clinical analysis using stochastic mode. By using the nanomaterials in amperometric sensor design, one can obtain from a certain point the same value for the active area like for a macrosensors based on macromaterials. Accordingly, the downsizing of materials and surface of sensors should be done with precautions. The modification of nanomaterials was done using either nano- or macro-inorganic or synthetic organic

Table 2 Applications of the most commonly nanomaterials used in design of the sensors

No	Nanomaterials	Sensor based on	Application	References
1	Graphene	Nitrogen-doped graphene	Determination of peroxide	[75]
		Graphene modified with a chitosan solution	Determination of hemoglobin	[80]
		Single- and multilayer graphene nanoribbons	Studies of the electrochemical reduction of 2,4,6-trinitrotoluene (TNT)	[17]
		Graphene nanosheet	Determination of serotonin	[35]
		Graphene as matrix modifier	Determination of glucose	[32]
			Determination of dopamine	[40, 74]
			Determination of DNA base	[4]
			Determination of H ₂ O ₂	[73]
			Determination of 4-aminophenol	[81]
			Determination of p-nitrophenol	[2]
			Determination of catechol and hydroquinone	[15, 61, 84]
Determination of paracetamol	[33]			
2	CNT	MWCNT-modified glassy carbon electrode (GCE)	Simultaneous determination of guanine and adenine	[78]
		MWNT-modified GCE	Determination of native DNA	[78]
		CNT and metal oxides	Determination of insulin	[71]
		MWCNT and dihydropyran polymer	Determination of insulin	[54]
		Antibody-modified CNT	Determination of prostate-specific antigen	[34, 47, 70]
			Determination of carcinoembryonic antigen	[69]

materials or using biomolecules such as enzymes or antibodies. Like for all sensors the advantages of modifications of the active surface with such molecules improved the selectivity of the sensors.

Acknowledgments The authors want to thank UEFISCDI, PN-II-CT-ERC-2012-1, contract number 3ERC/02.07.2012, for the financial support.

References

1. Arvand M, Anvari M (2013) A graphene-based electrochemical sensor for sensitive detection of quercetin in foods. *J Iran Chem Soc.* doi:10.1007/s13738-013-0219-3
2. Arvinte A, Mahosenaho M, Pinteala M, Sesay A-M, Virtanen V (2011) Electrochemical oxidation of p-nitrophenol using graphene-modified electrodes, and a comparison to the performance of MWNT-based electrodes. *Microchim Acta* 174:337–343

3. Bakker E, Telting-Diaz M (2002) Electrochemical sensors. *Anal Chem* 74:2781–2800
4. Bo Y, Yang H, Hu Y, Yao T, Huang S (2011) A novel electrochemical DNA biosensor based on graphene and polyaniline nanowires. *Electrochim Acta* 56:2676–2681
5. Brett Christopher MA, Oliveira-Brett AM (2011) Electrochemical sensing in solution—origins, applications and future perspectives. *J Solid State Electrochem* 15:1487–1494
6. Buffat P, Borel JP (1976) Size effect on the melting temperature of gold particles. *Phys Review A* 13:2287–2298
7. Byon HR, Choi HC (2006) Network single-walled carbon nanotube-field effect transistors (SWNT-FETs) with increased Schottky contact area for highly sensitive biosensor applications. *J Am Chem Soc* 128:2188–2189
8. Cash KJ, Clark HA (2010) Nanosensors and nanomaterials for monitoring glucose in diabetes. *Trends Mol Med* 16:584–593
9. Champion Y, Langlois C, Guerin-Mailly S, Langlois P, Bonnetien J, Hytch MJ (2003) Near-perfect elastoplasticity in pure nanocrystalline copper. *Science* 300:310–311
10. Chiroiu V, Stiuca P, Munteanu L, Donescu S (2005) Introduction to nanomechanics. Ed. Academiei Romane, Bucuresti
11. Choi W, Lahiri I, Seelaboyina R, Kang Y (2010) Synthesis of graphene and its applications: a review. *Crit Rev Solid State Mater Sci* 35:52–71
12. Coulter WH (1953) Means for counting particles suspended in a fluid. US Patent, 2656508
13. Daniel M-C, Astruc D (2004) Gold nanoparticles: assembly, supramolecular chemistry, quantum-size-related properties, and applications toward biology, catalysis, and nanotechnology. *Chem Rev* 104:293–346
14. Dey RS, Bera RK, Raj CR (2013) Nanomaterial-based functional scaffolds for amperometric sensing of bioanalytes. *Anal Bioanal Chem* 405:3431–3448
15. Du H, Ye J, Zhang J, Huang X, Yu CJ (2011) A voltammetric sensor based on graphene-modified electrode for simultaneous determination of catechol and hydroquinone. *J Electroanal Chem* 650:209–2013
16. Gan T, Hu S (2011) Electrochemical sensors based on graphene materials. *Microchim Acta* 175:1–19
17. Goh MS, Pumera M (2011) Graphene-based electrochemical sensor for detection of 2,4,6-trinitrotoluene (TNT) in seawater: the comparison of single-, few-, and multilayer graphene nanoribbons and graphite microparticles. *Anal Bioanal Chem* 399:127–131
18. Goldestien AN, Echer CM, Alivisatos AP (1992) Melting in semiconductor nanocrystals. *Science* 256:1425–1427
19. Gu LQ, Braha O, Conlan S, Cheley S, Bayley H (1999) Stochastic sensing of organic analytes by a pore-forming protein containing a molecular adapter. *Nature* 398:686–690
20. Gyurcsanyi RE (2008) Chemically-modified nanopores for sensing. *Trends Anal Chem* 27:628–639
21. Harris PJF (1999) Carbon nanotubes and related structures: new materials for the 21st century. Cambridge University Press, Cambridge
22. Hecht S (2003) Welding, organizing, and planting organic molecules on substrate surfaces—promising approaches towards nanoarchitectonics from the bottom up. *Angew Chem Int Ed Engl* 42:24–26
23. Heyrovsky J (1922) Elektrolysa se rtovou kapkovou Kathodu. *Chem Listy* 16:256–304
24. Holland ALR, Menard LD, Ramsey JM (2008) Stochastic sensing using chemically modified solid-state nanopores. In: Twelfth international conference on miniaturized systems for chemistry and life sciences, San Diego, 12–16 Oct 2008, pp 662–664
25. Holze R, Eftekhari A (2009) Nanostructured materials in electrochemistry. *J Solid State Electrochem* 13:1621–1622
26. Huang X-J, Choi Y-K (2007) Chemical sensors based on nanostructured materials. *Sens Actuators B* 122:659–671
27. Hulanicki A, Geab S, Ingman F (1991) Chemical sensors definitions and classification. *Pure App Chem* 63:1247–1250
28. Iijima S (1991) Synthesis of carbon nanotubes. *Nature* 354:56–58

29. Jacobs BC, Peairs MJ, Venton BJ (2010) Review: carbon nanotube based electrochemical sensors for biomolecules. *Anal Chim Acta* 662:105–127
30. Justino CIL, Rocha-Santos TA, Duarte AC (2010) Review of analytical figures of merit of sensors and biosensors in clinical applications. *Trends Anal Chem* 29:1172–1183
31. Justino CIL, Rocha-Santos TAP, Cardoso S, Duarte AC (2013) Strategies for enhancing the analytical performance of nanomaterial-based sensors. *Trends Anal Chem* 47:27–36
32. Kang XH, Wang J, Wu H, Aksay IA, Liu J, Lin YH (2009) Glucose oxidase–graphene–chitosan modified electrode for direct electrochemistry and glucose sensing. *Biosens Bioelectron* 25:901–905
33. Kang X, Wang J, Wu H, Liu J, Aksay IA, Lin Y (2010) A graphene-based electrochemical sensor for sensitive detection of paracetamol. *Talanta* 81:754–759
34. Kim JP, Lee BY, Lee J, Hong S, Sim SJ (2009) Enhancement of sensitivity and specificity by surface modification of carbon nanotube in diagnosis of prostate cancer based on carbon nanotube field effect transistors. *Biosens Bioelectron* 24:3372–3378
35. Kim KS, Kim D, Jeon S (2012) Electrochemical determination of serotonin on glassy carbon electrode modified with various graphene nanomaterials. *Sens Actuators B* 174:285–291
36. Lahiff E, Lynam C, Gilmartin N, O’Kennedy R, Diamond D (2010) The increasing importance of carbon nanotubes and nanostructured conducting polymers in biosensors. *Anal Bioanal Chem* 398:1575–1589
37. Leoni L, Desai TA (2001) Biocapsules for the encapsulation of insulinoma cells: biotransport and biocompatibility considerations. *IEEE Trans Biomedical Eng* 48:1335–1341
38. Lieber CM (2003) Nanoscale science and technology: building a big future from small things. *MRS Bull* 28:486–491
39. Lines MG (2008) Nanomaterials for practical functional uses. *J Alloys Compd* 449:242–245
40. Ling YY, Huang QA, Zhu MS, Feng DX, Li XZ, Wei Y (2013) A facile one-step electrochemical fabrication of reduced graphene oxide–multiwall carbon nanotubes–phosphotungstic acid composite for dopamine sensing. *J Electroanal Chem* 693:9–15
41. Mortimer RJ, Beech AAC (2002) Impedance characteristics of solid-state planar electrochemical carbon monoxide sensors with nafion as solid polymer electrolyte. *Electrochim Acta* 47:3383–3387
42. Novoselov KS, Geim AK, Morozov SV, Jiang D, Zhang Y, Dubonos SV, Grigorieva IV, Firsov AA (2004) Electric field effect in atomically thin carbon films. *Science* 306:666–669
43. Park C, Yoon J, Thomas EL (2003) Enabling nanotechnology with self-assembled block copolymer patterns. *Polymer* 44:6725–6760
44. Pumera M (2009) Electrochemistry of graphene: new horizons for sensing and energy storage. *Chem Rec* 9:211–223
45. Rao CNR, Cheetham AK (2001) Science and technology of nanomaterials: current status and future Prospects. *J Mater Chem* 11:2887–2894
46. Sailor MJ (1997) In: Canham L (ed) Properties of porous silicon, INSPEC, London. DERA, Malvern
47. Sardesai N, Pan SM, Rusling J (2009) Electrochemiluminescent immunosensor for detection of protein cancer biomarkers using carbon nanotube forests and [Ru-(bpy)₃]²⁺-doped silica nanoparticles. *Chem Commun* 33:4968–4970
48. Schedin F, Geim AK, Morozov SV, Hill EW, Blake P, Katsnelson MI, Novoselov KS (2007) Detection of individual gas molecules adsorbed on graphene. *Nat Mater* 6:652–655
49. Schneider R (2002) High-resolution analytical TEM of nanostructured materials. *Anal Bioanal Chem* 374:639–645
50. Seal S, Dahotre NB (2002) Nanostructured materials and the role of surface engineering. *JOM* 54:20–21
51. Shaw LL (2000) Processing nanostructured materials: an overview. *JOM* 52:41–45
52. Shioyama H, Akita T (2003) A new route to carbon nanotubes. *Carbon* 41:179–181
53. Siwy Z, Trofin L, Kohli P, Baker LA, Martin CR (2005) Protein biosensors based on biofunctionalized conical gold nanotubes. *J Am Chem Soc* 127:5000–5001

54. Snider RM, Ciobanu M, Rue AE, Cliffel DE (2008) A multiwalled carbon nanotube/dihydropyran composite film electrode for insulin detection in a microphysiometer chamber. *Anal Chim Acta* 609:44–52
55. Srinivasan C (2007) Graphene—mother of all graphitic materials. *Curr Sci* 92:1338–1339
56. Srivastava D, Menon M, Cho K (2001) Computational nanotechnology with carbon nanotubes and fullerenes. *Comput Sci Eng* 3:42–45
57. Stefan RI, Aboul-Enein HY, van Staden FJ (2001) *Electrochemical sensors in bioanalysis*. Marcel Dekker, New York
58. Stefan-van Staden RI, Moldoveanu I, Sava DF, Kapnissi-Christodoulou C, van Staden JF (2013) Enantioanalysis of pipecolic acid with stochastic and potentiometric microsensors. *Chirality* 25:114–118
59. Stetter JN, Penrose WR, Sheng Y (2003) Sensors, chemical sensors, electrochemical sensors, and ECS. *J Electrochem Soc* 150:S11–S16
60. Stradiotto NR, Yamanaka H, Zanoni MVB (2003) Electrochemical sensors: a powerful tool in analytical chemistry. *J Braz Chem Soc* 14:159–173
61. Su-Juan L, Yun X, Gui-Fang W (2012) A graphene-based electrochemical sensor for sensitive and selective determination of hydroquinone. *Microchim Acta* 176:163–168
62. Tang L, Wang Y, Li Y, Feng H, Lu J, Li J (2009) Preparation, structure, and electrochemical properties of reduced graphene sheet films. *Adv Funct Mater* 19:2782–2789
63. Theavenot RD, Toth K, Durst RA, Wilson GS (1999) *Electrochemical biosensors: recommended definitions and classification* (technical report). *Pure Appl Chem* 71:2333–2348
64. Vaseashta A, Erdem A, Irudayaraj J (2004) Nanoparticles, nanoporous and carbon nanotube based devices for bio-molecular detection, in *Nanostructured and Advanced Materials for Applications in Sensors, Optoelectronic and Photovoltaic Technology* (2005), 391–394, Springer, Netherlands
65. Vaseashta A (2003) Field emission characteristics of carbon nanotubes and their applications in photonic devices. *J Mat Sci Mater Electron* 14:653–656
66. Vaseashta A (2005) *Nanostructured materials based next generation devices and sensors*. Springer, Netherlands pp 1–30
67. Vashist SK, Zheng D, Al-Rubeaan K, Luong JHT, Sheu FS (2011) Advances in carbon nanotube based electrochemical sensors for bioanalytical applications. *Biotechnol Adv* 29:169–188
68. Viculis LM, Mack JJ, Kaner RB (2003) A chemical route to carbon nanoscrolls. *Science* 299:1361
69. Viswanathan S, Rani C, Anand AV, Ho JAA (2009) Disposable electrochemical immunosensor for carcinoembryonic antigen using ferrocene liposomes and MWCNT screen-printed electrode. *Biosens Bioelectron* 24:1984–1989
70. Wan Y, Deng W, Su Y, Zhu X, Peng C, Hu H, Peng H, Song S, Fan C (2011) Carbon nanotube-based ultrasensitive multiplexing electrochemical immunosensor for cancer biomarkers. *Biosens Bioelectron* 30:93–99
71. Wang J, Musameh M (2004) Electrochemical detection of trace insulin at carbon nanotube modified electrodes. *Anal Chim Acta* 511:33–36
72. Wang J, Yang S, Guo D, Yu P, Li D, Ye J, Mao L (2009) Comparative studies on electrochemical activity of graphene nanosheets and carbon nanotubes. *Electrochem Commun* 11:1892–1895
73. Wang K, Liu Q, Wu XY, Guang QM, Li HN (2010) Graphene enhanced electrochemiluminescence of CdS nanocrystal for H₂O₂ sensing. *Talanta* 82:372–376
74. Wang Y, Li Y, Tang L, Lu J, Li J (2009) Application of graphene-modified electrode for selective detection of dopamine-Short communication. *Electrochem Commun* 11:889–892
75. Wang Y, Shao Y, Matson D, Li J, Lin Y (2010) Nitrogen-doped graphene and its application in electrochemical biosensing. *ACS Nano* 4:1790–1798
76. Whitesides GM, Grzybowski B (2002) Self-assembly at all scales. *Science* (Washington, DC) 295:2418–2421
77. Whitesides MG, Kriebel KJ, Mayers TB (2005) *Self-assembly and nanostructured materials*. Spriger, US

78. Wu K, Fei J, Bai W, Hu S (2003) Direct electrochemistry of DNA, guanine and adenine at a nanostructured film-modified electrode. *Anal Bioanal Chem* 376:205–209
79. Wu X, Hu Y, Jin J, Zhou N, Wu P, Zhang H, Cai C (2010) Electrochemical approach for detection of extracellular oxygen released from erythrocytes based on graphene film integrated with laccase and 2, 2-azino-bis (3-ethylbenzothiazoline-6- sulfonic acid). *Anal Chem* 82:3588–3596
80. Xu H, Dai H, Chen G (2010) Direct electrochemistry and electrocatalysis of hemoglobin protein entrapped in graphene and chitosan composite film. *Talanta* 81:334–338
81. Yin H, Ma Q, Zhou Y, Ai S, Zhu L (2010) Electrochemical behavior and voltammetric determination of 4-aminophenol based on graphene-chitosan composite film modified glassy carbon electrode. *Electrochim Acta* 55:7102–7108
82. Zhang S (2003) Building from the bottom up. *Mater Today* 6:20–27
83. Zhou M, Zhai Y, Dong S (2009) Electrochemical sensing and biosensing platform based on chemically reduced graphene oxide. *Anal Chem* 81:5603–5613
84. Ma L, Zhao GC (2012) Simultaneous determination of hydroquinone, catechol and resorcinol at graphene doped carbon ionic liquid electrode. *International J Electrochem* 8

Stelian Lupu, Paul Cătălin Balaure, Cecilia Lete,
and Constantin Mihailciuc

Contents

Introduction.....	1162
Nanostructured Thin Films for Biosensors	1165
Spatially Organized Biocomposite Multilayer Structures	1165
Novel In Situ Sinusoidal Voltages Electrodeposition Procedures of BioComposite Materials	1180
Thick Films Based Biosensing Devices.....	1184
Conducting Polymers Based Biosensors	1184
Conclusions.....	1188
References.....	1189

S. Lupu (✉)

Department of Analytical Chemistry and Environmental Engineering,
Faculty of Applied Chemistry and Materials Science,
University Politehnica of Bucharest, Bucharest, Romania
e-mail: stelianl@yahoo.com

P.C. Balaure

Department of Organic Chemistry, Faculty of Applied Chemistry and Materials Science,
University Politehnica of Bucharest, Bucharest, Romania
e-mail: pbalaure@gmail.com

C. Lete

Laboratory of Electrochemistry, Institute of Physical Chemistry
“Ilie Murgulescu” of the Romanian Academy, Bucharest, Romania
e-mail: cecilia_lete@yahoo.com

C. Mihailciuc

Department of Physical Chemistry, Faculty of Chemistry,
University of Bucharest, Bucharest, Romania
e-mail: pc_mihailciuc@yahoo.com

Abstract

Biocomposite nanomaterials composed of biological receptors and various inorganic and organic components have recently attracted a great deal of interest due to their peculiar properties and use in electrochemical sensors and biosensors. Recognition systems based on biocomposite nanomaterials were developed as highly sensitive and selective elements for electrochemical biosensors technology. Since the development of the first marketed biosensor almost 25 years ago, the biosensor technology has benefited from the use of electrodes modified with nanostructured biomaterials that enhanced the selectivity and the sensitivity of the measurements. The use of electrochemical methods for in situ preparation and characterization of biocomposite nanomaterials resulted in the occurrence of unique electrocatalytic properties and enhanced analytical performances. In recent years, there has also been much progress in understanding the electrochemical behavior of biological elements, such as enzymes, antibodies, cells, tissues, peptides, and nucleic acids, immobilized within conducting polymer-based composite nanomaterials, as well as the synergy between their biocatalytic activity and affinity and the electrocatalytic activity of various inorganic/organic fillers towards the target analytes.

Keywords

Biocomposite nanomaterials • Conducting polymers • Electrochemical biosensors • Langmuir-Blodgett based biosensors • Layer-by-Layer based biosensors • Sinusoidal voltages

Introduction

Biosensors are analytical devices consisting of a biological sensing element either integrated within or in intimate contact with a transducer element which transforms the primary (bio)chemical information, resulted upon the interaction of the biological sensing element with the analyte, into a measurable signal. Typically, biosensor architecture comprises three parts: the biological sensing element which is usually immobilized on the surface of a suitable transducer, the transducer and an amplification or processing element. Actually, biosensors are a subset of chemical sensors, but are often considered as a distinct class of analytical devices. The key difference is that the sensing element in biosensors is biological in nature. Chemical sensors and biosensors are related with sensing and measuring various chemicals which may be biological themselves. These chemicals are referred to as *analytes*, although the term *substrates* is sometimes used. The design of biosensor architecture for a given analyte depends on various demands and analytical parameters such as selectivity, sensitivity, limits of detection and quantification, linear response range, time response, stability, reusability, precision, reproducibility, and the cost of the sought measurement. The research pursued in biosensors technology aimed to improve these analytical parameters by developing new sensing elements and transducer structures. The sensing element may be an enzyme, an antibody, a tissue, or a microorganism

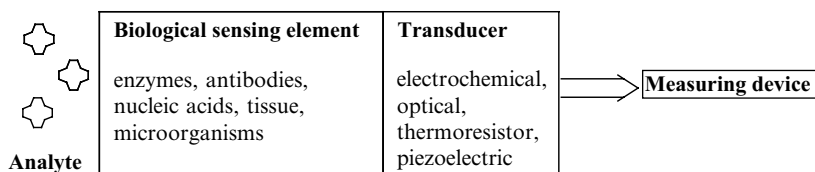


Fig. 1 A general biosensor architecture

which can specifically recognize species of interest (analyte). The transducer converts the biochemical signal into a measurable signal which is usually an electronic signal. Many forms of transducers were investigated during the last three decades such as electrochemical transducers, optical and optoelectronic detectors, field-effect transistors, mass sensitive devices, and thermistors. The most studied are electrochemical devices based on potentiometric, amperometric, voltammetric, and impedance transducers. These electrochemical transducers use the powerful features of the corresponding electrochemical methods, i.e., potentiometry, amperometry, cyclic and dynamic voltammetry, and electrochemical impedance spectroscopy. The use of electrodes modified with composite nanomaterials as electrochemical transducers proved to be a viable way in enhancing the selectivity and the sensitivity of measurements. A schematic picture of biosensor architecture is depicted in Fig. 1.

The biological sensing element should be in intimate contact with transducer surface. Moreover, the biological receptor immobilization step is crucial for the proper functioning of the resulting biosensor. The most used immobilization procedures are: adsorption, physical entrapment, cross-linking, and covalent bonding. Some of these immobilization procedures have benefited from the development of various pioneering nanotechnology approaches and their integration into advanced preparation techniques underpinned the biosensor technology. The main preparation techniques can be summarized as follows: (i) screen-printing technology; (ii) sol-gel method; (iii) self-assembled monolayers; (iv) Langmuir-Blodgett technique; (v) layer-by-layer assembling; (vi) photolithographic techniques. An overview of the use of these techniques in biosensors development together with some characteristics and applications is given in Table 1.

The aim of this chapter is to highlight *the importance of biocomposite materials and electrochemical transducers* in the field of electrochemical biosensors by giving an overview of the recent achievements. First, spatially organized multilayers of biocomposite materials will be discussed by giving reference to specific methods of preparation like Langmuir-Blodgett and layer-by-layer techniques. Then, new preparation procedures of biocomposite materials are presented in connection with the research activities carried out in our research group. Finally, a section is devoted to thick layer technology for biosensors development making reference to the use of conducting polymers as viable matrix for biological sensing elements immobilization. This chapter is also devoted to the *combination of biological molecules with nanomaterials* as well as to new strategies for nanoscale patterning electrode surfaces with *biocomposite materials* in the process of developing analytical devices for clinical, environmental, and food analysis.

Table 1 Overview of biosensors preparation techniques

Preparation technique	Sensing element composition/morphology	Type of transducer	Applications	Reference
Screen-printing	Silver and carbon inks, inorganic, organic and modifiers; enzymes, proteins, antibodies/thick film	Mainly electrochemical	Biomedical, environmental, industrial analyses	[1–3]
Sol-gel	Sol-gel matrix, enzymes, proteins/thin film	Electrochemical, optical	Biomedical, environmental	[4, 5]
Self-assembled monolayers	Alkanethiols, organosilanes, aryl diazonium salts; enzymes, proteins, DNA/thin film	Mainly electrochemical, optical, quartz crystal microbalance	Biomedical, environmental	[6, 7]
Langmuir-Blodgett	Lipids, enzymes/thin film	Electrochemical, optical	Biomedical, environmental	[8]
Layer-by-layer assembly	Polyelectrolytes; enzyme, proteins, DNA/thin film	Electrochemical, optical	Biomedical, environmental	[9]
Photolithographic techniques	Microelectrodes, inorganic and organic modifiers; enzymes, antibodies, DNA/thin film	Mainly electrochemical	Biomedical, environmental	[10]

Nanostructured Thin Films for Biosensors

Spatially Organized Biocomposite Multilayer Structures

The most important feature of electrochemical biosensors is their ability to detect the target analyte with high selectivity. Important advances in electrochemical biosensors technology have been achieved with the utilization of various nanomaterials such as nanoparticles [11], quantum dots [12], carbon-based nanostructures [13, 14], in connection with biological elements. The availability of advanced fabrication [15, 16] and characterization [17] techniques underpinned the development of commercially available biosensors.

Recent advances in nanobioelectrochemistry are related to the use of biocomposite nanomaterials as sensing elements in connection with modified electrodes, including new technologies for the fabrication and characterization of microelectrodes and their arrays [18–20]. The preparation of the sensing element as a thin film onto the transducer surface provides enhanced sensitivity of electrochemical biosensors. In this sense, the Langmuir–Blodgett approach [21–23] was the pioneering technique for the preparation of thin films formed by transferring the material film from air/water interface to a solid substrate. Another technique for preparing nanostructured thin films composed of multilayers was developed by Decher in the 1990s [24, 25]. This layer-by-layer technique provides a versatile strategy for fabrication of multilayers films with high control of thickness at nanoscale level. The main examples of Langmuir–Blodgett and layer-by-layer based biosensors are summarized in Table 2.

Langmuir–Blodgett Based Biosensors

The deposition of monolayers of organic molecules was firstly investigated by Katharine Blodgett and Irving Langmuir early in the beginning of twentieth century [21–23]. The Langmuir–Blodgett (LB) technique consists in the self-organization of amphiphilic molecules at the air–water interface in order to form a monolayer. The monolayer is compressed by moving two barriers throughout the Langmuir cube providing a more stable monolayer conformation. The formed monolayer can then be deposited onto a solid substrate. The amphiphilic molecules contain a hydrophobic (alkyl or perfluoro) side chain and a hydrophilic head group such as –OH, –COOH, –NH₂. The amphiphilic molecules dissolved in a water-immiscible solvent are cast on a clean water surface. After solvent evaporation, the disordered layer of amphiphilic molecules is compressed by two moving barriers which cause the molecules to pack more closely. At the end of process, a quasi two-dimensional monolayer film is obtained. The amphiphilic molecules are all aligned in the same direction with their hydrophilic head groups to the water surface. By dipping a solid substrate in the cube, the LB film is transferred onto the surface of the immersed substrate. By repeating the transfer step several times, multilayer LB films on solid substrates are built up. This process may be applied for other molecules by a proper design of the substrate surface functionalization.

Table 2 Langmuir-Blodgett and layer-by-layer based biosensors

Sensing element type	Sensing element components	Transducer	Analyte	Reference
LB ^a	Octadecyltrimethylammonium and Prussian blue; glucose oxidase	Electrochemical	Glucose	[29]
LB	Glucose oxidase, lipid	Electrochemical	Glucose	[31]
LB	Lipid-modified glucose oxidase, poly(pyrrole)	Electrochemical	Glucose	[35]
LB	Polyaniline, glucose oxidase	Electrochemical	Glucose	[37]
LB	Poly (3-hexylthiophene)/stearic acid, galactose oxidase	Electrochemical	Galactose	[41]
LB	Rabbit polyclonal antibody (Isotype-IgG) specific to <i>Salmonella</i> sp.	Magnetoelastic	<i>Salmonella typhimurium</i>	[44]
LbL ^b	Nitrate reductase	Electrochemical	Nitrate ion	[49]
LbL	Amino functionalized silica nanoparticles (ASNPs) and glucose oxidase	Electrochemical	Glucose	[64]
LbL	Gold nanoparticles, glucose oxidase	Electrochemical	Glucose	[65]
LbL	Gold nanoparticles, multiwalled carbon nanotubes-thionine, chitosan	Electrochemical	Carcinoembryonic antigen	[67]
LbL	Pentaerythritol-based metallodendrimer with Ru ^{II} terpyridine subunits, double-stranded-DNA	Electrochemical, optical	Styrene oxide	[68]
LbL	Multi-walled carbon nanotubes, DNA	Electrochemical	Bacterium <i>Neisseria gonorrhoeae</i>	[73]

^aLangmuir-Blodgett^bLayer-by-layer

The LB films present important properties, such as uniform thickness, molecule orientation, and electrical properties. These properties enabled the use of LB films in several applications including chemical sensors and biosensors, electronics, optics, and semiconductors. The key issue in preparing electrochemical biosensors is the preservation of the biocatalytic activity of the biological sensing elements after their immobilization onto the transducer surface. The use of biological sensing elements such as enzymes, antibodies, proteins, and DNA in the field of electrochemical biosensors has benefited from the advantages of LB technique [15, 26]. The main goal in using LB technique is the control of the thickness of the deposited layer and the study of various related properties like charge transport, optical effects, and the interaction of biological elements with the substrate.

Glucose is an analyte of significant importance due to the related disease diabetes. The most demanded approach nowadays in managing diabetes is the continuous monitoring of glucose level in blood by patients themselves. For this purpose, commercially available glucose sensors are used worldwide. These biosensors are based on electrodes (usually platinum or screen printed electrodes) covered with a gel or a polymer containing glucose oxidase (GOx). In the early stage, these analytical devices measure usually the hydrogen peroxide produced in the enzymatic reaction. Later, the use of mediators like organometallic compounds and redox or conducting polymers eliminated the drawback associated with the constant oxygen level required in the earlier biosensors. By their intrinsic properties, redox enzymes that are able to shuttle electrons between the redox-active sites and electrodes are the most used in electrochemical biosensors. Among redox enzymes, the oxidases and the dehydrogenases are extensively studied. The basic reactions of redox enzymes can be depicted according to the following scheme:



In the case of GOx (as oxidized and reduced forms E_{ox} , E_{red}), the S_{red} , S_{ox} , S'_{ox} and S'_{red} correspond to glucose, gluconolactone, oxygen, and hydrogen peroxide, respectively. The consumption of oxygen or the formation of hydrogen peroxide can be measured. However, several drawbacks associated with a constant level of oxygen or interferences due to the high operating potential values for hydrogen peroxide monitoring were encountered in practice. These drawbacks were eliminated by the use of redox mediators.

Due to their market availability, glucose biosensors are considered as reference devices in developing new biosensor technologies. For this reason, the use of LB technique will be focused on the glucose biosensors development. Consequently, it is also worth noting some historical aspects related to the birth of this biosensor. In 1956, Professor Leland C. Clark Jr. [27] published his important paper on the oxygen electrode. A couple of years later, Clark and Lyons [28] introduced the term enzyme electrode. Since then, there was a tremendous research interest in developing efficiently enzyme immobilization strategies. Several examples are

reported for the LB immobilization of GOx in glucose biosensors development. These strategies are based mainly on hybrid inorganic–organic materials and organic conducting materials. For instance, GOx was immobilized in an organic–inorganic hybrid LB films that consist of octadecyltrimethylammonium (ODTA) and Prussian blue (PB) nanosize clusters [29]. The ODTA positively charged molecules can adsorb PB clusters during the film formation on the water surface. The successful immobilization of GOx into LB films was confirmed by FTIR spectrometry. The PB is known as an excellent catalyst for hydrogen peroxide reduction and it has been extensively used in biosensors technology. In this case, the PB clusters are reducing the hydrogen peroxide produced by the enzymatic reaction of GOx. The biosensors prepared by using ODTA/PB/GOx LB films composed of six layers showed the best analytical performance toward glucose detection at a working potential of 0.0 V vs. Ag/AgCl in neutral buffered aqueous solution. The biosensor displayed a linear response up to 8 mmol/L glucose concentration. Ravaine and co-workers [30] previously reported the use of PB in LB films and demonstrated that the electrochemical and optical properties of PB-based hybrid LB films are strongly influenced by the number of deposited layers. In another example, LB films of Gox and lipid were transferred onto a PB-modified Pt electrode for biosensor preparation [31]. The LB-PB based biosensor displayed a linear calibration range from 5×10^{-6} to 6×10^{-5} M and a detection limit of 1.5×10^{-6} M. Further information related to the use of PB in sensors and biosensors preparation can be found in a review by Ricci and Pallechi [32]. The use of organic conducting LB films is another approach for GOx immobilization. Watanabe and coworkers [33] have used organic conductors based on radical and anion salts for GOx immobilization. The GOx-LB films were investigated by infrared absorption spectrometry. The change in the dc conductivity of the GOx-LB films after immersion in 3×10^{-2} mol/L glucose for 2 min was ranging from -13.4 to 7.9 %. It was demonstrated that GOx maintains its bioactivity and sensitivity after immobilization into LB films. Other conducting LB films based on conducting polymer for GOx immobilization have also been reported. Pyrrole derivatives were used to prepare derivatized polypyrrole Langmuir–Blodgett films characterized by shorter pathways for electron transfer reactions. Skotheim and coworkers [34] have prepared copolymers formed by chemical copolymerization of 3-alkylpyrrole and iron chloride ferrocene-modified 3-alkylpyrroles at the air–water interphase, with the subphase containing iron(III) chloride. After transferring the LB film on an electrode surface, the resulting modified electrode was used for reoxidizing reduced flavin enzymes such as GOx. Another LB film consisting of a lipid-modified GOx and poly(pyrrole) was used in the preparation of a multilayer enzyme electrode for detecting glucose [35]. The proposed biosensor response is based on the voltammetric detection of hydrogen peroxide produced by the modified enzyme layers. A linear response of the biosensor to glucose concentration ranging from 15 to 100 mM and a detection limit of 5 mM were obtained. Polyaniline (PANI) is an extensively studied organic conducting polymer for biosensor technology due to its high conductivity, rapid electron transfer, biocompatibility with biological sensing elements, and chemical stability in both organic and aqueous media [36]. LB films of the polyemeraldine base form

of PANI have been deposited on an indium tin oxide (ITO) electrode and then the GOx was entrapped between the LB layers [37]. The immobilized GOx retained its catalytic activity and the biosensor showed linear response toward glucose detection. Other examples of using LB technique for biological elements immobilization include enzymes, such as glutamate dehydrogenase [38], horseradish peroxidase [39], urease [40], and galactose oxidase [41], redox proteins [42], antibodies [43, 44], and DNA [45, 46]. Here some examples of using conducting polymers in LB films were presented. This approach has the advantage of controlled thickness and high quality of the prepared LB film, but the practical applications are limited due to the very specific experimental conditions and equipments for films growth. In a later section, the entrapment of enzymes within conducting polymers to produce thicker and more stable films is discussed. Finally, one can conclude that the LB technique proved over time to be an appealing approach for preparing highly ordered biological sensing elements for electrochemical biosensors used in biomedical, environmental, and food analysis.

Layer-by-Layer Based Biosensors

A critical step in the construction of electrochemical biosensors is designing of adequate molecular architectures able to assure a proper connection at the nanometer scale between the biological sensing and the surface of the working electrode (the transducer element of the biosensor) as biosensors work properly only if these two component elements are in close spatial proximity [47]. Immobilization of the bioreceptor on the transducer surface can be achieved by several methods such as: physical adsorption, Langmuir–Blodgett technique, layer-by-layer (LbL) deposition, entrapment, electrochemical doping, cross-linking, covalent binding and affinity binding [47, 48].

In its original version, LbL deposition is based on electrostatic immobilization of the bioreceptor as first described by Decher [24, 25]. In LbL technique, the deposition surface is first derivatized to produce a stable charge excess, and then multilayer films of polyelectrolytes of opposite electric charges are alternately deposited in virtue of electrostatic attractions. Figure 2 illustrates the principle of LbL deposition method in the case of an enzymatic electrochemical biosensor for nitrate ions [49]. In the first step, the gold electrode surface is functionalized with 2-mercaptoethanesulfonic acid (MESA) by chemisorption of the thiols groups; thus the gold electrode surface acquires a net negative charge due to the ionization of the sulfonic acid moiety at the working pH. The second step involves binding by electrostatic attractions of a cationic redox polymer, the polyviologen derivative denoted as PV. Now, a negatively charged enzyme, that is an enzyme having an isoelectric point below the working pH value, which in this case is nitrate reductase (NR), can be bound to the positively charged redox polymer surface (step three). Repeating steps two and three identically, multiple layers can be deposited on the electrode surface. The mechanism of the electrochemical sensing of the nitrate ion is depicted in Fig. 3. The formation of an organized PV/NR multilayer structure on the gold electrode surface was confirmed by cyclic voltammetry experiments that illustrated a proportional dependence of both cathodic and anodic peak currents to the

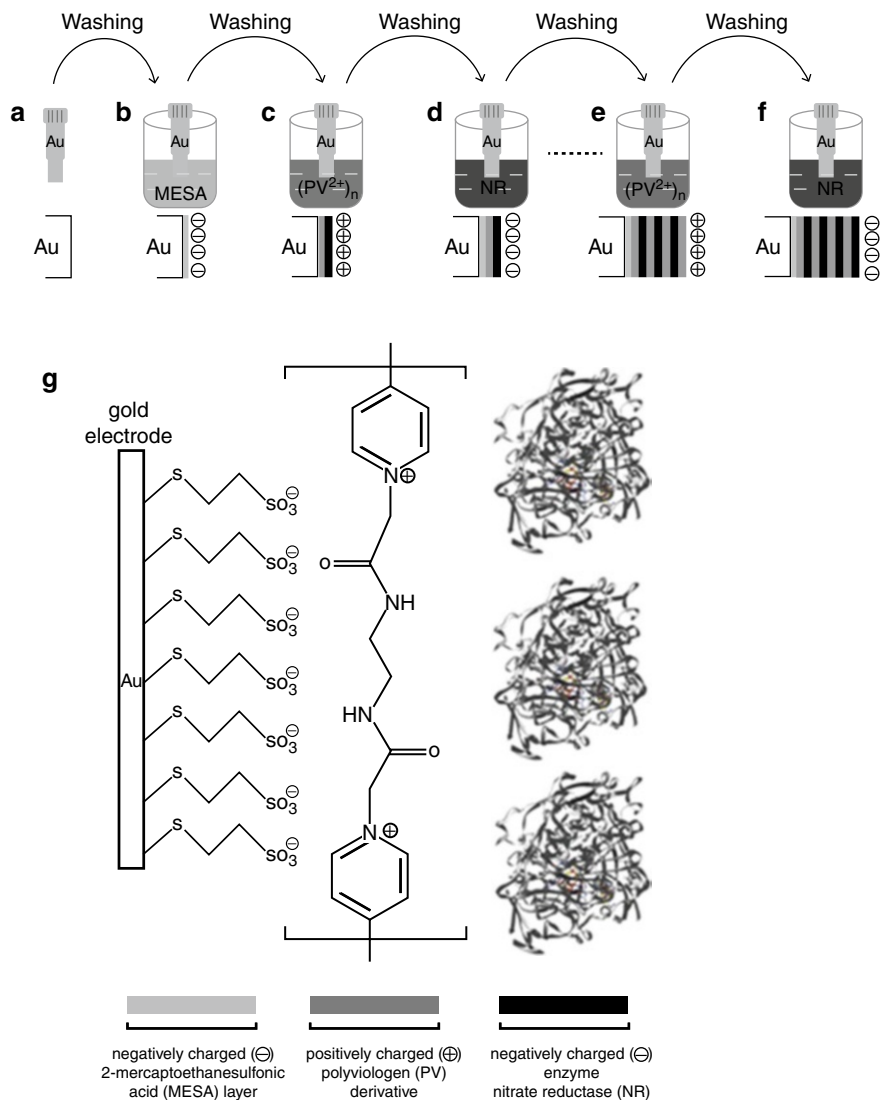


Fig. 2 LbL deposition procedure. Steps: (a) gold; (b) gold surface modified with MESA; (c) gold surface modified with MESA and PV; (d) gold surface modified with MESA and a bilayer of PV/NR; (e) gold surface modified with MESA, three bilayers of PV/NR and another PV layer; (f) gold surface modified with MESA and four bilayers of PV/NR; (g) chemical structures of the MESA layer and alternating PV/NR layers (Adapted with permission from Ref. [49] Copyright © 2007 Rev. Roum. Chim.)

potential scan rate in the range of 50–500 mV/s (see Fig. 4) [49]. Using an increment of 0.75 mM in the concentration of the nitrate ion, a linear amperometric response in the concentration range 0.75–3 mM was obtained (see Fig. 5) [49].

The LbL method to fabricate nanostructured films exhibits a series of important advantages when compared to other techniques. First of all, it is very versatile

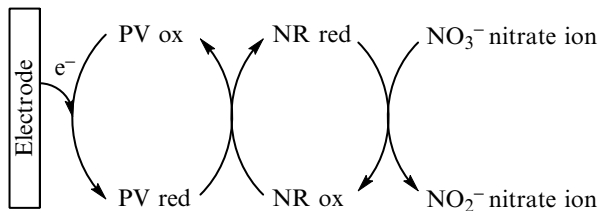


Fig. 3 Schematic diagram of the functioning principle of the nitrate biosensor. In the presence of the NR enzyme in its reduced state, nitrate ion is reduced to nitrite ion, while the enzyme gets oxidized. The reduced form of the enzyme is regenerated by the redox mediator (PV) that is converted from its reduced form to its polycationic oxidized form. The reduced form of the redox mediator can be regenerated by electron transfer from the electrode. Thus, the cationic redox polymer PV acts like a redox mediator facilitating the electron transfer between the redox enzyme and the electrode

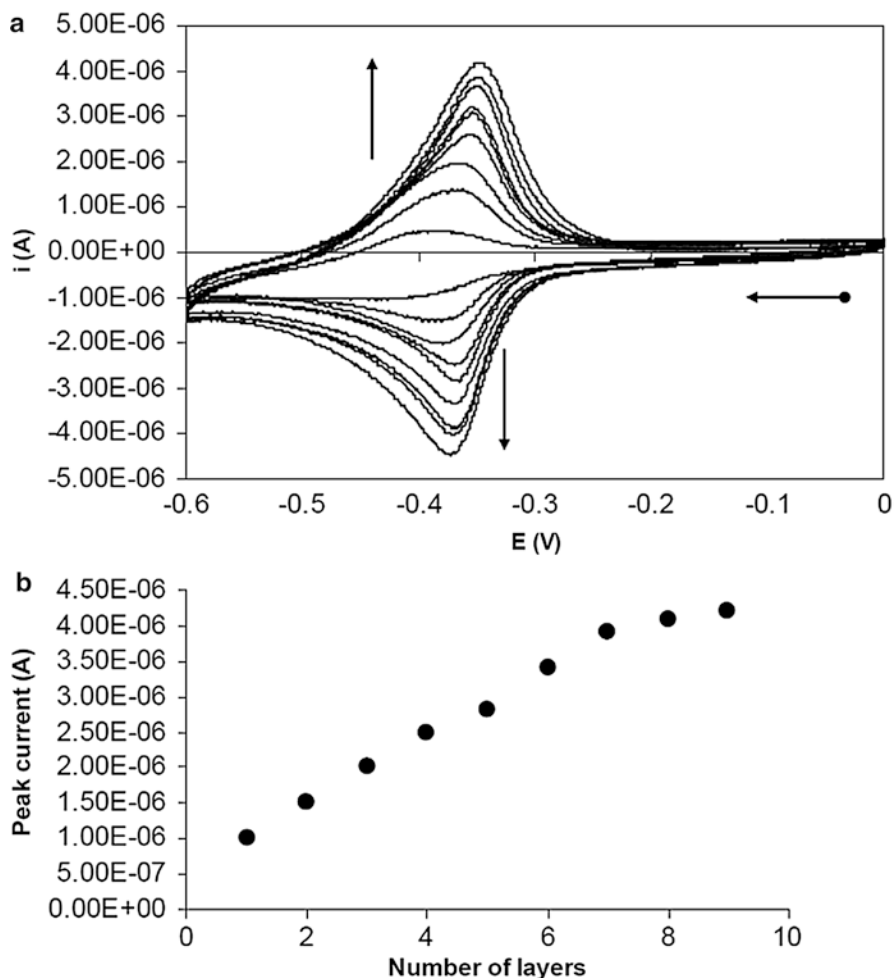


Fig. 4 Cyclic voltammograms of Au/MESA/(PV/NR)₉ modified electrode vs. sweep rates registered in 0.1 M phosphate buffer aqueous solution, pH=7.5 (a), and the dependence of the cathodic peak current on the number of PV/NR pair layers (b) (Reproduced with permission from Ref. [49] Copyright © 2007 Rev. Roum. Chim.)

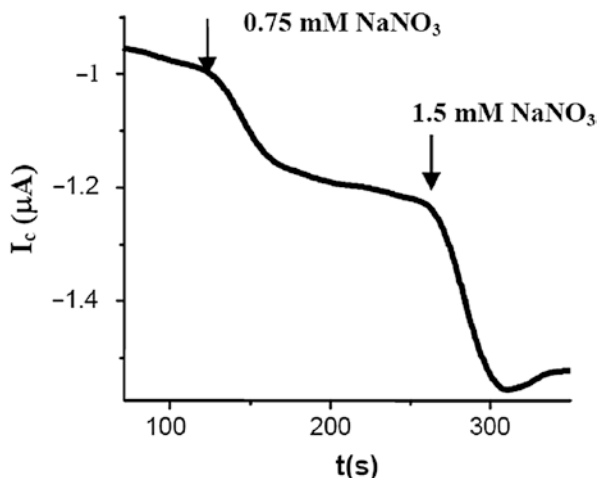


Fig. 5 Current response to nitrate of a Au/PV/NR electrode at -0.6 V vs. Hg/Hg₂SO₄ in 0.1 M phosphate buffer solution (pH=7.5). Nitrate was added to the stirred solution in the electrochemical cell at the time moments indicated by the arrows (Reproduced with permission from Ref. [49] Copyright @ 2007 Rev. Roum. Chim.)

allowing for utilization of a quite broad scale of different materials including polyelectrolytes, dendrimers, redox polymers, carbon-based materials, and biomolecules [50–53]. Second, it is a tunable method as it allows an effective control of important parameters such as thickness, roughness, porosity of films by modifying the film preparation conditions like pH, temperature, polyelectrolyte concentration, ionic strength of the media, and so on [54]. Although initially the construction of multilayer films by LbL method was restricted to electrostatic attractions between oppositely charged layers of polyelectrolytes, recently other types of binding like hydrogen bonding [51], π - π stacking between carbon nanotubes, and polyaromatic hydrocarbon derivatives [55] or even covalent linkage have also been developed. Figure 6 shows some representative examples from the different types of materials used in the preparation of nanostructured multilayers films for biosensing purposes. In the following, some selected relevant applications of the LbL method in the fabrication of electrochemical biosensors will be presented.

Enzymatic biosensors. The first biosensor was an enzymatic glucose sensor developed by Clark and Lyons in 1962 [28]. Although more than five decades have passed since Clark and Lyons reported their pioneering work, the detection principle is still valid and GOx remained one of the most used enzymes due to a series of favorable features such as high turnover rate, excellent selectivity, good thermal and pH stability, and low cost [56]. Several suggestive examples of GOx-based electrochemical biosensors are given below.

Layer-by-layer assembly through electrostatic attractions. An amperometric glucose biosensor was constructed using the LbL method by alternate deposition of

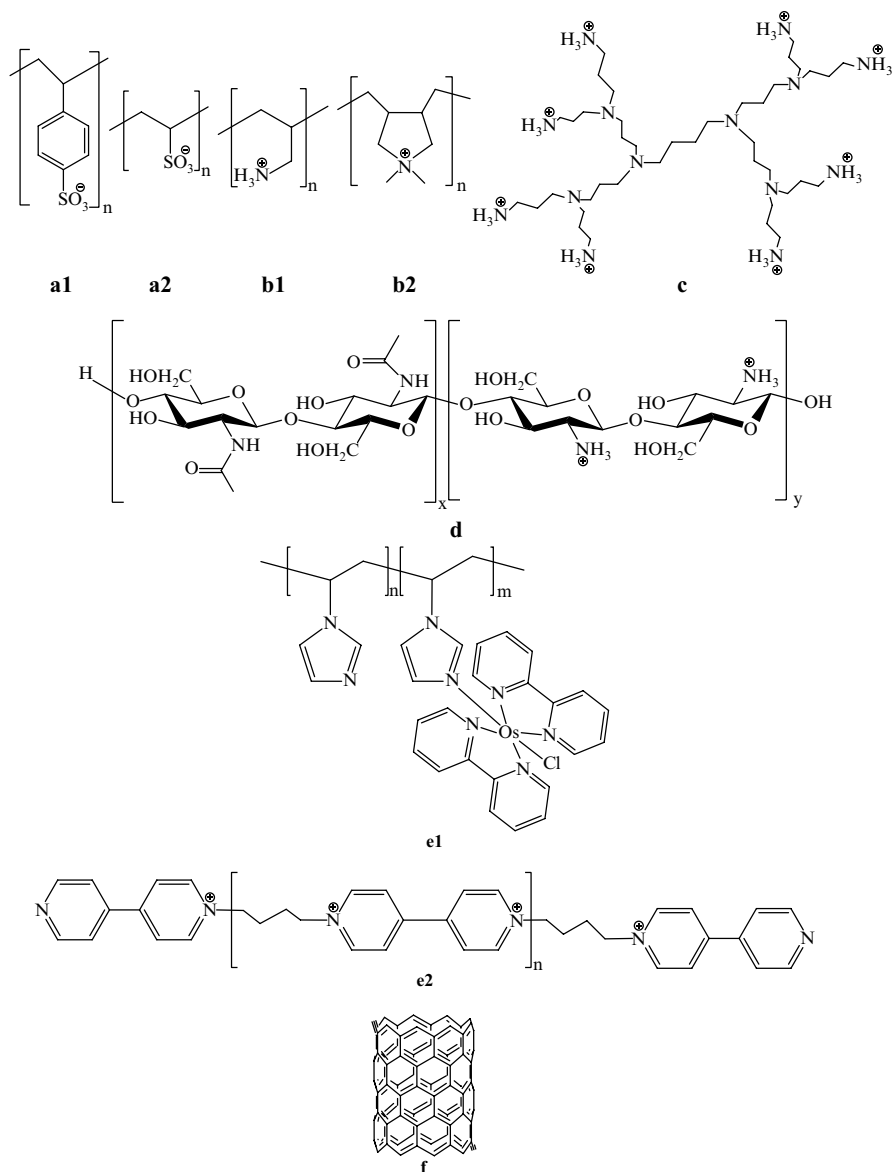


Fig. 6 Examples of different types of materials employed in the synthesis of nanostructured multi-layer films by LbL deposition method. **(a)** anionic polyelectrolytes; examples: **a1** – polystyrene sulfonate (PSS); **a2** – polyvinyl sulfate; **(b)** cationic polyelectrolytes; **b1** – polyallylamine hydrochloride (PAH); **b2** – polydiallyldimethylammonium chloride (PDADMAC); **(c)** dendrimers; example second generation (G2) of polypropyleneimine (PPI); **(d)** chitosan – a cationic polymer obtained by partial deacetylation of the natural polysaccharide chitin; **(e)** cationic redox polymers; examples: **e1** – a cationic redox polymer based on polyvinylimidazole and 2,2'-dipyridyl osmium complex designated as PVI-Os and **e2** – polyviologen a cationic polymer containing bipyridinium derivatives of 4,4'-bipyridyl; **(f)** carbon nanotubes. The counterions were omitted in the chemical structures

successive layers of the cationic redox polymer PVI-Os (see Fig. 6e1) and negatively charged glucose oxidase – single-walled carbon nanotubes conjugates (GOx-SWCNT) on a screen printed carbon electrode. The biosensor response was linear in a broad range from 0.5 to 8.0 mM, displayed a response time less than 5 s and a high sensitivity, these qualities making it a promising amperometric sensing device for the flow injection analysis of glucose [57]. In another example, carbon nanotubes (CNT) were first functionalized with carboxylic acid groups by oxidation, thus their surface becoming negatively charged. Then, the CNT suspension was deposited as a thin film on the surface of a glassy carbon (GC) electrode. The surface of the CNT modified GC electrode was further functionalized by alternatively assembling of successive layers of positively charged polyelectrolyte, polyethyleneimine (PEI), and negatively charged GOx. The so prepared PEI/{GOx/PEI}_n/CNT/GC electrode biosensor exhibited improved analytical performances such as greater stability, a high sensitivity of 106.57 $\mu\text{A mM}^{-1} \text{cm}^{-2}$, and is also able to measure as low glucose levels as 0.05 mM [58]. An interesting paper [59] is based on the synergy resulted from the combined utilization of multiwalled carbon nanotubes (MWCNT), gold nanoparticles (GNPs), conducting polymers (CP), and LbL assembly in order to obtain effective electron shuttling between the electrode (the transducer), and GOx (the bioreceptor). In this approach, an ITO electrode was drop coated with an aqueous solution of amine functionalized MWCNTs and dried. Then, poly(4-aminothiophenol) designated as PANI(SH) was grafted onto the MWCNT-NH₂ modified ITO electrode by electrochemical polymerization. Further, GNPs were electrodeposited onto PANI(SH)-MWCNT-NH₂ assembly. To this positively charged assembly, a layer of negatively charged GOx was stacked by virtue of electrostatic attractions. Repeating the above steps, the {GOx/GNPs-PANI(SH)-MWCNT-NH₂}_n/ITO biosensor was prepared. It showed fast electron transfer properties (rate constant 27.84 s⁻¹), a linear response to glucose in the concentration range 1–9 mM, and a low detection limit of 0.06 μM [59]. Another interesting achievement in the biomedical field is the use of polyethylene terephthalate (PET) as constructing material for artificial blood vessels in cardiovascular implants due to its excellent mechanical flexibility and moderate biocompatibility. Thin films of Ti and Au were successively deposited on the PET support by plasma immersion ion implantation and sputtering, respectively. Then, a negatively charged monolayer of sodium 3-mercapto-1-propane sulfonate (MPS) was attached on the gold surface by chemisorption. Further, a layer of the cationic polyelectrolyte polydiallyldimethylammonium chloride (PDADMAC; see Fig. 6b2) was adsorbed followed by a negatively charged sodium dodecyl sulfate (SDS) wrapped MWCNTs layer. Repeating the deposition steps, a film composed of three {SDS-MWCNT/PDADMAC}₃ bilayers was obtained. The LbL assembly process was further continued by successive deposition of alternately opposite charged layers of PDADMAC and GOx. Eventually, a nanostructured composite film {GOx/PDADMAC}₃/{SDS-MWCNT/PDADMAC}₃/MPS/Au/Ti/PET glucose biosensor was fabricated. The biosensor displayed a linear response in the concentration domain 0.02–2.2 mM and a detection limit of 10 μM [60]. Chitosan (CHT; see Fig. 6d) was also used as cationic

polyelectrolyte in preparation of biosensors by the LbL method. A polyelectrolyte multilayer film, composed of three bilayers of oppositely charged polyallylamine (PAA; see Fig. 6b1) and potassium polyvinyl sulfate (PVS; see Fig. 6a2), was deposited on the surface of a Pt electrode. The {PVS/PAA}₃/Pt modified electrode was further functionalized by chitosan conjugated multiwalled carbon nanotubes (CHT-MWCNT) and GOx resulting in the formation of the {GOx/CHT-MWCNT}_n/ {PVS/PAA}₃/Pt amperometric glucose biosensor. The analytical performances presented by this biosensor were a linear response in the range 1–10 mM, a response time less than 8 s, a sensitivity of 0.45 μA/mM, and a detection limit of 21 μM [61].

Layer-By-Layer Assembly Through Covalent Bonds

Multilayer films formed through electrostatic attractions between oppositely charged layers of polyelectrolytes have been widely used due to the simplicity and low cost of the synthetic procedure. However, they suffer from instability when changes in pH, ionic strength, or temperature occur during measurements [62, 63]. To overcome this lack of stability, multilayer films with covalent interlayer bonding have been synthesized. As covalent interlayer bond, formation of a Schiff base between an amino group and a carbonyl group is the most used method as it occurs in mild conditions and without need for additional reagents that could denature the enzyme bioreceptor. In an elegant synthetic procedure, multilayer films composed of alternately layers of amino functionalized silica nanoparticles (ASNP) and GOx have been deposited on the surface of a gold electrode which was first functionalized by treatment with cystamine dihydrochloride (step 1 Fig. 7). After this amino functionalization of the gold electrode surface, the electrode was treated with an aqueous solution of glutaraldehyde (step 2). Separately, an aqueous solution of ASNP was prepared by surface functionalization of silica nanoparticles with 3-aminopropyltrimethoxysilane (APTMS). In the third step of the synthetic procedure, the electrode modified in steps 1 and 2, was immersed in the ASNP solution. Then, after being washed with water, the electrode was again placed in aqueous glutaraldehyde solution (step 4). Finally, the electrode was immersed in a phosphate buffer solution (pH=6.8) of GOx (step 5). Thus, a GOx/ASNP bilayer was successfully assembled on the Au electrode. Repeating steps 2, 3, 4, and 5 identically, a film {GOx/ASNP}_n with the desired number of GOx/ASNP bilayers could be assembled on the surface of the Au electrode. The sensitivity of the biosensor increased with the number of GOx/ASNP bilayers from 1.87 μA mM⁻¹ cm⁻² for one bilayer to 5.11 μA mM⁻¹ cm⁻² for four bilayers. The detection limit was 9 μM, and the glucose biosensor showed also good long-term stability as the catalytic current response maintained over 90 % of the initial value after four weeks of storage in phosphate buffer solution (pH=6.8) at 4 °C [64]. In another similar approach, a glucose biosensor composed of several bilayers of covalently linked GOx and GNPs assembled on the surface of a gold electrode {GNPs/GOx}_n/Au was constructed. The biosensor exhibited a fast response time (less than 4 s) and a linear response in a wide concentration domain ranging from 10 μM to 13 mM [65].

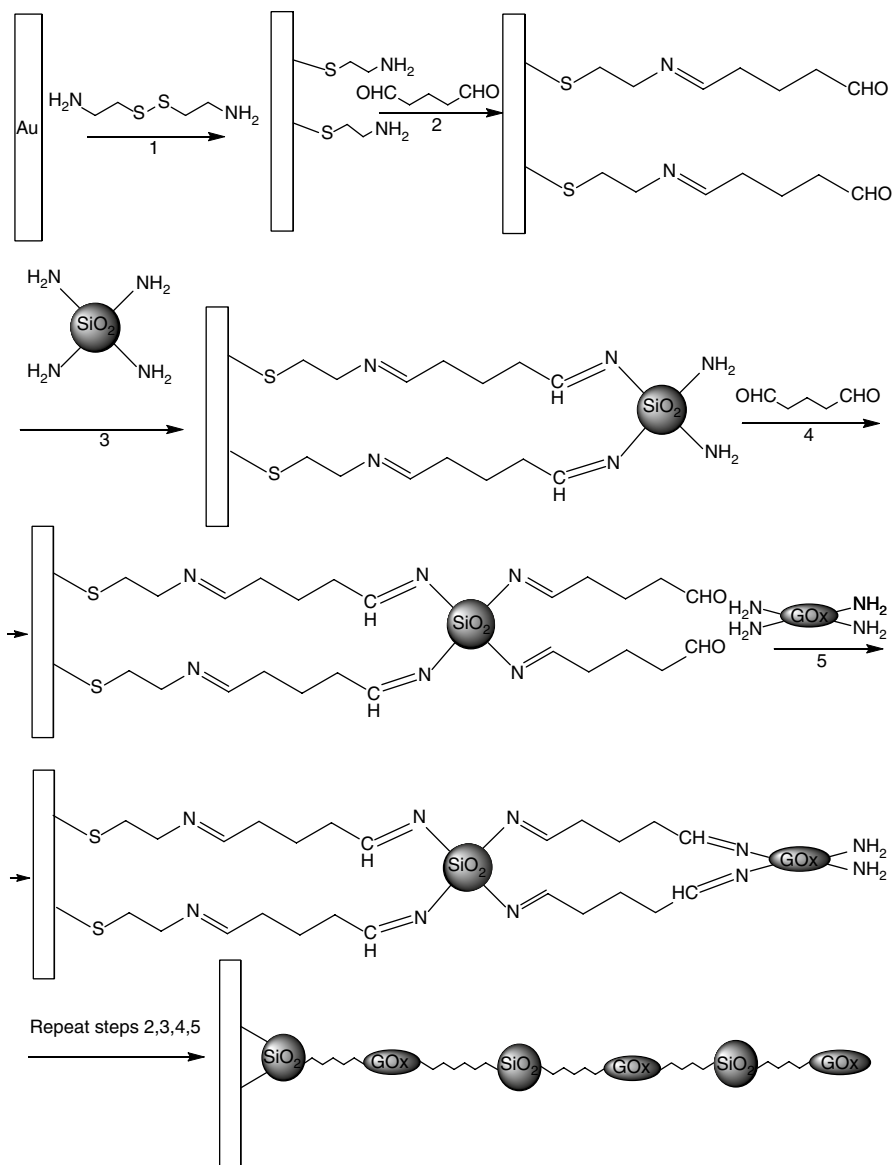


Fig. 7 LbL covalent assembly of multilayer $\{GOx/ASNPS\}_n$ film (Adapted with permission from Ref. [64] Copyright @ 2006 Biomaterials)

Immunosensors. Both amperometric and potentiometric immunosensors for determination of hepatitis B surface antigen (HBsAg) were constructed by the following synthetic protocol. The surface of a Pt electrode was modified with a negatively charged layer of plasma polymerized Nafion film (PPF) and subsequently positively

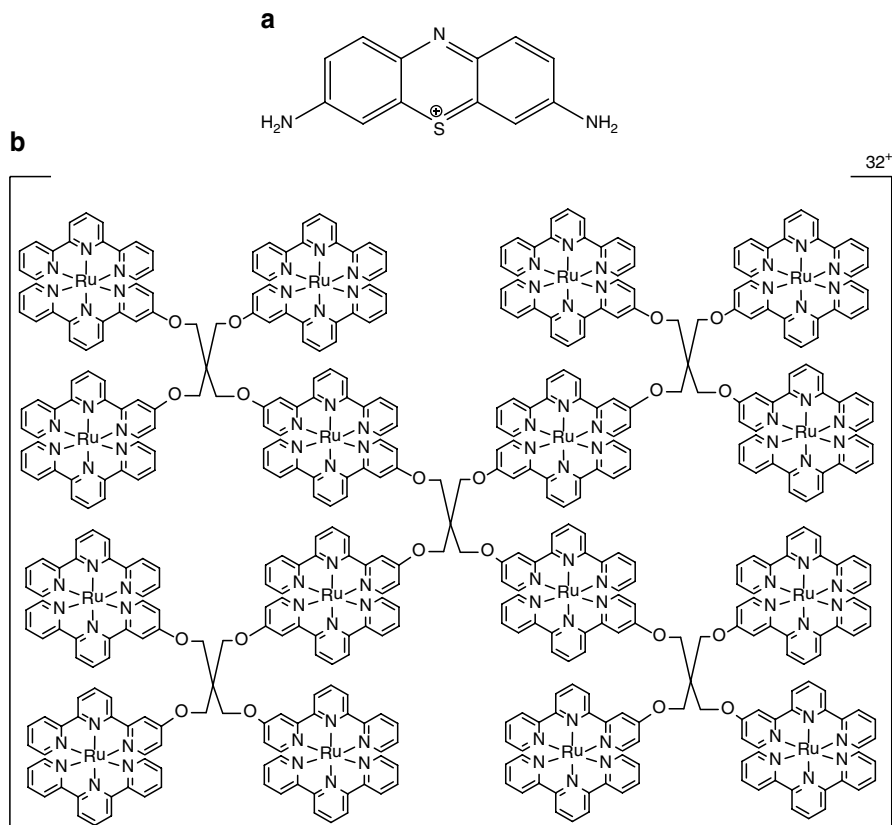


Fig. 8 Chemical structures of the redox dye thionine (THI) (a) and RuDen metallodendrimer (b)

charged tris(2,2'-bipyridyl)cobalt(III) ($\text{Co}(\text{bpy})_3^{3+}$) and negatively charged GNPs were sequentially adsorbed onto the modified electrode to form the nanostructured assembly $\{\text{GNPs}/\text{Co}(\text{bpy})_3\}_n/\text{PPF}/\text{Pt}$. Eventually, hepatitis B surface antibody (HBsAb) was electrostatically adsorbed on the GNPs surface. The resulted HBsAb/ $\{\text{GNPs}/\text{Co}(\text{bpy})_3\}_n/\text{PPF}/\text{Pt}$ immunosensor was used to analyze HBsAg in human serum with similar results as those obtained when the analysis was carried out by the standard ELISA method [66]. Another multilayered architecture was used in the construction of an amperometric immunosensor for the detection of carcinoembryonic antigen (CEA) which is well known as a tumor marker used for clinical diagnosis of colon, pancreas, breast, ovaries, and lung tumors. The immunosensor is based on LbL assembly of GNPs, MWCNTs, and CHT. First, MWCNTs were conjugated with thionine (THI, see Fig. 8a). THI is a redox dye which, acting as a mediator, has good electron conductivity. The driving force for formation of the MWCNTs-THI conjugate is the π - π stacking between these two conjugated frames. The MWCNTs were functionalized with carboxylic acid groups by oxidation with

nitric acids and then mixed with THI in water and sonicated to obtain the conjugate. CHT was solubilized in aqueous acetic acid solution and then mixed with GNPs solution to prepare the GNPs-CHT solution. By dispersing the MWCNTs-THI conjugate in the GNPs-CHT solution followed by sonication, an aqueous solution of the positively charged conjugate GNPs-MWCNTs-THI-CHT was obtained. In this solution, a gold electrode modified with a negatively charged self-assembled monolayer of MPS was immersed for 30 min followed by immersion of the modified electrode in negatively charged polystyrene sulfonate (PSS, see Fig. 6a1). The self-assembling process was completed by repeating the last two steps for several times to obtain the multilayer nanostructured film on which the anti-CEA antibody was eventually adsorbed. The resulting electrode was incubated in bovine serum albumin (BSA) solution. The detection limit of this immunosensor was 0.01 ng mL^{-1} and the electrode showed good stability, retaining 85.2 % of its initial response after a 60 days storage period due to the multilayer nanostructured assembly and to the biocompatibility of the microenvironment created by gold nanoparticles, multi-walled carbon nanotubes–thionine and chitosan matrix [67].

Genosensors. Development of DNA biosensors, also called genosensors, increased tremendously over the last decade. The LbL electrostatic deposition method was used to fabricate an electrochemical biosensor for monitoring the damage produced to DNA by styrene oxide. The surface of a GC electrode was coated with a negatively charged monolayer of aminobenzoic acid. Then, self-assembling of several bilayers of positively charged pentaerythritol-based metallodendrimer with Ru(II) terpyridine subunits (RuDen, see Fig. 8b) and ds-DNA (ds, double-stranded), which is negatively charged due to its sugar–phosphate backbone, led to the formation of a nanostructured multilayer film on the electrode surface. Any unraveling of the ds-DNA produced by damage was monitored by RuDen-catalyzed oxidation of exposed sites, e.g., guanine [68].

A different approach is based on the preferential binding of complementary single-stranded nucleic acid sequences. This system usually relies on the immobilization of ss-DNA (ss, single-stranded) probe onto a surface to recognize its complementary DNA target by hybridization [69]. Transduction of DNA hybridization can be measured electrochemically, for instance impedimetric by electrochemical impedance spectroscopy using a microarray configuration of interdigitated electrodes [70, 71]. The immobilized ss-DNA is surrounded by counter cations, which initially support ionic conductivity. After hybridization there is a reduction in the density of these cations leading to a corresponding increase in the overall electrical impedance between the interdigitated electrodes. Affinity binding can be used for DNA immobilization taking advantage of the high affinity of avidin (Avi) or streptavidin to biotin. Thus, DNA can be biotinylated as shown in Fig. 9 and then the biotin moiety binds strongly to avidin or streptavidin [72]. As Avidin and streptavidin are tetrameric proteins that have four identical binding sites for biotin, as much as four biotinylated DNA can be conjugated to these proteins. An Avi-CHT-MWCNTs/ITO electrode was prepared by the following procedure. A composite film composed of carboxyl functionalized MWCNTs and CHT was electrodeposited on the surface of an indium-tin-oxide (ITO) electrode. Then, using Avi as a

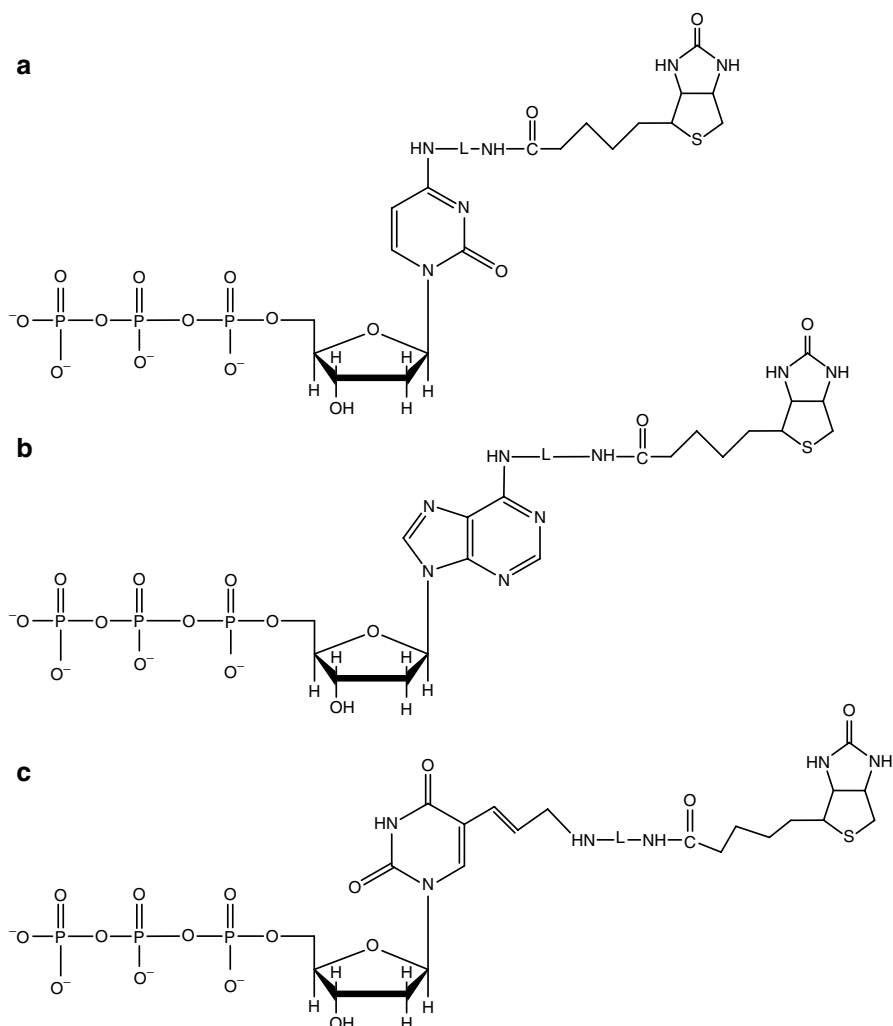


Fig. 9 Biotinylated deoxynucleotide triphosphates. (a) dCTP derivatives; (b) dATP derivatives; (c) dUTP derivatives. L can be a variable structure; e.g., $L = \text{CO}(\text{CH}_2)_5$ or $L = (\text{CH}_2)_6$

cross-linker, biotinylated DNA (BDNA) was further immobilized on the surface of the CHT-MWNT/ITO modified electrode. The amino groups of Avi were first activated by reaction with 1-ethyl-3-(3-dimethylaminopropyl)carbodiimide (EDC) and then covalently linked to the carboxyl groups on the surface of MWCNTs in the presence of *N*-hydroxysuccinimide (NHS). Thus, the biocomposite Avi-CHT-MWNT/ITO electrode was obtained. Then, the electrode, after washing previously, was incubated for 5 min with biotinylated oligonucleotide probes. The obtained BDNA-Avi-CHT-MWCNT/ITO bioelectrode was subjected to hybridization by incubation in the complementary target oligonucleotide solution and used as biosensor for the bacterium *Neisseria gonorrhoeae* [73].

Novel In Situ Sinusoidal Voltages Electrodeposition Procedures of BioComposite Materials

Recently, a great deal of interest has been devoted to the development of tyrosinase-based electrochemical biosensors for electroanalysis of biologically active compounds like catecholamines and phenolic compounds. Tyrosinase (Ty, polyphenol oxidase, E.C. 1.14.18.1) catalyzes the oxidation of *o*-diphenols (diphenolase or catecholase activity) to the corresponding *o*-quinones, in the presence of molecular oxygen, and the hydroxylation of monophenols to catechols (monophenolase or cresolase activity) and their subsequent oxidation to *o*-quinones [74]. The enzymatically generated *o*-quinone specie can be reduced at the electrochemical transducer surface at very low potentials, with the formation of *o*-diphenol (see Fig. 10, re-used from Ref. [75] with permission from MDPI under the MDPI Open Access Policy). The scheme depicted in Fig. 10 shows that there is an amplification of the measured signal, thanks to the regenerated analyte and this enables enhanced sensitivity of the analytical measurements. The Ty containing amperometric biosensors are based on this mechanism [76–80]. Several studies have indicated that there is a loss of enzymatic activity after enzyme immobilization and this issue was solved by incorporation of the enzyme into organic conducting polymer layers during the electrochemical polymerization of the corresponding monomers [81–84]. Usually, the polymeric coating is prepared via electrochemical polymerization by using electrochemical methods like chronoamperometry (potentiostatic method), cyclic voltammetry, and galvanostatic methods. In this context, we have investigated the development of a new enzyme immobilization method for biosensor fabrication. The principle of the proposed method is based on the application of sinusoidal voltages (SV) with various amplitudes and frequencies onto a fixed dc potential. The fixed dc potential is purposely chosen depending on the final goal, i.e., the electrochemical polymerization of a given monomer or synthesis of noble metal nanoparticles. As a consequence of the applied excitation signal, the current response displays a sharp transient at very high frequencies, followed by a constant value at medium

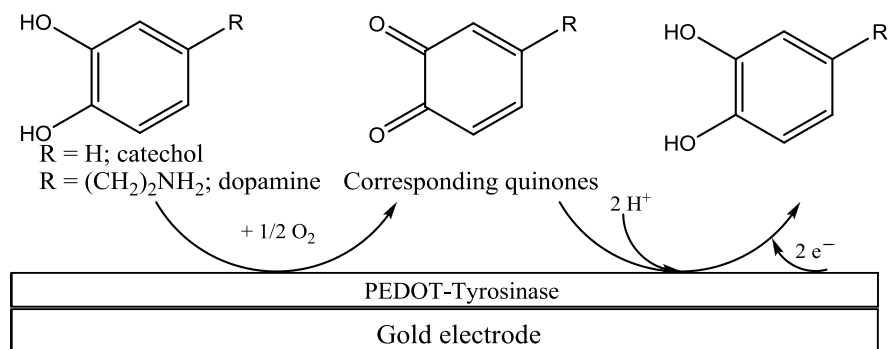


Fig. 10 Principle of functioning of amperometric biosensors based on immobilized tyrosinase (Re-used from Ref. [75] with permission from MDPI under the MDPI Open Access Policy)

frequencies, and a sinusoidal trend (current oscillations) at low frequencies. As will be shown below, these peculiarities proved to be very useful in the biosensors development. We have applied this new preparation method for the in situ electrodeposition of Pt nanoparticles onto poly(3,4-ethylenedioxythiophene) (PEDOT) layers [85], the electrodeposition of PEDOT coatings onto microelectrode arrays [86], and for the entrapment of Ty within PEDOT coating [75, 87].

The Ty-based amperometric biosensors were prepared via electrochemical polymerization of the 3,4-ethylenedioxythiophene (EDOT) monomer in phosphate buffer solution containing various amounts of Ty onto conventional-size Au disk electrodes and Au disk microelectrode arrays, respectively. The novel preparation procedure consists in the application of SV, with frequency in the range 100 kHz to 0.1 Hz and excitation amplitudes of 50 and 100 mV, respectively, onto a fixed dc potential value of +0.95 V vs. Ag/AgCl [75]. On the other hand, Ty-based amperometric biosensors were prepared via potentiostatic method (chronoamperometry, CA) at the same fixed dc potential value in order to compare the efficiency and the usefulness of the proposed preparation method. In order to perform the comparison between these two preparation procedures, the electrodeposition time was kept constant in both preparation methods, assuming that all the electrical charge is used in the electrodeposition of the PEDOT and/or PEDOT-Ty layers, respectively. Several experimental parameters such as, the amplitude of the sinusoidal voltages, the working detection potential, the enzyme concentration, and the pH of the deposition and the sample solutions, were optimized during the construction of the biosensors. The optimum experimental parameters were as follows: amplitude of sinusoidal voltages of 50 mV; working detection potential value of -0.2 V; enzyme concentration in the deposition solution of 2 mg/mL; pH of 7.5 for both deposition and sample solutions [75]. The morphology and the chemical structure of the prepared (bio) composite coatings were also investigated. During the optimization of the preparation procedure, the linear response range, the sensitivity, the repeatability, and the stability of the prepared biosensors were investigated. Finally, the electroanalytical determination of dopamine (DA) and catechol (CT) was achieved at the prepared amperometric biosensors in aqueous solutions.

The scanning electron microscopy (SEM) measurements [75] revealed that the PEDOT layer prepared by SV procedure has a higher roughness than that of the polymer coating obtained via CA method (see Fig. 11a, c). The proposed SV preparation procedure is characterized by current response oscillations, as a result of the applied sinusoidal signal, during the electrochemical polymerization process, and this influences the rates of the polymerization and the p-doping processes with clear effects on the roughness of the resulting polymer layer. In the case of PEDOT-Ty coating, the Ty incorporation takes place during the electrochemical polymerization of the EDOT monomer in the presence of Ty at a pH of 7.5. At this pH value, Ty is under anionic form and it is incorporated within the PEDOT layer as a counterion thanks to the electrostatic interactions with the positive charges of the polarons. As a result of the features of the SV approach and the enzyme incorporation within the polymer layer, the roughness of the PEDOT-Ty coating (see Fig. 11d) is smaller than that of the PEDOT-Ty coating deposited via CA method (see Fig. 11b).

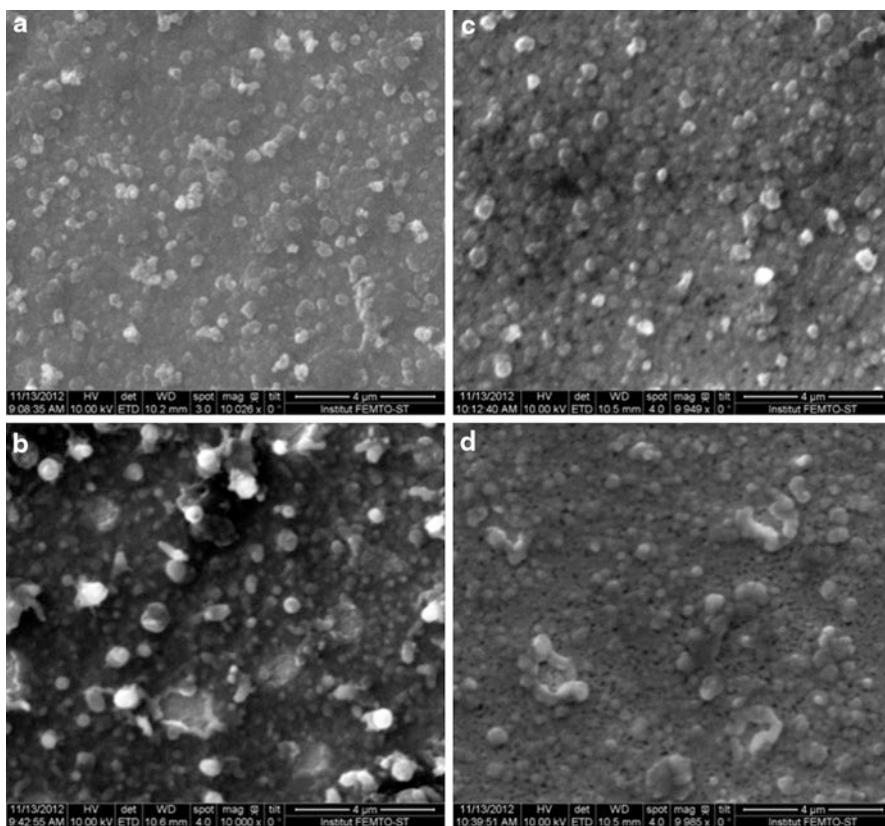


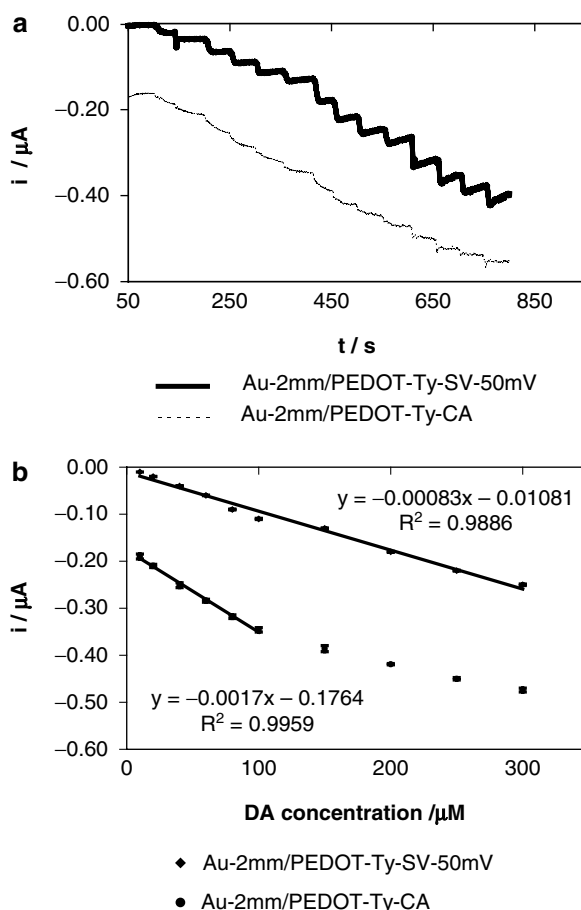
Fig. 11 2D SEM images of (a) PEDOT and (b) PEDOT-Ty layers prepared via CA method; 2D SEM images of (c) PEDOT and (d) PEDOT-Ty layers prepared via SV method (Re-used from Ref. [75] with permission from MDPI under the MDPI Open Access Policy)

Furthermore, the SV preparation procedure enabled a higher amount of immobilized enzyme and consequently better analytical performance of the proposed biosensor.

The DA electroanalysis was performed at biosensors obtained by both SV and CA preparation procedures using the amperometric detection method. The amperometric responses of both biosensors were recorded simultaneously using the bipot module of the potentiostat in the array operation mode. Figure 12a displays the responses of biosensors prepared by SV (Au-2 mm/PEDOT-Ty-SV-50 mV modified electrode) and CA (Au-2 mm/PEDOT-Ty-CA modified electrode) methods, respectively, in aqueous solution, at different DA concentrations [75]. The obtained results clearly demonstrate that the biosensor prepared via SV method has a better analytical response.

For instance, the new amperometric biosensor displayed a linear response for DA concentrations ranging from 10 to 300 μM , a sensitivity of 0.83 nA/ μM , as

Fig. 12 (a) Amperometric responses recorded simultaneously in array mode at a biosensor prepared via SV method (Au-2 mm/PEDOT-Ty-SV-50 mV modified electrode, *thick solid line*) and a biosensor prepared via CA method (Au-2 mm/PEDOT-Ty-CA modified electrode, *dotted line*), respectively, in aqueous phosphate buffer solution at various DA concentrations: 10, 20, 40, 60, 80, 100, 150, 200, 250, 300, 400, 500, 600, and 700 μM . Working detection potential: -0.20 V vs. Ag/AgCl; (b) Calibration plots obtained from the amperometric responses presented in (a) (Re-used from Ref. [75] with permission from MDPI under the MDPI Open Access Policy)



computed from the corresponding calibration plot depicted in Fig. 12b, and limits of detection (LD) and quantification (LQ) of 4.18 μM and of 13.95 μM , respectively. The amperometric biosensor obtained by CA method showed LD and LQ of 4.83 μM and 16.09 μM , respectively [75]. The repeatability and the stability of the biosensor prepared via SV procedure were superior with respect to those of a biosensor obtained by classical method. Furthermore, the biosensor based on microelectrode arrays was used in the simultaneous detection of DA and CT. A semiquantitative method for DA and CT monitoring was developed by using a PEDOT-Ty based biosensor prepared onto one electrode from the chip and a PEDOT-based electrochemical sensor prepared on the second electrode from the chip, respectively.

The array and bipot operation modes of the bipot module of the potentiostat were employed in the simultaneous analytical measurements. In conclusion, the obtained results pointed out that the SV preparation procedure has ensured enhanced immobilization of the enzyme within the PEDOT matrix and better analytical performance of the new biosensor.

Thick Films Based Biosensing Devices

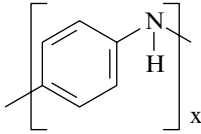
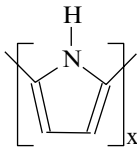
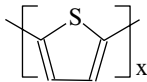
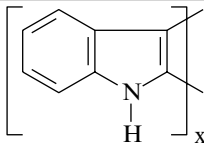
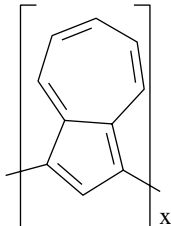
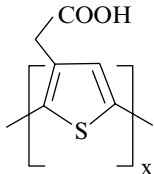
Conducting Polymers Based Biosensors

Conducting polymers (CPs) are polyconjugated polymers (extended π -conjugation along the polymer backbone) with a unique electronic structure which is responsible for their electrical conductivity, low ionization potentials, and high electron affinity. They can be prepared either by chemical or electrochemical oxidation, the latter being the preferred choice. In neutral state, they are insulators or semiconductors, but during doping the conductivity increases with several orders of magnitude. The doping process of CPs involves a partial oxidation (p-doping) or reduction (n-doping) of the π -system of the polymer chain. Simultaneously, ions from the supporting electrolyte diffuse into/out of the polymeric film in order to compensate the electronic charge. Polarons and bipolarons are the main charge carriers in CPs. A polaron is a radical cation or anion whereas a bipolaron is a dication or dianion. For low doping levels most of the charge carriers are polarons and for high doping levels are bipolarons. The conductivity of the polyconjugated polymers is influenced by the effective conjugation length, the overall chain length and by the charge transfer to adjacent molecules, which are determined by the synthesis experimental conditions. CPs possess switching ability to bind oppositely charged molecules in their oxidized conducting states and to release them in their neutral insulating state. In order to have a mediating electroactive coating, the electrons should be able to move through the modifying layer to/from the electrode surface, depending on whether an oxidation/reduction reaction is occurring. Owing to these distinguished properties they were used for obtaining light emitting diodes (LEDs) [88], electrochromic materials [89], antistatic coatings [90], solar cells [91], batteries [92], anticorrosion coatings [93], sensors [94], biosensors [95], and drug release systems [96].

Most of the electrodeposited CPs used for immobilization of biomolecules are polyaniline [97, 98], polypyrrole [99], polythiophene [100], polyindole [101], polyazulene [102, 103], and their derivatives [104]. The chemical structures of the most important CPs are presented in the Table 3.

The mechanism of electropolymerization of CPs can be explained by using poly(3-thiophene acetic acid) as an example. During the first step 3-thiophene acetic acid radical cation is formed at the electrode surface. This process is followed by dimerization with deprotonation. The dimer oxidizes more easily than the monomer and thus gets reoxidized to allow further coupling reaction to proceed. Figure 13 reports the electropolymerization of 3-thiophen acetic acid:

Table 3 Chemical structures of CPs used as matrix for enzyme immobilization

CP for immobilization of biomolecules	Chemical structure	Reference
Polyaniline		[97, 98]
Polypyrrole		[99]
Polythiophene		[100]
Polyindole		[101]
Polyazulene		[102, 103]
Poly(thiophene-3-acetic acid)		[104]

During the last years, a major challenge for the researchers was the development of the selective, sensitive, and fast biosensors as powerful tools for clinical and food analysis, drug and agricultural industries, and environmental monitoring. CPs are successfully used in biosensors manufacturing process owing to their outstanding properties concerning direct electron transport between oxidoreductase enzymes and electrode surface [98]. They are versatile materials for biosensors being easily produced with controlled thickness and porosity, and also can be selectively immobilized by electropolymerization over different sizes of surfaces of various morphologies. The sensitivity and response time of CPs-based biosensors are dependent on the film thickness, porosity, and the surface morphology. Therefore, a higher sensitivity and faster response time are expected for thinner films.

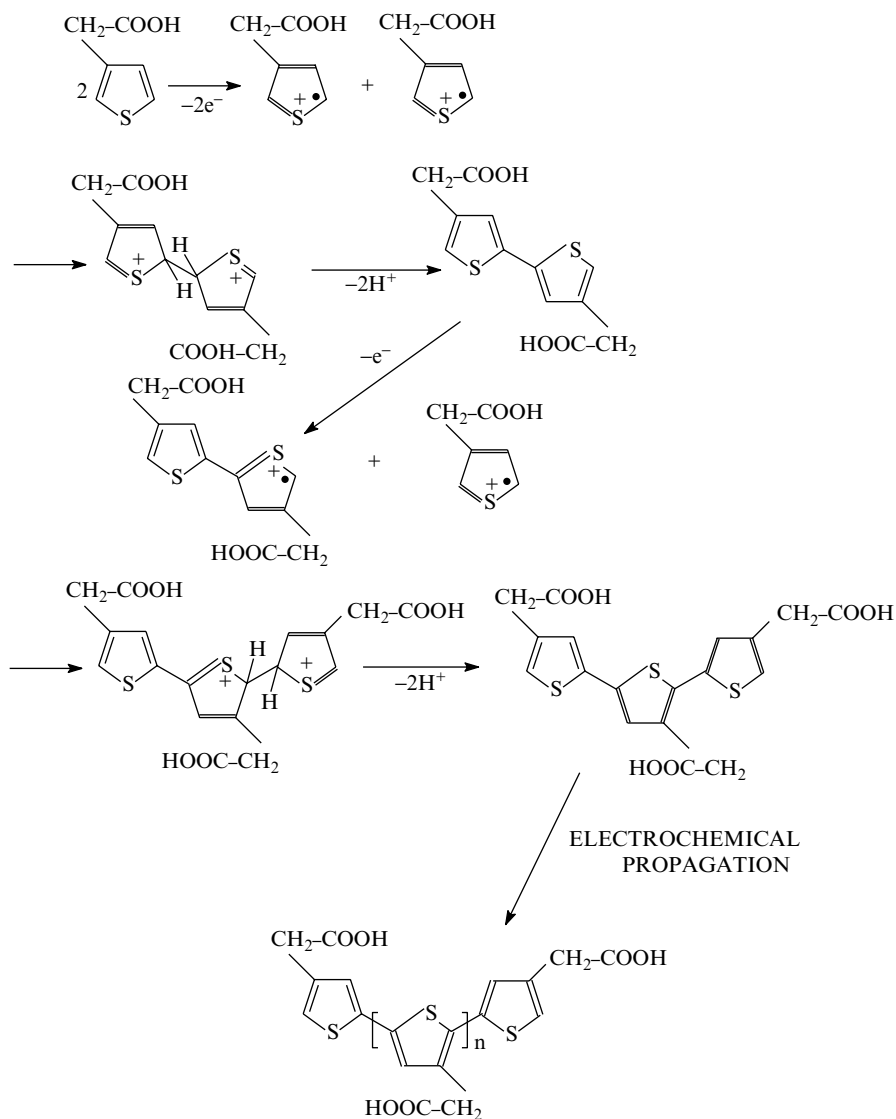


Fig. 13 The reactions scheme for the electropolymerization of 3-thiophenyl acetic acid

Often, CPs have been used to obtain either a simple carrier matrix for enzyme immobilization or a polymeric redox environment via copolymerization/polymerization of appropriate monomers, bearing chemical/affinity groups or redox moieties. The derivatization of the surface is very attractive and the resulting polymers possess high adherence on the surfaces without any surface activation. Obtaining of copolymers from a mixture of different monomers is a way to modify the structure

and the properties of CPs. By electrochemical copolymerization materials with controlled properties are obtained without the experimental disadvantages related to the preparation of new homopolymers [102].

The high selectivity of the biomolecular receptors as antibodies, enzymes, binding proteins, and nucleic acids is a key factor for the fabrication of electrochemical biosensors. These biomolecules can be integrated with an electrochemical, optical, or piezoelectric transducer. The immobilization of biomolecules in or on conducting polymer films is one of the few methods that have attracted interest for its electrochemical addressing property. By electropolymerization are obtained simple and reproducible films with precise spatial resolution over surfaces, whatever their size and geometry. CPs have an organized molecular structure on metal substrates, which permit them to function as a three dimensional matrix for the immobilization of biosensing molecule and preserve the activity for long duration. Conducting polymer films can be electrodeposited on a wide variety of electrode materials such as gold [105], platinum [106], glassy carbon [107], screen printed electrodes [108], thin oxide surfaces [109], and boron-doped diamond [110].

CPs-based biosensors can be divided into several categories depending on how the chemical signal is sensed and transmitted: amperometric (measures current), potentiometric (measures potential), optical (measures light absorbance or emission), impedimetric (measures change in conductivity), calorimetric (measures change in enthalpy), and piezoelectric (measures mechanical stress).

The immobilization of the biomolecules assumes: (a) simple adsorption onto polymeric films, (b) entrapment within the polymer matrix during its electrodeposition, (c) covalent binding between the biomolecules and functionalized polymers, and (d) attachment of the biomolecule by affinity interactions with the film. In the first approach, specific noncovalent immobilization of biomolecules is achieved by physical adsorption processes based on the electrostatic forces, hydrogen bonding, Van der Waal's forces, etc. This method is simple but has some limitations as desorption of biomolecule over time, limited control over immobilization and random orientation on surface. Obtaining of biosensor by entrapment of biomolecules during the polymerization is the most popular approach. The entrapment technique has several advantages as: it is simple (one step), faster than other immobilization techniques, good proximity between elements, the film thickness is well controlled through the charge involved in the electrodeposition step, the distribution of the immobilized enzyme is spatially controlled (no matter geometry, shape and dimension of the electrode), it allows a reproducible polymer film formation. Of course, even in this case there are some limitations such as: potential loss of enzyme activity, the need for high concentrations of enzyme. By covalent linking of biomolecules on transducer is obtained a strong and an efficient bonding between enzyme and the immobilizing material. Covalent linking of a biomolecule to polymer matrix is performed in a two steps, i.e., synthesis of functionalized polymer followed by covalent immobilization that takes place only on the outer surface of the polymer. The main advantages of this technique are: good control over biomolecule orientation, high accessibility of analytes, negligible enzyme loss over time, and a very accurate control during immobilization. The last approach, the attachment of the biomolecule by

Table 4 Analytical performance of various biological receptor's immobilization techniques

Method of immobilization	Biological receptor	Analyte	Limit of detection (M)	Type of transducer	Reference
Langmuir-Blodgett	GOx ^a	Glucose	1.5×10^{-6}	Amperometric	[31]
	GOx	Glucose	5×10^{-3}	Voltammetric	[35]
Layer-by-layer	GOx	Glucose	9×10^{-6}	Amperometric	[64]
Sinusoidal voltages	Tyrosinase	Dopamine	4.2×10^{-6}	Amperometric	[75]
Adsorption on CPs	Alcohol oxidase	Ethanol	5×10^{-6}	Amperometric	[97]
	Phytase	Phytic acid	1.5×10^{-4}	Amperometric	[99]
Covalent bonding to CPs	HRP ^b	Tamoxifen	7×10^{-11}	Amperometric	[98]
	GOx	Glucose	2.5×10^{-9}	Amperometric	[104]
Co-immobilization within CPs	HRP	H ₂ O ₂	6×10^{-8}	Amperometric	[105]
Affinity interactions	Streptavidin HRP	H ₂ O ₂	5×10^{-5}	Impedimetric	[111]

^aGOx glucose oxidase

^bHRP horseradish peroxidase

affinity interactions with the film allows a good control over molecule orientation, a high accessibility of analytes and a minimal loss of enzyme activity. A limitation of this immobilization procedure is that it requires preimmobilization of one of the affinity molecules. The analytical performance in terms of limit of detection for various biological receptors' immobilization techniques are listed in Table 4.

In the future, owing to excellent electrical, chemical, mechanical properties, it is expected that CPs based biosensors will likely find specific therapeutic applications in using as bioanalytical microelectrodes. CPs have an excellent flexibility, biocompatibility, and ability to be electrodeposited onto desired geometrical surfaces, they have a huge potential to be integrated into micro- or nanoscale devices for in vivo sensing and monitoring of bioanalytes (microfluidic lab-on-chip devices or lab-on-tube devices smart catheters used as smart medical diagnostic tools).

Conclusions

This chapter has presented the combination of biological molecules with nanomaterials in the process of developing electrochemical biosensors for clinical, environmental, and food analysis. Nanobioelectrochemistry is an interdisciplinary science covering various fields like bioelectrochemistry, nanotechnology, and materials science. The immobilization of biological molecules within nanostructured thin film was discussed in the light of classical approaches Langmuir-Blodgett and layer-by-layer techniques. The organization of biocomposite materials at nanoscale provided new insights in the interaction between biomolecules and various materials as well as improved analytical performances of the final analytical devices. Thick film technology based on conducting polymers showed a versatile and reliable approach for developing new electrochemical sensors. New biomolecules immobilization procedures developed in our

research group were also discussed in comparison with classical immobilization routes. Proof of concept, laboratory-based research and practical-oriented biosensor architectures were presented. The information presented throughout this chapter is based on recent achievements but also on classical and pioneering works in order to give a background overview of the use of biocomposite materials in biosensor technology. Therefore, this chapter devoted to various aspects of nanobioelectrochemistry may be used as a valuable source of information by students and scientists working in electrochemical biosensors field.

Acknowledgments S. L. greatly acknowledges the financial support by a grant of the Romanian National Authority for Scientific Research, CNCS-UEFISCDI, project number PN-II-ID-PCE-2011-3-0271.

References

1. Albareda-Sirvent M, Merkoçi A, Alegret S (2000) Configurations used in the design of screen-printed enzymatic biosensors. A review. *Sens Actuators B* 69:153–163. doi:10.1016/S0925-4005(00)00536-0
2. Hart JP, Crew A, Crouch E, Honeychurch KC, Pemberton RM (2004) Some recent designs and developments of screen-printed carbon electrochemical sensors/biosensors for biomedical, environmental, and industrial analyses. *Anal Lett* 37:789–830. doi:10.1081/AL-120030682
3. Hart JP, Wring SA (1994) Screen-printed voltammetric and amperometric electrochemical sensors for decentralized testing. *Electroanalysis* 6:617–624. doi:10.1002/elan.1140060802
4. Gupta R, Chaudhury NK (2007) Entrapment of biomolecules in sol–gel matrix for applications in biosensors: problems and future prospects. *Biosens Bioelectron* 22:2387–2399. doi:10.1016/j.bios.2006.12.025
5. Walcarius A (2012) Electrocatalysis, sensors and biosensors in analytical chemistry based on ordered mesoporous and macroporous carbon-modified electrodes. *Trends Anal Chem* 38:79–97. doi:10.1016/j.trac.2012.05.003
6. Davis F, Higson SPJ (2005) Structured thin films as functional components within biosensors. *Biosens Bioelectron* 21:1–20. doi:10.1016/j.bios.2004.10.001
7. Zhou Y, Chiu CW, Liang H (2012) Interfacial structures and properties of organic materials for biosensors: an overview. *Sensors* 12:15036–15062. doi:10.3390/s121115036
8. Arya A, Krull UJ, Thompson M, Wong HE (1985) Langmuir-Blodgett deposition of lipid films on hydrogel as a basis for biosensor development. *Anal Chim Acta* 173:331–336. doi:10.1016/S0003-2670(00)84973-9
9. Decher G, Lehr B, Lowack K, Lvov Y, Schmitt J (1994) New nanocomposite films for biosensors – layer-by-layer adsorbed films of polyelectrolytes, proteins or DNA. *Biosens Bioelectron* 9:677–684. doi:10.1016/0956-5663(94)80065-0
10. Hanazato Y, Nakako M, Shiono S, Maeda M (1989) Integrated multi-biosensors based on an ion-sensitive field-effect transistor using photolithographic techniques. *IEEE Trans Electron Devices* 36:1303–1310. doi:10.1109/16.30936
11. Saha K, Agasti SS, Kim C, Li X, Rotello VM (2012) Gold nanoparticles in chemical and biological sensing. *Chem Rev* 112:2739–2779. doi:10.1021/cr2001178
12. Willner I, Willner B (2010) Biomolecule-based nanomaterials and nanostructures. *Nano Lett* 10:3805–3815. doi:10.1021/nl102083j
13. Schnorr JM, Swager TM (2011) Emerging applications of carbon nanotubes. *Chem Mater* 23:646–657. doi:10.1021/cm102406h
14. Schwierz F (2010) Graphene transistors. *Nat Nanotechnol* 5:487–496. doi:10.1038/nnano.2010.89
15. Newman JD, Setford SJ (2006) Enzymatic biosensors. *Mol Biotechnol* 32:249–268. doi:10.1385/MB:32:3:249

16. Luong JHT, Male KB, Glennon JD (2008) Biosensor technology: technology push versus market pull. *Biotechnol Adv* 26:492–500. doi:10.1016/j.biotechadv.2008.05.007
17. Szunerits S, Pust SE, Wittstock G (2007) Multidimensional electrochemical imaging in materials science. *Anal Bioanal Chem* 389:1103–1120. doi:10.1007/s00216-007-1374-0
18. Davies TJ, Ward-Jones S, Banks CE, del Campo J, Mas R, Xavier Munoz F, Compton RG (2005) The cyclic and linear sweep voltammetry of regular arrays of microdisc electrodes: Fitting of experimental data. *J Electroanal Chem* 585:51–62. doi:10.1016/j.jelechem.2005.07.021
19. Tian J-H, Yang Y, Liu B, Schollhorn B, Wu D-Y, Maisonhaute E, Muns AS, Chen Y, Amatore C, Tao N-J, Tian Z-Q (2010) The fabrication and characterization of adjustable nanogaps between gold electrodes on chip for electrical measurement of single molecules. *Nanotechnology* 21:274012. doi:10.1088/0957-4484/21/27/274012
20. Varshney M, Li Y (2009) Interdigitated array microelectrodes based impedance biosensors for detection of bacterial cells. *Biosens Bioelectron* 24:2951–2960. doi:10.1016/j.bios.2008.10.001
21. Blodgett KB (1934) Monomolecular films of fatty acids on glass. *J Am Chem Soc* 56(2):495. doi:10.1021/ja01317a513
22. Blodgett KB (1935) Films built by depositing successive monomolecular layers on a solid surface. *J Am Chem Soc* 57(6):1007–1022. doi:10.1021/ja01309a011
23. Blodgett KB, Langmuir I (1937) Built-up films of barium stearate and their optical properties. *Phys Rev* 51:964–982. doi:10.1103/PhysRev.51.964
24. Decher G, Hong JD, Schmitt J (1992) Buildup of ultrathin multilayer films by a self-assembly process: III. Consecutively alternating adsorption of anionic and cationic polyelectrolytes on charged surfaces. *Thin Solid Films* 210–211:831–835. doi:10.1016/0040-6090(92)90417-A
25. Decher G (1997) Fuzzy nanoassemblies: toward layered polymeric multicomposites. *Science* 277:1232–1237. doi:10.1126/science.277.5330.1232
26. Higson SPJ, Vadgama PM (1994) Biosensors: a viable monitoring technology? *Med Biol Eng Comput* 32:601–609. doi:10.1007/BF02524233
27. Clark LC Jr (1956) Monitor and control of blood tissue O₂ tensions. *Trans Am Soc Artif Intern Organs* 2:41–48
28. Clark LC Jr, Lyons C (1962) Electrode system for continuous monitoring in cardiovascular surgery. *Ann N Y Acad Sci* 102:29–45. doi:10.1111/j.1749-6632.1962.tb13623.x
29. Ohnuki H, Saiki T, Kusakari A, Ichihara M, Izumi M (2008) Immobilization of glucose oxidase in Langmuir–Blodgett films containing Prussian blue nano-clusters. *Thin Solid Films* 516:8860–8864. doi:10.1016/j.tsf.2007.11.059
30. Ravaine S, Lafuente C, Mingotaud C (1998) Electrochemistry of Langmuir–Blodgett films based on Prussian Blue. *Langmuir* 14:6347–6349. doi:10.1021/la9808014
31. Lee D-Y, Kafi AKM, Choi W-S, Park S-H, Kwon Y-S (2008) Glucose sensor based on glucose oxidase-lipid LB film immobilized in Prussian Blue layer. *J Nanosci Nanotechnol* 8:4543–4547. doi:10.1166/jnn.2008.IC04
32. Ricci F, Palleschi G (2005) Sensor and biosensor preparation, optimisation and applications of Prussian Blue modified electrodes. *Biosens Bioelectron* 21:389–407. doi:10.1016/j.bios.2004.12.001
33. Watanabe N, Ohnuki H, Saiki T, Endo H, Izumi M, Imakubo T (2005) Conducting organic Langmuir–Blodgett films as chemical sensors. *Sens Actuators B* 108:404–408. doi:10.1016/j.snb.2005.01.048
34. Skotheim TA, Lee HS, Hale PD, Karan HI, Okamoto Y, Samuelson L, Tripathy S (1991) Derivatized polypyrrole Langmuir–Blodgett films. Applications to bioelectronics. *Synth Met* 42:1433–1437. doi:10.1016/0379-6779(91)871-7
35. Rikukawa M, Nakagawa M, Nishizawa N, Sanui K, Ogata N (1997) Electrochemical and sensing properties of enzyme-polypyrrole multicomponent electrodes. *Synth Met* 85:1377–1378. doi:10.1016/S0379-6779(97)80280-9
36. Dhand C, Das M, Datta M, Malhotra BD (2011) Recent advances in polyaniline based biosensors. *Biosens Bioelectron* 26:2811–2821. doi:10.1016/j.bios.2010.10.017
37. Ramanathan K, Ram MK, Malhotra BD, Murthy ASN (1995) Application of polyaniline-Langmuir–Blodgett films as a glucose biosensor. *Mater Sci Eng C3*:159–163. doi:10.1016/0928-4931(95)00113-1

38. Hourdou M-L, Besson F (1995) Enzymatic activities and infrared studies of glutamate dehydrogenase immobilized on Langmuir-Blodgett films. *Biotechnol Tech* 9:643–648. doi:10.1007/BF00156349
39. Schmidt TF, Caseli L, Viitala T, Oliveira ON Jr (2008) Enhanced activity of horseradish peroxidase in Langmuir-Blodgett films of phospholipids. *Biochim Biophys Acta* 1778:2291–2297. doi:10.1016/j.bbame.2008.05.012
40. Caseli L, Crespilho FN, Nobre TM, Zaniquelli MED, Zucolotto V, Oliveira ON Jr (2008) Using phospholipid Langmuir and Langmuir-Blodgett films as matrix for urease immobilization. *J Colloid Interface Sci* 319:100–108. doi:10.1016/j.jcis.2007.12.007
41. Sharma SK, Singhal R, Malhotra BD, Sehgal N, Kumar A (2004) Biosensor based on Langmuir-Blodgett films of poly(3-hexyl thiophene) for detection of galactose in human blood. *Biotechnol Lett* 26:645–647. doi:10.1023/B:BILE.0000023023.19651.01
42. Boussaad S, Dziri L, Archabaleta R, Tao NJ, Leblanc RM (1998) Electron-transfer properties of cytochrome c Langmuir-Blodgett films and interactions of cytochrome c with lipids. *Langmuir* 14:6215–6219. doi:10.1021/la980319i
43. Wang H, Brennan JD, Gene A, Krgll UJ (1995) Assembly of antibodies in lipid membranes for biosensor development. *Appl Biochem Biotechnol* 53:163–181. doi:10.1007/BF02788606
44. Guntupalli R, Lakshmanan RS, Wan J, Kim D-J, Huang TS, Vodyanoy V, Chin BA (2008) Analytical performance and characterization of antibody immobilized magnetoelastic biosensors. *Sens Instrum Food Qual* 2:27–33. doi:10.1007/s11694-007-9025-x
45. Minehan DS, Marx KA, Tripathy SK (1994) Kinetics of DNA binding to electrically conducting polypyrrole films. *Macromolecules* 27:777–783. doi:10.1021/ma00081a024
46. Komarova E, Aldissi M, Bogomolova A (2005) Direct electrochemical sensor for fast reagent-free DNA detection. *Biosens Bioelectron* 21:182–189. doi:10.1016/j.bios.2004.07.025
47. Sassolas A, Blum LJ, Leca-Bouvier BD (2012) Immobilization strategies to develop enzymatic biosensors. *Biotechnol Adv* 30:489–511. doi:10.1016/j.biotechadv.2011.09.003
48. Ahuja T, Mira IA, Rajesh DK (2007) Biomolecular immobilization on conducting polymers for biosensing applications. *Biomaterials* 28:791–805. doi:10.1016/j.biomaterials.2006.09.046
49. Lupu S, Fikai A (2007) Layer by layer deposition of redox polymers/enzyme assemblies onto electrodes surfaces for nitrate electrochemical sensing. *Rev Roum Chim* 52:1137–1143
50. Clark SL, Montague MF, Hammond PT (1997) Ionic effects of sodium chloride on the templated deposition of polyelectrolytes using layer-by-layer ionic assembly. *Macromolecules* 30:7237–7244. doi:10.1021/ma970610s
51. Zhang H, Fu Y, Wang D, Wang L, Wang Z, Zhang X (2003) Hydrogen-bonding-directed layer-by-layer of dendrimer and poly(4-vinylpyridine) and micropore formation by post-base treatment. *Langmuir* 20:8497–8502. doi:10.1021/la035036u
52. Olek M, Ostrander J, Jurga S, Mõhwald H, Kotov N, Kempa K, Giersig M (2004) Layer-by-layer assembled composites from multiwall carbon nanotubes with different morphologies. *Nano Lett* 4:1889–1895. doi:10.1021/nl048950w
53. Iost RM, Crespilho FN (2012) Layer-by-layer self-assembly and electrochemistry: applications in biosensing and bioelectronics. *Biosens Bioelectron* 31:1–10. doi:10.1016/j.bios.2011.10.040
54. Schönhoff M, Ball V, Bausch AR, Dejngnat C, Delorme N, Glinel K, Klitzing RV, Steitz R (2007) Hydration and internal properties of polyelectrolyte multilayers. *Colloids Surf A Physicochem Eng Asp* 303:14–29. doi:10.1016/j.colsurfa.2007.02.054
55. Chen RJ, Zhang Y, Wang D, Dai H (2001) Noncovalent sidewall functionalization of single-walled carbon nanotubes for protein immobilization. *J Am Chem Soc* 123:3838–3839. doi:10.1021/ja010172b
56. Wilson R, Turner APF (1992) Glucose oxidase: an ideal enzyme. *Biosens Bioelectron* 7:165–185. doi:10.1016/0956-5663(92)87013-F
57. Gao Q, Guo Y, Zhang W, Qi H, Zhang C (2011) An amperometric glucose biosensor based on layer-by-layer GOx-SWCNT conjugate/redox polymer multilayer on a screen-printed carbon electrode. *Sens Actuators B* 153:219–225. doi:10.1016/j.snb.2010.10.034
58. Deng C, Chen J, Nie Z, Si S (2010) A sensitive and stable biosensor based on the direct electrochemistry of glucose oxidase assembled layer-by-layer at the multiwall carbon nanotube-modified electrode. *Biosens Bioelectron* 26:213–219. doi:10.1016/j.bios.2010.06.013

59. Komathi S, Gopalan AI, Lee K-P (2009) Fabrication of a novel layer-by-layer film based glucose biosensor with compact arrangement of multi-components and glucose oxidase. *Biosens Bioelectron* 24:3131–3134. doi:10.1016/j.bios.2009.03.013
60. Yan XB, Chen XJ, Tay BK, Khor KA (2007) Transparent and flexible glucose biosensor via layer-by-layer assembly of multi-wall carbon nanotubes and glucose oxidase. *Electrochem Commun* 9:1269–1275. doi:10.1016/j.elecom.2006.12.022
61. Wu B-Y, Hou S-H, Yu M, Qin X, Li S, Chen Q (2009) Layer-by-layer assemblies of chitosan/multi-wall carbon nanotubes and glucose oxidase for amperometric glucose biosensor applications. *Mater Sci Eng C* 29:346–349. doi:10.1016/j.msec.2008.07.018
62. Kuhn A, Mano N, Vidal C (1999) Polioxometalate modified electrodes: from a monolayer to multilayer structures. *J Electroanal Chem* 462(2):187–194. doi:10.1016/S0022-0728(98)00410-0
63. Schlenoff JB, Ly H, Li M (1998) Charge and mass balance in polyelectrolyte multilayers. *J Am Chem Soc* 120(30):7626–7634. doi:10.1021/ja980350+
64. Sun Y, Yan F, Yang W, Sun C (2006) Multilayered construction of glucose oxidase and silica nanoparticles on Au electrodes based on layer-by-layer covalent attachment. *Biomaterials* 27:4042–4049. doi:10.1016/j.biomaterials.2006.03.014
65. Yang W, Wang J, Zhao S, Sun Y, Sun C (2006) Multilayered construction of glucose oxidase and gold nanoparticles on Au electrodes based on layer-by-layer covalent attachment. *Electrochem Commun* 8:665–672. doi:10.1016/j.elecom.2005.11.014
66. Tang D, Yuan R, Chai Y, Fu Y, Dai J, Liu Y, Zhong X (2005) New amperometric and potentiometric immunosensors based on gold nanoparticles/tris(2,2'-bipyridyl)cobalt(III) multilayer films for hepatitis B surface antigen determinations. *Biosens Bioelectron* 21:539–548. doi:10.1016/j.bios.2004.11.024
67. Ou C, Yuan R, Chai Y, Tang M, Chai R, He X (2007) A novel amperometric immunosensor based on layer-by-layer assembly of gold nanoparticles-multi-walled-carbon nanotubes-thionine multilayer films on polyelectrolyte surface. *Anal Chim Acta* 603:205–213. doi:10.1016/j.aca.2007.08.052
68. Pacey GE, Puckett SD, Cheng L, Khatib-Shahidi S, Cox JA (2005) Detection of DNA damaging agents, using layer-by-layer assembly. *Anal Chim Acta* 533:135–139. doi:10.1016/j.aca.2004.11.011
69. Sassolas A, Leca-Bouvier BD, Blum LJ (2008) DNA biosensors and microarrays. *Chem Rev* 108:109–139. doi:10.1021/cr068037a
70. Grieshaber D, MacKanzie R, Vörös J, Reimhult E (2008) Electrochemical biosensors – sensor principles and architectures. *Sensors* 8:1400–1458
71. Hang TC, Guiseppi-Elie A (2004) Frequency dependent and surface characterization of DNA immobilization and hybridization. *Biosens Bioelectron* 19:1537–1548. doi:10.1016/j.bios.2003.12.014
72. Diamandis EP, Christopoulos TK (1991) The biotin-(Strept)Avidin system: principles and applications in biotechnology. *Clin Chem* 37:625–636
73. Singh R, Sumana G, Verma R, Sood S, Sood KN, Gupta RK, Malhotra BD (2010) Fabrication of *Neisseria gonorrhoeae* biosensor based on chitosan-MWCNT platform. *Thin Solid Films* 519:1135–1140. doi:10.1016/j.tsf.2010.08.057
74. Decker H, Tuzek F (2000) Tyrosinase catecholoxidase activity of hemocyanins: structural basis and molecular mechanism. *Trends Biochem Sci* 25:392–397. doi:10.1016/S0968-0004(00)01602-9
75. Lupu S, Lete C, Balaure PC, Caval DI, Mihailciuc C, Lakard B, Hihn J-Y, Del Campo FJ (2013) Development of amperometric biosensors based on nanostructured tyrosinase-conducting polymer composite electrodes. *Sensors* 13:6759–6774. doi:10.3390/s130506759
76. Nistor C, Emneus J, Gorton L, Ciucu A (1999) Improved stability and altered selectivity of tyrosinase based graphite electrodes for detection of phenolic compounds. *Anal Chim Acta* 387:309–326. doi:10.1016/S0003-2670(99)00071-9
77. Cosnier S, Szunerits S, Marks RS, Lellouche JP, Perie K (2001) Mediated electrochemical detection of catechol by tyrosinase-based polycarbazole/electrodes. *J Biochem Biophys Methods* 50:65–77. doi:10.1016/S0165-022X(01)00176-2

78. Tembe S, Kubal BS, Karve M, D'Souza SF (2008) Glutaraldehyde activated eggshell membrane for immobilization of tyrosinase from *Amorphophallus campanulatus*: application in construction of electrochemical biosensor for dopamine. *Anal Chim Acta* 612:212–217. doi:10.1016/j.aca.2008.02.031
79. Lu L, Zhang L, Zhang X, Huan S, Shen G, Yu R (2010) A novel tyrosinase biosensor based on hydroxyapatite–chitosan nanocomposite for the detection of phenolic compounds. *Anal Chim Acta* 665:146–151. doi:10.1016/j.aca.2010.03.033
80. Apetrei IM, Apetrei C (2013) Amperometric biosensor based on polypyrrole and tyrosinase for the detection of tyramine in food samples. *Sens Actuators B* 178:4046. doi:10.1016/j.snb.2012.12.064
81. Ameer Q, Adejolu SB (2009) Development of a potentiometric catechol biosensor by entrapment of tyrosinase within polypyrrole film. *Sens Actuators B* 140:5–11. doi:10.1016/j.snb.2009.03.056
82. Teles FRR, Fonseca LP (2008) Applications of polymers for biomolecule immobilization in electrochemical biosensors. *Mater Sci Eng C* 28:1530–1543. doi:10.1016/j.msec.2008.04.010
83. Odaci D, Kayahan SK, Timur S, Toppare L (2008) Use of a thiophene-based conducting polymer in microbial biosensing. *Electrochim Acta* 53:4104–4108. doi:10.1016/j.electacta.2007.12.065
84. Akyilmaz E, Kozgus O, Türkmen H, Çetinkaya B (2010) A mediated polyphenol oxidase biosensor immobilized by electropolymerization of 1,2-diamino benzene. *Bioelectrochemistry* 78:135–140. doi:10.1016/j.bioelechem.2009.09.003
85. Lupu S, Lakard B, Hihn J-Y, Dejeu J (2012) Novel in situ electrochemical deposition of platinum nanoparticles by sinusoidal voltages on conducting polymer films. *Synth Met* 162:193–198. doi:10.1016/j.synthmet.2011.11.031
86. Lupu S, Del Campo FJ, Muñoz FX (2012) Sinusoidal voltage electrodeposition and characterization of conducting polymers on gold microelectrode arrays. *J Electroanal Chem* 687:71–78. doi:10.1016/j.jelechem.2012.09.035
87. Lupu S, Lete C, Balaure PC, Del Campo FJ, Muñoz FX, Lakard B, Hihn J-Y (2013) In situ electrodeposition of biocomposite materials by sinusoidal voltages on microelectrodes array for tyrosinase based amperometric biosensor development. *Sens Actuators B* 181:136–143. doi:10.1016/j.snb.2013.01.060
88. Lee HJ, Park TH, Choi JH, Song EH, Shin SJ, Kim H, Choi KC, Park YW, Ju B-K (2013) Negative mold transfer patterned conductive polymer electrode for flexible organic light-emitting diodes. *Org Electron* 14:416–422. doi:10.1016/j.orgel.2012.11.015
89. Jensen OW, Desai S, Shepherd RL, Innis PC, Jensen BW, Forsyth M, Wallace GG, MacFarlane DR (2010) Ion effects in REDOX cycling of conducting polymer based electrochromic materials. *Electrochem Commun* 12:1505–1508. doi:10.1016/j.elecom.2010.08.019
90. Soto-Oviedo MA, Araújo OA, Faez R, Rezende MC, De Paoli M-A (2006) Antistatic coating and electromagnetic shielding properties of a hybrid material based on polyaniline/organoclay nanocomposite and EPDM rubber. *Synth Met* 156:1249–1255. doi:10.1016/j.synthmet.2006.09.003
91. Lee UJ, Lee S-H, Yoon JJ, Oh SJ, Lee SH, Lee JK (2013) Surface interpenetration between conducting polymer and PET substrate for mechanically reinforced ITO-free flexible organic solar cells. *Sol Energy Mater Sol Cells* 108:50–56. doi:10.1016/j.solmat.2012.09.004
92. Wang CY, Tsekouras G, Wagner P, Gambhir S, Too CO, Officer D, Wallace GG (2010) Functionalised polyterthiophenes as anode materials in polymer/polymer batteries. *Synth Met* 160:76–82. doi:10.1016/j.synthmet.2009.10.001
93. Zeybek B, Pekmez NÖ, Kılıç E (2011) Electrochemical synthesis of bilayer coatings of poly(*N*-methylaniline) and polypyrrole on mild steel and their corrosion protection performances. *Electrochim Acta* 56:9277–9286. doi:10.1016/j.electacta.2011.08.003
94. Lupu S, Lete C, Marin M, Totir N, Balaure PC (2009) Electrochemical sensors based on platinum electrodes modified with hybrid inorganic–organic coatings for determination of 4-nitrophenol and dopamine. *Electrochim Acta* 54:1932–1938. doi:10.1016/j.electacta.2008.07.051

95. Soares JC, Brisolari A, Rodrigues VC, Sanches EA, Gonçalves D (2012) Amperometric urea biosensors based on the entrapment of urease in polypyrrole films. *React Funct Polym* 72:148–152. doi:10.1016/j.reactfunctpolym.2011.12.002
96. Ru X, Shi W, Huang X, Cui X, Ren B, Ge D (2011) Synthesis of polypyrrole nanowire network with high adenosine triphosphate release efficiency. *Electrochim Acta* 56:9887–9892. doi:10.1016/j.electacta.2011.08.063
97. Gvozdenović MM, Jugović BZ, Bezbradica DI, Antov MG, Knežević-Jugović ZD, Grgur BN (2011) Electrochemical determination of glucose using polyaniline electrode modified by glucose oxidase. *Food Chem* 124:396–400. doi:10.1016/j.foodchem.2010.06.046
98. Radhapyari K, Kotoky P, Khan R (2013) Detection of anticancer drug tamoxifen using biosensor based on polyaniline probe modified with horseradish peroxidase. *Mater Sci Eng C* 33:583–587. doi:10.1016/j.msec.2012.09.021
99. Rodrigues VC, Moraes ML, Brisolari A, Soares JC, Ferreira M, Gonçalves D (2011) Polypyrrole/phytase amperometric biosensors for the determination of phytic acid in standard solutions. *Sens Actuators B* 160:222–226. doi:10.1016/j.snb.2011.07.038
100. Maubane MS, Mamo MA, Nxumalo EN, van Otterlo WAL, Coville NJ (2012) Tubular shaped composites made from polythiophene covalently linked to Prato functionalized *N*-doped carbon nanotubes. *Synth Met* 162:2307–2315. doi:10.1016/j.synthmet.2012.10.020
101. Zhijiang C, Ruihan Z, Xingjuan S (2012) Preparation and characterization of polyindole nanofibers by electrospinning method. *Synth Met* 162:2069–2074. doi:10.1016/j.synthmet.2012.09.019
102. Teodorescu F, Lete C, Marin M, Munteanu C, Totir ND (2013) A novel glucose biosensor based on poly(azulene-co-3-thiophene acetic acid) conducting films. *Rev Chim* 64:15–21
103. Schuhmann W, Huber J, Mirlach A, Daub J (1993) Covalent binding of glucose oxidase to functionalized polyazulenes. The first application of polyazulenes in amperometric biosensors. *Adv Mater* 5:124–126. doi:10.1002/adma.19930050211
104. Abasiyamk MF, Şenel M (2010) Immobilization of glucose oxidase on reagentless ferrocene-containing polythiophene derivative and its glucose sensing application. *J Electroanal Chem* 639:21–26. doi:10.1016/j.jelechem.2009.11.001
105. Komathi S, Gopalan AI, Kim S-K, Anand GS, Lee K-P (2013) Fabrication of horseradish peroxidase immobilized poly(*N*-[3-(trimethoxy silyl)propyl]aniline) gold nanorods film modified electrode and electrochemical hydrogen peroxide sensing. *Electrochim Acta* 92:71–78. doi:10.1016/j.electacta.2013.01.032
106. Benyoucef A, Boussalem S, Ferrahi MI, Belbachir M (2010) Electrochemical polymerization and in situ FTIRS study of conducting polymers obtained from *o*-aminobenzoic with aniline at platinum electrodes. *Synth Met* 160:1591–1597. doi:10.1016/j.synthmet.2010.05.020
107. Mehretie S, Admassie S, Tessema M, Solomon T (2012) Electrochemical study of niclosamide at poly(3,4-ethylenedioxythiophene) modified glassy carbon electrode. *Sens Actuators B* 168:97–102. doi:10.1016/j.snb.2012.02.035
108. Wang Y, Xu H, Yang X, Luo Z, Zhang J, Li G (2012) All-solid-state blood calcium sensors based on screen-printed poly(3,4-ethylenedioxythiophene) as the solid contact. *Sens Actuators B* 173:630–635. doi:10.1016/j.snb.2012.07.064
109. Fang A, Ng HT, Li SFY (2003) A high-performance glucose biosensor based on monomolecular layer of glucose oxidase covalently immobilised on indium–tin oxide surface. *Biosens Bioelectron* 19:43–49. doi:10.1016/S0956-5663(03)00133-7
110. Martínez-Huitle CA, Suely Fernandes N, Ferro S, De Battisti A, Quiroz MA (2010) Fabrication and application of Nafion®-modified boron-doped diamond electrode as sensor for detecting caffeine. *Diamond Relat Mater* 19:1188–1193. doi:10.1016/j.diamond.2010.05.004
111. Esseghaier C, Bergaoui Y, Ben Fredj H, Tlili A, Helali S, Ameur S, Abdelghani A (2008) Impedance spectroscopy on immobilized streptavidin horseradish peroxidase layer for biosensing. *Sens Actuators B* 134:112–116. doi:10.1016/j.snb.2008.04.016

Development of Nanostructures by Electrochemical Method for Chemical Sensors

38

Surajit Kumar Hazra and Sukumar Basu

Contents

Introduction.....	1197
High Surface Area.....	1198
Effect of Nanocrystalline Grains.....	1198
Effect of Noble Metal.....	1199
Brief Review of Electrochemically Grown Sensing Materials.....	1201
Theory of Electrochemistry and Electrochemical Growth of Nanostructured and Nanoporous Thin Films.....	1205
Current Density Concern.....	1207
Growth Methods.....	1209
Basic Electrochemical Equations Highlighting Growth and Etching.....	1210
Structural, Morphological, Optical, and Electrical Characterizations of Electrochemically Grown Thin Films.....	1210
X-Ray Diffraction (XRD).....	1210
Morphological Studies (SEM, TEM, AFM).....	1212
Optical Studies.....	1220
Photocurrent Transient Measurement.....	1222
Hot Probe, Four-Probe Resistivity, and Hall Effect Measurements.....	1223

S.K. Hazra

Department of Physics and Materials Science, Jaypee University of Information Technology,
Waknaghat, Solan, HP, India

e-mail: surajithazra@yahoo.co.in

S. Basu (✉)

IC Design and Fabrication Centre, Department of Electronics and Telecommunication
Engineering, Jadavpur University, Kolkata, WB, India

e-mail: sukumarbasu@gmail.com

© Springer International Publishing Switzerland 2016

M. Aliofkhaezaei, A.S.H. Makhlof (eds.), *Handbook of Nanoelectrochemistry*,
DOI 10.1007/978-3-319-15266-0_23

1195

Fabrications of Nanochemical Sensors by Electrochemical Method.....	1226
Choice of Substrate	1226
Device Structure Fabrication.....	1226
Sensing Procedure	1228
Sensor Performance Using Different Gases and Chemicals.....	1229
Fundamentals	1229
Sensor Parameters	1231
Sensor Performance of Different Porous Materials	1231
Response of Electrochemically Grown Oxides to Volatile Organic Compounds.....	1237
Selectivity and Stability of the Chemical Sensors Fabricated from Electrochemically Grown Nanosized Oxide Materials	1237
Summary and Conclusion.....	1242
References.....	1243

Abstract

Innovations based on nanotechnology are introduced in the field of chemical sensors to reduce the sensor dimensions and increase the surface-to-volume ratio and for low power operation of a reliable sensor with faster response and quicker recovery. The formation of nanoporosity with controlled dimensions is another important parameter of the superior nanomaterials and thin films for chemical sensors. The response time can be reduced to as low as millisecond by the choice of appropriate nanostructures, and the selectivity can be improved to a large extent. Thus the material properties can be tailored to enhance the sensor performance. The electrochemical anodization is one of the modern techniques to meet the above challenges. This simple yet versatile method introduces a significant difference for achieving superb nanostructure morphology by manipulating the simple parameters like electrolyte composition, concentration, conductivity, and anodization voltage. It is realized by now that the electrochemical method can control the architecture from well-separated nanostructures to densely packed arrays where the aspect ratio can be monitored by selecting the appropriate electrolyte, the anodization voltage, and UV radiation. Moreover, the electrochemical anodization can be performed at room temperature that can avoid the grain growth and degradation of the grown materials, normally experienced in high-temperature growth technique. This chapter also highlights the appropriate characterization methods for nanocrystalline and nanoporous materials and thin films. The state-of-the art chemical sensors using electrochemically grown nanostructures of ZnO, TiO₂, SnO₂, and porous silicon are analytically discussed. The updated relevant literature references are included in the chapter.

Keywords

Electrochemistry • Anodization • Nanostructure • Thin films • Characterizations • Chemical sensors

Introduction

Electrochemistry is a classical branch of science. The electrochemical methods are applied commercially for decades in different arenas of technology. The electrochemistry and the electrochemical technology have also taken important roles in the material preparations because of their simplicity and economic advantages. Of late, the emergence of nanomaterials and nanotechnology has brought a revolution in almost all the technological aspects. Electrochemical technology has also shown its mettle in the preparation of high-quality nanomaterials and thin films. Nano-thin film formation by anodization is fairly popular nowadays. The thin films of nano-size semiconductor materials including the oxides are useful for electronic, optoelectronics, solar cells, and sensors. The special advantage of electrochemical deposition method over the other conventional physical and chemical methods is the ease of forming porous materials and thin films in the nanocrystalline form. Photoelectrochemical etching can facilitate the formation of nanoporous materials with well-defined pore size, pore volume, and thickness by illuminating the substrate surface during anodization. The aspect ratio of the nanoporous materials are much better controlled for solar cell and chemical sensor applications. In fact, the creation of porosity by photoelectrochemical etching has given birth to a new area of porous silicon technology. By controlling the etching rate during thin film growth, one can produce macro-, micro-, and nanoporous configurations useful for the fabrication of various electronic devices.

“Chemical sensors are devices that respond to external stimuli to convert it into an appropriate output signal mostly electrical in nature” [1]. Chemical sensors are mostly used in process industries, environmental monitoring, extraterrestrial exploration, defense, domestic safety, and biomedical diagnosis. Normally chemical sensors are widely known for gas, vapor, and humidity sensing; however, their sensitivity toward liquid analyte is also appreciable. They are active devices and need external power for their operations. A resistive sensor device is the simplest of its kind that manifests a change in resistance by interactions with analyte gases or vapor molecules. Generally, chemical gas sensors are widely used for safety applications, e.g., detection of poisonous (e.g., CO, NO_x) and/or inflammable gases (e.g., CH₄, H₂). They are also used to control climatic conditions inside the buildings and vehicles by monitoring the air quality. There is a growing interest to create large active surface area within a very small geometrical configuration to improve the efficiency of the gas sensors. The emergence of nanotechnology has made this task relatively easy. The use of nanocrystalline and nanoporous materials has considerably increased the surface area of interaction with the analyte, and therefore the device performance of sensors has also improved. The use of wide band gap oxides like ZnO, SnO₂, and TiO₂ is very lucrative to the researchers for the fabrication of chemical sensors. Apart from the oxides, abundantly available conventional semiconductor like silicon has been used ever since the Taguchi sensors were invented. Nowadays, emergence of nanotechnology has made possible the use of nanoporous silicon for sensing purposes.

Generally, nanostructure-based sensors are much faster and more efficient than the conventional solid state sensors. Kong et al. [2] has reported an increase of efficiency by almost an order of magnitude for single-walled carbon nanotube-based sensors. The factors to improve the performance of chemical gas sensors and the role of nanoelectrochemistry are discussed below. There are reports of varieties of thin films that have been deposited by electrochemical method. However, the present chapter is restricted to oxides and porous silicon thin films that are mostly used for chemical sensor applications.

High Surface Area

The main advantage of introducing nanodimensions in the sensor devices is the improvement of the sensor performance. Especially since the operating temperature has been reduced considerably, the sensitivity has been increased, and the response time and recovery time have been reduced due to the increased surface-to-volume ratio of the sensor configuration. For a solid spherical particle, the surface-to-volume ratio is inversely proportional to the particle radius, and its surface density (defined as area per unit mass) is $(6/\rho d)$, where “ ρ ” and “ d ” are density of material and diameter of the particle, respectively. This indicates that a change in particle diameter from micro- to nanodimension leads to an increase in surface density by an order of 10^3 . So, the decrease in particle size allows greater accumulation of atomic clusters on the surface compared to that in the bulk. This undoubtedly increases the catalytic effect of the material and improves chemical sensing. Parallely, it can be argued from theoretical point of view that for cylindrical pore (open at both ends) of wall thickness “ t ” and wall height “ h ,” the surface density, given by $(2/\rho t + 2/\rho h)$, increases with either the decrease in wall thickness or decrease in wall height. However, it is not feasible because the growth of porous nanostructure proceeds in a particular direction. So, it is obvious that wall thickness will have decreasing trend and wall height will have an increasing trend during growth. But the electrochemical anodization can achieve this by the self-adjustment of the etching process. In this technique, once well-defined pores are formed, the rest of the nanostructure growth is defined by the directional electrochemical etching. This directional etching is often amplified by optical illumination (usually UV radiations). Since for a hollow cylinder, the internal curved surface area is less exposed compared to the base of the pore to intense radiation, the etching is more significant at the base rather than the pore wall. As a result, the height increases with the increase in etching time.

Effect of Nanocrystalline Grains

The nanocrystalline grains display a monumental role in improving the performance of a chemical sensor. In fact, the selectivity of a chemical sensor can be conveniently controlled by nanocrystalline grains. A one-dimensional hollow tube can be

considered as a single phase or a multiphase with the reduced dimension. By reducing the grain size, an extra surface is exposed, and the boundary between two grains contains defects like vacancies and dangling bonds that control the transport properties of nanomaterials. By minimizing the interface energy either by exchanging or by sharing electrons with other atoms, the grain boundary interface can be stabilized. Thus, a space charge layer can be created, and it is dependent on the Debye length. The width of this space charge layer (L_S) is defined as follows:

$$L_S = L_D \left[\frac{2eV}{k_B T} \right]^{1/2} \quad \text{where Debye length, } L_D = \left[\frac{s_0 s k_B T}{2e^2 N_D} \right]^{1/2}, \quad (1)$$

where V is the barrier height, N_D is the ionized donor density, and ϵ is the permittivity.

At a particular temperature, the ionized donor density is constant, and so the width is proportional to the square root of the barrier potential. When the space charge is depleted of electrons, the barrier potential maximizes. During sensing, the electrons generated at the sensing electrode by solid–gas interactions traverse through the material, and the potential barrier height is reduced. The modulation of the barrier potential leads to the change in the space charge layer width, L_S , and three cases may arise out of this change, viz., D (grain size) $\gg 2L_S$, $D > 2L_S$, and $D \leq 2L_S$. For large grains ($D \gg 2L_S$), the grain remains unaffected by change in L_S , and therefore, the conductivity is governed only by the grain boundary contact. When D is slightly greater than $2L_S$, the space charge region extends deep into the grains, and the conductivity is now controlled by grain boundary area as well as by neck areas arising due to the space charge width. However, when $D \leq 2L_S$, the depletion region extends into the whole grain, and the conductivity is fully controlled by neck cross-sectional area. The electron transport is controlled by the charges generated during solid–gas interaction. So, it is obvious that the grain size can influence the size dependence sensitivity [3–7] (Fig. 1) and the nanomaterials can improve the sensor performance.

Effect of Noble Metal

The gas sensor performance can be significantly improved using noble metals which act as catalyst in the solid–gas interactions. Basically, these noble metals increase the rate of dissociation of analyte test gases without themselves getting chemically transformed. The noble metals can be incorporated in the nanostructure as (i) thin film electrode on the material surface and/or (ii) dispersed phase on the oxide or porous silicon surface. There are reports of the applications of nanoporous noble metal thin films as the electrode contact onto the metal oxides [9, 10]. M. Lofdahl [11] studied the role of noble metal gate morphology for sensing hydrogen and hydrocarbons. The other technique to use noble metal catalysts is to modify the material surface by dispersion. This is a wet chemical process, in which noble metal salt solutions are used. The dispersion is done either by dip coating in the

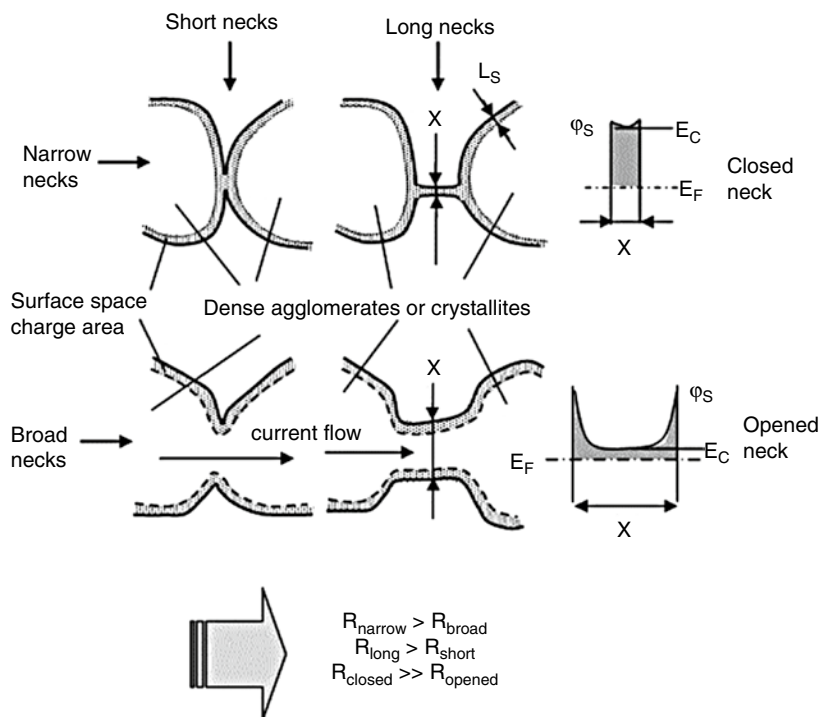
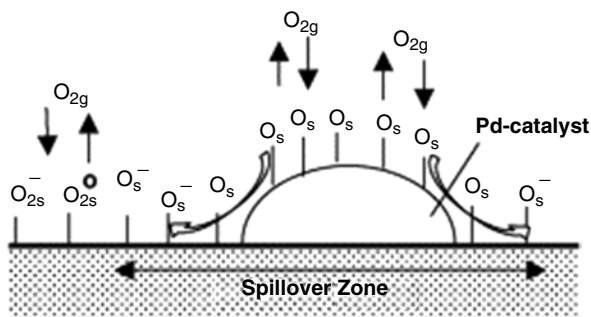


Fig. 1 Diagram illustrating the role of necks in the conductivity of polycrystalline metal oxide matrix and the potential distribution across the neck (Reprinted with permission from Korotcenkov [8]. Copyright: Elsevier)

noble metal salt solution or by putting a drop of the noble metal salt solution on the material surface, followed by low temperature drying. The dispersion can also be possible by electrochemical method. The noble metal solution can be added to the electrolyte to deposit the metal on the thin film substrate in the dispersive manner by cathodic deposition method. By the electrochemical method, the density of dispersion may be controlled more precisely by adjusting the concentration of the noble metal salt in the electrolyte. Moreover, nanoporosity of the dispersed noble metals may be better achieved by electrochemical means.

The surface modification passivates to a large extent the surface defect states which act as charge trapping sites during the sensing process. Basically, charges generated at the sensing electrode during solid–gas interaction must reach the receiving electrode for maximum response. However, if most of them get trapped during the charge transfer process, the response magnitude gets reduced and the sensor performance deteriorates. The catalytic additive used for surface modification segregates into microscopic islands on the materials surface and acts as the activator for the surface reactions. Such activation can be explained on the basis of “collective” and “local” site concepts. The idea of “collective” site along with the

Fig. 2 Spillover process on active surface
(Reprinted with permission from Korotcenkov [13].
Copyright: Elsevier)



chemisorption theory was proposed by F. Volkenstein [12]. It provides the concept of how the adsorbate affects the overall band structure of the modified semiconducting matrix. This theory correlates the catalytic activity of the modifier directly to the valence state of the dopant in the material and their influence on the charge carrier concentration in the semiconductor. In fact, the surface space charge develops due to chemisorptions on the modified semiconductors. In case of materials with the nanodimension, where the grain sizes are very small, the surface and the bulk properties merge due to the penetration of the space charge layer into the whole grain. So, the change in conductivity is mostly due to the catalytic effect of the modifier. On the other hand, the “local” sites approach is based on the consideration of a nonuniform semiconducting surface, whose interaction with the gas phase leads to the formation of surface complexes. In this model, the chemical nature of the modifier and its reactivity during the redox reactions play a vital role. The spilled-over species migrate to the intergranular contact as shown in Fig. 2. Fine dispersion of the catalyst on the semiconducting matrix ensures solid–gas interaction near all intergranular contacts. Moreover, the influence of dimensional effects such as the size of surface clusters and the average distance between two catalytic clusters does also play an important role. It has been reported that the surface cluster size should not exceed 1–5 nm and the optimal distance between the clusters should approximately be equal to the oxygen surface diffusion length at the suitable operating temperature [14–17]. The nanoelectrochemistry is one of the most promising technologies for achieving these optimal conditions.

Brief Review of Electrochemically Grown Sensing Materials

The prime concern in the development of sensor technology is the choice of materials. To achieve a useful sensing device, it is necessary to understand design parameters like size, cost, and durability. The transducer part, i.e., reading the sensor device output in terms of resistance, current, voltage, capacitance, etc., is also influenced by the choice of sensor materials. Basically all these concerns need to be addressed a priori to streamline the sensor parameters like sensitivity, response, recovery, selectivity, and drift. Obviously a single material cannot satisfy all the criteria [18].

Metal oxide materials are widely used due to their ability to sense a wide spectrum of test gases. They are able to operate at low as well as elevated temperatures and also in harsh environments without much deterioration. It is also possible to develop quantum confinement effect in the nano-oxides by controlling the grain size. Therefore, the tailor-made energy band gap can be developed. The oxides are relatively inexpensive and so are preferred for large-scale productions. Furthermore, it is easy to introduce nanomorphology onto metal oxide surfaces [19].

Titanium dioxide is an important material for chemical gas sensor applications in harsh industrial environments and at low as well as high temperatures by developing anatase or rutile crystal lattice. Titania-based devices are mainly used as oxygen sensors [20, 21]; however, their sensing property in the reducing ambient is also reported [22, 23]. With proper control of the microstructure, crystalline phase, and/or addition of impurities or surface functionalization, this material can also be used for the detection of reducing gases. Particle size reduction and generation of porosity from micrometer down to nanometer are positive approaches for improving the sensor performance [24]. Creation of nanopores or nanotubes is of utmost importance for highly sensitive and fast-responding chemical sensors.

A large section of the researchers have devoted toward the development of nanostructured ZnO since the reactions at the grain boundaries and a complete depletion of the carriers in the grains can strongly modify the material transport properties of ZnO. Nanocrystalline ZnO thin films have good gas-sensing properties when the crystallite size is of the order of Debye length. The response of nanograin ZnO is comparatively high because of the grain size effect. ZnO nanorod with Pd clusters showed very high and fast response toward hydrogen at relatively low power [25].

SnO₂-based gas sensors were developed in 1970 by Taguchi [26]. SnO₂ has high reactivity to reducing gases at relatively low operating temperatures due to the easy adsorption of oxygen on its surface because of the non-stoichiometry of SnO₂. Also, the possibility of tailoring SnO₂ sensing properties exists, by introducing nanocrystallinity and porosity. Surface modification using noble metals improves the properties of this material for sensing certain gases. The performance of tin dioxide is also related to its particle characteristics and composition which can be varied with dopant [27–32]. The gas sensitivity of SnO₂ can be explained on the basis of crystallite dimension and Debye length. By decreasing the crystallite size, the interparticle necks become thin and long. As a matter of fact, electrons might face resistance depending on the size of the necks. For SnO₂, if the particle size is less than 10 nm, the mechanical properties, viz., strength, is deteriorated [28]. Furthermore, as-prepared nanomaterials generally need some pretreatment at elevated temperatures before sensor applications, the nanoparticles may agglomerate thereby increasing the particle size. So, the whole purpose of reducing the particle size may be lost in such cases. However, an optimum particle size is desirable for efficient sensing.

It is found that porosity in the active matrix improves the sensor performance. However, the amount of porosity is directly related to the amount of surface.

Hence, a highly porous surface has very large surface area for solid–gas interactions. Electrochemical anodic oxidation is a convenient technique to grow microporous and nanoporous materials even at room temperature. Gong et al. [33] developed uniformly oriented porous titania nanostructures by anodic oxidation of high-purity titanium in hydrofluoric acid electrolyte under potentiostatic bias. The pore diameter as reported by Gong et al. varied from 15 nm to 30 nm. Varghese et al. [34, 35] reported hydrogen sensitivity of the titania nanostructures grown from high-purity titanium both at high temperature and at room temperature. For these sensor structures, the reduction of sensor temperature down to room temperature was achieved by incorporating Pd catalytic layer. Shimizu et al. [36] deposited TiO₂ films with nanosized holes on Ti plate by electrochemical anodization in 0.5 M H₂SO₄ aqueous solution at 20 °C. These porous films were then contacted with palladium for hydrogen sensor study. The structures were fast responsive and highly sensitive at 250 °C under a reverse bias of 0.1 V. Iwanaga et al. [37] prepared TiO₂ thin films by anodic oxidation of Ti plates in 0.5 M H₂SO₄ electrolyte at different temperatures and studied the hydrogen sensitivity with palladium catalytic contact under forward and reverse bias conditions. The current–voltage (I–V) characteristics of the sensor structures were ohmic in 0.8 % H₂ in N₂. Such nanostructures of the oxide materials not only have sensor applications, but it can be used for dye-sensitized solar cells [38–41], hydrogen generation by water photoelectrolysis [42–49], photocatalytic reduction of carbon dioxide [50], etc. These structures possess good charge transfer ability with negligible carrier annihilation. Porosity can also be generated in titania matrix by potentiostatic electrochemical as well as photoelectrochemical etching. Sugiura et al. [51, 52] fabricated TiO₂ nano-honeycomb structure in 0.1 M H₂SO₄ aqueous electrolyte under potentiostatic condition by illuminating the electrodes with a high-pressure mercury arc lamp for the applications as photocatalysts and dye-sensitized solar cells. Similar study was also reported by Hazra et al. [53] for hydrogen sensors.

Porous ZnO films have been prepared by electrochemical anodization process [54]. In the recent past, templating of colloidal crystals was one of the most attractive methods used to obtain a porous structure. Both two- and three-dimensional-ordered porous zinc oxide films were fabricated by electrodeposition using three-dimensional polystyrene opal templates and alumina templates. A template-free electrochemical deposition route to ZnO nanoneedle arrays and their optical and field emission properties were reported by Bingqiang Cao et al. [55]. A constant current supply method was studied by Atsushi Ashida et al. [56] for the preparation of ZnO thin films on sapphire substrate to study the growth rate of the films. It was found that samples grown with relatively larger currents showed small grains without sharp edges. Only the samples grown with currents in the range of 22–71 μA/cm² showed large XRD intensities and hexagonal grains with sharp edges. Chi-Jung Chang et al. [57] studied the electrochemical deposition of ZnO pore-array structures. ZnO films with hexagonal-packed pores were fabricated on indium tin oxide (ITO) from an aqueous solution of 0.1 M Zn(NO₃)₂ at 80 °C by the electrochemical deposition and microsphere lithography method.

There are reports of the fabrication of nanoporous tin dioxide film by electrochemical anodization technique [58]. Mesoporous SnO₂ has been used for ethanol sensing. The central pore sizes in mesoporous SnO₂ are 4.1 nm, 6.1 nm, and 8.0 nm [59]. These ethanol sensors exhibit fast response and recovery to low concentration of ethanol gas. Porous SnO₂ foam fabricated by electrochemical anodization was found to have good gas sensing properties [60]. The anodization was carried out in sulfuric acid and tin sulfate electrolyte. The working assembly used was tin film coated on SiO₂/Si substrate. Various test gases (H₂, CO, NH₃, NO_x, and C₂H₅OH) were used to study the response of SnO₂ foams. The foams showed selectively higher response toward ethanol vapor.

The different research groups have utilized the crystalline silicon or silicon carbide as the substrates to fabricate Schottky diodes for sensor applications [10, 61–64], keeping in mind the development of smart systems-on-chip using silicon IC technology. Since crystalline silicon is an insensitive sensing material due to negligible interactions with oxidizing and reducing chemicals and gases, nanocrystalline porous silicon (PS) is gaining importance as a potential platform for chemical sensors and photonic devices [64–70]. The extremely large surface-to-volume ratio of PS (≥ 500 m²/cm³), the ease of its formation, and the control of the surface morphology through variations of the formation parameters have drawn considerable attention for chemical sensors.

The most efficient and effective method to generate PS layer is the electrochemical etching of silicon crystal either in HF and methanol/ethanol [71, 72] or HF and water or HF and N,N dimethylformamide (DMF) [73] as the electrolyte. The pore geometry can be controlled by passing current for a fixed duration of time and by UV radiation. The pore morphology of the PS layer is characterized by the pore size distribution, the mean size of the pores, the void fraction or porosity, the interconnectivity of the pores, the passivation, and the mean size of the skeleton enclosing the pores. The quality of the PS depends on the additives in the electrolyte solution and doping concentration of the silicon wafer [74].

A simple and cheap supersensitive gas detector is based on resistive PS elements [75, 76]. Researchers at the University of Brescia, Italy, have patented a technique using a porous silicon membrane on alumina substrate which could sense NO₂ down to the concentrations of 100 parts per billion (ppb) at room temperature and at low power, with a minimum interference from the contaminant organic vapors [77–79].

Therefore, the branch of electrochemistry is so much useful for developing the nanomaterial and nanoporous thin films for the use in modern devices, e.g., optoelectronic, photonic, and chemical sensors. Some recent information on the development of chemical sensors using nanostructured and nanoporous thin films developed by electrochemical method are presented in this chapter. The electrochemical method is simple and relatively less hazardous as it can be operated in a close environment and at room temperature. Also, there are provisions for doping the materials and for creating porosity with defined dimensions by using the source of illumination during deposition. A brief description of the above discussions is summarized in Table 1.

Table 1 Brief summary in the tabulated format

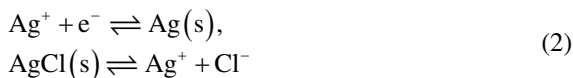
Characteristics/materials	Remarks
Nanomorphology	Nanostructured material morphologies make sensors faster and more efficient [2]
Nanocrystalline grains and their boundaries	The barrier potential is responsible for the width of the space charge layer, and the conductivity is modulated by the variation of the space charge [3–7]
Noble catalytic metals	Used as thin film electrode on the material surface [9–11] and/or dispersed phase on the material surface [14–17]
Metal oxide materials	Easy to introduce nanomorphology for better performance [18, 19]
Titanium dioxide	Suitable chemical sensor material for robust applications. Initially used as oxygen sensing material; however, it is useful for reducing gases as well [20–24] Easy to anodize in different electrolytes to generate nanolevel porosity for applications like chemical sensors, solar cells, etc. [33–53]
Zinc oxide	A versatile material for many applications and especially used to fabricate chemical sensor devices with surface-modified films [25] Nanostructures could be generated using both template-assisted and template-less techniques [54–56]
Tin dioxide	This oxide has high activity toward reactive gases. Also, the activity can be tuned by altering its material composition [27–32] Electrochemical anodization technique is implemented to enhance the solid–gas or solid–vapor interaction ability of tin dioxide [58–60]
Porous silicon	A smart and potential platform for applications in sensing and photonic devices due to very high surface-to-volume ratio [64–70] Electrochemical etching of crystalline silicon in acid medium is the preferred technique to generate porosity; the porous morphology can be modified by using suitable additives in the electrolyte [71–74]

Theory of Electrochemistry and Electrochemical Growth of Nanostructured and Nanoporous Thin Films

In an electrolytic conductor, the ions carry charges, unlike free electrons in metallic conductors. The conduction path in an electrolytic solution is completed with the metallic electrical contacts (electrodes) to and from the electrolyte. Such a system with immersed electrodes in an electrolytic solution constitutes an electrochemical cell assembly. This assembly is useful to grow and/or etch the oxide films at room temperature. The electrode where such deposition/growth/etching occurs is called the anode, and the other metallic electrode is called the cathode. So, this process is sometimes called anodization technique, and the anode and cathode are also called working and counter electrodes, respectively. However, the deposition of pure metal films or metallic dispersions on a substrate can be achieved on the cathode.

The two electrodes are often accompanied by a reference electrode. A reference electrode is an electrode which has a stable and well-known electrode potential with

respect to standard hydrogen electrode. The stability of the electrode potential is usually reached by employing a redox system with saturated concentrations of components. For example, Ag/AgCl reference electrode has a long Ag wire dipped in a solution saturated with AgCl. KCl is added to stabilize the AgCl solution. This combination functions as a redox system based on the equations written below:



The electrochemical potential is given by the Nernst equation:

$$E = E_o + \frac{RT}{nF} \ln a_i, \quad (3)$$

where E_o is the standard electrode potential, i.e., the potential difference between the electrode and the solution, when the activity, a_i , of the ions is unity. F , R , n , and T are Faraday's constant, gas constant, number of electrons involved, and temperature, respectively. For Ag/AgCl reference electrode, the Nernst equation is

$$E = E^o + \frac{RT}{F} \ln \frac{1}{a_{\text{Cl}^-}} = E^o - \frac{RT}{F} \ln a_{\text{Cl}^-}, \quad (4)$$

where E_o against standard hydrogen electrode (SHE) is $0.230 \text{ V} \pm 10 \text{ mV}$.

When the electrochemical potential varies from its standard value due to the application of an external potential, either a reduction (i.e., formation of solid) or an oxidation (i.e., formation of ions) takes place until the new equilibrium is reached. This difference in potential is called the overpotential or overvoltage. This overpotential has to be carefully controlled to avoid electrolysis of solvent or deposition of impurity phases; so electrochemical processes are normally performed using a good potentiostat which functions in the feedback mode with the help of the reference electrode.

Basically the reference electrode divides the electrochemical cell into two half cells. The reference electrode is used as a half cell to build an electrochemical cell. This allows the potential of the other half cell to be determined accurately. As a matter of fact, concepts like anodization under constant voltage condition (i.e., potentiostatic) and anodization under constant current (i.e., galvanostatic) arise from these electrochemical phenomena. In the potentiostatic condition, a fixed supply voltage is maintained between anode and cathode, and the current changes depending on the resistance of the path. Normally for oxide growth, potentiostatic conditions are preferable due to continuous increase in the path resistance owing to the growth of barrier oxide films. However, galvanostatic conditions can also be implemented for oxide growth provided we have higher power rating of the system.

The choice of the electrolytes for electrochemical deposition is important. The electrolyte must not dissolve the growing oxide or the rate of dissolution must be very slow, so that a substantial amount of oxide layer remains on the electrode after the process is completed. This is a prime concern when barrier oxide films are deposited. Sometimes, dissolution property of the electrolyte is necessary, if there is

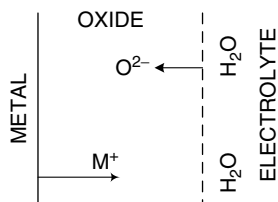
requirement to grow a porous matrix. Therefore, electrolyte composition also determines whether the film will be a barrier layer or a porous layer. Basically, barrier layers are formed in neutral solution (most commonly ammonium borate, phosphate, or tartrate compositions), which hardly has any dissolving power. For porous oxide growth, acid-based electrolytes are suitable because along with oxide deposition they also favor dissolution in certain directions to generate porous channels. The most common choice of acid electrolytes is dilute sulfuric acid, typically about 1 M or 10 wt% in concentration. Hydrofluoric acid (HF)-based electrolytes (0.5 wt%) are also used to generate porous morphology [33, 80–84]. Addition of acetic acid to 0.5 % HF electrolyte in a ratio of 1:7 yields robust nanostructures [85, 86]. A combination of 2.5 % HNO_3 and 1 % HF water solution (with or without boric acid) can be used to carry out anodization at 20 V. This will result in high current densities for the formation of oxide coatings [87]. In this way, several combinations can be made with fluoride-based electrolytes. So, far, the use of mixed electrolytes like ($\text{H}_2\text{SO}_4/\text{HF}$), ($\text{H}_2\text{Cr}_2\text{O}_7/\text{HF}$), ($\text{CH}_3\text{COOH}/\text{NH}_4\text{F}$, $\text{H}_2\text{SO}_4/\text{NH}_4\text{F}$), and ($\text{H}_3\text{PO}_4/\text{HF}$, $\text{H}_3\text{PO}_4/\text{NH}_4\text{F}$) have been reported [88–93]. If a very thin film is desired, the weak electrolyte like phosphoric acid is used for slow growth kinetics of the formation of oxide films [94].

Current Density Concern

Metals can be readily anodized under potentiostatic conditions. However, metals have the inherent tendency to develop a thin native oxide layer (2–3 nm thick) in air ambient to stabilize the surface against further reactions and thereby to protect the bulk purity. Such a piece of metal, when used for anodization, in a neutral electrolyte, will not allow much current to flow at low voltages due to the presence of the native barrier layer. So, a high voltage is applied to start the current conduction. This happens because the electric field is high enough to drive electrons. Also in the presence of such high field, oxidation of solvents like water can happen, and oxygen may evolve. However, oxygen evolution is not observed in the case of pure metals. So, it is obvious that the oxide blocks electrons moving into the direction from electrolyte to metal. Therefore, the high field drives metal and oxygen ions through the oxide layer. Basically, the current through the oxide is an ionic current, and these ions react to form the oxide layer. The process of high-field ionic conduction is the sole mechanism in anodization. Oxygen ions move inward to react with the metal, at the metal/oxide interface, to form oxide. Metal cation moves outward from the metal to react with water at the oxide/electrolyte interface to form oxide at that surface. The schematic of basic ion transport at metal–electrolyte interface is shown below (Fig. 3).

At the counter cathode, the electronic process is completed by the reduction of hydrogen ions to hydrogen gas. The rate of the oxide growth is proportional to the current density (A/cm^2). The field (V/m) inside the oxide layer remains constant with time if the potentiostatic conditions are employed. So, the voltage drop increases as the barrier oxide layer becomes thicker. If the voltage drop is not

Fig. 3 Schematic of ion transport through the oxide films



uniform, the current will change and as a result the current density will vary. So, a less resistive path, implying low voltage drop and hence high current density, will accelerate the barrier layer formation and vice versa. Therefore, for the uniformity of thickness across the surface of anodization, the voltage drop must be the same. This becomes significant when the barrier layer formation and dissolution in certain favorable directions occur to generate porous morphology. At the pore regions, the current density increases due to reduced barrier layer thickness. For an electrolytic composition at a certain temperature, there is a limit to the maximum voltage that can be tolerated before the breakdown of the dielectric barrier layer starts. At the breakdown, oxygen evolution, solute oxidation, or sparking due to electron avalanche through the oxide may occur in addition to the oxide growth. A dilute electrolyte enhances the ionization process by creating large number of mobile ions to maintain the high current density. Hence, the rate of anodization and the breakdown voltage are higher with the dilute electrolyte. However, it is not apparent from this discussion how the pores initiate. Usually, a surface has some degree of roughness. This may be due to the fabrication processes, such as rolling, chemical etching, cleaning, etc., prior to anodization or due to evaporation-assisted film deposition followed by annealing. Initially, the anodized oxide film growing on ridges and bulges becomes thicker than in the depressions because the ions move through oxide more easily at these ridge–bulge locations possibly due to higher film stress or high current concentration in these locations. Gradually, the oxide thickness becomes more uniform at the ridges and bulges, and the concentration of current shifts toward concave depressions where the oxide layer is thin and the electric field is high. Therefore, the field-assisted dissolution/breakdown is initiated. As a result, the thinning of the local oxide layer is likely to occur because of high current concentration at those locations. Thus, the pore formation starts, and as the steady state is reached, the size and the distribution of the pores are stabilized.

The development of the porous morphology due to the variation of potential and current density is also significant. Taveira et al. [95] anodized Ti foil using a constant current density, and they reported the tubular structure of the diameters in the range 40–50 nm and 60–90 nm by using the current density of 0.5 mA/cm² and 1.0 mA/cm², respectively. Basically, when anodization starts, a compact oxide layer is formed first, and the voltage drop maximizes. So, the current through the circuit slowly decreases from a maximum initial value to the saturation. At the point of dissolution, the growth rate balances the dissolution rate because of the change of the path resistance leading to the variations of potential and current and eventually reaches equilibrium. However, this equilibrium can be perturbed by an external optical irradiation. For example, the

oxides are wide band gap materials, and so their optical absorption is maximum in the ultraviolet (UV) range. If UV rays are incident on the anode surface during anodization, the additional positively charged holes are generated that increase the rate of dissolution, and so the equilibrium is disturbed.

Growth Methods

High-purity metallic foils of either titanium or zinc or tin (~0.2 mm thick) is usually chosen as the starting material for the growth of metal oxides by electrochemical method. The samples are cut to desired sizes and are thoroughly washed in acetone, methanol, dilute hydrochloric acid, and deionized water successively. They are then used as anode in a Teflon/quartz electrochemical cell containing the electrolyte. Normally, a platinum counter electrode and Ag/AgCl reference electrode (Fig. 4)

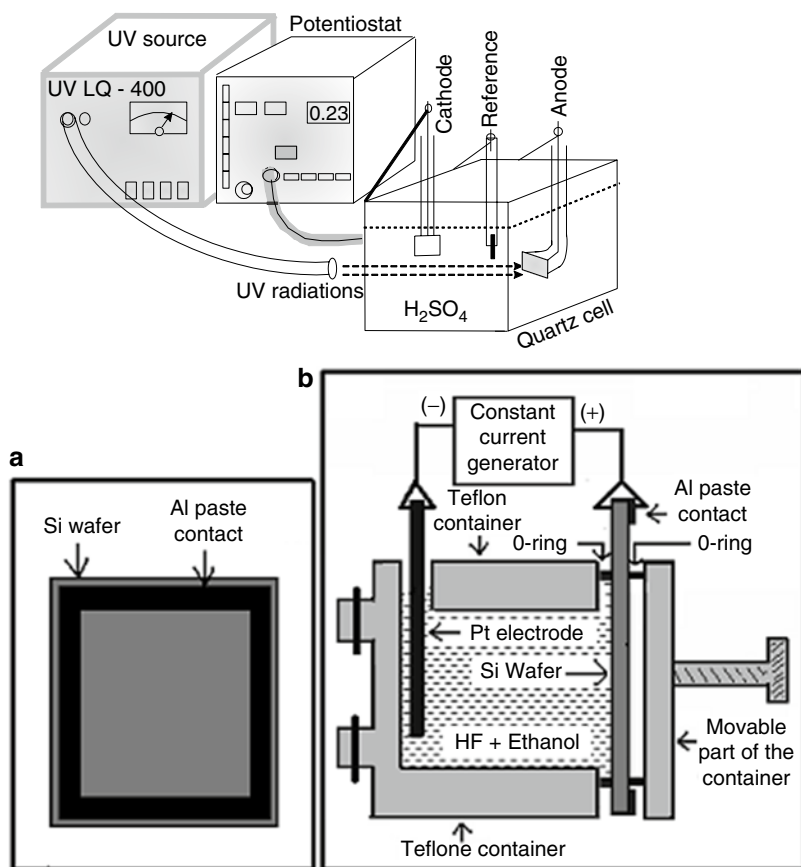


Fig. 4 Electrochemical etching assembly (Reprinted with permission from Hazra and Basu [96] and Kanungo et al. [98]. Copyright: Elsevier)

are used [96, 97]. The anodization can be carried out at a potentiostatic or a galvanostatic condition. For developing a porous structure, the oxide anode surface is illuminated with an ultraviolet (UV) radiation for photoelectrochemical etching. As mentioned earlier, UV radiation helps to generate excess holes in the material matrix, and this enhances the dissolution process. After the completion of oxide growth and etching, the samples need to be thoroughly washed with deionized water and dried in ambient air. The oxide surface may be annealed at a moderate temperature of 300–400 °C for 15–30 min to stabilize the surface structure.

For porous silicon formation, silicon wafers with the resistivity in the range of 2–5 Ωcm are normally chosen, and the anodization is carried out in a mixture of HF and ethanol as the electrolyte. The typical electrochemical etching assembly for porous silicon formation is shown in Fig. 4 [98]. Since, fluoride electrolytes attack glass and quartz, the Teflon container is used for porous silicon formation. For faster rate of pore formation a light of wavelength corresponding to the band gap energy of silicon (~ 1.1 eV) or higher may be used during the electrochemical etching process.

Basic Electrochemical Equations Highlighting Growth and Etching

From the above discussions, it is apparent that the electrochemical method is convenient and simple for the growth of nanomaterials and nanoporous thin films. Moreover, the thickness and the porosity of the nano-thin film may be better controlled by precisely adjusting the voltage or current and the time duration of anodization. The added advantage of the anodization is room temperature operation thereby minimizing the possibility of defect generation on the oxide surface at high temperature. The use of nanocrystalline and nanoporous oxides and nanoporous silicon thin films for the development of nanochemical sensors has demonstrated that the electrochemical deposition can produce much superior nanomaterials for efficient sensing of gases and volatile organic compounds (VOC). The steps of electrochemical depositions mentioned in Table 2 above clearly show the unique and versatile mechanism for thin film deposition without any intentional inclusion or doping of impurity.

Structural, Morphological, Optical, and Electrical Characterizations of Electrochemically Grown Thin Films

X-Ray Diffraction (XRD)

X-ray diffraction (XRD) technique is utilized to check the crystallinity and identify the phases of the anodized materials. Normal angle XRD is not adequate to reveal the detailed information of thin films, and therefore, the glancing angle x-ray diffraction (GAXRD) is used. The incident X-ray beam is focused at a small angle on

Table 2 Growth and etching reactions

Material	
Titanium	$\text{Ti} \rightarrow \text{Ti}^{4+} + 4\text{e}^-$ $4\text{H}_2\text{O} \rightarrow 4\text{OH}^- + 4\text{H}^+ \text{ (In acidic medium)}$ $\text{Ti}^{4+} + 4\text{OH}^- \rightarrow \text{Ti}(\text{OH})_4$ $\text{Ti}(\text{OH})_4 \rightarrow \text{TiO}_2 + 2\text{H}_2\text{O} \text{ (Oxide formation)}$ $\text{TiO}_2 + 2\text{SO}_4^{2-} + 4\text{h}^+ \rightarrow \text{Ti}(\text{SO}_4)_2 + \text{O}_2 \text{ (Etching in H}_2\text{SO}_4)$ $\text{Ti} + \text{H}_2\text{O} \rightarrow \text{TiO}_2 + 2\text{H}^+ + 4\text{e}^- \text{, (Oxide formation acidic medium)}$ $2\text{H}^+ + 2\text{e}^- \rightarrow \text{H}_2 \text{, (at cathode)}$ $\text{TiO}_2 + 6\text{F}^- + 4\text{H}^+ \rightarrow \text{TiF}_6^{2-} + 2\text{H}_2\text{O} \text{, (Etching in HF)}$ $\text{Ti}(\text{OH})_4 + 6\text{F}^- \rightarrow \text{TiF}_6^{2-} + 4\text{OH}^- \text{,}$ $\text{Ti}^{4+} + 6\text{F}^- \rightarrow \text{TiF}_6^{2-} \text{,}$
Zinc	$\text{Zn} \rightarrow \text{Zn}^{2+} + 2\text{e}^- \text{,}$ $2\text{H}_2\text{O} \rightarrow 2\text{H}^+ + 2(\text{OH})^- \text{, (In acidic medium)}$ $\text{Zn}^{2+} + 2(\text{OH})^- \rightarrow \text{Zn}(\text{OH})_2 \text{,}$ $\text{Zn}(\text{OH})_2 \rightarrow \text{ZnO} + \text{H}_2\text{O} \text{,}$ $\text{ZnO} + \text{C}_2\text{H}_2\text{O}_4 + 2\text{h}^+ \rightarrow \text{ZnC}_2\text{O}_4 + \text{H}_2\text{O} \text{, (Etching in Oxalic acid)}$ $\text{OH}^- + \text{OH}^- \rightarrow \text{H}_2\text{O} + \text{O}^- \text{,}$ $\text{O}^- + \text{O}^- \rightarrow \text{O}_2 + 2\text{e}^- \text{,}$ $2\text{H}^+ + 2\text{e}^- \rightarrow \text{H}_2 \text{, (at cathode)}$
Tin	$\text{Sn} \rightarrow \text{Sn}^{4+} + 4\text{e}^- \text{,}$ $4\text{H}_2\text{O} \rightarrow 4\text{H}^+ + 4(\text{OH})^- \text{, (In acidic medium)}$ $\text{Sn}^{4+} + 4(\text{OH})^- \rightarrow \text{Sn}(\text{OH})_4 \text{,}$ $\text{Sn}(\text{OH})_4 \rightarrow \text{SnO}_2 + 2\text{H}_2\text{O} \text{,}$ $\text{SnO}_2 + 6\text{F}^- + 4\text{H}^+ \rightarrow \text{SnF}_6^{2-} + 2\text{H}_2\text{O} \text{,}$
Silicon	$\text{Si} + 6\text{F}^- + 4\text{h}^+ \rightarrow \text{SiF}_6^{2-} \text{, (Etching in HF acid)}$ $2\text{H}^+ + 2\text{e}^- \rightarrow \text{H}_2 \text{,}$

the surface of the specimen under investigation. This requires a very small divergence of the primary beam or the use of a narrow parallel beam.

GAXRD performed at 0.2° glancing angle shows the crystalline character of the oxidized zinc surface as shown in Fig. 5 [99]. It is evident from the figure that the intensity of ZnO peaks [100] and [101] decreases and that of Zn peak increases with decreasing molar concentration of oxalic acid from 0.3 to 0.05 M because of the lower oxidation rate. Practically negligible ZnO formation occurs at 0.01 M electrolyte as observed from the plot of Fig. 5.

Glancing angle X-ray diffraction technique was used to find out the crystalline nature of the surface of anodized titania thin film at different incident angles (0.2° , 0.5° , 1° , and 10°) [53]. With the increasing incident angle, the penetration depth of X-rays increases. Figure 6 displays that at low incident angles, the surface peak intensity of the rutile TiO_2 is higher than the bulk Ti_xO phases ($\text{Ti}_x\text{O} \equiv \text{Ti}_3\text{O}$ and Ti_6O), which are titanium-rich non-stoichiometric phases and are isostructural to titanium. It is observed that the intensities of Ti_xO phases are almost negligible for 0.2° glancing incidence angle. So, we can infer that the minimum incidence angle

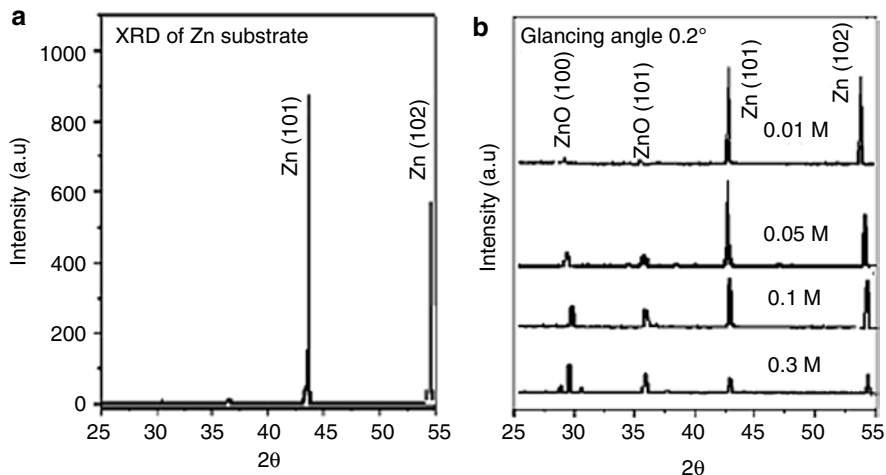


Fig. 5 XRD images of Zn substrate and deposited ZnO thin films at 0.2° glancing angle grown in different concentrations of aqueous oxalic acid electrolyte (Reprinted with permission from Basu et al. [99]. Copyright: Springer)

is required to obtain the surface information and, at higher incidence angle, the information for both bulk and surface are revealed by GAXRD.

Figure 7 [100] shows the GAXRD for as-prepared and modified porous silicon surfaces. The GAXRD analysis of the distribution of noble metals (Pt, Pd, and Ru) on the surface-modified porous silicon is also shown. The distribution of metal ions near the surface of porous silicon is apparent from the GAXRD plots.

Morphological Studies (SEM, TEM, AFM)

A field-emission cathode in the electron gun of a scanning electron microscope provides narrow probing beams at low as well as high electron energy, resulting in both improved spatial resolution and minimized sample charging and damage. FESEM produces distinct and less distorted images with spatial resolution down to 1–1/2 nm that is three to six times better than conventional SEM. Using FESEM, a high-quality and low voltage images are obtained with negligible electrical charging of the samples (acceleration voltages range from 0.5 to 30 kV).

Surface morphology of the ZnO thin films grown electrochemically using different concentrations of oxalic acid as electrolyte is shown in Fig. 8 [99]. The FESEM images reveal that ZnO thin film deposited in 0.05 M oxalic acid has poor crystalline feature and the sample in 0.01 M oxalic acid has only metallic Zn surface (Fig. 8c and d). This attributes to the lower oxidation rate at very low oxalic acid concentrations. On the other hand, nanocrystalline and nanoporous ZnO thin films were deposited in the increased oxalic acid concentrations (0.1 M, 0.3 M) as shown in Fig. 8a and b.

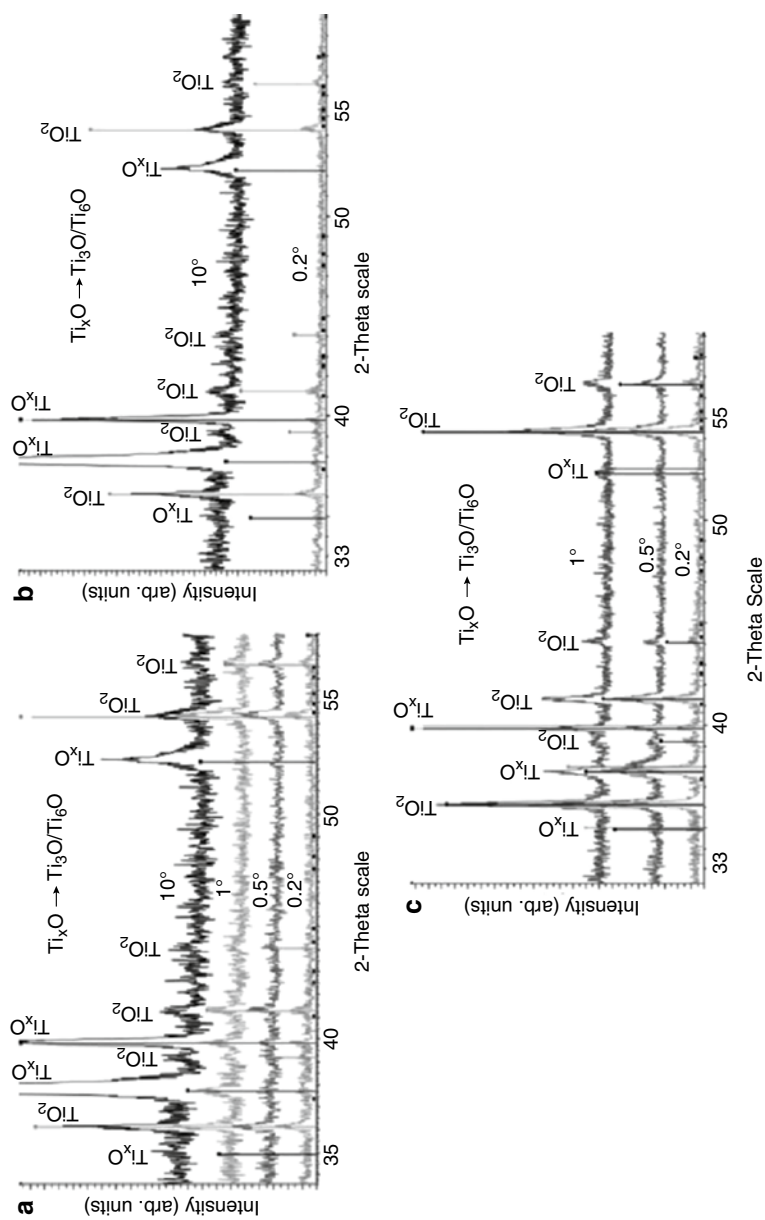


Fig. 6 GAXRD patterns of (a) the as-oxidized surface, (b) the dark etched surface, (c) UV light etched surface (Reprinted with permission from Hazra et al. [53]. Copyright: Elsevier)

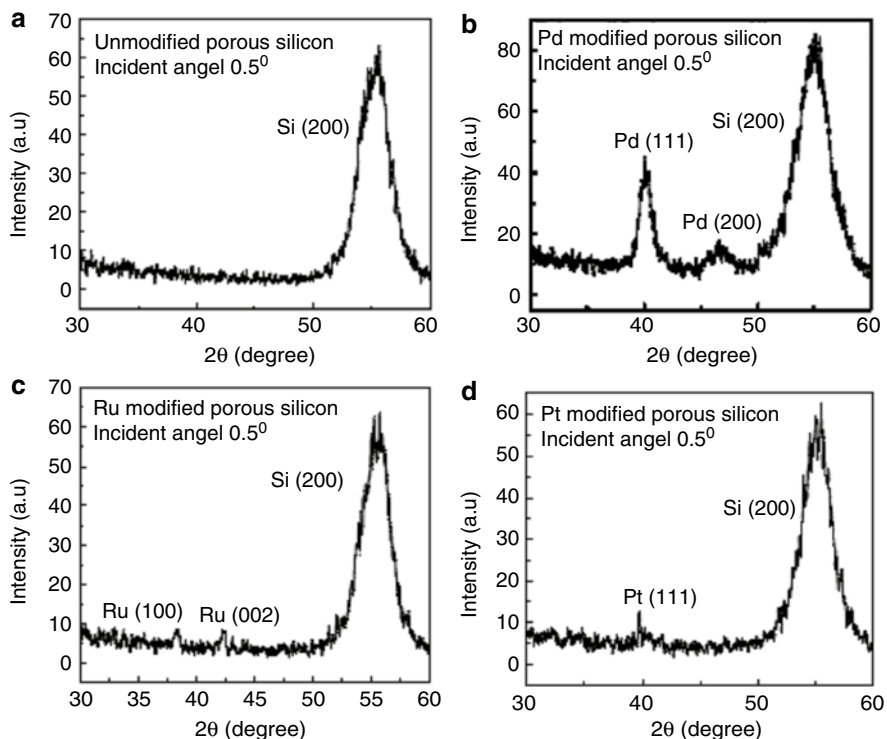


Fig. 7 GAXRD spectra at incidence glancing angle of 0.5° of (a) as-anodized porous silicon and metal-modified porous silicon using (b) 0.01 M PdCl_2 for 5 s, (c) 0.1 M RuCl_3 for 15 s, and (d) $0.01\text{ M K}_2\text{PtCl}_6$ for 15 s (Reprinted with permission from Kanungo et al. [100]. Copyright: Elsevier)

Scanning electron microscopy was employed to analyze the electrochemically etched titanium oxide surfaces using sulfuric acid electrolyte in the absence and presence of UV light illumination [53]. Figure 9 represents the polycrystalline nature of the oxide surface with tetragonal grains.

The tetragonal rutile grain size is reduced upon etching in acid medium. The grain size of the etched grains is in the range of 115–140 nm. Basically the electrochemical etching is governed by holes, and the grain boundaries or the bulk grains are selectively dissolved. A typical etching pattern appears on the oxide surface [51]. As the etching progresses in random directions, the oxide is removed from the surface, and the porosity is developed. However, the formation of uneven porosity is due to random surface orientations of the grains. When illuminated with UV light, the etching rate of the oxide surface is enhanced because of the excess holes generated in titania band. So, etching in the presence of UV light increases the depth of porosity. The grain size in the range of 100–250 nm was reported for UV-etched oxide samples.

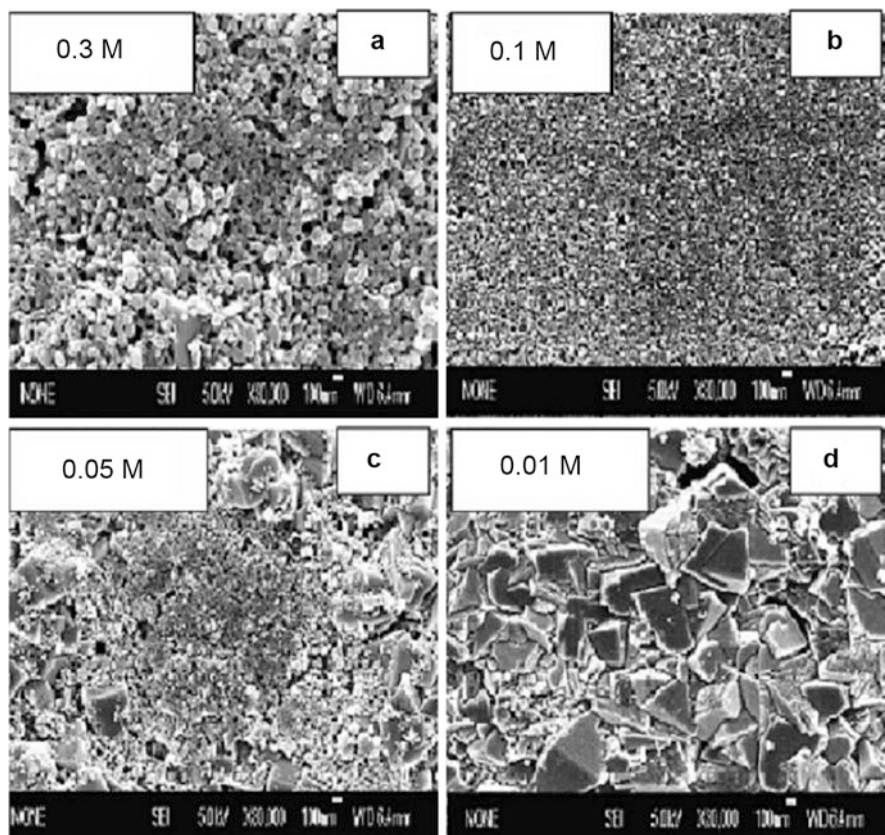


Fig. 8 (a–d) are the FESEM pictures of ZnO thin films obtained by anodic oxidation of Zn in different aqueous oxalic acid concentrations (Reprinted with permission from Basu et al. [99]. Copyright: Springer)

Due to the high etching rate in the presence of UV light, after a certain time, the underlying titanium layers may be exposed to the etching solution under the potentiostatic bias condition. Then the exposed titanium metal is anodically oxidized to titanium dioxide in 0.1 M sulfuric acid. However, the newly formed oxide cannot get strongly bonded to the substrate as it is etched once again. Hence, the newly formed oxide is deposited along the grain boundaries immediately after its formation and adheres to the skeleton porous structure. This may lead to nonuniform increase in the size of the grains as seen in Fig. 9.

Figures 10 and 11 represent the AFM pictures of the electrochemically etched surfaces. The rms roughness of the samples etched in the absence and presence of UV light are 36.309 nm and 123.04 nm, respectively. This is probably due to the fact that the etch pits are deeper and are frequently repeated on the surface. Basically surface roughness is defined as “the change in the profile of the surface in which the height and the depth of ridges and valleys vary in the nanometer order.”

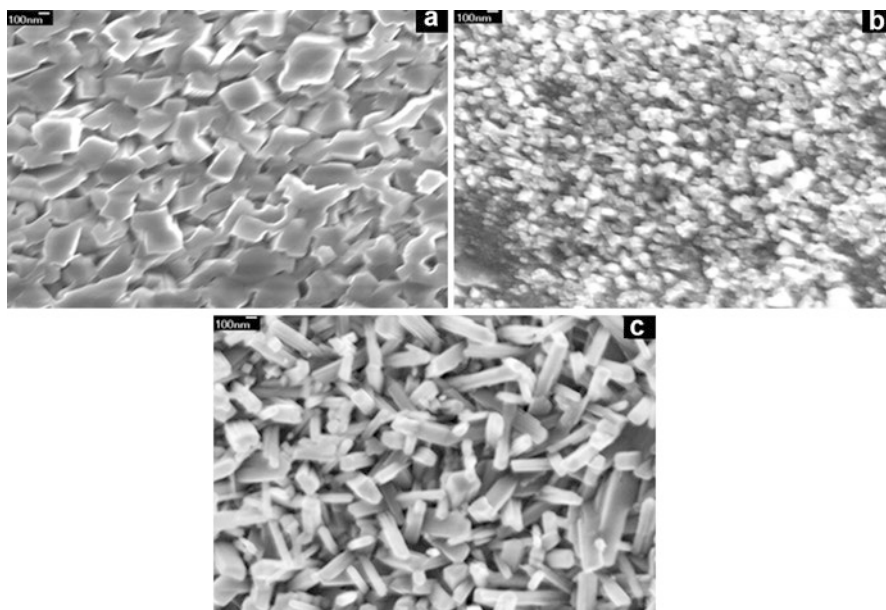


Fig. 9 Scanning electron micrographs of (a) as-grown oxide surface, (b) electrochemically etched surface, (c) photo (UV) electrochemically etched surface of titanium dioxide thin film (Reprinted with permission from Hazra et al. [53]. Copyright: Elsevier)

From the AFM data, the maximum height of a ridge/hill is 600 nm when the samples are etched without UV illumination. On the other hand, the minimum depth of samples etched in the presence of UV light is 1,000 nm. This demonstrates that the porous channels of the UV light-assisted-etched surfaces are deeper. But the width of the ridges/hills for the samples etched in the presence of UV light is relatively less as shown in Figs. 10b and 11b. So, the average aspect ratio (*height/width*) of a ridge/hill is high for the samples etched in the presence of UV light because “*h*” increases and “*w*” decreases. Since the increase in “*h*” is relatively higher than the decrease in “*w*,” the etching direction is more likely perpendicular to the surface.

The scanning electron microscopy technique was used to analyze the porous silicon (PS) surface modified with noble metals like Pd, Ru, and Pt [100]. Figure 12 shows the FESEM images of the PS surfaces before and after surface modifications. It is clearly observed that even after modifications, the porous silicon layer remains nanoporous in nature. For structural imaging, 10 KV accelerating voltage with In-lens detector was used, and all the images were taken without using any conducting coating over the sample surface in order to study the virgin state of the modified surface. The transverse section was investigated with EDX line scanning using Genesis EDAX Line Scan software for qualitative depth profiling. 20 KV potential and different magnifications were applied for identifying the metal particles/clusters. The agglomerated diameter of $\sim 5.8 \mu\text{m}$ was obtained for Pd island, whereas for

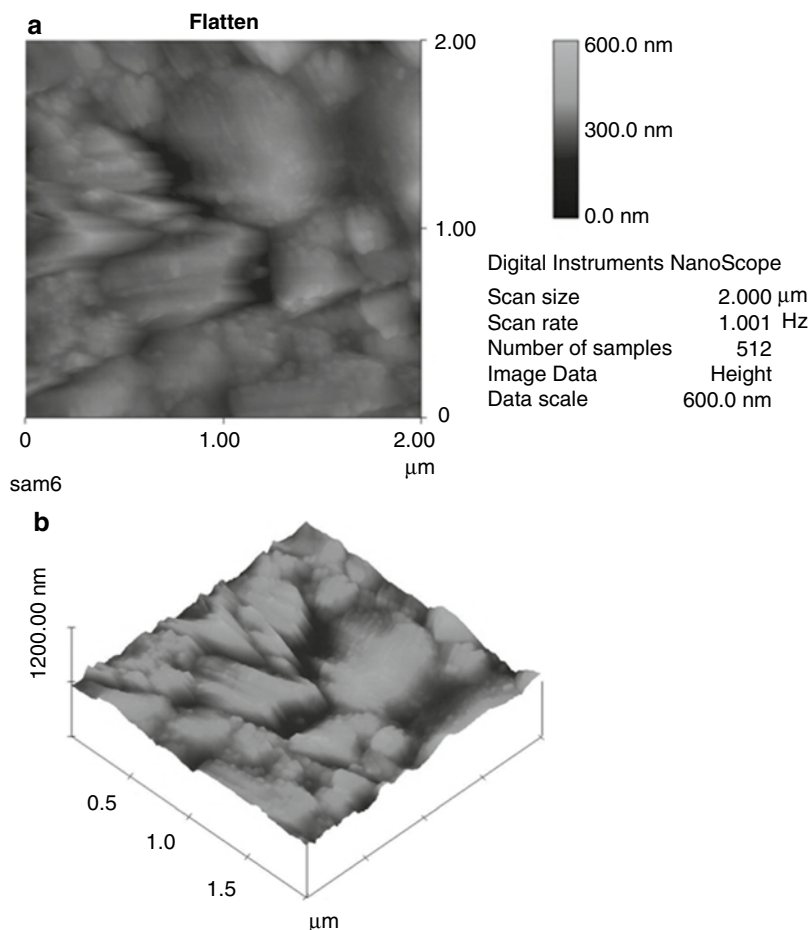


Fig. 10 AFM (a) topography and (b) surface image of the electrochemically etched titania surface without UV light (Reprinted with permission from Hazra et al. [53]. Copyright: Elsevier)

Ru and Pt, the size was reduced to $\sim 4.2 \mu\text{m}$ and $\sim 3.1 \mu\text{m}$, respectively. The Pd agglomerates are more frequently distributed over the uniform nanostructure of PS surface, whereas Ru and Pt are locally observed. Line scan analysis across the cross section of the modified PS sample confirms the presence of Pd and Ru in the surface structure but the rare presence of Pt. However, the presence of oxygen indicates the mild surface oxidation in the presence of noble metals. From the cross-sectional EDAX analysis shown in Fig. 13, the thickness of the PS layer (from the surface up to the depth where the Si intensity comes to a saturation value) was measured as $\sim 5 \mu\text{m}$.

Transmission electron microscopy (TEM) was employed to analyze the electrochemically grown single titania nanotube. The tube was grown at pH 5.0 and annealed at $600 \text{ }^\circ\text{C}$ [46, 101]. The TEM data revealed the anatase phase in the nanotube walls. Basically, titania exists in three phases, viz., brookite, anatase,

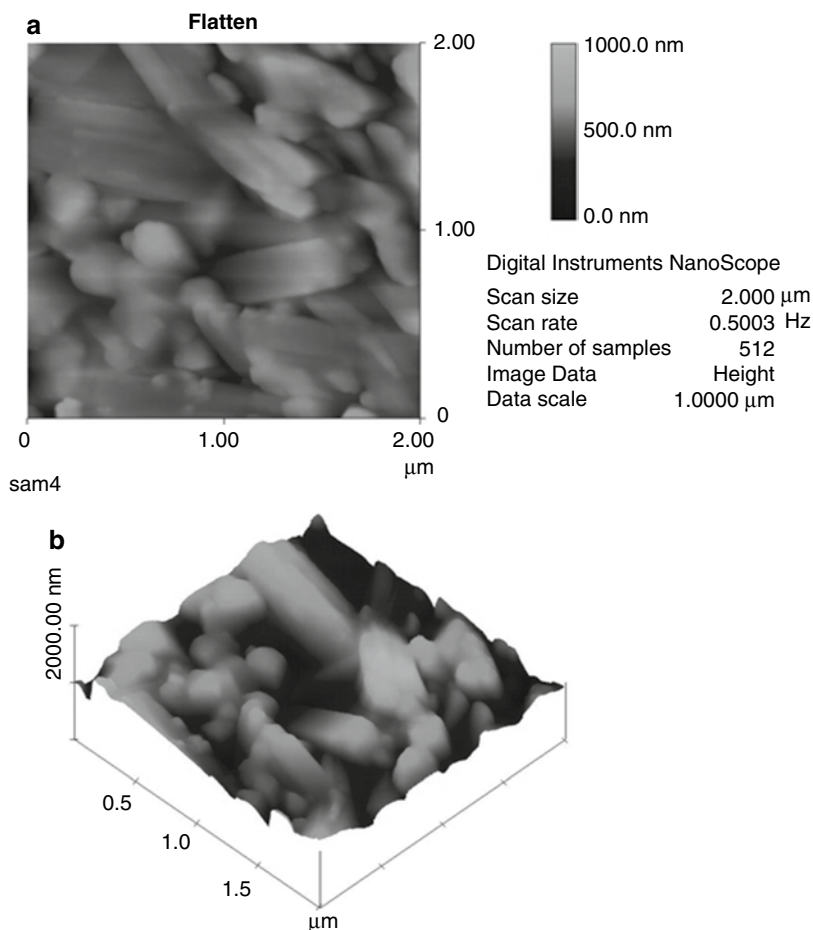


Fig. 11 AFM (a) topography and (b) surface image of the etched titania surface illuminated with UV light (Reprinted with permission from Hazra et al. [53]. Copyright: Elsevier)

and rutile. Brookite is the low temperature phase, anatase is the intermediate crystallinity (normally below 600 °C), and rutile is the most stable high-temperature phase. The conversion from anatase to rutile is irreversible. As-anodized titanium is amorphous and slowly derives its crystalline character upon annealing. This crystallinity in titania nanotube was reported using a model by Grimes et al. [102, 103]. As per this model, anatase crystals are formed at the nanotube–titanium interface due to high-temperature treatment. The rutile crystallites are then formed in the oxide matrix by phase transformation of anatase phase. The nanotube geometry also imposes some constraint on the phase transformation [46, 104, 105]. For annealing temperatures below 600 °C, it can be assumed that titania nanotubes have anatase crystallites stacked above rutile phase formed at the base of the nanotubes. Such results were also confirmed from high-resolution

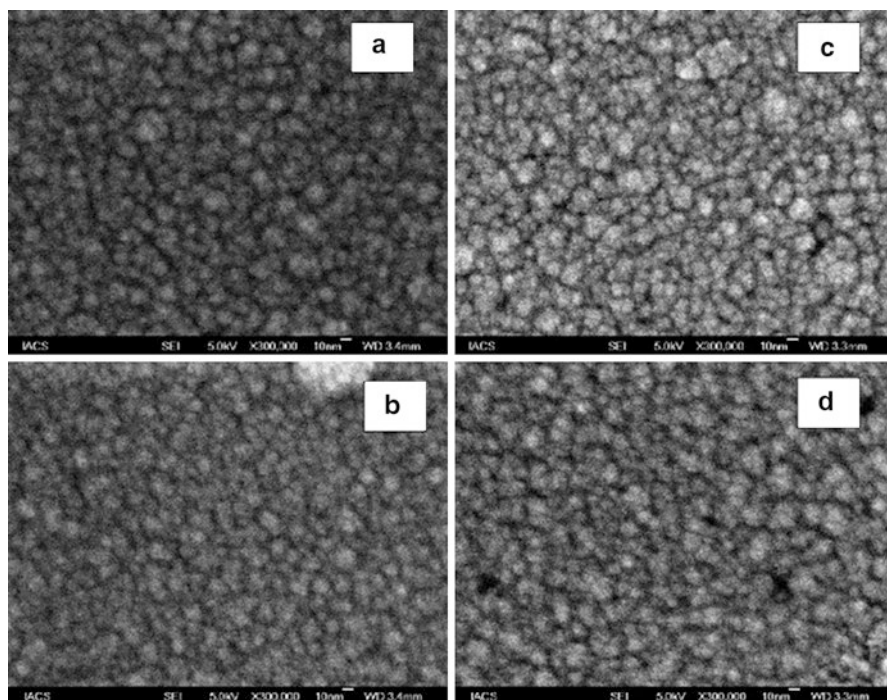


Fig. 12 FESEM of (a) unmodified, (b) Pd-, (c) Ru-, and (d) Pt-modified PS surfaces (Reprinted with permission from Kanungo et al. [100]. Copyright: Elsevier)

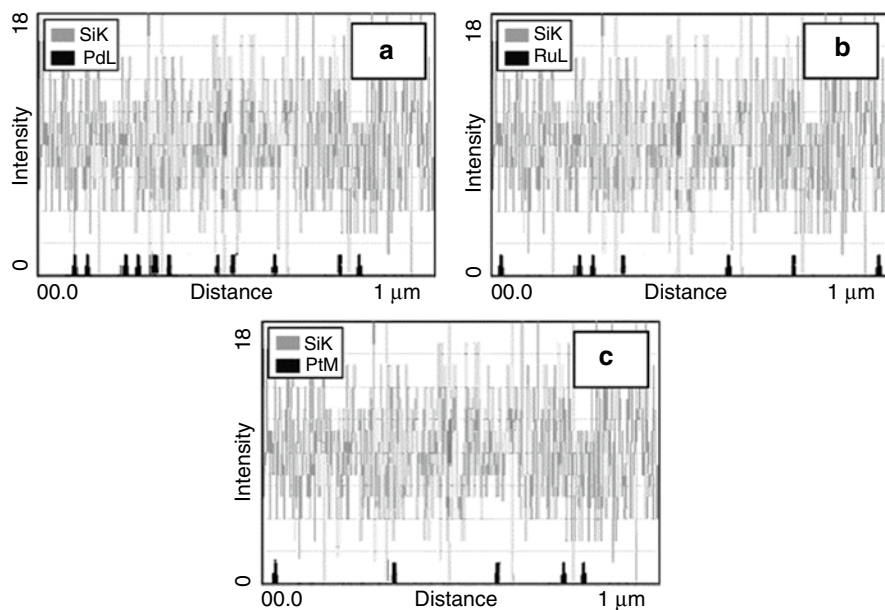


Fig. 13 EDAX line scan intensity distribution of (a) Pd-, (b) Ru-, and (c) Pt-modified PS surfaces (Reprinted with permission from Kanungo et al. [100]. Copyright: Elsevier)

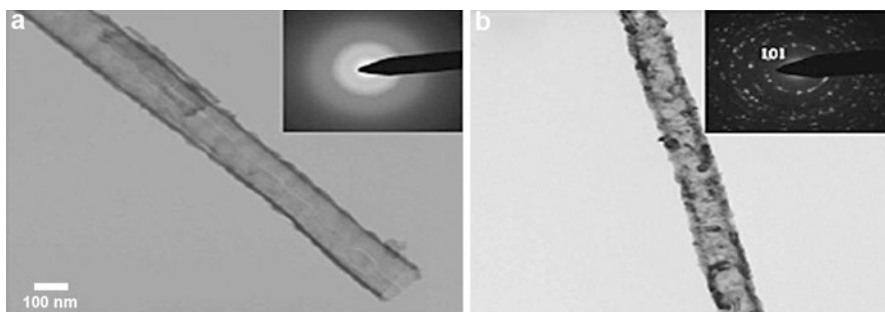


Fig. 14 High-resolution TEM images of a $\sim 45 \mu\text{m}$ long titania nanotube sample: (a) as-prepared and (b) after 550°C anneal in oxygen for 6 h. The corresponding selected area diffraction patterns are given in the insets (Reprinted with permission from Shankar et al. [38]. Copyright: IOP; doi:10.1088/0957-4484/18/6/065707)

transmission electron microscopy (HRTEM) studies carried out with $45 \mu\text{m}$ long titania nanotube grown electrochemically in mixed HF electrolyte at 40 V bias and are shown in Fig. 14 [38].

Optical Studies

The optical response of a material is used to determine its optical constant, required for various optical-related applications. The thin film of the material is normally used for the measurements of the optical reflectance, transmittance, and absorption. The optical data is generally evaluated by Swanepoel method [106], based on the idea of Manifacier [107] as the standard technique. According to this method, the envelope through the interference maxima and minima is drawn in the spectrum. The value of the refractive index of the thin film in the spectral region of medium and weak absorption is calculated by using the following expression:

$$n = \left[N + (N^2 - s^2)^{1/2} \right]^{1/2}, \text{ where} \quad (5)$$

$$N = 2s \frac{T_M - T_m}{T_M T_m} + \frac{s^2 + 1}{2}$$

and T_M and T_m are the transmission maxima and the transmission minima at a certain wavelength, λ , and “ s ” is the substrate refractive index. The basic equation for interference fringes is given by

$$2nd = m_o \lambda \quad (6)$$

The accuracy of the refractive index depends on the calculation of the thickness, d , of the film. “ m_o ” is an integer for maxima and a half integer for minima in the transmission spectra. If n_1 and n_2 are the refractive indices of two adjacent maxima

and minima at wavelengths λ_1 and λ_2 , the thickness of the film is given by the expression:

$$d = \frac{\lambda_1 \lambda_2}{2(\lambda_1 n_2 - \lambda_2 n_1)} \quad (7)$$

The extinction coefficient (k) can be obtained using the relation

$$k = \frac{\alpha \lambda}{4\pi}, \quad (8)$$

where α is the absorption coefficient [106] and is given by

$$\alpha = \frac{1}{d} \ln\left(\frac{1}{x}\right), \quad (9)$$

where “ x ” is the absorbance.

The optical behavior of the semiconductor and insulator materials can be utilized to calculate the optical band gap. However, the mode of measurement depends on the nature of the substrate on which the material is grown or deposited. For example, for glass, quartz, or any other transparent substrates, the transmission spectrum is recorded, but for nontransparent substrates the reflection/absorption spectra are considered.

The reflection spectrum of porous TiO_2 thin film deposited electrochemically on titanium substrate as obtained from UV–VIS–NIR spectrophotometer is shown in Fig. 15a. The absorption coefficient, α , and the optical band gap, E_g , of the material are related by the Tauc relation [108]

$$\alpha h\nu = A(h\nu - E_g)^n \quad (10)$$

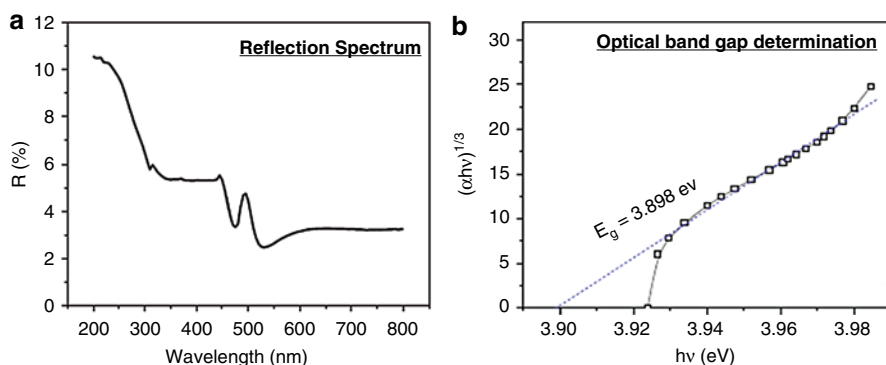


Fig. 15 Optical study of TiO_2 thin film grown electrochemically using soft drink electrolyte (a) reflection spectra and (b) optical band gap determination (Reprinted from Hazra et al. [94]. Copyright: Science and Engineering Publishing Company; OPEN ACCESS)

where “ E_g ” is the optical energy gap, “ A ” is constant, and the index “ n ” can have values 1/2, 3/2, 2, and 3, depending on the nature of electronic transition responsible for reflection. The absorption coefficient, α , is obtained from the relation,

$$2\alpha t = \ln\left[\frac{(R_{\max} - R_{\min})}{(R - R_{\min})}\right] \quad (11)$$

where “ t ” is the thickness of the film, R_{\max} and R_{\min} are maximum and minimum values of reflectance, and R is the reflectance at any photon energy, $h\nu$. Combining the above two equations,

$$\begin{aligned} \frac{1}{2t} \ln\left[\frac{(R_{\max} - R_{\min})}{(R - R_{\min})}\right] h\nu &= A(h\nu - E_g)^n \\ \Rightarrow h\nu \ln\left[\frac{(R_{\max} - R_{\min})}{(R - R_{\min})}\right] &= (2tA)(h\nu - E_g)^n \\ \Rightarrow \ln\left(h\nu \ln\left[\frac{(R_{\max} - R_{\min})}{(R - R_{\min})}\right]\right) &= n \ln(h\nu - E_g) + \ln(2tA) \end{aligned} \quad (12)$$

The above equation has a straight line characteristic, and the value of the power n can be obtained from the slope of the plot $\ln\left(h\nu \ln\left[\frac{(R_{\max} - R_{\min})}{(R - R_{\min})}\right]\right)$ versus $\ln(h\nu - E_g)$.

For the spectra shown in Fig. 15a, $n=3$ was obtained [94]. So, the optical band gap of the titania sample was determined by plotting $(\alpha h\nu)^{1/3}$ versus $h\nu$ and then extrapolating to $(\alpha h\nu)^{1/3} = 0$ (Fig. 15b).

Basu et al. reported the variation of the band gap of electrochemically grown nano-ZnO thin film by varying the molar concentration of the oxalic acid electrolyte [99] and showed that the band gap increases with the decreasing concentrations of oxalic acid. The widest band gap of 4.20 eV at room temperature was obtained by using 0.05 M oxalic acid electrolyte. This blue shift of the band gap of nanocrystalline ZnO film was further confirmed by photoluminescence spectra (Fig. 16) and was explained as due to the quantum size effect.

Photocurrent Transient Measurement

The nanostructures normally respond to light of appropriate wavelength. In transient photocurrent measurements, the porous layer is illuminated with a pulse of light, and the photo current generated is measured. Tsuchiya et al. [109] reported the photo current transient measurements of TiO₂ nanotubes using a light pulse of 350 nm wavelength. The exposure time was 10s. There was an initial increase of the current followed by a gradual decrease with time. The observed photocurrent was theoretically correlated with the equation

$$I_{ph}(t) = \{I_{ph}(t=0) - I_{ph}(t=\infty)\} \exp(-kt) + I_{ph}(t=\infty), \quad (13)$$

where k denotes a rate constant.

The annealed porous layer gave the lowest $k=0.14 \text{ s}^{-1}$ when compared with annealed compact layers. They found that the rate constants for the annealed compact layer and the as-formed compact layer were comparable (0.393 s^{-1} and 0.315 s^{-1}).

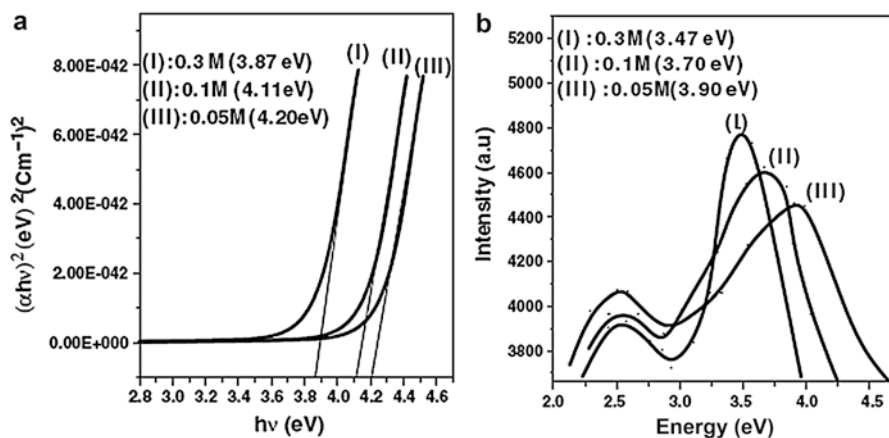


Fig. 16 Optical properties of ZnO thin films. **(a)** Optical absorption spectra and **(b)** PL spectra of nano-ZnO thin films obtained by anodization of Zn in different concentrations of oxalic acid. There is a significant increase in the optical band gap and PL energy of the film grown in 0.05 M oxalic acid due to blue shift (Reprinted with permission from Basu et al. [99]. Copyright: Springer)

Theoretically, the as-formed compact layer should have higher rate constant than annealed ones. Further, the samples without annealing showed continuous increase of the photocurrent with time during illumination. This phenomenon could be attributed to the filling of traps from the localized defect states introduced in the TiO₂ energy band gap during anodization and acting as the recombination centers. The unannealed porous layer could contain both shallow and deeper traps. During illumination the trap-filling behavior is prevalent, and the traps are preferentially filled with photogenerated charge carriers. So, to avoid the doubt and confusion, the above Eq. 13 was modified as

$$I_{ph}(t) = \{1 - \exp(-kt)\} \cdot \{I_{ph}(t = \infty) - I_{ph}(t = 0)\} + I_{ph}(t = 0), \quad (14)$$

and $k = 0.49 \text{ s}^{-1}$ was obtained for as-anodized porous layer by fitting the appropriate data. Photocurrent studies with porous ZnO, SnO₂, and silicon have been reported by other researchers [110–113].

Hot Probe, Four-Probe Resistivity, and Hall Effect Measurements

The semiconducting parameters of the grown nanostructures can be determined by hot electron probe, four-probe resistivity, and Hall effect measurements. Hot electron probe method is used to determine the type of conductivity of the semiconductors. A digital multimeter is attached to the sample, and a heat source (like soldering iron) is used to heat one terminal. The thermal energy causes charge carriers (electrons if n-type or holes if p-type) to move away from the heated lead. This generates

a voltage difference, and the sign of the voltage determines the type of conductivity. Four-probe arrangement with van der Pauw configurations is a convenient method to determine the material resistivity of a flat sample with arbitrary shape, because the resistivity can be measured without knowing the actual current paths. The sample needs to meet the following requirements:

1. The electrical contacts are on the perimeter of the sample.
2. The contacts are sufficiently small (compared to the dimensions of the sample).
3. The sample is uniformly thick.
4. The surface of the sample is singly connected, i.e., without isolated holes or other nonconducting macrodefects.

By this method, the measurements are quite accurate, and no additional correction factors have to be considered for the resistivity calculations.

As shown in Fig. 17 below, the two characteristic resistances R_A and R_B are related to the sheet resistance, R_S , by the van der Pauw equation

$$\exp\left(-\pi \frac{R_A}{R_S}\right) + \exp\left(-\pi \frac{R_B}{R_S}\right) = 1. \quad (15)$$

The current is passed between two adjacent contacts, while the voltage is measured between the two opposing contacts. The contacts are interchanged and the measurement is repeated. For accuracy, thus, for all possible combinations of adjacent contacts, four pairs of measurements are done. The two resistances are then calculated as an average of the respective resistances of the opposing pairs of contacts, e.g., $R_A = (R_{21;34} + R_{12;43} + R_{43;12} + R_{34;21})/4$ and $R_B = (R_{32;41} + R_{23;14} + R_{14;32} + R_{41;23})/4$,

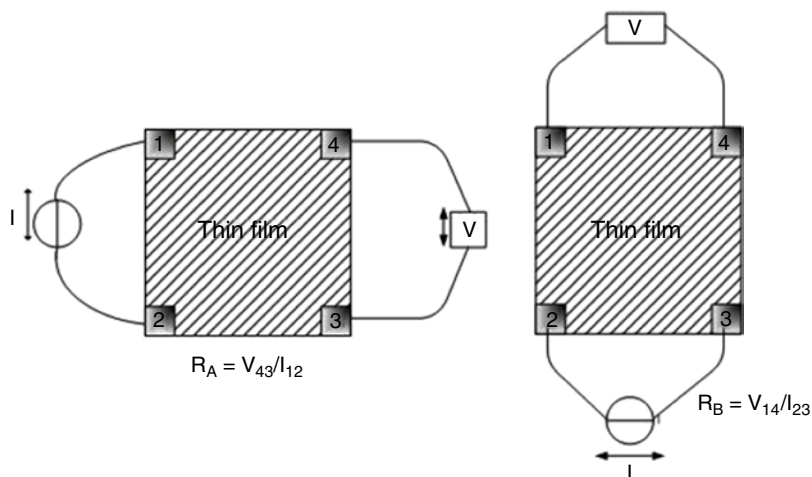


Fig. 17 van der Pauw geometry

respectively. If the sample has nonuniformity, the individual resistances belonging to R_A or R_B differ. However, for a uniform sample with symmetrically located contacts, the two resistances R_A and R_B may be nearly equal. In that case, $R_A = R_B = R$ and the van der Pauw equation reduces to

$$2 \exp\left(-\pi \frac{R}{R_s}\right) = 1 \Rightarrow R_s = \frac{\pi}{\ln 2} R. \quad (16)$$

The sheet resistivity, R_s , can be generally obtained from the van der Pauw equation. The bulk electrical resistivity (ρ) can then be calculated as $\rho = R_s d$, where “d” is the thickness of the thin film. Since bulk resistivity is directly proportional to the film thickness, the uniformity of the thickness across the sample and the measurement of accurate thickness value are the prime requirements for precise estimation of the bulk resistivity.

The van der Pauw configuration can be used to perform the Hall effect experiments in order to determine the carrier density and the carrier mobility. In this method, magnetic field is applied perpendicular to the current path. The voltage difference (i.e., the Hall voltage) across the material transverses to the electric current, and the magnetic field is measured. The Hall coefficient (R_H) is given by

$$R_H = \frac{V_H d}{IB}, \quad (17)$$

where V_H , d , I , and B are the Hall voltage, material thickness, current, and magnetic field, respectively. The carrier density, n , is obtained from the relation

$$R_H = \frac{1}{nq}, \quad (18)$$

where q is the charge of electron.

The carrier mobility is obtained from the equation

$$\sigma = \frac{1}{\rho} = nq\mu, \quad (19)$$

where σ , ρ , and μ are conductivity, resistivity, and carrier mobility, respectively.

The hot probe technique was used by Hazra et al. to determine the n-type conductivity of electrochemically grown porous titania using soft drink electrolyte [94]. Titania nanotubes grown electrochemically using ammonium fluoride (NH_4F) in glycerol as electrolyte showed the resistivity $\sim 1 \times 10^{-2} \Omega\text{-cm}$ [114].

The basic difference between microstructure and nanostructure can be realized from the characterization results. For surface morphology, SEM and AFM images reveal structural size variation either in micron order or in nanometer order. Normally, nanotechnology is limited to a maximum of 100 nm, which is 0.1 μm . So, the resolution of 1 μm is 10 times the maximum resolution for nanotechnology. As a matter of fact, the observation at micron resolution for nanostructures does not

have any contrast. Similarly, the observation of microstructure at nanoresolution lacks the clarity. Other than morphology, the subtle difference between micro- and nanodimensions is observed in the optical band gap. As the size is reduced, the band gap of nanomaterials increases, which is the quantum confinement effect [99]. Furthermore, the electrical properties, which are functions of defect states, grain boundaries, and stoichiometry, do also vary in micro- and nanoregimes. For a fixed device area, microdimensions have less grain boundaries and relatively less number of grains compared to nanostructures. Hence, the electrical transport parameters like mobility, carrier lifetime, etc. should be different for micro- and nanostructures.

Fabrications of Nanochemical Sensors by Electrochemical Method

Choice of Substrate

Both insulating and conducting substrates can be used for electrochemical anodization. The anodization process and subsequent device fabrication are easier for conducting substrates compared to the insulating ones, because the back surface of a conducting substrate can be directly used to make electrical contact with the control circuit. The important advantage of the conducting surface is that the whole front surface can be anodized and the rear surface is protected from the corrosive electrolyte. For titanium, zinc, tin, and other conducting substrates, high-purity thin sheets are used. Depending on the type of conductivity (p-type or n-type), the back side of the highly doped silicon substrate is coated with aluminum or antimony for good ohmic current transport. But for the insulating substrates like glass, quartz, alumina, and intrinsic silicon, a thin film of the material to be anodized is deposited on the insulating substrates, and the electrical connections are taken from one corner of the metal film by using conducting clips. Care must be taken so that the connecting clips do not touch the electrolyte or get immersed into it. In case the whole substrate needs to be immersed into the electrolyte, the clipped contact area is protected by epoxy coating which does not react with the electrolyte.

Device Structure Fabrication

The porous structure developed by electrochemical method is considered as the active layer favorable for sensor device fabrication. The most important part of the device fabrication is that the active porous layer must be properly connected electrically to the conducting circuit. Depending on the type of the substrate on which the porous layer is grown, two device configurations are generally very popular, viz., planar geometry and vertical geometry (Fig. 18). In planar configuration, two metal contacts are deposited closely on the same horizontal plane (laterally) such that the current path between the two contacts should be shortest. On the other hand, in vertical

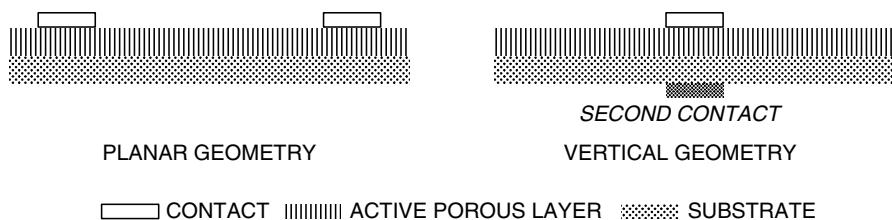
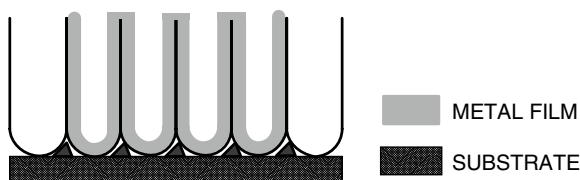


Fig. 18 Schematic view of *planar and vertical device geometries*

Fig. 19 Schematic presentation of the *deposited metal on porous film*



geometry, one contact is made on the top of the active layer, and the other one is taken from the back of the substrate (in case the substrate is conducting) so that the shortest charge carrier path is limited to the vertical gap between the two electrical contacts.

For the nonconducting substrates like glass, quartz, alumina, etc., planar geometry is the only choice. The main advantage of the vertical geometry is that the active layer thickness is the minimum distance between the two electrodes which is normally very short. The electrical contacts are mostly deposited by physical vapor deposition techniques, e.g., thermal and e-beam evaporation methods. So, the metal films percolate down to the base of the porous layer, and the electrical barrier is limited to a thin interfacial oxide layer as shown in Fig. 19 below.

The small current path in the vertical configuration ensures maximum transport of the charge carriers with negligible annihilation that normally occurs due to the traps present in the defective porous layer. As a matter of fact, the device performance of the vertical structure is expected to be better than the planar geometry.

The choice of the device geometry and the nature of the top contact material have serious relevance for the gas sensor performance. The nature of the top contact material also plays a significant role. For example, if palladium (Pd) is used for the metallic contact, it is considered as a catalytic contact material for hydrogen and oxygen gas sensors. During the deposition, the active porous layer may act as a template, and Pd is deposited on the wall of the tubes as shown in Fig. 19. So, a vertical device using Pd may be defined as *catalytic metal thin active layer/metal junctions* for sensor applications. In this case, the sensing is limited mainly to the area of the palladium film dimension. Therefore, the sensing will be directly proportional to the catalytic interaction over the area of Pd. This is also convenient for miniaturization of the sensor devices. However, for enhanced sensitivity, the area of Pd contact may be optimized for larger coverage by the catalytic contact. But for the

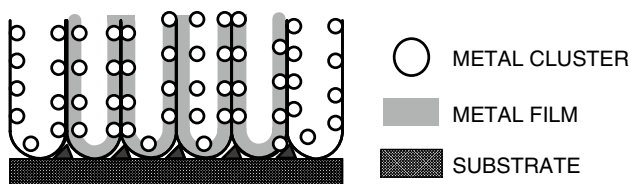


Fig. 20 Schematic presentation of *surface sensitization by dispersion of catalytic metal*

porous materials with high surface area, the contact area geometry is apparently not much significant. For all the practical purposes, 2–5 mm contact diameter is sufficient to study the sensing by a vertical device configuration. On the other hand, the planar geometry is more versatile due to the fact that the sensor devices can be fabricated with or without catalytic metal contacts. The porous layer between the two non-catalytic contacts may act as the active sensing area. The sensitivity of the oxides and porous silicon is proportional to the number of active sites available on the surface. It is worth mentioning that the number of active sites varies from material to material. So, for higher sensitivity of the planar geometry sensor devices, the surface modification of the active sensing layer by the catalytic metal salt solutions may be beneficial. By this process metal clusters are deposited on the wall of the porous layer (Fig. 20) and enhance the solid–gas interaction on the surface of the sensing material.

Therefore, the planar devices can be fabricated on a chemically modified porous surface with non-catalytic or catalytic contacts for higher sensitivity. The choice of the sensor configuration is determined by the ease of fabrication and the cost-effectiveness of the device for large-scale production. The electrical connections are completed by using very fine copper/gold wires bonded on the contacts either by spot welding or by using high-temperature silver paste.

Sensing Procedure

Normally, the resistance, current, and voltage of the device are the parameters which are monitored during sensing studies. Usually the change in resistance/current/voltage in response to the inclusion of low concentration of test gas mixed with air or an inert gas like nitrogen as the carrier gas is measured using an electronic multimeter. The multimeter can be interfaced with a computer for automatic data collections (Fig. 21).

The change in resistance/current/voltage in the porous devices is due to the chemisorptions of the test gases. Basically, the gas molecules are adsorbed on the surface sites of the sensing layer and dissociate to the ionic species, and the free charge carriers are transferred to the conduction band/valence band of the sensing material. Hence, there is a change in the resistance of the sensor assembly depending on the conductivity type of the active porous layer. If the sensing material is n-type and

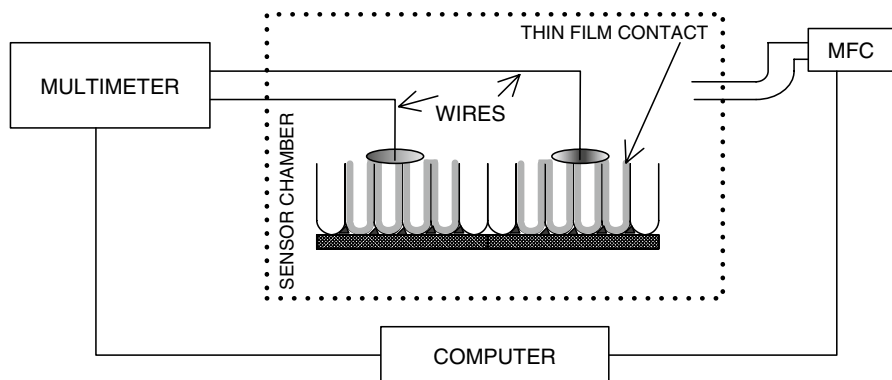


Fig. 21 Schematic diagram of a setup used for gas sensing

the sensing gas is reducing, e.g., H_2 , the resistance decreases due to *solid-reducing gas* interaction, and the opposite behavior is observed if the sensing layer is p-type material.

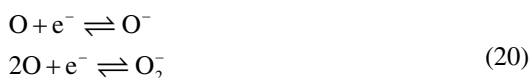
Sensor Performance Using Different Gases and Chemicals

Fundamentals

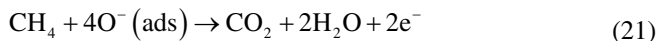
Hydrogen is the simplest reducing gas, and its molecule consists of two hydrogen atoms bonded covalently. The bond dissociation energy is 436 kJ/mol or 4.52 eV per molecule. This bond is strong, nonpolarizable, and cleaved only by catalytic metals or by strong oxidants present in the sensing layer. Although, the porous oxide matrix grown electrochemically is extremely sensitive to reducing gases, the sensing experiments with hydrogen are performed with the devices having catalytic metals like palladium, platinum, and ruthenium to enhance the sensitivity. The catalytic metal thin films may be used as the contact electrodes. The surface modification with the salt solutions of catalytic metals may also be incorporated into the sensor layer. Molecular hydrogen, despite its large bond dissociation energy, can easily dissociate in the presence of palladium or platinum [115]. The dissociated hydrogen atoms occupy tetrahedral/octahedral holes in the crystal structure of palladium. These hydrogen atoms have enough mobility to move from one hole to another. As a matter of fact, the surface chemisorbed atoms slowly move into the bulk of palladium, and the whole metal matrix is eventually saturated. The interaction of hydrogen with palladium in the presence of electric field leads to the formation of palladium–hydrogen complexes, PdH_x^+ ($x=1, 2, 3, 4$) [116]. The sensor device is operated at a specified applied voltage, which is not so high. So, the non-stoichiometric hydrides of palladium, PdH_x

($x = 0-0.7$), are likely formed [117, 118]. For low hydrogen concentration in PdH_x ($x = 0-0.02$), the hydride lattice and the pure palladium lattice are almost well matched, and this low concentration hydride phase is known as the α -phase. For higher concentration of hydrogen, β -phase of the hydride is formed. The β -phase makes palladium brittle due to lattice mismatch, and therefore the use of Pd-modified sensor is restricted to very low concentrations of hydrogen. However, to prevent the formation of β -phase of palladium hydride and make it more efficient for gas sensing, it is normally alloyed with an optimum percentage of silver ($\sim 12\%$ to $\sim 30\%$).

Both α - and β -phases readily release hydrogen by the reverse process of desorption mechanism as the partial pressure of hydrogen on the sensor surface is reduced. However, the α -phase has better reproducibility for the long-term sensing of ppm level of hydrogen. The sensing mechanism for bare oxide films can be realized in terms of electron exchange during solid-gas interactions. In a porous oxide, apart from lattice oxygen atoms, dangling oxygen ions can be found at the material boundaries. Further, not all dangling bonds are saturated. So, during sensing at elevated temperature, oxygen can be chemisorbed from the ambient by gaining one electron from the surface. Due to the chemisorptions and binding of free electrons from the surface, the resistivity of the material shows an increasing trend. The following equations support the above mechanism:



In the presence of the reducing gases like hydrogen, methane, etc., the chemisorbed oxygen reacts with them at the material grain boundaries and at the pore region with large surface-to-volume ratio. At higher temperature of sensing, the lattice oxygen can also migrate toward the surface and react with the reducing gases. Eventually, the bonded electron is released, and the resistance/resistivity decreases.



When the flow of the reducing gases is discontinued, the material again recovers its initial resistivity value by the oxygen chemisorptions' mechanism. However, this process is not so fast. When catalytic metal like palladium is used, the sensing process is the combined effect of two mechanisms. Since oxygen is an integral part of the ambient atmosphere, the catalytic metal surface will have weakly bonded oxygen, which is first removed by the reducing gas. The second step is dissociative adsorption of reducing gas into the metal matrix. For hydrogen, atomic hydrogen goes into the holes; for methane, both H and CH_3 radicals are produced upon dissociation. Hydrogen diffuses in and fills the holes in the metal lattice. These diffused hydrogen atoms form a dipole layer at the metal oxide

junction, which reduces the work function of the metal. The lowering of the metal work function lowers the barrier height of the metal/oxide junction resulting in an increase in the current flowing through the device at a fixed biased potential. However, CH_3 radical is bigger in dimension compared to hydrogen, and so its diffusion is not easy.

Sensor Parameters

The response is defined as the ratio of the change in resistance in the presence of test gas mixed with air/nitrogen ($R_{a,n}-R_g$) to the initial resistance in air/nitrogen ($R_{a,n}$) at the constant voltage and is expressed as

$$S = \left[\frac{(R_{a,n} - R_g)}{R_{a,n}} \right]_V, \quad (23)$$

where $R_{a,n}$ is the resistance in air/nitrogen and R_g is the resistance in the presence of test gas mixed with air/nitrogen. If current is monitored instead of resistance, the “ R ” in the above formula is replaced by current, “ I .” When resistance increases in the presence of test gas, the response is modified as

$$S = \left[\frac{(R_g - R_{a,n})}{R_{a,n}} \right]_V. \quad (24)$$

The response time of the sensor is calculated as the time taken by the sensor signal to reach 90 % of its saturation value upon exposure to test gas mixed with air/nitrogen gas, and the recovery time is calculated as the time corresponding to the decrease of the sensor signal by 90 % of its saturation value after the test gas supply is cut off.

Sensor Performance of Different Porous Materials

In this subsection, the sensor performance of the electrochemically grown porous oxide and porous silicon thin films is presented. A high change in resistance (3–9 orders of magnitude) was obtained for titania nanotube array-based sensors [119]. The normalized change in electrical conductance is shown in Fig. 22. The measurements were performed with 1,000 ppm hydrogen in nitrogen as carrier gas. As it appears from the figure, the conductance at lower temperature (180 °C) is minimum, and it maximizes at around 400 °C. The pore size has considerable influence on the sensitivity toward hydrogen. For smaller tube diameter, the conductance variation is maximum (Fig. 23) due to the increase in the surface area. As reported earlier [119], an increase in surface area by a factor of 2 increases the sensitivity by a factor of 200.

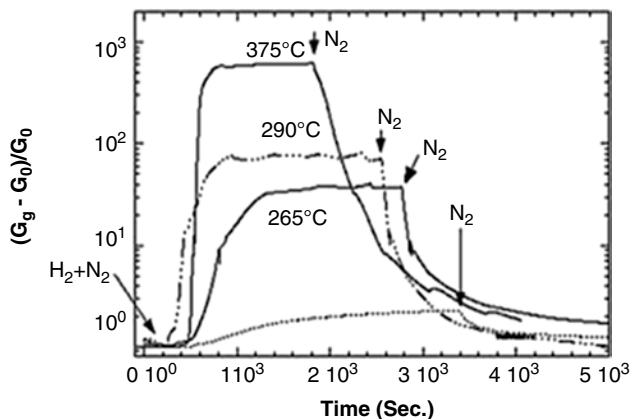
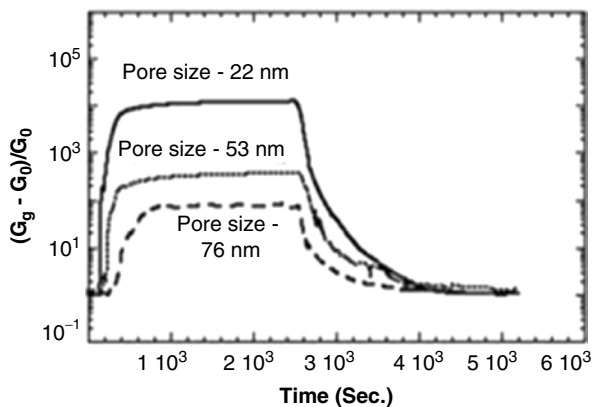


Fig. 22 Normalized change in electrical conductance of a 76 nm diameter TiO_2 nanotube array in 1,000 ppm hydrogen at different temperatures. G_g is the conductance in the presence of hydrogen and G_0 the base conductance in nitrogen only (Reprinted with permission from Varghese et al. [119]. Copyright: John Wiley & Sons, Inc.)

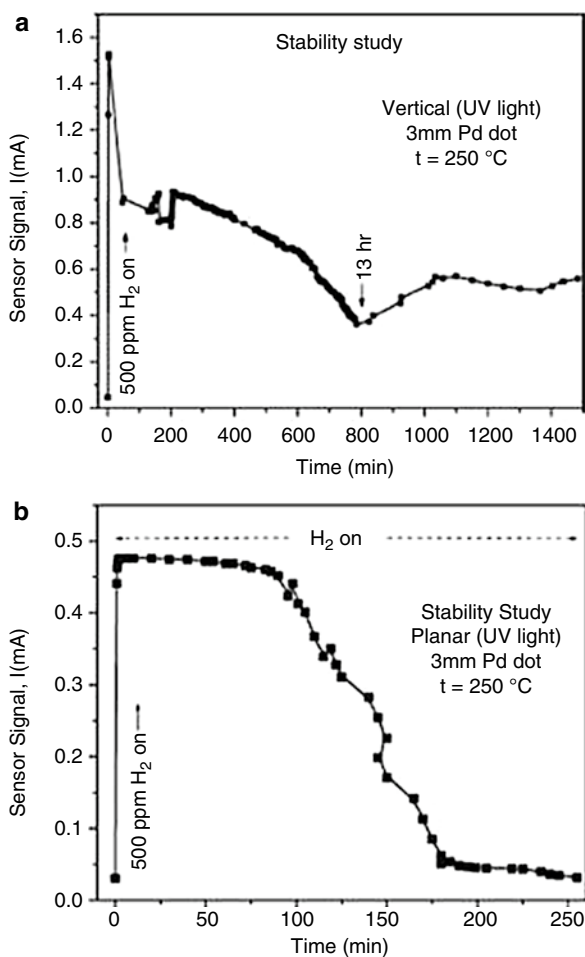
Fig. 23 Normalized change in electrical conductance of TiO_2 nanotube array of 76, 53, and 22 nm diameter in 1,000 ppm hydrogen at 290 °C (Reprinted with permission from Varghese et al. [119]. Copyright: John Wiley & Sons, Inc.)



Further, the nanotube wall thickness and tube length are important factors for the increase of sensitivity. When the wall thickness goes down the space charge layer created by hydrogen chemisorptions, it extends throughout the wall and reduces the overall resistance of the device leading to appreciably high conductance. For 1 μm tube length, the change in electrical resistance is almost 9 orders of magnitude in the presence of 1,000 ppm hydrogen, while for 20 μm tubes, a change of only 3 orders of magnitude in response is obtained with 2,000 ppm hydrogen [120].

Similar studies with electrochemically etched titania revealed high performance for both vertical and planar device geometries. The response time of 5 s was obtained for the vertical sensor configuration of $\text{Pd}/(\text{porous TiO}_2)/\text{Ti-Au}$ with UV-etched titania thin films in 1,000 ppm hydrogen at 300 °C [96]. Although there was not

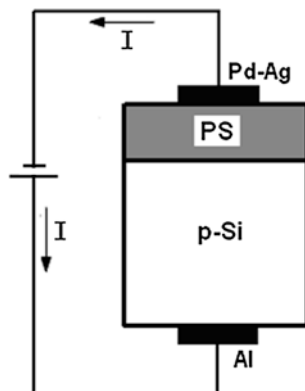
Fig. 24 Stability studies of photoelectrochemically etched titania hydrogen sensors at 250 °C for (a) vertical and (b) planar structures (Reprinted with permission from Hazra and Basu [96]. Copyright: Elsevier)



much difference in terms of response for planar and vertical devices, the stability of the planar geometry was poor in hydrogen (Fig. 24). This is due to the loss of electrons via recombination or trapping while traversing the least resistance path between the electrodes. For vertical configuration, the loss is reduced due to existence of a very thin tunneling oxide layer.

Porous silicon (PS) is a potential material for gas sensing applications mainly due to its large surface-to-volume ratio and strong adsorption of gases [121]. Khoshnevis et al. studied the effect of the anodization parameters during PS formation on the sensor response for oxygen [122]. For Pd-modified porous silicon-based hydrogen sensors, it was reported that the distribution of Pd over the porous silicon controls the sensor characteristics [123, 68, 124]. However, the distribution of Pd is related to the concentration of the binding sites, i.e., the porosity. The influence of the etching time, the anodization of current density, the effect of the catalytic layer

Fig. 25 Schematic of the PS-based sensor structure for hydrogen sensing (Reprinted with permission from Kanungo et al. [127]. Copyright: Elsevier)



thickness, and the stability of a Pd-doped hydrogen sensor were studied by Sekhar et al. [125]. Further, the effect of different parameters on the nucleation and growth of Pd particles on PS along with the gas response in hydrogen at room temperature was reported by Rahimi and coworkers [126].

The porous silicon surface was modified at room temperature using dilute PdCl_2 solution [127, 98]. The samples with different porosities were dipped into 10 % HF solution for 10 s to remove the native oxide layer from the PS surface. Then the samples were immediately soaked in the weakly acidic PdCl_2 solution (0.01 M) for 5 s, rinsed in DI water, dried, and annealed in air at 110 °C for 10 min. The decomposition of PdCl_2 produces Pd^{2+} which is subsequently reduced to Pd metal, and two holes (h^+) are released. The released h^+ oxidizes the PS surface to form a thin SiO_2 layer [128, 129].

A simple *MIS* vertical device configuration using nanoporous silicon was employed for gas sensor study (Fig. 25).

The gas sensor response is calculated as the ratio of the change in current in the presence of hydrogen mixed with nitrogen ($I_n - I_g$) to the initial current in nitrogen (I_n), at a constant voltage.

$$S = \left[\frac{I_n - I_g}{I_n} \right]_V, \quad (25)$$

where I_n , I_g are currents in pure nitrogen and in hydrogen mixed with nitrogen, respectively. The current magnitude depends on the type of porous silicon used. If p-type PS is used, the device current decreases in the presence of hydrogen ($I_g < I_n$), whereas for n-type, the current increases ($I_g > I_n$).

Figure 26 demonstrates that the response of palladium-modified PS increases with increasing porosity at room temperature for 1 % hydrogen. However, there is an optimum porosity of 55 % beyond which the response starts decreasing. The response and recovery time (Fig. 27) follow the similar trend. The effect of the variation of porosity on the sensor response is basically due to the defect states present. The increasing density of the defect states with increasing porosity provides

Fig. 26 Response versus porosity characteristics of unmodified and Pd-modified porous silicon sensors corresponding to their optimum biasing voltages at 27 °C (RT) for 1 % hydrogen in nitrogen as carrier gas (Reprinted with permission from Kanungo et al. [127]. Copyright: Elsevier)

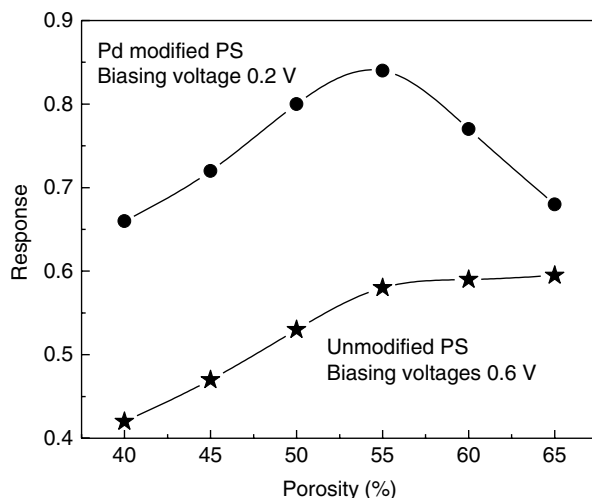
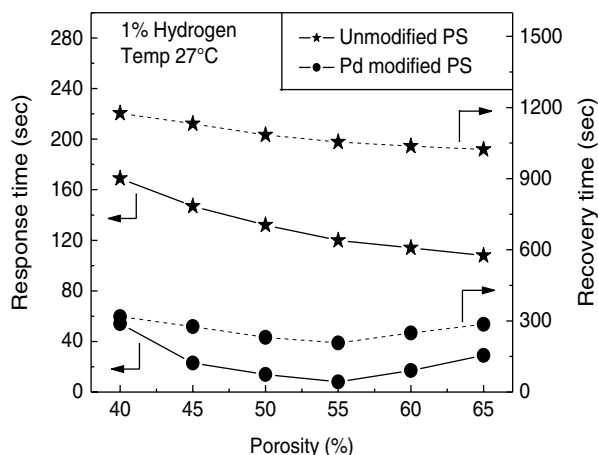


Fig. 27 Response time versus porosity and recovery time versus porosity characteristics of unmodified and Pd-modified porous silicon sensors corresponding to their optimum biasing voltages at 27 °C (RT) for 1 % hydrogen in nitrogen as carrier gas (Reprinted with permission from Kanungo et al. [127]. Copyright: Elsevier)

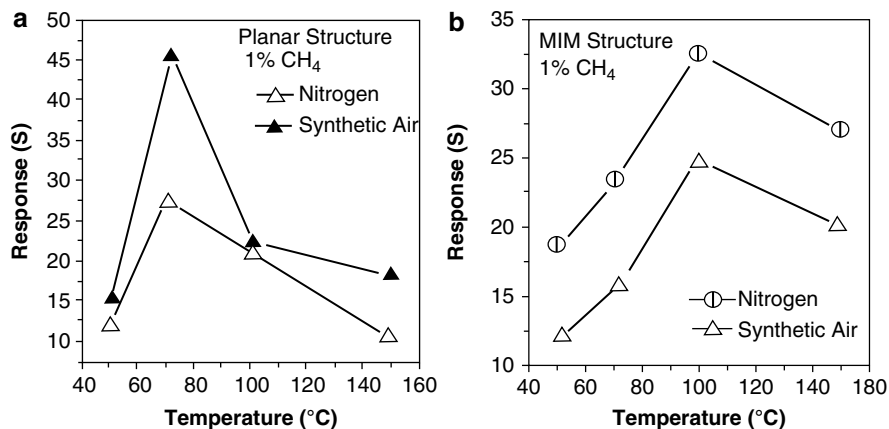


more nucleation sites for Pd dispersion. Hence, there is an enhancement of Pd density over the PS surface with increasing porosity.

However, there is an optimum loading of the Pd metal in PS [28] depending upon the porosity, and beyond the optimum (above 55 % porosity in this case), the increase in metal deposition may reduce the effective surface area of the dispersed Pd [28]. In the present investigation, the gas response behavior of PS was found to decrease with porosity higher than 55 %. Also a relative decrease in the recovery

Table 3 Response, response time, and recovery time without and with Pd sensitization

	Device: (Pd-Ag)-(Porous ZnO)-(Zn): MIM	
	Without Pd sensitizer	With Pd sensitizer
Response	3.85 (at 220 °C)	32 (at 100 °C)
Response time	5 s (at 220 °C)	2.7 s (at 100 °C)
Recovery time	16 s (at 220 °C)	16 s (at 100 °C)

**Fig. 28** Response versus temperature curves of (a) Planar and (b) MIM structures of electrochemically grown nano-ZnO sensors with 1 % methane in pure nitrogen and in synthetic air at the forward bias of 3 V (Reprinted with permission from Basu et al. [133]. Copyright: Elsevier)

time was observed after the optimum loading of Pd in PS with >55 % porosity. However, the measured value of the recovery time is appreciably large due to slow desorption kinetics (Fig. 27). In pure nitrogen and at room temperature, the desorption of hydrogen took long time after the hydrogen supply was cut off [127, 130, 131].

Normally, the sensors should operate in air for practical applications, and the desorption is much faster in air. But in this study, nitrogen was deliberately used to avoid the cross sensitivity due to oxygen [125]. The PS-based MIS device with a thin over layer of zinc oxide (ZnO) demonstrated an improved gas response behavior at relatively higher temperature (150 °C) [127, 131]. However, the temperature of sensing was reduced well (~55 °C), and the higher response for hydrogen was obtained after the Pd modifications of both ZnO and PS surfaces.

The potential of palladium sensitization of porous matrices is also evident from the studies performed with electrochemically grown nanoporous ZnO thin film for methane sensing. In two separate studies, reported by Basu et al. [132, 133], it was shown that the sensor parameters like the response, response time, and recovery time improved in the presence of dispersed sensitizers like palladium (Table 3). As reported by Basu et al. [133], the surface modification of nano-ZnO film by using an aqueous solution of PdCl₂ reduced the optimum operating temperature

from 220 °C to 70 °C and to 100 °C for planar resistive and for vertical MIM (metal–insulator–metal) configurations, respectively. The response of 48, the response time of 4.5 s, and the recovery time of 22.7 s were obtained for the planar structures, while the MIM structures showed the response of the order of 32, the response time of 2.7 s, and the recovery time of 16 s. The sensor studies were performed in the presence of 1 % methane in nitrogen and in synthetic air separately. The performance of the surface-modified device was somewhat reduced in synthetic air for both the sensor configurations at the respective optimum operating temperatures (Fig. 28). In the case of synthetic air as the carrier gas, oxygen is also chemisorbed on the Pd-catalyzed ZnO surface, and there is a competitive equilibrium between oxygen and methane adsorptions on ZnO; it may well be depicted that the adsorption sites for methane is reduced and also the chemisorbed oxygen traps hydrogen produced by the dissociation of methane. As a result, the current through the electrodes is reduced, and so a lower response to methane is obtained in synthetic air.

Fabrication of nanoporous SnO₂ is also possible by employing anodization technique. Reports are available on the use of porous tin oxides with honeycomb-like channels for lithium batteries [134]. However, very few reports are available on the use of nanoporous SnO₂ fabricated by electrochemical deposition technique for chemical sensor applications. Feng et al. fabricated mesoporous SnO₂ nanomaterials with the central pore sizes of 4.1 nm, 6.1 nm, and 8.0 nm by a novel carbon-assisted synthesis method (CAS) [59]. The pore size was regulated by adjusting the concentration of glucose in the precursor solution. The gas sensing properties of the mesoporous SnO₂ nanomaterials are reported, and the results reveal that this sensor exhibits short response/recovery time to ethanol gas and has ultralow detection limits of 50 ppb. The proper mesoporous nanostructure network (MNN) is responsible for the distinct response–recovery behavior and the mechanism to achieve the ultralow detection limit. However, more details on the numerical values of the sensor parameters are not available. Other than CAS method, microwave-assisted hydrothermal method is also reported to grow nanostructured SnO₂ to sense alcohol vapors at 240 °C [135].

Response of Electrochemically Grown Oxides to Volatile Organic Compounds

Electrochemically grown oxides have also been used to sense volatile organic compounds (VOCs). A two-step method was employed by Wu et al. [136] to grow TiO₂ nanotubes of ~400 nm in length and pore diameter of ~100 nm. These as-anodized TiO₂ nanotubes showed good sensitivity to formaldehyde at room temperature with or without UV illumination. The sensors responded linearly to 10–50 ppm concentration of formaldehyde under UV illumination. SnO₂ nanotubes synthesized using carbon nanotube template showed improved sensitivity to trace concentrations of methanol vapor compared to the compact tin dioxide thin films at quite high temperature [137]. This is due to the high active surface provided by porous SnO₂ surface (Fig. 29).

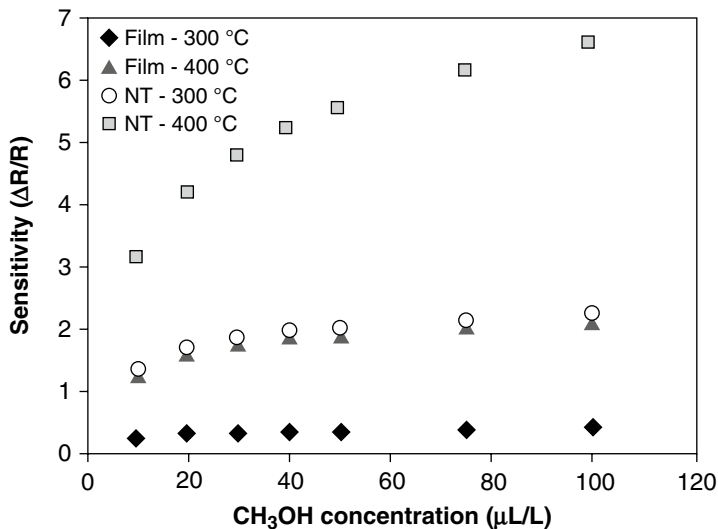


Fig. 29 Comparative sensitivities of porous SnO₂ nanotubes and compact SnO₂ thin films to methanol vapors (Reprinted with permission from Parthanga et al. [137]. Copyright: Materials Research Society)

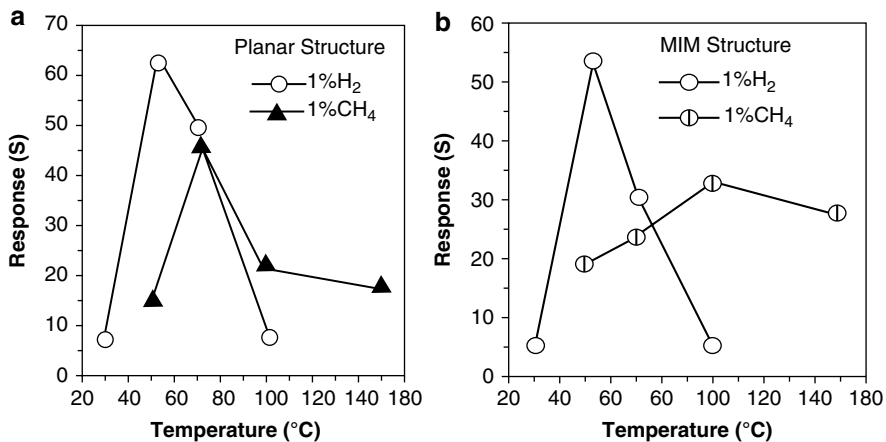


Fig. 30 Selective response of (a) planar and (b) MIM sensor structures with nanoporous ZnO in 1% H₂ and 1% CH₄ in pure N₂ atmosphere (Reprinted with permission from Basu et al. [133]. Copyright: Elsevier)

Selectivity and Stability of the Chemical Sensors Fabricated from Electrochemically Grown Nanosized Oxide Materials

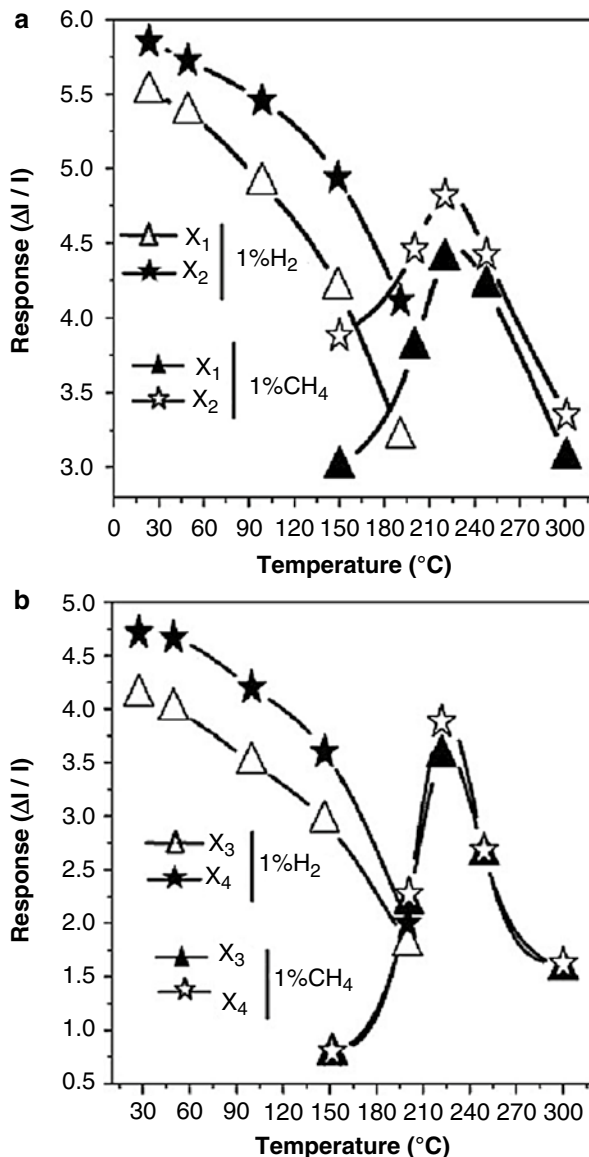
Oxide materials are sensitive to both reducing and oxidizing gases. Hence, the cross sensitivity toward other gases and chemicals is an important concern for sensor researchers. Since, the cross sensitivity cannot be eliminated, a suitable way out is

necessary to reduce the effect of cross sensitivity. Temperature is an important parameter. Basu et al. reported the temperature effect on the cross sensitivity of methane mixed with hydrogen for nanocrystalline and porous ZnO sensors [133]. The response of 1 % H₂ and 1 % CH₄ in nitrogen with the variation of temperature is shown in Fig. 30 for both planar and MIM sensor structures. At 50 °C hydrogen shows maximum response (more than 50) for both the structures, and methane shows >10. However, the selectivity for methane is better for MIM structure because at 100 °C, CH₄ shows maximum response (>30), and H₂ has almost no response. Actually, methane is a heavy molecule, and it needs higher activation energy for dissociation compared to that of hydrogen. Temperature selective sensing was also performed using different catalytic metal contacts (Fig. 31). Rh and Pd-Ag(26 %) contacts showed selective hydrogen sensing at room temperature, whereas methane was sensitive at 220 °C [132].

Porous titania-based chemical sensors also show cross-sensitivity effects. Wu et al. [136] examined the sensitivity of TiO₂ nanotube to ammonia, alcohols, and formaldehyde under UV illumination. The selectivity toward low concentration of formaldehyde was confirmed from the response data, which showed maximum response in the presence of relatively higher concentrations of ammonia, alcohol, and methanol vapors (Fig. 32). This was attributed to the enhanced diffusion of formaldehyde into the nanotubes relative to other analytes causing a large change in conductivity.

The stability of oxide-based sensors of different configurations needs to be verified in order to make the device reliable and compatible with the actuating electronics. If the resistance/current keeps on changing with time, it is difficult to use the device with standard electronic circuit. So, the stability of the sensor device needs to be checked in the presence of sensing gases mixed with air/nitrogen. We have shown in Fig. 24 that a porous morphology was developed by electrochemical etching of the thermally grown titania and it showed poor long-term stability specially for the planar device compared to the vertical device geometry [96]. This poor stability is often attributed to the defects present in the oxide matrix. Since titania was prepared thermally at high temperature, it is likely that a large number of defects were generated mainly due to migration of lattice oxygen from the bulk to the surface that is responsible for charge trapping/annihilation. However, the distance between the two electrodes of the sensor device plays a significant role in reducing the trapping effect. Since the vertical configuration provides the shortest path of charge transfer, it has relatively higher stability compared to the planar geometry [96]. But the good quality nanostructures developed electrochemically also show very high degree of stability for the planar devices [97]. Figure 33a shows that the electrochemically developed porous ZnO sensors in both planar and MIM configurations show long stability for sensing 1 % methane mixed with nitrogen [133]. The stability of the porous silicon MIS sensor was studied in 1 % hydrogen in nitrogen at 27 °C for 24 h in a discrete manner with 8 h duration per day at the biasing voltage corresponding to the maximum response and is shown in Fig. 33b. The stability is found to be quite good with time [138]. As shown in the figure, the Pd-modified PS sensor shows more stable sensing compared to the unmodified PS sensor over a long time. The deterioration of the unmodified PS sensor is due to loss of the charge

Fig. 31 Temperature selective response of electrochemically grown nanoporous ZnO MIM sensor structures for 1 % H₂ and 1 % CH₄ in pure N₂ atmosphere with different catalytic metals (a) Rh/ZnO/Zn [X1 and X2] (b) Pd-Ag(26 %)/ZnO/Zn [X3 and X4] (Reprinted with permission from Basu et al. [132]. Copyright: Elsevier)



carriers because of recombination at the defect states. Pd surface modification helps in eliminating the defect states to large extent, and so the stability is visibly improved. Similar stability study was performed with titania-based metal–active insulator–metal (MAIM) sensors, which showed negligible baseline fluctuations over a period of 7 days [97].

The titania nanoparticle sensors containing either anatase or rutile phase or both show appreciable sensitivity to hydrogen, and their response behavior is highly reproducible. Also, the sensitivity improves with temperature. Physical parameters

Fig. 32 Response of TiO_2 nanotube sensor toward gas and vapor at $\sim 19^\circ\text{C}$ and $\text{RH} \sim 33\%$ with UV illumination (Reprinted with permission from Guoqiang et al. [136]. Copyright: Elsevier)

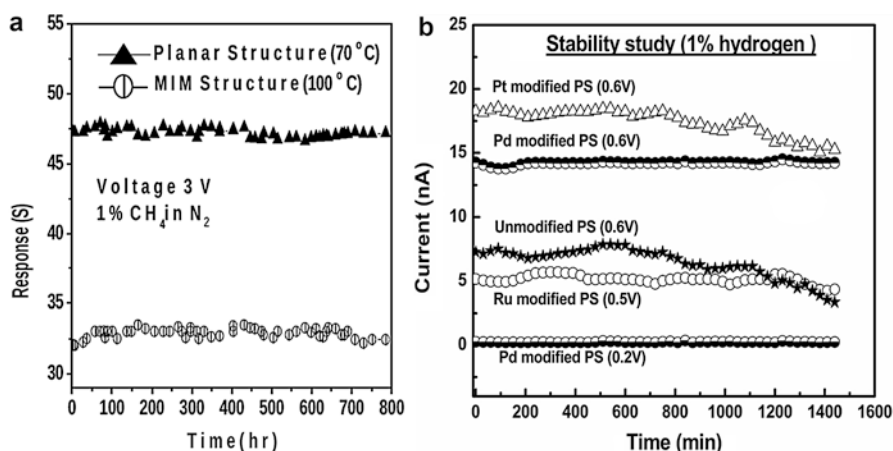
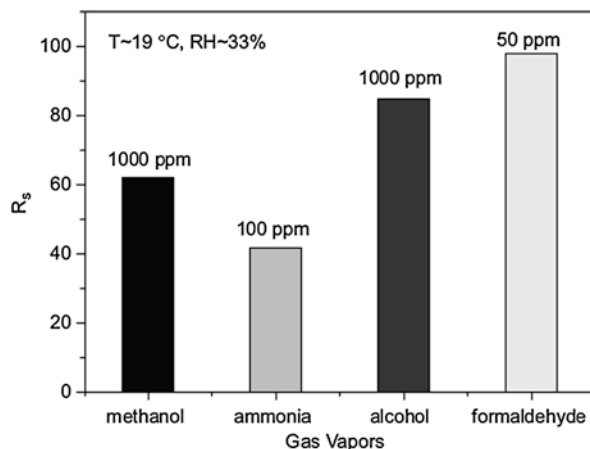


Fig. 33 Stability study of (a) porous zinc oxide and (b) porous silicon sensors (Reprinted with permission from Basu et al. [133] and Kanungo et al. [138]. Copyright: Elsevier)

like nanotube diameter and tube length affect the sensor performance. The sensors based on ZnO , SnO_2 , and porous silicon also respond well to hydrogen and methane. Although oxide-based sensors have high sensitivity toward hydrogen, the cross sensitivity toward oxygen in air (used as the carrier gas) reduces the overall response. The effect of oxygen can be eliminated by using inert carrier gases like argon and nitrogen. But for the field applications, air is imminent, and so the studies are to be carried out in air ambient. The cross sensitivity toward other oxidizing or reducing gases can also be diminished by controlling the operating temperature. For heavier molecules like methane, the reactions are feasible at higher temperatures, whereas for lighter gases like hydrogen, low temperature and even room temperature are sufficient to get appreciable response from these nanocrystalline- and

nanoporous oxide-based devices. The presence of moisture in ambient atmosphere can deteriorate the sensor performance. Therefore, calibration of the device to relative humidity is essential for all oxide-based sensors.

Nanoporous oxide sensors grown electrochemically have versatile applications in harsh industrial environments and over a long range of temperatures. The sensors can also be used in the biomedical area to detect disorders such as lactose intolerance. With respect to sensor design, the development of both theoretical model and experimental results are vital. CMOS (complementary metal–oxide–semiconductor) or CMOS-MEMS (complementary metal–oxide–semiconductor microelectromechanical system) has been presently employed in sensor technology for miniaturization of the devices, low power consumption, higher sensitivity, faster sensor response, batch fabrication at industrial standards, and low cost. From these considerations, electrochemically fabricated thin film oxides and porous silicon can play an important role.

Summary and Conclusion

In this chapter, theory of nanoelectrochemistry has been discussed for the development of nanostructures by electrochemical methods. Mainly the nano-oxides and nanoporous silicon have been focused because they are promising materials for chemical sensor application. The growth methodologies along with the chemical reactions have been discussed in detail. The optimum conditions to grow thin films on insulating and conducting substrates by varying the electrochemical parameters have been highlighted. The effect of UV illumination on thin film growth and etching has been discussed in details with special references to ZnO, TiO₂, and nanoporous silicon. The structural, electrical, and optical characterizations of the electrochemically deposited nanostructured thin films have been elaborated with the specific illustrations. The fabrication of sensor structures using the electrochemically deposited nanomaterials covers a major part of the chapter. A comparative study of the lateral and the vertical device geometry for gas sensing has been presented with special reference to ZnO and TiO₂ nanostructures developed by electrochemical method. The performance of the sensors made of electrochemically deposited nano-oxides, e.g., TiO₂, ZnO, SnO₂, and nanoporous silicon, has been discussed in great details with the reported results from the literature. Further studies on chemical modification of the surfaces of nanocrystalline materials are necessary to improve the magnitude of sensor parameters like response, response time, and recovery time. The selectivity and the stability of the sensor structures based on electrochemically developed nanocrystalline and nanoporous materials have been discussed for reliable sensor devices. Although some efforts to quantify and establish correlations between the nanostructure of materials and sensor performance are available in the published literature, there still remains the scope for better understanding of the fundamental mechanisms important for the surface-modified nanostructured and nanoporous materials. It is well known that defective and porous oxide matrices have high chemical sensor response owing to the presence of large number of active sites for the solid–gas/vapor interactions. But the carrier loss by recombination or

trapping is also important for defecting matrices. The surface sensitizers have indeed improved the sensor performance as reported in the published literature. Therefore, surface-sensitive characterizations can locate the state and the effect of sensitization of the oxide matrix. Using high-resolution TEM coupled with XPS and Raman spectroscopy, it may be possible to capture lattice defects and their passivation by surface sensitization.

In conclusion, the development of nanostructures by electrochemical method is indeed very convenient from the operational point of view because the method avoids the harsh conditions of high temperature and corrosive and polluting atmosphere; the growth process is largely hassle free, economic, and highly reproducible. The porous structures can be suitably grown by electrochemical method by illuminating the surface with the light of appropriate wavelength during anodization. The quality of the nano-thin films is of high standard for applications in chemical sensors and also in other technology. The electrochemical deposition method is specially suitable for the development of miniaturized chemical sensors with high efficiency and long-term performance.

References

1. Sze S (1994) *Semiconductor sensors*. Wiley, New York
2. Kong J, Franklin NR, Zhou C, Chapline MG, Peng S, Cho K, Dai H (2000) Nanotube molecular wires as chemical sensors. *Science* 287:622–625
3. Xu C, Tamaki J, Miura N, Yamazoe N (1990) Relationship between gas sensitivity and microstructure of porous SnO₂. *J Electrochem Soc* 58(12):1143–1148
4. Brynzari V, Korotchenkov G, Dmitriev S (1999) Simulation of thin film gas sensors kinetics. *Sens Actuat B* 61(1–3):143–153
5. Brynzari V, Korotchenkov G, Dmitriev S (2000) Theoretical study of semiconductor thin films gas sensors: attempt to consistent approach. *J Electron Technol* 33:225–235
6. Simon I, Brsan N, Bauer M, Weimar U (2001) Micromachined metal oxide gas sensors: opportunities to improve sensor performance. *Sens Actuat B* 73(1):1–26
7. Rothschild A, Komen Y (2004) The effect of grain size on the sensitivity of nanocrystalline metal-oxide gas sensors. *J Appl Phys* 95(11):6374–6380
8. Korotcenkov G (2008) The role of morphology and crystallographic structure of metal oxides in response of conductometric-type gas sensors. *Mater Sci Eng R* 61(1–6):1–39
9. Ding D, Chen Z, Lu C (2006) Hydrogen sensing of nanoporous palladium films supported by anodic aluminum oxides. *Sens Actuator B* 120(1):182–186
10. Lundstrom I, Sundgren H, Winquist MRC, Eriksson F, Spetz A (2007) Twenty-five years of field effect gas sensor research linkoping. *Sens Actuator B* 121(1):247–262
11. Lofdahl M, Utaiwasin C, Carlsson A, Lundstrom I, Eriksson M (2001) Gas response dependence on gate metal morphology of field effect devices. *Sens Actuator B* 80(3):183–192
12. Vol'kenshtein F (1960) *Electronic theory of catalysis on semiconductors* (In Russian). Fizmatgiz, Moscow
13. Korotcenkov G (2005) Gas response control through structural and chemical modification of metal oxide films: state of the art and approaches. *Sens Actuator B* 107(1):209–232
14. McAleer J, Moseley P, Norris J, Williams D, Tofield B (1988) Tin dioxide gas sensors. *J Chem Soc Faraday Trans* 1:84
15. Brinzari V, Korotcenkov G, Schwank J, Boris Y (2002) Chemisorptional approach to kinetic analysis of SnO₂: Pd-based thin film gas sensors (TFGS). *J Optoelectron Adv Mat (Romania)* 4:147

16. Korotcenkov G, Brinzari V, Boris Y, Ivanov M, Schwank J, Morante J (2003) Surface Pd doping influence on gas sensing characteristics of SnO₂ thin films deposited by spray pyrolysis. *Thin Solid Films* 436(1):119–126
17. Shinde V, Gujar T, Lokhande C (2007) Enhanced response of porous ZnO nanobeads towards LPG: effect of Pd sensitization. *Sens Actuator B* 123(2):701–706
18. Varghese O, Grimes C (2003) Metal oxide nanoarchitectures for environmental sensing. *J Nanosci Nanotechnol* 3:277–293
19. Paulose M, Varghese O, Mor G, Grimes C, Ong K (2006) Unprecedented ultrahigh hydrogen gas sensitivity in undoped titania nanotubes. *Nanotechnology* 17:398–402
20. Liaoying Z, Mingxia X, Tingxian X (2000) TiO_{2-x} thin films as oxygen sensor. *Sens Actuator B* 66(1–3):28–30
21. Atashbar MZ, Sun HT, Gong B, Wlodarski W, Lamb R (1998) XPS study of Nb-doped oxygen sensing TiO₂ thin films prepared by sol–gel method. *Thin Solid Films* 326(1–2):238–244
22. Devi GS, Hyodo T, Yasuhiro S, Egashira M (2002) Synthesis of mesoporous TiO₂-based powders and their gas-sensing properties. *Sens Actuator B* 87(1):122–129
23. Akbar SA, Younkman LB (1997) Sensing mechanism of a carbon monoxide sensor based on anatase titania. *J Electrochem Soc* 144(5):1750–1753
24. Vomiero A, Mea GD, Ferroni M, Martinelli G, Roncarati G, Guidi V, Comini E, Sberveglieri G (2003) Preparation and microstructural characterization of nanosized Mo–TiO₂ and Mo–W–O thin films by sputtering: tailoring of composition and porosity by thermal treatment. *Mater Sci Eng B* 101(1–3):216–221
25. Caihong W, Xiangfeng C, Mingmei W (2007) Highly sensitive gas sensors based on hollow SnO₂ spheres prepared by carbon sphere template method. *Sens Actuator B* 120(2):508–513
26. Taguchi N (1970) Gas detection device. UK Patent 1280809 and US Patent 3631436I
27. Gopel W, Schierbaum KD (1995) SnO₂ sensors: current status and future prospects. *Sens Actuator B* 26(1–3):1–12
28. Yamazoe N (1991) New approaches for improving semiconductor gas sensors. *Sens Actuator B* 5(1–4):7–19
29. Calderer J, Molins P, Sueiras J, Llobet E, Vilanova X, Correig X, Masana F, Rodriguez A (2000) Synthesis and characterisation of metal suboxides for gas sensors. *Microel Rel* 40:807–810
30. Xu C, Tamaki J, Miura N, Yamazoe N (1991) Grain size effects on gas sensitivity of porous SnO₂-based elements. *Sens Actuator B* 3(2):147–155
31. Krius FE, Fissan H, Peled A (1998) Synthesis of nanoparticles in the gas phase for electronic, optical and magnetic applications—a review. *J Aerosol Sci* 29(5–6):511–535
32. Zhang G, Liu M (2000) Effect of particle size and dopant on properties of SnO₂-based gas sensors. *Sens Actuator B* 69(1–2):144–152
33. Gong D, Grimes CA, Varghese OK, Hu W, Singh RS, Chen Z, Dickey EC (2001) Titanium oxide nanotube arrays prepared by anodic oxidation. *J Mater Res* 16(12):3331–3334
34. Varghese OK, Gong D, Paulose M, Ong KG, Grimes CA (2003) Hydrogen sensing using titania nanotubes. *Sens Actuator B* 93:338–344
35. Varghese OK, Mor GK, Grimes CA, Paulose M, Mukherjee N (2004) A titania nanotube-array room temperature sensor for selective detection of hydrogen at low concentrations. *J Nanosci Nanotechnol* 4(7):733–737
36. Shimizu Y, Kuwano N, Hyodo T, Egashira M (2002) High H₂ sensing performance of anodically oxidized TiO₂ film contacted with Pd. *Sens Actuator B* 83(1–3):195–201
37. Iwanaga T, Hyodo SY, Takeo EM (2003) H₂ sensing properties and mechanism of anodically oxidized TiO₂ film contacted with pd electrode. *Sens Actuator B* 93(1–3):519–525
38. Shankar K, Mor G, Prakasam H, Yoriya S, Paulose M, Varghese O, Grimes C (2007) Highly-ordered TiO₂ nanotube arrays up to 220 220 μm mu;m in length: use in water photoelectrolysis and dye-sensitized solar cells. *Nanotechnol* 18:065,707–065,717
39. Mor G, Shankar K, Paulose M, Varghese O, Grimes C (2007) High efficiency double hetero-junction polymer photovoltaic cells using highly ordered TiO₂ nanotube arrays. *Appl Phys Lett* 91:152111–152113

40. Shankar K, Mor G, Paulose M, Varghese O, Grimes C (2008) Effect of device geometry on the performance of TiO₂ nanotube array-organic semiconductor double heterojunction solar cells. *J Non-Cryst Solids* 354:2767–2771
41. Shankar K, Mor GK, Prakasam HE, Varghese OK, Grimes CA (2007) Self-assembly hybrid polymer-TiO₂ nanotube array heterojunction solar cells. *Langmuir* 23:12445–12449
42. Mor GK, Prakasam HE, Varghese OK, Shankar K, Grimes CA (2007) Vertically oriented Ti-Fe-O nanotube array films: toward a useful material architecture for solar spectrum water photoelectrolysis. *Nano Lett* 7:2356–2364
43. Mor GK, Varghese OK, Wilke RHT, Sharma S, Shankar K, Latempa TJ, Choi KS, Grimes CA (2008) p-type Cu-Ti-O nanotube arrays and their use in self-biased heterojunction photoelectrochemical diodes for hydrogen generation. *Nano Lett* 8:1906–1911
44. Chen SG, Paulose M, Ruan C, Mor GK, Varghese OK, Grimes CA (2006) Electrochemically synthesized CdS nanoparticle-modified TiO₂ nanotube-array photoelectrodes: preparation, characterization, and application to photoelectrochemical cells. *J Photochem Photobiol A* 177:177–184
45. Seabold JA, Shankar K, Wilke RHT, Paulose M, Varghese OK, Grimes CA, Choi KS (2008) Photoelectrochemical properties of heterojunction CdTe/TiO₂ electrodes constructed using highly ordered TiO₂ nanotube arrays. *Chem Mater* 20:5266–5273
46. Varghese OK, Paulose M, Shankar K, Mor GK, Grimes CA (2005) Water-photolysis properties of micron-length highly-ordered titania nanotube arrays. *J Nanosci Nanotechnol* 5:1158–1165
47. Paulose M, Shankar K, Yoriya S, Prakasam HE, Varghese OK, Mor GK, Latempa TA, Fitzgerald A, Grimes CA (2006) Anodic growth of highly ordered TiO₂ nanotube arrays to 134 134 μm μm; m in length. *J Phys Chem B* 110:16179–16184
48. Mor GK, Shankar K, Paulose M, Varghese OK, Grimes CA (2005) Enhanced photocleavage of water using titania nanotube arrays. *Nano Lett* 5:191–195
49. Grimes CA, Varghese OK, Ranjan S (2008) *Light, water, hydrogen: the solar generation of hydrogen by water photoelectrolysis*. Springer, New York
50. Varghese OK, Paulose M, LaTempa TJ, Grimes CA (2009) High-rate solar photocatalytic conversion of CO₂ and water vapor to hydrocarbon fuels. *Nano Lett* 9:731–737
51. Sugiura T, Yoshida T, Minoura H (1998) Designing a TiO₂ nano-honeycomb structure using photoelectrochemical etching. *Electrochem Solid State* 1(4):175–177
52. Sugiura T, Yoshida T, Minoura H (1999) Microstructural observation of photoelectrochemically tailored nano-honeycomb TiO₂. *Electrochem Commun* 67(12):1234–1236
53. Hazra SK, Tripathy SR, Alessandri I, Depero LE, Basu S (2006) Characterizations of porous titania thin films produced by electrochemical etching. *Mater Sci Eng B* 131(1–3):135–141
54. Hongwei Y, Yang Y, Zhengping F, Beifeng Y, Linsheng X, Shengquan F, Fanqing L (2005) Fabrication of 2D and 3D ordered porous ZnO films using 3D opal templates by electrodeposition. *Electrochem Commun* 7(11):1117–1121
55. Cao B, CaiW DG, Li Y, Zhao Q, Yu D (2005) A template-free electrochemical deposition route to ZnO nanoneedle arrays and their optical and field emission properties. *Nanotechnol* 16:2567–2574
56. Ashida A, Fujita A, Shim Y, Wakita K, Nakahira A (2008) ZnO thin films epitaxially grown by electrochemical deposition method with constant current. *Thin Solid Films* 517(4):1461–1464
57. Chang CJ, Hung ST (2008) Electrochemical deposition of ZnO pore-array structures and photoconductivity of ZnO/polymer hybrid films. *Thin Solid Films* 517(3):1279–1283
58. Yamaguchi A, Iimura T, Hotta K, Teramae N (2011) Transparent nanoporous tin-oxide film electrode fabricated by anodization. *Thin Solid Films* 519(8):2415–2420
59. Feng X, Jiang J, Ding H, Ding R, Luo D, Zhu J, Feng Y, Huang X (2013) Carbon-assisted synthesis of mesoporous SnO₂ nanomaterial as highly sensitive ethanol gas sensor. *Sens Actuator B* 183:526–534
60. Jeun JH, Kim DH, Hong SH (2012) Synthesis of porous SnO₂ foams on SiO₂/si substrate by electrochemical deposition and their gas sensing properties. *Sens Actuator B* 116(1):784–790

61. Spetz AL, Tobias P, Unus L, Svenningstorp H, Ekedahl LG, Lundström I (2000) High temperature catalytic metal field effect transistors for industrial applications. *Sens Actuator B* 70(1–3):67–76
62. Roy S, Jacob C, Basu S (2003) Ohmic contacts to 3C–SiC for schottky diode gas sensors. *Solid-State Electron* 47(11):2035–2041
63. Roy S, Jacob C, Basu S (2003) Studies on Pd/3C–SiC schottky junction hydrogen sensors at high temperature. *Sens Actuator B* 94(3):298–303
64. Usagawa T, Kikuchi Y (2010) A Pt–Ti–O gate si-metal-insulator-semiconductor field-effect transistor hydrogen gas sensor. *J Appl Phys* 108:74909–74916
65. Canham L (ed) (1997) Properties of porous silicon. INSPEC – The Institution of Electrical Engineers, London
66. Pavese L, Dubos P (1997) Random porous silicon multilayers application to distributed bragg reflectors and interferential fabry perot filters. *Semiconduct Sci Technol* 12(5):570–575
67. Dimitrov D (1995) Current–voltage characteristics of porous silicon layer. *Phys Rev B* 51(3):1562–1566
68. Tsamis C, Tsoura L, Nassiopoulou AG, Travlos A, Salmas C, Hatzilyberis K, Ndroutsopoulos G (2002) Hydrogen catalytic oxidation reaction on Pd-doped porous silicon. *IEEE Sensors J* 2(2):89–95
69. Archer M, Fauchet P (2003) Electrical sensing of DNA hybridization in porous silicon layers. *Phys Stat Solidi A* 198(2):503–507
70. Barillaro G, Nannini A, Pieri F (2003) APSFET: a new, porous silicon based gas sensing devices. *Sens Actuator B* 93(1–3):263–270
71. Saha H, Dutta SK, Hossain SM, Chakraborty S, Saha A (1998) Mechanism and control of formation of porous silicon on p-type Si. *Bull Mater Sci* 21(3):195
72. Kanungo J, Pramanik C, Bandopadhyay S, Gangopadhyay U, Das L, Saha H, Gettens RTT (2006) Improved contacts on porous silicon layer by electroless nickel plating and copper thickening. *Semiconduct Sci Technol* 21(7):964–970
73. Archer M, Christophersen M, Fauchet P (2005) Electrical porous silicon chemical sensor for detection of organic solvents. *Sens Actuator B* 106(1):347–357
74. Smith R, Collins S (1992) Porous silicon formation mechanisms. *J Appl Phys* 71(8):R1–R22
75. Pancheri L, Oton CJ, Gaburro Z, Soncini G, Pavese L (2003) Very sensitive porous silicon NO₂ sensor. *Sens Actuator B* 89(3):237–239
76. Seals L, Tse L, Hesketh PJ, Gole J (2002) Rapid, reversible, sensitive porous silicon gas sensor. *J Appl Phys* 91(4):2519–2523
77. Marsh G (2002) Porous silicon a useful imperfection. *Mater Today* 5(1):36–41
78. Foucaran F, Delannoy FP, Giani A, Scakda A, Comette P, Boyer A (1997) Porous silicon layers used for gas sensor applications. *Thin Solids Films* 297(1–2):317–320
79. Baratto C, Sberveglieri G, Comini E, Faglia G, Benussi G, La Ferrara V, Quercia L, Di Francia G, Guidi V, Vincenzi D, Boscarino D, Rigato V (2000) Gold-catalysed porous silicon for NO_x sensing. *Sens Actuator B* 68(1–3):74–80
80. Woo-Jin L, Alhoshan M, Smyrl W (2006) Titanium dioxide nanotube arrays fabricated by anodizing processes electrochemical properties. *J Electrochem Soc* 153:B499–B505
81. Perathoner S, Passalacqua R, Centi G, Su DS, Weinberg G (2007) Photoactive titania nanostructured thin films: synthesis and characteristics of ordered helical nanocoil array. *Catal Today* 122:3–13
82. Bai J, Zhou B, Li L, Liu Y, Zheng Q, Shao J, Zhu X, Cai W, Liao J, Zou L (2008) The formation mechanism of titania nanotube arrays in hydrofluoric acid electrolyte. *J Mater Sci* 43:1880–1884
83. Quan X, Yang S, Ruan X, Zhao H (2005) Preparation of titania nanotubes and their environmental applications as electrode. *Environ Sci Technol* 39:3770–3775
84. Zhao J, Wang X, Chen R, Li L (2005) Fabrication of titanium oxide nanotube arrays by anodic oxidation. *Solid State Commun* 34:705–710
85. Mor GK, Carvalho MA, Varghese OK, Pishko MV, Grimes CA (2004) A room-temperature TiO₂-nanotube hydrogen sensor able to self-clean photoactivity from environmental contamination. *J Mater Res* 19:628–634

86. Mor GK, Varghese OK, Paulose M, Grimes CA (2003) A self-cleaning, room-temperature titania-nanotube hydrogen gas sensor. *Sens Lett* 1:42–46
87. Ruan C, Paulose M, Varghese OK, Grimes CA (2006) Enhanced photoelectrochemical-response in highly ordered TiO₂ nanotube-arrays anodized in boric acid containing electrolyte. *Sol Energy Mater Sol Cells* 90:1283–1295
88. Vitiello RP, Macak JM, Ghicov X, Tsuchiya H, Dick LFP, Schmuki P (2006) N-Doping of anodic TiO₂ nanotubes using heat treatment in ammonia. *Electrochem Commun* 8:544–548
89. Prida VM, Hernandez-Velez M, Pirota KR, Menendez A, Vazquez M (2005) Synthesis and magnetic properties of Ni nanocylinders in self-aligned and randomly disordered grown titania nanotubes. *Nanotechnology* 16:2696–2702
90. Zwilling V, Aucouturier M, Darque-Ceretti E (1999) Anodic oxidation of titanium and TA6V alloy in chromic media. An electrochemical approach. *Electrochim Acta* 45:921–929
91. Zwilling V, Darque-Ceretti B-FA, David D, Perrin MY, Aucouturier M (1999) Structure and physicochemistry of anodic oxide films on titanium and TA6V alloy. *Surf Interface Anal* 27:629–637
92. Tsuchiya H, Macak JM, Taveira L, Balaur E, Ghicov A, Sirotna K, Schmuki P (2005) Self-organized TiO₂ nanotubes prepared in ammonium fluoride containing acetic acid electrolytes. *Electrochem Commun* 7:576–580
93. Bauer S, Kleber S, Schmuki P (2006) TiO₂ nanotubes: tailoring the geometry in H₃PO₄/HF electrolytes. *Electrochem Commun* 8:1321–1325
94. Hazra A, Hazra SK, Dutta D, Sarkar CK, Basu S (2013) Studies on hydrogen sensing by anodized nanoporous titania thin film using soft drink electrolyte. *Front Sensors* 1(2):17–26
95. Taveira LV, Macák JM, Sirotna K, Dick LFP, Schmuki P (2006) Voltage oscillations and morphology during the galvanostatic formation of self-organized TiO₂ nanotubes. *J Electrochem Soc* 153:B137–B143
96. Hazra SK, Basu S (2006) High sensitivity and fast response hydrogen sensors based on electrochemically etched porous titania thin films. *Sens Actuator B* 115(1):403–411
97. Hazra A, Hazra SK, Bontempi E, Lakshmi VN, Sinha S, Sarkar CK, Basu S (2013) Anodically grown nanocrystalline titania thin film for hydrogen gas sensors – a comparative study of planar and MAIM device configurations. *Sens Actuator B* 188:787–796
98. Kanungo J, Maji S, Saha H, Basu S (2010) Chemical surface modification of porous silicon with palladium and characterizations. *Mater Sci Eng B* 167:91–96
99. Basu PK, Bontempi E, Maji S, Saha H, Basu S (2009) Variation of optical band gap in anodically grown nanocrystalline ZnO thin films at room temperature-effect of electrolyte concentrations. *J Mater Sci Mater Electron* 20(12):1203–1207. doi:10.1007/s10854-009-9852-0
100. Kanungo J, Maji S, Mandal A, Sen S, Bontempi E, Balamurugan A, Tyagi A, Uvdal K, Sinha S, Saha H, Basu S (2010) Surface treatment of nanoporous silicon with noble metal ions and characterizations. *Appl Surf Sci* 256:4231–4240
101. Paulose M, Mor GK, Varghese OK, Shankar K, Grimes CA (2006) Visible light photoelectrochemical and water-photoelectrolysis properties of titania nanotube arrays. *J Photochem Photobiol A* 178:8–15
102. Varghese OK, Gong D, Paulose M, Ong KG, Grimes CA, Dickey EC (2003) Crystallization and high-temperature structural stability of titanium oxide nanotube arrays. *J Mater Res* 18:156–165
103. Mor GK, Varghese OK, Paulose M, Grimes CA (2005) Transparent highly ordered TiO₂ nanotube arrays via anodization of titanium thin films. *Adv Funct Mater* 15:1291–1296
104. Cai Q, Paulose M, Varghese OK, Grimes CA (2005) The effect of electrolyte composition on the fabrication of self-organized titanium oxide nanotube arrays by anodic oxidation. *J Mater Res* 20:230–236
105. Ohya Y, Saiki H, Tanaka T, Takahashi Y (1996) Microstructure of TiO₂ and ZnO films fabricated by the sol–gel method. *J Am Ceram Soc* 79:825–830
106. Swanepoel R (1983) Determination of the thickness and optical constants of amorphous silicon. *J Phys E Sci Instrum* 16:1214–1222

107. Manifacer JC, Gasiot J, Fillard JP (1976) A simple method for the determination of the optical constants n , k and the thickness of a weakly absorbing thin film. *J Phys E Sci Instrum* 9:1002–1004
108. Sirohi S, Sharma TP (1999) Bandgaps of cadmium telluride sintered film. *Opt Mater* 13: 267–269
109. Tsuchiya H, Macak JM, Ghicov A, Rader AS, Taveira L, Schmuki P (2007) Characterisation of electronic properties of TiO₂ nanotube films. *Corros Sci* 49:203–210
110. Hoyer P, Weller H (1995) Potential-dependent electron injection in nanoporous colloidal ZnO films. *J Phys Chem* 99(38):14096–14100
111. Moya M, Samantilleke AP, Mollar M, Mari B (2011) Nanostructured hybrid ZnO thin films for energy conversion. *Nanoscale Res Lett* 6:384. doi:10.1186/1556-276X-6-384
112. Li Z, Enqin G, Maizhi Y, Xuebin Q, Yanzhong H, Shengmin C (1999) Photoelectrochemical properties of the SnO₂ nanoporous film sensitized by cyanine dye. *Acta Phys-Chim Sin* 15(4):293–298
113. Rao P, Schiff EA, Tsybeskov L, Fauchet PM (1997) Electron time-of-flight measurements in porous silicon. In: Collins RW, Fauchet PM, Shimizu I, Vial J-C, Shimada T, Alivisatos AP (eds) *Advances in microcrystalline and nanocrystalline semiconductors-1996*, Materials Research Society, symposium proceedings, Pittsburgh, vol 452, pp 613–618
114. Alivov Y, Pandikunta M, Nikishin S, Fan ZY (2009) The anodization voltage influence on the properties of TiO₂ nanotubes grown by electrochemical oxidation. *Nanotechnology* 20:225,602–225,607. doi:10.1088/0957-4484/20/22/225,602
115. Mitsui T, Rose MK, Fomin E, Ogletree DF, Salmeron M (2003) Dissociative hydrogen adsorption on palladium requires aggregates of three or more vacancies. *Nature* 422:705–707
116. Tomaszewska A, Stepien ZM (2005) Hydrogen chemisorptions on palladium surface in a high electric field. *Optica Applicata XXXV*(3):375–383
117. Bartzczak WM, Stawowska J (2004) Interaction of dihydrogen with transition metal (Pd, Ni, Ag, Cu) clusters. *Struct Chem* 15(5):447–459
118. Greenwood NN, Earnshaw A (1984) *Chemistry of the elements*. Pergamon Press, Oxford
119. Varghese OK, Gong D, Paulose M, Ong KG, Dickey EC, Grimes CA (2003) Extreme changes in the electrical resistance of titania nanotubes with hydrogen exposure. *Adv Mater* 15: 624–627
120. Yoriya S, Prakasam HE, Varghese OK, Shankar K, Paulose M, Mor GK, Latempa TA, Grimes CA (2006) A transcutaneous hydrogen sensor: from design to application. *Sens Lett* 4:120–128
121. Deresmes D, Marissael V, Stievenard D, Ortega C (1995) Electrical behaviour of aluminium-porous silicon junctions. *Thin Solid Films* 255:258–261
122. Khoshnevis S, Dariani RS, Azim-Araghi ME, Bayindir Z, Robbie K (2006) Observation of oxygen gas effect on porous silicon-based sensors. *Thin Solid Films* 515:2650–2654
123. Polishchuk V, Souteyrand E, Martin JR, Strikha VI, Skryshevsky VA (1998) A study of hydrogen detection with palladium modified porous silicon. *Anal Chim Acta* 375:205–210
124. Luongo K, Sine A, Bhansali S (2005) Development of a highly sensitive porous Si based hydrogen sensor using Pd nano-structures. *Sens Actuators B* 111–112:125–129
125. Sekhar PK, Sine A, Bhansali S (2007) Effect of varying the nanostructured porous-Si process parameters on the performance of Pd-doped hydrogen sensor. *Sens Actuators B* 127:74–81
126. Rahimi F, Irajizad A (2006) Effective factors on Pd growth on porous silicon by electroless-plating: response to hydrogen. *Sens Actuators B* 115:164–169
127. Kanungo J, Saha H, Basu S (2010) Effect of porosity on the performance of surface modified porous silicon hydrogen sensors. *Sens Actuators B* 147:145–151
128. Jeske M, Schultze JW, Thonissen M, Munder H (1995) Electrodeposition of metals into porous silicon. *Thin Solid Films* 255:63–66
129. Kanungo J, Maji S, Saha H, Basu S (2009) Stable aluminium ohmic contact to surface modified porous silicon. *Solid State Electron* 53:663–668
130. Hung CW, Lin KW, Liu RC, Tsai YY, Lai PH, Fu SI, Chen TP, Chen HI, Liu WC (2007) On the hydrogen sensing properties of a Pd/GaAs transistor-type gas sensor in a nitrogen ambience. *Sens Actuators B* 125:22–29

131. Kanungo J, Saha H, Basu S (2010) Pd sensitized porous silicon hydrogen sensor—Influence of ZnO thin film. *Sens Actuators B* 147:128–136
132. Basu PK, Bhattacharyya P, Saha N, Saha H, Basu S (2008) The superior performance of the electrochemically grown ZnO thin films as methane sensor. *Sens Actuators B* 133(2): 357–363
133. Basu PK, Jana SK, Saha H, Basu S (2008) Low temperature methane sensing by electrochemically grown and surface modified ZnO thin films. *Sens Actuators B* 135(1):81–88
134. Shin HC, Dong J, Liu M (2003) Nano-porous tin oxides with honeycomb-like channels for lithium batteries. *The Electrochemical Society, Inc Abs.* 988, 204th meeting, 2003
135. Liying M, Jun Z, Jieqiang W, Hongyan X, Bingqiang C (2013) Microwave-assisted hydrothermal synthesis and gas sensitivity of nanostructured SnO₂. *Particuology* 11(2):242–248
136. Guoqiang W, Zhang J, Wang X, Liao J, Xia H, Akbar SA, Li J, Lin S, Li X, Wang J (2012) Hierarchical structured TiO₂ nano-tubes for formaldehyde sensing. *Ceramics Int* 38(8): 6341–6347
137. Parthangal P, Cavicchi RE, Meier DC, Herzing A, Zachariah MR (2011) Direct synthesis of tin oxide nanotubes on microhotplates using carbon nanotubes as templates. *J Mater Res* 26(3):430–436
138. Kanungo J, Saha H, Basu S (2009) Room temperature metal-insulator-semiconductor MIS hydrogen sensors based on chemically modified porous silicon. *Sens Actuator B* 140(1): 65–72

Razika Tala-Ighil

Contents

Introduction.....	1252
Classical Solar Cells	1252
Different Forms of Nanomaterials	1255
Nanomaterials in Inorganic Solar Cells	1260
Nanomaterials in Organic Solar Cells.....	1262
Photoanodes for Dye-Sensitized Solar Cells	1263
Nanomaterial-Based Solar Cell Performance	1265
Conclusion	1267
References.....	1267

Abstract

Reducing cost and improving conversion efficiency are the main tasks in order to make photovoltaic energy competitive and able to substitute traditional fossil energies.

Nanotechnology seems to be the way by which photovoltaics can be developed, whether in inorganic or organic solar cells. Wide-bandgap nanostructured materials (nanomaterials) prepared from II–VI and III–V elements are attracting an increased attention for their potential applications in emerging energy. They can be prepared in different geometric shapes, including nanowires (NWs), nanobelts, nanosprings, nanocombs, and nanopagodas. Variations in the atom arrangements in order to minimize the electrostatic energy originated from the ionic charge on the polar surface are responsible for a wide range of nanostructures.

This book chapter will focus on contribution of nanomaterials in solar cell technology advancement.

R. Tala-Ighil (✉)

Unité de recherche matériaux, procédés pour l'environnement, URMPE Institute of Electrical & Electronic Engineering, University M'Hamed Bougara, Umbb, 35000 Boumerdes, Algeria
e-mail: t_razika@hotmail.com

Keywords

Nanomaterials • Solar cells • Organic • Inorganic • Nanopillars • Nanowires • Nanobelts • Nanorods • Photocarrier collection

Introduction

Solar cells have known a big expansion these last years due to the voluntary move to cleaner energies like photovoltaics. Table 1 summarizes the chronological evolution of photovoltaic cells with their main characteristics.

After solid-state physics has shown its limits by reaching the maximum possible conversion efficiency for silicon, CdTe, and CuInSe₂, the highest conversion efficiency was obtained for triple-junction compound InGaP/GaAs/InGaAs solar cell with 37.9 % [6]. Chemistry seems to be another way by which an increase of the solar cell conversion efficiency is possible.

Nanomaterials made by chemical ways present high opportunity in efficiency enhancement by increasing light trapping and photocarrier collection without additional cost in solar cell fabrication.

The physical and chemical properties change from the bulk material to the nanomaterial. As an example, the melting point is lowest for the nanomaterial compared to its bulk one. This can be due to the high surface-to-volume ratio of atoms in a nanoparticle [7].

The main nanomaterial physical property is the large surface-to-volume ratio [6] due to different forms created; nanowires [8, 9], nanopillars [10, 11], nanocones [12], quantum dots [13].

It has been shown that light trapping is due to the increase of the photon path inside nanostructures [14–16] which enhance the electron–hole pair creation probability.

Quantum dots (QDs) have the particularity to have a size-dependent bandgap [13, 17, 18] so it can be adjusted to fit the maximum solar spectrum.

Classical Solar Cells

Before introducing the added value of nanomaterials in solar cells, a brief comeback should be presented to understand the work mechanism of solar cells.

Table 1 The four generations of solar cells and their characteristics

Solar cells evolution	Characteristics
First generation: bulk silicon	High cost with high efficiency [1]
Second generation: thin film solar cells	Amorphous or polycrystalline silicon, CIGS and CdTe [2, 3]
Third generation	Organic solar cells with nanocrystalline films [4]
Fourth generation	Combines the low cost/flexibility of polymer thin films with inorganic nanostructures [5]

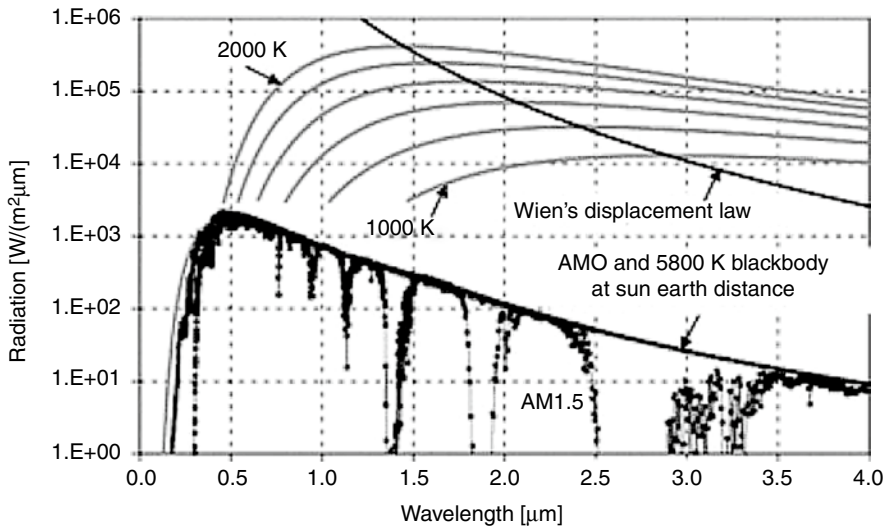


Fig. 1 Comparison of solar spectra at Sun-Earth distance and blackbody spectra in semi-logarithmic scale reprinted with permission from Ref. [20]

A solar cell is an electronic device, a P/N junction in its basic form, which has the ability to convert sunlight into electricity. This phenomenon was discovered by Edmond Becquerel in 1839 and is called the photovoltaic effect [19].

Not all materials can be solar cell components. Because the main feature should be the capacity to convert the visible spectrum of the sun into electricity, this can occur only by the creation of electron-hole pairs when the material absorbs photons corresponding to an energy greater or equal to its energy gap (Fig. 1).

The air mass (AM) is the level at which the atmosphere reduces the light reaching the Earth's surface [21].

AM0: The spectrum outside the atmosphere.

AM1.5: The used standard solar spectrum for terrestrial solar cells, it corresponds to a solar zenith angle of 48.2° .

From the figure, the blackbody radiation increases from 1,000 to 2,000 K in 200 K steps (small values overlapping with solar spectra are not shown). The blackbody maximum values are given by Wien's displacement law, also shown (black). The AM1.5 solar spectrum (black) shows strong absorption bands, whereas the AM0 spectrum (black) closely matches a 5,800 K blackbody at Sun-Earth distance (gray) [20].

One can see clearly that the blackbody maximum shifts toward higher wavelengths with its temperature according to Wien's displacement law. This law implies that a photovoltaic (PV) cell with a higher-energy bandgap corresponds to higher radiator temperature. The bandgap for silicon solar cells is $h\nu = 1.12$ eV (which responds up to 1.11 μm) and matches to the maximum of a blackbody at $2,610$ K [20, 22]. The most important part of the solar spectrum ranges in the visible light from 0.38 to 0.76 μm . It reaches its maximum at the wavelength of 4 μm [20].

So, the selection criterion of a photovoltaic absorbant is first its energy gap around 1 eV. Many materials fit with this bandgap energy. The most widely used is silicon, with its different forms: monocrystalline or multicrystalline, gallium arsenide GaAs, cadmium telluride CdTe, copper indium diselenide CIS, $\text{Cu}_2\text{ZnSnS}_4$ (CZTS), and other materials [23–25].

As cited above, a basic solar cell is a P/N junction. A P-type semiconductor has holes in excess while an N-type semiconductor has electrons in excess. There is free carrier migration from one side to the other until reaching equilibrium.

A built-in electric voltage is then created and, in consequence, electron–hole pairs. When the solar cell is connected to an electrical circuit, a current is formed across the PV cell [21] (Fig. 2).

The conversion efficiency (η) and the fill factor (FF) are calculated according to the equations listed below [26]:

$$\eta(\%) = \frac{V_{\max} \times J_{\max}}{P_{\text{in}}} \times 100\% = \frac{V_{\text{oc}} \times J_{\text{sc}} \times \text{FF}}{P_{\text{in}}} \times 100\%$$

$$\text{FF} = \frac{V_{\max} \times J_{\max}}{V_{\text{oc}} \times J_{\text{sc}}}$$

where

J_{sc} : The short-circuit current density (mAcm^{-2})

V_{oc} : The open-circuit voltage (V)

P_{in} : The incident light power

J_{\max} : The current density at the maximum power output in the J-V curves

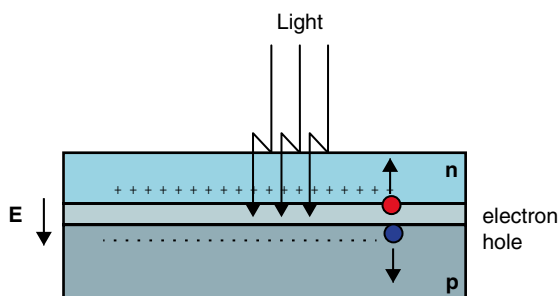
V_{\max} : The voltage at the maximum power output in the J-V curves

Each parameter has its specific influence on solar cell performance.

The fill factor, abbreviated *FF*, is a parameter which characterizes the nonlinear electrical behavior of the solar cell. Fill factor is defined as the ratio of the maximum power from the solar cell to the product of Open Circuit Voltage V_{oc} and Short-Circuit Current I_{sc} . The typical fill factor for commercial solar cells is usually 0.70 [27].

Classical solar cells require thicker materials to perform good optical absorption but loose carrier collection efficiency due to the higher minority carrier length [28].

Fig. 2 Basic solar cell structure and effect of light (Reprinted with permission from Ref. [21])



Different Forms of Nanomaterials

- **Nanowires** Different architectures have been proposed by researchers to improve the light absorption and carrier collection [10, 29, 30]

As an example, silicon nanowires enhanced the incident solar radiation path length up to a factor of 73 [31].

- It has been found that Ag nanowire mesh electrodes show low transparency and low sheet resistance. They match very well with flexible substrates in organic solar cells. An increase of 19 % in the photocurrent has been reported [32].
- The nanowires of silver can be deposited by a very low-cost method: simple brush painting, as performed by J.-W. Lim et al. with a conversion efficiency of 3.231 % [33].
- There are many deposition techniques for nanowire or nanocone arrays. One of the simplest is colloidal lithography, which is time effective, reproducible, and suitable for large-scale deposition [34]. Another one is the vapor-liquid-solid (VLS) method usually used for a core different from an outer shell (core-shell nanowires) [35].

The figure below illustrates the scanning electron microscopy (SEM) images for ZnO nanowires and nanorods [36] (Fig. 3).

- **Nanotubes**

- Carbon nanotube conductive layers were deposited on n-type silicon to form a Schottky junction photovoltaic cell with a conversion efficiency of 1.9 % under AM1.5 illumination. This efficiency has been increased to 8.6 % just by chemical charge transfer doping with bis (trifluoromethane sulfanyl) amide [(CF₃SO₂)₂NH] (TFSA) [37].

The main advantage of this solar cell type is that the graphene's work function can be varied to optimize the solar cell efficiency compared to the basic Schottky solar cell with indium tin oxide ITO over silicon (ITO/Si).

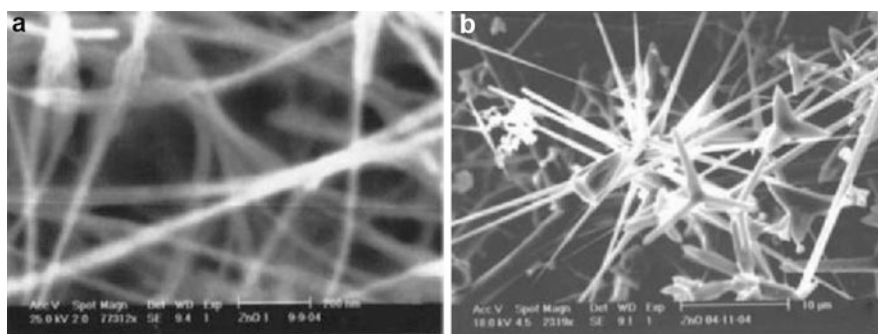
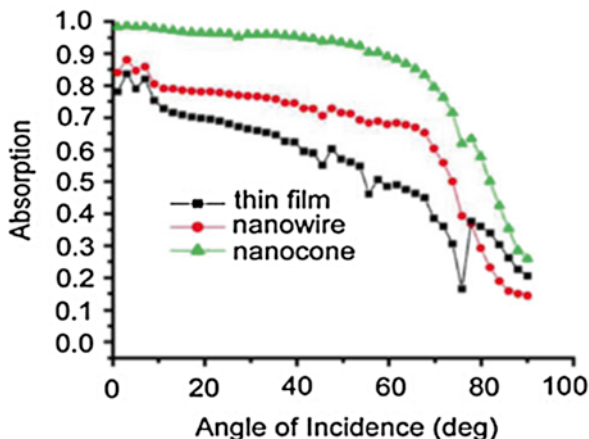


Fig. 3 Scanning electron micrograph from the different temperature zone showing (a) nanowires and (b) star nanorods (Reprinted with permission from Ref. [36])

Fig. 4 Absorption of ITO/a-Si:H samples with a-Si:H thin film, nanowire arrays, and nanocone arrays as top layer over different angles of incidence at wavelength $\lambda=488$ nm (Reprinted with permission from Ref. [28] (copyright 2011, Elsevier) and Ref. [12] (copyright 2011, American Chemical Society))



- Titanium dioxide nanotubes have been employed as transparent photoanodes for dye-sensitized solar cells. The nanotube shape for TiO_2 permits to have unequal electronic properties such as low carrier recombination, high electron mobility, and high surface-to-volume ratio [38]. It increases the electron transport by using direct pathways for the charge transfer [39, 40].

– **Nanococones:**

According to Fig. 4, one can remark that the absorption in a nanocone is greater than the absorption in a nanowire, which is greater in turn than a thin film. It is obvious that nanomaterials by their specific architectures contribute sensibly in conversion efficiency increase.

Silicon nanowires have shown a short collection length for excited carriers, which enhances considerably the carrier collection efficiency [14].

For classical hydrogenated amorphous silicon [a-Si:H] solar cells, there is an intrinsic problem which lowers the conversion efficiency. It is due to the high trap amounts that reduce the carrier lifetime.

An alternative is proposed by using a nanocone array structure as shown in Fig. 5.

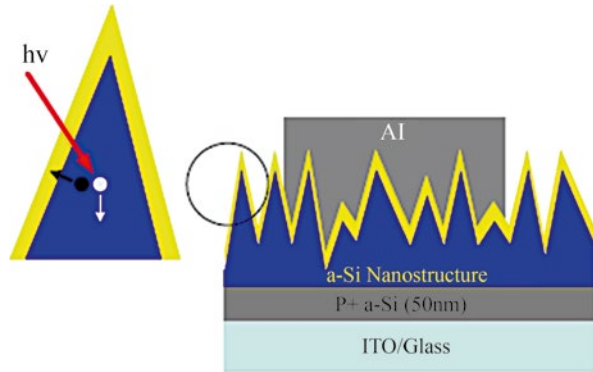
With carrier collection enhancement, an efficiency increase has been observed from 1.43 % to 1.77 % and so an enhancement of 24 % [41].

- **Nanopillars:** Nanopillar photovoltaics has many features that confer to it the capacity to replace classical photovoltaics due to its low cost. They can be listed below:

1. Growth of crystallized materials without using expensive techniques
2. Increase of carrier collection efficiency
3. Reduction of optical losses

The fabrication process of nanopillars is well illustrated in Fig. 5. There are four main steps: electropolishing, first anodization, wet etching, and finally the second anodization step [42] (Fig. 6).

Fig. 5 The schematic structure for a nanocone solar cell. Enlarged part of the a-SiH-nanocone structure describes the photogeneration and transport mechanism (Reprinted with permission from Ref. [41])



– Nanobelts

- Transparent graphene, i.e., carbon nanotube (CNT), layers have been used to cover CdSe nanobelts along certain positions. Really interesting solar cells based on Schottky junction have been made with this method by using different configurations and several connections from single or multiple assembled nanobelts [44].

The above solar cell has been fabricated by following three steps: the first one is the CdSe nanobelt deposition, then the graphene transfer, and finally the Ag paste contact formation.

The particularity of this solar cell is its low-cost manufacturing method based essentially on the chemical vapor deposition (CVD) process for both CdSe nanobelts and graphene films in addition to being a flexible thin-film photovoltaic cell [45].

A conversion efficiency of 0.1 % has been reached with an open-circuit voltage of 0.5 V and a short-circuit current density J_{sc} of 0.94 mA/cm² [44]. The cited photovoltaic structure is shown in Fig. 7:

One can remark that the small value of the conversion efficiency (0.1 %) is affected essentially by the weak value of the fill factor (FF) (less than 23.7 %) [44]. An improvement of this parameter is required to increase sensibly the conversion efficiency and to assess the position of this solar cell type as an alternative to the classical ones.

– Nanopagodas

Aligned ZnO nanopagoda arrays have been successfully carried out by Chang Yu-Cheng et al. [46]. They have very interesting properties in field emission devices and will permit to manufacture promising devices, especially dye-sensitized solar cells.

– Nanocombs

The nanocomb-shaped nanomaterials are represented in Fig. 8.



Fig. 6 R2R Al texturing system: **(a)** optical image of the R2R system used for Al texturization. The important components of the system are highlighted as (1) Al feeding roll, (2) electrical contact to the Al foil, (3) reaction chamber, (4) rinse bath, (5) capstan roll, and (6) rewinding roll. **(b)** Zoomed-in optical image of the reaction chamber, and **(c)** The rinse bath, respectively **(d)** Schematic diagrams of the process, and **(e)** The resulting surface structure after (i) electropolishing, (ii) first anodization, (iii) AAO wet etching and (iv) second anodization steps used for the fabrication of various surface textures (Reprinted with permission from Ref. [42] (copyright 2011, Elsevier) and Ref. [43] (copyright 2011, American Chemical Society))

– Nanorods

- Conjugated polymer donor and a ZnO acceptor have been used for elaboration of hybrid polymer solar cells. For this purpose, ZnO nanorods were grown on an indium tin oxide-coated glass from a mixture containing Zn^{+2} by using a hydrothermal method [47].

Fig. 7 Graphene – CdSe nanobelt schottky junction solar cells: illustration of a single layer graphene covered on the top surface of a CdSe nanobelt. The overlapped area forms the junction that is responsible for charge separation (Reprinted with permission from Ref. [44])

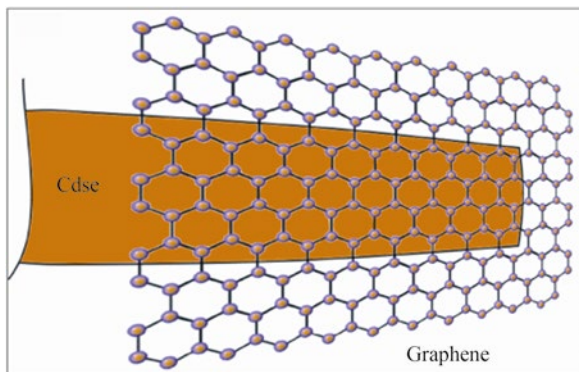
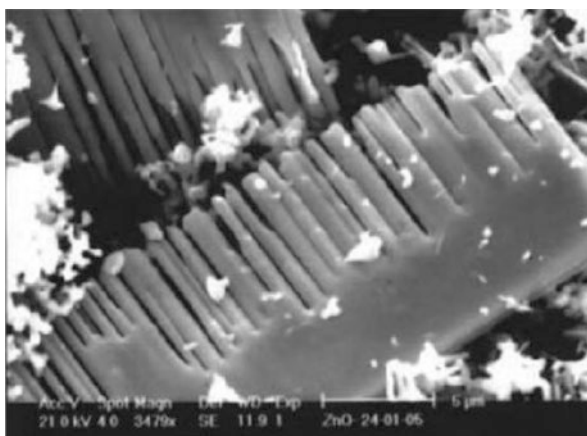


Fig. 8 Scanning electron micrograph of comb-like structures (Reprinted with permission from Ref. [36])



The ZnO nanorods which contain the filtered solution poly [1-methoxy-4-(2-ethylhexyloxy-2,5-phenylenevinylene)] form the active layer for the hybrid bulk heterojunction solar cells. An efficiency of only 0.045 % was obtained, which reveals that work should be done to reduce the high interior resistance of the PV cell [47].

Figure 9 illustrates the scanning electron microscopy images for different Zn^{+2} concentrations: 0.0125, 0.025, 0.05, and 0.1 mole. The ZnO nanorod diameter becomes bigger with increasing Zn^{+2} concentration [47].

It has been found that the electron mobility is 10^{-1} to $10^{-3} \text{ cm}^2 \text{ V}^{-1} \text{ s}^{-1}$ for nano zinc oxide and $100 \text{ cm}^2 \text{ V}^{-1} \text{ s}^{-1}$ for bulk zinc oxide. There is a considerable difference which explains the higher quality of nano ZnO compared to bulk ZnO [47].

The 0.3 eV energy level difference of zinc oxide with polymer donors leads to the efficient separation of excitons into free carriers [48, 49].

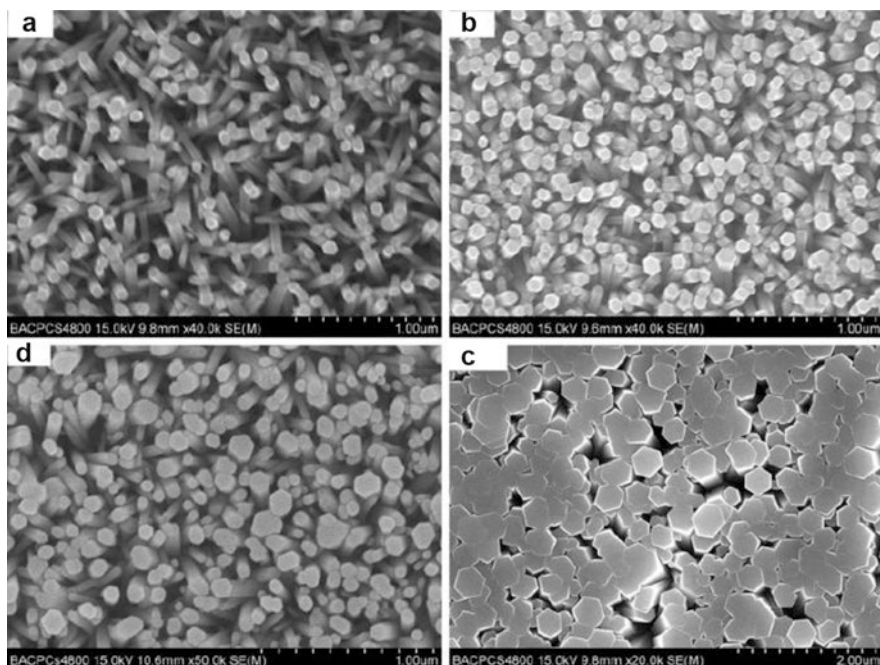


Fig. 9 SEM top-view image of ZnO nanorods under different Zn^{2+} concentrations: (a) 0.0125; (b) 0.025; (c) 0.05; and (d) 0.1 M (Reprinted with permission from Ref. [47])

Nanomaterials in Inorganic Solar Cells

- **Silicon:** Increase in silicon solar cell performance can be obtained by improving silver screen-printed contact. This can be done by introducing silver nanoparticles in the paste to increase contact compactness and consequently the fill factor and the conversion efficiency η .

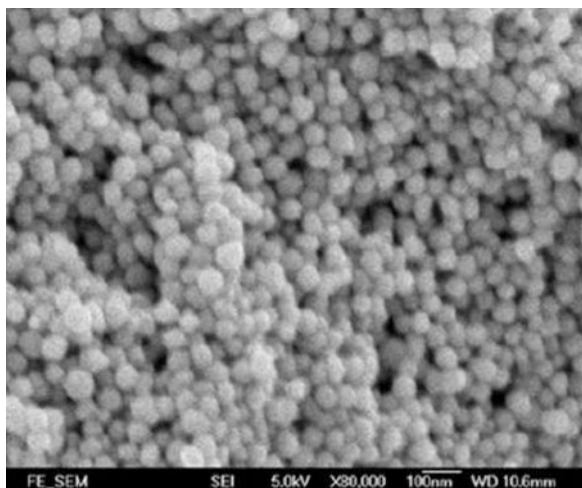
Silicon can be also used as nanowires in solar cells. Their diameters vary from 200 nm to 1.5 μm . It has been found that the minority carrier diffusion length is around 2 μm , the minimum carrier lifetime is 15 ns, while the maximum surface recombination velocity is approximately 1,350 cm s^{-1} [50].

These values are really different for silicon bulk material: the diffusion length is around 200 μm , the minimum carrier lifetime 30 μs , and finally the surface recombination velocity 8,600 cm/s [51].

The effect of nanomaterials in improving solar cell efficiency seems to be obvious when the previous data are compared. The recombination velocity is reduced with the nanomaterial structure, which means that photon collection is increased (Fig. 10).

- **CuInSe₂** Copper indium diselenide (CIS) thin layers represent another type of absorbant widely used in photovoltaics due to the fact that their energy gap matches perfectly the maximum solar spectra [53].

Fig. 10 FESEM micrograph of the as-prepared silver nanoparticles prepared by solvothermal process (Reprinted with permission from Ref. [52])



This type of material has the advantage compared to silicon of quantity of matter: the CIS is deposited as thin films with approximately 1 μm thickness while for silicon thick substrates of around 300 μm are required.

A second CIS advantage comes from the fact that to have type n or p semiconductor, there is no need of doping; just a small deviation of stoichiometry is necessary.

The classical CIS has generally the following structure: Mo/CuInSe₂/CdS/ZnO solar cell

Mo is molybdenum and represents the rear contact.

CuInSe₂ is the CIS pn junction CIS(p)/CIS(n).

CdS is the buffer layer

ZnO is the window layer

Many techniques have been used to deposit CIS layers: coevaporation and sputtering [54–56].

A conversion efficiency of 20.1 % has been reported for CIS films deposited by coevaporation [55].

The CIS morphology can be tuned just by changing the amount of strong and weak surfactants which passivate the surface. For example CIS nanowires can be obtained by using weakly binding dioctylphosphine oxide (DOPO), an impurity in trioctylphosphine oxide (TOPO) [57].

Band gap for spherical CIS nanoparticles can be adjusted according to the nanoparticles radius. While for CIS nanorods influence directly the energy gap, the diameter of the nanorods influence directly [57].

For p-type $\text{CuIn}_{1-x}\text{Ga}_x\text{Se}_2$ (CIGS) layers introduced in solar cells, electron mobilities vary from 0.02 to 0.05 cm^2/Vs . These values are less than those for n-type CIGS materials, which sweep from 2 to 1,100 cm^2/Vs [58].

An efficiency of 15 % for classical CIGS solar cells has been reported [58].

CdTe Cadmium telluride (CdTe) is one of the absorbant PV materials with its bandgap of 1.45 eV. It is used also combined to cadmium sulfide (CdS).

The solar cell structure ITO/CdTe/CdS/CNTs acts as front electrode/p-type semiconductor/n-type semiconductor/rear contact.

where CNTs: carbon nanotubes

ITO: indium tin oxide

A conversion efficiency from 3.5 % at orthogonal azimuthal angle to 7 % at 45° solar incidence [34].

– CdS

Cadmium sulfide (CdS) enters in the fabrication of the solar cells based on fluorine-doped tin oxide (FTO)/Au/TiO₂/CdS photoanode and polysulfide electrolyte. Gold nanoparticles have been used as an interfacial layer between FTO and TiO₂. Conversion efficiency increases from 0.86 % to 1.62 % for the structures FTO/Au/TiO₂/CdS and FTO/TiO₂/CdS respectively. So there is an enhancement of 88 % due basically to the Au nanoparticle incorporation [31].

Successive ionic layer adsorption and reaction (SILAR) techniques have been used for CdS deposition onto TiO₂ layers [59].

– CdSe

- The combination CdTe/CdSe core/shell structures have the particularity to emit in the near-infrared region, which doesn't exist for CdTe or CdTe nanoparticles taken apart [60].

The success of the structure core/shell depends directly on the lowest lattice mismatch between the used materials [61].

Polymeric solar cells with CdTe quantum dots (QDs) with single-wall carbon nanotubes (SWNTs) incorporated into a poly(3-octylthiophene)-(P3OT) composite have shown good exciton dissociation and carrier transport. An open-circuit voltage $V_{oc}=0.75$ V and short-circuit current density $J_{sc}=0.16$ $\mu\text{A}/\text{cm}^2$ have been obtained [62].

Nanomaterials in Organic Solar Cells

Organic solar cells have gained attention these last years. Key phenomena in PV cell manufacturing were consequently mastered like exciton generation effect, light trapping, and one-dimensional material for Schottky barrier arrays [63].

Organic solar cells, also called photoelectrochemical solar cells, are composed of photoactive electrode (semiconductor) and counter electrode (metal or semiconductor) immersed, both of them, in an electrolyte which contains redox couples. Electron/hole pairs are created when light with energy greater than those of the semiconductor is absorbed [64] (Fig. 11).

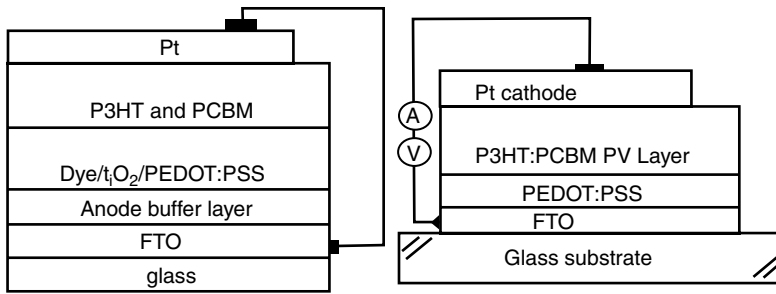


Fig. 11 Schematic diagram of FTO/TiO₂/dye/PEDOT:PSS/P3HT:PCBM (PSCs-1) and FTO/PEDOT:PSS/P3HT:PCBM (PSCs-2) heterojunction solar cells (Reprinted with permission from Ref. [65])

Table 2 Photoelectric performances for PSC-1 (Reprinted with permission from Ref. [65])

P3HT:PCBM (2:1)	V _{oc} (V)	J _{sc} (mAcm ⁻²)	FF	η (%)
Barrier	0.82	3.63	0.68	2.04
Atm. annealed	0.83	3.96	0.67	2.19
Vacuum annealed	0.83	4.30	0.67	2.37

Table 3 Photoelectric performances for PSC-2 (Reprinted with permission from Ref. [65])

P3HT:PCBM (2:1)	V _{oc} (V)	J _{sc} (mAcm ⁻²)	FF	η (%)
Barrier	0.80	2.83	0.65	1.48
Atm. annealed	0.78	3.27	0.62	1.58
Vacuum annealed	0.80	3.59	0.66	1.90

Photoanodes for Dye-Sensitized Solar Cells

– TiO₂

The corresponding solar cell performances are represented in Tables 2 and 3 [65].

TiO₂ nanomaterials can also be prepared by following a novel method, by combining dealloying process with chemical synthesis. A hierarchical nanostructure was obtained with a thickness of approximately 10 μm. It has the shape of nanoflower arrays and nanorods [66].

The nanoflower is composed of many nanopetals of 100–200 nm in diameter [66].

For titanium dioxide TiO₂, a new process called low-temperature solid-state dye-sensitized solar cell (LT-SDSC) has been carried out. As its name denotes, everything is obtained at low temperatures, which reduces directly the energy cost and yields cheaper solar cells [67].

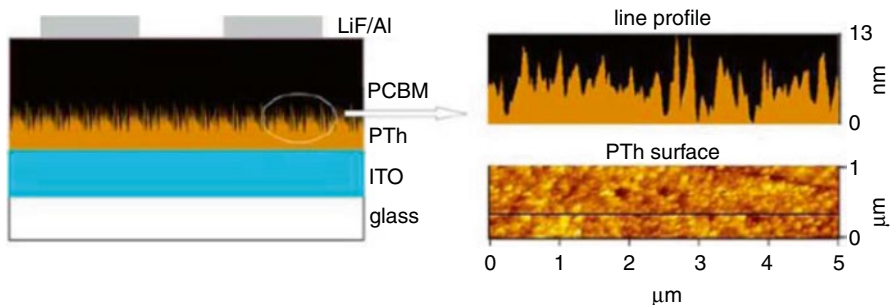


Fig. 12 The schematic structure of ITO/PTh/PCBM/LiF/Al organic solar cell (*left*) and AFM image (*bottom right*) of PTh/PCBM interface with profile line (*top right*) (Reprinted with permission from Ref. [68])

It consists in a mesoporous TiO_2 (mp- TiO_2) layer realized from a binder-free nanoparticle TiO_2 paste at room temperature. A conversion efficiency of 1.30 % was found for a photovoltaic cell with LT-SDSC 0.9 μm mp- TiO_2 and 20 nm ALD- TiO_2 [67].

- **ITO:** According to reference [68], an organic solar cell (OSC) has been prepared by using electrochemistry method.

The structure of this organic solar cell is presented in Fig. 12:

The bilayer heterojunction (OSC) had followed a two-step solution-based method: firstly electrodepositing polythiophene (PTh) and secondly a spin-coating chloroform solution of [6, 6]- phenyl C61-butyric acid methyl ester (PCBM) onto the PTh layer [68].

The PTh layer plays the role of a donor material due to its high hole mobility [68].

The conversion efficiency of this structure is around 0.1 % [68].

- **ZnO**

Hybrid solar cells based on the structure FTO/ TiO_2 /N719/P3HT:PCBM/Au have been fabricated [69] with

FTO: fluorine-doped tin oxide $\text{SnO}_2:\text{F}$

TiO_2 : titanium dioxide shaped as nanotube arrays

N719: Ruthenium (II) dye

P3HT: poly (3-hexyl-thiophene)

PCBM: [6, 6]-phenyl-C61-butyric acid methyl ester (PCBM)

TiO_2 nanotube arrays have been deposited on FTO by using a liquid-phase deposition method with ZnO template while the zinc oxide nanorods have been grown according to the method detailed in the references [70–73].

The hydrothermal process for ZnO nanorods can be summarized as follows:

$\text{Zn}(\text{CH}_3\text{COO})_2$ was added to water with stirring; after 10 min, citric acid was added to the previous mixture. After that, these solutions were sealed in stainless autoclaves at temperatures 120 °C, 160 °C, and 200 °C during 20 h. A white product was obtained and dried at 60 °C [71].

A conversion efficiency of 0.656 % was obtained [69].

Nanomaterial-Based Solar Cell Performance

- Anodic titanium oxide (ATO) nanotube-based dye-sensitized solar cells have shown a conversion efficiency of 2.9 %, 3.9 % and a fill factor of 0.51, 0.65 with and without bottom reductive doping treatment respectively [74].

I(V) characteristic for CdS NW core and Cu₂S shell [75] (Figs. 13 and 14).

Table 4 shows the organic solar cell performance [68]:

- Concerning the nanocone silicon solar cells, their performance is reported in Table 5 [41].

Thus, there is an efficiency increase when the nanocone architecture is adopted. The effect of the nanomaterial shape is confirmed.

- The characteristic of the structure FTO/TiO₂/CdS with and without gold nanoparticles is shown in Table 6.
- **SWNTs**, in other words “the semiconducting single-walled carbon nanotubes”: by using this material, Zhang et al. have achieved a solar cell with a conversion efficiency of 12.6 % [76].
- For dye-sensitized solar cells (DSSCs) based on TiO₂ nanocrystalline electrodes, Andréa de Morais et al. have improved their efficiency by introducing acid-treated multiwall carbon nanotubes (MWCNT-COOH). A conversion efficiency of 3.05 % was obtained for DSSC based on MWCNT-TiO₂ and 2.36 % for DSSC based on TiO₂ [77].

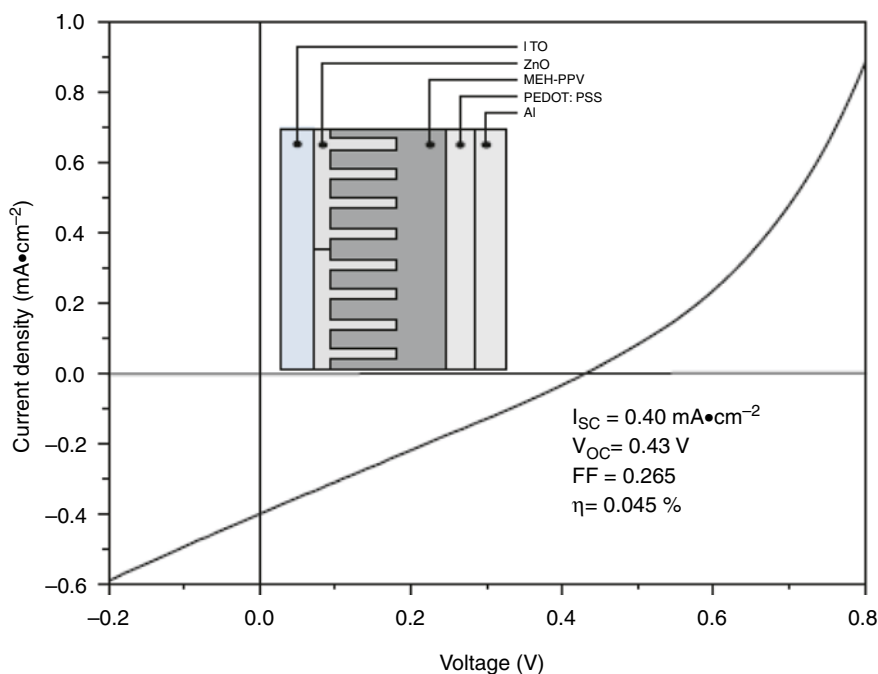


Fig. 13 I(V) characteristics of the MEH-PR/ZnO nanorod hybrid polymer solar cell illumination with a 100 mW/cm² light density (Reprinted with permission from Ref. [47])

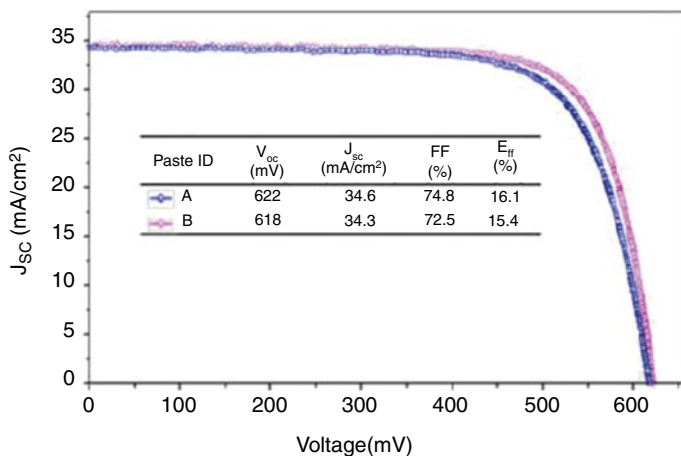


Fig. 14 I(V) performances of crystalline silicon solar cells based on different silver paste under AM1.5 (1,000 W/m²) (Reprinted with permission from Ref. [52])

Table 4 The performances of single-layer (PTh) and bilayer (PTh/PCBM) solar cell devices under illumination of AM1.5 (100 mWcm⁻²) (Reprinted with permission from reference [68])

Active layer	J_{sc} (mAcm ⁻²)	V_{oc} (V)	FF	PCE (%)
PTh	0.02	0.8	0.26	0.004
PTh/PCBM	0.4	0.6	0.42	0.1

Table 5 The detailed photovoltaic properties of a-Si:H nanocone solar cell, PCE power conversion efficiency, J_{sc} short circuit current density, R_{sh} shunt resistance, V_{oc} open circuit voltage, R_s series resistance (Reprinted with permission from Ref. [41])

Type	PCE (%)	J_{sc} (mA/cm ²)/ R_{sh} (Ω -cm ²)	Fill factor (%)	V_{oc} (V)/ R_s (Ω -cm ²)
PI/N	1.43	5.0/624	36.4	0.78/176
P/I(nanocone)/N	1.77	5.7/572	38.5	0.80/160
P/I(nanocone)/N (H2 Plasma)	2.0	5.8/800	41.4	0.83/62
P/I(nanocone)/N (H2 Plasma + 10 nm)	2.2	5.9/847	44.3	0.83/61

Table 6 Photovoltaic parameters of FTO/TiO₂/CdS and FTO/Au/TiO₂/CdS cells (Reprinted with permission from Ref. [59])

Electrode	V_{oc} (V)	I_{sc} (mA/cm ²)	FF	η (%)
FTO/Au/TiO ₂ /CdS	0.56	7.11	0.41	1.62
FTO/TiO ₂ /CdS	0.47	5.72	0.38	0.82

Conclusion

Solar cell performance is the perpetual challenge for researchers to make photovoltaic energy widely used in our daily life.

Nanoelectrochemistry seems to be a non-negligible alternative for widely used, high-performance, and low-cost solar cell fabrication by employing processes based essentially on chemistry.

It is due basically on the fact that these processes are carried out at low temperatures or at ambient temperature, which reduces sensibly the energy bill for photovoltaic cell manufacturing.

Despite the fact that the conversion efficiency obtained by conventional solar cells is relatively high compared to nanomaterial-based solar cells, they remain more attractive because of their low manufacturing cost and potential wide implementation in people's everyday life.

This shift to nanoelectrochemistry tends to overcome the limits encountered by solid-state physics. High opportunities to increase light trapping and photocarrier collection have been reached.

Different and interesting architectures were carried out like nanowires, nanorods, nanosprings, nanocones, nanotubes, nanopillars, nanobelts, nanopagodas, nanoflowers, nanopetals, and others.

But the real improvement is observed in inorganic solar cells rather than the organic ones.

Organic solar cells are promising next-generation solar cells but cannot be competitive with the inorganic ones. Their actual conversion efficiency is too small to provide electricity and to have large-scale application. Efforts should be made to make this possible.

References

1. Chiappafreddo P, Gagliardi A (2010) The photovoltaic market facing the challenge of organic solar cells: economic and technical perspectives. *Transit Stud Rev* 17:346–355. doi:10.1007/s11300-010-0148-0
2. Akl AA, Afify HH (2008) Growth, microstructure, optical and electrical properties of sprayed CuInSe₂ polycrystalline films. *Mater Res Bull* 43:1539–1548
3. Tauc J (2005) Optical properties of amorphous semiconductors and solar cells. In: Yu PY, Cardona M (eds) *Fundamentals of semiconductors: physics and materials properties*. Springer, Berlin/Heidelberg, pp 566–568. ISBN 3-540-25470-6
4. Wanzhu Cai, Xiong Gong, Yong Cao (2010) Polymer solar cells: recent development and possible routes for improvement in the performance. *Sol Energy Mater Sol Cells* 94:114–127
5. Imalka Jayawardena KDG, Rozanski LJ, Mills CA, Beliatis MJ, Aamina Nismy N, Silva SRP (2013) Inorganics-in-Organics: Recent developments and outlook for 4G polymer solar cells. *Nanoscale* 5:8411–8427. doi:10.1039/C3NR02733C
6. <http://sharp-world.com/Corporate/news/130424.html>. 24 Apr 2013
7. Goldstein AN, Echer CM, Alivisatos AP (1992) Melting in semiconductor nanocrystals. *Science* 256(5062):1425–1427
8. Garnett EC, Burthraw D (2005) Cost effectiveness of renewable electricity policies. *Energy Econ* 27:873

9. Yuhas BD, Yang P (2009) Nanowire-based all-oxide solar cells. *J Am Chem Soc* 131:3756
10. Fan ZY, Razavi H, Do JW, Moriwaki A, Ergen O, Chuch YL, Leu PW, Ho JC, Takahashi T, Reichertz LA, Neale S, Yu K, Wu M, Ager JM, Javey A (2009) Three-dimensional nanopillar-array photovoltaics on low-cost and flexible substrates. *Nat Mater* 8:3756
11. Cho K, Rurbrush DJ, Ergen O, Javey A (2011) Molecular monolayers for conformal, nanoscale doping of InP nanopillar photovoltaics. *Appl Phys Lett* 98:203101
12. Zhu J, Yu ZF, Burkhard GF, Hsu CM, Connor SH, Xu YQ, Wang Q, Mc Gehee M, Fan SH, Cui Y (2009) Optical absorption enhancement in amorphous silicon nanowire and nanocone arrays. *Nano Lett* 9:279
13. Peng ZA, Peng X (2001) Formation of high quality CdTe, CdSe, and CdN nanocrystals using CdO as precursor. *J Am Chem Soc* 123:183
14. Hu L, Chen G (2007) Analysis of optical absorption in silicon nanowire arrays for photovoltaic applications. *Nano Lett* 7(11):3249
15. Han SE, Chen G (2010) Optical absorption enhancement in silicon nanohole arrays for solar photovoltaics. *Nano Lett* 10:1012
16. Han SE, Chen G (2010) Toward the Lambertian limit of light trapping in thin nanostructured silicon solar cells. *Nano Lett* 10:4692
17. Peng X, Wickham J, Alivisatos AP (1998) Kinetics of II-VI and III-V colloidal semiconductor nanocrystal growth: 'focusing' of size distributions. *J Am Chem Soc* 120:5343
18. Rogach AL, Talapin DV, Shevchenko EV, Kowowski A, Haase M, Weller H (2012) Organization of matter on different size scales: monodisperse nanocrystals and their superstructures. *Adv Funct Mater* 12:653
19. Sze SM, Kwok KNg (2007) *Physics of semiconductor devices*. Wiley, USA
20. Bauer T (2011) *Thermophotovoltaic basic principles and critical aspects of system design, Green energy and technology*. Springer, Berlin/Heidelberg. doi:10.1007/978-3-642-19965-3_5
21. Pöde R, Diouf B (2011) *Solar lighting, Green energy and technology*. Springer, Berlin/Heidelberg. doi:10.1007/978-1-4471-2134-3_2
22. Modest MM (1993) *Radiative heat transfer*. Mc Graw Hill, New York
23. Compaan AD (2006) *Photovoltaics: clean power for the 21st century*. *Sol Energy Mater Sol Cells* 90:2170–2180
24. Xin Zhang, Xuezhao Shi, Weichun Ye, Chuanli Ma, Chunming Wang (2009) Electrochemical deposition of quaternary Cu₂ZnSnS₄ thin films as potential solar cell material. *Appl Phys A Mater Sci Process* 94:381–386. doi:10.1007/00339-008-4815-5
25. Takashi Jimbo, Tetsuo Soga, Yasuhiko Hayashi (2005) Development of new materials for solar cells in Nagoya Institute of Technology. *Sci Technol Adv Mater* 6:27–33
26. Nazeerudin MK, Péchy P, Renouard T, Zakeeruddin SM, Humphry-Baker R, Liska P, Cevey L, Costa E, Shklover V, Spiccia L, Deacon G, Bignozzi CA, Grätzel M (2001) Engineering of efficient panchromatic sensitizers for nanocrystalline TiO₂-based solar cells. *J Am Chem Soc* 123:1613
27. Nehaoua N, Chergui Y, Mekki DE (2011) A new model for extracting the physical parameters from I-V curves of organic and inorganic solar cells. In: Kosyachenko LA (ed) *Solar cells – silicon wafer – based technologies*. In-Tech Croatia. doi:10.5772/24854. ISBN 978-953-307-747-5
28. Rui Yu, Qingfeng Lin, Siu-Fung Leung, Zhiyong Fan (2012) Nanomaterials and nanostructures for efficient light absorption and photovoltaics. *Nano Energy* 1:57–72
29. Kelzenberg MD, Putnam MC, Warren EL, Spurgeon JM, Briggs RM, Lewis NS, Atwater HA (2010) Enhanced absorption and carrier collection in Si wire arrays for photovoltaic applications. *Nat Mater* 9:239
30. Spurgeon JM, Atwater HA, Lewis NS (2008) A comparison between the behavior of nanorod array and planar Cd(Se, Te) photoelectrodes. *J Phys Chem C* 112:6186
31. Garnett E, Yang P (2010) Light trapping in silicon nanowire solar cells. *Nano Lett* 10:1082
32. Lee JY, Connor ST, Cui Y, Peumans P (2008) Solution processed metal nanowire mesh transparent electrodes. *Nano Lett* 8:689–692
33. Jong-Wook Lim, Da-Young Cho, Jihoon-Kim, Seok-In Na, Han-Ki Kim (2012) Simple brush-painting of flexible and transparent Ag nanowire network electrodes. *Sol Energy Mater Sol Cells* 107:348–354

34. Mia Yu, Yun-Ze Long, Bin Sun, Zhiyong Fan (2012) Recent advances in solar cells based on one-dimensional nanostructure arrays. *Nanoscale* 4:2783
35. Yu PY, Cardona M (2010) *Fundamentals of semiconductors: physics and materials properties*. Springer, Berlin. ISBN 978-3-642-00710-1
36. Srivastava ON, Srivastava A, Dash D, Singh DP, Yadav RM, Mishra PR, Singh J (2005) Synthesis, characterizations and applications of some nanomaterials (TiO₂ and SiC nanostructured films, organized CNT structures, ZnO structures and CNT-blood platelet clusters). *Pramana J Phys* 64(4):581–592
37. Miao X, Tongay S, Petterson MK, Berke K, Rinzler AG, Appleton BR, Hebard AF (2012) High efficiency graphene solar cells by chemical doping. *Nano Lett* 12:2745, ArXiv: 1209.0432v1 [cond-mat.mtrl-sci]
38. Lamberti A, Sacco A, Bianco S, Manfredi D, Armandi M, Quaglio M, Tresso E, Pirri CF (2013) An easy approach for the fabrication of TiO₂ nanotube based transparent photoanodes for dye sensitized solar cells. *Sol Energy* 95:90–98
39. Baker DR, Kamat PV (2009) Photosensitization of TiO₂ nanostructure with CdS quantum dots: particulate versus tubular support architectures. *Adv Funct Mater* 19:805–811
40. Paulose M, Shankar M, Varghese OK, Mor GK, Grimes CA (2006) Application of highly ordered TiO₂ nanotube arrays in heterojunction dye sensitized solar cells. *J Phys D Appl Phys* 39:2498–2503
41. Thiyagu S, Pei Z, Jhong M-S (2012) Amorphous silicon nanocone array solar cell. *Nanoscale Res Lett* 7:172
42. Kapadia R, Fan Z, Takie K, Javey A (2012) Nanopillar photovoltaics: materials, processes and devices. *Nano Energy* 1(1):132–134
43. Lee MH, Lim N, Ruebusch DJ, Jamshidi A, Kapadia R, Lee R, Seok TJ, Takei K, Cho KY, Fan Z, Jang H, Wu M, Cho G, Javey A (2011) Roll to roll anodization and etching of aluminum foils for high-throughput surface nanotexturing. *Nano Lett* 11:3425
44. Luhui Zhang, Lili Fan, Zhen Li, Enzheng Shi, Xinming Li, Hongbian Li, Chunyan Ji, Yi Jia, Jinquan Wei, Kunlin Wang, Hongwei Zhu, Dehai Wu, Anyuan Cao (2011) Graphene- CdSe nanobelt solar cells with tunable configurations. *Nano Res* 4(9):891–900. doi:10.1007/s12274-011-0145-6
45. Zhang LH, Jia Y, Wang SS, Li Z, Ji CY, Wei JQ, Zhu HW, Wang KL, Wu DH, Shi EZ, Fang Y, Cao AY (2010) Carbon nanotube and CdSe nanobelt Schottky junction solar cells. *Nano Lett* 10:3583–3589
46. Chang Yu-Cheng, Yang Wei-Cheich, Chang Che-Ming, Hsu Che-Ming, Hsu Po-Chun, Chen Lin-Juann (2009) Controlled growth of ZnO nanopagoda arrays with varied lamination and apex angle. *Cryst Growth Des* 9(7):3161–6167
47. Zhang LN, Yan LT, Ai XD, Li TW, Dai CA (2012) Preparation of a hybrid polymer solar cells based on MEH-PPV/ZnO nanorods. *J Mater Sci Mater Electron*. doi:10.1007/s10854-012-0728-3
48. Zhang Q, Dandeneau CS, Zhou X, Cao G (2009) ZnO nanostructures for dye sensitized solar cells. *Adv Mater* 21:4087
49. Thorat JH, Kanade KG, Nikam LK, Chaudhari PD, Kale BB (2011) Nanostructured ZnO hexagons and optical properties. *J Mater Sci Mater Electron* 22:394
50. Kelzenberg MD, Turner-Evans DB, Kayes BM, Filler MA, Putnam MC, Lewis NS, Atwater HA (2008) Photovoltaic measurements in single nanowire silicon solar cells. *Nano Lett* 8(2):710–714
51. Tala-Ighil R (2013) Simulated multi-crystalline silicon solar cells with aluminum back surface field. *Mater Sci Indian J* 9(7):277–281
52. Quande Che, Hongxing Yang, Lin Lu, Yuanhoo Wang (2012) Nanoparticles-aided silver front contact paste for crystalline silicon solar cells. *J Mater Sci Mater Electron*. doi:10.1007/s10854-012-0941-0
53. Dongwook Lee, Yougwoo Choi, Kijing Yong (2010) Morphology and crystal phase evolution of doctor-blade coated CuInSe₂ thin films. *J Cryst Growth* 312:3665–3669
54. Ludwig C, Gruhn T, Felser C (2010) Indium – gallium segregation in CuIn_xGa_{1-x}Se₂: an ab initio-based Monte Carlo study. *Phys Rev Lett* 105:025702

55. Klenk R, Klaer J, Scheer R, Lux-Steiner MCh, Luck I, Meyer N, Rühle U (2005) Solar cells based on CuInS_2 - an overview. *Thin Solid Films* 480:509
56. Lux Steiner MCh, Ennaoui A, Fisher Ch-H, Jäger-Waldau A, Klaer J, Klerk R, Könenkamp R, Matthes Th, Scheer R, Siebentritt S, Weidinger A (2000) Processes for chalcopyrite-based solar cells. *Thin Solid Films* 361:533–539
57. Wark SE (2011) Simple chemical routes for changing composition or morphology in metal chalcogenide nanomaterials. Dissertation Doctor in Philosophy, Texas A&M University, May 2011
58. Dinca SA, Schiff EA, Shafarman WN, Egaas B, Noufi R (2012) Electron drift-mobility measurements in polycrystalline $\text{CuIn}_{1-x}\text{Ga}_x\text{Se}_2$ solar cells. *Appl Phys Lett* 100:103901. doi:10.1063/1.3692165
59. Guang Zhu, Fengfang Su, Tian Lv, Likun Pan, Zhuo Sun (2010) Au nanoparticles as interfacial layer for CdS quantum dot-sensitized solar cells. *Nanoscale Res Lett* 5:1749–1754. doi:10.1007/s11671-010-9705-z
60. Kim S, Fisher B, Eisler HJ, Bawendi M (2003) Type II quantum dots: CdTe/CdSe (core/shell) and CdSe/ZnTe (core/shell) heterostructures. *J Am Chem Soc* 125(38):11466–11467
61. Milliron DJ, Hughes SM, Cui Y, Manna L, Li JB, Wang LW, Alivisatos AP, Colloidal AP (2004) Nanocrystal heterostructures with linear and branched topology. *Nature* 430(6996):190–195
62. Landi BJ, Castro SL, Ruf HJ, Evans CM, Bailey SG, Raffaele RP (2005) CdSe quantum – single wall carbon nanotube complexes for polymeric solar cells. *Sol Energy Mater Sol Cells* 87:733–746
63. Yafei Zhang, Huijuan Geng, Zhihua Zhou, Jiang Wu, Zhiming Wang, Yaozhong Zhang, Zhongli Li, Liying Zhang, Zhi Yang, HueyLiang Hwang (2012) Development of inorganic solar cells by nanotechnology. *Nano Micro Lett* 4(2):124–134
64. Wei D (2010) Dye sensitized solar cells. *Int J Mol Sci* 11:1103–1113. ISSN 1422-0067
65. Yan Li, Gentian Yue, Xiaoxu Chen, Benlin He, Lei Chu, Haiyan Chen, Jihuai Wu, Qunwei Tang (2013) Application of poly(3,4-ethylenedioxythiophene): polystyrenesulfonate in polymer heterojunction solar cell. *J Mater Sci* 48:3528–3534. doi:10.1007/s10853-013-7147-6
66. Shengli Zhu, Guoqiang Xie, Xian Jin Yang, Zhenduo Cui (2013) A thick hierarchical rutile TiO_2 nanomaterial with multilayered structure. *Mater Res Bull* 48:1961–1966
67. Jiang CY, Koh WL, Leung MY, Chian SY, Wu JS, Zhang J (2012) Low temperature processing solid state dye sensitized solar cells. *Appl Phys Lett* 100:113901
68. Weili Yu, Bin Xu, Qingfeng Dong, Yinhua Zhou, Junhu Zhang, Wenjing Tian, Bai Yang (2010) A two-step method combining electrodepositing and spin-coating for solar cell processing. *J Solid State Electrochem* 14:1051–1056. doi:10.1007/s10008-009-0919-x
69. Rattanavoravipa T, Sagawa T, Yoshikawa S (2008) Photovoltaic performance of hybrid solar cell with TiO_2 nanotubes arrays fabricated through liquid deposition using ZnO template. *Sol Energy Mater Sol Cells* 92:1445–1449
70. Yu K, Zhang Y, Luo L, Ouyang S, Geng H, Zhu Z (2005) Synthesis of ZnO nanostructures on CuO catalyzed porous silicon substrate. *Mater Lett* 59:3525
71. Zhang H, Yang D, Li S, Ma X, Ji Y, Xu J, Que D (2005) Controllable growth of ZnO nanostructures by citric acid assisted hydrothermal process. *Mater Lett* 59:1696
72. Peterson RB, Fields CI, Gredd BA (2004) Epitaxial chemical deposition of ZnO nanocolumns from NaOH solutions. *Langmuir* 20:5114
73. Lee Y-J, Sounart TL, Scrymgeour DA, Voigt JA, Hsu JWP (2007) Control of ZnO nanorod array alignment synthesized via seeded solution growth. *J Cryst Growth* 304:80
74. Li D, Chang P, Chien C, Lu JG (2010) Applications of tunable TiO_2 nanotubes as nanotemplate and photovoltaic device. *Chem Mater* 22:5707
75. Kelzenberg MD, Turner Evans DB, Putnam MC, Boettcher SW, Briggs RM, Baek JY, Lewis NS, Atwater HA (2011) High performance Si microwire photovoltaics. *Energy Environ Sci* 4:866
76. Chen C, Lu Y, Kong ES, Zhang Y, Lee ST (2008) Nanowelded carbon nanotube based solar microcells. *Small* 4:1313
77. de Morais A, Loiola LMD, Beneditti JE, Gonçalves AS, Avellaneda CAO, Clerici JH, Cotta MA, Nogueira AF (2013) Enhancing in the performance of functionalized multi-walled carbon nanotubes into TiO_2 films: the role of MWCNT addition. *J Photochem Photobiol A Chem* 251:78–84

Characterization of Metallic Micro(Nano)cluster-Based Contacts for High-Effective Photovoltaic Devices

40

Viktor Laptev and Halyna Khlyap

Contents

Introduction.....	1272
Metallization of Electrical Contacts for Solar Cells	1272
Solar Cell as an Object of Investigation.....	1273
Cu Metallization from Water Solution.....	1280
Basic Reference Data.....	1280
Experimental Cu Metallization	1282
Results and Discussion	1293
Conclusions.....	1297
References.....	1298

Abstract

We present unique results on methods for producing electric contacts on the illuminated side of solar cells based on novel wet chemical processes [1]. We are describing about the copper–nickel–tin deposition on the silver pores in contradiction of the rule based on the standard electrode potentials (or the electrochemical series). The special feature of this process is the deposition of metal from a water solution on a silver surface and pores under the action of intrinsic electrical fields in solar cell absorber. Silver technologies are widely used for manufacture of crystalline silicon-based photovoltaic devices [2]. The role of small particles in solar cells was described previously [3]. The inclusion of nanoparticles into

Halyna Khlyap: Deceased.

V. Laptev (✉)

New Russian University, Moscow, Russia

e-mail: viktor.laptev@yahoo.com

H. Khlyap

University of Stuttgart, Kaiserslautern, Germany

e-mail: hkhlyap@yahoo.com; gkhlyap17@yandex.com

pores of photon absorbers increases their efficiency. Copper micro(nano)clusters were chemically introduced into pores of a silver contact. They changed the electrical properties of the contact: the dark current, which is unknown for metals, was detected [4]. The experimental data on electrical properties of the structures fabricated by the technique mentioned above are discussed in the framework of semiclassical nanoscaled metal–semiconductor junctions.

Keywords

Metall • Electroless • Deposition • Water solution • Dark currentcopper-nickel-tin • Micro(nano)clusters

Introduction

Manufacture of low-cost and reliable high-effective photovoltaic converters is still a challenge. Novel electrochemistry has developed unique methods not only for the production of various oxide-semiconductor nanoscaled structures (among them TiO and ZnO) but also for fabrication of effective photovoltaic devices (e.g., dye-sensitized solar cells). However, different chemical techniques (in particular, wet technology) based on intrinsic electrochemical processes in the components of the commercial silicon-based solar cells can significantly contribute to solution of the problem mentioned above. Chemical processes are widely employed in the fabrication of electrical contacts arranged at the irradiated surface of solar cells. Silver technology is extensively used in fabrication of silicon solar cells. The function of small particles employed in solar cells is described in [5–8]. Entering nanoparticles into the pores of photon absorbers enhances their efficiency. In this chapter, we describe how, for the first time, copper clusters were chemically entered into the micropores of a silver contact. The clusters have affected the electrical properties of the contact; a dark current, which was previously unknown in the case of metals, has been revealed. We have summarized these results in Table 1.

Metallization of Electrical Contacts for Solar Cells

The main task of the metallization of electrical contacts for solar cells is the enhancement of its efficiency. It means that the transformation of the radiation energy supplied by our Sun is to be maximal, and the principal way for reaching this goal is lowering the electrical resistance of the solar cell. To solve this problem, we propose to fill in the pores of the silver electrical contact with micro(nano)clusters of silver or other metals. The working-out technology is to be commercially profitable and consistent with the common technology of silicon wafer-based solar cells.

The manufacture of standard solar cells based on silicon wafers uses the silver paste in connection with porous printing. The paste film at the elevated temperatures is fired in the emitter layer through the antireflection coating. To provide the higher conductivity, the contact stripes of 140 μm width are fabricated. It leads to about 10 % shadowing effect of the surface of the solar cell and, consequently, to the considerable losses of produced electrical current and efficiency of the cell. These effects

Table 1 Summary of fundamental reference data

References	Result
[1]	Discovery of method allowing copper deposition on silver nanoclusters in metallic contacts for commercial Si-based solar cells
[2]	Discovery of unique structural and chemical characteristics of metallic Cu/Ag nanoclusters
[3]	Analysis of experimental data on structural characteristics of unique metallic Cu/Ag nanoclusters
[4]	Analysis of unique properties discovered under investigation of room-temperature electric characteristics of metallic Cu/Ag nanoclusters (room-temperature dark currents in metallic structure)
[5]	Formation of Si-based solar cells with front electrode consisted of porous network structure of double-walled carbon nanotubes (technology: chemical vapor deposition)
[6]	Demonstration of absorption and emission enhancement from Si solar cells by making use of the nanoscale properties of metals and demonstration of the effect of scattering by silver metal nanoparticles into Si devices
[7]	The vacuum pore-filling technique is applied to enhance efficiency of energy conversion in solid-state dye-sensitized solar cells (DSSCs) based on nanocomposite polymer electrolytes
[8]	Demonstration of photon recycling in strain-balanced quantum-well solar cells in both the dark current and the electroluminescence

can be eliminated by the very fine porous printing step with producing contact stripes of about 50 μm width and the following wet chemical deposition of metals as silver, aurum, and copper. This problem can be solved by the wet chemical current-free metal deposition with the rate of 1 mm/min under temperatures lower than 70 $^{\circ}\text{C}$.

The suitable wet chemical solution is to have the following features:

- A high selectivity, e.g., the metal deposition, is to be realized onto the front side of the solar cell and on the Al/Ag soldering pads of the backside only.
- The deposition of the metal on the antireflection coating as well as on the free silicon surface and Al layer is forbidden.
- The contact structures prepared early by the porous printing of the silver paste are to be not damaged, i.e., the parasite deposition on the edges of the contacts has not exceeded the 1.5 times magnified thickness value of the deposited metal layer.
- The contact resistance and the adhesiveness of the deposited contact are to be not affected.
- The process as a whole is to be environmentally friendly.

Solar Cell as an Object of Investigation

A solar cell based on the SiP/SiNx/SiB-crystal silicon structure with an aluminum contact made on the backside of a wafer and with a front-mounted silver contact was taken as a matter for inquiry; the silicon nitride layer was 70 nm thick. The principal construction of the common silicon-based solar cell is presented in Fig. 1.

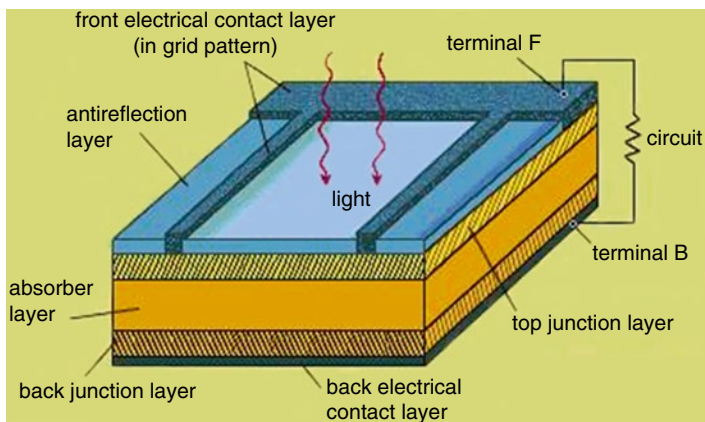


Fig. 1 Principal construction of common silicon wafer solar cell [4]

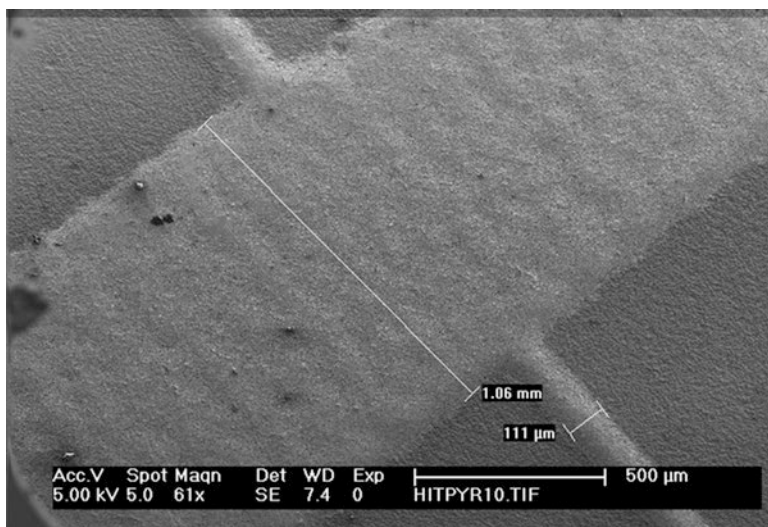


Fig. 2 Electron-beam image of the SGE contact surface – the bus bar and grid on the silicon wafer before the metal deposition. The width of the grid is 111 μm , and the width of the bus bar is no more than 1 mm (61 \times magnification)

A current-free enhanced metal layer serves as an electrical contact which represents a silver stripe-geometry element (further SGE) arranged at the silicon surface. The silver paste produced by DuPont was taken as a source material for obtaining the contact; the paste was deposited onto a silicon surface through a tungsten net-shaped mask. When drying was completed, the organic components of the paste were burned out in an inert atmosphere at 820–960 $^{\circ}\text{C}$. At the same time, silver was burned in silicon through a 70-nm-thick silicon nitride SiN antireflection coating (ARC).

The crossed silver contacts on the surface of the silicon wafer are of two kinds (Fig. 2). The narrow silver stripe is called “grid,” and the wide one is called “bus

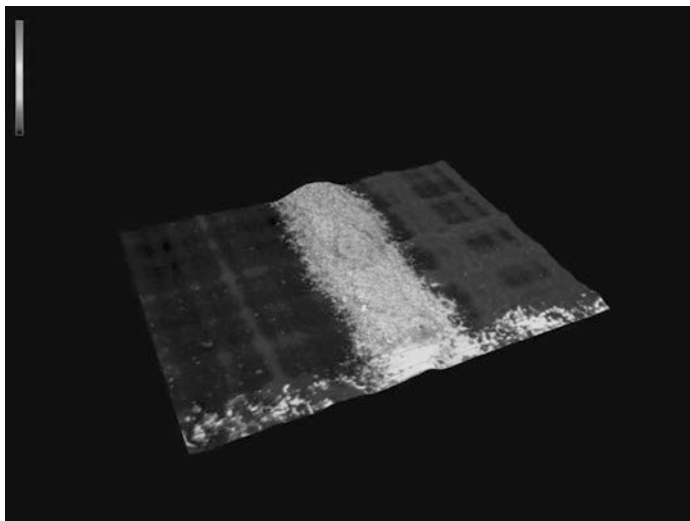


Fig. 3 Grid-contact morphology optical scanning area $430 \times 580 \mu\text{m}^2$; magnification $5000\times$

bar.” After annealing, the electric contact grid is made up from the silver SGEs of $10\text{--}20 \mu\text{m}$ thickness and $120\text{--}130 \mu\text{m}$ width. The bus bar has 1 mm width.

The morphology of the surface of the solar cell and the contact strips before and after copper deposition was investigated with a KEYENCE-5000 3D optical microscope. Figure 3 presents the result of computer processing of images of layer-by-layer optical scanning of the silver contact surface.

The porous structure of silver has been determined with the use of an electron microscope. The electron-beam image of the cleavage of a wafer with a SGE contact is shown in Fig. 4. It can be seen that the silver SGE is not bulk metal but a porous structure. Cavities are $1\text{--}2 \mu\text{m}$ in length. The electron-beam image of a contact SGE surface is shown in Fig. 5, where numerous pores are visible; the pores have access to these cavities.

The crystal structure of the metal phases was studied by grazing incidence X-ray diffraction (GIXRD). In a contact SGE $10 \mu\text{m}$ high and $120 \mu\text{m}$ wide, silver features the face-centered cubic structure referred to the $Fm\bar{3}m$ crystallographic space group of symmetry. The X-ray diffraction pattern obtained with the grazing incidence X-ray diffraction (GIXRD) technique is presented in Fig. 6. The X-ray beam incidence angle was 2° . For reference, the X-ray diffraction pattern of a silver structure is shown in the lower part of the figure. Single-crystal silicon wafers were aligned to (110). The associated X-ray diffraction peak with a significant half-width is shown in Fig. 6.

The crystal structures of the electrical collector (bus bar) and the contact on the backside of the wafer were examined by the GIXRD technique. The X-ray diffraction pattern of a silver structure is shown in Fig. 7. The silver features are demonstrated: the face-centered cubic structure referred to the $Fm\bar{3}m$ crystallographic space group of symmetry is shown in the lower part of the Fig. 6. The dash diagram of the Pb crystalline structure is shown in Fig. 7. As is seen, the contact contains some crystalline lead phases.

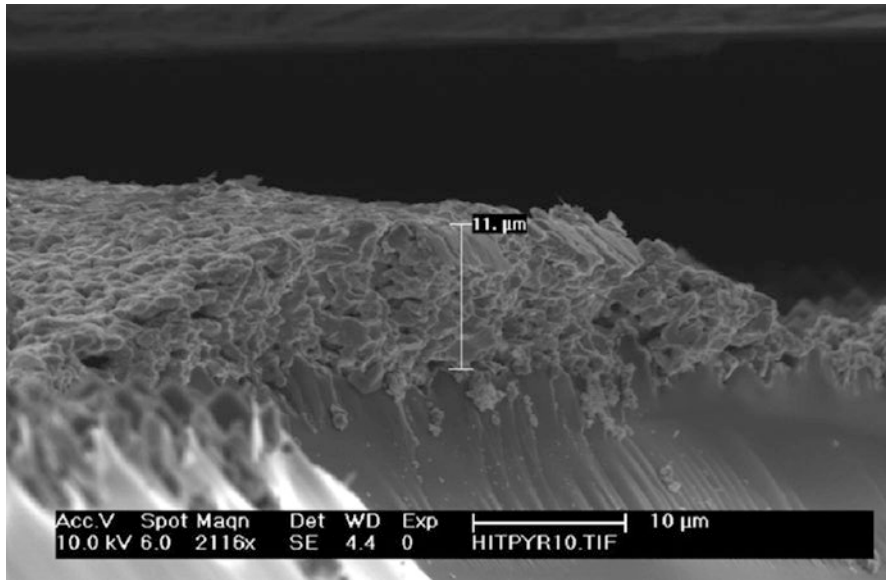


Fig. 4 Electron-beam image of a cross-section of a contact SGE made of porous silver and a cleavage of silicon wafer. The SGE is 11 μm in height; 2116× magnification

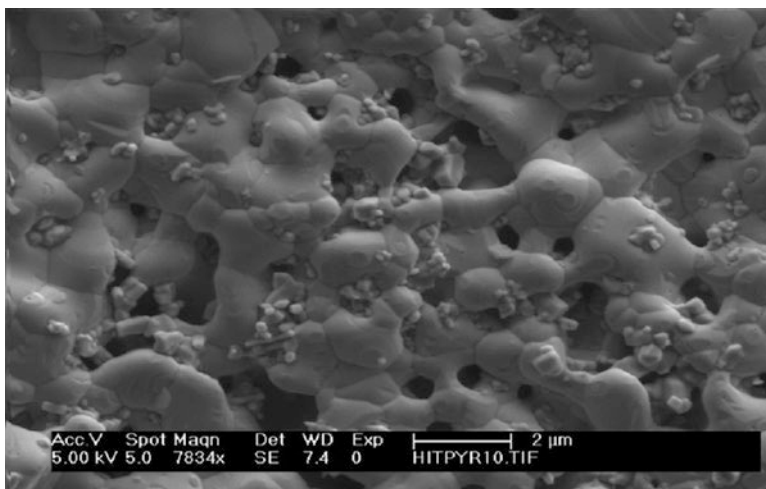


Fig. 5 Electron-beam image of surface of the contact SGE made of silver on a wafer. The linear size of pores occurring in silver is under 1 μm; 7834× magnification

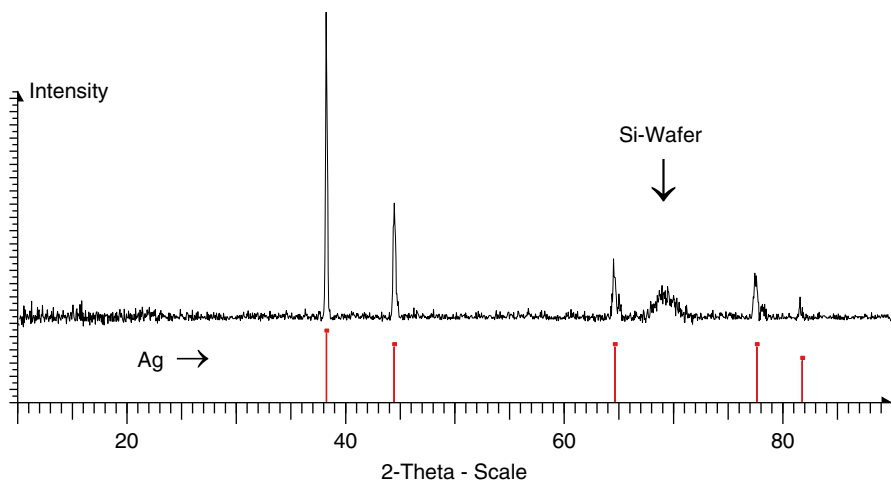


Fig. 6 X-ray diffraction pattern of a silver contact SGE and a single-crystal silicon wafer

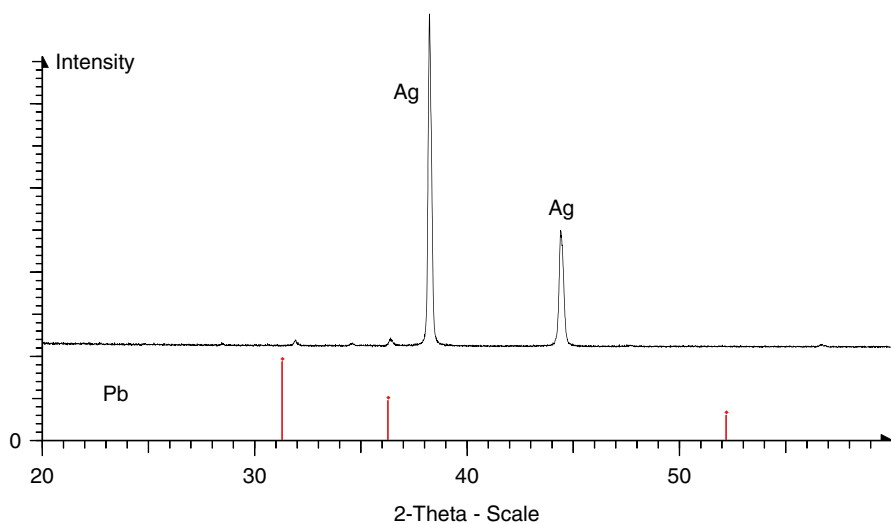


Fig. 7 X-ray diffraction pattern of a silver contact SGE (of the bus bar) and the back contact with the porous printing paste produced by DuPont. This pattern demonstrates the presence of both metals: silver and lead

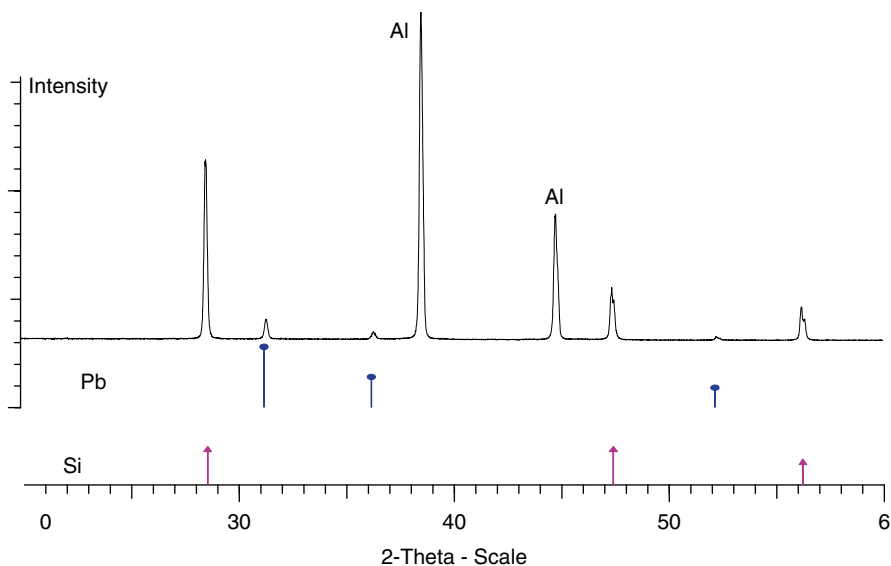


Fig. 8 X-ray diffraction pattern of the backside Al contact on the single-crystal silicon wafer

Figure 8 shows the X-ray diffraction pattern of the backside of the silicon wafer with an Al contact. The dash diagrams of crystalline structures for lead and silicon are presented in the lower part of Fig. 8. Its correspondence to the diffraction pattern indicates on the mixture of crystalline phases of Al and Pb.

At the next step, we have analyzed the reference samples with the EDX method. This technique allows analyzing the samples with two different values of the electron energy: the elemental analysis of the surface is made with 5 keV electron beam, and the deeper layers were studied with the 25 keV electron beam. The next three pictures present the results (Figs. 9, 10, and 11).

Thus, the EDX study carried out with two different voltages showed that the Ag paste contains no lead ($K\alpha = 10.55$ keV); zinc is registered in this paste. Furthermore, we can define the following properties of the reference sample:

- The grid and bus bar contain Ag + Zn phase mixture.
- There is no crystalline Zn phase in the Ag paste, and zinc is to be seemed as a doping agent only.
- Polycrystalline lead is placed between the grid and the wafer.
- Crystalline phases of Ag and Pb are mixed in the front and backside contacts.
- Crystalline phases of Al and Pb are mixed in the backside layer.
- Polycrystalline silicon is placed between the metal and Si wafer.
- The Ag layers have a porous structure.

Further, we will use these results for building the chemical model and description of chemical reactions taking place in the reference sample.

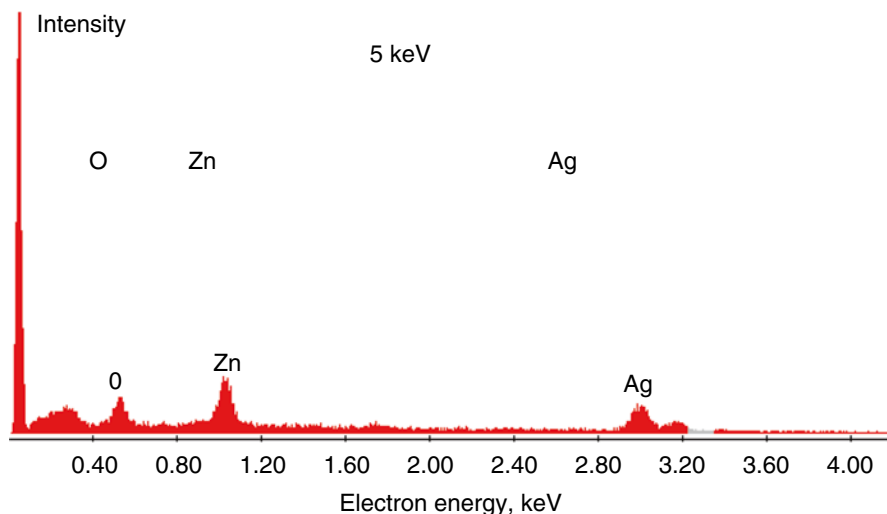


Fig. 9 EDX is registered with the acceleration voltage of 5 keV. The Pb-containing Ag paste from DuPont is deposited on the surface. This experiment showed no lead on the surface of the sample. The presence of zinc is found out

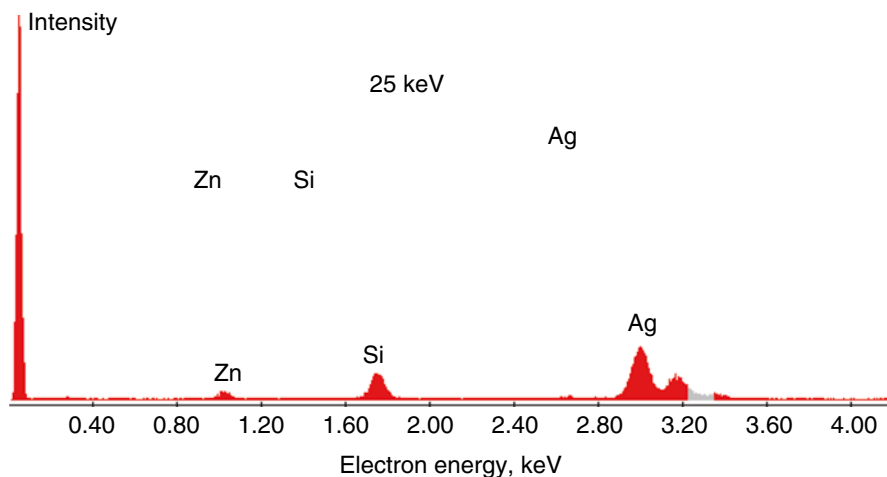


Fig. 10 EDX registered with the acceleration voltage of 25 keV. The Ag paste from DuPont is deposited on the surface. The deep regions of the surface are studied. The Si peaks force us to conclude that we examine the wafer through the double metal layer. No lead is detected in the semiconductor part of the sample

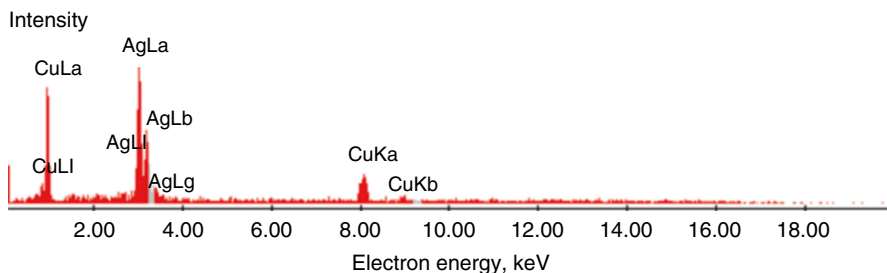


Fig. 11 EDX results for electron beam with energy 0–20 keV

Cu Metallization from Water Solution

Basic Reference Data

The topic “current-free deposition of copper on silicon, silver, and aluminum surfaces” is almost not investigated. We have to note that:

- “Copper is one of the most effective charge carrier lifetime killers in silicon” [9].
- “Copper does not penetrate through the thin chromium diffusion barrier at low temperatures” [10].
- Ni layer can serve as a protective coating for silicon against copper. The system “current-free Ni/Cu-halvanometallization of Si” is now studied [11].
- Organic salts are to be origins of metals Ag, Bi, Ti, and Nb for the silicon metallization [12].

For Cu deposition on silicon, we have applied the following process [13]:

- Copper hexanoate \rightarrow Cu + Cu₂O at 200 °C
- Cu + Cu₂O + H₂ + N₂ \rightarrow Cu (Metal) at 200 °C

The current-free Cu deposition on TiN/SiO₂/Si and WN/SiO₂/Si is carried out from organic solutions of copper sulfates with the help of the following reagents [14]:

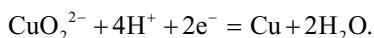
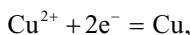
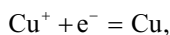
- EDTA – ethylenediaminetetraacetate
- Glyoxylic acid
- 2,2-dipiridine
- Polyethylene glycol
- Tetramethylammonium hydroxide

At the start of the process of Cu deposition, the electrical impulse is necessary. The parameters of the process are as follows: temperature 60–70 °C, time up to 15 min, thickness of the copper layer up to 0.5 μm, and pH ~11.

The laser beam irradiation of the alkali Cu solution ($\text{CuSO}_4/\text{H}_3\text{BO}_3/\text{NaH}_2\text{PO}_2$) leads to the metal film deposition at the following parameters: pH 9.2/60 °C/60 min [15].

As is known [16], the Firma SEG proposes the current-free Ni deposition and electrochemical technology for copper: “It should be now be clear that a specification that calls for “ELECTROLESS NICKEL” is totally inadequate. There are “horses for courses” and without knowledge of what the deposit has to do, the finisher is operating completely in the dark.” Going back to the history of chemistry, we should refer the reader to some important facts: in old Egypt, the Cu-covered mirrors were found out in the Pharaoh tombs. It also is known that in waters of many rivers in Altai Mountains (Russian Federation) iron precipitates were slowly covered by copper.

We also should remember that Cu-containing systems are available in three solid phases: metal, oxide, and hydroxide. So, in the solution, the following ions can be presented: Cu^+ , Cu^{2+} , HCuO_2^- , and CuO_2^{2-} . Then the following reactions are possible:



It is important that the value of the electrochemical potential of these reactions can be about zero. So, the wafers with contact stripes processed with porous printing technology have unavoidable micro-galvanic elemental pairs which are presenting immediately before the Cu metallization. We suggest the potential difference of these elemental pairs is very low. Thanking to this minimal value of the potential difference, the Cu deposition on the silver contact stripes is possible without applying additional electrical potential.

To conclude, we have to note that the current-free Cu deposition is possible without any additional conditions.

Now we briefly consider the most important requests for the metallization processes:

- Selectivity of the metallization
- High adhesion of the substrate
- Advantages compared to commercial baths
- Compatibility with industrial end processes and materials

The technological requests for the Cu metallization are as follows:

- Cyanide-free solutions.
- Deposition rates of the materials used in the process are to be about 1 $\mu\text{m}/\text{min}$.
- The temperatures in the technological chamber are to be about 40–60 °C.
- Using the most common (not rare components and compounds) materials in order to keep the cheapest process prices.

Let us consider the special requests:

- Material can be deposited only on the surface with contacts previously fabricated by the porous printing technique. The ARC-covered front side is not to be covered with any film.
- The long stability of the process.
- Safe and reliable recycling of the components after the process is finished.

Experimental Cu Metallization

Objects of investigations are the structures with 125×125 and 156×156 mm² active area (solar cells) with contacts on the front side and backside, ARC layers and edges, different porous printing stripes, Al and Ag pastes, and single-crystal and polycrystalline Si wafers. The principal chemical reagent is inorganic Cu-containing salt with 35.3 % Cu content. The experiments were carried out with the following copper-containing solutions:

Solution 1: 1.0 g Cu/100 ml H₂O

Solution 2: 0.5 g Cu/100 ml H₂O

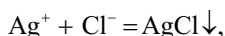
Solution 3: 0.2 g Cu/100 ml H₂O

Solution 4: 2.0 g Cu/100 ml H₂O

Solution 5: 5.0 g Cu/100 ml H₂O

These solutions have various reaction speeds.

The Cu-containing solution after Cu metallization was examined by the means of chemical analysis. The aim of this analysis was to establish how silver dissolves from the solution. The analytical method is based on the fact that the following reaction is possible:



and we have obtained the following:

(i) AgCl is not found in the solution for metallization; (ii) while the metallization of the bus bar and contacts takes place, no exchange reaction between Cu and Ag is registered; (iii) copper covers silver. Thus, copper covers silver without chemical reaction between the metals.

Crystalline copper clusters were deposited from aqueous solutions; they penetrated into pores and covered the silver contact SGE surface of a silicon solar cell. The deposition time varied within 160 min.

The morphology of the surface of the solar cells before and after Cu deposition was investigated by scanning electron microscope. Results are illustrated in Figs. 5 and 12. As is seen, all structures have the porous silver surface layer.

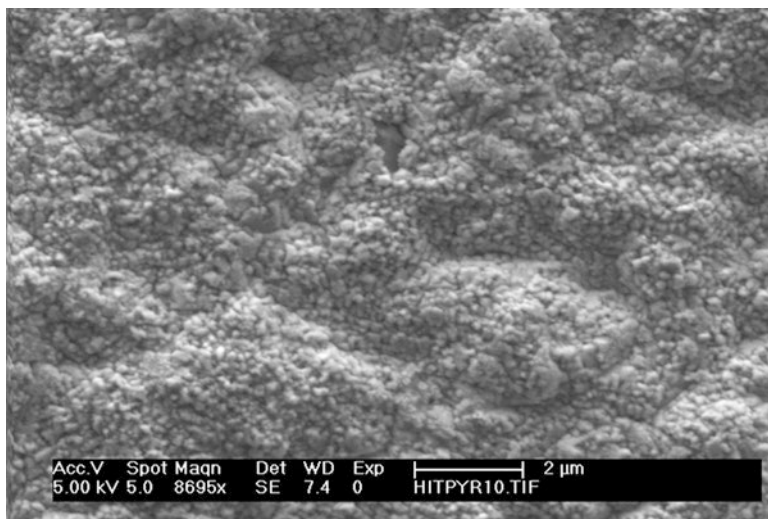


Fig. 12 The surface structure after the 5 min Cu deposition. 8695 \times magnification

The surface structure after the porous printing before the metallization is shown in Fig. 5. The electron-beam image of the surface of a silver contact SGE with copper deposited is presented in Fig. 12. This electron-beam image of the surface of a silver contact SGE was obtained on a wafer after 5 min copper deposition. As shown in Fig. 12, copper particles are smaller than 0.1 μm and smaller than the pore diameter in silver.

Comparison between the initial porous printed surface (Fig. 5) and the same surface after the Cu deposition from the solution (Fig. 12) shows the fine porous film on the porous printed layer. We have suggested that the pores in the Ag surface prepared by the porous printing are filled in with Cu particles.

Comparing this picture with Fig. 5, one also can conclude that copper particles are evenly distributed over the silver SGE. The copper particle size is below the pore diameter: copper penetrates into cavities of silver. The initial section of the curve shown in Figs. 13, 14, and 15 corresponds to the partial filling of the silver pores.

The deposited copper features a cubic face-centered crystal structure with Fm3m crystallographic point group of symmetry. For a contact SGE with a copper coating, an X-ray diffraction pattern with peaks of maximum intensity is shown in Fig. 14. As it can be seen, the copper reflections show an increase in the intensity with deposition time. Their intensities are compared in Fig. 15. It is noted that the intensity ratio steadily grows for 40 min. This means that the copper deposition rate is held constant for this period. The deposition rate decreases when copper has filled silver cavities; then, after 90 min, the copper deposition is essentially brought to completion.

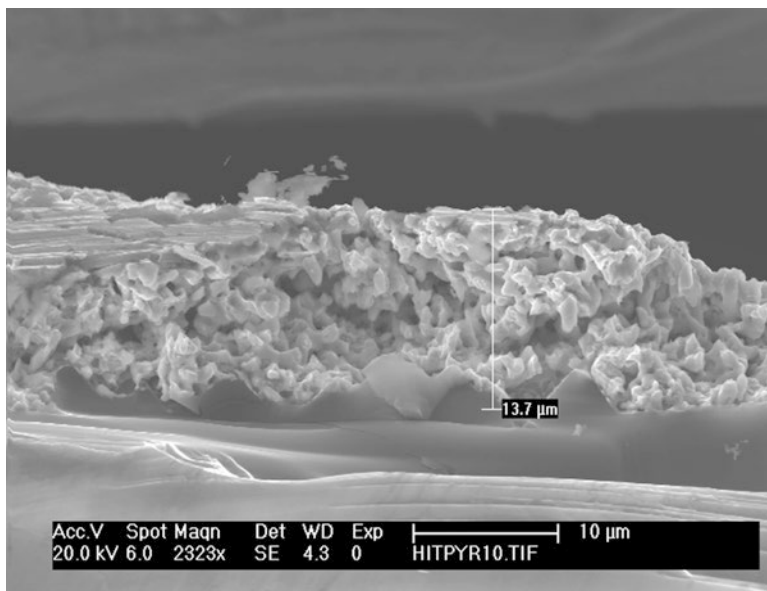


Fig. 13 Electron-beam image of cross-sectional cleavage of a silver contact SGE obtained on a wafer after 5 min copper deposition. The thickness is 13.7 μm , and it has increased up to 37 %

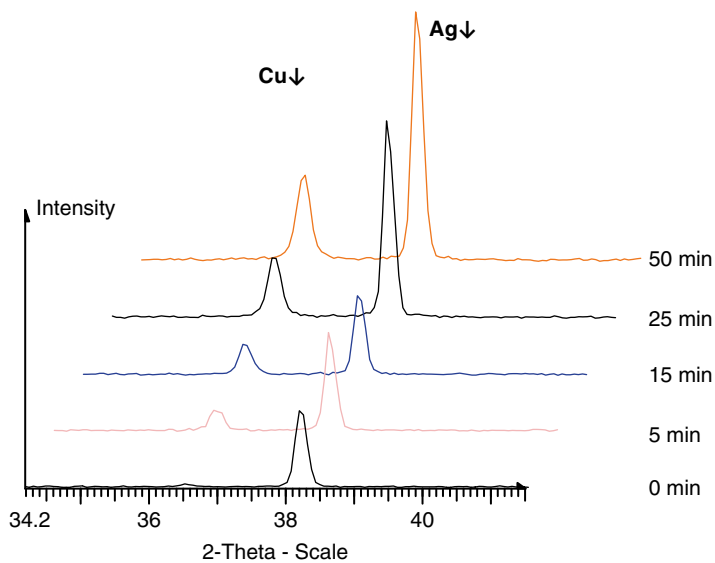


Fig. 14 X-ray diffraction pattern of a silver contact SGE obtained before and after copper deposition

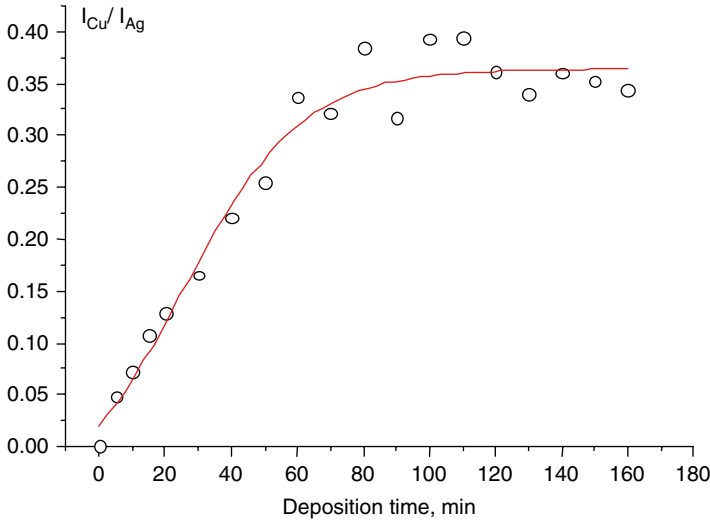


Fig. 15 Copper-to-silver peak intensity ratio depending on the deposition time

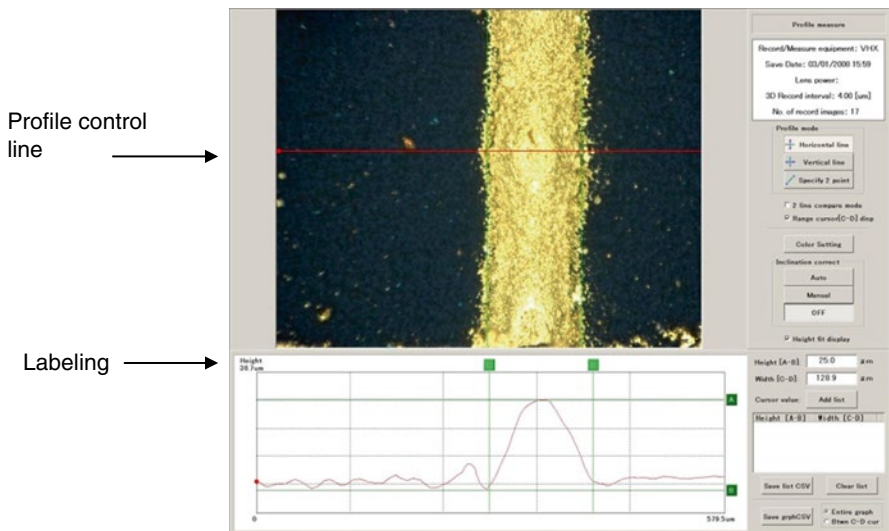


Fig. 16 Test record sheet on the imaging of the silver contact SGE with the use of a scanning optical microscope. The SGE is 25.0 µm in height and 129 µm in width

The morphology of the solar cell surface and contact SGEs was investigated before and after the deposition of copper with the use of a KEYENCE-5000 optical scanning microscope. The computer image processing of the data on the in-layer optical scanning of the surface obtained before and after the deposition gives the results presented in Fig. 16. The copper deposition onto silver SGE leaves the

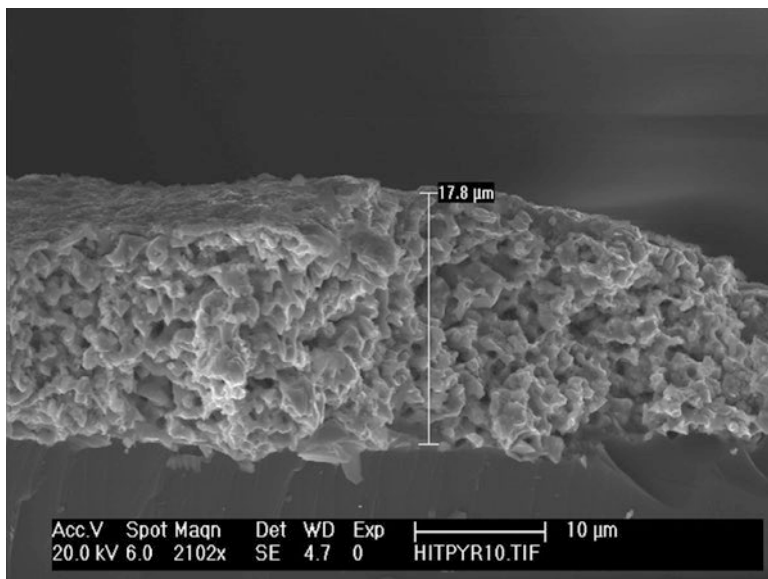


Fig. 17 Electron-beam image of cross-sectional cleavage of contact SGE made of silver on a wafer after 15 min copper deposition. The SGE is 17.8 μm in height, 2102 \times magnification; the pore diameter in silver is 1–2 μm , 8695 \times magnification

contact form and profile unchanged; the contact profile alone consists of regularly alternating thicker parts and contractions of a contact SGE. The difference in the height and width ranges up to 5 μm . In some instances, the thin copper layers were responsible for a modest size contraction throughout the height of the contact. It was found that, when copper layers up to 1 μm thick are deposited on a silver contact, they are able to initiate the thinning out of an SGE up to 10 %.

The electron-beam image of the cleaved facet of a silicon wafer with a contact SGE obtained with the copper deposition is given in Fig. 17. It is easily seen that the silver SGE remained a porous body. The SGE thickness grew up to 17.8 μm .

The chemical composition of the contact and the copper distribution over the contact depth were investigated by energy-dispersive X-ray (EDX) analysis, secondary ion mass spectrometry (SIMS), and X-ray photoelectron spectrometry (XPS). It was found that the copper composition in the silver pores declines with the contact depth. Copper was detected at the silicon–silver interface. Copper diffusion in the silicon escaped detection.

To examine the material properties of the contacts, we have used the EDX method (Fig. 18).

As we can see in Figs. 18 and 19, on the surface of the contact, only copper is registered. We note that the thickness of the copper layer cannot be measured by the EDX method.

Now we would like to describe our observations of changes taking place in profiles of the finger contacts and bus bar under the Cu metallization from water solutions without external electrical field. The parts of the standard solar cells with

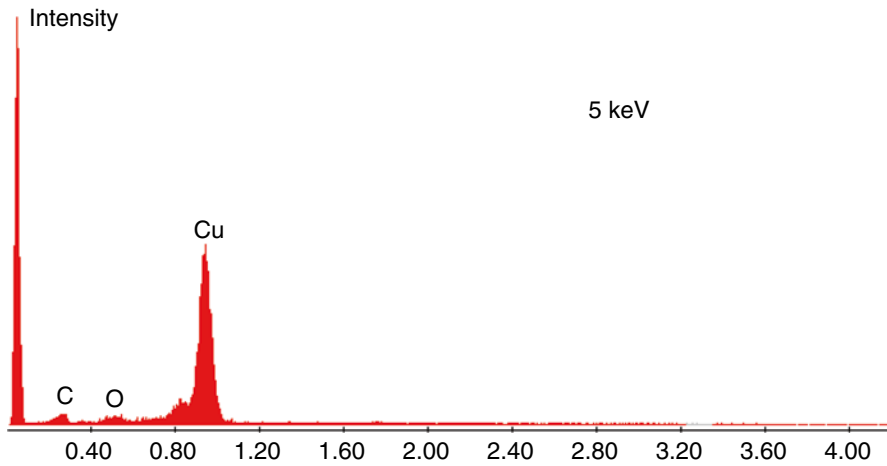


Fig. 18 EDX analysis with 5 keV. As is seen, copper (but not silver) is placed on the surface

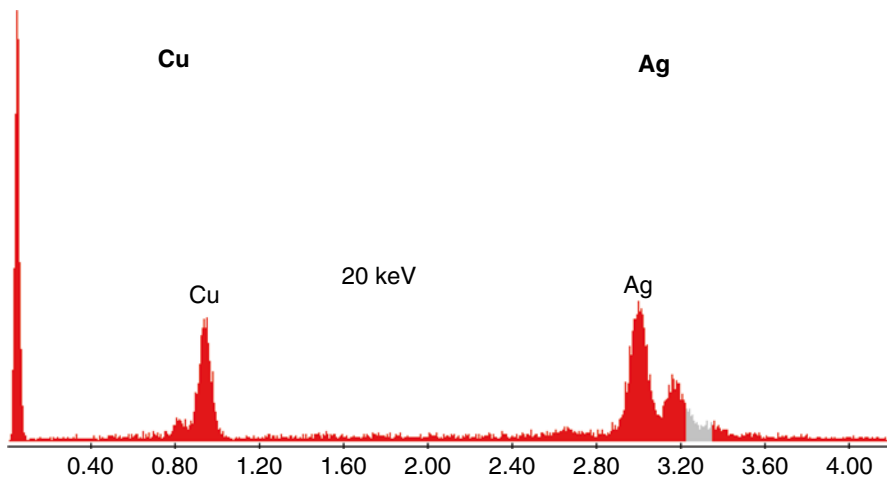


Fig. 19 EDX analysis using the electron beam with 20 keV energy. The deep layers of the sample are also investigated. The additional Ag signal is registered

dimensions 125×125 and 156×156 mm² were chosen as objects of examination. The deposition area did not exceed 15 cm².

The process of the Cu metallization was carried out at the room temperature. The samples were placed in the glass cuvette of 180 mm height and 1 l volume. The cuvette was filled in with 1.4 g/l Cu acetic acid solution and 0.02 N catalyst concentration. The time of the copper deposition was 5 min.

The next important question is the uniformity of the copper layer. We have studied the solar cells which were stored during various times after the screen printing (contact finger fabrication, the paste annealing was performed in the temperature

range 810–960 °C) and the chemical bath (Cu metallization of these contacts). First of all, we have to observe how uniform will be the copper layer produced by the metallization performed immediately after screen printing and paste etching. At the same time, we have found that the solar cells stored 6 months after the screen printing had poor copper covering (only at the edges of the grid), and in the middle of the solar cell, we also had seen no Cu layer. How one can explain this fact? We suppose the center of the solar cell has lower potential compared with the outside section of the cell. Why? Because the edge of the solar cell has got higher potential after the chemical bath than the area in the middle of the cell because the electromagnetic field is larger on the edges than that in the central part of the solar cell.

Besides that, the Ag contacts have various widths (from 80 μm to 120 μm). Our studies showed that the more slim contacts had larger Cu-covering ratio.

Many Ag pastes contain lead (Pb) as a component. We have checked the possible effect of lead on the formation of Cu layer on the silver contacts. Our investigations have showed no difference between metallization results for Ag contacts fabricated by using the Pb-free pastes and lead-containing ones.

We also have examined the uniformity of copper layer deposited on silver contacts immediately after the paste annealing and after 1 day storage of the industrially fabricated solar cells. The copper layer was completely uniform in the first case. For the set of the samples stored 24 h, we have registered lowering Cu deposition rate only for two samples; for other 98 structures, we have observed no changes either in uniformity of the copper layer or the rate of Cu deposition. Thus, we can conclude that the “fresh” samples (with storage times no more than 24 h) are the most suitable objects for Cu metallization in the sense of the layer uniformity and deposition rate.

The next stage of our experiments was studying the contact profiles before and after the metallization. Dektak measurement unit gave us a possibility to define the width and height of the contact fingers and, consequently, to calculate the cross section of the contacts. We have chosen two sets of the solar cells with various pastes:

- Solar cells from set 1: silver-containing paste DuPont with lead and DuPont Al-containing paste with lead
- Solar cells from set 2: silver-containing paste DuPont with lead and Heraeus Al-containing paste with lead

Tables 2 and 3 and Figs. 20 and 21 illustrate the results. The statistical working out was carried out for each experimental point (ten measurements for each point). The Dektak software allowed us to estimate the geometrical parameters of the Ag finger contacts.

What did we obtain? Let us analyze the experimental results. First of all, we see the sufficient mean variation of the geometrical parameters of the contact fingers. The height of the fingers produced using DuPont paste is varied between 11.1 μm and 17.1 μm . The statistically estimated mean value is about $14.0 \pm 1.6 \mu\text{m}$. The cross section of the fingers is in the range from 534 to 1,665 μm^2 , and the mean value is $1,234 \pm 242 \mu\text{m}^2$. The width of the contact finger is $125 \pm 3.5 \mu\text{m}$.

The similar statistical estimation was carried out for the height and cross section of the busbar. It was found that the height of the contact finger is $6.62 \pm 16.6 \mu\text{m}$ with

Table 2 Changes of width and thickness of the finger and bus bar before and after Cu metallization for the samples from set 1

Property	Finger		Bus bar	
	Reference	After Cu deposition	Reference	After Cu deposition
Height, μm	14.0 ± 1.6	16.5 ± 1.0	12.5 ± 1.5	16.6 ± 1.8
Δ , %	2.5 μm or 18 %		4.1 μm or 33 %	
Width, μm	125 ± 3.5	138 ± 7.2	$1,510 \pm 20$	$1,510 \pm 30$
Δ , %	8 μm or 10 %		0	
Cross-section, μm^2	$1,234 \pm 242$	$1,519 \pm 167$	$8,500 \pm 4,800$	$13,700 \pm 2,400$
Δ , %	$285 \mu\text{m}^2$ or 23 %		$5,200 \mu\text{m}^2$ or 61 %	

Table 3 Changes of width and thickness of the finger and bus bar before and after Cu metallization for the samples from set 2

Property	Finger		Bus bar	
	Reference	After Cu deposition	Reference	After Cu deposition
Height, μm	9.75 ± 1.22	12.2 ± 1.8	12.6 ± 1.2	14.0 ± 1.0
Δ , %	2.45 μm or 25 %		1.4 μm or 11 %	
Width, μm	114 ± 6	139 ± 17	$1,500 \pm 10$	$1,530 \pm 20$
Δ , %	24 μm or 21 %		30 μm or 2 %	
Cross-section, μm^2	746 ± 154	$1,110 \pm 180$	$11,800 \pm 1,700$	$13,900 \pm 1,400$
Δ , %	$364 \mu\text{m}^2$ or 49 %		$2,100 \mu\text{m}^2$ or 18 %	

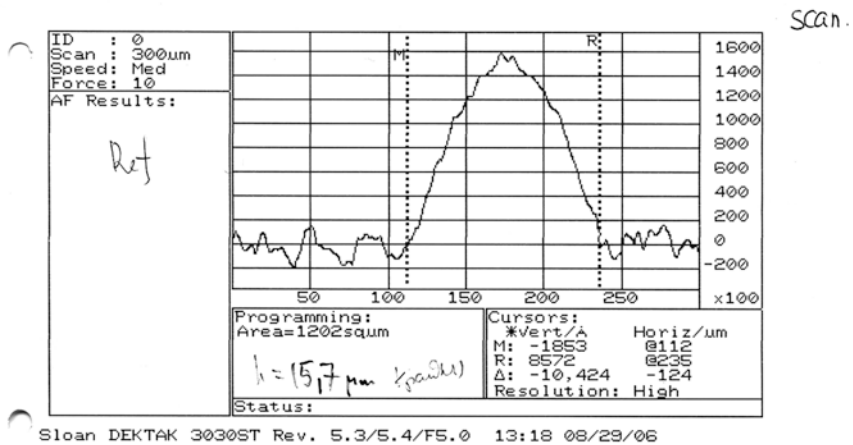


Fig. 20 Profile scan of the contact finger without copper. The height of the finger is 15.7 μm ; its width is 124 μm

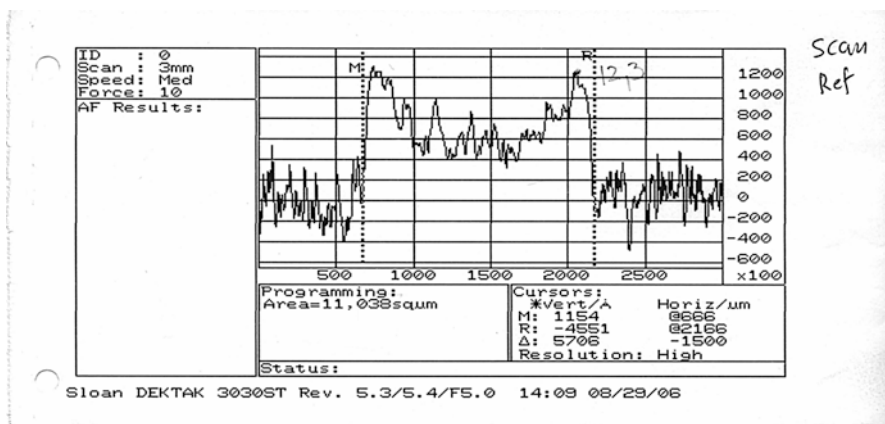


Fig. 21 Profile scan of the contact bus bar without copper. The bus bar height is $12.3 \mu\text{m}$; its width is 1.50 mm

the mean value of $12.5 \pm 1.5 \mu\text{m}$ (eight measurements for each point). The cross-section value changes from $6,913$ to $13,972 \mu\text{m}^2$. The width of the contact finger is estimated to be $151 \pm 0.02 \mu\text{m}$.

The analysis of the geometry of contact fingers showed no changes for narrow and wide contacts after the Cu metallization. The statistical dispersion of the contact parameters after the metallization has lowered. For example, the height of the finger has been decreased from 1.6 to $1.0 \mu\text{m}$. The range of the cross-section values for narrow contacts changed from 242 to $167 \mu\text{m}^2$, and for the busbar, this value decreased from $4,800$ to $2,400 \mu\text{m}^2$.

As is seen, the height and width of the contact finger are increased: 33% and 21% , respectively. The cross section of narrow contact fingers after the Cu metallization was increased in about 49% and that of the busbar up to 61% .

We should note that the aim of metallization carried out for the contact fingers is lowering of the specific resistance. The expression for calculating specific resistivity includes the cross-section value. It is impossible to estimate the efficiency of the contact metallization using the width and height of the copper layer. Our experiments showed the 60% effective increase of the cross-section surface of the contact finger. It means that the Cu metallization may enhance the efficiency of common solar cells.

However, it is important to know: is there a possibility to decrease the contact surface without minimizing the cross-section surface of the contact finger after the Cu metallization?

To answer this question, we had performed the profile measurements of the contact fingers using the Dektak profilometer. The results are plotted in Figs. 20, 21, 22, 23, 24, and 26.

It is seen that the contact height of the sample from set 1 increases, and its width decreases after Cu metallization. The same dependence is observed for the samples from set 2 (Figs. 18 and 19). Figures 21 and 22 show that the profile and height as well as the cross section of the plateau have been changed. Figure 24 demonstrates

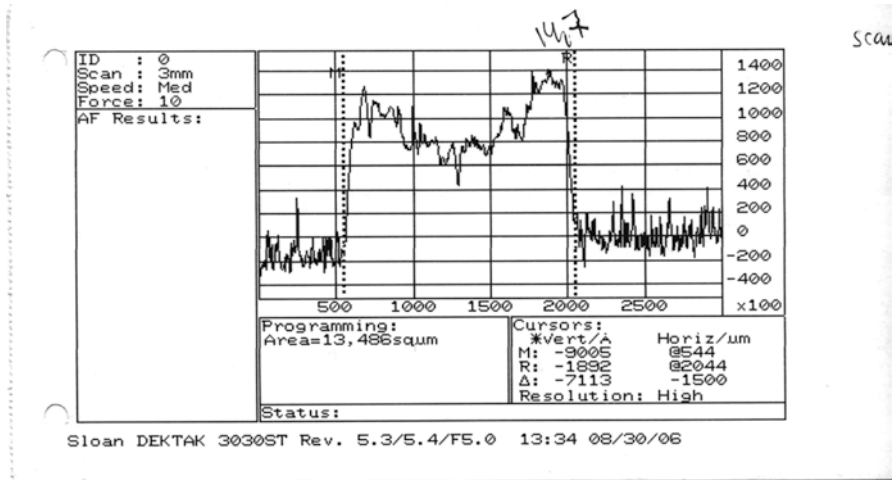


Fig. 22 Profile scan of the bus bar contact after Cu deposition. The bus bar height is 14.7 µm; the width is 1.50 mm

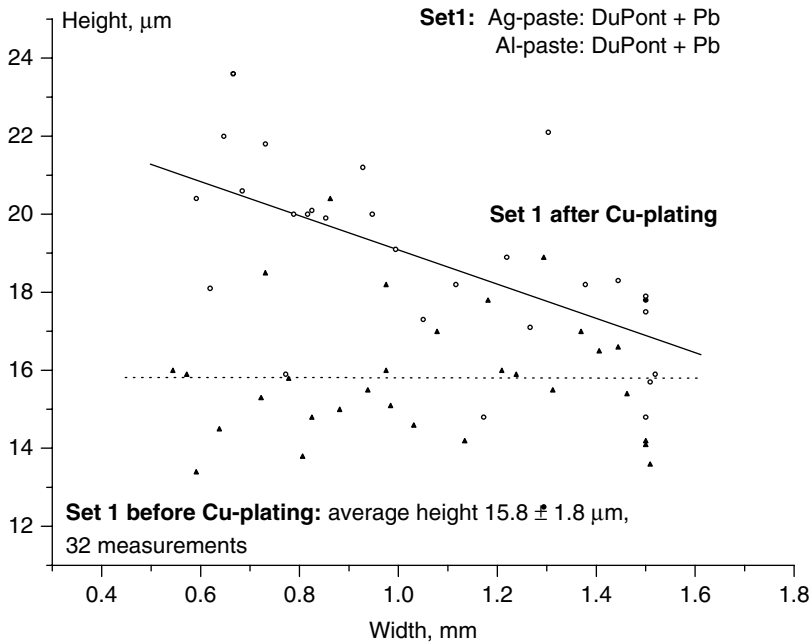


Fig. 23 Busbar height as a dependence of the width of the bus bar before and after metallization (set 1)

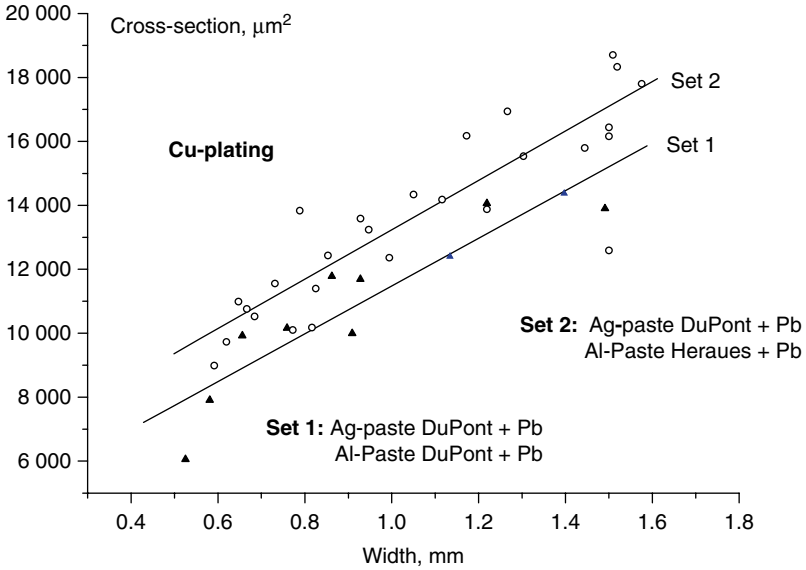


Fig. 24 Bus bar cross-sections of samples from set 1 and set 2 after Cu metallization

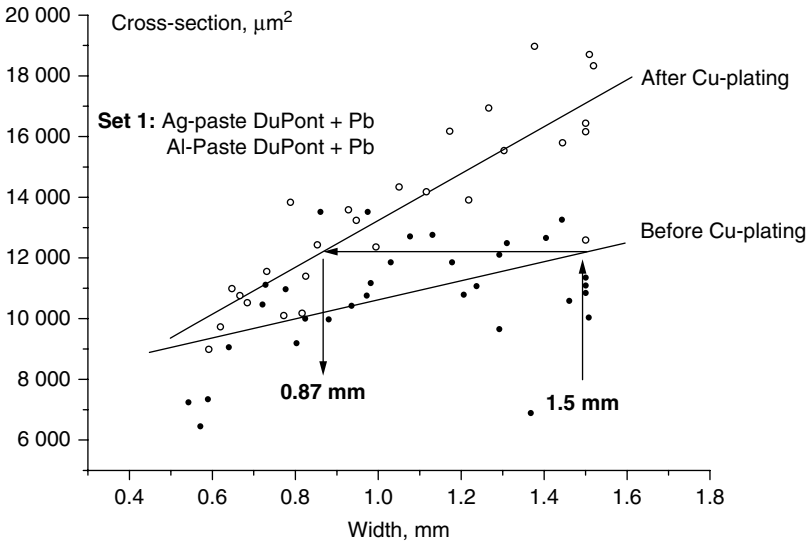


Fig. 25 Bus bar cross-sections of the samples of set 1 before and after Cu metallization

that the cross section of the plateau is changed after the Cu deposition. This feature of the process allows us to keep the contact cross section regardless of minimizing its width. Arrows in Fig. 25 point out that the cross section is kept ($12,000 \mu\text{m}^2$) without changes, and at the same time, the bus bar width has decreased from 1.50 mm to 0.87 mm.

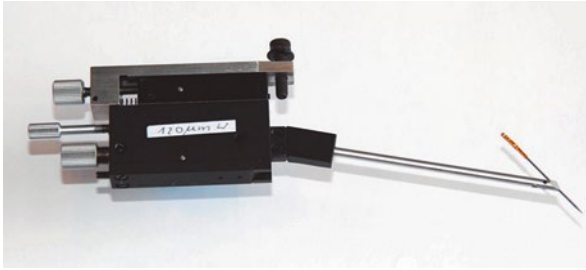


Fig. 26 Tungsten-measuring needle arranged in a holder and shown at the right of the figure

Results and Discussion

The resistivity of the contacts was measured at room temperature with the use of a Keithley 236 two-probe conventional meter. As shown in Fig. 26, two measuring probes were arranged at the contact SGEs which were 8 mm apart. The probe consists of a tungsten needle with a point of 120 μm in diameter (Figs. 26 and 27). The measurements were performed for two specimens placed in a box with black walls and a solar simulator. The experimental results are presented in Fig. 28.

Curve 1 is the current–voltage dependence for the initial silver contact SGEs arranged at a wafer surface. Other curves in Fig. 28 are the current–voltage dependences for contacts obtained after copper deposition. All the curves support the metallic conduction of the contact SGEs. The distinction between them resides in the fact that, in the case of contacts with copper clusters, these curves do not pass through the origin for either the forward current or for the back one. The phenomenon of a current flowing through a metal in the absence of an applied electric field is not outlined in the literature. In our experiment, the luminous current of 450 μA flows along the contact with copper clusters disposed only in silver pores and that of 900 μA flows along the contact with copper clusters disposed in the pores and at the silver surface.

Of fundamental importance is the fact that, in the absence of an applied electric field, the electric current continues to flow along the same samples when a solar simulator was taken out of service. The luminous and dark currents flowing along the contact SGEs are presented in Fig. 29. As can be seen, under the zero bias, in the case of darkness, the generation of charge carriers is kept constant in the duration of the experiment. In the silver contact, the dark current is associated with charge carriers generated in the contact itself. The silver clusters positioned in pores and at the silver surface serve as a source of charge carriers for the dark current.

We should note that various nanoscaled solar devices are proposed for high-effective photon harvesting [18–21]. Now let us describe our results.

As we have shown previously [17], the first attempt for explanation is to consider a Si-based p–n junction with Ag/Cu contacts with different heights of barriers formed at the metal–semiconductor interfaces: $\phi_{\text{Beff}} = \phi_{\text{Bn}} + \phi_{\text{Bp}} \sim 0.05$ eV (this value characterizes the effective barrier heights for electrons and holes,

Fig. 27 The point of tungsten needle seen through an optical scanning microscope. The point is 120 μm in diameter; 5000 \times magnification

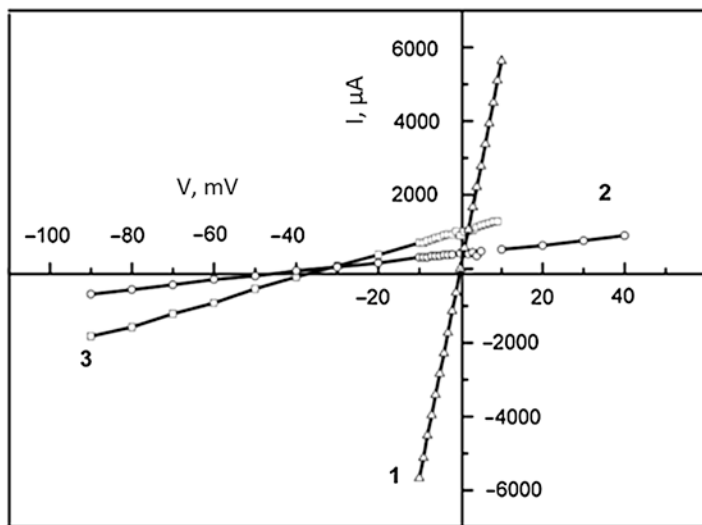
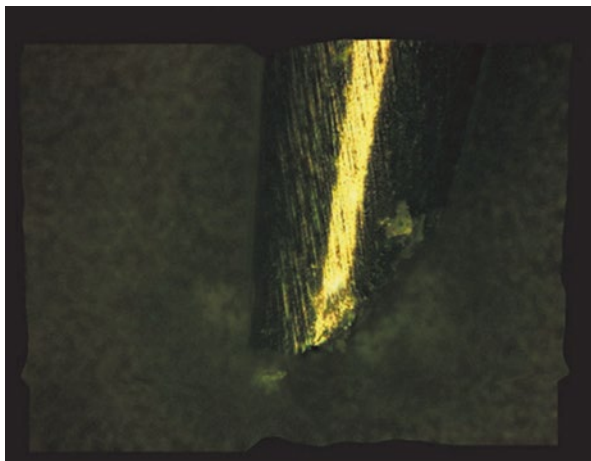


Fig. 28 Current–voltage dependences for 1 a contact SGE made of silver, 2 a contact SGE with copper clusters positioned in the silver pores, and 3 SGE with a copper layer positioned on the surface and with copper clusters positioned in the silver pores

respectively) [17 and Refs. therein], and, on the other side, the barrier may be formed due to the difference of work functions of the contact metals: $\varphi_{\text{B}} = \varphi_{\text{Cu}} - \varphi_{\text{Ag}} = 0.17 \text{ eV}$ [17 and Refs. therein]. Remembering how the solar cell operates (under illumination, the device harvests generated carriers, and in darkness, our

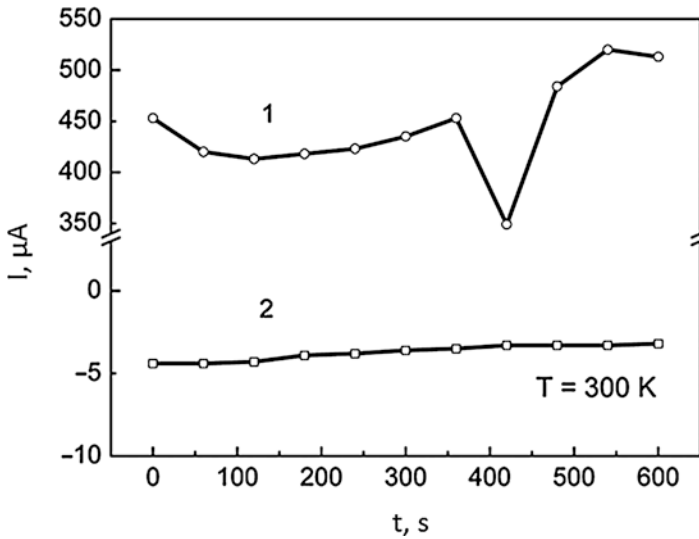


Fig. 29 Time dependencies of dark and luminous currents in the absence of applied bias at contact SGEs with copper clusters positioned in silver pores

active element produces practically no work; therefore, there should be no current!), we tried to calculate possible currents according to the semiclassical theory of semiconductor devices [17 and Refs. therein]:

$$I_{Cu} = A_{el} A^{**} T_{tun}^2 \exp(-e\phi_{Beff} / k_B T) \exp(eV_a / k_B T), \tag{1}$$

where I_{Cu} denotes the current produced by illumination of the sample where Cu atoms are in Ag pores, and on the surface of the Ag finger, A_{el} is an electrical area of the contact, A^{**} is the effective Richardson constant, T_{tun} is a coefficient of the barrier tunneling transparency, k_B is the Boltzmann constant, and V_a is an applied voltage.

What can we obtain for a dark current, when only the deformation of clusters in the contact stripe due to difference between the lattice constants of silver and copper can change the work function and the barrier height, respectively? The expression is as follows:

$$I_{Cu1} = A_{el} A^{**} T_{tun}^2 \exp(-e\phi_{B1f} / k_B T) \exp(eV_a / k_B T), \tag{2}$$

where I_{Cu1} denotes the current observed under illumination of the sample with Cu atom in Ag pores of the Ag finger only; we should note that values of the tunneling transparency coefficient are in the range 10^{-7} – 10^{-5} (they are determined numerically basing on the experimental data). Figures 30 and 31 show results of the numerical experiment.

As one can see, the numerical experiment performed in the region of very small applied bias (up to 40 mV) produces only a qualitative agreement with the measurements. First, there is no “solar cell feature” (calculated IVCs are beginning from

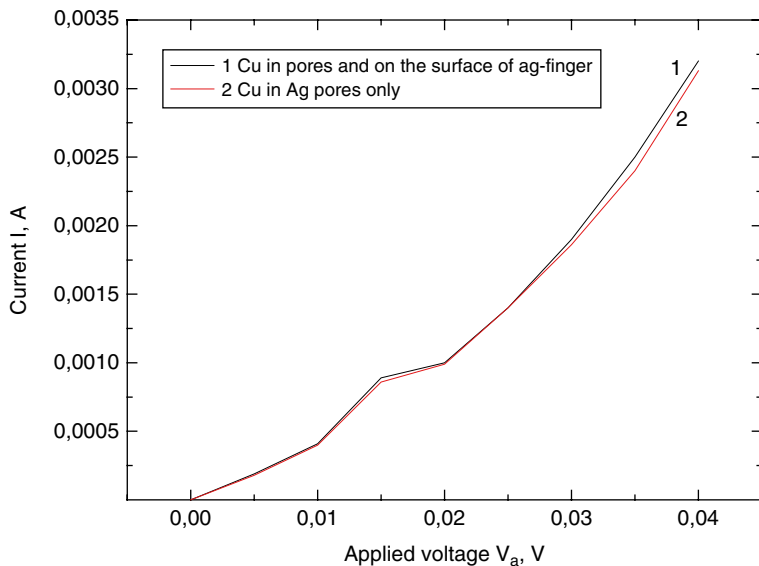


Fig. 30 Current–voltage characteristics (numerical experiment!) of the Cu/Ag cluster contacts of the Si-based solar cell: the calculation is performed according to the expressions (1, 2) and represents the “forward” sections of the experimental dependencies

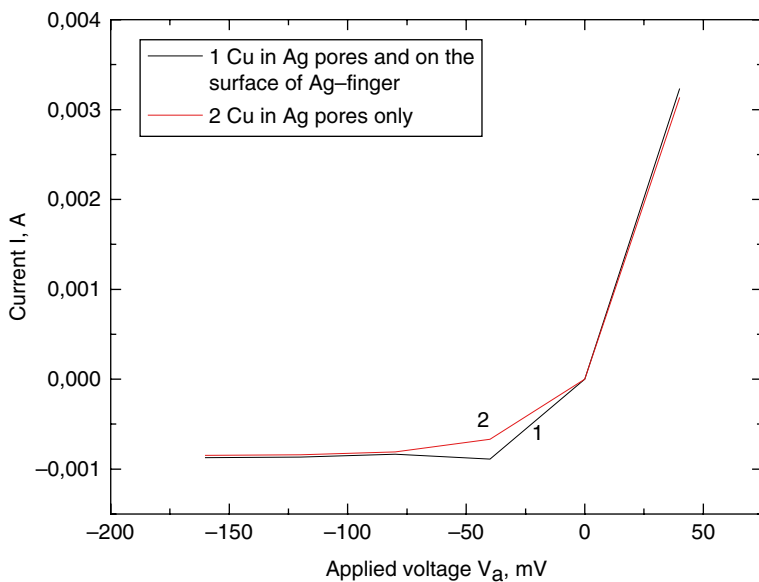


Fig. 31 Current–voltage characteristics (numerical experiment!) of the Cu/Ag cluster contacts of the Si-based solar cell: the calculation is performed according to the expressions (1, 2) and represents both sections of the experimental dependencies

zero unlike that of the illuminated solar cells); second, the values of experimental and calculated currents are also different. The semiclassical approximation (we introduced it by using the tunneling transparency coefficient) does not take into account all features of the conductivity of nanoscaled cluster structures. Before we discuss the further results, we would like to say some words about current–voltage dependencies of nanostructures. The overlap energy between different sites is related to the width of the energy bands. The second factor is disorder-induced broadening of the energy levels. If the ratio of these values is small, it is hard to match the width of the energy level on one site with that of a neighboring site so that the allowed energies do not overlap, and there is no appreciable conductivity through the sample. On the other hand, if the ratio is large, the energy levels easily overlap, and we have bands of allowed energy, so that there are extended wave functions and a large conductance through the sample [17 and Refs. therein].

The current flowing along a silver contact with copper clusters is induced by charge carriers generated in the semiconductor section of the wafer when the solar cell is illuminated. The density of carriers generated within the p–n junction is two orders of magnitude higher than that which occurred in the copper clusters, because the luminous current is two orders of magnitude larger than the dark one (Fig. 29).

Depositing copper onto silver does not result in the formation of the silver–copper solid solution. The contact between the crystal structures assures the electrical potential difference. The difference is inadequate to generate current carriers. However, the contact between the silver–copper crystal structures may result in the compressive deformation of a metallic SGE and in a decrease in the electron work function for copper clusters.

It is our opinion that, in darkness, charge carriers generated by copper clusters within a contact SGE, which is the component part of the solar cell, are governed by the deformation of the SGE [5]. It is known [6] that the deformation of metal cluster structures may result in high-temperature superconductivity. This is why it is necessary to investigate the behavior of the studied specimens in a magnetic field.

Conclusions

The conversion of the solar energy is in wide use in the production of electric power. In regular and industrial units, its efficiency depends on the grade of the component base [7]. As revealed in this paper, the dark current flowing along the silver contact arranged at the illuminated side of a silicon element makes it possible to produce additional electricity in the amount of 5 % of the averaged “light” value. Therefore, even with no changes in the semiconductor part of any solar cell, the efficiency of the solar energy conversion will be elevated when the copper–silver contacts are used in these units.

We have presented the method of metallization for silver contacts used under fabrication of commercial silicon wafer-based solar cells. This technique is applicable for covering the silver contacts with Ni, Sn, other metals, and their mixture layers.

References

1. Laptev VI, Demicheva OV (registration 20.02.2012). Patent of Russian Federation No. 2443037
2. Laptev VI, Demicheva OV (registration 20.05.2011). Patent of Russian Federation No. 104775
3. Kozar' TV, Karapuzova Na, Laptev GV, Laptev VI, Khlyap GM, Demicheva OV, Tomishko AG, Alekseev AM (2010) Silicon solar cells: electrical properties of copper nanoclusters positioned in micropores of silver stripe-geometry elements. *Nanotechnologies in Russia*, 2010, vol 5, Nos 7–8, pp 549–553. © Pleiades Publishing Ltd. (Original Russian text © Kozar' TV, Karapuzova NA, Laptev GV, Laptev VI, Khlyap GM, Demicheva OV, Tomishko AG, Alekseev AM (2010), published in *Rossiiskie nanotekhnologii*, vol 5, No 7–8)
4. Laptev VI, Khlyap HM (2012) Electrical Properties of copper clusters in porous silver of silicon solar cells. *Doklady physical chemistry*, 2009, vol 424, Part 2, pp 40–42. See also: “solar cell.” *Encyclopædia Britannica*. *Encyclopædia Britannica Ultimate Reference Suite*. *Encyclopædia Britannica*, Chicago
5. Greenwood MA (2007) Solar cells, array films constructed from nanotubes. *Photon Spectra* 41(9):114–116
6. Pillai S, Catchpole KR, Trupke T, Green MA (2007) Surface plasmon enhanced silicon solar cells. *J Appl Phys* 101(9):093105.1–093105.8
7. Han H, Bach U, Cheng YB, Caruso RA (2007) Increased nanopore filling: effect on monolithic all solid state dye sensitized solar cell. *Appl Phys Lett* 90(21):213510.1–213510.3
8. Johnson DC, Ballard LM, Barnham KWJ, Connolly JP, Mazzer M, Bessiere A, Calder C, Hill G, Roberts JS (2007) Observation of photon recycling in strain balanced quantum well solar cells. *Appl Phys Lett* 90(21):213505.1–213505.3
9. Pearton SJ, Corbett JW, Shi TS (1987) Hydrogen in crystalline semiconductors. *Appl Phys A* 43:153–198
10. Härkönen J et al (1997) 26th PVSC; Sept. 30–Oct. 3, pp 163–165
11. Lee EJ, Kim DS, Lee SH (2002) Ni/Cu metallization for low-cost high-efficiency PERC cells. *Solar Energ Mater Solar Cells* 74:65–70
12. Teng KF, Vest RW (1988) Metallization of solar cells with ink jet printing and silver metallo-organic inks. *IEEE Trans Comp Hybrid Manufact Technol* 11(N.3):291–297
13. Hong CM, Wagner S (2000) Inkjet printed copper source/drain metallization for amorphous silicon thin-film transistors. *IEEE Electron Device Lett* 21(8):384–386
14. Wang Z, Ida T, Sakaue H, Shingubara S, Takahagi T (2003) Electroless plating of copper on metal-nitride diffusion barriers initiated by displacement plating. *Electrochem Solid-State Lett* 6(3):C38–C41
15. Chu SZ, Sakairi M, Takahashi H (2000) Copper electroless plating at selected areas on aluminum with pulsed Nd-YAG laser. *J Electrochem Soc* 147(4):1423–1434
16. <http://www.secfinishes.co.uk>
17. Laptev VI, Khlyap H (2008) High-effective solar energy conversion: thermodynamics, crystallography and clusters. In: Carson JA (ed) *Solar cell research progress*. Nova, New York, pp 181–204
18. Qi W, Li Y, Yan X, Rathi M, Ropp M, Galipeau D, Jiang J (2008) Organic photovoltaic cells made from sandwich-type rare earth phthalocyaninato double and triple deckers. *Appl Phys Lett* 93(7):073303-1–073303-3
19. Zatirostami A (2011) Analysis parameters and waste output in nano structured solar cells. *J Appl Sci Res* 7(11):389
20. Kuznetsov AS, Tikhomirov VK, Shestakov MV, Moshchalkov VV (2013) Ag nanocluster functionalized glasses for efficient photonic conversion in light sources, solar cells and flexible screen monitors. *Nanoscale* 5:10065–10075
21. Zhang D et al (2013) Al-TiO₂ composite modified single-layer graphene as an efficient transparent cathode for organic solar cells. *NanoLetters* 7(2):1740–1747

Anodically Grown TiO₂ Nanotube Membranes: Synthesis, Characterization, and Application in Dye-Sensitized Solar Cells

Adriano Sacco, Andrea Lamberti, Stefano Bianco, and Elena Tresso

Contents

A Brief Overview on Photovoltaics	1300
Dye-Sensitized Solar Cells	1301
Nanoparticles and Nanostructures for DSC Photoanodes	1303
Anodic Oxidation.....	1305
Electrochemical Impedance Spectroscopy Characterization of DSCs	1308
The Transmission Line Model.....	1310
TiO ₂ Nanotube Membrane Fabrication and Characterization.....	1314
TiO ₂ Nanotube-Based DSCs	1316
Summary and Perspectives	1323
References.....	1323

A. Sacco (✉)

Center for Space Human Robotics@PoliTO, Istituto Italiano di Tecnologia,
Torino, Italy
e-mail: adriano.sacco@iit.it

A. Lamberti

Applied Science and Technology Department, Politecnico di Torino,
Torino, Italy
e-mail: andrea.lamberti@polito.it

S. Bianco • E. Tresso

Center for Space Human Robotics@PoliTO, Istituto Italiano di Tecnologia,
Torino, Italy

Applied Science and Technology Department, Politecnico di Torino,
Torino, Italy
e-mail: stefano.bianco@polito.it; elena.tresso@polito.it

Abstract

First proposed more than 20 years ago, dye-sensitized solar cells represent one of the most interesting non-silicon solar harvesters, with outstanding potential as low-cost devices with easy fabrication process. Their standard architecture is constituted by a dye-sensitized TiO₂ nanoparticle-based photoanode, a hole-conducting liquid electrolyte and a platinized counter electrode. Even if nanoparticles offer a high number of sites for dye molecule chemisorption, they exhibit limited transport and recombination properties with respect to 1D nanostructures such as nanowires or nanotubes. In view of increasing the dye-sensitized solar cell conversion efficiency, new one-dimensional metal–oxide nanostructures are suggested to be employed as photoanodes.

In this chapter the fabrication and characterization of free-standing TiO₂ nanotube membranes and their integration in front-side illuminated dye-sensitized solar cells are reported. Vertically oriented TiO₂ nanotube arrays are fabricated by anodic oxidation, a simple electrochemical technique. The charge transport and recombination mechanisms in the oxide nanostructures are studied by electrochemical impedance spectroscopy.

The first part of the chapter is devoted to describe the dye-sensitized solar cell working principles, the anodic oxidation process, and the electrochemical impedance spectroscopy measurements. In the second part the TiO₂ nanotube membrane fabrication and the results obtained on dye-sensitized solar cells are presented, showing the effectiveness of the use of 1D nanostructures as photoanode materials.

Keywords

Anodic oxidation • Dye-sensitized solar cells • Electrochemical impedance spectroscopy • Equivalent circuit • TiO₂ nanotubes

A Brief Overview on Photovoltaics

One of the major challenges that mankind has to face in the twenty-first century consists in passing the actual energy economy, essentially based on the diminishing fossil fuels (coal, oil, and natural gas) as primary energy sources. Such nonrenewable reserves require millions of years to be formed, and for this reason, alternative sources have to be found to allow the continuity of life when the reserves will finish. Moreover the continuous increase of prices, the delivery problems connected to geopolitics in the Middle East, and, most importantly, the pollutant and dangerous combustion products responsible of the greenhouse effect spur the research of new renewable energy solutions.

Till today solar energy is the only infinite, the most abundant, and clean renewable energy resource. The Earth's surface (at the upper atmosphere)

receives from the Sun something like 1.8×10^{11} megajoule per second (MW), and this value is many times larger than the actual rate of the global energy consumption. Photovoltaics (PV), the technology of harvesting solar radiation for generating electric power, is a renewable energy form that experienced an impressive growth over the past decade. In 2012 the world's cumulative PV capacity achieved 102 GW of installed electric power and, despite being in an economic crisis time, the global annual PV market is foreseen to grow, with estimated values that will reach more than installed 50 GW per year in 2017 [1].

Actually, the terms “photovoltaic cells” and “photovoltaic modules” indicate a wide group of different devices and technologies for the conversion of the sun energy into electric power. The principal parameter determining the effectiveness of the device is its power conversion efficiency (the ratio between the generated electric power produced by the cell and the solar power impinging on the cell itself). Due to thermodynamic considerations, the maximum theoretical efficiency of such energy conversion cannot overcome 81–82 %, but when considering a device, strong limitations arise, depending on the operation principles. For instance, when considering the traditional c-Si devices based on single p–n junction, this limit falls down to a value of about 31 % (Shockley–Queisser limit) [2].

Three different categories – the so-called first, second, and third generation – have recently been suggested [3] for classifying the solar cells. First-generation solar cells are silicon-based, large area, high-quality, and single junction devices. This technology is the most mature and currently leads the market, with an efficiency higher than 20 % that had been measured in the laboratory. The main drawback stands in the relatively costly technology for the module fabrication. The second-generation devices are obtained from a series of thin semiconducting films applied to a supporting substrate; the most employed semiconductors are amorphous or microamorphous silicon, cadmium telluride (CdTe), and copper indium gallium selenide (CIGS). The manufacturing of second-generation PV is made with techniques that permit a roll-to-roll processing and a noticeable cost reduction. However, performances are lower with respect to crystalline silicon counterparts, and some environmental issues related with waste disposal for some materials like cadmium or selenium have to be taken into account. The third generation is looking to find new solutions, alternative to the traditional p–n single junction, in order to achieve on one side efficiencies overcoming the 31 % limit (even if at higher production costs) and on the other side moderate efficiencies (15–20 %) at very low cost, with very cheap materials and process. Dye-sensitized solar cells belong to this category.

In Table 1 the best efficiencies measured for the different families of solar cells are reported.

Dye-Sensitized Solar Cells

Dye-sensitized solar cells (DSCs) are essentially photoelectrochemical devices that convert solar light into DC electric current [3]. Their name is due to the presence of the dye molecules, which have the task to capture the sunlight photons, playing a

Table 1 Best efficiencies for different families of photovoltaic devices [4]

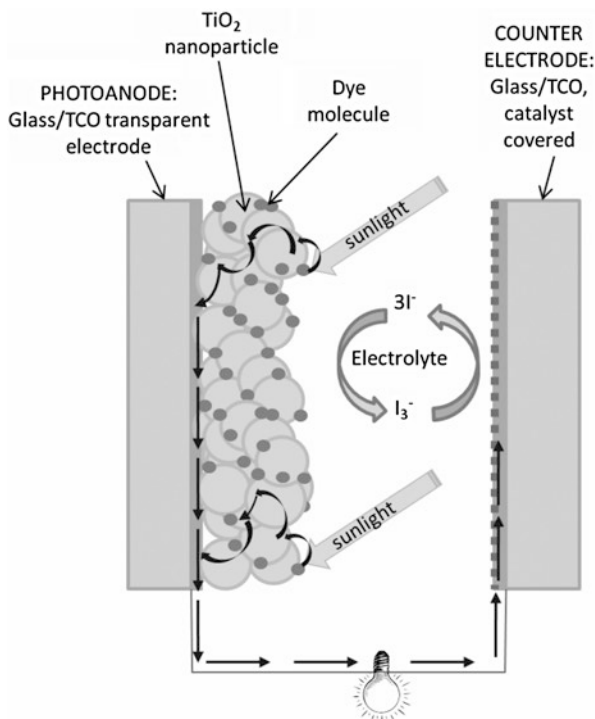
Cell	Efficiency (%)	Company/Institution
<i>Silicon</i>		
Crystalline	25.0	UNSW PERL
Multicrystalline	20.4	FhG-ISE
<i>III-V cells</i>		
GaAs (thin film)	28.8	Alta Devices
GaAs (multicrystalline)	18.8	RTI
InP	22.1	Spire
<i>Thin film</i>		
CIGS	19.6	NREL
CdTe	19.6	GE Global Research
Si (amorphous)	10.1	Oerlikon Solar-Lab
Si (nanocrystalline)	10.7	EPFL
<i>Emerging PV</i>		
Dye sensitized	11.9	Sharp
Organic (thin film)	10.7	Mitsubishi chemical
<i>Multijunction cells</i>		
InGaP/GaAs/InGaAs	37.9	Sharp
a-Si/nc-Si/nc-Si (thin film)	13.4	LG Electronics

role similar to that of the chlorophyll in green leaves. A typical DSC – as shown in Fig. 1 – is confined between two substrates, made in glass or polymer and covered by transparent conducting oxide (TCO) films: they constitute the anode and the cathode of the device, they provide the electron collection, and at least one of them (the front electrode) has to be transparent to sunlight. The essential elements of a DSC are:

- A molecular dye: ruthenium-based synthetic metal–organic molecules are actually the most employed, even if different natural dyes present, for example, in blackberries, raspberries or hibiscus flower can be employed.
- A nanostructured oxide semiconductor thick film, deposited on the front electrode and generally made in porous nanocrystalline titanium dioxide, TiO_2 in the anatase form, with nanocrystals that are electrically interconnected through a sintering process.
- A hole-conducting electrolyte: liquid or solid, containing ions for the reduction/oxidation reaction, typically the couple I^-/I_3^- .

In order to obtain a functioning device, also a catalyst, generally Pt, a sealant, and a packaging architecture are needed. The dye molecules are chemisorbed on the surface of the oxide film, forming a random network of sensitized TiO_2 nanoparticles (NPs), and the electrolyte impregnates the pores of such dye– TiO_2 layer. Upon light absorption electrons are excited in the lowest unoccupied molecular orbital of

Fig. 1 DSC structure and schematic working principle



the dye and fast injected from the dye into the conduction band of the semiconductor, leaving the dye molecule to an oxidized state. The electron possesses sufficient energy to migrate through the nanocrystalline TiO₂ and through the transparent conductive oxide layers to the external circuit. A closed circuit is required to enable electric current to flow and, so, to regenerate the molecules of dyes missing electrons: at the counter electrode, the electrons from the electricity-consuming device are transferred to the redox-couple ions present in the electrolyte. This process is enhanced by the catalyst presence. The ions carry the electrons through the liquid and the pores of the TiO₂ network until they meet with the dye molecules: electrons are transferred to the triiodide ions to obtain the iodide ions and the latter reduce the oxidized molecules of dye, to finally obtain the original molecule and the triiodide ion again. The “recharged” dye molecule is again capable of repeating the process of transforming light into electricity.

Nanoparticles and Nanostructures for DSC Photoanodes

In typical DSC photoelectrodes, the oxide nanoparticles are surrounded by the electrolyte, which impregnates the pores of the nanocrystalline film, forming an interpenetrated junction, with a very high contact area. Considering the typical low doping density of titania and the nanometric dimensions of the NPs, the

photoinjected electrons are essentially the only free carriers in the semiconductor, and in the oxide neither an electric field nor a significant band bending is present [5]. The ions in the redox mediator electrically compensate the electron excess; thus, the charge gradient is the main driving force for the electrons, which move by diffusion following a random walk. The motion of electrons in the semiconductor and ions in the electrolyte is capacitively coupled and an ambipolar diffusion occurs, which reduces the electron mobility. In a simplified picture, the motion of charges in the network of colloidal particles can be described as a sequence of hops from one crystallite to the adjacent one till the conducting electrode, where electrons are collected from the external circuit. More precisely, the charge dynamics is usually described with the Multiple Trapping Model that foresees the capture of electrons in localized states immediately below the conduction band and the subsequent release by thermal activation. The traps for electrons can be located either in the core of the NPs, at the interface between the semiconductor and the electrolyte, and in particular at the grain boundaries, where their density is significantly higher. It is obvious that such a trapping–detrapping process and the significantly tortuous path followed by the photogenerated electrons are associated with conspicuous charge losses. Therefore, experimentally the electron diffusion coefficient in mesoporous films is orders of magnitude lower with respect to that measured for single-crystalline anatase TiO_2 [6].

It is evident that to engineer the nanomorphology of a DSC photoanode with optimal performances, an equilibrium between conflicting requirements has to be found. A nanocrystalline network of particles takes benefit from the very high exposed area, which means the possibility to load a huge number of dye molecules linked to the surface of the semiconductor and thus harvest a large number of photons. On the other hand, when photogenerated, electrons need to survive without recombination until their collection at the electrode, and the tortuous path in the randomly oriented film is subjected to significant losses, notably limiting the achievable electron dynamics [7]. A more ordered structure with an optimized morphology could be beneficial, especially in conjunction with solid-state or quasi solid-state electrolytes, where the kinetics of the redox shuttles is limited. Thus, nanostructures with lower dimensionality like nanowires (NWs) and nanorods able to allow a direct and faster pathway for the photogenerated electrons have attracted consistent attention during recent years [8]. On that topic, zinc oxide emerged as a valuable alternative to titanium dioxide for the fabrication of photoanodes in dye-sensitized solar cells with controlled nanoshaped morphology. It presents a conduction band edge positioned approximately at the same level as in TiO_2 with respect to vacuum reference and higher electron mobility. More interestingly, it is almost an ideal material for the synthesis of an incredibly wide range of nanostructures, and it is thus particularly suitable to investigate the morphological effect in electron collection in DSC photoanodes [9]. In particular, ZnO is suitable for the fabrication of high-quality 1D single-crystalline structure in the wurtzite phase, and the first example of ZnO NW-based DSC was presented by Law et al. in 2005 [10], showing a very fast electron transfer. However, the strong reduction in surface area with respect to NP networks and the technological difficulties in synthesizing very long

Table 2 Efficiencies of some DSCs based on different kinds of nanostructured photoanodes (*NP* nanoparticle, *NW* nanowire, *NR* nanorod, *NT* nanotube)

Photoanode	Efficiency (%)	References
TiO ₂ NP	7.1	[3]
ZnO NW	1.5	[10]
ZnO hybrid NW/NP	1.3	[11]
ZnO/EosinY hybrid thin film	2.3	[12]
ZnO spongelike	6.7	[14]
Polymer-templated TiO ₂ film	4.0	[15]
TiO ₂ NR	5.4	[16]
TiO ₂ NT	7.6	[18]

NWs (up to tens of μm in length) strongly limit the possible applications. Synthesis and characterizations of materials with a more complex geometry, like branched nanorods [11], porous single crystals [12], or coral-shaped structures [13, 14], have been reported showing good conversion efficiencies, but still lower with respect to the ones achievable in TiO₂ mesoporous films. Coming back to titania, the synthesis of well-ordered films using technological approaches like polymer-templated synthesis [15] or impregnation of alumina templates [16] has been explored. In such field, the synthesis and application of TiO₂ nanotubes (NTs) grown by anodic oxidation of titanium emerged as probably the best compromise. In the following section, we present information on perhaps the most impressive and unexpected 1D metal-oxide nanostructure: the self-organized TiO₂ nanotube arrays. The synthesis is carried out by a simple, low-cost, and straightforward approach: the conventional electrochemical anodization of a metallic titanium substrate under a specific set of appropriate conditions. Currently, the publication rate on this topic shows an almost exponential increase, characterized by more than 1000 papers published over the last 5 years [17].

Some examples of the efficiencies obtained on DSCs based on different kinds of nanostructured photoanodes are reported in Table 2.

Anodic Oxidation

Anodic oxidation [19] is the process of forming an oxide (M_xO_y) on a metal surface by applying an electric current or potential through a cell containing a suitable electrolyte. The metals that can be anodized belong to the so-called valve-metal group (Al, Ti, Zr, Nb, W, Ta, etc.). The main feature of these metals is the possibility to grow compact oxide layers (some hundreds of nm in thickness) by anodization in aqueous electrolytes [20]. The characteristics of the layer obtained by anodic oxidation can vary according to the type and concentration of the electrolytes as well as the processing variables used during the oxidation. Compared with other synthesis approaches, electrochemical anodization is a simple and convenient technique to fabricate uniform layers of vertically self-oriented nanostructures.

The best investigated system, in which almost perfect self-organization of pores in oxide can be established, is the growth of anodic aluminum oxide (AAO). Over 50 years ago, Keller and coworkers [21] proved that electrochemical oxidation of aluminum in neutral or alkaline electrolytes allows compact oxide layer formation, while by employing acidic electrolytes, relatively regular hexagonal porous oxide structures could be produced. It has been widely accepted that the formation of the pores in anodic metal oxides is based on two continuous processes: the oxide dissolution at the electrolyte/oxide interface and the oxidation of metal at the oxide/metal interface.

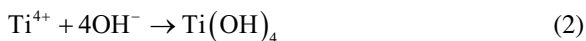
In the last decade several research groups proposed different models trying to provide an explanation to the formation of hexagonal self-arrangement of pores in AAO involving three possible causes: (1) stress at the metal–oxide interface (volume expansion/electrostriction) [22], (2) repulsion of electric fields [23], or (3) establishment of maximum current–flow conditions [24].

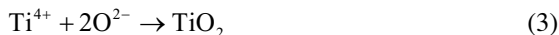
Particularly the case of anodic titanium oxide encouraged considerable interest, since TiO_2 is a material with unique properties employed in various functional applications. In general, the morphology and the structure of the ordered layer are strongly affected by the electrochemical conditions (anodization voltage, distance between the electrodes, temperature) and the electrolyte composition. Indeed, it is possible to differentiate three generations of TiO_2 nanotubes [25]. The first generation refers to TiO_2 nanotube arrays grown in acidic HF mixtures [26]. These tubular structures showed very rough walls, low-defined tube top, and a limited thickness that does not exceed 600 nm. The second generation is characterized by the use of buffered neutral electrolytes containing NaF or NH_4F instead of HF, and in this case, self-organized nanotube TiO_2 layers with thicknesses higher than 2 μm could be grown [27]. Lastly, third-generation nanotubes were grown in NH_4F -based electrolytes with a very small content of water. Earlier work carried out in glycerol showed tubes with extremely smooth walls, well-defined tube tops, and a tube length exceeding 7 μm [28], while using ethylene glycol electrolytes and by a further optimization of parameters, the nanotube length has reached 500 μm [29] and perfectly smooth walls. Water content in the electrolyte affects the growth rate and the etching speed (chemical dissolution rate) of the nanotubes; therefore, it is required for oxide formation (at the bottom), but it also accelerates the dissolution of the nanotube layer (particularly at the top).

The formation of TiO_2 nanotube membranes in fluorine-based electrolyte starts with the oxidation of the metallic surface which releases Ti^{4+} ions and electrons (Eq. 1):



An oxide layer is deposited on the metal surface from interaction of Ti^{4+} ions and O_2 or OH^- ions of water. Equations 2 and 3 describe the formation of hydrated anodic and oxide layers:

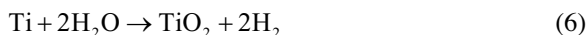




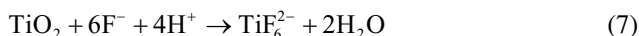
The titanium dioxide is produced from the hydrated anodic layer by a condensation reaction (Eq. 4):



At the cathode (Eq. 5), hydrogen evolution occurs and the entire process of oxide formation is expressed in Eq. 6:



The fluorine ions in the electrolyte attack the hydrated and oxide layers, where the F⁻ ions are mobile in the anodic layer and can react with Ti⁴⁺ under the applied electric field. Field-assisted dissolution of the oxide occurs therefore at the interface between oxide and electrolyte. Localized dissolution of the oxide creates small pits (Eqs. 7 and 8):



These locally etched pits act as pore-forming centers, which convert into pores uniformly distributed over the whole surface. The pores start to grow at the bottom with inward movement of the oxide layer, as depicted in the inset of Fig. 2. Ionic species migrate from the electrolyte toward the metal/oxide interface. The Ti-O bond undergoes polarization and is weakened to assist dissolution of the metal cations. Ions Ti⁴⁺ migrating from the metal to the oxide/electrolyte interface dissolve in the HF electrolyte (Eq. 9). The free oxygen anions migrate toward the metal/oxide interface and further interact with the metal:



The formation of the oxide can then be monitored by recording the current–time characteristics during growth. In Fig. 2 a typical current density–time curve for conditions that lead to nanotube formation is reported. The curve shows three regimes: In the initial stage I of anodization, a compact oxide layer is formed. In stage II, a current increase occurs, and nanoscale pores are initially formed penetrating the initial compact oxide (the current increases as the reactive area increases). In stage III, the current slowly drops again as a regular nanotube layer is formed.

The as-grown material is amorphous. The NT array grown onto the opaque Ti foil, once crystallized and dye sensitized, can be used as DSC photoanode employing a backside illumination setup [30, 31]. In this configuration, the cell is illuminated from the counter electrode side, so the number of incident photons that can be absorbed by dye molecules is partially reduced by the absorption and the reflection on the Pt thin film. Moreover, the iodine-based electrolytic solution between the two

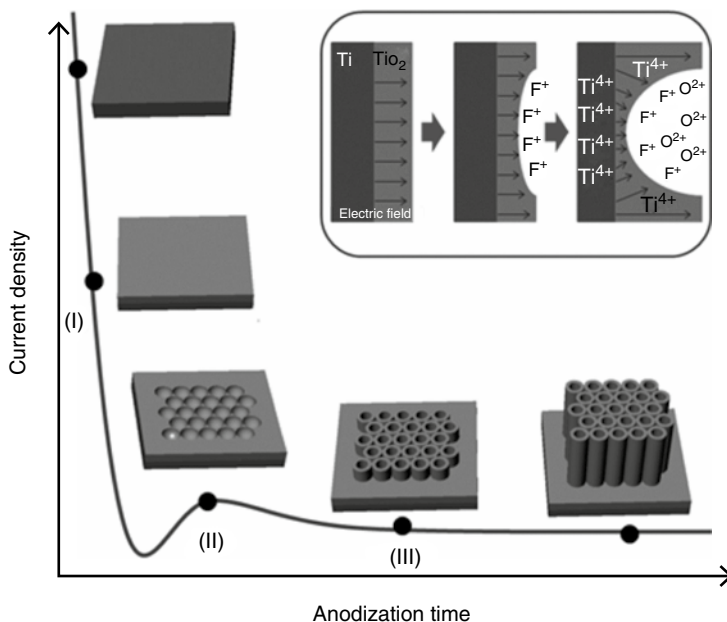


Fig. 2 Schematic representation of anodic oxidation process of Ti into fluorine-based electrolyte matched with the current density versus anodization time characteristics recorded during the process

electrodes can absorb in the UV-region, further reducing the device performances. A possible alternative is to fabricate front-side illuminated NT-based DSC starting by Ti thin films deposited on transparent conductive substrate [32]. In this case, the relatively low film thickness attainable with common sputtering or evaporation techniques in reasonable time limits the maximum NT length achievable. To overcome these constraints, self-standing TiO_2 NT membranes can be anodically grown on Ti foil, detached, and bonded on transparent sheet.

Since dye-sensitized solar cells found an ideal characterization tool in the electrochemical impedance spectroscopy, we briefly introduce the major features of such technique. Subsequently, the main aspects in the synthesis of TiO_2 nanotubes, their integration in DSC photoanodes, and the results of photovoltaic conversion are reported.

Electrochemical Impedance Spectroscopy Characterization of DSCs

Electrochemical impedance spectroscopy (EIS) is a well-established technique, widely used for the study of electrochemical devices and systems, being at the same time a simple but powerful tool; this technique is based on the analysis of the electric response of a cell to an applied periodic voltage of variable frequency superimposed

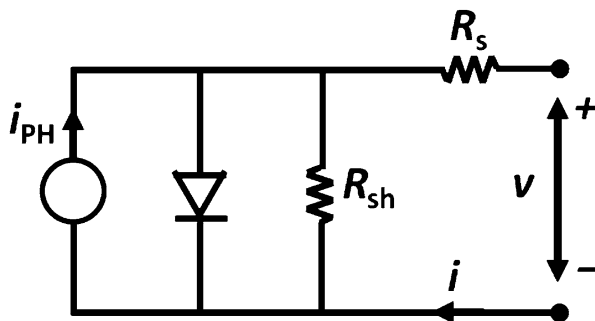
to a constant bias voltage [33]. Even if the transport and charge transfer processes occurring in real systems are described by nonlinear equations that connect the driving forces to the flux of the particles, in the case of excitation voltages with amplitude comparable with the thermal voltage (i.e., under small-signal condition), it is possible to describe all the processes by linear equations in which the coefficient between the potential and the current is the electric impedance [34].

EIS have been employed in a large variety of different fields, i.e., electrochemistry [35], biology [36], and physics [37], and for a wide range of applications, like energy storage [38] and production [39, 40] devices. In particular, this technique is a powerful tool in the characterization of dye-sensitized solar cells [14]. For a DSC, since the different transport and recombination processes occurring in the device are characterized by quite different time constants, this technique permits to distinguish all these mechanisms: the diffusion-recombination electronic processes in the TiO₂ layer and at the semiconductor/electrolyte interface, the diffusion mechanism of the redox species in the electrolyte, and also the charge transfer at the counter electrode [41]. In this framework, the electrochemical cell behavior can be described by an equivalent electric circuit. Usually the shape of the I–V curve of a solar cell can be fitted quite well exploiting the simple diode circuit model reported in Fig. 3 corresponding to the following equation [42]:

$$i = i_{\text{PH}} - i_0 \left(e^{\frac{v+iR_s}{m v_{\text{th}}}} - 1 \right) + \frac{v+iR_s}{R_{\text{sh}}} \quad (10)$$

where i_{PH} is the photocurrent modeled as an ideal current generator, i_0 is the diode reverse saturation current (the so-called dark current), v_{th} is the thermal voltage, m is the diode ideality factor, and R_s and R_{sh} are the series and shunt resistances of the cell, respectively. All these parameters can be determined by fitting the model to a measured solar cell I–V curve. However, in the fitting process, R_s needs to be assumed constant, but this is not the case in DSCs, because the series resistance takes into account also the contributions from the current-dependent resistances of charge transfer and mass transport at the counter electrode [42]. For this reason the modeling circuit that is usually adopted to fit the EIS data (the transmission line model, TLM) is more complicated, and it will be presented in the next section.

Fig. 3 Basic diode equivalent circuit model of a solar cell



The Transmission Line Model

Figure 4 shows the widely used equivalent circuit model of DSCs. In this picture, the representation of the nanostructured oxide has been simplified to a columnar model that represents the mesoporous layer (with thickness d) in which the electrolyte solution interpenetrates. The circuit components and their units are [43]:

- R_S (Ω): *ohmic series resistance* of the cell, accounting for the sheet resistance of the TCO substrates, and electric contacts and wiring of the cell.
- R_{CO} (Ω): *substrate contact resistance* at the interface between the TCO and the TiO_2 film.
- C_{CO} (F): *substrate contact capacitance* at the interface between the TCO and the TiO_2 film.
- R_{TCO} (Ω): *substrate charge transfer resistance* accounting for electron recombination from the uncovered layer of the TCO to the electrolyte.
- C_{TCO} (F): *substrate double-layer capacitance* at the TCO/electrolyte interface.
- r_t (Ω/m): *electron transport resistance* in the semiconductor layer. The total transport resistance of the film is $R_t = r_t \cdot d$.
- r_{ct} ($\Omega \cdot m$): *recombination charge transfer resistance* at the TiO_2 /electrolyte interface. The total recombination resistance of the film is $R_{ct} = r_{ct}/d$.
- c_μ (F/m): *photoanode chemical capacitance* that stands for the change of electron density as a function of the Fermi level. The total chemical capacitance is $C_\mu = c_\mu \cdot d$.
- Z_d (Ω): *electrolyte diffusion impedance*, accounting for mass transport of redox species in the electrolyte.
- R_{CE} (Ω): *counter electrode charge transfer resistance* at the Pt/electrolyte interface.
- C_{CE} (F): *counter electrode double-layer capacitance* at the Pt/electrolyte interface.

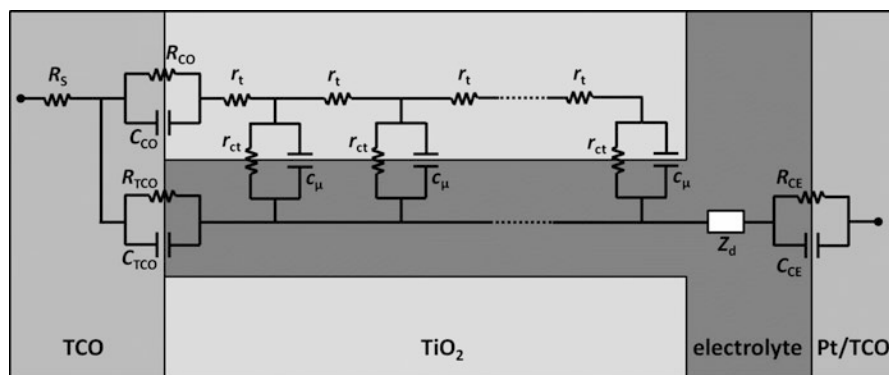


Fig. 4 Equivalent circuit based on the transmission line model for a DSC

Usually two assumptions can be made in order to simplify the above presented circuit [42]. First of all, the electron recombination through the TCO layer can be neglected if compared to the one occurring at oxide/electrolyte interface; this usually happens at normal light intensity (of the order of 1 sun, equivalent to 100 mW/cm²) and also at low intensity when a blocking layer is present onto the TCO substrate. Regarding the interface between the substrate and the oxide layer, it can be assumed that the contact has negligible resistance, since the effects of non-zero R_{CO} are present only for particular recombination blocking layer. Moreover, the ideal capacitors present in the circuit are often replaced by the constant phase elements (CPEs) that are a generalization of conventional capacitances included to take into account frequency dispersion that can be present in the impedance spectra, especially when dealing with porous interfaces. The equivalent impedance of a CPE is given by

$$Z_{CPE} = \frac{1}{Q(j\omega)^\beta} \quad (11)$$

where Q is called CPE prefactor, β is the CPE index, j is the imaginary unit, and ω is the small-signal angular frequency [34]. As for what concerns the components denoted in lowercase letter in the above list, which are r_t , r_{ct} , and c_μ , they are considered as material properties that are independent on the photoanode thickness, because they are distributed in a repetitive arrangement of a transmission line (this is the reason for the transmission line model name given to this circuit), with an equivalent impedance Z_{ph} . With the above reported considerations, by neglecting the electron recombination through the TCO substrate and the contact resistance between the TCO and the TiO₂ layer, and by replacing the ideal capacitors with the constant phase elements, the modeling circuit can be modified as reported in Fig. 5; the total cell impedance can be written as

$$Z = R_s + Z_{ph} + Z_d + Z_{CE} \quad (12)$$

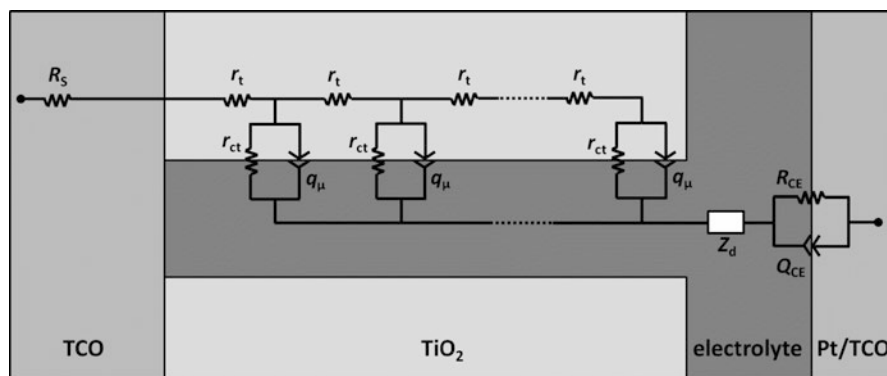


Fig. 5 Simplified equivalent circuit of a DSC

The components of this circuit (the series resistance, the photoanode impedance, the electrolyte impedance, and the counter electrode impedance) will be described in the following.

Series Resistance. The contribution of the series resistance is due to the sheet resistance of the substrates and also to the electric wiring; this value is constant for each frequency, and also it does not change upon illumination and by varying the bias voltage.

Photoanode Impedance. The impedance related to the oxide/electrolyte interface accounts for the so-called diffusion–reaction model, because it gives information about the electron transport properties of the semiconductor layer and about the recombination properties at the interface with the liquid solution. The general photoanode impedance has the form [44]:

$$Z_{\text{ph}} = \sqrt{\frac{R_{\text{ct}}R_{\text{t}}}{1 + (j\omega\tau_{\text{n}})^{\beta}}} \coth \left[(\tau_{\text{t}} / \tau_{\text{n}})^{\beta/2} \sqrt{1 + (j\omega\tau_{\text{n}})^{\beta}} \right] \quad (13)$$

where

$$\tau_{\text{t}} = (r_{\text{t}}q_{\mu}d^2)^{1/\beta} = (R_{\text{t}}Q_{\mu})^{1/\beta} \quad (14)$$

is the electron transport time in the semiconductor layer and

$$\tau_{\text{n}} = (r_{\text{ct}}q_{\mu})^{1/\beta} = (R_{\text{ct}}Q_{\mu})^{1/\beta} \quad (15)$$

is the electron lifetime. By fitting the experimental EIS curve using the circuit depicted in Fig. 5, the chemical diffusion coefficient D_{n} can be evaluated by using the formula

$$D_{\text{n}} = \frac{d^2}{\tau_{\text{t}}} \quad (16)$$

The transport and recombination properties can be summarized by means of a sole parameter, namely, the diffusion length L_{n} , which represents the mean path traveled by an electron inside the oxide layer before recombination. Its expression is given by

$$L_{\text{n}} = \sqrt{D_{\text{n}}\tau_{\text{n}}} \quad (17)$$

In order to have an efficient electron collection, L_{n} needs to be higher than the oxide thickness (or electron transport time lower than lifetime) [6]. By combining the Eqs. 14, 15, 16, and 17, the following relation can be found:

$$L_{\text{n}} = d \left(\frac{R_{\text{ct}}}{R_{\text{t}}} \right)^{\frac{1}{2\beta}} \quad (18)$$

Looking at Eq. 18, in order to have $L_{\text{n}} > d$, R_{ct} needs to be higher than R_{t} , i.e., the recombination resistance must be larger than transport resistance. In the opposite case,

which is when large recombination occurs, only a fraction of the photogenerated carriers is collected and the condition $R_t \gg R_{ct}$ applies; the general impedance of Eq. 13 becomes

$$Z_G = \sqrt{\frac{R_{ct}R_t}{1+(j\omega\tau_n)^\beta}} \quad (19)$$

known as Gerischer impedance [43]. This behavior corresponds to the diffusion in semi-infinite space, meaning that when transport resistance is large, the diffusion in the semiconductor becomes the limiting process in the device.

All the impedance elements related to the photoanode/electrolyte interface are strongly dependent on the distribution of conduction band electrons, and so their behavior depends on illumination and potential conditions. In particular the chemical capacitance, reflecting the density of states, is larger for high potential values but is quite independent from illumination. Regarding the transport resistance, its value remains constant as the light intensity varies for a given value of bias voltage; for this reason, the electron transport time (see Eq. 14) does not have an illumination dependency. On the other hand, while the applied potential is increasing, the TiO₂ Fermi level is displaced toward the band edge, thus increasing the free electron concentration and, as a consequence, the oxide conductivity. Accordingly, the transport resistance presents an exponential dependence on the bias voltage, becoming negligible for values around the open circuit voltage, because the oxide becomes sufficiently conductive. For what concerns the recombination resistance, also its value exhibits the same exponential voltage dependency of R_t , but it also depends on the illumination conditions: for example, under dark, its value is higher with respect to illumination, and correspondingly the dark electron lifetime is larger than under light. This can be explained with a difference of local I_3 concentration (which is responsible for the electron recombination). In fact under illumination, the I_3 can be formed near the oxide/electrolyte interface because of the large number of oxidized dye molecules, while under dark it is formed at counter electrode and then it can diffuse toward the semiconductor. The higher concentration of holes produced in proximity of the TiO₂ can be responsible for the reduction of the electron lifetime [41].

Electrolyte Impedance. As stated in section “Dye-Sensitized Solar Cells,” the charge transport in the electrolyte solution is a diffusion-driven process, which can be described by the so-called finite-length Warburg impedance equal to [41, 42]

$$Z_d = R_d \sqrt{\frac{\omega_d}{j\omega}} \tanh\left(\sqrt{\frac{j\omega}{\omega_d}}\right) \quad (20)$$

in which R_d is the electrolyte diffusion resistance and ω_d is the characteristic frequency of diffusion in the electrolyte solution:

$$\omega_d = \frac{D_{I_3}}{\delta^2} \quad (21)$$

The characteristic frequency ω_d depends on the diffusion coefficient $D_{I_3^-}$ and on the thickness of the diffusion layer δ (approximately equal to the half of the electrolyte layer thickness [45]).

Counter Electrode Impedance. The counter electrode impedance accounts for the charge transfer at the Pt/electrolyte interface; its expression is given by [42]:

$$Z_{CE} = \frac{R_{CE}}{1 + j\omega(R_{CE}Q_{CE})^{1/\beta_{CE}}} = \frac{R_{CE}}{1 + j\omega\tau_{CE}} \quad (22)$$

where

$$\tau_{CE} = (R_{CE}Q_{CE})^{1/\beta_{CE}} \quad (23)$$

is the counter electrode charge transfer time. The value of the counter electrode impedance is practically nondependent on the applied bias voltage.

TiO₂ Nanotube Membrane Fabrication and Characterization

Titania nanotube arrays were grown by a two-step anodic oxidation [18] of Ti foil in an electrolytic solution consisting of 0.5 wt% NH₄F and 2.5 vol.% deionized water in ethylene glycol. A Pt sheet was employed as cathode in a two-electrode configuration o-ring cell. A one-step anodic oxidation process can lead to the synthesis of disordered TiO₂ nanowires on the top of the TiO₂ nanotubes. The formation of NWs is due to the chemical dissolution of the tube top by means of the fluoride species, and it is detrimental to the DSC operation, since NWs can hamper the infiltration of dye molecules during the sensitization step [17]. In order to achieve a debris-free open-top nanotube morphology, a two-step electrochemical process was employed. The first 30 min anodization at 60 V forms a disordered sacrificial NT layer, which is subsequently removed by an ultrasonication treatment in acetone. Thus, the resulting Ti surface is patterned by almost periodic hollows that previously contained the removed NT bottom. This surface texture allows the electric field to be focused into each hole during anodic oxidation [46], and these hollows act as growth centers for the second electrochemical step leading to a more homogeneous debris-free NT distribution. This step was performed with different time intervals, and after this procedure hexagonal close-packed TiO₂ nanotube array was successfully obtained. Figure 6a shows the surface of the disordered NWs obtained on the top of the tubes after the first anodization. The surface of the Ti foil after the removal of the sacrificial NT layer is illustrated in Fig. 6b. The hollow-textured Ti surface was then again anodized, thus obtaining the well-ordered NT array shown in Fig. 6c (top view) and Fig. 6d (bottom view). The average external diameter of the tubes was 130 nm, with wall thickness of about 20 nm. After the anodization, the oxidized Ti substrates were repeatedly rinsed in deionized (DI) water and ethanol in order to remove the residual fluoride contaminants and other impurities. During this step a self-detachment of the NT array from the metal substrate was obtained avoiding crack occurrence.

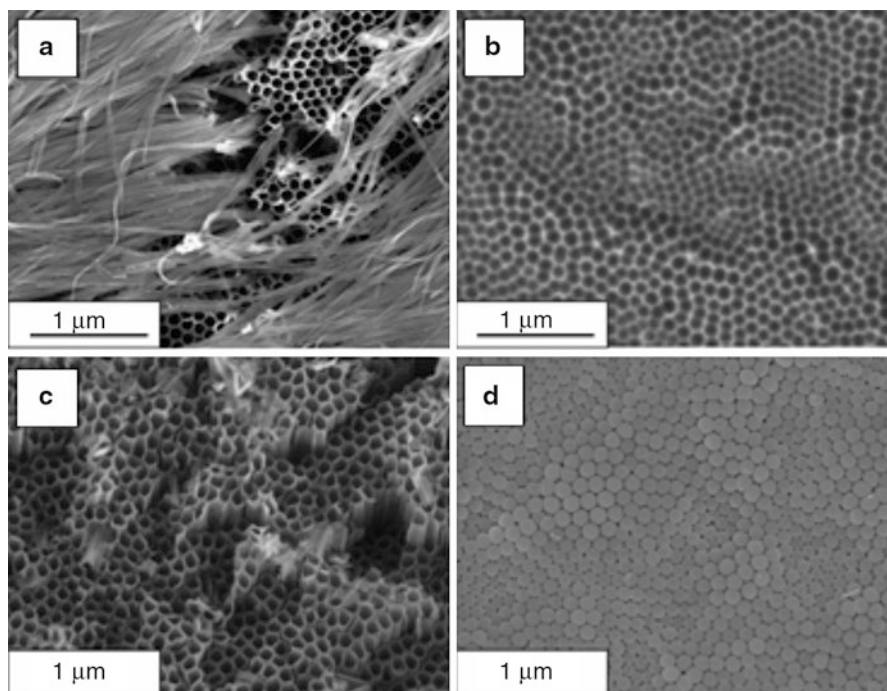


Fig. 6 FESEM micrographs showing the surface of the TiO₂ NT array after the first step of anodic oxidation (a) and the Ti surface after the growth and removal of the sacrificial NT layer (b); the top (c) and the bottom (d) of the TiO₂ NT array grown after the second anodization

The dependence of TiO₂ NT array length on the anodization time was investigated. The results obtained with the FESEM characterization are reported in Fig. 7. For the anodization times chosen (2, 3, and 4 h), TiO₂ NT membranes of different thicknesses were obtained (12, 22, and 30 μm, respectively, as shown in Fig. 7).

Chemical composition of the nanostructured thin film was investigated using energy-dispersive X-ray (EDX) analysis. The results on the as-grown material (reported in Lamberti et al. [47]) reveal the presence of fluorine and carbon atoms in addition to the expected titanium and oxygen atoms, as confirmed by the semi-quantitative standardless analysis. This contamination is consistent with the results of Albu et al. [48] that describe the TiO₂ NTs as composed by two layers: an outer shell of pure and dense TiO₂ and an inner porous core containing incorporated electrolyte components. However, EDX analysis shows that after the annealing at 450 °C, fluorine and carbon disappear, thus resulting in an optimal control of the oxide stoichiometry.

The specific surface area as measured by Brunauer–Emmett–Teller method is about 40 m²/g, in line with the value measured for TiO₂ nanotubes array obtained by anodic oxidation in organic electrolyte [17].

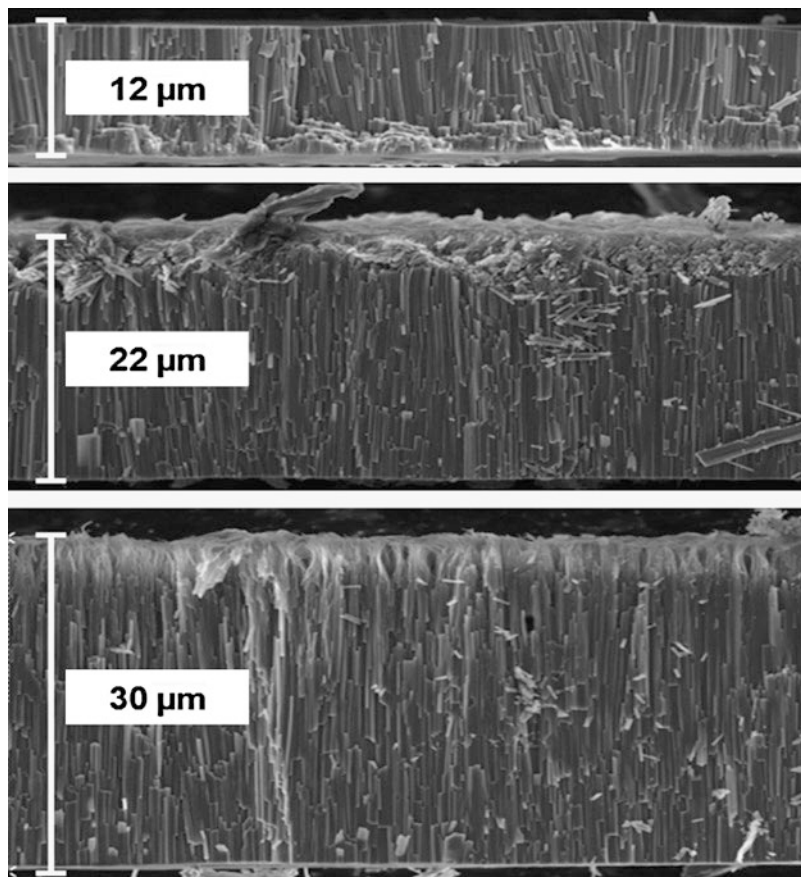


Fig. 7 Dependence of TiO₂ NT array length on the anodization time (2 h, 3 h, and 4 h from the *top* to the *bottom*)

The X-ray diffraction (XRD) pattern, reported in Fig. 8, shows the completely amorphous nature of the NT array after anodic oxidation while a crystalline anatase film was obtained after the thermal treatment.

TiO₂ Nanotube-Based DSCs

In order to fabricate DSC photoanodes, the TiO₂ NT membranes were transferred and bonded on fluorine-doped tin oxide (FTO) transparent substrates employing a drop of a TiO₂ sol, previously casted on the FTO surface. The sol of amorphous TiO₂ NPs (used to obtain a good interface between the FTO and the TiO₂ NT bottom) was prepared by sol-gel technique [18]. Afterwards, samples were heat treated at 450 °C for 1 h for crystallization, then treated with TiCl₄ for 20 min at 70 °C, and

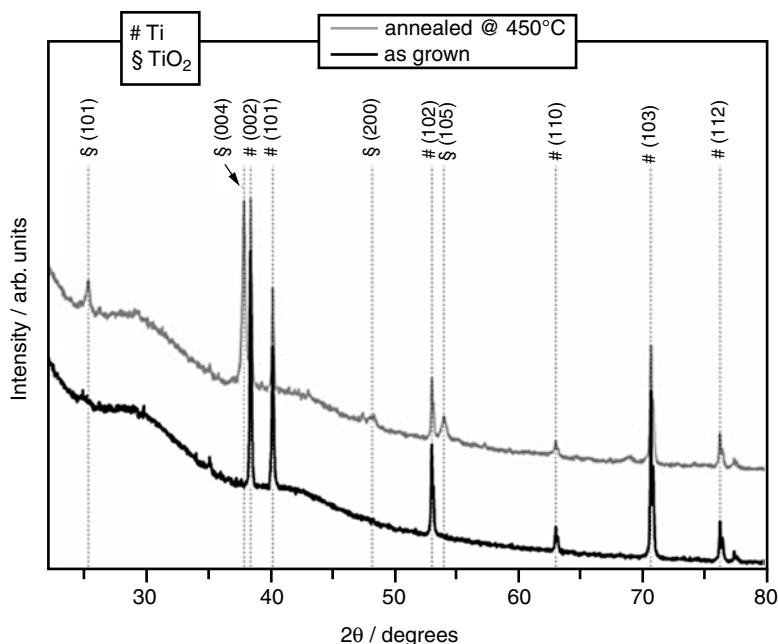


Fig. 8 X-ray diffraction pattern of as-grown and annealed TiO₂ NT array: the peak positions are in perfect agreement with JCPDS reference patterns (89–4921)

heat treated again at 450 °C. The various steps involved in the fabrication process of the NT-based transparent photoanode are summarized in Fig. 9. When the anodized Ti foil was removed from the electrochemical cell (Fig. 9a), NT membranes can be detached by the metal substrate without any crack following a self-detaching mechanism based on repeated rinsing in DI water and ethanol (Fig. 9b). This is a very simple procedure since it does not involve any chemical etching or mechanical splitting, unlike what has been proposed up to now. Subsequently the free-standing membranes were removed (Fig. 9c) and attached (Fig. 9d) on the transparent conductive substrates employing the sol as binding medium. Finally (Fig. 9e), a thermal treatment is performed for all the samples in order to crystallize both the nanotube array and the binding film of TiO₂ nanoparticles.

A FESEM micrograph of the multilayered structure showing the TiO₂ nanoparticle adhesion layer (derived from the sol) is presented in Fig. 10. There, a higher magnification of the interface confirms the good adhesion between the two layers. This process for membrane bonding is easier than others previously reported [49, 50] since just one thermal step is required for membrane crystallization and for interface formation.

The as-prepared photoanodes were incubated for 18 h into a 0.3 mM N719 ethanolic dye solution at room temperature. Then DSCs based on NT membrane photoanodes were assembled exploiting a microfluidic architecture [51].

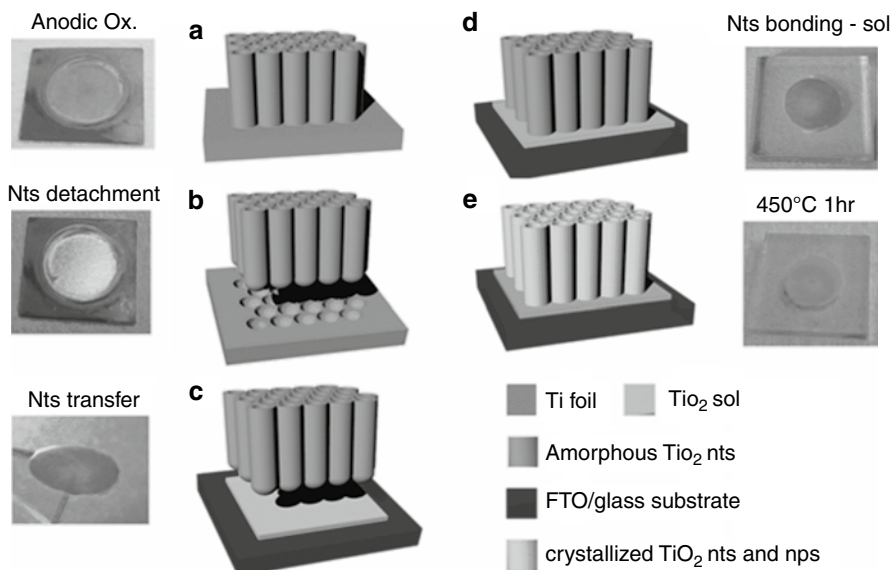


Fig. 9 Schematic of the fabrication process flow of transparent photoanode employing TiO_2 NT array

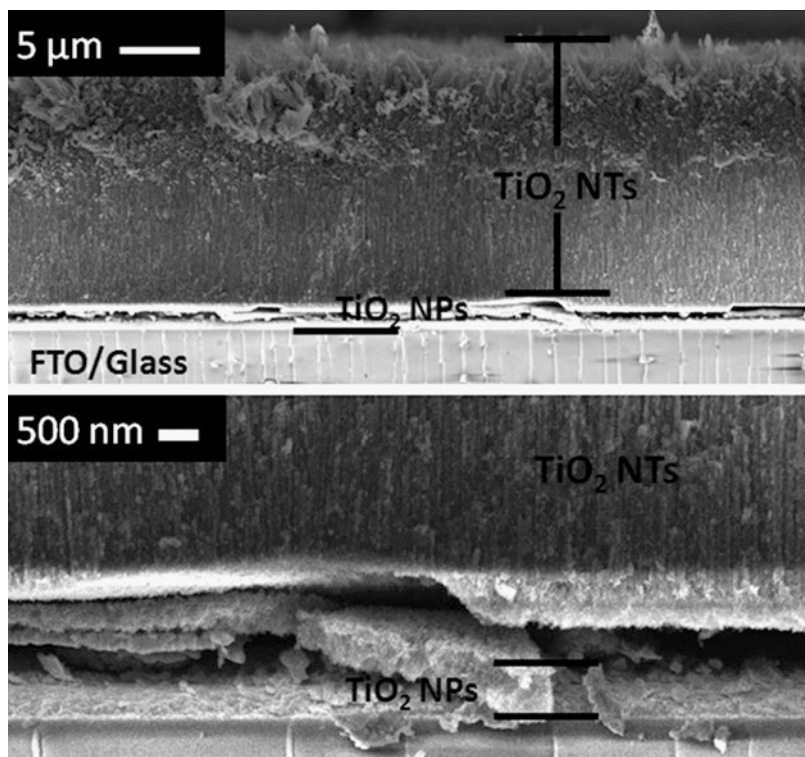


Fig. 10 Cross-sectional view of the multilayer structure consisting of glass/FTO/ TiO_2 -NP/ TiO_2 -NT layers at low (*above*) and high (*below*) magnification

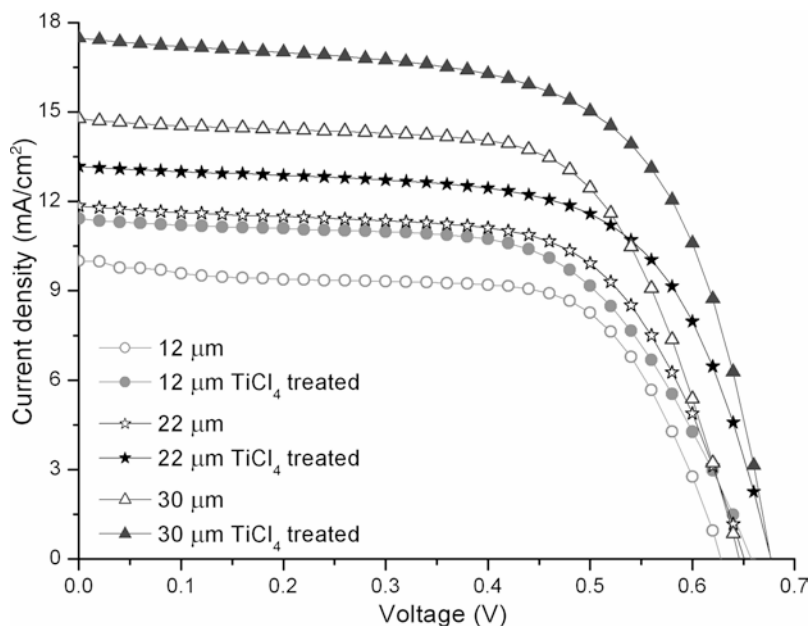


Fig. 11 Current density–voltage curves of TiO₂ NT-based DSCs with and without TiCl₄ treatment for different nanotube lengths (adapted from Lamberti et al. [18] with permission from the PCCP Owner Societies)

Table 3 Photovoltaic parameters of TiO₂ NT-based DSCs with and without TiCl₄ treatment for different nanotube lengths (J_{sc} short circuit current density, V_{oc} open circuit voltage, FF fill factor, PCE photoconversion efficiency)

Cell	J_{sc} (mA/cm ²)	V_{oc} (V)	FF	PCE (%)
12 μ m	10.07	0.628	0.66	3.64
12 μ m TiCl ₄	11.41	0.657	0.62	4.65
22 μ m	11.84	0.651	0.64	4.97
22 μ m TiCl ₄	13.17	0.677	0.65	5.82
30 μ m	14.77	0.646	0.66	6.26
30 μ m TiCl ₄	17.47	0.677	0.64	7.56

In Fig. 11 the I–V curves of the cells fabricated using the NT membranes with different nanotube lengths (namely, 12, 22, and 30 μ m) are reported; moreover, the effect of the TiCl₄ treatment is also presented. The photovoltaic parameters evaluated from the experimental data are reported in Table 3. An enhancement of the current density was obtained by increasing the nanotube thickness, leading to a higher photoconversion efficiency. This improvement has to be expected since an increase of the membrane thickness led to an enlargement of the total surface available for the dye molecule anchoring. Moreover, the TiCl₄ treatment is responsible for a further improvement of the photovoltaic performances of the cells. In fact, as

already reported in literature [52], the effect of this treatment is to downward shift the TiO_2 conduction band, thus enhancing the electron injection efficiency from the dye molecules to the semiconductor layer. In addition the light absorption is also amplified due to a higher number of charge separation interfaces [53]. The combination of the two effects is an increase of the short circuit current density values, and consequently of the photoconversion efficiency, with a maximum value of 7.56 % exhibited by the cell fabricated with TiCl_4 -treated 30 μm -thick membrane.

The incident photon-to-electron conversion efficiency (IPCE) measurements performed on the nanotube-based cells in order to evaluate the light harvesting and conversion efficiency [54] are reported in Fig. 12 for the TiCl_4 -treated cells. The already observed increase of short circuit current density while increasing the nanotube length was confirmed by these measurements. In fact, the spectra present an upward shift in the wavelength range from 400 to 750 nm, and in particular the 30 μm -length nanotube-based cell is characterized by a noticeable maximum value of 89 % at the wavelength of 530 nm.

The effect of the membrane thickness on the recombination kinetics was analyzed by the open circuit voltage decay (OCVD) technique [55]. The results of this measurement (reported in Fig. 13) show no difference in the exponential decay for the different NT membrane thicknesses, meaning that the recombination process is not dependent on nanotube length. On the other hand, TiCl_4 -treated cells exhibit a

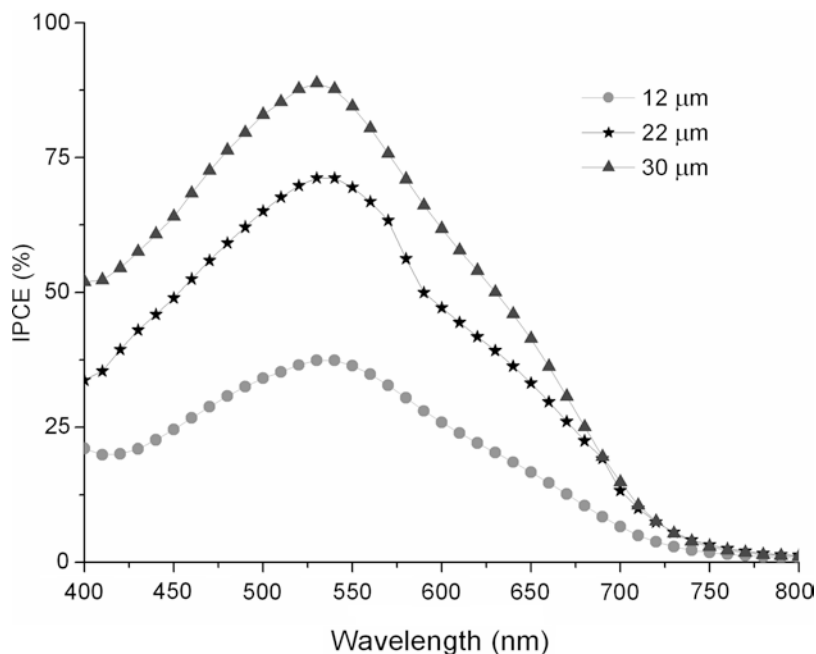


Fig. 12 Incident photon-to-electron conversion efficiency spectra of TiCl_4 -treated NT-based DSCs for different nanotube lengths (adapted from Lamberti et al. [18] with permission from the PCCP Owner Societies)

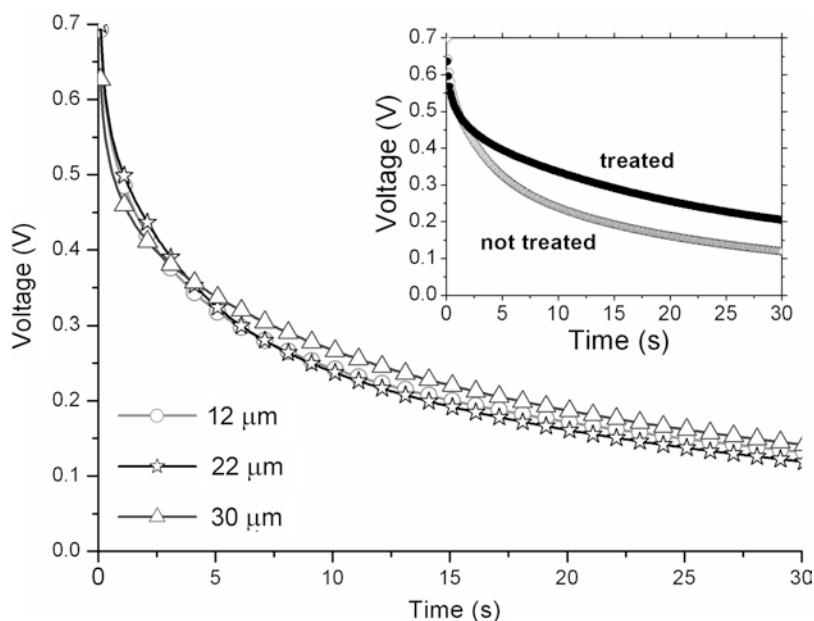


Fig. 13 Open circuit voltage decay curves of not-treated NT-based DSCs for different nanotube lengths. In the inset the comparison between the cells fabricated with 22 μm-thick NT membranes with and without TiCl₄ treatment is reported (adapted from Lamberti et al. [18] with permission from the PCCP Owner Societies)

slower decay of the photovoltage (i.e., a higher electron lifetime) if compared to not-treated devices, as witnessed by the curves presented in the inset of Fig. 13. In fact, after the treatment, the nanotube walls are covered by nanoparticles; these NPs could occupy surface impurities, defects, and grain boundaries [56], acting as a barrier for the interfacial recombination, thus increasing the charge lifetime [52].

A detailed study of the recombination and transport properties of the NT membranes was carried out by means of EIS measurements. The electron lifetime τ_n and the diffusion length L_n values were evaluated by fitting the experimental curves through the equivalent circuit reported in Fig. 5, and the results are reported in Figs. 14 and 15. For comparison, the same parameters were evaluated for a cell fabricated with a 8 μm-thick TiCl₄-treated layer of TiO₂ NPs. The increase of the carrier lifetime in the NT-based DSCs due to the TiCl₄ treatment observed from the OCVD was confirmed by impedance measurements; in the meanwhile, comparable values (about 70 μm at V_{oc}) were obtained for the L_n for treated and not treated samples, evidencing that the charge transport properties of the NTs are sufficient for electron collection even without the treatment [52]. With respect to the NP-based cells, both electron lifetime and diffusion length values of the membrane-based devices result significantly enhanced. Regarding the former, since the number of surface states is proportional to specific area, and the NT surface is one order of magnitude lower with respect to the NP one, the NT array presents a reduced number of defects and trap sites; for this reason the charge recombination rate

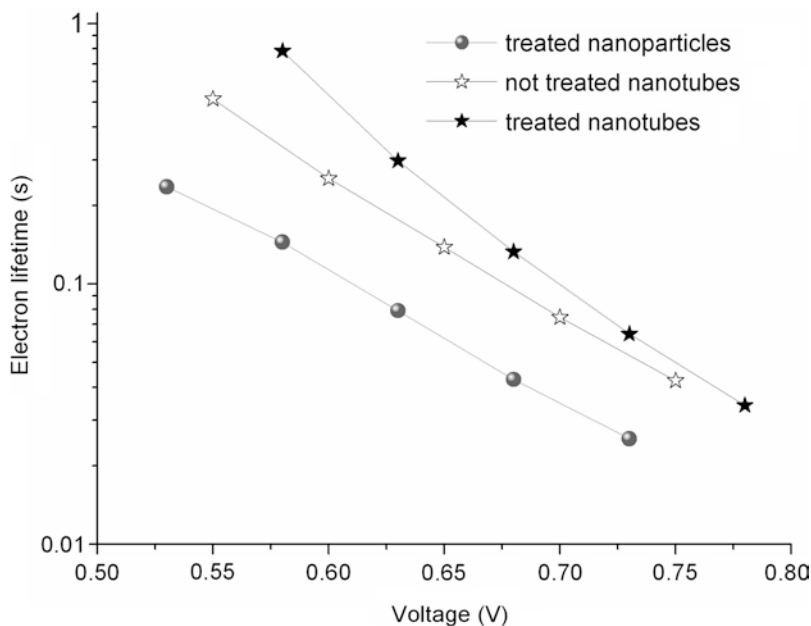


Fig. 14 Electron lifetime dependence on the bias voltage for the cells fabricated with 22 μm -thick NT membranes with and without TiCl_4 treatment and for a cell fabricated with 8 μm of TiCl_4 -treated TiO_2 nanoparticles (adapted from Lamberti et al. [18] with permission from the PCCP Owner Societies)

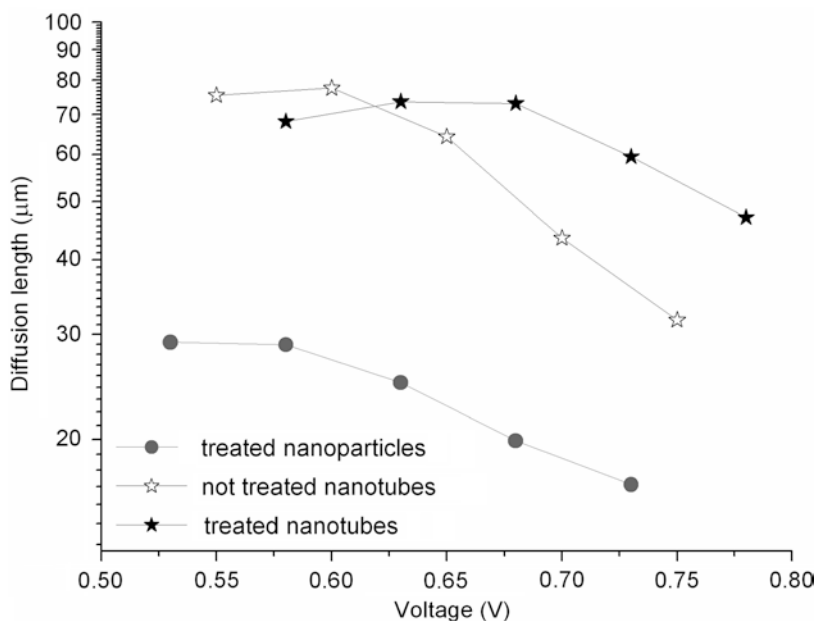


Fig. 15 Diffusion length dependence on the bias voltage for the cells fabricated with 22 μm -thick NT membranes with and without TiCl_4 treatment and for a cell fabricated with 8 μm of TiCl_4 -treated TiO_2 nanoparticles (adapted from Lamberti et al. [18] with permission from the PCCP Owner Societies)

is subsequently greatly reduced [57]. In addition, thanks to the NT monodimensional nature, the membrane-based DSCs are characterized by improved charge transport properties if compared to NP-based ones, in which the transport mechanisms result more complicated due to a longer pathway for the electrons: for the NP-based device, in fact, the calculated diffusion length values lie in the range 10–30 μm .

Summary and Perspectives

Free-standing NT membranes to be employed as DSC photoanodes have been fabricated through a two-step anodic oxidation of Ti foil. It has been possible to obtain a maximum efficiency equal to 7.56 %, in a DSC fabricated with a 30 μm -thick TiCl₄-treated nanotube membrane. The presented approach, with a simple self-detachment procedure, is innovative if compared to other photoanode fabrication processes: no chemical dissolution or mechanical splitting is involved for membrane separation, and membrane crystallization/attachment steps are coupled in the same thermal treatment.

Future applications of TiO₂ NT membranes can be envisaged in solid-state flexible DSCs: these devices will avoid the poor long-term durability mainly caused by leakage of the liquid electrolyte. Due to the open NT structure that allows the polymer electrolyte to easily penetrate inside the membrane, the coupling of TiO₂ nanotubes with such an electrolyte can lead to numerous advantages with respect to nanoparticle-based electrodes.

References

1. EPIA Global Market Outlook 2013–2017 (2013) http://www.epia.org/fileadmin/user_upload/Publications/GMO_2013_-_Final_PDF.pdf. Accessed 2 June 2013
2. Shockley W, Queisser HJ (1961) Detailed balance limit of efficiency of p-n junction solar cells. *J Appl Phys* 32:510–519
3. Green M (2003) *Third generation photovoltaics*. Springer, Berlin
4. Green MA, Emery K, Hishikawa Y et al (2013) Solar cell efficiency tables (version 42). *Prog Photovolt Res Appl* 21:827–837
5. O'Regan BC, Durrant JR (2009) Kinetic and energetic paradigms for dye-sensitized solar cells: moving from the ideal to the real. *Acc Chem Res* 42:1799–1808
6. Hagfeldt A, Boschloo G, Sun L et al (2010) Dye-sensitized solar cells. *Chem Rev* 110:6595–6663
7. Zhang Q, Cao G (2011) Nanostructured photoelectrodes for dye-sensitized solar cells. *Nano Today* 6:91–109
8. Gonzalez-Valls I, Lira-Cantu M (2009) Vertically-aligned nanostructures of ZnO for excitonic solar cells: a review. *Energy Environ Sci* 2:19–34
9. Anta JA, Guillén E, Tena-Zaera R (2012) ZnO-based dye-sensitized solar cells. *J Phys Chem C* 116:11413–11425
10. Law M, Greene LE, Johnson JC et al (2005) Nanowire dye-sensitized solar cells. *Nat Mater* 4:455–459
11. Baxter JB, Aydil ES (2006) Dye-sensitized solar cells based on semiconductor morphologies with ZnO nanowires. *Sol Energy Mater Sol Cells* 90:607–622
12. Yoshida T, Iwaya M, Ando H et al (2004) Improved photoelectrochemical performance of electrodeposited ZnO/Eosin Y hybrid thin films by dye re-adsorption. *Chem Commun* 4:400–401
13. Lamberti A, Gazia R, Sacco A et al (2014) Coral-shaped ZnO nanostructures for dye-sensitized solar cell photoanodes. *Prog Photovolt Res Appl* 22:189–197

14. Sacco A, Lamberti A, Gazia R et al (2012) High efficiency dye-sensitized solar cells exploiting sponge-like ZnO nanostructures. *Phys Chem Chem Phys* 14:16203–16208
15. Zukulová M, Zukal A, Kavan L et al (2005) Organized mesoporous TiO₂ films exhibiting greatly enhanced performance in dye-sensitized solar cells. *Nano Lett* 5:1789–1792
16. Bwana N (2008) Effects of the morphology of the electrode nanostructures on the performance of dye-sensitized solar cells. *Nano Res* 1:483–489
17. Roy P, Berger S, Schmuki P (2011) TiO₂ nanotubes: synthesis and applications. *Angew Chem Int Ed* 50:2904–2939
18. Lamberti A, Sacco A, Bianco S et al (2013) Charge transport improvement employing TiO₂ nanotube arrays as front-side illuminated dye-sensitized solar cell photoanodes. *Phys Chem Chem Phys* 15:2596–2602
19. Thompson GE, Xu Y, Skeldon P et al (1987) Anodic oxidation of aluminium. *Philos Mag B* 55:651–667
20. Young L (1961) Anodic oxide films. Plenum, New York
21. Keller F, Hunter MS, Robinson DL (1953) Structural features of oxide coatings on aluminum. *J Electrochem Soc* 100:411–419
22. Vanhumbeeck JF, Proost J (2008) On the contribution of electrostriction to charge-induced stresses in anodic oxide films. *Electrochim Acta* 53:6165–6172
23. Jessensky O, Muller F, Gosele U (1998) Self-organized formation of hexagonal pore arrays in anodic alumina. *Appl Phys Lett* 72:1173–1175
24. Ono S, Saito M, Ishiguro M et al (2004) Controlling factor of self-ordering of anodic porous alumina. *J Electrochem Soc* 151:B473–B478
25. Macak JM, Tsuchiya H, Ghicov A et al (2007) TiO₂ nanotubes: self-organized electrochemical formation, properties and applications. *Curr Opin Solid State Mater Sci* 11:3–18
26. Zwilling V, Darque-Ceretti E, Boutry-Forveille A et al (1999) Structure and physicochemistry of anodic oxide films on titanium and TA6V alloy. *Surf Interface Anal* 27:629–637
27. Macák JM, Tsuchiya H, Schmuki P (2005) High-aspect-ratio TiO₂ nanotubes by anodization of titanium. *Angew Chem Int Ed* 44:2100–2102
28. Macak JM, Tsuchiya H, Taveira L et al (2005) Smooth anodic TiO₂ nanotubes. *Angew Chem Int Ed* 44:7463–7465
29. Paulose M, Prakasham HE, Varghese OK et al (2007) TiO₂ nanotube arrays of 1000 μm length by anodization of titanium foil: phenol red diffusion. *J Phys Chem C* 111:14992–14997
30. Paulose M, Shankar K, Varghese OK et al (2006) Application of highly-ordered TiO₂ nanotube-arrays in heterojunction dye-sensitized solar cells. *J Phys D Appl Phys* 39:2498
31. Hwang HY, Prabu AA, Kim DY et al (2011) Influence of the organic electrolyte and anodization conditions on the preparation of well-aligned TiO₂ nanotube arrays in dye-sensitized solar cells. *Sol Energy* 85:1551–1559
32. Mor GK, Shankar K, Paulose M et al (2006) Use of highly-ordered TiO₂ nanotube arrays in dye-sensitized solar cells. *Nano Lett* 6:215–218
33. Fabregat-Santiago F, Bisquert J, Palomares E et al (2007) Correlation between photovoltaic performance and impedance spectroscopy of dye-sensitized solar cells based on ionic liquids. *J Phys Chem C* 111:6550–6560
34. Macdonald JR (1992) Impedance spectroscopy. *Ann Biomed Eng* 20:289–305
35. Macdonald JR (1974) Binary electrolyte small-signal frequency response. *J Electroanal Chem* 53:1–55
36. Pan S, Rothberg L (2005) Chemical control of electrode functionalization for detection of DNA hybridization by electrochemical impedance spectroscopy. *Langmuir* 21:1022–1027
37. Loyola BR, La Saponara V, Loh KJ (2010) In situ strain monitoring of fiber-reinforced polymers using embedded piezoresistive nanocomposites. *J Mater Sci* 45:6786–6798
38. Lamberti A, Garino N, Sacco A et al (2013) Vertically aligned TiO₂ nanotube array for high rate Li-based micro-battery anodes with improved durability. *Electrochim Acta* 102:233–239
39. Sacco A, Lamberti A, Quaglio M et al (2012) Electric characterization and modeling of microfluidic-based dye sensitized solar cell. *Int J Photoenergy* 2012:Article ID 216780

40. Borole AP, Aaron D, Hamilton CY et al (2010) Understanding long-term changes in microbial fuel cell performance using electrochemical impedance spectroscopy. *Environ Sci Technol* 44:2740–2745
41. Wang Q, Moser J-E, Grätzel M (2005) Electrochemical impedance spectroscopic analysis of dye-sensitized solar cells. *J Phys Chem B* 109:14945–14953
42. Halme J, Vahermaa P, Miettunen K et al (2010) Device physics of dye solar cells. *Adv Mater* 22:E210–E234
43. Fabregat-Santiago F, Bisquert J, Garcia-Belmonte G et al (2005) Influence of electrolyte in transport and recombination in dye-sensitized solar cells studied by impedance spectroscopy. *Sol Energy Mater Sol Cells* 87:117–131
44. Bisquert J, Garcia-Belmonte G, Fabregat-Santiago F et al (2000) Doubling exponent models for the analysis of porous film electrodes by impedance. Relaxation of TiO₂ nanoporous in aqueous solution. *J Phys Chem B* 104:2287–2298
45. Hauch A, Georg A (2001) Diffusion in the electrolyte and charge-transfer reaction at the platinum electrode in dye-sensitized solar cells. *Electrochim Acta* 46:3457–3466
46. Shin Y, Lee S (2008) Self-organized regular arrays of anodic TiO₂ nanotubes. *Nano Lett* 8:3171–3173
47. Lamberti A, Sacco A, Bianco S et al (2013) An easy approach for the fabrication of TiO₂ nanotubes-based transparent photoanodes for dye-sensitized solar cells. *Sol Energy* 95:90–98
48. Albu SP, Ghicov A, Aldabergenova S et al (2008) Formation of double-walled TiO₂ nanotubes and robust anatase membranes. *Adv Mater* 20:4135–4139
49. Dubey M, Shrestha M, Zhong Y et al (2011) TiO₂ nanotube membranes on transparent conducting glass for high efficiency dye-sensitized solar cells. *Nanotechnology* 22:285201
50. Chen Q, Xu D (2009) Large-scale, noncurling, and free-standing crystallized TiO₂ nanotube arrays for dye-sensitized solar cells. *J Phys Chem C* 113:6310–6314
51. Lamberti A, Sacco A, Bianco S et al (2011) Microfluidic sealing and housing system for innovative dye-sensitized solar cell architecture. *Microelectron Eng* 88:2308–2310
52. Sommeling PM, O'Regan BC, Haswell RR et al (2006) Influence of a TiCl₄ post-treatment on nanocrystalline TiO₂ films in dye-sensitized solar cells. *J Phys Chem B* 110:19191–19197
53. Yan J, Zhou F (2011) TiO₂ nanotubes: structure optimization for solar cells. *J Mater Chem* 21:9406–9418
54. Barnes PRF, Anderson AY, Koops SE et al (2008) Electron injection efficiency and diffusion length in dye-sensitized solar cells derived from incident photon conversion efficiency measurements. *J Phys Chem C* 113:1126–1136
55. Zaban A, Greenshtein M, Bisquert J (2003) Determination of the electron lifetime in nanocrystalline dye solar cells by open-circuit voltage decay measurements. *ChemPhysChem* 4:859–864
56. O'Regan BC, Durrant JR, Sommeling PM et al (2007) Influence of the TiCl₄ treatment on nanocrystalline TiO₂ films in dye-sensitized solar cells. 2. Charge density, band edge shifts, and quantification of recombination losses at short circuit. *J Phys Chem C* 111:14001–14010
57. Wang H, Liu M, Zhang M et al (2011) Kinetics of electron recombination of dye-sensitized solar cells based on TiO₂ nanorod arrays sensitized with different dyes. *Phys Chem Chem Phys* 13:17359–17366

Part VII

Future Prospects of Nanostructured Materials and Coatings

Frontiers of Nanoelectrochemistry and Application of Nanotechnology: A Vision for the Future

42

Sukanchan Palit

Contents

Introduction.....	1330
Vision, Innovation, and Progress in Macroscopic Electrochemistry	1331
Vision in the Field of Nanoelectrochemistry	1332
Application Areas of Nanotechnology in the Wider Domain of Electrochemistry and its Relevance to Human Society	1332
Doctrine Behind the Relevance of Nanoelectrochemistry to Mankind/Research Frontiers and Energy Sustainability	1333
Research Endeavor in the Field of Nanoelectrochemistry.....	1334
Emerging Trends, Visionary Hope, and Future Challenges.....	1337
A Deep Perspective into the Technological Applications of Nanoelectrochemical Science	1337
Required Skills and Vision of Implementation in Education	1337
Insight, Innovation, and Ideas in the Field of Nanoscale Electrochemistry	1338
Development of Electrochemical Science.....	1338
Vision of Future Research in the Far-Reaching Areas of Nanoelectrochemistry, Colloid Chemistry, and Environmental Engineering	1338
An Investigation in the Field of Application of Nanotechnology in Environmental Engineering	1339
Doctrine of Application of Electrochemistry in the Domain of Environmental Engineering.....	1340
A Critical and Rigorous Approach of Application of Nanofiltration in Environmental Engineering	1340
Nanotechnology as well as Developed and Developing Society.....	1340
The Invigorating and Coherent World of Nanoscience, Nanotechnology, and Molecular Nanotechnology	1341
Future Dimensions in the Field of Nanoelectrochemistry	1341

S. Palit (✉)

Department of Chemical Engineering, University of Petroleum
and Energy Studies, Dehradun, India

Haridevpur, Kolkata, India

e-mail: sukanchan68@gmail.com; sukanchan92@gmail.com

Engineering Vision, Engineering Innovation, and Vision of Tomorrow.....	1342
Challenges in Scientific Pursuit and Progress in the Domain of Nanoelectrochemistry	1343
The Visionary Challenges in the Domain of Nanoscience and Nanotechnology	1343
Scientific Vision, Scientific Truth, and the Progress in Nanotechnology	1344
March of Science in the Domain of Nanoscale Electrochemistry and the Future Scientific Vision	1344
Future Thoughts, Future Application Areas of Nanoelectrochemistry and Nanotechnology, and the Ultimate Vision for the Future.....	1345
Conclusion	1345
References.....	1345

Abstract

The vision and future of nanoelectrochemistry and application area of nanoelectrochemistry are wide, varied, and versatile. Nanotechnology is the ultimate engineering vision of tomorrow. Nanoparticle applications in bioanalysis, catalysis, and electrocatalysis and nanoparticles such as fullerenes, carbon nanotubes, and networks, semiconductor nanoparticles, and arrays of nanoelectrodes and nanopores are the vision of tomorrow's science, technology, and engineering. A scientist's vision is far-reaching and groundbreaking. For the range between 1 and 10nm, for the nanoparticles, progress has been stimulated by synthetic innovations and for single nanoelectrodes and single nanopores, similarly by advances in methods of innovation and also by the march of nanoscience. The author's endeavor is to highlight and review the advances in the field of nanoelectrochemistry and nanotechnology as a broad area. The application area of colloid chemistry also comes into play. Nanotechnology will help the million homes in years to come and will be a great boon to our mankind. Our vision is to delineate the advances in the vast domain of nanotechnology and nanoelectrochemistry as a whole. It will also touch upon the progress in colloid chemistry. The answers and fruits of scientific endeavor in the field of nanoscience and nanotechnology will be greatly enhanced. The vision and the objective of the treatise are targeted toward the application areas of nanotechnology, nanoelectrochemistry, and environmental engineering tools such as nanofiltration. An extensive review work is attempted with deep comprehension and cogent insight. An engineer's as well as a scientist's vision is emboldened with strong insight in the paper.

Keywords

Nano • Nanofiltration • Chemistry • Electrochemistry • Vision

Introduction

Application area of nanotechnology as well as nanoelectrochemistry is far-reaching and proven. Nanotechnology is breaking one scientific boundary over another. The world of unknown is opening up new and realistic domains of nanoscience and nanotechnology. This review highlights the importance of nanotechnology and

nano-electrochemistry in the future advancement of science, engineering, and technology. Nanoelectrochemistry refers to a dimensional scale of electrodes and electrochemical events as opposed to time or volume or mass.

Nano is a visionary terminology. Much of the contemporary and traditional chemistry focuses on small and minute structures, and indeed molecular science and molecular engineering is on the nanometer scale. Nano describes and delineates dimensional scale of electrodes and electrochemical events. Still, most of molecular and atomic chemistry is relevant within the 1–1000 nm range of dimensions, as does a larger body of charged or conducting substances, e.g., micro- and nanoparticles, colloids, and aerogels. The concerned geometry of conducting substances can have nanoscopic dimensions, with mesoporous materials such as aerogels and xerogels being contemporary examples. These are focal points and primordial issues as are nanoparticle applications in bioanalysis, catalysis, and electrocatalysis and nanomaterials such as fullerenes, carbon nanotubes and networks, semiconductor nanoparticles, nanoelectrodes, and nanopores [1]. The vision and objective is to delineate electrochemistry of nanoparticles and single nanoelectrodes and nanopores [1]. Murray [2] delineated in a phenomenal and a visionary review the ever-increasing truth and potential of the vast and visionary domain of electrochemistry. The author dealt with intuitive truth the application area of electrochemistry of metal nanoparticles. The intricacies of the linkages between colloid chemistry and nanoelectrochemistry are brought to the forefront of scientific vision. Oja et al. [3] dealt with accurate lucidity a review on the application area of nanoscale electrochemistry. The review elucidated on the varied, visionary, and proven applications of nanoelectrochemistry with incisive details. Electrochemical properties of nanoscale electrodes are delineated with extreme lucidity. The visionary definitions of this treatise will be incomplete without the application of nanotechnology on nanofiltration and environmental engineering. The visionary foundations are restructured and rebuilt in the area of nanofiltration and wastewater treatment. Hassani [4] dealt lucidly on the efficiency of nanofiltration and the application of nanofiltration membranes in water treatment. Visionary strides in the field of molecular nanotechnology have moved surpassing one barrier over another. So a detailed description on this area of nanotechnology is done with details. Nanoelectrochemistry and the application area of nanoelectrochemistry have an umbilical cord which is challenging as well as visionary.

Vision, Innovation, and Progress in Macroscopic Electrochemistry

Traditional macroscopic electrochemistry started 200 years ago with immense and effective technological, engineering, and scientific connection to energy technology and electrolysis [5]. In the last 10–15 years, electrochemical nanotechnology has been relevant, but in fact it is a domain of electrochemical science. As a link between these different fields, microelectrochemistry is fast and emerging growing part of electrochemistry forming interdisciplinary bridges to science, technology, and medicine. The emphasis of electrochemical micro- and nanotechnologies is an urgent and concerning activity since otherwise electrochemists do not realize the wide

application of their own field and on the other hand electrochemical methods are used without sufficient background and efficiency. Special developments in corrosion science and engineering need to be addressed with scientific vision. The vision is clear and sound to unravel the hidden truths of nanoelectrochemistry and colloid chemistry. In the path of success, there are a lot of scientific hurdles. Yet the truth and greatness of this vast domain of nanoelectrochemistry are revealed [5].

Vision in the Field of Nanoelectrochemistry

The determinant and vision of the science and engineering of nanoelectrochemistry are immense and varied. The question of application of nanoelectrochemistry to mankind comes into the horizon. A scientist's urge for knowledge is unquestionable. Nanoelectrochemistry is a relatively new branch of nanotechnology, so its vision is wide and visionary.

Nanoscale electrochemistry is critically important for modern electrochemical science as well as many other key research areas such as energy conversion and storage, catalysis, sensor development, and environmental science. Nanoscale electrochemical investigations have been successful in spite of the limitations of traditional methods [5].

New electrochemical phenomena, properties, and technological capabilities essential to reducing the dimensions of an electrochemical probe to the nanometer scale as well as electrochemical properties of new nanoscale electrode materials will be the focal point and a primordial issue of this journey through the frontiers of nanoelectrochemistry. Conventional definition of nanoscale refers to lengths between 1 and 100 nm.

Nanoscale electrochemical investigations have provided unique and genuine information unattainable by traditional methods. For example, nanoelectrodes can measure ultrafast electron-transfer kinetics that are often too fast to investigate with conventional electrodes. Nanoscale electrochemical materials, such as metal/semiconductor nanoparticles, have unique chemical and physical properties, and nanoscale electrochemical methods can be used to prepare advanced electrocatalytic materials. In addition, the use of nanoscale electrodes has envisioned electrochemical imaging with nanoscale spatial resolution, resulting in unique information for better understanding of heterogeneous electrode/solution interfaces [5].

Application Areas of Nanotechnology in the Wider Domain of Electrochemistry and its Relevance to Human Society

Application area of nanotechnology is wide and varied. The question of application of nanoelectrochemistry to the common man and his/her problems comes into the horizon of man's vision. The grit and determination on the researcher's point of

view is unrelenting and unequivocal. The world of unknown is unfolding into a world of known with proven scientific resources. Human society is today fragile in the question and aspects of environmental and energy sustainability. Here, the application of nanoelectrochemistry comes into immediate play. The answers to the burning question of environmental sustainability have brought our mankind in the brink of disaster. The willpower and strength of the researcher are visionary and far-reaching. Every step forward in the scientific endeavor is a giant step forward to human society and mankind.

The field of nanoelectrochemistry burgeoned about three decades ago shortly after the fast development and widespread development of microelectrodes. Since then this domain has generated enormous enthusiasm and has seen dramatic increase in scientific judgment and popularity in the last two decades. This growth is largely due to rapid developments in nanofabrication and characterization and the introduction of numerous bottom-up and top-down processes capable of preparing well-defined nanoelectrodes and nanomaterials [5].

Nanoscale electrochemistry has played a crucial and critical role in gaining a deep understanding of electron-transfer processes at the electrode/electrolyte interface and will effectively enhance and promote both fundamental, applied, and basic electrochemical research. Nanoscale electrodes are of central and vital importance in almost all aspects of nanoscale electrochemistry, from understanding electron-transfer kinetics and probing single catalytic nanoparticles to nanoscale electrochemical imaging.

Key challenges, thrust areas, and visionary-targeted domains in nanoscale electrochemistry have been the lack of structural control in nanoelectrode preparation and the need for advanced methods for structural characterization. This can be largely solved and addressed by the use of nanofabrication and nanocharacterization methods. Nanopore-based electrochemical methods have attracted global interest in research endeavor and will continue to grow rapidly and steadfastly in the near and distant future [5].

Doctrine Behind the Relevance of Nanoelectrochemistry to Mankind/Research Frontiers and Energy Sustainability

Energy sustainability is of major concern in today's world. The world is stepping toward a new vision of energy sustainability relevance. The concerns are exquisite and groundbreaking. The results are many. Here, comes the question of application of nanoelectrochemistry to energy scenario and energy sustainability. The depletion of fossil fuel resources is causing great burden to mankind. Renewable energy will be the researcher's main focus in days and years to come. The burden to mankind has also become a question of social responsibility. Nanoelectrochemistry can be an immediate vision of future in the area of energy sustainability, renewable energy, and application of solar energy.

Some thrust areas of nanoelectrochemistry in the present-day world is explained below [2]:

- (a) Nanoelectrodes
- (b) Extraordinary properties of electrodes
- (c) Nanoelectrode fabrication

Research Endeavor in the Field of Nanoelectrochemistry

Research pursuit in the field of nanoscale electrochemistry is far-reaching, ground-breaking, as well as visionary. The path of struggle in this domain is immature and latent yet widely proven.

- Over the last decade, several developments in electrochemistry have contributed significantly and effectively in the field of nanoscience and nanotechnology. Most important are the advances in nanoscale characterization of electrochemical interfaces, advances in electrochemical processing methods for the formation of micro- and nanostructures, and the rediscovery of electrochemical techniques, concepts, and future dimensions by the nanotechnology community, in particular for studying nanoscale structures (Table 1).

Murray [2] did a comprehensive, detailed, and visionary review on nanoelectrochemistry adding cogent insights on metal nanoparticles, nanoelectrodes, and nanopores. This is an absolutely phenomenal approach to nanoelectrochemistry. The author dealt extensively on the electrochemistry of each of the abovementioned nanomaterials.

Rauf et al. [6] did a phenomenal and groundbreaking research on the fabrication and characterization of gold nanohole electrode arrays. A fabrication method using photolithography, deep reactive ion etching, wet etching, and focused ion beam lithography techniques was discovered. According to the authors, due to good reproducibility, high accuracy, and miniaturization compatibility of the proposed fabrication technique, it has high, visionary, and proven potential in developing portable devices for bio-sensing.

Zheng et al. [7] dealt lucidly on electronic manipulation of DNA, proteins, and nanoparticles for potential circuit assembly. Using gold electrodes lithographically fabricated onto microscope cover slips, DNA and proteins are interrogated both optically (through fluorescence) and electronically (through conductance measurements).

Yang [8] dealt with intuitive observation on enzyme-based ultrasensitive electrochemical biosensors. This is an extensive review and a lucid treatise on enzyme-based biosensors. Signal amplification in conventional enzyme-based biosensors is not high enough to achieve the ultrasensitive detection of biomolecules. According to the authors, in recent years, signal amplification has been improved by

Table 1 A brief introspection on outstanding and far-reaching scientific endeavor in the field of nanoelectrochemistry

Investigators	Visionary scientific research pursuit in nanoelectrochemistry
Murray [2]	The research endeavor on a comprehensive treatise and review on the status of nanoelectrochemistry
Rauf et al. [6]	A deep insight on fabrication and characterization of gold nanohole electrode arrays
Zheng et al. [7]	Lucid details on electronic manipulation of DNA, proteins, and nanoparticles
Yang [8]	Description of enzyme-based ultrasensitive electrochemical biosensors
Mirksich [9]	Usage of self-enabled monolayers to model extracellular matrix
Taufany et al. [10]	Phenomenal work on the kinetically controlled autocatalytic chemical process
Janin et al. [11]	Formation of metallic nanowires via electrochemistry
Lin et al. [12]	Combined experimental and theoretical investigation of nanosized effects of Pt catalyst
Bard [13]	Single-size molecule electrochemistry
Miao et al. [14]	Review of new developments of assays for cholinesterase activity and inhibition
Oja et al. [3]	Review of recent advances of electrochemistry
Kraph et al. [15]	Report on the fabrication and characterization of nanopore-based electrodes
Zhan et al. [16]	Report on adsorption/desorption of hydrogen on Pt nanoelectrodes
Sun et al. [17]	Investigation of electrochemistry of individual molecules on Zeptoliter volumes
Amemiya et al. [18]	Report on generalized theory on nanoscale voltammetric measurements

combining enzymatic reactions with redox cycling or employing multienzyme labels per detection probe. A deep and cogent insight evolves newer vision in the field of electrochemistry and biotechnology.

Mirksich [9] dealt lucidly on usage of self-assembled monolayers to model extracellular matrix. This is a widely researched review dealing with applications of cell biology. Cell biology as in the research endeavor will go a long way in opening up new dimensions of nanotechnology and electrochemistry.

Taufany et al. [10] dealt in a phenomenal work on the kinetically controlled autocatalytic chemical process for bulk production of bimetallic core-shell structured nanoparticles. Although bimetallic core-shell structured nanoparticles (NP) are achieving prominence due to their multifunctionalities and exceptional catalytic, magnetic, thermal, and optical properties, the rationale underlying their design remains unclear, and the vision of this domain is immature. The authors of this scientific endeavor open up new vistas and newer vision in the application area of nanotechnology.

Janin et al. [11] dealt with severe precision on the subject of formation of metallic nanowires via electrochemistry in aqueous surfactant media. Atomic contacts between two copper microelectrodes, with conductance close to the conductance quantum, have been generated using simple electrochemical methods in aqueous

media containing various types of surfactants. Colloid chemistry and electrochemistry goes a long way in the successful future scientific endeavor. The authors delve deeply into these areas and unravel the hidden truths of this field of nanoelectrochemistry.

Lin et al. [12] dealt with impeccable scientific rigor on the subject of combined experimental and theoretical investigation of nanosized effects of Pt catalyst on their underlying methanol electrooxidation activity. The nanosized effects of Pt catalysts in terms of surface coverage, electrochemical response, and reaction kinetics during the electrocatalytic methanol oxidation reaction (MOR) have been extensively investigated. The areas of catalysis along with electrochemistry have widely opened up the visionary doors of innovation and scientific judgment.

Bard [13] delved deep into the science of single-enzyme molecule electrochemistry. Single-molecule studies, including those of single-enzyme molecules, have led to newer insights about the effects of environment and configuration on the behavior of these molecules. In this phenomenal and far-reaching review, scientific advancements toward studying a single-enzyme molecule by protein film voltammetry are dealt in details.

Miao et al. [14] dealt with cogent insight on the history and new developments of assays for cholinesterase activity and inhibition. They detailed with immense scientific rigor on the subject of cholinesterase which are key enzymes in the field of neurobiology and pharmacology.

Oja et al. (2012) [3] dealt with immense lucidity in a review on nanoscale electrochemistry. The review reports on the recent advances in electrochemistry. The specific focus and primordial issues were on new electrochemical phenomena, properties, and technological capabilities essential to reducing the dimensions of an electrochemical probe to the nanometer scale.

Krapf et al. [15] investigated in a report on the fabrication and characterization of nanopore-based electrodes with radii down to 2 nm. The authors reported on fabrication and characterization of gold nanoelectrodes with carefully controlled nanometer dimensions in a matrix of insulating silicon nitride.

Zhan et al. [16] reported on adsorption and desorption of hydrogen on Pt nanoelectrodes and evidence of surface diffusion and spillover. Nanoelectrochemical approaches were used to investigate adsorption/desorption of hydrogen on Pt nanoelectrodes. The world of challenges, difficulties, and barriers opened up new avenues of immense intuition and innovation.

Sun and Mirkin [17] dealt incisively on electrochemistry of individual molecules in Zeptoliter volumes. Electrochemical experiments were carried out in a nanometer-sized cylindrical thin layer cell (TLC) formed by etching the surface of a disk-type platinum nanoelectrode (5–150 nm radius).

Amemiya et al. [18] dealt lucidly on the subject of generalized theory of nanoscale voltammetric measurements. Investigations were done on a generalized theory of scanning electrochemical microscopy. This research work revolutionized the areas of nanoelectrochemistry and future visions of nanotechnology.

Emerging Trends, Visionary Hope, and Future Challenges

The unending and mindboggling questions in the field of nanoelectrochemistry are instinctive and far-reaching. The challenges are far and wide. The future trends are unchallengeable. Man's vision in the field of nanoscale electrochemistry and nanotechnology needs to be validated in future endeavors.

Emerging trends and future challenges are visionary as well as immature or latent. The questions arising in today's world are the application of nanotechnology and nanoscale electrochemistry to the common mass or the human society. Remediation of groundwater contamination in Southeast Asian countries particularly arsenic groundwater contamination is a serious challenge to mankind. Researchers worldwide are pondering over this vicious fact of nature. Arsenic in drinking water is directly linked to various ailments such as cancer which is a curse to mankind. The future of arsenic research is extremely bright, promising, as well as inspiring. The fruits of this area of research have already shaken mankind, and more results will follow. Besides another aspect of modern-day interest is the vicious question of environmental sustainability. The answers to sustainability are revolutionizing mankind.

A Deep Perspective into the Technological Applications of Nanoelectrochemical Science

Although an impressive and a wide range of electrochemical processes for nanostructure formation have been demonstrated already, only few of them have made it out of the laboratory. Many practical problems like reliability and compatibility with existing production methods must be addressed, specifically for methods based on nanoscale templates or self-ordering.

Technological advancements in the field of nanoelectrochemical science are far-reaching and has crossed several endless frontiers. It has taken the world by storm. Intensive research in the field of electrochemistry has revealed its enormous and visionary potentials. The world of unknown is slowly shedding its past to usher in a new generation science and technology [19].

Required Skills and Vision of Implementation in Education

All the abovementioned areas will provide ample opportunities for basic and applied sciences, i.e., jobs for scientists trained in electrochemistry [20, 2]. To prepare students, learners, and researchers adequately for these upcoming challenges is the task of modern electrochemical education, which brings us back to education and a vision of a classroom. Electrochemical education for students with different backgrounds may place the emphasis on slightly different aspects.

The visions of electrochemical education are as follows:

- Solid and sound working knowledge on every detail and every minute concepts
- Concepts of surface science, surface chemistry, and condensed matter physics
- Modern experimental and theoretical concepts

Insight, Innovation, and Ideas in the Field of Nanoscale Electrochemistry

The insight in the field of nanoscale electrochemistry is immense and varied. The innovation and ideas behind this phenomenon are of visionary importance. Science and technology are moving at a rapid pace in successive generations from now. The world of unknown is opening its doors to the world of known and vitality. The question of application area of nanoscale electrochemistry to the grassroots level and mankind is of vital importance.

Development of Electrochemical Science

Stimulated by substantial progress made in the study of surfaces under ultrahigh vacuum conditions, new concepts and innovations have started to emerge in interfacial electrochemistry in the 1980s. These have rapidly gained ground bringing in a new era in nanoscience and nanotechnology. The most important of these developments are as follows [21, 2]:

- Structurally defined electrodes
- In situ methods
- Modern theoretical approach

The answers to the various difficult hurdles of nanoelectrochemistry are obtained and validated by the scientific community by continuous and painstaking research endeavors. Nanoscale electrochemical science is the future vision of the science and engineering of nanotechnology. New methods of nanofabrication will surely revolutionize the scientific domain.

Vision of Future Research in the Far-Reaching Areas of Nanoelectrochemistry, Colloid Chemistry, and Environmental Engineering

The future of nanotechnology and nanoelectrochemistry is unquestionable and rigorous. Colloid chemistry nurtures nanoelectrochemistry. The world of nanotechnology is crossing visionary frontiers. The varied answers to the intricacies of

nanoelectrochemistry and colloid chemistry are slowly unfolding. The future will be truly visionary and far-reaching.

Colloid chemistry can cross unsurpassed frontiers. This area of science is advanced yet immature. The vision of potentialities in this branch of science is immense and groundbreaking. Application area of colloid chemistry to the grass-roots level needs to be addressed in view of the future of mankind.

Colloid chemistry is a discipline of great importance and of greater scientific vision to both science, engineering, and technology. In today's world, colloid chemistry is surpassing many visionary frontiers. The challenges and barriers in the domain of colloid chemistry are vast, varied, and far-reaching. The electrical behavior of colloidal dispersions in solutions classically encompasses colloidal nanoparticles with surface charges caused by adsorption of small ions, surfactants, or polyelectrolytes and with consequent electrokinetic properties. Such phenomena have great practical and visionary importance in chemical manufacturing and other chemical processes, in sanitary water treatment, and in ocean chemistry, among others [22].

The question and future of nanofiltration and application of nanotechnology in environmental engineering are truly unquestionable. The immediate future is bright in regard to the application areas such as desalination and industrial wastewater treatment. Intense environmental restrictions and regulations have urged the world order to reassess and revamp the environmental engineering paradigm. Man's vision will be validated in years to come with the successful projects of providing clean water to rural millions in developed as well as developing world [22, 2].

Here, the successful implementation of nanofiltration process to human society and the successful application of nanotechnology in environmental engineering come into play. In developing world, the question of contaminated water is a vicious and difficult problem. In such respect, nanofiltration and other membrane separation processes can change the horizon of nanotechnology research [22, 2].

An Investigation in the Field of Application of Nanotechnology in Environmental Engineering

Nanotechnology is crossing wide and immeasurable frontiers. Desalination and wastewater treatment are the relevant technologies of today and the visionary future. Nanofiltration as well as other membrane separation processes has insightful vision. It has been found to be extremely effective, visionary, and demanding in the years to come. Vision, hardship in scientific endeavor, and visionary truth will surely propel the scientific pursuit in the field of membrane separation processes. Engineering vision in the field of membrane separation processes will create wonders in the years to come.

Nanotechnology, nanofiltration, and environmental engineering are inseparable. In the similar vein, reverse osmosis, membrane separation processes, and desalination are bound by fetters of innovation. More research endeavor in advanced wastewater treatment will create waves in the scientific horizon.

Doctrine of Application of Electrochemistry in the Domain of Environmental Engineering

Electrochemistry and environmental engineering will be inseparable identities in years to come and in the distant future [20]. The question of application of electrochemistry to environmental engineering comes into the mind's horizon. The scientific world is moving at a rapid pace. The answers to the various intricate questions of the applicability of nanoscale electrochemistry to environmental engineering are dealt with in the present scientific scenario. The unknown world of nanoscale electrochemistry is opening up its new chapter of history and is unraveling the hidden facts [23, 2].

Scientific endeavor is immense and versatile. A short step in the path to destiny in nanoelectrochemical science can be a giant step toward environmental engineering horizon. The vision of the present is slowly changing with the rigors of question of environmental sustainability. Man's recreation of nature's gifts is awaiting. A large amount of research in the field of environmental sustainability can bring a revolutionary change to mankind [19, 24–26].

A Critical and Rigorous Approach of Application of Nanofiltration in Environmental Engineering

The world of environmental engineering is moving at a rapid and steadfast pace. The hurdles and barriers of the intricate science of nanofiltration are won in an equally unbelievable pace. The discovery of Loeb–Sourirajan model in membrane separation process has revolutionized the entire chemical engineering and environmental engineering paradigm [19, 27, 28]. The only question lies in the fact of the success of this technology to developing countries around the world with respect to desalination and provision of clean drinking water. Also the question of environmental sustainability comes into the mind's horizon. The truth of future of nanofiltration and membrane separation processes will be truly achieved in years to come with the invention of new technologies and newer vision [20, 27, 28].

Nanotechnology as well as Developed and Developing Society

Nanotechnology is the next-generation science. Its potential is immense and versatile [20]. The developed as well as developing world is gearing toward a next-generation scientific extravaganza in the field of nanotechnology [28]. Hurdles and barriers are won, and a new era is being expected in the near future. The only difficult question is the application of nanotechnology to the rural mass in developing nations throughout the world. In this endeavor, the world is not lagging behind. The vicious problem of groundwater contamination and arsenic contamination of drinking water in Southeast Asian countries has come to a scenario of resounding

success. Again one has to stress upon the fact that nanotechnology is breaking visionary barriers and is bearing fruits for countless millions [28].

Developed as well as developing society is moving briskly from one giant step over another in its progress in science. The question of validation of human knowledge is witnessing a new dawn and a new awakening. The world and human civilization today is witnessing a new chapter and a new era as regards the application of nanotechnology [28].

The Invigorating and Coherent World of Nanoscience, Nanotechnology, and Molecular Nanotechnology

The dimensions of nanoscience and nanotechnology are both invigorating and coherent to mankind and society [28]. It is opening up new vistas and new avenues. Unanswered questions in nanoscience and nanotechnology are dealt with lucidly with intellectual rigor and impeccable acuity. The application of nanotechnology and nanoscale electrochemistry to the area of immense engineering avenues and technological vistas will be the research for the future. Man's as well as scientist's vision will be successfully validated in the years to come with the advancement of nanoscale electrochemistry and nanotechnology.

The concern of the scientist is to unravel the intricate vision of nanotechnology and nanoscale electrochemistry. The future is wide and varied. The question of application of nanotechnology to the common mass and grassroots level will always be a forerunner in targets toward future scientific endeavors. A new world on the application of nanotechnology and nanofiltration is gearing up for the future. So in such a situation the answers to the varied questions need to be dealt with lucidity and intense scientific endeavor [20, 28].

In today's civilization, nanotechnology can be an immense boon to the application areas of environmental engineering such as monitoring, pollution prevention, and remediation methods. There are a number of avenues of applications such as contaminated water and air treatment, self-cleaning materials, energy applications, novel functionalized adsorbents for environmental and industrial applications, and nanomaterials for sustainable energy production [22, 29]. The definite and proven world of immense challenges in molecular level nanotechnology will surely be an eye opener to the major intricacies of research in nanoelectrochemistry and nanotechnology [22, 28, 29].

Future Dimensions in the Field of Nanoelectrochemistry

The future of nanotechnology is far-reaching and groundbreaking [2]. The questions are not unsurmountable. The vision of the future for the field of nanotechnology is extremely undoubtful. In a similar manner, nanoelectrochemistry can be the visionary technology of the future. The answers to nanoscale

electrochemistry can break barriers and cross frontiers. Today's urge and endeavor at every step of science are tomorrow's vision. Application area in grassroots level is not a mirage anymore. Nanoelectrochemistry will reach its vision in years to come [21].

Future dimensions in the field of nanoscale electrochemistry are instinctive and at the same time intuitive in nature [21]. The question of application to mankind and human society vibrantly comes into the mind's horizon and scientist's vision. Application areas are vast and visionary, but the applicability is immature and latent. So, here, the world of dedicated research endeavor comes into play. The developed as well as developing world is gearing up resources to tackle the intricate problems behind this widely unknown phenomenon. Time will soon be a witness to the immeasurable discoveries in years to come [21].

Engineering Vision, Engineering Innovation, and Vision of Tomorrow

The vision of today is the vision of tomorrow and the future. The greatness of today's research endeavor will bear fruits for a better tomorrow. New electrochemical phenomenon, properties, and technological capabilities essential to reducing the dimensions of an electrochemical probe to the nanometer scale as well as electrochemical properties of new nanoscale electrode materials are the ultimate vision of tomorrow. Lots of questions are unanswered, but the future of nanoscale electrochemistry is immense, bright, and inspiring [28].

The vision of tomorrow in the field of nanoscale electrochemistry lies at the hands of immeasurable endeavors of nanotechnologists. Nanoelectrochemistry has unquestionable resources and potential. The areas of nanoelectronics, nanoelectrodes, nanoparticles, and smart nanomaterials are opening up new vistas in the path to destiny. Visionary aims in the field of application area of nanoelectrochemistry to mankind will surely bear fruits in future generations with immense conviction and truth [28].

The methodical developments of the last two decades helped to establish electrochemistry as a modern and visionary nanoscience [28]. Current interfacial electrochemistry has many and widely oriented questions and often offers unique or superior possibilities heralding in a new era of nanoscience and nanotechnology. All these should be a bright future for this discipline and make it an interesting topic for students and researchers coming from diverse areas. To meet the challenges faced in future research, modern electrochemical education must convey a surface science-oriented, microscopic picture without sacrificing fundamental knowledge on electrochemical methods and electrode kinetics. Balancing and interconnecting these two sides are a delicate task that, in view of the ongoing rapid development of this field, requires continuous adaptation and depends to some extent on the background, interests, and vision of the audience [4, 30, 31].

Challenges in Scientific Pursuit and Progress in the Domain of Nanoelectrochemistry

Challenges in scientific pursuit, scientific progress, and scientific determination are immense and versatile [28]. The domain of nanotechnology and nanoelectrochemistry is moving and striving toward a newer generation of advancements of science and engineering [32, 33]. The visionary challenges and the intricacies in the field of nanoelectrochemistry need to be restructured and revamped. History of mankind and the future of human civilization are witnesses to the immense strides made in the field of nanotechnology. The visionary challenges will open a wide avenue of innovation in successive generations of immense scientific pursuit [28].

Challenges in the domain of electrochemistry and nanotechnology are moving toward a visionary era. The world of scientific determination is validated at every turn of human life. The vision of nanotechnology needs to be changed and reframed. The efficacies and the upshot will surely open up new generations of scientific thoughts [28].

The Visionary Challenges in the Domain of Nanoscience and Nanotechnology

Nanotechnology heralds in a new age and a resurgent era of science and engineering. The path to progress is surpassing many visionary frontiers [27, 28]. The answers to the intricacies in the field of nanoscience and nanoengineering have made our scientific domain to surge toward a new generation of scientific advancement. Hurdles, barriers, and immense vision will surely be the frontrunners to a new age of invention, innovation, and ideas in the field of nanotechnology. Nanotechnology has vast frontiers in diverse areas of scientific pursuit. Medical science in today's world is revolutionized and reframed. The restructuring has inputs from the ability to overcome serious and debilitating illnesses. Physicians would seriously delve into the depths of nanosurgery and be able to attack illness and injury at the molecular level. This would of course and surely eradicate cancer. Cancer cells would be identified and removed, and the surgical implantation of healthy cells would soon follow. Moreover, there would be an entire nanosurgical domain to help cure everything from natural aging to diabetes to bone spurs. The visionary frontiers of the application area of nanotechnology in diverse fields and engulfing diverse phenomena are vast and unimaginable. The application of basic science and the application of both nanotechnology and nanoelectrochemistry have an umbilical cord linked with great firmness. In today's civilization, validation of scientific knowledge and scientific innovation is the need of the hour in the progress of humanity. Nanoscience, nanotechnology, or nanoelectrochemistry will soon remove the barriers of scientific challenges as civilization plunges into the deep sea of the twenty-first century. Validation of knowledge will be surely restructured and rebuilt in years to come.

Scientific Vision, Scientific Truth, and the Progress in Nanotechnology

Nanotechnology in today's world is moving briskly and steadfastly toward one newer vision over another. Progress of science, technology, and engineering in today's scientific generation needs to be reassessed and re-envisioned. The scientific vision and the scientific truth will open up new areas in nanotechnology with years to come. The progress in nanotechnology is inspiring and immensely proven. In today's world, nanotechnology is inevitable connected with energy and environmental sustainability. Vision of the future needs scientific assessment and immense scientific fortitude. History of mankind will witness a new era in the domain of nanotechnology with the turn of this century of science and engineering.

Scientific truth and immense scientific resilience are the visionary prefixes or coin words of today's world of nanotechnology and its branches. Nanoelectrochemistry needs to be scientifically readdressed and restructured. This branch of science along with colloid chemistry is the torchbearer of the newer vision of nanotechnology. The scientific truth will pave the way for newer vision and newer scientific breakthroughs. The area of nanofiltration will be restructured with the immense application in wastewater treatment, desalination, drinking water treatment, and other areas of environmental engineering science. History of nanoscience and nanotechnology will witness a new revolution in a new era.

Nanotechnology in today's world has an umbilical cord with energy and environmental sustainability. Application of nanofiltration in environmental engineering science is a glorious example. Environmental catastrophes are boon to disaster to mankind. Stringent restrictions have urged scientific community to restructure their thoughts and plunge into the deep vision and strong comprehension of nanofiltration. The world of challenges will surely witness a new era in the application domain of nanotechnology.

March of Science in the Domain of Nanoscale Electrochemistry and the Future Scientific Vision

History of mankind is witnessing visionary challenges and ever-growing scientific challenges [28]. The doctrine of nanoscale electrochemistry is vast, versatile, and groundbreaking. The effectivity and greatness of the application areas of nanoelectrochemistry need to be restructured with the progress of science and technology. The burgeoning world of nanotechnology will surely surpass many visionary frontiers with years to come. The strong notion of validation of laboratory scale research to human society also needs to be envisioned with the turn of every decade as science progresses.

March of science and engineering is awesome and inspiring [28]. The application areas of nanoelectrochemistry and nanofiltration are surpassing visionary frontiers. The vision of application domain of nanofiltration in environmental engineering science will witness a dawn in science as civilization progresses [28]. Nanotechnology will also open up wide windows of futuristic vision and usher in

a definitive visionary scientific generation. It will truthfully absorb the immense barriers and overcome scientific frontiers with the passage of time and with progress of human civilization [28].

Future Thoughts, Future Application Areas of Nanoelectrochemistry and Nanotechnology, and the Ultimate Vision for the Future

Future thoughts, future application areas, and ultimate vision are wide and bright. Nanoelectrochemistry and nanotechnology need to be linked to nanofiltration and environmental engineering [32]. Water crisis and water shortage of our present-day civilization are boons to disaster. In such a crucial and critical juncture of history and time, application areas of nanoelectrochemistry and nanotechnology need to be restructured. The world of challenges and hurdles will open a new era of hope and immense vision if targets are achieved in the path to progress [27, 28]. The scientist's vision will be equally validated in years and generations to come [32].

Future vision in the domain of nanotechnology needs to be redrafted and rejudged with the immense application of nanoelectrochemistry. A scientist's vision will be only emboldened if scientific justification in scientific endeavor is addressed and scientific validation is envisioned.

Conclusion

The world of unknown is opening up the barriers of science and technology to the world of imagination of known. The fruits of nanotechnology are impressive and greatly visionary. Vision of nanoscience and nanotechnology is an unfinished journey. It is still latent and immature. The fruits of this domain of nanoscale electrochemistry are enviable and unquestionable. Daring ventures in the field of nanoscale electrochemistry particularly in environmental science can open up innumerable avenues in years to come, and then scientist's vision will be validated.

The treatise on nanoelectrochemistry will be incomplete if one does not acknowledge the vision of scientific endeavor and the immense hardship in the path to validation, success, and glory. The world of scientific challenges and scientific barriers will move into oblivion with the turn of the century along with validation of scientific endeavor. History of nanotechnology will then witness a new dawn of scientific breakthroughs.

References

1. Singh PS, Katelhon E, Mathwig K, Wolfrum B, Lemay SG (2012) Stochasticity in single-molecule nanoelectrochemistry : origins, consequences and solutions. *ACS Nano* 6(11):9662–9671
2. Murray RW (2008) Nanoelectrochemistry: metal nanoparticles, nanoelectrodes and nanopores. *Chem Rev* 108:2688–2720

3. Oja SM, Wood M, Zhang B (2013) Nanoscale electrochemistry. *Anal Chem* 85:473–486
4. Hassani AH, Mirzayee R, Nasseri S, Borghei M, Gholami M, Torabifar B (2008) Nanofiltration process on dye removal from simulated textile wastewater. *Int J Environ Sci Technol* 5(3): 401–408
5. Schultze JW, Bressel A (2001) Principles of electrochemical micro and nano system technologies. *Electrochem Acta* 47:3–21
6. Rauf S, Shiddiky MJA, Asthana A, Dimitrov K (2012) Fabrication and characterization of gold nanohole electrode arrays. *Sens Actuators B* 173:491–496
7. Zheng L, Brody JP, Burke PJ (2004) Electronic manipulation of DNA, proteins, and nanoparticles for potential circuit assembly. *Biosens Bioelectron* 20:606–619
8. Yang H (2012) Enzyme based ultrasensitive electrochemical biosensors. *Curr Opin Chem Biol* 16:422–428
9. Mirksich M (2009) Using self-assembled monolayers to model extracellular matrix. *Acta Biomater* 5:832–841
10. Taufany F, Pan C, Rick J, Chou H, Tsai M, Hwang B, Liu D, Lee J, Tang M, Lee Y, Chen C (2011) Kinetically controlled autocatalytic chemical process for bulk production of bimetallic core – shell structured nanoparticles. *ACS Nano* 5(12):9370–9381
11. Janin M, Ghilane J, Randriamahazaka H, Lacroix JC (2011) Formation of metallic nanowires via electrochemistry in aqueous surfactant media. *J Phys Chem C* 115:549–553
12. Lin Y, Chou H, Tsai M, Hwang B, Sarma SL, Lee Y, Chen C (2009) Combined experimental and theoretical investigation of nanosized effects of Pt catalyst on their underlying methanol electro-oxidation activity. *J Phys Chem C* 113:9197–9205
13. Bard AJ (2008) Toward single enzyme molecule electrochemistry. *ACS Nano* 2(12): 2437–2440
14. Miao Y, He N, Zhu J (2010) History and new developments of assays of cholinesterase activity and inhibition. *Chem Rev* 110:5216–5234
15. Krapf D, Wu M, Smeets RMM, Zandbergen HW, Dekker C, Lemay SG (2006) Fabrication and characterization of nanopore based electrodes with radii down to 2nm. *Nanoletters* 6(1):105–109
16. Zhan D, Velmurugan J, Mirkin MV (2009) Adsorption/Desorption of Hydrogen on Pt nanoelectrodes: evidence of surface diffusion and spillover. *J Am Chem Soc* 131:14756–14760
17. Sun P, Mirkin MV (2008) Electrochemistry of individual molecules in Zeptoliter volumes. *J Am Chem Soc* 130:8241–8250
18. Amemiya S, Nioradze N, Santhosh P, Deible MJ (2011) Generalized theory for nanoscale voltammetric measurements of heterogeneous electron-transfer kinetics at macroscopic substrates by scanning electrochemical microscopy. *Anal Chem* 83:5928–5935
19. Matsuura T (2001) Progress in membrane science and technology for seawater desalination- a review. *Desalination* 134:47–54
20. Palit S (2011) Ozonation associated with nanofiltration as an effective procedure in treating dye effluents from textile industries with the help of a bubble column: A review. *Int J Chem Chem Eng* 1(1):53–60
21. Palit S (2009) Ozonation of Direct Red – 23 dye in a fixed bed batch bubble column reactor. *Indian J Sci Technol* 2(10):14–16
22. Singh M, Naveen BP (2014) Molecular nanotechnology: a new avenue for environment treatment. *IOSR J Environ Sci Tox Food Technol* 8(1):93–99, Ver.1
23. Hilal N, Mohammad AW, Atkin B, Darwish NA (2003) Using atomic force microscopy towards improvement in nanofiltration membranes properties for desalination pretreatment- a review. *Desalination* 157:137–144
24. der Bruggen V, Manttari M, Nystrom M (2008) Drawbacks of applying nanofiltration and how to avoid them.-A review. *Sep Purif Technol* 63:251–263
25. Palit S (2012) Ozone treatment as an effective advanced oxidation process for the degradation of textile-dye effluents. *Int J Chem Anal Sci* 3(1):1293–1295
26. Hong S, Elimelech M (1997) Chemical and physical aspects of natural organic matter (NOM) fouling of nanofiltration membranes. *J Membr Sci* 132:159–181

27. Palit S (2012) A brief insight into advanced oxidation processes for wastewater treatment – a keen and far-sighted short overview. *Univ J Environ Res Technol* 2(3):106–109
28. Palit S (2013) Man's vision, mankind's vision and progress of science and technology-the inspirations and vision to target for the future. *Int J Sci Eng Res* August, 2013 (Editorial Article)
29. Senturk A, Yalcin B, Otles S (2013) Nanotechnology as a food perspective. *J Nanomater Mol Nanotechnol* 2:6
30. Ramesh Babu B, Parande AK, Raghu S, Premkumar T (2007) Textile technology, cotton textile processing-waste generation and effluent treatment. *J Cotton Sci* 11:141–153
31. Torabion A, Bihdendi GRN, Ranjbar PZ, Razmkhah N (2007) Efficiency evaluation of textile basic dye removal from water by nanofiltration. *Iranian J Environ Health Sci Eng* 4(3):177–180
32. www.technologia.gda.pl
33. www.sky.zjnu.edu.cn

New Insights in Nanoelectrodeposition: An Electrochemical Aggregative Growth Mechanism

43

Jon Ustarroz, Annick Hubin, and Herman Terryn

Contents

Introduction.....	1350
Early Stages of Electrochemical Nucleation and Growth: Classical Approach	1351
New Insights into Nanoelectrodeposition: An Electrochemical Aggregative Growth Mechanism.....	1355
Silver Electrodeposition.....	1355
Platinum Electrodeposition.....	1361
A Generalized Electrochemical Aggregative Growth Mechanism.....	1365
Conclusions.....	1373
References.....	1374

Abstract

Supported nanostructures represent the cornerstone for numerous applications in different fields such as electrocatalysis (fuel cells) or electroanalysis (sensors). In contrast to other methods, electrochemical deposition allows the growth of the nanostructures directly on the final support, improving the electron pathway within the substrate, nanostructure, and electrolyte. However, despite the increasing number of publications in the field, the early stages of electrochemical nanocrystal formation are still under discussion.

In this chapter, we first provide a survey on the traditional approaches to study the early stages of electrochemical nucleation and growth, together with the

J. Ustarroz (✉) • A. Hubin • H. Terryn

Department Materials and Chemistry, Research Group Electrochemical and Surface Engineering (SURF), Vrije Universiteit Brussel (VUB), Brussels, Belgium

e-mail: justarro@vub.ac.be; Jon.Ustarroz@vub.ac.be; justarro@gmail.com;

Annick.Hubin@vub.ac.be; Herman.Terryn@vub.ac.be

© Springer International Publishing Switzerland 2016

M. Aliofkhaezai, A.S.H. Makhlof (eds.), *Handbook of Nanoelectrochemistry*,

DOI 10.1007/978-3-319-15266-0_10

1349

classical theories used to understand them. Next, we describe our most recent findings which have led to reformulate the Volmer-Weber island growth mechanism into an electrochemical aggregative growth mechanism which mimics the atomistic processes of the early stages of thin-film growth by considering nanoclusters of few nm as building blocks instead of single atoms. We prove that the early stages of nanoelectrodeposition are strongly affected by nanocluster self-limiting growth, surface diffusion, aggregation, and coalescence.

Keywords

Supported nanoparticles • Electrodeposition • Nucleation and growth • Aggregative growth

Introduction

Supported nanostructures represent the cornerstone for numerous applications in different fields such as electrocatalysis (fuel cells) [1–3] or electroanalysis (sensors) [4–6] among others [7]. In both cases, supported metal nanoparticles (NPs) are the active materials whose development can boost both technologies to levels almost unimaginable a few years ago.

Metal nanoparticles can be synthesized by multiple methods either in solution or in the gas phase, as reviewed many times [3, 8, 9], colloidal synthesis and other solution-based methods being the most common approach [10–13]. Nonetheless, when generated particles are required to be attached to a surface, previously mentioned methods do not always provide the best solution. Physical vapor deposition methods such as sputtering or electron beam deposition require expensive high-vacuum facilities, whereas colloids may lose some of their properties due to the organic ligands used during the synthesis procedure or because of unwanted aggregation during deposition on a given support [14–16].

Alternatively, electrochemical deposition allows the growth of the nanostructures in one step, directly onto the final support, without needing further sample preparation, thus improving the electron pathway within the substrate, nanostructure, and environment. Consequently, the technique has been proven effective to obtain highly electroactive nanostructures with potential for fuel cell [17–20] or (bio)sensing [5, 4] applications. Moreover, the technique is surfactant free, highly selective, cost effective, and allows the nature of the nanoclusters to be easily tuned by changing electrolyte composition and deposition parameters [21, 22].

However, compared to other synthesis methods, the reliability of the synthesis procedures, size and shape tunability, or size dispersion control is far from being at the same level of development. The main reason for this is a lack of knowledge of the fundamental aspects of nanoscale electrodeposition. Despite the increasing number of publications in the field, the early stages of nanocrystal formation mechanisms in electrochemical processes are still under discussion.

Early Stages of Electrochemical Nucleation and Growth: Classical Approach

Nucleation and growth phenomena have been thoroughly studied since more than a century for colloidal syntheses [23], thin-film growth [24], and electrochemical deposition processes [25] among others, resulting in a classic nucleation and growth theory which predicts that nanocrystals grow irreversibly by atomic addition until the reaction is halted.

Contrarily to other nanoparticle synthesis or thin-film deposition methods, electrochemical deposition processes can be followed in situ by recording the current (or potential) transients after applying different potential (or current) pulses. In the case of potentiostatic single-pulse electrodeposition, the evaluation of the current-time transients, or chronoamperograms, provides invaluable time-resolved information about nucleation and growth processes and is hence performed and reviewed on countless occasions [26–30].

If we consider a homogeneous surface such as amorphous carbon, when a given overpotential, η , is applied, nuclei are supposed to form at random locations over the surface according to Eq. 1:

$$N(t) = N_0 [1 - \exp(-At)] \quad (1)$$

N_0 is the saturation number density (maximum number of nuclei within the surface), A is the nucleation rate constant, and AN_0 is the nucleation rate. In principle, all formed nuclei have $r \geq r_{\text{crit}}$, so they will grow irreversibly until the potential pulse is stopped or the concentration of active species in their surroundings decreases below a certain level. By considering that the only growth mechanism is that of direct reduction of ions onto the surface of three-dimensional hemispherical nuclei (direct attachment), plenty of theoretical work has been carried out to relate the chronoamperometric response $I(t)$ to the nucleation rate and $N(t)$ (Eq. 1) [26, 31–33, 28].

In short, the growth of each nucleus affects both the concentration of active species and the overpotential distribution in the cluster vicinity, creating zones of reduced concentration and overpotential and thus reduced nucleation rate. Then, if multiple clusters are considered, their local zones of reduced nucleation rate spread and gradually overlap. This is a very complex problem which is frequently solved by approximating the areas of reduced nucleation rate by overlapping planar diffusion zones in which nucleation is fully arrested. Then, if it is considered that these growth centers, which are randomly distributed on the electrode surface, grow under spherical diffusion control, the total electrochemical current can be expressed by

$$I(t) = Sj(t) = S\beta z Fc \left(\frac{D}{\pi t} \right)^{1/2} \times \left[1 - \exp \left(-\frac{1}{2} AN_0 \pi \gamma \left(\frac{8\pi cM}{\rho} \right)^{1/2} Dt^2 \right) \right] \quad (2)$$

if the nucleation is progressive, and

$$I(t) = Sj(t) = SzFc \left(\frac{D}{\pi t} \right)^{1/2} \times \left[1 - \exp \left(-N_0 \pi \left(\frac{8\pi cM}{\rho} \right)^{1/2} Dt \right) \right] \quad (3)$$

if the nucleation is instantaneous. It is important to note here that Eq. 1 accounts for progressive nucleation, but instantaneous nucleation can be thought as the limit $A \rightarrow \infty$ and then $N=N_0$, so N_0 nuclei are instantaneously formed at $t=0$. S is the electrode area, $j(t)$ is the current density, F is the Faraday constant, z is the number of transferred electrons, c is the electrolyte concentration, D is the diffusion coefficient, ρ is the density, M is the molar mass, β equals 1 according to references [26, 31] and 4/3 according to references [32, 33], and γ equals 4/3 according to references [26, 34] and 1 according to the other references. In the next sections, we will consider $\beta=1$ and $\gamma=4/3$. Equations 2 and 3 lead to $I(t)$ profiles which display a peaked shape, characteristic of 3D nucleation and diffusion-limited growth processes.

Other widely cited reformulations of the model have been developed by Scharifker and Mostany (SM) [31], Mirkin and Milov (MM) [32], and Heerman and Tarallo (HT) [33]. Additional theoretical approaches considered to study electrochemical nucleation and growth phenomena can be found elsewhere [35–38, 30]. It is not the purpose of this chapter to elaborate more on details of these theoretical models, but the reader can find more information in the bibliographic references provided in Table 1.

Table 1 Selected bibliographic references that describe theoretically the early stages of electrochemical nucleation and growth

Ref.	Year	Type of publication	Comments
1 [26]	1983	Journal paper	Scharifker-Hills Model (SH)
2 [31]	1984	Journal paper	Scharifker-Mostany Model (SM)
3 [32]	1990	Journal paper	Mirkin-Nilov Model (MN)
4 [35]	1998	Journal paper	Non-stationary nucleation approach
5 [36]	1998	Journal paper	Non-stationary nucleation approach
6 [33]	2000	Journal paper	Herman-Tarallo Model (HT)
7 [37]	2005	Journal paper	Model including proton co-reduction
8 [38]	2008	Journal paper	Multistep electrochemical reactions
9 [27]	1999	Review paper	–
10 [28]	2003	Review paper	–
11 [29]	2003	Review paper	–
12 [30]	2008	Review paper	–
13 [25]	1997	Book	Electrochemical nucleation and growth
14 [21]	2006	Book	Electrodeposition
15 [22]	2007	Book	Nanoelectrodeposition

The important feature to emphasize here is that independently of the slight modifications of the mathematical description of the processes, all the models describing three-dimensional electrochemical nucleation and growth are based on several assumptions that have no direct proof. One of them is the fact that **all nuclei are pinned to a specific site on the surface**, and another is that **they only grow by direct attachment**. This concept will be thoroughly discussed throughout this chapter. Further description of electrochemical nucleation and growth phenomena can be found in several books and review papers (see Table 1).

Qualitative agreement of the current transients with the referred models has been reported on countless occasions. However, the models allow a quantitative analysis which has been carried out on much less occasions. The most typical approach is to first fit the chronoamperograms obtained at different overpotentials. This way, if we take Eq. 2 as an example, the diffusion coefficient D and the nucleation rate AN_0 can be obtained by a standard least-squares algorithm. On the other hand, morphological characterization of the substrates is carried out to estimate the number of particles at different deposition times in order to get $N(t)$. The nucleation rate constant A and saturation number density N_0 can be inferred from Eq. 1 in order to compare the values with these obtained with the model fit and hence check the validity of the models for different experimental systems.

One important aspect which is emphasized here is related to the experimental determination of $N(t)$, N being the number of formed *nuclei* after a given deposition time. Obviously, an accurate determination of N will depend on the dimensions of the nuclei and on the size resolution of the characterization technique employed. Inherent to any electrochemical deposition system, the attachment of the nanoparticles to a surface has restricted traditionally the range of applicable techniques to surface analytical techniques such as Field Emission Scanning Electron Microscopy (FESEM) [19, 39, 40] or Atomic Force Microscopy (AFM)/Scanning Tunneling Microscopy (STM) [41–44]. In practice, however, the resolution of a FESEM is limited to particles with diameters larger than 5–6 nm, and AFM/STM can only be carried out accurately on very flat substrates, its lateral resolution being much affected by the geometry of the tip. Also, in situ Transmission Electron Microscopy (TEM) imaging has been developed and used to study the electrodeposition of copper nuclei on gold thin films [45–49]. Unfortunately, the fact that the electrons had to be transmitted through the electrolyte made their TEM spatial resolution rise up to about 5 nm, making it again impossible to detect smaller nuclei.

Several groups have reported quantitative analyses in which experimental observations agree [40, 41, 50, 51] or are in conflict with electrochemical nucleation and growth models [42, 44, 46, 52]. Further details and more bibliographic references are provided in Table 2. Anyhow, it is clear that even in the best of the cases, the presence or absence of nanoparticles of $d \leq 5$ nm cannot be ascertained. Critical clusters are known to be much smaller than 5 nm. Hence, it is doubtful to which extent experimental observations of particle number densities can be directly related to $N(t)$. Therefore, it can be asserted that *the early stages of electrochemical nucleation and growth are far from being fully understood*.

Table 2 Published data about the comparison of electrochemical nucleation rates obtained from $I(t)$ model fits and experimental observations of $N(t)$. GC glassy carbon, HOPG highly oriented pyrolytic graphite, SWNTs single-walled carbon nanotubes, GR graphene, OM optical microscopy

Ref.	Mat.	Substr.	Model	Fit parameters		Charact.	Exp. parameters		Exp/Theor
				$AN_0(p/cm^2s)$, $N_0(p/cm^2)$	$N_0(p/cm^2)$		$AN_0(p/cm^2s)$, $N_0(p/cm^2)$	$N_0(p/cm^2)$	
1[19]	Pd	SWNTs	SH	$N \ll \ll Exp.$		AFM, FESEM	$N = 1.5 \times 10^8$	$>>> 1$	
2[39]	Cu	GC	SH	$N = 2.6 \times 10^5$		SEM	$N = 9.7 \times 10^7$	4×10^2	
3[39]	Cu	GC	[53]	$N = 1.4 \times 10^{12}$		SEM	$N = 9.7 \times 10^7$	10^{-4}	
4[39]	Cu	GC	SH	$AN_0 = 9 \times 10^4$		SEM	$AN_0 = 1.5 \times 10^5$	1	
5[40]	Ag	GC	[40]	$N = 1 - 9 \times 10^9$		SEM	$N = 1 - 7 \times 10^9$	1	
6[41]	Ag	HOPG	SH	$N = 4 \times 10^8 - 2 \times 10^{10}$		NC-AFM	$N = 3 \times 10^9 - 1.2 \times 10^{10}$	1 - 10	
7[42]	Pt	HOPG	SH	$N = 1 - 2 \times 10^6$		STM	$N = 5 \times 10^9 - 1 \times 10^{10}$	10^3	
8[43]	Cu	Si	SH	$AN_0 = 4 \times 10^6$		AFM	$AN_0 = 3 \times 10^7$	10	
9[44]	Au	Si	SH	$N = 10^6 - 5 \times 10^7$		AFM	$N = 10^{10}$	$5 \times 10^2 - 10^4$	
10[44]	Au	Si	SH	$N = 10^6 - 10^8$		AFM	$N = 10^9$	$10 - 10^3$	
11[45]	Au	GaAs	SH	$N = 10^6 - 10^7$		SEM, TEM	$N = 10^9 - 10^{12}$	$10^3 - 10^5$	
12[46]	Cu	Au	SH	$N = 1 \times 10^4 - 1 \times 10^6$		TEM	$N = 1 \times 10^8 - 1 \times 10^{10}$	10^4	
13[50]	Ag	GC	SM	$N = 2 \times 10^5 - 7 \times 10^7$		OM	$N = 1 \times 10^6 - 2 \times 10^7$	1	
14[51]	Ag	H-Si	SH	$N = 2 \times 10^{10}$		NC-AFM	$N = 1 \times 10^9$	10^{-1}	
15[52]	Cu	TiN	SH	$N = 10^4 - 10^7$		AFM	$N = 10^8 - 10^{11}$	10^4	
16[54]	Au	GC	SH	$N = 3 \times 10^6$		FESEM	$N = 2 - 5 \times 10^8$	10^2	
17[55]	Hg	GC	SM	$N = 10^5 - 10^6$		OM	$N = 5 \times 10^5 - 10^7$	5 - 10	
18[56]	Pd	GR	SM	$N = 6 \times 10^7$		OM	$N = 3 \times 10^9$	50 - 100	

New Insights into Nanoelectrodeposition: An Electrochemical Aggregative Growth Mechanism

To clear the uncertainties derived from a lack of resolution, a novel approach has been introduced by our research group. Such an approach consists in using carbon-coated TEM grids (CCTGs) as electrochemical electrodes. In this way, an accurate determination of the nanoparticle size distributions and structural characterization at the atomic scale can be combined with electrochemical measurements. More details on the use of CCTGs as electrochemical electrodes can be found elsewhere [57–59]. The next two sections describe the studies, performed by means of this approach, of silver [58] and platinum [60] electrodeposition. The authors would like to acknowledge Prof. Sara Bals, Dr. Xiaoxing Ke and Thomas Altantzis for the excellent TEM analysis carried out at the Electron Microscopy for Materials Science (EMAT) research group of the University of Antwerp. The authors would also like to acknowledge Dr. Joshua Hammons for his active involvement in the research described in this chapter.

Silver Electrodeposition

Potentiostatic single-pulse depositions were performed by pulsing the electrode potential to $E = -0.4$ V vs Ag/AgCl, in a solution of 0.1 M $\text{KNO}_3 + 1 \times 10^{-3}$ M AgNO_3 , where the process should be diffusion controlled and no other reactions such as hydrogen evolution are present. The early stages of Ag electrochemical nucleation and growth were then analyzed according to the classical electrochemical models described in the section “[Early Stages of Electrochemical Nucleation and Growth: Classical Approach.](#)” More details on the experiments explained hereafter can be found elsewhere [57–59].

Comparison Between Theoretical Models and Experimental Data

On the one hand, the fact that the potentiostatic current transients satisfy the SH model for progressive nucleation implies that the dimensional chronoamperogram can be fitted to Eq. 2 so that the nucleation rate AN_0 is obtained. Good agreement is obtained with the best-fitting parameter being $AN_0 = 4.21 \times 10^{11} \pm 5.69 \times 10^9$ particles/cm²s. Figure 1a shows the experimental chronoamperogram and the theoretical model for the best-fitting parameters and different values of AN_0 .

On the other hand, it is possible to determine experimentally the evolution with time of the particle density, $N(t)$. Figure 1b shows $N(t)$, after analyzing FESEM pictures such as this of Fig. 2a. This means that it is possible to fit these data to an exponential curve to obtain A and N_0 , as shown in Fig. 1b.

We clearly identify an exponential behavior which agrees with Eq. 1, $A = 92 \pm 43$ s⁻¹ and $N_0 = 5.28 \times 10^9 \pm 8.85 \times 10^8$ particles/cm² being the best-fitting parameters. The product of these two values gives $AN_0 = 4.86 \times 10^{11} \pm 2.27 \times 10^{11}$ particles/cm²s, which is in good agreement with the value obtained from the fitting of the chronoamperometric curve to Eq. 2. This means that the evolution with time of the particle distribution agrees with the classical progressive nucleation model.

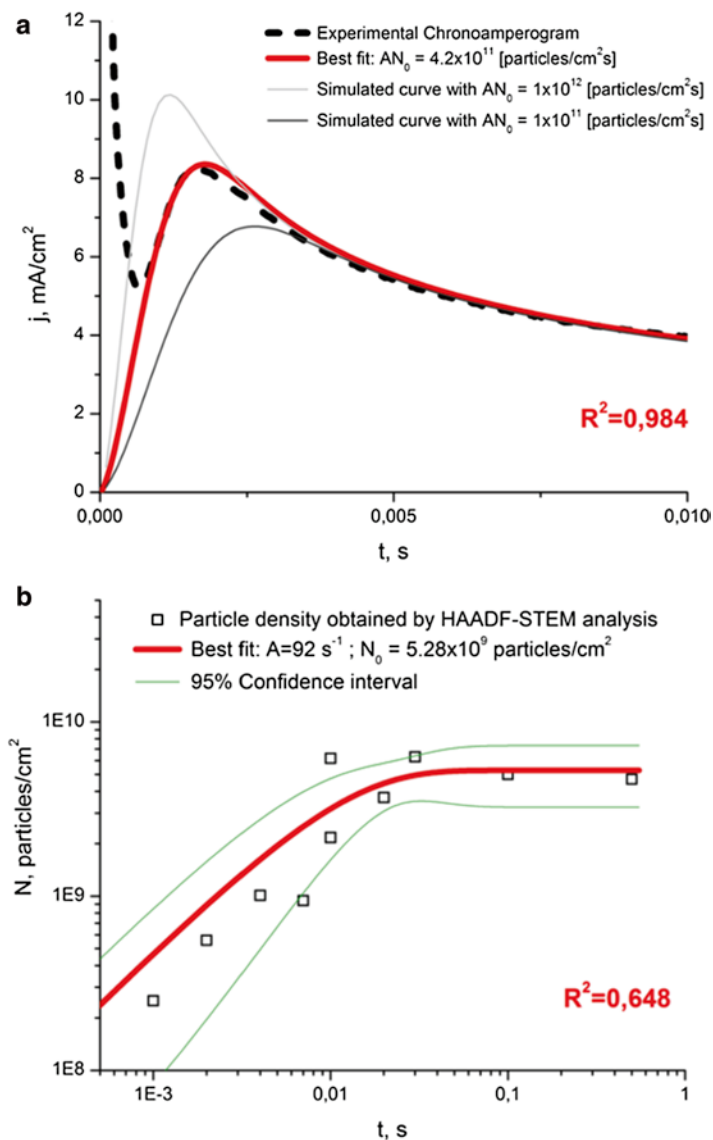


Fig. 1 (a) Experimental chronoamperogram of the potentiostatic electrodeposition of silver at $E = -0.4$ V vs Ag/AgCl and dimensional plots of the SH model for progressive nucleation (Eq. 2) with different values of the nucleation rate constant AN_0 . (b) Evolution of "large" nanoparticle number density with deposition time obtained from the analysis of HAADF-STEM pictures and the best exponential fit of 1

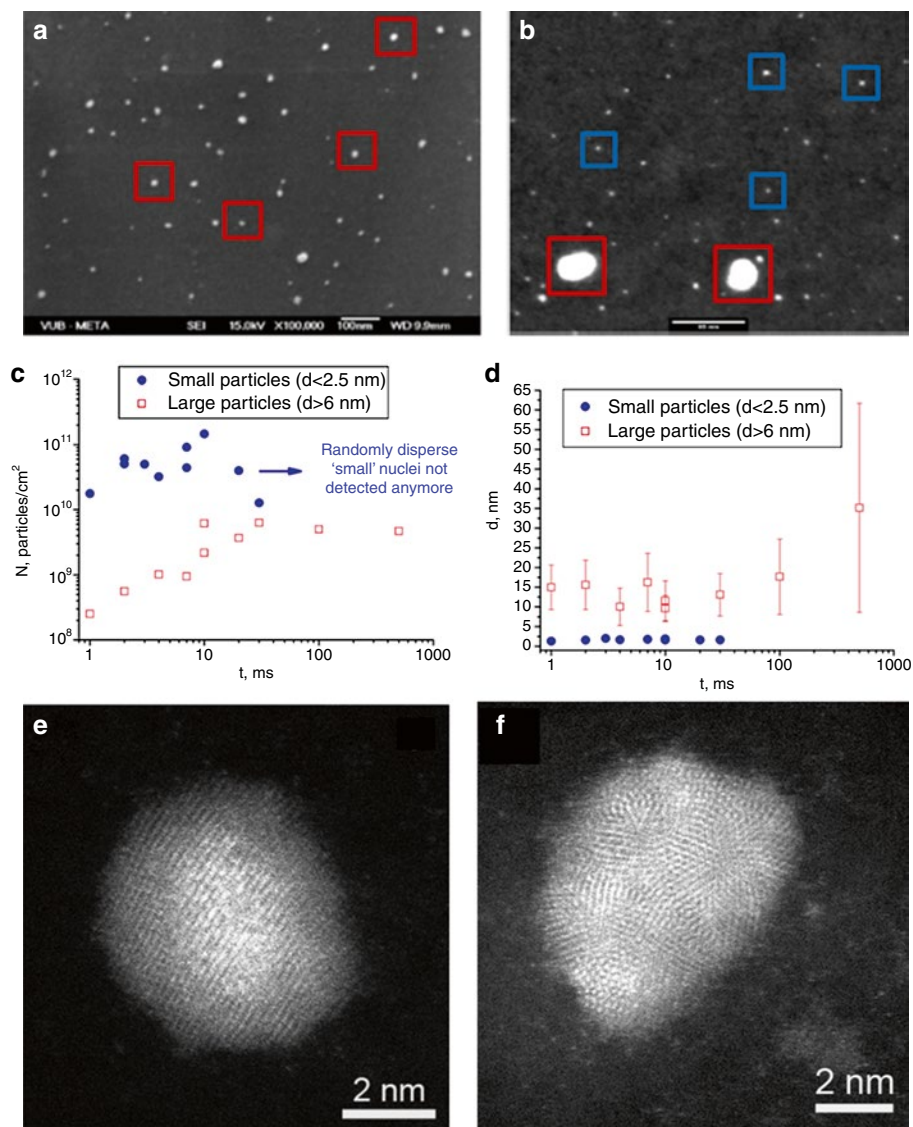


Fig. 2 Typical FESEM (a) and HAADF-STEM (b) pictures after potentiostatic electrodeposition of silver at $E = -0.4$ V vs Ag/AgCl during 10 ms. Evolution of “large” and “small” nanoparticle number density (c) and size (d) with deposition time obtained from the analysis of STEM pictures. Probe-corrected HAADF-STEM pictures of a monocrystalline (e) and polycrystalline (f) Ag nanoparticle

Particle Analysis: Bimodal Size Distribution and High-Resolution TEM studies

In this case, High-Angle Annular Dark-Field Scanning Transmission Electron Microscopy (HAADF-STEM) has also been used to analyze particle distributions after potentiostatic electrodeposition (see Fig. 2b). This way, no doubt should arise from the limits of resolution because this TEM mode can yield sub-Angstrom resolution.

In contrast with FESEM images (Fig. 2a), two populations are clearly distinguished corresponding to a bimodal size distribution in which “large” particles have $d \geq 6$ nm whereas the diameter of the “small” particles is always smaller than 2.5 nm. Figure 2 shows the evolution of particle density (c) and diameter (d) as a function of deposition time. The number of “large” particles grows exponentially with time until it becomes saturated after 30 ms. Accordingly, their average diameter and size dispersion also grow with time.

On the other hand, the number of randomly dispersed “small” particles also grows with time during the first 10 ms but then decreases during the following 20–30 ms. For longer times, the number of those kinds of particles is negligible. Surprisingly, the size of these particles remains constant with $d = 1.70 \pm 0.55$ nm, independently of the deposition time.

The presence of such a bimodal size distribution in the early stages of the process in which such “large” growing particles coexist with randomly dispersed nongrowing “small” clusters cannot be predicted by the classical models. It is logical that the nucleation of the “small” clusters is not reflected in the chronoamperograms because their contribution to the total current compared to the larger particles is very small, though the understanding of why these nuclei are present and which parameters may affect their size and number density is certainly of great importance for nanoscale electrodeposition.

In addition, probe-corrected HAADF-STEM was also used to investigate the atomic-scale structure of the particles. Contrarily to what would be expected from a growth mechanism based on direct attachment, most of the medium-sized particles ($6 \leq d \leq 15$ nm) obtained after short deposition times ($t_{dep} \leq 20$ ms) presented polycrystalline structures in which the crystalline domains had dimensions ranging from 1 to 3 nm (Fig. 2f). It must be pointed out that the dimension of these structural domains coincides with the size of the dispersed nongrowing shown in Fig. 2b. Only a small fraction of medium-sized nanoparticles (Fig. 2e) was found to be monocrystalline. This suggests that a mechanism such as aggregation–coalescence of small clusters governs the early electrochemical growth of the nanoparticles.

In contrast, larger particles obtained at longer deposition times ($t_{dep} \geq 20$ ms) showed in most of the cases monocrystalline structures with defects such as stacking faults and twinings, typical from coalescence events [61, 62]. This may be explained by the tendency of polycrystalline nanoparticles to reduce its internal energy by recrystallizing into a monocrystalline structure [63] and indicates that further nanoparticle growth is again governed by direct attachment because otherwise larger nanoparticles should present polycrystalline domains at least in their outer surface.

Ag Electrodeposition on Carbon: An Electrochemical Aggregative Growth Mechanism

The data here presented indicates that classical electrochemical nucleation and growth theories do not fully account for some nanoscale phenomena occurring during the early stages of silver electrodeposition. Hence, we have suggested that an Electrochemical Aggregative Growth Mechanism might be the clue to understand the observed phenomena on the early stages of electrochemical nanoparticle formation and growth. Figure 3 represents schematically the stages of the proposed mechanism. Further information about the discussion presented in this section can be found elsewhere [58, 59].

In the first instants after the application of a negative potential, very small clusters of $r \approx r_c$ are formed randomly distributed through the carbon substrate (particles such as 1 in Fig. 3a). Then, as the nucleation is progressive, more small clusters will be formed until the nucleation exclusion zones have overlapped and covered the entire surface. Although those small clusters do not dissolve because $r \geq r_c$, they are unstable and can easily move through the surface because of their small size [64] and the weak van der Waals (VDW) forces between carbon and silver atoms.

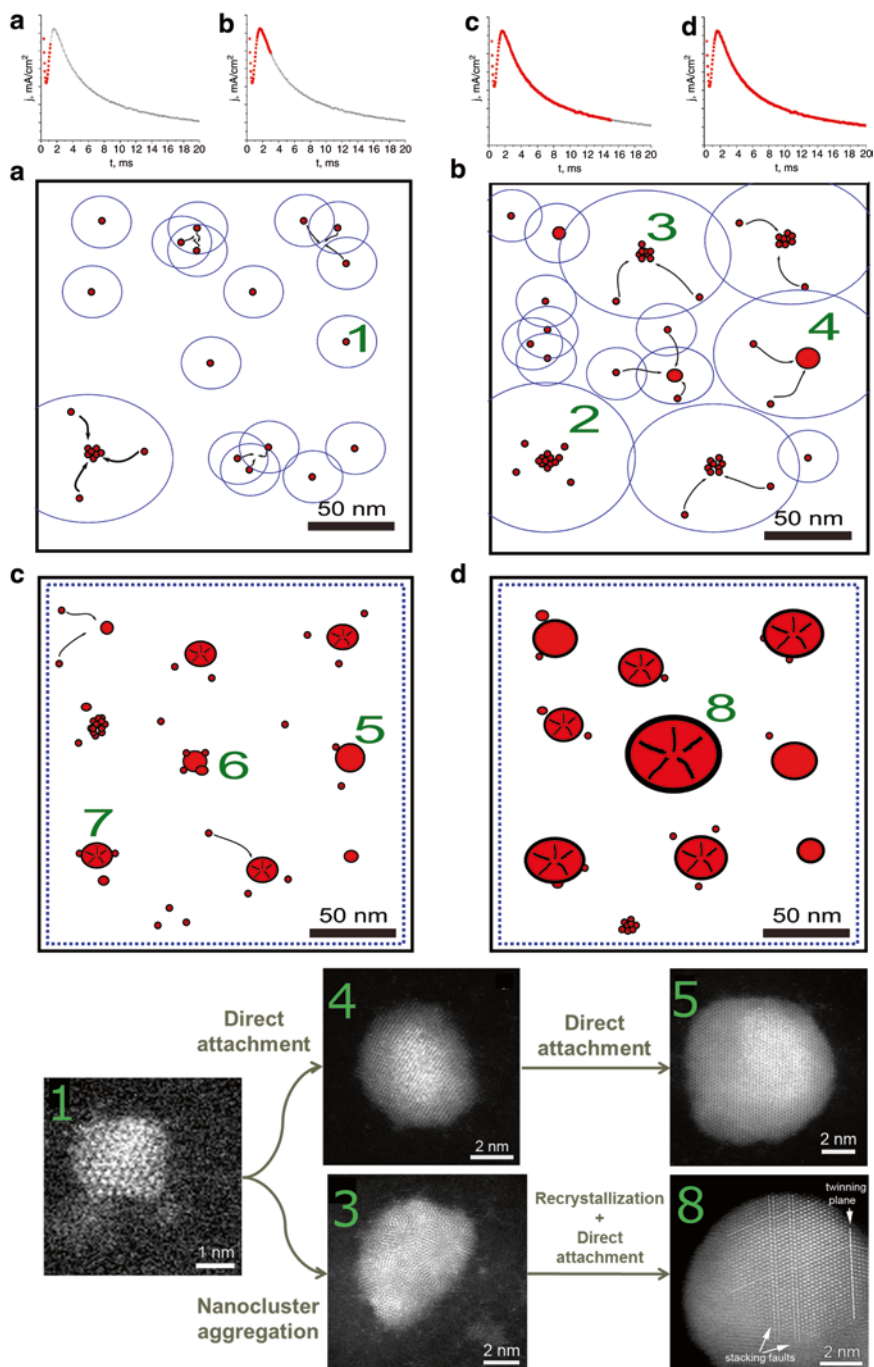
These small clusters aggregate with each other or with other aggregates. This aggregation mechanism takes place due to a thermodynamic driving force altering the system toward its lowest energy configuration, as small nuclei may move through the surface because of the same reasons that adatoms move toward edges or kink sites [64].

Then, until the conditions of planar diffusion are reached (i.e., when nucleation exclusion zones have overlapped and covered the entire surface as in Fig. 3c), three phenomena happen in parallel: nucleation of new small clusters, surface movement of small clusters which aggregate with each other or with other aggregates, and direct attachment (i.e., incorporation of Ag^+ ions onto aggregates and small clusters). A small fraction of monocrystalline structures (particles such as 4 in Fig. 3b) is also present. Therefore, we suggest that both aggregation and direct attachment are responsible for early nanoparticle growth, aggregation being predominant over the classical growth mechanism.

Afterward, when nucleation exclusion zones have completely covered the surface (Fig. 3c), no more nucleation is supposed to happen on the carbon surface so the concentration of the randomly dispersed small clusters decreases due to their aggregation or incorporation in the other aggregates.

Finally, when all the small clusters have been consumed (Fig. 3d), the number of aggregates reaches saturation. At this stage, previous polycrystalline and aggregated particles undergo recrystallization into monocrystalline structures so most of the larger particles are monocrystalline with a high amount of defects (particles such as 7 and 8 in Fig. 3c and d). In later stages, as no more small clusters are present on the carbon surface and nucleation exclusion zones cover all the carbon surface, further nanoparticle growth should be due to direct attachment.

The most significant feature introduced by the proposed mechanism is that in the early stages of electrochemical nucleation and growth, surface movement and aggregation of clusters of $d \approx 1-2$ nm cannot be considered negligible and



determine in great extent the size and structure of electrodeposited nanostructures. This is a striking result not only because these mechanisms had never been considered in the widely accepted electrochemical models for nucleation and growth but also because as a result, nanoparticles in the early stages of their electrochemical growth are polycrystalline instead of monocrystalline, which is the most commonly accepted hypothesis.

Platinum Electrodeposition

To get new insights into the electrodeposition of another metal, platinum deposition was studied with a similar strategy to the one described in the section “[Silver Electrodeposition](#).” Hence, potentiostatic single-pulse depositions were performed by pulsing the electrode potential to various potentials in a solution of 1×10^{-3} M $\text{H}_2\text{PtCl}_6 + 0.1$ M KCl. The early stages of Pt electrochemical nucleation and growth were again analyzed according to the classical electrochemical models described in the section “[Early Stages of Electrochemical Nucleation and Growth: Classical Approach](#).” More details on the experiments explained hereafter can be found elsewhere [60, 59].

Comparison Between Theoretical Models and Experimental Data

Contrarily to the case of Ag electrodeposition, the current-time transients obtained for the early stages of platinum electrodeposition, shown in Fig. 4a, do not always display the typical peaked-shape characteristic of the 3D island growth mechanism [26, 25].

However, for some potentials, such as $E = -0.5$ V, the peaked shape of the current transients allows an analysis according to the theoretical models described in the section “[Early Stages of Electrochemical Nucleation and Growth: Classical Approach](#).” In this case, a good fit is found for an instantaneous nucleation model, leading to a saturation particle density, $N \approx 4 \times 10^5$ particles/cm² [65]. It must be noted that platinum electrodeposition occurs together with different hydrogen reduction reactions catalyzed by the actual platinum surface. Therefore, the obtained current-time transients represent a convolution of both phenomena. If we take into account the effect of H adsorption in the model fit [37, 56], a good fit is in this case found for a progressive nucleation model. In this case, the nucleation rate is found to be approximately $AN_0 = 7.8 \times 10^4$ particles/cm².

On the other hand, it is possible to determine experimentally the particle density, N , for different potentials and times, as shown in Fig. 4b. For $E = -0.5$ V and $t = 20$ s, $N = 3 \times 10^{10}$ particles/cm², being approximately five orders of magnitude larger than the value obtained by fitting the chronoamperograms to the classical models. Although this reflects an important contradiction, a literature analysis reveals that for Pt electrodeposition, the difference in number density between experimental and calculated values has also been reported to rise up to several orders of magnitude [42]. Similar phenomena also occur with other metals such as Cu [46] or Pd [56].

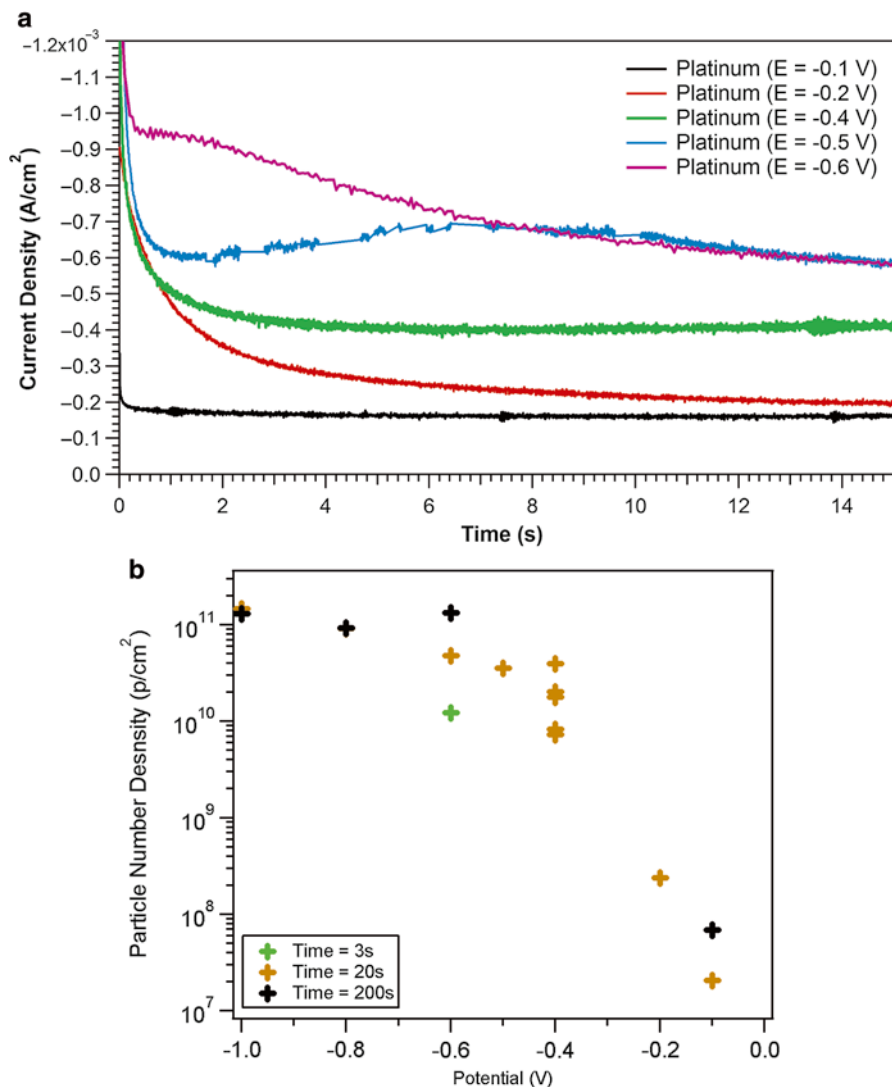


Fig. 4 (a) Chronoamperometric current transients obtained for the electrodeposition platinum onto CCTGs from a solution of 1×10^{-3} M $\text{H}_2\text{PtCl}_6 + 0.1$ M KCl. (b) Evolution of particle number density with applied potential for different deposition times

Particle Analysis: Bimodal Size Distribution and High-Resolution TEM Studies

To clear the doubts arising from a lack of resolution, HAADF-STEM was also used to analyze particle distributions. HAADF-STEM images at low magnification have shown that for high overpotentials ($E \leq -0.4$ V), a population of nanoclusters of $d \approx 2-4$ nm coexists with larger nanostructures regardless of deposition time. However, only large dendritic structures are observed at low overpotentials ($E \geq -0.2$ V) [60].

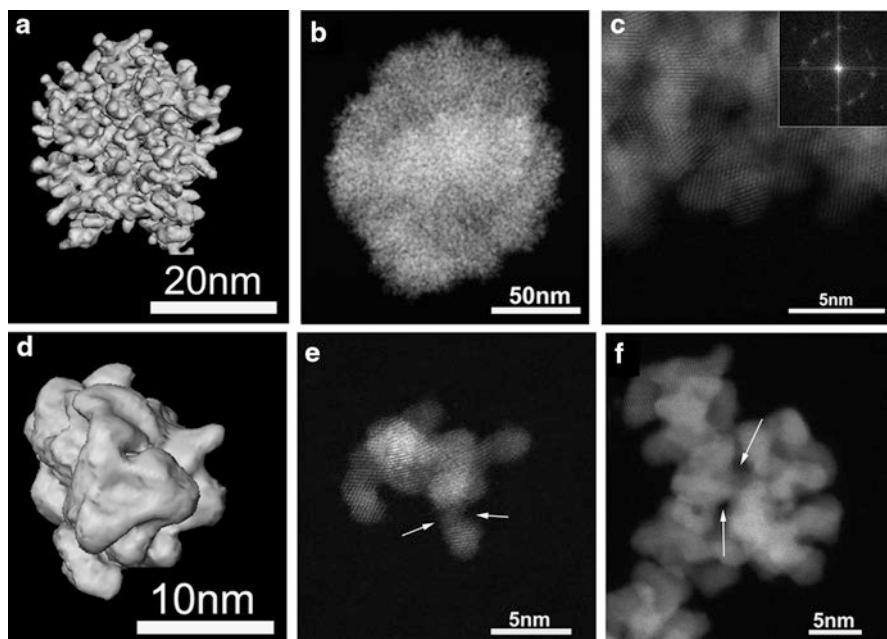


Fig. 5 Three-dimensional electron tomography reconstructions (*top views*: electrode surface below the particle) of platinum dendritic nanostructures obtained by electrodeposition at potential of (a) -0.1 V for 20 s and (d) -0.6 V for 200 s. High magnification HAADF-STEM images of platinum nanostructures obtained after electrodeposition at a potential of (b) -0.1 V for 200 s, (e) -0.6 V for 3 s and (f) -0.6 V for 200 s. (c) Region showing several domains with different crystallographic orientation, together with the corresponding FFT shown as inset

Although the morphology of the deposits and the current transients are very different from the ones obtained for Ag electrodeposition (section “[Silver Electrodeposition](#)”), bimodal size distributions for the early stages of Pt electrodeposition at certain potentials suggest that similar growth by nanocluster aggregation may be taking place.

To get more hints on their formation mechanism, electron tomography and HAADF-STEM at higher magnification were used to observe representative nanostructures obtained at the two potential regimes and different deposition times. Figure 5a–c are representative for the low overpotential regime, and Fig. 5d–f are representative for the high overpotential regime.

At low overpotentials, nanodendritic morphologies are depicted in all cases, consisting of many randomly oriented “branches” which build up a quasicircular shape (Fig. 5a, b). Different deposition times do not influence the dendritic morphology. In all cases, many spherical protuberances of $d \approx 2$ nm can be seen on the outer edges of the nanostructure, most of the times linked to the rest of the body by a narrower neck. Even if lattice fringes extend coherently through large domains within the nanostructure, domains with different crystallographic orientation coexist within the same “particle” as shown by Fig. 5c.

When deposited at high overpotentials, platinum nanoparticles also display an irregular porous shape but are more compact (Fig. 5d). After short deposition times, Fig. 5e shows that many spherical protuberances are again connected to the body of the structure by necks as narrow as few atomic layers. These protuberances have an equivalent diameter of 2–3 nm, just as in the case of low overpotentials. Figure 5e, f show that in contrast with the case of low overpotentials, an increase in deposition time leads to more compact structures and smoother edges. In these cases, lattice fringes are coherent within larger domains. However, structural defects such as twin planes or the open pores indicated by arrows in Fig. 5f point again toward nanocluster coalescence events [61, 62].

Pt Electrodeposition on Carbon: An Electrochemical Aggregative Growth Mechanism. Influence of Recrystallization and Coalescence

Traditionally, the growth of dendritic nanostructures had been associated to diffusion-limited growth [66]. However, pure epitaxial growth can be ruled out in the cases that spherical protuberances are linked through narrow necks (Fig. 5a or e) [67, 62, 61, 68, 69], that domains with different crystallographic orientation coexist (Fig. 5c) [70, 71, 62, 61, 72], or that structural defects such as twin planes or stacking faults are abundant [61, 62], as all these features indicate cluster coalescence events. At high overpotentials, the coexistence of large nanostructures with isolated nongrowing small nanoclusters points again toward nanocluster aggregation-mediated growth [71, 58] (see section “Silver Electrodeposition”). Accordingly, dendrite branch thickness, spherical protuberances, and isolated nanoclusters have the same dimensions ($d \approx 2$ nm), regardless of applied potential and deposition time.

This is an important concept to take into account as metal electrodeposition had traditionally been considered to proceed by nucleation and direct attachment, due to the assumption that growing nuclei would be pinned to the surface and motionless. Although some groups have found irregular Pt nanostructures and suggested that cluster aggregation could take part [73, 42, 74], cluster aggregation mechanisms and their influence in electrochemical growth have not been discussed in detail. Alternatively, the suggested growth mechanism is schematized in (Fig. 6).

At low overpotentials, even at later stages of the electrochemical deposition process, large nanostructures keep growing by the addition of clusters of the same size. This in turn indicates that a self-limiting growth mechanism stops the epitaxial growth of primary clusters and dendritic aggregates.

At high overpotentials, though, the situation is slightly different. After long deposition times, the electrodeposited nanostructures are more compact, less porous, and their lattice fringes extend over very large domains, indicating that they have undergone a higher degree of recrystallization and epitaxial growth by atomic incorporation. Firstly, this indicates that recrystallization kinetics are overpotential dependent and are accelerated at high overpotentials. Secondly, this indicates that a certain degree of nanocluster coalescence and recrystallization is needed to overcome the self-limiting growth mechanism and allow further growth by atomic incorporation.

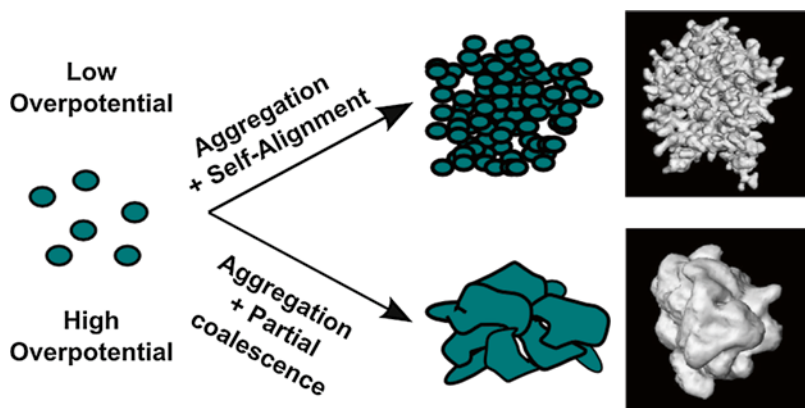


Fig. 6 Schematic representation of the electrochemical aggregative growth mechanism of platinum porous dendritic nanostructures

A Generalized Electrochemical Aggregative Growth Mechanism

Sections “[Silver Electrodeposition](#)” and “[Platinum Electrodeposition](#)” describe the discovery of new insights into Ag and Pt electrodeposition on carbon substrates, by using carbon-coated TEM grids as electrodes, and different TEM characterization modes. Although many differences exist between the growth mechanisms inferred for both materials, it has been shown in both cases that nanocluster self-limiting growth, surface diffusion, aggregation, and coalescence need to be taken account to understand the early stages of electrochemical growth. In this section, we analyze both systems together and elaborate on a Generalized Electrochemical Aggregative Growth Mechanism that can be used to describe the process of metal electrodeposition on low-energy substrates. More details can be found elsewhere [65, 59].

Evaluation of Different Growth Pathways

Figure 7 shows a summary of the different growth pathways of Ag and Pt electrodeposition on carbon.

When the main growth mechanism is atomic addition, monocrystalline defect-free nanoparticles are expected to be the most abundant species. However, in the case of silver electrodeposition, only a very small portion of particles are found to present such a structure. Contrarily, most of the silver nanoparticles are found to grow through a mechanism such as the one depicted by growth pathway “a” (see section “[Ag Electrodeposition on Carbon: An Electrochemical Aggregative Growth Mechanism](#)”). Platinum, though, forms irregular porous dendritic nanostructures rather than hemispherical nanoparticles, as indicated by the growth pathways “b” and “c” (see section “[Platinum Electrodeposition](#)”).

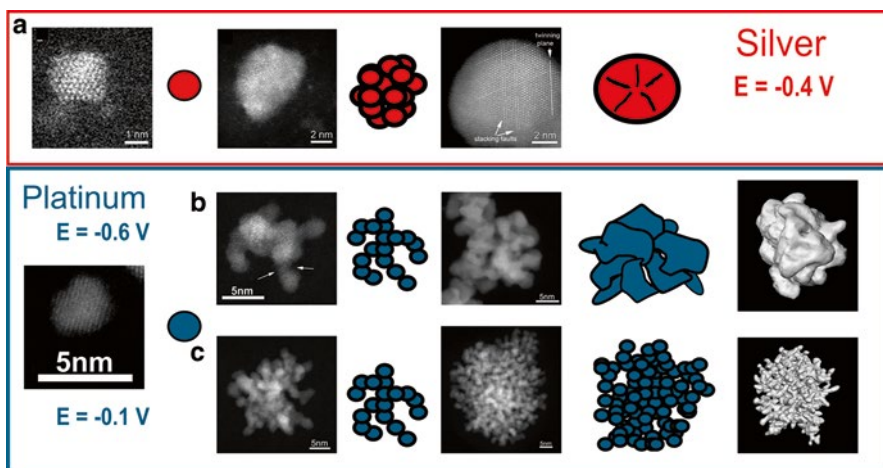


Fig. 7 Schematic diagram showing the growth pathways inferred by HAADF-STEM observation during the electrodeposition of silver (a) and platinum (b, c) onto CCTGs. (a) Growth by nanocluster aggregation and full coalescence resulting into monocrystalline nanoparticles with defects. (b) Growth by nanocluster aggregation and partial coalescence resulting in porous nanostructures. (c) Growth by nanocluster aggregation and small extent of coalescence resulting in ultra-porous dendritic nanostructures

A first important conclusion that can be derived from this analysis is that such an Electrochemical Aggregative Growth Mechanism is common for two metals from different rows and columns of the periodic table such as Ag and Pt. Therefore, it can be suggested as a general metal electrodeposition mechanism onto low-energy substrates such as carbon. Secondly, recrystallization and coalescence kinetics are dependent on material, overpotential, and adsorbed species and dictate the morphology of the final nanostructures to a large extent. Thirdly, direct attachment must not be excluded from the growth process, but its contribution is only noticeable after the aggregates have undergone a high degree of recrystallization.

To fully understand the described mechanism and its different growth pathways, an evaluation of electrochemical chronoamperograms and resulting nanoparticle size distributions is carried out in the next sections. Some concepts such as self-limiting growth, cluster surface diffusion, coalescence, and recrystallization will be used. Although they are common in other new phase formation fields, they are barely used in electrochemical systems. Therefore, the reader is encouraged to look up the discussion provided in a recent publication [65].

Evaluation of Nanoparticle Size Distributions

Figure 8 shows characteristic FESEM pictures presenting an overview of the distribution of silver (a–c) and platinum (d–f) nanoparticles electrodeposited at high overpotentials and different deposition times. Figure 8 shows also the corresponding evolution of average diameter (g) and particle number density (h) of both “large” and “small” particle populations for silver and platinum electrodeposition.

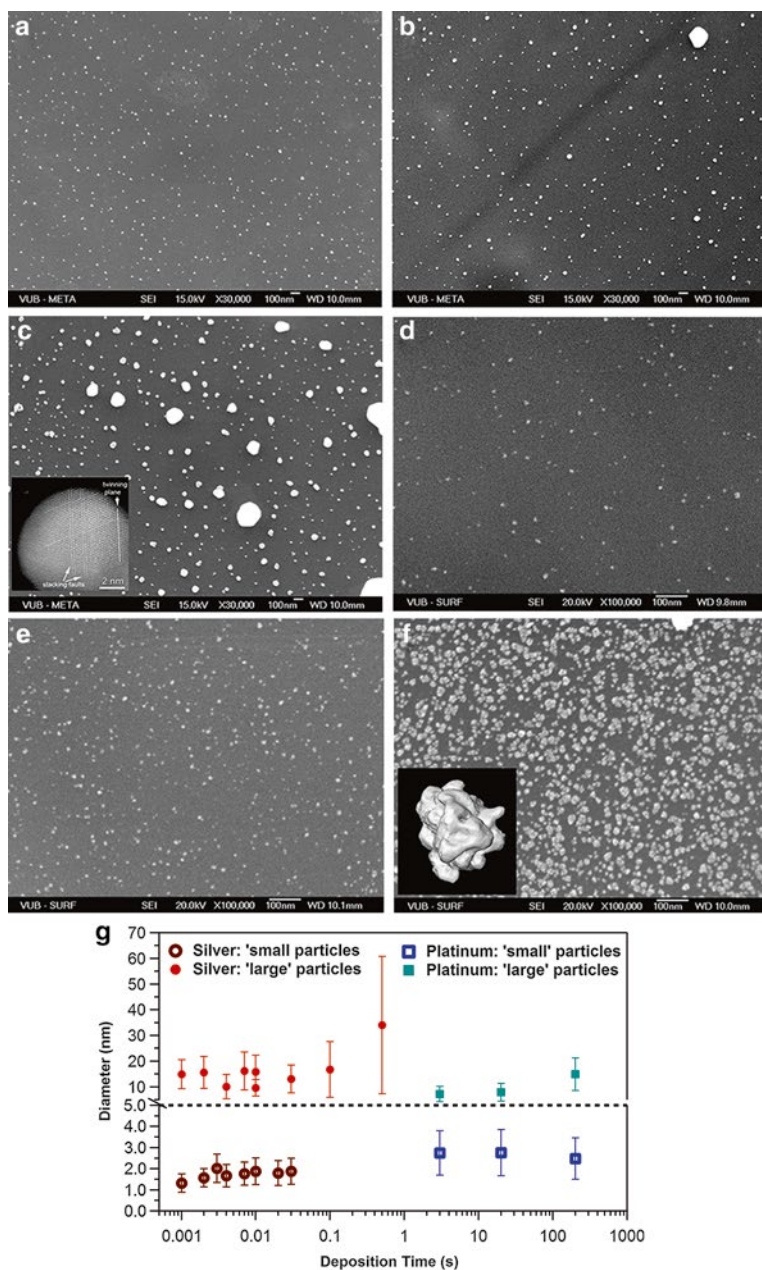


Fig. 8 Representative FESEM pictures after the electrodeposition of silver onto CCTGs at a potential of -0.4 V for (a) 10, (b) 100 and (c) 500 ms. Representative FESEM pictures after the electrodeposition of platinum onto CCTGs at a potential of -0.6 V for (d) 3, (e) 20 and (f) 200 s. Insets: high magnification HAADF-STEM figure of a monocrystalline silver nanoparticle (c) and 3D reconstruction of a porous platinum nanostructure (f). Time evolution of silver and platinum nanoparticle (g) average diameter and (h) number density after electrodeposition onto CCTGs at

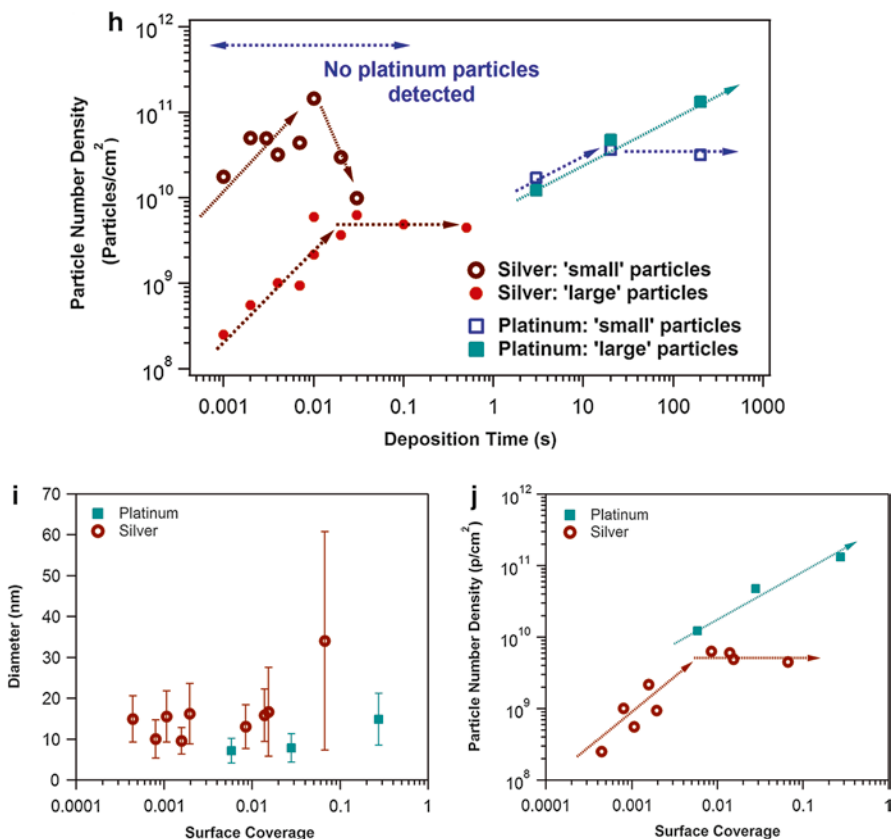


Fig. 8 (continued) potentials of -0.4 and -0.6 V respectively. Evolution of “large” particle (i) average diameter and (j) number density with surface coverage for silver and platinum electrodeposition onto CCTGs at potentials of -0.4 and -0.6 V respectively

Silver nanoparticles are formed at much shorter deposition times than platinum due to differences in reaction kinetics, and so the deposition time is represented in a logarithmic scale for the sake of comparability.

Figure 8g shows that small particles do not grow with deposition time in any of the cases. However, the size of such isolated small clusters is material dependent. This implies that a self-limiting growth mechanism prevents the growth of primary nanoclusters and stabilizes particles of different sizes depending on the material. On the other hand, we have shown that Pt aggregates which undergo a very small amount of recrystallization still show a self-limiting growth mechanism, whereas fully recrystallized aggregates do not (see section “[Platinum Electrodeposition](#)”) [60]. One possible explanation, linked to closed-shell magic sizes, would be that the nanoclusters have a metastable atomic configuration, which hinders epitaxial growth, but become unstable after coalescence. However, in all the cases, primary nanoclusters have relative large size dispersion (33 %), indicating that adsorption-driven stabilization is more plausible than closed-shell magic sizes. Therefore, another

possible explanation would be that stabilization is related to specific adsorption onto the exposed facets of the primary nanoclusters, which change after coalescence. On the other hand, Fig. 8g also shows that “large” Ag and Pt nanoparticles only start to grow after a certain induction time ($t_{ind} \approx 30$ ms for Ag; $t_{ind} \approx 10$ s for Pt); before this time, their size remains more or less constant ($d \approx 15 \pm 5$ nm for Ag; $d \approx 8 \pm 2$ for Pt). Such an induction time corresponds to the aggregation of primary nanoclusters onto larger entities which may grow at later stages [58]. Such a phenomenon, which can be considered an aggregative nucleation process, has been recently reported in the field of colloidal synthesis [71, 75, 76].

In the case of Ag electrodeposition, the induction time corresponds to the period in which the number of aggregates increases by the assembly of isolated primary nanoclusters. Figure 8h shows that after the induction period ($t_{ind} \approx 30$ ms), no more aggregates are created because the surface has been depleted of primary nanoclusters. In the case of platinum, large aggregates start to grow after $t_{ind} \approx 10$ s, but small primary clusters are continuously being formed on the carbon surface, and consequently, more and more large aggregates are also created continuously.

In fact, if one looks at the evolution of the aggregate diameter (i) and number density (j) with the surface coverage, shown in Fig. 8, it becomes clear that in the case of silver, the number of aggregates reaches saturation at small surface coverage of about 1 %, whereas for platinum, the large-particle number density keeps increasing even at large surface coverage of about 30–40 %. Correspondingly, for silver, the large-particle size starts to increase at low surface coverage, whereas platinum aggregates remain small even after large surface coverage has been reached. Under the assumption of growth by direct attachment, growth under diffusion control generates diffusion zones around growing islands of about 10 times their diameter [77]. This would imply that when diffusion fields cover the whole surface, surface coverage should be about 1 %. This is exactly the case for silver electrodeposition, indicating that silver aggregates grow by direct attachment under diffusion control. This behavior is confirmed by their monocrystalline structure after long deposition times, shown in the growth pathway “a” in Fig. 7. Such generation of diffusion zones around the growing aggregates implies that the concentration of ions close to the surface gets gradually smaller, which in turn implies that after a certain moment, no more primary clusters and hence no more aggregates can be generated. On the other hand, Fig. 8j shows that the number of platinum aggregates keeps increasing at high surface coverage, meaning that new primary nanoclusters are continuously generated over the carbon surface. This implies that no (or very small) diffusion fields are created around the aggregates, which in turn indicates that their growth by atomic incorporation is not limited by diffusion of active species toward the surface.

As shown in Fig. 7, the main difference between platinum and silver growth pathways is the fact that silver aggregates recrystallize into monocrystalline nanoparticles, whereas platinum forms porous dendritic structures which only seem to partially recrystallize at large overpotentials. Therefore, silver aggregates behave as traditional islands and grow by atomic incorporation once they have undergone total recrystallization. This is why the evolution of large-particle or aggregate distributions follows the trends established by conventional electrochemical nucleation

and growth theories and correlates with classical chronoamperometric models with good agreement (see section “[Silver Electrodeposition](#)”). On the other hand, partially recrystallized platinum dendritic nanostructures behave halfway between growing islands and small “stabilized” nanoclusters which cannot grow due to a self-limiting growth mechanism. Therefore, even under electrochemical diffusion control, the evolution of particle morphology and size distribution does not follow the assumptions of the Volmer-Weber 3D island growth mechanism.

Evaluation of Chronoamperometric Data

The potentiostatic current transients obtained for silver (a) and platinum (b) electro-deposition have been shown in previous sections (see Figs. 1a and 4a). The analysis of the silver current transients performed in the section “[Silver Electrodeposition](#)” leads to a calculated nucleation rate, AN_0 , in agreement with the number of “large” aggregates derived from HAADF-STEM analysis. Silver aggregates, which have fully recrystallized into monocrystalline islands, grow by direct attachment. Hence, the assumptions from the classical models are fulfilled, and good agreement between experimental and theoretical data is achieved.

On the other hand, it has been shown that most of the current-time transients obtained for the early stages of platinum electrodeposition do not display the typical peaked-shape characteristic of the 3D island growth mechanism [26, 25]. At $E = -0.1$ V, $I(t)$ has a constant value, characteristic of a charge transfer-limited electrochemical reaction. However, kinetically limited island growth should lead to an increasing current density due to an increasing active surface area, until physical island overlap is reached. This is not the case, indicating that the deposited islands do not act as active surface area for direct atomic incorporation. Under these conditions, platinum aggregates are ultraporous nanostructures which have not undergone almost any recrystallization and present no signs of growth by direct attachment (Fig. 7, growth pathway “c”). At $E = -0.2$ V, $I(t)$ shows long-term decaying characteristics that cannot be due to double-layer charging because they extend over ≈ 15 s. The current decay in this case is due to the fact that platinum reduction takes place in diffusion-limited or mixed-control regime. Still, no signs of current increase indicate that primary nanoclusters are being formed under planar diffusion limitations and that large aggregates are not contributing to an increase in active surface area for direct attachment. This is again correlated to the ultraporous nanodendritic morphology obtained at these potentials (Fig. 7, growth pathway “c”).

At $E = -0.4$ V, $I(t)$ starts by a long-term decay, followed by a slight increase in current, indicating that a certain degree of uncoupled diffusion toward growing active centers occurs. At $E = -0.5$ V and $E = -0.6$ V, current starts increasing at earlier times indicating an earlier onset of island growth by direct attachment. This is again linked with the fact that the obtained nanostructures have undergone a certain degree of recrystallization and are thus smoother and less porous than those obtained at smaller overpotentials (Fig. 7, growth pathway “b”).

We have shown in the section “[Comparison Between Theoretical Models and Experimental Data](#)” that the fitting of Pt chronoamperograms to classical models leads to a saturation particle density approximately five orders of magnitude smaller

than the value observed experimentally. The fact that we experimentally observe much more particles and much smaller than predicted by the models points again toward a self-limiting growth mechanism, which prevents primary nanoclusters to grow by atomic incorporation.

Revision of the Nucleation and Growth Mechanism: A Generalized Electrochemical Aggregative Growth Mechanism

In conclusion, the data presented throughout this chapter indicate that metal electrodeposition onto low-energy substrates, such as carbon, proceeds by an Electrochemical Aggregative Growth Mechanism instead of by a classical Volmer-Weber mechanism in which only direct attachment is considered. The proposed mechanism starts with the nucleation of primary nanoclusters that grow until a certain self-limiting growth mechanism stabilizes them at a given size. Then, electrochemical potential-driven surface diffusion of these primary nanoclusters leads to aggregation, which can be interpreted as aggregative-nucleation events. Finally, the degree to which aggregates undergo partial or full coalescence dictates to which extent further growth by direct attachment (or classical island growth) occurs. Figure 9 (top) schematically represents the stages of the proposed mechanism. Its implications on the interpretation of the potentiostatic current transients are shown in Fig. 9 (bottom).

In the first moments after the application of a negative potential, very small primary nanoclusters are formed, randomly distributed over the substrate as shown in Fig. 9.1. These clusters are single crystalline nanoparticles that grow by direct attachment until they reach a metastable size. These size-stabilized primary nanoclusters can diffuse over the carbon surface due to their small size and weak VDW forces between them and the carbon support. Due to particle-particle attractive VDW forces, primary nanoclusters stick together when they hit each other, resulting in aggregative-nucleation events, which give birth to aggregated particles from nanocluster building blocks (Fig. 9.2 and second column of Fig. 7). Silver aggregates (Figs. 9.2a and 7a) are much more compact than platinum ones (Figs. 9.2b, c and 7b, c) because they undergo more and faster recrystallization. Until this stage, new primary nanoclusters and consequently new aggregates are continuously formed on the substrate in both cases, because even under the assumptions of island growth by direct attachment, the diffusion zones of potentially growing nuclei would not have yet covered the whole carbon surface.

An important point here is related to the interpretation of the electrochemical current-time transients. Traditionally, the first decaying part is related to double-layer charging, whereas island nucleation and growth is correlated to hemispherical diffusion to an increasing active surface, leading to an increasing current. We have shown, though, that longer current decays should be of faradic origin, and hence we believe that such $I(t)$ feature reflects the formation of primary nanoclusters that do not grow beyond a given size. This period may be considered an induction time because large aggregates do not grow significantly yet. Such a phenomenon is normally correlated to a prenucleation stage where metal ions are being discharged before nuclei have been formed. However, we believe that such induction time corresponds to a preaggregation or precoalescence stage where primary nanoclusters have already

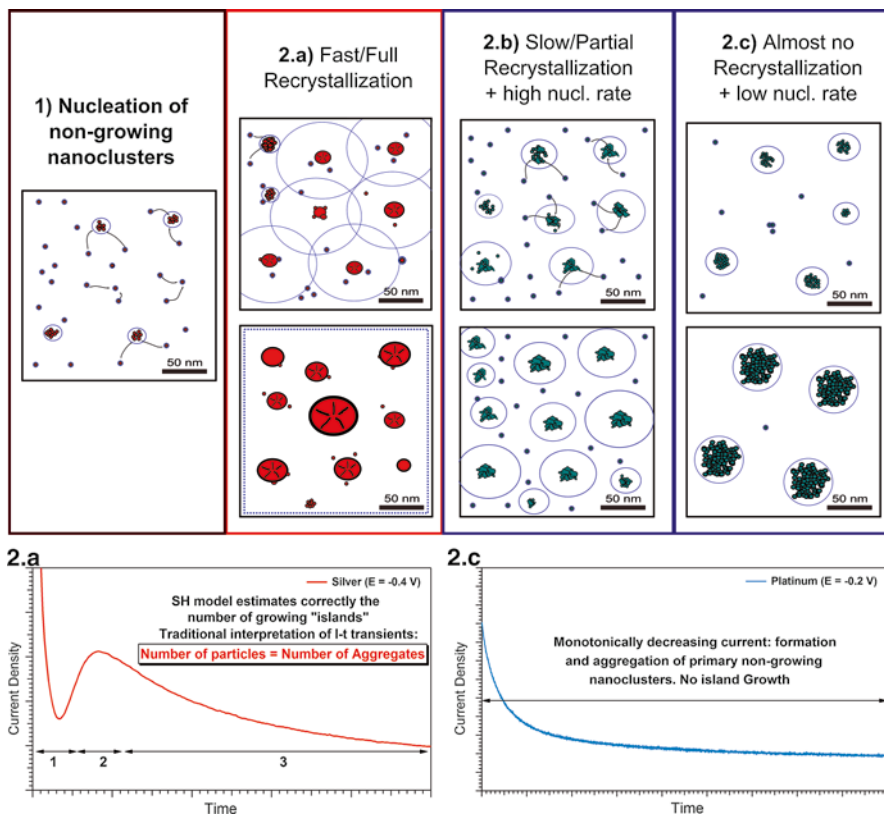


Fig. 9 *TOP*: Schematic diagram showing the different stages of the Generalized Electrochemical Aggregative Growth Mechanism and respective potentiostatic current transients. *Dots* represent the non-growing nanoclusters and *blue circles* around the aggregates represent the projection of their corresponding nucleation exclusion zones. *BOTTOM*: (2.a) Full recrystallization. (1) Induction time: Formation of non-growing primary nanoclusters, (2) Formation of primary nanoclusters + uncoupled "island" growth of completely recrystallized aggregates, (3) Coupled "island" growth of completely recrystallized aggregates. (2.c) Almost no recrystallization. Continuous formation and aggregation of non-growing primary nanoclusters

nucleated but cannot grow over a given size unless they undergo aggregation and recrystallization. Subsequent current rise and maximum are due to the growth of recrystallized aggregates. In fact, the degree to which such aggregates undergo coalescence and recrystallization dictates the subsequent growth pathways.

A first possibility is that the aggregates fully coalesce and recrystallize fast into monocrystalline nanoparticles (Figs. 9.2a and 7a), as it happens for silver electrodeposition. Then, the self-limiting growth mechanism vanishes, and the particles may grow by direct attachment. This is probably the most common case, and it implies that classical island growth concepts apply. Thus, diffusion zones are generated around growing particles until they cover the entire surface and particle number

density reaches saturation at small surface coverage of 1 %, while small primary nanoclusters are consumed. Therefore, a classical interpretation of the potentiostatic current-time transients can be carried out taking into account that the derived nucleation rate corresponds to an “aggregative-nucleation + recrystallization” rate rather than to primary nanocluster formation (Fig. 9.2a).

A second possibility is that aggregates undergo partial recrystallization as it happens for platinum electrodeposition at high overpotentials (Figs. 9.2b and 7b). In this case, classical growth concepts do not apply, as partially recrystallized aggregates behave halfway between traditional islands and nongrowing clusters. This way, small diffusion zones may be generated around growing aggregates, slowing down the nucleation rate of both primary nanoclusters and aggregates. However, the extent to which the particles grow by direct attachment is smaller than in the first case, and hence, diffusion zones do not cover the entire surface until longer deposition times. In this case, particle number density keeps increasing even at high surface coverage. The fact that many aggregates do not grow by atomic incorporation may favor the nucleation of new primary nanoclusters, as discharged atoms may be repelled by nongrowing particles, thus increasing their concentration on the carbon surface. In this case, the shape of the current transients depends on the degree of coalescence and recrystallization and growth by direct attachment.

A third possibility is that recrystallization happens to a very small extent leading to a lower degree of direct attachment (Figs. 9.2c and 7c). In these cases, highly porous dendritic nanostructures are obtained, ever decaying current transients are measured (Fig. 9.2c), and aggregates behave as nongrowing primary nanoclusters, which do not contribute to an increase in reactive surface area.

In conclusion, particle number density, size, and morphology depend on the balance between primary nanocluster nucleation, cluster surface diffusion, cluster aggregation, and coalescence kinetics. So do the obtained potentiostatic current transients and their interpretation.

Conclusions

Although the synthesis of supported nanostructures by electrochemical deposition offers many advantages compared to other synthesis methods, a lack of knowledge of the fundamental aspects of the early stages of electrochemical nucleation and growth had been identified. This book chapter summarizes the research which has been carried out in this field by using CCTGs as electrochemical electrodes, which has allowed to combine electrochemical characterization with structural characterization at the atomic scale.

By the combination of aberration-corrected HAADF-STEM, FESEM, and electrochemical characterization of different electrochemical deposition systems, a reformulation of the Volmer-Weber island growth mechanism for the early stages of metal electrodeposition on low-energy substrates has been provided. A Generalized Electrochemical Aggregative Growth Mechanism has been elaborated, which mimics the atomistic processes of the early stages of thin-film growth by considering

nanoclusters of a few nm as building blocks instead of single atoms. This way, the influence of new processes, such as nanocluster self-limiting growth, surface diffusion, aggregation, and coalescence, on the growth mechanism, morphology of the resulting nanostructures, and interpretation of potentiostatic current transients have been discussed.

This mechanism, apart from being an important scientific breakthrough from the fundamental point of view, is crucial to gain better control of electrochemical deposition processes in order to obtain supported nanostructures with desired morphology and enhanced properties. Besides, it provides exciting possibilities for electrochemical nanostructuring with nanoclusters as building blocks.

Acknowledgments The authors acknowledge the support from the Fonds Wetenschappelijk Onderzoek in Vlaanderen (FWO, contract no. FWOAL527), the Flemish Hercules 3 program for large infrastructure and the Société Française de Bienfaisance et d'Enseignement (S.F.B.E.) de San Sebastian-Donostia (Spain).

References

1. Campelo JM, Luna D, Luque R, Marinas JM, Romero AA (2009) Sustainable preparation of supported metal nanoparticles and their applications in catalysis. *ChemSusChem* 2(1):18–45
2. Yu W, Porosoff MD, Chen JG (2012) Review of pt-based bimetallic catalysis: from model surfaces to supported catalysts. *Chem Rev* 112(11):5780–5817
3. Chen AC, Holt-Hindle P (2010) Platinum-based nanostructured materials: synthesis, properties, and applications. *Chem Rev* 110(6):3767–3804
4. Welch CM, Simm AO, Compton RG (2006) Oxidation of electrodeposited copper on boron doped diamond in acidic solution: manipulating the size of copper nanoparticles using voltammetry. *Electroanalysis* 18(10):965–970
5. Campbell FW, Compton RG (2010) The use of nanoparticles in electroanalysis: an updated review. *Anal Bioanal Chem* 396(1):241–259
6. Rassaei L, Marken F, Sillanpää M, Amiri M, Cirtiu CM, Sillanpää M (2011) Nanoparticles in electrochemical sensors for environmental monitoring. *Trends Anal Chem* 30(11):1704–1715
7. Shipway AN, Katz E, Willner I (2000) Nanoparticle arrays on surfaces for electronic, optical, and sensor applications. *ChemPhysChem* 1(1):18–52
8. Burda C, Chen X, Narayanan R, El-Sayed MA (2005) Chemistry and properties of nanocrystals of different shapes. *Chem Rev* 105(4):1025–1102
9. Cuenya BR (2010) Synthesis and catalytic properties of metal nanoparticles: size, shape, support, composition, and oxidation state effects. *Thin Solid Films* 518(12):3127–3150
10. Murray CB, Sun SH, Gaschler W, Doyle H, Betley TA, Kagan CR (2001) Colloidal synthesis of nanocrystals and nanocrystal superlattices. *IBM J Res Dev* 45(1):47–56
11. Cushing BL, Kolesnichenko VL, O'Connor CJ (2004) Recent advances in the liquid-phase syntheses of inorganic nanoparticles. *Chem Rev* 104(9):3893–3946
12. Xia Y, Xiong Y, Lim B, Skrabalak SE (2009) Shape-controlled synthesis of metal nanocrystals: simple chemistry meets complex physics? *Angew Chem Int Ed Engl* 48(1):60–103
13. Mohanty A, Garg N, Jin R (2010) A universal approach to the synthesis of noble metal nanodendrites and their catalytic properties. *Angew Chem Int Ed Engl* 49(29):4962–4966
14. Narayanan R, El-Sayed MA (2005) Catalysis with transition metal nanoparticles in colloidal solution: nanoparticle shape dependence and stability. *J Phys Chem B* 109(26):12663–12676
15. Lee H, Susan E, Habas SK, Butcher D, Somorjai GA, Yang P (2006) Morphological control of catalytically active platinum nanocrystals. *Angew Chem Int Ed Engl* 45(46):7824–7828. New insights into nano-electrodeposition 25

16. Zhang B, Zhang C, He H, Yu Y, Wang L, Zhang J (2010) Electrochemical synthesis of catalytically active Ru/RuO₂ core-shell nanoparticles without stabilizer. *Chem Mater* 22(13): 4056–4061
17. Maillard F, Schreier S, Hanzlik M (2005) Influence of particle agglomeration on the catalytic activity of carbon-supported Pt nanoparticles in CO monolayer oxidation. *Phys Chem Chem Phys* 7:385–393
18. Tian N, Zhou Z-Y, Sun S-G, Ding Y, Wang ZL (2007) Synthesis of tetrahedral platinum nanocrystals with high-index facets and high electro-oxidation activity. *Science* 316(5825):732–735
19. Day TM, Unwin PR, Macpherson JV (2007) Factors controlling the electrodeposition of metal nanoparticles on pristine single walled carbon nanotubes. *Nano Lett* 7(1):51–57
20. Kibsgaard J, Gorlin Y, Chen Z, Jaramillo TF (2012) Meso-structured platinum thin films: active and stable electrocatalysts for the oxygen reduction reaction. *J Am Chem Soc* 134(18): 7758–7765
21. Paunovic M (2006) *Fundamentals of electrochemical deposition*. Wiley-Interscience, New York
22. Staikov G (2007) *Electrocrystallization in nanotechnology*. Wiley-VCH, Weinheim
23. Becker R, Döring W (1935) Kinetische Behandlung der Keimbildung in über sättigten Dämpfen. *Ann Phys* 416(8):719–752
24. Venables JA, Spiller GDT, Hanbucken M (1984) Nucleation and growth of thin films. *Rep Prog Phys* 47(4):399–459
25. Budevski E, Staikov G, Lorenz W, Keusler K (1997) *Electrochemical phase formation and growth*. Wiley-VCH, Weinheim
26. Scharifker B, Hills G (1983) Theoretical and experimental studies of multiple nucleation. *Electrochim Acta* 28(7):879–889
27. Scharifker BR, Mostany J, Palomar-Pardave M, Gonzalez I (1999) On the theory of the potentiostatic current transient for diffusion-controlled three-dimensional electrocrystallization processes. *J Electrochem Soc* 146(3):1005–1012
28. Hyde ME, Compton RG (2003) A review of the analysis of multiple nucleation with diffusion controlled growth. *J Electroanal Chem* 549:1–12
29. Milchev A, Heerman L (2003) Electrochemical nucleation and growth of nano- and microparticles: some theoretical and experimental aspects. *Electrochim Acta* 48(20–22):2903–2913
30. Milchev A (2008) Electrocrystallization: nucleation and growth of nano-clusters on solid surfaces. *Russ J Electrochem* 44(6):619–645
31. Scharifker BR, Mostany J (1984) 3-dimensional nucleation with diffusion controlled growth. I. Number density of active-sites and nucleation rates per site. *J Electroanal Chem* 177(1–2): 13–23
32. Mirkin MV, Nilov AP (1990) 3-dimensional nucleation and growth under controlled potential. *J Electroanal Chem* 283(1–2):35–51
33. Heerman L, Tarallo A (2000) Electrochemical nucleation with diffusion-limited growth. Properties and analysis of transients. *Electrochem Commun* 2(2):85–89
34. Correia AN, Machado SAS, Avaca LA (2000) Direct observation of overlapping of growth centres in Ni and Co electrocrystallisation using atomic force microscopy. *J Electroanal Chem* 488(2):110–116
35. Milchev A (1998) Electrochemical nucleation on active sites – what do we measure in reality? Part II. *J Electroanal Chem* 457(1–2):47–52
36. Milchev A (1998) Electrochemical nucleation on active sites – what do we measure in reality? Part I. *J Electroanal Chem* 457(1–2):35–46
37. Palomar-Pardave M, Scharifker BR, Arce EM, Romero-Romo M (2005) Nucleation and diffusion-controlled growth of electroactive centers. *Electrochim Acta* 50(24):4736–4745
38. Milchev A (2008) Nucleation and growth of clusters through multi-step electrochemical reactions. *J Electroanal Chem* 612(1):42–46
39. Zapryanova T, Hrussanova A, Milchev A (2007) Nucleation and growth of copper on glassy carbon: studies in extended overpotential interval. *J Electroanal Chem* 600(2):311–317

40. Gonnissen D, Simons W, Hubin A (1997) Study of the initial stages of silver electrocrystallisation from silver thiosulphate complexes. 2. Analysis of current transients. *J Electroanal Chem* 435(1–2):149–155
41. Zoval JV, Stiger RM, Biernacki PR, Penner RM (1996) Electrochemical deposition of silver nanocrystallites on the atomically smooth graphite basal plane. *J Phys Chem* 100(2):837–844
42. Gloaguen F, Leger JM, Lamy C, Marmann A, Stimming U, Vogel R (1999) Platinum electrodeposition on graphite: electrochemical study and STM imaging. *Electrochim Acta* 44:1805–1816
43. Ji C, Oskam G, Searson PC (2001) Electrochemical nucleation and growth of copper on Si(111). *Surf Sci* 492(1–2):115–124
44. Oskam G, Searson PC (2000) Electrochemistry of gold deposition on n-Si(100). *J Electrochem Soc* 147(6):2199
45. Jacobs JWM (1988) Note on a theory of three-dimensional nucleation with diffusion-controlled electrochemical growth. *J Electroanal Chem* 247:135–144
46. Radisic A, Vereecken PM, Hannon JB, Searson PC, Ross FM (2006) Quantifying electrochemical nucleation and growth of nanoscale clusters using real-time kinetic data. *Nano Lett* 6(2):238–242
47. Williamson MJ, Tromp RM, Vereecken PM, Hull R, Ross FM (2003) Dynamic microscopy of nanoscale cluster growth at the solid–liquid interface. *Nat Mater* 2(8):532–536
48. Radisic A, Ross FM, Searson PC (2006) In situ study of the growth kinetics of individual island electrodeposition of copper. *J Phys Chem B* 110(15):7862–7868
49. Radisic A, Vereecken PM, Searson PC, Ross FM (2006) The morphology and nucleation kinetics of copper islands during electrodeposition. *Surf Sci* 600(9):1817–1826
50. Serruya A, Scharifker BR, Gonzalez I, Oropeza MT, Palomar Pardave M (1996) Silver electrocrystallization from a nonpolluting aqueous leaching solution containing ammonia and chloride. *J Appl Electrochem* 26(4):451–457
51. Stiger RM, Gorer S, Craft B, Penner RM (1999) Investigations of electrochemical silver nanocrystal growth on hydrogen-terminated silicon(100). *Langmuir* 15(3):790–798
52. Radisic A, Long JG, Hoffmann PM, Searson PC (2001) Nucleation and growth of copper on TiN from pyrophosphate solution. *J Electrochem Soc* 148(1):C41
53. Abyaneh MY (1982) Calculation of overlap for nucleation and three-dimensional growth of centres. *Electrochim Acta* 27(9):1329–1334
54. Komsijska L, Staikov G (2008) Electrocrystallization of Au nanoparticles on glassy carbon from HClO₄ solution containing [AuCl₄][−]. *Electrochim Acta* 54(2):168–172
55. Serruya A, Mostany J, Scharifker BR (1999) The kinetics of mercury nucleation from Hg₂²⁺ and Hg²⁺ solutions on vitreous carbon electrodes. *J Electroanal Chem* 464:39–47
56. Rezaei M, Tabaian SH, Haghshenas DF (2013) Electrochemical nucleation of palladium on graphene: a kinetic study with an emphasis on hydrogen co-reduction. *Electrochim Acta* 87:381–387
57. Ustarroz J, Gupta U, Hubin A, Bals S, Terryn H (2010) Electrodeposition of Ag nanoparticles onto carbon coated TEM grids: a direct approach to study early stages of nucleation. *Electrochem Commun* 12(12):1706–1709
58. Ustarroz J, Ke X, Hubin A, Bals S, Terryn H (2012) New insights into the early stages of nanoparticle electrodeposition. *J Phys Chem C* 116(3):2322–2329
59. Ustarroz J (2013) New insights into nanoparticle electrodeposition: an electrochemical aggregative growth mechanism. PhD thesis, Vrije Universiteit Brussel
60. Ustarroz J, Altantzis T, Hammons JA, Hubin A, Bals S, Terryn H (2014) The role of nanocluster aggregation, coalescence, and recrystallization in the electrochemical deposition of platinum nanostructures. *Chem Mater* 26(7):2396–2406
61. Lim B, Kobayashi H, Camargo PHC, Allard LF, Liu J, Xia Y (2010) New insights into the growth mechanism and surface structure of palladium nanocrystals. *Nano Res* 3(3):180–188
62. Asoro MA, Kovar D, Shao-Horn Y, Allard LF, Ferreira PJ (2010) Coalescence and sintering of Pt nanoparticles: in situ observation by aberration-corrected HAADF STEM. *Nanotechnology* 21(2):025701

63. Zheng HM, Smith RK, Jun YW, Kisielowski C, Dahmen U, Alivisatos AP (2009) Observation of single colloidal platinum nanocrystal growth trajectories. *Science* 324(5932):1309–1312
64. Zhang ZY, Lagally MG (1997) Atomistic processes in the early stages of thin-film growth. *Science* 276(5311):377–383
65. Ustarroz J, Hammons JA, Altantzis T, Hubin A, Bals S, Terryn H (2013) A generalized electrochemical aggregative growth mechanism. *J Am Chem Soc* 135:11550–11561
66. Guo L, Oskam G, Radisic A, Hoffmann PM, Searson PC (2011) Island growth in electrodeposition. *J Phys D Appl Phys* 44(44):443001
67. Murray CB (2009) Watching nanocrystals grow. *Science* 324(5932):1276–1277
68. Colliex C (2012) Watching solution growth of nanoparticles in graphene cells. *Science* 336(6077):44–45
69. Yuk JM, Park J, Ercius P, Kim K, Hellebusch DJ, Crommie MF, Lee JY, Zettl A, Paul Alivisatos A (2012) High-resolution EM of colloidal nanocrystal growth using graphene liquid cells. *Science* 336(6077):61–64
70. Niederberger M, Cölfen H (2006) Oriented attachment and mesocrystals: nonclassical crystallization mechanisms based on nanoparticle assembly. *Phys Chem Chem Phys* 8(28):3271–3287
71. Shields SP, Richards VN, Buhro WE (2010) Nucleation control of size and dispersity in aggregative nanoparticle growth. A study of the coarsening kinetics of thiolate-capped gold nanocrystals. *Chem Mater* 22(10):3212–3225
72. Xu J, Wilson AR, Rathmell AR, Howe J, Chi M, Wiley BJ (2011) Synthesis and catalytic properties of Au-Pd nanoflowers. *ACS Nano* 5(8):6119–6127
73. Allongue P, Souteyrand E (1990) Metal electrodeposition on semiconductors: Part I. Comparison with glassy carbon in the case of platinum deposition. *J Electroanal Chem* 286:217–237
74. Plyasova LM, Molina IY, Gavrilov AN, Cherepanova SV, Cherstiouk OV, Rudina NA, Savinova ER, Tsirlina GA (2006) Electrodeposited platinum revisited: tuning nanostructure via the deposition potential. *Electrochim Acta* 51(21):4477–4488
75. Richards VN, Shields SP, Buhro WE (2011) Nucleation control in the aggregative growth of bismuth nanocrystals. *Chem Mater* 23(2):137–144
76. Njoki PN, Luo J, Kamundi MM, Lim S, Zhong CJ (2010) Aggregative growth in the size-controlled growth of monodispersed gold nanoparticles. *Langmuir* 26(16):13622–13629
77. Liu H, Penner RM (2000) Size-selective electrodeposition of mesoscale metal particles in the uncoupled limit. *J Phys Chem B* 104(39):9131–9139

Recent Advances in Synthesis, Modification, and Applications of TiO₂ Nanotube Arrays by Electrochemical Anodization

44

Jiaying Huang, Keqin Zhang, and Yuekun Lai

Contents

Introduction.....	1380
Electrochemical Anodization of TNAs.....	1384
Effects of Fabrication Factors on TNAs	1384
Growth Mechanism of Anodized TNAs	1388
Modification of TNA	1389
Doping.....	1390
Semiconductor Composites	1391
Noble Metal Nanoparticle Decoration	1391
Other Aspects.....	1393
Applications of TNA Materials.....	1393
Photocatalyst.....	1393
Solar Cells.....	1395
Water Splitting	1397
Biomedical Scaffold.....	1401
Wetting Template	1404
Other Applications.....	1406
Conclusion	1406
References.....	1407

J. Huang • K. Zhang

National Engineering Laboratory for Modern Silk, College of Textile and Clothing Engineering, Soochow University, Suzhou, People's Republic of China
e-mail: [jyhuang81@suda.edu.cn](mailto: jyhuang81@suda.edu.cn); [kqzhang@suda.edu.cn](mailto: kqzhang@suda.edu.cn)

Y. Lai (✉)

National Engineering Laboratory for Modern Silk, College of Textile and Clothing Engineering, Soochow University, Suzhou, People's Republic of China

Physikalisches Institute and Center for Nanotechnology (CeNTech),
Westfälische Wilhelms-Universität Münster, Münster, Germany
e-mail: [yklai@suda.edu.cn](mailto: yklai@suda.edu.cn); [yklai80@gmail.com](mailto: yklai80@gmail.com)

© Springer International Publishing Switzerland 2016

M. Aliofkhaezrai, A.S.H. Makhlof (eds.), *Handbook of Nanoelectrochemistry*,
DOI 10.1007/978-3-319-15266-0_17

1379

Abstract

Titania nanotube arrays (TNAs) as one of the hottest metal oxide nanomaterials has a unique one-dimensional highly ordered array structure, good mechanical and chemical stability, as well as excellent anticorrosion, biocompatible, and photocatalytic performance. It has been controllably synthesized by a simple electrochemical anodic oxidation in electrolytes containing small amounts of fluorine ions. In combination with our last research work, in this chapter, we review the recent advances of the new research achievements of TNAs on the preparation techniques, formation mechanism, and modification. In addition, we will review the potential and significant applications in the photocatalytic pollutant degradation, solar cells, hydrogen generation, biomedical implant, wetting template, and other aspects. Finally, the existing problems and further prospects of this renaissance and rapidly developing field are also briefly addressed and discussed.

Keywords

TiO₂ • Nanotube • Electrochemical Anodization • Photocatalyst • Solar Cells • Water Splitting • Biomedical Scaffold • Wetting Template

Introduction

Nanostructured materials with peculiar properties are not expected in bulk phase and have already led to a breakthrough in various fields of science and technology. Moreover, much of the current interest in one-dimensional (1D) nanostructures, such as nanotube, nanowire, nanorod, and nanobelts, initiated by the discovery of carbon nanotubes by Iijima in 1991 [1], the intensive researches of TiO₂-based nanotubes, therefore, attracted extensive and engrossing interest due to their merits of high specific surface area, ion-changeable ability, and photocatalytic ability. Over the past decades, nanostructured materials derived from TiO₂ have extensively been investigated for many promising applications, including solar cells/batteries, self-cleaning coatings, electroluminescent hybrid devices, and photocatalysis, owing to their peculiar chemical and physical behaviors. Currently developed methods of fabricating 1D TiO₂-based nanotubes comprise the assisted-template method [2, 3], hydrothermal treatment [4–6], and electrochemical anodic oxidation [7–10]. Detailed features description of each fabrication method is given in Table 1. Regarding the template-assisted method, high-quality anodic aluminum oxide (AAO) nanoporous membrane, which consists of an array of parallel straight nanopores with controllable diameter and length, is usually used as template. However, the template-assisted method usually encounters difficulties of prefabrication and post-removal of the previous templates and often results in impurities. Concerning hydrothermal treatment, the self-assembled TiO₂ nanotubes are based on the treatment of Ti foils or TiO₂ powders in a tightly closed vessel containing high concentrated alkaline solution (e.g., 5–10 M NaOH) to obtain TiO₂ nanotube layer or dispersed TiO₂-based nanoparticles [6, 11]. For comparison, electrochemical

Table 1 Comparison of typical TiO₂ nanotube synthesis method

Synthesis method	Resources and reagent	Crystal structure	Distribution	Main factor	Advantage and disadvantage	Ref.
Template-assisted methodological	AAO template and precursor solution	Amorphous, crystalline	Well order and vertically aligned	Temperature, concentration, pH, time	Difficulties of prefabrication and post-removal of templates and often results in impurities	[2, 3]
Hydrothermal synthesis	Metallic Ti, TiO ₂ nanoparticle powder, precursor solution, and alkaline solution	Titanate, anatase	Random distribution	Temperature, time, pressure	Vessel containing high concentrated alkaline solution and required high pressure	[4-6]
Electrochemical anodization	Metallic Ti, vacuum-sputter Ti film on conducting glass and F ⁻ ions containing electrolyte	Amorphous, anatase (higher anodizing voltage)	Well order and vertically aligned	Electrolyte, potential, water content, time	Relatively simple and efficient process to fabricate robust, pure TiO ₂ nanotubes	[7-10]

anodization is a relatively simple and efficient process to fabricate robust, vertically aligned, and highly ordered TiO₂ nanotube arrays. The demonstrated architecture of TiO₂ nanotube arrays (TNAs) by a facile electrochemical anodizing process is capable of an ordered alignment with high aspect ratio and establishment of pure-phase TiO₂ structure in one step under ambient environment. More importantly, the electrochemical anodization technique allows the growth of other oxides with self-ordering nanostructures for several transitional and valve metals, such as Ti, Al, Zr, Nb, V, Hf, Ta, W, and Fe, and their corresponding alloys, TiAl, TiZr, TiNb, Ti6Al4V, and so on [8, 10].

The self-ordered TiO₂ nanostructures were firstly reported in 1999 by Zwilling et al. by a simple electrochemical anodizing process in a fluoride electrolyte [12]. Since then, several anodizing approaches, mainly focused on finding the optimal electrolyte and experimental parameters, have been explored to efficiently achieve high-quality self-organized TNAs (Fig. 1) [13–18], such as short and rough TNAs [13], tapered and conical-shaped TNAs [18], smooth and high-aspect-ratio TNAs [16, 17], transparent TNAs [19, 20], free-standing and open-ended TNAs [21, 22], highly ordered TNAs by multistep anodization [23, 24], and TNAs with a sub-micrometer size in diameter [25, 26]. These results demonstrated that structure and morphology of TNAs, including tube diameter, length, wall thickness, and crystallinity, can be controlled by adjusting key parameters such as composition/shape of Ti substrate, electrolyte, pH, temperature, anodization voltage, current, and anodization time. It is, therefore, essential to understand the various factors influencing the characterizations of as-prepared amorphous TNAs. Also, it should be noted that either the annealing posttreatment or the modification of TiO₂-based nanotubes would dominate the corresponding features and the performance of TiO₂-based devices. The aim is to make the material more suitable for various applications that rely on specific electrical, optical, or chemical properties. In view of electronic properties, annealing to a crystalline structure mainly changes the conductivity and lifetime of charge carriers, while modification with active doping or band gap engineering by introducing other elements targets decreasing the optical band gap, thus enabling a visible light photoresponse [27].

Based on extensive literatures with regard to self-ordered TNAs, the authors have categorized three broad groups, preparation and formation mechanism, modifications, and applications, which are further subdivided according to their pertinent studies. First, the formation mechanisms and phenomenon of the electrochemical formation of nanopores and nanotubes by a self-ordering process are explained. Among the aforementioned experimental parameters, both electrolyte and anodizing voltage will be focused on and discussed. Then the properties and modification of the TNA materials are addressed briefly, including technique examples of doping, noble metal decoration, and semiconductor composite which are to be discussed. Finally, the current stage of knowledge and recent studies on their potential applications, such as photocatalysis, solar cell, water splitting, biomedical scaffold, etc, are introduced. The analysis of the physicochemical properties and recent advances in their modification and applications allow the identification of gaps in our knowledge and highlight the need for critical studies in the area of TNAs.

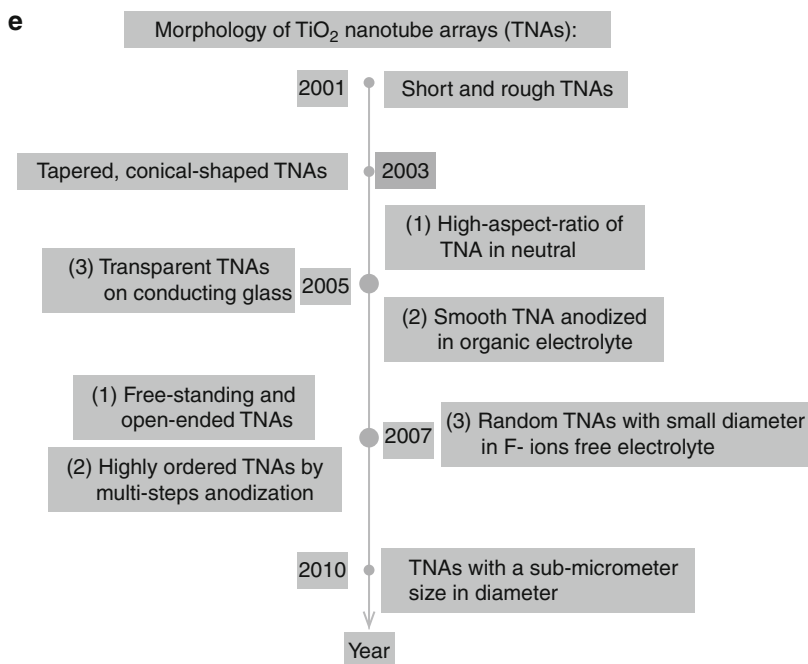
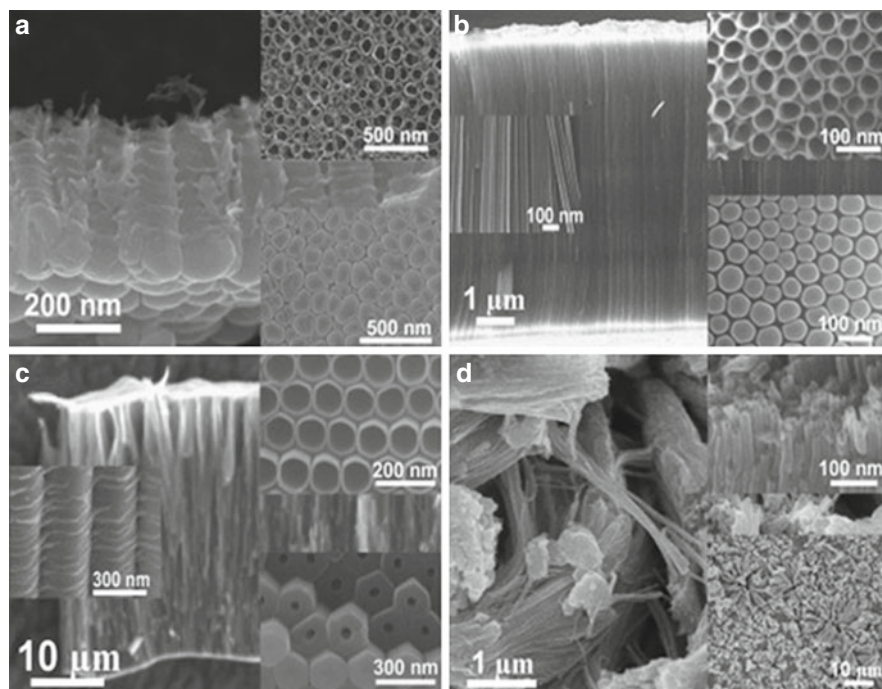


Fig. 1 SEM images of TNA layers grown with different electrolytes. (a) Typical morphology obtained in acidic fluoride or HF electrolytes, (b) glycerol/fluoride electrolytes, (c) ethylene glycol/fluoride electrolytes containing small amount of water. The *insets* show top views, bottom views, and side walls in detail. (d) Fluoride ions free electrolyte; these tubes grow in disordered bundles within seconds at comparably high anodic potentials. (e) Morphology of new type of TNAs with time

Electrochemical Anodization of TNAs

This section presents recent developments on the preparation of self-ordered nanoporous and nanotubular, focusing primarily on TNAs by electrochemical synthesis. First, the related statistics of the manuscript about TNAs and the phenomenon of the electrochemical formation of nanoporous TiO_2 materials by a self-organization process are introduced. Then some experimental parameters of synthesis, which are responsible for regulation of the morphology of TiO_2 nanostructures, are considered. Finally, the formation mechanisms of TNA materials fabricated by electrochemical anodization are presented.

The progressively increasing research interest in the TNA layers formed by electrochemical oxidation can be easily seen from publication statistics (see Fig. 2). Publication number and corresponding aggregated citations increased several times from the first work by Zwilling et al. [12], where only a tube length of a few hundred nanometers with a rough and high degree of disorder morphology could be obtained, to nowadays, where smooth and almost ideally hexagonally ordered arrays can be produced with individual nanotube lengths of hundreds of micrometers [22]. In other words, by controlling the electrochemical anodization parameters of Ti (temperature, potential ramping speed, applied potential, electrolyte species, electrolyte pH, viscosity, aqueous or organic electrolyte, etc.), one can obtain different titanium oxide structures such as a flat compact oxide, a disordered porous layer, a highly self-organized porous layer, or finally a highly self-organized nanotube layer (schematically shown in Fig. 3a).

Effects of Fabrication Factors on TNAs

Electrolyte

Hydrofluoric acid (HF) is the first and most widely studied electrolyte in titanium anodization to produce TiO_2 nanostructures. Since then, several optimized electrolytes of diverse acid/HF mixed electrolytes are put forward to successful fabrication of TiO_2 nanostructures [14]. A brief summary of various synthesis generations of TNAs is given in Table 2. However, the nanotube length in this first synthesis generation is limited to a few hundred nanometers. This second generation of TNAs was obtained with high aspect ratio, in a neutral type of electrolyte containing fluoride ions, e.g., $\text{Na}_2\text{SO}_4/\text{NaF}$ and $(\text{NH}_4)_2\text{SO}_4/\text{NH}_4\text{F}$ [28, 29]. The reason for the tube length increase is the limited dissolution on the top of nanotubes in the neutral electrolyte. The nanotubes by the above inorganic electrolyte always were accompanied with a rough external structure, i.e., “rings” or “ripples,” due to current oscillations along the anodization process. The third-generation electrolyte, organic electrolytes with additions of fluoride salts, allows construction of smooth and much taller TNAs to the regime of hundreds of micrometers. To date, the highest tube lengths can be up to 1000 μm in organic viscous electrolytes [22]. The pH of the electrolyte and the amount of water greatly influence the morphology, structure, and growth rate of the as-formed TiO_2 nanotube. Recent synthesis development of

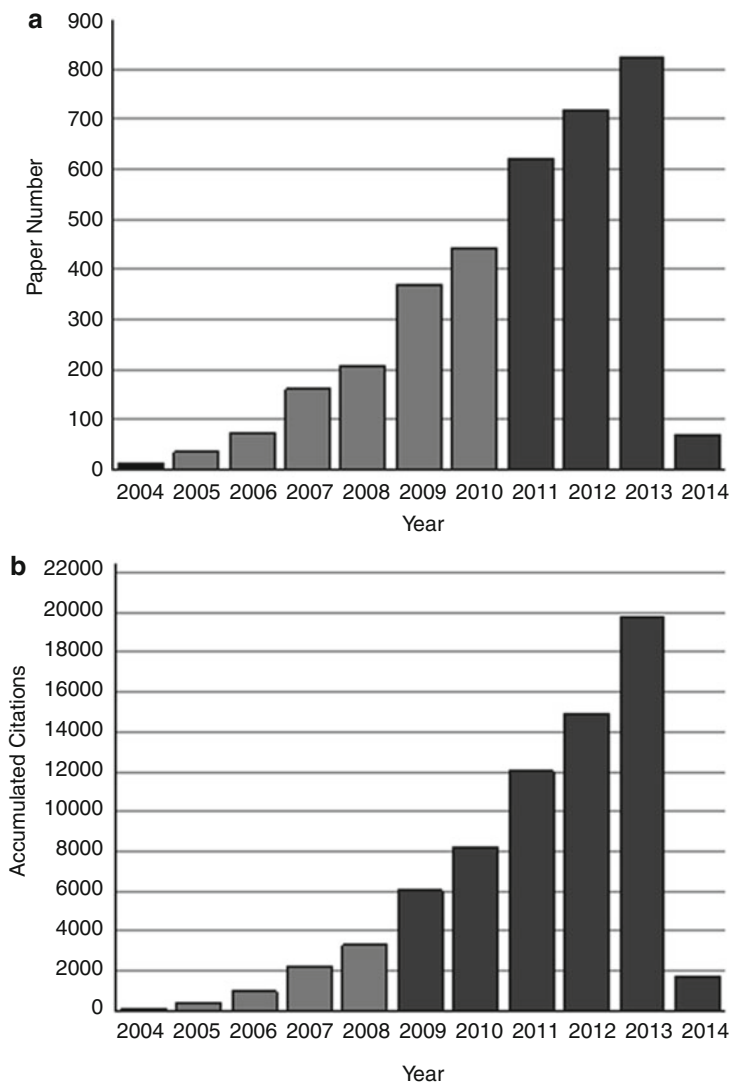


Fig. 2 The number of articles (a) published on the topic of TNAs formed by electrochemical anodization and corresponding aggregated citations (b) in the last decade. (Statistics analysis was obtained from the web of science database on May 30, 2013). Topic: TiO₂ nanotube, with the exclusion of nanotube by hydrothermal, sol-gel, template, or carbon nanotube

TNAs by using fluoride-free electrolytes is commonly considered as the fourth generation. The results of this rapid breakdown anodization (RBA) are also bundles of disordered nanotubes that grow within very short times (several minutes) [30, 31]. Depending on electrolyte nature, each electrolyte provides unique geometrical feature of the nanotubes and consequently varying surface properties; thereby a selection of electrolyte medium for the TNA fabrication is a primary concern.

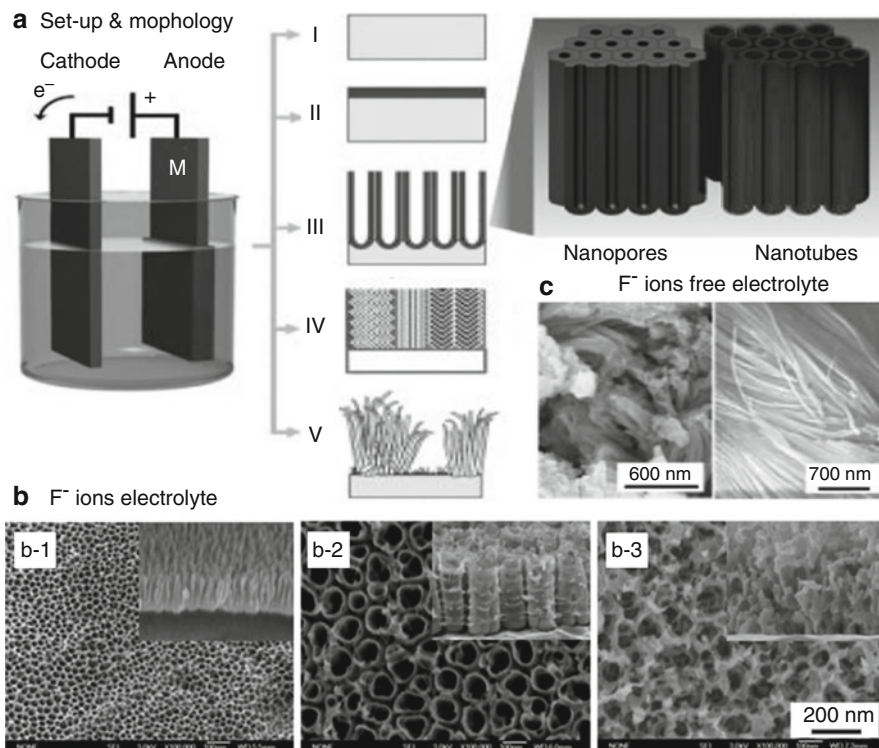


Fig. 3 (a) The electrochemical anodization process and typical morphologies: (I) metal electropolishing, (II) formation of compact anodic oxides, (III) self-ordered oxides (nanotubes or nanopores), (IV) ordered nanoporous layers, (V) rapid (disorganized) oxide nanotube formation. Examples of morphologies of obtained structures: (b) Classical ordered TiO₂ nanopores (b-1), nanotubes (b-2), sponge-like nanoporous structures (b-3) anodized in F⁻ ions containing electrolyte, (c) disordered TiO₂ nanotubes growing in bundles anodized in F⁻ ions free electrolyte

Voltage

The anodization voltage influences the morphology of formed nanostructures [34]: pores instead of tubes grow at low voltages of 5 V (Fig. 3b-1), while at voltages higher than 8 V, the diameter of the TiO₂ nanotubes is also influenced linearly by the applied voltage (Fig. 3b-2). However, at high anodization voltages (>50 V), breakdown events can be observed inside the nanotube resulting in the formation of sponge-like structures (Fig. 3b-3). At even higher anodization voltages (>80 V), electropolishing of the samples would take place at a high current density (>100 mA/cm²) in this electrolyte. Therefore, the retardation of breakdown events taking place is vital for the creation of larger tube diameter. Yin et al. reported TNAs with larger diameter about 600 nm can be obtained in ethylene glycol electrolytes containing 0.09 M ammonium fluoride and 10 vol.% water [35]. Albu and coworkers further increase the tube diameter to reach 800 nm. However, these tubes are not

Table 2 Brief summary of various synthesis generations of TiO₂ nanotubes

Generation	Electrolyte type	Potential	Anodized time	Morphology	Main factor	Ref.
First generation: Inorganic aqueous electrolytes (HF-based electrolyte)	0.5 wt% HF	10–23 V	≥20 min	Short nanotubes Length: 200–500 nm Diameter: 10–100 nm Wall thickness: 13–27 nm	Potential, electrolyte	[13]
	0.3–0.5 wt% HF + 1 M H ₃ PO ₄	1–25 V	2 h	Length: 20–1000 nm Diameter: 15–120 nm Wall thickness: 20 nm		[32]
Second generation: Buffered electrolytes (F ⁻ -based electrolytes)	1 M Na ₂ SO ₄ + 0.1–1.0 wt% NaF	20 V	10 min–6 h	Rough wall with rings Length: 0.5–2.4 μm Diameter: 100 nm Wall thickness: 12 ± 2 nm	Potential, pH, time	[28]
	1 M (NH ₄) ₂ SO ₄ + 0.5 wt% NH ₄ F	20 V	15–30 min	Length: 0.5–1.0 μm Diameter: 90–110 nm		[33]
Third generation: Organic electrolyte containing F ⁻ ions	0.5 wt% NH ₄ F + 0–5 wt% H ₂ O in glycerol	20 V	13 h	Smooth tube Length: 7.0 μm Diameter: ≈40 nm Wall thickness: 12 ± 2 nm	Potential, water content, time	[17]
	0.1–0.7 wt% NH ₄ F + 2–3.5 wt% H ₂ O in ethylene glycol	60 V	216 h	Ultra-long tube Length: 1000 μm Diameter: 120 ± 10 nm		[22]
Fourth generation: Fluoride-free electrolytes	0.01–3 M HClO ₄	1 min	15–60 V	Disordered tubes Length: 30 μm Diameter: 20–40 nm Wall thickness: 10 nm	Electrolyte, time	[30]

highly organized and seem loosely assembled in a mesoporous matrix rather than as a neatly defined nanotube array [26]. Recently, Jin et al. successfully demonstrated well-defined, large diameter (680–750 nm) TNAs, with the most uniform and clean morphology by using a higher voltage regime of up to 225 V [25].

Other Factors

In addition to the vital factor of the electrolyte and voltage to the high aspect ratio of the as-prepared nanotube, anodizing time and step, fluoride concentration, and pH and temperature also have a great synergistic effect on the morphology, structure, growth rate, and even crystallization of the as-prepared TNAs [8, 36–40]. For example, the transition from porous TiO₂ to a nanotubular structure is not only dependent on water content [41, 42] but also depends on the anodization voltage. The applied voltage directly determines the tube diameters but also strongly influences the rate of TNA growth, length, and crystallization.

Growth Mechanism of Anodized TNAs

Self-organized oxide tube arrays or pore arrays can be obtained by an anodization process of a suitable metal, such as transition metal, valve metal, etc. When metals are exposed to a sufficiently anodic voltage in an electrochemical configuration, an oxidation process will be initiated. Depending mainly on the electrolyte and the particular anodization parameters, essentially three possibilities for reactions exist (see illustration of Fig. 3a): (I) the metal is continuously dissolved (metal corrosion, or electropolishing); (II) the metal titanium ions (Mⁿ⁺) formed react with O²⁻ (provided by H₂O in the electrolyte) and form a compact oxide layer; (III) under some electrochemical conditions, competition between dissolution and oxide formation is established leading to porous structures. Under even more specific experimental conditions, a situation is established where self-organized growth of TNAs, formation of thick self-organized mesoporous layers (IV in Fig. 3a), or disordered rapid breakdown anodization (RBA) of nanotube bundles (V in Fig. 3a, c) can be observed [10].

In general, it can be concluded that all investigated organized oxide structures grown by anodization in fluoride-containing electrolytes on different metals or alloys seem to follow the same growth mechanism and influence by key factors [7, 8, 10]. Ti was firstly oxidized to form a thin barrier oxide layer of TiO₂ due to interaction of the metal with O²⁻ or OH⁻ ions. Then, the presence of electric field and fluoride ion led to the creation of random pits and small pores. Finally, self-ordered TNAs formed resulted from the allowance of optimal pores to grow continuously and wall opening by chemical dissolution. The tube diameter is determined by the anodization voltage, etching of the tubes (and thus the achievable length of the tubes) depends on the chemical resistance of the oxide against fluoride etching (in a particular electrolyte), and water plays the key role for providing the oxygen source for tube growth, splits pores into tubes, and is responsible for sidewall rings

formation. Obviously, anodization techniques in fluoride-containing electrolytes allow the fabrication of nanostructured oxide layers on an extremely wide range of valve metals and alloys that enable the controllable fabrication of mixed nanostructured oxides with virtually endless possibilities to create enhanced properties and therefore have also a very high and widely unexplored technological potential.

Modification of TNA

TiO₂ semiconductor material plays the most important role owing to its excellent chemical and physical properties. However, the higher band gap of the annealed TiO₂ between the valence band (VB) and conduction band (CB) makes them inactive under visible irradiation (Fig. 4a). In this regard, great efforts have been made to extend the absorption of the wavelength range into the visible light range via the modification of its electronic and optical properties. Over the past decade, considerable effort has gone into the modification of TiO₂ to exploit the solar spectrum much better. Up until now, several methods and techniques have been proposed to enhance the photoelectrocatalytic activity of TNTs, such as doping, filling, decoration, and others. For example, dye sensitization or doping TiO₂ using either nonmetal anions or metal cations is one of the typical approaches that have been largely applied (Fig. 4b).

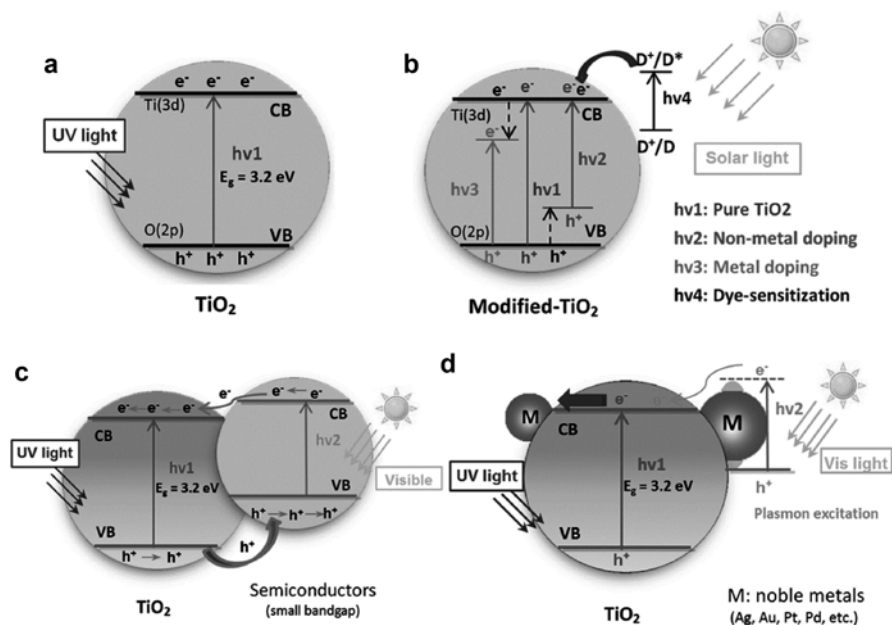


Fig. 4 Schematic energy level of pure TiO₂ (a) and corresponding modification (BD). (b) Doping or dye sensitization; semiconductors (c) and noble metal (d) coupling

Coupling TiO₂ with a narrow band gap semiconductor represents another approach (Fig. 4c). Decoration of noble metal particles with surface plasmon effects allows for more efficient charge transfer (Fig. 4d). In all of these cases, essentially three beneficial effects are expected: (I) promotion of the photogenerated separation between the electron–hole (e⁻/h⁺) and prevention of their recombination; (II) surface plasmon effects, leading to field enhancement in the vicinity of noble metal particles, thus allowing more efficient charge transfer and effective visible light absorption; and (III) heterojunction formation that either changes the band bending (metal clusters on semiconductor) or provides suitable energy levels for synergistic absorption and charge separation for enhanced utilization of solar energy.

Doping

Doping or sensitizing pure TiO₂ by introducing a secondary electronically active species into the lattice for sensitizing TiO₂ to visible light promotes the harness of the main range of the solar spectrum and also ensures the charge traps for effective photogenerated carrier separation (Fig. 4b). Asahi et al. firstly reported the nitrogen doping TiO₂ by sputtering in nitrogen containing gas mixture improves the photoelectrochemical reactivity under visible light irradiation [43]. In the following years, other doping species such as a number of nonmetals like carbon [44], fluorine [45], sulfur [46], and boron [47] have been introduced into TiO₂ by using various techniques, and these nonmetal elements showed positive effects in the visible absorption and higher photoelectrical transfer efficiency. The impurity states are normally near to the valence band edge but do not play the role of charge carriers [48–50]. Among all these anions, the doping of TNAs with nitrogen or carbon has been found to receive significant attention [51–58]. Highly promising N-doping approach for TNAs includes one-step direct electrochemical anodization of a TiN alloy or growing TNAs in a solution containing doping species [58]. High-energy ion implantation or sputtering in an atmosphere of doping species following an annealing process has been verified to be an effective doping method [59, 60]. However, these methods require special high-energy accelerators operated in a high-vacuum environment and the doping depth limited to several micrometers. Thermal treatment of TNAs in gas atmospheres of the doping species is regarded as a facile one-step doping technique [61, 62]. Moreover, such surface-modified nanotubes show a significant photoresponse in the visible range compared to nonmodified nanotubes.

At the same time, TiO₂ doped with transition metal cations (e.g., Fe, V, Cr, and Mn) [63–66] have also been reported to widen visible light absorption range, increase the redox potential of the photogenerated radicals, and enhance the conversion efficiency by extending the life of photogenerated electrons and holes. Although the metal cation doping of TiO₂ improves the visible light absorption of the host material to increase photocatalytic activity, a large amount of research also concluded that when the doping content is excessively high, extra defects can also act as recombination centers to decrease the photocatalytic activity. This adverse effect could be avoided by a suitable doping amount or annealing the doped TiO₂.

Semiconductor Composites

In the past decade, many efforts have been devoted to extend the light absorption range of TNAs and to alleviate the charge carrier recombination, such as the formation of semiconductor heterostructures with visible light excited narrow band gap semiconductors (Fig. 4c), e.g., CdS, CdSe, etc. [67–70]. However, it must be expected that the stability of many applied narrow band gap semiconductors fails quickly, not only due to corrosion or photocorrosion but also due to instability of some of the materials under applied voltage [71].

TNAs essentially provide a very versatile tool to fill or decorate other semiconductors to form composite electrode [72–74]. One of the most followed up schemes to establishing p-n heterojunctions for highly efficient photoelectrocatalytic devices is the direct deposition of p-type semiconductor onto TNAs [75–77]. For example, Lin et al. prepared Cu₂O/TiO₂ p-n heterojunction photoelectrodes by depositing p-type Cu₂O nanoparticles on n-type TiO₂ nanotube arrays via an ultrasonication-assisted sequential chemical bath deposition (Fig. 5a–d) [78]. The largely improved separation of photogenerated electrons and holes was revealed by photocurrent measurements. Consequently, p-n Cu₂O/TiO₂ heterojunction photoelectrodes exhibited a more effective photoconversion capability than single TiO₂ nanotubes (Fig. 5e). Furthermore, Cu₂O/TiO₂ composite photoelectrodes also possessed superior photoelectrocatalytic activity and stability in rhodamine B degradation with a synergistic effect between electricity and visible light irradiation (Fig. 5f–h).

Homogeneous TiO₂ nanoparticle decoration on TiO₂ semiconductor materials can enhance photoelectrocatalytic activity [20, 79, 80]. In DSSCs, the TNAs decorated with TiO₂ nanoparticles show higher solar cell efficiency in comparison to pure TNAs. The TiO₂ nanoparticles can be deposited inside as well as outside of the tube wall by hydrolysis of a TiCl₄ solution, which significantly increases the surface area and thereby improves the solar cell efficiency [81].

Noble Metal Nanoparticle Decoration

Another approach related to TiO₂ modification is the decoration of TiO₂ surfaces with noble metal nanoparticles (such as Ag, Au, Pt, Pd, or alloys) [82–87]. Noble metal loading is proved to be an effective way to restrain the recombination of photogenerated electron–hole pairs resulting in photoelectrocatalytic activity enhancement (Fig. 4d). Moreover, recent study reveals noble metal nanoparticles can improve the photoresponse ability of TiO₂ in the visible region based on the surface plasmon resonance (SPR) [88, 89]. It is known that the free electrons of metal can collectively oscillate, induced by light irradiation when the oscillation frequency of light electromagnetic field is in accordance with the free electrons, the SPR effect generates, and light energy is coupled into the metal nanoparticles in the meantime. For example, Ag nanoparticles can be deposited on the tube wall by a photocatalytically reducing process on a TiO₂ surface with UV illumination [90]. Other metal nanoparticles are preferably deposited by UHV evaporation,

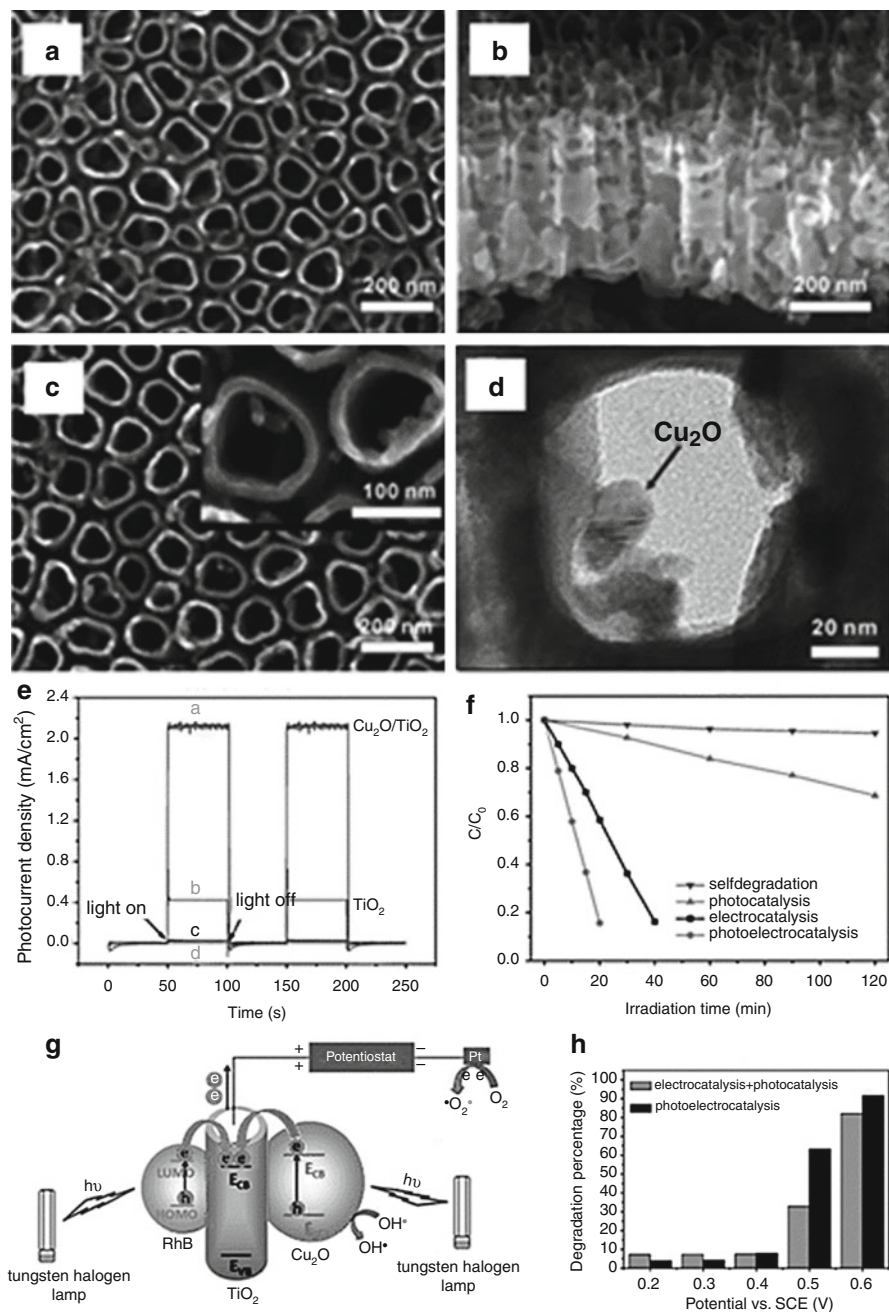


Fig. 5 SEM image of TNAs (a, b) and $\text{Cu}_2\text{O}/\text{TiO}_2$ NTAs (c). TEM image of $\text{Cu}_2\text{O}/\text{TiO}_2$ NTAs (d). (e) Photocurrent response of $\text{Cu}_2\text{O}/\text{TiO}_2$ NTAs (a, c) and TNAs (b, d) with (a, b) or without (c, d) a bias potential of 0.5 V (vs. SCE) under one sun visible light irradiation. (f) Comparison of photocatalytic, electrocatalytic, and photoelectrocatalytic degradation of RhB under visible light irradiation for $\text{Cu}_2\text{O}/\text{TiO}_2$ NTAs. (g) Schematic illustration of photoelectrocatalytic degradation of RhB under visible light irradiation. (h) Comparison of the RhB degradation efficiency using $\text{Cu}_2\text{O}/\text{TiO}_2$ NTAs in the process of photoelectrocatalysis (right) with the sum of photocatalysis and electrolysis (left)

sputtering, or chemical/electrochemical deposition techniques [82, 91]. Pt/TiO₂ or Pd/TiO₂ nanotubes also show a significantly higher photocatalytic activity and water splitting performance compared with plain nanotubes [83, 84].

Other Aspects

More recently work deals with decoration of graphene [92, 93], Ag/AgX (X=Cl, Br, I) [94, 95], other specific functional materials [96–98], or multiple hybrid composites [99–102] onto TiO₂ nanotube arrays to enhance their photocatalytic activity. Amorphous nanotubes synthesized by room-temperature electrochemical anodization are also reported to be annealed in oxygen-rich (O₂), oxygen-deficient (Ar, N), and reducing (H₂) environments, to modify TiO₂ crystal structure, morphology, and electronic properties [103, 104].

Applications of TNA Materials

Porous and tubular titanium dioxide nanostructures have attracted great interest because of their applications in photocatalysis, photovoltaic cells (solar cell), water splitting, biomedical scaffold, wetting template, and other aspects. This porous TiO₂ material is desirable for these applications because of its multifunctional semiconductor properties that are based on its excellent physical and chemical behavior, along with its specific nanostructured architecture that owns it high surface area, high surface activity, and fast carrier transfer path.

Photocatalyst

One of the most practical applications of TiO₂ today is in photocatalytic toxic pollutant decomposing. After Fujishima and Honda reported for the first time on light-induced water electrochemical photolysis on TiO₂ surfaces, this functional semiconductor material has been intensively investigated for applications in heterogeneous catalysis [105]. Since then, TiO₂ has shown to be an excellent photocatalyst due to the fact that the material has a set of good properties of long-term stability, low-cost preparation, and a strong enough oxidizing power to be useful for the decomposition of unwanted organic compounds [106–111].

The basic principles involved in the photocatalytic mechanism are shown in Fig. 6. UV light promotes electrons excited from the valence band to the conduction band, and then separated holes and electrons will transport to the semiconductor–environment interface and react with adsorbed molecules. In aqueous solution, highly reactive •OH radicals are generated by charge exchange at the valence band ($\text{H}_2\text{O} + \text{h}^+ \rightarrow \bullet\text{OH}$), whereas excited electrons at the conduction band mainly reduce dissolved molecular oxygen to superoxide anions ($\text{O}_2 + \text{e}^- \rightarrow \text{O}_2^-$). These •OH radicals and O₂⁻ ions are able to virtually oxidize all organic materials to CO₂ and H₂O.

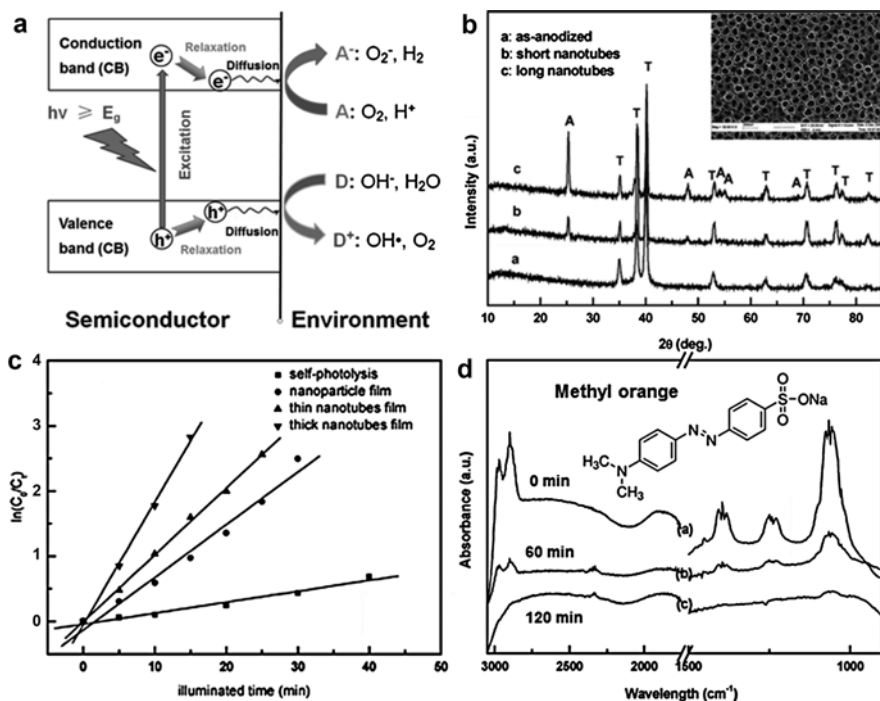


Fig. 6 (a) Scheme of photoinduced processes at a TiO₂ semiconductor/electrolyte interface. Light ($h\nu$) excites valence band electron to conduction band. Electron and hole react with environment acceptor (A) and/or donor (D). (b) XRD patterns of TNA film. (c) Comparison of photocatalytic degradation rates of MO for nanoparticle film and two different thicknesses of nanotube films under the high-pressure mercury lamp illumination. (d) ATR-IR spectra of MO before and after photocatalytic degradation

However, as discussed in previous sections, although TiO₂ has very suitable band edge positions for high photocatalytic activity, the band gap of about 3.2 eV allows only UV light to be efficiently used. In order to achieve maximal decomposition efficiency, in addition to adequate band edge positions, rapid charge separation, and high quantum yield, a large area of the catalyst is desired. TNAs fit these requirements comparably well [106–108, 112]. In previous work, we used anatase TNAs as the photoanode and verified such novel TNAs showed higher efficiencies than common TiO₂ nanoparticle photocatalysts (Fig. 6b–d) [107]. A similar work reported that a pulse current deposition of Ag nanoparticle-modified TNAs was used as the photoanode for photoelectrocatalytic decomposition of methyl orange (MO) pollutant [113]. In this case, we found that photocatalytic activity of titania nanotube layers can be significantly increased by applying an external bias [113]. In addition, Xie et al. performed photocatalytic decomposition of a model organic pollutant (methylene blue) in self-organized TNAs decorated with Ag and CdS nanoparticles.

The CdS–Ag–TiO₂ three-component nanotube array system exhibited superior synergy effect on both photoelectrochemical and photocatalytic activities to those of the pure TiO₂ and Ag or CdS-modified TiO₂ systems [114].

Solar Cells

One of the most promising applications of TiO₂ today is in dye-sensitized solar cells (DSSCs), a concept introduced by Grätzel and coworkers in 1991 [115]. The classical DSSCs operate with sintered or compressed nanoparticulate TiO₂ layers as electron harvesting material. Compared to agglomerate TiO₂ nanoparticle layer containing a high number of grain boundaries that can act as recombination sites, the new architecture of TNAs by electrochemical anodization has been verified to be an ideal photoanode in photoelectrocatalytic devices due to its improved charge-collection efficiency and short pathway for the photogenerated excitons along the vertically aligned tubes to the conducting substrate. As such, it may be expected that optimized TNAs can significantly increase the solar energy conversion efficiency.

Dye-Sensitized Solar Cells (DSSCs)

Owing to well-defined structural parameters and enhanced electronic properties, highly ordered TNAs have been employed to substitute TiO₂ nanoparticles for use in DSSCs [116]. Mor et al. reported the integration of TiO₂ nanoparticles modified transparent nanotube array (360 nm in length) architecture on fluorine-doped tin oxide (FTO) glass for front-side illuminated dye solar cell and displayed a photo-conversion efficiency (PCE) of 2.9 % (Fig. 7a) [20]. They also observed that solar cells constructed by longer nanotubes formed from titanium foils (back-side illumination) have superior charge transfer efficiency and more dye absorption in comparison with solar cells fabricated with transparent short nanotubes formed on FTO glass. However, the overall power conversion efficiency of dye-sensitized TNA solar cells remained relatively low as a result of incomplete coverage of dye molecules on the TNAs and insufficient infiltration of electrolyte into nanotubes. For example, back-side illuminated N719 DSSC based on 6 μm long TNA film on titanium substrate shows a PCE of 4.24 % under AM 1.5 sunlight source (Fig. 7b) [117]. To further improve the performance of dye-sensitized TNA solar cells, efforts have been directed toward the improvement of dye loading, charge transport, light absorption, and optimization of TiO₂ nanostructures [81, 118–122]. Recently, Misra and coworkers applied double-sided TNAs for bifacial dye-sensitized solar cells and reported that a photocurrent density of such bifacial DSSCs was almost twice that of one-sided illumination (Fig. 7c) [119]. Sun et al. demonstrated a new parallel configuration of DSSCs using double-sided TNAs as the photoanode and a dielectric mirror for sunlight to irradiate on both sides of TNA photoanode (Fig. 7d) [123]. An average 70 % increment in photocurrent and 30 % enhancement in PCE were obtained relative to those of the single cells. Zheng et al. constructed a layer-by-layer hierarchical photoanode consisting of TiO₂ particles and free-standing

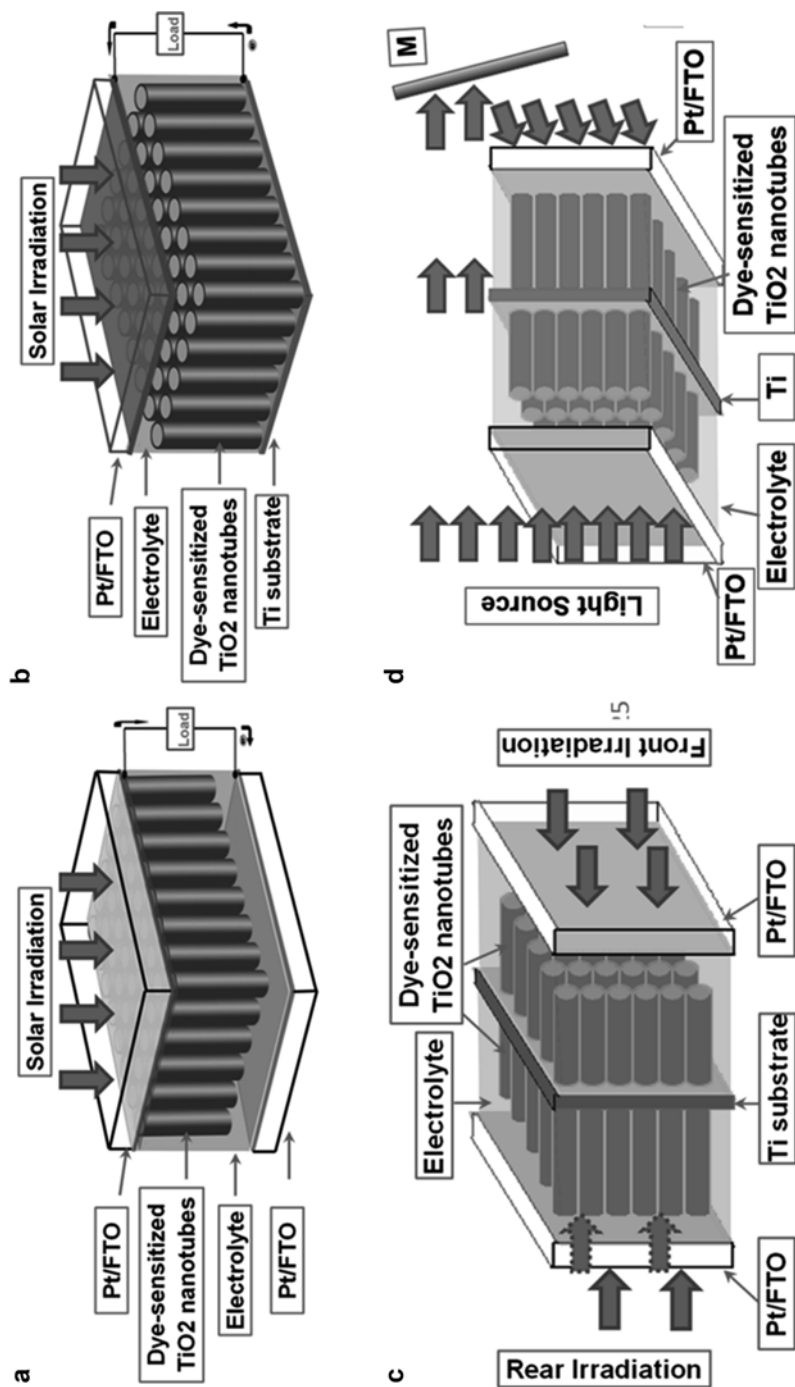


Fig. 7 Schematic illustration of front-side illuminated DSSC based on transparent TNAs on Ti substrate (a); back-side illuminated DSSC based on TNAs on Ti substrate (b); two light sources illuminated DSSC based on both sides of TNAs on Ti substrate (c); parallel configuration DSSC with one light source irradiation on double-sided TNAs by using a dielectric mirror (d)

TNAs for DSSCs with a PCE of 8.80 %, which exhibited increased light-harvesting efficiency, longer electron lifetimes, and more efficient electron extraction than those in single particle film or nanotube array-based devices [124].

Quantum Dot-Sensitized Solar Cells (QDSSCs)

Typically, CdX (X = S, Se, and Te) QDs with size-dependent band gaps provide new opportunities for harvesting light energy in the visible and infrared regions of solar light [125]. In addition, through the impact ionization effect, it is possible to generate multiple excitons from single-photon absorption in QDs [126]. In the case of the QDSSCs, excited electrons of CdX nanocrystals are injected into a large band gap semiconductor (e.g., TiO₂ and ZnO), and holes are reacted with a redox couple. Recently, Kang and coworkers prepared the CdS/CdSe coupled TiO₂ nanofibrous electrode with a maximum PCE of 2.69 % [127], while Shen et al. fabricated a CdSe QD-sensitized TNA photoelectrode with an optimal photovoltaic conversion efficiency of 1.80 % [128]. Recently, we report that a PCE of 2.74 % is achieved on a novel QDSSCs based on the CdS/CdSe QD co-sensitized TiO₂ nanocrystal arrays by a sealed annealing process (Fig. 8) [67]. We found that such coupled CdS/CdSe QDSSC exhibited a greatly enhanced short-circuit current density (Fig. 8e) as compared to pure TNAs and single CdS or CdSe QDSSC because the combination of CdS and CdSe QDs has a complementary effect in light harvest, surface area increment, and a stepwise band edge level structure of CdSe/CdS@TNAs benefited for electron injection into TNAs. Peng et al. reported a novel CdS QD-sensitized TNA photoelectrode by a sequential chemical bath deposition technique and found that the CdS QDs among the TNAs significantly increased the QDSSC efficiency up to 4.15 % [129]. These results clearly demonstrate that the unique nanotube structure can facilitate the propagation and kinetic separation of photogenerated charges, suggesting potentially important applications of the inorganic TNA QDSSCs in solar cell applications. However, compared to DSSCs with PCE up to 12 %, QDSSCs have not been demonstrated as an efficient inorganic dye than expected. Therefore, great efforts are still needed to inhibit charge recombination at the semiconductor surface for the efficiency improvement of QDSSCs [130].

Water Splitting

Considering that the principle of photoelectrolysis for water splitting is the same with photocatalysis, TNAs are considered as good candidates for high-efficient water splitting (see Table 3). The photoelectrolysis process using TiO₂ nanotube-fabricated cells as a photoanode is as follows: when the photoanode is immersed in water and exposed to light irradiation, it absorbs photonic energy over its band gap energy, and then electron-hole pairs are generated in it. The generated holes oxidize O²⁻ ions from absorbed water and produce oxygen gas and an electric current that moves through the external circuit to the conducting cathode in which it reduces H⁺ ions to produce hydrogen gas. Recently, TNAs prepared by anodization of titanium have attracted extensive interest in photocatalytic water splitting. Grimes et al. find

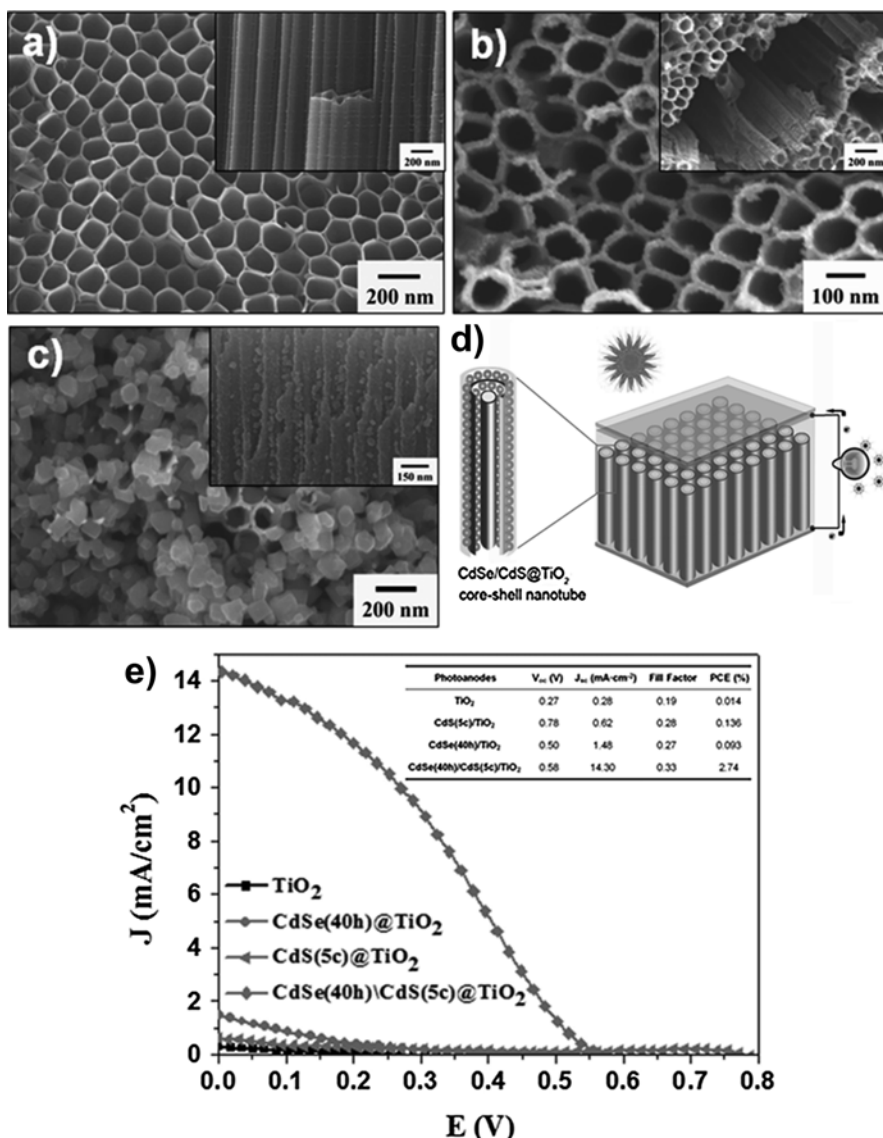


Fig. 8 Top view and cross-sectional SEM images of TNAs (a); CdS@TNAs (b); CdSe/CdS@TNAs (c). (d) Schematic of CdSe/CdS@TNAs for QDSSCs. (e) J-V characteristics of corresponding QDSSCs

a hydrogen generation rate of 96 $\mu\text{mol/h/cm}^2$ for the utilization of nanotube array (224 nm in length) for water splitting under a constant voltage bias of -0.4 V (vs. Ag/AgCl) [131]. Recently, we reported an enhanced hydrogen generation rate of 150 $\mu\text{mol/h/cm}^2$ by a three-step electrochemical anodized TNAs with a regular porous top layer (Fig. 9a, b) [132]. Moreover, we found that palladium quantum

Table 3 Summary of TNA-based materials in water splitting

Photoanode	Light intensity (mW/cm ²)	Electrolyte	Photocurrent (mA/cm ²)	Water splitting (μmol/h/cm ²)	Ref.
C-TNTs	N/A; 500 W Xe lamp	0.1 M Na ₂ S and 0.02 M Na ₂ SO ₃	N/A	1.6 (0.040 mL/h/cm ²)	[135]
TNT	70; 300 W Xe lamp	1 M KOH	0.58@0.6 V vs. NHE	7.1 (0.178 mL/h/cm ²)	[136]
C-TNT (C-containing TiO ₂ -based nanotube arrays)	12.7, 300 W Xe Lamp	1 M KOH	1.96@0 V vs. Ag/AgCl	11.28 (0.282 mL/h/cm ²)	[137]
TiO ₂ nanotubes with an etching pretreating	87, 300 W AM 1.5	1 M KOH	1.78@1.23 V RHE	(0.87 mL/h/cm ²)	[138]
Ru/TiO ₂ nanotube@0.05 at.% Ru	100	1 M KOH	1.78@0.4 V vs. Ag/AgCl	45 (1.08 mL/h/cm ²)	[139]
TiO ₂ nanotubes (224 nm length, 34 nm wall thickness)	100	1 M KOH	13.0@0 V vs. Ag/AgCl	96 (2.30 mL/h/cm ²)	[131]
TiO ₂ nanotubes	110	1 M KOH and 0.5 M H ₂ SO ₄ electrolytes	4.95	97 (2.32 mL/h/cm ²)	[140]
TiO ₂ nanotubes	74	1 M KOH	N/A	140 (3.28 mL/h/cm ²)	[141]
Leaflike TiO ₂ /TiO ₂ nanotubes	320	2 M Na ₂ CO ₃ +0.5 M ethylene glycol	16.3@0.9 V vs. SCE	150 (3.39 mL/h/cm ²)@-0.3 V vs. SCE	[132]
<i>Pyrococcus furiosus</i> /TiO ₂ nanotubes	74	1 M KOH	N/A	234.88@1.5 V vs. Ag/AgCl	[142]
TiO ₂ nanotubes	74	1 M KOH	32.8@1.5 V vs. Ag/AgCl	250	[143]
TiO ₂ nanotubes (three-step anodization)	320	2 M Na ₂ CO ₃ +0.5 M ethylene glycol	24@-0.3 V vs. SCE	420	[144]
Pt@TiO ₂ nanotubes	320	2 M Na ₂ CO ₃ +0.5 M ethylene glycol	24.2@-0.3 V vs. SCE	495	[84]
Pd@TiO ₂ nanotubes	320	2 M Na ₂ CO ₃ +0.5 M ethylene glycol	26.8@0.9 V vs. SCE	592	[83]

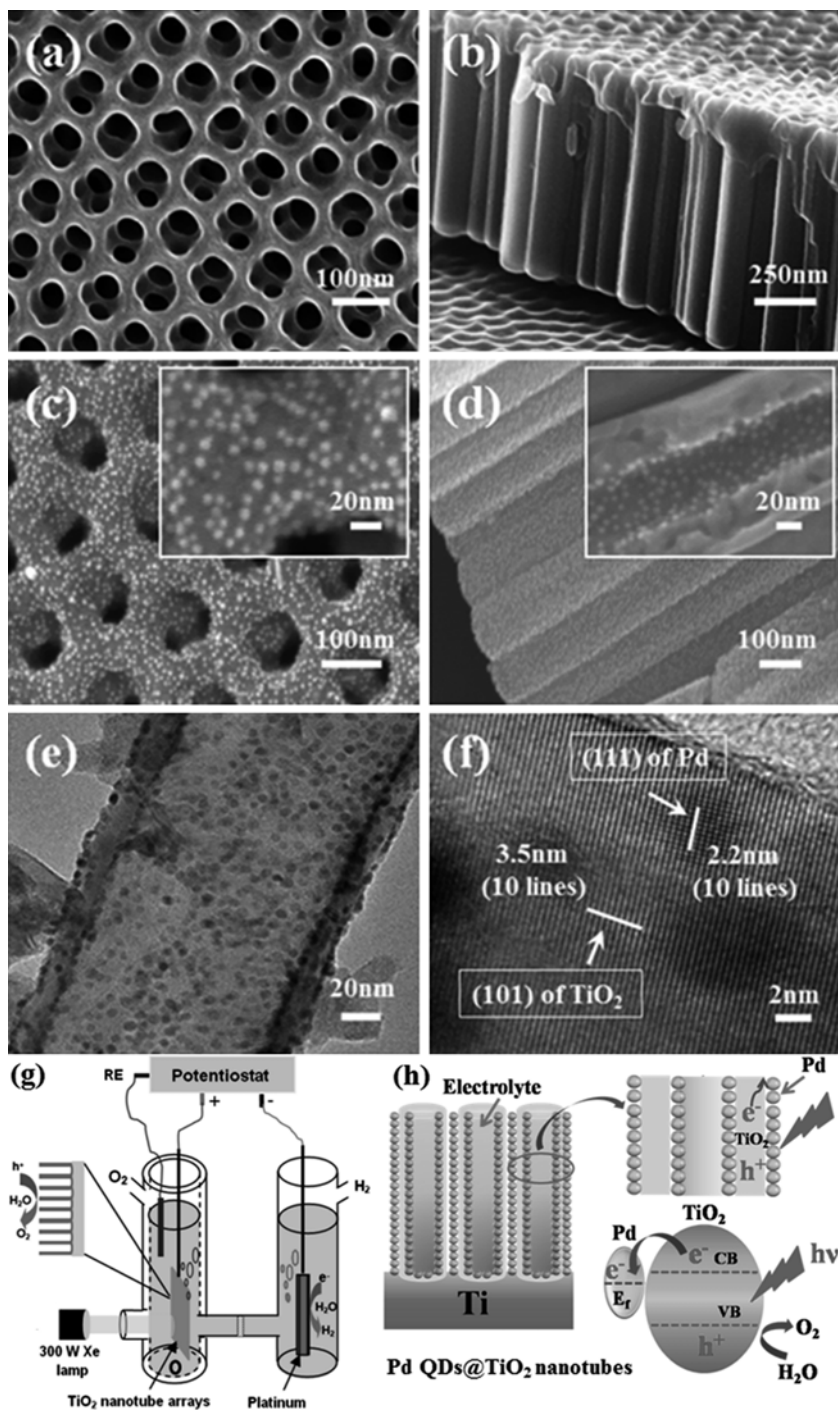


Fig. 9 Top and cross-sectional SEM images of pure TNAs (a, b) and Pd QDs@TNAs (c, d). The insets show the corresponding magnified images. TEM images of TNAs coated with Pd QDs. (g) Schematic of TNAs on photoelectrolytic water splitting for hydrogen production. (h) Schematic illustration of TNAs deposited with Pd QDs and the charge transfer process from TiO₂ to Pd (lower right panel)

dot-sensitized TNAs exhibited highly efficient photocatalytic hydrogen production rate of $592 \mu\text{mol/h/cm}^2$ under 320 mW/cm^2 irradiation (Fig. 9c–h) [83]. In general, the hydrogen production rate is greatly depending on the electrolyte, external bias, light intensity, TiO_2 morphology, and structure (e.g., exposed high reactivity crystal facets) [133, 134]. Therefore, it is important to optimize these parameters and fundamentally understand their possible correlations to clarify the approaches toward constructing high-efficient cell for hydrogen generation.

Biomedical Scaffold

Biocompatibility is a prerequisite for the application of new biomaterials, and it is defined in terms of cellular response and tissue integration of implantable biomaterials. Titania and its alloys have been proven as biocompatible and consequently widely used in biomedical implant materials due to their good biocompatibility and excellent mechanical and chemistry stabilities [8]. Efforts to use smooth-surfaced titania have been widely reported in the past, but recent studies have moved toward nanostructured TiO_2 , which shows better osteoblast cell attachment, activation, and bone formation [145–149]. However, the influence of surface micro- and nanotopography on osteogenesis is still not well understood. Therefore, studies on the TNAs and its modification with other bioactive inorganic materials or organic entities (mainly enzymes, proteins, or DNA) in regard to a biorelevant environment are of a very high significance. Mainly two directions have so far been explored with TNA substrates: (a) cell interactions and (b) hydroxyapatite growth.

Cell Interactions

Several studies have demonstrated that the nanotubular titania surface is a favorable template for bone cell growth and differentiation and provides clear evidence that osteoblast activity can be significantly enhanced using controlled nanotopographies [146, 147, 149–151]. Improved blood compatibility and anticoagulation on anodized titanium with nanotube structures compared with unanodized titanium have also been reported [152]. From the *in vitro* blood compatibility evaluation, it was observed that very few of platelets were attached onto the superhydrophobic surface than that on smooth counterpart (Fig. 10). Furthermore, the sparsely attached platelets were not activated on the nanotube surfaces with superhydrophobic property, suggesting that the superhydrophobic TNA layers exhibited excellent blood compatibility and remarkable performance in preventing platelets from adhering to the implant surface on superhydrophobic TNA surfaces.

In addition to surface wettability, the dimension of nanotube was also found to be an important parameter for cell adhesion, spreading, growth, and differentiation [153]. Two groups recently demonstrated that culture media prepared from TNAs can influence human and rat mesenchymal stem cells (MSC) [146, 147, 151]. Park et al. reported the adhesion, spreading, growth, and differentiation of mesenchymal stem cells increased on 15 nm nanotubes and dramatically decreased cell functions on 70 and 100 nm nanotubes [147]. This drastic effect of the nanoscale microenvironment on cell fate was ascribed to specific interactions between a specific

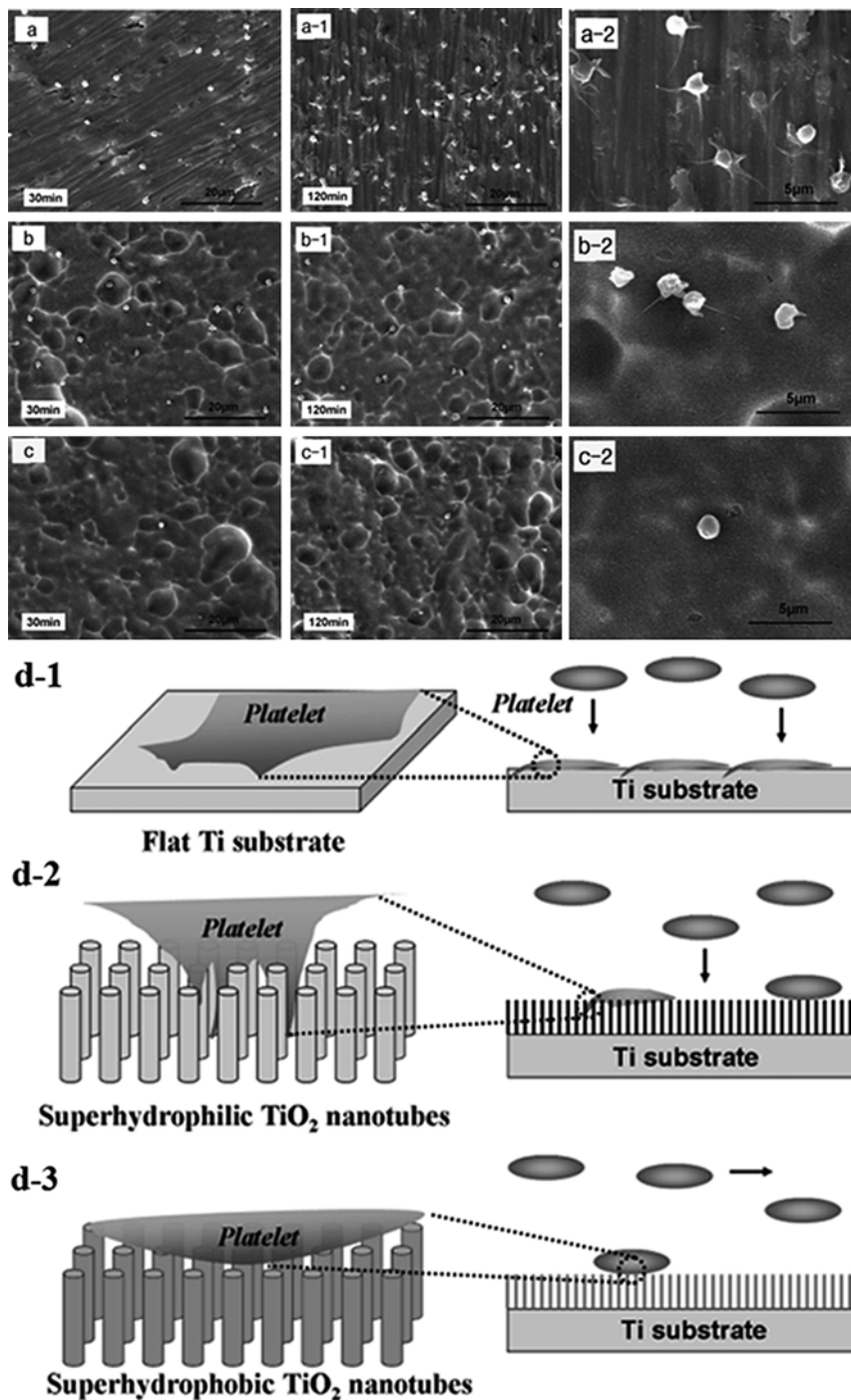


Fig. 10 SEM images of adhered platelets on three kinds of surfaces for different periods: (a–c) 30 min; (a-1, b-1, c-1) 120 min. (a-2), (b-2) and (c-2): magnified images of the corresponding images of (a-1), (b-1) and (c-1). Group (a) mechanically polished and cleaned Ti substrate; group (b), superhydrophilic TNA surface; group (c), superhydrophobic TNA surface; group (d), corresponding schematic illustration of platelet morphology and the corresponding interactions

nanotube size and the focal adhesion (FA) complex [146]. Recently, Oh et al. found that small (approx. 30 nm diameter) nanotubes promoted adhesion without noticeable differentiation, whereas larger (approx. to 70–100 nm diameter) nanotubes elicited a dramatic human mesenchymal stem cell (hMSC) elongation (approx. 10-fold increased), which induced cytoskeletal stress and selective differentiation into osteoblast-like cells [151]. These different findings motivated us that more systematic studies on the influence of TNA geometry, processing parameters, surface chemistry, crystal structure, and other differentiation approaches should be investigated on the response of various cells.

In addition to bioassay of cell viability, the TNAs are also desirable for certain applications to control drug release by environmental stimuli such as pH, temperature, light, voltage, magnetic field, or site-selective area drug release [154–158]. Song et al. reported the fabrication and use of an amphiphilic TNA structure that provides a highly controllable drug release system based on a hydrophobic cap on a hydrophilic TNA [154]. This hydrophobic cap prevents uncontrolled leaching of the hydrophilic drug into an aqueous environment. By exploiting the photocatalytic nature of TiO₂ for UV-induced chain scission of attached organic monolayers, the cap can be removed and a highly controlled release of drugs and proteins can be achieved.

In conventional uniform payload samples, the release of drugs usually follows a sustained kinetic mechanism that can be expressed in terms of diffusion of loading drugs without site selection. The microscale encapsulation of specific drug has received a great deal of attention because of the exciting possibilities of using these precious drugs in on-demand targeted place. For example, microscale silver nanoparticle patterns could be transported, released, and concentrated at pretargeted locations within the specific place in order to exert a specific function with high local and temporal precision. Lai et al. reported construction of microscale curcumin (a broad-spectrum anticancer drug) patterns on titania nanotube layers based on the utilization of the superhydrophilic–superhydrophobic templates and demonstrated the use of these patterned chip devices to targeted drug release for site-specific and high-sensitivity cancer cell bioassays [159]. Compared to that of the control group without payload, there exists significant difference in quantity and shape of cancer cell. With the curcumin site selectively loaded in the superhydrophilic regions that cancer cells preferentially adhered, few cells were found and most of the adhered MG-63 cells that remained spherical in shape indicated the cells were dead or inactivated. These *in vitro* anticancer results indicate that site-specific curcumin releasing can significantly inhibit MG-63 cell proliferation and migration and induce cancer cell apoptosis in superhydrophilic regions. This extraordinary example of using titania nanotubes as a biomedical scaffold for cell culture and the treatment of cancer cells opens many new opportunities for drug delivery applications, which need to be explored in the future [160].

Hydroxyapatite Growth

In biomedical field, another key feature of TNAs interacting with body fluids is that it can stimulate hydroxyapatite growth and enhance osseointegration [161, 162]. Tsuchiya et al. reported the nanotube layers significantly enhanced apatite formation compared with a flat TiO₂ compact layer, i.e., on the flat surface, no apatite was

formed even after 14 days soaking in simulated body fluid (SBF), whereas for the nanotubes after 14 days of soaking, a thick apatite coverage can be achieved. Moreover, compared to amorphous layers, anatase or a mixture of anatase and rutile enhances apatite formation. Apatite was initiated on both annealed crystalline layers already after 2 days soaking in SBF, whereas no apatite was formed on the amorphous nanotube layer [163]. The growth of the hydroxyapatite onto the TNAs was also achieved by a facile electrodeposition process, and the cell adhesion for the composite coating was observed to be greatly improved [164–166].

Wetting Template

For many applications of TiO₂ structures, alterations of surface topography and wetting behavior are of great importance for controlled drug delivery and biomedical engineering applications [167, 168]. Several approaches using UV light or organic monolayers have been reported to control the whole surface wettability or prepare the patterned wetting of TiO₂ nanostructures [34, 169, 170]. TNA structures show typically a superhydrophilic behavior, that is, quick spreading of water on the entire surface, penetrating into the aligned tubes due to side penetration of the liquid by capillary forces. In order to alter the surface properties, low-energy organic materials, e.g., fluoroalkylsilane or octadecylphosphonic acid molecules, can be attached to the TNAs [34]. The original hydrophilic surface becomes superhydrophobic with a water contact angle of about $158 \pm 2^\circ$ for the silane SAMs. However, the CA for the “flat” TiO₂ surface and its corresponding silane modified sample is about 46° (hydrophilic) and 115° (hydrophobic), respectively, indicating the rough nanotube structures have an amplification effect to construct surfaces with extreme wetting property, e.g., superhydrophilic or superhydrophobic (Fig. 11).

Using UV illumination the wetting behavior of the SAM-coated tube surface can be altered. After about 5 min irradiation for the silane SAM, the nanotube surface can be changed from superhydrophobic to superhydrophilic with a contact angle lower than 5° because the organic monolayers start to decompose as a consequence of the photocatalytic activity of TiO₂ films [159]. Moreover, the rough nanotube sample exhibited superhydrophobic character once again when it was assembled with low-energy materials. Therefore the surface can be reversibly switched between superhydrophobic and superhydrophilic by alternating SAM and UV photocatalysis on the rough TNAs (Fig. 11e).

The combination of organic modification with a controllable photocatalytic reaction of TiO₂ was used to create microscale patterning surfaces with any desired wettability value [159, 171]. Wetting micropatterns with different physical or chemical properties, without the need for ultraprecise positioning, have frequently been acted as templates for fabricating various functional materials in a large scale, such as CaP [165, 169], ZnO [172], CdS [173], Ag [174], drug and biomolecules in a highly selective manner [159]. Moreover, wetting patterns with tailored and improved properties for a wide range of applications have been reported [170]. For example, Ag@TNA micropatterns show not only the high-throughput molecular

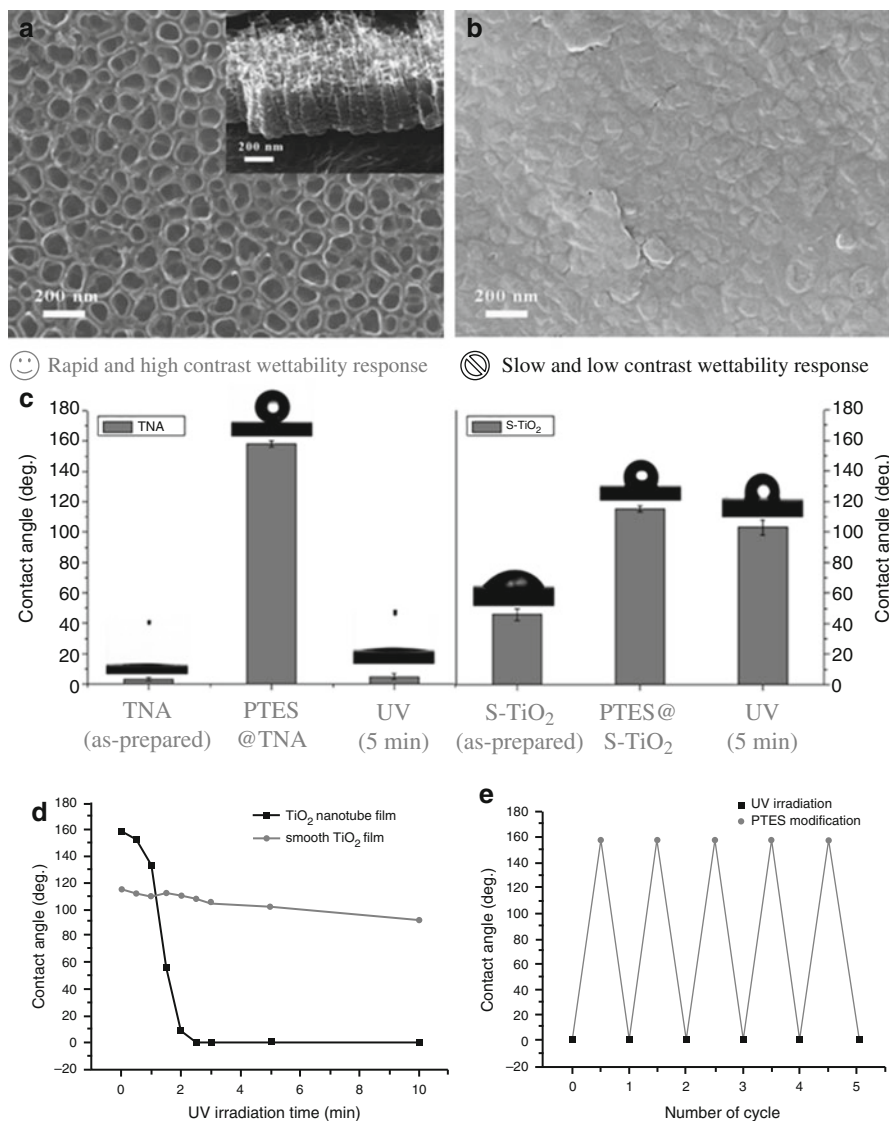


Fig. 11 Typical SEM image of a typical rough TNA film (a) and smooth TiO₂ (S-TiO₂) film (b) by electrochemical anodizing at 20 V for 20 min in 0.5 wt% HF solution and 1 M H₂SO₄ solution, respectively. (c) Contact angles of the as-prepared, PTES modified, following UV irradiated (5 min) rough TNA and S-TiO₂, respectively. (d) The effect of UV light irradiation (366 nm) on contact angle. (e) Reversible surface wettability on TNA film by alternating PTES modification and UV irradiation

sensing feature with high-sensitive, reproducible performance but also show promising targeted antibacterial properties [159]. The principle used to construct TiO₂ patterns with highly extreme wettability can be transferred to other semiconductor substrates.

Other Applications

As mentioned above, another special feature of TNAs or some other TiO_2 nanotube-based materials is its ability to serve as a host for small ion insertion, typically hydrogen ion or lithium ion, into the lattice, leading to the drastic change of electronic and optical properties for potential applications in lithium battery [175, 176], electrochromic devices [177, 178], and supercapacitor [179–181]. The kinetics, magnitude, and reversibility of the ion insertion and electrochromic reaction strongly depend on the ion diffusion length and therefore on geometry of the electrode surface. Due to the specific vertical alignment of the TNAs, a very high contrast can be obtained using vertically oriented nanotubes. By the deposition of Ag nanoparticles on the TNAs, a material can be created that shows considerable photochromic contrast [182]. Furthermore, the TNA has also been proved to be good support for Pt or Pt/Ru catalysts for enhanced methanol electrooxidation [183, 184].

Other applications of the TNAs for biomedical implant are specific gas/liquid (e.g., H_2 , CO, H_2S , NO_x , glucose, dopamine, insulin) sensing, electrochemical detection, photogenerated cathode protection [71, 185–193]. For instance, Grimes et al. have shown instant resistance response in order of several magnitudes for the TNA layer upon exposure to 1000 ppm H_2 containing nitrogen atmospheres at room temperature [187].

The applications of TNAs can significantly be expanded, if secondary material can successfully be deposited into the tubes. The TNAs can also be converted to other titanates MTiO_3 ($M=\text{Sr}$, Pd, Zr) with specific bioactive, piezoelectric, or ferroelectric properties and keep its original tube structure by a simple hydrothermal process in the corresponding precursor solution or a direct anodizing process in appropriate alloy substrates [194–197].

Conclusion

Till now, a large number of fundamental studies and application-oriented researches and developments are extensively carried out by many researchers for this low-dimensional nanomaterial due to the expected various properties of TiO_2 (high surface area and controllable nanotube dimensions, geometries, and surface chemistry). This chapter has presented the recent progress of preparation and modification on the electrochemically anodized TNA materials. These unique low-dimensional nanostructure materials have been shown to have many favorable properties for potential applications, including pollutant photocatalytic decomposition, photovoltaic cells, biomedical scaffold, and wetting template. On the other hand, extensive challenges to fabricate high-quality TNAs and develop various oxide nanotubes have been continued. For instance, rapid and high-efficient synthesis of anatase TNAs and other multicomponent nanotubes under ambient low-temperature conditions have recently been reported [198]. Some other aspects aim to encompass the new progress of TiO_2 for an efficient utilization in photocatalytic or photovoltaic applications under visible light, emphasize the future trends of TiO_2 in the

environment and/or energy-related fields, and suggest new research directions, including the preparation aspects for the development of this promising material [199–206].

Acknowledgements The authors thank the Alexander von Humboldt (AvH) Foundation of Germany, Natural Science Foundation of Jiangsu Province of China (No. BK20130313; BK20140400), National Science Foundation of China under Grant 91027039, 51373110 and 51203108, and Jiangsu Planned Projects for Postdoctoral Research Funds (No. 1302099B), Priority Academic Program Development of Jiangsu Higher Education Institutions (PAPD), and Project for Jiangsu Scientific and Technological Innovation Team (2013) for the financial support of this work.

References

1. Iijima S (1991) Helical microtubules of graphitic carbon. *Nature* 354(6348):56–58
2. Hulteen JC, Martin CR (1997) A general template-based method for the preparation of nanomaterials. *J Mater Chem* 7(7):1075–1087
3. Sander MS, Cote MJ, Gu W, Kile BM, Tripp CP (2004) Template-assisted fabrication of dense, aligned arrays of titania nanotubes with well-controlled dimensions on substrates. *Adv Mater* 16(22):2052–2057
4. Bavykin DV, Friedrich JM, Walsh FC (2006) Protonated titanates and TiO₂ nanostructured materials: synthesis, properties, and applications. *Adv Mater* 18(21):2807–2824
5. Sun XM, Li YD (2003) Synthesis and characterization of ion-exchangeable titanate nanotubes. *Chem Eur J* 9(10):2229–2238
6. Kasuga T, Hiramatsu M, Hoson A, Sekino T, Niihara K (1998) Formation of titanium oxide nanotube. *Langmuir* 14(12):3160–3163
7. Mor GK, Varghese OK, Paulose M, Shankar K, Grimes CA (2006) A review on highly ordered, vertically oriented TiO₂ nanotube arrays: fabrication, material properties, and solar energy applications. *Sol Energy Mater Sol Cells* 90(14):2011–2075
8. Macak JM, Tsuchiya H, Ghicov A, Yasuda K, Hahn R, Bauer S, Schmuki P (2007) TiO₂ nanotubes: self-organized electrochemical formation, properties and applications. *Curr Opin Solid State Mater Sci* 11(1–2):3–18
9. Grimes CA (2007) Synthesis and application of highly ordered arrays of TiO₂ nanotubes. *J Mater Chem* 17(15):1451–1457
10. Roy P, Berger S, Schmuki P (2011) TiO₂ nanotubes: synthesis and applications. *Angew Chem Int Ed* 50(13):2904–2939
11. Tian ZRR, Voigt JA, Liu J, McKenzie B, Xu HF (2003) Large oriented arrays and continuous films of TiO₂-based nanotubes. *J Am Chem Soc* 125(41):12384–12385
12. Zwilling V, Darque-Ceretti E, Boutry-Forveille A, David D, Perrin MY, Aucouturier M (1999) Structure and physicochemistry of anodic oxide films on titanium and TA6V alloy. *Surf Interface Anal* 27(7):629–637
13. Gong D, Grimes CA, Varghese OK, Hu WC, Singh RS, Chen Z, Dickey EC (2001) Titanium oxide nanotube arrays prepared by anodic oxidation. *J Mater Res* 16(12):3331–3334
14. Beranek R, Hildebrand H, Schmuki P (2003) Self-organized porous titanium oxide prepared in H₂SO₄/HF electrolytes. *Electrochem Solid State Lett* 6(3):B12–B14
15. Lai YK, Sun L, Zuo J, Lin CJ (2004) Electrochemical fabrication and formation mechanism of TiO(2) nanotube arrays on metallic titanium surface. *Acta Phys Chim Sin* 20(9):1063–1066
16. Macak JM, Tsuchiya H, Schmuki P (2005) High-aspect-ratio TiO₂ nanotubes by anodization of titanium. *Angew Chem Int Ed* 44(14):2100–2102
17. Macak JM, Tsuchiya H, Taveira L, Aldabergerova S, Schmuki P (2005) Smooth anodic TiO₂ nanotubes. *Angew Chem Int Ed* 44(45):7463–7465

18. Mor GK, Varghese OK, Paulose M, Mukherjee N, Grimes CA (2003) Fabrication of tapered, conical-shaped titania nanotubes. *J Mater Res* 18(11):2588–2593
19. Mor GK, Varghese OK, Paulose M, Grimes CA (2005) Transparent highly ordered TiO₂ nanotube arrays via anodization of titanium thin films. *Adv Funct Mater* 15(8):1291–1296
20. Mor GK, Shankar K, Paulose M, Varghese OK, Grimes CA (2006) Use of highly-ordered TiO₂ nanotube arrays in dye-sensitized solar cells. *Nano Lett* 6(2):215–218
21. Albu SP, Ghicov A, Macak JM, Hahn R, Schmuki P (2007) Self-organized, free-standing TiO₂ nanotube membrane for flow-through photocatalytic applications. *Nano Lett* 7(5):1286–1289
22. Paulose M, Prakasam HE, Varghese OK, Peng L, Popat KC, Mor GK, Desai TA, Grimes CA (2007) TiO₂ nanotube arrays of 1000 μm length by anodization of titanium foil: phenol red diffusion. *J Phys Chem C* 111(41):14992–14997
23. Macak JM, Albu SP, Schmuki P (2007) Towards ideal hexagonal self-ordering of TiO₂ nanotubes. *Phys Status Solidi Rapid Res Lett* 1(5):181–183
24. Zhang G, Huang H, Zhang Y, Chan HLW, Zhou L (2007) Highly ordered nanoporous TiO₂ and its photocatalytic properties. *Electrochem Commun* 9(12):2854–2858
25. Ni JH, Noh K, Frandsen CJ, Kong SD, He G, Tang TT, Jin SH (2013) Preparation of near micrometer-sized TiO₂ nanotube arrays by high voltage anodization. *Mater Sci Eng C Mater Biol Appl* 33(1):259–264
26. Albu SP, Schmuki P (2010) TiO₂ nanotubes grown in different organic electrolytes: two-size self organization, single vs. double-walled tubes, and giant diameters. *Phys Status Solidi Rapid Res Lett* 4(8–9):215–217
27. Mohamed AE, Rohani S (2011) Modified TiO₂ nanotube arrays (TNTAs): progressive strategies towards visible light responsive photoanode, a review. *Energy Environ Sci* 4(4):1065–1086
28. Macak JM, Sirotna K, Schmuki P (2005) Self-organized porous titanium oxide prepared in Na₂SO₄/NaF electrolytes. *Electrochim Acta* 50(18):3679–3684
29. Cai QY, Paulose M, Varghese OK, Grimes CA (2005) The effect of electrolyte composition on the fabrication of self-organized titanium oxide nanotube arrays by anodic oxidation. *J Mater Res* 20(1):230–236
30. Hahn R, Macak JM, Schmuki P (2007) Rapid anodic growth of TiO(2) and WO(3) nanotubes in fluoride free electrolytes. *Electrochem Commun* 9(5):947–952
31. Ishibashi K, Yamaguchi R, Kimura Y, Niwano M (2008) Fabrication of titanium oxide nanotubes by rapid and homogeneous anodization in perchloric acid/ethanol mixture. *J Electrochem Soc* 155(1):K10–K14
32. Bauer S, Kleber S, Schmuki P (2006) TiO₂ nanotubes: tailoring the geometry in H₃PO₄/HF electrolytes. *Electrochem Commun* 8(8):1321–1325
33. Taveira LV, Macak JM, Tsuchiya H, Dick LFP, Schmuki P (2005) Initiation and growth of self organized TiO₂ nanotubes anodically formed in NH₄F/(NH₄)₂SO₄ electrolytes. *J Electrochem Soc* 152(10):B405–B410
34. Lai YK, Gao XF, Zhuang HF, Huang JY, Lin CJ, Jiang L (2009) Designing superhydrophobic porous nanostructures with tunable water adhesion. *Adv Mater* 21(37):3799–3803
35. Yin H, Liu H, Shen WZ (2010) The large diameter and fast growth of self-organized TiO₂ nanotube arrays achieved via electrochemical anodization. *Nanotechnology* 21(3):035601
36. Albu SP, Roy P, Virtanen S, Schmuki P (2010) Self-organized TiO₂ nanotube arrays: critical effects on morphology and growth. *Isr J Chem* 50(4):453–467
37. Wang Y, Wu YC, Qin YQ, Xu GB, Hu XY, Cui JW, Zheng HM, Hong Y, Zhang XY (2011) Rapid anodic oxidation of highly ordered TiO₂ nanotube arrays. *J Alloys Compd* 509(14):L157–L160
38. Ghicov A, Schmuki P (2009) Self-ordering electrochemistry: a review on growth and functionality of TiO₂ nanotubes and other self-aligned MOx structures. *Chem Commun* (20):2791–2808
39. Regonini D, Bowen CR, Jaroenworarluck A, Stevens R (2013) A review of growth mechanism, structure and crystallinity of anodized TiO₂ nanotubes. *Mater Sci Eng R Rep* 74(12):377–406

40. Liao YL, Que WX, Zhong P, Zhang J, He YC (2011) A facile method to crystallize amorphous anodized TiO₂ nanotubes at low temperature. *ACS Appl Mater Interfaces* 3(7):2800–2804
41. Lai YK, Zhuang HF, Sun L, Chen Z, Lin CJ (2009) Self-organized TiO₂ nanotubes in mixed organic-inorganic electrolytes and their photoelectrochemical performance. *Electrochim Acta* 54(26):6536–6542
42. Song YY, Schmuki P (2010) Modulated TiO₂ nanotube stacks and their use in interference sensors. *Electrochem Commun* 12(4):579–582
43. Asahi R, Morikawa T, Ohwaki T, Aoki K, Taga Y (2001) Visible-light photocatalysis in nitrogen-doped titanium oxides. *Science* 293(5528):269–271
44. Park JH, Kim S, Bard AJ (2006) Novel carbon-doped TiO₂ nanotube arrays with high aspect ratios for efficient solar water splitting. *Nano Lett* 6(1):24–28
45. Li D, Haneda H, Labhsetwar NK, Hishita S, Ohashi N (2005) Visible-light-driven photocatalysis on fluorine-doped TiO₂ powders by the creation of surface oxygen vacancies. *Chem Phys Lett* 401(4–6):579–584
46. Umebayashi T, Yamaki T, Itoh H, Asai K (2002) Band gap narrowing of titanium dioxide by sulfur doping. *Appl Phys Lett* 81(3):454–456
47. Lu N, Quan X, Li JY, Chen S, Yu HT, Chen GH (2007) Fabrication of boron-doped TiO₂ nanotube array electrode and investigation of its photoelectrochemical capability. *J Phys Chem C* 111(32):11836–11842
48. Wang H, Lewis JP (2005) Effects of dopant states on photoactivity in carbon-doped TiO₂. *J Phys Condens Matter* 17(21):L209–L213
49. Liu YM, Liu JZ, Lin YL, Zhang YF, Wei Y (2009) Simple fabrication and photocatalytic activity of S-doped TiO₂ under low power LED visible light irradiation. *Ceram Int* 35(8):3061–3065
50. Ren WJ, Ai ZH, Jia FL, Zhang LZ, Fan XX, Zou ZG (2007) Low temperature preparation and visible light photocatalytic activity of mesoporous carbon-doped crystalline TiO₂. *Appl Catal B Environ* 69(3–4):138–144
51. Wang HY, Xu XJ, Wei JH, Xiong R, Shi J (2012) Structure and Raman investigations of nitrogen-doped TiO₂ nanotube arrays. *Liq Cryst Relat Mater II* 181–182:422–425
52. Antony RP, Mathews T, Panda K, Sundaravel B, Dash S, Tyagi AK (2012) Enhanced field emission properties of electrochemically synthesized self-aligned nitrogen-doped TiO₂ nanotube array thin films. *J Phys Chem C* 116(31):16740–16746
53. Li S, Lin S, Liao J, Pan N, Li D, Li J (2012) Nitrogen-doped TiO₂ nanotube arrays with enhanced photoelectrochemical property. *Int J Photoenergy* 2012:1–7
54. Lai YK, Huang JY, Zhang HF, Subramaniam VP, Tang YX, Gong DG, Sundar L, Sun L, Chen Z, Lin CJ (2010) Nitrogen-doped TiO₂ nanotube array films with enhanced photocatalytic activity under various light sources. *J Hazard Mater* 184(1–3):855–863
55. Xue Q, Guan YJ, Wang ZB, Bai SL (2010) Preparation of nitrogen doped TiO₂ nanotube arrays and its visible light responsive photocatalytic properties. *Acta Chim Sin* 68(16):1603–1608
56. Liu G, Li F, Wang DW, Tang DM, Liu C, Ma XL, Lu GQ, Cheng HM (2008) Electron field emission of a nitrogen-doped TiO₂ nanotube array. *Nanotechnology* 19(2):025606
57. Kim D, Tsuchiya H, Fujimoto S, Schmidt-Stein F, Schmuki P (2012) Nitrogen-doped TiO₂ mesosponge layers formed by anodization of nitrogen-containing Ti alloys. *J Solid State Electrochem* 16(1):89–92
58. Kim D, Fujimoto S, Schmuki P, Tsuchiya H (2008) Nitrogen doped anodic TiO₂ nanotubes grown from nitrogen-containing Ti alloys. *Electrochem Commun* 10(6):910–913
59. Ghicov A, Macak JM, Tsuchiya H, Kunze J, Haeublein V, Kleber S, Schmuki P (2006) TiO₂ nanotube layers: dose effects during nitrogen doping by ion implantation. *Chem Phys Lett* 419(4–6):426–429
60. Ghicov A, Macak JM, Tsuchiya H, Kunze J, Haeublein V, Frey L, Schmuki P (2006) Ion implantation and annealing for an efficient N-doping of TiO₂ nanotubes. *Nano Lett* 6(5):1080–1082
61. Vitiello RP, Macak JM, Ghicov A, Tsuchiya H, Dick LFP, Schmuki P (2006) N-Doping of anodic TiO₂ nanotubes using heat treatment in ammonia. *Electrochem Commun* 8(4):544–548

62. Hahn R, Ghicov A, Salonen J, Lehto VP, Schmuki P (2007) Carbon doping of self-organized TiO₂ nanotube layers by thermal acetylene treatment. *Nanotechnology* 18(10):105604
63. Sun L, Li J, Wang CL, Li SF, Chen HB, Lin CJ (2009) An electrochemical strategy of doping Fe³⁺ into TiO₂ nanotube array films for enhancement in photocatalytic activity. *Sol Energy Mater Sol Cells* 93(10):1875–1880
64. Tu YF, Huang SY, Sang JP, Zou XW (2010) Preparation of Fe-doped TiO₂ nanotube arrays and their photocatalytic activities under visible light. *Mater Res Bull* 45(2):224–229
65. Ghicov A, Schmidt B, Kunze J, Schmuki P (2007) Photoresponse in the visible range from Cr doped TiO₂ nanotubes. *Chem Phys Lett* 433(4–6):323–326
66. Xu ZH, Yu JG (2011) Visible-light-induced photoelectrochemical behaviors of Fe-modified TiO₂ nanotube arrays. *Nanoscale* 3(8):3138–3144
67. Lai YK, Lin ZQ, Zheng DJ, Chi LF, Du RG, Lin CJ (2012) CdSe/CdS quantum dots co-sensitized TiO₂ nanotube array photoelectrode for highly efficient solar cells. *Electrochim Acta* 79:175–181
68. Li GS, Wu L, Li F, Xu PP, Zhang DQ, Li HX (2013) Photoelectrocatalytic degradation of organic pollutants via a CdS quantum dots enhanced TiO₂ nanotube array electrode under visible light irradiation. *Nanoscale* 5(5):2118–2125
69. Liu YB, Zhou HB, Zhou BX, Li JH, Chen HC, Wang JJ, Bai J, Shangguan WF, Cai WM (2011) Highly stable CdS-modified short TiO₂ nanotube array electrode for efficient visible-light hydrogen generation. *Int J Hydrog Energy* 36(1):167–174
70. Bai J, Li JH, Liu YB, Zhou BX, Cai WM (2010) A new glass substrate photoelectrocatalytic electrode for efficient visible-light hydrogen production: CdS sensitized TiO₂ nanotube arrays. *Appl Catal B Environ* 95(3–4):408–413
71. Lin ZQ, Lai YK, Hu RG, Li J, Du RG, Lin CJ (2010) A highly efficient ZnS/CdS@TiO₂ photoelectrode for photogenerated cathodic protection of metals. *Electrochim Acta* 55(28):8717–8723
72. Macak JM, Gong BG, Hueppe M, Schmuki P (2007) Filling of TiO₂ nanotubes by self-doping and electrodeposition. *Adv Mater* 19(19):3027–3031
73. Lai CW, Sreekantan S (2013) Preparation of hybrid WO₃-TiO₂ nanotube photoelectrodes using anodization and wet impregnation: improved water-splitting hydrogen generation performance. *Int J Hydrog Energy* 38(5):2156–2166
74. Lai CW, Sreekantan S (2013) Incorporation of WO₃ species into TiO₂ nanotubes via wet impregnation and their water-splitting performance. *Electrochim Acta* 87:294–302
75. Hou Y, Li XY, Zou XJ, Quan X, Chen GC (2009) Photoelectrocatalytic activity of a Cu₂O-loaded self-organized highly oriented TiO₂ nanotube array electrode for 4-chlorophenol degradation. *Environ Sci Technol* 43(3):858–863
76. Dai GP, Yu JG, Liu G (2011) Synthesis and enhanced visible-light photoelectrocatalytic activity of p-n junction BiOI/TiO₂ nanotube arrays. *J Phys Chem C* 115(15):7339–7346
77. Hou Y, Li XY, Zhao QD, Quan X, Chen GH (2009) Fabrication of Cu₂O/TiO₂ nanotube heterojunction arrays and investigation of its photoelectrochemical behavior. *Appl Phys Lett* 95(9):093108
78. Wang MY, Sun L, Lin ZQ, Cai JH, Xie KP, Lin CJ (2013) p-n Heterojunction photoelectrodes composed of Cu₂O-loaded TiO₂ nanotube arrays with enhanced photoelectrochemical and photoelectrocatalytic activities. *Energy Environ Sci* 6(4):1211–1220
79. Xin XK, Scheiner M, Ye MD, Lin ZQ (2011) Surface-treated TiO₂ nanoparticles for dye-sensitized solar cells with remarkably enhanced performance. *Langmuir* 27(23):14594–14598
80. Huo KF, Wang HR, Zhang XM, Cao Y, Chu PK (2012) Heterostructured TiO₂ nanoparticles/nanotube arrays: in situ formation from amorphous TiO₂ nanotube arrays in water and enhanced photocatalytic activity. *Chempluschem* 77(4):323–329
81. Ye MD, Xin XK, Lin CJ, Lin ZQ (2011) High efficiency dye-sensitized solar cells based on hierarchically structured nanotubes. *Nano Lett* 11(8):3214–3220
82. Paramasivalm I, Macak JM, Schmuki P (2008) Photocatalytic activity of TiO₂(2)-nanotube layers loaded with Ag and Au nanoparticles. *Electrochem Commun* 10(1):71–75

83. Ye MD, Gong JJ, Lai YK, Lin CJ, Lin ZQ (2012) High-efficiency photoelectrocatalytic hydrogen generation enabled by palladium quantum dots-sensitized TiO₂ nanotube arrays. *J Am Chem Soc* 134(38):15720–15723
84. Lai YK, Gong JJ, Lin CJ (2012) Self-organized TiO₂ nanotube arrays with uniform platinum nanoparticles for highly efficient water splitting. *Int J Hydrog Energy* 37(8):6438–6446
85. Yang LX, He DM, Cai QY, Grimes CA (2007) Fabrication and catalytic properties of Co-Ag-Pt nanoparticle-decorated titania nanotube arrays. *J Phys Chem C* 111(23):8214–8217
86. Fu P, Zhang P, Li J (2012) Simultaneous elimination of formaldehyde and ozone byproduct using noble metal modified TiO₂ films in the gaseous VUV photocatalysis. *Int J Photoenergy* 2012:1–8
87. Mohapatra SK, Kondamudi N, Banerjee S, Misra M (2008) Functionalization of self-organized TiO₂ nanotubes with Pd nanoparticles for photocatalytic decomposition of dyes under solar light illumination. *Langmuir* 24(19):11276–11281
88. Xu ZH, Yu JG, Liu G (2011) Enhancement of ethanol electrooxidation on plasmonic Au/TiO₂ nanotube arrays. *Electrochem Commun* 13(11):1260–1263
89. Yu JG, Dai GP, Huang BB (2009) Fabrication and characterization of visible-light-driven plasmonic photocatalyst Ag/AgCl/TiO₂ TiO₂ nanotube arrays. *J Phys Chem C* 113(37):16394–16401
90. Sun L, Li J, Wang CL, Li SF, Lai YK, Chen HB, Lin CJ (2009) Ultrasound aided photochemical synthesis of Ag loaded TiO₂ nanotube arrays to enhance photocatalytic activity. *J Hazard Mater* 171(1–3):1045–1050
91. Lai YK, Zhuang HF, Xie KP, Gong DG, Tang YX, Sun L, Lin CJ, Chen Z (2010) Fabrication of uniform Ag/TiO₂ nanotube array structures with enhanced photoelectrochemical performance. *New J Chem* 34(7):1335–1340
92. Liu CB, Teng YR, Liu RH, Luo SL, Tang YH, Chen LY, Cai QY (2011) Fabrication of graphene films on TiO₂ nanotube arrays for photocatalytic application. *Carbon* 49(15):5312–5320
93. Wang P, Wang J, Wang XF, Yu HG, Yu JG, Lei M, Wang YG (2013) One-step synthesis of easy-recycling TiO₂-rGO nanocomposite photocatalysts with enhanced photocatalytic activity. *Appl Catal B Environ* 132:452–459
94. Hou Y, Li XY, Zhao QD, Chen GH, Rastor CL (2012) Role of hydroxyl radicals and mechanism of *Escherichia coli* inactivation on Ag/AgBr/TiO₂ nanotube array electrode under visible light irradiation. *Environ Sci Technol* 46(7):4042–4050
95. Hou Y, Li XY, Zhao QD, Quan X, Chen GH (2011) TiO₂ nanotube/Ag-AgBr three-component nanojunction for efficient photoconversion. *J Mater Chem* 21(44):18067–18076
96. Tang YH, Luo SL, Teng YR, Liu CB, Xu XL, Zhang XL, Chen L (2012) Efficient removal of herbicide 2,4-dichlorophenoxyacetic acid from water using Ag/reduced graphene oxide codecorated TiO₂ nanotube arrays. *J Hazard Mater* 241:323–330
97. Kang Q, Liu SH, Yang LX, Cai QY, Grimes CA (2011) Fabrication of PbS nanoparticle-sensitized TiO₂ nanotube arrays and their photoelectrochemical properties. *ACS Appl Mater Interfaces* 3(3):746–749
98. Wang MY, Sun L, Cai JH, Huang P, Su YF, Lin CJ (2013) A facile hydrothermal deposition of ZnFe₂O₄ nanoparticles on TiO₂ nanotube arrays for enhanced visible light photocatalytic activity. *J Mater Chem A* 1(39):12082–12087
99. Liu MJ, He L, Liu XN, Liu CB, Luo SL (2014) Reduced graphene oxide and CdTe nanoparticles co-decorated TiO₂ nanotube array as a visible light photocatalyst. *J Mater Sci* 49(5):2263–2269
100. Chen Y, Tang YH, Luo SL, Liu CB, Li Y (2013) TiO₂ nanotube arrays co-loaded with Au nanoparticles and reduced graphene oxide: facile synthesis and promising photocatalytic application. *J Alloys Compd* 578:242–248
101. Liu XN, Tang YH, Luo SL, Wang Y, Zhang XL, Chen Y, Liu CB (2013) Reduced graphene oxide and CuInS₂ co-decorated TiO₂ nanotube arrays for efficient removal of herbicide 2,4-dichlorophenoxyacetic acid from water. *J Photochem Photobiol A Chem* 262:22–27

102. Li JH, Lv SB, Liu YB, Bai J, Zhou BX, Hu XF (2013) Photoelectrocatalytic activity of an n-ZnO/p-Cu₂O/n-TNA ternary heterojunction electrode for tetracycline degradation. *J Hazard Mater* 262:482–488
103. Li S, Qiu JX, Ling M, Peng F, Wood B, Zhang SQ (2013) Photoelectrochemical characterization of hydrogenated TiO₂ nanotubes as photoanodes for sensing applications. *ACS Appl Mater Interfaces* 5(21):11129–11135
104. Chen XB, Liu L, Yu PY, Mao SS (2011) Increasing solar absorption for photocatalysis with black hydrogenated titanium dioxide nanocrystals. *Science* 331(6018):746–750
105. Fujishima A, Honda K (1972) Electrochemical photolysis of water at a semiconductor electrode. *Nature* 238(5358):37–38
106. Lai YK, Sun L, Chen YC, Zhuang HF, Lin CJ, Chin JW (2006) Effects of the structure of TiO₂ nanotube array on Ti substrate on its photocatalytic activity. *J Electrochem Soc* 153(7):D123–D127
107. Zhuang HF, Lin CJ, Lai YK, Sun L, Li J (2007) Some critical structure factors of titanium oxide nanotube array in its photocatalytic activity. *Environ Sci Technol* 41(13):4735–4740
108. Paramasivam I, Jha H, Liu N, Schmuki P (2012) A review of photocatalysis using self-organized TiO₂ nanotubes and other ordered oxide nanostructures. *Small* 8(20):3073–3103
109. Nakata K, Fujishima A (2012) TiO₂ photocatalysis: design and applications. *J Photochem Photobiol C Photochem Rev* 13(3):169–189
110. Yu JG, Wang B (2010) Effect of calcination temperature on morphology and photoelectrochemical properties of anodized titanium dioxide nanotube arrays. *Appl Catal B Environ* 94(3–4):295–302
111. Quan X, Yang SG, Ruan XL, Zhao HM (2005) Preparation of titania nanotubes and their environmental applications as electrode. *Environ Sci Technol* 39(10):3770–3775
112. Macak JM, Zlamal M, Krysa J, Schmuki P (2007) Self-organized TiO₂ nanotube layers as highly efficient photocatalysts. *Small* 3(2):300–304
113. Xie KP, Sun L, Wang CL, Lai YK, Wang MY, Chen HB, Lin CJ (2010) Photoelectrocatalytic properties of Ag nanoparticles loaded TiO₂ nanotube arrays prepared by pulse current deposition. *Electrochim Acta* 55(24):7211–7218
114. Xie KP, Wu Q, Wang YY, Guo WX, Wang MY, Sun L, Lin CJ (2011) Electrochemical construction of Z-scheme type CdS-Ag-TiO₂ nanotube arrays with enhanced photocatalytic activity. *Electrochem Commun* 13(12):1469–1472
115. Oregan B, Gratzel M (1991) A low-cost, high-efficiency solar-cell based on dye-sensitized colloidal TiO₂ films. *Nature* 353(6346):737–740
116. Zhu K, Neale NR, Miedaner A, Frank AJ (2007) Enhanced charge-collection efficiencies and light scattering in dye-sensitized solar cells using oriented TiO₂ nanotubes arrays. *Nano Lett* 7(1):69–74
117. Paulose M, Shankar K, Varghese OK, Mor GK, Hardin B, Grimes CA (2006) Backside illuminated dye-sensitized solar cells based on titania nanotube array electrodes. *Nanotechnology* 17(5):1446–1448
118. Zhu K, Vinzant TB, Neale NR, Frank AJ (2007) Removing structural disorder from oriented TiO₂ nanotube arrays: reducing the dimensionality of transport and recombination in dye-sensitized solar cells. *Nano Lett* 7(12):3739–3746
119. Liu ZY, Misra M (2010) Bifacial dye-sensitized solar cells based on vertically oriented TiO₂ nanotube arrays. *Nanotechnology* 21(12):125703
120. Wang J, Lin ZQ (2012) Dye-sensitized TiO₂ nanotube solar cells: rational structural and surface engineering on TiO₂ nanotubes. *Chem Asian J* 7(12):2754–2762
121. Wang J, Lin ZQ (2010) Dye-sensitized TiO₂ nanotube solar cells with markedly enhanced performance via rational surface engineering. *Chem Mater* 22(2):579–584
122. Zhong P, Que WX, Liao YL, Zhang J, Hu X (2012) Improved performance in dye-sensitized solar cells by rationally tailoring anodic TiO₂ nanotube length. *J Alloys Compd* 540:159–164
123. Sun LD, Zhang S, Wang X, Sun XW, Ong DY, Kyaw AKK (2011) A novel parallel configuration of dye-sensitized solar cells with double-sided anodic nanotube arrays. *Energy Environ Sci* 4(6):2240–2248

124. Zheng Q, Kang H, Yun J, Lee J, Park JH, Baik S (2011) Hierarchical construction of self-standing anodized titania nanotube arrays and nanoparticles for efficient and cost-effective front-illuminated dye-sensitized solar cells. *ACS Nano* 5(6):5088–5093
125. Kongkanand A, Tvrdy K, Takechi K, Kuno M, Kamat PV (2008) Quantum dot solar cells. Tuning photoresponse through size and shape control of CdSe-TiO₂ architecture. *J Am Chem Soc* 130(12):4007–4015
126. Klimov VI, McBranch DW (1998) Femtosecond 1P-to-1S electron relaxation in strongly confined semiconductor nanocrystals. *Phys Rev Lett* 80(18):4028–4031
127. Sudhagar P, Jung JH, Park S, Lee YG, Sathyamoorthy R, Kang YS, Ahn H (2009) The performance of coupled (CdS:CdSe) quantum dot-sensitized TiO₂ nanofibrous solar cells. *Electrochem Commun* 11(11):2220–2224
128. Shen Q, Yamada A, Tamura S, Toyoda T (2010) CdSe quantum dot-sensitized solar cell employing TiO₂ nanotube working-electrode and Cu₂S counter-electrode. *Appl Phys Lett* 97(12):123107
129. Sun WT, Yu Y, Pan HY, Gao XF, Chen Q, Peng LM (2008) CdS quantum dots sensitized TiO₂ nanotube-array photoelectrodes. *J Am Chem Soc* 130(4):1124–1125
130. Yang ZS, Chen CY, Roy P, Chang HT (2011) Quantum dot-sensitized solar cells incorporating nanomaterials. *Chem Commun* 47(34):9561–9571
131. Mor GK, Shankar K, Paulose M, Varghese OK, Grimes CA (2005) Enhanced photocleavage of water using titania nanotube arrays. *Nano Lett* 5(1):191–195
132. Gong JJ, Lin CJ, Ye MD, Lai YK (2011) Enhanced photoelectrochemical activities of a nanocomposite film with a bamboo leaf-like structured TiO(2) layer on TiO(2) nanotube arrays. *Chem Commun* 47(9):2598–2600
133. Jiang ZL, Tang YX, Tay QL, Zhang YY, Malyi OI, Wang DP, Deng JY, Lai YK, Zhou HF, Chen XD, Dong ZL, Chen Z (2013) Understanding the role of nanostructures for efficient hydrogen generation on immobilized photocatalysts. *Adv Energy Mater* 3(10):1368–1380
134. Liu GH, Hoivik N, Wang KY (2013) Small diameter TiO₂ nanotubes with enhanced photore sponsivity. *Electrochem Commun* 28:107–110
135. Jia FZ, Yao ZP, Jiang ZH, Li CX (2011) Preparation of carbon coated TiO₂ nanotubes film and its catalytic application for H-2 generation. *Catal Commun* 12(6):497–501
136. Li YK, Yu HM, Song W, Li GF, Yi BL, Shao ZG (2011) A novel photoelectrochemical cell with self-organized TiO₂ nanotubes as photoanodes for hydrogen generation. *Int J Hydrog Energy* 36(22):14374–14380
137. Sang LX, Zhang ZY, Bai GM, Du CX, Ma CF (2012) A photoelectrochemical investigation of the hydrogen-evolving doped TiO₂ nanotube arrays electrode. *Int J Hydrog Energy* 37(1):854–859
138. Smith YR, Sarma B, Mohanty SK, Misra M (2013) Single-step anodization for synthesis of hierarchical TiO₂ nanotube arrays on foil and wire substrate for enhanced photoelectrochemical water splitting. *Int J Hydrog Energy* 38(5):2062–2069
139. Roy P, Das C, Lee K, Hahn R, Ruff T, Moll M, Schmuki P (2011) Oxide nanotubes on Ti-Ru alloys: strongly enhanced and stable photoelectrochemical activity for water splitting. *J Am Chem Soc* 133(15):5629–5631
140. Sun Y, Wang GX, Yan KP (2011) TiO₂ nanotubes for hydrogen generation by photocatalytic water splitting in a two-compartment photoelectrochemical cell. *Int J Hydrog Energy* 36(24):15502–15508
141. Bae S, Shim E, Yoon J, Joo H (2008) Photoanodic and cathodic role of anodized tubular titania in light-sensitized enzymatic hydrogen production. *J Power Sources* 185(1):439–444
142. Yoon J, Bae S, Shim E, Joo H (2009) *Pyrococcus furiosus*-immobilized anodized tubular titania cathode in a hydrogen production system. *J Power Sources* 189(2):1296–1301
143. Park M, Heo A, Shim E, Yoon J, Kim H, Joo H (2010) Effect of length of anodized TiO₂ tubes on photoreactivity: photocurrent, Cr(VI) reduction and H-2 evolution. *J Power Sources* 195(15):5144–5149
144. Gong JJ, Lai YK, Lin CJ (2010) Electrochemically multi-anodized TiO(2) nanotube arrays for enhancing hydrogen generation by photoelectrocatalytic water splitting. *Electrochim Acta* 55(16):4776–4782

145. Popat KC, Chatvanichkul KI, Barnes GL, Latempa TJ, Grimes CA, Desai TA (2007) Osteogenic differentiation of marrow stromal cells cultured on nanoporous alumina surfaces. *J Biomed Mater Res A* 80A(4):955–964
146. Park J, Bauer S, Schlegel KA, Neukam FW, von der Mark K, Schmuki P (2009) TiO₂ nanotube surfaces: 15 nm – an optimal length scale of surface topography for cell adhesion and differentiation. *Small* 5(6):666–671
147. Park J, Bauer S, von der Mark K, Schmuki P (2007) Nanosize and vitality: TiO₂ nanotube diameter directs cell fate. *Nano Lett* 7(6):1686–1691
148. Burns K, Yao C, Webster TJ (2009) Increased chondrocyte adhesion on nanotubular anodized titanium. *J Biomed Mater Res A* 88A(3):561–568
149. Oh S, Jin S (2006) Titanium oxide nanotubes with controlled morphology for enhanced bone growth. *Mater Sci Eng C Biomim Supramol Syst* 26(8):1301–1306
150. Huang QL, Lin LX, Yang Y, Hu R, Vogler EA, Lin CJ (2012) Role of trapped air in the formation of cell-and-protein micropatterns on superhydrophobic/superhydrophilic microtemplated surfaces. *Biomaterials* 33(33):8213–8220
151. Oh S, Brammer KS, Li YSJ, Teng D, Engler AJ, Chien S, Jin S (2009) Stem cell fate dictated solely by altered nanotube dimension. *Proc Natl Acad Sci U S A* 106(7):2130–2135
152. Yang Y, Lai YK, Zhang QQ, Wu K, Zhang LH, Lin CJ, Tang PF (2010) A novel electrochemical strategy for improving blood compatibility of titanium-based biomaterials. *Colloids Surf B Biointerfaces* 79(1):309–313
153. Wang N, Li HY, Lu WL, Li JH, Wang JS, Zhang ZT, Liu YR (2011) Effects of TiO₂ nanotubes with different diameters on gene expression and osseointegration of implants in minipigs. *Biomaterials* 32(29):6900–6911
154. Song YY, Schmidt-Stein F, Bauer S, Schmuki P (2009) Amphiphilic TiO₂ nanotube arrays: an actively controllable drug delivery system. *J Am Chem Soc* 131(12):4230–4232
155. Moseke C, Hage F, Vorndran E, Gbureck U (2012) TiO₂ nanotube arrays deposited on Ti substrate by anodic oxidation and their potential as a long-term drug delivery system for antimicrobial agents. *Appl Surf Sci* 258(14):5399–5404
156. Shrestha NK, Macak JM, Schmidt-Stein F, Hahn R, Mierke CT, Fabry B, Schmuki P (2009) Magnetically guided titania nanotubes for site-selective photocatalysis and drug release. *Angew Chem Int Ed* 48(5):969–972
157. Song YY, Roy P, Paramasivam I, Schmuki P (2010) Voltage-induced payload release and wettability control on TiO₂ and TiO₂ nanotubes. *Angew Chem Int Ed* 49(2):351–354
158. Cai KY, Jiang F, Luo Z, Chen XY (2010) Temperature-responsive controlled drug delivery system based on titanium nanotubes. *Adv Eng Mater* 12(9):B565–B570
159. Lai Y, Lin L, Pan F, Huang J, Song R, Huang Y, Lin C, Fuchs H, Chi L (2013) Bioinspired patterning with extreme wettability contrast on TiO₂ nanotube array surface: a versatile platform for biomedical applications. *Small* 9(17):2945–2953
160. Schmidt-Stein F, Hahn R, Gnichwitz JF, Song YY, Shrestha NK, Hirsch A, Schmuki P (2009) X-ray induced photocatalysis on TiO₂ and TiO₂ nanotubes: degradation of organics and drug release. *Electrochem Commun* 11(11):2077–2080
161. Das K, Bose S, Bandyopadhyay A (2009) TiO₂ nanotubes on Ti: influence of nanoscale morphology on bone cell-materials interaction. *J Biomed Mater Res A* 90A(1):225–237
162. Oh SH, Finones RR, Daraio C, Chen LH, Jin SH (2005) Growth of nano-scale hydroxyapatite using chemically treated titanium oxide nanotubes. *Biomaterials* 26(24):4938–4943
163. Tsuchiya H, Macak JM, Muller L, Kunze J, Muller F, Greil P, Virtanen S, Schmuki P (2006) Hydroxyapatite growth on anodic TiO₂ nanotubes. *J Biomed Mater Res A* 77A(3):534–541
164. Kar A, Raja KS, Misra M (2006) Electrodeposition of hydroxyapatite onto nanotubular TiO₂ for implant applications. *Surf Coat Technol* 201(6):3723–3731
165. Lai YK, Huang YX, Wang H, Huang JY, Chen Z, Lin CJ (2010) Selective formation of ordered arrays of octacalcium phosphate ribbons on TiO₂ nanotube surface by template-assisted electrodeposition. *Colloids Surf B Biointerfaces* 76(1):117–122
166. Huang YX, Lai YK, Lin LX, Sun L, Lin CJ (2010) Electrochemical construction and biological performance of micropatterned CaP films. *Acta Phys Chim Sin* 26(8):2057–2060

167. Lai YK, Pan F, Xu C, Fuchs H, Chi LF (2013) In situ surface-modification-induced superhydrophobic patterns with reversible wettability and adhesion. *Adv Mater* 25(12):1682–1686
168. Lai YK, Tang YX, Huang JY, Pan F, Chen Z, Zhang KQ, Fuchs H, Chi LF (2013) Bioinspired TiO₂ nanostructure films with special wettability and adhesion for droplets manipulation and patterning. *Sci Rep* 3:3009
169. Lai YK, Lin CJ, Wang H, Huang JY, Zhuang HF, Sun L (2008) Superhydrophilic-superhydrophobic micropattern on TiO(2) nanotube films by photocatalytic lithography. *Electrochem Commun* 10(3):387–391
170. Lai YK, Huang JY, Gong JJ, Huang YX, Wang CL, Chen Z, Lin CJ (2009) Superhydrophilic-superhydrophobic template: a simple approach to micro-and nanostructure patterning of TiO(2) films. *J Electrochem Soc* 156(11):D480–D484
171. Wang DA, Liu Y, Liu XJ, Zhou F, Liu WM, Xue QJ (2009) Towards a tunable and switchable water adhesion on a TiO₂ nanotube film with patterned wettability. *Chem Commun* (45):7018–7020
172. Lai YK, Lin ZQ, Huang JY, Sun L, Chen Z, Lin CJ (2010) Controllable construction of ZnO/TiO(2) patterning nanostructures by superhydrophilic/superhydrophobic templates. *New J Chem* 34(1):44–51
173. Lai YK, Lin ZQ, Chen Z, Huang JY, Lin CJ (2010) Fabrication of patterned CdS/TiO(2) heterojunction by wettability template-assisted electrodeposition. *Mater Lett* 64(11):1309–1312
174. Huang YX, Sun L, Xie KP, Lai YK, Liu BJ, Ren B, Lin CJ (2011) SERS study of Ag nanoparticles electrodeposited on patterned TiO(2) nanotube films. *J Raman Spectrosc* 42(5):986–991
175. Ortiz GF, Hanzu I, Knauth P, Lavela P, Tirado JL, Djenizian T (2009) TiO₂ nanotubes manufactured by anodization of Ti thin films for on-chip Li-ion 2D microbatteries. *Electrochim Acta* 54(17):4262–4268
176. Ryu WH, Nam DH, Ko YS, Kim RH, Kwon HS (2012) Electrochemical performance of a smooth and highly ordered TiO₂ nanotube electrode for Li-ion batteries. *Electrochim Acta* 61:19–24
177. Ghicov A, Alba SP, Macak JM, Schmuki P (2008) High-contrast electrochromic switching using transparent lift-off layers of self-organized TiO₂ nanotubes. *Small* 4(8):1063–1066
178. Ghicov A, Yamamoto M, Schmuki P (2008) Lattice widening in niobium-doped TiO₂ nanotubes: efficient ion intercalation and swift electrochromic contrast. *Angew Chem Int Ed* 47(41):7934–7937
179. Kim JH, Zhu K, Yan YF, Perkins CL, Frank AJ (2010) Microstructure and pseudocapacitive properties of electrodes constructed of oriented NiO-TiO₂ nanotube arrays. *Nano Lett* 10(10):4099–4104
180. Salari M, Konstantinov K, Liu HK (2011) Enhancement of the capacitance in TiO₂ nanotubes through controlled introduction of oxygen vacancies. *J Mater Chem* 21(13):5128–5133
181. Yang F, Yao JY, Liu FL, He HC, Zhou M, Xiao P, Zhang YH (2013) Ni-Co oxides nanowire arrays grown on ordered TiO₂ nanotubes with high performance in supercapacitors. *J Mater Chem A* 1(3):594–601
182. Paramasivam I, Macak JM, Ghicov A, Schmuki P (2007) Enhanced photochromism of Ag loaded self-organized TiO₂ nanotube layers. *Chem Phys Lett* 445(4–6):233–237
183. Macak JM, Barczuk PJ, Tsuchiya H, Nowakowska MZ, Ghicov A, Chojak M, Bauer S, Virtanen S, Kulesza PJ, Schmuki P (2005) Self-organized nanotubular TiO₂ matrix as support for dispersed Pt/Ru nanoparticles: enhancement of the electrocatalytic oxidation of methanol. *Electrochem Commun* 7(12):1417–1422
184. Song YY, Gao ZD, Schmuki P (2011) Highly uniform Pt nanoparticle decoration on TiO₂ nanotube arrays: a refreshable platform for methanol electrooxidation. *Electrochem Commun* 13(3):290–293
185. Li XL, Yao JY, Liu FL, He HC, Zhou M, Mao N, Xiao P, Zhang YH (2013) Nickel/Copper nanoparticles modified TiO₂ nanotubes for non-enzymatic glucose biosensors. *Sens Actuators B Chem* 181:501–508

186. Zhang YH, Xiao P, Zhou XY, Liu DW, Garcia BB, Cao GZ (2009) Carbon monoxide annealed TiO₂ nanotube array electrodes for efficient biosensor applications. *J Mater Chem* 19(7): 948–953
187. Varghese OK, Gong DW, Paulose M, Ong KG, Dickey EC, Grimes CA (2003) Extreme changes in the electrical resistance of titania nanotubes with hydrogen exposure. *Adv Mater* 15(7–8):624–627
188. Varghese OK, Gong DW, Paulose M, Ong KG, Grimes CA (2003) Hydrogen sensing using titania nanotubes. *Sens Actuators B Chem* 93(1–3):338–344
189. Mahshid S, Li CC, Mahshid SS, Askari M, Dolati A, Yang LX, Luo SL, Cai QY (2011) Sensitive determination of dopamine in the presence of uric acid and ascorbic acid using TiO₂ nanotubes modified with Pd, Pt and Au nanoparticles. *Analyst* 136(11):2322–2329
190. Wang Y, Wu YC, Cui JW, Xu GB, Xu GQ (2013) Ag nanoparticles decorated TiO₂ nanotube arrays for ultrasensitive gas sensing. *J Nanosci Nanotechnol* 13(2):1453–1455
191. Joo S, Muto I, Hara N (2010) Hydrogen gas sensor using Pt-and Pd-added anodic TiO₂ nanotube films. *J Electrochem Soc* 157(6):J221–J226
192. Yang LX, Luo SL, Cai QY, Yao SZ (2010) A review on TiO₂ nanotube arrays: fabrication, properties, and sensing applications. *Chin Sci Bull* 55(4–5):331–338
193. Li HY, Bai XD, Ling YH, Li J, Zhang DL, Wang JS (2006) Fabrication of titania nanotubes as cathode protection for stainless steel. *Electrochem Solid State Lett* 9(5):B28–B31
194. Macak JM, Zollfrank C, Rodriguez BJ, Tsuchiya H, Alexe M, Creil P, Schmuki P (2009) Ordered ferroelectric lead titanate nanocellular structure by conversion of anodic TiO₂ nanotubes. *Adv Mater* 21(30):3121–3125
195. Xin YC, Jiang J, Huo KF, Hu T, Chu PK (2009) Bioactive SrTiO₃ nanotube arrays: strontium delivery platform on Ti-based osteoporotic bone implants. *ACS Nano* 3(10):3228–3234
196. Yasuda K, Schmuki P (2007) Formation of self-organized zirconium titanate nanotube layers by alloy anodization. *Adv Mater* 19(13):1757–1760
197. Yang Y, Wang XH, Zhong CF, Sun CK, Li LT (2008) Ferroelectric PbTiO₃ nanotube arrays synthesized by hydrothermal method. *Appl Phys Lett* 92(12):122907
198. Zhang J, Tang XH, Li DY (2011) One-step formation of crystalline TiO₂ nanotubular arrays with intrinsic p-n junctions. *J Phys Chem C* 115(44):21529–21534
199. Daghrir R, Drogué P, Robert D (2013) Modified TiO₂ for environmental photocatalytic applications: a review. *Ind Eng Chem Res* 52(10):3581–3599
200. Kowalski D, Kim D, Schmuki P (2013) TiO₂ nanotubes, nanochannels and mesosponge: self-organized formation and applications. *Nano Today* 8(3):235–264
201. Huang JY, Zhang KQ, Lai YK (2013) Fabrication, modification, and emerging applications of TiO₂ nanotube arrays by electrochemical synthesis: a review. *Int J Photoenergy* 2013:761971
202. Zhang Q, Xu H, Yan W (2012) Highly ordered TiO₂ nanotube arrays: recent advances in fabrication and environmental applications—a review. *Nanosci Nanotechnol Lett* 4(5): 505–519
203. Morales AGR, Guzman MOC, Arteaga CC (2011) A brief review on fabrication and applications of auto-organized TiO₂ nanotube arrays. *Corrosion Rev* 29(1–2):105–121
204. Wang KY, Liu GH, Hoivik N, Johannessena E, Jakobsena H (2014) Electrochemical engineering of hollow nanoarchitectures: pulse/step anodization (Si, Al, Ti) and their applications. *Chem Soc Rev* 43(5):1476–1500
205. Nah YC, Paramasivam I, Schmuki P (2010) Doped TiO₂ and TiO₂ nanotubes: synthesis and applications. *Chemphyschem* 11(13):2698–2713
206. Smith YR, Ray RS, Carlson K, Sarma B, Misra M (2013) Self-ordered titanium dioxide nanotube arrays: anodic synthesis and their photo/electro-catalytic applications. *Materials* 6(7):2892–2957

New Approaches to the Study of Spinel Ferrite Nanoparticles for Biomedical Applications

45

Noppakun Sanpo, Christopher C. Berndt, Cuie Wen,
and James Wang

Contents

Introduction.....	1418
Ferrites.....	1419
Cubic Ferrites.....	1419
Cobalt Ferrite.....	1420
The Sol–Gel Method.....	1421
History.....	1421
The Sol–Gel Processing Method.....	1422
Chelating Agents.....	1423
Synthetic Chelating Agents.....	1424
Polymeric Chelating Agent.....	1425
Humic or Fulvic Acids.....	1426
Organic Acids.....	1426
Amino Acids.....	1427
Approach and Methodology.....	1428
Fabrication of Spinel Ferrite Nanoparticles.....	1428
Analytical Techniques Employed.....	1428
Surface Charge Measurements.....	1429
Experimental Results.....	1430
Microstructure of Spinel Ferrite Nanoparticles.....	1430
Contact Angle Measurement.....	1431
Particle Size Analysis.....	1432
Zeta Potential.....	1433
XRD Analysis.....	1434
Antibacterial Activities of the Spinel Ferrite Nanoparticles.....	1435
Effect of the Chelating Agents.....	1438
Conclusion.....	1439
References.....	1440

N. Sanpo (✉) • C.C. Berndt • C. Wen • J. Wang
Faculty of Engineering and Industrial Sciences,
Swinburne University of Technology, Hawthorn, VIC, Australia
e-mail: Noppakuns@hotmail.com; cberndt@swin.edu.au; cwen@swin.edu.au;
jawang@swin.edu.au

© Springer International Publishing Switzerland 2016
M. Aliofkhaezrai, A.S.H. Makhlof (eds.), *Handbook of Nanoelectrochemistry*,
DOI 10.1007/978-3-319-15266-0_12

1417

Abstract

This chapter is prepared into six different sections. The first part will provide a brief introduction of spinel ferrite nanoparticles synthesis, the use of chelating agents in the sol–gel method, and applications of spinel ferrite nanoparticles in biomedical fields. The second part will cover an overview of the structure and magnetism of spinel ferrites. The third part will present a summary of different types of chelating agents. The fourth part will provide information of the sol–gel synthesis for ceramic nanoparticles. The fifth part will focus on the preparation of cobalt ferrite nanoparticles by sol–gel methods using polyvinyl alcohol (PVA) and citric acid (CA) as chelating agents. The influence of chelating agents on the physical properties and antibacterial property of cobalt ferrite nanoparticles will be highlighted in the last part. A discussion on chelating agent–metal ion formation and the antibacterial mechanisms of spinel ferrite nanoparticles will be presented.

Keywords

Antibacterial • Biomedical • Chelating agent • Nanoparticles • Sol-gel • Spinel ferrite

Introduction

Nanocrystalline metal oxides have been the focus of intense research for more than a decade due to their unique crystallographic structure and microstructure, e.g., high surface area and high volume fraction of atoms at interfacial regions. The resulting properties, such as superplasticity, catalytic activity, and increased hardness, as well as the processing route of the final products, are distinctly different from those of their micrometer-sized counterparts. The use of spinel ferrite nanoparticles has been summarized in Table 1.

Table 1 The use of spinel ferrite nanoparticles

Researchers	Year	Applications
Sugimoto et al. [1]	1999	Magnetic materials
Wang et al. [2]	2005	Refractory materials
Mathew et al. [3]	2003	Catalysts
Gupta et al. [4]	2005	Improved drug solubility and stability and reduced side effects
Kalambur et al. [5]	2005	Heat mediators in hyperthermia treatments
Nasongkla et al. [6]	2006	Magnetic guidance in drug delivery
Reddy et al. [7]	2006	Imaging agents and treatment of brain tumors
Byrappa et al. [8]	2008	Drug delivery carrier in biomedical treatment
Sun et al. [9]	2004	Improved bacterial activity of drug carrier
Buteică et al. [10]	2010	The carrier in drug delivery system for brain and kidney

Chelating agents can reduce the condensation reactions in liquid-phase synthesis. From this reason, it has been used in inorganic chemistry to prevent particle agglomeration. They have been proven to control the cobalt ferrite phase in sol-gel chemical synthesis [11]. Chelating agents can function as good selective flocculants because of their metal specificity and selectivity. From the synthesis point of view, chelating agents present advantages over conventional mineral processing in terms of metal selectivity. The variety of major donor atoms, such as sulfur, nitrogen, oxygen, and phosphorus, make chelating agents useful in several applications. It is important to understand the chemical behavior of donors to predict the properties of chelating groups. Normally the choice of a chelating agent or a group is made on the basis of its function in analytical metal separations.

The enhanced control of homogeneity, elemental composition, and morphology of nanoparticles can be achieved from sol-gel processes. Moreover, uniformly nanosized metal clusters can be obtained, which are crucial for improving the properties of the nanoparticles. These advantages make the sol-gel route a favorable alternative to other conventional methods for the preparation of ceramic oxide composites [12]. Hence, the objectives of this chapter are fourfold. The first section is to develop novel multifunctional magnetic iron-based nanoparticles that also exhibit biocompatible and antibacterial properties to fulfill the requirements of a drug delivery system. The second is to synthesize spinel ferrite nanoparticles (CoFe_2O_4) by the sol-gel process using polyvinyl alcohol (PVA) and citric acid (CA) as the chelating agents. The third is to investigate the effect of chelating agents on the physical and antibacterial properties of the synthesized spinel ferrite nanoparticles. And the final one is to discuss the formation between chelating agents and metal ions during the synthesizing period and explore the possible interaction mechanism of nanoparticles in a bacterial environment.

Ferrites

Ferrites are well-known ferrimagnetic materials that consist mainly of ferrimagnetic oxides and, therefore, are electrically insulating. Since an alternating current field does not induce undesirable eddy currents in an insulating material, then ferrites are broadly used in high-frequency applications [13].

When ferrites are determined by the size and charge of the metal ions, it can be divided into two different structural symmetries, so that the charge of the oxygen ions and their relative amounts is balanced [14].

Cubic Ferrites

The cubic ferrite has the general formula $\text{MO.Fe}_2\text{O}_3$ where M is a divalent metal ion. These ferrites crystallize in the spinel structure and the spinel lattice is composed of a close-packed oxygen arrangement in which 32 oxygen ions form the unit cell. These anions are packed in a face-centered cubic (FCC) arrangement leaving two

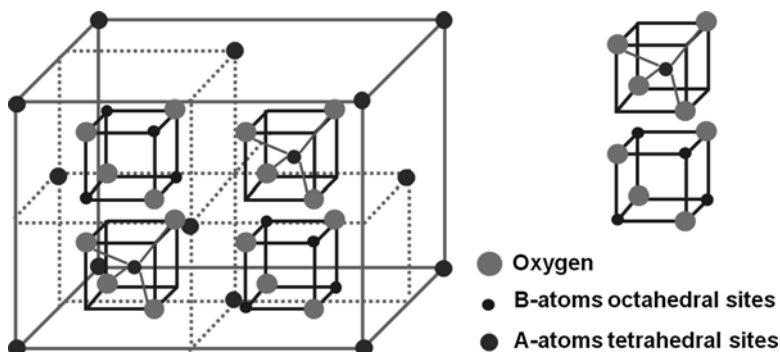


Fig. 1 The unit cell structure of spinel ferrite

Table 2 Anisotropy constants of some ferrites [14]

Ferrite	Anisotropy constant K_1 (erg/cm ³)
FeFe ₂ O ₄	-1.1×10^3
Co _{0.8} Fe _{2.2} O ₄	3.9×10^6
MnFe ₂ O ₄	-28×10^3
Co _{0.3} Mn _{0.4} Fe ₂ O ₄	1.1×10^6

types of space between anions: tetrahedrally coordinated sites (A), surrounded by four nearest oxygen atoms, and octahedrally coordinated sites (B), surrounded by six nearest neighbor oxygen atoms (Fig. 1). In total, there are 64 tetrahedral sites and 32 octahedral sites in the unit cell, of which only 8 tetrahedral sites and 16 octahedral sites are occupied, resulting in a structure that is electrically neutral [14].

Cobalt Ferrite

Some properties of the ferrites can be enhanced by incorporation of divalent metallic ions inside their structure. In the case of cobalt ferrite, the incorporation of cobalt ions results in an increase in coercivity due to an increased magnetocrystalline anisotropy resulting from the coupling of the spins of the cobalt and iron ions [15]. Cobalt ferrite (CoFe₂O₄) is a cubic ferrite with an inverse spinel structure where Co⁺² ions are located in B sites and Fe⁺³ in the A and B sites. This ferrite is characterized by having an anisotropy constant higher than the common ferrites (Table 2) such as magnetite and maghemite. The anisotropy constant of bulk cobalt ferrite is in the range of $1.8\text{--}3.0 \times 10^6$ erg/cm³, and the saturation magnetization is 80.8 emu/g at room temperature and 93.9 emu/g at 5 K. [16].

It has been observed that the magnitude of magnetic properties depends on the particle size. A decrease in particle size results in a decrease in coercivity and saturation magnetization; whereas the susceptibility and anisotropy constant have been reported to increase [17].

The Sol–Gel Method

History

The history of sol–gel technology has been summarized in Fig. 2.

The study of sol–gel processing on glass materials and inorganic ceramic started in the mid-1800s by Graham et al. [18]. These investigators found that the hydrolysis of tetraethyl orthosilicate under acidic conditions yielded SiO_2 in the form of a “glass-like material.” However, little technological interest was raised by these studies due to the long drying times required to obtain large monolithic pieces due to the discovery of the Liesegang rings phenomenon. The gels attracted the attention of chemists and researchers [19] in the late 1800s through to the 1920s. Despite the huge volume of descriptive literature published about these studies, understanding of physical–chemical properties of gels was limited. The second revival of the technique arose when the sol–gel method was employed by the ceramic industry in the 1950s and 1960s to synthesize a high number of novel ceramic oxide compositions (Al, Si, Ti, Zr, etc.). These ceramics were unavailable by traditional ceramic powder methods. The third boom came in the 1980s, when the sol–gel method was rediscovered by the micro-optical and heterogeneous catalytic industries. There are many key factors that made sol–gel gain its popularity such as the outstanding versatility, excellent control over the properties of the material, and the high degree of homogeneous component distribution. This phenomenon is indicated by the increase in the number of registered US patents using sol–gel elements, as depicted in Fig. 3.

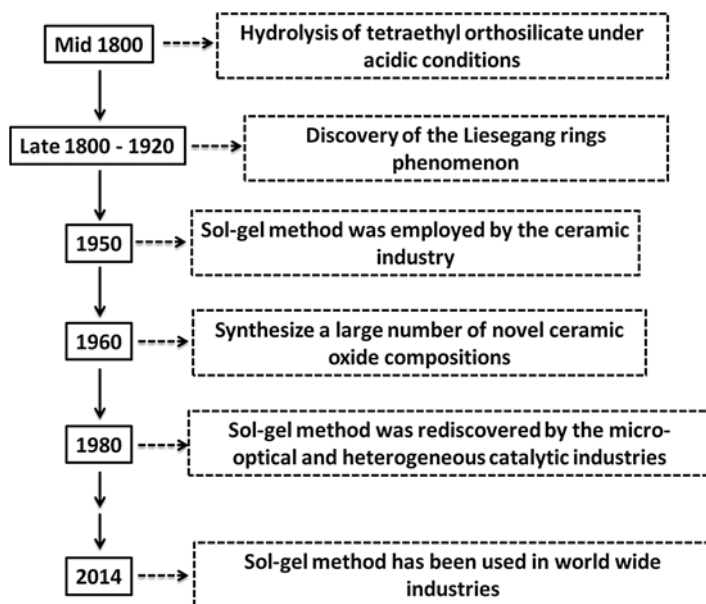


Fig. 2 The flowchart of sol–gel history

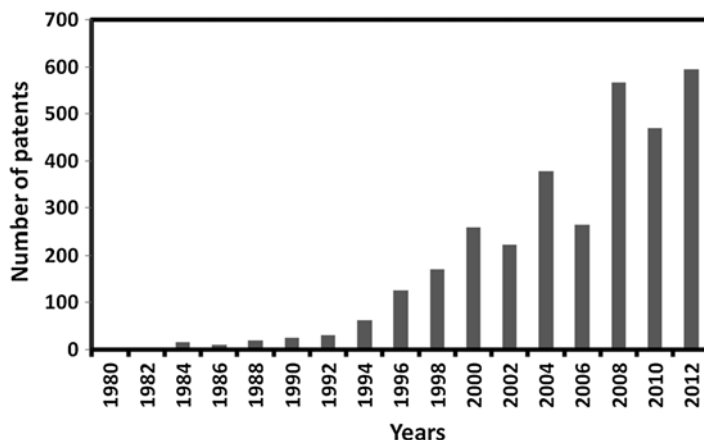


Fig. 3 Number of annually registered US patents related to the sol-gel method

The Sol-Gel Processing Method

In order to manufacture the ceramic oxide powders, sol-gel processing is considered one of the best chemical engineering. The term *sol* refers to the initial solution of the chemical components from which the final powder will eventually be derived. *Gel* is a term used to describe the final product of the ceramic material.

Ceramic method is the most broadly used synthetic technique for bulk metal oxides, which is based on the direct reaction of powder mixtures. The reactants and products controlled the diffusion of the atomic or ionic species. Both high temperature and small particle sizes are needed for solid-state processes in order to bring the reaction partners sufficiently close and to provide high mobility. The reaction conditions lead to thermodynamically stable phases, preventing the formation of metastable solids. There are various products that can be collected from the sol-gel process (Fig. 4), which depends on the synthesizing route.

Sol-gel procedures were successful in the nanoparticle synthesis for both inorganic and organic bulk metal oxides [20]. Liquid-phase routes represent the most promising alternatives for the size- and shape-controlled synthesis of nanoparticles [21]. The number of oxide nanoparticles obtained by sol-gel chemistry is small compared to the variety of compounds obtained via powder routes [12].

A synthesis procedure used for a bulk metal oxide may not be directly applied to the formation of its corresponding nanooxide. The reasons for this observation are manifold. Liquid sol-gel chemistry is considered a complex process because of the double role of water as ligand and solvent and the high reactivity of the metal oxide precursors toward water. However, there are many reaction parameters that must be controlled to provide good reproducibility of the synthesis protocol. Those parameters are the pH and temperature, the method of mixing, hydrolysis and condensation rate of the metal oxide precursors, the rate of oxidation, and the nature and concentration of anions [22].

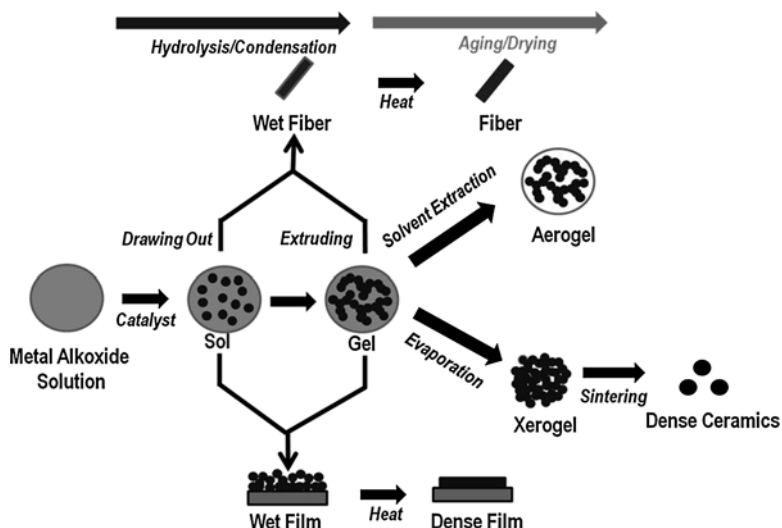


Fig. 4 Various steps in the sol-gel process to control the final morphology of the product

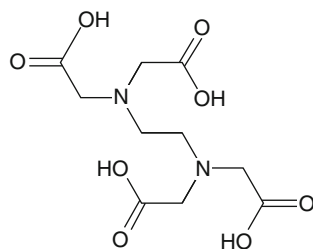
Chelating Agents

Chelating agents are chemical compounds that can form the stable metal complexes characterized by ring structures. Normally the choice of a chelating agent or a group is made on the basis of its function in well-known analytical metal separations. Several researchers have studied the application of using chelating agents in mineral processing [23].

Somasundaran et al. [24] studied the application of using chelating agents in mineral processing systems, the basis of the donor properties of the chelating groups and the metal species, and recent approaches to understand the chelation. Moreover, emphasis was given to the criteria for selection of chelating agents as collectors for various minerals and the predictability of the behavior of a chelating agent for a given mineral system. It was found that although chelating agents can be used effectively for the flotation of ores, they do not possess absolute specificity toward mineral species. The chelating agents must be carefully chosen in consideration of the conditions and mineral for beneficiation of the ore. Moreover, the chemical interaction between chelating agents and mineral species in the bulk and on the surface becomes more essential for understanding the mechanism. The reactions in the interfacial region might be understood only by use of new experimental approaches that will permit direct probing of this region.

Chelating agents can be classified either on the basis of donor atoms involved (O-O, N-O, N-N, S-O, S-S, S-N), ring size (4-, 5-, or 6-membered), charge on the complex (anion, cation, neutral), or number of bonds to the metal for every chelating molecule. However, there are five categories of compounds that are commonly mixed with minerals and that have been used in manufacturing. These chelating

Fig. 5 Chemical structure of EDTA



agents are (i) synthetic chelates, (ii) polymeric, (iii) lignosulfonates, humic or fulvic acids, (iv) organic acids, and (v) amino acids.

Each type of chelating agent has a different chemical structure, physical properties, and chelated mechanism to the minerals. The illustration of these chelating agents will be presented in sections “[Synthetic Chelating Agents](#),” “[Polymeric Chelating Agent](#),” “[Humic or Fulvic Acids](#),” “[Organic Acids](#),” and “[Amino Acids](#)” including the information that serves as a guide to understand the advantages and disadvantages of each type.

Synthetic Chelating Agents

Synthetic chelating agents have been used in many industrial applications, e.g., in the textile, detergents, metal cleaning, cosmetics, pharmaceuticals, agrochemicals, printing inks, concrete admixtures, photography, and pulp and paper industries as well as in electrochemical coating industries [25]. They are poorly degraded by microbes and present good water solubility. For these reasons, they are classified as environmentally acceptable. It has also been reported that the toxicity of the investigated synthetic chelating agents is low [26].

The most common form of a synthetic chelating agent is EDTA (ethylenediaminetetraacetic acid) which is usually used as the form of disodium salt of EDTA in agricultural mineral industry. A synthetically chelated mineral is the strongest form of chelation used in commercial agricultural applications [27]. The chemical structure of EDTA is presented in Fig. 5.

Normally alkaline earth divalent cations such as Ca^{2+} , Mg^{2+} , and Ba^{2+} form insoluble precipitates with carbonates, sulfates, and phosphates that may cause detrimental effects in several industrial processes. Moreover, the activation of corrosion process, the catalytic degradation, polymerization inhibition, redox reactivity, and changes in the coloring of products may be activated when the transition metal ions such as those of copper, iron, zinc, and manganese are added in the system [28]. Some of transition metal cations may also be added as a metal species for specific reasons, but they may later suffer undesired alterations due to changes in concentration, pH value, oxidation, or reactions with other ingredients during the process. Therefore, metal–EDTA complexes have been used as a chelate ligand with a high affinity constant.

In 1935, EDTA was patented in Germany by F. Munz. It is a powerful complexing agent of metals and a highly stable molecule which offered considerable versatility in industrial and household uses [28]. Since it is applied mostly in an aqueous medium, it is released into the environment through wastewaters. Moreover, the use of EDTA in agrochemical application may cause the presence of EDTA in soils or the disposal of products containing EDTA in landfill sites. It is highly unlikely to find the compound in air because it does not volatilize from waters or soils, even though this might arise during agrochemical use.

Polymeric Chelating Agent

Most chelating agents in the polymer group are considered to be water soluble and of low toxicity. Polymer, in this context, refers to the long-chain hydrocarbon backbone structure that consists of different functional groups such as hydroxyl, carboxylic, carbonate, and sulfonate groups.

Polyvinyl alcohol or PVA was first discovered from the experiment using polyvinyl acetate in ethanol and potassium hydroxide by Hermann and Haehnel in 1924 [29]. Polyvinyl alcohol is synthesized from the hydrolysis of polyvinyl acetate by ester interchange with methanol in the presence of anhydrous sodium methylate or aqueous sodium hydroxide.

Vinyl acetate monomer is the primary raw material used in the manufacture of polyvinyl alcohol. It is manufactured by the polymerization of vinyl acetate followed by partial hydrolysis. The process of hydrolysis is based on the partial replacement of the ester group in vinyl acetate with the hydroxyl group and is completed in the presence of aqueous sodium hydroxide. The addition of an aqueous saponification agent is required. Eventually, PVA is precipitated, washed, and dried. The degree of hydrolysis is determined by the time point at which the saponification reaction is stopped. Moreover, the degrees of hydrolysis and polymerization reaction are the main factors that specify the physical characteristics and its specific functional uses. Polyvinyl alcohol is classified into two classes of either partially hydrolyzed or fully hydrolyzed alcohol. Polyvinyl alcohol is the white or cream granular powder, odorless, tasteless, and translucent. PVA has several applications in the food industries as a binding and coating agent. It has been commercially used as a film-coating agent, especially in applications where moisture barrier and protection properties are required [30]. The food products in which PVA is intended to be used should have neutral pH and are stored at either low temperature or at room temperature conditions that would not have any impact on the stability of the PVA film. The repeating unit of polyvinyl alcohol is presented in Fig. 6.

Fig. 6 Chemical structure of PVA repeating unit

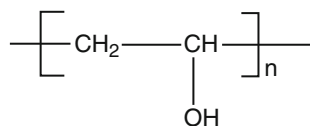
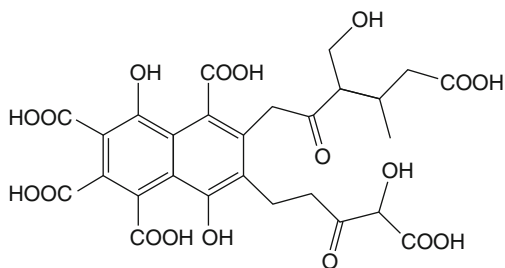


Fig. 7 Chemical structure of fulvic acids



Humic or Fulvic Acids

Fulvic acid is one of the most important compounds that constitutes the humic structure in rich composting soil [31]. There is no single fulvic acid chemical formula because it quickly forms into complex molecular combinations that may be needed to suit the varied environments. It is created in nature separately to fulfill many specific and essential functions. There are many publications concerning the chemical structure and the function of humic and fulvic acids [32]. Most of them debate the actual structure of these molecules; however, one commonly accepted structure is presented in Fig. 7.

The structure of fulvic acid is complex, and it is unable to be clearly identified and, therefore, synthesized by chemical methods. It is reported that fulvic acid has been applied in medical applications [32]. Many of these health examples have shown that fulvic acid is disease preventative and may enhance longevity. For this reason, fulvic acid potentially poses an opportunity to the future products of pharmaceutical companies, medical doctors, and health professionals.

Another interesting point of fulvic acid is about their absorptive interaction with environmental chemicals, either before or after they reach concentrations that are toxic to living organisms. Fulvic acid reacts strongly on the demise of organic compounds when it is applied to soil as a pesticide [32]. It has been found that fulvic acid is vital to aid the formation of new species of metal ions. It binds with organic pollutants such as pesticides and herbicides and catalyzes the breakdown of toxic pollutants [33].

Organic Acids

Organic acids are essential for the transportation and solubility of divalent elements (Zn^{2+} , Mn^{2+} , Fe^{2+} , and Cu^{2+}) in plants [34]. The organic acids can be called “anionic organic acids” because of their negative charge. One of the most popular organic acids used for manufacturing and agriculture is citric acid which is considered a weak organic acid. It is produced as a white crystalline powder and the chemical structure is presented in Fig. 8.

Fig. 8 Chemical structure of citric acid

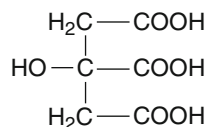
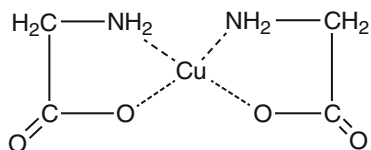


Fig. 9 Chemical structure of amino acid chelate of copper



The discovery of citric acid has been credited to Islamic alchemist Jabir ibn Hayyan in the eighth century [35]. Later, medieval scholars of the thirteenth century in Europe were aware of the acidic nature of lemon and lime juices. Citric acid was first extracted in 1784 by the Swedish chemist Carl Wilhelm Scheele [36], who crystallized it from lemon juice. Industrial-scale citric acid production began in 1890 and was based on the Italian citrus fruit industry.

Under the chemical structure consideration, citric acid presents the properties of other carboxylic acids. It decomposes through the loss of water and carbon dioxide when heated above 175 °C. The acidity of citric acid is slightly higher than other typical carboxylic acids because the anion can be stabilized by intermolecular hydrogen bonding from other protic groups.

Citric acid is one of the most useful ingredients in the food and beverage industries. The examples of the products that are produced using citric acid are jams, jellies, candies, preserved food, and frozen foods.

Amino Acids

In nature, plants produced amino acids for solubilizing and translocating minerals [37]. Amino acid compounds are produced from plants in order to make minerals biologically available in the cell. Although uncomplexed or unchelated minerals are sprayed on plants such as 10 % zinc sulfate, the mineral has to integrate with an organic compound such as an amino acid before it can be effectively used by the plant.

Moreover, amino acid compounds play a role in mineral uptake into plant tissue because of the increase in permeability effect of the amino acid on the cuticle. Figure 9 presents the complex structure of an amino acid chelate of copper:

The benefit of amino acid-chelated mineral systems is that they are considered less phytotoxic to plants, especially during stress points in plant development. In addition, iron glycinate complex, which is considered an iron amino acid, has been developed and used as a food fortifier and therapeutic agent in the prevention and treatment of iron deficiency anemia [38]. The most studied and broadly used chelate complex is ferrous bis-glycine chelate (FeBC). The primary experimental results have

shown that FeBC is efficacious in treating iron deficiency anemia. The ingestion of FeBC-fortified liquid milk, dairy wheat rolls, products, and multi-nutrient beverages is related with an improvement of iron status [39]. The limitations of using FeBC in widespread national fortification programs can be divided into two parts. The first one is the cost and the second issue is the efficiency for applying organoleptic changes in some food matrices. Moreover, the additional research is needed to establish the bio-availability of FeBC in different food matrices. Finally, there is a requirement for more rigorous potential trials designed to define the relative merits of amino acid chelates when compared with bioavailable iron salts such as ferrous sulfate and ferrous fumarate and to determine appropriate fortification levels.

Approach and Methodology

The prior background discussion has indicated the importance and need for focused studies concerning the influence of chelating agents on materials formed from nanoparticles such as spinel ferrites. Therefore, spinel ferrite nanoparticles were prepared via a sol–gel route using citric acid (CA) and polyvinyl alcohol (PVA) as a chelating agent. The influence of chelating agents on physical properties and anti-bacterial properties of these nanoparticles against *E. coli* and *S. aureus* was investigated. The intent of the following sections is to present data, the document, and the efficacy of such an approach that develops potentially therapeutic agents.

Fabrication of Spinel Ferrite Nanoparticles

The chelating agents, which are PVA and citric acid gel, were prepared by dissolving these powders in distilled water (5 %, 10 % and 15 % w/v) at 70 °C. The chelating agent solutions were maintained at 70 °C for 5 h or until the solution became clear. Cobalt nitrate ($\text{Co}(\text{NO}_3)_2 \cdot 6\text{H}_2\text{O}$) and iron nitrate ($\text{Fe}(\text{NO}_3)_3 \cdot 9\text{H}_2\text{O}$) powders were mixed with the chelating agent solution at ratios of cobalt nitrate weight (mol): iron nitrate weight (mol) : gel volume (ml) equal to 1:2:10. The sol–gel reaction was continued for about 3 h, and the temperature increased to 80 °C for 10 h or until the gel dried into the form of a powder. Finally, all samples were sintered at 800 °C for 4 h and then ground to a powder. Figure 10 diagrams the method employed.

Analytical Techniques Employed

Elemental composition analyses of the nanoparticles were carried out using energy-dispersive X-ray spectroscopy (EDX). Phase analyses of cobalt ferrite nanoparticles were conducted using X-ray diffraction (Bruker AXS D8 Advance XRD). Surface wettability, an indicator of the surface interaction of the metal oxide with a given solvent and an important measure for biomedical applications, was measured using the water contact angle technique (WCA-FTA200). The morphology (i.e., homogeneity

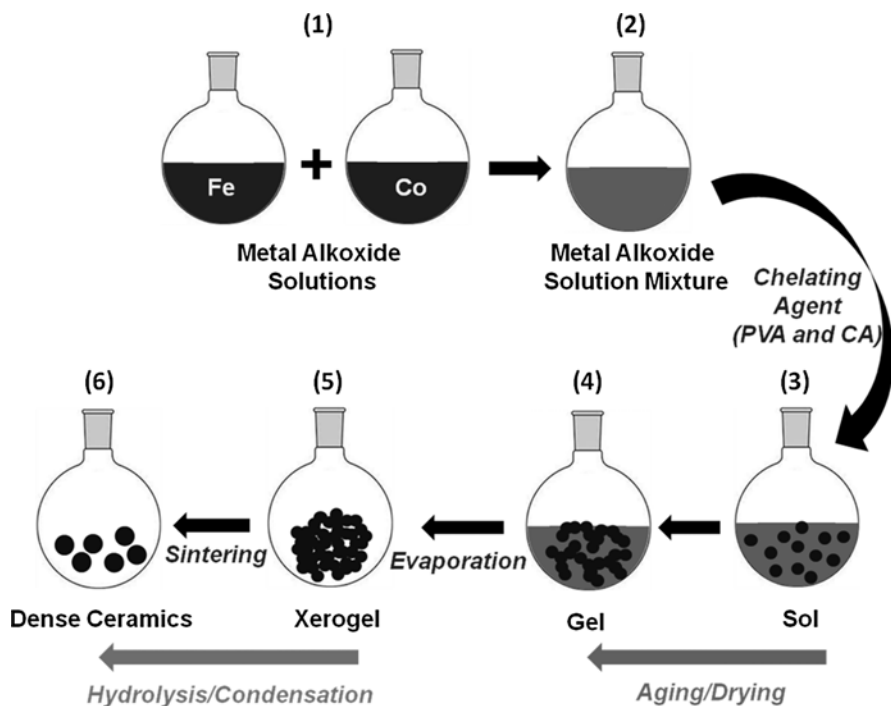


Fig. 10 The preparation of spinel ferrite nanoparticles

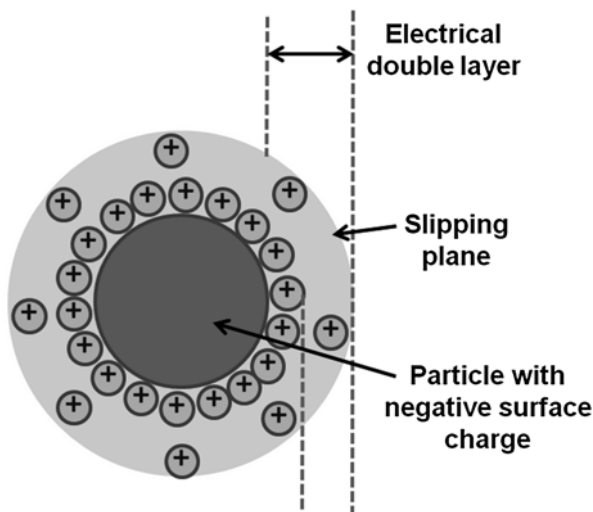
and particle size) of the materials was observed using a field emission scanning electron microscope (ZEISS SUPRA 40 VP SEM). Particle size characterization of nanoparticles was performed using a 90Plus Particle Size Analyzer (Brookhaven Instruments Corp., USA). The antimicrobial activity of cobalt ferrite nanoparticles was tested against gram-negative bacteria, *Escherichia coli* (*E. coli*), and gram-positive bacteria, *Staphylococcus aureus* (*S. aureus*).

For the modified Kirby–Bauer method [40], an equal amount of cobalt ferrite nanoparticles obtained from CA and PVA were coated on filter papers. All samples were placed on the *E. coli* growth lysogeny broth (LB) agar plate and incubated overnight at 37 °C. The zone of inhibition was measured in these studies.

Surface Charge Measurements

In order to determine the surface charge of nanoparticles, zeta potential analysis has been selected as the general experiment. Nanoparticles have a surface charge that attracts a thin layer of ions of opposite charge to the nanoparticle surface. This double layer of ions travels with the nanoparticle as it diffuses throughout the solution (Fig. 11). The electric potential at the boundary of the double layer is known as

Fig. 11 Electric double layer surrounding nanoparticles



the zeta potential of the particles which typically show the values between +100 mV to -100 mV. Zeta potential is considered an important method to interrogate the state of the nanoparticle surface and can be used to forecast the long-term stability of the nanoparticle. Zeta potential measurements were performed using a ZetaPALS Zeta Potential Analyzer BIC (Brookhaven Inst. Corp.).

Experimental Results

Microstructure of Spinel Ferrite Nanoparticles

Figure 12 reveals SEM images of the cobalt ferrites synthesized using different types and concentrations of a chelating agent. These micrographs indicate that the nature of the chelating agent influences the morphology of the synthesized nanoparticles. The nanoparticles synthesized using 5 % PVA as chelating agent (Fig. 12a) exhibit a sheet-type morphology. Meanwhile, the micrographs in Fig. 12b and c show irregular particles and some agglomeration where particles form large clusters. The nanoparticles prepared using 5 %, 10 %, and 15 % PVA as the chelating agent exhibit a polydisperse distribution with an average particle size of 350, 210, and 100 nm, respectively [41].

No difference for both microstructure and particle size was observed when using CA as the chelating agent at different concentrations as shown in Fig. 12d-f. However, they show an angular morphology along with a polydisperse distribution of an average particle size of 65, 55, and 48 nm for 5 %, 10 %, and 15 % CA, respectively.

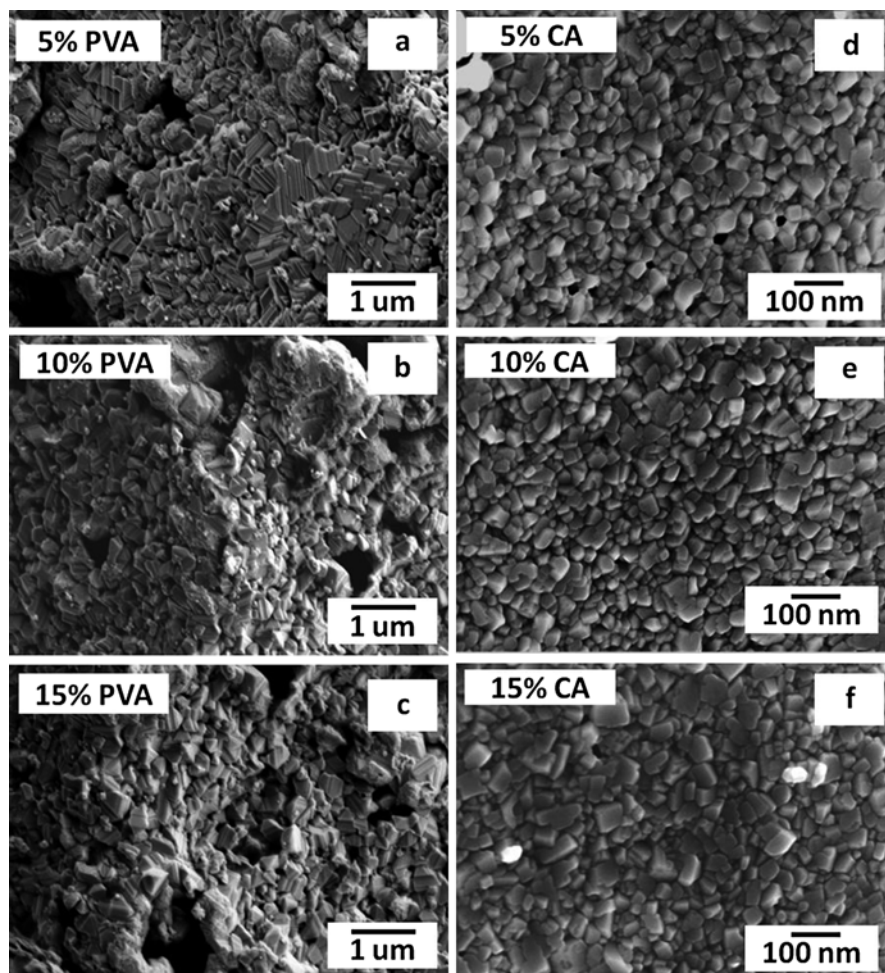


Fig. 12 SEM images of synthesized cobalt ferrite nanoparticles using (a) 5 % PVA, (b) 10 % PVA, (c) 15 % PVA, (d) 5 % CA, (e) 10 % CA, and (f) 15 % CA

Contact Angle Measurement

Figure 13 shows the contact angle measurements of cobalt ferrite nanoparticles obtained from CA and PVA and recorded with a CCD camera. Both images demonstrate that the water droplets were spread equally in all directions. The surface of cobalt ferrite was hydrophilic since the water contact angle was less than 90° .

Figure 14 depicts the stable water contact angle of the synthesized cobalt ferrite nanoparticles. The results indicate that cobalt ferrite nanoparticles obtained from CA as a chelating agent are marginally more hydrophobic than those prepared using PVA.

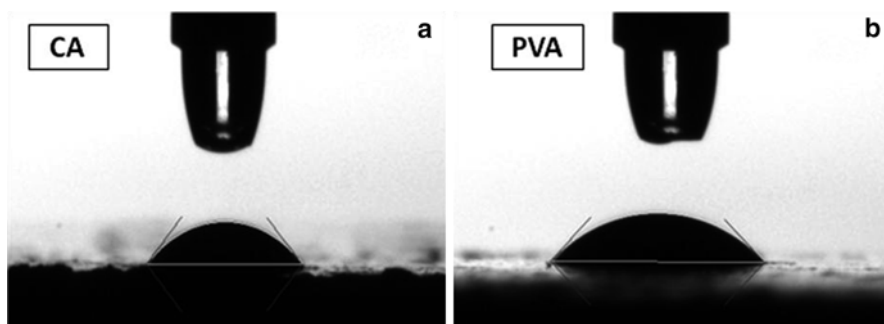


Fig. 13 The water contact angle images of cobalt ferrite nanoparticles obtained from (a) CA and (b) PVA

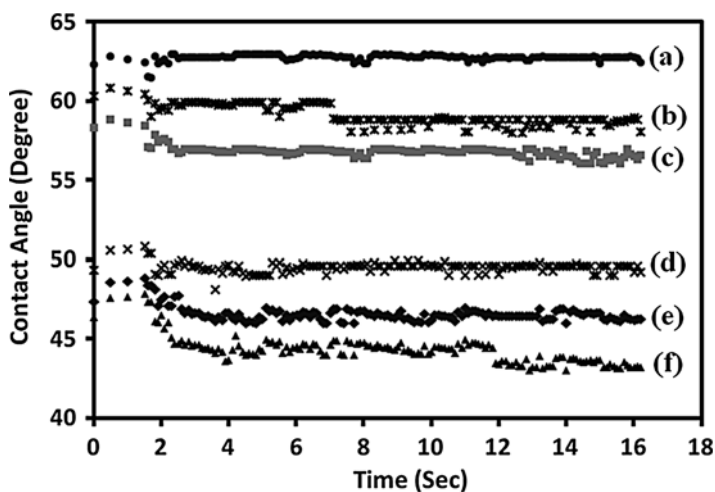


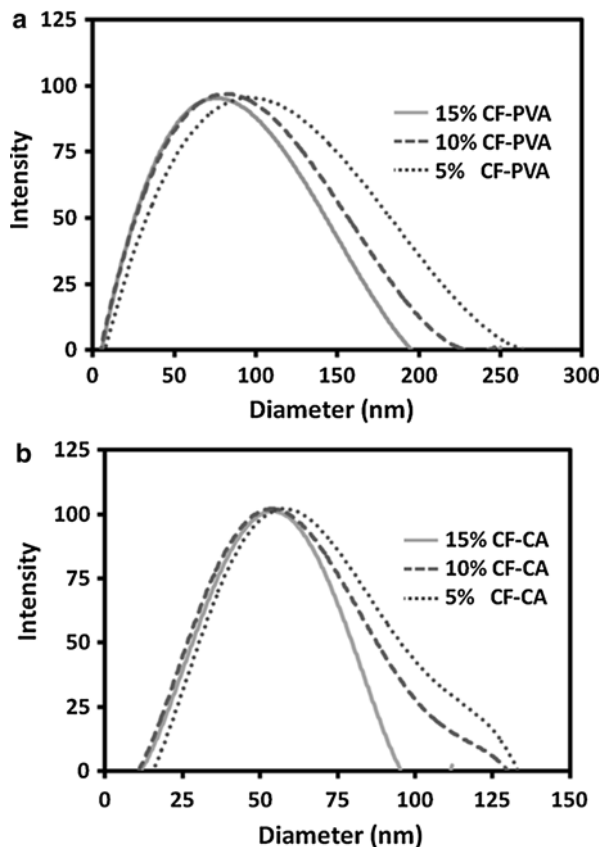
Fig. 14 The stability of water contact angles of the synthesized cobalt ferrite nanoparticles using (a) 15 % PVA, (b) 10 % PVA, (c) 5 % PVA, (d) 15 % CA, (e) 10 % CA, and (f) 5 % CA

Significant differences in the concentration of chelating agents have been noticed with respect to the contact angles of the cobalt ferrite nanoparticles. The water contact angles increase on increasing the concentration of the chelating agents [41].

Particle Size Analysis

Figure 15 shows the particle size distribution of cobalt ferrite nanoparticles prepared using PVA (a) and CA (b). Both types of nanoparticles present polydisperse particle size distributions.

Fig. 15 Particle size distribution of cobalt ferrite particles obtained from PVA (a) and CA (b)



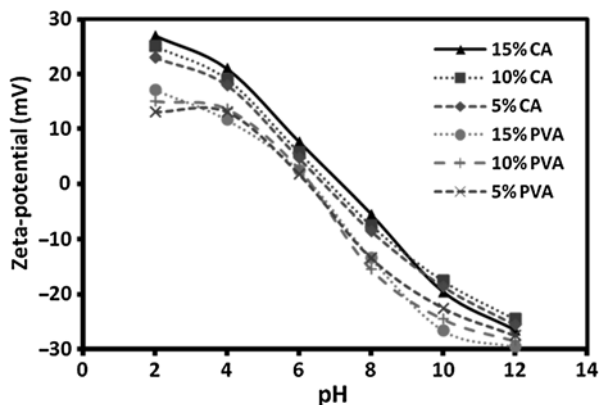
In Fig. 15a, the particle diameter ranges of cobalt ferrites prepared using 5 %, 10 %, and 15 % PVA are 25–260, 20–230, and 20–200 nm, respectively, and their average particle sizes are 112, 92, and 86 nm, respectively. In Fig. 15b, the particle diameter ranges of cobalt ferrites prepared using 5, 10, and 15 % CA are 20–135, 15–130, and 15–100 nm, respectively, and their average particle sizes are 62, 55, and 50 nm, respectively.

The particle size data indicates that the cobalt ferrite nanoparticles prepared using CA exhibit a smaller particle diameter distribution and average particle size than those prepared using PVA. Moreover, both particle diameter distributions and the average particle size decrease when increasing the concentration of PVA and CA.

Zeta Potential

Figure 16 shows the zeta potential of spinel ferrite nanoparticles prepared using different types and concentrations of chelating agents as a function of pH values. All the curves show isoelectric points (pH_{iep}) in the range of 6.5–8, which

Fig. 16 Zeta potential of cobalt ferrite particles as a function of pH in different NaCl concentrations



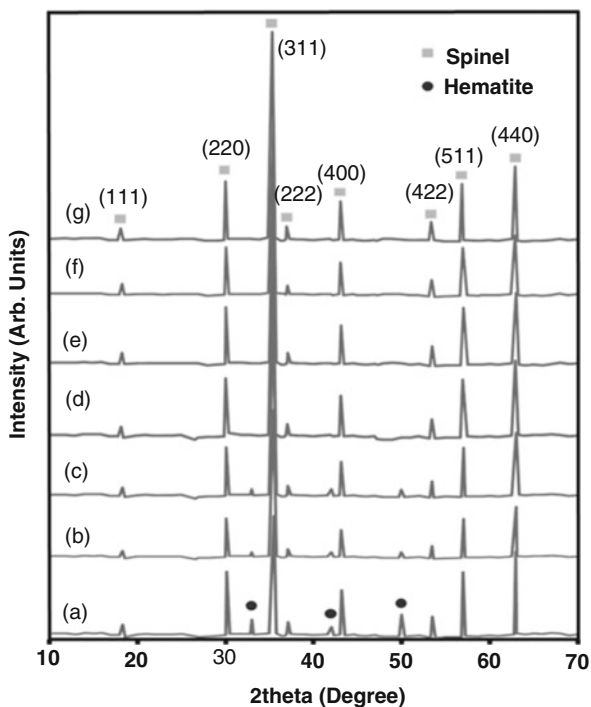
are in good agreement with previously reported data on these spinel nanoparticles [42]. The isoelectric point is the pH value at which a particular molecule or surface carries no net electrical charge. The results show that the pH_{iep} of cobalt ferrite nanoparticles decreased in the order of 5 % PVA < 10 % PVA < 15 % PVA < 5 % CA < 10 % CA < 15 % CA. Moreover, it can be seen that at a pH value below their pH_{iep} , cobalt ferrite nanoparticles carry a net positive charge, while they carry a net negative charge at a pH value above their pH_{iep} . This result unambiguously indicates that the electrical characterization of the cobalt ferrite surface can be used to identify different types and concentrations of chelating agents.

XRD Analysis

The XRD results of the cobalt ferrite nanoparticles prepared using PVA and CA are shown in Fig. 17. According to the literature [43], the spinel phase cobalt ferrite pattern exhibits eight peaks located between 15° and 70° .

The peaks at 18.29° , 30.08° , 35.44° , 37.06° , 43.06° , 53.45° , 56.98° , and 62.59° are indexed as the reflection planes of (111), (220), (311), (222), (400), (422), (511), and (440), respectively. The cobalt ferrite nanoparticles prepared using 5 %, 10 %, and 15 % CA (traces “e,” “f,” and “g” in Fig. 17) and 15 % PVA (trace “d” in Fig. 17) reveal that all peaks are related to the ideal spinel cobalt ferrite phase (JCPDS:00-002-1045). The appearance of these diffraction peaks demonstrates that single-phase polycrystalline cobalt ferrite nanoparticles can be formed by calcination of the precursor and chelating agent derived from the sol–gel process. However, additional peaks of an impurity hematite phase (JCPDS:01-089-2810) [21] were observed from cobalt ferrite nanoparticles prepared without using a chelating agent (trace “a” in Fig. 17) and 5 % and 10 % PVA (traces “b” and “c,” respectively, in Fig. 17) [41].

Fig. 17 X-ray diffraction patterns of cobalt ferrite nanoparticles synthesized at different conditions: (a) without chelating agents, (b) with 5 % PVA, (c) 10 % PVA, (d) 15 % PVA, (e) 5 % CA, (f) 10 % CA, and (g) 15 % CA



Antibacterial Activities of the Spinel Ferrite Nanoparticles

The contact biocidal property of cobalt ferrite nanoparticles prepared using PVA and CA was determined using a modified Kirby–Bauer technique. Filter papers are partially covered with and without cobalt ferrite nanoparticles and placed on a lawn of *E. coli* in an agar plate. The contact antibacterial property can be measured by the clear zone of inhibition around the filter papers after a 24 h incubation (Fig. 18). The diameter of inhibition zone for the cobalt ferrite nanopowders obtained from PVA is 17 mm, whereas that of cobalt ferrite nanoparticles prepared using CA is 25 mm (where the size of both filter papers is 5 mm). The result indicates that the cobalt ferrite nanoparticles prepared using CA have a more effective contact biocidal property than those prepared using PVA.

The antibacterial activities of the cobalt ferrite nanoparticles against *E. coli* and *S. aureus* are shown in Fig. 19. All tests were repeated ten times after culture incubation at 37 °C overnight for statistical studies. The concentration of cobalt ferrite nanoparticles was fixed at 1 g/L. Two typical cobalt ferrites prepared using PVA and CA were tested. Compared to the control, both types of cobalt ferrite nanoparticles inhibit the growth of *E. coli* and *S. aureus*, and the nanoparticles prepared using

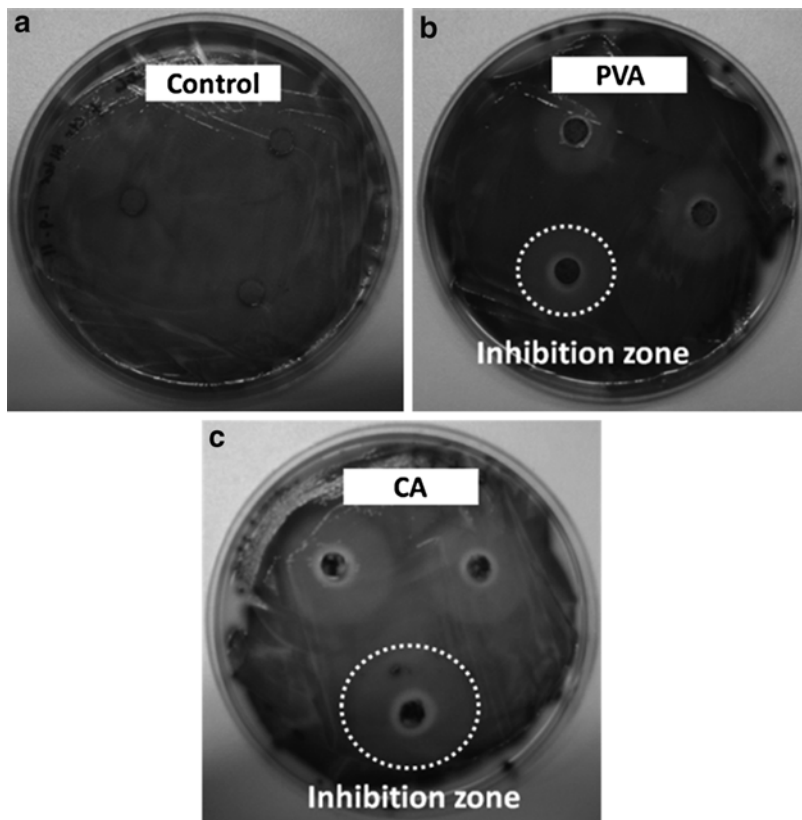
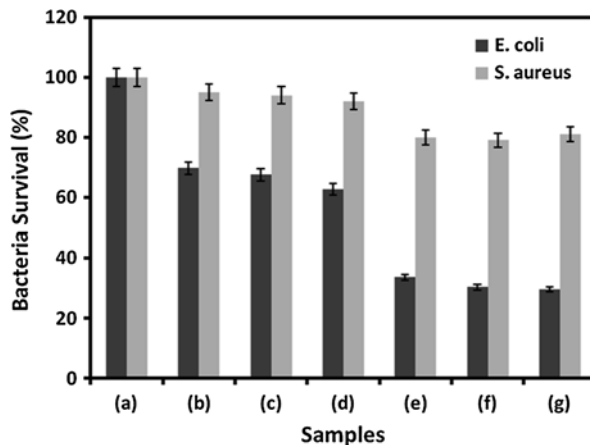


Fig. 18 Image of *E. coli* incubated for 24 h at 37 °C together with filter paper: (a) without cobalt ferrite nanoparticles, (b) with cobalt ferrite nanoparticles prepared using PVA, and (c) CA

Fig. 19 Antibacterial testing against *E. coli* and *S. aureus* of the cobalt ferrite nanoparticles synthesized at different conditions: (a) without cobalt ferrite nanoparticles, (b) with 5 % PVA, (c) with 10 % PVA, (d) with 15 % PVA, (e) with 5 % CA, (f) with 10 % CA, and (g) 15 % CA



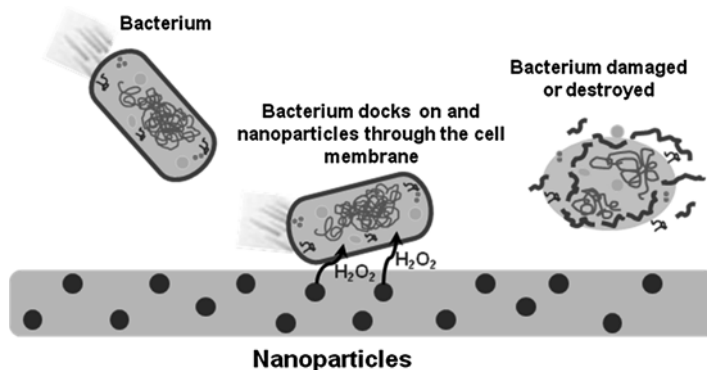


Fig. 20 The mechanisms for the antibacterial action of spinel ferrite nanoparticles

PVA showed 70 % of *E. coli* and 90 % of *S. aureus* survival, while 30 % of *E. coli* and 80 % of *S. aureus* survival were detected from nanoparticles prepared using CA. Their antibacterial abilities became slightly stronger with increasing chelating agent concentration [41].

There are several possible mechanisms for the antibacterial action to ceramic nanoparticles. It has been noted that ceramic nanoparticles bind to the membranes of microorganisms, similar to mammalian cells, prolonging the lag phase of the growth cycle and increasing the generation period of the organisms so that it takes each organism more time to make cell division finished [44]. Moreover, the main chemical species contributing to the occurrence of the antibacterial activity were assumed to be active oxide, hydrogen peroxide (H_2O_2), and superoxide (O_2^-), generated from the surface of these ceramics [45]. Hydrogen peroxide generated from the surface of ceramic nanoparticles can easily penetrate the cell wall of bacteria and cause cell destruction as presented in Fig. 20 [46]. The killing rate of ceramic nanoparticles against bacteria may depend on the penetration rate of an active oxide through the bacteria cell wall. Furthermore, the structure and the chemical composition of the cell wall are quite different between *E. coli* and *S. aureus*. That is, *E. coli* has a cell wall consisting of lipid A, lipopolysaccharide, and peptidoglycan, whereas the component of cell wall of *S. aureus* is peptidoglycan. These results indicate that active oxides generated from cobalt ferrite nanoparticles have more capability to penetrate the cell wall and decrease the cell division of *E. coli*. However, the interaction mechanism between cobalt ferrite nanoparticles and *E. coli* and *S. aureus* needs further investigation, and it is not intended to be the focus of the current contribution.

The *E. coli* and *S. aureus* killing rate of cobalt ferrite nanoparticles prepared using PVA is significantly lower than those prepared using CA. The first reason is that the killing rate is intimately associated with the surface area of nanoparticles dispersed into the *E. coli* and *S. aureus* suspension media. Since the cobalt ferrite nanoparticles prepared using CA exhibit a smaller crystalline size than those prepared using PVA as indicated in Fig. 15, these nanoparticles also exhibit a higher surface area, which leads to a higher killing rate of *E. coli* and *S. aureus*. These results are in good agreement with those reported by Ohira et al. [47].

A second effect may arise from the structural characteristics of the cobalt ferrite nanoparticles. XRD results (Fig. 17) indicate that cobalt ferrite nanoparticles prepared using CA present a single spinel cobalt ferrite phase, while those prepared using PVA exhibit a mixture of spinel and hematite phases. The spinel phase may play an important role in killing *E. coli* and *S. aureus*. It has been noticed that the sample with 15 % PVA demonstrates a higher *E. coli* and *S. aureus* survival rate than those with CA, even though they show the same single spinel cobalt ferrite phase. In this case the microstructural property may play a dominant role in killing *E. coli* and *S. aureus*.

Effect of the Chelating Agents

Chelating agents are used in inorganic chemistry to prevent particle agglomeration by reducing condensation reactions in liquid-phase synthesis [48]. From the point of chemical structure, PVA was used as a hydroxyl chelating agent, while CA was a carboxyl chelating agent. In this study, both types of chelating agents were used to chelate both inorganic precursors to form either a monodentate or bidentate metal complex as presented in Fig. 21 [49]. In addition, they prevent both metal cations from undesired spontaneous condensation reactions.

Powders without a chelating agent did not have a media through which they could interact with the mineral ions. Homogeneous sols were obtained by

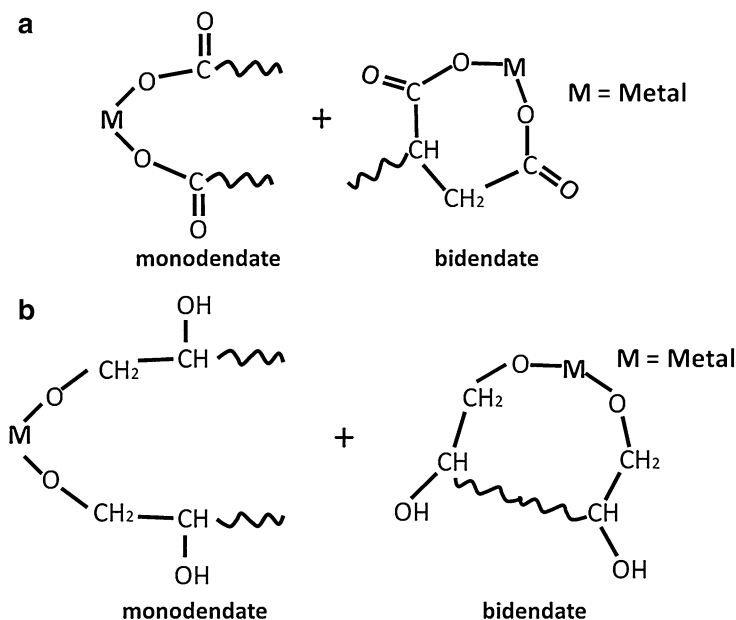


Fig. 21 Formation of monodentate and bidentate metal complexes obtained from (a) carboxyl chelating agent and (b) hydroxyl chelating agent

hydrolysis, but the time of homogeneity was on a small timescale compared to the overall reaction period. Phase separation usually took place at the gelling stage and resulted in a mixture of oxides. The random nature of the mixing process indicates that the final product contains a larger amount of the other oxides, for example, hematite as shown in Fig. 17a. Addition of PVA allows the formation of three oxide structures, i.e., cobalt–iron oxide, iron oxide, and cobalt oxide. On the other hand, CA permits the formation of individual molecular units that are free to diffuse so that the initial stoichiometry can be maintained as indicated in Fig. 17.

It has been observed that the addition of 5 %, 10 % and 15 % CA enables cobalt ferrite nanoparticles to be prepared under optimum processing conditions that result in the single-phase spinel cobalt ferrite without impurities. On the other hand, only the 15 % PVA formulation produces the same purity level of cobalt ferrite nanopowders that, however, exhibit a coarse microstructure. It can be concluded that a carboxyl chelating agent such as citric acid enables the manufacture of cobalt ferrites with a higher purity than those using a hydroxyl chelating agent (i.e., PVA). The variation in microstructure and morphology of the cobalt ferrite nanoparticles prepared from different chelating routes influences the *E. coli* and *S. aureus* survivor rate.

Conclusion

This work initially reviews the interrelationships between nanoparticles and chelating agents. It is emphasized that significant advances in material developments for many industries, i.e., mining, agricultural, and biomedical, have been implemented. Against this backdrop, a case is made concerning cobalt ferrite nanoparticles that have been modified by chelating agents of citric acid and polyvinyl alcohol.

A sol–gel technique for synthesizing cobalt ferrite nanoparticles using polyvinyl alcohol (PVA) and citric acid (CA) as chelating agents was developed. For the nanoparticles prepared using PVA, a crystal structure evolved from sheet to cube and presented a polydispersed distribution with an average particle size of 350, 210, and 100 nm as the PVA concentration increased from 5 % to 10 % to 15 %. However, those nanoparticles prepared under all concentrations of CA exhibited the same angular morphology along with a polydisperse of an average particle size of 65, 55, and 48 nm for 5 %, 10 %, and 15 % CA, respectively.

The cobalt ferrite nanoparticles prepared using CA as a chelating agent were marginally more hydrophobic than those prepared using PVA. Pure spinel cobalt ferrite nanoparticles were obtained when using CA and 15 % PVA. On the other hand, nanoparticles synthesized from 5 % and 10 % of PVA presented some impurities in the form of hematite phases. The results demonstrated that both types of cobalt ferrite nanoparticles exhibited effective antibacterial activity against *E. coli* and *S. aureus*. In the test of LB agar plates, the cobalt ferrite nanoparticles exhibited surface-dependent antibacterial activities and could be used as drug delivery systems and for other biomedical applications.

Acknowledgments The authors acknowledge financial support for this research through the Australia-India Strategic Research Fund (AISRF) ST060048. Mr. Sanpo acknowledges support from Swinburne University of Technology in the form of a postgraduate scholarship.

References

1. Sugimoto M (1999) The past, present, and future of ferrites. *J Am Ceram Soc* 82:269–279
2. Wang WG, Mogensen M (2005) High-performance lanthanum-ferrite-based cathode for SOFC. *Solid State Ion* 176:457–462
3. Mathew T, Malwadkar S et al (2003) Oxidative dehydrogenation of ethylbenzene over $\text{Cu}_{1-x}\text{Co}_x\text{Fe}_2\text{O}_4$ catalyst system: Influence of acid–base property. *Catal Lett* 91:217–224
4. Gupta AK, Gupta M (2005) Synthesis and surface engineering of iron oxide nanoparticles for biomedical applications. *Biomaterials* 26:3995–4021
5. Kalambur VS, Han B et al (2005) In vitro characterization of movement, heating and visualization of magnetic nanoparticles for biomedical applications. *Nanotechnology* 16:1221–1233
6. Nasongkla N, Bey E et al (2006) Multifunctional polymeric micelles as cancer-targeted, MRI-ultrasensitive drug delivery systems. *Nano Lett* 6:2427–2430
7. Reddy GR, Bhojani MS et al (2006) Vascular targeted nanoparticles for imaging and treatment of brain tumors. *Clin Cancer Res* 12:6677–6686
8. Byrappa K, Ohara S et al (2008) Nanoparticles synthesis using supercritical fluid technology-towards biomedical applications. *Adv Drug Deliv Rev* 60:299–327
9. Sun S, Zeng H et al (2004) Monodisperse MFe_2O_4 ($\text{M}=\text{Fe}, \text{Co}, \text{Mn}$) nanoparticles. *J Am Chem Soc* 126:173–279
10. Buteică AS, Mihaiescu DE et al (2010) The anti-bacterial activity of magnetic nanofluid: Fe_3O_4 /oleic acid/cephalosporins core/shell/adsorption-shell proved on *S. Aureus* and *E. Coli* and possible applications as drug delivery systems. *Dig J Nanomater Biostruct* 5:927–932
11. Sanpo N, Berndt CC et al (2012) Microstructural and antibacterial properties of zinc-substituted cobalt ferrite nanopowders synthesized by sol–gel methods. *J Appl Phys* 112:08433
12. De G, Mattei G et al (2000) Au–Cu alloy nanocluster doped SiO_2 films by sol–gel processing. *Chem Mater* 12:2157–2160
13. Callister WD (2007) *Materials science and engineering: an introduction*. Wiley, New York
14. Goldman A (2006) *Modern ferrite technology*. Springer, New York
15. Pillai V, Shah DO (1996) Synthesis of high-coercivity cobalt ferrite particles using water-in-oil microemulsions. *J Magn Magn Mater* 163:243–248
16. Tung LD, Kolesnichenko V et al (2003) Magnetic properties of ultrafine cobalt ferrite particles. *J Appl Phys* 93:7486–7488
17. Moumen N, Pileni MP (1996) Control of the size of cobalt ferrite magnetic fluid. *J Phys Chem* 100:1867–1873
18. Graham T (1864) On the properties of silicic acid and other analogous colloidal substances. *J Chem Soc* 17:318–327
19. Liesegang RE (1906) Einescheinbarchemische Fernwirkung. *Ann Phys* 324:395–406
20. Hench LL, West JK (1990) The sol–gel process. *Chem Rev* 90:33–72
21. Gul IH, Maqsood A (2008) Structural, magnetic and electrical properties of cobalt ferrites prepared by the sol–gel route. *J Alloys Compd* 465:227–231
22. Livage J, Henry M et al (1988) Sol–gel chemistry of transition metal oxides. *Prog Solid State Chem* 18:259–341
23. Parekh BK, Miller JD (1999) *Advances in flotation technology*. Society for Mining, Metallurgy & Exploration, Littleton
24. Somasundaran P, Nagaraj DR (1984) Chemistry and applications of chelating agents in floatation and flocculation. In: Jones MJ, Oblatt R (eds) *Reagents in minerals industry*. IMM, London, pp 209–219

25. Knepper TP (2003) Synthetic chelating agents and compounds exhibiting complexing properties in the aquatic environment. *TrAC Trends Anal Chem* 22:708–724
26. Islam A, ALaskar M et al (2013) Preconcentration of metal ions through chelation on a synthesized resin containing O, O donor atoms for quantitative analysis of environmental and biological samples. *Environ Monit Assess* 185:2691–2704
27. Neugschwandtner RW, Tlustoš P et al (2008) Phytoextraction of Pb and Cd from a contaminated agricultural soil using different EDTA application regimes: laboratory versus field scale measures of efficiency. *Geoderma* 144:446–454
28. Oviedo C, Rodríguez J (2003) EDTA: the chelating agent under environmental scrutiny. *Quim Nova* 26:901–905
29. Finch CA (1973) Polyvinyl alcohol: properties and applications. Wiley, New York
30. RajavardhanaRao T, Omkaram I et al (2013) Role of copper content on EPR, susceptibility and optical studies in poly(vinylalcohol) (PVA) complexed poly(ethylene glycol) (PEG) polymer films. *J Mol Struct* 1036:94–101
31. Van Tonder JT (2008) Effect of potassium humate on soil properties and growth of wheat. University of the Free State, New York
32. Gaffney JS, Marley NA, Clark SB (1996) Humic and fulvic acids: isolation, structure, and environmental role. American Chemical Society, New York
33. Pignatello JJ (1989) Sorption dynamics of organic compounds in soils and sediments. In: Sawhney BL, Brown K (eds) Reactions and movement of organic chemicals in soils. Soil Science Society of America, Madison, pp 45–80
34. Millaleo R, Reyes-Diaz M et al (2010) Manganese as essential and toxic element for plants: transport, accumulation and resistance mechanisms. *J Soil Sci Plant Nutr* 10:470–481
35. Flack H (2009) Louis Pasteur's discovery of molecular chirality and spontaneous resolution in 1848, together with a complete review of his crystallographic and chemical work. *Acta Crystallogr Sect A* 65:371–389
36. Verhoff FH (2000) Citric acid. In Ullmann's encyclopedia of industrial chemistry, Wiley-VCH Verlag GmbH & Co. KGaA, Indiana
37. Nowack B (2002) Environmental chemistry of aminopolycarboxylate chelating agents. *Environ Sci Technol* 36:4009–4016
38. Allen LH (2002) Advantages and limitations of iron amino acid chelates as iron fortificants. *Nutr Rev* 60:S18–S21
39. Hechtman L (2011) Clinical naturopathic medicine. Elsevier, Sydney
40. Wikins TD, Holdeman LV et al (1972) Standardized single-disc method for antibiotic susceptibility testing of anaerobic bacteria. *Antimicrob Agents Chemother* 1:451–459
41. Sanpo N, Wang J et al (2013) Influence of chelating agents on the microstructure and antibacterial property of cobalt ferrite nanopowders. *J Aust Ceram Soc* 49:84–91
42. Tamura H, Matijevec E (1982) Precipitation of cobalt ferrites. *J Colloid Interf Sci* 90:100–109
43. Choi EJ, Ahn Y et al (2003) Superparamagnetic relaxation in CoFe₂O₄ nanoparticles. *J Magn Magn Mater* 262:L198–L202
44. Radke LL, Hahn BL et al (1994) Effect of abscess fluid supernatants on the kinetics of *Candida albicans* growth. *Clin Immunol Immunopathol* 73:344–349
45. Yamamoto O, Sawai J (2001) Preparation and characterization of novel activated carbons with antibacterial function. *Bull Chem Soc Jpn* 74:1761–1765
46. Sawai J, Shoji S et al (1998) Hydrogen peroxide as an antibacterial factor in zinc oxide powder slurry. *J Ferment Bioeng* 86:521–522
47. Ohira T, Yamamoto O et al (2008) Antibacterial activity of ZnO powder with crystallographic orientation. *J Mater Sci Mater Med* 19:1407–1412
48. Oubaha M, Etienne P et al (2005) Sol–gel derived organic and inorganic hybrid materials for photonic applications: Contribution to the correlation between the material structure and the transmission in the near infrared region. *J Sol–Gel Sci Technol* 33:241–248
49. Varma PCR, Colreavy J et al (2009) Effect of organic chelates on the performance of hybrid sol–gel coated AA2024-T3 aluminium alloys. *Prog Org Coat* 66:406–411

Index

A

- AAO. *See* Anodic aluminum oxide (AAO)
- Absorption spectra, clusters
 - configurational average of signal, 747–748
 - multiple-scattering expansion, 744–747
 - photo-absorption process, 744
- AC voltammetry, 519–522
- Adenine, 254, 262–264, 266, 268
- Aggregative growth. *See* Nano-electrodeposition
- Alloys, nano-electrodeposited, 33–41
- Amperometry, 1134, 1135
- Anodic aluminum oxide (AAO)
 - anodization, 630
 - applications, 617–630
 - arrangement, influence on, 605–609
 - fabrication, 611, 625–626
 - formation, 594–602
 - luminescent properties, 609–611
 - nanodots, 618, 624
 - nanostructured sensors, 628–629
 - nanotubes, 617, 623
 - nanowires, 614–616, 620–621
 - silver plasmonic nanodots, 619
- Anodic eletrografting process, 857
- Anodic oxidation, 1305–1308
- Anodization, 1197, 1198, 1223, 1226, 1233, 1237, 1243
 - advantage, 1210
 - anodic aluminum oxide, 630
 - nanochemical sensor fabrications, 1226
 - nanoporous tin dioxide film fabrication, 57, 73, 1204
 - porous ZnO films, 1203
- Antibacterial properties, 1419, 1428, 1435–1438

B

- Bimetallic nanoparticles, 173–174
 - alloy-structured, 177–178
 - architectures, 177–181
 - characterization, 191–216
 - core-shell, 178–179
 - electrochemical aspects, 175–177
 - formation, 181–191
 - fuel cell reaction, electrochemical studies, 217–225
 - hollow-structured, 179–181
- Biochemistry, 261
- Biocomposite nanomaterials, 1180–1184
- Biofuel cells, 1014, 1015, 1025, 1028
- Biomedical analysis, 1135–1137
- Biomedical applications, spinel ferrite nanoparticles. *See* Spinel ferrite nanoparticles
- Biomedical materials
 - corrosion protection of implants, 584–585
 - EPD of bacteria, 583–584
 - forming biocompatible layers, 582–583
- Biomedical scaffold
 - cell interactions, 1401–1403
 - hydroxyapatite growth, 1403–1404
- Biosensors, 1074, 1126, 1130, 1135–1138
- Bridge-assisted superexchange, 505–506

C

- Cadmium selenide (CdSe), 105, 114
- Capacitance and nanoparticle's conductivity, 870, 871, 893–902, 907

- Carbon
 glassy electrodes, 257–258, 262
 materials for electroanalysis, 243–253
 NA detection, electrode material, 253–255
 paste electrodes, 257, 262
- Carbon nanostructures, 906, 917–925
- Carbon nanotube (CNT), 258–260, 262, 1150–1152, 1156
- Cathodic electrografting process, 857
- Ceramic materials, 570–572
- Characterization
 bimetallic nanoparticles, 191–216
 electrochemically grown thin films
 hot probe, four-probe resistivity, and hall effect measurements, 1223–1226
 morphological studies, 1212–1220
 optical studies, 1220–1222
 photocurrent transient measurement, 1222–1223
 X-ray diffraction, 1210–1212
- Charge transfer process
 carbon nanomaterial thin films, 893
 carbon nanotubes, 893–899
 graphene, 899–902
 mono- or multilayers of nanoparticles, 877
 two- and three-dimensional layer of nanoparticles, 889–893
- Chelating agents, 1423–1424
 amino acids, 1427–1428
 effects, 1438–1439
 humic/fulvic acids, 1426
 organic acids, 1426–1427
 polymeric, 1425
 synthetic, 1424–1425
- Chemical sensors
 choice of substrate, 1226
 description, 1197
 device structure fabrication, 1226–1228
 nanocrystalline grains, 1198
 selectivity and stability, 1238–1242
 sensing procedure, 1228–1229
- Chemistry, 1331, 1332, 1334, 1336, 1338–1339, 1344
- Chronoamperometry, 517–519
- Co nanoparticles, 772
- Coaxial nanorods, 126–131
- Codeposition, 401, 403, 405
- Composite coatings, 336, 338, 342–349
- Composites, nanomaterials, 18
- Conducting polymers (CPs), 419–420, 429, 1132, 1134, 1184–1188
 characterization of G-CP, 487
 FTIR spectra of G-CP, 491
 novel G-CP synthesis, 486
 synthesis of G-CP nanocomposite, 486–487
- Conductivity of nanoparticles, 883–889, 891, 900, 914, 915
- Core-shell particles, electrodeposition
 cobalt, 773–776
 platinum, 777–780
- Corrosion protection, 316–319, 325, 326
- Cu metallization
 basic reference data, 1280–1282
 experimental, 1282–1292
- Cyclic voltammetry, 510, 514–517, 1135
- Cylindrical particles, 1060–1062
- Cytosine, 254, 262–264, 266
- D**
- Deoxyribonucleic acid (DNA)
 multiplexed DNA visualization, 1081–1089
 thin films, 1079–1081
- Desorption/ionization on silicon (DIOS), 858–859
- Dielectrophoresis, 1129, 1131, 1136
- Doped graphene nanocrystalline layers, 161
- Doping, ZnO
 ECD growth conditions, 671
 n-type doping with Cl, 669
 p-type doping with Ag, 669–675
- Dye-sensitized solar cells
 electrochemical impedance spectroscopy
 characterization, 1308–1309
 equivalent circuit model, 1310
 essential elements, 1302
 nanoparticles and nanostructures,
 photoanodes, 1303–1305
 simplified equivalent circuit, 1311
 structure and schematic working principle, 1302–1303
 TiO₂ nanotube-based, 1316–1323
- E**
- Electrocatalytic properties, 771
- Electrochemical analysis of G-CP, 488
- Electrochemical anodization, TNAs
 electrolyte, 1384–1385, 1387
 growth mechanism, 1386, 1388–1389
 voltage, 1386, 1388
- Electrochemical biosensors
 amperometric glucose biosensor, 1172–1175
 enzymatic biosensors, 1172
 genosensors, 1178–1179
 immunosensors, 1176–1178

- Langmuir-Blodgett based biosensors, 1165–1169
- layer-by-layer based biosensors, 1169–1175
- Electrochemical etching, 286–287, 291–298
- Electrochemical fabrication, 357
- Electrochemical impedance spectroscopy (EIS), 522–527, 1308–1309
- Electrochemical materials, self-organized nano- and micro-structure of
 - See* Self-organized nano- and micro-structure, of electrochemical materials
- Electrochemical nucleation, 1063–1064
- Electrochemical promotion of catalysis (EPOC), 1102–1107
 - cell configurations and reactor design, 1109–1112
 - highly dispersed nano-catalyst preparation, 1107–1108
 - of nanostructured catalysts, 1112–1116
- Electrochemical sensors, 1147–1148
- Electrochemistry, 511–513, 1197, 1204–1210, 1331–1337, 1340, 1342, 1343
 - AC voltammetry, 519–522
 - bimetallic nanoparticles, 175–177
 - chronoamperometry, 517–519
 - cyclic voltammetry, 510, 514–517
 - electrochemical impedance spectroscopy, 522–527
 - fuel cell reaction, 217–225
 - metal electrodes, roughed, 50–54
 - peptide-based SAMs, 530–545
 - photocurrent generation measurements, 527–529
- Electrochromic device, 811–813
- Electrocrystallization, 26, 32
 - fundamentals, 138–141
 - nanostructured composites, 154–165
 - nanostructured copper, 141–151
 - nanostructured nickel, 151–154
- Electrodeposition. *See also* Nano-electrodeposition
 - Cd and Pb, 731–732
 - cobalt
 - growth loop characteristic, 773
 - of low charge, 774
 - reproducibility, 773
 - coinage and *sp* metals, 729
 - composite nanomaterials, 18
 - compound semiconductors, 734–735
 - elemental semiconductors, 732–734
 - for fabrication, 685–687
 - graphene nanomaterials synthesis, 11–17
 - magnetic metals, 725–727
 - nanostructured metal oxide electrodes
 - 2D and 3D doped MnO₂, 689–695
 - 3D branched dendritic structures, 702–706
 - composites carbon and metal oxides, 706–709
 - materials, 687–689
 - metallic foams, 695–701
 - platinum, 777–780
 - rare metals, 729–730
 - reactive metals, 723–725
 - semimetal elements, 727
 - surface-mediated, 7–11
 - zinc-nanoparticle composite coatings, 343–349
 - ZnO (*see* ZnO, electrodeposition of)
- Electroforming
 - continuous fiber-reinforced MMCs, 958–960
 - fundamentals of, 942–944
 - requirements for, 950–952
 - thick, complex 3D deposits, 948–952
- Electroless plating, 390, 392–397, 399–401
- Electroluminescence stabilization, 858
- Electrolytes, 484, 486
- Electromagnetic nanoresonators, surfaces, 50–54
- Electron hopping, 507
- Electron-transfer theory, 505–510
- Electrophoresis, graphene nanomaterials synthesis, 16–17
- Electrophoretic deposition (EPD)
 - bacteria, 583–584
 - batteries and electrochemical capacitors, 576
 - catalyst support and molecular sieves, 578–579
 - corrosion protection, 584–585
 - corrosion-resistant coatings, 578
 - dye sensitized solar cells, 575
 - forming biocompatible layers, 582–583
 - mechanisms, 566–567
 - multilayered composites, 572
 - nanotubes deposition, 574
 - oriented ceramic materials, 570–572
 - particle size separation, 574
 - piezoelectric actuators, 580–581
 - process parameters, 569–570
 - sensors, 579–580
 - SiC fiber reinforced composites, 575
 - solid oxide fuel cells, 576–578
 - suspension parameters, 567–569
 - thermoelectric thick films, 573
 - thick film optical modulators, 575–576

- Energy conversion, 74, 78
Energy storage, 73, 84
Environmental analysis, 1136–1138
Enzymes, 1015, 1027
Equivalent circuit, 1309–1311, 1321
EXAFS in condensed matter, 743, 759
- F**
Fibre metal matrix composites, 957–960
Formation, bimetallic nanoparticles, 181–191
Fuel cell, 74–75, 90–95
- G**
G-CPs. *See* Conducting polymers (CPs)
Galvanic replacement, 977, 982–985
Gold
 electrodeposition, 57
 electrodes, 52, 59
 nanostructured surfaces, 53, 56, 60
 surface, 1079–1084, 1086
 wire, 61–62
Graphene, 1152–1153, 1156
Graphene conducting polymers (G-CPs).
 See Conducting polymers (CPs)
Graphene oxide (GO)
 aqueous suspension, 16
 deposition, 9
 electrochemical prereduction, 10
 electroreduction, 8, 11, 12
Guanine, 254, 262–264, 266, 268
- H**
H-termination, 852
Hardness, 407
Heterogeneous catalysis, 1096–1102
High frequency soft magnetic material, 367
High-effective photovoltaic devices
 Boltzmann constant, 1295
 copper clusters, 1297
 Cu metallization, water solution,
 1280–1292
 current–voltage characteristics,
 1295–1296
 current–voltage dependences, 1293–1294
 energy level, 1297
 Richardson constant, 1295
 solar cells (*see* Solar cells)
 time dependencies, 1293, 1295
 tungsten-measuring needle, 1293–1294
Hybrid metal foams, 964–965
- I**
Impedance, 1135
 spectroscopy, 1084, 1085, 1088
Ink-jet-printing film
 electrochromic response, 807–810
 film forming, 807
 ink formulation and printability, 805–807
 printed electrochromic devices, 811–813
 shape impact, 805
 structure and morphology, 803–804
Inorganic solar cells, 1260–1262
Integrated inductor, 371, 379
Ionic conductivity, of zirconia solid solutions
 brick layer model, 820
 grain boundaries, 824
 grain size, 825
 particle size effect, 824, 825
 with different microstructures, 835–845
Ionic liquid, cation adsorption, 722
- L**
Langmuir-Blodgett based biosensors,
 1165–1169
Layer-by-layer based biosensors, 1169–1175
- M**
Magnetic-field assisted electroplating,
 953–957
Materials fabrication, 570, 571, 576
Metal
 Cd and Pb, 731–732
 coinage and *sp* metals, 729
 complex catalyzed reactions, 852–854
 electrodeposition, 988–990
 on planar surfaces, 991–994
 magnetic metals, 725–727
 nanoparticles
 AFM, 423, 426
 characteristics, 419–420
 electrochemical polymerization, 419
 FTIR, 424–425, 428
 routes of formation, 420–421
 sensing applications, 428–436
 surface and chemical
 characterization, 422
 XPS, 423–424, 426, 427
 XRD, 422, 425
 rare metals, 729–730
 reactive metals, 723–725
Metal oxide, nanoparticle engineering
 agglomerates, 797–799

- design rule outline, 801–802
- fluid control of printable dispersions, 799–801
- shaped nanocrystals, 795–797
- size–shape impact, 791–792
- small clusters, 792–795
- Metal-support interaction, 1096–1102
- Metallic micro(nano)cluster-based contacts
 - Boltzmann constant, 1295
 - copper clusters, 1297
 - Cu metallization, water solution, 1280–1292
 - current–voltage characteristics, 1295–1296
 - current–voltage dependences, 1293–1294
 - energy level, 1297
 - Richardson constant, 1295
 - solar cells (*see* Solar cells)
 - time dependencies, 1293, 1295
 - tungsten-measuring needle, 1293–1294
- Metallic nanoparticles
 - charge transfer process, 889, 891
 - components, 871
 - conductivity, 884, 886
 - electrochemical properties, 871, 877–881
 - Langmuir film, 884
 - organic monolayer-stabilized metallic nanoparticles, 872
 - quantized effects in thin films, 881–883
 - steady-state microelectrode voltammetry simulations, 874
- Metals, nano-electrodeposited, 33–41
- Mismatch detection, ds-DNA, 1079–1089
- Modification
 - electrode surface, 256
 - extrinsic, 257
 - intrinsic, 257
- Multi-nano-layer, 328, 367, 371
- N**
- Nano-electrodeposition
 - electrochemical nucleation and growth, 1351–1354
 - generalized electrochemical aggregative growth mechanism, 1365–1373
 - platinum electrodeposition, 1361–1365
 - silver electrodeposition, 1355–1361
- Nanobelts, 1257, 1259
- Nanocoatings, 314
- Nanocomposite, 25, 41
 - coating
 - applications, EL Ni–P, 411–412
 - corrosion resistance, 409–411
 - EL Ni–P, 391–401
 - hardness, 407
 - level of incorporation of nanoparticles, 404–405
 - nucleation, plating rate, and adhesion, 401–403
 - structure and composition, 405–406
 - surface appearance and roughness, 403
 - tribological characteristics, 407–409
 - CV characteristics of, 495
 - SEM images of, 489
 - synthesis of G-CP, 486–487
 - TEM images of, 490
 - TGA curves of, 492
- Nanocrystalline composites
 - with copper matrix, 163–165
 - with nickel matrix, 155–159
 - with nickel matrix and disperse phases built from carbon, 159–163
- Nanocrystalline materials in electrochemistry
 - transmission electron microscopy, 750–753
 - X-ray absorption spectroscopy, 743–748, 757–759
 - X-ray diffraction techniques, 748–749, 753–756
 - X-ray fluorescence, 749
- Nanocrystalline surface layers, 141, 156, 163
- Nanoelectrochemistry
 - application areas, 1332–1333
 - challenges, 1343
 - colloid chemistry, 1338–1339
 - developed and developing society, 1340–1341
 - education, 1337–1338
 - emerging trends, visionary hope, and future challenges, 1337
 - engineering vision and innovation, 1342
 - environmental engineering, 1338–1340
 - future dimensions, 1341–1342
 - insight, innovation, and ideas, 1338
 - invigorating and coherent world, 1341
 - mankind/research frontiers and energy sustainability, 1333–1334
 - march of science, 1344–1345
 - research endeavor, 1335–1336
 - scientific vision, scientific truth, 1344
 - technological applications, 1337
 - vision, 1332
- Nanoelectrode, 419
- Nanofiltration, 1331, 1339–1341, 1344, 1345
- Nanomaterials, 136, 137, 820, 845
 - classical solar cells, 1252–1254
 - inorganic solar cells, 1260–1262
 - nanobelts, 1257, 1259
 - nanocombs, 1257, 1259
 - nanocoones, 1256–1257

- Nanomaterials (*cont.*)
nanopagodas, 1257
nanopillars, 1256–1258
nanorods, 1258–1260
nanotubes, 1255–1256
nanowires, 1255
organic solar cells, 1262–1264
solar cell performance, 1265–1266
ZnO (*see* ZnO, electrodeposition of)
- Nanoparticle, 337, 341, 347, 349, 1096–1102
dendrimer-encapsulated nanoparticles, 985–988
electrochemical formation, 995–998
growth from preexisting seeds, 999–1003
spinel ferrite (*see* Spinel ferrite nanoparticles)
- Nanoparticle engineering
agglomerates, 797–799
design rule outline, 801–802
fluid control of printable dispersions, 799–801
shaped nanocrystals, 795–797
size–shape impact, 791–792
small clusters, 792–795
- Nanopillars, 1256–1258
- Nanopores, geometry control, 602–605
- Nanoporous membranes, 41
- Nanorods, 41, 118, 121, 1258–1260
CdSe, 114
CdTe, 115
coaxial, 126–131
fabrication, 114
segmented, 124–126
- Nanostructure
AFM, 1212–1220
based sensors, 1198
composites
desorption of SAM, 458–459
methods of SAM preparation, 456
micelles in aqueous medium, 437–438
nanostructured electrodes, 457–458
S-containing compounds, 454–455
sensor applications, 442–450, 460–469
surface modification mode, 438–442
surfactant on polymers/nanometallics, 451–454
surfactants at solid/liquid interface, 438
surfactants in solution, 437
effect of nanocrystalline grains, 1198–1199
effect of noble metal, 1199–1201
electrochemically grown sensing materials, 1201–1205
high surface area, 1198
hot probe, four-probe resistivity, and hall effect measurement, 1223–1226
materials, 1150–1153
nanoelectrochemical sensor fabrication, 1226–1229
noble metals, 1016
optical studies, 1220–1222
photocurrent transient measurement, 1222–1223
SEM, 1212–1220
sensor performance, 1229–1242
sensors, anodic aluminum oxide, 628–629
TEM, 1212–1220
theory of electrochemistry and electrochemical growth, 1205–1210
X-ray diffraction, 1210–1212
- Nanotechnology, 310, 356, 357.
See also Nanoelectrochemistry
- Nanothermodynamics, 977
- Nanothermodynamic stability, 988–1005
- Nanowire (NW), 25, 41, 73, 75, 1255
Ni/NiO, 76, 77, 81, 85–90
- Nucleation and growth, 26, 27, 1351–1354, 1369–1373
- Nucleic acid, 253–256
- O**
- Optoelectronics, 649, 650, 663
- Organic solar cells, 1262–1264
- P**
- Peptides
based SAMs, 529–530
electron-transfer theory, 505–510
self-assembled, 1126
nanostructure applications, 1135–1138
nanostructure fabrication and deposition, 1127–1131
nanostructure functionalization, 1132–1135
- Performance enhancement, 1045, 1054
- Phase transitions, 1058, 1063
- PhotocARRIER collection, 1252, 1267
- Photocatalyst, 1393–1395
- Photocurrent generation measurements, 527–529
- Platinum, electrodeposition, 777–780
- Porous indium phosphide
carrier concentration influence, 298–300
physicochemical regularities, 291–303
texturing, 302–303
- Porous templates, 116, 125, 127
- Printed electronics. *See also* Ink-jet-printing film

- electrochromic response, 807–810
- film forming, 807
- ink formulation and printability, 805–807
- printed electrochromic devices, 811–813
- shape impact, 805
- Printed films
 - morphology of, 787–789
 - required functionality, 789–790
 - structural influence, 790–791
- R**
- Radical induced hydrosilylation reactions, 854
- Reduction
 - chemical, 4
 - cyclic voltammetric, 7
 - electrochemical, 5, 8, 18
- S**
- Scanning electrochemical microscopy (SECM)
 - curve and tip geometry, 1077–1079
 - definition, 1074
 - DNA thin film applications, 1079–1092
 - feedback mode principle, 1075–1076
 - history of, 1074–1075
- Scanning tunneling microscopy (STM), 719–720
- Self-assembled monolayer
 - desorption of, 458–459
 - methods of SAM preparation, 456
 - micelles in aqueous medium, 437–438
 - nanostuctured electrodes, 457–458
 - peptide-based SAMs, 529–530
 - photocurrent generation measurements, 546–555
 - S-containing compounds, 454–455
 - sensor applications, 442–450, 460–469
 - surface modification mode, 438–442
 - surfactant on polymers/nanometallics, 451–454
 - surfactants at solid/liquid interface, 438
 - surfactants in solution, 437
- Self-assembly, 1127, 1132
- Self-healing, 310, 311
 - electrically conductive polymers, 323–326
 - layer-by-layer approach, 320–322
 - microcapsule-based coatings, 312–314
 - nanocapsule-based coatings, 314–320
- Self-organized nano- and micro-structure, of electrochemical materials
 - fabrication approach, design of, 1041–1053
 - material growth, defect analysis of, 1035–1038
 - structure control strategies, 1038–1040
- Self-organized two-step anodization, 598, 599
- Semiconductor
 - compound, 734–735
 - elemental, 732–734
 - etching, 290
 - porous, 284
 - structuring, 289
 - surface, 303
- Sensors, 418–419
 - electrochemical properties
 - morphology, sensitivity, selectivity, stability
- SERS. *See* Surface-enhanced Raman scattering (SERS)
- Silanization, 851
- Silver
 - electrochemical deposition, 59
 - electrode, 51, 52
 - morphological and electromagnetic properties, 55
- Sinusoidal voltages, 1180–1184
- Smart coatings, 310, 311
- Sol-gel method
 - history, 1421–1422
 - processing method, 1422–1423
- Solar cells
 - classical, 1252–1254
 - crossed silver contacts, 1274
 - dye-sensitized solar cells, 1395–1397
 - EDX, 1278–1280
 - grid-contact morphology, 1275
 - inorganic, 1260–1262
 - metallization of electrical contacts, 1272–1273
 - organic, 1262–1264
 - performance, 1265–1266
 - porous silver, 1275–1276
 - quantum dot-sensitized solar cells, 1397–1398
 - silicon-based, 1273–1274
 - silver, 1275–1276
 - X-ray diffraction, 1275, 1277–1278
- Spectro-electrochemistry, 1016, 1020–1022, 1027
- Spinel ferrite nanoparticles
 - analytical techniques, 1428–1429
 - antibacterial activities, 1435–1438
 - chelating agents (*see* Chelating agents)
 - cobalt ferrite, 1420
 - contact angle measurement, 1431–1432
 - cubic ferrites, 1419–1420

- Spinel ferrite nanoparticles (*cont.*)
 fabrication, 1428–1429
 microstructure, 1430–1431
 particle size analysis, 1432–1433
 sol–gel method, 1421–1423
 surface charge measurements, 1429–1430
 use of, 1418
 XRD analysis, 1434–1435
 zeta potential, 1433–1434
- Stabilized zirconia, 823, 826
- Structure, nanocrystalline materials
 transmission electron microscopy, 750–753
 X-ray absorption spectroscopy, 743–748,
 757–759
 X-ray diffraction techniques, 748–749,
 753–756
 X-ray fluorescence, 749
- Structure-function relationship, 1015
- Supercapacitor, 73, 77–78
 manganese oxide, 689–695
 nanostructured metal oxide electrodes
 2D and 3D doped MnO₂, 689–695
 3D branched dendritic structures,
 702–706
 composites carbon and metal oxides,
 706–709
 materials, 687–689
 metallic foams, 695–701
- Supported nanoparticles, 1350, 1373, 1374
- Surface energy, 1061–1064
- Surface nanostructures, 292
- Surface passivation, 857–858
- Surface plasmon resonances, 1014, 1016
- Surface-enhanced Raman (SER) spectroscopy,
 1014, 1015
- Surface-enhanced Raman scattering (SERS), 50
- Surfaces. *See* Gold, surface
- Surfactants
 adsorption, 440–441
 effects on electrochemical kinetics,
 439–440
 in electrochemistry, role, 442
 self-assembly at solid/liquid interface, 438
 self-assembly in solution, 437
 surface modification mode, 438–442
- Synthesis, 247–251
- T**
- Template-assisted nanofabrication, 602,
 611–613, 617
- TERS. *See* Tip-enhanced raman spectroscopy
 (TERS)
- Tethering by aggregation and growth (T-BAG),
 851–852
- Thermal stability Co-P, 379
- Thermally induced hydrosilylation, 854–855
- Thermoelectric materials, 573
- Thin films
 hot probe, four-probe resistivity, and hall
 effect measurements, 1223–1226
 morphological studies, 1212–1220
 of nanoparticle
 charge storage devices, 904–925
 charge transfer, 893
 conducting polymer-carbon
 nanostructure composites,
 917–925
 double-layer capacitors, 906–914
 metal oxide-carbon nanostructure
 composites, 917–925
 quantized effects in charging process,
 881–883
 supercapacitors, 904–906, 914–917
 optical studies, 1220–1222
 photocurrent transient measurement,
 1222–1223
 theory of electrochemistry and
 electrochemical growth, 1205–1210
 X-ray diffraction, 1210–1212
- Thymine, 254, 262–264, 266, 268
- TiO₂ nanotube
 DSCs, 1316–1323
 membrane fabrication and characterization,
 1314–1316
- TiO₂ nanotube arrays (TNAs)
 applications, 1406
 biomedical scaffold, 1401–1404
 doping, 1390
 electrochemical anodization, 1384–1389
 noble metal nanoparticle decoration, 1389,
 1391, 1393
 photocatalyst, 1393–1395
 self-ordered nanostructures, 1382
 SEM images, 1382–1383
 semiconductor composites, 1391–1392
 solar cells, 1395–1398
 synthesis method, 1380–1381
 water splitting, 1397–1401
 wetting template, 1404–1405
- Tip-enhanced raman spectroscopy (TERS), 61
- Titanium dioxide
 acid functionalization, 859–863
 wet chemical functionalization, 859
- Transition metal oxides
 2D and 3D doped MnO₂, 689–695

- 3D branched dendritic structures, 702–706
composites carbon and metal oxides,
706–709
materials, 687–689
metallic foams, 695–701
Transmission electron microscopy, 750–753
- U**
Underpotential deposition, 977–982, 1006
- V**
Vision
macroscopic electrochemistry, 1331–1332
nanoelectrochemistry
(*see* Nanoelectrochemistry)
- W**
Water splitting, 1397–1401
Wet chemical functionalization
of silicon, 850–852
of titanium dioxide, 859
Wetting template, 1404–1405
- X**
X-ray
absorption spectroscopy, 743–748, 757–759
diffraction techniques, 748–749, 753–756
fluorescence, 749
- Z**
Zinc
nanoparticle composite coatings, 343–349
Zirconia solid solutions, ionic conductivity.
See Ionic conductivity, of zirconia
solid solutions
ZnO, electrodeposition of
annealing effects, 666–668
bandgap tuning, 663
basics, 648
dissolved oxygen method, 651–653
electrochemical doping, 668–675
electrochemical growth, 650–651
electrochemistry-based characterization, 664
growth techniques, 648–649
optical quality and luminescence, 663
thin film transfer, 664
zinc nitrate method, 653–663